SLAC-R-839

Proceedings of the IXth International Conference on High Energy Accelerators,

Stanford, CA, May 2-7, 1974

9th International Conference On High-Energy Accelerators
Stanford, California
5/2/1974-5/7/1974

Stanford Linear Accelerator Center, Stanford University, Stanford, CA 94309

Work supported by Department of Energy contract DE–AC02–76SF00515.

CONF 740522
UC-28-Accelerators
(TID-4500, 60th Edition)

PROCEEDINGS
of the
IXth International Conference
on
High Energy Accelerators

Stanford Linear Accelerator Center
Stanford University, Stanford, California
May 2-7, 1974

International Union of Pure and Applied Physics
National Science Foundation
U.S. Atomic Energy Commission

This report was prepared as an account of work sponsored by the United States Government. Neither the United States nor the United States Atomic Energy Commission, nor any of their employees, nor any of their contractors, subcontractors, or their employees, makes any warranty, express or implied, or assumes any legal liability or responsibility for the accuracy, completeness or usefulness of any information, apparatus, product or process disclosed, or represents that its use would not infringe privately owned rights.

Printed in the USA. Additional copies of this volume are available at a cost of $13.60 each from the National Technical Information Service, U. S. Department of Commerce, **5285** Port Royal Road, Springfield, Virginia **22151.**

TABLEOFCONTENTS

Foreword vii

Conference Committees ix

Welcoming Remarks by W. K. H. Panofsky xi

Program Contents xiii

Session 1. Accelerators 1

Session 2. Storage Rings 32

Session 3. Superconductivity 115

Session 4. Collective Methods of Acceleration 214

Session 5. Special Ad Hoc Parallel Sessions 326

Session 6. Beam Dynamics: Theory. Experiments. New Devices and Controls (Part 1). 327

Session 7. Beam Dynamics: Theory. Experiments. New Devices and Controls (Part 2). 447

Session 8. Future Storage Rings and Major Accelerator Projects . . . 537

Session 9. Overall Perspective Talks 650

List of Participants - by country 693

List of Participants - alphabetically 695

Appendix - Catalogue of High-Energy Accelerators 703

Author Index 767

FOREWORD

The IXth International Conference on High Energy Accelerators was held at the Stanford Linear Accelerator Center on May 2 - 7, 1974. This conference was attended by 259 delegates from 14 countries, including the United States.

The technical program of the conference was presented during 8 regular sessions on Thursday and Friday, May 2 and 3, and on Monday and Tuesday, May 6 and 7. There were no parallel sessions during these dags. In addition to the regular scheduled sessions, several parallel ad hoc sessions were held on Saturday, May 4. Most of these special sessions were arranged during the Conference at the request of interested delegates.

During the regular sessions, the following papers were presented orally:

18 invited
8 rapporteur
37 contributed

In addition to these papers, 75 papers which could not be scheduled for oral presentation are published in the conference proceedings.

Reflecting recent trends, considerable emphasis was placed on receiving reports of storage developments during this conference. Sessions 2 and 8 were devoted to this subject with principal emphasis given *to* experience with existing rings in Session 2 and to future *storage* rings in Session 8. In addition, beam dynamics in storage rings received considerable attention in Sessions 6 and 9.

Other sessions of the conference were devoted to new large accelerators (Session 1), RF superconductivity and superconducting magnets (Session 3), collective methods of acceleration (Session 4), beam dynamics, new devices and controls (Sessions 6 and 7), and overall perspective talks (Session 9).

In this conference, more emphasis was placed upon the presentation of rapporteur papers than in past conferences. Each rapporteur was asked to divide his/her talk into two parts. The first part was an opening statement giving a state-of-the-art background and setting the stage for subsequent contributed papers. The second part came after the contributed papers and consisted of a summary of future problems and a discussion involving the audience *to* reconcile divergent points of view.

As an adjunct to the scientific aspects of the conference, the delegates participated in several interesting social events. These included an evening visit to the Lawrence Hall of Science in Berkeley (including a buffet dinner), a Sunday bus trip over the coastal hills to the redwood forests in the Henry Cowell State Park, followed by a visit to the Santa Cruz campus of the University of California where supper was served, and a reception at Hoover *House,* the home of Stanford University President and Mrs. Richard Lyman.

A separate social program was arranged for the ladies accompanying delegates to the conference. Their activities included a tour of the Sunset Magazine buildings and gardens, a visit to the Allied Arts Center in Menlo Park, an all-day trip to San Francisco, and a tour of the Paul Masson Winery followed by a visit to Old Town in Los Gatos. We are very grateful to Portia Hogg and other members of the Ladies Program Committee for arranging these events.

Many people participated in the planning and functioning of this conference. Because of the large number, it is not practicable to acknowledge each individual contribution. We are very grateful for the advice and assistance of the International Advisory Committee and to the Organizing/Program Committee. The names of members of these committees are given eisewhere in this Proceedings. The Scientific Secretaries were of great assistance to the Chairmen and Speakers and in the editing of remarks made during the technisal sessions. Finally, it is fitting to mention several people individually because of their extensive and indispensable contributions to the success of the conference. Coordination of all non-technical aspects of the conference including the editing of the Proceedings was ably handled by Ruth Nelson. Harry Hogg, a member of the Organizing/Program Committee, was principally responsible for the preparation of lhe program booklet. Joe Cobb was in charge of audio-visual services during the conference; he was assisted by William Johnson. Janette Pearl and Jane Peterson handled the main secretarial duties during the planning and preparation phase, as well as during the conference itself.

Richard B. Neal, Chairman
Organizing/Program Committee

CONFERENCE COMMITTEES

International Advisory Committee

The scope and format of the Conference followed recommendations made by the International Advisory Committee, members of which are named below:

Dr. John Adams
CERN, Switzerland

Professor Artem I. Alikhanian
USSR Academy of Sciences, USSR

Dr. Alick Ashmore
Daresbury Nuclear Physics Laboratory, Great Britain

Professor G. I. Budker
USSR Academy of Sciences, USSR

Dr. Bruce Cork
Lawrence Berkeley Laboratory, USA

Professor A. P. Lagarrigue
Ecole Normale Superieure, France

Professor Edward J. Lofgren
Lawrence Berkeley Laboratory, USA

Professor Alexander L. Mints
USSR Academy of Sciences, USSR

Professor A. A. Naumov
High Energy Physics Institute (Serpukhov), USSR

Professor Wolfgang K. H. Panofsky, Chairman
Stanford Linear Accelerator Center, USA

Professor Wolfgang Paul
DESY, West Germany

Dr. R. Ronald Rau
Brookhaven National Laboratory, USA

Professor Giorgio Salvini
University Degli Studi, Italy

Dr. G. H. Stafford
Rutherford High Energy Laboratory, Great Britain

Dr. William A. Wallenmeyer
U. S. Atomic Energy Commission, USA

Professor Robert R. Wilson
National Accelerator Laboratory, USA

Organizing Committee

All Conference arrangements were handled by the Organizing Committee composed of staff members of the Stanford Linear Accelerator Center and the Lawrence Berkeley Laboratory. The Organizing Committee was structured into the following sub-committees:

Organizing Committee Chairman

Richard B. Neal

Steering Sub-Committee

Richard B. Neal, Chairman
Joseph K. Cobb
Douglas W. Dupen
William B. Herrmannsfeldt
Harry A. Hogg
Charles J. Kruse
Gregory A. Loew
Ruth T. Nelson
Janette E. Pearl

Program Sub-committee

Gregory A. Loew, Chairman
Richard H. Helm
Glen R. Lambertson
John R. Rees
Burton Richter
Lloyd Smith

Secretariat Sub-committee

Harry A. Hogg, Chairman
Gerhard E. Fischer
Charles J. Kruse

Technical Arrangements Sub-Committee

James McEwan Paterson, Chairman
Hermann A. Grunder
Kenneth B. Mallory

Social Events Sub-committee

William B. Herrmannsfeldt, Chairman
Matthew A. Allen
Roger H. Miller
Phillip L. Morton
Steven J. St. Lorant
Perry B. Wilson

Scientific Secretaries

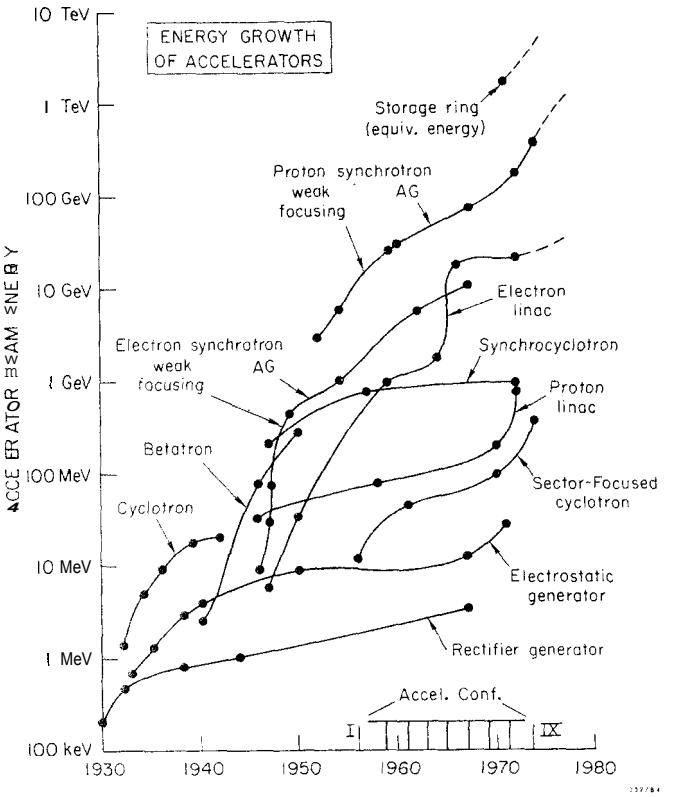
The following persons, staff members of the Stanford Linear Accelerator Center and the Lawrence Berkeley Laboratory, served as Scientific Secretaries:

Kenneth F. Crook
Z. David Farkas
John L. Harris
John M. Hauptman
Roland F. Koontz
Charles J. Kruse
Martin J. Lee
Christoph W. Leeman
Richard M. Mobley
Richard E. Morgado
Vernon G. Price
Daryl D. Reagan
Joseph B. Rechen
Andrew P. Sabersky
Steven J. St. Lorant
John W. Staples

WELCOMING REMARKS

W. K. H Panofsky

I would like to welcome all of you to the IXth International Conference on High Energy Accelerators. This is the first time this conference has been at SLAC, or even on the West Coast of the United States; we hope that you will be able to avail yourselves of this opportunity to become familiar with the accelerator installations in the San Francisco Bay Area.

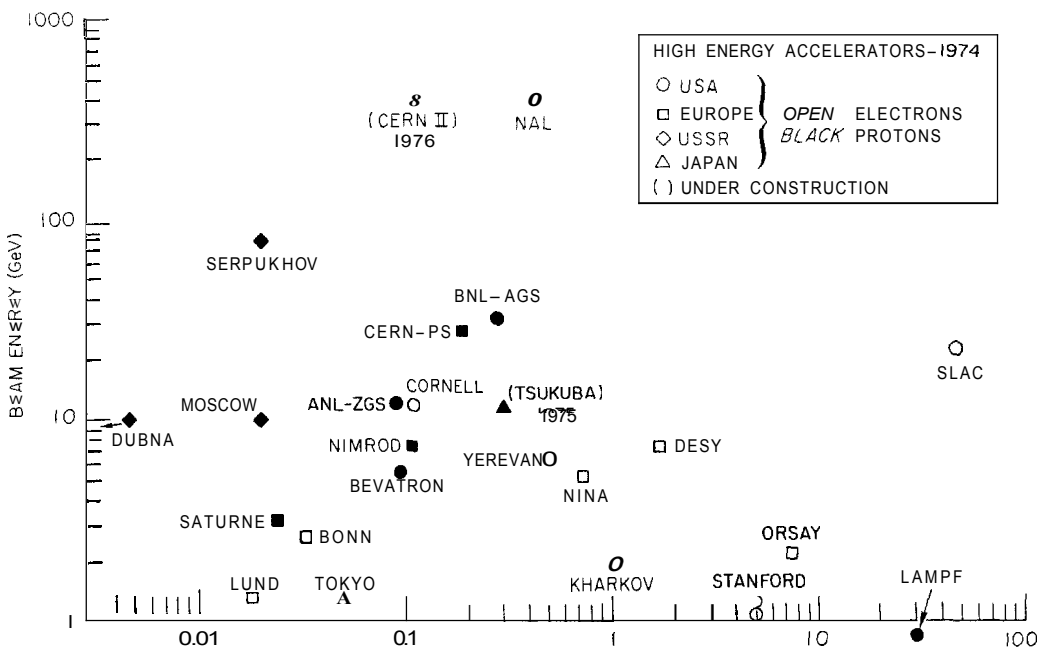


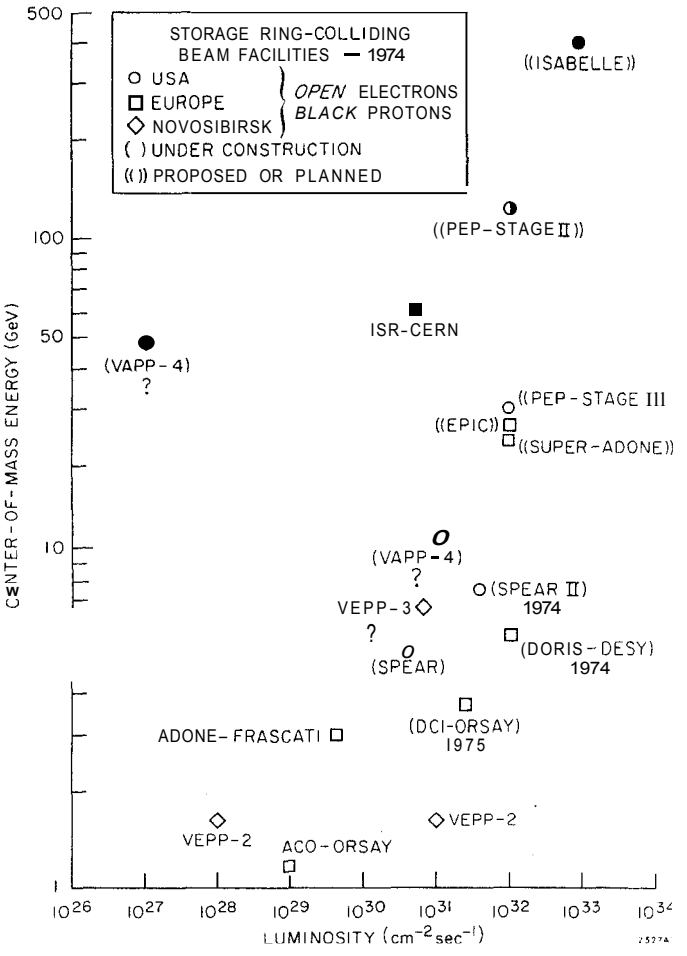
There has been much discussion about the interval between these conferences; the last conference was held two and a half years ago, and two-year intervals preceded that gap. To some this may appear to be too frequent, but I should like to remind you that the accelerator art is rapidly evolving indeed. The first figure is a chart which shows the growth over time of equivalent laboratory energy attained by accelerating or colliding beam devices. Note that if the exponential growth shown on this chart has continued, then the laboratory energy has risen by a factor of **2.6** since the time when this conference was last convened! At this rate "energy doublers"—whether for protons or electrons—will have to be built awfully fast!

Probably the most significant aspect of this chart is the clear indication it gives of the past richness of new ideas for the acceleration and storage of particles. Whenever any one technique appeared to saturate in terms of the energy which could he attained at reasonable cost, new ideas came to the forefront. I believe most elementary particle physicists would agree that the entire field of particle physics has been paced by the opportunities offered by accelerator technology rather than by the demands of high energy physicists. Today, however, I can not quite be sure whether this is still the case. Let *me* briefly review the situation.

The next two figures will show the laboratory energies and intensities of conventional accelerators and center-of-mass energies and luminosities of colliding beam devices. The data in these figures have been taken directly from the Catalog of High Energy Accelerators which compiles the information submitted by the various laboratories to this conference. * As you can see, the past advances have indeed been striking. However, we do not now discern how any genuinely new ideas appear to relate to the next generation

*The recent intensity record of 10^{13} particles/pulse reached by NAL has been included. Data on most Soviet installations is derived from earlier information.





of future accelerating devices. The various proposals for future accelerators and colliding beam devices which are appended to the catalog are based on what I might call parametric studies, that is, optimization of established principles and techniques rather than exploitation of genuinely new ideas. This does not mean that new ideas are absent; however, the effort needed to demonstrate whether, for instance, collective acceleration is promising for very high energy devices has proven to be so great that one cannot be too optimistic. So possibly for the next generation of accelerators or storage rings history may not repeat: It may be that the open problems of elementary particle physics rather than new technology will determine events. I can say that particle physics today has rarely been in a more "expectant" condition. Recent results, particularly at high momentum transfers, from the ISR, from the SPEAR hadron cross sections, from the high energy neutrino experiments at NAL, and from the initial evidence on neutral currents in the weak interaction all cry out for exploitation at higher energies and luminosities. So there is indeed great urgency about the further steps that might be taken in the evolution of accelerators and storage rings; I hope that the work of this conference can contribute to the wisdom of decisions in this respect.

PROGRAMCONTENTS

SESSION 1 - ACCELEXATORS

Chairman: Donald E. Young, National Accelerator Laboratory

Scientific Secretaries: Andrew P. Sabersky, Stanford Linear Accelerator Center
John L. Harris, Stanford Linear Accelerator Center

Invited Paper - "The IHEP 76-GeV Proton Synchrotron"
Yu. M. Ado, V. I. Kotov, K. P. Myznikov, A. A. Naumov, R. M. Suljaev, V. A. Tepljakov, E. F. Trojanov, V. I. Zaitsev, and A. A. Zhuravlev, Institute for High Energy Physics, Serpukhov 1

Invited Paper - "The NAL Accelerator and Future Plans"
The NAL Staff (presented by Paul J. Reardon), National Accelerator Laboratory 7

Invited Paper - "Progress on the 300-GeV Programme"
R. Billinge, CERN. 19

Invited Paper - "The Japanese 12-GeV Accelerator"
Tetsuji Nishikawa, National Laboratory for High Energy Physics 23

SESSION 2 - STORAGE RINGS

Chairman: Andrew M. Sessler, Lawrence Berkeley Laboratory

Scientific Secretaries: Martin J. Lee, Stanford Linear Accelerator Center
Charles J. Kruse, Stanford Linear Accelerator Center

Invited Paper - "Present Status and Future Plans for the ISR"
K. Johnsen, CERN. 32

Invited Paper - "SPEAR: Status and Improvement Program"
SPEAR Storage Ring Group: M. Allen, W. Davies-White, N. Dean, G. Fischer, J. Harris, R. Helm, L. Karvonen, M. Lee, R. McConnell, R. Melen, P. Morton, J. M. Paterson, J. Rees, B. Richter, A. Sabersky, P. Wilson, J.-E. Augustin, M. Harold, M. Matera, H. Wiedemann, Stanford Linear Accelerator Center 37

Invited Paper - "DORIS, Present Status and Future Plans"
DESY Storage Ring Group: J. Le Duff (visitor from Orsay), J. Maidment (visitor from Rutherford), E. Dasskowski, D. Degèle, H. C. Dehne, H. Gerke, D. Heins, K. Hoffmann, K. Holm, E. Jandt, R. D. Kohaupt, J. Kouptsidis, F. Krafft, N. Lehnart, G. Mulhaupt, H. Nesemann, S. Patzold, H. Pingel, A. Piwinski, R. Rossmanith, H.-D. Schulz, K. Steffen, H. Wiedemann, K. Wille, A. Wrulich, DESY 43

Invited Paper - "Design and Status of DCI"
P. Marin, Orsay 49

"Non-Destructive Diagnostics of Coasting Beams with Schottky Noise"
J. Borer, P. Bramham, H. G. Hereward, K. Hubner, W. Schnell, and L. Thorndahl, CERN. 53

"Beam Loading in High-Energy Storage Rings"
P. B. Wilson, Stanford Linear Accelerator Center 57

"A Search for a Beam-Beam Effect in the ISR"
K. Hubner, CERN 63

"Beam-Beam Coupling in SPEAR"
The SPEAR Group: R. H. Helm, M. J. Lee, M. Matera, P. L. Morton, J. M. Paterson, B. Richter, A. P. Sabersky, H. Wiedemann, P. B. Wilson, M. A. Allen, J.-E. Augustin, and G. E. Fischer, Stanford Linear Accelerator Center 66

"Vacuum Conditions for Proton Storage Rings"
R. Calder, E. Fischer, O. Grobner, and E. Jones, CERN. 70

"Influence of the Split Field Magnet Spectrometer on the CERN Intersecting Storage Rings"
P. J. Bryant and R. Perin, CERN. 75

'Dynamic Compensation During Stacking of the De-Tuning Caused by Space Charge Effects"
P. J. Bryant, CERN 80

"Tune Shift Computation for Storage Rings with Low-Beta Sections"
J. Buon, Orsay 83

"Experimental Investigation of Single-Beam and Beam-Beam Space Charge Effects"
P. J. Bryant and J. P. Gourber, CERN 87

"RF Systems for High-Energy e-e+ Storage Rings"
M. A. Allen and P. B. Wilson, Stanford Linear Accelerator Center 92

"Beam Dynamics Experiments at SPEAR"
The SPEAR Group: A. P. Sabersky, P. B. Wilson, H. Wiedemann, M. A. Allen, J.-E. Augustin, G. E. Fischer, R. H. Helm, M. J. Lee, M. Matera, P. L. Morton, J. M. Paterson, and B. Richter, Stanford Linear Accelerator Center 97

"Beam Enlargement by Mismatching the Energy-Dispersion Function"
R. H. Helm, M. J. Lee, and J. M. Paterson, Stanford Linear Accelerator Center 100

"Adone: Present Status and Experiments"
M. Bassetti, A. Cattoni, V. Chimenti. D. Fabiani, M. Matera, C. Pellegrini, M. Placidi, M. Preger, A. Renieri, S. Tazzari, F. Tazzioli, and G. Vignola, Frascati 104

"Resonant Methods for Beam Size Control in Storage Rings"
M. Bassetti, Frascati 108

"Direct Measurements on the Beam-Beam Interaction at SPEAR"
A. P. Sabersky, Stanford Linear Accelerator Center. 113

SESSION 3 - SUPERCONDUCTIVITY

Chairman: John P. Blewett, Brookhaven National Laboratory

Scientific Secretaries: Steven J. St. Lorant, Stanford Linear Accelerator Center
John W. Staples, Lawrence Berkeley Laboratory

Rapporteur Talk - "RF Superconductivity"
M. Kuntze, Karlsruhe 115

"Progress Report on the Stanford Superconducting Recyclotron"
M. S. McAshan, R. E. Rand, H. A. Schwettman, T. I. Smith, and J. P. Turneaure, High Energy Physics Laboratory, Stanford University 123

"Application of Superconducting RF Accelerating Sections to an Electron Synchrotron - A Progress Report"
R. M. Sundelin, J. Kirchgessner, H. Padamsee, H. L. Phillips, D. Rice, M. Tigner, and E. von Borstel, Cornell University 128

"Measurements on the First 20-Cell Deflector Sections for a Superconducting RF Separator"
W. Bauer, A. Citron, G. Dammertz, M. Grundner, L. Husson, H. Lengeler, and E. Rathgeber, Karlsruhe 133

"Breakdown Fields in a Superconducting Niobium Cavity at S-Band"
P. Kneisel, C. Lyneis, O. Stoltz, and J. Halbritter, Karlsruhe 140

"On the Preparation and a Thermal Breakdown Mechanism of Superconducting Niobium X-Band Cavities with High Magnetic Flux Densities"
B. Hillenbrand, H. Martens, K. Schnitzke, and H. Diepers, Research Laboratories Siemens AG 143

"Superconducting RF Cavity with Reactively Sputtered Niobium Nitride Surfaces"
S. Isagawa, Y. Kimura, Y. Kojima, S. Mitsunobu, and Y. Mizumachi, National Laboratory for High Energy Physics 147

"A 6-pass Microtron Using a Superconducting Electron Linac"
A. O. Hanson, J. R. Harlan, R. A. Hoffswell, D. Jamnik, and L. M. Young, University of Illinois, Urbana-Champaign 151

"Development and Testing of a Prototype Superconducting RF Separator"
A. Carne, R. G. Bendall, J. R. J. Bennett, B. G. Brady, J. A. Hirst, and J. V. Smith, Rutherford High Energy Laboratory. 154

"?Development of the Superconducting Helix for Heavy-Ion Acceleration"
J. Aron, R. Benaroya, L. M. Bollinger, B. E. Clifft, O. Despe, A. H. Jaffey, K. W. Johnson, T. K. Khoe, J. J. Livingood, P. J. Markovich, J. M. Nixon, G. W. Parker, and W. A. Wesolowski, Argonne National Laboratory. 159

Rapporteur Talk - "Superconducting Magnets"
D. B. Thomas, Rutherford High Energy Laboratory 164

"The Magnetic and Thermal Stability of Superconducting Accelerator Magnets"
W. B. Sampson, P. F. Dahl, A. D. McInturff, and K. E. Robins, Brookhaven National Laboratory 170

"Pulsed Superconducting Dipole Magnets of the GESSS Collaboration"
P. Turowski, Karlsruhe; J. H. Coupland, Rutherford High Energy Laboratory; and J. Perot, Saclay 174

"Experimental Superconducting Accelerator Ring (ESCAR)"
R. Avery, T. Elioff, A. Garren, W. Gilbert, M. Green, H. Grunder, E. Hartwig, D. Hopkins, G. Lambertson, E. Lofgren, K. Lou, R. Meuser, R. Peters, L. Smith, J. Staples, R. Thomas, and R. Wolgast, Lawrence Berkeley Laboratory 179

"Progress Report on the NAL Energy Doubler Design Study"
D. A. Edwards, W. B. Fowler, P. J. Reardon, D. E. Richied, B. P. Strauss, and D. F. Sutter, National Accelerator Laboratory 184

"Superconducting Stretcher Ring for the Zero Gradient Synchrotron"
E. A. Crosbie, T. K. Khoe, R. L. Martin, J. R. Purcell, and S. T. Wang, Argonne National Laboratory 193

"8° Superconducting Bending Magnet in a Primary Proton Beam"
J. Allinger, G. Danby, B. De Vito, H. Foelsche, S. Hsieh, J. Jackson, and A. Prodell, Brookhaven National Laboratory. 198

"Prediction of Radiation Effects on Accelerators Using Hadron Cascade Calculations"
J. Ranft, Karl Marx University, Leipzig 204

"Research Work on Pulsed Superconducting Magnets for Accelerators"
V. P. Alexeev, A. A. Vasiliev, E. A. Galstjan, L. I. Greben', and E. S. Mironov, Radiotechnical Institute of the USSR Academy of Sciences, Moscow 209

SESSION 4 - COLLECTIVE METHODS OF ACCELERATION

Chairman: Andrei A. Kolomensky, Lebedev Institute

Scientific Secretaries: Roland F. Koontz, Stanford Linear Accelerator Center
Joseph B. Rechen, Lawrence Berkeley Laboratory

Rapporteur Talk - "Electron Ring Acceleration"
G. R. Lambertson, Lawrence Berkeley Laboratory 214

"Acceleration of Electron Rings and Investigations on Ion-Electron Instabilities in the Garching ERA Experiment"
C. Andelfinger, W. Dommaschk, I. Hofmann, P. Merkel, U. Schumacher, and M. Ulrich, Max Planck Institute, Munich 218

"Energy Spreading and Energy Loss Due to Negative Mass Instability in an Electron Ring Experiment"
J. Fink, W. Herrmann, W. Ott, and J. M. Peterson, Max Planck Institute, Munich 223

"Observations on Collective Longitudinal Instabilities in Electron Rings"
A. Faltens, G. R. Lambertson, J. M. Peterson, and J. B. Rechen, Lawrence Berkeley Laboratory 226

"Experimental and Theoretical Studies of Electron Ring Formation and Ion Loading in the Maryland ERA"
W. W. Destler, A. Greenwald, D. W. Hudgings, H. Kim, P. K. Misra, M. P. Reiser, M. J. Rhee, and G. T. Zorn, University of Maryland 230

"The Electron Ring Program at Lawrence Berkeley Laboratory"
W. W. Chupp, A. Faltens, E. C. Hartwig, D. Keefe, G. R. Lambertson, L. J. Laslett, W. Ott, J. M. Peterson, J. B. Rechen, A. Salop, and R. W. Schmieder, Lawrence Berkeley Laboratory 235

"Compressor Design for Intense Electron Rings"
J. M. Hauptman, L. J. Laslett, W. W. Chupp, and D. Keefe, Lawrence Berkeley Laboratory 240

"Self-Consistent Equilibria of Accelerated Relativistic Electron Rings"
I. Hofmann, Max Planck Institute, Munich 245

"Report on the ERA Research at Karlsruhe"
C. H. Dustmann, W. Heinz, H. Krauth, L. Steinbock, and W. Zernial, Karlsruhe 250

Rapporteur Talk - "Other Collective Methods"
A. A. Kolomensky, P. N. Lebedev Physical Institute, USSR Academy of Sciences, Moscow 254

"Particle Acceleration by Intense Electron Beams"
D. Drickey, University of California, Los Angeles; B. Ecker and S. Putnam, Physics International Company 263

"Collective Ion Acceleration in Linear Electron Beams"
D. W. Swain, G. W. Kuswa, J. W. Poukey, and C. L. Olson, Sandia Laboratories 268

"Two New Collective Acceleration Schemes"
Craig L. Olson, Sandia Laboratories 272

"Electron Autoacceleration"
R. J. Briggs, T. J. Fessenden, and V. K. Neil, Lawrence Livermore Laboratory 278

"The Autoresonant Accelerator Concept"
M. L. Sloan and W. E. Drummond, Austin Research Associates, Inc. 283

Invited Talk - "The High Energy Polarized Beam at the ZGS"
T. K. Khoe, R. L. Kustom, R. L. Martin, E. F. Parker, C. W. Potts, L. G. Ratner, and R. E. Timm, Argonne National Laboratory; A. D. Krisch and J. B. Roberts, University of Michigan; and J. R. O'Fallon, St. Louis University. 288

"Intense Beams of 100 to 500 MeV Positrons"
B. Aune, M. Juillard, F. Netter, and A. Pacchioni, Saclay 295

"Second Harmonic RF Acceleration on Nimrod"
E. G. Sandels and I. S. K. Gardner, Rutherford High Energy Laboratory 297

"Accelerating Waveguides for High-Energy Accelerators"
A. V. Shalnov, International Atomic Energy Agency, Vienna, Austria 301

"Phase-Free Acceleration of Charged Particles by AC Fields"
W. Schott, H.-J. Winter, H. Hagn, K. Springer, H. Zinner, F. Brunner, and H. Daniel, Technical University, Munich 304

"Polarized Electron Source for the Stanford Linear Accelerator"
M. J. Alguard, R. D. Ehrlich, V. W. Hughes, J. Ladish, M. S. Lubell, and W. Lysenko, Yale University; K. P. Schiiler, Yale University and University of Bielefeld; and G. Baum and W. Raith, University of Bielefeld 309

"ITEP Experimental Assembly for ERA Collective Method Investigations"
I. V. Chuvilo, I. M. Kapchinsky, V. K. Plotnikov, and R. M. Vengrov, Institute for Theoretical and Experimental Physics, Moscow 314

"Present Performance of Collective Ion Acceleration in JINR"
L. S. Barabash, I. A. Golutvin, G. V. Dolbilov, I. N. Ivanov, A. D. Kovalenko, V. G. Novikov, N. B. Rubin, E. A. Perelshtein, V. P. Sarantsev, and V. A. Sviridov, Joint Institute for Nuclear Research, Moscow 318

SESSION 5 - AD HOC PARALLEL SESSIONS

Scientific Secretaries: Kenneth F. Crook, Stanford Linear Accelerator Center
Vernon G. Price, Stanford Linear Accelerator Center

An Ad Hoc Discussion Session - "Maximizing Productivity and Employee Morale in an Era of Tight Budgets"
Led by K. H. Reich, CERN 326

SESSION 6 - BEAM DYNAMICS: THEORY, EXPERIMENTS, NEW DEVICES and CONTROLS

Chairman: Gustav-Adolf Voss, DESY

Scientific Secretaries: Daryl D. Reagan, Stanford Linear Accelerator Center
Richard M. Mobley, Lawrence Berkeley Laboratory

Rapporteur Talk - "Collective Effects on Orbit Dynamics"
F. E. Mills, National Accelerator Laboratory 327

"Transverse Collective Instability in the NAL 500-GeV Accelerator"
R. Stiening and E. J. N. Wilson, National Accelerator Laboratory 329

"Transverse Single Particle Instability in the NAL 500-GeV Accelerator"
R. Stiening and E. J. N. Wilson, National Accelerator Laboratory 332

"Fast Damping of Transverse Coherent Dipole Oscillations in SPEAR"
J. M. Paterson, B. Richter, A. P. Sabersky, H. Wiedemann, P. B. Wilson, M. A. Allen, J.-E. Augustin, G. E. Fischer, R. H. Helm, M. J. Lee, M. Matera, and P, L. Morton, Stanford Linear Accelerator Center 338

"Head-Tail Type Instabilities in the CERN PS and Booster"
Part I (PS): J. Gareyte
Part II (Booster): J. Gareyte and F. Sacherer, CERN 341

"Transverse Bunched Beam Instabilities - Theory"
F. J. Sacherer, CERN 347

"Some Observations on Bunch Lengthening at SPEAR"
M. A. Allen, G. E. Fischer, M. Matera, A. P. Sabersky, and P. B. Wilson, Stanford Linear Accelerator Center 352

"Investigation and Cures of Longitudinal Instabilities of Bunched Beams in the ISR"
P. Bramham, S. Hansen, A. Hofmann, K. Hübner, and E. Peschardt, CERN 359

"Control of the Bunch Lengthening Phenomenon in Electron Storage Rings"
E. M. Rowe and W. S. Trzeciak, University of Wisconsin 365

"The Longitudinal Feedback System in Adone"
A. Renieri and F. Tazzioli, Frascati 370

"Fast Beam-Cavity Interaction and Its Effect on Bunch Shape in Storage Rings"
A. Papiernik, M. Chatard-Moulin, and B. Jecko, Orsay and University of Limoges 375

"Landau Damping by Non-Linear Space-Charge Forces and Octupoles"
D. Möhl and H. Schonauer, CERN 380

"The Effect of the Beam Self-Field on the Transverse Betatron Oscillation Frequency"
G. Parzen and K. Jellett, Brookhaven National Laboratory 385

"Acceleration by Phase Displacement in the ISR"
K. N. Henrichsen and M. J. de Jonge, CERN 390

Invited Paper - "Stochasticity"
L. Jackson Laslett, Lawrence Berkeley Laboratory 394

"Beam Loss in a Coasting Beam from a High Order Isolated Resonance"
M. Month, Brookhaven National Laboratory 402

"Intra-Beam-Scattering"
A. Piwinski, DESY **405**

"Detailed Study of the Beam-Beam Interaction at the Orsay Storage Ring (ACO)"
M. Bergher, J. Buon, A. Jejcic, J. Le Duff, P. Marin, M. Sommer, and H. Zyngier, Orsay 410

"Non-Linear Beam-Beam Effect Computer Simulation"
A. Renieri, Frascati 414

"Two-Dimensional Resonance Effects Due to a Localized Bi-Gaussian Charge Distribution"
A. G. Ruggiero, National Accelerator Laboratory 419

"Instabilities Detected in Saturne"
J. Faure, G. Leleux, J. L. Lemaire, and R. Vienet, Saclay 424

"Stochastic Effects in Longitudinal Phase Space"
I. Gumowski, CERN 429

"Gamma-Transition-Jump Scheme of the CPS"
W. Hardt, CERN 434

"Dipole Two-Beam Instability in Circular Beams with Azimuthal Non-Uniformity"
P. R. Zenkevich, D. G. Koshkarev, Institute for Theoretical and Experimental Physics, Moscow 439

"The Interaction of a Long Intensive Electron Bunch with a Passive Cavity"
G. V. Voskresensky and V. N. Kurdjumov, Radiotechnical Institute of the USSR Academy of Sciences, Moscow 444

SESSION 7 - BEAM DYNAMICS: THEORY, EXPERIMENTS, NEW DEVICES and CONTROLS

Chairman: David A. Gray, Rutherford High Energy Laboratory

Scientific Secretaries: Kenneth F. Crook, Stanford Linear Accelerator Center
Richard E. Morgado, Lawrence Berkeley Laboratory

Rapporteur Talk - "Beam Extraction"
H. T. Edwards, National Accelerator Laboratory 447

"Slow Resonance Extraction of Two Simultaneous Beams Without RF Structure"
Y. Cho, E. A. Crosbie, L. G. Lewis, C. W. Potts, and L. G. Ratner, Argonne National Laboratory 451

"Extraction for the Main Ring at NAL"
R. A. Andrews, H. T. Edwards, H. E. Fisk, F. Hornstra, J. D. McCarthy, H. Pfeffer, C. H. Rode, and J. Walton, National Accelerator Laboratory 456

"BNL Fast Shaving Extraction System"
L. Blumberg, G. Bagley, G. Bennett, J. Claus, J. Curtiss, R. Frankel, H. Hsieh, J. Keane, G. Levine, L. Repeta, J. Schuchman, and A. Soukas, Brookhaven National Laboratory 462

"Simulation of Simultaneous Beam Sharing Between Internal Targets and Slow Ejection at the CPS"
M. Bell and W. Kubischta, CERN 467

"Expected Energy-Spread in the Extracted Beam of Saturne II"
H. Bruck, J.-L. Laclare, and G. Leleux, Saclay 471

"Injection and Trapping of the Beam at 800 MeV in the CPS"
D. Boussard, M. Bouthéon, B. Carpenter, P. Lefèvre, and J. P. Potier, CERN. 475

"The CERN PS Booster: Design Expectation Confronted with Reality, Two Years after Start-up"
The PSB Staff (Reported by K. H. Reich), CERN 480

Rapporteur Talk - "Computer Control of Accelerators"
M. C. Crowley-Milling, CERN 485

"User's Assessment of the Computer Controls System of the CERN PS Booster"
G. Baribaud, G. Benincasa, A. Daneels, P. Heymans, C. Metzger, F. Pedersen, M. Rabany, K. Schindl, and J. Stark, CERN 490

"Use of a General-Purpose Time-shared Computer in Accelerator Control"
M. Q. Barton, B. B. Culwick, J. A. Curtiss, J. J. Dabrowski, R. S. Frankel, W. E. Harrison, F. R. Martin, J. D. Smith, R. J. Warkentien, and I. Weitman, Brookhaven National Laboratory 495

"The Operator Interface of the 300-GeV Accelerator"
F. Beck, CERN 499

"The Computer Control System for the SPS"
J. T. Hyman, CERN. 503

"The Impact of Computer Control on the Performance of the CERN Intersecting Storage Rings"
P. Wolstenholme, CERN 508

"Digital Control of Rectifier Firing Angles for the Zero Gradient Synchrotron (ZGS) Ring Magnet Power Supply"
M. J. Knott, L. G. Lewis, H. H. Rabe, Argonne National Laboratory 511

"PHASOR: A Control Computer Method for Displaying Amplitude and Phase of Ripple Components in the Ring Magnet Voltage"
L. G. Lewis, and A. D. Valente, Argonne National Laboratory 516

"Initial Experience with a Multi-Processor Control System"
K. B. Mallory, Stanford Linear Accelerator Center 521

"The CPS Improvements, 1965-1973 - An Assessment"
The CPS Staff, CERN 524

"Simultaneous Steering of H^+ and H^- Beams at LAMPF"
K. R. Crandall and W. E. Jule, Los Alamos Scientific Laboratory 529

"Fusion Reactions in Colliding Beams"
J. P. Blewett, Brookhaven National Laboratory 531

"Will Negative Hydrogen Ion Sources Soon Replace Proton Sources in High Energy Accelerators?"
Th. Sluyters and K. Prelec, Brookhaven National Laboratory 536

SESSION 8 - FUTURE STORAGE RINGS AND MAJOR ACCELERATOR PROJECTS

Chairman: Kjell Johnsen, CERN

Scientific Secretaries: Vernon G. Price, Stanford Linear Accelerator Center
Christoph W. Leeman, Lawrence Berkeley Laboratory

Invited Paper - "ISABELLE Design Study of Intersecting Storage Accelerators"
H. Hahn, Brookhaven National Laboratory 537

Invited Paper - "Design and Status of EPIC" .
EPIC Machine Design Study Group of the Rutherford and Daresbury High Energy Laboratories (presented by G. H. Rees) 548

Invited Paper - "The Proton-Electron-Positron Project - PEP"
L. Smith, Lawrence Berkeley Laboratory-Stanford Linear Accelerator Center Joint Study Group 557

Invited Paper - "The PEP Electron-Positron Ring - PEP Stage I"
J. R. Rees, Lawrence Berkeley Laboratory-Stanford Linear Accelerator Center Joint Study Group 564

"ISABELLE Antiproton Option"
C. Baltay, Columbia University; and R. Chasman, H. W. J. Foelsche, h. Hahn, M. Month, and A. Van Steenbergen, Brookhaven National Laboratory 572

"SLED: A Method of Doubling SLAC's Energy"
Z. D. Farkas, H. A, Hogg, G. A. Loew, and P. B. Wilson, Stanford Linear Accelerator Center 576

"A Preliminary Design of Tri-Ring Intersecting Storage Accelerators in Nippon, TRISTAN"
T. Nishikawa, National Laboratory for High Energy Physics, ... 584

"The Super-Adone Electron-Positron Storage Ring Design"
F. Amman, M. Bassetti, A. Cattoni, R. Cerchia, V. Chimenti, D. Fabiani, A. Marra, M. Matera, C. Pellegrini, M. Placidi, M. A. Preger, A. Renieri, S. Tazzari, F. Tazzioli, and G. Vignola, Frascati 588

"Bunched Beam Intersecting Storage Accelerators for Proton-Proton Collisions"
M. Month, Brookhaven National Laboratory 593

"Insertions for Colliding-Beam Storage Rings"
W. W. Lee and L. C. Teng, National Accelerator Laboratory 599

"Resonance Crossing in a Proton Synchrotron; Application to ISABELLE"
R. Chasman, Brookhaven National Laboratory; A. Garren, Lawrence Berkeley Laboratory; R. L. Gluckstern, University of Massachusetts; and F. E. Mills, National Accelerator Laboratory 604

"Main Ring Magnet System of KEK PS"
A. Ando, K. Endo, T. Kasuga, M. Kihara, and E. Takasaki, National Laboratory for High Energy Physics, ... 610

"Saturne 11: Proposal of a Renovated Proton Facility at Saclay"
H. Bruck, J.-L. Laclare, G. Leleux, and the "GERMA" Group 615

"The Electron Pulse Stretcher EROS"
N. R. Heese and R. Servranckx, University of Saskatchewan 618

"Preliminary Design Considerations for the Stage I PEP Lattice"
R. H. Helm and M. J. Lee, Stanford Linear Accelerator Center 622

"Design Considerations for a High Energy Electron-Positron Storage Ring"
H. Wiedemann, DESY 629

"High-Intensity Storage Rings for Meson Factory"
G. I. Batskikh, A. A. Vasiliev, A. A. Kuzmin, R. A. Meshcherov, B. P. Murin, V. S. Rybalko, Radiotechnical Institute of the USSR Academy of Sciences, Moscow; and Yu. Ya. Stavisskiy, Institute of Physics and Energetics 633

"Trends of the Development of Strong Current Cyclic Accelerators - Meson Factories"
V. P. Dzhelepov, V. P. Dmitrievsky, and V. V. Kolga, Joint Institute for Nuclear Research, Dubna 638

"First Beam Tests with the 590 MeV Ring Cyclotron at SIN"
J.-P. Blaser and H. A. Willax, Swiss Institute for Nuclear Research 643

"Basic Design Considerations on an Electron Beam Stretcher"
H. Herminghaus, Mainz 648

SESSION 9 - OVERALL PERSPECTIVE TALKS

Chairman: Karl Strauch, Harvard University

Scientific Secretaries: Z. David Farkas, Stanford Linear Accelerator Center
John M. Hauptman, Lawrence Berkeley Laboratory

Invited Paper - "Trends in Elementary Particle Theory"
M. Gell-Mann, California Institute of Technology (unfortunately this paper not available)

Invited Paper - "The Next Step: Accelerators vs Storage Rings"
L. M. Lederman, Columbia University 650

Invited Paper - "Perspectives on Colliding Beams"
E. Keil, CERN 660

Rapporteur Talk - "Synchrotron Radiation Sources"
S. P. Kapitza (presented by V. V. Elyan), Institute for Physical Problems, Moscow 671

Invited Paper - "Astrophysics and Elementary Particle Physics"
R. Ruffini, Princeton University 675

"A 2 GeV 1 A Electron Storage Ring Dedicated to the Production of Synchrotron Radiation"
D. J. Thompson, V. R. Atkins, J. C. Hopkins, E. A. Hughes, A. Jackson, J. B. Lyall, N. Marks, P. Moore, D. E. Poole, M. W. Poole, G. Saxon, V. P. Suller, T. E. Swain, K. Tarry, D. G. Taylor, and B. Trickett, Daresbury High Energy Laboratory 680

"The Stanford Synchrotron Radiation Project (SSRP)"
H. Winick, Stanford University 685

"The Conversion of the NBS 180-MeV Electron Synchrotron to a 240-MeV Electron Storage Ring for Synchrotron Radiation Research"
E. M. Rowe, M. A. Green, W. S. Trzeciak, and W. R. Winter, Jr., University of Wisconsin 689

THE IHEP 76 GEV PROTON SYNCHROTRON

Ado Yu.M., Kotov V.I., Myznikov K.P.,
Naumov A.A., Suljaev R.M., Tepljakov V.A.,
Trojanov E.F., Zaitsev V.I., Zhuravlev A.A.

Institute for High Energy Physics.
Serpukhov, USSR

Summary

This paper contains:
brief information on the accelerator operating characteristics; the activities for increasing accelerator beam intensity, including investigation of the proton beam space charge influence upon the betatron notions; the results of tuning secondary particles beam lines and the extracted proton beam.

The operation schedule for the IHEP Synchrotron complex is an annual one and it forsees normally 5 continuous runs with two-week intervals between them and one big summer shutdown.

Total operation time per year is about 4500 hours. 80% of this time is used for physics, 20% - for tuning and investigation of the accelerator. Time lost due to faults is about 11% averaged per year. The operation intensity of the accelerated beam can be maintained at the level of 2.2 x 10^{12} protons per pulse. Up to five experiments are carried out simultaneously. The investigations at the accelerator are aimed at increasing its efficiency along the following lines:

- increase of the accelerated proton beam intensity;
- creation and improvement of the particle extraction systems;
- development of new and improvement of the existing channels for transport of secondary particles.

1. The Synchrotron

a) The Linac - Injector

In the operation regime %heinjectors current can be increased up to 100 mA at the pulse length up to 40 μs. The maximum achieved current is 180 mA. The beam loading influence on the accelerating RF voltage is compensated by increasing the power amplifiers plate voltage during acceleration. This provides fairly stable beam parameters at the linac output. The normalized beam emittance does not exceed 1π cm.mrad at the 90% current level. The energy of particles after debuncher is of 100 $\pm$ 0.5 MeV.

b) The Ring Accelerator

The intensity restrictions take place during the protons' ecceleration in the ring accelerator. The main reason for this is the action of the beam particles own electromagnetic field on the betatron motion. To reduce its influence work has been performed to minimize the orbit distortion, to correct coupling between vertical and horizontal betatron oscillations and to narrow some resonances up to 4th order.

At present the following correction dc circuits are introduced at the accelerator:

- the 9th, 10th and 11th harmonics of the vertical magnetic field to correct the orbit horizontally;
- the 10th harmonic of the horizontal magnetic field to correct the orbit vertically.
- sextupole magnetic field component to control dependence of the betatron oscillation frequencies on the momentum (separately, in focusing and defocusing magnet units).
- the skew quadrupole magnetic field for narrowing the difference coupling $Q_r = Q_z$ resonance band;
- the 19th harmonic of the magnetic field gradient to narrow the stop-band $2Q_z = 19$;
- the 29th harmonic of the normal sextupole field to narrow stopbands $3Q_r = 29$ and $2Q_z + Q_r = 29$;
- the 29th harmonic of the skew eextupole field to narrow stop-band $3Q_z = 29$;
- the 39th harmonic of the normal octupole field and the 39th harmonic of the skew octupole field to narrow stop-bands $4Q_{r,z} = 39$; $3Q_{r,z} + Q_{z,r} = 39$; $2Q_r + 2Q_z = 39$.

To control betatron oscillation frequencies Q_r and Q_z the magnetic field gradient is corrected separately in focusing and defocusing magnet units. Gradient correction currents are changed according to the assigned program, which can LA easily varied.

Individual active correction, of Hz field is introduced into the magnet units where non-standard vacuum chambers with thick walls are installed (injection and extraction areas).

To smooth out fields in the magnet unite at injection, sbunting of additional windings by resistors is used as well[1].

As a result of the correction orbit distortions at small magnetic field levels (the Injection field is 76 Oe) were decreased down to $\pm$ 0.7 cm horisontally and $\pm$ 0.7 cm vertically in straight sections,

The necessity of narrowing stop-bands is illustrated in Fig.1, where the direction of the non-coherent betatron oscillation frequency shift is shown. The evaluations show that particle dynamics at high intensity can be influenced by resonances up to half-integral one.

The injected beam duration may be 34.5 μs (three-turn injection). The filling of the accelerator radial acceptance is performed by means of four electrostatic deflectore located symmetrically to the point of beam injection into the accelerator[2].

Fig.2 shows an oscillogram of the particle stack process at three-turn injection.

Fig.3a shows the dependence of the number of particles in the accelerator, one ms after Injection, on the number of particles injected into the accelerator chamber - for cases of 1, -2- and 3-turn injection,

The curves were taken at constant emittance and momentum spread of the injected beam. At low intensity the injection efficiency coincides with the calculated one. With the increase of the injection current its efficiency drops (Fig.3a shows decrease of curve slope at high current). This is due to the effect of the beam space charge. It should be noted that the slopes of these curves begin to decrease later if the filling of acceptance is more uniform.

The loss of particles after 1 ms (see Fig.3b) practically does not depend on the character of the phase space filling at the injection. This testifies to the fact that the character of the acceptance filling affects the loss of particles only at the initial stage of the acceleration, i.e. during beam bunching.

Further increase of the intensity is expected to be realized by improvement of longitudinal phase space filling. To achieve this the rate of magnetic field rise will be decreased at injection down to 500 - 1000 Oe/sec and quasi-adiabatic capture will be introduced [3].

Sharp intensity increase is planned upon completion of the 1.5 GeV fast-cycling booster[4] which will enable 70 GeV beam of intensity up to 5.10^{13} pppm to be obtained. The construction of the booster is expected to begin later this year.

2. Beam extraction system

Certain experiments were completed in 1973 with fast extraction of protons in the direction of the "Ludmila" 2-m hydrogen bubble chamber (channel 9)[5] and the extraction of protons in the direction of the neutrino channel was effected (channel 8). For these purposes a system of extraction magnets used earlier for fast extraction of protons in the direction of the "Mirabelle" 4.5 m hydrogen bubble chamber (channel 7) was applied[6]. A layout of the ion-optic system for focusing of the extracted beam in the channels is shown in Fig. 4.

Fig. 5 shows measured distribution of the beam intensity on the external target of channel No 9. Under operation conditions the beam dimensions on the target are 1 mm in the vertical plane and 1.5 mm in the horizontal one; stability of the beam position on the target is ± 0.1 mm, angular beam divergence is less than ± 2 mrad.

The channel No 8 ion-optic system is designed for extracted beam transport at a distance of 100 m and for beam focusing into the intermediate image point. Immediately after the channel goes out from the accelerator magnetic field a doublet is used enabling formation of a beam of small angular divergence. Beam focusing into the intermediate image point is performed using a triplet. At present work is being done to launch and optimize the system.

Great attention has been paid enabling double shot of the fast extraction system per cycle. Such a possibility had been conceived in the project of the system[7]. Fig. 6 shows the regimes which are either used in practice at present or will be used in the immediate future. Regime 6a enables double extraction of protons per cycle into channels No 8 and No 9. The extraction is performed whilst the magnetic field is rising; the flat top being fully used for internal targeting. Regime 6b makes it possible to perform double exposure of the bubble chambers to the beam extracted at intermediate energy; the interval between shots is 400 - 500 ms. Regime 6c enables double exposure of the chambers to the beam extracted at peak energy; the interval between shots is 1.5 - 2 s. In this case, the second shot extracts the debunched beam remaining after targeting.

Monitoring and stabilization of the remainder intensity is performed by ionization of residual gas in the accelerator vacuum chamber. The realization of double-shot fast extraction yielded a substantial increases in the accelerator operation efficiency.

Secondary particle berms generated on internal targets are widely used for electronics experiments. The interaction efficiency of the accelerated beam with beryllium targets was brought up to 90%[8]. The increase of the accelerator intensity, as well as the increase of extraction system efficiency, made it possible to raise the operation particle intensity in the channels. The extracted beam duration was increased to 1.8 s. Measures were taken to increase beam density homogeneity. For this purpose the ripple in the accelerator magnet current was substantially decreased. RF modulation was surely removed by cutting off accelerating voltage 20 - 30 ms before guiding the beam onto the target. HF structure of 26 MHz arising at the beam intensity of more than 5.10^{11}, as a result of its interaction with accelerating cavities, was removed by detuning the cavities after switching off RF[9]. The measures resulted in decreasing total density modulation down to 10-20%. This enabled the use of up to 10^7 particles per pulse in counter experiments.

Further increase in the accelerator operation efficiency was attained by increasing the number of targets used in each cycle and by combining their operation with fast extraction.

The consequent - parallel operation of targets is widely used. In such a regime at the initial part of the flat-top a target is set up to run the experiment, background - incompatible with others. Then the beam is guided simultaneously onto two other targets (Fig.6). Such a regime can be combined with the fast extraction.

At present, the double-shot fast extraction combined with consequent - parallel operation of 2 - 3 targets is a typical operating regime for the accelerator.

3. Particle channels

The general layout of the particle channels is shown in Fig.7.

The channels are located in the 159 x 90 m^2 experimental hall and in the adjacent gallery of 340 m length. It is 36 m wide in the initial 70 m length area and 24 m wide for the reminder of it.

principal channels for the negatively charged secondary particlea (channels No 2 and No 4, see Fig.7)[10,11] are designed so that the formed beams can be used for several experimental set-ups. There are four experimental set-ups in the channel No 2 area. The operating momentum range of secondary particles is 30-65 GeV/c at the accelerated proton energy E_p = 70 GeV; particle intensity at momentum spread $\Delta p/p$ = 1% and the intensity of the proton beam (interacting with the target) $I_o = 10^{12}$ ppp is of 10^6 - 10^4 respectively. The solid angle for capturing particles is of the order of 35 μsr. The dimensions of the formed particle beam in the central direction of channel No 2 are 2.3 x 2.5 cm^2 whereas those on the polarized target are 1 x 1.5 cm^2 (see channel No 14 on Fig.7). The extraction of positive particles from internal targets[12] has been also performed in this area. The intensity of the positive particle beams under the same conditions ae for negative particle beams is 10^6 particlee per cycle. Electron beams with 26.5 - 45.5 GeV/c momentum range have also been produced in the channel No 2 area[13]. The electron beam with momentum spread $\Delta p/p = \pm 3\%$ was formed on an experimental device into the image of 3 x 3 cm^2. 31 GeV electron beam intensity reaches 10^6 particles per cycle at E_p = 70 GeV and $I_o = 10^{12}$. The hadron admixture in the electron beam is less than 1%.

Five experimental set-ups are located in the channel No 4 area. This system of channels produces negative particle beams within 20-50 GeV/c momentum interval. Solid angle for capturing particles into these channels is of the order of 35 μsr. Particle intensity at $\Delta p/p$ = 1%, E_p=70 GeV and $I_o = 10^{12}$ is more than 10^6 per cycle.

A high intensity negative muon beam has been produced in the channel No 4 area (see channel No 16 on Fig.7)[14]. To increase muon intensity a muonguide is installed along the 70m decay path. The muonguide consists of a ferromagnetic tube (inner diameter 204 mm, thickness of wall 7.5 mm), supplied by dc up to 3 kA. It operates as a magnetic reflector and enables the μ-meson flux to be increased by a factor of 1.5. The flux of %'-mesons with average momen-

tum of 40 GeV/c and momentum spread $\Delta p/p \approx 25\%$ is $\sim 3.10^7$ particles per cycle (E_p= 70 GeV and $I_o = 10^{12}$). The flux of μ^--mesons onto the detector 24 x 24 cm^2 is more than 10^6 particles per cycle.

Another channel No 11 has been constructed to transport the 35 GeV/c muon beam to the rest. Notable feature of this channel is the application of magnetized iron eleaents to ensure focusing and braking of muons[15].

To run experiments with neutral particle beams a simple channel No 1 has been created (see fig.7). The neutron intensity in this channel depending on the experimental device geometry is of 10^6 - 10^7 particles per cycle at E_p = 70 GeV and $I_o = 10^{12}$.

Tuning of physics instruments is performed in channel No 6 using secondary particles with the momentum range of 0.8 - 20 GeV/c. Intensity of the 2 GeV/c beam in this channel is about 10^6 particles/cycle at Ep = 70 GeV and $I_o=10^{12}$.

The research program with the "Mirabelle" and "Ludmila" bubble chambers is carried out with beam channels No 7 and No 9 (see Big.7) where RF separators operating on the Panofaky - Montague - Schnally scheme were installed. The RF separators provide pure beams of anti-protons and kaons at the 17 - 40 GeV/c momentum interval (π^+-mesons to 50 GeV/c) in channel No 7[16] and at the 10 - 25 GeV/c momentum range in channel No 9[17-18].

The RF separator for channel No 7 was designed and built at CERN in the collaboration of soviet specialists. In agreement with the survey experiment program "Mirabelle" chamber was exposed to K^+-mesons and antiprotons with the momentum of 32.17 GeV/c as well as to π^+-mesons with 50 GeV/c momentum. For these purposes one of the 30 bunches vith the intensity of $\sim 6 \times 10^{10}$ protons was extracted from the accelerator and led onto an external copper target of 1.5 x 2 x 150 mm^3.

An average loading amounted to 4 - 6 particlea per picture, the background level being less than 2% (mostly muons).

The "Ludmila" bubble chamber was exposed to 23 GeV/C anti-proton beam. One of the 30 proton bunches, accelerated to the energy of 50 GeV, was extracted and guided onto a copper target of the same dimensions. An average loading was 4 particles per picture with a muon background of about 2%, hadron admixture being less than 1%.

Channels No 7 and No 9 also serve to produce for the bubble chambers beams of protons elastically scattered on internal targets.

Channel No 7 can form proton beams with the momentum of up to 70 GeV/c[19], whereas channel No 9 - with the momentum of up to 35 GeV/c[20].

The construction of channel No 8, designed for neutrino beam experiments, is nearing its completion.

The decay path is 140 m, the iron muon shielding is 58 m thick. A set of parabollic lenses[21] will be used as a focusing device. The construction of channel No 18 designed for the production of high-intensity secondary particle beams with a momentum r—— of 3 - 17 GeV/c[22] is also coming to an end. Fluxes of positive particles with the momentum of 5 - 10 GeV/c will be $\sim 10^8$ per cycle at E_p = = 70 GeV and $I_o = 10^{12}$.

References

1. Yu.M.Ado, A.A.Zhuravlev et al. IHEP preprint 69-98, Serpukhov, 1969.
2. Yu.M.Ado, V.I.Zaitsev, M.F.Ovtchinnikov. IHEP preprint 73-11, Serpukhov, 1973.
3. E.A.Myae, P.T.Pashkov. "Atomnaya Energiya", Vol.34, ed.6, p.465, 1973.
4. V.I.Balbekov, F.A.Vodopjanov et al. Proc. of the VIII Intern. Conf. on High-Energy Accelerators, CERN, 1971.
5. A.A.Aseev et al. IHEP preprint 73-27, Serpukhov, 1973.
6. A.A.Aseev et nl. Proc. of the IIIth USSR Conf. on Acc. Moscow, 1972, vol.2, p.160.
7. B.Kuiper, B.Langeseth, K.P.Myznikov. Proc. of the VIIth Intern. Coni. on High Energy Accel., Yerevan, 1969, p.549.
8. V.I.Gridasov, K.P.Myznikov, V.N.Tchepegin. IHEP preprint 73-73, Serpukhov, 1973.
9. A.I.Basov, V.V.Osipov et al. IHEP preprint 73-77, Serpukhov, 1973.
10. I.A.Alexandrov, M.I.Grachev, K.I.Gubrienko et al. "Atomnaya Energiya", Vol.29, ed.29, 1970.
11. M.I.Gratchev, K.I.Gubrienko et al. JETP, 41, 1812, 1971.
12. N.I.Golovin, M.I.Gratchev, K.I.Gubrienko et al. "Atomnaya Energiya", vol.32, p.244, 1972.
13. S.S.Gerschtein, A.I.Samoilov, Y.M.Sapunov, A.M.Frolov et al. "Atomnaya Energiya", vol.35, p.181, 1973.
14. M.I.Gratchev, A.I.Zaitsev, V,P.Kubarovsky et al. IHEP preprint 71-13, Serpukhov, 1971.
15. G.B.Bondarenko, V.A.Glukhich, Yu.P.Dobretsov et al. Proc. of the VIIIth Intern.Conf. on High Energy Accel. CERN, 1971, p.282.
16. Ph.Bernard, N.A.Galyaev, A.Grand et al. "Atomnaya Energiya", vol.35, ed.227, 1973.
17. A.V.Samoilov, Y.M.Sapunov, A.M.Frolov. Proc. of the IInd USSR Conf. on Charged Particle Accel., "Nauka", Moscow, 1972, vol.2, p.190.
18. V.N.Alferov, M.A.Bulgakov, A.M.Vyshnevskaya et al. Proc. of the IInd USSR Conf. on Charged Particle Accel. "Nauka", Moscow, 1972, vol.2, p.229.
19. V.A.Maksheev, A.V.Samoilov et al. IHEP preprint 73-7, Serpukhov, 1973.
20. N.A.Galyaev, N.I.Golovnya, M.I.Gratchev et al. JETP, vol.42, p.1437, 1972.
21. V.I.Voronov, I.A.Daniltchenko, V.A.Rzaev, A.V.Samoilov Nucl.Instrum. and Meth., 105, 142, 1972.
22. V.I.Belousov, A.M.Blick, V.G.Vassiltchenko et al. IHEP preprint 73-90, Serpukhov, 1973

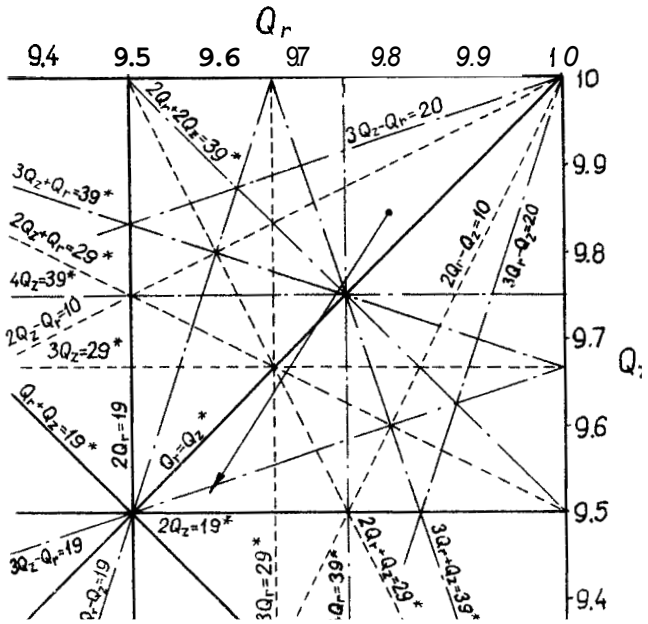


Fig.1. A tune space diagram. Asterisks mark resonances which can be corrected.. The arrow points to the betatron frequency shift direction caused by beam space charge.

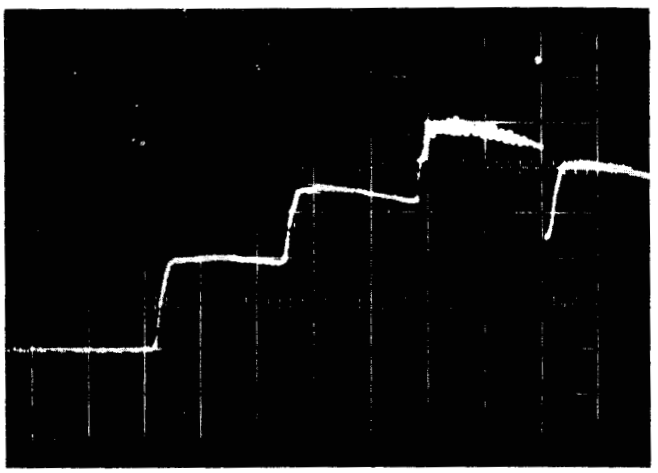


Fig.2. Particle stack oscillogram of 3-turn injection;
horizontal scale - 5 μs/div
vertical scale - 30 mA/div

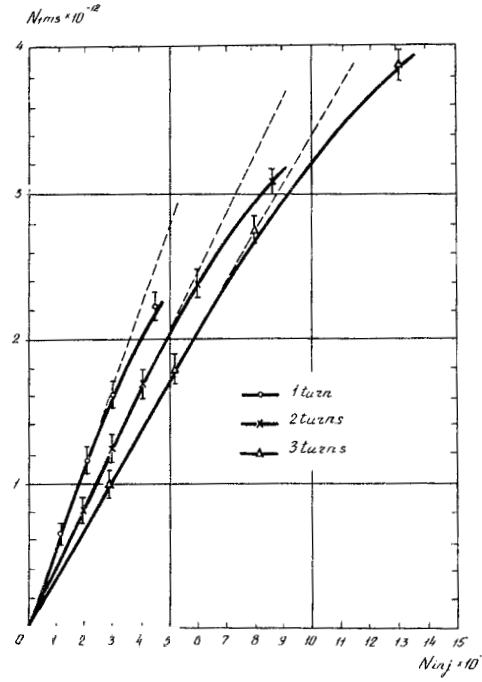


Fig.3a. Dependence of number of particles captured into the acceleration on the number of particles injected into the accelerator at different number of injection turns.

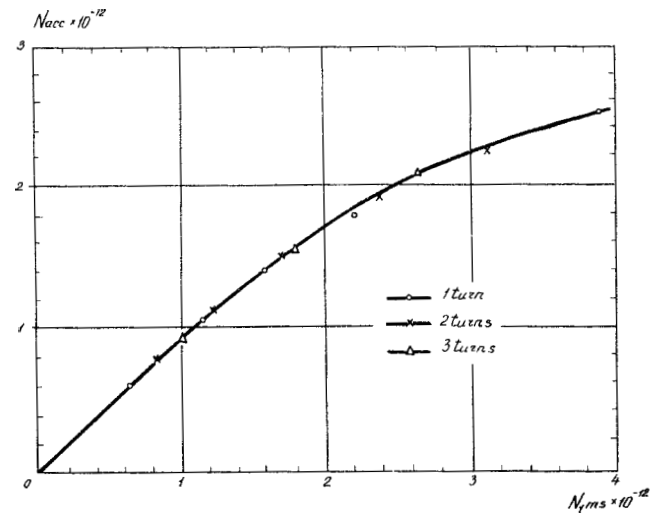


Fig.3b. Dependence of number of particles accelerated to the peak energy on the number of particles captured into acceleration.

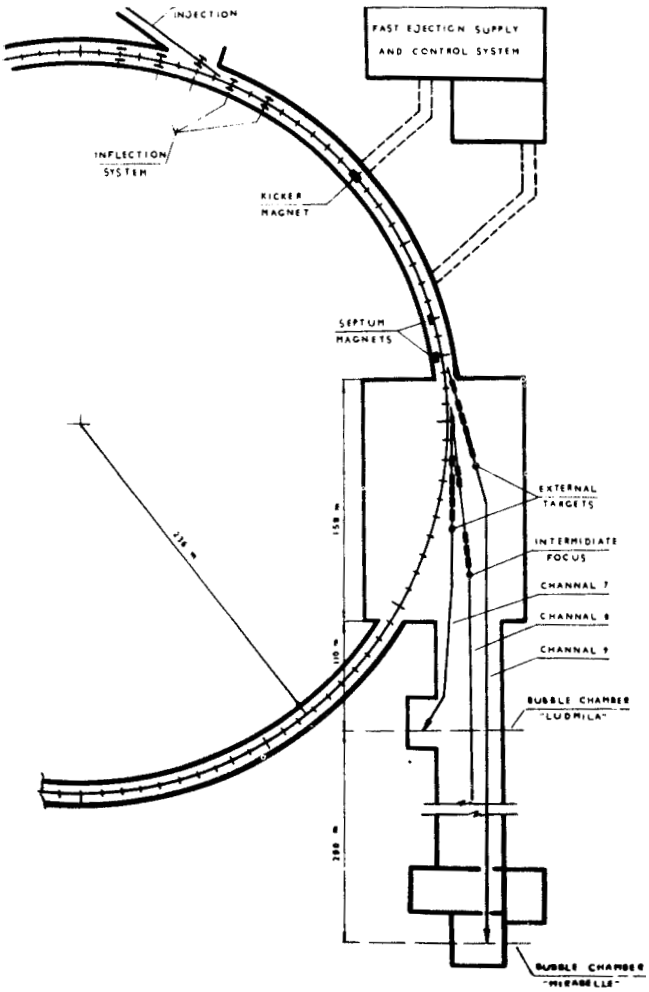


Fig.4. Extracted beam focusing system Layout.

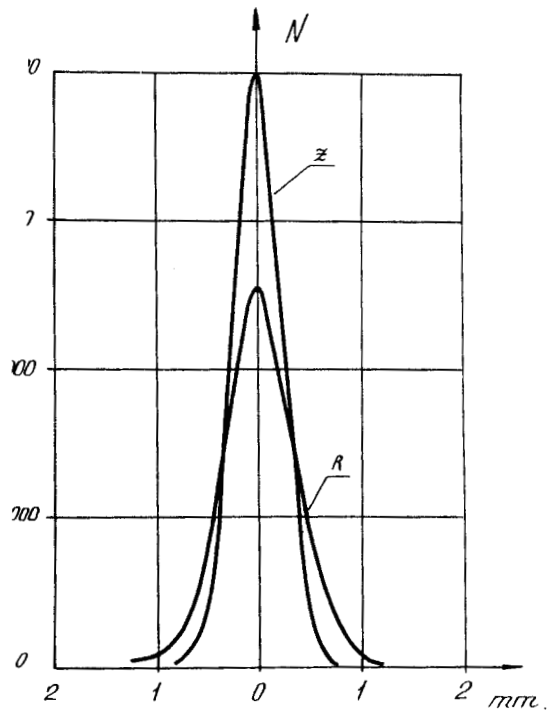


Fig.5. Intensity distribution on channel № 9 external target.

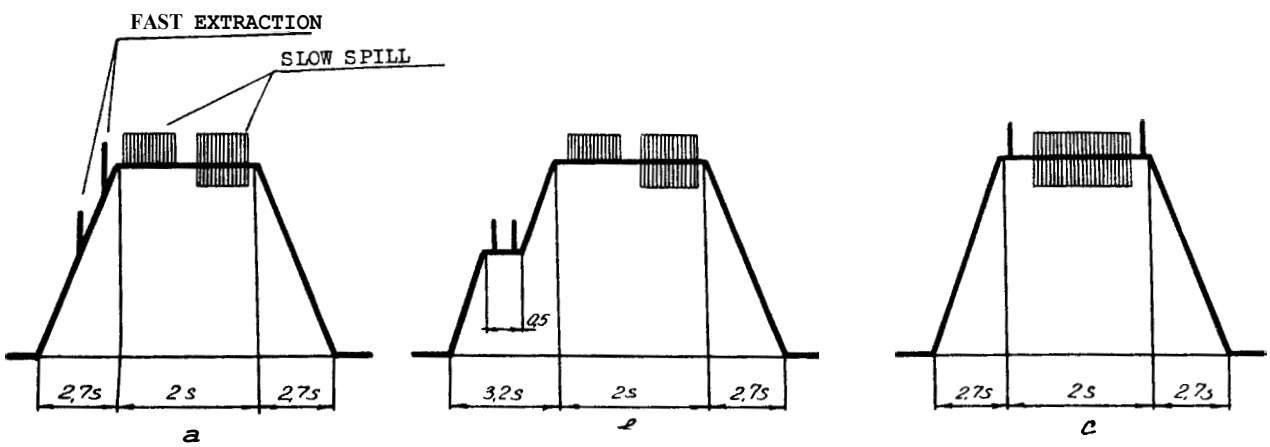


Fig.6. Standard operation regime for extraction devices.

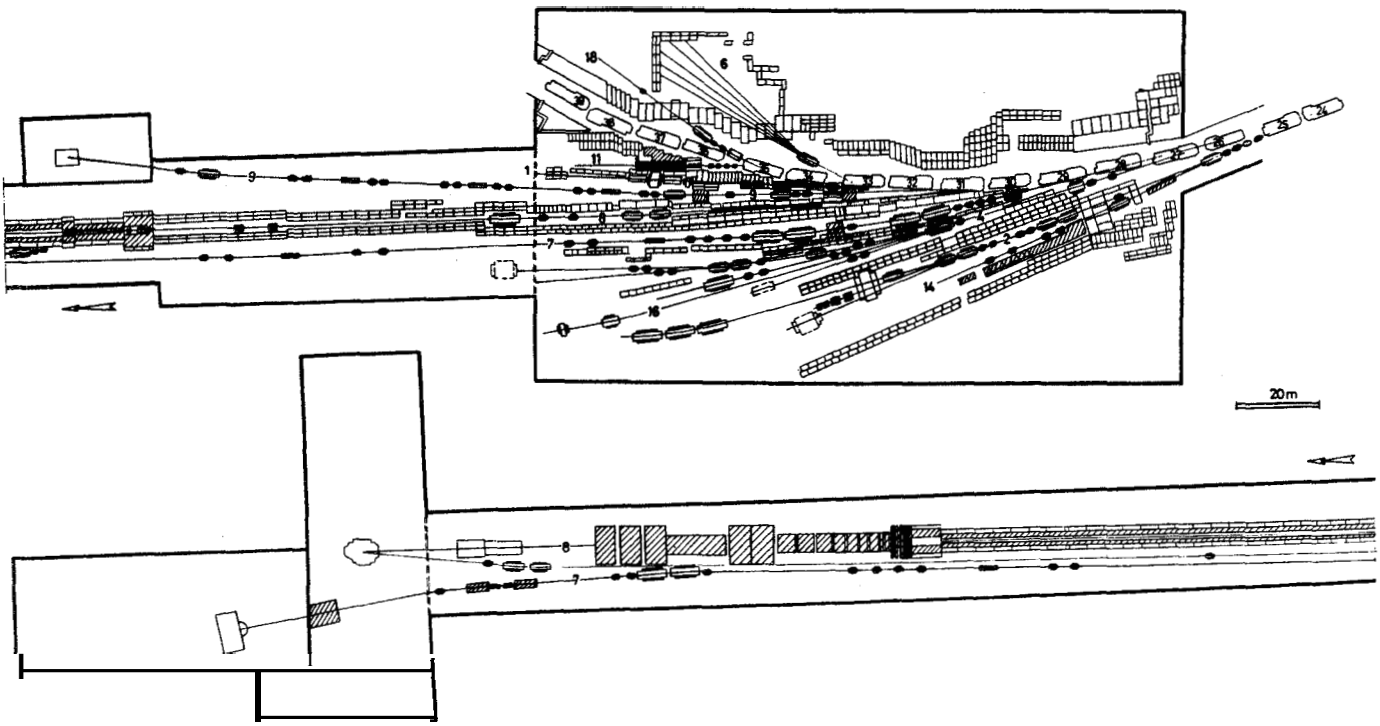


Fig.7. **Particle channels** location in **the** experimental hall and the **gallery.**

DISCUSSION

Lee Teng, (NAL): Would you say something more about your 1.5 GeV booster.

Ado: As I said, in this year we started the construction of the booster. It is a fast-scheme booster with a repetition frequency of **25** Hertz, the energy of particles is 1.5 GeV, and we have put them in the main ring during 1.2 sec. It is 25 bunches from the booster. The intensity after the completed tuning of the booster will be 5×10^{13} protons per pulse. The injection into the booster from the linac is at 30 MeV during 8 or 10 turns.

Milton White, (Princeton): Will the booster magnet power supply be a resonant system?

Ado: Yes

Milton White: With a flat top during injection?

Ado: During injection we have a flat top.

Shigeki Mori, (NAL): What is the residual radiation at the internal target?

Ado: We have some hot points in our ring near the internal targets. The maximum level of residual radioactivity is about 2 REM/hr. The main part of this is defined by short living isotopes.

Bruce Cork, (Berkeley): Do you plan a proton storage ring?

Ado: This is a question for which I have many answers. We have started to consider improvement of our accelerator, and we have many suggestions including accelerators from 1,000 GeV to 5.000 GeV, storage rings of protons, electrons and positrons, but it is not complete and is very preliminaiy.

Milton White, (Princeton): Do you have any plan for accelerating relativistic heavy ions, heavier than protons?

Ado: No. In Serpukhov we have no such plans.

THE NAL ACCELERATOR AND FUTURE PLANS

The NAL Staff
(Presented by P. J. Reardon)
National Accelerator Laboratory*
Batavia, Illinois

Summary

The NAL 300- to 500-GeV accelerator has achieved full operation with an intensive high-energy-physics experimental program in progress. The current operation of the accelerator and experimental areas is described as well as the present plans for improvement to achieve the design goals. The Laboratory is also working on longer range projects to achieve an accelerated beam of higher energy and to use this capability in a new experimental area and in a colliding-beam facility.

Introduction

The accelerator and experimental facilities of the National Accelerator Laboratory have been described previously. [1,2,3,4] This paper will summarize the present status of the Laboratory, including the performance of the major subsystems of the accelerator and plans for the improvements in these systems, the overall accelerator performance over the last fifteen months, and the goals for the future. At this time, all essential elements of the original project are now complete, although some upgrading of the experimental areas and the accelerators is continuing.

The overall accelerator is shown in an aerial view in Fig. 1. The injector system for the 1000-m radius main accelerator consists of a 750-keV preaccelerator, a 200-MeV linear accelerator and an 8-GeV rapid cycling (15-Hz) synchrotron (the "booster") with a circumference of 1/13.25 of the main accelerator. Normal operation consists of 12 booster pulses (in 0.8 seconds) injected head-to-tail into the main accelerator during the rest field, after which the field is increased at a rate of 100 - 125 GeV/sec to the final value of 300 or 400 GeV. At 300 GeV, the beam then is extracted over one second during a six-second pulse and sent to three external beam areas, shown in aerial view in Fig. 2. These experimental areas are called the Meson, Neutrino, and Proton areas. In addition, an Internal Target area, in the process of being enlarged. is located in one of the *six* 51-m long straight sections. Three of the other long straight sections are used for the beam-abort system, for the rf accelerating systems, and for the injection-extraction system.

A little over two years *ago,* on March 1, 1972, the accelerator reached the original design goal of 200 GeV. We now operate routinely at 300 GeV and have done several extended 400-GeV runs for high-energy physics. An intermediate intensity goal of 10^{13} protons per pulse was just reached a few weeks ago. A laboratory has been brought into being that, in terms of energy and active target stations, exceeds its design by a factor of two, with the other important goals of the project in sight, for about 90% of the funds allowed.

*Operated by Universities Research Association, Inc. under contract with the United States Atomic Energy Commission.

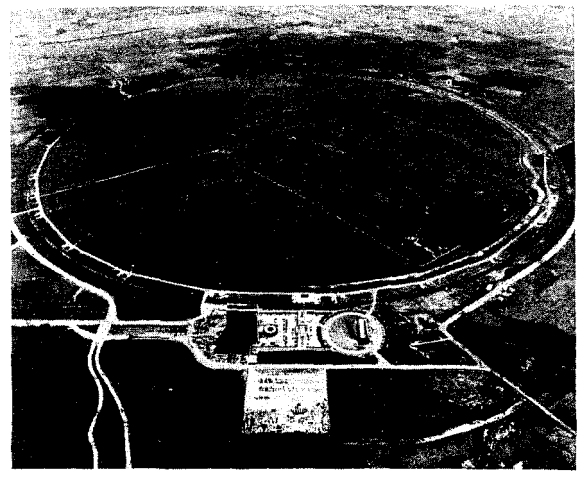


Figure 1. Aerial view of accelerator complex.'

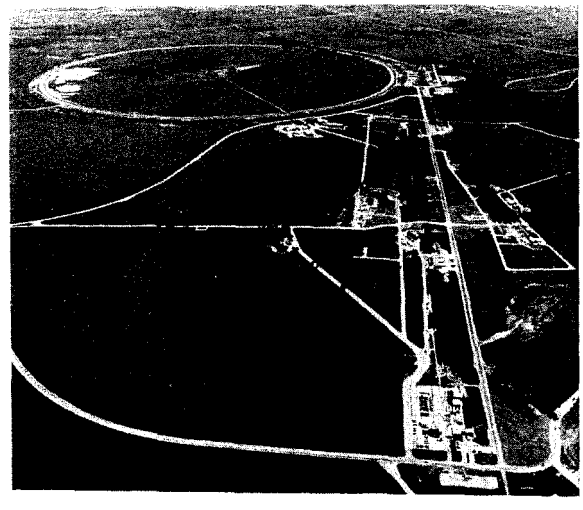


Figure 2. Aerial view of experimental areas (Proton, Neutrino, Meson from left to right).

We are looking forward now to the challenges of the future, which in the next year include attempts to operate the accelerator, extraction and switchyard systems at energies as close to 500 GeV as is possible, operations at 2 to 5 x 10^{13} protons per pulse, a front porch that will send a 300-GeV beam to the Meson Lab with a one-second flattop and at the peak of the same pulse, a 400-GeV beam to the Neutrino and Proton Laboratories, and a triple split in the Proton Laboratory, *so* that all eight proton target stations can be operated simultaneously.

In the longer run, say during the next four to seven years, we plan to design and install in the existing main-ring tunnel a superconducting ring of magnets that will enable us to bring the energy of the proton beam up to the region of 1000 GeV (the Energy Doubler), to complement the present facility with a new set of rings, two 1000-GeV proton rings and one 20-GeV

electron ring (POPAE) that will allow us to study the weak, electromagnetic, and strong interactions at a new energy scale where common characteristics might become apparent, and to construct a fourth external experimental area, the Quark Area, that will enable us to do counter experiments with high-intensity secondary beams with energy ranges up to 1000 GeV. We are also proposing, with the University of Wisconsin, the construction of a 1-MWH, 3600-MJ superconducting energy-storage device both to compensate for the energy droop to the utility system caused by our proposed 12-second, 500-GeV pulsed power load and to study some of the longer-range aspects of this form of energy-storage system as a potential competitor to other proposed systems for electrical-utility application.

Present Accelerator Operating Status

Program Status

The accelerator and the high-energy physics experimental program have been operating on a 24-hour, seven-day-per-week basis since April 1972. At present, approximately 75% of calendar time is scheduled for high-energy physics, 11% for accelerator studies, 5% for startup and tuneup, and 9% for scheduled maintenance and development. In recent months, the accelerator and extraction and switchyard systems have performed approximately 75% of the scheduled time, with highs of 93% for a week in March and 94% for a week in April.

The average intensity per 300-GeV pulse (with a 6-second cycle rate, including a 1-second flattop) is approximately 6×10^{12} protons per pulse and a peak intensity of 1×10^{13} protons per pulse has recently been achieved. Figure 3 shows main-ring beam intensity and main-ring magnet ramp over the 6-second 300-GeV cycle. The 12 beam pulses in the main ring are shown during injection in Fig. 4. Using the normal 12-pulse single-turn injection system from the booster into the main ring, transmission efficiencies of about 90% are regularly achieved and 100% transmission efficiencies have been observed during accelerator-physics experiments. The recent achievement of 1×10^{13} protons per pulse occurred using the multiple-turn booster injection system, with a transmission efficiency of 62% and 1.6×10^{13} protons injected into the main ring.

The extraction efficiency for slow extraction is now a solid 97% over periods of weeks at a time and the macroscopic spill duty factor during slow spill is about 70%. In both cases, the reproducibility and stability of operation are very good because of a computer-aided feedback system on extraction elements.

During high-energy physics running, we send protons to seven targets. Simultaneous operation of seven targets is possible because of the installation of four beam-splitting stations that use electrostatic septa and Lambertson magnets similar to those employed in the primary beam-extraction system.

When running neutrino experiments, approximately 50% of the beam is extracted in the fast mode at the end of the slow spill. Often, to reduce the instantaneous counting rate, we extract the beam for neutrino experiments in what we call the coherent fast mode for 100 to 300 microseconds. In all cases, any beam left in the accelerator after the various extraction modes are completed is deposited in a special beam dump through an abort system installed in the main ring. Typically, for operation near 10^{13} protons per pulse using a fast spill for the Neutrino-Area beam, half the beam is extracted in the slow-spill mode, split 15% to the Meson Area, 75% to the Neutrino Area, with four 1-msec high-intensity bursts for multiple pulsing of the bubble chamber, and 10% to the Proton Area, which is further split 80% to Proton East and 20% to Proton Center or 50% to Proton West and 50% to Proton Center. The two targets in the Internal-Target Area of course enjoy multiple traversals of the proton beam at any energy of interest from 8 GeV to 300 GeV, or at times 400 GeV.

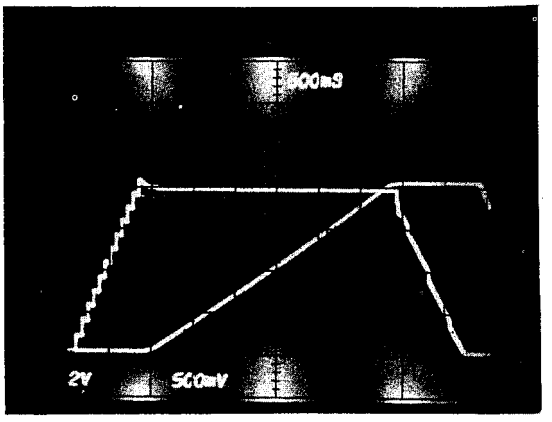


Figure 3. Main-ring ramp and beam. Twelve booster pulses, slow extraction with 4 fast bursts for multiple pclsing of 30-inch Bubble Chamber.

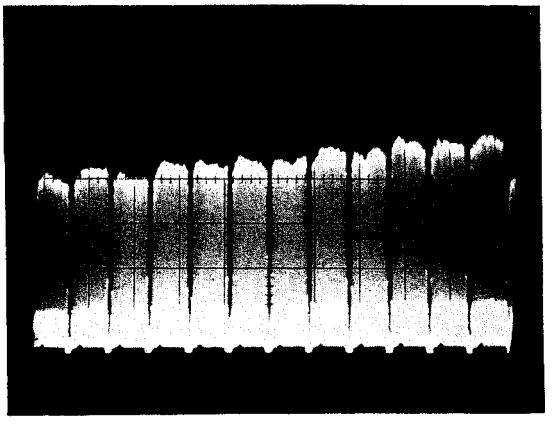


Figure 4. Twelve booster pulses during injection into the main ring.

We believe that with 8 proton target stations available, seven of which operate simultaneously, four experimental areas with about 25 experiments installed

at any given time, twelve to fourteen of which are usually operating at the same time, an operating intensity close to 10^{13} protons per 6-second pulse at 300 GeV (the intensity per pulse achievable at 400 GeV is the same as that achieved at 300 GeV), a good pulse-to-pulse stability in beam intensity, extraction efficiency and spill duty factor, a reliability factor over 70% and round-the-clock operation, that we have now achieved full operation. Corroborating this contention is the fact that some 49 experiments have been completed. Figures 5, 6, 7, and 8 show the progress of our program; Figure 5 shows the number of protons accelerated per month; Figure 6 shows the number of experiments set up and completed and the number of bubble-chamber pictures taken per month; and Figure 7 shows the experiments currently installed. Figure 8 gives the scheduled and actual high-energy physics and accelerator-studies utilization per month.

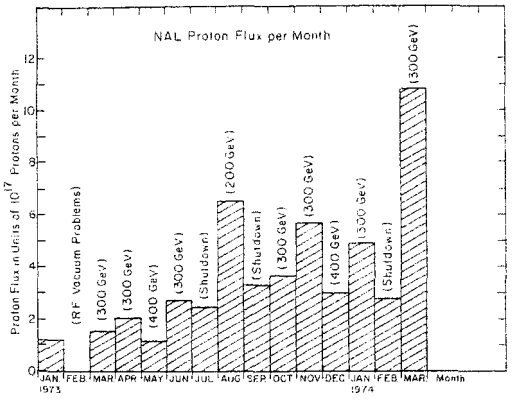


Figure 5. Accelerated protons per month.

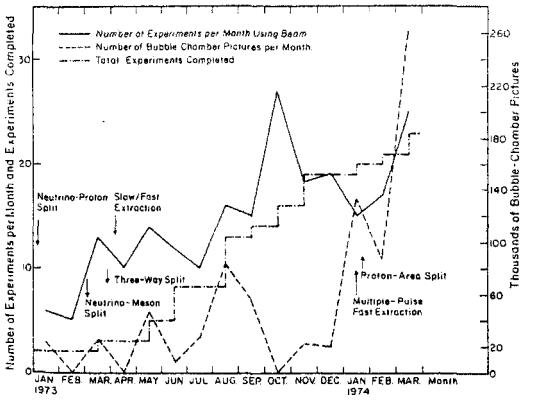


Figure 6. Progress of the NAL experimental program. (Approximately 20 emulsion experiments not included.)

Accelerator Reliability

The NAL accelerator contains many more systems than most accelerators. If operation is to be efficient, the reliability of each of these systems must be very good. We have therefore given intensive study to reliability problems. A reliability committee has been active in gathering and evaluating performance data and in developing recommendations for improvements of various systems. Considerable progress has been made. In the first half of 1973, the accelerator operated 49% of the scheduled operating hours, in the second half of 1973, 54% of the scheduled hours, and in the first quarter of 1974, 66% of the scheduled hours. Time for startup and tuning is not included in these totals.

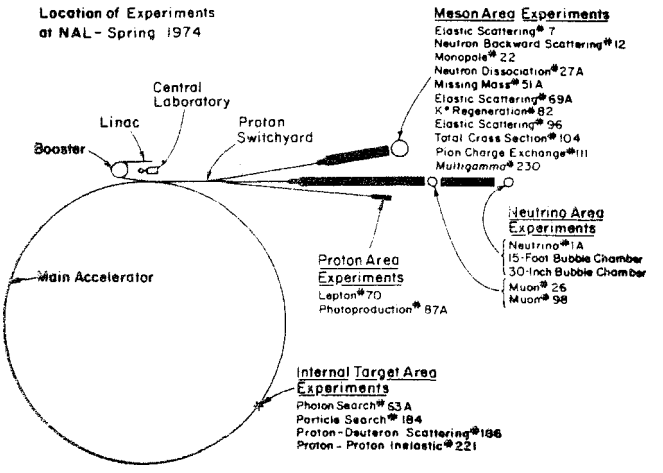


Figure 7. Experiments installed at NAL, Spring, 1974.

Our recording or reliability is divided into 14 major accelerator systems. For each of these, all downtimes longer than one minute are recorded by the operators. The downtimes as percentages of the total operating time for these 14 systems in the two halves of 1973 and the first quarter of 1974 are shown in Table I. Figure 9 summarizes the downtimes in five major systems groups as a function of time.

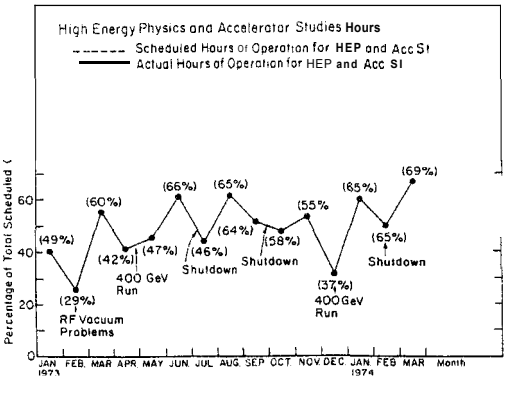


Figure 8. Scheduled and actual use of accelerator times.

The large downtime for main-ring rf in the first half of 1973 was almost all due to several catastrophic vacuum failures in February, the effects of which can

Table I

System Inefficiencies
(Percent of scheduled operating hours that systems failed.)

	First Six Mos. of 1973	Last Six Mos. of 1973	First Three Mos. of 1974
1. Preaccelerator	2.43	1.73	1.31
2. Linac	4. 86	4.22	2. 67
3. 200-MeV Line	1.74	0.86	0. 58
4. Booster	3.35	4. 65	2.06
5. Booster RF	3. 28	2. 88	0.93
6. 8-GeV Line	2. 28	1.67	1.19
7. Main-Ring Power Supply	10.31	3.43	2. 32
8. Main Ring	9. 38	8. 39	8.21
9. Main-Ring RF	18.16	4. 40	0. 85
10. Extraction	2. 25	0. 27	1.44
11. Switchyard	2.44	2.37	1.89
12. Controls	7.32	2. 67	3.30
13. Safety	1.24	0. 89	0. 24
14. Utilities	1.08	1.55	1. 71

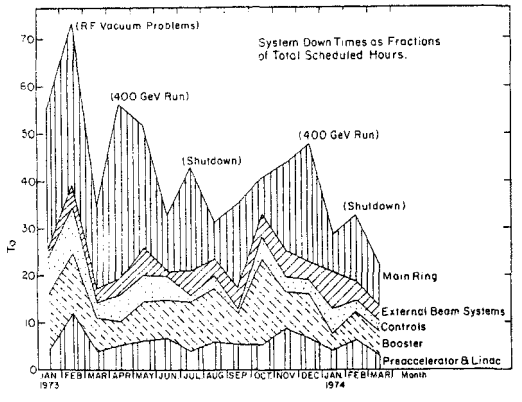


Figure 9. Accelerator-system downtimes per month.

be seen in the intensity and operations graphs in Figs. 5 and 8. Aside from this kind of failure, which has been cured by hardware improvements, the main-ring rf has been a very reliable system.

It can be seen from Table I that substantial improvements have been made in the reliability of preaccelerator, linac, booster, booster and main-ring rf, main-ring power supplies, extraction, switchyard, controls, safety. and beam-transfer systems. In all these systems, improvement programs are in progress and further improvements are expected. The main-ring reliability has not shown such dramatic improvement yet, but it is expected that current improvements in the techniques for rebuilding main-ring magnets and in upgrading water-system insulators and piping will improve the reliability of the main ring in the next year.

System Performance and Improvements

Preaccelerator and Linear Accelerator

The preaccelerator consists of a single 750-keV high-voltage supply with an accelerating column designed with appropriate gradient and electrode apertures to pass a parallel proton beam of 250 mA in a Pierce geometry. Although the ion source has operated at greater currents than this, a current of 180 to 200 mA, together with a simple single-gap buncher ahead of the linac, is adequate to produce a 100-mA proton beam out of the linac. The operational emittance of the preaccelerator beam is very near the design value of 50π mm-mrad. The preaccelerator and linac performance parameters are given in Table 11.

The linac typically operates with a beam current of about 90 mA, with the last accelerating cavity tuned to achieve a minimum momentum spread. This results in an output energy of the linac of 205 MeV. A beam chopper in the 750-keV transport system limits the length of the beam pulse accelerated in the linac to the length of pulse required for injection into the booster synchrotron and prevents the acceleration of protons that cause unnecessary radioactivity buildup elsewhere. For short beam pulses, the variation of the mean momentum during the pulse is small, but for the longer beam pulses required for multiple-turn injection into the booster, this variation results in an even greater voltage requirement on the booster rf system. The nominal operating emittance of the linac beam is close to the design, which recognizes a growth of a factor of 2 to 3 in the linac. This growth occurs mostly in the first accelerating cavity below 10 MeV, but there are no plans at present for redesigning this cavity, even though a smaller emittance would simplify multiple-turn injection in the booster.

A debunching cavity in the 200-MeV transport line

Table II
Preaccelerator and Linac Parameters

	Design	Nominal Operating	Best to Date	Improvement Expected
Preaccelerator				
Energy (keV)	750	750	--	
Beam Current (mA)	220-300	180-200	320(1)	
Emittance(2) (mm-mrad)	50π	50π - 60π	40π	
Linac				
Energy (MeV)	200.3	205	--	
Beam Current (mA)	75	90 - 100	120	
Beam Pulse Length (μsec)	up to 100	3 - 12	--	
Momentum Spread $\frac{\Delta p}{p}$ at the Booster				
(a) without debuncher	3.2×10^{-3}	$2\text{-}3 \times 10^{-3}$	2×10^{-3}	
(b) with debuncher	1.6×10^{-3}	Note (3)	Note (3)	$1.5\text{-}2 \times 10^{-3}$
Mean Momentum Variation	--	$3\text{-}6 \times 10^{-4}$	1×10^{-4}	1×10^{-4}
Emittance(2) (mm-mrad)	5π - 10π(2)	10π(2)	8π	

(1) Departure from Pierce geometry.
(2) For 90% of beam.
(3) The debuncher is being installed.

from the linac to the booster is presently being installed. It will consist of a 3-unit cell cavity placed 43 m from the end of the linac. When the debuncher is put into service, the linac will be retuned to increase the momentum spread (and the output energy wiil be lowered slightly), reducing space-charge effects in the 200-MeV transport system, but ultimately improving the momentum spread in the beam to the booster. The debunching cavity may also make possible slightly larger beam currents out of the linac without increase of the mean momentum variation of the beam, because it can be used to correct the momentum variation caused by beam loading during the beam pulse in the linac.

Booster Synchrotron

The booster synchrotron accelerates the beam from 200 MeV to 8 GeV in 33 msec, so that 12 pulses of beam can be injected into the rest field of the main accelerator to nearly fill the circumference. In order to achieve a design intensity of 5×10^{13} particles per pulse in the main accelerator, the booster must be capable of accelerating an intensity of about 4×10^{12} particles per booster pulse, assuming no losses in the main accelerator. At present, an intensity of 1.2×10^{12} particles per boosterpulse (i.e.1.8×10^{13} particles per sec) has been achieved using multiple-turn injection. In order to achieve the intensity design goal, improvements are required in both the transverse and longitudinal acceptance of the booster synchrotron. The parameters shown in Table III indicate the areas of improvement.

The design value for the rf bucket area is 3.0 eV-sec. Measurements indicate that the bucket area is 3.0 eV-sec at injection, but dips to approximately 1.6 eV-sec at 3 msec and then rises again. Measurements of the momentum spread of the coasting beam in the booster (using the Schottky scan techniques) give a $\Delta p/p$ of about 2×10^{-3} (full-width for 95% of the beam) before rf capture and about 3.5 to 4×10^{-3} after the rf capture. The reduction of the bucket area at 3 msec and the large momentum spread result in a loss of beam at this time in the acceleration cycle.

The installation of the debuncher in the 200-MeV transport between the linac and the booster to reduce the momentum spread of the injected beam and increasing the rf voltage to the design level during the first few milliseconds are expected to increase the transmission efficiency to about 90% for single-turn injection. Both of these improvement programs are well underway. It is expected that the total accelerating voltage at early times in the rf cycle can be increased by about 30% by modification of the ferrite tuners. In addition, two more rf stations are being installed, bringing the total to 18.

A measurement of the radial aperture of the booster by inducing betraton oscillations yields an acceptance of about 22π mm-mrad of "good transmission" with a decrease of transmission to zero for betatron amplitudes corresponding to an acceptance of 55π. These values for the acceptance are substantially less than the design value of 90π mm-mrad. The reduced acceptance of the booster results in a poor efficiency for multiple-turn injection. In the design, it was expected that four turns could be injected into radial phase space with good efficiency. At least three improvements are in progress to correct this situation. First, additional beam-position detectors are being installed in the upstream end of the long straight sections to provide information that should allow the elimination of misalignments as a source of aperture restriction. Second, additional quadrupoles are being installed in the transport system to the booster, so that the matching of the beam from the linac to the booster acceptance can be improved. Third, a new multiturn-injection bump-magnet power supply is being constructed with variable orbit-bump decay rate so that the filling of the available aperture can be optimized.

These improvements in the transverse and longitudinal acceptance of the booster are expected to improve the intensity. It is possible that other beam collective effects may cause difficulty before the design intensity is reached. The only beam instability from collective effects encountered so far is the head-to-tail effect which has been cured with sextupoles.[6]

Only one booster magnet has failed, at the feed-

Table III

Booster Synchrotron Parameters

	Design	Nominal Operating	Best to Date	Improvement Expected
Energy (GeV)	8 - 10	8	8	
Cycling Rate (Hz)	15	15	15	
Peak Intensity (protons per pulse)	3.5×10^{12}			
(a) Single-turn injection	x	0.70×10^{12}	0.74×10^{12}	1.5×10^{12}
(b) Multiple-turn injection	x	1.0×10^{12}	1.2×10^{12}	4.0×10^{12}
Acceptance (mm-mrad)				
(a) Horizontal	90π	22π - 55π(1)	--	85π
(b) Vertical	40π	22π		40π
Emittance (at extraction)	6.5s			
RF Bucket Area (eV-sec) (16 rf stations)	3.0	1.6(2)	1.7	2.8
Injection Momentum Spread	1.6×10^{-3}	$2\text{-}3 \times 10^{-3}$		1.6×10^{-3}
Transmission (percent)				
(a) Single turn		38	42	90
(b) Multiple turn		18	25	80

(1) The transmission decreases to zero between these two values.
(2) 3.0 eV-sec bucket area decreases to 1.6 eV-sec at 3 msec.

through insulator, in 3 years of service, and the magnet regulator' and power supply have been very reliable. The vacuum in the aperture of the magnets (which are inside the vacuum chamber) is in the low 10^{-7} torr range.

Main-Ring Synchrotron

Main-Ring Operation. During the first year of operation of the main-ring synchrotron, the major problems were hardware oriented. In the past year, as significant hardware improvements were completed and reliability of the magnets, magnet power supply, rf and cooling system improved, accelerator-physics studies of the main ring were started. A new set of beam-position detectors, and several types of beam profile and current monitors, including two loaned to us from CERN, were installed as diagnostic aids. The horizontal and vertical quadrupole power buses were separated so that they could be powered individually to allow the betatron frequencies, or tune, to be adjusted to slightly different values. In order to minimize closed-orbit distortion at higher fields, many magnets were realigned. Earlier this year, the tune was changed from the design value of about 20.25 to a new value of about 19.25 in order to operate in a more favorable tune diamond and to reduce quadrupole currents, thereby reducing saturation effects for future operation near 500 GeV.

At injection. the separated-function main-ring dipole field is approximately 400G and the closed-orbit distortion is caused principally by errors due to remanent fields. The distortions are corrected by computer-adjusted dc trim dipoles, five per betatron wave length, in each plane. An on-line program in the X-530 control computer takes the beam-position sensor readings and centers the orbit by 3-magnet local orbit bumps through an iterative procedure. Typically the orbit is centered to within the resolution of the sensors in three iterations (three pulses). The linear horizontal-vertical coupling resonance is eliminated at injection by using trim skew quadrupoles and at high field by slightly rotating about a dozen main quadrupoles about an axis along the direction of the beam. During injection time, when the accelerator must operate as a storage ring, beam intensities have been limited by transverse coherent[8] and single-particle instabilities.[9] The coherent instabilities have been successfully controlled by two active beam dampers. Single-particle instabilities have been controlled through the use of sextupole, skew-sextupole, and octupole correction magnets. These improvements were incorporated after a detailed study of third- and fourth-order resonances caused by remanent fields at injection. Subsequently, not only was the beam survival during the injection period increased by a factor of two, but, more significantly, stability of operation was markedly increased because of the resulting decrease in sensitivity to minor tune variation. Imperfect quadrupole-to-dipole tracking and transients from power-supply turn-ons occasionally cause a small amount of beam loss at the start of acceleration. These are being systematically investigated and remedied. There is no loss of beam in crossing transition and beyond.

Using the single-turn booster injection scheme, the main accelerator has regularly stored and accelerated to 300 GeV beams as large as 7×10^{12} with a loss of less than 10% of the injected beam. Main accelerator performance parameters are given in Table IV. Using the multiple-turn injection scheme, beams as large as 10^{13} ppp have been accelerated to 300 GeV with a somewhat greater loss, about 40%. Additional correction-magnet systems are being designed to further increase the transverse acceptance during the storage-ring mode to accommodate the wider multiple-turn booster beam.

Main-Ring Accelerating System. The main-ring accelerating cavity gap voltage has been limited to about 3 MV (15 cavities) by a tendency of the large alumina vacuum seal rf windows to crack. This has

Table IV

Main-Accelerator Parameters

	Design	Nominal Operating	Best to Date	Improvement Expected
Energy (GeV)	200	300	400	450 - 500
Peak Intensity (Protons per Pulse)	4.5×10^{13}	0.8×10^{13}	1.0×10^{13}	$2.5 - 5 \times 10^{13}$
Cycling Rate (sec)				
200 GeV (no flattop)	3.3	--	--	--
200 GeV (1-sec flattop)	4.3	4.8	4.5	4.2
300 GeV (1-sec flattop)		5.9	5.3	--
400 GeV (1-sec flattop)		12	12	7 (2-sec flattop)
500 GeV ($\frac{1}{2}$-sec flattop)		-	-	12
Rate-of-Rise (GeV/sec)	125	100	150	150
Slow Spill Flattop Length (sec)	1	1	1	
Peak RF Voltage per Turn (MV)	3.47	3		4
Momentum Spread $\frac{\Delta p}{p}$(1)	1×10^{-4}	$\sim 1 \times 10^{-4}$		
	$.09\pi$	$.06\pi$(2)		
	$.23\pi$(3)			
	≈ 20.25	≈ 19.4		
	100	90	100	100
	100	60	70	100

(1) Total spread measured at 100 GeV.

(2) Either horizontal or vertical with booster single-turn injection.

(3) In the accelerator for booster multiple-turn injection.

equivalent to 100 - 125 GeV/sec. Originally, the seals were made of 94% purity alumina. These will be replaced by seals composed of 99.5% purity alumina. High-power operation of the higher-purity seals indicates that they operate at temperatures about 100 degrees F lower than the 94% purity seals. Another problem has been an excessive failure rate of the ferrite tuners for the cavities. A modified tuner configuration in which the required tuner voltage is reduced by a factor-two is being tested. This modification will probably be introduced on all main-ring accelerating cavities.

Three additional rf cavities are being prepared for installation. The goal is to have a ring voltage of 4 MV with a two-cavity redundancy, making possible accelerator operation at 150 GeV per second with a synchronous phase angle of 50°.

Main-Ring Magnet Power Supply. The original master-substation transformer was designed for 200-GeV operation with a rating of 80 MVA rms and a peak of 160 MVA. At 500 GeV, the transformer is required to accommodate a 300-MVA peak and a 110 MVA rms for a reasonable repetition rate. A new transformer has been installed in the substation to allow 500-GeV operation. In addition, a series capacitor bank has been installed *so* that the voltage droop on the 345-kV mains will be less than 0.5%. The series capacitor bank will reduce the voltage droop so as to be consistent with the repetition rate at this energy (12 seconds). Most of the power-distribution system and the magnet power supplies are already rated for the higher energy levels, *so* that the accelerator can be operated at 500 GeV with a matched power system. Additional cooling capacity is being added to utilize the higher

With the new transformer and series capacitor, the main-ring magnets can be pulsed to a 500-GeV level with a 0.5-sec flattop at a repetition rate of 12 seconds. This newly-installed equipment will also make possible 400-GeV operation at a repetition rate of 7 seconds with a 2-second flattop or a 300 - 400-GeV dichromatic ramp. In these cases, the rate-of-rise of the magnet field would correspond to our new goal of 150 GeV/sec. Figure 10 shows these several main-ring cycles.

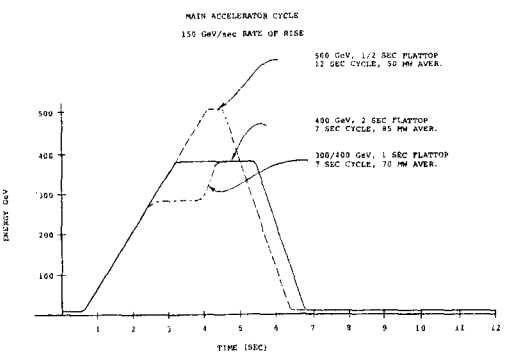


Figure 10. Planned higher-energy main-ring cycles.

Extraction and External-Beam Systems

Four modes of beam extraction from the main accelerator are presently used. They are shown in Table V. Typical operation consists of a long spill

(1 sec) for counter experiments, with four enhanced short spills (1 msec) spaced by 0.25 sec for bubble-chamber experiments, followed by a single high-intensity short spill for neutrino experiments. This final spike may be obtained by either coherent resonant extraction (100 - 400 psec) or by single-turn fast extraction (20 psec). The external beam from the accelerator has been split to provide simultaneous beams to as many as five primary targets in external areas, as well as two targets in the internal-beam area. Extraction efficiencies of approximately 97% are obtained for both fast and slow extraction.[9] Improvement in efficiency has been achieved by more careful assembly and alignment of the electrostatic septa wires, and thus a reduction in the effective septa thickness.

The slow-spill duty factor has been improved so that spills as long as 1 sec are available with about 70% duty factor, not including the rf structure. Fortunately, at the present beam intensity the 53-MHz rf bunching has not been a serious disadvantage for experimenters, and many have used the rf structure to their advantage. Main-ring power supply ripple is about 1×10^{-4}, predominantly at frequencies of 120 Hz and 360 Hz. Higher harmonics have been reduced by active filters. During extraction, two air-core quadrupoles are used to buck out the magnet ripple structure from the extracted beam. These quads are driven by two signal sources. First, a signal proportional to integral of $\dot{B}$ from the main quad bus is used to drive the bucking quads. Summed with this is a signal derived from the extracted spill structure averaged over a number of pulses and phase shifted ahead to offset the lag between ripple and correlated extracted beam. A PDP8 computer is used to provide this signal.

Enhanced spill for the bubble chamber is produced by pulsing an air-core quad with a 1-msec half-sine current waveform. This shrinks the stable phase space region for a short time, thus liberating a burst of particles into the unstable region. Coherent extraction is similar except that a dipole kicker is also fired, forcing the whole beam into the unstable region. This same kicker may be used for single-turnextraction. It has a rise time of 0.5 psec, a length of 20 psec and produces a displacement of 10 mm at 300 GeV.

Recent successful operation of dichromatic slow extraction at 200 and 300 GeV, shown in Fig. 11, has given us the confidence to schedule this mode of operation at 300 GeV for the Meson Area and 400 GeV for the Neutrino and Proton Areas this fall. Further use of the variable front-porch energy will undoubtedly be made by the Proton Area. A three-way splitting station for the Proton Area is also planned for installation in the next year. Development must continue on the wire septa and the four splitting-station septa now in continuous operation. Development of new wire installation and support techniques, automatic retraction devices for removing broken wires, better septum-alignment mechanisms, improved quick removal techniques, and investigation of different materials for septum wires must be pushed to improve septum reliability and further reduce beam losses and consequent radiation exposure to maintenance and operating personnel.

One of the most successful ventures we have had so far has been the implementation of the proton-beam splitting stations.

We now operate routinely with two primaryproton beam splits, neutrino-proton followed by neutrino-meson and two secondary proton beam splits, one in the Neutrino Area between the muon or neutrino beam and the hadron beam to the bubble chamber and the other between Proton Center and Proton East or Proton West.

Each splitting station consists of two electrostatic wire septa followed by Lambertson magnets appropriately sized to carry both beams to their respective targets. Including the extraction system, we now have a total of 10 electrostatic septa installed, which operate reliably at voltages up to 80 kV, and a total of 19 Lambertson magnets. The remaining elements of the proton beam are 110 conventional beam-transport dipoles. 41 quadrupoles and 35 trim dipoles. Diagnostic devices include 36 SWIC's (segmented wire ion chambers), 130 ionization loss monitors and 11 SEM's (secondary emission monitors). The redundancy and reliable operation of the diagnostics has played a major role in the switchyard operation. After tuneup, there are no significant beam losses in the switchyard, with the exception of the areas downstream of the splitting stations where loss on the wires in the septa is deposited on the Lambertson magnets.

Beam momentum spread $\Delta p/p$ is approximately 5×10^{-4} and the phase space transported to the experimental areas is approximately 0.3π mm-mrad. Targeting efficiency for a 1-mm cross section target is approximately 70%.

Accelerator Controls

The equipment associated with the accelerator and experimental areas is distributed throughout about ten miles of beam paths. The central computer control and monitoring system is configured around three Xerox 530 computers and fifteen Lockheed MAC 16 computers interconnected for the logical transmission of information between them.[10] An additional computer of each type is available for software and hardware development and for providing backup in case of a failure of one of the on-line systems. Switching to a backup computer requires approximately five minutes and generally does not require interruption of accelerator operation. Seven control consoles are connected to the X530 computers in the main control room, three for the injector and four for the main accelerator-extraction-external-beam systems. In addition, experimenter control consoles can be connected in the experimental areas through a CAMAC interface so that up to 192 bytes of relevant data can be transmitted on each pulse of the accelerator.

At the present time, there are approximately 1700 channels of analog control, 4500 channels of analog monitoring, 2400 digital-control points and 7500 digital-monitoring points connected to the system. There are approximately 80 CAMAC crates in the experimental area systems. These numbers are continuing to grow as the flexibility and requirements of the accelerator expand.

Major efforts now are directed to upgrading some of the earlier hardware and software systems, to provide more graphics, particularly of the type we call comfort displays, to improve alarms and limits, save

Table V
Extraction Modes At NAL

Spill	Method	Special Devices	Spill Duration	Intensity	Duty ?actor
Slow	ν_x = 19.5 resonant	2 ramped iron-core quads 1 spill feedback regulating iron-core quad 2 spill ripple-structure-reduction air-core quads 1 ramped iron-core octupole 3 ramped orbit-bump dipole pairs	1 sec	10% - 100%	70%
Enhanced Beam for Bubble Chamber	Resonant	Slow devices 1 air-core pulsed quad	1 msec	1×10^{10}-5×10^{11} P/b.c.p.	
Coherent Fast	Resonant	Slow devices 1 air-core pulsed quad 2 pulsed-orbit bumps 1 ferrite single-turn kicker	100-300 psec	< 80%	< 50%
Fast	Single-Turn	2 pulsed orbit bumps 1 ferrite kicker	21 psec	0 - 100%	

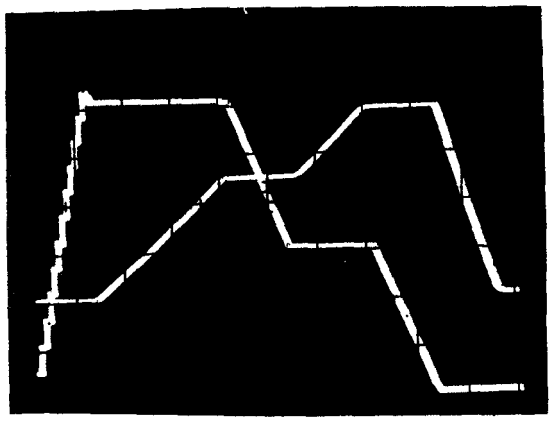


Figure 11. Dichromatic main-ring ramp and beam. 200 GeV to Meson and Proton areas, 300 GeV to Neutrino and Proton.

and restore, and data logging features, and to generate more automatic tuning programs. It has been clearly demonstrated that without the capabilityof the computer-control system, the performance and flexibility of the accelerator achieved to date would not have been possible.

Experimental Areas

Internal-Target Area

The internal-target area routinely operates with two of four experimental set-ups taking data on two targets simultaneously. The two targets, a supersonic hydrogen/deuterium jet furnished by our Soviet colleagues from Dubna and a rotating wheel with 2 to 5μ graphite and polystyrene fiber whiskers mounted on it, each absorb only about 5×10^9 protons per 5×10^{12} main-ring pulse, thereby causing no serious residual-radioactivity problems. (Present activities are 1 to 5 mrem per hour two hours after shutdown.) In order to optimize beam-on-target conditions in the internal-target area. limited local control of beam position is accomplished by the experimenters through a special rf beam bump. The experimentation with these targets in the internal-target area has been fruitful because experiments can be conducted in the same pulse with an energy spectrum of 8 to 400 GeV with almost a point source target.

We are now in the process of designing an expanded internal-target area. The expanded area, a room 50 x 50 feet, is to be built on the outside of the main ring with a transition section connecting it to the main-ring tunnel. We believe that this addition can be made with limited interference to accelerator operations.

Meson Area

Originally, the Meson Area was designed to operate at 200 GeV. The proton beam line has since been upgraded to transport 300-GeV beam to the Meson-Area proton target and this is now the routine mode of operation. There are five secondary-beam lines installed in the Meson Area, three charged-particle beams and two neutral beams, all originating from a single primary proton target. Two of these lines have branches at their ends so they can each switch between two experiments. There is now a total of eleven experimental set-ups installed in the Meson Area. A new target load for the area has recently been installed and when its cooling system is completed in a few months, it will be capable of accepting over 10^{13} protons per pulse. Within the next year or so, we plan to upgrade the proton beam line to the Meson Area to 400 GeV, probably by using superconducting magnets similar to

those of the proposed energy-doubler design. Prior to that change, the Meson Area will continue to operate by using a 300-GeV front-porch on a 400-GeV main-ring pulse.

Neutrino Area

So far, the Neutrino Area has used the lion's share of protons produced in the accelerator, devouring 50 to 80% of the proton beam each main-ring pulse. There are two simultaneous secondary beams in the Neutrino Area eminating from two primary proton targets. One target is the source of either the muon beam or of one of three possible neutrino beams. The three different neutrino beams are 1) a 100-μsec long spill using a pulsed horn; 2) a 1-sec long spill using a quadrupole-triplet focusing arrangement; and 3) a momentum-selected beam. At 300 or 400 GeV and an intensity of 10^{13} protons per main-ring pulse, the neutrino flux at the experiments is estimated to be 10^{11}. At 300 GeV and an intensity of 8×10^{12} protons, the muon beam has yielded 1.5×10^{6} 150-GeV/c positive muons and 0.5×10^{6} 150-GeV/c negative muons.

The second target, which can operate simultaneously with the first, is the source of a hadron beam that can be switched between the 30-in. or the 15-ft cryogenic bubble chambers. In 1972 and 1973, the 30-in. chamber took a total of 429,000 pictures. In the first 3 months of 1974, it took 486,000 pictures and has recently taken its millionth. This increase has resulted from the introduction of the quadrupole pulsing mentioned above and from the improved reliability in accelerator operation. The 30-in. chamber has completed all its approved hydrogen experiments and must now wait for the accelerator to operate at higher energies or change its hydrogen for deuterium or neon to go on to accomplish the approved experiments.

In November, a one-week test run was made on the 15-ft bubble chamber, the world's largest. There were a total of 80,000 pulses and several thousand good pictures were taken.

Proton Area

The Proton Area is different from the other two experimental areas in that the experimenters work directly from the primary proton targets. There are three separate areas and three separate targets in the Proton Area. At present, there is one splitting station in the primary-beam line, which can send beam simultaneously to two of these areas. In the next year, a triple-splitting system will be installed which will enable all three areas to operate simultaneously. The work of the Proton Area is closely coordinated with that of the Accelerator Division. since the three beam lines are primary proton beams. In the past year, extensive studies have been made by Proton-Area and Accelerator-Division personnel to measure the beam emittance and the beam-transport properties. As a result of these studies, installations are being modified to improve the transmission and reduce beam losses. This summer, manholes to hold focusing quadrupoles are being installed in the beam line to Proton Area West so that a very clean beam can be delivered there for the experiments with special requirements. In addition to these technical improvements, it is expected that a broad-band tagged-photon beam, a 0° high-flux pion beam and a two-stage electron beam will be added to the Proton Area.

At present there a total of three experimental set-ups installed in the Proton Area, with two operating simultaneously.

Future Laboratory Plans

Energy Doubler

As presently proposed, the Energy Doubler is a ring of relatively slow-pulsed superconducting magnets mounted on the ceiling of the main-ring tunnel so that the beam orbit is some 3 feet inside and 4 feet above the present main-ring orbit. The field can be ramped to 45 kG corresponding to a peak proton energy of 1 TeV (1000 GeV). The ring has a separated-function lattice essentially the same as that of the present main ring. The coil aperture of the dipole, determined principally and optimistically by extraction considerations, is oval with dimensions 2. 5 in horizontal and 1.74 in. vertical. To minimize ac heating effects, a rate of rise of 20 GeV/sec has been chosen for the Doubler. This leads to a 100-second repetition rate with injection at 200 GeV and a 20-second flattop. The 20-foot-long dipole magnets and 7-foot-long quadrupole magnets are of a cold-bore, warm iron design. The coil assemblies are suspended in the middle of the iron shield by a rigid suspension system. Figure 12 shows a refrigeration test loop.

The fields in two superconducting low-field (2. 5T) identical dipole magnet models, 30 inches long, connected in series, shown in Fig. 13, have been shown to be equal to at least within 10^{-3}. In order to gain operating experience and to study the effects of beam loss, this dual dipole-assembly has been installed in the external proton-beam line. Under ac (30-sec rep rate) conditions, these two dipole magnets also tracked each other to better than 10^{-3}.

The first 20-foot dipole model has been tested but the results on it so far are not fully understood.

The design heat load for the cryogenic system is 18 kW at 4. 4°K. In the present design concept, the magnets are their own transfer lines for the helium coolant. The liquid-helium supply and return flow is through a set of tubes surrounding the coil structure. Twelve helium refrigeration and recirculating systems will be located in existing service buildings distributed evenly around the main ring. One complete FODO cell consisting of eight 20-foot dipoles and two 7-foot quadrupoles is being constructed in the old protomain tunnel located in the NAL Village. Another paper entitled, "Progress Report on the NAL Energy Doubler Design Study," is being presented at this Conference. [11]

POPAE

The availability at NAL of 400-GeV protons, with extension to 500 GeV in the offing (and possibly higher energies, if the Energy Doubler proves to be feasible) makes it natural to ask what role storage rings might play in the Laboratory's future, particularly in view of the exciting results from the ISR and SPEAR.

In December of last year, the Laboratory's Long-Range Advisory Committee recommended that long-range planning at the Laboratory concentrate on a system of combined proton-proton and electron-proton storage rings capable of 1000 x 1000 $(GeV)^2$ for pp

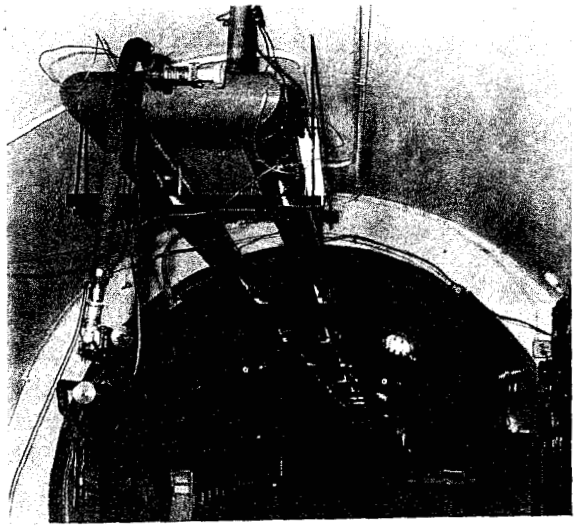


Figure 12. Energy-doubler refrigeration test loop installed in Protomain tunnel.

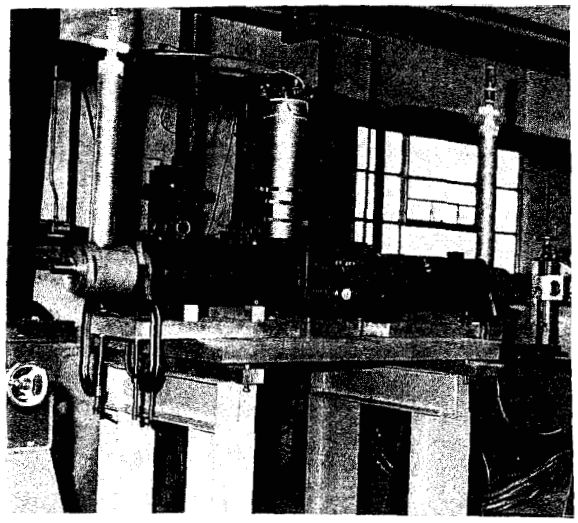


Figure 13. Superconducting 30-in. dual dipoles.

collisions and 20 x 1000 $(GeV)^2$ for ep. In selecting these particular energies, the Committee was guided to some degree by the maximum energy of protons that could conceivably become available at NAL in the next few years, but they stated that the largest step in collision energy consistent with technological and economic realities should be taken.

The project has been given the acronym POPAE (Protons on Protons and Electrons). A preliminary design study is beginning at NAL with the goal of having some tentative plans to lay before the high-energy-physics community for criticism and commentary.

Quark Area

By mid 1975, all the research facilities which were initiated in the early days of the project will be completed. Attention will then turn to new facilities that are needed to match the higher energy capabilities of the accelerator, up to 500 GeV as presently installed or up to 1000 GeV with the Energy Doubler. Consideration is being given to the concept of such an area, tentatively called the Quark Area, so that detailed designs can be formulated. As presently proposed, this area would lie to the east of the present Proton Area, The initial tunnels to carry beam to it have already been built. Our present thinking about the Quark Area envisions that it will be designed for operation with 1000-GeV protons and provide a number of high-energy secondary beams using a slow spill somewhat in the style of the present Meson Area, but with superconducting transport magnets for the higher energy.

If the accelerator runs at 400 to 1000 GeV, the Neutrino and Proton Areas can operate at those energies but the Meson Area cannot be upgraded easily and therefore the Quark Area will have as an important goal the provision of high-energy secondary beams. The design of the area is still in a very preliminary stage and will be influenced by our experience in building and operating the present experimental areas and more importantly by the physics questions raised by the present generation of experiments.

Acknowledgements

This work represents a large fraction of the effort the entire Laboratory has made to make these facilities function in the best possible manner to further the study of elementary-particle physics. Beyond that, this report is the work of some three hundred dedicated and hardworking people who are members of the NAL Accelerator Division. We would like to thank R. R. Wilson, Laboratory Director, and E. L. Goldwasser, Deputy Laboratory Director, for their inspiration. confidence and support.

References

1. R. R. Wilson, "The NAL Proton Synchrotron," Proc. of the 8th International Conference on High Energy Accelerators, CERN, 1971, 3-13 (1971).
2. The NAL Staff, "Operating Results from NAL." IEEE Trans. on Nucl. Sci., NS-20, No. 3, 191-197 (1973).
3. R. R. Wilson, "The Batavia Accelerator," Scientific American, 230, No. 2, 72. (Feb., 1974).
4. T. Toohig, "Design Description of the External Experimental Areas at the National Accelerator Laboratory," NAL Internal Report, TM-481, (Apr. 1974) (to be published).
5. J. Boere, P. Bramham, H. G. Hereward, K. Hübner, W. Schnell. L. Thorndahl, "Non-destructive Diagnostics of Coasting Beams with Schottky Noise," to be published, proc. of this conference.
6. E. L. Hubbard, R. E. Peters, and A. G. Ruggiero, "Correction of Intensity-Dependent Beam Loss in the NAL Booster Synchrotron," IEEE Trans. on Nucl. Sci., NS-20, No. 3, 863, (1973).
7. A. R. Donaldson and R. A. Winje, "The NAL Booster Synchrotron Magnet Power Supply Servo," IEEE Trans. on Nucl. Sci., NS-20, No. 3, 409, (1973).
8. R. Stiening, E. Wilson, "Transverse Collective Instability in the NAL 500-GeV Accelerator," to be published, proc. of this conference.

9. R. Stiening, E. Wilson, "Transverse Single-Particle Instability in the NAL 500-GeV Accelerator," to be published, proc. of this conference.

10. R. E. Daniels, R. W. Goodwin, and M. R. Storm, "The NAL Computer Control System," IEEE Trans. on Nucl. Sci., NS-20, No. 3, 505-509, (1973).

11. D. A. Edwards, W. B. Fowler. P. J. Reardon. D. E. Richied, B. P. Strauss, D. F. Sutter, "Progress Report on the NAL Energy Doubler Design Study," to be published, proc. of this conference.

DISCUSSION

Pierre Lehmann, (Orsay): Do you have to debunch to extract the lower energy when using the 200 GeV, 300 GeV dichromatic beam pulse?

Reardon: We simply run with the extraction system the same way as at 300 GeV for that one second and then we turn off the extraction system and continue to accelerate up to 300 GeV and then extract in the same way.

Andrei Kolomensky, (Lebedev Institute): Could you expand on your future plans, especially POPAE and the energy-doubler?

Reardon: I first have to talk about the energy doubler which was considered to be a prerequisite for POPAE as proposed at the summer study last year. The energy doubler is something that we are planning to undertake with approximately 10% of the funds that are left over from our $250 million construction project, mainly to make sure that a super conducting magnet system of that size would work. We are going about it slowly and in small steps because it is a difficult problem and we have learned that the technology for making the magnets is not as easy as we thought it might be. Our first effort will be to make approximately 10 - 20' long magnets work in a proto-type structure which is in the NAL village. We have built 2 - 20' long magnets, one of which has been tested. The results are not as hoped for, as I mentioned. We will continue that program to the tune of building 10 magnets over the next whatever it takes to make sure we can build them reliably and that they track each other under AC pulsed conditions. The repetition rate we are talking about is only in the order of 100 seconds. We will then go forward and try to build a larger number of magnets (approximately 150) and install them and test them with beam in one-sixth of the main ring. These are our present plans, however the technology limitations may change these plans very greatly. We are just getting into it. It is an exciting thing to try and understand superconducting magnets, but it's hard to find out what's going on inside the dewars. As far as POPAE is concerned -- POPAE is an outgrowth of last year's NAL summer study at Aspen, convened to in a general way come up with those projects which would appear fruitful for NAL to look at. I should have mentioned another earlier project that was talked about at the summer study; namely, a fourth experimental area for the quark lab which would enable us to run counter experiments at 400 GeV or higher (up to 1000 GeV). The present meson lab is limited to 300 GeV, although we hope to change that to 400 anyway.

The POPAE proposal is the result of the work of the summer study. So far there are no detailed plans for it, no definitive designs, and the current plan is to build a ring of approximately the same size as the present main ring, and inject into it from the energy doubler. It would include two DC proton rings and an electron ring either in the same tunnel or adjacent tunnels. Apart from these preliminary summer study suggestions there has been no detailed work done on this project.

PROGRESS ON THE 300 GeV PROGRAMME

R. Billinge
CERN, Switzerland

Before I begin, John Adams has asked me to convey to you his apologies for being unable to attend and describe the progress of the project in person.

I shall attempt in the short time available to give a brief outline of the salient features of the 300 GeV programme and report on the progress to date.

The programme, as approved by the CERN Council on February 19, 1971, covers a period of 8 years during which time we must design, construct and put into reliable operation, a machine of at least 300 GeV with an intensity of 10^{13} protons per pulse. (Figure 1).

The machine makes use of the existing CERN PS as injector and the West Experimental Area together with its two large detectors, Omega and BEBC. Experiments using this and other detectors are planned to begin in the West Area at the end of 1976. The West Hall will be fed with 200 GeV protons and the neutrino experiments in the West Area with 400 GeV protons. The North Area, which will be used for hadron and electron spectroscopy and muon physics using proton beams up to 400 GeV energy, is scheduled for operation in 1978.

The 8 years of the programme are each characterized by a main activity.

1971	Project team formation
1972	Review machine design
1973	Order main components
1974	Delivery of components
1975	Installation
1976	Testing and commissioning
1977	Operation with West Experimental Area
1978	North area operation

Turning now to the progress to date.

All the major decisions on the SPS programme have now been taken and these include two of particular note.

The first of these was the decision to equip the machine with a full set of conventional magnets allowing operation up to 400 GeV, rather than leaving space for superconducting magnets.

The second major decision concerned the layouts of the two Experimental Areas and the underground neutrino facility. This has enabled the two CERN Laboratories to put forward a complete plan for the SPS experimental facilities.

All the land covering the accelerator zone is now at our disposal together with the land necessary for the hadron and muon zones in the North Experimental Area.

The tunnel, which is being bored in molasse bed-rock at a depth which varies from 25 to 60 m, has now been bored around 3/4 of the machine circumference. The arrival accuracy of the 'Robbins' has been $\sim\frac{1}{2}$". The concrete lining and floor have started in the first half of the machine and the first sextant will be ready to begin installation of services during June. (Figure 2).

The main magnet system is now in the full production phase with 140 dipoles and 40 quadrupoles now delivered. about 120 dipoles have been measured magnetically and are now being prepared for installation. The results of the magnetic measurements show the bending field to be uniform over the whole aperture to within 2 or 3 in 10^4. The bending strength of the dipoles is adjusted by end shimming each magnet so that the rms variation is less than 2×10^{-4} over most of the cycle. (Figures 3 and 4).

Progress on the magnet Power Supply is good. The 380 kV line from a strong point in the French Electricity Network is almost complete and the two 60 MVA transformers are due to be delivered this summer. Half of the power supply components have been delivered and the first of the 12 Rectifier stations has been installed and tested.

The RF System is a 200 MHz travelling wave structure consisting of 2 @ 20 m long cavities. Delivery of the cavities and drift tubes is expected in the Autum. The power amplifiers have been constructed by industry and are now undergoing their acceptance tests. The low-level RF system is complete and has been tested on the CERN PS. (Figure 5)

The computer assisted Control and beam detection system is now fully specified. Half of the 24 computers required have been delivered, prototypes of the various interface modules and beam detectors have been checked out and the production quantities have begun to arrive. A prototype Control Desk has been built and is in use to develop interactive control devices and associated software.

The Injection and Extraction systems are completely designed and specified. Prototypes or models of each of the special elements have been constructed. These are undergoing lifetime tests while the final components are being manufactured by industry. (Figure 6)

To summarize: the design, prototype and ordering phases of the programme have been completed on time.

However, the delivery of components during the next year is critical. As Dr. Adams noted in the Progress Report to the CERN Council at the end of last year ". .... the present period of material shortages, fuel crises and monetary inflations is not the best in which to be building such a large project."

Nevertheless, the manufacturing phase has begun on time and if the deliveries match those in our contracts with industry, we believe we can start experimental research in the West Area using the SPS by the end of 1976.



FIG. 1--Aerial view of CERN site showing location of SPS.



FIG, 2--View of 4.5 metre diameter 'Robbins' boring machine.

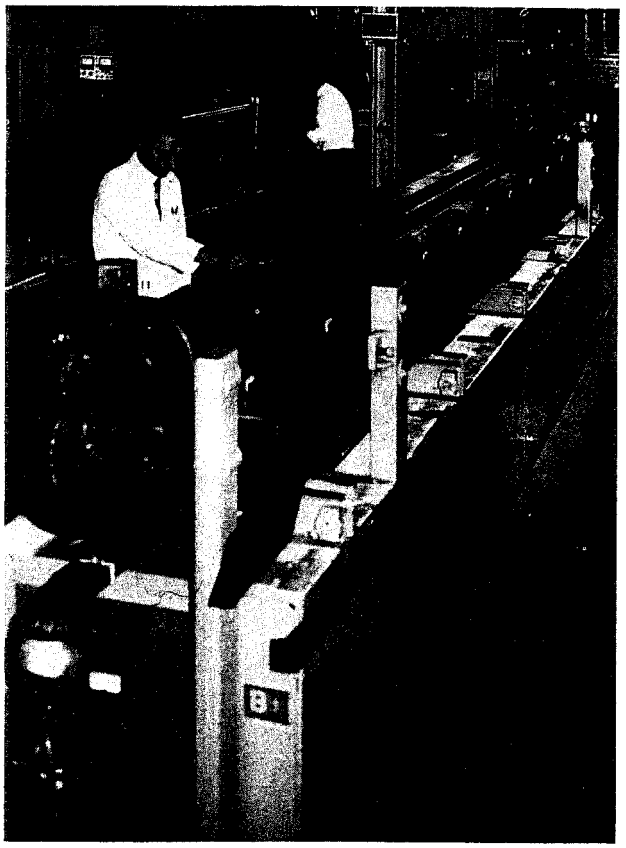


FIG. 3--Assembly of a 6.3 m dipole magnet.

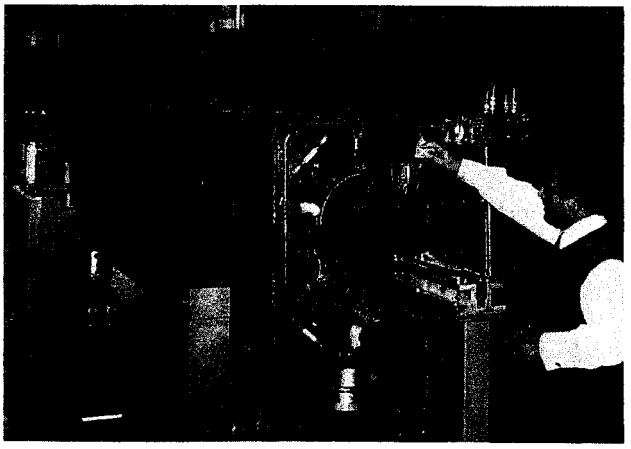


FIG. 4--Quadrupole magnet installed in the Measurements Area.

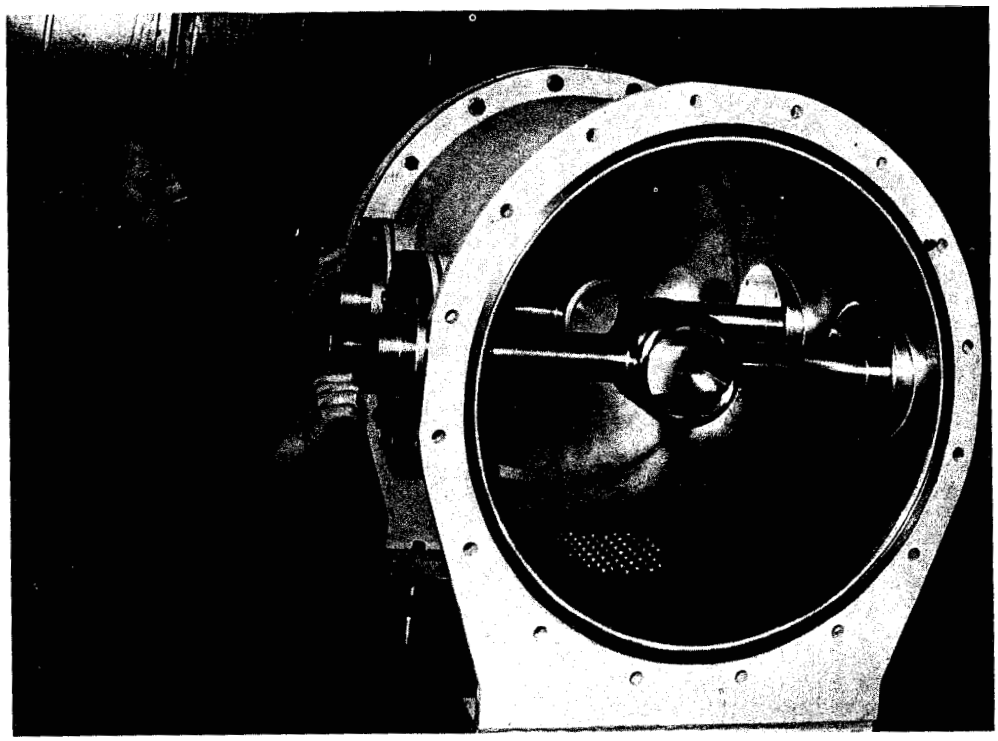


FIG. 5--Short-section prototype **of** RF Accelerating Cavity.

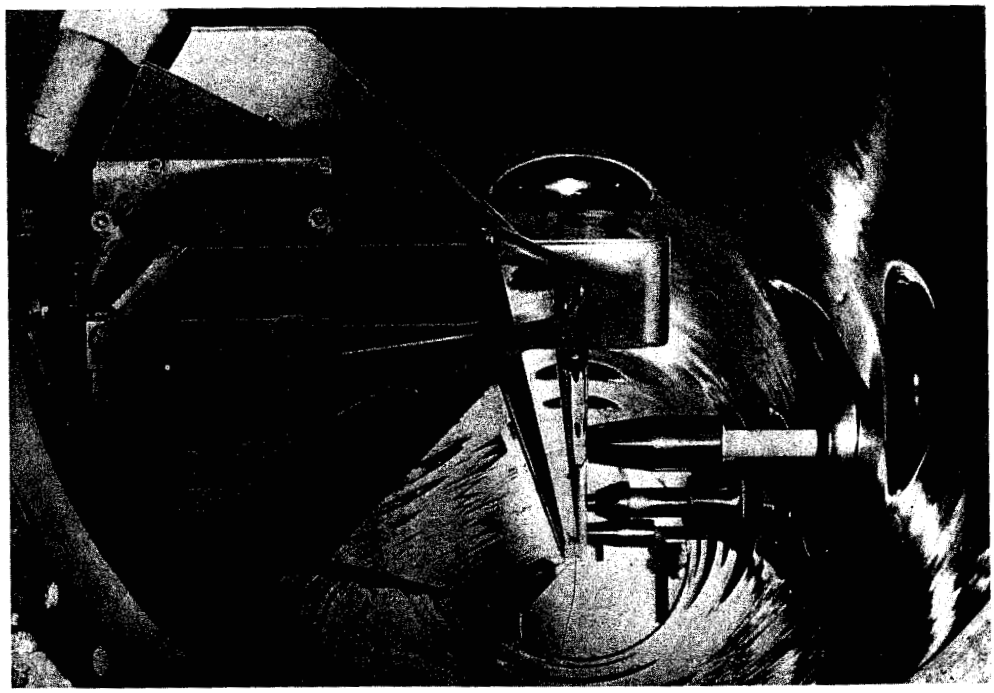


FIG. 6--Prototype Electrostatic Extraction Septum.

Andrei Kolomensky, (Lebedev Institute): (Referring to a slide of rockboring machine)

What is the diameter of the cutting head?

Billinge: 4.5 meters.

Milton White, (Princeton): How important is it to have magnetic measurements of higher-order components of the fields of the magnetic elements before installation?

Billinge: Well, certainly one thing that is very important is to measure them before they go in the ring because after that it is impossible. The important part of the measurement program first of all is to confirm that with the mixing of steel that we really do get the same remnant field in all the magnets to a very high precision. As I mentioned, by comparing every magnet with a standard magnet we actually end shim individual magnets to make their bending strength the same so the random variations in bending strength are down to an r.m.s. of one times 10^{-4}. Also, the measured field does allow one to predict which are the most likely troublesome resonances to occur, and I think this is very worthwhile.

Boyce McDaniel, (Cornell): Will you use the magnetic measurements to determine the location - the order of the magnets in the ring, or just as a check on the specifications?

Billinge: No, we will in fact use the high field characteristic, which of course the end shimming can do very little about. We are now grouping the magnets in groups of five of each type, so that as we begin to install the machine we will make a mixture of the magnets so that appropriate sets of say four magnets within a semi period will have the same bending strength at the 400 GeV level. So we do use the measurements for locating them based on the high field strength.

Boyce McDaniel, (Cornell): What is the ultimate limit of the useable field in your magnets?

Billinge: That depends a tittle on the present power crisis, but as you know, the basic cross sectional design is very similar to the design of the NAL magnets. The width of the aperture is larger so the corresponding good field width is larger and we have twice as much copper. Now, if one wants to invest in extra power supply and extra power, of course, it presumably will go to the 500 GeV level. It's not clear that is really required.

Lee Teng, (NAL): You said in the D quadrupole you have a round bore tube and in the F quadrupole you have an elliptical one. What is the reason for this?

Billinge: Just the aperture requirements. We use the same quadrupole for D and F. It's a four fold symmetry quadrupole. In fact, the aperture required for the F quadrupole actually protrudes in between the poles - so one can use a compromise size for the two types.

THE JAPANESE 12 GeV ACCELERATOR

Tetsuji Nishikawa
National Laboratory for High Energy Physics
Oho-machi, Tsukuba-gun
Ibaraki-ken, Japan

Introduction

After a long history, construction of the 12 GeV proton synchrotron started in 1971 at the National Laboratory for High Energy Physics in Japan (Ko-Enerugie-butsurigaku Kenkyusho, standing for KEK in the followings). The laboratory is located at about 70 km to the north-east of Tokyo. It is one of the major institutes in the new academic town, Tsukuba, dedicated to scientific research and education. The synchrotron will be completed in 1975; its energy was planned to be 8 GeV at the first design stage but now is expected to be increased to 12 GeV by saving budget.

Since this energy is still low in the present situation of the world high energy physics, we have worked out our design and construction plan according to the following philosophy of

1. Obtaining a high intensity beam with good quality for performing unique experiments in the possible energy range,

2. keeping flexibility both in the machine and its belongings for future improvements and refinements,

3. developing new technologies which will give distinctive feature of the machine and will make progress in the accelerator arts, and

4. leaving possibility for future extension to a higher energy range.

The main parameters of the KEK synchrotron are given in Table I. The synchrotron consists of four accelerators; i.e. a 750 keV Cockcroft-Walton preinjector, a 20 MeV injector linac, a 500 MeV fast-cycling booster and a main synchrotron. This scheme of the accelerator was chosen based upon the above design and construction philosophy. It will not only provide a high intensity beam but also notable experiences in the modern accelerator arts in Japan. An aerial photograph and the outline plan of the accelerator is shown in Fig.1 and Fig.2, respectively[1]

Table I. PARAMETERS OF KEK PROTON SYNCHROTRON

I.	Main Ring	
	Kinetic Energy	12 GeV
	Intensity	$>2\times10^{12}$ (1×10^{13}) p/pulse
	(Space Charge Limit)	
	Type	Separated-Function
	Focusing Order	FODO
	Average Radius	54 m
	Number of Superperiod	4
	Number of Betatron Oscillations	7.25
	Maximum Bending Field	17.5 kG
	Injection Energy	0.5 GeV
	Repetition Rate	0.5 Hz
II.	Booster	
	Kinetic Energy	500 MeV
	Space Charge Limited Intensity	2×10^{12} Combined-Function
	Type	
	Focusing Order	FDFO
	Average Radius	6.0 m
	Number of Cells	8
	Number of Betatron Oscillations	2.25
	Maximum Magnetic Field	11 kG
	Repetition Rate	20 Hz
III.	Linac	
	Energy	20 MeV
	Type	Single Tank D-T Linac
	Cavity Length	15.5 m
	Number of Cells	90
	Peak Current	-100 mA
	Repetition Rate	20 Hz
	Preinjector	750 kV Cockcroft-Walton

Ion Source and Preinjector

The Cockcroft-Walton high-voltage generator was constructed several years ago at the Institute for Nuclear Study, University of Tokyo and moved to Tsukuba in November 1971. After being assembled again and connected to the ion-source terminal, the high voltage system was tested up to 850 kV (Fig.3).

A high brightness ion source was developed by our ion source group in collaboration with Dr. Th. Sluyters, Brookhaven, the first alien visiting scientist. It is a modified duoplasmatron ion source with a nozzle-type expansion cup. The cup contour was designed by a consideration similar to supersonic nozzles for rarefied gas flows. By shaping or biasing the cup exit, we succeeded to reduce the aberrations due to the plasma boundary and get a brightness as high as 5×10^{10} A/m^2/rad' at 300 mA of the proton beam?) The shape of the plasma cup and a typical phase space distribution are shown in Fig.4 and Fig.5, respectively.

A high-gradient accelerating column with a mean accelerating field of about 38 kV/cm is used as the preinjector. One of the peculiar problems to our accelerator construction is the effect of earthquakes,. Vibration frequencies of the ground surface, the accelerator enclosures, and the accelerator components were carefully measured and most parts are safely designed against an earthquake of 0.2 g. In particular, for protecting the column from earthquakes we made it of a couple of large ceramic insulators, each 1.5 m in length and 1.1 m in diameter. The preinjector will be completed and come into operation in the course of this month.

Linac

The linac will provide a 100 mA beam with a 20 μs pulse duration at 20 MeV. The design feature of the linac is based on the extensive study on beam loading, space charge, and other high intensity effects carried out both by theoretical analyses and by measurements with model cavities?) Construction of the linac started in April, 1971, and the main components, i.e. the accelerator tank with drift tubes and quadrupole magnets, the RF power supply, the control system, the vacuum equipments, low and high energy beam transports, and other auxiliary components have been installed in the linac housing. The test of each component has almost been finished and the first linac beam will soon be obtained.

The accelerator tank is a 15.5 m long single cavity operating at 200 MHz with 3 MW RF power. This tank is

divided into 6 units and contains 88 drift tubes and 2 half-length drift tubes on the end plates.

In order to fabricate the linac tank and drift tubes with high RF conductivity and high mechanical precision, an electro-plating method of copper onto steel was developed and gave excellent results?) A copper bath with an organic brightening agent and bubble agitations was used. The surface roughness less than 0.3 μ of the plated copper of 1mm ± 0.1mm in thickness was obtained without any surface finishing after the plating. The measured unloaded Q-value was found to be as high as 90 % of the value calculated by using d.c. conductivity of copper (Fig.6). Field distributions along the cavity axis were measured by means of a perturbation method with a small metallic ball running through 50 cm/sec. The frequency perturbation was counted by a digital clock and displayed on a scope after a computer analysis (Fig. 7).

A new manufacturing process of drift tube quadrupole magnets was also developed leading to obtain the maximum field gradient of 11 kG/cm and the deviation of the mechanical bore center from the magnetic center within 20 μ.[5]) The quadrupole magnets are driven by the current of a half-sine shape (1.3 ms) with a flat top of 120 μs. The ripple and pulse to pulse fluctuations of the flat top are less than 0.1 %.

The linac tank and drift tubes were assembled and aligned better than ± 40 μ in the setting errors. The tank is supported by flat steel plates with preloaded U-shaped steel springs to ensure the tank setting against the earthquake vibrations as shown in Fig.6. The transverse and longitudinal natural vibration frequencies are set lower than the typical earthquake frequencies of 2 ~ 20 Hz.

The RF Dower supply consists of a master oscillator. a low level amplifier, two drivers with RCA 4616 tubes, and two final stage amplifiers of FIH 516 tubes. The RF power supply is installed in the service room paralleled the tank housing and the linac tank is driven at two points each located at a quarter of the total length from the end plates. Use of the double feeds has the advantage of compensating beam loading and transient effects along the cavity length!)

Booster

The booster is a fast cycling AG synchrotron operated at a repetition rate of 20 pulses per second. It accelerates protons to 500 MeV at the maximum guide field of 11 kG. Eight C-type magnets with a combined-function FDFO lattice are arranged around the circumference of 6 m in average radius. The average radius of the main ring is nine times larger than the booster, so that the booster injectes nine pulses into the main ring to fill up its total circumference. The number of betatron oscillations was chosen as $\nu_z = \nu_r = 2.25$ mainly from the requirement of tolerance for the magnetic fields at the beam transporting process from the booster to the main ring. The straight sections between the magnets are used for injection, ejection, and RP acceleration systems as shown in Fig.8.

The magnet cores are fabricated of oriented low-carbon steels laminated to 0.35 mm to reduce eddy current effect. The high permeability at high fields as ≳ 600 at 20 kG is obtained in the rolled direction of this specifically developed irons!) A soft epoxy resin was employed to reduce interlamination shorts and to fix a magnet core without a stress imposed by stacking process, however it was found that a careful thermal treatment is necessary to ensure the mechanical strength of the stacked blocks. Last October, all the magnets were set on the site with the rms error of about ± 60 μ in the radial direction, ± 90 μ in the height of median plane and ± 20 mrad in the twist of the median plane (Fig.9). The field measurements have been carried out upto the full excitation and the results obtained show good agreements with the design performance expected from computer calculations. The booster magnets were excited by using a series-parallel resonant circuit with dc-biased sinusoidal excitation (Fig.10). The same type core material as the magents was also used for the energy storage choke and produced -99.9 % coupling coefficients between secondary windings.

The useful aperture of the magnets is 12.6 cm in horizontal and 6.0 cm in vertical direction. Since the booster is a fast cycling machine, the eddy currents induced on the vacuum tube would cause a significant error in the magnetic field distribution. In order to reduce the eddy currents we have developed a corrugated stainless tube, whose effective wall thickness is 0.03 mm (Fig.11). The same type vacuum tube has been used in the 1 GeV electron synchrotron at the Institute for Nuclear Study and found to be satisfactory.

The fast-cycling low-energy .booster also requires a development of RF acceleration system which enables us to change the frequency and the voltage in a wide range with an adequate power loss. The harmonic number of the RF system was chosen as one from the consideration on the beam-transporting process as discussed later. A single cavity with two accelerating gaps is used, the resonant frequency of which is changed from 1.6 MHz to 6.0 MHz during the acceleration by an ordinary ferrite tuning system. A study on RF properties of various ferrites led to develop a material having large μQf values over the frequency range, however it was found that the Q value remarkably decreases by the fast repeating excitation. To avoid local heating of the stacked ferrites. is provided a cooling channel adiacent to everv ferrite sheet of 50 cm in outer-diameter and 2.5 cm in the thickness (Fig.12). The whole RF system consisted of RF power supply, ferrite bias supply and control units will be assembled during the next month. A computer calculation on the synchrotron oscillations led an RF voltage program capable of 80 - 90 % RF capture of the injected beam?) The proposed RF program is shown in Fig.13.

The linac beam is expected to be ready to inject into the booster by the fall of this year, so that the booster will come operation in the end of 1974.

Main Synchrotron

For flexibility, a separated-function type FODO lattice was chosen in the main synchrotron. There are four superperiods, each containing seven unit cells, two of which have a missing-magnet straight section of 5.5 m long. These straight sections are used for injection, fast and slow ejections and RF accelerations. Fig.14 shows the cell structure of the main ring. The average radius of the main ring is 54 m, and the nine pulses from the booster are injected into the main ring in 0.5 second while the main ring guide field is held constant at 1.5 kG. The acceleration takes place in the following 0.8 sec (0.5 sec), and a 12 GeV (8 GeV) proton beam will be obtained at the guide field of 17.5 kG (12 kG).

The main synchrotron enclosure and most of the auxiliary or the service buildings were completed in 1973 and sink of the foundation has been investigated. All of 48 bending and 56 quadrupole magnets have been installed in the main ring tunnel with setting error of about 1 mm (Fig.15). From orbit analysis, the position errors of magnets are required to be less than ± 0.1 mm, and precise alignments will hereafter be pursued.

In contrast to the usual separated-function synchrotron, we have decided to use the C-type bending magnet because of its better accessibility which makes beam handling and maintenance much easier than the H-type magnet machine?) By using oriented low carbon steels (lamination thickness = 1 mm) a maximum field of about 18 kG can be obtained at the gap of the bending magnets. The same material was also used for the quadrupole magnets. The design of magnets was done as a consequence of field computations with the magnetic field computer programs. For quadrupole magnet design, the computer program LINDA was modified to include the core-orientation effect?') The computations have been compared with the field measurements and the results show agreements within 0.5 % between computations and measurements?[1]) Typical results obtained by field measurements are given in Fig.16 - 18, where use of the oriented core also shows the advantage of reducing octupole components in the quadrupole magnets.

The main magnet power supply is manufactured in Fy '73 and '74" and will be installed in a service building. The bending magnet power supply is divided into 2 × 3 groups and operated in accordance with an inverter-converter combination program shown in Fig.19. The power supply for quadrupole magnets is also divided into two parts and operated at a similar condition. This system of power supplies was chosen to reduce the ripple voltage at the injection and flat-top operations in addition to the flexible programmable controls. One of the problem we met concerning the power provision is *a* negotiation with the electric company on cost estimates to the reactive power, protection of commercial lines from flickers and higher harmonics produced by a pulsed operation, and campaign of the inhabitants against the installation of high-voltage power transmission line to the laboratory. For protecting the voltage fluctuation, a thyristor reactive power compensator has been developed together with a large AC filter system against wave form distortions?') The commercial high voltage line is barely managed to reach the laboratory by October, '74, and after that the test of the power supply will be started.

The RF acceleration system is located in a long straight section and consists of three cavities somewhat similar to that of the booster. The RF frequency is varied over a frequency range from 6 MHz to 8 MHz corresponding to the harmonic number of 9. A beam-control system will be used to control the phase and radial position of accelerating particles.

Since we aim at a high intensity beam, a special attention should be paid on the problem of radiation damage. As an example, we decided to avoid any organic elements from the vacuum system of our synchrotron. For this purpose we have developed a new type of metal gasket called "H-type gasket", which is shown in Fig.20. The H-type gasket works well at a compressive force of less than 7 kg/mm, and can be used several times repeatedly. An all metallic gate-valve using the H-type gasket is also being developed and tested.

All of other equipments necessary for the main synchrotron operation will be constructed during this fiscal year *so* that we expect to have an accelerated proton beam by end of 1975.

Control and Beam Transporting System

The operation of KEK Synchrotron will be controlled from a central control system.[13]) A network computer system consisted of six Melcom-70 type computers will be used for data logging, processing and analysis, information display, and transmission of control commands. The main control computer with 16 bit w, 32 kw of core memory, 2.5 Mw disk memory and 2 magnetic tapes is assisted by five satellite computers each containing 8 kw core memory. The main computer communicates with the operator, stores the data collected from satellite computers, produces displays of accelerator parameters and develops various application programs. One of the satellite computers will assist data-collection at the control room and other four will collect data from or send commands to the distinct parts of the accelerator such as the linac with the preinjector, the booster, the east- and the west-part of the main ring. The main magnet power supply will be controlled by an additional computer system that communicates directly with the equipment.

All of the control modules such as on-off, up-down and interlock units have been standardized, and the monitoring equipments and information display system are being developed. A single control console at the central control room will be used for the entire machine operation, while several local control stations will also have their own consoles.

With the aid of computer programs, beam transport systems between the preinjector and the linac, between the linac and the booster, and between the booster and the main ring have been designed[**]) Each sub-system has successively been constructed from the low energy side. The low energy beam transport installed between the linac and the preinjector includes a prebuncher, beam monitors and emittance measuring devices (Fig.21). The beam from the linac is debunched by a debuncher to reduce longitudinal space-charge effect and passes through the phase-space matching section and achromatic system. The achromatic matched beam is injected into the booster by multiturn injection using a set of the septum and bump magnets. We left a space for a future increase of the linac energy between the linac and the booster. The linac beam can also be switched out to the beam measuring devices.

The proton beam accelerated by the booster is ejected by a set of the fast-kicker, bump and septum magnets, and injected into the main ring by a similar system consisted of the kicker and septum magnets. In the transport line between the booster and the main ring, the beam matching is performed not only for the transverse phase space but also for the momentum dispersion function.

In addition to the transverse matching, the bunched beam from the booster should be matched to the longitudinal phase space of the main ring. It is required for this to synchronize the phase of the booster bunch with the phase of the main ring RF bucket. Since the frequency of synchrotron oscillations in the booster is relatively low in such a low energy booster, the usual synchronization methods proposed or used for the NAL accelerator and other high energy machines would suffer from technical difficulties. Taking advantage of the single bunch acceleration in the booster (harmonic number ≈ 1), we shall use a new method utilizing phase slip due to a small difference between the RF frequency of the booster and that of the main ring.[14]) Near the maximum field of the booster, we switch off the booster beam feed-back control system and keep the booster RF frequency constant at about 10 kHz less than the main ring RF frequency which is synchronized with the design energy, i.e. 500 MeV. Then the booster bunch slips with respect to the main ring RF bucket and coincides with the latter once in every 100 μs. A coincidence circuit detects the phase coincidence and triggers the ejection system from the booster into the main ring. The variation of the magnetic field near the top energy is within 10^{-4} during 100 μsec and the shift of the radial beam

---

* Japanese fiscal year starts from April 1 and ends on March 31.

position due to keeping the RF frequency constant is within 0.1 mm. This synchrotronization method is simple, fast and independent of synchrotron oscillations.

Extractions and Experimental Facilities

The first proton beam accelerated by the KEK synchrotron is expected in the end of 1975 and the scheduled experiments will start from early 1977. Two experimental halls are designed, one of which will be used for bubble chamber experiments and the other for counter experiments. Three beam channels are planned for experiments; a fast extracted beam for the bubble chamber, a slow extracted beam and an internally converted secondary beam for the counter experiments. The fast extraction system from the main ring is planned to use an electrostatic septum combined with a fast kicker magnet, leading to produce a few us beam pulse with an improved emittance. The design study of the slow extraction system from the main ring is in progress including a choice of the resonance used.

A considerable amount of money for preparing and developing experimental instruments including a bubble chamber (.75 m/1mϕ) has been provided so that the experimental program can be started at the moment of the accelerator completion. The experiments will be performed not only by the KEK physics group but also by the scientists from other universities and institutions as the national accelerator for common use.

Future Option and Improvements

Since the total budget for machine construction is limited to 4000 M yen: first we aim at obtaining 8 GeV in energy and $\gtrsim 2 \times 10^{12}$ ppp in intensity. However, for performing unique experiments in the possible energy range, we will proceed with the successive improvements and refinements. The attainable energy will soon be raised up to 12 GeV with a small modification in the power supply and the cooling system. The intensity will be able to reach to 10^{13} ppp during a few more years. Beam quality and stability for experiments will also be improved gradually. In particular, we will make continued efforts on ensuring reliability and exploiting flexibility in the machine operations.

Although the design philosophy of employing a booster in our synchrotron is on rasing the space-charge limited intensity in the main ring, the booster will also be used for intermediate-energy nuclear science, pulsed neutron experiments, or medical applications as a future option. One of the straight sections in the booster is remained for extracting the beam to an experimental hall which will be constructed at that time. Possible acceleration of polarized protons both in the main ring and the booster are being studied;[15] and a serious resonance effect is pointed out in the booster caused by a choise of the ν value of 2.25. Such a high ν value was taken from the requirement that, in order to make beam transport easier, the transition energy of the booster should be much higher than the booster energy. However, some addiitonal quadrupole magnets for reducing ν value to 1.75 or less in the vertical direction will be necessary for accelerating polarized protons in the booster. Taking advantage of using a separated-function type lattice, the polarized beam may be accelerated upto the maximum energy in the main ring without any serious resonance effect. A development study of an intense polarized ion source is now started. Not only acceleration of protons, but acceleration of deuterons or polarized deuterons will also be studied for future applications to nuclear physics experiments.

At last, extension of the present synchrotron to higher energy range should be the most important goal of our project. In a separate paper, a preliminary design study on a possible plan of the future extension, i.e. so-called "Tristan project" will be reported in this Conference![6]

* 11-13 M$ depending upon the fluctuation of current currency.

Acknowledgement

The construction of the synchrotron reported here is a collaboration work in the KEK Accelerator Department and I would like to thank all of my good colleagues for their excellent collaborations. In addition, I am grateful to many outside collaborators, particularly to the visitors from foreign laboratories, for their valuable contributions in the various stages of our project.

References

1) Last November, the U.S.-Japan Seminar on High Energy Accelerator Science was held in Tokyo and Tsukuba. Details of some specialized topics reported here are available in the Proceedings of the Seminar (abbreviated Proc. U.S.-Japan Seminar in the following list) published by the Seminar Secretariat at KEK.

2) M. Kobayashi et al: Proc. U.S.-Japan Seminar, KEK, 1973, p.518, Proc. 1972 Proton Linac Conf., Los Alamos, 1972, p.365

3) H. Baba et al: Proc. 1970 Linac Conference, NAL, 1970, p.35, T. Nishikawa and S. Okumura, Proc. 6th Intn'l Conf. on High Energy Acc., Cambridge, 1967, p.162, S. Okumura, T. Nishikawa and H. Yoshikawa: Particle Accelerators 2 (1971) 279

4) J. Tanaka, T. Nishikawa and H. Baba, Particle Accelerators 2 (1971) 235, J. Tanaka, Proc. U.S.-Japan Seminar, KEK, 1973, 279

5) M. Kobayashi et al, Particle Accelerators 4 (1972) 87, Nucl. Instr. & Meth. 101 (1972) 187, 103 (1972) 493, J. Tanaka et al: Proc. 1972 Proton Linac Conf. LASL, 1972, p. 205

6) T. Nishikawa, Transients and Beam Loading Effect: P.M. Lapostolle and A.L. Septier ed. "Linear Accelerators", North Holland Pub. Co. 1970, p.809, see also BNL Rept., AADD 87, 1966

7) T. Doke et al, Nucl. Instr. Meth. 83 (1970) 300, M. Kihara, Proc. U.S.-Japan Seminar, KEK, 1973, p.134, H. Sasaki, K. Takikawa and M. Kumada, Proc. 4th Intn'l Conf. on Magnet Tech., Brookhaven, 1972, p.372

8) M. Kondo, Proc. U.S.-Japan Seminar, KEK, 1973, p.590

9) K. Endo and M. Kihara, Proc. 4th Intn'l Conf. on Magnet Tech., Brookhaven, 1972, p.363, see also ref.7

10) K. Endo et al, IEEE Trans. NS-20 (1973) No.3, p.716

11) A. Ando et al, Proc. 9th Intn'l Conf. on High Energy Acc., SLAC, 1974, p.

12) M. Masuda, IEEE Trans. Proc. 4th Intn'l Conf. on Magnet Tech., Brookhaven, 1972, p.709, Proc. U.S.-Japan Seminar, KEK, 1973, p.145

13) T. Kamei, Proc. U.S.-Japan Seminar, KEK, 1973, p.597

14) Y. Kimura, Proc. U.S.-Japan Seminar, KEK, 1973, p.574, T. Kamei et al, Proc. 8th Intn'l Conf. on High Energy Acc., CERN, 1971, p.120, see also L.C. Teng, KEK Pept. KEK-72-9, 1972

15) H. Sasaki, Proc. U.S.-Japan Seminar, KEK, 1973, p.247, see also T.K. Khoe, KEK Rept. KEK-73-8, 1973

16) T. Nishikawa, Proc. U.S.-Japan Seminar, KEK, 1973 p.209 and Proc. 9th Intn'l Conf. on High Energy Acc., SLAC, 1974, p.

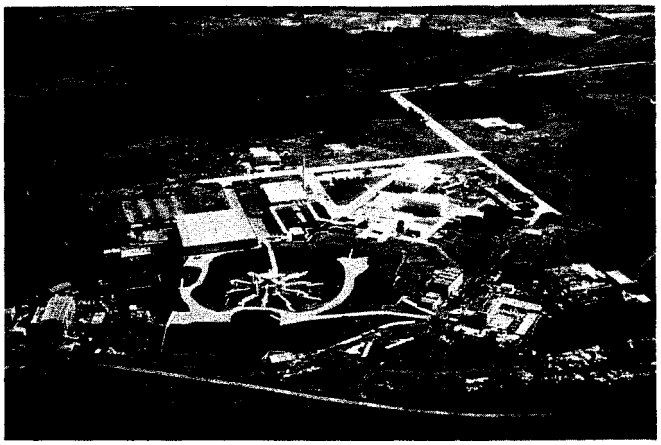


Fig.1 Aerial View of KEK Synchrotron

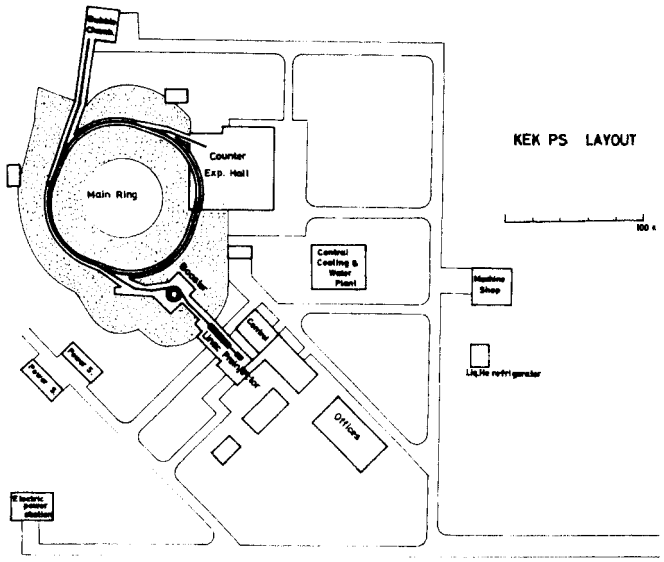


Fig.2 Layout of KEK Synchrotron

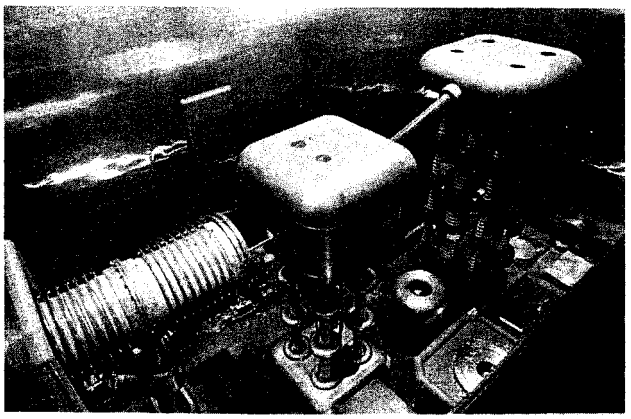


Fig.3 KEK Preinjector

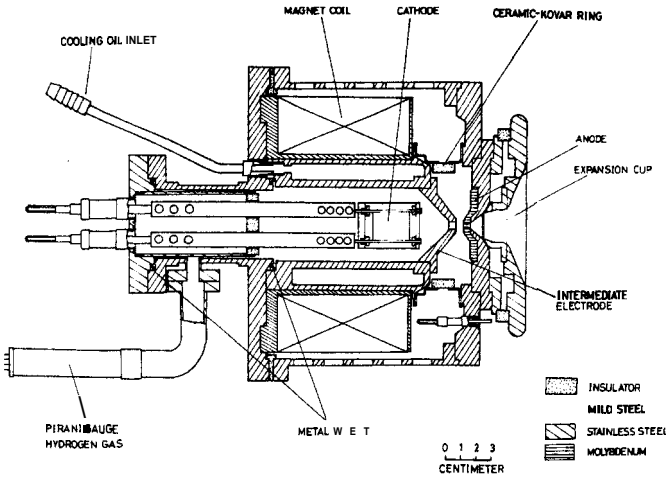


Fig.4 Duoplasmatron with a Nozzle-type Expansion Cup

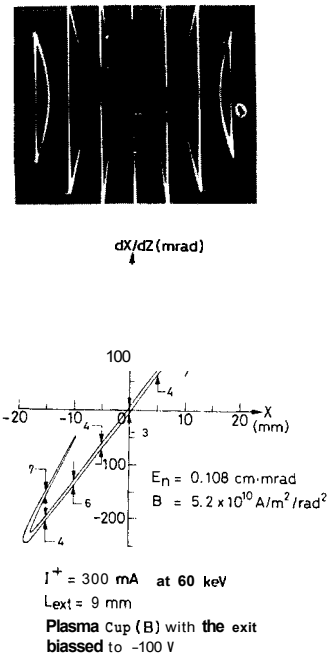


Fig.5 Beam Image and Emittance Diagram of a 60 kV, 300 mA beam

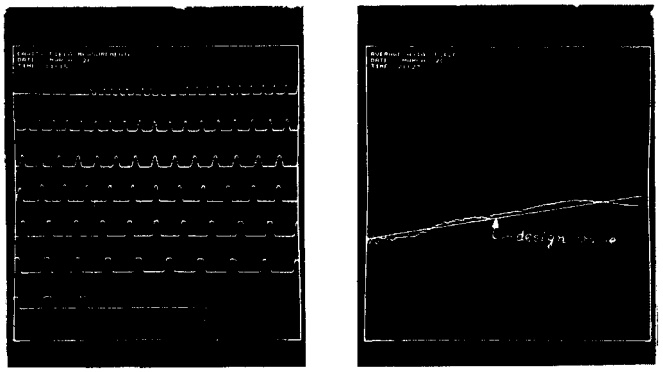


Fig.7 Field Distributions along Linac Cavity. Display of Frequency Perturbations (left) and Average Field in Comparison to Design Valve (right).

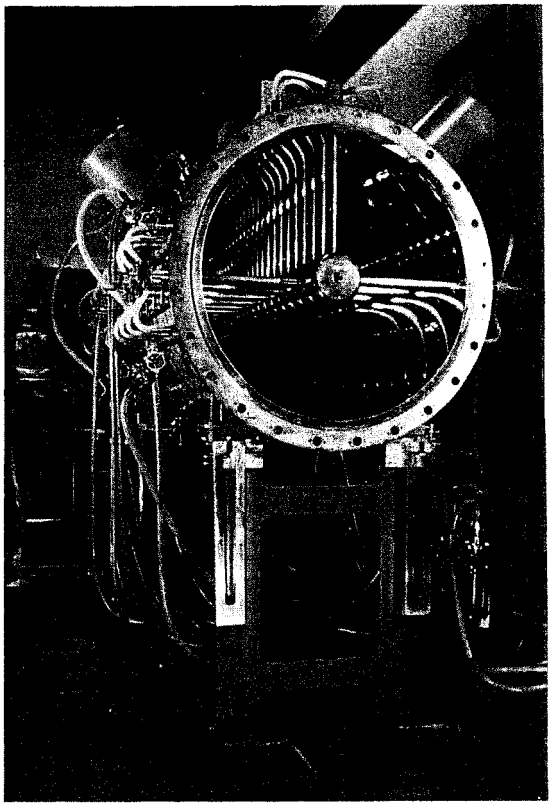


Fig.6 KEK Linac

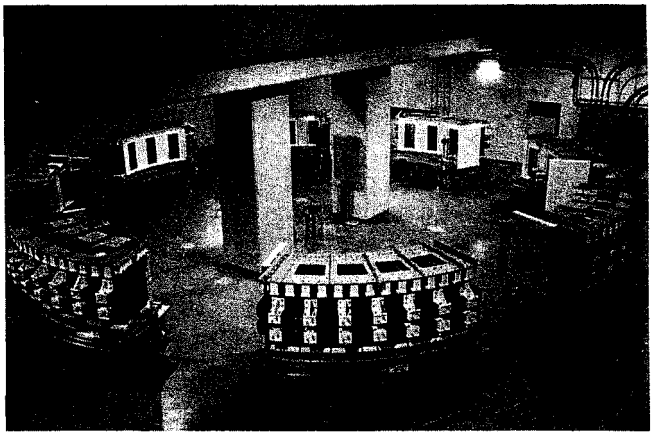


Fig.9 Photograph of KHK Booster

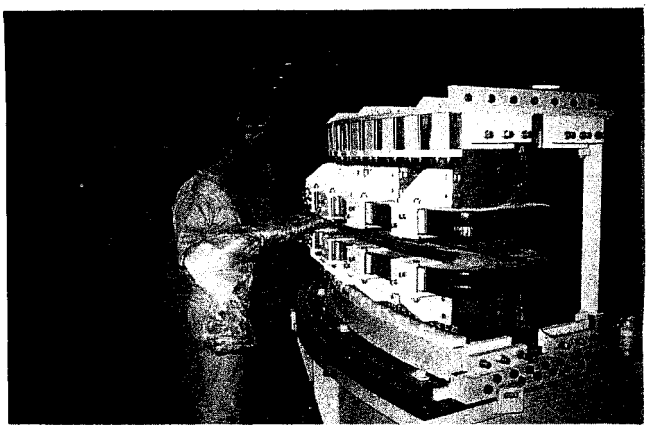


Fig.11 Corrugated Vacuum Chamber being installed between Magnet Gap of Booster

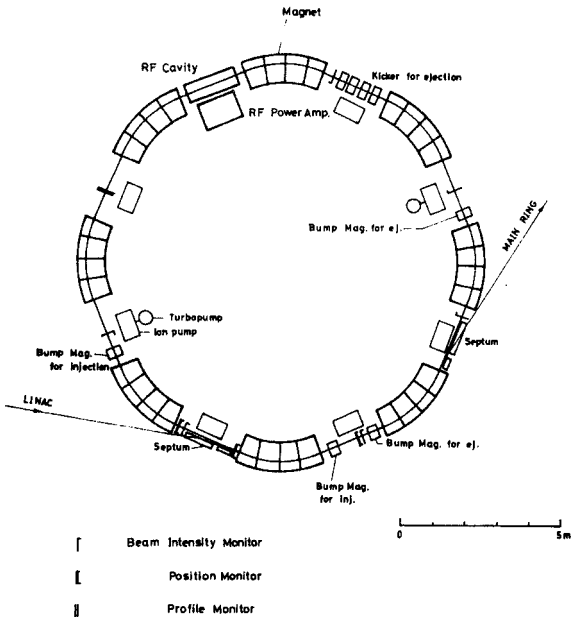


Fig.8 Layout of KHK Booster

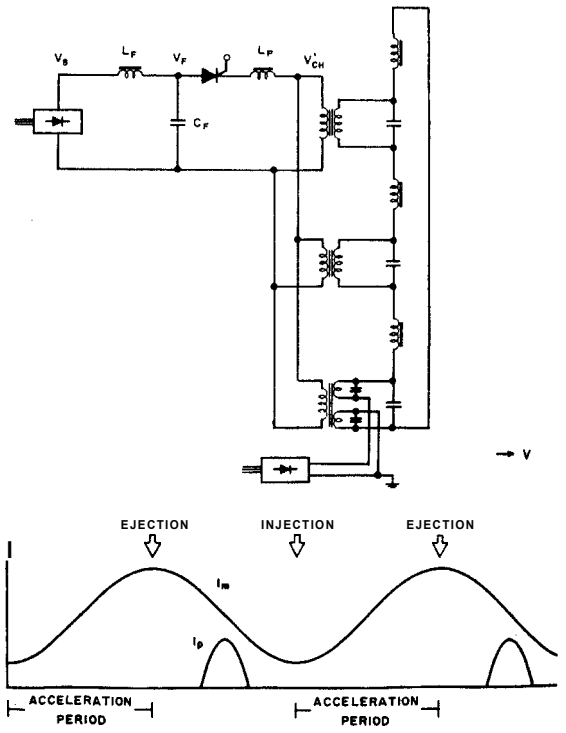


Fig.10 Basic Diagram of Booster Power Circuit

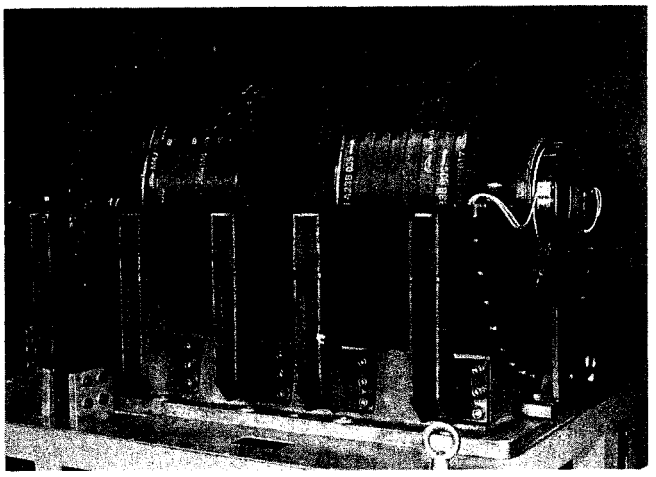


Fig.12 Booster RF Cavity

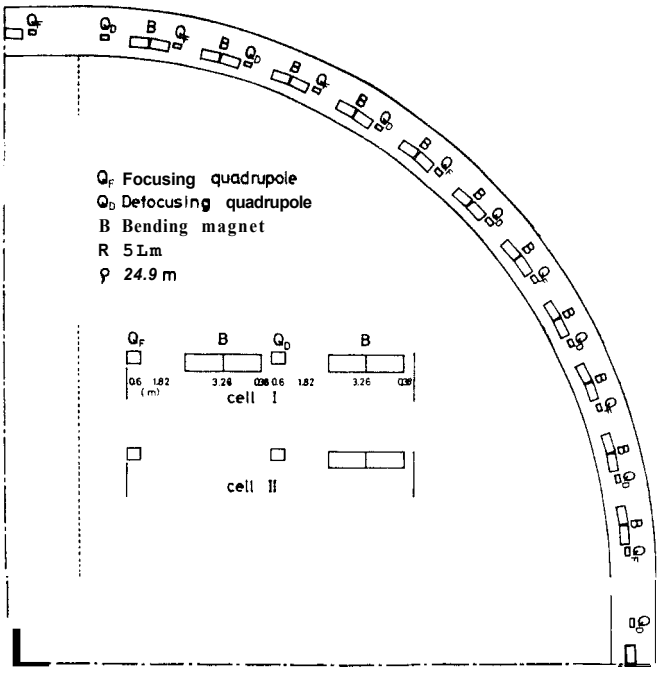


Fig.14 Cell Structure of KEK Main Ring



Fig.15 Photograph of KEK Main Ring

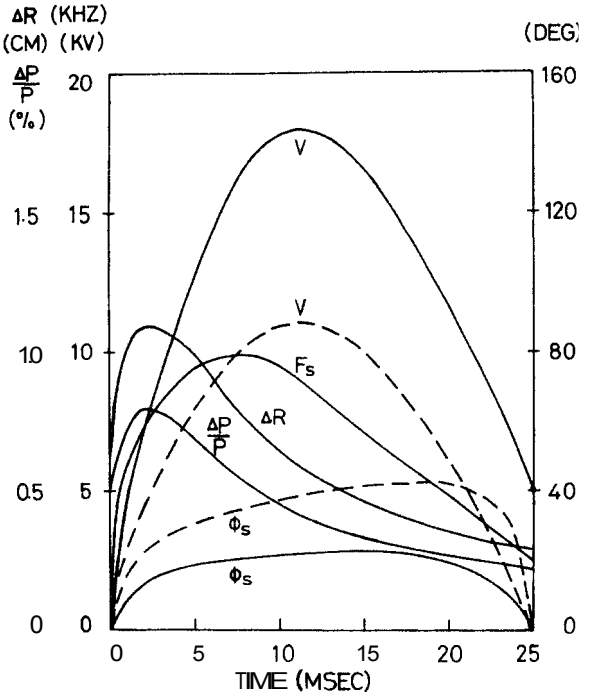


Fig.13 RF Program of Booster. Broken Curves show Necessary Minimum Voltage and Corresponding Phase Stable Angle. F_S gives Frequency of Phase Oscillations.

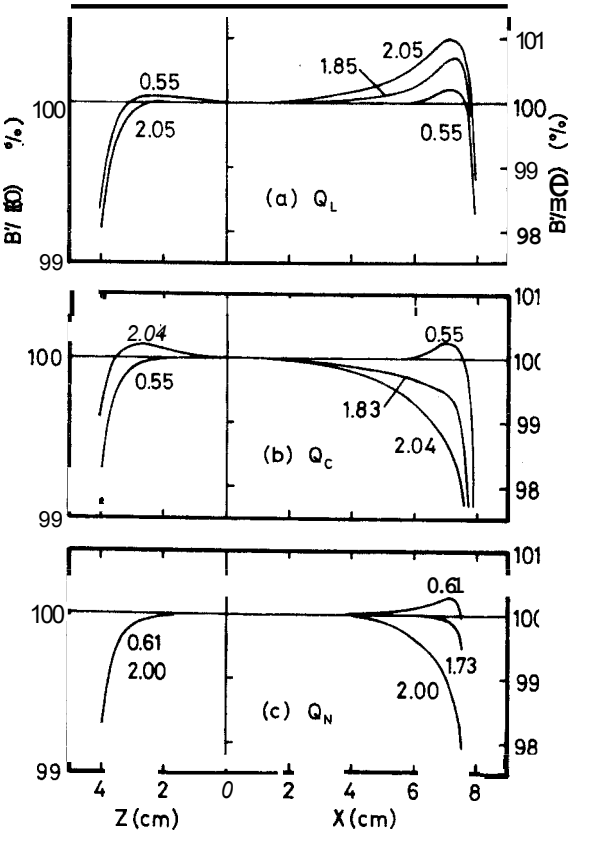


Fig.16 Horizontal and Vertical Gradient Distributions of Quadrupole Magnet. See ref.11.

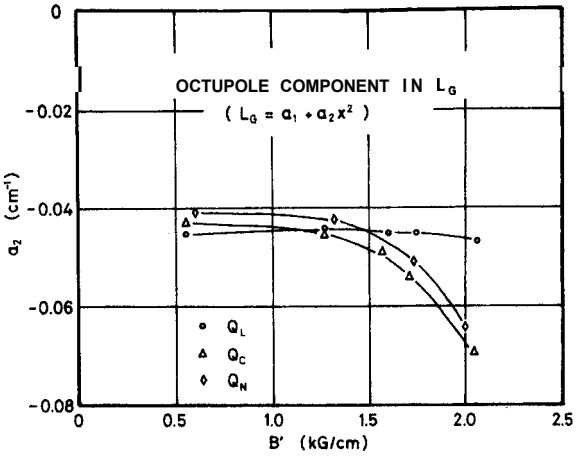


Fig.17 Octupole Component of Effective Length of Quadrupole Magnet

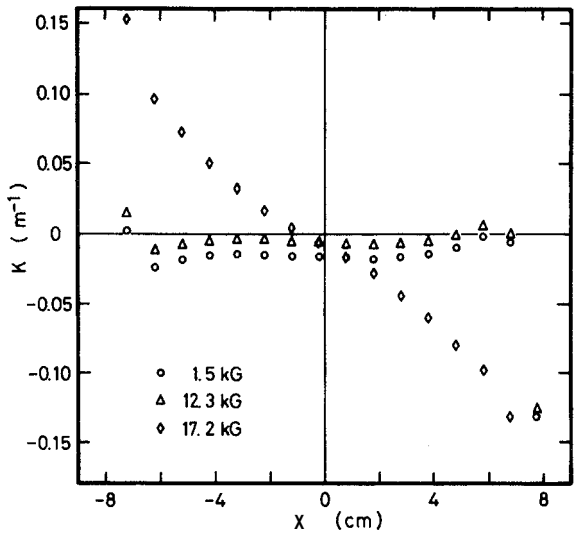


Fig.18 Gradient Distribution of Bending Magnet

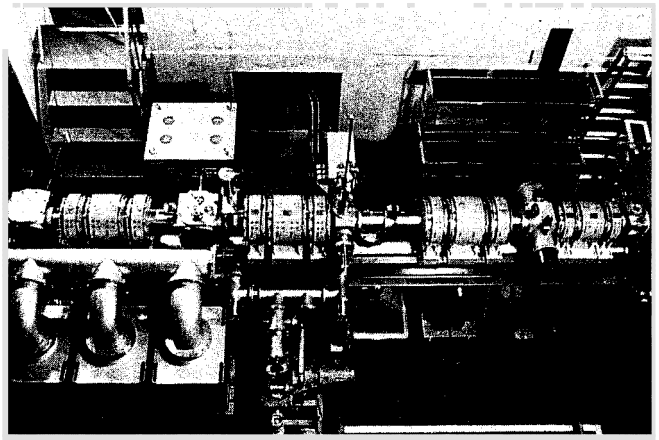
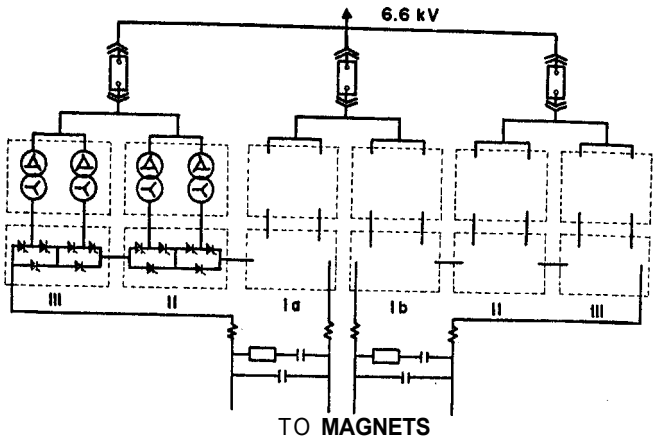
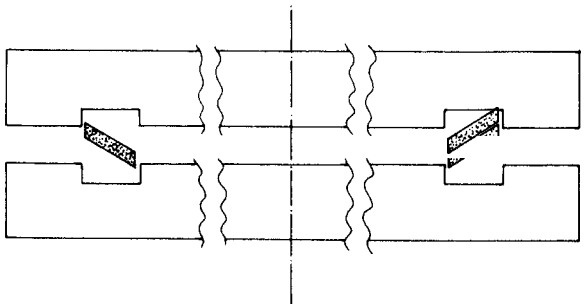


Fig.21 Low Energy Beam Line between Preinjector and Linac



RECTIFIER GROUP / PERIOD	I_a	I_b	II	III
Injection Porch	Conv.	Inv.	Bypassed	Bypassed
Acceleration	Conv.	Conv.	Conv.	Conv.
Flat Top	Conv.	Conv.	Bypassed	Bypassed
Deceleration	Inv.	Inv.	Inv.	Inv.

Fig.19 KEK Main Ring Power Supply and Operation Program



Merits :

- o Self-aligning structure
- o Sexless flange
- o Sealing point is hardly damaged.
- o Small force required ~ 7 kg/mm

Demerits :

- o Shape of gasket is complicated.
- o Deformation of gasket for ≳ 100 kg / mm

Fig.20 H-type Gasket

Andrei Kolomenskg (Lebedev Institute): Do you plan to do nuclear physics with this machine?

Nishikawa: We are also planning to use the machine for nuclear experiments, particularly using low-energy K-meson beams.

Milton White (Princeton): I didn't understand the vacuum chamber design in the booster.

Nishikawa: It is a corrugated vacuum chamber to reduce eddy current effects. The stainless-steel bellows of **0.2** mm in thickness are welded leading to the effective thickness of the wall of 0.03 mm.

Boyce McDaniel (Cornell): How much space do you lose in the magnet gap due to the corrugations?

Nishikawa: We lose 1.5 cm due to the corrugation.

Willard E. Jule (LASL): Were the field measurements in the linac made at high power and under vacuum?

Nishikawa: No, the measurements were made in air at a lower field level.

PRESENT STATUS AND FUTURE PLANS FOR THE ISR

K. Johnsen
CERN
Geneva, Switzerland

Summary

The CERN Intersecting Storage Rings (ISR) are in routine operation for about 3000 hours per year on the average. Of this time 75% is for colliding-beam physics or preparations for such runs, the rest for machine development. The starting luminosity for long physics runs, with acceptable background conditions, has been up to 5.4×10^{30} cm^{-2} s^{-1}. The longest run without refilling lasted 58 hours. During one of the last development runs in 1973, with the booster used as an injector for the CPS, a luminosity of 6.6×10^{30} cm^{-2} s^{-1} was achieved. It is hoped to reach still higher luminosities by further improvements in the vacuum, further developments of means to suppress instabilities and the effects of resonances, by improved phase space densities now available from the CPS, and by the insertions of low-β sections.

Introduction

The ISR has been in operation for three years with a heavy experimental programme and with rather little unscheduled down-time. As an example, it can be mentioned that in 1973 we had 3100 operating hours of which 2360 hours were for colliding-beam physics (including time for setting up and optimizing beams, luminosity measurements, etc.), and 740 hours were for developing the performance of the machine.

Luminosities for physics runs have reached somewhat over 5×10^{30} cm^{-2} s^{-1}, and, recently, with very good background conditions up to the highest luminosities. Long periods for taking physics data have been available, with several runs of 35 to 40 hours and one of 58 hours. During machine development currents of over 20 A have been obtained in each of the two rings.

During the same year, twelve experiments have been taking data at six of the ISR's intersection regions. A large spectrometer facility, the so-called Split-Field Magnet, has been put into operation without detrimental effects on the beams.

Acceleration of ISR beams has provided another standard operating momentum for physics at 31.4 GeV/c (equivalent to 2000 GeV on a fixed target) at luminosities up to 4×10^{29} cm^{-2} s^{-1}.

The machine is, however, not only a very exciting high-energy physics facility, but provides us also with the most fascinating experimental tool for studying particle beam behaviour under a variety of conditions. Such studies go on continuously in parallel with the high-energy physics programme and have given handsome rewards in the form of continuous improvement of the performance, a trend to which we do not *see*, as yet, the end.

I will, in what follows, sum up various effects we have met which have temporarily limited the performance and indicate some of the remedies that have been applied as well as their results. I will concentrate mainly on the latest developments.

Recent development of the performance

Recently, the performance of the ISR has mainly been influenced by the following effects:

- resistive wall instability
- non-linear resonances and coupling resonance
- space charge Q-shifts
- beam induced pressure bumps

Although the three first effects are of completely different nature, they influence each other *so* much, in particular through the remedies used against them, that it seems convenient to describe them together. The fourth effect will be dealt with separately. Finally, short remarks will be made about certain effects outside the above list.

Working line gymnastics *)

The main remedy against the resistive wall effect is Landau damping. The only practical way of creating this in the ISR, is to make $dQ_{v,h}/dp$ everywhere in the vacuum chamber larger than a critical value given by the current density in the stack, i.e. we must establish certain predescribed working lines across the machine aperture. Working lines can be conveniently classed as static or dynamic. The former are either made with a disregard for the space charge deformations, e.g. "FP" in Figure 1, or with a pre-stress that gives the line an ideal shape for a given space charge load, e.g. "5C" in Figure 1. These two lines have been extensively used for ISR operation and "FP" is still the principal low intensity line.

The philosophy of dynamic lines is to progressively correct the space charge deformations during the stacking *so* that the working line never departs very far from its ideal form. Operationally this is far more complicated and is only made possible by the very considerable flexibility of the poleface windings under computer control, but the results are amply rewarding.

Pre-stressed static lines require a lot of space in the tune diagram. This arises because the overall tune-spread has to be large enough to ensure that the local values inside the stack are sufficient for stabilization by Landau damping and secondly because the whole line sweeps across the tune diagram. For these reasons it was not possible to avoid the 5th order non-linear resonances which cross the stacking region on the "5C" line in Figure 1. These particular

*) For more details see Ref. 1).

resonances exhibit a somewhat variable excitation and can cause decay rates of up to 200 parts per million per minute, causing background so high that the experimentalists prefer lower luminosities. A feature with this working condition was also that the loss rates were very variable and unpredictable from run to run. This puzzled us at the beginning, but later we have found that since the excitation of the 5th order resonance comes mainly from the beam-beam effects, the losses became very sensitive to beam steering. A change in vertical beam position of a small fraction of a millimetre (having an insignificant effect on the luminosity) would change the background rather drastically [1]. Therefore, we try hard to avoid having a stack sitting across a 5th order resonance.

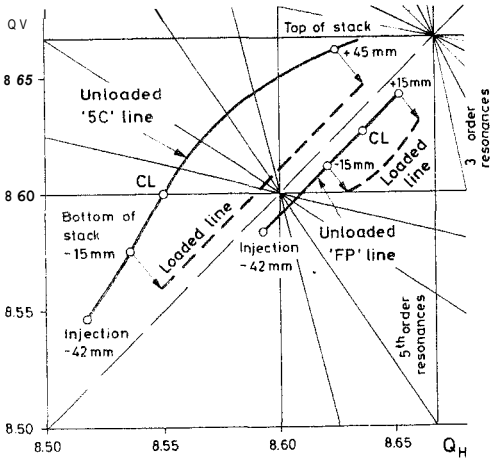


Fig. 1 - The static working lines "5C" and "FP" shown with and without a stack.

A dynamically compensated line can be much shorter, since the local tune-spreads inside the stack are maintained close to the maximum value and the line's excursions are very limited. Using the dynamically compensated line "8C", shown in Figure 2, full-aperture stacks of 17.6 A at 26 GeV/c can be made in the region between the 5th and 3rd order resonances, which is free of all resonances up to the 8th order. Compared to "5C", this line is shortened by a factor of 1.5 and the avoidance of the resonances lower than 8th order reliably gives excellent physics conditions.

When setting up a dynamically compensated line, the base line is first created and recorded in a file specifying all the relevant power supply currents. Realignment of the ISR and other changes make it necessary to periodically update this basic file. The pre-stresses, however, need no updating as they are in the form of small changes of tune derivatives, referred to the base line and are, therefore, invariant. When applying the pre-stresses, the ISR control computer changes all the power supplies in ratio so that the circulating beam sees a smooth transformation which takes only a few seconds. The stack does not show any sign of disturbance. The "8C" stack is built up in five steps. Prior to each step the line is pre-stressed (see Figure 2) and then the space charge is added bringing the line back to its ideal form. This procedure is controlled interactively by the ISR computer and it takes about one hour to fill both rings at 26 GeV/c to the maximum current of 17.6 A. At no time does the "8C" working line wander outside the limits shown and the stack always maintains a respectful distance from the diagonal ($Q_h = Q_v$), the 3rd order resonances and the 5th order resonances. If the full space charge pre-stress were applied in a single step, the stack would be swept across the 3rd and 5th order resonances and would be blown up and partially destroyed.

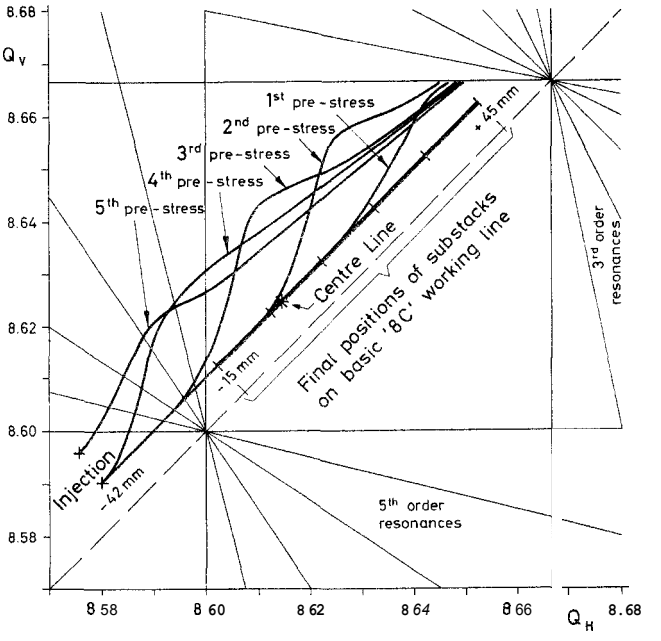


Fig. 2 - The "8C" family of pre-stressed working lines used at 26 GeV/c to stack 17.6 A in five steps of 3.52 A across the chamber from + 45 mm to - 15 mm (α_p average).

The "8C" line when loaded to its limit, is sufficiently stabilized by Landau damping to survive under very quiet conditions, but the slightest disturbance will cause the stack to be lost. The active transverse feed-back system is, therefore, used to ensure the stack's stability [3].

The space available for the "8C" line is very limited. It has been found prudent not to allow the tune-separation, $A = Q_h - Q_v$, to fall below 0.01. For example, at A = 0.005 the betatron coupling strongly perturbs the tune-values and an appreciable percentage (~ 17%) of the larger horizontal emittance is coupled into the vertical emittance. This is serious for the luminosity as we apply heavy beam shaving to reduce the effective beam height, and thus the horizontal to vertical emittance ratio is normally large in the stack. Once the tune-separation for the baseline is fixed, the size of a substack and the top and bottom of the main stack are fixed by the space between the base line and the 3rd and 5th order resonances. The tolerances aimed for on the positioning of these lines is ± 0.001. In order to maintain the tight tolerances on the stack's position in the tune-diagram, the current density has to be carefully controlled to give the correct space charge loading. The radial positions of the substacks

are maintained to ± 1 mm to avoid the resonances. The basic "8C" scheme can be converted to any energy and to different beam current densities.

It has also become normal practice to correct working line shifts during physics runs. This has been made possible by a method for measuring tunes based on the Schottky noise from the stack [4].

At 22 and 26 GeV/c, "8C" has been extensively used with the full five substacks. Typically, the starting luminosities were 5×10^{30} cm^{-2} s^{-1}. More recently, "8C" has been used at 26 GeV/c with the top and bottom substacks omitted giving 10.6 A and with the base line moved further from the diagonal ($Q_h = Q_v$). The most recent of these runs had a starting luminosity of 3.8×10^{30} cm^{-2} s^{-1} with a beam decay rate of 0.8×10^{-6} min^{-1}. During this 27-hour run, the luminosity fell to 2.7×10^{30} cm^{-2} s^{-1} and the decay rate rose to 1.1×10^{-6} min^{-1}. Approximately *40%* of the decay rate can be attributed to beam-beam interactions and the remainder to scattering on the residual gas. Although it is not a proven fact, it appears that the increased tune-separation improves injection optimization and the quality of the stacks. The maximum luminosity so far achieved in the ISR under physics conditions, 6.6×10^{30} cm^{-2} s^{-1}, has also been obtained on the "8C" line.

In order to stack still higher currents, an increased tune-spread is required. At present, an expanded "8C" line is being developed which extends across the 5th order non-linear resonances. At the crossing point, the tune-spread is locally increased so that the resonances are traversed more quickly in momentum space. By making separate stacks either side of the 5th order resonances, it is hoped that higher intensities can be reached.

RF knock-out of that part of the stack which is sitting across resonances has also been tried with encouraging results. A combination of these methods may make it possible to reach L = 10^{31} cm^{-2} s^{-1}.

Beam induced pressure bumps

The difficulties we have had with beam induced pressure bumps ever since we reached the *4* A level, are probably by now well known to everybody. The mechanism is briefly as follows:

Ions originating from collisions with the residual gas are driven into the chamber walls by the beam's electrostatic potential, which is about 1 kV at 10 A beam current. The ions liberate gas molecules from the surface layers adsorbed at the walls. It is easy to show that with such a process, where the pressure rise is proportional to the product of beam current and pressure, one has a critical current, above which the equilibrium pressure rises to infinity.

This effect has been thoroughly studied by now [5]. One remedy applied is to reduce the surface coverage of adsorbed molecules. As a first step we have adopted baking at 300° C for 24 hours everywhere and every time a sector has been exposed to atmospheric pressure, instead of only 6 hours at 200° C as used earlier. Surface treatment with ions from a glow discharge is applied to parts of the chamber where the pumping speed is small and difficult to increase. This is done in the laboratory, prior to installation. The beneficial effect survives a few hours at atmospheric pressure. Keeping the entire system in the 10^{-11} torr range of pressures also contributes to reducing the amount of beam-induced outgassing. In clean parts of the vacuum system we actually observe beam-induced pumping, i.e. the number of molecules desorbed per incident ion is smaller than one. Figure 3 shows an example of this beam pumping effect observed in a glow discharge cleaned section.

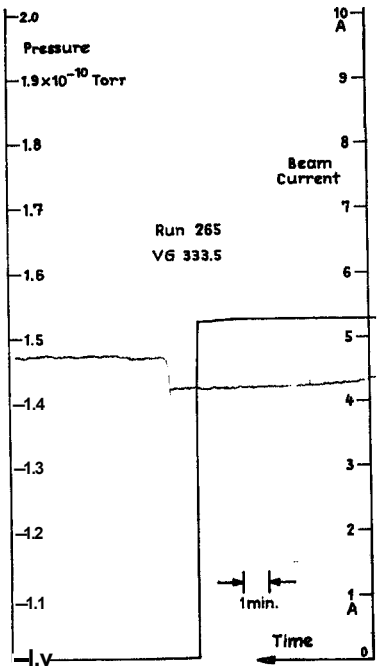


Fig. *3* - Beam pumping in a section which has been cleaned by glow discharge

An alternative way of reducing the desorption coefficient involves the use of other, cleaner materials to replace the traditional stainless steel chamber. We are actively investigating such possibilities and to date we have obtained the best results from titanium which has been given an 800° C vacuum bakeout prior to installation in the ISR. This has given consistently negative desorption coefficients and is comparable with the best results from glow discharged stainless steel.

The other, more universal, remedy is to increase the distributed pumping by means of a large number of additional titanium sublimation pumps. About 500 such pumps have been installed. As a result of these various remedies, the critical current had increased from about *4* A around the middle of 1971 to about 20 A in both rings. For most of this period this particular problem was the main performance limitation in the ISR and consequently a strain on our vacuum group. It was therefore quite a relief when they recently succeeded in bringing the critical beam current high enough that the other problems previously described came in the forefront of interest. We have good hopes in bringing the critical current still higher by the methods mentioned, say to 30 A, so that the vacuum system can keep pace with the improvements expected in the other problems.

Behaviour of bunched beams

Bunched beams have a tendency of behaving differently from unbunched beams, and in general not in a beneficial way. For instance, the injected beam exibits a longitudinal instability that leads to a considerable dilution of the longitudinal phase plane density. This is not yet a serious problem but in order to cope with the instability at the higher intensities that we expect in the future, possible cures have been investigated and tried with encouraging results. These will be reported on in a separate paper [6].

Another problem is that of lifetime and background. Bunched beams normally exibit orders of magnitude larger loss rates than unbunched beams. This is of no consequence to the ISR, but possibly of importance to future machines, and we are studying this effect. The indications are strong that it is the effect of non-linear resonances that is being enhanced by the bunching, and therefore we sometimes use even bunched beams for the specific purpose of studying non-linear resonance excitation. However, more studies are needed to understand these problems.

Acceleration to *31.4* GeV/c

The maximum particle momentum currently available from the PS is 26 GeV/c. At the price of much reduced luminosity, we have accelerated stacked beams from about 26 GeV/c to *31.4* GeV/c, the maximum our magnet power supplies can provide. The maximum luminosity achieved was 4×10^{29} cm^{-2} s^{-1}. Phase displacement acceleration was used for this [7].

During the acceleration process the shape and location of the magnetic working line must be kept constant while the field increases and saturation worsens. This is done by means of the poleface windings, the currents of which are continuously regulated by the controls computer. Serious beam losses due to beam-beam effects occur during the acceleration process. Only a small fraction of the stacked current is left after acceleration to *31* GeV/c if a beam is circulating in the other ring. When the beams are separated vertically by several beam heights in all intersections, these current losses can be avoided. This is another example of the importance of the non-linear resonances.

Some possible future developments of the ISR

Emittance exchanges in the transfer line

A new method of reducing the beam height was proposed by Schnell [8]. This can be done by a series of septum magnets in the beam transfer line. The vertical emittance ellipse is sliced into n parts which are then superimposed. The horizontal emittance is divided into n separate ellipses, which are placed side by side. With the choice of n = *4*, a worthwhile increase in luminosity can be obtained with a beam that still passes the horizontal aperture of the existing injection magnets. Altogether four septum magnets would be needed, otherwise no new elements.

The disadvantage of this method is the increased ratio of horizontal to vertical emittances. Although there may be space within the horizontal aperture, the coupling may become very serious, pushing us even further away from the diagonal in the working diagram. However, this means that the working lines have to be made shorter (Figures 1 and *2)*, and the corresponding, increased difficulty with instabilities may make it difficult to take advantage of this method.

Stochastic cooling of betatron oscillations

An even more speculative method of reducing the vertical beam height has been proposed by Van der Meer and has become known as "stochastic cooling" [9]. The method consists in observing, with a wide band pick-up, small statistical deviations of the centre of gravity from the closed orbit of a short longitudinal beam sample, containing a finite number of protons, and reducing the error 5/4 λ downstream with a fast kicker. New deviations of the centre of gravity are continuously created by the proton migration into and out of the sample, so that successive application of this correction leads to a progressive reduction of the rms betatron oscillation amplitude. The theory shows that it is marginal whether we shall, in practice, be able to reduce the beam height through this method. We feel that the idea is exciting and have therefore started an experiment. However, no conclusive results have been obtained yet.

High luminosity insertions

The most realistic way to increase the luminosity is, however, to change beam geometries by inserting and modifying beam optics elements near the crossing regions.

The simplest is to insert a system of quadrupoles that will reduce β_v, otherwise leaving the machine essentially unchanged. The first such system will consist of existing beam transport quadrupoles (partly borrowed from outside CERN), which will be installed this year. This system was analysed by Keil [10]. He arrived at $\beta_{min} \simeq 2.5$ m as compared with about *14* m in an unperturbed crossing region. This should therefore give a luminosity improvement of *2.3*. The obstruction-free space is ? 1.7 m which is just sufficient for the installation of a solenoid magnet, proposed by one of the experimental teams. The layout is shown in Figure 4.

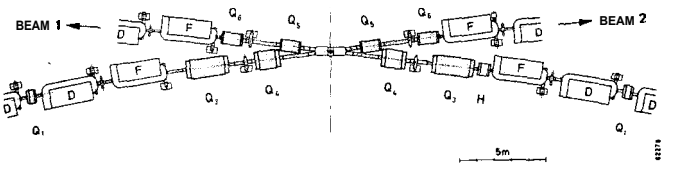


Fig. 4 - Low-β insertion with conventional quadrupoles.

Further improvements can be made with stronger lenses, which will require superconducting magnets. We have started working on plans for such a system as well, but naturally on a much longer time scale. The layout, illustrated in Figure 5, is not very different from the one with conventional lenses, but with the increased strength we hope to reach a $\beta_{min} = 0.6$ m and consequently a factor of five in luminosity [11]. Proto-

type work has started in close collaboration with other laboratories, in particular Rutherford High Energy Laboratory.

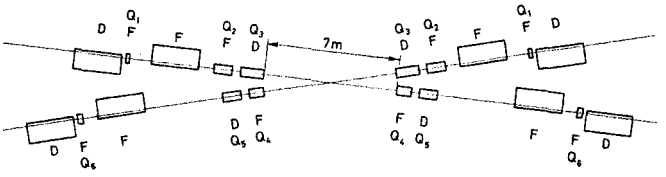


Fig. 5 - Example of low-β insertion layout with superconducting quadrupoles.

In addition to giving higher luminosity, such a superconducting low-β insertion will be a very realistic test facility of superconducting magnets under the most stringent conditions that we meet in accelerators. We therefore expect to gain an experience that will be very valuable for possible future projects.

Even more efficient insertions are possible if we attack the crossing angle as well as β. This cannot be done, however, without disturbing and modifying considerably the present ISR. This possibility has been considered by Montague and Zotter [12], and an example is illustrated in Figure 6. To achieve very small or zero crossing angle, it is necessary to displace ten magnets per ring. In addition, eight new bending magnets and 22 new quadrupoles would be required for the two rings. In this example some quadrupoles and the bending magnets would have to be superconducting to achieve the required strength. Montague and Zotter quote in their paper luminosity estimates in the neighbourhood of 10^{33} cm^{-2} s^{-1}. The main disadvantages of this kind of scheme are the modifications required in the main ISR structure, and the limited unobstructed space left along the beams from the crossing points. No decision is needed for the time being between the various schemes requiring superconducting magnets.

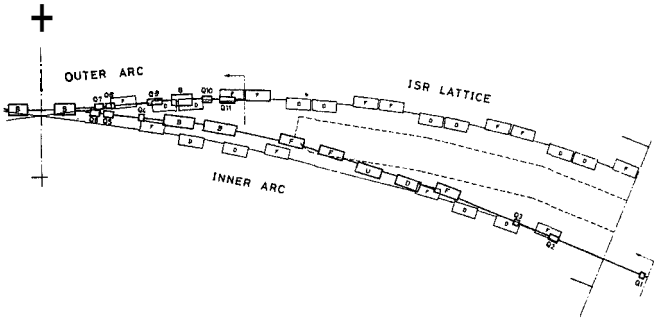


Fig. 6 - Example of high-luminosity insertion acting upon both β and crossing angle.

Superconducting ISR

A more spectacular use of superconductivity would be to replace all ISR magnets by superconducting magnets and thus being able to stack 100 - 150 GeV protons injected from the SPS. The ISR are conveniently situated for such a solution. This would, however, be a large project that would be for the far future. Its advantages and disadvantages would also have to be weighed against those of the even more ambitious project of constructing completely new 400 GeV storage rings attached to the SPS. Speculations on this is, however, outside the scope of this paper.

Concluding remarks

The ISR have fullfilled and partly surpassed all the hopes we had for this project when it was conceived. In some respect we have met problems, the difficulties of which we had not fully appreciated during the construction. However, the necessary remedies have been found and incorporated. In fact, we believe that the ISR have potentialities well beyond the present performance, in particular with respect to luminosity, where we hope that it will not be too long till we are operating in the $10^{31} - 10^{32}$ cm^{-2} s^{-1} range.

Our greatest hope is now that the ISR turn out to be only the first example of a series of such p-p facilities.

References

1) P.J. Bryant; Dynamic Compensation of the De-Tuning Caused by Space Charge Effects, Proc. of this Conference.

2) P.J. Bryant and J-P. Gourber; Experimental Investigation of Single-Beam and Beam-Beam Space Charge Effects, Proc. of this Conference.

3) L. Thorndahl and A. Vaughan; IEEE Trans. on Nuc Sci., Vol. NS-20, No. 3, p. 807 (1973).

4) J. Borer, P. Bramham, H.G. Hereward, K. Hübner, W. Schnell, L. Thorndahl; Non-Destructive Diagnostics of Coasting Beams with Schottky Noise, to be presented at this Conference.

5) R. Calder, E. Fischer, O. Gröbner, E. Jones; Vacuum Conditions for Proton Storage Rings, Proc. of this Conference.

6) P. Bramham, S. Hansen, A. Hofmann, K. Hübner, E. Peschardt; Investigation and Cures of Longitudinal Instabilities of Bunched Beams in the ISR, Proc. of this Conference.

7) K.N. Henrichsen and M.J. de Jonge; Acceleration by Phase Displacement in the ISR, Proc. of this Conference.

8) W. Schnell; CERN int. report, ISR-RF/73-42.

9) S. Van der Meer; CERN int. report, ISR-PO/72-31.

10) E. Keil; CERN int. reports, ISR-TH/72-52 and ISR-TH/73-39, and private communication.

11) B. Autin; CERN int. report, ISR-MA/72-45, and private communication.

12) B.W. Montague and B.W. Zotter; Very-High Luminosity Insertions for the CERN Intersecting Storage Rings, submitted for publication in Nucl. Instr. and Meth.

SPEAR: STATUS AND IMPROVEMENT PROGRAM*

SPEAR Storage Ring Group†
Stanford Linear Accelerator Center
Stanford University, Stanford, California 94305

Summary

Operating experience with the SLAC electron-positron storage ring over the past year is summarized. The control of several beam instabilities and the colliding beam performance over a wide operating range are described. The successful application of variable momentum dispersion to increase the beam size and luminosity is described. The improvement program to increase the energy to more than 4 GeV per beam is discussed and the results of testing the components of the new rf system are presented.

Introduction

The SLAC electron-positron colliding beam project SPEAR was completed in April, 1972. During the following year the operating characteristics of the ring were studied and, after approximately 20 weeks of testing, luminosities of greater than 10^{30} cm^{-2} sec^{-1} were attained in the operating-energy range, from 1.5 to 2.5 GeV per beam. Elementary particle experiments were installed in each of the two interaction regions, and since April, 1973 we have been routinely operating a high energy physics research program. The exciting results of this research program have already justified our efforts in the construction of SPEAR and encourage us in our next step of increasing the energy.

Every storage ring has incorporated in its design the lessons learned from earlier rings and is in itself a prototype for future higher energy rings. Although we have only begun to explore the characteristics and limitations of SPEAR we have already learned a great deal which has influenced the design of proposed electron-positron rings of higher energy, e.g., PEP.

General Description

In this section we summarize the salient features of the SPEAR project. Details of the design can be found elsewhere.[1,2] SPEAR is a single ring shown schematically in Fig. 1. Two arcs composed of standard modules connect two variable-dispersion, variable-beta, low-beta insertions. The lattice is extremely flexible in the choice of operating betatron tunes and in the choice of the momentum dispersion and beta values at the interaction points, The 51-MHz rf system operates on the 40th harmonic of the revolution frequency giving, in two accelerating cavities, a total voltage of 500 kV. This allows operation at present to 2.6 GeV.

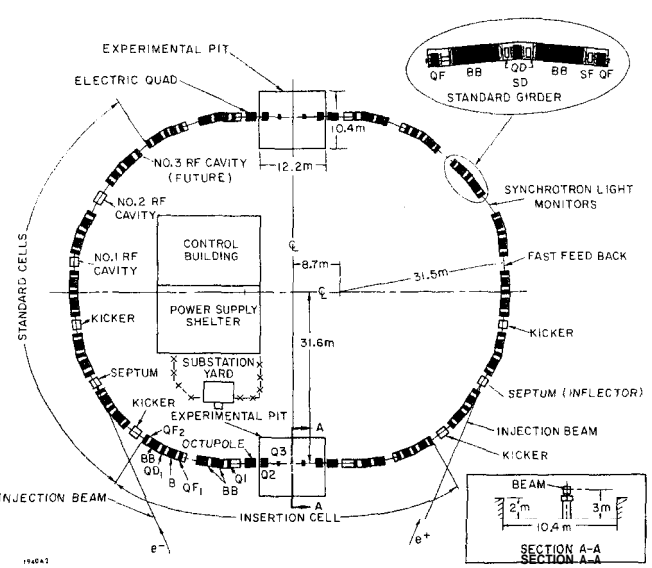


FIG. 1--Layout of SPEAR.

Injection of positrons from the SLAC linac is accomplished using a septum magnet and two kicker magnets, with a duplicate system for electrons. The injection repetition rate is 20 pps and a typical accumulation rate is 20 mA/min (10^{11} particles/min) into a single bunch. Under optimum conditions we have achieved 120 mA/min (6×10^{11} particles/min) into a single bunch. Injection takes place into a standard configuration of betatron tune and other lattice parameters and at a fixed energy of 1.5 GeV. The two counter-rotating bunches are vertically separated, using electric plates, as they pass in the low-beta insertions. After injection the energy of the ring is adjusted to the desired value and the lattice changed to the appropriate values for high-luminosity operation.

These lattice manipulations involve complex interrelations among the currents of eleven separate magnet systems and are much too difficult to accomplish under manual control. The control of the magnet system is accomplished by an XDS Sigma-5 computer. This computer system allows the operator to choose a wide range of values of tunes, betas, and dispersions and to vary any subset of these parameters while holding the other constant.[3] The computer handles most other instrumentation data-logging and control functions, e.g., closed-orbit measurement and control, and it also handles the data acquisition and on-line analysis of some of the physics experimental program.

Operating Experience

During this first year of routine running, SPEAR has operated on the SLAC schedule of 4- to 10-week running periods with similar maintenance and set-up periods. We have adopted a pattern of 5- to 6-day blocks of continuous operation for the research program with interruptions of 1 or 2 days for machine studies or equipment modification.

Figure 2 gives a breakdown of operating time during scheduled running for physics research over the past year. A typical fill takes of the order of 20 minutes with half the time being taken up by the lattice changes before and after injection. The beam lifetime is dominated in most cases by the beam-beam effect and varies from 2 to 8 hours. The luminosity decay rate is close to the beam-current decay rate as we operate in a region where the vertical beam size is greatly enlarged by the beam-beam effect and decreases as the beam current decays. In this region the luminosity is approximately proportional to current. The beams are maintained in collision for 2 to 4 hours before the injection cycle is repeated. We find that over a period of months the average luminosity delivered to the physics program is 25% of the peak achievable at the appropriate energy.

Two thirds of the SPEAR downtime occurred during an operating cycle when a vacuum loss led to contamination of approximately 30% of the ring, and necessitated an extensive bakeout to recover the required beam lifetimes and low backgrounds for the experimental program.

*Work supported by the U. S. Atomic Energy Commission.

†M. Allen, W. Davies-White, N. Dean, G. Fischer, J. Harris, R. Helm, L. Karvonen, M. Lee, R. McConnell, R. Melen, P. Morton, J. M. Paterson, J. Rees, B. Richter, A. Sabersky, P. Wilson, J. -E. Augustin, M. Harold, M. Matera, H. Wiedemann.

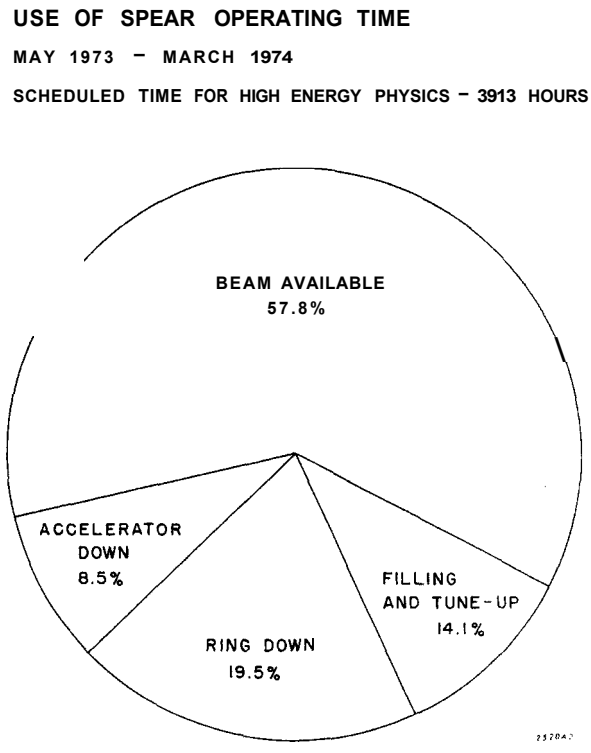


FIG. 2

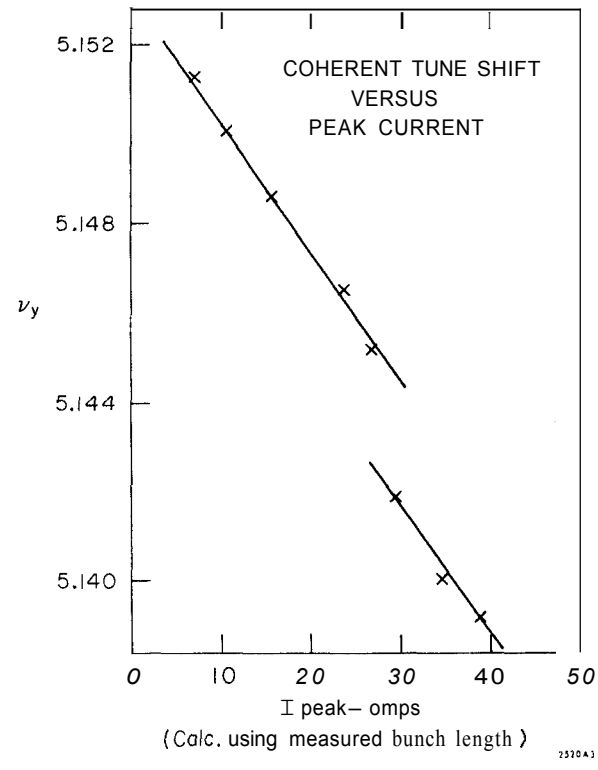


FIG. 3--Measured vertical betatron tune versus peak circulating current.

During the year the Stanford Synchrotron Radiation Project has built a laboratory which will use the synchrotron radiation emanating from one point on the SPEAR orbit.[4] It is planned to have several experiments in the field of solid state physics, chemistry, and biology operating in the upcoming running period. A pilot project using the x-ray beam was successfully completed in March of this year.

Single-Beam Performance

Several single-beam instabilities have been observed in SPEAR. They have been controlled, and currents of greater than 200 mA (10^{12} particles) have been stored in a single bunch at the injection energy of 1.5 GeV. Taking bunch lengthening into account, this corresponds to a peak current within the bunch of approximately 55 amps.

The first instability observed in SPEAR was a transverse betatron instability. The thresholds for the horizontal and vertical modes were similar and were 0.5 mA. The behavior of this instability as a function of the Chromaticity $[p(\delta\nu/\delta p)]$ is consistent with the theory of the barycentric mode 'head-tail' instability. The wake fields, which drive the beam, decay rapidly compared to the bunch separation in SPEAR, i.e., 20 nsec. When the lattice is adjusted to have positive chromaticity no instability is observed, but the wake fields then produce strong damping of coherent oscillations. This phenomenon has been studied and is discussed elsewhere in these proceedings.[5]

At higher currents, around 50 mA, a coherent vertical instability is again observed. A small increase in the chromaticity, to more positive values, raises the threshold to beyond 200 mA. A multi-bunch experiment shows that this is again a short wake-field effect as a second bunch, traveling 20 nsec behind an unstable bunch of higher current, is unaffected. The transverse coupling impedance of the beam to its surroundings leads to a tune shift for coherent oscillations. This has been measured and is shown in Fig. 3. The horizontal tune shift (not shown) is positive and five times smaller than the vertical. The magnitude of the tune shift is considerably larger than we would estimate from the known impedances (e.g., the chamber walls and ferrite kicker magnets)[6] in the vacuum system and may be due to the many transverse cavity-mode oscillations which the beam is observed to excite in each of the 20 SPEAR straight sections.[7] The break in the curve in Fig. 3 indicates a region where the shape of the tune spread line is complex and wide, $\Delta\nu$ FWHM $\simeq$ 0.005. At higher currents the tune spread line is again sharp. We do not understand this effect as yet, but it may be related to the vertical coherent instability which occurs at this current with appropriate chromaticity.

As has been reported previously, the phenomenon of bunch lengthening has been observed in SPEAR. Many measurements on this effect are reported elsewhere in these proceedings.[7] Briefly, it has been found that the ferrite injection kickers (now removed) made a significant contribution to the longitudinal coupling impedance and that many higher mode bunch-shape oscillations have been observed.

No intensity-dependent coherent phase instabilities (other than bunch lengthening!) have been observed. However, phase oscillations driven by higher order modes in the accelerating cavities and by rf system noise have been observed. They are controlled by either adjustment of the rf system or by phase feedback to the beam. Although not a single-beam effect, it is appropriate to include here the observation of coupled phase oscillations between counter-rotating bunches, Under certain operating conditions they have led to beam loss. The 0-mode oscillation, i.e., the bunches oscillating in phase, is strongly damped by the narrow-band phase feedback system, but the π-mode, out-of-phase oscillation, requires special treatment. Splitting the synchrotron oscillation frequencies of the bunches by a few per cent of the natural frequency completely removed these oscillations. The frequency splitting was achieved using a high-frequency cavity operating on the 122nd harmonic of the orbital frequency which was powered to give approximately 10 kV accelerating voltage.[8]

Coupled betatron oscillations have also been studied and are reported elsewhere in these proceedings.[9]

Colliding-Beam Performance

SPEAR has operated for physics experiments with colliding beam at 0.1-GeV intervals, between 1.2 GeV and 2.6 GeV per beam. The luminosity which was achieved over this energy range is shown in Fig. 4. With an almost constant lattice configuration the luminosity increases rapidly

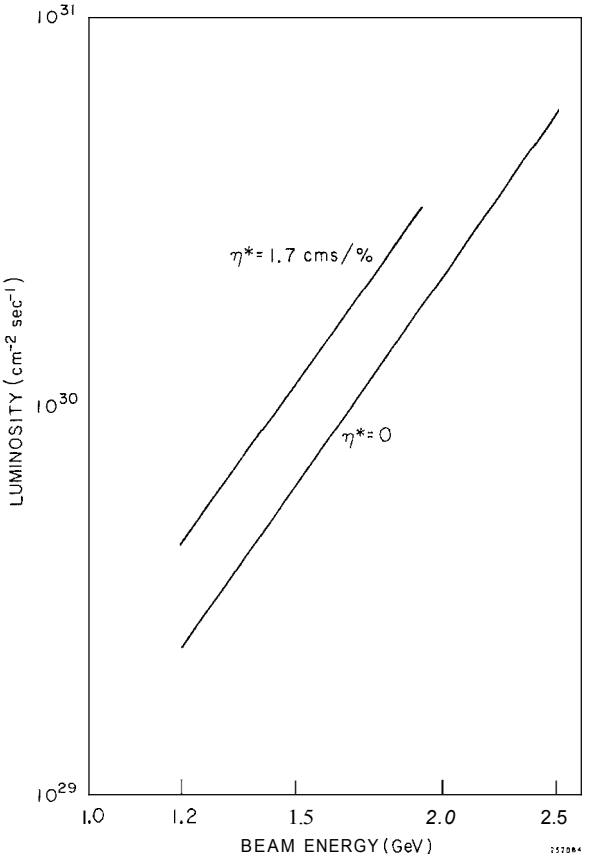


FIG. 4--Measured luminosity versus beam energy.

with energy, viz. , $L \propto E^4$ and the beam current (equal beams) at maximum luminosity increases approximately as the cube of the energy. These dependences are what one would expect for an energy-independent small-amplitude tune-shift limit and a 'natural' beam width, determined by quantum excitation, increasing linearly with energy.

This simple model is, however, complicated by the fact that the bunch length in SPEAR is comparable to the value of the vertical betatron function at the interaction point and the bunch length is a function of both the beam energy and the beam current.[7] We have found that the highest luminosity and highest colliding currents are achieved when the value of the vertical beta function equals the standard deviation of the bunch length, i.e. ,

$$\frac{\sigma_z}{\beta_y} \simeq 1, \quad \text{where } \beta_x >> \beta_y .$$

This means that at 1.5 GeV we operate with $\beta_y = 10$ cm and at 2.5 GeV $\beta_y = 20$ cm, and implies that the small-amplitude tune shift limit is higher at the higher energies. Calculations of the maximum tune shift can be done, using the the measured Iuminosity and currents as input.

$$\Delta\nu_y = \frac{2 e r_e \beta_y L F(\Delta\nu, \nu)}{\gamma I [1 + (\sigma_y/\sigma_x)]}$$

e is electronic charge,

r_e is classical electron radius,

γ is beam energy in units or rest mass.

The term $[1 + (\sigma_y/\sigma_x)]$ can be calculated from the luminosity and current, on the assumption that σ_x is unaffected by the beam-beam effect. To an accuracy of 10% in σ_x, this is consistent with our observations. The correction term $F(\Delta\nu, \nu)$ represents the perturbation to the lattice from the optical tune shift and, for the case of $\sigma_z/\beta_y \leq 1$ and $\nu_y \geq 0.1$, deviates from unity by no more than 10%. The value of $\Delta\nu_x$ can be calculated in a similar fashion. The calculated maximum tune shifts for a variety of lattice configurations and energies have been analyzed, and we find that the maximum $\Delta\nu_y$ is 0.025 ± 0.005 per interaction at 1.5 GeV and 0.035 ± 0.005 per interaction at 2.5 GeV. The complex dependence of luminosity and therefore $\Delta\nu$ on betatron tune at a fixed energy makes definitive analysis difficult, but we might say that the data suggest a trend. The calculated Av, is greater than the $\Delta\nu_y$ and can be as large as 0.06 per interaction in some configurations.

The complex nature of this problem and its importance in our understanding of the beam-beam limit has led us to attempt to measure directly the tune spread in colliding beams with the smallest perturbations possible to the interacting system of particles. The technique is still in development, but begins to show encouraging results. It is reported elsewhere in these proceedings.[10]

To increase the luminosity at the lower energies we must find a technique for enlarging the beam width at the interaction point. The beam height can be controlled by x-y coupling. However, in practice we find that the beam-beam effect enlarges the vertical size, maintaining an approximately constant particle density over a large range of current. The effective vertical height can also be controlled using small vertical crossing angles. SPEAR is equipped with the necessary electrostatic plates, but we have found that with the present bunch length and betatron function we cannot attain as high a luminosity using a crossing angle as with head-on collisions. It will be interesting to see whether this is still true in SPEAR II with its much shorter bunch lengths. (See below.)

When SPEAR was constructed, two techniques for beam enlargement were considered. One technique was a quasi-stochastic process, where a fast kicker magnet gave coherent kicks to the beam whose amplitudes were small compared to the beam size. Random application of these perturbations and the decoherence from the nonlinearities of the ring or from the other beam should lead to an enlarged beam. This technique worked well with single beams or with colliding beams of low current density. As the colliding currents were increased, the small amount of residual coherence led to instability, and independent control of the two beam sizes became impossible. No improvement in luminosity was achieved with this technique.

The other technique of beam enlargement is the introduction of momentum dispersion η^* at the interaction point.[1] As mentioned above, the complex lattice changes occur after injection with the beam stored. This proved troublesome at first until improvements in both hardware and software were made. Even now, we have explored only a small fraction of the lattice options which are available. During the past year the use of $\eta^* = 1.7$ m (i.e., 1.7 cm per percent became routine to increase the luminosity at the lower

energies. The luminosities obtained by this technique are also shown in Fig. 4.

A new technique of beam enlargement has been investigated recently and tested on SPEAR. This technique of 'mismatched η' is the subject of a separate paper in these proceedings,[11] and will not be discussed here in detail. The principle is that by allowing large variations in momentum dispersion through the standard lattice cells, while maintaining a constant average, one increases the natural betatron emittance given by quantum excitation and damping. Figure 5 shows the η function through one quadrant of SPEAR for two cases: matched-η with a non-zero η^* at the interaction region and a mismatched-η with $\eta^* = 0$ at the interaction region. These configurations give almost identical effective beam sizes, and the luminosities and currents agree with prediction. At a constant energy, the normal lattice $\eta^* = 0$, the $\eta^* = 1.7$ m and the 'mismatched η' give a constant ratio of maximum luminosity to current and therefore a constant maximum tune shift.

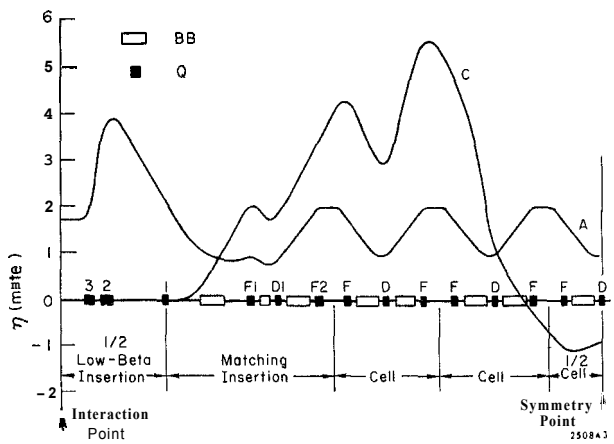


FIG. 5--Two lattice configurations used to increase the beam size at the interaction point
A 'Matched η' with $\eta^* = 1.7$ m
C 'Mismatched η' with $\eta^* = 0$.

In summary, the following table gives some typical SPEAR parameters which have been used over the past year.

TABLE I

	Colliding	Injection
Beam Energy	1.2—2.6 GeV	1.5 GeV
Max. Beam Current (single bunch)	45 mA × 45 mA (2.25×10^{11} particles)	>200 mA (> 10^{12} particles)
Max. Luminosity	$7 \times 10^{30} cm^{-2} sec^{-1}$	
Vertical Tune	5.10 - 5.13	5.15
Horizontal Tune	5.12 - 6.16	5.22
Vertical Beta Function at I.R.	0.1 - 0.2 m	0.1 m
Horizontal Beta Function at I.R	1.0 - 4.5 m	1.1 m
Momentum Dispersion at I.R.	0 - 1.7 cm/%	0

SPEAR II (Improvement Program)

The design of SPEAR incorporated the possibility of an eventual increase in maximum operating energy to between 4.0 and 4.5 GeV, limited by magnet saturation. To accomplish this goal, we need a substantial increase in rf and magnet power and vacuum improvements to handle the increased synchrotron-radiation load. We started on this improvement program 14 months ago and we will complete the installation of the equipment this summer. Testing of SPEAR II is planned for the SLAC operating cycle this fall and physics experiments are scheduled to begin at the higher energy in January, 1975.

RF System

The rf problems associated with the energy increase are considerable. A particle in SPEAR at 4.5 GeV loses 2.8 MeV per turn and still higher voltages are required to maintain an adequate quantum lifetime. Both the shunt impedance per unit length and the available straight-section length make it impractical to achieve these voltages at the present frequency of 50 MHz.

An analysis of cost versus frequency for a new rf system to meet the above constraints, gave a broad optimum around 300 MHz, and we selected 358 MHz (the 280th harmonic of the orbital frequency) for the new design. An accelerating system was designed around a cavity similar to that of the Los Alamos proton linac. A group of five a-mode, slot-coupled cavities is built into a single accelerator structure which matches the 3-meter straight-section length in SPEAR. Four such accelerators are being built.

One of the accelerators is shown in Fig. 6. They are machined from aluminum which has many cost and mechanical advantages over copper. One disadvantage of aluminum

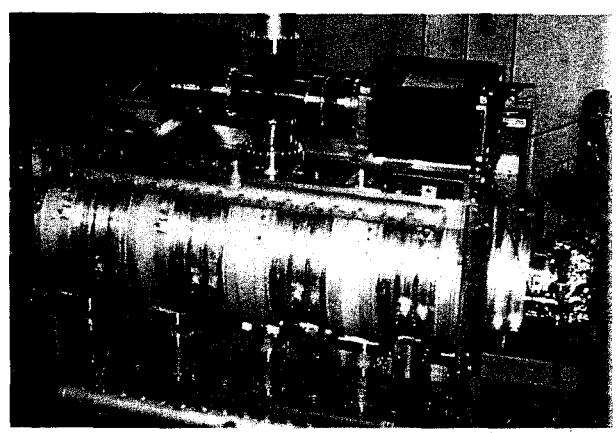


FIG. 6--Photograph of one of the four SPEAR II accelerator structures.

is that aluminum oxide has a high secondary-emission coefficient which can lead to multipactoring. This was overcome by coating the inside surfaces of the cavity with a few-hundred-angstrom layer of titanium nitride. The first accelerator section has been satisfactorily tested to its design limit of 75 kW of wall losses. The measured shunt impedance is 17.5 megohms per accelerator ($P = V^2/2R$) and this gives a transit-time-corrected accelerating voltage of 1.6 MV per accelerator. The four-accelerator rf system will therefore be capable of giving in excess of 6 MeV/turn to the beam.

There has been designed and developed at SLAC a 125-kW cw klystron and its associated power supplies. One klystron will feed each accelerator. The klystron is shown in Fig. 7. The first of the four klystrons has been tested to 125 kW cw into a dummy load and to 75 kW into an accelerator section. The klystrons operate at 41 kV with an efficiency of 50 to 55% as predicted by the design calculations. The assembly and testing program of this 500-kW rf system is under way and the system will be installed in SPEAR during July and August of this year.

A higher-frequency single cavity at 475 MHz is also being built and will be powered to 30 kW by an existing 50-kW transmitter. This system will be capable of splitting the synchrotron oscillation frequencies of the two counter-rotating bunches by 10% of the unperturbed frequency.

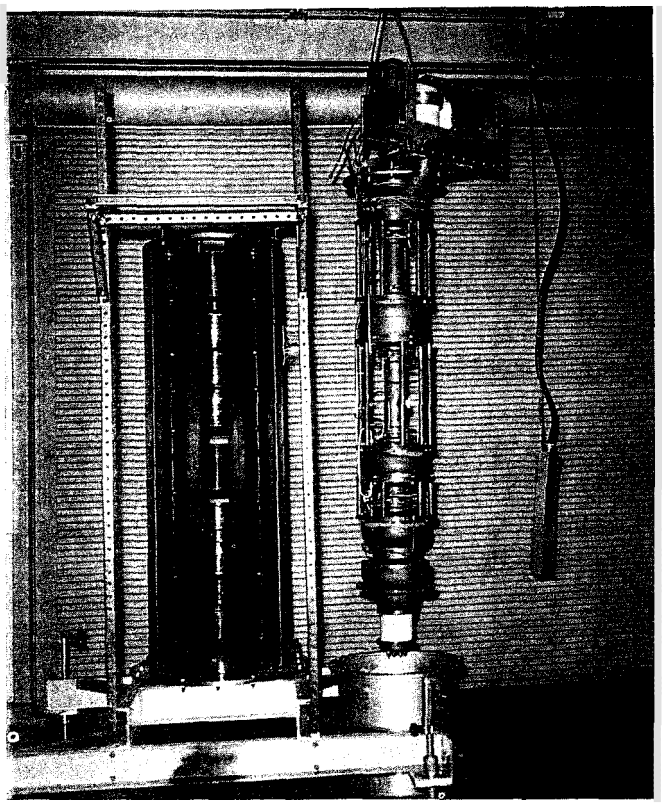


FIG. 7--Photograph of a SPEAR II, 125-kW cw klystron.

Magnet System

The only change to the magnet system itself is an increase in the water-cooling capacity. Most of this work has been completed. The additional 2.5 MW of dc power is obtained by adding a new power supply to the existing complement of power supplies and by a rearrangement in the utilization of these supplies. Although there is considerable work remaining, it involves no new technology. These changes will be made during July and August of this year.

Vacuum

To maintain good beam lifetime in the face of up to 300 kW of synchrotron radiation being deposited into the vacuum system, greater pumping capacity has been added to the SPEAR straight sections and interaction regions. The average pressure in the arcs was 6×10^{-11} torr/mA at 1.5 GeV and it increases approximately linearly with energy. The distributed ion pumps inside the bending-magnet chambers have adequate speed but the straight-section pumps have been increased from 100 ℓ/s to 400 ℓ/s.

The four ferrite injector kicker magnets absorbed considerable power[7] from the beam at high currents raising the pressures locally to the 10^{-7} torr range. These kickers have now been removed and replaced with an open-coil design.

Expected Performance

The single-beam performance is difficult to predict as we will be increasing the peak current densities because of the seven-fold increase in rf frequency. SPEAR's arsenal of beam-control devices and its flexibility may be needed to control instabilities and accumulate the high currents which we will be capable of colliding at the high energy. To maintain the present injection rates into a much shorter bunch, a new high-current, short-pulse gun is being developed for SLAC. An intriguing possibility lies in the fact that the fast coherent damping that we observe[5] may allow a faster injection repetition rate than the 20 pps, which is determined by the radiation damping at 1.5 GeV. Some tests of this indicated a possible 50% improvement in injection rate.

The two-beam performance is easier to predict ignoring any single-beam limitations. We believe that the luminosity will continue to increase as E^4 and the current as E^3 up to approximately 3.8 GeV. At that point the rf power to the beams equals 300 kW, and beyond that we will be rf-limited. The luminosity should peak at around 3 to $4 \times 10^{31} cm^{-2} sec^{-1}$ at 3.8 GeV. The extrapolation from the present performance is shown in Fig. 8 (cf. Fig. 4). We eagerly await the opportunity to study this new regime of SPEAR operation and of elementary particle physics.

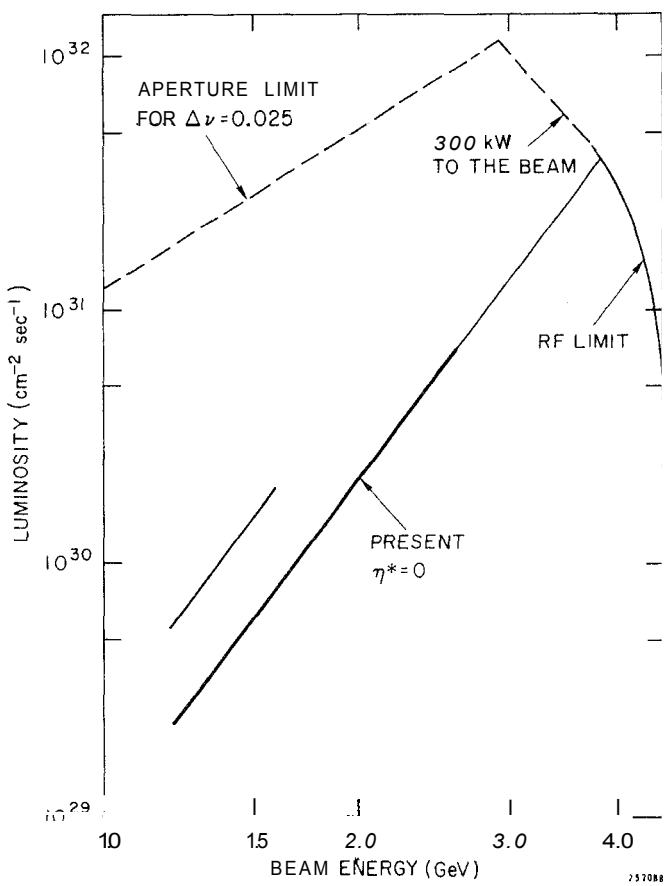


FIG. 8--Operating region of luminosity and energy in SPEAR II.

Acknowledgments

We wish to thank T. Taylor and the SPEAR operations group for their continuing excellent efforts, T. Gromme and A. King for their programming efforts and A. Gallagher for his general engineering coordination.

References

1. Stanford Linear Accelerator Center Storage Ring Group, Proceedings of the 8th International Conference on High Energy Accelerators, CERN 1971, p. 145.
2. SPEAR Storage Ring Group, Proceedings of the 1973 Accelerator Conference on Accelerator Engineering and Technology, IEEE Transactions, Vol. NS-20, p. 752.
3. Boyarski et al., Automatic Control Program for SPEAR Proceedings of 1973 Accelerator Conference on

Accelerator Engineering and Technology, IEEE Trans. NS-20, 580 (1973).
4. H. Winick, Stanford Synchrotron Radiation Project, these Proceedings.
5. SPEAR Group, Fast Damping in SPEAR, these Proceedings.
6. G. Fischer, Miscellaneous Single-Beam Observations, SPEAR-173 (1974, unpublished).
7. M. Allen et al., Observations on Bunch Lengthening in SPEAR, these Proceedings.
8. M. Allen et al., Operation of the SPEAR RF System, IEEE Trans. on Nucl. Sci. NS-20, 373 (1973).
9. SPEAR Group, Beam-Beam Coupling in SPEAR, these Proceedings.
10. A. Sabersky, Direct Measurement of Beam-Beam Tune Spread in SPEAR, these proceedings.
11. R. Helm et al., Beam Enlargement by Mismatching the Energy Dispersion Function, these Proceedings.

DISCUSSION

Mark Barton (BNL): In the single beam phenomenon, the ν shift vs. current has a series of breaks in it, isn't that what we expect from a single resonant structure with a deflecting mode resonant at that or one of the knock-out frequencies?

Paterson (SLAC): No, not a single mode, because these breaks are independent of the actual tune. You can operate at different tunes and still have the same behavior. It is not a single resonant system, it has to be a broad band system.

Gerhard Fischer (SLAC): If you're speaking of an rf deflecting mode in the box, yes, the single system in a box is a good model.

Barton: Yes, we're talking about a deflecting mode?

Paterson: Yes, if we look at any of our position monitors, we see not one, but many modes being excited in the straight sections as the 50 amps of peak current goes through, it is in the GHz frequency band. We see many sharp lines with Q's of several hundred. Now, we have not identified which one does bunch lengthening and which one causes transverse instabilities, but we certainly are convinced that they are all part of the structure of both transverse and longitudinal effects. Gerry Fischer will be talking on Monday about this.

Sergio Tazzari (Frascati): Did you say that the variation of luminosity versus energy was not quite E^4?

Paterson: The luminosity varies between E^4 and $E^{4.5}$

Tazzari: I wanted to remark that Bassetti has been working independently during this last year on this beam dimension control. We have some results and a preliminary paper on some work at Frascati on the same type of system.

It is a very interesting approach and it is being seriously studied for application in PEP.

DORIS, PRESENT STATUS AND FUTURE PLANS

DESY Storage Ring Group*

Deutsches Elektronen-Synchrotron DESY
Hamburg, Germany

Presented by D. Degèle

Summary

Experience with the double storage ring DORIS during its first *4* months of operation is described. The maximum average current of about 160 mA for positrons and *750* mA for electrons is limited by single beam instabilities due to interaction with higher modes in the rf cavities. The head-tail effect has not been observed so far. At currents of 130 mA and 300 mA, respectively, a luminosity of $2 \cdot 10^{29}$ $cm^{-2}sec^{-1}$ was measured.

Introduction

After **3** days of injection studies the first beam was stored in DORIS on December 20. During the first 4 months of this year, the properties of the storage ring were investigated, the stored beam currents were increased and the luminosity was measured.

The same *80* scientists, engineers and technicians who have designed and constructed the storage ring are now operating and developing the system further with the support of other DESY groups.

I shall report here on the machine physics investigations that have been done on our storage ring. A large fraction of our total effort was, at the same time, absorbed by technical investigations and difficulties.

Survey of DORIS parameters

DORIS is a double storage ring consisting of two vertically stacked single rings that are separated over most of their length. The beams stored in these two rings cross at two interaction points with a vertical crossing angle of *24* mrad.

The large aperture quadrupoles adjacent to the interaction points are the only magnets that are common to both beams (Fig.1). These magnets are followed by two bending magnets which vertically separate the beams and, after a drift space, by another two vertical magnets which make the beams parallel again at a vertical spacing of *80* cm. The subsequent straight section contains *4* rf cavities and *4* quadrupoles in each ring; it is followed by the curved quadrant consisting of *3x2* bending and *3x2* quadrupole magnets.

The ring circumference is *288* m, and the bending radius within the magnets is 12 m.

The rf accelerating frequency is *500* MHz, corresponding to a harmonic number of *480*. Thus, the machine can be filled with up to *480* bunches at a bunch separation of 60 cm.

*J. Le Duff (visitor from University of Paris, Orsay, France), J. Maidment (visitor from Rutherford Laboratory, Chilton, Didcot, England), E. Daßkowski, D. Degèle, H.C. Dehne, H. Gerke, D. Heins, K. Hoffmann, K. Holm, E. Jandt, R.D. Kohaupt, J. Kouptsidis, F. Krafft, N. Lehnart, G. Mülhaupt, H. Nesemann, S. Patzold, H. Pingel, A. Piwinski, R. Rossmanith, H.-D. Schulz, K. Steffen, H. Wiedemann, K. Wille, A. Wrulich.

DORIS Parameters

double storage ring with vertical crossing

crossing angle		*24* mrad
no. of interaction points		2
circumference		*288* m
radius of curvature in horizontal bending magnets		*12* m
rf frequency		*500* MHz
harmonic number		*480*
present operating conditions		
working point	Q_x	7,24
	Q_z	5,18
max. amplitude functions	x max	
	$\beta_{z\ max}$	60 m
amplitude functions at interaction point	β_x	0,3 m
	β_z	*1,3* m
beam dimensions at interaction point at *2* GeV	$2\sigma_x$	1 mm
	$2\sigma_z$	.4 mm
rf power per ring		*500* KW
no. of cavities per ring		*8*
shunt impedance		*24* MΩ
max. rf voltage		*4.5* MV
injection rate at *25* % efficiency	e^-	*30* mA/sec
	e^+	2 mA/sec

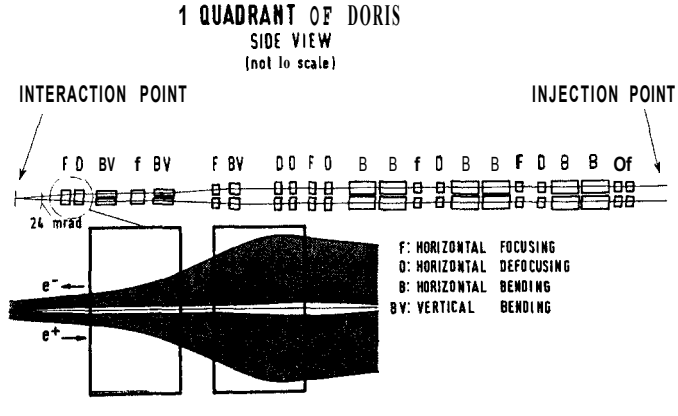


Fig. 1

Injection is done at 2 GeV from the DESY synchrotron. By employing the old *40* MeV linac as electron source and the new *400* MeV linac as positron source, we have available in a pre-selected pulse-to-pulse sequence up to 12 pulses of electrons and up to 25 pulses of positrons per second. During the remaining synchrotron cycles, electrons are accelerated for high energy physics experiments. The pulse currents obtained from the synchrotron are about 10 mA of electrons and *300* µA of positrons.

In order to allow a flexible choice of storage ring optics, the different quadrupole magnets are fed by individual power supplies. For both rings, we thus need 25 power supplies of high stability and good tracking accuracy during energy variation.

Present technical status of DORIS

Most of the components were delivered on schedule and could be assembled before the end of last year. I shall mention here only those parts that are not yet complete.

One third of the magnet power supplies is still missing. By connecting magnets in series that are planned to be powered independently, we are able to operate up to an energy of about 3 GeV.

The system of 60 position monitors is not yet operational. This system employs inductive loops detecting the 1 GHz component of the beam current. Difficulties arose from the large number of coax relais in the multiplexer system, which turned out to be unreliable. Therefore, a systematic measurement and correction of the closed orbit has not been possible *so* far,

The bake-out units for the vacuum system are only being delivered and assembled now.

The maximum currents

All investigations to be described here have been done at our injection energy of 2 GeV, for convenience. The energy variation with a stored beam was tried for some time and was difficult until we used a magnet training program, defining the magnetic history. In this way, it was possible to accelerate a stored beam to 3 GeV.

At present, our stored currents are limited by single beam instabilities. The maximum v-shift due to space charge forces by the other beam was measured during luminosity runs to be of the order of 10^{-3}; it has not yet been a limitation.

We have so far observed 3 types of single beam instabilities, all of them excited by higher modes in the rf cavities. Since these modes have high *Qs*, the threshold of the instability depends only on the average current. If only part of the ring is filled with bunches, a correspondingly higher current can be stored in this part. The cavity modes shown in Fig.2 have been observed to appear at the threshold of the instabilities; their frequencies were also observed in the beam spectrum.

The mode frequencies of the synchrotron and betatron oscillation modes in the beam are of the type [1]

$$(m \cdot B + n) \cdot f_o \pm f_{s,\beta} \qquad \begin{matrix} m,n \text{ integer} \\ m = 0,\ldots,\infty \\ n = 0,\ldots,B-1 \end{matrix}$$

with B being the number of bunches, f_s the synchrotron frequency, f_β the betatron frequency and f_o the revolution frequency.

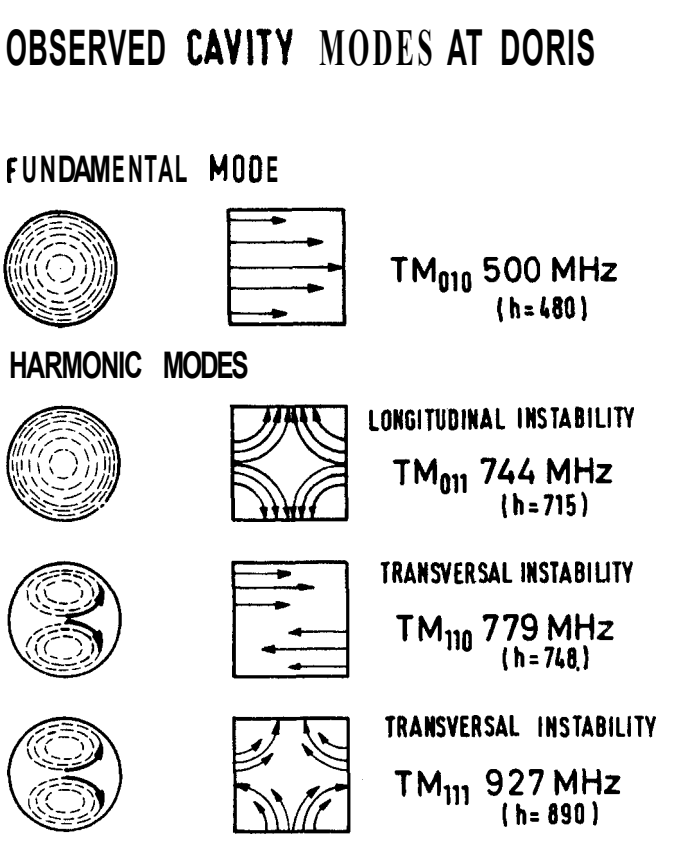


Fig. 2

Since our revolution frequency is close to 1 MHz and the betatron frequency is about (n + 0.25) MHz, the mode frequencies of the beam are rather uniformly distributed with a spacing of about 500 kHz, and, to avoid instability, none of these frequencies can be allowed to coincide with any of the parasitic modes in a cavity. With many cavities in a ring and high shunt impedances, unusually strong instabilities may ensue.

We fight the vertical instability with octupole magnets which produce Landau damping, thereby increasing the threshold from 10 mA to over 100 mA.

For the horizontal oscillations, we do not achieve a sufficient damping with the available octupole magnets. Here, an rf quadrupole is helpful which operates on the 15^{th} harmonic and shifts the betatron frequencies between subsequent bunches. So far, we have installed an rf quadrupole in the positron ring only. Its maximum v-shift is $Av = 1 \cdot 10^{-2}$. The decoupling, however, becomes effective at about $Av = 1 \cdot 10^{-3}$ already.

For suppressing longitudinal modes of oscillation, the synchrotron frequencies of subsequent bunches can

be decoupled by operating the two rf transmitters at frequencies corresponding to the harmonic numbers *480* and *481*. The sum of the rf voltages is then amplitude modulated by 1 MHz, and different bunches have different synchrotron frequencies.

In principle, electrons exhibit the same instabilities as positrons. However, the nonlinear field of the ions collected in the electron beam causes a coupling of horizontal and vertical betatron oscillations and also Landau damping. Thus, the vertical beam dimension of the electron beam is increased, the thresholds are higher, and the instability effects are less pronounced. A ν-shift due to the ions is observed, too; an example, measured at bad vacuum conditions, is shown in Fig.3. To keep this effect within limits, we must partly remove the ions. This is done with ∿ 120 pairs of small clearing electrodes operated at a few kilovolts.

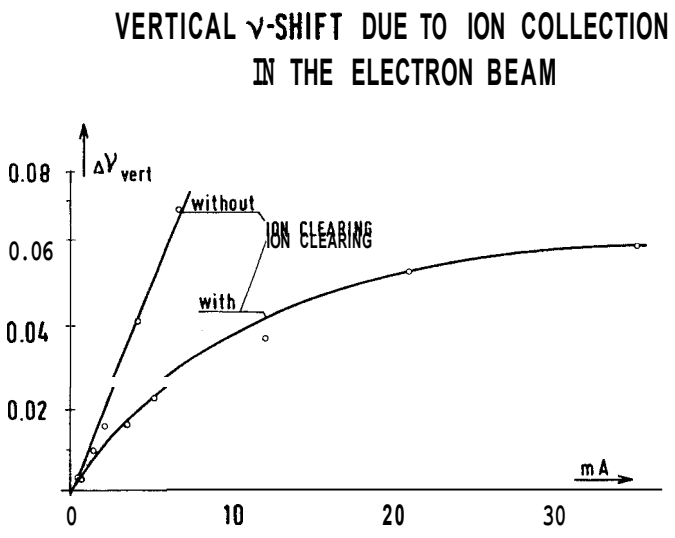


Fig. 3

With all this it is possible, at present, to store average beam currents of 750 mA electrons and 160 mA positrons.

With these currents, we had no indication of a head-tail effect; we do not normally compensate the chromaticity which is -14 in the horizontal and -7 in the vertical direction.

The beam life is limited by the vacuum. The first bake-out of about 3/4 of the vacuum system was done in April. Before baking, the pressure rise by the beam was about $3 \cdot 10^{-10}$ Torr/mA at 2 GeV; after baking, it reduced to $6 \cdot 10^{-11}$ Torr/mA. Thus, at 500 mA the typical pressure is $3 \cdot 10^{-8}$ Torr corresponding to a beam life of 1/2 hour. During the *4* months of operation, the vacuum improved steadily even without baking, being slightly influenced only by repeated let-up to air.

The injection efficiency is 25 % when injection is well adjusted. It is strongly affected by the choice of the $\nu_x - \nu_z - \nu_s$ working point. For an unfavourable choice, the large horizontal betatron oscillations at injection are coupled into the vertical direction where the acceptance of our machine is 5x smaller. Therefore, injection on a coupling resonance is as impossible as on a second or third order resonance. For all these resonances, we have observed satellite stop bands produced by coupling between synchrotron and betatron oscillations. In the vicinity of the coupling resonance $\nu_x - \nu_z = 2$, for example, injection is bad or impossible at a distance of one or two times ν_s on both sides (Fig.4).

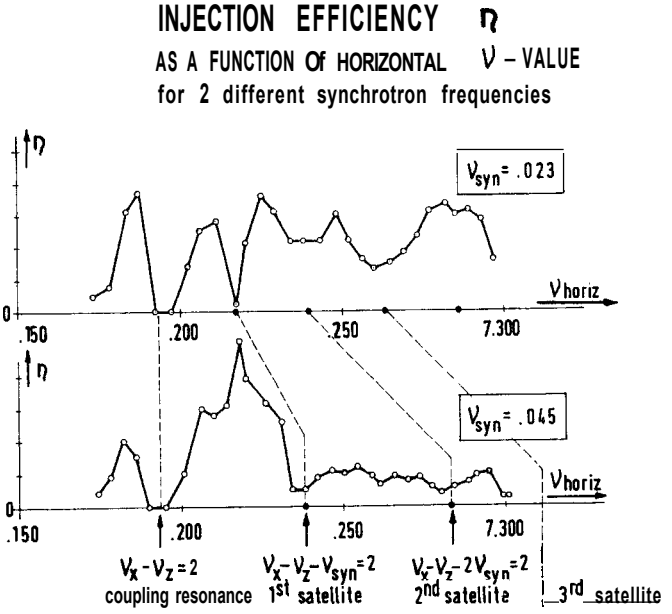


Fig. *4*

There is also a strong nonlinear coupling of betatron oscillations away from coupling resonances (Fig.5).

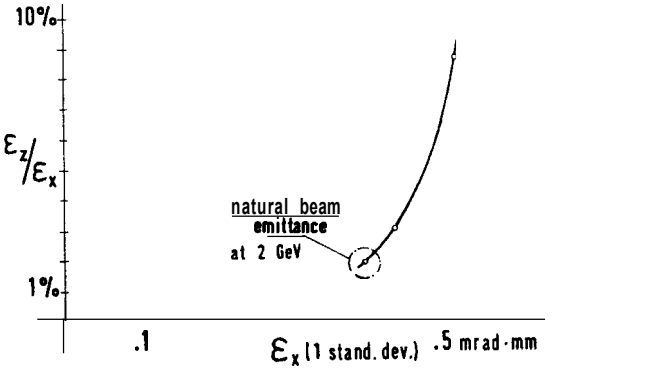


Fig. 5

In studying the rather strong resonances and coupling in our machine, we localized a strong non-linear effect in the large aperture quadrupoles, although the integral field of these magnets had been carefully linearized by shimming. When shifting the beam position in these magnets with a local beam bump, we observed variations of the v-value as shown in Fig.6. We believe that the effect is caused by the end fields of these quadrupoles, which are traversed by the beam off-center and at an angle (2). We shall try to correct the effect with additional magnets. This will be especially important when we go to a smaller beam size at the interaction point and to correspondingly larger amplitude functions in the quadrupoles.

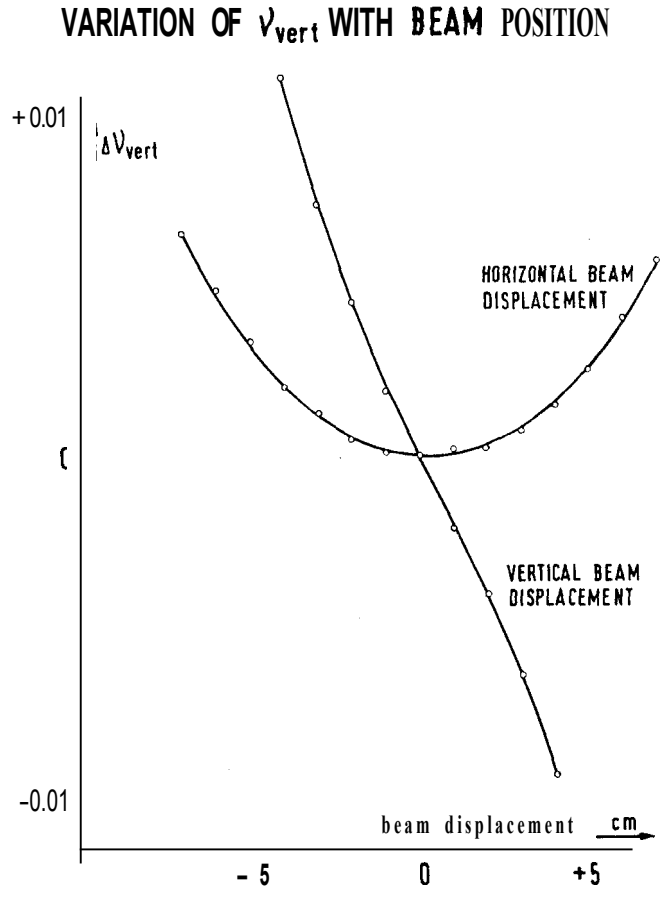
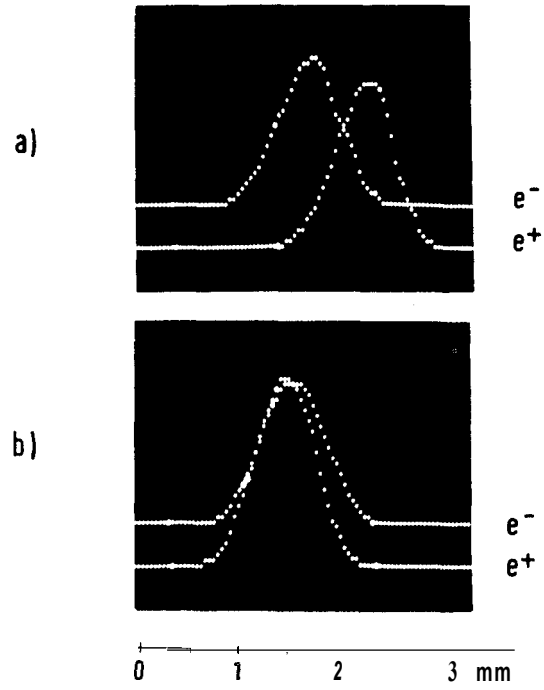


Fig. 6

Luminosity measurement

With the maximum currents reached so far, we did preliminary luminosity measurements. The positions and dimensions of the two beams at the interaction point are measured with a horizontal and a vertical carbon fibre, respectively, which is 5 μm thick and moves across the beam at a speed of 1.7 m/sec. The signals from 2 downstream gamma counters are used for adjusting both beams to the same position: they are shifted with local beam bumps until the two signals arrive simultaneously (Fig.7). - After transverse adjustment, the correct phasing between the two rings must be found. The simplest indication is the v-shift imposed on the positron beam by a strong electron beam.



SPILL COUNTER SIGNAL FROM CARBON FIBRE AT INTERACTION POINT

a). before
b). after
} horizontal alignment of the two beams

Fig. 7

The luminosity is determined from small angle scattering. Around each interaction point, 4 counter triplets are mounted at an angle of 52 mrad. The cross section of this counter assembly is $4.5 \cdot 10^{-30}$ $cm^2 GeV^2$.

The luminosity obtained at currents of 300 mA of e^- and 160 mA of e^+ is $2 \cdot 10^{29}$ $cm^{-2} sec^{-1}$. The measured value is in good agreement with the value derived from

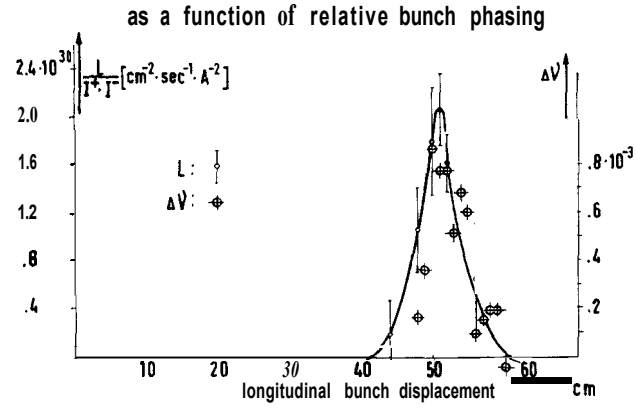


Fig. 8

the beam currents and cross sections. The variation of specific luminosity and ν-value with longitudinal bunch displacement is shown in Fig.8.

In order to increase the luminosity, first of all the stored beam currents must be increased . i.e. we must learn to control the effect of the parasitic cavity modes. In addition, we will aim at a smaller beam cross section at the interaction point. Since we are limited, at present, in the average current, a higher luminosity may also be obtained by reducing the number of bunches.

Status of experimental preparation

Along with our first storage attempts, counter background measurements have been done in the vicinity of the interaction points.

Near one of the interaction points the PLUTO magnet is being installed. This is a superconducting solenoid of **1.4** m diameter and 20 kG with additional solenoids at both ends to compensate the effect of the longitudinal field. By August of this year the magnet will be equipped with Charpak chambers and other detectors and will be wheeled into its final location.

At the other interaction region, DASP is being assembled, a double arm spectrometer incorporating a 500 t double gap magnet. This experiment is also scheduled to start in autumn of this year.

A smaller experiment on inclusive n^{O}-production has been set up and will take first data before the big assemblies are completed. Another small experiment with NaJ counters and without magnetic field is also being prepared.

Future plans for DORIS

At some time during the summer we plan to test the e^{-}-e^{-} operation. The problem is that, in this case, the common quadrupoles give opposite deflection and focusing to both beams and thus prevent a very low β at the interaction point. Consequently, the luminosity will be somewhat smaller than in the e^{+}-e^{-} case.

Next year we will increase the maximum energy which is now limited to **3.5** GeV by the magnet power supplies. A new main power supply, sufficient for magnet excitation up to 5 GeV, has been ordered and is to be installed in spring of 1975. Our present rf power is sufficient for 5 GeV if we can double the shunt impedance of the rf cavity system. To achieve this, we can choose between two alternatives: We can either restrict ourselves to a single ring, single bunch operation and transfer all our cavities into one ring, or we can build a new cavity system. Such new cavities could, for example, be of the same type as is needed for a 20 GeV storage ring which is presently being considered (3).

In order to avoid possible difficulties arising from energy variation with a stored beam, the maximum transfer and injection energy for DORIS will also be increased to **5** GeV (4).

Finally, preparations are on the way to inject protons into one of the DORIS rings (5) at about the middle of next year. We want to do storage ring studies on the collision between a bunched electron and a coasting proton beam as well as high energy physics experiments on e-p interaction.

References

(1) R.D. Kohaupt, **DESY** Interner Bericht **H1-74/2 (1974)**

(2) J. Le Duff, DESY Interner Bericht **H-74/1 (1974)**

(3) H. Wiedemann, DESY Interner Bericht **PET-74/1 (1974)**

(4) A. Wrulich, DESY Interner Bericht **H1-74/1 (1974)**

(5) Proceedings of the Seminar on e-p and e-e Storage Rings, DESY **73/66 (1973)**

Andrew Sabersky (SLAC): In the graphs for luminosity and $\Delta\nu$ shown separately as a function of longitudinal bunch displacement, how did you measure the $\Delta\nu$?

Degkle (DESY): We excited the beam with an rf exciter and we measured the ν value during the crossing of the two beams by observing the enlargement of the beam due to this exciter.

Harold Hahn (BNL): Could you say something about PETRA?

Degkle: No

Gus Voss (DESY): There is a study going on at DESY on the e--e+ storage ring which would go up to 20 GeV or a little higher depending on how much rf power is available. We think that from the progress and the set-up which we have, we can in such a scheme use DORIS as an intermediate storage ring to improve positron filling, but there are many ideas going around. We hope that perhaps by the middle of this year the tentative study could be concluded. There is also some talk about use of superconducting cavities.

Jean Buon (Orsay): What would be the reduction factor of luminosity with e^--e- operation mode of DORIS?

Degele: We have had no experience with e^--e- operation.

Buon: Yes, but that increases the beta function. What would the increase in the beta be?

Degkle: I could say five or two, but pi is a nice number.

Mervyn Hine (CERN): Do the SPEAR people expect to have trouble with transverse cavity modes?

Ewan Paterson (SLAC): Yes.

Hine: Why did you not say so?

Paterson: There is one bunch in SPEAR and any instability can be always controlled by feedback if the feedback is good enough; with the multibunch system you have a different problem. We do have longitudinal instabilities which are controlled by a feedback system in our present cavity—it is not a problem.

Ednor Rowe (University of Wisconsin): Did I understand you to say that the vertical beam dimension changed with chromaticity in the storage ring.

Degkle: Below the threshold, no. When we reach the threshold for vertical excitation of the beam by a higher mode then the sextupoles have damping in this mode so the beam size is somewhat smaller not larger.

Ronald L. Martin (ANL): What will you use for the proton source?

Degele: The linac and the Van De Graf and then accelerating the protons in the synchrotron DESY before transferring them to the storage ring.

Peter Schuler (Yale University): Have you had any experience with the compensation coils planned to replace the screening coil which shields the beams at the interaction point from the detector field?

Degele: We hope that there is no interaction which destroys our beams. But we have had no experience with those compensation coils. We have calculated the effect and from the calculation we see that it might be possible to compensate for the situation.

DESIGN AND STATUS OF DCI

P. Marin

Laboratoire de l'Accélérateur Linéaire
Université de Paris-Sud, Centre d'Orsay,
Orsay, France.

Summary

The main characteristics of DCI are first briefly reminded. The present status is then presented, as well as the schedule for the completion of Ring 1 and Ring 2. The expected performances are given for Ring 1 operating with e^+e^- beams and for Ring 1 and Ring 2 operating in the e^+e^+ and $e^\pm e^\pm$ mode of functionning. Typical aspects of these are emphasized concerning the use of DCI for high energy physics and synchrotron light research.

1. Description of the machine

DCI is a machine for intermediate energies, E_{max} = 1.8 GeV, aiming at a luminosity for e^+e^- annihilation in the range of 10^{32} cm^{-2} s^{-1}. It consists of two superposed rings with two circulating beams in each one. The space charge compensation scheme' should allow to reach the design luminosity with conventional β function in the meter range and stored currents below 1 A (see fig. 1).

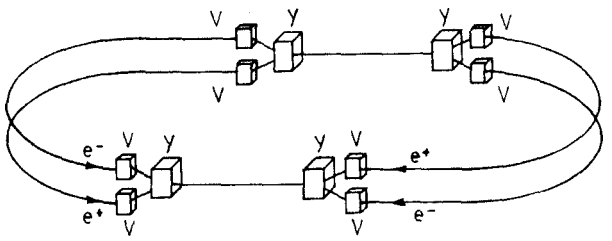


Fig. 1 : The four-beam charge compensation scheme.

Each ring has 4 half periods containing 3 horizontal 30" bending magnets (H), 2 vertical 10° bending magnets (V and Y) and 7 quadrupoles arranged in doublets except for the last one. Two straight sections 6 meter long, common to both rings, are used one for injection, the other for experimentation. The 4 beams will cross at the center of each of these. In practice, this limits the machine to the one-bunch mode operation.

Due to the lack of available space and to the maximum energy chosen for the machine, it has not been possible to incorporate in the design a matched insertion section. However the number of independant quadrupoles allows one to use different operating points with transition energies between 1.3 and 1.65 GeV for an RF power of 125 kW per beam.

The accelerating cavities work on the 8th harmonic of the revolution frequency. Injection of both beams will take place at the energy of 1.2 GeV. When filling one bunch only, the injection speed should be of the order of 6 A/h. For experiments which require one beam in each ring the filling of the 8 bunches should he made at the speed of 20 A/h.

2. Status

The general lay-out of the machine is given in fig. 2.

2.1 Injector

In order to produce a positron beam of energy 1.2 GeV, the Linac has been modified to a large extent. A positron converter is now installed at the end of the first 1 GeV part of the Linac. From recent tests carried out after only 4 accelerating sections one expects to reach on the target a peak current of 0.6 A with a pulse duration of 20 ns. The converter immersed in a focussing lens is followed by 6 accelerating sections surrounded by a 0.2 T solenoid. The positron beam is refocussed by doublets and triplets of quadrupoles over 1.2 GeV. A peak current of 1.6 mA is expected at the end of the Linac. Switching from a positron beam to an electron beam should be done in a few minutes. This part of the program is nearing completion.

2.2 Transport system

Two beam transport Lines will be used for injection in both ways. They match the emittance of the positron beam from the Linac to the acceptance of the machine. The optical magnification is about 1/5. The magnetic fields of the two transport lines can be reversed within a few minutes to switch from a positron beam to an electron beam. The North transport line should be completed at the end of 1974 and the South line 3 months later.

2.3 Magnets and quadrupoles

All the elements for both rings have been ordered. The bending magnets for Ring 1 are installed on their supports and connected. The last 9 magnets for Ring 2 which are not yet delivered are in a well advanced stage in the factory. 33 out of 48 quadrupoles are on the site and the rest is nearing completion. 8 special quadrupoles for the vertical arms of the 2 rings will arrive rather late in October or November this year. The machining of the bending magnets and of the quadrupoles is well within the tolerances (in fact $3\ 10^{-2}$ mm for the magnet gaps and 2 or $3\ 10^{-2}$ mm for the quadrupole aperture.

Besides the main coils, the quadrupoles are equipped with secondary quadrupolar coils for the separation of the wave numbers of the 2 rings. Furthermore 16 quadrupoles in each ring will have sextupolar windings.

2.4 Pulsed magnets

The pulse magnet system, which will work at the repetition frequency of 25 Hz, is made of 2 inflectors and 4 kickers. The inflectors are conventional iron cored septum magnet, 15 × 15 mm^2 useful aperture,

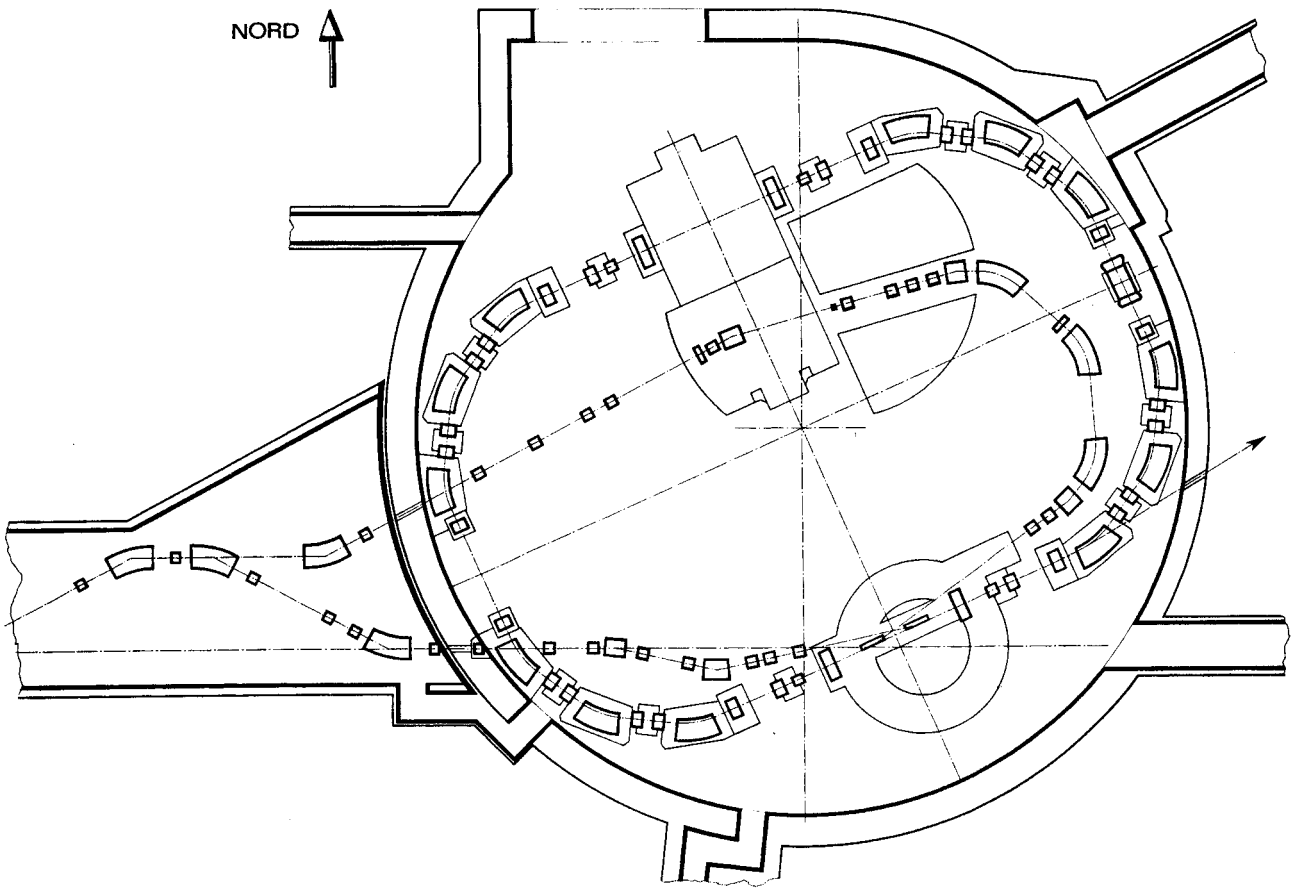


Fig. 2 : General lay-out of DCI

placed outside the vacuum chamber. The pulsed power supplies are completed and will soon be installed for tests.

The 2 kickers of each ring are separated by one half betatron wave length. They are of the full aperture type with an open ferrite circuit and will use CX 1192 thyratron switches. All the elements of the pulsed power supplies have been delivered except for the impedance transformer.

The whole system for Ring 1 should be ready in place at the end of the year.

2.5 RF

A 110 kW RF transmitter has been built in the laboratory and was tested at full power on a dummy load. An RF cavity has also been built and was tested at a power of 40 kW, corresponding to an accelerating voltage of 400 kV. The cavity is of a simple coaxial shape capacitively loaded by plates. It is made of pure aluminium and operates at 37° C. The cavity is completely evacuated. Power tests have shown that a good vacuum can be obtained after a reasonably short processing without baking out. Both the cavity and the RF transmitter are now installed in place. They will be connected by a 50 m long, 200 mm in diameter, coaxial line. The line has a characteristic impedance of 50 Ω and is matched at both ends by equivalent ideal transformers which also compensate for the loop impedance. The length of the line is $n\lambda/2$. It will be air cooled at full power.

The cavity for Ring 2 is being ordered just now. In the final stage each cavity will be driven by a 350 kW transmitter able to deliver 250 kW to the beams of each ring.

2.6 Vacuum chamber

Most of the elements of the vacuum chamber are made of stainless steel and have internal water cooled synchrotron light absorbers. The geometry of these absorbers is particularly complicated in the region between the horizontal and vertical magnets and has led there, to use copper chamber elements cooled from outside.

The total pumping speed for ring is 80 000 ℓ/s. At injection and during the process of rising the energy, high voltage electrodes are needed to separate electron and positron orbits. At 1.8 GeV, 50 kV would be needed. Until now a safe operation has been reached up to 40 kV.

At the moment 40 % of the vacuum chamber elements have been tested in the laboratory at the pressure of 1×10^{-10} Torr. The vacuum chamber for Ring I should be ready by the end of 1974.

2.7 Computer control and beam observation

The computer control system of DCI consists basically of a PDP 11/40 with a 48 k memory, associated with a one million word disk, a card reader and a magnetic tape unit. Two PDP 11/05 will manage for routine operation of the power supplies.

A real time monitor RSX 11 D will allow multiprogramming. Development of new programs will then be possible during normal machine operation. The interfacing of the computer system uses Camac modules.

The computer will do 4 essential jobs :

- Control of the power supplies, namely the main power supplies for the ring, correcting coils, sextupolar windings and part of the transport system power supplies. This includes the coupled variation of several element according to a predefined schedule.

- Control of the pulsed magnets : tuning, amplitude and commutation.

- Handling of the beam positron monitoring and display of the results.

- Interfacing with the operator through CRT screens allowing display of tables and curves and the selection of programs.

Two terminals consisting of an alphanumeric keyboard and two CRT screens will he provided.

Besides computer control, a manual operation of all the elements will be possible.

The computers have been already delivered. All the extra regulated power supplies and the Camac system should be delivered by September 1974. The software is expected to be operational next spring.

The beam control system includes the usual elements : beam positron monitor, measurement of beam profile and beam intensity. The power amplifier for beam excitation (wave number measurement, beam enlargement, feedback) delivers over 1 kV on a 10 pF electrode. A special system is designed to detect the beam positron in the interaction region with a reproducibility of a few 10^{-2} mm.

3. Expected performances

There will be 2 stages for DCI depending on the availability of Ring 1 and Ring 2.

- 1st Stage : Ring 1, e^+e^- beams

The luminosity curve and the current needed in each beam are given in fig. 3, for an available RF power of 35 kW/beam. The maximum luminosity is in the range of a few 10^{30} cm^{-2} s^{-1} at a transition energy variable between 1.4 and 1.7 GeV. During a long period of time the detectors for physics experiments on DCI will be somewhat shorter than the straight section. Two quadrupoles could therefore be installed in this section, as well as in the injection section, so as to reduce the β^*_s by a factor 2, in the hope of increasing the luminosity.

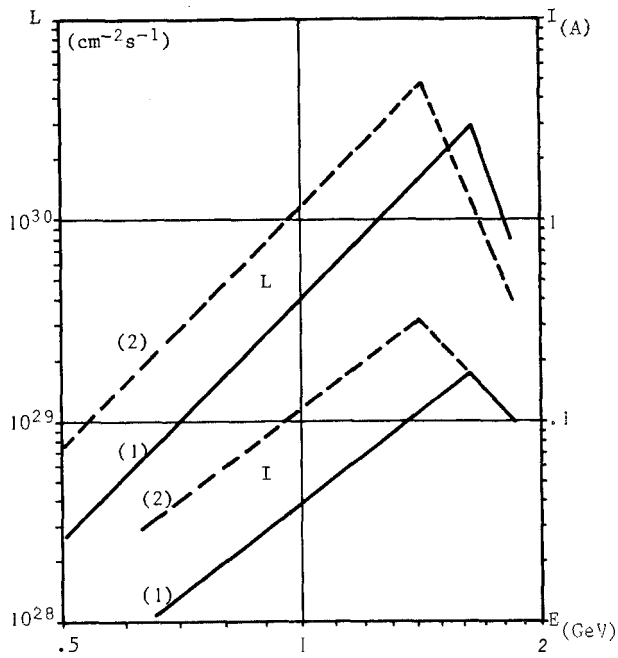


Fig. 3 : DCI - One Ring e^+e^-

$\beta^*_x = \beta^*_z = 2$ m — One bunch per beam

Av = .05 — P_{RF} = 35 kW per beam

Curves (1) $\nu_x = 4.155$ — Curves (2) $\nu_x = 3.845$

$\nu_z = 2.155$ — $\nu_z = 2.845$

- 2nd Stage : Ring 1 and Ring 2, e^+e^+ beams

The luminosity curve and the current needed in each beam are given in fig. 4, for an available RF power of 250 kW/ring. Each beam will have 8 bunches. The luminosity is in the range of 10^{31} cm^{-2} s^{-1}. This mode of functionning is envisaged for the use of DCI for two-photon experiments. Unwanted e^+e^- annihilation events are then suppressed. A rather good luminosity as well as a good duty cycle is obtained. Further, tagging systems can be used with maximum efficiency behind the Y magnets adjacent to the experimental section. In these three respects DCI is probably the best machine, if any, to carry out such experiments.

Ring I and Ring 2, e^+e^- collisions

Fig. 5 give the ultimate performances of the machine with an available power of 125 kW/beam. The luminosity is in the range of 10^{32} cm^{-2} s^{-1}. One feels at Orsay that even a factor 10 below these figures would still make DCI, a very attractive machine in its energy range.

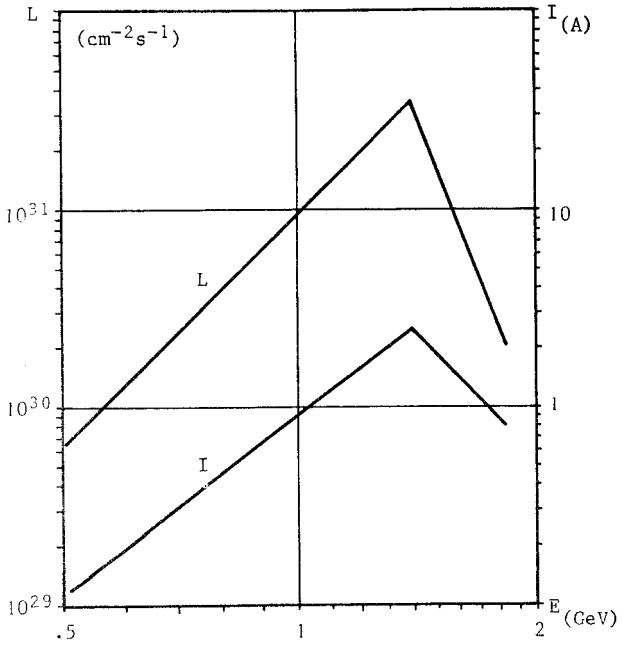


Fig. 4 : DCI - Two Rings e^+e^+

$\beta^*_x = \beta^*_z = 2$ m
$\Delta\nu = .05$
8 bunches per beam
$P_{RF} = 250$ kW per beam
$\nu = 3.845$
$\nu = 2.845$

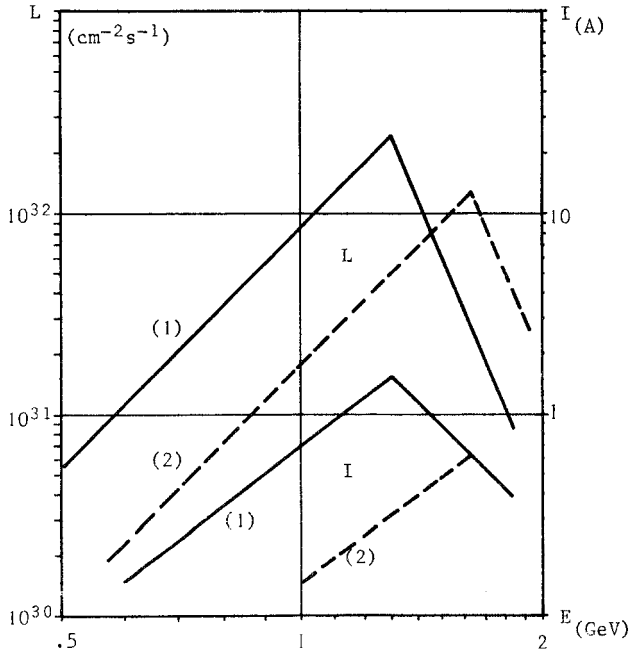


Fig. 5 : DCI - Two Rings $e^\pm e^+$

$\beta^*_x = \beta^*_z = 2$ m
$K\Delta\nu_o = .3$
Curves (1) $\nu_x = 3.845$
$\nu = 2.845$
One bunch per beam
$P_{RF} = 125$ kW per beam
Curves (2) $\nu = 4.845$
$\nu = 2.845$

4. Schedule and physics program

It is expected that the basic components for Ring 1 and the North transport line should be ready by the end of *1974* or the very beginning of next year and the South transport line, 3 months later. Ring 2 would then need another year to be completed.

One therefore hopes to start doing physics with one ring in September *1975* and with *2* rings in September *1976*.

A physics program is being laid down now. It will probably involve the use of a detector for charged and neutral particles and then a magnetic detector (actually in installation on ACO). Two-photon experiments are also proposed which would use, besides tagging systems, one of these two detectors. The building up of a large, weak field many purpose magnetic detector is also widely supported by Orsay physicists.

5. Synchrotron light research at Orsay

4 large effort is developping in France towards using synchrotron radiation from ACO and DCI. A beam line has been opened at the beginning of *1973* on ACO, which allows at the maximum energy of this machine *(540* MeV) , the use of synchrotron light down to *6* Å (max. at 20 Å). From *1976* on, this machine will be entirely devoted to this type of research and several others beams could be opened.

A similar effort is being made on DCI with the opening next year of a first beam line which will extend the use of very intense beams down to *0.65* Å (max. at *1.8* **8).** The construction of a hall for experimentation in the close vicinity of DCI will start this year together with the major components of the beam line. A national institution under the name of LURE* has been created for this purpose.

Reference

1. J.E. Augustin et al., Proceedings of the VIIth International Conference on High Energy Accelerators, Erevan (1969), vol. 2, p. 113.

*Laboratoire d'Utilisation du Rayonnement Electromagnétique (C.N.R.S. et Université Paris-Sud).

NON-DESTRUCTIVE DIAGNOSTICS OF COASTING BEAMS WITH SCHOTTKY NOISE

J. Borer, P. Bramham, H.G. Hereward, K. Hübner, W. Schnell, L. Thorndahl
CERN, Geneva, Switzerland

Summary

The finite number of protons in a circulating beam gives rise to statistical fluctuations in the beam current and beam's centre of gravity. This Schottky noise is used to monitor the distribution of particles in longitudinal momentum as well as to measure the extrema of the Q-values in a stack without any interference with the beam coasting for many hours. It is also instrumental in detecting the growth of betatron amplitudes at particular orbits of a stack, which helps to discern presence and strength of non-linear resonances.

Theory

The statistical noise due to the incoherent motion of particles in a coasting beam can be calculated from the signal of one particle. At the azimuth of a pick-up station the line charge density of the i'th proton is a sequence of delta-functions:

$$\lambda_i(t) = \frac{e}{R} \sum_{\ell=-\infty}^{+\infty} \delta(2\pi f_i t + \theta_i - 2\pi \ell) \qquad (1)$$

where e is its charge, f_i its revolution frequency, θ_i its azimuth at $t = 0$, and $2\pi R$ is the machine circumference. This can be Fourier analysed: in terms of non-negative frequencies:

$$\frac{\quad}{\quad}\left(1 \quad \sum_{n=1}^{\infty} \cos n(2\pi f_i t + \theta_i)\right)$$

it is a spectrum of lines with frequency spacing f_i and mean square values

$$2\left(\frac{e}{2\pi R}\right)^2$$

We have present particles with their f_i in some range, say f_o to $f_o + \Delta f_o$: then for any one given n the resulting frequencies of *(2)* are in a band of width $n\Delta f_o$. To avoid confusion we work in the region

$$n < f_o/\Delta f_o$$

so that this band does not overlap those belonging to the neighbouring n-values. In the ISR this means working below $n \sim 3000$, or 1 GHz. The signals contributing to this band are given by the n'th term in (2), summed over all the particles:

$$\sum_i \lambda_{i,n}(t) = \frac{2e}{2\pi R} \sum_i \cos n(2\pi f_i t + \theta_i) \qquad (3)$$

Let the spectrum of revolution frequencies be defined by $N(f_i)\, df_i$, the number present in an interval df_i at f_i. We take an idealised model of a spectrum analyser; when tuned to a frequency f it responds to all signals in a small interval δf , called its resolution, and evaluates their root mean square. The number of particles contributing is therefore

$$N\left(\frac{f}{n}\right)\frac{\delta f}{n} \qquad (4)$$

and the result is

$$\lambda_{rms}(f) = \frac{2e}{2\pi R}\left\langle \left[\sum_{\delta f} \cos n(2\pi f_i t + \theta_i)\right]^2 \right\rangle^{\frac{1}{2}} \qquad (5a)$$

$$= \frac{\sqrt{2}e}{2\pi R}\left[N\left(\frac{f}{n}\right)\frac{\delta f}{n}\right]^{\frac{1}{2}} \qquad (5b)$$

where the summation is restricted to the particles *(4)* A necessary assumption for going from (5a) to (5b) is that the particles in any group having all the same revolution frequencies f_i must have randomly distributed phases $n\theta_i$, so we are excluding cases where the beam has any coherent disturbance.

This (5b) is effectively Schottky's formula [1] for the statistical fluctuations of a d.c. currenr. It shows that the spectrum analyser gives out the spectrum of particle revolution frequencies, with a scale Eactor n in *the* abscissae and a square root function in the ordinates.

Now consider one particle making transverse betatron oscillations. At the azimuth of the pick-up station it will have a vertical displacement given by

$$z_i(t) = z_o + A_i \cos(2\pi Q_i f_i t + \phi_i) \qquad (6)$$

where z_o is the closed orbit displacement and A_i the particle's betatron amplitude at that azimuth.

A difference pick-up responds to the line dipole density, which we call d. d_i is given by multiplying (1) or (2) by (6), and its expansion in single frequencies is

$$d_i(t) = \frac{e}{2\pi R} z_o + A_i \cos(2\pi Q_i f_i t + \phi_i) + 2z_o \sum_{n=1}^{\infty} \cos n(2\pi f_i t + \theta_i) + A_i \sum_{n=1}^{\infty} \cos(n - Q_i)(2\pi f_i t + \psi_i) + A_i \sum_{n=1}^{\infty} \cos(n + Q_i)(2\pi f_i t + \chi_i) \quad (7)$$

Again it is possible to work in the region of n low enough that the bands belonging to different n values do not overlap, and to look with the spectrum analyser at any of the three n'th terms in (7), summed over all the particles.

We note in passing that information about the closed orbit z_o may be obtainable from the transverse signals in the "longitudinal", nf_i , frequency band. Calculating the root mean square in δf , as before, the $n \mp Q$ bands give

$$d_{rms}(f) = \frac{\sqrt{2}e}{2\pi R} A(f) [N_n(f)\, \delta f]^{\frac{1}{2}}$$

where $N_n(f)$ is the number of particles per unit interval of

$$f = (n \mp Q_i) f_i$$

and $A(f)$ is their rms amplitude.

In the general case Q-spread, f_i-spread and amplitude will all affect the spectra and need to be disentangled, but any marked feature like big amplitudes or missing particles occurring at some specific tune Q_k and revolution frequency f_k will show up as a spike or slot at the frequencies $f = (n \mp Q_k) f_k$ for every n.

Application

Figure 1 shows a scan in the frequency domain of the noise picked up from the coasting beam. It is the difference signal derived from two parallel plates located on opposite sides of the beam. The central peaks are enhanced by a resonant transformer which was used to form the difference. The small spikes arise from the longitudinal Schottky noise; they are harmonics of the revolution frequency f_o = 320 kHz. The transverse Schottky noise gives the large signals corresponding to Fourier expansion of the incoherent motion into slow and fast transverse waves. Their different spread in frequency is determined by the interplay between Q-spread and spread in revolution frequency. In the case of slow waves, $f = (n - Q) f_o$, the contributions of the two spreads add up if the accelerator is operated above transition and with positive chromaticity. Thus the signals are wider. The opposite holds for the fast waves, $f = (n + Q) f_o$. The Q-value was ~ 8,63 when this scan was made.

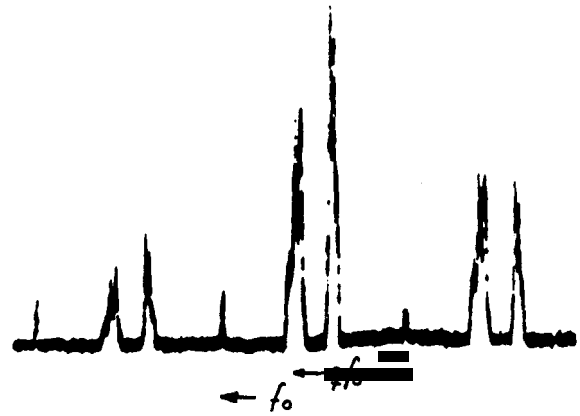


Fig. 1 - Frequency spectrum of the difference signal derived from two plates and induced by the Schottky noise in the beam. Small peaks harmonics of the revolution frequency. Large peaks fast and slow transverse waves.

Longitudinal Schottky scan

Scanning one of the harmonics of the revolution frequency in detail gives the longitudinal Schottky scan. The signal is taken from a sum pick-up, is amplified and displayed in the frequency domain by a HP 141 T frequency analyser. A substantial improvement in signal to noise ratio is achieved by averaging the analogue output of the analyser over many sweeps by means of a 1000 point HP 5480 B signal analyser. The choice of the harmonic is a compromise between conflicting requirements. At a too high frequency the harmonics start to overlap, at a too low harmonic the averaging takes too long because the sweep time of the analyser has to be increased for the same resolution.

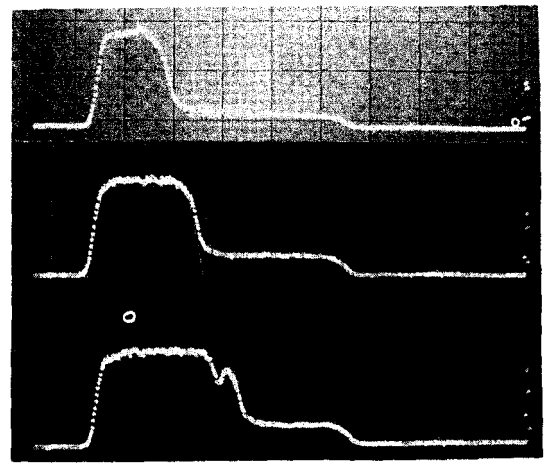


Fig. 2 - Longitudinal Schottky scan taken at different intensity levels during build-up of a stack (10 A, 15 A, 19 A). Average over ~ 2000 samples. $\Delta p/p$ = 6.4 % per hor. Division.

Figure 2 shows a sequence of longitudinal Schottky scans taken during the build-up of a stack. Typically, one averages over 2048 sweeps which takes 1,7 minutes. Figure 3 shows that a longitudinal Schottky scan provides the same information as a scan made by sweeping empty RF buckets through the stack. Moreover, the Schottky scan is not interfering with the beam in any way. This is an important point since the empty bucket scan turned out to be a rather gross perturbation of the coasting beams.

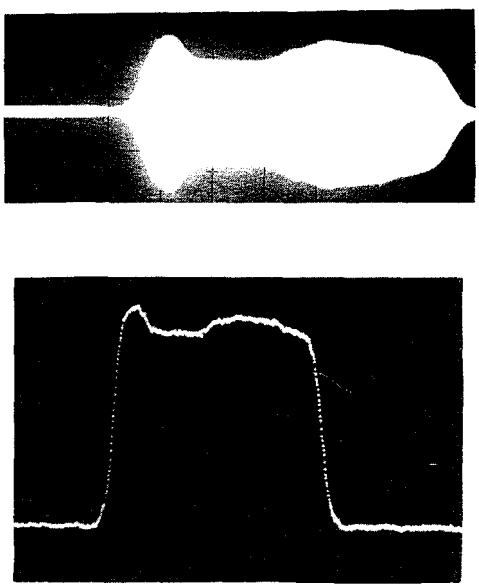


Fig. 3 - Scans of the longitudinal density in a stacked beam.

a) sweeping empty RF buckets through the beam

b) longitudinal Schottky scan

For these reasons the Schottky scan has becomethe standard technique in the ISR for measuring density in longitudinal momentum space. It is used operationally to monitor the mean momentum and the momentum spread of stacks coasting for many hours. It is also a valuable tool to detect the density variations due to beam loss at particular orbits caused by non-linear resonances, or due to diffusion in momentum space,

Transverse Schottky scan

Vertical Schottky signals in the low frequency range (5 - 20 MHz) are obtained with a resonant difference transformer connected to electrodes above and below the beam. Radial signals are obtained similarly from a pair of lateral electrodes. At higher frequencies (20 MHz - 2 GHz) where the capacitive coupling between beam and electrodes is increased, signals can be obtained with a 50 Ω hybrid transformer, using its difference output. The signals from the resonant transformer are fed to a high impedance low noise amplifier, those from the 50 Ω hybrid to a 50 Ω low noise amplifier. Then the signal is scanned in the frequency domain and suitably averaged as in the case of the longitudinal scan.

The transverse Schottky scans are mainly used to find the maximum and minimum Q-values of a stack. A large Q-spread in the stack is needed to prevent transverse coherent instabilities of the coasting beam. This Q-spread can be just accommodated between lower order non-linear resonances [2] known to be harmful. Hence, an accurate, "on line" monitoring of the stack extension in the Q-plane is imperative. The usual technique is to display scans of a slow and a fast wave, which are adjacent in frequency, on the same screen by mixing down the fast wave scan. Corresponding points of the stack will appear on opposite sides of each scan. By measuring the real frequency difference Δf between these points one can calculate the non-integral part of the Q-value

$$q = 0{,}5 + (\Delta f / 2 f_0)$$

where f_0 is the revolution frequency in the middle of the stack. Figure 4 shows two such scans. Each of them represents an average over 6000 sweeps of the frequency analyser. The sampling lasts 10 minutes in total. It is obvious from the figure that the ends of the distribution are quite well defined and that the frequency difference can be measured to better than 1 kHz. This means in turn a precision of 10^{-3} in the absolute value of q.

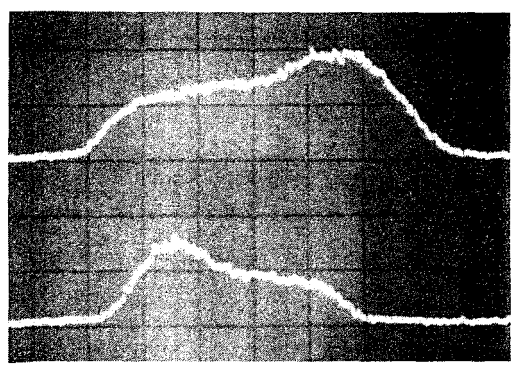


Fig. 4 - Transverse Schottky scan of a 6,5 A beam. Average over ∿ 6000 samples. 2 kHz/hor. Division.

upper trace: scan of slow wave $f = (43 - Q_V) f_0$

lower trace: scan of fast wave $f = (26 + Q_V) f_0$ displaced downwards in frequency by 76 kHz

Since the transverse Schottky scan gives the rms dipole moment as a function of the betatron frequency, one can observe changes in the rms betatron amplitude at a particular Q-value and orbit, provided that no beam loss occurs at this orbit; and the latter can be checked with the longitudinal Schottky scan. Figure 5a gives the vertical Schottky scan of a 15 A beam after stacking. Comparison with Figure 5b, a repetition of the scan after 80 minutes, shows a clear amplitude growth at distinct places. Figure 5c is identical to Figure 5b apart from the higher resolution of the former. The large peaks are due to 8th order resonances whereas 11th order resonances caused the smaller peaks.

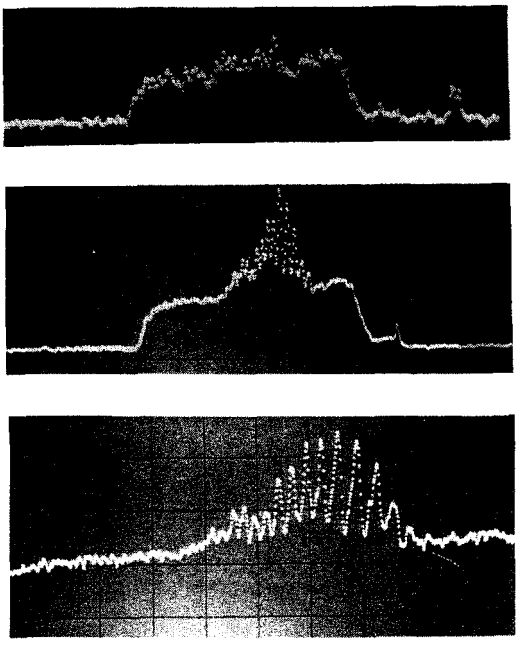


Fig. 5 - Transverse Schottky scan of the slow wave $f = (43 - Q)f_o$ showing amplitude growth due to 8th order and 11th order non-linear resonances.

a) after stacking $\Delta Q = 0{,}016$/hor. Division

b) 80 min. later $\Delta Q = 0{,}016$/hor. Division

c) same as b) $\Delta Q = 0{,}0063$/hor. Division

A further application is the monitoring of the position and extension of slots cut by RF knock-out in the particle distribution. Such a cleaning operation is needed if the beam position is so close to strong resonances that periodical removal is needed of those particles which diffused towards the resonances.

References

1) W. Schottky; Über spontane Stromschwankungen in verschiedenen Electrizitätsleitern. Ann. Physik 57, p. 541 (1918).

2) P. Bryant; Dynamic compensation during stacking of the detuning caused by space charge effects. Contribution to this conference.

BEAM LOADING IN HIGH-ENERGY STORAGE RINGS*

P. B. Wilson

Stanford Linear Accelerator Center
Stanford University, Stanford. California 94305

Summary

The analysis of beam loading in the RF systems of high-energy storage rings (for example, the PEP e-e+ ring[1]) is complicated by the fact that the time, T_b, between the passage of successive bunches is comparable to the cavity filling time, T_f. In this paper, beam loading expressions are first summarized for the usual case in which $T_b \ll T_f$. The theory of phase oscillations in the heavily-beam-loaded case is considered, and the dependence of the synchrotron frequency and damping constant for the oscillations on beam current and cavity tuning is calculated. Expressions for beam loading are then derived which are valid for any value of the ratio T_b/T_f. It is shown that, for the proposed PEP e-e+ ring parameters, the klystron power required is increased by about 3% over that calculated using the standard beam loading expressions. Finally, the analysis is extended to take into account the additional losses associated with the excitation of higher-order cavity modes. A rough numerical estimate is made of the loss enhancement to be expected for the PEP RF system. It is concluded that this loss enhancement might be substantial unless appropriate measures are taken in the design and tuning of the accelerating structure.

Summary of Beam Loading Expressions for $T_b \ll T_f$

We consider Hrst the case for which the time between bunch passages is short compared to the filling time for the fundamental and all higher-order cavity modes up to a cut-off frequency determined by the bunch length and the dimensions of apertures coupling the cavity to the outside world. We assume also that these higher-order mode frequencies are sufficiently removed from being integral multiples of $1/T_b = N_b f_0$ (where N_b is the number of bunches and f_0 is the revolution time) so that no higher-order mode is resonately excited. Beam loading can then be characterized by a continuous RF current at the fundamental mode frequency having a peak value (for short bunches) equal to twice the average circulating current. Beam loading in circular machines in this limit has been anaiyzed previously.[2] We will use here a somewhat different approach and notation. In this notation, a tilde is used to denote a complex (phasor) quantity, while a quantity without a tilde denotes absolute value. For convenience, $-\tilde{i}_0$ is taken as the reference direction (real axis), where $\tilde{i}_0$ is the beam current; the accelerating component of a phasor voltage is then obtained by taking the real part. All phasors are assumed to vary as $e^{j\omega t}$. In Fig. 1, $\tilde{i}_g$ gives the phase of the incident wave from the external generator. Angle θ is the phase of the external generator with respect to $-\tilde{i}_0$, and ϕ is the phase between $-\tilde{i}_0$ and the net cavity voltage, $\tilde{V}_c$. Using superposition, $\tilde{V}_c$ is the sum of a generator-produced voltage, $\tilde{V}_g$, and a beam-induced voltage, V_b. The vector addition $\tilde{V}_g + \tilde{V}_b = \tilde{V}_c$ is illustrated in Fig. 1.

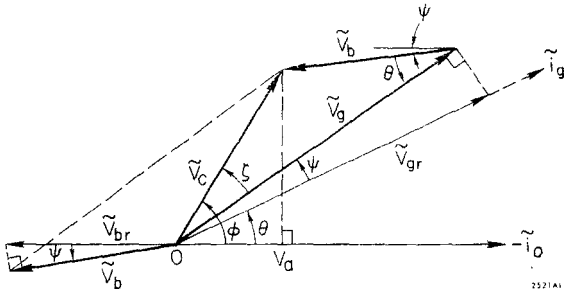


FIG. 1--Diagram showing vector addition of voltages in an RF cavity.

*Work supported by the U. S. Atomic Energy Commission.

The voltage $\tilde{V}$ produced across a parallel resonant circuit with shunt resistance R and driving current i is $V/R = \tilde{i}/(1+j\xi) = \tilde{i}\cos\psi e^{j\psi}$. In this expression ψ is the tuning angle shown in Fig. 1 and defined by $\tan\psi = -\xi = -2Q_L(\omega-\omega_0)/\omega_0$, where Q_L is the loaded Q, ω is the driving frequency and ω_0 is the cavity resonant frequency. We define now a coupling coefficient β, such that β/R is the internal shunt conductance of the external generator. Physically, β is the ratio of the power emitted from the coupling aperture to the power, P_c, dissipated in the cavity walls with the external generator off and the cavity internally excited (by beam loading, for example). The following expressions for the magnitudes of V_g and $\tilde{V}_b$ can now be derived:

$$V_g = V_{gr}\cos\psi; \qquad V_{gr} = \sqrt{RP_g}\,\frac{2\sqrt{\beta}}{1+\beta} \tag{1a}$$

$$V_b = V_{br}\cos\psi; \qquad V_{br} = \frac{i_0 R}{1+\beta} \tag{1b}$$

Here P_g is the incident (available) power from the generator, i_0 is the average circulating current, * and V_{gr} and V_{br} are the magnitudes of $\tilde{V}_g$ and $\tilde{V}_b$ at resonance.

From the vector diagram in Fig. 1, the basic expression for the accelerating voltage is

$$V_a = V_c\cos\phi = V_{gr}\cos\psi\cos(\theta+\psi) - V_{br}\cos^2\psi \tag{2}$$

In designing an RF system for a storage ring, we are normally given the syncnronous energy gain, eV_s, determined by the magnet lattice; the synchrcnous phase angle, ϕ, required to maintain an adequate quantum lifetime (alternatively, the peak cavity voltage $V_c = V_s/\cos\phi$ can be specified); and the circulating current i_0. We want to know the required generator power as a function of tuning angle and coupling coefficient. From Fig. 1 we have

$$V_c\sin\phi = V_{gr}\cos\psi\sin(\theta+\psi) - V_{br}\cos\psi\sin\psi. \tag{3}$$

Using this expression in Eq. (2) to eliminate $(\theta+\psi)$, and Eq. (1a) to express the result in terms of the available generator voltage $\sqrt{RP_g}$, we obtain

$$\sqrt{RP_g} = \frac{V_c}{\cos\psi}\left[\frac{1+\beta}{2\sqrt{\beta}}\right]\left\{\left[\cos\phi + \frac{i_0 R}{V_c(1+\beta)}\cos^2\psi\right]^2 + \left[\sin\phi + \frac{i_0 R}{V_c(1+\beta)}\cos\psi\sin\psi\right]^2\right\}^{1/2}. \tag{4}$$

Suppose now that a feedback system is available which can keep the reflected voltage wave in the input line to the cavity real by adjusting the cavity tuning; that is, to cancel out the reactive component of the induced beam-loading voltage. The reflected voltage wave can be real only if $\tilde{V}_c$ and $\tilde{i}_g$ as shown in Fig. 1 are co-linear. This condition in turn implies that $\zeta+\psi=0$. Since $\zeta+\psi+\theta=\phi$, then we must have also that $\theta=\phi$. Using the laws of sines on the vector triangle in Fig. 1 together with these relationships between

*The expression for V_{br} is valid in the limit of short bunches. For long bunches, i_0 must be multiplied by a bunch form factor, b_0, given in Appendix A. Note also that the shunt impedance is defined such that power and voltage are related by $P = V^2/R$.

angles, $V_{br}\cos\psi/V_c = \sin\zeta/\sin\theta = -\sin\$/\sin\phi$. The tuning angle for real reflected power becomes

$$\tan\psi = -\frac{V_{br}}{V_c}\sin\$ = -\frac{i_0R}{V_c(1+\beta)}\sin\$ \quad . \tag{5}$$

For this case, Eq. (4) reduces to

$$\sqrt{RP_g} = \frac{1+\beta}{2\sqrt{\beta}}\left[V_c + V_{br}\cos\phi\right] \quad . \tag{6}$$

If we now differentiate Eq. (6) with respect to β to find the value of coupling coefficient, β_m, which minimizes the required generator power, we obtain

$$\beta_m = 1 + \frac{i_0R\cos\phi}{V_c} = 1 + \frac{i_0R\,V_s}{V_c^2} \quad . \tag{7a}$$

The generator power at β_m is calculated, using Eq. (7a) in Eq. (6), to be $\sqrt{RP_g} = V_c\sqrt{\beta_m}$. The efficiency for the transfer RF power to the beam is $\eta = P_b/P_g = i_0V_s/P_g = (\beta_m-1)/\beta_m$. The power dissipated in the cavity walls is $P_c = V_c^2/R = P_g/\beta_m = P_b/(\beta_m-1)$. By conservation of power, the reflected power is in general $P_r = P_g - P_b - P_c$. It is seen that the reflected power reduces to zero for $\beta = \beta_m$. The tuning angle at $\beta = \beta_m$ is obtained, using Eq. (7a) in Eq. (5), as

$$\tan\psi_m = -\left[(\beta_m-1)/(\beta_m+1)\right]\tan\phi \quad . \tag{7b}$$

Phase Oscillations and Phase Stability

If the phase oscillations of the bunch about the synchronous phase angle are to be stable, then the above transition $dV_a/d(t-t_s)$ must be negative, where $(t-t_s)$ is the arrival time of the bunch at the cavity gap measured with respect to the arrival time of a synchronous particle. The arrival time of the bunch relative to a synchronous particle is related to their difference in phase by $\omega(t-t_s) = \theta-\theta_s$. Therefore, another way of saying the same thing is that $dV_a/d\theta$ must be negative. From Eq. (2) we then obtain the simple condition that $\sin(\theta+\psi) > 0$, or

$$0 < (\theta+\psi) < \pi \quad . \tag{8a}$$

It is easy to show that this condition is one of the stability conditions first derived by Robinson.[2] Using Eq. (3), this condition can be written

$$V_c\sin\phi + V_{br}\cos\psi\sin\psi > 0 \quad . \tag{8b}$$

If a feedback circuit adjusts the cavity tuning to keep the reflected voltage wave real in accordance with Eq. (5), then Eq. (8b) reduces to $V_{br}\cos\phi < V_c$. At optimum coupling, using Eq. (7a), this becomes $[(i_0R\cos\phi)/(i_0R\cos\phi + 2V_c)] < 1$. At optimum coupling the system is always stable.

The physical meaning of the stability condition of Eq. (8a) is clear when it is realized that $\theta+\psi$ is the phase angle between the bunch and the crest of the generator-produced wave. Since the beam-induced wave changes in phase with the bunch, only the generator wave is effective in producing a net restoring force on the bunch. Instability arises when $\theta+\psi = 0$ and the bunch lies at the crest of the generator-produced wave. Since the effective restoring force depends on $\theta+\psi$, and since this angle is a function of beam current for fixed V_s and V_c, then the synchrotron frequency will depend on beam current. From Eqs. (2) and (3),

$$dV_a/d\theta = V_{gr}\cos\psi\sin(\theta+\psi) = V_c\sin\phi + V_{br}\cos\psi\sin\psi$$

If cavity tuning is adjusted according to Eq. (5), and using also the fact that the synchrotron frequency is proportional to $(dV_a/d\theta)^{1/2}$, the change in synchrotron frequency with current can be written

$$\frac{\omega_s}{\omega_{s0}} = \frac{\omega_s(i_0)}{\omega_s(0)} = \left[\frac{1-(V_{br}/V_c)^2\cos^2\phi}{1+(V_{br}/V_c)^2\sin^2\phi}\right]^{1/2} \tag{9}$$

The high-current stability limit, $V_{br}\cos\phi = V_c$, is also the condition for $\omega_s = 0$.

The preceding analysis is strictly valid only in the limit in which the synchrotron oscillation frequency is small compared to the cavity bandwidth. If ω_s is large compared to the bandwidth, the induced beam voltage cannot respond to changes in phase of the driving beam current. The accelerating voltage is then simply $V_c\cos\phi$, and the stability condition is $V_c\sin\phi > 0$, independent of current. For synchrotron frequencies which are comparable to the cavity bandwidth, the dynamic response of the cavity field to phase changes in the driving current must be taken into account. This calculation is carried out in Appendix B. It is shown that for $\omega_s T_f \ll 1$, ω_s/ω_{s0} is given by Eq. (9), and that for $\omega_s T_f \gg 1$, $\omega_s = \omega_{s0}$. It is also shown that for $\xi > 0$ (or $\omega > \omega_0$) the oscillations are damped, while the opposite is true for $\omega < \omega_0$. This is the dynamic stability condition for a system without feedback, considered by Robinson.[2] Lee[3] has considered the case of a system with feedback.

It is worth point out that there are stability conditions similar to the ones just discussed in any high-frequency systems in which the stored energy can vary parametrically at a low frequency rate. Ceperley[4] has made a clear and concise analysis of a closely related problem, that of electromechanical (ponderomotive) oscillations which result from the modulation of the resonant frequency of a cavity by mechanical vibrations. He concludes that for these oscillations the system is antidamped (unstable) for $\omega > \omega_0$, and that on the opposite side of the resonance curve a "static" instability occurs in the limit of zero modulation frequency, corresponding to Eq. (8b) for the Case of phase oscillations.

Beam Loading for $T_b \sim T_f$

The energy per turn extracted by a bunch passing through a cavity is $\Delta W = qV_s = i_0T_bV_s = P_bT_b$, where q is the charge in the bunch. Using $Q_L = \omega T_f/2 = \omega W/[P_c(1+\beta)]$, together with $P_b/P_c = \beta_m - 1$ at optimum coupling, we have $\Delta W/W = (2T_b/T_f)[(\beta_m-1)/(\beta_m+1)]$. The ratio $\tau \equiv T_b/T_f$ is therefore an approximate measure of the fraction of the stored energy removed from the cavity by the passage of each bunch. This expression breaks down for $\tau \sim 1$, since ΔW cannot be greater than W. It is clear that the expressions for beam loading derived so far must be modified for $\tau \sim 1$.

Suppose charge dq crosses the cavity gap, producing an increment dV_b in the induced beam loading voltage. Using $R/Q = (V_c^2/P_c)/(\omega W/P_c) = V_c^2/\omega W$, the change in stored energy is $dW = 2V_c dV_c/[\omega(R/Q)]$. By conservation of energy this must be equal to $-V_c\cos\phi\,dq$. Since dV_b is in the direction of 10, the change in cavity voltage will be $dV_c = -\cos\phi\,dV_b$. Therefore $dV_b = (\omega/2)(R/Q)\,dq$. Assuming that all of the charge crosses the gap in a time short compared to the RF period, then

$$\Delta V_b = \frac{\omega}{2}\left(\frac{R}{Q}\right)q = \frac{i_0R\tau}{1+\beta} \quad . \tag{10}$$

For long bunches, the above expression must be multiplied by the bunch form factor given by Eq. (A. 1). The primary role of R/Q in determining the beam-loading characteristics for the passage of a single bunch is also clearly seen.

The steady-state excitation of the cavity by a periodic train of bunches is now readily calculated by taking the vector sum of the fields induced on successive passages.

The total induced beam voltage, calculated by taking the sum immediately after the passage of each bunch and denoted by $\tilde{V}_b^-$, is

$$\tilde{V}_b^- = \Delta V_b\left[1+e^{-\tau+j\delta}+e^{2(-\tau+j\delta)}\ldots\right] = \frac{\Delta V_b}{1-e^{-\tau}e^{j\delta}} \quad , \qquad (11)$$

where $\delta=(\omega_0-\omega)T_b=\tau\tan\psi$. In other words, between one bunch passage and the next, the residual field from the previous passage decays by a factor $e^{-\tau}$ and shifts phase by an angle 6. The average induced beam voltage is given by $\tilde{V}_b=\tilde{V}_b^- - \Delta V_b/2$. The relationship between these induced beam voltage vectors, and the transient behavior of the cavity field between bunch passages, is shown in Fig. 2.

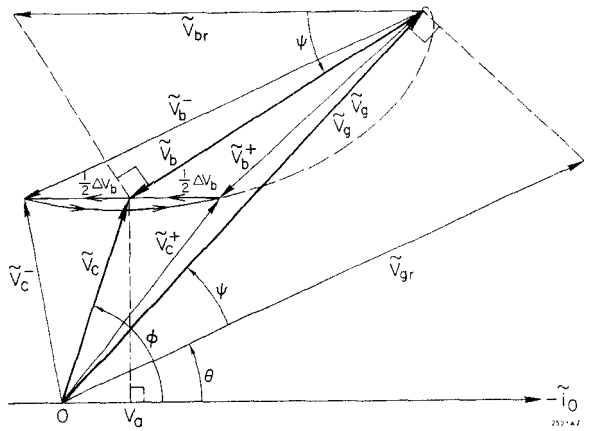


FIG. 2--Vector diagram showing transient behavior of cavity fields during beam loading for $\tau = 1$.

Using Eqs. (10) and (11) in this expression for $\tilde{V}_b$,

$$\tilde{V}_b = \left(\frac{i_0R}{1+\beta}\right)\left[F_1(\tau)+jF_2(\tau)\right] \quad , \qquad (12)$$

where

$$F_1(\tau) = \frac{\tau(1-e^{-2\tau})}{2\left[1-2e^{-\tau}\cos(\tau\tan\psi)+e^{-2\tau}\right]} \quad , \qquad (13a)$$

$$F_2(\tau) = \frac{\tau e^{-\tau}\sin(\tau\tan\psi)}{1-2e^{-\tau}\cos(\tau\tan\psi)+e^{-2\tau}} \qquad (13b)$$

In the limit $\tau \ll 1$, these relations reduce to $F_1=\cos^2\psi$ and $F_2=\sin\$\cos\psi$, as expected. The functions $F_1(\tau)/\cos^2\psi$ and $F_2(\tau)/\cos\psi\sin\psi$ are plotted in Fig. 3 as a function of τ.

All of the expressions listed previously for the case $\tau \ll 1$ can be corrected so that they are valid for any τ by using Eq. (12) wherever $\tilde{V}_b$ appears. In particular, Eq. (4) for the available generator voltage becomes

$$\sqrt{RP_g} = \frac{V_c}{\cos\psi}\left(\frac{1+\beta}{2\sqrt{\beta}}\right)\left\{\left[\cos\phi+\frac{V_{br}}{V_c}F_1(\tau)\right]^2+\left[\sin\phi+\frac{V_{br}}{V_c}F_2(\tau)\right]^2\right\}^{\frac{1}{2}} . \qquad (14)$$

This result can be applied to the proposed PEP RF system, for which $i_0=200$ mA, $R=950$ MΩ, $V_c=44$ MV and $V_s=26$ MV. We also define $\tau_0=\tau/(1+\beta)=T_b/T_{f0}$, where $T_{f0}=2Q_0/\omega$ is the unloaded filling time. For PEP, $T_{f0}=25$ psec, $T_b=2.4$ psec and $\tau_0=.096$. Using these parameters, the preceding expression can be minimized as a function of β and ψ. The result is $\sqrt{RP_g}=84.1$ MV for $\beta_m=3.41$ and $\psi_m=-37.3^o$. These values can be compared

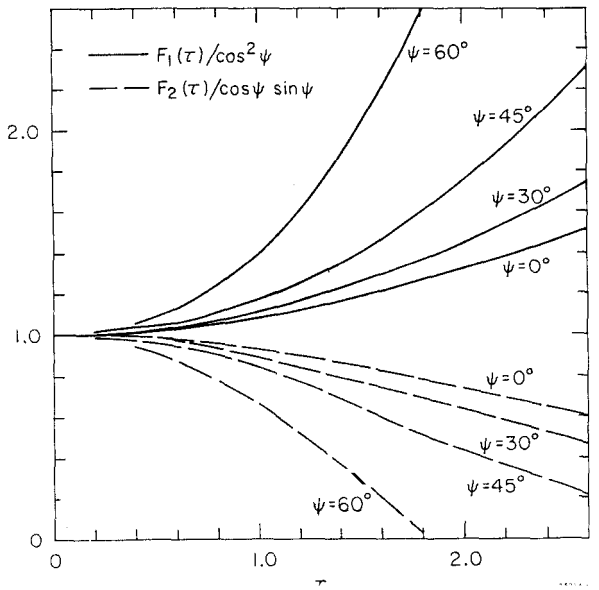


FIG. 3--The functions $F_1(\tau)$ and $F_2(\tau)$ for various values of ψ.

to $\sqrt{RP_g}=82.9$ MV, $\beta_m=3.55$ and $\psi_m=-37.4^o$ for $\tau=0$. Thus P_g is increased by 3% over that computed assuming $\tau=0$.

Beam-Loading Enhancement Due to Excitation of Higher Modes

From the analysis in the preceding section it is seen that the accelerating voltage can be written in the following *two* alternative forms:

$$V_a = V_{ga} - i_0\left(\frac{R}{1+\beta}\right)F_1(\tau) \quad ; \qquad (15a)$$

$$\Delta U = qV_a = qV_{ga} - q^2\left[\frac{\omega}{4}\left(\frac{R}{Q}\right)\right]\left[\frac{2F_1(\tau)}{\tau}\right] \quad , \qquad (15b)$$

where V_{ga} is the accelerating component of the generator voltage and **AU** is the energy gain per turn. For $\tau \ll 1$, $F_1(\tau)$ reduces to $\cos^2\psi$, while in the limit of large τ it is seen from Eq. (13a) that $F_1(\tau)$ approaches $\tau/2$. Thus $(\omega/4)(R/Q)$ represents the energy lost to the fundamental mode per unit charge for a single passage of the bunch, while the factor $2F_1/\tau$ takes account of the cumulative effect of a charge passing through the cavity on successive revolutions.

It is now simple to generalize the preceding expressions to take into account the additional loss due to the excitation of higher-order modes. This loss can be represented as an additional beam-loading voltage with real component

$$V_b(n>0) = \sum_{n>0}\frac{(w_n/q)\left(1-e^{-2\tau_n}\right)}{1-2e^{-\tau_n}\cos\delta_n+e^{-2\tau_n}} \quad . \qquad (16)$$

Here $\tau_n=T_b/T_{fn}$, $\delta_n=(\omega_n-\omega)T_b=\omega_nT_b$, $w_n=q2b_n^2(\omega_n/4)(R/Q)_n$ is the energy a single bunch would deposit in the nth mode in an "empty" cavity, and b_n is the bunch length correction factor of Eq. (A.1). For small τ_n, the ratio of the total beam-loading voltage, $V_{bt}=V_b(n>0)+V_{b0}$ to V_{b0} for the

fundamental mode at resonance is

$$f(\tau) = \frac{V_{bt}}{V_{b0}} = 1+\tau^2 \sum_{n>0} \frac{(w_n/w_0)(\tau_n/\tau)}{2(1-\cos\delta_n)}$$

For large τ, Eq. (16) shows that $f(\tau)$ approaches a limiting value of $f(\infty) = 1+\Sigma_{n>0}(w_n/w_0)$. Explicit expressions for the w_n's are given by Morton and Neil[5] for cylindrical cavities. As a function of τ, $f(\tau)$ should look like the curve in Fig. 4, with an inflection point at roughly $\tau \approx 1$. Shown also are resonances at particular values of τ for which higher-mode frequencies are exact multiples of $1/T_b$.

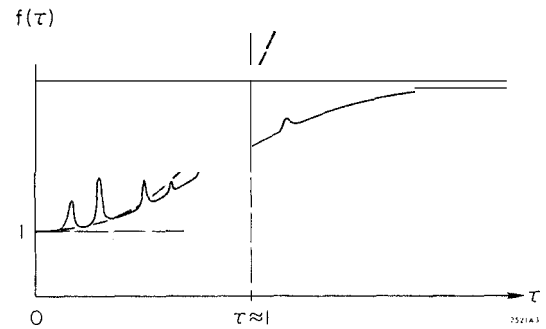


FIG. 4--The beam loading loss enhancement factor $f(\tau)$.

A measurement of V_{bt} in the limit $\tau >> 1$ has been made for a typical accelerating structure. An energy loss of 38 MeV has been measured[6] for a bunch of 10^{9} electrons passing through the SLAC structure. The loss if only the fundamental mode were excited would be $V_{b0} = q(\omega_0/4)(rL/Q)$. Substituting in $q = 1.6\times10^{-10}$, $\omega = 2\pi\times2856$ MHz, $L = 2880$ m and $r/Q = 4100\ \Omega/m$, we calculate that $V_{b0} = 8.5$ MV. Thus the single-bunch loss in the SLAC structure is enhanced by a factor of 4.5 due to the excitation of higher modes. This corresponds to the limit $f(\infty)$ in Fig. 4. For PEP, $\tau \approx 0.4$. If the PEP RF structure were to behave similarly to the SLAC structure, and if the enhancement factor for the SLAC structure were to behave as shown in Fig. 4, for PEP f would be about 1.5. Because the bunch length is relatively longer in a storage ring than in a linac, this is an overestimate of the enhancement factor. However, even an enhancement of f = 1.25 would make it necessary to increase the klystron power by 3.4 MW, or about 50% over the present design value of 7.2 MW. (See Appendix C for details.)

In principle, the enhancement factor f can be calculated for any value of τ using Eq. (16) if the frequencies, decay times and R/Q's of all modes with wavelengths longer than the bunch length are known. However, the measurement of these quantities with the necessary degree of completeness and precision is indeed a difficult problem. It may be necessary to measure the loss enhancement experimentally by sending a train of bunches at an energy of least several MeV, spaced apart in time by T_b, through a prototype structure. By adjusting the shapes of the cells within the structure and by trimming the higher-order mode frequencies with tuners, it should be possible to minimize the loss enhancement factor for a given value of T_b.

Acknowledgements

I would like to thank M. Allen, P. Morton, M. Lee, G. Loew and R. McConnell for helpful discussions on various aspects of the problem of beam loading in storage rings. Discussions with M. Sands and J. Rees were instrumental in the development of the analysis given in Appendix C.

Appendix A. The Bunch Form Factor

In Ref. 7 it is shown that the amplitude of the field induced in the nth mode of a cavity by the passage of a bunch having a current i(t) is reduced below the field induced by a short bunch by the factor

$$b_n = \left(I_{ns}^2 + I_{na}^2\right)^{1/2} , \qquad (A.1)$$

where

$$I_{ns} = \frac{1}{q\omega_n}\int i(t')\cos(\omega_n t')\, d(\omega_n t') \ ;$$

$$I_{na} = \frac{1}{q\omega_n}\int i(t')\sin(\omega_n t')\, d(\omega_n t') \ .$$

The phase of the induced field with respect to the real axis of a rotating coordinate system $e^{j\omega n t}$ is given by $\tan\theta_n = (I_{na}/I_{ns})$.

Appendix B

Assume a driving current i having a phase modulation of amplitude A, assumed small, such that $\tilde{i} = \tilde{i}_0(1+jA\cos\omega_s t)$. The response of a resonant circuit to this driving current is

$$\tilde{V} = R\, i_0 \left\{\frac{1}{1+j\xi} + \frac{jA}{2}\left[\frac{e^{j\omega_s t}}{1+j(\xi+\eta)} + \frac{e^{-j\omega_s t}}{1+j(\xi-\eta)}\right]\right\} ,$$

where $\xi = (\omega-\omega_0)T_f$ and $\eta = \omega_s T_f$. The terms in $e^{j\omega_s t}$ and $e^{-j\omega s t}$ represent two counter-rotating vectors with origins at the tip of the vector $Ri_0\cos\psi\, e^{j\psi}$, where $\tan\psi = -\xi$. It is readily shown that the resultant of the two rotating vectors traces out an ellipse with semi-major axis

$$a = (A/2)\left\{\left[1+(\xi+\eta)^2\right]^{-1/2} + \left[1+(\xi-\eta)^2\right]^{-1/2}\right\}$$

and semi-minor axis

$$b = (A/2)\left\{\left[1+(\xi+\eta)^2\right]^{-1/2} - \left[1+(\xi-\eta)^2\right]^{-1/2}\right\} .$$

The ellipse is rotated through an angle $\gamma = \pi/2 + (\psi_+ + \psi_-)/2$ with respect to the real axis, where $\tan\psi_+ = -(\xi+\eta)$ and $\tan\psi_- = -(\xi-\eta)$. This result is illustrated in Fig. 5.

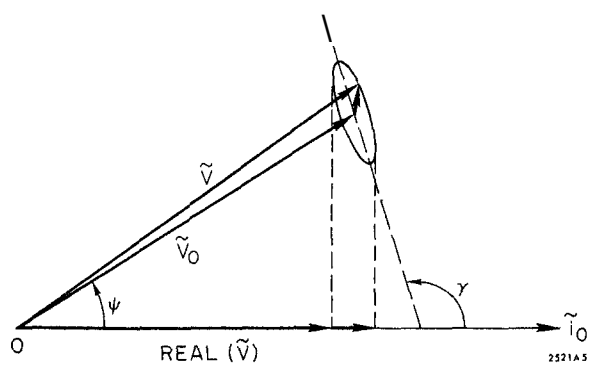


FIG. 5--Response of a resonant circuit to a phase-modulated driving current. Here $\tilde{V}_0$ is the unmodulated portion of the response, and REAL $(\tilde{V})$ is the projection of $\tilde{V}$ on $\tilde{i}_0$.

If $\tilde{i}_0$ is a beam-loading current, the projection of the ellipse on $\tilde{i}_0$ provides a component in the effective restoring force for phase oscillations. For ξ or $\eta = 0$ the ellipse collapses to a straight line, and the restoring force is in phase with the oscillations. For $|\xi| > 0$, the restoring force

is shifted in phase with respect to the oscillations, if η is also > 0, leading to a growth or decay of the oscillations.

Assume that the phase oscillations have the form $\mathbf{A} = \Delta_0 e^{(j\omega_s + \alpha)t}$. The differential equation for $\mathbf{A}$ can be written as

$$\frac{d^2\Delta}{dt^2} = -\omega_{s0}^2 \, \widetilde{T} \, A = (j\omega_s + \alpha)^2 \mathbf{A} \qquad \text{(B. 1)}$$

where ω_{s0} is the usual relation for the synchrotron frequency. The function $\widetilde{T}$ includes the effect of the cavity response on restoring force as mentioned above, and is

$$\widetilde{T} = \left\{ 1 - \frac{V_{br}}{V_c \sin\phi} \left[F_a(\xi,\eta) + jF_b(\xi,\eta) \right] \right\}$$

where

$$F_a = \frac{\xi(1+\xi^2-\eta^2)}{\left[1+(\xi+\eta)^2\right]\left[1+(\xi-\eta)^2\right]} \qquad \text{(B. 2a)}$$

$$F_b = \frac{2\xi\eta}{\left[1+(\xi+\eta)^2\right]\left[1+(\xi-\eta)^2\right]} \qquad \text{(B. 2b)}$$

Substituting for $\widetilde{T}$ in Eq. (B. 1), and equating real and imaginary parts, we obtain

$$\omega_s^2 - \alpha^2 = \omega_{s0}^2 \left[1 - \left(\frac{V_{br}}{V_c \sin\phi} \right) F_a \right] \qquad \text{(B. 3a)}$$

$$2\omega_s\alpha = \omega_{s0}^2 \left(\frac{\quad}{\quad} \right) F_b \qquad \text{(B. 3b)}$$

It is seen that, for $\xi \sim \omega - \omega_0 > 0$, the damping constant is negative and the phase oscillations are damped. In the limit of low oscillation frequency, $F_b = 0$ and $F_a = \xi/(1+\xi^2)$. Using also the real reflected power condition of Eq. (5), $\xi = (V_{br}/V_c)\sin\phi$, Eq. (B. 3a) reduces to the result obtained previously in Eq. (9). For $\eta >> 1$, $F_a = 0$ and $\omega_s = \omega_{s0}$. For $\eta \sim 1$, Eqs. (B. 3a) and (B. 3b) can be combined to give a fifth-order polynomial in ω_s. After solving this polynomial for ω_s, the damping constant is readily obtained from Eq. (B. 3b).

If $\Delta\omega_s = \omega_{s0} - \omega_s$ is small compared to ω_{s0}, we can write $\alpha/\Delta\omega_s \approx F_b/F_a = -2\eta/(1+\xi^2-\eta^2)$. Since α is also the half-width of the line for damped oscillations, this result shows that for $\eta \approx 1$ the line width is of the same order as the frequency shift.

Appendix C. Calculation of Power Loss due to Higher-Order Mode Excitation

A revised energy gain expression, which includes the additional energy loss due to higher-order cavity mode excitation, can be written as follows:

$$V_s + V_{hm} = V_{ga} - V_{b0} F_1(\tau) = V_c \cos\phi$$

The additional energy loss to higher modes, $qV_{hm} = q(f-1)V_{b0}$, is equivalent to an enhancement in the synchrotron radiation loss per turn in its effect on the synchronous phase angle and over-voltage ratio for the fundamental mode. The power transferred to the beam is increased by an amount $i_0 V_{hm}$. In addition, a higher peak cavity voltage is required to contain quantum fluctuations. It is shown by Sands[9] that, in the absence of higher-mode cavity losses, the height of the potential barrier which must be overcome by energy fluctuations is proportional to $V_s(\tan\phi - \phi)$. Thus, if the same potential barrier is to be maintained in the presence of higher-mode losses, a new synchronous phase angle ϕ' is required, where ϕ' is obtained from

$$\tan\phi' - \phi' = \frac{V_s}{V_s + V_{hm}} (\tan\phi - \phi) \quad . \qquad \text{(C. 1)}$$

The revised peak cavity voltage required to give the same quantum lifetime is then

$$V_c' = \frac{V_s + V_{hm}}{\cos\phi'} \quad , \qquad \text{(C. 2)}$$

and the revised rf power requirement is

$$P_g' = \frac{V_c'^2}{R} + i_0(V_s + V_{hm}) \quad . \qquad \text{(C. 3)}$$

For PEP, $V_{b0} = i_0 R/(1+\beta_m) = 42$ MV, using $i_0 = 0.2$A, $R = 950$ MΩ and $\beta_m = 3.55$. For $f = 1.25$, $V_{hm} = (f-1)V_b = 10.5$ MV. Using this value in Eq. (C. 1), together with $V_s = 26$ MV and $\phi = \cos^{-1}(26\text{ MV}/44\text{ MV}) = 53.8^\circ$, we calculate $\phi' = 49.4^\circ$. From Eq. (C.2) we obtain $V_c' = 56$ MV, which can be compared to $V_c = 44$ MV with $V_{hm} = 0$. From Eq. (C. 3) we find that $P_g' = 10.6$ MW, an increase by 3.4 MW over the power requirement for $V_{hm} = 0$. The cavity wall losses in the fundamental mode are increased from 2.0 to 3.3 MW as the result of the higher peak voltage requirement, and the power transferred to the beam is increased from 5.2 to 7.3 MW. However, this additional 2.1 MW also ends up as power dissipated in the cavity walls.

It must be emphasized that the preceding calculation is based on a very crude estimate of the enhancement factor f. The PEP structure, which consists of a chain of inductively-coupled shaped cells with re-entrant nose cones, may have a behavior which is quite different from that of the disk-and-cylinder structure measured at SLAC[6] and investigated theoretically by Keil.[8] Further experimental and theoretical work is clearly required to resolve this important question in detail.

References

1. J. R. Rees, "The PEP Electron-Positron Ring—PEP Stage I," invited paper, this conference.
2. Kenneth W. Robinson, Report No. CEAL-1010, Cambridge Electron Accelerator, Cambridge, Massachusetts (February 1964).
3. Martin Lee, IEEE Trans. Nucl. Sci. NS-18, No. 3, 1086 (1971).
4. Peter H. Ceperley, IEEE Trans. Nucl. Sci. NS-19, No. 2, 217 (1972).
5. P. L. Morton and V. K. Neil, Symposium on Electron Ring Accelerators, Report No. UCRL-18103, Lawrence Berkeley Laboratory, Berkeley, California (February 1968), p. 365.
6. R. F. Koontz, G. A. Loew and R. H. Miller, Proc. 8th Int. Conf. on High Energy Accelerators, CERN, Geneva (1971), p. 491.
7. P. B. Wilson, PEP Note 37, Stanford Linear Accelerator Center, Stanford, California (July 1973).
8. E. Keil, Nucl. Instr. and Methods 100, 419 (1972).
9. M. Sands in Physics with Intersecting Storage Rings, B. Touschek, editor (Academic Press, New York, 1971); p. 257f. Also available as Report No. SLAC-121, Stanford Linear Accelerator Center (November 1970).

DISCUSSION

James Leiss (NBS): Have you investigated what happens when bunches don't have the same population?

Wilson (SLAC): The answer is no. It seems to be messy enough for the case where the bunches have the same population, but it certainly should be looked into. The answer is, I have not.

Mark Barton (BNL): Have you investigated a case where the energy extracted by the beam in one pass is a sizeable fraction of the energy stored in the cavity?

Wilson: The expressions I showed are valid also in that case. In fact, they include the case where the stored energy goes through zero, and the beam induces a field of the opposite polarity.

Gordon Danby (BNL): If you have that case, where the loading is very heavy and the cavity fields haven't fully recovered by the time the next bunch arrives, then when you start, you have a different condition. How do you cope with that case?

Wilson: It is an equilibrium situation. In equilibrium the cavity recovers exactly back to the point where it was before the preceding bunch came by. If that does not happen by the time the next bunch comes by, you are not in equilibrium. Part of the calculation was to insure that that was exactly the case, that the cavity fields have recovered back exactly to the same point each time before the following bunch comes by.

A SEARCH FOR A BEAM-BEAM EFFECT IN THE ISR

K. Hübner
CERN
Geneva, Switzerland

Presented by Eberhard Keil

Summary

The lifetime of an aperture limited weak proton beam at 2 GeV/c was measured in the presence and absence of a strong 26 GeV/c beam colliding with it in eight intersection points. The typical intensity was 5 mA in the weak and 12 A in the strong beam. The lifetime of the weak beam, 30 min at 5 mA, was strongly intensity dependent. No effect of the other beam was detectable at this short lifetime. The Q-shift experienced by the weak beam was calculated to be $4 \cdot 10^{-3}$ per intersection.

Introduction

In electron-positron storage rings the limits imposed by beam-beam effects are well known and a wealth of data exists [1]. The situation is different for proton storage rings, where the ISR are the only source of experimental data. But in the ISR the beam-beam effect, usually characterized by the linear tune shift per intersection, is very small, and it is unknown whether it has any effect on the beams. Certainly, it does not limit the performance. Future proton rings, however, are supposed to work at a tune shift of $5 \cdot 10^{-3}$ which is an order of magnitude higher than the tune shift experienced by the beams in the ISR. In order to explore the beam behaviour under those conditions it was proposed to collide a very low energy beam with a strong beam in the ISR [2]. To gain the biggest factor in the tune shift the minimum momentum at which our injector, the CERN proton synchrotron, will still eject conveniently was chosen for the weak beam. The strong beam was an intense stack circulating in the other ring at an ISR standard energy,

Description of the expariment

Prior to the injection of the weak beam at 2 GeV/c a large, flat beam of 11,5 A and 26,5 GeV/c was stacked in the other ring and left circulating. The vertical FWHH of this beam, the strong beam, was measured with the beam profile monitor (gas curtain) to be $3,7 \pm 0,2$ mm at the intersection points ($\beta_v = 14$ m). The strong beam current decreased only by 150 mA during the actual experiment; the beam height did not change.

Then single pulses at a momentum of 2,01 GeV/c were injected and their lifetime was measured. In order to have well defined conditions the weak beam was aperture limited by a vertical and a lateral scraper. The scrapers were always set to the same position one after the other right after injection. The aperture was chosen such that about 10% of the beam was lost when one of the scrapers moved into position.

In order to measure the lifetime of the weak beam at different tune shifts we varied the intensity of the strong beam by radial scraping. Thus the vertical dimension of the strong beam, which is the other parameter determining the tune shift in the case of horizontal crossing, stayed approximately constant. In a first step, the intensity was reduced from 11,5 to 4,5 A, and finally to zero. Figure 1 shows the decay of the individual pulses.

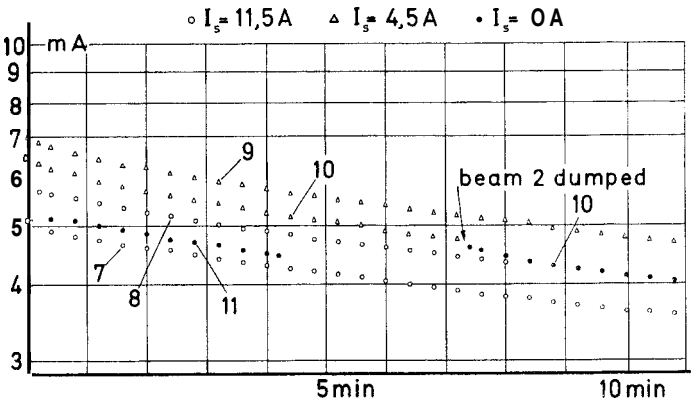


Fig. 1 – Decay of the weak beam for different strong beam intensities.

Table I gives the measured lifetime τ as a function of the calculated tune shift per intersection ΔQ and the strong beam current I_S. The lifetime τ_1 refers to a current of 5 mA in the weak beam, the lifetime τ_2 was measured 3 min after the aperture limits had been set. The accuracy of a lifetime measurement was approximately ± 10%.

Table I – Lifetime of the weak beams for different beam-beam tune shifts per intersection

ΔQ	I_S[A]	τ_1[min]	τ_2[min]	pulse No.
– 0,0043	11,5	21	30	7
– 0,0043	11,5	29	30	8
– 0,0017	4,5	34	29	9
– 0,0017	4,5	32	24	10
– 0,0	0	26	26	11

The tune shift given in the table was calculated from the following formula [3]

$$\Delta Q = -\sqrt{\frac{2}{\pi}}\,\frac{I_s\, r_o\, \beta_v}{e\beta c\gamma\alpha\sigma}\,\exp(-\,z_i^2/2\sigma^2)$$

The vertical beta value at the intersection β_v equals 14 m, α is the interaction angle which is 0,258 rad and β, γ are the relativistic constants. The spread σ is derived from the FWHH = 3,7 mm assuming a Gaussian distribution. One obtains σ = 1,5 mm. The exponential takes into account the vertical beam separation z_i in the intersections which is known from the measured closed orbits and shown in Table II.

Table II - Vertical beam separation in the individual intersection points

Intersection	1	2	3	4	5	6	7	8
z_i[mm]	0	0,6	0,6	1,6	5,3	3,6	2,0	1,6
$\exp(-\,z_i^2/2\sigma^2)$	1,0	0,9	0,9	0,6	0,0	0,1	0,4	0,6

Inspection of the table shows that the tune shift was not maximum in all intersection points. The average tune shift per intersection was 60% of the maximum one.

Discussion

It is apparent from Table I and Fig. 1 that we could not detect any dependence of lifetime on the tune shift within the precision of our measurement. The rather short lifetime of the weak beam may have masked a weak effect. Since the measured lifetimes varied between 20 to 30 min for a given tune shift, one could have discerned only effects yielding lifetimes of the same magnitude or less.

Two hypotheses can be put forward to explain the short lifetime of the weak beam in an aperture given by $A_h = 10\pi\cdot10^{-6}$ radm and $A_v = \pi\cdot10^{-6}$ radm.

The first one assumes that the beam was under the influence of isolated non-linear resonances. The working point in the presence of the strong beam was measured by inspection of the betatron frequencies after injection. We obtained for the non-integral part of the tune q_v = 0,662 and q_h = 0,725. This is quite close to a third and a sixth order resonance but only the latter is excited in a machine with a perfect median plane. Furthermore, scanning the lifetimes in the region around this working point by changing the tune of the machine with the help of the pole-face windings did not reveal any strong dependence on the tune as one would expect from non-linear resonances. Table III gives the results. The lifetime τ_1 was measured at a current level of 5,5 mA; τ_2 was obtained 4 min after the setting of the aperture limits.

When the strong beam was removed, the vertical tune increased by 0,02. Hence, the working point moved into a region where no lower than 7th and 11th order resonances were present. The lifetime, however, stayed the same even after this relatively large tune shift. This can be seen from Table I. Thus we can safely discard the first hypothesis because the lifetime did not depend on the tune of the machine.

Table III - Lifetime of the weak beam as function of external tune shifts

ΔQ_v	ΔQ_h	τ_1[min]	τ_2[min]
- 0,005	- 0,005	19	20
0	0	19	20
+ 0,01	+ 0,01	30	27
+ 0,01	0	27	26
0	0	18	19

A more likely explanation for the short lifetime is intra-beam scattering [4]. Although the theory has not yet been adapted to aperture limited beams, the strong intensity dependence of the lifetime supports this hypothesis. Table IV illustrates this point. It gives the lifetime at different current levels of an aperture limited 2 GeV/c beam, which decayed in the presence of the strong beam.

Table IV - Lifetime of an aperture limited 2 GeV/c beam as function of its current

I_w[mA]	6	5	4	3	2	1,5
τ[min]	14	20	23	29	35	39

Multiple scattering on the residual gas cannot account for the short lifetime. The N_2 equivalent gas pressure was only $2{,}7\cdot10^{-11}$ torr. This yields a lifetime of 280 min which is much longer than the observed one [5].

Acknowledgement

I am grateful to the CERN-PS crew, led by E. Brouzet and L. Henny, for the effort to prepare a stable ejection at this low energy. I thank for discussions with H.G. Hereward, E. Keil and W. Schnell. M.H.R. Donald assisted during the measurements and helped with useful comments.

References

1) F. Amman; Proc. 1973 Part. Acc. Conference, San Francisco, p. 858.

2) It is rumoured that B. Richter proposed it.

3) E. Keil, C. Pellegrini and A.M. Sessler; "Tune shifts for particle beams crossing at small angles in the low-β section of a storage ring", to be published in Nucl. Instr. and Meth.

4) C. Pellegrini; Frascati Report LNF 68-1 (1968).

5) W. Hardt; CERN int. report ISR-300/GS/68-11 (1968).

Henri Bruck (Saclay): Is the ingeneous idea of simulating the effect of the other beam by an external lens being pursued?

Keil (CERN): Actually, I have an abstract for a paper submitted to this Conference which I withdrew at the very last moment because the progress we have been making on that experiment was not as fast as we had expected. This idea is being pursued. There have been some very preliminary results and we hope to get better results sometime in the future.

Lee *Teng* (NAL): Did you say that the computed beam lifetime due to intrabeam scattering at 2 GeV agree with those experimental numbers?

Keil: I would say qualitatively yes, but we are not *so* sure that we have the right kind of theory to be very affirmative. They are in the right order of magnitude.

Alessandro Ruggiero (NAL): The first question is whether there was an official number for the limiting value electron-positron beam-beam tune drift?

Keil: I can not give a firm answer on that subject but the general feeling in the trade is that this number is in the vicinity of 5×10^{-2} or *a* little higher which means it is an order of magnitude higher than the accepted number for proton machines and two orders of magnitude higher than the actual number in the ISR, and that the electron-positron number is an experimental figure.

Ruggiero: The second question is whether the 0.05 was per intersection or not?

Andrew Sessler (LBL): Yes. We need an electron expert, someone from SPEAR presumably Ewan Paterson to respond to what the present situation is. Actually the next paper is on this subject.

Ewan Paterson (SLAC): There was some unfortunate errors in the luminosity monitors that we used to derive those calculations a year ago, so the agreement with the summation to 0.25 isn't as good as it was thought then. Concerning the number of interactions, the people you should ask to compare are from ADONE, where they have three interactions per turn compared with SPEAR's two interactions per turn. Both have very similar $\Delta\nu$ limits per crossing.

Sergio Tazzari (Frascati): We have measured small amplitude tune-shifts at ADONE with two crossings and six crossings. The ones measured with two crossings were higher than those with six crossings by a factor of about 1.5 and not by a factor of three.

Sessler (LBL): It is the $\Delta\nu$ per crossing.

BEAM-BEAM COUPLING IN SPEAR*

The SPEAR Group†

Stanford Linear Accelerator Center
Stanford University, Stanford, California 94305

Summary

The effect of the coupling upon the transverse coherent motion of two separated beams in SPEAR is presented in this paper. This effect has been studied for various parameters such as the separation and beta-values where the beams pass, the currents, energy and transverse betatron oscillation frequencies of the beams.

Introduction

When two single-bunched beams pass each other in a storage ring, they exert forces on each other which produce a coupling between the transverse motion of the beams. In SPEAR it is possible to vary the vertical separation of the two counter-circulating beams by means **of** an electrostatic beam bump[1] and thus alter the coupling between the beams. This coupling is also a function of the beta-values where the beams pass, the currents, energy and transverse betatron frequencies of the beams. It is possible to vary all of these parameters in SPEAR and to determine experimentally their effect upon the coupling between the beams by measuring the coherent beam response to an externally applied transverse electric field.

The linear theory for the coherent transverse motion of coupled beams is presented and the experimental results for the beam response to an external horizontal oscillating electric field are compared to the response predicated by this linear theory. For values of vertical separation large compared to the horizontal beam dimension, the experimental results agree with the linear theory. However, it is found that when the vertical separation between the beams is reduced to a value comparable with the horizontal beam dimension the non-linearities of the coupled motion become important and the linear theory is no longer adequate.

The deviation of the experimental results from the linear theory is thus a measure of the effect of the non-linear fields upon the coupled coherent motion.

General Equations of Motion

When two separated beams pass each other in a storage ring, each beam produces a transverse deflection of the other beam. In the linear approximation, this deflection results in both a change in the equilibrium positions of the two beams and a shift in the frequency of the transverse coherent oscillations. In the absence of any transverse coherent oscillation we take the equilibrium position at the passage point of beam two (including the static perturbation due to beam one) as $x = 0$, $y = h/2$, while the equilibrium position of beam one is taken as $x = 0$, $y = -h/2$. See Fig. 1.

In the "smooth approximation", the equations of motion for coherent oscillations of the centers of the two beams u_1 and u_2 are

$$u_1'' + \left(\nu_1^2 + \frac{p\nu_1\beta_1\Delta_1}{2\pi}\right) u_1 = \frac{p\nu_1\beta_1\Delta_1}{2a} u_2 + F e^{i\omega t}$$

and (1)

$$u_2'' + \left(\nu_2^2 + \frac{p\nu_2\beta_2\Delta_2}{2\pi}\right) u_2 = \frac{p\nu_2\beta_2\Delta_2}{2\pi} u_1 ,$$

*Work supported by the U. S. Atomic Energy Commission.

†R. H. Helm, M. J. Lee, M. Matera, P. L. Morton, J.M. Paterson, B. Richter, A. P. Sabersky, H. Wiedemann, P. B. Wilson, M.A. Allen, J. E. Augustin, G.E. Fischer.

where we have included a driving term for beam one with magnitude F and frequency ω and ignored the damping terms.

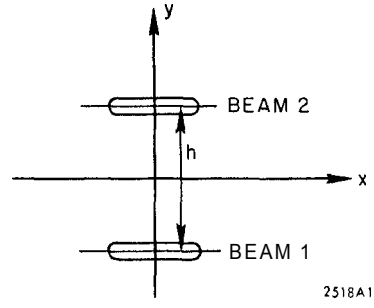


FIG. 1--Equilibrium position of two separated beams at point of passage.

The quantities (ν_1, β_1) and (ν_2, β_2) are the betatron oscillation frequencies and values of beta for beams one and two respectively at the passage point, p is the number of passage points (equal to two for SPEAR), Δ_1 and Δ_2 are the derivatives of the angular deflection for beams one and two respectively due to their passage. The explicit expressions for A are given in the appendix where it is seen that $\Delta_1 \propto N_2$ and $\Delta_2 \propto N_1$ with N_1 and N_2 the number of particles in beam one and two, respectively.

The steady state solution to Eq. (1) may be written in the form

$$u_1 = \hat{u}_1 e^{i\omega t} \quad \text{and} \quad u_2 = \hat{u}_2 e^{i\omega t} , \tag{2}$$

where the amplitudes $\hat{u}_1$ and $\hat{u}_2$ are given by

$$\hat{u}_1 = \frac{\left(\nu_2^2 + \frac{p\nu_2\beta_2\Delta_2}{2n} - \omega^2\right) F}{(w^2-\omega_\alpha^2)(w^2-\omega_p^2)}$$

$$\hat{u}_2 = \frac{\frac{p\nu_2\beta_2\Delta_2}{2n} F}{(w^2-\omega_\alpha^2)(w^2-\omega_p^2)} , \tag{3}$$

with ω_α and w_p the resonant frequencies.

Case of Equal Betatron Frequencies

One of the special cases we have studied in SPEAR is one in which the two beams have equal betatron frequencies and beta values at the passage points; i.e., $\nu_1 = \nu_2 = \nu$ and $\beta_1 = \beta_2 = \beta$.

The resonance frequencies are then given for a storage ring with two passage points by

$$\omega_\alpha = \nu \quad \text{and} \quad \omega_\beta \approx \nu + \frac{\beta}{2\pi}(\Delta_2 + \Delta_1) . \tag{4}$$

Near the resonance frequency $w \approx \omega_\alpha$ the oscillation amplitudes are given by

$$\hat{u}_1 \approx \left(\frac{F}{\omega_\alpha^2-\omega^2}\right)\left(\frac{\Delta_2}{\Delta_1+\Delta_2}\right) \quad \text{and} \quad \hat{u}_2 = \left(\frac{F}{\omega_\alpha^2-\omega^2}\right)\left(\frac{\Delta_2}{\Delta_1+\Delta_2}\right), \tag{5}$$

while near the other resonance frequency $w \approx \omega_\beta$ the oscillation amplitudes are given by

$$\hat{u}_1 \approx \left(\frac{F}{\omega_\beta^2-\omega^2}\right)\left(\frac{\Delta_1}{\Delta_1+\Delta_2}\right) \quad \text{and} \quad \hat{u}_1 = \left(\frac{F}{\omega_\beta^2-\omega^2}\right)\left(\frac{-\Delta_2}{\Delta_1+\Delta_2}\right). \tag{6}$$

If we assume the resonance widths as determined by the damping are the same at $w \approx \omega_\alpha$ and $w \approx \omega_\beta$, and since **A**, **a** N_2 and $\Delta_2 \propto N_1$, the amplitudes of the two beams at resonance frequencies are in the ratio of

$$|u_1(\omega_\alpha)| : |u_2(\omega_\alpha)| : |u_1(\omega_\beta)| : |u_2(\omega_\beta)|$$
$$= N_1 : N_1 : N_2 : N_1$$

At SPEAR' we detect the coherent response of the beams at the exciting frequency. This detected response is proportional to the product of the oscillation amplitude u and the number of particles in the beam N, and is a function of exciting frequency w, with the functional dependence displayed in Fig. 2. The labels over the resonance peaks denote their relative heights, and the distance between the peaks $(\omega_\beta - \omega_\alpha) \propto (N_1 + N_2)$.

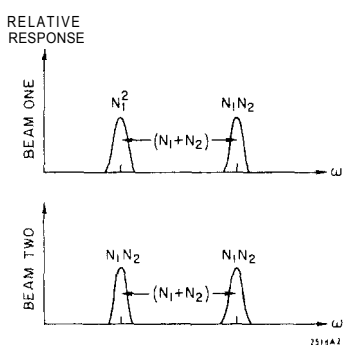


FIG. 2--Coherent response detected versus driving frequency.

For equal currents in each beam, the detected resonance peaks are all equal. If the current in beam one is decreased, the first peak for both beams remains at the same frequency $(\omega_\alpha = \nu)$, but for beam one, the first peak decreases in relative amplitude. The second peak moves toward the first peak and remains relatively large in amplitude for both beams. In the limit of a very weak beam one $(N_1 << N_2)$, the first peak for beam one disappears and both second peaks are shifted by one-half of the amount of frequency shift for the case of both beam currents equal to the current of the strong beam $(N_1 = N_2)$.

Conversely, starting with equal beams and decreasing the current in beam two, we again find that the second peak moves toward the first peak, but in this case, all peaks except peak one of beam one decrease in amplitude.

The experimental results from SPEAR on the positions and relative amplitudes of the resonance peaks for coherent horizontal motion of two separated beams are in excellent agreement with the above results when the beam is driven externally. It is interesting to note that the second resonance peak is often observed even without an externally applied oscillating field.

Case of Equal Beam Currents

Another specific case that has been studied at SPEAR is the case in which the beam currents are equal. For this case, when the difference between the betatron wave numbers is small compared to unity, we can assume that the beta values for the two beams are equal. Under these conditions, the values for the resonance frequencies w, and w_β are given by

$$\omega_{\beta,\alpha} = \frac{1}{2}\left[(\nu_1^2+\nu_2^2) + \frac{2\nu\beta\Delta}{\pi} \mp \sqrt{(\nu_2^2-\nu_1^2)^2 + \frac{4\nu^2\beta^2\Delta^2}{\pi^2}}\right]$$

For the case where the difference between the tunes is large compared to the tune shift; i.e., $(\nu_2 - \nu_1) >> \beta\Delta/\pi$, the values of ω_β and ω_α become

$$\omega_\beta \approx \nu_2 + \frac{\beta\Delta}{2\pi} + \frac{\beta^2\Delta^2}{4\pi^2(\nu_2-\nu_1)}$$
$$\omega_\alpha \approx \nu_1 + \frac{\beta\Delta}{2\pi} - \frac{\beta^2\Delta^2}{4\pi^2(\nu_2-\nu_1)} \tag{8}$$

The oscillation amplitudes near the resonance $w \approx \omega_\alpha$ are

$$\frac{\qquad}{(\omega_\alpha^2-\omega^2)} \quad \text{and} \quad \ddot{u}_\sim \approx \frac{\qquad}{\qquad}\frac{\qquad}{\qquad}$$

and near the resonance $w \sim \omega_\beta$ (9)

$$\hat{u}_1 \approx \frac{\beta^2\Delta^2}{4\pi^2(\nu_2-\nu_1)^2}\left(\frac{2F}{\omega_\alpha^2-\omega_\beta^2}\right) \quad \text{and} \quad \hat{u}_2 = \frac{-\beta\Delta}{2\pi(\nu_2-\nu_1)}\left(\frac{FF}{\omega_\beta^2-\omega^2}\right).$$

Thus, for the case where $(\nu_2 - \nu_1) >> \beta\Delta/\pi$, we expect to see *all* resonance response peaks from our detector disappear except for the response of beam one at a frequency ω_α.

This effect has been observed on the coupled horizontal motion at SPEAR, but it should be pointed out that if the tune shift $\beta\Delta/\pi$ becomes too large, it is difficult to obtain values for ν_1 and ν_2 by means of the electric quadrupole lenses that give sufficient tune splitting without being near a destructive machine resonance.

Summary of Experimental Results

Machine experiments have been done at SPEAR to determine the resonance frequencies of the coherent horizontal motion for two separated beams. In these experiments, the following parameters were varied: the currents in the two beams, the vertical separation of the two beams, the values of at the passage points, the separate betatron oscillation frequencies of the two beams and the energy of the two beams. The results of experiments with unequal currents and betatron tunes for the two beams driven externally has been discussed in the previous sections, and the results for the resonance amplitudes and frequencies are in agreement with the theory. In addition, we often observe the second resonance peak without an external driving field.

For most of the experiments, the currents and betatron oscillation frequencies of the two beams were equal. For this case, the frequency shift of the second resonant peak as predicted by the linear theory is given by

$$\omega_\beta - \omega_\alpha = \delta\omega = \frac{\beta\Delta}{\pi} .$$

where the expression for **A** is given in the appendix.

In Fig. 3, the frequency shift $\delta\omega$ is displayed as a function of current in the two beams for various values of vertical beam separation. The lines are theoretical values and the points are the experimental values. For this example,

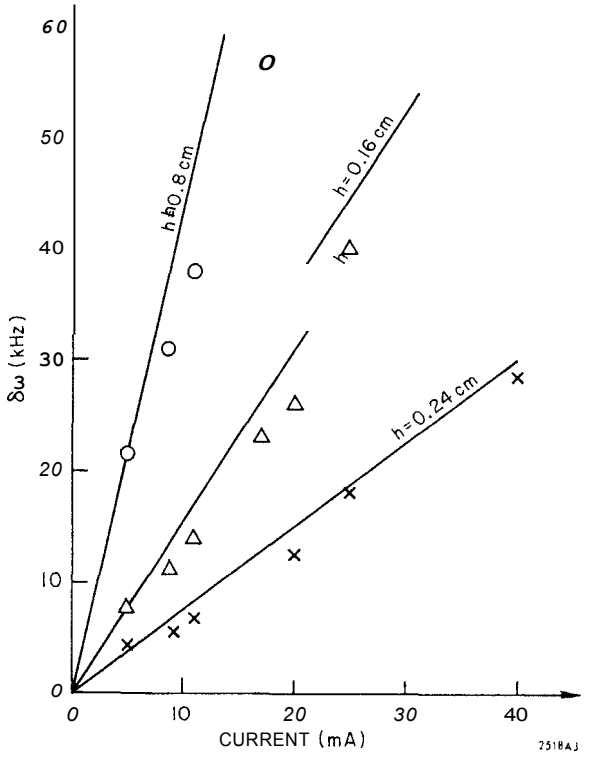


FIG. 3--Frequency shift vs. beam current.

the energy was equal to 1.5 GeV, the values of β_x at the passage points equal to 1.2 m, the betatron wave number ≈ 5.23 and the values of σ_x and σ_y = 0.0375 cm and 0.00315 cm respectively. Note that the agreement with theory is best for cases with large beam separation. Figure **4** shows the quantity $\delta\omega/I$ plotted as a function of beam separation h for the same values of energy, β, ν, σ_x and σ_y as those in Fig. 3. It can be seen that the theory breaks down when separation h is smaller than σ_x. The solid line is the theoretical value while the dotted line is the experimental results for two separated 5 mA beams. For values of h less than σ_x, the experimental results do not agree with linear theory and the experimental values for the frequency shift is considerably lower than the theoretical values. These differences have been obtained for several values of beam current, energy, β, and ν, and in all cases the experimental values for the frequency shift are lower than the theoretical values for $h < \sigma_x$, while for $h > 2\sigma_x$ their values agree.

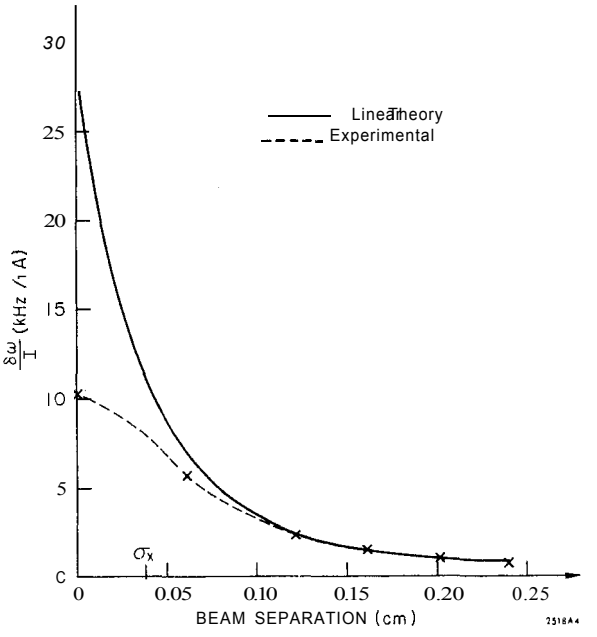


FIG. 4--(Frequency shift/current) vs. beam current.

This discrepancy can be understood if one remembers that the expression for the transverse deflection which has been used in this calculation is valid only for the particles in a beam that are near the beam center. When the separation of the beams is quite large compared to their width, this is a good approximation for all particles; however, as the separation between the beams decreases, the forces become more non-linear and the expression used for the transverse deflection yields a larger value than is actually experienced by many of the particles. Thus the experimental results deviate from the theoretical results obtained from the linear model. This deviation between the experimental and theoretical results is a measure of the amount of non-linearity of the beam-beam interaction for small separation.

Acknowledgments

It is a pleasure to thank the SPEAR Operation Group, who not only aided in the operation of the storage ring but also actively participated in the experimental measurements.

References

1. SPEAR Storage Ring Group (presented by B. Richter), IEEE Trans. Nucl. Sci., NS-20, No. 3, 752 (June 1973).
2. SPEAR Group, "Beam Dynamics Experiments at SPEAR," contribution to this conference.

Appendix

For the case of two beams that are separated in the vertical direction y by amount h, as shown in Fig. 1, the linear portion of the angular deflection of beam one due to beam two is given by

$$\delta\theta_{x1} = -A_{x1}(x_1 - x_2) \qquad \delta\theta_{y1} = -A_{y1}(v_1 - v_2)\,; \tag{A-1}$$

$$\delta\theta_{x2} = -A_{x2}(x_2 - x_1) \qquad \delta\theta_{y2} = -\Delta(v_2 - v_2)$$

with $v_1 = (y_1 + h/2)$ and $v_2 = (y_2 - h/2)$ the vertical deviations from their equilibrium positions. The quantities Δ_x and Δ_y are given by

$$= \frac{2 N_2 r_e}{\gamma(\sigma_x^2 - \sigma_y^2)} \left\{ g\left(\frac{h}{L}\right) - \frac{\sigma_y}{\sigma_x} e^{-\frac{h^2}{}} \quad g\left(\frac{h\sigma_x}{L\sigma_y}\right) \right\},$$

$$\Delta_{y1} = \frac{\quad 2 e}{\gamma(\sigma_x^2 - \sigma_y^2)} \left\{ -g\left(\frac{h}{L}\right) + \frac{\sigma_x}{\sigma_y} e^{-\frac{h^2}{}} \quad g\left(\frac{}{L\sigma}\right) \right.$$

$$\left. + \left(\frac{\sigma_x^2 - \sigma_y^2}{\sigma_x \sigma_y}\right) e^{-\frac{h^2}{2\sigma_y^2}} \left[1 - g\left(\frac{h}{L}\,\frac{\sigma_x}{\sigma_y}\right)\right] \right\}. \tag{A-2}$$

Δ_{x2} and A are obtained by substituting N_1 for N_2 in the above expressions, where

N_1 and N_2 are the number of particles in beams one and two respectively;

r_e is the classical radius of the electron;

σ_x and σ_y are the horizontal and vertical rms beam sizes of each beam (assumed to be equal);

$L = \sqrt{2(\sigma_x^2 - \sigma_y^2)}$;

γ is the relativistic energy parameter; and

$$g(z) = 1 - \sqrt{\pi}\, z\, e^{} \int e^{-u}\, du \,.$$

Note that deflection of beam one to beam two is proportional to the number of particles in beam two and vice versa.

DISCUSSION

Jean Buon (Orsay): Coupled beam oscillations have also been observed in ACO without external excitations and there have been frequency shifts with separation and the results agree with what you have seen in SPEAR.

Harold Hahn (BNL): The experiments were done with head-on collisions. Do you expect a difference if there is a small crossing angle?

A. Sabersky (SLAC): We don't know what to expect because the results are preliminary and we really have not fully interpreted what we have now, but certainly if we begin to believe these results, that they really are real tune spreads, then in fact we do expect to see a difference as is predicted theoretically.

Eberhard Keil (CERN): What is the revolution frequency in SPEAR II?

Sabersky: 1.28 MHz.

VACUUM CONDITIONS FOR PROTON STORAGE RINGS

R. CALDER, E. FISCHER, O. GRÖBNER and E. JONES

ISR Division - CERN

Geneva, Switzerland

Summary

The stability of coasting beams in storage rings depends critically on the vacuum. The beam is perturbed both by scattering on the residual gas molecules and neutralisation effects resulting from gas ionisation. Historically, these considerations were the only ones employed in the design of the ISR vacuum system. The operational experience with the ISR has shown that the vacuum itself may be perturbed by desorbed gas resulting from beam induced ion bombardment of the chamber wall. This can lead to an unstable chain reaction and to the destruction of the stored beam. The dynamic vacuum equation including stimulated desorption is applied to the conduction limited case. This shows the importance of the effective pumping speed at every given point and demonstrates the value of good conductance or quasi-distributed pumps. A vital factor is the state of the vacuum chamber wall and its response to low energy ion bombardment. Results of investigations on different materials, cleaning methods and recontamination problems are discussed in the light of their applicability and relevance to the design of large machines.

1. Introduction

The vacuum conditions necessary for proton storage rings are determined by the numerous interactions the beams can have with the residual gas. Not only the gas present in the volume of the vacuum chamber is important in this respect but also the gas adsorbed on the chamber walls. Some of the interactions were known and taken into account when the Intersecting Storage Rings (ISR) of CERN were designed. Others became apparent during the running-in of the machine.

Nuclear scattering is an important interaction of the protons with the residual gas molecules.[1] A scattered particle changes its direction or energy so much that it is lost from the beam. Hence the beam decay is given by

$$\frac{1}{I}\frac{dI}{dt} = -c\,\sigma\,n \qquad (1)$$

where I is the beam current, c the proton velocity, σ the total nuclear cross-section and n the atomic density of the rest gas. The decay rate in the ISR for quiet beams of up to about 10 A agrees to within ± 20% of that calculated from equation (1).

Coulomb scattering represents a second type of interaction of the circulating protons with the rest gas. The scattering angles due to Coulomb interaction with the electrostatic field of the nuclei are very small, but many successive events, i.e. multiple scattering, lead to a gradual blow-up of the beam. The process can be described as diffusion in betatron phase space.[1] The mean square betatron amplitude, $\langle x^2 \rangle$, of the freely circulating beam increases linearly with time according to

$$\langle x^2 \rangle = \langle x^2 \rangle_o + 7.2\cdot10^{-14}\,\beta\,\beta_{av}\,p^{-2}\,Z^{-2}\,n\,t \qquad (2)$$

where $\langle x^2 \rangle_o$ is the initial amplitude at the time t = 0, β and β_{av} the β-value in m at the given place and the average value respectively, p the proton momentum in GeV/c, Z the charge number and n the density of the scattering gas in molecules cm^{-3}.

With the gradual blow-up by multiple scattering the beam will finally occupy the whole aperture, A(mm^2) In this limiting case the decay rate is

$$\frac{1}{I}\frac{dI}{dt} = -\pi^2\,A^{-1}\,\frac{d}{dt}\langle x^2 \rangle \qquad (3)$$

where $\langle x^2 \rangle$ is taken from Eq. (2).

In the ISR, with a residual hydrogen pressure of 10^{-11} torr the beam does not fill the available aperture after a long run of 36 hours. Even so, the observed beam blow-up rates of a freely circulating beam in the ISR are, under best conditions, about one order of magnitude faster than calculated from equation (2). Hence, other perturbations also causing diffusion in betatron phase space are more important. One possible cause is again linked with the vacuum conditions, namely with the ionisation of the residual gas.

2. Beam Neutralisation

Ionisation of the rest gas by high energy protons produces ions, which are repelled from the beam and hit the chamber walls, and electrons which may stay trapped in the potential well of the beam if their energy is too low to escape. The partial neutralisation of the space charge causes a shift of the betatron frequencies.[2] Defining a neutralisation coefficient ε as the ratio of the number of electrons to protons and neglecting image effects, the Q-shift can be expressed as

$$\Delta Q = \frac{2\,R^2 r_p}{e\beta^3 c Q\,\gamma}\,\frac{I}{b(a+b)}\cdot\Delta\varepsilon \qquad (4)$$

Here R (m) is the machine radius, r_p the classical proton radius, e the electron charge, β and γ are the usual relativistic factors and c the velocity of light. 2a and 2b are respectively the horizontal and vertical beam dimensions. With typical ISR parameters one obtains from *(4)* to a good approximation

$$\Delta Q/\Delta\varepsilon \approx I/\gamma.$$

In proton storage rings one uses Q values which vary across the aperture and hence a "working line", which must be positioned between resonances in the Q_V, Q_H diagram to obtain low decay rates. An uncontrolled tune shift such as can be caused by partial neutralisation iarying with time must therefore be avoided. From permitted tolerances in working line shifts one can derive that the permissible variations of ε are of the order of 10^{-2} over a running period of, say, 24 h.

To keep the residual neutralisation low, the ISR have been equipped with an extensive system of electrostatic clearing electrodes.[3] Under stationary conditions ε can be expressed by the ratio of the electron production rate - in the ISR one finds a value of about $1.4\cdot10^9$ electrons/protons s^{-1} $torr^{-1}$ which is in good agreement

with calculation - and the clearing rate (s^{-1}). The latter depends on the longitudinal drift velocity of the electrons, the mean distance between clearing electrodes and, implicitly, also on E. For small degrees of neutralisation it is sufficient to assume a constant clearing rate and one finds[3] that ϵ is proportional to the residual pressure. Hence changes in the residual pressure which can occur due to beam induced gas desorption from the vacuum chamber walls, may shift the working line on to resonances and cause an increased decay rate.

3. Coupled Electron-Proton Oscillations

A further known mechanism which can modulate the residual neutralisation, is coupled oscillations of electrons and protons. This system can be described by a set of coupled oscillators and it has been shown[4,5] that there exists a threshold value for E above which the amplitudes become unstable and grow in a short time so that the electrons are lost on to the vacuum chamber. The calculated threshold neutralisation ranges from 10^{-3} to a few percent.[4,5] Apart from being a transport mechanism which can feed protons into non-linear resonances, successive electron-proton instabilities can also give rise to a gradual beam blow-up similar to multiple scattering on the residual gas.

Figure 1 shows a beam signal taken from a horizontal pick-up station, and one recognises the fast rise of the instability which lasts for about 5 ms. The repetition rate of this particular instability was 1.2 s. If one assumes that it was driven from a place in the ring with a pressure of 2×10^{-11} torr, a neutralisation of 3.5% can be estimated. This is in fair agreement with predicted values. Using equation *(4)* with the particular parameters I = 12 A and γ = 28, one finds a Q modulation of about $1.5 \cdot 10^{-2}$.

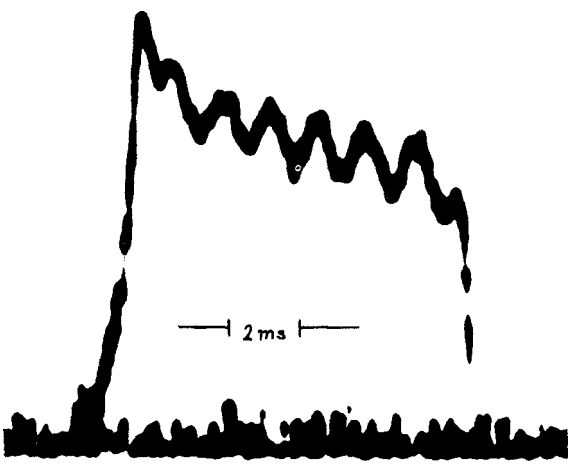


Fig. 1 Beam induced signal from a pick-up station showing a coupled electron-proton instability. Beam current is 12 A and a proton energy 26 GeV.

4. Beam Induced Pressure Rise

The most serious interaction between the proton beam of the ISR and its vacuum environment was only discovered during the early running-in period, When the beam current was increased beyond 4 A the static pressure of about 10^{-10} torr started to rise at several places around the ring until it reached 10^{-7} or even 10^{-6} torr and the beam was rapidly destroyed.

This pressure runaway has been explained by ion induced gas desorption from the vacuum chamber. A quantitative approach is obtained by solving a differential equation for the pressure in the vacuum tube as function of time and one-dimensional space[6], where one includes the desorption and readsorption of the residual gas on the walls. The gas density $n(x,t)$ and the surface coverage of adsorbed molecules $\theta(x,t)$ in an idealised module of the ISR vacuum system, are then described by

$$A \frac{\partial n}{\partial t} = a + C \frac{\partial^2 n}{\partial x^2} - w \frac{\partial \theta}{\partial t} \qquad (5)$$

$$\frac{\partial \theta}{\partial t} = \frac{\bar{v}}{4} n - \frac{\sigma}{e w} \eta I \qquad n - \theta/\tau$$

with the boundary conditions $C \frac{\partial n}{\partial x} \pm Sn = 0$ at the locations $x = \pm L$ where the pumps of speed 2S are connected to the system.

The vacuum chamber is characterised by its cross sectional area A, its perimeter w and a specific conductance C ($cm^4\ s^{-1}$). The wall is assumed to have a specific degassing rate a ($cm^{-1}\ s^{-1}$), and the gas molecules hitting the chamber wall a sticking probability *s*. The sojourn time of adsorbed molecules on the wall, which is a function of the binding energy in the adsorbed state is characterised by τ; furthermore $\bar{v}$ is the mean thermal velocity of the gas molecules, σ the ionisation cross section and e the electron charge. I is the stored beam current in amps and η the net desorption yield, defined as the number of released gas molecules per bombarding ion, minus the sticking probability of the ion itself.

In the presence of beam induced gas desorption from the walls, the gas density remains finite only as long as the product

$$\eta I < (\eta I)_{crit} = \frac{e}{\sigma} (C\omega^2 + w\bar{v}s/4 + A/\tau). \qquad (6)$$

Here, $\omega < \frac{\pi}{2L}$ is the first root of the transcendental equation

$$\omega \tan \omega L = S/C.$$

In the limit where the reaction of the residual gas with the surface can be neglected, that is for $s \to 0$ and $1/\tau \to 0$, this stability criterion gives a simplified pressure bump criterion.[6,7] When considering the pressure stability in a machine like the ISR it is probably safer to neglect all surface-sticking effects. This may however be different for a storage ring with a cryogenic vacuum chamber, where S can easily approach unity and the resulting increase in the stability limit would then become very important. In case of a cold ISR ($s \to 1$) the term $w\bar{v}s/4$ would account for an increase of about 10^4 in terms of the critical product ηI, and a much larger desorption yield could be tolerated than at present.

It follows from equation (6) that the beam-vacuum limit can be increased either by the installation of additional and somewhat larger pumps, or by increasing the aperture of the vacuum pipe. Alternatively, the net desorption yield of the walls may be reduced. From the definition, η can have negative values, implying that molecules are removed from the gas phase by the action of the beam and hence the pressure is decreased. This beam pumping can indeed be observed at many places around the ISR either in chambers which are sufficiently clean, or in those which have been conditioned successfully by one of the special surface treatments to be discussed.

Figure 2 shows η as measured on a well baked ISR chamber versus the energy of the bombarding ions. At low energies one observes $\eta < 0$, hence beam pumping, while above 800 V, the yield becomes positive and almost proportional to energy. Figure 2 was obtained with a constant beam current of 6 A and the ion energy could be varied with the help of a biasing electrode. Under normal conditions the ion energy is determined by the space charge potential of the beam which increases in the ISR by about 100 V per amp of stored beam.

5. Improved bakeout and additional pumps

The first effort to counter these pressure rises was to reduce the amount of adsorbed gas and hence η by increasing the bakeout temperature from 200°C to 300°C and lengthening the bakeout time from 5 to 24 h.

The second stage in the improvement of the ISR vacuum system consisted in installing some 500 additional sublimation pumps to raise the vacuum limit to about 20 A and to obtain $(\eta I)_{crit} = 40$ A at the weakest places. The sublimation pumps which have reduced the residual pressure by a factor of 10 to 100, gave at the same time also a reduction of η; from the observed Pressure runaway at 20 A one concludes $\eta \simeq 2$ as compared to the previous value of 4.

Tests in the laboratory have shown that a desorption coefficient of 2 molecules per ion is only observed on a contaminated stainless steel surface. A carefully cleaned and baked sample of stainless steel shows η-values of 0.1 and even lower. One can,

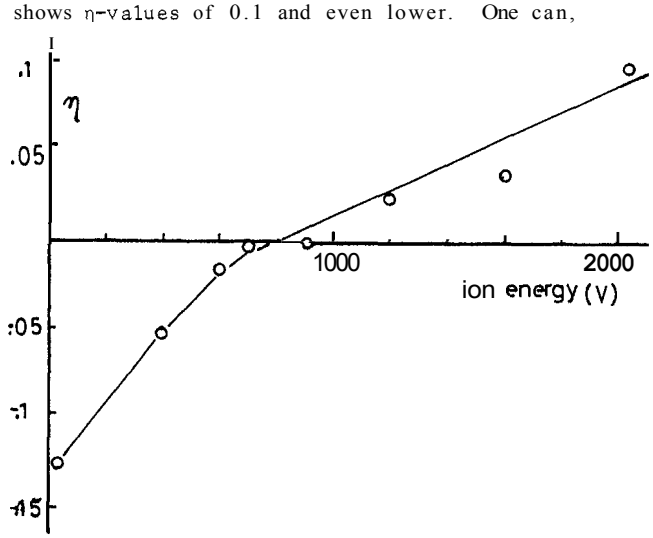


Fig. 2 Desorption coefficient η in molecules per ion versus bombarding ion energy for a stainless steel chamber after a 340°C bakeout of 24 h.

therefore, conclude that the vacuum limit is determined by that place around the one kilometre of circumference of an ISR ring where an accidental local contamination (high η) coincides with a low $(\eta I)_{crit}$, that is, with a place which is relatively poorly pumped.

6. Prevention of contamination

The most likely source of contamination in the present ISR, apart from the unavoidable leaks which are however surprisingly harmless as far as beam pressure bumps are concerned, seems to be from the roughing pumps. These stations, consisting of a rotary pump combined with a turbomolecular pump are used to provide the starting pressure for the ion pumps and provide also differential pumping for the double seal sector valves. The stations are valved-off from the main vacuum chamber except during the bakeouts. Nevertheless systematic measurements around the ISR have shown consistently increased desorption yields near the pumping stations and sector valves. To avoid or to reduce this source of contamination, the pumping stations are being prebaked before each use on the UHV system. It is furthermore planned to install titanium sublimators adjacent to all sector valves to stop any contamination from spreading out.

7. Results from surfaces and surface treatments with low ion desorption coefficient

As a third approach to overcome the beam vacuum limit, various methods yielding low desorption coefficients have been investigated. First results of this work have already been reported.[7]

The analysis of the beam desorbed gas shows primarily an increase of mass 28 (CO). This agrees with the results indicated by othermethods of surface analysis (Auger spectroscopy or secondary ion mass spectroscopy, SIMS) which show consistently an excessive carbon contamination on the stainless steel surface.

Studies have since been pursued in two main directions, namely by experiments and surface analyses in the laboratory (work which is reported elsewhere) and by in situ experiments in the ISR in the presence of high intensity beams.

The aim of the latter is to test the desorption properties of various samples in a realistic environment. This is important since the desorption yield depends on parameters which cannot, or only with difficulty, be reproduced in the laboratory. The long term behaviour of a given surface treatment is, next to the immediate desorption yield, one of its principal characteristics should it be applied on a large scale.

Treatments which can be applied prior to the installation are very attractive from a practical point of view. They are based on the fact that once the strongly adsorbed molecules are removed, the surface remains clean even after subsequent air exposure. Hence the requirements are :

- the fresh surface must have a low outgassing rate to obtain a low residual pressure and a low ion desorption yield.
- it should be insensitive to contamination and maintain the low desorption yield for a sufficiently long period of time.

- in case of accidental contamination it must be possible to regenerate the surface in situ, e.g. by a 300°C bakeout.

Following this general guide-line bakeouts at 350°C have been very effective in reducing the desorption yield and in regenerating a contaminated surface. Unfortunately the general application to the ISR vacuum chamber is difficult because many elements are not designed to withstand this high temperature.

Glow Discharge Cleaning

Glow discharge cleaning was one of the first treatments studied and applied to the ISR vacuum chambers. Although it does not yield consistently negative η values, the desorption coefficient obtained is always very low. The procedure itself is rather straight forward: the chamber is filled with about 10^{-2} torr of argon and a discharge is initiated by applying a few hundred volts to a wire electrode which is stretched along the chamber axis. The positive argon ions strike the wall and cause very intense gas desorption. To enhance the process, and to help to prevent readsorption, including argon, the chamber is held at 300°C. During the treatment one maintains a continuous flow of argon gas through the chamber which effectively transports the desorbed gas out of the system. The total dose applied is of the order of 10^{18} ions per cm^2, but may be reduced to 5×10^{16} ions cm^{-2} without significant loss in performance. Surface analyses and laboratory experiments show that the low desorption yield obtained immediately after the treatment is indeed preserved during several weeks of exposure to atmosphere. It is therefore not necessary to treat the chambers in situ, but the surface conditioning can be done more conveniently as the last step before the installation. This has become standard practice on all new vacuum chambers and up to now some hundred metres of the ISR vacuum system have been conditioned in this way. Figure 3 shows the desorption yield obtained by glow discharge cleaning versus the bombarding ion energy. Up to the maximum energy, 2200 V, corresponding to a beam intensity of about 20 A, the yield remains negative and the surface exhibits beam pumping.

Surface Oxidation

A possible method of removing the carbon contamination found on the surface has been investigated by oxidising the chamber and by pumping out the gaseous end products. The desorption coefficients so far obtained were positive, see Figure 3, but nevertheless sufficiently small to increase the beam-vacuum limit well beyond 20 A. In principle it should be rather easy to apply the oxidation in situ and this could become even part of a normal bakeout procedure.

800°C bake under vacuum

To overcome the temperature limitation of the in situ bakeouts high temperature bakeouts in a special vacuum furnace up to 800°C have been investigated. While laboratory tests and surface analysis on small samples show a considerable improvement in surface cleanliness and in the specific outgassing rate, the results from in situ experiments were so far rather disappointing. Measured desorption yields are shown in Figure 3.

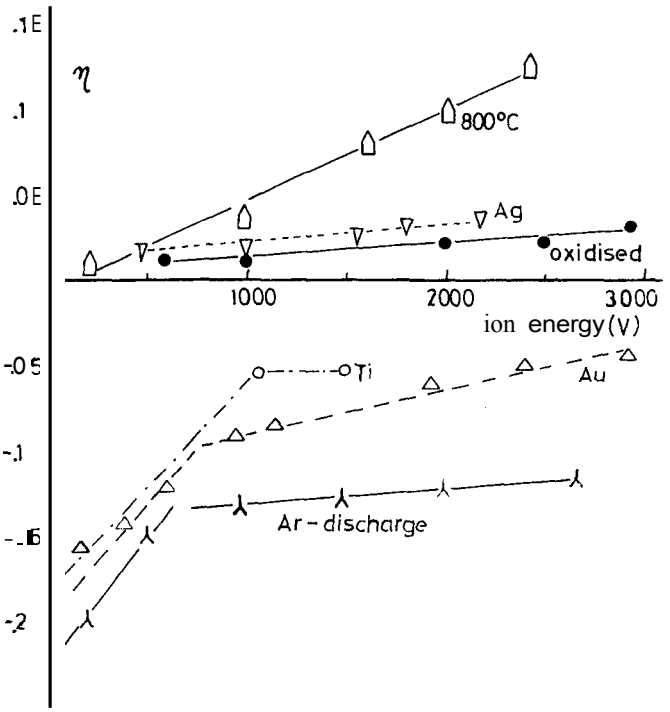


Fig. 3 Desorption coefficient η in molecules per ion versus bombarding ion energy as obtained by various surface treatments and surface coatings of stainless steel :

argon glow discharge cleaning,
oxidation at 400°C,
800°C bakeout under vacuum,
gold coating by evaporation,
layer of freshly sublimated titanium,
silver coating by sputtering.

Except for the titanium sample, all measurements were done after exposure to air and bakeout in the ISR.

Desorption yields of special surfaces

In the search for a surface material, other than stainless steel, we have investigated gold, silver and titanium, The latter material was tested in the form of an evaporated layer as well as in the form of liners made out of titanium alloy (13 Cr, 11 V, 3 Al), The coatings were produced by sputtering or sublimating the material under high vacuum on to the inner wall of a test chamber. The thickness of the layer, in some cases not very uniform, was of the order of 1 µm. In principle, this should be enough to cover the various contaminants on the stainless steel substrate and to protect them from the energetic bombarding ions. After the evaporation, the samples had to be exposed to atmospheric pressure before being installed in the ISR and baked at 300°C for 24 hours. The only surface which could also be deposited in situ under ultrahigh vacuum conditions and tested without prior exposure to air was the layer of sublimated titanium.[7]

Negative desorption yields were obtained for gold plating and for in situ deposited titanium; less favorable results were found with silver, see Figure 3. It could be shown that the gold and silver layers are fairly insensitive to recontamination by an air leak. After exposure their initial desorption properties could be reproduced, at least to a large extent, by a 300°C bakeout of 24 h. Figure 4 shows the desorption yields

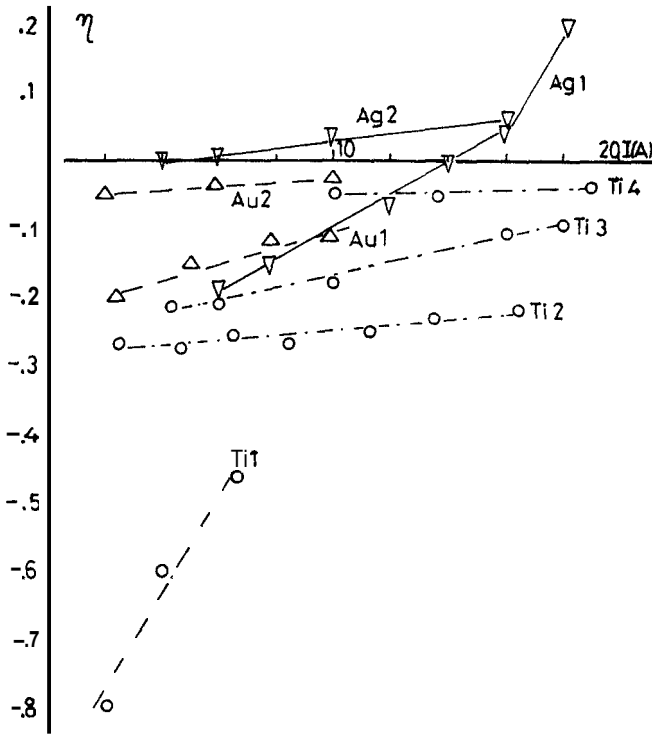


Fig. 4 Desorption coefficient η in molecules per ion versus proton beam intensity for titanium alloy (Ti(1) - Ti(4)), gold coating (Au(1) - Au(2)) and silver coating (Ag(1) - Ag(2)) each as measured after successive exposures to air and rebakes.

measured before and after exposure(s) to air and rebake. The same procedure, applied to the in situ deposited titanium layer which is shown in Figure *3*, gave, however, different results and the yield increased and remained high after the bakeout.

This behaviour is in strong contrast with the results obtained from liners made out of titanium alloy mounted inside the ISR vacuum chamber. The only pre-treatment which was given to this test surface consisted of a 3 hour bakeout at 700°C under vacuum. It has been found that this high temperature bake reduces the outgassing rate of the titanium sheet metal to at least one tenth of the value €or our normal degassed stainless steel, that is from about 2×10^{-13} to 2×10^{-14} torr ℓs^{-1} cm^{-2}. The initial desorption yield of these titanium liners, as measured after their first installation, turned out to be about **- 0.3**, see Figure *4*, curve Ti(1). Hence this chamber was strongly pumping in presence of beam. However, contrary to the previous experience with sublimated titanium, the alloy proved to be rather insensitive to contamination and maintained its negative desorption yield irrespective of several exposures to air and rebakes. The reason for this striking difference is not completely understood.

8. Long term behaviour of clean surfaces

When investigating the usefulness of various materials or surface treatments for low ion desorption yields, an important characteristic is their long term behaviour in an environment like the ISR. The test surfaces studied so far occupy a rather short length of the ISR circumference and have standard vacuum chambers on either side. It is therefore not excluded that, in the long term, contaminants are transferred from the normal chambers, where they are desorbed by the beam, to the specially cleaned test surface. This effect may well account for at least part of the gradual increase in η which is observed on the various chambers.

In this respect, the titanium alloy appears to be particularly promising. Over a period of 10 months and despite several bakeout cycles, its desorption yield increased from about **- 0.3** to - 0.03. It has therefore been decided to mount similar titanium liners in critical locations of the ISR where there is not enough space for additional pumps and a reduction of η remains the only possible way of obtaining stable vacuum. Effort goes, furthermore, into the development of titanium chambers for the intersecting regions to improve the vacuum conditions and to obtain chambers which are more transparent to high energy particles.

With the combined efforts of increasing the pumping speed and lowering the ion desorption yield η the ISR vacuum system has in the past steadily improved and the average pressure around the ring in the presence of stacked beams of up to 10 A has dropped to less than 10^{-11} torr. More important, however, the vacuum has become stable enough so that the original design aim of 20 A stable beams can now be obtained.

References

1) E. Fischer, ISR-VAC/67-16 (CERN, 1967)

2) L.J. Laslett, L. Resegotti, 6th Int. Conf. on High Energy Acc., 1967, p. 150

3) B. Angerth, E. Fischer, O. Gröbner, Proceedings of the VIII International Conference on High Energy Acc., CERN 1971, p. 298

4) H.G. Hereward, Coherent Instability due to electrons in a coasting proton beam, CERN-71-15, (1971)

5) E. Keil, B. Zotter, CERN-ISR-TH/71-58 (1971)

6) E. Fischer, K. Zankel, CERN-ISR-VA/73-52 (1973)

7) O. Gröbner, R.S. Calder, IEEE Transactions on Nuclear Science, Vol. NS-20, Nr. 3, June 1973, p. 760.

INFLUENCE OF THE SPLIT FIELD MAGNET SPECTROMETER ON THE CERN INTERSECTING STORAGE RINGS

P.J. Bryant and R. Perin
CERN
Geneva, Switzerland

Summary

The Split Field Magnet (SFM) is a general purpose spectrometer which has been functioning in an intersection of the CERN Intersecting Storage Rings (ISR) since summer 1973. Its equivalent field volume of 28 T.m^3 is crossed by the two circulating ISR proton beams. The bending action is compensated by two additional magnets per beam, and the focusing (— 2.4 T of integrated field gradient) by adjustable passive beam channels. The residual magnetic field effects were studied for tune changes across the aperture and the excitation of non-linear resonances, especially as the machine superperiodicity is reduced to one. Details are presented of these effects and of their compensation. The luminosity in the SFM is reduced by ~ 18 % due to an increase in the crossing angle of the beams, but the influence of the other factors has been limited to a few percent. Except for tune changes of the order of 0.004, which require minor modifications of working lines at the lower energies, and a small influence on high precision closed orbit bumps used for luminosity measurements, the ISR behave as if the SFM were not present. No operational restrictions have been encountered and all special facilities, such as acceleration to 31 GeV/c by phase displacement, remain unaffected.

1. Introduction and General Description

The Split Field Magnet, so called because it produces fields of opposite sign on either side of its vertical symmetry plane, is a large magnetic spectrometer installed in an intersection region of the ISR. The main requirements of the experimentalists were a large volume of magnetic field covering the full solid angle around the intersection and a bending power of at least 4 T.m in the forward beam directions. This field acts directly on the ISR beams.

With respect to the ISR machine, the system had to disturb the circulating beams as little as possible and had to be such that it could be switched off without hampering the regular operation. This implied that the existing ISR magnet structure could not be altered.

The above mentioned requirements led to a design which includes a number of unconventional solutions such as the pentagonal shape of the main magnet, the absence of a yoke to carry the return flux and to withstand the magnetic forces, the magnetic channels to protect the proton beams over part of their way through the magnet and the need to assemble completely the magnet outside the ISR and to transport it as a single unit to its working place.

A general layout of the installation is shown in Figure 1. Each proton beam passes through an upstream compensator, the main magnet and a downstream compensator magnet. The main magnet[1] can be regarded as composed of two horseshoe type magnets equidistant from the horizontal symmetry plane. At the beam crossing point, the magnetic field is zero and has opposite signs upstream and downstream of that point. The force of attraction between the poles and the weight of the top yoke and coils are supported by four pillars made from non-magnetic steel. Magnetic channels screen the ISR beams from the defocusing effects of the upstream edges of the magnet and compensate those occurring in its central part. They have the form of long rectangular tubes and are made from low carbon steel and aluminium. Their cross-section varies from point to point along their length in order to cope with the different field intensities and gradients. Over the last half meter, near to the beam intersection, the channels are provided with horizontal plates called "trim flaps" that can be inclined at a variable angle to the horizontal. With the trim flaps it is possible to produce, at will, field gradients to adjust the behaviour of the channels for different field levels and to compensate the edge focusing at the intersection.

The large compensators are H-type magnets with asymmetric return yokes. Besides compensating the deflection of the ISR beams, they are used for the analysis of high momentum particles produced at small angles. The small compensators are short window-frame magnets. All magnets are aligned in the ISR with an accuracy of 0.1 mm.

Table 1 summarizes the main features of the magnets.

TABLE 1

Main Magnet (SFM)			
- Nominal induction in median plane			1.14 T
- Gap height			1.10 m
- Length			10.50 m
- Width	at the end		2.00 m
	at the centre		3.50 m
- Weight			900 t
- Nominal power			4 MW
Compensators		**Large**	**Small**
- Nominal induction in median plane	(T)	1.5	1.8
- Gap height	(m)	0.4	0.075
- Steel length	(m)	1.5	0.435

2. Criteria Used in the Design and Assessment of the SFM

Every effort was made in the SFM design to minimize the loss of luminosity and the degradation of the ISR beams. For bending effects, this entails careful adjustment of the compensator magnets to prevent the residual orbit distortion from decreasing the maximum stack width. The local loss of luminosity of 18 % in the SFM itself, which arises from an increase in the beam crossing angle, is unavoidable. To evaluate the impact of the focusing effects on the whole ISR, the fractional

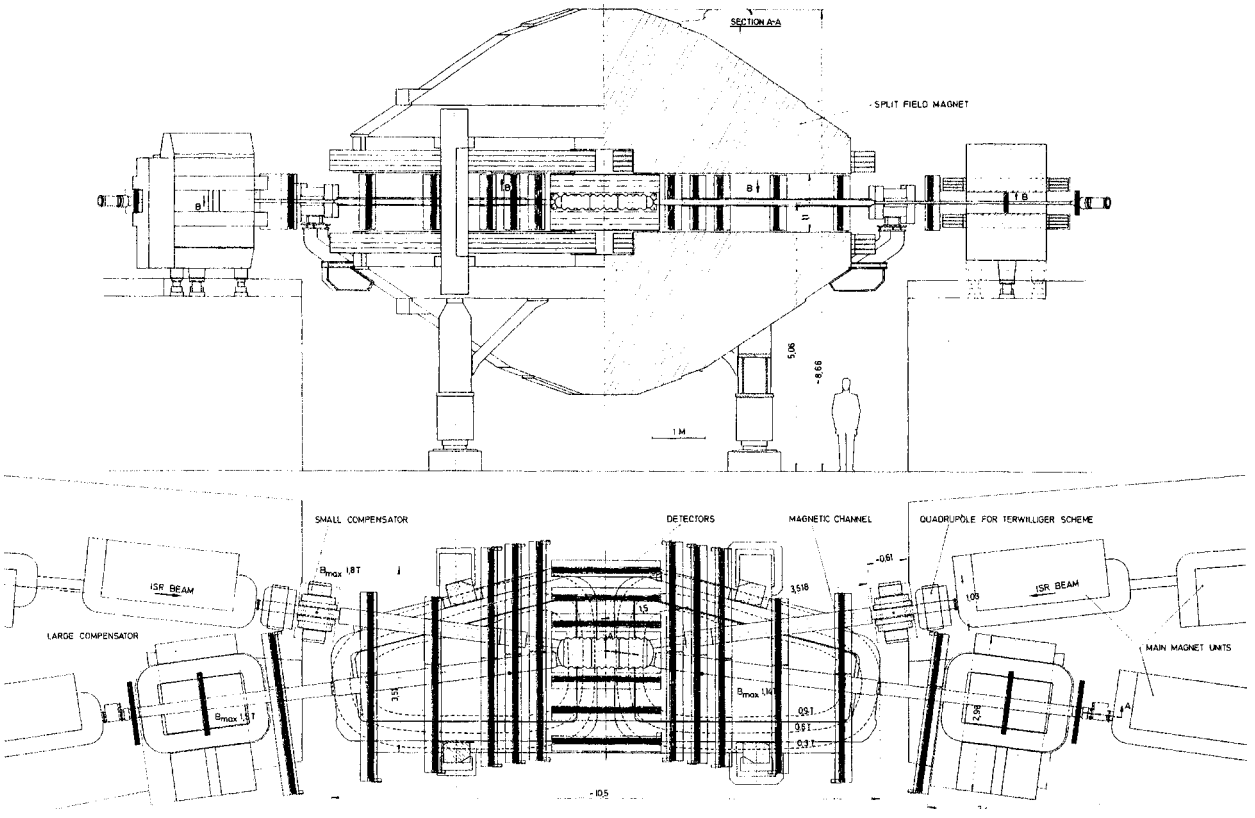


Figure 1. Schematic Layout of the Split Field Magnet Facility in the Intersection Region *I4*

change in a notional maximum luminosity was used, which assumes the vacuum chamber to be entirely filled by the beam[2]. This reduction of luminosity arises from an increased modulation of the momentum compaction function and from increased horizontal and vertical betatron oscillation amplitudes.

Finally, the effects of non-linear resonances have been estimated and evaluated in terms of the existing excitations in the ISR.

3. Bending Effects

Figure 2 shows the closed orbits in the SFM system with reference to the undisturbed beam trajectories. The compensator settings were calculated from the magnetic measurements at each field level. A mismatch of only *38* Gm at 25 GeV/c is sufficient to create a residual distortion in the *ISR* of ± 1 mm peak-to-peak. As can be seen from Table 2, this limit has been respected and, in most cases, improved upon. This level of distortion can be safely tolerated.

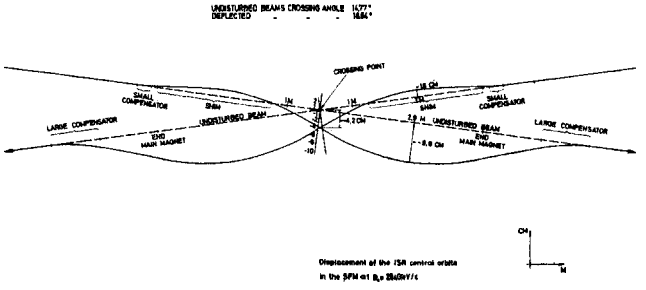


Figure 2. Displacement of the ISR central orbits in the SFM at p = 25 GeV/c and B_o = 1.14 T.

TABLE 2

Residual Closed Orbit Distortion Added to ISR

Energy GeV/c	26.588	22.505	15.376	11.780
Horizontal orbit distortion peak-to-peak	±0.5 mm	±0.65 mm	---	±1.1 mm

4. Focusing Effects

The beam enters the SFM on the upstream aide at an angle of $\sim 20^{o}$ to the pole edge and crosses the central region at -80^{o} to the plane of the field reversal (see Figure 1). At full field, the integrated transverse gradients in these regions are 2 T and *0.3* T, respectively (see Figure *3)*. According to the criterion mentioned in section 2, these gradients, if uncompensated, would cause 87 % loss in luminosity. The use of a compensating quadrupole directly upstream of the small compensator could reduce this loss to 35 %. This was still felt to be too high, especially since the luminosity in the SFM itself is further reduced by 18 % due to the increased crossing angle. For this reason, magnetic channels were adopted although they obstruct somewhat the physics equipment and create showers of secondary particles. Despite the widely different degrees of saturation in the magnetic channels between the maximum and minimum field levels, the transverse gradient seen by the beam when crossing the pole edge is virtually eliminated. The central gradient is compensated by the trim flaps. The overall effects at full and half field are shown in Figure 4.

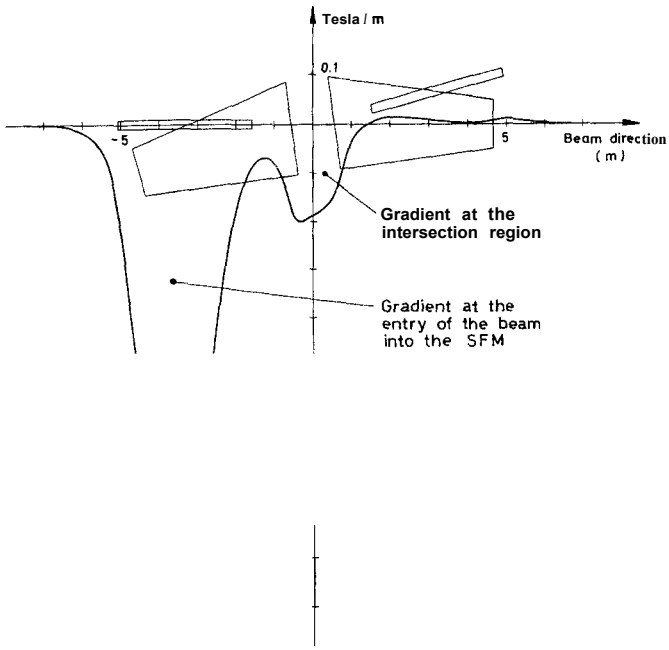


Figure 3. Transverse gradient without magnetic beam channels at maximum field level.

The small field gradients acting on the beam in the downstream half of the SFM depend upon the radial position of the magnet. Using the measurements made at full and half field on a fifth scale model, the variation of luminosity with the radial position of the SFM was evaluated in order to find the best balance between the various regions of gradient. On the basis of these calculations, it was decided to place the SFM so that its geometrical centre was shifted by 10 cm to the inside of the ISR with respect to the undisturbed beams' crossing point, Under these conditions, the loss in luminosity was estimated at 7 - 9 %.

A tracking program, using the magnetic measurements made at each field level, was used to integrate the residual field components along the beam trajectory. Table 3 summarizes the results for the central orbit and Table 4 gives the changes in the beam parameters derived from these measurements.

TABLE 3

Integrals of quadrupole and sextupole components along the beam trajectory (Ring 1)

SFM field level (T)	Corresponding momentum (GeV/c)	Integrated quadrupole (T)	Integrated sextupole (T/m)
1.14	26.588	- 0.0117	- 1.103
1.00	22.505	- 0.0056	- 1.141
0.65	15.376	0.0	- 0.900
0.50	11.780	- 0.0028	- 0.767

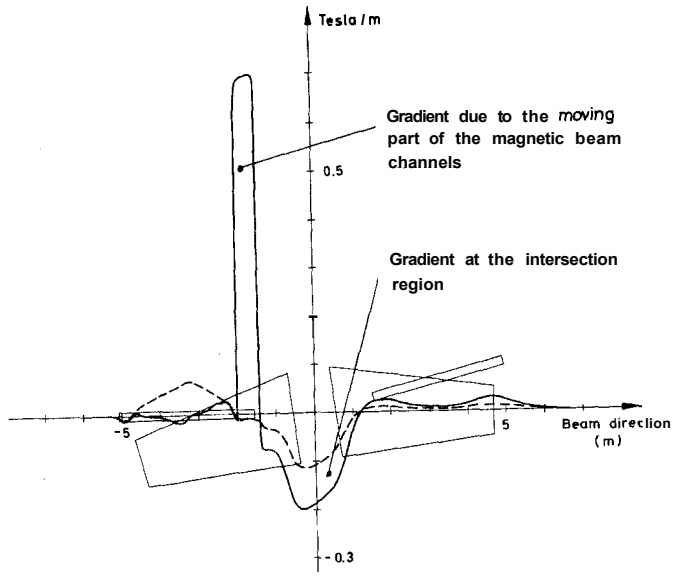


Figure 4. Transverse gradient with magnetic beam channels at :
- maximum field level (————)
- half field level (----------)

TABLE 4

Computed changes of ISR parameters with the SFM

	SFM field level (T)			
	Corresponding momentum (GeV/c)			
	26.588	22.505	15.376	11.780
ΔQ_H	0.0003	0.0003	0.0001	0.0001
ΔQ_V	0.0014	0.0015	0.0014	0.0012
$\Delta Q'_H$	0.048	0.060	0.076	0.082
$\Delta Q'_V$	- 0.030	- 0.038	- 0.044	- 0.048
$\Delta\beta_{H,max}$	0.07	0.06	0.08	- 0.12
$\Delta\beta_{V,max}$	0.67	0.80	0.85	0.86
$\Delta\alpha_{p,max}$	0.006	0.008	0.006	0.005
$\frac{L(S)}{L(0)}$	0.966	0.960	0.960	0.966

where :

- ΔQ_H, ΔQ_V are the changes in horizontal and vertical tunes,
- $\Delta Q'_H$ $\Delta Q'_V$ are the changes in horizontal and vertical tune spreads,
- $\Delta\beta_{H,max}$, $\Delta\beta_{V,max}$ are the changes in the maximum horizontal and vertical betatron amplitude functions,
- $\Delta\alpha_{p,max}$ is the change in the maximum momentum compaction function,
- $\frac{L(S)}{L(0)}$ is the fractional change in the luminosity due to the changes in β_H, β_V and α_p. "S" signifies the presence of the SFM and "0" its absence.

The parameter changes and loss of luminosity calculated in Table 4 are so small as to be practically unmeasurable in the machine and indeed the ISR performance has shown no degradation. However, it has been found necessary to make some minor tune changes *(0.004)* at injection to the ISR working lines at 11, 15 and 22 GeV/c and to modify by 1 - 2 % the excitation of the dipole magnets for the high-precision, vertical bumps used in the SFM itself for luminosity measurements.

5. Higher Order Effects

Equation (1) is the general condition for a non-linear resonance

$$n_1 Q_H + n_2 Q_V = p \qquad (1)$$

where :

$(n_1 + n_2) = N$, the order of the resonance,

p is the order of azimuthal harmonic of the magnetic imperfection exciting the resonance.

In the case of the SFM, the field on the median plane is purely vertical. This limits the resonances, which can be excited, to those for which n_2 is even. The measurements cannot give reliable results beyond the octupole term, so it is not possible to calculate the resonance excitation for the SFM beyond the 4th order resonances. A coefficient of excitation, d_p, can be defined[3] for a series of, m, localized errors?

$$|d_p| = \frac{1}{C} \left| \sum_m \beta_{H,m}^{n_1/2} \beta_{V,m}^{n_2/2} \ell_m e^{i(n_1 \mu_{H,m} + n_2 \mu_{V,m})} \left(\frac{\partial^{N-1} B_z}{\partial x^{N-1}} \right)_m \right| \qquad (2)$$

(for n_2 even)

where :

$\mu_{H,m}$, $\mu_{V,m}$ are the betatron phases in the m^{th} region

ℓ_m is the length of the m^{th} field error

C is the machine circumference

B_z is the vertical field

The SFM was sub-divided along the trajectory and the excitation coefficients as given by equation (2) were evaluated for the 3rd and 4th order resonances. The results are summarized in Table 5. These calculations are based on the intermediate field level of 0.65 T with a beam momentum of 15 GeV/c.

To give some idea of the meaning of these coefficients, the coefficient for the 4th order resonances ($N = 4$, $n_1 = 4$, $n_2 = 0$) arising from the main ISR magnet is [illegible]. Thus, the SFM adds approximately the same order of magnitude to the resonance excitation as the ISR main magnet. However, the beam-beam excitation of resonances is an order of magnitude stronger and remains the dominant effect[4]. The limitation to 4th order resonances, imposed by the accuracy of the magnetic measurements, left some uncertainty as to the higher order resonance excitations. Subsequent operation with the ISR has given no evidence of extra excitation arising from the SFM.

TABLE 5

The SFM excitation coefficients for 3rd and 4th order resonances on the equilibrum orbits for momentum deviations, $\Delta p/p$ = - 3 %, 0, + 3 %

(SFM field level = 0.65 T and beam momentum = 15 GeV/c)

Orbit $\Delta p/p$	Order of resonances n_1	n_2	N	Excitation $\lvert d_p \rvert$
	1			
	3			
0.0	2			0.0
	1	2	3	0.0
	3	0	3	0.0
- 3 %	2	2	4	6.1

Acknowledgements

The authors would like to thank all the people in the CERN ISR division who have contributed to the SFM project.

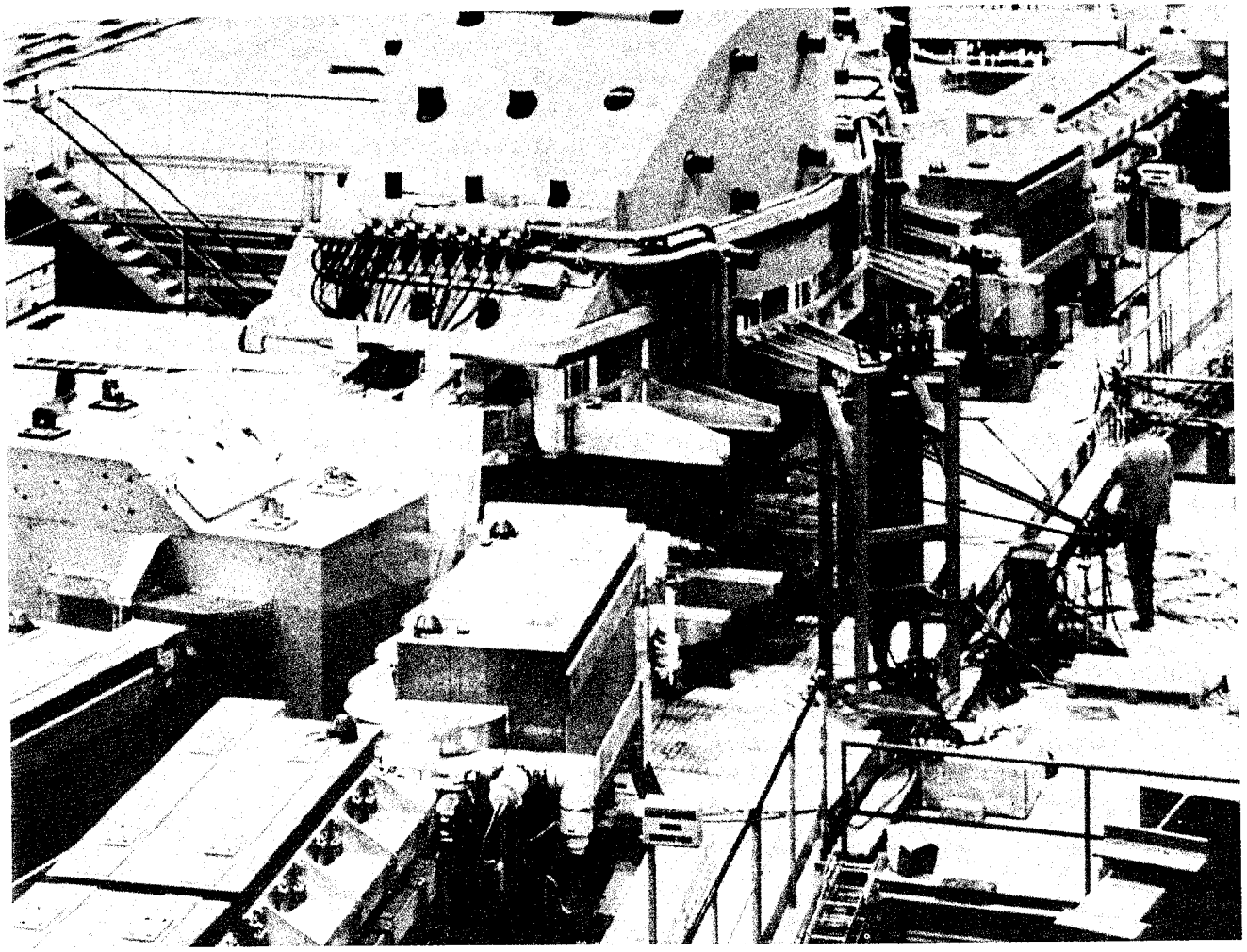


Figure 5. The SFM spectrometer installed in the ISR

References

1) B. Billan, R. Perin, V. Sergo - The Split Field Magnet of the CERN Intersecting Storage Rings - Proc. 4th Int. Conf. on Magnet Technology, Brookhaven (1972).

2) B. Couchman, B. de Raad, P. Strolin - Calculation of orbit perturbations and some remarks concerning the magnet system proposed for ISR experiments - ISR Divisional Report ISR-BT/68-57 (1968).

3) G. Guignard - Effets des Champs Magnétiques Perturbateurs d'un Synchrotron sur l'Orbite Fermée et les Oscillations Bétatroniques, ainsi que leur Compensation - Report CERN 70-24 (1970).

4) E. Keil - A comparison of non-linear resonances excited by magnet imperfections and by beam-beam space charge forces - (or Why be afraid of magnet imperfection resonances in high luminosity storage rings ?) - ISR Divisional Report ISR-TH/73-25 (1973).

DYNAMIC COMPENSATION DURING STACKING OF THE DE-TUNING CAUSED BY SPACE CHARGE EFFECTS

P.J. Bryant
CERN
Geneva, Switzerland

Summary

The incoherent tune-shifts, due to space charge, distort the tune values across the machine aperture (working line) and lead to the eventual onset of coherent instabilities. Until recently, for high intensity stacks in the CERN Intersecting Storage Rings (ISR), pre-stressed working lines have been used, which assume an ideal form under a given space charge load. Such lines require a lot of space in the tune diagram making it necessary to tolerate 5th order non-linear resonances inside the stack with a subsequent increase in decay rate and background. By correcting the incoherent tune-shifts during stacking by means of a progressive variation of the currents in the poleface windings, the line never deviates far from its ideal shape. In this way, practically the full tune-spread can be maintained throughout and the line requires less space in the tune diagram. This enables stacks occupying the full width of the vacuum chamber to be kept free of all resonances lower than the 8th order. The corrections are calculated according to the wanted stack position and intensity, so giving a high degree of flexibility. Working line measurements made inside the stack at each step have shown the calculation method to be very accurate. Despite the greater complexity, several variants have been made operational and the highest luminosity, which has been achieved under physics conditions (6.6×10^{30} $cm^{-2}s^{-1}$), has been obtained using this technique in conjunction with stabilization by transverse feed-back on the stacks.

Introduction

The distribution of the horizontal and vertical tunes (Q_H, Q_V) across the machine aperture (working line) is of extreme importance for ISR operation and for physics conditions. Working lines can be conveniently classed as static or dynamic. The former are either made with a disregard for the space charge deformations, e.g. "FP" in Figure 1, or with a pre-stress that gives the line an ideal shape for a given space charge load, e.g. "5C" in Figure 1. These two lines have been extensively used for ISR operation and "FP" is still the principal low intensity line. The philosophy of dynamic lines is to progressively correct the space charge deformations during the stacking so that the working line never departs very far from its ideal form. Operationally this is far more complicated and is only made possible by the very considerable flexibility of the poleface windings under computer control, but the results are amply rewarding.

The Advantage of a Dynamic Line over a Pre-stressed Static Line

Pre-stressed static lines require a lot of space in the tune diagram. This arises because the overall tune-spread has to be large enough to ensure that the local values inside the stack are sufficient for stabilization by Landau damping and secondly because the whole line sweeps across the tune diagram. For these reasons it was not possible to avoid the 5th order non-linear resonances which cross the stacking region on the "5C" line in Figure 1. These particular resonances exhibit a somewhat variable excitation and can cause decay rates of up to 200 parts per million per minute with the background so high as to make physics experiments very difficult if not impossible. In contrast, a dynamically compensated line can be much shorter, since the local tune-spreads inside the stack are maintained close to the maximum value and the line's excursions are very limited. Using the dynamically compensated line "8C", shown in Figure 2, full-aperture stacks of 17.6 A at 26 GeV/c can be made in the region between the 5th and 3rd order resonances, which is free of all resonances up to the 8th order. Compared to "5C", this line is shortened by a factor of 1.5 and the avoidance of the resonances lower than 8th order reliably gives excellent physics conditions.

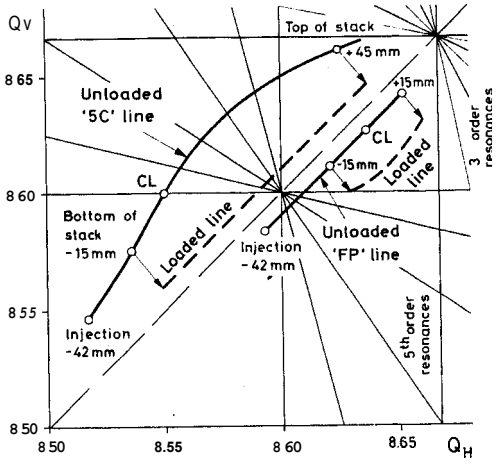


Figure 1. The Static Working Lines "5C" and "FP" shown with and without a Stack.

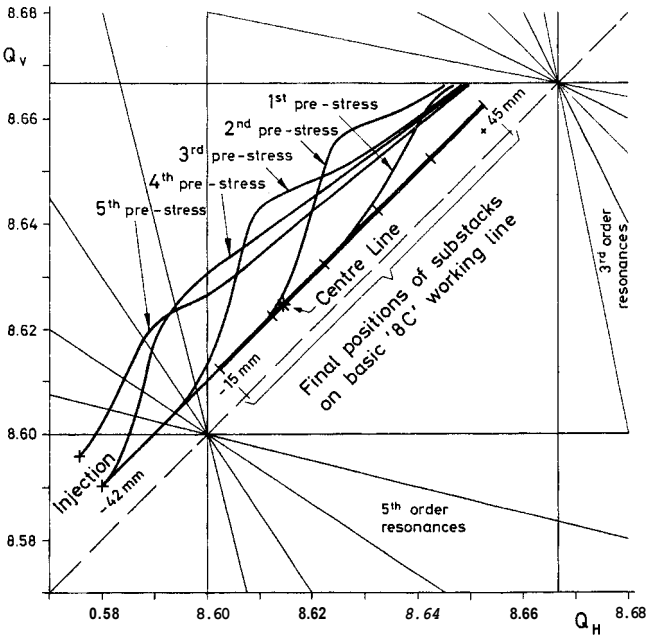


Figure 2. The "8C" Family of Pre-Stressed Working Lines used at 26 GeV/c to stack 17.6 A in 5 Steps of 3.52 A across the Chamber from +45 mm to -15 mm (α_p average).

Calculation of the "8C" Working Line

Equations 1 and 2 are an empirical fit to experimental data obtained in the ISR for the de-tuning caused by space charge. The equipment for measuring these incoherent tune shifts[1] has only recently become fully operational and so extensive measurements have not been made and no measurements yet exist outside the stack. Equations 1 and 2 fit the model shown in Figure 3.

$$\Delta Q_{H,\text{incoh.}} \quad \frac{0.04\ I}{\frac{2\pi}{\gamma}(r-a)}$$

$$\Delta Q_{V,\text{incoh.}} \quad \frac{0.04\ I}{\frac{2\pi}{\gamma}(r-a)}$$

where:

$\Delta Q_{H,\text{incoh.}}$ and $\Delta Q_{V,\text{incoh.}}$ are the incoherent tune-shifts

I is the beam current in ampere

γ is the total energy normalized by the rest energy

a, L, r are geometrical parameters defined in Figure 3.

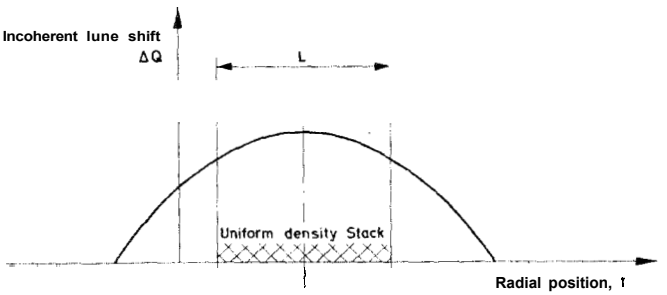


Figure 3. Space Charge Model for the Incoherent Tune-Shift.

Inside the stack these simple expressions work exceedingly well. Outside the stack they probably drop too rapidly to zero, but this is of less importance, except possibly for the injection optimization which depends upon stable conditions.

The necessary working line corrections are calculated by applying equations 1 and 2 to the complete stack after each substack is added. The difference between the overall corrections at each stage gives the pre-stress required for that substack. The pre-stresses are then expressed as an expansion of the tune derivatives with respect to the momentum deviation up to the octupole term. This is done independently for the inner and outer halves of the aperture. Finally, the coefficients are given to the ISR control computer which changes the poleface winding currents accordingly. A short computer program has been written to perform these calculations for any number, size and positions of the substacks.

Practical Realization of a Dynamically Compensated Line

The base line is first created and recorded in a file specifying all the relevant power supply currents. Re-alignments of the ISR and other changes make it necessary to periodically update this basic file. The pre-stresses, however, need no updating as they are in the form of small changes of tune derivatives, referred to the base line and are, therefore, invarient. Initially, the pre-stresses are checked by measuring the tune values on line[1] after each substack and making any corrections which are necessary. In the case of the "8C" working line (see Figure 2), some small changes in the sextupolar and octupolar terms were needed bat the calculated values proved surprisingly accurate. When applying the pre-stresses, the ISR control computer changes all the power supplies in ratio so that the circulating beam sees a smooth transformation which takes only a few seconds. The stack does not show any sign of disturbance. The "8C" stack is built up in 5 steps. Prior to each step the line is pre-stressed (see Fig.2) and then the space charge is added bringing the line back to its ideal form. This procedure is controlled interactively by the ISR computer and it takes about one hour to fill both rings at 26 GeV/c to the maximum current of 17.6 A. At no time does the "8C" working line wander outside the limits shown and the stack always maintains a respectful distance from the diagonal, ($Q_H = Q_V$), the 3rd order resonances and the 5th order resonances. If the full space charge pre-stress were applied in a single step, the stack would be swept across the 3rd and 5th order resonances and would be blown-up and partially destroyed. The "8C" line when loaded to its limit, is sufficiently stabilized by Landau damping to survive under very quiet conditions, but the slightest disturbance will cause the stack to be lost. The active transverse feed-back system is, therefore, used to ensure the stack's stability[2].

Operational Limits and Tolerances for "8C"

The space available for the "8C" line is very limited. It has been found prudent not to allow the tune-separation, $A = Q_H - Q_V$, to fall below 0.01. For example, at A = 0.005 the betatron coupling strongly perturbs the 'tune values and an appreciable percentage (—17 %) of the larger horizontal emittance is coupled into the vertical emittance. Once the tune-separation for the baseline is fixed, the size of a substack and the top and bottom of the main stack are fixed by the space between the base line and the 3rd and 5th order resonances. The tolerances aimed for on the positioning of these lines is $\pm$ 0.001. Working lines above the diagonal ($Q_H = Q_V$) have to be pre-stressed prior to loading, whereas the converse is true for lines below the diagonal. Thus, working above the diagonal minimizes the number of power supply changes made with the circulating beam. There is a region on the third pre-stress for the "8C" line (see Figure 2) where the horizontal tune-spread drops locally to virtually zero. This point and other similar points lie outside the stack. Only single pulses cross these regions and their stability has given no problems. The horizontal tune-spread is in any case less important than the vertical one. In order to maintain the tight tolerances on the stack's position in the tune-diagram, the current density has to be carefully controlled to give the correct space charge loading. The radial positions of the substacks are maintained to $\pm$ 1 mm to avoid the resonances. To prevent rounding errors accumulating, the maximum number of substacks is limited to eight.

Operational Flexibility with "8C"

At first sight, the "8C" line is rigidly defined and the standard recipe always has to be followed. This is only partially true. As can be seen from equations 1 and 2, the incoherent tune-shifts scale directly with the current and inversely with the normalized energy. With just a few hours for making test stacks, the basic

"8C" scheme can be converted to any energy and to different current densities. Even more simply, substacks and their corresponding pre-stresses can be omitted. Table 1 gives the basic range covered by the "8C" family. There is no intrinsic reason to terminate Table 1 at 3 substacks, except that the intensities given by 1 or 2 substacks are more usually stacked on the "FP" line (see Figure 1). The currents for 5 substacks represent about the operational limit for "8C". Some tests with a six substack variant of "8C", which was designed to support 18 A at 22 GeV/c, revealed a limit at 16 A where transverse instabilities caused the stack to be lost in spite of the active feedback system.

Table 1

Some Variants of the "8C" Working Line

Momentum (GeV/c)	11.780	15.376	22.505	26.588
Linear Current Density (A/mm)	0.14	0.17	0.25	0.29
1 + 2 + 3 + 4 + 5	8.1 A	10.4 A	15.0 A	17.6 A
1 + 2 + 3 + 4	6.5 A	8.3 A	12.0 A	14.1 A
			9.0 A	10.6 A

With such tightly specified lines as "8C", an operational problem arises from unexpected current losses or losses due to scraping. These losses upset the space charge loading on the line and can move it onto the resonances and any further loss on say the 3rd order non-linear resonances only accelerates the working line drift. However, in practice these stacks have extremely low decay rates and rarely require any scraping to improve physics conditions. It has also become increasingly normal practice to correct working line shifts during physics runs. This has been made possible by a method for measuring tunes based on the Schottky noise from the stack[3].

Operational Results

At 22 and 26 GeV/c, "8C" has been extensively used with the full 5 substacks. Typically, the starting luminosities were 5 x 10^{30} $cm^{-2}s^{-1}$. More recently, "8C" has been used at 26 GeV/c with the top and bottom substacks omitted giving 10.6 A and with the base line moved further from the diagonal ($Q_H = Q_V$) (see Fig. 4). The most recent of these runs had a starting luminosity of 3.8 x 10^{30} $cm^{-2}s^{-1}$ with a beam decay rate of 0.8 x 10^{-6} min^{-1}. During this 27-hour run, the luminosity fell to 2.7 x 10^{30} $cm^{-2}s^{-1}$ and the decay rate rose to 1.1 x 10^{-6} min^{-1}. Approximately 40 % of the decay rate can be attributed to beam-beam interactions and the remainder to scattering on the residual gas. Although it is not a proven fact, it appears that the increased tune-separation improves injection optimization and the quality of the stacks. The maximum luminosity so far achieved in the ISR under physics conditions, 6.6 x 10^{30} $cm^{-2}s^{-1}$, has also been obtained on the "8C" line.

Future Developments

Incoherent tune measurements outside the stack will help to predict the tune changes at injection. The stability of the injection optimization could then be improved, although there is still the problem of closed orbit shifts due to coherent tune changes.

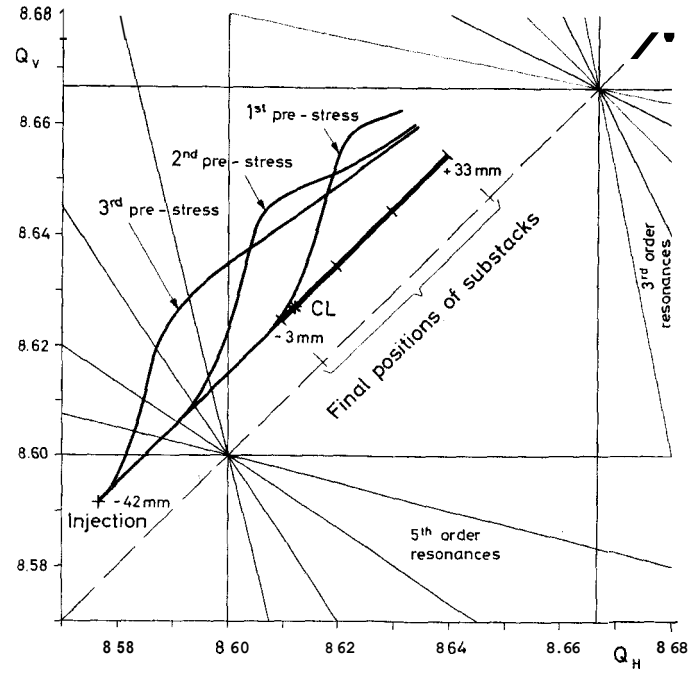


Figure 4. The "8C" Working Lines with the Top and Bottom Substacks omitted to give the Reduced Current of 10.6 A at 26 GeV/c and the Base Line moved away from the Diagonal to give $Q_H - Q_V = 0.015$

In order to stack still higher currents, an increased tune-spread is required. At present, an expanded "8C" line is being developed which extends across the the 5th order non-linear resonances. At the crossing point, the tune-spread is locally increased so that the resonances are traversed more quickly in momentum space By making separate stacks either side of the 5th order resonances, it is hoped that higher intensities can be reached.

Acknowledgements

The author would like to thank W. Schnell who suggested using a stepwise correction of the incoherent tune-shifts and who gave his full support and encouragement to this work. He also wishes to thank the large number of other people who combined their efforts to make this project possible.

References

1) B. Autin, J.P. Gourber, H. Laeger, L. Thorndahl - Measurement and Compensation of Space Charge Induced Q-shifts in the CERN Intersecting Storage Rings (ISR) - 1973 Particle Accelerator Conference Accelerator Engineering and Technology, IEEE Trans. on Nuc.Sci., June 1973, Vol. NS-20, No. 3, p. 802.

2) L. Thorndahl and A. Vaughan - Transverse Feedback for the ISR - 1973 Particle Accelerator Conference Accelerator Engineering and Technology, IEEE Trans. on Nuc.Sci., Vol. NS-20, No. 3, p. 807.

3) J. Borer, P. Bramham, H.G. Hereward, K. Hübner, W. Schnell, L. Thorndahl - Non-destructive Diagnostics of Coasting Beams with Schottky Noise - to be presented at this Conference.

TUNE SHIFT COMPUTATION FOR STORAGE RINGS WITH LOW-BETA SECTIONS

J. Buon

Laboratoire de l'Accélérateur Linéaire
Université de Paris-Sud, Centre d'Orsay,
Orsay, France.

Summary

On present rings with low-beta sections, the thin lens approximation for computing the betatron tune shift is no longer valid. Here the longitudinal distribution of the transverse electric field, generated by a stored bunch, is computed. The transfer matrix across the interaction region is obtained for small amplitude betatron motion. The linear betatron tune shift is derived for low-beta section.

Introduction

In a storage ring, one particle crossing an opposite bunch receives a transverse impulse from the electromagnetic field generated by the bunch. This effect leads to the beam loss observed at high intensity.

Usually the transverse impulse is computed within the thin lens approximation. Therefore, only the integral of the transverse electric field along the azimuthal direction Y is needed.'

For a particle with X and 2 transverse coordinates, the radial and vertical impulses, $\Delta\theta_X$ and $\Delta\theta_Z$, are :

$$\Delta\theta_{X,Z} = 4\pi\varepsilon \left(\frac{\xi^*}{\beta^*}\right)_{X,Z} f_{X,Z}\,(X,Z)$$

using the parameter :

$$\xi^*_{X,Z} = \frac{N\, r_e}{2\pi\gamma\,(\sigma^*_X + \sigma^*_Z)} \left(\frac{\beta^*}{\sigma^*}\right)_{X,Z}$$

N = number of particles in the bunch,

σ^*_X, σ^*_Z = transverse beam dimensions at the center of the interaction region,

β_X, β_Z = betatron amplitude functions at the center of the interaction region,

γ = ratio of the particle energy to the rest mass energy,

ε = + 1 for electron-electron interaction,

ε = - 1 for electron-positron interaction.

For small amplitude betatron motion ($X \ll \sigma^*_X$, $Z \ll \sigma^*_Z$), the functions f_X, f_Z are linear :

$$f_x \sim X \quad , \quad f_z \sim Z$$

In the last case, the betatron tune shift $\Delta\nu$ for each transverse direction is given by[2] :

$$\cos(\mu + 2\pi\,\Delta\nu) = \cos\mu - 2\pi\,\xi^* \sin\mu$$

where μ is the betatron phase shift between two crossing points.

On present rings with low-beta sections, the thin lens approximation is no longer valid for two reasons :

i) transverse beam dimensions vary along the interaction region,

ii) the radial or vertical displacement of the particle trajectory is not negligible during the crossing. This point is illustrated in Figure 1.

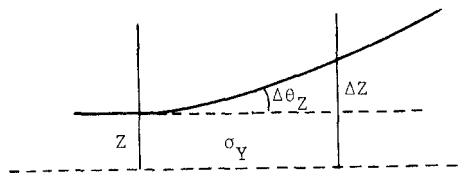


Fig. 1 : Vertical displacement A2 of a particle entering into the interaction region with a vertical coordinate Z.

Along the interaction length σ_Y, the vertical displacement ΔZ is approximately (Fig. 1) :

$$\Delta Z \sim \sigma_Y\, \Delta\theta_Z \sim 4\pi\varepsilon \frac{\xi^*_Z}{\beta^*_Z}\, \sigma_Y\, Z \quad .$$

The thin lens approximation assumes $\Delta Z \ll Z$, or :

$$\lambda^*_Z = 4\pi\, \xi^*_Z \frac{\sigma_Y}{\beta^*_Z} \ll 1 \quad .$$

On present rings ($\xi \lesssim .1$, $\sigma_Y/\beta^*_Z \sim 1$) this condition is not fulfilled.

For large values of λ_Z, the longitudinal distribution of the transverse electric field is needed in order to compute the kick. Therefore for a small betatron amplitude, the transfer matrix across the interaction region is obtained, by solving the linear differential equation of the motion. Finally, the betatron tune shift and the perturbation of β functions are computed.

Generally storage rings operate with two equal beams. Both beams influence each other. One must take into account the transverse dimension perturbation by the beam-beam interaction. On the contrary, one assumes here an interaction between a strong beam and a weak beam, with no perturbation of the former.

Longitudinal Distribution of the Transverse Electric Field

The electromagnetic field generated by one ultra-relativistic particle is almost entirely contained in the transverse plane of the particle. This provides a simple approximation for the field of any charged particle distribution.

More precisely the transverse electric field $E_\perp(t)$ created at the point M by one particle with uniform velocity along OY, located in A at time t, is[3] (Fig. 2) :

$$E = \frac{e}{\gamma^2\,(Y^2 + \frac{Z^2}{\gamma^2})^{3/2}} \times$$

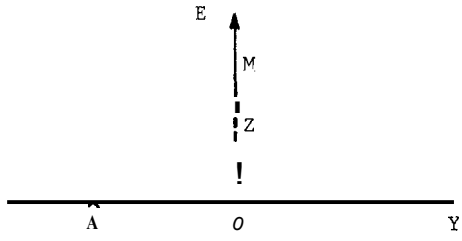


Fig. 2 : Transverse electric field created by one particle moving uniformly along the axis OY.

Two extreme cases can be distinguished :

i) $|Y| \ll \frac{Z}{\gamma}$ $\qquad E_\perp \simeq \frac{e}{4\pi\,\varepsilon_o} \times \frac{\gamma}{Z^2}$

ii) $|Y| \gg \frac{Z}{\gamma}$ $\qquad E_\perp \simeq \frac{e}{4\pi\,\varepsilon_o} \times \frac{Z}{\gamma^2\,Y^3} \ll \frac{e}{4\pi\,\varepsilon_o} \times \frac{\gamma}{Z^2}$.

Hence the field generated by particles at a longitudinal distance $|Y| > Z/\gamma$ can be neglected.

The Z-component of the electric field created at the point M (X,Y,Z) by a bunch of particles is approximated by :

$$E_Z \simeq \frac{e}{2\pi\,\varepsilon_o} \iint n(X',Y,Z') \, \frac{Z - Z'}{(X-X')^2 + (Z-Z')^2} \, dX' \, dZ'$$

where n(X',Y,Z') is the number of particles per unit volume at the point M'(X',Y,Z').

This approximation coincides with the exact value for a uniform linear density of particles along OY. For non-uniform particle density, the error is negligible at any point M not too far away from the bunch. In particular for a tri-gaussian bunch, the approximation is valid in the range $|Z| \ll .4\gamma\,\sigma_Y$, at a longitudinal distance $3\sigma_Y$ from the bunch center. For ultra-relativistic beams, the approximated expression for the transverse field can be used in order to compute the impulse given to one particle.

Longitudinal Distribution of the Transverse Impulse

Let one particle, at a longitudinal distance S apart from a synchronous particle, cross a tri-gaussian bunch of N particles :

$$n(X',Y',Z') = \frac{N}{(2\pi)^{3/2}\,\sigma_X\,\sigma_Y\,\sigma_Z} \times \exp\left[-\frac{1}{2}\left(\frac{X'^2}{\sigma_x^2} + \frac{(Y' + ct)^2}{\sigma_Y^2} + \frac{Z'^2}{\sigma_Z^2}\right)\right].$$

$\sigma_{X,Z}$ are the actual transverse dimensions, taking into account the longitudinal variation :

$$\sigma_{X,Z}(Y) = \sigma^*_{X,Z}\left(1 + \frac{Y^2}{\beta^{*2}_{X,Z}}\right)^{1/2}$$

The longitudinal distribution of the transverse impulse is :

$$\frac{d(P_X + iP_Z)}{dY} = \frac{2\varepsilon e}{c}(E_X + iE_Z)$$

$$\frac{d(P_X + iP_Z)}{dY} \simeq \frac{\varepsilon\,e^2}{\pi\varepsilon_o c} \times \frac{N}{(2\pi)^{3/2}\,\sigma_X\sigma_Y\sigma_Z} e^{-\frac{(2Y - S)^2}{2\sigma_Y^2}} \times \iint \exp\left[-\frac{1}{2}\left(\frac{X'^2}{\sigma_X^2} + \frac{Z'^2}{\sigma_Z^2}\right)\right] \frac{dX'\,dZ'}{X-X'-i(Z-Z')}$$

It is convenient to introduce dimensionless variables :

$$\frac{d}{dy}(\theta_x + i\theta_z) \simeq \frac{8\,\varepsilon\,N\,r_e}{(2\pi)^{3/2}\gamma} \times e^{-(2y - s)^2} \times \iint e^{-(x'^2+z'^2)} \frac{dx'\,dz'}{\sigma_X(x-x') - i\,\sigma_Z(z-z')}$$

Transfer Matrix Across the Interaction Region

For small amplitude betatron motion ($x \ll 1$, $z \ll 1$), the integral in the expression of the angular impulse is proportional to x + iz :

$$d(\theta_x + i\theta) \frac{8\,\varepsilon\,N\,r_e}{\sqrt{2\pi}\,\gamma\,(\sigma_X+\sigma_Z)} \times e^{-(2y - s)^2} (x + iz) .$$

In that case the X,Z equations of motion in the interaction region are linear :

$$\frac{d^2x}{dy^2} + K_X(y)\,x = 0$$

$$\frac{d^2z}{dy^2} + K_Z(y)\,z = 0 .$$

The radial and vertical gradients are :

$$K_{X,Z}(y) = -4\varepsilon\,\lambda_{X,Z} \times \frac{e^{-(2y - s)^2}}{\sqrt{2\pi}}$$

with

$$\lambda_{X,Z} = 4\pi\,\xi_{X,Z}\,\frac{\sigma}{\beta^*_{X,Z}}$$

The parameters $\lambda_{X,Z}$ depend on y through the transverse dimensions :

$$\xi_{X,Z} = \frac{N\,r_e}{2\pi\,\gamma\,(\sigma_X + \sigma_Z)}\left(\frac{\beta^*}{\sigma}\right)_{X,Z}$$

One can notice that the y-variation of the gradient $K_{X,Z}$ comes mainly from the exponential. The transverse dimension variation provides a slow dependence on y.

In the following, the vertical motion is studied in the case of a flat bunch : $\sigma_Z << \sigma_X$. For large values of λ_Z ($\lambda_Z \sim 1$), an approximated method cannot be easily found in order to solve the linear differential equation in z. A numerical method is used, and the transfer matrix across the interaction region is obtained.

Figure 3 shows numerical values of half the transfer matrix from y = - 1 to 0 for a synchronous particle (S = 0)†. The variation of the main diagonal elements a,d shows clearly the thick lens feature. The thin lens

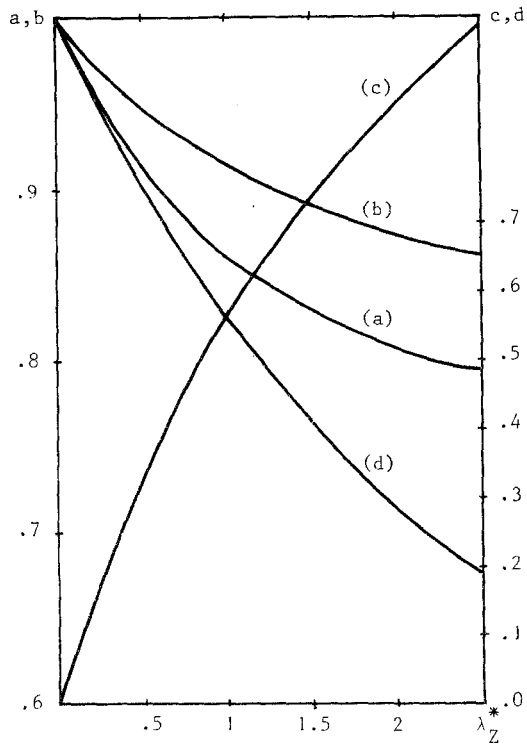


Fig. 3 : The elements of the transfer matrix $\begin{pmatrix} a & b \\ -c & d \end{pmatrix}$ versus the value λ_Z^* at the center of the interaction region.
$\xi_Z^* = .05$, $\sigma_Z << \sigma_Y$, s =.0

approximation is valid at the limit $\lambda^* = .0$, i.e. $\sigma_Y/\beta_Z^* = 0$.

At fixed λ_Z^*, the matrix elements depend also slightly on ξ_Z^*, on account of the vertical beam dimension variation with β_Z.

Ring Optics Perturbation

The transfer matrix across the interaction region is used in order to compute the linear betatron tune shift :

$$\Delta \cos\mu_Z = - p \cos\mu_Z - 2\pi q \xi_Z^* \sin\mu_Z \quad .$$

Figure 4 shows numerical values of p and q for different ξ_Z^*.

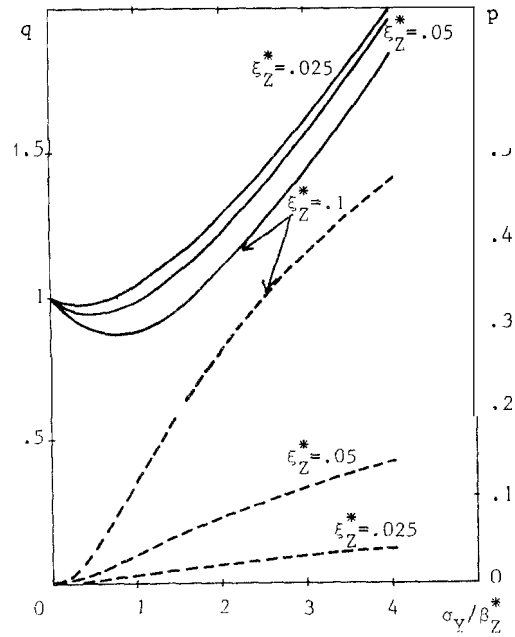


Fig. 4 : Coefficients p and q of the $\Delta\cos\mu_Z$ formula versus σ_Y/β_Z^* for different values of ξ_Z^*

——— : q ····· : p

For instance, in the case of SPEAR, at an operating point $\nu_Z \simeq 5.15$ the linear betatron tune shift increases with σ_Y/β_Z^* (Fig. 5). At $\beta_Z^* = \sigma_Y/2$ and $\xi_Z^* = .05$, the increase is about SO %. This can explain why the maximum luminosity decreases when the betatron amplitude function β_Z^* becomes smaller than the longitudinal dimension σ_Y.[4]

Non-synchronous particles ($S \neq 0$) cross the opposite bunch, at a distance S/2 on average from the interaction region center, where the amplitude function β_Z is somewhat larger than β_Z^*. Therefore the betatron tune shift is still larger for such particles (Fig. 5).

The betatron amplitude function, at the crossing point, is also perturbed :

$$\frac{\Delta \beta_Z^*}{\beta_Z^*} = \frac{p' \cos\mu_Z + (1+q') \sin\mu_Z}{\sin(\mu_Z + \Delta \mu_Z)} - 1 \quad .$$

† At longitudinal distance y < - 1 the impulse is negligible.

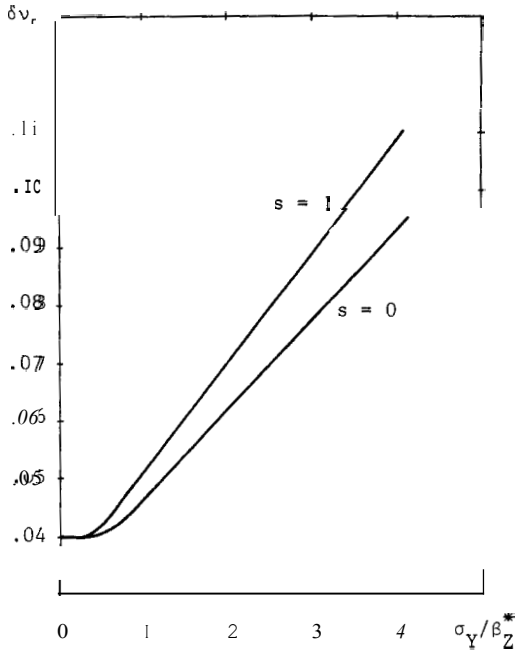


Fig. 5 : The linear betatron tune shift Δν, versus σ_Y/β^*_Z for a synchronous particle (s = 0) and a non-synchronous one (s = 1).

ν_Z = 2.575 ξ^*_Z = .05

Figure 6 shows numerical values of p' and q' for different ξ^*_Z. Contrary to the tune shift, there is no significant variation of β^*_Z with σ_Y/β^*_Z in the case of SPEAR, at ν_Z = 5.15.

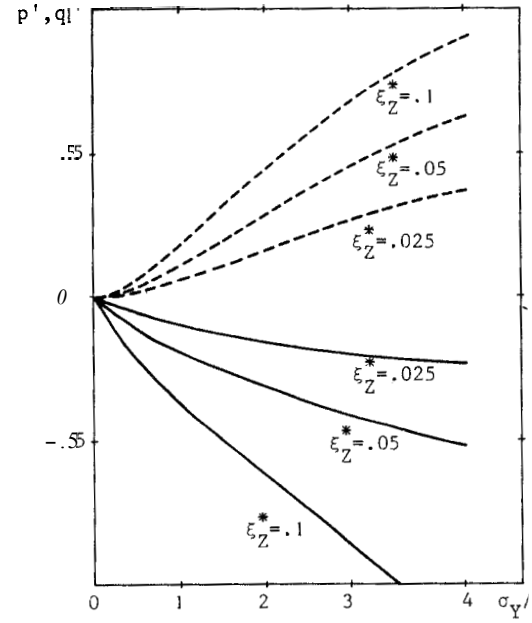


Fig. 6 : Coefficients p' and q' of the $\Delta\beta^*_Z/\beta^*_Z$ formula versus σ_Y/β^*_Z for different values of ξ^*_Z.

——— : q' ------- : p'

References

1. J.E. Augustin, RT/36-69, "Anneaux de Collisions", Laboratoire de l'Accélérateur Linéaire, Orsay (1969)

2. F. Amman and D. Ritson, Proceedings of the 111th International Conference on High Energy Accelerators, p. 471, Brookhaven (1961)

3. W.K.H. Panofsky and M. Phillips, Classical Electricity and Magnetism, p. 290

4. SPEAR Storage Ring Group, private communication.

EX MENTAL INVESTIGATION OF SINGLE-BEAM AND BEAM-BEAM SPACE CHARGE EFFECTS

P.J. Bryant and J.P. Gourber
CERN
Geneva, Switzerland

Summary

In order to improve the performance of the CERN Intersecting Storage Rings (ISR), it has become increasingly important to investigate experimentally the transverse space charge effects of both single-beam and beam-beam origin. The image-dominated, single-beam effects cause, in the first order, closed orbit distortions which have been measured and related to the coherent tune-shift variation across the aperture. Corrections for high precision bumps, used for luminosity measurements, have been calculated. This effect is also important when optimizing the beam-beam count rate. In the second order, these forces cause an incoherent tune-shift which is taken into account when adjusting the tunes across the aperture. The excitation of non-linear resonances by higher order effects has also been observed. The vertical closed orbit distortion due to beam-beam forces is one order of magnitude smaller than the corresponding single-beam effect. Measurements of this distortion have been related to the beam-beam tune-shift. Higher order effects are the strongest source of excitation for vertical non-linear resonances. The horizontal and coupled resonances are excited to a much lesser extent. It has been shown experimentally that by the appropriate adjustment of the beam-beam separations in the intersecting regions, this excitation can be minimized *so* reducing the decay rate and improving the physics conditions.

Introduction

Space charge effects in the ISR can be conveniently divided into single-beam effects and beam-beam effects. The single-beam effects are image-dominated and can be further sub-divided. Firstly, these image forces affect the motion of the beam as a whole, which can be conveniently studied in terms of a coherent tune-shift, and secondly, the motion of the individual protons is affected, which manifests itself as an incoherent tune-shift. To a lesser extent, the resonance excitation in the machine is also affected. The category of beam-beam effects can be similarly sub-divided. The effects on the closed orbits and tune-shifts are an order of magnitude less than for the single-beam case but the resonance excitation is, by contrast, a very important effect. The influence of space charge has become increasingly important as the operation of the ISR has become steadily more refined and sophisticated.

Single-Beam Coherent Tune-Shifts

The coherent tune governs the closed orbit, as well as the motion of the whole beam when it is disturbed. Thus, changes in the coherent tune directly affect the high precision closed orbit bumps[1] used for luminosity measurements[2]. Conversely, the closed orbit changes make it possible to measure the coherent tune-shift as a function of position with respect to the stack.

The closed orbit distortion can be expressed as a Fourier series in normalized co-ordinates (η, ψ):

$$\eta(\psi) = \sum_k F_k e^{ik\psi} \quad k = 0, 1, 2, \ldots \infty \qquad (1)$$

where:

- η is the orbit distortion normalized by the square root of the local betatron amplitude,
- ψ is the betatron phase normalized by the tune value,
- F_k is the kth azimuthal, harmonic amplitude of the orbit distortion.

The harmonics can be expressed as a function of the coherent tune, Q, and the corresponding azimuthal harmonics, f_k, of the magnetic imperfections[3].

$$F_k(Q) = \left(\frac{Q^2}{Q^2 - k^2}\right) f_k \qquad (2)$$

Providing the amplitude of the kth harmonic can be measured before and after any change in the space charge conditions, the coherent tune-shift ΔQ_c can be calculated from (2).

$$\Delta Q_c = \frac{Q}{2}\left[\frac{(1-E)(Q^2-k^2)}{E(Q^2-k^2) - Q^2}\right] \qquad (3)$$

where:

$$E = \frac{F_k(Q)}{F_k(Q + \Delta Q_c)} \qquad (4)$$

The method is most sensitive for k values close to Q which is 9 or 8 for the ISR.

The closed orbit measurements are made inside a stacked beam by detecting the position of empty scanning buckets in a way analogous to the closed orbit measurement made with single-beam pulses. By adding a thin tail to a dense beam, the empty scanning buckets can be "materialized" across the whole aperture and the variation of coherent tune-shift with position can be found. This has been done with a 10 A beam with a tail of 2.8 A spread across the aperture. Figure 1 gives the spatial variation of the 9th harmonic of the vertical closed orbit distortion with and without this stack. These results are used in the same Figure to give

$$\gamma \frac{\Delta Q_{c,\text{vertical}}}{\Delta I}$$

where:

- ΔI is the beam current exciting the ΔQ_c
- γ is the total energy normalized by the rest energy.

At the stack centre, $\{\gamma \Delta Q_{c,\text{vertical}}/\Delta I\}$ has its peak value of -0.15, which agrees well with other measurements made with the ISR[4].

The influence of space charge on half wavelength orbit bumps can now be investigated in some detail. Figure 2 shows a half wavelength closed orbit bump of amplitude F in the normalized co-ordinates (η, ψ). This deformation is expressed by:

$$\eta = F \cos(Q\psi) \text{ for } |\psi| \leq \pi/2Q$$
$$\eta = 0 \text{ for } |\psi| > \pi/2Q \qquad (5)$$

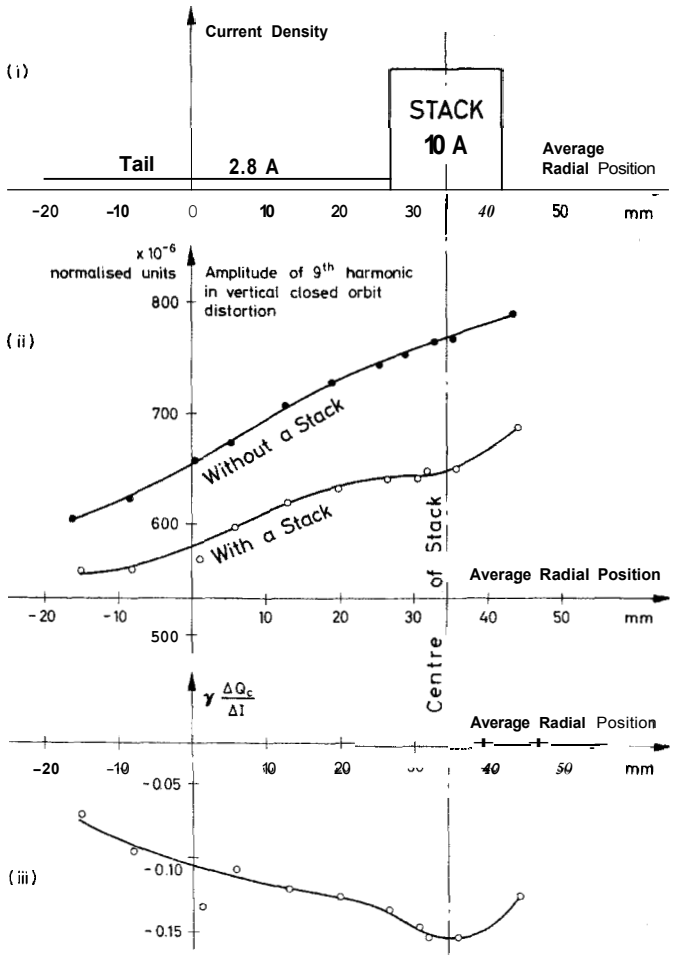


Figure 1. (i) Current Distribution in Stack
(ii) Variation of the 9th Closed Orbit Harmonic across Chamber
(iii) Variation of $(\Delta Q_{c,vertical}/\Delta I)\ \gamma$ across Chamber.

Giving harmonic amplitudes:

$$F_k = \frac{1}{\pi}\left[\frac{\sin\frac{\pi}{2}\left(1-\frac{k}{Q}\right)}{(Q-k)} + \frac{\sin\frac{\pi}{2}\left(1+\frac{k}{Q}\right)}{(Q+k)}\right] \qquad (6)$$

$$k = 1, 2, 3, \ldots \infty$$

Using (2), the effect can be calculated of a coherent tune-shift on the harmonic amplitudes given by (6). The resulting changes constitute a residual orbit distortion around the whole of the machine. Table 1 gives the errors arising in all intersections in the ISR from a single orbit bump in one intersection. These errors are expressed as a percentage of the height of the bump per ampere of circulating beam current with energy y. The effect is assumed to be linear for $|\Delta Q_c| < 0.2$. It is common practice in the ISR for luminosity measurements to take place simultaneously in several intersections. As can also be seen from Table 1, the compound errors can amount to a few percent when all bumps are excited with a beam of say 10 A. This does not favourably compare to the wanted accuracy of ± 0.5 %. By alternating the signs of the bumps in adjacent intersections, these residual effects are greatly reduced, but a more exact compensation is possible.

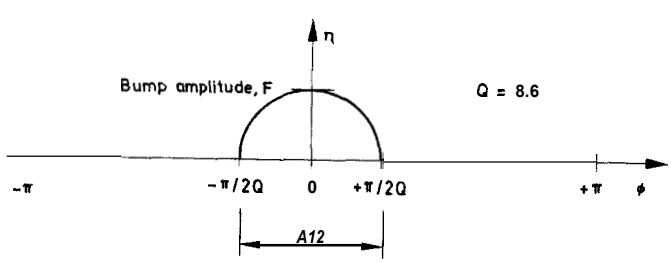


Figure 2. Half Wavelength Closed Orbit Bump in Normalized Co-ordinates.

Ring 2	I1*	I2	I3	I4	I5	I6	I7	I8
R	-0.35	1.17	1.56	3.20	3.45	1.29	1.56	-0.27

The ISR bumps are excited by two magnets separated by approximately half a wavelength with two more magnets acting as trimmers. Calculations were made to change the excitation of these magnets to compensate the mismatch in the 8th and 9th harmonics arising from the space charge, but this was found to be equivalent to the simpler procedure of calculating the orbit bumps with a tune-shift equal to the coherent one introduced into the computer program by modifying all the magnet gradients.

The stability or reproducibility of the closed orbit is also of great importance. It is usual practice to optimize the beam positions in the intersections and to measure the luminosity using 3 A stacks and then to re-stack high intensity beams. The new beams, however, are no longer optimized owing to the change in space charge conditions. This effect is found by summing over the harmonics in equation (2). The beam shift is not negligible. Consider a beam of 10 A at 22 GeV/c with a closed orbit dominated by a ± 3 mm peak-to-peak 8th order harmonic and a central non-space charge tune value of 8.6. Using (2) and $\gamma\ \Delta Q_c/\Delta I = -0.15$, an increase of 10 % is found in the 8th harmonic. If the peak falls at an intersection, there will be a shift of 0.3 mm in the orbit position. In addition to a small, and generally negligible reduction in luminosity, the change in the relative beam positions will produce an excitation of non-linear resonances. This is discussed later in this paper.

Single-Beam Incoherent Tune-Shifts

This is perhaps the best known space charge effect[5]. Recently, the dynamic compensation of the incoherent tune shift during stacking has become operational practice in the ISR. This is dealt with in detail in Reference 6 which is also presented at this Conference.

Single-Beam High Order Effects

The higher order moments of the single-beam space charge forces affect the excitation of non-linear resonances, which in turn are known to largely govern the decay rates and the background conditions in the ISR. However, resonance excitation is generally much stronger when the second beam is present. The investigation of these single-beam high order effects has only recently been started in the ISR. The experimental technique used consists of moving empty RF buckets across the machine aperture inside a stack. When the bucket position coincides with the position of a resonance, the surrounding particles are moved into that resonance. Aperture limiting the beam enhances the beam losses, which mark the resonances.

Beam-Beam Interaction

In the 8 intersecting regions of the ISR, the two beams interact electromagnetically. These forces have been studied theoretically for their influence on the tune values and on the excitation of non-linear resonances[1]. In these References, two extreme cases are generally considered; the case of head-on collisions between the two beams and the case of machines, such as the ISR, with a large crossing angle between the two beams. In the latter case, the two beams only interact over a short distance over which the variations of phases, betatron amplitudes and beam dimensions are negligible. Under these conditions, the electromagnetic forces cancel in the plane of crossing and add in the other plane, which explains why the main beam-beam effects in the ISR are observed in the vertical plane.

Dipole and Quadrupole Beam-Beam Effects

The vertical forces, $F_z(z,s)$ exerted by a beam on a test particle of the other beam is an odd function of the beam separation z and vanishes for $z = 0$. For the vertical motion, this is equivalent to a horizontal magnetic field. $B_x(z,s)$, the gradient of which imposes a tune-shift on the test particle of:

$$\Delta Q_V = \frac{1}{4s}\frac{1}{B\rho}\,\beta_V^{int}\int\left(\frac{\partial B_x(z,s)}{\partial z}\right)_{z=0} ds \quad \text{per intersection,} \tag{7}$$

where:

- $B\rho$ is the magnetic rigidity,
- β_V^{int} is the vertical betatron amplitude function at the intersection, and

the integral is extended over the whole interaction length, s being the distance along the beam.

For small values of z, the vertical force $F_z(z,s)$ produces a vertical closed orbit distortion given by:

$$\Delta z = \frac{1}{B\rho}\frac{\sqrt{\beta_V\,\beta_V^{int}}}{2\sin(\pi Q)}\, z\cos Q\,(\pi+\psi-\psi_{int})\int\left(\frac{\partial B_x(z,s)}{\partial z}\right) ds \tag{8}$$

The integral can be eliminated between the two equations (7) and (8) giving:

$$\Delta z = \frac{2\pi}{\sin(\pi Q_V)}\sqrt{\frac{\beta_V}{\beta_V^{int}}}\;\Delta Q_V\; z \quad \cos Q\,(\pi+\psi-\psi_{int}) \tag{9}$$

β_V and the normalized betatron phase ψ are at the point where Az is measured and β_V^{int} and ψ_{int} are taken at the intersection. Measurements of these effects in the ISR were made using a very sensitive magnetic beam detector. The vertical displacements of a coasting 6 A beam were measured near an intersection when vertically steering the other beam of 11.2 A by an amount z in all intersections at 26 GeV/c. The result $\Delta z/z = -6\cdot10^{-3}$ corresponds to a tune-shift of $-2.2\cdot10^{-4}$, which compares favourably with $\Delta Q_V = -2.7\cdot10^{-4}$ calculated using the theoretical formula[10]:

$$\Delta Q_V = \sqrt{\frac{2}{\pi}}\,\frac{\lambda r_o\,\beta_V^{int}}{\gamma\,\alpha\,\sigma_o} \tag{10}$$

where:

- $\lambda = \frac{N}{2\pi R}$ is the linear particle density
- r_o is the classical proton radius
- α is the crossing angle (14.77°)
- γ is the normalized energy
- σ_o is the r.m.s. half height of the beam (2.0 mm as measured by scraping the beam after the experiment).

In the case of high intensity beams, these vertical orbit distortions can introduce errors in luminosity measurements. For example, with two beams of 11.2 A at 26 GeV/c, the beam separations at the intersecting points would be increased by:

- 1.2 % when bumps of the same sign and amplitude are applied in all intersections simultaneously.
- 0.1 % when these bumps have alternate signs.

The comparison between the two cases gives an additional argument to use alternate humps in the ISR luminosity calibrations. By scaling these results to the lowest ISR energy and by keeping the same vertical beam dimensions, the error is less than 0.1 % for the usual 3 A beams used for luminosity measurements when alternate bumps are used.

Eeam-Ream Excitation of Non-Linear Resonances

In the approximation of a purely vertical resultant of the beam-beam forces and assuming a length of electromagnetic interaction short with respect to the wavelength of the azimuthal harmonic associated with the resonance, only vertical resonances $NQ_V = p$ can be excited, where N is the order of the resonance. The excitation term is the pth harmonic of the azimuthal angle 6 of the (N-1)th derivative of the force $F_z(z,s)$. The force $F_z(z,s)$ is an odd function of z as are its even derivatives. The contrary is true for the odd derivatives which are even functions of z, thus giving for the excitation produced by one intersection the curves of Figure 3. The contributions of all intersections have to be added according to their phase (i.e. $p\theta$ or $N\mu_V$ where μ_V is the vertical betatron phase). In a perfect machine ($z = 0$) and with a superperiodicity of 4, only vertical even order resonances are excited which have p as a multiple of 4. In a practical machine, as soon as z is different in all the intersections, all the vertical resonances occur.

The more sophisticated theories for the beam-beam interaction[9] lead to the same qualitative results: all the resonances $n_1 Q_H + n_2 Q_V = p$ where $(n_1 + n_2 = N)$ are excited but the excitation drops rapidly when n_1 increases from 0 to N. The excitation due to the beam-beam interaction is in general much stronger than that resulting from the magnetic imperfections of the ma-

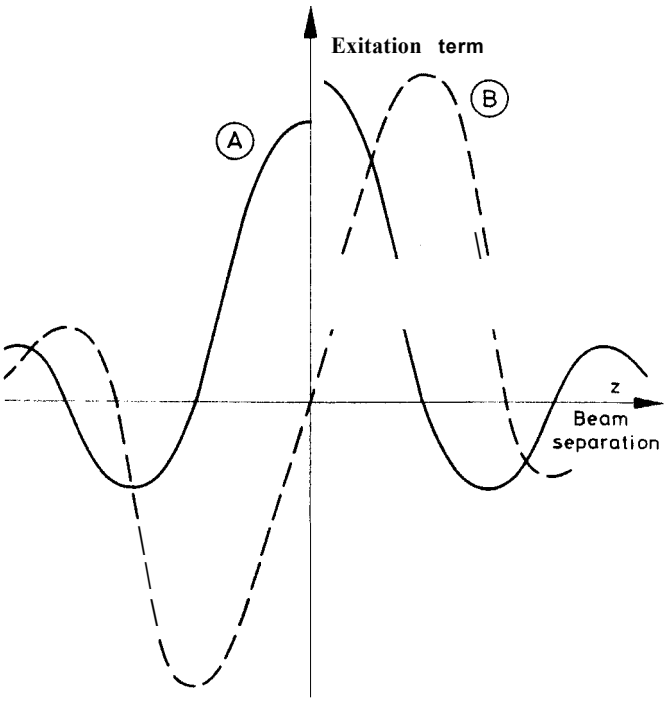


Figure 3. Variation of Resonance Excitation with the Beam Separation 'z' for an even order Resonance (A) or an odd order Resonance (B)

chine and in the ISR it was found to be the main cause of erratic decay rates and high background when using the 5C working line which crosses 5th order resonances (see Figure 4).

The method used to investigate these effects consisted mainly in displacing small beams from the injection orbit to the external orbit and vice versa by RF acceleration, and watching for beam losses when crossing resonances. Figure 4 shows such aperture scans made in Ring 1 in the presence of a stack of 14.5 A in Ring 2. As expected, only the purely vertical resonances $7\,Q_v = 60$, $5\,Q_v = 43$ and $8\,Q_v = 69$ are visible. The losses on $8\,Q_v = 69$ are one order of magnitude smaller than those observed on $5\,Q_v = 43$ which explains why a working line sitting across 8th order resonances rather than 5th order resonances gives improved decay rates and physics conditions[6].

However, as soon as only one resonance predominates in a stack, it is possible to zero the excitation of this particular resonance by suitably adjusting the beam separation in the intersections. This was done in Ring 1 for the resonance $5\,Q = 43$ (see Figure 4) by steering the beam in Ring 2 by 8.4 and 0.6 mm in two pairs of intersections, 14/18 and I2/I6. These intersections were chosen since they are separated by 90° for the 43rd harmonic in θ. This method of compensation greatly improves the decay rates and the background conditions of stacks. An experiment was carried out using the same 14.5 A beam in Ring 2 and a 12.5 A beam in Ring 1 placed on the working line 5C26 so as to avoid the 7th order resonances (see Figure 4). The vertical aperture of Ring 1 was reduced in order to increase artificially the decay rates and to simulate old physics stacks. When passing from the most unfavourable conditions of resonance excitation to a perfect compensation by vertical steering in Ring 2, the decay rate in Ring 1 was reduced by a factor 15. The required precision for the vertical steering was of the order of 1/10 mm. The gain observed in Ring 2 was smaller (a factor 3). This can be explained, since only two pairs of intersections were used to compensate the defects of 8 intersections. It follows that since the phase-shifts in internal and external arcs of the ISR are different, a compensation scheme which uses only two pairs of intersections cannot satisfy the requirements of both rings simultaneously. This problem can be overcome by distributing the corrections in all the intersections and experiments are continuing in this direction in the ISR.

The importance of these high order beam-beam effects have been recently demonstrated in relation with the acceleration of large intensity beams by phase displacement[10].

Acknowledgements

The authors would like to thank H.G. Hereward for many helpful discussions. They would also like to thank the many other people whose efforts have made the experimental work possible.

References

1) H.G. Hereward - Private communication.

2) S. Van der Meer - Calibration of the Effective Eeam Height in the ISR - ISR Divisional Report ISR-PO/68-31 (1968).

3) E.D. Courant and H.S. Snyder - Theory of the Alternating-Gradient Synchrotron - Annals of Physics, Vol. 3, p. 1-48 (1958).

4) K. Hübner, E. Keil and B. Zotter - Coherent Space Charge Phenomena in the ISR - Proc. 8th Int. Conf. on High Energy Accelerators, p. 295-297, CERN (1971).

5) L.J. Laslett and L. Resegotti - The Space Charge Intensity Limit Imposed by Coherent Oscillation of a Bunched Synchrotron Beam - Proc. 6th Int. Conf. on High Energy Accelerators, p. 150, Cambridge (1967).

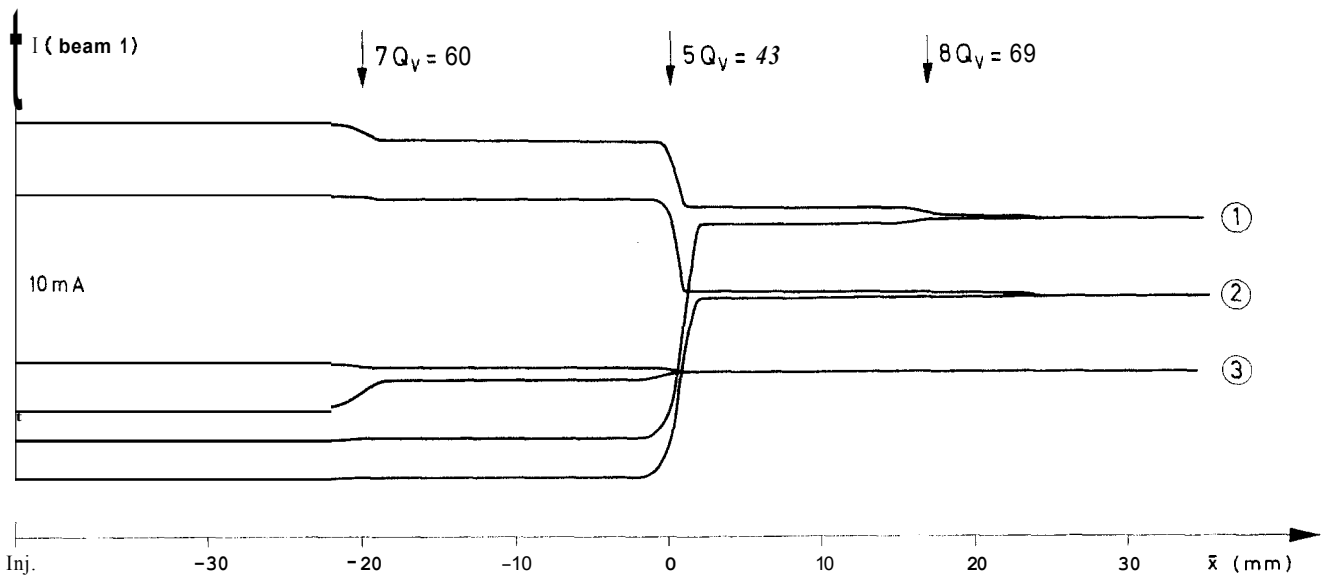
6) P.J. Bryant - Dynamic Compensation during Stacking of the De-Tuning Caused by Space Charge Effects - To be presented at this Conference.

7) E. Keil and A.M. Sessler - Space Charge Limits in the ISR - ISR Divisional Report ISR-TH/67-39 (1967).

8) E. Keil, C. Pellegrini and A.M. Sessler - Tune-Shifts for Particle Beams Crossing at Small Angles in the Low-β Section of a Storage Ring - Report CRISP 72-34 (1972).

9) P.M. Hanney and E. Keil - The Width of Non-Linear Resonances Excited by Beams Crossing at Small Angles in Low-β Sections - ISR Divisional Report ISR-TH/73-55 (1973).

10) M. de Jonge and K.N. Henrichsen - Acceleration by Phase Displacement in the ISR - To be presented at this Conference.



Vertical steering of **beam** 2 (mm) in the two pairs of intersections

	I 4	I 8	I 2	I 6
Scan 1	0	0	0	0
Scan 2			0.6	+ 0.6
Scan 3	+ 0.4	- 0 4	- 0 6	+ 0.6

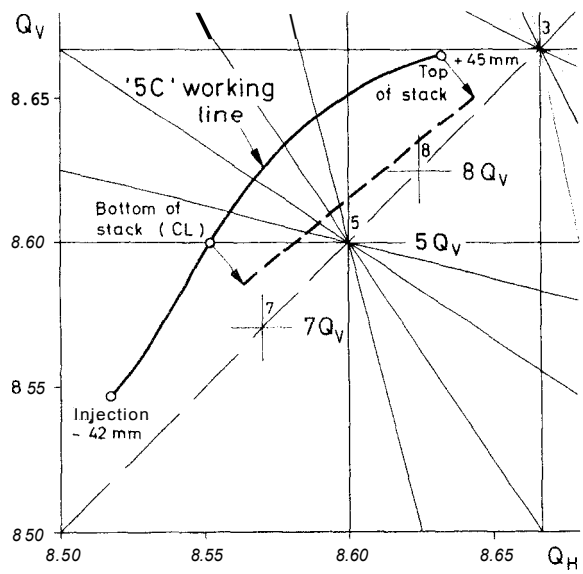


Figure *4*. Beam–beam excitation of resonances

Small beams of 75 mA were displaced across the aperture at a speed of 1.6 mm s^{-1}. The tune changes according to the 5C working line shown in the above Figure. Beam losses occur when crossing certain resonances. The broken working line is the 5C line deformed by the incoherent tune shift for a 12.5 A beam at 26 GeV/c.

RF SYSTEMS FOR HIGH-ENERGY e-e+ STORAGE RINGS*

M. A. Allen and P. B. Wilson
Stanford Linear Accelerator Center
Stanford University, Stanford, California 94305

Introduction

Electron or positron beams in a storage ring radiate electromagnetic energy at a rate proportional to the fourth power of the recirculating energy, and this loss must be supplied by an rf system. Furthermore, a substantial overvoltage is required to contain the stored beam against losses due to quantum fluctuations in the emitted photons. As an example, an improvement program, SPEAR II, is now underway to increase the energy of the SPEAR ring to 4.5 GeV.[1] At this energy, the radiation loss per turn is 2.8 MeV, and to maintain a reasonable lifetime against quantum fluctuations, a peak voltage of 7.5 MeV is required. Thus, the SPEAR II rf system is similar to a continuously-operating 7.5-MeV linear accelerator. Furthermore, the available straight-section space in the ring which is suitable for containing the accelerating structures is limited, and this means that a cavity design must be sought with a high shunt impedance per unit length so that the power dissipated in cavity wall losses will be held to a reasonable level. In the case of SPEAR, about 9 meters of straight section space is available for accelerating cavities, requiring a gradient of close to 1 MV per meter. The PEP 15-GeV ring would require peak accelerating voltages of around 50 MV, with about 60 meters of straight-section space available for accelerating structures.[2]

Choice of Frequency

The rf systems of e^-e^+ storage rings constructed until recently have operated at frequencies below 100 MHz; the present SPEAR rf system, for example, operates at a frequency of 51 MHz.[3] Although operation at this low a frequency has some important advantages, the shunt impedance per unit length of the cavities is only on the order of 1 MΩ/m. Thus, in order to attain the high peak voltages required for SPEAR II and PEP using such cavities, the length of the rf structures would need to be on the order of 50 meters and 500 meters respectively. By using a higher frequency, the geometric shape of the cavities can be optimized and the shunt impedance per unit length can be increased dramatically. On the other hand, as the operating frequency is increased, the overvoltage ratio (peak voltage divided by the synchrotron radiation loss per turn) required to give a reasonable quantum lifetime also increases. Taking tnese two competing factors into account, it can be shown that there is a rather broad optimum in the range 100 to 400 MHz for the SPEAR II and PEP rf frequencies. Above 400 MHz, the size of the beam hole, which is determined by beam excursions during injection, becomes large relative to the wavelength with a resulting loss in shunt impedance.

Within this frequency region, economic and engineering considerations dominate the choice of rf frequency. The structure diameter, weight and cost become unreasonably large below about 200 MHz. The availability of suitable rf power sources must also be considered. A careful study of the comparative advantages of klystrons vs gridded tubes was made in connection with the design of the rf system for SPEAR II, and it was concluded that klystrons were superior to tetrodes with respect to initial and annual operating costs, reliability and expected life. Klystron size and cost are lowest at the upper end of the 100 to 400 MHz range. This factor, together with the decrease in structure costs with increasing frequency, led to a choice of 358 MHz for the SPEAR II rf system. Similar reasoning applies to the PEP rf system, for which the SPEAR II system may be considered as a prototype.

Structure Design

As discussed above, the requirement of CW operation at high energy gain, together with the limited space available in the straight sections of a storage ring, demands an rf structure with a high shunt impedance per unit length. A high shunt impedance can be achieved by using a chain of shaped cells with nose cones, similar in design to the LAMPF accelerating structure.[4] There are, however, additional design requirements for structures for high-energy storage rings. These include: a large aperture to accommodate orbit distortions and beam excursions at injection; the need for tuning to compensate for reactive beam loading and for thermal detuning effects; the requirement to mask against intense synchrotron radiation; and adequate bandwidth to maintain reasonable field stability in the presence of differential thermal detuning.

Some structures of potential interest for high-energy storage ring applications are shown in Fig. 1.

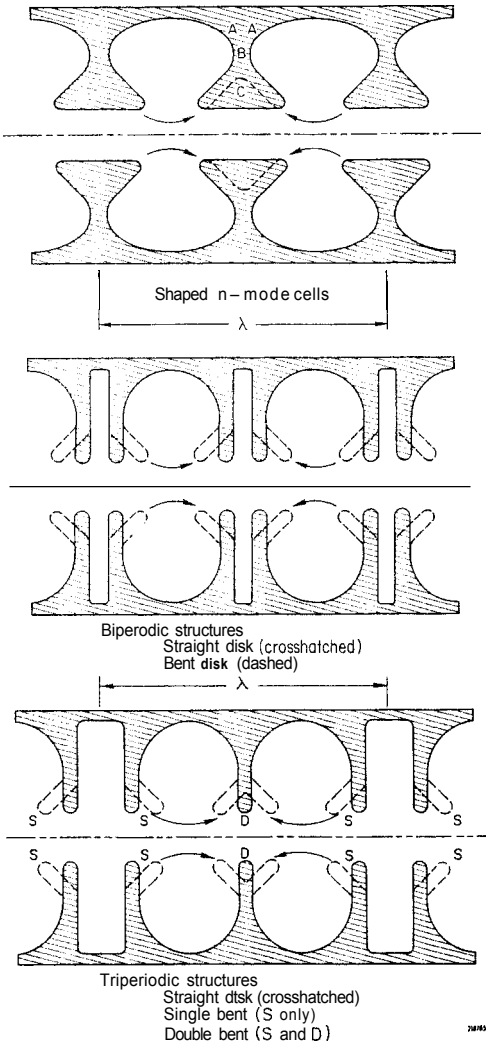


Fig. 1. Some structures of interest for high-energy storage ring rf systems.

*Work supported by the U.S. Atomic Energy Commission.

The top structure, Fig. 1a, is a chain of uncoupled cells spaced one-half wavelength apart. By optimizing the length and shape of the re-entrant nose cones to give the highest shunt impedance, and by adjusting the elliptical outer cavity boundary to hold the resonant frequency constant for different beam apertures, the top curve in Fig. 2, giving the shunt impedance per unit length (including transit time factor) as a function of beam aperture, is obtained. There is negligible coupling between neighboring cells in the structure as shown because the beam drift tubes are well below cutoff. A practical accelerating structure consists of a number of such cells, coupled together by one of several methods, fed from a single rf feedpoint. For example, by cutting a slot in the cavity wall at B, magnetic-field coupling makes possible operation in the π mode. By cutting slots at A-A, side-mounted cavities can be added to achieve resonant coupling and $\pi/2$ mode operation. A structure coupled in this way has a greater stability against perturbations in the tuning of individual cells, but entails a considerable increase in mechanical complexity. In either case, the addition of coupling slots increases the loss by perturbing the rf current flow, and the shunt impedance is reduced by perhaps 15% to that shown by the dashed curve in Fig. 2.

Several structures that have shunt impedances comparable to that of the side-coupled structure, hut which make use of on-axis electric-field coupling, are also shown in Fig. 1. On-axis coupling offers several advantages: first, cylindrical symmetry and mechanical simplicity makes construction easier; second, the maximum overall diameter is smaller than that of the side-coupled structure, an advantage at very low frequencies; and third, the loss associated with coupling slots is avoided. Nonresonant electric-field coupling can be achieved in the shaped-cavity structure of Fig. 1a by opening up the drift tube dimensions as indicated by the dashed line at C. Resonant on-axis coupling is achieved in the biperiodic and triperiodic structures shown in Fig. 1b and 1c. The corresponding shunt impedances at 2856 MHz are given in Fig. 2. In each of these structures, the disk width is 5 mm, and unless otherwise indicated, the length of the unexcited cells in both biperiodic and triperiodic structures is also 5 mm. For comparison, shunt impedances are also given for two cases in which the ratio of large-to-small cell lengths is 2:1. Finally, from the lowest curve in Fig. 2, it is seen that the structures shown in Fig. 1 give shunt impedances which are considerably higher than that, for example, of a simple $2\pi/3$ mode structure consisting of straight disks and an elliptical outer boundary (as viewed in a longitudinal cross-section).

Values of Q, shunt impedance per unit length and bandwidth for the various structures that have been discussed are listed in Table I for a beam aperture radius of 1.0 cm at 2856 MHz.

An additional parameter of importance in structure design is the relative bandwidth, k, defined as the frequency difference between the zero and π modes divided by the frequency of the $\pi/2$ mode. Expressions relating the stability of a structure against perturbations in tuning to the bandwidth have been given previously.5 Bandwidths for the various structures under discussion here are also listed in Table I.

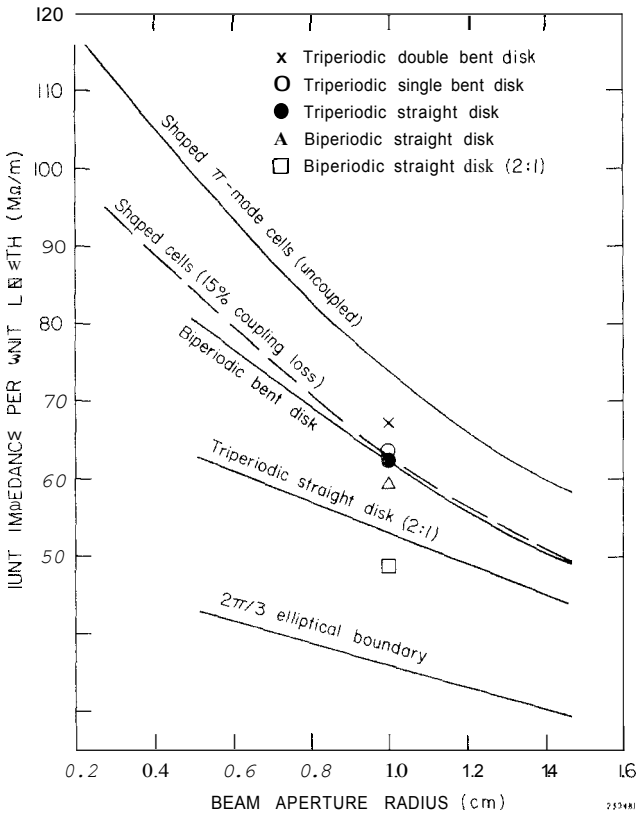


Fig. 2. Shunt impedance per unit Length at 2856 MHz as a function of beam aperture radius for various rf structures.

Table I.

Shunt Impedance per Unit Length, Q and Bandwidth for Various Structures at 2856 MHz for a Beam Aperture Radius of 1.0 cm

Structure	r (MΩ/m)	Q	k (%)
Shaped $\lambda/2$ Cells (uncoupled)	74.4	1.78×10^4	0
Triperiodic Double Bent Disk	66.9	1.84×10^4	0.35
Triperiodic Single Bent Disk	63.4	1.91×10^4	0.72
Shaped $\lambda/2$ Cells (15% coupling loss)	63.3	1.51×10^4	1-2
Biperiodic Bent Disk	62.5	1.73×10^4	0.74
Triperiodic Straight Disk	62.2	1.96×10^4	0.73
Biperiodic Straight Disk	59.3	1.81×10^4	1.00
Triperiodic (2:1) Straight Disk	53.1	1.79×10^4	0.83
Biperiodic (2:1) Straight Disk	48.4	1.56×10^4	1.23
$2\pi/3$ Shaped (elliptical) Boundary	36.6	1.57×10^4	0.89
$2\pi/3$ Straight (cylindrical) Boundary	32.6	1.40×10^4	0.90
$\pi/2$ Shaped Boundary	31.1	1.23×10^4	1.30

SPEAR II Rf System

To run SPEAR at energies up to 2.5 GeV, a peak rf voltage of about 7.5 MV is required. Four normal straight sections are available for the rf cavities. With allowance for position monitors, bellows, etc., the nominal three meters of length in each straight section is reduced to about 2.1 meters, giving a total of 8.4 meters of space available for cavities. Based on considerations discussed in previous sections, a frequency of 358 MHz was chosen (280th harmonic); 5 half-wave-length cavities at this frequency can fit into each of the straight sections. An accelerating structure consisting of five cavities of the high shunt impedance, shaped-cell design shown in Fig. 1a has been designed and built for the SPEAR II rf system. The cavities are coupled together with azimuthal slots in the common wall, and the structure is designed to run in the π mode. Rf power is fed into the structure by means of a loop in the center cavity. For ease of construction, the cavities were fabricated out of 6061 aluminum alloy. A schematic drawing of the cavities is shown in Fig. 3 and a picture of the cavities in Fig. 4. Tuners with a tuning range of over 1 MHz are provided in each cavity. In normal operation all five tuners are ganged together, but provision is made to allow the individual tuners to be adjusted independently. Each cavity has been provided with a pickup loop for sampling the field level. The unloaded Q of the cavities was measured to be 25,000. Using standard perturbation techniques, the shunt impedance was measured to be 7.0 MΩ per cavity (corrected for transit time effects). Adequate water cooling is important because of the high average power dissipation. Cooling is provided to the inner cavity surfaces by means of radial cooling channels in the common walls between cavities as shown in Fig. 3.

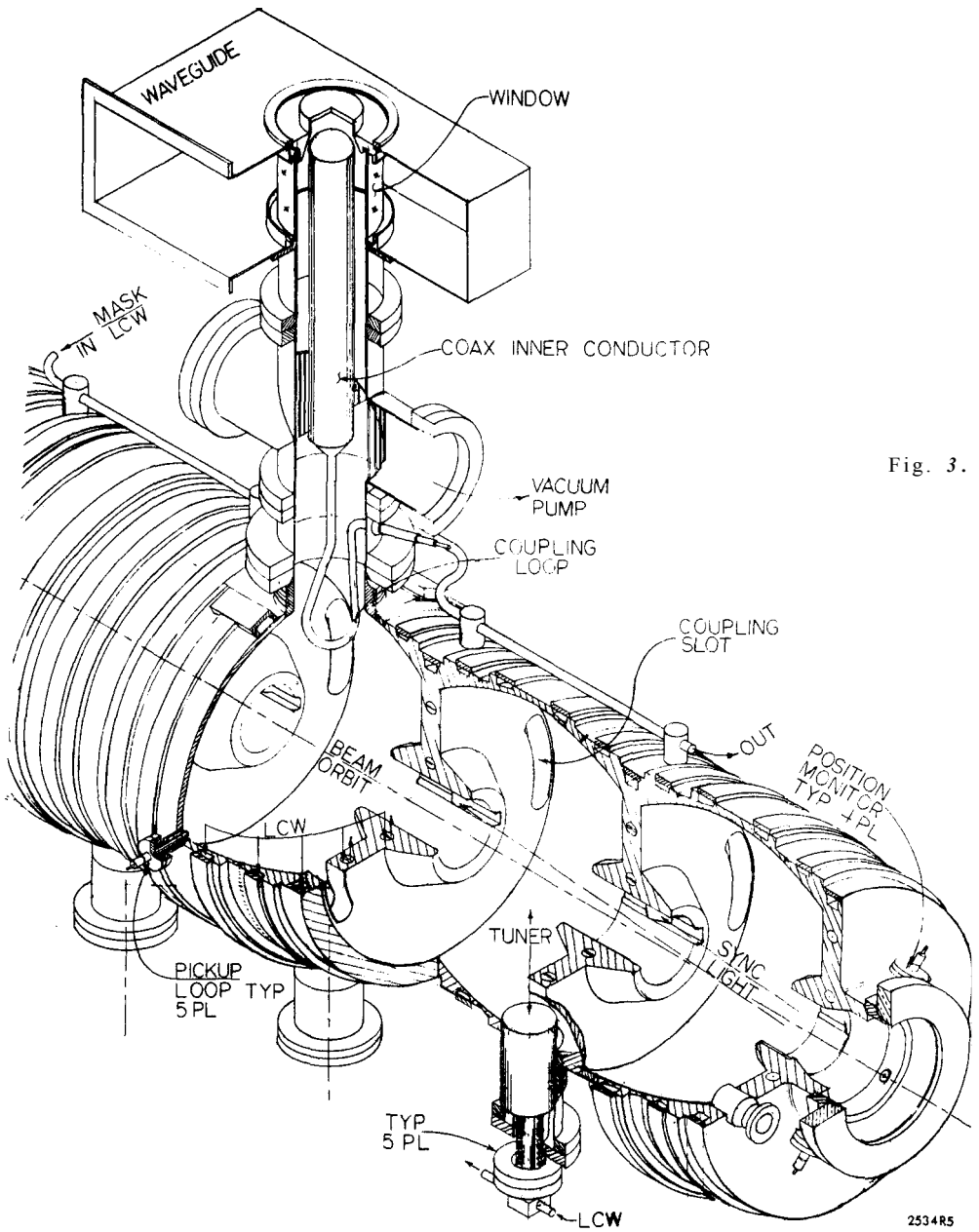


Fig. 3. Cut-away drawing of the SPEAR II accelerating structure.

The cavities have been tested up to 15 kW per cavity (75 kW for a structure of five coupled cavities) with very little thermal detuning (less than 100 kHz). Severe multipactor problems were encountered on initial testing, but these were overcome by coating the entire surface of the cavities (except for the synchrotron light masks) with titanium nitride. A layer between 100 and 1000 Å thick was applied by evaporating titanium from a source inside each cavity in a partial

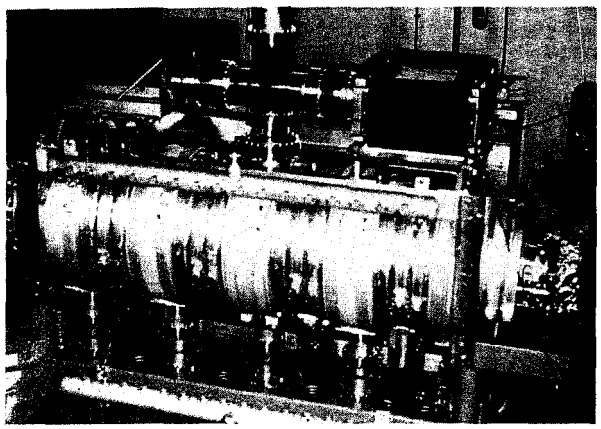


Fig. 4. Photograph of one of the four SPEAR II Accelerating structures.

pressure of about 2 x 10^{-5} Torr of nitrogen. The loop assembly and the tuners were similarly coated. Multipactoring ceased to be a problem after the coating was applied.

Figure 5 gives the frequencies of the five modes

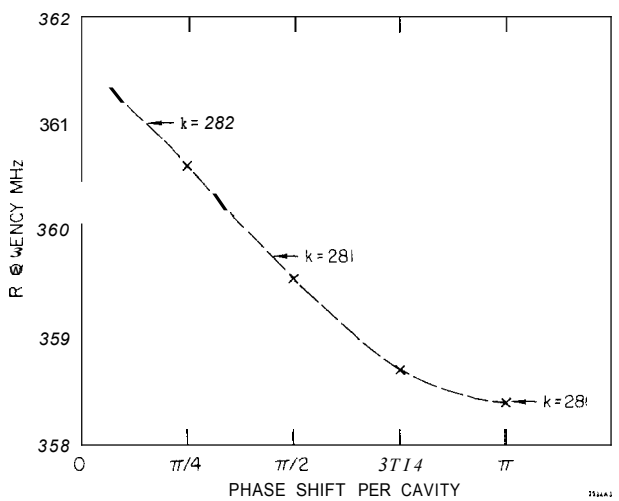


Fig. 5. Dispersion diagram showing the five resonances in the pass-band of the SPEAR II structure.

in the pass-band of the five-cell SPEAR II accelerating structure. Since these modes do not lie close to harmonics of the going-around frequency, they will not interact significantly with the beam during operation.

Each five-cavity structure is driven by a 130-kW CW klystron developed by the Klystron Group at SLAC. The klystrons have a measured efficiency greater than 50%. The present schedule calls for installation and operation of all four of the new 358-MHz structures in SPEAR by September, 1974.

PEP Rf System

As mentioned previously, the SPEAR II rf system is a prototype for the rf system proposed for PEP. The operating frequency is the same, and the rf structure for PEP is expected to be similar to the SPEAR II design. Before PEP is constructed, operational experience with the SPEAR II rf system will have served as a test of many aspects of the 358-MHz design. For PEP, however, the power output per klystron will be increased from 130 kW to 300 kW, and the klystron will be redesigned to achieve an efficiency of 70%. This high efficiency will be attained by the use of harmonic cavities, which produce sharper bunching and a higher rf current component.

It is expected that the accelerating structure for the PEP rf system will be fabricated from aluminum, following the SPEAR II design. A shunt impedance per unit length of 16.5 MΩ/m has been measured for a SPEAR II prototype cavity. Improvements in design and fabrication techniques are expected to bring the shunt impedance to about 19 MΩ/m for the PEP structure. The unloaded Q of the structure will be about 29,000. At the maximum operating energy, when the maximum beam current of about 200 mA (both beams) will be stored, the beams will extract more power from the rf source than is dissipated in the cavity walls. For optimum power transfer to the beam, and for zero reflected power, the cavities must therefore be overcoupled with a coupling coefficient of about 3.5. A cavity tuning angle* of -37° is required to achieve zero net reflected power for this value of coupling coefficient. The loaded Q for the structure is about 6,500, and the corresponding cavity filling time is about 6 μsec.

The parameters as presently proposed for the PEP rf system are summarized in Table II. The numbers

Table II.

PEP Rf System Parameters at 15 GeV[1]

Frequency	358.6 MHz
Harmonic Number	2592
Synchrotron Radiation Loss per Turn	26 MeV
Peak Rf Cavity Voltage[2]	44 MV
Particles per Beam	4.4 x 10^{12}
Circulating Current per Beam	100 mA
Synchrotron Radiation Power (both beams)	5.2 MW
Total Length of Accelerating Structure	60 m
Active Structure Length	50 m
Total Shunt Impedance[3]	950 MΩ
Unloaded Cavity Q	29,000
Total Cavity Power Dissipation	2.0 Mw
Number of 300 kW Klystrons	24
Total Rf Power	7.2 MW
Total Power Input to Rf Power Supplies[4]	11 MW

[1] These parameters are calculated without taking into account radiation loss into higher-order cavity modes.

[2] For a quantum lifetime of 12 hours,

[3] The shunt impedance used here is defined by $R = V_c^2/P_c$, when V_c is the peak cavity voltage and P_c the power dissipated in the cavity walls.

[4] Based on a klystron efficiency of 70% and a power supply efficiency of 95%.

shown should be considered an initial estimate. As will be discussed next, the final rf system design may need to be enlarged to provide power for additional loss mechanisms not taken into account by the usual beam loading expressions. These expressions are valid for the case of a small-diameter storage ring. More accurately, they are valid when the passage time between bunches is small compared to the cavity filling time. For a ring such as PEP which is large in diameter and has only a few circulating bunches, it is possible for the fields in the cavity to change substantially between successive bunch passages. When this transient

*The tuning angle is defined as $\tan^{-1}[2Q_L(\omega_0 - \omega)/\omega_0]$, where Q_L is the loaded Q, ω is the rf frequency and ω_0 is the cavity resonant frequency.

behavior is properly taken into account, it is found that additional power is required from the rf source beyond that calculated using the usual beam-loading relations.[6] For PEP, this additional power requirement is not large; at 15 GeV and 200 mA of circulating current, the increase in power is only 3%, or 0.2 MW. The cavity coupling coefficient for optimum coupling is decreased slightly to 3.4.

A far more serious problem arises as a result of the large time between bunch passages for PEP. For the PEP parameters, it is shown that substantial additional power may be lost due to the excitation of higher-order modes in the rf structure.[6] The power that must be transferred to the beam to make up for this loss is equivalent to an additional synchrotron radiation loss; consequently, in order to contain quantum fluctuations, a higher peak cavity voltage is necessary. Altogether, the additional power that must be furnished by the klystrons might be on the order of 50% of the design power of 7.2 MW. This result assumes that the energy loss to higher-order mode excitation is 42 i_0 MeV, where i_0 is the circulating current. If the circulating current is decreased to 132 mA (both beams), the power transferred to the beam and the peak cavity voltage requirement are both decreased, and the total rf power is reduced to the 7.2 MW design level. Alternatively, this same total power would be adequate for a circulating current of about 180 mA at *14* GeV. Considering the uncertainty in the estimate of the additional cavity losses due to the excitation of higher-order modes, it is not possible at present to specify exactly some of the parameters of the PEP rf system, such as cavity coupling coefficient and loaded Q. Theoretical and experimental work between now and the time that construction might begin on PEP will define more precisely the extent of the loss to higher-order modes for the proposed PEP structure. By making suitable modifications in the structure and by the addition of special tuners to perturb the frequencies of the higher modes, it may be possible to effect a substantial reduction in this loss. There is in addition the alternative of increasing the power capability of the rf system.

Control of Longitudinal and Transverse Instabilities

The N circulating bunches in a storage ring such as PEP can be considered as coupled harmonic oscillators with N normal modes. The in-phase (zero-mode) oscillations of the bunches can be controlled by a feedback loop coupling an amplified signal picked up from the beam to varactor diodes which phase-modulate the input drive to one or more of the klystrons. In order to damp the other (N - 1) possible modes, an additional rf cavity operating on a different harmonic of the revolution frequency is required. If such a cavity is installed in the proper location in the ring, the time derivative of the voltage seen by each of the bunches is different, leading to different synchrotron oscillation frequencies. If this "splitting" of the synchrotron frequencies is sufficiently large, the bunches are effectively decoupled against longitudinal phase oscillations, as has been demonstrated in other storage rings.

Single-beam instabilities have also been observed due to the interaction of the beam with transverse cavity modes.[7] The threshold for these transverse instabilities depends on average current, and the problem is therefore not as severe in a machine such as PEP which has only a few circulating bunches. In any case, the troublesome transverse deflecting modes may be selectively loaded, as has been demonstrated in connection with the elimination of beam breakup in a superconducting accelerator.[8]

Conclusions

Both theory and experimental observations have shown that there are two significant ways in which a bunched beam can interact with higher modes in the rf cavities of high-energy storage rings. First, the bunches can radiate power into higher cavity modes, leading to enhanced beam loading and a higher peak voltage design requirement. Second, higher cavity modes can lead to both transverse and longitudinal bunch oscillations. In addition, the bunch length is short in a storage ring with a high-frequency rf system. Shorter bunches imply that modes up to a higher limiting frequency (such that the mode wavelength is comparable to the bunch length) can be excited by the beam in vacuum chamber components around the ring.

Because of the large number of cavities employed in the rf system of a high-energy storage ring (e.g., 20 individual cavities for SPEAR II and 120 for PEP Stage I), the beam can interact strongly with any higher mode with a frequency close to a harmonic of the revolution frequency. It may be advisable to give each individual cavity in a five-cavity structure a somewhat different shape, while maintaining the same fundamental mode frequency. Each cavity would then have a different spectrum of higher modes, and the possibility would be avoided of a strong interaction between the beam and all 20 or 120 cavities at any higher-mode frequency. This result can be achieved to a limited extent by staggering the individual tuners on the cavities in a five-cavity structure, but at some cost in shunt impedance at the fundamental frequency. An additional tuner could also be added to each cavity; by appropriate adjustment of the two tuners in a given cavity, the spectrum of higher-order modes can be perturbed while maintaining the frequency of the fundamental mode.

The "rigid-bunch" beam-loading enhancement due to power radiated into higher-order cavity modes, and potential transverse and longitudinal instabilities arising from the interaction of the beam with these modes, pose the greatest problems in the design of the rf system for a high-energy storage ring. In addition to the various techniques discussed above for perturbing the higher-mode frequencies, active feedback can be employed for damping bunch oscillations.

Acknowledgements

The authors are indebted to R. McConnell, L. Karvonen, N. Dean and R. Culver for the design, construction and testing of the SPEAR II cavities; to K. Bane for making the calculations which provided the data for Fig. 2; to K. Welch for suggesting the use of titanium nitride as a multipactor suppressor, and to E. Hoyt for developing the deposition technique; and to G. Loew for helpful discussions.

References

1. SPEAR Storage Ring Group, "SPEAR: Status and Improvement Program", these Proceedings.
2. J. R. Rees, "The PEP Electron-Positron Ring -- PEP Stage I", these Proceedings.
3. M. A. Allen and R. A. McConnell, IEEE Trans. Nucl. Sci. NS-20, No. 3, 373 (June 1973).
4. E. A. Knapp, B. C. Knapp and J. M. Potter, Rev. Sci. Instr. 39, 979 (1968).
5. M. A. Allen and P. B. Wilson, Proceedings of the 1972 Proton Linear Accelerator Conference, Report No. LA-5115, Los Alamos Scientific Laboratory, Los Alamos, New Mexico (November 1972), p. 279.
6. P. B. Wilson, "Beam Loading in High-Energy Storage Rings", these Proceedings.
7. DESY Storage Ring Group, "DORIS, Present Status and Future Plans", these Proceedings.
8. K. Mittag, H. A. Schwettman and H. D. Schwartz, IEEE Trans. Nucl. Sci. NS-20, No. 3, 86 (June 1973).

BEAM DYNAMICS EXPERIMENTS AT SPEAR*

The SPEAR Group†
Stanford Linear Accelerator Center, Stanford University, Stanford, California 94305

Introduction

The single-particle properties of beams in storage rings are well understood, but high density single and colliding beams suffer from a variety of instabilities due to self-forces and interactions with their surroundings. The chief experimental problems in the study of stored beams arise from the difficulty of devising beam-diagnostic probes which do not affect the stored beams or disturb the phenomena being studied, and which give unambiguous results when different phenomena act on the probes simultaneously.

In the SPEAR electron-positron storage ring, we have apparatus and methods for measuring center-of-mass motions of our beams on all three axes, as well as motions with higher moments. The shapes of the beam bunches can also be accurately measured. We will describe the techniques we have used to study instabilities and measure operating characteristics.

Center-Of-Mass Motions

There are directional antennas (striplines) inside the vacuum envelope[1] which detect the electromagnetic field of the whole bunch. When the beam executes betatron oscillations, there is a small amplitude modulation of the signals from the striplines. We detect and measure this modulation to give us information on betatron wave numbers, line strengths and widths.

In an electron storage ring, most types of longitudinal and transverse motion damp out, with a characteristic damping time, due to synchrotron radiation. Thus, we can excite the beam transversely with external electromagnetic fields to a finite, stable amplitude in contrast with the "rf knock-out" techniques used in proton machines. Combining coherent excitation with the coherent detection referred to above allows us to measure the transverse properties of the beam in much the same way that electrical engineers measure linear networks.

Typical electrode structures, because of their small size, low capacitance and inductance, have a very poor sensitivity to betatron frequencies, which are usually in the sub-megacycle range. At SPEAR, the rotation frequency is 1.28 MHz, and the bunch length is 1 ns, thus, the frequency spectrum of a signal from a stripline has a line structure with a spacing of 1.28 MHz, extending out to ≈500 MHz. It is possible to observe betatron sidebands on the individual harmonic lines with a high frequency analyzer, but not with any great accuracy or ease. By using a microwave diode or a fast switching diode to detect the signal from a stripline, we convert the original spectrum, having very small amplitude at low frequencies and no dc component, to one which has a dc component and the betatron frequencies at baseband from 200-600 KHz. A simple low-pass filter blocks out the higher harmonics and their sidebands and the frequencies are scanned by a low-frequency wave analyzer of a type designed for testing communications and audio-frequency equipment.‡ The accuracy of frequency measurement is limited only by the stability of the storage ring power supplies, as is the resolution of line widths. Excepting these effects, we can resolve betatron lines to 1 part of 10^5 of betatron frequency, and our sensitivity to transverse motion is 10^{-1} mm mA^{-1} circulating current.

*Work supported by the U. S. Atomic Energy Commission.

† A. P. Sabersky, P. B. Wilson, H. Wiedemann, M.A. Allen, J.-E. Augustin, G. E. Fischer, R.H. Helm, M. J. Lee, M. Matera, P. L. Morton, J. M. Paterson, B. Richter.

‡ Hewlett-Packard Mod. 3590A — sensitivity ≈1μV.

The wave analyzer has an oscillator which automatically tracks the center of the receiver pass band. By connecting this oscillator to the beam excitation system and sweeping the receiver and exciter simultaneously, we observe directly resonant responses of the beam with freedom from harmonic or intermodulation responses. (Fig. 1). A similar technique has been used at the Bevatron,[2] to measure the phase response of the beam.

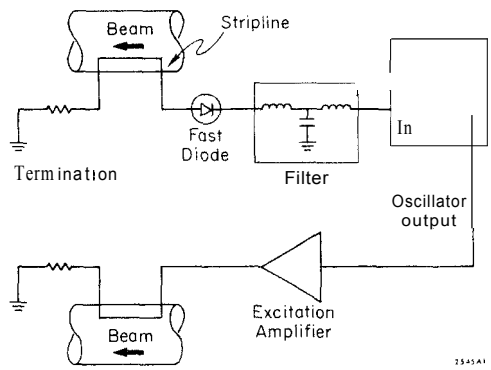


FIG. 1--The system for betatron and synchrotron-frequency response measurement. The oscillator is not used when observing self-excited lines.

We have been able to measure several rather subtle effects with this equipment, including tune shift with increasing circulating current, anomalous line-splitting at the threshold of instabilities, and coupled two-beam effects.[3]

Using only the detector system and an oscilloscope (Fig. 2) we can see the coherent damping of the beam due to large transverse kicks.[4] The incoherent damping is observed using the optical monitors, which will be discussed later.

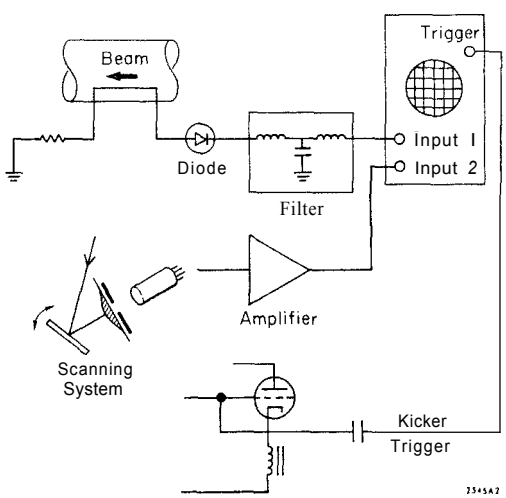


FIG. 2--Measurement of coherent and incoherent damping. The scanner system is described in Ref. 10.

Due to the dispersion (η (s)),[5] of any synchrotron, the sinusoidal energy oscillations (synchrotron oscillations) are translated into sinusoidal transverse oscillations at ω_s, the synchrotron frequency. The detector system described above for betatron oscillations picks up these oscillations as well. We can phase-modulate the rf driving voltage to our cavities

with a voltage-controlled phase shifter.[6] Using the local oscillator of the low-frequency wave analyzer, as above, we can measure the transverse response of the beam as a function of frequency. In the linear approximation, the response of the beam is identical with an L-C-R tuned circuit about resonance frequency and the damping time due to rf system stability[7] and the active phase-feedback system[6] can be measured directly from the frequency-response curve

$$\tau_{damping} = \frac{1}{\pi \Delta f}$$

where Δf is the full width at 0.707 amplitude relative to peak response.

Longitudinal Size and Motions

Bunch length and high-order modes of bunch oscillation have been studied extensively at SPEAR.[8] The apparatus used to measure the higher modes was the same as that used to measure betatron and synchrotron oscillations.

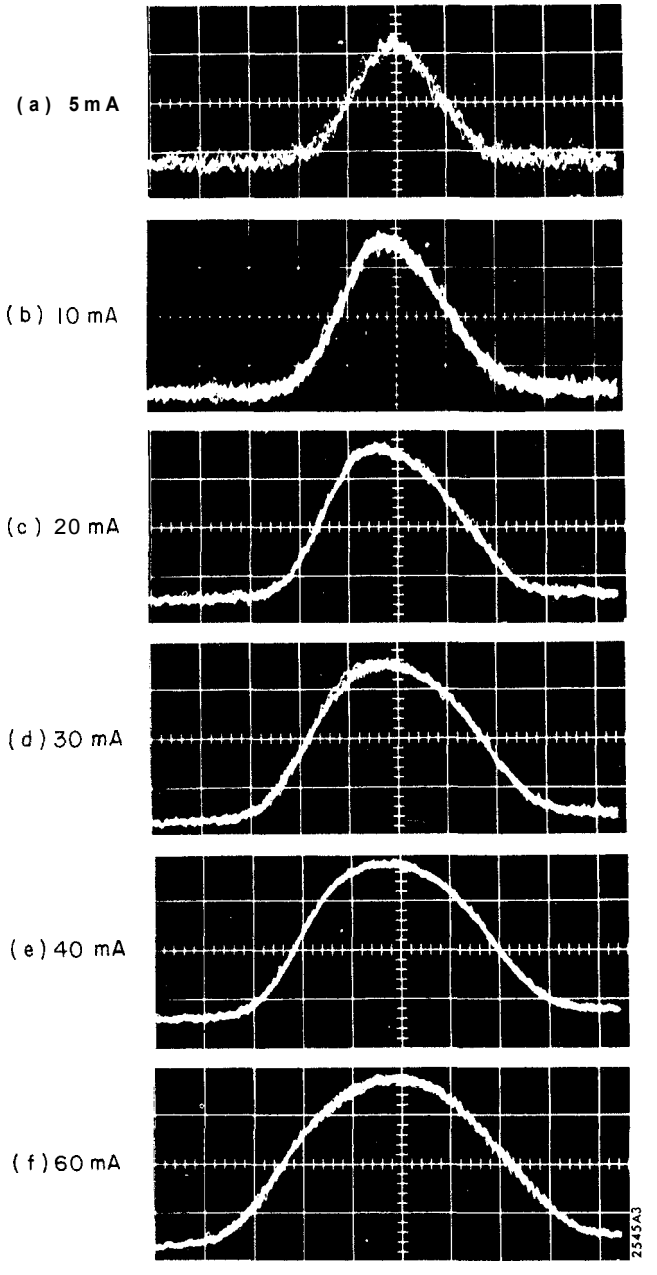


FIG. 3--Bunch shape with respect to a fixed rf time. Horizontal scale is .5 ns/division, vertical scale is amplitude.

Higher-order modes of bunch shape oscillation[9] have no amplitude-modulating frequency components at their fundamental frequency, and our system responds to them only due to the imperfectness of the detector diodes, which are peak-detecting to some degree. Higher modes have also been observed as sidebands of rotation-frequency harmonics at CEA.[10]

Bunch-length measurement methods have already been described.[11] The quality of the bunch-length data is very important in detailed studies, and there is an excellent discussion of applicable fast-pulse techniques in Ref. 12. The use of an x-y plotter to read out bunch-length traces makes a significant difference in the accuracy of the data: the absolute accuracy of bunch lengths and reproducibility is ±5%.

In order to see the distribution of current within the rf "bucket" for asymmetric bunches (Fig. 3) the sampling oscilloscope was triggered with radiofrequency taken from a pick-up loop in one 51.2 MHz main cavity. This loop sampled the actual fields,

The quadrupole mode of bunch oscillation could be excited by strongly phase-modulating the rf drive to the cavities, and this mode was directly observed on the bunch length by synchronizing the oscilloscope triggers with the Q-mode excitation wave form (Fig. 4).

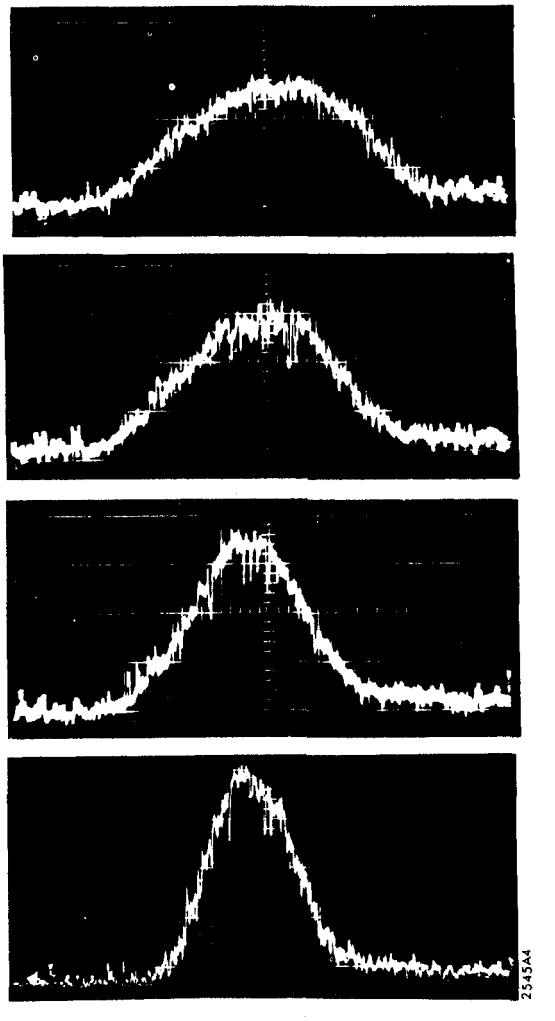


FIG. 4--Longitudinal quadrupole-mode oscillations. The horizontal scale is 1 ns/division.

Transverse Size

The optical monitors for measuring x and y transverse profile have been described in detail.[11] One modification has been the use of noise-averaging integrator (boxcar-integrator)

to convert the rapidly-scanned (100 Hz), rather noisy signal into an accurate x-y tracing (Fig. 5). The reproducibility

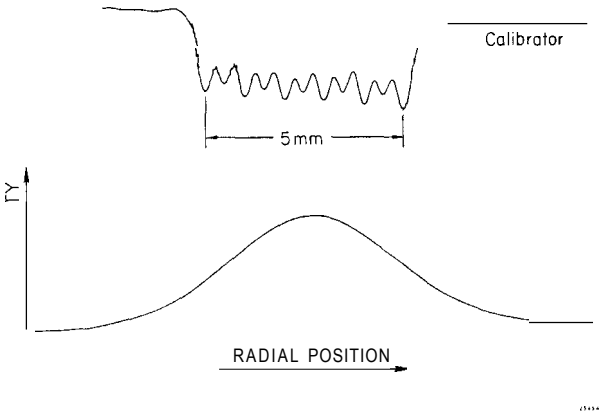


FIG. 5--A tracing of particle density versus radial position taken from the profile scanners with the scanning integrator.

of the size measurements is ±1% and the accuracy is ±3%, limited only by errors in the calibrator system and in the construction of the optical monitors. This accuracy allows us to measure small beam-size effects such as: (1) horizontal broadening due to the excess energy spread associated with bunch lengthening, (2) shape distortions resulting from the effect of colliding beams.

The amplitude of the profile pulses is inversely proportional to the beam width for a constant beam current, thus time-resolved measurements of the pulse amplitudes can show charges in beam width. The beam profiles are scanned at 100 Hz, but this yields 200 pulses/sec, since the profile is scanned twice per cycle. This is a rapid enough rate to allow measurement of beam decoherence and damping times. For the damping time measurements, the pulses are displayed at some slow sweep rate (e.g., 10 ms full sweep) on an oscilloscope which is synchronized with the initial beam displacement, i.e., the kicker pulse.

The combination of rapid profile scans and broadband amplifiers allows us to see the first three modes of beam longitudinal-transverse motion on the horizontal profile scan. This allows us to accurately measure the amplitude of these modes with respect to the beam size.

References

1. J.-L. Pellegrin, Nucl. Instr. and Meth. 108, 365 (1973). For theory of striplines, see Q.A. Kerns and D.B. Large, University of California Rad, Lab. UCRL-11511 (1964).
2. H.A. Grander and G.R. Lambertson, "Transverse Beam Instabilities at the Bevatron," IEEE Trans. Nucl. Sci. NS-18, No. 3, 308 (1971).
3. The SPEAR Group, "Beam-Beam Coupling in SPEAR," these proceedings.
4. The SPEAR Group, "Fast Damping of Transverse Coherent Dipole Oscillations in SPEAR," these proceedings.
5. M. Sands, Introduction to the Physics of Electron Storage Rings, Proceedings of International School of Physics "Enrico Fermi", Course 46, Vienna (1969). Also published as Stanford Linear Accelerator Center Report No. SLAC-PUB-121.
6. M. A. Allen, R. A. McConnell, "Operationof the SPEAR RF System," IEEE Trans. Nucl. Sci. Vol. NS-20, No. 3 (1973).
7. K. W. Robinson, "Stability of Beam in Radiofrequency System," Cambridge Electron Accelerator, CEAL-1010 (1964).
8. M. A. Allen et al., "Some Observations on Bunch Lengthening in SPEAR," these proceedings.
9. F. J. Sacherer, "A Longitudinal Stability Criterion for Bunched Beams," IEEE Trans. Nucl. Sci. NS-20, No. 3, 825 (1973).
10. R. Averill et al., "Dependence of Phase Instabilities On Bunch Length at the Cambridge Electron Accelerator," IEEE Trans. Nucl. Sci. NS-20, No. 3, 765 (1973).
11. A. P. Sabersky, "Monitoring the Beams in SPEAR with Synchrotron Light," IEEE Trans. Nucl. Sci. NS-20, No. 3, 638 (1973).
12. N. J. Norris and R. K. Hanst, "Picosecond Beam Monitors and Data-Acquisition System," IEEE Trans. Nucl. Sci. NS-16, No. 3, 927 (1969).

BEAM ENLARGEMENT BY MISMATCHING THE ENERGY-DISPERSION FUNCTION†

R. H. Helm, M. J. Lee and J. M. Paterson

Stanford Linear Accelerator Center
Stanford University, Stanford, California 94305

Summary

The natural beam size at the interaction point of a storage ring can be increased by operating the machine in a configuration in which the energy-dispersion function (η-function) is nonrepetitive in the periodic cells of the machine lattice. This mode of operation has been studied in SPEAR and is being considered in the PEP design. The usual method of beam enlargement in SPEAR has been to operate the machine in a configuration with a large value of the η-function at the interaction point, bit with periodic η-function in the cells. Some of the results of this study will be described,

Introduction

For a given operating configuration and energy, the maximum luminosity $\mathscr{L}_m$ is proportional to the product of the beam currents at the beam-beam limit as characterized by the value of the maximum incoherent tune shift $\Delta\nu_m$. Since the value of $\Delta\nu_m$ is proportional to the beam current density, higher values of $\mathscr{L}_m$ can be obtained for configurations with larger natural beam size at the interaction point. The natural beam size is determined by two terms: one depends on the square of the value of energy dispersion η^* at the interaction point and the other depends on the value of beam emittance due to betatron motion. It can be shown that configurations with nonperiodic η-functions in the cells (η mismatched) give higher values of beam emittance than those with periodic q-functions (η matched).

In order to get higher luminosity at the lower operating energies, SPEAR has been operated in high-η^* configurations with η matched. Recently we have tried operating SPEAR in a mismatched-? configuration with $\eta^*=0$. The maximum value of luminosity obtained for this mismatched-configuration has been found to be comparable to those of the normal high-η^* configuration. In practice, operation in the mismatched-? mode is limited by the available machine aperture in the lattice since the η-function varies over a large range of values and the betatron oscillation amplitudes are increased by the greater emittance.

In the following sections, we will describe the effect of mismatching η upon the luminosity, present some configurations for SPEAR with η mismatched and discuss some experimental results.

Luminosity

The dependence of luminosity upon the various machine parameters will be studied in this section. It will be shown that luminosity can be increased by mismatching the η-function in the lattice cells.

Consider a storage ring consisting of several superperiods. Each superperiod is composed of periodic cells and insertions. An example of a superperiod can be seen in Fig. 1 which shows the lattice for half of a superperiod of SPEAR.

For an electron storage ring with N_b equal bunches in each beam, the luminosity is[1]

$$\mathscr{L} = \frac{N_b N^2 f}{4\pi\sigma^*_{xt}\sigma^*_{yt}} \tag{1}$$

where f is the revolution frequency, N is the number of electrons in a bunch, σ^*_{xt} and σ^*_{yt} are the effective beam widths and height in the interaction region. At the beam-beam limit, the number of electrons as limited by horizontal tune shift is given by

$$N_m = \frac{2\pi\,\Delta\nu_m}{r_e\beta^*_x}\left(\frac{E}{mc^2}\right)(\sigma^*_{xt}+\sigma^*_{yt})\,\sigma^*_{xt} \tag{2a}$$

or the vertical tune shift

$$N_m = \frac{2\pi\,\Delta\nu_m}{r_e\beta^*_y}\left(\frac{E}{mc^2}\right)(\sigma^*_{yt}+\sigma^*_{xt})\,\sigma^*_{yt}\ , \tag{2b}$$

where r_e is the classical electron radius, β^* is the value of the p-function at the interaction point and (E/mc^2) is the beam energy.

For simplicity, we will assume that there are no vertically bending fields and that all the horizontally bending fields are uniform. Under this condition it can be shown (see Appendix) that the maximum value of luminosity for a given $\Delta\nu_m$ is given by

$$\mathscr{L}_m = \frac{\pi N_b f\,\Delta\nu_m^2}{r_e^2}\left(\frac{E}{mc^2}\right)^2\left(\frac{1}{\beta^*_x}+\frac{1}{\beta^*_y}\right)\left(\epsilon_0+\frac{\eta^{*2}\delta^2}{\beta^*_x}\right) \tag{3}$$

where ϵ_0 = the horizontal beam emittance in the absence of x-y betatron coupling = $\sigma^{*2}_{x\beta}(0)/\beta^*_x$

δ = energy spread in the beam = $(\Delta E/E)$.

In particular, for a storage ring with M identical zero-gradient bending magnets of length ℓ,

$$\mathscr{L}_m = \frac{\pi N_b f\,\Delta\nu_m^2}{r_e^2\rho}\left(\frac{E}{mc^2}\right)^4\left(\frac{\hbar}{mc}\right)\frac{55}{32\sqrt{3}}\left(\frac{1}{\beta^*_x}+\frac{1}{\beta^*_y}\right)\left(\langle\bar{H}\rangle+\frac{\eta^{*2}}{2\beta^*_x}\right), \tag{4}$$

where ρ is the radius of curvature in the bend and $(\hbar/mc)$ is the reduced Compton wavelength;

$$\langle\bar{H}\rangle = \frac{1}{2\pi\rho}\sum\int_i H(\eta,\eta')\,ds\ ; \tag{5}$$

$$H(\eta,\eta') = \frac{1}{\beta_x}\left[\eta^2+\left(\beta_x\eta'-\frac{1}{2}\beta'_x\eta\right)^2\right] \tag{6}$$

The $\sum$ denotes summation over all of the bending magnets and $\int_i$ denotes integration over the ith bending magnet.

To see the effect of mismatching η on the value $\mathscr{L}_m$, it will suffice to consider its effects on $\langle\bar{H}\rangle$. For this purpose we let

$$\eta(s) = \eta_0(s) + \eta_1(s) \tag{7}$$

where η_0 is the η-function for the corresponding storage ring composed of only the repeated cells. In the cells, both η and η_0 satisfy the same inhomogeneous differential

†Work supported by the U. S. Atomic Energy Commission.

equation

$$\eta''(s) - K(s)\,\eta(s) = \frac{1}{\rho} \tag{8}$$

where K(s) is the focusing function in the cells.

The function $\eta_1(s)$ satisfies the homogeneous differential equation

$$\eta_1''(s) - K(s)\,\eta_1(s) = 0$$

so that the function $H(\eta_1,\eta_1')$ is a well-known invariant;[3] i.e.,

$$H_1 = H(\eta_1,\eta_1') = \text{constant.}$$

It can be shown' that the function $\eta_0(s)$ varies approximately as $\sqrt{\beta_x(s)}$ so that

$$\beta_x(s)\,\eta_0'(s) - \frac{1}{2}\beta_x'(s)\eta_0(s) \approx 0$$

and the function $H(\eta_0, \eta_0')$ is also approximately an invariant; i.e.,

$$H_0 = H(\eta_0, \eta_0') \approx \text{constant.}$$

Making use of these properties of η_0 and η_1, we find for the cells

$$H(\eta, \eta') \approx H_0 + H_1 + \frac{2\eta_0(s)\,\eta_1(s)}{\beta_x(s)} \tag{9}$$

For a machine with many cells, the last term gives a small contribution to the value of $\langle \bar{H} \rangle$ because η_1 oscillates about η_0, and most of the contribution to the value of $\langle \bar{H} \rangle$ comes from the cells. In addition, if there is a point of symmetry in the cell lattice ($\beta_{xs}' = \eta_s' = 0$) then the value of $\langle \bar{H} \rangle$ is approximately given by

$$\langle \bar{H} \rangle \approx \frac{\eta_{0s}^2}{\beta_{xs}} + \frac{\eta_{1s}^2}{\beta_{xs}} \tag{10}$$

with the subscript s denoting the symmetric point. Since $\eta_{1s} = \eta_s - \eta_{0s}$, η_{1s} is a measure of how much η is mismatched in the cells. The increase in luminosity varies as η_{1s}^2 for a mismatched configuration.

Computed Results

The values of luminosity for a family of mismatched-? configurations have been computed for SPEAR using Eq. (4). Since SPEAR has a superperiodicity of two and each superperiod is symmetric about its midpoint, it is convenient to characterize these configurations by the value of η at that symmetry point as discussed in the previous section. Figure 1 shows a schematic layout of the magnets in SPEAR for half of a superperiod starting at the interaction point and ending at the symmetry point. There are five cells in each superperiod. Each cells contains two focusing quadrupole magnets, one defocusing magnet and two bending magnets. The values of η at different points along the machine for a typical matched-η configuration (A) and a typical mismatched-7) configuration (C) are shown in Fig. 1. It can be seen that the 7-function is periodic in the cells for configuration A with $\eta^* = 1.75$ m. The η-function for the configuration C has no periodicity within a superperiod of the machine, and $\eta^* = 0.0$ m.

Figure 2 shows a plot of $\mathscr{L}_m$ as a function of η_s for a family of configurations with $\Delta\nu_m = 0.025$, E = 1.5 GeV, $\beta_x^* = 1.2$ m, $\beta_y^* = 0.1$ m, $\nu_x = 5.15$, $\nu_y = 5.11$ and $\eta^* = 0$, 1.0, 1.5, 1.75 and 2 m. The values of $\mathscr{L}_m$ for the matched-η configuration lie along the curve between points A and B. It can be seen that for the matched configurations $\mathscr{L}_m$

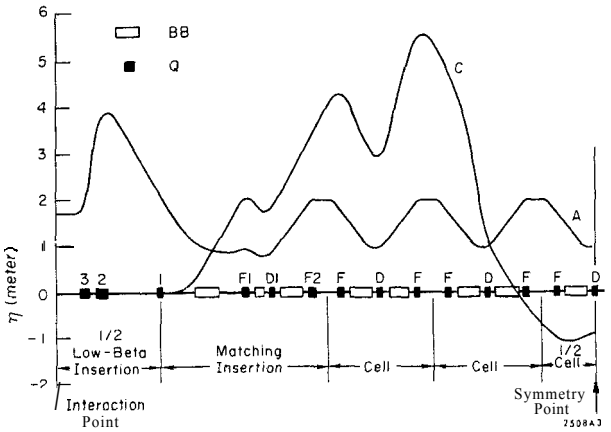


FIG. 1--A schematic layout of the magnets in SPEAR for half of a superperiod. The matching section consists of quadrupole magnets F1, D1 and FZ. The low-beta insertion consists of quadrupole magnets 1, 2 and 3. A cell is composed of quadrupole magnets F, D and F.

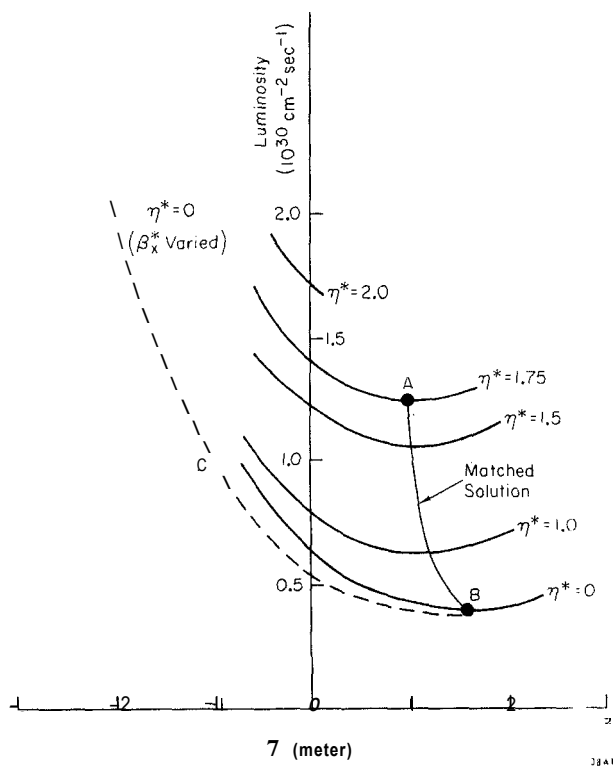


FIG. 2--Computed values for the maximum value of luminosity for some SPEAR configurations with $\Delta\nu_m = .025$. The machine parameters for these configurations are: $\nu_x = 5.15$, $\nu_y = 5.11$, $\beta_x^* = 1.2$ m, $\beta_y^* = .1$ m and different values of η^* and η_s. For the values on the dashed line, the value of β_x^* varies linearly from 1.2 m at the matched-? configuration B to 4.5 m at the mismatched-η configuration C. (E = 1.5 GeV.)

increases as η^* increases as expected. Furthermore, for a given value of η^*, the value of $\mathscr{L}_m$ is very close to a minimum as a function of η_s at the matched configuration. Although SPEAR has only five cells per superperiod, the gain in $\mathscr{L}_m$ by using the mismatched-η configurations and the approximate validity of Eq. (10) can be seen from this plot.

From Eqs. (4) and (10), it can be seen that the value of $\mathscr{L}_m$ is not appreciably affected by the value of β_x^* for $\eta^*=0$ configurations if $\beta_x^* >> \beta_y^*$. The dashed line in Fig. 2 shows the values of $\mathscr{L}_m$ for configurations with $\eta^*=0$ and with β_x^* increasing linearly from 1.2 to 4.5 m between configurations B and C. It has been observed that as the value of η_s gets more negative, maximum β values in the matching section become very large. However, by using larger values of β_x^*, it is possible to keep the maximum beam size within the allowable machine aperture up to some large values of η-mismatch.

Since the rate of change of the machine damping time constant with RF frequency depends on the momentum compaction factor α, Fig. 3 shows a plot of α for some of the configurations shown in Fig. 2. It can be seen that α is relatively independent of β_x^* for $\eta^*=0.0$ configurations.

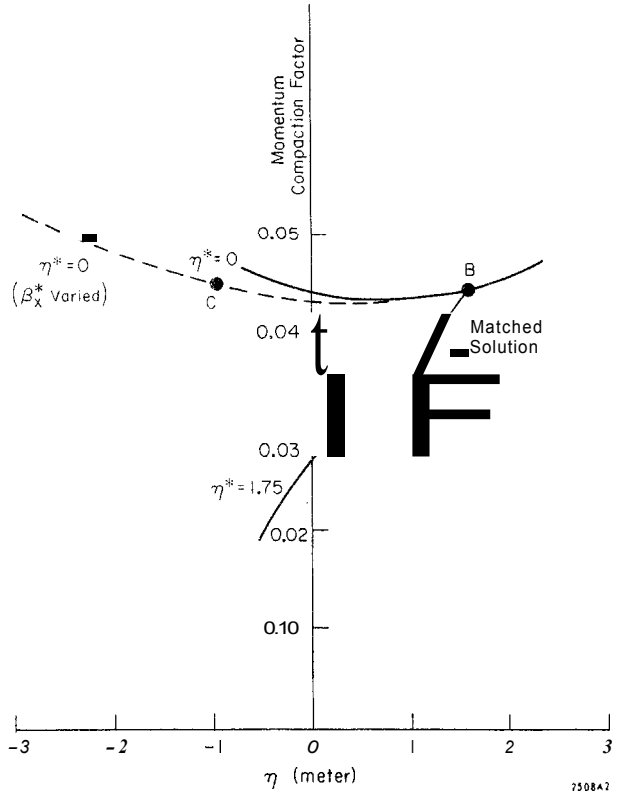


FIG. 3--Values of momentum compaction factor for some typical configurations shown in Fig. 2.

Experimental Results

Luminosity for different beam currents has been measured for configurations A, B and C at 1.5 GeV. The results are shown in Fig. 4. Configuration A is a matched-η configuration with $\eta^*=1.75$ m, B is also a matched-η configuration with $\eta^*=0.0$ and C is a mismatched-η configuration with $\eta^*=0.0$ and $\beta_x^*=4.5$ m. The values of $\mathscr{L}_m$ at the beam-beam limit for these cases are shown in Fig. 4. $\mathscr{L}_m$ is largest for A and smallest for B, which is consistent with the computed results (see Fig. 2). It may be interesting to note that at the limit the ratio of $\mathscr{L}_m$ to beam

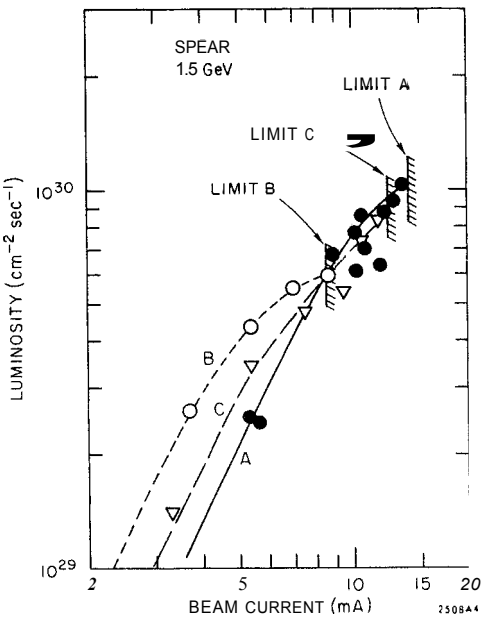


FIG. 4--Measured values of luminosity for three configurations A, B and C. The values of machine parameters for these configurations are given in Fig. 2.

current is nearly the same for all three cases; i.e., the values of $\Delta\nu_m$ are independent of configurations.

The beam width at one point in the cell has been measured for A and C. The measured values are in general agreement with the computed values. The variation of damping time constant for different values of RF frequency has been measured also for A. The result is consistent with the computed results in the order of magnitude. We expect from the computed result that the change in damping time with frequency should be nearly the same for both A and C. Further decrease in the values of η_s beyond the value for C has been tried. Beam life-time becomes poorer for these configurations as we approach the limit imposed by the machine aperture at locations of large η and β values.

Conclusions

It may be concluded from this study that mismatched-? configurations can produce higher luminosity values than matched-η configurations and are a viable alternative to matched-?), high-η^* configurations, provided that there is sufficient machine aperture to allow for the increase in beam width.

For a given machine the optimum operating configuration may be one with mismatched-7, finite η^* and a judicious choice for the value of β_x^*.

Acknowledgements

The authors wish to thank the other members of the SPEAR Group, M. Allen, G. Fischer, P. Morton, B. Richter, A. Sabersky, P. Wilson and the operating and engineering staff for their assistance.

Appendix

The expressions for the maximum value of luminosity [Eqs. (3) and (4)] will be derived in this section. For this derivation, we assume that there are no vertically bending fields in the machine and that the horizontally bending fields are uniform within each magnet. The effective beam width and height are then given by

$$\sigma^*_{xt} = \sqrt{\sigma^{*2}_{x\beta} + \eta^{*2}\delta^2} \tag{A.1}$$

and

$$\sigma^*_{yt} = \sigma^*_{y\beta} \tag{A.2}$$

where * denotes the values at the interaction point, the subscript β denotes the contribution to the beam dimension due to betatron motion, and δ is the energy spread in the beam ($\Delta E/E$). The value of $\sigma^*_{y\beta}$ comes from the coupling between the x and y betatron motion of the particles. Let the coupling constant be defined by

$$A = \frac{\sigma^*_{y\beta}}{\sigma^*_{x\beta}} \sqrt{\frac{\beta^*_x}{\beta^*_y}} \tag{A.3}$$

If we assume[1] that

$$\frac{\sigma^{*2}_{x\beta}}{\beta^*_x} + \frac{\sigma^{*2}_{y\beta}}{\beta^*_y} = \frac{\sigma^{*2}_{x\beta}(0)}{\beta^*_x} \tag{A.4}$$

where $\sigma^*_{x\beta}(0)$ is the effective beam width for zero coupling, then

$$\sigma^*_{x\beta} = \frac{1}{\sqrt{1+A^2}}\, \sigma^*_{x\beta}(0) \tag{A.5}$$

and

$$\sigma^*_{y\beta} = \frac{A}{\sqrt{1+A^2}}\, \sigma^*_{x\beta}(0) \sqrt{\frac{\beta^*_y}{\beta^*_x}} \tag{A.6}$$

The expression for luminosity may be written in terms of $\sigma^*_{x\beta}(0)$ and A as

$$\mathscr{L} = \frac{N_b N^2 f \sqrt{1+A^2}}{4\pi A \sigma^*_{x\beta}(0) \sqrt{\sigma^*_{x\beta}(0) + \eta^{*2}\delta^2(1+A^2)}} \tag{A.7}$$

The maximum value of luminosity $\mathscr{L}_m$ is determined by the maximum number of electrons in a bunch as given by Eq. (2).

If we assume that the value of the incoherent tune shift for both x and y oscillations are the same, we find from Eq. (2) that at the beam-beam limit,

$$\frac{\sigma^*_{xt}}{\beta^*_x} = \frac{\sigma^*_{yt}}{\beta^*_y} \tag{A.8}$$

Substituting the expression for σ^*_{xt} and σ^*_{Yt} into Eq. (A.8) and solving for the value of A, we obtain

$$A = \sqrt{\frac{\beta^*_y}{\beta^*_x}} \sqrt{\frac{\left(\sigma^{*2}_{x\beta}(0) + \eta^{*2}\delta^2\right)}{\left(\sigma^{*2}_{x\beta}(0) - \eta^{*2}\delta^2 \frac{\beta^*_y}{\beta^*_x}\right)}} \tag{A.9}$$

Combining Eqs. (2), (A. 7), and (A.9), we find at the beam-beam limit the expression for $\frac{\sigma^*_{x\beta}}{\beta^*_x}$ in terms of ϵ_0 and 6 as given by Eq. (3). The values $\sigma^*_{x\beta}(0)$ and δ may be expressed in terms of the synchrotron integrals[2] I_2, I_3, I_4 and I_5

$$\epsilon_0 = \frac{\sigma^{*2}_{x\beta}(0)}{\beta^*_x} = \frac{55}{32\sqrt{3}} \left(\frac{\hbar}{mc}\right)\left(\frac{E}{mc^2}\right)^2 \frac{I_5}{I_2 - I_4} \; ; \tag{A.10}$$

$$\delta^2 = \frac{55}{32\sqrt{3}} \left(\frac{\hbar}{mc}\right)\left(\frac{E}{mc^2}\right) \frac{I_3}{2I_2 + I_4} \; , \tag{A.11}$$

where $\hbar/mc$ is the reduced Compton wavelength.

For the special case of equal zero gradient bending magnets of length ℓ:

$$I_2 = 2\pi/\rho \; , \quad I_3 = 2\pi/\rho^2, \quad I_4 \approx -\frac{\pi\ell^2}{6\rho^3} \ll I_2 \; ,$$

$$I_5 = \langle \bar{H} \rangle \frac{2\pi}{\rho^2} \; ,$$

we find the expression for $\mathscr{L}_m$ as given by Eq. (4).

References

1. M. Sands, "The Physics of Electron Storage Rings, an Introduction," Proceedings of the International School of Physics "Enrico Fermi", Course XLVI, ed., B. Touschek (Academic Press, New York, 1971); also Report No. SLAC-121, Stanford Linear Accelerator Center.
2. R. H. Helm, M. J. Lee, P. L. Morton and M. Sands, "Evaluation of Synchrotron Radiation Integrals," IEEE Trans. Nucl. Sci. NS-20, No. 3 (1973).
3. E. Courant and H. Snyder, Ann. Phys. (N.Y.) 3, 1 (1958).

ADONE: PRESENT STATUS AND EXPERIMENTS

M. Bassetti, A. Cattoni, V. Chimenti, D. Fabiani, M. Matera, C. Pellegrini, M. Placidi, M. Preger, A. Renieri, S. Tazzari, F. Tazzioli, G. Vignola
Laboratori Nazionali di Frascati del CNEN
Frascati, Italy

Abstract

The present status of the electron-positron storage ring Adone is reported, together with the foreseen improvements. Some recent measurements are also reported.

Status

The second generation experimental setups were installed on the ring during a five-month shutdown. Among other, a 4 Kgauss, 2 MW, 1 meter inner radius transverse field magnetic detector (MEA)[1] has beer, installed and is now running.

Major improvements were also carried out on the machine: a feedback on the longitudinal relative oscillations, and a distributed pumping system in the magnets on both sides of three experimental sections, have been installed; the control system has been further improved.

Tests on the magnetic field distribution of MEA performed before the installation of the magnet on the ring, were repeated with the first circulating beam with satisfactory results as far as a single beam is concerned. The detector magnetic field is compensated by means of two compensating magnets mounted on the same straight section; integrated field compensation is such that a residual closed orbit of the order of 1mm in the vertical plane is easily reproduced at $Q_x = Q_z = 3.05$, E = .5 GeV and with the detector running at its maximum field (4 KGauss). The corresponding compensation error is of the order of 1.5 Gauss x meter over the 2.5 m length of the section, versus a specified figure of 2.5 Gauss x meter. The quadrupole component integral is also within specifications: the $\Delta Q/Q$ is of the order of $.6^{o}/oo$ per KA/GeV.

The sextupolar component integral changes the machine natural cromaticity by approximately 10% versus a specification of 20% (maximum).

The detector is at present running for experiments, although for reasons not yet fully understood, at low machine energies the maximum luminosity can not be attained when the detector is running at high current.

The feedback system to cure longitudinal relative oscillations of the three bunches[2] has been brought into operation. The system makes use of two R F cavities running at 8^{th} harmonic of the revolution frequency (22.8 MHz), not a multiple of the R F frequency (8.568 MHz). The system prevents destructuve oscillations from occurring and makes storage of currents as high as 60 mA/beam much easier.

A complete bakeout of the vacuum chamber has not yet been carried out and the average pressure without beams is $\sim 5 \cdot 10^{-10}$ torr.

Beam lifetime is nevertheless quite good because of the installation of distributed pumping in six out of twelve magnets (~ 8 ÷ 10 hours depending on energy).

Distributed pumping has also appreciably improved the pressure in the experimental sections: data taken at E = 1.2 GeV, with a total current of 78 mA are given in the following table:

Exp. Section	pressure with distr. pump.	pressure without distr, pumping
5	.53 ntorr	1.2 ntorr
9	1.9 "	4.1 "
11	2 "	5.6 "

A complete bakeout of the chamber, plus the installation of the rest of the distributed pumping system, should further improve both local and average pressures by at least a factor of 2 or 3.

Experiments on beam size control.

Some preliminary tests on the possibilities afforded by the method proposed by M. Bassetti[3], who suggested that natural beam transverse dimensions can be controlled by modifying the ring magnetic structure, were recently carried out.

As discussed in detail in Ref. 3, transverse beam dimensions can be modified by acting on the average value in the dipoles ($\overline{H}$) of the well known function[4]

$$H(s) = \frac{1}{\beta_x(s)} \left[\psi^2(s) + \left(\beta_x(s)\psi'(s) - \frac{1}{2}\beta'_x(s)\psi(s) \right)^2 \right] \quad (1)$$

The original magnetic structure of Adone was modified by introducing a third harmonic resonant perturbation.

The actual way to do it is to lower the strength of three pairs of radial focussing quadrupoles located at the ends of three equally spaced, non-interaction straight sections. The $\psi(s)$ function is thus distorted, causing H to grow.

The measurements were done by shunting away a fixed amount (3%) of the quadrupole excitation currents.

The $\beta(s)$ and $\psi(s)$ functions, for the modified structure ($\beta^{*}(s)$ and $\psi^{*}(s)$) are shown in fig. 1,2 and compared with the same functions for the imperturbed machine.

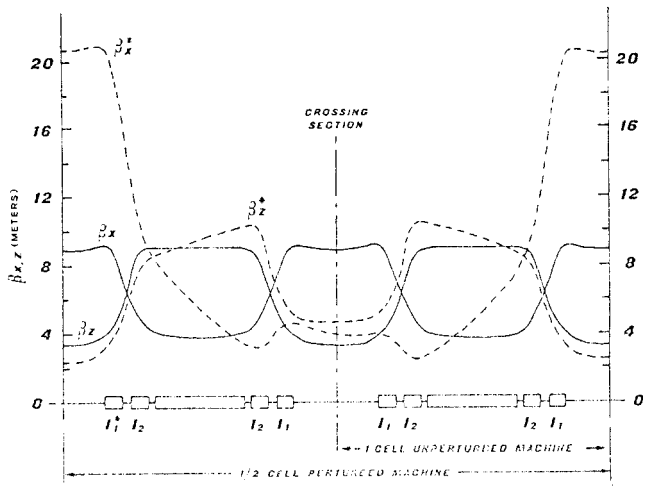


Fig. 1 - /?functions with (β_x^*, β_z^*) and without (β_x, β_z) shunted quadrupole perturbation.

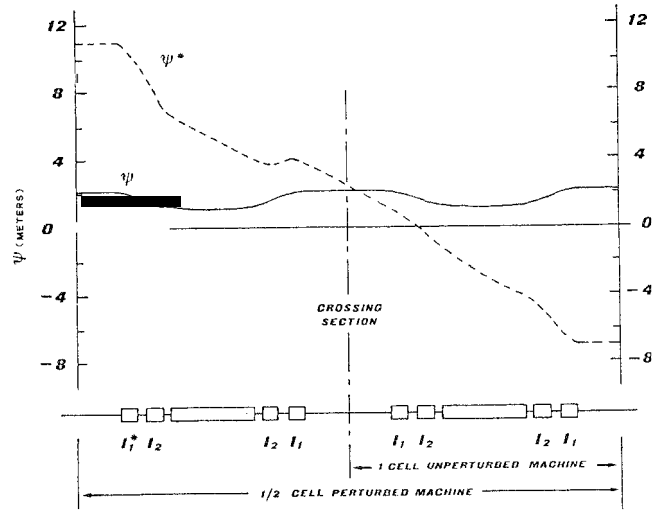


Fig. 2 - Off-energy function with (ψ^*) and without (ψ) shunted quadrupole perturbation.

The maximum currents that could be stored in a stable two-beam configuration, without beam "flipping" or short lifetimes were measured, in the energy range from .5 to .6 GeV. Luminosity measurements were also carried out.

Luminosity values obtained with the Bhabha scatteringluminometer were corrected to account for the bunch lengthening effect which, at a given energy, is larger than for the original structure, mainly due to the increase of the stored currents.

Preliminary results seem to be in rough agreement with expectations. In the .5 to .6 energy range, currents higher by a factor of ~ 2 were stored and brought into head-on collision: the maximum obtained luminosities were higher by a factor of 1.5 than the corresponding unperturbed machine values, in rough agreement with what expected under the hypothesis that the maximum attainable value of ξ_z (the beam-beam interaction parameter) is the same as for the unperturbed machine.

Further experimenting is needed, to obtain more accurate data and to actually check whether the behaviour of the structure has been fully understood.

An interesting aspect of the perturbed machine is that, due to the large distortion of function $\psi^*(s)$, radiation losses in the quadrupoles are larger, and the RF frequency range beyond which antidamping of the sychrotron or the betatron modes occurs should therefore be narrower by large factors. This would open the possibility of changing the damping partition numbers, and therefore beam dimensions (see references 5 and 6), by working at a slightly different frequency.

Strong beam - weak beam interaction measurements

The behaviour of a positron beam colliding with an electron beam of much lower intensity has been studied in same detail.

We first measured the maximum attainable strong beam current (defined as the value I_L at which the weak beam shape begins to change) as a function of energy. We then measured luminosity at several energies, with strong beam currents lower than but near to I_L.

Measurements were carried out with three bunches in the strong beam and one bunch in the weak beam. This because more accurate beam shape measurements can be carried out with our present detection apparatus on a single-bunch beam.

It should also be recalled that, with our machine parameters, higher current densities are obtained with one bunch per beam [8], so that one could argue that, for a given weak beam current per bunch, the strong beam is less perturbed by a single-bunch weak beam.

All measurements were carried out with the machine tuned at $\nu_x = \nu_z = 3.05$.

A definition of how weak the weak beam should be, in order not to affect the strong beam, is needed,

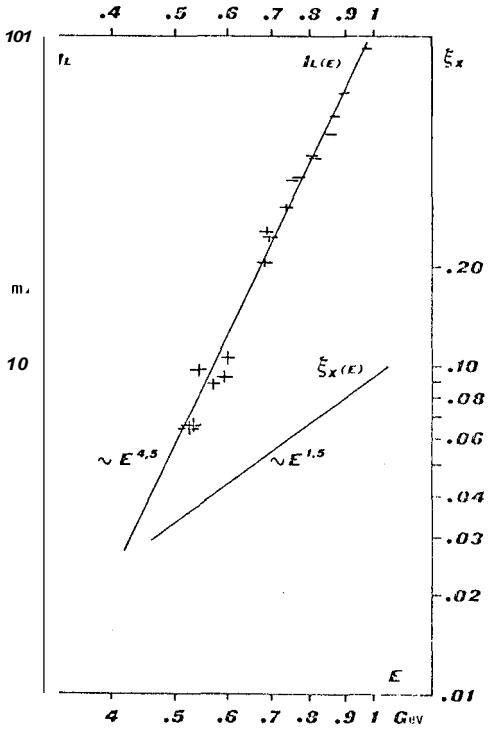
Recalling from our strong beam/strong beam work that $I/E^{4.5}$ is a good parameter to characterize beam-beam interaction-induced shape modifications (see discussion in ref. (8)), we assume that a relevant parameter could in our case be

$$R = \frac{(I \cdot i)^{1/2}}{E^{4.5}} \qquad (2)$$

I and i being the strong and the weak beam currents respectively.

Under this tentative assumption we then choose to define the weak beam intensity to be negligible when (I being only slightly lower than I_L) R is $\leq$ 25 $mA/GeV^{4.5}$, a figure that can be deduced from the data of Fig. 5 of Ref. (8) by somewhat arbitrary arguments.

Experimental values of I_L versus E, for $R \leq 25$ $mA/GeV^{4.5}$ are shown in fig. 3.



Fig, 3 - Maximum current in the strong beam I_L versus energy.

Measurements were carried out over a period of approximately one month and were found to be reproducible to within the experimental uncertainties.

A power-law best fit through the data shows that

$$I_L = I\, E^{4.34}$$

with a χ^2/N value of 1.3 (N = 18).

Luminosity measurements performed at different R values and at several energies were used to calculate the ratio of the effective interaction cross section to σ_p^2, S_o^M, defined as

$$S_o^M = K \frac{I \cdot i}{LE^2} \qquad (4)$$

σ_p being the r.m.s. energy spread in the beam and K being equal, For our tune values, to 2.5 10^{30} GeV^2/mA^2 . s. We also define S_o^o as the natural single beam radiation cross section on the coupling resonance divided by σ_p^2 8.

Fig. 4 shows a plot of S_o^M/S_o^o versus R.

The data are not incompatible with the assumption that the interaction effective measured cross section in the vicinity of the weak beam space-charge limit is proportional to E^2, and that the strong beam cross section is equal to $S_o^o \cdot \sigma_p^2$, at least for $R \leq 25$ $mA/GeV^{4.5}$. Given the large experimental errors on most points a more refined analysis of the data would not be meaningful. Further measurements should however be carried out on this important point, with greater accuracy.

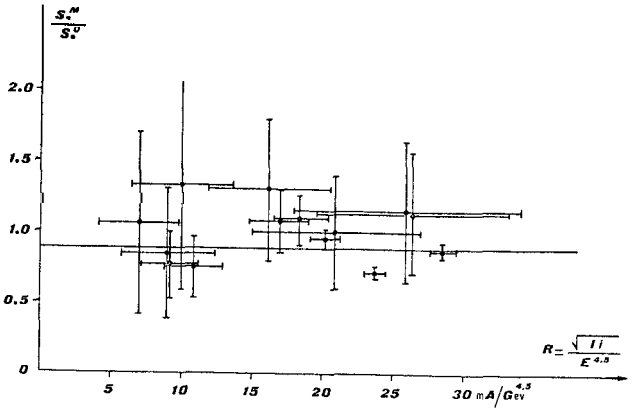


Fig. 4 - Behaviour of S_o^M/S_o^o as a function of R.

A possible explanation for the slightly lower value one gets fitting a horizontal straight line through the data (.88) is that, due to beam-beam interaction, the actual weak beam tune is Par off coupling (see Ref. 9).

If the strong beam has its natural on-coupling resonance dimensions, we know how to calculate the value of the interaction parameter ξ_x (as seen by the weak beam) corresponding to I_L, as a function of energy (with our parameters and for natural on-coupling beam dimensions, $\xi_x \approx 1.07\, \xi_z$). The result is shown in fig. 3.

The data presented here are incompatible with the $I_L \propto E^3$ law we deduced for strong beam/weak beam interaction in Ref. 8 and that one would expect from a simple thin lens model for the interaction. A fit through the present data with an E^3 dependence has a χ^2/N value of 14.5, and is therefore highly improbable.

A best fit with $I_L \propto E^{4.5}$ which is our strong beam/strong beam energy dependence, gives a χ^2/N value of 1.5 and is therefore still compatible with the data.

It should be said however that previous measurements were carried out with three bunches per beam and over a very narrow energy range (.5 i .6 GeV); control system improvements have since allowed the energy range to be extended, and more accurate current measurements to be performed. We also can not exclude that the exact definition of I_L has an important role.

It should also be borne in mind that the fact that the actual weak beam tune is far off-coupling, so that the weak beam density is by no means well known, is an unaccounted-for part of the picture that may be important.

Future improvements.

In the attempt to eliminate the problems arising from the several modes of longitudinal oscillation which take place with the present RF system, the installation on Adone of a new 200 KV single-gap cavity, operating at 51.4 MHz is planned. The RF driver system will be delivered in September and the cavity is expected to be delivered at the end of this year.

Accompanying changes will have to be made on the Linac beam choppering system which will have to provide 10 ns long pulses at a repetition frequency ranging from ~3 MHz (1 bunch) to~1 7 MHz (6 bunches) (upto six bunches are required to be stored in Adone when used as a booster for the SuperAdone project ring[7]).

To compensate for the decrease in the injection rate due to the reduced R F time acceptance, a factor of two in the peak Linac current has to be provided, together with an increase in the positron injection energy from .31 to .36 GeV allowing theinjection repetition rate to be increased by a factor of approximately 1.5.

This also involves a substantial improvement in the control instrumentation of the beam transfer lines from the Linac to the ring.

Aknowledgments.

All members of the Adone group have contributed to the work reported in this paper. We would like to aknowledge in particular the contribution of M. Vescovi who, besides participating in all measurements, was mainly responsible for the proper operation of the machine.

References.

1 - A. Catitti, A. Cattoni, G. Sacerdoti: A magnetic analyzer for colliding beam experiments in a storage ring. - Proceeding of the Fourth Int. Conf. on Magnet Tech. - Brookhaven 1972.

2 - A. Renieri, F. Tazzioli: The longitudinal feedback in Adone (This Conference).

3 - M. Bassetti: Beam dimensions control in storage rings. (This Conference).

4 - M. Sands: The physics of electron storage rings. SLAC Rep. 121 (1970).

5 - C. Pellegrini: Non linear effects of the damping constants of electron oscillations in a synchrotron. Frascati, NI 62/96.

6 - M. Bassetti: Internal memorandum T-65 (unpublished).

7 - F. Amman et al.: The SuperAdone electron-positron storage ring design. (This Conference).

8 - F. Amman et al.: Remarks on two beam behaviour of the 1.5 GeV electron-positron ring Adone. VIII International Conference on High Energy Accelerators, CFRN (1971), p. 132.

9 - R. Belbeoch et al.: Beam-beam interaction at the e^+e^- Orsay Storage ring ACO. - L.A.L. Rapport Technique 3-73 (June 1973).

RESONANT METHODS FOR BEAM SIZE CONTROL IN STORAGE RINGS

M. Bassetti

Laboratori Nazionali di Frascati del CNEN

Frascati, Italy

Abstract.

Three methods for varying the magnetic structure of a storage ring at constant betatron number Q_x, in order to vary the natural beam dimensions, are discussed. It is also shown that beam-beam interaction in the thin lens approximation, and dipole or gradient errors can be interpreted as magnetic structure modifications of the kind discussed.

Introduction.

In colliding beams storage rings physics, the function[1]

$$H(s) = \frac{1}{\beta(s)}\left[\psi^2 + (\beta\psi' - \frac{1}{2}\beta'\psi)^2\right] \tag{1}$$

ψ being the periodic solution (continuous with its derivative) of equation

$$x'' + K(s)\,x = \frac{1}{\varrho(s)} \quad , \tag{2}$$

is particularly important. The local value of H(s) at the crossing point is simply given, due to the symmetry of the optical functions, by

$$H_o = \frac{\psi^2}{\beta} \tag{3}$$

and its average value in the bending magnets is given by

$$\bar{H} = \frac{1}{2\pi}\int \frac{ds}{\varrho(s)}\,H(s) \tag{4}$$

The importance of $\bar{H}$ and H_o stems from the dependence of beam dimensions at the crossing point on these parameters (we assume $J_S = 2$, $J_X = J_z = 1$), namely

$$\sigma_x = \sigma_p\sqrt{\beta_x\left[\frac{2\bar{H}}{1+\varepsilon^2} + H_o\right]} \tag{5}$$

$$\sigma_z = \sigma_p\sqrt{\beta_z\bar{H}\,\frac{2\varepsilon^2}{1+\varepsilon^2}} \tag{6}$$

ε being the coupling parameter between radial and vertical betatron oscillations ranging from 0 (no coupling) to 1 (maximum coupling).

In order to obtain a satisfactory behaviour of luminosity in the low-energy range, it is necessary to increase the beam cross-section at the interaction point. It is apparent from 5) and 6) that this can be obtained by the increase of $\bar{H}$ or of H_o (high ψ). In this paper we propose a resonant method to control parameter $\bar{H}$.[2]

It is convenient to transform formulas (2) and (4) by means of the Floquet transformation

$$\begin{cases} \eta = \dfrac{\psi}{\sqrt{\beta}} \\ \phi = \dfrac{1}{Q_x}\displaystyle\int \frac{ds}{\beta} \end{cases} \tag{7}$$

Formulas (2) and (4) become:

$$\frac{d^2\eta}{dQ^2} + Q_x^2\eta = Q_x^2\beta^{3/2}\left(\frac{1}{\varrho}\right) \tag{8}$$

$$\bar{H} = \frac{1}{2\pi}\int \frac{ds}{\varrho}\left[\eta^2 + \frac{1}{Q_x^2}\left(\frac{d\eta}{d\phi}\right)^2\right] \tag{9}$$

Starting from a symmetry point, the right hand side of *(8)* can be written as

$$Q_x^2\beta^{3/2}\,\frac{1}{\varrho} = f(\phi) = \sum_{k=0}^{\infty} A_k\cos k\phi \tag{10}$$

and the solution of equation *(8)* is:

$$\eta = \sum_{k=0}^{\infty}\frac{A_k}{Q_x^2 - k^2}\cos\phi \tag{11}$$

It should be kept in mind that the independent variable in formula (11) is ϕ and not s.

Resonant methods.

It can be seen from (9) and (10) that, keeping Q_x constant, $\bar{H}$ is a function of coefficients A_k, in particular of those corresponding to k values near to Q_x: this observation suggests that, to control $\bar{H}$, it is necessary to have a degree of freedom in the ring magnetic structure allowing to modify the value of coefficients A_k near to Q_x.

The machine magnetic structure can be varied in three different ways, which will be illustrated referring as an example to the structure of the preliminary project of Super Adone [3], and namely:

A) Variation of the standard cells and the low-β insertion relative contributions to Q_x.

B) Modification of the standard cell dipole term $1/\varrho(s)$[4].

C) Modulation of the standard cell gradient function k(s).

In our example we have 32 standard cells, each beginning from the center of a straight section in between two defocusing quadrupoles Q_D and two inser-

tions defined by the conditions to which they must' satisfy.

A) Starting from a configuration with $Q_x = 10.2$ (8.2 from the standard cell and 2.0 from the two low-β insertions), the total standard cell contribution to Q_x is raised to 9.2 and that of the two insertions decreased from 2.0 to 1.0, thus keeping the total value of 10.2 constant. We also assume that the insertions do not contain bending magnets.

In addition to producing the low-β at the interaction points, the insertions must allow to obtain:

1) Variable Q_x values
2) Fixed Q_z values.

In this case we do not want any matching between the ψ values at the end of the low-β insertion and at the beginning of the standard cells: the periodic solution of equation (2) must be calculated on the whole machine.

Let us consider the quarter of the ring, extending from symmetry point A to low-β point B at the center of the experimental straight section. Function ψ can be considered as being the sum of two terms: the first (ψ_1) is a solution of eq. (2), as applied to the standard cell only: if ψ_1 were propagated inside the low-β insertion, it would have a non-zero derivative at the crossing point; the second term (ψ_2) is a free betatron oscillation, whose amplitude at point A, is such that at points B its derivative has the opposite sign with respect to the derivative of ψ_1. The sum of the two terms is still a solution of eq. (2) and represents the total y. The increase of $\bar{H}$ is due to ψ_2.

The behaviour of $\bar{H}$ and of the momentum compaction α_c as a function of Q_{xp} (contribution to Q_x of standard cells) is shown in Fig. 1. In this case the degree of freedom is Q_{xp}.

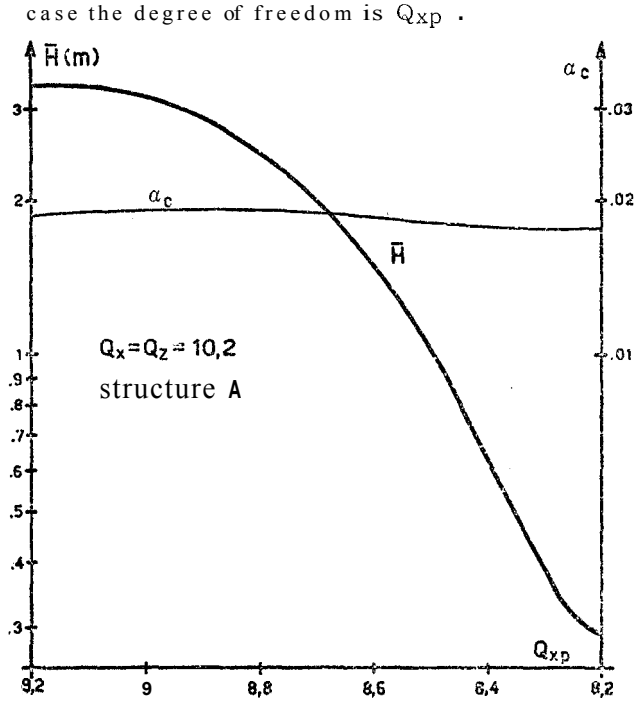


FIG. 1

B) The variation of the standard cell dipole term $1/\varrho$ can be obtained by replacing parts of the bending magnets with straight sections and viceversa. This can be achieved [illegible] by introducing either a high superperiodicity (e.g. a superperiod af 4 standard cells in which the length of each magnet is slightly changed) or a low superperiodicity, equal to the number of insertions in which some whole standard cell has the bending magnets replaced by straight sections.

As an example we refer to the periodic structure described above and consider a 4-cell superperiod. We assume that the magnets of the first and of the fourth cell are ,2 m longer, and those of the second and third cell. 2 m shorter than thoseof the normal structure. The natural degree of freedom of this second kind of magnetic structure would be the lengthening of the magnets, and is obviously impossible to adopt in practice: the lengthening (and shortening) of the magnets will therefore be kept fixed and equal to .2 m; as one degree of freedom we choose the standard cells contribution to Q_x, the total Q_x being kept constant, by properly varying the low-β insertion contribution to Q_x. The same 2 conditions of case A) and a third condition, namely (3) matching of the standard cells ψ value to that of the low-β insertion have to be satisfied.

This condition requires that some bending magnets exist in the low-β insertion: the bending magnet radius must therefore be changed, to compensate for the additional bending angle of the insertion magnets.

The behaviour of $\bar{H}$ and of the momentum compaction α_c as a function of Q_x are shown in Fig. 2.

C) The variation of the standard cell gradient function K(s) is suggested by the observation that in formula (10) function $f(\phi)$ can be modified either by changing the dipole term $1/\varrho(s)$ or function $\beta(s)$ (which is influenced by the gradient function K(s)). It should be pointed out that according to (7) the change in $\beta(s)$ entails a change of function $\phi(s)$ so that functions $1/\varrho(\phi)$ and $\beta(\phi)$ are both modified.

We introduce (as in case b)) a superperiod of 4 cells. In this case a degree of freedom is obtained in the following way: if we call K_F and K_D the values of the gradient function in the focusing and defocusing quadrupoles of the first and the fourth cell, the corresponding values in the second and third cell are replaced by:

$$K_F(1-p)$$

$$K_D(1+p)$$

p can be easily varied by properly varying the quadrupole currents, and the low-β insertions are very simple, because is sufficient for the insertions to correspond to an identity matrix to obtain the proper matching of functions $\beta(s)$ and $\psi(s)$.

Among the three possible kinds of struc-

ture modification, this seems to be the most promising, and will therefore be analyzed in some detail.

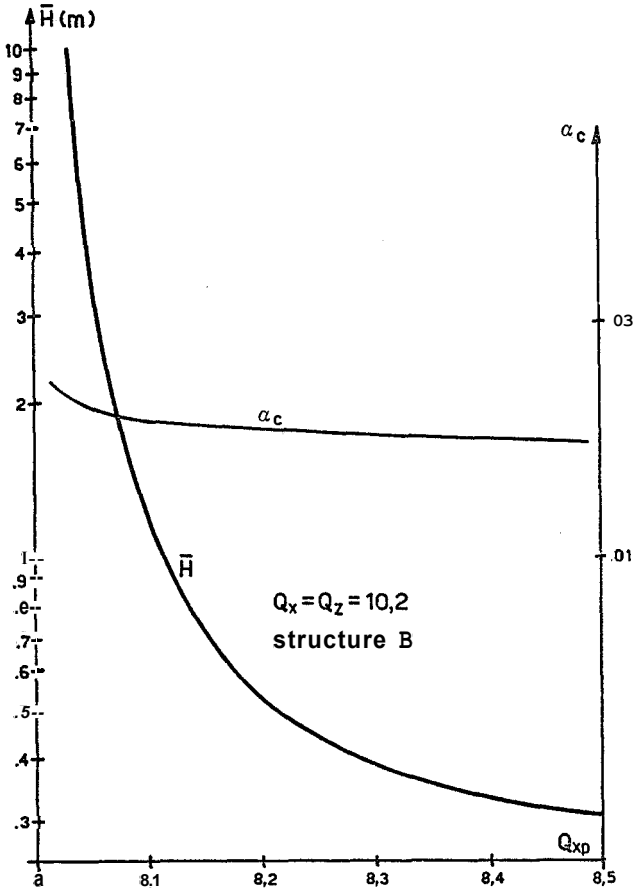


FIG. 2

We assume $Q_x = Q_z = 10.2$. The behaviour of $\bar{H}$ and α_c as a function of p are shown in Fig.3, while σ_x, the maximum r. m. s. radial dimension divided by the energy (in GeV) along the periodic structure, and σ_z, the maximum r. m. s. vertical dimension on the coupling resonance are shown in Fig, 4. In order to get an idea of the requirements on the low-β insertions functions β_x, β_z and the off-energy function ψ, evaluated at the beginning of the low-β insertion are shown, as a function of p, in Fig. 5. The same quantities for $Q_x = Q_z = 11.2$ are shown in Figs. 6, 7, 8. It can be seen from Fig. 5 and Fig. 8 that beam dimensions can be easily increased by factors of the order of 4.

Effect of beam-beam interaction on beam dimensions.

Let A and B be the same points defined above. Following the optical model, we assume that beam-beam interaction can be described by means of a thin lens defined by the approximate tune shifts ξ_x and ξ_z in the radial and vertical planes.

Labelling with an asterisc the functions modified by beam-beam interaction, it is easy to obtain the following formulas[5].

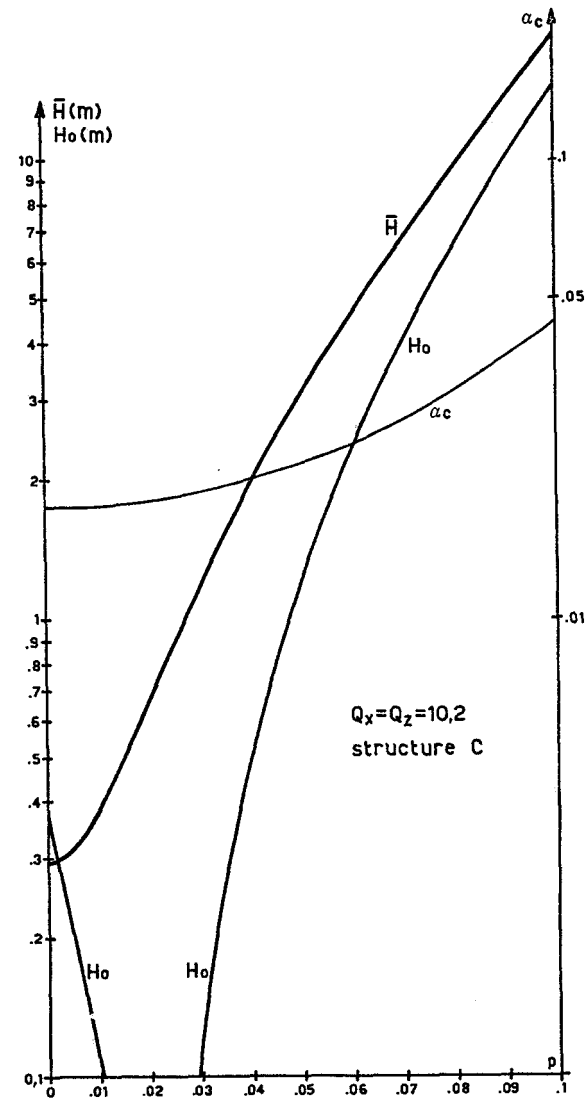


FIG. 3

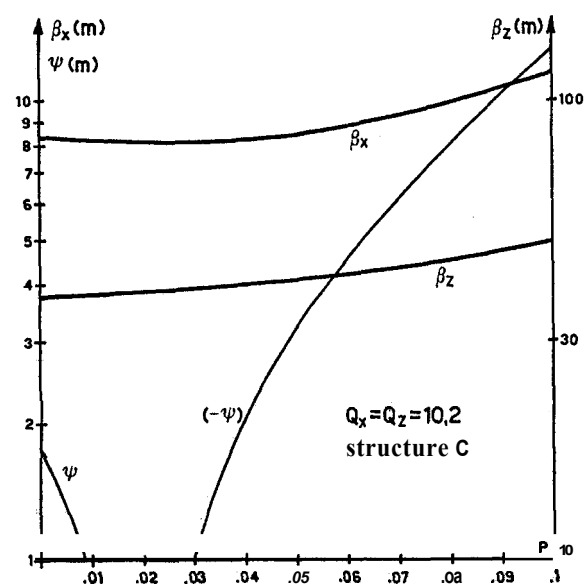


FIG. 4

$$\psi^{*}_{A} = \psi_{A} - \psi\left(\frac{\beta_A}{\beta_B}\right)^{1/2} \frac{2\pi\xi_x}{\operatorname{sen}\frac{\pi}{2}Q_x + 2\pi\xi_x \cos\frac{\pi}{2}Q_x} \qquad (13)$$

$$\psi^{*}_{B} = \frac{\psi_B}{1 + 2\pi\xi_x \operatorname{cotg}\frac{\pi}{2}Q_x} \qquad (14)$$

$$\frac{d\psi^{*}_{B}}{ds} = \frac{2\pi\xi_x}{\beta_x}\psi^{*}_{B} \qquad (15)$$

$$\cos\pi Q^{*}_{x,z} = \cos\pi Q_{x,z} - 2\pi\xi_{x,z}\operatorname{sen}\pi Q_{x,z} \qquad (16)$$

$$\beta^{*}_{A_{x,z}} = \beta_{A_{x,z}}\left(\frac{\operatorname{tg}\frac{\pi}{2}Q_{x,z}}{\operatorname{tg}\frac{\pi}{2}Q^{*}_{x,z}}\right) \qquad (17)$$

$$\beta^{*}_{B_{x,z}} = \beta_{B_{x,z}}\left(\frac{\operatorname{sen}\pi Q_{x,z}}{\operatorname{sen}\pi Q^{*}_{x,z}}\right) \qquad (18)$$

We want to show how the interaction entails a variation of $\bar{H}$ with a mechanism similar to A). At point B there is a thin lens with an intensity given by $4\pi\xi_x/\beta$: the derivative of function $\psi^{*}(s)$ at point B must therefore be given by eq. (15) in order to mantain the required symmetry. On the other hand, nothing has changed in the ring, magnetic structure except for point B, so that the difference between functions ψ and ψ^{*} can only be a free betatron oscillation, symmetric with respect to A and with an amplitude such as to have the right derivative in B. The difference between ψ_A and ψ^{*}_{A} and the variation of function $\beta(s)$ modify the value of $\bar{H}$. The variation of H, ψ_B and β_B shows that beam-beam interaction (in the thin lens approximations) strongly changes the beam dimensions. It should be pointed out that for $\xi_x = 8 \times 10^{-2}$ the quantity $2\pi\xi_x$ has a value of 0.5. All these effects strongly change if Q_x is near an even rather than to an odd integer; the choice between an even and an odd integer is therefore difficult: as an example with Q_x even, the longitudinal beam-beam limit is less severe but the value of ψ at the crossing point is strongly decreased.

Effect of dipole or gradient errors on beam dimensions.

For completeness, we want to point out that errors in the dipole function $1/\varrho(s)$ and in $K(s)$ can be interpreted as applications of methods B) and C): it would seem that the methods we have described do not apply to the case of a single dipole perturbation, which gives an error orbit in the form of a betatron oscillation along the ring, but it is sufficient to make a transformation into the reference system of the error orbit to get a term $1/g(s)$ on the right hand side of eq. (2), which represents the bending effect of the off-axis quadrupole modulated by the betatron oscillation: the situation is therefore similar to that described in B).

In Adone a vertical error orbit[6], due to a single dipole perturbation with a maximum amplitude of 2 cm, gives, for $Q_z = 3.05$ a value of $\bar{H}_z$ leading to the same vertical dimensions as full coupling. For the case of gradient errors, it can be shown that the maximum tolerated gradient error in the experimental magnetic detector (MEA), which is equivalent to a ξ_x value of $3.\,10^{-3}$, entails a 12% variation in the function ψ for $Q_x = 3.05$: this can be seen from (14), taking into account that there is only one perturbation, This perturbation therefore excites a betatron oscillation in ψ, with an amplitude equal to 12% of the unperturbed ψ. The ψ value at two successive crossing regions, about half a betatron wavelength apart, differ therefore by 25%.

Conclusions.

In this paper some resonant methods to control beam dimensions through the variation of the parameter $\bar{H}$ defined by (1) and (4) have been illustrated. Among the 3 proposed methods, the third, namely a modulation of the gradient function K(s), seems to be the most

Studies on this subject have been also carried out at SLAC, by D. Helm[7].

Obviously, this solution for beam dimension control must be compared or integrated with other proposed methods, like the high ψ value at the crossing point and the variation of Q_x with energy, as proposed initially by F. Amman[8] for the Super Adone project, and adopted for the SLAC 15 GeV electron-positron storage ring project[9] and for EPIC[10], for which the variation of J_x and J_z (partition numbers of betatron damping constants) or a vertical $\bar{H}_z$ are also proposed.

The first and the third methods, in particular the third, can also be applied to existing machines. In ref. [11] experiments on Adone with a configuration of 6 shunted quadrupoles are described. It would be desirable to make similar experiments at other machines in order to look for possible difficulties not at present foreseen.

References.

1 - M. Sands, The Physics of electron storage rings, Report SLAC-121 (1970).

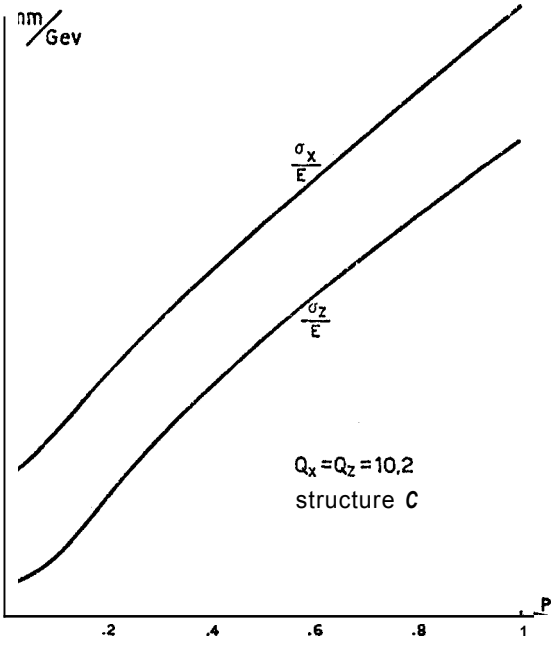
2 - M. Bassetti, Resonant methods for $\bar{H}$ control (In Italian) ADONE Int. Memo. T-61 (1974).

3 - F. Amman et al., The Super ADONE (SA) Electron-Positron Storage Ring Design, This Conference.

4 - M. Bassetti, How to change $\bar{H}$ (In Italian), ADONE Int. Memo. T-56 (1973).

5 - M. Bassetti, Zero-order optical effect of beam-beam interaction (In Italian), ADONE Int. Memo. SM-10 (1973).

6 - M. Bassetti, Generalization of ψ (off-energy function), due to dipole field (In Italian), ADONE Int. Memo. T-52 (1972); Effect of a vertical closed orbit on beam dimensions (In Italian), ADONE Int. Memo. T-59 (1974).
7 - J. Rees, SLAC, private communication.
8 - F. Amman, Luminosity, current and specific luminosity, ADONE Int. Memo. T-55 (1973).
9 - J. Rees and B. Richter, Preliminary design of a 15 GeV electron-positron variable-tune storage ring, Report SPEAR-167 (1973).
10 - G. H. Rees, Variable damping and tunes in the $e^{\pm}$ ring, Report EPIC/MC/39 (1974).
11 - M. Bassetti et al., ADONE: Present status and future improvments, This conference.



-FIG. 5

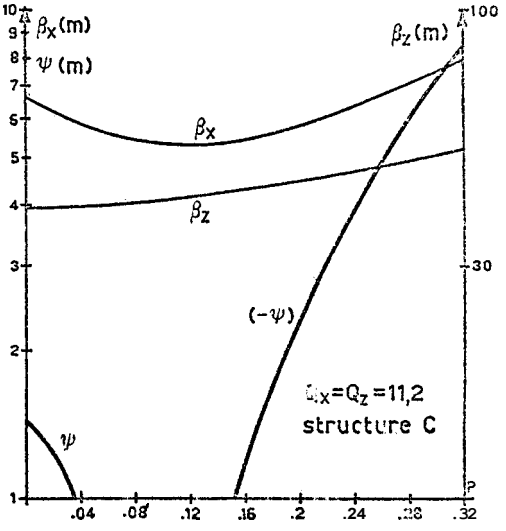


FIG. 7

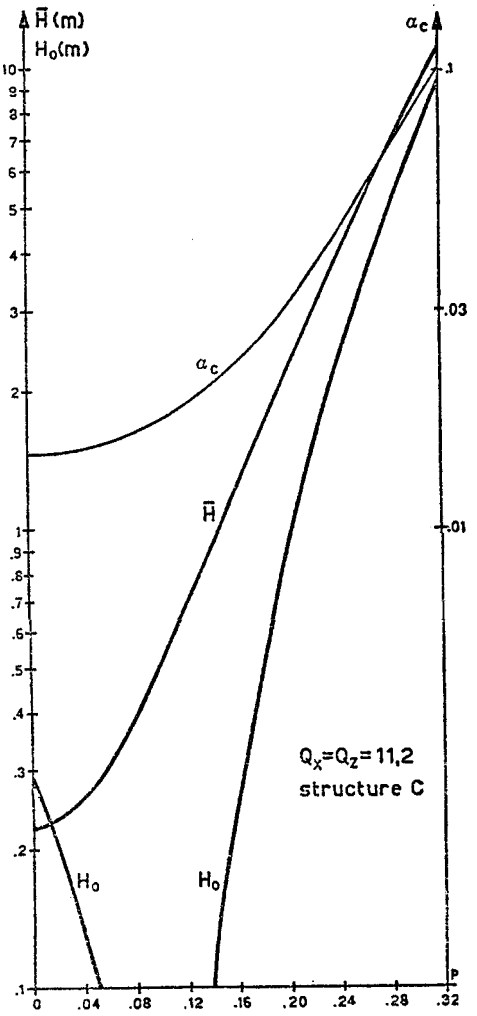


FIG. 6

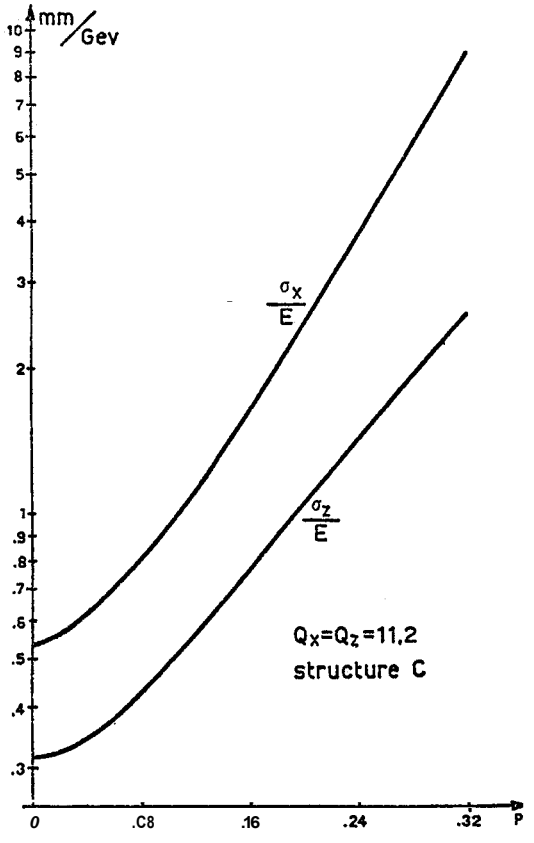


FIG. 8

DIRECT MEASUREMENTS ON THE BEAM-BEAM INTERACTION AT SPEAR*

A. P. Sabersky
Stanford Linear Accelerator Center
Stanford University, Stanford, California 94305

Introduction

The electromagnetic field of one colliding beam on another acts as a strong nonlinear lens, causing a spread in wave number (ν). Both the ν spread and its upper limit, $\Delta\nu_0$, have been invoked as causes of the beam-beam current limit in storage rings.[1,2] The extent of the spread has been searched out at other rings by studying workable operating regions in ν_x, ν space.[3,4] We have studied small changes in the sizes of chiding beams caused by external transverse excitation of one beam over a range of betatron frequencies. The results of the measurements are interpreted as tune shifts and tune spreads.

Measurement Technique

A single stored beam at equilibrium can be excited into betatron oscillations by applying a transverse oscillating electric field at the betatron frequency f_β or at frequencies sufficiently nearby.

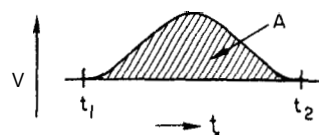
$$f_\beta = f_r |n-\nu| \quad ,$$

where f_r is the revolution frequency in the ring, ν is the betatron tune and n is any integer; in practice, the first integer above ν. Such a resonance has a finite width, often dominated by power-supply ripple, and includes damping phenomena and nonlinearities in the magnet lattice.

Usually it is the coherent resonance width which is measured, with antennas which detect the spatially average electromagnetic field of the particle beam. It is also possible to measure the response of the beam transverse size to transverse or longitudinal excitation.

An optical profile monitor using synchrotron radiation is a standard device in electron-positron machines.[5] In SPEAR,[6] we have an image-dissecting system which produces a train of profile scans for display on an oscilloscope. For a constant beam current, the area of each of the voltage pulses,

$$A = \int_{t_1}^{t_2} V(t)\,dt \quad ,$$



is constant, independent of changes in beam dimension. Thus the peak amplitude is inversely proportional to pulse width. With a peak-detecting circuit whose output feeds a recorder (Fig. 1h), one may plot the size response of the beam to excitation. This response is often quite different from the coherent response.**

The output of the optical monitors is often noisy, and the beam itself can be unstable, so one must use noise-suppression techniques in order to see small beam-size changes clearly, We use a lock-in technique (Fig. 2) in

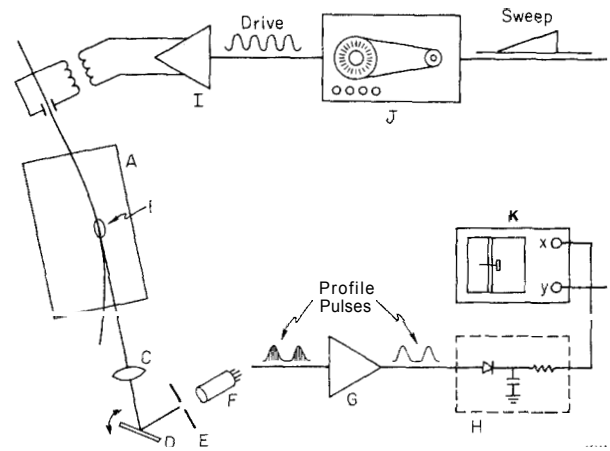


FIG. 1--Experimental equipment excluding lock-in

A. bend magnet
B. beam
C. lens
D. oscillating mirror
E. slit
F. photomultiplier
G. amplifier
H. peak-detector circuit
I. excitation amplifier
J. sweeping oscillator
K. x-y recorder

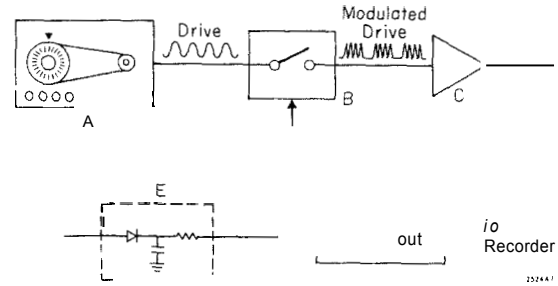


FIG. 2--Synchronous modulation of beam excitation and demodulation

A sweeping oscillator
B. electronic switch
C. beam excitation system
D. lock-in amplifier
E. peak detector

which the beam excitation is modulated with a square wave at approximately 1Hz and the output of the peak detector circuit (Fig. 2e) is synchronously demodulated.

When this size response technique is applied to a beam in collision with another, we see a broad peak (Fig, 3) which we interpret as a tune-spread response. In general, there is no detectable broad coherent response when one stimulates colliding beams, only isolated resonant responses. The limiting sensitivity of our tuned receiver[7] is such that we can detect coherent signals which are 10^3 times smaller than the resonant response of the same beam not in collision.

The strong nonlinearities of the field of one beam on another cause a spread of wave numbers, the upper limit of which is the optical tune shift.[8] We observe that the exciting field couples to the beam, for the beam-size changes, but it does not couple in a coherent way. Rather, the particles whose f_β lie close to the exciting frequency gain

*Work supported by the U. S. Atomic Energy Commission.
**The germ of the ideas which led to this measurement technique originated in discussions with M. Matera of Frascati.

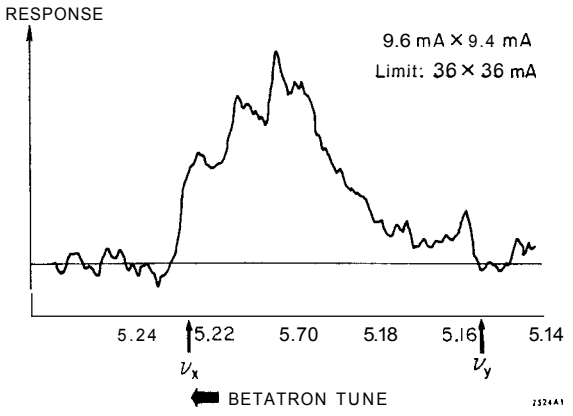


FIG. 3--Beam size response to excitation.

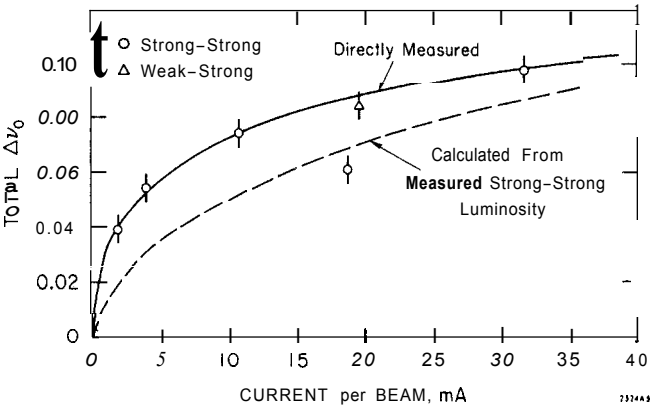


FIG. 4--Measured tune shifts.

transverse energy, change frequency and are replaced by other particles which move into the same region of f_β. Some time after the excitation is switched on, the colliding beams reach a new equilibrium, with the entire excited beam having more transverse energy and being wider.

Although we have no analytic treatment of this effect, it seems that the magnitude of the coupling of the exciting field to the beam is proportional to the local density of particles near that f_β or the coupling strength of the particles at that frequency, or both.

In all measurements, the excitation has been kept small enough so that the beam sizes change by less than 10%, and we have observed no changes in measured luminosity to within ±5%.

As one beam widens, the other shrinks. Under some conditions, energy couples to beam B when beam A is being excited, and beam A shrinks. This effect can be confusing and is usually eliminated by reducing the amplitude of the exciting field.

Another problem is the coupling of energy between horizontal and vertical motions in colliding beams. We have not yet measured the magnitude of this coupling, but it may lead to difficulty when ν_x and ν_y are close enough so that the tune spreads in the two planes overlap.

There can be no problem with "pulling" of particles with the excitation, since the frequency sweep is very slow, and the lock-in modulation period is long enough to allow the particles to attain complete equilibrium with excitation off. A typical sweep rate is $\Delta\nu/\Delta t = 2\times10^{-4}$/sec and a typical lock-in modulation rate is 1 Hz.

Experimental Results

There are still many difficulties with the measurement technique, and the results we present are preliminary. Figure 4 shows tune shifts per interaction region for 1) colliding beams with the same currents (strong-strong), 2) a large-current beam colliding with a weak beam. The tune shift of the weak beam is plotted versus current in the strong beam.

At all equal-current points, the tune shift of the more diffuse beam, as seen on the optical monitors, was measured. There is no measurable difference in the weak-strong and the strong-strong case. Tune shifts for the equal-beam case, computed from lattice parameters, beam currents, and measured luminosities, are also plotted.

Several of the response peaks in Fig. 2 are not noise, but repeat over many measurements at the same operating point, with different colliding currents. Most data show pronounced, repeatable structure of this type, and while we have no certain explanation, we suspect they may be due to resonances.

In some of the weak-strong measurements, strong, isolated responses appear with tune shifts more than twice the calculated tune shift. The peaks of these mysterious resonances do not have any harmonic relationship with the lower-tune responses.

Acknowledgements

I would like to thank the members of the SPEAR group for their help and the SPEAR operations group for excellent running of the machine.

References

1. E. D. Courant, IEEE Trans. Nucl. Sci. NS-12, 550 (1965).
2. F. Amman, Proceedings of the 8th International Conference on High Energy Accelerators, CERN, 1971, p. 63.
3. V. L. Auslander et al., Proceedings of the 5th International Conference on High Energy Accelerators, CERN, 1965, p. 335.
4. R. Belbeoch et al., "Beam-Beam Interaction at the e^+e^- Orsay Storage Ring," Report No. LAL-RT-3-73, Orsay (1973).
5. E. T. Zinin et al., Proceedings of the 5th International Conference on High Energy Accelerators, CERN, 1965, p. 276.
6. A. P. Sabersky, Proceedings of the National Particle Accelerator Conference, San Francisco, 1973.
7. The SPEAR Group, "Beam Dynamics Experiments in SPEAR," these proceedings.
8. A. Jejcic and J. LeDuff, Proceedings of the 1971 National Particle Accelerator Conference, San Francisco, p. 355.
9. The SPEAR Group, Proceedings of the 1971 National Particle Accelerator Conference, San Francisco, p. 838.

RF SUPERCONDUCTIVITY

M. Kuntze

Universität and Gesellschaft fiir Kernforschung, Karlsruhe
Karlsruhe, Germany

Summary

Superconductors used for the microwave accelerating structures held the promise of a drastic reduction in RF power requirement at comparable or higher field strengths with respect to conventional ones. Technically applied accelerating structures have sufficiently low RF losses at high fields, whereas the maximum achievable RF field is still below expectations. However, the theoretical limit for the RF field has nearly been reached in some test resonators at a laboratory scale. Further improvement in high RF fields is expected.

Introduction

The new technology of RF superconductivity originally developed, as in the case of many other things, out of the field of accelerator research. Conventional linacs with high beam intensities for the acceleration of electrons, protons and heavy ions have been built (e.g. Stanford, Los Alamos, GSI-Darmstadt). They are expensive in operation because of the very high RF power requirements and must be pulsed, in general. Superconductors used for the microwave accelerating structures held the promise of a drastic reduction in RP power requirement and hence a reduction in operating cost due to the much lower RF losses at comparable or higher field strengths. In addition, continuous beam acceleration is available which results in higher beam quality and more abundant production of secondary particles. Therefore, nearly ten years ago, some enthusiastic physicists started to develop the new technology of RF superconductivity.

Some milestones in the history are:

1964 electrons were accelerated for the first time with a superconducting lead plated test-resonator by a group at Stanford'. The existence proof for a superconducting linear accelerator (SCA) had been given.

1967 the construction of prototype Components for an electron SCA was first begun at Stanford[2].

1968 the attention was directed towards Nb as a superconductor which had been shown to be superior to Pb by the Stanford group[3,4].

1970 the construction of prototype components for a proton SCA was first begun by a group at Karlsruhe[5].

1971 electron beam tests with the first part of the Stanford SCA were carried out successfully[6].
The first part of an electron SCA as part of a microtron was operated as an accelerator by a group at the university of Illinois'.

1972 proton beam tests with the first part of the Karlsruhe SCA were carried out successfully',

Today, in the field of accelerator technology, about 8 technical projects with superconducting RF devices are well underway. Among them are superconducting cavities for electron and proton acceleration[9-12] and for heavy ion acceleration[13,14]. Moreover, superconducting particle separators[15-17] are under construction for the separation of pions and kaons. A superconducting RF separator is the only economic possibility for particle separation above a certain particle momentum, especially for long beam pulses[15,16].

More than 10 other laboratories view their work as applied research on RF superconductivity. Unfortunately, detailed information about the work in this field which is going on in the UdSSR has not come to the authors attention.

This broad interest in RF superconductivity is motivated not from accelerator technology alone. Beyond basic nuclear research superconducting RF accelerators with its high beam current and continuous operation offer novel possibilities in biomedical research[18-22]. Basically, the use of particle accelerators in radiotherapy and radiodiagnostic has the advantage, that the global radiation exposure of the patient is reduced to a large extend, if pions or protons are used instead of X-rays, gamma rays or electrons. The existence of RF superconductivity held the promise of energy economized accelerators. It thus may contribute to the production of more useful particles for medical applications.

Small and compact SCA's in the MeV range could also be used advantageously in high voltage electron microscopes[23].

Superconducting cavities for high field applications must have low losses R (high Q-values) as well as high peak RF surface fields, E_{max} and B_{max}. However, the high Q-value alone permits various interesting low field applications. I am refering to the field of measurement of extremely small quantities (dielectric losses, small frequence shifts, small changes in length etc.). Recently at Stanford" another milestone has been achieved. A superconducting cavity stabilized a Gunn-effect oscillator with a short term frequency stability of 10^{-15}.

In principle, the scope of application of this new technology is nearly the entire field of electrical engineering, The additional expenditures for cryogenics limits the application of RF superconductivity, however, to problems where superconductivity offers particular advantages. For example, in the field of communications applications include low noise receivers of extremely weak signals, extremely narrow bandwidth, RF filters, and low loss delay lines. A particular example is the application of superconducting coaxial cable for communications[25]. Superconducting transmission lines are nearly lossless and have low distortion. They are superior to conventional coaxial cables, but have a competitor in the glass optical waveguides[26].

There have been several summary papers in recent years concerning RF superconductivity and its application to particle accelerators at different conferences[27-30]. In this paper I would like to discuss the present situation with superconducting RF cavities and the currently operating superconducting accelerator prototypes. Fabrication and processing techniques being utilized for the production of superconducting structures have been summarized two years ago in the excellent paper by J.P. Turneaure[27]. Progress in this field since that time will be summarized in this paper.

Present situation with superconducting RF cavities

The behavior of superconductors at high frequencies can be characterized by the following facts:
1. In contrast to dc fields ac fields still cause losses which are lowest in the Meissner state.
2. In the Meissner state shielding currents flow only near the surface and the RF losses are concentrated within this very thin surface layer of about 50 nm thickness.

According to the BCS-theory[38] the ac losses should vanish exponentially with temperature (see Fig. 1). Experimentally the losses in superconducting RF cavities have been reduced to the theoretical value at all temperatures above 1.5 K. This progress can be seen from Fig.1. At temperatures below 1.5 K a constant residual resistance, R_{res}, is obtained. The origin of this R_{res} is not completely understood, although surface effects which are localized directly at the metal oxide interface[39] are thought to be responsible.

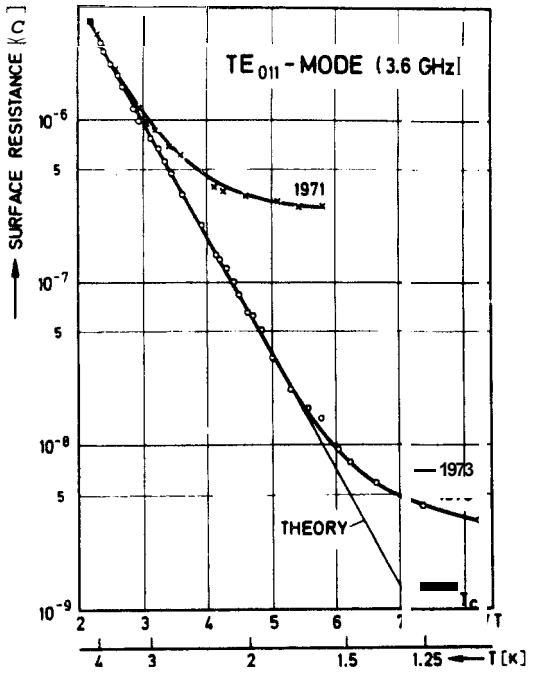


Fig. 1: Surface resistance as function of temperature for a TE-mode Nb cavity.

Obviously surface preparation and protection techniques are of great significance. The improvement of these techniques has led to the present situation with RF losses on the order of 10 nΩ (Fig.1). Results of simple cavities at 1.5 K are given in Table I[36,37].

Table I: Results of simple Nb cavities at 1.5K

Frequency	Mode	R	B_{max}	E_{max}	Reference
GHz		nΩ	mT	MV/m	
9.6	—	20	193	—	BCS-Theory
9.6	TE_{011}	39	160	—	Siemens
9.6	TM_{010}	140	150	70	Siemens
3.6	—	5	193	—	BCS-Theory
3.6	TE_{011}	8	81	—	Karlsruhe
2.1	TM_{010}	50	38	29	Karlsruhe
0.09	—	0.008	193	—	BCS-Theory
0.09	Helix, π	10	100	24	Karlsruhe

The residual resistance is sufficiently low, though it is sometimes an order of magnitude higher than the theoretical limit, especially in modes which have strong electric fields terminating on the cavity surface. Even in actual accelerating structures the RF losses at high fields do not exceed thermal insulation losses of the cryogenic system. For example, at an energy gradient of 3.0 MeV/m in a 6 m long 1300 MHz Nb accelerating structure at Stanford' the RF power dissipated at helium temperature was 8.6 watts. The total insulation loss of the cryogenic system was on the order of 10 watts.

The situation, in general, with respect to RF losses hence is satisfactorly even on a technical scale. However, the situation with respect to maximum achievable RF field is different. The theoretical limit is thought to be the thermodynamic critical magnetic field B_c. With the type I superconductor Pb this limit has been reached at RF frequencies[44,45]. For type II superconductor Nb the thermodynamic critical magnetic field is B_c = 193 mT at 1.5 K, while the lower critical field is B_{c_1} = 127 mT at 1.5 K.[37] With simple Nb cavities the measured RF peak values at 1.5 K, B_{max}, are slightly lower than the thermodynamic limit (see Table I), but clearly higher than B_{c_1}. This is in agreement with expectations of Halbritter[36,40], according to which the value of B_{c_1} is meaningless within the microwave range, because the generation and penetration of magnetic flux takes too much time. Therefore, other hard superconduc-

tors such as Nb_3Sn or NbN become interesting for superconducting RF cavities due to their substantially higher B_c.

There exists, however, especially with respect to peak fields, a discrepancy between simple cavities and large Nb structures. In actual Nb accelerating structures the standard surface RF fields obtained are much lower than the best values obtained in these structure~~''~'. This is shown by the results given in Table II, which summarizes standard values, best values and standard energy gradients for large Nb structures.

Table II: Results of actual niobium accelerating structures.

TYPE OF STRUCTURE	FREQUENCY	SURFACE RF-FIELDS STANDARD	BEST VALUE	ENERGY GRADIENT STANDARD	REFERENCE
	GHz	MV/m / mT	MV/m / mT	MeV/m	
SINGLE λ/2 -HELIX	0.1	151 60	251 100	2 - 3	KARLSRUHE [31,32]
REENTRANT CAVITY	0.35	12 /	26 /	–	STANFORD [33]
IRIS	1.3	10.8 / 16.2	18/27	3 - L	STANFORD [9,34]
DEFLECTOR IRIS	2.8	14.5 / 40	30 / 85	2.6 - 5.5	KARLSRUHE [35]
SINGLE CELL OPEN CAVITY	3.0	–	–	6	CORNELL [1]
TM-CAVITIES	2.1	–	29 / 38	–	KARLSRUHE [36]
	2.9	20 /	35 /	–	STANFORD [34]
	8.6	40 / 61.5	70 / 108	–	STANFORD [4]
	9.6	–	70 / 150	–	SIEMENS [37]

The situation with respect to accelerator applications is indicated in Fig.2. Peak electric fields and energy gradients are given for different types of accelerating structures. Further improvements in the achievable energy gradient seem possible.

For all the real progress in superconducting RF cavity work the essential requirement for high RF fields and Q's have still not been determined with assurity. Still one gets varying results for B_{max} and Q with resonators which have been fabricated and treated in a similar way. In particular, in real accelerating structures the results fluctuate for identical resonators as a result of similar repeated surface preparation procedures. This points to different surface states which we are not yet able to parameterize.

Two problems which are related to the surface condition are the following[36,41]. One problem is magneto-thermal breakdown. Precipitates of bad superconductors or surface roughness, for instance, will locally lower the critical magnetic field and thus lead to a premature magneto-thermal breakdown. Already at medium macroscopic field levels the spot goes normal conducting. Due to a factor of 10^6 higher

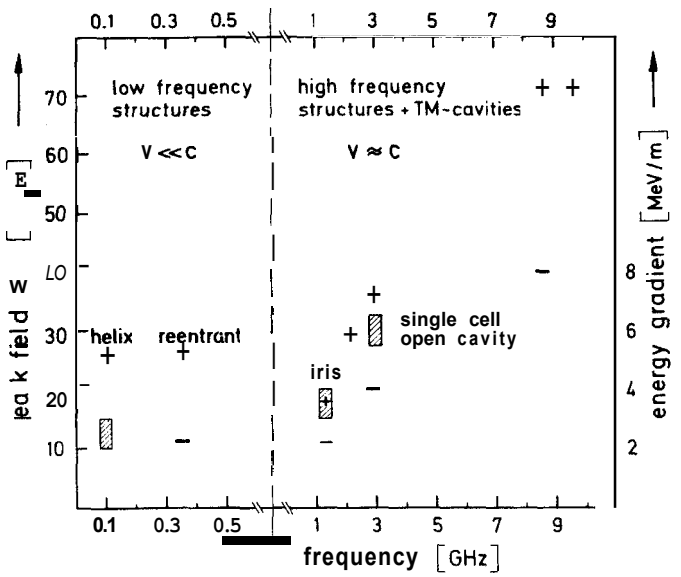


Fig. 2: Peak electric field (±) and achievable energy gradient (▨) for different types of accelerating structures. Standard values are indicated with dash (-), best values are indicated with cross (+).

losses the normal conducting nucleus is heated up and spread out within microseconds until at least a large part of the resonator surface goes to the normal-state.

Another problem which has become apparent in recent years is that of electron loading[41,43] for cavity modes which have strong electric fields terminating on the cavity surface, as is the case for all accelerating modes. Electron loading is a primary reason for field limitation and degradation in accelerating structures. In particular, surface damage due to electron impact can cause RF breakdown. Furthermore charging of the oxide coating by electron impact will change the residual losses and will enhance the secondary electron emission[41]. The experimental evidence is taken from the big difference in obtainable peak magnetic RF fields in TE- and TM-mode cavities. TM-mode cavities- subjected to electron loading- have significantly lower breakdown fields than TE-mode cavities. Results of $B_{max}(TE_{011})$ = 80 mT and $B_{max}(TM)$ = 40 mT in a S-band cavity show[44], that the hypothesis of an area-[27] or frequency-dependent[28] B_{max} cannot describe the experiments. Instead, a model derived on electron loading can explain $B_{max} \propto \omega$ in similar shaped cavities, e.g. the value B_{max} (2.2 GHz) = 40 mT corresponds to B_{max} (9.6 GHz) = 150 mT, which has in fact been measured in a 9.6 GHz Nb cavity[37].

Current activities in RF superconductivity

Laboratory	SCA projects underway
Stanford University (High Energy Physics Lab) ref. 9	electron linac (4 orbit recirculation system), 350 MeV, >100 μA superconducting structure: 4x6 m long 1300 MHz niobium structure of the iris-loaded type (multiperiodic)
University of Illinois ref. 10	electron microtron (recirculation of beam for 6 turns), 600 MeV, 10 μA superconducting structure: 4.6 m long, 1300 MHz Nb structure of the iris-loaded type (multiperiodic)
Cornell University ref. 11	electron synchrotron, 25 - 40 GeV superconducting structure: 10 - 500 m, 3000 MHz Nb structure which is completely open in the horizontal mid-plane
Rutherford High Energy Lab. ref. 17	RF-separator for pions and kaons with a central momentum of 4GeV/c superconducting strucutre: 2×1.25 m long lead-plated cavities separated by a distance of 7.5 m and operated at 1.3 GHz
Karlsruhe / CERN ref. 15, 35	RF-separator for kaons and antiprotons up to a momentum of 30GeV/c superconducting structure: 2×2.7 m long Nb deflectors of 104 cells each and separated by a distance of 90 m and operated at 2.855 GHz
Karlsruhe Institut fiir Experimentelle Kernphysik ref. 12, 30	proton linac (2-stage-pilot accelerator) 10 - 15 MeV, >100 μA superconducting structure: 4.8 m long 90 MHz Nb helices, 2 m long 720 MHz Nb structure (eventually of Alvarez-type)
Argonne National Lab. ref. 13	heavy-ion postaccelerator 10 MeV/N superconducting structure: 90 MHz niobium helices
California Institute of Technology ref. 14	heavy-ion postaccelerator superconducting structure: niobium spiral resonator

Laboratory	applied SCA research
Stanford University ref. 34	niobium TE- and TM-mode cavities at 1.3 GHz, 2.6 GHz and 8 - 10 GHz (stable oscillators)
Stanford University/ Weizmann Institute of Science ref. 33	niobium reentrant cavities at 433 MHz
Karlsruhe/Heidelberg (Max-Planck-Institut fiir Kernphysik)	niobium single λ/2-helix resonators at 50/100 MHz
Karlsruhe ref. 36	niobium TE- and TM-mode cavities at 2-5 GHz
Siemens (Erlangen) ref. 37	niobium TE- and TM-mode cavities at 8-10 GHz
Bonn	niobium cavities at 8-10 GHz
DESY	niobium cavities at 1.3 GHz
Orsay (Institut d'Electronique Fondamentale)	niobium cavities at 2-3 GHz
Tokyo (National Lab. for High Energy Physics)	niobium cavites at 6.5 GHz
Osaka University ref. 46	lead-plated cavities at 3.8 GHz

The listing presented here does not pretend to be complete. For example, many laboratories are interested in developing superconducting cavities if they can possibly increase the energy of their accelerator. In the past there has been work on superconducting cavities at SLAC[47].

Fabrication and surface preparation of Nb cavities

Nb products can be supplied commercially with low enough impurity content, free of voids and inclusions, and annealed. The standard specification is now named "Stanford grade"[27]. The price per kg still is constant at about 80 $/kg. Drawn tubing for helices are mechanically polished, solid ingots are forged and sometimes prerolled or premachined. Generally, Nb products can be formed by most of the standard forming techniques.

The method of cavity fabrication depends very much on the type of cavity. The most direct way to fabricate cavities is to machine the parts from solid Nb bar and join the parts with either demountable seals or electron beam (EB) welds. This method is used for 3 GHz and 10 GHz test-cavities[36] and even for 3 GHz particle separator structures[15]. It has been used for 720 MHz test cavities for proton acceleration. This method is relatively expensive for a long SCA, and therefore HEPL has used another approach to manufacture Nb cavities for their bigger structures. 20 cm diameter cavities are fabricated from Nb square sheets about 5 mm thick. Half cells are made by hydroforming into cups and then machining. These cups are finally EB welded together to form the cavity[9,27].

But what decides the matter above all, is the preparation of the niobium surface. The surface preparation procedures are chemical polishing, electropolishing with subsequent anodizing, and ultra-high-vacuum (UHV-)firing.

Chemical polishing: The usual surface treatment after-final machining is chemical polishing with a mixture of HNO_3 and HF. Up to about 100 µm are to be removed from the surface to get rid of the damage layer and smooth the surface.

Electropolishing: The best surface smoothness is obtained by electropolishing with a H_2SO_4 and HF solution[49]. Starting at a certain dc voltage current oscillations occur, due to a repetitive process which involves the formation of oxidation products (SO4 ions etc.) in a thin oxide layer of high resistance, which is then dissolved by HF. Because of the high resistance layer peaks are preferentially removed. As a result, a surface roughness as low as 30 nm has been achieved.

Anodizing: The electropolished Nb surface is very often subsequently covered with a dense (about 0.1 µm thick) layer of amorphous Nb_2O_5. This is done by anodic oxidation[50] in a NH_3- or H_2SO_4-solution. Anodizing results in an increase of B_{max} and Q, even if the resonator has not been handled before under particularly clean conditions. The reason for this improvement is thought to be that, when the oxide layer is grown, the Nb surface is shifted to a deeper and cleaner niobium layer. In addition, this method allows to get rid of a large amount of chemicals. Handling under particularly clean conditions is not always possible with the relatively large accelerating structures, therefore anodizing seems to be advantageous. At least transportation and storage of Nb structures may be much easier with anodized cavities. The only disadvantage of the oxide layer seems to be its sensitivity to electron loading and its enhanced secondary electron emission. These effects have to be studied in more detail.

UHV-firing: UHV-firing the Nb cavity at temperatures in the range of 1400°C to 1800°C for several hours not only removes gaseous contaminations, mainly oxygen, but it also stress relieves and dissolves precipitates. Especially, if the surface has been anodized first, UHV-firing can remove some carbon[36,47], because CO can be evaporated. Again UHV-firing is necessary for welded and complicated Nb structures because welds always need some annealing and complicated structures are otherwise difficult to clean from chemicals, In addition, rapid cooldown of the UHV furnace and ventilation with nitrogen at 400°C has shown to give better results in small test cavities[41].

Other performance considerations

We are able to design and manufacture superconducting Nb cavities with similar or better CW energy gradients than with conventional RF cavities. We maintain the required deflecting and accelerating fields continuously, because the power loss on the surface of the cavities is reduced up to a factor of 10^6 compared to normal-state conductors. Although some improvements still remain to be made, especially increasing the energy gradient in Nb accelerating structures, the major difficulty has been shifted to the economy and reliability question of the compound system of superconducting electrical engineering with cryogenics.

Nb RF structure: As already indicated, the fabrication and processing of large Nb cavities is sometimes expensive because a rather complex surface preparation technique is needed. Simplifying the processing procedure and developing new methods for mass production will essentially contribute to a more economic solution.

Further SCA development should be towards

- improved surface preparation techniques to achieve higher fields,
- simplified surface preparation techniques for mass production,
- surface protection for long term stability,
- radiation resistivity,
- other superconducting materials with higher T_c.

RF-system: In general, unless very high beam currents are required, the RF system of a SCA is simpler than conventional ones. Conventional RF transmitters in the range of 50 W to 1 kW are needed, only. The only problem which will remain in some cases is probable tuning of individual cavities with extremely narrow bandwidth, In particular, for a high current proton accelerator one major problem is to couple adequately the microwave power out of the cavity to an external tuner[51] without large dissipation into the helium.

Cooling: The power loss on the surface of superconducting accelerating structures is in the order of W/m. One must remember, however, that this heat loss must be removed at 1.8 K. When the Carnot efficiency and the refrigerator efficiency are taken into account, the refrigerator must have a power input of about 2000 W per W of power dissipated at 1.8 K.

It seems clear, that the cost of the refrigerator and that of the cryogenic appendages play a major role in the total cost of a superconducting accelerator. These cost are dominated by the necessary size of the refrigerator, which in turn must be adequate to handle the total power dissipated at 2 K. The latter is composed of the RF power loss on the cavity surface, the RF dissipation into the helium down the RF transfer lines, and the insulation loss of cryostats, helium transfer lines and fittings. Optimization with respect to economy and reliability of cryogenic components must be given particular attention. The choice of operating temperature and the design of an adequate cooling system have to be taken seriously into account.

Refrigerators and cryostats: Rapid progress has been made in cryogenics, and the state of cryogenic engineering permits the manufacture of helium refrigerators in the range of very small (<1 W) up to large ($\geq$ 1 kW) machines. However, refrigerators so far have not been particularly optimized to special applications and continuous operation at a constant heat load. It seems to be clear, that an optimization of refrigerator, cryostat and transfer lines for every special application is necessary.

Helium cryostats and transfer lines do have insulation losses, at this time, in the range of 0.2 W/m^2 up to 0.7 W/m^2 [52]. With the rapid progress in reduced RF power losses on the surface of superconducting structures in recent years, it seems to be clear, that a reduction in insulation losses also will contribute to a more economic superconducting solution. The cost for cryostats [6] (3-6 m^3) are nowadays in the range of 8000 $\$/m^3$ up to 40000 $\$/m^3$.

References

[1] J.M.Pierce, H.A.Schwettman, W.M.Fairbank, P.B.Wilson
Proc. 9th Inter.Conf.on Low Temp.Physics - Part A (Plenum Press, New York, 1965) p.396

[2] H.A.Schwettman, J.P.Turneaure, W.M.Fairbank, T.I.Smith, M.S.McAshan, P.B.Wilson, E.E. Chambers
IEEE Trans. NS-14, No.3, 336 (1967)

[3] J.P.Turneaure, I.Weissman
J.Appl.Phys. 39, 4417 (1968)

[4] J.P.Turneaure, N.T.Viet
Appl.Phys.Lett. 16, 33 (1970)

[5] A.Citron
Proc. 1970 Proton Lin.Acc.Conf., Batavia 1970, Vol.I, p. 239

[6] L.R.Suelzle
IEEE Trans. NS-18, No.3, 146 (1971)

[7] A.O.Hanson
IEEE Trans. NS-18, No.3, 149 (1971)

[8] A.Brandelik et al.
Part.Acc. 4, 111 (1972)
A.Citron et al.
Proc.1972 Proton Lin.Acc.Conf.,(Los Alamos LA 5115, 1972) p. 93
H.Klein, M.Kuntze
IEEE Trans. NS-19, No.2, 304 (1972)
M.Kuntze
Proc. US-Japan Seminar, Tokio, Nov.1973

[9] J.P.Turneaure, H.A.Schwettman, H.D.Schwarz, M.S.McAshan
HEPL-report 728, Feb.1974 (to be published in Appl.Phys.Lett.)

[10] Lloyd M.Young
IEEE Trans. NS-20, No.3, 81 (1973)

[11] R.Sundelin, E.vonBorstel, J.Kirchgessner, D.Rise, M.Tigner
IEEE Trans. NS-20, No.3, 98 (1973)

[12] A.Citron et al.
Proc. 8th Int.Conf.High Energy Acc., CERN (Geneva 1971, CERN), p. 278
M.Kuntze
IEEE Trans. NS-18, No.3, 137 (1971)

[13] R.Benaroya et al.
Appl.Phys.Lett. 21, 235 (1972)
R.Benaroya et al.
Proton Lin.Acc.Conf. (Los Alamos LA 5115, 1972), P. 168
J.Aron et al.
IEEE Trans. NS-20, No.3, 76 (1973)

[14] A.Sierk, C.J.Henner, T.A.Tombrello
Part.Acc. 2, 149 (1971)
T.A.Tombrello et al.
Proc.1972 Proton Lin.Acc.Conf.,(Los Alamos LA 5115, 1972), p. 256
G.J.Dick, K.W.Shepard
Appl.Phys.Lett.24, 40 (1974)

[15] W.Bauer et al.
IEEE Trans. NS-20, No.3, 59 (1973)
W.Bauer et al.
Proc.Conf.Instr.High Energy Physics, Frascati 1973, p. 716

[16] J.R.Aggus, W.Bauer, S.Giordano, H.Hahn, H.J.Halama, Appl.Phys.Lett.24,144(1974) and IEEE Trans NS-20, No.3, 95 (1973)
S.Giordano, H.Hahn, H.J.Halama, C.Varmazis, L.Rinderer
J.Appl.Phys.44 , 4185 (1973)

[17] A.Carne, R.G.Bendall, B.G.Brady, R.Sidlow, R.L.Kustom
Proc.8th Int.Conf.High Energy Acc., Geneva CERN (1971), p. 248

[18] H.S.Kaplan, H.A.Schwettman, W.M.Fairbank, D.Boyd, M.A.Bagshaw
to be published in Radiology (1973)
D.Boyd, H.A.Schwettman, J.Simpson
Nucl.Instr. and Meth. 111, 315 (1973)

[19] P.B.Wilson, C.S.Nunan
IEEE Trans. NS-20, 1018 (1973)

[20] K.Scheer, U.Schmidt-Rohr
report of the german cancer research center (DKFZ), Heidelberg and the Max-Planck-Institut für Kernphysik, Heidelberg (1973)

[21] B.P.Murin, A.P.Fedotov, V.G.Kulman, G.I. Batskikh, B.T.Polyakov
Proc.1972 Proton Lin.Acc.Conf.,(Los Alamos LA 5115, 1972), p. 387

[22] E.A.Knapp
Proc. US-Japan Seminar, Tokio, Nov.1973
L.Rosen
Science Journal 5A, p.29 (1969)
IEEE Trans. NS-20, No.3, 10 (1973)

[23] C.Passow
Ext.report KFK 957 (Karlsruhe, 1969)

[24] J.P.Turneaure
private communication

[25] N.Chiba, Y.Kashiwayanagi, K.Mikoshiba
Proc.IEEE 61, 124 (1973)
W.Hartwig
Proc.IEEE 61, 58 (1973)
H.G.Unger
private communication

[26] D.B.Keck, R.D.Maurer, P.C.Schulz
Appl.Phys.Lett.22, 307 (1973)

[27] J.P.Turneaure
Proc.1972 Appl.Superconductivity Conf., (IEEE, New York, 1972) p. 621

[28] P.B.Wilson
Proc.1972 Proton Lin.Acc.Conf., (Los Alamos LA 5115, 1972) p. a2

[29] L.R. Suelzle
IEEE Trans. NS-20, No.3, 44 (1973)

[30] M.Kuntze
IEEE Trans. NS-20, No.3, 49 (1973)

[31] J.E.Vetter, B.Piosczyk, J.L.Fricke
Proc.1972 Proton Lin.Acc.Conf., p.145
Los Alamos Sci.Lab. (1972)
J.L.Fricke, B.Piosczyk, J.E.Vetter, H.Klein
Particle Acc.3, 35 (1972)

[32] B.Piosczyk
Ext.report 3/74-7, Karlsruhe (1974)

[33] I.Ben-Zvi, J.G.Castle Jr., P.H.Ceperley
IEEE Trans. NS-19, No.2, 226 (1972)

[34] C.Lyneis, Y.Kojima, J.P.Turneaure, Nguyen Tuong Viet
IEEE Trans. NS-20, No.3, 101 (1973)

[35] H.Lengeler et al.
this conference

[36] P.Kneisel, O.Stoltz, J.Halbritter
IEEE Trans. NS-20, No.3, 63 (1973)

[37] H.Martens, H.Diepers, B.Hillenbrand
Phys.Lett. 44A, 213 (1973)
K.Schnitzke, H.Martens, B.Hillenbrand, H.Diepers
Phys.Lett. 45A,241(1973) and this conference.

[38] J.Halbritter
Z. Phys. 238, 466 (1970)
Z. Phys. 266, 209 (1974)

[39] J.Halbritter
J.Appl.Phys. 42, 82 (1971)

[40] J.Halbritter
Proc.1972 Appl.Superconductivity Conf., Annapolis (IEEE, N.Y.,1972), p. 662

[41] P.Kneisel, O.Stoltz, J.Halbritter
to be published in J.Appl.Phys.45 (May 1974)

[42] B.Piosczyk, P.Kneisel, O.Stoltz, J.Halbritter
IEEE Trans. NS-20, No.3, 108 (1973)

[43] P.Kneisel, O.Stoltz, J.Halbritter
J.Appl.Phys. 44, 1785 (1973)

[44] Y.Bruynseraede, D.Gorle, D.Leroy, P.Morignot
Physica 54, 137 (1971)

[45] T.Yogi
Cryogenics 13, 369 (1973)

[46] A.Takaoka, K.Ura
Techn.rep.Osaka University 23, No.1111, 223 (1973)

[47] M.A.Allen, Z.D.Farkas, H.A.Hogg, E.W.Hoyt, P.B.Wilson
IEEE Trans. NS-18, No.3, 168 (1971)
P.B.Wilson, Z.D.Farkas, H.A.Hogg, E.W.Hoyt
IEEE Trans. NS-20, No.3, 104 (1973)

[48] Siemens, Erlangen
Laborbericht 1973

[49] H.Diepers, O.Schmidt, H.Martens, S.F.Sun
Phys.Lett. 37A, 139 (1971)

[50] H.Martens, H.Diepers, R.K.Sun
Phys.Lett. 34A, 439 (1971)

[51] G.Hochschild, D.Schulze, F.Spielböck
IEEE Trans. NS-20, 116 (1973)

[52] P.Flecher
J.Vac.Sci.Techn. 9, 46 (1972)
W.Barth et al.
Proc. 4. ICEC, Eindhoven, May 1972

T. Khoe, Argonne National Laboratory: When you anodize the accelerating cavities, do you have any problems with multipactoring ?

M. Kuntze: We had problems with multipactoring but so far we have always been able to overcome it. But electron loading seems to limit the cavities at high fields. We have not gone completely through it up to now, but what will happen at the surface will happen with or without anodizing, because there is a 40 to 50 Angstrom thick oxide layer on the niobium surface. What happens on the surface will happen in the first 10 or 15 Angstroms, so an oxide layer of 500 Angstroms makes no difference. It will enhance electron secondary emission a little, but I don't think that that is a problem.

M. White, Princeton University: Do you have any problems with whiskers ?

Kuntze: No, we have developed a surface preparation method called "electro-polishing" which is extremely sensitive just to whiskers, so we can get a very plane surface. I think that this was the real progress of the last two years.

A. Schwettman, Stanford University: I'd like to respond briefly to the last two questions. There are still field emission problems in superconducting cavities but these problems appear at higher energy gradients than are achieved in large-scale structures at the present time. If we make progress in the magnetic breakdown problem and reach higher and higher fields, we are still going to be confronted with the problem of field emission which is enhanced both by geometrical projections and by an absorption of gases on the surfaces of the cavity and consequent resonant tunneling.

The first question had to do with multipactoring and I'd like to point out that there is one effect of multipactoring which we at Stanford had not clearly perceived before. Multipactoring is usually looked upon as a barrier in getting to high field levels and if you once get through the multipactoring levels you don't worry about them any longer. We have found upon occasion, however, in our electron accelerator tests at Stanford that you can have small-level multipactoring taking place which couples r.f. energy from the accelerator mode into one or another of the longitudinal modes of the accelerator structure. If you are trying to achieve very high energy resolution such as in one part in 10^4, it is possible to excite these other modes by the secondary electron currents, despite the fact they don't represent a limitation to the field itself. I don't think that's a serious problem, but it is only one aspect of multipactoring that we have only recently become aware of.

H. Hahn, Brookhaven National Laboratory: Why don't most cavities reach H_{c1} ?

Kuntze: There is a difference between the results one gets with small test resonators and with actual accelerating structures. In actual accelerating structures one has electron loading which does damage to the surface lowering the breakdown below H_{c1}. But the proof you can go above H_{c1} has been given by a small test resonator.

Hahn: But you have not reached H_{c1} ?

Kuntze: It depends on the H_{c1} of the material.

J. Blewett, Brookhaven National Laboratory: I have the impression that H_{c1} is not that clearly defined.

B. Cork, Lawrence Berkeley Laboratory: Is there an application of r.f. superconductivity to high-voltage electron microscopes ?

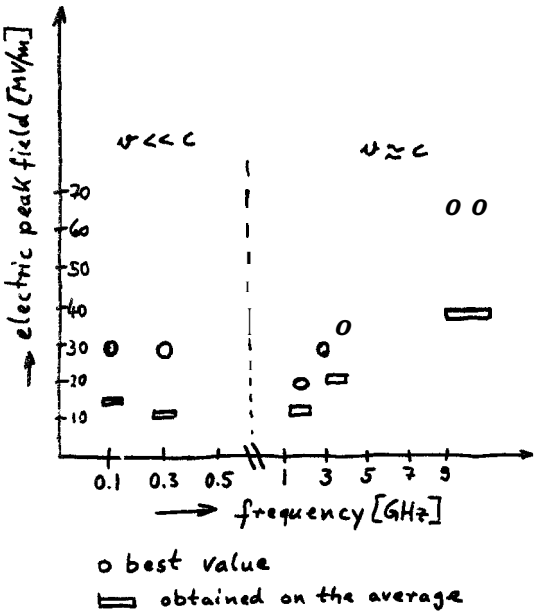
Kuntze: Yes. One thinks about a 10 MeV electron microscope that uses a superconducting accelerator structure and superconducting lenses. The ultimate goal is to achieve a very good energy resolution and spatial resolution on the order of 1 Angstrom.

R. Wideroe, Swiss Institute for Nuclear Research: Could you say something about the surface treatment of the niobium ? Must there still be a bake at 1800°C or more in vacuum ?

Kuntze: It's a very critical procedure. I will come back to this in the second part of my talk.

D. Gray, Rutherford High Energy Laboratory: Would you give sane numbers for the magnetic fields you reach at various frequencies in large-scale structures ?

Kuntze: As you can see from the drawing, for low-β structures the best values are around 30 MV/m, but the average standard value is about a factor of 2 lower. In the S- or L-band structures, the normal gradient is about 10 MV/m peak field, and one has reached nearly 20 MV/m. In X-band test cavities, peak fields as high as 70 MV/m have been seen, but on the average they are about 40 MV/m.



Gray: These are peak fields ?

Kuntze: Yes. You can derive from the peak fields the possible energy gradient vs frequency. In the low-β region the accelerating field is between 2 and 4 MV/m, and in the electron structure Cornell obtained nearly 6 MV/m at 3 GHz. The energy gradient obtained at Stanford is between 3 and 4 MV/m. This is where we are now. We have peak values which are roughly a factor of 2 higher.

PROGRESS REPORT ON THE STANFORD SUPERCONDUCTING RECYCLOTRON*

M.S. McAshan, R.E. Rand, H.A. Schwettman, T.I. Smith, J. P. Turneaure

High Energy Physics Laboratory

Stanford University

Stanford, California 94305

Summary

A prototype superconducting recyclotron is being constructed at Stanford High Energy Physics Laboratory (HEPL). It is designed to accelerate electrons to an energy of 700 MeV with a beam current of 100 μA at a duty factor of unity and with an energy resolution of one part in 10^4. In recent tests the superconducting linac has achieved the following beam parameters: maximum energy 37 MeV; maximum peak current 500 μA at a duty factor of 0.33 and at an energy of 25 MeV; energy resolution (FWHM) < 5×10^{-4} at 25 μA and 28 MeV; emittance < 1.2×10^{-4} π mc-cm at 25 μA and < 4×10^{-4} π mc-cm at 500 μA . Three 6-meter accelerator structures have achieved average energy gradients of ~ 3.0 MeV/m and Q-values of ~ 3×10^9 with CW operation. Two of these structures have been operated with beam currents 25-200 μA for about 1000 hours without significant deterioration. The four-orbit recirculation system is under construction.

I. Introduction

The primary objective of the HEPL superconducting accelerator program is to produce an intense high-quality beam of electrons in the energy range 500 MeV to 2 GeV, where some interesting and unique applications to nuclear and particle physics are possible. Specific objectives are shown in Table I. We are aiming at a beam current of 100 μA with a duty factor of unity and an energy resolution of one part in 10^4.

Such beam qualities are only feasible in a superconducting accelerator. Conventional high current linear accelerators are limited by power requirements to duty factors of a few percent, while the improvement of energy resolution (usually ~ 0.2%) by stabilization of the field levels is difficult with the short time constants involved. Beam break-up problems are more severe in a high Q superconducting linac, but by selective external loading of the break-up modes, it has been shown that the starting currents for regenerative beam break-up can be raised above 500 μA.[1,2] The most critical portion of a superconducting linac with regard to maximum beam current and ultimate energy resolution is the injector, which consists of a superconducting capture section and a superconducting preaccelerator. Successful operation of this part of our machine has already been reported.[3] Energy spectra from the injector are shown in Fig. 1.

Recirculation of the beam was considered early on in the superconducting accelerator program as an economical method of increasing the beam energy. The superior beam quality and unit duty factor make this a particularly attractive possibility. In the last two years it has been shown that a multi-orbit recirculation system is indeed feasible and that beam quality can be conserved in such a system. Moreover the complete accelerator is then considerably more economical than a superconducting linac, as shown in Fig. 2. Construction of a prototype recirculation system (or recyclotron) capable of a final energy of 700 MeV has begun at HEPL.[4]

Table I

Objectives of HEPL SCA Program

Energy	500 - 2000 MeV
Current	100 μA
Duty Factor	~ 1.0
ΔE/E	
Long term stability	~ 10^{-5}
Long term reliability.	

II. Results of Recent Tests

Recently two 6-meter sections of the superconducting accelerator have been operated together with the superconducting injector.

Figure 3 shows the injector and accelerator dewars set up in the tunnel. One of the niobium L-band structures complete with beam break-up probes, etc. installed insideits dewar, is shown in Fig. 4.

Table II summarizes the beam parameters which have been achieved during the last two runs.

Table II

SCA Achievements for Runs 12 and 13

No. of 6m Sections	1	1	1	1	2
Energy (MeV)	25	22	28	28	37
Duty Factor	0.33	CW	0.15	0.15	0.10
Pulse Length (msec)	30	-	15	15	10
Peak Current (μA)	500	25	25	100-200	25
ΔE/E (FWHM)	-	-	<5 x 10^{-4}	-	-
Emittance (π mc-cm)	<4 x 10^{-4}	-	<1.2 x 10^{-4}	-	-
Duration	~ hour	-hour	~week	~week	~hour

Using one 6-neter section, peak currents up to 500 μA with a duty factor of 0.33 and pulse length 30 msec at 25 MeV have been successfully achieved demonstrating that the regenerative beam break-up problem has been adequately controlled. This section has also been used in the CW mode to accelerate a beam to 22 MeV .

An energy resolution (FWHM) of better than 5×10^{-4} has been attained at an energy of 28 MeV with a peak current of 25μA . However, some difficulty - now understood - has been found in maintaining this resolution at higher currents. The beam emittance has exceeded all expectations and in fact has been impossible to measure accurately due to monitor saturation. The magnitude of the emittance (< 0.024 π mm mr) means, for instance, that a 25 MeV beam with a 1 mm waist only doubles in size after a drift of 72 meters. It has proved relatively simple to transport this beam a distance of 240 m to a dump in the HEPL end station. Beam currents up to 200 μA at 28 MeV have been run routinely for periods up to 3 weeks.

Using the second 6-meter section a total energy of 37 MeV has been obtained. Unfortunately this section could not be used extensively due to a problem with a mechanical tuner.

The properties and endurance of the accelerator structures themselves have been carefully monitored over the last few runs. Some results are shown in Table III. CW energy gradients average ~ 3 MeV/m with somewhat higher values in pulsed operation.

Two 6-meter sections have both been used in two runs of several weeks each. Between the runs they were kept under vacuum at room temperature and were not reprocessed. Energy gradients over this period have not deteriorated. Q-values degrade during a 3 week run (e.g. from ~ 7×10^9 to ~ 4×10^9) but recover between runs while the structure is at room temperature. This effect is almost certainly due to poor beam line vacuum, the structure itself being the best pump in the systen, so that its surface gradually becomes contaminated with air, hydrocarbons, etc. Steps are being taken to improve this situation. These two sections have now run for about 1000 hours without significant deterioration. The pre-accelerator structure suffered a vacuum accident well over a year ago when a considerable amount of oil vapor was pumped through it. This immediately degraded its Q-value to 2×10^8 , but since then it has been used without reprocessing in 3 runs without any further degradation and is stable in operation.

The superfluid helium refrigerator has been operated continuously for many periods of 3 - 4 weeks and has now accumulated a total of 8000 hours of operation. This machine which is shown in Fig. 5 delivers 300 W at 1.9 K . We now have considerable confidence in both the reliability and stability of the whole accelerator and cryogenic system.

During the coming year we expect to complete and operate two more 6-meter structures and to obtain more data on the system's longevity.

III. Recirculation and Future Plans

It has already been shown that recirculation of the beam is an economically sensible way to increase the final energy of the superconducting accelerator. Such a recirculation system must satisfy the following conditions:

(a) multi-orbit capability
(b) possible extension to energies of a few GeV;
(c) final energy resolution better than 10^{-4} .

These conditions require that the main bending magnets themselves be multi-channel devices with very uniform fields in each channel and minimum field volume. A magnet configuration which satisfies these requirements by means of a split coil winding is shown in Fig. 6.

Table III

L-Band Niobium Accelerator Structure Performance

fin	6m Structure	Energy Gradient MeV/m	Duty Factor	Q Initial	Q Final
# 11	# 1	3.8	CW	2.5×10^9	
	# 2	2.0	CW	3.0×10^9	
# 12	# 3	3.0	CW		
	# 4	4.2	0.15	9×10^9	3.3×10^9
	# 2	2.0	CW	2.3×10^9	1.9×10^9
# 13	# 3	3.0	CW		
	# 4	4.2	0.15	6.9×10^9	4.1×10^9

A four-channel prototype recirculation system for a minimum final energy of 700 MeV has now been designed using this principle. The main magnets each bend the beam by 167° with orbits separated radially by 7.7 cm and with a gap of 15 mm . The rather stringent beam properties necessary to utilize such small apertures (as shown in Table IV) have already been exceeded in all respects. The beam current with a 4 orbit system will be restricted to ~ 100 μA by RF power limitations.

Table IV

Mininum Beam Specification for Prototype Recirculation

Minimum Energy	50 MeV
Maximum Emittance	0.05 π mm mr
	(5×10^{-4} π mm cm)
Maximum ΔE/E	$\pm 2 \times 10^{-4}$
Maximum Phase Spread	$\pm 1^0$
(Beam Current	~ 100 μA)

A general layout of the complete prototype recyclotron in the accelerator tunnel is shown in Fig. 7. The way in which the beams of different energies ere separated at the output end of the linac is shown in some detail in Fig. 8. The steering coils at the entrance and exit of each magnet channel are situated at optically conjugate points and provide a means for fine tuning of the path length of each orbit and hence the acceleration phase of each pass through the linac.

Ideally, each orbit of the system should be isochronous so that optically the complete recyclotron would be equivalent to a continous linac. However, such a system would require at least 11 quadrupoles per orbit with splits in the main bending magnets, Now, since the initial beam emittance has proved to be so small, a compromise design using only 5 quadrupoles

per orbit is possible. This system operates on the longitudinal phase space of the beam as shown in Fig. 9, in such a way that provided the initial phase ellipse from the beam filter is suitably adjusted, a waist in longitudinal phase space can be maintained during each pass through the accelerator. Thus the final energy spread is better than 1 part in 10^4 and not significantly worse than that of a continuous linac as shown in Table V. The system does have an advantage over a continuous linac in that the initial phase spread of the beam can be somewhat larger.

The present status of the recirculation program is that all the small magnets for 2 orbits exist, while the multi-channel magnets are being manufactured. It will soon be possible to install two orbits with 4 sections of superconducting accelerator which should give a final energy in excess of 200 MeV.

References

K. Mittag, H. A. Schwettman and H. D. Schwarz, Proceedings of the 1972 Proton Linear Accelerator Conference, (Los Alamos Scientific Laboratories, Los Alamos, N. M.), p. 131.

K. Mittag, H. A. Schwettman and H. D. Schwarz, IEEE Trans. Nucl. Sci., NS-20, 3,86 (1973).

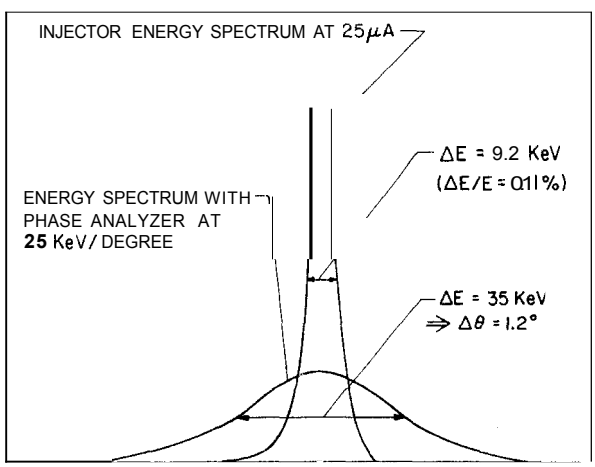
M. S. McAshan, K. Mittag, H. A. Schwettman, L. R. Suelzle and J. P. Turneaure, Applied Physics Letts. 22, 605 (1973).

R. E. Rand, IEEE Trans. Nucl. Sci., NS-20, 3, 938 (1973).

J. P. Turneaure, H. A. Schwettman, H. D. Schwarz and M. S. McAshan, Applied Physics Letts., (to be published).

Work supported by NSF GP 39029.

Alfred P. Sloan Fellow.

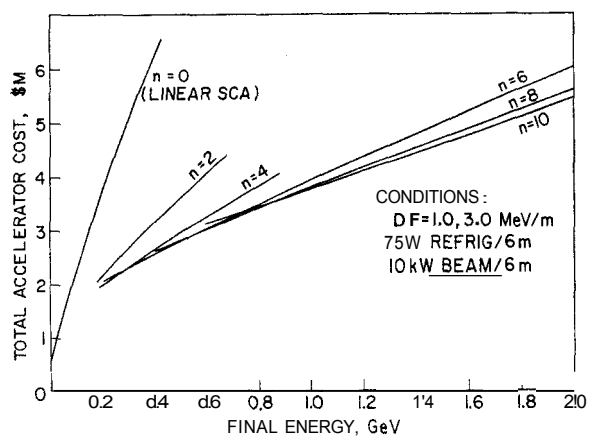


1. Energy Spectra obtained with the superconducting injector.

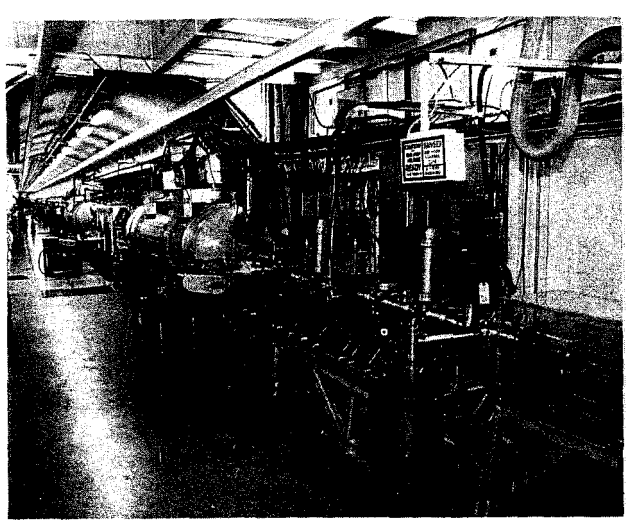
Table V

Calculated Energy Resolution From Prototype Superconducting Recyclotron And Superconducting Linac

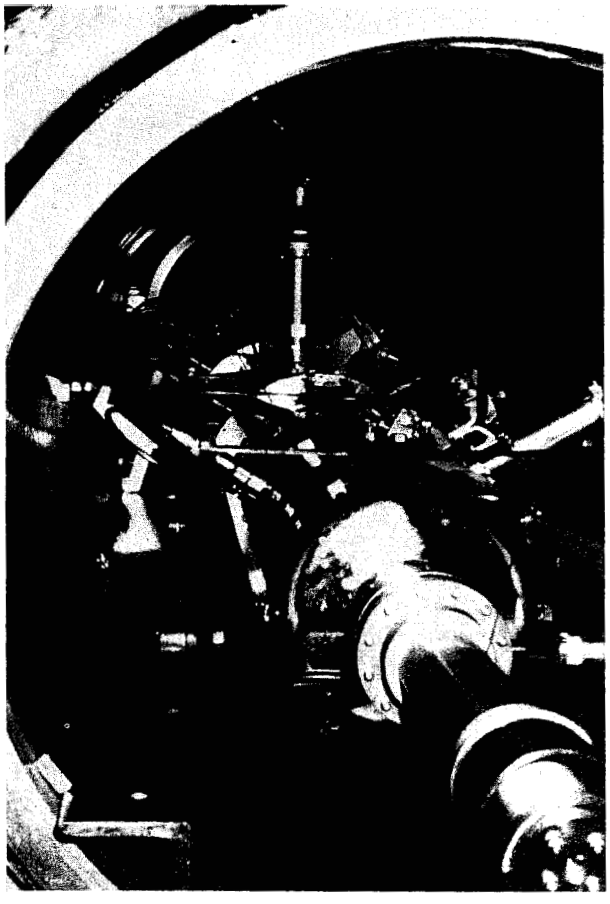
		at Beam Filter (9 MeV)	at 349 MeV
SCR	$\Delta\phi$	$\pm 0.70^{\circ}$	$\pm 0.64^{\circ}$
	$\Delta E/E$	$\pm 8.2 \times 10^{-4}$	$\pm 0.63 \times 10^{-4}$
SC Linac	$\Delta\phi$	$\pm 0.41^{\circ}$	$\pm 0.41^{\circ}$
	$\Delta E/E$	$\pm 14.0 \times 10^{-4}$	$\pm 0.44 \times 10^{-4}$



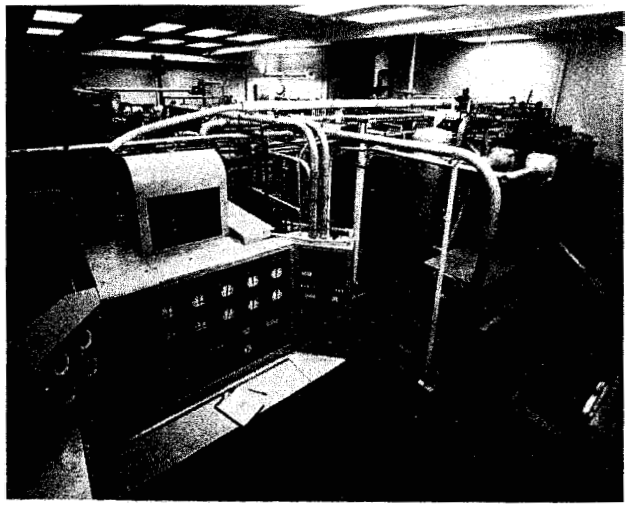
2. Estimated costs of superconducting recyclotron with various numbers of orbits (n) as a function of final energy.



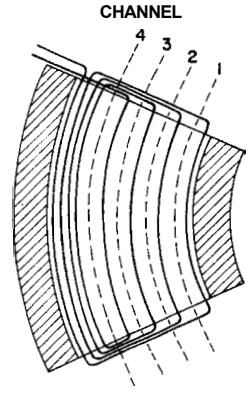
3. Photograph of superconducting accelerator installed in tunnel.



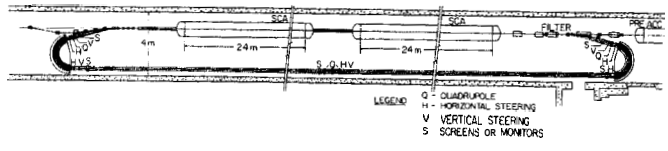
4. Photograph of Niobium accelerator structure complete with beam break-up probes installed in dewar.



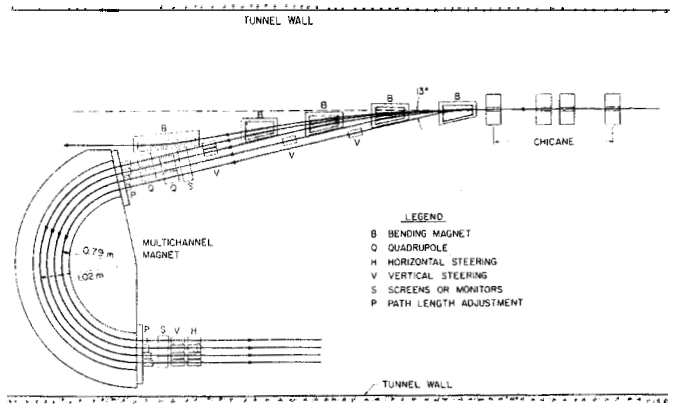
5. Photograph of superfluid helium refrigerator.



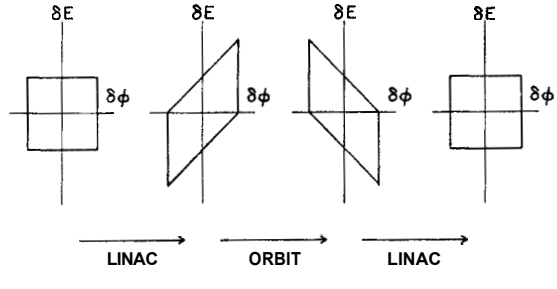
6. Principle of multi-channel bending magnet.



7. Schematic layout of prototype 700 MeV recyclotron.



8. Details of beam separation and multi-channel magnet.



9. Rotation of longitudinal phase space by re-circulation.

Discussion

W. Panofsky, Stanford Linear Accelerator Center: I have a question about the beam breakup situation. You said at 500 pa that you have been able to avoid the beam breakup problem by lowering the Q of the element at the various high modes. But the beam breakup threshold depends also on the length and you do recirculate. In your superconducting linac the radial regeneration is coherent turn-by-turn, producing an effective length of the beam length times the recirculation number. Have you investigated this ?

Rand: We are looking into these problems but we have come to the conclusion that probably the best way to investigate them is to build the first two orbits of the machine.

Panofsky: It's a very fundamental problem. If you write down the beam breakup equations, the threshold goes as Q/ℓ^2. One obtains coherence on a turn-by-turn basis producing a rather significant situation. Maybe there is a way with active feed-back to cure it.

A. Schwettman, Stanford University: We have taken a look at the relatively simple problem of cumulative beam breakup. We have not done any more complicated analysis for a recirculating system. The problem that you identify is analyzable in the sense that you describe, but we haven't really quantitatively analyzed what the current limitations will be in the recyclotron, yet.

H. Blosser, Michigan State University: One of your slides showed 28 MeV from one six meter section and I think 37 MeV from two. Why does the second section do so little ?

Rand: The 28 MeV includes the energy gain from the pre-accelerator which is 7 MeV and the second 6-meter section had a gradient of 2 MeV/meter. This is due to a poor cell in the second section, which is a statistical effect.

E. Michaelis, CERN: What is the effect of synchrotron radiation on your bending magnets ?

Rand: There is no serious problem until we get to 3 GeV.

Kuntze: I thought you had problems with your tuner.

Rand: We did have problems with the tuner. That's not the reason for the low gradient.

Kuntze: Do you get 3 MeV/meter reproducibly with your sections if you do not have trivial problems with tuners or leakage ?

Rand: Yes.

Kuntze: So it was statistical problems depending on the surface.

APPLICATION OF SUPERCONDUCTING RF ACCELERATING SECTIONS TO AN ELECTRON SYNCHROTRON - A PROGRESS REPORT*

R.M. Sundelin, J. Kirchgessner, H. Padamsee, H.L. Phillips, D. Rice, M. Tigner, E. von Borstel
Cornell University
Ithaca, New York 14850

Summary

This is a progress report on our efforts to apply superconducting RF accelerator technology to an electron synchrotron. Using a 60 cm length of an open type of pi-mode structure operating at S-band, a beam has been stably accelerated to 2 GeV in the Cornell Electron Synchrotron. Characteristics of the RF accelerator are described and the results of the first beam tests are given. Problems revealed by these tests are listed.

Introduction

To achieve energies in the neighborhood of 25 GeV in an electron synchrotron of the size of the Cornell machine, RF peak powers of the order of hundreds of megawatts would be required if normal copper accelerating cavities were used. Since the chief advantage of a synchrotron is its inherent high duty factor, the average power corresponding to this high peak power will be of the order of tens if not hundreds of megawatts. The use of superconducting cavities offers the possibility of reducing this power by two orders of magnitude, thus making practical high duty factor electron acceleration in the 20 to 25 GeV range. Building on the pioneering and excellent work at other laboratories,[1] we have been pursuing this possibility for the past two years at Cornell.

In addition to the gross power problem there is the problem of handling the synchrotron radiation into which the RF power has been converted. This radiation must not be allowed to strike the cold surfaces. Because the synchrotron radiation will fan out into the straight sections as shown in Fig. 1 and because we need to get as much RF accelerator as possible into each straight section, the aperture through at least the downstream part of the accelerating section must be quite wide if intermediate water cooled synchrotron radiation traps are not used. For a machine of the Cornell size, i.e. 120 m gross radius, this required aperture is more than 20 cm at the end of a 5 m straight section.

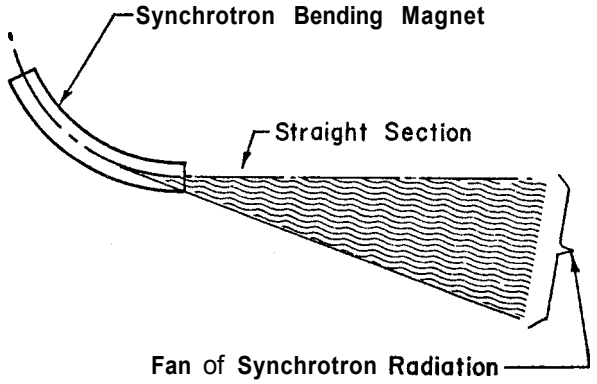


Fig. 1 Synchrotron radiation geometry

Rather than try a large, low frequency structure with slotted irises, we have decided to try a high frequency cavity which has, in principle at least, no material in the mid-plane. A cutaway view of a single cell of such a structure is shown in Fig. 2.

*Work supported by the National Science Foundation

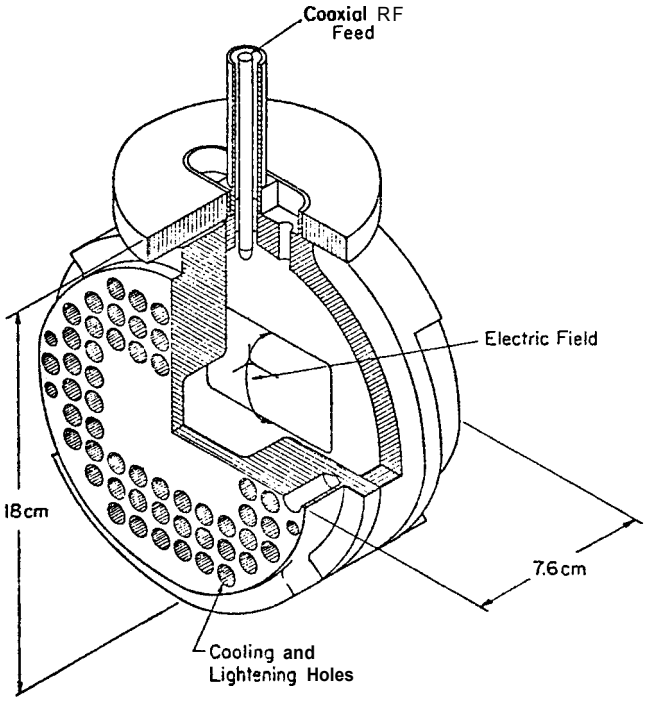


Fig. 2 Test arrangement for single cell

The two rectangular half cavities face each other across a gap of 2.5 cm. In these single cell devices we consistently get Q's of 2 to 5 x 10^9 and breakdown fields of 6 to 15 MeV/m effective accelerating field. The conceptual extension of this idea to a multiple cell structure is shown in Fig. 3. Figures 4 and 5 are photographs of a partially assembled 11 cell structure and the completely assembled structure ready for insertion into the cryostat. Note that this first multiple cell model is not completely open but mounted on a rim which forms simultaneously a convenient mechanical support and vacuum chamber for the accelerator. S-band was chosen for our first attempts because of the generally better results had with superconducting cavities at the higher frequencies. Aperture limitations and the penalties of high harmonic numbers make it inconvenient to use frequencies higher than S-band.

Properties of the Structure

Because of the open nature of the cavity, the shunt impedance is not as large as it would be in the case of a standard iris loaded guide. The shunt impedance of this muffin tin structure at room temperature is 45 M ohm/m. For a side coupled structure at the same frequency with an iris hole of 2.5 m, the theoretical[2] shunt impedance is about 60 M ohm/m. The shunt impedance is defined by the relation $P'L = V^2/r_1$ where V is the max. energy gain per unit length, L is the active length of the accelerator, and P is the power dissipated in the walls. Taking out the Q factor, the muffin tin cavity has $r_1/Q = 3.1 \times 10^3$ ohm/m. The geometry factor for this structure is G = 233 ohms where G divided by Q gives the surface resistance. The ratio of peak surface magnetic field to effective accelerating field is B_{pk}/E_{eff} = 44 Gauss/MeV/m.

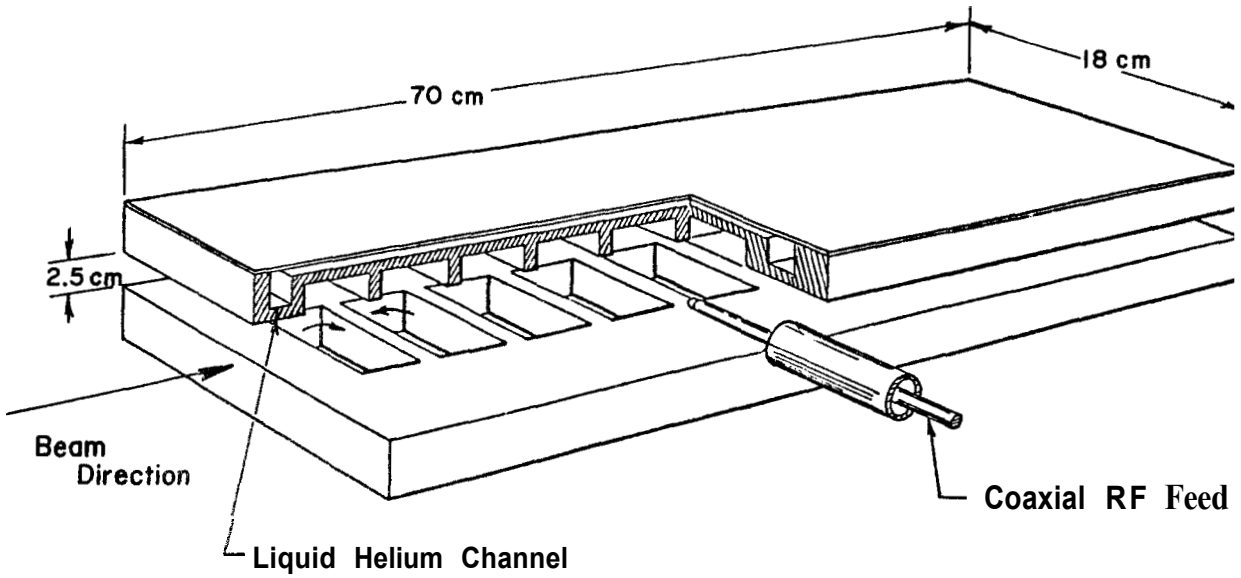


Fig. 3 Line drawing of the muffin-tin structure

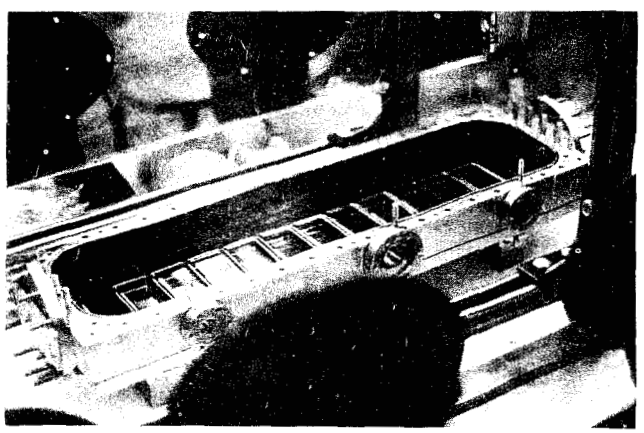


Fig. 4 Partially assembled 60 cm cavity

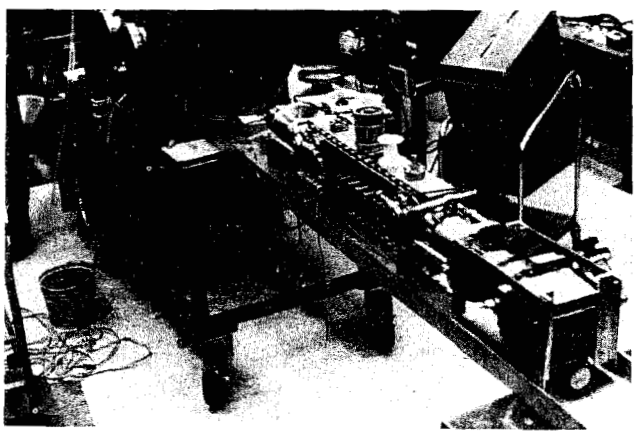


Fig. 5 Assembled cavity and cryostat

Our first structure is designed to operate in the pi-mode for simplicity. Because of the openness of the cavity, however, there is relatively tight coupling between the cells giving a fractional bandwidth of 4.7 percent. Coupled with practical machining tolerances, such a bandwidth probably restricts the length of a single piece of pi-mode structure to about 25 cells. Since the length may also be restricted by RF power coupling and synchrotron radiation handling considerations, it is not clear whether it will be necessary to use a quasi-pi-mode structure to reduce the error sensitivity. This question is under active consideration at present.

Another feature of the cavity in this form is that the light velocity component of the accelerating field is not uniform across the accelerating gap as it would be in a circularly symmetric device but has approximately a cos dependence in the horizontal direction and a cosh dependence in the vertical direction, the origin being taken at the beam axis. In the cavity described here a particle 1.3 cm off the beam axis would receive 10 percent less energy than an on-axis particle. While this is not particularly important for a synchrotron, it could be unpleasant for a linac where high energy homogeneity was required if the beam had an appreciable size compared to the aperture. The situation could be retrieved if the gap were very small and the beam hole were cut through the irises.

As with periodic structures now in use for accelerators, this structure supports a large number of modes capable of beam deflection. Because no vertical currents can flow across the gap, any deflections will tend to be in the horizontal plane. The first pass band above that containing the accelerator mode is one supporting these modes. The Q's of these modes are of the same order as that of the accelerating mode. However, for several reasons these modes are not expected to be worrisome. First, these modes being of higher frequency than the accelerating mode will not be as strongly cut-off in the gap region so that if they are excited they can be heavily loaded by probes in this region without loading the accelerating mode. Secondly, since the injector into the synchrotron is a 150 MeV linac, the beam is already quite stiff when it enters the accelerator, thus requiring rather high fields to build up before significant deflection takes place in contrast to the case of a superconducting linac injected into at energies in the 100 KeV range. Thirdly, for the deflection modes to interact coherently with the synchrotron beam, they must lie at one of the so-called shaker frequencies, those frequencies at which the deflection field is synchronous with the betatron frequencies in the beam's reference frame.

$$f_{shaker} = f_{revolution}\ (\nu \pm N)$$

where ν is the betatron number and N is an integer. At the frequencies we are talking about N is of the order of 10^4 and Landau damping will be very powerful in suppressing the interaction. For example, if the difference in betatron number between two electrons in the Cornell synchrotron is 3×10^{-3} and one of them is in the correct phase with respect to the deflecting mode, the other will have slipped 90^o in phase with respect to the deflecting field in one revolution around the orbit. The natural octupole moment alone in our synchrotron will give a dispersion of 2×10^{-3} at 1 mm of betatron amplitude. There will also be a spread in revolution frequencies due to the energy oscillations.

A further characteristic of this open structure which is of great importance is that while the accelerator mode is strongly cut-off in the gap region, any asymmetry in the structure which tends to make a vertical field component will drive the eigenmodes of the gap region surrounding the cavities even though the eigenfrequencies of these modes do not coincide with that of the accelerating mode. Any such excitation will couple energy from the accelerator mode and some of it can radiate out the open edges of the structure. While experiments show it not difficult to maintain the necessary symmetry in the single cell models, we have found it difficult to maintain the required symmetry in the multiple cell cavity. Top to bottom symmetries evidently need to be held to the order of 0.01 mm throughout. In the end we shall have to make some compromise between realizable manufacturing tolerances, empirical tuning to minimize excitation of the gap, and conducting the radiated power to a room temperature load where it can be dissipated harmlessly.

Accelerator Fabrication

The open nature of the structure gives several advantages in fabrication. First, there need be no welds where RF currents flow. Second, such a geometry gives an ideal electropolishing configuration and differential electropolishing can easily be applied for tuning. Third, there being no hidden areas or inside weld cracks, cleaning is relatively easy. Last but very important, one can inspect the surfaces in detail after final processing to see that there are no chemical deposits or blemishes. Our first multi-cell cavity has been machined from solid niobium slabs 76 cm x 23 cm x 3 cm using a tape controlled milling machine. Most of the cutting was done with ordinary tool steel cutters. For the final cuts the slabs were immersed in trichloroethane. Subsequent to machining, the slabs were electropolished, removing 0.15 mm of material. The Siemens formula[3] was used. Differential electropolishing was used to tune individual cells. A frequency accuracy of 25 kHz and a field flatness of ± 0.004 were obtained. After this polishing, the slabs were cold chemically polished at -10^oC in the standard $40\%HF-60\%HNO_3$ solution. Before assembly to the holder frame the slabs were anodized using the NH_4OH solution and rinsed in distilled water and electronic grade methyl alcohol. During assembly the surfaces were kept wet with alcohol in as far as possible and the completed assembly was flushed with electronic grade alcohol several times in the manner of the Karlsruhe lab.[4] These procedures are the same as used in our single cell experiments. No heat treatments or stress annealing of the multi-cell model have been done. The results quoted for the single cell tests were obtained without annealing or vacuum outgassing.

Control System

In order to maintain the necessary stability, three control loops are being used at present. They are shown in Fig. 6. To be sure of ample accelerating field while simultaneously limiting the field to values below breakdown, the field level in the cavity is monitored and fed back to control the klystron drive. Because the phase between the RF drive and the beam must be properly related to the linac injector, a phase control loop is used to stabilize the phase shift from the oscillator to the klystron output. The crucial feed-back loop is the one that regulates the frequency. The cavity itself is used as the frequency determining element in the system. The cavity is tuned to the desired frequency by mechanical distortion of the entire structure. (The cavity frequency is very stable in time, mechanical vibrations etc. disturbing the frequency less than 500 Hz. Since the loaded Q under heavy beam loading conditions will be less than 10^6, the 500 Hz is a small fraction of the bandwidth and is not troublesome. It appears that for an ensemble of these cavities it will be sufficient to use slow mechanical tuning to keep them in synchronism.) The oscillator frequency is then controlled by comparing the phase angle of the RF into the cavity to the phase of the RF transmitted through the cavity. This comparison is made only when the beam is not in the cavity and the control voltage to the oscillator is held clamped until after the next acceleration cycle to avoid confusion due to the beam induced signal. The tuning angle is adjusted by means of a phase shifter in the phase comparison circuit used for frequency control. This scheme should be sufficient to maintain acceleration stability. To maximize acceleration efficiency and allow smooth beam spill during beam extraction when beam loading is changing substantially, a feed-back loop designed to control both amplitude and phase of the cavity fields is being developed.

Laboratory Tests

Prior to insertion into the synchrotron the completed cavity was tested in the laboratory. The first measurement showed a Q of 10^4. A measurement of the helium boil-off, however, showed no increase in the boil-off rate when an RF power equal to the equilibrium heat leak was applied. Since the error in the measurement of helium gas evolution was less than 10%, we concluded that the Q_0 was at least a factor of 10 higher than the effective Q determined from the energy decay time constant. This in turn meant that the RF was being radiated out the beam holes into the stainless steel bellows which connect the cavity to the outside world. A hasty attempt to remedy the situation was made by bolting niobium beam tubes onto the cavity with an indium wire gasket to make the RF joint. This attempt was ill-conceived as the Q was still 10^7 while all of the RF power put in showed up in helium boil-off. There were complicating circumstances but the preponderance of the evidence indicates that the beam tubes were acting as absorbers for the RF rather than reflectors. This conclusion is bolstered by the fact that visual observation down the beam pipe under high field conditions showed a blue glow around one of the cut-off tubes and disassembly after the beam tests showed that the indium gaskets were making poor contact. These matters are of course under active investigation at the moment.

By using reduced duty cycle, it was possible to study the high field behavior of the cavity. A coaxial power probe whose length is adjustable permitted the required power to be coupled into the cavity with various coupling factors. Effective accelerating fields of 4.5 MeV/m were obtained before thermal breakdown occurred. No X-rays were detectable outside the cavity. Windows on the beam tubes permitted visual observation of the cavity interior. In addition to the blue glow at the cut-off tube mentioned above, a few luminescent points were seen at high electric field points in the cavity. A dc voltage applied to an auxiliary probe in the gap between the cavity halves revealed the presence of multipactoring electrons in the cavity at accelerating gradients above

2.2 MeV per meter, consistent with similar observations in the single cell model. No loading due to these electrons was observed below 4.5 MeV/m, however. The pulse energy to cause breakdown was 1 joule.

In order to be useful for our electron synchrotron, a superconducting cavity should exhibit a Q_0 in excess of 10^8 and a gradient in excess of 3 MeV/m.

Beam Tests

Since under synchrotron operating conditions the appropriate loaded Q of the cavity is 10^6 or less, most tests involving the beam-cavity interaction could be carried out despite the problems referred to above. The only significant test that we could not make is evaluation of the long term effects of the synchrotron environment on the surface resistance of the cavity. The chief objectives of beam tests in the synchrotron were to see that the cavity could accelerate the beam properly, to look for instabilities at large beam currents, to evaluate the control system and to look for unexpected problems.

The Cornell 12 GeV electron synchrotron has a 60 Hz sinusoidal magnet excitation. The linac beam is injected at 136 MeV and the acceleration demand at injection is 0.78 MeV/revolution. The acceleration time is 6 to 8 msec depending upon the final energy.

With no power applied to the normal acceleration system, the 60 cm superconducting cavity successfully captured the injected beam and accelerated it throughout a normal acceleration cycle to an energy of 2 GeV. This was done with a computed accelerating gradient of 1.9 MeV/m, the required gradient being 1.8 MeV/m. The phase error tolerance for beam capture was $\pm 21^o$. The synchronous phase angle was 140^o at injection.

Although the cavity reached 4.5 MeV/m, this limit being imposed by multipactoring, heating due to the poor effective Q prevented the cavity from being operated for a full acceleration cycle at this gradient. In order to test the cavity at a higher gradient in the presence of the beam, the magnet was set for 4 GeV and the beam carried almost to the maximum dE/dt point with the normal RF system. This RF was then switched off and the superconducting cavity alone carried the beam for 1 msec past the maximum dE/dt point. Under these conditions the cavity operated at 3.7 MeV/m.

Stability of the beam-cavity system against coherent phase oscillations was studied by varying the tuning angle between -10^o and $+12^o$, the possible range being limited by available cavity voltage. Neither instability nor tendency to instability were observed although the shunt impedance of the superconducting cavity is some 50 times higher than that of the present RF system.

Circulating currents of 110 microamperes were accelerated with the superconducting cavity. At this current no anomalous phase or betatron oscillations were observed. By means of an auxiliary RF probe, excitations of beam deflection modes up to 4 GHz were looked for. Excitations of two of the modes were seen at about 70 db below the beam induced acceleration mode signal on the same probe. At these frequencies the auxiliary probe is 20 db more tightly coupled to the deflection modes than to the accelerator mode. Another measurement was made by passing a 380 microampere beam through the cavity, the beam being accelerated by the normal acceleration system at a frequency just off the accelerator mode frequency. No sign of transverse instability was observed and longitudinal interactions were observed only when the frequency difference of the two systems equalled the synchrotron oscillation frequency.

The control system operated satisfactorily. When regulating on cavity field, the field remained stable as long as the power demanded by the beam was less than the maximum available power. The mechanical tuner, which elastically squeezes the structure over a $\pm$ 500kHz range, provided adequate resolution to tune the cavity to well within 1 kHz of the desired value.

One unexpected problem was encountered as a result of the beam tests. Upon moving the cavity back into the lab, it was found that there was a substantial quantity of dust on the bottom and side surfaces. Since the dust was not there prior to installation and since the cavity at no subsequent time had a substantial gas flow through it, we hypothesize that dust particles are transported around the synchrotron vacuum system when the beam is on under the influence of induced electric forces. In addition to the obvious relevance of this phenomenon to our circumstances, it may have some relevance for storage rings.

Outstanding Problems to be Solved

Top priority in our next test will be given to checking the longevity of high Q surfaces in the synchrotron environment. In addition, before applying this technology to the synchrotron on a large scale, there are a number of other problems that need solving and a number of developments that would be desirable as is clear from our initial experiences. The coupling of RF energy into the gap region must be brought under control as previously discussed. The transport of dust onto the cavity surfaces must be severely limited. Electrostatic precipitators in the beam line will be tried first. Waveguide coupling will have to be developed to avoid the severe limitations on power handling capacity of coaxial lines at high frequency. There are also developments which would ease the manufacturing process. Among these are the use of stress annealing to reduce the required electropolishing and the use of sheet metal techniques for rapid forming of the cavity bodies. Both of these subjects are being pursued now.

Despite the manifest engineering problems, we believe that our first tests show the basic practicality of applying superconducting RF technology to the electron synchrotron.

Acknowledgements

It is a great pleasure to acknowledge the important contributions to this work made by many members of the Cornell Accelerator staff and in particular by M. Banner, R. Bower and J. Stimmell. We are also most appreciative of the help given us by our Cornell colleagues in low temperature physics and in the Department of Materials Science and Engineering.

References

[1] Work at HEPL, SLAC, Karlsruhe, Siemens and Brookhaven has provided the foundation and inspiration for our work. See rapporteur talks at recent accelerator conferences such as the one at this conference by Kuntze for detailed information and further bibliography.

[2] M. Allen and P.B. Wilson, Linac Type Structures for High Energy Store Rings, SLAC publication 1142, Oct. 1972.

[3] H. Diepers et al., A New Method of Electropolishing Niobium, Physics Letters 37A number 2 p. 139 ff.

[4] P. Kneisel, private communication.

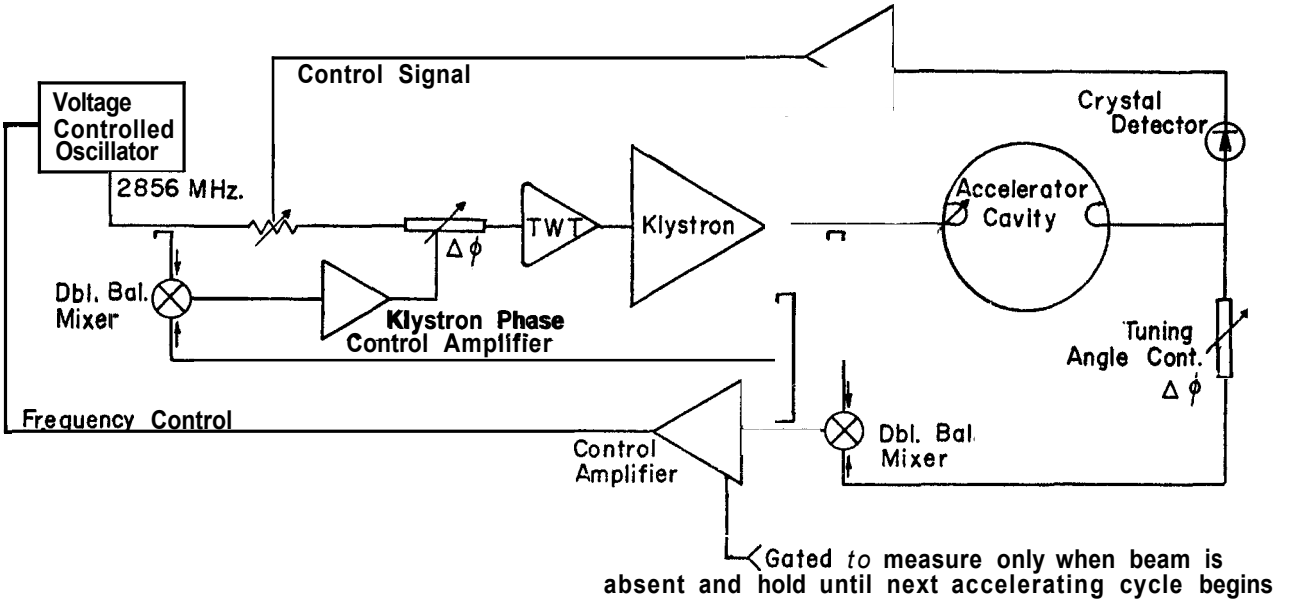


Fig. 6 Control system for accelerator cavity. In this version only the magnitude of the cavity field is controlled. Phases are measured directly by means of double balanced mixers. Two auxiliary probes are used for monitoring. Main coupling is done by an electric probe with variable penetration.

MEASUREMENTS ON THE FIRST 20-CELL DEFLECTOR SECTIONS FOR A SUPERCONDUCTING RF SEPARATOR

W. Bauer, A. Citron, G. Dammertz, M. Grundner, L. Husson, H. Lengeler *, E. Rathgeber
Universität and Kernforschungszentrum Karlsruhe
Karlsruhe, Germany

Summary

Experimental results on the first 20-cell Nb deflector sections for an S-band superconducting RF separator are given. A sequence of surface treatments including electropolishing, anodizing and high temperature UHV-annealing has allowed to obtain repeatedly high field Q-values up to $1.8 \cdot 10^9$ and peak magnetic fields up to 400 Oe. This corresponds for the operating mode ($\pi/2$) to deflecting fields of 2.6 MV/m and to electric peak-fields of 14 MV/m. With the same surface treatments we have obtained in a 4 cell test deflector a Q-value of $2.5 \cdot 10^9$ and a peak magnetic field of 850 Oe which corresponds to a peak electric field of 30 MV/m. A new method for localizing cells with high surface resistance in multicell cavities has been applied successfully. It also has been tried to localize the cells where a magnetic breakdown takes place. Perturbation measurements have been performed for a large number of modes and it is shown that the fabrication tolerances ensure a sufficient field-flatness in the $\pi/2$-mode. A movable RF coupling system using a bellow as an outer conductor and a new type of RF joint are shortly described.

Introduction

At Karlsruhe a superconducting RF particle separator is currently under construction' which will be installed in a particle beam with an intercavity distance of 80-90 m allowing separation of kaons and antiprotons in the range of 10-30 GeV/c.[2] The design frequency of the separator is 2855 MHz (S-band) and its two iris loaded and uniform periodic niobium deflectors are operated in a $\pi/2$-standing wave mode. Each deflector has an effective length of 2.74 m corresponding to 104 cells. It is intended to reach deflection fields of at least 2 MV/m corresponding to magnetic peak fields at the surface of 310 Oe. In order to avoid safely a thermal breakdown during operation at these field levels, a minimum quality factor $Q_o = 5 \cdot 10^8$ has to be reached. Experiments on several test-deflectors[1,3-6] allowed us to fix all parameters, the fabrication and welding techniques and the surface treatments to be applied. As a UHV-treatment at temperatures around 2000°C seems essential for obtaining sufficiently good performances it was decided to assemble each deflector from 5 sections of about 60 cm length which can be heat treated in the existing high-temperature UHV-furnace. The fabrication of the first deflector at Siemens, Erlangen has been finished and we report in the following on experimental results obtained with the first 20-cell sections (called hereafter D1 - D5). In Fig.1 the geometry of the deflector cells is shown.

1. The experimental layout for cold measurements; surface treatments.

For the low temperature measurements on the deflector sections we have used the experimental layout shown in Fig.2. The sections are hanging vertically inside the cryostat. They are connected to a coupling unit with the help of an RF joint of the same type as will be used later on for the assembling of the different sections to form one deflector.[7] During the first experiments the coupling unit was situated above the sections but it turned out that there is a danger of dust or small particles falling from the movable coupling lines into the first (coupling) cell of the coupling unit. Therefore, we changed the layout by coupling from below as it is shown in Fig.2. The pumping of the structure is always done via a pumping line and a bend from below. This pumping system has several advantages. It avoids dust particles falling from above into the sections. At the beginning of cooling down for a cold measurement, it acts as a cryopump for the sections and at the same time as a trap for degassing products (or leaks) from the upper warm part of the vacuum system. Rough-pumping of the system is done by using a turbomolecular pump, Once a vacuum of the order of 10^{-5}Torr is obtained, pumping is continued with an ion-pump which is normally not exposed to atmospheric pressure. Many experiments on test-deflectors[1,3-5] have led us to a sequence of surface treatments which allow to reach reliably Q-values and magnetic peak fields in excess of what has been assumed a lower limit for the application at CERN. The sequence has been described in ref.5 and we list here only the surface treatments applied to each section

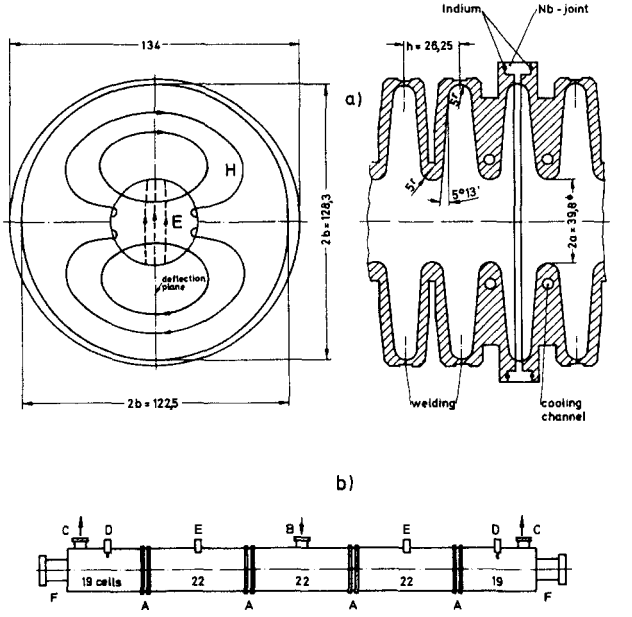


Fig.1a: Geometry of the normal cells and a joint cell of one deflector section. Some field lines are indicated. For mode stabilisation the cells have an elliptical cross-section.
1b: Schematic layout of one deflector assembled from 5 sections. A: RF joints, B: RF-in, C: RF-out, D: fine tuner, E: coarse tuner, F: beam tube

* on leave of absence from CERN, Geneva

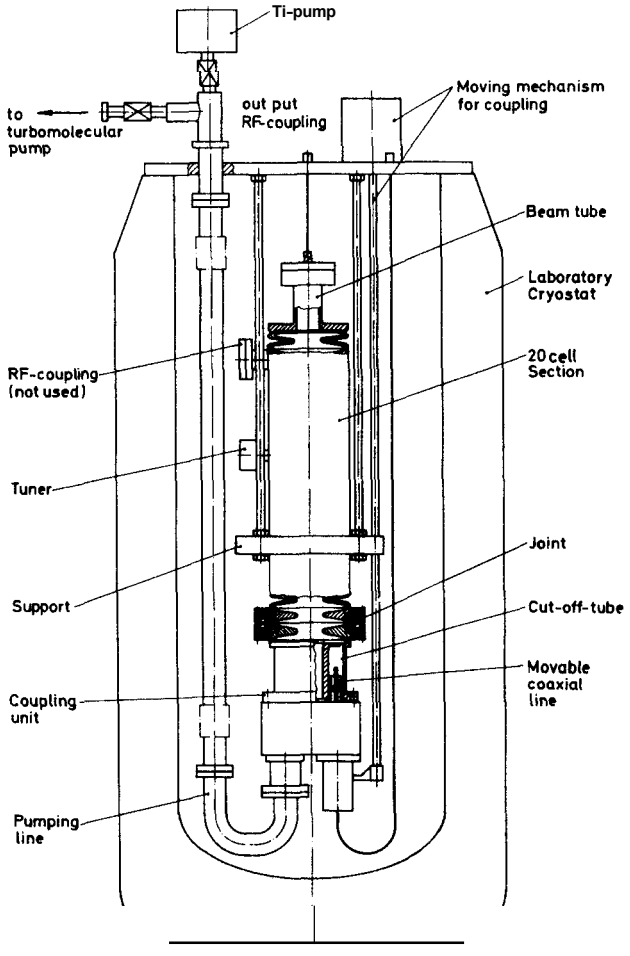


Fig. 2: Experimental layout for cold measurements. In the layout shown the RF power is coupled from below. For the first measurements the RF power was coupled from above.

before the first cold RF measurement (basic treatment).

1. Electropolishing of about 25 µm
2. Anodizing and subsequent removal of the oxide in hydro fluoric acid
3. Second anodizing
4. High temperature annealing in a UHV-furnace at 1850°C for 24 h
5. Electropolishing of about 75 µm
6. Anodizing as in point 2 and 3
7. Second high temperature annealing as in point 4.

After the high temperature treatment the sections are carefully flooded with dry and clean N_2 inside the furnace, then brought under a protective plastic cover to a dust-free glove box where they are assembled with the coupling unit and where all extra flanges are mounted under streaming clean air. Finally the sections are connected to the pumping system.

Whenever the sections have been exposed for longer periods to air or protective gases an additional treatment is applied before the following cold measurement. This consists of an electropolishing of about 10 µm, an anodizing and a high temperature annealing (as in point 4). The treatment described above also is applied to the coupling units. As they cannot be mounted immediately after the last high temperature treatment to a 20-cell section, they are stored for a few days under clean air or in a stainless-steel box which is evacuated to about 10^{-2} Torr. Before assembling with the sections they are flooded eventually with dry and clean nitrogen gas and then stored inside the dust free box.

2. The dependence of Q-values on modes and bad cells[3]

In the course of low temperature measurements on the 20-cell sections we have found not only unloaded Q-values well below the theoretical values at 1.8 K but also a mode dependence of the unloaded Q exceeding greatly the normal 20% variation which is predicted by theory and measured at room temperature. This is explained by localized regions where the surface resistance is greatly increased. The Q-value of an RF cavity is defined by the relation

$$\frac{1}{Q} = \frac{P_o}{\omega W} = \frac{\frac{1}{2}\int RH^2 dS}{\omega W} \qquad (1)$$

with $\omega = 2\pi f$, and
f: frequency of the mode used
W: stored RF energy inside the cavity
P_o: RF power absorbed inside the cavity
H: magnetic field amplitude
R: surface resistance.

If the quality factors in a multi-cell cavity are dominated by the RF losses of one bad cell one can write[8]

$$\frac{1}{Q_{i,k}} = K_i' \frac{(H_{i,k})^2}{W_k} \qquad (2)$$

where $Q_{i,k}$ is the quality factor determined by the RF losses in cell "i" and for the mode "k", $H_{i,k}$ is the magnetic field amplitude at the bad region of cell "i" and for the mode "k", W_k is the stored energy for the mode "k", K_i' is a constant independent of mode (but not of cell number!).

In our disk loaded waveguides we expect that bad regions are located mainly at the weldings, the RF joints and the holes for tuning and RF coupling. All these regions are situated inside the slot region where the deflecting mode is described well by a TM_{110} coaxial mode and where losses are due to the magnetic field components H_θ and H_r. On the other hand, in a disk loaded waveguide the longitudinal electric field component E_z can be easily measured by pulling a perturbating needle parallel to the axis of the waveguide and in the disk hole region. It has been shown' that there exists for every point inside the slot region a proportionality between $H_{i,k}$ and the maximum of the electric field component E_z inside the disk hole region of cell "i" and for the mode "k". We therefore may write

$$H_{i,k} = K E_{z\,i,k} \qquad (3)$$

where K, for a given point, is independent of mode and cell number. By combining (2) and (3) one gets

$$\frac{1}{Q_{i,k}} = K_i \frac{(E_{z\,i,k})^2}{W_k} \qquad (4)$$

where the constant K_i is again independent of mode. Formula (4) is convenient for calculating the mode distributions for any bad cell "i". One obtains for every "i" a characteristic $1/Q_i$-distribution and one can try to fit the low temperature Q-distributions by one distribution or by a superposition of distributions thereby identifying the position of the bad

cell(s). The only free parameter for this fit is the value of the constant K_i and in many cases it was possible to get a good fit with a single distribution showing that the Q-value was determined mainly by one bad cell. In Fig.3 and Fig.4 a few fits are illustrated.

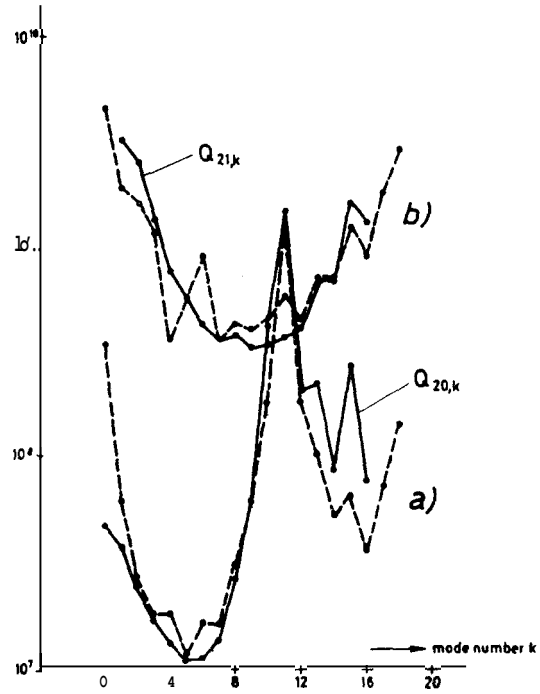


Fig.3: Fit of the measured mode dependence in D5 for the unloaded Q-values at low temperatures (dashed line) with the calculated values (full line).
a) coupling from above, bad joint. Fit for the joint cell.
b) coupling from above, better joint. Fit for the coupling cell.

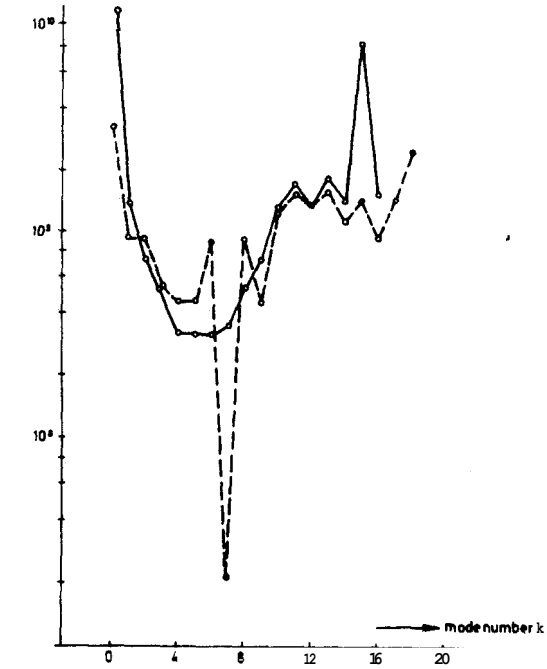


Fig.4: As Fig.3, good joint, coupling from below. Fit by a superposition of contributions from the joint- and the coupling-cell. The deep minimum for k=7 is not understood.

3. Results of cold measurements

In Table I some results of cold measurements are given. For more details see ref. 9.

Table I: Some experimental results for the π 12-mode

$Q_o \cdot 10^{-9}$ at low field	$Q_o \cdot 10^{-9}$ at H_p	H_p (Oe)	Remarks
	D 1 + M		(20 cells)
0.72	0.54	385	additional treatment*
2.5	1.6	400	warmed up and joint retightened.
2.2	1.8	390	4 weeks under vacuum
	E + D 3 + M		(24 cells)
1.6	>0.72	330	additional treatment
	D 5 + M		(20 cells)
0.72	0.5	340	additional treatment
1.25	1.2	370	warmed up and joint retightened
	Test deflector (4 cells)		
3.6	2.5	850	additional treatment

*before the additional treatment (10 µm electropolishing, anodizing, high-temperature annealing) each deflector has been submitted to a basic treatment (see chapter 1); coupling always from below.
M: coupling unit (2×1/2 cell)
E: end unit with beam hole (2×1/2 cell)

Q-values

Whenever possible we have measured the Q-value for all modes of a section (Fig.3 and Fig.4). As the mode dependence is in all cases largely exceeding the calculated range for a uniform surface resistance the analysis of the preceding chapter was applied in order to localize cells with bad regions. As an example of such an analysis we choose the first measurements on D1 and D5 which were done by coupling from above. It turned out that for both deflectors the first cooling down cycle after a surface treatment and assembly did not give very high Q-values. An analysis of the mode dependence of Q showed that this was always due to a bad RF joint. (Fig.3a). After a warming up and a retightening of the joint the Q-values improved but the analysis of the Q-distribution showed for both deflectors bad regions in the coupling cell (Fig.3b). After a dismounting of the section D1 a few small metallic particles were found lying in this cell. These particles presumably had fallen into the cell from the coupling region above. Therefore, in the next experiments the sections were turned by 180° in order to couple from below. The mode-distributions obtained after this change show an additional improvement and are described essentially by a superposition of contributions from the joint- and coupling-cell (Fig.4). The contribution from the coupling cell now could be explained by the fact that before assembling the coupling sections are stored for a few days under vacuum or air. This storage period and the following exposure to air may give an increase of the surface resistance of the coupling cell.

At very low Q-values one always is limited by thermal breakdown but there is no consistent relation between Q and the breakdown field levels. In fact such a relation cannot be expected as long as very inhomogeneous surface

resistances are found. Once the Q-values at high fields exceed our design value of $5 \cdot 10^8$ we are no longer limited by thermal breakdowns and we are always able to reach magnetic field levels above our design value of 310 Oe. We finally note that our deflectors showed only a moderate multipacting (a few hours at most) and a degradation of Q-values towards higher fields not exceeding 50% of the low-field values. The multipacting barriers are always restored by a warming-up cycle under vacuum.

Peak magnetic fields and breakdown field levels

Peak field levels between 350 and 400 Oe have been obtained repeatedly in the 20 cell-deflectors. This corresponds to electric peak fields between 12.5 and 14.3 MV/m and to deflecting fields between 2.3 and 2.6 MV/m, the design value for this latter being 2 MV/m.* We have tried to localize during a low temperature measurement the cells where breakdowns occur. If one assumes that the breakdowns are caused by the weldings or by bad regions near the weldings the method described in ref.8 may be applied. We use formula (3) in order to obtain for the mode "k"

$$\frac{(H_{i,k})^2}{W_k} = K^2 \frac{(E_{z_{i,k}})^2}{W_k} \qquad (5)$$

This may be written with the relation (1)

$$(H_{i,k})^2 = \frac{K^2}{\omega} \frac{(E_{z_{i,k}})^2}{W_k} \cdot P_{o_k} Q_k \qquad (6)$$

If one replaces in formula (6) P_{o_k} by the RF power at which a magnetic breakdown occurs in the mode "k" and Q_k by the corresponding low temperature Q-value and $(E_{z_{i,k}})^2/W_k$ by the value obtained from a perturdation measurement one can determine with the K-value of a given but arbitrary point in the slot region the magnetic field level corresponding to this breakdown. If for different modes the magnetic field levels are equal for a given cell "i" one can suspect that the breakdown occurs somewhere in the slot region of this cell and if it is assumed that the breakdown takes place at a definite point e.g. at the welding region one may determine with the corresponding K the critical breakdown field-level H_{crit}. During one low temperature measurement we have found two possible cells where the breakdown levels are nearly equal for three different modes. We therefore suspect that the field levels were limited by a magnetic breakdown at the weldings of these cells.**
We mention another simple method of localizing RF breakdowns in multi-cell deflectors lying horizontally in a He-bath. By raising the He-temperature slightly above the λ-point (2.17 K) we were able to see directly a bubble production in the He-bath which sets in when a breakdown with sufficient energy production occurs. In a 4 cell test-deflector a breakdown occuring at a peak field level of the order of 200 Gauss and a stored energy of 1/100 Wsec could be clearly localized.

* We have obtained recently in a 4 cell test deflector magnetic peak fields of 850 Oe with a corresponding quality factor of $2.5 \cdot 10^9$.

4. Coupling system and RF joints

Coupling system[11]

The RF power is fed to the cavity by a system using a vertically movable coaxial transmission line with the center conductor acting as a probe in a circular waveguide below cut-off and an off-center aperture coupling to the magnetic field of one deflector cell (Fig.5). In the layout used previously (Fig.5a) sliding spring contacts were used so to avoid radiation of RF power between the outer conductor of the movable coaxial line and the cut-off cylinder. As there was a danger of small metallic pieces rubbed off from the (niobium) cut-off cylinder and falling inside the deflectors and, at high power levels, of excessive currents across the contacts we replaced the sliding contacts by a bellow forming the outer conductor of the movable coaxial line (Fig.5b). It was found experimentally that the impedance of the bellow was not changed by more than ±1% over the moving range of the bellow (± 5 mm for a normal length of 50 mm). From measurements with a prototype coupling system using a stainless-steel bellow and an inner conductor made of copper we anticipate that the coupling losses with a niobium conductor cooled by HeII will be negligible for the working conditions we foresee with 3m-deflectors (unLoaded and loaded 8-factor $\geq 5 \cdot 10^8$ and $5 \cdot 10^6$ respectively). In order to reduce even more the coaxial line losses we intend to replace the stainless-steel bellow in the final version by a niobium bellow. The dependence of the coupling coefficient and the coupling losses on the

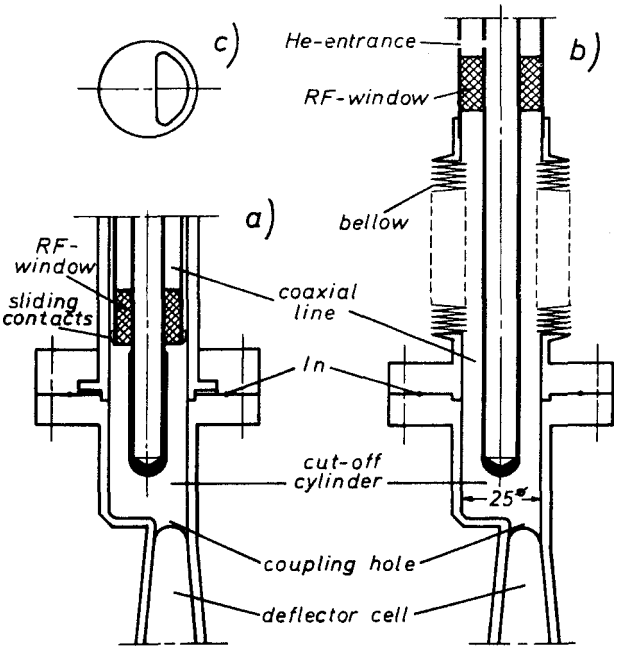


Fig.5: RF coupling system. Only the vacuum-tight lower part is shown.
a) old layout with sliding spring contacts
b) new layout with bellow
c) shape of the coupling hole.

distance of the inner conductor from the coupling hole shows that the coupling coefficient is dominated by a TM_{01}-mode and, at very small distances, by a TM_{03}-mode whereas the largest contribution to the coupling losses stems from a TM_{11}-mode. One therefore can try to optimize the system by giving the coupling hole an adequate shape. As a result of theoretical calculations and RF measurements the shape of the coupling hole shown in Fig.5c has been adopted.

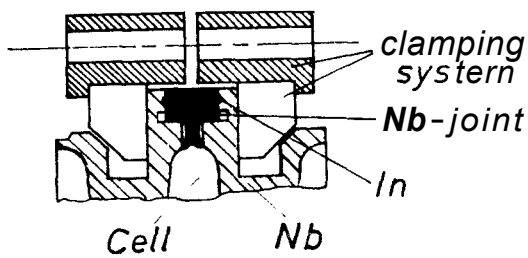


Fig.6: Layout of RF joint

RF joints'

The 3m deflectors will be assembled from 5 sections by using RF joints of the type shown in Fig.6. The RF' contact is obtained by a specially shaped niobium ring and vacuum tightness is insured by two indium-joints. Before mounting the joint is chemically polished or cleaned in hydrofluoric acid. This type of joint has been used by now many times and turned out to be reliable and easily exchangeable. No remachining of the end flanges of the sections is necessary. Its RF performances have been tested both in a simple cavity and during the measurements on the different deflector sections and it was found that the joint - which normally is placed at a field-free cell of the deflectors - does not deteriorate the Q-value of the deflectors below the design value of $5 \cdot 10^8$ even for modes where it is submitted to nearly the full RF current. This will simplify considerably the frequency tuning requirements on the different sections of a deflector.

Acknowledgements

The authors would like to express their gratitude to their technicians H. Budig, R. Dlttmann, D. Ewert, F. Kröner, R. Lehm and H. Skacel for the very competent and careful work. The help of our cryogenics, vacuum and furnace groups and of our workshops is greatly appreciated. This work would not have been possible without the collaboration of Siemens, Erlangen, especially Dr. H. Diepers, during the fabrication period of the deflectors.

References

[1] W. Bauer, A. Citron, G. Dammertz, M. Grundner, H. Lengeler and E. Rathgeber - Proc. Int.Conf. on Instr. for High Energy Physics, Frascati 1973, p. 716

[2] A. Michelini, G. Petrucci - CERN Internal Report NP 72-13 (1972)

[3] W. Bauer, G. Dammertz, H.C. Eschelbacher, H. Hahn, W. Jüngst, E. Rathgeber, J. Votruba, and H. Diepers - Trans. IEEE, NS-18, No.3, 181 (1971)

[4] W. Bauer, A. Citron, G. Dammertz, H.C. Eschelbacher, H. Hahn, W. Jüngst, H. Miller, E. Rathgeber, and H. Diepers - Proc.Conf.High Energy Accelerators, CERN, 1971, p. 253

[5] W. Bauer, A. Citron, G. Dammertz, H.C. Eschelbacher, W. Jüngst, H. Lengeler, H. Miller, E. Rathgeber and H. Diepers - Proc. 1972 Applied Superconductivity Conf., Annapolis (IEEE, N.Y.) 1972, p. 653

[6] W. Bauer, A. Citron, G. Dammertz, H.C. Eschelbacher, H. Lengeler, H. Miller, E. Rathgeber and H. Diepers - Proc. 1973 Particle Acc.Conf., San Francisco, 1973 (IEEE Trans.on Nuclear Science NS-20,) p. 59

[7] E. Rathgeber - to be published

[8] G. Dammertz, L. Husson, H. Lengeler, E. Rathgeber - to be published in Nucl.Instr. and Methods

[9] A. Citron, G. Dammertz, M. Grundner, L. Husson, H. Lengeler and E. Rathgeber - GfK Karlsruhe Internal report No. 74-33-SEP (1974) and to be published as GfK External Report

[10] J. Aggus, W. Bauer, S. Giordano, H. Hahn, and H.J. Halama - BNL Informal Report AADD 73-14 and Appl. Phys.Letters, 24, p. 144 (1974)

[**] G. Dammertz, L. Husson - to be published

D. Gray, Rutherford High Energy Laboratory: Dr. Kuntze mentioned the cost of the refrigerator. We have seen niobium with these low Q's at 1.85°K. One might think that perhaps one could get the same Q and field values with niobium at 4.2°K. Carne operated a cavity 1.2 m long at 1.2 GHz and he found that he could achieve a Q of about 10^8 and a field of 2.5 MV/m at both 1.850 and 4.2°K.

Kuntze: I completely agree with you as far as different actual accelerating structures are concerned because we are already in the region of 10 nano-ohms, which we reach sometimes at 4.2°K. However mechanical considerations introduce additional constraints. With the helix we have to use super fluid helium for cooling to avoid bubbles. We do not see much improvement between 4.2° and 1.80 in actual structures. In small test resonators we get an improvement of 50 to 80 between 4.20 and 1.8°.

Gray: You get 2.5 MV/m in actual structures ?

Kuntze: Yes. It's not necessary to reduce the surface resistance to a tenth of a nano-ohm.

L. Bollinger, Argonne National Laboratory: We have recently tested a helix with a bare surface at both 1.8°K and also 4.2°K to an accelerating field in excess of 3 MV/m. There is almost no difference in the Q for these two temperatures, Therefore, in planning a small heavy ion energy booster we are planning to operate at a temperature in the neighborhood of 4.2°K and using forced flow.

A. Schwettman, Stanford University: Temperature dependence of Q is strongly dependent on frequency. Now, Kuntze at Karlsruhe and the group at Argonne are talking about helical structures which operate at frequencies on the order of 100 MHz where there is very little difference between the Q at 4.2°K and 1.8°K. For the electron accelerator structures at 1.3 GHz the Q of our structure at 4.2°K would be about 3×10^8 whereas the Q that we achieve at 1.9°K is 7×10^9, a factor of more than 20. The conclusion that you reach depends very strongly on the operating frequency.

H. Lengeler, CERN: I would like to confirm fully what Schwettman is saying. For similar cavities at the same frequency, we also have an improvement of at least a factor of 20 between 1.8 and 4%.

Kuntze: It's a question of economy. A refrigerator for 4.2°K is very much less expensive than 1.8°K so if one can live with the Q value at 4.2°K I think one should give it a chance.

T. Khoe, Argonne National Laboratory: What experience have you had with indium seal joints ?

Kuntze: Very good.

Khoe: What is the best surface treatment of the indium joint region ?

Kuntze: The cavity structure is electro-polished before we put it together and then sometimes it is anodized and fired. I see no difference in the joint region. Structures should be fired. It depends upon the frequency as Alan Schwettman said.

M. Green, Lawrence Berkeley Laboratory: This is a question that I would like to direct to both Schwettman and Kuntze. How important is temperature stability in the accelerator ? Is this an argument in favor of the superfluid helium refrigeration system ?

Schwettman: I would have to answer that we' ve not experimentally studied that question because we already have good tempsrature stability. But there would be several things that might be considered. First, with our feedback circuitry which samples both the amplitude and the phase of the r.f. fields temperature stability is not so important. Also, there will always be some advantage in reducing magnetic breakdown in having as low a temperature as possible. The question is not the stability of the thermal environment but how big a AT you have at the conducting surface at its operating temperature. The question of temperature stability is probably less important than we originally thought.

Kuntze: With the helix, I think temperature stability might be really essential because we have bubbles. The helix is mechanically a very weak structure and bubbles in the helium vibrate the helix. So far we haven't tried to run it at 4.2°K. We were just able to run it at a fixed frequency at 1.8°K.

Bollinger: The point of Tat Khoe's remark was that we have recently gotten some evidence that occasionally at the joint there is a failure to have a good r.f. contact. Cornell has found that, also. The way in which you treat the surface at the joint can be quite important.

Kuntze: We haven't done any special treatment.

T. Nishikawa, National Laboratory for High Energy Physics: I would like to mention the preliminary result on NbN cavities done by the staff at KEK. Using NbN cavities they got a Q of about 10^7 at 4°K.

Kuntze: It may be important to go to another superconductor with a substantially higher H_c and this would be the case of NbN as Dr. Nishikawa said.

M. Tigner, Cornell University: I'd like to comment about the surface treatment. In single cells we have gotten Q's of 5×10^9 and fields of 10 to 15 MV/m with no heating, not even to annealing temperatures. We just machined and electropolished it and then chemically polished and anodized it.

Kuntze: In my opinion, firing is needed in actual big accelerating structures where cleanliness is harder to obtain than with small cavities. We got good results with r.f. separator structures only if we put them in the furnace for final treatment. These are 60 cm sections and together with the 3 meter section we need the furnace for cleanliness.

G. Loew, Stanford Linear Accelerator Center: If you want to get beyond the barrier of 3 or 4 MeV/meter is the only hope right now to try nitride compounds and if so, is anybody trying ?

Kuntze: Yes, Japan is trying. At KEK they have fabricated the first NbN cavities and work has also been done at SLAC. Brookhaven is trying Nb_3Sn. Could Dr. Hahn comment ?

H. Hahn, Brookhaven National Laboratory: Since we are extremely limited in funds and personnel, everything goes extremely slowly. The procedure to generate Nb_3Sn was to put a small piece of tin in a cavity, to close it off, and to heat it to 900°C. In this procedure we don't know exactly what we are generating, but we did detect the Nb_3Sn pattern with x-rays. We measured the Q's and they were in the middle range and we were able to see something like 120 gauss. Now, at the same time I would like to mention that we are working on a NbTi cavity to establish if type-II materials have a limit H_{c1} or not. We chose NbTi because this is the easiest material to handle and still have all of

the properties of very high conductivity.

Kuntze: I would like to put a question to Dr. Sarantsev. Unfortunately, I have no information about the work in Russia which is going on in this field, but I know that there has been work in the past on different super-conductors. Do you know something about it ? At Dubna and Kharkov work has been done in this field.

V. Sarantsev, Joint Institute for Nuclear Research: There have been no results.

BREAKDOWN FIELDS IN A SUPERCONDUCTING NIOBIUM CAVITY AT S-BAND

P. Kneisel[†], C. Lyneis[*], O. Stoltz, J. Halbritter
Universität and Gesellschaft für Kernforschung, Karlsruhe
Karlsruhe, Germany

Summary

The measurements of the RF breakdown and its localization in different modes of an S-band niobium cavity gave new insight about the thermal magnetic breakdown. Especially the TE_{011} mode, where the initial peak RF field of 810 Oe deteriorated to about 400 Oe after the cavity has been subject to the electron loading of TM modes causing surface damage. After damaging the surface by electron impact at He temperatures, the field level in all modes is limited to about 400 G. For TM modes this field level corresponds to a surface electric field of about 25 MV/m.

Introduction

In the past several years considerable progress has been made in the field of superconducting cavities.[1-8] For example, this is shown by the high breakdown fields H_{crit} at frequencies between 8 and 10 GHz up to 1600 Oe in a TE_{011} mode cavity and 1500 Oe in a TM_{010} mode cavity.[1] At lower frequencies, between 1-4 GHz, the breakdown fields have been considerably lower,[2-4] especially in TM mode cavities, with $H_{crit} \leq 600$ Oe. These low RP critical fields are not related to bulk properties but are due to weak or heated spots at the surface as discussed in [3,9]. These spots become normal at a field level below the bulk thermodynamic critical field ($H_c(0) = 1990$ Oe). In this normal conducting region the RF dissipation is more than a factor of 10^5 higher than in the surrounding superconducting region which cause a thermal explosion,[9] i.e. the thermal magnetic breakdown.

Several causes for the nucleation of RF breakdown have been proposed[3,6,8-10] e.g. localized impurities, especially at welds, trapped flux or direct electron impact. The results on the multimode cavity - especially the reduction of the breakdown field and the motion of the breakdown spot - show that none of these proposed models can explain our results. Instead the measurements support a model of thermal magnetic breakdown initiated by surface damage and caused by electron impact in TM modes. This surface damage seems to be larger for wet oxidized or contaminated surfaces than surfacesprepared in a UHV furnace; and, seems to saturate for moderately clean surfaces. In similarly shaped cavities for one type of mode the electron loading strength[11] and the surface damage by those electron scales with f^{-1}. Hence, this surface damage can explain the reduced H_{crit} in low frequency cavities.[1]

[†] Present address: HEPL, Stanford University, Stanford, California
[*] On leave of absence from HEPL, Stanford University, Stanford, California

Measurements and results

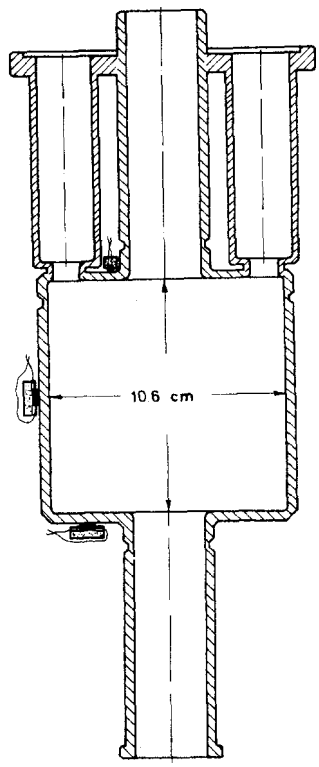


Fig. 1: Schematic drawing of S-band cavity with beam tubes. The cavity is constructed out of several niobium parts that have been electron beam welded together. The welds are shown as thinned walls in the drawing. Carbon resistors used to detect heat pulses are indicated schematically.

The measurements discussed here were made on a beam hole cavity (see Fig.1) in which a number of modes can be excited between 2 and 5 GHz. The addition of beam holes to the cavity allows better chemical surface treatments because it gives better access to the interior surfaces. The various parts of the cavity were electropolished before final electron-beam welding. The surface treatments after welding have included cold chemical polishing, oxipolishing, and high temperature annealing in a UHV furnace. A more detailed description of the surface treatments is given in Ref.4. The best results in terms of H_{crit} and R_{res} were attained after an high temperature anneal at 1750°C for 20 hours. During the cool-down cycle N_2 at one atmosphere was introduced at 400°C which increases the cooling rate at low temperatures by about a factor of 10. The cavity is tested in a vertical position as indicated in Fig. 1. The microwave coupling is provided by two coaxial lines which are pumped by a sputter-ion pump located on top of the dewar. It is possible that gases from the warm portion of the vacuum system condense on the cold cavity

walls when the cavity is at helium temperature.

The microwave measurements made on the multimode cavity include the measurement of H_{crit} and R_{res} in the TE_{011}, TE_{012}, TE_{111}, TM_{010}, TM_{011}, TM_{012}, TM_{013}, TM_{110} and TM_{111} modes. The effect of electron impact was studied by measuring the electron free TE_{011} mode before and after electron loading was produced by exciting TM modes. Measurements have also been made to study the location of the thermal magnetic breakdown as a function of mode and electron surface damage. The position of breakdown was found by detecting the heat pulse produced by breakdown with carbon resistors as described previously by one of the authors.[2]

Table I:

The minimum RF surface resistance, the surface resistance at the limiting fields and the limiting fields in the TE_{011} mode. In each test the values are given for the initial measurement and for the measurement after electron damage was produced by excitation of the TM modes. The surface preparations prior to each measurement were:

a) chemically polished, anodized, rinsed, and assembled while wet with CH_3OH
b) chemically cleaned, annealed at 1750°C in UHV furnace. During cool down N_2 at 1 atm. was introduced at 400°C to increase the cooling rate.
c) chemically polished, rinsed in NH_3OH, H_2O and CH_3OH and assembled while wet with CH_3OH.

Test	TE_{011} Initial		H_{crit} (Oe)
	Min. R_{res} (nΩ)	R_{res} at H_c (nΩ)	
a	6.9		650
b	6.6	8.8	810
c	10.5	10.5	780
	TE_{011} values after γ's		
a	40	40	430
b	17	19	510
c	73	78	330

In Table I data are shown illustrating the effect of surface damage on R_{res} and H_{crit} in the TE_{011} mode. The basic test procedure was first to measure the surface resistance as a function of RF field level in the electron free TE_{011} mode up to H_{crit}. Then various TM modes were excited and both electron multipacting and electron field emission were observed. The TE_{011} mode was remeasured after γ-radiation was produced in one of the TM modes. The reduction of H_{crit} in the TE_{011} mode shown in Table I cannot be explained by a model where electron impacts directly cause thermal magnetic breakdown by localized heating or the breaking of Cooper pairs because the TE_{011} mode has no surface electric fields.

A systematic study of the sensitivity of the niobium surface to electron damage as a function of surface treatment has not been made. However, anodized and wet prepared surfaces seem to be more sensitive to electron impact than surfaces for which heat treatment is the final step in the cavity's preparation. As discussed below, the lower end plate of the cavity had a lower H_{crit} than the upper end plate as has also been reported in sealed TM_{010} mode cavities.[2] This indicates that contamination or absorbed gas may play a role in the surface damage mechanism.

Table II:

Summary of the best results in terms of field level in various modes. The values are taken from several different tests on the cavity. Only the results of the TE_{011} mode change significantly with test.

Mode	Frequency [GHz]	H_{crit} [Oe]	E_{max} [MV/m]
TE_{011}	3.7	810	-
TM_{010}	2.1	380	29
TM_{011}	2.6	400	26
TM_{012}	3.6	415	20
TM_{110}	3.4	410	22

In Table II a summary of the highest fields achieved in various modes is given. The difference between H_{crit} in the TE_{011} mode and H_{crit} for the TM modes is very clear. However, if one compares the values of H_{crit} in the TE_{011} mode after γ's (see Table I) with H_{crit} for the TM mode the differences are smaller. In run c the values of H_{crit} in the TE_{011} and TM modes were all comparable after significant γ's had been produced. This indicates that the field levels reached in TM mode are influenced by self-induced electron damage to the surface.

Experiments were done to study the location of the thermal magnetic breakdown as a function of mode and electron damage. Measurements in a TM_{010} mode S-band niobium cavity have been previously made by one of the authors,[2] but the measurements in the multimode cavity have yielded new clues about the mechanism causing thermal magnetic breakdown. The thermal magnetic breakdown in a particular mode will occur at the point where the magnetic field first exceeds some local H_{crit} at the surface. The location of the maximum magnetic field is dependent on mode. Therefore different areas of the cavity can be sampled by measuring more than one mode. If the surface RF properties are inhomogeneous then the breakdown will not necessarily occur in the region of maximum field. The surface inhomogeneities can be precipitates of NbO, carbides or surface damage due to electron impact.

A series of measurements on the cavity have demonstrated that the location of breakdown in the TE_{011} mode can be altered by exciting TM modes between measurements of the TE_{011} mode. The fields in the TE_{011} mode are not dependent on the azimuthal angle and the points of the maximum H-field lie on a circle around the middle of the cylinder wall. The ratio of maximum H-field on the cylinder wall to the maximum H-field on the endplates is 1.6 for the TE_{011} mode. Before the excitation of the TM modes the TE_{011} mode breakdown was in the middle of the cylinder wall. After measurements on the TM_{111} mode during which electron multi-

pacting was observed, the TE_{011} breakdown was found in a new location on the cylinder wall. The TM_{110} mode was excited and y-radiation caused by the impact of field emitted electrons with the cavity walls was observed. Before further γ's were produced the location of breakdown was checked and found unchanged from the previous measurement. Then the cavity was operated for 15 min in the TM_{110} mode at H_{max} ~ 400 Oe and E_{max} ~ 20 MV/m with the production of γ's. After this the breakdown in the TE_{011} mode was found in a 3rd location in the middle of the cylinder wall. The mechanism involved in the relocation of breakdown appears to be the creation of a new weak spot in the surface of the superconducting niobium rather than an improvement in the properties at the former location of breakdown. This follows from the observation that each change in location was accompanied by a decrease in the H_{crit} in the TE_{011} mode. In this set of measurements the value of H_{crit} in the TM mode did not decrease significantly during the measurements.

The results of the measurements on breakdown as a function of mode show different breakdown locations for different modes. For example the TE_{011} breakdown occurred on the cylinder wall as described above, while the TE_{012} breakdown occurred on the lower endplate in the region of maximum H-field. The breakdowns in the TM_{012} and TM_{013} mode were located on the lower endplate also in the region of highest fields but in a slightly different location than for the TE_{012} mode.

Discussion

In this paper we reported on RF breakdown and their location. As witnessed by the deterioration of TE_{011} mode results due to electron loading in TM modes, electron impact damages Nb surfaces. This surface damage should be differentiated from bulk radiation damage, which for slow electrons consists in point defects[9] and cannot explain the observed deterioration of R_{res} and H_{crit}. This was already discussed in[13] where a model for surface damage was proposed consisting in the formation of (normal) conducting precipitates of some niobium oxides. This damage of the superconductor oxide interface saturates after some hours electron impact depending, e.g., on the thickness of the dielectric oxide. Hence, anodized and wet oxidized Nb, which is covered at least by 50 Å Nb_2O_5,[14] show more surface damage, than sealed cavity surfaces oxidized during cooling in a UHV furnace, where Nb_2O_5 is thinner (≤ 20 Å).[15] But there are indications[16] that Nb covered only with a thin oxide layer (≤ 20 Å)[15] becomes fairly reactive by electron impact at He temperatures and deteriorates if contaminents or gases are present. The bottom of the cavity is more easily contaminated than the top endplate and this could explain the observation, that the breakdowns occur preferentially at the bottom endplate. In the multimode cavity after electron loading for several hours, the breakdown spot was localized in the region of maximum magnetic field for each mode. This indicates, that the surface damage is quite homogeneous and that inhomogeneities present from the beginning play no significant role. It should be mentioned, that near the welds no breakdown was observed, in contrast to [6].

References

[1] J.P. Turneaure, Nguyen Tuong Viet
Appl.Phys.Lett. 16, 333 (1970)

[2] C. Lyneis, M. McAshan, Nguyen Tuong Viet
Proc. 1972 Proton Linear Accelerator Conf.
(Los Alamos, 1972) p. 98
C. Lyneis, Y. Kojima, J.P. Turneaure,
Nguyen Tuong Viet
IEEE NS-20, No.3, 101 (1973)

[3] J.P. Turneaure
Proc. 1972 Appl.Superconductivity Conf.,
Annapolis (IEEE, N.Y., 1972) p. 621;
P.B. Wilson
Proc. 1972 Proton Linear Accelerator Conf.
(Los Alamos, 1972), p. 82

[4] P. Kneisel, O. Stoltz, J. Halbritter
IEEE Trans. NS-20, No.3, 63 and
J.Appl.Phys. 45, May (1974)

[5] H. Martens, H. Diepers, B. Hillenbrand
Phys.Lett. 44A, 213 (1973)
K. Schnitzke, H. Martens, B. Hillenbrand,
H. Diepers
Phys.Lett. 45A, 241 (1973) and this conference

[6] J.R.Aggus, W.Bauer, S.Giordano, H.Hahn,
H.J.Halama, Appl.Phys.Lett.24, 144 (1974)

[7] e.g. B. Piosczyk, P. Kneisel, O. Stoltz,
J. Halbritter
IEEE Trans. NS-20, No.3, 108 (1973)

[8] P.B. Wilson, Z.D. Farkas, H.A. Hogg,
E.W. Hoyt
IEEE Trans. NS-20, No.3, 104 (1973)

[9] J. Halbritter
Proc.1972 Appl.Superconductivity Conf.,
Annapolis (IEEE, N.Y., 1972), p. 662

[10] R. Sundelin, E.von Borstel, J. Kirchgessner,
D. Rice, M. Tigner
IEEE Trans. NS-20, No.3, 98 (1973)

[11] J. Halbritter
Part.Accel. 3, 163 (1972)

[12] H. Ullmaier in: Defects and Defect Clusters
in bcc Metals and their Alloys, Nuclear
Metallurgy, Vol.18 (NBS, 1973)

[13] P. Kneisel, O. Stoltz, J. Halbritter
J.Appl.Phys. 45, May (1974)

[14] G. Beranger, P. Boisot, P. Lacombe, G. Amsel,
D. David,
Revue Phys. Appl. 5, 383 (1970)

[15] P.B. Sewell, D.F. Mitchell, M. Cohen
Surface Science 29, 173 (1972)

[16] C.M. Lyneis, P. Kneisel
to be published

ON THE PREPARATION AND A THERMAL BREAKDOWN MECHANISM OF SUPERCONDUCTING NIOBIUM X-BAND CAVITIES WITH HIGH MAGNETIC FLUX DENSITIES *

B. Hillenbrand, H. Martens, K. Schnitzke, H. Diepers

Research Laboratories Siemens AG
Erlangen, Germany

Summary

Performing only a surface treatment of Nb-X-band cavities we could obtain high magnetic breakdown flux densities B_c^{ac} up to 159 mT (TE_{011}-type) and 149 mT (TM_{010}-type) with high field Q values in the order of 10^{10}. The preparation consists of electropolishing, oxipolishing and, in many cases, a final anodizing, but includes no degassing. For oxipolishing special conditions are reported to prevent the formation of gray stains. Thus prepared surfaces are stable against degradation by gas exposure even if not anodized. B_c^{ac} values of 100 mT and more could be reached with different materials (coarse and fine grained), but not with cold worked niobium. We repeatedly observed a strong temperature dependence of B_c^{ac} which we interpret as a thermal breakdown independent from the critical fields of superconducting niobium. Calculations on the basis of this mechanism are carried out and compared with experimental results.

I. Introduction

For some applications of superconducting resonators it is important to have a high quality factor Q_o and a high breakdown flux density B_c^{ac} which are stable for a long time. For type I superconductors the field limit[1] is given by the thermodynamical critical flux density B_c, which for all these materials is less than 100 mT. Investigations were concentrated on the type II superconductor niobium which has higher critical fields and a higher transition temperature. Two different methods of material preparation are used. The first one[2] influences both the bulk and surface properties by degassing the cavities at about 2000 °C in ultra high vacuum. The second one is restricted to a mere surface treatment, as the electromagnetic fields penetrate only to a depth of some ten nm. We chose the second method and succeeded in reaching $B_c^{ac} \approx 160$ mT with $Q_o = 1 \cdot 10^{10}$ for TE_{011}-type[3] and $B_c^{ac} = 149$ mT with $Q_o = 3 \cdot 10^9$ for TM_{010}-type cavities, both at 1.4 K and 9.5 GHz. These are our best results, but a number of cavities could sustain flux densities in the range between 110 and 160 mT.

II. Surface preparation and stability tests

Our preparation and installation method has been published to a great part earlier, therefore we will give here only a short description.

Each cavity was machined from niobium in a single piece. Then the damaged sheath was removed to a depth of about 100 µm by electropolishing in a solution of 9 parts of H_2SO_4 (95 - 97 %) and of 1 part HF (40 %) with oscillating current[4]. Thereafter the cavities were oxipolished[5], that means they were anodized and the oxide layer was dissolved again, this procedure being repeated several times.

Anodizing was done in a NH_3-solution at a current density of 10 mA/cm² and was stopped at a voltage drop at the oxide layer of 100 V. This amorphous oxide was dissolved in 50 % HF. Then the cavity was rinsed first with diluted H_2O_2 (6 % by weight) thereafter with H_2O and finally with acetone, The dissolving and H_2O_2-rinsing were done in an ultrasonic bath. Our investigations have shown that all these conditions have to be met to prevent the formation of gray stains (crystalline oxide?) which are hard to remove afterwards. For the same reason the current density during anodizing should be greater than 1 mA/cm²[2]. Often the cavity remained anodized, e.g. the last oxide layer was not removed.

When the cavity was connected to the measuring equipment it was continuously rinsed with acetone, the vapor of which streams out through the remaining opening thus keeping clean the inner niobium surface. In many cases the cavity was baked at 100 °C for some hours. After installation the cavity was continuously pumped through the waveguides, the form of which was chosen such that gases penetrating through leakages would freeze out before reaching the cavity, and that dust could not fall down into the cavity[12].

Niobium surfaces prepared in this manner proved stable when being exposed to air, CO, CO_2, and CH_4 at room temperature and at atmospheric pressure, even without the anodic oxide layer[3,6]. This is in contrast to the degradation found by Wilson et.al.[7] for degassed niobium.

* This work has been supported by the technological program of the Federal Department of Research and Technology of the FRG. The authors alone are responsible for the contents.

We have made one experiment to date to test a welded cavity. It could be shown that the described surface preparation was also successful for the welded cavity. Before welding, we had B_c^{ac} = 85.8 mT with $Q_o = 3.4 \cdot 10^9$. Welding was done in a poor vacuum > 10^{-4} torr, and the cavity showed annealing colours afterwards. Removing a thin layer of about 0.7 um by oxipolishing 7 times, we only could reach 16.2 mT and $1.8 \cdot 10^9$. After electropolishing, however, (50 um removed) the values increased to 91.4 mT and $3.3 \cdot 10^9$. From this we conclude that heat treatment is not necessary even after welding.

III. The influence of the niobium bulk constitution

To test the influence of different bulk constitution we fabricated cavities from niobium with different pretreatments performed by the suppliers (Wah Chang Corp. and Kawecki-Berylco Corp.).

Niobium I was an electron-beam molten, coarse grained material (grain size ca. 1 cm) without internal stresses.
Niobium 11, in addition, has been cold worked and therefore is severely strained (from Wah Chang Corp. only).
Niobium 111, in a further step, has been stress annealed by the supplier at 1200 °C and is fine grained (grain size < 1 mm).

Most of these experiments were made with TM-cavities. To obtain high field strengths with this type of resonator we usually had to do some He-processing[4] with periodic breakdown. In order to obtain some of the following results, He-gas had to remain in the cavities during the measurement.

With Nb III in every case (eight TM-cavities) B_c^{ac} values between 110 and 150 mT were reached, the values being uniformly distributed over this range. Nb I was used only for two cavities which, after a single preparation, gave B_c^{ac} values of about 100 mT. We believe that further oxipolishing will raise B_c^{ac}. Therefore we conclude that with Nb I and Nb III generally B_c^{ac} values of 100 mT and more can be obtained.

With Nb 11, however, we attained critical flux densities no higher than 30 - 40 mT ($Q_o \approx 5 \cdot 10^4$). Later we will demonstrate that this is probably due to bad thermal conductivity. Annealing in ultra high vacuum at 1440 °C and for 5 hours resulted in a considerable increase of B_c^{ac}, but 80 mT was not exceeded, presumably because electropolishing was not yet applied.

With TE_{011}-cavities, which have no electrical surface fields, we obtained higher B_c^{ac} values. For niobium III the best results were 159 mT with $Q_o = 1 \cdot 10^{10}$ at this flux density.

IV. The mechanism of thermal breakdown

For well prepared cavities made from type I superconductors, B_c^{ac} coincided with the thermodynamical critical flux density[1]. This implies a temperature dependence proportional to $1-(T/T_c)^2$, T_c being the transition temperature. The same temperature dependence was measured for niobium[5]. When we changed the He-bath temperature from 1.4 to 2.0 K, a weak temperature dependence was sometimes noticable, which can be interpreted as a $1-(T/T_c)^2$-law. Repeatedly, however, for cavities with a high B_c^{ac} (> 130 mT), we observed a much stronger temperature dependence. An example will be given in fig. 2.

Such a strong temperature dependence of B_c^{ac} can be explained by a mechanism in which no critical field of the superconductor is involved, but only the temperature dependence of the surface resistance R_S. In the relevant temperature range R_S can be written

$$R_s(T,B) = [R_{res} + R_0 \exp(-A/T)][1 + \gamma(B/B_c)^2] \quad , \qquad (1)$$

where R_{res} is a temperature independent resistance. $R_0 \cdot \exp(-A/T)$ equals approximately the BCS-part[9] of the resistance ($A \approx \Delta/k_B$, Δ energy gap, k_B Boltzmann constant). The field dependence is taken into account by a factor $(1 + \gamma(B/B_c)^2)$.

γ should be[10] of order 1. The local magnetic fields cause a heat production which is given by $(1/(2\mu_0^2))R_S B^2$ (μ_0 permeability of vacuum). This heat raises the temperature T_i of the inner surface until there is a balance between the heat produced and that conducted away through the cavity wall to the helium bath. In this case we have the equation

$$\frac{1}{2\mu_0^2} R_s(T_i,B)\, B^2 = \kappa\, |\mathrm{grad}\, T| \qquad (2)$$

(κ thermal conductivity). For simplicity we will consider only the heat flow normal to the surface. Also we will take for κ a constant mean value $\bar{\kappa}$. This makes, as we have checked, no great difference in comparison to a temperature dependent κ. Then we obtain for the cavity wall with inner radius r_i, outer radius r_a

$$\frac{1}{2\mu_0^2} R_s(T_i,B)\, B^2 = \frac{\bar{\kappa}}{r_i \ln(r_a/r_i)} (T_i - T_a) \, . \qquad (3)$$

T_a is the temperature of the outer wall. If the wall thickness $d = r_a - r_i$ is small compared to r_i we can replace $r_i \cdot \ln(r_a/r_i)$ in equation (3) by d.

Because of the Kapitza resistance R_K there is a temperature jump ΔT at the interface between the outer cavity surface and the He-bath with the temperature T_B. Mittag[11] has measured the Kapitza resistance of a niobium-He11 interface. We take his value for polished niobium $1/R_K = 0.02 \cdot T_B^{4.65} \cdot f(\Delta T)$ (dimension $Wcm^{-2}K^{-1}$, $\Delta T = T_a - T_B$) and put for our calculation $f(\Delta T) = 1$ (in reality $f(\Delta T) = 1 + 1.5 \cdot \Delta T/T_B + \ldots$). Then we can add up the temperature differences in the niobium wall

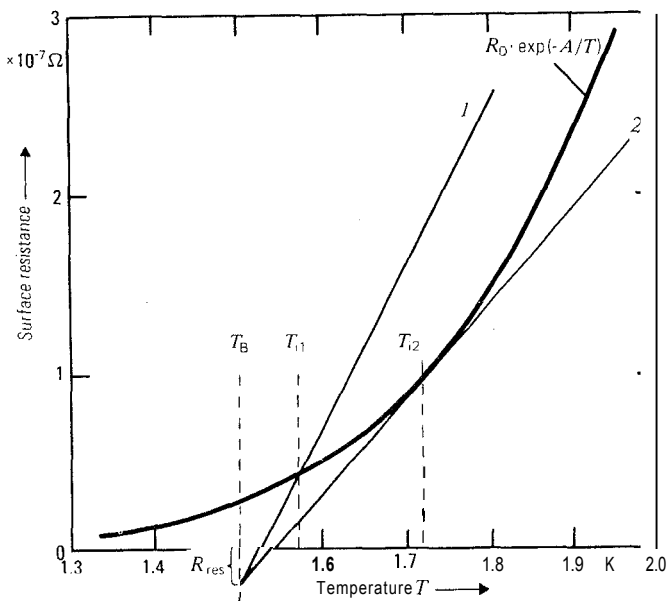


Figure1
Plot for the graphical solution of equation (5) with $A = 15.6\ K^{-1}$, $R_0 = 9.6 \times 10^{-4}\Omega$, $R_{res} = 2 \times 10^{-8}\Omega$ and $T_B = 1.5$ K. Line 1 represents a stable situation, line 2 the limit of stability. From the slope of line 2 the critical flux density B_c^{ac} can be determined, if all other parameters are known.

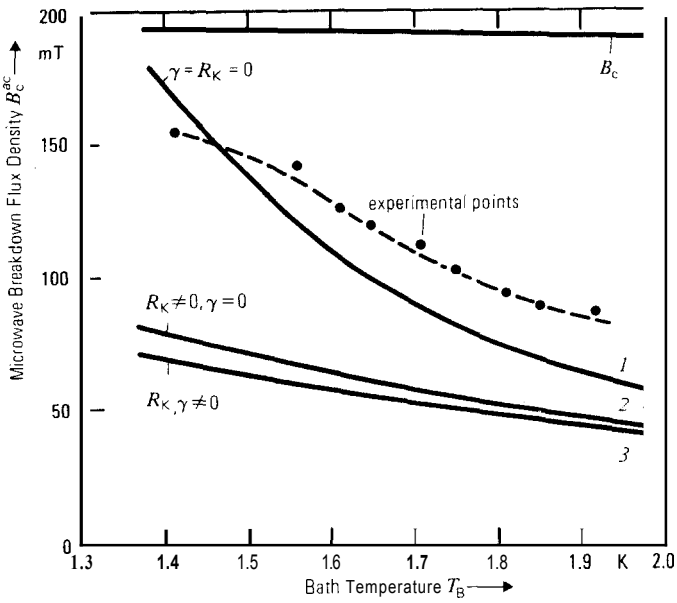


Figure2
Comparison of an experimental $B_c^{ac}(T_B)$-curve with curves calculated under different assumptions. Curve 1: $\gamma = R_K = 0$, Curve 2: $\gamma = 0$, $1/R_K \approx 0.02 \times T_B^{4.65}$, Curve 3: $\gamma = 3.7$, $1/R_K$ as in curve 2. $B_c(T)$ is taken from[16].

and at the interface and obtain

$$\frac{1}{2\mu_0^2} R_s(T_i,B)\, B^2 = \frac{1}{(r_i/\bar{\kappa})\ln(r_a/r_i)+R_K}\,(T_i - T_B)$$

or for $d \ll r_i$

$$\frac{1}{2\mu_0^2} R_s(T_i,B) B^2 = \frac{1}{d/\bar{\kappa}+R_K}\,(T_i - T_B)\,. \qquad (4a)$$

After replacing R_s according to equation (1) we can put (4a) into the form

$$R_0 \exp(-A/T_i) = \frac{2\mu_0^2}{(d/\bar{\kappa}+R_K)\ (1+\gamma\,(B/B_c)^2\, B^2}\,(T_i - T_B) - R_{res}\,.$$

In fig. 1 there is a plot of the functions of both sides of equation (5). The left hand side represents the BCS-part of the surface resistance of niobium. The other cavity parameters (R_{res}, χ, R_K, d) and the magnetic flux density B enter into the parameters of the straight line at the right hand side of equation (5). We have drawn two straight lines. Line 1 shows a stable situation. At the temperature T_{i1} of the intersection point of line 1 with the BCS-curve, the heat produced by the microwave flux density B at the inner surface, is stationarily conducted to the He-bath. If B is increased, the slope of the straight line is decreased, and finally there is no point of intersection. That means we have a thermal runaway, and the energy stored in the cavity breaks down. Breakdown just occurs if the straight line (line 2) is the tangent of the BCS-curve. This critical slope is given only by the BCS-curve, T_B and R_{res}. To obtain high B_c^{ac} values, one must make R_K and d as small and $\bar{\kappa}$ as great as possible.

In fig. 2, we have compared an experimental curve $B_c^{ac}(T_B)$ of a TE_{011}-cavity with calculated curves. For our calculations we chose $\bar{\kappa} = 0.21$ W (cmK)$^{-1}$ and R_K according to Mittag[11], $R_0 = 9.6 \cdot 10^{-4}\Omega$, $A = 15.6\ K^{-1}$, $R_{res} = 2 \cdot 10^{-8}\Omega$ and d = 0.6 cm were taken from our own measurements. Fig. 2 contains three calculated curves, curve 1 with $R_K = \gamma = 0$, curve 2 with $\gamma = 0$ and $R_K \neq 0$ and curve 3 with both γ and $R_K \neq 0$. All three curves exhibit a temperature dependence much stronger than $1 - (T/T_c)^2$, in agreement with the experimental curve.

Curve 2 and 3, however, are considerably lower than the experimental curve, while curve I agrees much better. We believe that the discrepency is due to a great part to our simplifications, for instance neglecting the increase of the factor f in R_K with AT, the lateral heat flow, and to a minor extent, to the cylindrical form of the cavity. Furthermore we do not know $\bar{\kappa}$ and R_K of our niobium, and these data are necessary to perform more accurate calculations.

We can mention two further observations which corroborate our model of thermal breakdown:

We decreased the wall thickness of a cavity by a factor of 2 and then found an increase of B_c^{ac}. At the lowest bath temperature ($\approx$1.4 K) we then had another type of limitation which was only weakly or not temperature dependent. At higher temperatures ($\approx$1.8 K) we had a strong temperature dependence and the increase of B_c^{ac} was roughly a factor of $\sqrt{2}$. This is to be expected if the corrections for γ and R_K are small.

For cold worked niobium (Nb 11) we have to expect a much lower value of κ, and therefore the thermal limit should be considerably lower than for annealed material, In fact, with Nb 11, we observed the strong temperature dependence of B_c^{ac}, typical for thermal breakdown, for a low field level.

The model of purely thermal breakdown can also explain weakly temperature dependent fields. If one assumes a thin normal conducting film at some small area of the inner surface of, for instance, 10 nm thickness, then it can be taken into account by adding a term $\alpha \cdot R_f$ to R_{res}. R_f is the microwave surface resistance of that normal conducting material and may amount e.g. to 10^{-5} to $10^{-3}\Omega$. The factor α accounts for the fact that this film is much thinner than the penetration depth of the film material and that only part of the heat is conducted perpendicular to the surface. We estimate α to be of the order 10^{-2} to 10^{-1}, and $\alpha \cdot R_f = 10^{-4}$ to 10^{-7} Looking at fig. 1, one can see that this will result in an only weakly temperature dependent breakdown flux density. The tangent to the BCS curve starts from a point far below, and the influence of the bath temperature on the slope of the straight line becomes small. This area of increased losses, of course, will generally not be in the region of the maximum field. Therefore B_c^{ac} which is always taken as the maximum surface field may be considerably higher than the triggering flux density.

In a similar way the model is open to include at least qualitatively other types of "weak" surface regions as low T_c areas, normal conducting spots etc.

A strong temperature dependence of B_c^{ac} was already observed by Wilson et.al.[7]. They interpret this result as a thermal runaway of a normal conducting small region generated at a flux density of 70 mT.

V. Conclusions

Our investigations have shown that it is possible to produce Nb-cavities with stable high B_c^{ac} values solely by a surface treatment, even after welding. The limitation often is given by a thermal breakdown which is due to the exponential temperature dependence of the BCS surface resistance and not to critical fields of the superconductor which might be locally surpassed. With special precautions, for instance thin walls, one should reach the thermodynamical critical field for homogeneous surfaces.

It is favourable to have a high thermal conductivity of the bulk niobium, and that may be obtained by a degassing treatment. However, another severe limitation is given by the Kapitza resistance, and therefore special care should be given to the outer cavity surface. A degassing treatment may be useless if the Kapitza resistance is large.

At T = 1.5 K, the BCS resistance $R_0 \cdot \exp(-A/T)$ is about $3 \cdot 10^{-8}\Omega$. Therefore it will bring no essential improvement in B_c^{ac} to prepare surfaces with R_{res} much better than $10^{-8}\Omega$.

If the above discussed thermal breakdown is avoided, for ideal surfaces B_c and not B_{c1} seems to be the limiting flux density [13,14,3], and one can try to make use of high B_c superconductors as Nb_3Sn ($B_c \approx 330$ mT, calculated from $(dB_c/dT)_{T_c} \approx 36$ mT/K[15]). In the case of Nb_3Sn being produced as a surface layer on bulk niobium thermal conductivity and Kapitza resistance should be essentially those of niobium. Therefore one has to expect severe problems with thermal stability at high field levels. But the greater energy gap will result in a considerably lower BCS resistance and one can hope to obtain higher B_c^{ac} values, provided one can fabricate homogeneous Nb_3Sn-surfaces with sufficiently small R_{res}.

References

1. Y. Bruynseraede, D. Gorle, D. Leroy and P. Morignot, Physica 54, (1971) 137
   J.P. Turneaure, Proc. 8th Intern. Conf. on High Energy Accelerators, CERN, 1971
2. J.P. Turneaure, Proc. of the Applied Superconductivity Conf., Annapolis, May 1972, 621
3. K. Schnitzke, H. Martens, B. Hillenbrand and H. Diepers, Phys. Lett. 45A, (1973) 241
4. H. Diepers, O. Schmidt, H. Martens and F.S. Sun, Phys. Lett. 37A, (1971) 139
5. H. Martens, H. Diepers and B. Hillenbrand, Phys. Lett. 44A, (1973) 213
6. K. Schnitzke, H. Martens, B. Hillenbrand and H. Diepers, to be published
7. P.B. Wilson, L.D. Farkas, H.A. Hogg, E.W. Hoyt, IEEE Trans. NS-20, (1973) No. 3, 104
8. P. Kneisel, O. Stoltz and J. Halbritter, Proc. of the Applied Superconductivity Conf., Annapolis, May 1972, 657
9. J. Bardeen, L.N. Cooper and J.R. Schrieffer, Phys. Rev. 108, (1957) 1175
10. J. Halbritter, KFZ Karlsruhe, Germany, Externer Bericht 3/69-6, (März 1969)
11. K. Mittag, Cryog. 13, (1973) 94
12. H. Diepers and H. Martens, Phys. Lett, 38A, (1972) 337
13. P. Kneisel, O. Stoltz and J. Halbritter, IEEE Trans. NS-20, (1973) No. 3, 63
14. J. Halbritter, KFZ Karlsruhe, Germany, Externer Bericht 3/72-2, (Marz 1972)
15. G. Meyer, Z. Phys. 219, (1969) 397
16. D.K. Finnemore, T.F. Stromberg and C.A. Swenson, Phys. Rev. 149, (1966) 231

SUPERCONDUCTING RF CAVITY WITH REACTIVELY SPUTTERED NIOBIUM NITRIDE SURFACES

S. Isagawa, Y. Kimura, Y. Kojima,
S. Mitsunobu* and Y. Mizumachi

National Laboratory for High Energy Physics
Oho-machi, Tsukuba-gun
Ibaraki-ken, Japan

Abstract

A technique to make a superconducting RF cavity with niobium nitride (NbN) surfaces has been developed. Niobium nitride is deposited on inner surfaces of Al and Nb cavities by the reactive dc sputtering method. The sputtering is performed by applying high voltage of about 5.2 kV between a Nb cathode and a Cu or Nb anode in an atmosphere of N_2 and Ar. The deposited NbN film is about 5 μm thick and shows a critical temperature of about 15°K. A preliminary Q measurement for a C-band NbN cavity of TE_{011} type gives $Q = 0.9 \times 10^7$ at 4.2°K.

Introduction

Aiming at the construction of superconducting linear accelerators, considerable amount of theoretical and experimental works have been done to develop a superconducting surface. By these works niobium has been found to be the most favorable material, but a technique to form stable surfaces has not yet been established. Recently niobium nitride (NbN) has attracted special attentions on stabilizing Nb surfaces. For example it is formed by nitriding Nb surfaces and expected to work as a very thin protecting layer.[1,2,3] However, NbN itself is also a very interesting superconductor.[4,5,6] There are many phases of niobium nitride and some of them show very high transition temperatures as given in Table 1. Although superconductor with high T_c has not always low RF surface impedance, higher T_c is desirable. RF characteristics of NbN films are not clear now.

To investigate a use of NbN as a stable RF superconducting material, we have developed a reactive dc sputtering technique to form thick NbN layers on inner surfaces of Al and Nb cavities. In this paper we describe details of the NbN deposition method and a preliminary result on the Q measurement for a C-band TE_{011} cavity with NbN surfaces sputtered on Nb substrates.

Deposition of NbN on Cavity Surface

Reactive dc Sputtering Method

In the reactive dc sputtering method, glow discharge is built up in an atmosphere of N_2 and Ar between a Nb cathode and a Cu or Nb anode. Niobium is sputtered from the cathode and reacts with N_2 on a substrate surface. The apparatus is schematically shown in Fig. 1. The sputtering process is done as follows. First of all the system is pumped to ~10^{-6} Torr. Then N_2 and Ar gases are introduced and the discharge is turned on. Initially the substrate is covered by an Al shutter for 2 ~ 3 hours. This presputtering process is necessary to clean the surface of the Nb cathode and to warm up and bake out the apparatus. Finally the shutter is removed and deposition on the substrate is carried out. Small pieces of glass plate are placed for reference at the side of the substrate to know the thickness and critical temperatures of the deposited films. The deposited film is required to have high T_c, thickness of about 1 μm and uniformity over the substrate surface. Sufficient film thickness (much larger than the penetration depth) is necessary since the initially deposited part of film contains a great deal of impurities than the later deposited one.[7,8,9] Superconducting properties of the film depends greatly on the gas pressures and discharge voltage. Moreover, the geometrical disposition of the electrodes and substrate must be carefully arranged to obtain uniform film over the cavity surface. We have made systematic studies of the substrate materials and sputtering techniques.

Materials for the Substrate

This method was originally developed for the deposition on small glass plates. We must use metal substrate to make RF cavities. It must have
(1) low vapor pressure at deposition temperature (200 ~ 500°C),
(2) high thermal conductivity at liquid helium temperature, and
(3) no residual magnetization.
Copper, aluminum and niobium satisfy these conditions. However, we found that NbN film deposited on copper came off like blisters when it was taken out of the vacuum and left in the air (Fig. 2). The poor adhesion between NbN and Cu substrate will be due to the difference of thermal expansion coefficients. When aluminum is used for the substrate, some chemical reaction seems to occur on the aluminum surface under the deposited film. A number of white spots appear uniformly on the surface. In microscope these spots look like transparent glass beads, and we can observe slow growth of these spots. It seems that they come from the oxidization of aluminum through pin holes in NbN film. The growth of white spots can be inhibited by anodizing surfaces of Al substrates before deposition of NbN. The proper thickness of the anodized layer is found to be about 3 μm. A good NbN surface has been obtained for Nb substrate. In the case of Nb substrate the deposition temperature can be made as high as 500°C. The high deposition temperature is one of the essential conditions to make high T_c NbN films.[9,11] For NbN layers formed on Nb material, we have not found such problems as described above. Figure 2 shows a photograph of NbN films sputtered on Cu, Al and Nb substrates.

Film Deposition on Plain Substrate

Figure 3 shows the apparatus to sputter NbN on plain substrates. The distance between cathode and substrate surface is taken to be about 3 cm.[10] Substrates were heated up to 350°C with a stainless steel wire heater before presputtering, and kept at about 400 ~ 500°C during discharge. Our sputtering conditions are as follows.

Presputtering time	-4 hrs.
P_{N_2}	-9.5×10^{-5} Torr
P_{Ar}	-5.3×10^{-2} Torr
Target potential	-5.2 kV
Discharge current	-35 mA
Deposition time	-3 hrs.

For NbN films sputtered on the Al plain substrate, we have measured transition temperature (T_c), transition temperature width (ΔT_c), resistance ratio (β =

---

* Laboratory of Nuclear Science, Tohoku University

$R_{300°K}/R_{77°K}$), and film thickness (t) as a function of the distance along the radial direction from the center of the disc substrate. An example of the data is shown in Fig. 4. Thickness, T_c and β tend to decrease and ΔT_c slightly increases as the distance increases. Critical temperatures of the films are close to, or as high as those of the bulk materials; the highest value is $T_c = 14.8°K$ and the dispersion is rather small. The fact that the onset of a plateau is located near the wall position of our cavity is most favorable.

Film Deposition on Inner Surface of Cylindrical Substrates

The substrate is a hollow cylinder with an inner diameter of 60 mm and a length of 65 mm. In this case the coaxially disposed electrodes were used (Fig. 5). The cylindrical substrate was used as the anode at earth potential and a niobium rod of 10 mm in diameter was used as the cathode. Figure 6 shows the data of the films deposited on Al substrates by this method at the following pressure and voltage conditions.

No. of curves	1	2	3	4
Presputtering time (hrs.)	4	3	3	3
P_{N_2}	0	4.5×10^{-5}	9.6×10^{-5}	9.4×10^{-5}
P_{Ar}	5.5×10^{-2}	5.5×10^{-2}	5.5×10^{-2}	8×10^{-2}
Target potential (kV)	4.6	5.4	5	2
Discharge current (mA)	18	18	15	18
Deposition time (hrs.)	1 44	4	4	$4\frac{1}{4}$
Substrate temperature (°C)	335	335	325	325

Curve 1 corresponds to the data for sputtering of Nb in a pure Ar atmosphere. The degradation of T_c of the curve 4 is probably due to the low target potential.

Preliminary Results on Q Value of the NbN Cavity

Using the reactive dc sputtering method described in the previous section, we have constructed a C-band NbN cavity of TE_{011} type. The NbN layer of about 5 μm thick is formed on the inner surfaces of the Nb cavity. The cavity consists of three parts, a hollow cylinder (inner diameter = 60 mm, length = 65 mm) and top and bottom plates. A photograph of the cavity is shown in Fig. 7. To investigate RF superconducting properties of the NbN cavity, the Q value has been measured at 6.512 GHz by using the decrement method. In the preliminary experiment an unloaded Q value of 0.9×10^7 has been obtained at 4.2°K in the low RF power region. Improving the deposition technique and also the microwave and low temperature systems to measure Q values, we are making further experimental studies on NbN cavities.

Acknowledgement

The authors wish to express their thanks to Professor Y. Onodera and Dr. T. Yamashita of Research Institute of Electrical Communication of Tohoku University for their kind helps and encouragements. They also thank Messrs. G. Oya, K. S. Keskar and S. Kohsaka for their helpful discussions and technical aids.

References

1) J. M. Dickey et al.: Phys. Letters 32A, (1970) 483

2) M. Strongin, H. H. Farrell, H. J. Halama, O. F. Kammerer, C. Varmazis and J. M. Dickey: Particle Accelerators 3, (1972) 209

3) P. B. Wilson: SLAC-TN-71-7, May 1971

4) T. Mitsuoka, T. Yamashita, T. Nakazawa, Y. Onodera, Y. Saito and T. Anayama: J. Appl. Phys. 39, (1968) 4788

5) G. Oya and Y. Onodera: J. Vac. Science Techn. 7, (1970) 544

6) B. W. Roberts: Progress in Cryogenics IV

7) J. R. Gavaler, M. A. Janocko, J. K. Hulm and C. K. Jones: Superconductivity, ed. by F. Chilton, 585 (1971)

8) J. R. Gavaler, J. K. Hulm, A. A. Janocko and C. K. Jones: J. Vac. Science Techn. 6, (1969) 177

9) C. A. Neugebauer and R. A. Ekvall: J. Appl. Phys. 35, (1964) 547

10) Symposium on the present situation and the future of superconductivity, 1970, Tohoku University

11) H. J. Spitzer: J. Vac. Science Techn. 9, (1972) 333

Table 1 Stable Phases of NbN_x and T_c

NbN_x	Crystal Structure	T_c (°K)
NbN	whiskers	10 - 14.5
NbN	diffusion wires	16.1
NbN	film, cubic, f.c.	6 - 9
$NbN_{0.824-0.988}$	film, cubic, f.c.	14.4 - 15.3
$NbN_{0.70-0.795}$	cubic, tetragonal	11.3 - 12.9
$NbN_{0.91}$	cubic, tetragonal	~16
Nb_xNO_y	cubic, f.c.	13.5 - 17.0
Nb-N-C		~17
Nb-Ti-N		~18

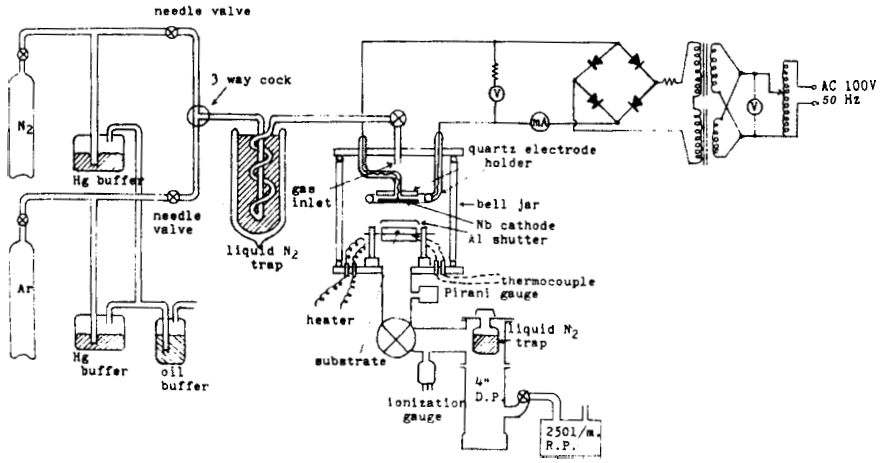


Fig. 1 Apparatus for reactive dc sputtering.

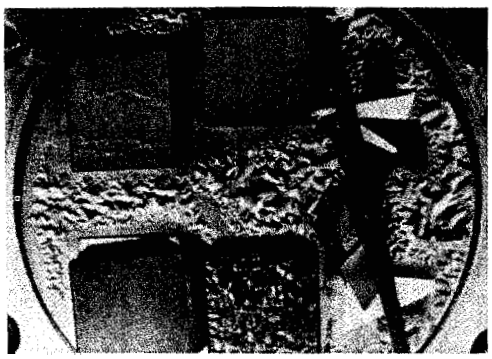


Fig. 2 NbN films sputtered on various substrates.

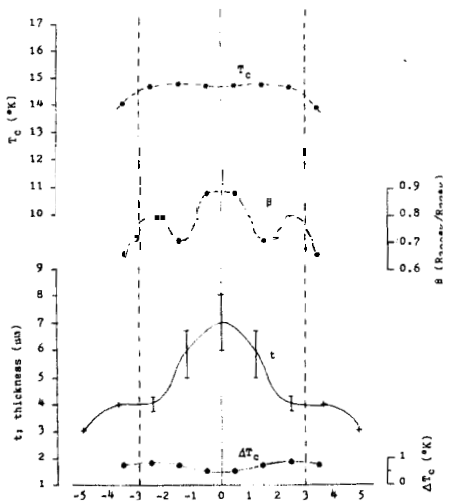


Fig. 4 Characteristics of the NbN film deposited on the Al disc substrate measured along the radial direction. Vertical broken lines indicate the boundary of the C-band TE_{011} cavity.

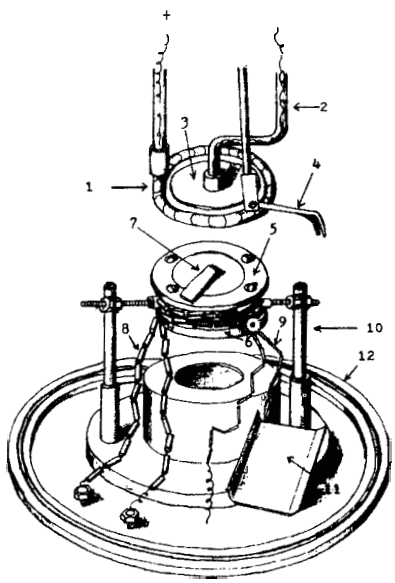


Fig. 3 Apparatus for reactive sputtering on plain substrates (1-anode, 2-cathode, 3-fused quartz cover under which Nb cathode disc is suspended, 4-magic hand, 5,6-substrates, 7-glass slide substrate for monitoring, 8-stainless steel wire heater, 9-thermocouples, 10-substrate holder, 11-Al shutter, 12-vacuum flange).

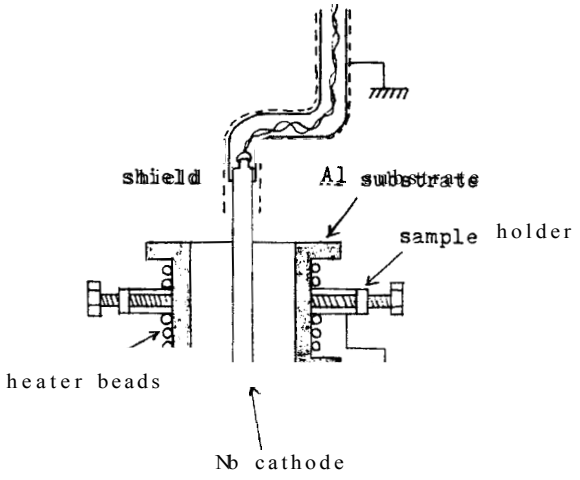


Fig. 5 Apparatus for reactive sputtering on cylindrical substrates.

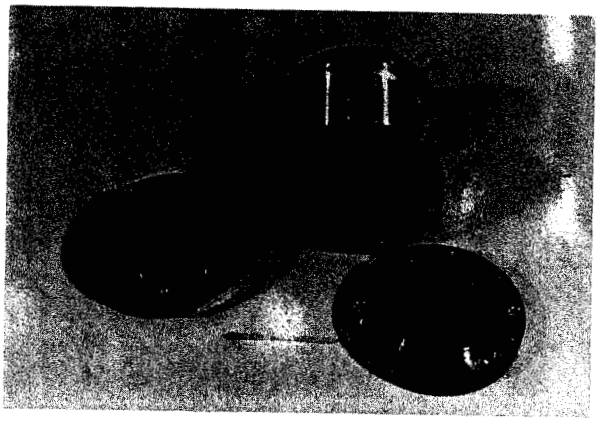


Fig. 7 C-band TE_{011} cavity with reactively sputtered NbN surfaces.

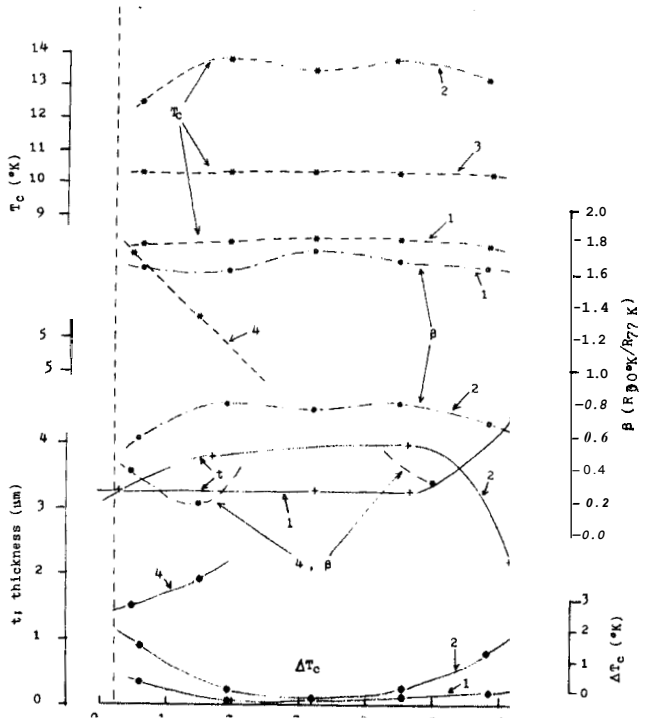


Fig. 6 Characteristics of the NbN film deposited on the inner surface of the Al cylindrical substrate measured along the axial direction. Vertical broken lines indicate the boundaries of the C-band TE_{011} cavity.

A 6-PASS MICROTRON USING A SUPERCONDUCTING ELECTRON LINAC

A. O. Hanson, J. R. Harlan, R. A. Hoffswell, D. Jamnik* and L. M. Young
University of Illinois, Urbana-Champaign, Illinois U.S.A.

Summary

Electrons have been recirculated six times through a 1.5 meter superconducting linac to a final energy of 19 MeV with an energy resolution of 0.1 percent. The recirculation system is based on a racetrack microtron arrangement. Novel features include active reverse magnetic field clamps at the entrances to the turn-around magnets to compensate for the vertical defocusing by the fringe fields, cylindrical lenses for vertical focusing on the return paths, and a phase adjusting bypass to guide the first return beam around the cryostat. At this time the system is operated about 40 hours per week with a three pass beam of 5 microamperes at 9.5 MeV for resonance fluorescence, photon scattering, and photofission experiments.

Introduction

The design of a 600 MeV microtron to guide electrons through a 30 MeV superconducting linac for 20 passes was discussed in previous reports[1]. Experience in recirculating electrons three times through a superconducting linac was described about a year ago together with plans to extend the system to six passes[2]. The six pass system has been completed and it has been operated to produce an electron beam for experimental purposes.

General Arrangement

A plan view of the linac cryostat and the associated recirculation system is presented in Fig. 1. Electrons of 270 keV are chopped, bunched, and deflected onto the linac axis where they are accelerated to 0.7 MeV by 3/2 λ section and to 3.5 MeV by the 13/2 λ section. Since the effective phase difference between the two sections is about 70 degrees for the return beams, little energy is contributed by the 3/2 λ section and the energy gains on the subsequent passes is only 3.1 MeV.

The recirculation system in its present form is shown to scale in the figure. It can be seen to be terminated by uniform field magnets whose pole pieces are 114 cm wide and 56 cm deep. The active magnetic clamps extend along the entire entrance edge of the turn-around magnets and provide a reverse field of about 10 percent of the main field to compensate for the defocusing of the fringe fields as well as some additional vertical focusing. There are a number of cylindrical lenses made up of uniform field triplets which are useful in adjusting the vertical focusing on the separate return paths. One can identify the bypass for the first return beam which also provides for a phase adjustment of 40 to 160 degrees in its return path. A bypass of only 4 degrees carries the second return beam around the other side of the cryostat. The special features of these components were described briefly in the previous report on recirculation[2]. All the magnets in the system are simple rectangles which have a focusing effect only in the vertical direction. The horizontal focusing takes place only on the common linac axis by means of the linac fields and by two quadrupole singlets at the ends of this axis.

The phases of the returning first, second, and third pass beams are adjusted by means of the bypass angle, the magnetic field in the end magnets, and the spacing between them. The return phases of the fourth and fifth pass beams need only small corrections which are made with pole face currents affecting the magnetic fields in strips covering only the outer portions of their semicircular paths.

The beam, after 3, 4, 5, or 6 passes through the linac can be deflected by 17 degrees into a common channel leading to the two 36.5 degree rectangular magnets which bend the beam into the experimental area. These exit magnets have no horizontal focusing and their spacing is adjusted to remove the focusing in the vertical direction. The exit magnets have a useful dispersion of 30 mm for a 1 percent momentum change at a point about 2 meters away.

By observing the structure of the beam on a view screen at this point it is usually possible to adjust the phases of the return beams to reduce the energy spread in the beam to less than 0.1 percent. Optimization of the adjustments, however, is not straightforward since the phase adjustments for the first three returns are interrelated and can be optimized only by successive readjustments of a number of components.

Computer Simulation

The beam optics of the system can be presented most easily by a computer simulation in which beam is taken step by step through each element with its location and field given by the actual operating conditions. Trajectories simulated for a linac energy gain 0.4 percent above the nominal gain are shown in Fig. 2. The rays start at the linac and emerge at the next vertical line. The rays enter the end magnet at the second line and emerge from the opposite magnet back onto the linac axis on the third. Two rays, one starting 2 mm off the axis and the other on the axis at an angle of one milliradian, are shown to illustrate the nature of the trajec-

tories. The beam can be seen to be rather strongly confined in the vertical direction. The narrow excursions from the nominal return lines in the horizontal plane are associated with the bypasses, the inflector triplet and the cylindrical lens triplets. The inflector triplet introduces recurrent vertical focusing on the linac axis and compensates to some extent for the vertical defocusing of the quadrupole singlets. The discontinuities in the horizontal trajectories, on the bypass and other return paths, are associated with the 0.4 percent mismatch in the energy gradient.

The phases at which the beams return to the linac as referred to the phase at which the energy gains would be a maximum are shown in the center part of the figure. In the simulation as well as in the actual operation of the system it is possible to find nominal return phases which reduce the energy spread associated with small variations in input phase and in the energy gain in the linac. Even for the small number of returns represented by this system the optimization is reflected by the fact that the return phases oscillate about an average value. The phase changes in the simulation are not ouite typical since the energy gain mismatch is very large.

Operating Experience

The 3/2 λ and the 13/2 λ niobium sections have operated reliably without disassembling the cryostat and without any major difficulties for about two years. These sections which were processed only by chemical polishing had initial Q values above 10^8 but now have values of $4\ 10^7$ and $8\ 10^7$ respectively. These are operated at 4.2 K with energy gains of 2 MeV per meter and would require 100 watts of cooling at that temperature if operated continuously. The practical duty factor is limited to 40 percent by the capacity of the refrigerating system.

The liquid helium for cooling the linac is supplied by an 8 liter per hour helium liquefier which can supply 800 liters of liquid helium per week. Of this amount about 400 liters per week are spent in supplying the standby losses. The remaining 400 liters per week are used in operating the linac about 40 hours per week with a 40 percent duty factor. The cryostat is filled twice a week with a maximum of 400 liters which initially covers the niobium structure by 30 cm. The cooling available from the liquid is enhanced by a factor of 4 by a heat exchanger mounted at the top of the cryostat which utilizes the cooling supplied by the escaping vapor. At 40 percent duty an average of 40 watts are required which boils off 10 liters of liquid per hour. The heat exchanger required a flow of 10 standard liters per second of helium gas entering the top of the heat exchanger at 12 atmospheres.

When the linac is operated routinely the gas flow through the heat exchanger is adjusted to maintain its top temperature near to the room temperature. When so adjusted the linac structure can be operated without adjusting the tuning between sections for several hours. Operation can be continued at the same duty factor until there is essentially no liquid helium left in the cryostat. Apparently the 40 watts of cooling required by the structure at 4.2 K is supplied without liquid contact with the niobium.

Recirculation of the electron beam has been straightforward with no major difficulties. There are, however, many magnetic elements which must be precisely adjusted to control the sizes, positions, and phases of the returning beams at critical points. The optimization of these elements is complicated by the many adjustments which interact and it requires a highly skilled operator to set up the system. When it is optimized the beam has often remained stable and reliable on an experimental target for several hours without operator intervention. Under these conditions the beam is confined within a radius of 6 mm in any of the 6 meter straight sections in the return paths and there is no loss of beam in the recirculation system.

Plans

We are presently involved with the installation of a larger system using a 3 MeV Van de Graaff as an injector. The superconducting linac will be a 6 meter section that is being made for us at Stanford University using their designs and facilities. The initial recirculation system will be similar to the one described here. If larger end magnets could be obtained the system could be expanded to handle 10 to 20 passes in a straightforward way.

Acknowledgements

We want to express our appreciation to C. McGuire, H. Miller and D. Vermillion for their assistance with the operation and maintenance of the microtron and to F. Witt who has been responsible for the operation of the cryogenic system.

The work has been supported in part by The National Science Foundation,

References

* Permanent address, Institute Josef Stefan, Ljubljana, Yugoslavia.

1. J. S. Allen, P. Axel, A. O. Hanson, J. R. Harlan, R. A. Hoffswell, D. Jamnik, C. S. Robinson, J. W. Staples, and D. C. Sutton. Particle Accelerators 1, 239-245 (1970). See also, Proceedings of the 7th International Conference of High Energy Accelerators, Aug. 29, 1969, p. 284-290.

2. L. M. Young, IEEE Trans. Nucl. Sci. NS-20, 81, (1973).

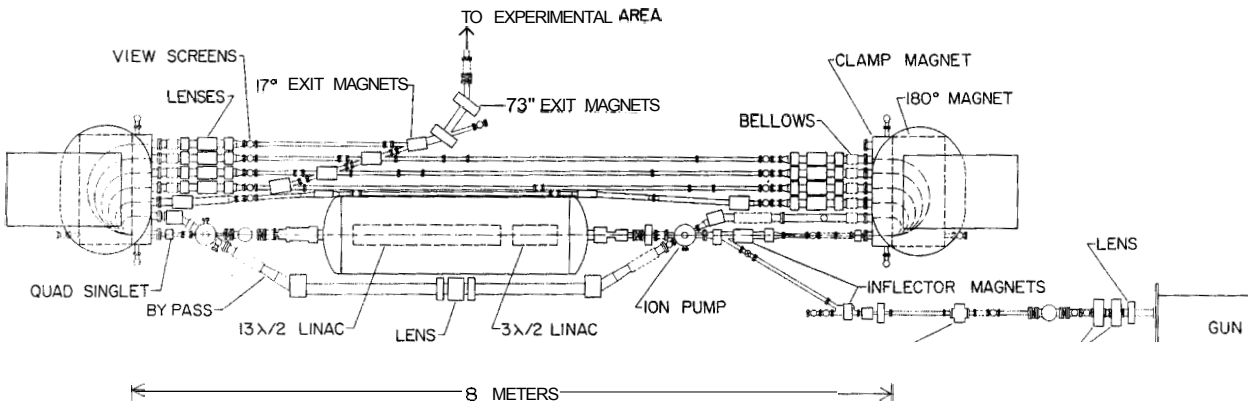
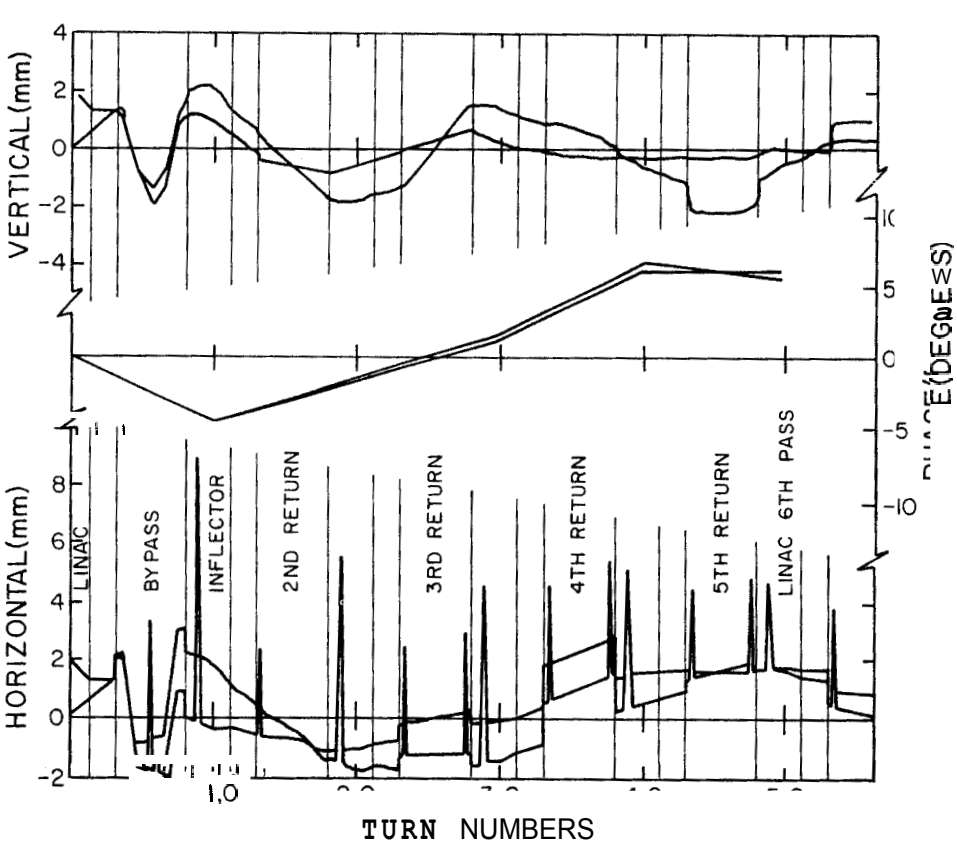


Fig. 1, Experimental arrangement of the six pass microtron.



Magnet Separation
790.82 cm
Magnet Fields
1268.7 gauss
Clamp Fields
-11.46 percent
Strip Fields
1.32 percent
2.04 percent
Phase Between Linac Sections
30 degrees
Injection Phase
-53 degrees
Bypass Phase Advance
100.6 degrees
System Optimized For
Linac Energy Gradient
1.968 MeV/meter
Nominal Final Energy
18.247 MeV
Linac Energy Gradient
1.976 MeV/meter
Energy Gains

inject.	0.270 MeV
1st	3.394 MeV
2nd	2.959 MeV
3rd	2.949 MeV
4th	2.927 MeV
5th	2.861 MeV
6th	2.885 MeV
total	18.244 MeV

Fig. 2. Simulation of trajectories in the six pass mlcrotron for a linac energy gain 0.4 percent above the nominal value. The narrow excursions are associated with the inflector and the cylindrical lens triplets. The phase is referred to the phase for maximum energy gain on each pass.

DEVELOPMENT AND TESTING OF A PROTOTYPE SUPERCONDUCTING RF SEPARATOR

A Carne, R G Bendall, J R J Bennett, B G Brady, J A Hirst and J V Smith

Rutherford Laboratory, Chilton, Didcot, Oxon. England

1 Introduction

For several years the Rutherford Laboratory has been developing superconducting RF Separators, the main purpose of which was to provide separated kaon beams from Nimrod, in the 2-4.5 GeV/c momentum range. During 1971 tests were performed on a 2-cell full scale frequency model cavity[1]. The results were sufficiently encouraging to warrant proceeding to a full size operational 'prototype' separator to be developed and tested as the first stage of a possible 2-cavity RF separated beamline. The superconductor chosen was lead, electrodeposited onto an OFHC copper substrate. Tests with the prototype have confirmed that lead can sustain the fields required for an operational separator. It is the purpose of this paper to describe some of the aspects of the design and development of the prototype separator, the tests and results obtained.

2 Cavity and Cryostat

The cavity in its cryostat is shown schematically in Figure 1. The cavity contains 10 cells (in three sections of 3, 4 and 3 cells) operating in uniform periodic π-mode, $v_{ph} = c$, frequency 1.305 GHz. Main parameters are:

Aperture 2a	=	10.5cm
Disk thickness t	=	3.95cm
Outside diameter 2b	=	26.172cm
Cell length $D = \lambda_o/2$	=	11.53cm
Aperture radius curvature = t/2	=	1.975cm
Radius curvature disk/outer wall	=	1.588cm
Q_o(Cu,300K)	=	2.37×10^4
η/Q	=	$0.409 \times 10^3 \Omega/m$
E_p/E_o	=	3.83
H_p/E_o	=	145 G/MV/m
E_o	=	2 MV/m

The low frequency and large aperture were dictated by the need for large acceptance for Nimrod secondary beams. Operation in π-mode was chosen since it gives maximum shunt impedance in standing wave, least peak surface magnetic (H_p) and electric (E_p) fields, and least number of disks. The main disadvantage of tight dimensional tolerance is hardly met in this 10-cell structure[2]. The choice of disk thickness was made to minimise H_p and E_p[3], but also to anticipate any degradation of Q-value due to non-linear dependence of surface resistance on field amplitude[4]. Thus a compromise value t = 3.95 cm was chosen. The radius of curvature was simply t/2 at the disk aperture; at the junction of disk to outer wall it was made as large as possible to ensure good plating. The length of the end cells was chosen to cancel the reactive loading of the beam pipes (of diameter = 2a = 10.5 cm), and extended the length of the terminal half cells by about 4 cm. Losses due to the end cells reduce the overall Q-value by 6% (there is also field enhancement at the adjacent disks, but this has been ignored in evaluating the results of chapter 5).

The mechanical joints between the three sections of the cavity were designed to provide simultaneously a good RF joint and vacuum seal. The joint is shown in figure 2 in its final version. The vacuum seal was provided by 1.6 mm indium wire crushed between the flexible cantilever and the opposite flange. Because of the flexibility of the cantilever the clamping force between sections was taken wholly through the RF joint. The RF joint was a simple rectangular spigot (2.25 mm by 0.13 mm) opposite a plane flange, both lead plated. The clamping force was 80% of the yield strength of copper at room temperature.

Along the top of the cavity are five ports, the central one for the RF feed, the others for two mechanical tuners, and two fine RF tuners. These components are all moveable to vary the coupling to, or tuning of, the cavity, and are controlled from stepping motors mounted in a rigid 'A' frame above the cryostat. Beneath the cavity are two fixed RF sampling loops. All RF components were designed to give a good match (with VSWR < 1.03), and utilize choke joints to give low RF and thermal loss. As a typical component the RF feed is shown in some detail in figure 3. Heat loss was reduced by the use of a choke joint on the inner conductor, and thin-wall stainless steel on the outer. There are two coaxial vacuum windows of ultra-pure alumina, the lower one being clamped by copper braiding to the liquid nitrogen shield at 77 K to provide a thermal conduction path for the coupling loop. The overall VSWR of the RF feed assembly was 1.2, the RF loss was 17 mW/W of transmitted RF power, and a coupling range of 10^4 was available. The RF feed transmitted up to 300 W without breakdown. The operation of the tuners is discussed in chapter 4. The total thermal load of the above components was about 0.12 W to liquid helium.

The cavity is immersed in a bath of liquid helium and surrounded by an evacuated cryostat with super-insulation and a liquid nitrogen shield to reduce the heat load to liquid helium. Ten layers of super-insulation were used between the helium container and the liquid nitrogen shield, fifteen layers between the liquid nitrogen shield and the outer vessel. Additionally there were two mu-metal shields to reduce the ambient magnetic field to less than 10 mOe in the vicinity of the cavity. All RF and cryogenic components were clamped to the liquid nitrogen shield to reduce the conductive heat load to liquid helium. The helium container and shields were suspended from the flat lid of the cryostat in a cradle of thin stainless steel wires which were adjustable from the outside for alignment purposes. The beam pipe connections to the outer vessel were thin-wall stainless steel bellows, with an inner copper shield held at 77 K to reduce the radiation load. The total thermal loads were about 20 W to liquid nitrogen and 1-2 W to liquid helium.

In the test arrangement for the cavity the temperature of the helium was reduced below 4.2 K by pumping on the liquid through the horizontal 'culvert'. A small heat exchanger and Joule-Thomson valve were incorporated to augment the refrigeration available from the pumps to about 7 W. This low value limited the duty cycle available in the tests described in chapter 5. In operation in a beamline, this system would be replaced by a refrigerator, with the culvert carrying the liquid and return gas,

3 Brazing, Plating and Assembly Stages

To facilitate plating, the OFHC copper cavity was built in three sections, one of four, and two of three

cells. External diameters of the cells were machined to the same dimensional tolerances ($\sim 5 \times 10^{-3}$ mm) as the internal ones, so the cells of a section could be properly aligned using external jigs. The brazing metal (copper-silver eutectic, MP 778° C) was chosen so that no spillage occurred during vacuum brazing, to reduce the risk to the eventual lead plated surface. Many tests were performed to determine the correct quantity of eutectic, the condition of the flat mating surfaces, and the optimum temperature cycle for brazing.

The open-bath plating system used earlier[1] had several disadvantages, not least of which was the risk of contamination of the plated surface from either the atmosphere or dust during transfer operations. To overcome these risks the enclosed plating system was developed, shown schematically in figure 4. The various liquids which are stored in closed polythene tanks are piped to a common control, whence they are fed via a manifold and flexible pipe to the cavity section. The cavity section acts as its own plating bath, and only the internal surface is involved in any process. The solutions are driven round the system by pure nitrogen gas. Nitrogen is also bubbled through the solutions in their tanks to remove dissolved oxygen, since it is believed that the oxygen in the final water washes in particular is one of the causes of staining.

Once the whole plating process was started, the internal surfaces were never exposed to the atmosphere. All filling, emptying and eventual drying of the cavity section were done with the cavity axis vertical. At each stage, gas bubbles were removed from the liquid by agitation and evacuating the space above the liquid in the domed end-cap. This was particularly important for removing trapped bubbles on the horizontal undersides of the disks. The actual lead plating was done with the axis horizontal, the cavity section rotating about the fixed anodes.

The anodes themselves were made of 6 N's pure lead, and bagged in fine weave crimplene. An anode was wedge-shaped in the plane parallel to the disks, and shaped to follow an equipotential surface in a plane perpendicular to the disks. This shape was obtained using a computer program[5], and verified using an electrolytic tank. In the plane perpendicular to the disks the field was uniform within the ratio 1.3:1, and this set the limit to the uniformity of plating thickness. In each cell 5 anodes were used, the resulting variation of field around a circumference being 11.2:1. With the cavity section rotating about the anodes, this allowed a peak current density 2.69×10^{-3} A/cm^2, considered optimum, yet with a continuing deposition at field minima. A mean thickness of 1.25×10^{-2} mm of lead was deposited.

Fuller details of the plating system and schedule are to be given in a separate paper[6], suffice it here to report the final lead plating was bright, smooth, fine grained (~ 1 mm^2) and free of blemishes. When the plating system was fully developed, a successful plating could be achieved at the first attempt. Indeed the confidence in the plating system has become such that it is believed a successful plating could be obtained in the whole 10-cell cavity, obviating the need for the inter-section joints.

After plating and vacuum drying, each cavity section was let up to pure nitrogen in a glove box, and the lead surface inspected using mirrors. After inspection, each section was blanked-off and mounted on a specially prepared lathe bed. The sections were aligned on the lathe bed to a tolerance 2×10^{-3} mm on radius, after which the whole system was enclosed by a perspex glove box cover and the enclosed atmosphere changed to pure nitrogen. The blanking plates were removed and the sections hydraulically rammed together and bolted using precalibrated brass bolts and load washers. After this stage the lead plated beam pipes, RF samplers, and temperature monitoring resistors were added, and the whole slid into the helium container. The top RF components were fitted, and the cryostat was built up to the completed assembly described in chapter 2. At no time from the beginning of the plating process to the completed assembly of the cavity in the cryostat were the lead surfaces exposed to the atmosphere.

Prior to cooldown the cavity and external beam pipe assemblies were evacuated to a pressure typically 1.5×10^{-7} torr, from which pressure less than 1 monolayer of residual gas condenses on the lead surface. The cryostat insulation vacuum was typically 1.0×10^{-5} torr.

4 RF System

Dynamical requirements of a 2-cavity RF separated beam calls for an amplitude stability $(\delta A/A) < 1\%$, and a frequency stability $(\delta\omega/\omega) < 3 \times 10^{-10}$ with corresponding phase errors <2° per cavity, <6.7° between cavities. With a cavity loaded Q-value 5×10^7 an incident power of 200 W per cavity is required. An RF system based on a single power source and output split to feed the two separately controlled cavities has been developed and is shown schematically in figure 5.

A solid state voltage controlled oscillator was phase locked to a reference oscillator having a stability $< 2 \times 10^{-10}$. The output of the VCO was controlled by a PIN diode modulator. A TWT amplifier (gain 30 db, 20 W output) was used as a driver for the single 3-cavity CW klystron power amplifier. The RF output level was sampled by a directional coupler and crystal detector. The crystal output voltage was compared with a reference voltage in an ALC unit. The resultant error signal was amplified and used to vary the bias current in the PIN diode modulator to regulate the drive power to the klystron. The reference voltage could be switched between zero and any required level to pulse modulate the RF supply. An output power of 800 watts into 50Ω, with amplitude stability <0.6%, was available from this stage, adequate for two cavities and transmission losses. The output power was split by a T-section variable power divider between the prototype separaior and a matched load for the tests described in chapter 5.

Cavity phase must be correct to within 2°, ie, 0.45 Hz at 1.3 GHz. This is achieved by tuning a cavity to the standard reference frequency by means of a) mechanical plungers (coarse tuners), position controlled by stepping motors, and b) reactive loading by varactor diodes (fine tuners). The mechanical tuners were measured to have a linear tuning range of 160 kHz per 5 cells, four times that needed from cavity dimensional tolerance requirements, and a sensitivity 1.8 Hz per step (6×10^{-5} mm) per 5 cells. The fine tuners were varactor diodes tightly coupled to the cavity, their tuning range depending on total power loading. For cavity powers corresponding to $E_0 = 2$ MV/m, the tuning range was found to be 1-2 Hz per tuner per 10 cells, with a sensitivity about 0.5". Phase detection was taken from forward and refiected power in the main feed via a bridge circuit. Control to the required 2° was through the varactor diode tuners, overlapped by the mechanical tuners for greater phase errors.

Amplitude control of a cavity was obtained by using a multiple 4-arm bridge network, with a varactor diode and 3-port circulator to control phase between bridges. A field level signal taken from a fixed sampling loop, was rectified and compared with a standard d.c. reference, the resultant error signal being used to vary the bias on the varactor diode. In principle, a system using 4:1 bridges should be able to control power from P_o to 0.85 P_o, however due to losses in the various components a power range P_o to 0.93 P_o was obtained, with the varactor diode absorbing about 1½% of the forward power.

5 RF Tests

Three series of tests have been performed, though the results reported here are mainly from the third. In the first series of tests, a low power Q-value 1.5-2.0 x 10^8 at 2.0 K, and fields up to $E_o \sim 1$ MV/m were obtained. Precise high power measurements were limited by the low E-field coupling of the RF feed. The mechanical tuners performed satisfactorily, giving the expected tuning range of 160 kHz, though it was suspected the RF dissipation was a little high. The RF feed has been modified to a loop as shown in figure 3, giving coupling factors up to 100 in the expected Q-value range. The mechanical tuners have been modified to reduce the possibility of high order coaxial mode excitation. In the second series of tests the Q-values were poor due to the inter-section joints becoming distorted. On examination the joints were found to be distorted in the plane parallel to the disks, and oval up to 2 x 10^{-1} mm on diameter. The joints were modified as shown in figure 2, and remachined flat, requiring a reduction in the coupling cell lengths of 1.8 x 10^{-1} mm (with a resultant field distortion of less than 1.5%, an effect which has been ignored in the calculations below); but nothing could be done about the ovality, and this inevitably contributed to the actual Q-values obtained.

For the third series of tests, the initial room temperature cavity vacuum was 1.5 x 10^{-7} torr. No vacuum leaks were encountered on cooldown to 1.85 K or during the tests, though there were large pressure excursions on cooling to 77 K with liquid nitrogen. These were thought to be due to movement of the beam-pipe joints, the inter-section joints being too massive to be affected. On cooling through the critical temperature of lead, the temperature differences across the cavity were 0.16 K, 0.05 K, 0.04 K for the three runs comprising the third series. Between runs the cavity was warmed to 77 K, as would happen in normal standby operation.

In the RF measurements the RF feed and one RF tuner as a variable detector were used, and both sampler loops were terminated with matched loads. The low power asymptotic Q_L at 4.2 K was 1.31 x 10^8, which, allowing for coupling factors, was 75% of theoretical Q. At 1.85 K the highest Q_L-value was not less than 2.1 x 10^8 (the asymptotic value could not be found since it was not possible to withdraw the RF feed loop sufficiently). On the application of only a few watts of RF power the Q-values degraded permanently by a factor roughly 2½ (to 5.7 x 10^4, and 8 x 10 respectively), but remained roughly constant up to the highest cavity powers, as can be seen in figure 6. The coupling factors were measured by powering each loop in turn: thus at loop q

$$P_c = \{r_q P_{inc} - P_{refl}/r_q\} - \Sigma'_s P_{trans}/r_s \qquad \text{i)}$$

Where the transmission loss factor $r = (P_{refl}/P_{inc})^{\frac{1}{2}}$ off resonance. All powers P (except P_c) refer to the point of measurement. In the above equation the quantity $\{\}/P_c = A-Bq$, where $A \simeq 1+\Sigma\beta$. Summing over the number of loops n gives $[(n-1)A+1]$, hence A and the β's could be calculated. Although not completely consistent values were obtained in this way, it was found the sum of the coupling factors (without the RF feed which was varied) was 0.03 at 4.2 K and 0.05 at 2.0 K or less, and these values were used throughout. Low power Q measurements against cavity mode were taken at 1.85 K and 4.2 K and gave the following results, expressed as a fraction of Q_o at n-mode.

	0.9π	0.8π	0.6π	0.511
Practical	0.72	1.40	1.03	1.10
Theoretical	0.93	0.88	0.75	0.66

Due to various aspects of the cavity geometry, interpretation of these numbers is not easy, however it can be broadly stated that within a factor 2 the joints operated satisfactorily, especially with the limitations stated earlier.

Three high power runs were made, and their results are summarised in figures 6 and 7. Due to the limited refrigeration available, temperatures during the runs were not constant but lay in the ranges 2.03 K - 2.17 K, ie, just below the helium A-point (run A), 1.84 K - 2.04 K (B); and 4.2 K (C). In run A 1.5 sec pulses, 1/10 pps were used; in the other two runs 0.5 sec pulses, 1/6 pps were used. In run A, incident and reflected powers were measured by power meters, together with a calibrated crystal detector to record reflected signals

$$(P_{inc} = P_{refl}(\text{instantaneous}),\ P_{refl},\ P_e)$$

Coupling factors in the range 0.4 - 0.6 were used: β-values obtained from power meters and the crystal detector gave good agreement, improving with higher cavity powers with error less than 10%. With increasing power, some conditioning was required, by operating with short pulse, high repetition rate for a few minutes. During this run radiation levels in a horizontal plane containing the cavity axis were typically 60 - 70 mR/hr with occasional bursts to 300 mR/hr on voltage breakdown. The highest field obtained during this run was E_o = 2.07 MV/m. Field levels were obtained from

$$E_o = 0.189\ (P_c\ Q_o(H))^{\frac{1}{2}}, \qquad \text{ii)}$$

with P_c in watts, $Q_o(H)$ in units of 10^8

where the high field unloaded Q-value was obtained from $Q_L(L)$

$$Q_o(H) = (1+\beta_1+CF)\ Q_L(L)\ (P_e/P_{inc})_H^{\frac{1}{2}}/(P_e/P_{inc})_L^{\frac{1}{2}} \qquad \text{iii)}$$

where CF is the 'coupling factor' given above, and $Q_L(L)$ and $(P_e/P_{inc})_L$ were measured from decay and extrapolated (P_e/P_{inc}) values.

During run B, incident power and crystal detector signals only were measured. Higher β's (~0.8) were used to increase the cavity power. Radiation levels were lower at 10-20 mR/hr, with bursts to 80 mR/hr. The highest field obtained was E_o = 2.51 MV/m, with corresponding peak surface fields H_p = 364 gauss, E_p = 9.2 MV/m. At fields approaching E_o = 2.5 MV/m, conditioning took longer, though it is felt that with prolonged conditioning these maximum fields could have been exceeded. In all, the cavity operated for several hours at field levels greater than E_o = 2 MV/m.

With the good fields obtained, but relatively low Q-values, it was decided to try operation at 4.2 K, and the results are also shown in figures 6 and 7 (run C). The high power performance turned out to be

little worse than below 2.0 K. The highest field measured was E_o = 2.40 MV/m, limited by the available power. Again the cavity operated for several hours over 2 MV/m. The unloaded Q-value was only about 30% lower than at 1.85 K at an operating field level E_o = 2 MV/m. The thermodynamic performance at 4.2 K was little affected compared with 1.85 K. Whereas the indicated temperature rise at 1.85 K was typically 0.1 K, it was more like 0.4 K at 4.2 K, with an accompanying pressure rise up to about 2 torr. During all the power measurements some changes of frequency were seen. However, providing the temperature was well below the helium A-point the frequency appeared to be independent of cavity power, and the frequency drift could be accounted for by the slow temperature drift and the mechanical sensitivity of the structure (measured to be 5.26 Hz/torr). Around the λ-point, the frequency shift was greater, and could not be adequately accounted for either in terms of the above or skin depth, thermal expansion or non linear effects. At 4.2 K the detune occurred during the pulse (and had to be corrected), but could be again accounted for by the mechanical sensitivity.

6 Conclusions

The tests performed on the full prototype separator have demonstrated that superconducting lead electrodeposited onto a copper substrate can sustain the fields required for an operational separator. The RF system and cryostat have performed satisfactorily, and little further development is required to bring them to operational status. The results have shown that an operational field E_o = 2 MV/m is perfectly feasible, with reliable performance up to 2.5 MV/m. The limitation is possibly field emission, but conditioning could increase the operational fields. With the relatively low Q-values obtained, in part due to the distorted joints, the operating temperature could be 1.85 K or 4.2 K. Indeed there would be a major advantage that though 30% more peak power would be needed at 4.2 K with E_o = 2 MV/m, the refrigerator required would be cheaper by a factor $2\frac{1}{2}$-3. A 2-stage beamline for Nimrod operating at 2 MV/m, 0.5 second pulses, 20% duty cycle would require a refrigerator of 80-100 W at 4.2 K. Work is continuing towards such a beamline.

7 Acknowledgements

We gratefully acknowledge the contributions to this project of members of the Nimrod Design Group, Messrs. A R Mortimer, K H Roberts, D Craddock, J Rimen and G Simms; also Messrs. B J Goodenough, R Sidlow and K W Smith. We should also like to thank D A Gray for his support in this project.

8 References

1. A Carne, R G Bendall, B G Brady, R Sidlow and R L Kustom, "High Field Tests in a Model S/C RF Separator at 1.3 GHz". Proc. 8th International Conference on High Energy Accelerators, CERN. Sept. 1971.

2. P B Wilson, "Structures for S/C Electron Linacs and RF Separators". 1969 Particle Accelerator Conference, Washington DC. IEEE Trans. Nucl. Sc. NS-16(3) June 1969.

3. V Vaghin, Ph. Bernard and H Lengeler, CERN report CERN./D.Ph.II/RF-Sep. 70-2.

4. J Halbritter, "Dependence of Surface Resistance on Field Level in Pure Superconductors". KFK Report 3/70-14 and J.Appl.Physc. 41, 4581 (1970).

5. P J Stening and C W Trowbridge, "The Pathfinder Program and its Application to Ion Optics". Rutherford Laboratory Internal Report. RU/RL 1. 1968.

6. R G Bendall, A Carne and J A Hirst, "An Enclosed System for High Quality Lead Plating". To be published.

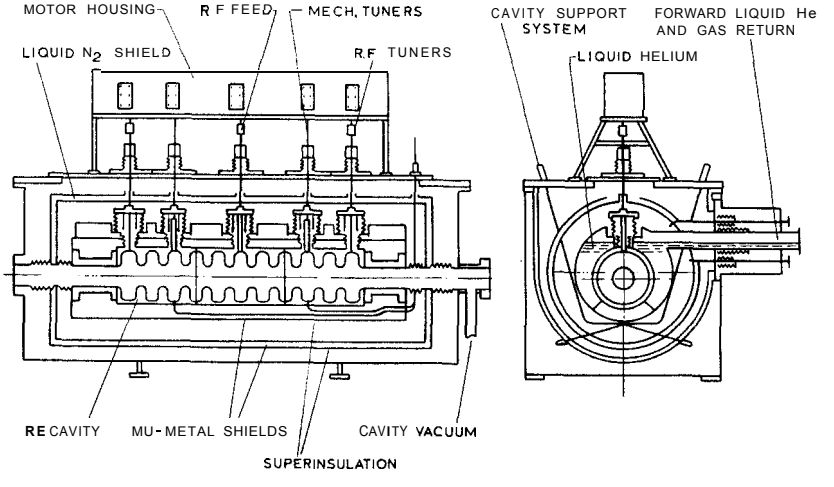


FIG 1. LAYOUT OF SUPERCONDUCTING R F. SEPARATOR CAVITY IN ITS CRYOSTAT

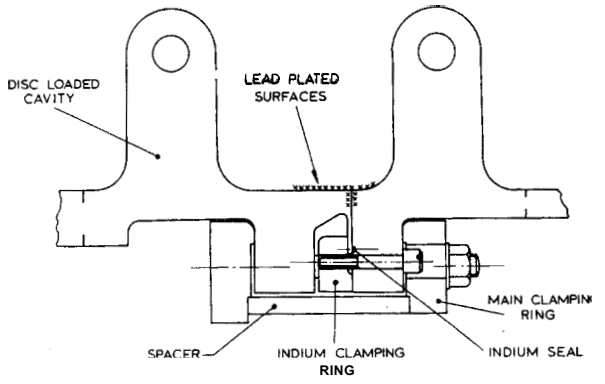


FIG 2. MODIFIED CANTILEVER JOINT.

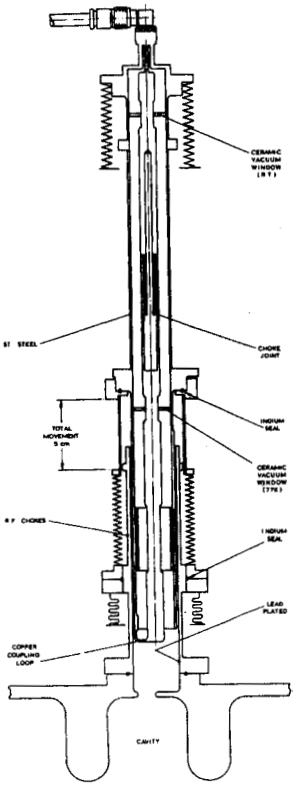


Fig 3 R.F. FEED

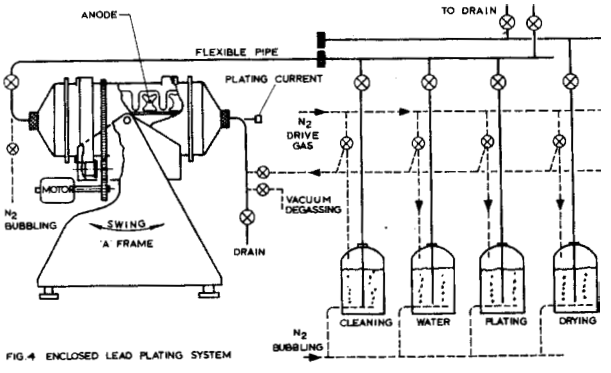


FIG.4 ENCLOSED LEAD PLATING SYSTEM

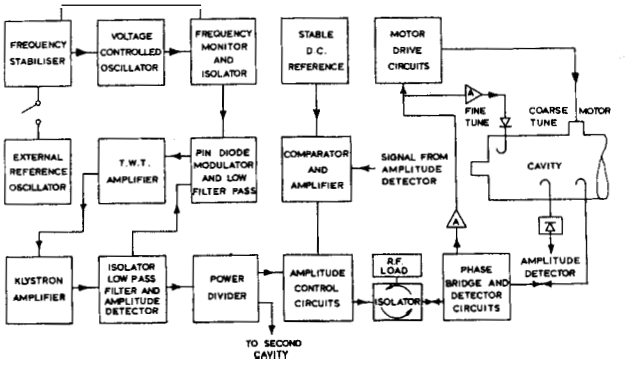


FIG.5 R.F. POWER SUPPLY AND CAVITY PHASE AND AMPLITUDE CONTROL

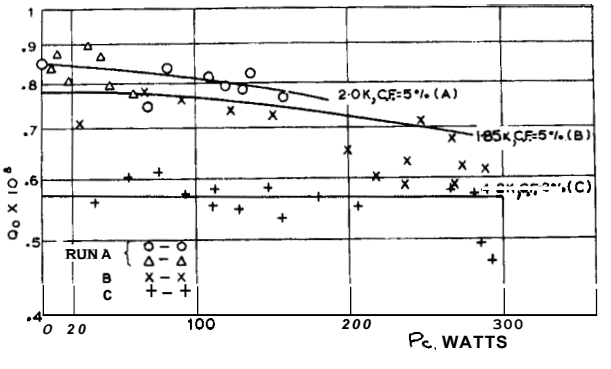


FIG.6 Q_0 AGAINST CAVITY POWER

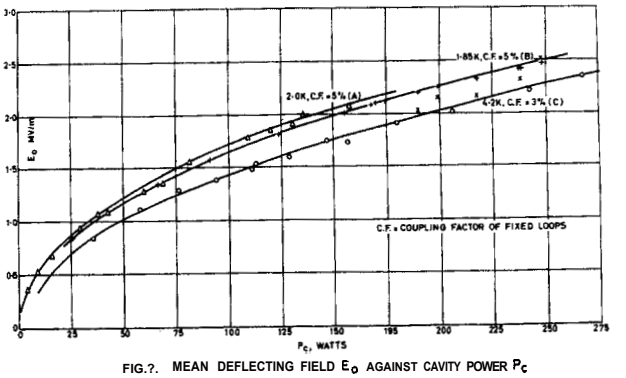


FIG.7. MEAN DEFLECTING FIELD E_0 AGAINST CAVITY POWER P_c

little worse than below 2.0 K. The highest field measured was E_o = 2.40 MV/m, limited by the available power. Again the cavity operated for several hours over 2 MV/m. The unloaded Q-value was only about 30% lower than at 1.85 K at an operating field level E_o = 2 MV/m. The thermodynamic performance at 4.2 K was little affected compared with 1.85 K. Whereas the indicated temperature rise at 1.85 K was typically 0.1 K, it was more like 0.4 K at 4.2 K, with an accompanying pressure rise up to about 2 torr. During all the power measurements some changes of frequency were seen. However, providing the temperature was well below the helium A-point the frequency appeared to be independent of cavity power, and the frequency drift could be accounted for by the slow temperature drift and the mechanical sensitivity of the structure (measured to be 5.26 Hz/torr). Around the λ-point, the frequency shift was greater, and could not be adequately accounted for either in terms of the above or skin depth, thermal expansion or non linear effects. At 4.2 K the detune occurred during the pulse (and had to be corrected), but could be again accounted for by the mechanical sensitivity.

6 Conclusions

The tests performed on the full prototype separator have demonstrated that superconducting lead electrodeposited onto a copper substrate can sustain the fields required for an operational separator. The RF system and cryostat have performed satisfactorily, and little further development is required to bring them to operational status. The results have shown that an operational field E_o = 2 MV/m is perfectly feasible, with reliable performance up to 2.5 MV/m. The limitation is possibly field emission, but conditioning could increase the operational fields. With the relatively low Q-values obtained, in part due to the distorted joints, the operating temperature could be 1.85 K or 4.2 K. Indeed there would be a major advantage that though 30% more peak power would be needed at 4.2 K with E_o = 2 MV/m, the refrigerator required would be cheaper by a factor $2\frac{1}{2}$-3. A 2-stage beamline for Nimrod operating at 2 MV/m, 0.5 second pulses, 20% duty cycle would require a refrigerator of 80-100 W at 4.2 K. Work is continuing towards such a beamline.

7 Acknowledgements

We gratefully acknowledge the contributions to this project of members of the Nimrod Design Group, Messrs. A R Mortimer, K H Roberts, D Craddock, J Rimen and G Simms; also Messrs. B J Goodenough, R Sidlow and K W Smith. We should also like to thank D A Gray for his support in this project.

8 References

1. A Carne, R G Bendall, B G Brady, R Sidlow and R L Kustom, "High Field Tests in a Model S/C RF Separator at 1.3 GHz". Proc. 8th International Conference on High Energy Accelerators, CERN. Sept. 1971.

2. P B Wilson, "Structures for S/C Electron Linacs and RF Separators". 1969 Particle Accelerator Conference, Washington DC. IEEE Trans. Nucl. Sc. NS-16(3) June 1969.

3. V Vaghin, Ph. Bernard and H Lengeler, CERN report CERN./D.Ph.II/RF-Sep. 70-2.

4. J Halbritter, "Dependence of Surface Resistance on Field Level in Pure Superconductors". KFK Report 3/70-14 and J.Appl.Physc. 41, 4581 (1970).

5. P J Stening and C W Trowbridge, "The Pathfinder Program and its Application to Ion Optics". Rutherford Laboratory Internal Report. RU/RL 1. 1968.

6. R G Bendall, A Carne and J A Hirst, "An Enclosed System for High Quality Lead Plating". To be published.

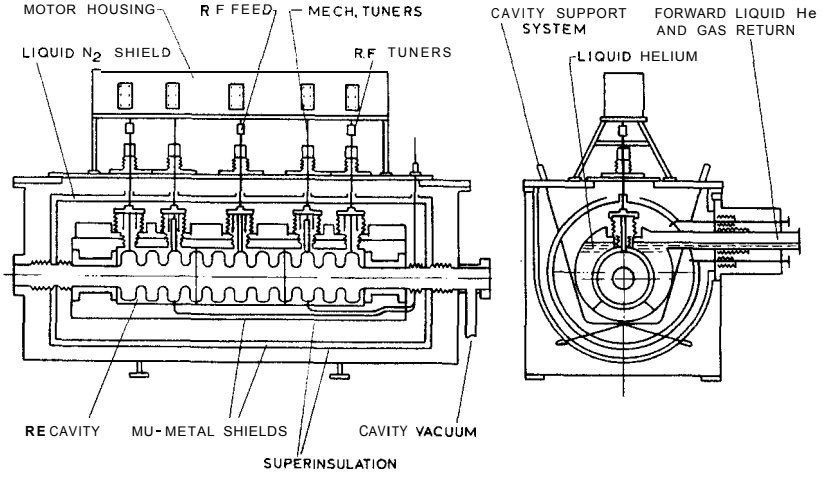


FIG 1. LAYOUT OF SUPERCONDUCTING R F. SEPARATOR CAVITY IN ITS CRYOSTAT

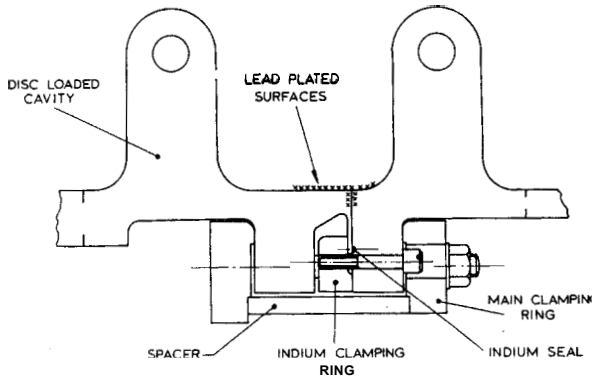


FIG 2. MODIFIED CANTILEVER JOINT.

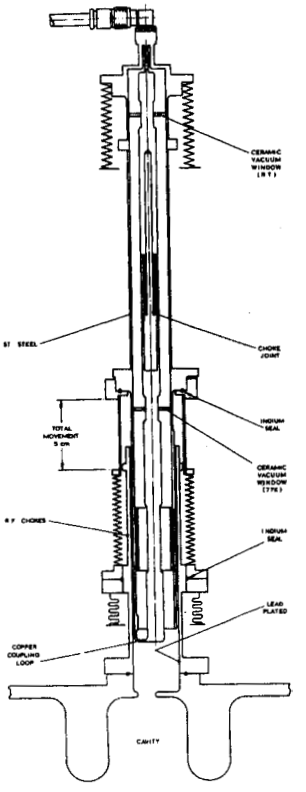


Fig 3 R.F. FEED

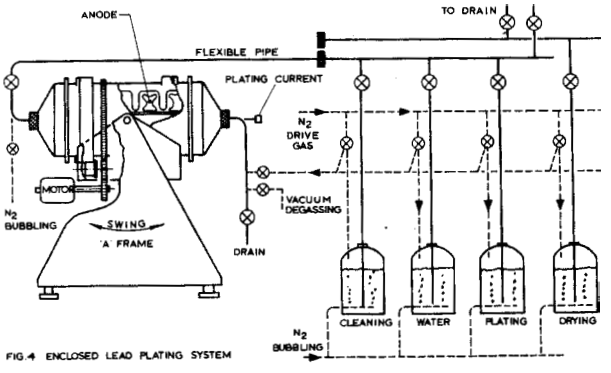


FIG.4 ENCLOSED LEAD PLATING SYSTEM

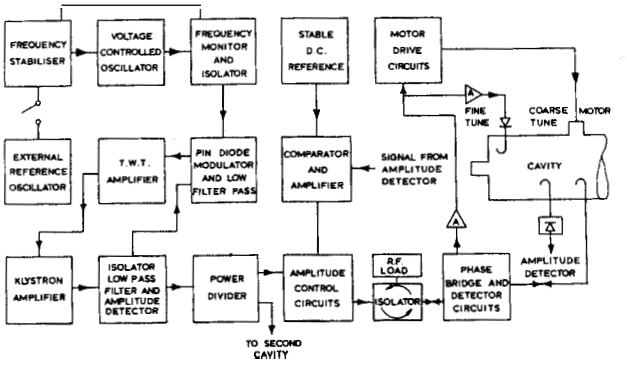


FIG.5 R.F. POWER SUPPLY AND CAVITY PHASE AND AMPLITUDE CONTROL

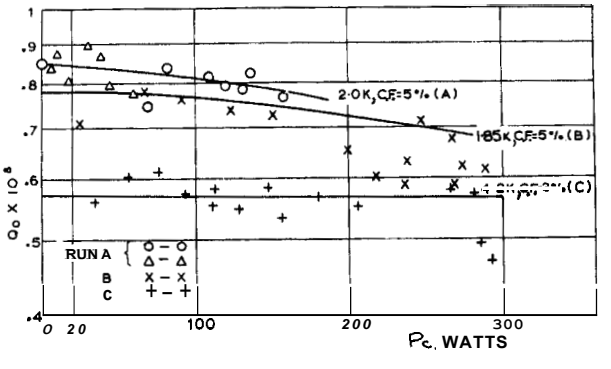


FIG.6 Q_0 AGAINST CAVITY POWER

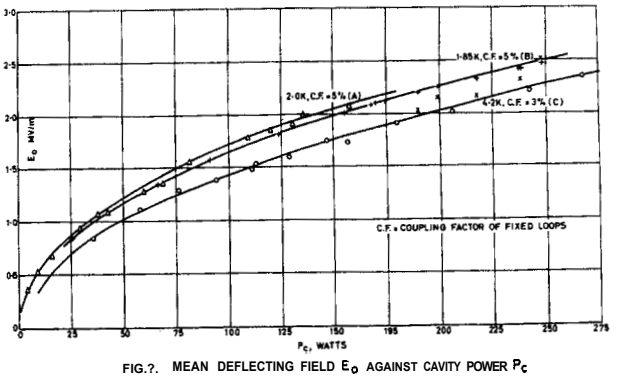


FIG.7. MEAN DEFLECTING FIELD E_0 AGAINST CAVITY POWER P_c

DEVELOPMENT OF THE SUPERCONDUCTING HELIX FOR HEAVY-ION ACCELERATION*

J. Aron, R. Benaroya, L. M. Bollinger, B.E. Clifft, O.Despe, A.H.Jaffey, K. W. Johnson, T. K. Khoe, J. J. Livingood, P. J. Markovich, J.M.Nixon, G. W. Parker and W. A. Wesolowski

Argonne National Laboratory, Argonne, Illinois 60439 U.S.A.

SUMMARY

Recent progress in the development of the superconducting helix for heavy-ion acceleration is reported. Accelerating fields in $\lambda/2$ resonators have been pushed up to 4.6 MV/m. Phase control by means of a voltage-controlled reactance has been refined to the extent required for helix structures appropriate for projectiles with $\beta \gtrsim 0.07$. Protons have been accelerated in a prototype accelerator consisting of two independently-phased resonators; phase control was maintained with ease, and no unforeseen problems were encountered. A prototype accelerator consisting of three independently-phased resonators, one of which is a $5\lambda/2$ unit, is nearing completion. This system will accelerate O^{5+} ions from an FN tandem.

I. INTRODUCTION

An attractive concept for heavy-ion acceleration is a tandem electrostatic accelerator injecting into a superconducting linac. The tandem provides the high initial velocity and charge state needed to minimize the design problems and the length of the linac, and superconductivity in the linac minimizes the RF problem and assures CW operation. Also, the characteristics of the tandem allow the linac to have an output beam of the highest quality.

A broad investigation of the technology required for the tandem-superconducting linac concept is being carried out at Argonne. This development program includes 1) investigations of the most important individual questions concerning the superconducting accelerating structures, 2) the construction and testing of several prototype accelerator systems, and 3) a search for economical solutions to engineering problems. This paper is a brief summary of highlights of the program for the past year. Earlier results are given in Ref. 1-3.

To date, all of our experimental work has been concerned with the helix accelerating structure, for which the range of optimum performance is well matched to the velocity range of interest for a tandem-linac heavy-ion accelerator — the range β = 0.04-0.2. These investigations have been carried out with $\lambda/2$ units made of niobium metal. RF resonance frequencies have ranged from 60 to 100 MHz. Illustrations of such units and some of the fabrication procedures have been reported previously.[1,2] The next step, the fabrication of a $5\lambda/2$ resonator, is nearing completion.

The design parameters of the helix resonators tested to date are summarized in Table 1. Note that most of these units have undergone many cycles of surface preparation (typically polishing and anodization) followed by tests of resonator performance. Thus, the total number of sets of active surfaces that have been studied is quite large — over 50.

II. ACCELERATING FIELD

In October 1972, we reported that accelerating fields of about 2.7 MV/m had been obtained with a superconducting-helix structure and that the performance characteristics could be stabilized by anodizing the niobium surfaces. Since that time, the maximum field has been substantially increased, and most other aspects of resonator technology have been improved and are better understood. The present status is summarized below.

Maximum Field

Recently the axial accelerating field E_{ax} of a helix resonator was pushed up to 4.6 MV/m, the highest field reported yet for a structure operating near 100 MHz. Also, as shown in Fig. 1, the Q of the system (Unit C) is extremely high — about 10^{10} at low fields, which corresponds to a surface resistance of about 5×10^{-10} ohm. It is believed that the sharp drop in Q above E_{ax} = 3 MV/m results from electron field emission from the central turns of the helix, since the drop in Q is accompanied by high-energy X rays. Note (in the caption of Fig. 1) that the superconducting surfaces used in the measurements were bare (not anodized),

A resonator (Unit A) with anodized surfaces has also given $E_{ax}(max)$ = 4.5 MV/m, although with much lower Q than for Unit C. In view of the high Q obtained previously with Unit A, it seems probable that the low-Q behavior is not intrinsic but rather results from some surface flaw that has not yet been identified in continuing investigations.

The cause of the extraordinarily high fields exhibited by Units A and C has not been established. However, it might be significant that these two units are (in their present form) the only two units that have undergone two heat treatments with electropolishing after each treatment. Investigations of this question are continuing.

Helium Discharge Conditioning

Following the lead of workers at Stanford and at Siemens, we now routinely use helium discharges in operating superconducting resonators to "condition" the active surfaces. For anodized surfaces, this process almost always increases the maximum achievable field (typically by 30%) and the process also makes it easier to penetrate a low-field multipacting barrier.

A typical example of the improvement achieved by means of helium conditioning is given in Fig. 2. Here one sees that the process gradually and reproducibly extends the Q vs E_{ax} curve toward higher fields. Associated with this extention is a dramatic decrease in the intensity of X rays generated at a given field.

Table 1. Design parameters of $\lambda/2$ helix resonators that have been studied. The last column gives the number of new sets of surfaces studied in each unit.

Unit	Helix Radius (cm)	Helix Length (cm)	Helix Pitch (cm)	No. of Turns	Cavity Radius (cm)	Cavity Length (cm)	RF Frequency (MHz)	Max E_{ax} (MV/m)	No. of Test Cycles
A	3.25	11.0	1.00	11	9.75	20	96.9	2.7	2
B	3.25	11.0	1.00	11	9.75	20	99.4	1.7	5
B'	3.25	11.0	1.00	11	9.75	20	96.7	3.5	13
A'	3.25	11.0	1.00	11	9.75	20	95.8	4.5	4
C	3.25	11.0	1.00	11	6.5	20	91.9	4.6	10
E_1	4.40	12.2	1.016	12	8.8	16	62.9	1.3	1
E_2	4.40	12.2	1.016	12	8.8	16	63.1	1.1	1
G_1	3.30	12.2	1.016	12	8.8	16	91.6	2.5	9
G_2	3.30	12.2	1.016	12	8.8	16	91.6	3.2	7

For bare surfaces (for which our experience is not very extensive yet), the beneficial effects of helium-discharge conditioning are less consistent. When a unit with a bare surface is first put into service, the response to helium conditioning is similar to that for an anodized surface — that is, clearly beneficial. However, when the unit has been used and then exposed to air, helium conditioning usually does not increase the maximum field.

Stability of Bare and Anodized Surfaces

We have repeatedly demonstrated that resonators with anodized surfaces do not deteriorate when exposed to the atmosphere or when operated for long times at high fields. Indeed, high-field operation usually causes the performance to improve, probably from effects that are similar to those involved in the helium conditioning. This improvement may result from the movement of absorbed gas from sensitive surfaces to less sensitive parts of the resonator.

Recent studies of resonators with bare surfaces indicate that the bare surfaces are not as unstable as we had previously thought. For example, in Unit C, which gave a maximum field of 4.6 MV/m with a newly prepared bare surface, the maximum field dropped to 3.0 MV/m after the unit had been exposed to the atmosphere for several hours. The maximum field remained stable at the level of about 3.0 MV/m after further exposure to air.

Reproducibility of Fabrication Techniques

There are two aspects to the question of resonator-fabrication reproducibility. One involves the performance of a set of resonators of the same design, and the other involves the performance of a set of resonators with similar but differing designs.

Most of our experience to date is for resonators with the same or almost the same design. Experience of this kind includes repeated tests on single resonators whose surfaces are reprocessed (polished and anodized) before each test. Originally, the reproducibility of performance characteristics was poor. However, this problem has been largely eliminated by using greater care in surface preparation and assembly. Key elements in the present procedure are thought to be (1) rigid control of parameters in the electropolishing process, (2) the use of oxypolishing (anodization followed by stripping of the oxide) to remove surface impurities that may be left after electropolishing, and (3) final assembly of the resonator components in a dust-free "clean room".

The reproducibility of units with differing geometries is not yet satisfactory. In particular, the G-type units of Table 1, which differ from the others principally in having a smaller distance between the helix and the end plates, have not consistently performed well. This is not understood with certainty, but some of the curves of Q vs E_{ax} have characteristics that suggest that multipacting may be responsible. In any case, poor behavior of the two G-type units strongly suggest that it is inadvisable to have the end plates close to the helix.

III. VIBRATION CONTROL

Even when a helix resonator is carefully isolated from its surroundings, mechanical vibrations cause the RF resonance frequency to fluctuate more than can be tolerated if the RF phase must be controlled. To date, our approach to this problem has been to use a voltage-controlled reactance (VCX) to modulate the resonance frequency in such a way as to maintain a constant average frequency. The VCX consists of a $3\lambda/8$ transmission line terminated by a PIN-diode switch. The operation of the switch causes the impedance seen by the helix to change by $\pm jz_o$, where z_o is the characteristic impedance of the line; and this impedance change causes a change Δf_o in the resonance frequency of the helix-VCX system. A full description of our initial experience with the VCX technique of phase control is given in Ref. 3.

Nonlinear Effect

During the past year it has become clear that the principal limitation on a VCX is not set by the total RF-power loss in the system but rather by a nonlinear component in the loss, an effect that tends to enhance the mechanical vibrations whose effects one is trying to control. Although the cause of the

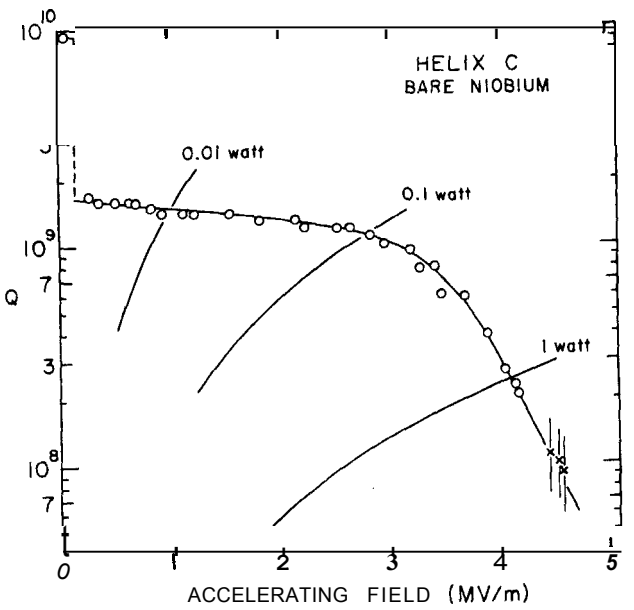


Fig. 1. Best performance of resonator C. The niobium surfaces were bare (not anodized) for these measurements.

nonlinear effect is not weil understood, the magnitude of the effect can be reduced substantially by operating several diodes in parallel. This approach has probably not been pushed as far as it could be, but systematic measurements have shown that 6 diodes in parallel are better than any lesser number for our diode pulser. Presumably, the optimum number of diodes depends on the switching current available from the pulser.

Cooled Diodes

Another significant development has been the demonstration that the switching time of a PIN diode can be reduced by an order of magnitude by cooling it with liquid nitrogen. For example, the Unitrode type-4010 diode, which normally has a carrier lifetime of about 7 μsec, has the lifetime reduced to about 1.5 μsec when it is operated at liquid-nitrogen temperature. This enables one to use diodes that have higher power ratings than the type-7206 diode, which was originally thought to be the only useable type.

Test Results

The λ/2 helix resonator (Unit G_2) that happened to be operational during the final tests of the VCX system was defective and could provide an accelerating field of only 1.7 MV/m. The frequency changes caused by mechanical vibrations in this system were controlled with ease. Specifically, the vibration-induced Δf_o was only about ± 125 Hz, whereas the VCX-induced modulation was about ± 400 Hz. Thus, since the VCX control range is inversely proportional to the square of the accelerating field, it seems certain that the G_2 resonator could have been controlled at an accelerating field of 2.5 MV/m.

During the acceleration tests described in the next section, some attention was devoted to the influence on the VCX of a fluctuating beam load. It was found that phase control could be maintained up to a proton-beam current of 14 μA for a wildly fluctuating beam. This level of performance is near that required for a practical heavy-ion accelerator.

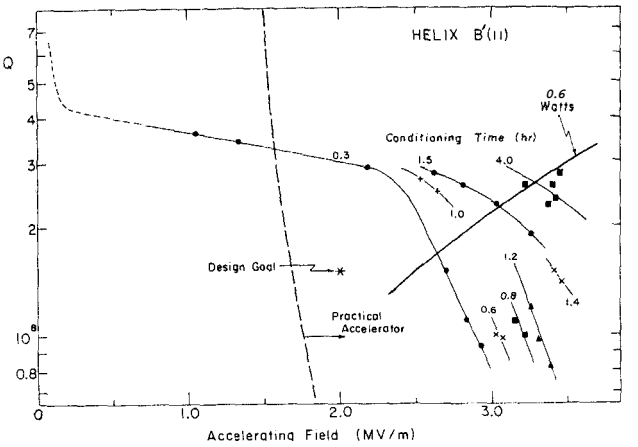


Fig. 2. Influence of helium-discharge conditioning.

Tubing Diameter

A recent conceptual advance has been the development of a quantitative understanding of the relationship between the mechanical stiffness of a helix and its vibration control. Since the vibration amplitude depends on the parameters involved in different ways for various modes of excitation, the relationships cannot be stated concisely. However, typically the amplitude depends on d^3, where d is the diameter of the helix tubing. Consequently, vibration controllability is greatly improved if the tubing diameter can be increased. This consideration has led us to increase to 3/8 inch the tubing diameter of a 5λ/2 resonator now near completion, whereas from an electrical point of view 1/4 inch is better. It is expected that two VCX units of the tested design will be able to control the phase of this large resonator up to $E_{ax} \leq 2.0$ MV/m.

Summary of Present Status

Our conclusion from the considerations and results outlined above is that the VCX technique is adequate for the control of accelerating structures of the kind required for heavy-ion beams with $\beta \gtrsim 0.07$. The technique is borderline for lower velocities. Development of another technique has started.

PROTOTYPE ACCELERATORS

The prototype-accelerator program now in progress has three phases: (1) acceleration tests with single λ/2 helix resonators, (2) acceleration tests with a system of two independently-phased λ/2 helix resonators, and (3) acceleration tests with a system of three independently-phased resonators, one of which is a 5λ/2 unit.

Individual Resonators

The work on the individual λ/2 units was described in Ref. 2. The experimental arrangement was the same as is shown in Fig.3 except

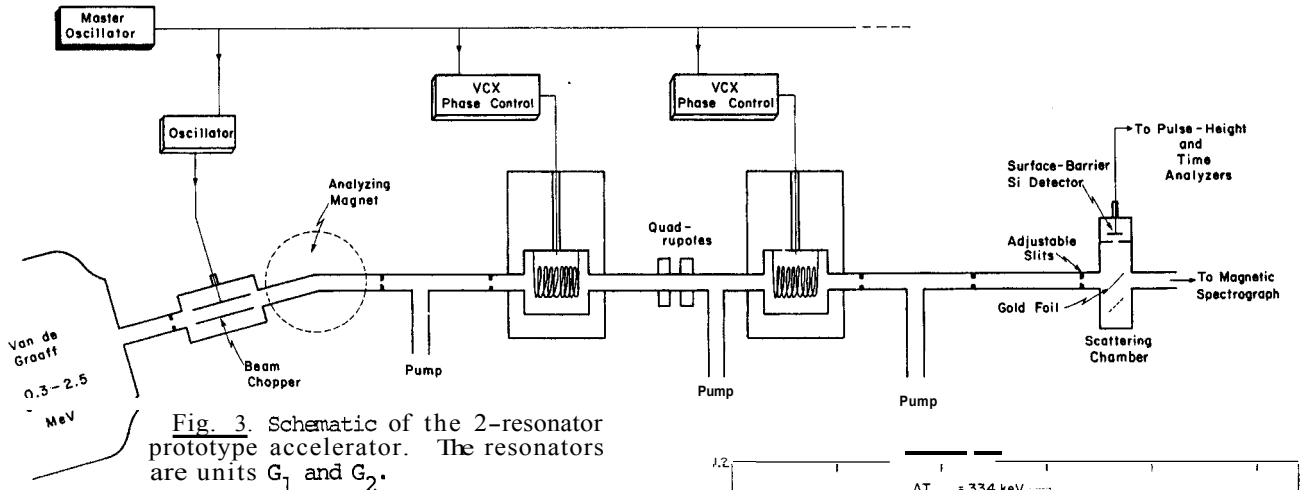


Fig. 3. Schematic of the 2-resonator prototype accelerator. The resonators are units G_1 and G_2.

that only one resonator was used. Proton beams were accelerated in two different kinds of structures for long periods of time (a total of about 130 hours of beam time), and no unexpected problems were encountered. The measured energy gains are in good agreement with what is calculated from measurements on a copper model at room temperature.

The measured dependence of the transit-time factor on projectile energy is given in Fig. 4, where the relative energy gain $\Delta T/\Delta T_s$ is plotted as a function of the energy $(T_i + \frac{1}{2}\Delta T)$ of the proton at the center of the helix; here the normalizing constant ΔT_s is the energy gain for a synchronous particle, and T_i is the incident energy. As is indicated by the smooth dependence of $\Delta T/\Delta T_s$ on projectile energy, the measurements were quite accurate and reproducible.

The curves associated with each set of data points were calculated from the field distributions measured in copper models at room temperature. The good agreement indicates that the field distributions of the copper model and the superconducting structure are closely the same, as expected.

2-Resonator System

A schematic of the 2-resonator prototype is given in Fig. 3, and the system is described in Ref. 2. The main objective of the tests with this prototype was to study phase control in a working system of resonators. The phases of both accelerating units were locked to the phase of a master oscillator by means of VCX control units of the kind described in section III.

Since we do not yet have any means of coarse tuning a resonator after it is placed within its cryostat, when the two resonators have frequencies which are matched at low fields, they must always operate at the same field; otherwise, differences in radiation pressure will cause the two resonance frequencies to be different, and phase control is impossible. This limitation will not be present in a full-scale accelerator, of course, because in it each resonator will have a coarse tuner, probably an externally-controlled mechanical adjustment. However, because of the lack of coarse tuning on the prototype

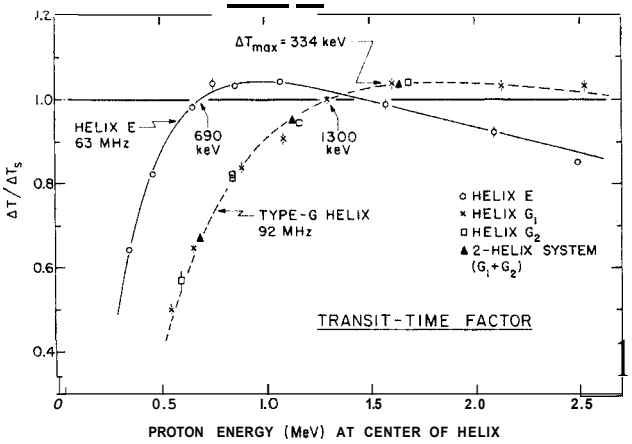


Fig. 4. Results of energy-gain measurements.

units and because of the poor performance of one of the resonators, in the tests carried out to date the accelerating field was limited to 1.0 MV/m. This limit could be greatly increased now, but it has not seemed worthwhile to repeat the measurements because of the effort being devoted to the preparation of the multiple-helix resonator described below.

An interesting detail concerning the 2-helix system was the ease with which the two units were tuned to approximately the same RF resonance frequency before they were placed in their cryostats. A simple mechanical device was used to deform the helices and in this way to match the two frequencies within about 10^3 Hz - that is, to one part in 10^5.

Objective evidence of the successful operation of the two-helix system is provided by a measurement of energy gain AT as a function of incident energy. Since the energy gain was small compared to the incident energy, the energy dependence of ΔT should be the same for the two-helix pair as it is for an individual unit. This was found to be the case, as is shown by the data in Fig. 4.

The 2-helix system was operated with phase control €or several hours, and no unexpected problems were encountered. The energy gain of the system was shown to be equal to the sum of the energy gains of the individual resonators. Phase control of the system could be maintained up to a beam current of 10 μa.

Multiple-Helix Prototype

Construction of a multiple-helix prototype consisting of two single $\lambda/2$ resonators and one $5\lambda/2$ resonator is nearing completion, and components are beginning to be assembled on a beam line at the FN-tandem injector. The main objective of the project is to gain engineering experience with a multiple-wavelength resonator of the type needed for a practical accelerator.

The design of the $5\lambda/2$ resonator is optimized for the acceleration of O^{5+} ions with an incident energy of about 2.8 MeV per nucleon. The maximum energy gain of the accelerator system is expected to be about 2 MeV per charge. The beam current will be low because the pulsed beam is formed by a simple chopper.

The phases of the resonators will be controlled by VCX units of the type described earlier — one unit for each $\lambda/2$ resonator and two units for the $5\lambda/2$ resonator. As mentioned in section III, the helix in the $5\lambda/2$ resonator is made of 3/8 inch tubing in order to limit the amplitude of mechanical vibrations. Also, for the same reason, the supporting stubs are short and very rigid.

The cryostat for the $5\lambda/2$ resonator is a helium-pumped system in which the temperature of the liquid-helium bath is designed to operate at about 1.8°K. The principles of operation are the same as for the cryostats of the $\lambda/2$ units (see Ref. 2) except that the insulation vacuum and the resonator vacuum are separate.

As far as is foreseeable, the principal question about the proper functioning of the $5\lambda/2$ resonator is whether the technique of surface preparation that has worked well for the $\lambda/2$ units can be successfully applied to the larger $5\lambda/2$ unit.

References

*Work performed under the auspices of the U.S. Atomic Energy Commission.

1 R. Eenaroya, A.H.Jaffey, K. Johnson, T. Khoe, J. J. Livingood, J. M. Nixon, G. W. Parker, W. J. Ramler, J. Aron, K. E. Gray, and W. A. Wesolowski, in Proc. 1972 Proton Linear Accelerator Conference (Los Alamos Scientific Laboratory Report LA-5115),p. 168

2 J. Aron, R. Benaroya, L. M. Bollinger, K. E. Gray, A. H. Jaffey, F. J. Lynch, K. W. Johnson, T. K. Khoe, J. J. Livingood, J. M. Nixon, G. W. Parker, W. J. Ramler, and W. A. Wesolowski, in Proc. of the 1973 Particle Accelerator Conference (IEEE Trans. on Nucl. Sci. NS-20, No. 3) p. 76

3 O. D. Despe, K. W. Johnson, and T. K. Khoe, in Proc. of the 1973 Particle Accelerator Conference (IEEE Trans. on Nucl. Sci. NS-20, No. 3) p. 71

SUPERCONDUCTING MAGNETS

D B Thomas
Rutherford Laboratory, Chilton, Nr. Didcot, Berkshire, England.

1. INTRODUCTION

Progress in superconducting magnet technology over the past few years has been steady rather than dramatic with the principal emphasis centred on the construction and commissioning of fully engineered prototype magnets, some of which have now seen several thousand hours of reliable operational service on high energy physics experiments. Filamentary niobium-titanium composite superconductors have established themselves firmly as the universal choice for use in such magnets. They can now be obtained commercially in the USA, Europe and Japan in forms suitable for dc and pulsed magnets and in a variety of current ratings and cross-sectional shapes. Magnets using this material will comfortably produce magnetic fields of 4 to 5 T thus in general giving at least a factor of two advantage over conventional magnets in this respect.

High energy physics has continued to be the main user of superconducting magnets and hence the main springboard for developments in the technology since industrial applications have not yet materialised to any extent. This dominant position is likely to be maintained over the next few years with the building of larger and more complex superconducting systems for beam line and accelerator applications using the conductors that are available today and also by the initial exploitation in prototype magnets of the higher field filamentary superconductors that are now nearing completion of development.

The papers selected for oral presentation in the Conference Session on Superccnducting Magnets, for which I am acting here as rapporteur, are all concerned with the use of pulsed magnets in accelerators and accelerating storage rings. No magnets of this type have yet seen true operational experience and thus the papers will be mainly concerned with the future of the subject rather than its present status. To achieve a correct balance and to provide scope for a wider discussion following these papers, my contribution will aim at establishing the present state of knowledge in superconducting magnet technology.

2. SUPERCONDUCTING COMPOSITE DEVELOPE

2.1 Conductors for dc Magnets.

Since their introduction in 1968, intrinsically stable conductors of the twisted multifilament variety[1] have been adopted for virtually all superconducting coils with overall current densities above about 100A/mm^2. Niobium-titanium superconducting alloy is capable of sustaining a current density in the region of 1000 to 1500A/mm^2 at 5 T and 4.2°K. The multifilament conductor takes the form of a number of individual filaments embedded in a pure copper matrix, the copper-to-superconductor ratio varying in general between 2:1 and 1:1 depending on the application. The copper with its good electrical and thermal conductivities at 4.2°K serves two purposes, coil protection during an accidental transition of the coil to a non-superconducting state (by encouraging the propagation of the resistive region so that the energy dumped into the coil by the collapsing magnet field is distributed as uniformly as possible) and also to provide a measure of dynamic stabilisation (to damp out any sudden local magnetic field changes due to unwanted microscopic conductor movement). When account is taken of the space occupied by interturn insulation and imperfect conductor packing, overall current densities in coils wound from multifilament niobium-titanium composites can be expected to range roughly from 200A/mm^2 to 300A/mm^2 in designs with peak magnetic fields of 5 T, and indeed this is found to be so in practice. Some improvement in overall current density can be achieved by operating the coils at a temperature below 4.2°K. For example reducing the temperature to 3.0°K increases the critical current density of Nb-Ti at 5 T by about 30%.[2] Only limited use has yet been made of this increased performance in magnets for high energy physics applications.

The theory of multifilament superconductors, well supported by experiment, requires that individual filaments of Nb-Ti shall not be greater than about 50μm in diameter. A single filament of this size will carry approximately 2.5A at 5 T so that conductors with typically hundreds of individual filaments are needed for dc superconducting magnets such as beam line elements where energising currents in the 100 to 1000A region are appropriate. In the higher current ratings it is advantageous to ease coil winding problems and to obtain the best packing factor in the windings by using a conductor of rectangular cross-section rather than a round wire. So long as the aspect ratio of the finished conductor is not too great, say two to one, the current carrying properties are not degraded to any excessive extent but some anisotropy (15 to 25%) can be detected in such a conductor by measuring the critical current with the field aligned first parallel to its wide face and then parallel to its narrow face.

The use of superconducting cables consisting of many individual composite wires in parallel, sometimes soldered together for mechanical integrity, seems to have come into disfavour with magnet designers since solid conductors with many hundreds of filaments became available. One disadvantage of the large cross-section solid conductor is the limited length in which it can be obtained. At the time of writing piece weights of conductor in the range 70 to 120 kg can be processed industrially. Allowing for wastage during processing and assuming that no conductor breakage occurs in any one of the many stages of production (an assumption already shown to be statistically optimistic) then single pieces of superconductor weighing 50 kg and occasionally 100 kg can be obtained. This is sufficient to allow for example a single pole of a quadrupole of 25 cm cold bore and of 1 to 2 m length to be constructed without internal joints. (Internal joints however well made will be somewhat resistive since no method has yet been devised nor seems likely to be devised for joining two lengths of multifilament conductor in a truly superconducting manner.)

Magnets wound from the type of conductor described above are in general energised to full field over a period of some minutes. The hysteresis loss in the superconductina filaments themselves amounts to about 150 mJ/cm^3 in charging a coil from

zero field to 5T if 50 μm filaments are used. Heat generated in the coil at this level is easily conducted away to the surrounding liquid helium refrigerant without increasing the internal coil temperature unless charging times of less than one minute are called for. When such a requirement is specified conductors with finer filaments should be used.

One potential reason why filaments finer than the 'standard' 50 μm size may be required in special dc magnets is the remanent field which arises from the diamagnetic persistent currents left circulating in every individual filament of the magnet winding when it is returned to zero current after excitation. The magnitude and harmonic content of this residual field will of course depend crucially on the geometry of winding configuration used. As an example the measured remanent field of a dipole of 9 cm bore wound from a conductor with 12 μm filaments was measured to be about 1.2 mT after de-energisation from 4 T. The cold iron yoke surrounding the coil was found to contribute 0.2 mT of this total.[3]

This effect is only likely to be important in magnets which as part of their normal operating role must be held near zero field with particle beams passing through them and where field quality is of the utmost importance. Once the magnet is energised even partially, the critical current density of the superconductor will be substantially reduced from its zero field value ($\sim 10^4 A/mm^2$) and with it the strengths of the dipole persistent current systems in the filaments and the field distortions which they cause.

No composite conductors with tens of thousands of 5 to 10 μm filaments are known *to* have been produced specifically for dc magnet applications. Rather more complicated composites for pulsed magnet work with these numbers and size of filament have been produced by the 'double stack' method and these will be described in the next section. There seems no reason to suppose therefore that simpler dc versions of these conductors could not be developed quickly if the need arose.

For dc superconducting magnets therefore, a complete range of Nb-Ti filamentary conductors(with the one possible exception noted above) is already commercially available for all anticipated applications.

2.2 Conductors for pulsed magnets

The term pulsed superconducting magnets must first be defined as describing coils that can be charged to full field in times between 1 and 100s. The applications most frequently mentioned for such magnets are in synchrotrons and accelerating storage rings but switching applications in beam lines have also been suggested.

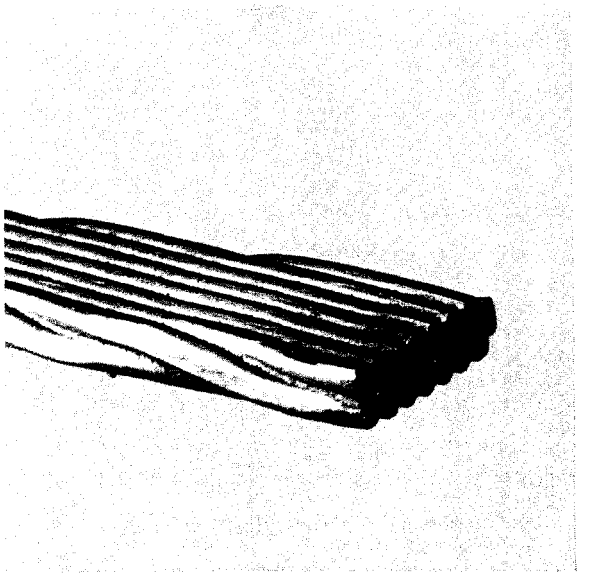
The so-called 'ac losses' which occur in composite superconductors arise from three sources, hysteresis losses in the individual filaments, matrix losses and self-field losses.[4]

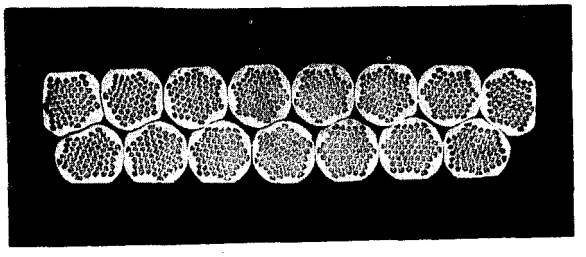
The hysteresis losses incurred per unit volume of superconductor are directly proportional to the diameter of the filaments used. Thus decreasing the size of filament from 50 to 5 μm (and perhaps increasing the number of filaments in the composite by a factor of 100 to maintain the same current rating) produces a conductor in which the magnitude of the loss rate due to hysteresis is acceptable with field rise times as low as 1s. (The average rate of heating per cm^3 of superconductor is of order 20 mW in a coil energised to 5 T in 1s if 5 μm filaments are used: typically 25% of the volume of the windings would be Nb-Ti.)

Matrix losses occur because of coupling between individual filaments in the twisted array. Unlike filament hysteresis losses, matrix losses are field rate dependent in that the total losses incurred in changing from one magnetic field level to another are directly proportional to the rate at which this change takes place. Twisting the conductor more tightly about its longitudinal axis reduces the matrix losses but it becomes progressively more difficult to achieve the twist pitch required for field rise times of a few seconds as the current rating and therefore the size of the conductor increases. The introduction of a partial resistive barrier between filaments in the composite is therefore indicated. An ideal conductor geometry from the standpoint of losses in the matrix would consist of a number of Nb-Ti filaments each surrounded by a sheath of pure copper, the whole embedded in a matrix of high resistivity alloy such as cupro-nickel and then twisted tightly. No such conductor is commercially available presumably because of the difficulty in processing on any reasonable scale a composite with a high volume percentage of cupro-nickel.

Self field losses occur in twisted composites essentially because the filaments are not fully transposed; those near the longitudinal axis stay near this axis and do not interchange position with filaments near the outer diameter of the composite. There is then always a self field flux enclosed between the outer filaments in the wire and those near the centre. This flux tends to couple the filaments together and increases the losses which are incurred. Self field losses are proportional to the square of the diameter of the superconducting composite and are only of practical importance in the largest composites.

For pulsed magnets with rise times of 10 to 100s, rate dependent matrix losses in conductors with a copper matrix are not sufficiently high to preclude their use. A typical conductor for such a magnet might be a cable or braid of 25 composite wires of 0.6 mm diameter each with 1000 filaments of 10 μm. For pulsed magnets with rise times of 1 to 10s, superconducting composites with cupro-nickel in the matrix are used in the same cabled form. To obtain the highest overall current density, a cable with a small number of large diameter wires is preferred to a cable with a large number of small wires because of the higher packing factor obtained with the former. The latter are also more fragile in handling. The optimum cable is probably a simple flat helix of the type shown in Figure 1. For multi-thousand ampere applications such a flat tape conductor requires composites with many thousands of filaments for use at the fastest rise times. Such composites are now available. Figure 2 shows a cross sectional view of a conductor with 14,000 filaments. A pulsed magnet is under construction using a flat tape conductor comprising 15 composite wires each with 9000 filaments.[5]





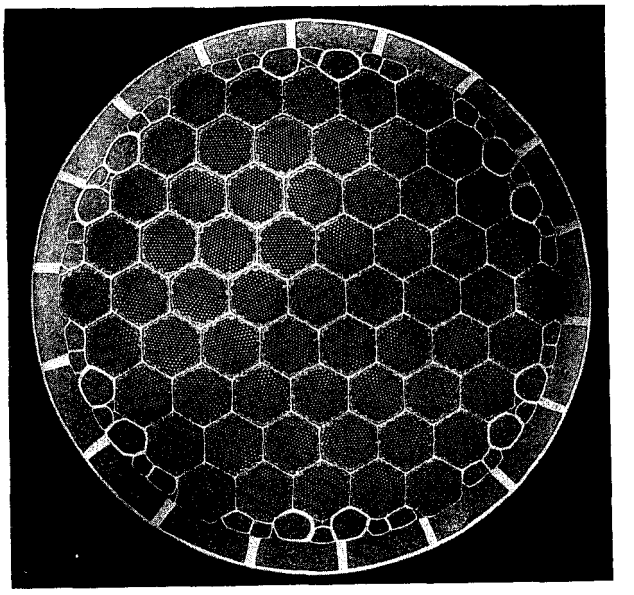
(b)

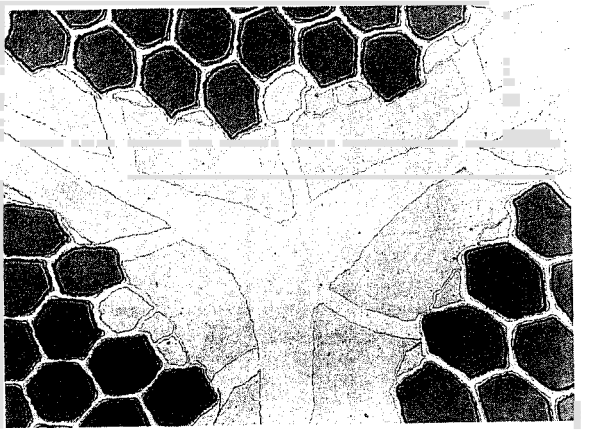
FIGURE 1 - A TYPICAL SUPERCONDUCTING CABLE

(a) General view

(b) Cross sectional view

15 strands; 1.06 mm strand diameter; 8917 filaments per strand; 7.2 μm filaments; Cu and Cu-Ni matrix; 6300 A at 5 T; compacted to 95% metal in cross section.





(b)

FIGURE 2 - CROSS-SECTION OF A 14701 FILAMENT NIOBIUM-TITANIUM COMPOSITE SUPERCONDUCTOR

(a) General view

(b) An enlargement of a region of the cross-section

1.06 mm dia; 5.3 μm filaments; ~430A at 5 T; copper matrix with cupro-nickel barriers. [Imperial Metal Industries]

The final step to be taken to eliminate the cabling of wires to form conductors for pulsed magnets is to produce a solid conductor with about 10^5 filaments. Such a conductor with 180,000 filaments has been produced in experimental quantities for evaluation.

For pulsed magnets therefore an adequate range of composite conductors is available for field rise times down to 1s but some further development work can be foreseen.

2.3 New Filamentary Composites with Higher Field Properties.

During the past few years the development of filamentary composites based on niobium-tin and vanadium-gallium has been under way. A measure of the difficulty in developing these new conductors is the time that has been taken to produce them even in sample form. When they become available in quantity it is clear that a whole new range of problems will have to be faced by the magnet designer. These materials are brittle when reacted and cannot be subjected to elongation strains greater than about one half percent without their performance being degraded by filament fracture. The indications are that coils will have to be wound with the unreacted ductile materials, essentially fine filaments of niobium on a copper-tin bronze or fine filaments of vanadium in a copper-gallium alloy. Subsequent reaction of completed windings at temperatures in excess of 500°C will produce the superconducting intermetallic compounds as well as a number of interesting and challenging problems for the magnet

designer! The potential advantages of gaining a further factor of two in field strength (from the 5 T of Nb-Ti to the 10 T of Nb_3Sn and V_3Ga) are such however that preparations are already being made in several high energy physics laboratories to exploit these new materials.

An example of an experimental filamentary Nb_3Sn conductor is shown in Figure 3. In spite of the high matrix to superconductor ratio of this conductor (5.5:1 compared with the usual 2:1 or 1:1 of Nb-Ti composites) the overall current density is expected to exceed 1500A/mm^2 at 5 T.[6] Such an overall current density would represent about a factor two to three increase over that obtainable from Nb-Ti composites. Because of the fineness of the filaments in this composite and the resistive nature of the bronze matrix material between the filaments, this conductor should be equally suitable for pulsed as well as dc applications. Similar work on these A15 filamentary conductors is known to be under way at a number of laboratories including Brookhaven National Laboratory.[7]

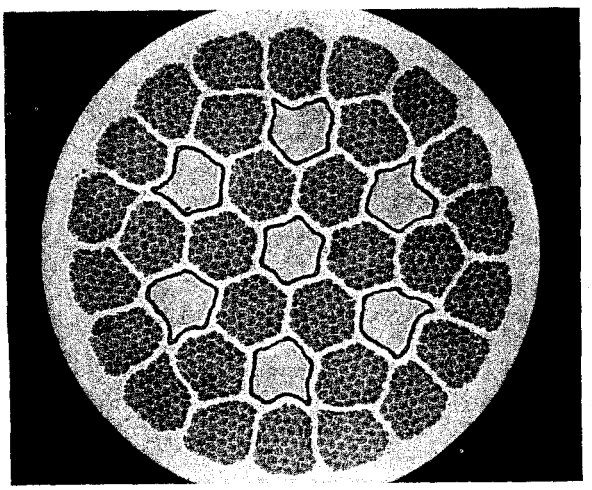


FIGURE 3 - CROSS-SECTION OF A 41,070 FILAMENT NIOBIUM-TIN COMPOSITE SUPERCONDUCTOR

1 mm diameter; 2 μm filaments; bronze matrix; 7 pure copper strands protected by diffusion barrier. Overall current density expected to be 1500 A/mm^2 at 5 T and 4.2°K.
[A.E.R.E. Harwell]

3. MAGNET DESIGN AND COIL PERFORMANCE

3.1 dc Magnets

The number of superconducting magnets that have been built as prototypes for high energy physics applications is now so considerable, probably approaching one hundred, and the number of designers that have been involved so large, that most possible coil configurations and constructional techniques have already been tried. From the results obtained it is clear that no one technique is to be preferred above all others. Coils are still built with liquid helium coolant in direct contact with the conductors whilst others employ epoxy resin impregnated windings for mechanical strength which are only cooled by conduction through the coil body. Virtually all the coils built by these methods to provide magnetic fields of 4 T or above show 'training' effects. They do not reach their design current on first energisation but 'quench' prematurely. Subsequent energisations result in progressively higher fields being reached on each occasion until in general the design figure is exceeded. 'Re-training' may be necessary after each magnet cooldown. Such premature quenching behaviour is believed to be due to a local rise in temperature in a region of the coil caused by any one of a number of effects. The movement of one section of the coil with respect to another or with respect to its supporting structure will, for example, cause sufficient temperature rise by frictional rubbing even when movements of only a few microns are involved, Micro-cracking in the resin impregnant under the action of the electromagnetic forces in the coil can also release mechanical energy locked in by differential contraction during the cooldown to 4°K.

'Training' then is now the principal problem left to the designer of superconducting magnets and is really a question of quality of the detailed engineering design. All constructional materials used should ideally have well matched thermal contractions and the coils should be completely constrained against movement, objectives more difficult to meet than to state.

In this context there is a relevant question that must be asked - "Is the magnet designer expecting too much of the available superconducting materials and not allowing a sufficient margin of safety between the chosen design current of the magnet and the critical current of the conductor he is using?" The critical temperature of Nb-Ti at 5 T is 7°K when zero current is flowing in the conductor. In a conductor already carrying 80% of its critical current at 5T and 4.2°K the effective critical temperature is reduced to about 4.6°K. This means that in the $(5T)_{peak}$ field region of a coil working under these conditions the temperature margin below 'quench' is only 0.4°K if liquid helium boiling at atmospheric pressure is used as refrigerant. Possibly a greater margin on temperature should be allowed by operating the magnet at reduced temperature or alternatively lower fields. Discussion at the Conference could perhaps bring light to bear on this question.

One novel approach to the problem of curing training has been suggested but not yet tested in practice.[9] The idea is to enclose the magnet windings in what is essentially an aluminium pressure vessel and then to inject epoxy resin under high pressure to fill the small voids between the windings and the vessel. In this way it is hoped that the windings can be held in compression at all times, even when the forces associated with energisation of the magnet are being taken. There is some supporting evidence in favour of this technique which arises from an investigation of 'training' in race-track coils. =Depending on the degree of pre-compression applied, these coils can be made to 'train' or not 'train' in a reproducible fashion.

Most of the superconducting magnets constructed to date have used iron shields to contain the stray field of the magnet which could otherwise influence surrounding equipment. The iron does indeed make a contribution to the field produced by the magnet. In a dipole magnet operating at 4.5 T, the use of an iron shield which fits closely around the windings contributes 1.5 T itself.[10] The use of iron does however increase the weight of material that has to

be cooled down to 4°K by about an order of magnitude. In the future, as the fields attainable with superconducting magnets increase, iron shields will probably be relocated outside the magnet cryostat since the contribution to the total field made by the iron becomes less significant. The introduction of additional spacing between the coil and iron shield would then more easily be accepted.

There is one property of iron, its coefficient of thermal contraction, that makes it somewhat unsuitable for positioning directly adjacent to the coils. Iron contracts by only 2 parts in 10^3 in cooling from room temperature to 4°K whereas superconducting composites, stainless steels and other constructional materials in general have coefficients at least 50% higher. If the situation were reversed, a cold iron shield could be used to generate compressive forces on the coil as it cooled to its working temperature as has been suggested above as being desirable. In practice in a magnet with a cold iron shield, the coils tend to shrink away from the iron and some external clamping system must be devised to make the iron, suitably split, follow up on the coil as it contracts. This adds a complexity to the coil design which is better avoided if 'training' is to be overcome.

3.2 Pulsed Magnets

The engineering problems associated with pulsed superconducting magnets for synchrotron applications are in general similar to those of dc magnets with several important differences as listed below.

a) Conductors are rated in thousands rather than hundreds of amperes (in keeping with the requirements of a superconducting synchrotron).

b) Finer filament conductors are used than in dc magnets to avoid excessive 'ac losses'.

c) Cooling channels are incorporated into the coils to aid removal of the heat generated during pulsing.

d) Iron yokes must be laminated to reduce eddy current losses in the iron.

e) Winding tolerances are more stringent because of the higher quality field requirements of the synchrotron or storage ring.

f) Potential fatigue problems in the magnet structure are introduced by repeated pulsing over millions of cycles.

The prototypes to be described in detail in the papers which follow in this Session meet the requirements of a), b), c) and d) completely. Under point e), a dipole has been built in which the unwanted sextapole component of magnetic field is less than 5×10^{-3} times that of the dipole throughout the entire excitation range, 0 to 5 T.[3] (The field uniformity depends almost entirely on the accuracy with which individual conductor blocks can be positioned in a superconducting magnet. This is in contrast to a conventional magnet where tolerances on the shaping of the iron poles are of paramount importance.) Two magnets built to the same design have been tested and show excellent agreement between measured field distributions.[11] On point f), the life testing of these two prototypes under repeated pulsing has been carried out over a period of six months without their condition deteriorating.

The next obvious stage in pulsed magnet development is to build and run a larger number of such magnets under operational conditions and assess their suitability for use in high energy synchrotrons and storage rings.[12,13,14] When this objective is achieved the necessary technological expertise to undertake a full scale superconducting accelerator project will be available.

3.3 Operational dc Superconducting Magnets

In the last few years real progress has been made in the operational aspects of dc superconducting magnets. A number of systems, each comprising two or three separate magnets, have together seen many thousands of hours of successful service on high energy physics experiments.[15,16,17,18] These systems are either coupled to a closed loop helium refrigerator or use dewar-dispensed liquid. An example of one system is shown in Figure 4.

These tests have shown that the superconducting coils themselves present no problems in operation, thus allowing interest to be focussed on the secondary cryogenic, refrigeration and vacuum systems. Here there is considerable scope for development. Refrigerators with longer periods between maintenance shut-downs than the present *4000* hours would be advantageous. Improved cryogenics giving lower heat leaks would mean smaller refrigerators. Permanently connected vacuum systems could be dispensed with if sealed cryostats with self-cryopumping could be used (as is now customary in liquid helium transport dewars). Permanently connected magnet power supplies could be dispensed with in many applications in favour of flux pumps if these were developed to the required level of reliability. It is in these and associated regions that some effort should now be concentrated.

4. GENERAL CONCLUSIONS

The considerable investment made by the high energy physics community in superconducting magnet technology is now beginning to show a return. Superconducting dc magnets are already in daily operation in accelerator beam lines, albeit in small numbers. Pulsed magnets have reached the stage of development where immediate operational use can be envisaged. This objective should be pursued with vigour as a precursor to the next logical step in high energy accelerator development, the superconducting synchrotron or storage ring.

As the proposed applications for superconducting magnets extend into other branches of science and electrical engineering, the contribution made to this subject via the high energy physics programme is becoming increasingly recognised. The present work in progress within this programme on higher field materials and magents is also likely to be of wider benefit in the future.

5. ACKNOWLEDGEMENTS

In preparing this paper I have relied heavily on information which has been supplied to me by personnel in the various laboratories engaged in superconducting magnet development, and on their published work. Without their help this paper could not have been compiled. I wish to extend my thanks to all those who have helped in its preparation.

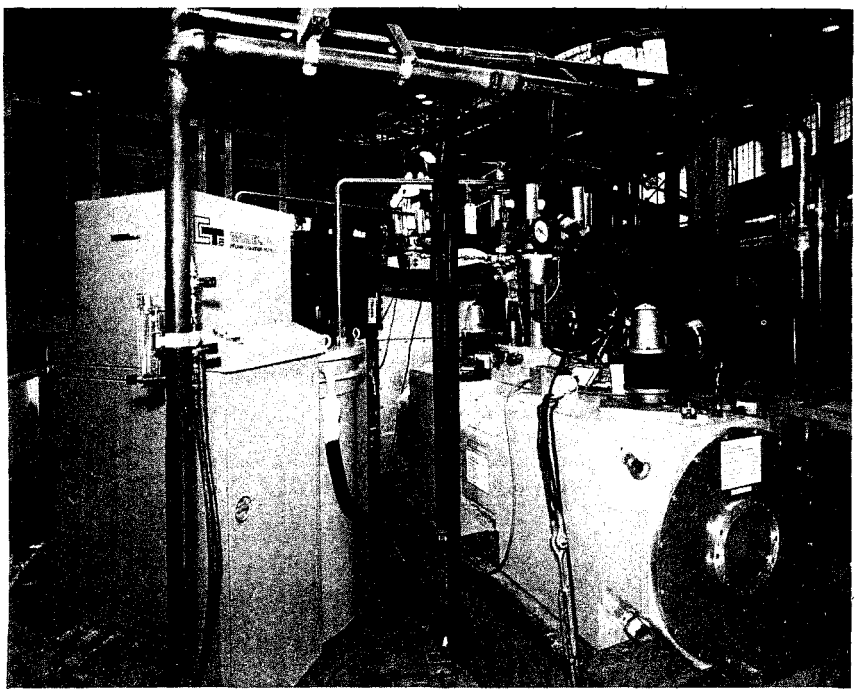


FIGURE 4 - SUPERCONDUCTING ELEMENTS IN A BEAM LINE AT LAWRENCE BERKELEY LABORATORY

The system consists of a 4 T dipole of length 80 cm and of 20 cm warm bore in one cryostat and a pair of quadrupoles each 60 cm long producing 20 T/m in a 20 cm warm bore in a second separate cryostat. The closed loop helium refrigerator coupled to the magnets can be seen on the left in the photograph. The system has been in operation since March 1973.

6. REFERENCES

1. P F Smith et al. J.Phys.D. 3,1517(1970)
2. P E Hanley, M N Biltcliffe. Proc. 4th Int. Conf. Cryogenic Eng., Eindhoven, 224 (1972).
3. J H Coupland, D E Baynham. Proc. Int. Conf. Magnet Tech., Brookhaven, 737 (1972).
4. M N Wilson, Proc. Conf. Appl. Superconductivity Annapolis, 385 (1972).
5. The GESSS Collaboration (Gfk Karlsruhe, Saclay, Rutherford Laboratory), GESSS-2 (May 1973).
6. J A Lee. A.E.R.E., Harwell - Private Communication.
7. M Suenaga, W B Sampson. Proc. Conf. Appl. Superconductivity, Annapolis, 481 (1972).
8. R Hampshire, J Sutton, M T Taylor. Proc. Conf. Low Temperatures and Electric Power, London (1969) (Commission I of Int. Inst. of Refrig. and British Cryogenics Council).
9. M N Wilson, RL - Private communcation.
10. J H Coupland, J S Simkin, T C Randle. Nucl. Inst. & Meth. 106, 595 (1973).
11. W B Sampson, et al. BNL - these Proceedings.
12. T Elioff et al, LBL - these Proceedings.
13. E A Crosbie et al, ANL - these Proceedings.
14. D A Edwards et al, NAL - these Proceedings.
15. W S Gilbert et al, LBL. Proc. Conf. Particle Accel., San Francisco (1973).
16. J Allinger et al, BNL - these Proceedings.
17. Report on operation of Saclay OGA quadrupoles CERN Courier 12,12,422 (December 1972).
18. Report on superconducting quadrupoles for CERN hyperon beam - CERN Courier 9,10,281 (September 1970).
19. Report on superconducting dipoles for BEBC beam line - CERN Courier 5, 13,144 (May 1973)

THE MAGNETIC AND THERMAL STABILITY OF SUPERCONDUCTING ACCELERATOR MAGNETS*

W.B. Sampson, P.F. Dahl, A.D. McInturff and K.E. Robins
Accelerator Department
Brookhaven National Laboratory
Upton, New York 11973

Summary. The two model superconducting storage ring magnets ISA I and II[1] have been subjected to extensive magnetic and thermal cycling to determine the effect of long term operation on their field distribution. The magnets were pulsed using the cycle proposed for ISABELLE (i.e. 100 sec rise, 100 sec fall) but substituting a 10 sec flat top *so* that a large number of pulses could be run in a relatively short time. The harmonic content of the magnets was measured periodically during the test. No significant changes were observed after a total of 5500 pulses. During the test, which lasted approximately six months the magnets were allowed to warm up to 150 K several times for refrigerator maintenance. They were also cycled to room temperature (300 K) twice after the pulsing test. Again no change in the harmonic coefficients was observed.

I. Introduction

In recent years improvements in materials and design techniques have made the construction of very high energy accelerators and storage rings using superconducting magnets technically feasible. However, very little is known about the long-term effects of the cyclic magnetic forces and thermal stresses that will be experienced by these magnets in day-to-day operation. Magnets whose field configuration changes with time would considerably complicate machine design, perhaps even making it impossible. *The* object of the ISA model magnet program is to demonstrate that superconducting magnets of accelerator quality can be built with the required reproducibility at reasonable cost and that such magnets can withstand the forces encountered during operation for the expected lifetime of an accelerating storage ring structure such as ISABELLE. A secondary objective was to gain experience in operating such magnets and their associated cryogenic hardware over an extended period under simulated accelerator conditions.

II. Magnet Design

The ISA model magnets are dipoles of the cos θ type; wound from a single layer of wide braided superconductor. They are approximately 1 m long and have an aperture of 8 cm. The construction details have been presented elsewhere.[1] The coil halves are pressure molded at elevated temperature to form a monolithic structure which is then clamped around the beam tube which contains sextupole and decapole correction windings. A photograph of a coil end is shown in Fig. 1. The complete coil assembly is cooled in liquid N_2 and then inserted in a warm iron core to insure that the conductors are under compression at all temperatures. This method of construction is thought to be largely responsible for the exceptionally small amount of training experienced with these magnets.

III. Magnet Performance

Both magnets were initially tested individually while vertically positioned in an open mouth dewar at *4.18* K. The magnets were quenched several times to check for possible training and extensive magnetic measurements were made. After these tests had been completed the magnets were mounted in a horizontal cryostat and connected in series. Figure 2 shows both magnets just prior to insertion in the dewar. The cryostat is fitted with a room temperature aperture containing two sets of magnetic measuring coils on a common shaft. The magnetic and thermal cycling tests were performed in this configuration.

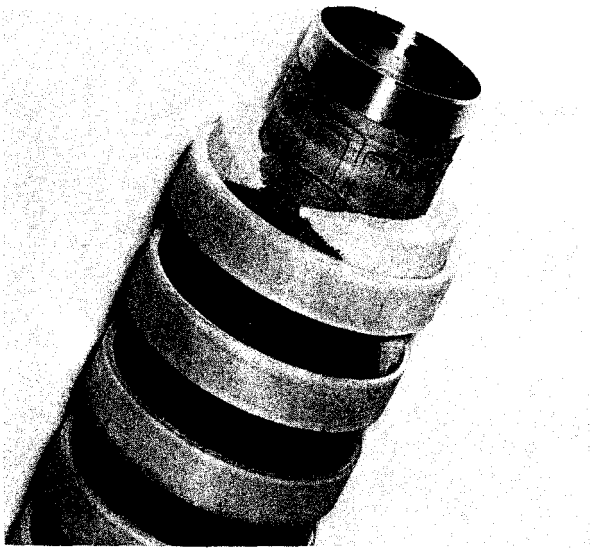


Fig. 1. End configuration of ISA dipole. The 3θ and 5θ correction windings are built into the central tube.

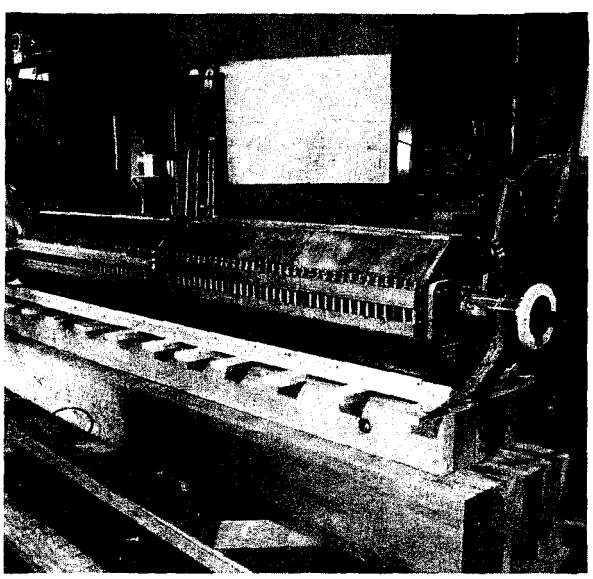


Fig. 2. ISA I and II just before insertion in horizontal cryostat.

1. Training

Remarkably little training was observed in either magnets. In Fig. 3 the load line for the magnets is shown on a current vs field plot for the conductor used and the first seven quench points are marked for ISA I. The two curves indicate the maximum and minimum currents observed in the wires used to make the braided conductor. $I(10^{-12}\ \Omega\text{-cm})$ is the current at which the effective overall resistivity is $10^{-12}\ \Omega$-cm and is generally taken as the highest practical operating current for conductors

*Work performed under the auspices of the U.S. Atomic Energy Commission.

containing very small filaments. Even the first quench exceeded the design current *(3450* **A)** and subsequent quenches resulted in about 10% higher current. The field plotted in Fig. **3** is the central field and no allowance has been made for the fact that the peak field is about 5% higher at some positions in the coils. The quench history of both magnets is shown in Fig. 4.

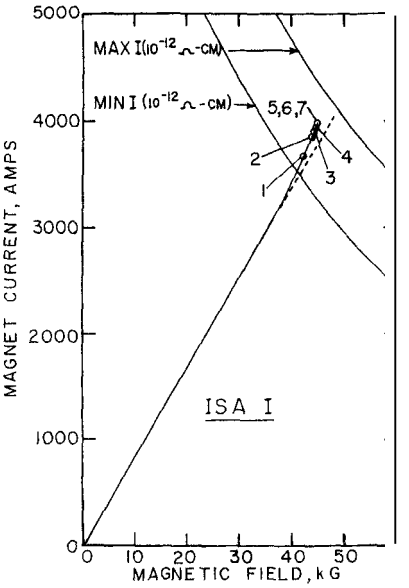


Fig. **3.** Current vs field curves for the conductor in **ISA** I the maximum and minimum values for the individual wires used in the braid are shown for an effective overall resistivity of 10^{-12} Ω-cm. The number points are the first seven quenches.

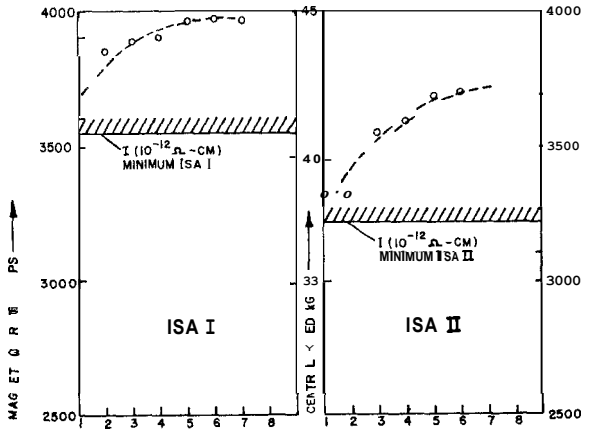


Fig. *4.* The quench history of **ISA I** and II at 4.2 K. The horizontal line indicates the minimum current at 10^{-12} Ω-cm for the wires used to make the braids in each magnet.

The conductor used for **ISA II** is not quite as good **as** that used for **LSA I** resulting in a somewhat lower field. After warm-up the magnets reached their highest previous current on the first energizing.

2. Current Density

The performance of the two model magnets is even more remarkable when the high current density required in this design is taken into account. The total radial winding thickness is only 1.9 cm and the overall current density at 40 kG on the median plane is 30 kA/cm^2. This corresponds to 60 kA/cm^2 in the wires used to form the braid and 130 kA/cm^2 in the superconductor itself.

3. Temperature Dependence

When mounted in the horizontal cryostat the magnets are at a somewhat higher temperature than in the vertical test dewar because of refrigerator back pressure. The temperature can be as low as 4.25 K when the system is free of impurities. The dewar pressure increases with time as impurities collect in the return line until a temperature of 4.9 K is reached at which time the system is usually warmed for cleaning. It takes approximately three weeks for the system to collect enough impurities to require warm-up, and the clean-up process itself requires about 24 hours. Because the magnets are in series the quench current is set by ISA II, which has the lowest quench current. Figure 5 **shows** some quench points obtained at different temperatures and compares them with the expected values based on an extrapolation of the 4.18 K value (the dashed line). The scatter in these points is probably due to the fact that we have used the dewar pressure as a temperature monitor rather than the actual magnet temperature.

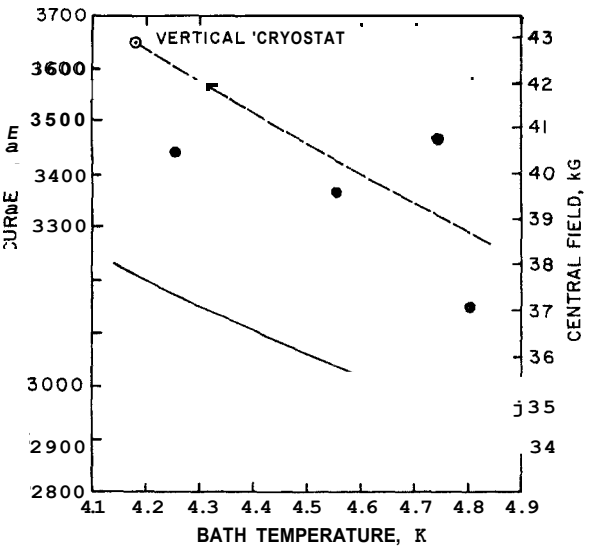


Fig. 5. Maximum current as a function of temperature for the two magnets in series with the closed loop refrigeration system. The dashed curve **is** the expected performance based on the results obtained at 4.18 K.

IV. Magnetic Measurements

During the vertical test, magnetic measurements were made using a set of Morgan2 coils of 6.9 cm diameter. This set contained dipole, quadrupole, sextupole, decapole, 14-pole and 18-pole windings. The results are shown in Table I for 6 kG (injection), 24 kG and at a high field, 40 kG, where the effect of iron saturation is evident. Calculated values for the harmonic coefficients are also given in Table I. These calculated values take into account the actual dimensions of the wedges used and the differential contraction of the coils on

cooldown and represent the built-in or "construction" harmonics. Only the in-phase (b_n) terms are affected by these symmetric construction displacements of the current blocks. *The* calculated values for the out-of-phase (a_n) term are based on a random error in block placement of 50 μm. The b_n terms are also subject to random errors, Since the calculated values do not include the effect of superconductor magnetization or iron saturation they are only valid at medium fields where the magnetization is small and iron saturation is not important. In general, the measured values fall within the range allowed by the assumed error. **The** quadrupole component (28) is sensitive to coil centering in the iron shield and shows considerably more variation from magnet to magnet.

shown as a function of dipole field in Fig. 7.for a cycle to 40 kG and back to 1 kG. From Fig. 7 it can be seen that the sextupole component returns to the original increasing field curve at approximately injection field. This curve is for dc excitation; under pulsed conditions the harmonics are altered considerably by currents induced between wires in the braid. It is expected that newer conductor types with faster dynamic response will eliminate this problem in the model magnets now under construction. An electronic scheme for automatic control of the harmonics is also under development.

A fixed frequency *NMR* set-up has been used to compare the two magnets. This device has two probes so

Table I. Harmonic Coefficients for ISA I and II

ISA I

Harmonics	Measured 6 kG b_n	a	Measured 24 kG b_n	a	Measured 40 kG b_n	a	Calculated 24 kG b_n	a	Units
3θ	- 3.1	- 0.2	- 2.7	- 0.1	+ 2.8	- 0.1	- 2.6	± 0.3	$10^{-4}/cm^2$
59	- 3.1	- 0.5	- *3.4*	- 0.5	- 8.7	- 1.4	- 1.4	± 2.6	$10^{-6}/cm^4$
79	11	7	7	7	4	4	11	± 19	$10^{-8}/cm^6$
98	- 230	< 1	- 170	< 1	- 120	< 1	- *300*	± 170	$10^{-10}/cm^8$
2θ	0.9	3.5	1.1	3.7	0.7	5.4	± 1.1*	± 1.1	$10^{-4}/cm$

ISA II

Harmonics	Measured 6 kG b_n	a	Measured 24 kG b_n	a	Measured 40 kG b_n	a	Calculated 24 kG b_n	a	Units
39	- 3.6	- 0.1	- 3.3	- 0.1	+ 2.2	0.0	- 2.8	± 0.3	$10^{-4}/cm^2$
59	- 5.1	- 0.4	- 4.6	- *0.4*	- 9.4	- 0.8	- 1.9	± 2.6	$10^{-6}/cm^4$
79	7	11	7	4	- *4*	- *4*	8	± 19	$10^{-8}/cm^6$
9θ	- *400*	< 1	- 350	< 1	- 290	< 1	- 350	± 170	$10^{-10}/cm^8$
2θ	2.7	0.9	2.2	2.0	2.5	0.2	± 1.1*	± 1.1	$10^{-4}/cm$

*No allowance made in the calculation for noncentering of coil in iron core.

In the horizontal test configuration two sets of Morgan coils were used in the warm bore. These coils were mounted on a common shaft and centered in each magnet. Only dipole, quadrupole, sextupole and decapole (10θ) coils were used because of the small diameter available. The shaft was driven by a stepping motor under the control of a small computer (HP 9100B) which also read the signals and computed the harmonics. The system is completely automatic and is shown schematically in Fig. 6. The sextupole component of **ISA I** is

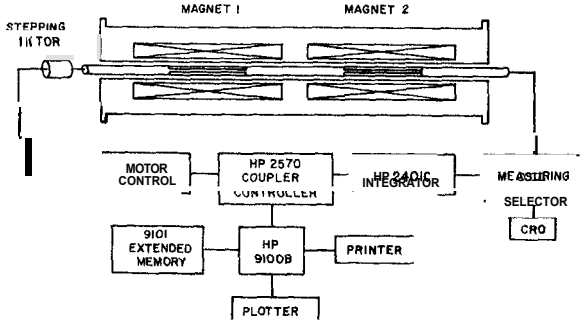


Fig. 6. Block diagram of automatic harmonic analysis apparatus.

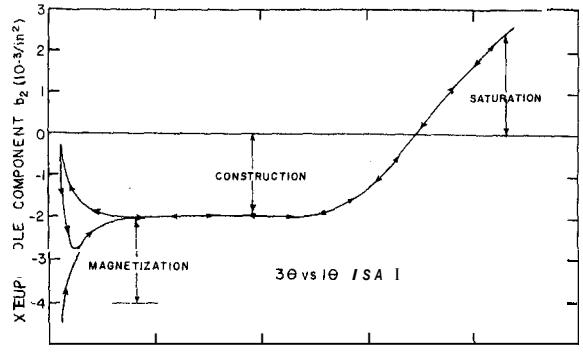


Fig. 7. Dependence of sextupole coefficient on dipole field for increasing and decreasing dc fields; ISA I.

that one can be mounted in each magnet and small differences in the fields observed directly. Since the magnets are in series, it is possible to compare them directly to a few parts in 10^5 despite the difficulty of determining the absolute current to much better than a part in 10^3. The measured magnetic constant for both magnets at the aluminum resonance field (20.72 kG) was

11.73 gauss/A. The calculated value using the program MAGFLD is 11.762. The difference between these two values is less than the uncertainty in current determination.

V. Magnetic Cycling

The magnets were cycled using a 100 sec current rise and fall and a 10 sec flat top and dead time. The idealized waveforms for the current and voltage are shown in Fig. 8 (a) and (b) and the actual waveforms are shown in Fig. 8 (c) and (d). A total of 5500 pulses were run to simulate the lifetime of an accelerating storage ring such as ISABELLE. Almost all of these pulses were to approximately 35 kG which was the highest field at which the magnets would operate for long periods without quenching due to low liquid level or high dewar temperature. The operation was completely automatic and proceeded with remarkably little difficulty. The harmonic coefficients were checked periodically during the run. No changes were observed within the accuracy of the measurement. The resolution possible from the measuring setup is $1 \times 10^{-5}/cm^2$ for the sextupole component and $5 \times 10^{-7}/cm^4$ for the decapole component. Considerable care must be taken in making the measurements since the dynamic effects can easily give differences of this magnitude if a precise measuring sequence is not followed.

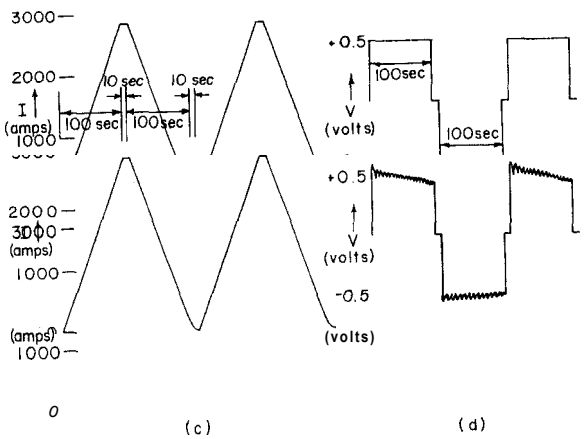


Fig. 8. Ideal and observed current and voltage waveforms for pulsing test.

VI. Thermal Cycling

As mentioned previously, the magnets were warmed up periodically for refrigerator maintenance. The maximum temperature reached during these periods varied from 50 K to 150 K. The system would reach a temperature of 150 K if allowed to warm unattended for one week. After completion of the pulsing test the magnets were purposely warmed to room temperature by circulating helium gas and then recooled. Again no appreciable changes in the harmonic coefficients were observed during this thermal cycling. Quenching of the magnets produces a rapid temperature rise in the coils and considerable thermal shock, but this did not effect the field distribution either.

VII. Conclusions

Both magnets performed well throughout the test. They exhibited very little training and could be operated successfully in series. The reproducibility from magnet to magnet was quite good and indicates that mass produced magnets of this type would meet the tolerances required for storage ring applications. The magnetic and thermal cycling tests indicate that no significant changes in field quality or magnet performance would be encountered during the life of a machine like ISABELLE.

Acknowledgments

The authors wish to thank the following people for their considerable assistance: R. Damm and C. Lasky, mechanical engineering; M. Thomas and S. Giordano, electrical engineering; R. Gibbs, J. Jensen, S. Kiss, and R. Rohrbach, cryogenic engineering and support. Also instrumental in the construction and testing were F. Abbatiello and R. Atkins. C. Walters (visiting from Rutherford) and G. Morgan were active participants in the testing and provided many useful ideas.

References

1. P.F. Dahl, et al., IEEE Trans. Nucl. Sci. NS-20, No. 3, p. 688 (1973).

2. G.H. Morgan, Proc. 4th Intern. Conf. Magnet Tech., Brookhaven, p. 787 (1972).

PULSED SUPERCONDUCTING DIPOLE MAGNETS OF THE GESSS COLLABORATION

P. Turowski (IEKP, Karlsruhe, Germany), J.H. Coupland (RL, Didcot, England), J. Perot (CEN/Saclay, France)
Presented by P. Turowski

Summary

The three laboratories of the GESSS Collaboration have biult dipole magnets which approach synchrotron conditions, all show a field homogeneity of a few parts in 10^3 up to a field level of 4.5 T, are capable of a rise time of at least 5 seconds with losses less than 20 W/m at a rise time of 10 seconds. For the next magnets the changes in designs are mainly towards a more homogeneous thermomechanical structure to overcome training effects, which are seen as the main problem of superconducting magnets today after meeting the requirements for field homogeneity.

I. Introduction

The three laboratories of the GESSS Collaboration IEKP Karlsruhe, Rutherford Laboratory and CEN Saclay have biult pulsed superconducting magnets of different designs, but all with the aim to fulfill the conditions of a synchrotron dipole magnet with high field homogeneity and operation under a pulsed mode. The three magnets D2a (SEKP), AC 4 (RL) and Moby (Saclay) have several design features in common, such as cold iron yoke or epoxy resin impregnated coils. Other details, current density distribution, the type of cable, the cooling conditions and the clamping of the coil are different. It is a difficult task to draw final conclusions from the test runs completed so far because of the many different parameters which influence the operational behaviour of each of the magnets.. This paper aims at summarising the most important conclusions drawn from the comparison of the three dipoles.

II. Main Design Features of the Three Magnets

Some geometric data of the magnets are given in Table I.

Moby:[1)]

The coil configuration of the Moby magnet is shown in Fig. 1. The slope of the parallelogram shaped current block was determined, so that the sum of all multipole terms in the-median plane gives a $\Delta B/B$ of less than 1×10^{-3} over 50%of the aperture. The cable the coil was wound from has organic insulated strands which are hollow braided and than flattened. The end contours of the coil are wound in constant perimeter fashion on the cylindrical surface. By choosing the slope of the end block it is possible to avoid a field enhancement in the end. The heat generated under pulsed load is removed by heat drains made of copper wires. The coil was wet impregnated during winding. The finished coil was mounted in the bore of the iron yoke, adjusted and finally moulded with epoxy resin to get a good fit to the iron yoke. The laminated iron is not split.

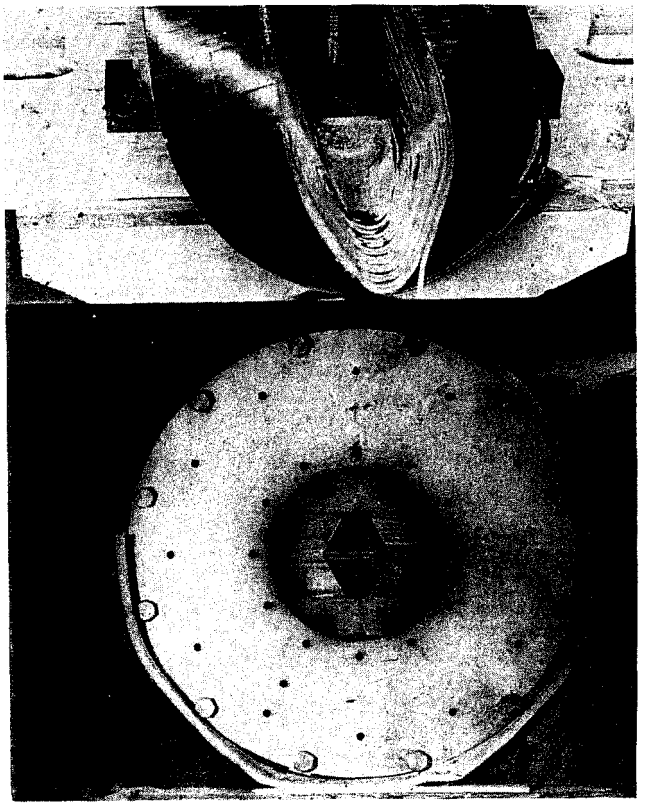


Fig. 1. End winding and cross-section of Moby.

AC 4:[2)]

The dipole field in AC 4 is generated by a current distribution very similar to overlapping ellipses shown in Fig. 2. The coil consists of two cylindrical double layers which are vacuum impregnated with epoxy resin and than stacked together. Between all the layers and on the outside surfaces there are annular cooling channels to provide a free circulation of liquid helium. The end was spread with the bending of 90° made in two steps. The lay-out of the ends is designed so that the field integral is correct with respect to multipoles. The strands of the 25 strand cable are inorganically insulated by copper oxide and the entire cable insulated by a terylene braid. The cylindrical and laminated iron yoke is split vertically. Therefore the magnetic forces acting on the coil have to be carried by the bolts which hold the iron halves together. On the other hand, one can prestress the coil by the bolts and compensate radially the differential contraction of the iron and the coil. The inner surface of the iron yoke is chamfered at the poles, see Fig. 2, to control the variation in sextupole due to iron saturation.

TABLE I. Main Features of Pulsed Dipoles Built and Tested by GESSS

Laboratory	RHEL	CEN-Saclay	IEKP-Karlsruhe
Dipole Designation	AC 4	Moby	D2a
Magnet Parameters			
Cold bore diameter (m)	0.093	0.1	0.08
Outside coil diameter (m)	0.15	0.23	0.152
Coil length (overall) (m)	0.725	0.66	1.3
Iron bore diameter (m)	0.1676	0.275	0.172
Iron outside diameter (m)	0.432	0.475	0.38 × 0,3
Iron length (m)	0.91	0.8	1.46
Current density in winding at 5 Tesla ($A \cdot cm^{-2}$)	2.03×10^4 (6000 A)	1.281×10^4 (6 T) (1230 A)	2.1×10^4 (1576 A)
Inductance (mHy)	4.8	200	136
Conductor			
Type	cable	braid	cable
Number of strands	25	24	12
Number of fil. × fil. size	2035 × 12 μ	1000 × 10 μ	1000 × 12 μ
Matrix	Cu/CuNi	cu	cu
Strand insulation	copper oxide	organic	In/Sn
Twist pitch (mm)	4.4	2	4
Transposition pitch (mm)	63.8	63	35
Performance			
Short sample field (Tesla)	5.4 (6200 A)	6.5 (1330 A)	5.4 (1800 A)
Max. auench field (Tesla)	5.4	5.0	5.3
Pulse field at 0.1 cycle/sec. (Tesla)	5.4	3.7	4.5
Losses at 4.0 Tesla and 0.1 Hz (Joule/cycle)	65	126 (3 T)	360
Effective magnetic length (m)	0.55	0.5	1.24

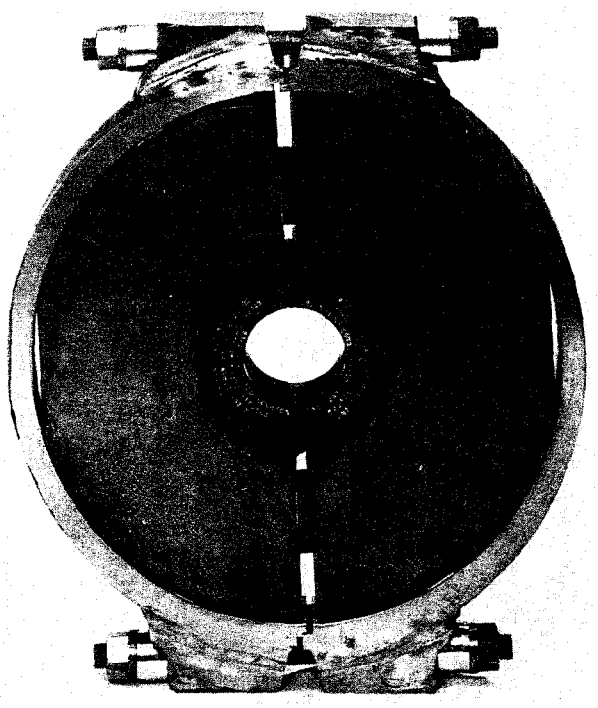


Fig. 2. Cross-section of AC 4.

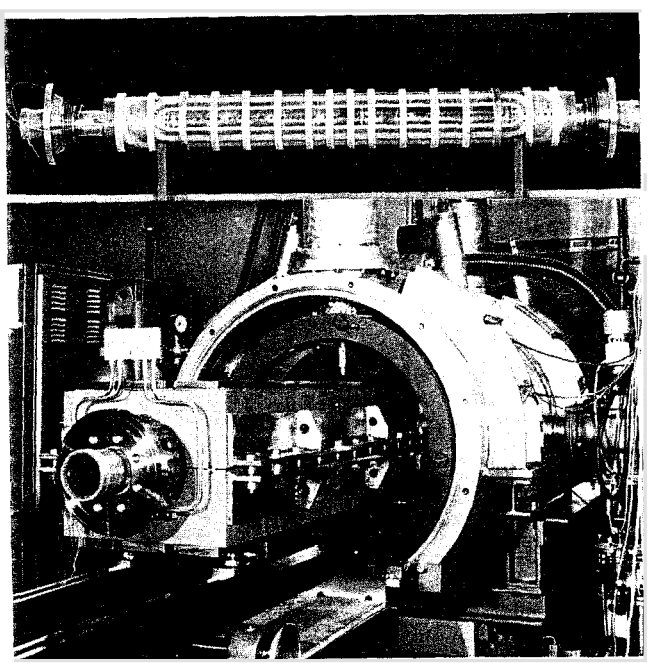


Fig. 3. Coil of D2a and the assembled magnet half inside its cryostat.

D2a:

The dipole field in D2a is generated by a modified sector geometry with constant current density distribution, see Fig. 3. The whole coil consists of five cylindrical shells each containing a double layer winding vacuum impregnated with epoxy resin. Between each shell cooling channels are provided for a free convection of liquid helium. The end of the coil is spread axially with a circular bending around the end. This contour is shaped in such a way, that the error in the field integral is smaller than 1 part in 10 . The

TABLE 11. Harmonic Coefficients C_n from Measurements of B_r *) in the Central Region

	B_o(T) / C_n							
AC 4:		0.85	1.69	2.57	3.51	3.86	4.26	4.61	4.91
	C_2	0.0017	0.0017	0.0017	0.0017	0.0017	0.0017	0.0017	0.0018
	C_3	-0.0053	-0.0050	-0.0049	-0.0045	-0.0042	-0.0038	-0.0043	-0.0047
	C_4	0.0004	0.0004	0.0004	0.0005	0.0004	0.0005	0.0004	0.0005
	C_5	-0.0050	-0.0049	-0.0047	-0.0040	-0.0033	-0.0025	-0.0020	-0.0016
Moby:	B_o(T) / C_n	0.025	0.1	0.25	0.5	1	2	3	4
	C_2	0.012	0.003	0.0019	0.0019	0.0019	0.0019	0.0019	0.0019
	C_3	0.025	0.0038	0.0062	0.0105	0.0125	0.0138	0.0147	0.0152
	C_4	0.002	0.002	0.002	0.002	0.002	0.002	0.002	0.002
	C_5	-0.038	-0.046	-0.046	-0.046	-0.046	-0.046	-0.046	-0.046
D2a:	B_o(T) / C_n	0.68	1.36	2.03	2.7	3.36	3.96	4.26	4.54
	C_2	0.0032	0.0032	0.0033	0.0034	0.0033	0.0032	0.0032	0.0031
	C_3	0.00072	0.00064	0.00063	0.00059	0.00062	0.00069	0.00077	0.00092
	C_4	0.00080	0.00077	0.00077	0.00074	0.00071	0.00071	0.00070	0.00068
	C_5	0.00098	0.00084	0.0011	0.00105	0.00107	0.00074	0.00067	0.00072

*) $B_r = B_o \sum_{n=2}^{\infty} C_n \left(\frac{r}{a}\right)^{n-1} \sin(n\Theta - \beta_n)$

cable contains 12 strands transposed around a central copper wire all soldered with indium-tin. It is therefore geometrically very stable and guarantees a good winding accuracy.

The iron yoke has a cylindrical bore but a rectangular outer contour with the ratio of the sides such that the influence of iron saturation on the central field is as small as possible. It is split in the horizontal plane so that the iron yoke itself can assist in the support of the magnetic forces; but there is no possibility for prestressing the coil. The 10 half shells were made to fit together exactly and clamped by a prestressed epoxy resin impregnated glassfibre tape. These bandages contain the total magnetic force of about 130 t.

III. Field Accuracy

In Table 11, some results are listed of field shape measurements. The field measurements are done in a very similar way in all three laboratories by rotating a bucked coil system.

For AC 4, a very exact calculation of the field coefficients in the case of iron saturation had been performed in the design stage. A good agreement was found between the measured and calculated values for the sextupole enhancement due to iron saturation.

In Moby, the measured sextupole *is* increasing with field whereas the decapole is practically independent of field. The summation of the sextupole (3.5×10^{-3}) and the decapole (-3×10^{-3}) at 4 T at half the aperture shows that these terms just compensate to a total field error of $\Delta B/B = 5 \times 10^{-4}$.

In D2a, a slight increase of the sextupole coefficient from 5.8×10^{-4} at low fields to 9×10^{-4} at 4.5 T may be observed. A calculation of field errors due to random distribution of 0.1 mm for tolerances in coil manufacturing shows that a sextupole coefficient of 5×10^{-4} is to be expected. This indicates that the limit in field accuracy was reached as given by possible tolerances of 0.1 mm. At 5 T the field reduction due to iron saturation amounts to about 5%, see Fig. 4.

All three magnets show an undesired quadrupole term. It seems that slight errors in symmetry during the winding process and during positioning of the coil into the iron yoke can cause these deviations. In the case of D2a there is a radial deviation of the outer cylindrical shell with respect to the other four shells of about 0.3 mm, which causes a quadrupole term of 3×10^{-3} independent of B_o. It is believed that this field error can be reduced to about 5×10^{-4} by correcting this misalignment.

The remanent fields, depending on the filament size and on the amount of superconductor, are in the range of $1 - 2 \times 10^{-3}$ T. Within a factor of 1.5 to 2, they agree with the values expected by calculations.

IV. The Pulse Mode Operation

The pulse mode operation and the loss measurements have shown that the predicted and the experimentally measured values are in

good agreement. The exact calculation is troublesome because the field distribution inside of the winding area has to be integrated over all elementary volumes. In Fig. 5 the measured values of ac losses are shown normalized per kg of NbTi. The losses in Moby and D2a are measured with a Hall-multiplier whereas in AC 4 the hysteretic loop of the entire magnet was studied and used for evaluating the losses. AC 4 and Moby show mainly hysteretic losses with only a small contribution from eddy currents, see Fig. 5. In the indium-tin soldered cable of D2a the eddy current contribution amounts to 290% at 0.1 cycle/sec and 4 T. In spite of these high eddy current losses all the magnets meet the conditions of 10 - 20 Watts/m for pulse times of 20 sec. The eddy current losses, e.g. in the D2a cable, can only be calculated roughly because of the lack of knowledge of resistivity and critical length dimensions. For an estimateone can use the decay time of the eddy currents which can be measured. It was found to be 5 msec for the D2a cable.

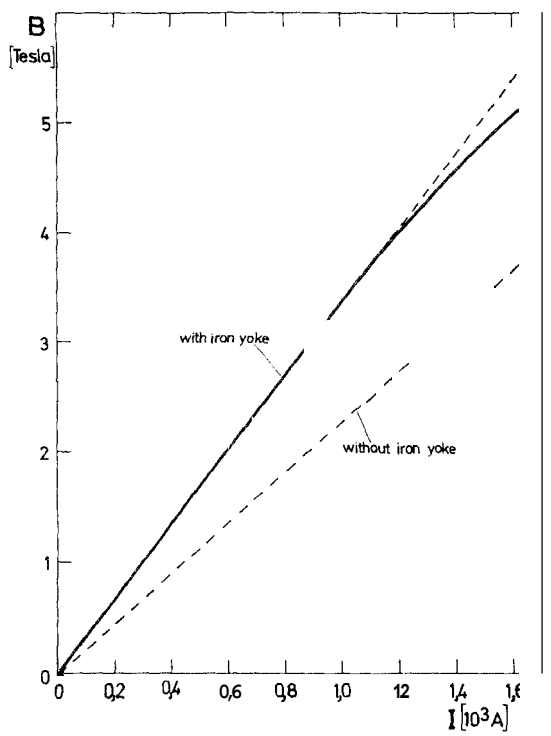


Fig. 4. The continuously measured central induction of D2a up to quench versus current.

In pulsed operation the three magnets demonstrate a somewhat different behaviour. Moby has a significant reduction in maximal field with increasing frequency whereas AC 4 and D2a do not show nearly as much frequency dependence up to 1 Hz for AC 4 and up to 0.1 for D2a, both rates being limited by the power supply. The cause of this frequency dependence is not the heat generated in the coil as shown by detailed temperature measurements in Moby during pulsing. A comparison of the losses per unit volume in Moby and D2a, shows that in spite of the higher losses in D2a(7.3×10^{-3} W/cm^3) against 1.4×10^{-3} Watt/cm^3 at 0.1 Hz), there is no reduction in maximum field. An experiment with D2a shows, that cooling conditions and temperature enhancement are not decisive factors for early quenches: it was possible to pulse the magnet (4 T, 0.1 Hz) at 4.9 K temperature of the bath just as well as at 4.2 K. The reason for the poor pulsed behaviour in Moby is due to eddy currents in the cable, which are the more marked the higher the frequency.

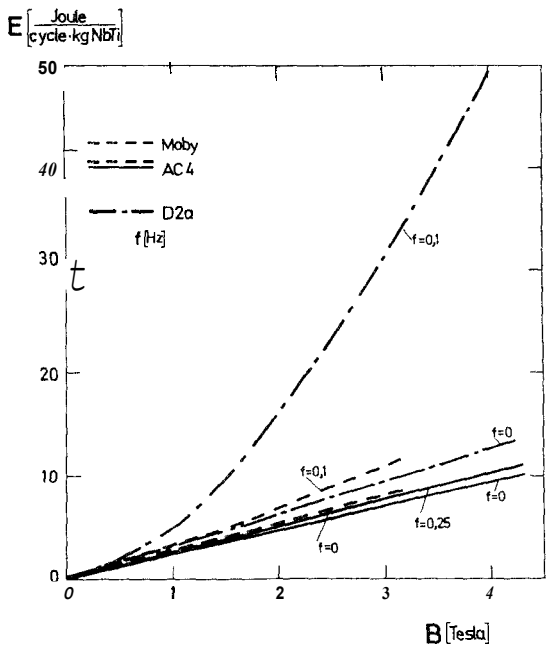


Fig. 5. Losses of the three magnets versus field amplitude at different frequencies.

Experiments in Karlsruhe have shown, that these induced currents collapse abruptly when critical current and field conditions are reached and cause a macroscopic flux jump. Obviously, well insulated strands in cables are susceptible to such loop currents by intermittent shorts in conjunction with soldered end connections.

V. Training

Though the magnets are different in mechanical assembly, different epoxy resins and different clamping, they needed many quenches to reach the maximum field value and demonstrate a very similar training behaviour. AC 4 started in training at 75% of the maximum value whereas Moby and D2a had their first quench at 40 - 50% of the maximum value finally reached. It is assumed that this difference is due to prestressing in AC 4.

The cooling of the coils does not appear to influence the training behaviour, since Moby and D2a exhibit very similar training inspite of their very different cooling methods. The heat release which causes a magnet to quench is obviously very quick, and so close to or in parts of the superconductor, that time constants of 10^{-2} s for heat transfer through 0.3 mm thick epoxy resin coatings are too slow.

The magnets AC 4 and D2a have proved robust and reliable during operation. The magnet D2a has experienced more than 250 quenches and has been pulsed 2×10^5 times up to a field level of 4.5 T. The AC 4 cable, with its inor-

ganic insulation and the indium-tin soldered cable of D2a are obviously more able to withstand overload during the quick event of a quench. Unfortunately, in Moby 8 strands of the cable were burnt out during early quench tests but it was quenched many times later quite successfully using the remaining 16 strands, each fed with a individual resistor.

VI. New Designs

For the latest magnets Alec, D2b, AC 5 to be constructed in the GESSS-Laboratories several changes or improvements in the designs have been made.

For Alec, the main changes from Moby are:

1. Instead of the braid, a 6 × 6 cable (4.65 × 2.7 mm^2) copper oxide insulated will be used.

2. The coil is to be assembled into the "non-split" iron in a special way to support the electromagnetic forces and accomodate the differential thermal contraction in the radial direction.

3. The wet lay-up technique for bonding the layers of the winding is replaced by a dry "B-stage" epoxy resin. Each layer is then bonded by minimal heating so as to leave a porous structure for subsequent vacuum impregnation of the whole coil into its outer sleeve.

4. The coil shape is chosen to give a better field homogeneity in the central section. In the horizontal or mid plane of the magnet the field deviation is less than 4×10^{-4} within 70% of the full aperture.

5. The magnet is being constructed entirely in industry to a collaborative design.

6. Principal parameters are: coil aperture 110 mm, coil length 1.66 m, overall length 1.8 m, effective magnetic length 1.5 m. Operational field is 5 T (0.1 Hz; 2100 A).

D2b differs from D2a in the following points:

1. The cable will be a flat helix made from three component conductor with inorganic insulation, like copper oxide.

2. There will be two double layers of winding, vacuum potted together in a "one-piece" construction. The coil has a thick glass fibre outer bandage which is later machined to suite the "split-iron" yoke.

3. The conductor will be wound into specially machined slots in carbon fibre reinforced epoxy formers so that at cooldown, the coil blocks are compressed on all sides.

4. Helical cooling channels will be formed in the windings between the layers by pulling out teflon strips from the winding after potting. Supercritical helium circulates through these channels when the magnet is pulsed.

5. For economic reasons, a short magnet is planned: length of coil 0.6 m.

AC 5, design differences from AC 4 are:

1. The four layers of the windings will be in a "one-piece" potted construction with no split at the equator. The same system of annular cooling channels remains, but they will be made by dissolving out preplaced wax strips.

2. The layers are thicker radially to include more conductor or increase the safety margin at 4.5 T.

3. The use of high density flat strip conductor (polyimide coated) leads to a lower thermal contraction overall for the winding especially as the conductors are wound into tight rectangular groups of six. It is hoped to get an overall contraction of 250×10^{-5} to 77 K or 375×10^{-5} to 4.2 K. This allows the application of shrunk-on stainless steel bands around the coil to contain it under compression and facilitate fitting into a whole, but laminated iron yoke.

4. With the increased gap between coil and iron there is no need th chamfer the inside of the iron yoke to control the sextupole variation due to iron saturation.

5. Because the conductor is a flat strip, round ends have to be used to enable winding.

6. It *is* planned to correct any residual quadrupole error in the winding by eccentric assembly of the iron; 0.25 mm is allowed for in the design.

VII. Conclusions

The magnet tests have shown that the achieved field qualitity in the range of some parts in 10^3 is due to errors in the symmetry of coil assembly; more care in maintaining the symmetry would lead to errors in the full bore of less than 1 part in 10^3. When pulsed, the losses are below 20 W/m at 0.1 Hz. In fully insulated cables, the losses are mainly hysteretic and can be predicted reliably. The eddy current losses in soldered cables are surprisingly low; they can only be estimated by additional information on the decay time of eddy currents. The iron losses measured are small and there is no reason to avoid a cold iron yoke.

Apart from training, all the magnets have achieved in d.c. operation between 70% and full short sample values of the currents. Under pulsed operation, magnets D2a and AC4 have run at the design value of 4.5 T. The Moby magnet had the misfortune of shorts in the cable which limit the performance for pulsed operation. The phenomena in a cable made of organic insulated strands are not fully understood. Current sharing between the strands is an important factor of stability.

From experience gained in the magnet tests, it seems clear that training may be reduced or eliminated by avoiding internal rubbing surfaces and shear forces which may arise from electromagnetic forces as well as from differential contraction. So, the aim is to construct a "one-piece" superconducting magnet with well matched materials in order to avoid all kinds of internal stresses.

References

1. A. Berruyer et al., "The Superconducting Pulsed Dipole 'Moby' ", 4th Int.Conf. of Magnet Technology, Brookhaven, 1972
2. J.H. Coupland, "The Design, Construction and Testing of the Superconducting Magnet AC 4", Rutherford Laboratory Report RL-73-105
3. P.Turowski, to be published as KFK-Report, Karlsruhe, Germany

EXPERIMENTAL SUPERCONDUCTING ACCELERATOR RING *

(ESCAR)

R. Avery, T. Elioff, A. Garren, W. Gilbert, M. Green, H. Grunder, E. Hartwig, D. Hopkins, G. Lambertson, E. Lofgren, K. Lou, R. Meuser, R. Peters, L. Smith, J. Staples, R. Thomas, R. Wolgast

Lawrence Berkeley Laboratory
Berkeley, California

Introduction

The ESCAR project is an accelerator technology development for which the primary goal is the fabrication and operation of a relatively small proton synchrotron and storage ring employing superconducting magnet elements for the main ring. The purpose is to gather data and experience to insure that the planning and design of future large superconducting synchrotrons and storage rings may proceed in a knowledgeable and responsible manner.

The proposed project will not only provide the experience of fabricating and operating a complete cryogenic magnet system with a significant advancement beyond present experience, but it will also provide a comprehensive accelerator system from which can be learned the realities of the interaction between the cryogenic components and the many other elements of an accelerator. The extent to which these elements (e.g., rf, injection, vacuum, control systems, etc.) are compatible with the cryogenic features of the accelerator, and to which they force modifications of the design, will be determined.

The ESCAR circulating beam will permit experimentation on important aspects of the dynamics of high-current stored proton beams. In this area there are many unresolved issues of importance to future storage rings. The flexibility to carry out a program of beam experiments will be incorporated in the design. Finally, the ESCAR system may indeed prove suitable for an experimental program with high-energy heavy ions, or as a booster-injector for future high-energy proton systems.

Design Goals

The following general parameters express the intended scope of ESCAR.

Maximum Energy	-	4.2 GeV
Intensity	-	5×10^{12} protons
Pulse Rate	-	6/minute
Pressure	-	10^{-11} torr
Injection Energy	-	50 MeV.

The maximum energy is chosen to permit a realistic test of high-field magnets at a reasonable cost. The intensity evolves from the characteristics of the existing injector, the desire to avoid excessive apertures in the main-ring magnets, and the desire to investigate high-current beam effects. The pulse rate is determined (initially) by power supply and refrigerator capabilities. The magnet system will be capable of faster pulse rates; additional refrigeration capacity can be added if higher pulse rates are desired. Of course, d.c. operation will be provided, and the low pressure expected from cryogenic pumping will permit beam storage times of several hours.

Physical Location

The overall layout with respect to the Bevatron is shown in Fig. 1. ESCAR will utilize the existing 50 MeV linac which is in close proximity. The linac is used also as a proton injector for the Bevatron. A pulsed magnet will direct the 50 MeV beam either to ESCAR or to the Bevatron. ESCAR is located at the rear of the existing Bevatron experimental hall which provides roof coverage, 30-ton-crane facilities, and heavy-duty floor and foundation. Adequate power and water distribution systems are located in tunnels below the experimental hall. No major interference with the Bevatron-Bevalac program is anticipated.

Machine Geometry

An expanded view of the ESCAR system is shown in Fig. 2. The ring, of 15 m average radius, has 4 long straight sections, each 6 meters in length. The lower straight section is occupied by the injection and beam dump system, the right straight section contains the normal accelerating rf system, and the other straight sections are available for experiments, monitoring, and diagnostics. High-frequency cavities which might be used for longitudinal bunch compression are indicated as a future possibility on the left side of the ring.

The magnet layout in a quadrant, or cell, of the lattice is shown schematically in Fig. 3. It is a separated function structure with focusing provided by the groups of 4 quadrupoles. Six dipoles, each $\sim$ 1 meter long, form the 90° arc of each quadrant. This arrangement provides adequate straight sections and a loosely-packed lattice structure which is desired for diagnostics and general flexibility. The betatron functions are shown in Fig. 4, corresponding to betatron tune values of $\nu_x = \nu_y = 3.25$. The structure allows arbitrary values for the transition energy. The nominal value chosen, $\gamma_t \approx 8$, is well above the peak energy--as it would be difficult at best to cross transition with 5×10^{12} protons. The high value of γ_t has been achieved by the action of the strong Q4 lenses that reduce the excursion of off-momentum particles in the curved regions (see Fig. 4). Independent variations of ν_x, ν_y, and γ_t may be obtained by adjustments of the quadrupoles. γ_t can be brought within the machine energy range if experimentation on crossing γ_t is desired. Table I summarizes the nominal value of most of the machine parameters. Other physical paramenters are shown in Fig. 3. Further optimization of these parameters can be expected as the detailed design evolves,

* Work supported by the U.S. Atomic Energy Commission.

Table I

Design Momentum	P	5 GeV/c
Kinetic Energy	T	4.2 GeV
Dipole Field	B_o	4.6 T
Quadrupole Gradients:	dB/dr	
Q1		12 T/m
Q2		-13 T/m
Q3		-15 T/m
Q4		18 T/m
Aperture Radius (dipoles & quads)	A_r	8.2 cm
Number of Cells	N	4
Betatron Tunes	$\nu_x = \nu_y$	3.25
Transition Energy	γ_t	7.8
Beta Function (maxima)	β_x	16.4 m
	β_y	20.2 m
Dispersion (maximum)	$\hat{n}_x$	3.3 m
Injection (vertical stacking)		
Energy	E_{inj}	50 MeV
Linac Emittance	ε_L	2s cm-mrad
Linac Current	I_L	100 mA
Number of Injected Turns	n	~20
Captured Intensity	N_p	5×10^{12} protons
Stacked Emittances	ε_H	2π cm-mrad
	ε_V	16π cm-mrad

Injection and Ejection

To obtain the intensity of 5×10^{12} protons, one must use multiturn injection and stack about 12 effective turns, of which about 70% will be captured by the accelerating rf. The stacking will be done in vertical betatron space using programmed kicker-magnets. If needed for additional intensity and to make the beam cross-section more round, the beam from the linac may be split vertically and recombined radially before injection to reduce the vertical emittance.

For an experimental accelerator, it is particularly desirable to minimize radioactivation by the accelerated beam. Normal operation will include deceleration of the beam and controlled internal dumping at an energy below 150 MeV. The primary goal of the project and studies of single-particle dynamics can be done with an intensity reduced to 10^{11} or less protons. For emergency beam dumping at high intensity, a pulsed magnetic ejector is planned.

Accelerating Radiofrequency System

For the greatest flexibility in beam experiments, the particles shall be accelerated in one bunch at the first-harmonic frequency. After acceleration, if desired, the beam can be more tightly bunched or divided into a few bunches by a second, higher-frequency system. It is possible that a single drift tube may serve for both frequencies; that is, it will act as an accelerating drift tube at the fundamental frequency and also act as a half-wave resonator at a higher harmonic; e.g., the 10th or 11th. For experiments with extremely short bunched beams, it will be possible to add other high-frequency cavities.

Magnets and Cryosystem

The magnets and associated equipment are central to the ESCAR experiment and will include many features appropriate to a full-scale high-energy ring. Although certain adaptations to the magnets are required by the smaller scale of ESCAR, the experience gained with the complete system will be directly applicable to future systems. Hence, the magnet system must not be regarded as an exact prototype but a realistic test of the technology.

The preliminary design for the dipole magnets is illustrated in Fig. 5. The quadrupoles will have a similar structure. Each dipole is ~1 meter long, with a design field of 4.6 T. The magnet design incorporates intrinsically stable, fine filament, NbTi superconductor that is well cooled with liquid helium and rigidly supported. The high-vacuum region is enclosed by a cold beam tube upon which the multi-layered coil is wound. Circular symmetry is used in all inner regions to yield the best possible structural and magnetic properties.

The cold-bore system will be continuous through each quadrant of the ring containing 6 dipoles and 8 quadrupoles. Helium at 4.4°K is introduced at the quadrant entrance magnet, flows through the quadrant elements, and then flows back, at reduced pressure and temperature in the outer annular region of the cryostats, as in a counter-flow heat exchanged. This system is surrounded by evacuated super-insulation and an 80° temperature shield, The magnet iron at room temperature surrounds the cryostat. The cryostats of three dipoles will be welded together, forming a single unit to be assembled into the main ring. Two such units are required in each quadrant. In addition, there will be two straight cryostats, each containing 4 quadrupoles to complete each quadrant.

The maximum required quadrupole gradient is 20 T/m. The quadrupoles will be separately controlled to vary focusing conditions. Initially the magnets will have a 5 second rise time to full field, as determined by the capacities of the power supply and the refrigeration system, Shorter rise times as low as one second are possible and will not complicate the magnet fabrication or the conductor requirements, Without flattop the pulse rate will be six per minute, or the power supply can hold full current continuously for studies with coasting beam,

In the straight sections, it is planned to maintain the beam tube at ~4.4°K, except where a warm section is required for special equipment. The magnets may remain cold while straight sections are warmed and opened. The refrigeration capacity required is 1500 watts. The choice of the optimum refrigerator system is presently under investigation.

Vacuum

The vacuum system will be designed for 10^{-11} torr. It is believed that this can be economically obtained via distributed cryopumps at 4.4°K. This is the operating temperature of the superconducting magnets and provides practically unlimited pumping capacity for all gases except helium and hydrogen. Hydrogen can be pumped effectively by bare-surface cryopumps up to a coverage of eight-tenths of a monolayer. The only helium gas loads which could arise come from leaks from the

refrigeration system. Helium is pumped by bare-surface cryopumps at a pressure of 10^{-11} torr to only 1/1000 of a monolayer before saturation. Because of the large area of cold surface available, about 200 minimum detectable leaks can be pumped effectively for a number of weeks.

The straight sections contain the accelerating cavities, the injection and extraction systems, and diagnostic equipment. These elements will present additional gas loads for which the geometry and size of the cryopumps must be designed. Distributed cryopumping will be used where possible. The hydrogen and helium pumping capacity of the straight section cryopumps can be increased as required by operation at a lower temperature, by a permanent electro-deposit of porous silver, or by a replaceable condensation deposit of CO_2. The C02 deposit could be especially useful in the valved cryopumps used for finish roughing and conditioning. These pumps could be operated steadily to remove small helium leak loads. Gas loads that could enter from the straight sections into magnet sections will be intercepted by short lengths of tubular cryopumps that are easily cycled.

While a cold bore through most of the system provides excellent cryopumping, the surfaces surrounding a high-intensity beam are a concern with respect to gas desorption, the electrical impedances presented to the beam, and the potential need for ion-clearing electrodes. Consequently, various liners for the bore are being considered.[3] Fig. 6 illustrates some examples. These vacuum system questions are an important part of the ESCAR mission. The cold-bore system visualized here would greatly simplify the design and reduce costs[4] of future large proton storage rings.

Accelerator Research

In addition to the primary goal of obtaining a workable superconducting accelerator system, it is expected that ESCAR can be effectively utilized to investigate phenomena related to high-current stored proton beams. Some of the present design considerations for high-energy colliding beam devices are making new demands, for example, on beam densities, magnet tolerances, and rf systems. ESCAR should be able to provide additiondl information with regard to some of the beam effects in question. The relatively long straight sections would permit the addition of special diagnostic components, low-β insertions, or rf systems to accomplish strong bunching, as required, for example, in the PEP device[5].

In the 1973 PEP Summer Study, a number of problems were discussed for which various existing and proposed devices would provide important contributions toward future proton storage rings. Listed below are suggested studies[6] for ESCAR:

-- Methods for achieving ultra-short bunches. Can high-frequency passive cavities be used for self-bunching?

-- Bunch stability: coupling of the beam to cryogenic surroundings, bunch-broadening phenomena (transverse and longitudinal), multi-bunch effects, rf noise, intrabeam scattering.

Beam-vacuum interaction. What are the differences with bunched and unbunched beams?

Investigation of cold-bore vs. warm-bore vacuum systems.

Investigation of new diagnostics for beam measurements in a cryogenic environment.

-- Investigation of methods for correction elements; i.e., superconducting or conventional, lumped or distributed?

-- Determination of radiation damage effects and fatigue effects on superconducting elements. Also beam-heating effects.

Some of the above examples are a logical part of the primary ESCAR goal, such as the feasibility of the cold-bore vacuum system, It is expected, however, that many other phenomena will arise and require investigation when a real circulating high-peak current beam is at hand.

Other Research Potential

Aside from the potential value for experiments in beam effects, ESCAR could provide unique physics research facilities for ultra-heavy ions. In Fig. 1, it is seen that it would be relatively easy to inject ions as heavy as Uranium from the SuperHILAC, whose output-beam line is near the 50 MeV linac which serves as the ESCAR proton injector. Due to the excellent ESCAR vacuum system, the unstripped SuperHILAC output could be accelerated in ESCAR to ∿300 MeV/nucleon, which is nearly two orders of magnitude more energetic than any existing system. Partially stripped outputs could reach more than 1200 MeV/nucleon. Apart from obvious uses in nuclear science and in biomedical studies, the interest in such energies has been heightened by recent theories[7] which indicate the possibility of new superheavy states of nuclear matter which might be achieved by heavy ion collision at these energies.

Another possibility is the use of ESCAR as a booster injector for future proton storage rings, The ESCAR parameters are well matched to the proton injector requirements of PEP Stage II. In any case, its components could provide a compact injector for a future high-energy storage ring.

Schedule and Plans

The nominal parameters and systems outlined above are presently being investigated in detail. A preliminary engineering design for all system components is planned for completion in July 1974. Final design and fabrication of components can begin at that time, coincident with the beginning of FY 75. Based on expected funding levels, 2.5 years are projected to fabricate ESCAR and begin operational testing.

The AEC has appointed an ESCAR advisory board having members from other accelerator laboratories. It is intended that this group help guide the scientific planning of the project. It is recognized that the primary goal of ESCAR is to gain information on superconducting accelerator design and system operation. For this purpose alone, the entire project could be considered as an experiment that would end with successful operation as an accelerator and storage ring. But it is also apparent that the ring has potential value as a tool for experiments in beam effects and controls, as well as for physics research.

At this time, when funding is limited and progress requires the extrapolation of our understanding to ever more complex and costly machines, it seems that ESCAR will be a very appropriate and productive experiment in accelerator science.

References

1. W. Gilbert, R. Meuser, and F. Toby, Proceedings of the International Conference on Magnet Technology, BNL, Upton, N.Y., September 19-22, 1972.
2. Refrigeration System for the NAL Energy Doubler, Cryogenic Consultants Incorporated, April 26, 1973 (Unpublished).
3. Superconducting Accelerator Miniproject (Concept & Intent), LBL Accelerator Study Group, Proposal #1, Sept. 1973.
4. J. R. J. Bennett, Hot or Cold Bore for a Superconducting EPIC Ring, Rutherford Internal Report EPIC/MC/42.
5. L. Smith, The Proton-Electron-Positron Project, Proceedings of the 9th International Conference on High Energy Accelerators, Stanford, May 2-7, 1974.
6. 1973 PEP Summer Study Report, LBL-SLAC Study Group, PEP Note #66, March 1974.
7. T.D. Lee and G. C. Wick, Physical Review D, April 15, 1974.
8. This method is related to that utilized by V. V. Vladimirskii and E. K. Tarasov, "Problems of Cyclic Accelerators," USSR Academy of Sciences, Moscow, 1955.

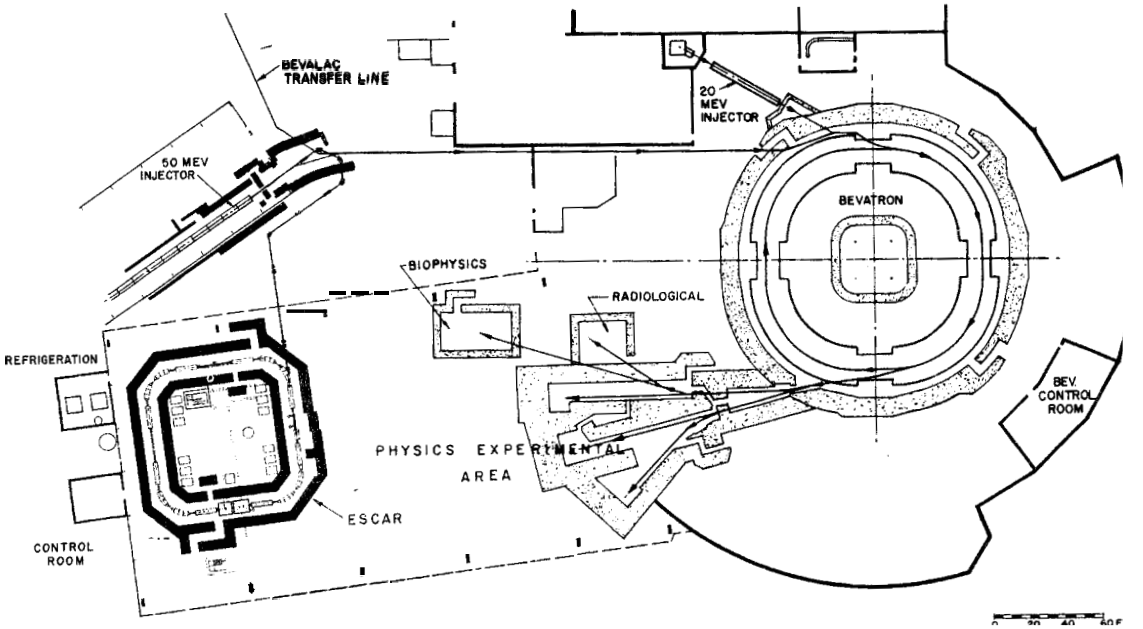


Fig. 1
ESCAR Location

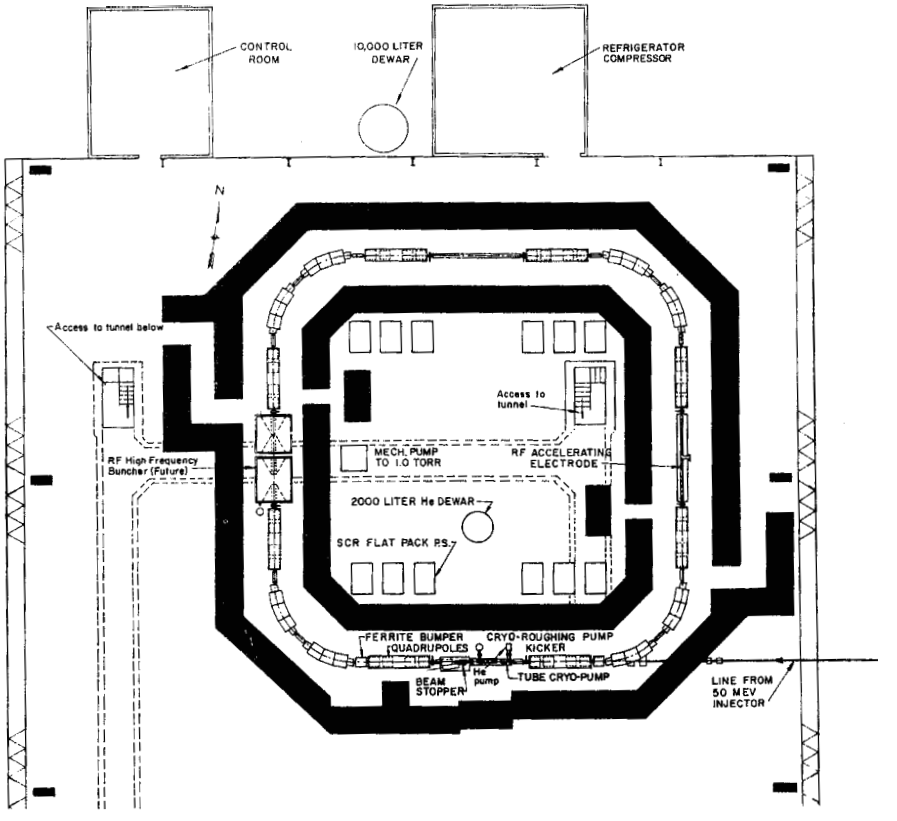


Fig. 2
Ring Geometry

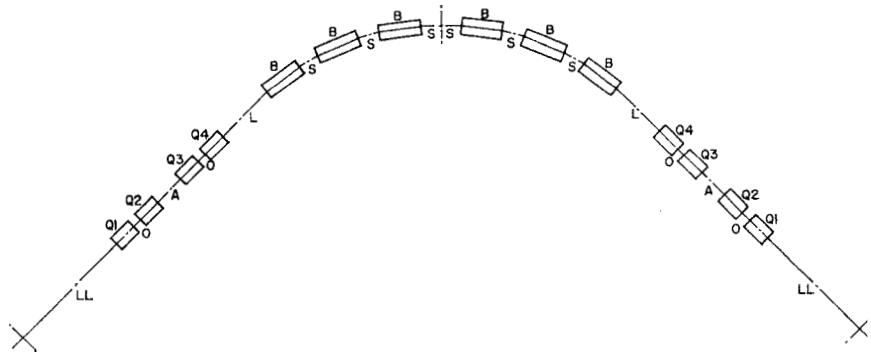
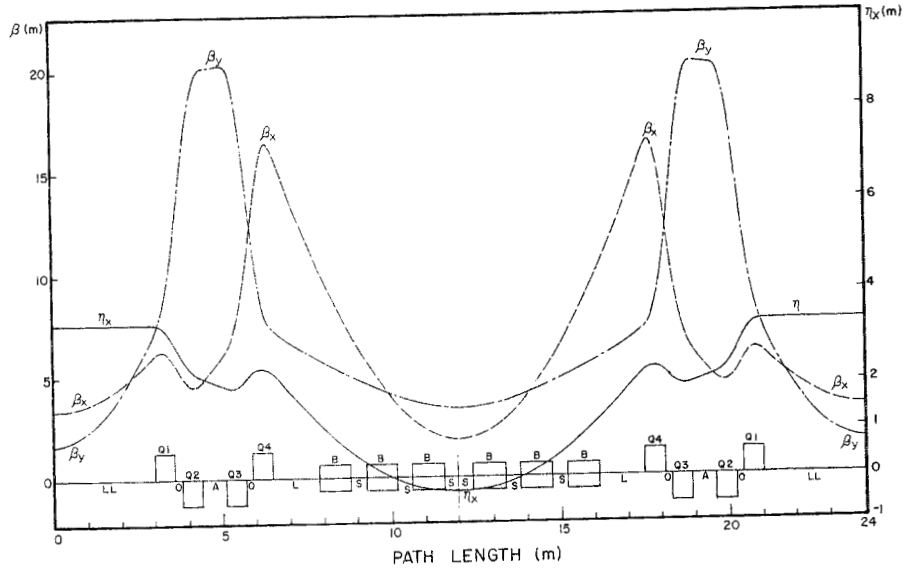


Fig. 3 - ESCAR
Quadrant Schematic

Radius (Circ./2π)	R	15.29	m	**Drift Lengths (Effective):**	
Magnetic Radius	ρ	3.6287	m	LL	3.00m
Cell Length	Lc	24.0	m	O	0.20m
Quadrupole Effective Length	ℓ_Q	0.6	m	A	0.70m
Dipole Effective Length	ℓ_B	0.95	m	L	1.36m
				S	0.43m

Fig. 4
Betatron Functions



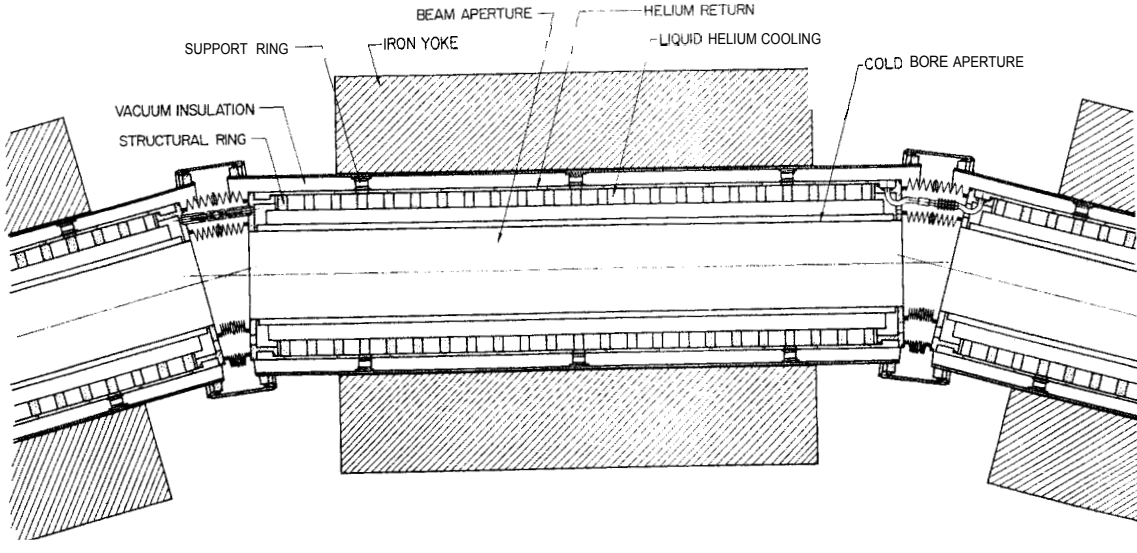


Fig. 5 - Dipole
Magnet Structure

PROGRESS REPORT ON THE NAL ENERGY DOUBLER DESIGN STUDY

D, A. Edwards, W. B. Fowler, P. J, Reardon, D. E. Richied, B. P. Strauss, D. F. Sutter
National Accelerator Laboratory*
Batavia, Illinois 60510

Summary

For close to a year and a half, a study has been in progress at NAL to examine the feasibility of constructing the "Energy Doubler" - an accelerator employing superconducting magnets which would increase the energy of protons available at the Laboratory substantially above that provided by the present accelerator system and possibly to 1000 GeV. In this paper, we report on the progress to date and on plans for continuing the study in the immediate future.

The Energy Doubler Concept

The design parameters of the NAL accelerator were set primarily by the funds available for construction. There was no sharp guideline of an energy threshold at which some crucial physics hypothesis could be tested, nor did accelerator technology dictate a limit to the energy that could be achieved. Thus, there was considerable incentive to build a potential for higher energies and to conserve funds *so* that this potential could be realized within the initial $250 million construction authorization for the Laboratory.

The NAL proton synchrotron was initially intended to be a 200 GeV machine. It now regularly operates at 300 GeV and has occasionally produced protons at 400 GeV. In the near future, tests at energies up to 500 GeV are planned.

It was recognized early in the project that an even higher energy or an improved duty cycle was conceivable if a ring of superconducting magnets were to be installed in the same enclosure as the present main accelerator, which would then act as the proton source for the superconducting ring. Space in the tunnel and in the service buildings has been saved for just such a possibility, Because superconducting bending magnets might be expected to reach 45 kG, twice the field of the conventional magnet ring at 500 GeV, the superconducting ring has been designated an "Energy Doubler."

Origin of The Design Study

After the accelerator came into operation in 1972 and high energy physics experiments got underway, it was not only possible to devote some attention to the Doubler idea but it was also timely. Of the funds authorized for construction of the Laboratory some $30 million remained uncommitted at that time. Of course, it was expected that a significant portion of this sum would be needed to bring the accelerator and experimental areas to a reasonable state of completion and some $10 million has since been spent for those purposes. But if it were possible to obtain the major components of the Doubler - the magnets and their associated refrigeration system - at a cost in the neighborhood of say, $20 million then the opportunity would present itself for a further increase of the energy capability of the Laboratory within the initial authorization. The design effort to date represents a first step in the exploration of this possibility.

Though the next section offers comments on the various roles that the Doubler might play at the Laboratory, the purpose of those remarks is intended only to provide a context within which to view the subsequent discussion, since the emphasis of the work thus far has been on magnets and refrigeration. There are many other accelerator-related topics that deserve study, but given the limited resources that could appropriately be diverted from far higher priority activities associated with bringing the accelerator performance up in terms of intensity, reliability, proton splitting and beam spill and with initiating the ambitious experimental program at the Laboratory, it was clear that the focus of the study should be on those aspects of the Doubler most intimately associated with new technology. [1]

At the outset, a number of tentative design principles were established, among which are:

- the Doubler cycle time will not exceed 100 seconds but in order that thermal loads originating from time varying currents not be the major factor in determining refrigeration system capacity and cost, shorter cycle times are not essential.
- the magnet dewars will themselves play the role of transfer lines carrying coolant from and back to the refrigerators located at the service buildings.
- the magnets will have a cold beam tube since the relatively low Doubler beam current will have less stringent vacuum and surface cleanliness requirements than a storage ring.
- the magnet enhancement iron will be at room temperature and non-saturating, two criteria intended to provide magnets whose fields are linear with excitation and within the smallest possible total cross-section, including dewars and to reduce the refrigeration requirements for reasonable cool down times.
- the superconducting material will be NbTi since this is the only material which industry presently is able to provide in a filamentary configuration in large quantity.
- the current in the conductor will be consistent with utilization of existing main accelerator power supplies for Doubler excitation at the highest practical current density.

The discussion below will summarize the work thus far in developing cryogenic systems and magnets consistent with the above.

General Descriptions of the Energy Doubler

Location and Magnet Distribution

The position that the Doubler might occupy is shown in Fig. 1; at the top of the tunnel its orbit would be some 3 feet inside of and 4 feet above that of the main ring. Only limited variations from the disposition of magnets in the present accelerator is possible for the doubler lattice, having selected the enclosure. For

* Operated by Universities Research Association, Inc. under contract with the U. S. Atomic Energy Commission.

example, the doubler geometry must duplicate the *six* long and six short straight sections of the main ring. Some of the flexibility that remains may be used to advantage to facilitate injection and extraction, but for the purpose of this discussion it is sufficient to think that the Doubler replicates the main accelerator bend-for-bend and quadrupole-for-quadrupole.

We have adopted a length of 20 feet for our superconducting dipole prototypes - the same length as the conventional dipoles in the main accelerator. A total of 744 such magnets would be required. A duplication of the main ring lattice implies 192 normal cell quadrupoles and 48 long straight section matching quadrupoles. If the tune of the Doubler is to be the same as that of the main ring, then $B'\ell$ for the normal cell would be 1260 kG-m at 1000 GeV, and just over 60% of that figure for the matching quads. Thus a total of 1014 superconducting magnets are needed for the Energy Doubler.

Uses for the Doubler

As a Conventional Accelerator. In its basic form, the Energy Doubler idea is that of a slow-cycling machine with a period of 100 seconds or less at 1000 GeV, but not an order of magnitude less, Today the typical operating intensity of the NAL accelerator is 6×10^{12} protons per pulse with a 6 second cycle at 300 GeV. If, by the time the Doubler is functioning, the accelerator has achieved its design goal of 5×10^{13} protons per pulse and if this charge can be conveyed to, accelerated in, and extracted from the Doubler without significant loss, then a 60 second cycle time Doubler would deliver to the external beam lines approximately the same average intensity as the accelerator produces at present. Of course, for internal target experiments causing negligible diminution of the circulating beam current, the effective intensity is independent of cycle time. Fig. 2 shows how the accelerators might operate in this mode. In this and the following examples let's assume that the Doubler ramp rate is limited to 20 GeV/sec. One out of every ten 300 GeV main ring pulses is injected into the Doubler; the remaining nine are extracted and used as at present. The Doubler accelerates to 800 GeV at which energy the beam is extracted. Higher energies would imply longer Doubler cycle times.

As an Energy Saver. The present accelerator system, operating at 300 GeV with a 6 second repetition rate and a 1 second flat-top, requires an average power of somewhat over 40 MW. This already substantial demand increases rapidly with higher energy or duty factor. It is easy to think of ways in which a superconducting ring may help in this situation. Fig. 3 illustrates two approaches to a 12 second 400 GeV cycle each having a duty factor of $\sim 1/6$. The dotted line represents the main accelerator going to 400 GeV with a 2 second flat-top. The average power required is 60 MW. In contrast, the solid lines depict an acceleration in the main ring to 300 GeV, fast transfer to the Doubler, acceleration in the Doubler to 400 GeV, and subsequent extraction using a 2 second flat-top. We estimate the average power required in this case to be 22 MW, almost a factor of three less than that associated with the present accelerator system alone.

As a Beam-Stretcher. In this mode, the Doubler does not accelerate at all. Rather, the beam is transferred to it from the main ring at the peak of the cycle of the latter, and slow extraction from the Doubler lasts, hopefully, until the next pulse is available for injection. In principle, a auty factor of close to 100% could be obtained.

As an Injector to Storage Rings. The NAL Long Range Advisory Committee has recently recommended that the Laboratory's long term planning center around the design of "POPAE" storage rings, (Proton On Proton And Electron), with the proton rings to accomodate energies of 1000 GeV. The Doubler could be the proton injector to POPAE, thereby providing protons at the storage energy and making it unnecessary to contemplate acceleration of the high current in the storage rings thereby simplifying their construction.

Dynamical Questions

Since the Energy Doubler as pictured here closely resembles the main accelerator in number and disposition of magnets, many of the aperture arguments are the same for the two machines and need not be detailed here. Finding and improving a closed orbit, provided a suitable beam position monitoring system is available, is a well-understood problem. Given reasonable magnetic measurement data, a careful survey, and a means for beam steering, it is likely that a circulating beam can be obtained without unusual difficulty insofar as magnetic length and placement effects are concerned.

Efficient extraction imposes a more severe aperture requirement. In a resonant extraction scheme the aperture has to be large enough in the extraction plane to permit a betatron oscillation of sufficient amplitude to develop so that the amplitude-dependent step size becomes sufficient to jump an extraction septum with high efficiency. A measurement made at 300 GeV in February of this year indicated that the extraction system of the main accelerator uses 1.3 inches of aperture in which the unstable betatron oscillation builds up. To this we add twice the septum channel width of 0.4 inch, and arrive at an aperture requirement of 2.1 inches. At present, the extraction efficiency is typically 97% and is limited by effective septum thickness.

The full scale Doubler prototype dipoles discussed below have a geometrical (in contrast to good-field) aperture in the horizontal plane of just under 2.2 in. Though the fundamental guide line in the doubler proposition is the acceleration of protons to the 1000 GeV range at minimum cost, clearly their effective delivery to external experimental areas is a most desirable feature, and it remains a subject for further study to determine whether or not improvements in the extraction scheme or in the good field width of the magnets can be made to compensate for the aperture constraints considered here. As the design progresses it may also be necessary to make the magnets slightly wider in order to accomplish high efficiency slow extraction from the Doubler.

The second principal accelerator related question associated with the Doubler magnet design concerns non-linear effects. Interpretation and correction of non-linear resonances in the main accelerator has proved to be a difficult and time-consuming process. Measurements on field quality of the superconducting

magnet prototypes produced thus far give cause for concern. The cost trade-off between increasing the coil aperture to improve field quality versus an elaborate correction system remains to be assessed.

Refrigeration System

The design principles upon which the magnet cooling system is based were reported at the 1973 Particle Accelerator Conference in San Francisco.[2] Very briefly, the idea is that subcooled liquid helium will be pumped from 12 *(or* 24) refrigeration stations, located at 12 (or 24) main accelerator service buildings into the coil volume of magnets situated upstream and downstream of each such station. At the point halfway to the next refrigeration station, the coolant will pass through a Joule-Thompson pressure reduction valve, and flow back toward the refrigerator as boiling liquid in an annular space surrounding the subcooled liquid helium coming from the refrigerator. One of the 12 *(or* 24) modules of the system is sketched in Fig, 4. The realization of this scheme with the magnets is discussed under Magnet Development below. In this section we report on experimental work on the pumped helium feature.

Liquid Helium Pump Loop

Large pumped helium systems of the sort required for the Energy Doubler have not been built. Accordingly, a significant effort in the design study is the construction and testing of a liquid helium pump loop on a scale large enough to provide experimental verification of Energy Doubler refrigeration concepts. A detailed report on the pump loop will be published shortly;[3] here we summarize this activity.

The basic pump loop system is sketched in Fig. 5. Refrigeration is provided by a 150-200 ℓ/hr helium liquefier [equivalent to $\sim$ 600 W of refrigeration at 4.5°K) purchased from Gardner Cryogenics, Inc., which makes liquid into a reservoir. The reservoir contains a liquid helium pump which circulates liquid helium through the pump loop. In addition to the liquid helium pump, the reservoir contains a heat exchanger, which (together with a vacuum pump) will make it possible to operate the loop at temperatures as low as 3.6°K.

The loop itself consists of 2 lengths of 200 feet of coaxial pipe forming a total length of 400 feet (space constraints required that the line doubles back on itself). The helium pump forces liquid through the inner tube. At the end of the 400 feet, the liquid is expanded through a Joule-Thompson valve and low pressure liquid helium returns through the outer annulus to the reservoir. Typical temperatures of the subcooled supply and low pressure return streams are 4.6°K and 4.4°K respectively. The pressure difference between the two streams lies in the range of 5-15 lb/in^2. The loop is equipped with temperature, pressure and flow monitors, heaters that simulate the thermal loads of magnets, and valves to simulate the pressure drops of the magnets.

It is intended that Energy Doubler magnets will be inserted in the loop by removing sections of pipe and replacing these with magnets. Even without magnets, however, an interesting and useful test program has carried out.

The system has been operated for three runs of 109, 70 and 106 hours duration. These tests were very valuable in giving experience in the operation of a cryogenic system on this scale. As noted above, discussion of the results will appear elsewhere;[3] we only enumerate some of the subjects of study here.

Pump Characteristics. The liquid helium pump was purchased from Sunstrand Aviation and was developed for this application based on their experience with liquid hydrogen pumps. Measurements of flow rate versus developed head are in agreement with predictions of the manufacturer. To illustrate a typical operating condition, a flow of 215 lbs/hr corresponds to a pressure rise of 10.4 lbs/in^2 across the pump.

The electrical power measurements compare favorably to the power measured by the fluid properties. Heat input to the liquid for the aforementioned condition is approximately 64 watts.

Pressure Drops. Under all flow conditions, as expected, pressure drops were quite low. Measured psi drop on the liquid line as measured by the pressure gauges for the 400 foot loop are in the region of 20" of H_2O.

The pressure drop as measured on the 2 phase return line, with an unknown quality, is approximately 42" of H_2O.

Precise measurements will be made with the installation of improved instrumentation.

Heat Transfer. By energizing heaters in the subcooled helium pipe and observing temperatures in the two streams, the heat transfer coefficients between the subcooled and two-phase regions can be determined. The measurements are in agreement with calculations, the principle uncertainty being in the duality of the two-phase flow.

Thermal Oscillations. In the first run, thermal oscillations, sometimes of magnitude sufficient to cause visible motion of the entire pump loop, were frequently observed. Modifications - principally the conversion to cold check valves - eliminated these oscillations at design flow parameters by the time of the third run.

Magnet Development

Superconducting Wire

For our first full scale prototype magnets, we settled on a multi-filament NbTi wire, consisting of about 2300 filaments 35 μm in diameter embedded in a Cu matrix, with outside dimensions of 0.075 inch x 0.150 inch including a 0.002 inch layer of polyvinyl and formvar insulation. The short sample test requirement was specified to be 3500 A in a 50 kG field at 4.2°K. This configuration offered the high current and high current density desired for our magnets (2815 A and 43.6 kA/cm^2 at 45 kG) yet was also felt to be achievable with present technology.

Since we are interested in developing magnets with coils that can be wound by more *or* less conventional techniques in industry, the conductor should resemble a "stiff" copper wire. Initially, this presented some

problems at the current densities desired since most conductors offered when this project began optimized the critical current density by cold working the wire. In response to our invitations for proposals, Magnetic Corporation of American recommended the use of superconducting alloys that would optimize the critical current by the solid state precipitation of submicroscopic normal particles within the filaments. An order was placed with this vendor, and the conductor that they have supplied has met our specification with regard to critical current insofar as our preliminary tests have indicated.

With its relatively large filament size and low-resistivity matrix, this conductor is not suited to high repetition rates. Calculations indicate that hysteresis losses dominate at a 100 second repetition rate and it is not until cycle times shorten to about 10 seconds that hysteresis and coupling losses become comparable.[4] Insofar as the initial conductor order was concerned, we felt that the more important goal was to establish that a high current density wire could be made and that later industry could develop a similar wire but with smaller filaments. We also have on order a quantity of cable conductor sufficient for the fabrication of two full scale dipole prototypes; this cable is to be made of seven wires each containing filaments less than 20 μm in diameter and separated one from another by a high resistivity material (cupro-nickel).

The Energy Doubler would require 6 million feet of superconducting wire. An order of this size would have considerable impact on the industry. We expect that for these lengths, the cost per foot would come down to an asymptotic level approaching less than half of present costs. Additionally, the cost difference between a relatively sophisticated small filament cable and a larger filament wire may be small. Fig. 6 shows our estimate of cost per foot as a function of total length.

Magnet Design and Fabrication

Here we will only summarize work on dipole magnets. A full-scale quadrupole prototype is nearing completion: however, the emphasis *so* far has been on dipoles. Fig. 7 shows a transverse section through a magnet.

The Bore Tube. The bore tube forms both the vacuum chamber and the locating surface for mounting the coils. In cross-section, the tube geometry consists of two semi-circles joined by flat portions top and bottom to provide a proton beam aperture measuring 2.2 inches horizontally by 1.4 inches vertically. The bore tube is a composite of an inner 0.032 inch stainless steel pipe with a molded epoxy-fiberglass coating to provide a reproducible insulating base for the coils.

Coils. The coils are wound as three concentric shell-like layers, with conductor placement calculated to provide a field uniform to 0.1% within a region similar in shape to the inner surface of the coils but 25% to 30% smaller in linear dimensions. The conductor is graded in size for economy; a smaller cross section wire (0.050 inch x 0.150 inch) formed by an additional drawing of the basic conductor is used in regions of sufficiently lower field. Prior to winding, the wire is keystoned so that it may be close-packed into the shell configuration. Winding is performed on a specially designed fixture in which the mandrel oscillates about its longitudinal axis while the conductor supply reel "walks" at a programmed speed around the table on which the mandrel is mounted.

Coil Cooling Passages. Liquid helium flows along the length of the magnet in the spaces above and below the coil. The conductors are to be cooled by vertical convection through passages between the innermost coil and the bore tube, between the inner shell and the second shell, and between the third shell and the wall of the vessel. It is intended that at least 40% of one edge of every conductor be exposed to the convective flow, that fraction representing a compromise between the demands for cooling on one hand and for adequate rigidity of the structure to withstand the magnetic forces on the other. The passages are formed by circumferential grooves on the bore tube, by G-10 spacers between the first and second coil shell, and by the banding on the outer coil bundle as described below. In the present design the passages extend 0.25 inch in the dimension parallel to the axis of the magnet. The two inner passages are 0.062 inch in depth.

Coil Banding. The coils are held against the beam tube by pretensioned bands, with a periodicity and width determined by the cooling passage requirements mentioned above. Until recently, a thin high strength mylar was used as the banding material, applied at a tension of ~ 80% of its breaking strength. As this material was available in a thickness of only .00075 inch, 210 layers were needed to produce the required strength resulting in an overly costly and time-consuming stage in magnet fabrication. At present, we are using stainless steel as the banding material.

Cryostat. The helium vessels are formed by two concentric stainless steel cylinders, separated by a corrugated structure to transfer electromagnetic forces on the magnet to the suspension members. These, containing the coil, form the 4-5°K volume of the magnet. A precisely centered energized coil is in unstable equilibrium with respect to the shield; at 45 kG, the "negative spring constant" is ~ 750 lb/in^2. Thus a strong, low heat loss suspension must be interposed between the inner chambers and the outer cryostat jacket. The use of an intermediate temperature (15-20°K of gaseous helium) shield makes this problem more tractable and is now being incorporated in prototype magnets. Prototypes completed to date have, for simplicity, not included a heat shield, and although considerable effort has gone into the development of a suspension which would be adequate for use without the shield, the results have not been encouraging.

Iron Shield. The iron enhancement shields consist of two laminated half cores stacked on one of the original main ring magnet fixtures with a precamber to compensate for the subsequent deflection under gravity. The laminations are first roller coated with a room-cure epoxy and stacking of a 20 foot half-core is then easily accomplished within the three hour pot life of the resin.

Ends and Interconnections. In a sense, the transverse section described above is the simple part of the magnet. Space does not permit us to describe present designs for ends and interconnections, which

may be fortunate, since ideas concerning these aspects of the magnets are changing daily.

Magnet Tests

Prior to the construction of the first full scale prototype dipole, seven short magnets (6 dipoles and 1 quadrupole with lengths ranging from 12 inches to 40 inches) were built. The first five were in a sense fabrication studies.[5] Two coil geometries were in competition - the shell configuration described above and a pancake style. Tests in both vertical and horizontal dewars suggested that the shell offered a geometry more appropriate to effective cooling. As a result, the shell coil was adopted for further development.

The last two of this seven magnet series were a pair of 30 inch long dipoles intended to be identical. Compartive measurements of magnetic length and field duality were made in order to determine whether or not the magnets were indeed identical insofar as the design goals established for them were concerned. Their magnetic lengths did in fact agree at the 0.1% level, however a significant quadrupole component in both magnets (~ 0.4%/inch) indicated that some symmetry had been lost in construction.[6]

In general, results on this set of short prototype magnets were quite encouraging. The superconducting wire procured for the full scale magnets was not yet available, *so* the coils of these magnets were wound from a variety of conductors available at the time. These conductors did not permit excitation to the 45 kG level demanded of the Doubler, however, in all cases, these short prototypes were capable of excitation at ~ 90% of the short sample current for the materials used in their fabrication. In all cases, magnets were tested in pool-boiling helium.

In February of this year, a full scale, 20 foot long prototype was ready for test. This was the first magnet wound from the wire intended for use at 45 kG. Also, it was the first magnet incorporating the complete counter flow cooling scheme proposed for the Doubler. Thus far, the performance of this magnet has been, in general, unsatisfactory. It has quenched repeatedly at low current levels - less than 50% of design current. Though the current at quench has been increasing gradually, whether or not the magnet would eventually reach its design current is an academic question, for the processing of a large number of magnets in this way is impractical. Nevertheless, the construction of a full scale magnet at the earliest possible time in our program was very valuable in suggesting improvements in fabrication methods.

In order to isolate and identify the source, or sources, of difficultv in the full scale magnet we are now engaged in a program of testing 30 inch long dipoles. These magnets have geometrical cross sections similar to the 20 foot doubler magnet but allow us to make changes in magnet construction in a known and controlled way - for example, operating with one, two or three shells. To date, a three shell version identical to the 20 foot magnet except for length and stainless steel (vs. mylar banding) has exhibited behavior similar to the 20 foot magnet and a single, inner shell version impregnated with epoxy and banded with stainless steel has gone to the short sample limit, 4500 A at 23 kG, in a vertical dewar. This program is continuing in full force and is expected to shortly provide the engineering data that will allow us to resume construction of the 20 foot magnets.

Plans for the Near Future

As the discussion of the preceeding paragraphs would imply, our immediate goal is the production of full scale dipole magnets capable of excitation to fields in the neighborhood of 45 kG without excessive processing.

The next phase will bring the magnet and refrigeration systems programs together by installation of a series of magnets in the pump loop. Actually, a step in this direction is already underway, for the second full scale prototype is being readied for insertion in the loop. This magnet does not differ significantly from the first, *so* its excitation characteristics are likely to be the same, however, useful experience will be gained in the loop system by this exercise. Completion of this phase will be marked by the insertion in the loop of a complete basic lattice period of the Doubler - 8 dipoles and 2 quadrupoles.

As indicated earlier, the design effort to date has been highly concentrated on the magnet and refrigeration system for the Doubler in order to establish their feasibility for a cost of something like $20 million. *So* far, in order of descending confidence, we have had industrial estimates made on the refrigerator, the superconducting wire and the magnets. On this preliminary basis, it appears barely possible to talk about these items being accomplished for the funds we have allowed. We have a long way to go, however, in completing the design and building satisfactory prototypes and production models before we can say something more definite. We, like everyone else, are also experiencing shortages and higher costs for raw materials, and the current state of uncertainty in the economy will no doubt play an as yet unknown role in the final estimate for the doubler, particularly in view of the instability of the superconducting wire business.

Acknowledgements

Many more members of the Laboratory staff have contributed to this effort than is reflected in the authorship of this particular paper. Magnet design and fabrication has been carried out by Technical Services headed by H. Hinterberger; G. Biallas, R. Brocker, and W. Hanson have devoted much of their time *to* this activity during the past year. S. Snowden of the Accelerator Theory Group has performed a number of the more difficult calculations relating *to* the magnets. W. Gilbert and the LBL Superconductivity Magnet Group have provided valuable assistance to this effort with measurements on our wire. We are indebted *to* R. R. Wilson for his support and guidance.

References

1. The basis for the design study are described more extensively in NAL Technical Memorandum TM-421-0428, edited by P. J. Reardon and B. P. Strauss.
2. P. C. Vander Arend and W. B. Fowler, IEEE Transactions on Nuclear Science, Volume NS20, No. 3, 119 (1973).
3. To be presented at the 1974 Applied Superconductivity Conference, September 30, 1974.
4. W. Gilbert, LBL, Private Communication.

Tests on the first two magnets of this series were reported by P. J. Reardon et al, IEEE Transactions on Nuclear Science, Volume NS20, No. 3, 744 (1973).

NAL Technical Memorandum TM-456-0428, by B. P. Strauss and D. F. Sutter, "Evaluation of Matched Superconducting Dipoles."

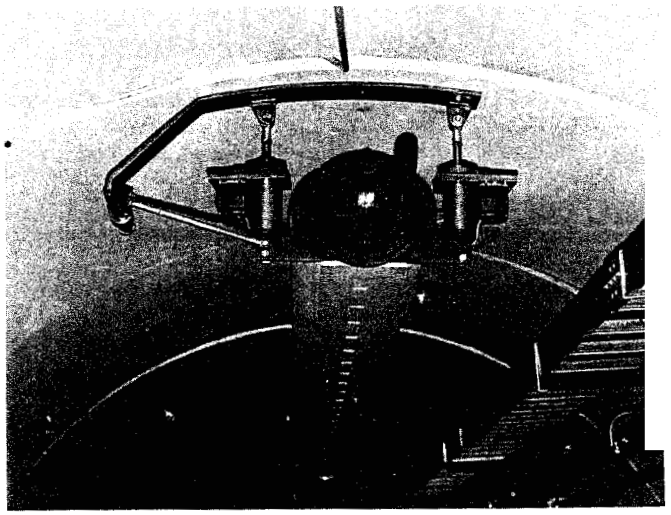


Fig. 1. A model magnet and suspension system hung in the present NAL Main Ring.

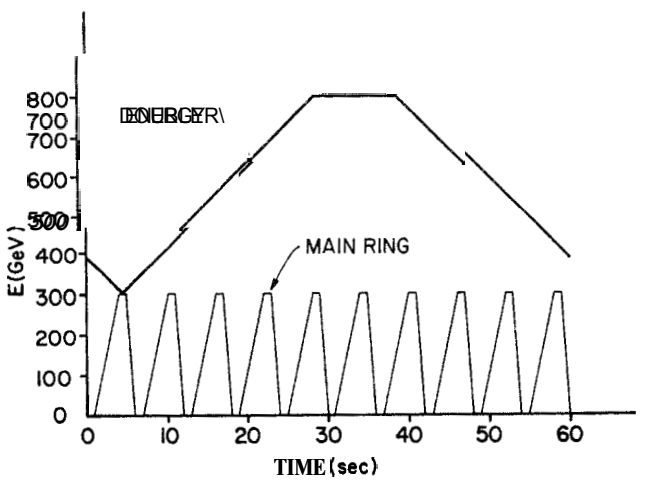


Fig. 2. The proposed Energy Doubler cycle superimposed on the present Main Ring cycle.

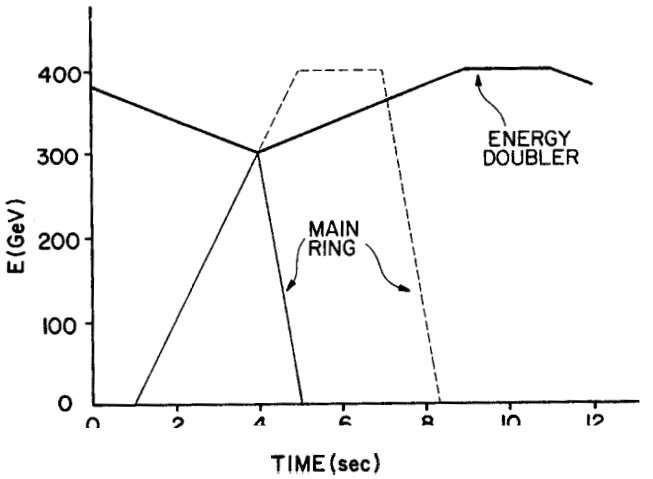


Fig. 3. The proposed energy saver cycle. Here the Energy Doubler is used to accelerate protons from 300 to 400 GeV and provide an extended flat-top.

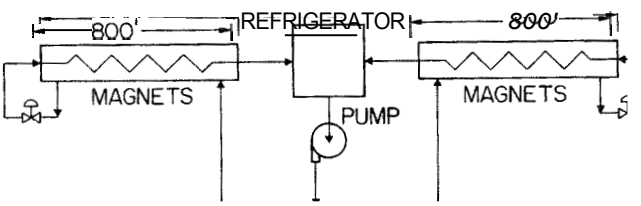


Fig. 4. Schematic diagram of the pump loop showing one refrigerator servicing the magnets between two service buildings. Note the main features of the pump and the Joule-Thompson expansion valves at the end of each string of magnets.

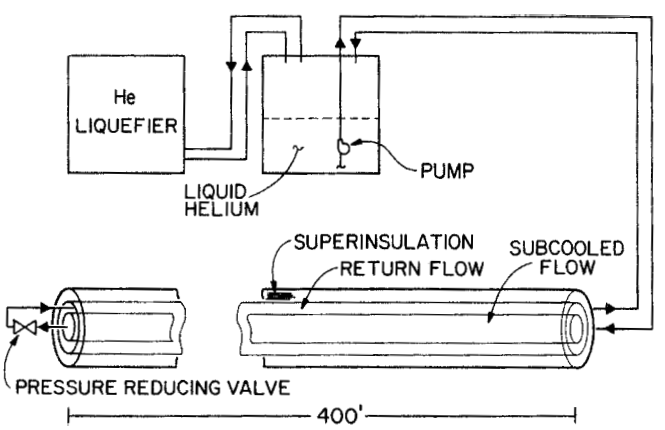


Fig. 5. Schematic diagram of the pump loop presently installed in a prototype tunnel at the NAL Village. This is basically the same system shown in Fig. 4 except for the elimination of the magnets.

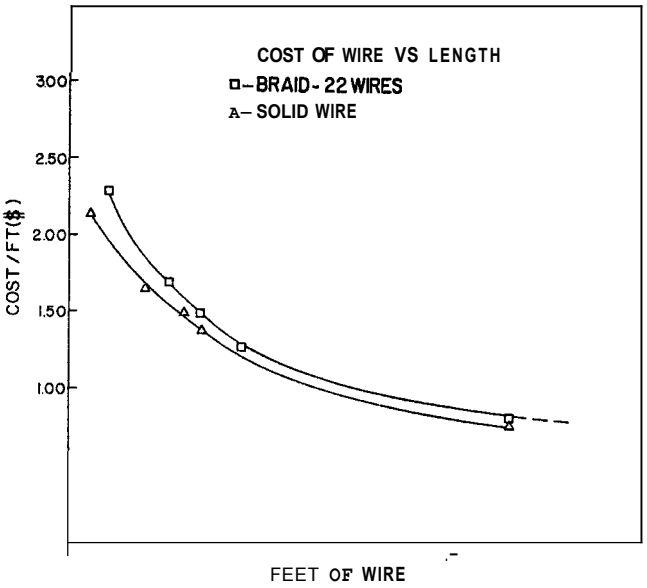


Fig. 6. The estimated cost of the present conductor for the Energy Doubler as a function of the total order is shown. It is assumed that at high quantities sufficient economies of scale will bring the price down to less than half of the present cost.

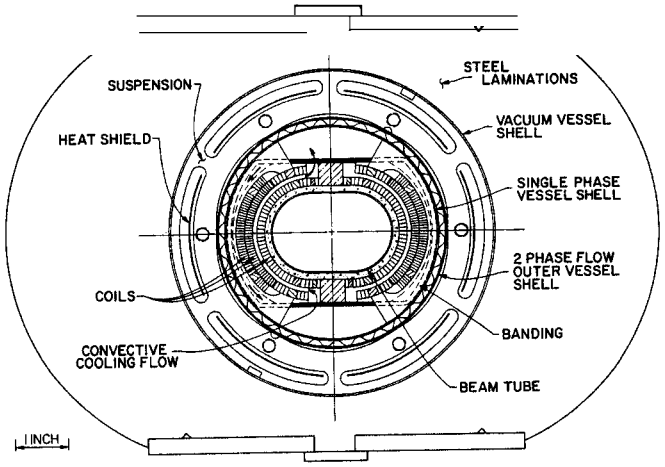


Fig. 7. Transverse section through the latest version of the Energy Doubler dipoles. This shows a fully shielded magnet. Note the features of warm iron, counter flow dewar, heat shield and low loss suspension.

P. Reardon, National Accelerator Laboratory: You made a point about the availability of superconducting wire. Would you comment on that.

D. B. Thomas, Rutherford High Energy Laboratory: In Europe we have three manufacturers, one in Britain, one in France, and one in Germany, and the conductors I showed are available from them in small quantities and unfortunately with longer deliveries than we would like. But, the European magnets you have seen have been built from these materials and there is no reason to believe that they are not entirely satisfactory.

Reardon: Have the European producers of wire built cables or braid, or just provided the solid wire?

Thomas: In some cases yes. The braid I showed was produced by a German company, but on the whole the laboratories who are using this material tend also to do the cabling. The cable and flat tape were actually made in the laboratory. The cabling operation is really not terribly significant. I think producing the composite is the difficult part I should say the very advanced composite I showed with the 14,000 NbTi filaments is available only in experimental quantities and the 180,000 filament composite is hardly available at all, though we do have some.

R. Videroe, Swiss Institute for Nuclear Research: Are there no difficulties with the radiation damage?

Thomas: On the superconductor itself? Lots of tests have been made and we do not believe radiation damage itself will be a severe problem in a synchrotron. I mean, long term damage due to radiation. Of course, one must ask the question what happens if the protons beam ploughs into the magnet. It will quench, I think. I don't know whether Gordon Danby who runs the Brookhaven magnet is here. He has some experience with magnets quenching due to 5×10^{12} protons ploughing into them due to some malfunction.

G. Danby, Brookhaven National Laboratory: I'll comment briefly. We plan to do more quantitative experiments, but I'll describe what we know qualitatively: we have been quite pleasantly surprised. The magnet over the entire running period has been quenched four times. The first two quenches have positively been identified. They were at the beginning of the running periods and were due to gross malfunctions upstream of the magnet. They were effectively due to a direct hit, if you want to call it that, the reason being the upstream collimation. The *two* other quenches took place late in the running period when new operators were operating during the night. We cannot positively attest to what happened but it seems obvious that it could have been either human or equipment malfunction. We do know that we can run with some very gross errors. For example, upstream quadrupoles have gone wrong, and it was clear from both logic and from measuring the instantaneous pressure rise of the pulse in the dewar that we were dumping several hundred Joules into the cryostat. We have some confirmation of this number from considerations of the forward peaking of the scattering and so forth. In fact, the pressure rise in the cryostat to 10 psi, which is about $4.8^{\circ}K$, is sort of used as a beam monitor, to tell people to take a look at the alignment. Basically, the magnet can stand some rather brutal things, like a beam flux of some 6×10^{12} protons striking the jaws of the collimator roughly twenty feet from it.

Thomas: The problems are likely to be operational rather than questions of radiation damage to the materials themselves.

L. M. Bollinger, Argonne National Laboratory: Is anyone doing anything about developing helium pumps?

Thomas: Not that I know of. There is one operating of course at NAL.

Bollinger: That one loses lots of energy in the pump itself, as I understand.

D. A. Edwards, National Accelerator Laboratory: May I make a comment? The helium pump that is used in the NAL system dumps about 60 W into the flow. There is a reciprocating pump being built by another outfit. This one is designed with the motor outside the cold flow and I understand that this will reduce the problem.

Bollinger: And what heat loss is in that?

Edwards: I don't how.

Thomas: It is not essential to have a pumped system. One can have one that is simply working in pool boiling with natural convection.

M. Kuntze, Institut fur Experimentelle Physik, Karlsruhe: As far as I know in your laboratory a helium pump has been developed.

Thomas: Yes, we have a small one, but not of the size one would think of for an accelerator.

R. L. Martin, Argonne National Laboratory: We have tested a superconducting dipole in a proton beam line and observed that it quenches a lot earlier than one calculates from the amount of heat that could be deposited by the beam. It seems to me that it is important for superconducting accelerators that in fact one can't work very close to the peak of the amount of heat flux that the magnet can stand. I'd like also to ask a question of Bill Sampson about the magnets that he has built. You seem to have quite different currents limits in them.

W. B. Sampson, Brookhaven National Laboratory: I don't think that is true if you look at the displaced scale I presented: there is only a 5 percent difference in the current.

Martin: That does not represent problems, this 5 percent variation?

Sampson: No, as both magnets are more than 10 percent away from the design, particularly at the operating point.

G. K. Green, Brookhaven National Laboratory: The available material had a 5 percent variation as many materials will have. Bill used up his best material when he made the first magnet and when he made the second one he used his second best material.

Reardon: Bill, was this second best material tested to the basic short sample value of the wire you received to make the braid or after braiding?

Sampson: No, it was the material as it came. It was delivered in different lengths and we checked them all and selected them in descending order.

Reardon: Let me repeat my earlier question concerning what we mean by conductor availability.

Thomas: If you are talking about tonnage qualities, nothing has been produced. A typical order I would say these days is 100 kg.

Reardon: The quality control of an industrial volume production is a very crucial issue.

Sampson: Well, that is so of the old material. The newer materials are a lot more uniform. I don't think that is a real problem.

Green: I would like to underline a comment by Dr. Thomas on A15 compounds, and emphasize very much the importance of temperature. Temperature has not been mentioned. Superconductors of course have 3 parameters: field, current and temperature. NbTi has a critical temperature of $9^{o}K$ at zero field, zero current. At 4T, this critical point is already at $7^{o}K$, at 6T it's less than $6.5^{o}K$ for no field or for field but no current. So a NbTi magnet built with any economy will be operating with only a few tenths of a degree K reserve against going normal. Now, there is no mystery whatever about particles quenching a magnet, it is simply thermodynamics. The problem is including the particle flux. If you know the particle flux, you can predict the result. In general, the way one runs a superconducting magnet, a flux on the coil of the order of 10^{9} protons/cm^{2} will quench it. And that is a bit too small a flux. The very important thing about the A15 compounds is their higher initial temperature. I would urge that people forget the business that with A15's we can go to 8T. With the A15 compounds we can go to 5T, but we can have 5 degrees of temperature reserve. And I think that that 5 degrees of temperature reserve will make a superconducting *ring* practical, profitable, and entirely usable. So, the A15 compounds are of enormous importance because one gets the temperature reserve. Of all things that is one I believe, in our business, to be more important than higher fields.

SUPERCONDUCTING STRETCHER RING FOR THE ZERO GRADIENT SYNCHROTRON*

E. A. Crosbie, T. K. Khoe, R. L. Martin, J. R. Purcell, and S. T. Wang
Argonne National Laboratory
Argonne, Illinois

Introduction

A superconducting (beam) stretcher ring (SSR) has been designed for the Argonne National Laboratory 12-GeV Zero Gradient Synchrotron (ZGS). The SSR would be installed in the existing ZGS tunnel outside the present ring accelerator. With fast injection at 12 GeV from the *ZGS*, a slow resonant extraction from the SSR could supply protons continuously into the two existing external proton beam lines during the time required for the ZGS to cycle and accelerate more protons. Nearly 100% duty cycle could be achieved. Since practically no flattop is required, the ZGS could be run at approximately double the present 4.6 s repetition rate resulting in a corresponding increase in the average beam intensity supplied to the experimental areas. Provisions could also be made to extract the beam into a new third external beam line in the meson building (see Fig. 1).

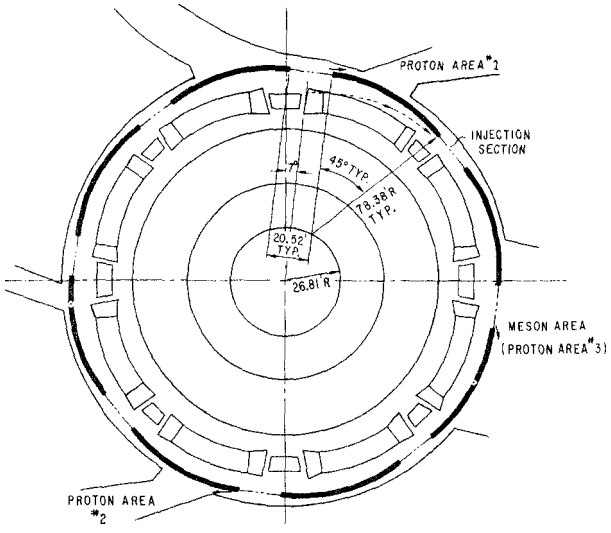


Fig. 1 Layout in *ZGS* Ring Building

The layout of the proposed SSR is shown in Fig. 1. The outside wall of the ZGS ring building is roughly described by a circle having a radius of 110 ft. Four rather valuable survey monuments are located near the outside wall and limit the outer radius of the SSR to about 106 ft. The ZGS extends outward to 96 ft. The SSR has been designed to be as circular as possible in order to provide enough space for the magnets required for the ZGS to SSR beam transfer line.

A separated function focusing design has been chosen to make the superconducting magnet design as simple as possible and to provide easy tune control to move away from undesirable tune resonances. Simultaneous resonant extraction from three straight sections (located at 90° intervals) can be achieved if the radial tune is near $4n/3$, where n is any integer not divisible by 3. The choice of n equal to 4 and 32 sectors per revolution produces an adequately strong focusing machine having a phase advance per sector of nearly $\pi/3$. With one focusing and one defocusing quadrupole per sector, the required quadrupole focal lengths are about. 7 times the length of the sector.

Eight straight sections have been created by eliminating the dipole magnets from every fourth sector and requiring that each of the remaining 24 magnet sectors produce 15° of bend. Thus a periodicity of 32 exists in the vertical plane and 8 in the radial plane. However, since the dipole magnets in each of the 24 magnet sectors do not provide much radial focusing compared to the quadrupoles, the radial tune structure still remains very nearly 32. Special matching quadrupoles in the 8 straight sections are not required. The straight sections have the same lengths (246.24 in) and quadrupole positions and strengths as the magnet sections.

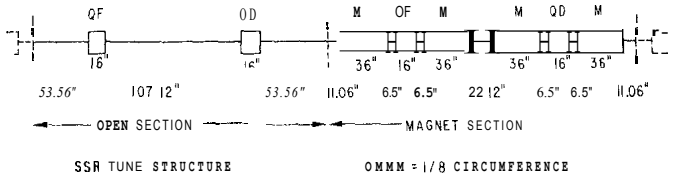


Fig. 2

This basic OMMM (= 1/8 circumference) is shown in Fig. 2. At 12 GeV, each 16-in quadrupole requires a gradient of ~ 8.7 kG/in. Each of the four 36-in dipoles in each M section produces 3.75° of bend and requires 30.8 kG of magnetic field strength. Two dipole magnets and a quadrupole magnet will be constructed as a single unit and housed in the same cryostat as illustrated in Fig. 3. Since the sagitta for each 3.25° bend is only .3 in, the dipole magnets are straight.

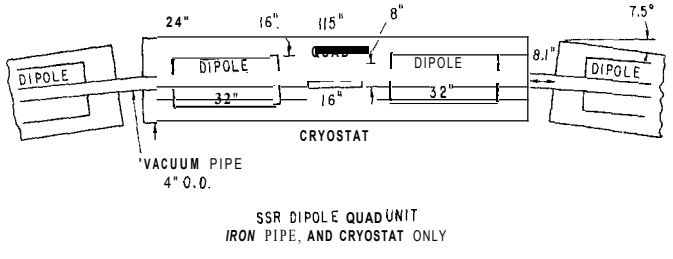


Fig. 3

The calculated horizontal and vertical beta functions for $\nu_x = 5.3$, $\nu_y = 5.25$ are shown in Fig. 4. Assuming a $3\pi \times .3\pi$ (mrad.in)^2 beam from the *ZGS*, the maximum horizontal and vertical beam sizes in the SSR would be 2.3 in and .7 in respectively. The calculated momentum error function shown in Fig. 5 more clearly shows the 8-sector structure of the lattice.

*Work performed under the auspices of the U. S. Atomic Energy Commission.

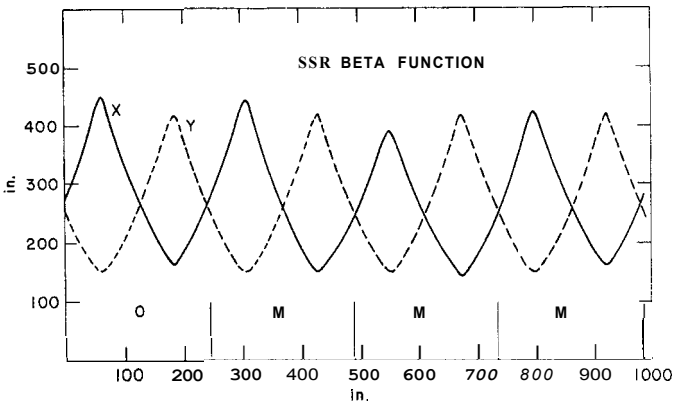


Fig. 4

10^{-4}

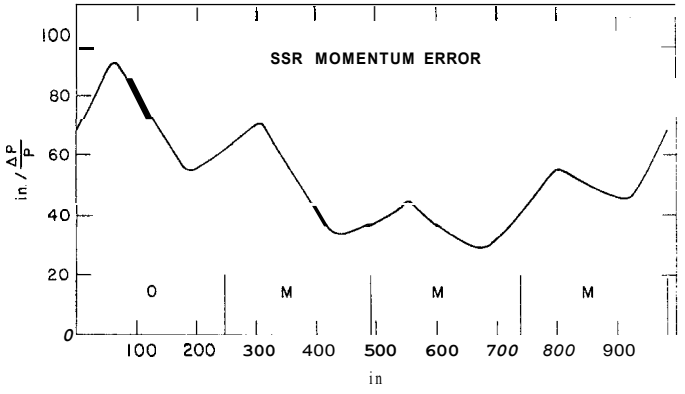


Fig. 5

Injection and Extraction

Because of the radial size of the beam in the ZGS, a single turn bumper magnet radial extraction and injection into the SSR does not appear to be feasible. However, a very fast 50 turn (30 μsec) resonance extraction from the ZGS has already been demonstrated. This beam could be resonantly injected into the SSR using an integral resonance and a single sextupole and dipole magnet'. The dipole field is initially large enough to cause the stable phase space region to disappear completely. During injection, the dipole field is rapidly decreased so that the stable region reappears and increases in size. The injected particles must be injected at the right slope into an appropriately located septum inflector magnet. The radial tune used for this type of injection would be about 5.1.

It has recently been proposed that the beam in the ZCS can be extracted vertically in a single turn[2] The plane of the SSR would then be five or six ft above that of the ZGS and a combination of radial and vertical bending magnets would be used to transport the beam to the SSR from below where injection would occur using a septum magnet and a fast vertical bumper magnet.

The extraction from the SSR must be done very slowly and simultaneously into two and perhaps three external proton areas. Four sextupole and dipole magnets would be placed in four straight sections to form and control the size of the 16/3 resonance phase space. Septum magnets in the two (or three) straight sections would alternately intercept the unstable beam for extraction. The spill rates and distributions of the extracted beam can be controlled by feedback from the external proton areas to the four dipole magnets. When used in this way, the SSR would not use an rf system to contain the beam An rf cavity would be required to contain the beam during initial tuneup and uncontrolled extraction[3].

Table I

SSR Parameters	
Magnet Section Structure	OMFMOOMDMO
Open Section Structure	OFOODO
No. of Magnet Sections	24
No. of Open Sections	8
Periodicity	8 radial (almost 32), 32 vertical
Length of Magnet Sections	246.24 in. (6.254m)
Length of Open Sections	246.24 in. (6.254m)
Average Radius of Octant	940.56 in. (23.89m)
Magnet Length	36 in. (.914 m)
No. of Magnets	96
Bending Radius	550 in. (13.97 m)
Magnetic Field Strength	30.8 kG
Design Energy	12 GeV
No. of Quadrupoles	64
Quadrupole Lengths	16 in. (.406 m)
Quadrupole Strengths (focus)	8.67 kG/in. (3.41 kG/cm)
(defocus)	8.81 kG/in. (3.47 kG/cm)
Phase Advance per Sector	238.725° radial, 59.152° vertical
Betatron Frequencies	5.305 radial, 5.258 vertical
β max	447 in. (11.35m)
Momentum Compaction	.033
Maximum Energy Error	
Orbit Deviation	91 in. (2.31 m) per unit Aplp
Injected Beam Quality	$3\pi \times .3\pi$ (mradin.)^2 ($.76\pi$ x $.76\pi$ mrad cm)^2
Δp/p	
Rotation Period	.67 μsec

Aperture Requirements

Allowance must be made for the curved equilibrium orbit within the straight dipole magnet. The effects of the sextupole component of the field are minimized if the equilibrium orbits enter the dipole magnet at the position -.2 in.

The effects of random field errors and misalignment can be treated as a random walk problem. With 90% probability, the equilibrium orbit displacement will be less than

$$X_{mis} = 70\,\Delta_{rms} \quad .$$

Assuming $\Delta_{rms} = .004$ in for the quadrupole magnet misalignments gives

$$X_{mis} = .28 \text{ in}$$

The random field errors give, with the same (90%) confidence level, and

$$\left(\frac{\Delta B}{B}\right)_{rms} = 5 \times 10^{-4} \quad ,$$

ield

The momentum spread of the ZGS bunch is of the order of $\pm 10^{-4}$. On the other hand, the pulse-to-pulse momentum spread is estimated to be $\pm 5 \times 10^{-4}$, the required contribution to the vacuum chamber width is

$$X_P = .055 \text{ in}$$

The ZGS radial emittance is assumed to be 3π mrad in. This corresponds to a SSR betatron amplitude of

$$X_{bet} = 1.2 \text{ in} \quad .$$

The total aperture requirement is

$$X_{tot} = X_{sag} + \sqrt{X_{field}^2 + X_{mis}^2} + X_p + X_{bet}$$
$$= 1.75 \text{ in}$$

SSR Magnet Design

Introduction

The ZGS dc SSR will require about 96 dipoles and 64 quadrupoles. Each dipole will provide 30 kG $\times$ 37 in integral bending power, Each quadrupole will provide 8 kG/in $\times$ 18 in integral focusing power. A prototype dipole and a prototype quadrupole were first constructed. Extensive tests have shown that both beam magnets have very good field quality despite the fact that the coil winding was carefully but randomly wound and the coil support and the iron shield were very economically designed. These measures plus the economical low cost cryostat design have reduced the construction cost of the SSR to the minimum. To obtain further experience in the practical aspects of fabricating these beam magnets, we are currently constructing an SSR test section of 10 dipoles and 5 quadrupoles. All 10 dipoles and 5 quadrupoles have been completely wound and assembled. We are presently undergoing the complete performance test of these 15 beam magnets. After these tests, they will be assembled into five SSR beam magnet module cryostats. Each magnet module cryostat will house a dipole at each end and a quadrupole in between. Fabrication of the five cryostats is nearly completed. After the magnets are assembled into module cryostats, further tests will be performed to determine the final field quality and magnetic characteristics due to the field interaction between adjacent magnets.

Detailed Considerations for Magnet Design and Construction

SSR Dipole

The dipole was designed to produce 30 kG at a current of 190 A. The required integral field homogeniety is $\pm 0.1\%$ over a 3" diameter. A coil cross section of two equal radii intersecting circles was chosen because this configuration is a good geometry in that each curve is a portion of a circle, the coil forms and winding fixtures can be easily and accurately machined, and the field inside the aperture due to such a dipole coil of constant current density is a constant uniform field within the entire aperture. Furthermore, the distortions in the coil shape due to the clamping forces of the coil support produce small effects on the field uniformity. The cross section of the coil ends is also overlapping circles. This provides a uniform end field across the entire aperture.

Several copper coils were wound and epoxy potted first to establish the winding techniques and the techniques of epoxy vacuum impregnation and to check field uniformity with various coil end configurations. From these experiences, it was decided to use a 40 mil diameter superconductor with 400, 24 μ formvar coated filaments, twisted one turn per inch, and a copper to superconductor ratio of 3:1. The short sample characteristic is greater than 300 A at 40 kG.

The dipole consists of two half dipole coils. Each half coil consists of 1300 turns. The coil is randomly wound with coil form filler and winding fixtures guiding the surface of the intersecting circles. The direction of coil winding was changed several times to smooth out the unevenness of coil winding near the corners of coil ends, After winding was accomplished, it was vacuum impregnated with a room temperature cure epoxy (EM 308 and Verse 120). The packing factor of the winding is 62%, resulting in an overall current density of 15,000 A/cm^2. The two half-dipole coils were then clamped onto a 4-in bore tube, type 304 stainless steel with 0.22 in wall, by tightly spiral-wrapping with aluminum wire. The aluminum contracts more than the coil during cooldown increasing the preloading. The assembly is shown in Fig. 6. Note also that the coil ends are well supported and well cooled by potting aluminum end plates on each coil end.

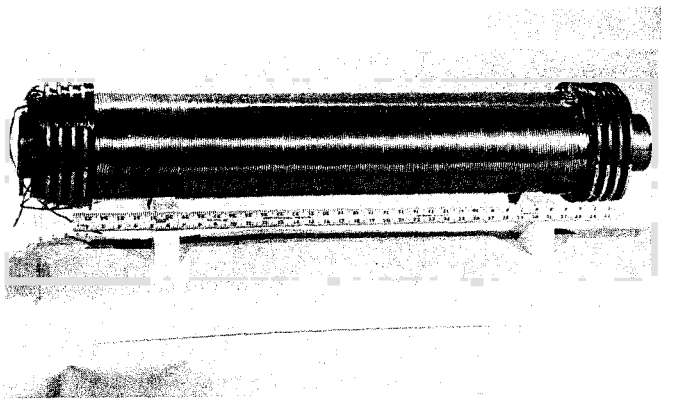


Fig. 6 Dipole Coil Winding Assembly and Support

To solve the problems associated with strong stray fields, each dipole is shielded with cold iron. The TRIM computer program[4] was used to determine the dimensions of the least amount of iron compatible with the required field uniformity. It turns out that to produce 30.5 kG with iron, with an operating current of 190 A, a coil winding build of 1.1 in is required. The iron is spaced 1½ in away from the coil in order to avoid the iron saturation effect on field uniformity. A wall thickness of 3-5/8 in is required to provide complete shielding. The entire dipole cross section is illustrated in Fig. 7. Nesting standard size iron pipes were used to build up the required amount of iron shield. The iron pipe also contributes about 6.5 kG to the field strength. Although the magnet has not been pulsed or the loss accurately measured, no increase in the boil-off rate can be detected with a rapid charge at 10 V. It appears that laminated iron is not required for the SSR magnets where the magnets will not be cycled rapidly and will take about 2 min to charge up.

The coil form fillers were made of molded composite consisting of small glass beads and epoxy resin. The composite was designed to have strong compressive strength and a low thermal expansion coefficient.

It was quite a challenging problem to provide

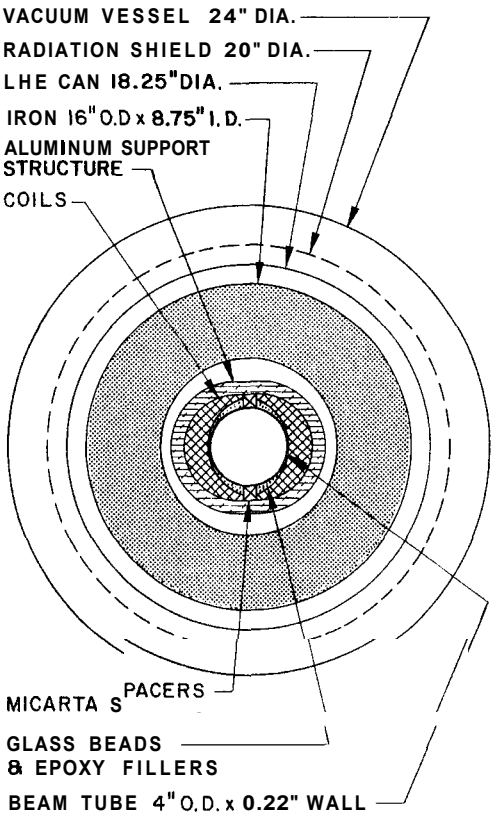


Fig. 7 Schematic of Cross Section View of Dipole Assembly

adequate coil support for dipoles of this kind. It was decided to avoid an external support structure with bolted type compression on the 0.22-in-wall bore tube. Deformation of the bore tube will distort the coils and produce poor quality dipole fields. Thus, it is desirable to have a coil support structure that produces uniform compression on the coils. Various types of supporting schemes were tried and the final decision was made to wrap the dipole coils with aluminum alloy wires. Iron bolts, 45° equally spaced, were used to enforce the support by threading through the iron pipe and bearing on the aluminum wrapping wire.

SSR Quadrupole

Since each quadrupole is housed together with two dipoles in a cryostat, it is desirable to use the same type of contuctor and to have near the same operating current as the dipoles. The quadrupole was designed to have a field gradient of 8 kG/in at operating current of 190 A. The required integral gradient uniformity is ± 0.270 over a 3-in diameter. A Panofsky type[5] quadrupole was decided upon. Many air core superconducting quadrupole designs exist in which the field gradient is shaped by means of appropriate current distributions. However, all these configurations require more superconducting material than a Panofsky quadrupole. The Panofsky quadrupole also requires a smaller amount of iron than a conventional quadrupole and thus a large reduction in the outer dimensions and in the total cold weight is possible. Furthermore, the mirror iron walls in contact with current sheets serve as the convenient supporting structure as well as shielding.

The Panofsky quadrupole produces an ideal quadrupolar field in an entire square or rectangular aperture. The required thickness of coil windings is determined by the Panofsky formulae[4]. The width of the winding square bore is four in. An average current density of 15,000 A/cm^2 was adopted as a reasonable figure in view of past experience. These led to a winding thickness of 0.4 in. The TRIM computer program was used to determine the least amount of mirror iron wall thickness compatible with the required good field quality. A special computer program, PANOF,[6] which is based on the method of magnetic images, was used to determine the mechanical tolerance of winding, tolerance of positioning of each coil section, size effect of the spacers, etc., in accordance with the required field gradient uniformity.

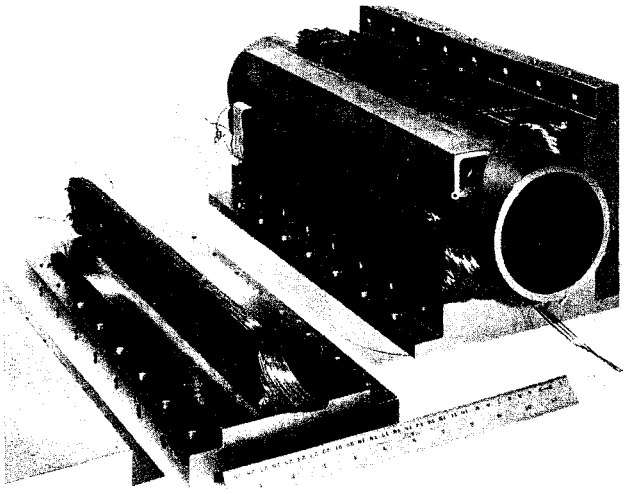


Fig. 8 Quadrupole Assembly

The same winding technique developed for the SSR dipoles was used for the winding of the SSR quadrupoles. Each quadrupole magnet consists of four quadrant section coils. Each section coil is randomly wound and vacuum impregnated with epoxy. The four quadrant coils are then assembled onto a 4-in-square flat surface surrounding the 4-in diameter bore tube. Four carbon steel imaging walls, each 1.5 in thick, are firmly pressed onto the coil windings with spring loading compression. Final assembly is shown in Fig. 8. The packing factor is 63%. Each section coil consists of 400 turns.

Performance Tests

SSR Dipole Tests

A long search coil connected in series bucking with a stationary reference coil was developed to have $\sim 10^{-3}$ sensitivity to map the dipole field under low ac excitation at room temperature. It turns out that the gap between two dipole half-coils could be shimmed properly with G-10 sheets of various thickness to obtain the most favorable field pattern. The same ac field measurement was repeated after the dipole winding was wrapped tightly with aluminum alloy wire.

A 44-in long search coil is used along with a high gain low drift Miller integrator to map the field of the dc dipole at liquid helium temperature. The dipole

bending power is obtained by flipping the calibrated search coil 180°. The integral field nonuniformity is obtained by translating the search coil step by step across the useful bore. These field measurements were done at several different magnet currents. These integral field maps showed that field deviation within ±0.1% over 3 in useful bore has been achieved.

The hysteresis effect on the integral field was very small. The remnant field was measured by a point field search coil and was about 20 G for each dipole. We are currently setting up accurate methods to measure ac pulsing loss.

There is no provision for cooling passages within the vacuum impregnated coils. Despite this fact, the dipole coils could be charged up to 30 kG within two minutes. No change in quench current was found for charging voltage from 0.2-10 V. Past tests showed that the dipole with iron shield first quenched at ~ 170 A. After the first quench, it is possible to charge up to an operating current of 190 A. After five quenches or so, it is possible to achieve 34 kG (~ 210 A).

We have tested the radiation heating effects of our prototype dipole. Results were that the 12 GeV ZGS well-focused beam directly impinging on the superconducting winding immediately quenches the magnet. With partial impinging on the coil winding by a 6-in diameter defocused beam, the heating effect was still enough to quench the magnet after many pulses if the beam intensity was greater than 10^{11} protons per pulse. However, if the beam is properly aligned so that beam travels through the 4-in cold bore, no noticeable heating effect was observed.

SSR Quadrupole Tests

A pair of long narrow rotating search coils were used with a wave analyzer to measure the harmonic coefficients of the quadrupole. The pair of coils were designed to suppress the quadrupole components and thus enable one to measure other harmonics with high sensitivity. Because of possible rotational wobble with a long search coil, it was decided to use a shorter search coil to measure the harmonic content in half focusing power. The harmonic field measurements showed that within the useful bore, a 6-pole component of the integral focusing power is 0.27%, 8-pole component is 0.28%, and 12-pole component is 0.35%. All other multipole components are well below 0.1%. The relative percentage of the multipole components was found to be independent of excitation.

The quadrupole could be charged to 10 kG/in (~ 225 A) without training. The operating gradient is 8 kG/in (~ 190 A). At 225 A, the quadrupole produces more than 10 kG/in.

SSR Magnet Module Cryostat

After the dipole field direction and the quadrupole field center have been determined, the dipole-quadrupole-dipole will be assembled to form an angle of 1.875° between each dipole and the quadrupole.

The 3-magnet assembly is suspended by two "U" straps. The three magnets will be energized in series requiring only two vapor-cooled current leads and some smaller leads to "trim" the current in each magnet. The helium vessel is surrounded with multilayer insulation of aluminized mylar. The bore tube is at liquid helium temperature. Insulation vacuum of ~ 10^{-9} torr will be achieved through cryopumping. The liquid helium reservoir will have a capacity large enough so that one transfer per 24 hours is sufficient.

The shield cooling is by two parallel sets of continuous liquid nitrogen flow from the liquid nitrogen reservoir.

To minimize the construction cost and sealing problems, the cryostat is an all welded construction. The cryostat is designed to provide freedom of alignments between two adjacent cryostats.

Conclusion

The design and construction of the Argonne SSR magnets represent a significant step forward in the development of low cost, high quality dc superconducting beam magnets. Extensive performance tests have demonstrated the successful design and use of economical materials in high quality superconducting magnets. The results gathered from the construction of SSR test section will be valuable in the investigation of the feasibility of superconducting magnets as high quality proton storage rings and as superconducting accelerators.

[1] T. K. Khoe and R. J. Lari, "Resonance Injection in the Superconducting Stretcher Ring," IEEE Transactions on Nuclear Science, Vol. NS-20, No. 3, p. 392 (June, 1973).

[2] R. L. Kustom, "One-Turn Extraction from the ZGS," Argonne National Laboratory, Accelerator Research Facilities Division report SSR-1 (April 1, 1974).

[3] More details on the injection, beam transfer, and extraction for the SSR will be presented in a forthcoming SSR proposal report.

[4] Argonne TRIM Program, adapted by R. Lari.

[5] L. H. Hand and W. K. H. Panofsky, Rev. Sci. Instr. 30, 927-930 (1959).

[6] Written by H. Desportes.

8° SUPERCONDUCTING BENDING MAGNET IN A PRIMARY PROTON BEAM*

J. Allinger, G. Danby, B. De Vito, H. Foelsche, S. Hsieh,
J. Jackson, A. Prodell
Brookhaven National Laboratory
Upton, New York

Abstract

A large superconducting bending magnet system is in operation in the new beam from the Brookhaven AGS to the 7-ft. Bubble Chamber. Two dipole modules excited to 37kG with a total magnetic length of 4m bend 30 GeV primary protons by 8 . The system has operated routinely for several months, traversed in 3μs by 6 ∧ 10^{12} protons with a beam power of 30kJ. The magnet modules have been proven to be very rugged and were found immune to operational beam difficulties which give rise to occasional bursts of radiation heating. The system is designed for on-line operation and computer monitoring of parameters with closed loop He refrigeration. The magnets have demonstrated very little training and have been operated to 44kG with both modules identical to computed field predictions to an accuracy of ~ 1 × 10^{-4} over the useful aperture. These are the first superconducting magnets used in a primary proton beam, and are of a type which can be used in future accelerators.

1. Introduction

The 8° magnet project has met all its design goals. The combination of a very simple conductor with high conductivity corrugated aluminum sheets results in an economical and mechanically precise coil structure which provides very rapid and efficient heat exchange to helium. A solid iron core was used to avoid a stamping die. The same coil construction technique can be used with a laminated split core. Pulsed models with similar construction have demonstrated excellent behavior, with field properties identical to dc for rise rates of ~ 4kG/sec. Errors due to construction and magnetic pressure are evidenced by the magnitude of quadrupole, octupole, and other error fields, and by the non-identity of sextupole, etc. between modules. These fields show the 8° to be considerably more accurate and predictable than other superconducting magnets built to date. Later designs will produce much higher fields combined with the field quality of the best conventional magnets. The method of construction produces a very economical magnet.

2. Magnet Design

The two magnets employ a rectangular "window-frame" iron core surrounding a rectangular cross-section dipole coil package. The magnet cross section, shown in Figure 1, is 37.8cm high by 43.5cm wide. The iron core, which is closely coupled around the coil, reduces the ampere turns required for magnetic fields below saturation by a factor greater than 2. The magnetic images of the coil in the iron simulate extended dipole sheets, producing very uniform fields below 20kG. Above this field the systematic aberrations due to saturation require an auxiliary correcting coil which is approximately an air core sextupole. The excitation required of this correcting coil commences at ~ 20kG and increases linearly to several percent of the dipole ampere turns at 40kG. The combination of the two separate coils, the dipole and the sextupole, permits the generation of precision fields at all levels as well as providing sextupole tuning when desired.

The dipole coil is wound with 340 turns of a conventional NbTi superconducting composite with a rectangular cross section of ~ 1.4mm by 2.9mm. This contains 361 NbTi filaments, 75 microns in diameter, imbedded in copper, and the whole matrix is twisted one turn per inch. The copper to superconductor ratio is 1.25 to 1. A sheet of anodized high purity aluminum is placed between each of the vertical layers of the dipole and correcting coils. These aluminum sheets are grooved to provide helium coolant channels over 50% of one face of the conductor layer and the anodized surface of the aluminum provides additional interlayer insulation in the coil. The good diffusivity and conductivity of the high purity aluminum provides excellent thermal and dynamic stability.

In order to locate the dipole and sextupole coil turns precisely in the magnet, the stainless steel cold bore block of the magnet was machined with grooves to contain the top and bottom racetrack correcting coils, and the outside of the cold bore block was used as a winding fixture to wind the mid plane correcting coil and the dipole coils. Since the superconductor was relatively uniform in size and the aluminum sheets were rolled to close thickness tolerances, the location of each layer of superconductor in the coils was established during winding. Figure 2 shows the coil winding around the end blocks. Iron plates were assembled around the coil package after winding and torqued to provide precompression of the coil package before assembly in the core blocks. Any residual horizontal motion under magnetic pressure is constrained to coherent motion of the coil layer as a whole and results in very small field errors. Coolant channels were provided at the top and bottom of each coil package and liquid helium supply grooves were machined wherever necessary in the cold bore block. Vent holes were also drilled through the magnet core block and inner iron plates at 3.8cm intervals to provide flow paths for helium gas venting.

Liquid nitrogen precooling channels are welded to the core to provide rapid magnet cooldown through a closed loop LN system. Heating coils are also mounted on the outside surface of the magnet iron to provide rapid warm-up of the system if maintenance is required.

The magnet parameters for the 8° dipole are shown in Table I. Figure 3 shows a completed magnet unit.

TABLE I. MAGNET PARAMETERS (4° MODULE)

Aperture (I.D. warm vacuum pipe)	7.3cm
Magnetic field intensity	40kG
Ampere turns (dipole coil)	408,000
Ampere turns (sextupole coil)	18,000
Current (dipole coil)	1200A
Current (sextupole coil)	300A
Current density (dipole coil conductor)	3.05 × 10^4 A/cm²
Current density (sextupole coil conductor)	3.0 × 10^4 A/cm²
Stored energy	150kJ per unit
Inductance (dipole coil)	0.2h per unit

3. Test Performance

The superconducting magnets are immersed in liquid helium at a temperature of 4.5°K. They were designed

*Work performed under the auspices of the U.S. Atomic Energy Commission.

to operate at a field of 40kG. The first module reached 44kG after four training quenches; the second after only two, both at about 40kG. An earlier full-scale cross section model 0.5m long, which was much more poorly constructed, required about ten quenches to attain this level.[1,2] Although this model was designed for 40kG, it has been operated to ~ 50kG at which level there is 57kG in the coil due to excessive saturation, and requires essentially 100% of short sample current.

None of these three magnets has ever quenched after its first operation to a given field, except when subjected to extreme proton radiation heating. This observation is based on much experience with repeated thermal cycles between ambient temperature and liquid helium temperature, charging and discharging the magnets in seconds, and discharging the magnet from 25kG very rapidly into a 0.5 Ω resistor by opening a 500A circuit breaker. No potting is used in these coils which are free to shrink azimuthally with respect to the core, and to move into a final position, or set, under magnetic pressure. After initial testing to its highest field, this type of magnet could be assembled for beam or accelerator applications and no subsequent training would occur.

4. System Description

Since this system was envisioned as a forerunner of more extensive superconducting magnet beam transport lines, considerable attention was given to making it a complete "on-line" pilot plant which would require little direct supervision. A 7kW helium refrigerator separated from the magnet by ~ 10m of earth shielding and connected to the magnet dewars by 40m of liquid nitrogen shielded transfer lines provides the necessary cooling. The magnet dewars and refrigerator comprise a closed loop system to which auxiliary equipment has been added for the recovery and storage of the helium gas. The magnet, refrigeration, and recovery systems are instrumented for automatic operation and provisions have been made for computer monitoring.

If required, the two magnets (~ 4082kG total mass) can be heated from 4.5°K in ~ 30 hours and can be cooled down from 300°K to 4.5°K in ~ 16 hours so that the total recycling time in case of a magnet warm-up is quite modest.

These magnets have been in operation whenever needed since late October 1973. Although they have been quenched on four occasions due to problems occurring in other beam transport components, they still operate reliably and with no difficulty. Figure 4 shows the 8° magnet in the proton beam.

5. Radiation Heating

Since this system was designed for use in a primary beam, uncertainty existed as to whether or not the external beam pulse would be sufficiently free of stray particles to limit heating of the superconducting coil. These magnets have operated successfully for long periods of time at beam intensities of ~ 6×10^{12} protons per pulse even under abnormal heating conditions. On occasion, during malfunction of other beam transport components; e.g., a trip-out of the upstream quadrupoles, the magnets absorbed several hundred joules of radiative energy in a period of 3μs for a series of pulses without quenching while small incremental pressure increases were observed in the helium dewars. Moreover, operation has been sustained while one jaw of a collimator located ~ 6m upstream from the magnet was protruding into the beam and intercepting about one-half of the beam. On the other hand, gross malfunctions in steering have quenched the magnet. The capacity of these magnets to absorb large beam losses is very significant since hoped-for future superconducting accelerators depend on a reasonable capacity of the magnets to operate with heating due to beam loss. This is the first experimental evidence anywhere bearing on this fundamental question. It should be noted that this type of construction permits very rapid heat exchange and extreme cooling of the coil. The acceptable maximum exposure in 3μs to the coil itself will have to await more controlled experimentation.

6. Magnetic Measurement Results

The two magnet modules were measured separately, prior to final assembly with their warm bore beam tubes which define the maximum aperture of $r_m = 3.653$cm, using a harmonic coil device. These radial field measurements were made at $\rho_c = 3.825$cm which is 76% of the 5cm radius to the superconductors. Each magnet was repetitively cycled to 38kG. Long integrating and internal point measurements were made on both rising and falling sides of the cycle. The radial field is expressed as

$$B = B_o \sum_n \left[a_n \frac{r^n}{\rho_c^n} \cos (n+1)\theta + b_n \frac{r^n}{\rho_c^n} \sin (n+1)\theta \right] \quad (1)$$

carried out to n = 11. The reference angle, θ = 0, is set at the magnet horizontal midplane. Considerable data were accrued in intensive periods which were restricted to a few days on each magnet by the construction schedule. Simultaneous measurements on the magnets in series are planned when they are not in use for the physics program. The identity of the units can then be more easily and accurately checked, especially for the sextupole component which can be affected by slight differences in excitation currents. Nevertheless, quite accurate conclusions can already be drawn.

Analysis focuses on three parts:

1. With equal excitation currents in each magnet, as if in series, the agreement of the sextupole terms b_2 with each other and with computer predictions.

2. With the auxiliary coil tuned to cancel the sextupole (b_2) in each magnet, the identity of the field aberrations with computer predictions and with each other.

3. The magnitude of terms not allowed by symmetry due to construction and measurement errors. The most critical effect is on the quadrupole terms (2θ), followed by sextupole, etc.

The identity and mechanical precision of the two units are, in fact, very good and appear to be comparable to high quality conventional magnets. The absolute field uniformity, while reasonable when compared with other superconducting magnets constructed to date and being more than adequate for its purpose, is not as good as high quality conventional magnets. These modules were the first magnets of their type designed, It is now known how to make the field below 20kG arbitrarily uniform by design, and how to correct for saturation at high fields with much less aberration resulting.[3] It is believed that a second generation of such magnets should be of conventional magnet field quality from both a conceptual and practical construction point of view.

Table II shows calculated and measured field multipolarities at 24kG for module 1 on a rising field cycle. Column 1 lists the computed multipoles for the "perfectly constructed" magnet. Column 2 gives the corresponding measured internal fields. Column 3 gives the long coil results. Column 4 is the difference

(i.e., Columns *3-2)* or the contribution due to the ends. Column *5* lists results of a separate experiment wherein the short coil and the long coil were hooked in series opposition to measure end effects directly, This should be more accurate than Column *4*. The agreement gives some measure of precision.

TABLE II. 8^{o} MAGNET (#1) B_o = 24kG

(n+1)θ / 1θ	1 Computer		2 Measured Point Coil		3 Measured Long Coil		4 (3-2)		5 Measured Long-Point	
	a	b_n	a_n	b_n	a_n	b_n	a	b_n	a_n	b_n
3θ/1θ	*0*	+12.2	*1.1*	+ *2.5*	*0.3*	+1.3	*1.4*	*-1.2*	*2.3*	*-3.4*
5θ/1θ	*0*	+ *9.2*	0.1	+11.4	*0*	+6.8	0.1	*-4.6*	*0.7*	*-4.6*
7θ/1θ	*0*	- *6.2*	0.1	- *7.4*	0.1	*-4.8*	*0*	+2.6	*1.0*	+2.5
9θ/1θ	*0*	- *3.4*	0.1	- *5.2*	*0*	*-4.4*	0.1	+0.8	*1.0*	+0.9
11θ/1θ	*0*	+ 1.0	*0*	- 0.1	0.1	+0.2	0.1	+0.3	*0.2*	*0*
2θ/1θ	*0*	*0*	*1.7*	+ *3.3*	*2.8*	+3.4	*1.1*	+0.1	0.7	+0.2
4θ/1θ	*0*	*0*	*0.9*	- *0.8*	*1.4*	*-0.4*	*0.5*	+0.4	*0*	+0.2
6θ/1θ	*0*	*0*	*1.3*	+ *0.2*	*0.9*	+0.1	*0.4*	-0.1	*0.4*	*0*
8θ/1θ	*0*	*0*	*0.8*	+ *0.3*	*0.6*	*tO.2*	*0.2*	-0.1	*0.2*	*-0.3*
10θ/1θ	*0*	*0*	*0.3*	- 0.1	*0.2*	-0.1	0.1	*0*	0.1	-0.1

Note: Field multipolarities expressed relative to the dipole field *(1e)* in terms of 10^{-4} parts at the measurement radius (p = 3.825cm).

The amplitudes in Columns *2* and *3,* which are zero in 1, are a measure of magnet construction errors, complicated by measurement errors. Comparison of the many runs, both on the up and down cycle, long and short coil, gives a quadrupole b error of $\sim 3 \times 10^{-4}$ at $r = \rho_c$ *(0.8* $\times 10^{-4}$ cm^{-1}). 'This is present at all field levels. The skew quadrupole term, a_1, is $\sim 1.5 \times 10^{-4}$ *(0.4* $\times 10^{-4}$ cm^{-1}). The quadrupole error happens to be roughly equal in both magnet modules. The higher order terms not allowed by symmetry, when data from all the $\sim$ *50* runs both up and down are examined, show no systematic presence and are consistent with being measurement errors. At the measurement radius the quadrupole is about three times larger than the estimated measurement error. This is consistent with higher order errors due to mechanical asymmetry being equal or smaller than measurement accuracy. The difference between predictions and measurement for terms allowed by symmetry will be discussed later. Briefly, in Columns 1 and *2,* the *(38)* b_3 offset is due to iron hysteresis common to both magnets. It is small, well behaved with field, and is well known in conventional magnets. Computations ignore hysteresis which can be corrected by a slight change of the auxiliary coil current,

Table III lists, for both units at three fields on a rising cycle, the internalmultipoles b_n allowed by symmetry, plus their out-of-phase equivalent a_n, as a rough indicator of accuracy. For these, and all the runs, the difference between the two units is small and well predicted by computations. (The *38kG* b_3 difference shown in Table III happens to be the largest discrepancy found.)

There exists a small design field difference between the two magnets. After the winding of a dipole coil vertical layer, a few thin shims are located between conductors in known positions so that the layer is tight in predetermined locations between its boundaries. The size of the initial length of the Formvar coated rectangular conductor used for the inner layers of the first magnet varied along its length. Thereafter the size settled down to a constant tolerance. When the second magnet was started, it required different shims consistent with the outer layers of number 1. The correct shim locations were computed rapidly when the problem arose, using block approximations to the coil, and gave an arrangement with essentially identical field multipoles. Later, more accurate calculations using actual location of the conductor layers revealed a small difference between the magnets. In retrospect, this problem presented a method for fine tuning. A few predetermined calculations permit the location of spacings to be used in both the design and construction to flatten the low field properties to great accuracy. It should be noted that following a lead burnout and resulting coil arc, number 1 module had the outer layers of the coil removed. The coil was spliced and rewound

TABLE III. COMPARISON OF UNITS 1 AND 2

(n+1)θ / *1e*	Magnet Unit	*6kG*		*24kG*		*38kG*	
		a_n	b_n	a_n	b_n	a_n	b_n
38/18	1	2.7	+ *4.0*	1.1	+ *2.5*	*0*	- *6.4*
	2	*0.1*	+ *4.3*	*0.3*	+ *1.7*	0.1	- *1.9*
58/18	1	*0.1*	+17.6	*0.1*	+11.4	*0.4*	*-15.6*
	2	0.4	+18.0	*0.3*	+12.5	*0.1*	*-14.1*
78/18	1	0.1	-10.1	0.1	- *7.4*	*1.4*	- *2.0*
	2	*0.2*	*-11.0*	*0.2*	- *8.5*	0.9	- *2.1*
9θ/1θ	1	*0.5*	- 1.8	0.1	- *5.2*	0.1	*-32.6*
	2	*0.2*	- *1.6*	*0.2*	- *4.9*	*0*	*-32.5*
11θ/1θ	1	*0.1*	- 1.0	0	- 0.1	*0.5*	+ *3.9*
	2	*0.2*	- *1.2*	*0*	+ 0.1	*0.4*	+ *2.9*

Note: Field multipolarities expressed relative to the dipole field (1e) in terms of 10^{-4} parts at the measurement radius (p = 3.825cm).

without difficulty. It was after the repair that the magnet module was measured and put to use.

We return to the question of the precision and identity of the two units. The largest error is the quadrupole, $G/B_o \sim 0.8 \times 10^{-4}$ cm^{-1} for each magnet. The next largest effect expected is on the identity of the sextupoles. Figure 5 shows point coil sextupole data for identical current excitations of both magnets. The baseline corresponds to average $b_2 = 0$ for the computed magnets. Because of the computational errors during construction described earlier, these excitations more accurately produce the computed b_2 values shown in curves (L_1) and (L_2). For rising fields, experimental b_2 are plotted and their average, curve (M). Also plotted is the corresponding falling field data and curve (N). The offset of curve (M) from the baseline is due to hysteresis on a rising cycle. The offset between curves (M) and (N) is the width of the single sided hysteresis loop. Note that the downside is further than the upside from the computed baseline, as it should be, since the computed magnets have no hysteresis. For comparing the two magnets the down-cycle is as valid as the up cycle. The difference between magnets as measured and computed is in agreement to a very small error consistent with measurement accuracy €or the great bulk of the data. It is evident that the module 2 point at 18kG on curve (M) is in error. The other points at 18kG on curves (M) and (N) are normal. An identical graph for long coil results (not shown) has no irregularity at *18kG* and constant loop width between the up and down cycles. The 38kG data shows some deviation beyond expected measurement accuracy, as also seen in b_2, Table III. The long coil data suggests that if this magnet difference is real, it is considerably smaller than indicated in Figure 5. Separate run data taken at 40kG does not show this deviation. Further experimentation will have to clarify if there is a very small high field difference. Since these magnets have solid iron rather than mixed and stacked laminations, some small permeability effects are possible. Finally, if the 1-2 differences for all runs are averaged and compared with the equivalent computed differences, agreement is good to a number small compared to 1×10^{-4}. The evidence strongly suggests that real sextupole magnet errors are less than measurement errors and are $\leq 1 \times 10^{-4}$ (0.06×10^{-4} cm^{-2}) to go along with the quadrupole error of $\sim 3 \times 10^{-4}$ (0.8×10^{-4} cm^{-1}) This is respectably small even for conventional magnets.

Consider next the higher multipoles from the viewpoint of predictability and of absolute field quality. The 5θ, point coil, field measurements show very small hysteretic effects ($\sim 1 \times 10^{-4}$). The up and down cycles are mutually displaced as in Figure 5, but only by about 0.5×10^{-4}. The absolute agreement of computer and experiment for both magnets is very good with a constant offset of 3×10^{-4}. This includes any small hysteresis, plus systematic permeability or computer fitting effects, etc. The amplitude of 5θ varies considerably with field level, and this is followed exactly by the computations. The fact that the computer predicts the shape of 5θ very accurately is important, since the 8° magnets have a large built-in 5θ, considerably larger than in the later designed 20-in. long model.

The 58 term has the only significant superconducting diamagnetism in this magnet design. Internally, $b_4 \sim 6 \times 10^{-4}$ is produced on the up-cycle at 6kG, and is very small by 12kG. This diamagnetism is due to the correcting coil used.[4] Diamagnetism in the dipole coil returns primarily through the iron to high approximation.

For 78, 98, and 11θ no hysteretic or diamagnetic effects are evident, and the magnet differences are predicted to better than 1×10^{-4}. Again, as the amplitude changes with field, the predictions of absolute value follow the shape closely. Systematic offsets at the level of a few parts in 10^4 occur, as in 5θ.

With sextupole tuned to zero, the magnetic field uniformity of each magnet at 6kG *is* shown in Figure 6B. The horizontal midplane field (H1) of magnet 1 and (H2) of magnet 2 was reconstructed at several radii and this data plotted, Points (V1) and(V2) are the equivalent vertical midplane data. The computer predictions are shown by the two solid curves. For clarity of presentation, the computed fields of magnets 1 and 2 were averaged. Thus HCOMP is the average computed horizontal midplane, and VCOMP is the vertical equivalent. For perfect predictability and measurement, HCOMP should pass through the average of H1 and H2. Quadrupole field is not included and must be treated as a superposition. The absolute field nonuniformity is $\leq 10 \times 10^{-4}$ at the beam tube on both midplanes and at all angles θ. At the measurement radius ρ_c, computer and experimental average deviate by $\sim 1.5 \times 10^{-4}$. It is important to note that the model, which was of a somewhat later conceptual design, was uniform to $\pm 1 \times 10^{-4}$ up to the beam tube; i.e., ~ ten times more uniform than the 8°.

While absolute field quality is reasonably good, Figure 6A shows the predictability is of a much higher order. This contains the same information, but now only the differences between the two magnets are plotted. Note the scale change. The differences are very small and predicted to $< 1 \times 10^{-4}$.

Figure 7 gives the same information at 30kG. The field nonuniformity is now somewhat larger and the deviation from prediction is larger. The vertical computer curve, VCOMP, lies quite close to the experimental points. The HCOMP curve is off even at r = 60%. This is due to the systematic offsets between experimental and computed multipoles described earlier. However, the magnet difference data in Figure 7A is again predicted to $< 1 \times 10^{-4}$.

Figure 8 gives the same results at 38kG. The useful field radius is shrinking, due mainly to the large 9θ produced by the correction coil design. Again VCOMP agrees quite well with both magnets, but *HCOMP* by $r = \rho_c$ differs considerably. However, in Figure 8A the differences between magnets are predicted very accurately with an error $< 1 \times 10^{-4}$. It should be noted that, as was the case at low fields, the field uniformity of the model was much better than the 8°. The field uniformity $\Delta B/B_o$ was within 1×10^{-4} to 62% of aperture at 38kG. Nevertheless, the differences between the measured and the predicted model were about equal to those in the 8° case, showing the same systematic effects due to hysteresis, computer program, etc.

In summary, except for small hysteretic and other effects common to both, the 8° magnets have shown allowed multipoles which are predictable to high accuracy. The predicted small difference between the two magnets due to construction problems which are now under control comes very close to the difference between the two magnets as measured separately. This means that the construction and measurement errors are very small, and the ability to iterate, in the future, small absolute deviations between computations and reality is ensured. This was the first design of this type. The full cross section model was a considerable improvement, and later designs provide very uniform fields at all levels. With the same precision of construction as in the 8°, field quality equivalent *to* the best of conventional magnets seems feasible.

Finally, a brief comment on end effects. No attempt was made to design the ends for field shaping.

Nevertheless, the b_2 contribution of ends to the field integral remains within $\sim 10 \times 10^{-4}$ parts over all excitations. This, like the iron hysteresis of similar magnitude, can simply be absorbed into the defined auxiliary coil current required for all magnets so that the b_2 integral is made zero at all fields. The 5θ contribution is roughly constant, at -4×10^{-4}. To the extent this is constant, it can be handled simply by a compensating internal offset in computed design. The low field 5θ end effects due to diamagnetism in the superconductor happen to cancel the internal contribution of 6×10^{-4} at 6kG, so that the 5θ integral on the rising field is equal at 6kG and 12kG. The 7θ term measures $+2.5 \times 10^{-4}$ and is very constant over the entire field range, so it can be taken care of by internal design. The 9θ and 11θ have negligible end effects. Without any attempt at end shaping, end effects should be smaller than in typical conventional magnets used in beams and accelerators.

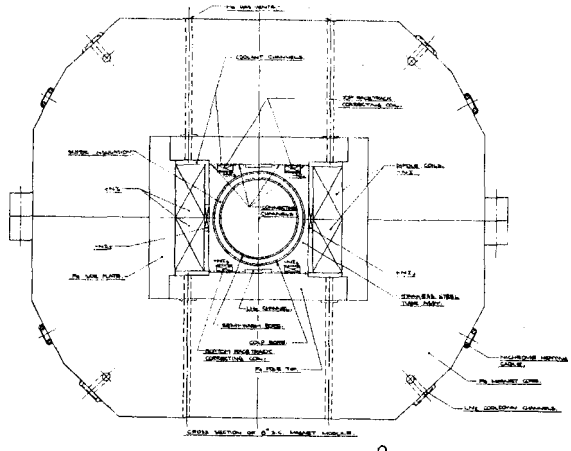


Fig. 1. Cross section of the 8° superconducting magnet.

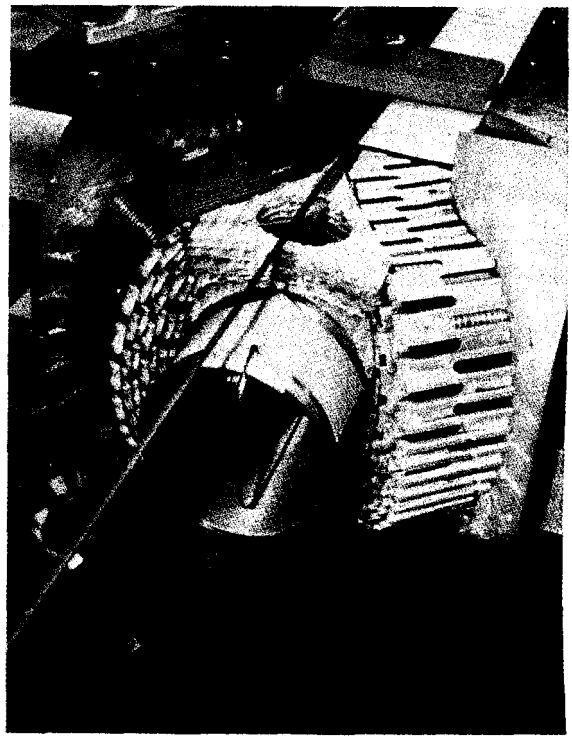


Fig. 2. Superconductor being wound around magnet end blocks.

References

1. J. Allinger, et al., IEEE Trans. Nucl. Sci. NS-20, No. 3 (1973).
2. J. Allinger, et al., in Proc. of the Fourth Intl. Conf. on Magnet Technology (CONF-720908) p. 637 (1972).
3. J. Allinger, et al., Proc. of this Conference.
4. G. Danby, et al., in Proc. of the Fourth Intl. Conf. on Magnet Technology (CONF-720908) p. 334 (1972).

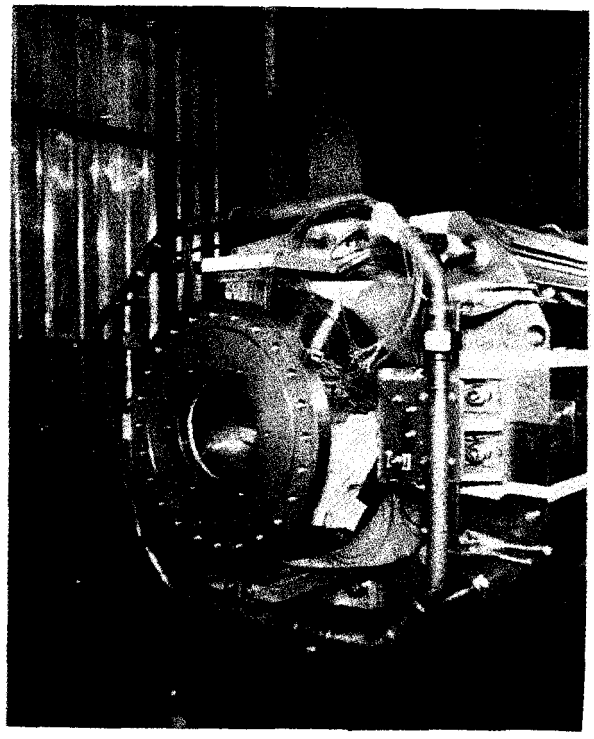


Fig. 3. End view of 8° superconducting magnet module.

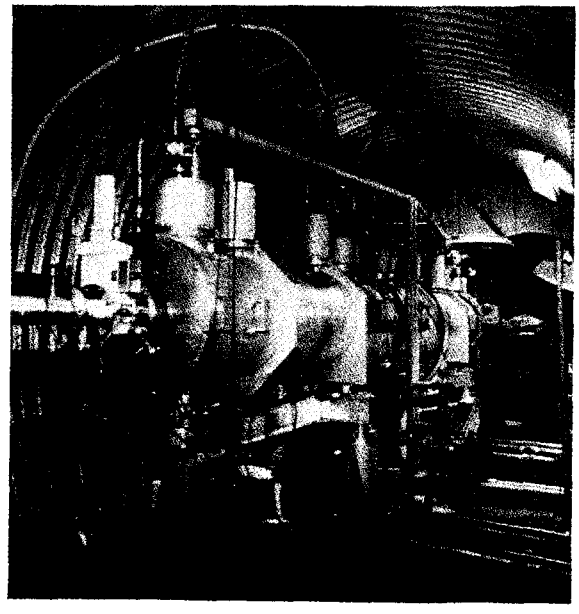


Fig. 4. 8° magnet system installed in North Area tunnel.

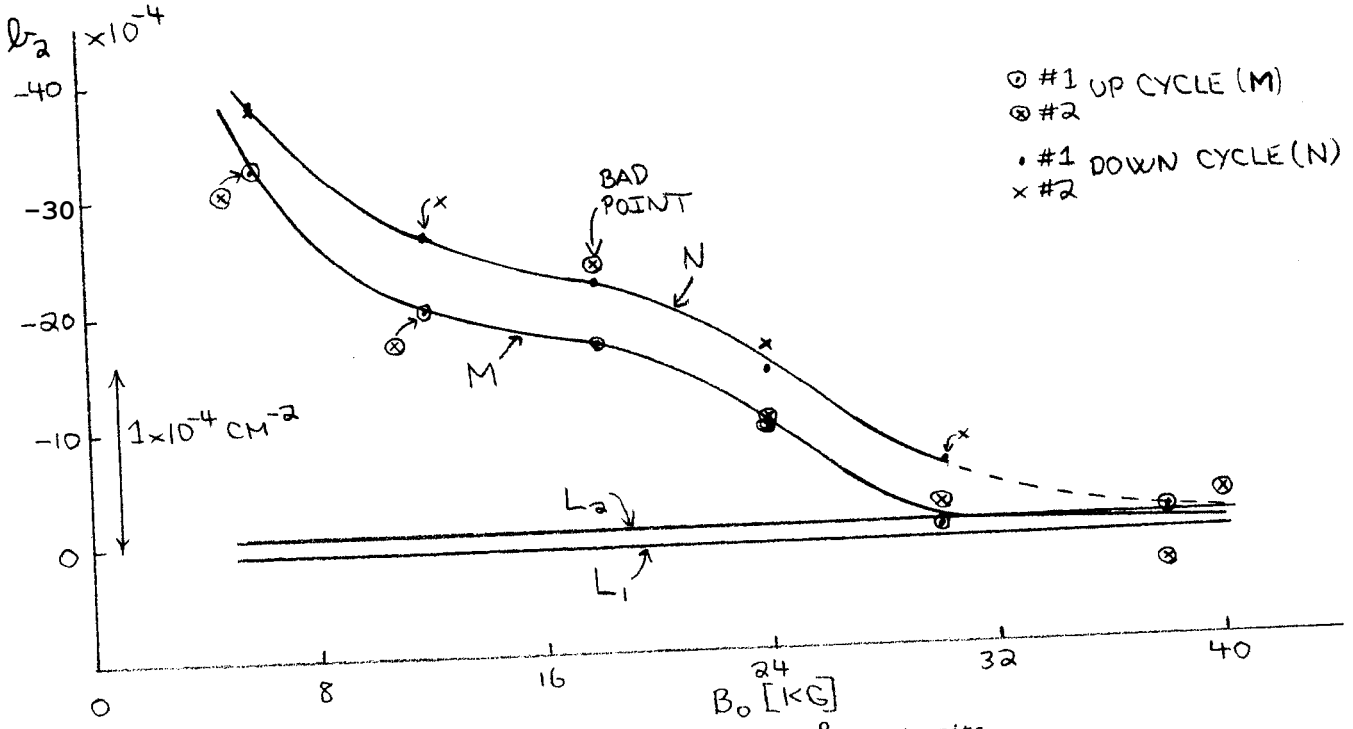


Fig. 5. Sextupole identity of 8° magnet units.

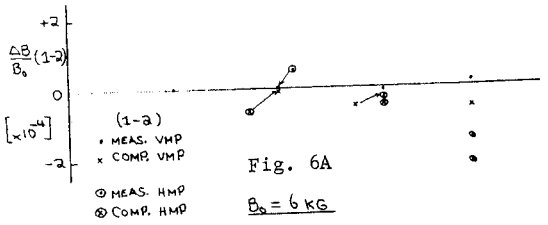


Fig. 6A

$B_0 = 6$ KG

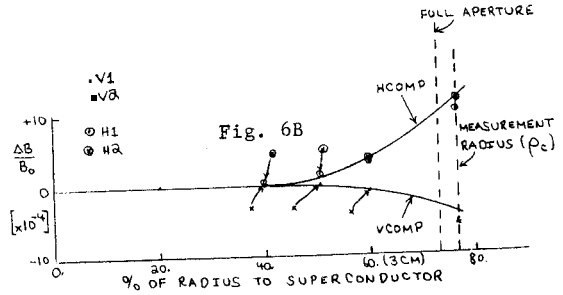


Fig. 6B

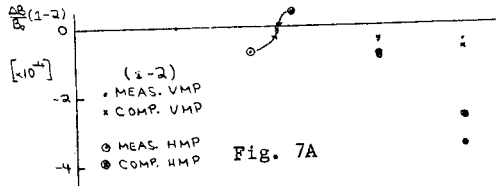


Fig. 7A

$B_0 = 30$ KG

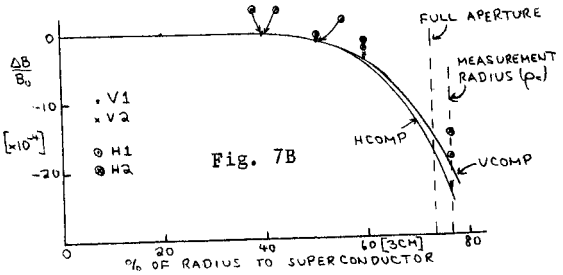


Fig. 7B

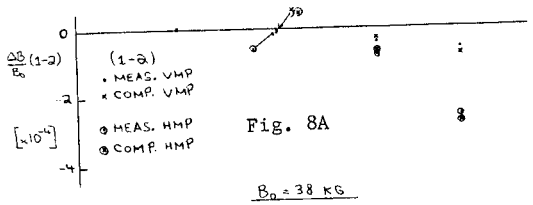


Fig. 8A

$B_0 = 38$ KG

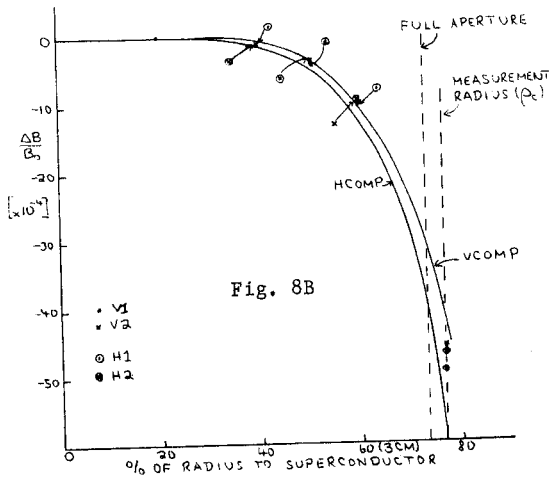


Fig. 8B

PREDICTION OF RADIATION EFFECTS ON ACCELERATORS USING HADRON CASCADE CALCULATIONS

J. Ranft
Sektion Physik, Karl-Marx-Universität,
Leipzig, DDR

Summary

Radiation effects, especially radiation heating, radiation doses and induced activities on accelerator components as septa, targets, beam dumps and accelerator and beam line magnets are predicted using hadron cascade calculations. There is good agreement to measurements in the 10-20 GeV energy range, the same is found in a comparison to first measurements at 300 GeV at NAL.

1. Hadron cascade calculations

Hadron cascade calculations and their application to radiation problems around high energy accelerators were described in detail by Ranft.[1] Here we report on recent experimental comparisons and applications of these calculations.

The cascades considered are initiated by primary hadrons in the energy range of tens and hundreds of GeV. The characteristic feature of collisions in this energy range is the abundant production of new hadrons, a process which is rather independent on wether Hydrogen or heary material like Fe or Cu is used as target material. The number of newly produced secondary particles rises logarithmically or with a small power of the laboratory energy of the primary particle

$$n_s \approx \log E_p \quad \text{or} \quad n_s \approx E_p^{1/4} \qquad (1)$$

In extended matter these secondaries produce in turn more particles in their collisions and so on. This process comes to an end only when finally the energies of all particles are small enough so that particle production is no longer possible.

In most materials the cascade of high energy hadrons is the dominant mechanism of energy transport. For many applications of hadron cascade calculations nuclear excitation processes like the intranuclear cascade and nuclear evaporation, which give rise to large numbers of low energy secondaries - mostly neutrons - are relatively unimportant and can be treated approximately. In the well developed cascade the fluxes of these low energy particles are related to the flux of high energy particles, collisions of high energy hadrons are the main source of the low energy component.

There are three dominant mechanisms of energy deposition by the hadron cascade. These are:

(i) the ionization energy loss of high energy charged hadrons,
(ii) electromagnetic cascades initiated by γ quanta from π^0 decay and
(iii) low energy nuclear fragments depositing the energy component which we call nuclear excitation energy.

The three mechanisms are roughly of equal importance. The proportion of energy deposited by the electromagnetic cascade rises with energy and the proportion of nuclear excitation energy decreases with primary energy.

For most applications the three dimensional development of the cascade initiated by a narrow beam of primary particles is of interest. The elementary events in the cascade are rather complicated, particle production is strongly anisotropic. There are different kinds of processes to be considered, elastic and ineiastic collisions, ionization energy loss, electromagnetic cascades etc. Different kinds of particles are involved, we consider protons, neutrons, and charged and neutral pions.

In this situation three dimensional analytic calculations are extremely difficult no such calculations have been performed yet. Analytic calculations of the one dimensional development of the hadronic cascade using a simplified description of the contributing processes were however performed.[2] Such calculations are valuable for the general understanding of the cascade process but only of

limited use for practical applications.

Physical input data for the cascade calculations are the following: elastic and inelastic cross sections of hadrons on nuclei, inclusive particle production cross sections for hadrons colliding with nuclei and ionization energy losses, multiple Coulomb scattering, nuclear excitation energies and energy deposition by the electromagnetic cascade. All input data used are discussed in Ref. [1] and [3]. Technical details of the Monte Carlo calculation are discussed in Ref. [1,3,4] and [5].

Computer programs using different methods, for different applications and for different geometries are available [5-9].

The most important results of the hadron cascade calculations are presented in the form of three dimensional hadronic cascade star densities and energy deposition densities. Star densities are of use to estimate the production of radioactive isotopes in the material and from this the remanent dose rates from induced radioactivity after the end of irradiation by the high energy particles. Energy deposition densities are related to direct radiation dose and to heat deposition in the material as well as to signal size in scintillation detectors.

2. Recent comparisons of results of hadron cascade calculations with experimental data

The confidence in the predictive power of the rather complex hadron cascade calculations is to be justified by comparison of the results with experimental data obtained in a wide variety of situations. Such comparisons done up to 1971 were reported in [1], here we discuss recent work done since the completion of the paper. [1]

The computer programme FLUKA [5,8] was used by Henny and Potier to calculate the heat deposition in external targets. The results of the calculation were compared with experimental data obtained at the CERN-PS with a proton beam of 24 GeV/c incident on external targets with the length $l = 180$ mm and a diameter of 12 mm. In Table 1 we compare the measured heat deposited by a beam of 10^{12} protons with the hadron cascade results. It is to be noted that the heat deposition in heavy materials is up to five times larger than due to the ionization energy loss of primary particles alone. The calculated heat depositions agree rather well with the experimental data.

Table 1

heat deposition in cal/10^{12} protons by a proton beam of 10^{12} particles incident on targets of $l = 180$ mm length and 12 mm diameter [10]

Target material	Al	Ti	Cu	Mo	W
primary ionization alone	3.5	5.5	10.5	11.2	19.0
experiment	4.7	10.8	38.0	47.0	93.5
hadron cascade calculation, FLUKA	7.0	13.3	28.6	38.8	89.0

Deep penetration hadron fluxes measured with activation detectors and dose meters in the large muon filter of the CERN neutrino experiment were compared by Goebel, Ranft and Routti [11] with hadron star densities and energy deposition densities calculated with the programme TRANKA. [5] Good agreement of experimental and calculated results was found up to a depth of 400 cm in iron and up to radial distances of 200 cm from the beam axis. The hadron fluxes in this region are attenuated by about 7 decades. This agreement was found in spite of the rather inhomogenous composition of the muon back stop used.

In the same paper Goebel, Ranft and Routti compare the results of TRANKA with activation detector measurements in a more homogenous Fe backstop irradiated with 28 GeV protons at BNL. [12] In Fig. 1 we compare the hadron flux density calculated with the BNL results. The data at $r = 60$ cm outside the beam axis might be influenced by the halo of the beau.

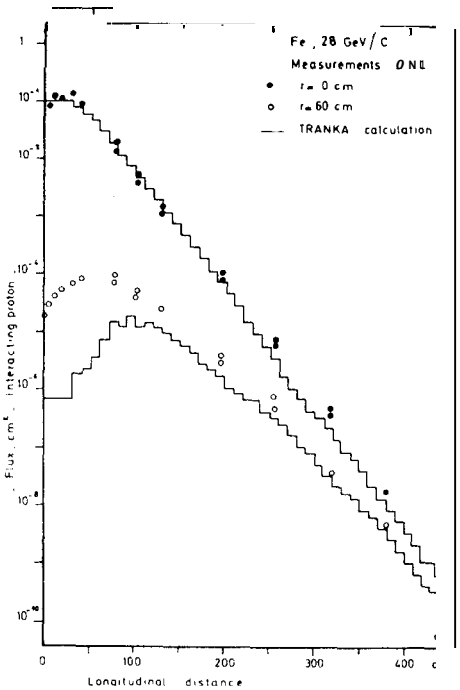


Fig. 1 Comparison of hadron flux densities calculated with the Monte Carlo programme TRANKA[5] with BNL measurements using ^{11}C activation detectors.[12]

As described in[1] and[5] the programme FLUKA can also be used to simulate the action of total absorption detectors. A modified version of FLUKA was used by Engler et al.[13] in order to optimise the energy resolution of neutrons or other strongly interacting particles with sampling total absorption counters (STAC). In Fig. 2 we compare the energy resolution measured by Engler et al.[13] using a particular STAC counter with the energy resolution calculated with the modified version of FLUKA by the same group,

A first experiment measuring the propagation of the hadron cascade initiated by 300 GeV protons interacting in a target which was positioned inside a beam line bending magnet was performed at NAL.[14] Preliminary results of this experiment were compared with hadron cascade calculations using the programme MAGKA.[8] In Fig. 3 we compare the energy deposition density as calculated by MAGKA with the results of dose measurements inside and outside the magnet yoke. Good agreement is found.

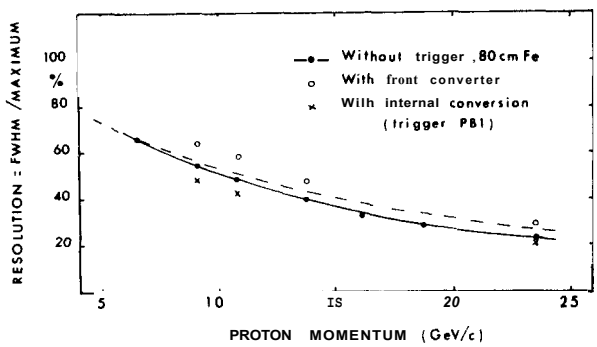


Fig. 2 The energy resolution measured with a sampling total absorption counter as function of the proton momentum for different trigger conditions. The full line is drawn through measured points without special trigger conditions. The dashed line was obtained from hadron cascade calculations using a modified version of the programme FLUKA.[13]

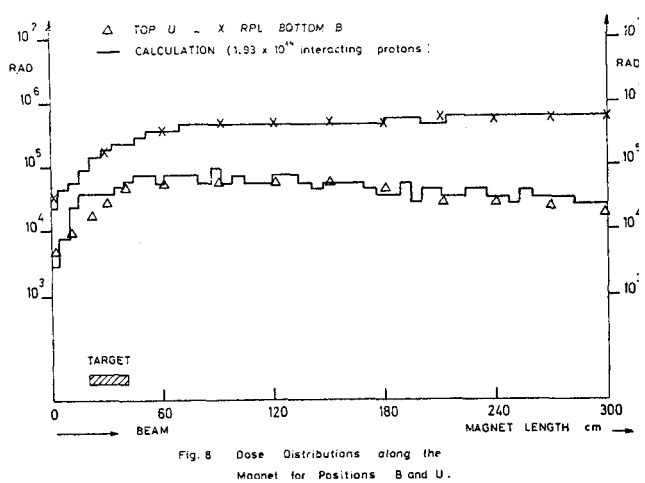


Fig. 8 Dose Distributions along the Magnet for Positions B and U.

Fig. 3 Comparison of calculated and measured doses inside and outside the yoke of a beam line magnet. A target inside the magnet was irradiated with 300 GeV/c protons at NAL.[14,15]

Particle fluxes measured at large angles around massive targets in external proton beam lines were compared by Ranft and Routti[6] with results obtained with the computer programme FLUKU simulating the hadron cascade inside the target. Good agreement was obtained.

Hadron fluxes in a side shield near to a target in an external proton beam line were measured at BNL for 15.5 and 28 GeV/c incident protons.[16] The results of this experiment were compared by Ranft[7] with results of the hadron cascade programme BIAGKO.

In situations where particle fluxes and doses perpendicular to the incident proton beam are of interest it is of advantage to use the programmes FLUKU[6] and MAGKO.[7] In these programmes the protons and neutrons resulting from the intranuclear cascade are considered in more detail than in other coinputer programmes.

3. Prediction of radiation effects around future accelerators using hadron cascade calculations

Many applications of hadron cascade calculations for the estimation of radiation problems around high energy accelerators are discussed in Ref.[3]. Such applications include estimation of dose to components and induced radioactivity in ejection regions and external target areas of proton accelerators, prediction of target heating and heat deposition in beam dumps, calculation of longitudinal and transverse hadron shielding requirements. We discuss here some recent applications mostly for problem around the 300 GeV accelerator of CERN-Laboratory II.

The thermal effects which accur in external targets when irradiated by fast and slow extracted beams of 400 GeV/c and 10^{13} protons per pulse were studied by Kalbreier, Middelkoop and Sievers[17] using the programme FLUKA.[5,8] Temperature and thermal stress distributions in targets of different materials were derived from the calculated energy deposition density. The incident beam was assumed with a Gaussian density distribution with 92% of all protons within a diameter of 2 mm. In Table 2 we give as an example temperatures calculated for targets with a length of one nuclear interaction length and 2 mm diameter.

Table 2

Target temperatures in °C for 10^{13} protons of 400 GeV interacting in a one interaction length, 2 mm diameter target compared to the melting temperatures of the target materials T_{melt}. T_o is the maximum temperature rise in the centre of the target for the case of a fast extracted beam. $\bar{T}$ is the average temperature rise at the end of a slow extracted pulse in the absence of cooling. T_R is the steady state temperature of the target at the end of the thermal cycle evaluated for cooling by radiation only. The maximum target temperatures are $T_R + \bar{T}$ for slow extraction and $T_R + T_o$ for fast extraction.

Material	T_o	$\bar{T}$	T_R	T_{melt}
Be	490	190	730	1280
BeO	950	420	830	2570
B_4C	1190	550	750	2430
C	1250	510	600	3320
SiC	840	310	910	2700
Al	670	400	660	660
Al_2O_3	1060	450	850	2040
Ti	1670	1070	880	1670
cu	2900	1910		1080
Mo	9300	4000		2610
W	39000	20000		3380

The numbers in Table 2 exclude the use of heavy target materials and forced cooling by convection seems to be adviceable.
The dynamic stresses created in the targets due to the rapid heating in fast extracted beams have to be reduced by subdividing the total target length into several parts. In fast extracted beams also the quasistatic stress produced in the target due to the radial temperature gradient exceeds the elastic limit.

The thermal problems arising in bean dumps are also investigated using the hadron cascade programmes FLUKA and MAGKA.[18]

Dose to components and remanent dose rates from induced radioactivity were estimated at CERN-Laboratory II for the ejection region of the main ring and for the target areas in the 'Nest, North and Neutrino zones[19,20] using the programmes MAGKA and FLUKA. The results indicate very high dose and radiation levels in critical positions. Therefore it seems adviceable to develop special radiation hard components for these regions.

The remanent dose rates estimated for the CERN-SPS ejection region are in good agreement with the first experience around the NAL accelerator.[19]

The hadron cascade programmes MAGKA[8] and MAGKO7 are well suited to study the effect of the heating due to beam losses in superconducting synchrotrons and storage rings. A preliminary study of this kind is beeing performed by Schönbacher and Van de Voorde.[21] The effect of radiation heating due to beam losses is not important for the refrigeration requirements but the sudden temperature rise due to the hadron cascade in the supraconducting windings can lead to a sudden loss of supraconductivity. The beam loss which can be tolerated depends on the arrangements of the supraconducting magnets but it seems that a loss of 10^{12} protons in or near to a s.c. magnet could affect its operation. For these reasons the operation of supraconducting synchrotrons and storage rings requires a control of beam losses well beyond the present state of the art.

Acknowledgements

Most of the work reported was done while visiting CERN-Laboratory II. I thank very much Dr. J. Adams and Dr. K. Goebel for their kind hospitality. Like wise I would like to thank the radiation groups of CERN-Laboratory II and NAL as well as the beam transfer group of CERN-Laboratory II for the permission to present some material from unpublished laboratory reports.

References

1. J. Ranft, Particle Accelerators 3, 129 (1972).
2. C. Passow, DESY-Notiz A 2.85 (1962); R. G. Alsmiller jr., Proc. Symposium on Accelerator radiation dosimetry, BNL (1965) p. 327; K.O'Brien, J.E. Mc Laughlin, Nucl. Instr. Meth., 60, 129 (1968); K.O'Brien, Nucl. Instr. Meth. 72, 93 (1969).
3. K. Goebel (ed.), Report CERN 71-21 (1971).
4. J. Ranft, Comp. Phys. Comm. (1973).
5. J. Ranft, J.T. Routti, CERN-Lab. II-RA/PP/73-1 (1973) to be publ. Comp. Phys. Comm.
6. J. Ranft, J.T. Routti, Particle Accelerators 4, 101 (1972).
7. J. Ranft, CERN-Lab. II-RA/73-2 (1973).
8. J. Kanft, J.T. Routti, CERN-Lab. II-RA/71-4 (1971).
9. J. Ranft, CERN-Lab. II-RA/Note/74-1 (1974).
10. L. Henny, J.P. Potier, CERN/MPS/CO i3-2 (1973).
11. K. Goebel, J. Ranft, J.T. Routti, Nucl. Instr. Meth. 113, 43% (1973).
12. G.W. Eennett, H.N. brown, H.W.J. Poelsche, J.D. Fox, D.M. Lazarus, G.S. Levine, T.E. Tookig, R.H. Thomas, J. Xostoulas, BNL preprint (1972).
13. J. Engler, W. Flauger, B. Gibhard, F. Mönnig, K. Runge, H. Schopper, Nucl. Instr. Meth. 106, 189 (1973).
14. Radiation groups of NAL-Batavia and CERN-Lab. II, report in preparation (1974).
15. I. Klanner-Jarstorff, K. Lambert, J. Ranft, CERN-Lab. II-RA/73-7 (1973).
16. W.H. Morre, G.S. Levine, G.W. Bennett, BNL report BNL 16409 (1971).
17. W. Kalbreier, W.C. Middelkoop, P. Sievers, CERN-Lab. II/BT/74-1 (1974).
18. P. Sievers, CERN-Lab. II/BT/74-3 (1974); P. Sievers, K. Teutenberg, CERN-Lab. II/BT/ in preparation (1974).
19. K. Goebel, J. Ranft, J.T. Routti, G.R. Stevenson, CERN-Lab. II-RA/73-5 (1973).
20. M. Ellefsplass, K. Goebel, J. Ranft, H. Schönbacher, CERN-Lab. II-RA/74-1 (1974)
21. H. Schönbacher, M. Van de Voorde, personal communication (1974).

RESEARCH WORK ON PULSED SUPERCONDUCTING MAGNETS FOR ACCELERATORS

Alexeev V.P., Vasiliev A.A., Galstjan E.A., Greben' L.I., Mironov E.S.

Radiotechnical Institute of the USSR Academy of Sciences
Moscow, USSR

Abstract

Research work on precise and reliable superconducting magnets for accelerators is presented.

Accelerator magnet requirements, design, and related topics are considered.

Some features of superconducting magnets usage in high-energy accelerators are discussed.

Introduction

During several last years a research work on the creation of superconducting magnets for particle accelerators is carried out at the Radiotechnical Institute of the USSR Academy of Sciences. The study was intended to examine the feasibility of superconducting cybernetic high energy accelerator [1-3].

Investigation of the topic in different accelerator laboratories [4-8] demonstrates that problems of a.c. losses, field accuracy etc. prove to be solvable. Several accelerator projects with superconducting magnets are known to-day. But still a lot of problems remains in the design and production of reproducible fail-safe superconducting magnets.

Our activity on superconducting magnets may be subdivided into 3 domains of research: theoretical, experimental and that of superconducting accelerator design as a whole including cryogenic and power supply systems.

Theoretical work is concentrated now on the magnetic field calculations. The effects of iron shield saturation, persistent currents in superconducting filaments and eddy currents are considered.

Technique of the iron shield influence calculation is based on computation of local magnetization of iron in a considerable number of shield elements by use of integral iterative method. Magnetic field intensity in the center of an element with uniform magnetization is obtained from the reccurence formula

$$\vec{H}_n^{(\ell)}\left[1-c_\ell\left(\mu_{n-1}^{(\ell)}-1\right)\right]=\vec{H}_c^{(\ell)}+\sum_{K\neq\ell}c_{\ell K}\left(\mu_{n-1}^{(K)}-1\right)\vec{H}_{n-1}^{(K)}$$

where n = iteration step number,
ℓ, K = element's numbers,
$H_c^{(\ell)}$ = field intensity of the magnet coil in a given point,
$c_{\ell K}$ = tensors of mutual magnetic influence of elements,
c_ℓ = coefficients corresponding to demagnetization of element ℓ,
μ = magnetic permeability, which depends on local magnetic induction.

The $c_{\ell K}$ and c_ℓ coefficients are determined by choice of dimensions and shape of shield elements and depend on a given field symmetry.

Zero approximation is taken in the following form:

$$\vec{H}_0^{(\ell)}=\vec{H}_c^{(\ell)}/\left(1-c_\ell\left[\mu\left(H_c^{(\ell)}\right)-1\right]\right)$$

Field intensities in shield elements obtained from the iterative procedure are used in calculation of iron shield influence on the field distribution in magnet aperture. The technique requires a tabulated permeability as a function of magnetic inductance or some approximation of the function.

Much consideration is given also to the performance of braided and twisted superconducting cables. Transposition of insulated strands in composite conductor provides total current capacity of individual strands only in uniform field. But in nonuniform field, which is just the case of frontal parts of accelerator magnets, and in some other cases

the critical current of the composite conductor may be less than the net critical current of its strands.

Our experimental program includes development and testing of dipole magnets and different types of conductors. In solenoids made of the conductor with 10μ superconducting filaments in complex Cu-CuNi matrix the measured critical current differed from that of a short sample less that 5 per cent. Rate of magnetic field rise was 4T/sec. Measured qualities of the solenoids (Q up to 1500) were in close agreement with calculations.

Superconducting dipole SPD-2

Length of the magnet is – 70 cm, coil i.d. is 78 ma. Cryostat and magnet design provides either 70 mm cold os 50 mm warm aperture.

Multilayer coil is placed layer after layer on stainless steel pipe. Each layer is fixed by capon fishing line wound with some pitch so as to provide continuous channels for helium. The magnet produced pulsed 4T field with 10 sec rise time [9].

No special mesures were taken to obtain good field accuracy. Nevertheless the measured field distribution in 40 mm aperture differed from the calculated one less than 0.2 per cent.

Dipole SPD-2 and its cryostat are shown in Pig. 1.

Superconducting dipole SPD-3

IMI transposed conductor with 24 strands is used in the magnet coil. Cross-section of the conductor is 2.5 x 3.5 mm^2, each strand contains 10μ Nb-Ti filaments in copper matrix. Magnet length is abt 70 cm, coil i.d. is 85 am. Cross-section of SPD-3 is presented in Fig. 2. The coil consists of eigth cylindrical layers which are grouped in pairs in four circular sectors with different angular spread.[10] For given magnetic field (4T in our case) the design scheme requires minimum amount of superconductor. Four boundary angles of circular sectors were determined by two computer programs? The first one used an assumption of constant current density in coil layers.Boundary angles were chosen so as to minimize the sum of absolute values of 3-d, 5-th, 7-th and 9-th field harmonics within the aperture. The second program performs approximate angle calculation with due allowance for the given conductor dimensions and the number of turns in each layer. Calculated field pattern is presented in Fig. 3. The figure gives field distributions along horizontal *(x)* and vertical (z) axes within the limits of 0.7 coil i.d.

Turns of the coil are fixed in the same way as in SPD-2 but instead of capron fishing line an insulated 1mm copper wire is used. It enables to improve fabrication accuracy of coil layers. Radial tolerances range from 0.05 mm to 0.2 mm in different layers. Angle tolerances also differ in coil layers. Mean angle tolerance is 10'. Uniformity of turns positioning in a layer is of great importance. The tolerance of turn positioning proves to be closest- in the first layer where a long-wave variation of conductor density is practically inadmissible . Calculations indicate that it is necessary to take some special steps to provide uniform distribution of conductors in coil layers.

In azimuthal direction the layers lean against seven supports. Dielectric spacers are placed between the supports. The spacers prevent from noncircular deformations of the coil during layer fixing by copper wire. The wire is wound with some pitch providing annular cooling channels. Openings in the dielectric spacers anable free liquid helium access to the coil.

End part of SPD-3 is similiar to that of previous dipole SPD-I, i.e. the turns are placed in special grooves. In the design three turns are laid in a groove. Dielectric components of the magnet are made of epoxy resin with filler. Cooling down to 4.2K causes relative contraction of the material ranging from $3.5 \cdot 10^{-3}$ to $10 \cdot 10^{-3}$ as a function of amount of filler. Proper choice of filler amount enables to fit relative contraction of the dielectric to that of the coil in radial and azimuthal directions.

Expected deviation of the real field distribution from the calculated one is 0.1 per cent in the aperture that is equal to 0.7

coil i.d. We intend to construct two such magnets and investigate their indentity. The magnets are under manufacturing now.

Magnetic system design for high energy accelerators

In the development of superconducting accelerators many particular problems arise. The problems are caused by the fact that magnets are operated at very low temperatures. So, e.g. the contraction of a 6 m long magnet due to the cooling down from 300K to 4.2K amounts 20-30 mm. Magnet adjustment system also has to operate at low temperatures.

A peculiar problem is that of accelerator vacuum chamber which may be either "warm" or "cold". The second alternative is preferable since it simplifies considerably the design of cryostat and vacuum chamber. Besides the inner pipe of helium vessel may serve as a vacuum chamber. If the cryostat and the accelerator chamber have separate vacuum systems the vacuum chamber may have a form of a thin cold partition. In both cases the cold chamber serves as a cryopump. With cold vacuum chamber the i.d. of magnet coil is less and hence the superconductor expenditure and cost are less. But final option of the chamber depends upon the careful examination of the interaction processes between the beam and cold chamber. Desorption of molecules from the surface and some other problems have to be considered.

In the case of cold vacuum chamber it is reasonable to arrange magnet units in separate helium vessels and join several units in a common demountable vacuum vessel with liquid nitrogen screen.

Magnet unit positioning and adjustment may be realized by use of thin rods. Length of the rods has to provide enough stress after cooling down.

Cross-section of the magnet in cryostat and the arrangement of several magnet units are presented in Fig. 4. In the figure the adjustment rods are also shown, some of them (5) bearing the magnet weight.

Heat transfer to cryostats may be reduced by connection of coils of different magnet units with superconducting cables. In the case current leads will be installed only in those points of ring where a whole group of magnets connects with power supply system. The superconducting cables may be accomodated in helium vessels of magnets. In straight sections with small number of magnets the interconnecting cables may be placed in the helium supply manifold.

Later on we plan to develop a number of alternatives of magnets and cryostats and choose the optimal design scheme for accelerators under consideration in our Institute.

Acknowledgements

The authors wish to thank L.A.Popokin for his contribution to the design of SPD-2 and SPD-3; V.F.Aleshin for his Q measurement data; V.P.Nashchekin and A.E.Danilova for development of dielectric with contraction coefficients close to that of a coil.

References

1. Burshtein E.L., Vasiliev A.A., Mints A.L. Proc. VII Int. Conf. High Energy Accelerators, v. I, p. 60, Yerevan, 1970.
2. Alexeev V.P., Meshcherov R.A., Mironov E.S., Vasiliev A.A. Proc. E-th Int. Conf. High Energy Accelerators, p. 228, Geneva, 1971.
3. Alexeev V.P., Meshcherov R.A., Mironov E.S., Vasiliev A.A. Proc. VII Int. Conf. High Energy Accelerators, v. 11, p. 735, Yerevan, 1970.
4. Smith P.F., Lewin J.D. Nucl. Instr. Meth. v. 52, p. 296, 1967.
5. Ado J.M. et al. Proc. of the 3-d USSR National Conf. on Particle Accelerators, v. 11, p. 275, Moscow, 1973.
6. NALREP, NAL-73/10, September 1973.
7. GESSS-2, A second report of the work of GESSS-Colaboration, May 1973.
8. CERN Courier, v. 13, n. 7-8, p. 223, 1973.
9. Alexeev V.P., Galstjan E.A., Mironov E.S., Popokin L.A., Vasiliev A.A. Proc. of the 3-d USSR National Conf. on Particle Accelerators, v. I, p. 163, Moscow, 1973.
10. Alexeev V.P., Greben' L.I., Mironov E.S., Vasiliev A.A. Proc. of the Radiotechnical Institute of the USSR Academy of Sciences, N 15, p. 91, Moscow, 1973.
11. Galstjan E.A., Greben' L.I., Mironov E.S. Proc. of the Radiotechnical Institute of the USSR Academy of Sciences, N 15, p.100, Moscow, 1973.

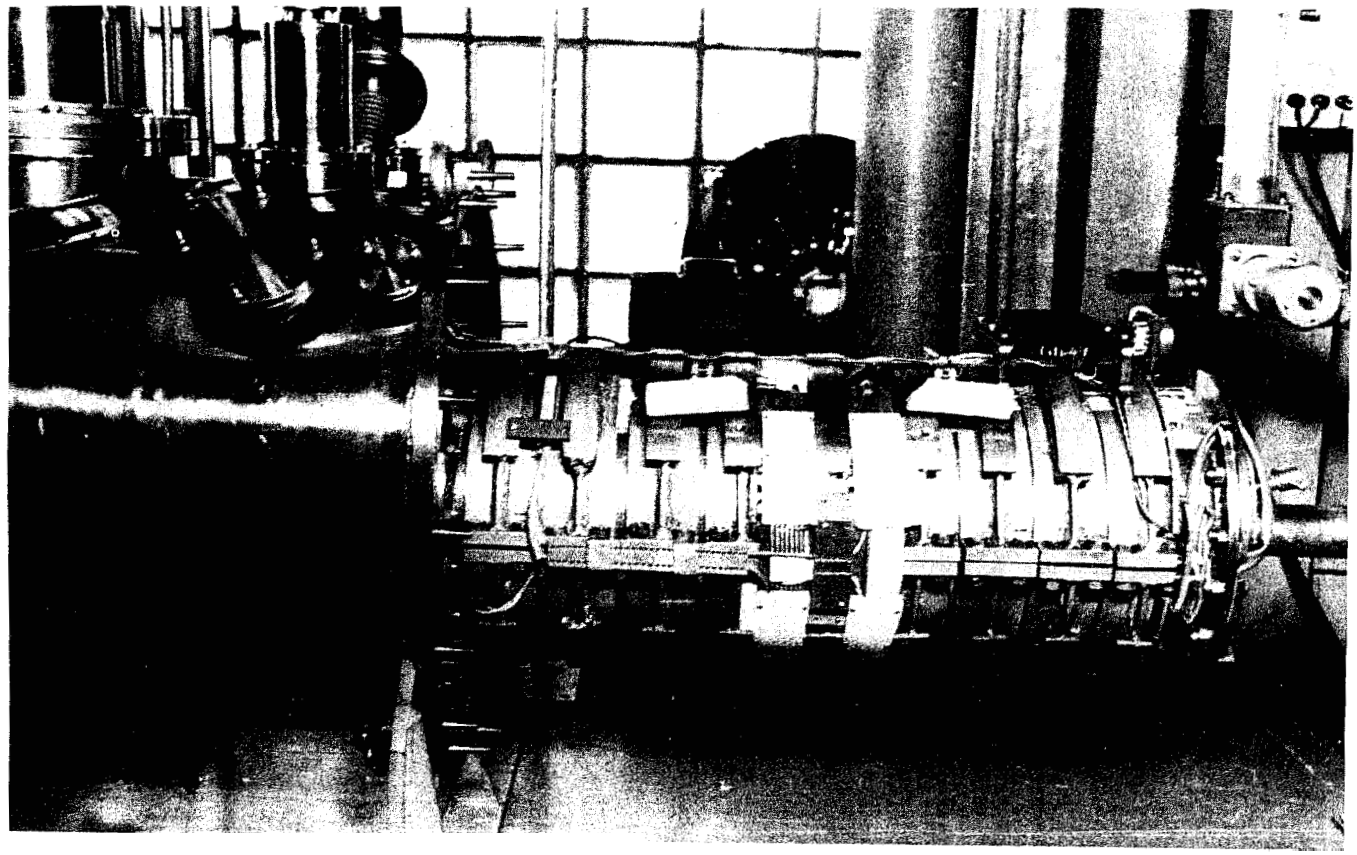


Fig. 1. Superconducting dipole magnet SPD-2 with cryostat



Big. 2. Cross-section of superconducting dipole magnet SPD-3

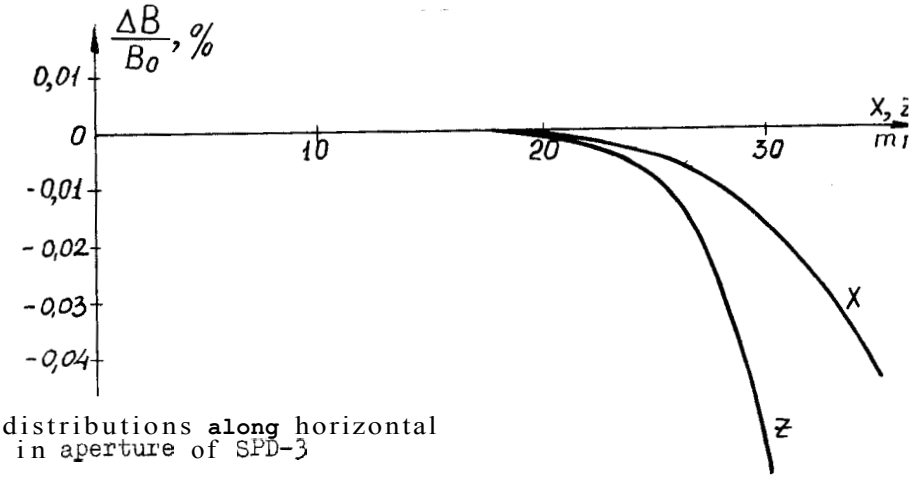
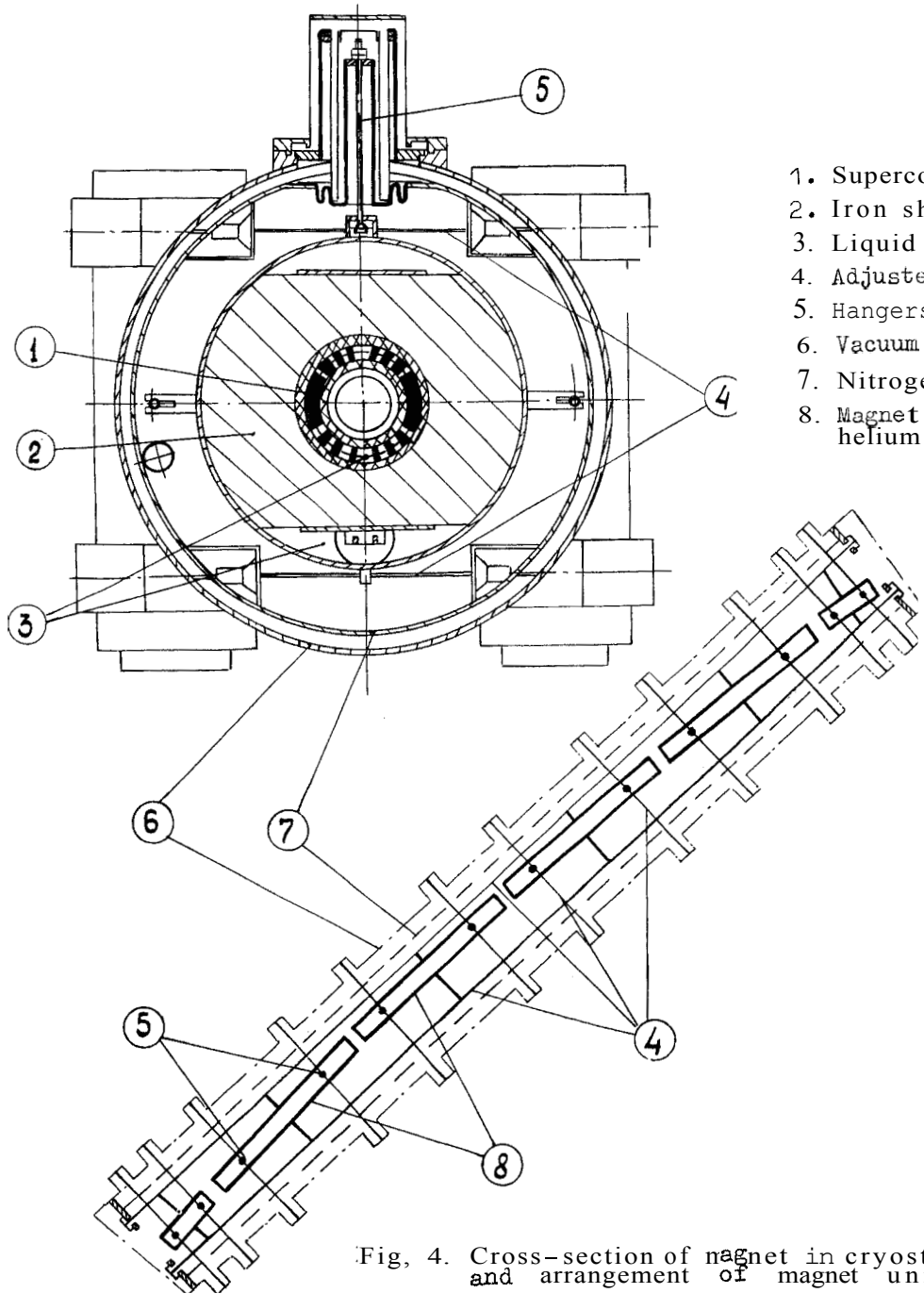


Fig. 3. Calculated field distributions along horizontal and vertical axes in aperture of SPD-3



1. Superconducting coil
2. Iron shield
3. Liquid helium
4. Adjustement rods
5. Hangers
6. Vacuum vessel
7. Nitrogen screen
8. Magnet units in helium vessels

Fig, 4. Cross-section of magnet in cryostat and arrangement of magnet units

RAPPORTEUR TALK ON ELECTRON RING ACCELERATION

Glen R. Lambertson

Lawrence Berkeley Laboratory
University of California
Berkeley, California

The work on electron rings is characterized by the conflict between (1) the desire to maximize and utilize the collective fields of the ring and (2) the necessity of suppressing instabilities propagated through those same collective fields. The search for this balance has resulted in some analyses of the limitations one may expect on ring parameters. I want to give as an example a particularly simple illustration of this that was presented by Jackson Laslett.[1] This concerns the maximum rate of acceleration for ions in an electron ring. Acceleration is limited by the maximum electric holding field expressible as

$$\mathcal{E} = \frac{\mu_0 c I}{2\pi\beta(\sigma_a+\sigma_b)}$$

for a ring having I amperes of electrons of energy E and velocity βc distributed over an elliptical ring cross section with standard deviations σ_a and σ_b. The ring is considered to be circulating in a conducting cylinder the radius of which exceeds by $4\sigma_a$ the ring major radius R.

For longitudinal stability, one requires

$$I\,\frac{|Z_m|}{m} \leqslant \frac{E}{e}\,\beta^2\,\left(\frac{\Delta p}{p}\right)$$

where the momentum spread $\frac{\Delta p}{P}$ is limited by the radial deviation σ_a according to

$$\frac{\Delta p}{P} \leq 2.36\,\frac{\sigma_a}{R}\ ;$$

the energy is related to the magnetic field B by

$$\frac{E}{e} = \frac{cBR}{\beta}$$

and the longitudinal impedance Z_m at mode m is given approximately by[2]

$$\frac{|Z_m|}{m} \approx 300\,\frac{4\sigma_a}{R+4\sigma_a} \approx 1200\,\sigma_a \text{ ohms.}$$

To maximize the holding field $\mathcal{E}$, assume that $\sigma_b \ll \sigma_a$. Combine the equations to obtain the following expression for $\mathcal{E}$ where $\mathcal{E}/2$ represents the useful accelerating field, a factor of two less to avoid loss of most of the accelerating ions:

$$\mathcal{E}/2 < 41.7 \times 10^6\ B$$

Let B = 2 Tesla to obtain

$$\mathcal{E}/2 < 03\ \text{MV/m}.$$

This should illustrate the close relationship between the useful and the disruptive aspects of the collective fields.

The conducting walls we need to stabilize the ring have been shown by a number of workers to exert a retarding effect on the moving ring. From a recent evaluation of this by Merkel[3] I show in Fig. 1 a diagram of the functional behavior of the retarding field on a ring in a conducting cylinder. If the walls are thin with resistivity of a few ohms/□ this can be a prohibitively large drag force. The walls must be made with high conductivity to reduce this problem.

Walls of intermediate resistivity were also shown by the LBL group to introduce transverse instabilities.[1,4] Laslett showed that even with nominally adequate Landau damping, a transient growth of amplitude may occur for portions of the injected beam before the damping can suppress it. In this case, walls of higher conductivity were a convenient cure.

Oscillations between the ions and the electrons can also arise and we shall hear of such observations in paper 4-2 today.

The question of what degree of acceleration can be imparted to the loaded ring before ions are lost from the potential well has been analyzed by Hoffman in paper 4-8 of the Proceedings. He maintains self-consistent and realistic distributions of electrons and of ions under various accelerating conditions. He evaluates the advantage of a squirrel cage of axial conductors by showing that a ring primarily focussed by images in such a cage can carry all its ion load to an acceleration of 40% of the maximum e-field and a few survive up to 80%. In contrast, the ring relying upon ion-focussing alone has lost its payload in the region of 25% of maximum electric field.

An approach toward understanding collective longitudinal motion including the non-linear coupling between harmonic modes that is implied by the Vlasov equation has been proposed by Pellegrini and Sessler.[5] In order to give tractable equations, they found an approximation concerning mean square momentum widths was necessary. The multi-mode, coupled behavior predicted has been a useful guide in the LBL studies of longitudinal instabilities. No change in stability criteria is indicated but the consequences of instability under given conditions can be pursued computationally.

I now wish to review briefly the electron ring programs that are in progress, with some notes from papers not to be heard today.

At Dubna in the Soviet Union there is a broad program on electron ring development. The compressor in which the acceleration of a-particles was reported at our last conference has been modified with the object of injecting rings into electric accelerating structures. In a paper submitted for this conference the Dubna group reports that a series of accelerating cavities lined with NbTi for frequency 1.3 GHz is being developed. A second electron ring system intended for the acceleration of heavy ions is being assembled. As injector, they have built a novel high-current electron linac, named Silund. Four of an eventual 5 sections of this induction linac have been operating at 600-700 amperes. The cold cathode in the first section is at 10^{-2} torr pressure with ~ 10^{-5} torr

pressure downstream. The complete injector will produce pulses of 3.0 MeV electrons at 10 Hz. The compressor configuration is shown in Fig. 2. The vacuum chamber walls of 0.5 mm stainless steel closely confine the ring to provide control of instabilities. Figure 3 shows this chamber. It is built for high vacuum; on test it has reached 5×10^{-9} torr. The compressor is intended to form rings of 1-to-5×10^{13} electrons.

Nearby, at ITEP in Moscow, and electron ring facility is being set up. Operation of a 1.5 MeV injector and the compressor will start by mid-1974. A 5 MeV injector will be ready next year.

The program at the Max Planck Institute near Garching, Germany in 1972 completed their first experiment on compressing rings. Improvements in their injector, since the 1971 Conference, helped them obtain an intensity of 5×10^{12} electrons in their compressed ring. Evidences of damages from betatron resonances stimulated their construction of a new compressor having a very short compression time of about 100 nsec. In another apparatus, they have studied intensity effects upon injection into a chamber. Papers 4-2 and 4-3 concern these experiments.

At Karlsruhe, Germany the IEKP has had a group working on the formation of intense rings. I am told they will not continue an electron ring program. Their work on achieving energy spread in their injector and on stacking a ring is given in a report 4-9 in the Proceedings.

The electron ring program at LBL will soon be discontinued. The interest there in electron rings has moved away from the acceleration of protons toward heavy ion work and it will no longer be supported by high-energy physics funds.

For some time, the LBL work was concerned with the suppression of instabilities near injection and in the early stage of compression; paper 4-4 to be presented today will report on longitudinal instability studies from that work. Last fall a compressor capable of full compression was assembled and paper 4-6 of the proceedings will describe that. Rings in this device have just been compressed to 4-cm radius where synchrotron light becomes a convenient diagnostic tool. Resonant betatron disturbances appear and have been seen to widen the ring axially. First and second harmonic field correction coils have been adjusted to reduce the ring width but there is still loss of electrons during compression from, at this time, uncertain causes.

The electron ring in the previous compressor at Berkeley was used in an experiment to see if x-rays from ions formed and trapped in the ring could be detected above background. Xenon was admitted to the compressor and the K and L x-rays of Xenon were clearly identified and measured.

This result stimulated the consideration of the electron ring as a device for studying the atomic spectra of highly stripped *ions*. For this use, one wishes a dense electron ring current, very high vacuum, and a long lifetime of the order of one second. In this case, considerable energy is radiated as synchrotron light but the loss can be utilized to increase the electron density. Paper 4-7 submitted for the proceedings describes how this can be done by the proper selection of field index, n. A diagram (Fig. 4) from this report shows how the compressed ring first radiates and becomes more dense; at that point it is near the longitudinal instability limit and it is necessary to reduce the magnetic field thereafter to allow some growth in momentum spread. In such a ring the progressive ionization of Argon would appear as in Fig. 5. (6)

The electron ring group at the University of Maryland has started experiments with their novel ring-forming system. Paper 4-5 to be presented will describe that work. They plan to start experiments on acceleration this summer.

Now, let us hear these reports.

[After the oral presentations, the following concluding comment was delivered.]

We see from these reports that those working with electron rings can find their activities both tantalizing and frustrating.

It is *my* reaction that experimental effort that may be characterized as a rush toward a workable accelerator has not been the most productive approach. In a complex field, complexities arise and we have had to fall back to firmer ground and new techniques.

It is interesting to contrast the approaches pursued by the various groups, all working on the same problem, but with different emphasis. The Soviets have had the broadest program, strengthened and encouraged by their early successes. At Berkeley, concern centered on collective instabilities. The Garching workers chart a path around betatron resonances and vacuum problems. Maryland has a particularly fast version of the static compressor. And there are still untried parameters such as azimuthal magnetic field, With these differences in approach, there have been difficulties in applying one group's findings to another group's problems.

To handle this communication problem and make steady progress, we should try to have better diagnostics and more control of experimental variables. In this way, we can build up the shared store of data and knowledge that we separately have been seeking.

Finally, I am encouraged to see new and less demanding applications appearing for the electron ring. I mentioned the atomic spectroscopy. Even simpler would be use of the electron ring to get basic ionization and cross-section data for use in the development of heavy-ion sources. Through new applications, the new user will profit while contributing to a steady and orderly development of electron ring technology.

References

1. L.J. Laslett, "Current Understanding of ERA", IEEE Trans. Nucl. Sci. NS-20, No. 3, 271-275 (June 1973).
2. A. Faltens and L.J. Laslett, "Longitudinal Coupling Impedance of a Stationary Electron Ring in a Cylindrical Geometry", Particle Accelerators, 4, 151 (1973).
3. P. Merkel, private communication.
4. G.R. Lambertson, et.al., 'Experiments on Electron Rings at Berkeley", Particle Accelerators, 5, 113-120 (1973).
5. C. Pellegrini and A. Sessler, "Theory of the Non-Linear Negative-Mass Instability", Lawrence Berkeley Laboratory Report - ERAL{-203, January 1973 (unpublished).
6. J. Hauptman et.al., "Compressor Design for Intense Electron Rings", Lawrence Berkeley Laboratory Report LBL-2489, (1974).

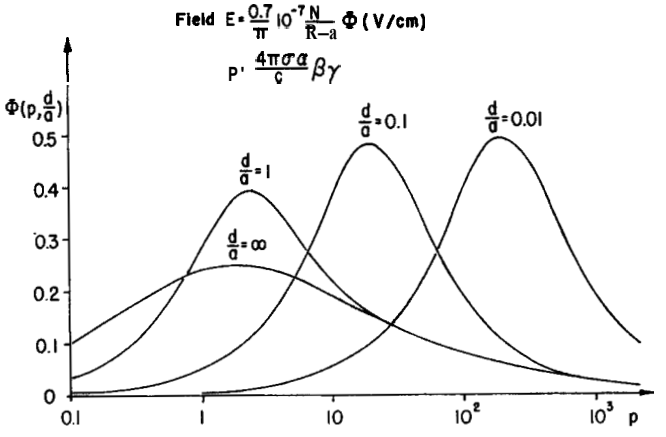


Figure 1 - Axial retarding field E for a ring of N electrons moving in a metallic cylinder. R[cm] is radius of ring; R + a[cm] is radius of cylinder wall; d(cm) is thickness of wall of conductivity $\sigma[sec^{-1}]$.

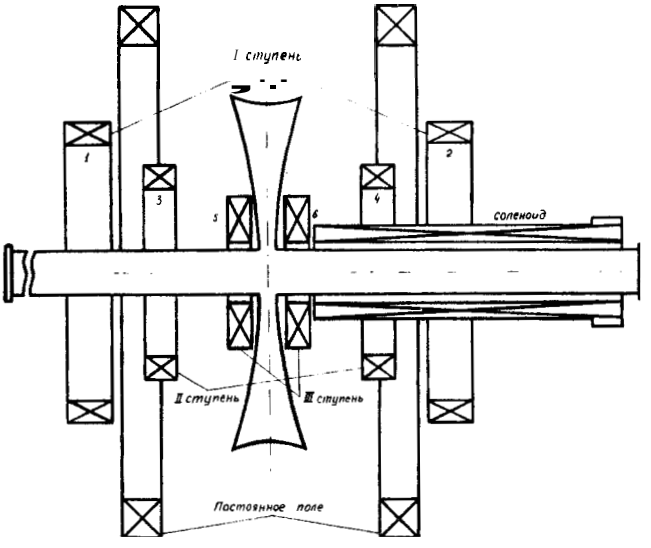


Figure 2 - Coils and chamber of collective ion accelerator at JINR.

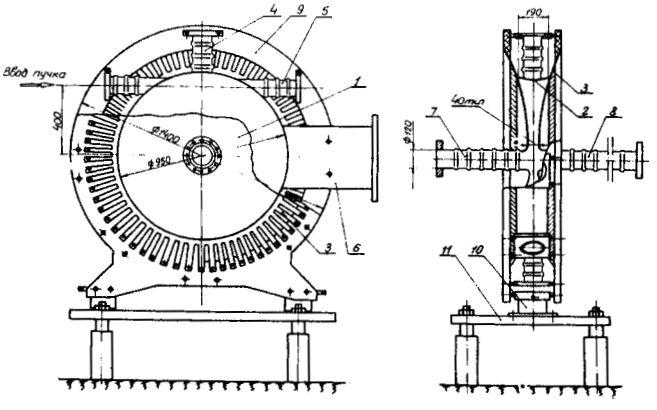


Figure 3 - Thin-wall steel vacuum chamber of JINR compressor.

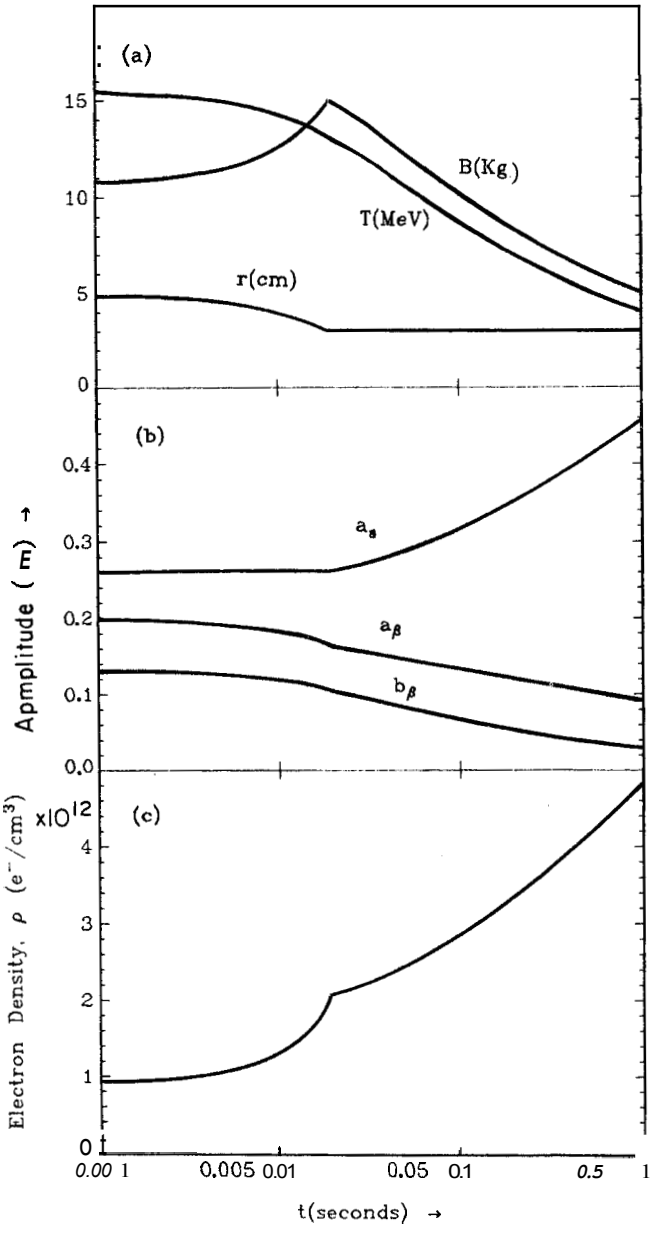


Figure 4 - Changing parameters of a stored electron ring intended for study of atomic spectra.

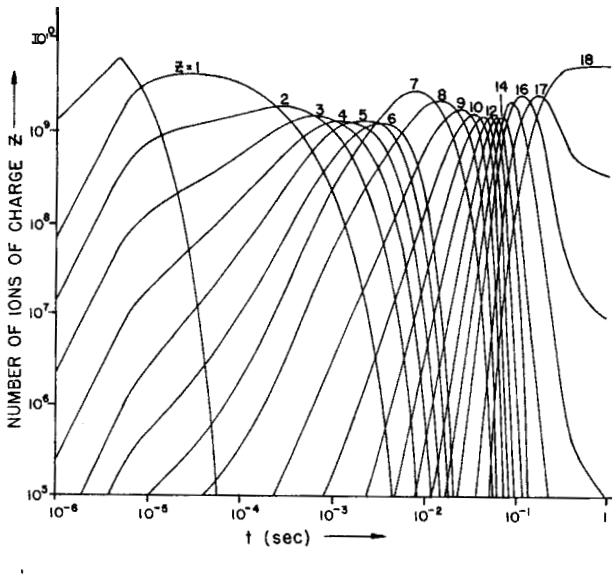


Figure 5 - The progressive abundances of ionized states of Argon, approaching equilibrium with the background gas *at* one second.

ACCELERATION OF ELECTRON RINGS AND INVESTIGATIONS ON ION-ELECTRON INSTABILITIES IN THE GARCHING ERA-EXPERIMENT

C.Andelfinger, W.Dommaschk, I.Hofmann, P.Merkel, U.Schumacher, M.Ulrich
Max Planck-Institut fiir Plasmaphysik, Garching bei München/BRD

In the Garching ERA device ("Schuko") with fast ring compression electron rings have recently been accelerated in a slightly non-uniform field. Near the end of electron ring compression and during the roll-out phase, collective radial oscillations were observed. They showed an obvious dependence on the amount of ion loading and on azimuthal distortions of the electromagnetic field. For the compression phase, these oscillations were suppressed successfully by changing the magnetic field index and increasing the Landau damping coefficient. There occur still losses near the spill-out point. Further investigations will be carried out to suppress these losses, possibly by applying an additional B_φ -field.

1. Introduction

The Garching ERA experiment is made to study the fast magnetic compression of electron rings and the acceleration of ions trapped by these rings in a smoothly expanding magnetic field. The compression of the rings is done very fast in order to reduce broadening of the minor ring dimensions due to single particle resonances, which necessarily have to be crossed, and to reduce the requirements on the base pressure in the apparatus. As the acceleration of electron rings has to be done carefully in order to keep the ions, a smooth expansion acceleration structure is used. The combination of the fast compression with a smooth acceleration section is performed by one single turn axially extended magnetic field coil[1], with which the forming, compressing and the acceleration of electron rings has partly been successfully performed. The apparatus is schematically shown in Fig.1.

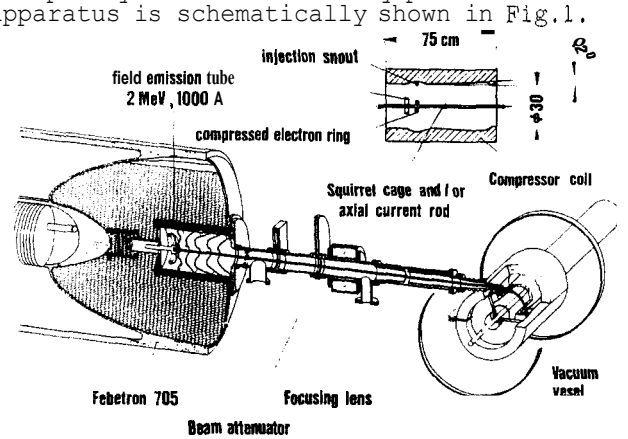


Fig.1 A schematic view of the experimental arrangement and a cross section of the magnetic field coil

The single turn coil has a bump in the electron injection plane to provide a magnetic field index of $n \approx 0.55$ around the injection radius. The ring compression is very fast (initially about .2 cm per electron revolution) so that all dangerous single particle resonances are crossed in less than 100 ns, for which the growth is negligible. Fig.2 shows the time dependence of the electron ring radius R and the magnetic field index n.

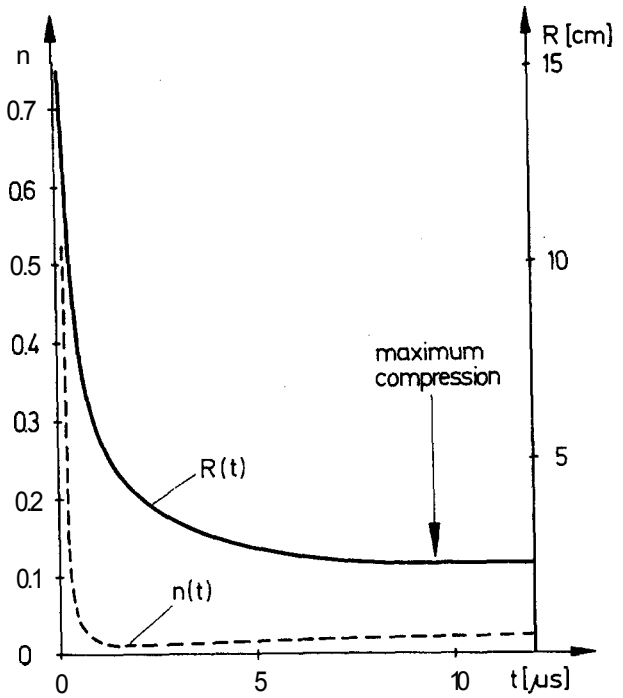


Fig.2 The time dependence of the electron ring radius R and the magnetic field index n during compression

The compressed electron ring is accelerated in the z-direction by providing a B_r-component of a few Gauss, which is mainly formed by a slight radial expansion of the magnetic field coil along the axis (see Fig.1). The transfer of the ring from the compressed state to the acceleration section, the "roll-out" process, is provided by an axially short additional coil inside the main coil, which "blows" the ring (at nearly constant radius) for some 10 to 20 cm in the z-direction towards the "spill-out" point. The magnitude of B_r in the acceleration section as well as the magnetic field index n and its radial derivative $\partial n/\partial r$ during compression and roll-out of the ring can be varied by putting specially formed axi-symmetric passive conducting structures on the coil axis.

The experiments were performed with different injected beam currents (up to 450 A). The electron number in the compressed phase is $N_e = (5 \pm 2)10^{12}$, the major radius is R = 2.3cm and the minor axial and radial radii are about a = b = 0.3 cm.

In the first experiments[2] with the new device, strong collective radial oscillations were observed near the end of compression. The frequency of these oscillations was found to be $\omega = 2\pi f = \omega_{ce}(1-\nu_r)$, corrected for ion loading. ω_{ce} is the electron gyrofrequency and ν_r is the radial betatron tune, calculated from the external magnetic field as $\nu_r \approx \sqrt{1-n}$. The observed oscillation frequency shifted to smaller values with increased ion loading, while simultaneously the growth rate of the instability went up appreciably.

The following experiments were concentrated on the origin of the transverse oscillations. Radial collective oscillations can be excited by the collective electron-ion dipole instab-, first studied by Koshkarev and Zenkevich, and can be driven by a disturbance in the external electric or magnetic field.

Solving the dispersion relation of the coupled motion of the relativistic electrons and ions for small values of the magnetic field index n, one finds an unstable region[4], which is plotted in Fig.3 as function of Q_i and Q_1.

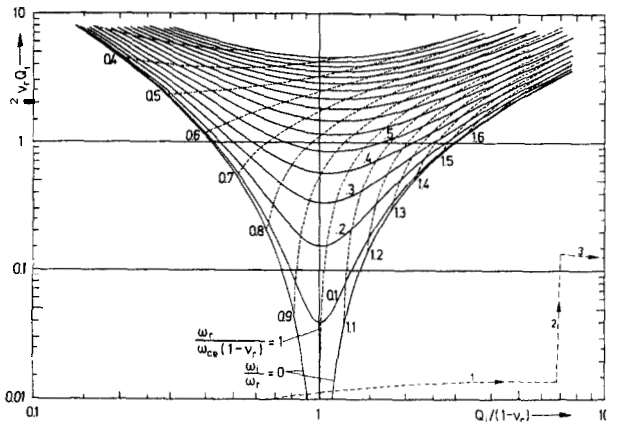


Fig.3 The stability diagram of ion-electron dipole oscillations. ω_i, ω_r are the imaginary and real part of the oscillation frequency. The normalized diagram is exactly correct for $\nu_r = 0.9$.

The Q_1 and Q_1 are the coupling coefficients of electrons and ions, defined as

$$Q_i^2 = \frac{2 r_e m_e}{m_p} \cdot \frac{N_e Z R}{A a(a+b)} \qquad Q_1^2 = 2 r_e N_i \frac{Z R}{\gamma a(a+b)}$$

(r_e = classical electron radius, Z = ion charge number, A = mass number, m_e, m_p = electron and proton mass, resp., N_e, N_i = electron and ion number, resp., a, b = minor radial and axial half-axis, resp.) The curves in Fig.3 also give the growth rate ω_i/ω_r and the frequency $\omega_r/\omega_{ce}(1-\nu_r)$ of the unstable oscillations. The growth rate has its maximum when the frequency of the ion oscillations in the potential well of the electrons is nearly equal to the collective electron oscillation frequency $\omega_{ce}(1-\nu_r)$ in the external magnetic field. In this diagram the influence of image focusing and Landau damping on the instability is neglected. The dotted line demonstrates schematically how the crossing of the instability region should occur: number 1 during compression; number 2 for the ion loading; and number 3 for the roll-out process. The curves are normalized, so that they can be used for different values of ν_r. Furthermore an asymmetry of the field can cause a collective radial oscillation at the end of compression and in the roll-out phase. The amplitude of the m = 1 mode is found to be inversely proportional to its frequency. Hence it is particularly dangerous when this collective frequency becomes very low.

B. Experimental Investigations of the Radial Collective Oscillations

The instability was observed by three different diagnostic methods:

1. A thin wire was brought at radii smaller than that of the compressed electron ring. The occurance of an unstable radial oscillation is indicated by the X-rays, produced when the electrons hit the wire.

2. The measurement of the magnetic self-field gives the current in the electron ring and furthermore the frequency and amplitude of the collective transverse oscillations.

3. The spatial resolved synchrotron radiation measurement gives the direction (radial and axial), the frequency, and the amplitude of these oscillations.

These diagnostic methods showed that for the compressor without conducting structures on the axis strong collective oscillations occured with radial amplitudes comparable with the electron ring radius ($R \approx 2.5$ cm), while the axial amplitudes remained less than 0.1 cm. The electron ring precesses around the magnetic field axis with the frequency $\omega \approx \omega_{ce}(1-\nu_r)$. For small values of n (i.e.near the end of ring compression) both the occurrence and growth of these collective radial instability depended strongly

1. *on* the magnitude of the deviation from axisymmetry of the fields when the collective frequency was less than $5 \cdot 10^{-3} \cdot \omega_{ce}$,
2. on the amount of ion loading of the ring, which depends on the pressure of the rest gas and on the elapsed time.

The dependence of the radial collective instability on the magnetic field parameters could be shown by putting small axisymmetric conducting structures on the compressor axis.

Fig.4a demonstrates the influence of the gas pressure on the amplitude of the collective oscillation. A small structure on the axis (see Fig.7, profile I), stops the growth of the oscillation due to its field shaping properties at small radii R.

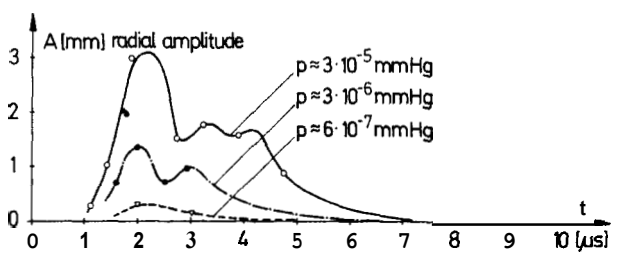


Fig.4a The radial oscillation amplitude for different base pressures

In Fig.4b the measured collective frequencies are plotted and compared with the calculated values of $1-\nu_r$. For small ion loading fractions the measured frequencies are nearly equal to the calculated ones. In cases with higher gas pressure, when the ion loading increases with time due to further ionization by the electrons, the inertia of the ring increases and the measured frequencies deviate towards smaller values.

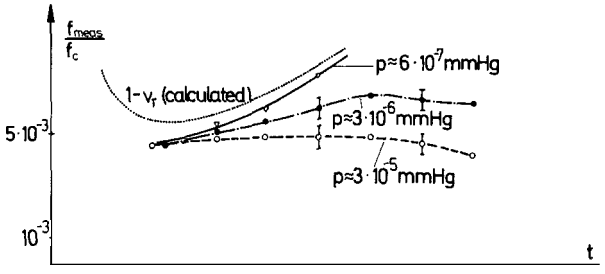


Fig.4b The measured frequencies for different base pressures in comparison with the calculated collective radial frequency

The oscillations start as soon as the Landau damping coefficient of the electrons becomes small, and disappear later, when the damping Coefficient increases. Synchrotron radiation profile measurements in the compressed-state show an increase of the radial width after the oscillations have disappeared by about the amplitude of the previous radial collective oscillation (see Fig.5).

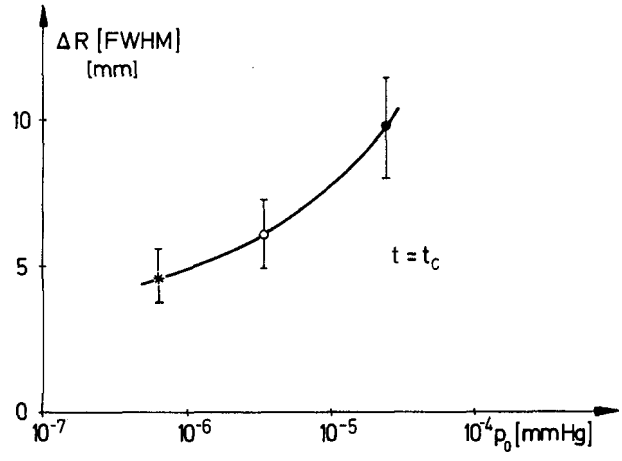


Fig.5 The radial width of the Synchrotron radiation profile for the compressed electron rings as a function of base pressure

In the Q_i, Q_1-diagram of Fig.6, for four different times and three different gas pressures the Q_i, Q_1-values of the electron rings are plotted. During compression Q_i is only slightly changed, while Q_1 increases with time. The time dependence of the Landau damping is only qualitatively considered (line below hatched area). The unknown contribution of the ion Landau damping has been set equal to unity. The Landau damping of the electrons with a $\Delta E/E = 5\%$ has been equated with the calculated growth rate of the instability.

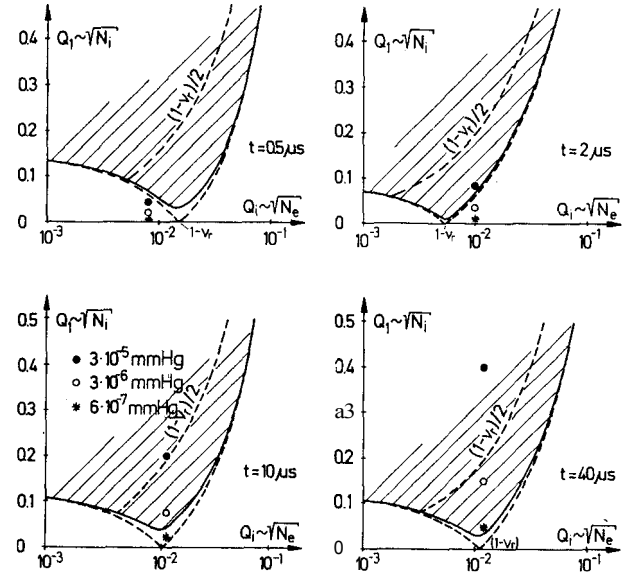


Fig.6 The coupling coefficients Q_i, Q_1 of the electron ring in the stability diagram of the ion-electron dipole instability are plotted for different times and different base pressures. The hatched areas are the unstable regions, taking Landau damping approximately into account.

In accordance with theory we find

1. that the instability starts (1-1.5 μs after injection), when the instability area crosses the Q_i, Q_1 value of the ring,
2. that the frequency decreases with higher ion loading. For t = 10 μs and $p \approx 3 \cdot 10^{-5}$ mm Hg the observed frequency is $(1-\nu_r)/2$.

The influence of different magnetic field parameters, n and the Landau damping coefficient $\varepsilon \partial S/S \partial \varepsilon$ (with $S = \omega_{ce}(1-\nu_r)$) and the ion loading, $Z N_i/N_e$, on the instability behaviour are collected in Fig.7. For different n-spoiler structures (profile I-IV) used in the experiments and sketched below, the time behaviour of the occurence and amplitude of the oscillations are shown. The vertical width of the drawn streaks is a measure of the observed amplitudes.

The empirical results are:

1. The instability occurs mainly at small values of $1-\nu_r$.

2. The growth rates and the amplitudes increase with the ion loading in agreement to the theory of ion-electron instability.

3. The instability occurs, when the Landau damping coefficient has passed through small values and it is stopped and damped when the coefficient has increased sufficiently (see Fig.7, profile I, III, IV).

4. In the case where no n-spoiler is used stationary large amplitudes have been ob-

served. The saturation of the amplitude may be explained by nonlinear effects, which are neglected in the above mentioned theory.

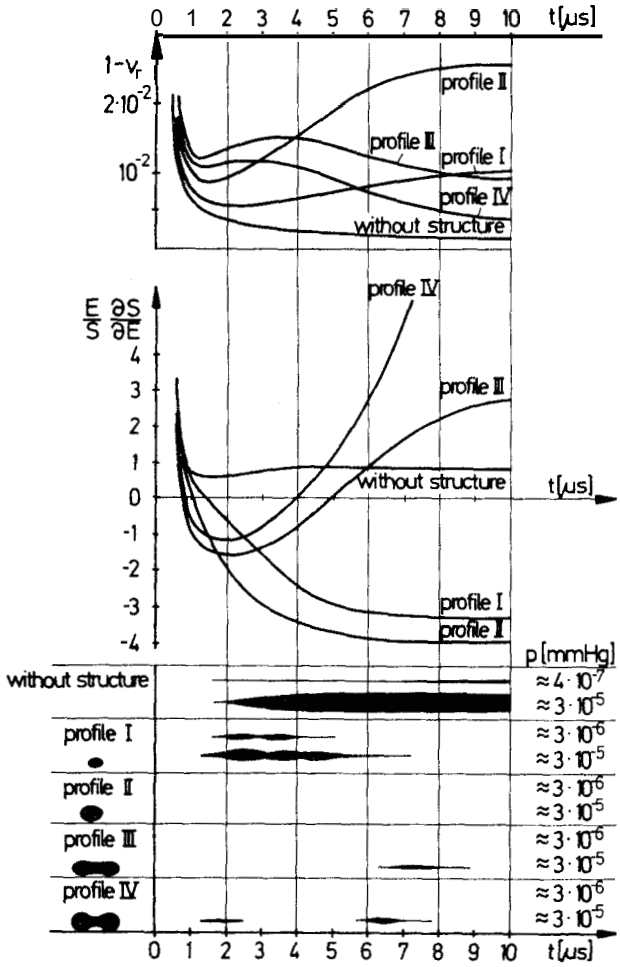


Fig.7 The occurence of radial collective oscillations for different field-shaping profiles

C. Acceleration of the Electron Rings

Experiments without Image Focusing

By taking the n-spoiler I and switching the "blow-coil" to unbalance the magnetic field transfer of the ring to the acceleration section is possible. But with this arrangement the ring was destroyed before having reached the spill-out point, earlier for higher electron numbers, later for smaller values. The reason may be a lack of axial focusing or crossing of the $\nu_r = 1$ resonance and subsequent radial losses; the destruction of the ring is indicated by a relatively broad X-ray burst; but it is not yet investigated where these losses occur.

Experiments Using Image Focusing

As it turns out that focusing is necessary to get beyond the spill-out point, different types of image cylinders were used: inner cylinders with thin conductive layers ($1\Omega/\square$), "squirrel cage" type cylinders of conductive strip layers on a glass cylinder and a "squirrel cage" type made of thin copper strips.

The structure of the "squirrel cage" type seems to work best. The image cylinders with uniform conducting layers showed cracks after some experiments, leading to electron ring destruction. This uniform conducting layer should act to reduce the coupling impedance of the compressed electron ring, in order to suppress the negative mass instability.

Ion-electron instabilities have been observed during the roll-out process especially at higher base pressures. The mechanical adjustment of this image cylinder and the coaxial field shaping structures has to be very accurate, as a disturbance as small as $\Delta B/B \approx 10^{-3}$ leads to destruction of the ring during roll-out.

In order to have a time dependence of the tunes during the roll-out process, which should prevent collective radial instabilities even during roll-out, the image focusing with a "squirrel cage" (R = 1.5 cm) is combined with an axially elongated field-shaping structure ("asparagus-type"). This structure (1.0 cm in head diameter, appr. 0.5 cm in tail diameter) changes also the B_r-field in the acceleration section

In recent experiments with these long field; shaping structures and with a "squirrel cage the electron rings were brought beyond the spill-out point to the acceleration section and accelerated.

The first diagnostic tools to investigate the accelerated ring behaviour are Faraday cups and magnetic probes measuring the B_z when the ring passes by. From the time of flight between two cups, a small one (0.2 cm in dia.) and a big one (1.0 cm thickness), or from the time of flight between the magnetic probe and the big Faraday cup, the axial velocity was found as a function of axial position.

The measured v_z agree within 20% with the calculated values assuming a pure electron ring. The measured values range from $v_z = (8 \pm 2) \cdot 10^8$ cm/s at $\Delta z = 5$ cm to $v_z = (2 \pm .4) 10^9$ cm/s at $\Delta z = 25$ cm in the acceleration section. Δz is the axial distance measured from the spill-out point.

These values can be checked by the shape of the $\dot{B}_z(r = 0)$-signal. Fig.8 gives an oscillogram with 5ns/div time sweep of the addition of the B_z-signal and the signal from the Faraday cup situated further downstream.

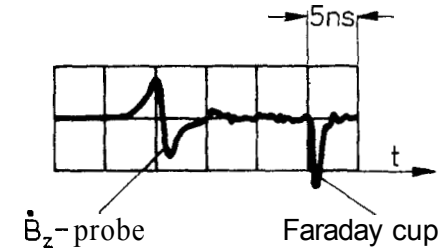


Fig.8 An oscillogram of the addition of the $\dot{B}_z$ and the Faraday cup in the acceleration section

From the time difference A t of the maximum and the minimum of the B_z-signal one obtain the velocity $v_z = R/A\ t$, where R is the major electron ring radius.

From the width of the Faraday cup signal and the local axial velocity one gets an axial half width of the accelerated electron ring, which is less than 1 cm. The Faraday cup pulse may still be broadened by the time constant of the cup, the frequency dispersion of the signal cable and the rise time of the oscilloscope.

The preliminary results at present (April 74) are:

1. The elctrons are accelerated as rings of nearly expected axial width (less than 1 cm)

2. The electron number within the ring seems to be much smaller (at present 3×10^{11}) than in the compressed state (5×10^{12})

3. As no change of axial ring velocity with ion loading is observed, at most only a few ions could have been accelerated in the main part of the acceleration section. The holding power seems to be too low yet. The peak field is in the order of 1 MV/m, which is too low for keeping many ions.

Future plans

The main problems to be solved in the next future therefore are:

1. Reduction of losses during the roll-out process.

2. Reduction of B_r in the acceleration section

3. Detection of accelerated ions by nuclear reactions.

4. Increase of the holding power by the use of conducting side walls[5].

5. Application of an additional azimuthal magnetic field B_φ .

There are some reasons to apply an additional B_φ -field[6] to avoid dangerous single particle resonances[7] and the radial collective instabilities* and to increase the Landau damping coefficients for transverse collective instabilities[8]. Furthermore, the ion-electron instability area can be shifted far away from the experimentally relevant parameter regions.

Since by this work it has been proven that electron rings can be accelerated as intactly coherent entities and since there are clear possibilities to improve their performance we feel certain of the viability of the ERA scheme.

References

1 U. Schumacher, MPI für Plasmaphysik, Garching, Report 0/10 (March 1972)

2 C. Andelfinger, W. Herrmann, D. Jacobi, A.U. Luccio, W. Ott, U. Schumacher, M. Ulrich, IEEE Transactions on Nuclear Science, Vol.NS-20, No.3, June 1973, p.276

3 D.G. Koshkarev and P.R. Zenkevich, Inst.f. Theor.and Exp.Physics, Moscow, USSR, Dec. 1970

4 W. Dommaschk, MPI fiir Plasmaphysik, Garching, Report IPP 0/19 (Dec. 1973)

5 J. Fink, W. Herrmann, W. Ott, J.M. Peterson, next paper in these proceedings

6 A.G. Bonch-Osmolovskii et al., JINR-P9-4135 (Dubna, USSR, Nov.1968)

7 P. Merkel, MPI für Plasmaphysik, Garching, Report IPP 0/4 (March 1971)

8 L.J. Laslett and U. Schumacher, Proc.VIII. Int.Conf.on High Energy Accelerators, Geneva, Sept.20-24, 1971

Acknowledgements

The authors should like to thank G. Weber, E. Zellner and all the members of the workshop for carefully preparing the hardware of this experiment, E. Springmann for various computer programming and Prof. A. Schlüter for many helpful discussions.

This work was performed under the terms of the agreement on association between the Max Planck-Institut fur Plasmaphysik and EURATOM.

ENERGY SPREADING AND ENERGY LOSS DUE TO NEGATIVE MASS INSTABILITY IN AN ELECTRON RING EXPERIMENT

J.Fink, W.Herrmann, W.Ott, J.M.Peterson+
Max Planck-Institutfür Plasmaphysik++
Garching bei München/BRD

A. Introduction

The aim of the experiment described here was to find limitations for the conductivity of the walls surrounding the ring. To suppress the negative mass instability or transverse resistive wall instabilities, highly conducting walls are necessary[1]. On the other hand, the rising magnetic field in fast compression requires a low enough conductivity for almost undisturbed penetration of the field. For the relatively slow compression of the Berkeley experiment a surface resistances of $1/30\,\Omega/\square$ has been sufficient[1]. For compressors like the Garching fast ERA-device[4] (Schuko) with compression nearly 100 times faster, surface resistances of at least $1\,\Omega/\square$ will be required. It seemed worthwhile finding out in a separate experiment whether such sidewalls are compatible with the above mentioned requirements for stability.

B. Description of the Experiment

The experiment was performed in the so-called "Unkompressor", a system with a static main magnetic field where ring formation is possible without compression (see Fig.1). Rings have been studied with no conducting sidewalls nearby, with highly conducting copper walls at a distance of f3 cm from the ring and with walls with $1\,\Omega/\square$ and $6\,\Omega/\square$.

The injected beam had an energy of almost 2 MeV, the maximum peak current was 220 A and the full halfwidth was 10 ns. The energy spread was 3 to 4% and the maximum closed orbit was set between R = 16.5 and 17 cm at a field index of n = 0.55, corresponding to a radial tune of 2/3. The Landau damping coefficients $(E/S)(\partial S/\partial E)$ and the field index n are displayed in Fig.2 as function of the radius. The vacuum vessel is a lucite chamber whose inner walls are 6 cm from the ring, have a thickness of 2 cm and a dielectric constant $\varepsilon \approx 2.4$. There are nearly no electric image effects and the experiment without conducting sidewalls is supposed to be very similar to the free spacecase.

C. Free Space Case

In free space with more than 5×10^{11} electrons and an energy spread $\Delta E \approx 4\%$, beam widening and losses due to negative mass instability are expected. The surprising result was the large amount of energy lost during the instability. This energy loss can be understood as coherent synchrotron radiation of the lower harmonic bumps, which develop during the negative mass instability. As long as the minor dimensions of the ring (especially the radial dimension) are small compared to the radiated wavelength, the radiation is coherent. If only 10 to 50% of the particles have a sinusoidal density distribution in the first harmonics, radiation powers of 10 MW - as corresponds to the observed energy loss in 20 ns - can be expected. Beam widening, energy losses and particle losses have been observed by three methods: 1. Scraper technique; 2. Self-field measurement with two loops; 3. Radiation frequency.

Fig.3 shows the result of an experiment in which a 0.5 mm Kapton wire was positioned at different radii R_K. The wire was so thin that it did not noticeably influence the ring during the instability phase (say the first 50 ns) but it did eject all particles which crossed the radius R_K in the course of time. Fig.3 gives the ratio of the number of the eliminated to the total number of particles in the ring for different injected beam levels. At full beam a large widening and reduction of the mean radius compared with 1/50 of the beam is apparent. At 1/50 beam almost no HF radiation was observed and the resultant distribution is consistent with the injected energy spread. At full beam average radii as low as 11 cm were often observed.

Fig.4 gives the result of the two-loop measurement. One loop on the axis and another at R = 24 cm measure the self-field of the ring. The combination of the two signals gives the average radius and particle number. At full beam part of the particle losses occurs immediately after injection and cannot be analyzed because of noise on the signals. The relatively growing noise level at low beam intensities limits the accuracy at 1/50 beam. There are nearly no particle losses at 1/10 beam although the radius still changes. At 1/3 beam drastic losses and reduction in radius occur. At full beam a change of radius is seen, whereas the particle losses apparently already occur during the first 20 ns after injection. (The particle losses are probably due to radial widening and subsequent scattering at the snout.)

The third method determining the radius as a function of time was by measuring the first-harmonic RF signal of the gyrofrequency. It was mainly applicable for the higher beam levels and gave in these cases the best time resolution. All three methods gave consistent results and indicate that negative mass instability in free space is accompanied by powerful radiation.

D. Experiments with Conducting Side Plates

35 μ copper plates ($0.6\,m\Omega/\square$) and silvercarbon plates with $1\,\Omega/\square$ and $6\,\Omega/\square$ were used. The inflection voltage was connected directly to a hole in the plates at 180°, which itself was covered with a $50\,\Omega/\square$ plate. With the copper plates no resistive wall effect was expected. Possible negative mass effects would hopefully be not too different in all side plate cases.

No difference could be seen in the experiments with the $0.6\,m\Omega/\square$ and $1\,\Omega/\square$ cases. The beam

+On leave from Lawrence Berkeley Laboratory University of California, Berkeley/Cal.

++This work was performed under the terms of the agreement on association between the Max Planck Inst.f.Plasmaphysik and EURATOM

trapping efficiency was the same in both cases and led to rings with $3\text{-}4\times10^{12}$ electrons. The closed orbits after trapping corresponded well to the energy of the injected particles. In the copper case the radius was determined by the scraper method and from gyrofrequency oscillations. These oscillations probably do not indicate negative mass instability, but are rather the consequence of imperfect inflection, azimuthally asymmetric distributions or wrong energy slopes in the injected beam. In the $1\,\Omega/\square$ case the radius was additionally determined from the two-loop signals. There is apparently no coherent radiation. Fig.5 gives the results of the scraper method. Both curves have the same shape. The full radial halfwidth is 4 cm, and the peak of the curve is at a radius corresponding to the peak in the injected energy. The curve for 1/10 beam level and the $1\,\Omega/\square$ plates has the same shape inside the estimated error limits as the displayed curves. The curves are apparently wider than the 1/50 beam case in free space. This might be due to slightly different injection conditions, e.g. different trapped particle radii.

The situation is quite different in the $6\,\Omega/\square$ case. Here only 1×10^{12} electrons could be trapped at full beam level. At lower beam levels the trapping efficiency was higher as can be seen in Fig.6. The particle loss occurs very early, probably at the end of the third turn. This effect is similar to the one observed in Berkeley with the high-resistance side plates and was probably caused by transient resistive wall effects[2]. In our experiment it could at least be ruled out that the losses are caused by crossing of the n = 0.5 resonance. This was done by changing the coil geometry in such a way that at all closed orbits the field index n was smaller than 0.5. In the same Fig.6 the number of trapped particles at full beam for the better conducting side-plates is given. It does not indicate collective instabilities. If for higher particle numbers collective effects show up, a larger energy spread or increased Landau damping coefficients might help to suppress the instability.

E. Self-Inflection

In free space a large fraction of the injected electrons could be trapped by self-inflection. With the sideplates no self-inflection was possible. According to the calculations of I. Hofmann[3], this might be explained by a reduction of the radial forces due to the images in the sidewalls.

F. Conclusion

Although during the course of the experiments many new questions arose, the main question could be answered: Sideplates with $1\,\Omega/\square$ did not disturb the trapped ring. It is therefore also possible in a fast compression experiment like Schuko to use sideplates to advantage. The mechanism of the losses found in the experiments with $6\,\Omega/\square$ sideplates has not yet been investigated in detail. It is therefore still open whether this is the result of a resistive wall instability or not.

References

1 L.J.Laslett, 1973 Particle Accelerator Conf., San Francisco, IEEE Transactions NS 20, 271, (1973)(contains further references)

2 G.R.Lambertson, Particle Accelerators 5, 119, (1973)

3 I. Hofmann, private communication

4 C. Andelfinger et.al., 1973 Particle Accelerator Conference, San Francisco, IEEE Transactions NS 20, 276, (1973)

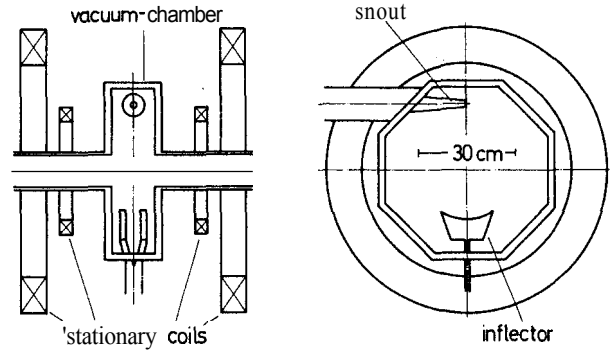


Fig.1 Sketch of the "Unkompressor" experiment

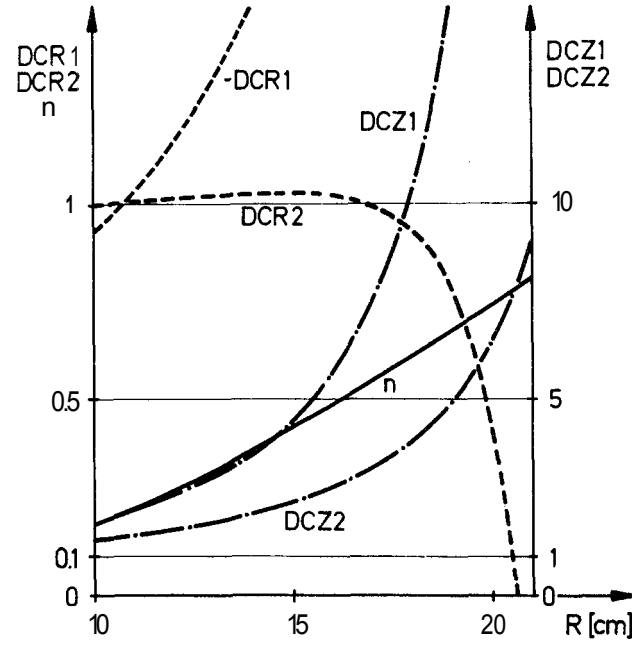


Fig.2 Landau damping coefficients $\xi\frac{\partial S}{\partial \mathcal{E}}$ and field index n as a function of radius R around the injection closed orbits. DCR1, DCR2, DCZ1, DCZ2 are the damping coefficients for the first and second radial, first and second axial collective betatron oscillations resp. $S = (m-\nu_{r,z})\cdot\omega_0$ with m an integer, $\nu_{r,z}$ the radial or axial tune and ω_0 the cyclotron frequency. $\mathcal{E}$ is the particle energy.

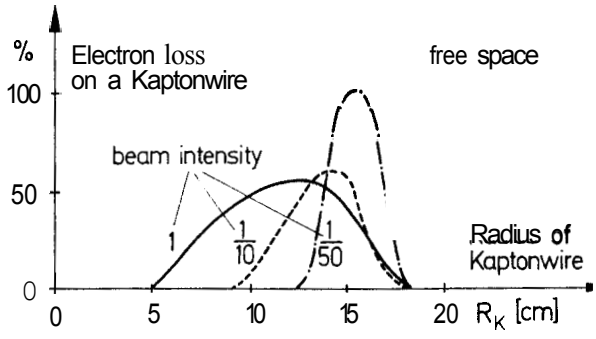


Fig.3 Percentage of lost particles in the scraper experiment in "free space" for different beam intensities

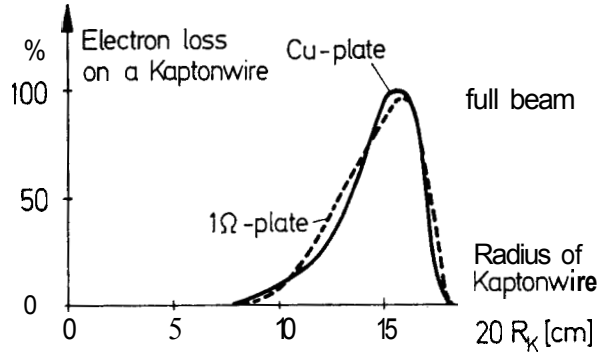


Fig.5 Result of scraper experiment for a ring between conducting sideplates at full beam level. The 1/10 beam curve is inside the estimated error limits of the displayed curves

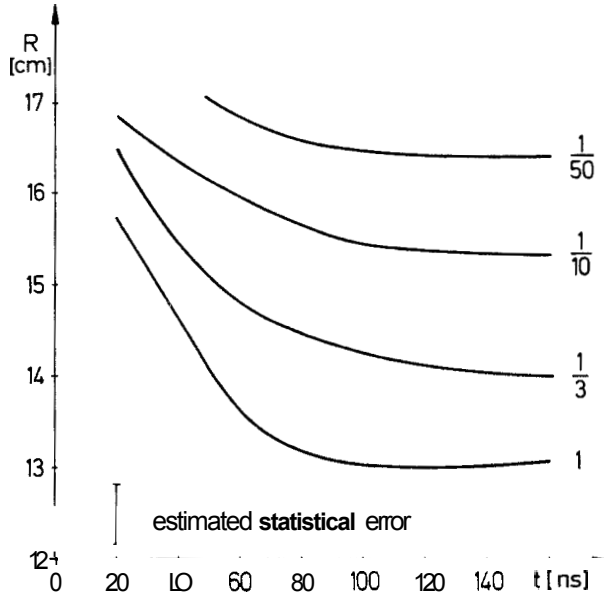


Fig.4 Dependence of mean radius a a function of time after injection for different beam levels (1; 1/3; 1/10; 1/50)

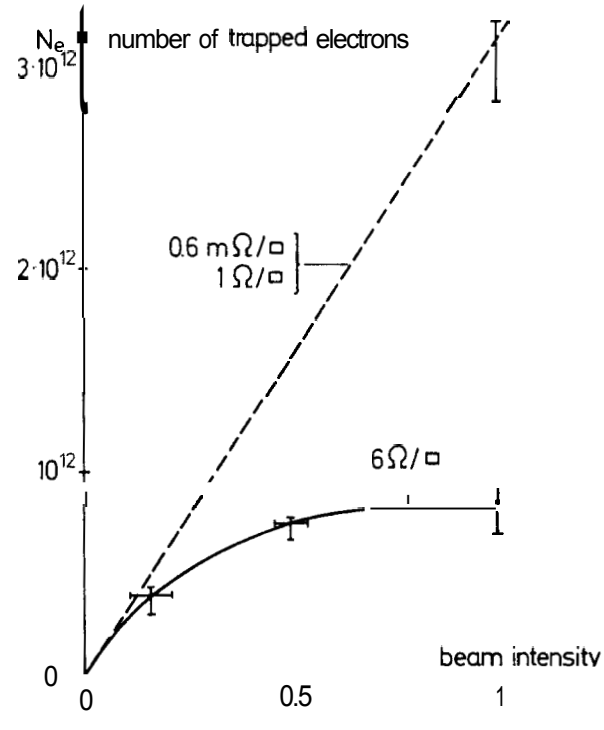


Fig.6 Number of trapped electrons as a function of beam intensity for different sideplate resistivities

Observations on Collective Longitudinal Instabilities in Electron Rings

A. Faltens, G.R. Lambertson, J.M. Peterson, J.B. Rechen

Lawrence Berkeley Laboratory
University of California
Berkeley, California

The longitudinal collective instability, or negative-mass effect, has been observed in a wide variety of particle beams. It has been a particularly bothersome effect in electron-ring systems. In order to understand its complicated, non-linear behavior and to find means of controlling this instability, we have made a series of radio-frequency and momentum-spread observations.

The theory of the negative-mass effect predicts a threshold intensity for the onset of growth of the instability -- namely, that the number of electrons N_e at which the electromagnetic bunching forces predominate over the dispersing action produced by an energy spread ΔE is given by[1]

$$N_e = |\eta| \frac{\gamma R Z_0}{2\beta^3 r_e |Z_n|/n} \left(\frac{\Delta E}{E}\right)^2$$

where η is the chromaticity (relative change in revolution frequency per unit momentum change), γ is the total energy in units of the rest mass, R is the major radius of the electron ring, Z_0 is 377 ohms, β is the electron velocity in units of velocity of light, r_e is the classical electron radius, $\Delta E/E$ is the fractional energy spread (FWHM), and Z_n is the longitudinal coupling impedance seen by the electron ring for azimuthal modulation at the nth harmonic of the electron revolution frequency. Z_n is defined by the relationship $I_n Z_n = 2\pi R \mathcal{E}_n$, where $\mathcal{E}_n$ is the nth harmonic electric field strength at the ring, and I_n is the amplitude of the nth harmonic of the ring current. The key parameters at our disposal were the energy spread of the electron beam and the longitudinal coupling impedance.

The instantaneous energy spread of the electron beam from the 3.6 MeV injector was found to be less than 0.2% (FWHM). Spreads of 1, 2, or 4% were produced by passing the beam through non-uniform energy absorbers with sawtooth thickness profiles.

The longitudinal coupling impedance was controlled by means of conducting side plates, or "liners", placed inside the vacuum chamber rather close to the electron ring. The geometry of that inner section of our electron-ring compressor is illustrated in Figure 1.

The coupling impedance of an electron ring in this system is compared in Figure 2 with the impedance for a ring in free space and also with that of a ring between infinite sideplates. The use of close sidewalls of infinite extent would lower the impedance at all frequencies for which the axial spacing is less than or comparable to a half wavelength. With sidewalls separated by 5 cm, this critical frequency is about the 10th harmonic of the revolution frequency of an electron ring of 17 cm radius. At higher frequencies waves can propagate in this semi-infinite system, and the impedance approaches the free-space impedance. Our sideplates were not infinite in extent but rather were terminated by a conducting wall at a radius of about 22 cm and thus formed a resonant cavity having TE modes at frequencies higher than the 10th harmonic. The lowest mode resonant with an electron ring at 17 cm occurs at the 16th harmonic of the revolution frequency. The impedance in this resonance region is qualitatively indicated in Fig. 2 as very structured and having a typical value some Q times the impedance of the infinite side-plate case. We reduced the Q by the use of resistive material and holes. The inflector window and its attached cable assembly complicated the impedance picture throughout the frequency spectrum; its resonances were reduced in some assemblies by shunting the inflector window with resistive material. The conducting walls were usually stainless steel of about 12 micron thickness, which had effectively high conductance at radio frequencies and yet did not distort significantly the pulsed compressor field.

In our experiments we varied the following parameters: incident beam intensity (without change of emittance), pulse length (1/2-turn and 2-turn incident beam lengths), instantaneous energy spread (0.2 to 4% FWHM), energy ramp (up to 2% per turn), beam-to-sidewall spacing ($\pm$ 1.5, $\pm$ 2.0, and $\pm$ 2.5 cm), and frequency of observation (all harmonics up to n = 40, usually in broad bands).

Radiofrequency activity was often seen to occur very soon after the formation of the electron ring. At the highest beam intensities the instability could be seen to develop even during the injection process, where it was strong enough to have a noticeable effect on the inflection process. Either lower intensity or greater injected energy spread resulted in later onset, slower growth rate, and smaller peak amplitude of the r.f. signal. The latest onset observed before the signal became undetectably low was as late as 1 microsecond. Typical envelopes of the radio-frequency signals are shown in Figure 3. One striking feature of these patterns of radio frequency amplitudes is that they appear to be independent of frequency over a broad range of observation -- i.e., for a given ring intensity and amount of energy spread, the R.F. envelope at the 12th harmonic, for example, had very closely the same shape and timing as that at the 20th or the 40th harmonic, which indicates strong coupling between the longitudinal bunching modes.

The variation of the peak r.f. activity with frequency qualitatively followed the impedance curve of Fig. 2. Typical data for a ring of 1.1 x 10^{12} electrons are shown in Fig. 4 for side-walls at $\pm$ 2.5 cm. With this sidewall spacing growth in the first few harmonics was not seen, which is consistent with the low coupling impedance expected at these frequencies. When the spacing to the sidewall was reduced to $\pm$ 1.5 cm, the peak activities at the high harmonics decreased, as expected, but here strong activity in the 2nd and 3rd harmonics did appear. The growth of low harmonic activity is seen also at a sidewall spacing of $\pm$ 2.0 cm, but in this case it was less severe and was reduced by shunting the inflector window with resistive material. Apparently at the closer spacings to the beam, the ring couples more strongly to the inflector window and finds a substantial coupling impedance due to resonances in the inflector system. Although the low harmonic behavior is worse in the $\pm$ 2.0 cm sidewall system, the high harmonic activity is, as expected, better (approximately by a factor of 5) than in the $\pm$ 2.5 cm case.

The radiofrequency voltage from the pick-up loops is interpreted as a measure of azimuthal modulation of

of the electron density. The maximum relative modulation is shown in Fig. 5 as the ratio of the maximum r.f. signal to the electron current. These data as well as measurements at other frequency bands display no threshold behavior; the modulation appears to be proportional to a power of the current, However, it is notable that the current that produces a given modulation increases in proportion to ΔE^2 in apparent but unexplained similarity to the threshold formula. The rule appears not to apply in the case of 0.2% ΔE because with this small energy spread, the spread of azimuthal frequencies is predominantly contributed by betatron amplitude spread. At injection, the betatron oscillations are quite non-linear and hence the effective equivalent energy spread for this case is at least 1/2%. This effective spread has been confirmed from observations of the damping rate of stable, low-frequency modulation at low intensity.

In a further effort to determine the threshold for the instability we measured the growth rate by observing the doubling time τ_2 (see Fig. 3). One expects the growth rate $1/\tau_2$ to be zero at threshold current, I_{th}, and to approach zero as a smooth function of I that depends on the distribution of energies in the beam. In Figs. 6 and 7 values of $1/\tau_2$ are shown. One sees that larger growth rates arise for lower energy spread, as expected, but threshold currents indicated by extrapolating to zero do not exhibit the variation with energy spread that is expected from instability theory.

An alternate attempt to find a sensible threshold behavior was tried using the time τ_1 from injection to a standard low level of modulation [defined by $V_{RF}(volts) = .025\ I_{RING}(amps)$]. An example of these data plotted again as growth rate, $1/\tau_1$, is shown in Fig. 8. Again, for zero growth rate, the data converge toward indicated thresholds near 2 or 3 amperes and show little dependence on energy spread.

The question next arises as to the significance of these longitudinal instabilities with respect to electron ring properties. What momentum spread is produced, and what damage is done to the beam? One damage caused by the negative-mass effect is the limitation in intensity that can be achieved. With high impedance sidewalls we were limited typically to about 1×10^{12} electrons trapped, whereas with the conducting sidewalls at ± 25 cm, we have had at least 5 times as much. The amount of energy spread was measured by the two-probe method;[3] the results are shown in Figure 9. We see that with very little incident energy spread the instability at high ring intensities can produce energy spread in excess of 5%. At this level it is beginning to be unacceptable because it increases the ring radial width to such an extent that the holding power is seriously reduced. With injected energy spreads of 1 and 2%, the instabilities are not strong enough to increase the energy spread further, even at ring intensities considerably higher than the calculated thresholds assuming $|Z_n|/n$ of 100 ohms.

The conclusions that we can draw from these studies are as follows:

1) A conducting enclosure can be designed to suppress longitudinal instability in the electron ring. Resonant responses of the enclosure appear but can be limited in strength.

2) The longitudinal instability is still a limiting but not necessarily prohibitive factor in achieving high electron density during the ring formation and start of compression. Throughout subsequent stages of the ring manipulation it is expected to require control.

3) The instability arises at many frequencies simultaneously and appears to be a non-linear phenomenon involving many coupled modes.

4) One does not observe a threshold for bunching that follows the usual linear predictions for a smooth energy distribution. Growing modulation is seen over a wide range of conditions.

5) Even in the presence of r.f. activity, deterioration of ring quality is moderate until intensities exceed the expected threshold to a significant degree. There is reason to believe that the commonly-accepted intensity limitations can be achieved or exceeded.

References

1. K. Hübner, E. Keil, and B. Zotter, Proc. VIII International Conf. on High Energy Accelerators, 295-297 (CERN, Geneva, Switzerland; 1971).

2. D. Möhl, LBL Internal Report ERAN-178, 1977 (unpublished).
P. Channell, LBL Internal Reprot ERAN-240, 1974 (unpublished).

3. JM. Peterson and J.B. Rechen, 1973 Particle Accelerator Conference, IEEE Trans. on Nucl. Sci. NS-20, #3, p. 790 (1973).

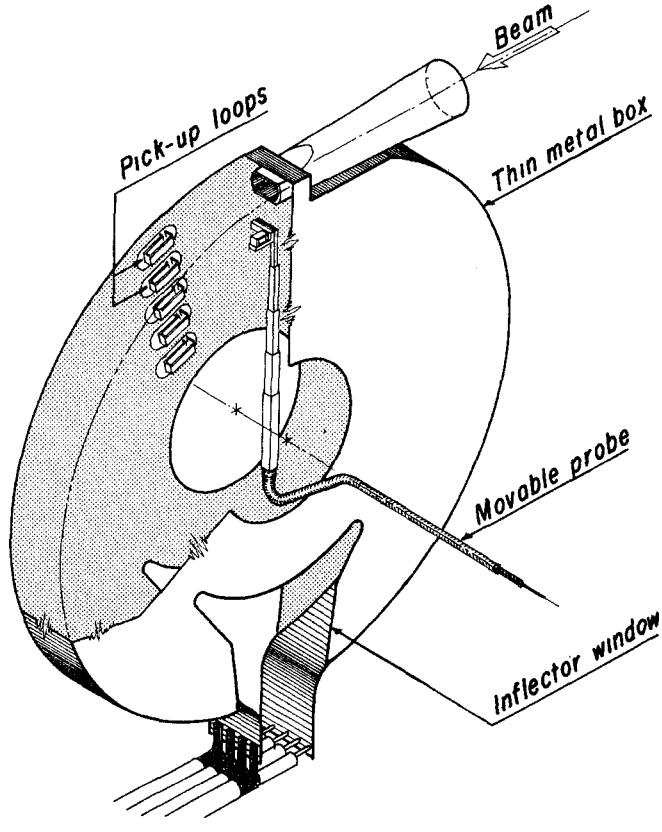


Figure 1 - Drawing of a typical conducting enclosure used in Compressor 4. The walls are 12 micron stainless steel. The pickup loops monitored beam level and radio-frequency activity. The movable probe functioned as a movable obstacle, a current collector, and a magnetic pickup loop.

LONGITUDINAL COUPLING IMPEDANCE

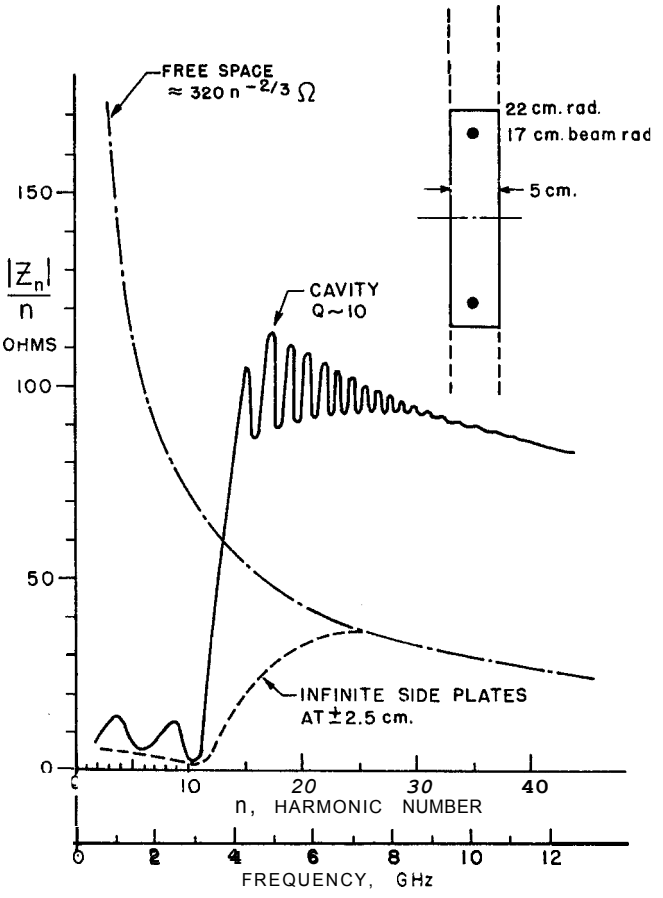


Figure 2 - Approximate variation of the longitudinal coupling impedance of an electron ring (a) in free space, (b) between infinite sideplates, and (c) in an enclosed cavity.

ENVELOPES OF TYPICAL RF SIGNALS

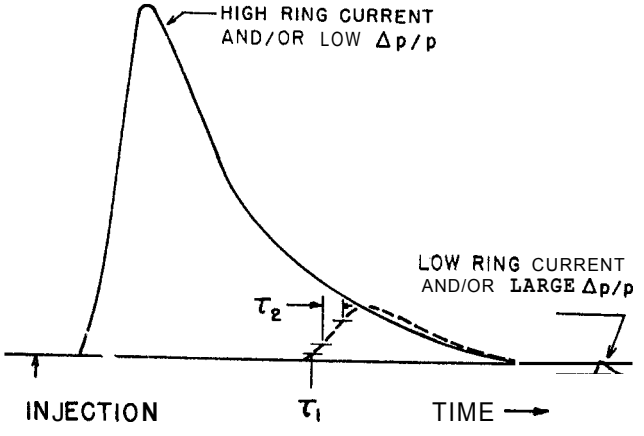


Figure 3 - Sketch of the envelopes of typical R.F. signals. With increasing beam level and/or decreasing incident momentum spread the signals became earlier, stronger, and had faster rates of growth. The shape and timing of the envelopes were the same at all frequency bands where observed.

LONGITUDINAL ELECTRIC FIELD
FOR 50 AMPERE RING (N_e = 1.25x10^{12} ELECTRONS)

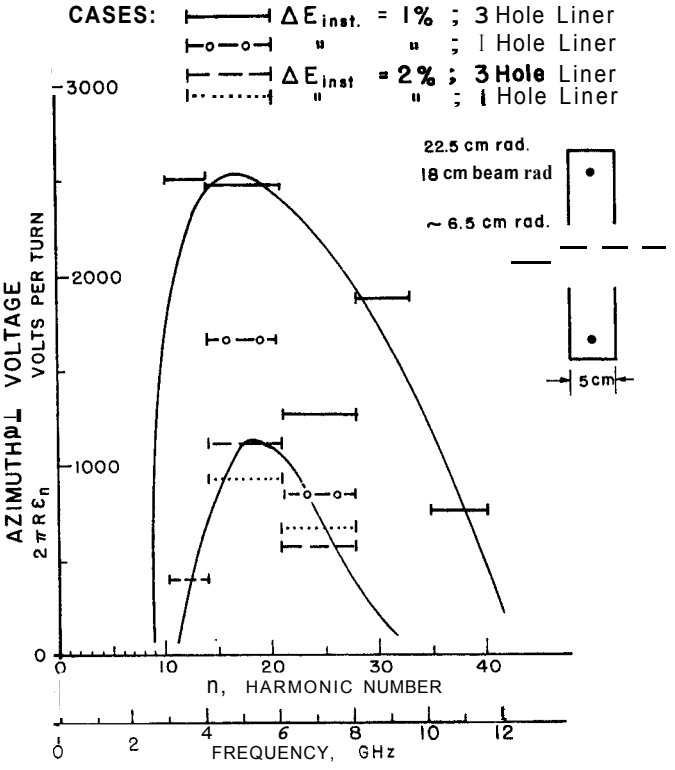


Figure 4 - Plots of maximum radio frequency signal strength for an electron ring current of 50 amperes versus frequency of observation for incident energy spreads of 1% and 2%. The differences between liners having 1 and 3 inflector holes did not appear to be significant.

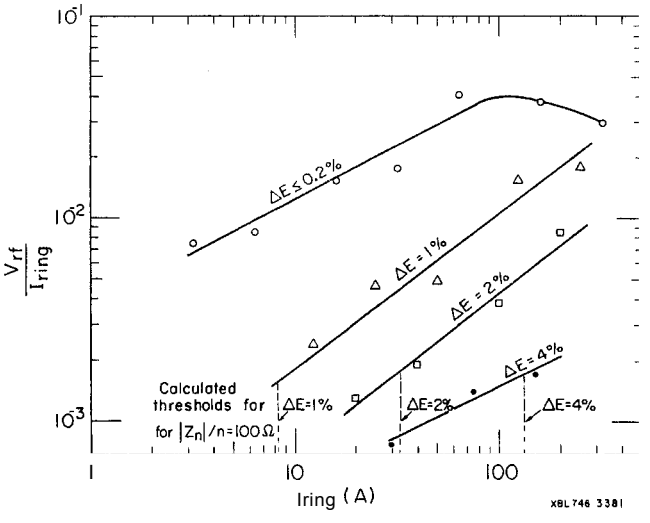


Figure 5 - Plots of relative beam modulation versus trapped ring current for energy spreads of 0.2, 1, 2, and 4%. Observations were in the 2 to 4 GHz frequency band (harmonics 7 to 14) with a two-turn incident beam with energy ramp in a three-hole conducting enclosure,

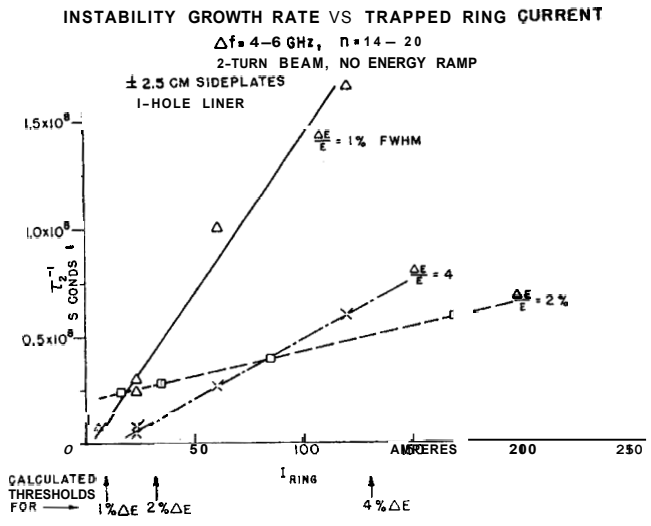


Figure 6 - Plots of growth rate $1/\tau_2$ versus trapped ring current for incident energy spreads of 1 and 2%. Observations in the 4 to 6 GHz frequency band (harmonics 14 to 20) with the two-turn beam without energy ramp in a one-hole enclosure with walls at ± 2.5 cm from the beam mid-plane. The calculated current thresholds for growth of the longitudinal instability assumed $|Zn|/n$ of 100 ohms.

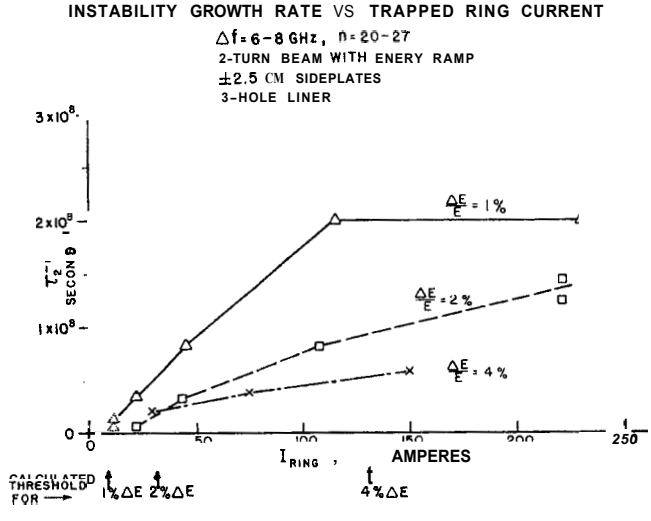


Figure 7 - Plots of growth rate $1/\tau_2$ versus trapped ring current for incident energy spreads of 1 and 2%. Observations in the 6 to 8 GHz frequency band (harmonics 20 to 27) with the two-turn beam with energy ramp in a three-hole enclosure with side-walls at ± 2.5 cm from the beam mid-plane.

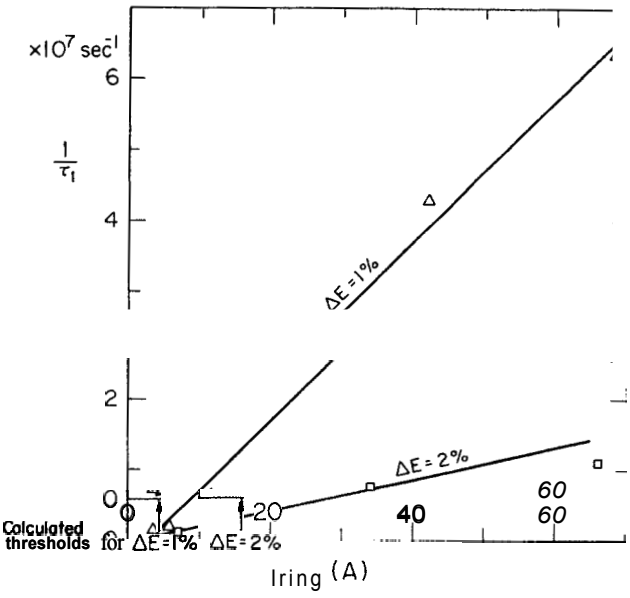


Figure 8 - Plots of growth rate $1/\tau_1$ versus trapped ring current for incident energy spreads of 1 and 2%. Observations in the 4 to 6 GHz frequency band (harmonics 14 to 20) with the half-turn beam in a three-hole enclosure.

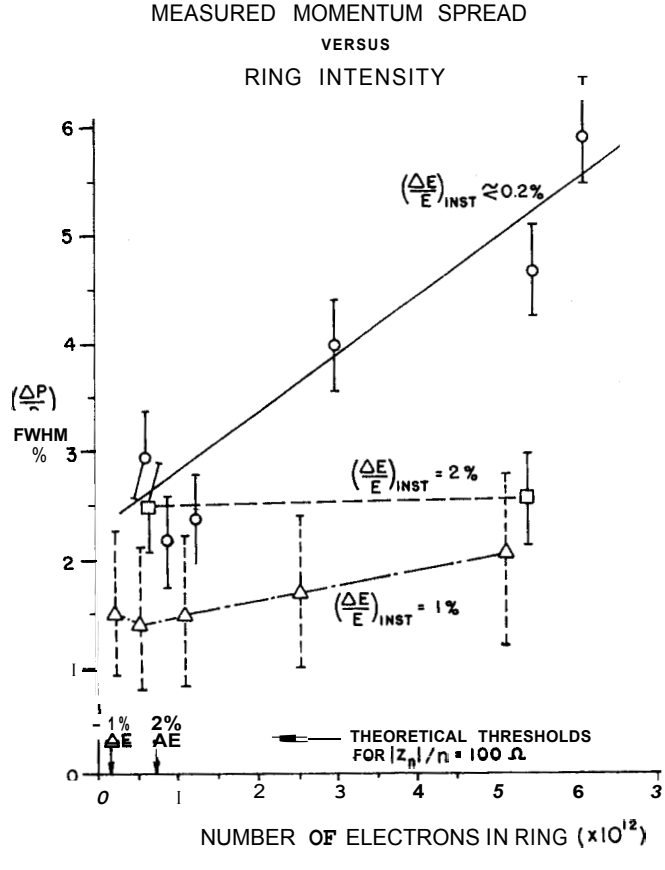


Figure 9 - Plots of the measured final momentum spread versus electron ring intensity for injected instantaneous energy spreads of 0.2, 1, and 2%.

EXPERIMENTAL AND THEORETICAL STUDIES OF ELECTRON RING FORMATION AND ION LOADING IN THE MARYLAND ERA*

W. W. Destler, A. Greenwald, D. W. Hudgings, H. Kim, P. K. Misra
M. P. Reiser, M. J. Rhee, and G. T. Zorn

University of Maryland
College Park, Maryland 20742

Summary

In the University of Maryland ERA experiment, a rotating electron ring beam is formed by passage of a hollow cylindrical beam through a cusped magnetic field geometry. The initial research objectives, present status of the project, and recent results of experimental and theoretical studies are described. Electron beams with peak currents up to 3 kA and peak voltages of 2 MV have been passed through the cusp. Pulse width, coherent and incoherent radial motion is in relative good agreement with single-particle theory. Transmission efficiency and radialwidth of the beam are strongly dependent on peak current, magnetic field and kinetic energy. Electrons with energies appreciably higher than those corresponding to the injector voltage were observed downstream from the cusp. This "auto-acceleration" effect is an indication that beam compression occurs which produces strong space-charge fields as is desired for collective ion acceleration. A neutral gas pulse is injected from a puff valve. Positive ions created by electron collision have a significant focusing effect on the electron beam.

Research Objectives and Present Status

The first objective of the University of Maryland ERA experiment is to form an intense rotating electron ring by passage of a hollow cylindrical beam through a static cusped magnetic field system which transforms axial into rotational velocity. Positive ions which are formed in the collisional interaction of the electrons with a gas cloud are to be trapped in the potential well created by the space charge of the electron beam. For collective acceleration of the ions the expansion method (which was used successfully in the Dubna ERA experiment[1]) will be employed.

The basic concept of the Maryland ERA scheme and the general design features of the facility were described elsewhere[2,3,4]. The five major components of the facility are (a) the electron beam injector, (b) the cusped magnetic field system, and (e) a fast-trapping coil system. Presently components (a) through (c) are in operation (though we encountered some problems with the injector as will be mentioned below). The 14 coils for system (d) have been built, vacuum chamber and mechanical support are in the design phase, and assembly of this part of the ERA facility is planned for late summer or early fall this year. Theoretical studies concerning the trapping system (e) are under way; some earlier studies relating to this have been reported elsewhere[5]. The engineering design is scheduled for the latter part of this year, and we hope to put the trapping system into operation by spring of 1975.

The most important component in our ERA facility is the electron beam injector which was a special developmental project designed and built in a collaborative arrangement by the Plasma Physics Division of the Naval Research Laboratory with cooperation from members of our group[4]. It was designed to generate short electron pulses with peak energies in the range of 1 to 5 MV, peak currents of 1 to 10 kA and a pulse width in the range of 20 ns. Initial tests during the spring of 1973 revealed some high-voltage breakdown problems which primarily affected the operation of the switches in the pulse-shaping Blumlein section and the radial insulator between the vacuum diode region and the oil-filled transmission line section. This problem limited the output voltage to about 1.6 MV for the initial phase of experiments which were conducted during the summer and fall of 1973. After this period the injector was modified to allow operation at higher voltage and to obtain a shorter pulse width by incorporating a pulse-sharpening switch. Experiments were resumed in March of this year and are initially confined to a range of 2-3 MV output voltage. The upper voltage limit for the injector should be near 3.5 MV. In recent weeks, we have had several failures of the radial diode insulator (see Fig. 1). The failures seem to be of mechanical origin probably caused by dynamical stress due to shocks when the switches are fired and followed by electrical breakdown (or vice versa). Analysis of this phenomonon is in progress, and we hope to solve it by appropriate mechanical modifications.

In the following sections we will present a brief summary of the experimental studies performed during last fall and in the past few weeks after modification of the injector. The results of theoretical considerations and studies which provide interpretation of the data are included.

Diode and Magnetic Field Geometry

In the initial experiments that have been conducted so far we are trying to obtain an understanding of the injector diode and beam characteristics, the passage of the beam through the cusp (which is the key element of our ERA scheme), the beam properties downstream, and the interaction with the gas cloud. Figure 1 shows schematically the diode end of the injector, the magnetic coil system with iron plate and the vacuum chamber. The curves below the coil system represent the magnetic field B_z versus distance z (measured at the beam radius of r=6 cm) for three different compressor coil configurations. The diode coils to the left of the iron plate remain unchanged. The initial experiments of last fall were conducted in Field I geometry. Subsequently the compressor coils were changed to the positions (indicated in the figure) which produce the Field IIA configuration; Field IIB is obtained by shorting out the second coil to the right of the iron plate. Both Diode coils and compressor coils are in series, and the current for each system can be independently varied. The field is normalized by the cusp condition, $B_z(z_c) = -B_z(-z_c)$, where $-z_c$ represents the axial distance of the cathode from the center of the iron plate ($z = 0$, $B_z = 0$). Field IIB conforms to the desired design shape on the compressor side: after a short plateau the field increases by about 40% until it reaches a peak where maximum compression occurs and the ion-loaded ring is to be formed. As mentioned above, 14 coils will be added downstream later this year to form the expansion-acceleration field. These coils will add approximately two meters to the length of the present system.

Beam Transmission through Cusp

The electron beam is produced by field emission when the high voltage pulse arrives at the diode. A knife-edge tantalum ribbon (diameter of 12 cm) which is bent into a circular shape and protrudes several millimeters from the cathode disk forms the emitter for the hollow cylindrical beam. As indicated in Fig. 1, the beam passes through an annular slit (radial width 5 mm) in the anode and iron plate. The latter serves to shorten the length of the cusp transition in which the magnetic field reverses polarity.

According to single-particle theory[6-8], the cusp transforms axial into rotational motion. If v_{z1} is the axial velocity on the diode side of the cusp, r_o the cathode radius, v_{z2} the axial velocity downstream, one finds

$$v_{z2}^2 = v_{z1}^2 - r_o^2\omega_c^2, \qquad (1)$$

where $\omega_c = (eB_z/\gamma m)$ is the electron cyclotron frequency and $(\gamma - 1)mc^2 = eV$ represents the kinetic energy. Eq. (1) predicts a threshold velocity

$$v_{zth} = r_o\omega_c \qquad (2)$$

below which electrons are reflected at the cusp. The corresponding threshold energy is determined by

$$\gamma_{th} = [1 - (v_{th}/c)^2]^{-1/2} \qquad (3)$$

or

$$E_{th} = eV_{th} = [(m_oc^2)^2 + c^2e^2r_o^2B_z^2]^{1/2} - m_oc^2 \qquad (4)$$

For a typical diode voltage and current pulse with finite rise time, one would therefore expect that the beam pulse at the downstream side of the cusp is shortened in time. This effect is indeed observed experimentally. A low-inductance Faraday cup was used to measure the beam current pulse upstream and downstream of the cusp in Field I geometry. Two typical oscilloscope traces are shown in Fig. 2 together with a self-explanatory illustration of this "cutoff" effect. (The voltage pulse, V(t), is measured on the diode side of the cusp by a separate voltage probe). By raising the magnetic field on both sides of the cusp, it is possible to decrease the width of the downstream current pulse or to stop the beam entirely from passing into the compressor region.

The loss in peak current amplitude seen in the downstream pulse of Fig. 2 is largely due to the slit aperture in the iron plate and collective effects as will be explained below.

A second important result of single-particle theory for particle motion through cusped magnetic field is the coherent radial off-centering experienced by the particles due to the $v_\theta B_z$ force term. If one approximates the B_z curve across the cusp by

$$B_z(z) = B \tanh \frac{z}{\lambda}, \qquad (4)$$

one finds for the amount of off-centering, ΔR, the relation[8]

$$\Delta R = \frac{\lambda}{2} \sin^{-1}\frac{1}{b}. \qquad (6)$$

In these equations λ is a scale factor for the effective width of the cusp which can be determined experimentally; in our case $\lambda = 0.9$ cm. The parameter b in (5) represents the ratio of total particle velocity v_t to azimuthal velocity $v_{\theta 2}$ after passing the cusp, i.e. $b = v_t/v_{\theta 2}$. Obviously $1 < b < \infty$ corresponds to $\frac{\pi}{2} > \sin^{-1}\frac{1}{b} > 0$. In a series of careful measurements using a pinhole technique[7,8] we found experimental data to be in good agreement with the theory. Depending on the ratio $v_t/v_{\theta 2}$, which is adjustable via the magnetic field, we measured typical values for ΔR between 2 and 6 mm.

At peak currents of several kiloamperes collective effects (space charge and image fields) play an important role in the beam dynamics. The radial width of the straight hollow beam before entering the cusp is determined by the emittance at the cathode, kinetic energy after acceleration, beam current and magnetic field strength. A non-relativistic theory of the space charge effects which neglects the emittance and the image forces due to boundaries gives the following scaling law.[9]

$$\Delta r = \text{const}\,\frac{I}{B^2 V^{1/2}} \qquad (7)$$

A relativistic analysis is more involved; however the basic feature remains that Δr increases with current I and decreases with magnetic field B and voltage V. Measurements by Rhee and Zorn[10] with the relativistic beam from a Febetron 709 showed a B^{-2} dependence of Δr. In our case the slit width, Δr_s, in the iron plate limits the peak current that can be transmitted as long as $\Delta r > \Delta r_s$. Figure 3 shows Faraday-cup measurements of peak current in Field I at a distance of z = 5 cm from the center of the iron plate. The injected diode current was varied by changing the cathode-anode spacing d from 1.5 to 3 inches; this unfortunately also changed the peak voltage from 1.5 MV (for d = 3") to 1.05 MV (for d = 1.5"). Note that the current in a relativistic diode varies as V^α/d^2 where α is between 3/2 (non-relativistic case of Child's Law) and 1 for the extreme relativistic case.[11] From Fig. 3 it is clear (at least for the higher energy beams) that the current rises as B_z is increased and then drops rapidly as the theoretical cutoff values is reached. The higher B_z (provided it remains below threshold) and the higher the voltage, the higher is the peak current transmitted through the cusp, consistent with theoretical expectations of decreasing Δr.

One very interesting phenomenon, not yet completely understood in detail is the experimental observations of electrons above the theoretical cutoff value.[12] Thus, for instance we have observed in Faraday-cup measurements electron peak currents of up to 200 A substantially above the cutoff field of about 1.1 kG for a diode voltage of 1.5 MV peak. The "pinhole" experiments, mentioned above, also showed this effect. As illustrated in Fig. 4, the entire beam was masked by a copper plate with the exception of a small hole (of typically 1 mm^2 area). The electrons emerging from this pinhole follow a helical path downstream of the cusp transition with the pitch angle depending on their kinetic energy in accordance with Eqs. (1) to (4). A film placed in an r-z plane at some azimuth angle away from the pinhole intercepts the electrons, and the traces give information on energy, radial width, coherent off-centering, and particle density. The film track shows that the beam density peaks at the front or high-energy end; also, the energy at this point is in agreement with the single-particle "cutoff" value. However, we have consistently observed a thin trace of electrons whose energy is a factor 1.5 to 2 above the threshold as is evident in the figure which is an independent confirmation of the Faraday-cup measurements. Our tentative interpretation is that these are electrons at the beam front which are accelerated by the space charge field of the particles behind them The so-called "ram effect", first discussed by Raudorf,[13] would be responsible for this auto-acceleration mecha-

nism. As the electrons cross the cusp, their forward motion is slowed down and the space-charge density increases rapidly. Energy associated with the center and rear parts of the advancing hollow beam is transferred to the electrons at the front of the beam. This auto-acceleration effect is also found in our computer simulation studies.[14] The experimental observation of "ram effect" electrons is direct evidence of the strong potential well which is formed on the downstream side of the cusp and which we want to utilize for positive ion acceleration.

Radial Beam Profiles and the Effects of Interaction with Gas

The radial cross section of the beam downstream from the cusp was measured with time-integrated photographs of the scintillation-light emitted when the electrons strike a glass plate. To mask out the light from the diode the glass plates were coated with graphite. Figure 5 shows such a picture at a distance z = 32 cm from the iron plate in Field I. The dense "core" (of radial width 2-4 mm) surrounded by a "halo" is typical for the pictures obtained. With increasing magnetic field, as the threshold is approached, the halo seems to disappear.

Time-resolved pictures of the radial beam width were obtained with the aid of an image converter camera operating in the streak mode. In this case the beam was hitting a thin scintillating glass rod. A typical picture, shown in Fig. 6, indicates that the front of the beam arriving early in time has a well defined narrow width. Clearly this part of the beam forms the dense "core" observed in Fig, 5 while particles arriving late show considerable spreading in radius and thus constitute the "halo". It is the dense, early part of the beam which we want to separate from the halo and use as the potential well for the positive ions. The time-resolved radial beam profile of Fig. 5 was reasonably well explained by Rhee[8] on the basis of a single-particle model of electron motion for different starting conditions at the cathode.

For injection of gas into the rotating electron beam a special puff-valve was built, and the pressure profiles in time and space were measured with a fast ionization gauge. A rotationally symmetric gas cloud is injected radially from the tip of a cylindrical pipe protruding from the end flange along the axis of the vacuum chamber as schematically illustrated in Fig. 7. This figure also shows curves of constant pressure (with argon, numbers are in torr) at the peak of the gas pulse, 1.4 ms after opening of the puff valve. The number of positive ions N_i created by electron collision is given by the approximate relation[6]

$$N_i = 0.1\, Z_m N_e p \Delta t$$

where Z_m = number of electrons per molecule, N_e = total number of electrons, p = gass pressure in torr, Δt = interaction time (duration of electron pulse) in nanoseconds. The positive ions play an important role in self-focusing of the beam and the fraction $f = N_i/N_e$, which gets trapped in the electron ring, must be greater than the Budker limit, or $f > 1/\gamma^2$. In our case γ is between 5 and 8, f in the range of 10 to 20%, As between 10 and 100 ns; hence we need pressures in the range of 10^{-3} to 10^{-2} depending on the type of gas used.

To study the effects of ionization on the radial cross section of the beam, we took time-integrated photographs with the scintillation plate technique. A typical shot, which was taken under similar conditions as that in Fig. 5 except that argon gas was added, is shown in Fig. 8. The peak of the gas cloud was approximately 20 cm downstream from the iron plate in the Field I compressor coil geometry. In this experiment the electrons still had an appreciable axial velocity. The hollow beam passes through the gas region and strikes the scintillator glass plate which was approximately 10 cm beyond the gas peak. Comparison of Figs. 5 and 8 illustrates that positive ions produce strong pinching (in this case radial focusing) of the electron beam. Figure 9 shows a time-integrated photograph of the light emitted by the ionized gas cloud viewed at an angle perpendicular to the direction of beam travel.

In addition to the diagnostic techniques described so far we are also using non-intercepting magnetic probes. A B_z probe located on the axis measures the self-magnetic field generated by the rotating component of the electron beam current while a B_θ probe at a radius outside of the beam measures the field due to axial beam current. Figure 10 shows typical magnetic probe signals obtained in one of our experiments. The ratio B_θ/B_z indicates the degree to which the beam has been slowed down in axial velocity. From the pulse shape and amplitude we hope to learn something about the electron current distribution in space and time. The amplitudes of B_z and B_θ in Fig. 10, for instance, are consistent with Faraday cup measurements of peak currents in the range of 1.5 to 2 kA.

A more detailed experimental study of beam profiles and effects of ion focusing for various conditions using multifinger probes is underway.[15] We have also started theoretical work to simulate our ERA system by computer. Poukey and Freeman of Sandia Laboratories, in a collaborative effort, have adapted a self-consistent computer program to our specific requirements and preliminary results were reported recently.[16] A less sophisticated program has been developed at the University of Maryland by Kalnins and Greenwald[14] which has some versatility and requires less computer time at the expense of accuracy and self-consistency. In preliminary simulation runs with this computer program we calculated the magnetic field at the two probe positions and found relatively good agreement with the experiment. The calculations so far also demonstrate that a dense part of the beam is formed in the region near the peak magnetic field. We hope that either by collective effects (ion loading, image forces, etc.) or with the aid of auxiliary-pulsed coils we will be able to separate this dense part from the rest of the electron beam and use it as the vehicle for positive ion acceleration.

References

1. V. P. Sarantsev, Proc. of 8th Int. Conf. on High Energy Accelerators, CERN, 1971, p. 391.
2. M. Reiser, IEEE Trans. NS-18, 460 (1971); IEEE Trans. NS-20, 310 (1973).
3. J. G. Kalnins, H. Kim, and D. L. Nelson, IEEE Trans. NS-18, 473 (1971).
4. J. K. Burton, J. J. Condon, W. H. Lupton, F. L. Desrosier, A. C. Greenwald, J. M. Henness, M. J. Rhee, and G. T. Zorn, IEEE Trans. NS-20, 321 (1973).
5. J. G. Kalnins, H. Kim, and J. G. Linhart, IEEE Trans. NS-20, 324 (1973).
6. M. Reiser, IEEE Trans. NS-19, 280 (1972).
7. M. J. Rhee, W. W. Destler, D. W. Hudgings, M. P. Reiser, H. S. Uhm, and G. T. Zorn, Bull. *APS*, Series II, Vol. 18, 1265 (1973).
8. M. J. Rhee and W. W. Destler, Technical Report No. 74-065, Jan. 1974, Physics & Astronomy, University of Maryland; to be published in Physics of Fluids.
9. P. T. Kirstein, G. S. Kino, W. E. Waters, Space-Charge Flow, McGraw-Hill, 1967, p. 158.

10. M. J. Rhee and G. T. Zorn, Proc. of 8th Int. Conf. on High Energy Accelerator, CERN 1971, p. 481.

11. H. R. Jory and A. W. Trivelpiece, J. Appl. Phys. 40, 392 (1969).

12. D. W. Hudgings, Bull. APS, Series II, Vol. 19, 534 (1974).

13. W. R. Raudorf, Wireless Engr. 28, 215 (1951).

14. A. C. Greenwald and J. G. Kalnins, Bull. APS, Series II, Vol. 19, 534 (1974).

15. P. K. Misra, Bull. APS, Series II, Vol. 19, 534 (1974).

16. J. W. Poukey, J. R. Freeman, and G. T. Zorn, *APS* Bull., Series II, Vol. 18, 1283 (1973).

*Research supported by the National Science Foundation

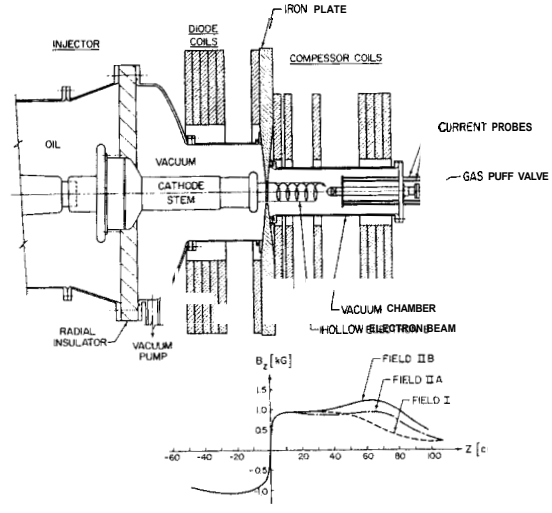


Fig. 1 Diode and magnetic field geometry.

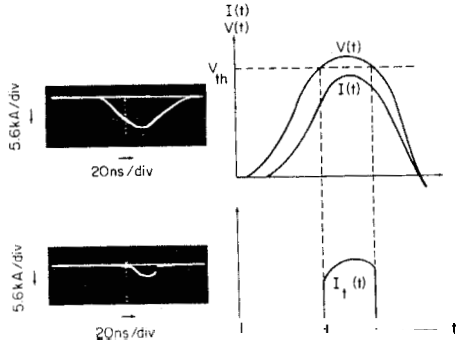


Fig. 2 Current pulse before and after beam passage through cusp.

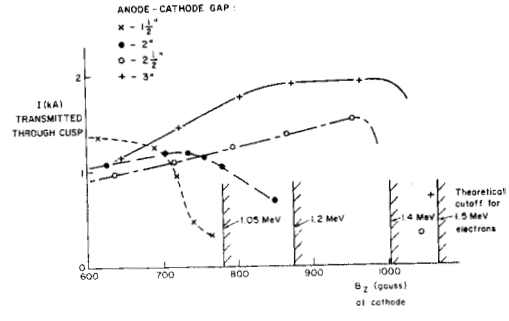


Fig. 3 Peak current versus B_z at z = 5 cm for different beam energies.

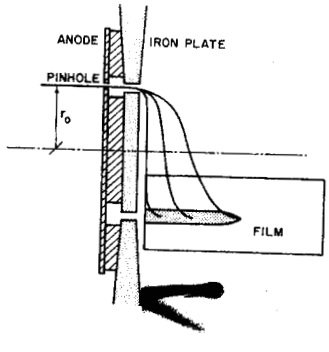


Fig. 4 Geometry of "pinhole" experiment and film traces of electron beam.

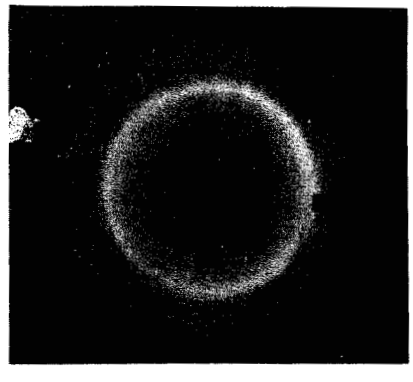


Fig. 5 Beam cross section at z = 32 cm.

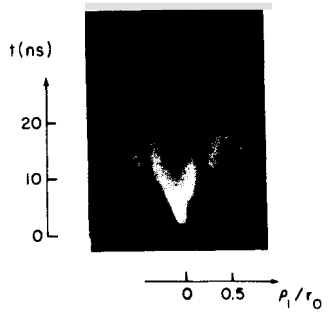


Fig. 6 Streak photograph of beam cross section.

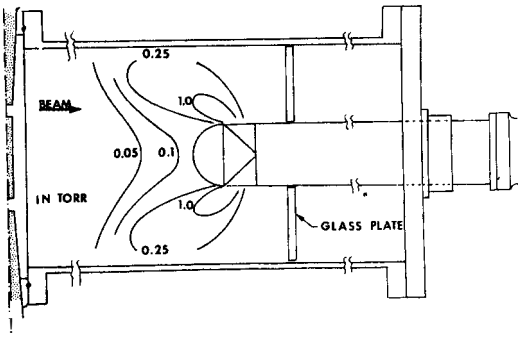


Fig. 7 Puff-valve geometry and pressure profiles.

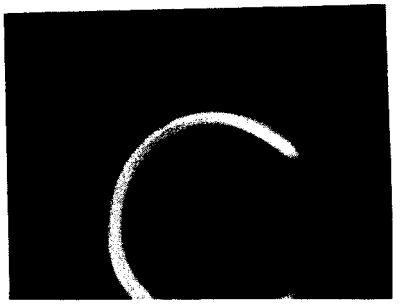


Fig. 8 Beam cross section in the presence of gas (pinching due to positive ions).

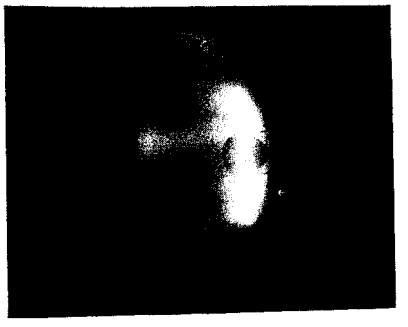


Fig. 9 Transverse view of beam interaction with gas.

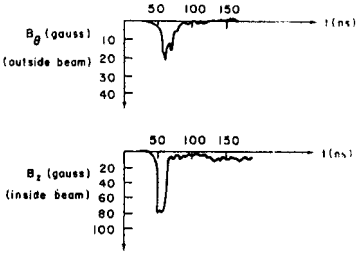


Fig. 10 Typical magnetic probe signals.

THE ELECTRON RING PROGRAM AT LAWRENCE BERKELEY LABORATORY*

W.W. Chupp, A. Faltens, E.C. Hartwig, D. Keefe, G.R. Lambertson, L.J. Laslett, W. Ott,† J.M. Peterson, J.B. Rechen, A. Salop, and R.W. Schmieder**

Lawrence Berkeley Laboratory
University of California
Berkeley, California

Introduction

The Electron Ring Program[1-3] at Lawrence Berkeley Laboratory has been recently concerned principally with the study of collective instabilities and their control and has led to the injection, trapping, and compression of rings intense enough and compact enough for studies of acceleration and ionization processes.

Experimental Arrangement

The injector accelerator and compressor have been described previously.[4-6] For orientation, we review the principal features of the apparatus and the goals of the program.

Electrons originate at a field-emission cathode in a pulse 40 nanoseconds long, 1100 amperes in intensity, and of 1.2 MeV energy produced by a unit made up of five stages of the induction accelerator. The pulse is then accelerated to 3.6 MeV by twelve additional induction acceleration stages. A beam transport system further modifies the pulse to approximately 25 nanoseconds full duration, 400 amperes maximum intensity. Portions of the pulse of shorter duration, and fractions of the full intensity may be selected. A time-varying and an instantaneous energy spread may be imposed on the pulse also.

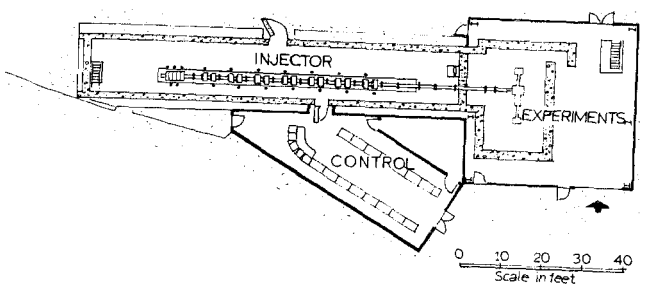


Figure 1 - Electron Ring Facility-Plan View

This tailored electron pulse is then injected into the rising transverse magnetic field of the compressor through a compensated input snout. This field and the inflector form and trap the electrons into a ring at a radius typically of 17.5 centimeters major radius, 2 cm axial width and 4 cm radial extent. It is then further compressed by 3 sets of pulsed coil pairs to the final radius of 3.9 cm and energy of 18 MeV in approximately 700 microseconds.

The compressor vacuum chamber contains a conducting liner, which establishes the electromagnetic environment of the ring, and diagnostic devices in-the form of obstacle probes, single-turn loops both movable and fixed, current measuring coils, and a pulsed gas-input valve. A window for viewing synchrotron light is provided on the periphery.

Most of the injection, trapping, and collective instability problems have been studied in the limited apparatus called Compressor 4. It was not designed for full compression, ion loading, or rollout for magnetic expansion acceleration. This compressor was no longer used after August 1973, and Compressor 5A, which could accommodate additional experimental advances, was brought into operation in October, 1973. The details of its design relied heavily on the results of the prior experiments with Compressor 4.

The vacuum capability of Compressor 5A, while better than that of Compressor 4, is not in the pressure range desired for controlled ion loading and acceleration. An improved vacuum chamber of polyimide-glass laminate material was designed and pursued actively, but fabrication methods have not yet been developed to produce a bakeable high-vacuum structure from this material.

The principal goal of the experimental program remains to form intense, stable electron rings of high holding power which may then be accelerated very strongly while loaded with a useful number of the desired ions. A secondary goal is to form intense rings which may be retained for times approaching one second, in a suitably designed compressor, for the production and study of very high ionization states in heavy ions.

Experimental Observations

The principal problem that had to be analyzed and attacked was the intensity-dependent radial broadening of the ring shortly after injection. The effects were increasingly more severe at high beam intensities, and initially the number of electrons that could be formed into a compact ring was small (about 10^{12}) because the broadening led to large losses of beam particles on surrounding structures. Most of the effects occurred within 20 to 100 nanoseconds of injection.

One useful technique adopted was to use a low-intensity, short input pulse which could be easily identified and pursued through the inflection process, which allowed the inflector to be adjusted properly.

Several effects were observed.3 One effect was a coherent, transverse, intensity-dependent oscillation of the ring as a whole at a frequency $(1-\nu_R)f_0$, where ν_R is the radial betatron tune and f_0 is the electron gyro-frequency. Another observation was that the ring developed a momentum spread, larger at high beam intensities, shortly after injection, accompanied by radio-frequency emission at harmonics of the electron gyro-frequency. The analysis of this phenomenon is the subject of another paper in this session.7 Under some circumstances an axial oscillation at a frequency $(1-\nu_Z)f_0$ was observed.

An additional complication was the effect of the single-particle resonance at a field index value of $n = 0.5$. We chose, at first, to inject at a radial tune of 2/3, ($n = 0.55$) in order to achieve high inflection efficiency. However, this entailed crossing the $n = 0.5$ resonance very shortly thereafter, which broadened the ring and caused additional growth and beam loss at other resonances.

*Work supported by the U.S. Atomic Energy Commission.
†On leave from MPI für Plasmaphysik, Garching, Germany.
**Sandia Laboratory, Livermore, Calif.

These problems were attacked in several ways. One of the conclusions drawn in Reference 1 was that the compressor liner should have low resistivity to suppress the resistive wall transverse instability and aid in the suppression of the longitudinal instability and yet be resistive enough to allow the fast inflector field to operate through it. Various attempts were made to optimize separately the radial and azimuthal conductivities of liners, but none had the desired effect, as combinations of instabilities still dominated ring behavior, leading to enlarged ring dimensions and losses on surrounding structures.

A drastic change was then made to a thin stainless steel liner of less than 0.1 ohm per square resistivity, with a hole in both side-walls, whose edges formed the current conductors for the inflector pulse. Thus the environment for the electron ring could be varied by means of wall spacing and conductivity, while the inflection process was essentially decoupled from such adjustments. This arrangement was aimed at improving the early growth and loss situation. It was hoped that the inflector holes were a small perturbation, and in a friendly direction, to the impedance presented by the liner to low harmonics of the electron gyro-frequency.

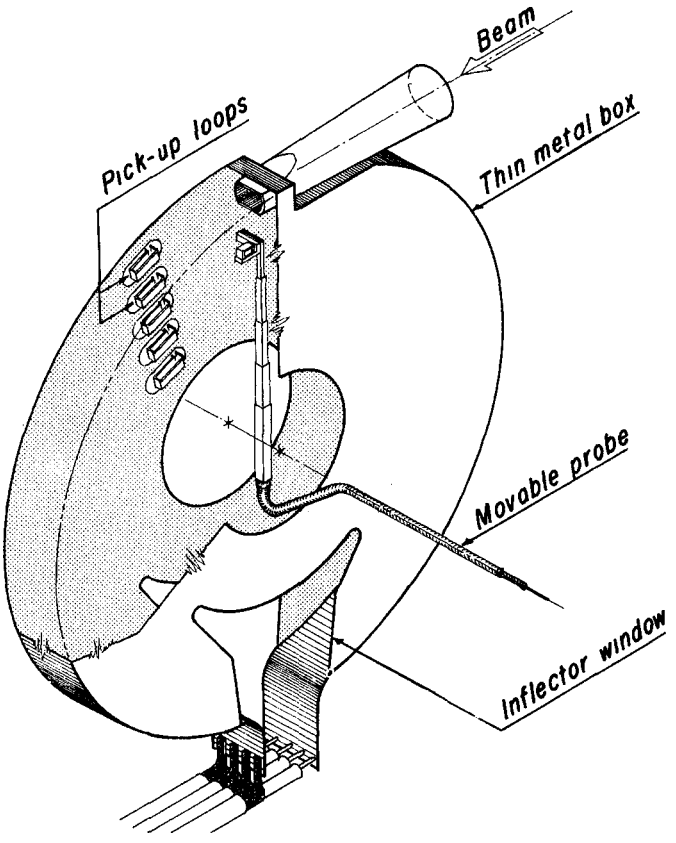


Figure 2 - Compressor metal liner

The opacity of the metal liner to R.F. signals necessitated the introduction of internal loops for high-frequency observations.

In a series of experiments in which we varied wall spacing and conductivity and the low-frequency behavior of the inflector holes and peripheral band, it was found possible to suppress the coherent transverse instabilities, reduce R-F radiation from the ring at high and low harmonics separately, and improve trapping.

One coherent transverse instability was traced to cancellation of terms in the Landau damping coefficients due to eddy currents induced in the windings of the second compression coil pair. A change, first to stranded conductors and then to stainless steel has eliminated this problem.[8]

Another coherent transverse instability was found to be due to full neutralization of the electron ring by ions[9] either from background gas or from gas evolved from arcs or electron impact on unstable materials. The removal of organic materials, careful attention to electrical connections, and improvement of the vacuum have minimized this contribution.

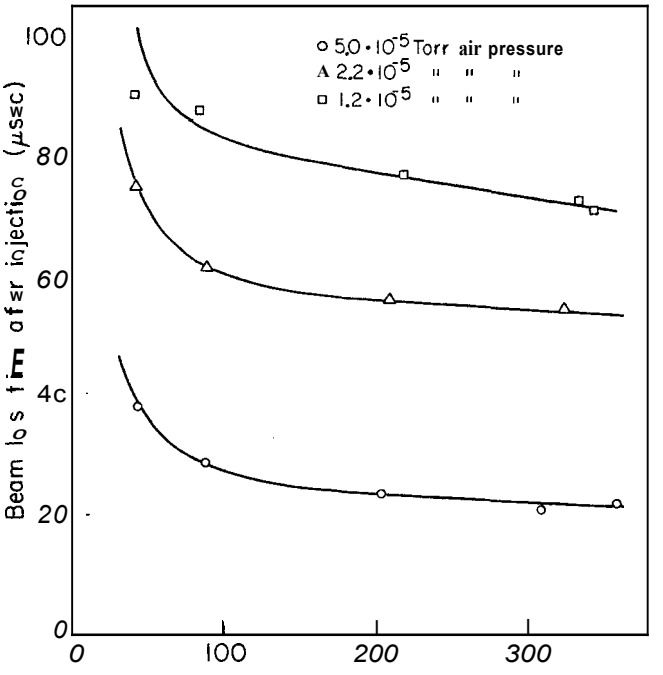


Figure 3 - Beam loss due to neutralization

Another coherent transverse instability is influenced by the spacing and resistivity of the wall material close to the ring.[3] Lowering the resistivity of the wall material below about 0.1 ohm per square raised the intensity threshold for this instability beyond the current levels we inject, and caused a dramatic increase in the maximum current we could trap into a stable ring from 80 Amperes to 300 Amperes (about 7×10^{12} electrons).[2]

The prompt energy spread increase observed' was assumed to be caused by the "negative mass", or coherent longitudinal instability, and was approached on that basis. Existing theories[3] predict the onset of the instability at a number of particles N

$$N = |n| \frac{\gamma R}{2\beta^3 r_e} \frac{Z_0}{|Z_M|/M} \left(\frac{\Delta E}{E}\right)^2,$$

where $|n| = \left|\left(\frac{1}{1-n}\right) - \gamma^{-2}\right|$, $\tilde{=} \frac{1}{(1-n)}$ for the electron ring, n = magnetic field index, R = major ring radius, r_e = classical electron radius, Z_0 = impedance of free space, $\Delta E/E$ = full-width at half maximum energy spread in the beam and Z_M is the longitudinal coupling impedance of the mode or harmonic number, M. In this threshold formula the only parameters available for effective variation were the energy spread and the coupling impedance. As noted above, the side-wall impedance is a factor also

in a transverse instability, and in earlier experiments was limited by the inflector pulse requirements. It has been found that low impedance metallic side-walls, relatively close to the ring can reduce the R.F. activity observed at high electron gyro-frequency harmonics and also the energy spread produced in the electron ring. Careful bridging of the inflector holes with resistive material reduces some of the lower harmonic activity. However, threshold currents do not appear to follow the linear theory, and the R.F. activity seen, in terms of the inferred degree of modulation of the beam current, is never large relative to the observed increase in energy spread. Growth rates predicted by simple theories of mode coupling also do not agree with observations in a qualitative sense. Another paper, No. 4-4,[7] presented at this conference, discusses these observations more fully.

As soon as experiments had progressed to the stage of reliably trapping intense, compact rings, Compressor 5A, incorporating this accumulated knowledge and additional experimental possibilities as outlined above was installed and began operation in October 1973. It was found that the inflector holes and other structures were perturbing the main magnetic field to a significant degree. Inductors were bridged across the inflector holes to carry induced eddy currents more symmetrically in the compressor liner, and perturbations due to other causes also were reduced as much as possible.

The electron ring, during compression, must cross several single-particle resonances. To minimize the growth of ring dimensions and loss of beam particles caused by these resonances, each has been examined to ascertain the riving terms and the factors involved in growth rates." The resonances involved and the corresponding integral tune relationships are:

n = .50	$\nu_R - \nu_z = 0$
n = .44	$3\nu_z = 2$
n = .36	$\nu_R + 2\nu_z = 2,\ 2\nu_R - \nu_z = 1$
n = .25	$2\nu_z = 1$
n = .20	$\nu_R - 2\nu_z = 0$

Our inflection system was designed for 3-turn injection with a closed orbit radial tune just above $\nu_R = 2/3$ (n = .556). While the inflection process performs best here, the ring must cross n = .5 immediately thereafter. Attempts to delay this crossing and then perform it rapidly involved extra coils and did not show much promise.

This problem could be avoided completely if the inflection were performed at n less than 0.5. Trapping efficiencies with the inflector optimized here were not as high as previously, but the lack of beam damage due to the resonance was considered as acceptable compensation.

Presently, small beam losses accompanied by broadening of the ring are seen at approximately 20 and 40 ysec after injection. These have been tentatively associated with the resonances at n = .44 and n = .36. They may be minimized by careful adjustment of injection parameters and by the use of harmonic correction coils designed to counteract the known first and second harmonic distortions of the compressor magnetic fields due to eddy currents, injection snout and inflector holes.

The resonance at n = .25 is crossed immediately after the second coil-pair is turned on, giving a maximum crossing rate for this resonance, If the ring is allowed to reach this resonance slowly, as at the end of the first coil's cycle, the entire beam may be lost. This

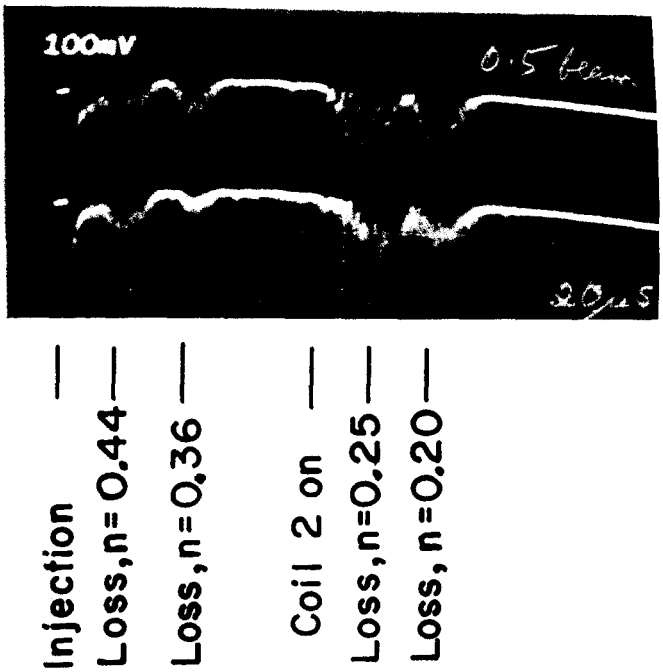


Figure 4 - X-ray loss pattern

resonance also responds to the use of the harmonic correction coils.

The n = .20 resonance is observed to cause X-ray losses also. These may also be minimized by use of the field harmonic correction coils, as growth on this resonance has a field second-harmonic term.

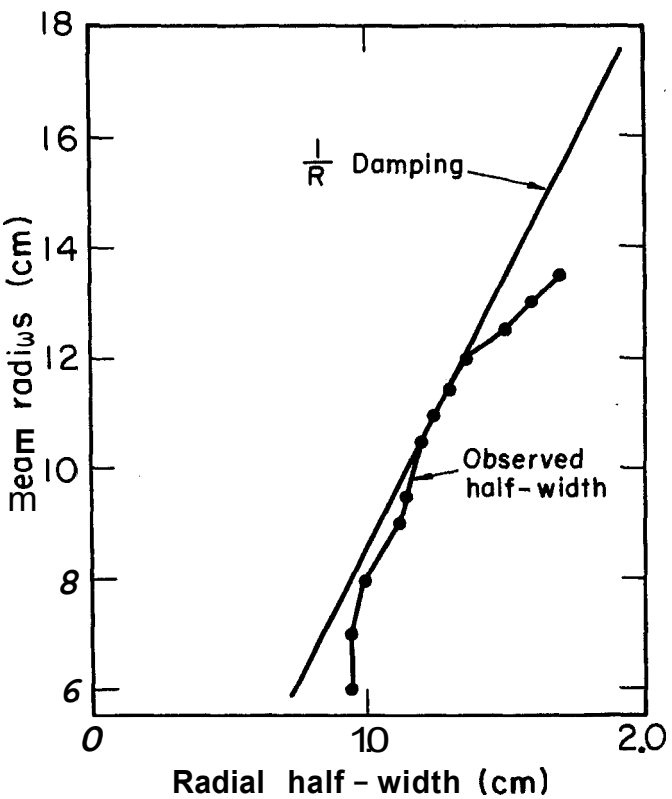


Figure 5 - Radial half-width vs. radius

Taken together, these ring-growth minimizing measures have been successful. The final ring dimensions, as seen by synchrotron light from the fully compressed ring show diffuse rings of low intensity without resonance-crossing assistance. Many of these rings are observed to have an oscillating, multiple-ring appearance also. When the measures outlined above are optimized, it is found that practically all of the trapped electrons survive to form a final compressed ring whose dimensions, at present, are:

Major radius	4.2 cm
Minor radial half-width	0.2–0.3 cm
Minor axial half-width	0.3–0.4 cm

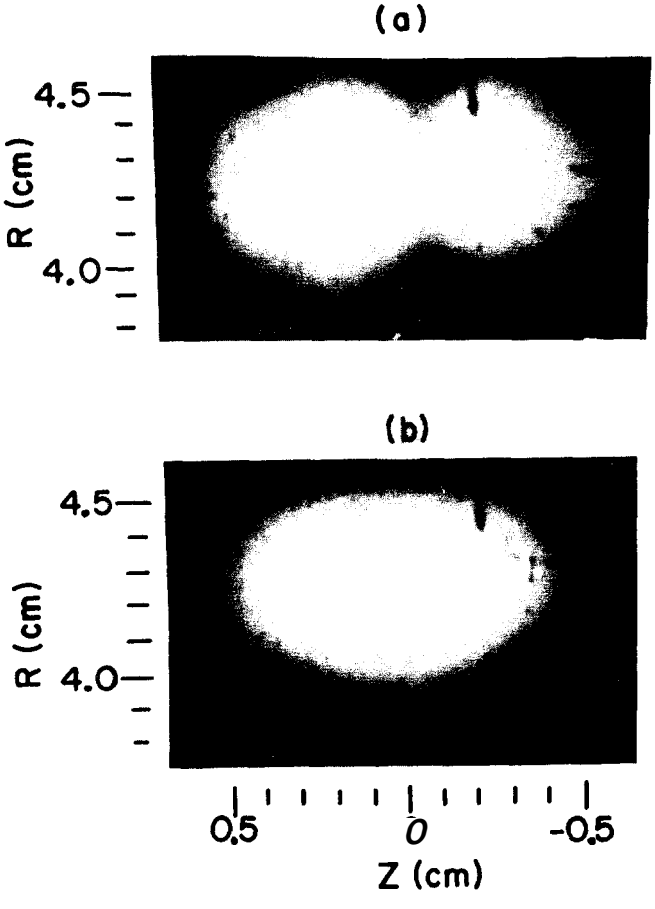


Figure 6 - Synchrotron light
(a) No harmonic compensation
(b) With harmonic compensation

A smaller major radius was planned, but a capacitor bank voltage limitation at present prevents full use of the third coil-pair.

Other Experiments

An experiment on the observation of K and L x-rays from atoms undergoing ionization in the electron ring was performed on the Compressor 4 apparatus.[11] Detection was by means of a cooled lithium-drifted silicon diode, collimated to view a small portion of the fully-compressed ring. The detector was heavily shielded against the copious x-rays and electrical and magnetic disturbances present near the compressor. The characteristic K and L x-rays of Xenon were successfully observed and identified (Fig. 7). It is believed that the ionizing capabilities of an intense electron ring are unique and could enable research on the ionization process and on the spectroscopy of highly-stripped ions.[12] A conceptual design for such a compressor is the subject of another paper to appear in the proceedings of this conference.[13] A typical calculated progression of the ionization of argon in an intense electron ring is shown in Figure 8

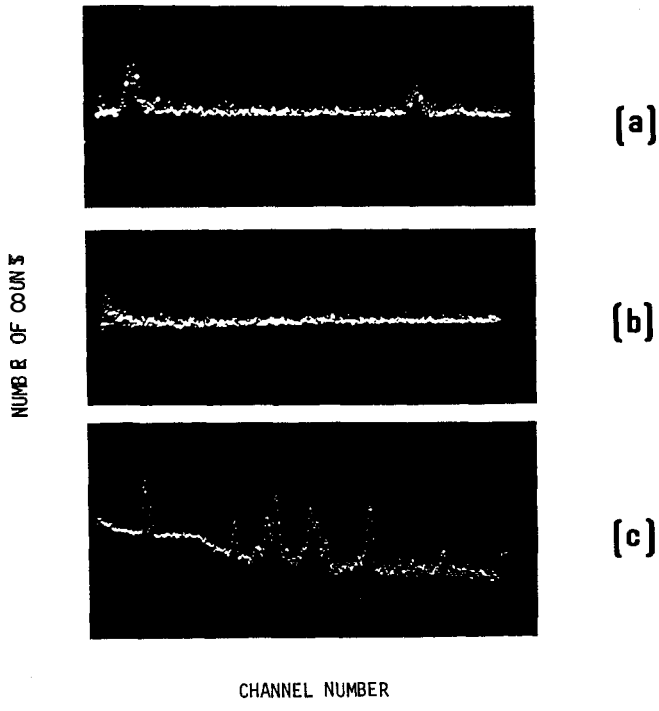


Figure 7 - Xenon x-ray observations
(a) K and L x-rays of Xenon
(b) X-rays, Xenon gas absent
(c) Calibration

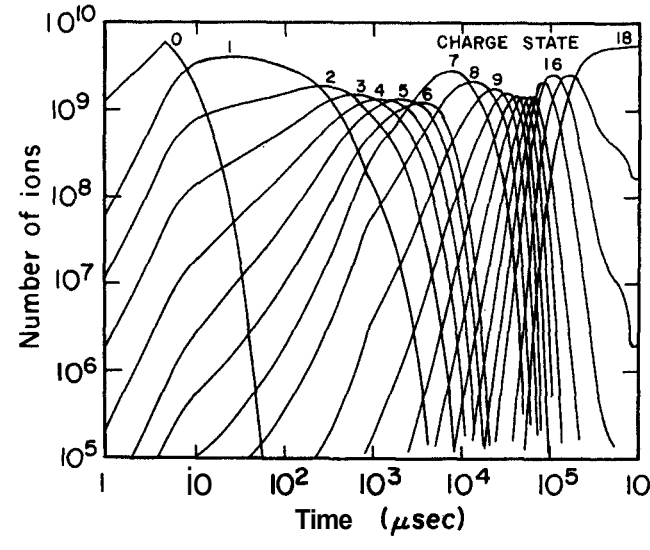


Figure 8 - Progress of ionization, Argon in electron ring

Theoretical and Calculational Work

An extensive calculational program has served and guided the experimental program throughout. Most of the results appear as internal reports (ERAN). Topics which have been treated recently are:

Minimization of field coil eddy currents[4]

The transverse resistive wall instability[15]

The negative-mass instability[16]

The full neutralization instability[9]

Ring stability and behavior during acceleration[17]

An electron ring as a spectroscopic source for ion study[11,12]

Ionization of heavy atoms by electron impact[18,19]

Conclusions

The LBL Electron Ring Program has demonstrated the injection and efficient trapping of rings of 7×10^{12} electrons without significant losses or dimensional broadening due to instabilities. The instabilities have been identified and either eliminated or ameliorated to the extent that their effects are acceptable. Most of the ring initially trapped can be compressed to a radius of 4 cm. The radial width of the rings show the expected adiabatic damping but the axial width shows blow-up caused by resonances. The next stages, ion loading and magnetic expansion, are ready to be undertaken except for the requisite vacuum of less than 10^{-8} torr.

Because of funding limitations, the Berkeley Electron Ring Program will be suspended after June, 1974.

References

1. D. Keefe, Proc. VIII International Conf. on High Energy Accelerators, 397-402 (CERN, Geneva, Switzerland; 1971).
2. Glen R. Lambertson, et.al., Particle Accelerators, 5, 113-120 (1973).
3. L. Jackson Laslett, IEEE Transactions on Nuclear Science, NS-20, No. 3 June 1973, pp. 271-275.
4. R. Avery, et.al, IEEE Trans. Nucl. Sci. NS-18, No. 3, 479 (1971).
5. E.J. Lofgren, IEEE Trans. Nucl. Sci. NS-18, No. 3, 456 (1971).
6. G.R. Lambertson, el.al., IEEE Trans. Nucl. Sci. NS-18, No. 3, 50 (1971).
7. A. Faltens, et.al., Paper 4-4 presented to this conference.
8. R.T. Avery and L.J. Laslett, Proc. VIII International Conf. on High Energy Accelerators, 465-467, (CERN, Geneva, Switzerland; 1971).
9. W. Ott, Lawrence Berkeley Laboratory Internal Report, ERAN-216, September 1973 (unpublished).
10. L.J. Laslett and W.A. Perkins, Nucl. Instr. and Meth. 97, pp. 523-538 (1971).
11. R.W. Schmieder, Lawrence Berkeley Laboratory Report LBL-2476 (1973) (unpublished).
12. R.W. Schmieder, LBL Report Internal report ERAN-221 (1973) (unpublished).
13. J.M. Hauptman, et.al., Paper 4-7 presented to this conference.
14. W. Ott and L.J. Laslett, LBL Internal Report ERAN-234 (1974)(unpublished).
15. L.J. Laslett, LBL Internal Report ERAN-209 (1973) (unpublished).
16. The negative-mass instability has been addressed recently by our group in several LBL internal ERAN reports (unpublished):

    A. Sessler and C. Pellegrini, ERAN-203, January 1973

    A. Sessler, ERAN-207, April, 1973

    P. Channell, ERAN-222, Nov. 1973; ERAN-226, Oec. 1973; ERAN-240, April, 1974.
17. Ring stability under acceleration and the performance as an accelerator has been addressed by the Berkeley group in the following LBL internal ERAN reports (unpublished):

    L.J. Laslett - ERAN-206, March 1973; ERAN-208, May, 1973; ERAN-211, July, 1973; ERAN-214, August, 1973; ERAN-228, January, 1974.

    W. Ott and L.J. Laslett - ERAN-234, February, 1974.
18. A. Salop, Phys. Rev. A 8/6, p. 30-32 (1973).
19. A. Salop, Lawrence Berkeley Laboratory Report LBL-2440, Dec. 1973 (to be published in Phys. Rev. A, June 1974).

COMPRESSOR DESIGN FOR INTENSE ELECTRON RINGS*

J.M. Hauptman, L.J. Laslett, W.W. Chupp, and D. Keefe

Lawrence Berkeley Laboratory
University of California
Berkeley, California

Introduction

An electron ring compressor is being designed for the purpose of obtaining very highly-stripped, high-Z ions. This effort may constitute a necessary step for development of a possible heavy ion accelerator, is expected to lead to useful basic ion-source information, and independently will permit obtaining interesting spectroscopic information concerning such ions. The primary design objective is the achievement of a ring of high electron density that must retain this density and remain stable for a sufficient time to develop the desired highly-stripped ions. A density-time product in the vicinity of 10^{13} electron-sec/cm^3 may be required. Vacuum requirements become undesirably stringent if the time interval exceeds 1 sec. Synchrotron radiation over such time periods plays a dominant role in the design, and a proper shaping of the magnetic field is presented which employs synchrotron radiation to enhance ring quality while avoiding both single particle resonances and the onset of negative-mass instability.

The attainment in an electron ring device of high electron density extended over a time of order 1. sec. requires the following two conditions. Firstly, the electron beam from a linac must be formed into a large radius ring in a magnetic field, and pulsed to small major radius in order to obtain a necessary degree of adiabatic damping of the minor ring dimensions. Secondly, the magnetic and electric environment of the beam must be such that the beam amplitudes are stable, and remain small, against both transverse and longitudinal instabilities for several tens of synchrotron radiation time constants. Specifically, the radial and axial betatron tunes must not lie near, nor cross, strong resonant values. The requirement that the beam be stable with respect to longitudinal (negative-mass) instability demands that, at all times, the beam maintain an energy spread in excess of a few percent (FWHM). In the present design, we choose to limit the number of circulating electrons only by the brilliance of the injector, and adjust the energy spread in the beam so that the limit imposed by longitudinal stability is always larger.

The long confinement time makes it impractical to support the magnetic field of this device with air-core coils as previously done in the ERA program at LBL. We envision the use of ferromagnetic pole tips to shape the field, and limit the flux density at 3.0 cm radius on the median plane to 15. Kgauss.

We have investigated the performance of such an electron ring device by dividing the entire cycle into three sequential stages of operation. The first is pulsed field compression with

$$B^m r = \text{constant} \quad \text{(Stage 1)}$$

along the compression trajectory. Familiar cases are $m = 0$ (betatron), $m = \frac{1}{2}$ (scaling field $B \sim r^{-n}$ compressor), and $m = 1$ (static magnetic field compressor). The second is synchrotron radiation by the ring in a static magnetic field

$$B(r,z,t) = \text{constant}, \quad \text{(Stage 2)},$$

and in the final stage the ring is maintained at a constant major radius

$$r(t) = \text{constant}. \quad \text{(Stage 3)}.$$

The general differential equations governing r,z motions of an electron in a cylindrical magnetic field are

$$\dot{r} = \frac{-r\left(\dot{B}_z \frac{\partial B_r}{\partial z} - \dot{B}_r \frac{\partial B_z}{\partial z}\right) + \frac{\partial B_r}{\partial z}\left(\dot{A} - \frac{U_\gamma}{\beta}\right)}{D} \qquad (1a)$$

$$\dot{z} = \frac{r\left(\dot{B}_z \frac{\partial B_r}{\partial r} - \dot{B}_r \frac{\partial B_z}{\partial r}\right) - \dot{B}_r B_z - \frac{\partial B_r}{\partial r}\left(\dot{A} - \frac{U_\gamma}{\beta}\right)}{D}, \qquad (1b)$$

where

$$D = \frac{\partial}{\partial z}(B_r B_z) + r\left[\left(\frac{\partial B_z}{\partial z}\right)^2 + \left(\frac{\partial B_z}{\partial r}\right)^2\right]. \qquad (1c)$$

U_γ is the rate of electron energy loss by synchrotron radiation,

$$U_\gamma = \frac{C_\gamma P^4}{r^2}, \qquad (2)$$

with C_γ an electromagnetic constant

$$C_\gamma = \frac{2}{3}\frac{r_e}{(m_e c^2)^3} \simeq .04223655 \ (\text{cm}^2/\text{MeV}^3 \ \text{sec}).$$

It is convenient to define a quantity ξ as the fractional rate of change of momentum,

$$\xi \equiv -\frac{U_\gamma}{P\beta} = \frac{\dot{P}}{P} < 0, \qquad (3)$$

whose negative inverse is an instantaneous decay time constant for the radiation process.

During stages 2 and 3 we consider the possibility of employing a flux bar through the ring such that $\frac{\partial A}{\partial t} \neq 0$ on the equilibrium orbit. If we define f to be the fraction of momentum lost to radiation which is restored by the flux bar (FB) on the equilibrium orbit,

$$f \equiv -\frac{\dot{A}_{FB}}{\xi P}, \qquad (4a)$$

then the flux change at a radius r is

$$\dot{A}_{FB}(r) = -f\xi_o P_o \left(\frac{r_o}{r}\right)^\alpha, \qquad (4b)$$

where the subscript (o) refers to the equilibrium orbit, and $a = 1$ if all flux succeeds in threading the orbit. During stage 3 a magnetic field varying at a rate

$$\frac{\dot{B}}{B} = \lambda \frac{\dot{P}}{P} = \lambda\xi \qquad (5a)$$

will produce a flux change at r given by

* Work supported by the U.S. Atomic Energy Commission.

$$\dot{A}_{FM}(r) = \frac{\partial}{\partial t}\left[\frac{1}{r}\int_{R_L}^{r} RB_o\left(\frac{R}{r_o}\right)^{-n} dR\right]$$

$$= \frac{\lambda \xi_o P_o}{2-n}\left[1 - \left(\frac{R_L}{r}\right)^{2-n}\right] \equiv \xi_o P_o \,\dot{\varkappa}, \quad (5b)$$

where the lower limit R_L reflects the deviation from an r^{-n} field at small r. We estimate that $R_L \cong 1.0$ cm.

A. Pulsed Field Compressor

A compression scheme in which the relationship between ring radius r and axial magnetic field B is specified to be $B^m r$ = constant along the compression trajectory yields the following scaling laws[1] for the beam momentum and synchrotron (a_s) and betatron (a_β, b_β) amplitudes. Let subscript i denote quantities at injection; then for compression from radius r_i to r

$$a_s = a_{s_i}\left(\frac{1-n_i}{1-n}\right)\left(\frac{r}{r_i}\right)^{\frac{1}{m}-1} \quad (6a)$$

$$a_\beta = a_{\beta_i}\left(\frac{1-n_i}{1-n}\right)^{1/4}\left(\frac{r}{r_i}\right)^{\frac{1}{2m}} \quad (6b)$$

$$b_\beta = b_{\beta_i}\left(\frac{n_i}{n}\right)^{1/4}\left(\frac{r}{r_i}\right)^{\frac{1}{2m}} \quad (6c)$$

and

$$P = P_i\left(\frac{r}{r_i}\right)^{1-\frac{1}{m}}. \quad (6d)$$

The injected electron current and the initial betatron amplitudes are taken to be those realized in the present ERA compressor at LBL.

B. Radiation in a Static Magnetic Field

The median plane symmetry of the compressor and the static field maintained in stage 2 requires, respectively, that

$$\frac{\partial}{\partial z} = -\frac{\partial}{\partial r} = 0 \text{ and } B_z = B_r = 0 \quad (7)$$

Hence from (1b)

$$z = 0,$$

and from (1a) we are left with

$$\dot{r} = \frac{\frac{\partial B_r}{\partial z}\left(\dot{A} - \frac{U_\gamma}{\beta}\right)}{\frac{\partial B_z}{\partial r} + r\left(\frac{\partial B_z}{\partial r}\right)^2}$$

$$= \left(\dot{A} - \frac{U_\gamma}{\beta}\right)\frac{-nB_z/r}{B_z(-nB_z/r) + r(-nB_z/r)^2},$$

where we have substituted the n-value, $n = -\frac{r}{B_z}\frac{\partial B_z}{\partial r}$, and employed the curl condition $\nabla \times B = 0$ to obtain $\frac{\partial B_z}{\partial r} = \frac{\partial B_r}{\partial z}$. Then

$$\dot{r} = \left(\dot{A} - \frac{U_\gamma}{\beta}\right)\frac{1}{P}\frac{r}{1-n} \quad (8b)$$

or

$$\frac{\dot{r}}{r} = \frac{1}{1-n}(\xi + \dot{A}/P) = \frac{\xi}{1-n}(1 - f).$$

The rate of change of momentum is

$$\frac{\dot{P}}{P} = \xi + \frac{\dot{A}}{P} = \xi(1 - f) \quad (9)$$

C. Radiation at Constant Ring Radius

Applying the same symmetry requirement to (1a) as before, we obtain

$$\dot{r} = \frac{-r\dot{B}_z\left(\frac{\partial B_z}{\partial r}\right) + \left(\frac{\partial B_z}{\partial r}\right)(\dot{A} + \xi P)}{B_z\left(\frac{\partial B_z}{\partial r}\right) + r\,(-nB_z/r)\left(\frac{\partial B_z}{\partial r}\right)} \quad (10)$$

or

$$\frac{\dot{r}}{r} = \frac{1}{1-n}\left[\xi + \frac{\dot{A}}{P} - \frac{\dot{B}_z}{B_z}\right].$$

The total flux change $\dot{A}$ is due to both the flux bar and the time-varying magnetic field in the ferromagnet,

$$\dot{A} = \dot{A}_{FB} + \dot{A}_{FM} = -f\xi P + \dot{\varkappa}\xi P = \xi P(-f + \dot{\varkappa}). \quad (11)$$

Noting that we have defined λ such that $\frac{\dot{B}_z}{B_z} = \lambda\xi$,

$$\frac{\dot{r}}{r} = \frac{\xi}{1-n}\{1 - f + \dot{\varkappa} - \lambda\}, \quad (12)$$

which is zero as desired if

$$\lambda = \frac{(1-f)(2-n)}{(2-n) - \left[1 - \left(\frac{R_L}{r}\right)^{2-n}\right]} \quad (13)$$

and where we have employed the definition of $\dot{\varkappa}$ in (5b). Finally, we have in stage 3 that

$$\frac{\dot{P}}{P} = \xi + \frac{\dot{A}}{P} = \xi\{1 - f + \dot{\varkappa}\} \quad (14)$$

on the equilibrium orbit.

D. Radiation Damping of the Betatron Oscillations

The axial betatron displacement z, according to Bruck[2] (eqn. 23.8), satisfies the damped harmonic oscillator equation

$$\ddot{z} + \left[\frac{U_\gamma}{E} + \frac{\dot{E}}{E}\right]_o \dot{z} + \omega_z^2 z = 0, \quad (15)$$

where E is the total energy, U_γ the rate of energy loss, and the bracket is to be evaluated on the equilibrium orbit. The amplitude of these oscillations damps as

$$b_\beta \propto \exp\left\{-\frac{1}{2}\int\left[\frac{U_\gamma}{E} + \frac{\dot{E}}{E}\right]_o dt\right\}, \quad (16a)$$

so that in the absence of radiation ($U_\gamma = 0$)

$$b_o \propto \exp\left\{-\frac{1}{2}\int \frac{\partial}{\partial t}\ln E\, dt\right\} = \frac{1}{E}. \quad (16b)$$

There is additional damping due to changes in the oscillation frequency $\omega_z^2 = \beta c \nu_z / r$, so that for $\nu_z = \sqrt{n}$ = constant

$$b_\beta \propto \frac{1}{\sqrt{\beta}}. \quad (16c)$$

Then the axial betatron amplitude has a time-dependence

$$\frac{\dot{b}_\beta}{b_\beta} = -\frac{1}{2}\left[\frac{U_\gamma}{E} + \frac{1}{B}\frac{\partial B}{\partial t}\right]_o = \frac{1}{2}\left[\xi_o - \frac{1}{B}\frac{\partial B}{\partial t}\right]. \quad (17)$$

This reduces to $\frac{\dot{b}_\beta}{b_\beta} = \frac{\xi_o}{2}$, as required in a constant field betatron ($A = 0$) with RF cavity flux compensation ($f = 1$, $a = 1$).

The radial displacement is similarly governed by the equation (Bruck 23.12)

$$\ddot{x} + \left[\frac{U_\gamma}{E} + \frac{\dot{E}}{E}\right]_o \dot{x} + \omega_x^2 x = -\ddot{x}_R , \quad (18)$$

where $\ddot{x}_R$ expresses the shrinkage of the orbit due to radiation and also possibly flux change acceleration. We calculate the radial acceleration in the following manner. From Bruck eqns. 23.16 and 23.17, we have

$$\dot{x}_R = -\frac{1}{1-n}\frac{r_o}{P_o}\left[\dot{P}\left(1 + \frac{x}{r_o}\right) - \dot{P}_o\right] , \quad (19)$$

where P and P_o are the rates of momentum loss on, respectively, a betatron excursion of amount x and the equilibrium orbit. The above expression gives the radial velocity due to the differential-rates of azimuthal momentum loss. Since $\dot{P}_o = P_o\xi_o$, P and $\dot{P}_o$ are for small excursions from the equilibrium orbit

$$\dot{P} = \xi_o P_o\left(1 - 2n\frac{x}{r_o}\right) - f\xi_o P_o\left(1 - a\frac{x}{r_o}\right) + \varkappa\xi_o P_o\left[1 + (1-n)\frac{x}{r_o}\right]$$

$$= \xi_o P_o\left[(1 - f + \varkappa) + (-2n + fa + \lambda(1-n))\frac{x}{r_o}\right] \quad (20a)$$

and

$$\dot{P}_o = \xi_o P_o[1 - f + \varkappa]. \quad (20b)$$

Substitution into (19) yields

$$\dot{x}_R = \xi_o\left[\frac{(1 - f + \varkappa) - 2n + fa + \lambda(1-n)}{1-n}\right]x, \quad (21)$$

where the entire bracket is a constant so that $\ddot{x}_R \propto x$. Finally the radial equation becomes

$$\ddot{x} + \left[\frac{U_\gamma}{E} - \frac{U_\gamma}{E}\left\{\frac{(1-f+\varkappa) - 2n + f\alpha + \lambda(1-n)}{1-n}\right\} + \frac{\dot{E}}{E}\right]\dot{x} + \omega_x^2 x = 0. \quad (22)$$

Hence the damping rate for the radial betatron amplitude is

$$\frac{\dot{a}_\beta}{a_\beta} = \frac{1}{2}\left[\xi_o\left\{\frac{f(1-\alpha) - 2\varkappa + (1+\varkappa)n}{1-n}\right\} - \frac{1}{B}\frac{\partial B}{\partial t}\right], \quad (23)$$

which reduces to

$$\frac{\dot{a}_\beta}{a_\beta} = \frac{\xi_o}{2}\frac{n}{1-n}$$

as required for the usual betatron with RF cavity ($f = 1$, $a = 1$) in a static magnetic field ($\lambda = 0$).

E. Radiation Damping of the Momentum Spread in the Beam

Consider an electron on the equilibrium orbit r_o with momentum P_o. An achromatic electron of momentum P has an equilibrium orbit at

$$r = r_o\left[1 + \frac{1}{1-n}\frac{\Delta P}{P}\right] = r_o\left[1 + \frac{1}{1-n}\left(\frac{P-P_o}{P}\right)\right]. \quad (24)$$

The rate of change of momentum spread is just

$$\frac{\partial}{\partial t}\left(\frac{\Delta P}{P}\right) = \frac{P}{P_o}\left[\frac{\dot{P}}{P} - \frac{\dot{P}_o}{P_o}\right] ,$$

where

$$\frac{\dot{P}}{P} = -\frac{C_\gamma}{\beta}\frac{P^3}{r^2} + \frac{\dot{A}(r)}{P}$$

$$= \xi_o\left[(1-f+\varkappa) + \left(\frac{1-3n}{1-n} - \frac{1}{\gamma^2} + \frac{f\alpha}{1-n} + f\right)\frac{\Delta P}{P}\right]$$

and

$$\frac{\dot{P}_o}{P_o} = -\frac{C_\gamma}{\beta_o}\frac{P_o^3}{r_o^2} + \frac{\dot{A}(r_o)}{P_o} = \xi_o[1-f+\varkappa] .$$

Hence (defining $\varepsilon \equiv \Delta P/P$) the damping rate for momentum spread is

$$\frac{\dot{\varepsilon}}{\varepsilon} = \xi_o\left[\frac{(1+f(\alpha+1)) - (3+f)n}{1-n} - \frac{1}{\gamma^2}\right]$$

Quantum fluctuations are negligible in our domain of interest. The time-dependence of the synchrotron amplitude in a constant n field is

$$\frac{\dot{a}_s}{a_s} = \frac{\dot{r}}{r} + \frac{\dot{\varepsilon}}{\varepsilon} .$$

For the usual betatron case ($f = 1$, $\alpha = 1$, $\lambda = 0$), we obtain

$$\frac{\dot{a}_s}{a_s} \equiv \xi_o\frac{3-4n}{1-n} ,$$

which is twice the rate in a betatron. Our case, however, differs from a betatron in that the electron trajectory is the envelope, rather than an oscillatory trajectory within the envelope. The usual sum rule for radiation damping rates does not maintain in the present case.

F. Longitudinal (Negative-mass) Instability

The number of circulating electrons allowed for longitudinal stability has been calculated by L.J. Laslett *to* be

$$N_e < 1.57 \times 10^{12}\,\gamma(1-n)\frac{s}{\Delta R} , \quad (28)$$

where $\gamma = E/m_e c^2$ for the electrons and ΔR_M is the axial displacement of electric side plates about the beam. We have chosen $\Delta R_M = 2b_\beta$ at injection, and taper the side-plates according to

$$\Delta R_M \propto \frac{1}{\sqrt{B}} \propto r^{n/2}. \quad (29)$$

As previously stated, we have chosen the energy spread of the injected beam so that the quantity of eqn. (28) is just larger than the brilliance limit of the injector. A smaller value of (28) at any time will limit the number of circulating electrons whereas a larger value of (28) implies an unnecessarily large value of a_s and a consequent reduction in electron density. The most favorable circumstance is where the limit (28) always remains slightly larger than the number injected. The conditions under which the limit (28) is constant are straightforward to obtain in a constant n field. In stage 2, $N_e \propto \gamma a_s^2/\Delta R_M \propto p^{3/2} r^{3/2}\varepsilon^2$, so that

$$\frac{\dot{N}_e}{N_e} = \frac{3}{2}\left[\frac{\dot{p}}{p} + \frac{\dot{r}}{r}\right] + 2\frac{\dot{\varepsilon}}{\varepsilon}$$

$$= \frac{\xi}{2(1-n)}\left[\begin{matrix}(10+f(4\alpha-2) - 4/\gamma^2) \\ -(15+f-4/\gamma^2)n\end{matrix}\right], \quad (31)$$

using (8), (9), and (26).

Then the number of circulating electrons allowed for longitudinal stability is constant if n is a "critical value",

$$n_c = \frac{10 + f(4\alpha-2) - 4/\gamma^2}{15 + f - 4/\gamma^2} \quad \text{tage 2)}, \quad (32)$$

which reduces to $n_c = 2/3$ in the absence of a flux bar and for γ large. Similarly for stage 3, $N_e \propto \gamma a_s^2 \propto P\varepsilon^2$ and

$$\frac{\dot{N}_e}{N_e} = \frac{\dot{p}}{p} + 2\frac{\dot{\varepsilon}}{\varepsilon}$$

$$= (1 - f + \pi) + 2\left[\frac{1 + f(\alpha+1) - (3+f)n}{1-n} - \frac{1}{n}\right] \quad (33)$$

The stage 3 condition that r = constant requires that we take

$$\pi = \frac{(1-f)\left[1 - \left(\frac{R_L}{r}\right)^{2-n}\right]}{(2-n) - \left[1 - \left(\frac{R_L}{r}\right)^{2-n}\right]}. \quad (34)$$

The resulting equation for n_c is complicated if $R_L \neq 0$ and $f \neq 1$. The critical n-value in stage 3 ranges from $n_c = 3/4$ (f=1) down to $n_c \cong 0.48$ (f = 0, R_L = 1.5 un). Figure 1 displays the dependence of n_c on the strength of the flux bar, f, during stages 2 and 3.

G. Compressor Design

The above solutions have been employed to calculate the perfoimance expected of an electron ring device with the intent of maximizing the density-time product

$$\int_0^1 \frac{N_e}{\text{Volume}}\, dt = \text{figure-of-merit (FM)},$$

where the volume is calculated from the ring parameters as

$$\text{Volume} = 2\pi^2\, r b_\beta \sqrt{a_s^2 + a_\beta^2}.$$

It will be convenient, and probably necessary in an operational device, to maintain a constant n-value at the orbit radius everywhere during stages 2 and 3. The ring will then never cross a betatron resonance line (where the growth rates are much larger than the typical rates of change $\sim\xi$ in this device), and the rates of change (31) or (33) of the longitudinal stability limit can be kept very near zero for the duration of the stage by an appropriate choice of f.

Two cases have been considered: case A without use of a flux bar, and case B with a flux bar. A case without a flux bar is attractive experimentally due to its simplicity. In regard to case A, it is evident from Figure 1 that if f = 0 at all times, one cannot have the rate (31) zero in stage 2 and the rate (33) zero in stage 3 without the ring crossing a single particle resonance at n = 0.64. Hence we choose a case A with only stages 1 and 3, and an n-value everywhere constant and equal to $n_c = 0.526$ (for the choice R_L = 0.75cm). Results of this calculation are tabulated in Table I and displayed in Figure 2. The figure-of-merit for this case is 2.59×10^{12} e⁻sec/cm³.

A case employing a flux bar during stage 3 only, if it is to maintain the rate (31) zero during stage 2, must have n = 2/3 by (32). By inspection of Figure 1, this demands that f ≅ 0.625 during stage 3 so that the rate (33) is zero. This is case B, from which relevant quantities are listed in Table II and displayed in Figure 3. The figure-of-merit for case B is 3.97×10^{12} e⁻sec/cm³

Finally, there are many possible cases of interest in which a flux bar is employed during both stages 2 and 3. The operating n-value would then be chosen in the range 2/3 < n < 3/4 for this device.

References

1. Electron Ring Accelerator Proceedings, L.J. Laslett, p. 270 (1968).

2. Introduction to the Theory of Circular Particle Accelerators, H. Bruck (1966).

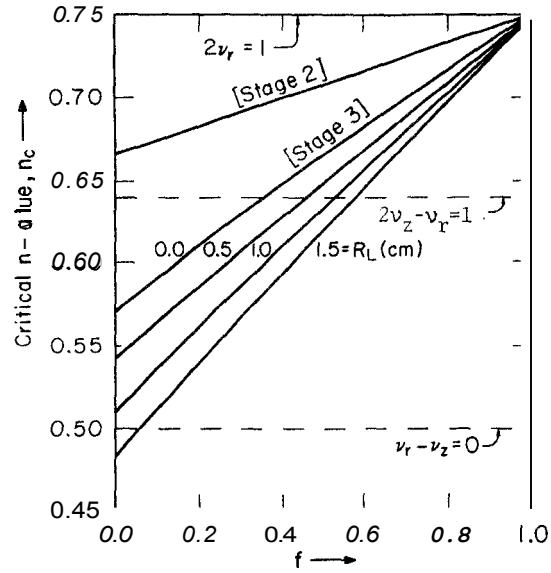


Fig. 1 - Critical n-values as function of flux bar strength, f, for stages 2 and 3. In stage 3, four choices of R_L are shown. The horizontal dotted lines are locations of prominent single particle betatron resonances.

Table I. Case A (no flux bar) $N_e = 1.04 \times 10^{12}$ electrons

	Stage 1		Stage 2	Stage 3
	Injection	End of Compression		
t(sec)	0.	.001		1.0
r(cm)	40.	3.0		3.0
B(Kg)	.0842	15.0	(none)	3.396
KE(MeV)	.621	12.96		2.586
n-value	5/9	.525		.526
a_s(cm)	1.350	.095		.200
a_β(cm)	1.495	.110		.074
b_β(cm)	1.115	.085		,029
$\frac{\Delta P}{P}$	.015	.015		.0316
$\rho(e^-/cm^3)$	6.09×10^8	1.42×10^{12}		2.80×10^{12}

Table 11. Case B(with flux bar) $N = 3.90 \times 10^{12}$ electrons

	Stage 1		Stage 2	Stage 3
	Injection	End of Compression		
t(sec)	0.	.001	.0202	1.00
r(cm)	40.	4,999	3.000	3.00
B(kg)	.167	10.678	15.009	4.978
KE(MeV)	1.553	15.50	12.997	3.995
n-value	2/3	2/3	2/3	2/3
a_s(cm)	2.100	.262	.262	.457
a_β(cm)	1.607	.201	.162	.090
b_β(cm)	1.066	.133	.103	.029
$\frac{\Delta P}{P}$	.0175	.0175	.029	.051
$\rho(e^-/cm^3)$	1.75×10^9	8.98×10^{11}	2.07×10^{12}	4.84×10^{12}

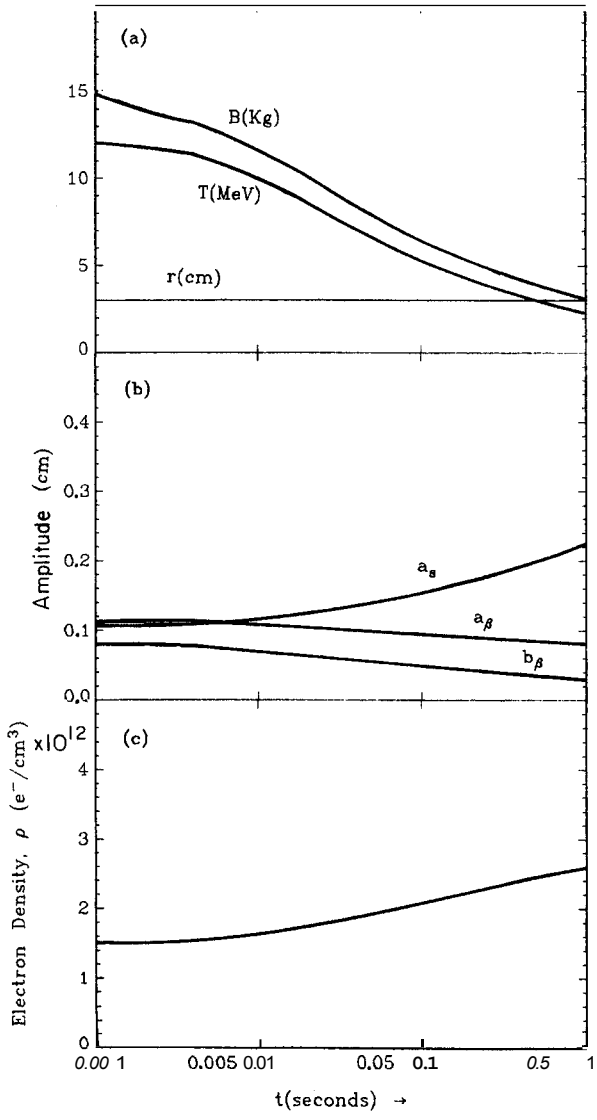


Fig. 2 - Ring parameters for Case A. (a) equilibrium orbit radius, r(cm), magnetic field at r, B(kg), and kinetic energy of electrons at r, T(MeV); (b) synchrotron, a_s, radial betatron, a_β, and axial betatron, b_β, amplitudes; and (c) electron density as function of time. The figure-of-merit for this case is $\cong 2.59 \times 10^{12}$ e⁻sec/cm³.

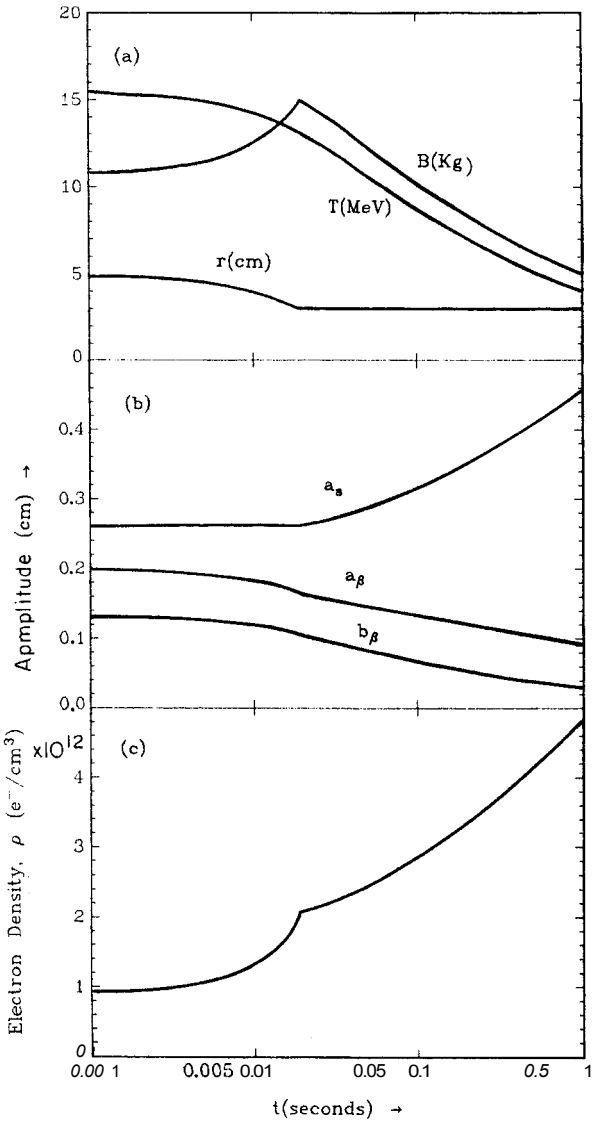


Fig. 3 - Ring parameters for Case b; the figure-of-merit is $\cong 3.97 \times 10^{12}$ e⁻sec/cm³.

SELF-CONSISTENT EQUILIBRIA OF ACCELERATED RELATIVISTIC ELECTRON RINGS

I.Hofmann
Max Planck-Institut fiir Plasmaphysik+
Garching bei München/BRD

Summary

A self-consistent model and numerical code for a relativistic electron ring loaded with ions was developed, using realistic distribution functions for adiabatically changing equilibria.. The main result is that in an ion-focussed ring the "holding power" $e\mathcal{E}_R$ is only about 20% *of* the ring peak electric field, whereas an additional electric image cylinder ("squirrel cage") allows ion acceleration up to 80% of the peak electric field.

A. Introduction

Collective ion acceleration by the strong electric fields in a ring of relativistic electrons has been the subject *of* many investigations in the past few years.

In order to establish performance characteristics for an electron ring accelerator (ERA), one has to consider instability problems as well as the equilibrium state. Instabilities turned out to impose severe limits on the effectiveness of ion acceleration [1]. The study of equilibrium is not only the starting point for instability investigations, but is also necessary for the basic question of the "holding power", which will be treated in this paper. Equilibrium models have been used in the past which often showed a substantial lack of self-consistency from the point of view of the Vlasov equation. Most of the theoretical work has been done along the following lines:
1. self-consistent particle codes'; with present-day computers they are restricted to short physical times and thus inappropriate for adiabatically changing equilibria.
2. virial theorems and macroscopic fluid models[2,3,4].
3. models based on the Vlasov equation; simple models *for* rings at rest use uniform densities and harmonic betatron oscillations[5,6,7] while others study nonuniform density effects without being self-consistent[8,9], or calculate realistic ion distribution functions for uniform electron density[10], whereas accelerated equilibria are treated numerically employing microcanonical distribution functions and approximating ring cross-sections by ellipses[11].

The present paper is free from the simplifications of the above-mentioned models and gives numerical solutions of accelerated ring equilibria that are self-consistent within the framework of the Vlasov-Maxwell equations. In particular, it uses physically relevant distribution functions for either particle species and takes into account their time-dependence by means *of* appropriate adiabatic invariants.

+This work was performed under the terms of the agreement on association between the Max Planck Institut fiir Plasmaphysik and EURATOM

B. Stationary Vlasov Equilibria for an Electron Ring with Ions

I. Basic Equations

For axisymmetric fields the electron motion is governed by the relativistic Hamiltonian in cylindrical coordinates

$$H_e=(m_0^2c^4+c^2\underline{p}^2)^{1/2}-e\phi(r,z)\quad,\quad \frac{\partial H_e}{\partial\theta}=0$$

with (1)

$$\underline{p}=\{p_r,p_z,p_\theta\}\quad,\quad p_\theta=\frac{P_\theta}{r}+\frac{e}{c}A_\theta(r,z)\quad,\quad P_\theta=0$$

and particle velocities $\underline{v}=\underline{p}/m_0\gamma$, $\gamma^2=(1-\underline{v}^2)^{-1}$
A_θ is the only non-vanishing component of the vector potential and ϕ the scalar potential, including self-fields $A_\theta=A_\theta^{ext}+A_\theta^s$, $\phi=\phi^s$
Ion motion is prescribed by the nonrelativistic Hamiltonian

$$H_i=\underline{p}^2/2m_i+e\phi(r,z)\qquad(2)$$

where magnetic field effects are neglected and $p_\theta\equiv 0$.
Distribution functions $f_{e,i}(r,z,p_r,p_z,p_\theta)$ satisfy the steady-state Vlasov equation

$$d/dt\,f_{e,i}=0\qquad(3)$$

solved with A_θ^s, ϕ^s self-consistently calculated from the equations

$$\partial/\partial r\left(r^{-1}\partial/\partial r(rA_\theta^s)\right)+\partial^2/\partial z^2\,A_\theta^s=\frac{4\pi}{c}j_\theta\qquad(4)$$

$$r^{-1}\partial/\partial r\left(r\,\partial/\partial r\,\phi^s\right)+\partial^2/\partial z^2\,\phi^s=4\pi e(n_e-n_i)$$

with

$$n_{e,i}=(2\pi r)^{-1}\int d^3p\,f_{e,i}\quad\text{and}\quad j_\theta=e\,n_e\,v_{\theta_0}\equiv\int d^3p\,v_\theta f_e$$

Hence we obtain two coupled nonlinear integro-differential equation?

$$L^*A_\theta^s=J(A_\theta^s,\phi^s)\quad,\quad L\phi=Q(\phi^s,A_\theta^s)\qquad(4^+)$$

with appropriate boundary conditions to be imposed at infinity or on finite conductors.

11. Exact Stationary Distribution Functions

To determine the $f_{e,i}$ a knowledge of constants of motion is most useful since an arbitrary (differentiable) function of them solves (3). In the stationary case the total energy $H_{e,i}$ and, for electrons, P_θ are constants that allow for a class of exact solutions of (3) which can be written as

$$f_e=f_{e\perp}(H_e)\,g(P_\theta)\qquad(5)$$

$$f_i=f_i(H_i)\qquad(6)$$

where $g(P_\theta)$ prescribes the momentum spread of the electrons, and $f_{e\perp}$ is typically Gaussian-like for an ER, in contrast with other papers [7,11] where a δ-function leading to a uniform density inside a sharp boundary was chosen.

Whether distribution functions (5), (6) are sufficiently general for an ER is a question of basic importance. In fact, it seems impossible in general to give explicitly an additional exact constant of motion comparable to the energy. Certain approximations are possible, however, which can be discussed more transparently in a model where transverse (r,z) and longitudinal (θ) energies are decoupled.

III. Decoupling of Transverse and Longitudinal Energies

For a given value of P_θ an equilibrium radius $R(P_\theta)$ and corresponding minimum energy $E_{e\,min}(P_\theta)$ are given for electrons according to the

following variational principle:

$$\delta_{p_r=p_z=0,\ r,z} \left(H_e(r,z,p_r,p_z,p_\theta) = 0 \right) \qquad (7)$$

Since in ER applications the "transverse" energy $E_e - E_\parallel$ is nonrelativistic, we may expand the square root in (1) to obtain a transverse Hamiltonian $\mathcal{H}$ with nonrelativistic features. We define a zero-order (i.e. neglecting self-fields) equilibrium radius R_0 and minimum energy $E_{e\min_0}$ for which we obtain from (7) (for B_z^{ext} symmetric in r):

$$\partial/\partial r\, P_\theta^2 = 2P_\theta\left(-P_\theta/R^2 + e/c\, \partial A_\theta^{ext}/\partial R\right) = 0\ , \quad E_{e\min_0} = \left(m_0^2c^4 + c^2\left(\frac{P_\theta}{R_0} + \frac{e}{c}A_\theta^{ext}(R_0)\right)^2\right)^{1/2}$$

The desired expansion to first order is

$$H_e = \left(m_0^2c^4 + 2c^2P_{\theta_0}\,\delta\left(P_\theta + e(A_\theta^s + A_\theta^{ext})\right) + c^2(P_r^2 + P_z^2)\right)^{1/2} - e\Phi^s$$

$$= m_0^2\gamma_0c^2 + (P_r^2 + P_z^2)/2m_0\gamma_0 + v_{\theta_0}\left(\left(P_\theta/R^2 + e/c\,\partial A_\theta^{ext}/\partial r\right)_0 \delta r + e/c\,\partial^2 A_\theta^{ext}/\partial z^2\, z\right) + e/c\,(A_\theta^s)_0 - e\Phi^s$$

with $\gamma_0 \equiv E_{e\min_0}/m_0c^2$, $v_{\theta_0} \equiv P_{\theta_0}/m_0\gamma_0$, $P_{\theta_0} \equiv P_\theta/R_0 + e/c\, A_\theta^{ext}(R_0,0)$ and $v_{\theta_0}^2 = 1 - 1/\gamma_0^2$ where it is assumed that higher variations of P_θ than second order are negligible compared with self-field variations. Thus, we find with $n \equiv -R/B_z^{ext}\cdot \partial/\partial R\, B_z^{ext}/_{R=R_0}$, $x = \delta r$, $z = \delta z$:

$$H_{e\perp} = \frac{P_r^2 + P_z^2}{2m_0\gamma_0} + \frac{m_0\gamma_0v_{\theta_0}^2}{2R_0^2}\left((1-n)x^2 + nz^2\right) + \frac{e}{c}v_{\theta_0}A_\theta^s - e\Phi_0^s \qquad (8)$$

IV. Approximate Solutions for Distribution Functions of a More General Nature

The exact solutions (5), (6) expressed in $H_{e\perp}$, H_i prescribe densities in $(x, p_x, t p_z)$-phase space uniform on surfaces of constant energy. Let us consider an ensemble of phase points uniformly distributed on the surface $H = E_0$. Let us now assume a change in the external field B^{ext} which deforms the energy surface. Clearly, a rapid change in B^{ext} may lead to nonstationary phase space flow. The considered ensemble then lies in general on a fluctuating surface different from any energy surface. Filamentation may lead after sufficiently long time to an effective stationary phase space distribution, which one can determine in general only by following the particle trajectories.

Next, let us consider a change $B^{ext}(0) \to B^{ext}(\tau)$ which is slow (τ the slowly varying time) compared with the short oscillation times of the system such that the instantaneous distribution is free from short-time fluctuations. Two situations are of interest at the time τ

(I): the original ensemble $H(0) = E(0)$ is transformed into a new ensemble uniform on $H(\tau) = E(\tau)$ with $H(\tau)$ the new Hamiltonian

(II): (I) is not true

In case (I) typically ergodic behaviour is present. More recent works on ergodic theory[12, 13, 14] and computer calculations for two-dimensional particle motion[15] have shown that even in quite general situations - depending on the amount of coupling between different degrees of freedom - an energy surface is separated into invariant tori with Lebesgue measure greater than zero. There exist distribution functions nonuniform on energy surfaces. To determine them, one needs the additional invariants of the motion. Such invariants can in general be represented only in terms of asymptotic series, which were introduced in theories on adiabatic invariants relevant for confinement of particles in magnetic fields[16,17]. (A simple exception is rotational symmetry in x, z which shall be excluded here.) With increasing (nonlinear) coupling in x, z computer calculations[15] have shown that "stochastic" trajectories which wander all over the whole energy surface dominate over the ordered motion (confined to invariant sections). In this case the usual asymptotic series expansions for invariants cannot be applied. There is pronounced ergodic behaviour and case (I) appears to give the appropriate prescription of the phase space flow.

A rough estimate of the amount of nonlinear x, z-coupling in particle motion in realistic electron rings (with collective field strengths within the present limits) justifies the following treatment: 1) ions are described according to (I) with distribution functions (6) uniform on energy surfaces; 2) electron motion is weakly coupled and depends on still another invariant. The detailed form of the distribution functions will be established in the next section.

C. Adiabatically Changing Equilibria

Compression, ion loading and acceleration may be treated as slow processes compared with oscillation times of electrons and ions. The time-dependence of f_e, f_i during such adiabatic changes described by the parameter τ can be established by using adiabatic invariants in accordance with the conclusions at the end of B IV.

I. The Ion Distribution Function

According to (I) ions on a surface $H_i(0) = E(0)$ are redistributed on a new surface of $H_i(\tau)$. Because of Liouville's theorem the 4-dimensional phase space volume

$$I(E,\tau) \equiv \int_{H_i(p_x,p_z,x,z,\tau)\,\le E} dp_x\, dp_z\, dx\, dz\ , \quad \frac{dI}{d\tau} = 0 \qquad (9)$$

is invariant and permits us to determine $E(\tau)$. Hence we obtain an (adiabatically) invariant distribution function for ions (for constant ion number)

$$F_i(I)\, dI \equiv f_i\left(I(H_i,\tau)\right) dI \qquad (10)$$

which is related to (6) according to

$$F_i(I)\, dI = \int_{E \le H_i \le E + \frac{\partial E}{\partial I} dI} f_i$$

From (6) we obtain for $H_i = \frac{p_x^2 + p_z^2}{2m_i} + V_i(x,z,\tau)$

$$I(E,\tau) = 2m_i\pi \int_{E - V \ge 0} \left(E - V_i(t)\right) dx\, dz \qquad (9')$$

and

$$n_i(x,z)\, dx\, dz = 2m_i\pi \int_0^\infty F_i\left(I(T + V_i, \tau)\right) dT$$

For rest-gas ionization ions are produced with zero kinetic energy (neglecting their small azimuthal velocity) in the potential trough built up by the instantaneous electric space charge. The ionization probability is proportional to the electron density; the ionization rate α_i may be time-dependent. Hence we obtain the following differential change of the distribution function

$$\frac{\partial F_i(I,t)}{\partial t} dI = \alpha_i(t) \int_{E(I,t) \le V_i(x,z,t) \le E(I,t) + \frac{\partial E}{\partial I} dI} n_e(x,z,t)\, dx\, dz \qquad (11)$$

The integral can be transformed into a line integral along equipotential lines of V_i

The functional determinant for transformation into curvilinear coordinates V_i, σ is derived as $\partial(x,z)/\partial(V,\sigma) = |\nabla V_i|^{-1}$ and with $dV_i = \partial E/\partial I\, dI$ we find

$$\partial F_i(I,t)/\partial t = \alpha_i(t)\, \partial E(I,t)/\partial I \int \frac{n_e(x,z,t)}{|\nabla V_i|}\, d\sigma \qquad (11')$$

II. The Electron Distribution Function

To determine an invariant distribution function for electrons, we require two adiabatic inva-

riants instead of one for the ions. Taking into account nonlinear x,z -coupling, asymptotic series for the invariants should be the only correct procedure, but this is not useful for a straightforward numerical code. We therefore neglect x,z -coupling and obtain the simple separate adiabatic invariants

$$I_x(E_x,\tau) \equiv \int_{H_x \le E_x} dp_x\,dx \quad , \quad I_z(E_z,\tau) \equiv \int_{H_z \le E_z} dp_z\,dz \qquad (12)$$

with $H_{e\perp}(p_x,p_z,x,z,\tau) = H_x(p_x,x,\tau) + H_z(p_z,z,\tau)$

A better approximation could be obtained by using the scaling law for radial and axial betatron oscillations: $\nu_x/\nu_z \gg 1$, which is valid for the present experiments. In this case the radial phase space volume I_x is again an invariant. The second invariant follows from the z-motion averaged over rapid oscillations due to the coupling with x.

With (12) the invariant distribution function can be written as

$$F_e(I_x,I_z)\,dI_x\,dI_z \equiv F_{e\perp}\big(I_x(H_x,\tau),I_z(H_z,\tau)\big)\,dI_x\,dI_z \qquad (13)$$

and the density (apart from integration over p_θ) is $n_e(x,z)\,dx\,dz = \int F_{e\perp}(I_x,I_z)\,dp_x\,dp_z$

III. Polarization and Particle Loss During Acceleration

When an accelerating B_r^{ext} or E_z^{ext} field is applied, forces acting on ions and electrons tend to polarize the ring in the z-direction. For sufficiently high acceleration particles evaporate from the ring as a result of the decreasing axial focussing. This results in a truncation of the distribution function (10) or (13) at a limiting value of I or I_x corresponding to the energy where the potential has a pass.

For magnetic acceleration we have in a coordinate system moving with the ring

$$\bar{H}_{e\perp} \equiv H_{e\perp} + (e\,v_{e0}/c\;B_r^{ext} - m_e\gamma_0 b)z = H_{e\perp} + \kappa' z$$
$$\bar{H}_i \equiv H_i - m_i b z = H_i - \kappa z \qquad (14)$$

where nonrelativistic axial velocity is assumed. Force balance yields $(e\,v_{e0}/c - m_e\gamma_0 b)N_e = m_i b N_i$ and thus $\kappa' = N_i/N_e\,\kappa$, $b = e\,v_{e0}/c\;B_r^{ext}/(m_i N_i/N_e + m_e\gamma_0)$

D. Iterative Solution of the Self-Consistency Problem by a Numerical Code

For given invariant distribution functions (10), (13) the integro-differential equations (4') assume the following form, using (9') and (12)

$$\Box A_\theta^s = -\frac{2e}{c\tau}\int dp_\theta\, g(p_\theta)\, v_{e0} \int F_{e\perp}(I_x,I_z)\,dp_x\,dp_z$$
$$\Box \phi^s = \frac{2e}{\tau}\int dp_\theta\, g(p_\theta) \int F_{e\perp}(I_x,I_z)\,dp_x\,dp_z - 8\pi^2 e m_i \int F_i(\bar{I})\,d\tau \qquad (4'')$$

Self-consistent solutions for A_θ^s, ϕ^s are supposed to exist for physical reasons. Equations (4'') have to be solved taking into account possible truncation of F if there is insufficient focussing. Convergence of an iteration scheme to solve (4") depends critically on the mathematical properties of the operator defining the iteration, i.e. its eigenvalue spectrum. The following physical quantities are expected to influence convergence: number of particles to be confined, attractive or repulsive self-forces, several particle species interacting with each other, variable total particle numbers, boundary conditions. As far as the author knows, no mathematical criteria are available concerning convergence of an appropriate iteration scheme for the present coupled equations problem.

The simplest "direct" iteration was attempted in the numerical code. In most of the cases it was convergent after few ($\lesssim 5$) iteration cycles. When iteration failed relaxation was introduced which connects subsequent iteratives according to $\psi^{(n+1)} \equiv (1-\alpha)\psi^{(n)} + \alpha\,\psi^{(n+1/2)}$ ($0 < \alpha \le 1$). This "first-order relaxation" is convenient if direct iteratives oscillate about some solution.

In the present code divergence of both methods was used to indicate the nonexistence of an equilibrium solution. This is important for defining the maximum admissible accelerating force (holding power).

The numerical code has the following characteristics (details see[18]):

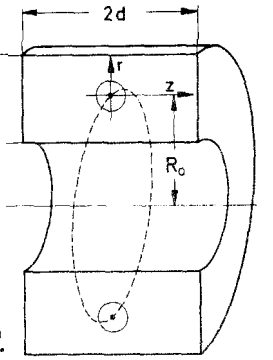


Fig.1 Geometry

1) Toroidal geometry with an infinite conductivity boundary of rectangular cross-section to solve the Poisson and vector potential equations (on a 128 x 128 grid). Different electric and magnetic boundaries were allowed for to simulate a squirrel cage, which is transparent to magnetic but not electric fields[19,20].

2) After each step of differential ion production $\Delta = \partial F_i/\partial t\,\Delta t$ (11') self-consistency is re-established according to (4").

3) At difl'erent stages of a full compression cycle, ion loading cycle and acceleration cycle the contribution of instabilities may be taken into account by increasing the occupied phase space volumes (9), (12).

E. Results

Computer runs are presented here with data adapted to the Garching ERA experiment (compressed rings): $N_e = 5\cdot10^{12}$, $R_0 = 2.3$ cm, $\gamma_0 = 27.2$, $n = 0.021$ (at the end of compression); no momentum spread for simplicity.

The electron distribution function was chosen as $F_{e\perp} \sim \exp\!\left(-I_x/\mu + I_z/I_{max}\right)\cdot\Theta(I_x/\mu + I_z - I_{max})$, with Θ the step function and $\mu = 6$ to obtain nearly circular ER cross-sections (small semi-axes $\bar{a} \approx \bar{b} \approx .3$ cm).

These initial conditions are common to all examples listed below. The ring is then loaded with ions ($f = N_i/N_e$, $0 < f \lesssim 0.05$) and afterwards studied in two different surrounding structures (with acceleration):

a) boundary CYL; two cylinders at $r_{1,2} = R_0 \pm 1.25$ cm closed axially at $z = \pm 2.5$ cm (already present before ion loading)

b) boundary SQC; cylinder at $r_2 = R_0 - 1.25$; electric image cylinder at $r_{1e} = R_0/p_{sqc}$ ($0.6 \lesssim p_{sqc} \lesssim 0.8$), magnetic image cylinder at $r_{1m} = R_0 + 3(r_{1e} - R_0)$. p_{sqc} is a measure of the focussing strength of the "squirrel cage" simulated hereby.

Table 1 shows characteristic ring data for the unloaded ER and loaded rings in CYL and SQC

(for $n = 0$, no accel.). $2\bar{a}$, 26 axial and radial electron ring width at half maximum density; $e\mathcal{E}_{z\,peak}$, $e\mathcal{E}_{z\,edge\ ions}$ peak electric field and the electric field at the edge of the ion subring that are produced by electron space charge; $\Delta_e \nu_z^2$ self-field contribution to squared axial tune of the electrons (including toroidal and image effects); N_e/N_{e0} confined electrons as fraction of originally ($n=.021$) present electrons.

Conclusion

1) Inhomogeneous electron and ion densities.

Fig.2-4 show that the half-width of the density profiles of the ions is a factor 2 smaller than that of the electrons.

2) Toroidal effects.

In relativistic electron rings an axial defocussing force occurs5 which is usually much stronger than the $1/\gamma^2$ -repulsion of straight beams. Table 1 shows that without a squirrel cage an $f \gtrsim 0.5$ (Ex. ②) is necessary to keep all electrons confined (at $n = 0$, zero accel.).

3) "Squirrel Cage" focussing.

With a SQC the electron contribution $\Delta_e \nu_z^2$ can be made positive, which guarantees axial focussing of the electrons independent of the ion loading fraction (f), provided that p_{sqc} is larger than0.65 (Table 1).

4) Acceleration and "holding power".

We define the maximum "holding power" here as the highest admissible accelerating force κ (acting on the ions, see (14)) at which at least a residue of ions remains trapped in the ring. On acceleration an electron-ion ring is polarized, as a result of which the axial focussing of either particle species is reduced.

Two principal situations can then be distinguished:

a) Insufficient image focussing if the electron self-field contribution $\Delta_e \nu_z^2$ is nearly zero or negative (for very small f) as in ex. ②-④ and with the weak SQC in ex. ⑫, ⑬. In this case electrons are gradually lost from the ring with increasing acceleration until complete ring disintegration and spontaneous loss of all ions (Fig.7). Without SQC nearly no acceleration is possible for $f = .0175$. The maximum "holding power" is typically $\lesssim 25\%$ of the peak electric field $e\mathcal{E}_{z\,peak}$.

b) Dominant image (SQC) focussing is present if $\Delta_e \nu_z^2$ is sufficiently positive as in ex. ⑥-⑪, where electrons are well-focussed even for very small f. In this case ions are gradually lost from the ring above a threshold acceleration (≈ 7.5 MeV/m). The maximum "holding power" is about 75% of $e\mathcal{E}_{z\,peak}$ (Fig.7).

Acknowledgements

The author is indebted to Prof. A. Schlüter and Dr. P. Merkel for discussions and to E. Springmann for computer programming.

Bibliography

1 J.P.Boris, R.Lee, NRL-Rep.2284(1971)
2 W.H.Kegel,Plasma Physics 12,105(1969)
3 S.Yoshikawa,Princeton-MATT-816(1972)
4 P.Merkel,MPI f.Plasmaphysik IPP 0/18 (1973)
5 L.J.Laslett, LRL Berkeley, ERAN 30(1969)
6 W.A.Perkins, LRL Berkeley, ERAN 97(1970)
7 R.C.Davidson.J.D.Lawson, Univ.of Maryland-Rep.204P029(1972)
8 L.J.Laslett, Symp.on Electr.Ring Accel.ERA19
9 C.Bovet, LRL Berkeley, ERAN 88 (1970)
10 A.A.Drozdovskii,Rep.ITEF-10,Moscow(1973)
11 N.Y.Kazarinov,E.A.Perelshtein, Symp.on Coll. Meth.of Acceleration, Dubna(1972)
12 V.I.Arnold,in V.I.Arnold a.A.Avez,Problèmes Ergodiques de la Mécan.Classique,Paris(1967)
13 J.Moser,Nachr.Akad.Wiss.Göttingen 1,1(1962)
14 A.N.Kolmogorov,in R.Abraham, Found.of Mechan. App.D, New York(1967)
15 M.Hénon,C.Heiles, Astron.J.69, 73(1964)
16 M.Kruskal, J.Math.Phys.3,806(1962)
17 B.McNamara,K.J.Whiteman,J.Math.Phys.8,2029 (1967)
18 I.Hofmann, IPP 0/21 (1974)
19 G.V.Dolbilov et.al.,JINR-P9-4737,Dubna(1969)
20 I.Hofmann, IPP 0/16 (1973)

Figures

(list of examples see Table 1)

Fig.
1 Electron density profiles, ex. ① (densities with maximum normalized to 1)
2 Electron a.ion (dashed) dens.prof. ex. ②
3 Electron a.ion (dashed) dens.prof. ex. ④
4 Electron a.ion (dashed) dens.prof. ex. ⑧,⑨
5 Axial potent.f.electr.a.ions(dashed)ex.②④
6 Axial potent.f.electr.a.ions(dashed)ex.⑧⑨
7 N_e/N_{e0} or N_i/N_{i0} (fraction of confined particl. to originally-before roll out-pres.particl.) as function of accelerating force. The left-side curves show examples with prevalent electron loss ($N_e/N_{e0} \to 0$; insufficient image focussing), the right-side curves prevalent ion loss ($N_i/N_{i0} \to 0$; dominant image focussing). The hatched regions cover $0.001 \leq f \leq .025$. The dotted appendices indicate (numerical) ring disintegration.
8 Density plots for electrons and ions in (x,z)-cross-sections, for ex.③,⑧,⑨: a)before ion loading ($n=0.021$, $R_0 = 2.3$ cm); b) loaded ring at $n=0.005$; accelerated rings. The plots show lines of constant density $n_e(x,z)$ and $n_i(x,z)$ with uniform level difference Δn. The ion subring is thinner than the electron ring and slightly shifted to smaller radius.

Table 1

	f	bound.	$\bar{a}$ [cm]	$\bar{b}$[cm]	$e\mathcal{E}_{z\,peak}$	$e\mathcal{E}_{z\,edge\ ions}$ [MeV/m]	$\Delta_e \nu_z^2$	N_e/N_{e0}
ex.①	before ion loading $n=.021$		.32	.29	24	–	-.0067	1
ex.②	.05	CYL	.23	.30	22	22	-.0069	.97
ex.③	.025	"	.25	.30	15	15	-.0047	.66
ex.④	.0175	"	.23	.31	12	9	-.0036	.51
ex.⑥	.025	p_{sqc}=.8	.25	.29	25	23	.026	1
ex.⑦	.001	"	.29	.29	24	22	.025	1
ex.⑧	.025	p_{sqc}=.7	.30	.29	21	21	.0010	1
ex.⑨	.001	"	.50	.29	17	17	.0022	1
ex.⑩	.025	p_{sqc}=.65	.31	.29	19	19	-.0018	1
ex.⑪	.001	"	.70	.29	13	13	.002	1
ex.⑫	.05	p_{sqc}=.6	.20	.29	29	27	.0053	1

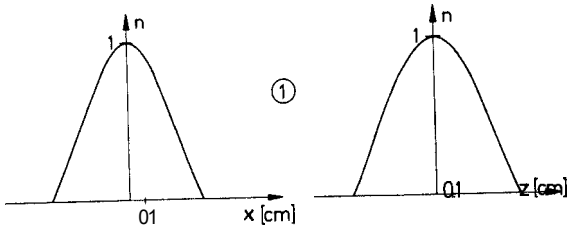


Fig.1

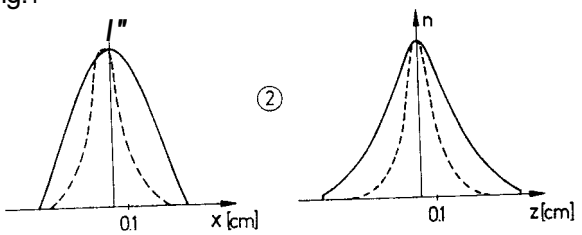


Fig 2

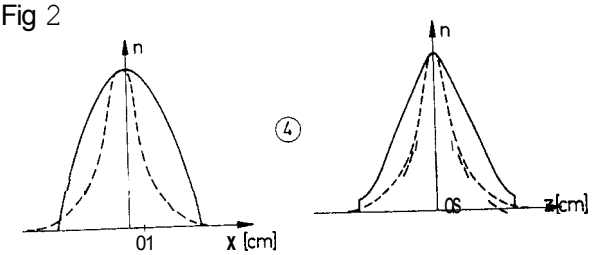


Fig.3

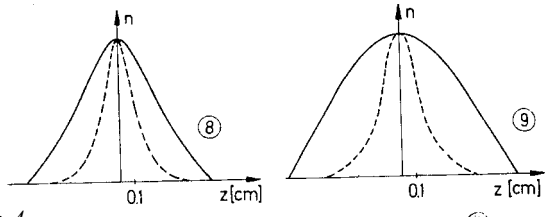


Fig.4

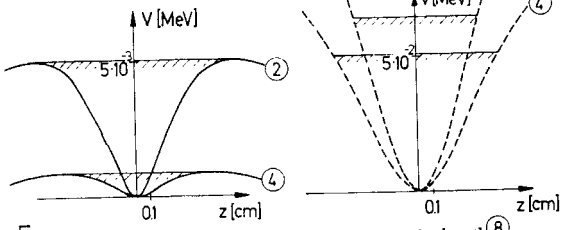


Fig. 5

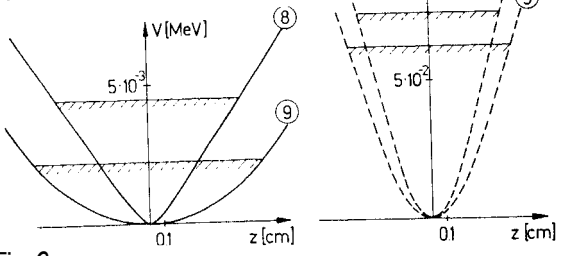


Fig.6

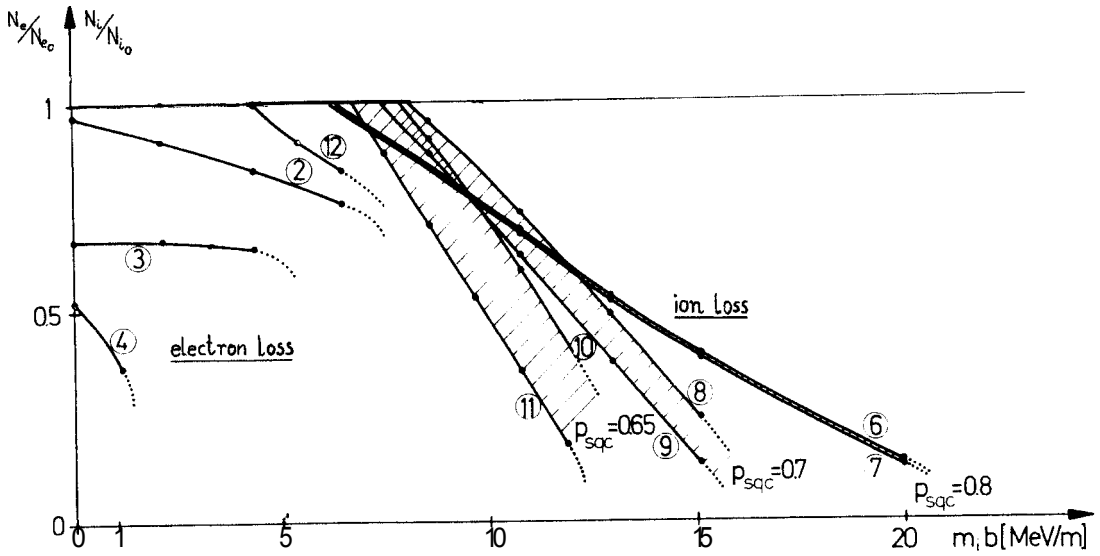


Fig 7

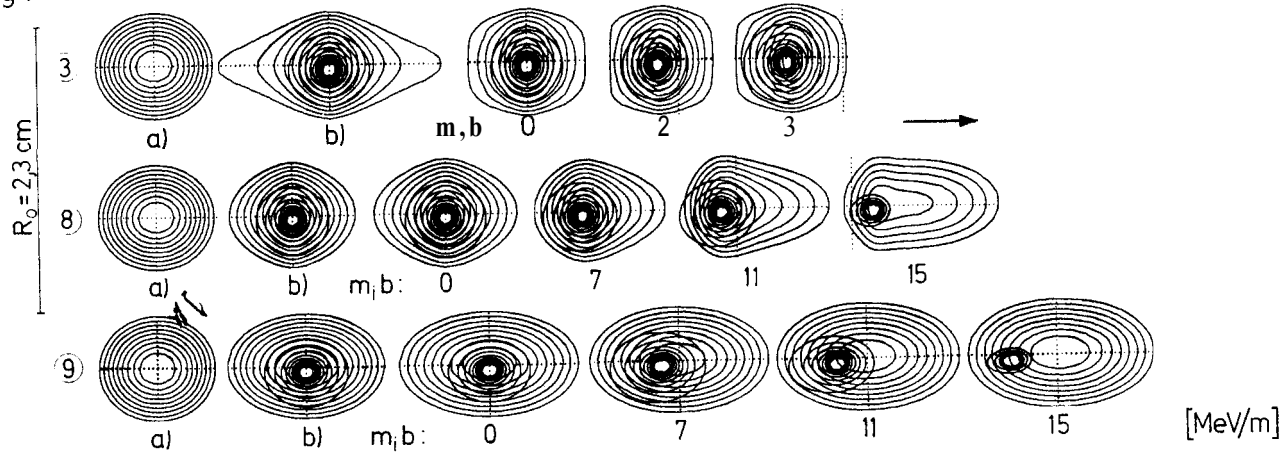


Fig. 8

REPORT ON THE ERA RESEARCH AT KARLSRUHE

C.H. Dustmann, W. Heinz, H. Krauth,
L. Steinbock, W. Zernial

Institut für Experimentelle Kernphysik, Kernforschungszentrum
und Universität, Karlsruhe, Germany

Abstract

An overall review of the experiments on ERA at Karlsruhe is given. In a first part the improvements done on the injector are reported. Maximum current in the acceptance of the electron ring compressor is about 650 A with a pulse width of 8-10 nsec. In the second part the inflection and compression experiments are described. The maximum number of electrons inflected was higher than $6 \cdot 10^{12}$. Best compressed rings contained about $3 \cdot 10^{12}$e at a radius of R = 4 cm with minor radii of about .6 cm.

I. Injector

For the generation of the electron pulse the FEBETRON 705 is used, which consists of a 160-stage Marx-generator and delivers a 2.3 MV pulse with a half-width of 50 nsec into a matched load of 400 Ω. For this pulse generator a new diode has been developed because the commercial diode had only a lifetime of some 100 pulses and did not fit the current-specifications of the ERA. In fig. 1 a cross section of the new diode is shown with the main design-principles.

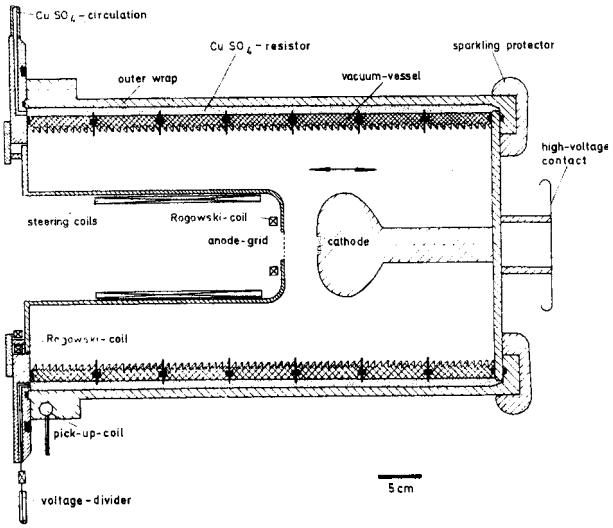


Fig. 1: Schematic drawing of the diode

1. The internal load resistance of the diode can be matched to the generator impedance by a variable CuSO4-resistor for each value of the electron current up to 6000 A.

2. The two electrode system is easily exchangeable and is dimensioned in such a way that the electrons cannot hit and damage the vacuum vessel. The cathode-anode spacing is small to reduce the space charge influence.

3. The anode is formed by a grid, made out of a 0.022 mm diameter stainless steel wire with 0.5 mm spacings. The 2 cm diameter multi-needle cathode is produced by electrolytically etching a tungsten wire system.

The investigation of the diode behaviour proved the validity of the Child's law $i \alpha U/d^2$. A plasmacloud is created at the emitting peaks because the large current density vaporizes part of the material. This cloud acts as the real electron source. Fig. 2 shows a scanning electron microscope picture of the melting zones at the tip of one of the needles after about 1000 pulses.

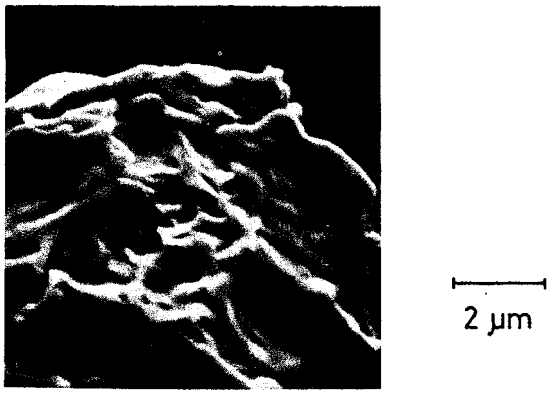


Fig. 2: Scanning electron microscope picture of a needle

The plasma smoothes the ripple of the electric field in needle region. This results in a good emittance of the beam, so that for the ERA a usable current of 650 A was obtainable in $\varepsilon = 0.05\ \pi$ cmrad. The lifetime of the diode is increased by at least one order of magnitude. The diode is now running for 9000 pulses without any failure. The instantanuous energy spread turned out to be smaller than 0.4 %. Therefore a so called resistive cathode was constructed to produce the necessary energy spread without increasing the transverse emittance. The principle idea is to put different resistors between the needles and the cathode stem to produce different potentials of the needles according to the value and the current trough the resistor. Two things have to be regarded.

1. The distance between needles of different potential must be big enough to avoid that the plasma does short circuit them.

2. There must be as many needles as possible to get a reproducible beam.

One version producing a stable energy spread of about 1 % could be operated in the compression experiments. Another cathode delivered

up to 3 %, but not yet stable. A further version is in construction from which a stable operation With 3 % is expected.

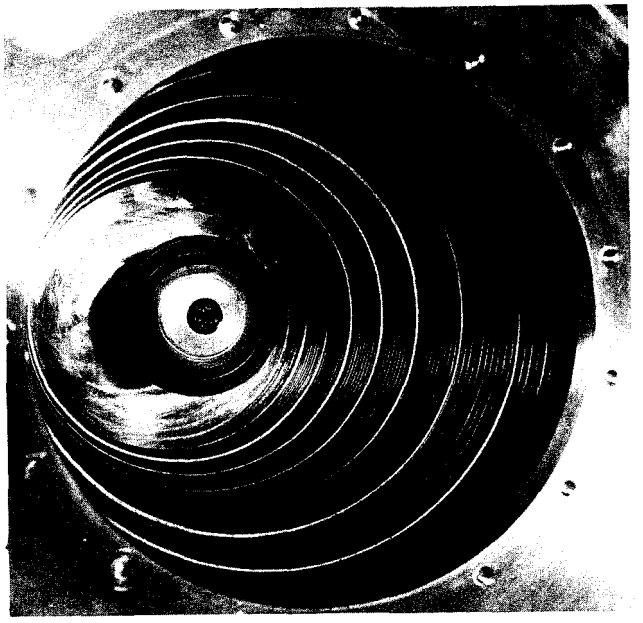


Fig. 3: View of the diode showing cathode stem and groups of needles of a resistive cathode

IT. Formation and Compression of the Electron Ring

1. Mechanical and electrical features

In fig. 4 the electron ring compressor is shown together with the injector and the beam line. The beam line consists of a focusing solenoid and a device to attenuate the bear? intensity to investigate current dependant effects without changing other beam parameters.

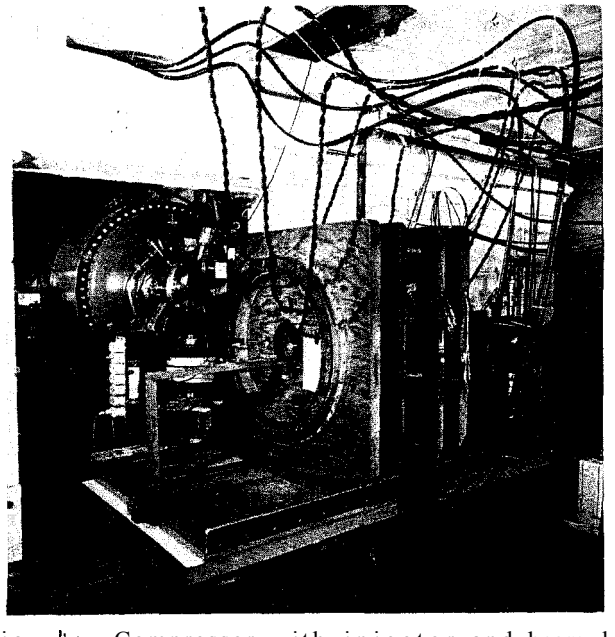


Fig. 4: Compressor with injector and beam line

a) Inflection system. The electron ring is inflected on a closed orbit in a weak focusing magnetic field by a quickly varying magnetic field distortion produced by the inflector coils. Fig. 5 shows the system in case if conducting side plates are used. In this case the inflector coil is formed by a small hole (≃ 30° in azimuthal direction) in the side plates. The inflector is fed by a cable pulse generator shown in fig. 6.

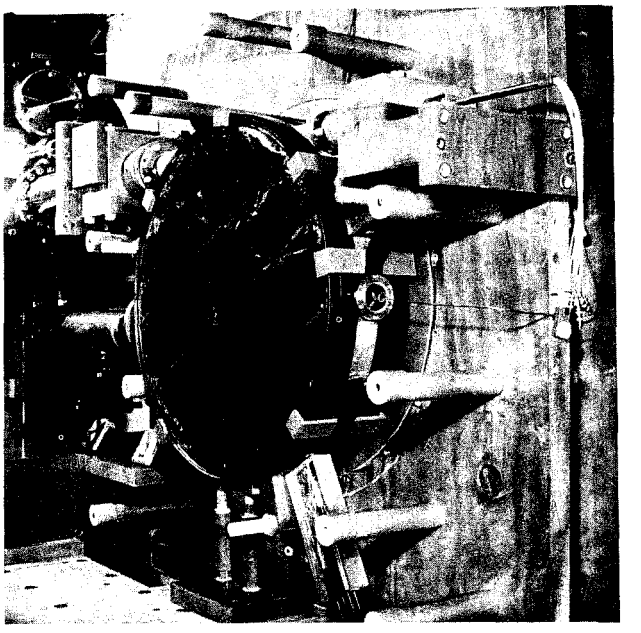


Fig. 5: Compressor, one half removed, with vacuum chamber and conducting side plates

The two spark gaps are fired simultanuously and the cables are discharged in both directions. The pulse on the right side is transformed to a high impedance by the cable transformer to get a steep current pulse at the inductivity of the inflector. Any reflection from this load is absorbed in the 8 Ω resistor.

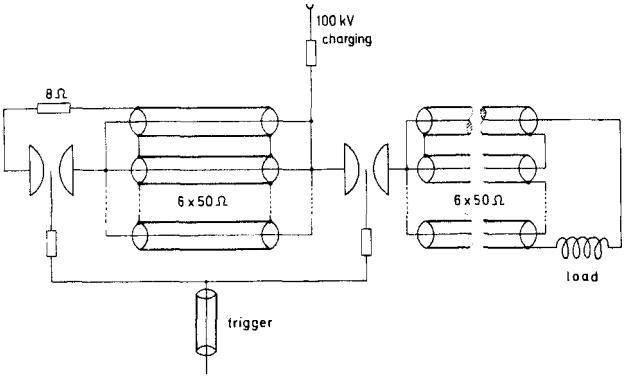


Fig. 6: Inflector circuit

The decay time of the magnetic field is about 10 nsec, the jitter is smaller than 1 nsec. At a charging voltage of 100 kV the dB/dt = 15 G/nsec. Best performance of this inflection system is found experimentally at

about 40 kV.

b) Compression system. The compressor consists of a system of 4 nested multiturn Helmholz-coils. These coils are fed by condensor banks (25-70 µF) through spark gaps at a maximum voltage of 30 kV. The current rise time in one coil is about 40-80 psec, giving a total compression time in the order of 150 psec. This medium fast timing is a compromise between the demand for fast crossing the resonances and for the virtually unimpeded penetration of the pulsed compression field through the conducting side plates. The system is flexible in the sense that the field index pattern can be changed easily by changing the timing program and by changing the axial distances of the coils.

The ring is injected with a $\gamma \simeq 5$ at a radius $R \simeq 20$ cm and can be compressed to $R \simeq 4$ cm and a $\gamma \simeq 20 - 30$.

c) Diagnostics. For the diagnostics of the electron ring mainly magnetic loops are used picking up the signals of the ring. 'Fast' and 'slow' loops are used to measure the ring current. Other loops are used to detect rf-signals emitted by the ring indicating collective instabilities. The synchrotron light is used to measure the minor ring radii in the compressed phase. In addition x-ray signals are observed to detect electron losses, sometimes in connection with a scraper to measure ring radii.

2. Beam behaviour during the first turns

Inflection experiments showed a nonlinear dependance of the inflected beam (measured about 200 nsec after injection) on the injected current above a certain limit. In addition a degradation of the beam quality was observed: The radial minor ring radius (at R ~ 20 cm) increased from 1.5 cm to 2.5 cm at high current indicating an energy loss or energy spreading. A further symptom is the amount of self inflection beginning with a few percent and going up to 2/3 at full current. In addition rf-bursts have been observed during the first hundreds of nsec.

One possible explanation of this behaviour could be a longitudinal instability. Regarding the formula for the threshold of this instability'

$$N_e \leq \frac{1}{1-n} \cdot \frac{\gamma R}{2 r_e} \frac{Z_0}{|Z_M|/M} \left(\frac{\Delta E}{E}\right)^2 \qquad (1)$$

one finds two possible cures:

1. increasing the energy spread and
2. reducing the longitudinal coupling impedance.

Because of the pulse shape of the injector the injected beam has no constant energy but a time distribution with a FWHM of about $\Delta E/E = 5$ % for the pulse width of 8 nsec. The instantanuous energy spread has been measured to be smaller than 0.4 % During the first revolutions only this instantanuous energy spread is effective. An additional energy spread must be introduced by using energy spreading foils - which reduced the usable current drastically - or by using the resistive cathodes.

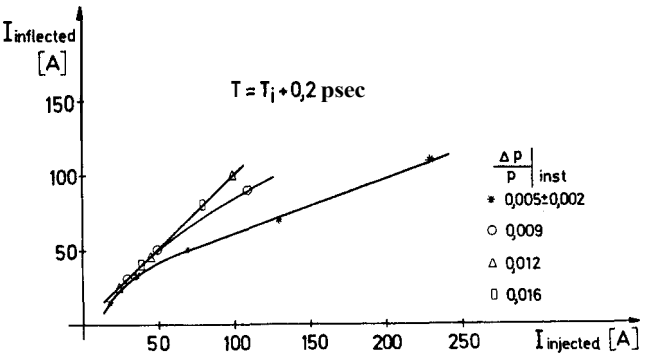


Fig. 7: Inflection in a glass chamber, H = 5 cm

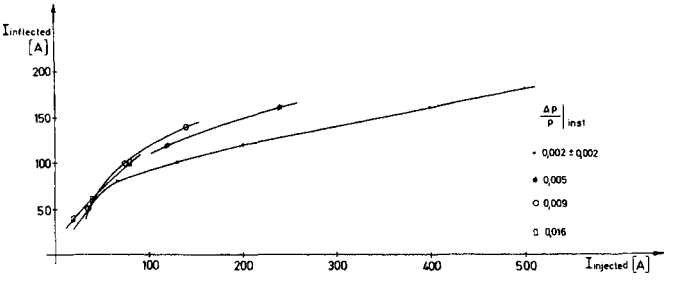


Fig. 8: Inflection in a metallic pillbox, H = 5 cm

Figures 7 and 8 show the influence of an instanuous spread on the number of electrons inflected. In both cases an influence of the energy spread can be seen, but there is no quantitative agreement with (1). The measurements of fig. 7 have been done with a vacuum chamber with glass plates of a separation H = 5 cm, this means Z is comparable to the impedance of free space. In the other case (fig. 8) a pillbox has been used consisting of a 5 µm stainless steel foil (180 mΩ per square) with the same separation of 5 cm. This should give a maximum impedance of about 30 Ω. The measured improvement is not so big as expected by (1).

The variation of the spacing between the side plates without changing the other parameters yielded a puzzling result, shown in fig. 9. It is hard to explain the increase of the inflected current at bigger spacing by a longitudinal effect. May be, that this effect is due to the increasing Q-shifts produced by image effects reducing the incoherent space charge limit and enhancing drastically the growth rate $\tau = 1/V$ of the LNS-theory of the transverse instability[2].

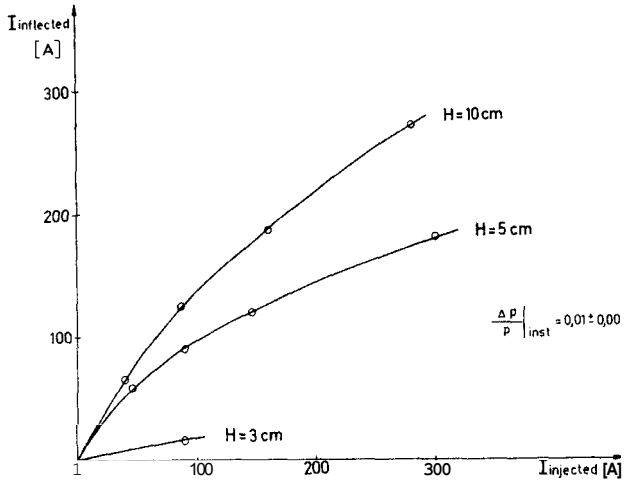


Fig. 9: Pillbox with different spacings of the side plates

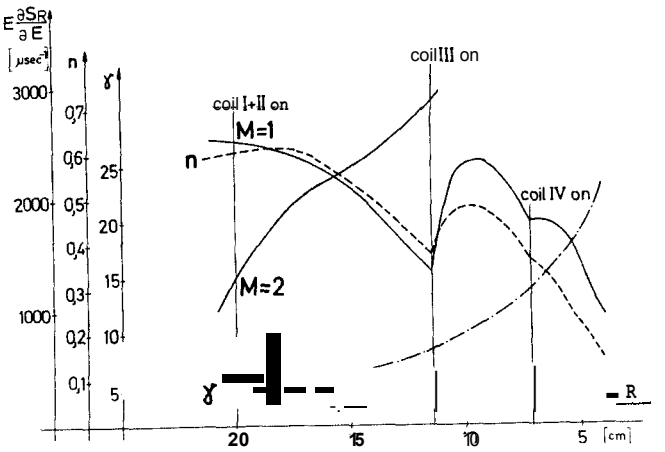


Fig. 10: Typical compression program

3. Fieldindex pattern

The stability in radial transverse direction during the compression is governed by the value of the Landau damping coefficient'

$$E\,\frac{\partial S}{\partial E} = \omega_o\left[\frac{M-\nu_r}{1-n} - \frac{R}{2}\,\frac{1}{\nu_r^3}\,\frac{\partial n}{\partial R}\right.$$

This value is kept high for all M throughout compression by having high values for both n and $\partial n/\partial r$ for a longer time and then decreasing n relatively quickly. This guarantees automatically that the resonances at n = 0.36 and n = 0.25 are crossed at small radii where the distortions of the magnetic field are very small,

By computational and experimental optimization we got the compression program shown in fig. 10. Comparing the Landau damping coefficients with the driving terms U,V for the resistive wall instability with an energy spread of 1 % a number of more than 10^{12} e should be kept stable during cornpression.

4. Parameters of the compressed ring

The experiment showed a further blow up of the ring (in axial direction) and electron losses during compression, especially at a radius R = 5.5 cm. Up to now it is not clear whether this is due to the n = 0.2 resonance or to the fact that the conducting side plates had a hole in the center at about this radius. This will be checked in the near future. At R = 4 cm the compressed rings contained a number of electrons $N_e \simeq 3\cdot10^{12}$ with minor dimensions of a ≃ b ≃ 6 mm, starting with an electron number of $6\cdot10^{12}$ after inflection.

Conclusion

The intention of the group was to demonstrate the feasibility of the ERA as an ion accelerator, as reported in previous papers[3,4] and in ref. cited there. To give a simplified idea of the quality of the compressed rings for such an application one can combine the datas given above by calculating the holding field

$$E_H[V/m] = 120\,\frac{I}{a+b}\;[A/m]$$

where I is the circulating current. The resulting value of 6 MV/m is too small by about one order of magnitude for the acceleration of ions. An improvement is expected by

1. increasing the instantanuous energy spread to a value of 3-4 % of the injected beam,
2. suppressing the blow up at R = 5.5 cm.

This will be the subject of additional experiments.

Acknowledgement

The authors wish to thank Dr. H. Kim, University of Maryland, for many helpful discussions and his continuous interest for the experiment during his sabbatical year at Karlsruhe.

References

1) L.J. Laslett, IEEE Trans. NS 20, 3 (1973) 271-275

2) L.J. Laslett, V.K. Neil, A.M. Seßler, Rev. Sci. Instr. 36 (1965) 436

3) C.H. Dustmann et al., Proc. VIII Int. Conf. on High Energy Accelerators, 408-414 (CERN, Geneva, 1971)

4) C.H. Dustmann et al., IEEE Trans. NS20, 3 (1973) 283-285

OTHER COLLECTIVE METHODS

A. A.Kolomensky

P.N.Lebedev Physical Institute, Academy of Sciences, Moscow, USSR

Summary

A review of the collective methods of particle acceleration is presented. The electron rings method (ERA) is not considered, and most of the other collective methods are reviewed very briefly. The main attention is paid to two new directions: "electron autoacceleration" and ion acceleration in a gas caused by electron beam passage. The contributed papers of this session concern just these methods.

Introduction

'Chis International Conference on Accelerators is the ninth such event, But even at the first Conference, which took place at CRRN in I956 there were already presented reports on various types of collective acceleration methods. These were the fundamental paper by V.I.Veksler /I/, and also papers by G.I.Budker /2/ and Ya.B.Fainberg /3/, which all contain in addition to the authors' ideas information on work conducting in their laboratories on collective methods. These papers stimulated further activity in this direction. To these should be added the work of H.Alfven and P.Wernholm /4/ on ion acceleration by shifting electron focus and W.H. Bennett /5/ on relaticistic self-focusing of beams, which were published earlier, but attracted special attention on this time.

Since that time many modifications and new schemes of collective acceleration have been proposed by various authors and considerable experimental and especially theoretical work has been done. The focusing and/or acceleration of particles in collective methods must be provided by electromagnetic fields created by joint (collective) action of numerous charged particles (electrons and ions) in beams or in a plasma. In creating and amplifying these fields the accelerated particles themselves can take part. The main interest in such methods is that by their means one can create very strong electric (and magnetic) fields. These fields in principle may be much higher, than in usual methods in which fields are created by charges and currents in conducting solid walls. In the latter case the discharge breakdown and field wall emission determine limits which can be considerably displaced in the case of collective fields. In addition in ordinary accelerators electric and magnetic fields in accelerating space must have divergence and curl practically equal to zero. This circumstance limits significantly the focusing and accelerating possibilities. In collective methods these limitations can be cancelled too.

The history of collective methods is not simple and straightforward with alternating periods of optimism and pessimism. Among recent achievement one can mention:

a) A good understanding level of the collective effects in accelerators and storage rings of the ordinary types.

b) Construction of a series of highcurrent pulse electron accelerators with beam energy in the range of kilojoules and higher.

c) Obtaining of intense circulating relativistic beams (in the ERA-methods).

d) Progress in plasma physics, in particular in investigation of beam-plasma interaction.

Inspite of these achievement the practical realization of collective methods is not proceeding as rapidly, as one could wish. This is due to part to certain pecularities of these methods such as complexity of the processes involved, diagnostics difficulties, cumbersomeness of injector systems, low frequency repetition rate etc. There are however also some serious difficulties of a principle physical character, the scale of which one can feel by comparison of collective and ordinary accelerators: the action of the latter is essentially disturbed because of collective effects due to fields of several orders of magnitude less than in collective methods. One of the main difficulties is perhaps the neccessity to suppress a variety of dangerous instabilities which are connected with collective interactions of electrons and ions, in themselves on the other hand useful mechanisms of acceleration.

There are many papers concerning collective acceleration methods and, as one can note, the limits of this field are to some extent indefinite. In recent times there appeared several review papers /6-I0,39/ which present the history and status quo of the subject. Therefore we shall only list the basic ideas and systems in the field without claiming to be exhaustive.

List of collective acceleration methods

I. Plasma and highcurrent electron beam (HEB) as a medium for exciting accelerating waves and fields.

A. Linac-type systems

I) Acceleration in longitudinal waves excited in plasma or beam.

a) Excitation of accelerating waves in plasma by HEB, by external RF-sources /I0/ - see below.

b) Acceleration in solitary nonlinear waves (solitons) moving in a plasma or in uncompensated electron beams (particularly in E-layer) /I0,25/.

c) Acceleration of ions by the waves excited during HEB passage through special structures or longitudinal magnetic field /I8,28,8,5I/.

d) Plasma betatron (linear) - an analog of ordinary linear betatron, but based on a runway electron phenomenon in plasma under action of longitudinal electric field /I0/.

2) Acceleration in plasma waveguides or rods analogous to linear accelerator with low losses /3,I0/.

3) Acceleration of ions in vacuum and plasma diodes /46-49,39/ - see below.

4) Acceleration of ions during passage of HEB through gas /34-4I/ - see below.

5) Autoacceleration of electrons during

passage of HEB through passive structures /28-33 8/ - see below.

6) Acceleration of ions in the focus (crossover) of the electron beam by its scanning /4,12,13/, i.e. by means of rapid displacement of the beam in a direction approximately perpendicular to the direction of electron motion.

7) Impact self-acceleration by transferring of the beam magnetic energy to beam particles /14-16/.

8) Mametic-dissipation mechanism of particles acceleration /17/ in a plasma by means of electric field created on account of a dissipation of a constant magnetic field energy.

B. Systems of the cyclic accelerator type

1) Acceleration of particles in a strong magnetic field generated in a closed-circuit high-current relativistic beam stabilized due to the presence of ions /2/. The purpose was to create a collective analog of a very strong-focusing synchrotron.

2) Plasma betatron (cyclic) based on phenomenon of runaway electrons under action of a vortical induction electric field in toroidal chamber filled with plasma /19,20/.

3) Acceleration of ions in systems of HIPAC-type /21/, containing and accelerating ions, particularly multiple charged, in a potential well of toroidal form. The well is formed by electrons drifting in the meridional plane under the action of an external, azimuthal magnetic field and self-electric field due to space charge.

11. Use of moving plasma bunches or electron beams and bunches for acceleration of particles.

A. Linac-type systems

1) Acceleration of ions captured by electron bunches, which in turn are accelerated by ordinary means (in particular ERA-method /22/).

2) hcceleration of charged or plasma bunches by a "wind" due to moving plasma or beam. In speaking about such mechanism one can not fail to recall the pioneering works of I.E.Tamm /11/ and V.I.Veksler /1/ on reversing Cherenkov and polarization losses,

3) Acceleration of charged or plasma bunches by RF-fields (radiative method of acceleration) /1,23/. The mechanism is in principle analogous to light pressure acting on a charge or oscillator, but the rigid "bunch" model appears to be too idealized and kinetic effects and instabilities play an important and dangerous role.

4) Impact method of acceleration due to collisions of bunches /1/. The simplest variant consists in using the collision of a "heavy" relativistic bunch with a "light" bunch at rest. As a result a large energy can be transmitted to ions forming a part of the light bunch. The use of compact electron rings containing some ions (as in ERA-method) may open up new perspectives for the impact method although there are serious difficulties /24,25/.

B. Systems of the cyclic accelerator type

1) Rotating "infinite" electron beam (ray) which makes the captured ions accelerate /26/. Ions slip along the beam and go over to larger radii.

2) Collective cyclic accelerator-gyrotron /8,27/. By using a rotating electromagnetic field an electron beam of close space configuration is forced to rotate as a whole. The ions are captured and experiencing a reaction of constraint increase their energy. In principle an electron beam can be used repeatedly and ion acceleration can be realized in a continuous regime.

Some of the above methods were proposed a relatively long time ago (~15-20 years), others quite recently. All are still considerably less developed than the ERA method and, as a rule, have not yet reached the construction stage. Directions which can lead in the future to the construction of effective installations are still being sought.

In the limited space available, we can not consider all methods listed, but shall deal briefly rather only wish several of them which are beeing investigated extensively (theoretically and experimentally) in recent times and arc dealt within contributed papers, presented at this conference. We shall deal, in particular with acceleration in plasma, autoacceleration of electrons, ion acceleration during passage of HEB through gas and in diodes.

Excitation of accelerating wave:: in a plasma by highcurrent electron beams

Particle acceleration by means of waves excited in a plasma by HEB or external RF-Sources is being developed for a number of years particularly in Kharkov Physical-Technical Instutute (see a series of detailed reviews /10/. The beam particles entering plasma can lose their energy rapidly due to beam-plasma interaction. In order to realize effective particle acceleration in plasma one must find methods to hinder the natural development of beam-plasma interaction, which leads to heating and anomalous plasma diffusion. One must provide conditions in which waves with regular phases and narrow frequency spectra will be excited, because only they are suitable for regular acceleration of considerable length. One can note for completeness that in turbulent plasma along with deceleration processes stochastic acceleration may occur but it can play some role only for multiply-charged ions.

The power of excited waves is determined by beam power and effectiveness of its transformation. As theoretical and experimental research for relatively low power levels of 10^7-10^9 watts have shown this effectiveness may be quite high (~tens of percent). In experiments with HEB having power of 10^{10}-10^{11} watts which began recently such high efficiency is not achieved but there is no principle prohibition in this respect.

One of the methods to increase the wave excitation effectiveness and to make spectra narrower consists in using preliminary beam modulation either by means of external RF-sources or by passive retardation systems. Several methods of stream instability control and of spectra narrowing (in particular by relatively weak signal) were checked experimentally in Kharkov.

Autoacceleration concept

For some time considerable attention has been paid to the new collective acceleration

concept - the so called autoacceleration of particles. Corresponding investigations /8, 28-33/ are proceeding in a number of laboratories in USSR and USA after this concept and some of its specific schemes were first proposed in our Laboratory of New Accelerator Problems /28-31,8/ at the Lebedev Physical Institute. We proceeded from the appearance of highcurrent pulse electron accelerators. The maximum energy of particles in such accelerators has been limited by high voltage engineering problems and lies usually in the region up to several megaelectronvolts. At the same time the acceleration of large pulsed current to larger energies is very desirable, but is very difficult to achieve by conventional methods,

We speak about the acceleration of electrons whereas one considers usually collective methods in the application to acceleration of ions by means of electron beams and bunches, But it is undoubtedly of interest to accelerate electrons themselves. In autoacceleration this is achieved by decreasing the integral charge of the beam and/or pulse duration while maintaining or slightly decreasing the instantaneous value of current and total energy of the beam. For this purpose there can be used passive elements (resonators, waveguides, diaphragms), interaction with which leads to a redistribution of energy within the beam: some of the particles are accelerated at the expense of a decrease in energy of others.

As first illustration /28,8/ let us consider a metallic tube in which there is a short-circuited line with a hollow central conductor (Fig.Ia). The characteristic impedance of the line is ρ and velocity of propagation of the waves in the line v. Through this system there passes a bunch of relativistic electrons of duration t_u, energy W and current I_0. If the length of line is $l=0.25t_u v$, then when the bunch reaches cross-section A-A at the input of the line there appears the voltage U. This voltage has the form of a bipolar pulse of amplitude $\alpha\rho I_0$, where α is the coefficient of coupling between the beam and line. The voltage at the input of the line retards the leading particles of the beam to energy $W-\alpha\rho I_0 e$ and accelerates the particles of the trailing half to energy $W+\alpha\rho I_0 e$, where e is the electron charge (Fig.Ib). To avoid a destruction of the beam at the input of the line one must choose $\rho < W/I_0\alpha e$. Thus, it is possible to increase the energy of the leading half of the beam by a factor of two.

For autoacceleration one can also use the passage of a relativistic bunch through a cylindrical resonator of length d and radius R (see /28,29/). We can characterize the beam energy redistribution after cavity passage by means of the effective impedance in ohms, i.e. by quantity W/eI_0. The results of calculations show that the impedance is modulated along the axis approximately with the period of the fundamental mode of the resonator. The impedance depends essentially on the value d/R and the optimal value is about $d/R \simeq 2$. The autoacceleration effect may be significant even for this simple variant. For example in the case of a bunch with initial energy - 2-3 MeV and current $\sim 2\times10^{4}$ A the part of a beam will have energy 4-5 MeV. One should mention, that with such beam current the total losses expended on the cavity excitation still will represent a small fraction of a beam energy.

In order to amplify the autoacceleration effect one must either increase the level of the field excited (it is limited because of breakdown) or increase the interaction length. The latter may be achieved by cascade connection of autoacceleration elements or by using waveguide systems in which propagation of waves with phase velocity near to beam velocity is possible. As is known if slow waves ($v_{phase} \lesssim c$) can be propagation in the given structure a uniform electron beam is unstable and excites longitudinal electric fields. It corresponds to inductive impedance. The maximum fields will be achieved in the stage when the beam will tend to self-phase state as a result of the instability development. Theory and numerical calculations /29,30/ for the case of diaphragmed waveguide show, that this process consists of the following stages (see also Figs.2-4) x/.

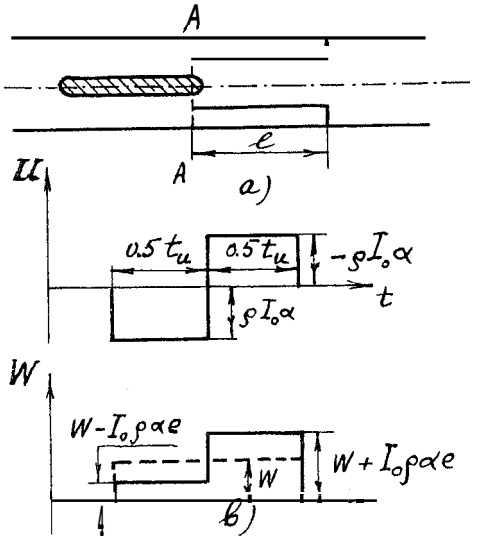


Fig.I

1. The limear stage. Instability developes and the amplitude of a wave having phase velocity near to the beam velocity rises exponentially with increment $\sim I^{1/3}/\gamma$, where I, γ are beam current and energy of particles. The interaction of the beam with the excited field leads to essential redistribution of the particle energies, and particles appear the energies of which are two-three times larger then initial energy.

2. The nonlinear stage. The process of particle capture by a wave developes, and the wave amplitude begins to ffel the effect of saturation accompanied by beats, The major part of the beam begins to be decelerated but a certain part continues to be accelerated.

3. The saturation stage. The quasistationary regime of energy exchange between beam and field is established. Autoacceleration, i.e. particle energy increase ceases.

4. The nonlinear wave decay stage. The higher wave harmonics generation occurs and also stochastization of the particle distribution in the phase plane.

In our concrete calculation we assumed that parameters are near to those used in

x/ We can mention that the results obtained are to some extent analogous to known results of the theory of beam propagation in a plasma.

autoacceleration experiments /31/:

Waveguide radius	4.35 cm
Cell length	2.5 cm
Wavelength of the main mode	10 cm
Ream radius	1.5 cm
Initial beam energy	$\gamma_0 = 3$
Momentum spread [x7]	2%
Ream current (three variants)	0.8; 2.7; 6.4kA

Some results of calculations are given in Fig.2, where time dependence of the longitudinal field 'amplitude E_m and the maximum momentum $\beta\gamma_m$ is shown up to the saturation stage. For simplicity the same premodulation wave length λ =12.5 cm for each current value is considered. As one can see, E_m and $\beta\gamma_m$ rise approximately during 2-4 HF periods. Then during transition to the nonlinear stage the maximum pulse increase rate is slowed down and the field amplitude begins to experience pulsations. For currents having practical interest in experiments the establishment time is of the order of ten HF period:;. The Fig.3 shows the particle phase plane locations corresponding to the beginning (curve I) to the end of the linear stage (curve 2) and to the nonlinear stage close to saturation (curve 3).

Let us consider briefly the experimental works in the field of autoacceleration. In our Laboratory a series of experiments on autoacceleration in a cavity was carried out /31/. The basic idea of these experiments consists in comparison of two electron energy spectra: one obtained immediately after the gun anode grid and the other obtained after the beam had passed the cavity. Using an initial electron beam with parameters: E_e=0.5-0.6 MeV, I_e=10kA, $\tau \simeq$ 40 nsec we obtain that after the resonator the electron spectrum dictinctly extends to energy I.0--1.2 MeV. The portion of electrons with energy exceeding the initial maximum energy is approximately equal to I%. We can mention that results was improved by using a sequence of two equal resonators, separated by some distance: the first of them excites initial modulation of the beam energy and density and the second - amplifies this effect. Now experiments with a diaphragmed waveguide are under way. The waveguide and beam parameters were listed above.

Analogous experiments were conducted at the Naval Research Laboratory /33/ on the base of above mentioned idea illustrated in Fig.I. The mean electron energy was incresed from about 0.5 to 25 nsec. The beam current was~10 kA.The total energy efficiency of the process was ~ 75%.

Autoacceleration effect was observed also in Lawrence Livermore Laboratory /32/. The beam having current about 12 kA and electron energy 2-2.5 MeV propagates down the diaphragmed waveguide with outer radius 15 cm, radius of holes 2.5 cm, length 120 cm, A longitudinal magnetic field up to 8 kG was used to guide the beam. Under such conditions the energy distribution of electrons after passage of waveguide extends beyond 3 MeV.

One can raise the question about the improvement of autoacceleration effectiveness, in particular in waveguide, i.e. about the maximum possible particle energy increase for a given initial energy. One of the possibilities consists in beam current increase, although as calculations show, beginning from a current of the order of I kA and higher there must be no considerable rise in for 3. Roughly speaking it is connected with the development of decay processes which begin to affect the current propagation earlier when the beam current is greater. The autoacceleration effectiveness should be also increased if one uses a special form of beam current initial modulation I(t), in particular of the asymmetric saw-shaped form /32/.

The other more radical way to increase the maximum particle energy is cutting of the low energy part of the beam spectrum. The physical mechanism of limiting maximum energy by a value of 2-3 γ_0 is as follows: the main part of the particles which have lost energy passes to the accelerating phase and takes energy from the wave, decreasing the electric field. If one withdraws such particles from the interaction space in proper time we can expect that the wave amplitude will rise continuously, and the maximum energy in a beam spectrum will rise as well. The numerical calculation in one-mode approximation proves these considerations and show that the value of γ_m when cutting will be several times more than in the case of freely moving electrons (see Fig.4).

In conclusion, the following should be noted. We have seen that for autoacceleration purposes a certain stage of beam instability is used. For relatively short waveguides and not large energy gain the "useful" property of this instability prevails over harmful onea. But in order to achieve large energy gain of the order of ten MeV or more the wavegiude must be sufficiently long. In this situation the development of various instabilities can lead to "beam break up" and to disturbance of the regular acceleration process. Some symptoms of such behavior were observed during experiments referred to in /31,32/. So the problem of beam stabilization apparently arises here too as in other collective methods.

Collective ion acceleration in highcurrent diodes

The reports on ion acceleration in diodes are not presented to this conference. We shall concern this question briefly taking into account its connection with ion acceleration from gas. We can note in particular that first experimental results on collective ion acceleration in general were obtained by Plyutto and collaborators /46,47/ in Sukhumi Institute. These investigations were continued in recent years /48/ and new works were started in other places /49/. Conditions of experiments vary widely: voltage 30-2000 kV electron current 0.1-50 kA, energy of accelerated protons 0.1-4.0 MeV, number of protons per pulse 10^{10}-10^{12} with large energy spread. Ions are accelerated in diod gap in the direction from cathode to anode up to energies much more then applied voltage. This took place in plasma-filled diodes and in vacuum diodes as well. In the last case the ion acceleration was observed when diod gap was closed by plasmas formed

[x7] The greater the spread - the smaller the increment because of Landau damping.

at cathode and anode respectively, when current density rises sharply due to beam pinching.

Different mechanisms were considered to explain the observed effects, among them moving virtual cathode model /42/, coherent acceleration mechanism /I,47/ and local pinch model /43/. All these mechanisms will be considered in the next sectiod. It seems to us that one of the most probable mechanism in diod acceleration is based on excitation of longitudinal waves due to two-beam instability in a system, consisting of an electron beam and slow ions /50/.

Ion acceleration due to electron beam passage through a gas

Some time ago the IPC-group /34/ and then the PIC-group /35/ in the USA observed that a relatively large number of ions are accelerated up to several MeV per nucleon as a result of passage of a HEB through a gas. Later on an analogous phenomenon was observed in Sandia Laboratories /36/ and in the Lebedev Physical Institute /37/. The general physical picture of the phenomenon is as follows: HEB generates ions by means of gas ionization and at the same time creates a field, which accelerates these ions. However the processes which accompany beam passage through a gas and lead finally to ion acceleration are rather complicated and not completely clear. The results obtained by the above mentioned groups and even by one group at different times are at times not consistent.

Let us recall briefly certain general properties, which characterize the process of ion acceleration in a gas (see also /39/ and Table I).

Table I (see ref./ 39/ and /35b,37/)

Peak voltage MV	Peak current kA	Current rise-time/Pulse duration nsec	Proton yield	Proton Energy MeV	'Acceleration' length cm	Reference
I.5	40	25/50	$I0^{I2}$	5.0	30	34a
I.7	30	25/50	$I0^{I2}$	5-I0	30	34b
0.2-I.0	200-I00	35/80	$I0^{I2}$	2.0	I0	35a,40
I.5-2.0	I00-50	70/90	$-^{I2}$	I-5	6	36
1.0	I00	~15/50	$\gtrsim I0^{I2}$	12	~I0	35b
0.65	20	50/I00	$\sim I0^{I2}$	2-4	30	37

a) Ion acceleration is observed for a wide range of electron energy (0.2-2.0 MeV), current (200-20 kA) and also ν/γ parameters (0.4-5.0).

b) There is a narrow range of pressure (about 0.1 torr), which corresponds to ion acceleration. As a rule, there is only a slight dependence of ion energy on pressure in this range,

c) The constancy of ion energy per unit charge and independence of this energy on ion mass is more or less fulfilled.

d) In the last experiments the final velocities of accelerated ions coincide with the beam front velocity /38,4I/. But while in /4I/ the ion bunch is localized at the front, in the majority of experiments (see /38/ in particular) one observes a spatial and temporal division: the ion bunch moves behind the beam front at a certain distance.

e) Protons with energies from 2 to I2 MeV were obtained, the last figure corresponding to the case of an electron beam having low temperature achieved by the use of a smooth cathode. Almost monoenergetic ions /34,4I/ and ions with wide energy spread /40/ as well (mostly recently) have been observed.

f) The acceleration region is localized either near the anode at a distance of 6-11 cm from it /35,36/, which is about drift tube diameter, or at a rather larger distance ~30 cm /34,37/; the estimates for accelerating fields are 0.I-I.0 MV/cm.

g) Ion pulse duration (3-I0 nsec) is considerably less than electron pulse duration (30-60 nsec).

Several attempts to find an explanation for the experimental results have been made.

I. A simple one-dimensional model has been proposed in /42/ based on the following considerations. If a beam enters a vacuum after the anode it will be decelerated because of potential "sagging". It is accompanied by creation of a virtual cathode - at a distance $d \sim c/\omega_p$ with height of potential barrier ~ MeV (γmc^2), where ω_p is the beam plasma frequency. But if a gas is present it will be ionized by the beam, the electrons appearing will be pushed out in the radial direction and therefore the space charge forces will decrease. As a result the virtual cathode will move from the anode with velocity $u=d/\tau_I$, where τ_I is the ionization time of a unit volume $\tau_I \cong (n\sigma v)^{-1}$, n is gas density, v is electron velocity and σ is ionization cross-section. Electrons will be decelerated and ions can be accelerated on the moving virtual cathode front.

In such a simple form (see also 42a, 42b), this model disagrees with certain experimental data in particular concerning pressure dependence. Then the velocity u corresponding to real τ_I is too small ~ $I0^8$ cm/sec. Therefore one must suppose the existence of some additional mechanisms which can diminish τ_I, in particular the preionization by Bremstrahlung from the anode or by the fast electrons which overtake the main part of the beam. But question of the acceleration effectiveness remains open even if these additional assumptions are fulfilled, because in particular ions due to preionization can be created not at the proper place, which corresponds to their capture and acceleration in a potential well. One of the main objections to this model is that it assumes ion acceleration at the head of the beam only, but the majority of experiments shows acceleration inside the beam.

Simultaneously an other electrostatic model was proposed /38/ in particular to explain the ion bunch formation and acceleration behind the beam front. This model proceeds from the assumption that the avalanche discharge may act as a main mechanism. At the boundary between discharge (plasma) and beam a potential well will be formed in which ions can be accelerated. However the actual possibility of accelerated discharge front has not been proved, The velocity of the corresponding potential well appears to be approximately constant and equal to $\sim d/\tau_d$, where d is the distance from anode to virtual cathode in the model /42/. The discharge time τ_d was calculated and is $\tau_d > \tau_I$. Therefore the velocity of "discharge well" turns out to be less than the velocity of "beam front well". Perhaps the effective discharge time can be reduced because of gas preionization by electrons or newly generated ions.

Let us note that for both one-dimensional models the potential well motion does not depend on the existence of accelerated ions and therefore this motion is not self-consistent and not self-synchronized.

An other physical phenomenon constitutes the bases for the so-called localized pinch model /43/. When a value n_i/n_e near the anode is of the order $I/\gamma^2 \beta_{beam}$ pinching on the ionization front begins. Inductive longitudinal electric field E_{ind} arises due to a change in the inductance L and electrostatic field E_{el} arises when there is a surplus of negative charges before the ion bunch: $E_{ind} \sim I\, dL/dt \sim I\, dr_{beam}/dt$, $E_{el} \sim \partial r_{beam}/\partial z$. The electric field decelerates the beam electrons and accelerates the ions, situated in the pinch region. The accelerated ions cause a movement of this region ahead and the mechanism can be self-synchronized, The actual realization of such a regime requires a definite rate of elimination of the electrons and this does not neccessarily occur in practice. There are certain reasons which lead to cessation of the acceleration process. A part of the ions can fall out of the accelerated bunch, and as a result there will be another region of higher negative charge density. Due to this situation the pinch begins to dissipate, and the acceleration process too.

Some other models have been considered, among them the coherent acceleration of a proton bunch "fanned" by an electron stream /44/. This model however is in contradiction to the experimental results: small dense ion bunches are not present, the proportionality of ion energy to bunch charge squared has never been observed etc.

Quite recently a new modification of the electrostatic model /42/ has been proposed /42b/. The new feature taken into account is the ion motion inside and outside the potential well and the back influence of ions on the beam head dynamics. At first ions are formed inside the beam front by means of impact ionization by electrons. Due to electric fields in the accelerated beam front the newly generated ions are in turn accelerated. The energy of ions depends on the place in the potential well where they have appeared. Part of the ions lag behind the beam front. The other part achieves a velocity which exceeds the beam front velocity and passes ahead of the beam front. These ions generate additional ions ahead of the electron beam front. Estimations show that this can decrease the ionization time τ_I by several times and increase correspondingly the beam front velocity. The authors /42b/ have made many simplified assumptions, and their results partly agree and partly disagree with experimental data. But they have shown convincingly that ionization which is provided by newly created ions can play a significant role and electron beam dynamics is closely connected with ion generation and acceleration.

We have seen that all proposed theoretical models are incapable of understanding and explaining the whole complex of problems of ion acceleration in a gas. Apparently the future theory must take into account the variety of different phenomena accompaning the electron beam propagation through gas: electron and ion ionization, electron and ion avalanche breakdown, different preionization effects, secondary electron behavior etc. These phenomena must be considered in a self-consistent manner and not in a plane but in a cylindrical geometry too. It is very important to calculate the spatial and temporal characteristics of ion capture in the acceleration regime. The question of the capture and effectiveness of the acceleration process is not simple even in the case of ordinary accelerators, and in the given case it is especially complicated but must be solved.

We must emphasize that ion acceleration in a gas was discovered "accidentally", and attempts to explain it were undertaken only post factum. Therefore considerable experimental and theoretical work is required to more definitely determine several important characteristics and dependences. This will help to overcome phenomena disturbing or breaking down the acceleration process. In the first place one must obtain the dependence of accelerated ion beam characteristics (energy and its spread, intensity) on initial electron beam characteristics (energy, current, geometry) and ion beam propagation conditions in a drift chamber. The further development of the method requires the creation of special conditions leading to the most effective use of electric fields (which in principle may be very large) escited by beams in a gas.

In particular one can attempt to make the acceleration process more effective by means of gas pressure change along the drift chamber. Under certain simplifying assumptions (one-dimensional picture) one can obtain synchronized ionization front movement and accelerated ion motion if the pressure rises proportionally to the square root of distance.

The other possibility is the introduction of an additional external ion source, which can help the localized pinch to propagate in a self-synchronized manner with ion motion. It is of some interest to continue investigations with a longitudinal magnetic field to the drift chamber. Perhaps one can find such a magnetic field longitudinal dependence which will give an additional possibility to synchronize the accelerating wave propagation and ion motion. At the same time the magnetic field will magnetize the secondary electrons and provide additional difficulties for pinch creation. In order to find a reasonable compromise separate work is re-

quired.

There are other more sophisticated possibilities to control a potential well motion in a gas to synchronize it with ion motion. For this purpose one can combine different methods of acceleration as is sometimes the case in traditional accelerators. In particular we can use the scanning and rotation of an electron beam according to neccessary law /I3,26/ not in a vacuum but in a gas or in a plasma, Such proposals were made in /45,52/, in the latter case with using laser beam too. We can note also that the gas can serve not only as a medium for potential well propagation, but also provide the required conditions of electron beam and well propagation by means of a gas focusing.

In conclusion one can say that there are two general problems: one more physical and the other more technical. The first problem is to utilize the electric field created in a gas along a possible larger interaction length in order to obtain ion energy of the order of tens or hundreds of MeV and also a large number of ions per pulse ($\sim 10^{14}$-10^{15}). The second problem consists in a considerable increase of the pulse repetition rate up to tens or hundreds of times per second. This requires considerable work in order to construct fast-acting spark gaps and a corresponding energy supply system.

The solutmon of these two problem can transform ion acceleration in a gas into an effective and reliable method of acceleration,

References

1. V.I.Veksler, Proc.CERN Symp.Accell., I, 80 (I956).
2. G.I.Budker, ibid., 68.
3. Ya.B.Fainberg, ibid., 84.
4. H.Alfven and P.Wernholm, Ark.Fys., 5, I75 (I952).
5. W.H.Bennett, Phys.Rev., 45, 89(I934); 98, I584(I955).
6. A.M.Sessler, Proc.VII Int. Accel.Conf., 2, 43I, Yerevan, USSR (I969).
7. M.S.Rabinovich, Proc.Ist.Nat.USSR Accel. Conf., 2, 473, VINITI, Moscow (I970).
8. A.A.Kolomensky, Coll.Papers Symp.Coll. Meth.Accel., JIPJR, Dubna, 79(I972); Particle Accelerators, 5(2), 73(I973).
9. J.D.Lawson, Particle Accelerators, 3(I), 2I(I972).
10. Ya.B.Fainberg, Soviet physics Uspekhi, I0, 750(I968); Proc.VII Int.Accel.Conf., 2, 465, Yerevan, USSR (I969); Particle Accelerators (in press).
11. I.E.Tamm, J.Phys.USSR, I, 439(I939).
12. R.M.Johnson, Symp.ERA, LRL, Rep. 18103,219 (I968).
13. A.A.Kolomensky and I.I.Logachev, Proc.2 Nat.USSR Accel.Conf.I970, Moscow, I, 204 (I972).
14. I.J.Billington and W.R.Raudorf, Wireless Engineer, 3I, 287(I954).
15. G.A.Askarjan, Atomnaya Energiya, 6, 658 (I959).
16. A.A.Kolomensky, Yu.T.Zozulya, 4 Nat.USSR Accel.Conf., Moscow (I974).
17. S.U.Syrovatsky, JETP, 50, II33(I966).
18. N.A.Khyzhnjak and M.S.Repalov, Proc.I Nat. USSR Accel.Conf., Moscow, 2, 522(I970).
19. G.I.Budker and A.A.Naumov, Proc.CERN Symp. Accel., I, 76(I956).
20. T.G.Linhart et al., Proc.2 Int.Accel.Conf., p.I39, CERN, Geneva (1959); K.C.Rogers et al., ibid., p.I45.
21. G.S.Janes, R.H.Levy, H.A.Bethe, B.T.Feld, Phys.Rev., I45(3), 925(I966).
22. V.I.Veksler, V.P.Sarantsev et al., Proc. VI Int.Accel.Conf., p.289(I967).
23. V.I.Veksler, I.R.Gekker, M.S.Rabinovich et al., Proc.IV Int.Accel.Conf., p.II0, Dubna (I963).
24. A.G.Bonch-Osmolovsky, Atomnaya Energiya, 3I, I27(I97I).
25. M.S.Rabinovich and V.N.Tsytovich, Particle Accelerators, 5(2), (I973).
26. A.A.Kolomensky and I.I.Logachev, Proc. VITI Int.Accel.Conf.CERN, Geneva, 587 (I97I); Coll.Papers Symp.Coll.Meth.JINR, Dubna, I9(I972).
27. A.A.Kolomensky, Brief Phys.Commun.Leb. Phys.Inst., No.8, p.67(I972); Preprint No. I4I, Leb.Phys.Inst.(I972).
28. L.N.Kazansky, A.V.Kisletsov, A.N.Lebedev, Proc.VIII Int.Accel.Conf.CERN, 592(I97I); Atomnaya Energiya, 30(I), 27(I97I).
29. N.E.Belov, A.V.Kisletsov, A.N.Lebedev, htomnaya Energiya, 36(3), 20I(I974).
30. V.C.Gapanovich, A.A.Kolomensky, A.N.Lebedev, 4 Nat.USSR Accel.Conf., Moscow(I974).
31. A.A.Kolomensky, B.N.Yablokov et al., 4 Nat.USSR Accel.Conf., Moscow (I974).
32. V.K.Neil, A.A.Mirin, Rep.UCID-I643I, Lawrence Livermore Lab.(1973).
33. M.Friedman, Phys.Rev.Lett., 3I, II07(I973).
34. a) S.Graybill, J.Uglum, J.A.P., 4I, 236 (I970); b) S.Graybill, IEEE Trans.Nucl. Sci., NS-I9(2), 292(I972).
35. a) J.Rander, B.Ecker, G.Yonas, D.Drickey, Phys.Rev.Lett., 24, 283(1970); b) B.Ecker, S.Putnam, D.Drickey, IEEE Trans.Nucl.Sci., NS-20(3), p.30I(I973).
36. G.Yonas, L.P.Bradley, G.W.Kuswa, ibid., p.305.
37. A.A.Kolomensky, L.M.Likhachev, I.V.Sinilschikova, O.A.Smith, 4 Nat.USSR Conf. (I974).
38. R.Uglum, S.E.Graybill, W.N.McNeil, Bul. Am. Phys. Soc., I4(II), I047(1969).
39. G.Yonas, Coll.Papers Symp.Coll.Meth.Accel., JINR, Dubna, I37(I972); Particle Accelerators, 5(2), 81(I973).
40. G.Yonas, IEEE Trans.Nucl.Sci.NS-I9, No. 2 p.297(I972).
41. J.Rander, Phys.Rev.Lett., 25, 893(I970).
42. N.Kostoker, Proc.VII Int.Accel.Conf., 2, 509, Yerevan, USSR (I969); a) S.E.Rosinskii, A.A.Ruchadze, V.G.Rukhlin, JETP Lett., I4, 53(I97I); b) K.F.Alexander, E.Hantzsche, P.Siemroth, Rep.Zentralinstotut für Elektronenphysik(I973), Berlin, DDR.
43. S.Putnam, Phys.Rev.Lett., 25, II29(I972); IEEE Trans.Nucl.Sci., NS-I8(3), 496(I97I).
44. D.Eastlund, J.Wachtel, Bull.Am.Phys.Soc., I4, I047(I969).
45. A.A.Kolomensky, I.I.Logachev, 4 Nat.USSR Accel.Conf., Moscow (I974).
46. A.A.Plyutto, Sov.Phys.JETP, I2, 6, II06(I96I).
47. A.A.Plyutto, K.V.Suladze, V.N.Ryzhkov, Proc. VII Int.Accel.Conf., 2, 505, Yerevan(I969).
48. A.A.Plyutto et al., Zh.Tekh.Fiz., 43(8), I627(I973).
49. L.P.Bradley, G.W.Kuswa, Phys.Rev.Lett., 29 I44I(I972).
50. S.P.Gary, H.W.Bloomberg, Appl.Phys.Lett., 23(2), II2(I973).
51. M.L.Sloan, W.E.Drummond, Phys.Rev.Lett., 3I (20), I234(I973).
52. C.L.Olson, SLA-74-5I00, Conf.on Confinement of Plasmas and Rel.El.Beams, New York (I974).

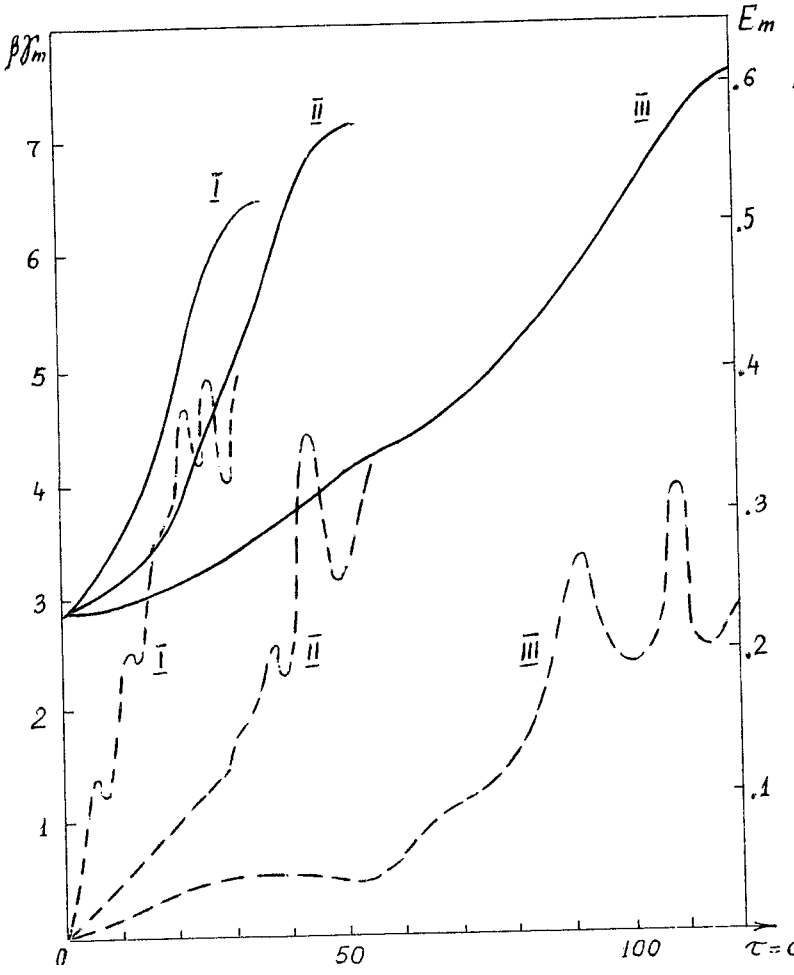


Fig. 2. Time dependence of $\beta\gamma_m$ (solid curves) and E_m (dashed curves): $\gamma_0 = 3$; **I** - 6.4 kA, II - 2.7 kA, III - 0.8 kA.

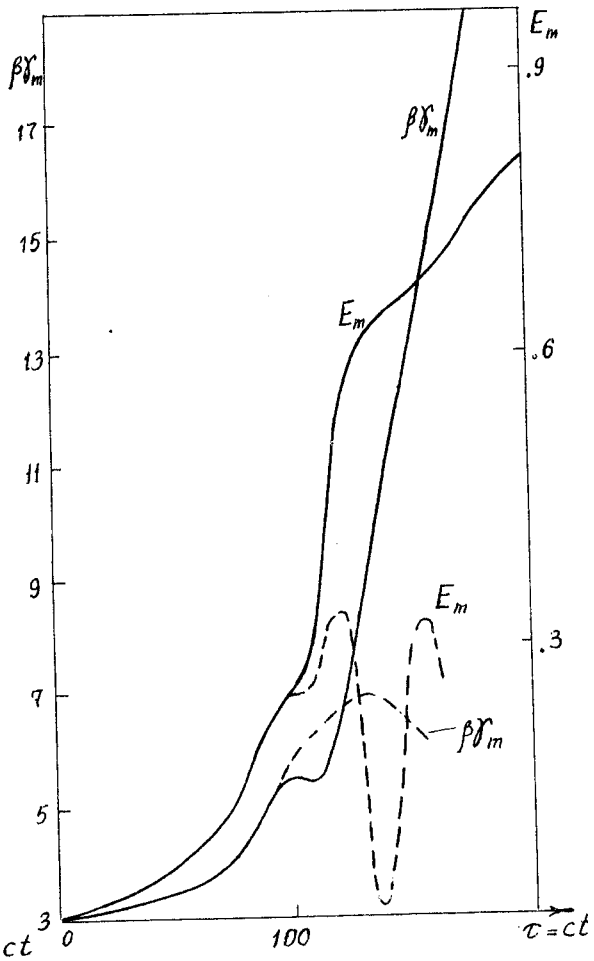
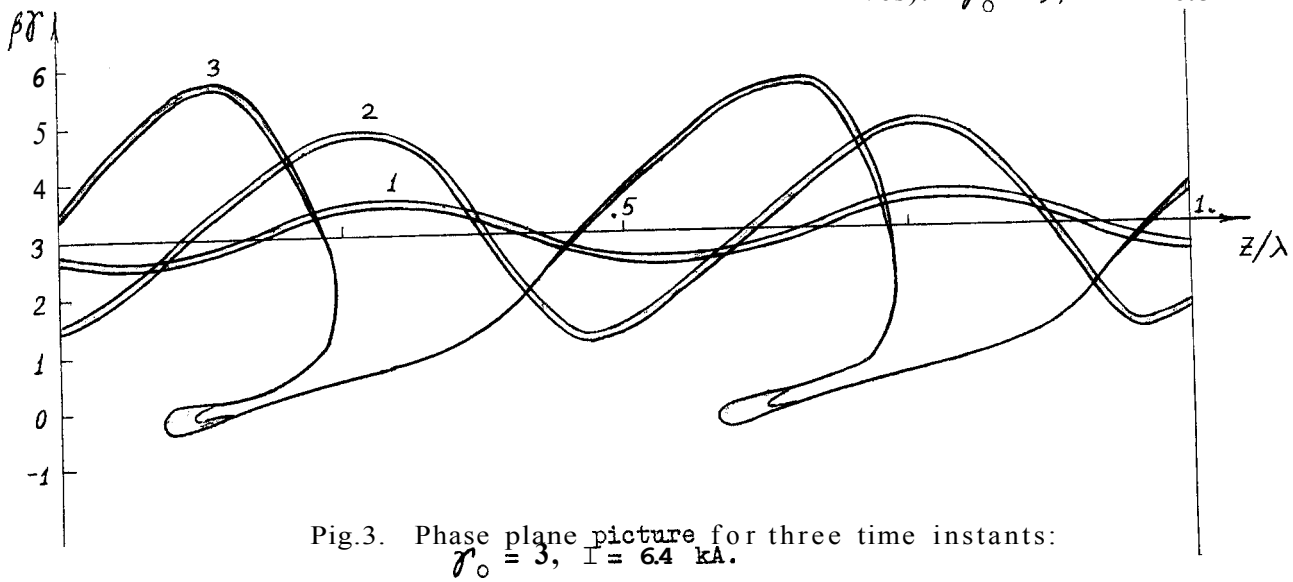


Fig.4. Time dependence of $\beta\gamma_m$ and E_m in the case of freely moving electrons (dashed curves) and in the case of low-energy electrons cutting (solid curves): $\gamma_0 = 3$, I = 0.8 kA.



Pig.3. Phase plane picture for three time instants: $\gamma_0 = 3$, I = 6.4 kA.

Millard Sloan (Austin Research Associates Corporation): I have a question for Dr. Kolomensky. You mention in the two stream instability case the concept of driving the two stream instability with a small RF signal to obtain a very narrow electric field spectrum. Does this produce a wave coherent enough to be used as a traveling wave accelerating field?

A. A. Kolomensky (Lebedev Institute): Yes, it does produce a wave coherent enough for accelerating purposes, but it is very low power and is not useful for acceleration. It is only useful for training.

Millard Sloan: What was the power amplification and the RF input power into your system?

A. A. Kolomensky: The beam power was 40 kilowatts, and the RF input driving power was about 1 watt.

PARTICLE ACCELERATION BY INTENSE ELECTRON BEAMS

D. Drickey
Department of Physics
University of California, Los Angeles
Los Angeles, California 90024

B. Ecker and S. Putnam
Physics International Co.,
San Leandro, California 94577

Further results on the process of coherent acceleration of positive particles by intense electron beams injected into an initially neutral gas are presented. Accelerating fields of the order of one MV per centimeter and proton intensities of 10^{12} protons per pulse have been observed. Proton energy as a function of cathode and gas parameters are also presented. Agreement between the beam current velocity and proton velocity is seen. Acceleration cutoff occurs in a pressure region where beam current velocity increases sharply.

Introduction

In this paper we report on a study of coherent acceleration of protons by intense relativistic electron beams injected into initially neutral gas. As this study is a continuation of previously reported work,[1] we include both new data and, where appropriate for comparison, a compilation of all of the data taken on the Physics International 738 Pulserad electron beam generator. Although many different positive particles have been accelerated (up to 29 MeV N^{+7} ions when nitrogen was used as the gas), the present study concentrated on using hydrogen gas and observing the accelerated protons, since the unique charge to mass ratio of the proton provides a valuable diagnostic tool in understanding the acceleration mechanism.

Apparatus

The vacuum diode of the 738 Pulserad consisted of a flat circular cathode and an aluminized mylar transmission anode. Cathode diameters of 1, 2, and 3 inches and cathode materials of carbon or conductive epoxy were used. Use of a 3/8 inch anode-cathode spacing gave a beam current increasing at 7.5×10^{12} A/sec for 10 nsec, a peak current of more than 100 kA after 35 nsec, and zero current at 100 nsec. Two diode voltages were used, corresponding to peak voltages of 1.0 MV and 750 kV at about t = 10 nsec and decreasing to zero volts at 90 nsec. For these differing diode voltages, peak diode currents were virtually the same although details of risetimes and other injected beam parameters were slightly different. We use the nomenclature 1.0 MV and 750 kV to refer to these two beams but caution that these are nominal values only *so* far as detailed parameters are concerned, The beam was injected into the proton acceleration chamber, a 3 inch diameter copper tube filled with the hydrogen gas at various pressures. Chamber length was 82 cm for the 750 kV beams and 73 cm for the 1.0 MV beams. Transmitted electron beam current wave forms and the position of the beam front versus time were measured using four Rogowski coils recessed in the tube wall at 1, 5, 14.7 and 49.4 cm from the anode. A 1.1 cm diameter tube, 20 cm long, separated the acceleration tube from the low vacuum proton diagnostic region and served as an impedance for differential pumping or, at the higher pressures, was covered with a 2.5 micron mylar foil for the same purpose. Electrons traversing this tube were stripped away from the protons by space charge forces and by a transverse 1 kG field extending 6 inches along the proton path. The field reversed midway *so* that proton trajectories would be deviated negligibly. Our previous studies[1] used a magnetic spectrometer with emulsions for positive identification of ion species and momentum. Particle energy determined in that way agreed well with energy determined by time-of-flight measurement done simultaneously, using two collector screens to generate proton current wave forms. In the present work, the proton data were taken using the collector screens only. The first screen was 125 cm from the anode and 64.3 cm from the second collector. Reference 1 contains further details of the experimental arrangement.

Results

Data from each pulse consisted of eight or nine photographs of oscilloscope traces. Clearly it is impossible to present all of the details of these traces here. Instead, we have attempted to group the data into families of curves, extracting, to the best of our knowledge, the relevant part of the data for presentation. In this analysis, we have used the data only from the first pulse when multiple proton pulses were present.

Perhaps the most important data are summarized in figure 1a where observed proton energy is plotted as a function of hydrogen gas pressure for three cases. We tend to attribute the highest energy case (2 inch cathode, 1 MV beam) to the lowest temperature beam. This curve contains our highest observed proton energy (12.2 MeV) and has been previously reported.[1] The bell-shaped curve is especially interesting; unfortunately, Rogowski coil information is incomplete for these data. Figure 1b shows similar 1 inch cathode data (and one 3 inch cathode point) using a nominal 750 kV beam, but the scatter and inconsistency of these data are *so* great that we have chosen to concentrate on analysis of the 2 inch cathode 1 MV and 750 kV curves. The reasons for this scatter are unknown. Apparently, certain diode configurations and certain pressure regimes are stable while others are not.

Figure 2 shows the beam current front velocities for these two cases, measured between the 5 and 14.7 cm points, where β_b^2 is plotted versus pressure. The similarity between these curves and the proton energy curves is dramatic; this behavior has been noticed previously.[1,2] Here we have defined the beam front as the leading edge of the current pulse, which in most cases is very sharply defined (sub-nsec) on the Rogowski coil wave forms. In all of our data, the proton bunch (typically 10 cm in length at the first collector) is always behind this leading edge, based on a linear proton trajectory extrapolation to the anode computed from observed proton arrival time and velocity in the diagnostic region. (Previously we confirmed that the proton bunch does have its origin quite near the anode.[1])

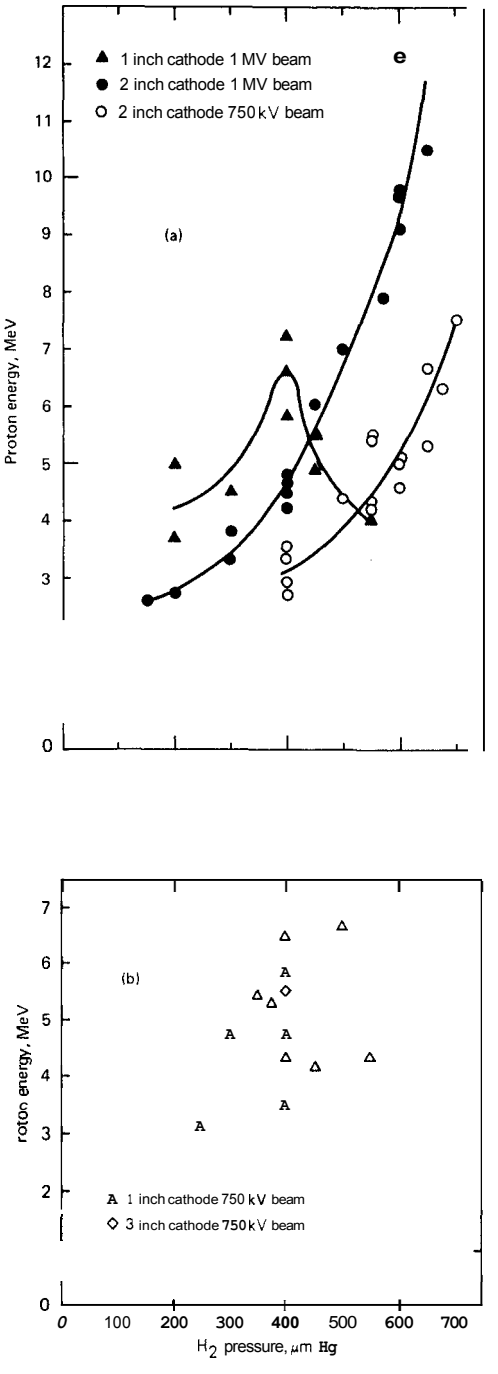


Figure 1 Proton energy versus hydrogen pressure, determined by time-of-flight of the peak amplitude of the proton waveform. Smooth curves are drawn through the data in this and subsequent figures.

We have computed a relative measure of total proton flux by integrating the proton current waveforms. These data, in figure 3, are given in most cases as pressure-bin averages because the individual values showed great fluctuation, occasionally by more than an order of magnitude at unchanged hydrogen pressure. Whether this reflects real variations in the total number of accelerated protons, or whether the spatial distribution of protons was off-axis and, as a result, not well sampled by our 1.1 cm aperture, is uncertain; the latter effect has been observed in other studies.[3] The implication of figure 3 along with figure 1 is that the upper limit on the pressure regime for acceleration involves a dwindling particle flux.

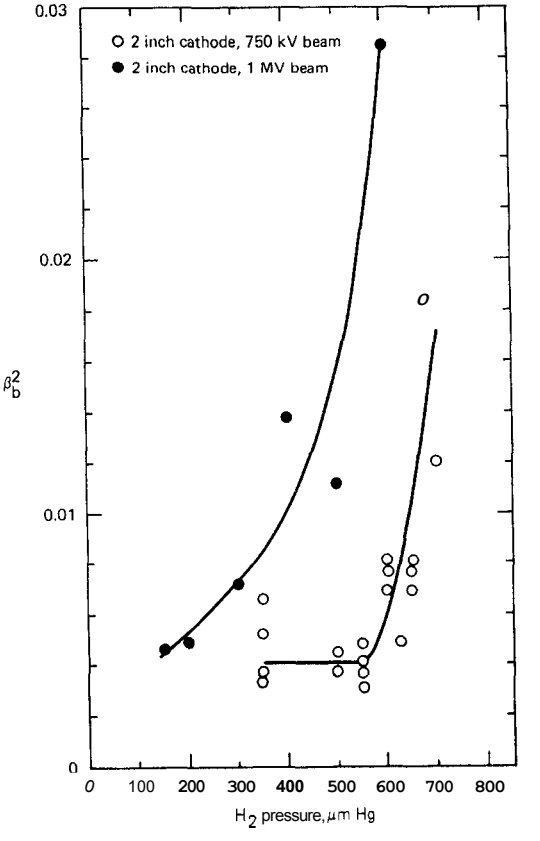


Figure 2 The square of the beam front velocity β_b versus hydrogen pressure. β_b was measured by the leading edge of Rogowski coils at 5 and 14.7 cm from the anode.

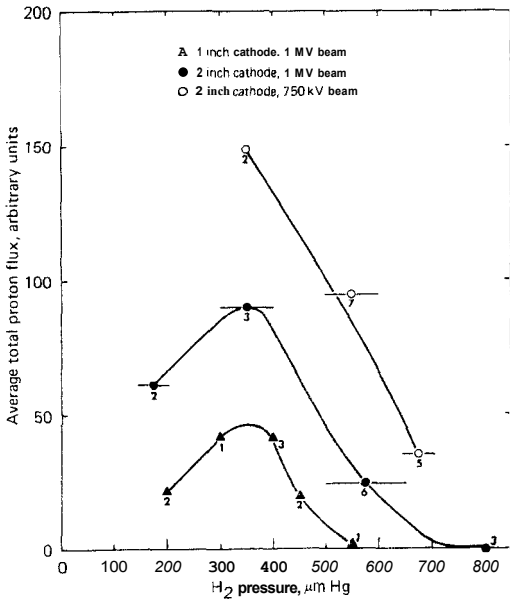


Figure 3 Average relative proton flux versus pressure, computed by integration of proton waveforms. Horizontal bar shows pressure bin in which the number of data points indicated, were averaged. The two 1 MV curves have the same absolute normalization.

The electron current in the acceleration tube has a well-defined rise time (typically 3 to 10 nsec), which we term the beam head. The extrapolated proton trajectories are always either within the beam head (most cases), or closely behind it. In view of this, we exhibit in figure 4 the calculated energy $\mathcal{E}_o$ given to a positive charge by the induced longitudinal electric field in the beam head, where dI/dt (typically 0.4 to 2.0 x 10^{13} A/sec) was measured versus distance by the four Rogowski coils. For protons the expression for $\mathcal{E}_o$ is

$$\int eE_{ind.}\,dz = \frac{e\mu_o}{2\pi}\,\frac{dI}{dt}\,(1 + 2\ell n\,\frac{r_w}{r_b})$$

where e is the proton charge, r_w is the radius of the cylindrical chamber wall, and r_b is the radius of the beam (assumed to be uniform). We have set $r_b = r_w$ in computing $\mathcal{E}_o$ to account for radial expansion of the beam head due to incomplete charge neutralization. Note that the energy $\mathcal{E}_o$ would be transferred only if the protons were in step with the beam head along the entire length of the chamber. Of course, in experimentally selecting out and confining our study to pressures that gave the highest energies, we may have empirically chosen that parameter range where the protons are accidentally in step; or alternatively, a trapping or synchronizing mechanism may be operating. In either case, the correlation of higher proton energy with higher dI/dt is very apparent, as is the downturn in this calculated integral near those pressures where beam front velocity increases sharply and where proton acceleration cuts off. As a precautionary note, we point out that this calculation is sensitive to the exact interpretation of the beam current wave forms and may be too high by a factor of about two due to instrumental effects. The relative error seems smaller and is perhaps represented by the scatter of the points. We note that as a rule, dI/dt decreases away from the anode, in some cases by as much as a factor of four over the length of the chamber.

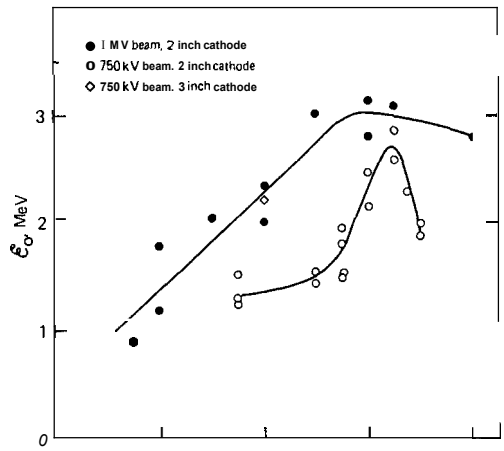


Figure 4 The energy gain $\mathcal{E}_o$ calculated from the induced electric field at the beam head versus pressure.

We have attempted to summarize important aspects of these data in the final two figures. Figure 5 is a correlation plot for all of our data of current front velocity versus proton velocity. General agreement is seen although the correlation is not precise. Of course, since in most cases the beam current front is mildly accelerating once it leaves the anode region, this comparison of proton velocity with beam velocity at one part of its trajectory could not be expected to be complete. Figure 6 shows the correlation plot of "inductive" energy versus observed particle energy for all of our data. A correlation is seen, as is the fact that the inductive energy contributes only a part of the final proton energy. We know that fields of at least 300 kV/cm exist near the anode (see ref. 1 where at least 3 MeV protons were seen to come from the region within 10 cm from the anode). This seems to be at least three to six times larger than the strongest fields induced by dI/dt observed in the anode vicinity. We interpret these data as indicating that the observed acceleration is due to both induced and space charge fields, and that the latter (i.e., electrostatic) field of order 10^6 V/cm predominates near the anode.

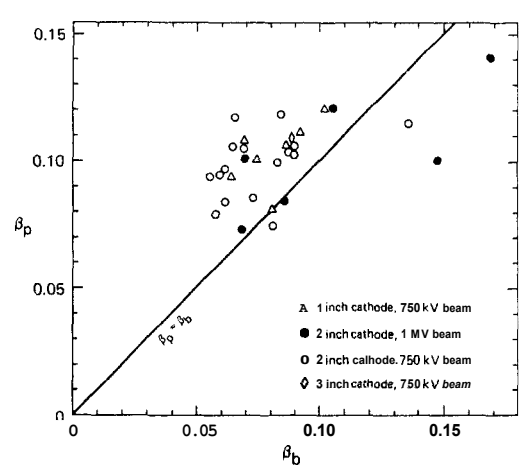


Figure 5 Proton and beam front *velocity* correlation plot.

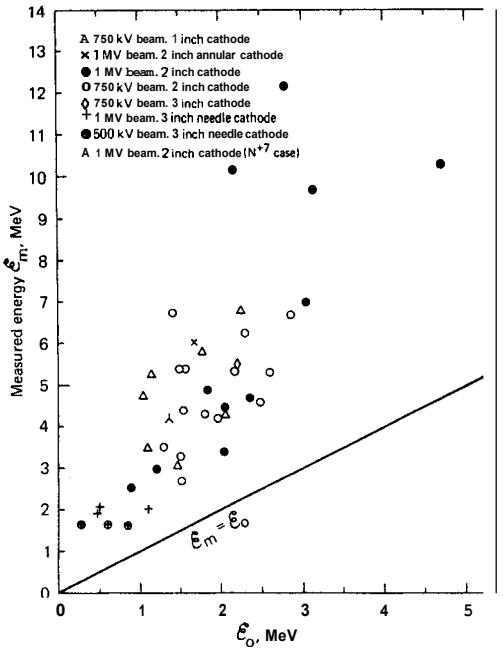


Figure 6 Correlation plot of measured particle energy $\mathcal{E}_m$ and calculated energy $\mathcal{E}_o$. Data refer to accelerated protons in all cases except the point marked A, which refers to 29 MeV N^{+7} ions. For this case, energies are MeV/Z.

Conclusions

Our experimental results, new and previously reported (marked below by an asterisk*), can be summarized as the following tentative conclusions:

1. Agreement between the beam current front velocity and proton velocity exists. (See also reference 1 and 2.)
2. Part of the proton energy apparently is generated by the induced medium strength electric field in the beam head over the length of the beam propagation chamber.
3.* There is evidence that a high field, short-distance launch occurs near the anode: at least 300 kV/cm, perhaps 1 MV/cm, over 10 cm.[1]
4.* The proton bunch has a small longitudinal extent, typically 10 cm after moving more than a meter, and is associated with the beam head, consistent with the idea of a high-field launch near the anode.[1,6]
5.* Weak longitudinal magnetic fields (≃500 G) drastically reduce proton flux without affecting proton energy.[1]
6. An upper limit pressure region exists, near 600 to 700 microns in hydrogen for our 2-inch beams, where
   a) beam front velocity increases dramatically,
   b) proton energies are highest but proton flux decreases severely, perhaps to zero.
7.* Ion energies are Z times proton energies, where Z is observed ionic charge.[1,6]
8.* Multiple pulses are observed under certain appropriate beam and pressure conditions.[5,6]
9.* The number of accelerated protons per beam pulse is 10^{12} to 10^{13}, and protons up to 12.2 MeV and N^{+7} ions at 29 MeV have been observed.[1]

With the detection of coherent electrostatic accelerating fields of order 10^6 V/cm, the usefulness of the technique depends upon the extension of the acceleration length, which in our work was of order 10 cm. How this can be done depends upon the physics of the electron charge cloud that causes the field. The space charge structure may be produced by primarily longitudinal effects,[7] and/or radial effects may be involved.[8] Our observation1 that weak longitudinal magnetic fields (—500 gauss) severely affected the acceleration process means that two-dimensional effects must be involved.

The observed velocity agreement between beam front and proton bunch and the fact that beam front velocities of up to $\beta_b = 0.7$ have been observed in hydrogen at uniform pressure[9] indicate that a way to take advantage of the increasing beam velocity with increasing pressure may be to use a pressure gradient in the acceleration tube. This would avoid the proton flux cut-off by starting acceleration at a pressure that gives high flux, and then proceeding continuously to higher pressures where beam front and bunch velocity increase.

Kuswa[10] and Swain, Kuswa, Poukey and Olson[11] have performed pressure gradient experiments along these lines, and did not detect increased proton energy. However, they had significantly slower electron beam risetime than used in the present studies, and according to the theory of Olson,[12] this would mitigate the effect of the gradient.[3] The very broad proton pulses of Swain et al. is further indication that their study and ours have treated significantly different parameter regimes.

The observation of multiple ion bunches (2 to 4 bunches arriving at the collector screens up to 60 nsec apart) may have significant implications about the acceleration and charge production processes. If, for example, these bunches are associated with time-separated space charge fields, then space charge neutralization cannot be complete behind the first bunch or, indeed, behind the risetime portion of the beam.

We conclude with a discussion of energy balance. Since the bunch velocity appears limited by the beam front velocity, we examine the energetic constraints on beam front velocity. The beam power injected from the diode is $P_d = I_d V$, where I_d is diode current and V is diode voltage. This power, which represents purely beam kinetic energy at the anode plane, is distributed during beam propagation into plasma energy (ionization, the driving of plasma currents, and plasma heating), the kinetic energy of an accelerated proton or ion bunch, electromagnetic waves (e.g., microwaves), electric fields, and magnetic fields. Here we treat only the last of these, which with our parameters turns out to imply by itself a velocity limitation.

Consider a simple model in which the beam front has reached its final propagation velocity $\beta_b c$. This velocity is less than the electron longitudinal streaming velocity $\beta_{\parallel} c$, which in turn is less than the total electron velocity $\beta_e c$. The distance from anode to beam front is $\ell = \beta_b ct$. For simplicity, we assume a sharp beam front. Ignoring end effects, the conversion rate of beam kinetic energy into magnetic field energy is

$$P_m = \frac{\partial}{\partial t}\int \frac{B^2}{2\mu_o} d^3x = \frac{\partial}{\partial t}\frac{1}{2} LI_n^2,$$

where L is the inductance of beam propagation and I_n is the net beam current. Explicitly,

$$P_m = \frac{\partial}{\partial t} k\ell I_n^2 = k\,(\ell I_n \dot{I}_n + I_n^2 \dot{\ell}),$$

where $k \equiv (\mu_o/4\pi)\,[1+2\ell n(r_w/r_b)]$ and a dot $(\cdot)$ signifies $\partial/\partial t$. With $\dot{\ell} = \beta_b c$, energy conservation (neglecting all the other possible losses) requires

$$\frac{P_m}{P_d} = \frac{k(\ell I_n \dot{I}_n + \beta_b c I_n^2)}{I_d V} < 1 \qquad (1)$$

assuming that injected beam energy is not stored over time and then quickly converted to magnetic field energy by some unknown process. We choose the time $t = 7$ nsec to evaluate the above ratio, because Rogowski coil data shows that typically the beam front has by this time accelerated away from the anode and attained a "final" velocity that increases slowly thereafter, if at all. Then $\ell \simeq 0.2$ m, $I_n \simeq 65$ kA, $\dot{I}_n \simeq 10^{13}$ A/sec, $\beta_b \simeq 0.09$, $I_d \simeq 70$ kA, $k = 10^{-7}$ henry/m and $V \simeq 6\times10^5$ volts. These figures give $P_m/P_d = 0.58$. In addition it is to be noted that the energy for P_m comes fron the beam's longitudinal kinetic energy, which with $\nu/\gamma = 2$ must be assumed to be substantially less than the total kinetic energy.[13] It therefore appears very probable that in our study the beam front (and proton bunch) velocity was limited by power input. This effect has also been deduced in other studies.[1,14] If true, this is a promising result because P_m is quite sensitive to I_n; for example, decreasing I_d (and therefore $\dot{I}_n$ and I_n) by a factor of 2, and increasing V by the same factor, allows an increase of β_b by a factor of 8 in equation (1) without increasing the ratio P_m/P_d. These effects may explain why in figure 1 the 1 MV, 2 inch beam gave higher proton energies than the 750 kV, 2 inch beam, and why in figure 2 the beam front velocity increases so sensitively with pressure. The clear implication of the energetic constraints is that beam voltage and current profiles must be properly tailored to achieve higher particle energies.

References

1. B. Ecker, S. Putnam, D. Drickey, IEEE Trans. Nuc. Sci. NS-20, Series 3, 301 (1973).
2. J. Rander, Phys. Rev. Letters, 25, 893 (1970).
3. G. Kuswa, Sandia Laboratories (private communication).
4. S. Putnam, Phys. Rev. Letters 25, 1129 (1970).
5. S. Putnam, IEEE Trans. Nuc. Sci. NS-18, 496 (1971).
6. J. Rander; B. Ecker, G. Yonas and D. Drickey, Phys. Rev. Letters 24, 283 (1970).
7. N. Rostoker, "Acceleration of Ions in Intense MeV Electron Beams," VII International Conference on High Energy Acceleration, Yerevan, Armenia, USSR (1969); S. Graybill, et al., DASA Report No. 2477, Defense Nuclear Agency, Washington, D.C. (1970).
8. Radial electrostatic effects include both the mechanism of localized pinch model (references 4 and 5) and radial blowup in the beam head due to beam space charge forces.
9. J. Rander et al., Physics International Company Report No. FIIR-2-71 (unpublished).
10. G. Kuswa, Annals of the New York Academy of Science, 1974 (to be published).
11. D. Swain, G. Kuswa, J. Poukey and C. Olson, to be published in the Proceedings of the IXth International Conference on High Energy Accelerators, Stanford, California, May 1974.
12. C. Olson, to be published in the Proceedings of the IXth International Conference on High Energy Accelerators, Stanford, California, May 1974.
13. The observed net currents in our studies were typically 84 kA, which is twice the Alfven limiting current, so $(\nu/\gamma)_{net}=2$. Radial electrostatic fields can relax the Alfven current limitation, and this observation may be evidence of the existence of such fields over substantial portions of the beam pulse width.
14. G. Yonas, P. Spence, B. Ecker, Current Neutralization in High ν/γ Relativistic Electron Streams, Physics International Company Report No. PIIR-8-70 (1969).

COLLECTIVE ION ACCELERATION IN LINEAR ELECTRON BEAMS*

D. W. Swain, G. W. Kuswa, J. W. Poukey, and C. L. Olson

Sandia Laboratories

Albuquerque, New Mexico

Summary

Collective acceleration of ions by intense relativistic electron beams injected into low pressure neutral gases has been observed at several laboratories over the past six years.[1-4] A theory recently proposed by Olson has been successful in explaining the existing data.[5] In the experiments reported here, the acceleration mechanism is studied for a beam injected into a guide tube containing (i) vacuum, (ii) neutral gas with uniform pressure, and (iii) neutral gas with a pressure gradient (both positive and negative gradients are considered). A unique feature of these experiments is that time-resolved energy measurements of the ions were made. The results are explained in relation to the Olson theory, and numerical simulation results are given which confirm this explanation. In all cases, ion acceleration occurs in the electric fields of a time-dependent, 2D, electrostatic, potential well.

Experimental Apparatus

A 2 MeV electron beam which rose to $\sim$ 100 kA in $\sim$ 70 ns was produced by Reba.[6] Current and voltage wave forms are shown in Fig. 1. The 1.9 cm diam Aquadag-coated aluminum cathode was spaced 1.1 *cm* from the 0.0025 *cm* thick aluminum anode foil. The beam emerged from the foil and entered a 5 cm diam stainless steel or copper-lined glass drift section 1 m long. A 1.5-3 mm diam aperture at the end of the drift tube served as the first collimator for particles entering a mass spectrometer, and served as part of a differential vacuum *pumping* system which could maintain 10^{-6} Torr in the spectrometer with 1 Torr in the drift tube. A second aperture 0.33 mm diam was placed at the input to the mass spectrometer; an admittance solid angle of $\sim 10^{-7}$ steradians was defined by the two apertures together.

The Thomson parabola momentum and energy analyzer has been described in detail previously.[7] For constant fields, particles with charge Ze and mass Mm_p (where m_p = proton mass) are deflected so that the trace formed by each M/Z species falls on one branch of a unique parabola. This apparatus is shown in Fig. 2. An example of typical spectrometer data obtained by injecting the electron beam into an evacuated drift region is shown in Fig. 3. Electric deflections along the x axis and magnetic deflections along the y axis are related to the energy $\mathcal{E}$ in eV and the potential across the deflector plates φ, by:

$$E = ZV_s \varphi/x$$

$$\mathcal{E} = Z^2 B_s / My^2 \quad , \quad \text{where } V_s \text{ and } B_s \text{ are constants.}$$

Simultaneous solution of these equations gives the mass/charge ratio M/Z; $\mathcal{E}$ can then be found from either equation.

The time of arrival of particles was determined by applying a fast-rise, slaw-fall ramp voltage to the deflector plates, which was accurately timed in relation to the electron beam.[7] The traces, which deviated strongly from the parabolic shape, were interpreted by the following method: (1) $\mathcal{E}$ was found from magnetic deflections y of points on a curve of known mass; (2) from $\mathcal{E}$ and measured values of x,φ was determined for each such point; (3) from the known $\varphi(t)$ waveform, arrival times at the analyzer were found.

A puff of gas (usually H_2 or D_2) could be introduced into either end of the drift tube by firing a "puff valve"[8] that was connected to a side port in the tube. The resulting pressure gradient changed with time; varying the delay time between opening the puff valve and firing the beam allowed the beam interaction with various pressure distributions (Fig. 4) to be examined.

Experimental Data

Energy Spectra and Species

The vacuum shots were taken with a drift chamber pressure $\leq 10^{-3}$ Torr. A typical vacuum shot picture from the energy analyzer is shown in Fig. 3. The parabolas shown, starting from the top, correspond to M/Z ratios of 1.0, 3.0, 4.0, 6.1, 8.0, 11.8, and 15.2. We attribute the M/Z = 1 to H^+, and the M/Z = 3, 4, 6.1, and 11.8 to C^{4+}, C^{3+}, C^{2+}, and C^+, respectively. M/Z = 8 and 15.2 may be O^{2+} and O^+ (determination of M/Z becomes less accurate for higher M/Z; the measured value of 15.2 is probably 16). This shot is representative of results obtained for pressures $\leq$ 0.015 Torr at the anode foil. For such shots many ion species were accelerated and broad energy continua ranging from 0.1 to, 5 MeV were observed. As pressure was increased above 0.015 Torr, impurity ions began to disappear; above 0.050 Torr, only ions of the fill gas were observed.

Time Resolved Data

The quantities determined from an energy analyzer data point (x_i, y_i) are the ion energy $\mathcal{E}_i$ (and velocity), and the arrival time t_i at the analyzer. These data are shown by the dots at z = 2.2 m on Fig. 5, with lines on the z-t plot representing the ion velocity at the analyzer drawn through these points. In the differential pumping section (between z = 1.0 and 2.2 m) the ions should move at constant velocity since the space charge is small and electric fields in this region are low. In the drift region, we have no reason *a priori* to assume that the ions move with constant velocity. However, the extrapolation of the constant velocity lines back into the drift region as shown in Figs. 5-7, indicates that the ions may have been accelerated in a fairly localized region (10-20 cm), and at approximately the same time. This acceleration cannot occur until the beam current exceeds a certain critical current (see theory) which in our case is about 40 ns after the start of the beam pulse. In addition, numerical simulation results indicate that the bulk of the acceleration (although not all) should occur in a region 10-20 cm long.

Figure 5 is a vacuum shot for which time resolved data of accelerated H^+ and D^+ was obtained. The D was supplied from TiD_2 powder coated on the drift tube side of the anode foil. Figure 6 is a uniform pressure shot at 0.065 Torr. In both cases, acceleration appears to occur within 20 cm of the anode. The arrival time of the ions is known to within $\pm$ 5 ns for the higher energy ions. For the slower ions (< 0.2 MeV), the uncertainty in arrival time gradually increases to

Work supported by the U.S. Atomic Energy Commission.

± 20 ns due to the exponential decay of the voltage pulse applied to the deflector plates. The ion energy is known to within 5%. However, the point of intersection of two z-t lines which are nearly parallel can be changed significantly by a small change in either $\mathcal{E}_i$ or t_i for one line. Therefore, the intersections of the z-t lines on the figures are subject to rather large errors, particularly for the low energy ions.

Gradient Shots

The effect of a pressure gradient along the drift tube has not been investigated previously. We have performed a series of experiments to measure the influence of this parameter on the ion acceleration process. Pressure gradients measured in the drift tube are shown in Fig. 4 and the results of ion observations are listed below.

Pressure increasing away from anode. 1. For pressures at the anode of less than approximately 0.015 Torr, the accelerated ions had all the characteristics of a vacuum shot (Fig. 3). Higher pressure farther down the tube due to the gradient did not modify these characteristics, so we infer that the acceleration process occurred locally near the anode. Mean free paths for 1 MeV ions are much longer than the tube length; scattering of accelerated ions with drift tube gas was therefore negligible.

2. For H_2 (or D_2) pressures at the anode of 0.02 - 0.1 Torr, H^+ and H^+_2 (or D^+ and D^+_2) ions were observed, with intensities and maximum energies comparable to shots in which the uniform drift tube pressure was in this range.

3. For all the conditions that we examined, no significant enhancement over the results of uniform pressure shots of the maximum ion energy, or the number of accelerated ions, was observed. Streak camera photos of the beam indicated that the front velocity did not change significantly as a function of position down the tube in any of these experiments.

Pressure decreasing away from the anode. In this series of experiments the beam propagated first into a high pressure region and then into vacuum as it moved down the tube.

1. The number of ions recorded by the analyzer increased over the steady fill shots by a factor of 2 or more.

2. The energy spectrum was broad (0.1 to ≥ 1 MeV) and only the ions of the filling gas (usually H_2 or D_2) were seen. Maximum energy was laver than in the steady pressure shots (1 - 1.5 MeV vs. 3 - 4 MeV).

3. Time-resolved measurements for different puff valve delay times were made. Sample results are shown in Fig. 7. The intersection points of the extrapolated ion trajectories suggest that the ions are accelerated as the beam propagates out of the pressure front. Two distinct ion species, H^+ and H^+_2, are observed on some traces; the solid trajectory lines are calculated for $M/Z = 1$ and the dashed trajectories are calculated for $M/Z = 2$.

Theory and Numerical Simulation

The recently proposed theory of ion acceleration by Olson[5] has been successful in explaining the collective acceleration of ions observed in drifting beam experiments with uniform neutral gas pressures. In this theory, ion acceleration occurs in the electrostatic fields of a 2D potential well whose time-dependent motion is governed by the self-consistent coupling between the bean dynamics and the ionization processes of the neutral gas. Here we note that the acceleration mechanism is operative only if the injected current I is greater than the space charge limiting current I_ℓ, which in our case is ≈ 40 kA. For $I \geq I_\ell$, a stationary well forms near the anode With a depth of 2 to 3 times the beam energy. As the beam becomes charge neutralized, a non-adiabatic transition occurs, the well depth drops to the order of the beam energy, and the beam begins to propagate. In the context of the present experiments, charge neutralization may occur in several distinctly different ways: (i) ions *may* be drawn *from* the anode plasma, (ii) ions may be created by ionization of the neutral gas, and (iii) in a decreasing pressure gradient, ions from the higher pressure region may be drawn out into the low pressure region. These three cases correspond, respectively, to vacuum shots, constant fill pressure shots, and negative pressure gradient shots (for steep gradients). Brief discussions of each case follow.

Vacuum Shots

In this case the beam remains stopped at the anode until a sufficient number of ions (created in the anode plasma) can be drawn into the deep well region. When the dynamic ion background density is sufficient to provide approximate charge neutrality, the beam may begin a "quasi-propagation" stage in which beam "propagation" is consistent with the drawn-out, dynamic ion background. The highest ion energies are predicted to be of order 2 to 3 times $Z\mathcal{E}_e$ (where Z is the ion charge, and $\mathcal{E}_e$ is the beam electron energy).

Constant Pressure Shots

In this regime, the neutral gas is ionized faster than anode plasma ions can be drawn off, and the usual drifting beam acceleration phenomena (as observed at several laboratories) occurs. In the experiments here, the transition between "vacuum-type" shots and true "constant-pressure" shots occurs at about %hepressure p = 0.015 Torr H_2, i.e., below this pressure anode ions dominate the charge neutralization process and the event looks like a vacuum shot. Above this pressure, gas ions determine the moving beam front speed and ion energies of order 2 to 3 times the beam energy (for protons) result. For pressures above a critical pressure %, the beam becomes charge neutralized during the beam risetime before the limiting current I_ℓ is reached; consequently the beam never stops at the anode, a deep well never forms, and no accelerated ions should occur. Because the beam risetime is so large here (~ 70 ns), p_R is comparatively low ($p_R \approx 0.15$ Torr H_2). For a fast current rise, the 2-D well theory predicts a high pressure regime for which the final accelerated ion velocity is proportional to the pressure in the drift region." However, this regime was not accessible in this experiment because p_R was so low. This means that increase of the ion energy above 2 to 3 times $Z\mathcal{E}_e$ should not occur with the given beam parameters.

Gradient Shots

For pressure increasing away from the anode, the results will depend mainly on the pressure at the anode, and the results should be similar to those for constant fill pressure. Although the high pressure regime discussed above is not accessible due to the long beam risetime, theory indicates that even if the high pressure regime were accessible, ion energies would not be substantially increased for slowly-varying pressure gradients. For presswe decreasing from the anode, the situation is physically different since the beam eventually encounters a vacuum region. If $p > p_R$ in a region between the anode and some position downstream, then essentially no ion acceleration will occur in that

region. Beyond this position, conventional well acceleration occurs.

To aid in understanding the above experiments, a number of numerical simulations were performed using a $2\frac{1}{2}$-dimensional, finite-size particle code, in which cylindrical symmetry and quasistatic fields (E_r, E_z and B_θ) are assumed. The electron-beam park of the code was described previously.[10] The ions are followed as weighted particles, the weight being determined at the time of the particular ion's creation by solving a rate equation which includes production by both primary electrons and ion avalanche. Charge exchange is taken into account by allowing only ions whose kinetic energy exceeds a given threshold to contribute to further ionization.

Although a variety of cases (vacuum, constant gas pressure, pressure gradient) have been studied with the code, we will here describe *only* one example. Here the drift chamber was 40 cm long, 5 cm in diameter, the H_2 gas pressure was 0.7 Torr at the entrance (anode) end and fell linearly to zero at 20 cm. The 2 cm diam electron beam was injected parallel to the z *axis* with a *small* perpendicular energy spread (to correspond to scattering in the anode foil). The input beam energy was 1.8 MeV, and the current was assumed to rise linearly in 5 ns to 40 kA. A relatively short risetime was used here to minimize the computer time required. However, the results should indicate the main features expected for longer risetime beams. The result was that the beam blew up radially near the anode for a few nsec until charge neutralization occurred, then the beam, together with the potential well it produced, moved dawn the tube until it approached z = 20 cm (where the gas pressure becomes zero). For times $\geq$ 15 nsec, a quasi-stationary state existed in which the beam propagated to slightly less than 20 cm, then blew up radially, while the minimum of the potential well remained (except for small fluctuations) fixed at about z = 20 cm. The ions were accelerated by this potential well (whose depth varies from 1 to 2 MV) in agreement with the Olson model. The code calculated the number and energies of the ions as they would be seen by a detector at z = 2.2 m. Figure 8 shows z - t lines for ions reaching this detector at various times. In rough agreement with experimental results the code predicts ion energies of $\sim$ 3 MeV at early arrival times ($\sim$ 100 nsec), and monotonic —— decreasing energies thereafter. Note that the 3 MeV ions have energies greater than the electron beam energy (1.8 MeV) or the potential well depth (which never exceeds 2 MeV).

Conclusions

Collective ion acceleration by intense relativistic electron beams has been examined for conditions of vacuum, uniform pressure, and pressure gradients in the drift tube. The highest ion energies attained are of the order of 2 to 3 times the beam energy, in accordance with the model for the parameter regimes cosidered. Numerical simulation results were also given in *support* of our explanation of the observed results. The theoretical results also indicate that no great enhancement of ion energy should be observed when shooting into pressure gradients; no enhancement was observed experiment ——.

It is concluded that the initial deep well can be used to attain ion energies of order αZe_e where $2 < \alpha < 3$, and e_e is the injected electron beam energy. Since e_e may be up to 10 MeV in existing machines, ion energies per nucleon up to 30 Z/M appear attainable from proper use of the deep well. In order to permit acceleration of ions to very high energies, it appears that artificial means must be invoked to create a steep well and to control its speed. Two new acceleration schemes, which do precisely this, are discussed in the following paper.

References

1. S. Graybill, J. Uglum, J. Appl. Phys. 41, 236 (1970).
2. J. Rander, B. Ecker, G. Yonas, D. Drickey, Phys. Rev. Letters 24, 283 (1970).
3. G. W. Kuswa, L. P. Bradley, G. Yonas, IEEE Trans. on Nuclear Sci. NS-20, 305, (1973).
4. B. Ecker, S. Putnam IEEE Trans. On Nuclear Sci. NS-20, 301 (1973).
5. C. L. Olson, Bull. Am. Phys. Soc. 18, 1356 (1973); C. L. Olson, Annals of the New York Academy of Sciences, to be published (1974), presented March 1974; New York City, New York. C. L. Olson (to be published).
6. D. L. Johnson "Reba, A Pulsed Electron Beam Generator." Sandia Laboratories Report SC-DR-70-872, Albuquerque, New Mexico (1970).
7. G. W. Kuswa, to be published, Annals of the New York Academy of Sciences, (1974); presented March 1974 New York City, New York.
8. G. W. Kuswa, Charles Stallings, Alfred Stamm, Rev. Sci. Instr. 41, 1362 (1970).
9. C. L. Olson, J. W. Poukey, Phys. Rev. A, June (1974) (to be published).
10. P. A. Miller, J. B. Gerardo and J. W. Poukey, J. Appl. Phys. 43, 3001 (1972).

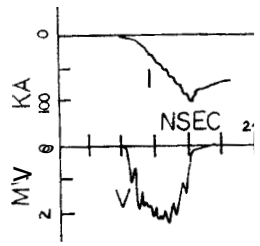


FIGURE 1
Current and voltage waveforms for Reba

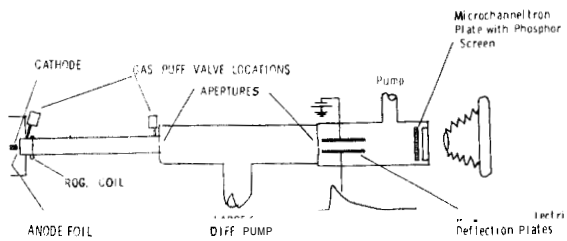


FIGURE 2
Experimental setup

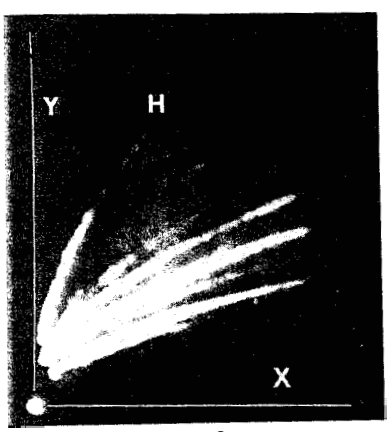


FIGURE 3
Thomson analyzer data for a vacuum shot

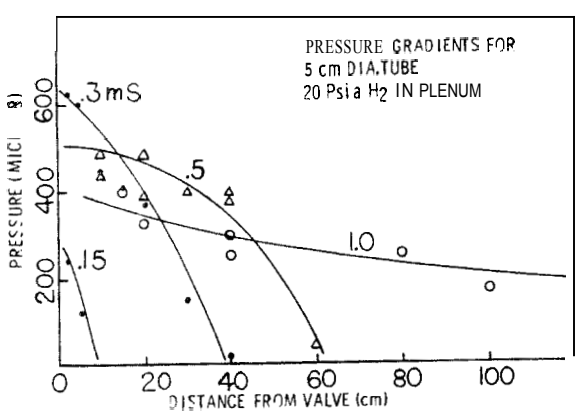


FIGURE 4
Pressure vs. distance from the puff valve for different delay times

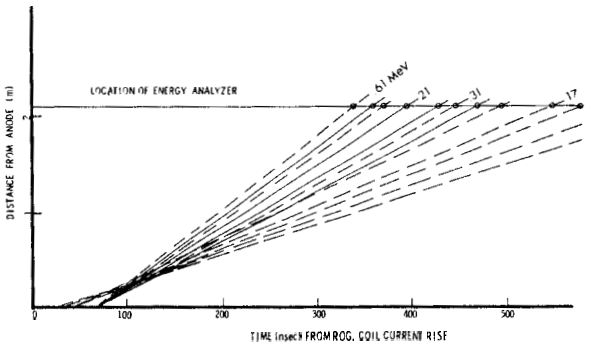


FIGURE 5
Plot of constant velocity ion trajectories for a vacuum shot. Solid lines are H^+, dashed lines are H_2^+ or D^+. Beam current starts at t = 0. Ti_1D_2 powder was coated on the drift tube side of the anode foil. Ion energies are shown for several points.

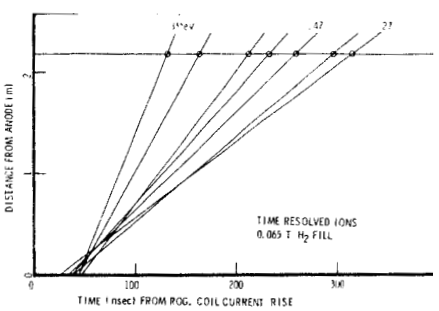


FIGURE6
Ion trajectories for 0.065 Torr H_2 pressure in the drift tube

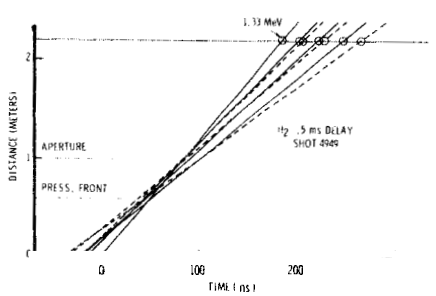


FIGURE 7
Ion trajectories for a pressure gradient shot, pressure decreasing *from* anode. Solid lines are H, dashed lines axe H_2^+.

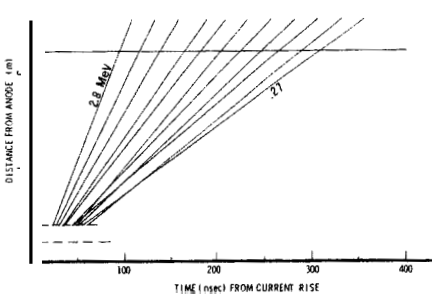


FIGURE 8
Numerical simulation results for ion trajectories

TWO NEW COLLECTIVE ACCELERATION SCHEMES*

Craig L. Olson
Sandia Laboratories
Albuquerque, New Mexico

1. Introduction

Two new ion acceleration schemes are proposed here that utilize the collective fields of an intense relativistic electron beam to provide both the accelerating fields and the focusing fields required to accelerate ions to high energies. Under appropriate conditions, existing intense electron beams can produce accelerating and focusing fields greater than 10^8 V/cm. Also, existing intense beams have the required power and pulse lengths to permit acceleration of protons to energies above 1 GeV and heavy ions to energies above 10 A MeV for $\zeta/A \geq 0.1$ (where A is the atomic mass number and ζ is the actual ion charge number). However, realization of these ion acceleration goals does not appear possible using conventional methods of intense beam propagation, or simple variants thereof. Thus the new schemes presented here invoke artificial means to achieve these goals. With these schemes, a new generation of compact, relatively inexpensive, ion accelerators appears feasible.

It has already been demonstrated experimentally that intense electron beams drifted in low pressure neutral gases can collectively accelerate ions to energies greater than the beam energy.[1-11] Accelerating fields of the order of 10^6 V/cm over a few cm have been reported. Various theories involving space charge fields,[12-17] inductive fields,[18-21] and collective wave fields[22] have been proposed to explain this phenomenon. However, it has been shown[23-25] that these theories are unable to account for the existing data,[1-8] and a new theory[25-27] was recently proposed which has been successful in explaining the existing data. In this theory, ion acceleration occurs in the time-dependent space charge fields of a 2D potential well, whose motion is governed by the self-consistent coupling of the beam dynamics with the ionization processes of the background gas. This theory predicts that there are several limitations to the observed acceleration process[27] (including well slip-out, beam front runaway, and charge exchange cutoff processes). Also axial variation of the pressure or guide tube radius does not appear to permit an effective increase in the ion energy.[28-30] In addition, to maintain a steep, moving potential well requires that the propagating beam front current risetime length $\beta_f c t_r^*$ be of order r_b, where $\beta_f c$ is the beam front speed, $r_b \beta_f c \ll \beta_e c$, $\beta_e c$ is the electron speed, t_r^* is the current risetime associated with the beam Front, and r_b is the beam radius. (The time t_r^* is determined from equilibrium beam front conditions, and it may be substantially different than the injected beam current risetime.) For typical parameters ($\beta_f \approx 0.1$, $r_b = 1$ cm), this would require $t_r^* \approx 0.3$ ns, whereas $t_r^* \sim 10$ ns is observed.[5,8] Thus it appears that artificial means must be employed to create a small risetime (to maintain large accelerating fields) and to control the well speed (to permit ion acceleration over substantial distances).

We now present the new schemes, their characteristic parameters, and some numerical examples based on existing intense beam machines. Then these schemes are compared briefly with conventional accelerators (linacs, synchrotrons) and other collective acceleration methods (ERA, auto-resonant acceleration, inverse coherent Cerenkov radiation, impact acceleration, and non-linear wave methods).

2. New Collective Acceleration Schemes

The basic concept involves creating a single steep potential well and controlling its motion.[31] If a beam with fractional space charge neutralization f_e is propagating inside a metallic drift tube whose radius equals the beam radius, then the potential difference between the guide tube wall and the center of the beam is[24]

$$\phi = \frac{I_o}{\beta_e c}\left\{1 + \frac{\nu}{\gamma}\left[1 - (1 - f_e)\,\beta_e^{-2}\right]\right\} \qquad (1 - f_e) \ . \quad (1)$$

Here I_o is the injected beam current, the Budker parameter ν is the number of beam electrons per classical electron radius, $\gamma = (1 - \beta_e^2)^{-1/2}$, and $\nu/\gamma < 1$ is assumed. A radial electric field of order $E_r = \phi/r_b$ is thus associated with the beam. If axially a sharp charge neutralization front is created so that f_e drops suddenly from unity to zero over an axial distance $z \leq r_b$, then an axial electric field of order

$$E_r = I_o(1 + \nu/\gamma)^{1/2}\,(\beta_o c\, r_b)^{-1} \qquad (2)$$

will be produced. The schemes below use different means to achieve the field (2). The desired well motion corresponds to constant acceleration of a particle, i.e., the well location z(t) should be (relativistically)

$$z = (c^2/a^*)\left\{\left[1 + (a^* t/c)^2\right]^{1/2}\right. \qquad (3)$$

where $a^* = d(\gamma_i M \beta_i c)/dt$ is a constant and $a^* \leq \zeta e\, E_z/M$ (*e* is the charge of an electron, M is the ion rest mass, and $\beta_i c$ is the ion speed). In the non-relativistic limit ($\beta_i \ll 1$), (3) reduces to the classical result $z = (1/2)a^* t^2$. The schemes below use different means to achieve the desired well motion (3).

Linear Collective Accelerator

The basic concept is indicated schematically in Fig. 1. An intense beam is injected into a metallic drift tube of radius $R \approx r_b$. The tube is filled with an appropriate working gas at a pressure low enough that ionization by the beam is essentially negligible. An external "ionizer" is then used to ionize the gas as indicated, and a steep moving potential well is created at the beam front. Excess secondary electrons escape to the walls essentially instantaneously.[26] The beam front speed $\beta_f c$ would be the same as the ionizer speed $v_i(t)$, while the beam electrons would continually stream through the beam front and diverge to the walls since $\beta_f \ll \beta_e$. The densities n_b, n_i^s, nf, n_e^{net} [which

* This work supported by the United States Atomic Energy Commission.

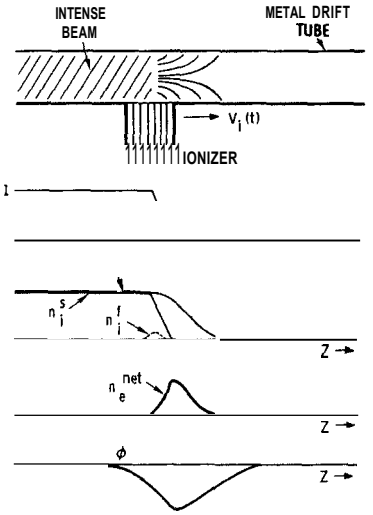


FIGURE 1. **LINEAR COLLECTIVE ION ACCELERATOR**

corresponds to the beam electrons, the background ions, the (fast) moving ions, and the net electron density] would be as indicated in Fig. 1. Many forms have been considered for the "ionizer," the most viable one to date being UV laser photo-ionization of a suitable background gas. [Note that a W window would be necessary along the side(s) of the guide tube]. Several methods of producing a well-controlled sweep of the laser along the guide tube have been considered. One such method entails irradiating several optical paths simultaneously, where each path terminates at a successive position along the guide tube. By having the path lengths increase systematically, the laser could be made to appear to sweep down the drift tube with a motion approximating (3).

Transverse Collective Accelerator

The basic concept is indicated schematically in Fig. 2. Here the intense beam is transported a distance in a charge neutralizing medium (a plasma of density $n_p \approx n_b$) and then injected transversely

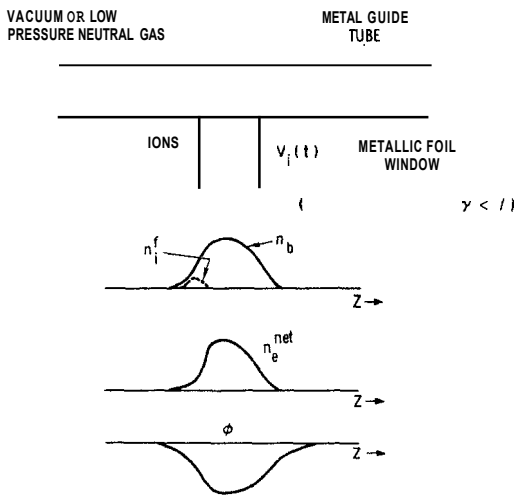


FIGURE 2. **TRANSVERSE COLLECTIVE ION ACCELERATOR**

through a metallic foil window into a metallic guide tube of square cross section (the length of each side being about equal to $2r_b$). A vacuum, or gas at a pressure low enough that beam ionization is negligible is contained in the drift tube. Inside the drift tube, the unneutralized beam blows up, and creates a steep potential well as indicated. The well is made to move by deflecting the beam in the region prior to its injection into the ion drift tube. Several methods for deflecting the beam have been considered. One such method involves a rising, external magnetic field $B_o(t)$ over the whole drift region prior to the ion drift tube. With this method, the ion drift tube could be curved to help maintain approximately normal injection.

Both schemes use the beam electrons just once to contribute to the accelerating field. Both schemes use the intense beam with its injected radius r_b; no focusing of the beam to smaller radii is required. In both schemes, the steep potential well is created rather easily. The main difficulties involve sweeping the W laser (linear scheme), or sweeping the intense beam (transverse scheme).[32] The ion bunch output from either scheme would be a very short (subnanosecond), high intensity (kA), ion bunch.

3. Characteristic Parameters

The intense beam (for either scheme) should have $\nu/\gamma < 1$ to permit propagation in the charge-neutral (but not current-neutral) state. For proton acceleration to high energies, it is necessary to have $\nu/\gamma \ll 1$ to insure the electrons have $\beta_z > \beta_i$. On the other hand, ν/γ as large as possible is desirable to maximize I_o, and therefore E_z [see (2)]. Thus typically, ν/γ would be in the range $0.1 \leq \nu/\gamma \leq 0.7$, and the corresponding beam impedance $30(\gamma - 1)(\beta_e\nu)^{-1}$ would be 50 Ω or larger. Intense beam quality would not be a problem since the drift tube acceptance for a charge-neutral beam typically matches the injected beam emittance reasonably well.

The ions would have energy $\mathcal{E}_i = \zeta\, eE_zL$ where E_z is given by (2) and L is the acceleration length, consistent with the beam pulse Length t_b. The number of ions per pulse would be $N = \xi(4/3)\,\pi r_b^3\, n_b\, \zeta^{-1}$ where $0.01 \leq \xi \leq 0.1$ ($\xi \approx 0.25$ has been observed in drifting beam experiments[1-3]). The ion pulse length would be $t_i \approx r_b/(\beta_i c)$. The emittance and energy spread would, of course, depend on the mode of operation (see examples below). The macroscopic duty cycle would be very small as in the ERA.

The energy required for the UV laser (linear scheme), or $B_o(t)$ (transverse scheme), would be but a very small fraction of the intense beam energy. For the linear scheme, the background gas must he easily obtainable, the photoionization cross-section σ should be as large as possible, and windows and mirrors must he available for the wavelength λ chosen. For direct photoionization, the optimum choice presently is to use Cs vapour ($\lambda \leq 3184$ Å, $\sigma \approx 0.2$ Mbn[33]). Typically the required laser power is high ($\sim 10^8$ W) but the total laser energy needed is low (< 0.1 joule). For the transverse scheme, $B_o(t)$ would be required to rise from zero to about 100 G over a time scale of tens of nanoseconds. Again, the required power would be high ($\sim 10^8$ W) but the total field energy would be low (a few joules). The obvious choice for power to supply $B_o(t)$ would be to tap a small portion of the intense beam power supply (since existing intense beams can easily create kilogauss fields on nanosecond time scales).

The relative energy efficiency $\eta \equiv$ (ion energy out)/(intense beam energy in) is $\eta = N\mathcal{E}_i(\pi r_b^2\, n_b c\beta_z t_b \mathcal{E}_e)^{-1}$. For $\mathcal{E}_i = 1$ GeV, $\xi = 0.01$, $\eta \sim 0.3\%$ typically. This can

be compared, e.g., with the equivalent η for RF systems ($\eta < 1\%$) in conventional proton linacs. The great advantage here is that a REB power system is less expensive and much simpler than an equivalent RF power system.

In regard to possible power loss mechanisms, we have considered instabilities (e.g., the relativistic two-stream instability[34]), radiation losses [e.g., accelerated ion bremsstrahlung losses in the linear scheme (esp. for a high Z background gas), and synchrotron radiation losses in the transverse scheme], charge exchange losses (esp. for heavy ions), and gas scattering losses. In general it appears that all of these effects will not grossly affect the basic pro osed ion acceleration scheme. Also, it has been shown[**] that once the potential well is moving, background ions should not interfere with the acceleration process since they will not be picked up by the moving well.

4. Numerical Examples

Several examples of both schemes have been investigated. Two examples of the linear scheme are given here.

1 GeV Proton Accelerator

Consider a beam with $\mathcal{E}_e$ = 3 MeV, I_o = 30 kA, t_b = 70 ns, and r_b = 1 cm. The drift tube has R = 1 cm and L = 10^3 cm, and the working gas is Cs (produced by heaters) at pressure p = 0.01 Torr. The laser is Nd frequency quadrupled with power $\sim 10^9$ W. Protons (either injected at very low velocity at the beginning of the drift tube, or produced by beam ionization of a small puff of H_2) will attain energy $\mathcal{E}_i$ = 1 GeV. Assmming ξ = 0.01, the ion pulse has current $I_i \approx$ 0.3 kA, pulse length $t_i \approx$ 0.04 ns, and number $N \approx 10^{11}$. The emittance is less than 20 cm mrad, and the energy spread $\Delta\mathcal{E}_i/\mathcal{E}_i \approx 0.1\%$. The total energy in the beam, the accelerated ions, and the ionization energy (required for the laser to permit complete charge neutralization) are 6.3 kJ, and 16 J, and 0.01 J, respectively. Note that a very small amount of laser energy is required to control the very large amount of beam energy to accelerate the ions.

Heavy Ion Accelerator ($\geq$ 10 A MeV for $\zeta/A \geq 0.1$)

The beam front velocity can be controlled to provide essentially any desired well velocity. Consider a beam with $\mathcal{E}_e$ = 1.5 MeV, I_o = 30 kA, t_b = 70 ns, and r_b = 1 cm. Then ions with $\zeta/A \geq 0.1$ (either injected at low energy, or produced by beam stripping of a small puff of gas at the beginning of the drift tube) will attain energy $\mathcal{E}_i \geq 10\,A$ MeV. The acceleration length scales as ζ/A, and would be L = 10^2 cm for ζ/A = 0.1.

5. Comparison with Other Schemes

The electric fields in several different collective acceleration methods, and in conventional accelerators, are compared with those of the new schemes in Table I. Three sets of intense beam parameters are considered. In addition, it should be noted that the new schemes require no external magnetic focussing system, nor do they require a high vacuum system [compare, e.g., proton synchrotrons which have magnet systems of 1000's of tons of steel, and high vacuum systems ($p < 10^{-5}$ Torr)]. The high electric fields in the new schemes permit GeV proton energies in lengths of a few meters (compare, e.g., proton linacs which require about a half mile to achieve 1 GeV). Following are some brief comments on other collective methods, in reference to Table I.

(i) The autoresonant accelerator scheme[35] is based on the assumption that a single, large-amplitude, wave of the desired type (lower cyclotron mode) can be created when an un-neutralized intense beam propagates along a strong (but spatially decreasing) external magnetic field B(z). In keeping with the linear theory used, an estimate of E, is

$$E_z \ll (\Omega/c)[1 + (\omega_o/\Omega)]\, I_o(\beta_e c)^{-1} \qquad (4)$$

where $\Omega = eB(z)(\gamma mc)^{-1}$, and ω_o is the constant frequency of the mode. Also, in meeting several sufficiency conditions for equilibria and stability,[35] one finds that the required B(z) is typically very large [B(0) $\geq$ 100 kG], and that the total external magnetic field energy required is of the order of the total beam energy.

(ii) Inverse coherent Cerenkov radiation, as proposed by Veksler,[36,37] can produce a field

$$E_z = N\zeta e\, \omega_b^2\, F\, V^{-2}\, \ell n[1 + (V/V_\theta)^2] \qquad (5)$$

where $N = (4/3)\,\pi\,\ell^3\, n_i$, $\omega_b^2 = 4\pi n_b\, e^2(\gamma m)^{-1}$, $n_b(n_i)$ is the beam (ion bunch) density in the laboratory frame, ℓ is the bunch dimension, and $V(V_\theta)$ is the ion bunch (beam thermal) velocity in the beam frame. Validity of (5) requires[23]

$\ell \ll \lambda_d$	(coherent radiation)
$\ell \ll r_b$	(bunch immersed in beam)
$n_i \ll n_b$	(so bunch is small perturbation; and also so no gross space charge spreading)
$\lambda_d \ll r_b$	(so wave picture correct)

Here, the Debye length $\lambda_d = 2\pi k_d^{-1}$, $k_d^2 = 4\pi n_b\, e^2 T_e^{-1}$, and T_e is the average beam transverse energy in the beam frame. In Table I, we assumed ℓ is the smaller of $\lambda_d/3$ or $r_b/3$, $n_i = n_b/10$, F = 1 (a form factor), and the ℓn term equals unity.

(iii) Impact acceleration, as proposed by Veksler,[36,37] involves a collision between a fast (y), heavy bunch N_1M_1 (dense electron bunch) and a light bunch N_2M_2 (ions). Each ion receives energy $2\gamma^2 M_2c^2$ provided the bunches remain intact during the collision, and provided

$$\gamma N_2 M_2 \ll N_1 M_1 \qquad (6)$$

$$p^* \leq N_1 N_2 e^2 (M_o c^2)^{-1} \qquad (7)$$

$$\ell < p^* \qquad (8)$$

where $M_o \equiv (M_1M_2N_1N_2\gamma)(M_1N_1 + \gamma M_2N_2)^{-1}$. In Table I, we consider the projectile bunch N_1M_1 to be a spherical segment of the intense beam, with $N_1 = (4/3)\pi r_b^3 n_b$. The peak current associated with this bunch is $I = \pi r_b^2 n_b e\beta_e c$, or $I = (3/4)\beta_e c N_1 r_b^{-1}$. But (6)-(8) combine to give $r_b = \ell < N_1 e^2(\gamma M_2 c^2)^{-1}$. Thus it is required that

$$I > (3/4)\,\beta_e\gamma\, M_2 c^3 e^{-1} \qquad (9)$$

or

$$I > \beta_e\gamma\,(23.4)\ \text{MA} \qquad (10)$$

for M_2 equal to the proton rest mass. Roughly, (9) is $I > M_2 M_1^{-1} I_A$ where the Alfvén-Lawson limiting current is $I_A = \beta_e \gamma M_1 c^3 e^{-1}$. The current required by (9) is considerably above that available with present intense beam technology.

(iv) Relativistic solitons and nonlinear waves have been studied extensively in the Soviet Union (see, e.g., Rabinovich and Tsytovich[38]). However, assessibility of these methods is not yet possible, since neither solitons nor nonlinear waves (for ion acceleration) have been demonstrated experimentally.

(v) Electron ring research has been actively pursued for many years now. Here we only note that several instabilities limit the holding power, and Möhl et. al.[39] recently concluded that the maximum holding power of an electron ring should be (with no safety factors) $E < 4.5 \times 10^5$ V/cm.

In summary, Table I shows that the new schemes could produce very high accelerating electric fields, and that these schemes offer distinct advantages in relation to other collective acceleration methods or conventional acceleration methods.

6. Conclusions

Two new methods of collective ion acceleration have been given. Both utilize an intense relativistic electron beam to create an accelerating field and a focusing field. Both should permit the realization of a compact, relatively inexpensive, high energy ion accelerator. It is emphasized that accelerating fields of order 10^8 V/cm have already been demonstrated experimentally. In addition, existing intense beams have the power *and* pulse lengths required to accelerate protons to GeV energies and heavy ions to energies above 10 A MeV for $\zeta/A \geq 0.1$. Even higher ion energies appear possible, using state of the art intense beam technology [as in case (2) of Table I] or future technology [as in case (3) of Table I]. Experiments designed to study the validity of the acceleration methods proposed here have been planned.

ACKNOWLEDGEMENTS

Comments from G. Kuswa, D. Swain, J. Poukey, J. Freeman, and G. Yonas are gratefully acknowledged.

		CASE 1	CASE 2	CASE 3
	INTENSE e-BEAM $\mathcal{E}_e$	1.5 MeV	15 MeV	15 MeV
	INTENSE e-BEAM I_o	30 kA	300 kA	300 kA
	INTENSE e-BEAM r_b	1 cm	1 cm	0.1 cm
	INTENSE e-BEAM n_b	$\sim 2.5 \times 10^{12}$ cm^{-3}	$\sim 2.5 \times 10^{13}$ cm^{-3}	$\sim 2.5 \times 10^{15}$ cm^{-3}
NEW	NEW SCHEMES	$\sim 10^6$ V/cm	$\sim 10^7$ V/cm	$\sim 10^8$ V/cm
COLLECTIVE ACCELERATION METHODS	AUTO-RESONANT ACCELERATION	$\sim 10^5$ V/cm	$\sim 10^6$ V/cm	$\sim 10^7$ V/cm
COLLECTIVE ACCELERATION METHODS	INVERSE COHERENT CERENKOV RADIATION	$\sim 10^4$ V/cm	$\sim 10^5$ V/cm	$\sim 10^6$ V/cm
COLLECTIVE ACCELERATION METHODS	IMFACT ACCELERATION	method not possible due to insufficient current [requires $I_o > (23.4)\ \beta_e \gamma$ MA; see (10)]		
COLLECTIVE ACCELERATION METHODS	SOLITONS	method not assessible yet; need experimental demonstration of relativistic soliton		
COLLECTIVE ACCELERATION METHODS	ELECTRON RING ACCELERATORS	maximum holding power is limited by various instabilities [39] to $< 4.5 \times 10^5$ V/cm		
CONVENTIONAL ACCELERATORS	PROTON LINACS	$\sim 10^4$ V/cm		
CONVENTIONAL ACCELERATORS	PROTON SYNCHROTRONS	$\sim 5 \times 10^5$ V/(cm circumference), i.e., 0.1 - 1 V/cm but particles make 10^5 - 10^6 passes via cyclic nature		

TABLE I.

Comparison of effective electric field produced by various ion acceleration methods for three *sets of* intense e-beam parameters ($\zeta = 1$). Cases 1, 2, and 3 represent respectively, a typical existing beam, a state-of-the-art beam, and a beam that would require future technology to permit its existence and propagation over sizeable distances.

REFERENCES

1. S. E. Graybill and J. R. Uglum, J. Appl. Phys. 41, 236 (1970).
2. S. E. Graybill, IEEE Trans. Nu. Sci. NS-18 (#3), 438 (1971).
3. S. E. Graybill, IEEE Trans. Nu. Sci. NS-19 (#3), 292 (1972).
4. J. Rander, B. Ecker, G. Yonas, and D. J. Drickey, Phys. Rev. Lett. 24, 283 (1970).
5. J. Rander, Phys. Rev. Lett. 25, 893 (1970).
6. J. Rander, J. Benford, B. Ecker, G. Loda, and G. Yonas, Physics International Company Report PIIR-2-71.
7. B. Ecker and S. Putnam, IEEE Trans. Nu. Sci. NS-20 (#3), 301 (1973).
8. G. Kuswa, L. P. Bradley, and G. Yonas, IEEE Trans. Nu. Sci. NS-20 (#3), 305 (1973).
9. A. M. Sessler, Comments on Nuclear and Particle Physics 3, 93 (1969).
10. J. D. Lawson, Particle Accelerators 3, 21 (1972).
11. G. Yonas, Particle Accelerators 5, 81 (1973).
12. N. Rostoker, Bull. Am. Phys. Soc. 14, 1047 (1969).
13. N. Rostoker, VII Int. Conf. on High Energy Accelerators, Yerevan, Armenian SSR; N. Rostoker, Cornell University Report LPS 21 (1969).
14. J. R. Uglum, S. E. Graybill, and W. H. McNeill, Bull. Am. Phys. Soc. 14, 1047 (1969).
15. S. Graybill, W. McNeill, and J. Uglum, in Record of Eleventh Symposium on Electron, Ion, and Laser Beam Technology, edited by R.F.M. Thornley (San Francisco Press, San Francisco), 577 (1971).
16. S. E. Rosinskii, A. A. Rukhadze, and V. G. Rukhlin, Zh. Eksp. Teor. Fiz. Pis. Red. 14, 53,(1971); Engl. Trans. In JETP Lett. 14, 34 (1971).
17. J. W. Poukey and N. Rostoker, Plasma Physics 13, 897 (1971).
18. S. Putnam, Bull. Am. Phys. Soc. 14, 1048 (1969).
19. S. Putnam, Phys. Rev. Lett. 25, 1129 (1970).
20. S. Putnam, IEEE Trans. Nu. Sci. NS-18 (#3), 496 (1971).
21. S. Putnam, Physics International Company Report PIFR-72-105 (1972).
22. J. M. Wachtell, and B. J. Eastlund, Bull. Am. Phys. Soc. 18, 1356 (1969).
23. C. L. Olson, "Mechanisms of Ion Acceleration by Drifting Intense Electron Beams," to be published.
24. C. L. Olson and J. W. Poukey, Phys. Rev., to be published.
25. C. L. Olson, Bull. Am. Phys. Soc. 18, 1356 (1973).
26. C. L. Olson, "Theory of Ion Acceleration by Drifting Intense Electron Beams," to be published.
27. C. L. Olson, Annals of the New York Academy of Sciences, to be published.
28. D. W. Swain, G. W. Kuswa, J. W. Poukey, and C. L. Olson, preceding paper.
29. G. Kuswa, Annals of the New York Academy of Sciences, to be published.
30. C. L. Olson and J. W. Poukey, to be published.
31. C. L. Olson, Bull. Am. Phys. Soc. 18, 1369 (1973); C. L. Olson, Sandia Laboratories Report SLA-73-0864 & 5 (1974).
32. Swept beam methods different than that proposed here are mentioned in A. A. Kolomensky, Particle Accelerators 5, 73 (1973). Also, use of a highly-focused, low-current, swept beam was considered by R. M. Johnson, Symp. on ERA, UCRL 18103, 219 (1968).
33. G. Marr, Photoionization Processes in Gases, (Academic Press, New York, N. Y., 1967), p. 115.
34. A. J. Toepfer and J. W. Poukey, Phys. Lett. A, 42, 383 (1973).
35. M. L. Sloan and W. E. Drummond, Phys. Rev. Lett. 31, 1234 (1973).
36. V. I. Veksler, CERN Symposium on High Energy Accelerators, 1, 80 (1956).
37. V. I. Veksler, Atomnaya Energiya 2, 525 (1957).
38. M. S. Rabinovich and V. N. Tsytovich, Particle Accelerators 5, 99 (1973).
39. D. Möhl, L. J. Laslett, and A. M. Sessler, Particle Accelerators 4, 159 (1973).

Darrell Drickey (UCLA): In these collective methods there must be some kind of radial motion of the protons and to my knowledge that is not known very well experimentally. You can extrapolate the longitudinal length, but if everything drops out radially it doesn't work. In order to have any kind of accelerator there must be some kind of radial confinement also. Are there any comments on this?

Craig Olson (Sandia Laboratories): The basic picture is if you have a moving space charge well it looks like a ball of charge which contains both longitudinal and radial fields. These fields tend to concentrate things in the center of the ball. You have decisive accelerating fields and you have focusing in the order of 10^6 volts per centimeter. I don't think confinement should be a problem. We have looked at things numerically shooting beams into gases. Things may oscillate but they stay confined.

I have two other brief comments. The cross sections that I used for the lasser schemes are well known and are published in a book by G. Marr called "Photoionization Processes in Gases". Lastly, these new schemes should not be affected by the usual instabilities since the electrons are only used once. This is one advantage of this scheme over the electron ring accelerator. In the electron ring accelerator you recirculate the electrons many times and many instabilities arise because of this.

A. A. Kolomensky (Lebedev Institute): The electron beam must propagate. During the propagation of this electron beam there arise many instabilities of a very simple nature. These instabilities are both hydrodynamic and kinetic. The electrons may pass through only once, but they are the same electrons passing through the gas and instabilities will arise.

ELECTRON AUTOACCELERATION*

R. J. Briggs, T. J. Fessenden, and V. K. Neil

Lawrence Livermore Laboratory, Livermore, California 94550

Summary

In this paper we describe theoretical and experimental studies of autoaccelerating electrons in an iris loaded pipe. The theory is based on a self consistent one dimensional hydrodynamic model. The computational results indicate that some particles may be accelerated to several times their initial energy provided the proper current vs time is injected, and the initial particle energy is high enough to limit the growth of longitudinal density fluctuations to a tolerable level. An experimental study of the interaction of an intense 3 MeV electron beam with a simple multicavity structure is described, where autoacceleration of some particles by the excited longitudinal r.f. fields was observed.

1. Introduction

The concept of autoacceleration entails the transfer of energy from one group of particles to another. This transfer of energy may he accomplished by means of large electrostatic fields generated by the particles,[1] or by means of electromagnetic energy stored in the surrounding structure by the front portion of a pulse of relativistic particles and subsequently imparted to narticles in the tail of the pulse. With relativistic particles, the energy exchange can proceed over a considerable path length before axial phase oscillations occur.

One conceptually simple example is in a low frequency limit where the structure storing the energy presents an inductive impedance to the beam, so that the axial electric field $E = -LdI/dt$, with L the inductance per unit length and I the beam current. Particles at the trailing edge of the current pulse, where $dI/dt < 0$, are accelerated when passing throuh such a structure.

Other concepts involve the excitation of resonant modes, where the structure may be a single resonant cavity,[2,3] a transmission line,[3,4] or a series of resonant cavities. The possibilities have also been discussed by Kolomensky.[5] The iris loaded pipe studied in this work is in fact a series of resonant cavities, since we treat the case where the electromagnetic coupling between cavities is weak. Note that the excitation of the individual cavities by the beam head results in an automatic phasing of the r.f. fields, thus producing a traveling wave that is automatically synchronous with the relativistic beam particles.

The model used for the computational study of the behavior of the particles in the iris load pipe is described in Sect. 2, where some results of the computations are also presented. The experiments are described in Sect. 3. The main goal of the experiments was to determine if the RF modes excited by the beam could be controlled in such a way that autoacceleration of some particles would occur. In particular, the transverse beam break-up mode was observed and suppressed by alterations in the cavities, while the longitudinal modes were allowed to persist and provide an autoaccelerating mechanism. Section 4 contains a discussion of the instabilities apparent in the theoretical results and observed in the experiment.

2. Theoretical Calculations

We first calculate the axial electric field generated by an electron beam travelling down the axis of an iris loaded pipe. Each section of the structure is treated as a separate cavity with characteristic eigenmodes. The modes contributing to exchange of energy among particles are the azimuthally symmetric TM modes. In each cavity, only these modes with no axial (z) dependence will be considered. In describing the electromagnetic fields in each cavity, we neglect the presence of the hole, consequently neglecting the transfer of energy between cavities by all means except the electron beam.

The model of the beam has uniform current density out to a radius r = a and zero beyond. The current density varies with z and t. The electrostatic field generated by the beam's charge is not considered. This electric field will terminate near the inner edge of the disks and have little effect on the particles' axial motion if the variation in charge per unit length is small over a distance comparable to the radius of the hole.

To calculate the electromagnetic fields, we represent the normal modes of the cavity by their vector potentials $\bar{A}_\ell(\bar{r})$. For the pertinent modes we have

$$\bar{A}_\ell(\bar{r}) = N_\ell J_o(\omega_\ell r/c)\hat{r}, \tag{1}$$

with N_ℓ a normalization constant and ω_ℓ the eigenfrequency of the mode. The eigenfrequencies are determined from the condition $J_o(\omega_\ell b/c) = 0$, where b is the radius of the pipe wall. The vector potential in the cavity, $A(r,t)$, may be expressed as a sum over the eigenmodes. We have

$$A(r,t) = \sum_\ell q_\ell(t) N_\ell J_o(\chi_\ell r/b), \tag{2}$$

in which χ_ℓ is the Rth root of J_o. The electric field from the kth mode is given by $\bar{E}_\ell(r,t) = -(\dot{q}_\ell/c)\bar{A}_\ell(r)$, in which c is the speed of light. Gaussian units are employed in this work, but both theoretical and experimental results are given in practical units.

The method used for determining the time dependent coefficients $q_\ell(t)$ is described in detail in Ref. 6 and will not be given here. We evaluate E_ℓ at the beam radius (r=a) and obtain

$$E_\ell(r=a,t) = -\frac{8J_o(\chi_\ell(a/b)J_1(\chi_\ell a/b)}{ac\chi_\ell^2 J_1^2(\chi_\ell)}\Psi, \tag{3}$$

$$\text{with } \Psi = \int_o^t I(y)e^{-\omega_\ell(t-y)/2Q_\ell}$$

$$\chi[\omega_\ell\cos\omega_\ell(t-y) - (\omega_\ell/2Q_\ell)\sin\omega_\ell(t-y)]dy. \tag{4}$$

We consider only the axial motion of electrons. This simplification is in part justified by the presence of a large (several kG) axial magnetic field. It is convenient to employ the hydrodynamic equations in their Lorentz invariant form. We introduce the variables u and μ by the definitions

$$u = \gamma v/c, \qquad \mu = r_o n/\gamma, \tag{5}$$

in which v is the particles' speed, γ is the particles' energy in units of rest energy, n is the number of particles per unit length in the beam, and r_o is the classical radius of the electron. In terms of these quantities, the beam current I is given by

*Work sponsored by ARPA Order #1377 and U.S. Dept. of Navy, ONR, Govt. Order #NAONR-13-74.

$$I = ec\mu u/r_o, \tag{6}$$

with e the particles' charge, taken to be positive. The quantities μ and u are functions of z and t, and γ and u are related by $\gamma^2 = 1 + u^2$.

The Eulerian equation of motion is

$$\left(\frac{\gamma}{c}\frac{\partial}{\partial t} + u\frac{\partial}{\partial z}\right)u = \frac{e\gamma E}{mc^2}, \tag{7}$$

with m the particles' rest mass. The electric field E is a sum over the electric fields of the eigenmodes. For any z_i, we have

$$E(z_i,t) = \sum_{\ell} E_{\ell}(z_i,t), \tag{8}$$

where $E_{\ell}(z_i,t)$ is found from Eq. (3) with Eq. (6) inserted for I. The continuity equation has the form

$$\frac{1}{c}\frac{\partial}{\partial t}(\mu\gamma) + \frac{\partial}{\partial z}(\mu u) = 0. \tag{9}$$

Equations (7) and (9) are integrated numerically, with u(o,t) and μ(o,t) specified for all time.

We first treat a beam current rising linearly with time at the rate of 1700 A/ns. The initial energy of the particles is $\gamma = 6$. It was found that the values of Q_{ℓ} chosen had little influence on the results if $Q_{\ell} \gtrsim 50$. We choose $Q_{\ell} = 50$ and use the first 20 modes in our calculation. At 2 ns after the start of injection, the electric field is very nearly that calculated for a given current (i.e., neglecting the effect of the field on the particles' motion). For example, Eq. (3) yields $E_1 = -4(1-\cos\omega_1 t)$ kV/cm.

Results of the calculation at 9 ns after the start of injection are shown in Fig. 2. The peaks in the linear charge density are so narrow that the validity of the results is somewhat questionable. The electrostatic field has not been included in the calculation, and the axial component of this field would tend to suppress the formation of these peaks. Nevertheless, the results give some insight into the behavior of the unstable longitudinal bunching. The largest values of E and γ are found around halfway between the injection point and the head of the beam, a behavior consistent with linear theory.

The same calculation was performed using the first mode only, and the results are qualitatively the same. No sharp peaks have occurred at 9 ns, and the peak electric field is enhanced by about a factor of 4 over that at 2 ns. The results suggest that large accelerating electric fields may be achieved by allowing unstable axial motion to occur, but relying on instabilities may impose fundamental limits in the ultimate particle energy multiplication. One of the main goals of the experiment was to investigate this regime.

For $Q_1 = \infty$, it is theoretically possible to choose a current profile I(t) such that the lowest mode of the cavities transfers energy from the front of the beam to the back, and furthermore, no energy is left in the lowest mode after the beam passes. Some energy will be left in the higher modes. For example, we choose a current rising linearly to a value I_{max} in a time T equal to p periods of the fundamental mode, then falling linearly back to zero in one period. It can be verified that for $Q_1 = \infty$, this current shape leaves no energy in the first mode. The electric field of the first mode is of the form

$$E_1 = \begin{cases} -E_o(1-\cos\omega_1 t), & \text{during rise,} \\ pE_o[1-\cos\omega_1(t-T)], & \text{during fall,} \end{cases} \tag{10}$$

with E_o a constant determined by the rate of rise of the current. Thus the accelerating field is p times the decelerating field, and ideally a maximum energy of p times the initial energy may be achieved before stopping the front electrons.

To illustrate the current shaping concept, we choose p = 8 with dI/dt = 1700 A/ns during the rise, To help suppress the longitudinal bunching, we choose $\gamma = 12$ at injection. Results are shown in Fig. 3 at 16 ns after start of injection, We see that the longitudinal bunching is present, even at $\gamma = 12$, but the results at this time are still believable. The particles in the tail of the pulse have an energy ranging from $\gamma = 11$ to $\gamma = 38$. About 2% of the total number of particles in the pulse have energy greater than 90% of the peak energy. The calculation was continued, and at 18 ns the longitudinal bunching still had not affected particles in the tail of the pulse. At this time the peak value of γ was 50. Even though the longitudinal instability occurs during the rise of current, the acceleration of the particles in the tail proceeds as though the electric field were as calculated from the given current profile.

3. Experimental Study

The pulsed diode device (Physics International 422) we used injects a beam of up to 50 kAmp at 2.5-3 MeV with a 30 nsec half width into a 30 cm inside diameter aluminum drift tube that is 130 cm long. The total beam energy measured with a calorimeter at the anode was approximately 2.6 kJ. All experiments were performed at the best obtainable vacuum in the system ($p \approx 10^{-4}$ torr).

The autoaccelerating structure consisted of a series of 30 cm diameter aluminum disks separated by 2.54 cm placed inside the drift tube. A 5 cm diameter hole was punched on axis through the disks to form an iris loaded waveguide structure. The electron beam was fired through these holes and guided by an axial magnetic field of up to 8 kG.

A diagram of the experimental apparatus is presented in Fig. 1. The net beam current flowing in the structure was measured by placing resistive shunts (RS) in the wall of the drift tube and measuring the return current at each side of the anode plane and at the drift tube-end plate junction. In this way the current emitted by the cathode, the current injected into the drift tube and the current leaving the drift tube were monitored. The level and frequency of the r.f. oscillations induced in the autoaccelerating structure were monitored at two axial points with the aid of a Tektronix 7904 direct access oscilloscope and an r.f. coupling loop. This oscilloscope has a 3 db cutoff frequency of 1 GHz. The loop was calibrated with a known signal and it was determined that over the frequency band from 0.5 to 1.0 GHz, the loop calibration varied from .6 to 1 Volt/Gauss.

Beam Drifting Experiments

Initial experiments were performed in which the beam was propagated the length of the drift tube in the presence of a strong (B_z = 8 kGauss) axial magnetic field, with no accelerating structure within the tube. These experiments initialized the beam parameters for the autoacceleration experiment, and essentially repeated the experiment of Mkheidze et al.[7] It was found that only 10-12 kAmps could be propagated as measured with resistor shunt 3. For these experiments the peak diode voltage was 3.0 MV and approximately 600 joules were transfered to a calorimeter on the end plate of the drift tube. In the presence of the space charge potential, the beam current is limited to the value given by Eq. (1) of Ref. 7, namely $I = 17{,}000 \times (\gamma_o^{2/3}-1)^{3/2}/[1 + 2\ln(b/a)]$, with $\gamma_o = 1 + eV_d/mc^2$ and V_d the diode voltage. At this limiting current, $\gamma = \gamma_o^{1/3}$. According to this relation, the space charge limited current is 10.7 kA, in good agreement with the experimental result.

An approximate energy distribution function of the beam at the end plate was obtained by allowing the beam to strike a magnesium target and measuring the flux of energetic electrons in the metal. Details of this technique are given in Ref. 8. This data is presented as a dashed curve in Fig. 4. Note the sharp cutoff of the energy distribution at an energy corresponding to the peak diode voltage.

Autoacceleration Experiments

Initial autoacceleration experiments with 24 disks placed in the drift tube revealed that an intense oscillation at 1.2 Ghz was being strongly excited by the beam. Figure 5 shows reproductions of oscillograms obtained with the aid of the r.f. loops. It was verified by both calculations of the eigenfrequency for our cavity dimensions and bench tests of the structure that this oscillation resulted from excitation of the TM_{110} mode. Bench testing showed that typical "Q's" of the TM_{110} mode at 1.2 Ghz and the TM_{010} mode at 0.8 GHz were 300 to 500. As seen in the oscillograms this oscillation strongly disrupted the beam and limited the transmitted beam current. In order to suppress the excitation of the TM_{010} mode, the disks were sliced along six radii approximately 60° apart from the center hole to within approximately 3 cm of the outer radius. As a result of these slices the TM_{110} mode could no longer be detected even in bench tests, whereas the TM_{010} mode "Q" was reduced by less than a factor of two. With the sliced disks, the disruption of beam propagation and intense 1.2 GHz oscillations were eliminated.

The configuration that produced the most easily detectable autoacceleration in our experiments consisted of the system shown in Fig. 1. A 1.5 cm diameter collimator was placed just after the anode foil, and the beam was drifted a distance of 29 cm in the empty tank before entering the autoaccelerating structure. Figure 4 shows a measurement of the effect of the structure on the beam distribution function obtained with the technique mentioned above. Oscillograms of the signal detected by r.f. loop 2 are shown in Fig. 6. This signal results from the excitation of the TM_{010} mode (as identified by its frequency). Note that the scope gain has been increased by a factor of 25 over that used in obtaining the oscillogram of Fig. 5. In Fig. 6 we also show oscillograms of the current detected by resistor shunt 3. Of particular interest is the prolonged decay of the signal, which suggests that an appreciable number of electrons are being slowed to very low energies by the fields of the structure. Estimates of the r.f. fields in the cavities as obtained from Fig. 6 give an oscillating field of 3×10^4 V/cm on axis. This measurement is consistent with an energy gain or loss of 2-3 MeV over the 90 *cm* length of the structure.

Comments on the Experimental Observations

In a structure of this type, the TM_{110} mode is easily excited and, if not decoupled from the system, will build up to a sufficient amplitude to destroy the electron beam. Under these conditions we found that little or no autoacceleration occurs.

With the disks located close to the anode, autoacceleration effects are barely detectable. When a 29 cm drift space (30 cm tube diameter) separated the disks from the anode plane, the results displayed in Fig. 4 were obtained. The most plausible explanation for the difference between these two configurations is the change in the initial kinetic energy of the beam electrons in the iris structure itself. With the disks placed close to the anode, $\gamma = \gamma_0^{1/3} \simeq 1.8$ in the iris structure. Reducing the beam current from this value (by placing a current limiting drift space in front of the disks) reduces the space charge potential depression in the iris section causing γ to increase in this section. With the latter configuration, γ is estimated to be approximately 4.5 in the structure, and the autoacceleration evidenced in Fig. 4 is observed. (It is also important to note in this connection that when the electrons approach the end plate (ground potential), they recover a kinetic energy equal to the potential depression in the structure.)

The above interpretations suggest a strong dependence of the autoacceleration effect on the initial kinetic energy of the electrons inside the structure. The computational models have also indicated this general trend.

4. Discussion of Instabilities and Limitations On the Energy Gain

Our calculations and experiments have dealt primarily with autoacceleration in a series of relatively high-Q cavities excited by the beam pulse. Amplification of beam density modulations by the beam-cavity interaction can lead to large amplitude electric fields, but it is not clear to the authors that the longitudinal instabilities can be controlled in a way that will produce significant kinetic energy multiplications with reasonable efficiency (i.e., much more than a factor of two). The experiments, although preliminary, also indicate that a broad energy spectrum is produced under these circumstances. Significant energy multiplication before instability growth occurs can be achieved at high γ with special current waveform tailoring, according to the computations presented in Section 2, but the instability still imposes an upper limit to the multiplication. In this section, we briefly review the linear instability picture with a series of cavities. We also discuss the "low frequency" (non-resonant) form of autoacceleration, and its potential limitations.

The linear theory of the instabilities arising from interaction of the beam with the TM_{110} and TM_{010} modes of the iris structure is contained in Ref. 6. The theory is not directly applicable to either the theory or experiment described here, because it assumes a constant injected current, but it provided a useful guide. According to the theory of Ref. 6, the amplitude of longitudinal density fluctuations from the TM_{010} mode interaction and the amplitude of transverse oscillations from the TM_{110} mode both behave as

$$A(z,\tau) \propto e^{-\omega_\ell \tau/2Q_\ell} f(W^{1/3}), \tag{11}$$

in which τ is the time since a local perturbation passed a point z. For interaction with the TM_{010} mode, the quantity W is given by

$$W_L = \frac{2r_o n \omega_\ell \tau}{\beta^2 \gamma^3 J_1^2(\chi_\ell)} \left(\frac{z}{b}\right)^2 \tag{12}$$

The function f is relatively flat for $W^{1/3} \lesssim 4$, then it becomes exponential. For $W^{1/3} > 5$, the behavior of f is given approximately by $f \simeq \exp[1.15(W^{1/3}-5)]$. Exponential growth of the amplitude will therefore not occur at a position z until at time τ such that the condition $1.15(W^{1/3}-5) - \omega_\ell \tau/2Q_\ell > 0$ is satisfied. With the geometry of our apparatus, for a current of 17,000 A, Q = 100, and γ = 6, the theory predicts that exponential growth would set in at z = 120 cm, τ = 20 ns, and at z = 240 un, τ = 3.4 ns. The theoretical results show growth faster than this, if τ is the time since the front of the beam passed the point z. Some growth was also observed in the experiment at times shorter than that predicted by linear theory.

For interaction with the beam break-up (TM_{110}) mode, the quantity $W_T = 1.3\,\gamma^2 W_L$. For the same parameters, we find exponential growth at z = 60 *cm* in less than 1 ns, so this mode clearly must be sup-

pressed. The linear theory of both instabilities suggests that higher values of γ and lower values of Q are desirable to reduce the growth of unstable motion. The stabilizing effect of higher y was demonstrated in the computational results and the use of mode suppression techniques on the TM_{110} mode in the experiment successfully suppressed the transverse instability.

The use of non-resonant structures producing autoacceleration of a pulse tail by their inductive low-frequency behavior ($E_z = -L\, dI/dt$) might be expected to suffer less from instability limits. This nonresonant behavior might be effected by staggering the structure's resonant frequencies or loading the cavities with absorbing material. This type of structure will still be subject to an inductive wall instability, however. If we assume a longitudinal density perturbation of the form exp(ikz-iωt), and an electric field dependence $E_z = -L\, dI/dt$, we ohtain the dispersion relation

$$\omega - kc = \pm i\omega\left[eLI_o/\gamma^3 mc\right]^{1/2}, \qquad (13)$$

where I_o is the unperturbed current and $v_z \approx c$. This calculation is only approximate, of course, because y and I both vary with z and t.

If we consider a triangular current waveform rising linearly in a time T_r to I_o and falling linearly to zero in a time T_f, the particles in the tail will be accelerated by the electric field

$$E_{acc} = LI_o/T_f. \qquad (14)$$

With $T_f \ll T_r$, an energy gain of T_r/T_f could be approached before the front electrons lose all their energy.

From a stability standpoint, the most critical element is the front part of the beam where γ is decreasing with z. The total number of e-foldings over a length ℓ is of order

$$N = \frac{\omega \ell}{c}\left[\frac{LI_o e}{\gamma_i^3 mc}\right]^{1/2} \qquad (15)$$

where γ_i represents a mean value of $\gamma(z)$ for the decelerated front electrons. The inductive characteristics of the structure must hold up to $\omega = 2\pi/T_f$ to operate in the desired mode, so we use $\omega = 2\pi/T_f$ as a conservative upper bound to ω in Eq. (15). Defining $W_f = eE_{accel}\ell$ as the final kinetic energy of the accelerated electrons, and using Eq. (14), we can estimate the number of e-foldings as

$$N \gtrsim \frac{2\pi}{\gamma_i}\left(\frac{W_f}{W_i}\right)^{1/2}\left(\frac{\ell}{cT_f}\right)^{1/2} \qquad (16)$$

As an example, with $W_i = 5$ MeV, $W_f = 50$ MeV, $T_f = 10$ ns, $T_r = 50$ ns, and $\ell = 3$ meters, at least 2 e-foldings of longitudinal growth would occur. Stability considerations can, therefore, impose an important constraint on the possible energy amplification in an inductive mode of autoacceleration as well.

REFERENCES

1. N. R. Heese and W. R. Raudorf, Rev. Sci. Instr. 43, 1594 (1972).
2. T. A. Grishaev and A. M. Shenderovich, Sov. Phys.-Tech. Phys. 17, 1871 (1973).
3. L. N. Kazanskii, A. V. Kisletsov, and A. N. Lebedev, Atomnaya Energiya 30, 27 (1971).
4. M. Friedman, Phys. Rev. Letters 31, 1107 (1973).
5. A. A. Kolomensky, private communication, 1970.
6. V. K. Neil and R. K. Cooper, Particle Acc. 1, 111 (1970).
7. G. P. Mkheidze, V. I. Pulin, M. D. Raizer, and L. E. Tsopp, JETP 36, 54 (1973).
8. T. J. Fessenden and R. J. Briggs, "Experiments on the Autoacceleration of a Relativistic High Current Electron Beam", Lawrence Livermore Laboratory Report No. KID-16487, April 18, 1974.

ACKNOWLEDGMENTS

The authors wish to thank E. J. Lauer, R. E. Hester and W. A. S. Lamb for their active participation in the experiments, as well as A. A. Mirin for his assistance in the computer calculations. The assistance of Ross Spoerlein in film scanning and Al Chesterman in the design of the experiment is also gratefully acknowledged.

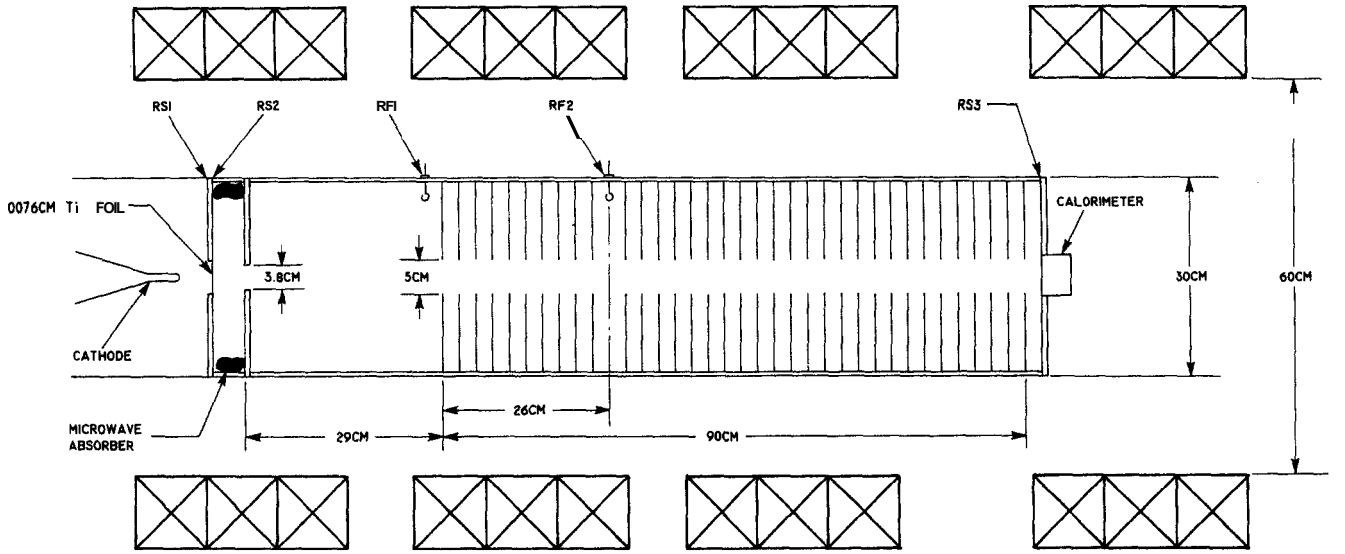


Fig. 1: Schematic drawing of the experimental apparatus

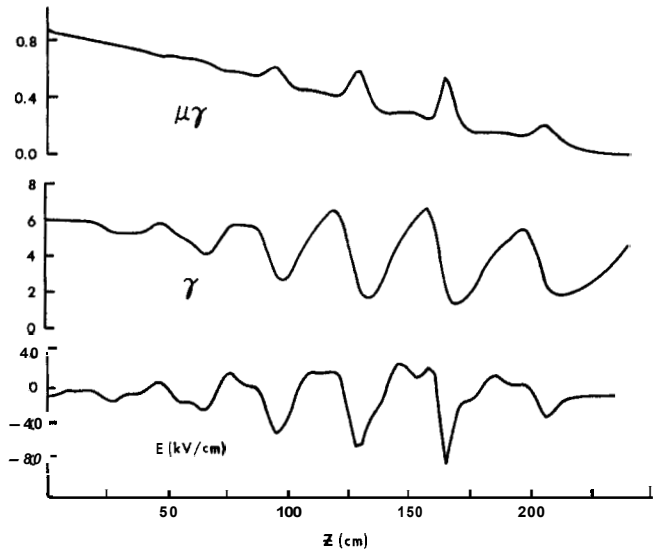


Fig. 2: The quantities μγ, y, and E vs z at 9 ns after start of injection for a current rising linearly with time and with γ = 6.

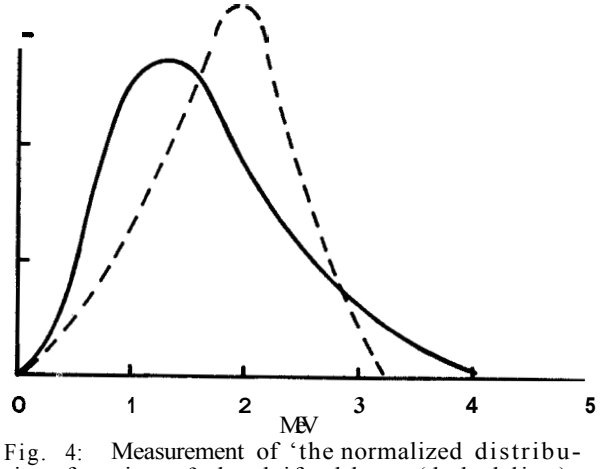


Fig. 4: Measurement of 'the normalized distribution function of the drifted bean (dashed line) and the autoaccelerated beam (solid line).

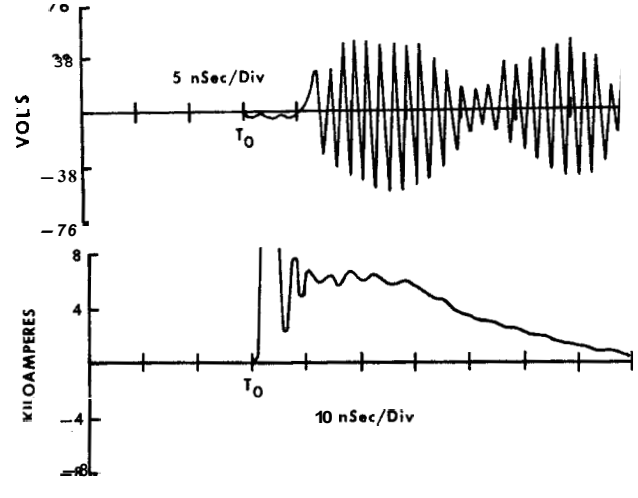


Fig. 6: Oscillograms of the TM_{010} magnetic field detected by RF 2 (a) and of the transmitted current (b) under autoaccelerating conditions. Signal levels in (a) correspond to an axial electric field of approximately 30 kV/cm.

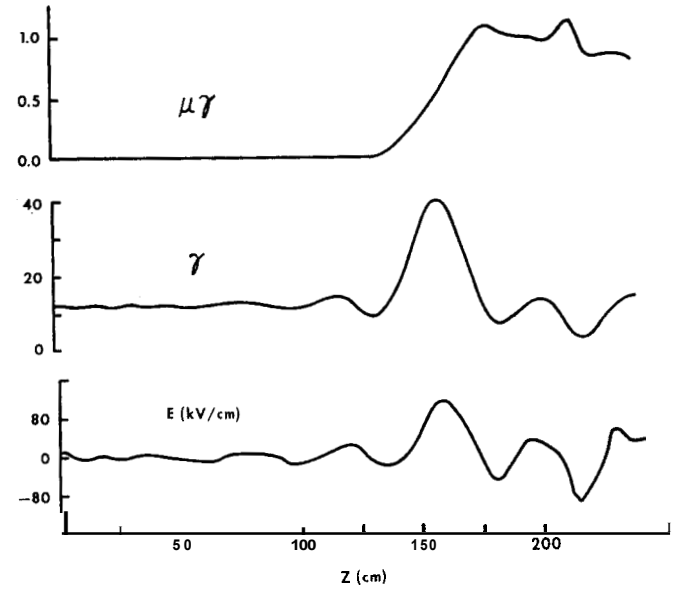


Fig. 3: The quantities μγ, y, and E vs z at 16 ns after start of injection for a "triangular" current and with γ = 12.

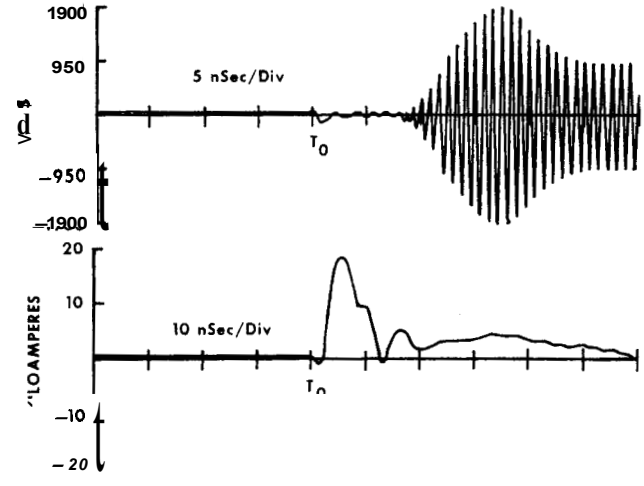


Fig. 5: Oscillograms of the TM_{110} magnetic field detected by RF 2 (a) and of the transmitted current (b) under beam break-up conditions. Signal levels in (a) imply transverse oscillating magnetic fields on axis greater than 1 kG.

THE AUTORESONANT ACCELERATOR CONCEPT

M. L. Sloan and W. E. Drummond
Austin Research Associates, Inc.
Austin, Texas

I. Introduction

The autoresonant accelerator principle[1] offers a conceptually simple and compact method for the generation of energetic pulsed ion beams in the multi-ampere current range. This accelerator scheme utilizes the lower branch of the Doppler shifted cyclotron mode of a relativistic electron beam propagating along a guide magnetic field inside a cylindrically symmetric conducting guide to serve as a traveling wave for the acceleration of ions loaded into the potential troughs of such a wave. This accelerator scheme thus combines the basic concepts of traveling wave and collective acceleration,[2,3] in that while a traveling wave is used for the acceleration process, this wave is a collective eigenmode of the electron beam-magnetic guide field-cylindrical guide system rather than a vacuum wave guide mode as in conventional traveling wave accelerators.

Due to the collective nature of the medium of propagation much higher effective accelerating fields can be sustained than in a conventional accelerator, allowing a substantial economy of machine size. Two further characteristics of the lower branch of the Doppler-shifted cyclotron mode make it well suited for use as the traveling wave €or the acceleration process:

1) Of the 8 eigenmodes of the electron beam system, this mode is the only one with a phase velocity variable from zero to (asymptotically) the velocity of the electron beam. Hence, proton energies upwards of 10 GeV (and larger energies for heavier ions) would be achievable using present day electron beam devices which typically operate in the 5-10 MeV energy range.[4]

Furthermore, the phase velocity can be varied simply by spatially varying the magnetic field along the length of the accelerator, the phase velocity of the wave varying inversely with the strength of the magnetic guide field. Thus control of the phase velocity is relatively easy to achieve.

2) Conventional traveling wave accelerators employing vacuum wave guide modes must supply large amounts of RF power to the wave to compensate for losses since such waves are positive energy waves and hence their electric field energy is degraded by dissipative processes, such as the acceleration process or cavity losses. However, the cyclotron wave used in the Autoresonant Accelerator is a negative energy wave. Hence in the acceleration process where energy is delivered to the ions, rather than being degraded, the electric field energy of the wave actually grows. The reason this can occur is that the wave is not propagating in a passive medium, but rather an active medium with a large free energy source; namely the relativistic electron beam. The process of acceleration automatically extracts energy from the electron beam to both accelerate the ions and to increase the electric field energy of the wave. Hence the need for large RF sources to maintain the wave is removed. Furthermore, present day pulsed relativistic electron beam devices output pulsed power typically in the range of 10^{12} watts over a pulse time of typically 10^{-7} s, with the larger machines achieving power levels well over 10^{13} watts.[5] Thus, if the autoresonant accelerator achieves only a few percent efficiency of conversion of electron beam energy to ion energy, one could anticipate pulsed ion currents in the tens of ampere range or larger.

In the following sections, a technical discussion of the accelerator proper and its operating parameter constraints, methods of generation of the desired eigenmode, and problem areas remaining to be investigated are presented. In Section II, the equilibrium and stability requirements for the electron beam configuration are presented. Section III contains a discussion of the eigenmodes, with the basic operating principles of the accelerator discussed in Section IV. In Section V a method €or generation of the wave is presented. Section VI contains an example of the performance one might optimistically expect from such an accelerator. Problem areas one might anticipate in the efficient operation of such an accelerator are also briefly discussed.

11. Electron Beam Propagation Requirements

We consider a cold relativistic electron beam of current I_e and relativistic factor γ propagating interior to an azimuthally symmetric conducting vacuum wave guide along a guide magnetic field. $\vec{B} = B\hat{z}$, where $\hat{r}$, $\hat{\theta}$, $\hat{z}$ comprise the usual cylindrical coordinate unit vector triad. Let the electron beam radius be given by a and the radius of the conducting guide given by $b \geq a$, where we shall consider b a a. We further specialize to the case $\gamma >> 1$.

It is well known, both from theoretical inve tigation[6,7] and experimental verification,$ that such an electron beam may be propagated provided that the equilibrium and stability conditions of such a beam are satisfied.

In equilibrium, the beam propagates along the *z* axis with a velocity v_e while undergoing an azimuthal rotation with velocity v_θ. For such an equilibrium to exist, it is necessary that the $\vec{v} \times \vec{B}$ restoring force, including the self magnetic field, be larger than either the destabilizing forces due to the self radial electric field or the centrifugal force associated with the azimuthal rotation. The following conditions can be shown to be sufficient for such an equilibrium *to* exist:[9]

$$\omega_p^2 < \gamma\Omega c/a \qquad \text{or} \qquad I_e < 5BaY \quad (1a)$$

$$2\omega_p^2 < \gamma^2\Omega^2 \qquad I_e < .6B^2a^2\gamma \quad (1b)$$

Here $\omega_p^2 \equiv 4\pi n_o e^2/(\gamma m)$ is the usual relativistic plasma frequency, where n_o is the beam density as measured in the laboratory frame: m, the electron mass, and e, the magnitude of the electron charge. The quantity $\Omega \equiv eB/(\gamma mc)$ is the usual relativistic electron gyrofrequency.

The equilibrium equations have also been stated in terms of the total electron current I_e, beam radius a, and guide magnetic field strength B, where I_e is measured in kiloamperes; a, in centimeters; and B, in kilogauss.

Furthermore, if we consider the anode of the electron beam diode as electrically connected to the walls of the conducting guide so that it resides at the same potential as the conducting guide, then the electron beam must have sufficient energy to overcome its own self potential as it propagates away from the anode plane. This leads to the usual Lawson criterion

$$\omega_p^2 a^2 < 4c^2 \qquad \text{or} \qquad I_e < 17\gamma \quad (1c)$$

Such an electron beam equilibrium has furthermore been investigated for stability both for the special case of electrostatic perturbations[10] and the more general case of electromagnetic perturbations.[11] A sufficient condition for stability is given by:

$$\omega_p^2 < \gamma\Omega c/b \qquad \text{or} \qquad I_e < 5Ba^2\gamma/b \quad (2)$$

which reduces effectively to Eq. (1a) for $b \approx a$.

III. Electron Beam System Eigenmodes

The linearized fluid equations governing the electron beam coupled with Maxwell's equations and boundary conditions at r=a appropriate to a conducting wall boundary ($E_z(a) = E_\theta(a) = B_r(a) = 0$) allow a determination of the linear eigenmodes of the system. Expanding the z component of the electric field in an appropriate Fourier-Bessel series:

$$E_z = \sum_n E_n J_o(k_\perp r) \exp(-i\omega t + ik_z z)$$

and expressing the $\hat{r}$ and $\hat{\theta}$ components in a similar suitable fashion, one obtains an eigenvector equation of the usual form:

$$\vec{\vec{T}} \cdot \vec{E} = 0$$

with the dispersion relation given by:

$$\varepsilon(\omega,k) \equiv \|\vec{\vec{T}}\| = \frac{\omega^2}{\Delta\omega^2(\Omega^2-\Delta\omega^2)} \left\{ \Omega^2(\omega^2-k^2c^2) \left[\Delta\omega^2(\omega^2-k^2c^2) - \omega_p^2/\gamma^2(\omega^2-k_z^2c^2) \right] - \Delta\omega^2(\Delta\omega^2-\omega P^2/\gamma^2)(\omega^2-k^2c^2-\omega_p^2)^2 \right\} \quad (3)$$

Here the quantity $\Delta\omega \equiv \omega - k_z v_e$ and $k^2 \equiv k_z^2 + k_\perp^2$.

The boundary conditions require that

$$J_o(k_\perp a) = 0 \quad (4)$$

We now wish to determine the zeroes of $\varepsilon(\omega,k)$ and the appropriate sign of the wave energy of various modes.

A. Definition of Wave Energy

The energy density and energy density flux of a vacuum electromagnetic wave is given by the usual formulas

$$(E^2+B^2)/8\pi \quad (5)$$

and

$$\frac{c}{4\pi}(\vec{E}\times\vec{B}) \quad (6)$$

respectively. However, for waves propagating in an active medium, such as in the electron beam background here considered, energy resides not only in the bare electric and magnetic fields, but also in the "sloshing" motion of the particles comprising the background medium, i.e., the relativistic electrons, as they move under the influence of the electric and magnetic field.

The wave energy of such a system is defined as the change in total energy of the electric and magnetic fields plus particles from the state where the wave is absent to the state where the wave is present. If this change is positive, then the wave is defined as a positive energy wave; if negative, then a negative energy wave. In coordinate systems in which the active medium is at rest, the introduction of a wave always causes an increase in the sloshing energy of the particles and hence is a positive energy wave in that reference frame. However, in reference frames where the medium is not at rest, the introduction of a wave, in addition to increasing the sloshing energy of the particles, may also tend to slow the velocity of the beam. If this second effect is strong enough, then the introduction (or growth) of such a wave actually results in less energy in the system than before. Such waves are called negative energy waves. The introduction of any dissipative effect into such a system will then result in the growth of this wave, rather than its damping as in the case of a positive energy wave.

In terms of the Fourier components of the electric field, the wave energy and wave energy flux can be found in the following simple manner:[12,13,14]

$$U = \text{wave energy} = \frac{\partial G}{\partial \omega}$$

and

$$\vec{S} = \text{wave energy flux} = -\vec{\nabla}_k G$$

$$\text{where } G \equiv \frac{E_k^2}{8\pi} \frac{\varepsilon(\omega,k)}{\omega \sum_i [\text{cofactors of } T_{ii}]}$$

The quantities U and $\vec{S}$ obey the usual energy conservation law

$$\partial_t U + \vec{\nabla}\cdot\vec{S} = R \quad (7)$$

where R is the energy density loss rate due to dissipative effects.

The above definitions reduce to the usual case Eqs. (5) and (6) for vacuum electromagnetic waves.

B. Character of the Eigenmodes

The 8 eigenmodes of Eq. (3) may be identified as follows:

1) Four electromagnetic modes of the general form

$$\omega^2 = k^2c^2 + \text{[correction terms due to the presence of the electron beam]} \quad (8)$$

where the effect of the electron beam is to remove the degeneracy in the forward traveling and backward traveling electromagnetic modes. The phase velocity of these waves is always greater than c for this wave guide configuration, and hence they cannot serve as traveling waves for acceleration for this configuration. These are furthermore all positive energy modes, which might be expected since they are nothing more than slightly modified vacuum electromagnetic modes.

2) Two Doppler-shifted plasma modes, with a dispersion relation appropriate for a strong magnetic field limit. For such a case the magnetic field effectively prevents transverse oscillation (except near the cyclotron frequency) and hence the mode involves longitudinal electron mass effects:

$$\omega = k_z v_e \pm (\omega_p/\gamma_e)(k_z/k) \quad (9)$$

The phase velocity of the upper branch (positive sign) is always greater than v_e, the electron flow velocity. Furthermore, it is a positive energy mode. The lower branch (negative sign) which is a negative energy mode, unfortunately has a phase velocity range bounded by $c(1-\frac{1}{\gamma}) < v_\phi \leq v_e \approx c$, so that it is not useful as a traveling wave.

3) The final two modes are the Doppler shifted cyclotron modes. The dispersion relation for this mode is to good approximation given by

$$\omega \cong k_z v_e \pm \Omega \frac{k^2c^2}{k^2c^2 + \omega_p^2} \quad (10)$$

The upper branch suffers from the same deficiencies as the upper branch of the plasma mode. However, the lower branch (negative sign) has the proper features of being both a negative energy wave and having a phase velocity variable from $\Omega \leq v_\phi < v_e$. Of the 8 eigenmodes, this wave alone is suitable for use as the wave of a traveling wave accelerator for the electron beam configuration considered.

IV. Principle of Acceleration

We now consider the acceleration process proper. Let the electron beam be traveling from left to right, with the low phase velocity cyclotron wave with the ions trapped in the troughs of the wave entering the system at the left also. Furthermore, let the magnetic field be slowly decreased spatially from its initial value B_0 at the left hand boundary to a final value B_1. The electron beam, because it tends to be tied to the magnetic field lines, will expand in a flux preserving manner, i.e., "a" will scale as $B^{-\frac{1}{2}}$. The walls of the conducting guide are thus also considered to be expanded spatially in a similar manner, $b \approx a \propto B^{-\frac{1}{2}}$.

Because only a spatial change is being made in the magnetic field, the frequency of the mode stays fixed at its initial frequency ω_o, while the wave vector changes in order to continue to satisfy the dispersion relation:

$$\omega_o \cong k_z v_e - \Omega \quad (11)$$

and the boundary condition $k_\perp a = 2.4$, the first zero of J_o. Thus the phase velocity is given by:

$$v_\phi = \frac{\omega_o}{k_z} = v_e \frac{\omega_o}{\omega_o + \Omega} \hat{z} \quad (12)$$

and, therefore, the phase velocity of the wave increases down the accelerator. By tailoring the magnetic field appropriately so that there is no sudden acceleration which would cause the ions to be spilled from the potential well in which they are trapped, the ions may be brought up to a velocity comparable to v_e.

Equations (11) and (12) govern the adiabatic change in wave number and phase velocity of the wave. In order to calculate the change in the electric field amplitude, Eq. (7) must be used. For the temporally independent system considered here we obtain

$$\vec{\nabla} \cdot \left[\frac{E_k^2}{8\pi} \frac{\vec{v}_g \frac{\partial \varepsilon}{\partial \omega}}{\omega \Sigma \text{ cofactors of } T_{ii}} \right] = R = -\vec{\nabla} \cdot \left[\hat{z} \frac{1}{2} M_i n_i v_\phi^3 \right] \quad (13)$$

where the acceleration of the ions provide the dissipation. Here M_i, n_i are the mass and density of the accelerated ions, respectively. Integrating Eq. (14) over the volume of the accelerator, we obtain the following equation governing the change of the electric field strength down the accelerator:

$$\pi a^2 \left[\frac{E_k^2}{4\pi} c \frac{\omega_o(\omega_o - k_z v_e)\, k^2}{\omega_p^2 k_\perp^2} + \frac{1}{2} M n_i v_\phi^3 \right] = \text{constant} \quad (14)$$

In the foregoing analysis the response of the electrons was considered within the linear approximation. We therefore require that the perturbed velocity and position of the electrons remain small compared to the equilibrium values. Such consideration gives rise to the following constraints:

$$e\phi << \gamma m_e c^2 \quad (15)$$

and

$$I_e > 1.68\gamma \left[e\ell / (\gamma m c^2) \right] \quad (16)$$

where ϕ is the electric potential of the wave. Furthermore, total energy flux must of course be conserved; which places a kinematical upper bound on the ion energy:

$$I_e \gamma m >> I_i M_i (\gamma_i - 1) \quad (17)$$

where γ_i is the final ion relativistic gamma factor.

Equations (11), (14)-(17), along with the equilibrium and stability constraints, Eqs. (1) and (2), delineate the parameter range of operation of the accelerator.

V. Generation of the Cyclotron Eigenmode

It is evident that rather large amounts of power must be invested in the traveling wave to effect the acceleration of ions in the relatively short distances the extremely high electric fields would indicate possible. The pulsed electron beam source provides a convenient source of energy for growing the desired eigenmode at the desired amplitude and phase velocity through use of the negative energy character of the wave, without having to rely on large amounts of external RF power and attendant coupling problems.

The introduction of a resistive liner within a section of the guide introduces a dissipation within the system and hence renders all negative energy modes unstable. Analysis indicates that such a scheme can indeed be employed to grow the desired eigenmode.

In particular, it was found that a resistive liner must be constructed to be highly conducting in the $\hat{\theta}$ direction, but with a predetermined conductivity σ in the $\hat{r}$, $\hat{z}$ directions. The high conductivity in the $\hat{\theta}$ direction is required to stabilize the non-axisymmetric m=1 kink instability which, for a scalar conductivity, has a higher growth rate than the purely axisymmetric mode. Such a liner could be constructed, for example, by using metallic rings of high conductivity alternated with rings of material with the sppropriate resistivity. Another possibility for partially quenching the growth of the m=1 mode has been offered by M. Rosenbluth, who suggests that the resistive liner be surrounded by a highly conducting material, with the liner chosen thinner than the skin depth of the cyclotron wave. Such a configuration would partially short out the $\hat{\theta}$ electric field component associated with the m=1 mode, thereby lowering its growth rate below that for the axisymmetric mode.

Here we only consider the growth of the axisymmetric mode. For a low phase velocity, the electric field is given roughly as the gradient of a potential

$$E = -\nabla\psi, \quad \psi = \Phi(r)\exp(ik_z z - i\omega t) \qquad (18)$$

Interior to the beam ($r<a$) we have $\Phi(r) \propto J_0(k_\perp r)$, while in the interior of the resistive liner ($r>a$) $K_0(k_z r)$ is the appropriate form for $\Phi(r)$.

Using the appropriate matching conditions across the beam-liner interface, one arrives at the following dispersion relation for $k_\perp$:

$$\frac{k_z^2}{k_\perp^2}\,\frac{\partial_a J_0(k_\perp a)}{J_0(k_\perp a)} = -\left(1 + i\,\frac{4\pi\sigma}{\omega}\right)\frac{\partial_a K_0(k_z a)}{K_0(k_z a)} \qquad (19)$$

where the frequency ω is governed by the cyclotron dispersion relation

$$\omega \cong k_z v_e - \Omega\frac{k^2c^2}{k^2c^2 + \omega_p^2} \qquad (20)$$

Equations (19) and (20) can be solved approximately in the limit that $4\pi\sigma/\Omega << 1$ by expanding $J_0(k_\perp a)$ about its first zero to obtain the following estimate for the growth rate Γ of the wave:

$$\Gamma \approx 2\Omega\,\frac{I_e}{4\nu}\,\frac{k_z a}{(6+k_z^2a^2)^2}\,\frac{4\pi\sigma(k_z v_e-\Omega)}{16\pi^2\sigma^2+(k_z v_e-\Omega)^2} \qquad (21)$$

which is strongly peaked about $k_z v_e \approx \Omega$. By choosing $\frac{\Omega a}{v_e} = 1.4$ this growth rate can be maximized to yield:

$$\Gamma_{max} \approx \frac{I_e}{1288}\,\frac{c}{a} \quad \text{at } Ba \cong \sqrt{6}\,\gamma \qquad (22)$$

The phase velocity of the most unstable wave is given by:

$$v_\phi \cong c\,\frac{4\pi\sigma}{\Omega} \qquad (23)$$

Thus by an appropriate choice of $4\pi\sigma/\Omega$, the phase velocity of the wave may be chosen as required. Furthermore, the amplitude of the wave may also be selected by an appropriate choice of the length of the liner. Finally, we note that such a resistive liner also renders the negative energy plasma wave unstable. However its growth rate can be shown to be substantially smaller and hence the inclusion of an appropriately tailored resistive liner interior to the conducting guide allows a cyclotron mode with the proper phase velocity and amplitude to be generated.

VI. Operating Parameters and Problem Areas

As an example to illustrate the operating parameters for the autoresonant accelerator, we consider a 12 MV, 100 kamp electron beam with an initial beam radius of 1 centimeter. Then with a magnetic field decreasing from 200 kG to 2.5 kG, acceleration of upwards of 500 amperes of ions to the 1 GeV energy level can be achieved in an accelerator length of less than 5 meters. Of course, the electron beam and magnetic field requirements are fairly severe for this case; however, these numbers are meant only to be exemplary of the performance one might expect from an autoresonant accelerator.

There are of course numerous problem areas that remain to be completely investigated. Of particular concern are 1) nonlinear instabilities associated with the electron response to the cyclotron eigenmode for large values of electric field strength, and 2) trapped particle instabilities between the electrons and the ions trapped in the potential troughs of the accelerating electric field. The so-called decay instability has been briefly examined for the cyclotron mode and appears not to be a case of concern. Furthermore, because the electrons are used in a one pass fashion, one might anticipate that most instabilities would be convective in nature and possibly convect out of the system before

growing to an amplitude large enough to be disruptive. However, the complete answer to such questions of stability and performance will have to await further analysis, computer simulation, and experimental determination.

This work was supported by ARALCO, Austin, Texas.

References:

[1] M. L. Sloan and W. E. Drummond, Phys. Rev. Letter 20, 1234 (1973).

[2] V. I. Veksler, in Proceedings of the CERN Symposium of High Energy Accelerators and Pion Physics, Geneva, 1956, Vol. 1, p. 80 (1956).

[3] M. S. Rabinovich and V. N. Tsytovich, Lebedev Physical Institute Report No. 55, 1973 (to be published).

[4,5] S. E. Graybill, IEEE Transaction on Nuc. Sci. NS-18, 438 (1971).

[6] D. A. Hammer and N. Rosotoker, Phy. Fluids 13, 1831 (1970).

[7,9] W. E. Drummond, J. R. Thompson, and H. V. Wong, AFOSR report No. I-ARA-73-U-88, Sec. III (unpublished).

[8] Private communication with Ken Fowler, LLL; and A. Kolb, Maxwell Corporation.

[10] R. C. Davidson and N. A. Krall, Phys. Fluids 13, 1543 (1970).

[11] H. V. Wong, M. L. Sloan, J. R. Thompson, A. D. Drobot, Phys. Fluids 6, 902 (1973).

[12] B. Kadomtsev, Plasma Turbulence, p. 18 ff, Academic Press, New York, N.Y. 1965.

[13] L. Landau and E. Lifshitz, Electrodynamics of Continuous Media, p. 253 ff, Pergamon Press, New York, N.Y. 1960.

[14] S. Weinberg, Phys. Rev. 6, 1899 (1962).

THE HIGH ENERGY POLARIZED BEAM AT THE ZGS*

T. K. Khoe, R. L. Kustom, R. L. Martin, E. F. Parker
C. W. Potts, L. G. Ratner, and R. E. Timm
Argonne National Laboratory
Argonne, Illinois

A. D. Krisch and J. B. Roberts
University of Michigan
Ann Arbor, Michigan

J. R. O'Fallon
St. Louis University
St. Louis, Missouri

Introduction

The possibility of accelerating polarized protons in the Zero Gradient Synchrotron (ZGS) had been considered for many years, and our plans were presented at a previous accelerator conference.[1] Today, we are presenting the results of the successful operation of a high energy polarized beam.

The behavior of a polarized beam in a high energy synchrotron was studied by Froisart and Stora[2] in 1960. The problem was also studied by D. Cohen[3] at Argonne National Laboratory, E. Courant[4] at Brookhaven National Laboratory, and Lobkowicz and Thorndike[5] at Rochester. Froisart and Stora concluded that there would be depolarizing resonances and suggested two procedures to overcome them.

One was to "stop down" the beam in the vertical direction at the approach of the resonance, and the other was to "jump" the resonance by suddenly displacing the orbit radially. Cohen's computer study for the ZGS showed that 12 depolarizing resonances existed during the ZGS acceleration cycle. He suggested that these resonances could be avoided by producing a fast vertical tune shift using pulsed quadrupoles.

During the following years, the advent of good polarized targets at Berkeley, CERN, and Argonne and the experiments[6, 7, 8] done with them maintained the interest in spin dependence in high energy physics. The development of a high current polarized proton source by Glavish,[9] which is now commercially available from ANAC[10] of New Zealand, made experiments using both polarized beams and polarized targets seem possible. Such experiments can study pure spin states and could eventually measure all the amplitudes in the proton-proton interaction and even check parity and time reversal invariance in high energy strong interactions.[11]

With this background, we made some further theoretical studies[12, 13] which confirmed the earlier work and led to the decision to purchase a source and to fabricate a pulsed quadrupole system.[14] A second preaccelerator[15] was constructed for this source to minimize interference with the normal operation of the ZGS. The complete system first operated in July 1973. In Section I we describe the various systems that are necessary for polarized proton acceleration; and in Section II, the measurements of beam polarization.

Section I

A. Polarized Proton Ion Source and Preaccelerator

Figure 1 shows a photograph of the first item of the system, the polarized proton source before installation in the dome. The source was purchased from Auckland Nuclear Accessory Company of New Zealand. It is a ground state source which takes advantage of the hyperfine structure of hydrogen atoms in the ground state to produce polarized protons. As originally constructed, it operated dc

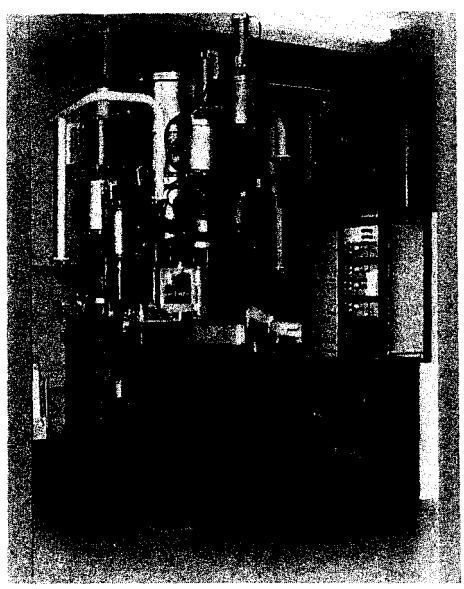


Fig. 1. Photograph of source and control racks before installation in the preaccelerator dome.

with an average output current of 8-10 μA and a polarization of 70-75%. However, we discovered by accident that if we pulsed the dissociator RF supply

*Work performed under the auspices of the U. S. Atomic Energy Commission.

instead of running it dc, we could increase the output beam to 20 μA and the polarization to 75-80%. The source also produces polarized deutrons, and we expect to accelerate them sometime in the future.

The source requires 15 continuously variable controls, 16 on-off controls, and 64 monitor points. Since the source is mounted in the Cockcroft-Walton dome at a potential of 750 kV, the control signals and readouts are transmitted by four fiber optic bundles.

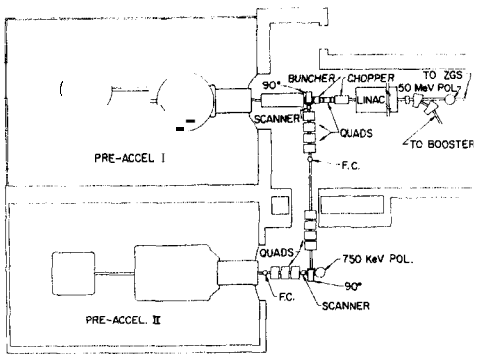


Fig. 2. Layout of the ZGS preaccelerator and linac areas.

Figure 2 shows the ZGS preinjector area with two preaccelerators. The polarized proton ion source (PPIS) is mounted in the PA-II dome, which is 8 x 11 x 14 1/2 ft. This is significantly larger than the normal proton source dome.

The 20 keV beam from the source is matched into the 750 keV accelerating column by an electrostatic quadrupole doublet. After the column, the beam transfer line consists of 14 dc magnetic quadrupoles and two pulsed 90° bending magnets. The last quadrupole triplet is common to both preaccelerators, and the beam tune must allow for this. The pulsed bending magnets allow injection of negative hydrogen ions from preaccelerator I into the booster during the same pulse the ZGS is accelerating polarized protons from preaccelerator II.

The beam current is monitored at two places along the beam line by plunging Faraday cups. The current for each pulse is read by a sample-and-hold circuit and displayed in the Main Control Room and is used to maximize the transport efficiency to the linac, which is typically 85%. The normal system is used to accelerate the beam through the linac and inject it into the ZGS. Faraday cups measure beam current at the entrance and exit of the linac.

B. 50 MeV Polarimeter

Figure 3 shows a schematic of the 50 MeV polarimeter. This polarimeter gives an absolute measurement of the beam polarization after the linac and before the ZGS.

It detects 50 MeV protons which are elastically scattered from carbon at a laboratory angle of 55° where the analyzing power is about 85% and the cross section is 10 mb.[16,17] The polarimeter consists of two symmetric 3-counter scintillator telescopes looking at a thin carbon target which is 0.05 cm x 7.5 cm x 0.08 g/cm^2 thick. All but elastic events are ranged

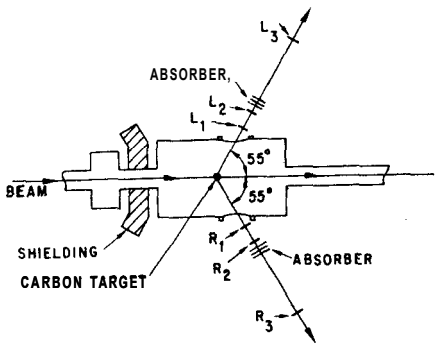


Fig. 3. 50 MeV polarimeter showing the two symmetric 3-counter scintillator telescopes.

out before the last scintillator. The first two counters in each telescope are 1/8 in. thick scintillators giving a total energy loss of about 20 MeV. The third counter is 1/16 in. thick x 1.5 in. wide by 3 in. high and 26 in. away, and defines the lab solid angle of 6.7 x 10^{-3} sr.

Just after the second counter is a dE/dx energy absorber composed of 3/16 in. of polyethylene sheets. The elastic protons leave the absorber with a kinetic energy of about 13 MeV and a velocity of ~ 0.15 c. After a 14 in. flight path, they stop in counter 3. A combination of pulse height discrimination, time of flight, and range discrimination cleanly separates the elastic signal from the background.

The measured asymmetry is the difference between the left and the right counts divided by their sum. The beam polarization is then given by the ratio of the measured asymmetry A_m to the asymmetry parameter A_p (= 0.85 ± 0.07)

$$P_B = \frac{A_m}{A_p} = \frac{(N_L - N_R)}{A_p(N_L + N_R)} .$$

The left and right counts can be directly read from scalers, but during normal operation these numbers are fed into the Main Control Room computer.

Figure 4 shows the polarization consolette. This is the remote control panel which gives a readout of source parameters and allows remote tuning of the source.

This system has provisions for handling a 750 keV polarimeter, a 50 MeV polarimeter, and also a high energy polarimeter. The consolette interfaces to the computer and allows the A_p parameter to be entered at each energy. In addition, the operator can display:

1. A_P for each polarimeter.

2. Pulse-to-pulse N_L, N_R data and the calculated polarization for each.

3. Also, the polarization accumulated averages for the three polarimeters are sent to the experimenters via the CUPID system. The accumulation in the computer is reset whenever polarity is changed or a new run started.

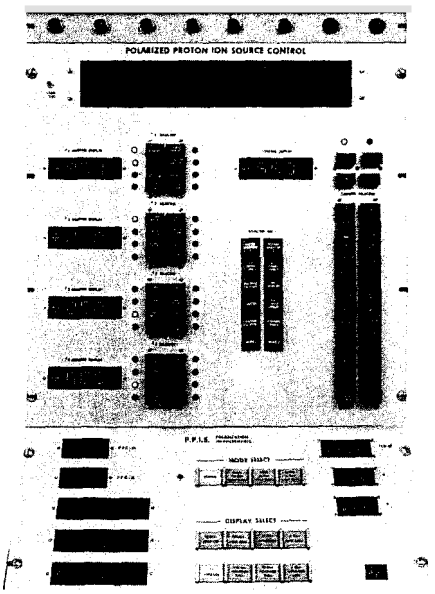


Fig. 4. Photograph of the polarization consolette showing the source control panel and readouts and the polarization input/output data panel.

C. Machine Diagnostics

A bare minimum of machine diagnostics was made operational for low intensity: an injected charge measurement, a circulating beam measurement, and a beam bunch signal for RF phase feedback compensation.

The *ZGS* circulating intensity Q electrode provides a signa; of a few millivolts at levels of $1\text{-}3 \times 10^8$ protons/pulse.

The segmented wire ion chambers[18] (SWIC) extracted beam position monitors are quite important for the operation of the ZGS extracted beams. While the SWIC's are not usable at polarized proton intensities, proportional chambers are. Fortunately, the scanning electronics can operate with either, *so* enough proportional chambers were built to instrument extracted beam lines for three simultaneous polarized proton experiments. These new chambers provide the same type of beam profiles as SWIC's and greatly facilitate beam line tuneup.

D. Pole Face Windings

To minimize the nonlinear depolarization arising from field terms such as

$$\frac{\partial^2 B_y}{\partial x \partial y}\, x\, y,$$

the pole face windings[19] are set to produce a flat vertical tune over as much of the aperture of the ZGS as possible.

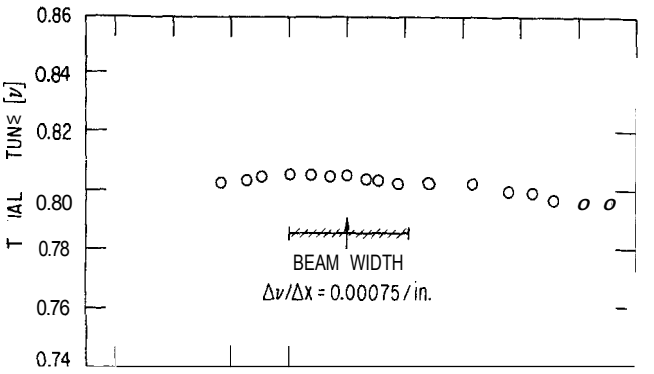


Fig. 5. Typical *ZGS* vertical tune profile as a function of radius.

Figure 5 shows a typical profile. The change in vertical tune as a function of radial position is $\frac{\Delta \nu}{\Delta x}_y = 0.00075/\text{in.}$ over the width of the accelerated beam (4 in.).

Tune measurements were made at 1 kG intervals throughout the ZGS cycle. Up to 14 kG, the tunes remain flat *to* ≤ 0.001/in. and then increase to 0.004/in. by 16 kG and remain at this level to full field 19.8 kG.

E. Pulsed Quadrupoles

In order to create the fast vertical tune change to pass through the depolarizing resonances, a pair of pulsed quadrupoles spaced 180° apart was installed

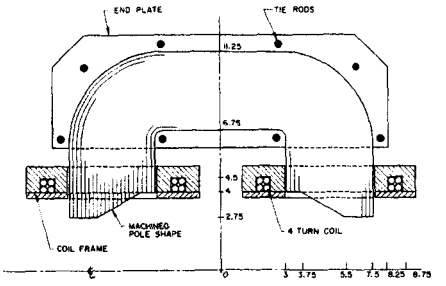


Fig. 6. Top half of pulsed quadrupole showing computer-designed pole profile and copper placement.

in the ZGS ring. These were built with a yokeless figure-8 design, using the TRIM computer program, to fit inside the ZGS aperture, as shown in Fig. 6.

The quadrupoles produce up to 50 G/in. gradient over a useful aperture of 2 in. vertically and 10 in. horizontally. Rise times can be as fast as 10 μs. After the fast pulse, a flattop of 2-10 ms can be sustained, as shown in Fig. 7. The quadrupoles have an effective length of 25 in. each, and both operate at the same polarity to give a maximum gradient length of 2500 G-in/in. Figure 8 shows the pulsed quadrupole control panel. The pair must be pulsed with opposite polarity on successive resonances. Therefore, two power sources are used; one to provide t pulses and the other - pulses. The quadrupoles could be pulsed up to 12 times, 6 t and 6 - pulses. The start time of each pulse was set by programming the ZGS computer, and the fall time and quadrupole strength could be independently varied for each of the 12 pulses by using the control potentiometers.

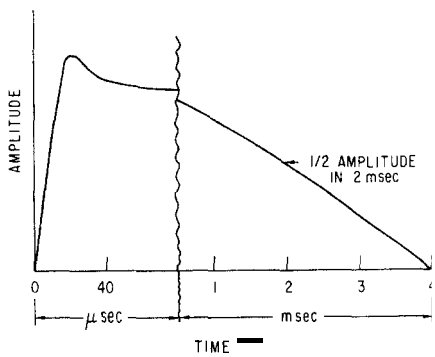


Fig. 7. Quadrupole pulse shape showing fast rise time and slow decay.

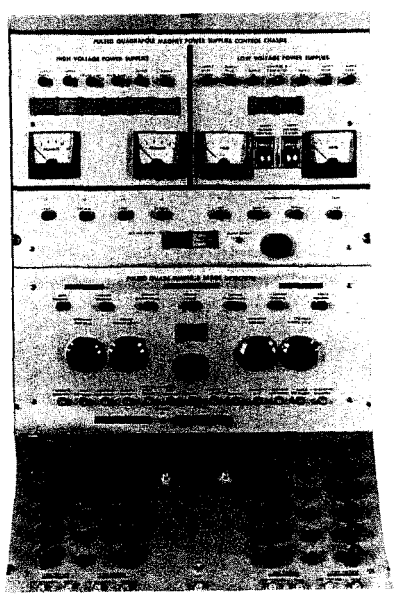


Fig. 8. Control panel for pulsed quadrupole power supplies.

F. Extraction from the ZGS

To tune through the depolarizing resonances, we must extract the beam before and after each resonance and measure beam polarization. Figure 9 shows a typical ZGS field cycle which was used for the 6.0 GeV/c polarized proton run.

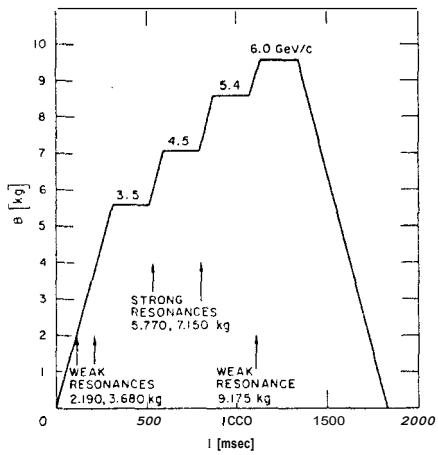


Fig. 9. ZGS magnet field cycle used for tuneup of polarized proton beam.

The beam is extracted on the front porches which are set just after each resonance. The quadrupoles are then tuned for each resonance separately to maximize the polarization measured in the high energy polarimeter. Beam was first extracted using the normal ZGS systems" with an energy loss target and slow spill. The energy loss target causes no depolarization since the scattering angle is small.[21] We have since then found that resonance extraction[22] also gave no depolarization. For our next run, we are planning to use a slow resonance extraction which should gain about a factor of three in extracted beam intensity.

G. Experimental Areas

As shown in Fig. 10, the ZGS has the capability of providing polarized beam to seven experimental setups simultaneously. To date, only beams 1 and 21 have had experimental setups, and they both have run during the two periods of operation for polarized protons. During the spring 1974 run, we expect to run the 12 ft bubble chamber in addition to beams 1 and 21. As more experiments come on the floor, we expect to increase the beam use factor.

H. High Energy Polarimeter

Figure 11 shows the experimental layout in beam 1 and the high energy polarimeter. This polarimeter was used both to tune the ZGS and to measure the beam polarization during the data runs. It consists of two double-arm spectrometers, each containing magnets and scintillation counters, which each measure proton-proton elastic scattering from a liquid hydrogen target (one measures the scattering of the forward particle to the left while the other measures the scattering to the right). They both run

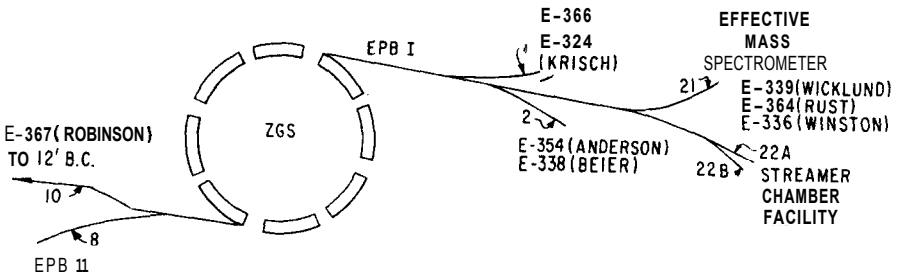


Fig. 10. Experimental areas showing beam lines which can be used for polarized proton experiments.

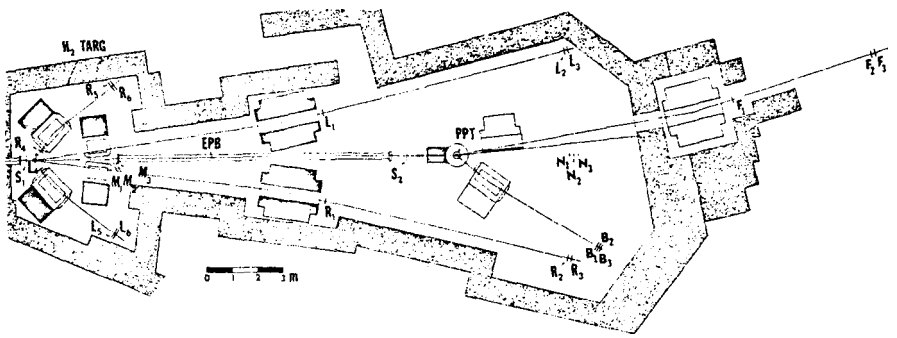


Fig. 11. Beam 1 experimental area showing the high energy polarimeter and experiment **E-324.**

simultaneously and continuously and are as identical as possible. The solid angle is defined by the counters L_3 and R_3, 6 x 5 in^2 at 850 in. from the target;

$$\Delta\Omega_{LAB} \approx 4 \times 10^{-5} \text{ sr}.$$

The momentum bite defined by L_3 and R_3 is

$$\frac{\Delta P}{P} = \pm 6\%.$$

The overmatched counters L_6 and R_6 detected the recoil protons. Measuring both scattered particles gave a very clean elastic signal. Target-empty runs and magnet curves showed that the background was 2% or less.

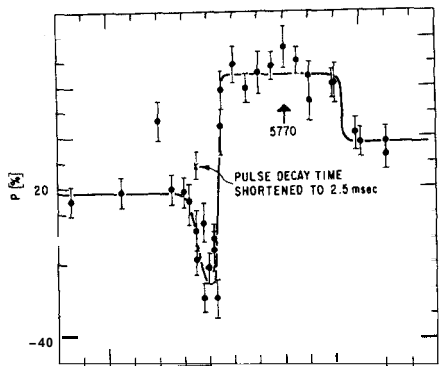
The polarimeter contained steering magnets so that at each momentum we could choose a $P_\perp^2 = 0.4 \rightarrow 0.5$ [GeV/c^2]. The six magnets contain three pairs of identical magnets run in series on three power supplies so the currents are identical. The central fields were measured and agree within 0.2'7'0. The main systematic asymmetry apparently comes from misalignments of the incident beam. The beam direction was monitored using two segmented-wire ion chambers (S_1 and S_2) which measured the beam position. This systematic asymmetry was studied by flipping the beam polarization P_B between up and down (↑ and ↓) at the source. The value of P_B was monitored by the 50 MeV polarimeter and was independent of direction within 1%. When the beam was kept aligned within a few millimeters, the systematic asymmetry was 2% or less.

Section II

A. Locating the Depolarizing Resonances

Since the resonances are given by $(\frac{g}{2} - 1)\gamma = k \pm \nu_y$, we must determine ν_y and γ to locate them. For each point in the *ZGS* acceleration cycle, the value of γ can be calculated and the tune measured. The *ZGS* cycle is controlled by a "B" clock after being initiated by an electron resonance signal which occurs at **433.0** G. Since we must locate the resonance to better than 1/2 ms, we need a good calibration of the "B" clock. We used the resonance itself to calibrate the "B" clock, which gave a precise value (± 0.1%) of the extracted beam momentum of the ZGS.

The beam was extracted on a front porch above the resonance and the quadrupoles were pulsed as a function of time in the neighborhood of the resonance. The polarization in the extracted beam was then measured. The start time of the quadrupole pulse was varied until the beam polarization was maximum. Using the measured time at this point, the "true" value of the field could be calculated. This result from the search of the two k = 8 harmonics shown in Fig. 12, was then used to predict the fields at which the higher harmonic resonances occurred. The next strong resonance at k = 16 was within 1/2 ms (~ 7 G) of the predicted value.



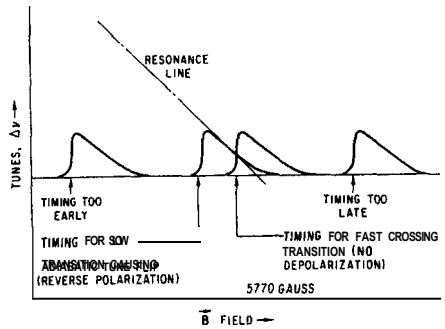


Fig. 13. Schematic representation of quadrupole pulse time for adiabatic transition.

B. Passage Through the Depolarizing Resonances

1. Passage with Spin-Flip. There is a region where the sign of polarization reverses. This is due to an adiabatic rapid passage[23] through the resonance and occurs about 2 ms before the quadrupoles compensate for depolarization without spin-flipping. We can see this in Fig. 12. In Fig. 13, the tune is plotted against the magnetic field. The sloping line is the tune value at which a depolarizing resonance occurs for each value of γ, and depolarization occurs when this resonance line crosses the solid line, which is the actual tune. When the pulsed quadrupoles are properly timed, the resonance line passes through the rapid rising edge of the pulse; the depolarization condition lasts for only a few microseconds, and there is no significant depolarization. When the quadrupole pulse trailing edge matches the resonance line, the protons stay on the resonance for a longer time, and a partial spin reversal occurs.

2. Passage with Compensation for Depolarization and No Spin-Flip. As seen in Fig. 12, when the resonance is crossed rapidly at the proper γ value, there is no loss of depolarization. Spin-flip does not occur because the resonance is crossed during the fast rise time, and there is no appreciable dwell time on the resonance. The width of the plateau in Fig. 12 is about 2 1/2 ms, and is related to the $\Delta\nu$ caused by the quadrupole fast pulse, which was typically 0.04 for the 20 μs rise time. Earlier runs made with a 10 μs rise time gave about a 1 ms plateau. The data in Fig. 12 are results from tuning the quadrupole at the 3.65 GeV/c resonance and measuring the polarization at 4.39 GeV/c and 6.0 GeV/c. These runs were made at different times with different ZGS conditions, yet they give remarkably consistent results.

C. Beam Polarization Measurements

1. 50 MeV Polarization. At 50 MeV, the measured beam polarization is 73% ± 6%. The amount of depolarization in the linac is estimated to be ≤ 3%. A measurement of this will have to await the completion of the 750 keV polarimeter. The

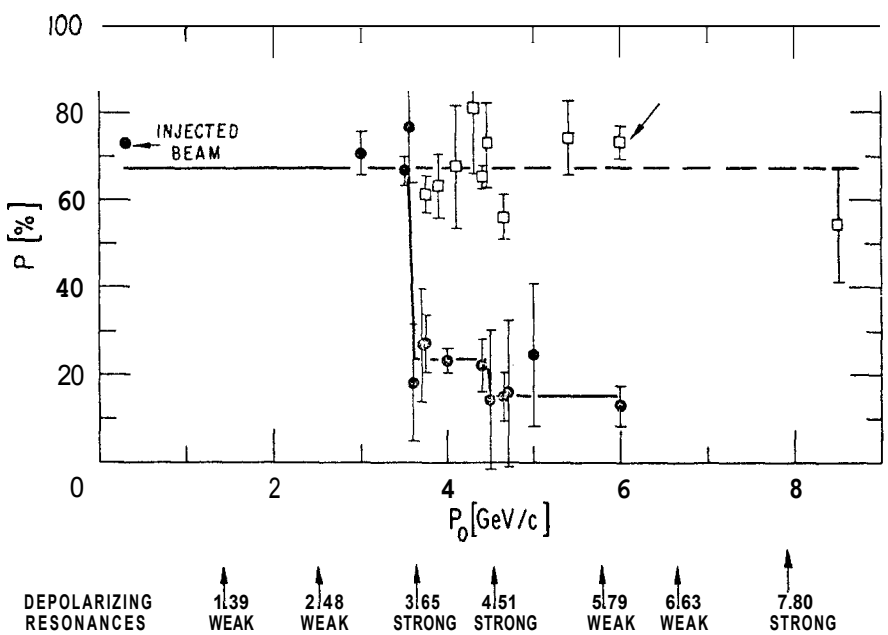


Fig. 14. Measured polarizations as a function of momentum. Open squares are with quadrupoles compensating for resonances and black dots are with the quadrupoles off.

polarization remains stable over a period of a day to better than 2%, but varied by about 5% throughout the run, probably due to long-term drifts in the polarized source.

2. High Energy Polarization. The extracted beam polarization has been measured at several energies, both with and without the pulsed quadrupoles. Figure 14 shows the results. The measured depolarization agrees with the theoretical calculations if we assume an rms vertical amplitude of about 3/4 in. at injection. This agreement suggests that the theoretical treatment is valid and that only the linear resonances are significant in the ZGS. Moreover, it appears that the *ZGS* magnetic field, midplane, and gradient fields are close to their theoretical design values. At 6.0 GeV/c, we measure optimally 73 ± 8% for an injected beam polarization of 73 ± 6%. The quoted errors include the statistical errors in quadrature with an uncertainty in the asymmetry parameter of ± 10% at 6.0 GeV/c and ± 8% at 50 MeV.

At the end of the last physics run at 6.0 GeV/c, we were able to accelerate to 8.5 GeV/c and obtain an extracted polarized beam after correcting for the 16th harmonic resonance. Peak extracted beam was 10^8 protons/pulse. We will attempt to accelerate to higher energies during the next operating period.

Acknowledgements

We are especially grateful to Dr. Bruce Cork for his support of this project. We would also like to thank S. B. Andrews, B. C. Brown, W. deBoer, R. C. Fernow, S. W. Gray and H. E. Miettinenfor their help in constructing and operating the polarimeter. We also thank Dr. G. Marmer for his efforts in the early stages of this project. We are also grateful to the many people of the ZGS staff, without whose contributions this project could not have succeeded. Among these are J. Bogaty, D. Bohringer, F. Brumwell, J. Bywater, Y. Cho, W. Chyna, A. Creer, K. DeVries, R. Lari, L. Lewis, J. Madsen, R. Nielsen, A. Passi, W. Praeg, A. Rauchas, N. Sesol, V. Stipp, R. Stockley, P. Walker, A. Wright, and R. Zolecki. We also thank Dr. L. C. Teng, Dr. E. D. Courant and Dr. R. Serber for their comments.

References

1. L. G. Ratner and T. K. Khoe, Argonne National Laboratory, IEEE Trans. Nucl. Sci., 20, No. 3 (1973) p. 217.
2. M. Froisart and R. Stora, Nucl. Instr. Methods I, (1960) p. 297.
3. D. Cohen, Rev. Sci. Instr. (1962), 33, p. 161.
4. E. Courant, Accelerator Dept. Internal Report EDC-45, January 22, 1962, Brookhaven National Laboratory (Unpublished).
5. F. Lobkowicz and E. H. Thorndike, Rev. Sci. Instr. (1962), 33, p. 454.
6. P. Grannis, et al., Phys. Rev. (1966), 148, p. 1297.
7. M. Borghini, et al., Phys. Letters (1967) 24B, p. 77, and (1970) 31B, p. 405, and (1971) 36B, p. 501; M. G. Albrow, et al., Nucl. Phys. (1970) B23, p. 445.
8. N. E. Booth, et al., Phy. Rev. Letters (1968), 21, p. 651, and (1969), 23, p. 192, and (1970), 25, p. 898, and Phys. Rev. (1973) D8, p. 45.
9. H. F. Glavish, Nucl. Inst. (1968), 5 , p. 1.
10. Auckland Nuclear Accessory Company, Ltd., PO Box 16066, Auckland 3, New Zealand.
11. A. D. Krisch, Experiments with Polarized Beams and Targets, Proceedings of the 1972 Canadian Institute of Particle Physics Summer School, Edited by R. Henzi and B. Margois (McGill University, Montreal) (1972), p. 209.
12. T. Khoe, "Acceleration of Polarized Protons in the ZGS" Internal Report TKK-10, Argonne National Laboratory, Accelerator Division, Argonne, Illinois. (Unpublished)
13. L. G. Ratner and T. K. Khoe, Argonne National Laboratory, IEEE Trans. Nucl. Sci. (1973), 20, No. 3, p. 217.
14. J. Bywater, et al., Argonne National Laboratory, IEEE Trans. Nucl. Sci. (1973), 20, No. 3, p. 869.
15. E. F. Parker, et al., Argonne National Laboratory, IEEE Trans. Nucl. Sci. (1973), 20, No. 3, p. 395.
16. R. M. Craig, et al., in Proceedings of the Second International Symposium on Polarized Phenomena of Nucleons, Karlsruhe, 1965, edited by P. Huber and H. Schopper (Birhaüser Verlag, Stuttgart, Germany, 1966), pp. 322-323.
17. M. P. Fricke, E. E. Gross, B. J. Morton, and A. Zucker, Phys. Rev. (1967), 156, p. 1207.
18. F. Hornstra, et al., Argonne National Laboratory, IEEE Trans. Nucl. Sci. (1969), 16, No. 3, p. 823, and Nucl. Instr. and Methods (1969) 11, p. 4062.
19. E. A. Crosbie, et al., Argonne National Laboratory, IEEE Trans. Nucl. Sci. (1971), 18, No. 3, p. 1000.
R. L. Kustom, et al., Argonne National Laboratory, IEEE Trans. Nucl. Sci. (1973) %, No. 3, p. 253.
D. E. Suddeth, et al., Argonne National Laboratory, IEEE Trans. Nucl. Sci. (1973), , No. 3, p. 397.
20. L. G. Ratner, et al., Argonne National Laboratory, IEEE Trans. Nucl. Sci. (1967), 14, No. 3, p. 688.
21. L. Wolfenstein, Phys. Rev. (1949), 75, p. 1664; E. Heilberg, U. Kruse, J. Marshall, L. Marshall, F. Solmitz, Phys. Rev. (1955), 97, p. 250.
22. L. G. Ratner, et al., Argonne National Laboratory, IEEE Trans. Nucl. Sci. (1971), 18, No. 3, p. 1002.
23. T. K. Khoe, Accelerator Division Technical Report, October 29, 1973, Argonne National Laboratory, Argonne, Illinois (Unpublished).

INTENSE BEAMS OF 100 TO 500 MeV POSITRONS

B. AUNE, M. JUILLARD, F. NETTER and A. PACCHIONI

Département de Physique Nucléaire
CEN Saclay, B.P. 2, 91190 Gif-sur-Yvette, France

Present status of the acceleration of positrons at the high intensity Saclay's electron linac is described. Availability of average currents of 1 μA for 100 MeV positrons and higher than 0.5 μA for 450 MeV positrons is demonstrated. Major improvements are including the use for the first acceleration of the positrons of a new section with a 1.5 m long triperiodic standing wave structure, feeded with the full RF power of one arm of a TV2013 klystron (2 MW peak - 30 kW average power).

Average currents up to one microampere of 100 to 500 MeV positrons are now available as a consequence of the high duty cycle electron linacs actual operation associated with very efficient system of high power conversion target, magnetic lenses and specifically designed accelerating wave guide. The high intensity positron beam producing system now completed at the Saclay's 600 MeV electron linac is described and the various factors involved by the high flux operation are discussed.

Intense, high quality electron beam

An improvement of the emittance of the electron beam by a factor of 5 was obtained recently as a consequence of studies on the gun. The emittance is now of the order of $5 \times \pi \times 10^{-3}$ $m_o c \times$ cm, permitting acceleration from 80 MeV (section 6) to 600 MeV (section 30) without any focusing and beam diameter is smaller than 10 mm. Neither the high voltage of the gun (35 kV) nor the prebunching and bunching system were changed.

High power target (1)

The incident electron current on the target is limited by peak heating rather than average power dissipation in the target itself.

The duty cycle of 1% is made with pulses of 10 μs and repetition rate of 1000 c/s. The conversion system was designed in such a way that two successive impacts of electrons with spot diameter of 1 to 2 mm are well separated on the target. As a consequence, the speed of the target must be greater than 1 m/s.

The target itself is made of gold, electron-beam welded on the periphery of a rotating wheel of 64 cm in diameter. The speed of rotation is 30 to 50 t.p.m.

Destructive effects on the next section of the electromagnetic shower produced by the impact of the electron beam is reduced by adjusting strongly cooled collimators.

A 24 hours run with an average electron current of 350 μA (E = 80 MeV) has been carried out without damage.

Focusing devices

The matching of the emittance of the positron source to the acceptance of the linac is achieved by the mean of a short focal length lens. The focusing of the beam over the 12 sections following the target is made by an axial magnetic field of about 2500 gauss, followed by a set of quadrupole triplets from section 18 to section 30.

The short lens is made of two coils, giving a field of 18000 gauss over a distance of 6 cm. It was designed to provide a large angular acceptance for positrons of energy within the range 8 - 12 MeV.

In addition we have two quadrupole triplets between sections 12 and 13 (100 MeV positrons) where there is a gap of about 4 m in the magnetic field due to the beam handling system for the low energy experimental area.

With this focusing system, transverse momenta up to 0.7 $m_o c$ are accepted, giving a theoretical acceptance of 0.7 π $m_o c$.cm for the linac.

Newly designed standing-wave accelerating section

High accelerating field and special technology for reducing the effect of the electromagnetic shower produced in the conversion target, associated with high radial acceptance, are the two goals of the design for the first section accelerating positrons from 10 MeV to 20 MeV or more. The choice of a standing-wave structure offers the opportunity to set the RF coupler, very sensitive to radiation heating, at the end of the section.

This section is a 1.5 m-long, triperiodic structure with iris diameters of 22 mm for the coupling cavities and 26 mm for the main cavities. The iris thickness is 10 mm.

The shunt impedance, measured in Thomson-CSF labs, is 43 MΩ/m and the unloaded Q value is 12,000. The section was designed to give maximum energy at zero current (critical coupling).

Tests at full duty cycle were made with the following characteristics : 2 MW peak, 30 kW average RF power (1 kW average power dissipated per cavity).

The repetition rate was 1000 c/s and the pulse length of RF power detected in the section was 11 μs at 10% from maximum.

For these values of RF power the accelerating voltage in the main cavities is greater than 10 MeV/m.

Beam diagnostics

Due to the low peak current of electron in the linac, and to the yield of conversion e^-/e^+ (of the order of 10^{-3}) the measurement of positron current is not easy. We have developed two types of monitors :
i) ferrite monitors associated with low-noise amplifier, permitting measurement of peak currents down to 4 μA. Two ferrite monitors are located in the linac (section 12 and 30 and other ones in the beam handling system ;
ii) cavity monitors detecting peak currents down to 0.5 μA (If necessary the use of an RF amplifier could lower this limit). Ten cavities can detect and measure positron current from section 12 to section 30.

In addition we have developed a system of scintillator associated with photomultiplier which can detect peak currents as low as 10^{-2} μA.

Operating results

We have not yet tested the entire conversion facility : target + new section. The results mentioned were obtained without the standing-wave section. We hope they will be improved in the future.

1. Low energy beam (20 to 100 MeV) is delivered after section 12 (6 accelerating sections for positrons) in the low energy station. At this point we have obtai-

ned a maximum yield of 3×10^{-3} e^+/e^- at 100 MeV which can give an average current of 1 @when using an incident electron current of *350* μA.

2. The maximum yield at the end of the linac was 2×10^{-3} e^+/e^-. The discrepancy between this result and the figure at the level of section 12 is due **to** poor steering, stray magnetic fields, or quadrupole misalignment , the transmission factor from 100 MeV to 500 MeV can be improved.

From the total current at the end of the linac, about 70:% is concentrated in an energy width of 1 %.

With the whole assembly including the standing wave section and with the incident electron current of *350* μA it would be then realistic to expect *500* MeV positron average current higher than 0.5 μA in an energy width of 1 *X*.

(1) B. Aune et al. IEEE Trans. on Nucl. Sc. 20, *3*, *934* (1973).

SECOND HARMONIC R.F. ACCELERATION ON NIMROD

E G Sandels and I S K Gardner, Rutherford Laboratory, Chilton, Didcot, Oxon. England

Introduction

The R.F. power circuits, the drift tube and the ferrite tuning system have already been described[1]. Subsequently high voltage biasing plates, along the vertical internal walls of the straight section box containing the drift tube, were added to suppress multipactoring. The present paper will describe the low power R.F. electronic circuits and the commissioning of the complete system.

The possible beam intensity improvement for Nimrod by the use of two R.F. cavities operating at harmonic numbers h and 2h for the acceleration of protons has been computed[2] and the optimum accelerating field amplitudes and phases obtained. Let the combined accelerating field be represented by

$$Va = V[\sin h\omega t - \delta \sin (2h\omega t + \theta)]$$

where

V = amplitude of the first harmonic accelerator voltage
$\omega = 2\pi$ x proton rotational frequency
t = time
h = harmonic number = 4
δ , θ consts.

The optimum values obtained for δ and θ were $\delta = 0.6$ and $\theta = -60°$ with the constraint that V cannot be increased. The permissible errors on δ and θ were ±10% and ±10° respectively. The predicted increase in accelerated beam intensity was 45%.

The Phase Lock System

Some characteristics of the two R.F. systems are listed in table 1. From the above considerations, and the fact that to affect capture the two R.F. systems must be locked together in a period short compared with 1/4 of a phase oscillation (50 psec on Nimrod), the specification for the phase lock system were set as follows.

i) Accuracy of lock ±5° of 2nd harmonic
ii) Bandwidth of lock servo 30 kHz
iii) Loop gain sufficient to reduce 90° to 1° at D.C.

Mode of Operation

Hereafter, to save words, the fundamental and 2nd harmonic R.F. systems will be referred to as the 4f and 8f systems respectively.

A block diagram of the phase lock system is shown in figure 1. The 8f input signal for the 2nd drive chain is derived by doubling the synchrotron master oscillator output RF signal in a squarer circuit, thus making use of the relation $\sin^2 h\omega t = \frac{1}{2}(1 + \cos^2 h\omega t)$. The error signal for the phase lock servo is developed by a phase detector comparing the phase of the doubled 4f gap volts with the 8f gap volts. The two signal paths from the identical gap voltage monitors to the input of the phase detector have equal delays over the R.F. bands. Phase shifts at the 8f frequency occur as follows. The drift tube introduces an additional 90° of phase shift to the accelerating field relative to the cavity. The frequency doubler introduces an additional 90° of phase shift. The phase shift detector gives zero out when the two inputs are 90" out of phase. A constant phase shift of 30° therefore has to be introduced prior to the phase detector to give zero out when $\theta = 60"$. This is done with the 15° lead and lag circuits.

The equality of the signal delays, the accuracy of the 15° lead and lag circuits and the accuracy of the phase detector determine the overall system error.

The phase shifter can alter the phase of the 4f R.F. by ±45°, thus the 8f output of the frequency doubler can be altered by ±90°. A graph of the delay and the equivalent phase shift through the 4f drive chain is shown in figure 2. This has a maximum value of 150° at 2.4 MHz and the required phase shift at the output of doubler 2 would be 300° at 8f. (The linear delays from point A to the 4f and 8f gap volts are made equal). The variable delay unit which is programmed by a function generator throughout the machine cycle is used to compensate for the change in delay with frequency through the 4f drive chain. The circuitry of the 8f drive chain has negligible delay variation. The variable delay unit is programmed to give as small an error as possible throughout the acceleration cycle, and keeps the open loop error within ±20°. The maximum error signal to the phase shifter is limited to ±40° and this in conjunction with the programmed error of ±20° prevents the sign of the loop being reversed as the phase detector's sign reverses if the inputs move more than 90° apart.

Unit Descriptions

1 The Frequency Doubler and Doubler Simulator

These units each consist of a discrete component variable transconductance multiplier. When both inputs are coupled together it acts as a frequency doubler, but when driven with R.F. in one input and a D.C. bias in the other, it acts as a doubler simulator providing similar delay characteristics for both the 4f and 8f channels. The circuit bandwidth is 50 MHz.

2 The Automatic Level Control Units

These are open loop level control units in that the R.F. output is provided from a multiplier, the gain of which is controlled by the amplitude of the input to the unit. The voltage analogue of the input level is fed via a divider (which forms the reciprocal) to the multiplier gain control input. This enables the unit to combine a fast response time with the ability to handle larger variations in input signal, than could be accommodated in a closed loop A.L.C. system. The R.F. bandwidth is 50 MHz and the level control response time 20 μs. The A.L.C. units are required to keep the inputs to the frequency doublers constant as the 4f and 8f gap voltages are varied.

3 The Phase Shifter

The phase shifter output is the sum of two signals which are 90° out of phase, figure 3. By altering the relative amplitude of both these signals with multipliers the output phase may be varied through ±45°. The signals with 90° relative phase difference are produced from the incoming master oscillator signal, by passing it through two parallel all pass filters, the outputs of which are 90° apart over the 1-8 MHz band[3]. Diode shaping is used on the gain control voltages of the multipliers to reduce the amplitude modulation introduced with the phase

modulation. This approximates the locus of the vector sum of the R.F. signals to a circle. The R.F. bandwidth of this unit and its phase modulation are both 50 MHz.

4 Phase Detector

The phase detector is of the overlap pulse type. A block diagram is shown in figure 4. With this circuit the output is zero when the two inputs are 90° out of phase. One channel of the phase detector rejects even harmonic distortion on the input signal. The bandwidth of the phase detector to phase modulation is determined by the quantity of R.F. which can be tolerated on the output, since too high a level saturates the inputs of the subsequent D.C. amplifiers. On this system the low pass filters were set to cut off at 100 kHz.

5 The Lead and Lag Circuits

The lead and lag circuits are identical units. A block diagram of one unit is shown in figure 5. The incoming R.F. signal is passed through two all pass networks whose outputs are 90° apart over the band 1-20 MHz. These two signals are passed through variable attenuators and then summed. Thus with two units, two outputs of constant relative phase difference in the range ±90° can be produced over the 1-20 MHz frequency band.

6 Variable Delay Unit

This unit contains eight sections of R.F. delay (varying from 1-128 ns) which can be switched into the R.F. signal path with diode gates, figure 6. The number of delays in circuit is selected by an 8-bit A.D.C. whose input is a function generator. The function generator is programmed throughout the acceleration and extraction cycle giving a variable delay range of 0-255 ns. The A.D.C. output is updated at 100 kHz.

System Performance

The syste- was checked statically with the set up shown in figure 7, the assumption being made when choosing the delay equivalent of the doubler that the delay on the two channels of the oscilloscope used were equal for 4f and 8f. The scope bandwidth was 1 GHz. The error output of the phase detector did not exceed ±3°.

The system was checked during the normal R.F. sweep using the X-Y scope as shown in figure 1. Again the assumption was made that the two channels of the scope (which were identical) had equal delays for 4f and 8f frequencies. The X and Y channel bandwidths were 50 MHz. The results showed errors of less than ±5° over the band and the lock-in time of the system was less than 20 psec.

Acceleration with 4f and 8f

First attempts at combined harmonic acceleration produced the following results.

i) A larger beam was trapped and accelerated for 10-70 msec with the 2nd harmonic set at its predicted amplitude and phase. The amount of beam 30 ms after trapping was increased from 3.0-3.5 x 10^{12} protons with the 4th harmonic only to 4.0-5.0 x 10^{12} protons with the combined harmonics.

ii) Beam loss occurred at 40-100 msec and the final accelerated beam was usually about 1.0 → 2.0 x 10^{12} protons as compared with a final beam of 3.0 → 3.5 x 10^{12} protons with the 4th harmonic only.

iii) The beam loss at 40-100 ms could be eliminated by two methods:-

(a) Cutting down the quantity of accelerated beam either by reducing the injected beam or by radially mis-steering the beam at 2-3 msec., when steady final accelerated beams of 2.5 x 10^{12} protons could be achieved.

(b) Altering the phase of the 8f R.F. relative to the 4f R.F. to reduce the beam bunch length. This gave steady accelerated beams of 2.5 → 3.0 x 10^{12} protons. The bunch length had to be reduced by 20°-30° (at 4f).

iv) The beam bunches had the predicted shape during the first 30 ms of acceleration. Photographs 1 and 2.

Properties of the loss mechanism

The loss was accompanied by longitudinal oscillations in the beam bunches. A beam mean bunch length detector showed oscillations at about 10 kHz (ie, twice the phase oscillation frequency) growing to about 35° (at 4f) peak to peak. Photograph 3.

The machine was run without beam radial or phase control loops and the longitudinal oscillations still occurred.

Damping system for bunch length oscillations

A bunch length oscillation damping system was built as shown in figure 8[4,5]. This by-passed the normal beam control point (the frequency modulation of the master oscillator) allowing a higher bandwidth.

The bunch length oscillation frequency was found on the output of the existing beam phase detector which was fitted with integrators prior to the limiting stages[6]. This allowed a parallel feedback path for the bunch oscillation frequency and prevented the damping system from working.

A new beam phase detector whose output was unaffected by the phase and amplitude of even harmonics on one input channel was built. With the beam signal in this channel the damping system prevented bunch length oscillations and steady beams of greater than 4.0 x 10^{12} protons were accelerated.

The mean bunch length detector consists of a series of 3 limiters followed by an R.C. filter with a cut off frequency of 100 kHz. Photographs 3 and 4 show the bunch length detector outputs with the damping on and off.

Extraction

The increase in accelerated beam intensity due to the addition of the 2nd harmonic system is always (at present beam levels) about 40%, which is in good agreement with the predictions[2].

Two modes of extraction have been used (to date) with the combined harmonic acceleration, although only small beams (2.0 x 10^{12}) were available during these tests. In the first mode the 8f R.F. was switched off at the start of flat top and the

extraction efficiency dropped by 15%. In the second mode both the 8f and 4f R.F's were operated throughout flat top producing the same extraction efficiency as for the normal 4f extraction.

Acknowledgements

The authors wish to thank J M Dickson, D A Gray and G H Rees for helpful discussions during the commissioning of the 2nd harmonic acceleration system.

References

1 E G Sandels, R A Church, I S K Gardner, H C Whitby.
A Second R.F. System for Nimrod.
1973 Particle Accelerator Conference,
San Francisco. IEEE Transactions on Nuclear Science. Vol. NS20, No.3, p.418.

2 G H Rees, J V Trotman.
Acceleration with combined use of R.F. Harmonic Numbers h and 2h.
Rutherford Report SCS/Machine/10, (internal note ABT Group 1970).

3 H J Orchard.
Synthesis of Wide Band Two Phase Networks.
Wireless Engineer, March 1950.

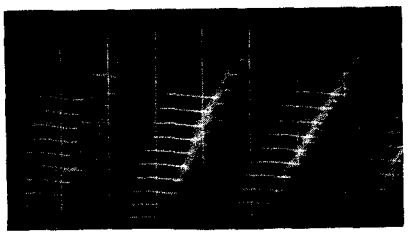
4 H G Hereward.
Second Order Effects in Beam Control Systems of Particle Accelerators.
Proc. 1961. international Conf. on High Energy Accelerators, Brookhaven. pp236-243.

5 E C Raka.
Damping Bunch Shape Oscillations in the Brookhaven AGS.
1969 Particle Accelerator Conference,
Washington. IEEE Transactions on Nuclear Science. Vol. NS16, No.3, p.182.

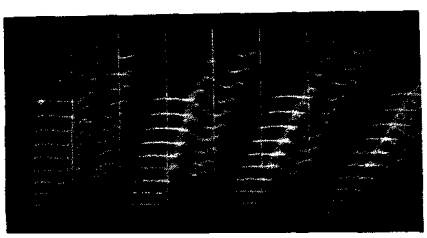
6 I S K Gardner, G H Rees, E G Sandels, G Soulby, R A Swales.
Beam Sensing, Radial and Phase Control Systems for Nimrod.
Rutherford Laboratory Report NIRL/R/89. 1965.

TABLE 1

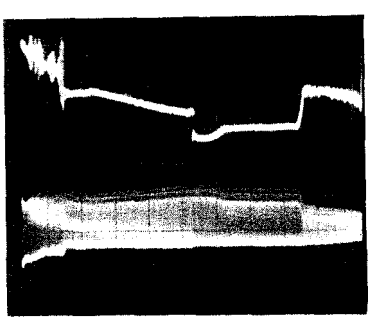
Parameter	Fundamental ! Cavity System	2nd Harmonic Drift Tube System
Start Frequency	1.4 MHz	2.8 MHz
Top Frequency	8.0 MHz	16.0 MHz
Ferrite Bias Supply Band-width at start frequency	300 Hz	4 kHz
Peak Gap Volts	6 kV	10 kV
Initial Phase Transient at start of acceleration	-20° for 2 msec	±10° for 5 msec



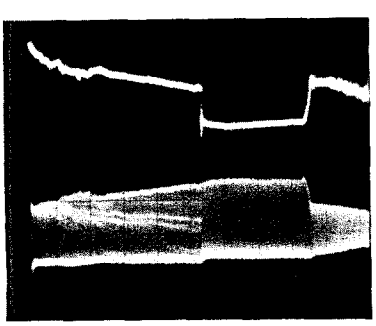
PHOTOGRAPH 1: BEAM BUNCHES, 4f ONLY.



PHOTOGRAPH 2: BEAM BUNCHES, 4f AND 8f.



PHOTOGRAPH 3: TOP-BUNCH LENGTH DETECTOR OUTPUT
BOTTOM 4f AND 8f BEAM SIGNAL



PHOTOGRAPH 4: TOP-BUNCH LENGTH DETECTOR OUTPUT
BOTTOM 4f AND 8f BEAM SIGNAL

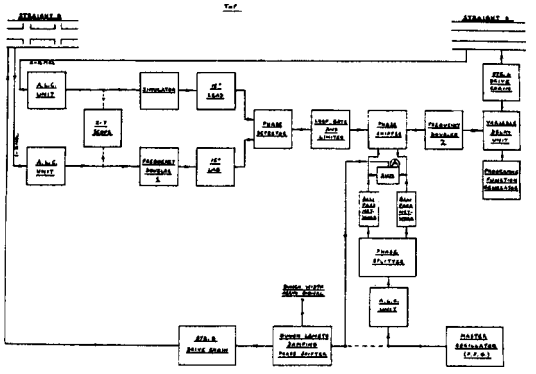


FIG. 2ND HARMONIC I LOAD LOOP

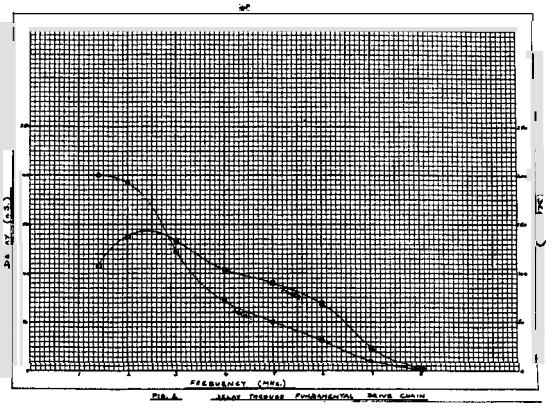


FIG. 2 DELAY VERSUS FUNDAMENTAL DRIVE CHAIN

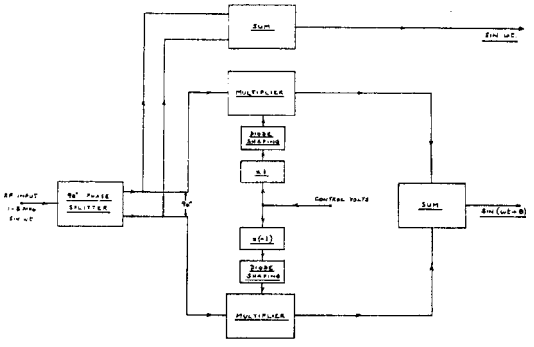


FIG. 3 PHASE SHIFTER

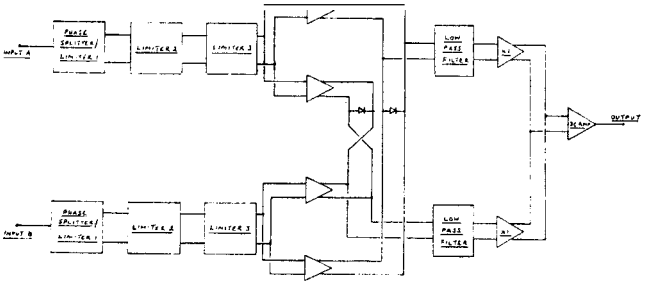


FIG 4 PHASE DETECTOR

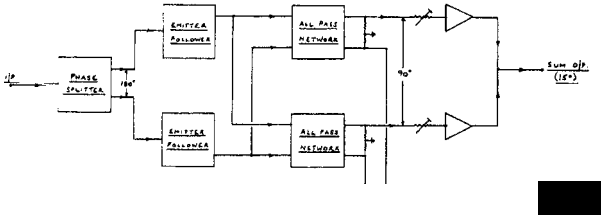


FIG. 5 LEAD AND LAG CIRCUIT

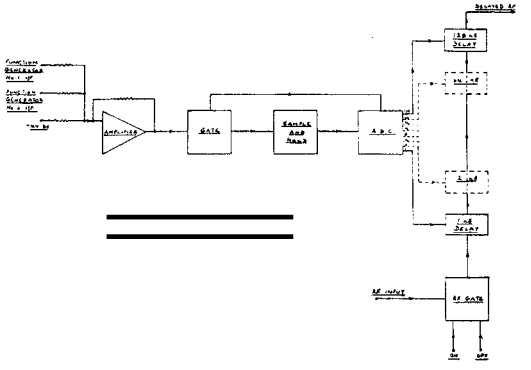


FIG. 6 VARIABLE DELAY UNIT

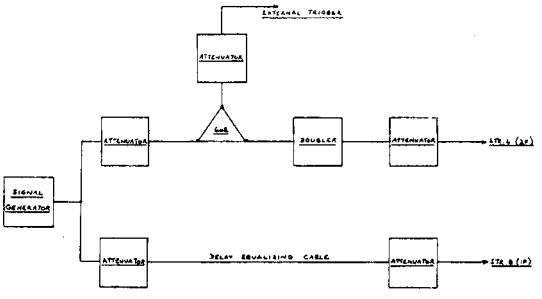


FIG. 7 SYSTEM PERFORMANCE MEASUREMENT

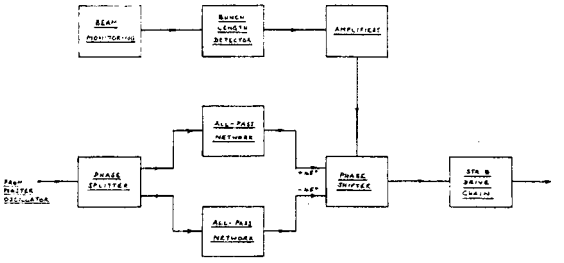


FIG 8 BUNCH LENGTH OSCILLATION DAMPING SYSTEM.

ACCELERATING WAVEGUIDES FOR HIGH-ENERGY ACCELERATORS

A.V. Shalnov
Director of the Research and Laboratories
Division of the I.A.E.A., Vienna, Austria

Summary

Accelerating waveguides are used for both high-energy and low-energy electron accelerators and can also be applied to synchrotrons. High-energy synchrotrons have a very narrow frequency band(due to the high energy of injection), use a high frequency supply and require a significant energy gain per turn and therefore non-tuned accelerating waveguides can be used. This application was proposed at CERN and then was extended to high intensity accelerated beams, For the last case, heavy beam loading, bunched in an equilibrium phase, must be taken into account. Uniform waveguides are considered and some recommendations from the energetical point of view are discussed. Some general remarks are made concerning non-uniform waveguides.

Introduction

In high-energy synchrotrons the frequency of the accelerating voltage is increased to assure resonant acceleration for an equilibrium particle. Owing to the dispersion of non-tuned waveguides, a shift of the equilibrium particle relative to the travelling wave created by a high-frequency generator exists inside the waveguide. Such process practically takes place during the whole time of acceleration, excepting only one specific moment when the shift is equal to zero.

When the intensity of the accelerated beam is as high as it is for modern synchrotrons, it is quite necessary to take into account the action of the field having the same pattern as the field of generator, but irradiated by bunches. This field irradiated by each separate bunch is stationary with respect to the bunch and has a different main frequency in comparison with the generator frequency. Both frequencies only coincide at the very same moment mentioned above, when the bunch velocity and the phase velocity of the travelling wave become equal.

The frequency of the irradiated field after a build-up time becomes equal to the generator frequency. Therefore the bunches accelerated inside the non-tuned waveguide are shifting relative to their own irradiated field. Finally, there is the essential difference between the waveguides implemented for linear electron accelerators: the bunches are located at the crest of the accelerating wave, while in synchrotron waveguides the bunches are in a certain equilibrium phase.

The application of non-tuned waveguides to synchrotrons with variable frequency was first suggested by Schnell at CERN[1]. In this article the phase shift of bunches with respect to the travelling wave was also considered. But at the same time, attenuation of the electron-mametic field inside the waveguide and beam loading were neglected. On the other hand, Lichtenberg[2] took into account the field irradiated by the bunches located in the certain equilibrium phase. But in the last article, since it was concerned with linear electron accelerators, the author neglected the shifting of bunches with respect to the field created by the high-frequency genarator as the field irradiated.

In previous investigations fulfilled by the author of this report in co-operation with his collaborators, both the shifting of bunches relative to the generator field and the irradiated one and the location of the bunches in the equilibrium phase were considered. To be convinced in the correctness of the main preconditions, some experiments were performed at the linear accelerator for 360 MeV of the Kharkov Physical-Technical Institute of the Ukrainian Academy of Sciences. There, special conditions were artificially created for shifting bunches relative to the irradiated field. Close accordance was shown between theory and experiment for both frequencies and amplitudes of the irradiated fields. Results of these investigations were published as monograph[3].

Using the model presentation of physical. processes inside the waveguides, one can solve problems concerning energetical efficiency, find out conditions of optimal. efficiency, and choose accelerating structure for a certain synchrotron. The very same calculations were used for one alternative version of accelerated systems, for the "cybernetic accelerator", with output energy up to 1000 BeV.

Field superposition

As it is known[2] for an achievement of the right presentation for energetic field balance of generator and irradiated fields, the vector superposition is used. For accelerating waveguides of synchrotrons it is more convenient to employ the standard presentations and replace the waveguide for the equivalent accelerating gap with a monoharmonic voltage U.

For uniform waveguides such equivalent voltage can be easily deduced by integrating the generator electric field E_g and induced field E_i:

$$E_g = E_{go} \exp(-\alpha Z) \left[\cos(\varphi_o + K_s Z) + i \sin(\varphi_o + K_s Z)\right] = \mathrm{Be}\, E_g + \mathrm{Im}\, Eg \qquad (1)$$

$$E_i = \left\{ IR_s Z \Big/ \left[(\alpha Z)^2 + (K_s Z)^2\right]\right\} \left[(\alpha Z - \alpha Z \exp(-\alpha Z) \cdot \cos K_s Z + K_s Z \exp(-\alpha Z) \sin K_s Z) + i\,(K_s Z - K_s Z \cdot \exp(-\alpha Z) \cdot \cos K_s Z - \alpha Z \exp(-\alpha Z) \sin K_s Z)\right] = R_e E_i + \mathrm{Im}\, E_i \qquad (2)$$

The amplitude of the generator equivalent voltage can be determined by:

$$U_{og} = \sqrt{(\mathrm{Re}U_g)^2 + (\mathrm{Im}U_g)^2} \qquad (3)$$

where $ReU_g = \int_0^\ell Re\ E_g\, dz$; $ImU_g = \int_0^\ell Im\ E_g\, dz$

The same can be done for the induced field. Here the index "o" is used to indicate the amplitude of fields and voltages.

Below one can find the list of terms:

Z - co-ordinate along the waveguides axes

φ_o - particle phase in respect to the travelling wave crest for Z = o ;

α - attenuation coefficient ;

K_s - shifting coefficient ;

$$K_s = \frac{2\pi}{\lambda}\left(\frac{1}{\beta_w} - \frac{1}{\beta_p}\right) ; \qquad (4)$$

λ - free-space wavelength ;

β_w - relative wave velocity (in units of the light velocity - c) ;

β_p - relative particle velocity ;

I - accelerated current ;

R_s - waveguide series resistance ;

$$R = \frac{E_o^2}{2P} ; \qquad (5)$$

P - high-frequency power.

The voltage acting to any particle of the bunch is given by:

$$U = U_{og}\cos(\varphi_o + y) - U_{oi}\cos(\varphi_o - \varphi_{os} + \delta) =$$

$$= U_o \cos(\varphi_o + \theta) \qquad (6)$$

The corresponding vector diagramme is shown in Fig.1. Values of U_{og} and U_{oi} obtained by integrating can be found from the next equations:

$$U_{og} = (2R_s P)^{\frac{1}{2}}\ell\, A(X,Y) ; \qquad (7)$$

$$U_{oi} = IR_s\ell^2\, G(X,Y) ; \qquad (8)$$

$$A(X,Y) = \left\{\left[1 - 2\exp(-X)\cos y + \exp(-2X)\right]/(X^2+Y^2)\right\}^{\frac{1}{2}}$$

$$G(X,Y) = \left[2/(X^2+Y^2)\right]\cdot\left\{Y^2 - (1-X)^2 - 2\exp(-X)\times\right.$$

$$\left.\times\left[(1-X)\cos y + Y\sin y\right] - \exp(-2X)\right\}^{\frac{1}{2}}$$

Here $X = \alpha\ell$ and $Y = K_s\ell$ - the total attenuation and total phase shift correspondently. The phase angles can be determined with the help of the next expressions:

$$\gamma = \tan^{-1}\frac{Y - \exp(-X)(X\sin Y + Y\cos Y)}{X - \exp(-X)(Y\sin Y - X\cos Y)} \qquad (9)$$

$$\delta = \tan^{-1}\frac{Y(X^2+Y^2) - 2XY - \exp(-X)\cdot}{X(X^2+Y^2) + Y^2 - X^2 - \exp(-X)}$$

$$\cdot\left[(Y^2 - X^2)\sin Y - 2XY\cos Y\right]$$

$$\cdot\left[(Y^2 - X^2)\cos Y + 2XY\sin Y\right] \qquad (10)$$

$$\theta = \tan^{-1}\frac{U_o\sin\gamma - U_{oi}\sin\delta}{U_{og}\cos\gamma - U_{oi}\cos\delta} \qquad (11)$$

The voltage applied to the equilibrium particle in accordance with Fig.1, is given by:

$$U_\sim = U_{\sim\sim}\cos(\qquad\qquad_{oi}\cos\delta = U_o\cos\varphi \qquad (12)$$

The analogical relations can be obtained far non-uniform waveguides if the well-known supposition about linear dropping of the group velocity along the waveguide is applied to have the constant electric field acting to the bunch in any point of the waveguide. This can be done either for the zero accelerated current or for a certain nominal value. For both cases shifting of the bunch with respect to the accelerating wave becomes non-linear and voltages are described by much more complex formulae.

If for linear accelerator waveguides one considers that increasing of the waveguide length is useless beyond the point where the acting electric field is equal to zero, for synchrotron waveguides this condition can be written in the form $-\cos\varphi_s < 1$. This requirement is determined by the whole accelerator and the equilibrium phase can be found out by

$$\varphi_s = \tan^{-1}\left\{\frac{1}{U_s}\left[\pm\sqrt{U_{og}^2 - (U_s + U_{oi}\cos\delta)^2} - \right.\right.$$

$$\left.\left. - U_{oi}\sin\delta\right]\right\} \qquad (13)$$

Significantly, the last expression includes δ, U_{oi}, U_{og} which are dependent on the total phase shift Y and, consequently, the equilibrium phase will be varied if the high-frequency power is constant during the accelerating cycle. The equations considered allow these variations to be investigated.

Optimization and choice of accelerating structure

Using the relations obtained, the optimal efficiency of the accelerating waveguides to achieve the minimum of high-frequency power supply can be found. As a result, we determine the condition which corresponds to maximum transformation of high-frequency power into beam power. For uniform waveguides, for instance, we can find the requirements on the accelerating structure. For the highest efficiency the accelerating structure would have the series resistance:

$$(R_s)_{opt} = \frac{2U_o}{I\ell^2\, G(X,Y)} \qquad (14)$$

which gives the efficiency:

$$\eta_{max} = \frac{2A^2(X,Y)\cos\varphi_s}{G(X,Y)\left[1+\cos(\varphi_s-\delta)\right]} \qquad (15)$$

A very helpful simplification can be obtained supposing that $X = 0$ and $Y = 0$. In this case $\delta = 0$ and $A(X,Y) = G(X,Y) = 1$. For non-uniform waveguides, the corresponding expressions have rather complicated forms[3] and therefore are omitted here.

Parameters contained in the equation written above are not mutual independent. For example, the phase shift γ depends not only on the waveguide length but on the group velocity (β_g). If the value of β_w and the mode of oscillation are fixed, it appears that for any high-frequency structure the dependence R_s (β_g) can be plotted.

On the other hand, if the values of the parameters for the accelerating waveguide are fixed (length ℓ, X, φ_s, U_s etc) the equation (14) can be plotted in the same form. An intersection of two curves, one of which belongs to the accelerating system of the synchrotron and the other to the structure, presents the optimal waveguide.

For example, for one of the variants of the 1000 BeV "cybernetic accelerators", optimal systems are: "clover-leaf" and "corrugated" waveguide with additional radial slits. The cylindrical corrugated waveguide employed for linear electron accelerators is not a high-frequency structure providing optimal conditions (14).

At the same time the possibility to achieve optimal conditions by this waveguide is not excluded if other parameters of the accelerating system are suitably chosen.

It is necessary to notice that there is not an essential benefit in efficiency for accelerating waveguides without feedback if the attenuation tends to zero. For instance, the waveguide efficiencies for $X = 0$ in comparison with $X = 0{,}25$ have the benefit not more than 10% and this circumstance does not allow the conclusion that the application of superconducting waveguides is advantageous.

Conclusion

The above analysis shows that in principle accelerating, non-tuned waveguides can be applied with high efficiency for synchrotrons with variable frequency. Nevertheless, some phenomena which have not been considered here must be taken into account. The first of these is a variation of the high-frequency voltage, connected with changes of shifts for particles relative to the accelerating wave. The second major problem is connected with achieving the proper performance at the transition energy, because of the long build-up time for the waveguides. Sped attention must be paid to the possibility of generating asymmetrical waves, which can destroy the accelerated beam. In linear electron accelerators it is known to produce a shortening of the beam pulse, (the "beam blow-up effect"). It cannot be eliminated by focusing magnets, because of the high-frequency modulated structure of the beam. This effect must be further studied, especially if tne structure used is asymmetric and excites the asymmetric type of electromagnetic wave. Implementation of non-uniform waveguides decreases the last effect.

References

1. Schnell, CERN Report AR/Int. SG/65-16, 1965.
2. Lichtenberg, RSI, Vol. 33, p.395, 1962.
3. O.A. Valdner, A.V. Shalnov, A.W. Didenko "Accelerating Waveguides", Moscow, Atomizdat, 1973.

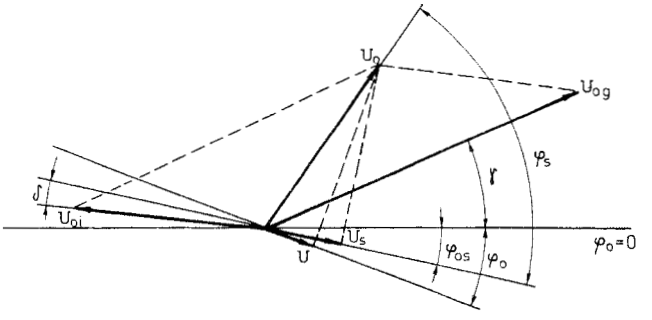


Figure 1.

PHASE-FREE ACCELERATION OF CHARGED PARTICLES BY AC FIELDS

W. Schott, H.-J. Winter, H. Hagn, K. Springer, H. Zinner, F. Brunner and H. Daniel

Physik-Department, Technische Universitat München, Munich, Germany

Summary: Two methods for acceleration of charged particles that do not require a phase relation between the accelerating ac field and the incoming particles are investigated. With such a system a continuous particle beam can be accelerated. One system uses time-of-flight differences in triangular-shaped hollow electrodes on which ac voltages are applied. In the other system particles are accelerated perpendicular to an electric and a magnetic ac field whose phase difference is $\pi/2$. The time averaged energy gain of both methods is relatively small corresponding to a shunt impedance of several kΩ for electrons at small energies. In the first system the energy gain decreases with increasing particle energy whereas the energy gain for heavier particles is practically constant up to high energies ($\approx$600 MeV for protons) in the second system.

The whole accelerating device of the first method is shown in fig. 1 schematically. By means of an RF dipole magnet D_1 and a quadrupole doublet consisting of the quadrupoles Q_1 and Q_2 a periodic movement of the parallel beam in x-direction at the entrance of an hollow electrode system is established. After having passed the electrode system the beam is made parallel again by D_2 and focused to the axis by a second quadrupole doublet Q_3 - Q4. Using a third RF dipole magnet the beam could be deflected into the axis again. At the position of the third RF magnet we measured the energy of the beam by a retarding field analyzer. If D_2 is driven by a dc current the deflections caused by the electrode system are not compensated resulting in a slim ellipse at the position of the analyzer. Thus, it is possible to measure the energy of the beams belonging to different phases.

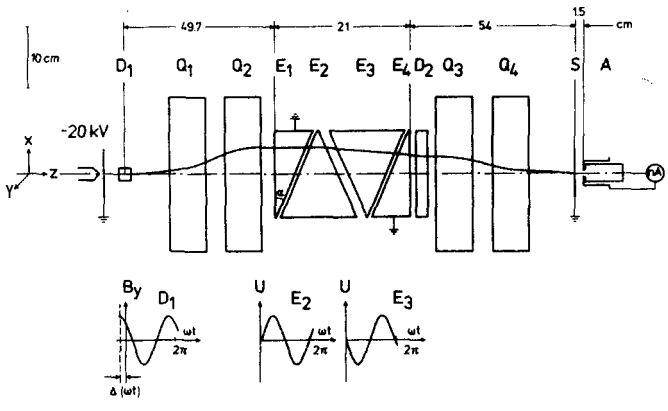


Fig. 1. Experimental setup of the hollow electrode accelerating system; D dipole magnet, Q quadrupole magnet, E electrode, A analyzer

In fig. 2 the principle of the method' is described. The hollow electrodes and particle beams of different phases are sketched. The outer electrodes are grounded. RF voltages with a phase difference π are applied to the inner ones. For simplicity it is assumed that the electric field inside the electrodes is perfectly shielded. The potential ϕ_o on the dashed line between the electrodes 2 and 3 is always zero. The period of the RF voltage must be large compared to the time needed by the particles to pass the electrode system. Considering negatively charged particles, e.g., the parallel incoming beam is moved up and down in x-direction with a phase difference $\pi/2$ to U_2 before entering the electrodes. All beams pass four regions within the electrode system where they are accelerated and retarded. Due to the proposed phase relation between the electrodes and the x-coordinate on the entering beams a net energy gain results. The electrons entering at phase O, e.g., are

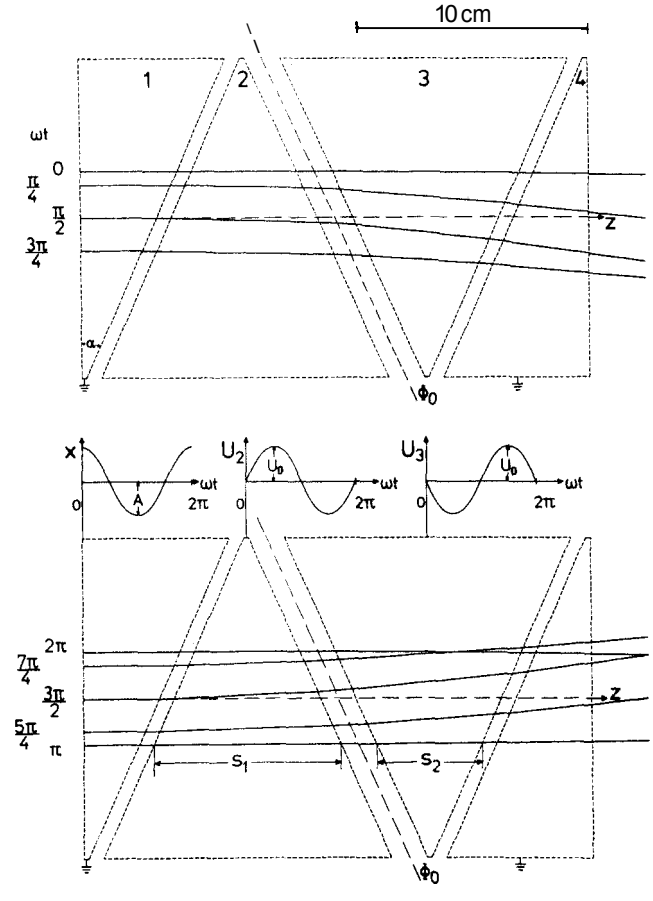


Fig. 2. Principle of hollow electrode accelerating system

accelerated in the gap between the electrodes 1 and 2, retarded between 2 and 3 and accelerated again between 3 and 4. The accelerating effect between ϕ_o and electrode 4 is larger than the retarding effect between 1 and ϕ_o. This can be seen as follows: the particles cover a longer distance within electrode 3 than in electrode 2, hence the voltage drop of 3 is larger during passing 3 than the voltage rise of 2 during passing 2. For the second half of the period the electrodes 2 and 3 change their rolls. The maximum deflected beams gain the maximum energy. In fig. 2 the distances of the beam s_1 and s_2 within the electrodes 2 and 3, respectively, are shown for a phase of entrance π of the beam into the electrode system. Therefore, the accelerating effect depends on the absolute value of the difference of the time-of-flight within the electrodes 2 and 3 and is zero for the phases $\pi/2$ and $3\pi/2$. The energy gain ΔE is approximately given by

$$E = |q| U_o \omega \cdot \frac{|s_o|}{v} \cos^2 \omega t, \qquad (1)$$

where U_o is the maximum voltage of the electrodes, s_o is the difference between s_1 and s_2, and v is the particle velocity. The energy gain does not depend on the sign of the particle charge q.

Due to the triangular shape of the electrodestheparticle beams are deflected from being parallel to the axis (fig. 2). The deflection angle at the end of the electrode system, ϕ , is $\phi \propto \sin\omega t$ and can be corrected by an RF magnet.

The energy gain versus phase is seen in the upper part of fig. 3 for 20 keV electrons with U_o = 3 kV, a maximum displacement of the beam at the entrance of the electrode system A = 2 cm and a frequency of 13.55 MHz. The maximum energy gain is 140 eV. The drawn lines are calculated assuming the field within the electrodes to be zero. The deviation from the $\cos^2\omega t$-curve comes from the deflection of the beams within the electrode system from being parallel to the axis. Using a second accelerating system with a phase difference $\pi/2$ to the

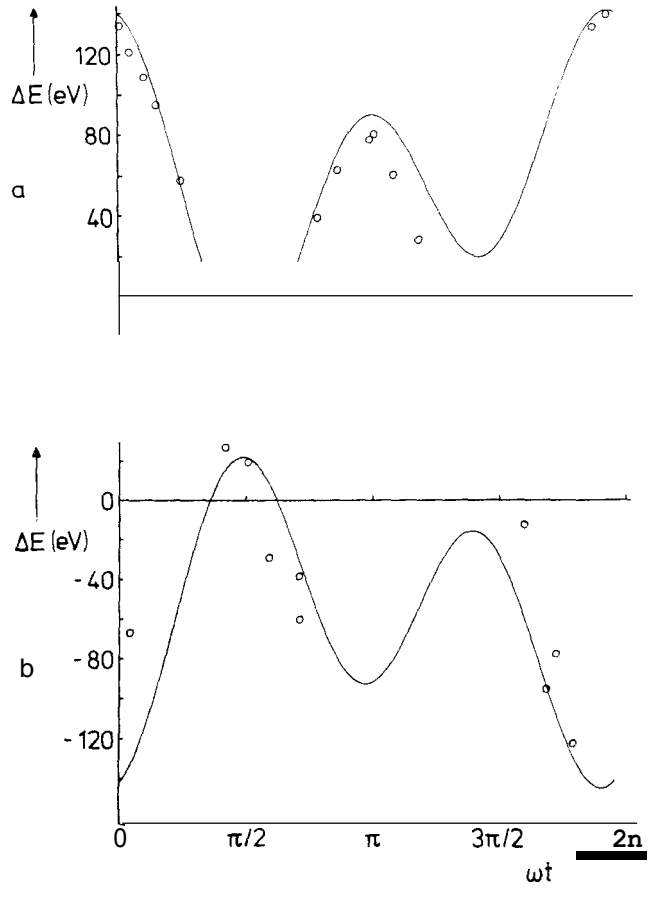


Fig. 3. Energy measurements versus phase of the hollow electrode system. a) The electrons are accelerated on the time average, the system works as an accelerator. b) The phase of the electrode system is shifted by π compared to a). The electrons are retarded on the time average. The parameters of the measurements are given in fig. 2.

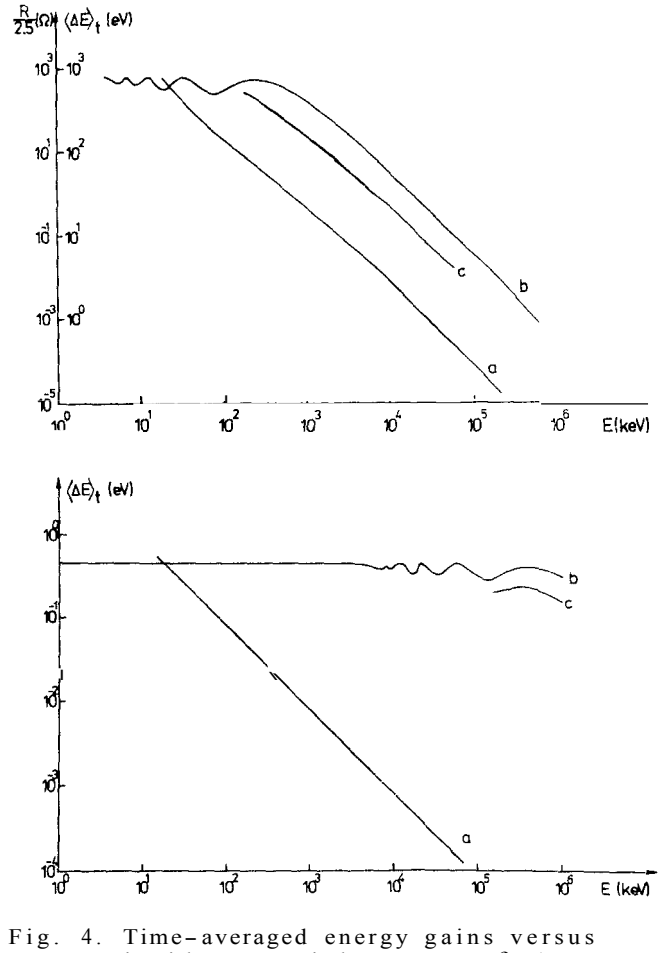


Fig. 4. Time-averaged energy gains versus incident particle energy of the accelerating system. Upper graph: Electrons. a) Hollow electrode system. b) Resonator system (ideal field calculation). c) Resonator system (calculation using measured fields). Lower graph: the corresponding results for protons. The power loss of the hollow electrode system and the resonators were taken to be 400 W.

first one the energy gain of particles having passed two such stages is nearly constant. In order to study the dependence of ΔE on the incident particle energy E eq. (1) can be written as

$$E = \text{const} \frac{P_{loss}}{v \cdot p} \cdot \cos^2 \omega t, \qquad (2)$$

where the constant is given by quantities like the Q-factors of the resonant circuits of D_1 and the electrodes E2 and E3 etc. P_{loss} is the total power loss and p the particle momentum. In our experiment the constant has a value of 0.142 where the energy gain is measured in eV, the power loss in W, the velocity in units of c, and the momentum in MeV/c. In fig. 4 (curve a) the time averaged energy gain $\langle \Delta E \rangle_t$ versus E is shown for electrons and protons for P_{loss} = 400 W. In both cases a large decrease of $\langle \Delta E \rangle_t$ with increasing E results. The lower part of fig. 3 shows the result when the phase between D_1 and the electrodes is shifted by π. In this case the system retards the electrons on the time average.

The second method[2] uses two orthogonal E- and B-fields with a-phase difference π/2, say $E_y = \tilde{E} \sin\omega t$, $B_x = B \cos\omega t$, for accelerating particles in the z-direction. Taking E and B to be constants, an energy gain for slow particles after an accelerating distance d/2 is easily derived in the nonrelativistic approximation to be

$$\Delta E = \frac{q^2 d}{4m\omega} \tilde{E}\tilde{B}, \qquad (3)$$

where m is the particle mass. Replacing m by $m/\sqrt{1-\beta^2}$ eq. (3) gives the right order of magnitude even in the relativistic case.

A similar combination of E- and B-fields can be realized by a rectangular cavity resonator (fig. 5). When the resonator is operated at the TE 101-mode we have the two fields in the plane x = a/2

$$E_y = E_o \sin\left(\frac{\pi}{d} z\right) \sin\omega t$$
$$B_x = -B_o \cos\left(\frac{\pi}{d} z\right) \cos\omega t. \qquad (4)$$

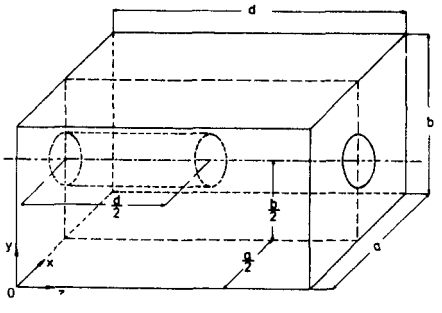


Fig. 5. Cavity resonator, schematically. The dimensions were chosen to be a = 25.4, b = 30, c = 55.3 cm. The drift tube has a diameter of 10 cm.

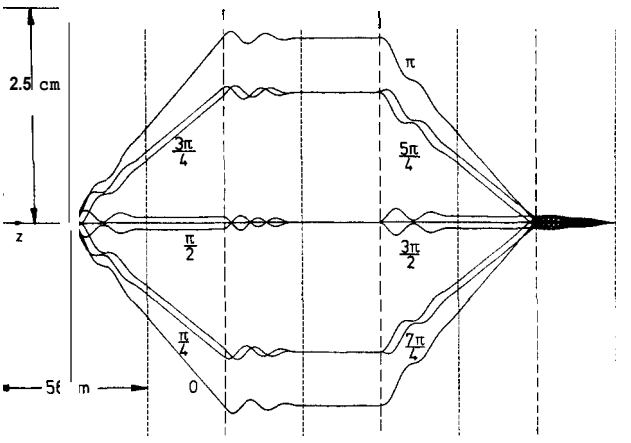


Fig. 6. Electron trajectories within the cavity resonators for different phases of entrance of the particles into the first resonator (ideal field calculation). Incident energy E = 20 keV, power loss in one resonator P_{loss} = 30 W. The broken lines represent cavity resonator boundaries. The large spaced broken lines notify the middle of the cavities.

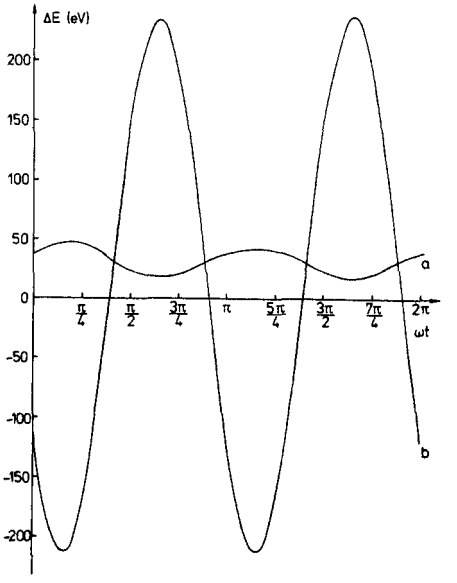


Fig. 7. Total energy of electrons after having passed four resonators versus phase. a) Ideal field calculations. b) Calculation using measured fields; E = 20 MeV, P_{loss} = 400 W.

Because of the z-dependence of the fields we see from eq. (3) that AE < O for O < z < d/2 and AE > O for d/2 < z < d. Therefore, if the fields of the first half of the resonator are shielded by a drift tube, the fields of the second half can be used for continuous particle acceleration.

The beams which enter the resonator in the plane x = a/2 are deflected by the fields within that plane. The deflection angles at tne end of the resonator depend on the phases of entrance of the particles into the accelerating fields. If an ideal field distribution exists, it can be shown that the deflections of the beams at the end of the resonator can be compensated by three additional identical resonators which have phase differences of π, π, and O, respectively, to the first one. An ideal field distribution means that there are an E_y- and a B_x-component as given by eq. (4) in the second half of the resonator and the fields are perfectly shielded in the first half.

In fig. 6 results of a numerical calculation of electron trajectories through four resonators at different phases of entrance into the first resonator are shown. An ideal field distribution was assumed. In fig. 7 (curve a) the total energy gain of electrons after having passed four cavities is drawn against the phases of entrance into the first resonator. The dependence on the phase is much smaller in this ideal case than in the hollow electrode system. There is, however, a fact which greatly disturbs this behavior. The drift tube which shields the field in the first half of the resonator disturbs the ideal field distribution. Therefore, the electric

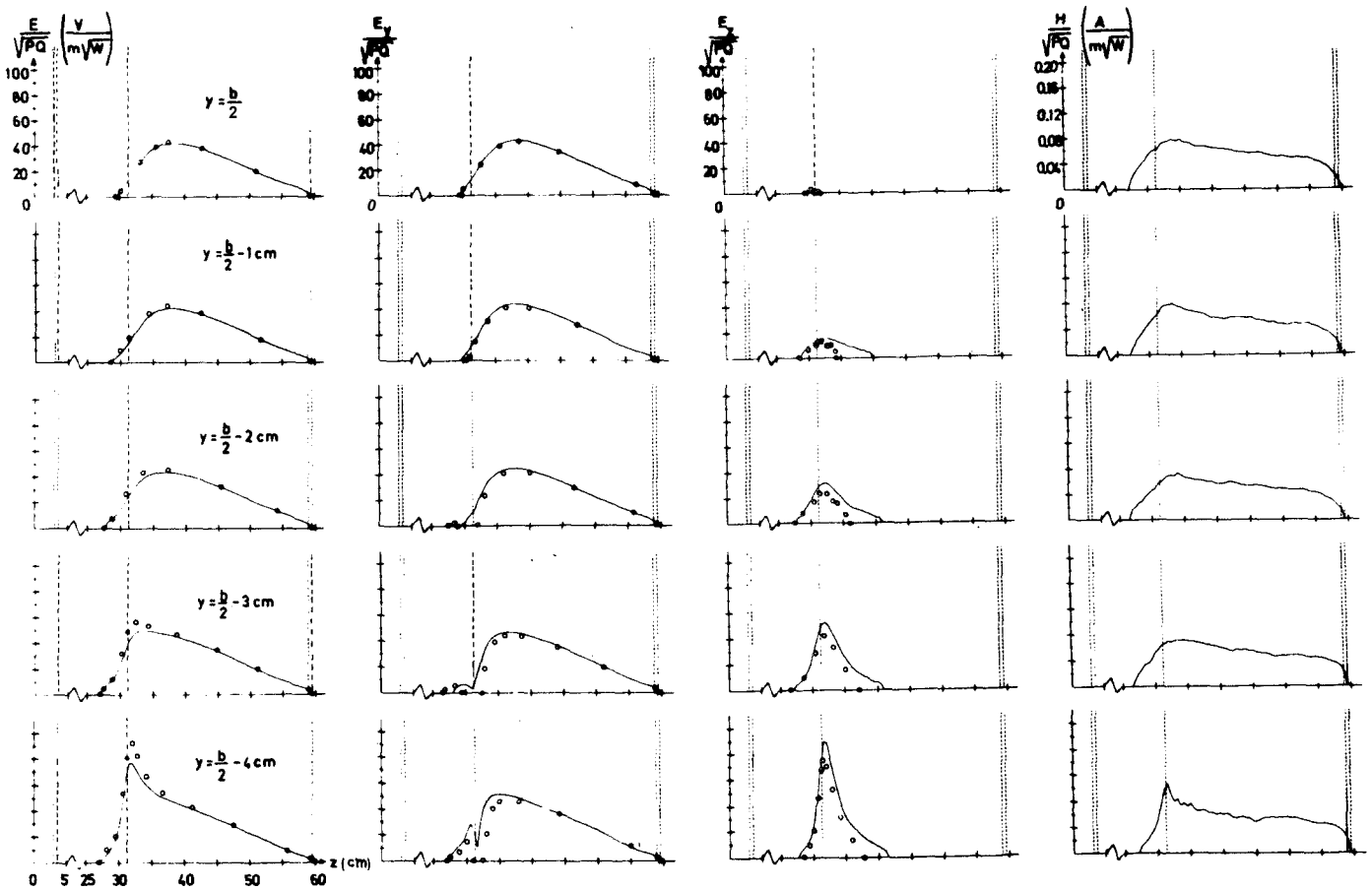


Fig. 8. Results of perturbation object measurements of E, E_y, E_z, and H_x versus the z-coordinate of the resonator at different distances from the axis in the plane x = a/2. The drawn lines represent direct measurements. The circles represent values which were composed from different electric field component measurements. P is the power loss and Q the Q-factor of the resonator. The double dotted lines represent the front and rear plate, the single dotted line the middle of the cavity or the end of the drift tube, respectively.

field lines are slightly bent at the end of the drift tube causing a nonvanishing electric field component E_z at both sides of the axis. Fig. 8 shows perturbation object measurements of electric fields E_y and E_z, and the magnetic field H_x versus the z-coordinate within the $x = a/2$ plane at different distances from the axis. A drift tube of 10 cm diameter was used. No further field components have been found. Taking into account the measured fields the energy gain of electrons after having passed four resonators versus phase of entrance were calculated and are shown in fig. 7 (curve b). The large deviations from the ideal behavior is caused by the additional E_z-component. Fig. 9 shows a corresponding numerical calculation of electron trajectories within the cavities using the measured fields. On the time average, the mean values of the energy gains over all phases of entrance are nearly equal to the ideal energy gain mean values. This is true in a wide range of incident energies as can be seen from fig. 4 (curve c).

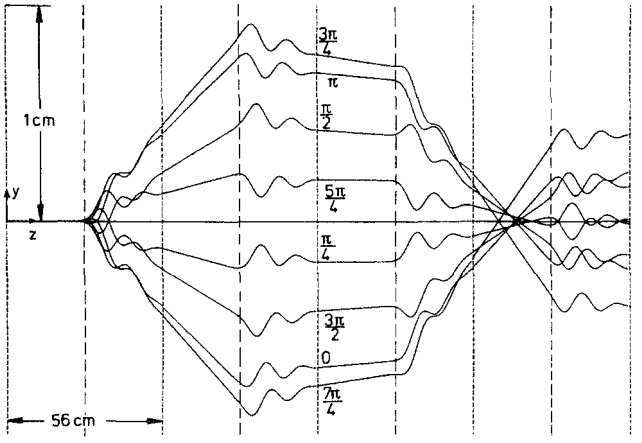


Fig. 9. Calculations analog to fig. 6 where the measured fields were taken into account. The parameters of the calculation being the same as in fig. 6.

In the x-direction the cavities have a slight defocusing effect on the particles even in the ideal field case, i.e., the particles are deflected off the plane $x = a/2$ by means of the magnetic field B_z of the cavity which is different from zero for $x \neq a/2$. Writing $\xi = x - a/2$ and $\zeta = z - d/2$ we get for ξ within the second half of a cavity

$$\xi = (1+\tfrac{\varepsilon}{2}f(\zeta,\omega t_o))(C_1 \cdot e^{\sqrt{\frac{\varepsilon}{2}}\zeta} + C_2 \cdot e^{-\sqrt{\frac{\varepsilon}{2}}\zeta}), \quad (5)$$

where C_1 and C_2 are constants depending on the initial values. For ε we get

$$\varepsilon = q^2 B_o^2 (1+\beta^2)/2m^2c^4R^2,$$

where B_o is the maximum of the B_z-field.

References

1 H. Daniel, Z. Physik 236 (1970) 166.

2 H. Daniel, P. Halfar and K. Springer, Contributed paper to the IV. Int. Conf. on High Energy Physics and Nuclear Structure, Dubna (1971).

POLARIZED ELECTRON SOURCE FOR THE STANFORD LINEAR ACCELERATOR*

M.J. Alguard, R.D. Ehrlich, V.W. Hughes, J. Ladish, M.S. Lubell and W. Lysenko
J.W. Gibbs Laboratory, Yale University, New Haven, CT 06520

K.P. Schüler
J.W. Gibbs Laboratory, Yale University, New Haven, CT 06520
and University of Bielefeld, Bielefeld, West Germany

G. Baum and W. Raith
University of Bielefeld, Bielefeld, West Germany

A polarized electron source suitable for injection into the 20 GeV Stanford Linear Accelerator has been developed and is currently being installed at SLAC. Based on a prototype built a number of years ago,[6] the polarized electron source (PEGGY) relies on the photoionization of an intense spin polarized beam of Li^6 atom by putsed uv Light. When final installation is completed, PEGGY should deliver 10^9 electrons/pulse in a 1.5 μsec pulse with a polarization of 0.9 at a repetition rate of 180 pulses/sec.

Introduction

The method of producing polarized electrons by photoionization of a polarized atomic beam. originally suggested by Fues and Hellmann in 1930,[1] led to one of the earliest successful developments of a low-energy source of polarized electrons in 1965.[2] Since then the method has been studied extensively, and a detailed description of the underlying principles has been published.[3,4] The present paper contains a brief review of these principles, a more detailed description or' the apparatus used in PEGGY, and a summary of the results obtained with PEGGY to date.

Principles

A schematic diagram of the method of producing polarized electrons is shown in Fig. 1. A beam of Li^6 atoms is produced by heating lithium metal in *an* oven and passing the emerging atoms through a collimation system. Polarization of the Li^6 beam is then achieved by high-field state selection of the $m_J = +\frac{1}{2}$ atoms in a six-pole magnet. The polarized atoms pass into the ionization region in which there is a 200 G longitudinal magnetic field, with the atomic states adiabatically following the magnetic field seen by the atom. In a magnetic field of 200 G the hyperfine interaction reduces the electronic polarization of the Li^6 atoms to 0.95 of the high-field value.[4] The electronic polarization of the atoms transmitted Lo the ionization region can thus be written as function of the magnetic field, H, as

$$P_{e,atom} = \langle \sigma_z \rangle = sf(H), \tag{1}$$

where σ_z is the z component of the Pauli spin operator and s is the six-pole magnet state selection parameter given by

$$s = (\Omega^+ - \Omega^-)/(\Omega^+ + \Omega^-) \tag{2}$$

with $\Omega^\pm$ the effective solid angle for transmission of the $m_J = \pm\frac{1}{2}$ atoms through the six-pole magnet. The hyperfine structure coupling function, f(H), is given by[4]

$$f(H) = \frac{1}{2I+1} \sum_{m=-I+\frac{1}{2}}^{I+\frac{1}{2}} \frac{2m/(2I+1) + X}{\left\{1+[4m/(2I+1)]X + X^2\right\}^{\frac{1}{2}}}, \tag{3}$$

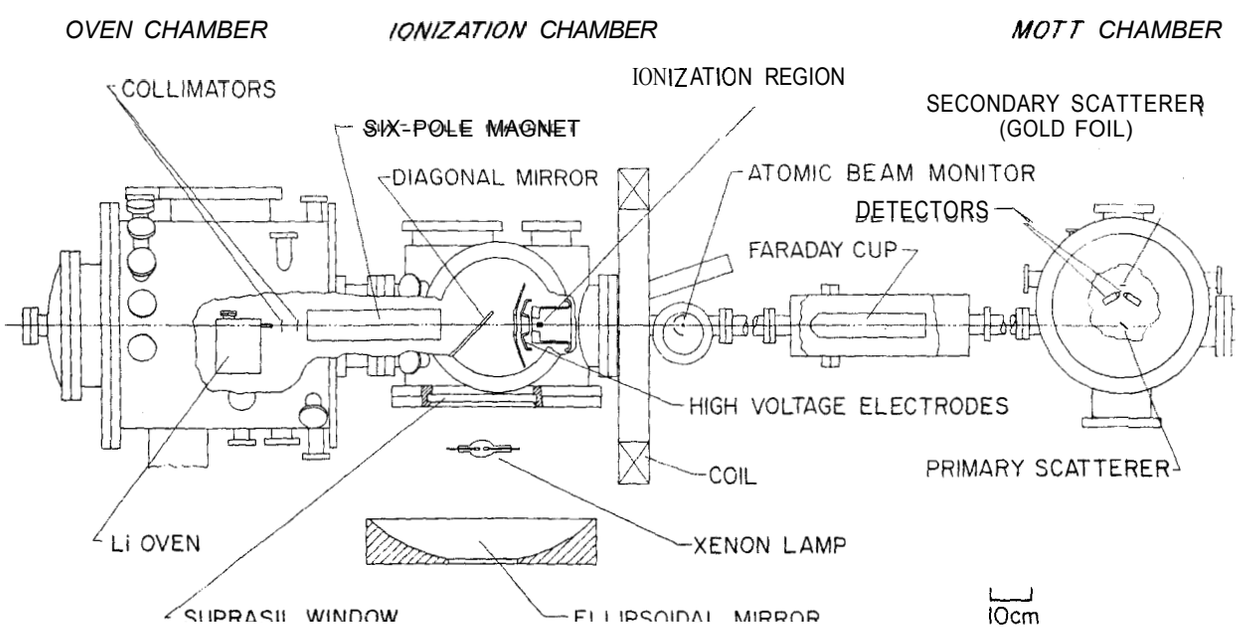


FIG 1. Schematic diagram of PEGGY.

where

$$X = (g_J - g_I)\mu_B H/\Delta W \qquad (4)$$

and I is the nuclear spin, μ_B is the Bohr magneton, ΔW is the hyperfine structure (hfs) splitting, and g_I and g_J are the nuclear and electronic g values respectively. In strong fields where the nuclear and electronic spins are decoupled, Eqs. (3) and (4) show that f(H) approaches unity; at zero field f(H) takes on the value $1/(2I+1)$. Thus Li^6 was chosen as the optimum alkali atom because it has a very small hfs splitting ($\Delta W/\mu_B$=163G) and a correspondingly small nuclear spin (I=1), thereby maximizing f(H). At H=200 G, f(H) takes on a value of 0.95. In addition, lithium was chosen because it has the highest photoionization cross section (2 Mb) of all the alkali atoms.

The polarized Li^6 atoms are photoionized in the ionization region by pulsed uv light ($\lambda \leq 2300$ Å) which is focused onto the lithium atomic beam by an ellipsoidal mirror and a plane mirror (denoted by "diagonal mirror" in Fig. 1) which reflects the light through 90° to maximize the atom-photon interaction region. Since lithium does not display any depolarization associated with a final continuuin state spin-oroit interaction,[4-6] the ejected photoelectrons are characterized by $P_{e,atom}$ given by Eq. (1). The ionization region is maintained at a potential of -70 kV, and the ejected photoelectrons are accelerated to ground potential during extraction. Depolarization of the electron beam during extraction is estimated as being at the 1% level.

Downstream from the ionization region the characteristics of the lithium atomic beam can be monitored by a removable oxidized tungsten hot wire surface ionization (Langmuir-Taylor) detector.[7,8] The intensity of the Longitudinally polarized 70 keV electron beam can be monitored as well by a Faraday cup which has a door at its downstream end. With the door open, the electron beam is transported further downstream for either injection into the accelerator or for polarization analysis into a Mott scattering device. Mott scattering results in a scattering asymmetry ϵ given by[10,11]

$$\epsilon = \frac{I(+\theta)-I(-\theta)}{I(+\theta)+I(-\theta)} = \vec{P}\cdot\vec{A} = S(\theta)\,\vec{P}\cdot\hat{n}, \qquad (5)$$

where $I(+\theta)$ is the intensity of electrons scattered in the direction (θ,φ) and $I(-\theta)$, the intensity scattered in the direction $(\theta,\varphi+\pi)$. In Eq. (5), P is the polarization ($\vec{P} = \langle\vec{\sigma}\rangle$) of the incident beam, A is the analyzing power of the interaction, $S(\theta)$ is the analyzing function,[12] and $\hat{n}$ is a unit vector perpendicular to the scattering plane. In terms of the non-flip and spin-flip scattering amplitudes, f and g respectively, S can be written as

$$S = i(fg^* - gf^*)/(|f|^2 + |g|^2). \qquad (6)$$

From Eq. (5) it is seen that ϵ is non zero only if the polarization vector of the incident electrons has a transverse component. A 90° scattering by transmission through a primary foil is used therefore to convert the longitudinal polarization into transverse polarization, which is subsequently measured by 120° Mott scattering from a secondary gold foil.

Description of the Apparatus and Results

Thus far PEGGY has been operated at Yale University at a repetition rate of 1 pulse/sec which was limited by the modulator available at Yale for operating the pulsed uv lamp. Table 1 contains a summary of the results of the Yale tests as well as the projected PEGGY characteristics for operation at SLAC and the source characteristics obtained with the prototype.[4] During the Yale tests PEGGY produced 3×10^{11} electrons/pulse for extended periods. The atomic beam necessary to achieve this intensity was maintained over a continuous period of 60 hours and was limited only by the charge of lithium inserted in the oven. For brief periods the peak current of the uv light source was increased from its normal operating value of 3.3 kA to 5.0 kA with a resultant increase of electron intensity to 5×10^{11} electrons/pulse.

One of the major advances required to make PXGGY a viable source for SLAC was the davelopment of a short arc uv flash lamp with a long Life-time, defined as time to half intensity. As seen in Table 1. the lamp used in the prototype had a life-time of less than 10^4 pulses. The lamp finally developed for PEGGY contains 5 atm of xenon gas sealed in a Suprasil envelope. The electrodes are fabricated from sintered tungsten, with the cathode being impregnated with $BaSrAl_2O_3$ to reduce sputtering, and are 4 mm apart. The lamp is operated in a pulsed mode at 180 pulses/sec with a pulse length of 1.5 μsec and is capable of withstanding peak currents of 3.5 kA and peak voltages of 17 kV for 10^7 pulses before clouding of the envelope reduce the light output in the spectral range 2300 Å-1900 Å to half its initial intensity. Extensive lifetime tests of the lamp were carried out at SLAC at the 180 pulse/sec repetition rate using a modified klystron modulator; thus, once installation at SLAC has been completed, PEGGY will be capable of being operated at 180 pulses/sec as indicated in Table 1. Detailed measurements of tne spectral characteristics of the lamp were carried out at a 1 pulse/sec repetition rate at Yale.[13] The average spectral radiance for a point midway between the electrodes was found to be 7×10^{13} photons/sr cm² Å at 2100 Å.

The optical system consisting of flash Lamp, MgF_2 overcoated front surfaced aluminized ellipsoidal. and diagonal mirrors, and Suprasil window was designed to provide light at the ionization region in the spectral range 2300 Å - 1800 Å since the photoionization threshold for lithium occurs at 2300 Å. In order to avoid the O_2 absorption bands at wavelengths shorter than 2000 Å, a sealed housing filled with dry nitrogen was placed around the lamp, window, and ellipsoidal mirror assembly. This dry atmosphere also served to protect the front surfaced ellipsoidal mirror from degradation due to condensed water vapor. The overall optical efficiency of the mirrors and window averaged over the spectral range of interest was found to be 0.5 ± .05.

The polarized lithium beam system consists of an oven fabricated from Armco iron (which is the most nonreactive material for use with lithium metal) with a capacity of 250 g of lithium. a collimation system containing two heated collimators, and a six-pole magnet. The oven is typically operated at a temperature of 1150 ± 50°K at which the vapor pressure of lithium is in the range 5-15 Torr. The lithium consumption rate under these conditions has been experimentally found to be about 2.5 g/hr. Thus a fully charge oven will Last about 100 hrs. The lithium used to charge the oven is 95.4% Li^6 and 4.6% Li^7 and is produced and shipped oil free under an argon atmosphere by Oak Ridge National Laboratory.

The six-pole magnet is 34.3 cm long with a bore diameter of 3.2 mm and has Alnico 8a drivers and Permendur pole tips. With a pole tip field strength of 8.6 kG computer calculations show that the six-pole magnet state selection parameter, s, defined in Eq. (2) has a value of 0.993. Thus with f(H) = 0.95, Eq. (1) shows that $P_{e,atom}$=0.94. If the 4.6% Li^7 contamination is taken into account, f(H) decreases to 0.93 and $P_{e,atom}$, to 0.93. A Lithium atomic beam profile measured at the

Table 1. Characteristics of Polarized Electron Source for Use with SLAC

Characteristic	Prototype[4]	PEGGY Vale Test	PEGGY Projected
Mean energy	100 keV	70 keV	70 keV
Energy spread (calc.)	<1.5 keV	<1.5 keV	<1.5 keV
Emittance at mean energy (calc.)	1 mrad cm	10 mrad cm	10 mrad cm
Pulse length	1.5 μsec	1.5 μsec	1.5 μsec
Repetition rate	10 pulses/sec	1 pulse/sec	180 pulses/sec
Lamp Lifetime	$<10^4$ pulses	$\sim 10^7$ pulses	10^7 pulses
Electron intensity	2×10^8 electrons/pulse	3×10^8 electrons/pulse	10^9 electrons/pulse
Electron polarization	0.73 ± 0.03	0.7 ± 0.2	0.90 ± 0.03

ionization region for an oven temperature of 1000°K is shown in Fig. 2. Table 2 contains a comparison summary of the lithium and electron beam intensity parameters for PEGGY and the prototype source.

Detailed electron optics calculations were carried out using a SLAC computer program[14] to insure that the polarized photoelectrons would be extracted with the proper emittance and energy spread. Space charge effects on electron extraction were found to be negligible at intensities of 10^9 electrons/pulse. The separation of background (photoelectrons ejected from the electrode surfaces) trajectories from those of the polarized electrons is shown in Fig. 3. The electrode structure consists of a cathode maintained at -70 kV. a repeller maintained at -76 kV to prevent electrons from being extracted upstream (to the left in Fig. 3), and aground shield to protect the front surfaced diagonal mirror from discharges. Not shown in Fig. 3 is a movable mesh that can be rotated under vacuum into the ionization region to provide an intense (10^{10} electrons/pulse) test beam of unpolarized electrons. As indicated in Table 1, the energy spread is calculated to be <1.5 keV and for a 200 G magnetic field at the ionization region the emittance is calculated to be 10 mrad cm for electrons extrnctad from an ionization region whose radial extent is 2.3 mm. From Pig. 3 it can be *seen* that more than 90% of the lithium atoms lie inside this region. As shown in Fin 3 the 200 G magnetic field is provided by a single large coil mounted 24 cm downstream from the ionization region. Further downstream are mounted additional coils for focusing and steering the electron beam.

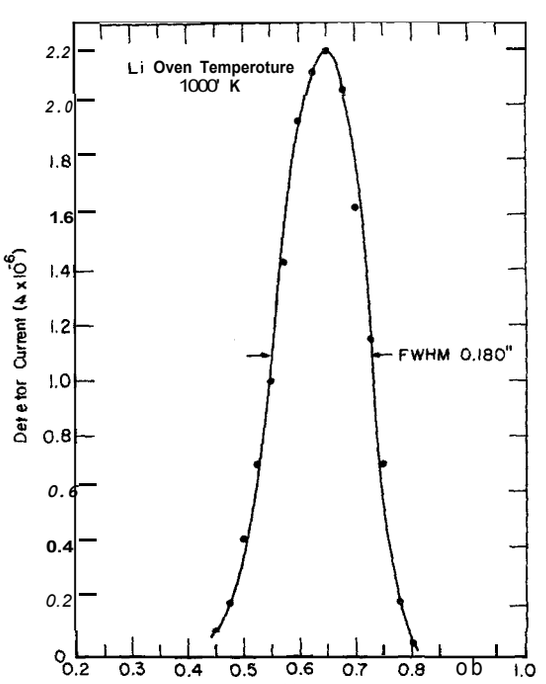


FIG 2. Typical atomic beam profile measured at the ionization reglon for an operating oven temperature of 1000°K. An oxidized tungsten hot wire detector with a 0.012 diam. wire 1.2 cm long was used.

A preliminary polarization measurement of the extracted electron bean was performed at Yale at a repetition rate of 1 pulse/sec. The Mott scattering apparatus used is equipped with two silicon surface barrier detectors mounted 180° apart in azimuthal angle φ and at a scattering angle θ of 120° measured from the direction of incidence on the secondary foil. To facilitate measurement of instrumental asymmetries, the detectors are mounted on a wheel whose axis of rotation coincide. with the direction of the electrons incident on the secondary foil. The primary and secondary foils are both mounted on target wheels which can be rotated under vacuum to place any one of six foils in position for each of the primary and secondary scatterings. During the preliminary measurements at Yale only one 60 μg/cm² gold foil was used for the secondary scattering; two gold foils, one 2.90 μg/cm² and one 3.5 μg/cm², were used for the primary scattering. All foils were evaporated onto Formvar backings with thicknesses of approximately 20 μg/cm². Charge sensitive preamplifiers, shaping amplifiers, discriminators, scalers and a pulse height analyzer were used for data aciuisition. A composite pulse height spectrum is snown in Fig. 4. The polarization, P, was calculated according to

$$P = \delta(1 + \alpha d)/SD, \qquad (7)$$

where δ is a foil thickness correction tern, d is the thickness of the second foil in μg/cm², S is *the* analyzing function, D is the depolarization due to spin rotation in single and plural scattering at the primary foil, and ε is the measured asymmetry already corrected for oackground and instrumental asymmetries. At 120° and 70 keV, the calculated value[15] of S is 0.37; D is estimated to be[10,11,15] 0.89. Since no foil thickness dependence was studied in the preliminary measurement, α is taken as[16,17] 0.0045. The polarization thus obtained is 0.7 ± 0.2. More detailed polarization measurements will be made after PEGGY has been installed at SLAC and can be operated at 180 pulses/sec.

Table 2. Intensity of Polarized Electron Source *Using* A Lithium-6 Atomic Beam

	PROTOTYPE	PEGGY
Flux from oven source in forward direction	10^{18}/sec x sr	5×10^{18}/sec x sr
Acceptance of magnet for atoms *in* m_J=+1/2 states	6×10^{-4} sr	4×10^{-4} sr
Fraction of atoms *in* m_J=+1/2 states	0.5	0.5
Flux of polarized atoms to photoionization reglon	3×10^{14}/sec	10^{15}/sec
Most probable beam velocity	2×10^5 cm/sec	2.2×10^5 cm/sec
Length of ionization reglon	2.5cm	3.7 cm
Photaionlzation efficiency	5%	2%
Intensity of polarized electrons/pulse	2×10^8/1.5μsec	3×10^8/1.5μsec

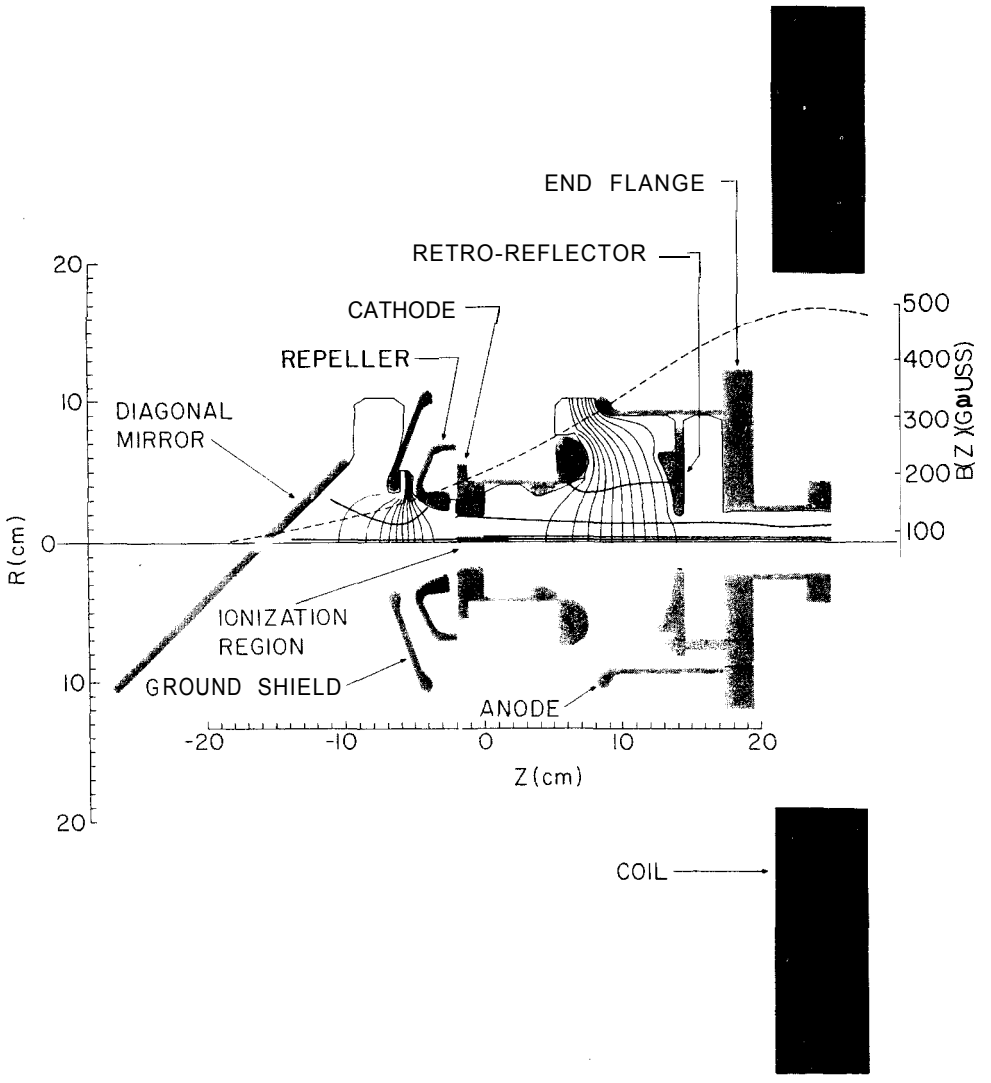


FIG 3. Scale drawing of electron optical components at the ionization region together with the results of tne electron trajectory calculations. The gray areas are cross sections of the electrodes and other surfaces exposed to the electrons. The thin line which bounds them (shown in the upper half only) are the different boundaries used in the computer calculation of the electron trajectories. The cathode potential was set at -70 kV, the repeller at -76 kV and all other surfaces at, ground. The tnin curved lines are 10% equipotential tines with the two lines on either side of the ionization region and closest to it being -70 kV Lines and with each adjacent Line differing from its neighbor oy 7 kV. The six heavier Lines, two starting from the ionization region and extending downstream (positive z direction), one starting from the ionization region and extanding upstream (negative z direction), and three starting at points along the repeller and cathode surfaces are typical electron trajectories. The dasned line is the value of the magnetic field on axis produced by the coil shown in cross section by the black area.

were fabricated from stainless steel and cleaned to meet the SLAC ultra-high vacuum requirements; vacuum

During the installation of PEGGY at SLAC, the optical system will be modified with the incorporation of a retro-reflector to send the uv light back a second time through the ionization region, as shown in Fig. 3, in order to increase the ionization probability. Additional improvements planned for the near future include the fabrication and instaliation of a larger bore six-pole magnet, which will increase the atomic beam flux at the ionization region, and the development of a vortex stabilized flash lamp[19] which will tolerate the higher peak currents necessary for increased uv light output. With the incorporation of these improvements it is estimated that PEGGY will produce in excess of 10^9 electrons/pulse.

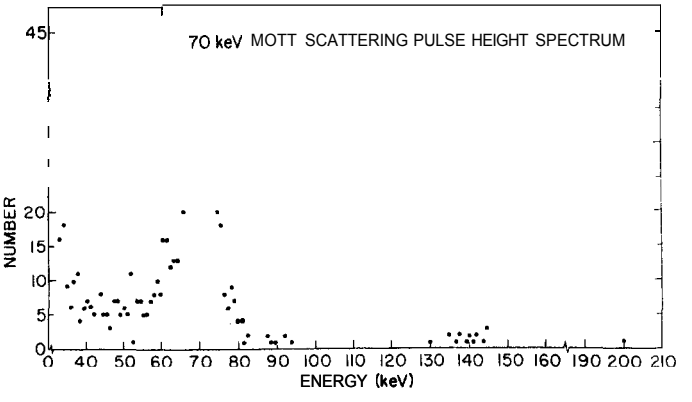


FIG 4. Composite Mott scattering pulse height spectrum showing one, two and three electron events. The primary scattering targets used were 290 $\mu g/cm^2$ and 385 $\mu g/cm^2$ gold foils for spin rotation. The secondary scattering target used for Mott scattering was a 60 $\mu g/cm^2$ gold foil.

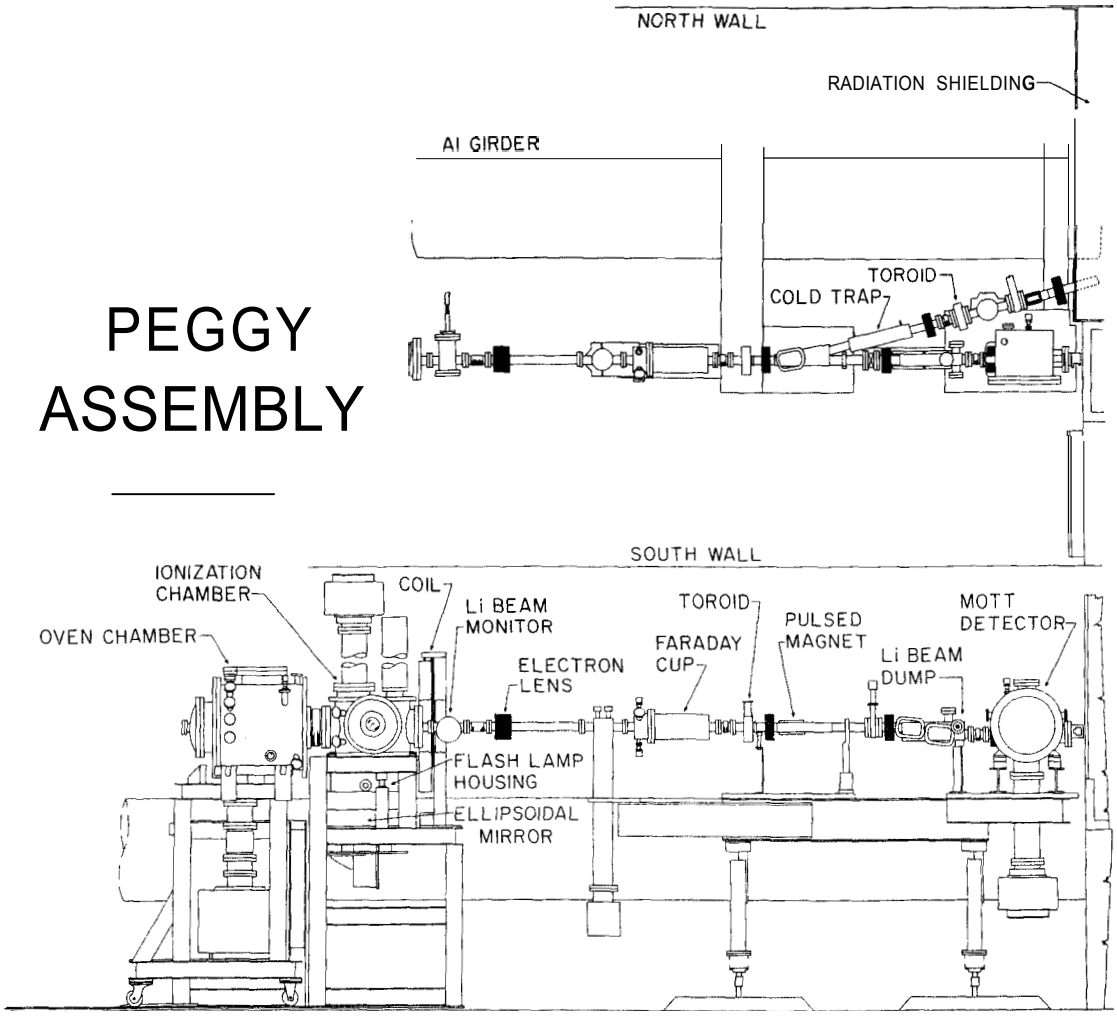


FIG 5. Scale drawing of PEGGY installation at SLAC, showing a top view and an elevation. The top view shows the 14° switch into the beam transport to the injector. The switching is accomplished by a pulsed magnet to allow some of the pulses to be transported directly to the Mott detector for polarization analysis at 70 keV.

Following measurement of the electron polarization at high energy by means of Møller scattering,[20,21] two high-energy experiments are planned and have been approved for SLAC. One experiment, SLAC/E80,[22] will measure the asymmetry in deep inelastic scattering of polarized electrons by polarized protons and will utilize a hydrocarbon, longitudinally polarized proton target operated at 1°K and 50 kG. The second experiment, SLAC/E95,[23] will search for parity violations $(\vec{a}\cdot\vec{p}_e)$ in the scattering of longitudinally polarized electrons by unpolarized protons in a liquid hydrogen target.

*Research (Yale Report COO 3075-76) supported in part by the U. S. A. E. C. Contract No. AT(11-1)3075, the U. S. Office of Naval Research Contract No. N00014-67-A-0097-0015, the German Federal Ministry of Research and Technology and the University of Bielefeld.

1. E. Fues and H. Hellmann, Physik. Z. 31, 465 (1930).
2. R. L. Long, Jr., V. W. Hughes and W. Raith, Phys. Rev. Letters 15, 1 (1965).
3. V. W. Hughes, M. S. Lubell, M. Posner and W. Raith in Proceedings of the Sixth International Conference on High Energy Accelerators, Cambridge, Mass. (CEA Laboratory, Cambridge, Mass., 1967). p. A144.
4. V.W. Hughes, R.L. Long, Jr., M.S. Lubell, M. Posner, and W. Raith, Phys. Rev. A 5, 195 (1972).
5. U. Fano, Phys. Rev. 178, 131 (1969); 184, 250 (1969).
6. G. Baum, M.S. Lubell and W. Raith, Phys. Rev. A 5, 1073 (1972).
7. P. Kusch & V. W. Hughes, Enc. of Phys. 37/1, Springer Verlag (1959).
8. W. Schroen, Z. Physik 176, 237 (1963).
9. N.F. Mott, Proc. Roy. Soc. (London) A124, 425 (1929); A135, 429 (1932).
10. M.F. Mott and H.S.W. Massey, The Theory of Atomic Collisions, 3rd Edition (Oxford, 1965), pp. 226-236.
11. L.S. Rodberg and R.M. Thaler, Introduction to the Quantum Theory of Scattering (Academic Press, 1967), Ch.11.
12. N. Sherman, Phys. Rev. 103, 1601 (1956); N. Sherman and D.F. Nelson, Phys. Rev. 114, 1541 (1959).
13. M.J. Alguard and M.S. Lubell (to be published).
14. W. Herrmannsfeldt, SLAC-166. The calculation was carried out with the help of Mr. C.W. Tu.
15. G. Holzwarth and H.J. Meister, Tables of Asymmetry, Cross Section and Related Functions for Mott Scattering of Electrons by Screened Au and Hg Nuclei (Universityof Munich, Munich, Germany, 1964); Nucl. Phys. 59, 56 (1964).
16. L. Mikaelyan A. Borovoi and E. Denisov, Nucl. Phys. 47, 328 (1963).
17. H. Wegener. Z. Phys. 151, 252 (1958).
18. R.H. Helm and W.P. Lysenko, SLAC TN 72-1.
19. M.E. Mack, Appl. Optics 13, 46 (1974).
20. H. Frauenfelder and A. Rossi in Methods of Experimental Physics, edited by L.C.L. Yuan and C.S. Wu (Academic Press, New York, 1963), Vol. 5, p. 214.
21. "Test of PEGGY Polarization at High Energy," V.W. Hughes et al., SLAC/T133.
22. "Measurement of Asymmetry in Deep Inelastic Scattering of Polarized Electrons by Polarized Protons," V.W. Hughes et al., SLAC/E80.
23. "Experimental Test for an Electromagnetic Axial-Vector Current of Hadrons in Inelastic Scattaring of Polarized Electrons," C.Y. Prescott et al., SLAC/E95.

ITEP EXPERIMENTAL ASSEMBLY FOR ERA COLLECTIVE METHOD INVESTIGATIONS

I. V. Chuvilo, I. M. Kapchinsky, V. K. Plotnikov, and R. M. Vengrov
Institute for Theoretical and Experimental Physics, Moscow, USSR

The most promising branch of the ERA collective method seems to be nowdays the acceleration of heavy ions and construction of an effective high current nucleon accelerator. In both cases the block scheme of the accelerator seems to have the following form. The electron beam, after acceleration in an injector, is injected into compressor, the formed ring is compressed in it, is filled with ions and accelerated in a static magnetic field decreasing towards acceleration direction due to energy accumulated by electrons in azimuthal motion. Every electron ring is used in one cycle at maximum energy transformed from electrons to ions.

All the effects related to particle dynamics in the ring may be divided into two main groups. The first group effects are those which define the parameters of the ring during the compression and filling with ions. These effects restrict the possibility of obtaining the electron-ion rings with high electric fields of electrons and given number of nucleons in the ring. The second group effects are those holding in the electron-ion ring acceleration. The modern theory allows one to point out the existence of these effects and to estimate the regions of their emergence but does not allow to find accurate qualitative criteria for definition of the bounds of stability and instability regions. Theoretical estimates give a very wide range of the collective accelerator parameters starting with the types of accelerators with the parameters much better than those of the "classic type" and finishing with the types beyond any criticism. Therefore the experimental study of the above effects is of special importance.

At present in ITEP the assembly for investigation mainly of the first group effects has been constructed. After some reconstruction and building up of the acceleration channel it will allow us to study the effects arising during acceleration. The experimental program will consist of azimuthal coherent instability study and of the study of mutual resonant coupling of electrons and ions betatron oscillations. The investigation of the electron-ion rings polarization by modelling this process in external electric field, and, after constructing an arrangement for rings extraction, study of the "cylindricity" effect and of the focusing by "image" forces is planned.

The assembly consists of an injector, electronguide with the apparatus for measuring the beam parameters, compressor and a system for beam diagnostics.

As an injector, we use a 1.5 MeV linear induction electron accelerator with the beam current 100÷200 A (LIA-1.5). This accelerator will be used for adjusting the compressor and other assemblies of the installation. In future the LIA-1.5 will be replaced by a 5 MeV LIA with the beam current 2+4 kA. It is proposed that the main part of the experimental program will be made with this new accelerator.

The length of the electron guide is 7 m. The electron beam focusing is performed by short longitudinal field lenses with the 1 m distances from one to another. Between the lenses there are: magnetic analyzer of instantaneous particle spectrum which makes it also possible to measure the electron mean energy during a pulse, a phase volume meter, a measuring revolver unit with six different masking apertures, collimators and grids, beam transformers, scintillation screens and pulse bending magnets.

The walls of the dynamical type compressor are made of stainless steel sheets, 0.8 mm gauge. Seven pairs of coils forming the main magnetic field are placed outside the compressor chamber in special rims made of glass-fabric laminate to perceive mechanical impact at the moment of switching the current into the coils. The current pulses in the coils are of the semi-sinusoidal form. Each next coil is putting into operation with the phase shift $\pi/3$ relative to the previous one. The pulse shape of the current is defined by an oscillatory discharge of condensers to the coils. The switching on of the current is fulfilled by thyristors. Three-turn injection of the beam into compressor is made by fast displacement of injected electrons from the inlet nozzle by the magnetic field of special injection coils mounted inside the chamber of the compressor. During the process of injection the electron momentum spread of about 3÷5% must occur. The compression chamber has eight flanges at its perimeter and two at the center. The flanges are intended for the beam injection, for putting in the current pulses for injection coils, fixing of the coils, pumping out of the chamber and for diagnostic apparatus. One of the central flanges will be used for mounting of a pulse source of "tube" form flow of neutral gas. When estimating the accessible quantity of electrons from the coherent azimuthal instability point of view it was assumed that the compressor chamber shunt-impedance will be not worse than that in Berkeley and the momentum spread not less than 0.03.

The diagnostic system consists of different means of ring parameter measuring devices. There will be used movable X-ray pick-ups and Faraday cups for measuring big radius and every radial dimension of the ring, beam transformers of the ring currents, wide ban receivers for measurements of the spectrum of electromagnetic oscillations excited in the chamber by the ring, image converter to measure the synchrotron radiation density along the cross section of the ring and thus the distribution of electrons along the cross section for the periods of some nanoseconds with the interval of some tens of nanoseconds.

The main parameters of the LIA-1.5, LIA-5 and of the compressor are given in Tables I and 11. The diagrammatic drawing of the compressor and calculated time characteristic curves of the ring big radius, field on the radius of the ring and n-trajectory are shown in Figs. 1 and 2. The photographs (Figs. 3 and 4) show the total view of the LIA-1.5 as viewed from the compressor and the compressor itself.

By the time that this report was ready the production and mounting of the LIA-1.5, the electron guide and the compressor were mainly completed. The adjusting of the LIA-1.5 and leading of the beam through the electron guide are carrying out. Works of adjusting the compressor operation and forming of the rings will start in the first half of 1974. The LIA-5 is now in the process of fabrication, the design and the shop drawings were made in the D. V. Efremov Scientific Research Institute of Electrophysical Apparatus. This accelerator must be ready for operation in 1975.

The development, construction and adjustment of separate systems and blocks were supervised by V. Y. Bobylev, E. N. Daniltzev, A. A. Drozdovsky, A. M. Kozodaev, V. V. Kurakin, N. V. Lazarev, Yu. F. Pavlytchev, N. Ya. Popova, Yu. B. Stasevich.

Table I

The main parameters of the LJA-1.5 and the LIA-5

No.	Parameter	Symbols and Units of Measurement	Value LIA-1.5	LJA-5
1.	Output energy (max)	W, MeV	1.5	5
2.	Beam current	I, kA	0.1+0.2	2+4
3.	Emittance	E, cm rad	0.03	0.01
4.	Beam pulse duration	τ_i, nsec	20	50
5.	Beam top slope (at the length of 15+20 nsec)	$\frac{dw}{dt}$, $\frac{MeV}{nsec}$	0.07	0.2
6.	Pulse repetition (max)	f, 1/sec	0.07	1
7.	Acceleration length	L_{LIA}, m	3	10

Table II

The main parameters of the compressor

No.	Parameter	Symbols and Units of Measurement	In operation with LIA-1.5	LIA-5
1.	Injected electron energy	W_{inj}, MeV	1.5	4.5
2.	Type of injection		three-turn	three-turn
3.	Injection radius	R. ., cm	25	25
4.	Radius of a compressed ring	R_{comp}, cm	3.2	3.2
5.	Injection induction of the magnetic field	B_{inj}, kgs	0.27	0.67
6.	Induction at the end of compression	B_{comp}, kgs	16	40
7.	Number of electrons in the ring	Ne	5.1012	10^{14}
8.	Big-small radii ratio	α	0.07	0.07
9.	Momentum spread of electrons in the ring	$\Delta p/p$	0.03+0.05	0.03+0.05
10.	Relativistic factor of electrons at the end of compression	$\gamma_{\theta\ comp}$	31	78
11.	Rings ejection		not provided	not provided
12.	Duration of compression	τ_{comp}, msec	1	1
13.	Current pulse duration in the main coils	$\tau_{main\ coil}$, msec	0.5	0.5
14.	Current pulse duration in the injection coils	$\tau_{inj\ coil}$, nsec	20	20
15.	Pressure in the chamber of the compressor	P, mm Hg	10^{-9}	10^{-9}
16.	Injection nozzle acceptance (in radial direction)	A_r, cm rad	0.01	0.01

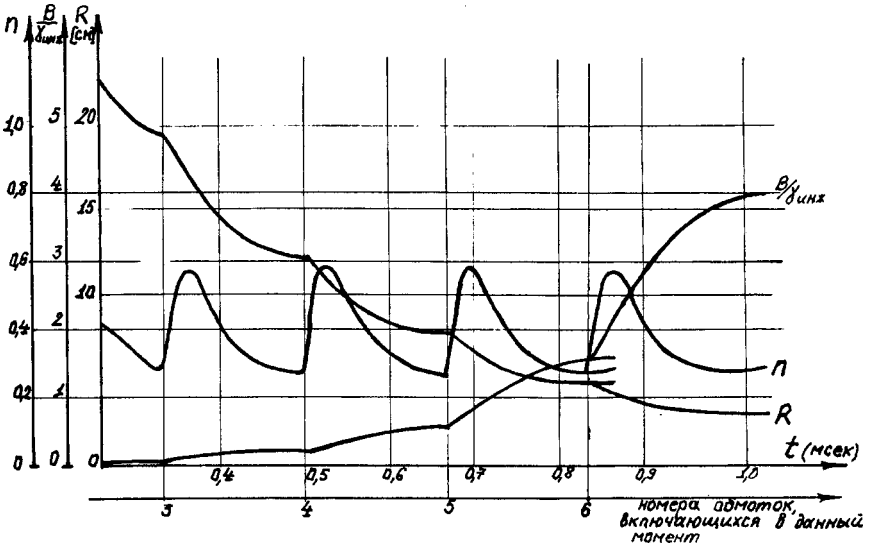


FIG. 1--Big radius of the ring R, induction at the radius of the ring B and slope factor of the field at the radius of the ring n dependences of time (γ_{inj} is the relativity factor of electrons at the moment of injection; in operation with the LIA-1.5 $\gamma_{inj} = 4$, in operation with the LIA-5 $\gamma_{inj} = 10$).

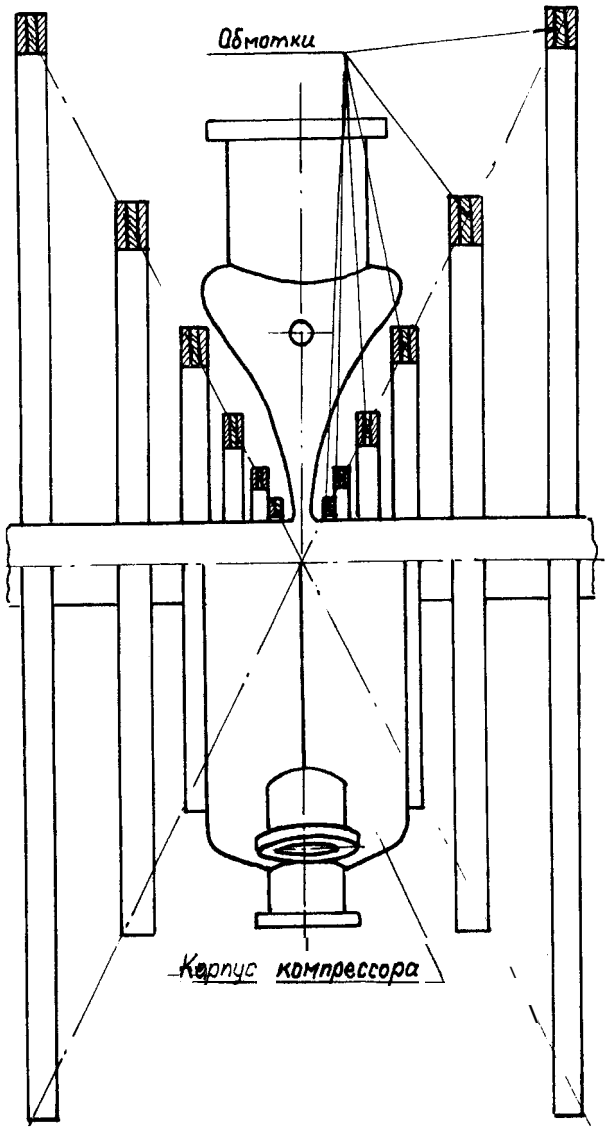


FIG. 2--Arrangement of coils near the compressor chamber.

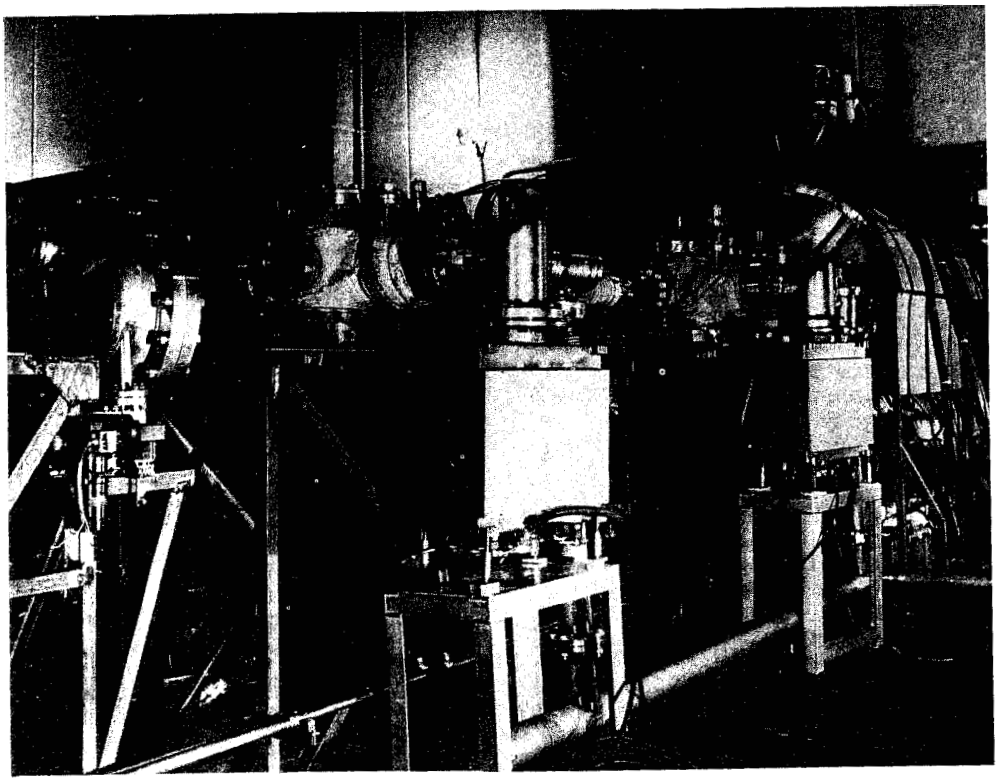


FIG. 3--The LIA-1.5 and the electron guide.

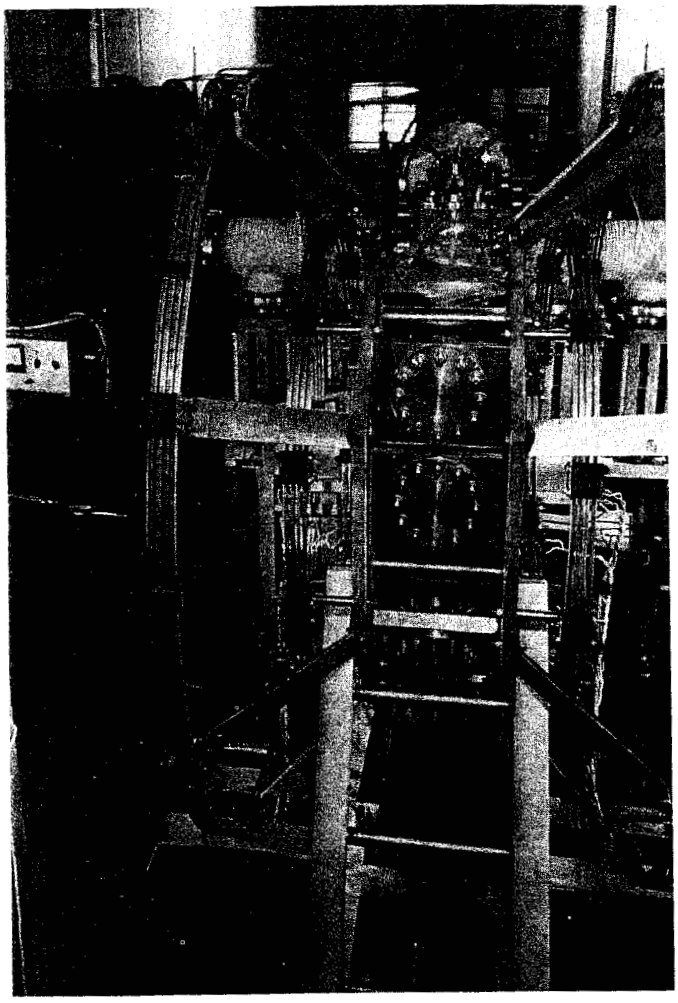


FIG. 4--The compressor.

PRESENT PERFORMANCE OF COLLECTIVE ION ACCELERATION IN JINR

L. S. Barabash, I.A. Golutvin, G.V. Dolbilov, I. N. Ivanov, A.D. Kovalenko,
V. G. Novikov, N. B. Rubin, E.A. Perelshtein, V. P. Sarantsev, V.A. Sviridov
Joint Institute for Nuclear Research, Moscow, Union of Soviet Socialist Republics

Thoughout the last few years all the laboratories investigating and studying collective ion acceleration method paid a great attention to theoretical as well as experimental possibilities of the accelerator. However, to come to final conclusion a progress towards greater densities of electrons in the ring and specified experimental studies of the main effects accompanying by the electron ring formation and electron-ion acceleration are necessary. If the results of the last year studies are summarized it appears that one can avoid the known limitation for heavy ion accelerator using a specified scheme of the ring formation. It allowed us to start investigations of the scheme individual elements so that to create a prototype of heavy ion accelerator and a possibility of studying the behaviour of dense electron ring with ions under different conditions.

I. Accessible Estimations of Heavy Ion Accelerator Parameters.

For multi-charged ion collective accelerator the following two parameters are the most determinative:
1. Energy storage per nucleon per the unity of the length

$$U = k \cdot \frac{N_e}{\pi r_0 (a_r + a_z)} \cdot Z^*/A \quad \left(\frac{Mev}{cm}\right) \qquad (1)$$

where N_e - electron number in the ring, r_0 - major radius, $a_{r,z}$ - radial and axial sizes of the ring cross section, Z^* - ion charge, k - the ratio of acceleration to its limit value. 2) Accelerated ion number - Bi.

If our task is obtaining energy ~7 MeV per nucleon at the number of accelerated ions ~10^{11} per pulse then inserting in (1) the ring parameters which seem to be real nowadays $a_r \sim 1.2$ mm, $r_0 \sim 4$ cm and choosing $(Z^*/A) \simeq 1/10$ and $K \sim 1/4$-$1/5$ (there's no ion loss during acceleration at such K) we'll realize that the required electron number in the ring should be about $5 \cdot 10^{13} \div 10^{14}$. During adiabatic compression of such intense beams in ADHEZATOR and their acceleration it is too difficult to provide their stability. Azimuthal instabilities are presented as the most dangerous ones. The threshold particle number N_e for such inatabilities is proportional to electron energy epread in the ring and inversely proportional to the so-called ring impedance in the chamber Z_c.

The growth of the energy spread is unreasonable since it leads to the growth of a_r and in accordance with (1) to U decrease. So N_e increasing is provided by impedance decrease. Since Z_c value characterizes the ratio of azimuthal electric fields to created currents the decrease of 2, might be attainable by locating metallic screens close to the ring. On the screens and close to them the electric fields are significantly small than in free space. The location of the screens close to the ring while being compressed has undesirable consequences. Firstly, the metallic compreesor chamber screens the external magnetic fields which compress the ring that limits the admittable external field frequency (for the chosen chamber the admittable frequency is now $f \lesssim 1000$ cps). Secondly, the chamber side-wall closer to the ring location deteriorates the condition of the single-particle stability because of the field image in the walls which are necessary to be compensated by the appropriate choice of the external field geometry.

At the final stags of the ring compression and its acceleration there appears a danger of resonance instabilities on the chamber self-modes and wave resonances. For euppression of the in-stabilities a metallic tube is expected to be used with radius less than r_0 and the quality-factor at resonance modes is supposed to be decreased to the value $Q \sim 40$.

Among electron-ion instabilities the hosing one is the moat dangerous, The accelerated heavy ion number that is defined by theoratical threshold condition of sinuous instability at typical electron ring parameters is about 10^{11}. A more strong restriction on ion number is connected with magnetic method of ring acceleration. In order no to change the ring sizes significantly $(N_i/N_e) \lesssim 10^{-3}$ is required. The similar estimations are based on the choice of the arrangement parameters.

II. Present Performance of Heavy Ion Accelerator,,

Heavy ion accelerator baeed on collective method consists in fact of the two large arrangements. The high-current induction linear accelerator of electrons is an injector for collective accelerator, Adiabatic charged toroid generator - ADHEZATOR is intended for electron ring formation, their ion loading and initial ring acceleration. The acceleration of the ring to the final energy is produced by solenoid with the decreasing magnetic field. Magnetic system of ADHEZATOR accelerator allows the formation of the rings with the electron number $N_e = 10^{13} - 5 \cdot 10^{13}$ and eleotron density $n_e \sim (0.5\text{-}2.5) \cdot 10^{11}$ 1/om. The other expected accelerator parameters are defined by the figures.

I. Injector - High-Current Pulsed Linear Accelerator of Electrons - SILUND.

Electron pulsed accelerator ueed as

an injector was constructed due to the requirements of providing the following parameters of the accelerated beam.
Particle energy in the beam - E=3.0 MeV
Peak current in pulse - I=1000 a
Pulse length τ 010 ÷ 15 nsec.
Pulse repetition frequency f=10 Hz
Energy electron spread at E=3MeV ($\Delta E/E$)=3
Emittance at E=3.0 MeV
$\varepsilon = \pi a\theta \lesssim 0.1$ cm·rad

Accelerator consists of 5 accelerating sections containing 18 accelerating element-inductors each and fed by nanosecond pulse generators (fig.?). A more detailed description of the linear accelerator system was reviewed earlier /4/. The most complicated stage in the adjustment of electron accelerator appeared to be a reasonable configuration of the source - autoemissive cathode operating at high pressure with the accelerating eystem of accelerator. In the Initial experiments there was pressure gradient along the whole accelerating system so that to provide the conditions of focusing. Under such routines of accelerator operation current to 1.5 ka was registrated at the output of the system. However, the studies of the current showed that the main part of it contained electrons - 200--300 kev. Taking into consideration the analysis of the obtained data one can draw the conclusions:
the acceleration occurs in the last section and the source is ionized electrons produced in the result of collisions with gas atoms. Further experiments were carried out under normal vacuum conditions along the whole acceleration (operating pressure - 10^{-5} torr.). Normal electron source operation was provided by higher pressure in the first section. Cathode was associated with the first accelerating eection (fig.2). Operating pressure in cathode region was 10^{-2} torr, and it decreased towards anode at the first section output to 10^{-5} torr. The studies of the electron beam behind anode showed that the whole potential of the first section at the pulee moment applied to charge region near cathode and electron energy correlated with the applied voltage. The choice of magnetic field parameters and operating pressure allowed to monitor the value of electron current from 300 a to 1.5 ka. Thus the first accelerating sectfon was used as an electron source. The source operation is clearly seen in the plots of the current and voltage given in figure 3.

The investigations of loading features of pulsed accelerating system (fig.4) witnessed that loading influence did not change the magnitude of accelerating voltage for the chosen formation system significantly at the currents of loading to 1000 a. The calculated energy dependence of the accelerated beam on the current (without a glance at the energy of injection is shown in figure 5 It is clear that the change of the beam current of an order $\Delta I/I = \pm 10\%$ will lead to energy variation not greater than ± 2%. The studies of the beam current passing along the accelerator gave quite satisfactory results. Under optimal conditions current passing contains 90%. After three acceleration sections current (600-700 a) with the energy correlating with the summarized pulse voltage (fig.6) is registrated'. Presently the operations of the studies of the probe characteristics of the electron beam and its injection into chamber are being carried out. One more accelerating section is expected to be installed for increasing electron beam energy and its intensity. Operations on the beam trapping and injecti.on will be carried out with the mentioned above parameters until an additional section is installed.

System of the Rinn Bunch Formation - - ADHEZATOR.

The design of the chamber and magnetic field system were chosen due to conditions to provide electron ring stability in the process of its formation,

Metallic chamber of ADHEZATOR represents the welded construction made of stainless steel with thickness of 0.5 mm (fig.7). The side-wall surfaces of the chamber are spherical. In the rim there is a number of snouts intended for the input of the electron ring from SILUND, placing the measurement devices and the electron path corrector, vacuum chamber pumping out.

In the center of side-walls two anouta are placed (7 and 8). They are intended due to injection of a Plow of neutral atoms into the electron ring and for output of the accelerated electron-ion ring from the chamber,

The forces produced onto the chamber surface by the atmosphere pressure and interaction of inducted eddy currents in the metal of chamber with the external magnetic fields are transmitted through the ring crested expanders 3 made of 0.8 mm stainless steel onto two glass-textolite rings 9 mounted on the support II and rigidly connected with each other.

On the support table (II and IO) made of textolite besides the chamber a rigid framework made of glass-textolite is placed. In the rigid framework the windings forming dc and ac fisIda are mounted. The design of the chamber, support and framework includes the device for adjustment and rigid fixation of the median plane of the chamber and the windings in respect to based axes of heavy ion accelerator. At the previous test runs vacuum 5.10^{-9} torr. was obtained. A general scheme of the chamber is shown in fig.8. The magnetic field system consists of dc field coils, three-stage compression coils forming ac magnetic fields and the solenoid

* The beam currant along the acceleration was measured by Rogovsky coils installed between accelerating sections and movable Faraday cup.

which is intended for output end acceleration. Their locations and currents were selected due to magnetic fields by means of metal walls of the chamber. For passing the dangerous resonance regions of ν-path of the ring correcting loops are expected to be used.

The magnetic field sources are multi-turn coils poured by epoxy compound. The main parameters of the coils are given. in the table (variant A).

Coils	Mean Radius (cm)	Distance from the median plane of the chamber	Winding Number	Section Sizes (cm)	
dc field	67	31	2 x 80	10,5	10,5
I stage	38	48	2 x 28	a	4
II stage	26	24-29	2 x 48	8	6
III stage	14,3	8-10	2 x 71	6	12

In figure 10 the measured curvature H(R) is given for the magnetic field coils shown in Table I. In the process of magnetic field formation a significant influence of the broken three stage coil on n-path was found. The influence is shown in figure 2 which indicates the chosen geometry does not provide the required parameters. The alteration of the third stage geometry of pulsed field resulted in the significant alterations in n-path (fig.12),

The final R-path of the ring is given in figure 13, In figure 14 one of the n-paths of the electron ring for two stages of the magnetic field is shown.

At the present time the operations on electron injection into ADHEZATOR system have been begun. Preliminary test runs with various injector types have been carried out (with magnetic screening, electric pulsed, magnetic pulsed). These test runs indicated that the best conditions for trapping and the most small value of distortions can be obtained with the magnetic-screening injection system.

Present Performance on KOLTSETRON.

The first cryogen start up was in December 1972, During the start up one cavity of KOLTSETRON with Nb-Ti coating and copper stark as well as one gradient superconducting solenoid (with length of 40 cm, diameter 17 cm, 16 sections) were operative. The stable cooling regime of KOLTSETRON cavity was not obtained. Gradient solenoid was cooled and its probe test runs were performed. The start up indicated that in a number of cryogenic systems of KOLTSETRON there are significant warm flows coming from the environment. By the present time the warm flows have been decreased. The part of the warm flows with nytrogenic screening of Helium pipelines contains only 0,2 w/m.

Operations on sample cylindrical cavities on E-wave with frequency 1,3 . IOHz with Nb-Ti coating showed that the improvement of the stark design made the hopes of obtaining quality-factor in operating cavities of KOLTSETRON true,

In June 1973 the detailed investigations of gradient solenoid at independent current test runs of 16 coils were carried out. Well operative stabilization of power supplies provided the required current stability and allowed to avoid the expected difficulties.

By the present time the design of the main external solenoid of KOLTSETRON (with length of 2,4 m) has been finished. Helium test runs of the solenoid in KOLTSETRON under operative conditions are being prepared.

REFERENCES :

1. I.N. Ivanov et al. Preprint JINR Dubna 1970 P9-5335,
2. Yu.I, Aleksahin et al. Preprint JINR P9-7065, P9-7066 Dubna 1973.
3. Yu.I, Aleksahin , V.P. Sarantser Preprint JINR P9-7357 Dubna 1973,
4. LJ. Laslett IEEE Vol, NS-20, NO 3, p.271
5. V.P. Sarantsev VIII International Conference on Accelerators CERN 1971,

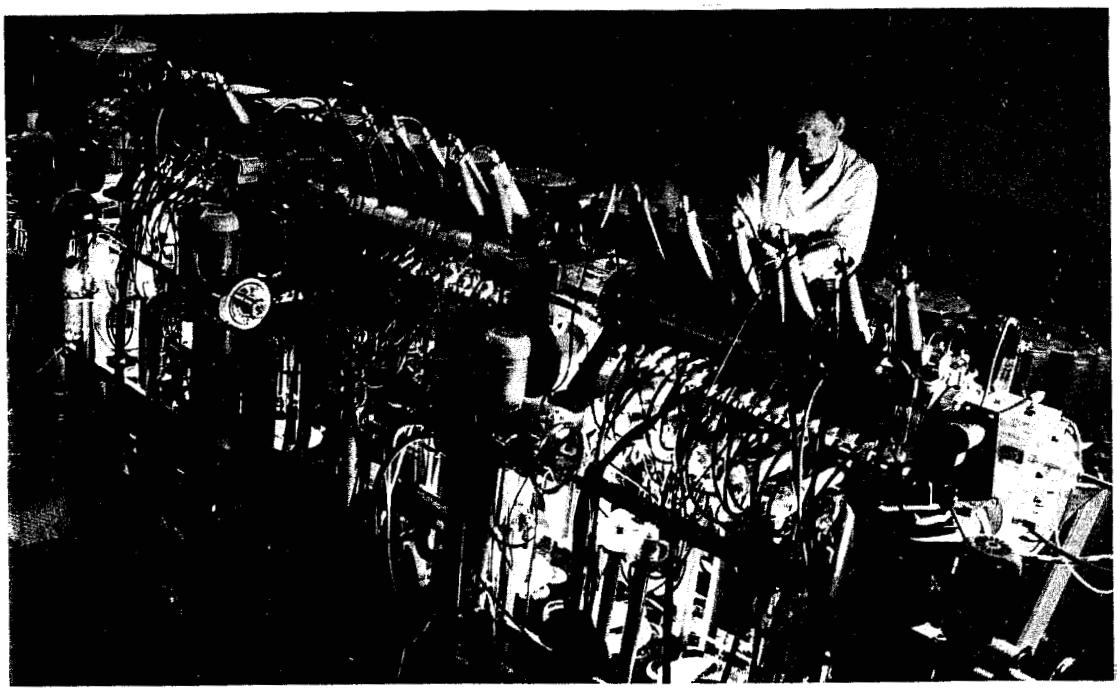


Fig.1 General scheme of electron accelera tor - SILUND.

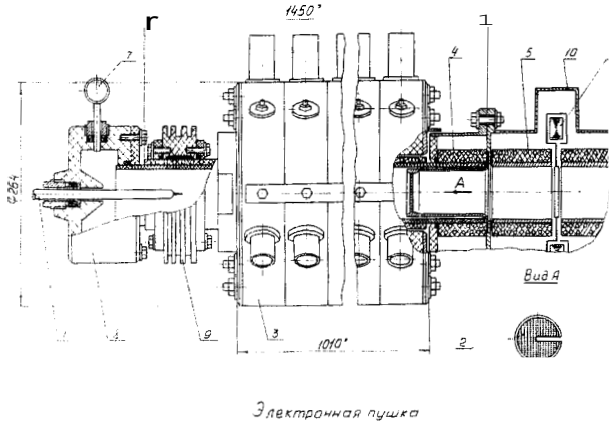


Fig.2 Electron *gun* of the accelerator.

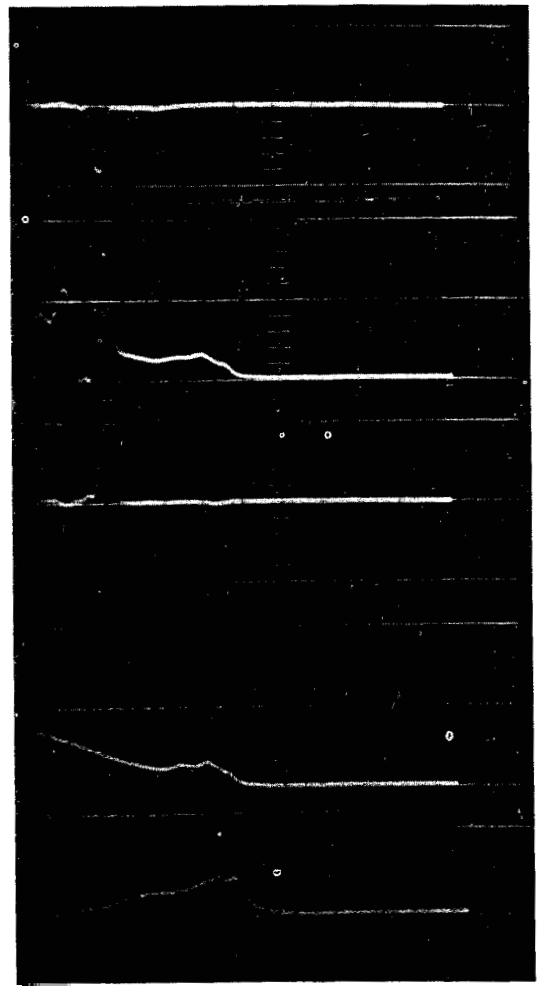


Fig.3 Oscillograms of operative electron source.
a) Voltage pulse on cathode.
b) Charge current of cathode.
c) The pulse of accelerating voltage on the inductors of the first section.
d) Charge current of cathode at the presence of voltage pulse on the inductor.
e) Electron current at the output of the first section.
Rate - 200 nsec/fission.

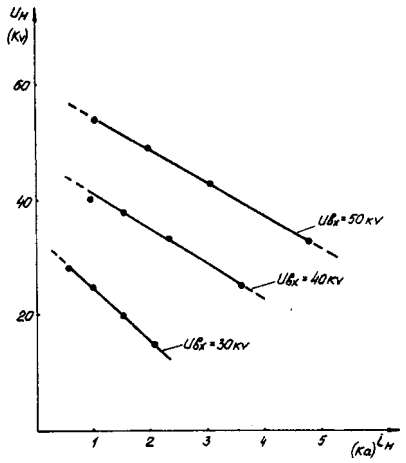


Fig.4 Loading characteristics of the inductor.

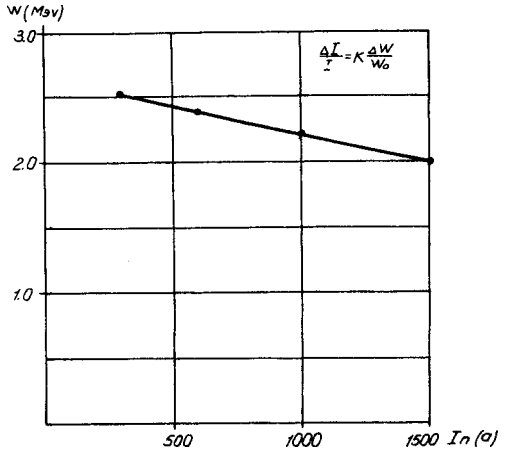


Fig.5 The dependence of electron accelerator energy on accelerated current.

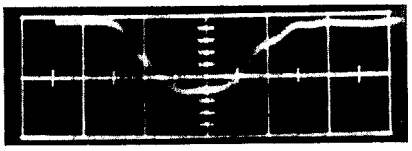


Fig.6 The shape of accelerated current of electrons.
(Rate - 20 nsec/fission)
Vertical Scale - 800 a/fission.

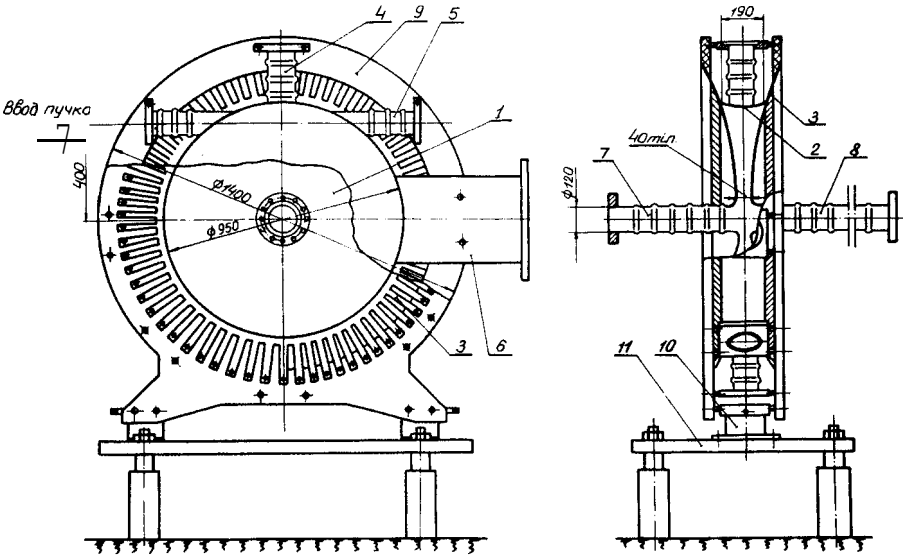


Fig.7 Constructive scheme of ADHEZATOR chamber.

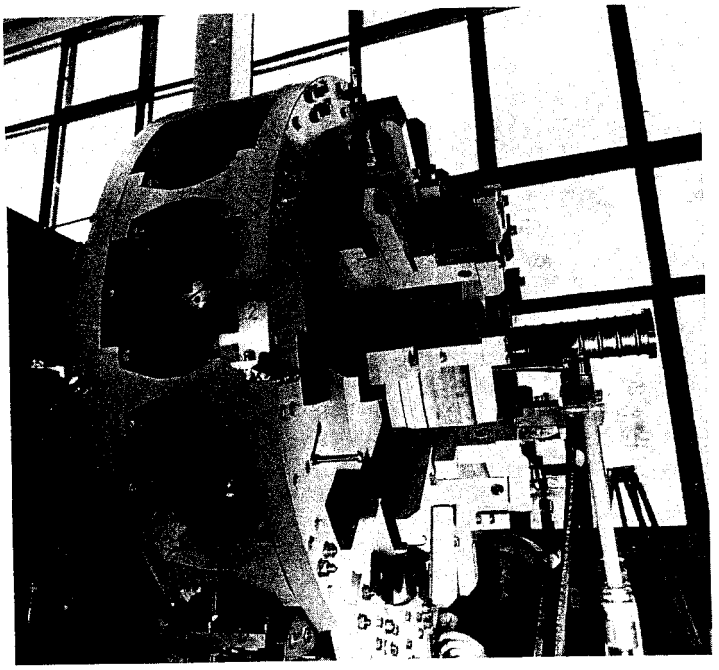


Fig.8 General scheme of ADHEZATOR.

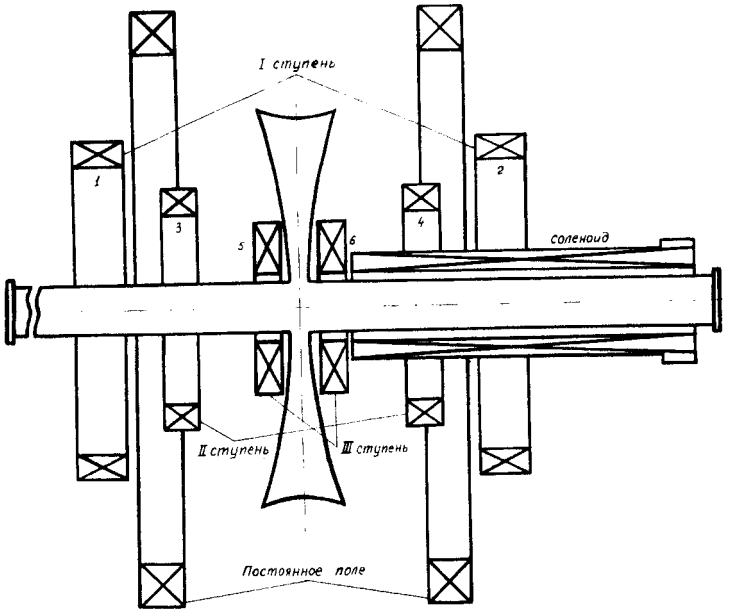


Fig.9 Scheme of winding location of magnetic field.

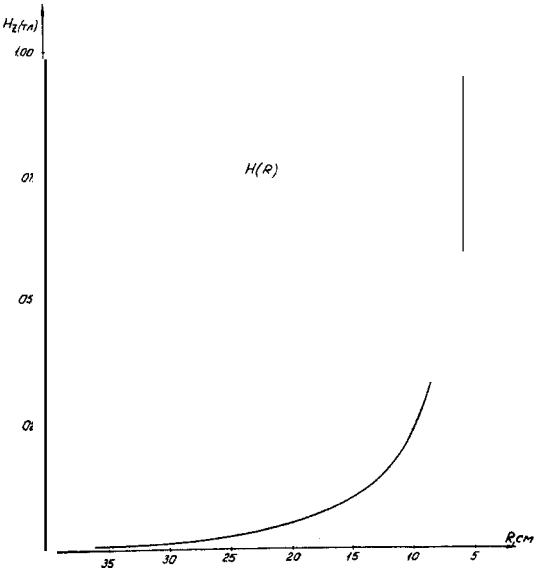


Fig.10 Magnetic field values at different radii of ADHEZATOR H(R).

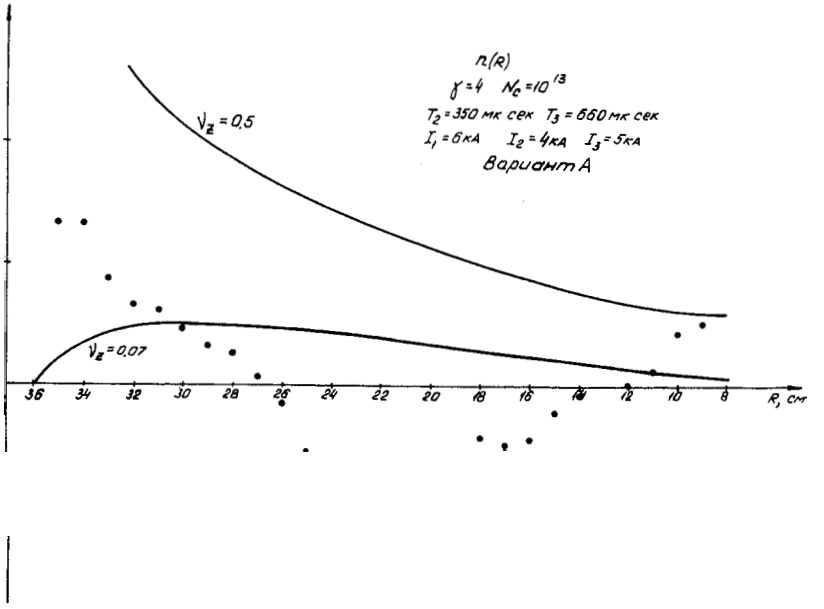


Fig. 11

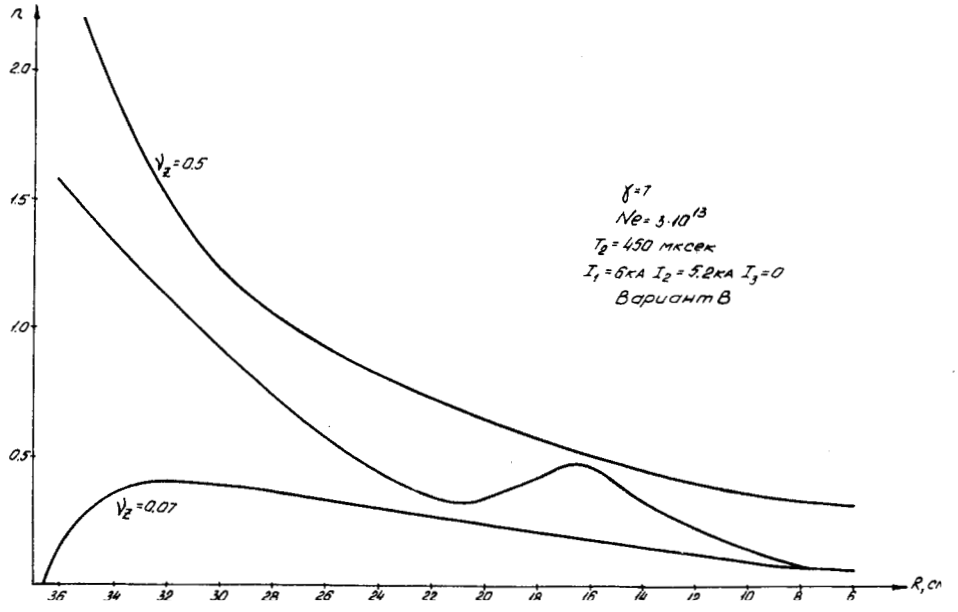


Fig. 12

Fig. 11, 12 — The influence of different broken coils of the third stage on n-path of the magnetic field. (Variant A and Variant B).

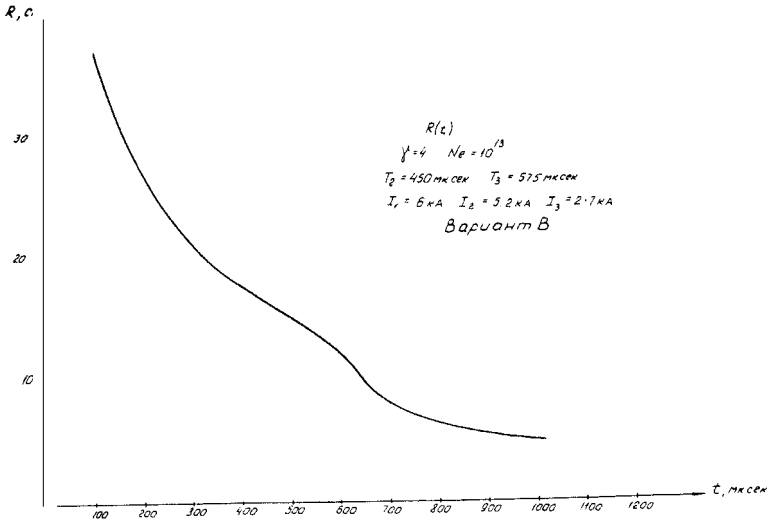


Fig. 13 Radius change of the electron ring in time.

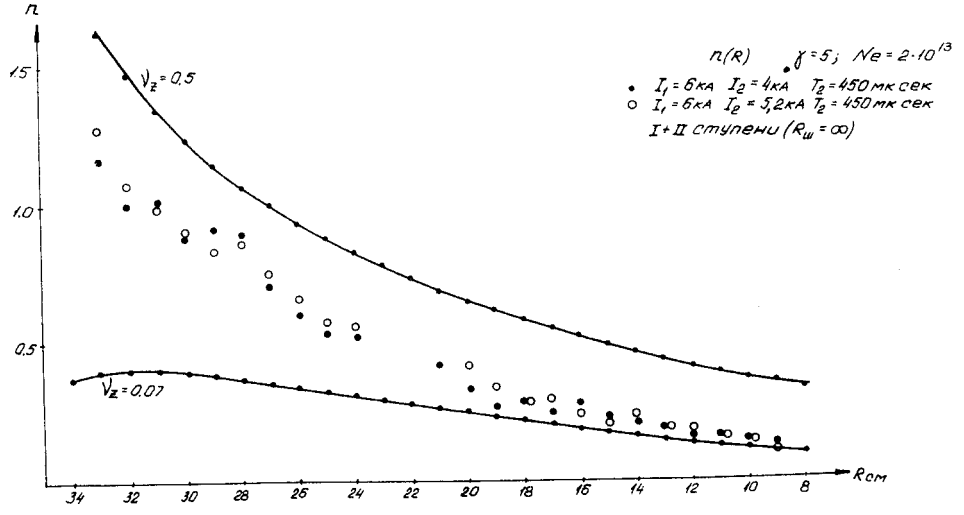


Fig. 14 The change of the external magnetic field index in ADHEZATOR.

AD HOC DISCUSSION SESSION

K. H. Reich
CERN
Geneva, Switzerland

I. Maximizing Productivity and Employee Morale in an Era of Tight Budgets

Judging from experience in recent years, the following actions and attitudes of the different echelons of management were considered likely to produce good results (if a given echelon fails to make its particular contribution, the echelon(s) below still should and will try to do their best, but the margin for appropriate action may have become so narrow that the chances for success are reduced):

1. Top Echelons (Government Departments and Agencies, Laboratory Top Management)

--Making and keeping a given laboratory a world leader at least for part of its activities.

--Provision of sufficient funds for (i) operating effectively existing facilities and adapting them to changing needs and technologies, and (ii) paying competitive salaries and social fringe benefits.

--Giving adequate advance warning (up to several years) and planning appropriately where phasing out of programs, closing down of facilities or worsening of employment conditions become unavoidable.

2. Middle Echelons (Laboratory Directors and Department/Division Heads)

--Continuous updating of targets to be reached, in say, the next 6, 12, 24 and 36 months and announcing them to all concerned.

--Developing, improving and making known participative mechanisms for allocation of resources, and for reaching and maintaining common standards concerning staff (in particular as regards hiring and layoff, promotions, etc.).

--Associating as many people as reasonable and possible with new projects, even on a part-time basis (to keep people in the main stream and to minimize the creation of first and second class citizens). These projects should preferably have built-in stretch capacity and possibilities for ulterior development.

--Using occasions arising (e.g., the recent Technology meeting at CERN, the breaking of the 10^{13} ppp barrier by NAL, etc.) for emphasizing the unity of purpose of the various Divisions of the Laboratory, for putting into the limelight the work usually done backstage, and for sharing success.

--For a Director or Head, to be visible and approachable regularly (notably to be available for answering questions by any person in charge; at SLAC this is done twice a month). The general feeling was that as much information concerning the future as available and clearly established—even if bad news—should be passed on as soon as possible (both to assist people in making their own decisions and to reduce rumour-mongering) with the exception of really catastrophic developments which should only be announced once they have become absolutely certain, and irreversible (if that can be done!). Particularly in times of stress the realistic confidence and leadership of the Director (including solving particular personnel problems with humanity and imagination) were considered of special importance for productivity and morale.

3. Lower Echelons

--Ensuring a good match between a given person and his job, if at all possible at his individually right level of challenge. This may involve (re-)training, prolonged tutoring and medium to long term career planning.

--Despite reduced staff numbers for continuing tasks, trying hard to keep the ratio wanted/unwanted duties and responsibilities above the individual good-morale subsistence level for the largest number of people.

--Although obliged to spend increased time on budget reviews, justification of expenditure, etc., time should remain available for discussing the problems with people in charge contributing to the solution.

11. Operation of Accelerators

Only (too) little time remained available for this subject. Common features of several laboratories appear to be that (i) operators (particularly graduates) share their time about equally between operation and machine hardware or software development, and (ii) rotation (after some years) from operation to other activities is encouraged.

The introduction of control computers has often meant a heavy load of training and has not always been an easy adaptation. Once accepted, these new facility are usually appreciated.

Payment of appropriateshift allowances, etc., and particular attention to operation motivation were generally considered indispensable for success.

RAPPORTEUR - "COLLECTIVE EFFECTS ON ORBIT DYNAMICS"

F. E. Mills
Fermi National Accelerator Laboratory*
Batavia, Illinois

Introduction

Much of the work of this conference is concerned with collective phenomena in plasmas and particle beams. Here we are concerned with the onset of collective phenomena, primarily the appearance of growing oscillations, that tends to limit the performance of devices which rely on the maintenance of high-phase space density in particle beams. These phenomena can cause degraded performance of the devices, sometimes loss of beam, but rarely in themselves, keep the devices from performing at all. Further, since the beam motions involved are rather simple, ameliatory measures are available and are usually successful, unless technology limited (usually) bandwidth).

There are several ways to characterize these instabilities but two points should be made. First, the source of energy needed to create the fields which cause the unwanted motion of the beam is the directed energy of the beam itself. Thus the fields in question will have an electric field in the direction antiparallel to the beam. Also one must find currents in the beam which have the same multipolarity as the fields driving the motion. A second point is that there is no shielding of the fields by the beam itself. Then no complicated internal motion of the beam is necessary to get the simple "coherent" modes. Every particle is subjected to the same form of field, independently of its position in phase space.

Description of Motion, Source of Fields

Our usual goal in accelerators is to provide focussing in two or three dimension and to populate regions of phase space as in Figure 1 with the expectations that the particles will remain in these regions. In these regions the particles describe orbits which are, with appropriate units, circles in the three projected phase spaces. Then particles move around these circles with frequency ν_x, ν_z, ν_s. Typically the frequencies may depend upon amplitude, that is, the area of the circle in question; or upon momentum, that is, the total momentum of the particle in question.

Let us now superpose upon this picture, say for the x motion, fields of the following character: dipole fields with frequency ν_x, quadrupole fields with frequency 2 ν_x, sextupole with 3 ν_x, etc., and let us suppose that these fields have been turned on slowly. We notice that these are just the same form of field which drive the usual heirarchy of resonances of the single particlemotion. Then the circles of Figure 1 are changed into the lobed regions of Fig, 2. Projections of the resulting charge and current distributions on the coordinate axis clearly show appropriate multipole currents flowing at the required frequency to act as a source of the fields. As **energy** flows out of the longitudinal motion into the perturbing fields, the lobes get larger, and the motion is "unstable." That is, the phase space is diluted and some beam may be lost on the aperture stops of the system.

Now the question of when the motion is unstable requires a more careful look at the fields themselves, Typically, in addition to the local fields generated by the beam, fields from the induced currents and charges in the wall by one segment of the beam will influence later segments of the beam - the so called "wake field", due to the finite resistivity of the wall. In addition, resonant structures will be excited by the beam and leave fields to deflect later particles. Thus the longitudinal description of the fields and particles motion determine whether energy is transmitted to or from the beam. In the simplest case, that of the unbunched beam, the instability arises as a simple wave phenonmena, that is, the phase of the motion varies linearly with azimuth (mode description). When the beam is bunched, then modes exist within the bunch (head-tail) and the chromaticity of the device determines which modes are susceptible to growth (have strong multipole currents). In addition, some of these head-tail modes leave strong wake fields, others do not, so that the long range modes may enter the picture as well, in which each bunch acts as though it were simply part of a uniform beam, in addition to suffering its internal motion.

Stabilization, Onset of Instability

The onset of instability is determined in a simple way. If, for example, in Figure 2, ν_x varies with amplitude, then the lobes drawn will smear out, leaving no multipole currents, so there will be no growth of the peturbing field. Similarly in an unbunched beam, chromaticity will cause the same smearing to take place. The situation is similar to a group of coupled oscillators of different frequencies. The coupling "drags" the frequency of the oscillators and a collective oscillation can take place when the collective force (coupling strength) is strong enough to drag all the oscillators to the same frequency. Since the collective force is proportional to the number of particles, stability for intense beams is gained by providing a spread of frequencies (ν_x, ν_z, ν_s) for the beam. This is done by variations of the tunes with amplitude, by octupoles for transverse motion or by the nonlinear waveform of the rf for longitudinal motion. In addition space-charge forces are themselves nonlinear, and for an unbunched beam, chromaticity provides stabilization.

In addition to these dynamic effects, the time average fields produced by the beam causes a change in the "potential well" in which the beam travels. This change causes a shift in the particle oscillation fre-

*Operated by Universities Research Association, Inc. under contract with the United States Atomic Energy Commission.

quency, and an effective change in the β function for that motion. In the transverse motion this is called the "Laslett shift" and limitation is presumably due to resonance effects when the shift is sufficiently large. In the longitudinal motion, where the focussing is (usually) much weaker, presumably the limit is zero focussing, in which case the longitudinal β function becomes large and the longitudinal size of the beam grows. This can seriously reduce the current density in the beam and lower the luminosity of colliding beam devices. The point is made in two papers here that both this effect and the excitation of unstable longitudinal modes are required to explain the bunch lengthening (and shortening) seen in electron-positron storage rings.

Summary

The papers presented in the session help clarify several old mysteries, demonstrate some new methods and raise some new problems.

The PS-PS Booster results with head-tail instability help clarify the role of the wake field and chromaticity in that motion. The agreement between experiment and calculation is encouraging.

The results from SPEAR and Tantalus shed long-needed light on the bunch lengthening phenomenon which has plagued storage rings. Further exploration of the character of the longitudinal modes, at a level of sophistication comparable to the ISR work reported should clarify the mechanism of turbulent excitation of these modes and reduce this phenomonon to the status of a designers problem (as apparently has been done at the ISR).

Finally, the work at NAL demonstrates the emergence of problems of large rings. The difficulty of simultaneous control of both nonlinear resonance phenomena and instability phenomena is demonstrated by this work. Contradictions between the needs of the two stability aspects will plague designers of high-energy rings and can be expected to play a critical role in their design.

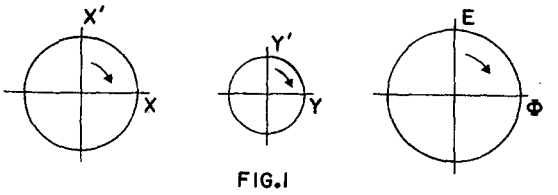


FIG.1

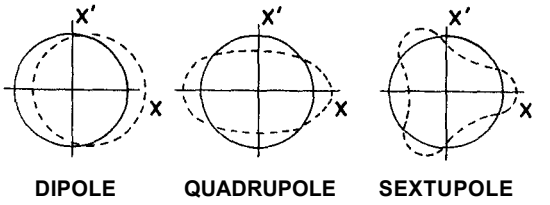


FIG.2

TRANSVERSE COLLECTIVE INSTABILITY IN THE NAL 500-GeV ACCELERATOR

R. Stiening and E.J.N. Wilson*
National Accelerator Laboratory, Batavia, Illinois, U.S.A. §

Abstract

Vertical collective beam instability occurs during 8-GeV injection into the NAL main accelerator with an intensity threshold of approximately 10^{12} protons and a tune spread of 0.01. Horizontal collective instability has been observed at 5×10^{12} protons with a 0.01 tune spread. Sextupole, octupole, and active feedback damping have been used to control these instabilities. A brief description of these methods and the results obtained is given.

Discussion

Above an intensity of 10^{12}, proton beams in the NAL 500-GeV main accelerator suffer from destructive collective transverse instabilities. AS the azimuthal intensity distribution is a significant factor in these instabilities, we begin with a description of the manner in which the accelerator is loaded with beam from the booster synchrotron.

Injection is accomplished by a sequence of twelve booster cycles, during which time the main accelerator is operated as a storage ring at 8.89 GeV/c. RF voltage is held at a fixed frequency (52.813 MHz) at a level sufficient to preserve the 2-ns longitudinal bunch structure of the booster beam. In each cycle 82 of the available 1113 RF buckets are filled. (The 82 buckets filled in a single cycle are known as a batch.) After twelve booster cycles have been completed, 984 of the RF buckets are filled. There is one gap of unfilled buckets between the first and the last booster batch, and a gap of nine unfilled buckets between all other batches.

Both radial and vertical beam breakup have been observed. The vertical instability has a lower threshold, and can occur at any time in the acceleration cycle. The radial instability has not been observed above 50 GeV. We shall focus the discussion of this paper on the vertical instability, as it has the lowest threshold and the most rapid growth rate.

The vertical instability is observed during the loading of the accelerator. After a number of booster batches have been injected, part of the circulating beam breaks into coherent vertical oscillations and is subsequently lost. The growth time for the disturbance is a few tens of milliseconds. A frequency analysis of the signal from a pickup electrode which responds to coherent vertical motion shows a strong peaking at the frequencies of the coherent normal modes:

$$f_c = f_o\,(n - \nu_y)$$

with f_o = 47.5 KHz (revolution frequency)

and ν_y = 19.3 (vertical tune).

Only those modes with $n > \nu_y$ are observed. Although there is considerable fluctuation from event to event and mode numbers as high as 40 are seen, the modes with n close to 20 are usually the strongest. The wide range of mode numbers is a consequence of the fact that the disturbance is usually confined to a portion of the machine azimuth. The azimuthal distribution of coherent betatron oscillation amplitude during the development of a breakup which occurred after ten booster batches had been injected is shown below in Figure 1.

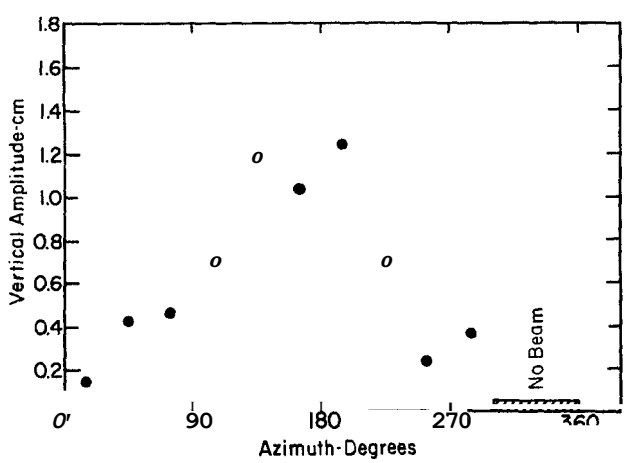


Figure 1. The azimuthal distribution of coherent vertical betatron oscillation amplitude during a well developed beam breakup. Ten booster batches had been injected into the main accelerator with stabilizing octupoles turned on. After injection of the tenth batch, the octupoles were turned off. The azimuthal distribution of the resulting disturbance indicates that a number of low-order normal modes are excited.

* Visitor from CERN, Geneva, Switzerland.

'Operated by Universities Research Association Inc., under contract with the U.S. Atomic Energy Commission.

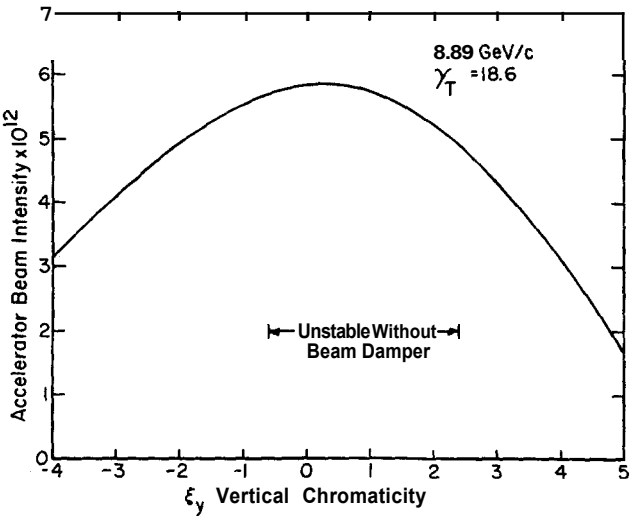


Figure 2. In this experiment the accelerated beam intensity was measured for various values of ξ_y loss with active feedback damping in use. The loss of intensity for non-zero values of ξ_y is due to extraction on non-linear resonances. Without active damping, the region shown was unstable against vertical coherent oscillations.

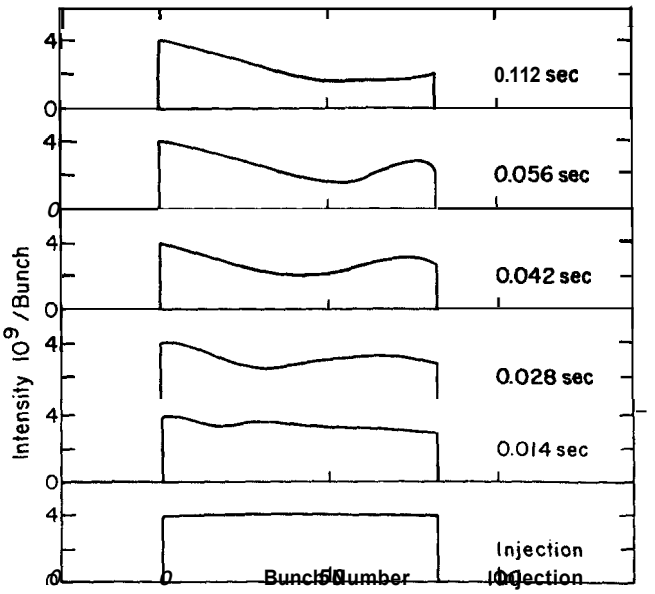


Figure 3. The intensity distribution within a batch of 82 RF buckets at various times during a vertical breakup of the beam. A disturbance originating near the leading edge of the batch began to cause beam loss by 0.014 seconds. It propagated toward the trailing edge of the batch, and was finally stabilized after quite a loss in intensity.

One of the mechanisms which contributes to the instability appears to be a dipole mode head-to-tail interaction within the RF bunch due to a short range wake field. Such an instability has been described by Pelligrini.[1] As the data in Figure 2 show, the instability occurs at the lowest threshold, when

$$\xi_y = \frac{P}{\nu_y}\,\frac{\partial \nu_y}{\partial P}$$

is positive ($\gamma < \gamma_t$). A similar condition applies to the radial instability. Furthermore, if the beam is allowed to debunch with RF turned off, it is stable at all intensities. We have explored the regions $19.2 < \nu_y < 19.4$ and $20.2 < \nu_y < 20.4$, and have found that the threshold is essentially independent of tune except in the vicinity of strong non-linear resonances. From this we conclude that the wake field comes either from an object resonant at the RF frequency or from a broadband source such as the vacuum chamber wall. The latter is more likely.

In addition to the short range dipole instability, there is a longer range coupling between bunches. An oscillating bunch will drive bunches following in its wake. In this manner a disturbance originating near the leading edge of a group of filled RF buckets is propagated with amplification toward the trailing edge. An example of such a breakup is shown in Figure 3. We have determined the range of the coupling between bunches by injecting two batches of filled buckets separated by a gap of empty buckets. At an intensity of 4×10^9/bunch, a gap of 20 unfilled buckets is sufficient to significantly reduce the coupling between batches. We have investigated the coupling across gaps as large as 2000 m. At that distance there is still evidence for a weak coupling. This we interpret as a signature of the resistive wall effect. We conclude that both head-to-tail and resistive wall effect are present, and feed one upon the other.

We have used sextupole, octupole, and active feedback damping to suppress this instability. Initially we used sextupole or octupole damping to destroy the coherence of the beam by introducing a tune spread, but it was found that the tune spread required had a detrimental effect because it became comparable with the spacing between non-linear resonances which extract the beam. This is illustrated in Figure 2, for the case of sextupole damping. In that experiment we varied the strength of the zeroth-harmonic correction sextupoles in a manner in which ξ_x was held constant while ξ_y was varied. During the experiment the average vertical tune was ν_y = 19.30. The momentum spread of the coasting beam was approximately $\delta P/P = 10^{-3}$ full width at half maximum. As the tune spread was increased to the extent that constituents in the beam periodically crossed sextupole and octupole resonances, they were slowly extracted. The region of instability thus occurs at those values of ξ_y which are most desirable from the viewpoint of single particle stability.

In order to be able to store stable beams having very small tune spreads, we have constructed an active damping system. The layout of this system is shown in Figure 4. At

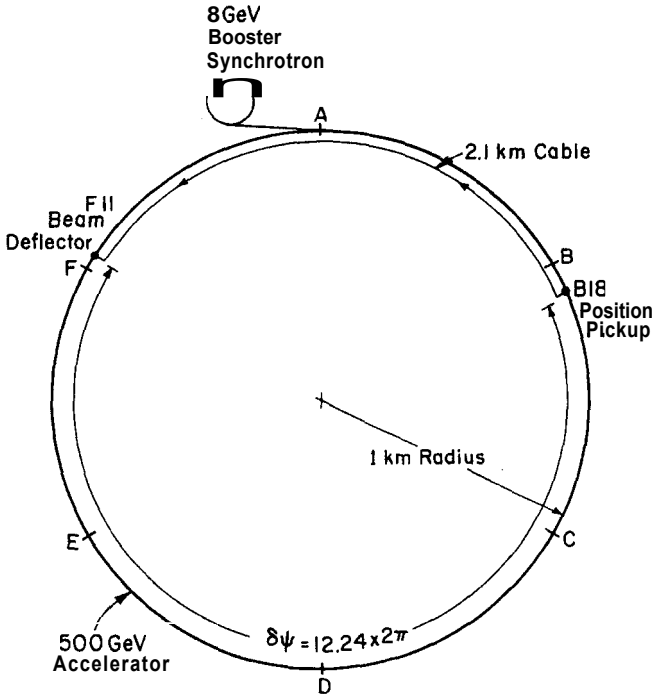


Figure 4. Diagram of the active damping system. The proton beam circulates in a clockwise direction.

station B18, 53-MHz RF signals from a pair of pickup plates are converted into a 3-MHz bandwidth, intensity independent, vertical position signal by electronic circuitry developed by E. Higgins. This signal is sent in a direction opposite to the beam through 2.1 km of coaxial cable. The beam deflector, which was developed by Q. Kerns, is a pair of 1.2-m long plates with a 5-cm separation. It is capable of producing a peak electric field of ±400 V/cm at frequencies up to 2.5 MHz. The betatron phase shift between the pickup and the damper is 12.24 × 2π at a tune of 19.287.

We operate the damper with a gain of 8×10^{-4} mrad/mm. For this gain, the absolute value of the eigenvalues of the once-around-the-ring matrix is $|\lambda| = 0.92$. The measured damping of an induced betatron oscillation agrees with the calculated damping rate.

At present, we employ both radial and vertical active feedback damping systems in the NAL main accelerator. No low mode number instabilities are observed. As a desirable by-product, the dampers remove the betatron oscillations caused by injection errors. As the intensity of the injected beam increases, we intend to extend the bandwidth of the damping system.

References

1. C. Pellegrini, Nuovo Cimento 64A, 447 (1969).

2. E.D. Courant and A.M. Sessler, Rev. Sci. Inst. 37, 1579 (1966).

TRANSVERSE SINGLE PARTICLE INSTABILITY IN THE NAL 500 GeV ACCELERATOR

R. Stiening and E.J.N. Wilson†
National Accelerator Laboratory, Batavia, U.S.A.

Abstract

Experiments reveal that single particle resonances, driven by field imperfections limit the 8 GeV acceptance of the NAL main accelerator to protons with betatron oscillation amplitudes less than 8 mm. It is observed that resonances driven by random azimuthal field fluctuations are much weaker than those driven by average field errors acting in concert with the superperiodicity of the accelerator. This consideration dictates the choice of operating tune. Correction magnets are installed to compensate zero harmonic skew quadrupole, sextupole and octupole errors. Separate control of $d\nu_x/dp$, du_y/dp, $d^2\nu_x/dp$, and $d^2\nu_y/dp$ is possible in an energy-dependent manner. High azimuthal harmonic patterns correction magnets are used to eliminate, dipole, quadrupole, sextupole and skew sextupole resonances adjacent to the operating point. A description of these systems and the improvements obtained are given.

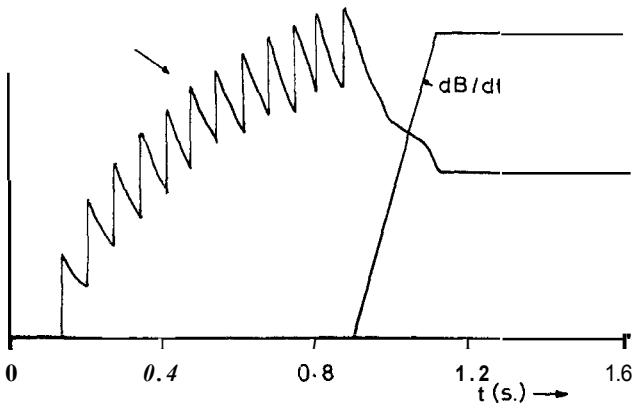


FIG.1 Loss during main ring loading and parabola

1. Introduction

The NAL main ring is fed with twelve batches of 8 GeV protons delivered at 15 Hz repetition rate by the fast cycling booster, These are loaded head to tail to fill the circumference of the main ring and during the loading sequence which lasts 0.8 seconds the main ring must act as a d.c. storage ring. Once the loading is complete the guide field rises parabolically until, at about 20 GeV, the maximum acceleration rate is reached and sustained to full energy.

Soon after this injection scheme was first implemented it became clear that a considerable fraction of the injected beam was lost during the loading sequence. Each batch decayed exponentially with a time constant of less than 1 second and this loss continued during the parabola, tailing off to zero near 20 GeV (Fig. 1). The fraction of the injected beam which survived to full energy was rarely higher than 35% and the peak intensity was limited to 10^{12} protons per pulse,

Improvements in the intensity delivered by the booster, which inevitably resulted in a larger transverse emittance, did little to raise the high energy intensity but merely augmented the losses.

Preliminary experiments showed that switching off the r.f. did not affect the loss rate nor was the loss diminished on those days when the brightness of the injected beam was low. This suggested that the loss was due to a transverse single particle acceptance limitation rather than a longitudinal or collective phenomenon.

The acceptance limitation seemed not to be a purely mechanical obstruction. Measurements of beam profile and the closed orbit distortion after correction revealed that the beam occupied only a 20 mm diameter central care of the 100 mm x 50 mm section vacuum chamber. Moreover, one could bump the beam locally at any point in the machine almost to the vacuum chamber wall before any mechanical obstacle killed the beam.

On the other hand we found that the loss rate was very sensitive to the current in the main quadrupoles of the FODO lattice which affect the tune (ν_x, ν_y) and *to* the strength of the sextupole magnets which had been installed to reduce the large chromatic time spread in the injected beam.

We suspected that there were strong resonance lines in the working diamond driven by non linear imperfections in the guide field and that these were responsible for the losses. We therefore commenced a program of studies, which included improvements in techniques for measuring betatron motion and the installation of multipole correction magnets, with the intention of compensating the non linearities and reducing the tune spread in the beam. The remainder of this report describes this work which, at the time of writing, has improved the main ring to the point that it will accept and accelerate over 10^{13} protons per pulse rejecting under the best conditions only 10 to 20% of the beam presented by the booster.

† Visitor from CERN.

2. Exploration of the NAL Working Diamond

Figure 2 shows the position of the nominal injection tune of the main ring in relation to the more important resonance lines. The lines are excited by random azimuthal variations in the non linear imperfections in the guide field.

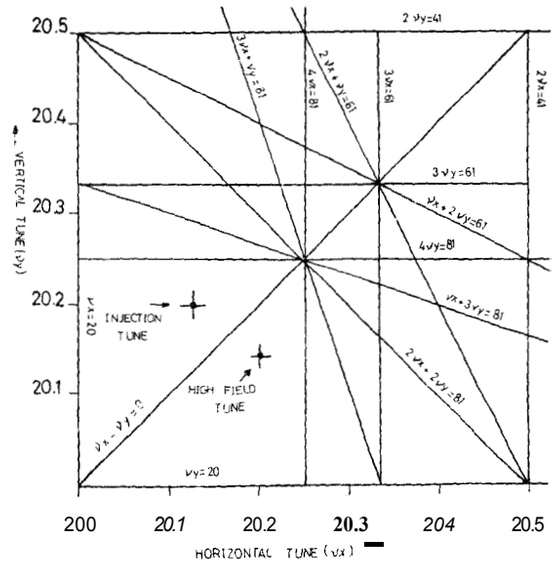


FIG 2 Working diagram

The F and D sets of main ring quadrupoles are connected in series but are powered independently of the dipoles. By changing the ratio of quadrupole to bending magnet current we were able to scan the working point *along* a line $\nu_x - \nu_y = -0.08$, parallel to the diagonal coupling resonance $\nu_x - \nu_y = 0$. The small difference in the tunes is due to bide field imperfections. The configuration of the F and D quadrupole bus bars allowed us to shunt a small fraction of the current from the F to the D system through a pulsed vacuum tube power supply: the tune splitter. In this way we were able to control the tune split, $\nu_x - \nu_y$, and scan along a variety of lines mapping the working diamond at injection.

We calibrated these manipulations of the F and D quadrupole currents against measurements made by kicking the beam with a "pinger" dipole. This consisted of two turns of copper pulsed within a machine revolution from a small capacitor bank. By injecting a single booster batch and photographing an oscilloscope trace of the signal from one of the standard capacitive beam position detectors one could examine the beat frequency of the coherent betatron oscillations and calculate the fractional part of ν_x or ν_y, dividing the number of beats by the number of machine revolutions. We also deduced the tune spread in the beam from the rate of decay of the coherent signal and from the vertical oscillations induced by a radial kick could measure coupling between the two planes. We did not feel we could entrust disentangling these three signatures to a more convenient automated process at this stage.

Since we were interested in the influence of the resonances on beam loss we measured the fraction of the beam surviving by sampling and digitising a beam intensity monitor just after the injection of a single booster batch and again 400 milliseconds later. This quantity, the transmission, we measured with steady 8 GeV magnet excitation and with the r.f. switched on. It proved to be a powerful probe in exposing the resonance lines and reliable index of the overall transmission of the main ring to high energy.

We were fortunate in that we were able to make these injection studies parasitically with a special booster batch injected each machine cycle before the main batch sequence destined for acceleration to high energy.

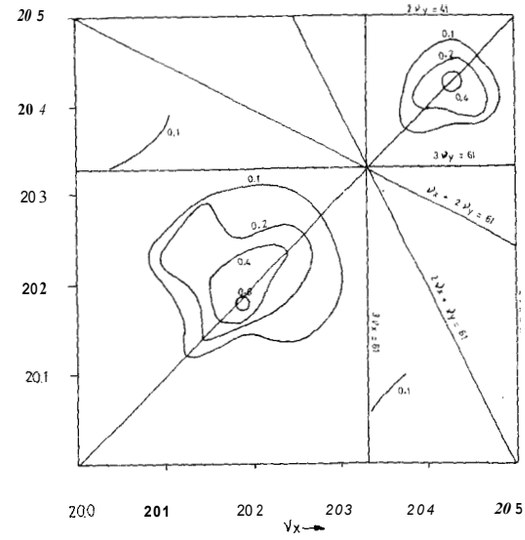


FIG 3 Contours of transmission for 0.4 sec at 8 Gev with original air cored sextupole pattern

Figure 3 shows a contour plot obtained at the outset of these studies by measuring 8 GeV transmission as a function of ν_x and ν_y. Clearly the influence of the resonance line: extends over the whole working space and there is no one place where more than 70% of the beam survives. .

Beam survival is best close to the diagonal coupling resonance $\nu_x - \nu_y = 0$. But in this region there is a danger that this coupling will transfer a large horizontal emittance into the vertical plane and our method of ν measurement became confused. One of the first corrections applied was to compensate the skew quadrupole imperfections in the guide field which drive this coupling.

3. Correction of Skew Quadrupole Coupling

Coupling between vertical and horizontal phase planes can be driven by systematic skew quadrupole imperfections in the guide field such as might result if all the quadrupoles of one type were rotated by a fraction of a milliradian about the beam axis. An

average roll of this magnitude could quite easily creep in during the surveying of the ring but could be compensated by rolling a few quadrupoles in the opposite sense. Significant coupling is to be expected in a region centred on the line $\nu_x - \nu_y = 0$, of width:

$$\nu_x - \nu_y = \frac{1}{2(B\rho)} \int \sqrt{\beta_x \beta_y}\, k\, ds$$

where: k is the skew quadrupole $\partial B_x/\partial x$, $\partial B_Y/\partial y$
$B\rho$, the magnetic rigidity
$\beta_x \beta_y$, the betatron functions

Within this band a vertical ping would generate a coupled horizontal coherent oscillation of frequency $\nu_x - \nu_y$ and of amplitude:

$$\frac{\Delta b}{a} = \frac{1}{2(B\rho)(\nu_x - \nu_y)} \int_o^c \sqrt{\beta_x \beta_y}\, k\, ds$$

where Δb is the coupled amplitude horizontally
a is the pinged amplitude vertically.

and the oscillograms clearly showed the beat frequency $\nu_x - \nu_y$ (ten turns per wavelength for $\nu_x - \nu_y = 0.1$). These beats were of opposite phase in the two planes, Using above expression we calculated the angle of roll, about 8 milliradians, *to* be applied to 12 equally spaced quadrupoles *to* neutralise the coupling. This adjustment reduced the coupling effect by almost an

4. Correction of Chromaticity

Magnetic measurements show that the NAL main ring dipole magnets have a remanent field whose predominant imperfection is a sextupole term. The field falls parabolically towards the edges of the poles. The average derivative is:-

$$d^2B_Y/dx^2 \simeq 0.05\ T\ m^{-2}$$

This field distortion can be understood qualitatively if one remembers that flux lines in the iron rooted at the centre of the poles are longer than those from the edge. The remanent magneto motive force, $\int H_c\, d\ell$, is larger near the pole centre.

The chromaticity in each phase plane produced by this sextupole shape is

$$(d\nu/\nu)/(dp/p) = 9$$

seven times larger than that due to the momentum dependence of the focusing strength of the lattice. Uncorrected it would introduce a tune spread of $\Delta\nu = \pm 0.09$ for a momentum spread within the beam of ± 0.5 o/oo, measured by observing the time taken for the coasting injected beam to lose its 53 MHz r.f. structure. The half widths quoted are those at the half height of the distributions.

During the early commissioning *of* the machine air cored sextupoles had been installed to correct this large chromaticity. These had been placed in all but a few of the short straight section spaces which follow each main ring quadrupole. Those near F quadrupoles and those near D quadrupoles should ideally have been separately powered to neutralise $\partial\nu/\partial p$ and $\partial\nu_y/\partial p$ independently but for practical reasons all sextupoles were in series and powered with a simple square pulse covering only the injection period and the parabola. They were therefore not ideal tools for accurate chromaticity control.

We measured the ν spread in each plane at a number of points in the acceleration cycle by counting the number of machine revolutions that a pinged coherent betatron oscillation took to smear to half its original signal strength. For a Gaussian tune distribution the reciprocal of this number is a measure of the extreme (2σ) spread in tune. Figure 4 shows the way in which

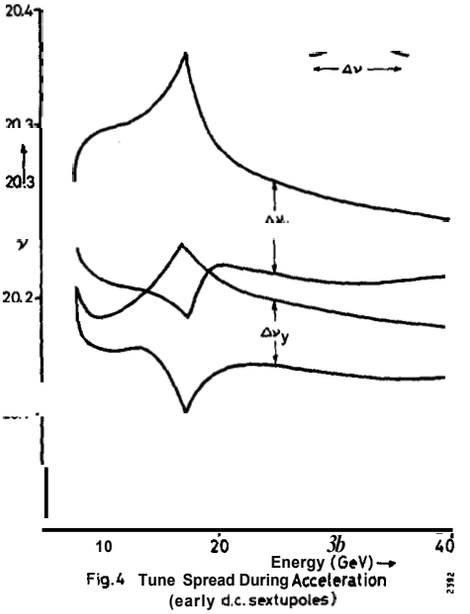


Fig.4 Tune Spread During Acceleration (early d.c. sextupoles)

from almost perfect compensation in the vertical plane the chromaticity changes in each plane during the parabola as eddy current sextupole fields develop in the vacuum chamber. The momentum spread also swells, peaking at almost double its injection value in passing through transition. This further adds to Av. The edges of the proton population cross the third and fourth order stopbands.

We therefore installed a new set of iron cored sextupoles with independent control of the set next to F quadrupoles and the set next to D quadrupoles. The currents in F and D sets are related to the $d\nu_y/dp$ and $d\nu_y/dp$ via a simple 2 x 2 matrix transformation which was built into the control software to give independent orthogonal control in the two planes.

The time development of sextupole imperfections contained three components: a steady one due to remanent fields, a component proportional to magnet excitation (B) and due to the geometry of the main ring dipoles and finally a component growing as dB/dt, generated by eddy currents in the vacuum chamber. We therefore powered the correctors with a current waveform:

$$I = a + \frac{bdB}{dt} + cB$$

deriving the dB/dt and B signals from the main ring reference magnet.

Each of the coefficients, a, b, c multiplied by the 2 x 2 matrix could be controlled directly from a page on the main ring console display.

We set up each coefficient in turn at energies at which its influence predominates (8, 17 and 60 GeV), maximising the decay time of pinged betatron oscillations and, repeating the tune spread experiments, we found $\Delta\nu < \pm 0.005$ throughout the acceleration cycle,

As expected beam survival improved as a result of this correction and the machine became much less sensitive to adjustments in the ratio of quadrupole to dipole current during the parabola.

5. Correction of Third Order Stopbands

Our early transmission experiments had revealed the strong influence of the four third order stopbands which intersect at $\nu = 20.33$ close to the nominal working point:

$$3\nu_x = 61\ ,\quad \int \beta_x^{3/2} (\partial^2 B_y/\partial x^2) e^{i61\theta}\, d\theta$$

$$\nu_x + 2\nu_y = 61\ ,\quad \int \beta_x^{\frac{1}{2}} \beta_y (\partial^2 B_y/\partial x^2) e^{i61\theta}\, d\theta$$

$$2\nu_x + \nu_y = 61\ ,\quad \int \beta_x \beta_y^{\frac{1}{2}} (\partial^2 B_x/\partial y^2) e^{i61\theta}\, d\theta$$

$$3\nu_y = 61,\quad \int \beta_y^{3/2} (\partial^2 B_x/\partial y^2) e^{i61\theta}\, d\theta$$

The table lists the resonances and their driving terms which are all 61st Fourier harmonics of the azimuthal pattern of sextupole imperfections weighted according to the local betatron functions. The first two resonances are driven and may be corrected by regular sextupoles with symmetry about a vertical plane; the same symmetry as one expects from the main ring dipoles. The last pair are driven by skew sextupoles of symmetry about the median plane. *To* correct all four stop bands one must use sextupole magnets of both regular and skew types.

The weighting factors are such that a further subdivision of correctors into those near F quadrupole locations where β_x is large and β_y small and those near D locations where the opposite is gives one almost orthogonal control of each resonance.

To generate the correct phase and amplitude of the 61st harmonic and neutralise the driving term the current settings of the individually powered sextupoles were ganged up through the control system to increment the sine or cosine amplitude in the strength pattern.

Tuning the machine to sit exactly on one of the stopbands we could adjust the amplitudes of the sine and cosine components to achieve 70% transmission. A contour plot versus the two variables revealed a simple maximum.

We calculated the width of the stopband from the strength of the correctors. For a proton at the periphery of the beam (1 cm amplitude at $\beta = 100$ m) $\Delta\nu$ is greater than $\pm$ 0.01. We had expected these stopbands to be due to variations in the azimuthal pattern of the remanent sextupole fields responsible for the chromaticity. We knew that the remanent fields in the dipole magnets constructed from unshuffled laminations varied by as much as $\pm$ 40%. Yet this could only account for a stopband $\Delta\nu \approx \pm$ 0.002.

Clearly other, stronger sextupoles were present and we soon discovered that the uneven pattern of chromaticity correction sextupoles determined by the need to leave room in some short straight sections for other equipment contained driving terms of the appropriate magnitude and phase to explain the observed widths.

We redeployed these chromaticity sextupoles in a pattern considerably less rich in 61st harmonic taking into account the differing weighting factors in the Table and repeated our transmission scan. The line widths had clearly become very much smaller and this was reflected in an improvement from 1.8 *to* 3.4×10^{12} in the intensity which could be accepted from the booster and accelerated to full energy.

We went on to compensate these much thinner resonances and from the corrector strength deduced a width commensurate with the theoretical estimate based on magnet measurements.

Our transmission scan showed all four lines to be comparable in width. We presume that sextupole fields of the skew configuration were present coming from assembly errors in the quadrupoles upon which we had little measurement data. We therefore installed F and D sets of skew sextupoles and set about compensating each of the four resonance lines scanning through each in turn along a line $\nu_x - \nu_y = -0.1$ where they are clearly resolved in the transmission scan. Figure 5 shows the effect of this compensation which raised the intensity which could be accepted and accelerated intensity a further 502.

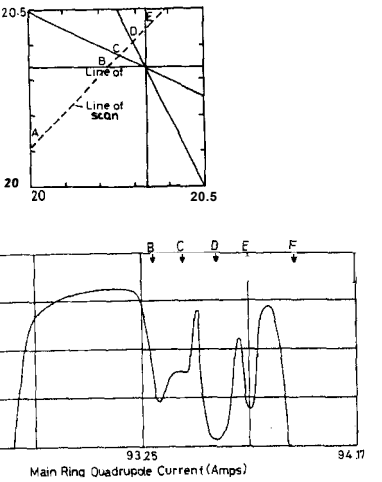


FIG 5(a). 8Gev transmission with harmonic sextupole correction off

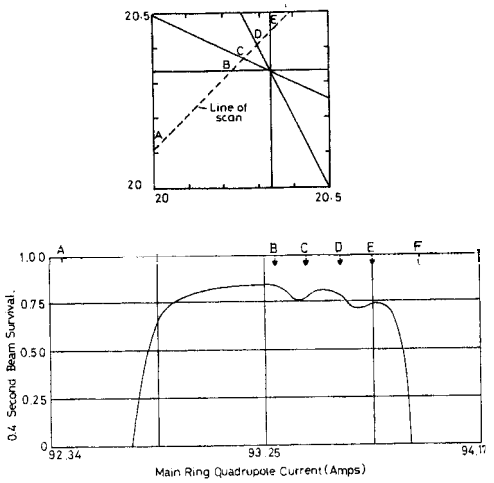


FIG 5(b). 8Gev transmission after harmonic sextupole correction

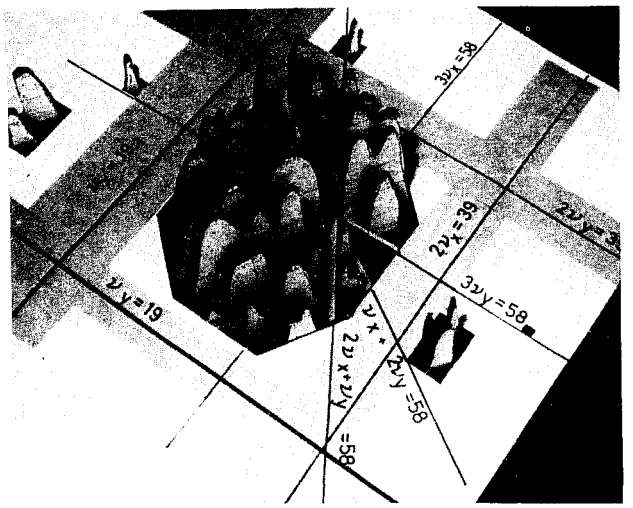


Fig. 6 - Contour model of transmission.

6. Compensation with Octupoles

Seeking to improve the linearity of the machine still further we measured the amplitude dependence of the tune by pinging coherent oscillations of a range of amplitudes and adjusting a set of d.c. series powered octupoles to make $\partial^2\nu/\partial a^2$ zero. Zero harmonic octupole imperfections in the lattice also generate a curvature to the chromaticity $\partial^2\nu/\partial p^2$. We measured the shape of $\nu(p)$ by pinging and steering to various mean radii with an r.f. bump. We optimised the octupoles to give a flat curve. Both techniques arrived at the same octupole strength. They proved effective in improving the tune spread. One could maintain coherent oscillations undiminished for several hundred turns indicating a $\Delta\nu$ of a few x 10^{-3}. Not surprisingly the machine became so linear at this point that a resistive wall instability emerged. The diagnosis and cure of this instability is the subject of another paper in this conference.

7. Alternative Working Point

The definition of our resonant scans had improved Sufficiently by this time that we were able to construct three dimensional models of the transmission over the diamond: $20 < \nu_x, \nu_y < 20.5$ and could identify the valleys of the third integer resonances as well as less well defined depressions at the location of fourth and higher order resonances.

The integer stopbands $\nu_x, \nu_y = 20$ were very wide and we suspected that one of their main components was the systematic resonance

$$3\nu = 60 = 10\ S$$

where S is the superperiodicity of the long straight sections and thence of the systematic sextupole imperfection.

Such systematic relations reoccur at all even ν values for S = 6 and give rise to very wide stopbands. We therefore decided to explore the diamond just above 19 to see if the integer was less strong.

Figure 6 shows a model of this diamonds contours with no harmonic correction applied. The integer has a width of $\Delta\nu = \pm 0.05$ compared with ± 0.1 in the original diamond. The region around 19.2 gives somewhat higher transmission and much more elbow room to accommodate changes in the working point due to magnet ripple and quadrupole power supply regulation. Accordingly, it was decided to change the operational working point permanently from 20.2 to 19.2 and improvement in accelerated beam has resulted.

Conclusions

These experiments demonstrated the deleterious effect of non linear field imperfections in the guide field. It is apparent from transmission scans like Fig. 5 that beam survival is affected over a much wider band than the classical stopband width even when the measures have been taken to reduce the momentum and amplitude dependence of the tune. The reason for this line broadening is still being investigated. It may be due to ripple in the excitation of the dipoles and quadrupoles.

As a result of these experiments and improvements the four dimensional acceptance of the main ring increased by almost an order of magnitude to match improvements in Booster intensity and reduce the fraction of the beam lost after injection.

Yet even when the third order resonances had been corrected the acceptance was barely larger than the diameter of the booster beam. To enlarge this still further to be commensurate with the geometrical size of the vacuum chamber will require correction of fourth and higher order stopbands which are not resolved in transmission scans at injection but which we know are there from measurements at higher energy.

Andrei Kolomensky (Lebedev Institute): Do you know the mechanism of the pressure instability?

R. Stiening (NAL): No, we do not. We haven't explored it in great detail because the instability occurs under conditions which are very far from our normal operating conditions.

Karl Reich (CERN): Is the narrowing of stop-bands done just during the low energy period or further on in the cycle?

Stiening: Some are and some aren't. The average sextupole corrections are made throughout the cycle. It's necessary to carry them up to about 50 GeV. It doesn't matter, at present, whether the octupole corrections are made or not.

FAST DAMPING OF TRANSVERSE COHERENT DIPOLE OSCILLATIONS IN SPEAR*

The SPEAR Group**
Stanford Linear Accelerator Center
Stanford, California

Summary

The fast damping phenomenon observed in SPEAR is discussed in this paper. Some of the effects of various beam parameters such as chromaticity, rf voltage, octupole lens strength and beam current upon the fast damping are presented.

Introduction

Fast damping of coherent transverse oscillations of the center of charge of a single bunch beam has been observed in VEPP-2[1] and SPEAR. This damping for horizontal oscillations has been studied in SPEAR and the results seem to be consistent with those predicted by the "Head-Tail" theory for wake fields that vary rapidly over the length of the bunch.[2,3,4,5] This phenomenon was investigated experimentally by shock-exciting the beam horizontally and then observing the decay of the amplitude of the coherent signal. In order to establish that the decay of the coherent signal corresponds to a decay in particle amplitude and not to a randomization of phases of the coherent motion, the transverse particle density was also observed as a function of time. This damping rate has been measured for various parameters of the beam. It has proven possible to eliminate this fast damping of particle amplitude by means of octupole fields which produce a spread in the particle betatron frequencies, leading to Landau damping of the coherent motion.[6]

Experimental Observations

The two kickers which produce the required beam bump during injection were used to produce an initial amplitude of the horizontal oscillation for the center of charge of a stored beam.[7] By varying the relative strength of the kicker pulses, it was possible to excite horizontal amplitudes that were large enough to be detected and studied.

The response of the beam after the kick is observed by two types of detectors.[8] The first of these is a strip-line monitor that gives a signal proportional to the position of the center of charge of the beam. The second is a profile monitor that scans the synchrotron light emitted by the beam; the maximum output signal from this monitor is proportional to the maximum density of the beam averaged over times longer than the transverse betatron oscillation period. Thus the maximum signal from the profile monitor is inversely proportional to the beam width. The beam width derived from the profile monitor includes the contribution from the incoherent particle motion and coherent motion at the betatron frequency. An example of the fast damping as observed by the two detectors is shown in Figs. 1 and 2. The two figures are for identical beam parameters but different sweep speeds. The top traces are the envelope of the coherent beam motion while the bottom traces are the evolution of the peak particle density.

If the peak particle density increases while the coherent signal decays, then this would be evidence that the amplitude of the oscillation decays, while if the peak particle density does not increase, this would be evidence that the decay of the coherent signal is due to a randomization of the phases of the coherent motion. Figures 1 and 2 are thus evidence that the amplitude of the oscillation decays. Since the active feedback system was off during these experiments and the radiation damping time is long (~60 msec for beam parameters in Figs. 1 and 2) compared to the fast damping times measured in SPEAR, there must be a feedback field produced by the beam in its passive surroundings.

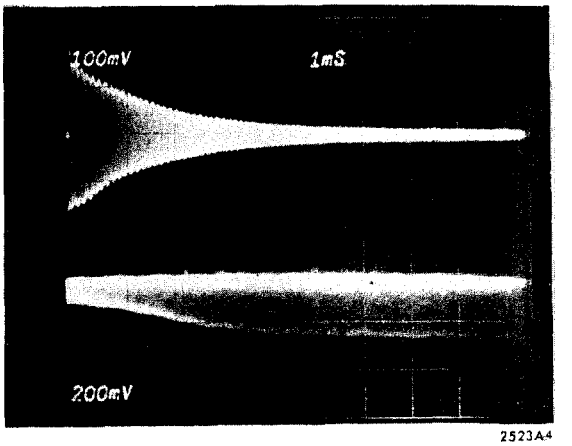


Fig. 1. Fast Damping

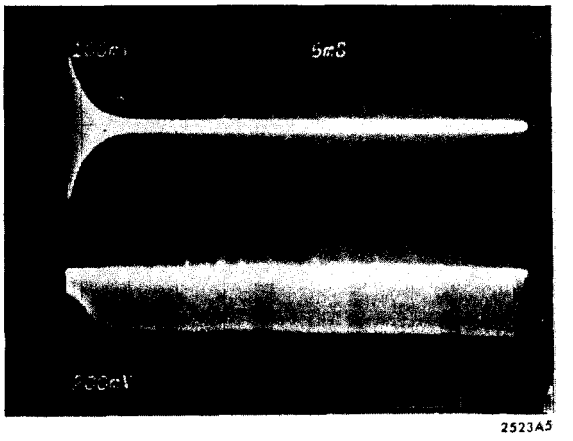


Fig. 2. Fast Damping

Low Current Phenomena

In this section, the fast damping phenomenon discussed will be for currents in a single bunch < 40 mA. The fast damping rate of horizontal coherent oscillations as a function of horizontal chromaticity ξ_x is shown in Fig. 3 for three values of the rf voltage.

In this figure, the energy was 1.5 GeV, the average current 20 mA and the chromaticity ξ_x is defined by $\Delta\nu_x = \xi_x(\Delta p/p)$. One can see from Fig. 3 that the fast damping rate is a linear function of the chromaticity.

The bunch length in SPEAR shortens with increasing rf voltage; hence the results in Fig. 3 show that the variation of the damping rate with chromaticity, $d\alpha/d\xi_x$, decreases with increasing bunch length. This last fact is consistent with the "Head-Tail" instability with fast varying wake fields.

* Work supported by the U. S. Atomic Energy Commission.

** J. M. Paterson, B. Richter, A. P. Sabersky, H. Wiedemann, P. B. Wilson, M. A. Allen, J. E. Augustin, G. E. Fischer, R. H. Helm, M. J. Lee, M. Matera, P. L. Morton

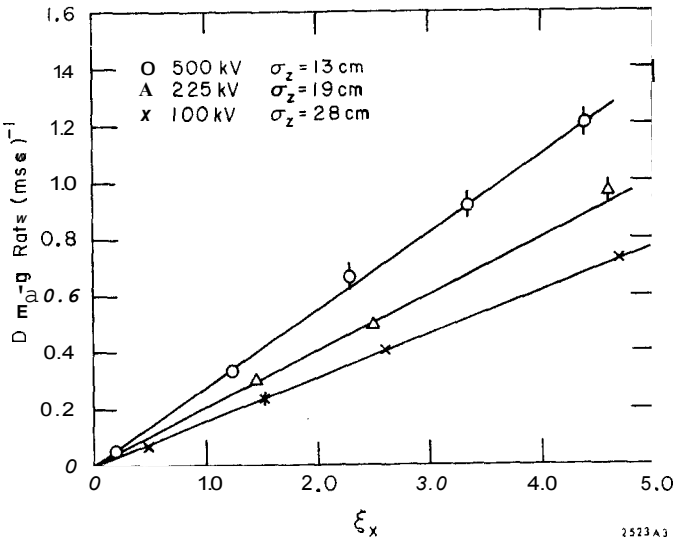


Fig. 3. Fast Damping rate versus chromaticity. E = 1.5 GeV; I = 20 mA

Below currents of *40* mA, the decay of the coherent oscillation signal observed is similar to the decay presented in Figs. 1 and 2. The damping rate versus the average current is shown in Fig. 4 for various values of the rf voltage with an energy of 1.5 GeV and chromaticity ξ = *2.4.* Due to the bunch lengthening phenomenon in SPEAR, the length of the bunch increases with current and is probably the explanation of why the fast damping rate varies more slowly than linearly with current.

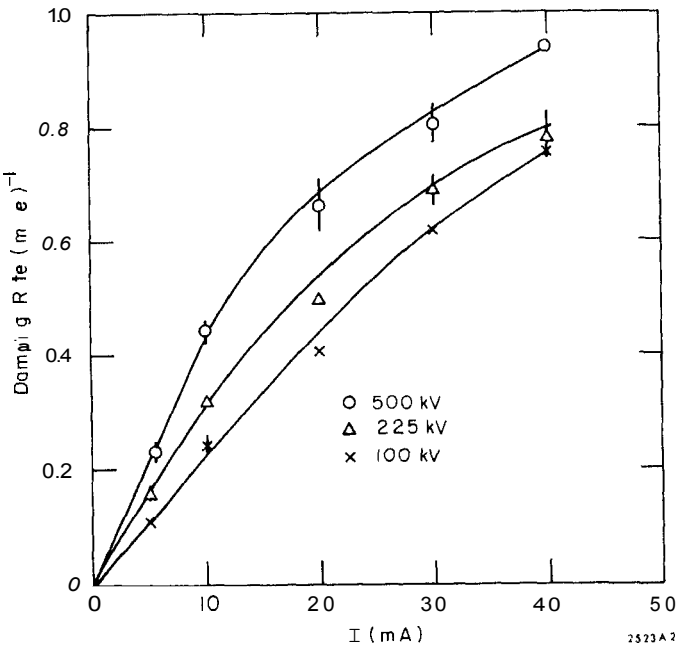


Fig. *4.* Fast damping rate versus average current. E = 1.5 GeV; ξ_x = *2.4*

The fast damping rate, α, is normally expected to be inversely proportional to the energy so that the decay rate is plotted as a function of (1/E) in Fig. 5. Because the bunch length decreases as (1/E) increases (i.e., as the energy decreases), we see from Fig. 5 that α increases faster than (1/E).

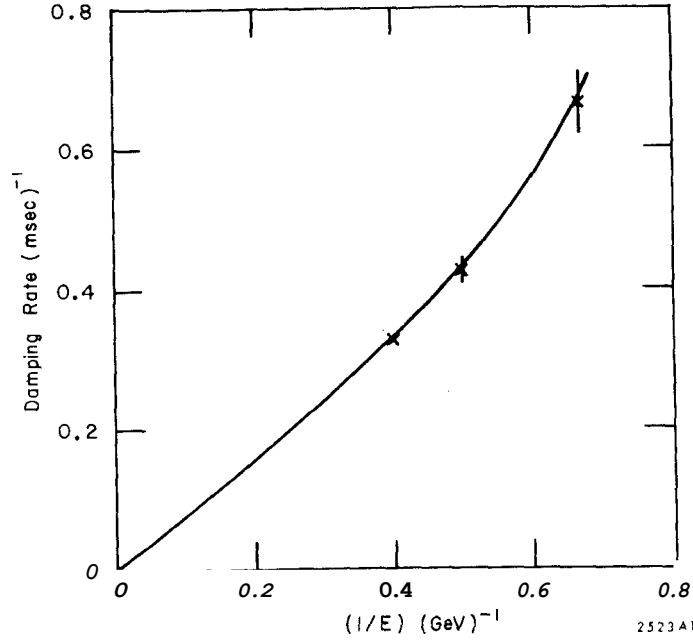


Fig. 5. Fast damping rate versus (Energy)$^{-1}$ I = 20 mA; V = 200 kV; ξ_x = *2.4*

High Current Phenomena

When the current in a single bunch circulating in SPEAR exceeds *40* mA, the fast damping phenomenon is not as simple to interpret as it was for the lower current. The response of a 100-mA beam is shown in Figs. 6, 7 and 8. Again, the top traces are the envelope of the coherent horizontal motion for the center of charge in the beam while the bottom traces are the peak particle density averaged over the transverse betatron period. In all three figures, the beam parameters were identical except for the chromaticity and the rf voltage. The horizontal chromaticity ξ_x = 2.1 in both Figs. 6 and 7, but the rf voltage was 100 kV in Fig. 6 and 225 kV in Fig. 7. The rf voltage was 100 kV in Figs. 6 and 8, but ξ_x was 2.1 in Fig. 6 and *4.2* in Fig. 8. The motion displayed in Figs. 6, 7 and 8 seems to indicate that the center of charge is oscillating horizontally at more than one coherent frequency, and that the difference between these frequencies produces a beating that depends upon the bunch length and the chromaticity.

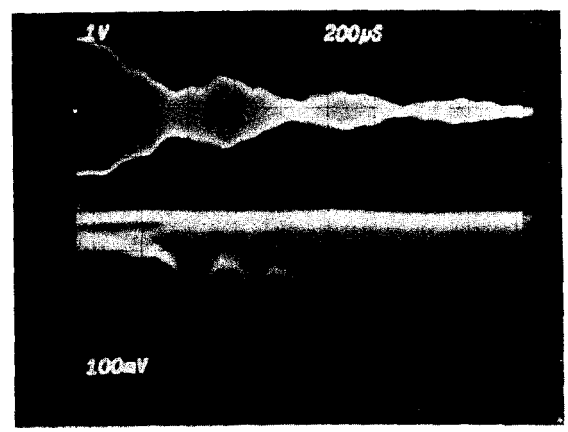


Fig. 6. I = 100 mA; ξ_x = *2.4;* V = 100 kV

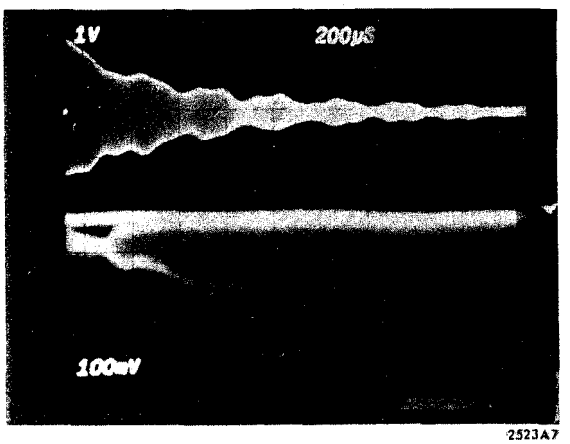


Fig. 7. I = 100 mA; ξ_x = 2.4: V = 225 kV

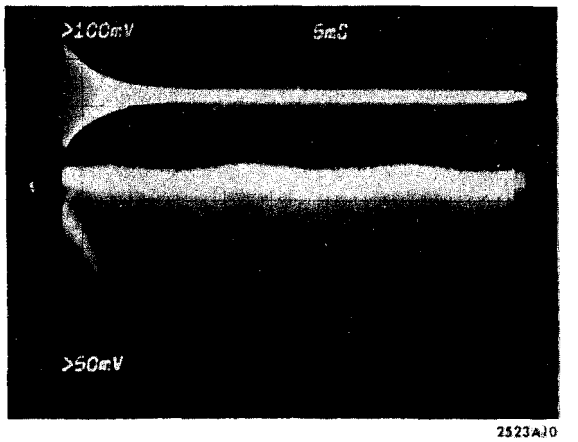


Fig. 9. $I_{oct} > -3A$

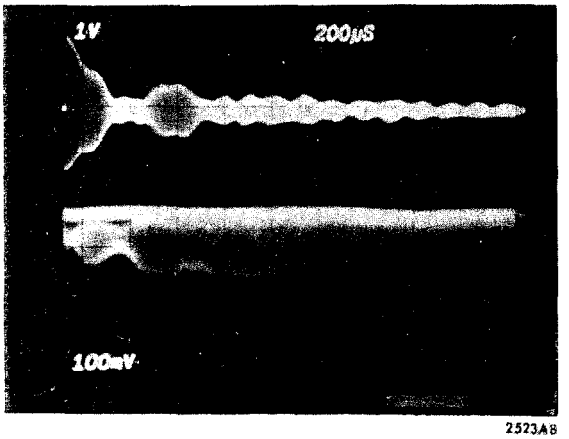


Fig. 8. I = 100 mA; ξ_x = 4.2; V = 100 kV

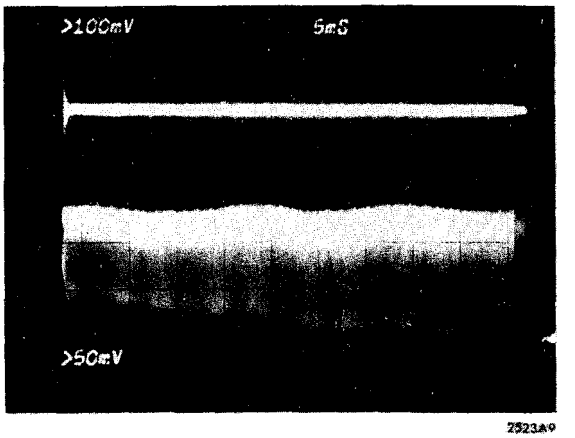


Fig. 10. $I_{oct} = -5.6A$

For the case where the "Head-Tail" instability theory assumes a hollow bunch in longitudinal phase space, there should be only one frequency for the transverse coherent oscillation of the center of charge. However, if the bunch is not hollow in longitudinal phase space, it is possible to have several transverse coherent dipole modes with slightly different frequencies[2,4] and it is possible that these are what we observe in SPEAR for high current.

Landau Damping

In the SPEAR lattice, there are octupole lenses that can be powered to produce a variation of the transverse oscillation frequency with particle amplitude, a.

The octupole may be powered with up to ±20 amps, which yields up to $(\Delta\nu/a^2) = \pm 0.004/cm^2$ for an amplitude variation of betatron wave numbers. The fast damping has been observed as a function of the octupole lens strength. It has been found that for a 10-mA beam, the fast damping is independent of the octupole lens strength in the range $-3A < I_{oct} < 12$ A. On the other hand, if the octupole lens strength is sufficiently negative; i.e., $I_{oct} < -5.6A$, the fast damping disappears. This is shown in Figs. 9 and 10.

In Fig. 9, the $I_{oct} > -3A$, and we see that we have the usual fast damping; however, in Fig. 10, the $I_{oct} = -5.6A$, and we see that the coherent signal decays rapidly and the peak particle density is lower than was obtained for the fast damping case. We have interpreted these results as a Landau damping of the coherent motion. When the Landau damping is sufficient to damp the coherent motion, the resulting beam size is larger (peak particle density smaller) and the oscillation amplitudes are damped by the slower radiation process.

Acknowledgements

It is a pleasure to thank the SPEAR Operations Group, who not only aided in the operation of the storage ring but also actively participated in the experimenta 1 measurements.

References

1. V. L. Auslender et al., Proc. International Symposium on Electron and Positron Storage Rings, SACLAY, IV-4 (1966).
2. C. Pellegrini, Nuovo Cimento 64 A, 477 (1969).
3. M. Sands, SLAC-TN-69/85 and SLAC/TN-69/10 (1969).
4. F. Sacherer, CERN/SI-BR/72-5 (1972, unpublished).
5. A. G. Ruggiero, NAL Report FN-254 (1973, unpublished.
6. J. Landau, J. Phys. USSR 10, 25 (1946).
7. SLAC Storage Ring Group, Proc. 8th International Conference on High-Energy Accelerators, CERN, Geneva, 145 (1971).
8. The SPEAR Group, "Beam Dynamics Experiments at SPEAR", contribution to this conference.

HEAD-TAIL TYPE INSTABILITIES IN THE CERN PS AND BOOSTER

PART I on the PS, by J. Gareyte
PART II on the Booster, by J. Gareyte and F. Sacherer

CERN, Geneva, Switzerland

Summary

A single-bunch instability of the head-tail type has been observed for several years in the PS. Only mode zero is seen eventhough the phase shift between head and tail is changed from zero to over 100 radians by varying the machine chromaticity. According to theory', the bunch spectrum is centered on the "chromatic" frequency f_ξ = phase shift/bunch length, and has a width of about 100 MHz (inverse bunch length). Near transition, f_ξ can be varied over a range of 2 GHz, thus providing an excellent probe of the transverse coupling impedance seen by the beam. One finds a broad-band spectrum with a flat maximum near 1 GHz. This is consistent with the absence of higher modes. Thresholds versus octupole strength and beam emittances have been measured and compared with theory. The present cure is octupoles, but reduction of the chromaticity to zero is foreseen for higher intensities ($\sim 10^{13}$ ppp).

In the Booster, head-tail modes zero, one, two and three occur, the higher modes occuring for large chromaticities and mode zero for zero or small chromaticities. The growth rate increases rapidly as the Q-value approaches 5 from below. This is a coupled-bunch multi-turn phenomenon that is well explained by the resistive wall effect. The e-folding times of a few ms require a total wall resistance of about one Ohm at low frequencies, in agreement with the resistance of the thin walled vacuum chamber.

PART I : THE CPS

History

Already in 1967 when the CPS accelerated intensity exceeded 0.8×10^{12} p/p, the beam was from time to time deteriorated by a vertical instability. The phenomenon manifested itself as partial or total disappearance of some of the 20 bunches. The cure was to lengthen the bunches by means of a dilution in the longitudinal phase space, obtained by mistiming transition phase jump.

Soon after, the accelerated intensity increased to 2×10^{12} p/p and the ISR asked for a CPS longitudinal density as high as possible. The Q-jump method was devised to cure transition problems and maintain nominal phase-space area up to the available peak intensity. The result of this was a catastrophic vertical explosion of the beam soon after transition (~ 7 GeV/c), leading to complete loss of the particles. Fortunately, some of the octupolar lenses foreseen during construction of the CPS were still in the ring, and proved to be sufficient to Landau damp the instability. A systematic study programme was then launched with the aim of controlling the instability even at the increased intensity of 10^{13} p/p.

Observations

Single-Bunch Instability

Usually several, if not all, of the twenty bunches become unstable. Nevertheless, a regular pattern, which is the signature of coupled motion, was never observed. Also, working near the threshold, one can observe situations where only one bunch oscillates (Fig. 1).

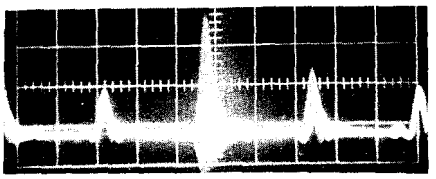


Fig. 1 : A single bunch instability

Dependence on bunch length

Increasing bunch length, either by increasing longitudinal emittance or by lowering longitudinal focussing, reduces growth rate and increases the threshold of the instability.

Dependence on octupoles and emittances

Octupoles are currently used in operation to suppress the instability. A rule of thumb which can be drawn from dispersion relation analysis[1,2] is that the spread in betatron number Q due to octupoles must exceed $|\Delta Q_{inc} - \Delta Q_{coh}|$, the difference between incoherent and coherent Laslett Q-shifts. In fact, half this value is sufficient to avoid any beam blow-up under operational conditions. During the experiment described below, the required spread was found to be even much smaller.

The experiment : Threshold was determined in terms of octupole current needed to suppress the instability for given energy and intensity, and varying emittances. Vertical instability was investigated, horizontal and vertical emittances being varied by means of multiple pulsing of a fast kicker followed by filamentation in the presence of strong non-linearities. The clear and reproducible threshold values obtained are plotted on Figs 2 and 3. Minimum spread is about 20 times smaller than $|\Delta Q_{inc} - \Delta Q_{coh}|$.

Dependence on chromaticity

At medium energy ($P < 15$ GeV/c), the CPS is a linear machine with both horizontal and vertical chromaticities

$$\xi = \frac{\partial Q}{Q} \Big/ \frac{\partial P}{P} = -1$$

In this case, instability grows in the vertical plane. At high energies, ξ_H and ξ_V become respectively -2 and zero due to saturation, and instability grows in the horizontal plane. Above transition, it was found by varying the chromaticities with sextupoles that the instability grows in the plane in which $|\xi|$ is the largest ($\xi < 0$). For zero or positive chromaticities, no instability has ever been seen up to intensities of 5×10^{12} p/p. Below transition, the same behaviour is

found for the reverse sign of chromaticity (unstable for $\xi > 0$).

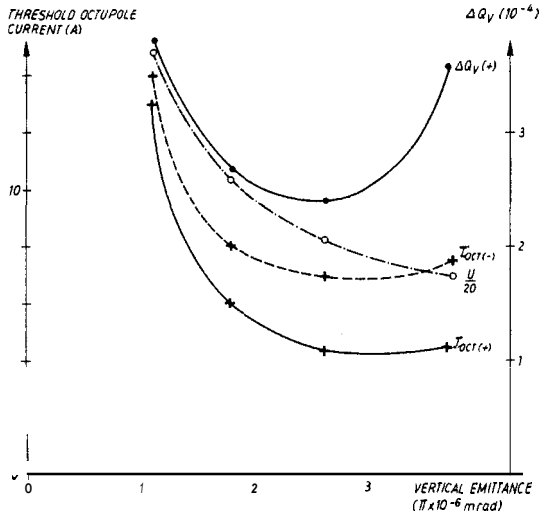
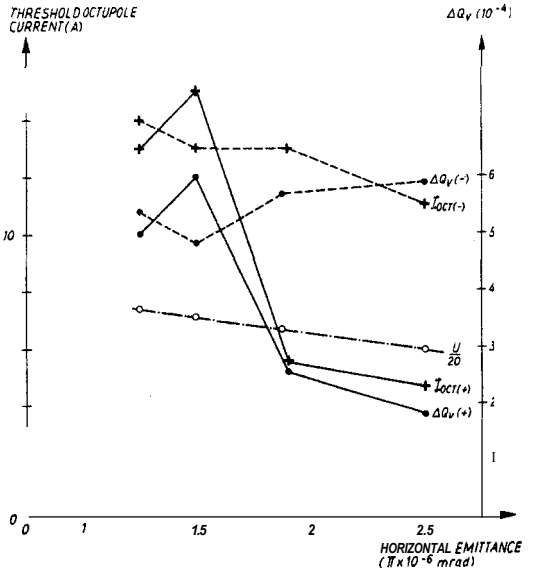


Figure 2

Octupole current and estimated Q_V spread at threshold versus vertical emittance (10 GeV/c, 1.7 x 10^{12} p/p) :

——————— positive current
– – – – – – – – – – negative current

- ΔQ_V is the quadratic sum of the Q_V spreads induced by the octupoles via both vertical and radial betatron amplitudes. Each of these contributions corresponds to full-width at half-height of the considered distribution.
- $|\Delta Q_{inc} - \Delta Q_{coh}| = U$ is plotted, divided by 20 for reasons of scale.
- Emittances correspond to twice the r.m.s. radius of the beam.



Fin. 3 same as 2, but for varying horizontal emittance.

Fig. 4 shows the signal of a single bunch coming from a position observation station (APU) on five consecutive passages. According to theory[1], such a signal should be

$$p(t) = P_m(t)\, e^{j\omega_\xi t + j2\pi kQ} \qquad (1)$$

on the k^{th} revolution, where $w_\xi \simeq \frac{\xi}{\eta} Q\, \omega_o$,

$\eta = \gamma_T^{-2} - \gamma^{-2}$

ω : revolution angular frequency,

and P_m is approximately sinusoidal with m nodes for head-tail mode m (Fig. 7). The phase shift from head to tail of the bunch due to non-zero chromaticity is

$$\chi = \omega_\xi\, \tau_L \text{ radians} \qquad (2)$$

(τ_L = bunch length in seconds).

Fig. 4 shows a bunch oscillating in mode m = 0, with $\chi \simeq 12$ radians. For smaller values of χ, oscillations approaching rigid-bunch motion are observed; the instability disappears for $\chi = 0$. One can check that the oscillation mode is m = 0 up to $\chi \simeq 15$ radians or chromatic frequency $f_\xi \simeq 200$ MHz, which is the bandwidth limit of the APU. For higher values of χ, the instability can be monitored (Fig. 5) by the Ionization Beam Scanner (IBS[3]), but a signal is no longer visible on the ΔPU. This is expected if mode 0 is still the dominant mode at these high chromatic frequencies; low frequency signals would be observed if higher order modes grew (see Fig. 9).

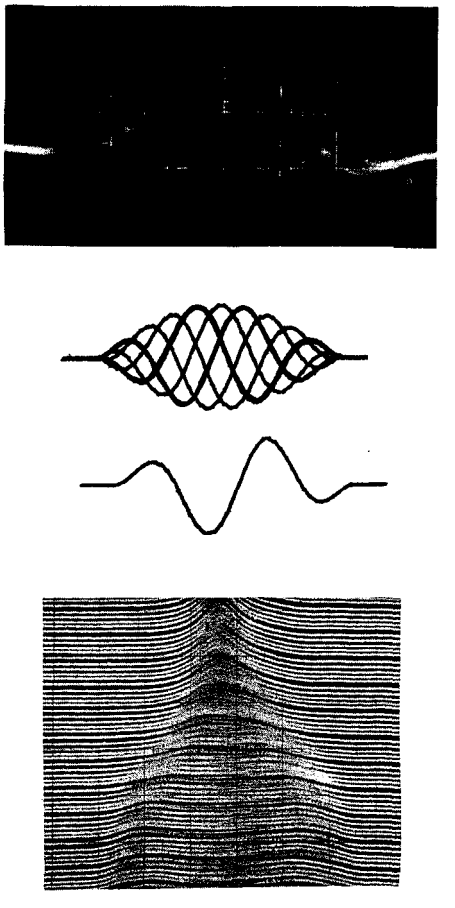


Figure 4 : Δ signal for a single bunch on 5 consecutive revolutions :
a) mode 0 observed for χ = 12 radians (2 ns/div.)
b) computed from equation 1.
- 5 traces
- 1 trace

Figure 5 : Mountain range display (5 ms/cm) of the Ionic Beam Scanner during the instability.

Growth rate measurements versus chromaticity

Very large phase shifts ($\chi > 100$ radians, chromatic frequencies f_ξ in the GHz range) can be investigated, on a magnetic flat-top near to transition energy (η small). Growth-rates have been measured as a function of f_ξ. Different energies (hence different η) have been used to look more closely at one region or the other of the frequency spectrum. For $f_\xi < 200$ MHz, the growth rate was monitored using the signal from our P.U. station. Above 200 MHz, the IBS was used. It was set to collect electrons from a small region centered on the beam - the rate of decrease of this signal is related to the growth-rate. This is a rather crude measurement, but it has the advantage of being independent of frequency. At low frequency, it agreed quite well with the P.U. measurements. Fig. 6 shows the results of these investigations : the striking feature is that the growth rate increases markedly with frequency.

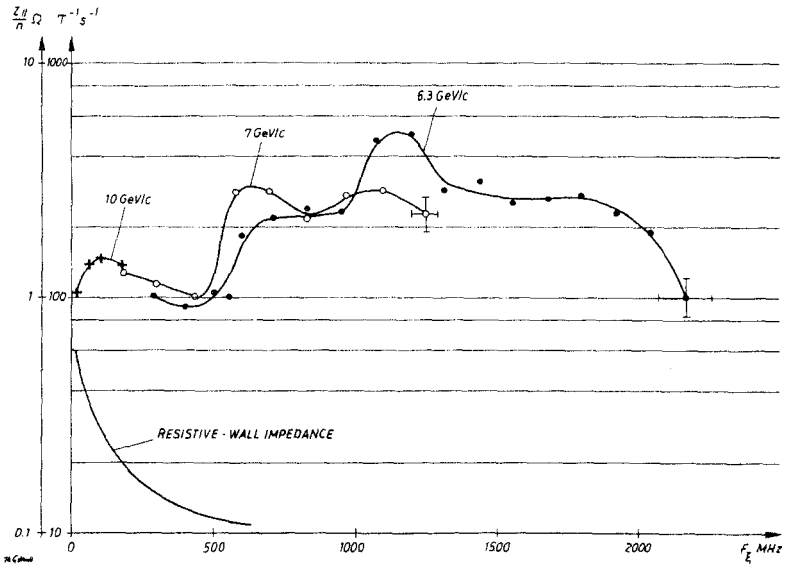


Figure 6 :

Growth rate as a function of chromatic frequency f_ξ was measured for three energies (error bars are drawn only for last point of each curve). The impedance deduced from eq. (4) is indicated as well as the resistive-wall impedance ($n = \omega/\omega_o$).

Discussion and Interpretation

The single-bunch feature and the disappearance of the instability at zero chromaticity is well explained by the head-tail mechanism described by Pellegrini[4] and Sands'. For short-range wake fields, the growth rate for mode m is given by[1] :

$$\tau_m^{-1} = \frac{-1}{m+1}\,\frac{1}{2Q\omega_o}\,\frac{e\beta}{\gamma m_o}\,\frac{I_o}{L}\,\frac{\int_{-\infty}^{+\infty} \mathrm{Re}\ Z_\perp(\omega)\ h_m(\omega-\omega_\xi)\ d\omega}{\int_{-\infty}^{+\infty} h_m(\omega)\ d\omega} \qquad (3)$$

where $Z_\perp$ is the transverse coupling impedance which can often be related to the usual longitudinal impedance $Z_{/\!/}$ (see eq. 6); $h_m(\omega)$ is the frequency spectrum of mode m (Fig. 9); m_o is the rest mass of the proton; I_o is the current in one bunch of length L meters. This formula can be applied with the hollow-bunch modes of Pellegrini and Sands, or with the more realistic sinusoidal modes defined by Sacherer[1].

The experimental observations are consistent with the assumption that $Z_\perp$ is a broad-band impedance, slowly varying with frequency. Then (3) can be simplified for mode 0 to

$$\tau_o^{-1} = \frac{-1}{2Q\omega_o}\,\frac{e\beta}{\gamma m_o}\,\frac{I_o}{L}\ \mathrm{Re}\ Z_\perp(\omega_\xi) \qquad (4)$$

which is the coasting beam result for ω_ξ, but increased by the bunching factor.

Measuring τ gives then Re $Z_\perp(\omega)$ with a resolution of order $\delta\omega = 2\pi/\tau_L$, which is the width of the frequency spectrum for mode 0. On Fig. 5, a double vertical scale shows the correspondence between growth rate and impedance, according to this interpretation. The resistive-wall impedance is plotted for comparison : it cannot explain the observed phenomena.

An impedance that increases with frequency is also consistent with the absence of higher-order modes. A search for equipment that could explain Fig. 5 has been made. It was concluded[6] that ceramic vacuum chamber sections, introduced to allow fast field penetration from pulsed magnets, and ferrite structures used in fast kickers, are good candidates. Unfortunately, it is hard to see how to modify them to reduce their impedance without affecting the CPS capabilities.

Damping with octupoles : It seems likely that non-linear space-charge fields of the beam contribute to the useful Q-spread[2], and can help or counteract the action of octupoles : this can perhaps explain why the necessary spread is sometimes much smaller than what is expected and the rather complicated behaviour observed. The subject needs more study, both theoretical and experimental, to be understood in detail.

Acknowledgements

Thanks are due to C.D. Johnson, builder of the IBS, for his participation in growth rate measurements.

PART II : THE PS BOOSTER

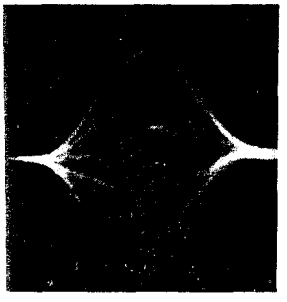
Observations

Dependence on Q-value

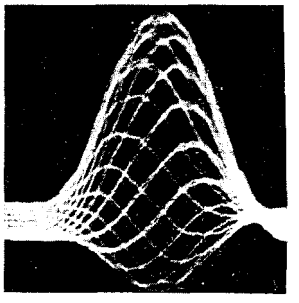
The Q-value can be varied over the range 4 to 5.3. One finds that both horizontal and vertical instabilities depend strongly on Q-value, with the growth-rate increasing rapidly as Q_V or Q_H approaches 5 from below. Other conditions being equal, the horizontal instability grows faster.

Dependence on chromaticity

The chromaticities can be varied over the range $-2 > \xi_H > +.5$ and $-4 > \xi_V > +1$ with the zero-harmonic sextupoles. For zero chromaticity, rigid-bunch motion occurs (Fig. 7a). As $|\xi|$ increases, a phase-shift develops between head and tail of a bunch (Fig. 7b). For larger $|\xi|$, the higher-modes start to grow (Figs 7c-f). The demarcation between modes is not sharp, with often two or thee modes growing for the same value of ξ. The higher modes appear to grow less fast than the lower modes.



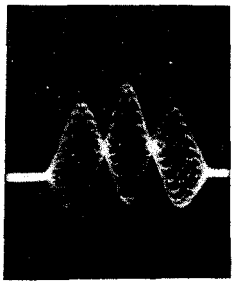
a) mode m = 0, χ = 0



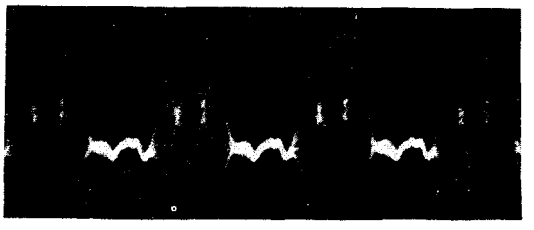
b) m = 0, χ = 2.3 radians



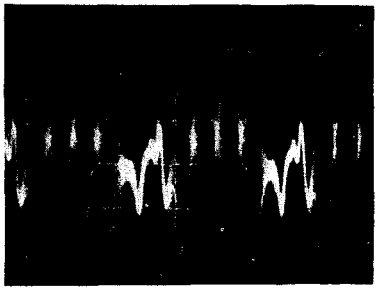
b) m = 1, χ = 6.9 radians



d) m = 2, χ = 6.9 radians



e) m = 2, χ = 8.9 radians



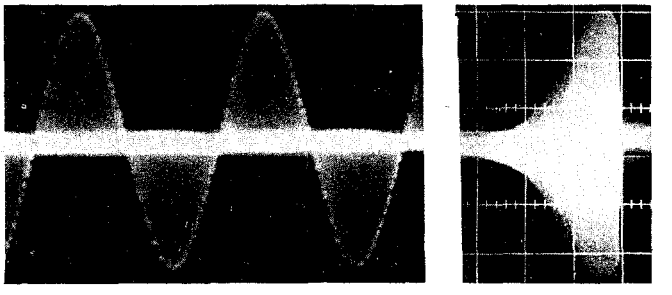
f) m = 3,
χ not recorded.

Fig. 7 : A single bunch seen on about 20 consecutive revolutions. Vertical axis : APU signal. Horizontal axis : time (50 ns/div.).
a-b-c-d : with wide-band PU (bandwidth ≃ 150 MHz)
e-f : with normal PU (bandwidth ≃ 40 MHz, and baseline restitution circuit acting).

Coupled-motion : Fig. 8a shows coupled motion for rigid-bunches (ξ_V = 0) with Q_V = 4.96. The frequency observed is

$$f_n = |n - Q_V| \, f_{rev} = 25.6 \pm 1 \text{ KHz}$$

for a revolution frequency f_{rev} = 678 kHz, and therefore the coupled-bunch mode number is n = 5. The evidence for coupled motion of the higher modes is less direct, but it appears from photos such as Fig. 7e that the motion is coupled. In any case, when the growth rate is reduced by lowering the Q-value, the motion is less strongly coupled with sometimes only two of the five bunches growing.



a) 10 μs/div. b) 5 ms/div.

Fig. 8 : Coupled bunch mode pattern a) and growth rate b).

Dependence on octupoles : Small currents in the hero-harmonic octupoles cure the instability except for Q-values near to but below 5 where larger currents are required. In all cases, the required spread in Q is less than the expected value $|\Delta Q_{coh} - \Delta Q_{incoh}|$.

Discussion

The growth-rates fit a resistive-wall impedance, or in general a narrow bandwidth impedance centered at zero frequency. The fact that the higher modes grow as the chromaticity is increased is explained by the frequency spectrum of the various modes (Fig. 9). One sees that increasing $|\chi|$ displaces the spectrum so that progressively higher-order modes overlap the assumed high impedance region at the origin. The numerical value of the phase-shift χ necessary for a given mode to grow agrees reasonably well with the theory (Eq. 5).

The frequency spectrum shown in Fig. 9 is actually discrete with lines at $f_n = (n+Q)f_{rev}$. The strong dependence on Q-value and the long-range nature of the wake fields imply that the impedance is sufficiently narrow that only the line f_n nearest the origin contributes (Fig. 10). In this case, the growth-rate for mode m is [1] (MKS units)

$$\tau^{-1} = -\frac{1}{1+m}\,\frac{e\,\beta\,I}{2Q\omega_o\,\gamma m_o}\,\frac{\mathrm{Re}\,Z_\perp(f_n)}{2\pi R}\,F'_m(\chi) \qquad (5)$$

which is just the coasting beam result but reduced by the factors $(1+m)^{-1}$ and $F'_m(\chi)$. Here, $F'_m(\chi)$ is proportional to the amplitude of the Fourier component at f_n (Fig. 9 and Fig. 7 of Ref. 1). The other quantities are : $\beta = v/c$, $\omega_o = v/R$, I = total current for coupled motion or the current in one bunch for decoupled motion, m_o = rest mass of particles, $2\pi R$ = machine circumference, and $Z_\perp$ is the transverse coupling impedance in Ohm/meter. For a circular pipe of radius b and surface resistivity R_{surf}, it is related to the more familiar longitudinal coupling impedance $Z_\parallel$ by

$$Z_\perp(\omega) = \frac{2c}{b^2}\,\frac{Z_\parallel(\omega)}{\omega} \qquad (6)$$

where

$$Z_\parallel(\omega) = \frac{2\pi R}{2\pi b}\,R_{surf} \qquad (7)$$

and $R_{surf} = (1+j)\rho/\delta$ provided the wall thickness ℓ exceeds the skin depth δ, or $R_{surf} = \rho/\ell$ if $\delta > \ell$. Here ρ is the resistivity in Ohm-meters. It follows that the growth-rate varies as $|n-Q|^{-\frac{1}{2}}$ for thick walls, or as $|n-Q|^{-1}$ for thin walls and that the modes with $|n|$ larger than Q are unstable. In the limit $\chi = 0$ and for the thick-wall impedance, (5) reduces to the familiar Courant and Sessler[7] result for mode m = 0.

Measurements of growth rate for different Q-value are shown in Fig. 11. The chromaticity was set to zero so that only mode m = 0 grows. The frequency $|n-Q|f_{rev}$ was determined to an accurary of 1 or 2 kHz (Fig. 8a), and the growrh rate to about ± 5% (Fig. 8b). The results have the thin-wall form with $\overline{Z}_\perp = 10.2\times10^5$ Ohm/m at 30 kHz, or $Z_\parallel = 321\ b^2$ Ohms independent of frequency. On the other hand, the major contribution to the vacuum chamber impedance in the Booster comes from the 52 m of thin-walled ($\ell = 0.4$ mm, $\rho = 1.3\ 10^{-6}$ Ohm-meters) chamber in the bending magnets'. The skin depth is much Larger than the wall thickness ($\delta \geq 1.7$ mm for $Q_y \geq 4.8$) so one expects $Z_\parallel = 0.027/b$ Ohms independent of frequency. This agrees with the measured value for b = 4.4 cm, which is about what one expects for the actual rectangular chamber of half-height 3 cm and half-width 6.6 cm.

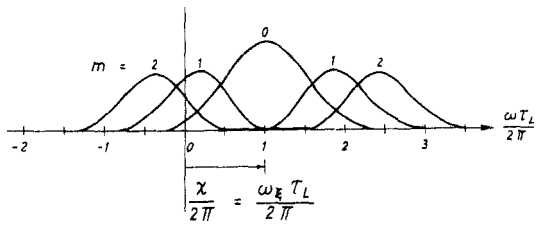


Fig.9 Frequency spectrum for modes 0, 1 and 2 drawn for $\chi = 2\pi$

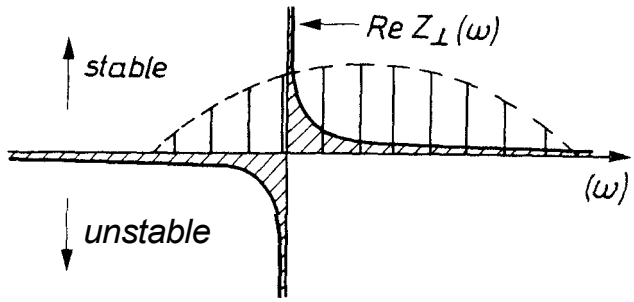
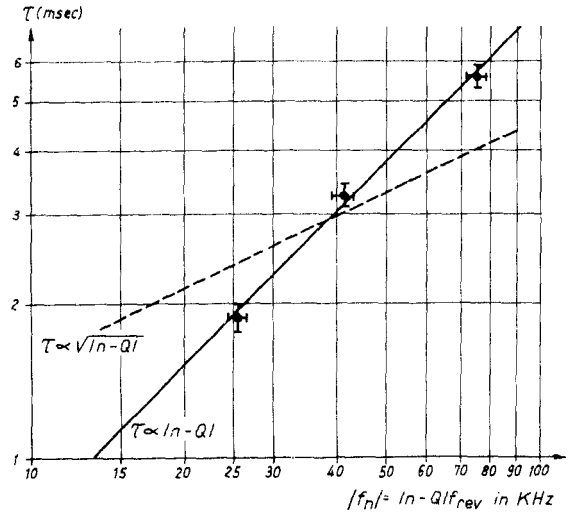


Fig. 10 : Spectrum lines for mode m = 0 and Q just below an integer.

Fig.11 e-folding time vs Q on 70 MeV flat top normalized to I = 100 mA



References

1. F.J. Sacherer, Transverse bunched beam instabilities - Theory, This Conference.

2. D. Mohl, H. Schönauer, Landau damping by non-linear space-charge forces and octupoles, This Conference.

3. C.D. Johnson, L. Thorndahl, The CPS gas ionisation beam scanner, Proceedings of U.S. Particle Accelerator Conference (Washington, 1969).

4. C. Pellegrini, On a new instability in electron positron storage rings (the head-tail effect), LNF 69/45 (Frascati, Italy).

5. M. Sands, The head-tail effect, an instability mechanism in storage rings, SLAC-TN-69-8.

6. D. Möhl, Equipment responsible for the transverse beam instability in the PS, CERN-MPS/DL/Note 74-6.

7. E.D. Courant, A.M. Sessler, Rev. Sci. Instr. 37, 1579 (1966).

8. K.H. Reich, H. Schönauer, Transverse stability of a coasting PSB beam, CERN-SI/Int.BR/72-2.

Gus Voss (DESY): I see that there are no questions anymore about the existence of higher modes of the head-tail instability.

Lee Teng (NAL): In what way does the bunched beam resistive wall effect differ from that on an extended beam? Assume the beam is continuous and just take a section and add the appropriate boundary conditions. Wouldn't that be exactly the same thing?

Frank Sacherer (CERN): If you put all the boundary conditions on it's probably the same. It's the same electromagnetic fields, and the particles move in the same ways. You can get quite confused if you use coasting beam theory in the case of bunched beams. The growth rates are bigger by the bunching factor, for example. But the electrodynamics and all that are roughly the same, although that's certainly not the way it was arrived at.

Alessandro Ruggiero (NAL): Now let me comment on that. The difference depends on the synchrotron motion. If you take a coasting beam, chopped, but with no synchrotron motion, there is one kind of instability. If you take a bunched beam with synchrotron motion, there is another kind of instability.

TRANSVERSE BUNCHED BEAM INSTABILITIES - THEORY

F.J. Sacherer, CERN, Geneva, Switzerland

Introduction and Summary

A glance at Figs. 1 and 2 shows some of the contortions that a single bunch can undergo as it progressively destroys itself. The instability is driven by the surrounding environment, which extracts energy from the longitudinal directed motion of the bunch and converts it into growing transverse oscillations. As pointed out by Pellegrini[1] and Sands[2], simple rigid-bunch motion is possible only in the exceptional case of zero machine chromaticity; otherwise there is always a phase-shift between head and tail of a bunch. While the original and still widely used theory of Courant and Sessler[3] is restricted to rigid-bunch motion driven by long-range wake forces, the more recent head-tail theory of Pellegrini and Sands is restricted to the opposite limit of short-range wakes that act only from head to tail of a bunch, and not from bunch to bunch or over many revolutions. In addition, it was developed mainly for the unrealistic hollow-bunch distribution (see Fig. 3).

This paper presents a unified approach for a parabolic bunch that includes both single-turn and multi-turn effects. The main ingredients are

i) oscillation modes
ii) transverse coupling impedance $Z_\perp(\omega)$
iii) stability criterion.

The derivations are given in other papers[4,5] and only the results are presented here. A companion paper[6] presents the recent experimental observations in the CERN PS and Booster.

Classification of modes

If all particles have the same betatron frequency $\omega_\beta = Q\omega_0$ and synchrotron frequency ω_s, and we ignore the transit time of the bunch past a fixed observer, the first few head-tail modes appear as in Fig. 1a. The difference signal from a position monitor has the form

$$\text{A-signal} \propto p_m(t) e^{j2\pi kQ} , \qquad (1)$$

for the k^{th} revolution.

Usually both Q and the revolution frequency ω_0 depend on momentum, so ω_β varies as a particle moves around a synchrotron orbit, The important quantity is the betatron phase of a particle at each position along the bunch as compared with the phase of the synchronous particle. The total phase-shift χ between head and tail has contributions from the Q-variation, the ω_0 variation, plus the finite transit time. In fact, the last two contributions cancel, and we are left with

$$\chi = \frac{\xi}{\eta} Q\omega_0 \tau_L \quad \text{(radians)} , \qquad (2)$$

where $\xi = (dQ/Q)/(dp/p)$ is the chromaticity, $\eta = \gamma_T^{-2} - \gamma^{-2}$, and τ_L is the bunch length in seconds. The difference signal has the form (Figs. 1b and 1c)

$$\Delta\text{-signal} \propto p_m(t) e^{j\omega_\xi t + j2\pi kQ} , \qquad (3)$$

where

$$\omega_\xi = \frac{\chi}{\tau_L} = \frac{\xi}{\eta} Q\omega_0 . \qquad (4)$$

Note that for the example shown in Fig. 1c, mode 2 has appreciable contre-of-mass motion and would leave a long-range resistive-wall wake whereas mode 0 would not.

For a parabolic bunch, the modes pm(t) are approximately sines and cosines as shown in Fig, 1, while for a hollow bunch they appear as in Fig. 3 with

$$p_m(t) = \frac{T_m(t/\tau_L)}{\pi\sqrt{1 - (t/\tau_L)^2}} , \qquad (5)$$

where T_m is a Chebychev polynomial.

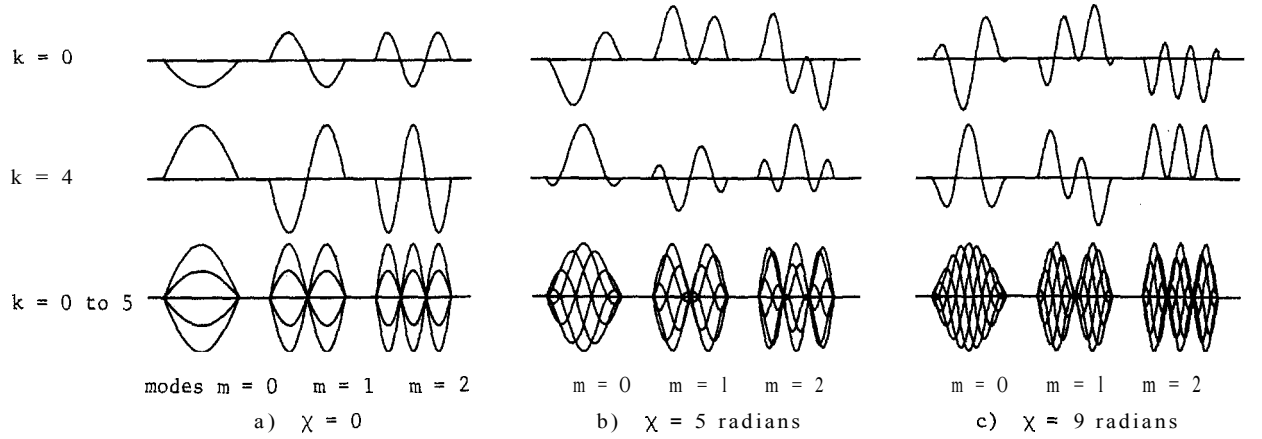


Fig. 1 Contortions of a single bunch on separate revolutions, and with six revolutions superimposed. Vertical axis is difference signal from position monitor, horizontal axis is time, and Q = *4.833*.

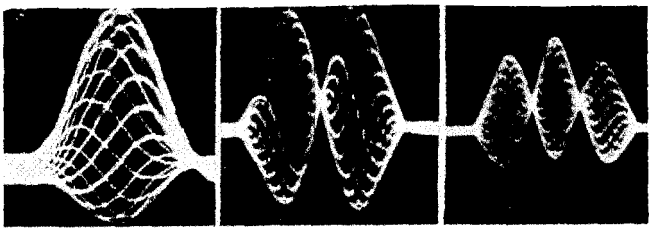


Fig. 2 Head-tail modes observed in the CERN Booster[6].

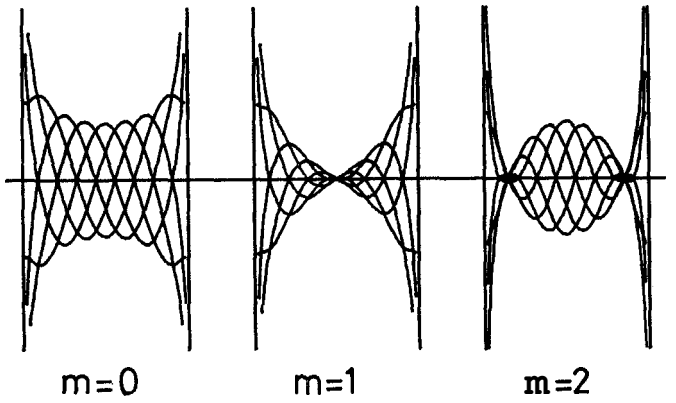


Fig. 3 Hollow-bunch modes for the same parameters as in Fig. 1c

Coupling impedance

Longitudinal

$$Z_{\parallel} \simeq \frac{2\pi R}{2\pi b}\mathcal{R}_{surf} \qquad (6)$$

where $2\pi R$ = machine circumference, b = vacuum chamber radius, and $\mathcal{R}_{surf}$ is the surface impedance in ohms per square. In this case the beam sees a uniform longitudinal electric field set up by the return currents flowing in the vacuum chamber walls.

Transverse

The wall currents flow in opposite directions on either side of the vacuum chamber (or whatever is enclosing the beam) and set up a transverse magnetic field and a longitudinal electric field that varies in strength across the aperture (Fig. 4). Energy extracted from the directed motion of the beam by the longitudinal electric field drives the wall currents, which set up the dipole magnetic field, which deflects the beam. Expressed in equations, the power lost per unit length by the beam is

$$\int E\cdot J\,dx\,dy = -\frac{E_0}{b}\,\Delta \int y\,\frac{\partial J_0}{\partial y}\,dx\,dy \qquad (7)$$
$$= \frac{E_0\Delta}{b}\,I$$

while the power flow into the walls is $-2l_W E_0$, and therefore

$$I_w = -\frac{1}{2}\frac{\Delta}{b}\,I\ . \qquad (8)$$

This current is related to the electric field at the wall by the wall impedance,

$$E_0 = 4\,\frac{I_w Z_{\parallel}}{2\pi R}\ , \qquad (9)$$

where in place of the actual current distribution in the wall, we assume that I_W is confined within a strip of width $\frac{1}{4}$ the pipe circumference. This gives the correct result for a circular pipe, which has a cos θ current distribution. The deflecting magnetic field is (from Fig. 4)

$$B_x = -j\,\frac{2\Delta}{\omega b^2}\,\frac{Z_{\parallel} I}{2\pi R}\,e^{j\omega t}\ , \qquad (10)$$

and when this is inserted into the definition

$$\frac{\int \left[E + v\times B\right]_{\parallel} ds}{\qquad} \qquad \text{(ohms/metre)}$$

one finds

$$Z_{\perp} \simeq \frac{2c}{b^2}\,\frac{Z_{\parallel}}{\omega}\ , \qquad (12)$$

where c is the speed of light (3×10^8 m/sec) and $\beta = v/c$. The definition (11) was introduced by Hereward, and is used extensively by the ISR group.

The convenient relation (12) between $Z_{\perp}(\omega)$ and $Z_{\parallel}(\omega)$ is strictly valid for a round pipe with surface impedance $\mathcal{R}_{surf}$ and for frequencies sufficiently below cut-off that the fields have the simple form shown in Fig. 4. On the other hand, for perfectly conducting walls ($\mathcal{R}_{surf} = 0$)

$$Z_{\perp} = -j\,\frac{RZ_0}{\beta^2\gamma^2}\left(\frac{1}{a^2} - \frac{1}{b^2}\right)\ , \qquad (13)$$

where Z_0 = 377 ohms, a = beam radius, and b = pipe radius. The additional contribution due to wall resistivity can be found from (6) and (12) with

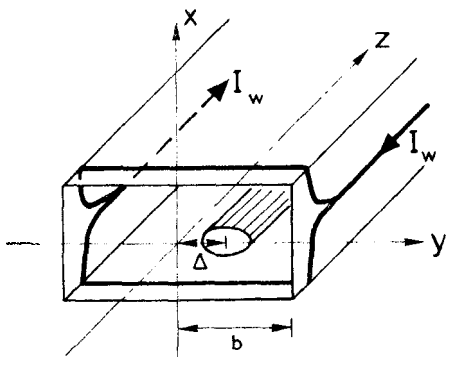
$$\mathcal{R}_{surf} = (1+j)\frac{\rho}{\delta} \qquad \text{(thick-wall)}\ , \qquad (14)$$

where ρ is the resistivity (ohm-m) and δ is the skin depth, which is assumed to be smaller than the wall thickness. At low frequencies where δ > wall thickness ℓ,

$$\mathcal{R}_{surf} = \frac{\rho}{\ell} \qquad \text{(thin-wall)} \qquad (15)$$

provided the impedance of the outside material (air, magnets, etc.) is sufficiently high that all currents

Fig. 4



Currents:

I_W = wall current

$J_0(x,y-\Delta e^{j\omega t},z)$ = beam current density

$$\simeq J_0(x,y,z) - \frac{\partial J_0}{\partial y}\,\Delta e^{j\omega t}$$

with I = beam current = $\int J_0(x,y,z)\,dx\,dy$.

Fields:

$$E = E_0\,\frac{y}{b}\,e^{j\omega t} \qquad \text{(median plane)}$$

$$B_x = \frac{j}{\omega}\,\frac{E_0}{b}\,e^{j\omega t} \qquad (\text{from } \nabla\times E + \dot{B} = 0)\ .$$

flow through the walls. At low frequencies, $Z_\parallel$ is just the d.c. resistance of the vacuum chamber, typically about one ohm for stainless steel, and increases with frequency as $\sqrt{\omega}$ owing to the skin effect. Interruptions in the conducting vacuum chamber for ceramic or ferrite sections leads to much larger impedances. More elaborate and accurate calculations of $Z_\parallel$ and $Z_\perp$ or equivalently U and V can be found elsewhere[7-10], but the above approach is often sufficient.

Growth-rates in the absence of frequency spreads

The growth-rate is

$$\frac{1}{\tau} = -\mathrm{Im}\,\Delta\omega \qquad (16)$$

and the motion is unstable if Im $\Delta\omega$ is negative. For purpose of comparison, the coasting-beam growth-rate is found from

$$\Delta\omega = \frac{j}{2\omega_\beta}\frac{e\beta}{\gamma m_0}\frac{Z_\perp(\omega)I}{2\pi R} \qquad \text{(coasting beam)} \qquad (17)$$

$$= U + (1-j)V$$

with $\omega = (n+Q)\omega_0 + \Delta\omega$ for the mode with $|n|$ wavelengths around the machine circumference $2\pi R$, beam current I, particle rest mass m_0, $\beta = v/c$, and $\omega_\beta = Q\omega_0$. MKS units are used throughout with an assumed time dependence exp (jωt). To compare with papers using exp (-iωt), replace j with -i in all formula.

For a bunched beam, the growth-rate involves a sum over the bunch spectrum. We need

$$h_m(\omega) = |\tilde{p}_m(\omega)|^2$$

where $\tilde{p}_m(\omega)$ is the Fourier transform of $p_m(t)$ (see Fig. 5). The spectrum is discrete with lines at $\omega_p = (p+Q)\omega_0$, $-\infty < p < \infty$ for a single bunch or several bunches oscillating independently. For coupled motion of M bunches, only every M^{th} line occurs with $p = n + kM$, $-\infty < k < \infty$, where n is the coupled-bunch mode number. It specifies the phase difference $2\pi|n|/M$ between adjacent bunches.

The growth-rate for mode m is found from

$$\Delta\omega_m = \frac{1}{1+m}\frac{j}{2\omega_\beta}\frac{e\beta}{\gamma m_0}\frac{I_0}{L}\frac{\sum_p Z_\perp(\omega_p)h_m(\omega_p-\omega_\xi)}{\sum_p h_m(\omega_p-\omega_\xi)}, \qquad (18)$$

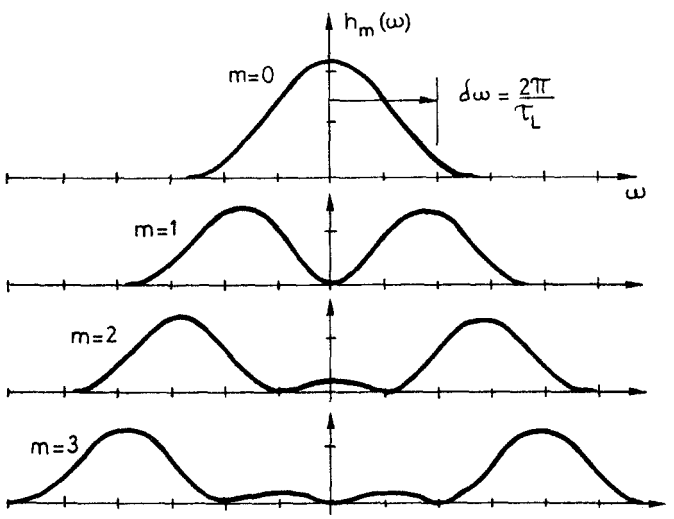


Fig. 5 Frequency spectrum for modes 0 to 3 with $\chi = 0$.

where I_0 is the current in one bunch of length L metres. The factor $(1+m)^{-1}$ arises because the motion for the higher-order modes is constrained more and more to the few particles with large synchrotron amplitudes; this factor is absent for the hollow-bunch. Equation (18) is the general result. In the limit of short-range fields or smoothly varying $Z_\perp(\omega)$, it reduces to the classic head-tail effect, while in the opposite limit of long-range fields or rapidly varying $Z_\perp(\omega)$, it gives the multiturn contribution.

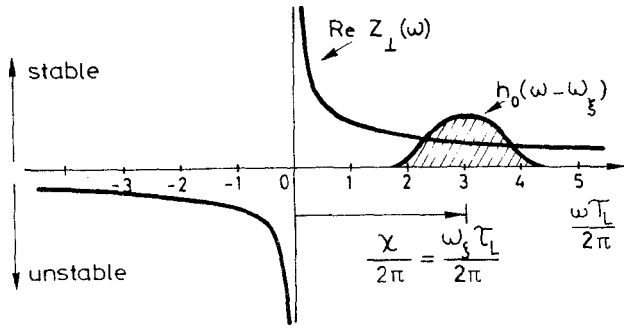


Fig. 6

As an example, consider Fig. 6, which is drawn for a positive phase shift χ so one is above transition with $\xi > 0$ or below transition with $\xi < 0$. The phase shift $\chi = 3 \times 2\pi$ corresponds to three oscillations along the bunch. Only the resistive or real part of $Z_\perp(\omega)$ causes instabilities, and this is drawn for a resistive-wall type impedance. Regardless of the type of impedance, the resistive part of $Z_\perp$ is positive for positive frequencies and negative for negative frequencies [from Eq. (12)]. From the figure, one sees that mode m = 0 is stable for χ positive and unstable for χ negative, and that this is true for any type of impedance.

If $Z_\perp(\omega)$ is sufficiently smooth that the sum in (18) can be replaced by an integration (discrete spectrum replaced by continuous spectrum), the growth-rate is independent of betatron frequency. In fact, the impedance shown is sufficiently smooth that it can be removed from the sum, and we find

$$\Delta\omega_0 = \frac{j}{2\omega_\beta}\frac{e\beta}{\gamma m_0}\frac{Z_\perp(\omega_\xi)I}{2\pi RB} \qquad (19)$$

which is just the coasting beam result (17) for the frequency ω_ξ with a bunching factor included ($B = ML/2\pi R$; $I = MI_0$).

It is convenient to rewrite (18) as

$$\Delta\omega_m = \frac{1}{1+m}\frac{e\beta I}{2\omega_\beta}\frac{}{\gamma m_0\, 2\pi R}\times \left[\frac{\frac{1}{B}\int_{-\infty}^{\infty} Z_\perp(\omega)h_m(\omega-\omega_\xi)\,d\omega}{\int_{-\infty}^{\infty} h_m(\omega)\,d\omega} + Z_\perp\left(\omega_n\right)F_m'\left(\chi-\omega_n\tau_L\right)\right] \qquad (20)$$

near field, independent of Q, $\to 0$ or $\xi \to 0$

multiturn fields, depend on Q, multiply by 1/M for independent bunch motion

with the slowly varying part of $Z_\perp(\omega)$ separated from the rapidly varying part, where only one or a few lines $\omega_n = (n+Q)\omega_0$ contribute. The form factor $F_m'(\chi)$ is plotted in Fig. 7.

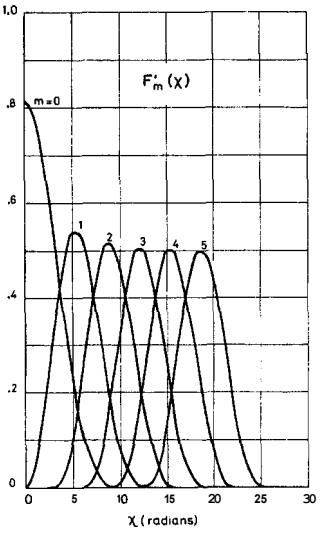


Fig. 7

If only a single line is important as for the narrow spectrum shown in Fig. 8, Eq. (20) again leads to the coasting beam result (17), but reduced by the factors F'_m and $(1 + m)^{-1}$.

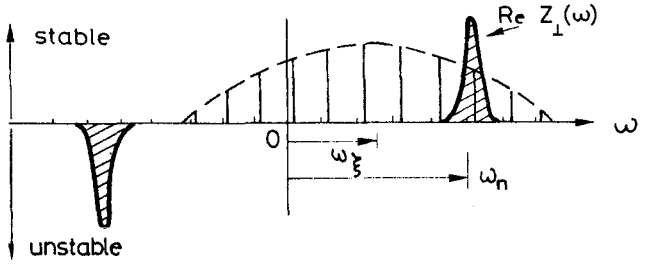


Fig. 8

A less obvious case is the resistive-wall impedance shown in Fig. 9, but here also only a single line contributes strongly to the long-range wake, namely the line $\omega_n = (n + Q)\omega_0$ nearest the origin. One easily recovers the usual rule that the mode number $|n|$ just above Q grows fastest. In the limit $\xi \to 0$ and for the thick-wall impedance (14), the multiturn part of (20) reduces to the familiar Courant and Sessler formula[3] (as corrected by Morton[11,12]). However, ξ is rarely zero, and often the frequency $|n-Q|\omega_0$ is sufficiently small that the thin-wall impedance (15) applies with consequently larger growth-rates. Although Fig. 9 is drawn for mode 0, for large enough χ the spectrum of

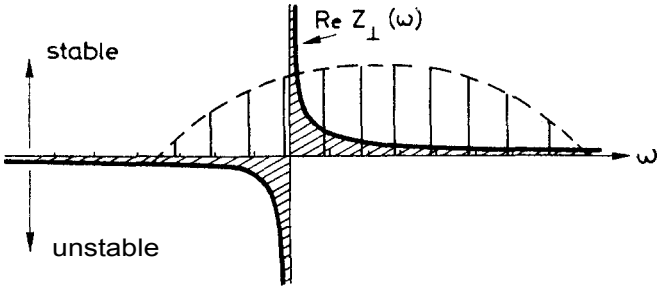
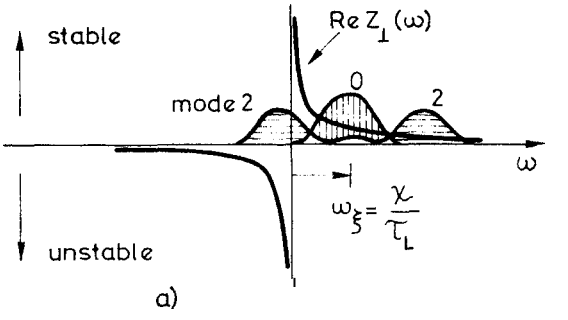


Fig. 9 The frequencies $\omega_n = (n + Q)\omega_0$ drawn for mode m = 0 and Q just below an integer

mode m overlaps the high impedance region near the origin: for example for $\chi = 9$ radians, mode m = 2 grows fastest (see Figs. 1c and 7).

Now consider only the near-field part of (20). As an illustration of the graphical approach, the growth-rates of modes 0 and 2 for a resistive-wall impedance are sketched in Fig. 10b. As pointed out above, mode 0 is stable for positive χ, but one sees that mode 2 is unstable for small positive χ, and the reason is evident



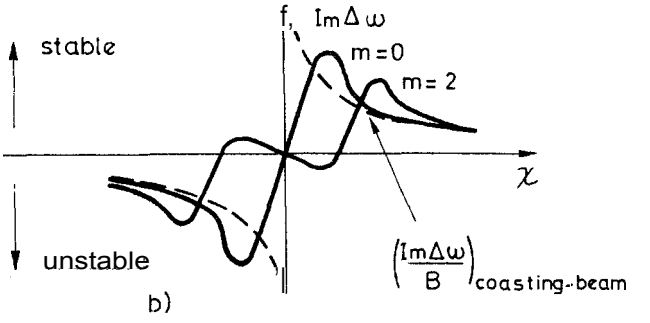


Fig. 10

from Fig. 10a. For χ sufficiently large, both modes have the same stability character as the coasting beam. The exact result for the thick-wall impedance *(14)* and sinusoidal modes is shown in Fig. 11, and the growth-rate is found from

$$\Delta\omega_m = \frac{j}{1+m}\,\frac{e\beta I}{2\omega_\beta}\,\frac{}{\gamma m_0}\,\frac{}{2\pi R}\times \tag{21}$$

$$\times\left[\sqrt{\frac{2\pi}{MB}}\,Z_\perp(\omega_0)F_m(\chi) + Z_\perp(\omega_n)F'_m(\chi-\omega_n\tau_L)\right].$$

At this point some history is in order. The formula of Pellegrini' and Sands' is just the near-field part of (20), but expressed in the time domain and written explicitly for the hollow-bunch modes (5) and the resistive-wall impedance *(14)*. They simplified the integration by considering only small χ, and found that the modes with $m > \hat{m}$ are unstable when mode $\hat{m}$ is stable, and vice versa. Later Zotter[13] carried out the integration numerically and found results similar to Fig. 11. However, the resistive-wall impedance is not sufficient to explain the fast growth-rates or absence of higher-order modes in electron storage rings. This is also true for the PS: Gareyte[6] has made detailed measurements of growth-rate as a function of phase-shift χ and has deduced from (19) that above 100 MHz the impedance rises slowly with frequency to a broad maximum around 1 GHz. Such an impedance can result from the several metres of ceramic and ferrite elements required for extraction magnets[8]. A slowly rising impedance also explains the absence of higher-order modes: from

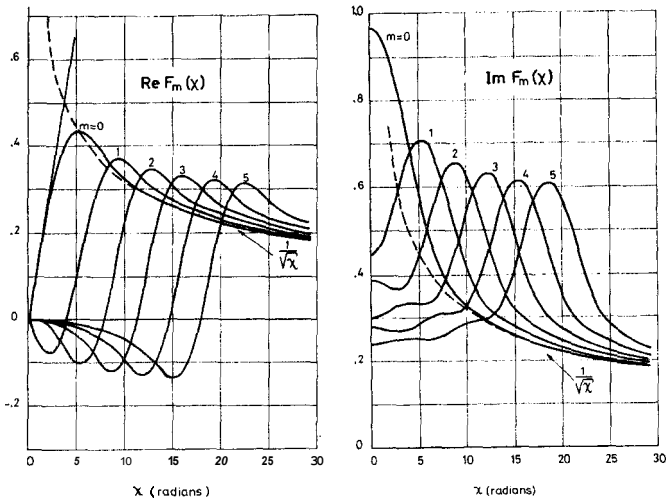


Fig. 11

Fig. 12 one sees that in this case the broad positive part of the spectrum contributes more than the narrow region of negative frequencies near the origin. This was also pointed out by Ruggiero[14]. One should have no trouble imagining other types of impedance and estimating the corresponding growth-rates.

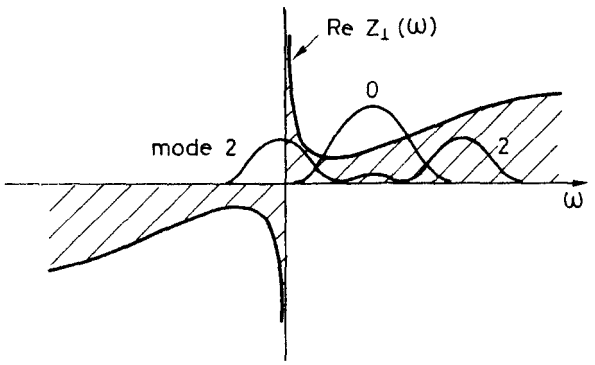


Fig. 12

Stability criterion

A sufficient spread in bunch frequencies prevents the coupled-bunch type instability. Such a spread may arise from a difference AN in bunch populations, via the coherent Laslett frequency shift $\Delta\omega_c = \Delta Q_c \omega_0$. For decoupled motion, the r.m.s. spread in bunch frequencies should exceed the growth-ratel*

$$|\Delta\omega_c| \left(\frac{\Delta N}{N}\right)_{rms} > |\tau^{-1}| \ , \qquad (22)$$

and this may occur for large space-charge forces.

Octupoles cure either single-bunch or coupled-bunch instability if they produce enough frequency spread within a bunch to prevent its coherent motion, that is provided the spread in betatron frequencies exceeds the frequency shift $\Delta\omega_m$,

$$\text{/full-spread at half-height of } Q\omega_0| > |\Delta\omega m| \ . \qquad (23)$$

Sextupoles or changes in machine chromaticity change the phase-shift χ, but do not contribute to Landau damping. For the long-range resistive-wall instability observed in the PS Booster, increasing χ shifts the instability to higher-order modes which have slower growth-rates. The opposite occurs for the PS or electron storage rings, namely the growth-rate increases as χ is made more negative.

Acknowledgements

I have profited very much from discussions with J. Gareyte, H.G. Hereward, K. Hübner, D. Möhl, and B. Zotter.

References

1. C. Pellegrini, Nuovo Cimento 64A, 477 (1969).
2. M. Sands, SLAC-TN-69/8 and 69/10.
3. E.D. Courant and A.M. Sessler, Rev. Sci. Instr. 37, 1579 (1966).
4. F.J. Sacherer, Methods for computing bunched-beam instabilities, CERN/SI BR/72-5.
5. F.J. Sacherer, Dispersion relations for head-tail modes, CERN/BR/74-4.
6. J. Gareyte and F. Sacherer, Head-tail type instabilities in the PS and Booster, these proceedings.
7. B. Zotter, CERN 69-15, CERN 69-16, CERN/ISR-TH/70-52, CERN/ISR-TH/71-13, and Particle Accelerators 1, 311 (1970).
8. R.J. Briggs and V.K. Neil, Plasma Physics 8, 255 (1966).
9. D. Möhl, Equipment responsible for transverse beam instability in the PS, CERN MPS/DL/Note 74-6.
10. L.J. Laslett, V.K. Neil and A.M. Sessler, Rev. Sci. Instr. 36, 436 (1965).
11. P.L. Morton, An investigation of space-charge effects for the booster injector to the CPS, CERN SI/Int. DL/68-3.
12. F.J. Sacherer, Spring Study on Accelerator Theory, 1972, Report to the 300 GeV Advisory Machine Committee, CERN, p. 159.
13. B. Zotter, The head-tail effect in the ISR, CERN-ISR-TH/69-60.
14. A.G. Ruggiero, The head-tail effect enhanced by a fast oscillating or fast decaying wake field, NAL report FN-254 (1973).

SOME OBSERVATIONS ON BUNCH LENGTHENING AT SPEAR*

M. A. Allen, G. E. Fischer, M. Matera, A. P. Sabersky, and P. B. Wilson

Stanford Linear Accelerator Center
Stanford University, Stanford, California 94305

I. Introduction

The phenomenon of current dependent bunch lengthening discovered at ACO and ADONE about seven years ago can be used as an engineering diagnostic tool to examine how the longitudinal electromagnetic field of a beam couples to its surroundings.[1] The importance of isolating such coupling factors is that they may give rise to damaging instabilities. Another practical reason for studying the effect is that if bunch lengths grow anomalously beyond those calculated on the basis of classical theory,[2] the effective luminosity of storage rings, particularly those employing low beta insertions, may be reduced.[3] As in most other electron storage rings, the effect at SPEAR is observed to be large and may play a role in proton rings if the beam is highly bunched.

Two sets of theories explaining the effect exist. In one set it is suggested that the effect results from modification of the effective azimuthal potential well by beam loading. These theories can also lead to bunch shortening but not to an increase in the energy spread of the beam. A very general treatment, together with many examples of coupling impedance is put forth, for example, by Pellegrini and Sessler.[4] The theoretical calculation of specific coupling impedances has received a great deal of attention in the last several years.[5] On the other hand, an alternative explanation of bunch lengthening was advanced by Lebedev[6] in which the effect arises due to instabilities of internal coherent synchrotron oscillations of the bunch. This concept has recently been extended to include the turbulent motion of the collective higher modes.[7] The latter theories predict that the anomalous bunch lengthening is directly related to an increased energy spread of the beam. We believe that some ingredients from both sets of theories contribute.

In the following section we compare the functional dependence of the SPEAR bunch length with those of the various theories. In Section III the potential distortion model is used to extract a coupling impedance. The existence of coherent bunch shape oscillations is demonstrated in Section IV. Frequency shifts with current, and line widths are discussed. The excitation of theoretically predicted vacuum chamber modes is shown in the next section after which we estimate beam power absorption to those elements of the structure believed to cause bunch lengthening. In the final section, the prediction that the ferrite kicker magnet cores are presently the dominant elements is confirmed.

II. Bunch-Length Measurements and Data Reduction

The rms length σ_z of a single circulating bunch was measured as a function of wide-ranging values of average current I, total rf cavity voltage V_0, and machine energy E_0, by observing on a fast sampling oscilloscope the output from a specially mounted light-sensitive diode exposed to the optical part of the synchrotron-radiation spectrum. Details of this technique are reported elsewhere.[8] A typical output scan is shown in Fig. 1. It is noted that at high currents the distribution tends to deviate from a purely Gaussian shape, and at times displays an asymmetric tail so that the values of σ_z calculated from the measured full width at half-maximum tend to lose their traditional meaning. (A discussion of bunch shape was recently presented by Haissinski. 9) The data were corrected for instrumental rise time. The correction ranged from 30 percent at very low currents and very high voltages to an average of a few percent over most of the points taken.

*Work supported by the U. S. Atomic Energy Commission.

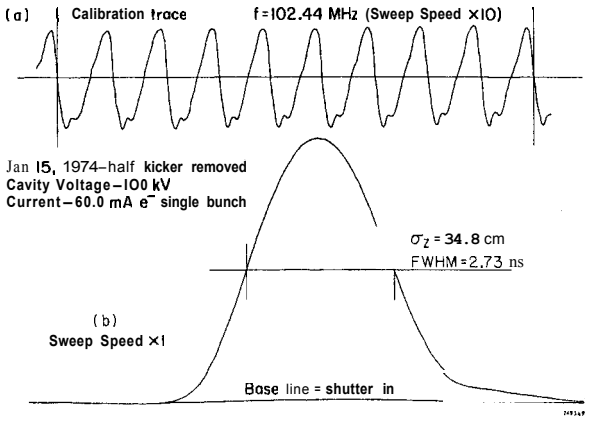


FIG. 1--A typical bunch length recording and calibration trace.

The so-called "natural bunch length" σ_{z0}, which results from the balance of quantum fluctuation and radiation-damping terms is calculated following the analysis of Sands[2] and is proportional to $E_0^{3/2}\alpha^{1/2}(V_0\cos\phi)^{-1/2}$ and is of course independent of I. (Symbols used throughout this paper are identified in Table I.) The momentum compaction factor α and V_0 are singled out here because, in contrast to other machine parameters, they are not so well known and must be measured. Fortunately, the quantum lifetime near zero current, and the synchrotron frequency have a functional dependence on both α and V_0 and by a series of measurements of these quantities the cavity voltage readout was calibrated and α determined. The value of α found in this way differed from that calculated by the magnet-lattice program by only a few percent. Measurements taken over a span of one year with various different kinds of equipment reproduced to better than 10 percent.

Values of $R=(\sigma_z/\sigma_{z0})$ are plotted in Figs. 2, 3, and 4 as functions of I, E_0, and V_0, respectively. Some of the points shown in Fig. 2 were interpolated by less than 10% in

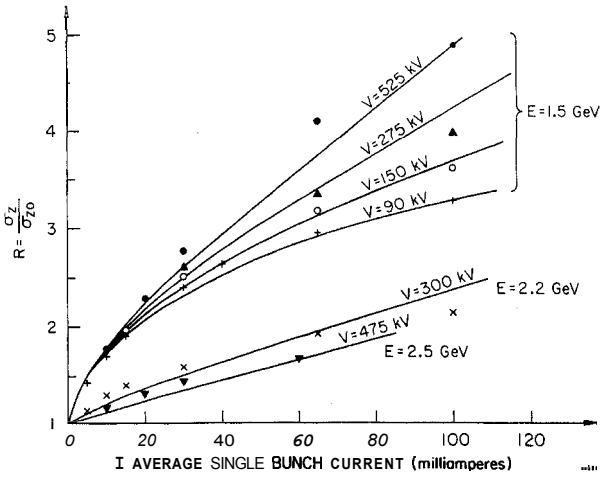


FIG. 2--The ratio $R=\sigma_z/\sigma_{z0}$ at various rf voltages and energies vs average single bunch current.

either current or voltage to facilitate intercomparison. For large R, the data demonstrate an $I^{1/3}$ dependence, which is also found at ACO[10] and ADONE,[11] and which is common to

both sets of theories. For large I, the $E^{-5/3}$ dependence shown in Fig. 3 is also consistent with data from ACO and

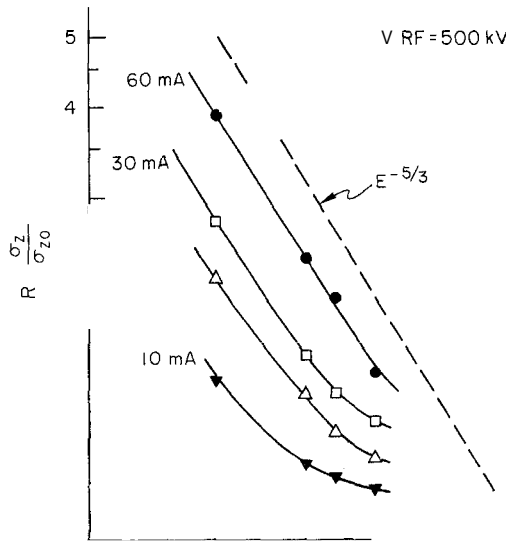


FIG. 3--R vs E_0 for various currents.

and ADONE. The potential distortion model[4] predicts $E^{-3/2}$, the coherent synchrotron oscillation model $E^{-8/3}$ and the simplified turbulent higher-mode model[7] $E^{-3/2}$. The dependence of R on cavity voltage is not so easily deciphered. Figure 4 shows that it is independent of voltage at very low

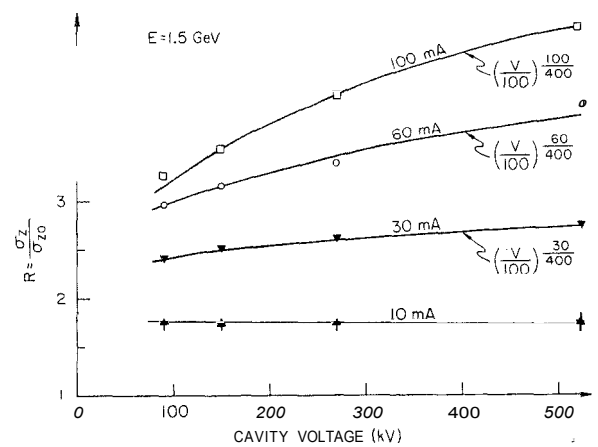


FIG. 4--R vs rf voltage at 1.5 GeV and various currents. The fit to the data indicates a power-law dependence on voltage, the exponent of which is proportional to current.

currents, but that it rises to as much as $V^{1/4}$ for higher currents. The ACO and ADONE results are fi approximately by $V^{1/6}$ while the existing theories predict V^{1} 6, $V^{1/2}$, $V^{1/6}$, respectively. From these considerations only, therefore, it is hard to distinguish between the various models.

To fit the data over a wide range of the ratio R, which must tend to 1 as the current approaches zero, the function

$$R = \frac{2}{\sqrt{3}} \cos(1/3 \arccos KI) \qquad (1)$$

derived in Ref. 6 as formula (24) was chosen.

For large R, $R \approx (KI)^{1/3}$. A reasonable phenomenological fit to all SPEAR data is

$$KI = 0.92\, I_{mA} \left(\frac{1.5}{E_{GeV}}\right)^5 \left(\frac{V_{kV}}{100}\right)^{\frac{3I_{mA}}{427}} \qquad (2)$$

in which only the constant and the power of V were adjusted.

The solid lines drawn in Fig. 2 obtain from the formula for R shown above. Relevant machine parameters are listed in Table I.

TABLE I. SPEAR I Parameters

r	= average ring radius = 37.3 meters
$\omega_0/2\pi$	= revolution frequency = 1.28 MHz
ρ	= magnetic radius = 12.7 meters
α	= momentum compaction factor = 0.04124 (configuration INJEQ)
h	= harmonic number = 40, rf frequency = 51.22 MHz
j_ϵ	= energy partition constant = 2
τ_{rad}	= synchrotron damping time at zero current = 33 msec at 1.5 GeV
U	= radiation loss per turn in kV
Ω_0	= synchrotron frequency in kHz
ϕ	= synchronous phase angle in degrees
σ_{ϵ_0}	= rms energy spread at zero current in GeV
σ_0	= rms bunch length at zero current in cm
R	= the ratio σ_z/σ_{z_0}
V_{rf}	= total cavity voltage
$\mathscr{R}$	= resistance

Gev	kV		kV	degrees	kHz	cm
1.5	35	0.539	100	159	5.05	13.6
			300	173	9.03	7.6
			500	176	11.68	5.9
2.0	111	0.958	300	157	7.56	12.1
			500	167	10.00	9.2
2.5	270	1.49	500	147	8.2	13.8

III. Application of Bunch-Length Data

Two calculations have recently been performed using the previously published SPEAR data.[12] Sessler[7] has found a surprisingly good fit using the turbulent mode model and finds a value of coupling impedance $Z_n = i46n$, where the integer n indicates the coupling frequency in multiples of the revolution frequency. However, the derived values of energy spread are about a factor of 3 larger than those actually found at SPEAR from measurements of the quantum lifetime of large current beams. Further attempts at measuring the energy spread are under way. Sacherer,[13] on the other hand, applied the potential distortion model[4] (no increased energy spread is contained in this theory) and found either $Z_n = i30n$, or $i360n^{1/2}$ to fit the data. He pointed out that this is much too large to be caused by the conductivity of the vacuum-chamber walls. More will be said on this point further on. It may be instructive to follow his analysis in a very simplified form.

Formula (2.8) of Ref. 4 relates the current dependent synchrotron frequency shift with bunch length as follows:

$$\left(\Omega^2 - \Omega_0^2\right)/\Omega_0^2 = 1 - \left(\frac{\sigma_{z_0}}{\sigma_z}\right)^2 = 1 - \left(\frac{1}{R}\right)^2 \equiv x \qquad (3)$$

In terms of an effective impedance Z_{eff}, x is also the ratio of the beam-induced voltage to the impressed voltage, i.e., $x = I Z_{eff}/hV_0 \cos\phi$.

In the case when Z_{eff} is dominated by the high frequency components of the beam one can write

$$Z_{eff} = i \sum_n n Z_n e^{-1/2 n^2 \sigma_z^2 \omega_0^2}$$

in which ω_0 is the revolution frequency for a single bunch machine and σ_z is in time units. If, for example, one assumes that Z_n is of a nonresonant form and can be fitted by a power law $Z_n = -i\mathcal{R}|n|^s$, then the sum over n may be simply carried out and, for s=1, yields

$$Z_{eff} = \frac{2.5\mathcal{R}}{(\sigma_z \omega_0)^3} \quad . \qquad (4)$$

Substituting this in the above, we have

$$x = \frac{2.5\mathcal{R}}{hV_0 \cos\phi\ \omega_0^3}\left(\frac{I}{\sigma_z^3}\right) \quad \text{or} \quad \mathcal{R}I = \frac{x\sigma_z^3 V \cos\phi\ h\omega_0^3}{2.5}. \qquad (5)$$

For Eq. (3) one notes for large $R = \sigma_z/\sigma_{z_0}$, x approaches 1 and from Eq. (5) the bunch length should then vary as $I^{1/3}$, consistent with observation. $\mathcal{R}I$ is plotted in Fig. 5, which

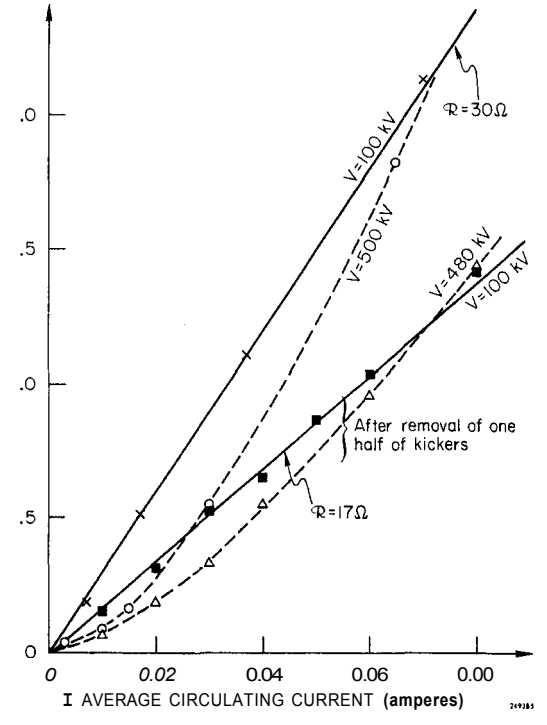


FIG. 5--The quantity $\mathcal{R}I = \dfrac{x\sigma_z^3 V \cos\phi\ h\omega_0^3}{2.5}$ vs average current I.

demonstrates that a single value of $\mathcal{R}=30\Omega$ fits the data quite well at low rf voltage so that simple assumption made about the form of Z_n is borne out. Data in the very short bunch regime, i.e., high voltage, low current regime, however, does not fit this simple model,

Several comments may be made at this point. First: Since σ_z is of the order of nanoseconds, very high harmonics of the revolution frequency are involved in the above sum and Z_{eff} is quite large, in fact, around 10^8 ohms, and one would expect the beam to lose a good deal of power somewhere around the ring. Second Since x approaches 1, one would expect large shifts of the synchrotron frequency of particles in the bunch with current. These shifts will not be observed for the coherent center-of-mass motion or dipole frequency because the induced defocusing force of the beam on itself can be thought to be traveling around the ring with the bunch, but might be seen in the frequencies of high-order shape oscillations. [6, 14]

IV. Observation of Coherent Bunch-Shape Oscillations

In summer of 1973, a high-gain low-frequency spectrum analyzer* was installed to permit more accurate measurement of betatron frequencies. This instrument can also be used to measure the frequencies of synchrotron oscillations, either those occurring naturally or those excited by frequency-modulating one main rf cavity driver. Again, the details of technique are reported elsewhere.[8] Under certain operating conditions, especially for low cavity voltage and high beam current, a rich spectrum of naturally occurring lines was observed. Typical sweep traces are shown in Fig. 6. The

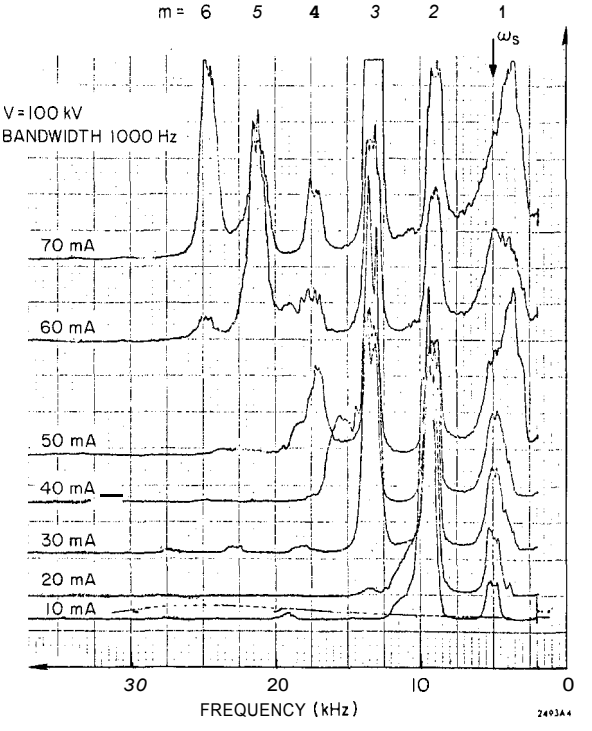


FIG. 6--Higher mode frequency spectrum tracings taken at 1.5 GeV, V_{rf}= 100 kV, and various currents.

frequencies of the lines seen are proportional to $(V\cos\phi)^{1/2}$ and arise from high-mode synchrotron oscillations. The current dependence of the frequencies is shown in Fig. 7. One may note that the shifts, down from integral multiples of the dipole synchrotron frequency, vanish at zero current. Also, at higher currents the frequency shifts become constant. We do not believe that the coherent dipole frequency shifts significantly with current at current levels below 60 mA.

During these measurements the cavity gap voltage was stabilized to compensate for beam loading. [15]

*Hewlett Packard Model 3950A.

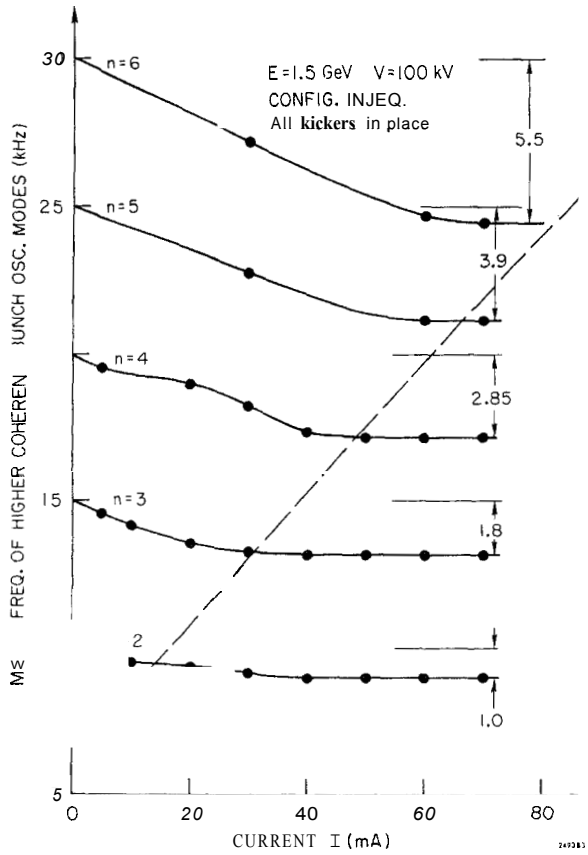


FIG. 7--Higher mode frequencies vs single bunch average current. The shifts from multiples of the synchrotron frequency are indicated on the right in kHz.

Further demonstration that the lines arise from shape oscillation stems from the following experiment. One main rf cavity was externally phase-modulated at the shifted frequency $\Omega_Q - 2\Omega_s = \Delta\Omega$ and the bunch shape was photographed using the sampling oscilloscope with its trigger locked to the modulating frequency. A series of photographs taken at various fixed times in the modulating cycle therefore represent a slow motion sequence of the oscillation and clearly showed the "breathing" nature of the quadrupole mode. Under certain conditions of cavity voltage and beam current, specific naturally occurring modes become dominant. A multiple trace photograph of a bunch executing sextupole oscillations is shown in Fig. 8. This shape is preciselythat

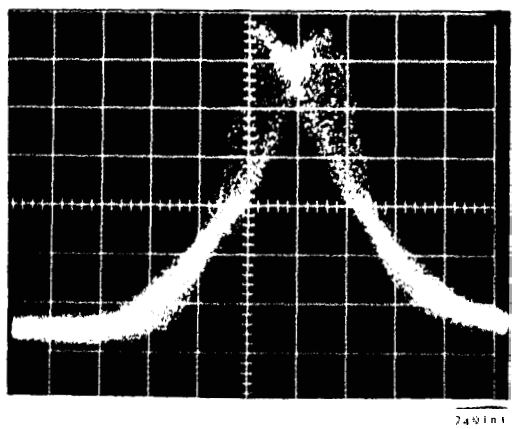


FIG. 8--Multiple sweep photograph of sampling oscilloscope showing self-excited coherent sextupole oscillations of the bunch shape. Sweep speed= 1 nsec/cm. Single bunch e^- current 134 mA at 1.5 GeV. Cavity voltage 235 kV.

outlined by Sacherer (Fig. 1, m=3 in Ref. 14). The octupole mode could also be seen in this way.

We turn now to the magnitude of the frequency shifts as a function of mode number m. The convention used is: For the dipole, m=1, quadrupole, m=2, etc. The importance of examining this dependence is that various impedance structures would yield differing results.[14] Examining Fig. 7, one sees that the frequency shifts do not bear a fixed relationship to each other until high currents are reached. Something more complicated must be going on. In spite of this, the higher mode frequencies at large current are well fitted by expression (45) of Ref. 18, $\omega_{mn} = n\Omega_z + 2nC_{mn}\Delta Q$ in which $Q_z = Q_{z0} - \Delta Q$ and we have set m=n for the fastest growing modes. The coefficients C_{mn} used were those calculated by Sacherer for the so-called Legendre modes that arise from a parabolic charge distribution. From the fit, one finds $\Delta Q = 0.83$ kHz at $Q_z = 5.0$ kHz. Since $C_{11} = 0.5$ the dipole frequency does not shift with current in this theory.

As stated before, specific modes are preferentially excited at certain currents. In fact, this is observed to occur for those currents at which the dashed line in Fig. 7 intersects the frequency of that mode. Even harder to understand is the appearance in the spectra of a relatively broad line, whose frequency is given by this dashed line. The first observation might be explained as follows. Suppose there exists in the ring a beam-excited resonant gap of spacing $D = \lambda/2$, so that when the total bunch length $4\sigma_z = m\lambda/2$, the mth mode is preferentially coupled. This picture corresponds to the form-factor treatment of Ref. 14. Unfortunately the predicted even spacing in bunch length with m is not borne out. The second observation suggests that there exists inside the bunch a separate population of particles, which oscillate coherently at frequencies linearly proportional to the total current and when frequencies coincide, preferential mode excitation occurs. Although the observed modes are clearly coherent, it is not yet possible to tell precisely what fraction of the bunch population is oscillating coherently.

The above discussion concerns the real part of the frequency shift. A measure of the imaginary part was obtained in two ways: swept line widths and decoherence times following shock excitation. The techniques are reported elsewhere[8] and were first tried out on the dipole line. Near zero current, this line displays a proper Lorentzian shape and yields the proper classical amping time. Both cavity detuning, producing Robinson" damping and phase feedback (when used),[15] broaden the line correctly, Both instrumental methods give the same results. Although rf-system damping should be different for the quadrupole mode, the observed line shape, taken with high resolution, is not understood, Moreover, the full width at the base is too narrow to fit the generally accepted stability criterion[14] that the spread be greater than the shift. This last fact may, however, be consistent if mode mixing, suggested in the turbulent equilibrium theory,[17] contributes. At the highest operating energies (2.5 GeV) quantum fluctuations appear to wash out the coherent modes.

V. Observation of Vacuum-Chamber Resonances

In SPEAR, the aluminum-extruded, curved vacuum chambers that thread through the bending magnets are connected to each other by round, 2-meter long 20-cm-diameter stainless-steel tubes. The tubes house a variety of machine elements. Common to each straight section is a subsection containing a set of beam position pickup electrode buttons. Signals from these electrodes were observed to contain very

high frequency components which were found not to be characteristic of the electrodes and their associated circuitry.[19] A detailed spectrum-analyzer examination of all twenty stations showed lines at 1.1, 1.4, and 1.8 GHz (Fig. 9). These

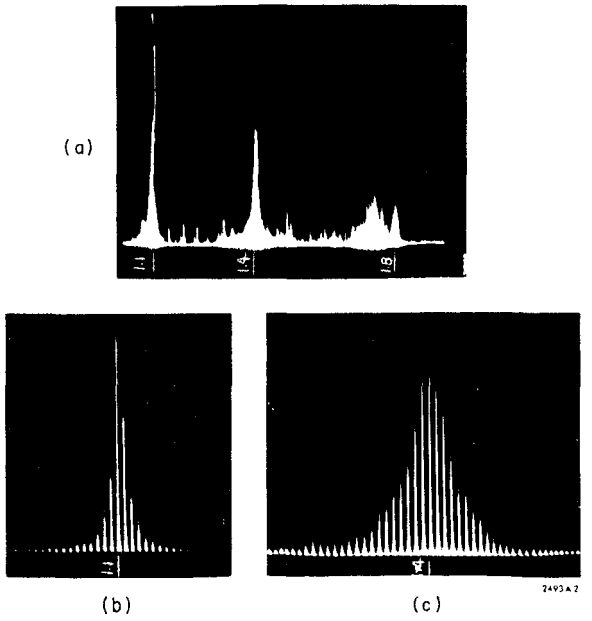


FIG. 9--Spectrum analyzer traces showing resonances in cylindrical vacuum-chamber straight sections at 1.1, 1.4, and 1.8 GHz. (a) 100 MHz/cm, (b) and (c) expanded scales showing lines which are high harmonics of the 1.28 MHz revolution frequency. The ordinates are proportional to power. Taken at 20 mA, 1.5 GeV, 500 kV.

frequencies are just those of the so-called "waveguide modes," which are independent of cavity length and are mentioned in Ref. 4. Their usual designation is TM_{010}, TE_{210}, $(TM_{110}-TE_{010})$, respectively. Transverse magnetic modes certainly could be excited by the axial electric field of the beam, and the cavity impedance for these modes can be estimated. In fact, one of the first calculations explaining bunch lengthening correctly was due to Robinson[20] who considered the fields due to vacuum chamber discontinuities. For the TM_{010} mode for example, one has the relation,

$$\frac{R}{Q} = 308 \sin(\pi \ell/\lambda) \qquad (5)$$

where ℓ is the length of the cavity and λ the resonant wavelength. The Q of the 1.1 GHz mode is estimated from Fig. 9 to be about 400. For twenty elements having a length $\ell \sim \lambda/2$, the preceding relation then gives a total impedance of about 2.5×10^6 ohms, a significant value.

Since the purpose of this investigation is to attempt to determine which machine elements couple strongly to the beam, further miscellaneous tests were performed. The electric separation plates (normally terminated) and the electric quadrupole conductors were shorted to ground or opened. The 3rd harmonic cavity[15] shorting bar was removed. The tuning paddle in an idling rf cavity was moved to resonance. None of these impedance changes affected the bunch length measurably.

VI. Beam-Power-Loss Estimates

A. Kicker Magnets

Following Sacherer,[13] one may write for the power dissipation

$$P = \frac{1}{2} I^2 \sum_n \mathrm{Re}\, Z_n\, e^{-n^2\sigma_z^2 w_0^2} \qquad (6)$$

Assuming the resistive part of Z_n to be of the same order as the reactive part, i.e., $\mathrm{Re}\, Z_n = \mathscr{R} \ln|$, substituting, and performing the sum gives

$$P = \frac{1}{2} \frac{I^2 \mathscr{R}}{(\sigma_z \omega_0)^2} \quad . \qquad (7)$$

For a beam current of 50 mA and using the value of $\mathscr{R}$ obtained from the fits in Fig. 5, one finds a loss of between 400 and 800 watts, the higher figure obtained from shorter bunches obtained with higher cavity voltages. The elements most likely to be responsible for this loss are the ferrite-kicker magnet cores which have been observed to have a large thermal outgassing rate, not associated with synchrotron radiation, in the presence of high current beams. The power dissipated per unit volume in the ferrite core at frequency ω is

$$P(\omega)/v = \frac{1}{2} \omega \mu'' \mu_0 H^2(\omega) \qquad (8)$$

in which μ'' is related to the loss tangent and relative permeability by $(\mu''/\mu_r) = \tan\delta$. Using values of μ'' and μ_r for the 4C4 Ferroxcube material found in the literature,[21,22] one can perform the sum over the high-frequency components of the beams numerically and find a power loss of about 100 watts for each of the four kickers, the loss peaking very broadly at frequencies of about 100 MHz. Unfortunately, it is not known exactly what material the manufacturer actually provided, so this rather good agreement is only qualitative but is consistent with core heating times.

B. Cavity Modes

An estimate of power loss to the cylindrical cavity modes can also be made. In this case, one is dealing with low-Q resonators at specific high frequencies. The excitation of, for example, the 1.1 GHz TM_{010} mode depends strongly on bunch lengths, which in turn is a function of current. The total beam loading voltage due to all twenty resonantors can be written

$$V_T = I R_T f_1(\sigma_z)\, f_2(T_0/T_F) \qquad (9)$$

where $f_1 = e^{-\omega^2\sigma_z^2/2c^2}$ gives the component of the current at frequency ω resulting from the finite bunch length. The function f_2 gives the enhancement in the energy loss which results when the bunch revolution time, T_0 becomes comparable to the decay time, T_F, for the mode in question. For SPEAR, T_0 is 0.78 μsec, for a cavity with a Q of 400 at 1.1 GHz, $T_F = 0.12$ psec giving $T_0/T_F = 6.6$. In Ref. 23 it is shown that for $T_0/T_F \gg 1$, $f_2 \sim 1/2\,(T_0/T_F) = 3.3$. The function f_1 decreases rapidly with increasing current because of the increase in bunch length. The product $I f_1$, in fact, reaches a maximum value of 0.9 mA at a current I = 5 mA. Using $R_T = 2 \times 10^6$ ohms as previously calculated, V_T is about 6 kV. The total power dissipation is $I f_1 V_T = 5$ W. The power dissipated in all of the cavity modes might be several times this, or about 15 W. In contrast to the situation at DORIS,[24] resistive losses due to the aluminum vacuum chamber wall with these bunch lengths amount to no more than a few watts.

VII. Effect of Removing Half the Kicker-Magnet Core

In January, 1974, two of the four magnets were replaced with ferriteless magnets of a new design. Bunch lengths and frequency shifts were remeasured. The results are shown best in Fig, 5. If the ferrite cores were the dominant bunch-lengthening component and half of them were removed from the ring, one should expect the slope of $\mathscr{R}$I to be halved. This is indeed nearly the case. For higher voltages, i.e., short bunches, the effect is less dramatic. The resultant ~ 20 percent reduction in bunch length (recall Eq. (5)) also shows up in the mode spectra. The rich spectrum up to 6th order previously seen at 70 mA now contains prominent lines only up to order 2, but can be reproduced at 170 mA. The frequency shifts of the higher modes are also uniformly reduced by 25 percent. Removal of the remaining two kicker cores is scheduled for May, 1974, at which time large further reduction of bunch length is expected. How close to the theoretical value it becomes will depend then on the influence of the aluminum-chamber impedance, cavity-mode excitation, and as yet unidentified elements whose effects have been masked by those of the kickers. Further, an entirely new regime will obtain after conversion of SPEAR to higher energies. The present RF system will be replaced with one of seven times the frequency and capable of providing accelerating voltages up to 7 MeV/turn. The resulting extremely high peak currents of a single bunch will no doubt raise interesting new problems.

VIII. Conclusions

On the basis of the data obtained at SPEAR, ACO, and ADONE, we conclude that no single theory presently explains the bunch lengthening effect, however, use of existing theories has lead us to identify the dominant element responsible in SPEAR. The search for other elements will continue after all the ferrite kicker magnet cores have been removed. We find that the existence of higher order bunch-shape oscillations, and measurements of their real and imaginary frequency shifts provide an additional, perhaps simpler tool for the study of the electromatic beam-environment interaction. It remains to compare such observations with theory in a quantitative way.

Acknowledgments

We wish to thank the other members of the SPEAR Group, R. Helm, M. Lee, P. Morton, J. M. Paterson, B. Richter, and the operating staff for their assistance.

References

1. A. M. Sessler, IEEE Trans. Nucl. Sci. NS-18 (1971) 1039.
2. M. Sands, Physics with Intersecting Storage Rings, ed. by B. Touschek (Academic Press, New York, 1971), p. 257 or Report No. SLAC-121, p. 129, Stanford Linear Accelerator Center (1970).
3. G. Fischer, SPEAR-154 (internal note), Stanford Linear Accelerator Center (1973); E. Keil, CERN/ISR-TH/72-33.
4. C, Pellegrini and A. M. Sessler, Nuovo Cimento 3A (1971) 116.
5. For examples, see references listed in 1, above.
6. A. N. Lebedev, Physics with Intersecting Storage Rings, loc. cit., p. 184.
7. A. M. Sessler, PEP Note 28, Lawrence Berkeley Laboratory (April 1973) (unpublished).
8. A. P, Sabersky, these proceedings.
9. J. Haissinski, Nuovo Cimento 18B (1973) 72.
10. R. Belbeoch et al., Proceedings of the National Conference on Particle Accelerators No. 1, Moscow, USSR, 1968; p. 129.
11. F. Amman, Proceedings VIIIth International Conference on Accelerators, CERN, Geneva, 1971; p. 68.
12. B. Richter et al., IEEE Trans. Nucl. Sci. NS-20 (1973) 755.
13. F. Sacherer, PEP Summer Study Note No. 45 (August, 1973).
14. F. Sacherer, IEEE Trans. Nucl. Sci. NS-20 (1973) 825.
15. M. A. Allen, R. A. McConnell, IEEE Trans. Nucl. Sci. NS-20 (1973) 373.
16. K. Robinson, CEAL 1010 (1964) unpublished.
17. A, M. Sessler, IEEE Trans. Nucl. Sci. NS-20 (1973) 856.
18. F. Sacherer, CERN/SI-BR/72-5, unpublished.
19. W. Dumond, R. Melen, M. Matera, SPEAR-168 (internal note), Stanford Linear Accelerator Center (1973).
20. K. Robinson, CEAL-TM-183 (July 1969) unpublished.
21. H. P. J. Wijn et al., Rev. Mod. Phys. 25 (1953) 91.
22. F. G. Brockman et al., Philips Technical Review 30 (1969) 324.
23. P. B. Wilson, PEP Note 37, SPEAR-163 (internal note), Stanford Linear Accelerator Center (1973).
24. A. Piwinski, DESP Report 72/72 (December, 1972).

Karl Reich (CERN): Could you give some recipe on what should be done about the ferrites?

Gerry Fischer (SLAC): At SPEAR we have decided to remove them, and at PEP we have also decided not to use them.

Reich (CERN): Then replace them by what?

Fischer: Air core magnets.

Andrei Kolomensky (Lebedev Institute): What do you expect with your new machine which will go up to 4 GeV? There may be new resonant instabilities as well as the present ones.

Fischer: The bunch will be considerably shorter because the harmonic of the cavities has been raised a factor of 7, and the voltage will go up.

Kolomensky: So, it will improve?

Fischer: No. The bunch will be shorter, and therefore the bunch spectrum will now overlap the higher order resonances in the vacuum boxes, and I imagine that one should design mode suppressors for these boxes to prevent the impedance from having a bad'effect. I'd just like to comment on the impedance that Sacherer mentioned. The longitudinal and transverse impedances are very much tied together, and if you have a bad impedance longitudinally you can probably get into trouble transverse.

Gus Voss (DESY): I think the data on the energy widening may perhaps be consistent with the observed bunch lengthening, if one keeps in mind that the bunch lengthening is observed with a photodiode where you observe plus or minus one or two standard deviations, whereas the energy spread is inferred from the quantum lifetime where one observes what happens at five standard deviations. If we no longer have a Gaussian distribution one would underestimate the energy widening in the center. If I understand it correctly, in all other storage rings the bunch lengthening data is consistent with an energy widening, and I believe it still might be here too.

Fischer: Our present thought is that the bunch energy widening is only a factor of two down from what is required to explain bunch lengthening. I really believe in potential distortion because at very high energies where the coherence seems to wash out, we have no bunch widening but we have bunch lengthening.

Andrew Sabersky (SLAC): There is strong evidence for potential well distortion which was not explicitly mentioned. That is, the bunch under certain conditions becomes highly asymmetrical. The tail is much longer than the head. This has been carefully checked to be sure that it's not an instrumental effect. We think that the only way to explain such an asymmetry is very strong potential well distortion.

Fischer: From the SPEAR magnetic detector data, looking at the time of arrival of Bhabha events, we feel that the leading edge is sharper than the tail.

INVESTIGATION AND CURES OF LONGITUDINAL INSTABILITIES OF BUNCHED BEAMS IN THE ISR

P. Bramham, S. Hansen, A. Hofmann, K. Hübner and E. Peschardt
CERN
Geneva, Switzerland
(Presented by W. Schnell)

Summary

The present status of longitudinal bunched beam instabilities in the ISR is described. Experiments to test the theory have been conducted with a tunable, passive cavity. In order to cope with the instability at higher intensities we expect in the future, possible cures were investigated. A bunch-by-bunch feedback system has been built. It damps dipole and quadrupole oscillations of individual bunches. Stabilization by means of a passive cavity was also successfully demonstrated.

1. Introduction

The RF system in the ISR is mainly used to accelerate the injected beam for stacking in longitudinal phase space[1]. It works at the 30th harmonic of the revolution frequency. The injector, the CERN proton synchrotron, has the same RF frequency but its circumference is only 2/3 of the ISR. Hence, the injected beam consists normally of 20 consecutive bunches. They are trapped on the injection orbit in 20 large, stationary buckets with the help of a phase lock system; the remaining 10 buckets are left empty. Each bunch covers a longitudinal phase space area of 0.16 eVs The phase oscillation frequency is around 60 Hz and the injected beam current equals ∿75 mA. The bunches stay in these large buckets for approximately 10 phase oscillation periods until the shutter protecting the stack from the stray field of the inflector magnet has opened. Subsequent acceleration with the same voltage displaces the beam towards the stack. Before the beam approaches the stack the voltage is reduced to fit the buckets tightly to the bunches. This avoids bringing empty phase space into the stack, which would dilute its density. The stable phase angle, whose typical value is 350, is kept constant during the whole acceleration. After a final acceleration with the reduced voltage to the stacking orbit the voltage is cut off abruptly. Fig. 1 shows the voltage and frequency programmes. The total length of such a stacking cycle is determined by the repetition rate of the injector. It is around 2 s.

During the time the bunch spends in the large bucket, phase oscillations develop and subsequent filamentation leads to dilution of the longitudinal phase space density. Since the maximum current which can be stacked is proportional to the longitudinal phase space density, performance will be reduced. Therefore, a study of these oscillations as well as of possible cures was in order.

2. Observation of Phase Oscillations

In order to observe these phase oscillations we kept the beam usually on injection orbit with a constant RF voltage, rather than going through the normal RF programme. A wide-band, fast intensity monitor and a "mountain range" display were our main tools for beam observation. With this set-up the longitudinal position

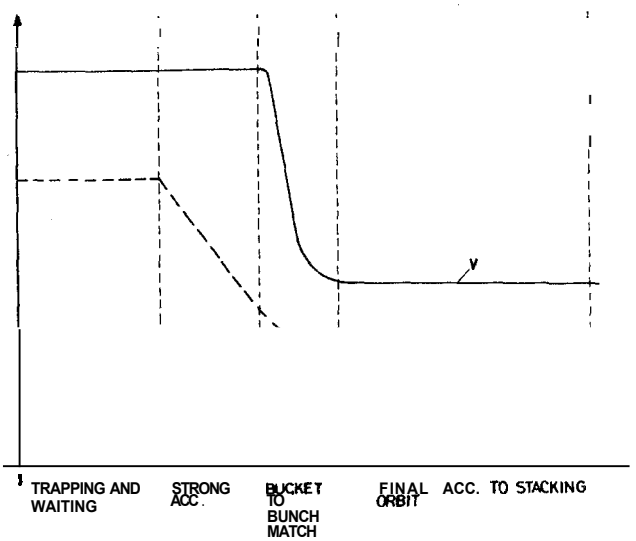


Fig. 1. Voltage and frequency programmes during an acceleration cycle.

of a bunch as well as its shape could be observed during the development of the instability.

The first objective of our investigation was to find the mode of the oscillation of a particular bunch. The dipole mode (rigid bunch mode) oscillation. which is described here with the mode number m = 1, was usually dominant, but also some quadrupole mode, m = 2, could be observed. Fig. 2 shows these oscillations for two different RF voltages ∿3.8 s after injection on a "mountain range" display.

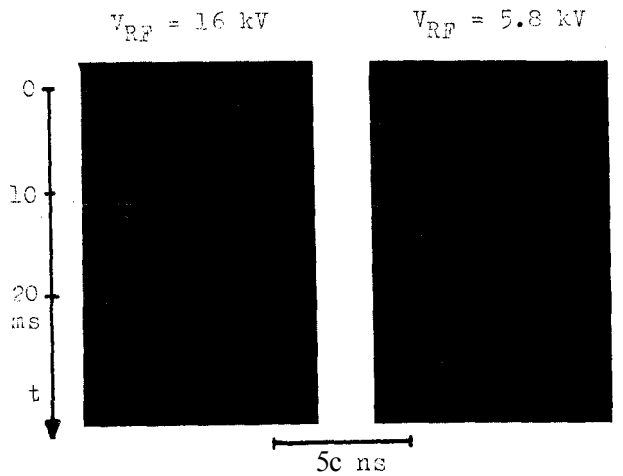


Fig. 2. "Mountain range " display of bunch oscillations for two different RF voltages

For the lower RF voltage, the bunch is longer and the quadrupole mode is more pronounced, as expected.

As a next step we studied the coupling between the bunches which is characterized by the phase relation between the oscillations of different bunches. An obvious such relation can be seen in Fig. 3 which shows the dipole oscillations of four bunches ∿3.8 s after injection.

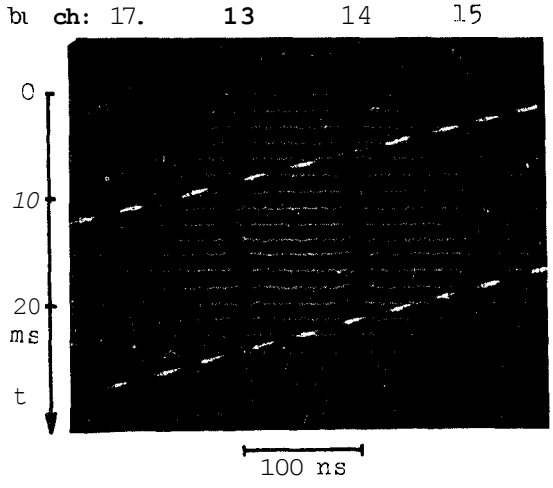


Fig. 3. Coupled bunch oscillations. Bunches with the same phase are connected by the oblique, dashed line.

On this picture the phase difference from one bunch to the next is

$$\Delta\phi \sim \frac{25}{30}\,271.$$

This phase difference can be described by a mode number n so that

$$\Delta\phi = 2\pi\,\frac{n}{h}$$

where h is the harmonic number of the RF.

Finally we measured the growth rate $\Delta\omega_m$ of the instability. By taking "mountain range" pictures at different times after injection we can observe the growth of the amplitudes of the different modes m. In the case where the dipole mode is dominant, we took "mountain range" pictures with many sweeps, triggered every revolution, on the same trace. Each trace then shows in superposition several phase oscillations and the growth of their amplitude can be measured directly from a single picture (Fig. 4).

These methods were used to investigate the longitudinal instability we presently observe for bunched beams in the ISR. We found that for standard conditions (V_{RF} = 16 kV, I ∿80 mA) our instability is a coupled bunch phenomenon consisting mainly of dipole mode oscillations with a growth rate of

$$\Delta\omega_1 \sim 1.6\ s^{-1}$$

and some weaker quadrupole oscillations.

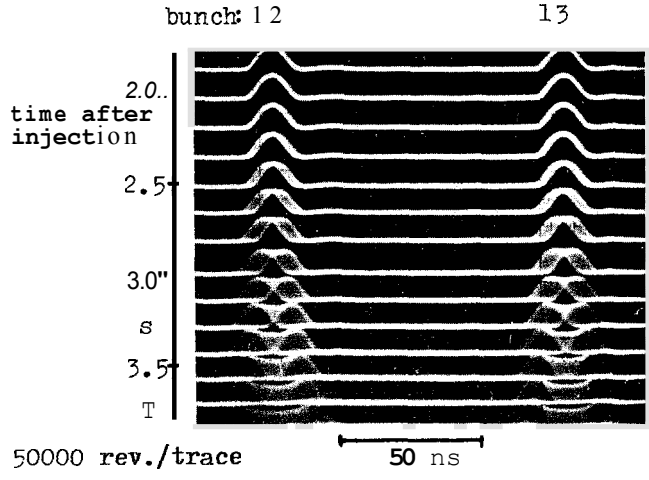


Fig. 4. Growth of dipole instability

3. Comparison of Theory and Experiment

Review of the Theory

Basically the longitudinal stability of the bunches in the ISR is determined by two effects: (a) the spread S of phase oscillation frequency ω_s due to the non-linearity of the RF waveform; (b) the longitudinal space charge force which shifts the coherent phase oscillation frequency with respect to the incoherent distribution and hence can make ineffective the Landau damping due to the spread S.

For typical ISR bunches in stationary buckets this space charge effect is quite large and Landau damping is ineffective. The situation is therefore potentially unstable which means that a resonator of arbitrarily small shunt impedance can cause an instability.

A theory describing the effect of such resonators on bunched beams has been worked out by F. Sacherer[2]. Below we summarize it briefly and apply it to the ISR. This theory applies to beams with equidistant bunches and gives the modes m and n as well as the growth rates of the oscillations which are excited by a resonator having a resonant frequency f_{res} and a shunt impedance R_s. Since we have in the ISR 20 bunches followed by 10 empty buckets, rather than equidistant bunches, Sacherer's theory is not directly applicable and a correct treatment is complicated. However, for a resonator which has a quality factor Q large enough for its signal not to decay too much during the time of ∿1 μs while the empty buckets pass by, we can use this theory as a good approximation. For the ISR beam in stationary buckets the growth rate of the instability is then:

$$\Delta\omega_m \approx \frac{\omega_s\, R_s\, I\, D\, F_m(\Delta\phi)}{271\, V_{RF}\, B}$$

where

I = beam current,
V_{RF} = RF voltage and
B = bunching factor = full bunch length/distance between bunches.

The form factor $F_m(\Delta\phi)$ specifies how efficiently the resonator can drive a certain mode m. It depends on

the phase change $\Delta\phi = 2\pi \times$ bunch length in seconds $\times f_{res}$, which occurs during the passage of a bunch (cf. Fig. 5). The term D depends on the attenuation of the resonator signal between two bunches and on the ratio

$$k = \frac{f_{res}}{f_o}$$

between the resonant frequency f_{res} and the revolution frequency f_o. This factor D has in general an imaginary part which is, for our assumption of large Q, of about value 1 if

$$k \approx \text{integer} \times h \pm n,$$

but of value zero for the coupled modes n = 0 and n = 15.

The above equation determines which coupled bunch mode n will be excited. How well it has to be satisfied depends on the bandwidth of the resonator.

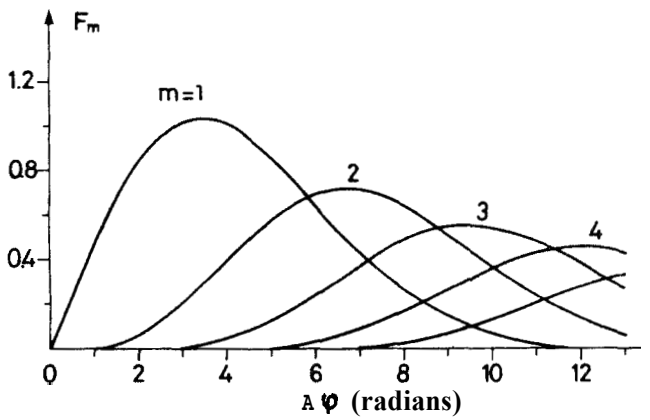


Fig. 5. Form factors $F_m(\Delta\phi)$ (from F. Sacherer[2])

Experimental Test of the Theory

We tested the theory and its validity for the ISR case using a cavity[3] with variable shunt impedance and resonant frequency. The excited modes and their growth rates were measured using the methods described in the last chapter. The experimental results are listed in Table 1 and compared with the calculations. The agreement is quite good considering the rather large measurement errors. For each case in Table 1 only the mode with the strongest oscillation is shown, because its presence may change the condition for the weaker modes and also makes their measurement difficult.

Application of the Theory

Having now tested the theory (at least for some range of resonant frequencies) we can use it to derive a criterion for the maximum shunt impedance R_{max} a resonator in the ISR is allowed to have, if a certain instability growth rate $\Delta\omega_{max}$ is tolerated. We assume a beam current of I = 0.1A, stationary buckets with V_{RF} = 16 kV and we approximate the curves $F(\Delta\phi)$ by their envelope and get for k > 75:

$$R_{max} \sim 40\sqrt{k}\,\Delta\omega_{max} \qquad \Omega$$

Since we assumed $|D| = 1$, this criterion might be pessimistic.

Table 1

Comparison of Theory and Experiment

beam energy GeV	26	26	26	22	22
beam current mA	90	30	90	90	90
RF voltage kV	16	16	5.8	16	16
bunch length ns	16.5	15.5	22	17.5	17.5
shunt impedance kΩ	5.2	5.2	5.2	13	13
$k = f_{res}/f_o$	175	175	175	153	177
strongest observed mode m	2	2	2	2	2
growth rate					
observed s^{-1}	12.5	2.7	2.4	11.8	16.7
calculated s^{-1}	6.9	2.6	8.5	16.8	11.4
mode n					
observed	-	5	-	27	
expected	5	5	5	27	3

As a further application of the theory we can use instability observations to estimate the parameters of the possible resonator. By measuring the growth rate of the dominant modes m for different RF voltages and hence bunch lengths, we get some idea of where on the curves $F_m(\Delta\phi)$ we are operating. This determines $\Delta\phi$ which is directly related to the resonator's frequency. Observation of the coupled bunch mode n may give additional information about f_{res}. A comparison between the oscillation amplitudes of the first bunch (after the gap of the 10 empty buckets) and later bunches can be used to estimate the quality factor Q. The measured growth rate and Q determine the shunt impedance of the resonator. This method has been successfully used in the past to identify an instability-causing resonator in the ISR which then could be shorted out. The present instability observations, as described in the last chapter, indicate a resonator with $R_s \sim 1.5$ kΩ, $f_{res} \approx 20$ MHz and $Q \sim 15$, if the instability is caused by only one resonator.

4. Increase of the Landau Damping with a Cavity Operating at a Harmonic of the RF Frequency

A cavity operating at a harmonic p of the RF frequency can increase the Landau damping and provide longitudinal stability for bunched beams[4]. With a passive cavity we made some experiments to study this method. While dipole and quadrupole mode oscillations can be damped with the feedback system described in the next chapter, a cavity could be used to damp possible higher modes. Ideally such a cavity should be driven by an oscillator and have a low shunt impedance. Operating with the correct phase and with a voltage V_p it would produce a spread S_p in phase oscillation frequencies of approximately[4]

$$S_p \sim S_o\left[1 + \frac{V_p}{V_{RF}}(p^3 - p)\right],$$

where S_o is the spread obtained with the normal RF system alone. This is a good approximation as long as the bunch length is smaller than the wavelength of the higher harmonic oscillation and $V_p/V_{RF} < 1/p$.

It is also possible to work with a passive cavity which is driven by the beam. For optimum operation it has to be tuned to a frequency which is about half a bandwidth below $p \cdot f_{RF}$ so that the phase ψ between this cavity oscillation and the bunch is $\sim 45^o/p$ as shown in Fig. 6,5. The spread obtained is then

$$S_p \sim S_o\left[1 + \frac{I_p R_s}{2V_{RF}}(p^3 - p)\right]$$

where I_p is the $p \cdot f_{RF}$ - Fourier component of the beam current. Due to the shunt impedance R_s and the finite bandwidth such a cavity can itself excite instabilities. The damping provided by the cavity has to cope with their growth rates and the space charge frequency shift.

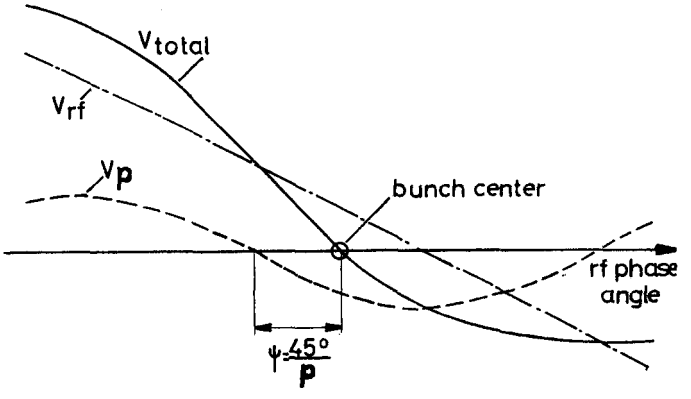


Fig. 6. Phase relation between the oscillation of the higher harmonic cavity, the bunch and the RF voltage.

In our experiments we used a cavity with variable shunt impedance operating at the 6th harmonic of the RF frequency. With p = 6 this cavity is not quite ideal because the wavelength of its oscillation is shorter than the bunch length at the end of the acceleration cycle. This cavity can therefore not be used for stacking and all the experiments were done with bunches in stationary buckets.

With this method all bunches could be kept stable for a long time as shown in Fig. 7. Usually some oscillations showed up after some time. We do not know if they are caused by a real instability or by noise. Such oscillations either got damped out (as in Fig. 7) or they upset the driving of the cavity, in which case a violent instability occurred. The lowest shunt impedance of the cavity necessary to provide stability was measured and found to be in good agreement with theory. To appreciate the damping effect of the cavity Fig. 7 should be compared with Fig. 4 which refers to normal conditions.

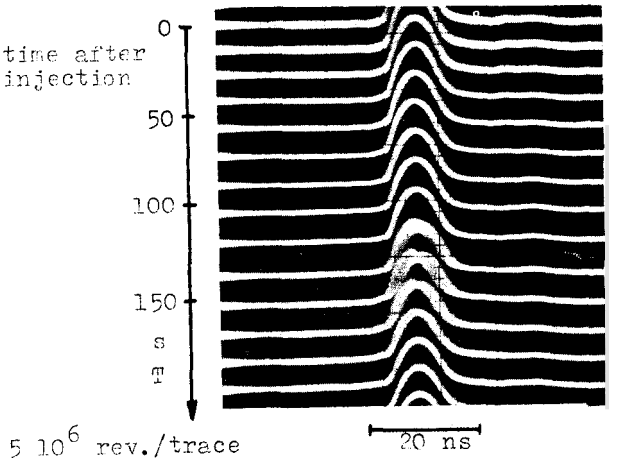


Fig. 7. A bunch stabilized with the higher harmonic cavity.

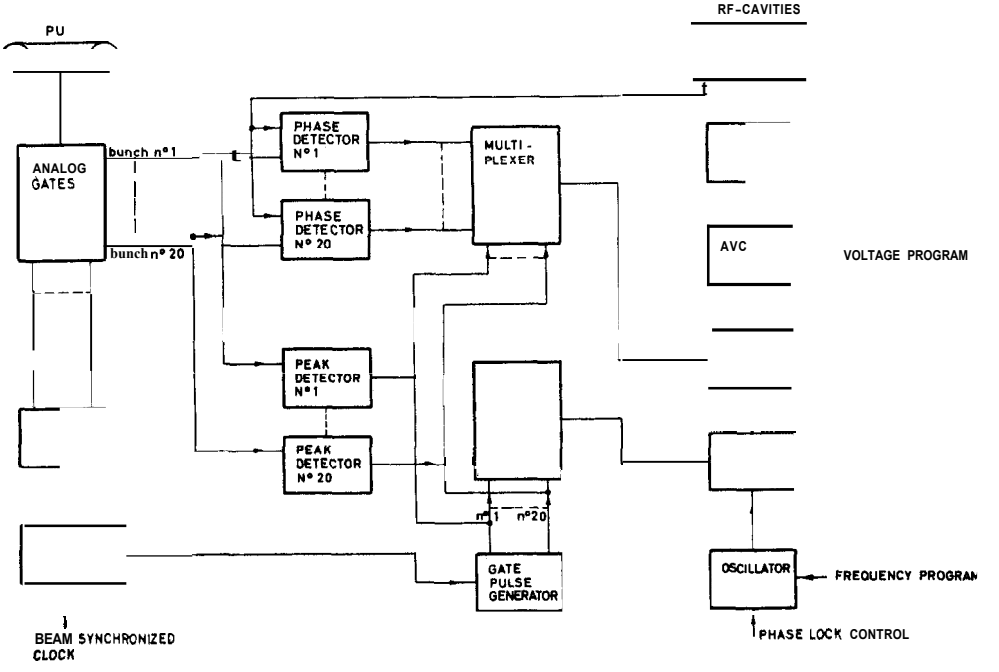


Fig. 8. Block diagram of the feedback system

5. The Bunch-by-Bunch Feedback System

One method of damping bunch oscillations of the dipole and quadrupole mode is to act directly on the phase and amplitude of the RF voltage. The ISR RF system works with beam control[1] (missing bunch phase-lock), where the beam phase-reference is taken from one single bunch. The dipole mode of bunch oscillations thus appears as a phase-modulation of individual bunches with respect to the reference bunch, with a frequency ω_s equal to the synchrotron frequency. A pure quadrupole oscillation appears as an amplitude modulation of the individual bunches. The frequency of the amplitude modulation is $2\,\omega_s$.

By detecting these phase and amplitude modulations of individual bunches and using the detected signals to modulate the RF wave seen by the same bunches, these oscillations can be damped. Such a system has been built for the ISR.

Fig. 8 shows a simplified block diagram of the feedback system. The signal induced on a pick-up station is fed into an analogue gating system, where the 20 bunches are separated. Twenty phase-detectors measure the instantaneous phase difference between each individual bunch and the RF voltage on the cavities. In the multiplexer, the error signal from each detector is sampled once per revolution for approximately 105 ns (one RF period). The output signal from the multiplexer is a signal representing the phase-deviation between the individual bunches and the RF voltage. This signal is applied to a fast phase-modulator that varies the phase of the RF cavity voltage.

Due to a relatively low Q-value of the RF cavities[6], fast changes of phase and amplitude of the RF voltages are possible, when these changes are small.

Twenty peak-detectors measure the amplitude modulation of individual bunches. An identical multiplexing system as described above is used to extract a signal related to the amplitude of the bunch oscillations for each individual bunch. This signal modulates the amplitude of the RF voltage.

All the switching processes are guided from the beam-synchronized timing system.

Experimental Results

The feedback system is built so that any number of bunches from 1 to 20 can be damped individually. Dipole oscillations of 1 and 2 of the 20 bunches have been successfully damped, in the presence of violent oscillations of both the leading and lagging neighbouring bunches. Fig. 9a shows two neighbouring bunches when no feedback is applied. Fig. 9b shows the same bunches when feedback is applied only to the last bunch.

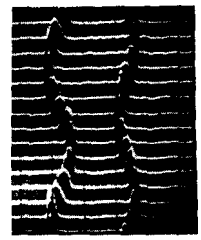


Fig. 9a. Dipole oscillations without feedback

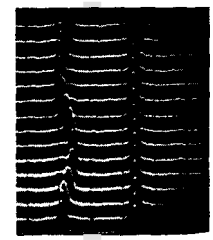


Fig. 9b. Second bunch stabilized by feedback

An experiment measuring the overall effect on the final phase plane density in a stack when feedback is applied to all 20 bunches has not yet been performed.

References

1. S. Hansen, M.J. de Jonge: "Beam control and RF stacking in the ISR." Proc. of the 8th Int. Conf. on High Energy Accelerators, CERN 1971, p.505.

2. F. Sacherer: "A longitudinal stability criterion for bunched beams." Proc. of the 1973 Particla Accelerator Conference, San Francisco, p.825. This paper also gives an extensive list of references.

3. B. Zotter and P. Bramham: "Experimental investigation of the coherent longitudinal instability of relativistic particle beams." Proc. of the 1973 Particle Accelerator Conference, San Francisco, p.830.

4. R. Averill et al.: "Synchrotron and betatron inst. of stored beams in the CEA." Proc. of the 8th Int. Conf. on High Energy Accelerators, CERN 1971, p.301.

5. G.A. Voss, private communication.

6. F.A. Ferger and W. Schnell: "The high power part of the RF system for the CERN Intersecting Storage, Rings (ISR)." USSR 2nd Nat. Conf. on Particle Accelerators, 1970, Vol. 11, p.129.

Matt Sands (UCSC): Can you explain how the feedback system works for the quadrupole mode?

Wolfgang Schnell (CERN): First, there is a separate detector and separate channel for each bunch with multiplexers. I *think* that's not what you wonder about. The other thing is rather well known, the basic principle, the quadrupole oscillation means that the bunch gets long and short periodically. When it's short, it's dense and so the peak induced voltage in the pickup is high. When it's long, it's low. The next stage is that you modulate the rf voltage with twice the phase oscillation frequency and you find that it spirals in phase space. This is well known and is used in several machines. I know it's used in the PS and the AGS for many years. The new thing for us is that it's individual from bunch to bunch.

Gus Voss (DESY): At the PS it is called Aragon damping, is it not?

Schnell: Yes. I believe it's called Racah damping at Brookhaven.

Arie Van Steenbergen (BNL): Would you give us some more detail on your injection kicker which has no shutter.

Schnell: We are working on this—the beam height is smaller than we expected and we usually make it even smaller by shaving away a lot of beam. Then instead of having a moving shutter you can perhaps get away with having the beam in a narrow slot where the field attenuates very rapidly when it penetrates into the slot. The trouble is that we can probably not use it at the lowest energies that we have to run, so we will try to work this into the moving shutter and then have both systems.

Gus Voss (DESY): You lose a little bit of radial aperture, I guess, with such an arrangement.

Schnell: A few millimeters, yes. This doesn't work yet, this is under development.

Alberto Renieri (Frascati): What is the order of magnitude of modulation of the rf for damping the quadrupole mode?

Schnell: A few percent. I think it's no more than two or three percent.

CONTROL OF THE BUNCH LENGTHENING PHENOMENON IN ELECTRON STORAGE RINGS*

E. M. Rowe and W. S. Trzeciak
Physical Sciences Laboratory - University of Wisconsin
Stoughton, Wisconsin

Introduction

A dependence of the bunch length on the bunch total charge in electron storage rings was first reported by the Orsay group[1]. Since that time, the phenomenon has been observed at Frascati[2], Kharkov[3], and SLAC[4]. The phenomenon was not observed at the Stanford electron-electron storage rings[5], VEPP I and VEPP II[6] at Novosibirsk and, until recently, on Tantalus I[7], the 240 MeV electron storage ring at the Physical Sciences Laboratory of the University of Wisconsin.

Because of the importance of bunch lengthening in determining the luminosities achievable in electron-positron storage rings, a considerable amount of theoretical work aimed at explaining the phenomenon has been carried out[8-11]. In 1971, Pellegrini and Sessler[12] gave a general theory of the equilibrium length of high current bunches in electron-positron storage rings. This theory requires inductive coupling between the beam and its surroundings for bunch lengthening to occur above transition energy. Here, the term inductive coupling means that the impedance seen by the beam is inductive, i.e. the structure with which the beam interacts is driven at a frequency below resonance. The theory also allows for the possibility of bunch shortening to occur through the same coupling mechanism, though, to our knowledge, before this present work no such observations have been reported.

Subsequently, Sessler extended this work and developed a dynamic theory which describes the turbulent steady state associated with stable non-zero amplitude collective modes[13].

Recently, bunch lengthening has been observed at Tantalus I. A series of measurements, to be described below, have been made of the bunch length dependence on both current and energy which are in good agreement with both the original Pellegrini-Sessler Theory and the more recent development by Sessler. Further, bunch shortening has also been observed and, while the measurements made so far on this manifestation of the phenomenon are not as complete as those made of bunch lengthening, they have been included because of their possible importance.

I. Theory

In this section we give a brief summary of the theory developed in Ref. 12. The theory makes use of the concept of self fields arising from the interaction of the bunch itself with components of the accelerator or storage ring near the particle path such as RF cavities, clearing electrodes, pick up loops, etc. These self fields then modify the accelerating potential seen by the electrons in the bunch and there then results a change in the synchrotron oscillation frequencies of the electrons in the neighborhood of the synchronous particle. The oscillation amplitudes of the electrons, now oscillating at some new synchrotron oscillation frequency Ω, change, and this results in the bunch taking on a new length.

*Work performed under the auspices of the AFOSR-Contract No. F44620-70-C-0029.

The dependence of the mean square of the half bunch length, Δ^2, on the synchrotron oscillation frequency, Ω, as given by Bruck[14], is

$$\Delta^2 = A/R^2 \tag{1}$$

where A is a quantity dependent on machine parameters and energy. Thus, the perturbed bunch length Δ can be related to the unperturbed bunch length Δ_o through

$$\Delta^2 = \Delta_o^2 [1 + (\Omega^2 - \Omega_s^2)/\Omega_s^2)]^{-1} \tag{2}$$

where Ω, the synchrotron oscillation frequency in the presence of the self fields, is calculated by including a term of the form $e\, dU/d\phi$ to account for the fluctuation in energy gain per turn arising from the self fields in the usual equation for Ω[14].

The frequencies of the self fields may be either lower or higher than a critical frequency defined as $\omega_{crit} = \beta c/A = R_s \omega_s/\Delta$. We will confine the discussion to the case $\omega >> \omega_{crit}$. In this case, Ref. 12 gives the dependence of Ω on the impedance $Z(\omega)$ which gives rise to the self fields as

$$(\Omega^2 - \Omega_s^2)/\Omega_s^2 = F I C \Delta^{-3} \tag{3}$$

where

$$\frac{Z(\omega)}{} d\omega + \int^{\omega_{crit}} \frac{Z(\omega)}{} d$$

and C is a constant that depends only on machine parameters and energy. Pellegrini and Sessler show that with the use of this expression, Eq. 2 can be written in the form

$$\Delta^2 = \Delta_o^2 (1 + KI/E_s^3 \Delta) \tag{5}$$

where the constant K is proportional only to F.

The impedance $Z(\omega)$ may arise from several structures in the machine or it may be presented to the beam by one high impedance object. In the work being reported here the latter is the case. If $\Delta >> \Delta_o$, the following development of the theory is pertinent. Equation 5 becomes under these conditions

$$\Delta^3 = \Delta_o^2 KI/E_s^3 \tag{6}$$

Thus, in this limit, the parametric dependence of Δ itself becomes $\Delta \propto (I/V_{rf} \cos \phi_s)^{1/3}$ and is independent of energy.

In Ref. 13, Sessler derives a similar expression for the standard deviation, σ_Δ, as

$$\sigma_\Delta^3 \propto I \left| Z_n/nZ_o \right| V_{rf}^{-1} \tag{7}$$

where Z_n is the coupling impedance of the nth mode of the structure interacting with the beam and Z_o is the impedance of free space.

II. Observation

The theoretical root mean square bunch length in Tantalus I, calculated from 4.1 is .22 nsec. The observed RMS bunch length is .54 nsec and normally is constant for a range of beam currents of over *two* orders of magnitude (100 PA- 20 mA). The reasons for the discrepancy between theory and observation are not known at the present time.

Recently (1972), the injection system of the machine was modified and the original fixed, septumless inflector was replaced with an inflector with septum, which is remotely controllable in position. A plan view of the new inflector and its associated section of vacuum chamber is shown in Fig. 1. The inflector and its stem are made of OFHC copper and it is grounded *to* the vacuum chamber by spring fingers at the point of stem penetration. The fundamental resonant mode of the inflector and stem occurs at a frequency near 240 MHz, which is approximately three times ω_{crit} for the storage ring. However, it is clear from the geometry of the inflector that it can support higher modes; certainly up *to* several kMHz. Finally, because of the shape of the inflector, it is reasonable *to* believe that the beam may couple to the inflector structure either magnetically or electrostatically, depending on the standing wave distribution along the inflector in the region of closest approach of the electron beam. The standing wave distribution will be determined by which mode the beam happens *to* excite. Movement of the inflector tunes the structure through two effects: first, by changing the length of the inflector stem protruding beyond the ground point and, second, by changing the capacitative loading *to* ground at the other end of the inflector body.

During the adjustment of this new inflector it was noted that the beam bunch length became either longer or shorter than normal, depending on radial position of the inflector.

These observations of the bunch length were carried out by processing the signal from an electrostatic induction pickup mounted in the storage ring vacuum chamber through a Tektronix 1S1 sampling system and displaying the composite signal on an oscilloscope. The signal observed, then, was not a "real time" signal and questions concerning the reality of bunch length measurements based on these observations may legitimately be raised. However, beam lifetimes on Tantalus I, at beam currents of more than one or *two* mA, are strictly a function of bunch density. Thus, the fact that beam lifetimes reflected the observed bunch length variations make a reasonably convincing argument for the accuracy of the bunch length observations. Fig. 2 shows the normal bunch and Fig. 3 shows a typical lengthened bunch. A beam decay curve showing the beam lifetime for normal and long beam bunch lengths appears in Fig. 4-A.

A series of measurements of the beam bunch length as a function of circulating current have been made under both normal and lengthened bunch conditions. The results of these measurements appear in Fig. 5. The curve shown for the long bunch is a least squares fit of Eq. 5 to the observational data. The fit is sufficiently good so as to argue strongly for the correctness of the functional form of Eq.8.

From these data, the derived value of the quantity F is 9.9×10^{7} MHz^{-1}. Taking $\omega = 1.4 \times 10^{9}$ sec^{-1}, which corresponds *to* the fundamental mode of the inflector, gives a value for $Z(\omega) = 2.4 \times 10^{3}\ \Omega$.

The value of $|Z_n|/n$ calculated on the basis of Eq. 7 for large beam currents and taking $n = 1$, is $2.2 \times 10^{3}\ \Omega$. This is not unreasonable, considering the expected electrical properties of the perturbing structure. Further, for constant circulating current, $|Z_n|/n$ is reasonably constant as is shown by the small variation in bunch length with energy displayed in Fig. 4-B. We note the agreement of this result with that obtained on the basis of the theory developed in Ref.12.

Finally, the variation of bunch length as a function of accelerating voltage is shown in Fig. 4-C. Once again, the theory tends to predict the observational data. The discrepancy at low accelerating voltage may well be the result of the fact that the total bunch length has become almost equal *to* $\lambda_{RF}/4$.

As one expects, the beam is a strong source of radio frequency signals up to at least the 100th harmonic of its revolution frequency. When operating with normal bunch length the spectrum of the beam signal in the region of the fundamental and any of its harmonics, appears as shown in Fig. 6. When the inflector is positioned so as *to* excite bunch lengthening, the spectra exhibit very little change at the fundamental and the lower harmonics. However, beginning at the eighth harmonic, ($\omega = 1.4 \times 10^{9}$ sec^{-1}) the spectra take the form shown in Fig. 7. This spectrum is typical of a frequency modulated signal. The modulating frequency is 60 kHz which is the small amplitude synchrotron oscillation frequency of the beam at 240 MeV. As can be seen, the level of the sidebands fluctuate violently. At higher harmonics the spectra become richer in structure as is shown in Fig. 8. Again, the prominent sidebands occur at 60 kHz intervals but other sideband spacings can be seen. These spectra suggest that the electron motion within the bunch is to some extent collective and is, indeed, strongly turbulent.

Since the bunch length is longer, it is reasonable to expect, and, indeed, the theory developed in Ref. 13 predicts that the beam should be wider. Observation once again confirms this prediction. The data are not as extensive as in the previous measurements, however, Fig. 9 shows that the standard deviation of the beam width increases by a factor of approximately 2 between the normal and perturbed conditions.

As was mentioned above, the bunch lengthening phenomenon was not seen in Tantalus I during the first several years of its operation. However, bunch shortening was observed several times. Unfortunately, the observations were misinterpreted at the time (1969) and we have only recently begun *to* study this effect. For the sake of historical completeness, we show Fig.10. Here, the *total* beam bunch length is less than one nsec. The structure that the beam was interacting with is not known, but it is suspected that it was the original inflector which was not very different in form from the one presently installed.

Recently, the oscillogram shown in Fig. 11 was obtained. To produce this reduction in total bunch length (from 2.5 nsec to approximately 1 nsec) adjustment of the inflector position both vertically and radially was necessary.

III. Conclusions:

Controlling the bunch length in order to control beam lifetime is now standard practice at the Synchrotron Radiation Center of The University of Wisconsin. In developing this technique we studied the effects of the interaction of a specific resonant structure with the electron beam circulating on Tantalus I. The effect of this interaction is usually *to* cause the bunch length *to* increase but under some circumstances the interaction can cause the bunch length *to* decrease. The observational data are in good agreement

with the predictions of the theory developed by Sessler and Pellegrini. As a result, there appears to be reason to believe that passive resonant structures could be developed that would reduce the bunch length in large electron and positron storage rings and thus increase the luminosities attainable in these machines. The capability of reducing bunch length would also be of some use at electron storage rings used as synchrotron radiation sources for measurement of short fluorescence lifetimes.

References

1. R. Jolivot: Private Communication (1970).
2. F. Aman, Electron-Positron Storage Rings: Status and Present Limitations, Proceedings of the 1969 Particle Accelerator Conference, IEEE, trans. Nucl. Sci. NS-16, No. 3, 1073 (1969).
3. Grigoriev, et al., Investigations Made on a Storage Ring for Electrons of 100 MeV in Physical Technical Institute of Ukrainian Academy of Sciences, Proceedings of the 7th International. Conference on High Energy Accelerators, Vol. 11, p. 121, Yerevan, 1969.
4. M. Allen: Private Communication (1973).
5. B. Richter: Private Communication (1969).
6. V. L. Auslender: Private Communication (1969).
7. E. M. Rowe, F. E. Mills, Tantalus I: A Dedicated Storage Ring Synchrotron Radiation Source, Particle Accelerators, Vol. 4, pp. 211-227 (1973).
8. E. Ferlenghi, Nuovo Cimento, 48 B, 73 (1967).
9. H. Zyngier, Allongement des Paquets pas Une Tension Induite, Orsay Laboratoire de l'Accélérateur Linkaire, Internal Technica Note HZ-FB 21-67, Nov. 1967.
10. K. W. Robinson, Bunch-Lengthening in Storage Rings, Cambridge Electron Accelerator Internal Report CEAL-TM-183, July 1969.
11. A. N. Lebedev, On the Bunch-Lengthening Effect in Storage Rings, Laboratori Nazionali di Frascati, preprint (1970).
12. C. Pellegrini, A. M. Sessler, The Equilibrium Length of High-Current Bunches in Electron Storage Rings, Il Nuovo Cimento, Vol. 3A, N. 1, pp. 116-134, 1 Maggio 1971.
13. A. M. Sessler, Strongly Turbulent Collective Motion and the Anomalous Size of Stored Particle Beams, PEP Note 28, Lawrence Berkeley Laboratory, April 26, 1973.
14. H. Bruck, Accélérateurs Circulaires de Particules, (Paris, 1966), p. 231.

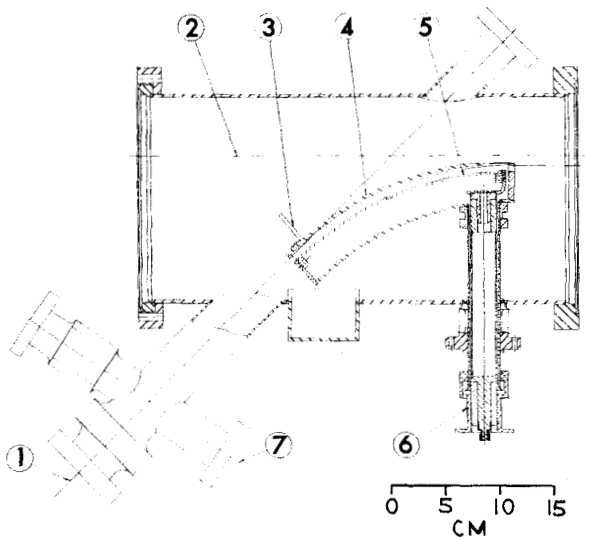


FIG. 1--Plan view of inflector. 1. Injection beam path; 2. Electron orbit; 3. Scintillator; 4. Inflector body; 5. Inflector electrode; 6. High voltage terminal; 7. Photon beam line from upstream magnet.

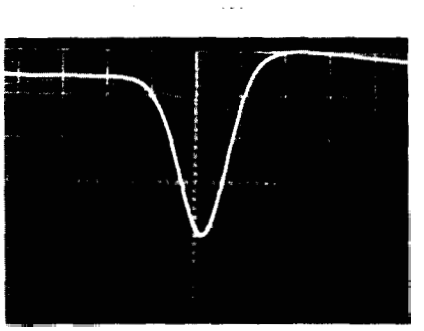


FIG. 2--Normal bunch. Sweep speed: 10^{-9} sec cm^{-1}.

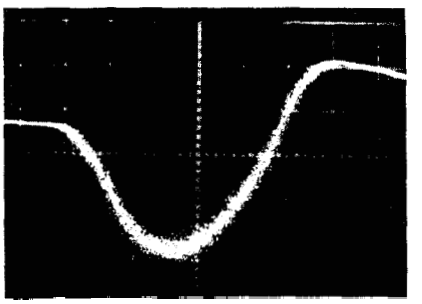


FIG. 3--Wide bunch. Sweep speed: 10^{-9} sec cm^{-1}.

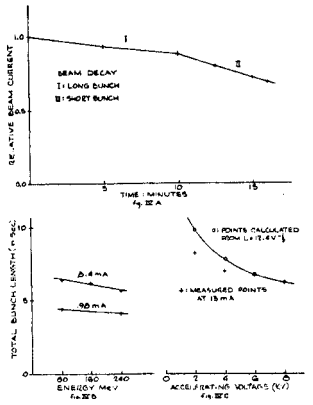


FIG. 4--A. Beam decay, long and short bunch. B. Bunch length dependence on energy. C. Bunch length dependence on accelerating voltage.

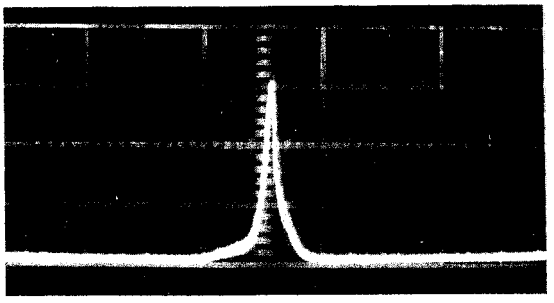


FIG. 6--Bunch signal spectrum at sixth harmonic of particle revolution frequency, normal bunch length. Dispersion: 10^5 hertz cm^{-1}.

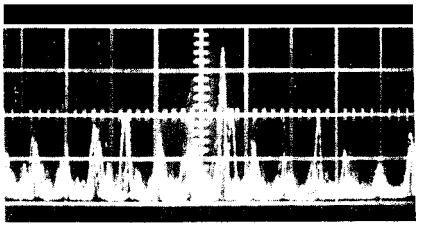


FIG. 8--Bunch signal spectrum at thirtieth harmonic of particle revolution frequency, long bunch length. Dispersion: 10^5 hertz cm^{-1}.

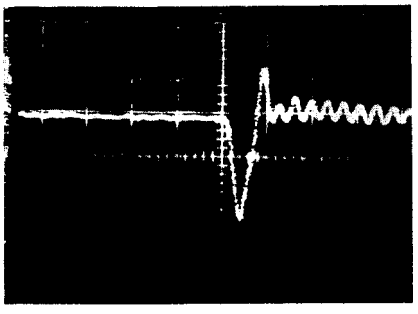


FIG. 10--"Historical" short bunch signal, Ca 1969. Sweep speed: 10^{-9} cm sec^{-1}.

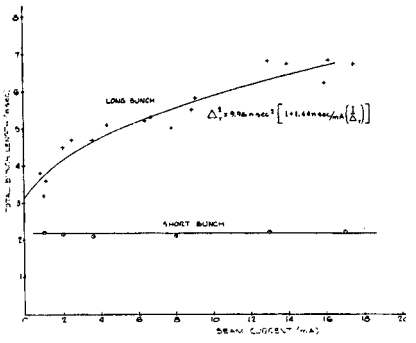


FIG. 5--Bunch length dependence on circulating current for normal and long bunches.

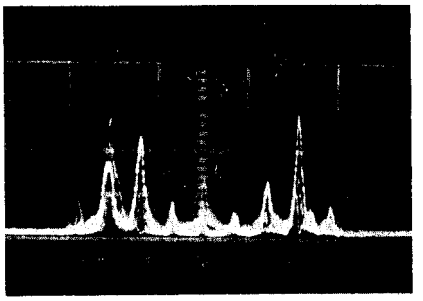


FIG. 7--Bunch signal spectrum at eighth harmonic of particle revolution frequency, long bunch length. Dispersion: 10^5 hertz cm^{-1}.

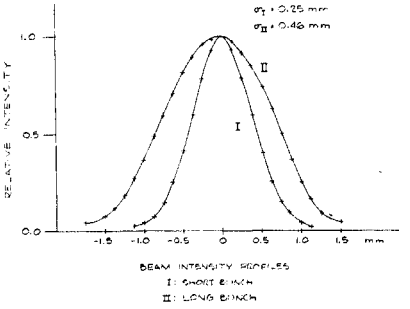


FIG. 9--Beam width, normal and long bunch length,

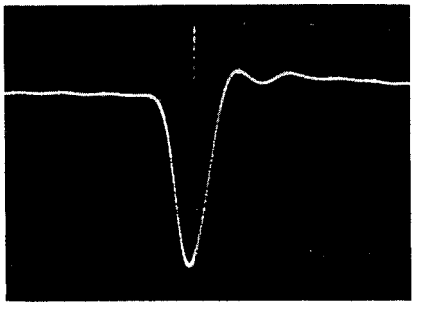


FIG. 11--Short bunch. Sweep speed: 10^{-9} cm sec^{-1}.

Phil Morton (SLAC): You showed a curve of the bunch decay for shorter and longer bunches. Why did a short bunch decay faster?

E. Rowe (University of Wisconsin): The density of the charge in the bunch is very much higher for the short bunch. and apparently our lifetime is determined by the Touschek effect.

Andrew Sessler (LBL): Do you have observations of the radial bunch width at the same time that you see shortening in length?

Rowe: That was shown on about the third slide from the end.

Sessler: That was while the beam was getting long.

Rowe: There were two curves there. One showed the width in the normal, short bunch mode, and the other curve showed the width in the long bunch mode. We don't have data on the super-short mode. We're trying to get it, These observations are difficult. We are fortunate that our machine is rather small and operates at a rather low energy so that some of these effects tend to be gross, like the bunch length going up by a factor of 7 or 8.

THE LONGITUDINAL FEEDBACK SYSTEM IN ADONE

A. Renieri and F. Tazzioli

Laboratori Nazionali del CNEN

Frascati, Italy

Summary. In the paper is described the feed back system, actually working on Adone, that acts on the longitudinal relative modes of oscillation of the two e^+, e^- beams, of three bunches each. The stability condition for small oscillations of rigid bunches is analitically found. The system, implemented with two resonators tuned at the 8^{th} harmonic of the revolution frequency, is described. The results are discussed.

1. - Introduction

The instabilities of the synchrotron oscillations of particle bunches in a circular accelerator are known and their mechanism has been discussed by many authors[1,2,3] together with the means to counteract them. However the damping systems designed or implemented for storage rings up to the present time were made for beams containing only one bunch. In this work we shall describe the damping system for the e^+, e^- beams in Adone, containing three bunches each.

As it is known, the longitudinal modes of oscillation of the bunches of a beam may be classified in center of mass mode and relative modes. The latter are the most difficult to deal with and may be damped in two ways. One way is to split the synchrotron frequencies of the various bunches by means of a sinusoidal voltage whose frequency is a multiple of the revolution frequency but not of the main radio-frequency. In Adone we have introduced 2KV peak by means of a small resonator tuned at 71.4 MHz which is the 25^{th} harmonic of the revolution frequency. This voltage alone has not been sufficient to damp the instabilities of the relative modes, especially at low energy, and it has been necessary to introduce the feedback damping system illustrated hereafter.

The centre of mass mode of oscillation of one beam has been damped by a feedback system that uses the main accelerating cavities to interact with the beam. This system has already been mentioned elsewhere[4] and will not be described in this paper. The mode of oscillation of the centers of mass of the two beams in phase opposition cannot be acted upon by any of the systems here described. However it can be influenced by splitting the synchrotron frequencies of the two beams. This can be achieved in Adone by varying suitably the phases of the R.F. voltages on two adjacent main accelerating gaps.

2.1. - Description of the feedback system for relative modes.

The block scheme of the feedback system is shown in Fig. 1. For the symbols used see Appendix A.

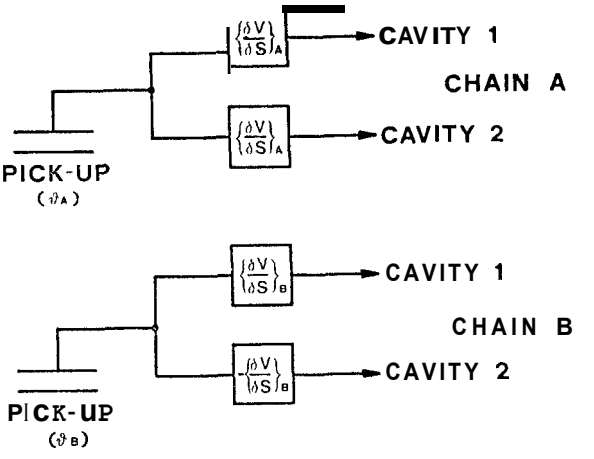


FIG. 1

As shown in the scheme, the system is made of two amplifying chains (A and B) and two cavities. The two amplifier chains correspond to two different equivalent positions of the pick-ups on the circumference of the accelerator and two different gains $(\Delta V/\Delta S)_A$ and $(\Delta V/\Delta S)_B$. From pick-up A the same signal is sent to the two cavities, from B the signal to cavity 2 is inverted w.r. to that sent to cavity 1. The signals from the two beams (e^+, e^-) are separated by a gate system, so that it is possible to shift the equivalent position of the pick-up for each beam merely by inserting delays. The pick-up gives a signal proportional to the radial displacement of the beams. There are various reasons for employing a transverse position pick-up instead of a longitudinal one. The most immediate one is that the radial displacement signal has a 90^o phase shift w.r. to the longitudinal displacement, so that its phase is already the correct one to be fed back on the beam. There is however5 a fundamental reason that excludes the use of a longitudinal position pick-up in a feedback system on many bunches, because with such a signal it is impossible to damp simultaneously all the modes of oscillation.

2.2. - Equations of motion.

The linearized motion equations, in the absence of radiation damping and noise, written as iterative equations turn by turn, are[3]:

$$\phi^{\pm}_{l,m} - \phi^{\pm}_{l,m-1} = \varrho\, \varepsilon^{\pm}_{l,m} \qquad (1)$$

$$(l=1,2,3\ldots,\ -\infty < m < +\infty)$$

$$\varepsilon^{\pm}_{l,m} - \varepsilon^{\pm}_{l,m-1} = -\frac{\Omega^{2\pm}}{\varrho}\,\phi^{\pm}_{l,m} +$$

$$+N\sum_{k=1}^{3}\sum_{n=-\infty}^{+\infty}\left(C^{\mp}_{k-l,n-m}\,\phi^{\mp}_{k,n} + C^{o}_{k-l,n-m}\,\phi^{\pm}_{k,n}\right) + \qquad (1)$$

$$+N\sum_{k=1}^{3}\sum_{n=-\infty}^{+\infty}\left(S^{\mp}_{k-l,n-m}\,\varepsilon^{\mp}_{k,n} + D^{\pm}_{k-l,n-m}\,\varepsilon^{\pm}_{k,n}\right)$$

The meaning of the symbols is the following:

$\phi^{\pm}_{k,m}$, $\varepsilon^{\pm}_{k,m}$ — Displacement from synchronous phase and energy of the k^{th} bunch $e^{\pm}$ at the m^{th} turn.

$$\varrho = \frac{2\pi a}{E}$$

a = momentum compaction
E = energy of synchronous particle
$\Omega^{\pm}$ = synchrotron frequency of $e^{\pm}$ beam in unities of the revolution frequency ω_o.
$C^{\pm}_{r,s}$, $C^{o}_{r,s}$ — coefficients that give a weight to the signals left in the cavities in the preceding turns.
$D^{\pm}_{r,s}$, $S^{\pm}_{r,s}$ — coefficients that take into account the action of feedback.

In Appendix A are reported the expression of:

$$\Omega^{2\pm},\ C^{\pm}_{r,s},\ C^{o}_{r,s},\ D^{\pm}_{r,s},\ S^{\pm}_{r,s}$$

Equations (1) are obtained using the approximation of rigid bunches. We also suppose that in the accelerator are circulating 3 bunches per beam with an identical number of particles, and that the synchronous phase is equal for the various bunches.

2.3. - Damping coefficients.

Neglecting the difference $(\Omega^{2+} - \Omega^{2-})$ and sup posing the two feedback cavities identical, we obtain from equations (1) the damping coefficients (see again ref. 3) for the four relative modes:

$$\delta^{\pm}_{r} = 3N\left\{g_A\left[\cos(m_o(\theta_A-\theta_1)) + \cos(m_o(\theta_A-\theta_2))\right] + \right.$$

$$+ g_B\left[\cos(m_o(\theta_B-\theta_1)) - \cos(m_o(\theta_B-\theta_2))\right] + \qquad (2)$$

$$\left. + \gamma\,\mathrm{Re}\left(\alpha_{r\pm}\sqrt{\Delta_r}\right)\right\} \qquad r = 1,2$$

with: Re( ) = real part of( ).

$$\Delta_r = \left\{g_A\left[\cos(m_o(\theta_A+\theta_1)) + \cos(m_o(\theta_A+\theta_2))\right] + \right.$$

$$+ g_B\left[\cos(m_o(\theta_B+\theta_1)) - \cos(m_o(\theta_B+\theta_2))\right] + \gamma\,\alpha^{c}_{r}\Big\}^2 + \qquad (3)$$

$$+\left\{g_A\left[\mathrm{sen}(m_o(\theta_A+\theta_1)) + \mathrm{sen}(m_o(\theta_A+\theta_2))\right] + \right.$$

$$\left. + g_B\left[\mathrm{sen}(m_o(\theta_B+\theta_1)) - \mathrm{sen}(m_o(\theta_B+\theta_2))\right] + \gamma\,\alpha^{s}_{r}\right\}^2 -$$

$$-\left\{g_A\left[\mathrm{sen}(m_o(\theta_A-\theta_1)) + \mathrm{sen}(m_o(\theta_A-\theta_2))\right] + \right.$$

$$\left. + g_B\left[\mathrm{sen}(m_o(\theta_B-\theta_1)) - \mathrm{sen}(m_o(\theta_B-\theta_2))\right]\right\}^2$$

where:

$$g_{A,B} = \frac{e\psi}{4E}\left(\frac{\Delta V}{\Delta S}\right)_{A,B}, \qquad \gamma = \frac{e^2\,\omega_o\,\varrho}{2\,\Omega_o}$$

ψ = closed orbit function at the pick-up position;
$\theta_{1,2}$ = longitudinal abscissa of the feedback cavities 1, 2;
$\theta_{A,B}$ = equivalent longitudinal abscissa of pick-up for chains A, B;
$\Omega_o \approx \Omega^{+} \approx \Omega^{-}$
m_o = harmonic of the revolution frequency to which are tuned the feedback cavities;
α_r, α^{c}_{r}, α^{s}_{r} $(r = 1, 2)$ = coefficients that depend on the impedances of the resonant modes of the cavities interacting with the beam along its path; for their expressions see Appendix A.

In order that the four relative oscillation modes be stable, it is necessary that the four coefficients δ^{+}_{1}, δ^{-}_{1}, δ^{+}_{2}, δ^{-}_{2} be positive.

As the sign before the term $\sqrt{\Delta_r}$ is ambiguous, it is convenient to choose the parameters of the feedback system so that the dependance of Δ_r on g_A and g_B disappears.

If we choose:

$$a_A = \frac{n\,n}{m_o} + \frac{\theta_1+\theta_2}{2}$$

$$\theta_B = \frac{\pi s}{m_o} + \frac{n}{2m_o} + \frac{\theta_1+\theta_2}{2} \qquad (4)$$

$$g_A = (-1)^n g\,\mathrm{sen}\left(m_o\,\frac{\theta_1-\theta_2}{2}\right) \qquad n = 0, \pm1, \pm2, \ldots$$

$$g_B = (-1)^s g\cos\left(m_o\,\frac{\theta_1-\theta_2}{2}\right) \qquad s = 0, \pm1, \pm2, \ldots$$

we obtain for $\sqrt{\Delta_r}$ an expression that is independent from gain parameters:

$$\sqrt{\Delta_r} = \gamma\sqrt{(\alpha^{c}_{r})^2 + (\alpha^{s}_{r})^2}$$

and we have:

$$\delta^{\pm}_{r} = 3N\left[2g\,\mathrm{sen}(m_o(\theta_2-\theta_1)) + \gamma\,\mathrm{Re}\left(\alpha_{r\pm}\sqrt{(\alpha^{c}_{r})^2 + (\alpha^{s}_{r})^2}\right)\right] \qquad (5)$$

The physical meaning of the choice made above is that the equivalent pick-up for chain A is placed, with respect to the intermediate point between the two feedback cavities $(\theta_1+\theta_2)/2$, in a crossing point for the displacement of the bunches at the harmonic m_o of the revolution frequency, while pick-up B is placed in a non-crossing point. Thus chain A sees only the in-phase modes of the two beams, while B sees only the ones in pnase opposition. The conditions on g_A and g_B exclude effects arising from interference between in-phase and counter-phase modes.

3.1. - Implementation of the system.

With reference to the scheme of Fig. 1, and to equations (4) the feedback system can be implemented with two cavities tuned at the harmonic m_o of the revolution frequency ω_o, where m_o is not a multiple of the main radio frequency and with two pick-ups placed one at a crossing point and the other one at a non crossing point at frequency $m_o\omega_o$. From the same equations we see that the gains of the two chains, g_A and g_B, are equal if the distance between two feedback cavities along the circumference is a whole number of half wavelengths plus one quarter wavelenght, still at frequency $m_o\omega_o$. Imposing the latter condition, as it simplifies the system, and given the physical distance L between the two gaps, the harmonic m_o is determined:

$$2\pi m_o \frac{L}{C} = \frac{\pi}{2} + k\pi \qquad k = 0, 1, \ldots$$

Where C is the perimeter of the accelerator. In Adone C = 105 m, L = 16.5 m, so, for k = 2 it results $m_o \approx 8$ with an error of about 3 degrees on the angular distance. As $\omega_o = 2.856$ MHz the resonant frequency of the cavities results $m_o\omega_o = 22.8$ MHz. Another condition on the cavities is that their bandwidth be large with respect to the synchrotron oscillation frequency.

Furthermore the pick-ups must behave as magnetic ones, i. e. the signal must depend only on transverse displacement and not on the sign of the particle. The two pick-ups can be reduced to only one by means of suitable delays added in the chains, as it was already mentioned. To see this let us choose the origin of coordinates in the mid point between feedback cavities as in Fig. 2, where θ_1, θ_2 are the coordinates of the cavities, θ_A, θ_B those of the pick-ups.

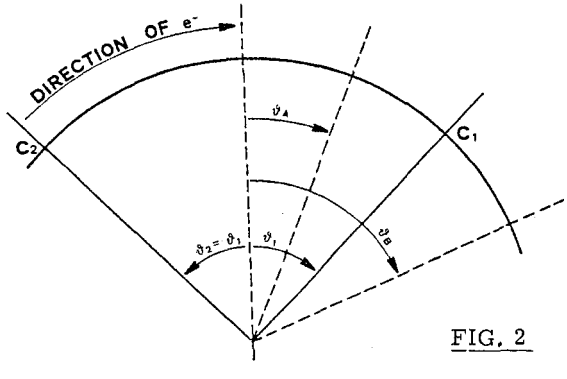


FIG. 2

We may write, for the signals from two e^+, e^- bunches on a pick-up situated at an abscissa θ^x, at frequency $m_o\omega_o$, using phasor notation:

$$w^+(\theta^x) = w^+ e^{i\varphi^+} e^{+im_o\theta^+} = W^+ e^{+im_o\theta^x}$$

$$w^-(\theta^x) = w^- e^{i\varphi^-} e^{im_o\theta^x} = W^- e^{-im_o\theta^x}$$

where φ^+, φ^- are the phases of each bunch through the origin; w^+, w^- are proportional to the bunch intensities. Remembering that $\theta_A = n\pi/m_o$, $\theta_B = (s\pi/m_o) + (\pi/2m_o)$ we may write:

$$w^+(\theta A) = W^+(-1)^n; \qquad w^-(\theta_A) = W^-(-1)^n$$

$$w^+(\theta_B) = +iW^+(-1)^s; \qquad w^-(\theta_B) = -iW^-(-1)^s$$

Calling v_1, v_2 the voltages on cavities C_1 and C_2 and choosing n, s both even or odd, we obtain:

$$v_1 \propto W^+(1+i) + W^-(1-i) \propto W^+ e^{+i\pi/4} + W^- e^{-i\pi/4}$$

$$v_2 \propto W^+(1-i) + W^-(1+i) \propto W^+ e^{-i\pi/4} + W^- e^{+i\pi/4}$$

We may rewrite these equations as follows:

$$v_1 \propto \left[W^+ e^{+im_o\theta^x} e^{-i(-\frac{\pi}{4} + m_o\theta^x)} + W^- e^{-im_o\theta^x} e^{-i(\frac{\pi}{4} - m_o\theta^x)} \right]$$

$$v_2 \propto -i\left[W^+ e^{im_o\theta^x} e^{-i(-\frac{\pi}{4} + m_o\theta^x)} - W^- e^{-im_o\theta^x} e^{-i(\frac{\pi}{4} - m_o\theta^x)} \right] \qquad (5)$$

If the signals due to e^+, e^- are separated by means of gates, they can be delayed independently and equations (5) can be translated into the block scheme of Fig. 3.

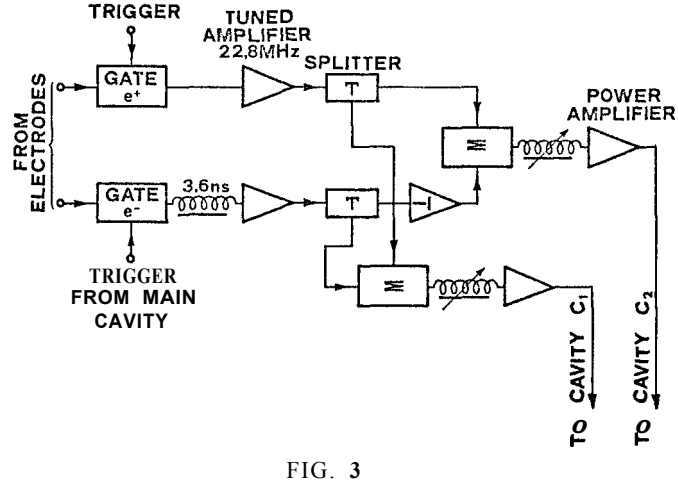


FIG. 3

In Fig. 3 the signals are taken from one only pick-up placed in θ^x, the e+ and e⁻ channels are separated by gating and the signals are combined according to equations (5). Taking into account the effective position of the pick-up as it results from Fig. 4, the shown values of the delays turn out.

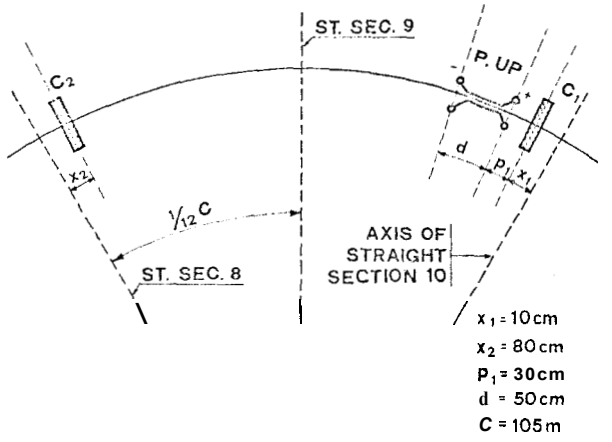


FIG. 4

3.2. - Pick-up sensitivity and loop gain.

The signals proportional to transverse displacement are taken from a strip-line pick-up similar to that already used in Stanford'. The difference between the signals from the two electrodes is made by means of hybrid junctions, as illustrated in Fig. 5.

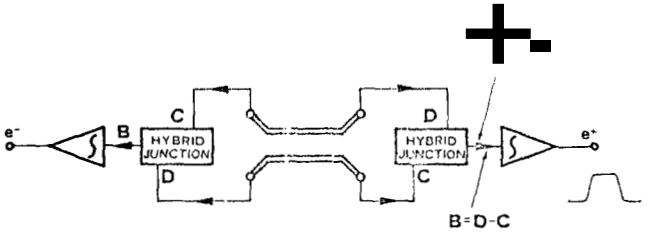


FIG. 5

The pick-up system therefore behaves as a magnetic pick-up, i.e. the polarity of the signal depends only on the transverse displacement and not on the sign of the particle. The wave form, after integration, is a train of approximately rectangular pulses, whose width is about 5 nsec (of the order of twice the transit time of a wavefront along the electrodes and whose period is 350 nsec. The peak voltage is $S = \approx 4,2$ mV/ < mA > bunch. The 8th harmonic of such a waveshape is $\approx 2.7 \times 10^{-2} S$, the gain of the chains has resulted about 100 db, therefore $(1/e\omega_o)(\Delta V/\Delta S) = \approx 11.5$ V/mm < mA > bunch. Supposing the oscillations to be caused by one only resonant line at ≈100 MHz, and remembering that

$$g = \frac{e}{4}\left(-\frac{\Delta V}{\Delta S}\right)\frac{\psi}{E} \gtrsim \gamma\, a_s$$

with

$$\gamma = \frac{\pi\, a\, e^2\, \omega_o}{\Omega\, E}, \quad \left(\text{hB-s-}\frac{\Omega}{2\pi}\right) \approx 35$$

$a_s \gtrsim 35\, Z(35\,\omega_o)$, $a = 10^{-2}$, $\Omega = 3,3 \times 10^{-3}$ at 1 GeV, $\omega_o^s = 2\pi \times 3$ MHz, $\psi = 2$m, we obtain $Z(35\,\omega_o) = 17$ KΩ i.e. the instability could be caused by a spurious mode of the cavities of shunt impedance 17 KΩ at 100 MHz.

4. - Conclusions.

The adjustment of the system is simple enough. It is made with only one beam and with only one feedback cavity working at a time, by acting separately on the variable delays shown on each chain.

The feedback system described is working on Adone. In Fig. 6 we show a photo of straight section 10 with one of the feedback cavities and the synchrotron frequency splitting cavity.

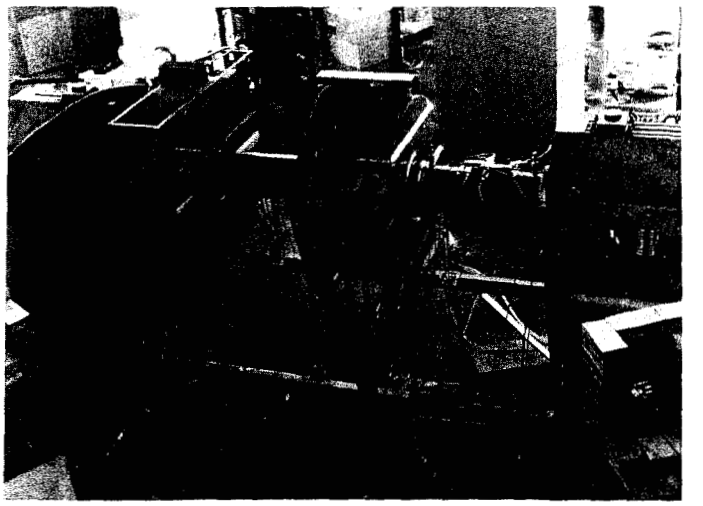


FIG. 6

Straight section with 71.4 MHz cavity and one of the feedback cavities.

The system has resulted essential for a good injection and to avoid sudden beam losses, especially at low energies. Care must be taken that the signal level, depending on the stored current level, does not saturate the amplifiers.

Acknowledgments.

Thanks are due to all the Adone staff and particularly to D. Fabiani for collaboration.

Appendix A.

Definitions:

B = n° of bunches per beam (in Adone B=3)
N = n° of particles per bunch
N_C = number of spurious cavities
N_{RF} = n° of accelerating cavities
v_j, ψ_j = peak voltage and phase of the j^{th} accelerating cavity.
$\varrho = 2\pi a/E$, a = momentum compaction, E = energy of synchronous particle.
e = charge of the electron
ϕ_o = synchronous phase (supposed equal for all bunches)
$\theta_{A,B}$ = azimuth of pick-up of chain A, B.
$Z_j(\omega)$, θ_j = impedance and azimuth of j^{th} cavity (indexes 1, 2 refer to the feedback cavities).
$\omega_o = 2\pi/T$ = revolution frequency.
$i = \sqrt{-1}$

$$\mu_{A,B} = \frac{e\psi}{2E\,\omega_o Z^x}\left(\frac{\Delta V}{\Delta S}\right)_{A,B}$$

$\left(\frac{\Delta V}{\Delta S}\right)$ = voltage in cavity (chain A, B) for a radial displacement ΔS at the pick-up.
β_y = closed orbit function at the pick-up.
Z^x = real part of feedback-cavities impedance at their harmonic frequency.

From reference 3 we have:

$$\Omega^{2\pm} = -e\varrho B \sum_{j=1}^{N_{RF}} V_j \cos\left[B(\phi_o \pm \theta_j) - \psi_j\right] + ie\varrho BN \sum_{j=1}^{N_C} \sum_{h=-\infty}^{+\infty} hB\,\omega_o Z_j(hB\,\omega_o)(1+e^{\mp 2ihB\theta_j})$$

$$C^o_{r,s} = \frac{ie^2}{\omega_o} \sum_{j=1}^{N_C} \int_{-\infty}^{+\infty} \omega\, d\omega\, Z_j(\omega)\, e^{i\omega(s+\frac{r}{B})T}$$

$$C^{\pm}_{r,s} = \frac{ie^2}{\omega_o} \sum_{j=1}^{N_C} \int_{-\infty}^{+\infty} \omega\, d\omega\, Z_j(\omega)\, e^{i\omega(s+\frac{r}{B}\pm\frac{\theta_j}{\cdot})T}$$

$$D^{\pm}_{r,s} = \sum_{j=1}^{2} \int_{-\infty}^{+\infty} d\omega\, Z_j(\omega) e^{i\omega(s+\frac{r}{B})T} \left(\mu_A e^{\pm i\omega\frac{\theta_A-\theta_j}{2\pi}T} - (-1)^j \mu_B e^{\pm i\omega\frac{\theta_B-\theta_j}{2\pi}T}\right)$$

$$S^{\pm}_{r,s} = \sum_{j=1}^{2} \int_{-\infty}^{+\infty} d\omega\, Z_j(\omega) e^{i\omega(s+\frac{r}{B})T} \left(\mu_A e^{\pm i\omega\frac{\theta_A+\theta_j}{2\pi}T} - (-1)^j \mu_B e^{\pm i\omega\frac{\theta_B+\theta_j}{2\pi}T}\right)$$

$$a_r = \sum_{j=1}^{N_C} \sum_{h=-\infty}^{+\infty} (hB-r-\frac{\Omega_\varrho}{2\pi}) Z_j\left[(hB-r-\frac{\Omega_\varrho}{2\pi})\,\omega_o\right]$$

$$\alpha^c_r = \sum_{j=1}^{N_C} \sum_{h=-\infty}^{+\infty} (hB-r-\frac{\Omega_o}{2\pi}) Z_j\left[(hB-r-\frac{\Omega_o}{2\pi})\,\omega_o\right] \cos\left[2(hB-r-\frac{\Omega_o}{2\pi})\theta_j\right]$$

$$a^s_r = g \sum_{j=1}^{N_C} \sum_{h=-\infty}^{+\infty} (hB-r-\frac{\Omega_o}{2\pi}) Z_j\left[(hB-r-\frac{\Omega_o}{2x})\,\omega_o\right] \operatorname{sen}\left[2(hB-r-\frac{\Omega_\varrho}{2\pi})\theta_j\right]$$

References.

1 - F. Amman, IEEE Trans. NS-16, 1073 (1969).
2 - D. Boussard and J. Gareyte, Proc. 8th Intern. Conf. on High Energy Accelerators - CERN (1971).
3 - C. Pellegrini and A. Renieri, Frascati Internal report MEMO-T 64 (1974).
4 - F. Amman et al., Proc. 8th Intern. Conf. on High Energy Accelerators CERN (1971).
5 - M. Bassetti, Frascati Internal report MEMO-T 34 (1971).
6 - J.L. Pellegrin, Nuclear Instr. and Meth. 108, 365 (1973).

FAST BEAM-CAVITY INTERACTION AND ITS EFFECT ON BUNCH SHAPE IN STORAGE RINGS†

A. Papiernik, M. Chatard-Moulin, and B. Jecko

Laboratoire d'Electronique et Microondes
U.E.R. des Sciences, Limoges, France

Summary

When a bunch of stored particles passes a gap, it induces fields which affect the energy of the particles, and hence the bunch shape. An analytical formula giving the transient voltage is derived for a short bunch of any shape. The equilibrium bunch shape is calculated using Haïssinski's self consistant theory. The bunch lengthens, but comparison with experiment shows that beam-cavity fast interaction is not the main reason for bunch lengthening in rings having only one cavity.

Introduction

The longitudinal equilibrium shape of a bunch circulating in a storage ring is related to the effective accelerating voltage by[1]

$$I(\tau) = K \exp \left\{ \frac{}{} \left[eV(y) - U_o \right] dy \right\}$$

where τ is the time displacement between a particle of the bunch and an origin which will be defined below,

$I(\tau)$ is the instantaneous intensity in the bunch,

$V(\tau)$ is the effective accelerating voltage,

U_o is the average energy loss per turn,

T_o is the revolution period in the ring,

$K = I(0)$ is a constant which, as we shall see, is related to the total charge of the bunch,

H_o is a constant which depends on ring characteristics and energy.

The effective accelerating voltage $V(\tau)$ is the sum of two terms : the sinusoidal voltage $V_{RF}(\tau)$, and a transient voltage $U(\tau)$ due to the self fields induced by the bunch

$$V(\tau) = V_{RF}(\tau) + U(\tau) \quad . \qquad (2)$$

$V_{RF}(\tau) = \hat{V} \sin(\omega\tau + \phi_s)$ is the accelerating voltage, taking into account sinusoidal beam loading.

The time origin $\tau = 0$ is defined such that $eV_{RF}(0)$ compensates exactly the average energy loss U_o.

Since the bunches are much shorter than the wavelength, V_{RF} may be linearized :

$$eV_{RF}(\tau) = U_o + e\,\dot{V}_{RF} \times \tau \qquad (3)$$

where $\dot{V}_{RF} = w\,\hat{V} \cos\phi_s = \omega \sqrt{\hat{V}^2 - (U_o/e)^2}$ is the slope of the sinusoidal voltage at origin.

At low current, the transient self fields are weak, and $U(\tau)$ may be neglected.

Under such conditions, the instantaneous equilibrium current has a gaussian shape :

$$I(\tau) = K \exp(-\tau^2/2\sigma_o^2)$$

where $\sigma_o = \sqrt{T_o H_o / e\,\dot{V}_{RF}}$ is the standard deviation of the gaussian distribution.

At higher currents, the bunch shape depends on the transient induced voltage $U(\tau)$:

$$I(\tau) = K \exp\left[-\frac{\tau^2}{2\sigma_o^2} - \frac{1}{\sigma_o^2\,\dot{V}_{RF}} \int_0^\tau U(y)\,dy \right] \quad . \qquad (4)$$

The transient voltage $U(\tau)$ results from interaction between the bunch and the elements of the ring (accelerating cavity, vacuum chamber, ...). Then it depends on $I(\tau)$ and geometrical environment.

We give here below an analytical formula of $U(\tau)$ expressing only bunch-cavity interaction. Then we obtain the shape, length and position of the bunch for DCI and ACO. Finally, we compare the results with measurements on ACO.

Evaluation of the transient voltage $U(\tau)$

The detailed calculations have been reported in the reference[2]. We restrict ourselves here to the main points.

Geometry of the cavity gap

Figure 1 shows the DCI cavity. The apertures for the beam are neglected. The field front generated by the bunch propagates radially at light velocity ; the influence of the radius R_o of the gap plate appears on the axis only after a time $2R_o/c$. Thus, if the bunch is short enough, the cavity may be replaced by any cylinder of height g and radius $R > R_o$ (fig. 2).

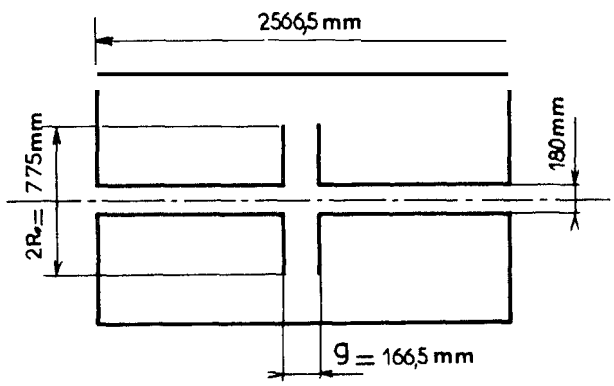


Fig. 1 : Actual geometry of the DCI cavity.

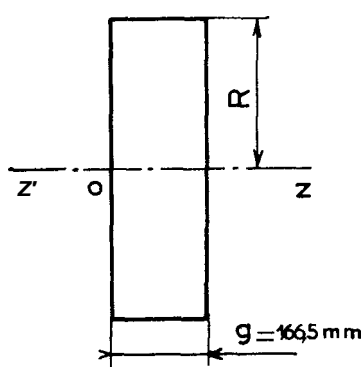


Fig. 2 : Equivalent simplifies geometry.

Self field and voltage generated by the bunch are calculated by summing the response to a unit step of current

We denote by $U_H(x)$ the transient voltage acting on the particle entering the cavity at a time x later than the head of the unit step of current to which it belongs. If the actual instantaneous intensity $I(\tau)$ in the bunch is zero outside the interval $[-b, +b]$ and continuous inside, the transient voltage $U(\tau)$ is :

$$U(\tau) = -\int_0^{b-\tau} U_H(x)\, \dot{I}(\tau + x)\, dx \qquad (5)$$

$U_H(x)$ is evaluated by eigenmode method [3,4,5]

We obtain :

$$U_H(x) = \frac{-1}{\pi \varepsilon_o c} \sum_{p=0}^{\infty} \sum_{n=1}^{\infty} \frac{\alpha_p}{v_{on}^2 J_1^2(v_{on})\, \omega_{onp}} \left\{ 2 \sin \omega_{onp} x - (-1)^p \sin\left[\omega_{onp}\left(x - \frac{g}{c}\right)\right] - (-1)^p \sin\left[\omega_{onp}\left(x + \frac{g}{c}\right)\right] \right\} \qquad (6)$$

$\alpha_p = 1$ if $p = 0$ and $\alpha_p = 2$ if $p \neq 0$.

v_{on} is the n^{th} root of Bessel function J_o and $\omega_{onp} = c\sqrt{(v_{on}/R)^2 + (p\pi/g)^2}$.

Using properties of Fourier series and Fourier-Bessel series, we find :

$$\sum_{p=0}^{\infty} \sum_{n=1}^{\infty} \frac{\alpha_p}{v_{on}^2 J_1^2(v_{on})} \frac{\sin \theta \sqrt{\left(\frac{v_{on}}{R}\right)^2 + \left(\frac{p\pi}{g}\right)^2}}{\sqrt{(v_{on}/R)^2 + (p\pi/g)^2}} = \begin{cases} -\frac{g}{2} \ln \frac{\theta}{R} & \text{when } 0 < \theta < 2g < R \\ -\frac{g}{2}\left(\ln \frac{\theta}{R} + \ln \frac{\theta^2 - 4g^2}{R^2}\right) & \text{when } 2g < \theta < 4g < R \end{cases} \qquad (7)$$

$$\sum_{p=0}^{\infty} \sum_{n=1}^{\infty} \frac{(-1)^p\, \alpha_p}{v_{on}^2 J_1^2(v_{on})} \frac{\sin \theta \sqrt{\left(\frac{v_{on}}{R}\right)^2 + \left(\frac{p\pi}{g}\right)^2}}{\sqrt{(v_{on}/R)^2 + (p\pi/g)^2}} = \begin{cases} 0 & \text{when } 0 < \theta < g < R \\ -\frac{g}{2} \ln \frac{\theta^2 - g^2}{R^2} & \text{when } g < \theta < 3g < R \\ -\frac{g}{2}\left|\ln \frac{\theta^2 - g^2}{R^2} + \ln \frac{\theta^2 - 9g^2}{R^2}\right| & \text{when } 3g < \theta < 5g < R \end{cases}$$

Using (7), the double sum (6) simplifies into :

$$U_H(x) = \begin{cases} -\frac{1}{2\pi\varepsilon_o c} \ln\left(1 + \frac{2g}{cx}\right) & \text{when } 0 < x < \frac{2g}{c} \\ -\frac{1}{2\pi\varepsilon_o c} \ln\left(1 + \frac{2g}{cx+2g}\right) & \text{when } \frac{2g}{c} < x < \frac{4g}{c} \end{cases}$$

We can take for $U_H(x)$ practically without appreciable error :

$$U_H(x) = -\frac{1}{2\pi\varepsilon_o c} \ln\left(1 + \frac{2g}{cx}\right) . \qquad (8)$$

Expression for $U(\tau)$

From (5) and (8) we get :

$$U(\tau) = \frac{1}{2\pi\varepsilon_o c} \int_0^{b-\tau} \ln\left(1 + \frac{2g}{cx}\right) \dot{I}(x + \tau)\, dx . \qquad (9)$$

Determination of the bunch shape equilibrium

From the formulas (4) and (9), we obtain the equation satisfied by $I(\tau)$:

$$I(\tau) = K \exp\left[-\frac{\tau^2}{2\sigma_o^2} - \frac{1}{2n\varepsilon_o c \sigma_o^2 V_{RF}} \left| \int \ln\left(1 + \frac{2g}{cx}\right) \dot{I}(x + y)\, dx\, dy \right|\right]$$

This equation may be written in the form $I(\tau) = F[I(\tau)]$ where F is the operator defined on the rhs of (10). $I(\tau)$ is determined by iteration as the limit of the set of functions

$$I_n(\tau) = F[I_{n-1}(\tau)]$$

where $I_0(\tau)$ is an arbitrary function ; for example $I_0(\tau) = 0$, then $I_1(\tau) = K \exp(-\tau^2/2\sigma_o^2)$.

Equation (10) is solved numerically using an IBM 1130 computer by noticing that :

(i) given σ_o and V_{RF}, the solutions $I(\tau)$ of (10) depend on K. For each value of K, we can solve $I(\tau)$ and find the bunch charge

$$Q = \int_{-b}^{} I(\tau)\, d\tau$$

It can be noticed that K determines finally the value of Q.

(ii) according to the latter remark and to the form of (10), it follows clearly that the ratio $I(\tau)/Q$ depends only on the two parameters σ_o and $Q/\dot{V}_{RF}$.

σ_o is the standard deviation of the gaussian distribution when the self fields are disregarded. $Q/\dot{V}_{RF}$ depends on the parameters of the storage ring

$$\frac{Q}{\dot{V}_{RF}} = \frac{i\, T_o^2}{2\pi\, h\, \left[\hat{V}^2 - (U_o/e)^2\right]^{1/2}}$$

where $i = Q/T_o$ is the mean current in the ring, and h is the harmonic number.

	T_o (ns)	h	i (mA)	$\hat{V}\cos\phi_s$ (kV)	$Q/\dot{V}$ (10^{-20} C s V^{-1})
ACO	73	2	30	17.5	.0726
ADONE	350	3	60	120	.325
SPEAR	780	*40*	50	*400*	.0302
DCI	316	8	350	350	.198

Table I gives the value of the parameter Q/V for some storage rings.

Application to DCI

With the above assumption we have calculated the bunch shape in DCI using the following characteristics :

- number of accelerating cavities : 1,
- operating frequency of the cavity : 25.352 MHz (h=8),
- transit time through the gap g/c = .555 ns,
- order of magnitude of $\dot{V}_{RF}(0) \simeq 10^{13}$ V/s,
- order of magnitude of charge Q : 10^{10} to 10^{12} particles.

The exact hunch shape and the transient voltage are shown in figures 3 and *4* for the particular case $\sigma_o = 0.2 \times 10^{-9}$ s and $Q/\dot{V}_{RF} = .115 \times 10^{-20}$ C.s.V^{-1}.

In figure 3, it can be noticed that the gaussian distribution which describes the bunch shape when the self fields of the cavity are disregarded is modified : the bunch is longer and the center of charge is shifted forward. The dotted straight line on figure *4*, whose slope is $\dot{V}_{RF}/Q$, allows comparison between the transient voltage and the RF voltage. We systematically study the deformation effect of the bunch versus σ_o and Q/V_{RF} by calculating the following parameters :

- half height bunch length ℓ (for the gaussian bunch, this length is $\ell_o = 2.35\ \sigma_o$),
- position τ_o of the center of charge defined by

$$\tau_o = \frac{1}{Q}\int_{-b}^{+b} \tau\, I(\tau)\, d\tau$$

- average energy loss $\langle U(\tau) \rangle$ defined by

$$\langle U(\tau)\rangle = \frac{1}{Q}\int_{-b}^{+b} U(\tau)\, I(\tau)\, d\tau \quad .$$

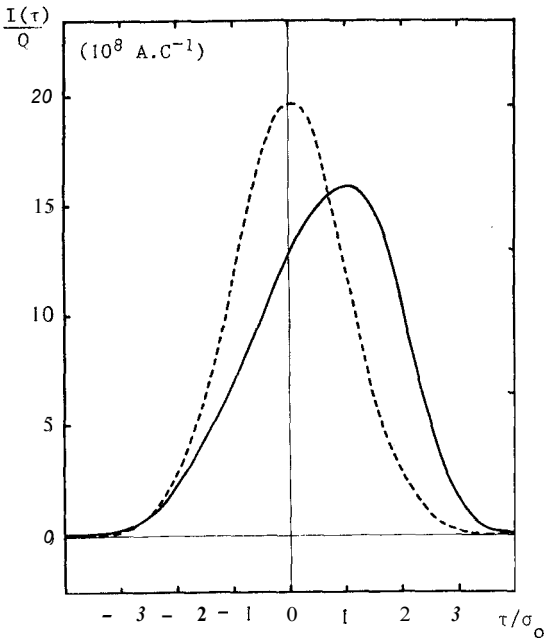


Fig. 3 : Bunch shape for σ = .2 ns.
$Q/\dot{V}_{RF} = .115 \times 10^{-20}$ C.s.V^{-1}.
The dotted curve represents the gaussian obtained by neglecting the self-fields.

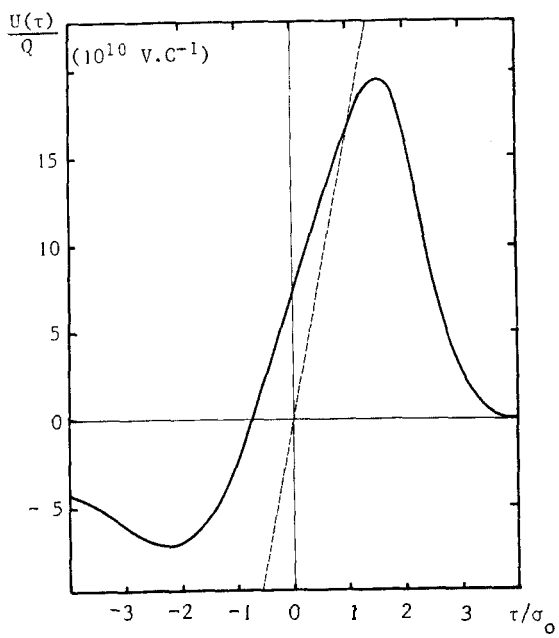


Fig. *4* : Transient voltage for σ = .2 ns,
$Q/\dot{V}_{RF} = .115 \times 10^{-20}$ C.s.V^{-1}.
The dotted line represents the sinusoidal voltage of the cavity.

The results are summed up in the curves of figures 5, 6 and 7 obtained by solving (10) for different values of σ_o and Q/V_{RF}. These curves stop where the iteration method becomes divergent and does not permit solutions. Notice in these conditions that the relative lengthening $(\ell - \ell_o)/\ell_o$ is at most 30 % and the relative center of charge shift τ_o/ℓ_o can reach 30 %.

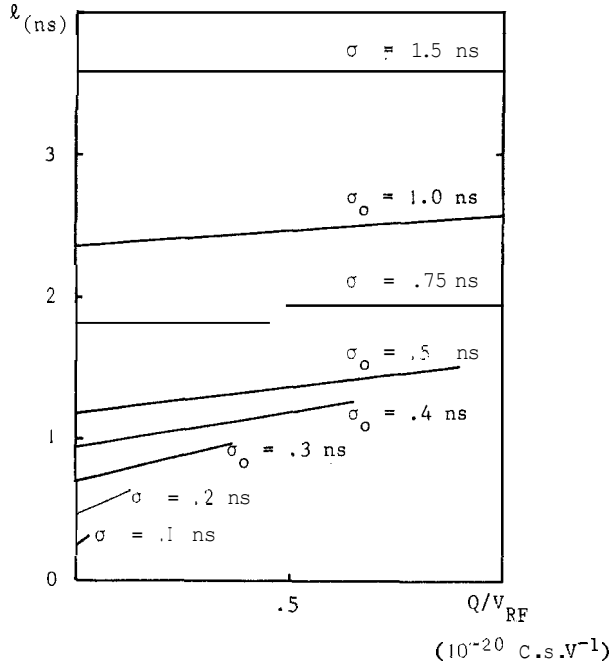


Fig. 5 : Evolution of bunch half-height length.

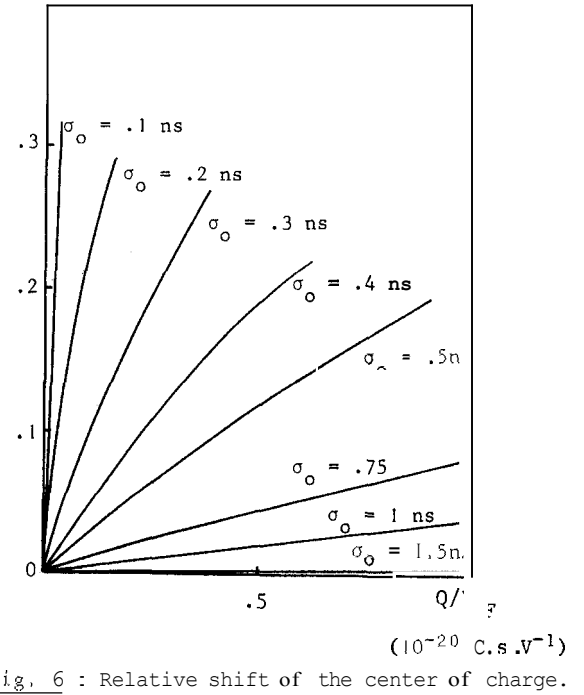


Fig. 6 : Relative shift of the center of charge.

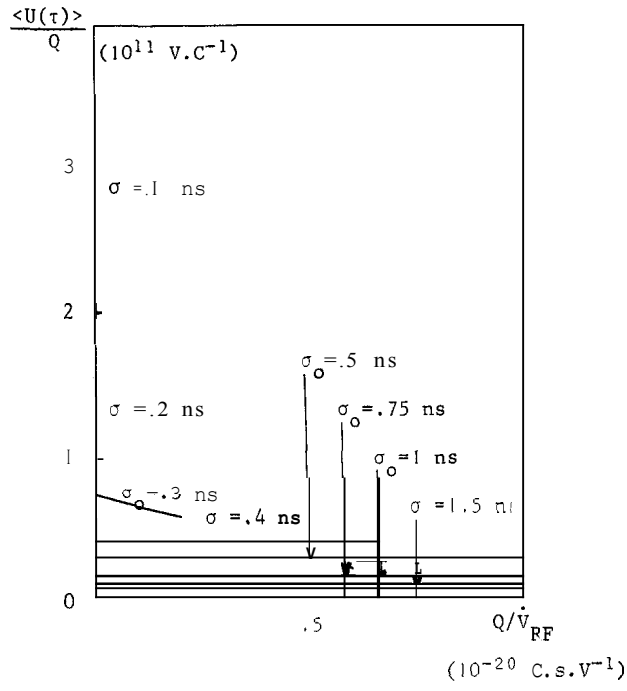


Fig. 7 : Average energy loss.

Application to ACO

The gap shape of ACO is quite complicated and can hardly be regarded as a cylindrical cavity.

However, since the expression of $U(\tau)$ only depends on the transit time g/c, we determined the lengthening on ACO using $g/c = 0.35$ ns.

Comparing with experimental results[6] (fig. 8), we notice that the bunch-cavity interaction does not explain more than 25 to 40 % of the total lengthening.

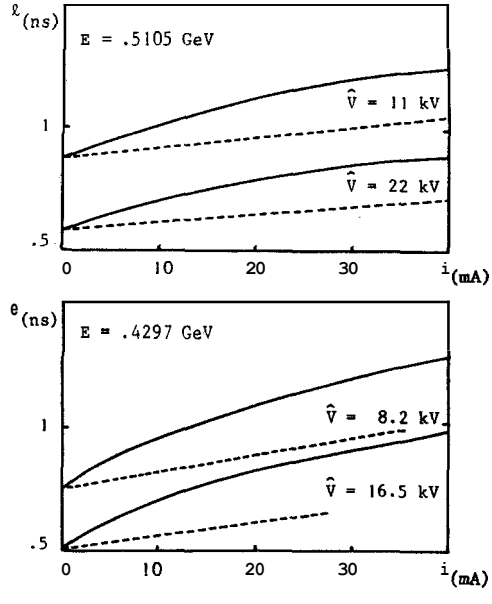


Fig. 8 : Evolution of the ACO bunch length versus beam intensity.

——— experimental length

- - - - - calculated length

Conclusion

The bunch-cavity interaction is not the main cause of bunch lengthening observed at high intensity in storage rings using only one cavity. Actually, at each discontinuity of the vacuum chamber, the bunch loses energy and a transient voltage similar to those we have studied appears. The geometry of the vacuum chamber being very complicated, even a simplified calculation is difficult. However, when storage rings are equipped with several accelerating cavities, the bunch-cavity interactions can generate important bunch lengthening.

Acknowledgments

We wish to express our thanks to Professor Haïssinski, Dr P. Brunet, Dr D. Potaux and Dr H. Zyngier for their encouragement and helpful suggestions.

† Work supported by the Laboratoire de l'Accélérateur Linéaire d'Orsay.

References

1. J. Haissinski, Il Nuovo Cimento 18 B, N° 1, pp 72-82 (1973)
2. M. Chatard-Moulin, B. Jecko and A. Papiernik, Rapport 73/A-1 Laboratoire d'Electronique et Micro-ondes, Université de Limoges, France (1973)
3. K. Kurokawa, LEEE Transactions on Microwave Theory and Techniques, MTT-6, pp. 178-187 (1958)
4. Van Bladel, Electromagnetic Field (Mc Graw-Hill), p. 308
5. M. Chatard-Moulin, B. Jecko and A. Papiernik, Rapport 73/A-2, Laboratoire d'Electronique et Micro-ondes, Université de Limoges, France (1973)
6. Groupe "Anneaux de Collisions", RT/34-69, Laboratoire de l'Accélérateur Linéaire, Orsay (1969)

LANDAU DAMPING BY NON-LINEAR SPACE-CHARGE FORCES AND OCTUPOLES

D. Möhl and H. Schönauer,
CERN, Geneva, Switzerland

Summary and Conclusions

Increasing the PSB and CPS intensities to 10^{13} ppp will require more powerful octupoles in order to overcome the transverse instabilities that are to be expected. Unfortunately, theory fails tc give quantitative predictions at low energies, where direct space-charge forces dominate over image forces. To be able to specify the future needs more precisely, an extension of the theory would be desirable, particularly since experimental evidence is such that it is hard to extrapolate to higher intensities.

The theory presented here solves the dispersion relation, including the influence of external and space-charge induced non-linearities in both transverse dimensions as well as a spread in the LNS coefficient U. Results are preliminary in the sense that modulation of the space-charge forces due to synchrotron motion is not included. They show that the combined effect of external and space-charge non-linearities in the two transverse planes can considerably enhance Landau damping in low-energy machines (up to 10 GeV, say). The sign of the octupole current is important especially for a flat beam, and should be chosen in such a way that ν increases with amplitude in the direction where the beam is wide.

Stability diagrams for several typical conditions are presented and applied to the PSB.

1. Introduction

Octupole lenses have been installed both in the CPS and its Booster years ago, and they have successfully cured transverse instabilities. It is planned to use more powerful lenses in the CPS, and possibly in the Booster too, in order to tame future intensities. It is puzzling, however, to observe that the currents needed to avoid instabilities are considerably lower than predicted by theory[1,2]. In addition, lower thresholds for radial rather than for vertical resistive wall instability were observed frequently in the PSB. These observations suggest that the influence of space-charge non-linearities and the spreads due to motion in the second transverse direction might be important.

An attempt to include these effects[3] already showed the importance of the variations due to the betatron amplitudes in the second transverse plane. This approach, however, still predicted too high octupole strengths and failed to give the correct behaviour in the limit of vanishing external octupole force. In this limit incoherent space-charge forces should have no influence on dipole motion, a fact which can be deduced from the single particle-equation[4] and is fully confirmed by computer simulation[5].

To make more reliable extrapolations, it was felt necessary to extend the theory in order to remove these deficiencies. The main difference of the present work in comparison with Ref. 3 is that we include space-charge non-linearity in both the driving term (the U-term of Ref. 1) and in the single-particle frequency.

A general model would have to include:

i) frequency spreads due to external non-linearities in both transverse (x and y) directions;

ii) spreads due to x- and y-non-linearities of space-charge forces;

iii) spreads due to the energy distribution of the beam;

iv) spreads due to longitudinal variation of transverse space-charge forces;

and probably other effects. In the present paper we content ourselves with considering the effects (i) and (ii). This is a valid approximation at least for the coasting beam experiments which were performed in the Booster and which exhibited the "anomalities" discussed above. We shall find that the combination of external and space-charge non-linearities can considerably enhance the stability conditions. and that the spreads from both transverse directions are important.

2. Dispersion Relation

Let us discuss dipole oscillations in one transverse (x) direction. Neglecting energy spread, the dispersion relation of Laslett, Neil and Sessler (LNS) can be written as

$$(U + V + iV)\int_0^\infty \frac{-\frac{1}{2}\, h'(a)a^2\, da}{\omega - (n - \nu_x)\Omega} = 1 \ . \qquad (1)$$

Here the tune $\nu_x = \nu_x(a)$ depends on a, the amplitude of the incoherent betatron oscillation; h(a) is the corresponding distribution function, $\int_0^\infty h(a)a\, da = 1$. The coefficient U + V + iV can be expressed in terms of the revolution frequency (Ω) and the incoherent ($\Delta\nu_{ic}$) and coherent ($\Delta\nu_c$) Laslett tune shifts (generalized to include wall resistivity and equipment interaction) :

$$U + V + iV = \Omega(\Delta\nu_c - \Delta\nu_{ic}) \ . \qquad (2)$$

Finally $\omega = (n - \nu)\Omega$ is the mode frequency (coasting beam mode n) to be obtained by solving Eq. (1); $\mathrm{Im}(\omega)$ is the growth rate, ν being the collective betatron frequency.

To include space-charge non-linearities as well as y-variation of ν_x we can use the derivation of Eq. (1) given by Hereward[6]. We start from the single-particle equation

$$\ddot{x}_i + \Omega^2\left[\nu_i^2(x_i,y_i) - 2\nu_0\Delta\nu_{ic}(x_i,y_i)\right]x_i = 2\Omega^2\nu_0\left[\Delta\nu_c - \Delta\nu_{ic}(x_i,y_i)\right]\bar{x} \ , \qquad (3)$$

where $\bar{x}$ is the dipole motion of the beam and x_i the motion of the test particle (coherent and incoherent). The corresponding dispersion relation is

$$\int_0^\infty \frac{(U + V + iV)(a,b)\ \ (-\frac{1}{2}\, h'(a)a^2)\, b\, g(b)\ da\, db}{\omega - [n - \nu(a,b)]\Omega} = 1 \ . \qquad (1a)$$

Here b is the incoherent y-amplitude, g(b) the corresponding distribution, $\int_0^\infty g(b)b\, db = 1$. The tune $\nu(a,b) = \nu_0(a,b) - \Delta\nu_{ic}(a,b)$ includes the incoherent tune shift, and so does U + V + iV through Eq. (2). The terms $\nu(a,b)$ and $(U + V + iV)(a,b)$ are obtained by averaging over the incoherent betatron motion.

To evaluate Eq. (1a) we make some further approximations: We assume that only the incoherent tune shift is non-linear, whereas the image term $\Delta\nu_c$ is the same for all particles. This is a valid approximation at low energy, where $\Delta\nu_c \ll \Delta\nu_{ic}$ and/or for thin beams. The case where both $\Delta\nu_c = \Delta\nu_c(a,b)$ and $\Delta\nu_{ic} = \Delta\nu_{ic}(a,b)$ but where external non-linearities are negligible (ν_i = const) was discussed in Ref. 4. We shall further expand $\nu(a,b)$ and only retain terms up to the octupole moment :

$$\Delta\nu_{ic}(a,b) = \Delta\nu_{ic}(0) + \frac{\partial\Delta\nu_{ic}}{\partial a^2}\,a^2 + \frac{\partial\Delta\nu_{ic}}{\partial b^2}\,b^2$$
$$= A - A\,a' - \Delta_b b^2 \ , \qquad (4)$$

and

$$\nu_0(a,b) = \nu_0(0) + \frac{\partial\nu_0}{\partial a^2}\,a^2 + \frac{\partial\nu_0}{\partial b^2}\,b^2$$
$$= \nu_0 + \nu_a a^2 + \nu_b b^2 \ .$$

The symbols A, Δ_a, Δ_b (all positive) and ν_a, ν_b are hereby defined and will be used throughout the rest of the paper. Quantities such as $\nu_a\hat{a}^2$, $\Delta_a\hat{a}^2$, etc., will be denoted as "external spread" and "space-charge spread", respectively; $\hat{a}$ and $\hat{b}$ are typical amplitudes to be defined below; "a "corresponds to the plane of the instability.

3. Results

Here we shall present the solution of the dispersion relation (1a) for two different distributions and for several typical conditions. We assume $\nu_a = 0$, $\nu_b = 0$ in Section 3.1; $\hat{a} >> \hat{b}$ in Section 3.2 and Figs. 1 and 2; $22 = \hat{b}$ in Section 3.3 and Figs. 3 and 4; and $\hat{a} << \hat{b}$ in Section 3.3 and Fig. 5.

3.1 No external non-linearities (i.e. $\nu_a = 0$, $\nu_b = 0$)

In this case incoherent space-charge has no effect, as was found already in Ref. 4. In fact it is easily verified from the single-particle equation (3) that $x_i = \bar{x}$ is a solution provided that $\nu_i^2 = \nu_0^2 - 2\nu_0\Delta\nu_c$ is the same for all particles. Under this condition $\Delta\nu_{ic}$ simply drops out from Eq. (3).

3.2 ν-spread due to betatron amplitudes in the plane of the instability only (i.e. $\hat{a} >> \hat{b}$)

3.2.1 "Semicircular" distribution

It is instructive to start with the distribution which -- without space charge forces -- leads to a circular range of stability and gives the rule-of-thumb criterion

$$4\,\frac{|U + V + iV|}{\Omega} \lesssim \delta\nu_{FWHH} \qquad (5)$$

for the stabilizing ν-spread. The derivative of this function which enters into Eq. (1a) is a half circle:

$$-\frac{1}{2}\,h'(a^2)\,da^2 = \frac{2}{\pi\hat{a}^2}\sqrt{1 - \left(\frac{a^2}{\hat{a}^2} - 1\right)^2}\,da^2, \qquad (6)$$
$$0 \le a^2 \le 2\hat{a}^2$$

Including now space-charge, the solution of the dispersion relation gives the stability boundary

$$V^2 + \frac{(U + V)^2}{\left(1 + \frac{2}{q_a}\right)^2} = \frac{\Omega^2}{4}\,(\nu_a\hat{a}^2)^2 \simeq \frac{\Omega^2}{16}\,(\delta\nu_{FWHH})^2 \ . \qquad (7)$$

Here we have introduced a parameter $q_a = \nu_a/\Delta_a$, the ratio of external spread to space-charge spread. U involves an average of $\Delta\nu_{ic}$

$$\frac{U}{\Omega} = \Delta\nu_c - (A - \Delta_a\hat{a}^2)\cdot \qquad (8)$$

For $1/q_a = 0$ we recover the rule of thumb (5). With space-charge spread, the stability circle is distorted into an ellipse with real half-axis:

$$\hat{U} = (\Omega/4)\,\delta\nu_{FWHH}\,(1 + 2/q_a) \ .$$

The stable range is thus increased or decreased depending on the sign of q_a, i.e. depending on the polarity of the octupoles. Typically the space-charge non-linearity is such that $2/q_a = \pm\,|U|/(\Omega\nu_a\hat{a}^2)$ (see Appendix). Hence for $V << |U|$ -- the case of interest in the PSB and in the CPS below 10 GeV -- the stability condition reduces to

$$4\,\frac{|U|}{\Omega} \le \frac{\delta\nu_{FWHH}}{1 \pm \frac{1}{2}} \simeq \delta\nu_{FWHH}\begin{cases}2\\0.67\end{cases}, \qquad (9)$$

and the stabilizing octupole ν-spread is about 0.67 or twice the value obtained from conventional theory $(1/q_a = 0)$.

Normalization: In the following we shall use a suitable normalization to reduce the number of parameters. We normalize frequencies (U,V) and spreads to the space-charge spread $S = \Omega\Delta_a\hat{a}^2$ in the plane of the instability We denote

$$u = \frac{U + V}{S}\bigg|_{\text{beam centre}}, \qquad v = \frac{V}{S} \ . \qquad (10)$$

This normalization is convenient because the range over which u can reasonably vary is small (values between-3 and-5 depending on the emittance ratio and the plane considered, are typical for the PSB), see Appendix.

Figure 1 displays stability boundaries' for the distribution (6) in this normalization. Note that the normalization (10) shifts the ellipse (7) towards more negative u-values because u refers to the beam centre.

The reduction of the stable area for the "wrong" octupole polarity ($q_a < 0$) can be seen from a comparison between Fig. 1a and Fig. 1b for given $|q_a|$, and is obviously due to cancellation of external and space-charge spread.

3.2.2 Parabolic distribution

Figure 2 gives similar results for a parabolic distribution:

$$h(a) = \frac{1}{2\hat{a}^2}\left[1 - \frac{a^2}{2\hat{a}^2}\right], \qquad 0 \le a^2 \le 2\hat{a}^2 \ . \qquad (11)$$

Again for negative q_a the stable area is largely reduced. One particularity of Fig. 2 is that all curves intersect the point $v = 0$, $u = -2$. It appears that this effect is due to the sharp cut-off of this distribution.

3.3 ν-spread due to betatron amplitudes in both transverse directions (parabolic distribution in each plane)

Now we have to introduce another two parameters:

$$p = \frac{\nu_b\hat{b}^2}{\nu_a\hat{a}^2}, \qquad r = \frac{\Delta_b\hat{b}^2}{\Delta_a\hat{a}^2}\ ; \qquad (12)$$

p denotes the ratio of the two external spreads and r the ratio of the space-charge spreads; $\hat{b}$ is the equivalent of $\hat{a}$ for the second transverse direction. Note that r is determined by the emittance ratio and varies from 0 for $\hat{a} >> \hat{b}$ to about 2 for $\hat{a} << \hat{b}$; $r = 1$ corresponds to $\hat{b} = 2\hat{a}$.

Figures 4 and 5 refer to parabolic distributions h(a) g(b) in Eq. (1a) and demonstrate the influence of the second transverse plane. In Figs. 3 and 4, $r = 1$, i.e. the same spreads $\Delta_a\hat{a}^2$ and $\Delta_b\hat{b}^2$ have been assumed.

The case $p = 1$ as taken in Fig. 3 assumes that two sets of octupoles (in F- and D-sections say) are used such that ν_a and ν_b have the same sign. In this case we recover the reduction of the stable area for negative q as for the one-dimensional case (Figs. 1 and 2).

In Fig. 4, ν_a and ν_b have been taken of opposite sign, which is typical for simple lens arrangements.

In this case, the reduction of stable areas is less noticeable, because the tendency of cancellation for the one octupole polarity is to some extent smoothed out : cancellation in one plane goes together with addition in the other plane.

Finally Fig. 5 corresponds to a beam which is wide in the direction perpendicular to the plane of instability ($\hat{b} >> \hat{a}$), as is usually the case for vertical instability of a multiturn beam. Hence we take $r = 2$ and assume in addition "simple octupoles" with large negative p.

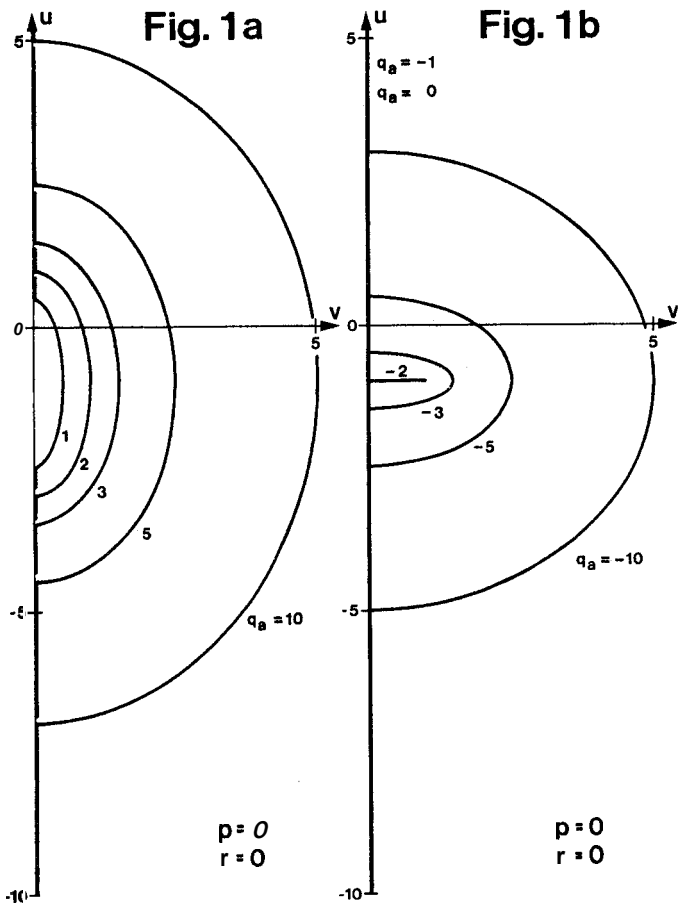
One finds again that one octupole polarity is favourable although the "right" sign is now the opposite to the preferred one in the case of a beam which is wide in the other direction ($p = 0$, $r = 0$). We conclude that the octupole moment in the direction where the beam is wide should be chosen with care.

Application to the PSB

The coasting beam and bunched beam instabilities observed in the PSB[7,8] occur sometimes horizontally, sometimes vertically, in an apparently irregular way. In order to explain this feature, we apply the results of Section 3.3. to the PSB. We compute the thresholds for both planes as a function of the emittance ratio E_H/E_V, assuming the product $E_H E_V$ and hence the area of the beam cross-sections to be a constant. We include image forces and averaging over the strongly varying beam dimensions within a machine period. The arrangement of the octupoles is as described in Ref. 9. Tresholds are expressed by the octupole currents required to stabilize the beam.

Figure 6 shows the result for $N = 2.5\ 10^{12}$ p/p and $E_H E_V = 5200$ (π mrad mm)^2 at 50 MeV. One observes that positive octupole current ($\partial\nu/\partial r^2 > 0$) is more favourable and that for this polarity vertical stability requires stronger octupole currents for $E_H/E_V \lesssim 1.7$ whereas horizontal stability is more critical for $E_H/E_V \gtrsim 1.7$. The intersection point $E_H/E_V = 1.7$ falls into the region of emittance ratios actually observed in many machine experiments. This might explain why slight differences in beam parameters can favour the one or the other direction.

The predicted octupole currents are still higher than measured values. This is probably owing to the neglect of synchrotron motion in our model for the case



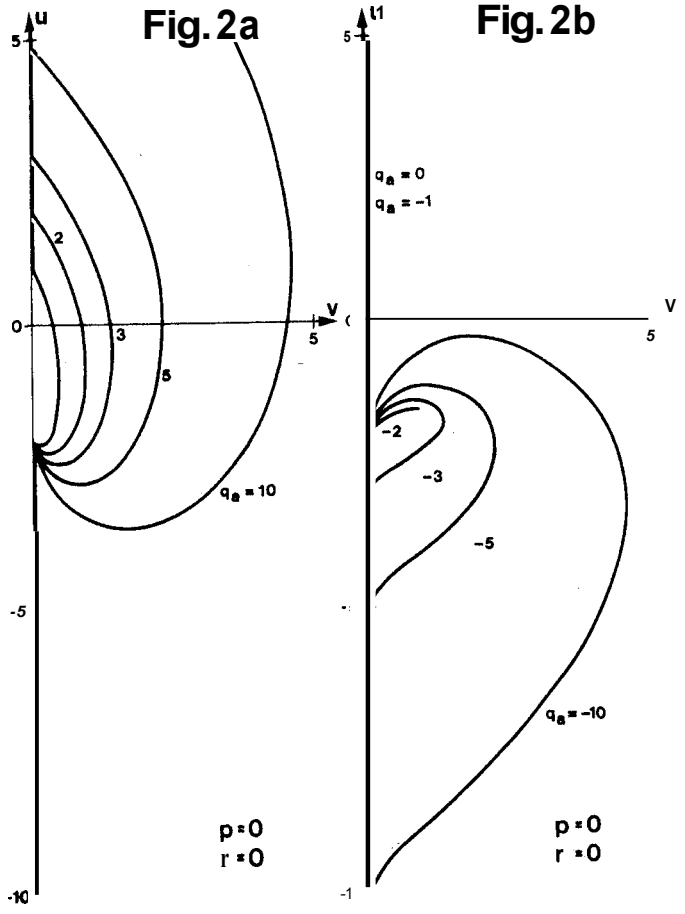
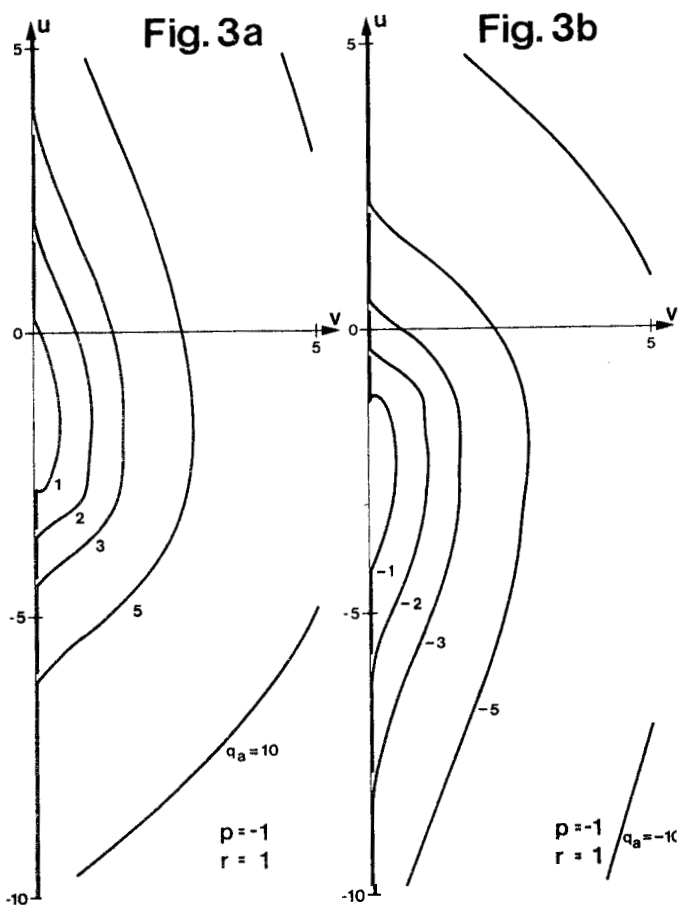


Fig. 1 : Stability diagram for a beam with amplitude distribution (6). The LNS-coefficients u and v are normalized to the space-charge v-spread (for this distribution and vanishing image forces, u is around -3). The beam is stable if the point (u,v) is on the left-hand side of the curve.

Fig. 2 : Same physical conditions as in Fig. 1, but parabolic amplitude distribution (11). For this distribution u is typically between -3.5 and -5.

q_a is a measure of the octupole v-spread due to betatron oscillations in the plane of the instability. Parts (a) and (b) of Figs 1-5 refer to the two polarities of the octupoles, respectively; p is the ratio of the octupole u-spreads due to incoherent motion in the two transverse directions; r is the corresponding ratio for space-charge v-spreads. In Figs 1 and 2, p and r are 0 because the beam is wide in the direction of the instability ($\hat{a} >> \hat{b}$).



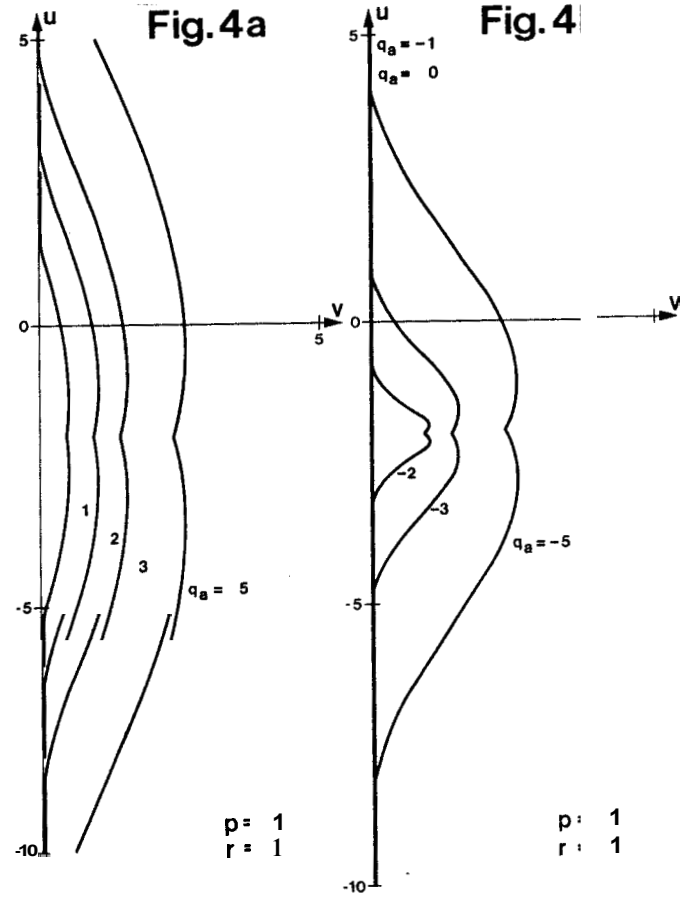


Fig. 3 : Parabolic amplitude distributions (11) in both transverse directions : r=1 means $\hat{b} \simeq 2\hat{a}$; $p \simeq -1$ is typical for one set of octupoles and not too flat a beam

Fig. 4 : As for Fig. 3, but $p \simeq 1$ requires two sets of octupoles.

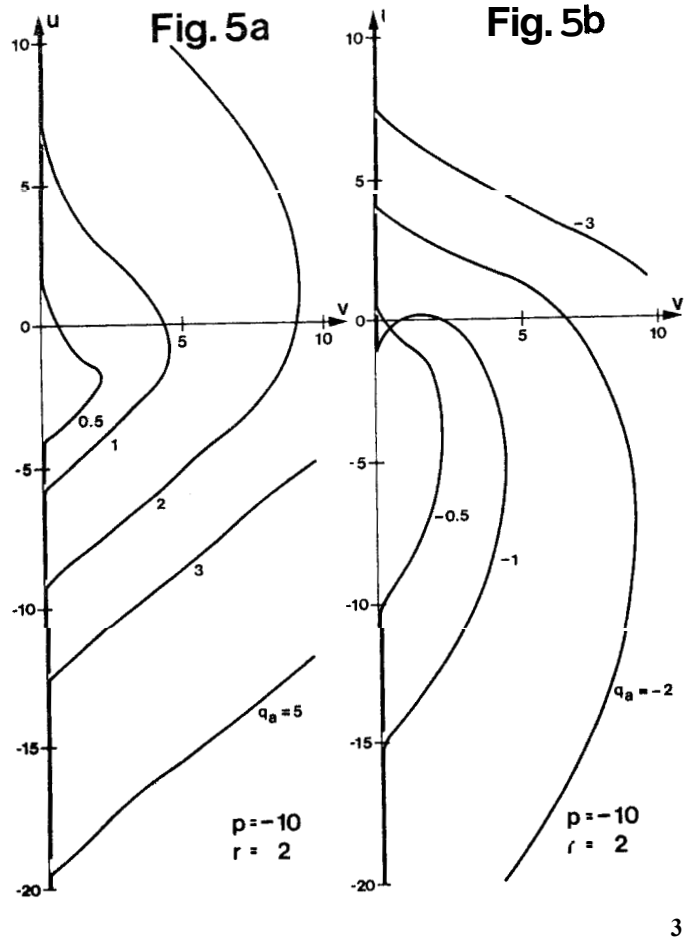
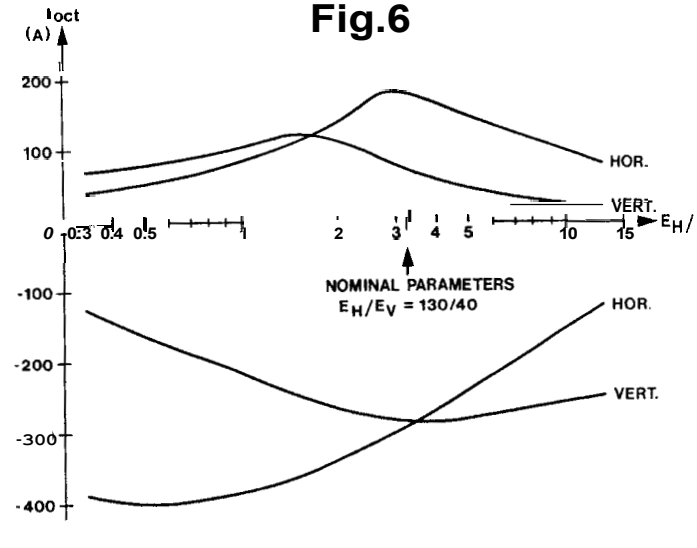


Fig. 5 : As for Fig. 3, but for a beam wide in the direction perpendicular to that of the instability ($\hat{b} >> \hat{a}$).

Fig. 6 : Octupole currents required to stabilize the PSB beam versus emittance ratio, calculated for parabolic amplitude distributions (11) in both transverse planes. Nominal parameters at 50 MeV : $E_H E_V$ = 130x40 (π mrad mm)^2, N = 2.5 10^{12} p/p.



of bunched beams and because of neutralization in the coasting beam case. To conclude, let us make a comparison with conventional theory (external spread in one transverse direction, no spread in $\Delta\nu_{ic}$) : the latter requires stabilizing octupole currents of 400 A (horizontal) and 520 A (vertical instability), for the nominal E_H/E_V = 130/40, all other parameters as for Fig. 6. This is to be compared with the values of 180 A and 70 A taken from Fig. 6.

References

1) L.J. Laslett, V.K. Neil and A.M. Sessler, Rev. Sci. Instrum. 36, 436 (1965).

2) K. Hübner, A.G. Ruggiero and V.G. Vaccaro, Proc. 7th Int. Conf. on High-Energy Accelerators, Yerevan, 1969, p.343.

K. Hübner and V.G. Vaccaro, CERN/ISR-TH/70-44.

3) K.H. Reich, H. Schönauer, CERN/SI/Int.BR/72-2.

4) G. Merle and D. Möhl, CERN/ISR/300/GS/69-66.

5) G. Besnier, Thesis, University of Rennes, France.

6) H.G. Hereward, CERN/MPS/DL 69-11.

7) The PSB Staff (reported by K.H. Reich), The CERN PS Booster, design expectations.., this conference.

8) J. Gareyte and F. Sacherer, Head-tail instabilities in the CERN PS and Booster, this conference.

9) C. Bovet, K.H. Reich, CERN/SI/Int.DL/69-3.

Appendix

Calculation of incoherent ν-shift and ν-spreads

In order to assure self-consistency with the parabolic distribution that we mainly use, we should solve the potential problem for the corresponding charge distribution. This seems to be difficult for the kind of factorized amplitude distribution h(a)g(b) assumed above, which represents a beam of rectangular cross-section. Hence we restrict ourselves to the computation of ν-shifts and ν-spreads for a beam of elliptical cross-section and parabolic density

$$\rho(x,y) = \frac{\lambda}{\hat{a}\hat{b}\pi}\left[1 - \frac{(x-\bar{x})^2}{2\hat{a}^2} - \frac{y^2}{2\hat{b}^2}\right], \qquad (A1)$$

where λ is the linear density and $\hat{a}\sqrt{2}$, $\hat{b}\sqrt{2}$ are the beam radii, corresponding to the ellipse $\rho(x,y) = 0$, which contains all particles. This choice provides at least approximate self-consistency: projected densities obviously do agree with those obtained from the factorized amplitude distribution.

Neglecting image forces, the force in the x-direction is given by

$$eF_x = \frac{e^2\lambda}{\pi\varepsilon_0}\frac{1}{\hat{a}(\hat{a}+\hat{b})}\left\{(x-\bar{x}) - \frac{1}{6}\frac{2\hat{a}+\hat{b}}{\hat{a}^2(\hat{a}+\hat{b})}(x-\bar{x})^3 - \frac{1}{2\hat{b}(\hat{a}+\hat{b})}y^2(x-\bar{x})\right\}. \qquad (A2)$$

Performing an averaging process over incoherent betatron motion (e.g. by the method of harmonic balance), $x - \bar{x} = a\cos(\nu_x\Omega t)$, $y = b\cos(\nu_y\Omega t)$, we take

$$\langle(x-\bar{x})^3\rangle = \frac{3}{4}a^3\cos\nu_x\Omega t = \frac{3}{4}a^2(x-\bar{x})$$
$$\langle y^2(x-\bar{x})\rangle = \frac{1}{2}b^2 a\cos\nu_x\Omega t = \frac{1}{2}b^2(x-\bar{x}), \qquad (A3)$$

and obtain for $\Delta\nu_{ic}(a,b)$:

$$\Delta\nu_{ic}(a,b) = \frac{Nr_pR}{\varepsilon_0\pi\beta^2\gamma^3}\frac{1}{\hat{a}(\hat{a}+\hat{b})}\left[1 - \frac{2\hat{a}+\hat{b}}{8(\hat{a}+\hat{b})}\frac{a^2}{\hat{a}^2} - \frac{\hat{b}}{4(\hat{a}+\hat{b})}\frac{b^2}{\hat{b}^2}\right], \qquad (A4)$$

where the r.h.s. should be averaged over the circumference. We identify the quantities introduced in Eq.(A4):

$$\Delta = \frac{Nr_pR}{\varepsilon_0\pi\beta^2\gamma^3}\frac{1}{\hat{a}(\hat{a}+\hat{b})}$$
$$A \simeq \frac{A}{\hat{a}^2}\frac{1+\frac{a}{\hat{a}+\hat{b}}}{8} \qquad (A5)$$
$$\Delta_b \simeq \frac{\Delta}{\hat{b}^2}\frac{1}{4}\frac{\hat{b}}{\hat{a}+\hat{b}}.$$

This gives a rough estimate of the order of u [of Eq.(10)] to be expected. For our parabolic distribution, u represents the normalized ν-shift in the beam centre:

$$u = \frac{\Delta - \Delta\nu_c}{\Delta_a\hat{a}^2} \simeq -\frac{\Delta}{\Delta_a\hat{a}^2} = \frac{8}{1+\frac{\hat{a}}{\hat{a}+\hat{b}}}.$$

This would imply values of u between -4 and -8, which is valid only for a machine of small wiggle in the β-functions.

Computed values for the PSB, assuming nominal emittances ($E_H = 130\pi$, $E_V = 40\pi$ mrad at 50 MeV) and including image contributions, give values of

u = -3.8 (horizontal) and u = -4.8 (vertical).

Note that r is approximately given by $r = 2\hat{b}/(2\hat{a}+6)$ and can only take values of $0 < r < 2$ (Eqs.(12), (A5)).

For the semicircular distribution (6), a numerical estimate gives $u = -\Delta/\Delta_a\hat{a}^2 \simeq -3$.

This value of u is used to derive the stability criterion (9). From (8) and (10) we obtain for $V \ll |U|$

$$\frac{1}{q_a}\frac{A_a\hat{a}^2}{v\hat{a}^2}\frac{U/\Omega + A}{v\hat{a}^2}\frac{u}{\Omega\nu_a\hat{a}^2}\frac{u}{q_a}, \quad -\frac{}{}$$

and

$$\frac{2}{q_a} = \pm\frac{U}{|u+1|} = \pm f\left|\frac{U}{\Omega\nu_a\hat{a}^2}\right|, \qquad (A6)$$
$$f = \frac{2}{|u+1|} \simeq 1.$$

Hence

$$|U| < \hat{U} = \frac{\Omega}{2}\nu_a\hat{a}^2\left|1 - \frac{2}{a}\right|,$$

$$2\frac{|U|}{\Omega}\left|1 \pm \frac{f}{2}\right| \leq \nu_a\hat{a}^2 \sim \frac{1}{2}\delta\nu_{FWHH},$$

or

$$4\frac{|U|}{\Omega} \leq \delta\nu_{FWHH}\frac{1}{\left|1 \pm \frac{f}{2}\right|} \simeq \delta\nu_{FWHH}\begin{cases}2\\0.67\end{cases}.$$

Acknowledgements

We are grateful to K.H. Reich for the encouragement to carry out the work presented here, and to Mrs. M. Lelaizant for carrying out numerical computations.

THE EFWCT OF THE BEAM SELF-FIELD * ON THE TRANSVERSE BETATRON OSCILLATION FREQUENCY

G. Parzen and K. Jellett
Accelerator Department
Brookhaven National Laboratory
Upton, New York

Summary

The electric and magnetic fields generated by the accelerator beam are computed using a mesh-iteration program. This allows the self-fields to be computed for beams having any desired charge or current distribution, and for vacuum chambers and magnet pole faces of any desired shape. The shift of the transverse betatron oscillation frequencies due to the self-fields of the beam can then be computed. The results are applied to various beam geometries including ISABELLE, the AGS, and a small aperture conventional storage accelerator. Comparisons are made with the results found using the analytical results for simple geometries.

I. Introduction

The electric and magnetic fields generated by an accelerated beam, the self-field of the beam, give rise to forces on individual particles in the beam which change their betatron oscillation frequencies, ν_x and ν_y. Depending on the distribution of charge and current within the beam, the shift in ν_x and ν_y caused by the self-field of the beam will vary across the cross section of the beam.

The fields produced by the beam also depend on the surroundings such as the vacuum tank and the iron pole face of the magnet. Calculations have been done of the change of the v-value by Kerst,[1] Laslett,[2,3,13] Resegotti,[3] Lapostolle,[4] Gluckstern,[5,6] Month,[6] Claus,[7] Zotter[8] and Hardt.[9] These were calculations usually involving some simplification of the charge and current distribution or of the vacuum tank or pole face geometries.

In this paper, the change in the v-value caused by the beam self-field and the beam images are computed using a mesh-iteration program, GRACY,[10] which allows the calculation to be done for any distribution of current and charge and for any geometry of the vacuum tank and the pole face. Generally, one finds that results found using the simple analytical formulas are fairly good. However, in some instances, appreciably different results are found using the more exact mesh-iteration calculation.

II. Theory

The beam will generate an electric field E_x, E_y and a magnetic field H_x, H_y which will give rise to a force F_x, F_y acting on the individual particles of the beam where

$$F_Y = e(E_Y + \beta H_x) \quad ,$$

$$F_x = e(E_x - \beta H_y) \quad ,$$

At any instant of time, the charge distribution longitudinally is given by

$$\lambda = \lambda_o + \lambda_1 \cos kZ$$

where λ is the charge per cm in the beam, λ_o is the average charge/cm around the accelerator and the bunching factor is given by

$$B = \lambda_o/(\lambda_o + \lambda_1) \quad ,$$

B is the ratio of the average charge per cm to the peak charge per cm.

The beam has both a time varying component and a steady component which have different boundary conditions. Following the usual treatment,[2] we write

$$E_y = E_{y,ac} + E_{Y,dc}$$

$$H_x = H_{x,ac} + H_{x,dc} \quad .$$

Then

$$E_{y,ac} = \frac{\lambda_1}{\lambda_o} E_{y,dc} = (1/B - 1)E_{y,dc} \quad ,$$

$$H_{x,ac} = \beta E_{y,ac} = -\beta(1/B - 1)E_{y,dc} \quad ,$$

since E_{ac}, H_{ac}, and E_{dc} satisfy the same boundary conditions that the tangential components of E and H vanish on the surface of the vacuum tank.

We thus find

$$E_y = (1/B)E_{y,dc}$$

$$H_x = -\beta(1/B - 1)E_{y,dc} + H_{x,dc} \quad .$$

H_{dc} satisfies a more complicated boundary condition on the iron surface. We find for the force F_y

$$F_Y/e = E_{y,dc}\frac{1}{\gamma^2 B} + \beta^2 [E_{y,dc} + H_{x,dc}/\beta] \quad .$$

In the absence of the vacuum tank, and the iron surface, $E_{y,dc}$ and $H_{x,dc}/\beta$ would exactly cancel each other. The presence of the image fields due to the surroundings gives the result

$$F_Y/e = E_{y,dc}\frac{1}{\gamma^2 B} + \beta^2 [E_{y,image} + H_{x,image}/\beta] \quad .$$

This force leads to a change in the ν_v by the amount

$$2\nu \Delta\nu = -\frac{NRr}{2\pi\gamma\beta^2}\left\{\frac{1}{\gamma^2 B} EG_{y,dc} + (EG_{y,image} + MG_{x,image}/\beta)\beta^2\right\},$$

where EG_y and MG_x stand for the components of the electric and magnetic gradients for a beam having a unit charge per cm.

There are various simplifications in the above expression for $\Delta\nu_y$ which could be removed if desired. The magnetic image term $MG_{x,image}$ needs to be reduced by the factor ρ/R because the magnet iron only covers ρ/R of the circumference, where ρ is the magnet radius of curvature and R is the average radius of the accelerator. The various gradients are varying around the accelerator ring as the beam dimensions change. As a first approximation one should use the average dimensions of the beam around the ring, or the beam dimensions where the β-factor has its average value.

*Work performed under the auspices of the U.S. Atomic Energy Commission.

A similar expression can also be found for the horizontal force F_x. Since, as in the above

$$E_x = (1/B)E_{x,dc} \quad ,$$

$$H_y = \beta(1/B - 1)E_{x,dc} + H_{y,dc} \quad ,$$

$$Fx/e = \frac{1}{\gamma^2 B} E_{x,dc} + \beta^2 [E_{x,dc} - H_{y,dc}/\beta] \quad ,$$

$$F_x/e = \frac{1}{\gamma^2 B} E_{x,dc} + \beta^2 [E_{x,image} - H_{y,image}/\beta] \quad ,$$

and

$$2\nu_x \Delta\nu_x = - \frac{NRr_p}{2\pi\gamma\beta^2} \left\{ \frac{1}{2} \frac{1}{\gamma B} EG_{x,dc} + (EG_{x,image} - MGy,image/\beta)\beta^2 \right\}.$$

Finding the electric field generated by the beam for the geometry shown in Fig. 1 is fairly simple. One simply solves the equation

$$\nabla^2 V = - 4\pi\rho \quad ,$$

with the boundary condition that V = constant on the surface of the vacuum tank. To find the image field, the GRACY program also computes the free space electric field when no vacuum tank is present. It does this by subdividing the beam into small rectangles and adding up the electric fields due to each rectangle which it computes using an analytical result for the electric field due to a rectangular beam with a uniform charge density.

Finding the magnetic field generated by the beam shown in Fig. 1 is somewhat more complicated. The vector potential satisfies the equation.

$$\nabla^2 A = - 4\pi S \quad ,$$

where S is the current density. However, the usual boundary condition that the tangential component of H vanish at the surface of the iron is not valid,[2,6] for this would imply that $\int H d\ell = 0$ along the surface of the iron, which cannot be true as there is a non-zero net current enclosed by the iron.

One approach to solving this problem is to solve the problem with a finite permeability of about $\mu = 10$ or $\mu = 100$ in the iron, and then find the limit as $\mu \to \infty$. The boundary condition at the iron is then

$$(\partial A/\partial n)_{air} = 1/\mu \ (\partial A/\partial n)_{iron} \quad .$$

This approach usually involves some convergence problems when one tries to run the mesh-iteration program with large value of μ in the iron.

III. Results

In this case the magnet is circular with an inner iron surface with a radius of about *8* cm, and the vacuum tank is circular with an inner radius of *4* cm. The beam is assumed to 2 cm wide and 0.8 cm high. The charge distribution in either direction is taken as

$$f(x) = 1 \ , \quad x \le W_x \quad ,$$

$$f(x) = 0.5(1 - \sin Z) \quad , \quad W_x \le x \le W_x + H_x \quad ,$$

$$Z = n(x - W_x - H_x/2)/H_x \quad ,$$

which represents a beam which has a uniform distribution over the distance W_x and falls gradually to zero over the distance H_x. All the results given here assume that the fall-off region H_x is 20% of the beam extent.

The circular vacuum tank has the property that the image fields vanish for a circular charge distribution. However, during the stacking process, the ISABELLE beam will be moved off center.

Figure 1 shows the variation of the image electron gradient, $EG_{x,image}$ across the horizontal extent of the *beam.* Results are shown when beam is moved $\Delta x = 1$ cm off center, and $\Delta x = 2$ cm off center. Also shown are the simple analytical results found using the image field for a point charge concentrated at the center of the beam. For the proposed geometry and injection procedure of ISABELLE, R = 427 m, I = 10 A, v = 20, γ = 30 $r_p = 1.535 \times 10^{-18}$ m, the $\Delta\nu$ caused by $EG_{x,image}$ is

$$\Delta\nu_x = - 0.48 \ EG_{x,image} \quad .$$

The analytical result for a circular vacuum tank is

$$EG_{x,image} = 2/(x - a2/x_o)2 \quad ,$$

where x_o is the center of the beam, a is the radius of the vacuum tank and the beam has unit charge per unit length.

In storage rings, the v-variation across the beam becomes important especially in connection with the "brick wall" effect. One sees that in particular one is interested in the quadratic variation of v with x, since this may require correction with octupole coils. One sees from Fig. 1, that the simple analytical result is fairly good, except when the beam gets close to the vacuum tank and the v-variation with x becomes increasingly nonlinear.

Table I lists the magnetic and electric gradients across the beam in the median plane. The magnetic gradient is given for a case when the inner radius of the iron is *4* cm. The proposed ISABELLE magnet will have an inner iron radius of *8* cm, for which the image magnetic field is about 50 times smaller than for the 4 cm radius case, and produces a negligible effect.

Warm ISABELLE Magnets

The case considered here is that of the storage accelerator using warm conventional magnets. We assume that the magnet is a window frame magnet with an iron aperture of 4 X 20 cm. The vacuum tank is assumed to be elliptical and 3 X 14 cm. The beam is assumed to be 2 cm wide and 1 cm high, with the same kind of charge distribution assumed for the cold superconducting ISABELLE magnets.

Table II lists the results for the electric and magnetic gradients along the horizontal x-axis and along the vertical y-axis of the beam. The electric results are for a beam having a unit charge per cm of beam, and the magnetic results are divided by β.

Figure 2 shows the variation of the image electric gradient $EG_{x,image}$ and the image magnetic gradient $MG_{y,image}$ across the horizontal extent of the beam. The analytical result for $MG_{y,image}$ is also shown which result is obtained assuming a point current between 2 parallel iron surfaces. This analytical result is[12]

$$MG_{y,image} = \frac{2n^2}{g^2} \ \sinh^{-2}(\pi x/g) - \frac{2}{x2} \quad ,$$

where g is the gap between the iron surfaces, and a unit

current is assumed.

For a possible 100 GeV storage accelerator using warm H-magnets, with R = 428.2 m, I = 3 A, ν = 15, r_p = 1.535 x 10^{-18} m, p = 218 m, γ = 30, $\Delta\nu_x$ generated is

$$\Delta\nu_x = -0.19\ (EG_{x,image} - 0.45\ MG_{y,image}/\beta)\ .$$

AGS Magnets

The AGS beam at injection is assumed to be 6 x 10 cm. The vacuum tank is elliptical whose dimensions are 3 x 6 in. or 7.5 x 15 cm. The pole is roughly hyperbolic with a gap at the center of 3 in. or 7.64 cm. The same charge and current distributions are used as in the previous 2 cases.

Table III lists the results for the electric and magnetic gradients along the horizontal x-axis and along the vertical y-axis for a beam having unit charge per cm. The magnetic results are divided by β. In this case since the injection occurs at 200 MeV, and $\gamma \simeq 1$, and the field term $EG_{x,dc}$ plays an important role.

Figure 3 shows the variation of the electric gradient across the horizontal extent of the beam. Also shown is the magnetic gradient $MG_{y,image}$ computed using the AGS pole face, and computed by replacing the complicated AGS pole with a window frame pole which is 3.75 x 30 cm in aperture.

For the AGS, R = 120 m, I = 0.7A, ν = 8.75, p = 87 m, $\gamma \simeq 1$ and the $\Delta\nu_x$ generated is

$$\Delta\nu_x = -0.32\ \left\{\frac{1}{B}\ EG_{x,dc} + \beta^2 (EG_{x,image} - 0.72 \times MG_{y,image}/\beta)\right\}.$$

Acknowledgments

We wish to thank J. Claus for drawing our attention to this problem.

References

1. D.W. Kerst, Phys. Rev. 60, 47 (1941).

2. L.S. Laslett, Brookhaven Summer Study on Storage Rings, 1963, p. 324.

3. L.J. Laslett and L. Resegotti, Proc. 6th Int. Conf. on High Energy Accelerators, Cambridge, Mass. 1967, p. 150.

4. P.M. Lapostolle, CERN Report AR/Int SG/65-27 (1965).

5. R.L. Gluckstern, BNL Report, CRISP 72-33 (1972).

6. M. Month and R.L. Gluckstern, BNL Report AADD 73-8 (1973).

7. J. Claus, BNL Report, AGS DIV 73-4 (1973).

8. B. Zotter, CERN Report, CERN-ISR-TH/72-36 (1972).

9. W. Hordt, CERN Report, CERN-ISR/Int 300/GS/66-2 (1966).

10. G. Parzen and K. Jellett, Particle Accelerators 2, 169 (1971).

11. J.H. Van Bladel, Amer. Am. J. Phys. 29, 732 (1961).

12. B. Hague, Principles of Electromagnetism Applied to Electrical Machines, Dover Publications (1962).

13. L.J. Laslett, Proc. VII Intern. Conf. on High Energy Accelerators, 1970, Vol. II, p. 324.

Table I. Field gradients due to the beam self-field for a cosine magnet. The vacuum tank radius is 4 cm; the iron inner radius is 4 cm. The beam is 0.8 x 2 cm and off-center by 2 cm. Gradients are in cm^{-2}.

X	EG_x	$EG_{x,image}$
0.75	-1.98	0.043
1	-1.02	0.046
1.25	3.55	0.051
1.5	3.16	0.056
1.75	2.59	0.062
2	2.44	0.068
2.25	2.61	0.077
2.5	3.19	0.087
2.75	3.59	0.099
3	-0.95	0.112
3.25	-1.9	0.122

X	MG_Y	$MG_{y,image}$
1.0	-1.09	-0.030
1.2	2.25	-0.035
1.4	3.46	-0.043
1.6	2.76	-0.047
1.8	2.42	-0.052
2.0	2.32	-0.060
2.2	2.41	-0.065
2.4	2.74	-0.073
2.6	3.43	-0.079
2.8	2.21	-0.090
3.0	1.15	-0.100

X	EGY	$EG_{y,image}$
0	7.28	-0.0685
0.1	7.30	-0.683
0.2	7.98	-0.0680
0.3	4.90	-0.0675
0.4	1.20	-0,0665
0.5	-1.31	-0.0655
0.6	-1.78	-0.0647

Y	MG_x	$MG_{x,image}$
0	-2.32	-0.059
0.126	-2.30	-0.058
0.251	-2.27	-0.055
0.377	-2.07	-0.050
0.503	-1.66	-0.041
0.628	-1.43	-0.028
0.754	-1.21	-0.027

Table II. Field gradients due to the beam self-field for a window frame magnet with a 4 x 20 cm aperture. The beam is 1 x 2 cms and the elliptical vacuum tank is 3 x 14 cm. Gradients are in cm^{-2}.

X	EG_x	$EG_{x,image}$
0	1.982	-0.328
0.25	2.119	-0.322
0.5	2.586	-0.304
0.75	2.801	-0.276
1	-1.089	-0.241
1.25	-1.974	-0.202

X	MG_y	$MG_{y,image}$
0	2.57	0.253
0.2	2.65	0.251
0.4	2.92	0.247
0.6	3.44	0.238
0.8	2.29	0.227
1.0	-0.64	0.214
1.2	-1.75	0.198

Y	EG_y	$EG_{y,image}$
0	5.78	0.320
0.1	5.80	0.324
0.2	5.86	0.328
0.3	5.96	0.336
0.4	0.415	0.348
0.5	0.420	0.352
0.6	-1.35	0.364

Y	MG_x	$MG_{x,image}$
0	-5.31	0.253
0.1	-5.33	0.255
0.2	-5.39	0.258
0.3	-5.48	0.259
0.4	-3.66	0.262
0.5	+0.084	0.267
0.6	+1.88	0.272

Table 111. Field gradients due to the beam self-field for the AGS magnet. The beam is 6 x 10 cm. The elliptical vacuum tank is 7.5 x 15 cm. Gradients are in cm^{-2}.

X	EG_x	$EG_{x,image}$
0	0.0594	-0.0301
1	0.0620	-0.0302
2	0.0703	-0.0306
3	0.0863	-0.0305
4	0.0464	-0.029
5	-0.0516	-0.0245

X	MG_y	$MG_{y,image}$
-5.08	0.032	0.064
-3.81	0,159	0.071
-2.54	0.180	0.071
-1.27	0.159	0.065
0	0.144	0.054
1.27	0.134	0.040
2.54	0.134	0.025
3.81	0.099	0.011
5.08	-0.033	-0.002

Y	EG_y	$EG_{y,image}$
0	0.199	0.0301
1	0.203	0.0315
2	0.208	0.0293
3	0.024	0.0280

Y	MG_x	$MG_{x,image}$
0	-0.115	0.054
1.27	-0.118	0.056
2.54	-0.028	0.062
3.18	0.100	0.067

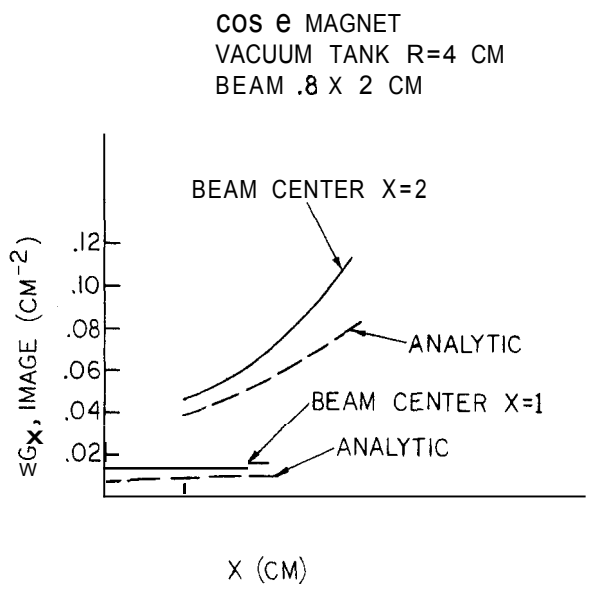


FIG. 1

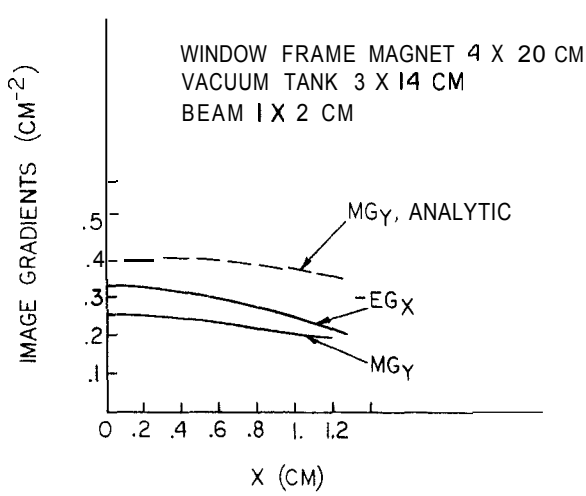


FIG. 2

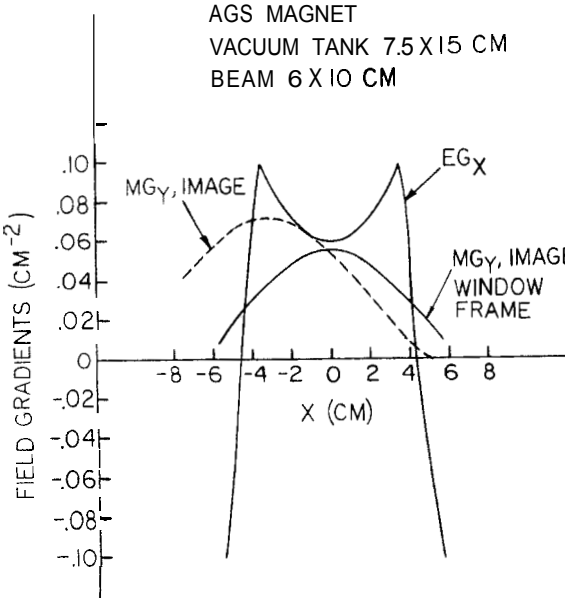

AGS MAGNET
VACUUM TANK 7.5 X 15 CM
BEAM 6 X 10 CM
FIELD GRADIENTS (CM^{-2})
.10
.08
.06
.04
.02
0
-.02
-.04
-.06
-.08
-.10
-8 -6 -4 -2 0 2 4 6 8
X (CM)
MG$_Y$, IMAGE
EG$_X$
MG$_Y$, IMAGI
WINDOW
FRAME

FIG. 3

ACCELERATION BY PHASE DISPLACEMENT IN THE ISR

K.N. Henrichsen and M.J. de Jonge

CERN

Geneva, Switzerland

Summary

Acceleration by phase displacement is used in the ISR to accelerate stacked protons from 26 GeV/c to *31.4* GeV/c. In the phase displacement process empty RF buckets are moved through the stack from higher to lower momentum which results in a shift of the stacked beam towards higher momentum. The total momentum shift is determined by the available RF voltage, the stable phase angle ϕ_s and the number of passages of the empty buckets through the stack. The stable phase angle ϕ_s should be as small as the time and RF noise permit, in order to reduce the dilution of longitudinal phase space density inherent in the process. One of the main difficulties encountered was the synchronisation of the magnetic field adjustments and the RF system. Twenty-six power supplies are adjusted simultaneously by the control computer in order to keep the betatron frequencies constant during the acceleration. To reduce losses resulting from beam-beam effects, the betatron frequency band used must be free of resonances and the beams have to be separated in the intersections during acceleration.

Introduction

The first attempts to accelerate stacked protons in the ISR to 31.4 GeV/c were made by means of rebunching. The available RE voltage, however, limits the total current that can be accelerated to *31.4* GeV/c to about 1A[1]. In order to overcome this limitation the method of phase displacement acceleration has been developed. This method is at present operational and currently used in the ISR for preparation of colliding beams for physics experiments at 31 GeV/c.

Beam currents of up to 6A have been accelerated by this method. The highest luminosity so far achieved has been 0.36 $10^{30}cm^{-2}sec^{-1}$, but a luminosity of 10^{30} $cm^{-2}sec^{-1}$ seems well within reach.

Phase displacement acceleration

Large stacks can be accelerated or decelerated with a medium power radio frequency system by means of "phase displacement". In this process the frequency of the radio frequency system is modulated in such a way that empty RF buckets are generated which are carried all the way through the stack repetitively. The change in momentum which the stack experiences when an empty bucket is carried through is however accompanied by a reduction in the longitudinal phase-space density, which is the main disadvantage of the process.

The choice of the RF parameters - stable phase angle, sin ϕ_s, and RF voltage V - for the phase displacement process is a compromise between an acceptable density reduction and the total time spent during the process.

The density reduction, which can be described by the root mean square momentum spread - δp_{rms} - introduced in the stack by the passage of n empty buckets, is given by

$$\delta p_{rms} = \sin \phi_s \cdot \delta p_o(p,V)\sqrt{n} \qquad (1)$$

where $2\pi\delta p_o(p,V)$ is the area of the stationary bucket that would be generated by the actual RF voltage V at sin $\phi_s = 0$. This relationship, which was derived theoretically2 and studied with a computer simulation[3], has been verified experimentally and good agreement has been found, as can be seen from Fig. 1.

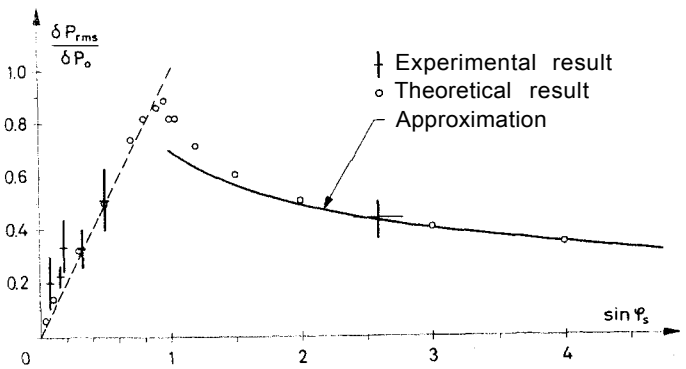


Fig. 1. Normalised r.m.s. momentum spread as function of sin ϕ_s.

The time t spent by one passage of an empty bucket through the stack is given by

$$t = \frac{s\Delta p}{\dot{p}} = \frac{s\Delta p \cdot 2\pi R \cdot m_o c}{V \sin\phi_s} \qquad (2)$$

where Ap is the width of the stack in momentum at the beginning of the process and $\dot{p}$ is the rate of change of momentum of the empty bucket, which is independent of p when sin ϕ_s and V are kept constant during the process.

The safety factor s has to be introduced since the total momentum bite traversed by the empty buckets should always be considerably bigger than the width of the stack in order to allow for the growth in Ap inherent in the process and to avoid additional density reduction due to switching transients, which occur when the RF voltage is switched on and off at the beginning and the end of the empty bucket sweeps.

The total number of passages n required to change the average momentum of a stack from p_1 to $p_2 (p_2 > p_1)$ is given by

$$n = \frac{p_2 - p_1}{\delta p_o(p,V) \cdot \alpha(\sin \phi_s)} \qquad (3)$$

with $\alpha(\sin \phi_s)$ the bucket area parameter.

Combining (1) and (3) one finds

$$\delta p_{rms} = \frac{\sin \phi_s}{\sqrt{\alpha(\sin \phi_s)}} \cdot \sqrt{p_2 - p_1} \cdot \sqrt{\delta p_o(p,V)} \qquad (4)$$

which shows a strong dependence of δp_{rms} on the choice of $\sin \phi_s$ and a weak influence of the voltage V since δp_o is proportional to $\sqrt{V}$. The dependence of δp_{rms} on momentum p is also very weak when p is well above transition energy.

To minimize time and density reduction the highest possible RF voltage should be used together with the lowest value of $\sin \phi_s$ which seems practical from the point of view of the total time spent.

The working line

The band covered by the tune in the stack is shown in Fig. 2. This working line is similar to the line frequently used for the preparation of medium intensity stacks for physics.

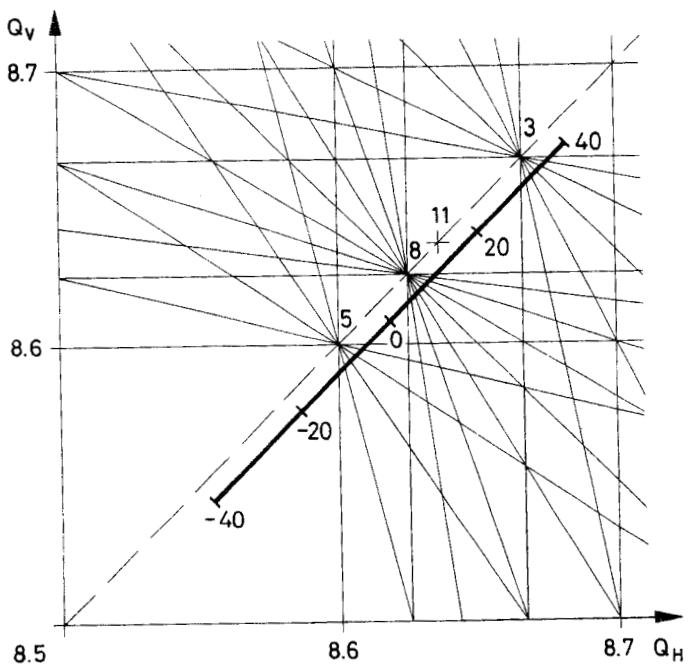


Fig. 2. The working line used for the phase displacement acceleration.

The chosen region provides 35 mm of radial space, free of resonances of an order lower than 8. Space-charge effects limit the region slightly but no compensation has been necessary hitherto. The series of 8th order resonances, $nQ_V + (8-n)Q_H = 69$, and the series of 11th order resonances, $mQ_V + (11-m)Q_H = 95$, are those of the lowest order present.

Beam loss due to the excitation of these resonances is not observed during the normal operation of the ISR. However, during the acceleration process these resonances are excited much more strongly, especially by beam-beam effects[4] when a beam is present in the other ring.

Furthermore the resonances will move slightly relative to the stack because of the imperfections when tuning the magnet. This movement can cause serious beam losses depending directly on the precision in controlling the magnetic field distribution.

Tuning the magnet

The configuration of the magnetic field is kept proportional to the beam momentum at central orbit over the full energy range by the excitation of the pole-face windings, the focussing and defocussing magnet units, as well as the excitation of the localized sextupole lenses[5]. The corrections are highly non-linear due to the saturation in the magnet core. An example of the distribution of the pole-face winding currents as function of radial position and momentum is shown in Fig. 3.

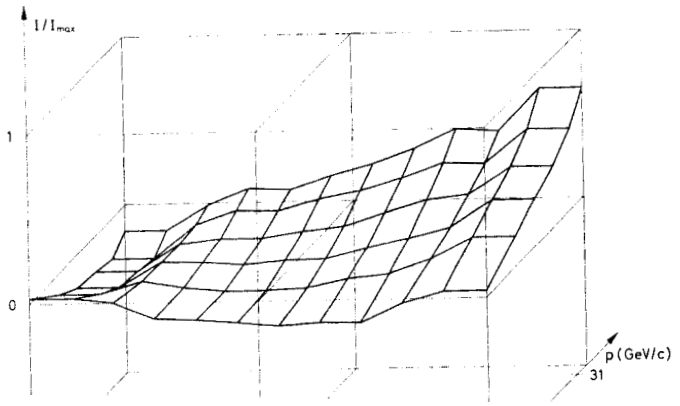


Fig. 3. Normalized currents in the pole-face windings of the focussing magnet units as function of radial position and momentum.

The resulting compensation of the magnetic field gradient is shown in Fig. 4.

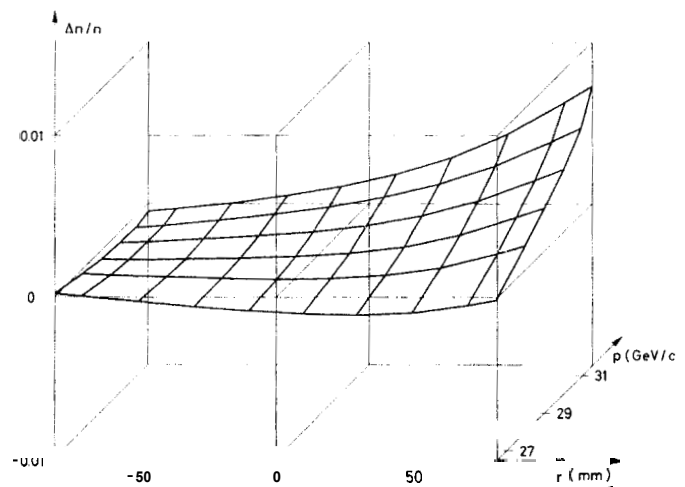


Fig. 4. Normalized field-gradient compensation as a function of radial position and momentum.

The working lines were measured and adjusted for six different values of beam momentum. To establish working lines at intermediate beam momenta linear interpolation is used.

Application of the phase displacement acceleration in the ISR

In the ISR the phase displacement method of acceleration is used to accelerate stacked proton beams from 26.5 GeV/c to *31.4* GeV/c.

The maximum voltage that can be generated by the ISR RF system is 20 kV which, however, cannot be used due to severe beam loading of the RF cavities. This beam loading is the result of the modulation of the stack by the empty buckets carried through, which results in induced voltages, equivalent to what would be induced by about 1A beam current, on the cavity gap. At present 12 kV is used which has proved to be a safe value.

The safety factor *s* has been chosen *so* that the total momentum bite travelled by the empty bucket is approximately three times the initial stack width.

The value of sin ϕ_s has been set to 0.1 which yields a total time for the acceleration process of about 20 minutes which is acceptable for routine operations. The bucket area for 12 kV RF voltage and sin ϕ_s = 0.1 is 0.168 ($\Delta p/m_o c$, ϕ_{RF}) at 26 GeV/c and increases to 0.177 ($\Delta p/m_o c$, ϕ_{RF}) at 31 GeV/c. A total of *184* empty bucket traversals is required to change the average momentum from 26.5 to *31.4* GeV/c. In Fig. 5 the RF empty bucket scans are shown at the beginning and at the end of a typical acceleration process, whereby an initial stack of 11.9A gave 6.2A at *31.4* GeV/c.

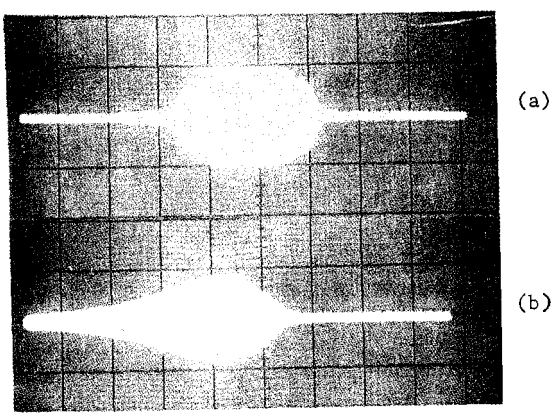


Fig. 5. Empty bucket signal induced on p.u. station
(a) initial 11.9A stack at *26.5* GeV/c
(b) 6A stack at 31 GeV/c after phase displacement

The acceleration process is at present performed under complete computer control. Main field and pole-face winding currents are changed in small steps, derived by linear interpolation from the currents measured at six different momenta. The magnitude of the steps is such that the increase in central orbit momentum due to main field change and one empty-bucket traversal are identical. The current changes in all power supplies and the empty-bucket sweep are initialized at the same time by the computer.

Synchronization of main field adjustments and RF system is guaranteed since field changes can only be applied when a signal, indicating the end of the empty bucket sweep, has been received by the computer.

The matching between empty bucket sweeps and field changes is, however, still not perfect since the variation of the bucket area as function of momentum has up till now not yet been taken into account.

Current losses during the acceleration process

During the acceleration process a considerable amount - typically between *40* and 50% - of the current stacked at 26 GeV/c is lost, which makes the process less efficient than would be expected from the density reduction described above.

The current losses seem to depend on both density and/or intensity, since the losses are always much bigger at the beginning of the acceleration process than towards the end (see Fig. 6).

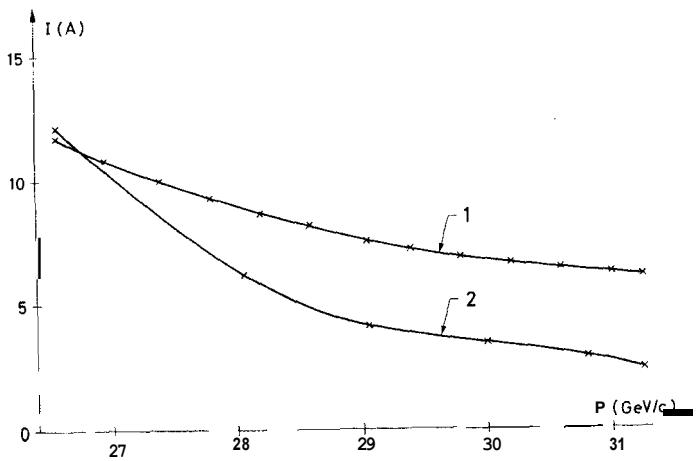


Fig. 6. Current as function of momentum
(1) single ring acceleration
(2) acceleration in presence of a stack

Several sources can be evoked for these current losses.

(a) Current loss due to RF noise

Due to noise in the RF system, which modulates both the phase and the amplitude of the RF voltage, particles are collected in the buckets when passing through the stack. If a significant number of particles is collected in the buckets, a bunched-beam-like signal should be observed on the pick-up stations *as* the bucket emerges from the stack. A signal of this nature can indeed be observed on a sufficiently sensitive pick-up. The particles collected in the buckets are most likely to be found near the sepatrix and since sin $\phi_s \approx 0.1$ the bunching factor of the particles in the bucket will be small. The peak value of the signal induced on the pick-up stations, together with the low bunching factor, indicates that a total number of particles is trapped in the buckets corresponding to approximately 10 mA, which shows that RF noise is only partially responsible for the heavy current losses during the acceleration.

The number of particles collected in the bucket is a function of the density in the stack and the time the bucket spent in the stack. The RF noise is thus setting a lower limit to the value of sin ϕ_s. When sin ϕ_s is lowered to minimize δp_{rms} more time will be spent per empty bucket passage and the current loss due to particles trapped in the bucket will thus increase.

(b) Current losses due to non-linear resonance excitations

When an empty bucket moves through a stack heavy current losses occur even when the magnetic field is kept constant. These losses can be as high as 200 mA for a single empty bucket sweep through a stack which only contains relatively high order - 8th and 11th - resonances.

The reasons for these types of losses are the following: The presence of an empty bucket in the stack influences the particle trajectories and particles on orbits near the non-linear resonances are moved into the resonances and lost. Furthermore, the moving bucket does modulate the space charge detuning and as a consequence the resonances are not kept at the same position during the empty bucket sweep.

During the actual phase displacement the movements of the stack due to imperfect synchronisation between the RF system and magnetic field changes add to the losses.

The increase in momentum spread inherent in the process also contributes to the current losses since particles are moved into the 3rd and 5th order resonances which are the boundaries of our present "resonance free" region.

The relative strength of the different loss mechanisms is at present unknown and will be studied in the future.

The beam losses due to non-linear resonances are very much enhanced by beam-beam effects. Only about 1A of beam current is left after acceleration to 31 GeV/c if a beam of 5A is circulating in the other ring (see Fig. 5, curve 2). These losses are biggest in the region of the 8th order resonances. When separating the beam vertically by 10 mm in all the intersections, these losses can be avoided.

That the empty bucket in the stack is at the origin of the heavy current losses has been very clearly demonstrated by the beam-beam effect mentioned above, which appears during acceleration much more strongly than during normal stacking.

Acknowledgements

We are very indebted to many colleagues, in particular to R. Keyser who wrote all the necessary computer programs both for the incremental field changes and the synchronisation with the RF system.

References

1. S. Hansen, K.N. Henrichsen, M. de Jonge. "Extension of the CERN ISR Energy by Acceleration of Stacked Beams." 1973 National Particle Accelerator Conference, San Francisco.

2. E.W. Messerschmid. "Scattering of Particles by Phase Displacement Acceleration in Storage Rings." CERN/ISR-TH/73-31.

3. E.W. Messerschmid. "Dispersion of Stacked Protons in Synchrotron Phase Space by a Modulated RF Voltage." CERN/ISR-RF/72-28.

4. P.J. Bryant and J.P. Gourber. "Experimental Investigation of Single-Beam and Beam-Beam Space Charge Effects." Paper presented to this Conference.

5. J.P. Gourber and K.N. Henrichsen. "Adjustment of the Working Lines in the ISR." Proc. International Conference on High Energy Accelerators. CERN, Geneva (1971), p. 518.

"STOCHASTICITY"*

L. Jackson Laslett

Lawrence Berkeley Laboratory
University of California
Berkeley, California

Detailed examination of computed particle trajectories has revealed a complexity and disorder that is of increasing interest to accelerator specialists. To introduce this topic, I would like you to consider for a moment the analysis of synchrotron oscillations for a particle in a coasting beam, regarded as a problem in one degree of freedom. A simple analysis replaces the electric field of the RF-cavity system by a traveling wave, having the speed of a synchronous reference particle, and leads to a pair of differential equations of the form

$$dy/dn = -K \sin \pi x, \tag{1a}$$

where y measures the fractional departure of energy from the reference value, πx measures the electrical phase angle at which the particle traverses the cavity, and K is proportional to the cavity voltage; and

$$dx/dn = \lambda' y, \tag{1b}$$

in which λ' is proportional to the change of revolution period with respect to particle energy. It will be recognized that these equations can be derived from a Hamiltonian function

$$H = (1/2)\lambda' y^2 - (K/\pi) \cos \pi x . \tag{2}$$

Because this Hamiltonian function does not contain the independent variable explicitly, it will constitute a constant of the motion and possible trajectories in the x,y phase space will be just the curves defined by H = Constant, namely the familiar simple curves in phase space that are characteristic of a physical (non-linear) pendulum.

If we note, however, that a localized cavity can affect the energy of a particle only when the particle encounters the cavity, it is natural to replace the differential equations by difference equations. Thus, measuring energy y_n at the n^{th} entry to the cavity, we write the transformation

$$\left.\begin{aligned} y_{n+1} &= y_n - K \sin \pi x_n \\ x_{n+1} &= x_n + \lambda' y_{n+1} \end{aligned}\right\} \tag{3a,b}$$

(which can readily be shown to be area-preserving). Although alternatively the motion in this case could again be expressed by differential equations derivable from a Hamiltonian function, the Hamiltonian now would contain a periodic δ-function of the independent variable as a factor multiplying the term $-(K/\pi) \cos \pi x$ and hence could not be taken as a constant of the motion. (The differential equations, moreover, would be non-linear, so that Floquet theory could not be applied.) The use of such a Hamiltonian formulation nonetheless can be helpful in analytic work, but difference equations of course are attractive for computational investigations.

It is of interest to take a quick look at some computational results obtained through use of a transformation equivalent to (3a,b) but written in terms of working variables $Y = y - (K/2) \sin \pi x$, $X = x$, so that the transformation assumes the form

$$\left.\begin{aligned} X_{n+1} &= X_n + \lambda' [Y_n - (K/2) \sin \pi X_n] \\ Y_{n+1} &= Y_n - (K/2)[\sin \pi X_n + \sin \pi X_{n+1}] \end{aligned}\right\}, \tag{3a',b'}$$

with the result that the resulting phase diagrams will necessarily have a desirable symmetry about both the X- and Y-axes. With $K/\pi = 0.1$ and $\lambda' = 0.1$ we find what appear to be conventional bucket diagrams with buckets separated in Y by $2/\lambda'$ for successive harmonic modes, although we may wish to return to the question of whether the bucket boundaries are as simple and definite as appears on Fig. 1.

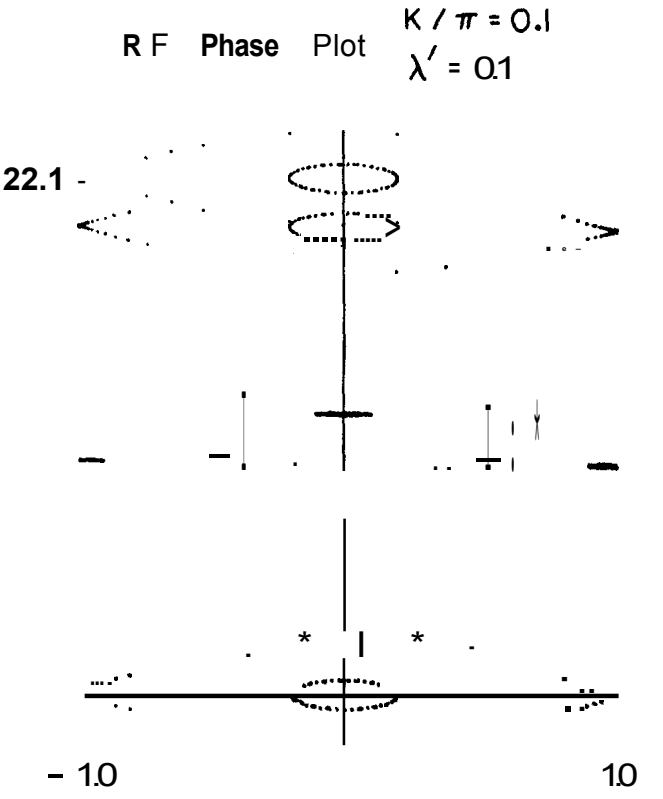


Fig. 1. - X,Y phase plot for a coasting beam under the influence of an R.F. cavity with $K/\pi = 0.1$, $\lambda' = 0.1$ - - as computed by Eqns. (3a',b'). X is plotted mod. 2.

We also find evidence of some "sub-harmonic" structure (with higher order fixed points) that, if enlarged some 60X, has the appearance shown in Fig. 2.

Work supported by the U.S. Atomic Energy Commission.

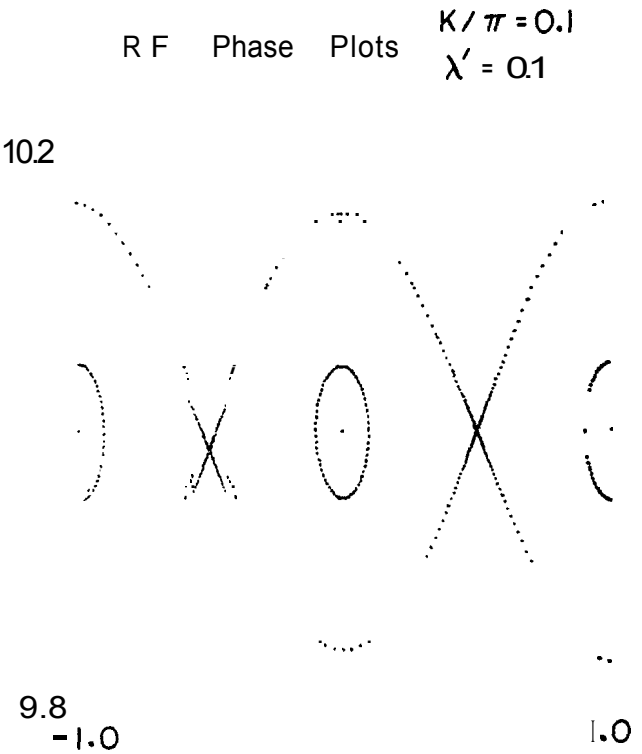


Fig. 2. - Circa 60-fold vertical enlargement of central portion of Fig. 1, near Y = 10.0, showing sub-harmonic structure.

If the cavity voltage is increased eight-fold (so $K/\pi = 0.8$), the bucket areas are expected to become larger, and we indeed find this to be the case (Fig. 3), with an accompanying very marked increase of complexity

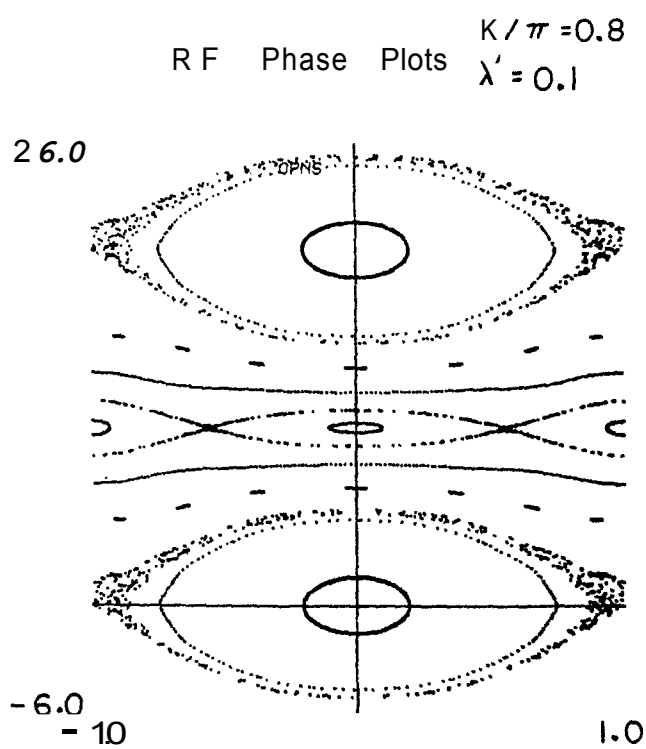


Fig. 3. - Phase plot similar to Fig. 1, but for operation with $K/\pi = 0.8$, showing the obvious development of complex structure.

that is immediately apparent in the phase plot. Of particular interest is the evident diffuse character of phase trajectories generated by points launched close to the first-order unstable fixed points situated at $X = \pm 1$, since the bucket boundary in consequence no longer appears clearly defined.

In the first example ($K/\pi = 0.1$), on the other hand, where the bucket width is some two and one-half times smaller in relation to the bucket separation, the presence of structure in the separatrix can be revealed computationally only with considerable care.[4] To do this, one can extend from the unstable fixed points the eigenvector directions of the transformation linearized about these fixed points, and examine whether such curves intersect smoothly. One finds in fact that they do not quite do so, but generate loops (of a nature to be illustrated later) that in this instance ($K/\pi = 0.1$) have a very small area that amounts to only about $1/(5 \times 10^{11})$ of the area of the bucket itself.

Similar questions concerning the character of phase trajectories and the possible erratic or stochastic behavior of canonical mappings can arise in problems with more than one degree of freedom. As an example, Hénon and Hiles[5] and subsequently Walker and Ford[6] studied a model of an astronomical system, for which the Hamiltonian function was taken to be

$$H = \frac{1}{2}(p_1^2 + p_2^2 + q_1^2 + q_2^2) + q_1^2 q_2 - \frac{1}{3} q_2^3 . \qquad (4)$$

The cubic terms appearing here as coupling terms become increasingly significant for increasingly large values of H -- which is itself a constant of the motion. With the coupling terms present, however, and in the absence of any simple constant of the motion other than H, a given phase trajectory might be expected to wander (ergodically) over virtually all of a three-dimensional surface specified by H = Constant (and that will be a closed surface for values of H below the dissociation energy). If, on the other hand, some additional integral of the motion were in fact also acting, the phase points of a given trajectory then would be constrained to lie on a two-dimensional surface, and graphs of the intersection of such surfaces with some selected plane or other surface (a "surface-of-section") would lead to simple curves in this plane rather than to a scattering of points. Computations of this nature indicated that for sufficiently small values of energy (e.g., $H \lesssim 1/12$) only curves that to computer accuracy were smooth (and relatively simple) were formed by intersection with the plane $q_1 = 0$ (and $p_1 \geq 0$). Examples in which the energy of the particles was successively raised, however, resulted in the development of ragged island structures or of apparent stochastic behavior over increasingly large portions of this surface-of-section (Fig. 4).

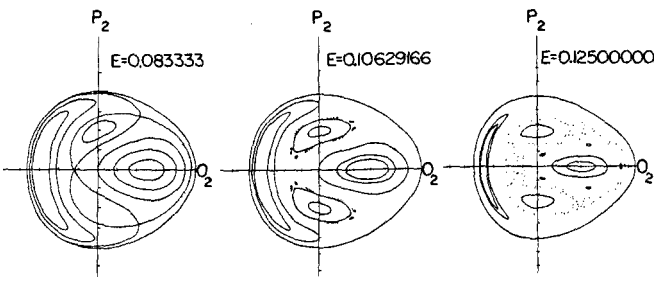


Fig. 4. - Phase plots, in the surface of section $q_1 = 0$, resulting from the equations implied by the Hamiltonian function (4) -- for increasing values of the energy. [After Walker and Ford.[6]]

Such behavior appears concordant with the "KAM" (Kolmogorov-Arnol'd-Moser) theory (see Refs. 58, 59, & 60 of our Ref. 1c), which suggests that many of the invariant curves or surfaces present in the absence of the perturbation will persist, with only minor distortion, in the presence of a sufficiently small perturbation (see, however, Note 7). It is of interest, of course, to determine or to estimate the circumstances (e.g., perturbation strength) at which the KAM theory becomes inapplicable and extended regions of erratic (or stochastic) behavior develop. As was suggested by our first examples, and has been e o ded more extensevely by Zaslavskij and Chirikov, one means for obtaining such estimates may be by determining the ratio of resonance width $[\delta\omega=(d\omega/dI)_r\delta I]$ to the distance $(\Delta\omega)$ to the nearest neighboring resonance.

Additional tests (to be mentioned below) may be required to determine the degree of disorder associated with the movement of phase points in such stochastic regions. We may first note, however, that the existence of nested closed invariant curves in a plane -- as suggested by the KAM theorem for a problem in one degree of freedom -- prevents phase points from moving outward or inward to regions of substantially different "amplitude" (in the absence of noise). With more than one degree of freedom, however, stochastic layers may intersect, to form an intricate system of channels along which a phase point can slowly diffuse and result in instability. The possibility of such "Arnol'd diffusion" has been demonstrated by Arnol'd [Ref. 35 of our Ref. 1c; stated simply the example considered by Arnol'd is comprised of a physical pendulum and a simple-harmonic oscillator, with a time-dependent coupling (that also depends on the phases, or angle variables, of these oscillations)].

It should be pointed out that some non-linear transformations -- say for a system with one degree of freedom -- will not lead to the disappearance of some or all of the invariant phase curves at substantial amplitudes. Thus for transformations of the form

$$x_{n+1} = y_n; \quad y_{n+1} = -x_n + f(y_n), \qquad (5a,b)$$

McMillan[9] has shown that if $f(y)$ can be written as $\Phi(y) + \Phi^{-1}(y)$ (where Φ^{-1} denotes the function inverse to Φ), then the curves $y = \Phi(x)$ and $x = \Phi(y)$ will constitute invariant curves. Such curves will pass through the first-order fixed point(s) situated at the intersection(s) of $y = (1/2)f(x)$ with the principal diagonal. An enclosed area can thereby be formed from which phase points cannot escape even if the behavior in portions of the interior becomes highly stochastic. This is illustrated by an example (Fig. 5) in which

$$f(y) = \tfrac{1}{2}(3y-1) - \frac{1}{2}\frac{k^2}{y+1+\sqrt{y^2+k^2}} \qquad (6a)$$

and

$$\Phi(x) = x - 1 + \sqrt{x^2+k^2}\ . \qquad (6b)$$

Such a situation also can develop when $f(y)$ is a stepwise linear function of y with discontinuities of slope, as has been noted by Dr. Judd [see, for example, Figs. 13 and 14 (pp. 27-28) of Ref. 10]. If $f(y)$ is of the form

$$f(y) = -(By^2 + Dy)/(Ay^2 + By + C), \qquad (7)$$

moreover, the entire phase plane will be covered by a family of simple invariant curves -- see, for example, the cases[9] $f(y) = 2ky/(1+y^2)$, with the invariants $x^2y^2 + x^2 + y^2 - 2kxy$ = Constant, and $f(y) = 2ky/(1-y^2)$, with the invariants $x^2y^2-x^2-y^2+2kxy$ = Constant, illustrated by Figs. 6-8.

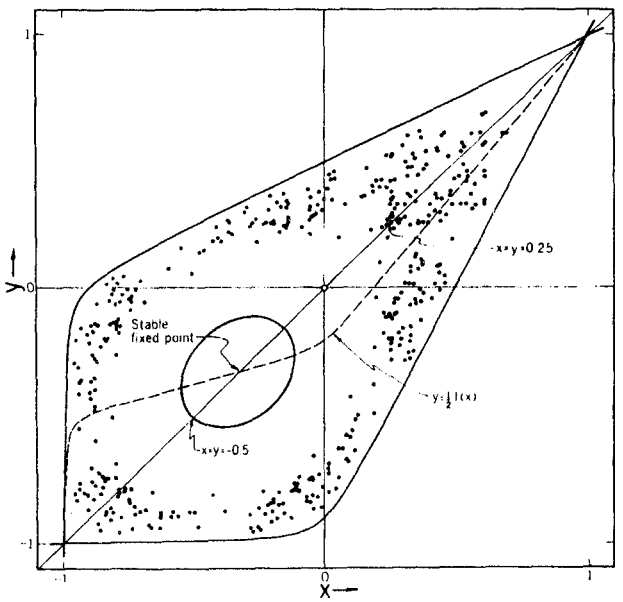


Fig. 5. - Phase diagram for the transformation (5a,b), with f(y) given by Eqn. (6a). The scattered points result from computations initiated with $x_0 = y_0 = 0.25$, but must remain within the separatrix defined by the function Φ [Eqn. (6b)]. k=0.1

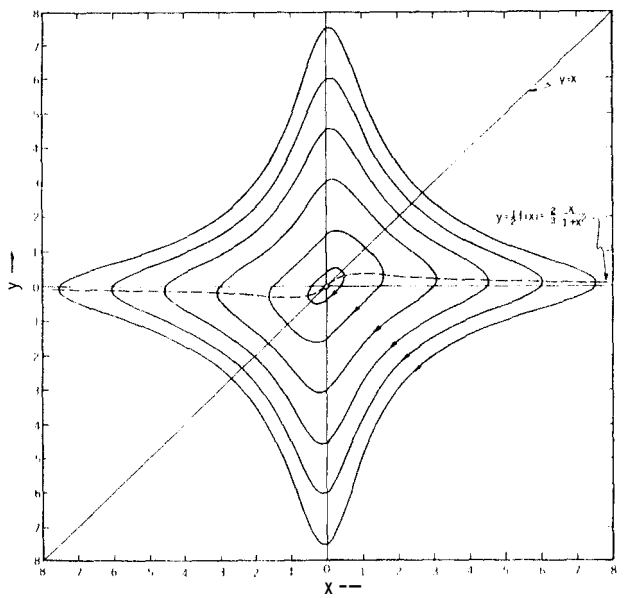


Fig. 6. - Invariant curves for the transformation (5a,b) with $f(y) = 2ky/(1+y^2)$ and $k = 2/3$. [Figs. 6-10 after McMillan.[9]]

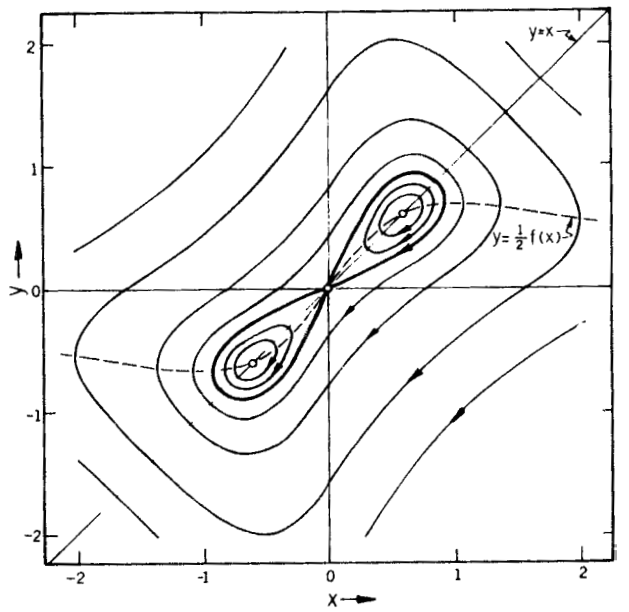


Fig. 7. - Invariant curves for the same transformation as in Fig. 6, but with k = 1.36.

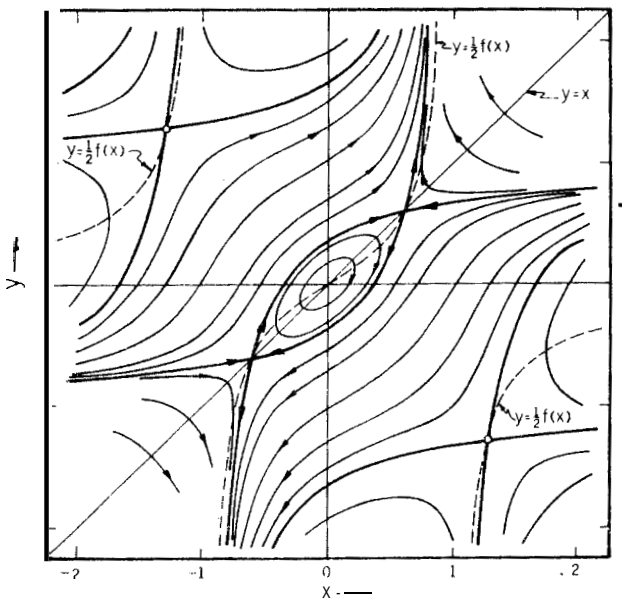


Fig. 8. - Invariant curves for the transformation (5a,b) with $f(y) = 2ky/(1-y^2)$ and k = 0.64.

It is of interest to examine the mechanism whereby irregular behavior can develop in the neighborhood of unstable fixed points, taking as an illustration an example suggested by Progessor deVogelaere that [when generalized and rewritten in variables leading to the form (Sa,b) advocated by McMillan] employs

$$f(y) = 2[Ty + (1 - T)y^2]. \qquad (8)$$

First-order fixed points appear at (0,0) and at (1,1). For T = 0, this transformation, when linearized about the unstable fixed point at (1,1), can be represented by the matrix $\begin{pmatrix} 0 & 1 \\ -1 & 4 \end{pmatrix}$, with eigenvalues and eigenvector slopes

$$\lambda = 2 \pm \sqrt{3}, \quad dy/dx = \lambda. \qquad (9)$$

A line segment extending downward from the fixed point (1,1) with the slope $2 + \sqrt{3}$, if subjected to repeated applications of the transformation, generates the loops shown in Fig. 9; similarly a line segment of slope $2 - \sqrt{3}$, if extended by the inverse transformation, generates the mirror-image curve (mirrored about the principal diagonal). Points such as A, B, C ... progress toward the fixed point in smaller and smaller steps and, since the transformation is area-preserving, the associated loops clearly must become increasingly elongated as they become increasingly narrow from repeated applications of the forward transformation. The evolution of such loops clearly will become quite intricate (Fig. 10),

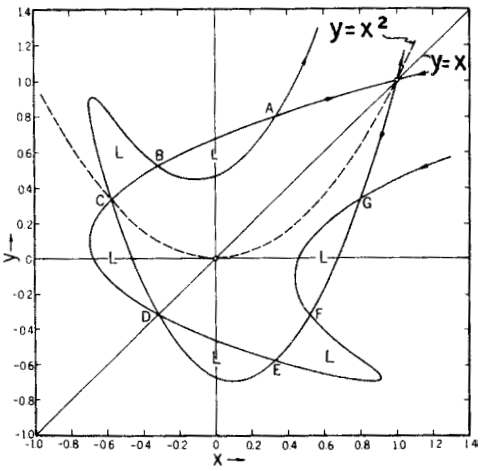


Fig. 9. - Plot of the extensions of the eigenvector directions from the unstable fixed point at (1,1), for the deVogelaere transformation expressed in McMillan's variables [Eqns. (5a,b) and (8), with T = 0]. The areas of the loops marked L are all equal, by virtue of the area-preserving character of the transformation and the inherent symmetry about the principal diagonal.

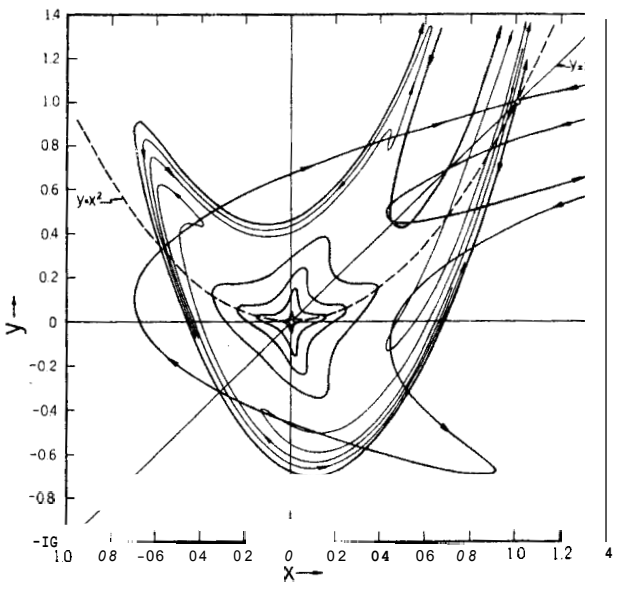


Fig. 10. - A partial extension of the curves shown on Fig. 9.

but the loops apparently need not permeate the entire "interior" -- portions of an inward loop can, in fact, enter, on a later iteration, into the interior of an outward-lying loop (as indicated on Fig. 10).[11] It is clear, however, that the development of such a loop system can readily give rise to an apparent stochastic motion of phase points in portions of the phase diagram -- most particularly near an unstable fixed point such as that mentioned here.

The existence of a firm separatrix, or of an extensive family of invariant curves generally, can be extremely sensitive to the exact form of the transformation.[12] A case of some physical interest arises in computational studies relating to the Toda Lattice.[13] This one-dimensional lattice consists of particles interacting through exponential pair potentials and can propagate certain non-linear wave forms ("solitons") without change of shape. One computational investigation[14] of stability for a three-particle lattice (with periodic boundary conditions) has commenced with a Hamiltonian function

$$H = \tfrac{1}{2}(P_1^2+P_2^2+P_3^2)+e^{-(Q_1-Q_3)}+e^{-(Q_2-Q_1)}+e^{-(Q_3-Q_2)}. \quad (10)$$

By a canonical transformation of variables, in recognition of the invariance of this system to translation -- so that $I_1 = P_1 + P_2 + P_3$ constitutes a constant of the motion -- the Hamiltonian (10) becomes expressible as a function of two pair of conjugate variables in the form

$$H = \tfrac{1}{2}(p_1^2+p_2^2)+\tfrac{1}{24}[e^{(2q_2+2\sqrt{3}q_1)}+e^{(2q_2-2\sqrt{3}q_1)}+e^{-4q_2}], \quad (11)$$

which is identical to the Hénon-Heiles Hamiltonian function (4) through terms of third order. It is of interest to examine whether in the present case constants of the motion other than H act to restrict the motion. Computationally it was found -- again using the surface-of-section $q_1 = 0 (p_1 > 0)$ -- that in this case simple invariant curves apparently continued to exist in the q_2p_2 plane, even for very large values of H. Stimulated by this result, Hénon[15] has directed attention to an additional integral of the motion that is valid in this case; the constants of the motion for the three-particle lattice then can be written in a form that we may express as[16]

$$H = \text{Constant} \quad (12a)$$

$$P_1 + P_2 + P_3 = \text{Constant, and} \quad (12b)$$

$$P_1P_2P_3 - P_1e^{-(Q_3-Q_2)} - P_2e^{-(Q_1-Q_3)} - P_3e^{-(Q_2-Q_1)} = \text{Constant}. \quad (12c)$$

[Evidently" further analytic work in fact has now established that the n-particle Toda lattice with periodic boundary conditions (or with fixed ends) is a "completely integrable" system.]

It is of some interest to seek means for anticipating whether stochastic behavior will occur in various portions of a phase diagram and to examine the character of such stochastic behavior as does occur. What we here have loosely termed stochastic behavior can be catalogued with respect to a hierachy of properties (ergodicity, mixing, ···), indicative of increasing disorder, that are fundamentally significant for statistical mechanics.[1a,e] Of particular interest to the accelerator designer, of course, is the determination of a threshold beyond which stochastic behavior will set in and may act to carry a phase point to unacceptably large amplitudes. As noted earlier, stochastic behavior appears to be associated with overlapping resonances,[1c] and this concept has served as the basis for some analytic estimates of stochasticity limits.[1c,17] It has been noted by René deVogelaere and confirmed in subsequent computations[18] that for a particular class of fixed-point families -- say those with rotation of the form $m/(4m+1)$ -- there is a closely linear relationship between the order of the resonance $(4m+1)$ and $\ln|1 - \frac{1}{2}\,\text{Trace}|$ through many decades ("Trace" denoting the trace of the tangential-mapping or differential matrix associated with the 4m+1 iterations required to map a given fixed point onto itself). Such regularities, and others relating to the apparent size of the stable areas about high-order fixed points (e.g., as estimated from the intersection angle of eigenvectors), have been considered useful indicators of the change in character of a mapping at certain amplitudes.[19,8,20]

A computational procedure of considerable interest for recognizing stochasticity is that in which one follows the evolution of the distance between two initially very close points in phase space. In practice it can prove desirable to reduce the separation from time to time by a recorded factor whenever the separation becomes excessive during the computations, or, perhaps preferably, to evaluate the growth of an infinitesimal vector through use of the cumulative tangential-mapping matrix. A high degree of stochasticity can be ascribed to the behavior of the transformation if there are such vectors whose length generally grows beyond the first iteration by a factor greater than unity (while others may similarly contract). (Ref. 1a, p. 55; for examples, see Ref. 21.) An analogous procedure -- that can be more attractive, although possibly of a less direct basic significance -- is an investigation of the growth of the eigenvalue(s) of the cumulative tangential mapping. Such eigenvalues can change sign repeatedly during the course of many iterations, and hence will be seen to decrease from time to time, but an exponentially increasing trend in eigenvalue magnitude is likely to be associated with a similar type of increase for the lengths of the vectors mentioned previously. The nature of eigenvalue growth has been illustrated by Froeschlé[22] for the transformation[23]

$$\left.\begin{aligned} x_{n+1} &= x_n\cos a - (y_n - x_n^2)\sin a \\ y_{n+1} &= x_n\sin a + (y_n - x_n^2)\cos a \end{aligned}\right\} \quad (13a,b)$$

The general characteristics of this transformation, expressed in variables such that the transformation has the symmetry of McMillan's form, is seen on Fig. 11. On an expanded scale (X10), we see (Fig. 12) the sudden onset of erratic behavior as the starting values for the transformation are successively increased (in steps $\Delta x_0 = 0.0025$, for $y_0 = 0$), and on a scale expanded by a further factor 100/6 we see (Fig. 13) the presence of a great deal of additional structure within a portion of this "stochastic" region. Associated with the transition to the stochastic region there appears to be a marked change in the manner of growth of $\psi_n = \log|\lambda_n|$ (linear, vs. n, in the stochastic case -- indicative of an exponential trend for $|\lambda_n|$) or of the "Cesaro mean" $\mu_n = \frac{1}{n}\sum_{m=1}^{n}\frac{1}{m}\psi_m$ (constancy in the stochastic case, monotonically decreasing otherwise -- Fig. 14).[24] Such methods indeed may prove useful in investigating computationally the possible development of stochastic motion in storage-ring devices. Extended computations of this nature can present challenging problems with respect to computer accuracy.[25]

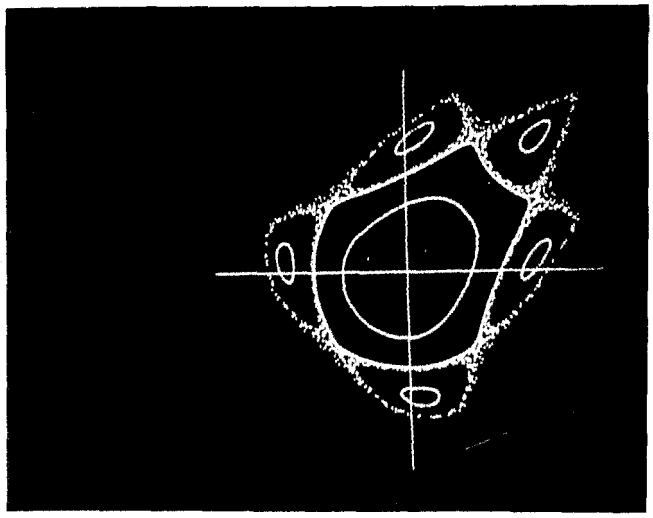


Fig. 11. - Apparantly-smooth phase curves and a scattering of points resulting from iteration of the transformation (11a,b), with cos α = 0.22 and coordinates X,Y appropriate to expressing the transformation in the form (5a,b).[23] Five islands of stability (containing stable fixed points of order 5) are seen surrounding the area associated with the order-1 fixed point at the origin. The outermost smooth curve, shown as bounding this inner area, resulted from the starting values x_0 = 0.5350, y_0 = 0 (Froschlé notation), and the scattered points result from x_0 = 0.5375, y_0 = 0. Scale (as indicated by the coordinate axes): -1.0 to 1.0

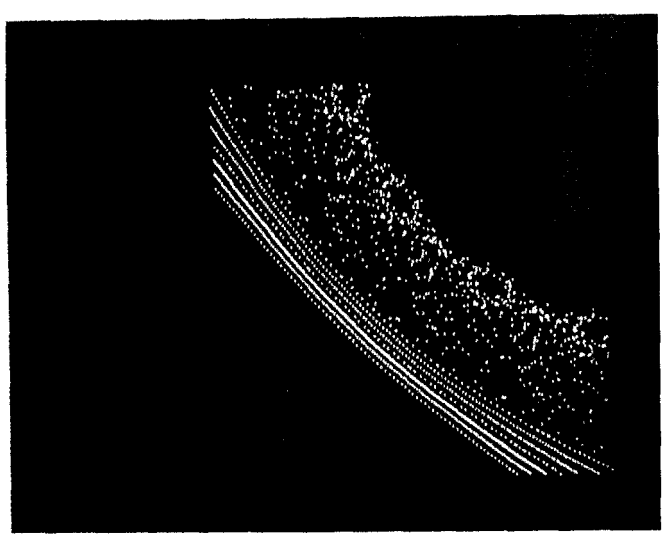


Fig. 12. - Enlarged portion (10X) of Fig. 11, showing seven smooth phase trajectories resulting from starting values x_0 = 0.5200, 0.5225, ... 0.5350 (and y_0 = 0) and a scattering of points resulting from x_0 = 0.5375, y_0 = 0. Note the occurrence of open areas within the region covered by the scattered points -- for example the area surrounding an (unplotted) stable fixed point of order 65 at X ≅ 0.476, Y ≅ 0.521
Scale: 0.38 to 0.58



Fig. 13. - Detailed multiple-island structure in the immediate neighborhood of an order-65 stable fixed point (shown here just below the center of the diagram) of which mention has bten made in the caption to Fig. 12. Scales: 0.470 to 0.482 for X, 0.516 to 0.528 for Y.

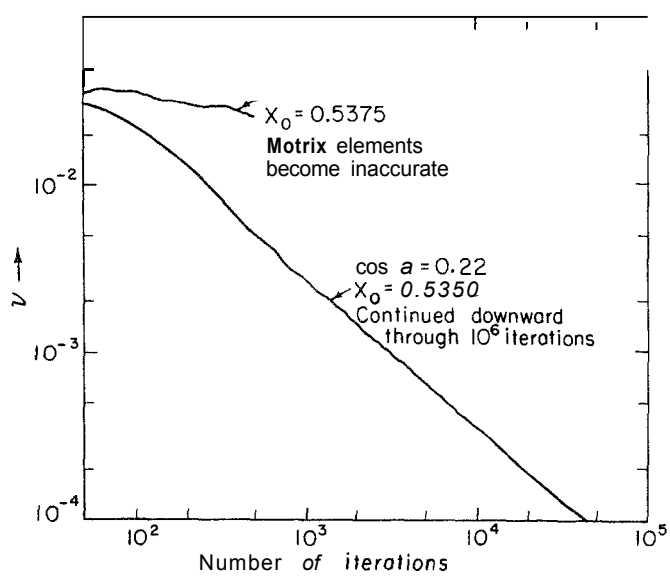


Fig. 14. - Plots of the "sliding mean", ν_n (Note 24), vs. n, obtained from computations begun (i) with initial conditions leading to the last smooth curve of Fig. 12 (x_0 = 0.5350) and (ii) with initial conditions leading to the scattered points on that Figure (x_0 = 0.5375), of which only the results for the latter case indicate a general exponential upward trend of $|\lambda_n|$.

References and Notes

1. (a) An authorative treatment of the mathematical aspects of the problems discussed here is given by V.I. Arnol'd and A. Avez, "Ergotic Problems of Statistical Mechanics" (Benjamin, New York, N.Y.; 1968) and (b) by Jiirgen Moser, "Stable and Random Motions in Dynamical Systems" (Princeton Univ. Press, Princeton, N.J.; 1973); (c) an extended discussion of which portions relate more immediately to those of interest to an accelerator designer is presented, with many references, by G.M. Zaslavskij and B.V. Chirikov, Uspekhi Fizicheskikh Nauk 105 and Engl. Transl. Sov. Phys. Usp. 14, 549-568 (1972), with further discussion and examples (d) by B.V. Chirikov in Nucl. Phys. Inst. Report 267 (Novosibirsk, USSR) with Engl. Transl. by A.T. Sanders, CERN Trans. 71-40 (CERN, Geneva, Switzerland; October 1971); and (e) related questions of ergotic theory in statistical mechanics are summarized by J.L. Lebowitz and O. Penrose, Physics Today, pp. 23-29 (February 1973).

2. CNRS Internat. Conf. on Point Transformations and their Applications, Laboratoire d'Automatique et d'Analyse des Systèmes, Toulouse, France (10-14 September 1973).

3. K.R. Symon and A.M. Sessler, Proc. CERN Symposium on High Energy Accelerators and Pion Physics 1, 44-58 (CERN, Geneva, Switzerland; 1956).

4. L. Jackson Laslett, ERAN-57 (Lawrence Berkeley Laboratory; 1970).

5. M. Henón and C. Heiles, Astron. J. 69, 73-79 (1964).

6. G.H. Walker and J. Ford, Phys. Rev. 188, 416-432 (1969).

7. The present example in fact is exceptional in that the unperturbed frequencies, being equal, are "rationally connected" and the analysis requires special treatment -- see F.G. Gustavson, Astron. J. 71, 670-686 (1966); J. Moser, "Lectures on Hamiltonian Systems", Memoirs Amer. Math. Soc., No. 81, 1-60 (1968).

8. See also V.K. Mel'nikov, Soviet Math. 4, 266-270 (1963).

9 Edwin M. McMillan, "A Problem in the Stability of Periodic Systems", in "Topics in Modern Physics -- A Tribute to Edward U. Condon", pp. 219-244 (Colorado Asso. University Press, Boulder, Colorado; 1971). A transformation written in the form (5a,b) is convenient for the study of area-preserving transformations in the plane because of the "double symmetry" pointed out by McMillan (p. 225). The transformation can be interpreted as describing the effect of a simple linear focusing system supplemented by a periodic sequence of thin non-linear lenses that introduce at such points a Ay specified by f(x).

10. Laslett, McMillan, and Moser, Courant-Institute Report NYO-1480-101 (New York University, N.Y.; 1 July 1968).

11. A wealth of island structure of course can develop throughout the area of such phase diagrams. In some instances a family of unstable fixed points for which the eigenvalues are negative may arise (in place of a stable family, for which λ is purely imaginary), and the appearance of phase trajectories can thereby be drastically affected -- see Ref. 10, esp. Fig. 2 (p. *35)* of the Appendix, drawn for $T = -1/8$. For discussion of the occurrence and consequences of loop systems, see S. Smale, "Diffeomorphisms with Many Periodic Points ...", (Princeton Univ. Press, Princeton, N.J.; 1965); E. Zehnder, Comm. Pure Appl. Math. 26, 131-182 (1973); Ref. 1c, Sect. 6.1; and Ref. 1d, Sect. 2.6.

12. The loss of a firm separatrix can be illustrated computationally for the transformation (5a,b) by modifying the function $f(y)$ of (6a) so as to introduce the quantity $1 - b$ as a factor multiplying the second term on the right and setting $b \neq 0$ (for example, $b = 0.05$) -- L. Jackson Laslett, ERAN-239 (in preparation; 1974).

13. See, for example, M. Toda, Prog. Theoret. Phys. (Kyoto) Suppl. 45, 174-200 (1970); references cited therein; and related papers in this issue of the Supplement.

14. J. Ford, S.D. Stoddard, and J.S. Turner, Prog. Theoret. Phys. (Kyoto) 50, 1547-1560 (1973).

15. Cited in Ref. 14, p. 1558.

16. The validity of these (time-independent) expressions as constants of the motion of course can be confirmed directly by forming their Poisson-bracket expressions with the Hamiltonian function (10).

17. B.V. Chirikov, E. Keil, and A.M. Sessler, CERN Report ISR-TH/69-59 (CERN, Geneva, Switzerland; 15 October 1969).

18. E.g., Ref. 10, pp. 42-43, where is also listed a quantity $\lambda_I = A - 1$ for fixed-point families that have rotation $\frac{m}{4m+1}$.

19. John M. Greene, J. Math. Phys. 9, 760-768 (1968).

20. James H. Bartlett, "Stability of Area-Preserving Mappings", Paper III-3 of Ref. 2.

21. J. Ford and G.H. Lunsford, Phys. Rev. A1, 59-70 (1970).

22. C. Froeschlé, Astron. and Astrophys. 9, 15-23 (1970); C. Froeschlé and J.-P. Scheidecker, ibid. 22, 431-436 (1973); and other references cited therein.

23. This transformation can be put into McMillan's form[9] by the change of variables $x = \sqrt{\sin\alpha}\,Y$, $y = (X - Y\cos\alpha)/\sqrt{\sin\alpha}$, with $f(Y)$ then becoming $2Y\cos\alpha + Y^2\sin^{3/2}\alpha$.

24. The curves of Fig. 14 are plots of

$$\nu_n \equiv \sum_{m=1}^{n} \frac{1}{m}\,\psi_m \exp\left(-\frac{n-m}{\tau}\right) \Big/ \sum_{m=1}^{n} \exp\left(-\frac{n-m}{\tau}\right) \text{ with}$$

$1/\tau = 0.015$, the sliding exponential factor being designed *to* provide some smoothing of the results (L. Jackson Laslett, unpublished LBL Report). Extended comuutations of this nature can present challenging problems with respect to computkr accuracy. (Refs. 24 & 25).

25. C. Froeschlé and J.-P. Scheidecker, J. Comp. Phys. 11, 423-439 (1973); ____, Astrophys. & Space Sci. 25, 373-386 (1973).

26. I am deeply indebted to Paul J. Channell (LBL) for many stimulating and helpful conversations concerning topics discussed here. Responsibility for the views expressed in this paper, however, remains exclusively *my* own.

Lee Teng (NAL): Are you proposing the parameter ν as the parameter which specifies whether you are close to this stochastic paradox?

Jackson Laslett (LBL): I would like to propose that for the consideration of anyone doing this. I have noticed recently that people in this country have been concerned with whether interacting beams, a weak beam on a strong beam, give stable or unstable motion. Some of these people have taken two points a finite distance apart, followed them with the equations, and then tried to see how the distance between two points grows. We see the structure in some cases can be very detailed, so if one took two points, not an infinitesimal distance apart, but a considerable distance apart to get some computer accuracy on the difference, one might worry whether one should continue too long before they would get on opposite sides of the diagram. I think that Chirikov has suggested that one occasionally push them back together and keep a record of which one is pushed back. It might seem more reasonable to use infinitesimal vectors, and do this by means of keeping track of this tangential mapping transformation. One does get into computational difficulties in that connection and the same would apply for the eigenvalues. I don't know that it makes too much difference. Froeschlé has discussed the use of eigenvalues, and he has done some very nice work in transformations in two spatial degrees of freedom where he had four phase variables, and in that case he insisted that one should look not only at the growth of the largest eigenvalue but also at the next fellow, and that put very difficult computational requirements on his program. So, I am not sure whether that's a practical thing to do or not. In fact, in a plane I think if you have a scope presentation you could see the erratic behavior developing about as quickly as you could see the evolution. On the other hand, people interested in statistical mechanics are sometimes interested in the qualitative manner in which the erratic behavior develops. So I'm not sure. It's an open question to me. I'd be interested in your opinion.

Teng: Have you checked that this indicator behaves the same way as some others usually used to assess whether the distance between infinitesimally separated particles grows.

Laslett: I think that's what Froeschlé is suggesting and I've been trying to see whether I believe it, and I'm beginning to believe it from some of my computer experiments. That is to say, it's correlated with the scatter points, or with the evolution at least of the infinitesimal distances. The matrix elements sort of control both these things.

Francis Cole (NAL): One of the transformations that flashed by, I think it was the one right after de Vogelaere's, when it was put into MacMillan's form, seemed to be linear. It had sin α and cos α. Was it linear?

Laslett: No, it was not linear. There was a $(y-x_n)^2$, quadratic term in it.

Henry Blosser (Michigan State University): Occasionally, in tracking orbits in a computer. one's near the limit. I have seen-them be well behaved for a long period of time and then sort of go into the stochastic sort of behavior. Do you think that's a really physical possibility, that it would change behavior? Or that it just might be round-off?

Laslett: I would think it could be either. I mean one certainly has to be on guard against computer artifacts, and there are ways of trying to check on those things, as I'm sure you very well know. However, one can imagine situations where, for example, if one is extending one of these eigenvector directions from an unstable fixed point, in the manner indicated, the extensions of such a segment will generate a curve which only after some time may develop noticeable loops of the sort that we saw so readily with Professor de Vogelaere's transformation, And any single point of course ultimately would show a greater scatter as a result of following along on those loops. I don't know whether you feel differently. I think it's an open question in any particular instance. One just has to check his computations carefully and see whether it's right.

BEAM LOSS IN A COASTING BEAM FROM A HIGH ORDER ISOLATED RESONANCE*

M. Month
Brookhaven National Laboratory
Upton, New York

Abstract

It is well known that nonlinear detuning stabilizes high order isolated nonlinear resonances. On the other hand, for a system with changing tune, small amplitude particles can "lock-into" a resonance and be carried to large amplitudes. In coasting beams, such as the ISR beams, there is no obvious dynamic process to provide tune changes. However, it has been pointed out that scattering processes, such as intrabeam p-p scattering, induce momentum diffusion and, through the chromaticity, tune diffusion. In this way, particles can "pass through resonances". Using a random-walk model of the diffusion process, a simple expression for the fractional current loss rate is derived. Estimates for the loss rate are compared with ISR observations and are found to be in agreement. It might be emphasized that the model of beam loss presented here uses only the classical theory of nonlinear resonances.

1. Introduction

The stacked coasting beams in the ISR storage rings exhibit a loss ratel which cannot be explained by a single, direct mechanism. A typical fractional beam loss rate might be 10^{-5}/min. This is much faster than can be described by the existing diffusion processes in the ISR, e.g. scattering of protons off the residual gas in the chamber or the electromagnetic scattering of protons off each other (intrabeam scattering). On the other hand, it is apparent from ISR observations that the beam loss is associated with resonances of high order. In fact 5th and 8th order resonances have been identified and correlated with the loss of beam.' The difficulty here is that single, isolated nonlinear resonances, by themselves, cannot cause beam loss. Actually, it is well known that nonlinear detuning stabilizes these high order nonlinear resonances.' Here, then, is the dilemma: In the first place, there are diffusion processes which can cause beam growth and loss to the aperture. But, these are too slow to explain the observed beam loss rate. Secondly, the beam loss is correlated with high order resonances; but, in a coasting beam, the particles should be stable against these.

To resolve the situation, two basic approaches have been tried. One is to discard the traditional resonance picture and replace it with a multi-resonance model.[3,4] Under the influence of many nonlinear resonances, particles are (so it is suggested) driven into complex pathways in the four-dimensional betatron phase space, pathways which can transport particles to large betatron amplitudes and thereby to the aperture limit. The transport process, known as Arnold diffusion, is thought to be related to the stochastic nature of strong nonlinearities. Thus, it is suggested that the combination of many nonlinear resonances can manifest itself as a diffusive beam growth, with the time scale determined by the quasi-random nature of the multiresonance system. The ISR observation that beam loss is associated with single high order resonances presents somewhat of a problem in this model. It is conceived, however, that certain strong single resonances may act as feeding mechanisms for the Arnold diffusion pathways. The final word on this rather elegant and radical approach is not yet in and we will not pursue it further here. The second approach to an explanation of storage ring beam loss is more conventional. It follows simply from the fact that, although isolated high order resonances are stable in a static system, for a system with changing tune, particle amplitudes may grow. Thus, it is suggested that diffusion processes, such as intrabeam scattering, can feed resonances which then transport particles to the aperture limit.[5] We will here take this approach and present a model for beam loss in the ISR, utilizing a diffusion process which feeds a resonance which in turn transports particles to the aperture limit.

The ingredients of our model are as follows: Intrabeam scattering induces a diffusion of momentum and, through the machine chromaticity, a diffusion in particle tune. In this way, particles "pass through resonances". Under certain conditions, particles may "lock-into" a resonance during their passage through it and thereby be carried to large amplitudes. Thus, we have, in our model, the two essential features, feeding and transport." The feeding process is described by a random-walk model of the tune diffusion due to intrabeam scattering, while particle transport during resonance passage will be described by a trapping mechanism[7], obtained using only the classical theory of nonlinear resonances. Combining the feeding and transport processes, we derive an expression for the fractional beam loss rate.[8]

Our analysis applies to one-dimensional resonances. The extension to two dimensions has not been done. However, in the coupling resonance case, the excitation width and nonlinear detuning are still the dominant characteristics; and, we believe that, by an appropriate redefinition of tune and a proper interpretation of resonance width and detuning strength, our one-dimensional results are also applicable in the coupling resonance case.

In Section 2, we discuss the trapping mechanism, while in Section 3, we present our beam loss model, and compare our predicted loss rates for the ISR with experimental observations. We find that they are in agreement. We conclude that a combination of intrabeam scattering and classical resonance theory provides an adequate explanation of beam loss rates at the ISR.

2. Particle Trapping in Resonance Passage

A particle passes through resonance when its linear tune passes through some rational fraction. As this occurs, the particle's phase-space topology is transformed. If the passage through resonance is in the proper direction, stable islands appear at the origin and begin to move outward to regions of larger betatron amplitude as the tune changes. As these islands move outward, they also grow in phase-space area. The moving, growing islands can trap particles in their migration. This therefore represents a particle transport mechanism. Note that under quasi-static (adiabatic) conditions, particles can stream into the stable islands through the regions around the unstable fixed points, since these are intrinsically nonadiabatic phase-space regions. If a particle is trapped in one of these islands, and if the island reaches a physical aperture, then the trapped particle will be deposited

*Work performed under the auspices of the U.S. Atomic Energy Commission.

on the boundary walls and be lost. This process can be formally described by a trapping efficiency, which is simply the fraction of particles trapped (i.e. capable of being transported to "large" amplitudes) during a single resonance passage.

The detailed trapping mechanism is clearly a complex one; thus, the trapping efficiency is a complicated function of the resonance crossing parameters. First, there is the speed of resonance crossing. In the limit of fast crossing, we expect no trapping. Now, this is not to say that in the fast crossing limit, there is no influence on the beam. However, the time scale for beam growth, in this case, is far different from what exists under conditions when trapping occurs. In any case, we ignore the effect on the "remaining" beam. In other words, we presume that the only significant effect of resonance crossing is trapping. The question we confine ourselves to is, then, what is the trapping efficiency as a function of crossing speed? A second characteristic which influences trapping is the beam distribution. In this regard one might ask, is the trapping probability dependent on the particle phase-space position at the time the islands pass? Are particles near the outside of the beam more easily trapped than those near the center? For our purposes here, the influence of beam distribution can be neglected. Finally, we must determine the dependence of the trapping efficiency on the two nonlinear parameters: the resonance width and the nonlinear detuning strength.

The evaluation of the trapping efficiency has been considered in detail elsewhere.[7] The results of that analysis allows us to make substantial simplifications in order to obtain an expression for the trapping efficiency. The main point is that the trapping efficiency can be approximated by the area of the moving islands (relative to the beam area) near the exit of these islands from the beam. The crossing speed has been taken into account and enters through a multiplicative factor with an exponential fall-off. If we take for the island area the area at the amplitude corresponding to one rms beam emittance, ε_{rms}, we find for the trapping efficiency,

$$P_T = \frac{\sqrt{2}\,\pi}{\sqrt{p}} \left|\frac{\Delta_e}{\Delta_{NL}}\right|^{\frac{1}{2}} e^{-\gamma} \qquad (2.1)$$

where p is the order of the resonance, Δ_e is the resonance excitation width at $E = \varepsilon_{rms}$, Δ_{NL} is the nonlinear detuning at $E = \varepsilon_{rms}$, and γ is a function of the crossing speed given by

$$\gamma = \left[\frac{\delta\nu_{rev}}{4\pi\left|\Delta_e\,\Delta_{NL}\right|}\right]^{2/p} , \qquad (2.2)$$

with $\delta\nu_{rev}$ the average tune change per particle revolution. It is demonstrated in Ref. (7), that this expression for the trapping efficiency is in remarkable agreement with a computer simulation of a 5th order resonance crossing.

3. Beam Loss Rate

To produce beam loss from the trapping mechanism described in the previous section, there must be a process which causes a particle's tune to vary with time. In a coasting beam, of course, there is no synchrotron motion. However, in a high intensity beam, scattering processes may be strong enough to produce significant momentum diffusion. Through the machine chromaticity, this momentum diffusion translates into tune diffusion. In applying our model to the ISR, we will use p-p intrabeam scattering, which is a substantial effect in the ISR, as the diffusion source.[1,5]

Let us assume a momentum diffusion process, with a diffusion coefficient

$$D_p = \frac{d}{dt}\left(\frac{\Delta p}{p}\right)^2_{rms} . \qquad (3.1)$$

The tune diffusion arising from this can be described by

$$D = (\nu')^2 D_p , \qquad (3.2)$$

where ν', the change in ν per unit fractional momentum change, is proportional to the chromaticity. We consider the diffusion process as a simple random walk in tune. However, there is a boundary condition: If the particle is trapped by the stable outward moving islands, then at a certain tune distance from the resonance, say δ, the particle will be deposited at the aperture and be lost. If we consider a set of n particles at resonance at time $t = 0$, then some fraction of these will be lost. In fact, if the trapping efficiency is P_T, then the beam loss rate at time $t = T$ can be written[8]

$$\frac{\dot{n}}{n} = -\frac{P_T\,\delta}{2T(\pi D_\nu T)^{\frac{1}{2}}}\, e^{-\delta^2/4D_\nu T} \qquad (3.3)$$

For a beam with uniform density in tune, we can find the fractional loss rate at time T by integration (some care must be exercised in performing this integration since only particles which cross the resonance in the proper direction are to be included):

$$\frac{2P_T}{\Delta}\sqrt{\frac{D_\nu}{\pi T}}\, e^{-\delta^2/4D_\nu T} \qquad (3.4)$$

where Δ is the total tune spread in the beam, and N is the total number of particles in the beam. Since this function has a maximum at

$$T = \frac{\delta^2}{2D_\nu} , \qquad (3.5)$$

the maximum percentage loss rate is

$$\left(\frac{\dot{N}}{N}\right)_{max} = -0.97\,\frac{P_T D_\nu}{\Delta\delta} \simeq -\frac{P_T D_\nu}{\Delta\delta} . \qquad (3.6)$$

Note that the loss rate as a function of T falls off slowly, like $T^{-\frac{1}{2}}$ and so we can use this last expression as a measure of the average loss rate.

Thus, the beam loss rate is a simple function of *4* parameters: 1. The trapping efficiency, P_T; 2. the tune diffusion coefficient, D_ν; 3. the total beam tune spread, Δ; and *4*. the change in tune as trapped particles move from *the* resonance to the aperture, δ. The quantity δ is just the change in linear tune which causes the stable fixed points at the island centers to move from the origin of the betatron phase space to the aperture limit. It can be approximated by the nonlinear detuning at the aperture--that is,

$$\delta = \Delta_{NL}\,\frac{\varepsilon_{ap}}{\varepsilon_{rms}} , \qquad (3.7)$$

where ε_{ap} is the emittance value corresponding to the aperture amplitude. The average tune change per revolution is determined by the diffusion process. The relation between the diffusion coefficient D_ν and $\delta\nu_{rev}$ is easily found to be

$$\delta\nu_{rev} = (2D_\nu T_{rev})^{\frac{1}{2}} , \qquad (3.8)$$

where T_{rev} is the revolution period of the machine.

Let us now apply this theory to the ISR. We try to estimate the required parameters for a 5th order resonance. Using a head-on collision model and noting that the 5th order resonances are excited only if the various interactions are not identical, we estimate the resonance excitation and nonlinear detuning (at one rms beam width) to be[4]

$$\Delta_e = 0.1\ \eta\ \Delta_{bb} \quad ,$$

and

$$\Delta_{NL} = 3/8\ \Delta_{bb} \quad ,$$

where η is a factor (< 1) describing the departure from symmetry of the interaction points, and Δ_{bb} is the linear beam-beam tune shift. Typically, for the ISR, we can take $\Delta_{bb} = 3.5 \times 10^{-4}$, which leads to $\Delta_e = 3.5 \times 10^{-5}\ \eta$ and $\Delta_{NL} = 1.3 \times 10^{-4}$. Taking $D_\nu = 4 \times 10^{-11}$ sec^{-1}, we have $\delta\nu_{rev} = 1.5 \times 10^{-8}$. For 5% symmetry breaking, $\eta = .05$, $\Delta_e = 1.75 \times 10^{-6}$, which leads to $\gamma = 1.94$ and $P_T = 0.033$. If we assume the aperture limit to be 3 times the beam size, $\delta = 1.2 \times 10^{-3}$. Thus, if $\Delta = 0.01$, we have the loss rate $\dot{N}/N = \dot{I}/I = -0.7 \times 10^{-5}$ min^{-1}. If η is as high as 10%, the loss rate increases to 1.5×10^{-5} min^{-1}. These loss rates are consistent with observations made at the ISR.[1]

4. conclusions

We have proposed a model which can account for the beam loss rate observed at the ISR. The model is composed of a mechanism for beam loss due to a high-order isolated nonlinear resonance fed by a diffusion process, which was taken to be intrabeam scattering. It is perhaps important to emphasize that only the classical theory of nonlinear resonances was used.

References

1. The basic experimental facts relating to ISR beam loss have been obtained from, E. Keil, CERN Report, CERN/ISR-TH/73-38 (1973): Lectures given at the International School of Applied Physics, Erice, Italy, June 5-16, 1973. See also, ISR Performance Reports, Run 376 (Oct. 30, 1973) and Run *400* (Dec. 6, 1973).
2. A Schoch, CERN Report, CERN 57-23 (1958).
3. For studies relating to the multiresonance approach, stochasticity and Arnold diffusion, see: G.M. Zaslavskii and B.V. Chirikov, Usp. Fiz. Nauk 105, 3 (1971)[translation, Soviet Physics USPEKHI, 14, 549 (1972)]; E. Keil, Proc. 8th Int. Conf. High Energy Accel., Geneva 1971, 372 (1971); and Ref. (4).
4. E. Keil, CERN Reports, CERN/ISR-TH/72-7, 72-25 (1972).
5. E. Keil, III All-Union National Conf. on Part. Accel., October, 1972; H.G. Hereward, CERN Report, CERN/ISR-DI/72-26 (1972).
6. The basic notions of resonance feeding and "lock-in" are, of course, well known and are considered in Refs. (5) and (2), respectively.
7. A.W. Chao and M. Month, BNL Informal Report, CRISP 74-9 (1974).
8. A more detailed derivation of the loss rate is given in, M. Month, BNL Informal Report, CRISP 73-25 (1973). It should, however, be combined with Ref. (7), where a more accurate treatment of the trapping efficiency is given.
9. S. Chandrasekhar, Rev. Nod. Phys., 15, 1, p.1 (1943).

DISCUSSION

Rae Stiening (NAL): Have you studied more extreme cases? Where more of the beam goes away faster? In particular with regard to what the situation is with the remaining core of these dips.

Melvin Month (BNL): No, in fact, this calculation is only an onset calculation. It doesn't attempt to look at the beam distribution dynamically as the process is proceeding. In one of the slides I showed, there was the beginning of an attempt to see the effect on the distribution.

Andrei Kolomensky (Lebedev Institute): Besides this process of scattering of proton on proton, there can be other processes. Is there an effect of other random processes to shift the tune?

Month: I'm afraid I'm not familiar with detailed calculations. I've just used the results from the ISR reports, where it is claimed that the dominant process of this nature is the intra-beam scattering, and I think that's correct.

Kolomensky: About 10 years ago we tried to use stochastic modulation in the ν_r, ν_z plane to detune this resonance. But we got diffusion separation, and the harm was greater than the benefit. So we cancelled this work. But maybe, in principle, with a controlled stochastic mechanism one could counteract resonances. But in our machine in the USSR, this stochasticity did more harm than good.

Month: I think it's true here, too.

Andrew Sessler (LBL): In a bunched beam there will be a very systematic and large variation of the synchrotron motion. And I wonder if you have tried to calculate that, and put it into your theory because then you can make comparisons with experiments which have already been tried on the ISR. It would be a stringent test of your theory, and interesting as a predictive thing for other machines.

Month: No, I haven't tried that.

Mervyn Hine (CERN): There is another feeding mechanism, which I believe can contribute in some conditions. As you lose current, the space-charge ν-shift changes, so the whole beam slips fairly sideways across resonances.

Month: That's certainly a possibility. I haven't looked at that.

INTRA-BEAM-SCBTTERING

A. Piwinski
Deutsches Elektronen-Synchrotron DESY
Hamburg, Germany

Summary

The excitation and damping of betatron oscillations and the energy spread due to intra-beam scattering is investigated. It is shown that below transition energy an equilibrium for the particle distribution exists which does not depend on the number of the particles. The rise times and damping times for betatron oscillations and energy spread are calculated. The investigation shows that this effect sets a limit to the intensity of stored proton beams at energies below a few GeV.

Introduction

The intra-beam scattering or multiple scattering, i.e. the scattering of the particles within the beam, was investigated in several reports[1-8]. The result of these investigations showed an increase of all beam or bunch dimensions and an increase of the energy spread. But in these investigations two facts have been disregarded, the energy spread within the beam and the influence of the coordinates of the scattered particle on the scattering angle.

The energy spread in the beam, i.e. the energy difference of two colliding particles before the collision, leads to an excitation of betatron oscillations which is, for small energies, the main contribution to the increase of the beam dimensions.

The second point, the linear dependence of the change of the coordinates on these same coordinates, leads to a damping of the betatron oscillations and to a reduction of the energy spread. Without this damping one obtains an infinite increase of the beam dimensions and the energy spread. This seems to be impossible for particles below transition energy.

Far below transition energy the influence of the dispersion can be neglected as will be shown later, and the particles in the beam behave like the particles of a gas in a closed box. Here the focusing forces play the same role as the walls of the box. Since the collisions within a gas cannot lead to an increase of the temperature the collisions within the beam cannot , below transition, lead to an increase of the total oscillation energy and the energy spread. One can only expect a transfer of oscillation energy from one direction into another. Thus, there must exist an equilibrium distribution where the intra-beam scattering does not change the beam dimensions. It is shown that the equilibrium distribution is a Gaussian distribution.

Above transition energy the situation is changed by the property of the particles that is often characterized by the so called "negative mass" behaviour. Here the comparison with a gas in a closed box is not valid, and the calculation shows that the total oscillation energy can increase. The behaviour of the beam can be described with help of an invariant which is given by

$$\frac{1}{n}\left(\frac{1}{\gamma^2}-\alpha_M\right)\left\langle\frac{\Delta p}{p^2}\right\rangle^2+\langle x'^2\rangle+\langle z'^2\rangle=\text{const} \qquad (1)$$

with

p, Δp = momentum and momentum deviation, respectively
x', z' = betatron angles for horizontal and vertical direction, respectively
γ = particle energy divided by its rest energy
α_M = momentum compaction factor
n = 1 for bunched beams, 2 for unbunched beams

The momentum compaction factor α_M is, in Eq.(1), precise only for a weak focusing machine. For a strong focusing machine α_M is a good approximation for the mean value of D^2/β_x^2, where D denotes the dispersion and β_x the amplitude function.

If $1/\gamma^2-\alpha_M$ is positive, i.e. below transition, the three mean values in Eq.(1) are limited. But for negative $1/\gamma^2-\alpha_M$ the three mean values can increase so far as they do not exceed other limitations, and an equilibrium distribution does not exist.

In case of an equilibrium the three terms of the sum in Eq.(1) are equal and one can calculate the equilibrium dimensions starting from the initial dimensions. Eq.(1) further shows that the equilibrium dimensions do not depend on the number of particles, but only on the initial mean values. The number of particles determines the relaxation time for the equilibrium and the rise time for the increase above transition energy.

Kinematics

If s, x and z denote the longitudinal, horizontal and vertical coordinates, the momenta of two particles before a collision are given by (see fig.1)

$$\vec{p}_{1,2}=p_{1,2s}\{1,\ x'_{1,2}\ z'_{1,2}\}_{s,x,z} \qquad (2)$$

$x'_{1,2}$ and $z'_{1,2}$ are the betatron angles, and we consider in this investigation only linear and quadratic terms of $x'_{1,2}$ and $z'_{1,2}$. We define a coordinate system {u,v,w} with help of the unit vectors

$$\vec{e}=(\vec{p}_2+\vec{p}_1)/|\vec{p}_2+\vec{p}_1|,$$
$$\vec{e}_v=\vec{p}_1\times\vec{p}_2/|\vec{p}_1\times\vec{p}_2| \qquad (3)$$
$$\vec{e}_w=\vec{e}_u\times\vec{e}_v$$

The momenta can then be written in the form

$$\vec{p}_{1,2}=p_{1,2}\{\cos\alpha_{1,2},\ 0,\ \pm\sin\alpha_{1,2}\}_{u,v,w} \qquad (4)$$

The angles α_1 and α_2 are defined by

$$p_1\sin\alpha_1=p_2\sin\alpha_2 \qquad (5)$$

and

$$\alpha_1+\alpha_2=2\alpha=J\sqrt{(x'_1-x'_2)^2+(z'_1-z'_2)^2} \qquad (6)$$

A Lorentz transformation parallel to the u-axis gives the representation of the momenta in the center of

mass system

$$\vec{\bar{p}}_{1,2} = \pm \{ \bar{p}_u, 0, \bar{p}_w \}_{\bar{u},\bar{v},\bar{w}}$$

$$= p_{1,2}\{\gamma_{tr}(\cos\alpha_{1,2} - \beta_{tr}/\beta_{1,2}), 0, \pm \sin\alpha_{1,2}\}_{\bar{u},\bar{v},\bar{w}} \quad (7)$$

where β_{tr} and γ_{tr} are defined by

$$\beta_{tr} = \frac{\beta_1\gamma_1\cos\alpha_1 + \beta_2\gamma_2\cos\alpha_2}{\gamma_1 + \gamma_2} \quad (8)$$

$$\gamma_{tr} = \frac{1}{\sqrt{1-\beta_{tr}^2}}$$

The bar denotes all quantities in the center of mass system. After the collision the momenta are changed by the polar angle $\bar{\psi}$ and the azimuthal angle $\bar{\phi}$, and the momenta are

$$\vec{\bar{p}}'_{1,2} = \pm \{\bar{p}_w \sin\bar{\psi}\cos\bar{\phi} + \bar{p}_- \cos\psi \ , \ \bar{p}\sin\bar{\psi}\sin\bar{\phi}$$

$$\bar{p}_w \cos\bar{\psi} - \bar{p}_- \sin\bar{\psi}\cos\bar{\phi} \}_{\bar{u},\bar{v},\bar{w}} \quad (9)$$

where the prime denotes all quantities after the collision. The inverse Lorentz transformation gives the momenta in the {u,v,w}system, and the change of the momenta has the form

$$\vec{p}'_{1,2} - \vec{p}_{1,2} = p_{1,2}\{\gamma_{tr}(\pm\sin\bar{\psi}\cos\bar{\phi}\sin\alpha_{1,2} +$$

$$+ (\cos\bar{\psi}-1)\gamma_{tr}(\cos\alpha_{1,2} - \beta_{tr}/\beta_{1,2})) \ ,$$

$$\pm \sin\bar{\psi}\sin\bar{\phi}\bar{p}/p_{1,2}, -\sin\psi\cos\phi\gamma_{tr}(\cos\alpha_{1,2} - \beta_{tr}/\beta_{1,2})$$

$$\pm (\cos\bar{\psi}-1)\sin\alpha_{1,2}\}_{u,v,w}$$

We now assume that the velocity of the particles in the center of mass system is non relativistic. Then the relation

$$\bar{\beta}^2 = \tfrac{1}{4}\beta^2\gamma^2((\eta_1 - \eta_2)^2/\gamma^2 + (x'_1 - x'_2)^2 + (z'_1 - z'_2)^2) << 1$$

with

$$\eta_{1,2} = \frac{\Delta p_{1,2}}{p}$$

is satisfied, and one obtains

$$\gamma_{tr} = \gamma \ , \quad \cos\alpha_{1,2} - \beta_{tr}/\beta_{1,2} = \pm \frac{\eta_1 - \eta_2}{2\gamma^2} \ .$$

The change of the momenta can now be written in the form

$$\vec{p}'_{1,2} - \vec{p}_{1,2} = \pm \frac{p}{2}\{2\alpha\gamma\sin\bar{\psi}\cos\bar{\phi} + \gamma\xi(\cos\bar{\psi}-1),$$

$$\left(\zeta\sqrt{1+\xi^2/\alpha^2/4}\sin\bar{\phi} + \xi\Theta/\alpha/2\cos\bar{\phi}\right)\sin\bar{\psi} + \Theta(\cos\bar{\psi}-1),$$

$$\left(-\Theta\sqrt{1+\xi^2/\alpha^2/4}\sin\bar{\phi} + \xi\zeta/\alpha/2\cos\bar{\phi}\right)\sin\bar{\psi} + \zeta(\cos\bar{\psi}-1)\}_{s,x,z}$$

with

$$(\eta_1 - \eta_2)/\gamma = \xi, \quad x'_1 - x'_2 = \Theta, \quad z'_1 - z'_2 = \zeta \ .$$

Change of the emittances and the momentum spread

The emittance ε is defined by

$$\beta_x\varepsilon_x = x_\beta^2 + \beta_x^2 x'^2$$

where we have neglected β'_x. The change of the emittance due to a scattering event is

$$\beta_x\delta\varepsilon_x = 2x_\beta\delta x_\beta + \delta^2 x_\beta + 2\beta_x^2 x'\delta x' + \beta_x^2\delta^2 x'$$

$$= -2x_\beta D\frac{\delta p}{p} + D^2\frac{\delta^2 p}{p^2} + 2\beta_x^2 x'\frac{\delta p_x}{p} + \beta_x^2\frac{\delta^2 p_x}{p^2} \quad (11)$$

For the vertical oscillations one obtains

$$\beta_z\delta\varepsilon_z = 2\beta_z^2 z'\frac{\delta p_z}{p} + \beta_z^2\frac{\delta^2 p_z}{p^2} \quad (12)$$

For the momentum spread one can define the following invariant

$$H = \begin{cases} \eta^2 + \dot{\eta}^2/\Omega^2 & \text{for a bunched beam} \\ \eta^2 & \text{for an unbunched beam} \end{cases}$$

where Ω is the synchrotron frequency and η the relative momentum deviation. The change of H due to a scattering event is in both cases

$$\delta H = 2\eta\frac{\delta p}{p} + \frac{\delta^2 p}{p^2} \quad (13)$$

Determination of an invariant

Since the particle velocity should be non relativistic in the center of mass system we may employ the Rutherford cross section which has the form

$$d\bar{\sigma} = \left(\frac{r_o}{4\bar{\beta}^2\sin^2\bar{\psi}/2}\right)^2 \sin\bar{\psi}d\bar{\psi}d\bar{\phi} \quad (14)$$

with r_o = classical particle radius.

The impact parameter for the smallest scattering angle $\bar{\psi}_m$ is given by

$$\tan\frac{\bar{\psi}_m}{2} = \frac{r_o}{2\bar{\beta}^2\bar{b}} \quad (15)$$

We assume $\bar{b}$ to be equal one half of the average distance between the particles in the center of mass system

$$\bar{b} = \tfrac{1}{2}(\gamma/\rho)^{1/3} \quad (16)$$

To calculate the mean value of the change of the emittance or the momentum deviation for one particle we have to average with respect to all betatron angles and momentum deviations of the second particle. For the total mean value of the change of the emittance and momentum deviations of all particles we have to average additionally with respect to all betatron angles , momentum deviations and positions of the first particle. Thus, we have to integrate with the following density function

$$P = \rho_s^2(s)\rho_{x\beta}(x_{\beta 1})\rho_{x\beta}(x_{\beta 2})\rho_z^2(z)\rho_\eta(\eta_1)\rho_\eta(\eta_2)$$

$$\cdot\rho_{x'}(x'_1)\rho_{x'}(x'_2)\rho_{z'}(z'_1)\rho_{z'}(z'_2)$$

since

$$s_1 = s_2 = s \ , \quad z_1 = z_2 = z$$

but

$$x_{1\beta} + \eta_1 D = x_{2\beta} + \eta_2 D$$

The functions ρ_i are normalized to one. We replace the variables $x_{\beta 1,2}$, $\eta_{1,2}$ $x'_{1,2}$, $z'_{1,2}$ by the variables x_β, η, x', z', ξ, Θ, ζ with help of the relations

$$x_{\beta 1,2} = x_\beta \mp D\gamma\xi/2 \ , \ \eta_{1,2} = \eta \pm \gamma\xi/2$$

$$x'_{1,2} = x' \pm \Theta/2 \quad , \ z'_{1,2} = z' \pm \zeta/2$$

The function P is now symmetric with respect to ξ, Θ and ζ. The relative velocity between two colliding particles in the center of mass system is $2c\bar\beta$. The mean value of the change of the emittances and the momentum deviation per unit time is then given by

$$\int 2c\bar\beta \, P \int_{\bar\psi_m}^{\pi} \int_0^{2\pi} \frac{d\bar\sigma}{d\bar\omega} \begin{pmatrix} \delta H_1 /\gamma^2 \\ \delta\varepsilon_{x1}/\beta_x \\ \delta\varepsilon_{z1}/\beta_z \end{pmatrix} \sin\bar\psi d\bar\phi d\bar\psi d\tau =$$

$$= \frac{\pi}{2} c \, r_o^2 \gamma \int P \begin{pmatrix} \Theta^2 + \zeta^2 - 2\xi^2 \\ \xi^2 + \zeta^2 - 2\Theta^2 + \frac{D^2\gamma^2}{\beta_x^2}(\Theta^2+\zeta^2-2\xi^2) \\ \xi^2 + \Theta^2 - 2\zeta^2 \end{pmatrix} \ln\left(\frac{2\beta^2 b}{\ldots}\right) \frac{d\tau}{\ldots}$$

$$d\tau = ds \, dx\,dz \, d\eta dx' \, dz' \, d\xi d\Theta d\zeta$$

$$4\bar\beta^4 \bar b^2 / r^2 >> 1$$

From Eq.(17) we get

$$\int_{\bar\psi_m}^{\pi} \int_0^{2\pi} P\left[\left(\frac{1}{\gamma^2} - \frac{D^2}{\beta_x^2}\right) \delta H_1 + \frac{\delta\varepsilon_{x1}}{\beta_x} + \frac{\delta\varepsilon_{z1}}{\beta_z}\right] \frac{d\bar\sigma}{d\bar\omega} \bar\beta \sin\bar\psi d\bar\phi d\bar\psi d\tau = 0 \qquad (18)$$

and

$$\left(\frac{1}{\gamma^2} - \frac{D^2}{\beta_x^2}\right) \langle H\rangle + \langle\varepsilon_x\rangle/\beta_x + \langle\varepsilon_z\rangle/\beta = \text{const.}$$

where the brackets denote the average with respect to all particles of the beam. With the relations

$$\langle H\rangle = \begin{cases} 2\langle\frac{\Delta^2 p}{p^2}\rangle & \text{for bunched beams} \\ \langle\frac{\Delta^2 p}{p^2}\rangle & \text{for unbunched beams} \end{cases}$$

$$\langle\varepsilon_x/\beta_x\rangle = 2\langle x'^2\rangle \ , \ \langle\varepsilon_z/\beta_z\rangle = 2\langle z'^2\rangle \qquad (19)$$

we obtain finally for the invariant the expression

$$\frac{1}{n}\left(\frac{1}{\gamma^2} - \frac{D^2}{\beta_x^2}\right)\langle\frac{\Delta^2 p}{p^2}\rangle \quad x'^2\rangle + \langle z'^2\rangle = \text{const.}$$

Rise times and damping times

For the calculation of the rise time and damping time we assume a Gaussian distribution for x_β, z, η, x' and z'. The distribution in longitudinal direction may be uniform or Gaussian-like. With Eq.(17) one gets for the change of the mean value of the emittances and the momentum spread per unit time

$$\begin{pmatrix} \frac{d}{dt}\frac{\langle H\rangle}{\gamma^2} \\ \frac{d}{dt}\frac{\langle\varepsilon_x\rangle}{\beta_x} \\ \frac{d}{dt}\frac{\langle\varepsilon_z\rangle}{\beta_z} \end{pmatrix} = 2c \int P \int_{\bar\psi_m}^{\pi} \int_0^{2\pi} \bar\beta \frac{d\bar\sigma}{d\bar\omega} \begin{pmatrix} \frac{\delta H_1}{\gamma^2} \\ \frac{\delta\varepsilon_{x1}}{\beta_x} \\ \frac{\delta\varepsilon_{z1}}{\beta_z} \end{pmatrix} \sin\bar\psi d\bar\phi d\bar\psi d\tau$$

$$= 2A \int_{-\infty}^{\infty}\int\int \exp\left\{-\frac{\xi^2\gamma^2}{4}\left(\frac{D^2}{\sigma_{x\beta}^2} + \frac{1}{\sigma_\eta^2}\right) - \frac{\Theta^2}{4\sigma_{x'}^2} - \frac{\zeta^2}{4\sigma_{z'}^2}\right\} \cdot \begin{pmatrix} \Theta^2 + \zeta^2 - 2\xi^2 \\ \xi^2 + \zeta^2 - 2\Theta^2 + \frac{D^2\gamma^2}{\beta_x^2}(\Theta^2+\zeta^2-2\xi^2) \\ \xi^2 + \Theta^2 - 2\zeta^2 \end{pmatrix} \cdot \ln\left(\frac{q^2}{4}(\xi^2+\Theta^2+\zeta^2)\right) \frac{d\xi d\Theta d\zeta}{(\xi^2+\Theta^2+\zeta^2)^{3/2}} \qquad (20)$$

with

$$A = \frac{c\, r_o^2 \Lambda}{16\pi\sqrt{\pi}\, \sigma_{x\beta}\sigma_z\sigma_\eta\sigma_{x'}\sigma_{z'}\beta^3\gamma^4}$$

$$\Lambda = \begin{cases} \frac{N_b}{2\sqrt{\pi}\sigma_s} & \text{for bunched beams} \\ \frac{N}{C} & \text{for unbunched beams} \end{cases}$$

$\sigma_{s,x,z}$ = standard deviations for longitudinal, horizontal and vertical bunch dimensions

N_b, N = number of particles in a bunch and in the beam, respectively

C = circumference, $c\beta$ = particle velocity

With Eq.(19) one obtains

$$\frac{1}{\tau_\eta} = \frac{1}{2\sigma_\eta^2}\frac{d\sigma_\eta^2}{dt} = nA\left(1 - \frac{\eta}{\sigma_x^2}\right) f\left(\frac{y}{\sigma_{x'}}, \frac{y}{\sigma_{z'}}, q\sigma_y\right)$$

$$\frac{1}{\tau_{x'}} = \frac{1}{2\sigma_{x'}^2}\frac{d\sigma_{x'}^2}{dt} = A\left[f\left(\frac{\sigma_{x'}}{\sigma_y}, \frac{\sigma_{x'}}{\sigma_{z'}}, q\sigma_{x'}\right) + \frac{D^2\sigma_\eta^2}{\sigma_x^2} f\left(\frac{\sigma_y}{\sigma_{x'}}, \frac{\sigma_y}{\sigma_{z'}}, q\sigma_y\right)\right]$$

$$\frac{1}{\tau_{z'}} = \frac{1}{2\sigma_{z'}^2}\frac{d\sigma_{z'}^2}{dt} = A\, f\left(\frac{\sigma_{z'}}{\sigma_y}, \frac{\sigma_{z'}}{\sigma_{x'}}, q\sigma_{z'}\right)$$

with

$$\sigma_y = \frac{\sigma_\eta\sigma_{x\beta}}{\gamma\sigma_x} \quad , \quad q = \beta\gamma\sqrt{2\,\frac{\bar b}{r_o}}$$

The function f is defined by

$$f(a,b,c) = 2\int_0^{\infty}\int_0^{\pi}\int_0^{2\pi} \exp\left\{-\rho\left(\cos^2\mu + (a^2\cos^2\nu + b^2\sin^2\nu)\cdot \sin^2\mu\right)\right\} \cdot \ln(c^2\rho)(1-3\cos^2\mu)\sin\mu d\nu d\mu d\rho \qquad (21)$$

f cannot be evaluated analytically. It is calculated by a computer program and plotted in fig.2 and 3. To reduce the range of numerical values for f one can use the relations

$$f(a, b, c) = f(b, a, c)$$

$$f(a,b,c) + \frac{1}{a^2} f\left(\frac{1}{a}, \frac{b}{a}, \frac{c}{a}\right) + \frac{1}{b^2} f\left(\frac{1}{b}, \frac{a}{b}, \frac{c}{b}\right) = 0$$

One can proof that

$$f(1, 1, c) = 0 \ .$$

Thus, with

$$\sigma_\eta\sqrt{\frac{1}{\gamma^2} - \frac{D^2}{\beta_x^2}} = \sigma_{x'} = \sigma_{z'}$$

an equilibrium is reached and the Gaussian distribution

remains stable, This equilibrium can only be reached for

$$\gamma < \left(\left\langle \frac{D^2}{\beta_x^2} \right\rangle\right)^{-1/2} \approx \frac{1}{\sqrt{\alpha_M}}$$

i.e. below transition energy.

References

1) H.Bruck, J.Le Duff, Labor.Accel.Lin.,Orsay, Rap.Techn.,24-64 (1964)

2) J.Le Duff, Labor.Accel.Lin.,Orsay, Thesis (1965)

3) C.Pellegrini, Proceeding of the International Symposium on electron and positron storage rings, Saclay, 1966.

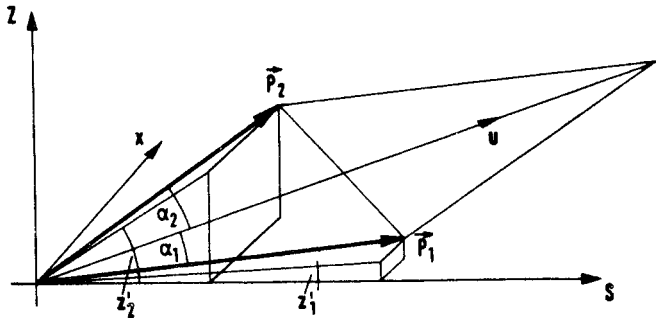
4) C.Pellegrini; Nota Interna, LBF-68/1 (1968)

5) J.-E.Augustin; PEP Note-26, SPEAR-I47

6) E.Keil; ISR Performance Report, ISR-TH/EK/anb

7) K.Hübner; ISR Performance REport, ISR-TH/KH/ps

8) H.G.Hereward; ISR Performance Report, ISR-TH/HGH/anb



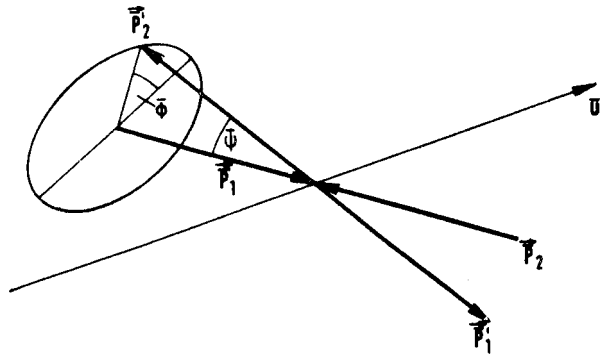


Fig. 1

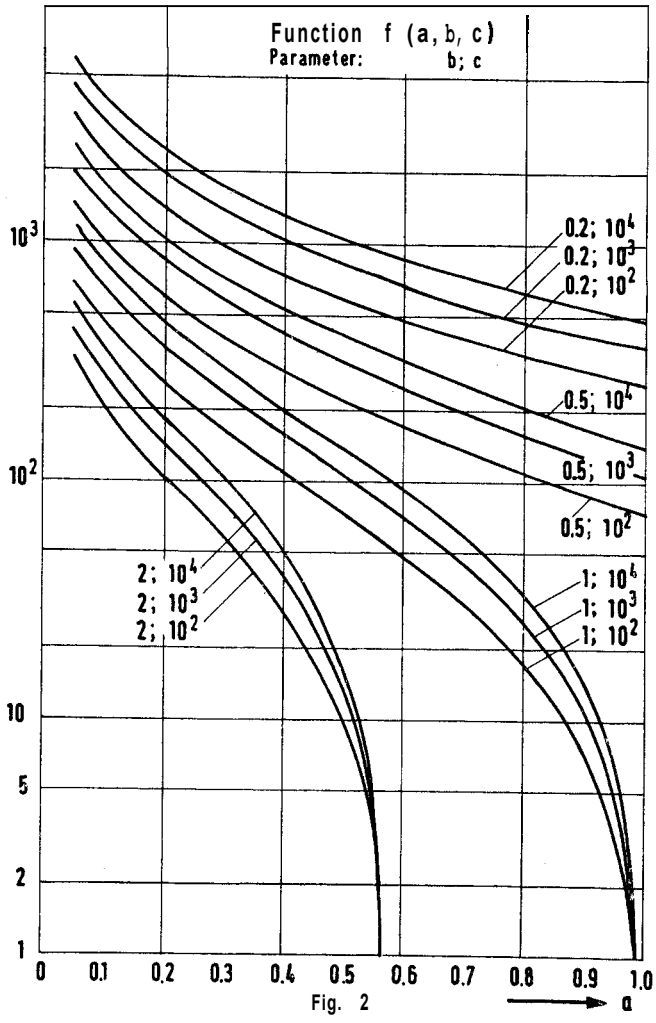
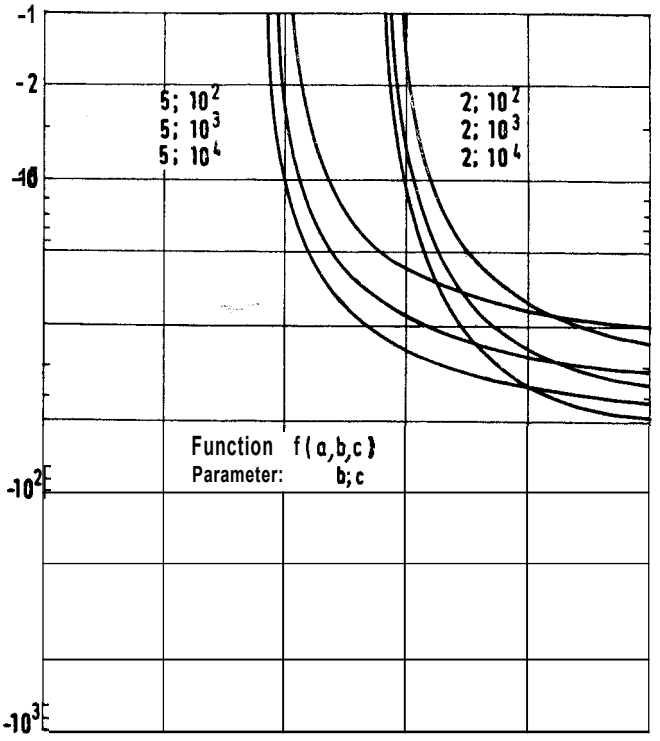


Fig. 2



Andrew Sessler (LBL): Could you remind me how the rise time goes with γ, as one goes to higher energy.

Anton Piwinski (DESY): The risetimes are proportional to $1/A$, and A is proportional to $1/\gamma^4$, so the risetimes are proportional to γ^4. But, there is also a $\nu\gamma$ weaker γ dependence in the function f.

Andrei Kolomensky (Lebedev Institute): Are the risetimes independent or are they connected by some rule?

Piwinski: There is a linear relation between $1/\tau_n$ and $1/\tau_z$, but multiplied with certain factors.

Wolfgang K. H. Panofsky (SLAC): How *is* the numerical agreement with the 2 GeV tests made in the ISR?

Piwinski: Buchner has made an estimate and calculation, and he found that the values that come from measurement have the right order of magnitude, but I don't remember the exact measurement.

DETAILED STUDY OF THE BEAM-BEAM INTERACTION AT THE ORSAY STORAGE RING (ACO)

M. Bergher, J. Buon, A. Jejcic, J. Le Duff, P. Marin, M. Sommer, and H. Zyngier

Laboratoire de l'Accélérateur Linéaire
Université de Paris-Sud, Centre d'Orsay,
Orsay, France.

1. Abstract and Introduction

In the normal operating conditions of ACO the two beam behaviour is dominated by the beam-beam interaction. Single beam behaviour in the range of energy and current described below ($250 \leq E \leq 510$ MeV, $I \leq 35$ mA) exhibits no effect such as resonances, beam losses, etc..., in comparison with the ones observed with two beams. In this clear situation a detailed study of the beam-beam interaction has been performed on ACO in 1973.

The normal operating conditions are : one bunch per beam, two crossing points and head-on collisions. Radial and vertical wave numbers per turn are set just below an integer, near the coupling resonance $\nu_x - \nu_z = 2$ (usually $\nu_z \sim .835$, $\nu_x \sim 2.845$). Table 1 shows some relevant ring parameters at the crossing points.

The main result obtained is the important part played by high order non-linear resonances in the beam loss induced by the beam-beam interaction. This appears in the study of the beam-beam limit as a function of the operating point in the wave number diagram.

Other results are reported on :

- The tune shift parameter ξ at the beam-beam limit.
- The influence of the number of bunches.
- The absence of any difference between the interaction of two strong beams versus the strong beam-weak beam interaction.
- Coherent motion induced by small vertical separations at the crossing points.

More details can be found in recent ACO reports'.

Betatron amplitude function β^*	radial		$\sim$ 2 m
	vertical		$\sim$ 4 m
Off-momentum function η^*			$\sim$ 2 mm
Transverse beam dimensions	radial	σ_x^*	$\sim$ .5 mm
	vertical	σ_z^*	$\sim$ .5 mm
Longitudinal beam dimension		σ_ℓ	$\sim$ 15 cm
Single beam lifetime at 30 mA		τ	$\sim$ 35 h

Table 1 : Ring parameters at E = 510 MeV and V_{RF} = 17.5 kV.

2. Operating points and non-linear resonances

It has been studied how the operating point can be moved in the ν_x, ν_z plane as a function of the intensity for two equal beams at 510 MeV.

The ν_x, ν_z diagram has been explored in the region[†]

$$.67 < \nu_z < .90 \qquad 2.67 < \nu_x < 2.90$$

According to the intensity, three cases can be distinguished :

2.1 Low current : $I^+ \sim I^- < 5$ mA

Whatever the tune, the beam-beam interaction does not affect the beam lifetime. Away from the coupling resonance $\nu_x - \nu_z = 2$, many beam transverse enlargements are observed, indicating the excitation of non-linear resonances. No enlargement is observed with only one single beam stored in the ring. Hence we may infer that these resonances are excited by the beam-beam interaction. Between two well separated non-linear resonances, the beams are flat, but the beam-beam limit (very short lifetime) is already reached at $I \sim 5$ mA.

2.2 High current : $I^+ \sim I^- > 10$ mA

Using a lifetime criterion ($\tau > 1$ h), the possible tunes are found to be restricted to small areas along the coupling resonance $\nu_x - \nu_z = 2$. Figure 1 shows 4 different areas which were specially investigated. They are separated by stopbands near rational numbers p/q. Other areas between rationals may exist, but were not searched for.

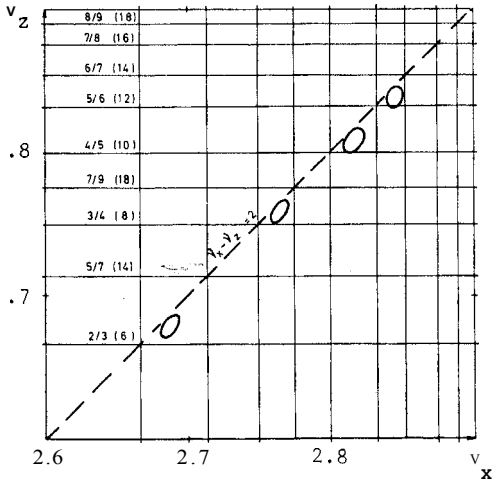


Fig. 1 : ν_x, ν_z diagram

Studied operating points are indicated by small circles.

Rational values of ν_x and ν_z are indicated by vertical and horizontal fines.

The number between parenthesis gives the order 2n of the non-linear resonances associate6 to the rational number m/n.

[†] The values ν_x, ν_z are determined by the quadrupole settings, calibrated with a single beam stored in the ring. This calibration does not take into account the small perturbation of wave numbers on the coupling resonance.

The existence of such stopbands can be attributed to the influence of non-linear resonances in the beam loss mechanism induced by the beam-beam interaction.

High order resonances seem to be involved. For instance the stopband near 5/6 is related to 12^{th} order resonances in the case of two crossing points per turn*. Many 12^{th} order resonances cross at $\nu_x = 2+5/6$, $\nu_z = 5/6$. The stopband may be due to a single or a cluster of such resonances. There is no experimental answer to this question.

2.3 Medium current : 5 mA < $I^+ \sim I^-$ < 10 mA

The size of the area is larger than for higher currents, but still restricted to the neighbourhood of the coupling resonance (Figure 2). Beam enlargements appear when ν_z is approaching a rational value. Sometimes these resonances can be crossed, by varying ν_z, without beam loss.

For instance, at $I^+ \sim I^- \sim 7$ mA, three groups of resonances have been observed (Figure 2), corresponding to $\nu_z = 6/7$, 5/6 and 4/5. One may guess that the strength of these resonances is too low to reduce the lifetime. For higher current (I > 10 mA), their strength increases and the lifetime is reduced before a beam enlargement appears.

At high current, the boundary of the area available for an operating point is characterized by a sharp decrease of the beam lifetime (from a few hours to much less than one hour). For a fixed value of ν_x, the beam lifetime remains almost constant as ν_z is varied, and a sharp decrease is observed when the boundary is reached.

The size of the ν_x, ν_z area decreases when the current is increased (Figure 3). At the same time, its center shifts below the coupling resonance.

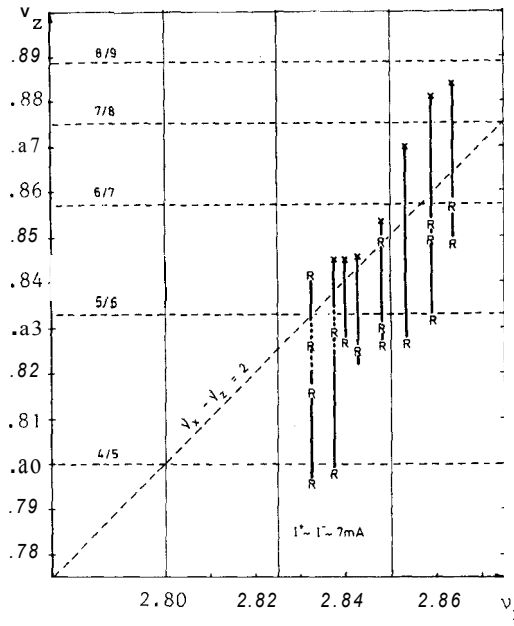


Fig. 2 : Range of ν versus the radial wave number ν.

Enlargement of one bean near a resonance is indicated by R or R.

Low order rational values ν = m/n are indicated by horizontal dotted lines.

(× : limit of the ν_z range when the lifetime drops)

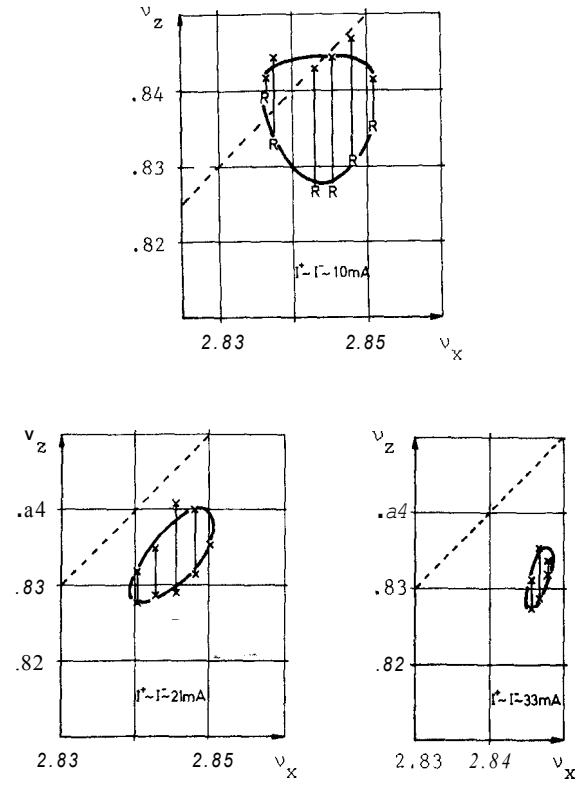


Fig. 3 : Pange of ν versus the radial wave number ν for different intensities.

The coupling resonance $\nu_x - \nu_z = 2$ is indicated by a dotted line.

Enlargement of one beam at an end point of the ν_z range is indicated by R.

*Here the order of a resonance is defined as the smallest degree of the terms which excite this resonance in the Taylor expansion of the space charge potential. The wave number $\nu = k \times p/q$ (k : the number of crossing points, p and q : relatively prime integers) corresponds to a resonance of the order either q (q even) or 2q (q odd), since the potential parity is even. For k = 2, and writing $\nu = m/n$, the resonance order is 2n.

Figure 4 shows how the limits of the ν_z range vary with the intensity I for three different operating points. The lower bound $\nu_{z\ min}$ is almost independent of I, but the upper bound $\nu_{z\ max}$ decreases as I increases.

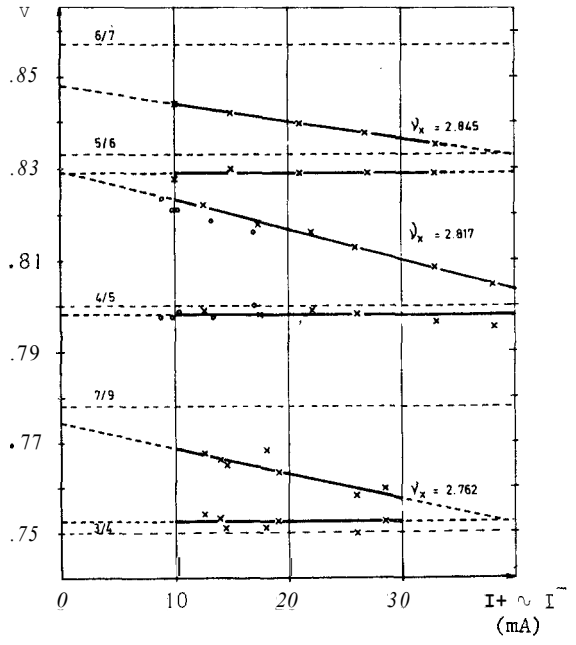


Fig. 4 : Limits of ν_z range versus the intensity of each beam and for 3 values of ν_x.

Low order rational values ν = m/n are indicated by horizontal dotted lines.

x : one bunch per beam.
o : two bunches per beam.

The $\nu_{z\ min}$, $\nu_{z\ max}$ bounds, extrapolated to zero current, are quite close to rationals, as shown in table 2. The same behaviour has been found for the ν_x bounds.

ν_x	$\nu_{z\ min}$	$\nu_{z\ max}$
2.162	.752 ∿ 3/4	.774 ∿ 7/9
2.817	.798 ∿ 4/5	.830 ∿ 5/6
2.845	.829 ∿ 5/6	.848 ∿ 6/7

max,

All these experimental results can be summarized as follows :

a) At high intensity, operating points are separated by stopbands near rational numbers.

b) Beam enlargements appear at low and medium current near such values.

c) The I = 0 extrapolated values of the ν_x,ν_z bounds are also close to rational numbers.

The excitation of high order non-linear resonances by the beam-beam interaction may explain such a behaviour.

The beam-beam limit is said to be reached at an intensity for which the beam lifetime is less than one hour, inside the available area of the operating point. At this limit, the ν_x or ν_z range is about 3.10^{-3}.

Since the operating point is set below an odd integer, and the beam-beam interaction shifts the tune upwards, it is currently believed that the half integer resonance is responsible of the beam-beam limit observed on ACO[2,3]. The experimental result reported here is not inconsistent with this idea, but it shows that the limit is also due to the excitation of non-linear resonances.

At 510 MeV the intensity limit, and the maximum luminosity, are about the same for the three operating points studied : ν_x = 2.845, 2.817 and 2.762.

$$I_{max} \sim 35 - 40 \text{ mA}$$
$$L_{max} \sim 10^{29} \text{ cm}^{-2} \text{ s}^{-1}.$$

These maximum values scale with the energy like :

$$I_{max} \sim E^{3.5 \pm .2} \qquad L_{max} \sim E^{5.4 \pm .6}$$

in the ACO energy range : 250-540 MeV. The I_{max} scaling law appears to be inconsistent in the cubic law ($I_{max} \sim E^3$) predicted by a simple model[4]. It is worth point out that the measured beam cross section varies as $E^{2.1 \pm .2}$

3. Tune shift parameter

The tune shift parameter :

$$\xi_{x,z} = \frac{N r_e}{2\pi\gamma\ (\sigma_x^* + \sigma_z^*)} \times \left(\frac{\beta}{\sigma}\right)^*_{x,z}$$

(N is the number of particles per bunch, and γ the ratio of the particle energy to their rest mass energy) has been derived from the luminosity measurements with a double Bremsstrahlung monitor.

At 510 MeV, and at the two operating points ν_x = 2.817 and 2.345, the maximum ξ values are :

$$\xi_{x\ max} = .021 \qquad \xi_{z\ max} = .030$$

Systematic errors on these values, due to biases on the intensity and luminosity measurements, are less than 30 %.

These values disagree with former values derived from transverse beam dimensions measured inside a bending magnet : $\xi_{x\ max} \simeq .03$, $\xi_z \simeq .055$.

It is believed that the new measurments, using a luminosity monitor, are more reliable. A bias on the former values could arise from the correcting factor

relating the measured dimensions to the actual beam dimensions at the crossing point. The factor used does not account for optical perturbations due to the beam-beam interaction.

From the energy law of the maximum intensity and luminosity, a slight dependance of ξ_{max} is deduced :

$$\xi_{max} \sim E^{1/2}.$$

The exponent is smaller than the one observed at ADONE.

4. Beam-beam interaction with two bunches per beam

Assuming a constant ξ_{max}, the maximum luminosity should be proportional to the number of bunches. Already at the first stages of ACO[5], it has been observed that the maximum luminosity is the same with two bunches per beam, at the usual operating point $\nu_x = 2.845$.

This result has been confirmed at the other operating point $\nu_x = 2.817$. More precisely the ν_z range as a function of the intensity is about the same with one or two bunches per beam (Figure *4)*.

5. Strong beam-weak beam interaction

Simple models for the beam-beam interaction study the motion of one particle crossing an opposite beam. Such models are only relevant for strong beam-weah beam interaction.

Since storage rings operate with two equal beams, it is important to check if there is any qualitative difference.

The strong beam-weak beam interaction has been studied at the usual operating point $\nu_x = 2.845$, and at 510 MeV. The weak electron beam intensity was about 1/20 of the strong positron beam intensity. No qualitative difference has been observed.

The ν_x, ν_z range, and its variation with the strong beam intensity, are about the same than those obtained with two equal beams. In particular the conclusion about the excitation of non-linear resonances is the same.

6. Coherent motion induced by the beam-beam interaction

In the head-on collision mode, only a very small coherent motion of the beams can be observed (about 3 % of $\sigma_{x,z}$) whatever the operating conditions[6]. The coherent frequency is approaching the revolution frequency at the beam-beam limit, but with no amplitude increase. Therefore it is difficult to imagine haw such a small amplitude motion can participate to the beam loss mechanism.

When the two beams are slightly separated in the vertical direction at the crossing points, the situation is quite different.

A large amplitude (about $\sigma_{x,z}$) coherent motion appears in a small range of ν_z, when the beam separation reaches a threshold around $\frac{\sigma}{20}$. At high intensity (above 20 mA) this coherent motion leads to a poor lifetime*.

It is worth to try to relate the observation of the difficulties encountered in various rings with beams crossing at angle'. Obviously a longitudinal displacement of the crossing point leads to a small separation, which in itself has already a bad effect, as observed on ACO.

References

1. R. Belbéoch et al., RT/3-73, "Anneaux de Collisions" Laboratoire de l'Accélérateur Linéaire, Orsay (1973)
   R. Belbéoch et al., NI/52-73 "Anneaux de Collisions" Laboratoire de l'Accélérateur Linéaire, Orsay (1973)
2. F. Amman, D. Ritson, Proc. of the Int. Conf. on High Energy Accelerators, Brookhaven, p. 471 (1961).
3. F. Amman, Proc. of the Particle Accelerators Conf., San Francisco, p. 858 (1973).
4. Coppelia : Projet d'anneaux de collisions électron-positron d'énergie maximale 3 GeV à charge d'espace compensée. Laboratoire de l'Accélérateur Lindaire, Orsay (1969).
   J. Haissinski, Proc. of the Int. School of Physics "Enrico Fermi", Course 46, p. 150 (Academic Press 1971).
5. The Orsay Storage Ring Group, RT/26-67, "Anneaux de Collisions", Laboratoire de l'Accélérateur Linéaire, Orsay (1967).
6. The Orsay Storage Ring Group, Proceedings of the 8th Intern. Conf. on High Energy Accelerators, p. 127, CERN, Genève (1971).
7. The Orsay Storage Ring Group, Proc. of the 1973 Particle Accelerator Conference, San Francisco, p. 768 (1973).
8. ADONE Group, LNF/70-48, Frascati (1970).
   SPEAR Storage Ring Group, private communication.

*Preliminary results, published at the San Francisco Conference[7] must be corrected on this point.

DISCUSSION

Sergio Tazzari (Frascati): What parameters did you measure with the strong beam-weak beam?

J. Buon (Orsay): We have measured the ν_x, ν_z areas.

Alberto Renieri (Frascati : What is the threshold for radial coherent motion of'separated beams?

Buon: There is a sharp threshold, true, but the result at the moment is not very reliable. But it's quite small, something like the transverse dimension divided by 10.

Gerhard Fischer (SLAC): Is the value of ξ that you quote per interaction region or total?

Buon: It's per interaction region.

NON-LINEAR BEAM-BEAM EFFECT COMPUTER SIMULATION

A. Renieri

Laboratori Nazionali di Frascati del CNEN

Frascati, Italy

Abstract.

The motion of a single particle colliding with a strong beam in a storage ring is studied by computer simulation, under the assumptions that there is no radiation noise and no damping and that the strong beam has a gaussian transverse charge distribution. The phase space regions of stochastic motion and the corresponding minimum ΔQ values are determined. There is evidence that the motion stochasticity is due to overlapping of neighbouring resonances (Chirikov criterion).

1. - Introduction.

The stochastic phase space behaviour of many one-dimensional non-linear conservative dynamic systems has been extensively studied by I. Gumowski and C. Mira[1,2,3], E. Keil[4,5], using the resonance overlapping Zaslavskii-Chirikov[6] criterion, evaluated the transverse amplitude and ΔQ limit for beam-beam non linear space charge effect.

In this paper we investigate the one-dimensional transverse phase space motion of a single particle colliding with a strong beam in a storage ring. The ΔQ threshold for the stochastic motion and the stochastic phase space regions are found using the properties of the phase space periodic points (cycles). The investigation is performed under the following conditions,

- head-on collision,
- strong beam shorter than β value at crossing point,
- the space charge forces from the strong beam are simulated by δ-function-like kicks given to the weak beam particle (point-like strong beam),
- no radiation noise and no damping,
- off energy closed orbit $\eta = 0$ at interaction point,
- no chromaticity,
- gaussian charge distribution function of the strong beam

$$f(x,z) = \frac{1}{2\pi a^2}\, e^{-\frac{(x^2+z^2)}{2a^2}} \qquad (1)$$

- only one transverse mode excited.

We will use the following notations,

β = betatron 8-value at crossing point,
μ = betatron phase difference between two neighbouring ring crossing points,
x = transverse displacement,
$x' = dx/dS$, where S is the machine longitudinal coordinate,
$\theta(x)$ = transverse kick experienced by the particle with x transverse displacement.

For the strong beam distribution function (1), $\theta(x)$ is given by the eq.

$$\theta(x) = -\frac{r_o N}{\gamma \sigma^2}\left\{x\left(\frac{1-e^{-\frac{x^2}{2\sigma^2}}}{\frac{x^2}{2\sigma^2}}\right)\right\} \qquad (2)$$

Where r_o is the particle classical radius, γ is the ratio between the total and the rest energy, N is the number of particles of the strong beam. Note that all computations have been carried out with at least 14 digits.

2. - Motion equations.

We write the motion equations as recurrences between the middle of one crossing and the middle of the next one. We assume that the machine is perfect, and that all crossing points are identical. We have,

$$\begin{pmatrix} x \\ x' \end{pmatrix}_{n+1} = \begin{pmatrix} \cos\mu, & \beta\sin\mu \\ -\frac{1}{\beta}\sin\mu, & \cos\mu \end{pmatrix} \begin{pmatrix} x \\ x' + \frac{1}{2}\theta(x) \end{pmatrix}_n + \frac{1}{2}\begin{pmatrix} 0 \\ \theta(x) \end{pmatrix}_{n+1} \qquad (3)$$

where n labels the crossing.

If we put,

$$\xi = \frac{r_o N \beta}{4\pi\gamma\sigma^2} \qquad F(y) = \frac{1-e^{-y}}{y}$$

equations (3) become (see eq. (2)),

$$\begin{aligned} x_{n+1} &= x_n\cos\mu + \beta x'_n\sin\mu - 2\pi\xi F\left(\frac{x_n^2}{2a^2}\right)\sin\mu\, x_n \\ x'_{n+1} &= -\frac{x_n}{\beta}\sin\mu + x'_n\cos\mu - \\ &\quad - 2\pi\xi F\left(\frac{x_n^2}{2a^2}\right)\cos\mu\, x_n - 2\pi\xi x_{n+1} F\left(\frac{x_{n+1}^2}{2a^2}\right) \end{aligned} \qquad (4)$$

ξ is related to the linear ΔQ shift by the eq.,

$$\cos(\mu + 2\pi\Delta Q) = \cos\mu - 2\pi\xi\sin\mu$$

3. - Phase space variables,

The recurrence equations (4) can be derived

from the Hamiltonian,

$$H(q, q\ S) = \frac{1}{2}(p^2+(\frac{\mu}{L})^2 q^2) + \\ + \frac{4\pi\xi\mu\sigma^2}{L} G(\frac{q^2}{2\sigma^2}) + \sum_{n=-\infty}^{\infty} \delta(s-nL) \qquad (5)$$

Where we have put,

$$q = x, \qquad p = \frac{\mu\beta x'}{L}$$

L = longitudinal distance between two neighbouring crossing points.

$\delta(s)$ = Dirac function

$G(x) = \int_0^x F(y)\,dy$

In order to obtain variables more manageable than (q, p), let us define,

$$H_0(q, p) = \frac{1}{L}\int_0^L H(q, p|\bar{S})dS = \frac{1}{2} p^2 + \frac{\mu^2\sigma^2}{L^2} V(\frac{q^2}{2\sigma^2}) \qquad (6)$$

$$(V(x) = x + \frac{2\xi}{\mu} G(x)).$$

From this Hamiltonian we derive two new variables (T, W) that will be used in describing the motion derived Prom the complete time-dependent Hamiltonian (5). We define,

$$T(q, p) = \frac{1}{\mu}\int_{-\lambda_M(q,p)}^{\lambda_M(q,p)} \frac{d\lambda}{\sqrt{V(\lambda_M^2(q, p)) - V(\lambda^2)}}, \qquad (7)$$

$$W(q, p) = \frac{|p|}{p}\frac{2\pi}{T(q, p)}\int_{q/\sqrt{2}\sigma}^{\lambda_M(q,p)} \frac{d\lambda}{\sqrt{V(\lambda_M^2(q, p)) - V(\lambda^2)}}, \qquad (8)$$

where $\lambda_M(q, p)$ is the solution of the equation,

$$V(\lambda_M^2(q, p)) = (\frac{L}{\mu\sigma}) H_0(q, p). \qquad (9)$$

The physical meaning of T, λ_M and W is obvious. T is the motion period, in units d L, $\lambda_M = A/\sqrt{2}\sigma$ where A is the maximum q value, W is the phase conjugate variable. The solutions of the dynamic equations derived from the time-independent Hamiltonian H_0 are,

$$T(S) = T(0)$$
$$W(S) = W(0) - \frac{2n}{T(0)}(\frac{S}{L}) \qquad (\text{mod } 2\pi) \qquad (10)$$

In the following we restrict our investigation to the phase space strip enclosed between W = 0 and W = $\pi/2$. This is allowed by the simmeiry of recurrence equations (4) with respect to the x and x' axis, that is, in terms of (T, W), with respect to W = 0, $\pi/2$, π, 2π.

4. - Cycles and separatrices.

With the new (T, W) variables, the recurrence equations (4) become,

$$T_{n+1} = A(T_n, W_n)$$
$$W_{n+1} = B(T_n, W_n).$$

Let us define the functions,

$$A_k(T_n, W_n) = T_{n+k}$$
$$Bk(Tn, W_n) = W_{n+k}, \qquad (12)$$

We call cycles of order N, the points (T_n, W_n) satisfying the equations,

$$T_n = A_N(T_n, W_n)$$
$$W_n = B_N(T_n, W_n) \qquad n = 1, 2, \ldots, N \qquad (13)$$

A further property of a cycle, beside N, is the number of turns (rotational number) made around the origin (x = x' = 0) by the pnase space representative point. In the following we use the notation "cycle N/r" for a cycle of order N and rotational number r. The characteristic matrix of a cycle N/r is,

$$\hat{C} = \begin{pmatrix} \frac{\partial A_N(T, W)}{\partial T}, & \frac{\partial A_N(T, W)}{\partial W} \\ \frac{\partial B_N(T, W)}{\partial T}, & \frac{\partial B_N(T, W)}{\partial W} \end{pmatrix} \qquad (14)$$

The determinant of $\hat{C}$ is always 1, because our recurrence is conservative. If the absolute value of the trace of $\hat{C}$ is lower (greater) than 2 the cycle is stable (unstable) and is called centre (saddle). Separatrices start from saddles. They divide the phase space into stable and unstable phase regions. As an example we have, in Fig. 1, cycles 6/1 and 5/1 with their separatrices. Inside the 6/1 separatrices we have stable motion (particle E), while outside the phase motion is unstable (particle A and H). In the computer graphs we use the notations, x = saddle; 0 'centre; N = separatrix of cycle N/1; * = overlap between two or more separatrices. The vertical scale on the right (A/σ) is related to T by eq. (7) (A = $\sqrt{2}\lambda_M\sigma$). Roughly speaking A is the "instantaneous motion. amplitude". From the physical meaning of T and W, we have, for a cycle N/r,

$$T_1 \approx T_2 \approx \ldots \approx T_N \approx \frac{N}{r}$$

$$W_n - W_{n-1} \approx -\frac{2nr}{N}$$

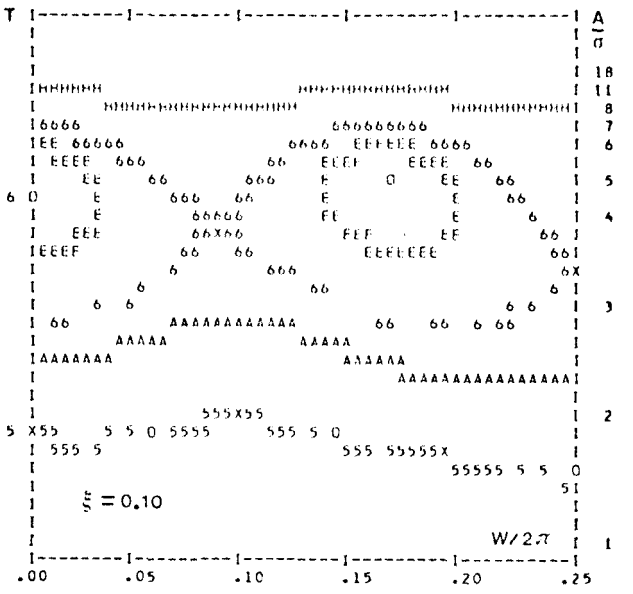


FIG. 1

5. - Stochasticity threshold.

The phase space pattern of N/1 cycles, for $\mu/2\pi = 0.15$, is given in Figs. 2, 3 and 4,

Fig. 2, $\xi = 0.10$ ($\Delta Q = 0.087$); we have cycles 6/1 and 5/1,

Fig. 3, $\xi = 0.16$ ($\Delta Q = 0.136$); there is an overlap region between cycles 6/1 and 5/1; a new cycle (4/1) appears,

Fig. 4, $\xi = 0.20$ ($\Delta Q = 0.171$); the whole phase space region between cycles 6/1 an 4/1 is stochastic, with the exception of the stable phase islands around the centres.

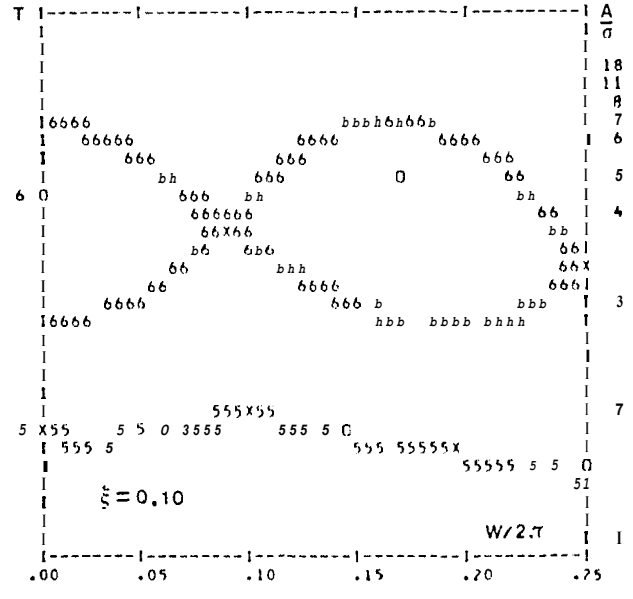


FIG. 2

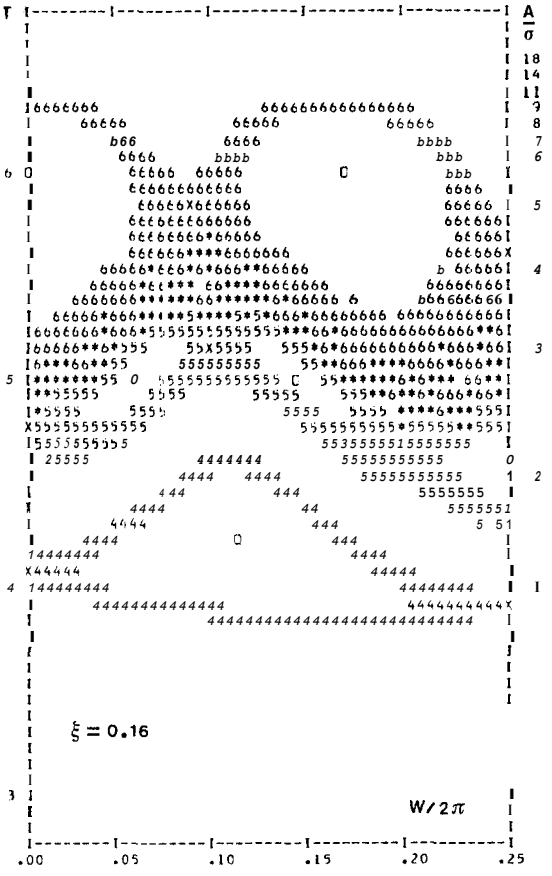


FIG. 3

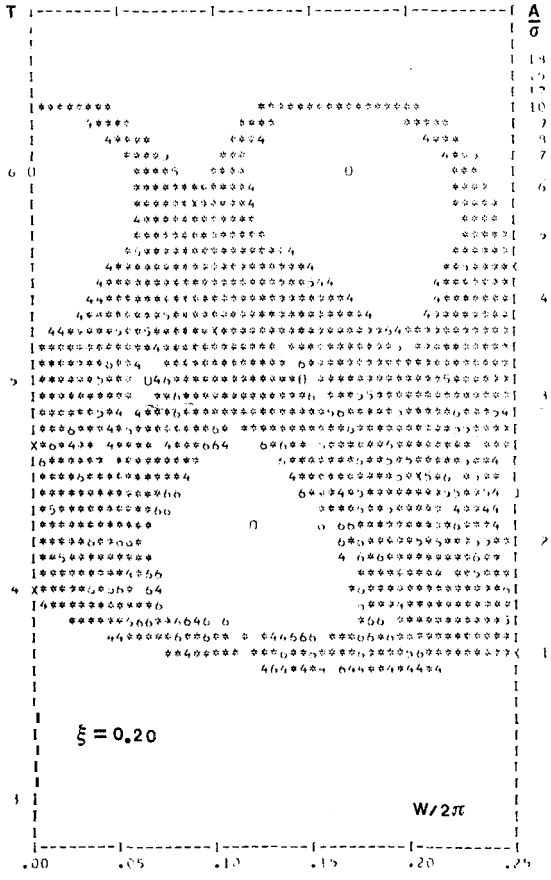


FIG. 4

In Fig. 5 ($\xi = 0.20$) we have the phase space trajectories of particles A, B, H outside and W inside the stochastic region. From the vertical right scale we see that A/σ ranges, for particle W, from 1 to 10, *so* that this stochastic region may be very dangerous.

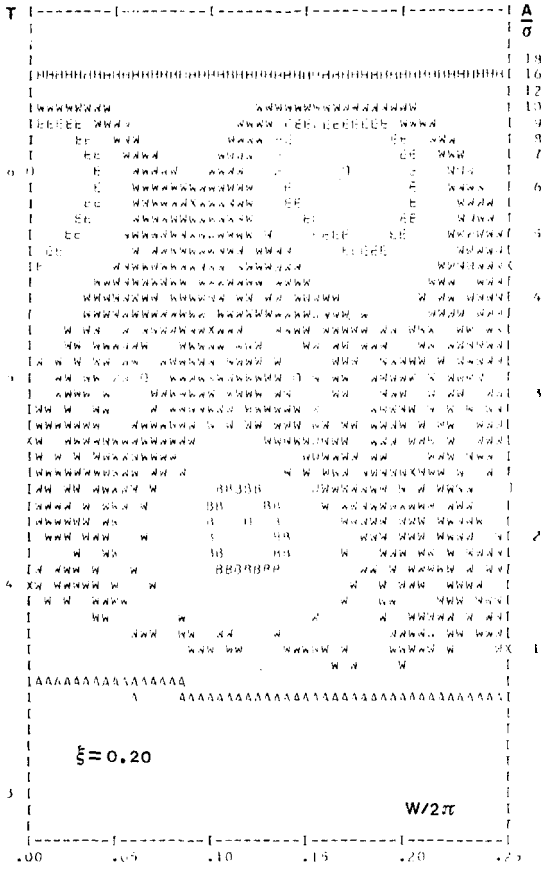


FIG. 5

If we add, in somehow artificial way, radiation noise and damping to our model, we obtain that the r.m.*s.* transverse dimension of the weak beam does not change until stochastic regions appear (See Fig. 6). When the phase space between 6/1 and 4/1 is fully stochastic, the weak beam enlarges by a factor of five. This behaviour does not depend on the damping time value (τ), in the range

$$10^2 \lesssim \frac{\tau}{\delta} \lesssim 10^4$$

where δ is the time distance between two neighbouring crossing points. From this observation we may derive the energy independence of ξ in the weak beam-strong beam incoherent limit. However, we must remember rhat our model is very rough. The minimum require ment, for taking into account experimental data, is to have a bi-dimensional model (four-dimensional pha se space).

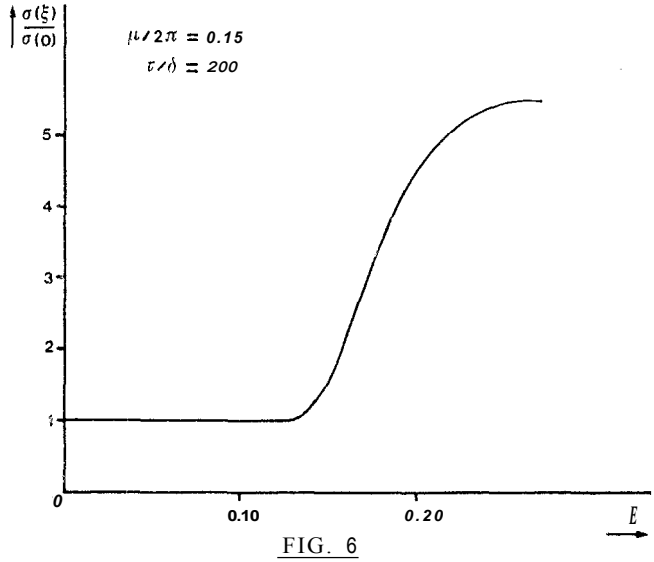


FIG. 6

6. - Conclusions.

According to Zaslavskii and Chirikov[6], we may say that the stochastic region in Fig. 3 and 4 is due to the overlapping of the stochastic layers of neighbouring resonances. On the other hand, as showed by Gumoski[2,3], when a centre bifurcates into a saddle, the region in the neighbourhood of such a cycle becomes stochastic. We 'nave indeed that the phase spa ce between cycles 5/1 and 4/1 becomes stochastic just when centres 19/4 and 17/4 bifurcate into saddles. Equally we have that the bifurcation of centre 23/4 (21/4) makes the region between 6/1 and 11/2 (11/2 and 5/1) stochastic. Fig. 7 shows the plot of ξ bifurca tion values versus μ of the centres 19/4 and 17/4. We have tested this behaviour for

$$0.05 \lesssim \mu/2\pi \lesssim 0.15;$$

for this range of μ we may write the following empirical rule.

The phase space region between cycles N/1 and (2N±1)/2 becomes stochastic when the centre (4N±1)/4 bifurcates into a saddle.

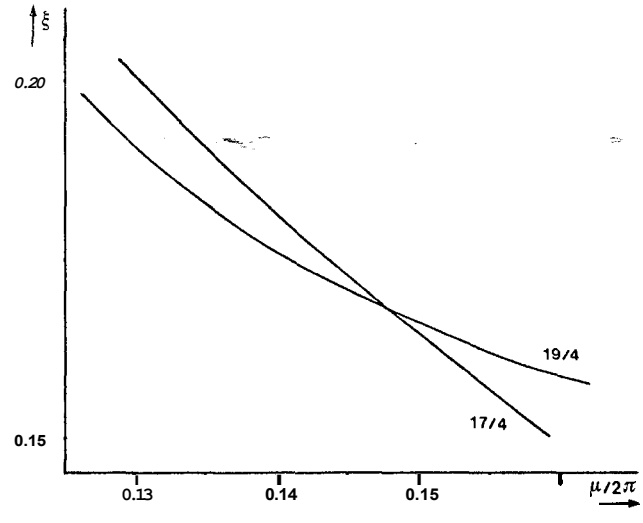


FIG. 7

References. -

1 - I. Gumosky and C. Mira, Proc. 8th Intern. Conf. on High Energy Accelerators, CERN (1971), page 374.
2 - I. Gumosky, CERN/SI/INT.BR/72-1 (1972).
3 - I. Gumosky, CERN/SI/INT.BR/72-7 (1973).
4 - E. Keil, CERN/ISR-TH/72-7 (1972).
5 - E. Keil, CERN/ISR-TH/72-25 (1972).
6 - G.M. Zaslavskii and B.V. Chirikov, Sov. Phys. - -Uspekhi 14, 249 (1972).

TWO-DIMENSIONAL RESONANCE EFFECTS DUE TO A LOCALIZED BI-GAUSSIAN CHARGE DISTRIBUTION*

A. G. Ruggiero
National Accelerator Laboratory
Batavia, Illinois

The effect of a nonlinear kick supplied by one beam to the other in a colliding device had already been investigated by E. Keil' and J. LeDuff[2]. The nonlinear kick was multiple analyzed and a single resonance was considered, but only the average term and the lowest Fourier mode driving the resonance were taken into account. More recently, A.G. Ruggiero and L. Smith[3] approached the problem again, but with a different technique, They found that it is possible to describe a single resonance taking the exact analytical expression of the nonlinear kick and the contribution of all the higher Fourier modes driving the same resonance. Nevertheless, their calculation was limited to the one-dimensional case. The purpose of this paper is to extend this kind of calculation to the bi-dimensional case. We shall still assume a round beam with bi-gaussian distribution of standard deviation σ. The nonlinear kick is taken to occur lumped over a zero length interval. The main application is the calculation of the motion in proximity of a single, isolated and weak resonance; the calculation of the resonances width; 2nd of the stochasticity limit. Our result for the stochastic limit is higher than the one obtained by Keil. Because of the amount of the topics we shall report here the essential results. The details of the calculations can be found in another paper[4].

Equations of Motion

The equations of motion are

$$x''(s)x \qquad \xi_x \frac{1-e^{-u^2}}{}$$

and similarly for y,

$$u^2 = \frac{x^2+y^2}{2\sigma^2} .$$

Both beams are considered ultrarelativistic i.e. $v \sim c$. k_x and k_y are the two unperturbed linear focusing functions. δ_{int} is the periodic delta function which represents a kick every revolution of circumference $2\pi R$. Also, it is

$$\xi_x/\beta_x^* = \xi_y/\beta_y^* = \xi/\beta^* = Nr_o/4\pi\sigma^2\gamma$$

N is the number of particles in the strong bunch, r_o the classical radius of the test particle, to be taken as positive for charges of equal sign and negative for charges of opposite sign, γ the ratio of the total energy to the rest energy. β_x^* and β_y^* are constant and denote the values of the beta-functions at the crossing point. ξ_x and ξ_y are the usual linear tune shifts per interaction.

*Work Supported by the U.S.A.E.C.

We perform the transformation to the two pairs of angle-action variables ψ_x, I_x and ψ_y, I_y. The angle $\theta = s/R$ is the independent variable and prime denotes derivative with respect to θ. By performing a triple Fourier expansion we obtain

$$\psi_x' = \nu_x + 2\xi_x \sum_{nm\ell} f_{nm}(I_x,I_y) \cdot e^{i(n\psi_x+m\psi_y-\ell\theta)}$$

$$I_x' = -2\xi_x I_x \sum_{nm\ell} g_{nm}(I_x,I_y) \cdot e^{i(n\psi_x+m\psi_y-\ell\theta)}$$

and similarly for y, where

$$f_{nm} = \frac{1}{4\pi}\int_{-\infty}^{+\infty} e^{i\omega(\tau_x+\tau_y)}\left(\log\frac{\omega^2+1}{\omega^2}\right)(-i)^{\frac{m+n}{2}} \cdot J_{\frac{m}{2}}(\omega\tau_y)\left\{J_{\frac{n}{2}}(\omega\tau_x) - iJ_{\frac{n}{2}}'(\omega\tau_x)\right\}d\omega$$

$$g_{nm} = \frac{1}{4\pi}\int_{-\infty}^{+\infty} e^{i\omega(\tau_x+\tau_y)}\left(\log\frac{\omega^2+1}{\omega^2}\right)(-i)^{\frac{m+n}{2}} \cdot J_{\frac{n}{2}}(\omega\tau_x)\, J_{\frac{m}{2}}(\omega\tau_y)\,\frac{n\,d\omega}{\omega\tau_x}$$

for n and m both even numbers, otherwise $f_{nm} =$

Single Isolated Resonance

We now define a resonance by choosing three integer numbers, with no common divisor, such that the quantity, $X = p\psi_x+q\psi_y-r\theta$, can be considered as slowly varying, and retain in the triple sum only terms of the form, $\exp[is(p\psi_x+q\psi_y-r\theta)]$. It can be proven that one invariant of the motion is

$$W_1 = qI_x-pI_y = \text{constant.} \qquad (2)$$

The other invariant is the Hamiltonian W_2 which relates the action variables I_x and I_y to the new angle variables $\alpha_x = \psi_x - \frac{r}{p}\theta$, $\alpha_y = \psi_y$

$$W_2 = (\nu_x-\frac{r}{p})I_x+\nu_y I_y+2\sigma^2\left(\frac{\xi}{\beta^*}\right)\int_o^1 \frac{dt}{t}\left\{1 +\right.$$

$$- e^{-t(\tau_x+\tau_y)} \sum_{\ell=-\infty}^{+\infty} I_{\ell p_o}(t\tau_x) I_{\ell q_o}(t\tau_y) \cdot$$

$$\cdot \cos(\ell X_o) \Big\}^{*} \qquad (3)$$

where p_o, q_o and X_o equal, respectively, p, q and 2X in the case at least one of p and q is odd, and equal, respectively, p/2, q/2 and X in the case both p and q are even. Also it is

$$\tau_x = \frac{\nu_x}{p} \qquad \tau_y = \frac{\nu_y}{q} \ ,$$

In the case of a single resonance the motion is bounded, because for large τ_x and τ_y the dependence of W_2 on X_o vanishes.

The equations of motion are easily derived from (3)

$$I_x' = -4p_o\sigma^2\left(\frac{\xi_x}{R}\right) \int_o^1 \frac{dt}{t}\, e^{\cdots}$$

$$\cdot \sum_{\ell=-\infty}^{+\infty} \ell I_{\ell p_o}(t\tau_x)\, I_{\ell q_o}(t\tau_y) \sin(\ell X_o) \qquad (4)$$

and similarly for y.

In particular we derive

$$X' = p\alpha_x' + q\alpha_y' = \varepsilon_{pq} +$$

$$+ p\xi_x \int_o^1 dt\, e^{-(\tau_x+\tau_y)} \sum_{\ell=-\infty}^{+\infty} \Big[I_{\ell p_o}(t\tau_x) +$$

$$- I_{\ell p_o}'(t\tau_x) \Big] I_{\ell q_o}(t\tau_y)\cos(\ell X_o) +$$

$$+ q\xi_y \int_o^1 dt\, e^{-t(\tau_x+\tau_y)} \sum_{\ell=-\infty}^{+\infty} \Big[I_{\ell q_o}(t\tau_y) +$$

$$- I_{\ell q_o}'(t\tau_y) \Big] I_{\ell p_o}(t\tau_x)\cos(\ell X_o) \qquad (5)$$

where $\varepsilon_{pq} = p\nu_x + q\nu_y - r$.

Fixed Lines

The equation of a fixed line is obtained by setting

$$I_x' = I_y' = o \qquad \text{and} \qquad X' = o.$$

From eq. (4), we notice that there are two fixed lines, namely for $X_o = o$ and $X_o = \pi$. From eq. (5), then, the equations of the two fixed lines are, respectively,

$$p\xi_x \int_o^1 dt\, e^{-t(\tau_x+\tau_y)} \sum_{\ell=-\infty}^{+\infty} \Big[I_{\ell p_o}(t\tau_x) +$$

$$- I_{\ell p_o}'(t\tau_x) \Big] I_{\ell q_o}(t\tau_y) +$$

$$+ q\xi_y \int_o^1 dt\, e^{-t(\tau_x+\tau_y)} \sum_{\ell=-\infty}^{+\infty} \Big[I_{\ell q_o}(t\tau_y) +$$

$$\ell q_o'(t\tau_y) \Big] I_{\ell p_o}(t\tau_x) + \varepsilon_{pq} = o$$

and

$$p\xi_x \int_o^1 dt\, e^{-t(\tau_x+\tau_y)} \sum_{\ell=-\infty}^{+\infty} \Big[I_{\ell p_o}(t\tau_x) +$$

$$- I_{\ell p_o}'(t\tau_x) \Big] I_{\ell q_o}(t\tau_y)(-1)^{\ell} +$$

$$+ q\xi_y \int_o^1 dt\, e^{-t(\tau_x+\tau_y)} \sum_{\ell=-\infty}^{+\infty} \Big[I_{\ell q_o}(t\tau_y) +$$

$$- I_{\ell q_o}'(t\tau_y) \Big] I_{\ell p_o}(t\tau_x)(-1)^{\ell} + \varepsilon_{pq} = o. \qquad (7)$$

The motion around the fixed lines can be investigated by expanding the right hand side of eqs. (4) and (5), respectively, around $X_o = o$ and $X_o = \pi$. It is found that the $X_o = \pi$ fixed line is a stable line and the $X_o = 0$ fixed line is an unstable line. It has been proven that the condition for existence of the fixed lines is, for $p > 2$

$$-1 < \frac{\varepsilon_{pq}}{p\xi_x + q\xi_y} < o \ . \qquad (8)$$

Let us consider the three-dimensional space with ε_{pq} on the abscissa and I_x, I_y on the other two axis. Eqs. (6) and (7) represent two surfaces in this space. For fixed I_x and I_y we can go from one surface to another moving parallel to the ε_{pq}-axis. The distance $\Delta\varepsilon_{pq}$ which separates the two surfaces defines the "width" of the resonance at amplitude I_x and I_y. This is obtained by simply subtracting (7) from (6).

The general feature of the motion in the presence of a single resonance (p>2) is that the phase space is clearly divided in two regions, one close to the origin and the other reaching the infinite. In both regions, a particle executes stable betatron oscillations with little amplitude and frequency modulation. This modulation vanishes as the unperturbed amplitude gets either smaller or very large. These two regions confine with an intermediate region. In this, the perturbation of the resonance is the largest and several islands appear. The motion inside an island is also stable, but on top of the betatron frequency another frequency of precession movement appears; this is the resonance frequency. The precession movement disappears when (8) is not satisfied.

This is pretty much all that we can say, from a general point of view, about a single

*I_n is the modified Bessel function.

resonance. To have a better insight of the motion one should have a more compact expression for the summation

$$R = \sum_{\ell=-\infty}^{+\infty} I_{\ell p_o}(t\tau_y) I_{\ell q_o}(t\tau_y)\cos(\ell X_o)$$

which we have been able to derive only for some special cases such as (a) $q = o$ and (b) $p = |q|$, or $\tau_y = o$ (see ref. [3]).

First Mode Approximation

Taking into account all the higher Fourier modes, we have found that even as well as odd order resonances are possible. This is in contrast to what we get by using the "first mode approximation" where only the average term $R = o$ and the next $|\ell| = 1$ are retained. In this case, only even order resonances are possible. On the other hand, in the more exact approach, a resonance is defined only when the three integer numbers p, q and r do not have a common divisor. In contrast, in the "first moue approximation", the (p,q,r)-resonance is considered independent of the $(\ell p, Rq, \ell r)$-resonance.

In the "first mode approximation" the width of a resonance is

$$\xi_x \int dt\, e^{\quad\quad\quad

$$I_x = pW+W_1 \quad , \quad X = p\alpha+q\alpha_y$$

$$I_y = qW \quad , \quad X_1 = \alpha_x .$$

We shall investigate here only the case $P = |q|$.

We have

$$W_2 = (\nu_x - \frac{r}{p})I_x+\nu_y I_y+\frac{2\sigma}{p_o}(\frac{\xi}{\beta^*}) \sum_{s=1}^{\infty} \int_o \frac{d1}{t} \Big| - e^{-t(\tau_x+\tau_y)} I_o(\sqrt{\tau_x^2+\tau_y^2+2\tau_x\tau_y\cos\frac{X-2\pi s}{p_o}}) \Big] .$$

Let us consider the lowest orders $p_o = 1$ and the case $\xi_x = \xi_y$, i.e. $\beta_x^* = \beta_y^*$.

Difference Resonance, $q < o$

We have the invariant $\tilde{W}_1 = \tau_x+\tau_y$ and the new variable $\tilde{W} = \frac{1}{q}\tau_y$.

On the $(X, \tilde{W})$-plane there are two fixed points. The origin $\tilde{W} = o$ is the unstable fixed point, and the stable fixed point is obtained by solving the following equation

$$1 + \frac{\varepsilon_{pq}}{2p\xi}(2p\tilde{W}+\tilde{W}_1)-e^{-\tilde{W}_1}(1+\tilde{W}_1)I_o(2p\tilde{W}+\tilde{W}_1) + - e^{-\tilde{W}_1}(2p\tilde{W}+\tilde{W}_1)I_1(2p\tilde{W}+\tilde{W}_1) = o.$$

Observe that the location of the unstable fixed point depends on the invariant W_1. The picture of the motion on the $(X, \tilde{W})$-plane is thus similar to the one shown in Fig. 1.

Sum Resonance, $q > o$.

We have the invariant $W_1 = \tau_x-\tau_y$ and the new variable $W = \tau_y/q$. On the (X, W)-plane there are two fixed points. The stable one has for coordinate the solution of

$$\varepsilon_{pq} + 2p\xi e^{-(2p\tilde{W}+\tilde{W}_1)}\left[I_o(\tilde{W}_1)+\frac{\tilde{W}_1 I_1(\tilde{W}_1)}{2p\tilde{W}+\tilde{W}_1} \right] = o$$

and the unstable one has for coordinate the solution of

$$\varepsilon_{pq}(2p\tilde{W}+\tilde{W}_1) + 2p5 \Big[1 t - e^{-(2p\tilde{W}+\tilde{W}_1)} I_o(2p\tilde{W}+\tilde{W}_1) \Big] = o.$$

Also here, the location of the fixed points depends on the invariant $\tilde{W}_1$. The picture of the motion of the $(X, \tilde{W})$-plane is shown in Fig. 3.

Several Crossings Per Turn

The generalization to n_c crossings per turn or to n_r revolutions between crossings is easily done. The only changes are: (a) ξ_x and ξ_y are now replaced by $\xi_x n_c$ and $\xi_y n_c$ or ξ_x/n_r and ξ_y/n_r, (b) the only possible resonances are those with the third integer number r that is an algebraic multiple of n_c or $1/n_r$. Thus the strength of a resonance is either increased by the factor n_c or decreased by a factor n_r. But the density of the resonances is also, respectively, decreased or increased by the same amount.

The Stochasticity Limit

According to Chirikov[5] the stochasticity limit is reached when many nonlinear resonances overlap. As done by Keil[1], we take as criterion for resonance overlapping that the area covered by resonances in a square region in the (ν_x, ν_y)-plane of unit area becomes unity. The extension of a resonance in the (ν_x, ν_y)-plane is given by the quantity $\Delta\varepsilon_{pq}$ we have calculated above. This quantity gives the range of $p\nu_x+q\nu_y-r$ which is locked to the resonance. The extension of the same resonance along the ν_x-axis is obviously given by $\Delta\varepsilon_{pq}/p$, and the extension along the ν_y-axis by $\Delta\varepsilon_{pq}/|q|$. The sum of the areas occupied by resonances is obtained by summing all $\Delta\varepsilon_{pq}/p$ for resonances $p > |q|$ and all $\Delta\varepsilon_{pq}/|q|$ for resonances $p < |q|$. The width of a resonance, $\Delta\varepsilon_{pq}$, does not depend on the number r, also in the "first mode approximation". For assigned p and q there are exactly p resonances all with the same width, in a square region of the (ν_x, ν_y)-plane of unit area, if $p > |q|$ and $|q|$ resonances if $p < |q|$. Also, to calculate the sum of the area we should use eqs. (6) and (7) for the width $\Delta\varepsilon_{pq}$. Nevertheless, one should take into account in the sum only those triplets (p, q, r) that have no common divisor. Since the "first mode approximation" gives an accurate estimate of the resonance width, we shall use eq. (9). But in this way, odd order resonances do not give any contribution. To balance this, we shall sum over all possible triplets (p, q, r) including those that do have common divisors.

Denoting the sum by S, we have

$$S = 4\xi_x T(\tau_x)+4\xi_y T(\tau_y) \qquad (11)$$

where the function

$$T(x) = e^{-x}\left[I_o(x)+I_1(x) \right]$$

is plotted in Fig. 4. The details of the summation can be found in [4]. All the contributions to S come only from the one-dimensional resonances, namely the $q = o$ resonances with $I_y = o$ contribute to the first term, in ξ_x, and the $p = o$ resonances with $I_x = o$ to the second term, in ξ_y.

In the case one of β_x^* and β_y^* is much smaller than the other, the corresponding term at the right hand side of (11) can be neglected. The stochasticity limit (S=1) is then reached for $\xi \sim 0.25$. Conversely, if $\beta_x^* = \beta_y^*$, the stochasticity limit is reached

for $\xi \sim 0.125$. In both cases, the limit occurs at $x = y = o$.

Observe that most of the contribution to the function T(x) comes mostly from the lowest order resonance p = 2 or q = 2. Indeed if the contribution of this resonance is ignored, T(x) is smaller and given by the lower curve in Fig. 4. In this case the stochastic limit is reached at, $\tau_x = \tau_y = 2.5$, for $\xi \sim 0.8$ if, say, $\beta_x^* >> \beta_y^*$, and for $\xi = 0.4$ if' $\beta_x^* \sim \beta_y^*$.

This result is in disagreement with Keil's results. We found that the contribution of the higher order resonance is smaller than the contribution of the few lowest order resonances. Keil found just the opposite. The discrepancy can he due to (a) the different definition of the resonance width, and/or (b) to the fact that Keil performs multiple expansion of the nonlinear kick and stops the summation to the order 30.

If we are to believe our result, (which is in much better agreement with the experimental observations) we infer that the experimental beam-beam limit is mainly caused by few low-order resonances, and that it is rather below the stochastic limit.

In the case of one kick every n_r revolutions or n_c kicks every revolution, we would still obtain the same *result* if the summation of the resonance widths is taken over a square of area, respectively, $1/n_r^2$ and n_c^2.

Clearly, what is more important, especially in the second case, is a local summation of the widths. Likely the stochastic limit is a function of a tune. To prove this, we limited ourselves to the one dimensional case ($\beta_y^* = o$ and $\tau_y = o$), then we summed the widths of those resonances that fall in a smaller interval of tune, let us say, between 0.1 and 0.2, or 0.2 and 0.3, and so on. The results are shown in the next table where the maximum tune shift ξ_{max} allowable is reported versus the tune. The amplitude τ_{max} is also shown in the table.

Range of the Tune (incl.) - (excl.)	ξ_{max}	$2\tau_{max}$
0.0 - 0.1	0.050	0.0
0.1 - 0.2	0.984	4.9
0.2 - 0.3	0.473	1.4
0.3 - 0.4	0.984	4.9
0.4 - 0.5	2.884	19.0
0.5 - 6.6	0.050	0.0
0.6 - 0.7	0.984	4.9
0.7 - 0.8	0.473	1.4
0.8 - 0.9	0.984	4.9
0.9 - 1.0	2.884	19.0

References

1. E. Keil, CERN/ISR-TH/72-7 and CERN/ISR TH/72-25

2. J. LeDuff, Laboratoire de l'Accélérateur Linéaire, Groupe Anneaux de Collisions, Rapporte Technique 6-72.

3. A.G. Ruggiero and L. Smith, 1973 PEP Summer Study, PEP Note #52.

4. A.G. Ruggiero, NAL Internal Report, FN-258 (1974).

5. B.V. Chirikov, CERN Trans. 71-40.

FIG. 1

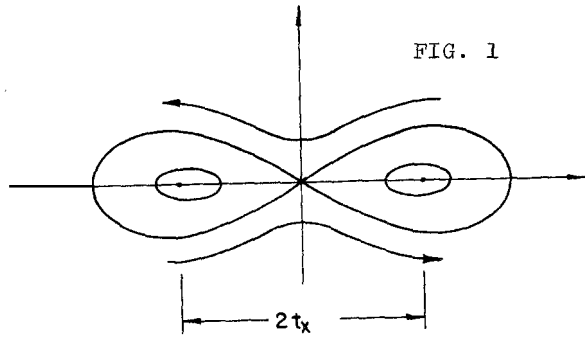


FIG. 2

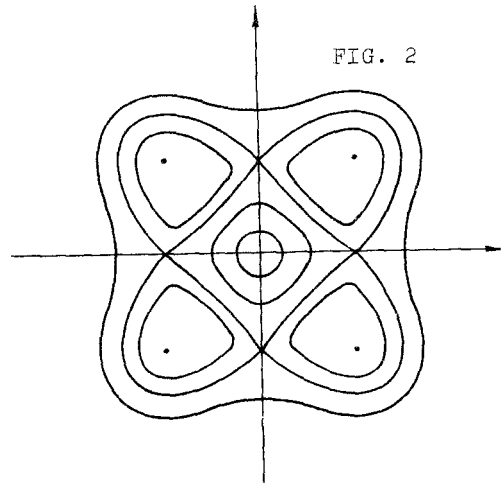
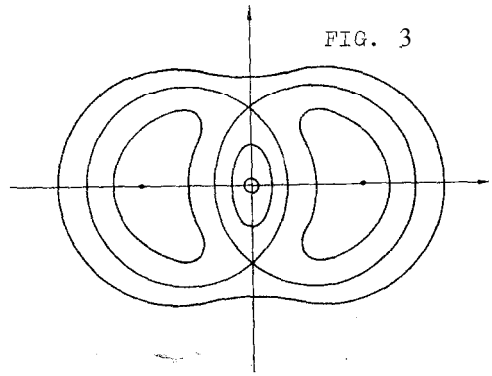


FIG. 3



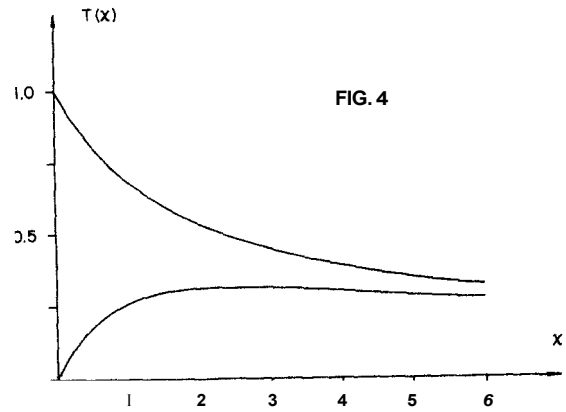


FIG. 4

INSTABILITIES DETECTED IN SATURNE

J. FAURE, G. LELEUX, J.L. LEMAIRE, R. VIENET,
Saclay, (France)

1. Introduction

After the injection energy had been increased from 3.6 MeV to 20 MeV, some problems arised at Saturne.

The theoretical number of captured particles is about $6.10^{\bullet\bullet}$. This figure corresponds to a ν_z shift from 0.88 to 0.5. But we did not succeed to accelerate more than $1.6 - 2.10^{\bullet\bullet}$. Moreover it was very difficult to keep particles up to the end of the accelerating process. Strong losses appeared in the first 100 ms together with, occasional coherent oscillations phenomena in both directions. In order to overcome these difficulties, we empirically created horizontal magnet field index variation for coherent oscillations damping and we had to work out some cumbersome radial exploration during the acceleration process.

This refined tuning depended upon the beam intensity and was unstable from pulse to pulse. These difficulties were especially inconvenient for resonant extraction because of the necessary good optical properties of the beam needed for this extraction type and of the imposed magnetic field index variation.

For these reasons we have undertaken the experimental and theoretical studies described in this paper.

2. Experimental study

In order to get the machine characteristics the measurements were made by means of the beam itself, in the following way. [1]

At a given time of the cycle, the beam is accelerated on a given radius $R_o + x$. Then, by means of the current i of the pole face windings, we change the n-value continuously. If we measure the intensity of the beam before and after the field index n changes we know the variation loss versus i. Maxima losses appear for a few i values. Then this measurement is repeated for different x positions. If we plot the i values giving maximum loss versus x, we see that we obtain parallel straight lines. Moreover, the ν_z is measured and is used to obtain n-value from the formula $\nu_z = \sqrt{n(1+k)}$. From these measurements we deduce machine characteristics as shown on figure n° 1.

The magnetic field index (integrated on one turn) varies with x ($n' \sim 0.5$ meter). Losses occur when the field index n reaches the indicated values. Later, we shall see what kind of resonances are concerned.

The same investigations have been made at various times during the cycle. On figure n° 2 one can see how the magnetic field index varies. We have not yet found a good explanation of this phenomena : remanent magnetic field, eddy currents, saturation effect, etc..

3. Resonances

According to the instabilities theory we have to deal with relations such as $a\nu_z + b\nu_z = c$, where $(|a| + |b|)$ is the resonance order. On figure n° 4 we can see the stability diagram (ν_x, ν_z) with the resonance lines up to the fourth order and the circle $\nu_x^2 + \nu_z^2 = 1 + k$, wich represents operating points of the machine. [2] [3]

Instabilities occur at the intersection of the circle with the lines. If one refers to figure n° 3, one can see that there is a precise correspondance with experimental results.

Sextupolar or octupolar defects responsible for instabilities proceed from non linear index variation versus x inside the quadrant and from end effects of the quadrants. We tried to correct this last defect. But this correction cannot be perfect and the first defect remains and hence we did not notice a very important improvement.

4. Coherent oscillations

Experimental results show that coherent oscillation can'occur together with incoherent oscillation . We have not yet found any theoretical explanation but it seems that the induced signal on the vacuum chamber walls due to the increase of the beam dimension helps the coherent oscillation to develop.

Moreover if the $\frac{dn}{dx}$ value is decreased in order to improve acceleration or ejection process, the beam becomes immediatly unstable whatever is the n-value. This is due to the lack of n-value dispersion inside the beam.

5. Consequences on the beam behaviour

We are, now, able to understand losses occuring at injection and beam instabilities during acceleration. We can then consider the

possibility of improving the performances.

Let us consider figures n° 2 and 3.

The beam closed orbit dispersion due to energy spread from injection up to 150 ms is larger than 10 cm. Hence each particle crosses resonance lines many times during synchrotron motion.

The $3\nu_x + \nu_z = 3$ resonance is the most dangerous since the betatron amplitudes can increase infinitely. We understand then why we can avoid losses by changing beam position during the acceleration process. But if the injection itself is not exactly reproducible from pulse to pulse, the capture efficiency changes, the energy spread too and the beam becomes unstable.

Referring to figure n° 2, we can see that the beam would be more stable if we could inject particles between n = 0.561 and n = 0.5 and attempt to keep the beam inside this range during the whole acceleration process. The losses would occur in the few first ten milliseconds and the beam would remain stable. If there is any emittance increase the betatronic damping would begin earlier so that the beam diameter would be smaller at the time we intend to eject. We could check experimentally this assumption and we now inject, at n-value = 0.55.

Unfortunately we have to achieve a n-value = 0.658 for the resonant ejection process and we have again to cross resonances. But another experiment shows that the emittance increase is small if we stay for less than a few millisecond in the resonance vicinity. Therefore we are studying a power supply able to change n-value from n = 0.55 to n = 0.658 within 10 ms.

A more accurate analysis of phenomena occuring at injection, taking into account space charge, has been made and shows another particle intensity limitation. The operating point moves in the stability diagram inside the cercle : $\Delta\nu_x = -4.10^{-5} \times N$,

$$\Delta\nu_z = -1.3.10^{-4}\ N,$$

if N is the number of particles. Whatever the n-value between n = 0.5 and n = 0.7, the operating point reaches the $2\nu_x + 2\nu_z = 3$ resonance line and the N value we calculate from $\Delta\nu_x$ or $\Delta\nu_z$ corresponds exactly to the maximum amount of particles captured i.e. $1.6.10^{12} - 2.10^{12}$.

In figure n° 5 we have plotted the beam extension in the (ν_x, ν_z) diagram taking into account the energy spread, as the n-value depends on radial position or energy. Since this extension is a parallel line to $2\nu_x + 2\nu_z = 3$ we understand why we cannot cross this line because all the particles are unstable at the same time.

6. Conclusion

All these theoretical and experimental studies show that. resonances are the limiting factors for improving Saturne performances. Further developments have been recently stopped due to the decision to strongly increase the performances of Saturne : the magnetic components of the main ring will be rebuilt, leading to a version number 2 of the Saturne accelerator.

The new magnetic structure will be a strong focusing separated function scheme. [4]

7. Bibliography

[1] C. FOUGERON,
Internal report - AS 261
Influence de l'indice sur la stabilité du faisceau

[2] JL. LEMAIRE,
thesis
Etude des phénomènes responsables des instabilités de faisceaux dans Saturne

[3] G. LELEUX,
Internal report - SOC 73-06
Non linéarité dans une machine type Saturne

[4] H. BRUCK, JL. LACLARE, G. LELEUX and the "GERMA" group,
Saturne II : Proposal of a renovated proton facility at Saclay
IXth International Conference on High Energy Accelerators, 1974.

FIG 1 MAGNETIC FIELD INDEX AND RESONANCES

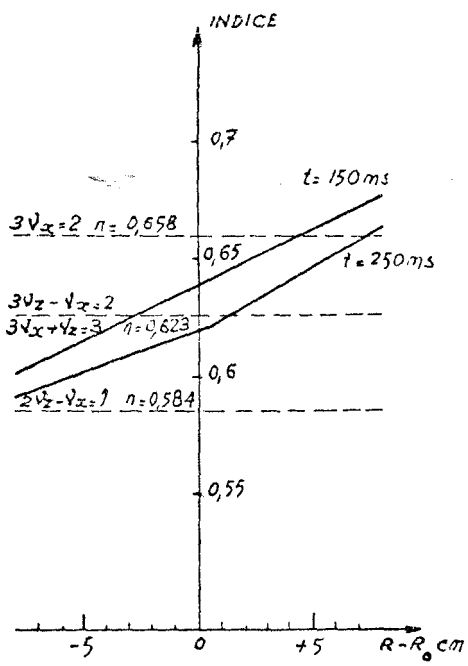


FIG 2 INDEX VARIATION VERSUS TIME

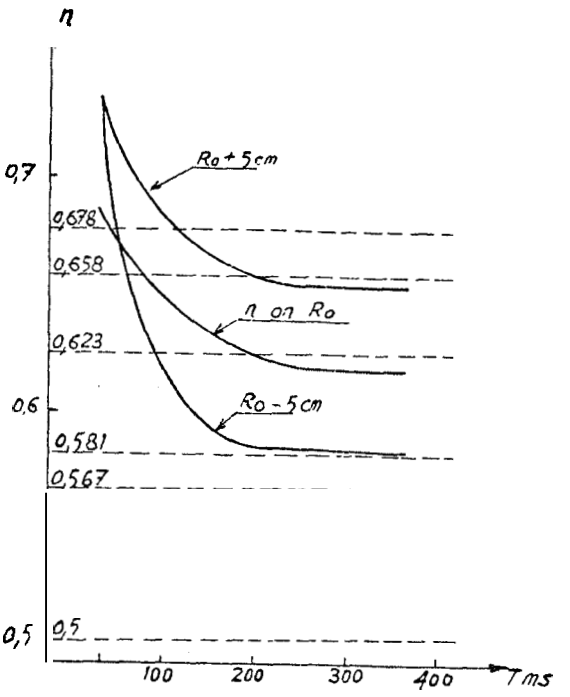


FIG 3 RESONANCES IDENTIFICATED IN SATURNE

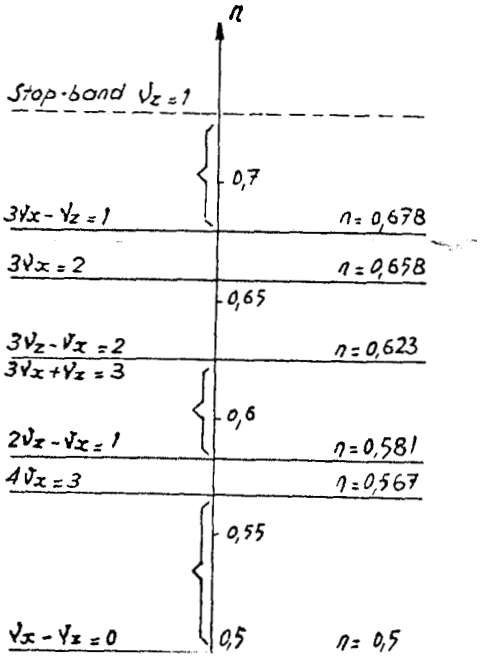


FIG 4 STABILITY DIAGRAM

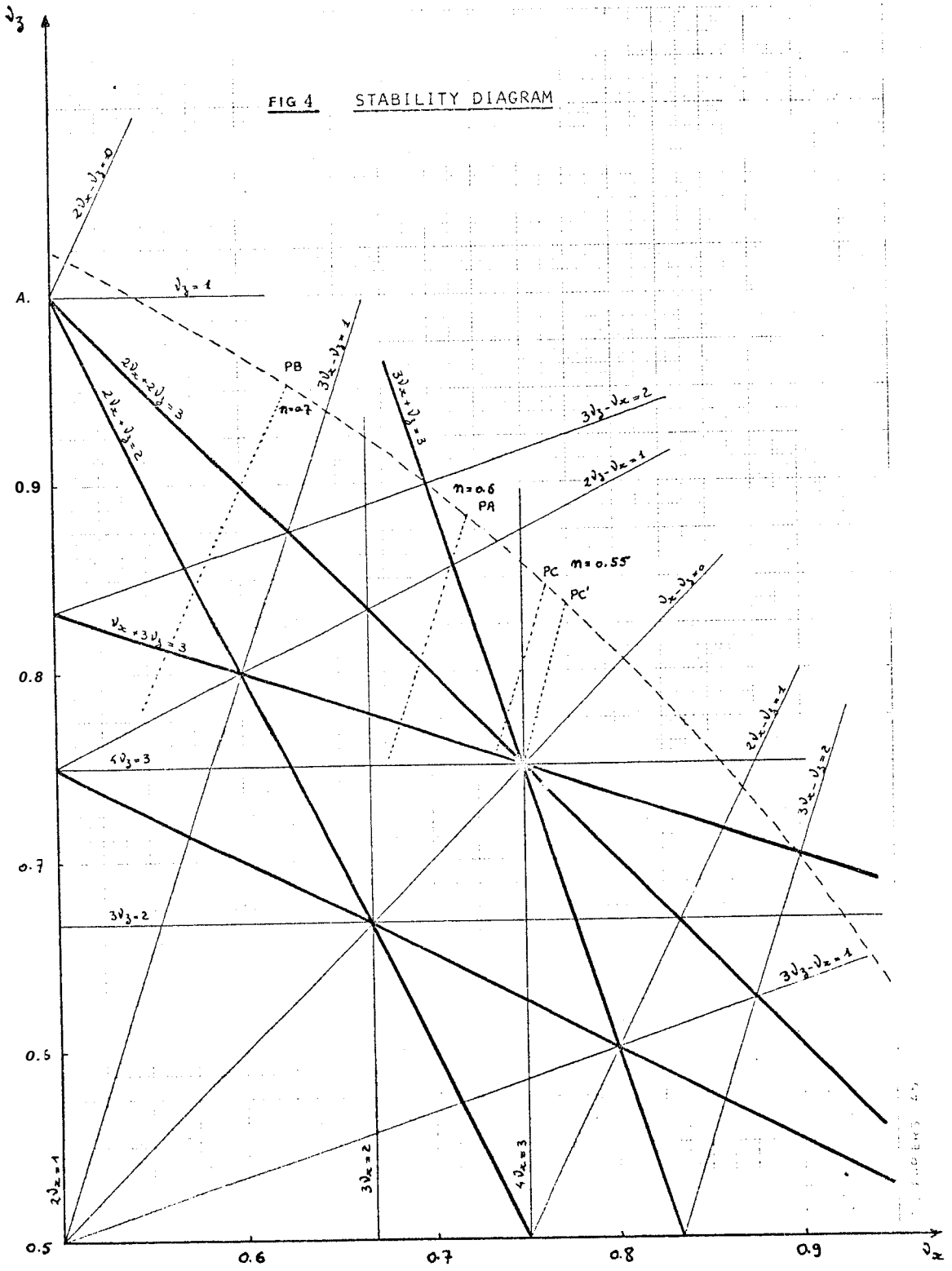
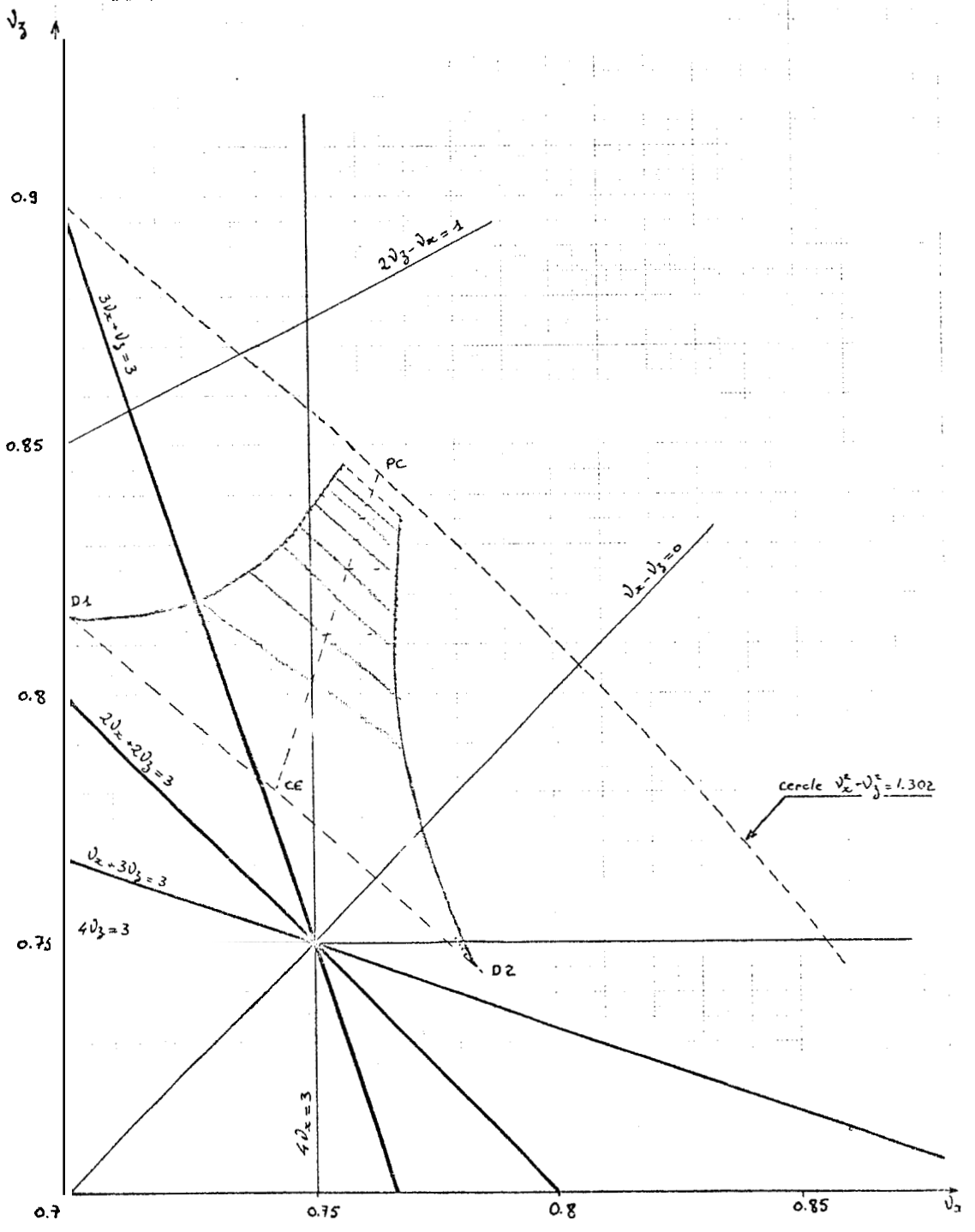


FIG 5 OPERATING POINT VARIATION DUE TO SPACE CHARGE



STOCHASTIC EFFECTS IN LONGITUDINAL PHASE SPACE

I. Gumowski

CERN, Geneva, Switzerland

Some estimates of the stochasticity domain of a particular Hamiltonian dynamic system with a continuously increasing non-linearity have been given elsewhere's'. These estimates are not directly applicable to longitudinal motion in a circular accelerator because in the latter case the non-linearity is periodic and bounded, An extension of the method used in Refs. 1 and 2 shows that in accelerators such as the CERN PS and PSB the accelerating voltage non-linearity produces stochastic behaviour only in the close vicinity of the separatrix. The usual description of a microtron is shown to imply the existence of a large stochastic domain.

Introduction and Statement of the Problem

The longitudinal motion in an accelerator can be described in a straightforward manner if the assumption is made that the ring is composed of discrete elements only. One formulation without space charge, taking into account one RF-cavity gap, is[3]

$$\Delta p_{n+1} = \Delta p_n + \frac{eV}{\beta_s c}(\sin\phi_n - \sin\phi_s)$$
$$\phi_{n+1} = \phi_n + \frac{2\pi h}{p_s}(\alpha - \gamma_s^{-2})\,\Delta p_{n+1} \qquad (1)$$

where p is the particle momentum, Ap the momentum deviation, α the momentum compaction factor, $ the phase, n the number of cavity gap traversals, V the amplitude of a sinusoidal accelerating voltage, h the harmonic number, e the particle charge, and β, γ, c the usual relativistic quantities. The subscript s refers to synchronous values. When radiation damping is taken into account, the recurrence (or point-mapping) (1) is equivalent to the known alternate forms[4,5]. It is also equivalent to the differential equation[6]

$$\frac{d\phi}{d\tau} = \psi \quad , \quad \frac{d\psi}{d\tau} = \Omega^2\left(-\sin\phi + 2\,\mathrm{tg}\,\phi_s \cdot \sin^2\frac{\phi}{2}\right)\left(1 + 2\sum_{m=1}^{\infty}\cos m\tau\right) \qquad (2)$$

where τ and Ω are the normalized time and small-amplitude synchrotron frequency, respectively.

The object of this paper is the determination of the solution structure of the recurrence (1) in the discrete phase plane Δp_n, ϕ_n, and the application of the results to the CERN PS and PSB. When the differential eouation (2) is solved by a method of series truncation[6] (perturbations with averaging, or a finite number of canonical transformations which reject the explicit time-dependence toward higher-order terms), the solution structure so obtained is valid only in the region where the recurrence (1) admits closed trajectories (invariant curves without "stochastic" intersections). The region where the invariant curves of (1) intersect is called stochastic, because the intersection pattern is so complex that superficially it appears to be random. Since this pattern is unambiguously defined by (1), it is of course completely deterministic.

Determination of the solution structure of the recurrence (1)

The approach used in this paper is based on the previously tested conjecture that the qualitative features of the solution structure of (1) can be deduced from the distribution in the phase plane of zero- and one-dimensional singular solutions (point- and line-singularities) [1,2,7-11]. Consider, in fact, the particular conservative recurrence

$$x_{n+1} = y_n - F(x_n) = g(x_n, y_n)$$
$$y_{n+1} = -x_n + F(x_{n+1}) = f(x_n, y_n) \qquad (3)$$

where F(x) is an arbitrary differentiable function. From (3) it is possible to construct unambiguously the iterated recurrence

$$x_{n+k} = g_k(x_n, y_n) \quad , \quad y_{n+k} = f_k(x_n, y_n)$$
$$g_1 = g \quad , \quad f_1 = f \quad , \quad k = \text{integer} \qquad (4)$$

The simplest point-singularity of *(3)* is a cycle of order k (periodic point of order k), defined by a real root x,y of the two algebraic equations

$$x_{n+k} = x_n = x \quad , \quad y_{n+k} = y_n = y \qquad (5)$$

deduced from (4), provided x,y is not simultaneously a root of (5) when k is replaced by one of its divisors. A cycle of order k=1 is called a fixed point.

An invariant curve of (3) is described by G(x,y) = const. if the function G(x,y) satisfies the functional equation

$$G\left(g_k(x,y), f_k(x,y)\right) = G(x,y) \qquad (6)$$

If the curve G(x,y) = const. has at least one single-valued branch $y = \theta(x)$ passing through a point (x_0,y_0), then an equivalent formulation of (6) for this branch is

$$f_k\left(x, \theta(x)\right) = \theta\left[g_k\left(x, \theta(x)\right)\right] \quad , \quad y_0 = \theta(x_0) \, . \qquad (7)$$

The function $\theta(x)$ and a sufficient number of its derivatives are assumed to possess at least an asymptotically convergent Taylor series at and near x_0. The simplest line-singularity of (3) is an invariant curve passing through a point of a cycle.

Cycles are classified according to the eigenvalues $\lambda_{1,2}$ of their characteristic equation. The special form of (3) implies $\lambda_1 \cdot \lambda_2 = 1$. The indices are so chosen that either $\lambda_1 > +1$ or $\lambda_2 < -1$. Cycles are called saddles (or hyperbolic points) if the λ are real (of type 1 if $\lambda > 0$ and of type 3 if $\lambda < 0$) and centres (or elliptic points) if $\lambda = \exp(\pm i\phi)$. The constant ϕ is called the rotation angle of the centre. An additional property of a cycle is its rotation number r (integer), describing the least number of turns made around an interior point when following the k successive points of the cycle in the phase plane. For conciseness, a cycle of order k and rotation number r is designated by $k_{(r)}$.

If the point (x_0,y_0) is a saddle, a singular invariant curve segment passing through (x_0,y_0) can be sought in the form

$$y = \theta(x) = y_0 + \sum_{i=1}^{\infty}\beta_i\,(x - x_0)^i \quad , \qquad (8)$$

where the β_i, i = 1,2, ... are real constants. Because of the postulated smoothness of $\theta(x)$, β_1 is equal to one of the eigenslopes p_1,p_2 at (x_0,y_0). A known segment $y = \theta(x)$ can be continued by means of *(4)*. The slope β_1 can be continued by means of the recurrence

$$dx_{n+k} \left(a + b\,\frac{dy_n}{dx_n}\right)^{-1} \cdot \left(c + d\,\frac{dy_n}{dx_n}\right) \quad , \quad \frac{dy_0}{dx_0} = \beta_1 \quad , \qquad (9)$$

where a,b,c,d are elements of the Jacobian matrix of (4), whose determinant is unity for any k. Similar recurrences exist for the continuation of the β_i, i > 1. If b > 0, the eigenslopes of a saddle are given by $p_{1,2} = (A_1, - a)/b$.

It is straightforward to show that the recurrence (1) can be transformed into the form *(3)*. In fact, when $\theta_n = b(\phi_n - \phi_s)$, $\psi_n = b(\phi_{n-1} - \phi_s)$, $b = \pi - 2\phi_s$, (1) becomes

$$\psi_{n+1} = \theta_n \quad , \quad k_0 = \frac{heV}{E_0} \cdot \frac{\alpha \gamma_s^2 - 1}{\gamma_s (\gamma_s^2 - 1)}$$
$$\theta_{n+1} = -\psi_n + 2\theta_n + \frac{2\pi k_0}{b}\left[\sin(b\theta_n + \phi_s) - \sin\phi_s\right] \qquad (10)$$

where E_0 is the particle rest energy. The parameter k_0 is negative below transition. Comparing (10) to the diagonal form of (3):

$$x_{n+1} = u_n \quad , \quad u_{n+1} = -x_n + 2F(u_n) \qquad (11)$$

obtained by means of the transformation $u_n = y_n + F(x_n)$, yields the required equivalence relation

$$F(x) = x - \frac{1-\mu}{b\cos\phi_s}\left[\sin(bx + \phi_s) - \sin\phi_s\right]$$
$$\mu = 1 + \pi k_0 \cos\phi_s \quad , \quad 0 \le \phi_s \le \frac{\pi}{2} \quad , \quad -1 < \mu < +1 \qquad (12)$$

The function F in (12) involves two independent parameters μ and ϕ_s, rendering a graphical display of the singular solutions of (3), (12) very inconvenient. A preliminary study has shown, however, that the stochastic features of (3), **(12)** do not change qualitatively as long as $\phi_s \neq 0$. For the purposes of this paper it is therefore possible to choose ϕ_s arbitrarily. For convenience ϕ was fixed as follows:

$$\phi_s = \frac{\pi}{2} - \text{arc tg}\,\frac{1-\mu}{\pi} \qquad (13)$$

The recurrence defined by (3), (12), (13) is periodic in x. In order to assure uniqueness of the graphical representation for a fixed μ, a cylindrical phase space may be used, i.e. the phase plane is thought to be wrapped around a cylinder of radius $1/\pi$ centred on $x = 0$.

Some of the singularities of (3), (12), (13) are easily found, such as the two fixed points at (0,0) and (1,0). The former is a centre of rotation angle $\phi = \arccos\mu$ and the latter a saddle of type 1. The locations of other singularities depend on the value of μ and must be sought numerically. A partial list of cycles is given in Tables 1–3. The invariant curves passing through the "main" saddle (1,0) are shown in Figs. 1–3.

From an inspection of Figs. 1–3 it is clear that the recurrence (2), (12), (13) admits homoclinic points. Hence by a theorem of Birkhoff[12] it admits an infinity of cycles. An inspection of Tables 1–3 suggests that the cycles found so far form well-ordered sets. Some properties of the ordering can be found by rearranging the tables so that the ratio **k/r** is roughly constant, or by tracing the locations of the points in the phase plane, together with the "main" invariant curves traversing the saddle (1,0), as illustrated in Figs. 1–3. The first deduction is that the points of the cycles are located on curves which approach a discrete set of homoclinic points'. In addition to the x-axis, one such curve is $y = x - F(x)$. A more fundamental way consists, however, in ordering the cycles according to conditions of their appearance, disappearance, or other change of properties, i.e. in ordering them from the point of view of Poincaré's theory of bifurcation.

By present knowledge, bifurcations take place only when the eigenvalue of a cycle satisfies

$$\lambda^q = +1 \quad \text{or} \quad \lambda^q = -1 \quad , \quad q = \text{integer} \geq 1 \qquad (14)$$

The case q = 1 is called a critical case[13] and the case q > 1 an exceptional one[14,15]. The latter arises in (3) whenever $\phi = 2\pi p/q$, p = integer. In the case (3), (12), (13) an exceptional case occurs at (0,0) whenever

$$\mu \to \bar{\mu} = \cos(2\pi r/k) \quad , \quad k > r \text{ and relatively prime} \qquad (15)$$

It has been found' that the traversal of $\bar{\mu} \neq -\frac{1}{2}$ in the direction of decreasing μ (increasing strength of nonlinearity) releases from (0,0) a cycle saddle $k_{(r)}$ of type 1 and a cycle centre $k_{(r)}$. The "bifurcated" cycles $k_{(r)}$ exist only for $\mu < \bar{\mu}$ and they merge with (0,0) when $\mu \to \bar{\mu}$ from below. Furthermore

$$k/r < \text{finite constant}, \quad \lambda_1(k_{(r)}) \to +1$$
$$p_1 - p_2 \to 0 \quad , \quad \phi(k_{(r)}) \to 0 \quad \text{as} \quad \mu \to \bar{\mu} \quad , \qquad (16)$$

where $\lambda(k_{(r)})$, $\phi(k_{(r)})$ designate the eigenvalue and rotation angle of the cycles $k_{(r)}$, respectively. The first enumerable set of cycles of (3), (12), (13) consists therefore of cycles bifurcated from (0,0) at the exceptional values (14), provided r/k # 1/3, according to the schematic rule:

$$\text{centre } (0,0) \to \text{centre } (0,0) + \text{centre } k_{(r)} + \text{saddle } k_{(r)} \text{ of type } 1 \qquad (17)$$

The geometric distance s(x,y) between points of a cycle $k_{(r)}$ *so* bifurcated and (0,0) is found to increase simultaneously with the parametric distance $s(\mu) = p - \bar{\mu}$. The parameters $\lambda_1(k_{(r)})$ and the angle between p_1, p_2 also increase with $s(\mu)$.

For any given $\mu \neq -\frac{1}{2}$ the centre (0,0) is thus surrounded by an infinite but enumerable set of concentric cycle pairs $k_{(r)}$, bifurcated according to the scheme (17), with k/r verifying the inequality $\mu < \cos(2\pi r/k)$. When the difference $\lambda_1(k_r) - 1$ is sufficiently small, the computed invariant curves passing through the saddles $k_{(r)}$ are for all practical purposes indistinguishable from regular invariant curves, i.e. from invariant curves not traversing any singular points. The assumption that these invariant curves are not "analytically" closed for arbitrarily small values of s(x,y) implies that homoclinic points can exist arbitrarily close to (0,0). It is, however, known' that homoclinic points $(\bar{x},\bar{y})$ are accumulation points of a set of cycles $k_{(r)}$ of coordinates $(x_m,y_m)_k$, and that the "effective" order k/r, as well as the eigenvalues $\lambda_1(k_{(r)})$ of the saddles of type 1 of this set increase indefinitely as the geometric distance between $(\bar{x},\bar{y})$ and $(x_m,y_m)_k$ decreases, i.e.:

$$k/r \to \infty \ , \ \lambda_1(k_{(r)}) \to \infty \text{ and } p_1 - p_2 \to \text{finite constant as } (x_m,y_m)_k \to (\bar{x},\bar{y}) \ . \qquad (18)$$

The assumption that sufficiently near (0,0) the invariant curves are not (truly) closed leads to a contradiction between the properties (16) and (18). A small neighbourhood of (0,0) is therefore filled with an infinite but enumerable set of island structures [formed by the invariant curves which traverse the saddles $k_{(r)}$ of type 1, surround the centres $k_{(r)}$ and join without other intersections]. Since two close island structures have been bifurcated from (0,0) at two distinct values of $\phi = 2\pi r/k$, and thus of μ (because k and r are relatively prime) the area between them contains either regular closed invariant curves or closed invariant curves passing through an infinity of singular points [points of cycles $k_{(r)}$ for which $k \to \infty$, $r \to \infty$, $\lim k/r <$ < finite constant, $\lambda_1(k_{(r)}) \to 1$, $p_1 - p_2 \to 0$, $\phi(k_{(r)}) \to 0$]. The distribution of closed invariant curves near (0,0) is thus extremely irregular in theory but quite smooth in practice.

Because the construction of an iterated recurrence like *(4)* does not produce any intrinsically new data, the solution structure near a centre $k_{(r)}$, $k > 1$, is the same as near the centre (0,0), i.e. one has a "box within a box" behaviour. The growth of the rotation angle as a function of $s(\mu)$ of the centre $\bar{k}_{(\bar{r})}$, bifurcated from the-centre $k_{(r)}$ and characterized by the property that k/r contains the factor k/r, is much faster than the growth of $\phi(k_{(r)})$. In other words, the bifurcation speed is higher inside the inner boxes.

Since the rotation angle of a centre increases with the parametric distance from its generating bifurcation, it may eventually reach the value $\phi = \pi$. If the

traversal (in the direction of decreasing μ) of the corresponding critical case $\lambda = -1$ is examined from the bifurcation point of view, it is found[**] that the cycle centre $k_{(r)}$ turns into a cycle saddle $k_{(r)}$ of type 3 with a simultaneous release of a cycle centre $(2k)_{(2r)}$, or schematically

$$\text{centre } k_{(r)} \rightarrow \text{saddle } k_{(r)} \text{ of type 3} + \text{centre } (2k)_{(2r)} \qquad (19)$$

Since the companion saddles $k_{(r)}$ of type 1 remain unchanged, the bifurcation (19) converts the centre-saddle of type 1-pair into a saddle of type 3-saddle of type 1-pair. Several examples of such saddle-saddle pairs appear in Tables 2 and 3. The presence of cycles generated by means of the bifurcation (19) appears to be a sufficient condition of the presence of local stochasticity, i.e. of the presence of interesting invariant curves in the neighbourhood of the saddle-saddle pair. Small islands of closed trajectories may persist near the centres $(2k)_{(2r)}$.

The bifurcations (17) and (19) are insufficient to explain the origin of all cycles of the recurrence (3), (12), (13). There are, for example, two cycles saddle $13_{(2)}$ of type 1 in Table 3, and it is found that the cycle pair $3_{(1)}$ exists also when $\mu > -\frac{1}{2}$, whereas according to (17) it should appear at $\mu = -1$. The study of this difficulty has disclosed the existence of two additional bifurcations, related to the critical case $\lambda = +1$ ($\phi = 0$)[11]. The first is of the type:

$$\text{composite cycle } k_{(r)} \rightarrow \text{centre } k_{(r)} + \text{saddle } k_{(r)} \text{ of type 1} \qquad (20)$$

The composite cycle $k_{(r)}$ appears as an isolated double root of (5), and is unrelated to any close simple root. After traversal of the bifurcation the double root separates into two simple ones, giving rise to the usual pair centre $k_{(r)}$-saddle $k_{(r)}$ of type 1. The second cycle saddle $13_{(2)}$ of Table 3 and the cycle pair $3_{(1)}$ originate in this way (at $\mu \approx 0.23$ and $\mu \approx 0.41$, respectively).

When $\mu \rightarrow \bar{\mu} = \cos(2\pi/3) = -\frac{1}{2}$, only the $3_{(1)}$ saddles merge with the centre (0,0), the $3_{(1)}$ centres remaining some distance away [one point at (-0.33,0)] Furthermore, $\lambda_1(3_{(1)}) \rightarrow 1$ as $\mu \rightarrow \bar{\mu}$. The bifurcation is of the type

$$\text{saddles } k_{(r)} \text{ of type 1},\ \text{centres } \bar{k}_{(\bar{r})} \rightarrow \left\{ \text{composite cycle } \lambda(k_{(r)}) = 1,\ \varphi(\bar{k}_{(\bar{r})}) = \frac{2\pi p}{q} \right\} \rightarrow \ldots \rightarrow \text{saddles } k_{(r)} \text{ of type 1},\ \text{centres } \bar{k}_{(\bar{r})},\ k \neq \bar{k} \qquad (21)$$

with $k = 3$ and $\bar{k} = 1$. Six invariant curve segments traverse the composite singular point (0,0) when $\mu = \bar{\mu}$, resulting from the coalescence of the three saddles $3_{(1)}$ of type 1. The bifurcation (21) produces an unstable point singularity.

Consider now the structure of invariant curves of (3), (12), (13) when $\mu \neq -\frac{1}{2}$. According to the theory of Birkhoff[16] the island structures around (0,0) should turn into instability rings (degenerate island structures formed when the invariant curves traversing the saddles of type 1 have other intersections but remain nevertheless inside a domain bounded by a finite closed curve) as their geometric distance from (0,0) increases. Stochasticity thus exists inside an instability ring, but it does not lead to an "orbital" instability. Since instability rings require the existence of a centre-saddle pair, they must give way to a different configuration when the bifurcation (19) is reached. The corresponding geometric distance from (0,0) can be estimated from Tables 1-3. It has been found, however, that instability rings cease to exist sooner',". From Tables 1-3 it can be seen that $\lambda_1(k_{(r)})$ and the angle between p_1 and p_2 increase simultaneously with the effective order k/r. Beyond a critical value the geometric distance between (0,0) and a point on a singular invariant curve through a saddle $k_{(r)}$ is found to increase first at an algebraic rate and then at an exponential one. The slow increase has been called diffusion and the fast one stochastic instability',".

Application to longitudinal motion

When the solution structure of the recurrence (3) (12), (13) is expressed in the terminology of accelerator theory [recurrence (1)], RF acceleration is found to produce bunches with a dense structured core (region of closed trajectories, including island structures), surrounded first by a dense but unstructured shell (instability rings) and then by a halo (diffusion region). Since the separatrix of the RF bucket (main invariant curve) is not closed, random particle losses occur from the halo (stochastic instability). The size of each region depends on the specific accelerator parameters. The RF acceleration process is unstable at the 1/3 parametric resonance between the synchrotron and beam revolution frequencies [exceptional case $\phi = 2\pi/3$ at (0,0)].

As far as the PSB is concerned, all longitudinal stochastic effects are negligible ($\mu \geq 0.99$). Analogous circumstances prevail in the CPS ($\mu \geq 0.90$). Stochastic effects may, however, occur inside self-buckets produced by beam-induced high-frequency voltages.

An accelerator likely to be subject to considerable stochastic effects is the microtron. Assume that the recurrence[4,17,18]

$$x_{n+1} = x_n + y_n \quad , \quad y_{n+1} = y_n + 2\pi\left(\frac{\cos x_{n+1}}{\cos\phi_s} - 1\right) \qquad (22)$$

is a valid description of the longitudinal motion (some doubts have been expressed in a paper by Turrin[19]). By a linear change of variables (22) transforms into

$$\zeta_{n+1} = v_n \quad , \quad v_{n+1} = -\zeta_n + 2v_n + \frac{2\pi}{\cos\phi_s}\left[\cos(v_n - \phi_s) - \cos\phi_s\right] \qquad (23)$$

Since an RF voltage V sin ϕ below transition is equivalent to $-V \sin(\phi - 2\phi_s)$ above transition[**], transforming (22) into an equivalent form "below transition" and replacing cos ϕ by sin ϕ yields the recurrence (3), (12), (13) with $0 < \phi_s < \text{arctg}\,(2/\pi) \approx 32.5°$. The solutions of (22) therefore exhibit considerable stochasticity even for relatively small ϕ_s. Figure 3 corresponds to $\phi_s = 15.6°$; on the x-axis, stochastic instability starts at $x \approx 0.51$.

References

1. I. Gumowski and C. Mira, Proc. 8th Int. Conf. on High-Energy Accelerators, CERN 1971, p. 374.
2. I. Gumowski, Proc. Int. Colloq. on Point Mappings, Toulouse 1973 (CNRS, Paris, 1974).
3. H.G. Hereward, CERN 66-6 (1966).
4. G. Bathow and E. Freytag, DESY Report 69/29 (1969).
5. C. Pellegrini, private communication (1968).
6. K.R. Symon, J.D. Steben and L.J. Laslett, Proc. 5th Int. Conf. on High-Energy Accelerators, Frascati 1965 (CNEN, Rome, 1966), p. 246.

7. I. Gumowski and C. Mira, Proc. 6th Conf. on Non-linear Oscillations, Poznan 1972 (Polish Academy of Science, 1973).

8. I. Gumowski and C. Mira, CR Acad. Sci. A, 274, 1271 (1972).

9. I. Gumowski and J.K. Trickett, CR Acad. Sci. A, 275, 147 (1972).

10. I. Gumowski and C. Mira, CR Acad. Sci. A, 275, 869 (1972).

11. I. Gumowski, CR Acad. Sci. A, 275, 939 (1972).

12. G.D. Birkhoff, J. de Math. (Liouville) 7, 345 (1928).

13. A.M. Liapunov, Ann. Fac. Sci. Univ. Toulouse 9 (1907).

14. T. Levi-Civita, Annali di Matematica (1901), p. 221.

15. A.R. Cigala, Annali di Matematica (1904), p. 67.

16. G.D. Birkhoff, Acta Math. (Uppsala) 43, 1 (1922).

17. L.B. Lugansky, Elektronika Bolshikh Moshchnosti 6, 130 (1970).

18. V.N. Melekhin, Zh. Eksper. Teor. Fiz. 61, 1319 (1971).

19. A. Turrin, Frascati Report LNF 72/33 (1972).

20. I. Gumowski and K.H. Reich, CERN Report SI/Int. DL/70-6 (1970).

Table 1

Cycles of the recurrence (3), (12), (13), μ = 0.8

k	r	x	Centres or Saddles of type 3: Y	φ or λ2 (>0) (<0)	p1	p2	Saddles of type 1: x	y	λ1	p1	p2
10	1	0.250529									
11	1	0.541454	0	0.0001			0.241025	0.036592	1.0001	-1.900	-1.893
12	1	0.701253	0.049673	0.0037			0.553773	0	1.0037	38.1	
13	1	0.784250	0	0.0103			0.690883	0.042725	1.0103	-2.135	-2.021
14	1	0.852864	0.033848	0.0188			0.792358	0	1.0190	48.78	
15	1	0.869912	0	0.0296			0.846697	0.025965	1.0300	-2.269	-2.023
16	1	0.923864	0.019596	0.0434			0.894539	0	1.0444	25.71	
17	1	0.942225	0	0.0616			0.920418	0.014651	1.0635	-2.425	-1.964
18	1	0.958820	0.010888	0.0859			0.944776	0	1.0897	14.19	
19	1	0.969314	0	0.1187			0.957934	0.008060	1.1258	-2.706	-1.840
19	1	0.969314	0.005949	0.1631			0.970704	0	1.1767	7.818	

k	r	Centres or Saddles of type 3: x	y	φ or λ2 (>0) (<0)	p1	p2	Saddles of type 1: x	y	λ1	p1	p2
7	1	-0.453247	0	0.4374			0.611988	0	1.531	2.349	
8	1	-0.519721	0	1.1355			0.763198	0.090499	2.766	1.084	-4.284
9	1	-0.541178	0	2.9517			0.872783	0	5.685	1.277	
10	1	-0.548847	0	-9.366	30.47		0.915006	0.038910	13.10	1.057	-1.375
11	1	-0.551694	0	-29.21	25.90		0.931111	0.054332	32.41	1.040	-1.419
12	1	0.971773	0	-81.08	-1.043		0.968120	0.015436	82.94	1.120	-1.082
13	1	0.961612	0.037471	-216.9	-1.072	0.881	0.973774	0.021412	215.3	1.127	-1.086
13	2	-0.364999	0	0.0319			0.455575	0		36.39	
15	2	-0.495642	0	0.5326			0.707595	0		5.355	
17	2	-0.532975	0	-2.357	128.0		0.848055	0		1.665	
19	2	0.899388	0.024261	-43.33	-0.732	1.318	0.885209	0		1.345	
19	3	-0.313851	0	0.0013			0.375926	0		386.2	

Table 2

Cycles of the recurrence (3), (12), (13), μ = 0.5

Table 3

Cycles of the recurrence (3), (12), (13), μ = 0.125

k	r	Centres or Saddles of type 3: x	Y	φ or λ2 (>0) (<0)	p1	p2	Saddles of type 1: x	Y	λ1	p1	p2
5	1	-0.502858	0	2.525			0.551511	0	3.849	1.011	
6	1	-0.577941	0	-25.97	2.731		0.754058	0.163018	20.18	1.297	-1,084
7	1	-0.594668	0	-114.5	2.511		0.892309	0	80.35	1.347	
8	1	0.953152	0	-423.3	-1.458		0.932867	0.054883	291.3	1.423	-1.446
9	1	-0.600442	0	1494	2.452		0.970033	0	1024	1.514	
9	2	-0.288774	0	0.1467			0.318515	0	1.157	4.245	
11	2	-0.545848	0	-85.46	3.311		0.621978	0	70.28	1.259	
12	2	0.861806	0.02997;	-395.1	-1.282	1.141	0.641711	0	251.8	1.377	
13	2						0.647291	0	874.8	1.418	
13	2						0.802214	0.226028	1611	1.202	
14	3	0.455590	0	0.4915			0.440250	0.052857	1.617	-4.440	-1.292
15	3	-0.460141	0	-8.748	1.772		-0.511499	0	5.072	-4.768	
16	3	0.608929	0	-286.8	-1.183		0.597869	0.029811	253.1	1.089	-1.300
17	3						0.613179	0.040647	802.0	1.117	-1.527
19	4	-0.387920	0	1.048			0.505232	0	2.615	1.917	
20	4						-0.525779	0	40.96	-0.413	
25	5	-0.504186	0	0.0378							

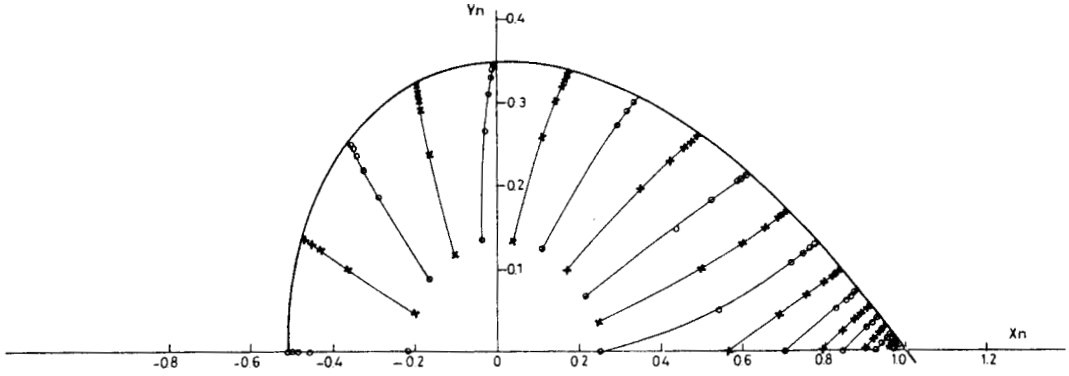


Fig. 1 $\mu = 0.8$. Main invariant curves and positions of some cycle

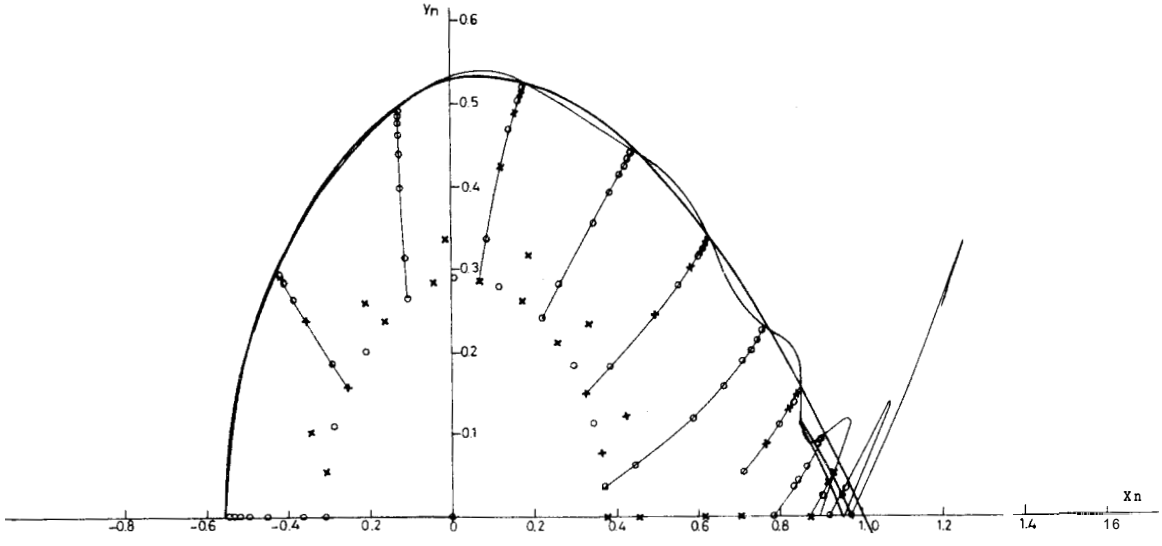


Fig. 2 $\mu = 0.5$. Main invariant curves and positions of some cycles

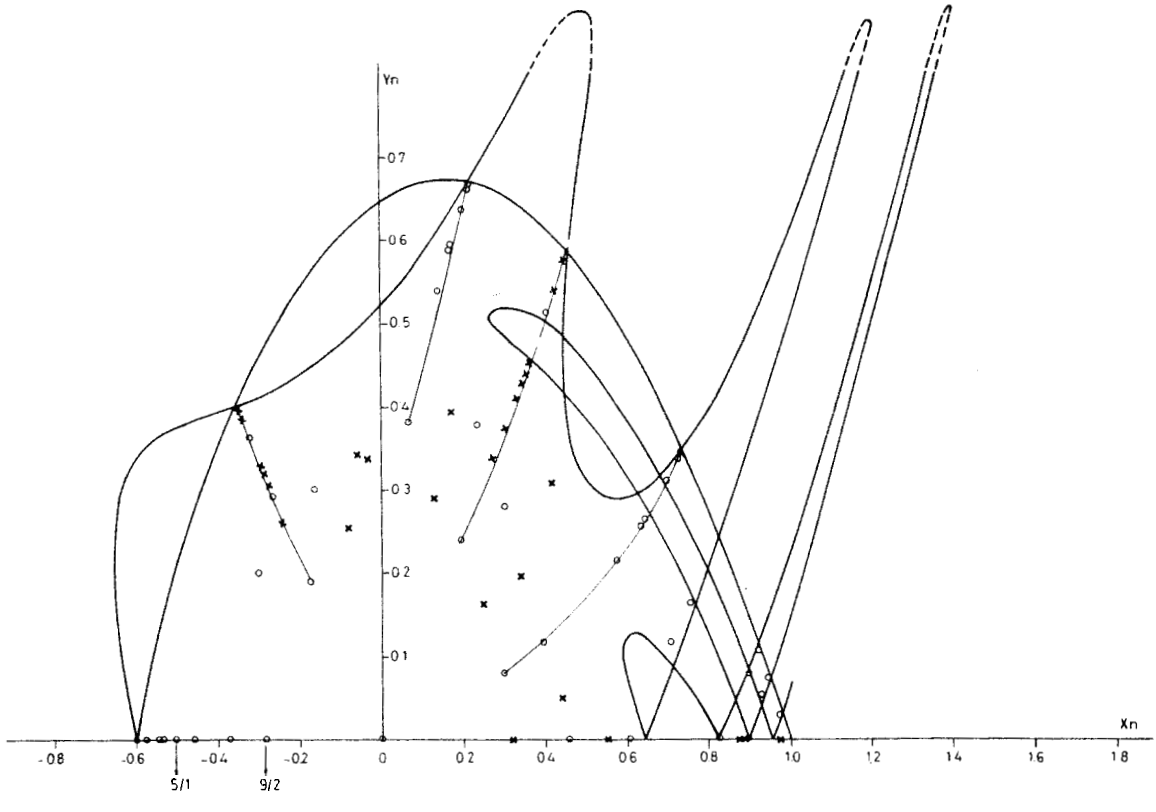


Fig. 3 $\mu = 0.125$. Main invariant curves and positions of some cycles

GAMMA-TRANSITION-JUMP SCHEME OF THE CPS

W. Hardt
CERN, Geneva, Switzerland

Summary

In 1973, the former Q-jump system has been replaced by 8 fast and 6 slowly pulsed quadrupoles forming 4 doublets and 2 triplets respectively. They allow presently a change of γ_t by $\simeq 2.3$ (instead of $\simeq 0.23$), limited only by the power supply within 0.8 ms (< 0.4 ms with a new supply under construction). Transition is crossed 50 times (instead of 5 times) faster than without jump. More than $5\ 10^{12}$ p/p have been accelerated operationally and brought through transition within a bunch area of $\simeq 10$ mrad. In the future, it should be possible to handle 10^{13} p/p within the same bunch area. The scaling laws for achievable longitudinal density Ψ (apart from logarithmic terms $\Psi \propto N^{1/3} |\Delta\gamma_t|^{\frac{1}{2}}$ for bunch matching and $\Psi \propto N^{1/5} |\dot{\gamma}_t|^{2/5} |\Delta\gamma_t|^{-1/10}$ for negative mass instability) are in good agreement with experiments.

1. Introduction

High longitudinal phase space density is of particular importance in the CPS as it serves as injector for the ISR and, in the future for the SPS. The most severe limitation occurs at transition where a blow-up due to negative mass instability must be avoided. As shown in chapter "The negative mass instability", the only efficient method to achieve this at high intensity is to cross transition much faster than it would be crossed without special precautions. The method used to manipulate the transition energy is the subject of chapters 2 to 5. Chapter 6 deals with bunch matching, chapter 7 with the negative mass instability leading to a simple criterion for avoiding blow-up trouble. Chapter 8 summarizes the practical experience with the new scheme.

2. The Lens Configuration

A convenient way to influence γ_t without affecting the betatron tune is to form doublets : two lenses of opposite polarity are placed half a betatron wavelength apart. The phase advance per cell of the CPS being $\pi/4$ and the structure being FOFDOD, the doublet lenses can all be placed in mid-F straight sections. A doublet leaves the amplitude function β_H unperturbed outside but not the dispersion function x_p. Two consecutive doublets of opposite polarity form a triplet whose center lens is twice as strong as the outer lenses.

The lens configuration consists of two superperiods, each containing : 1 triplet, 2 cells, 1 doublet, 1 cell, 1 doublet, 6 cells. In the following three chapters, expressionsfor β, x_p and γ_t are derived for a machine assuming :

i) all unperturbed β and x_p values at the lenses are equal to β_F and x_{pF} respectively;

ii) the phase advances are precisely as required.

3. The Excursion of the Amplitude Function

The knowledge of β is not really needed for obtaining γ_t but we want an expression for $\hat{\beta}$ and we shall prove that the Q-value remains constant. As a measure for the lens strength we introduce the dimensionless parameter :

$$q = \beta_F / f \qquad (f : \text{focusing length})$$

With $\psi = \int \frac{ds}{\beta}$ the phase advance of the unperturbed machine counted from the first quadrupole, we have in short lens approximation with initial conditions

$$\Delta\beta = 0 \quad \text{and} \quad \frac{d}{d\psi}\left(\frac{\Delta\beta}{\beta}\right) = 0$$

just before the lens :

$$\Delta\beta = -\beta\, \Delta q \sin 2\psi \quad \text{for small } \Delta q.$$

For large q, we have :

$$\frac{\partial \tilde{\beta}}{\partial q} = -\tilde{\beta} \sin 2\tilde{\psi} \tag{3.1}$$

where $\tilde{\beta}$ and $\tilde{\psi}$ are the new values such that

$$ds = \tilde{\beta}\, d\tilde{\psi} = \beta\, d\psi$$

It follows together with (3.1)

$$\frac{d^2 \tilde{\gamma}}{d q^2} = \frac{d\tilde{\psi}}{dq} \sin 2\tilde{\psi} \tag{3.2}$$

The system (3.1, 3.2) has a solution which can be written :

$$q = \operatorname{ctg} \psi - \operatorname{ctg} \tilde{\psi} \qquad \text{from which}$$

$$\tilde{\psi} = \pi \text{ for } \psi = \pi \qquad \text{q.e.d.}$$

$$\frac{\tilde{\beta}}{\beta} = \cosh \chi - \sinh \chi \sin(2\psi + \operatorname{arctg} \frac{q}{2})$$

$$\frac{\delta}{\beta} = \cosh \chi + \sinh \chi \sin(2\tilde{\psi} - \operatorname{arctg} \frac{q}{2})$$

$$\frac{q}{2} = \sinh\left(\frac{\chi}{2}\right)$$

It follows :

$$\left(\frac{\tilde{\beta}}{\beta}\right)_{\substack{\max \\ \min}} = e^{\pm\chi} = 1 + \frac{q^2}{2} \pm q\sqrt{1 + \frac{q^2}{4}}$$

4. The Excursion of the Dispersion Function

A simple way of treating x_p is to consider $\Delta x_p = x_p - x_{po}$ as a betatron oscillation excited by kicks at the lenses, the magnitude of the kick being proportional to x_p. A convenient measure for Δx_p is

$$\xi = \frac{\Delta x_p}{\sqrt{\beta}}$$

ξ must obey the differential equation

$$\frac{d^2\xi}{d\psi^2} + \xi = -q_k(1 + \xi_k)\ \delta(\psi_k)$$

With complex notation $z = \xi + i\frac{d\xi}{d\psi}$ and the initial conditions $z(\psi_1) = z_1$ at $\psi_1 = 0$, one finds after a lens of strength q_1 at $\psi_1 = 0$

$$z = \left(z_1 - iq_1(1+\xi_1)\right)\ \exp(-i\psi)\ ;\ 0 < \psi < \pi \qquad (4.1)$$

and after the second doublet lens of strength $-q_1$ at $\psi = \pi$:

$$z = (z_1 - 2iq_1)\ \exp(-i\psi) \qquad ;\ \pi < \psi \qquad (4.2)$$

The term $-q_1\xi_1 \sin\psi$ which occurs inside the doublet deserves particular attention. As we shall see in chapter 5, this term causes the γ_t change. With $\varphi_k = \psi_{k+1} - \psi_k$, the tracing law is

$$z_{k+1} = (z_k - 2iqk)\ \exp(-i\varphi_k) \qquad (4.3)$$

For n doublets within a superperiod, the periodicity condition leads to

$$z_1 = \left(-\ \mathrm{ctg}\ \frac{\phi}{2} + i\right) \qquad \exp\left(i \qquad\right)$$

where $\$ = \sum_{k=1}^{n} \varphi_k$ is the phase advance over the superperiod.

In the CPS, there are two sets of lenses powered differently. Let $q_1 = -q_2 = T$; $-q_3 = q_4 = D$. The choice $\varphi_3 = \$$ eliminates the term containing D^2 in the characteristic polynominal P_2 (see 5.2) and simultaneously maximizes the term containing DT if φ_2 is put $3\pi/2$ (mod 2π) and $\varphi_4 = 5\pi/2$ (mod 2π). Modifications arise from shifting doublets by π and reversing the polarity. The scheme

$$(T)\ \pi\ (-T)\ \frac{371}{2}\ (-D)\ \phi\ (D)\ \frac{5n}{2}$$

yields with *(4.3)* and (4.4)

$$\begin{cases} \frac{z_1}{2} = \frac{z_T}{2} = \left(-\ \mathrm{ctg}\ \frac{\phi}{2} + i\right) T+D\ ;\ \frac{z_2}{2} = \frac{z_{-T}}{2} = \mathrm{ctg}\ \frac{\phi}{2}\ T-D \\ \frac{z_3}{2} = \frac{z_{-D}}{2} = \left(-1 + i\ \mathrm{ctg}\ \frac{\phi}{2}\right) T-iD\ ;\ \frac{z_4}{2} = \frac{z_D}{2} = \left(1 + i\ \mathrm{ctg}\frac{\phi}{2}\right) T \end{cases} \qquad (4.5)$$

from which results

$$\sum_{k=1}^{4} q_k\ \xi_k = 4T\ \left(2D - \mathrm{ctg}(\tfrac{\phi}{2})\ T\right)$$

In the CPS, $|-\mathrm{ctg}\ \phi/2|$ could be kept small by going to the antisymmetric disposition which makes

$$\phi = \frac{6.25 - 1}{2}\ 2\pi$$

and

$$-\mathrm{ctg}\ \frac{\phi}{2} = \mathrm{tg}\ \frac{\pi}{8} = \sqrt{2} - 1$$

(a corresponding scheme for the AGS is feasible with $\phi = 8.75/2\cdot 2\pi$ or $-\mathrm{ctg}\ \phi/2 = -(\sqrt{2} - 1)$ with lenses placed in FD or DF straights for which the desired phase distances can be approximated rather closely i.e. : $\pi \sim 3\frac{1}{2}$ cells; $3\pi/2 \simeq 5$ cells; $7\pi/4 \simeq 6$ cells).

5. The new Transition Energy

As γ_t is defined by $1/\gamma_t{}^2 = \Delta C/C$ where ΔC is the additional circumference of a particle with unit momentum displacement $\Delta p/p = 1$ we have to sum over the contributions of all elements $\Delta C = \Sigma \delta C_k$. The kth doublet contributes to this sum

$$\delta C_k = \int \frac{\Delta x}{\rho}\ ds \simeq \frac{x_{pF}}{R\sqrt{\beta_F}} \int_o^{\pi} \beta^{3/2} \left[\xi_k \cos\psi + \left(\left(\frac{d\xi}{d\psi}\right)_k - q_k(1+\xi_k)\right) \sin\psi\right] d\psi$$

$$\frac{x\ \overline{\beta^{3/2}}^{\psi}}{pR\sqrt{\beta_F}}\ 2\left(\left(\frac{d\xi}{d\psi}\right)_k - q_k(1+\xi_k)\right) \qquad (5.1)$$

When summing over the whole circumference the only remaining terms involve the combinations $q_k\xi_k$ leading to

$$\left(\frac{\gamma_{to}}{\gamma_t}\right)^2 = 1 - cP\ P_2$$

$$c_p = 8\ \frac{\overline{pF}}{\pi\ R^2\sqrt{\beta}} \qquad \text{for the CPS}$$

$$P_2 = T\ (2D + (\sqrt{2} - 1)\ T$$

With this P_2, γ_t can be changed to either side as with a first order perturbation by keeping one set (triplets T) fixed and pulsing the other set (doublets D). Applying reasonable criteria, this scheme is superior to those studied previously[1,2].

An additional application has arisen which helps to ease debunching the beam prior to the continuous transfer into the SPS [3]. The combination $|Z|\ I\ \eta^{-1}\ (\Delta p/p)^{-2}$ should be small (Z : coupling impedance; I : beam current). As long as $|Z|$ is rather high as at present, it is helpful to increase η via a decrease of γ_t. The phase advance over the superperiod ϕ can be made 6.25 π by reversing the polarity of one triplet and of one doublet within each of the two superperiods so that P_2 becomes

$$P_2 = -\ T\ \left(2D + (\sqrt{2}+1)\ T\right)$$

The quadratic term is so efficient now that with the (water-cooled) triplet lenses alone, a gain of 2.5 in η is obtained with $T \simeq 1$; $\gamma_t \simeq 4.32$; $\hat{\beta} \simeq 60$ m; $\hat{x}_p = 23$ m. The peak excursion of x_p is high, but as for this application $\Delta p/p$ is small, the synchrotron width of the beam is not excessive. Also betatron width and synchrotron width add in quadrature to the total beam width; this is rigorous for the rms values of symmetric and uncorrelated distributions, and 4σ are a good measure for the total beam width.

The scheme is fairly flexible and allows for other modes of operation if the criteria (e.g. permissible $\hat{\beta}$, $\hat{x}_p$) are altered.

6. Bunch Matching

Since we shall describe the features of the negative mass instability also in terms of the matching theory, it is justified to recall briefly the most important facts of the matching theory[4]. They are

i) RF forces are linearized, so trajectories are elliptic ;

ii) Space-charge forces are also linearized by assuming a parabolic shape for the linear density which results from phase space density of semi-circle shape across trajectories ;

iii) Time is measured in units of the non-adiabatic time τ for ordinary transition crossing

$$\tau = \left(\frac{\gamma_{cr}^4 \, |tg\ \phi_s|}{4\pi\, \nu_{RF}\, \dot{\gamma}_s^2} \right)^{1/3}$$

and the new time given by $x = t/\tau$; $d/dx = '$; γ_{cr} is the γ at which transition crossing occurs (i.e. γ_t equals γ_s the value of the particles), ϕ_s the synchronous phase angle and ν_{RF} the RF frequency.

iv) Manipulations on γ_t are described by a function $f(x) = \eta/\eta_s'$ where

$$\eta = \frac{1}{\gamma_t^2} - \frac{1}{\gamma_s^2} \quad \text{and} \quad \eta_s' = -\frac{d}{dx}(\gamma_s^{-2}) \simeq \frac{2Y}{\gamma_{cr}}$$

Note that $f(x) \simeq x$ for $\gamma_t = \text{const.}$

v) A longitudinal space-charge parameter n_o is introduced by

$$n_o = \frac{3\pi^2}{2} \frac{r_p\, N\, g_o}{R\, A^{3/2}} \left(\frac{\nu_{RF}}{\dot{\gamma}_s} \right)^{1/2}$$

$$n = 0.772334\ n_o(0)\ ;\ n_o(0) \text{ of ref. } 4.$$

r_p = classical proton radius; $2\pi R$ = machine circumference; N = number of particles; A = bunch area in units of $\Delta(\beta\gamma)$·RF-angle (cut-off value); $g_o \simeq 1 + 2\ \ell n\ b/a$ (see 7.i).

vi) A variable θ is introduced denoting the half length of a normalized bunch of area π. θ is related to the physical bunch half length $\hat{\phi}$ by

$$\hat{\phi} = \frac{2\sqrt{A\, \nu_{RF}\, \gamma_s'\, \tau}}{\gamma_s^2}\, \theta .$$

θ obeys a second order differential equation. Far away from transition, the equilibrium values of θ are below (-) and above (+) transition given by

$$|f_\pm| = \theta_\pm^4 \pm n_o\, \theta_\pm \qquad (6.1)$$

A large and fast **jump** is aimed at such that θ_- is re-established $\theta_+ = \theta_- = \theta$. For this case, summation and subtraction of (6.1) yields

$$\theta = \left(\frac{\Sigma f}{2} \right)^{1/4} \quad \text{and} \quad n_o = \left(\frac{\Delta f}{2\theta} \right) \qquad (6.2)$$

with $\Sigma f = f_+ + |f_-|$ and $\Delta f = f_+ - |f_-|$. For $f_- = 0$, the minimum jump size[5] is $\Sigma f = f_+ = 2(n_o)^{4/3}$.

The system installed now in the CPS allows at least twice this jump.

The advantages of such a "superjump" are :

i) The mismatch is little sensitive against space-charge parameter variations. This is important at the CPS since each of the four Booster rings has some individuality. Roughly one has :

$$\frac{\partial}{\partial n_o} \left(\frac{\Delta\theta}{\theta} \right) \propto \left(\Sigma f \right)^{-3/4}$$

ii) For systematic intensity modulations from cycle to cycle, as planned, it is sufficient to change only the timing. This is much simpler than to change current amplitudes too.

iii) The negative mass unstable region is crossed near the peak of $|\dot{\gamma}_t|$, a very important aspect which leads us to the next chapter.

7. The Negative Mass Instability

The linear region of negative mass (n.m.) instability[6] is characterized by the fact that (small) modulations of the linear density grow exponentially with a growth rate which is a function of both the mode number and, in our case, of time, since we change η rapidly with the aim of reaching the threshold before the modulations have grown too much. In order to treat the phenomenon conveniently, we shall make a few assumptions and simplifications none of which are unrealistic or too rough.

i) The dependence of the geometrical factor g on the mode number is given for a beam of radius a, within a perfectly conducting pipe of radius b, at the axis by

$$g = \frac{4}{w} \left(\frac{1}{w} - K_1(w) - I_1(w)\, \frac{K_o\left(\frac{wb}{a}\right)}{I_o\left(\frac{wb}{a}\right)} \right)$$

with $$w = \frac{a\, k_c}{\gamma_{cr} R} = \frac{\pi\, a\, h\, k_b}{\gamma_{cr} R\, \hat{\phi}}$$

k_c, k_b : mode number per circumference or per bunch length respectively.

I_o, I_1, K_o, K_1 : modified Bessel functions.

The space-charge parameter n_o contains :

$$g_o = \lim_{w \to 0} g = 1 + 2\ \ell n\ \frac{b}{a}$$

For larger arguments w and b/a not too big, g is approximated by

$$g = \frac{g_o}{1 + \frac{w}{(1.6\ a/b + 0.52)^2}} \qquad (7.1)$$

$$g = \frac{g_o}{2} \quad \text{at} \quad k_{c\frac{1}{2}} = \gamma_{cr} R \left(\frac{1.6}{b} + \frac{0.52}{a} \right)$$

using the simplified kernel' for the space-charge potential, together with a numerical fit.

ii) From inspecting the Vlasov equation, it can be concluded that for $k_b >> 1$, the coasting beam model is a good approximation as proposed earlier by Pease[8].

iii) For the unperturbed density, the same distribution is assumed as in chapter 6.

iv) The initial modulation is assumed to be given entirely by statistical fluctuations due to the finite number of particles within the bunch $N_b = N/h$. The small amplitude approximation being based on Fourier decomposition, we can calculate the expectation value of the modes when referred to the average linear density $\hat{A} = N/2\hat{\phi}$ and find them independent of the mode number and the distribution function to be (see the Appendix)

$$|c_k(0)| = \frac{2}{\sqrt{N_b}}$$

A detailed study of the initial value problem shows that the behaviour after transition crossing as function of the growth rate G(x,k) is

$$|c_k(x)| \simeq |c_k(0)| \cosh \int G(x,k)\, dx$$

so that after a short time

$$|c_k(x)| \simeq \frac{\exp \int G(x,k)\, dx}{\sqrt{N_b}} \qquad (7.2)$$

With these assumptions, the growth rate and the threshold can be found via the Vlasov equation and the dispersion relation. The threshold can be expressed conveniently by the parameters of chapter 6 except that

$$n = \frac{g}{g_o} n_o \quad \text{is to be used (7.1)} \quad : \frac{\eta}{\eta_{th}} = \frac{f}{n\theta} \qquad (7.3)$$

This relation is valid along the whole bunch and allows to define a threshold value $f_{th} = ne$ which is always smaller than f_+ the value to be reached for matching. The growth rate varies along the bunch as the square root of the linear density and involves additional parameters. At the bunch center, the growth rate is

$$G(x,k_c) = \frac{k_c n}{h} \sqrt{\frac{A\,|tg\,\phi_s|}{\pi\,\gamma_s'}} \; \frac{1 - \left(\frac{f}{n\theta}\right)}{\sqrt{2\,\frac{n\theta}{f} - 1}} \qquad (7.4)$$

For θ = const. and f = f'x, the integral throughout the unstable region which measures the accumulated e-folding times of the n.m. instability is

$$E_{acc}(k_c) = \int G(x,k_c)\, dx = \frac{k_c\, n^2 \theta}{h\, f'}\left(1 - \frac{\pi}{4}\right) \sqrt{\frac{A\,|tg\,\phi_s|}{\pi\,\gamma_s'}} \qquad (7.5)$$

E_{acc} has a maximum $\hat{E}_{acc}$ for $k_c = k_{c\frac{1}{2}}/\sqrt{3}$, yielding

$$k\, n^2 = \frac{3\sqrt{3}}{16} k_{c\frac{1}{2}}\, n_o^2$$

$\hat{E}_{acc}$ must remain smaller than some critical value E_{crit} in order to avoid a blow-up which happens when

$$(\Sigma |c_k|^2)^{\frac{1}{2}}$$

of equation (7.2) approaches unity.

The implied summation

$$\sum_k \exp\left(2E_{acc}(k)\right) = N_b$$

can be carried out by second order expansion of $E_{acc}(k)$ around E_{crit}

$$E_{acc}(k_b) \simeq E_{crit}\left(1 - \left(\frac{3}{4}\frac{\Delta k_b}{k_{b\frac{1}{2}}}\right)^2\right)$$

$k_{b\frac{1}{2}}$ has to be taken in order to achieve the proper mode spacing within a bunch. The sum may then be approximated by the error integral yielding the transcendental equation for E_{crit}

$$\frac{k_{b\frac{1}{2}}}{3}\sqrt{\frac{8\pi}{E_{crit}}}\, \exp(2E_{crit})\, \underbrace{\operatorname{erf}\left[3\sqrt{\frac{E_{crit}}{8}}\right]}_{\simeq 1} = N_b$$

An approximate solution is

$$E_{crit} = \tfrac{1}{2}\left[\ln N_b - \ln\left(\frac{k_{b\frac{1}{2}}\sqrt{8\pi}}{3\sqrt{\tfrac{1}{2}\ln N_b}}\right)\right] \simeq \quad 10$$

($\frac{1}{2}\ln N_b$ is E_{crit} for only one mode; the second term arises from the presence of many modes).

The criterion for no blow-up due to n.m. instability is then

$$\boxed{\frac{k_{eff}\, n_o^2\, \theta}{h\, f'}\left(1 - \frac{\pi}{4}\right)\sqrt{\frac{A\,|tg\,\phi_s|}{\pi\,\gamma_s'}} < E_{crit}} \qquad (7.6)$$

with $k_{eff} \simeq \frac{\tilde{\gamma}_{cr}^R}{3}\left(\frac{1.6}{b} + \frac{0.52}{a}\right)$; $k_{eff}(\text{CPS}) \simeq 2\,10^4$

This should be considered as a condition for f' indicating how much faster transition energy is to be crossed by the jump. If f' prooves to be insufficient, the magnitude of the blow-up might be estimated by applying Dory's law[9] together with *(7.4)*.

The inequality (7.6) allows also to study other methods, for example, playing with ϕ_s. Since they only provide factors of the order unity, at least in the good direction, we conclude that a fast jump is indispensible*.

If we put $\theta = (\frac{\Sigma f}{\Sigma})^{\frac{1}{4}}$ and note that n_o^2 contains A^{-3}, we see that the longitudinal phase-space density scales as $N/A \propto N^{1/5}\,(f')^{2/5}\,(\Sigma f)^{-1/10}$. The scaling law for bunch matching taken from (6.2) goes as $N/A \propto N^{1/3}\,(\Delta f)^{2/3}\,(\Sigma f)^{-1/6}$ and simplifies to $N/A \propto N^{1/3}(\Sigma f)^{\frac{1}{2}}$ if $\Sigma f/\Delta f$ remains constant.

* A promising method at a first glance seems to be passive compensation[10], i.e. reducing n_o via g_o. As we need really to reduce n(k) via g(k), a critical frequency characteristic of the wall impedance over a wide range is required to achieve this without over-compensation[11]. Since that is also sensitive to the density distribution, an awkward problem would have to be mastered.

8. Experimental observations

All quadrupoles are compact in length (< 0.25 m), the doublet quadrupoles (except one) are also compact in cross-section. The present power supplies allow for $|D| \simeq 0.45$ and $T \simeq 0.82$ corresponding to $\hat{\gamma}_t \simeq 7.9$ and $\check{\gamma}_t \simeq 5.6$, the jump is performed within 0.8 ms corresponding to $f' \simeq 50$. ($\dot{\gamma}_s = 50\ s^{-1}$; $\gamma_s' \simeq 0.09$).

The scheme came into operation smoothly. Some initial beam loss due to closed orbit perturbation could be cured by centering carefully the mean radial position of the beam. The pulse form of the triplet current is rather uncritical, the peak should approximately coincide with the jump. The doublet current should not rise too quickly after the jump (see Fig. 1). The triple switch on the RF phase gives perfect bunch matching but a single switch is sufficient (see Fig.2). The bunch size of the booster seems to decrease with increasing intensity. Above 6 10^{12} p/p in the CPS, a negative-mass instability blow-up was sometimes observed at $A \simeq 8$ mrad (in quantitative agreement with (7.6)). In order to improve the situation, more powerful supplies are under design for a larger jump and more than doubled speed aiming at $|D| \geq 0.55$, $T \geq 1.0$, $f' \simeq 200$–400. 10^{13} p/p could then be handled within a bunch area of 10 mrad or less. The betatron tunes Q_H and Q_V change only by ΔQ = a few 10^{-3} in agreement with computations by a lattice programme which also show that the real CPS yields the analytical results of chapters 3–5 very closely, in particular for γ_t.

Appendix

Let N_b = number of particles per bunch, $2\hat{\phi}$ = bunch length, $F(\phi)$ = bunch distribution function normalized by

$$\int_{-\hat{\phi}}^{\hat{\phi}} F(\phi)\, d\phi = 2\hat{\phi}$$

Subdivide the bunch into M bins indexed by m (or n). Each bin contains $F(\phi)$ ΔN particles where $\Delta N = N_b/M$ is the average number of particles per bin. Random fluctuations lead to particle numbers per bin different by δN from that determined by the distribution function. The expectation value of that difference is assumed to be given by

$$E\left\{ \frac{\delta N}{\Delta N}(m)\, \frac{\delta N}{\Delta N}(n) \right\} = \frac{F}{\Delta N}\, \delta_{m\,n}$$

The implied step function $f(\phi) = (\delta N/\Delta N)(m)$ for $(m-1)/M < (\phi+\hat{\phi})/2\hat{\phi} < m/M$ represented by Fourier expansion is to be

$$f(\phi) = \sum_{k=-\infty}^{\infty} c_k \exp\left(\frac{i2\pi k}{2\hat{\phi}}\,\phi\right) \rightarrow c_k = \frac{1}{2\hat{\phi}} \int_{-\hat{\phi}}^{\hat{\phi}} f(\phi)$$

$$\exp\left(-\frac{i2\pi k}{2\hat{\phi}}\,\phi\right) d\phi = \frac{1}{2\hat{\phi}} \sum_{m=1}^{M} \int_{\frac{m-1}{M}2\hat{\phi}}^{\frac{m}{M}2\hat{\phi}} \frac{\delta N}{\Delta N}(m)$$

$$\exp\left(-\frac{i2\pi k}{2\hat{\phi}}\,(\phi + \hat{\phi})\right) d\phi$$

$$= \frac{1}{M} \sum_{m=1}^{M} \frac{\delta N}{\Delta N}(m) \exp\left(-\frac{i2\pi km}{M}\right) \rightarrow E\left\{ c_k\, \bar{c}_k \right\}$$

$$= \frac{1}{M^2} \sum_{m=1}^{M} \sum_{n=1}^{M} E\left\{ \frac{\delta N}{\Delta N}(m)\, \frac{\delta N}{\Delta N}(n) \right\} \exp\left(-\frac{i2\pi k}{M}(m-n)\right)$$

$$= \frac{1}{M^2} \sum_{m=1}^{M} \frac{F}{\Delta N} = \frac{1}{2\hat{\phi}} \int_{-\hat{\phi}}^{\hat{\phi}} \frac{F}{N_b}\, d\phi = N_b$$

The modulus of the Fourier coefficient c_k is composed of c_k and c_{-k} so that $|c_k| = 2/\sqrt{N_b}$ q.e.d.

Acknowledgements

The hardware for the present γ_t-jump system was provided under the responsibility of F. Rohner, the power supply built by H. Dijkhuizen. The scheme was brought into operation by M. Bôle-Feysot, E. Brouzet, J. Gareyte, J. Guillet, R. Ley, F. Rohner, G. Roux and further people. With D. Möhl and F. Sacherer, I had fruitful discussions on the theory. B. Schorr contributed to the subject in the appendix.

References

1. W. Hardt, H. Schönauer, A. Sdrenssen, Passing transition in the future CPS, Proc. of the 8th Int. Conf. on High Energy Acc., 323, CERN, 1971.
2. H. Schönauer, Lens configurations for the CPS to provide a large and fast γ_{tr}-jump without Q-change, Int. report, CERN-MPS/DL 72-7, 1972.
3. W. Hardt, Proposal to ease debunching for the continuous transfer, Internal report, MPS/DL/Note 74-5, CERN, 1974.
4. A. Sdrenssen, Longitudinal space-charge forces at transition, Proc. 6th Int. Conf. on High Energy Acc., 474, Cambridge/Mass., 1967.
5. D. Möhl, Compensation of space-charge effects at transition by an asymmetric Q-jump - A theoretical study, Internal report CERN-ISR/300/GS/69-62, 1969.
6. V.K. Neil, A.M. Sessler, Longitudinal resistive instabilities of intense coasting beams in particle accelerators, Rev. Sci. Instrum., 36, 429, 1965.
7. P.L. Morton, Longitudinal space-charge effects in standing wave Linacs, Rev. Sci. Instr. 36,1826, 1965.
8. R.L. Pease, Longitudinal instabilities in synchrotrons at transition, Internal report, BNL/AADD-147, Brookhaven, 1968.
9. R.A. Dory, Azimuthal space-charge effects in particle accelerators, MURA report, Wisconsin, 1962.
10. R.J. Briggs, V.K. Neil, Stabilization of intense coasting beams in particle accelerators by means of inductive walls, Plasma Physics - Accelerators - Thermonuclear Research (J. Nuclear Energy, Part C), 8, 255, 1966.
11. H.G. Hereward, Limitations on beam quality and intensity, Proc. of 8th Int. Conf. on High Energy Acc., 548, CERN 1971.

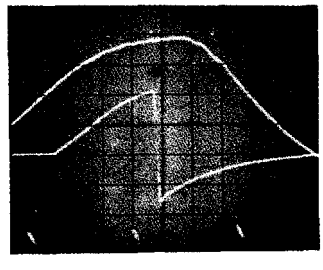


Figure 1
Triplet current (upper trace). Doublet current (lower trace). Sweep : 5 ms/div.

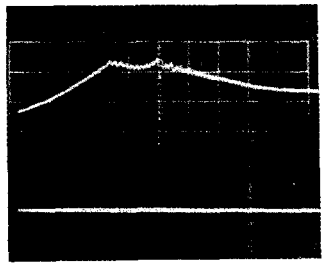


Figure 2
Wide-band pick-up station signal, inversely proportional to bunch length. First peak : doublet current starts rising. Second peak : Jump. N = 5.5 10^{12} p/p. Sweep : 10 ms/div.

DIPOLE TWO-BEAM INSTABILITY IN CIRCULAR BEAMS WITH AZIMUTHAL NON-UNIFORMITY

P.R.Zenkevich, D.G.Koshkarev

USSR, Moscow, ITEP

Summary. The modulation of the beam tranversal dimensions in the strong focusing accelerators causes the spead of the oscillation frequency of the electrons or ions which are created by ionization of residual gas. This paper will discuss the influence of such frequency spead on the stability of the two-beam dipole transversal oscillations.

After publication of paper [1] on two-beam instability in electron-ion rings some theoretical [2-5] and experimental investigations on two-beam instabilities in circular accelerators and storage rings have been made (such instabilities appear due to the interaction of the rotating beam with ionization of the rotating beam with ionization particles-electrons or ions created by ionization of residual gas). It seems that the growth of the beam transversal dimensions observed at the Bevatron [6] and at the CERN storage ring [7] is due to two-beam instabilities.

It is evident that in high energy accelerators and storage rings such instabilities have some specific features which are beyond the theory developed in paper . In this work we will mainly deal with the effects which are connected with azimuthal non-uniformity of interacting beams. Besides, some other effects have been considered qualitatively.

1. Influence of Transversal Dimension Modulation of Rotating Beam

In paper [4] it is noted that the transversal dimension modulation causes the spread of the oscillation frequency of the ionization particles and, consequently, affects the instability increment and the intensity limits.

Let us consider this problem by means of the linear hydrodynamical theory neglecting the image forces and forces of the coherent interaction between particles with the same charge sign. Besides, let us restrict ourselves by the vertical motion and suppose that the longitudinal density of the rotating beam is uniform.

Under these assumptions the transversal motion equation of the rotating particles (index 1) and equation of ionization particles (witn index 2) will be of the following form

$$\frac{d^2 z_1}{dt^2} + \Omega_1^2(x) z_1 = \Omega_{12}^2(x)\,\bar{z}_2 \qquad (1)$$

$$\frac{d^2 z_2}{dt^2} + \Omega_2^2(x) z_2 = \Omega_2^2(x)\,\bar{z}_1 \qquad (2)$$

In (1) t - the time, z - transversal coordinate, z - the beam centre gravity coordinate, x - the length along the equilibrium trajectory, $\frac{d}{dt}$ - the time derivative.

Supposing the first and the second beam to have the uniform longitudinal densities and. the same elliptical cross sections we get the following expression for $\Omega_2^2(x)$ and $\Omega_{12}^2(x)$:

$$\Omega_2^2 = (\Omega_2^*)^2 \mathcal{X}^2(x)$$
$$\Omega_{12}^2 = (\Omega_{12}^*)^2 \mathcal{X}^2(x) \qquad (3)$$

where $\mathcal{X}(x)$ is the coefficient describing the azimuthal modulation of transversal dimensions, Ω_2^* and Ω_{12}^* are the values of Ω_2 ana Ω_{12} corresponding to the beam with the circular constant radius cross section, Ω_2^* and Ω_{12}^* being determined by

$$(\Omega_2^*)^2 = (1-\eta_1)\Omega^2 \frac{m r_e Z_2 Z_1 N_1 Q_1}{\pi M_2 V}$$

$$(\Omega_{12}^*)^2 = \eta_1 \Omega^2 \frac{m r_e Z_2 Z_1 N_1 Q_1}{\pi M_1 \gamma_1 V} \qquad (4)$$

where η_1 - the neutralization factor, N_1 - the number of particles in the chamber, the transversal phase volume of the rotating beam, z_1 and z_2 axe the particle char

ges, M_1 and M_2 are the particle masses, γ_1 - the relativistic factor, r_e and m are the classic radius and the mass of the electron, Q_1 - the vertical oscillation betatron frequency*

Neglecting the Floquet function modulation due to the random harmonics of the magnetic field gradient we obtain:

$$\varkappa^2_{(x)} = \frac{2R\Delta}{Q_1 g_z (g_r + g_z)} = \frac{2}{\left\langle \frac{1}{g_z^2} \right\rangle g_z (g_r + g_z)} \qquad (5)$$

where $2\pi R$ the acceleator length, Δ =1 m, g - the Floquet function modulus, $\langle\ \rangle$ means the averaging over the accelerator length. Note that $\varkappa^2$ is the periodic function of x with the period length $2\pi R/S$ (S is the number of magnetic structure periods along the accelerator length).

In the variables

$$y = \frac{z}{g_{z(x)}}, \quad d\Psi = \frac{\Omega R\, dt}{Q_1\, g^2_{z(x)}} \qquad (6)$$

eq. (1) has the following form

$$\frac{d^2 y_1}{d\Psi^2} + Q_1^2 y_1 = \frac{Q_1^2 g_z^4(\Psi)\, \Omega_{12}^2(\Psi)}{R^2 \Delta^2 \Omega^2}\, \overline{y_2} \qquad (7)$$

If the right-hand part of eq.(7) is time-independent, then the solution of this equation cannot be represented as orthogonal Fourier series in Ψ. Let us try to solve the system including eqs.(2) and (7) in the following form

$$\overline{y_{1,2}} = \sum_{n=-\infty}^{\infty} \overline{y^n_{1,2}}\, \exp[i(n\Psi - \omega t)] \qquad (8)$$

Substituting $z_1 = g_z \sum_{n=-\infty}^{\infty} \overline{y_1^n} \cdot \exp[i(n\Psi - \omega t)]$ into eq.(2) and taking into consideration that all the ionization particles have the same frequency for given Ψ we find

$$\overline{y_2} = \sum_{n=-\infty}^{\infty} \frac{\overline{y_1^n}\, \Omega_2^2(\Psi)}{\Omega_2^2(\Psi) - \omega^2} \exp[i(n\Psi - \omega t)] \qquad (9)$$

After the substitution (9) into (7) we get the following equation for y_1

$$\frac{d^2 y_1}{d\Psi^2} + Q_1^2 y_1 = \sum_{n=-\infty}^{\infty} \frac{\overline{y_1^n}\, \Omega_2^2 \Omega_{12}^2 g_z^4 Q_1^2}{R^2 \Delta^2 \Omega^2 (\Omega_2^2 - \omega^2)} \cdot \exp[i(n\Psi - \omega t)] \qquad (10)$$

The general solution of eq.(10) is determined by the following system of equations

$$\overline{y_1^{n+Ks}} = \sum_{K=-\infty}^{\infty} c_{K-K'}\, \overline{y_1^{n+Ks}} \cdot \left\langle \left[Q_1^2 \Omega^2 - (n\Omega + K'S\Omega - \omega)^2 \right]^{-1} \right\rangle \qquad (11)$$

where $K' = 0, \pm 1, \pm 2 \ldots$, the sign $\langle\ \rangle$ means the averaging over longitudinal momentum **Thus**, the amplitudes of harmonics with the numbers 'differing by ks are connected by an infinite system of linear equations; supposing that the determinant of this system is equal to zero we get the exact dispersion relation. The resonance condition

$$\omega \approx (n + KS)\Omega - Q_1 \Omega \qquad (12)$$

may be, however, realized only for one value of K. Besides, if the focusing is not too strong, $|C_0| \gg |C_{K-K'}|$ (for $|K-K'| \neq 0$). Taking into account of these considerations we may neglect **all** the harmonics except the resonant one starting with $K = K' = 0$; then after substitution (3) and (4) into (11) we get the following dispersion equation

$$1 = -(\Omega_2^* \Omega_{12}^*)^2 \int_{-\infty}^{\infty} \frac{f(p)\, dp}{Q_1^2 \Omega^2 - (n\Omega - \omega)^2} \cdot \int_0^L \frac{dx}{[\omega^2 - \Omega_2^2(x)]} \frac{2\Delta}{\pi Q_1 (g_z + g_r)^2} \qquad (13)$$

where $f(p)$ is normalized p distribution function.

Of course, without dimension modulation the dispersion relation coincides with that for nonmodulated beam obtnined in [1]. Taking into account only resonant terms in the denominator let us write the dispersion equation (13) as

$$1 = -\varepsilon^2 \int_{u_1}^{u_2} \frac{\varphi_1(u)\, du}{\alpha - u - \eta} \int_{v_1}^{v_2} \frac{\varphi_2(v)\, dv}{\alpha - v} \qquad (14)$$

where

$$\alpha = \frac{\omega}{\Omega_0} - Q_2^*, \quad u = \frac{(n - Q_1)\Omega}{\Omega_0} - (n - Q_1^0), \quad \eta = n - Q_1^0 - Q_2^*, \quad v = Q_2 - Q_2^*, \qquad (15)$$

$Q_2 = \Omega_2 / \Omega_0$, φ_1 and φ_2 are normalized distribution functions, index "o" corresponds to the central particle of the rotating beam. Here we supposed that the shape modulation is not very strong and therefore

$$\frac{2\Delta}{\pi Q_1 (g_z + g_r)^2} \approx (2\pi R)^{-1}$$

If longitudinal ion density does not depend on x we obtain the following formula for the function $\varphi_2(v)$

$$\varphi_2(v) = \left|\frac{dv}{dx}\right|^{-1} S\,(2\pi R)^{-1} \qquad (16)$$

Parameter Δ — the frequency shift with respect to the resonance line center, ε — the monochromatic beam increment divided by the rotation frequency;

$$\varepsilon^2 = \frac{Q_2^* Q_{12}^2}{4Q_1} \simeq \frac{Q_2^* \Delta Q_{12}}{2} \qquad (17)$$

where ΔQ_{12} is the rotating particle frequency shift due to the ionization particles. It is seen from (14) and (16) that the beam dimension modulation results in Landau damping. However, this damping has some specific features because $\varphi_2(v) \to \infty$ near the Floquet function extremum (when $\frac{dQ}{dx} \to 0$). It is known, that the Landau damping becomes small if the distribution functions have infinite magnitude. To illustrate this effect let us consider a simple example

$$v = \Delta Q_2 \cdot \cos\left(\frac{sx}{R}\right), \qquad (18)$$

$$\varphi_2(v) = \frac{1}{2\pi}\left(|\Delta Q_2|^2 - v^2\right)^{-1/2} \qquad (19)$$

Substituting (19) into (14) we obtain

$$1 = -\varepsilon^2 \left[\lambda^2 - (\Delta Q_2)^2\right]^{-\frac{1}{2}} \int_{u_1}^{u_2} \frac{\varphi(u)\,du}{\lambda - u - \eta} \qquad (20)$$

Here λ is tile complex variable with $\mathrm{Im}\,\lambda > 0$.

For $\varphi(u) = \delta(u)$ eq. (20) has the following form

$$\sqrt{\lambda^2 - (\Delta Q_2)^2}\,(\lambda - \eta) = -\varepsilon^2 \qquad (21)$$

The solution of eq.(21) depends on the parameters $A = \Delta Q_2 / \varepsilon$ and $B = \eta / \varepsilon$. It may be shown that the stability limit is determined by

$$|B| \leq B_{lim}(A) \qquad (22)$$

The graph $B_{lim}(A)$ is given in Fig.1.

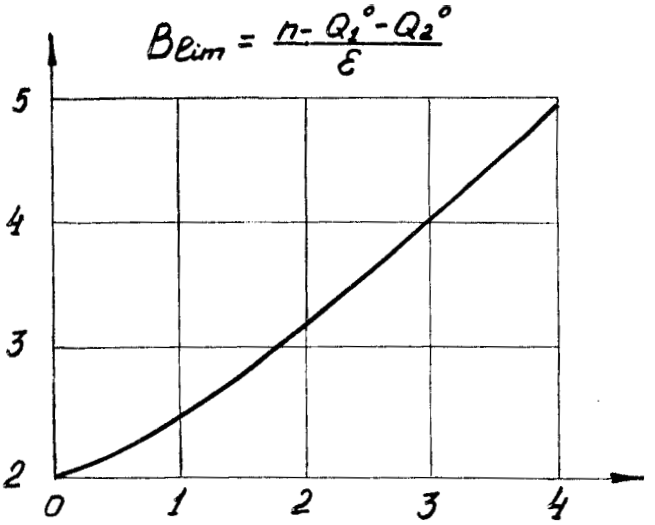


Fig. 1

It is seen that at A = 0 B_{lim}=2. When A increases the instability region is expanded and if $A \gg 1$

$$B_{lim}(A) \approx A + 1{,}5A^{-1/3} \qquad (23)$$

Within the instability region for one of the roots $9\,\mathrm{m}\,\lambda > 0$.

Fig.2 shows the dependence $\chi = \mathrm{Im}\,\lambda / \varepsilon$ on B and A.

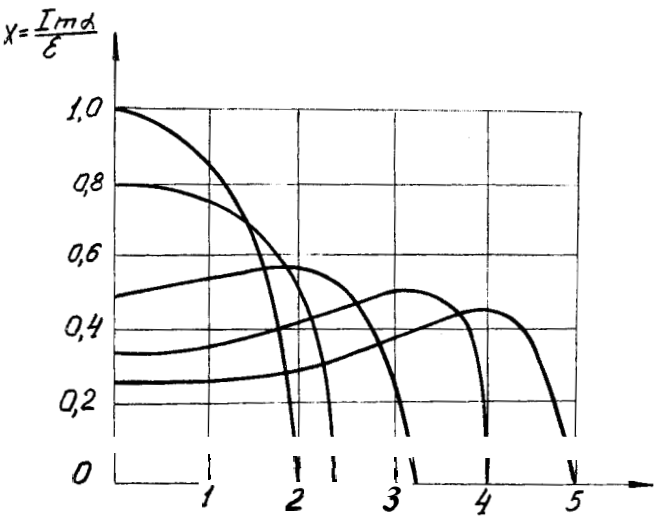


Fig. 2 $A = \frac{n - Q_1^\circ - Q_2^\circ}{\varepsilon}$

It is seen from the graph that if $A \gg 1$ χ achieves its maximum value at $B \approx A$; this maximal value of χ is determined by

$$\varepsilon \chi = Im \frac{\omega}{\Omega_0} \approx \frac{\sqrt{3}}{2} \frac{\varepsilon^{5/3}}{(2\Delta Q_2)^{1/3}} \qquad (24)$$

So we can see that the frequency spread in one of the beam results in the increase of the resonance width accompanied by some reduction of the increment value. The value of these changes depends on the form of the distribution function.

It seems that this effect causes "Landau antidamping" mentioned by Chirikov [8].

Analysis of eq.(20) shows that for nonmonochromatic beams the stability condition has the form

$$\langle \Delta Q_1 \rangle \geqslant \frac{K_1 \varepsilon^2}{\sqrt{(\Delta Q_2)^2 - \eta^2}} \qquad (25)$$

where K_1 is the coefficient of order of 1 depending on the form of distribution in u and $\langle \Delta Q_1 \rangle$ is the dispersion of this distribution.

It is seen from (25) that if the rotating particle oscillation frequency coincides with the oscillation frequency of ionization particles in the Floquet function extremum(i.e. at $n = Q_1 + Q_2^* \pm \Delta Q_2$) the dipole oscillations are unstable for any rotating particle frequency spread.

If we formally introduce an additional frequency spread of the ionization particles depending on variable τ, the corresponding dispersion integral in eq.(15) will have the modified form

$$\int_{v_1}^{v_2} \frac{\varphi_2(v)dv}{\alpha - v} \to \int_{v_1}^{v_2}\int_{\tau_1}^{\tau_2} \frac{\varphi_2(v)\varphi_2(\tau)dv\,d\tau}{\alpha - \tau - v} \qquad (26)$$

where $\varphi_2(\tau)$ is the distribution function in τ.

The stability condition(25) is also modified and for the most dangerous modes (with $n = Q_1 + Q_2 \pm \Delta Q_2^*$) is determined by

$$K_2 \langle \Delta Q_1 \rangle \sqrt{\Delta Q_2 \langle \Delta Q_2 \rangle} \geqslant \varepsilon^2 \qquad (27)$$

where $\langle \Delta Q_2 \rangle$ is the "trial" ionization particles frequency spread connected with variable K_2 is the coefficient depending on $\varphi_2(\tau)$.

In fact, $\langle \Delta Q_2 \rangle$ may appear only due to nonlinearity of the potential well which stabilizes the ionization particles motion, and consequently $\langle \Delta Q_2 \rangle$ depends on many factors, such as the rotating particles distribution in phase space, the Energy distribution of ionization particles and so on.

If $\eta_1 \ll 1$ and the transversal phase space density of rotating particles is uniform $\langle \Delta Q_2 \rangle / Q_2^* \sim 0.03$. Substituting in to (28) $\Delta Q_2 / Q_2^* = 0{,}2$, $\langle \Delta Q_2 \rangle / Q_2^* = 0.03$, and $K_2 = 2$ we get the following stability condition:

$$1{,}5 \langle \Delta Q_1 \rangle \geqslant \Delta Q_{12} \qquad (28)$$

where ΔQ_{12} is the betatron frequency shift of rotating particles due to the interaction with the ionization particles

Of course, formula(28) is approximate as it is derived from the hydrodynamical theory. Eesides, it should be reminded that this analysis was made neglecting the image force effects resulting in appearance of the shift between the coherent frequency and the incoherent oscillation frequencies. It seems that the Landau damping disappears if this frequency shift exceeds the corresponding incoherent frequency spread.

2. Aeutralization Factor and Ionization Particle Life-Time.

The calculation of the neutralization factor is a nontrivial problem. Firstly let us first consider a debunched beam; if the ionization particle life-time is equal to τ_1, then the neutralization factor is determined by

$$\frac{d\eta_1}{dt} = \mu(\eta_1) - \eta_1 / \tau_1 \qquad (29)$$

where μ is the ion birth-rate depending on η_1 due to the variation of the potential well depth(at $\eta_1 \to 1$ $\mu(\eta_1) \to 0$). Thus, the equilibrium value of is derived from the expression

$$\mu(\eta_1)\tau_1 = \eta_1 \qquad (30)$$

Particularly, at $\tau_1 \to \infty$ $\mu(\eta_1) \to 0$ and $\eta_1 \to 1$.

If the "clearing" is absent the ion life-time is determined by the various coherent and incoherent effects, while in the presence of "clearing" the life-time is determined by the drift time up to the "clearing" electrodes.

If the instability has already appeared the ionization particle life-time begins to depend on its increment. The character of this dependence is sophisticated. For example, if the instability takes place at some definite points of the ring, the longitudinal components of the ionization particles field results in their motion to the loss place. On the other hand, these ionization particles induce the desorbtion of the molecules in the molecular layer and thereby deteriorate the local vacuum and increase the leakage rate [7]. Note that the influence of finite life time leads to variation of the particles dynamics [10]. With the account of this effect eq.(16) is modified

$$\int_{\nu_1}^{\nu_2} \frac{\varphi_2(\nu)d\nu}{\lambda-\nu} \to \int_{\nu_1}^{\nu_2} \frac{\varphi_2(\nu,d\nu}{\lambda+i\delta-} \qquad (31$$

The analysis of the modified dispersion equation(31)shows that outside the region of the coupling resonance this effect results in appearance of weak instability; inside the resonance region this effect,formally analogous to coherent radiation[10] diminishes the increment.

The situation considerably changes with the presence of the r.f.field because the rotating particles bunching creates some"alternating field focusing" for electrons or ions 5. Of course, the bunching influence may be neglected if

$$Q_2^* \ll q \qquad (32)$$

where q is tile harmonic number.

If inequality (32)is not fulfilled, then to determine η_1 one needs in detail calculation of the stability regions [5]. We believe that the electrons may be accumulated only in the first stability region due to the fluctuation of density from bunch to bunch (such fluctuation may be artificially increased that allows one to check the presence or the absence of effects caused by the electrons oscillating in the high order stability regions.

As a rule, the inequality(32) is correct for electrons and therefore in the positive ion circular accelerator a great number of electrons may be accumulated only in the debunch-regime or if the accelerated ions are injected at the constant magnetic field (with synchronous phase $\Psi_s = 0$). Consequently, the use of such regimes requires a special attention to "proton-electron" instability.

Conclusion

We see that the ionization particle frequency spread due to the dimension modulation of the rotating beam does not stabilize the dipole two beam instability even in the presence of momentum and frequency spread of the rotating bean. Let us remind that according to the results of paper [1] , the stability region may exist only if the frequency spread is present in both beams. Consequently the given necessary condition is insufficient to provide the stability.

The evaluation shows that the two-beam instability may essentially affect the beam parameters in the accelerators and the storage rings if the circulating beam have the uniform density during some nonzero time interval (for example, during the constant field injection or slow ejection).

Correct calculations of the instability limit is complicated due to the difficulties in the evaluation of the neutralization factor. However, it is possible to give a simple expression to evaluate the maximal beam disturbance due to the electron-proton dipole interaction in the proton synchrotrons.

Note that in the electron-proton instability the electron oscillation amplitudes exceeds the proton oscillation amplitudes. On the other hand, the electron coherent oscillation amplitude is limited by the chamber dimensions This allows one to make a simple estimate of a maximal possible effect during the time interval t_0 after the proton injection. Substituting $y_2 = y_{max}$, $\eta_1 = \mu t$ into (2) we get

$$\frac{y_1}{y_{max}} = \frac{\mu \Omega_0 t_0^2 r_e Z_1 Z_2 N_1}{2\pi M_1 \gamma_1 V} \qquad (33)$$

Substituting the ITEF proton synchrotron data into (33) ($Z_2=Z_1=1$, $=200sec^{-1}$, $V=7\cdot10^{-5}$ m.rad, $N_1=10^{12}$, $\Omega_0 = 2\pi \cdot 2{,}5\cdot10^5$ sec^{-1}) we find

$$\frac{y_1}{y_{max}} = 10^7 t_0^2 sec^{-2}$$

i.e. the instability begins to be dangerous at to 0,1msec. Accounting for the difficulty of the correct calculation, the formula (33) may be useful for evaluation of the possible effect in the positive ion circular accelerators.

References

1. P.R.Zenkevich, D.G.Koshkarev, Proceedings of the II-nd USSR Conference on Charged Particle Accelerators, 1970,p.219,Moscow. (1972); "Particle Accelerators",3,p. 1(1972).
2. D.Mo'hl, A.M.Sessler, ERAN 180 (1971).
3. E.Keil, B.Zotter, ISR-TH/71-58 (1971).
4. B.Zotter, "Proceedings USA Conference on High Energy Accelerators" p.847 (1973).
5. H.Shönauer, ibid., p.866.
6. M.Grunder, G.Lamberston, CERN Conf.1971, p.308.
7. E.Keil, Proceedings of the III-d USSR Conference on Charged Particle Accelerators, p.328 (1973).
8. B.V.Chirikov, Atomnaya Energiya,19,239 (1965).
9. E.Fisher, Proceedings of the III-d USSR Conference on Charged Particle Accelerators, p.101 (1973).
10. H.G. Hereward , CERN/71-15 (1971).
11. P.R.Zenkevich et al., Atomnaya Energiya 33, 1, 56 (1972).

THE INTERACTION OF A LONG INTENSIVE ELECTRON BUNCH WITH A PASSIVE CAVITY

Voskresensky G.V. , Kurdjumov V.N.

Radiotechnical Institute of the USSR Academy of Sciences
Moscow, USSR

Abstract

The change of energy distribution in an initialy monochromatic long electron bunch due to radiation field induced by the bunch in a passive cavity is investigated. The characteristics of "autoacceleration" for a long bunch is obtained, the "head-tail" effect dependence on energy for a short intensive bunch is evaluated and electron ring defocusing averaged over the trajectory is calculated.

The charged bunch passing through a cavity resonator induces the radiation field. Due to this field the bunch as a whole is being retarded. For a long bunch the distribution of the radiation reaction force on a separete particle is not uniform along the bunch. The analisis of this radiation reaction force distribution is of great importance in several applications. It may be noted three of them.

1. The possibility of "autoacceleration" of an electron beam passing through a cavity by the induced field [1]. If the sign of energy which transfered to the separate particle by the longitudinal component of the radiation field changes along the bunch some part of the particles will be accelerated.

2. The influence of radiation also must be taken into account in design of the electron accelerator with intensive bunches [2]. The action of radiation field results in an energy spread of the particles, that may be comparable to energy gain due to the accelerating field.

3. The diffraction radiation may have a significant effect upon longitudinal ring stability in electron ring accelerator. The approximate estimation [3] shows that for the periodical structure diffraction radiation defocusing force is proportional to the total energy loss of the electron ring.

The points in question will be investigated for a model of cylindrical cavity (radius b, length 2d) with entrance and exit tubes of radii a [4]. Let the bunch with total charge Q is an uniformly charged filament of length 2h, that moves along the axis of structure with constant velocity $v=\beta c$. We introduce the coordinate ξ along the bunch with the origin in its centre and normalised to its length ($-1\le\xi\le 1$).

The diffraction radiation reaction force on electron with coordinate k in the z point of trajectory is equal

$$T(\xi,z)= e E_z(\vec{r},t)\Big|_{\substack{r=0\\ t=(z-\xi h)/v}} \qquad (I)$$

where E_z is longitudinal component of electric field induced in the structure by the bunch. We will investigate the radiation reaction force work upon a separate electron during the flight through the structure

$$F(\xi) = \int_{-\infty}^{\infty} T(\xi,z)\,dz \qquad (2)$$

The electromagnetic radiation field may be found following the references [4, 5], where the exitation of cavity with tubes by given current have been investigated.

The total field is presented as a sum $\vec{E}^0+\vec{E}^1$ and only the radiation field $\vec{E}^1$ have been taken into account in calculations of radiation reaction force work: this field for each frequency may be presented by the superposition of waveguide modes. The expression of radiation reaction force work upon the separate charge with coordinate ξ is

$$F(\xi) = -4ea\int_{-\infty}^{\infty} d\omega\, e^{i\frac{\omega}{v}\xi h}\sum_{n=1}^{\infty}\left\{\frac{\nu_n}{J_1^2(\nu_n)\left[(\Gamma a)^2+\nu_n^2\right]}\times\right.$$

$$\left[F_n\left(ih_n\sin\frac{\omega}{v}d-\frac{\omega}{v}\cos\frac{\omega}{v}d\right)+G_n\left(h_n\cos\frac{\omega}{v}d-i\frac{\omega}{v}\sin\frac{\omega}{v}d\right)\right]+$$

$$+i\frac{\beta}{a}\frac{\nu_n\exp(ig_nd)}{(\Gamma\beta)^2+\nu_n^2}\left[K_n\left(\frac{\omega}{v}\sin g_nd\cos\frac{\omega}{v}d-g_n\cos g_nd\sin\frac{\omega}{v}d\right)+\right.$$

$$\left.+L_n\left(g_n\sin g_nd\cos\frac{\omega}{v}d-\frac{\omega}{v}\cos g_nd\sin\frac{\omega}{v}d\right)\right]\Bigg\}, \qquad (3)$$

where $\Gamma=k/\gamma\beta$, $k=\omega/c$, $\gamma=(1-\beta^2)^{-1/2}$, $g_n=\sqrt{k^2-(\nu_n/\beta)^2}$, $h_n=\sqrt{k^2-(\nu_n/a)^2}$ and the coefficients F_n, G_n, K_n, L_n can be found from the infinite set of linear algebraic equations, which was outlined in [5]. This coefficients have the simple poles at the resonant frequencies of the structure and the integration path in ω-plane in (3) must come above those poles through a small semicircles. Thus the integral *(3)* may be expessed in terms of the principal value of integral and half of residues in those poles. The determination of coefficients and evaluation of principal value of integral and the residues in poles have been found by numerical methods.

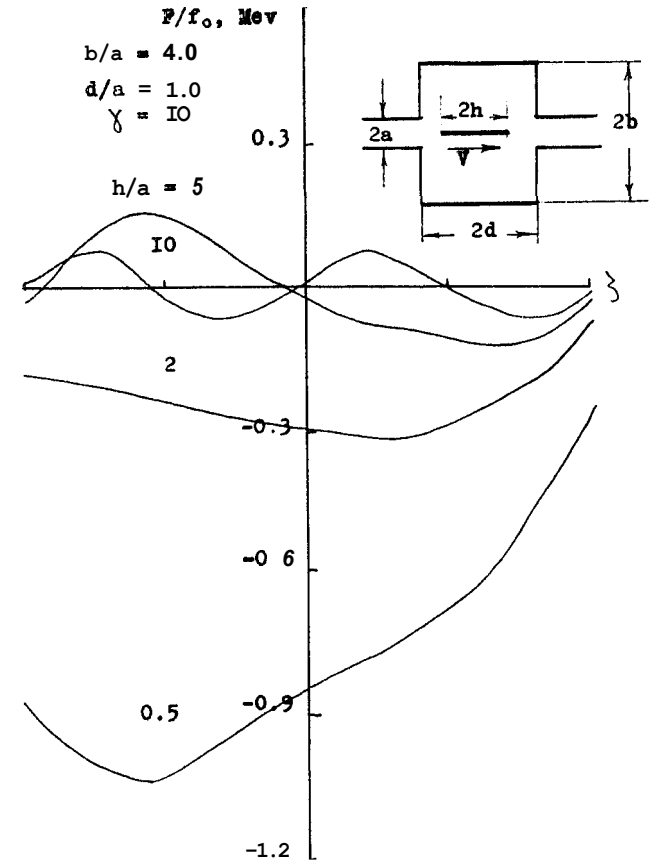
We begin to consider the results of calculation with discussion of "autoacceleration" possibility. The plot of reaction force work $F(\xi)$ for different length bunches is presented in the Pig. 1. The function $F(\xi)$ is normalised by factor $f_0=\frac{N}{N_0}\beta^{-1}$, where N - the total number of particles in the bunch, $N_0=10^{12}$, β -is expressed in santimeters; then the value $F(\xi)$ is in MeV. The autoacceleration becomes possible for $h>\beta/2$. For $h\gg\beta$ the beam after passing a passive resonant cavity is turned out to be energy modulated at the frequency close to main resonant mode ones. If the total bunch charge is fixed, then the modulation amplitude varies inversly as its length. If we will determine the acceleration efficiency as the total energy gain of all accelerated particles then this quantity represents by integral $\int F(\xi)d\xi$, where the integration region include only that ξ for which $F(\xi)>0$. Fig. 2 shows the total energy of accelerated particles vs bunch length. Optimal case is $h\approx\beta$.

As it can be seen from Fig. ■ for length of bunch much less than the wavelength of main resonant mode (this case is tipical for using of a resonator as an active accelerating device) the action of radiation reaction force gives the energy spread in the beam. For example, the energy spread for the 20 sm length bunch with $N = 10^{12}$ after passing the resonator with b=20 cm, d=a=5 cm is equal 40 KeV for γ ■ The energy spread vs relativistic factor γ is shown in Pig. *3;* it quickly reaches the limiting value as γ increases.

The bunches in the electron ring accelerator have a small axial extent, which is constant in the ring frame. Our calculation shows that the radiation field gives a defocusing effect and for realistic ring dimension the distribution of the radiation force work $F(\xi)$ is approximately linear. The ratio of average over the trajectory magnitude of defocusing force due to the radiation $T=[F(\xi=1)-F(\xi=-1)]\gamma/2h$ to the total energy loss $W=\frac{1}{2}\int_{-1}^{1}F(\xi)d\xi$ in function of γ is shown in Fig. 4. The date are obtained for a thin electron ring with radius $\rho=0.2a$. For a single cavity the presented ratio increases hearly linear with γ as distinguished from results in [3]. This discrepancy may be explain by different character of the radiation loss energy dependence for a single cavity and a periodic waveguide structure.

References

1. Kazansky L.N., Kisletsov A.V., Lebedev A.N. Atomnaya Energia, 30, N 1, ■ (1971).
2. Alikhanian A.I., Orlov Yu.F. et al. Proc. of the VII International Conference on Accelerators, Yerevan, v. 11, p. 103. (1970).
3. Pellegrini C., Sessler A.M. Lawrence Had. Lab, Raport ERAN-93, Berkeley (1970).
4. Voskresensky G.V., Kurdjumov V.N. Proc. of the VII International Conference on Accelerators, Yerevan, v. 11, p. 568, (1970).
5. Voskresensky G.V., Kurdjumov V.N. Journal Technitcheskoy Fiziki, XLI, N 10, 2103 (1971).



Pig. I

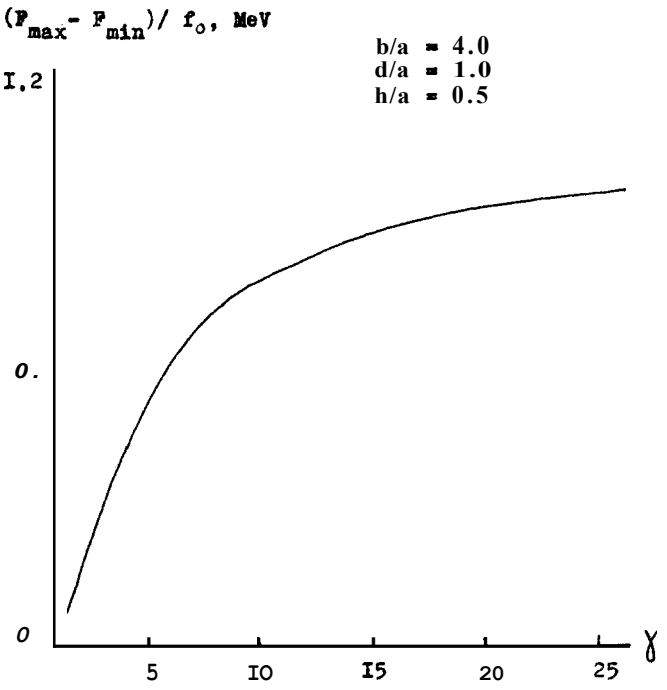


Fig. 3

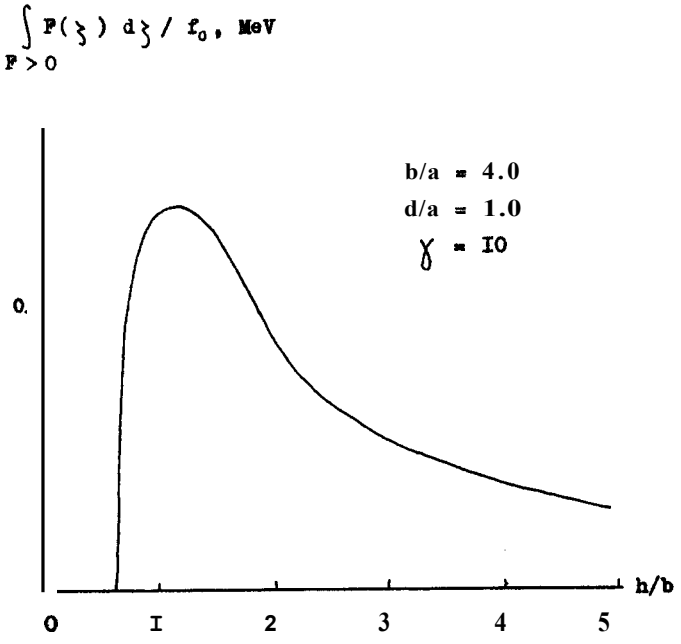


Fig. 2

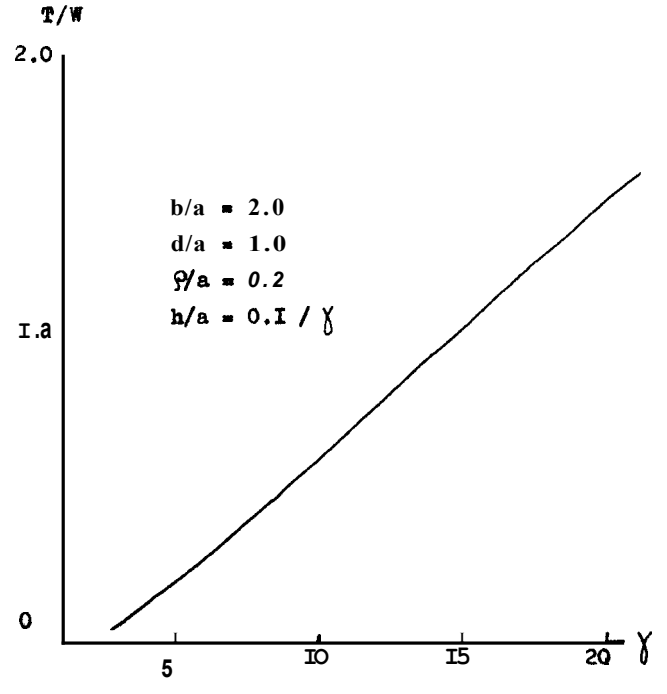


Fig. 4

BEAM EXTRACTION

H.T. Edwards
National Accelerator Laboratory
Batavia, Illinois

Introduction

Extraction of beams from synchrotrons has progressed over the past few years from an interesting accelerator-physics problem to an important engineering problem, the success of which determines in one sense the ultimate intensity at which machine operation is feasible. The original Piccioni extraction was a natural step away from internal-target physics. Resonant extraction then provided more efficient extraction with less loss and induced radioactivity. The extraction process could be more easily understood and analyzed. Simultaneous extraction to as many as two external lines has been accomplished[1,2] as has the simultaneous use of an internal target and an extracted beam.[3,4,5,6] Fast spill necessary for neutrino and bubble-chamber experiments has been obtained by fast kickers[6] and more recently by shaving[7,8] and fast resonant extraction.[9]

With the advent of large machines, the philosophy of extraction has changed. Effort has been made to isolate the various experimental areas from the machine proper. No longer are hadron beams made directly in the machine and radiation problems associated with targeting intense high-energy primary beams have been relegated to the various laboratories in the experimental area, where designs specifically directed at the radiation problem can be carried out more easily. The only severe radiation problem associated with the accelerator proper thus becomes the beam-extraction efficiency. The invention of the wire electrostatic septum[10] has been a major step in pushing the extraction efficiency from around 80% using magnetic septa to approximately 97%. Large machines have a slow cycle rate and it has become necessary to provide in each cycle slow extracted beam, bubble-chamber beam, and high-intensity fast extracted beam for weak interaction physics.

Large machines and storage rings have also produced a different type of extraction problem, that is, the problem of extracting from a booster, transporting, and injecting into a larger higher-energy machine or storage ring.

Resonant Extraction

Three types of resonant extraction are used in accelerators at the present time; they are integer, half-integer, and third-integer. Integer and half-integer modes are similar in that they are linear resonances to which a nonlinear perturbation has been added in order to obtain a gradual slow spilling of the beam. The third-integer resonance is nonlinear and does not produce any intrinsic linear instability.

Integer and half-integer extraction rely on a perturbing quadrupole or set of quadrupoles to both shift the machine tune toward 2ν = integer and to generate a stopband such that if the perturbing quadrupole is increased sufficiently or if the unperturbed machine tune is changed, it is possible to get inside the stopband. In this case, the solution of the equations of motion predicts exponential growth of all particle orbits (except for an unstable fixed point of zero phase-space population). Tuning to the integer has the disadvantage that equilibrium-orbit distortions may become large. In both the integer and half-integer cases the amplitude function around the machine is modified by the perturbing quad and a superperiodicity of @($) and $\alpha(\phi)$ established. This structure has a repetition rate of 2ϕ, where @ is the normal betatron phase advance. The β distortions are analytically similar to equilibrium-orbit distortions and the phase of the perturbed amplitude can be rotated by changing the ratio of strengths of two or more perturbing quads. Beta distortions produced by main quadrupole errors are probably better behaved at the half-integer than dipole equilibrium-orbit distortions at the integer produced by main dipole errors. This is especially true for separated function machines where there are a great many more dipoles than quadrupoles. The change in β with the excitation of the perturbing quad produces phase space ellipses that are very long. At the azimuthal location of the extraction septum, the ellipses should lie approximately along the x axis of the x, x' phase plot. When the stopband is entered, the phase ellipse becomes hyperbolic.

For slow extraction, it is necessary to generate a phase-stable region that slowly shrinks so that only a few particles become unstable in any short time interval. To generate this region, a nonlinear element (either intrinsic to the machine or introduced for this purpose) must be used. In the case of integer extraction, this element is generally a sextupole and thus produces one fixed point and one extraction phase-space trajectory. (An octupole nonlinearity could possibly produce the trajectories for simultaneous extraction of two beams.) In the half-integer system, the octupole must be used because the sextupole effect would be cancelled on successive turns.

The third-integer extraction relies on sextupoles themselves to supply both the nonlinearity and to set the phase of the extraction trajectory. The size of the stable region is controlled by how far the tune is from $\nu = 1/3$ or $2/3$. In some cases, a "semi-quad" or similar magnet is used instead of a sextupole, but has the same function.[4,11]

It is not clear what criteria should be used in selecting one particular resonance over the others. The integer resonances have

possible equilibrium-orbit problems. In half-integer extraction, the separatrix can be considerably curved; consequently the extracted beam phase space will be diluted. In third-integer extraction, octupole components of the guide magnetic field may make extraction difficult. Because there is no stopband, it is also possible to pass through the resonance and either leave some unextracted particles or extract from the other side of the resonance and thus dilute the extracted phase space and increase the extraction losses. Third-integer extraction is presumably least sensitive to magnet ripple, because the growth of the resonant beam near the fixed points is slower that for the other two cases, but the ripple should not sweep the beam tune back and forth through the resonance.

Third integer extraction seems to be better than integer if beam is shared with an internal target. Apparently this is so because of the small momentum aperture of the integer scheme.[3] Simultaneous third- and half-integer extraction to two experimental areas has succeeded.[1,12] Fast spill must also be provided in accelerators; linear resonances make some forms of fast extraction very easy and inexpensive.

In separated-function machines, new considerations enter. There are usually substantially fewer machine quadrupoles than bending magnets. It is therefore likely that the machine octupole moment will be much less important than the sextupole moment. The octupole moment will then be easily controlled for half-integer extraction and the sextupole moment will not matter except for its effect on tune changes caused by bending-magnet power supply ripple. For third-integer extraction, both sextupole and octupole field components may have to be corrected out. Another factor to consider is that quad and bend magnets may be separately powered and the sensitivity to the magnetic-field ripple in both types of magnets should be investigated. CERN has undertaken a study of all three resonant extraction modes for the SPS and probably quantitative comparisons will be forthcoming.[13,14]

Beam Spill Structure

The reduction of slow-beam spill structure to the point where effective spills are a large fraction of the available spill time is important to the experimental program at all accelerators doing counter experiments. Typically, one or more of the following approaches are used to reduce the spill structure. Power supply ripple is reduced by active or passive filtering and phase adjustment of thyristors or ignitrons. This is done either through feedback from devices which measure the voltage, current, or magnetic field ripple or through manual correction. At the AGS, for instance, the ripple is analyzed in terms of frequency components and manual correction is made by the operators. In some cases an auxiliary device is used to compensate for ripple from the main supply. In most cases, rf structure is not a problem because either the beam has been purposely debunched or the rf has been turned off so that it naturally debunches. At NAL, the rf frequency is high enough that rf structure has not yet become as important as other spill-factor problems. Betatron acceleration is proposed in a paper at this conference as a means of obtaining beams of small instantaneous momentum spread with good spill structure.[20] Typical power-supply ripple is approximately 10^{-4} in $\Delta B/B$ at frequencies between 10 and 1000 Hz. At higher frequencies than this where filtering is easier, the ripple is much less. The beam-spill structure itself can be used in feedback loops. This use is discussed in two papers at this conference and is also done at other laboratories.[2,9] Debunching the beam by the rf to produce a wide momentum spread is used at the AGS and the PS to help control spill.

Rf structure can often be used for time of flight and its quantization of the beam leads to ease in setting up coincidence-circuit gate widths. At the Bevatron, rf knockout to drive coherent betatron oscillations has been suggested as a means of producing sharp bursts of extracted particles.[16]

Most laboratories can obtain what they consider to be a good spill structure with a peak-to-valley ratio of at least 3 to 2. What path is taken and how it is pursued to improve the spill depends to a great extent on personal preference and cost considerations. (Straightforward power-supply filtering is expensive in large systems and at low frequencies.)

In high-energy, high-intensity machines it is likely that only a fraction of the beam will be used in the slow spill. Beam-structure problems will probably become very difficult when say only 10% of the beam is slow extracted over the magnetic flat top of the order of 1 second. Usually the beam phase space in the machine does not. grow linearly with intensity. However, extraction of a small fraction of the beam must come from a small fraction of the phase space and the rate of change of phase space will determine the spill quality.

Extraction Efficiency

To first order, the extraction efficiency is given by the septum thickness divided by the resonant step size for n turns of a particle with an oscillation amplitude equal to the distance of the septum from the equilibrium orbit. (n is 1, 2, or 3 depending on whether the resonance is integer, 1/2 or 1/3.) For semitransparent septa such as wire electrostatic septa, the extraction efficiency is expected to be better than the purely geometrical prediction.

Extraction efficiencies in machines with magnetic septa are usually 70 to 80%. At Brookhaven, for instance, the calculated efficiency of 85% is also the best observed efficiency.[6] Internal targets are used in some laboratories to produce secondary-particle beam lines. These targets are relatively thick and have a non-negligible effect on the extracted beam efficiency and emittance. (These targets should not be confused with those of the NAL internal-target area, which uses very light thin targets like 25 microns of polyethylene fibers and does not interfere

with the machine operation and extraction.) Generally, the extraction efficiency drops another 20% if internal targets are used to interact with 10 to 20% of the beam.[5] CERN (PS) uses an electrostatic septum and obtains 97% extraction efficiency with no internal target. The efficiency with internal targets using up to 40% of the beam stays above 90% and agrees very well with calculations.[4]

Extraction efficiency at NAL, where a wire electrostatic septum is used is also estimated to be about 97%. Calculations[10] had predicted considerably higher efficiencies, but probably there is no cause for alarm, both because the efficiency measurement is very elementary and because residual radioactivity appears to be under control. Probably improvements of the inefficiency of a factor of 2 or 3 are still forthcoming even without the shield suggested in Ref. 10. Possibly of more significance to future machine design is the catastrophic wire failures that have been experienced at NAL at intensities an order of magnitude below the design intensity. These failures are not yet understood.

Fast Extraction

Fast extraction is becoming increasingly more important. It is used at low intensities for conventional bubble-chamber experiments and at very high intensities for neutrino experiments. It is used for the transfer of beam from one machine to another. There are different requirements placed on the time structure, phase space, intensity, and extraction efficiency of the fast beam, depending on its final use. Bubble chambers tend to need 0.5-msec spill with low intensity that should not be disruptive to the slow extraction process because they can be most efficiently mixed with slow spill. Neutrino horns do not have long high-efficiency pulse times and requires spill times of approximately 0.1 msec at very high intensity. Weak-interaction physics often needs high-intensity spills of the order of 1 msec but not as short as 0.1 msec to reduce cosmic-ray background while still not producing too many accidentals. Injection from boosters to larger rings need single turn, very-fast rise and fall-time kickers so that the rings can be efficiently filled.

Fast kickers for extracting beams traditionally have been single-turn or fractional-turn devices that extract a number of rf bunches at one time and can be fired a number of times during one acceleration cycle.[17] They have tended to be rather extravagant and electrically complicated devices so as to ensure flexibility and fast rise time. Actually? for applications simultaneous with slow spill or internal targeting, kickers are not particularly well matched, because they put holes in the circulating-beam structure and consequently in the experimenters beam. The more recent use of beam shaving and enhanced slow spill are more reasonable solutions to the problem of supplying low-intensity fast spikes. The intensity range is much greater and slow spill is not affected.

For high-intensity fast spill at high-energy accelerators, single-turn kickers have the advantage that the beam should cleanly jump the septum with only low losses resulting. At intensities above 10^{13}, the fraction of the beam required in the fast spill will probably become larger and single-turn extraction may be one of the most effective ways to minimize radioactive buildup. The kicker necessary for fast extraction probably does not have to have a rise time shorter than about 0.5 μsec because of the long revolution time (20 μsec) of particles in large rings. Notching of the beam could be done so that losses do not occur during the kicker rise time. Thus the fast kicker is probably a reasonably straightforward device, even though it is acting on particles with momentum in excess of 200 GeV. Of course orbit-bump magnets (either pulsed or slow) and a thin septum are also a necessary part of single-turn extraction or injection.

Fast kickers have become all important in extraction and injection between boosters and large accelerators. Here, ferrite delay-line magnets are used. Rise times of less than 60 nsec have been achieved. Such systems have been very successful and reliable at NAL. A more complicated but similar system is used for transfer of beam from the four ring PS Booster to the PS at CERN.[18,19]

Beam shaving has been developed at CERN[7] over the past few years as the means of extracting from the PS for injection into the SPS. Here it is necessary to peel the beam from the PS in eleven revolutions in order to fill the SPS azimuthally.

Beam shaving is conceptually the next step after fast single-turn extraction and consists of a fast-kicker orbit-bump system, the field level of which can be changed quickly on successive turns. The standard slow bumps and septum are of course part of the system. Reasonably large transverse beam size and thin electrostatic septa to peel the beam out are necessary or efficiencies will not be tolerable. An added bonus of the method is that the phase space injected into the SPS will be considerably reduced from that in the PS.

Though the CERN system is complicated in order to produce uniform filling of the SPS, less-complex applications may easily be found.[8] For instance, beam shaving can be applied to extraction of small fractions of the beam either over a fraction of a turn, a single turn, or a number of turns. Two great advantages of this system over single fast kickers are that the rise time of the shaving magnets does not have to be exceptionally fast, and that, when the beam is not totally extracted, coherent oscillations are not induced from the kicker magnets.

Fast extraction from a resonant machine condition is also possible.[9] The half-integer resonance with its intrinsic stopband seems exceedingly flexible. Small fast quadrupoles can extract or aid in the extraction of large fractions of the beam. Coherent extraction relies on the resonant build up of a betatron oscillation produced by a fast kicker. One other form of fast resonant extraction that should be mentioned involves the third-integer

resonance and an octupole nonlinearity.[21] In this scheme, particles are trapped in stable island regions along the arms of the separatrix as the v value is tuned through the third integer. Three-turn extraction can then be obtained with the use of a fast-kicker orbit bump that lasts over a time interval of three revolutions. It is possible that this type of extraction could be done a number of times in a beam cycle. It would have the advantage of good extraction efficiency because of the isolation of the beams in phase space islands.

Conclusions

Extraction of beams for experimental use will continue to be dominated by the need to reduce beam losses as much as possible. Historically, every particle extracted from a machine first passed a number of times through an internal target before being extracted. Then, with the change to resonant extraction, 20 to 30% of the beam hit the magnetic septum. Now, with the electrostatic septa, 3% of the particles are lost. Possible future advances may involve even further reduction of material in the beam or possibly a way may be found to remove completely the septum material.

Beam-transfer systems from boosters to high-energy machines, from accelerators to storage rings, and beam-abort systems of storage rings probably will continue to use various permutations of fast-kicker and beam-shaving schemes. The more complicated beam-transfer problems will, however, involve rf manipulations necessary for phase locking, or debunching and stacking in longitudinal phase space.

References

1. E.A. Crosbie, et al., IEEE Transactions on Nuclear Science (June, 1973) Vol. NS-20, No. 3, p. 434.
2. Y. Cho, et al., This conference - IXth International Conference on High Energy Accelerators.
3. W. Kubischta, Proc. 8th Int. Conf. on High Energy Accelerators, CERN, 1971, p. 110.
4. M. Bell and W. Kubischta, This conference,
5. L.N. Blumberg, et al., Proc. 7th Int. Conf. on High Energy Accelerators, Yerevon, 1969, p. 615.
6. M. Barton, et al., IEEE Transactions on Nuclear Science (June, 1973) Vol. NS-20, No. 3, p. 226.
7. C. Bovet, et al., IEEE Transactions on Nuclear Science (June, 1973) Vol. NS-20, No. 3, p. 438.
8. L. Blumberg, et al., This conference.
9. R. Andrews, et al., This conference.
10. R. Andrews, et al., IEEE Transactions on Nuclear Science (June, 1969) Vol. NS-16, No. 3, p. 262.
11. R. Allison, et al., Proc. 7th Int. Conf. on High Energy Accelerators, Yerevan, 1969, p. 675.
12. B. McDaniel, Private communication.
13. The 300 GeV Programme, CERN 1050, Jan., 1972.
14. K.H. Kissler, Private communication.
15. R. Yarema and R. Cassel, IEEE Transactions on Nuclear Science (June, 1973) Vol. NS-20, No. 3, p. 414.
16. K. Crebbin, et al., This conference.
17. R. Bossart, et al., Proc. 7th Int. Conf. on High Energy Accelerators, Yerevon, 1969, p. 624.
18. C. Bovet, IEEE Transactions on Nuclear Science (June, 1973) Vol. NS-20, No. 3, p. 221.
19. K. Reich, This conference.
20. H. Bruck and G. LeLeux, This conference.
21. A. VanSteenbergen and M. Month, Proc. 7th Int. Conf. on High Energy Accelerators, Yerevan, 1969, p. 578.

SLOW RESONANCE EXTRACTION OF TWO SIMULTANEOUS BEAMS WITHOUT RF STRUCTURE*

Y. Cho, E. A. Crosbie, L. G. Lewis, C. W. Potts, and L. G. Ratner
Argonne National Laboratory
Argonne, Illinois

Abstract

The installation of a digital phase angle control system for the Zero Gradient Synchrotron (ZGS) magnet power supply firing circuits reduced the low frequency ripple to the point where a magnetic beam spill mode with RF off has become feasible. Orbit warping magnets using feedback from the extracted beam are used to compensate for remaining ripple, and main magnet flattop control is used to move the beam to the $\nu_r = 2/3$ extraction point. To date, a combined extraction efficiency for the two beams of 50% has been achieved. There is 0% RF structure and about 20% of low frequency modulation.

Introduction

The primary experimental areas of the ZGS are supplied from *two* extracted proton beam lines lying 180° apart around the machine circumference as shown in Fig. 1. Under these conditions, it appeared to be very time effective to consider simultaneous extraction to these two areas by using the $\nu_r = 2/3$ resonance extraction scheme. With the $\nu_r = 2/3$ extraction, three separatrices are formed in phase space and beam is extracted into each area every turn and a half around the machine. Since the majority of experiments use counters and spark chambers, their data accumulation rate is sensitive to the time structure of the extracted beam. It was therefore necessary to use magnetic field feedback, rather than RF, to control the beam spill.

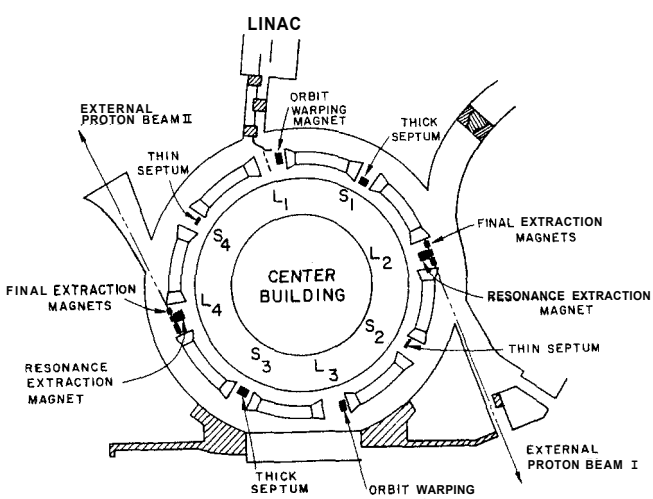


Fig. 1. Layout of the ZGS ring showing extraction system components.

*Work performed under the auspices of the U. S. Atomic Energy Commission.

In Section I we describe the resonance extraction scheme and in Section II the method of beam spill control.

I. Description of the *ZGS* Resonance Extraction

Use of the $\nu_r = 2/3$ resonance to provide simultaneous extraction into the two ZGS external proton beam lines has already been described.[1] At the present time, with the two sextupole magnets located in straight sections L-2 and L-4 (Fig. 1), the locations of the separatrices in the septum magnet straight sections S-2 and S-4 are shown in Fig. 2.

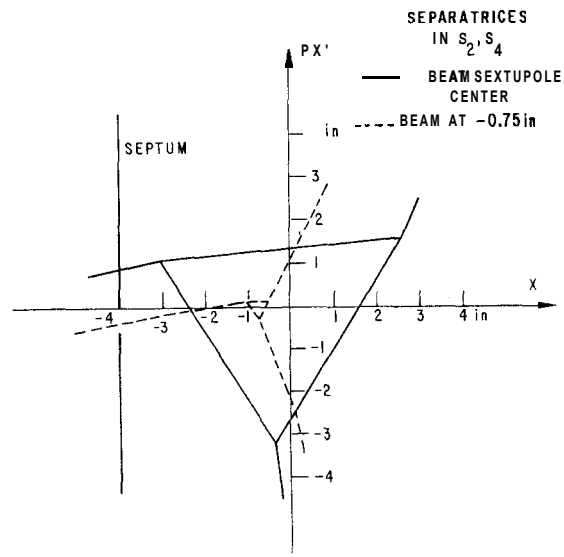


Fig. 2. Phase space plot of extraction in straight sections S-2 and S-4.

Protons move away from the unstable fixed points and are eventually intercepted by the *two* thin septum magnets located on the inside of the straight sections *S-2* and S-4. Those protons which pass close to the septum magnet in either S-2 or S-4 will, after 3/2 turns, find themselves within the magnet apertures in S-4 or *S-2* respectively. There they receive inward kicks to arrive within the apertures of the thick septum magnets located further radially inward in S-1 and *S-3* respectively. The S-1 and *S-3* magnets in turn kick the particles outward into the outside extraction chains located in *L-2* and L-4 respectively.

The beam is extracted slowly by driving the circulating beam radially inward which causes the radial stable phase space to decrease in area. For spills with no RF structure, the RF is turned off and the inward movement of the beam is accomplished by allowing the main magnetic guide field to increase slowly. Feedback from the spilled beam to *two*

warping magnets located in L-1 and L-3 provides fine control and takes out most of the slow structure.

As described in Ref. 1, the sharing ratio of the amount of beam into each proton area can be controlled either by adjusting the relative positions of the two septum magnets in S-2 or S-4 or by adjusting the strengths of the two dipole fields that are a part of the two resonance extraction magnets (REX) in L-2 and L-4. The warping magnets in L-1 and L-3 can also be used to control the share ratio to a limited extent. Difference signals from the spilled beams in the two proton areas may eventually be fed to these magnets to maintain the desired share ratio during the entire extraction time.

We had anticipated that moving the REX magnets from the positions described in Ref. 1 to their present location would increase the extraction efficiency. We have found, however, that the increase in their septum current necessitated by this move has produced sufficiently strong fringe fields, which have increased the effective septum thickness of the magnet from about 0.1 in. to 0.2 in. In addition, the higher temperature gradient across the septum sheet gives rise to radial field components which affect the vertical size of the beam. Our present plans are to correct these fringe fields. This should improve the extraction efficiency from its present peak of 50%.

II. Magnetic Beam Spill Control

The *ZGS* has operated its slow spills since 1963 with extraction from energy loss targets. Appropriate choice of the parameters of the target damping lip allows such a spill to come out with little RF structure. Since the RF can be left on during extraction, a closed-loop spill feedback control is utilized which uses the RF to control the rate the beam impinges on the target. This system is used to establish the rate of spill required by the experimenters and to minimize the structure caused by guide magnet field ripple and nonlinear radial beam distribution.

Since a slow, resonantly-extracted beam is most usable when free of RF structure, we have developed methods of magnetic spill control with RF off.

The ZGS guide magnet power supply is a 12-phase, 50-Hz system. The control elements are excitrons. Theoretically, no frequency components less than 600 Hz should be present. Detailed studies of the guide field ripple showed 50 Hz components that sometimes were as large as ± 1 G out of 19,800. These are probably created by supply transformer unbalances. Due to adjustment limitations on our 1963-vintage phase control system, these 50 Hz errors could not be eliminated. Other frequency components were present above their expected levels.

Originally, we had planned an active filter for the guide magnet power supply system to reduce ripple for magnetic spill control of slow resonant extraction. The 50 Hz components drastically increased the power dissipation requirements for the proposed active ripple filter. It was therefore necessary to improve the guide magnet phase control system. This has been completed with a significant reduction in ripple, as described in companion papers.[2,3]

Even with this improvement, an active ripple filter would require several hundred water-cooled transistors. It would be expensive, take two man-years of effort, and force a two-month shutdown for installation. An inexpensive alternate method using small warping magnets and feedback control was proposed to eliminate spill structure caused by guide field ripple. This method has the additional advantage of compensating for REX magnet field ripple and radial beam distribution nonlinearities.

A system consisting of two small medium-frequency (dc to 2 kHz) magnets, two 3 kW bipolar transistor power amplifiers, and appropriate beam feedback sensors has been built, installed, and successfully operated in the ZGS. These magnets warp the beam orbits at the REX magnets in response to beam spill signals. A more accurate description might be "the rate at which the stable phase is decreased is modulated by these magnets to control spill structure." As shown below, these magnets are not powerful enough to spill the beam by themselves. The low frequency spill rate is set by ramping the guide field magnets. A tandem spill regulation system is used. That is, the low frequency rate is set by spill feedback into the guide magnet phase control system, while structure is regulated by spill feedback to the warping magnets. Each by itself is inadequate, but together they do a rather nice job, as Figs. 3, 4, and 5 demonstrate.

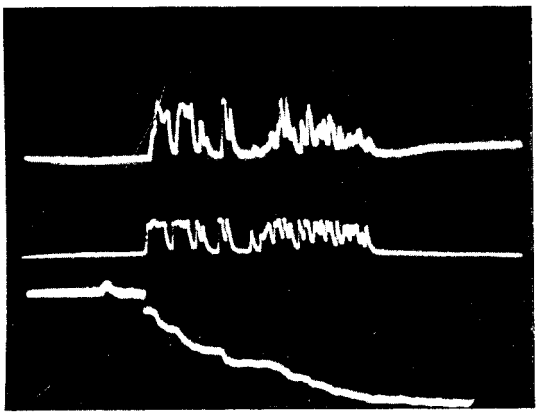


Fig. 3. Open loop spill.

Trace 1: EPB-I ion chamber readout.
Trace 2: EPB-II ion chamber readout.
Trace 3: Ion Q at 1 x 10^{12} protons/cm.

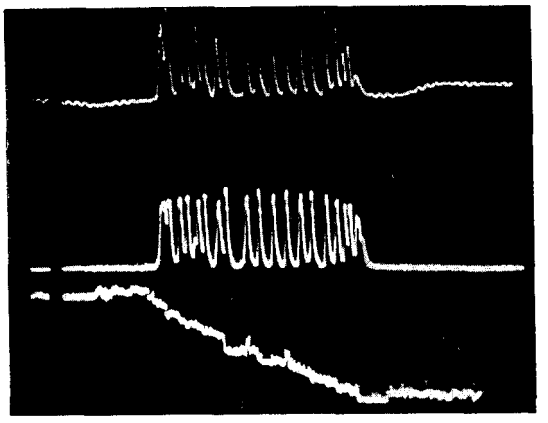


Fig. 4. Guide magnet spill feedback.

Trace 1: EPB-I ion chamber readout.
Trace 2: EPB-II ion chamber readout.
Trace 3: Ion Q at 1 x 10^{12} protons/cm.

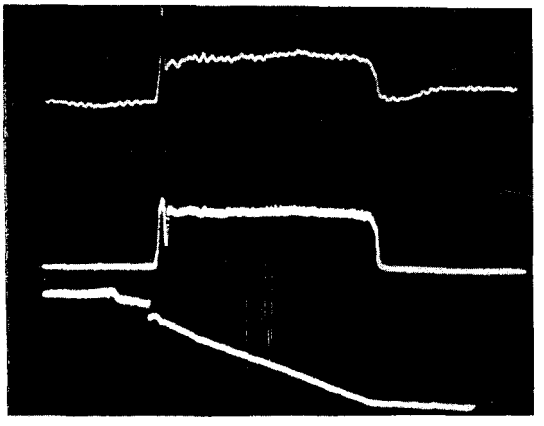


Fig. 5. Tandem spill feedback.

Trace 1: EPB-I ion chamber readout.
Trace 2: EPB-II ion chamber readout.
Trace 3: Ion Q at 1 x 10^{12} protons/cm.

Effect of Guide Field Ripple

It is difficult to appreciate the effect of a small amount of ripple in a weak focusing synchrotron. A few numbers point up the problem.

A 4-inch wide beam in the ZGS can be completely extracted on a 2/3 resonance with a radial movement of 0.7 in. Extracting that beam in 0.7 s gives a rate of beam movement of 1 in./s.

A disturbance modulation $\left(\frac{dE}{dt}\right)$ of ± 0.3 in./s superimposed on a 1 in./s programmed spill movement creates a spill structure of * 30%. This disturbance can be defined as that created by guide field ripple, and the allowable ripple for 30% modulation can be computed. With appropriate ZGS parameters for 12.3 GeV/c operation we have for 30% modulation, an allowed ripple field rate of

$$\frac{dB_r}{dt} = \frac{\nu_r B}{R} \times \frac{dE}{dt} = \frac{(0.7)(19,800)}{1080} \times 0.3 = 3.85 \text{ G/s}.$$

If the ripple has frequency f, the allowed ripple field is

$$B_r = \frac{1}{2\pi f} \frac{dB_r}{dt} = \frac{3.85 \text{ G/s}}{2\pi f} .$$

For 50 Hz, this gives an allowable peak-to-peak ripple of 0.024 G out of 19,800 G. Only ± 0.001 G of the basic 600 Hz ripple of the ZGS would be acceptable. Such small values indicate that a pretty good active filter would be required. The warping magnet fields to compensate for this ripple are not quite so awesome.

Warping Magnets

The radial movement resulting from the 1 G 50 Hz ripple field at 12.3 GeV/c is:

$$\Delta R = \frac{(\Delta B)\, R}{\nu_r B} = \frac{1(1080)}{(0.7)(19,800)} = 0.078 \text{ in.}$$

Two warping magnets located 180 machine degrees from each other and 90° from the REX magnets can produce in-phase warps at each of the REX magnets, which will remove structure from the spill to each of the extracted proton lines. The required warp magnet strengths to compensate for the 0.078 in. movement are:

$$BL = \frac{(B\rho)(2\nu)(AX)\sin\frac{\pi}{2}\nu}{R}$$

$$BL = \frac{(1400)(2x0.7)(0.078)\sin 63^\circ}{1080}$$

$$BL = 0.126 \text{ kG ft}$$

This modest requirement is exceeded by our magnet and amplifier design which produces a dc warp of ± 0.297 in. and a 50 Hz warp of ± 0.101 in. at each REX magnet.

Each of the magnets has a tape-wound, 12-mil Selectron "C" core which has a 6 in. x 6 in. cross section. The half cores are symmetrically cut to have a 5.25 in. air gap when assembled. Thirty-six turn coils are mounted at the pole tips. These are wound out of No. 4 AWG square copper. No special cooling is provided since the rms value of the pulsed currents is only about 25 A. When the coils are connected in series, the magnets have an inductance of about 2 x 10^{-3} H at 60 Hz. The magnets are operated at a peak flux density of 800 G.

Simple "C" magnets such as these have an almost Gaussian flux distribution. Gradients of

154 G/in. can be measured 2 in. from the pole tip. These, of course, combine with the sextupole fields of the REX magnets in an undesirable way. However, the levels are such that they distort the REX fields less than 10%.

Power Amplifier

Each magnet is driven by a *3* kW dc coupled complementary symmetry amplifier. Each side of the amplifier has 24 air-cooled transistors in parallel. Emitter degeneration is used to force the paralleled currents to be equal within * 10%.

The magnet and connecting cable form a load impedance of *0.66* ∠ 72.4° ohms at 50 Hz. The load time constant is about 20 ms. Driving such an inductive load as part of a feedback system presents stability problems. The amplifier is operated with about 30 dB of current feedback so that the phase shift does not build up until the output transistors saturate. This results in a gap flux corner frequency of about 200 Hz.

The power amplifier is gated on only during the spill period of the *ZGS*. Several protective and warning circuits are included in the amplifier. Most are to protect the amplifier and magnets, but two circuits are intended to alert the *ZGS* operator of problems. One of these detects warping magnet current during beam injection and alerts the operator if current is present. The other detects transistor saturation during the beam spill. The presence of saturation implies beam structure, and most likely means the *two* spill rate controls in the tandem system are not matched to each other. A flashing warning light alerts the operator that the rates need adjusting.

The Closed Loop

Figure *6* is a semischematic diagram of the loop. The warping magnet loop is quite conventional. Lead stabilization is provided by a simple network, as shown. As noted before, the current feedback tends to make the magnet load look resistive out to several hundred cycles.

Coupling the beam feedback into the guide magnet power supply is somewhat more complicated. The *ZGS* magnet flattop is smoothed by a closed loop system. The normal operation of this closed-loop system (without spill feedback) compares B to a reference input (usually zero) and the difference is applied to an analog-to-digital converter (ADC). The output of this ADC is gated into the guide magnet phase control system only on *ZGS* flattop. The B comparison amplifier is very heavily filtered with an upper corner frequency at about 20 Hz. This frequency was chosen to be below an existing *MG* set shaft resonance which is at *36* Hz.

In the spill feedback application, the input reference to the $\dot{B}$ comparison amplifier is the output of the spill rate comparison amplifier. This signal consists of $\dot{B} = 0$ commands until spill is desired. At that point, the guide magnet field is ramped to move the beam toward the unstable fixed point. As the beam comes out, spill feedback controls the rate of guide field ramp to regulate the rate of spill. The ZGS programmer can gate in up to three different rate commands during a pulse.

Figure *3* shows the open-loop proton spill. The spill structure is mostly caused by phase control commands attempting to maintain the flattop flat.

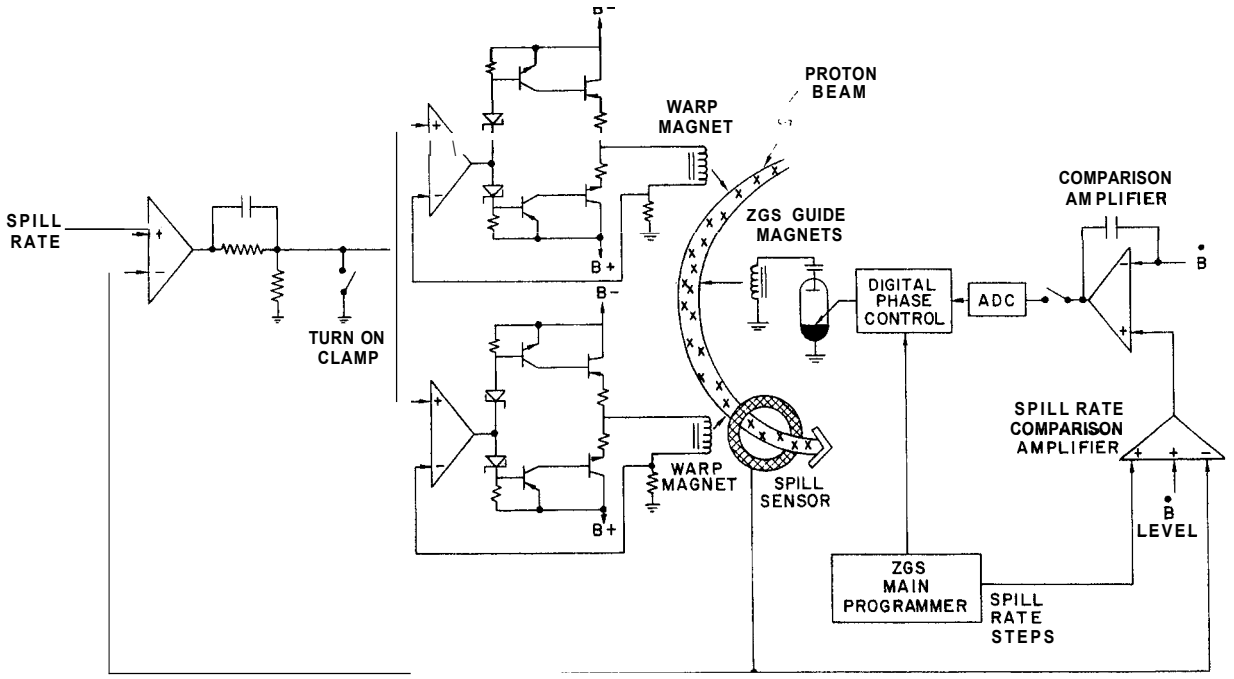


Fig. 6. Spill feedback control system.

Fig. 4 shows the spill down the beam lines with only the guide magnet loop closed. Note the instability caused by the 20 Hz response limit of *the* system. Figure 5 shows the proton spill with both loops closed. The feedback source for spill control was obtained from an ion chamber signal in the EPB-II line. The spike at the beginning is caused by resonant magnet turn-on. The two loops complement each other so well because the frequency response limits are so far apart. The warping magnets can operate more than ten times higher in frequency than the guide magnet systems.

Operating Experience

While we have only operated in a HEP mode for a few days with this system, Figs. 3, 4, and 5 seem *to* speak for themselves as to its success. Despite the apparently good spills of Fig. 5, the HEP experimenters are complaining of troublesome accidental rates between 800 and 1,000 Hz. Since our spill sensors do not show this rate, the feedback loop cannot work to correct it. Further effort must be spent to determine the sensing, cause and cure of this problem. At the present time, these frequencies produce a 50% spill modulation.

Acknowledgements

Quite a few people have been involved with the development *of the* warping magnet system. Our thanks go to M. Faber, R. Zolecki, K. DeVries, R. Lari, T. Quarnstrom, and L. Donley and last, but certainly not least, F. Brumwell.

References

1. E. A. Crosbie, et al., Argonne National Laboratory, Simultaneous Resonance Extraction, IEEE Transactions on Nuclear Science, San Francisco, California, March 5-7, 1973, NS-20 (June 1973) pp. 434-437.

2. L. G. Lewis and A. D. Valente, Argonne National Laboratory, Phasor: A Control Computer Method for Displaying Amplitude and Phase of Ripple Components in the Ring Magnet Voltage, IXth International Conference on High Energy Accelerators, Stanford, California, May 2-7, 1974.

3. M. J. Knott, L. G. Lewis, and H. H. Rabe, Argonne National Laboratory, Digital Control of Rectifier Firing Angles for the Zero Gradient Synchrotron (ZGS) Ring Magnet Power Supply, IXth International Conference on High Energy Accelerators, Stanford, California, May 2-7, 1974.

DISCUSSION

Lee Teng (NAL): How thick is the thin septum?

Crosbie: This is somewhat a matter of controversy at the present time. It was supposed to be on the order of 50 - 60 mils. From indirect measurements on the extracted beam, we know that it is thicker than that. It might effectively be as much as 150 - 200 mils.

EXTRACTION FOR THE MAIN RING AT NAL

R.A. Andrews, H.T. Edwards, H.E. Fisk, F. Hornstra, J.D. McCarthy,
H. Pfeffer, C.H. Rode and J. Walton
National Accelerator Laboratory
Batavia, Illinois

Summary

Significant improvements have been made in the efficiency, duty factor, and flexibility of the NAL Main Accelerator extraction system, consistent with the increasing intensity of the synchrotron and the growing diversity of the experimental program. Currently, a typical extraction mode will include a one-second period of slow extraction punctuated by four higher intensity bursts for bubble chamber use, followed by a high intensity fast terminal spike for neutrino experiments. The extraction efficiency - now some 97% - is such that radioactivity levels in extraction system components are not increasing despite operation of the accelerator at record currents. A modified septum design is expected to lead to further gains. A computer-assisted feedback system has raised the spill duty factor to 70%. Recently, the synchrotron has been operated with a front porch, with two periods of slow extraction, each of one-second duration, at two different energies within the same accelerator cycle.

Introduction

When a slow extracted beam was initially obtained from the Main Accelerator at NAL in September of 1972, the synchrotron was operating at an intensity of less than 10" protons per pulse and only one experimental area was in operation. Under those circumstances, the demands placed upon the extraction system were modest, and a low efficiency spill with a ragged time-structure was tolerable for the time being. Today, however, the accelerator intensity has risen by two orders of magnitude and a rich and diversified experimental program is underway at the three experimental areas simultaneously, each receiving a share of the protons from every acceleration cycle, and the demands on the extraction system have risen correspondingly. It is the purpose of this paper to describe the evolution of the extraction system during this period.

The basic features of the extraction system have been reported previously.[1,2] In brief, half-integral resonant extraction is employed for the slow spill, at a horizontal (extraction-plane) tune of $\nu_x = 39/2$. (Until recently, $\nu_x = 41/2$ was used, but a few months ago, the operating point of the Main Accelerator was lowered by one unit for reasons not associated with extraction.) Prior to extraction, the currents in the Main Accelerator quadrupole busses are adjusted to bring ν_x close to the half-integer. To initiate extraction, a stop-band is created by the excitation of two quadrupoles, *so* situated that by varying their relative currents a rotation of the phase space area of the extracted beam can be effected. The non-linearity required to differentiate between stable and unstable particles and to give adequate growth rate to betatron oscillation amplitude of the particles to be extracted is provided by the intrinsic octupole moment of the Main Accelerator, aided when necessary by a single iron-core octupole of adjustable strength. A proton whose unstable betatron oscillation amplitude has grown sufficiently (2 cm typically) will enter the extraction channel, the initial component of which is an electrostatic septum.[2] Localized orbit bumps are used to adjust the position and angle of the Main Accelerator central trajectory with respect to the extraction channel.

We distinguish three main categories, into which the subsequent discussion is divided, on which our system development efforts have been concentrated. First, the improvement of extraction efficiency has been essential, in order to control the buildup of residual radioactivity in accelerator and extraction system components. Second, a smoothing of the initially ragged time structure of the spill had to be achieved so that experiments utilizing electronic detectors might benefit from increases in accelerator intensity. Third, the various requirements of the three experimental areas had to be satisfied within each beam spill.

Efficiency

Once the various elements of the extraction channel have been carefully aligned with respect to one another and with respect to the beam, the dominant source of losses in the extraction process becomes the first splitting device - the electrostatic septum. The alignment process raised the extraction efficiency above 90% over a year ago; since that time, considerable attention has been given to identifying and correcting septum losses.

The beam splitting surface of the septum consists of a row of vertical tungsten wires having a diameter of 0.002 in. spaced at 0.050 in. intervals. The wires are at ground potential.

Parallel to the plane of the wires, at a distance of 1 cm., a titanium cathode is placed which is charged to a negative high voltage (72 kV at 300 GeV) with respect to the wires. The extraction septum consists of two separate 10 foot units which can be individually positioned or replaced. Within each unit, the wire planes and cathodes are divided into five 2 foot modules. Protons passing between the wire plane and the cathode experience a horizontal deflection of 0.14 mrad, sufficient to enter the gap of a Lambertson magnet 100 feet downstream.

For half-integral resonant extraction, a step size of 1 cm per two turns would imply extraction losses of ~ 1% for ideally fabricated wire septa with our wire thickness. In contrast, a year ago losses were at the 6 - 7%

level. The source of these losses have been studied using two techniques.

At the outset, the origin of extraction inefficiency could not be clearly attributed to any single element of the system. To study the extraction process, a number of remotely operable horizontal and vertical targets were installed in the extraction straight section and external beam line. The first horizontal target is located 0.5 m upstream of the electrostatic septum. The second and third horizontal targets are positioned between the septum and the Lambertson magnets. The fourth horizontal and first vertical targets are located near the downstream end of the long straight section while the fifth horizontal and second vertical targets are situated in the extracted beam line. Ionization chambers are used to detect particles scattered by these targets, and a plot of normalized ionization chamber signal versus target position yields a measure of proton flux as a function of position across the beam. Figure 1 shows a plot of ionization chamber signals as the targets are scanned across the beam. Scattering from targets downstream of the electrostatic septum clearly outline the shadow cast by the septum and from these data effective septum thicknesses were found to be considerably larger, typically a factor of five, than that suggested by wire size alone. Subsequently, mechanical measurements of the septa verified these results, The target scan plots can be used also to estimate the phase space of the extracted beam. Typical results give areas of 0.14 mm - mr vertically and 0.25 mm - mr horizontally. The phase space measured 1000 meters downstream gives numbers of the order of three times larger and to date the discrepancy is not well understood.

The mechanical technique for measuring septa thickness is illustrated in Figure 2. A wire is stretched from one end of the septum to the other, and electrical contact is maintained with the septum wires as the position of the two ends of the stretched wire are moved in the direction perpendicular to the plane of the septum wires. A graph of the position of one end of the stretched wire versus the other while electrical contact is preserved can then be interpreted to yield the septum thickness. In Figure 3, we show results of measurements by this method before and after straightening a crooked septum (0.030 inch thick) which had exhibited a poor extraction efficiency. By external welding on the septum vacuum skin, to introduce compensating stress, for seam welds, the effective thickness of the septum was reduced to 0.005 ± 0.003 in. A modified wire septum constructed on a single 10 ft. wire frame promises to be straighter, to be constructed more rapidly, and to automatically retract broken wires without the necessity of accelerator shutdown.

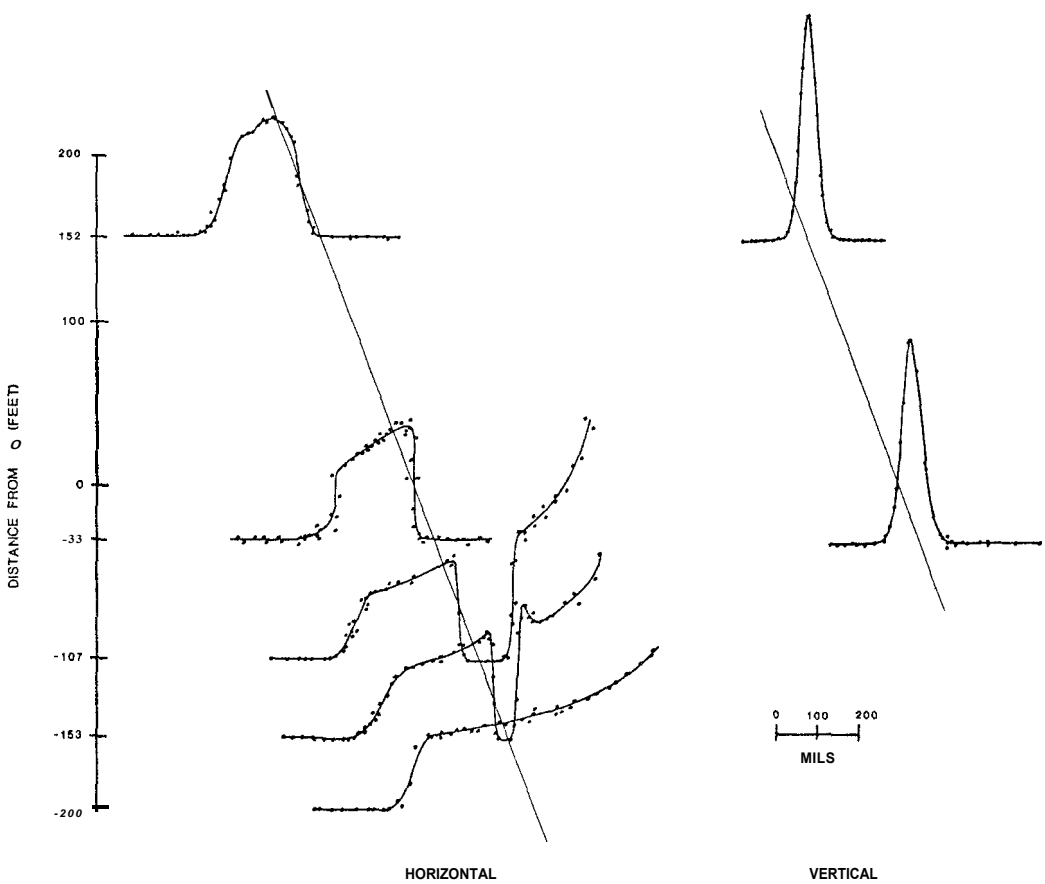


Figure 1 **EXTRACTED BEAM PROFILE**

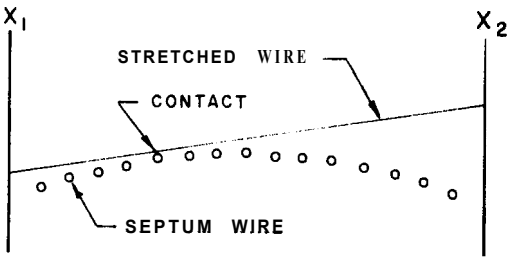


Figure 2
Diagram of Method Used to Measure Effective Thickness of Septa

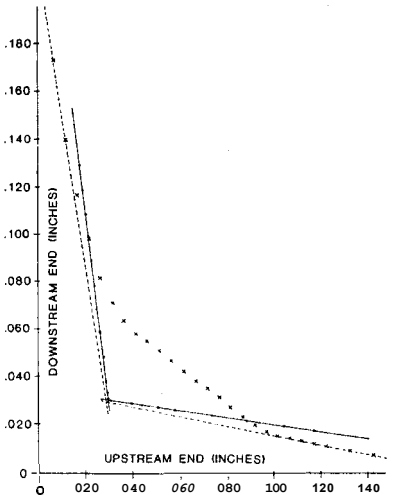


Figure 3
Septum Thickness Measurements. Data before straightening are represented by curve with the points designated x.

Present extraction losses of approximately 3% are sufficiently low that excessive radioactivity buildup in system components is not anticipated at average accelerator intensities close to the 10^{13} protons per pulse.

Absolute calibration of the losses has not been developed to date. In one sense the residual radioactivity is the only meaningful observable. As long as the diagnostic equipment give signals which indicate how to improve the efficiency absolute calibrations have not been necessary, and it is quite possible the extraction efficiency is higher than 97%.

It is clear, however, that as the accelerator intensity rises toward its design goal of 5×10^{13} protons per pulse, corresponding improvements in extraction efficiency must be achieved, and our major effort in this direction is focussed on the septum designs discussed above.

It should be mentioned that, twice in the past three months, the extraction septum has failed catastrophically where all the wires over the first two to four feet of the upstream module have broken. It is believed thermal heating from short duration high losses on the wires is responsible. These failures point out the need to understand high temperature behavior of the septa wires and also show the necessity for very clean fast or coherent extraction in which no major portion of the beam hits the wires.

Duty Factor

The time structure of the slow extracted beam arises from two sources; rather low frequency current ripple, principally in the quadrupole magnets which leads to tune variation, and the 53 MHz radio frequency bunch structure of the beam. To date, the radio frequency structure has not been a serious disadvantage for experimenters, and a number of experiments have found it useful for timing purposes. Current ripple in the main ring power supply system at 360 Hz and below, however, requires compensation. Higher harmonics are reduced to negligable proportion by the active filters on the main quadrupole supplies.[3] For the present, we have chosen to define the duty factor, F, by

$$F = \frac{\left[\int_0^T I(t)dt\right]^2}{T\int_0^T I^2(t)dt}$$

where T is the duration of the slow spill, I (t) is the instantaneous extracted beam current as a function of time t, and the radio frequency structure is ignored. This definition of F is suggested by the expression for the chance coincidence rate in a two counter telescope.

To counteract the tune variation brought about by ripple, two air-core quadrupoles have been placed in the accelerator. Their excitation currents are derived from a combination of signals which have been found to be effective in improving the duty factor. Each is driven by a current proportional to the ripple compenent of field in neighboring main ring quadrupoles. The two so called "bucker" quadrupoles are far from each other in the ring so that their signal sources sample potentially different ripple contributions to the overall tune variations. (The accelerator magnet circuit forms a rather complex delay line, so that ripple terms in the current may be non-uniform around the machine.)

In addition, one of these air-core quadrupoles receives an excitation current derived from the actual beam spill. A detector composed of a scintillator and light sensitive diode is placed so as to intercept spray from the extracted beam. The signal from this detector is digitized and sampled by a PDP-8 computer at a rate of 8 x 720 Hz. A learning algorithm, similar in principle to that used in the Main Accelerator power supply control system[4], determines the appropriate correction signal which is delivered to the bucker quadrupole advanced in time on subsequent cycles by an amount corresponding to the time delay between a perturbation in the tune and its modulation of the spill (about 1/2 ms). A calculation of the duty factor is made in the computer and displayed to the operators.

The improvement in duty factor effected by the bucker quadrupoles is shown in Figure 4. Figure 4a shows typical ripple signals on the main quadrupole (top) and bend (bottom) busses and Figure 4b the associated spill if no correction signal is sent to the buckers. In Figure 4c, the buckers are receiving their excitation from the local ripple field in the main quadrupole ($\int \dot{B} dt$ signal), while in Figure 4d the computer processed spill signal alone is used. In Figure 4e both the integrated B signal and computer processed spill signals are used to drive the buckers. In the last case, a duty factor of about 70% has been achieved in contrast with the 15% or so of Figure 4b.

Clearly, many avenues for duty factor improvements remain to be explored. For example, no compensation for ripple on the dipole busses has been introduced as yet, and no real time spill feed back tried. Recognizing that subharmonics of the twelve-phase power supplies must arise from phase unbalance, the 360 Hz and lower components may be removed by power supply improvements, such as trying to induce ripple on the regulating supplies to compensate for the over all ripple and the addition of phase balance compensating circuits in the individual unregulated supplies. Finally, manipulations of the accelerated beam such as spreading the momentum with the r.f. may make extraction less sensitive to power supply ripple.

Extraction Modes

Currently, four extraction modes are in use, combined during each accelerator cycle in a way that reflects the needs of the experimental program.

Slow Spill

Normally, most of the beam is extracted by the slow, resonant, process. The regulation of the spill insofar as its gross time structure is concerned (that is, exclusive of the higher frequency structure discussed in connection with duty factor above) is performed by a feedback system consisting of a MAC-16 mini-computer and an iron-core quadrupole. The intensity of the beam circulating in the accelerator is digitized and sent to the computer. The desired dependence of circulating beam on time throughout the spill is stored in memory; the computer compares the actual

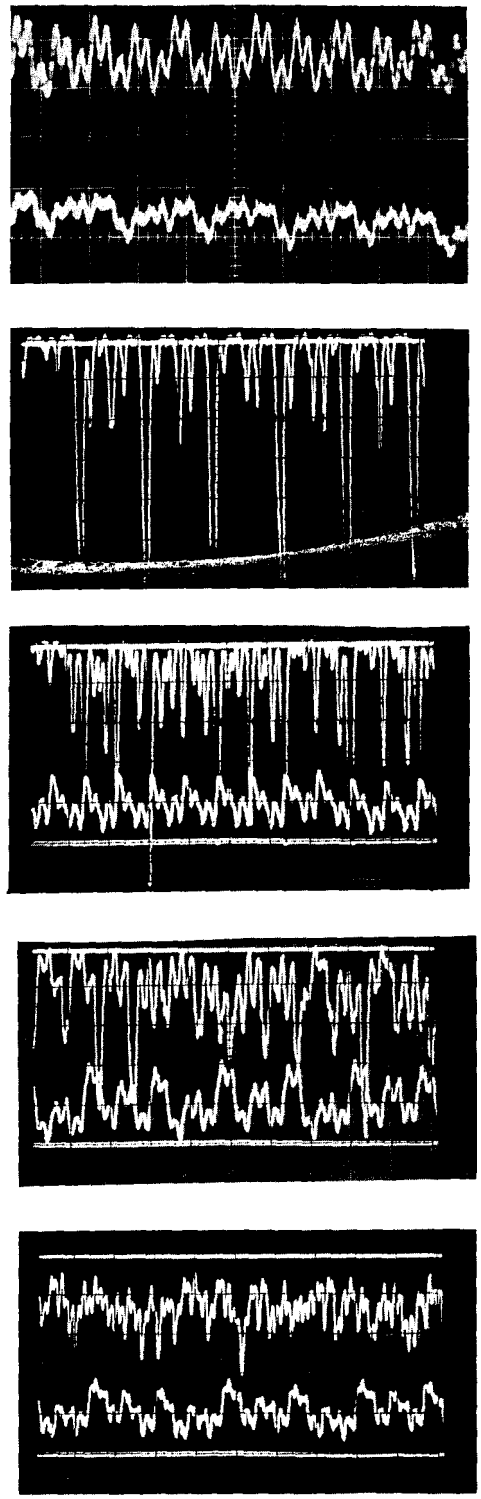


Figure 4
Magnet Ripple, Spill Structure & Bucker Drive Signals
(10 ms/div)
4a Top-Main Ring Quadrupole Bus 1 div = 0.8×10^{-4}
Bottom-Main Ring Bend Bus
4b Uncompensated Spill
4c through 4e; Top trace is the output of the diode spill monitor and bottom trace is the bucker drive input signal.
See text for details.

intensity with that desired and delivers a correction signal to the quadrupole excitation circuit. A learning algorithm similar to that employed for duty factor improvement is also used here. The use of the computer allows for rather complicated time structures like front porch operation and enhanced spill.

Enhanced Spill

The 30 inch bubble chamber is capable of expansion every quarter of a second during a beam pulse. The normal slow spill intensity does not provide sufficient flux for the bubble chamber when exposures with secondary particles, such as negative pions, are being made. In order to provide spill rate enhancement during the chamber's sensitive period, an air core quadrupole is driven with a half-wavelength sinusoidal current pulse. This causes a shrinkage of the stable region in phase space for a short time, thus forcing a number of particles beyond the separatrix and causing them to be extracted. Depending on bubble chamber requirements, typically 10^{10} to 5×10^{11} particles are extracted in each burst, though this method has been used to provide up to 2×10^{12} protons in its 1 msec spike. (See Figure 5.) Pulsed beam line magnets are being constructed to avoid sending this intensified spill to laboratories wishing only slow spill.

The computer maintaining the slow spill rate need only be informed of the times at which spill enhancement occurs. After each such event, it renormalizes its model of the circulating beam intensity to the current remaining after the burst, and continues as before.

Fast Extraction

Fast extraction represents one of two ways to achieve a fast spill of the beam remaining in the synchrotron at the end of the slow extraction period. The fast spill, extracted in one turn, is intended primarily for use with the bubble chamber and neutrino focusing horn (125 μs pulse width). The fast spill is accomplished by using pulsed orbit bumps to place the beam near but not on the wire septum a few ms before the ferrite kicker is fired. The ferrite kicker gives the beam a large amplitude betatron oscillation and causes it to jump across the septum which is located half way around the ring from the kicker. To achieve the 0.5 ps rise time and 20.5 μs duration of the ferrite magnet field a lumped element delay line charged to 50 kV is discharged into a matched 12 ohm load consisting of ferrite magnets and terminating resistors. A picture of the kicker is shown in Figure 6.

Coherent Extraction

If a spill of duration somewhat longer than 20 ps, but still fast, is desired the beam is coherently extracted. As in the enhanced spill described above an air core quadrupole is pulsed to shrink the stable area of phase space while at the same time the ferrite kicker and orbit bumps referred to above are pulsed at a magnetic field reduced from the single turn case. The beam is thus perturbed coherently in phase space so that it starts to come out after several turns and proceeds to spill on every other turn until all the beam is expelled. Figure 7 shows an example of the integrated spill and extraction SEM intensity for a beam which has been coherently extracted in 200 ps,

Front Porch

The Proton and Neutrino experimental areas can receive proton beams up to 500 GeV. However, the Meson area is limited, by design, to 300 GeV operation. For this reason and for the potential advantages of sending two energies to the proton laboratory a front porch test has been completed in which the front porch and flat top operated at 200 and 300 GeV, respectively. For both levels the beam was spilled with the MAC 16 computer feedback discussed in the slow spill section above. Each of the two spills had a duration of one second with the ripple bucker magnet working over each spill duration (See Figure 8.) Many devices in the external beam lines including the extraction electrostatic septum were ramped. The front porch test showed that this mode of operation was reasonable and that the relative intensities of the two energy extracted beams could be varied over a range of about 5 to 1.

Conclusion

The NAL Main Ring half integer resonant extraction system has operated satisfactorily over the past year with steadily improving performance. The extraction efficiency and duty factor are 97% and 70%, respectively. A front porch test was concluded with no difficulties and suggests it may be a useful way to run as the machine achieves higher energies.

References

1. H.T. Edwards, W.W. Lee, J.D. McCarthy, S. Ohnuma, and L.C. Teng, IEEE Transactions on Nuclear Science (June, 1973) NS-20, 3, p. 424 (1973).

2. C.H. Rode, R.A. Andrews, A.W. Maschke, and R.M. Mobley, IEEE Transactions on Nuclear Science NS-18-3, 984 (1971).

3. R.J. Yarema, R.L. Cassel, IEEE Transactions on Nuclear Science NS-20-3, p. 414 (1973).

4. R. Cassel, LEEE Transactions on Nuclear Science NS-20-3, p. 355 (1973).

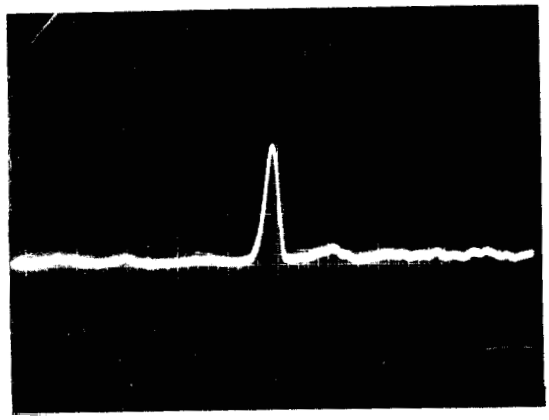


Figure 5a
Typical Enhanced Spill
(2ms/div)

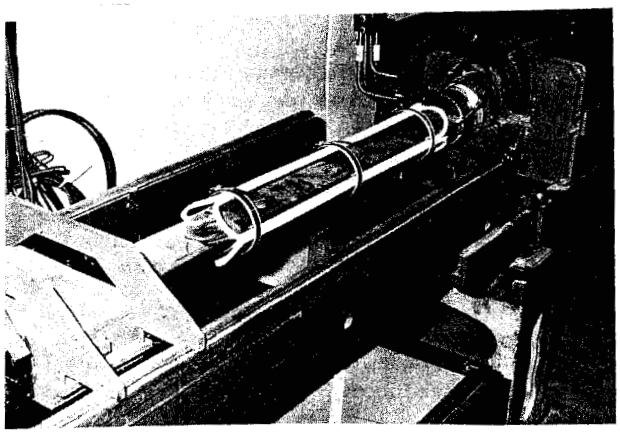


Figure 5b
Air Core Quadrupole Used
for Enhanced and Coherent Spill

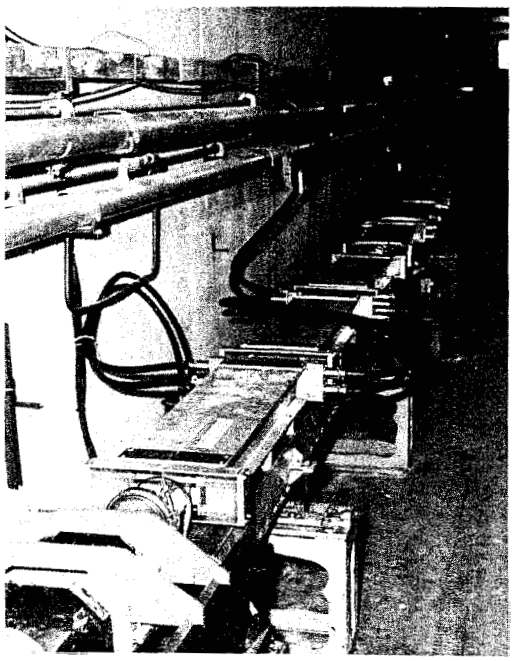


Figure 6
Main Ring One Turn
Extraction Ferrite Pulsed Magnet

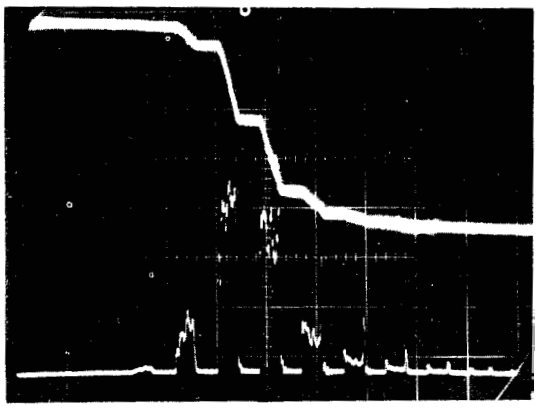


Figure 7
Coherent Spill (50 μs/div)

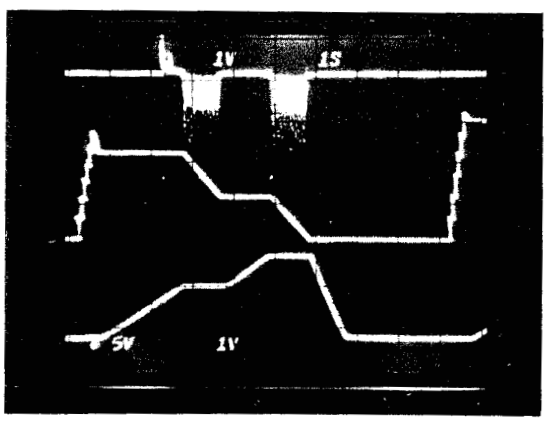


Figure 8
Front Porch
Top trace is the spill; middle trace is the main ring intensity; bottom trace is the magnet ramp.

BNL FAST SHAVING EXTRACTION SYSTEM*

L. Blumberg, G. Bagley, G. Bennett, J. Claus, J. Curtiss, R. Frankel,
H. Hsieh, J. Keane, G. Levine, L. Repeta, J. Schuchman, A. Soukas
Brookhaven National Laboratory
Upton, New York

Summary

Design and performance of a recently commissioned fast extraction system to serve the requirements of the bubble chamber programs at the AGS are discussed. Several of the major components are described along with the diagnostic instrumentation and system performance. Extraction of various fractions of the internal beam, including total extraction in an essentially single-turn mode, has been accomplished with the AGS beam either bunched or debunched. The expected extraction efficiency, ~ 95%, has been observed and transport losses in the 258 m, 10-cm aperture external beam are ≤ 1 %.

I. Shaving Extraction Method

In a previous paper,[1] we presented the orbit calculations, configuration and component parameters of the extraction system. A similar system has been developed at CERN[2] for extraction from the PS. Briefly, the method consists of producing a rapid, local orbit deformation at the azimuth of a thin septum magnet in straight section E10. The fraction of beam displaced across the septum is deflected into the aperture of a septum ejector magnet at straight section H10, approximately 2¼ betatron wavelengths (λ_β) from E10. The rapid orbit deformation is produced by two full aperture, single-turn, ferrite core kicker magnets located in straight sections C15 and E15 with a separation of approximately 1½ λ_β. In the fractional extraction mode, the kickers are powered by a half sinusoid current waveform of 2.5 μs duration. For full extraction, the waveform duration is ~ 6 μs with amplitude of ~ 8000 A. At 5000 A in the kickers, and at typical extraction momentum 28.7 GeV/c, the measured deflection at E10 is 1.4 cm, which is adequate for complete displacement of a 1.3 cm wide[3] AGS bunch across the 0.3 mm E10 septum. A 1.0 mrad deflection at E10, provided by a current pulse of 3000 A peak and 200 μs duration in the single-turn magnet deflects the shaved fraction across the 2.25 mm H10 ejector septum with a measured separation between circulating and shaved beam of 7.6 mm, in good agreement with calculations. The H10 ejector, also a single turn magnet, provides a 1.5 ms current pulse of 21,000 A peak, and deflects the beam by 22 mrad into the external channel for the 7-ft bubble chamber neutrino beam. The E10 and H10 septa are fixed at mean radial positions relative to the AGS central orbit of 4.6 and 5.6 cm respectively, during the entire accelerating cycle; slower orbit deformations of 9 ms duration in a 1/2 λ_β configuration centered at the septa are energized prior to extraction and provide measured displacements of 3.95 and 3.7 cm at E10 and H10 respectively, for a 1000 A peak current through backleg windings on selected AGS magnets. We have determined that the septa are not machine apertures at injection energy, even for intensities up to 9 x 10^{12} protons/pulse.

Another operating mode, presently being commissioned, involves a polarity reversal of the H10 magnet and deflection of the shaved beam by -3 mrad, back into the AGS aperture, for extraction 3/4 λ_β downstream at I10 for the 80-in. bubble chamber. The I10 ejector magnet, originally used for single-bunch extraction,[4] has been reduced in septum thickness to 2.0 cm and a backleg winding 1/2 λ_β orbit deformation has been deployed in the I superperiod for the present application. In this mode, we will extract only ~ 2% of the 6 × 10^{12} p/p circulating beam; the system is capable of four extractions per second at 200 ms intervals. We have achieved the required spill duration of ≤ 1.5 μs imposed by the present pulse duration of the rf beam separator for the 80-in. chamber. Also, we have extracted the beam both during the acceleration and flat top part of the AGS cycle.

II. Extraction Components

Kicker Power Supply

For the fractional shaving mode, a deuterium thyratron switches a 0.2 μF capacitor charged to 30 kV, generating a 5 kA peak pulse with 2.5 μs base. In the full extraction mode, four thyratrons are triggered, each switching a 0.2 μF capacitor at 30 kV onto the common load. Two thyratrons are triggered initially; 0.6 μs later, the other two are triggered. The resulting pulse has an 8 kA amplitude and 0.5 μs rise time with 6 μs base. This triggering method produces an optimum waveshape for the given constants of cable and magnet.

Ejector Power Supply

The H10 magnet supply consists of an energy discharge system in which magnet inductance and power supply capacitance oscillate with a period of 3 ms. The stored energy is 5500 J and the peak current is 21.5 kA at 800 V. The power supply is completely solid state, featuring water cooled SCR's (thyristors) and silicon rectifiers. The charging supply is a three phase, constant current type utilizing resonant monocyclic networks. This system eliminates the need for a lossy series charging resistor.

Ejector Magnet

The ejector magnet, located at the H10 straight section, has been designed to serve two purposes. The magnet assembly consists of two segments; the length ratio is one-third for the upstream segment and two-thirds for the downstream segment. With a current of 21.5 kA flowing in the same direction in both segments, the beam is deflected 22 milliradians out of the AGS, aiming toward the 7 ft. chamber. With a current of 8 kA flowing in the opposite direction in the downstream segment, the beam is displaced across a thick septum (20 mm) at the I10 straight section. A further kick by the I10 ejector magnet causes the beam to exit from the AGS aiming toward the 80-in. bubble chamber.

* Work performed under the auspices of the U.S. Atomic Energy Commission.

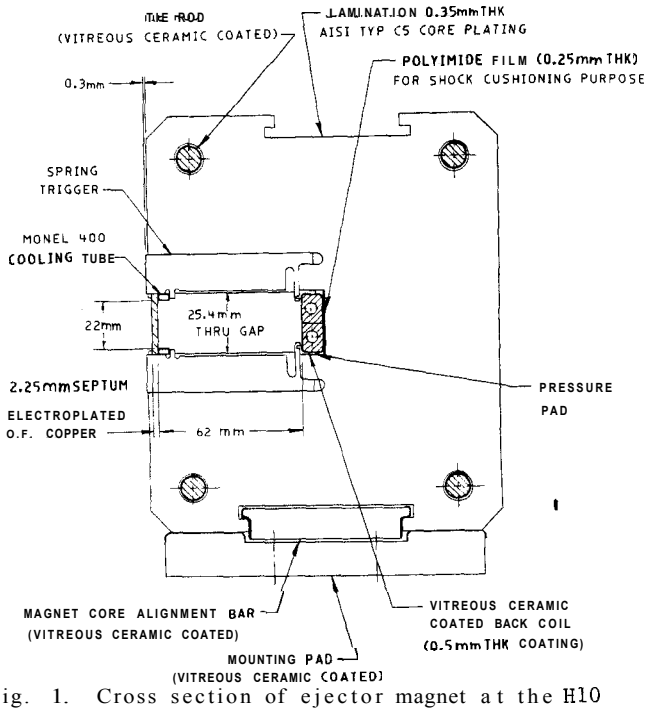


Fig. 1. Cross section of ejector magnet at the H10 straight section.

The cross section of the magnet is shown in Fig. 1. The septum is of copper 2.25 mm thick. The nominal design current is 21.5 kA at induction of 1.05 tesla in the gap. Thermal heating of this septum is rather low due to the short pulse width (1.5 ms). However, the mechanical stress due to magnetic pressure is rather severe. The septum is edge cooled by attaching two monel 400 rectangular tubes at the top and bottom of the septum. The resistance ratio of each tube to septun is only in the order of 0.27%; this results in nearly uniform current density in the septum. The septum is very carefully hand fitted into the magnet gap, so that the clearance between the septum and core can be kept at 0.025 mm. The laminations are made of intermediate silicone steel, 0.35 mm thick. The end plate is 31 mm thick, made of welded laminations. The laminations are held together by 4 ceramic insulated tie rods. The tightening torque is kept as low as possible (0.1 kG-m in our case). The stray field 6 mm from the middle of the septum was found to be 0.08% of the central internal field; 6 mm from the end of the septum the value was 1.4%.

III. External Optics

The design of the beam transport was dictated largely by the presence of two superconducting dipoles[6] at the 8° bend point located ~ 96 m from the ejector magnet and downstream of a 4¼° bend with conventional magnets as shown in Fig. 2. The superconducting dipoles are 1.83 m long with a 7 cm ID vacuum pipe; the additional length of the dewar and vacuum chamber increased the length of the vacuum pipe to 2.62 m. Sagitta in the magnet accounted for 3.2 cm of the aperture. Calculations' indicate that as few as ~ 3 X 10^8 hadrons/cm^2/AGS cycle impinging on the Nb-Ti superconducting ribbon might cause the critical temperature to be exceeded and the magnet to revert to normal conductivity. It was therefore necessary to provide a beam of small horizontal size at this point with stability against momentum changes or variations in strength of the 4¼° bend. We accomplished this by designing an achromatic system giving momentum recombination at the 8°; the five quadrupoles Q3 through Q7, between the 4¼° and 8°, powered in series accomplish this objective. In addition, protective collimation upstream of the 8° bend was provided at a betatron phase shift of 180° at positions U5 and U12 in Fig. 2 to remove halo which might quench the superconductor. Antiscattering collimators were also provided at U170 and U259. The expected collimator images have been observed on scintillating screens upstream of the magnet, and the expected beam size there, 9 mm horizontal X 26 mm vertical, based on full extraction emittances of E_H = 2.42 π mm-mrad and E_V = 1.86 π mm-mrad, have been qualitatively confirmed.

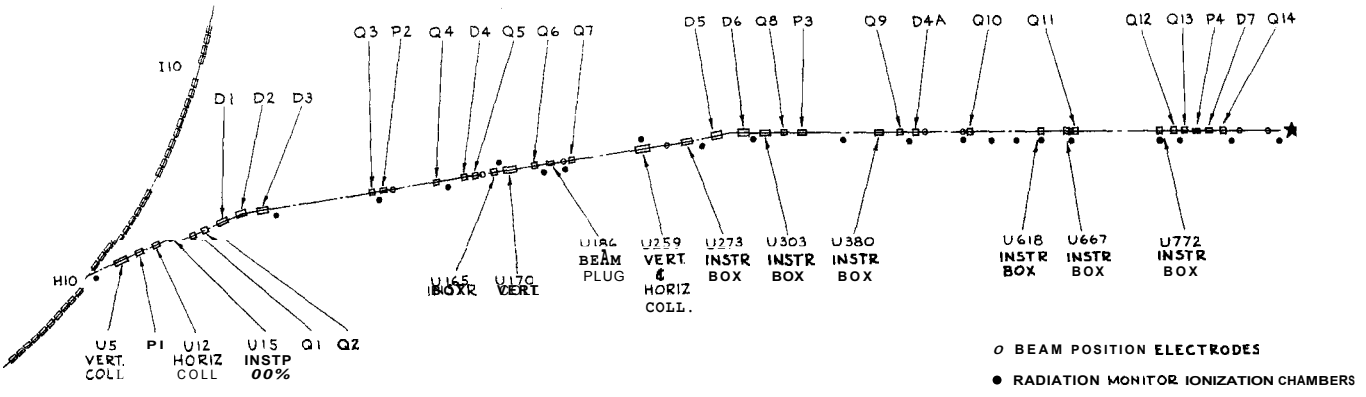


Fig. 2. Plan view of external beam line from ejector magnet to neutrino production target for 7-ft bubble chamber.

The transport downstream of the 8° is intended to provide a minimum spot size at the 5 mm dia. X 45.7 cm long sapphire production target. Qualitative observation on a BeO screen indicate that we have achieved the expected 1.7 mm horizontal X 1.2 mm vertical spot, which is minimum size for the given target length and emittances.

IV. Diagnostic Instrumentation

Instrumentation was designed to measure beam intensity, position and spatial distribution. All signals are presented as quasistatic analog levels at the computer interface. No electronic components are located within the primary radiation shield. Intensity is measured by current transformers at six locations. These consists of tape wound permalloy cores with n = 100 turn secondaries. The signal is fed via coaxial cable to an integrator/peak reader (Fig. 3). The integrators have an output calibration of

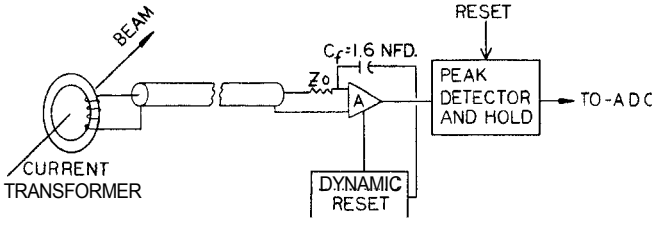


Fig. 3. Schematic diagram of beam current transformer and integrator.

$$Q/V = nC_f/1.6 \times 10^{-19} = 10^{12} \text{ protons/volt.} \quad (1)$$

The integrator incorporates a dynamic reset circuit which prevents runaway drift due to low source impedance but is slow enough (500 μs) to have a negligible effect over the 3 μs extraction interval. Bench calibration using a pulser or capacitor discharge source and a dielectric loaded coaxial fixture to minimize reflections showed less than 1% departure from the theoretical value in Eq. (1). Another calibration compared the integrator output with the beam charge determined from ^{11}C activation of polyethylene foils. This also agreed with the theoretical calibration to within the ± 4.6% uncertainty in the ^{11}C production cross section.[7] A current transformer with a 24 turn secondary has also been used to observe the temporal distribution of the beam (see Fig. 7 below).

Beam position is measured by insulated plates and split transverse ion chambers (STIC). Insulated plates in the AGS ring are situated in the shadows of the extraction magnet septa. The plates are charge sources by virtue of the knock-on electrons ejected by the proton beam. The efficiency is about 10%, i.e. one electron per 10 incident protons. The signal is transported via coaxial cable to integrators similar to those for current transformers; however, the peak detector and dynamic reset circuits are omitted because the source impedance is large. The plates are used to optimize extraction magnet position and skew-angle. Insulated plates are also located upstream of collimator jaws in the external transport, but suffer in this application due to ion collection in the rough vacuum (10^{-3} to 10^{-2} T). The residual gas ionization is exploited in the STIC (Fig. 4). The ions are propelled along field lines transverse to the beam axis to triangular collection electrodes. For uniform ionization density, the relative signal strength is proportional to beam position. The beam position is given by D·W/2, where W is the effective width of the electrodes and D is the normalized difference in integrated signals, (A-B)/(A+B).

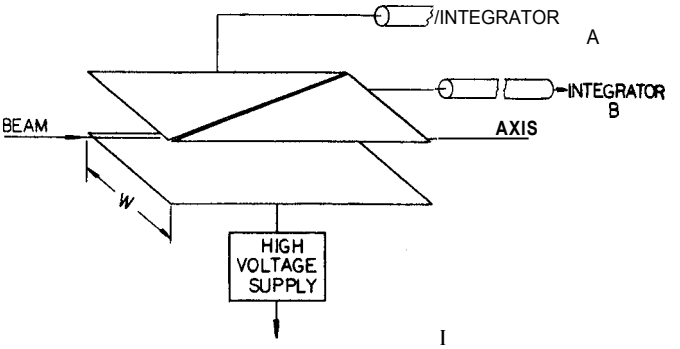


Fig. 4. Sketch of split transverse ion chamber (STIC).

Spatial distribution is provided by closed circuit TV viewing scintillating screens of "Radelin" (a fluoroscopy screen from U.S. Randium Corp.) or beryllium oxide, and by multiwire profile monitors. The usefulness of the screens is limited since they are easily damaged by the beam and optical and electronic components of the cameras suffer radiation damage. The profile monitors consist of 16 Al strips, 0.6 mm thick and 5 mm center-to-center spacing, attached to a rotatable frame. A 0.05 mm Al bias electrode is included upstream and downstream of the strips to comprise 16 parallel strip ionization chambers. Screens and profile monitors are mounted on remotely controlled actuators and are removed from the beam when not required. Future designs of the profile monitor will use thinner electrodes and bias foils. The charge from each electrode is stored on the coaxial signal cable which sees > 10^9 Ω impedance at the FET multiplex switch at the computer interface. In the "on" state, each switch FET has < 100 Ω resistance and the charge from each cable is sequentially transferred to an integrator and ADC. The read time per channel is 75 μs. The integrator gain is remotely varied over a 36:1 range by means of a switchable integrating capacitor. Typical beam profile displays are shown in Fig. 5.

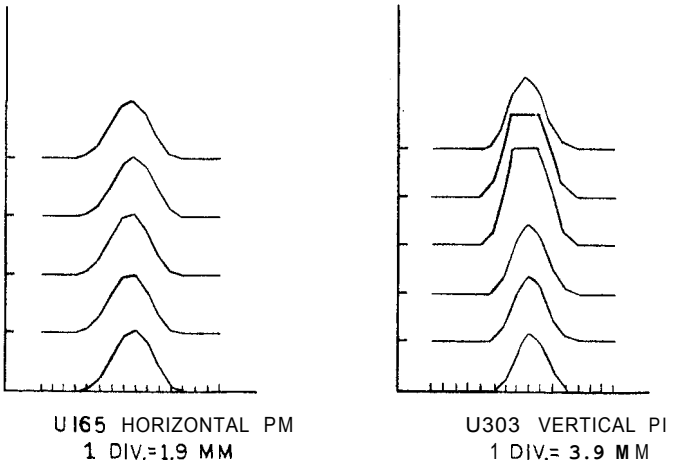


Fig. 5. Typical beam profile monitor displays for successive machine cycles. The profiles at right show saturation at low values for the remotely switched integrating capacitor.

We have also deployed 22 ionization chambers along the beam line to measure the longitudinal distribution of beam loss. The associated electronics include discriminators and alarm circuits which activate interlocks to turn the beam off should excessive losses occur. An illustration of the computer-generated loss pattern from these detectors is given in Fig. 6. The readout and display utilizes an amplifier and FET multiplex switch similar to the profile monitor circuit. The data readout and transfer is accomplished by a single-coax digital system, Datacon 11, controlled by a PDP-8E computer interfaced to the AGS control room PDP-10 computer. The system is described elsewhere.'

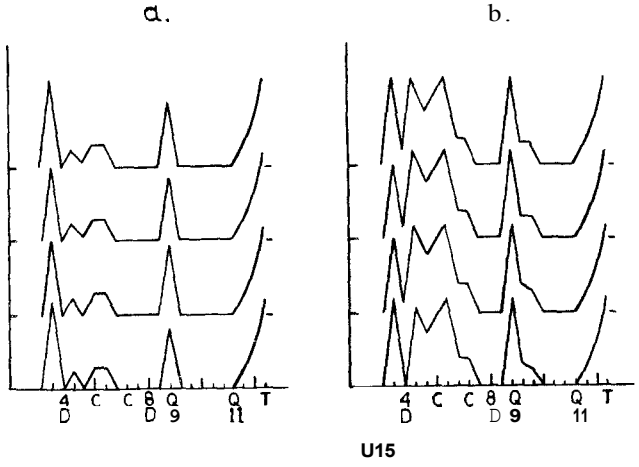


Fig. 6. Computer generated display of radiation monitor signals along the beam line. The ejector magnet is at the left, and the production target, T, at the right of each abscissa. a - Beam tuned for minimum loss. b - Scintillation screen (— 72 mg/cm^2) inserted at U15.

V. Beam Performance

Extraction efficiency for the full extraction mode was measured by comparing the internal AGS "pick-up" electrode beam monitor to an external current transformer, and a monitor foil using carbon-eleven activation. During the calibration run, the measured efficiency was only 85%; however, ~ 90% is indicated by the current transformer at a circulating beam intensity of ~ 5 X 10^{12} when the beam is well tuned, and ~ 95% is observed at lower circulating beams of ~ 2 X 10^{12} p/p. Assuming that three AGS bunches are shaved by the E10 septum due to the finite rise time of the beam kicker pulse, the expected' theoretical efficiency is ~ 98%. Indirect evidence from bunch amplitudes from current transformer signals indicate an efficiency of 96%. Thus, the measurements are well within the ± 5% uncertainty in calibration of the internal beam monitor.[••]

Transport efficiency was measured by comparing current transformers and foil calibrations at the upstream and downstream end of the beam. The result under optimum conditions was 100 +0/-1%. Note that for this case, the coil activation results do not suffer from the ± 4% absolute uncertainty in the ^{11}C activation cross section.

The observed spill duration fur total and fractional extraction in a bunched and unbunched mode were observed on an external current transformer and is shown in Fig. 7. For the full extraction case, it is seen that a fraction of the first bunch was shaved by the E10 septum; part of the remainder was extracted on the second turn. For the fractional extraction cases illustrated, the internal beam was only ~ 2 X 10^{12} p/p and we extracted about 25% of the beam. The spill duration for smaller fractions will be correspondingly less.

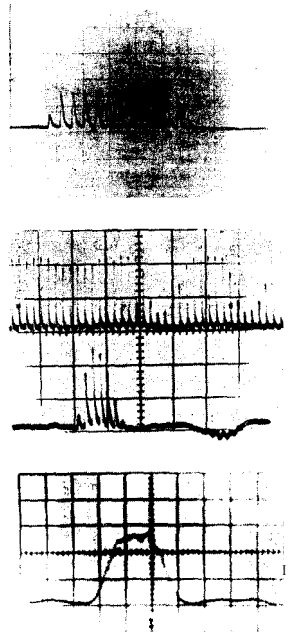


Fig. 7. Top photo - Oscillogram of external beam current transformer signal-full extraction mode, bunched beam (0.5 μsec/div). Middle photo - Fractional extraction mode, bunched beam. Upper trace shows AGS circulating beam intensity during extraction process. Lower trace shows external current transformer signal (1 μsec/div). Bottom photo - Current transformer oscillogram for fractional extraction mode, debunched beam (0.5 μsec/div).

The beam has been successfully utilized for both bubble chamber and spark chamber neutrino experiments. In these applications, position stability has been of importance for optimum neutrino production as well as to minimize neutron and muon background resulting from transport losses. We have noted that the position variation, ΔX, at an observation station — 14 m from the ejection magnet for a change, Δr, in the radial position of the internal beam is $\Delta X/\Delta r \approx 6.4$ mm/mm. The corresponding sensitivity at the production target is $(\Delta X)_{targ}/\Delta r = 2.2$ mm/mm. Thus, a radial shift Δr = 1 mm will move the spot at the production target by more than its diameter. We therefore had to optimize the gain of the AGS radial position servo, and have achieved long-term stability of $\Delta r \sim 0.1$ mm. Similarly, we have maintained the momentum drift at extraction time to 0.1% by careful adjustment of the motor-generator speed control. The extraction process is also sensitive to internal beam size. The beam size is in turn affected by longitudinal and transverse instabilities in the machine during acceleration. The instabilities are intensity and tune-dependent. We have observed both vertical and horizontal beam blow-up from coherent dipole oscillations and higher order resonances. To avert these difficulties, it is necessary to program the machine radius by a sequence of radius shifts during acceleration, as well as introduce a larger than optimal momentum spread by detuning the rf phase shift at transition energy. This procedure results in a beam loss at transition of ~ 15% from a circulating beam of ~ 6 X 10^{12} p/p. We also find that the available aperture at extraction time is only 3 mm. Typical machine tune at the extraction radius is $\nu_H = 8.74$, $\nu_V = 8.66$.

Spot size measurements in the external channel have been in qualitative agreement with calculations based on earlier emittance measurements." However, we plan new measurements to define the emittance better under various extraction conditions. For the new measurements, we plan to measure the beam half widths, W_1, W_2 and W_3 at three different positions downstream of the 8° bend. It can be shown" the emittance area $\varepsilon = E/\pi$ and the ellipse parameter α_1 and β_1 at point one are given by

$$\varepsilon = \frac{(D_1 + D_2 + D_3) - 2\,(D_1^2 + D_2^2 + D_3^2)}{2\,|a_2 b_3 - a_3 b_2|\,b_2 b_3} \qquad (2)$$

$$\alpha_1 \varepsilon = \frac{\left[W_1^2\,(a_2^2 b_3^2 - a_3^2 b_2^2) - D_2 + D3 \right]}{2(a_2 b_3 - a_3 b_2) b_2 b_3} \qquad (3)$$

$$\beta_1 \varepsilon = W_1^2 \qquad (4)$$

where $D_1 = W_1^2\,(a_2 b_3 - a_3 b_2)^2$; $D_2 = W_2^2\,b_3^2$; $D_3 = W_3^2\,b_2^2$

and a_2, b_2 and a_3, b are matrix elements of the transport matrix

$$M = \begin{pmatrix} a & b \\ c & d \end{pmatrix}$$

from point one to points two and three respectively.

Acknowledgements

We thank R. Adams and W. Gefers for the beam security system; R. Glasmann, J. Gabusi and E. Raka for valuable help in machine studies; D. Easler, W. Harrison and J. Schirmer €or expert construction of external power supplies and computer interfaces; J. Balsamo, J. Guthy, E. Tombler and M. Zguris for invaluable contributions to the instrumentation; and A. Pendzick for excellent cooperation in facility installation. We are grateful for much support and consultations from J.G. Cottingham, B. Culwick, G. Danby, H. Foelsche, J. Grisoli, A. van Steenbergen and H. Williams.

References

1. L.N. Blumberg, J.G. Cottingham, J.W. Glenn, J.J. Grisoli, M. Month and A. van Steenbergen, Proc. U.S. Nat'l. Part. Accel. Conf., IEEE Trans. Nucl. Sci. NS-18, No. 3, 1009 (1971).
2. C. Bovet, D. Fiander, L. Henny, A. Krusche and G. Plass, Proc. U.S. Nat'l. Part. Accel. Conf., IEEE Trans. Nucl. Sci. NS-20, No. 3, 438 (1973).
3. J. Herrera, private communication, 1973.
4. E. Forsyth and C. Lasky, BNL Report BNL-910 (1965).
5. G. Danby et al., Proc. of this Conference.
6. Y.Y. Lee, BNL Accel. Dept. Int. Report EP&S 73-1 (1973).
7. J.B. Cumming et al., Phys. Rev. 125, 2078 (1962).
8. M.Q. Barton et al., Proc. of this Conference.
9. L. Blumberg and F. Krausz, BNL Accel. Dept. Int. Report, AGS DIV 71-1 (1971).
10. E.C. Raka, BNL Accel. Dept. Int. Report ECR-4 (1961); ECR-6 (1962).
11. L. Blumberg, M.Q. Barton, J.D. Fox, J.W. Glenn and L. Repeta, BNL Accel. Dept. Int. Report AGS DIV 69-12 (1969).
12. H. Ploss and L.N. Blumberg, BNL Accel. Dept. Int. Report AGS DIV 68-4 (1968).

SIMULATION OF SIMULTANEOUS BEAM SHARING BETWEEN INTERNAL TARGETS AND SLOW EJECTION AT THE CPS

M. Bell and W. Kubischta
CERN, Geneva, Switzerland

Summary

The slow ejection of the CPS, going either to the West or East Hall, shares the beam regularly with one of the two internal targets feeding the South Hall. A simulation program has been written, in order to understand the process of sharing, especially the losses (about 5% to 7% for typically 30% to 50% on the internal target; the efficiency of the ejection itself is 95% to 97%) and the emittance blow-up (about a factor 2 for the vertical emittance) associated with it. In this program, a number of particles are followed through the resonant extraction process, while the target is treated using a Monte-Carlo method. Calculated values for efficiencies and emittance blow-up are given and compared with measured values.

1. Introduction

The CPS provides protons for counter experiments in four areas : East Hall (slow ejection from s.s. 62), West Hall (slow ejection from s.s. 16), and two internal targets in the South Hall (one in s. ~ .1, one in s.s. 8). In order to make efficient use of these facilities, the two slow ejection areas are served turn about (runs of 3 weeks), always sharing the beam with one of the internal targets.

First machine experiments' and calculations' had shown that with the former integer resonant extraction system the efficiency of the sharing process would have been unacceptably low, but with a third integer resonance test scheme, rather favorable results could be obtained[3]. In parallel with the installation of the final system, which has been running now for almost two years, the sharing process was studied by computer.

2. The Sharing System

The ejection system is schematically shown in Fig. 1. The required sextupolar component is provided by one non-linear lens (semi-quadrupole, SQ 53). A quadrupole (AQ 23) together with the quadrupolar component of the semi-quadrupole shifts the Q-value at the centre of the vacuum chamber from about 6.235 to the resonance 6 1/3. The accelerated beam is put in the inside half of the aperture, then debunched, and drifts into the resonance due to a slope on the flat-top of the main magnetic field.

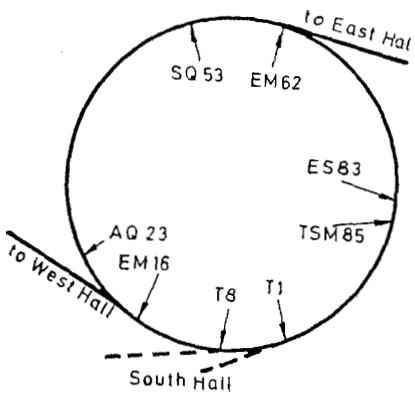


Fig.1 : Layout of the system.

SQ : semi-quadrupole
AQ : auxiliary quadrupole
ES : electrostatic septum
TSM : thin septum magnet
EM : extractor magnet
T : internal target (orbit bumps are omitted for the sake of simplicity)

The phase of the separatrices is chosen so as to have the maximum jump at the first septum, which is electrostatic (foil ∿ 0.15 mm effective thickness). 1/8 betatron wavelength downstream there follows a thin septum magnet (1.5 mm septum). Depending on the required operation, the beam then enters either the extractor magnet in s.s. 16 (to West Hall), or s.s. 62 (to East Hall), Except for the extractor magnet and the corresponding orbit deforming dipoles, the system is identical for both channels. Further details on some of the extraction channel elements are given in Ref, *4*.

The internal target is put at a position as required by the secondary beams, and by means of a servo-loop acting on two orbit deforming dipoles, the sharing ratio is adjusted.

The servo-system for the ejection acts on a separate quadrupole and works independently of the target servo.

3. Description of the Program

The program is an extensively modified version of the program of ref. 5, treating the target similarly to ref. 6.

At the beginning, radial and vertical co-ordinates are chosen corresponding to an approximately Gaussian beam profile. All particles are given the same momentum, as we assume that the sharing process is independent of momentum within the momentum spread of the debunched beam.

After each machine turn, the radial position and accordingly the Q-values are changed to simulate the drift of the beam, and checks are made to see if the target is hit, if the particle enters the field of the first septum or if it is lost on the walls of the vacuum chambers.

While the magnetic septa are taken into account with their actual septum thickness, the thickness of the electrostatic one is neglected. This is justified by the experience that the losses on this septum are proportional to the ejected beam intensity.

3.1 Internal target

As in ref. 6, each particle is assumed to represent a large number of protons, given by its "intensity" μ_i, which is set to 1 at the beginning. If a superparticle hits the target or its support, a certain fraction $\Delta\mu$ is lost by nuclear interactions

$$\Delta\mu = \mu_i \left(1 - e^{-\frac{D\rho}{\lambda}}\right) \qquad (1)$$

D is the length of the target (or support), λ the total nuclear mean free path, and ρ the density of the target material. The surviving part loses energy by ionisation

$$\Delta E = - L.D.\rho \qquad (2)$$

where L is a material constant characterizing the ionisation energy loss.

Moreover, the angle of the super-particle is changed by multiple Coulomb scattering. The distribution of the projected scattering angles is assumed to be Gaussian with r.m.s. θ (Rossi formula)

$$\theta_s^2 = \left(\frac{E_s}{\beta cp}\right)^2 \frac{D\rho}{X_o} \qquad (3)$$

with E_s = 15 MeV, βcp measured in MeV, and X_o the radiation length depending on target material.

3.2 Definition of efficiencies

In the program, a superparticle can have the following "fates" :

- after many target traversals, its betatron amplitudes may have grown such that it hits the vacuum chamber either vertically or horizontally; or
- after having passed through the deflecting field of the electrostatic septum, it may hit one of the septum magnets either radially or vertically; or
- after having passed through the deflecting field of the electrostatic septum, it may be extracted.

The sum of the intensities of the latter superparticles divided by the original total intensity, gives the extracted fraction n_e. The sum of all Ap's (eq. 1) divided by the original total intensity, gives the fraction n_t lost by nuclear interactions.

In a separate run, with all ejection lenses switched off, the fraction n_{to} has been computed as reference value. We define then the relative fraction of the beam on the target by

$$f_t = \frac{n_t}{n_{to}} \qquad (4)$$

and the computed sharing efficiency by

$$n_c = n_e + f_t \qquad (5)$$

This corresponds to the efficiency n_m as defined in [3] for measurement purposes

$$n_m = \frac{n_{es}}{n_e} + \frac{\alpha_{st}}{\alpha_t} \qquad (6)$$

with n_e the measured ejection efficiency without target, n_{es} the measured ejection efficiency with sharing, α_t and α_{st} being the integrated and normalised signals from a counter near the internal target, the former measured when all ejection lenses are switched off (reference), the latter measured during sharing. All efficiencies and fractions are to be understood with respect to the beam after all preceding operations like fast ejections or short target bursts.

3.3 Emittances

As emittance, two times the mean squared betatron amplitude is taken.

$$\varepsilon = 2 < a^2 > = 2 \frac{\Sigma \mu_i a_i^2}{\Sigma \mu_i} \qquad (7)$$

with, for the vertical co-ordinates,

$$a.2 = \beta y_i'^2 + 2\alpha y_i y_i' + \gamma y_i^2 \qquad (8)$$

For a Gaussian distribution, this emittance contains 86.5 % of all particles; 95%of a measured profile (projected distribution) are between $\pm \sqrt{\beta\varepsilon}$.

The radial emittance in the case of a slow ejection is, of course, not at all elliptic, and the distribution is not Gaussian. Nevertheless, a formula similar to (8), with empirical constants, was used to calculate a "betatron amplitude" and the emittance calculated using formula (7).

4. Results

We have concentrated mainly on three systems (for the main parameters see Table 1). While systems I and II correspond essentially to the present situation, system III assumes larger emittances for the internal beam as expected for a future operation at higher intensity[7]. All computations were done for 24 GeV/c. The target dimensions used for calculations are slightly different from the dimension of the targets now used in operation (usually 2 x 1 x 10 mm, 100 to 200 mrad angle), but by a few computer runs we could verify that the influence of target dimension is small. The same argument is valid for a change in target material from Be to B_4C. The material constants used are given in Table 2.

System	Ejection Channel (s.s.)	Emittances of int. beam hor. (10^{-6} π m.rad)	Emittances of int. beam vert. (10^{-6} π m.rad)	Target s.s.*	Target Mat.	Target width (mm)	Target height (mm)	Target length (mm)
I	16	1.	1.	1	Be	1.	1.	20.
II	16	1.	1.	8	Be	1.	1.	20.
III	62	3.	1.7	8	Be	1.	1.	20.

Table 1 : Main parameters of systems

* Straight section 1 is radially focussing, straight section 8 radially defocussing.

Material : Be		
Ionisation loss L	2.	MeV/(g/cm^2)
Radiation length X_o	62.5	g/cm^2
Nuclear mean free path λ	56.5	g/cm^2
Density ρ	1.84	g/cm^3

In order to keep the use of computer time at an acceptable level, the calculations were done with relatively small numbers of superparticles (usually 300).

4.1 The process in general

Already for rather modest fractions on the internal target, practically all ejected protons have passed through the target or support at least once (90% for $f_t \sim 0.1$). Some of them have lost so much energy that they become unstable at a radial position outside the normal range (see Fig. 2 for a typical example). They reduce the width of the hole created by the first septum, and a certain part is lost radially on the magnetic septa.

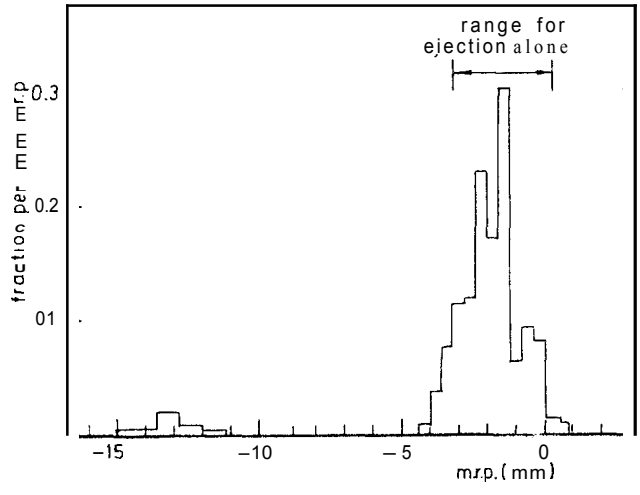


Fig. 2 : Mean radial position of superparticles entering the electrostatic septum. (Typical case).

Some protons are "locked in" to the target, they lose energy so fast that they do not become unstable in spite of the drift and their emittance growth. A small fraction of these protons, however, is scattered across the first septum (mrp $\sim$ -13 mm in Fig. 2), creating a diffuse vertical halo around the ejected beam, and is usually lost vertically on one of the magnetic septa (as it has no yoke, the electrostatic septum is no obstacle in the vertical direction).

4.2 Efficiencies and emittances

All results are presented on Figs 3 to 6 as a function of f_t, the relative fraction on the internal target, as defined in section 3.2.

For the sharing efficiency (Fig. 3) we give two curvesfor each system. The lower curve assumes a rather poor alignment of the septa, while the upper curve assumes no radial losses on the septa at all. By careful alignment of all septa, efficiencies between the two curves can be expected. A slightly smaller efficiency seems to result when a target in a D-section is used, but this difference has not been found experimentally. The measured points correspond to system I, but with different target dimensions (see above 4.).

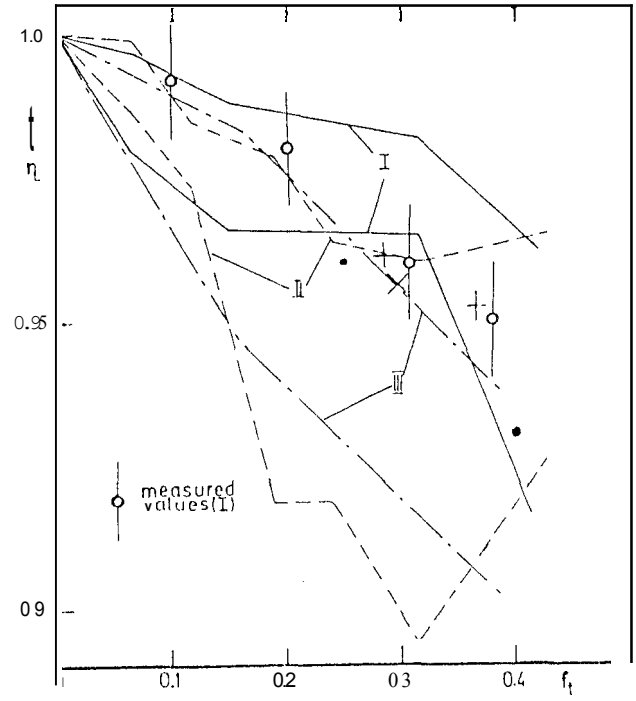


Fig. 3 : Calculated and measured sharing efficiencies (Roman numbers are system numbers from Table 1). Single points, which are not measured points, correspond to the pessimistic curve of system I, but with different targets : ∘ Be, 1x1x10mm
+ Be, 4x1x10mm
× B_4C, 1x1x20mm

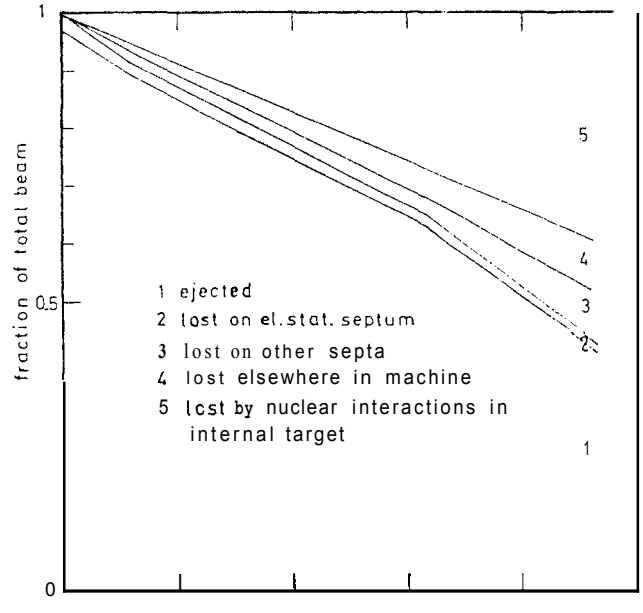


Fig. 4 : Repartition of protons as function of f_t. Unlike the rest of the report, the losses on the electrostatic septum are shown explicitly.

Fig. 4 presents the results for system I in a different way (only the conditions corresponding to the pessimistic curve in Fig. 3 are shown). From the point of view of radiation damage to the whole machine', the additional losses due to the sharing process (region 3 and a small part of 4) are small compared to the damage due to the use of any internal target at all (region 5 and most of 4). Even if the losses on the magnetic septa can partially be avoided by careful alignment, the irradiation of these delicate magnets represents however one of the most important limitations of the sharing scheme.

Figs 5 and 6 show the blow-up of the emittances by the sharing process. Again, it seems that a target in a D-section is slightly worse than a target in an F-section. Measured points for system II[9] are probably too optimistic, as they have been measured rather far downstream in the ejected beam line, and there are indications that a small part of the beam might have been shaved off on the way (in our calculation, all particles passing through the extractor magnet have been included).

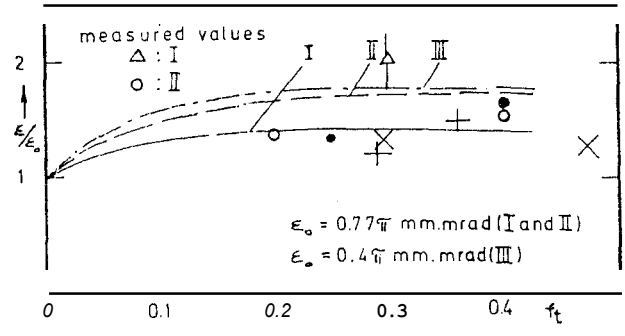


Fig. 5 : Blow-up of radial emittance. Single points other than measured points have the same meanings as in Fig. 3.

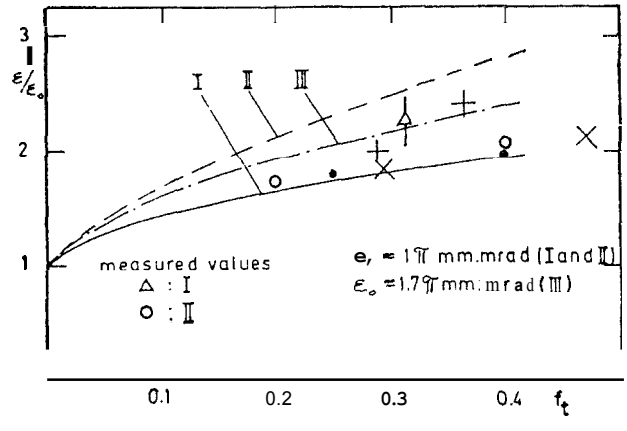


Fig. 6 : Blow-up of vertical emittance. Single points other than measured points have the same meaning as in Fig. 3.

5. Conclusions

On paper, beam sharing between slow ejection and internal targets at the CPS looks rather efficient, and experience supports this result. Under the conditions prevailing at CERN, it allows an optimal use of experimental facilities.

Taking the machine as a whole, the difference in radiation damage between an operation with an internal target alone and a sharing operation is small. The additional losses however occur mainly on the magnetic septa, as these are the aperture Limitations in the first part of the extraction channels (both radially and vertically). The growth of the radial emittance of the extracted beam is small, but the vertical emittance is blown up considerably (by about a factor 2 for $f_t \sim 0.3$), which leads to losses in the external beam transport and increases the spot size on the external target.

In order to keep these effects tolerable, usually one choses f_t not bigger than about 0.35 (fraction of the beam after all previous operations), which corresponds to about 20% to 30% of the total accelerated beam.

6. Acknowledgements

We would like to thank Mrs. D. Dumollard and D.J. Simon for their emittance measurements, and G. Cuisinier, Ch. Serre and Ch. Steinbach for their help during machine development sessions.

References

1. Kissler K.H. , CERN/MPS/SR/MD 70-4.

2. Baconnier Y., "Sharing the CPS Beam between an Internal Target and a Slow Extraction", CERN/MPS/DL Note 70-18.

3. Kubischta W., "A Multiple Target-Extraction Sharing Scheme at the CPS", Proc. of the 8th Int. Conf. on High Energy Accel., CERN, 1971.

4. The CPS Staff, "The CPS Improvements 1965-1973, An Assessment", Proc. of this Conference.

5. Barbalat O., "Fortran Programs for the CPS Resonant Extraction Calculations", CERN/MPS/Int.DL/69-1.

6. Hereward H.G., Ranft J., Richter W., "Efficiency of Multi-Traversal Targets", CERN 65-1.

7. Barbalat O., "Beam Emittance Estimates", CERN/MPS/DL Note 72-42.

8. Gouiran R., "High Intensity Running Implication on Magnet Irradiation and Radioactivity", CERN/MPS/SR/Note 73-43.

9. Dumollard D., Simon D., "Caracteristiques du Faisceau SE 62 et des Branches e_9 en 1973", CERN/MPS/MU-EP/Note 74-6.

EXPECTED ENERGY-SPREAD IN THE EXTRACTED BEAM OF SATURNE II

H. Bruck, J. -L. Laclare, G. Leleux

Section d'Optique Corpusculaire, Centre d'Etudes Nucléaires de Saclay.

Abstract.

Nuclear spectroscopy in the range of medium energy (~ 1 GeV) needs a good duty cycle and extracted beam little dispersed in energy ($< 10^{-3}$). To meet these requirements it is possible to slowly extract the beam in a resonant mode so as to give an instantaneous momentum spread small compared to the stored one. For this purpose we propose to slowly push the stored beam into the resonance $3\nu = 11$ by means of a betatron acceleration in order to avoid the creation of structure. In the frame work of this method we develop a simple formula in good agreement with computer results giving the dispersion in energy of the beam as a function of the principal parameters of the extraction. A numerical example is given applicable to the new design of Saturne II (proton accelerator in the range 0. 5 -2. 7GeV).

A large part of the experimental program around Saturne II is based on spectrometry facilities for nuclear physics studies in the range of medium energy (. 5 to 2. 7 GeV). The new synchrotron will have to provide experimental areas with high quality proton beams slowly extracted.

The beam will be extracted in a resonant mode excited by the 11^{th} harmonic of sextupolar fields in the neighbourhood of $\nu_H = 11/3$.

At a given amplitude, the particles encounter a septum magnet and are extracted. This extraction septum must be outside the stored beam particularly at injection. Reciprocally, the injection septum must not interfere with the unstable particles before they enter the extraction channel. Generally one can get rid of this problem by a local closed orbit deformation [1] or by moving the extraction septum towards the damped beam. In the present case, it has been possible to choose a suitable location of sextupoles with respect to injection and both extraction points (fig. 1) so that particles do not strike injection septum before entering extraction magnet which is set radially outside the injected beam.

In this scheme, during the last three turns, particles reach large amplitudes beyond the "good field" region.

Extraction is achieved by 2 sextupoles of equal strength but different polarities, set diametrically opposite in the machine. Another pair of chromaticity sextupoles of equal strength and same polarities makes it possible to act on :

$$K_H = \frac{d\nu_H}{(dp/p)}$$

and consequently, because of the sensitivity of the separatrix size tu deviation of ν_H, they allow for adjustment of the instantaneous momentum range in the extracted beam.

Debunched beams with small momentum spread are requested. Therefore, on the flat top, we plan to extract with ν_H highly dependant on momentum and to push the debunched beam towards the resonance by means of a betatron acceleration.

Typically, at 1 GeV, the stored beam is characterized by its emittances $\mathcal{E}_H \simeq 10$ mm x mrd, $\mathcal{E}_v \simeq 25$ mm x mrd and its momentum range $\Delta p/p \simeq \pm 1.6\ 10^{-3}$.

For a deviation $|\Delta\nu_H| = 3.3\ 10^{-3}$ of ν_H value from its value at resonance the triangular separatrix encloses the beam. The corresponding extraction sextupole strength allows a jump $\sigma \simeq 2.5$ cm at 8 cm from the axis during the last three turns.

Total emittance and instantaneous momentum spread in the output depend on chromaticity. A range

$$\left(\frac{\Delta p}{p}\right)_{ext} = \frac{|\Delta\nu_H|}{K_H}$$

is extracted at the same time. The corresponding total emittance is $\mathcal{E}_x = \sigma \Delta x'$ (fig. 2).

One can easely establishes formulae for $(\Delta p/p)_{ext}$ and $\mathcal{E}_x$ with σ as a parameter. Using K. R. Symon's results one finds :

$$\left(\frac{\Delta p}{p}\right)_{ext} = \frac{3^{1/2}\, X_o\, \sigma \cos^2\varphi}{9\pi K_H (X_s^2 - X_o^2 + X_s\sigma)}$$

$$\mathcal{E}_x = \frac{\sin(\varphi-\alpha)}{\beta_x \cos\varphi} \left\{ \sigma R \left[g^2 + \left(\alpha_x g + \beta_x g'\right)^2 \right]^{\frac{1}{2}} - \frac{2\sqrt{2}}{3} K_H \times \right.$$

$$\left. \times \left(X_s^2 - X_o^2 + X_s\sigma\right) \frac{1}{\cos\theta\,(\sqrt{3} - \mathrm{tg}\theta)} \right\} \left(\frac{\Delta p}{p}\right)_{ext}$$

where :

$$X_o = \sqrt{\frac{\mathcal{E}_H \beta_x}{3^{1/4}}} \cos\varphi$$

X_s : distance from beam center to extraction septum

R : mean radius

α_x, β_x, g, g' : usual orbit parameters

φ, a are represented in figure 3

$\theta = \varphi - \alpha + \pi/3$

Numerical results are given in fig. 4.

However for increasing chromaticity values which correspond to smaller and smaller extracted momentum range, ν_H is more and more amplitude dependant and extraction is entirely suppressed by separatrix distorsion.

It is well known that non resonant terms can perturb the extraction mechanism. In the present case, we have to deal with sextupolar and octupolar components in magnets (extraction is very sensitive to quadrupole fringing fields) and especially with non resonant components created by extraction sextupoles and strong chromaticity sextupoles.

Results from analytical derivations and numerical computation lead to the same chromaticity limitation 3 :

$$-12.5 \leq K_H \leq 3$$

(these two values are symmetrical with respect to the intrinsic K_H).

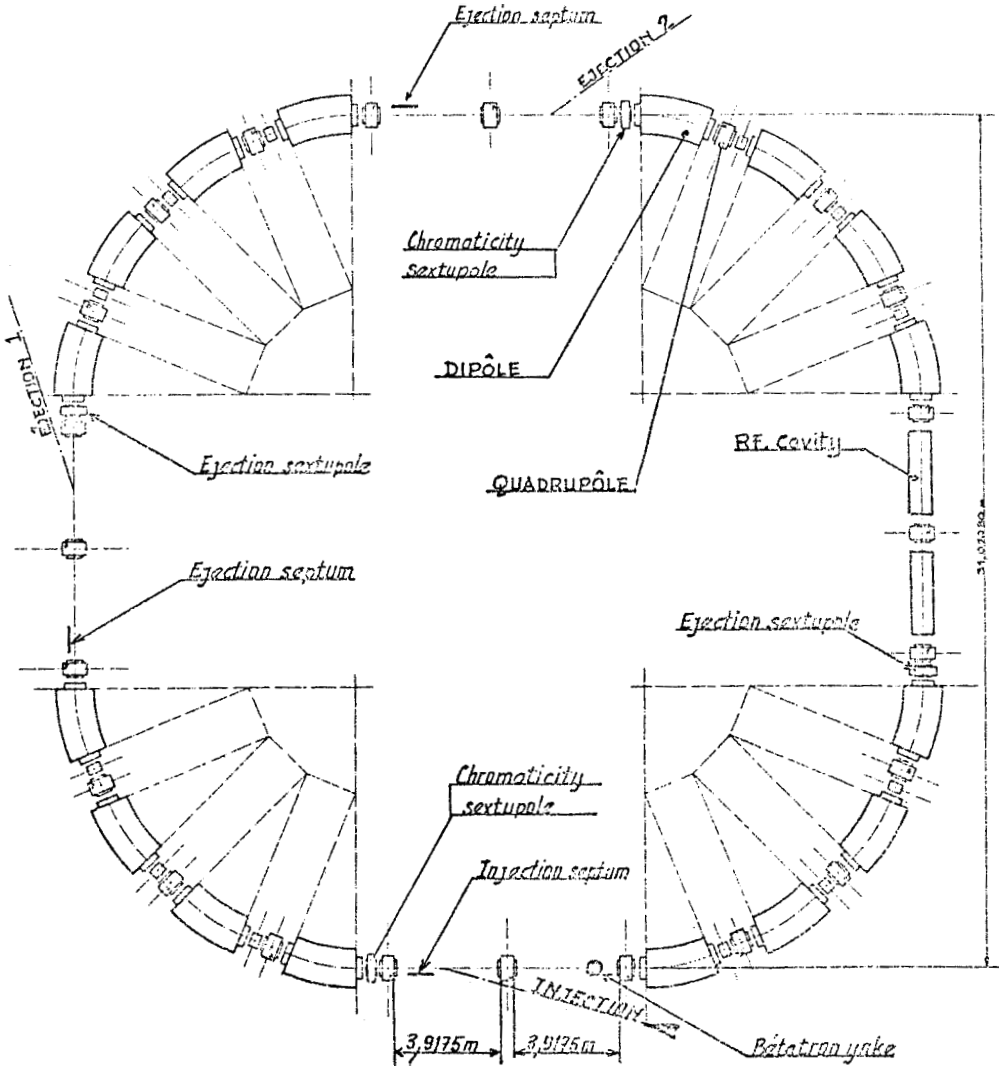
Consequently the instantaneous extracted momentum dispersion cannot be less than :

$$\left|\frac{\Delta p}{p}\right|_{\substack{ext \\ total}} \gtrsim 3 \cdot 10^{-4} \text{ at 1 GeV}$$

Octupolar zero harmonic components will be used for widdenning the range of allowed K_H values, but with large stored beam $\Delta p/p$ the ν spread within the beam could become excessive. In fact $\Delta p/p = \pm 1.5\,1^{-4}$ will be the possible minimum.

References.

1. J. Faure, "Déformation d'orbite fermée", SEFS TD 73/63, MS 7, RS 21, 26/06/1973.
2. H. Bruck, J. -L. Laclare, G. Leleux, "Extraction à l'aide d'une accélération bétatron", DSS/SOC. RS-73. 19, 06/04/1973.
3. J. -L. Laclare, G. Leleux, A. Tkatchenko, "Résonance d'extraction, influence des composantes octupolaires", DSS/SOC. RS. 74. 96, 04/04/19 74.



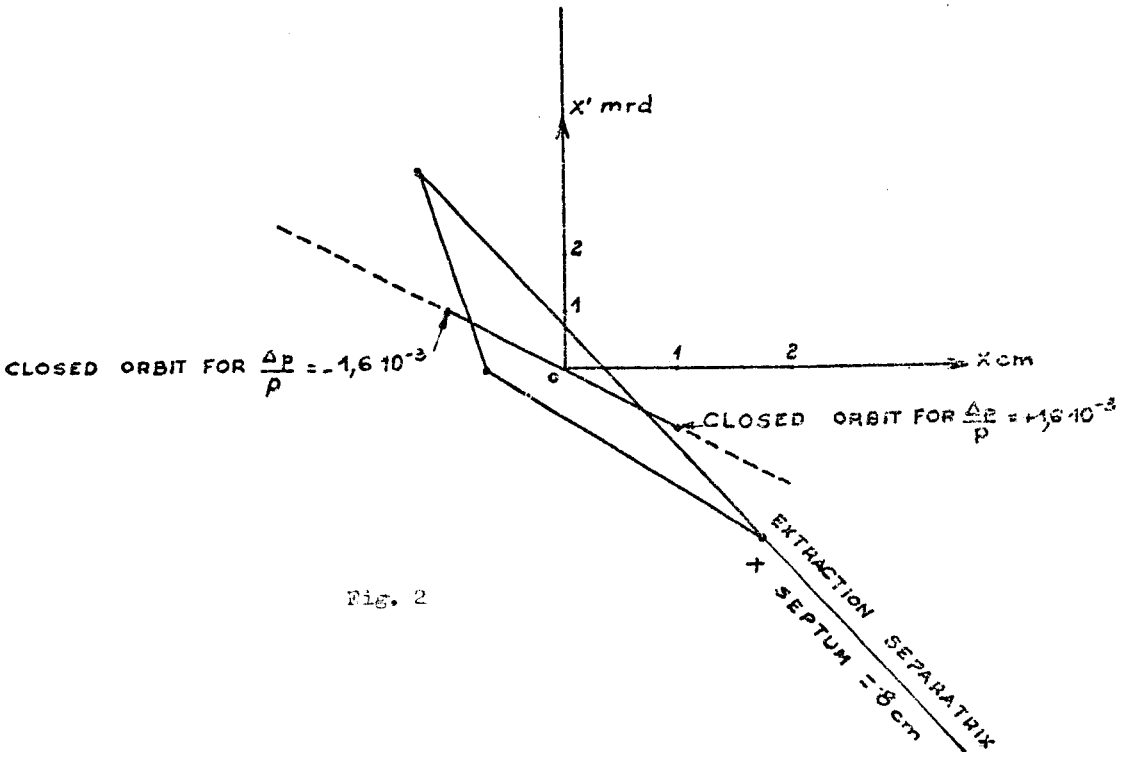

x' mrd
2
1
1
2
x cm
CLOSED ORBIT FOR $\frac{\Delta p}{p} = -1{,}6\,10^{-3}$
CLOSED ORBIT FOR $\frac{\Delta p}{p} = +1{,}6\,10^{-3}$
EXTRACTION SEPARATRIX
SEPTUM = 8 cm

Fig. 2

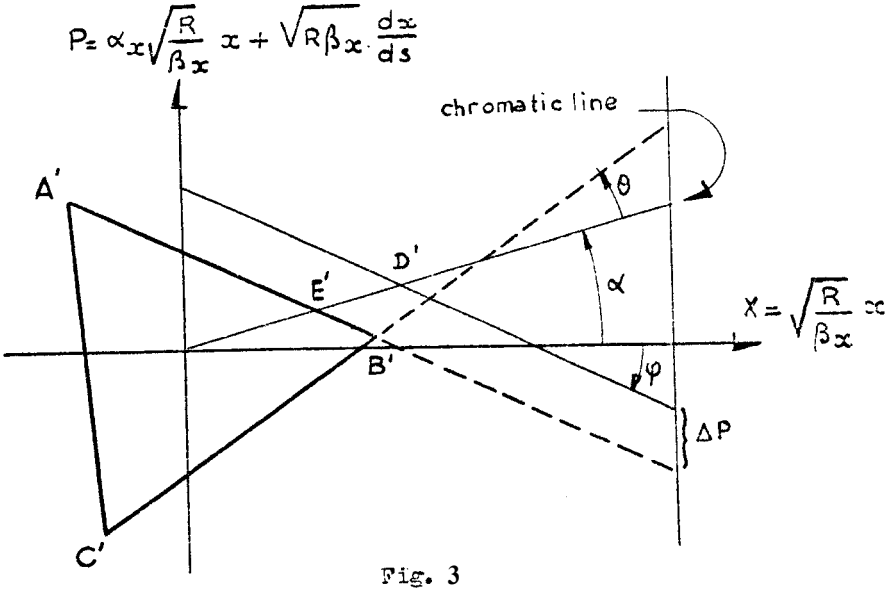

$P = \alpha_x \sqrt{\frac{R}{\beta_x}}\, x + \sqrt{R\beta_x}\cdot\frac{dx}{ds}$
chromatic line
A'
D'
E'
B'
C'
θ
α
φ
ΔP
$X = \sqrt{\frac{R}{\beta_x}}\, x$

Fig. 3

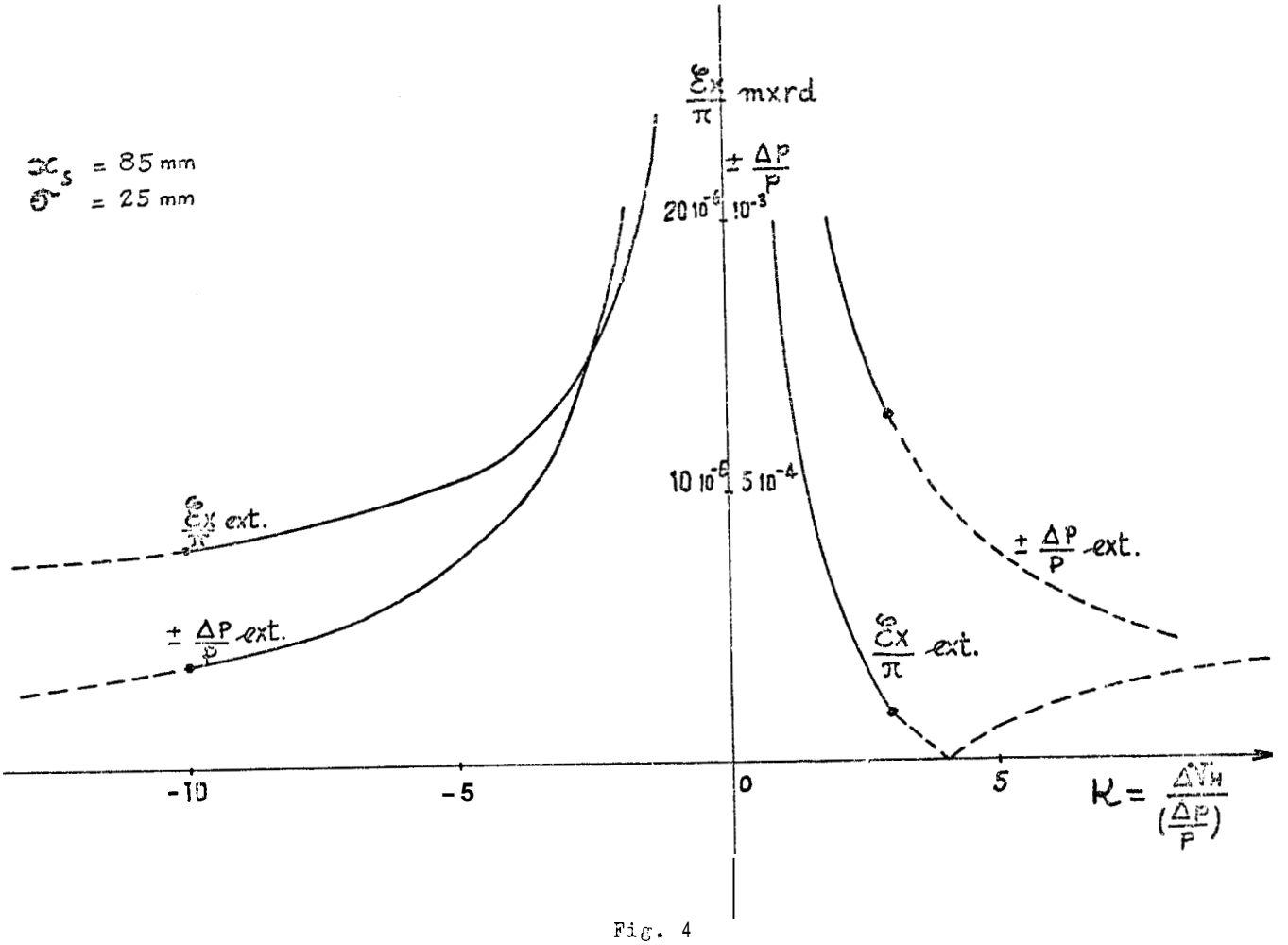

σ_s = 85 mm
σ = 25 mm
$\frac{\varepsilon_x}{\pi}$ mxrd
$\pm \frac{\Delta P}{P}$
$20\,10^{-6}$
10^{-3}
$10\,10^{-6}$
$5\,10^{-4}$
$\frac{\varepsilon_x}{\pi}$ ext.
$\pm \frac{\Delta P}{P}$ ext.
$\pm \frac{\Delta P}{P}$ ext.
$\frac{\varepsilon_x}{\pi}$ ext.
-10
-5
0
5
$K = \frac{\Delta \nu_H}{(\frac{\Delta P}{P})}$

Fig. 4

INJECTION AND TRAPPING OF THE BEAM AT 800 MeV IN THE CPS

D. Boussard, M. Bouthéon, B. Carpenter, P. Lefèvre, J.P. Potier
CERN, Geneva, Switzerland

Summary

The principles of injection and trapping of the 800 MeV beam from the CERN PS Booster are briefly described. A local deformation produced by a set of four bumpers displaces the closed orbit on the edge of a septum magnet, while the incident beam is made to jump the septum thickness by a full aperture kicker. The PS buckets are matched to the incoming bunches; the normal accelerating conditions are then reached adiabatically. A short review of the equipment needed for inflection, longitudinal trapping, acceleration and beam measurements is made. Results obtained in running-in sessions and operation are summarized.

Introduction

The CPS improvement programme] was essentially completed in the second half of 1973 by the successful increase of the accelerated proton intensity using the Booster injector.

This paper describes the injection equipment and operating procedures. Two kinds of system are used, a specific one for the 800 MeV PSB beam inflection, and a general-purpose one adjusted for this usage. This is necessary because the CPS has two modes of operation: one at 50 MeV from the Linac and one from the PSB. The computer has proved to be a great help for these applications.

Injection

Principle

The slow-cycling injector synchrotron (PSB) has been described elsewhere[2,3] as well as its performance [4,5,6]. The beam extracted from the 4 PSB rings is recombined and measured in a transfer line[7,8,9]. Matching is also achieved there by a set of 6 quadrupoles and drift spaces.

The principle of monoturn injection[10] is rather simple. A localized deformation of the CPS closed orbit allows using a fixed septum magnet, lying outside the synchrotron acceptance, as an input point in the machine. Four horizontal dipoles (septum bumpers) produce a forced closed orbit deformation over two magnet periods (1 betatron period = 8 magnet periods). Currents are calculated to produce the desired displacement with no residual deformation outside the inflection region. Local fluctuations of the focusing betatron function (β) were taken into account since a 2 10^{-3} error on one deflection leads to a 1 mm residual deformation. The incoming beam is brought on the closed orbit by a fast deflection at half a wavelength away from the end of orbit deformation,

Initial inflection conditions are achieved horizontally by a dipole in the transfer line and the septum magnet and vertically by two dipoles before the CPS input. Energy adjustment is made by a synchronization between the two machines, based on a very accurate pulse train linked to the magnetic field of the CPS (10 μT resolution with 3 μT jitter)[11].

The aim of the procedure is to achieve the conditions given in Fig. 3. The emittance of the incoming beam, suitably matched, determines the jump to be made at the level of the septum. Synchronization is fixed by the PSB energy; it is only necessary to adjust the local closed orbit deformation so as to avoid any residual betatron oscillation. The usual strong focusing synchrotron matrix calculations show that only the closed orbit angle and position at the septum level have to be adjusted. The use of 4 dipoles gives an additional degree of freedom which is used to cater for some possible future acceptance-limiting conditions (vertical stacking, two-turn radial injection). The hardware specifications allow incoming beam emittances (95% of the particles) of E_H = 33 π 10^{-6} rad.m and E_V = 12 π 10^{-6} rad.m, on closed orbits which at the input point can vary horizontally between + 15 and − 7.5 mm in position, ± 0.6 mrad in angle, and vertically between ± 5 mm and ± 0.25 mrad.

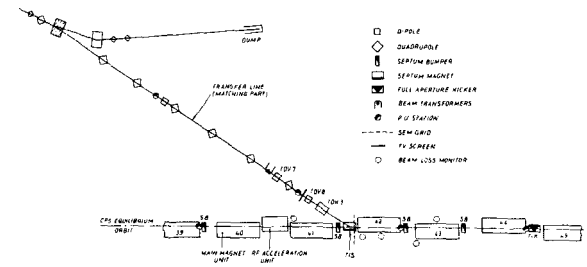


Fig. 1 Layout of inflection region

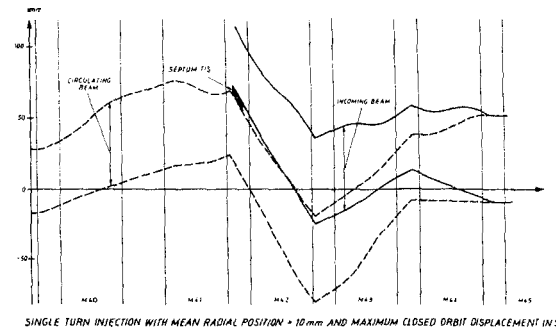


Fig. 2 General optics for 800 MeV injection

Control of magnetic state of the CPS

This system comprises the set of magnetic corrections of up to the 3rd order to control the CPS magnetic state up to about 6 GeV/c for both 50 and 800 MeV injections.

The general policy adopted for the upgrading of this system[12] was to provide independence by using one supply for each lens. The various compensating circuits (in particular harmonics) are achieved by computer programming.

The location of the various elements in the machine is such as to ease some compensation by avoiding dangerous harmonics and minimizing bothersome secondary effects. The corrections enable adjustment of the working point and to act on all stopbands up to the 3rd order in the given energy range. This is necessary

because of the working point chosen and the space charge effects observed[13,14]. The effect of octupolar resonance has not yet been demonstrated at these low energies but has been studied above transition[15]. The low-energy magnetic corrections are summarized in the following table.

Lens type	No	Description	Maximum strength per lens	Power supply	Use and performance (at 800 MeV)
Horizontal dipoles	20	2-turn windings on the main magnet yoke	10^{-3} Tm (4 mm)	± 10 A 50 V	local + 6th, 7th harmonics radial closed orbit < 8 mm ptp
Vertical dipoles	20	air core on araldite frame *	$2.6\ 10^{-3}$ Tm	± 10 A 30 V	local + 6th, 7th harmonics vertical closed orbit < 5 mm ptp
Normal quadrupoles	40	air core (L = 15 cm) * 20 at β_{Hmax} locations 20 at β_{Vmax} locations	$5.6\ 10^{-2}$ T	± 10 A 40 V	zero harmonic: $\Delta Q_{max} = 0.35$ 13th harmonic, horizontal and vertical (stopbands $2Q_i = 13$)
Skew quadrupoles	40	idem * on the same frame as the vertical dipoles	$3.5\ 10^{-2}$ T	± 10 A	zero harmonic ($Q_R = Q_V$) and 13th harmonic ($Q_R + Q_V = 13$)
Normal sextupoles	16	air core, in the straight sections 8 at β_{Hmax} locations 8 at β_{Vmax} locations	$2\ T.m^{-1}$	± 20 A 60 V (± 40 A for enlarged lenses)	zero harmonic (chromaticity variation ± 0.5) 19th harmonic (stopbands $3Q_R = 19$, $2Q_V + Q_R = 19$)
Skew sextupoles	16	idem on the same frame and concentric with the normal sextupoles	$2\ T.m^{-1}$	idem (± 60 A for enlarged lenses)	zero harmonic, 19th harmonic (stopbands $3Q_V = 19$, $2Q_R + Q_V = 19$)

* located between the main magnet coil head

These lenses are excited by medium-power amplifiers steered by programmed voltages which can be time-dependent functions or linked to the magnetic field. These voltages are produced by computer-driven function generators[16]. All the parameters are digitized and acquired by the computer.

Inflection system

This whole set of elements[17,18,19,20,21] was specifically designed for the injection of the beam coming from the Booster and is also entirely computer-controlled. The name and location of the various elements can be found on Fig. 1. Their characteristics are summarized below.

Type of element	Main characteristics	Power supply	Performance	Use and remarks
Transfer dipole (TDH3, TDV7, TDV8)	± 8 mrad	dc ± 20 A	stability: $\leq 10^{-2}$	determination of initial conditions
Septum magnet (TIS)	gap height: 60 mm gap width: 100 mm septum thickness: 6 mm 66 mrad	dc 1960 A	field homogeneity: $\pm 2.10^{-3}$ stability: $\leq 10^{-4}$	located in a β_{Hmin} straight section, adjustable in radial and vertical positions and in angle
Septum bumpers (SB)	gap height: 90 mm gap width: 212 mm on metallized ceramic chamber 23.2 mrad	condenser discharge half sine wave current (f = 240 Hz) 4000 A	accuracy: $\leq 10^{-3}$ stability: 3.10^{-4}	4 in CPS straight sections; the discharges are balanced to limit the residual closed orbit to a few 1/10 mm during the pulse
Fast kicker (TIK)	delay line kicker gap height: 54 mm gap width: 150 mm 3.7 mrad	60 kV delay line 2.5 μs pulse length	stability: 2.10^{-3} ripple: 2.10^{-2} fall time: 50 ns	the discharge instant is stabilized by feedback

The general synchronization of the injection is derived from a master pulse linked to the main CPS magnetic field. This master pulse defines the injection timing. Pre or post pulses synchronize the PSB ejection transfer and the CPS injection. To synchronize the bunches, pulses linked to the PSB accelerating voltage are used (fine tuning of recombinations, TIK, etc.). Most of the adjustments are made via a computer.

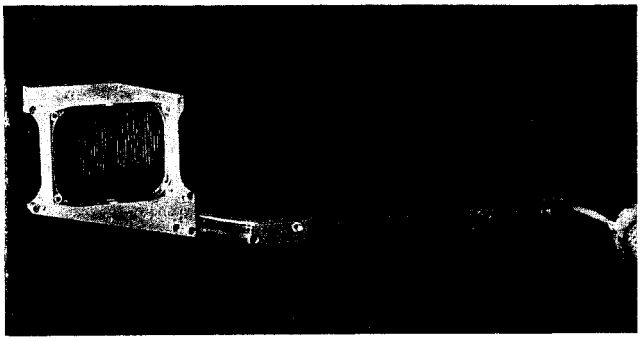
Transverse beam observation and measurements[22]

Beam position is checked by a few TV screens but mainly by electrostatic PU electrodes (two at the end of the transfer). The usual CPS trajectory measurement system23 is the main tool for fine tuning of the inflection, thanks to the 1st turn synchronization in a given bunch.

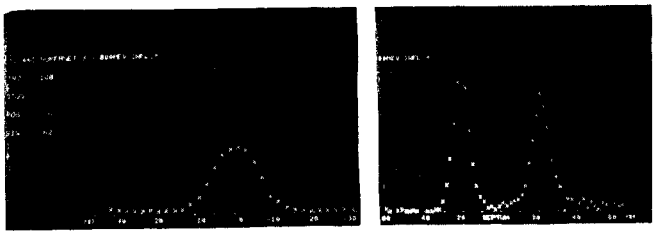
Independently of the data given by the PSB instrumentation[24], a set of current transformers[25], located at the end of the transfer line and in the CPS, measure the beam intensity. The signals are used for analog observation and are afterwards integrated and digitized (for elaborate numerical display. The frequency range of interest is covered by passive (60 MHz) or active transformers with various integration ranges (with the possibility of independent digitizing of the first 6 turns).

Signals of 6 beam loss monitors with ACEM-type photo-multipliers[26] are used to detect the likely cause of an inflection loss: analog observation and integration digitization, gated to choose the timing of the measurement (n turns after h^{th}).

The most sophisticated apparatus is for emittance and matching measurements. A set of 10 secondary emission wire monitors (SEM grids[27]) is used with a double monitor on the incoming and circulating beam at the septum exit, and 3 monitors at 3 λ/8, 5 λ/8 and 6 λ/8 from the inflection point in both transverse planes The measuring grid is made of 32 0.1 mm Cu-Be wires, spaced by 2 mm. The charge on each wire is integrated over one CPS turn and digitized. The data are processed by computer to reconstruct the beam profile and with 3 profiles the injected beam emittance can be computed and its matching checked. The double monitor is also used to check whether the injection is correct.



SEM grid and its mechanical positioning device



Measured beam profiles. Left: circulating beam. Right: both incident/circulating beams

Longitudinal Trapping

Principle

The PSB bunches have to be matched to the CPS RF buckets by modifying the main magnet B and the RF voltage, and normal conditions are then reached rapidly but adiabatically. Several methods were possible, depending upon the dilation allowed. The following was chosen as the best compromise between various requirements (accuracy of synchronization from magnetic field

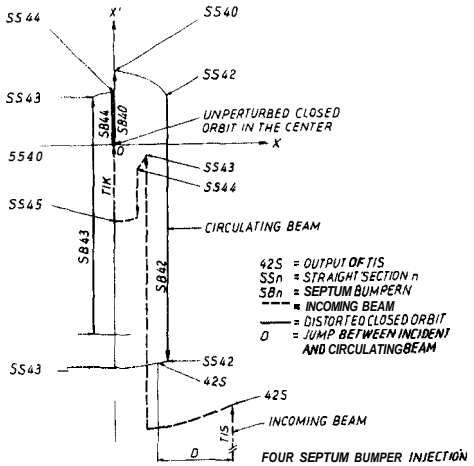
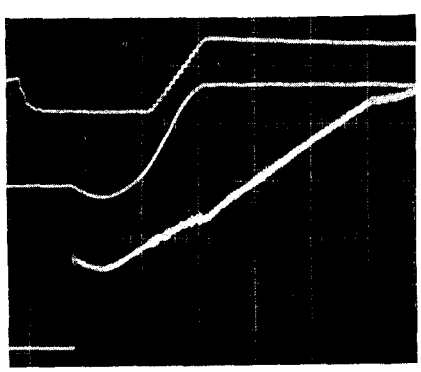


Fig. 3 Inflection trajectories in a normalized phase diagram

derived pulses among others): $\dot{B} = 0.22\ Ts^{-1}$, initial bunch length 145°; RF voltage: 37.5 kV, stable phase angle 15°, which give a theoretical 5% dilation after matching. B is kept constant for 20 ms, then raised linearly to 2.3 Ts^{-1} in 20 ms, which is compatible with the adiabaticity condition (synchrotron period of 0.4 ms). The RF voltage is simultaneously adjusted to prevent the bunch length decreasing faster than $(\beta\gamma^2)^{-1}$ in order not to increase the transverse space charge forces.

Moreover, the accelerating voltage is adjusted so that the buckets are almost filled in order to prevent possible instabilities by Landau damping.



a = main magnet B, b = RF voltage envelope,
c = wide-band pick-up signal (detected)

Equipment and measurements

The general phase and radial CPS beam control system[29] has not been modified. The usual adjustments are used and are not described here. The only elements specific to the 800 MeV injection are the initial accelerating voltage programming and the synchronization with the RF of the PSB.

The latter is achieved before injection proper by replacing the PS phase PU signal by one coming from the reference oscillator of the PSB, which is properly phase matched. The usual observations related to the acceleration (radial position error, stable phase, etc.) and to the feedback loops, are used. Beam behaviour is observed with wide-band (1 GHz) electrostatic PU electrodes which enable the evolution of the longitudinal density and its stability during acceleration to be followed. Fast sampling and digitization of these signals is also possible[30].

Operator Interaction

All controls are made using an IBM 1800 computer and its data transmission system[31], with the exception of those for longitudinal capture and acceleration. In consequence all operator access is concentrated at one console[32], which is centred on an alpha-numeric and graphical display. Adjustments and beam observations are made by using the display with the aid of a keyboard and four shaft encoders. The basic software tool is an interpretive syntax, ISAAC (Interpretive System for Automated Accelerator Control[33]). This makes it possible to establish a setting-up procedure employing the calculations mentioned above, and displaying theoretical parameters to the operator in normalized units and in a decoupled form. This has been a significant factor in the success of this injection. For example, the closed orbit is adjusted relative to the injection septum, while keeping the resultant deformation automatically at zero, without the operator having to concern himself with the actual currents in the various dipoles. In addition, it is possible to store reference measurements on the computer's disk store, and by subtracting the present values to display in real time such features as the residual betatronic oscillation at the injection. Since this constitutes the difference between the closed orbit and the actual trajectory, its minimization via the console is, in fact, the fine tuning of the injection.



The injection console

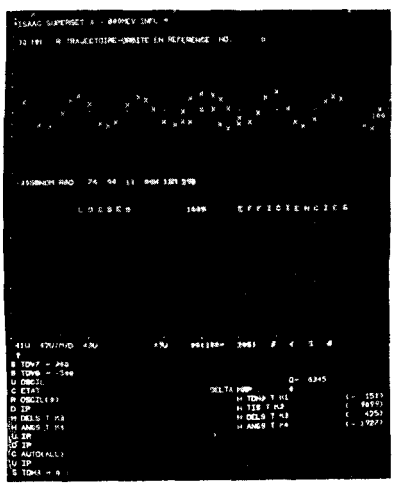
A complete description of the console is outside the scope of this paper. It is however worth noting that all the relevant analog signals are under computer control, providing centralized multiplexing, selection and identification of 225 signals up to 2 MHz and 225 more up to 30 MHz. The simultaneous availability of a large number of analog, numeric and graphical data has been of incomparable help in the understanding, running-in and operation of the injection from the PSB.

Results

After the usual equipment checks for the running-in of a system of this complexity, study sessions (12 hours per month on average) gave the following results in 1973.

"Nominal" beam (from a single PSB ring)

Initial conditions at transfer: intensity $\sim 10^{12}$ p^+/p, E_H = 21 10^{-6} π rad.m, E_V = 9 10^{-6} π rad.m, obtained by target collimation; radial and vertical positions $\leq$ 2 mm, longitudinal emittance 9 mrad ($\Delta p/m_o$ c, RF rad). Transverse trapping: 97 ± 2%, longitudinal trapping 100%, residual oscillation < 1 mm. Matching: at its best leads to a dilation of about 10% horizontally and 20% vertically (controlled by SEM grid at injection and targets at 10 GeV/c). Loss-less acceleration of $\sim 10^{12}$ p^+/p. Transition crossed without losses or longitudinal blow-up, thanks to the use of the γ-transition jump[34]. Longitudinal instabilities avoided by careful optimization of the accelerating voltage[35]. Longitudinal density twice as large as a 50 MeV injected beam. Transverse instabilities damped by octupoles[36].

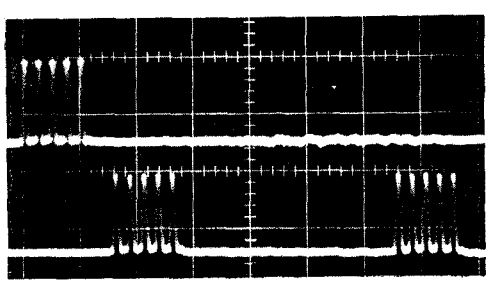


oscillation (first turn)

losses and efficiencies

some instructions of current use

Example of use of alpha-numeric and graphic display



500 ns/div

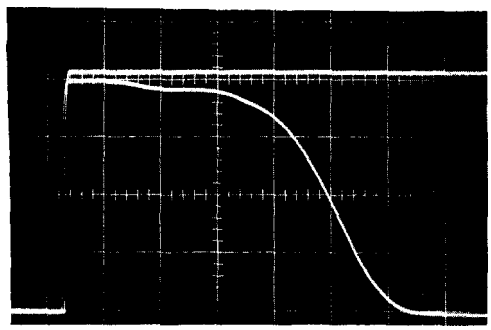
a

b

5 bunches (one PSB ring) at end of transfer (a) and two first turns in CPS (b)

"Intermediate intensity" (4 PSB rings)

PSB beams without collimation give: E_H = 24 to 30 10^{-6} π rad.m; E_V = 14 to 20 10^{-6} π rad.m; intensity = 1 to 1.5 10^{12} p^+ by ring, depending on the ring. Losses at inflection ∿ 15%. Longitudinal trapping 100%. Loss-less acceleration giving about 5 10^{12} p^+/p at 26 GeV/c. In addition to the dilation mentioned Above, an initial blow-up occurs due to differences between the rings; after this, no noticeable blow-up 'appears until 10 GeV/c. However, from 10 to 26 GeV/c, ,there is an unexplained vertical emittance increase by a factor $\leq$ 2. Successful tests of fast extraction (26 GeV/c, efficiency $\geq$ 97%) and slow extraction (6 1/3 resonance, 200 ms spill at 24 GeV/c, efficiency $\geq$ 90%) preceded operational use of the system,



a

1 ms/div

b

"Slow" transformer signals: a = with acceleration b = coasting beam.

Operation

The "intermediate intensity" has been used several times essentially for the neutrino channel. During these periods the overall PSB - CPS reliability proved to be reasonably good (same failure rate as usual). The peak intensity reached was 6.5 10^{12} p^+/p and 5.58 10^{12} p^+/p was averaged over two weeks.

Near future

Some improvements are planned to achieve reliable operation at 10^{13} p/p:

- to obtain this intensity within the nominal emittances and to refine the matching, avoiding the initial losses at inflection
- to improve the stabilization process of intense beams to maintain high density
- to complete computerization[37,38] providing automatization of procedures and monitoring
- to complete density distribution measurements and studies of their perturbations from injection to medium energies[39].

Acknowledgements

This work, and in particular the hardware, is the result of the teamwork of many people from the CERN MPS Division

References

1. The CPS Staff, CERN, CPS Improvement Programme 1965-1973. An Assessment. This Conference.
2. REICH, K.H., The CERN Proton Synchrotron Booster. Round-table discussion on booster synchrotron injectors, 1969 Particle Accelerator Conference, Washington
3. REICH, K.H., The PSB seen as a particle accelerator, CERN internal note SI/Note DL 72-2
4. KOZIOL, H., Results from the running-in of the CERN 800 MeV PS booster, 3rd USSR National Accelerator Conference, 1972, Moscow
5. PSB Staff (reported by C. BOVET), Recent performance of the CERN 800 MeV Booster, 1973 Particle Accelerator Conference, San Francisco

6. PSB Staff (reported by K.H. REICH), The CERN PS Booster: design expectations confronted with reality two years after start-up. This Conference

7. SCHAFF, F., Injection PSB CPS. Beam optics and matching parameters, CERN internal note SI/Note MAE/69-13

8. WEISSE, E., Optics of the Booster CPS transfer system, CERN internal note SI/Note MAE/69-5

9. BARIBAUD, G., METZGER, C., The 800 MeV measurement line of the CERN PS Booster, 1973 Particle Accelerator Conference, San Francisco

10. LEFEVRE, P., Principes et procedures d'injection à 800 MeV (report in preparation)

11. MAZELINE, C., Projet du système formateur de l'impulsion WTR précédant le transfert PSB - CPS, CERN internal note MPS/SR/Note 71-27

12. LEFEVRE, P., Corrections transversales dans le PS à basse énergie, CERN internal note MPS/DL Note 72-23

13. BACONNIER, Y., GAREYTE, J., LEFEVRE, P., High intensity phenomena observed at the CPS, 1971 Particle Accelerator Conference, Chicago

14. BOUTHEON, M., GAREYTE, J., Adiabatic capture in the CERN PS, VIII International Conference on High Energy Accelerators, 1971, CERN, Geneva

15. GAREYTE, J., Etude des résonances non linéaires sur un palier à 10 GeV/c au CPS, CERN internal report CERN/MPS/DL 73-1

16. ASSEO, E., Etude d'un générateur de fonctions banalisé en terminal STAR, CERN internal report MPS CERN/MPS/CO 72-5

17. JACOB, U., The injection of the PSB beam into the CPS in transverse phase space (summary of the results achieved by the Transversal Working Party), CERN internal note MPS/SR Note 70-17

18. KEYSER, R.I., Prototype 12-turn septum magnet (T-SV) for the PSB - CPS transfer line, CERN internal report CERN/SI/int. MAE/71-4

19. VLOGAERT, J., Further development of the prototype for the septum bumpers for the 800 MeV PS injection, CERN internal note SI/Note MAE 71-13

20. GRUBER, J., Specifications techniques pour les alimentations pulsées destinées aux nouveaux "Septum Bumpers" pour l'injection PSB - CPS, CERN internal note MPS/SR/SPEC 71-2

21. BRUCKNER, A., Kicking proton, fast and cheap, 1571 Particle Accelerator Conference, Chicago

22. LEFEVRE, P., Spécifications pour l'injection à 800 MeV, CERN internal note MPS/DL Note 70-27 (A,B,C,D,E)

23. BOUCHERON, J. et al, The CERN PS orbit display, Particle Accelerators, Vol. 2, pp 315-324

24. KOZIOL, H., REICH, K.H., Beam diagnostics at the CERN PS Booster, 1971 Particle Accelerator Conference, Chicago

25. BATTISTI, S., Booster beam transformers, CERN internal note MPS-SI/Note CO/70-8

26. The aluminium cathode elctron multipliers, Technology Note B33, Meeting on Technology arising from High Energy Physics, 1974, CERN, Geneva

27. BATTISTI, S., Moniteurs à émission secondaire (report in preparation)

28. BOUSSARD, D., Adapatation longitudinale adiabatique PSB - PS, CERN internal note, MPS/SR Note 70-1

29. BOUSSARD, D., Une presentation élémentaire du système beam control du PS, CERN internal note MPS/SR Note 73-10

30. FRAMMERY, B., private communication

31. ASSEO, E. et al, The computer-assisted control and data acquisition system for the CERN PS Booster, Proceedings of the 1971 Particle Accelerator Conference, Chicago, pp 354-358

32. BOUTHEON, M., La console injection du PS, CERN internal note MPS/CO Note 73-35

33. CARPENTER, B., Experience with interactive control software at the CPS, IEE Conference Software for Control, 1573, Warwick

34. HARDT, W., Gamma-transition jump, scheme of the CPS. This Conference

35. BOUSSARD, D., GAREYTE, J., Damping of longitudinal instabilities of the CERN PS, VIII International Conference on High Energy Accelerators, 1971, CERN, Geneva

36. GAREYTE, J., SACHERER, F., Head tail type instabilities in the CERN PS and Booster. This Conference.

37. MADSEN, J.H.B., The expansion of the PS control system, CERN internal note MPS/CO Note 72-6/Rev.

38. ASSEO, E., BIDUL: Principes, caractéristiques, performances dynamiques et résultats des essais, CERN internal report CERN/MPS/CCI 74-1 (in preparation)

39. LEFEVRE, P., Utilisation des sextupoles pour le CPS à basse énergie (report in preparation)

THE CERN PS BOOSTER: DESIGN EXPECTATION CONFRONTED WITH REALITY, TWO YEARS AFTER START-UP

The PSB Staff *(reported by K.H. Reich)*
MPS Division, CERN, Geneva, Switzerland

Summary and Introduction

At the 6th International Conference (1967), higher energy linacs and booster synchrotrons, cycling fast or slow, were discussed as a means for raising the intensity of the main proton synchrotron. Today one machine of each of these types is in operation: the 200 MeV AGS Linac; the 8 GeV NAL Booster; and the 800 MeV slow-cycling four-ring CERN PS Booster (PSB). It is still too early to assess the full PSB capabilities, but at present the design expectations seem, on the whole, to be realizable, as far as intensity (10^{13} ppp), machine systems performance, and reliability are concerned. Not unexpectedly, obtaining and preserving beam density has been more difficult, and we are almost a factor of 2 below the design values.

This report consists of two parts. First, the major design options are assessed in the light of the experience gained over the last two years. Secondly, the efforts to obtain and to preserve beam density are reported; in particular, optimization of multiturn injection, choice of the working point in the Q_H, Q_V diagram, compensation of stopbands, adiabatic RF trapping, and avoidance or damping of various instabilities. The concluding remarks contain data on the latest performance as a CPS injector, and an outlook into the future.

Assessment of Some Major Design Choices

For 50 MeV injection, the CPS intensity is space-charge limited to about 2×10^{12} ppp. The purpose of the new CPS injector is to raise the intensity to about 10^{13} ppp with only moderate increase in transverse and longitudinal emittances. Major choices concerning this injector (Fig. 1) and their assessment are listed in Table 1. While good progress was made during the last two years[21,8], resulting in successful runs for neutrino physics, the original performance aims have not yet been reached completely. (Because of the reduction in resources available, it was decided to operate the PSB for part of the CPS time only, and at an intermediate intensity level of about 5×10^{12} ppp, until higher intensity is required by the SPS.) Thus some of these assessments may need to be updated and/or eventually completed.

Multiturn Injection[8,21]

Extensive computational studies•• showed that horizontal multiturn injection with stacking in transverse phase space is a promising method for obtaining beams of high transverse density in the PSB. With a stable Linac beam of good quality it was found that the measured efficiency values, typically in the region of 30 to 50% (depending on such parameters as number of turns, Linac beam emittance, acceptable PSB beam emittance, value of Q_H, etc.) agree remarkably well (to within 5%) with the predicted figures. Unfortunately, lack of usable observation equipment for the trajectory at injection led to rather lengthy setting-up procedures by trial and error. With a Linac be of 50 mA (half the design intensity), 8 to 9×10^{12} p p (total of the four rings) are now routinely injected into the nominal horizontal emittance ($\varepsilon_H = 130\pi\ 10^{-6}$ rad m at 50 MeV). Recent experimental and theoretical studies[23] demonstrated that for small values of $|Q_H - Q_V|$ a substantial improvement of the efficiency (up to 60%) can be achieved by means of a linear coupling introduced by zero-harmonic skew quadrupoles. After reinventing•• this technique for the PSB, we used it in operation for some time. Although leading to an unwanted vertical emittance increase (due to $\varepsilon_V < \varepsilon_H$) it is nevertheless considered an interesting way of obtaining higher beam intensities for making machine experiment, for instance on beam loading.

Choice of Working Point, Stopbands

At the design stage it was unclear whether the working point should be above 4.5 or below. On the one hand, transverse resistive wall instabilities are more serious above. (Ionic instabilities are more serious below, but because of the low pressure of $< 10^{-7}$ Torr, they were not expected to occur.) On the other hand, for a Q-value below 4.5, there is not much working room available for accommodating larger (incoherent) Q-shifts. Furthermore, the space-charge driven fourth-order difference resonance $2Q_H - 2Q_V = 0$ was expected to lead to beam blow-up for $|Q_H - Q_V| < 0.2$[25].

The final choice was $Q_H = Q_V = 4.5$ for zero quadrupole trim currents and to rate the trim supplies such that the entire area $4.0 < Q_{H,V} < 5.0$ and some outside regions could be reached. On account of the high current, high proton density goal, slightly more weight was, however, given to providing room for the Q-shifts. Hence, the first lenses for stopband narrowing were planned with $4.5 < Q_{H,V} < 5.0$ in mind and the running-in started with working points in that area.

While the PSB could then be made to accelerate beams of good intensity, their vertical emittance was up to two or three times larger than the design value ($\varepsilon_V = 9\pi\ 10^{-6}$ rad m at 800 MeV). The most likely explanation is that a combination of the Laslett Q-shifts with the synchrotron oscillations causes repeated crossing of several stopbands. When a working point was found in this area that avoids stopbands, denser beams could be accelerated but then the beam became unstable transversely. Head-tail modes 1, 2, and 3 were observed for the first time[26]. Moderate to strong octupole fields cured this instability, but widened some stopbands as expected'.

Most of these problems were overcome by moving the working point to the region $Q_H \approx 4.18$, $Q_V \approx 5.24$ for the following reasons[27]: i) both Q-values are above integers, hence resistive-wall instability growth rates are slower; ii) the difference line $2Q_H - 2Q_V = -2$ was expected to be narrower than the $2Q_H - 2Q_V = 0$ line since both space-charge forces and Landau damping octupoles [which can anyway be weaker because of (i)] are essentially zero harmonic; iii) because of (ii), more room for Laslett shifts should be available even without narrowing of stopbands. These points were confirmed by experiments, and for the time being this is the usual working point leading to the transverse densities reported in Table 1.

The measured widths of the stopbands agree remarkably well (to within 20% in many cases)•• with those computed from the actual azimuthal distribution of the measured magnet errors.

Though exploring and narrowing stopbands is tedious (and needs more correction lenses than we have at present) we may have to come back to the area $4.5 < Q_{H,V} < 5.0$ for accommodating larger Q-shifts. (At present it is only used to produce high intensity beams when a vertical blow-up can be accepted exceptionally.)

RF Trapping and Acceleration

For the adiabatic voltage rise used'•• trapping efficiencies above 90% are expected theoretically[29,30].

Experimental results[31] are shown in Fig. 2. The values obtained for a beam of 1.2×10^{12} p/ring thus agree with the estimates. Corresponding figures (lower efficiencies for larger Linac beam energy spreads) apply to 2.5×10^{12} p/ring, as long as no instabilities occur (see below). Acceleration and synchronous transfer into the CPS buckets[32] are almost lossless, i.e. total loss about 5%, since the time that the beam control and synchronization system[33] became fully operational[34]. Under normal conditions the bunch area of a 6×10^{12} ppp beam is 9 mrad in units of $(\Delta p/m_0 c) \times$ RF radians.

Instabilities and their Cure

At the present level of operational beam intensity, instabilities, both transverse and longitudinal, are not harmful with either working point, provided the Linac beam energy spread is $\Delta E \approx \pm 150$ keV (design value) and that appropriate zero-harmonic octupole fields are applied. In machine experiments where different working points, other magnet cycles, and/or smaller energy spreads are used, various types of instabilities were studied. An example of a horizontal instability occurring with a 50 MeV coasting beam is shown in Fig. 3. Note the presence of a longitudinal structure, as yet unexplained. Bunched beam instabilities have already been referred to when discussing the working point; they are reported elsewhere in this Conference[26]. These instabilities appear to be driven by the long-range resistive-wall forces[35]. In general, the growth rates are as expected from theory, but the threshold intensities tend to be higher than those calculated, possibly because of neutralization (for coasting beams) or the additional frequency spreads introduced by the strong non-linear space-charge forces[36].

For large intensities and Linac beam energy spreads $\pm < 150$ keV, bunch position and bunch shape oscillations' occur soon after injection; so far, studies have brought out neither pure modes nor exponential growth. Instrumentation for more detailed observation is being developed[31].

Conclusions and Outlook

During the two neutrino physics runs in 1973 with the PSB-CPS beam[37], the average number of protons delivered to the external target was about 5×10^{12} ppp, thus fully meeting the intermediate intensity goal. The beam was remarkably stable (Fig. 4) and operation reliable. All studies made so far have not disclosed any difficulties of a basic nature which would prevent us from attaining the original performance aims. Hence the major design options chosen appear to have been sound.

Besides the completion of the beam observation apparatus and the expansion of the computer control system" already mentioned, we list among the necessary improvements: i) more protons from the Linac (a new 50 MeV accelerator is under construction[39]); ii) extra multipoles[12] for stopband compensation (being ordered); iii) refined RF voltage amplitude control[12] (under way); and iv) a faster Linac beam distributor to facilitate trajectory studies at injection and equal filling of the four rings (being built).

The anticipated capacity for accommodating new requirements has already shown up in two ways: i) the planned use of the PSB as pulse-to-pulse intensity modulator when the CPS will supply sequentially various users (25 GeV physics, ISR, SPS) with intensities differing by a substantial factor; and ii) simultaneous and independent use of each of the four rings for machine experiments, operator training, and hardware and software tests.

Acknowledgements

We are indebted to many members of the PS Department, past and present, who were not, or no longer are, members of the PSB staff, in particular to H.G. Hereward who participated actively in the PSB studies, and to G. Brianti, who led the Construction (SI) Division. We would also like to thank the other CERN Divisions for their collaboration, in particular SB Division. Finally, we gratefully acknowledge the contribution of European Industry, without whose competence and enterprising spirit the PSB could never have been built.

References

1. K.H. Reich (Editor), Progress report on the new CPS injector, CERN Internal Report MPS/DL/66-6 (CERN/SPC/227).
2. C. Bovet and K.H. Reich, Proc. 6th Int. Conf. on High-Energy Accelerators, Cambridge (Mass.), 1967, p. 315.
3. W. Hardt, Proc. 5th Int. Conf. on High-Energy Accelerators, Frascati, 1966, p. 151.
4. U. Bigliani et al., Proc. 7th Int. Conf. on High-Energy Accelerators, Yerevan, 1970, Vol. I, p. 433.
5. E.D. Courant, E. Keil and A.M. Sessler, Proc. 6th Int. Conf. on High-Energy Accelerators, Cambridge (Mass.), 1967, p. A-163.
6. A. Asner et al., Proc. 3rd Int. Conf. on Magnet Technology, Hamburg, 1970, p. 418.
7. C. Bovet et al., Proc. 8th Int. Conf. on High-Energy Accelerators, Geneva, 1971, p. 380.
8. The PSB Staff (presented by C. Bovet), Proc. 5th Particle Accelerator Conference, San Francisco, 1973 (IEEE, Vol. NS-20, No. 3), p. 221.
9. D.W. Lamotte and K.H. Reich, CERN Internal Report SI/DL/70-8.
10. I. Gumowski, Proc. 8th Int. Conf. on High-Energy Accelerators, Geneva, 1971, p. 360.
11. F.J. Sacherer, Proc. 5th Particle Accelerator Conference, San Francisco, 1973 (IEEE, Vol. NS-20, No. 3), p. 825.
12. G. Nassibian et al., private communication.
13. J.D. Pahud, Proc. 4th Int. Conf. on Magnet Technology, Brookhaven, 1972, p. 718.
14. U. Bigliani et al., Proc. 4th Particle Accelerator Conference, Chicago, 1971 (IEEE, Vol. NS-18, No. 3), p. 233.
15. G. Nassibian, CERN Internal Report SI/EL/69-3.
16. A. Brücker, Proc. 4th Particle Accelerator Conference, Chicago, 1971 (IEEE, Vol. NS-18, No.3), p. 976.
17. C.E. Rufer and W. Unterlerchner, Proc. 4th Particle Accelerator Conference, Chicago, 1971 (IEEE, Vol. NS-18, No. 3), p. 649.
18. H. Koziol and K.H. Reich, Proc. 4th Particle Accelerator Conference, Chicago, 1971 (IEEE, Vol. NS-18, No. 3), p. 347.
19. A. Asseo et al., Proc. 4th Particle Accelerator Conference, Chicago, 1971 (IEEE, Vol. NS-18, No. 3), p. 354.
20. G. Baribaud et al., this Conference.
21. The PSB Staff (presented by H. Koziol), Proc. 3rd All-Union Accelerator Conference, Moscow, 1972.
22. G. Bovet et al., Proc. 8th Int. Conf. on High-Energy Accelerators, Geneva, 1971, p. 102.

23. K. Schindl and P. van der Stock, CERN Internal Report MPS/BR/74-2.
24. M.H. Blewett et al., Rev. Sci. Instrum. 24, 861 (1953).
25. B.M. Montague, CERN 68-38 (1968).
26. G. Gareyte and F.J. Sacherer, this Conference.
27. F.J. Sacherer, private communication.
28. J. Gareyte and K. Schindl, private communication.
29. C.G. Liliequist and K.R. Symon, MURA 491 (20 July, 1959).
30. U. Bigliani, CERN Internal Report SI/EL/68-2.
31. F. Pedersen, private communication.
32. D. Boussard et al., this Conference.
33. U. Bigliani, Proc. 4th Particle Accelerator Conference, Chicago, 1971 (IEEE, Vol. NS-18, No. 3), p. 352.
34. G. Gelato, private communication.
35. F.J. Sacherer, this Conference.
36. D. Möhl and H. Schönauer, this Conference.
37. The CPS Staff, this Conference.
38. G. Plass et al., private communication.

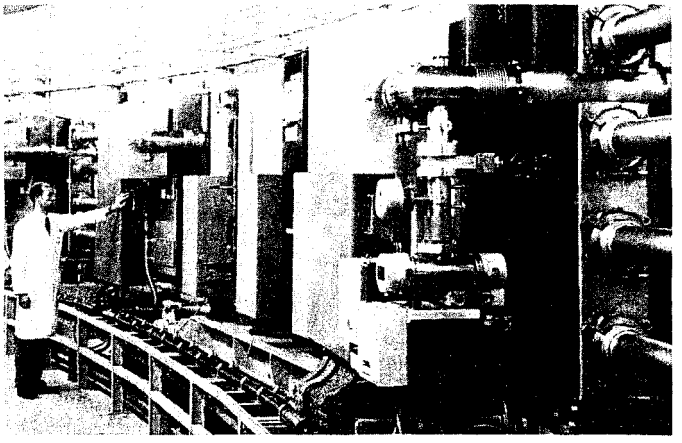


Fig. 1 View into PSB tunnel showing (from right to left) long straight section, bending magnet (with vacuum pumps), triplet, bending magnet, long SS.

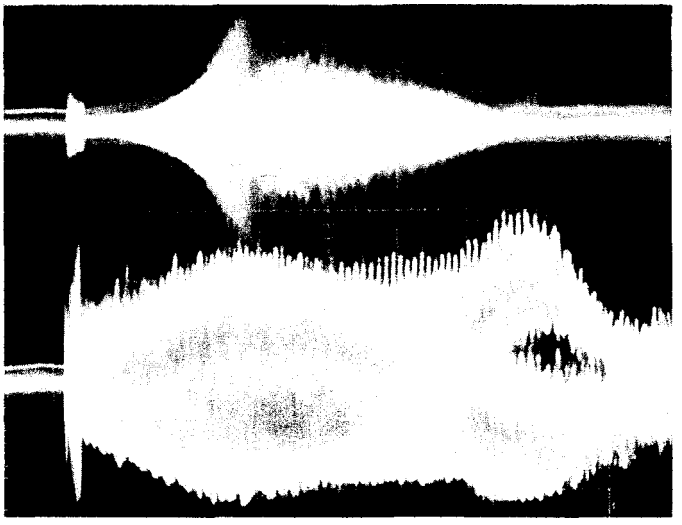


Fig. 3 Horizontal instability observed with a 10^{12} p per ring beam coasting at 50 MeV.
ΔE Linac = +60 keV; Q = 4.18, Q_V = 5.24;
time scale 20 msec per division.
Upper trace: difference signal from electrostatic pick-up electrode.
Lower trace: sum signal.

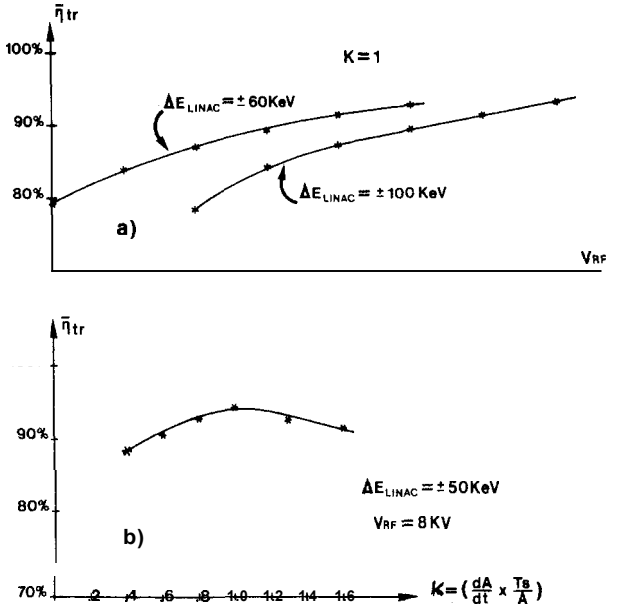


Fig 2 Measured efficiency of RF trapping η_{tr} of a 1.2×10^{12} p/ring beam using an adiabatic voltage rise from 1 kV to final RF voltage indicated (K = 1 means rise-time equal to sychrotron oscillation period T_s), a) as a function of RF voltage (for two Linac beam' energy spreads); b) as a function of K.

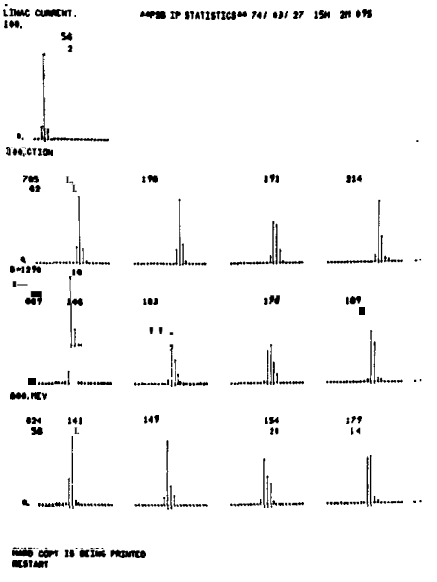


Fig. 4 Histogram (for 100 acceleration cycles) of Linac current and PSB intensities. (At injection 100 mA circulating correspond to ∿ 10^{12} p). From top to bottom: Linac current, intensities accepted by PSB before trapping (rings one to four from left to right), intensities trapped, and intensities accelerated to 800 MeV and synchronized. The figures indicate mean values and standard deviations, respectively. The left-hand column gives the average of the total intensities (of the four rings). The PSB was not optimized when this photograph was taken; during the neutrino runs the intensities were about 20% higher (with the same distribution).

Table 1

Assessment of some major PSB design choices

Aim	Choice, including reasons given in 1966–1969	Consequences of choice	Particular actions taken	Assessment in March 1974
10^{13} ppp	800 MeV slow-cycling circular injector: for about the **same** cost as a 200 MeV Linac, higher beam quality; spare capacity for contingencies and improvements'[1,2] ($\beta\gamma_{800\ MeV}/\beta\gamma_{200\ MeV} \approx 3.5$)	Need to study, select, and design the first slow-cycling "Booster" synchrotron[3], a fairly complex machine in which collective effects were expected to be significant, particularly in longitudinal phase space.	Taking into account beam intensity effects from the start[4]; emphasis on simple design and easy, reliable operation.	Final cost indeed very comparable to that of a 200 MeV Linac; too early for comparing performance limits; with a 50 mA Linac beam $\sim 8 \times 10^{12}$ ppp were accelerated to 800 MeV ($\sim 5 \times 10^{12}$ ppp within design emittances),
High phase-space density, adjustable within some range	a) Four rings: comparatively modest extrapolation of transverse phase-space density beyond the 1966 state of the art; favourable numerology including the possibility of combining two beams for better ISR performance'[1,5].	Need to compare horizontally interlaced version with vertically stacked version; higher complexity and probably cost than with two or three rings; need to distribute the Linac beam and to recombine the four beams prior to transfer into the CPS.	Vertical stacking whenever possible; use of combining (magnet yokes, pumping of vacuum systems etc.) and multiplexing (beam observation, data treatment, and display, etc.); emphasis on simple and reliable design for beam distribution and recombination.	Distribution of the beam to the four PSB levels and precision recombination present no particular problems ***per se***, but the load of running in and setting up four almost independent rings was underestimated; vertical stacking is definitely beneficial.
	b) Lattice with 16 periods and no super-periods; separate function magnet: no systematic resonances for $4.0 < Q_{H,V} < 5.3$; ease of moving the working point; good probability of providing a magnet system of high quality, notably through the use of a computer simulation program'.	Larger number of magnet units than in the case of a combined function magnet; occupation of a larger fraction of the machine circumference in the present case of relatively low peak magnet fields.	No remedy possible or needed in view of the relatively small total number of magnet units and the relatively large PSB circumference, determined independently as $4R_{PSB} = R_{CPS}$.	Performance aims achieved; distortions of the uncorrected closed orbit do not exceed a few millimetres peak to peak; half integer stopband widths were measured as $\delta Q \approx 0.01$, and the four rings were found* to be within the narrow tolerances specified'.
	c) Provision of a number of correction lenses from the beginning: faster running in; improved final lens order.	Need to anticipate most wanted types of lenses and their strength without much quantitative experience available on which to base oneself.	Extensive calculations and machine measurements; provision of two extra lenses of a different type for experiments.	On the whole successful approach (see text); the need for skew sextupole corrections was underestimated.
	d) Decision to design equipment from the start with a low beam-coupling impedance: faster running in; better final phase-space density.	Need to specify acceptable impedance values without much quantitative experience for judging beforehand the effect on beam; this led in some cases to awkward decisions whether or not to change a given prototype design.	Calculations[g-,1] and measurements" on prototypes and final equipment (RF cavities, fast kicker and septum magnets, quick-connect vacuum couplings, beam detectors, etc.); assessment and modifications to the best of one's knowledge.	Since so far no beam interaction with a fixed-frequency parasitic resonator has been observed, and the impedances cannot be adjusted, assessment is not easy; in view of the difficulty of later changes the course of action adopted appears justified.

	Choice, including reasons given in 1966–1969	Consequences of choice	Particular actions taken	Assessment in March 1974
	a) Magnet power supply fed directly from the electricity mains: no rotating machinery (i.e. less wear, no continuous manning of power house); model for SPS.	Lengthy negotiations with the local Electricity Authority including simulated tests with the grid; electrical coupling with other users inside and outside CERN.	Provision of adequate a.c. compensating and filtering networks[13], appropriate regulation of power supply.	Supply gives entire satisfaction from all points of view: stability, reproducibility, ease of control, freedom from creating perturbations (outside tolerances).
	b) Triplet focusing: resulting beam cross-section comparable to that in the CPS in the long straight sections, hence use of some proven existing CPS designs and even equipment; reduced energy storage in PSB magnets.	Sixteen extra lens units (compared to FODO lattice).	(None possible.)	Exact value somewhat difficult to assess; main advantage probably reduction of energy exchange with electricity mains; also appreciated: possibility to install borrowed CPS equipment in PSB.
	c) Air-cooled RF accelerating cavity having only final amplifier stage in machine tunnel: low failure rate.	New development[14] based on restricted experience; possibility of thermal runaway of ferrites[15].	Adoption of sufficiently low working temperature; individual measurement and stacking of ferrite rings according to properties.	So far entirely satisfactory performance from all points of view.
	d) Standardization and modularization: general economy; less spare parts; easier training of operating and maintenance staff.	Unless standardization is based on a full knowledge of all cases to be covered, difficulties arise; standardization may adversely affect individual inventiveness.	Appropriate organization of Project Division, including Parameter and Technical Coordination Committees.	Unqualified success where applied (injection and ejection lines, power supplies, kicker system[16], vacuum components[17], naming of PSB components from drawings to software, etc.).
	e) No electronics or power supplies in machine tunnel (unless indispensable): no irradiation; spread of maintenance in time.	Degradation of signal quality and power loss due to longer cable transmission.	Construction of auxiliary tunnel and equipment rooms above machine tunnel; appropriate equipment design.	Aims achieved; easy addition of extra equipment appreciated.
	f) Centralized controls, located in the CPS main control room (MCR): easier running-in; faster take over by CPS operating team.	i) Lack of space and specialized facilities during running-in. ii) MCR and PSB systems activities separated by 400 m distance.	i) Basically none, in the future possibly rebuilding of MCR. ii) Intercom and public address, TV and other communication links.	Completion of the centralized controls was clearly a major progress compared to the earlier (temporary) stage of distributed controls; CPS team has not yet taken over PSB operation.
	g) Powerful beam observation apparatus[18]: faster running-in; better beam quality; easier fault diagnosis.	i) Largish cost item (∿ 10% of total). ii) Dilemma of what priority to give: not required before main machine components but much less useful if not ready from the start-up	i) Multiplexing wherever possible (e.g. one camera for looking at two screens, etc.); cheap solutions where possible (e.g. beam loss monitors) ii) Building by industry (e.g. measurement targets).	Nearly all facilities for the measurement of beam position, beam current, bunch shape, emittance, energy spectrum, closed orbit, and betatron frequency meet expectations and are in use almost continually.
	h) Computer assistance for data acquisition and control: faster measurements; improved beam quality; better reproducibility; easier operation[19], hardware tests".	i) Limitations due to existing IBM 1800 (used because of available capacity and time pressure). ii) No manual back-up foreseen (to save cost).	i) Short term: change over to MPX, addition of core memory and a satellite computer for on-line work; long term: new system. ii) Diagnostic means for fault finding.	Data acquisition, treatment and display even more powerful than anticipated; helpful for control after teething troubles[20] were overcome; too early to assess full capability for reducing PSB down time.

COMPUTER CONTROL OF ACCELERATORS

A Review Paper

M.C. Crowley-Milling

CERN Lab II, Geneva, Switzerland

I should like to start by paraphrasing some notes I circulated at the start of the European 300 GeV project, now known as the SPS. In these notes I said that there were four main purposes a control system for an accelerator has to serve.

1. Requirements

An accelerator control system has to provide facilities for :-

(i) Normal operation of the accelerator

(ii) Interaction with the experimenters

(iii) Experiments on the accelerator (machine development)

(iv) Keeping records

There is no longer any argument about the advantages of adding computers to control systems, but there is some conflict between the requirements for these different facilities, and it is clear that in the past the designers of some systems have concentrated more on one aspect than on the others.

For normal operation of the accelerator, we want a system that is simple to operate and that allows the normal setting up or changing of operating conditions to be carried out with the minimum possibility of error, It is quite possible to provide a system that, once the desired operating conditions had been inserted, could run up an accelerator from cold, but this would be unnecessarily complicated, and could lead to a system that is too inflexible to serve the other purposes. It seems sufficient to provide a system that leads the operator through the correct steps to run up the accelerator, and tells him what actions to take in the event of some failure.

For the interaction with the experimenters, the first requirement is a good means of communication, together with provision for the transfer of the control of some elements in the beam lines to these, when this is permissible. It is also advantageous to be able to transfer some data periodically from the accelerator control system to the experimenters' data acquisition systems, for subsequent use in the analysis.

For machine development the utmost flexibility is required, and it is in this area that the largest amount of computing power is likely to be required. This is shown particularly in the case of the AGS. Some control of the machine was already carried out using PDP 8 computers at the time when the purchase of a PDP 10 was justified mainly on the effect it could have in speeding up machine development.

Lastly, for record keeping we want selection. It is all too easy to record masses of data that no one looks at.

2. Control Actions

Turning from the overall areas of control to the control actions that can be assisted by computers, I think the most important actions include :

(1) Complicated setting up

(2) Supervisory control

(3) Multiple acquisition and treatment

(4) Closed-loop control

(5) Function generation

The first thoughts of most people in the early days was that one of the main contributions that computers would make was in the area of closed-loop control, and the earliest application was in this field. This was the closed-loop control of the Bevatron guide field. It had been pointed out previously, that some people who tried closed-loop control found that by the time the system concerned had been analysed in sufficient detail for the loop to be closed by a computer, the causes of instability had been found and eliminated, and so the closed-loop control became unnecessary. This is not always true, and closed-loop control can improve significantly the performance, or drastically reduce the setting up time, as in the case of the injection steering in the ISR[1]. In other cases, such as the r.f. control for the Bevatron, it would be more correct to call it self-adaptive function generation.

In most cases where a computer was added to an existing accelerator, its first duty was supervisory control, by which I mean the checking of status or

values against those demanded, and providing some warning of unwanted changes. Other facilities were added later. One of the most useful of these is the one I have called complicated setting up. The facility to set up a system of many power supplies either to predetermined values from a table, or according to some mathematical relationship, has saved the operators a lot of tedious work, and has enabled some things that would not otherwise be possible, such as acceleration of the stored beams in the ISB, and the β and tune control on SPEAR, where a very considerable amount of computing is required.

However, it is in the multiple acquisition and treatment of data from the accelerator that the most spectacular (literally!) advances have been seen. The ability to acquire masses of data from the beam instrumentation system, manipulate it and produce sophisticated displays of emittance etc. has been shown at a number of laboratories, of which Argonne was amongst the pioneers, and it was said at one of the recent Linac conferences that a linac that did not have an on-line emittance display was way behind the times.

Thus we have seen a tendency away from direct closed-loop control, except in the function generator, and a concentration on the supervisory control and complicated setting up to assist the operator in normal operation, and on the acquisition and presentation of data to assist the machine development.

3. Hardware

Turning from the types of operations, let us now look at the development of the hardware and software needed to meet these requirements, and see if there are any trends from which we can make predictions. Taking the hardware first, we naturally start off with the computers themselves.

3.1 Computers

When computers were first applied to control accelerators they were relatively expensive and so a lot of effort was expended in making small machines do the maximum amount of work. As prices came down, or the control budget went up, larger machines could be afforded, notably the CDC 924 at the ZGS, and the general idea seemed to be to couple as many things as possible to the largest single computer one could afford. However, it was found that a number of routine tasks were taking up an unreasonable amount of CPU time, and, with the advent of the so-called mini-computer, the idea of using a dedicated processor for performing some routine task became practicable. A number of systems that started with a single computer have had small dedicated processors added to them, such as the function generators at the AGS and CPS.

The next stage was that the satellites became larger and more powerful so that they could be used to operate some part of the equipment under the command of the main computer, and may also have some stand-alone capability. This increase in the size of the system can be seen by quoting a few examples.

The AGS started off with 2 PDP 8 computers and later added a PDP 10 and more PDP 8's. This is the exception to my generalization - in this case a large main computer was added after the satellites had been operating in a stand-alone fashion for some time. This system is described in one of the papers to be presented at this session[2].

The Bevatron started with a single PDP 5 and now has added PDP 8's and a PDP 9.

The CPS started with an IBM 1800, added a Varian 620 and is now in the process of adding 3 PDP 11's, with the prospect of further additions later.

SLAC started with a PDP 9 for the machine, which was then coupled up to the SDS 975 controlling the beam lines and now 9 PDP 8's are being added[3].

Even at LAMPF, which started with one of the largest single computer configurations of any machine, a NOVA 620 and a PDP 11 have been added for special purposes.

More recent accelerator systems have been planned to use a number of computers from the start, but even then the number of computers has increased. For example, NAL started with two Sigma 2 and eight Mac 16, and the latest plans include four Sigma 2 and over twelve Mac 16.

Almost all these systems are arranged so that a control computer acts as master, the others being satellites. The next stage, which we have adopted in the SPS, is to split the duties of the central computer amongst a number of processors, of which none is absolute master. In order to do this, one has to have an effective message transfer system to sort out the intercommunication problems. This system is outlined in a paper to be printed in the proceedings[4].

Summarizing the progress, we have proceeded from single computers to the addition of dedicated satellites, then the stand-alone satellites to a true multicomputer computer system. The next stage seems to be the addition of dedicated processors to the multicomputer system. These could be the so-called micro processors, but more likely will be peripherals with some processing power such as the CAMAC units described below.

This development can be paralleled with the Business ADP scene. Here also, a single computer, as big as possible, was used to provide a service to a number of "dumb" terminals. The single computer was increased in size until it began to suffer from organizational indigestion. The dumb terminals were then replaced by "intelligent" terminals and now proposals are being made that the big computer should be replaced by a network of mini-computers, some acting as "super-intelligent" terminals, and others dividing the duties of the control computer between them, working on a common base.

Thus the picture on the computer side shows an increase in the number of processors, and the consequent need for a good means of inter-computer communication. However, it is also seen that as the number of computers increases, the number of tasks to be carried out by each computer does not decrease - the total load increases to use up all the additional power! This can be illustrated by the case of the SPS. We started out with the idea of having a large number of very small computers, each doing a relatively simple task and having the very

minimum operating system. We have ended up with the same number of computers, but now these are fairly powerful processors with a multiprogramming operating system in each, when all the requirements have been taken into account.

3.2 Interface to the equipment

The next most important thing after the computers is the interface system. In the earlier systems either the manufacturers standard interface, or some special system developed in the laboratory concerned, was used. I think we can now say that we are well on the way towards standardization on CAMAC, with NAL, Triumph, Los Alamos, Daresbury, Rutherford and the CERN machines, amongst others, using it for at least part of the interfaces. CAMAC may not be the ideal interface for control use, but it is a recognized standard that has been accepted by the experimental physics community, and is being used more and more in control outside this field, including medical and some industrial applications. Sufficient different modules are now available to cover almost all requirements.

The main disadvantages of CAMAC are that the miniature plugs and sockets, which have to be used because of the narrow panels, cannot be used with normal sized cables, so that, for transmission over distances of more than a few metres, junction boxes have to be used, and relays, transformers or opto-couplers inserted to minimize pick-up where standard CAMAC modules serve several different pieces of apparatus. There are also problems in having the CAMAC crates any appreciable distance from the computer with most existing systems, but this will be solved when the serial highway alternative gets going.

On a large accelerator, these disadvantages can be overcome, without losing too many of the advantages, by using a second level of multiplexing for acquisition and control where the timing is not too critical. The system for the SPS, which uses CAMAC as the primary interface, is outlined in a paper in these proceedings[4].

I mentioned earlier the trend towards putting some processing power into the peripherals. The SPS system has a CAMAC autonomous function controller that can be loaded with a simple program to cause it to perform a repetitive action. An example of its use is for status checking via the multiplex system. When initialized, it can scan a list of addresses and desired status in the core of the host computer, via DMA, and check the actual status of the equipment connected to the multiplex system. If the status is correct, it will step through the whole table. The CPU is not involved, unless an error is found and in such a case an interrupt is raised and the address of the offending unit is passed to an alarm program. Other simple processors in CAMAC are under development in other laboratories.

3.3 Interface to the operator

Another area where there have been some developments is that of the computer/operator interface. Gone are the days when all action was through a teletype. More and more systems are using visual displays with various means of interaction. The light pen found a few friends, and we were told about the LAMPF card-programmable buttons and the SLAC cross-wire touch-screen at the National Accelerator conference last year[5,6]. A further development on this theme is the capacitive-change touch-screen described in a paper in these proceedings[7]. Various systems have used knobs connected to incremental encoders that could be hooked to control variables in the system, and the latter paper also describes a knob with feedback to the operator, as it can have variable resistance to being turned, or can become a multiway switch, or a rate-control, spring loaded to zero.

4. Software

I have taken up rather a lot of my space with the hardware, but this does not mean that I think it is more important than the software. In fact, it is in the software that I think the accelerator community has made the greatest contributions to computer technology.

The earlier machines were small, and so programming had to be carried out in assembly language. Following the practice of the computer engineers, the programs were written to carry out a particular function and the specialized handlers for the hardware were considered as part of the program. Gradually, as more than one program acted on the same variables, the handlers were made re-entrant and concentrated data bases were introduced. There are certainly some advantages in using a single massive data base with a system using a single computer, as in the system for the CPS Booster described in one of the papers presented at this conference[8]. In the case of a multi-computer system, I think that to concentrate the data into a single area will result in too great a traffic on the data links, and so with a distributed computer system the active data base should be distributed, but there should be a master copy kept centrally, which is updated relatively infrequently, for reference or in case of accident.

The next stage, where computers increased in size somewhat, was the introduction of higher level languages for the production of applications programs, mainly on pressure from the machine physicists. The further development on this theme was the use of a real time interpreter, with a suitable command language, so the operator could interact in a simple way with the control system, and changes could be made on-line. These ideas were first developed in the Rutherford Laboratory in England, and some parallel work was going on in the early days of NAL.

I shall return to the subject of interpreters in the second part of my talk.

Rapporteur's Summing up

In the first part of my talk I traced the evolution of computer control of accelerators up to the present, and now let us see if we can look into the future.

On the hardware side, there seems to be general agreement that, except for the smaller systems, a multicomputer arrangement is the best, with some satellites carrying out the true real-time functions tied to the accelerator time scale, and one or more central computers working in the operator time scale. Whether we should use a single large computer like at Brookhaven, or LAMPF, or many small ones, like at the SPS, is more controversial, and so a point for further discussion.

On the interface side, obviously laboratories which have already developed successful systems for interfacing, such as the DATACOM at Brookhaven, will continue to use them, but for those starting from scratch on future accelerators, I think the pressure to standardize on CAMAC for at least the primary interface will be very strong. A point of discussion could be how much of the routine processing should be carried out by such devices as the autonomous function controller in CAMAC.

Turning to the operator-computer interaction, I think that the accelerator control community is in the forefront of this field, and so I hesitate to predict the next stage. The idea of an accelerator being controlled by verbal instructions from the operator is not too far beyond present technology, but I cannot see any justification for putting any effort into it.

It is on the software side that the biggest differences exist - whether one should use only compiled or assembled programs, or should use an interpreter. For those not steeped in the computer jargon, I should explain that an interpreter is a program that takes statements in a command language and forms the links between the appropriate subroutines at the time of execution. This allows changes to be made without going through the stages of compiling or assembling, linking and loading normally needed.

Thus the operator can interact fully with the system, even programming on-line, seeing the effect of each statement before going on to the next, protected by the interpreter from doing things fatal to the system.

One pays for these advantages by slower execution, but this has not proved a major problem so far. One can have very simple subroutines and a relatively long command language program, which gives the maximum flexibility but slow execution, or more complicated subroutines and a shorter command program, which is less flexible but runs faster.

For the SPS we are basing our software very heavily on an interpreter for a very powerful control language, NODAL, which is mentioned in one of the papers to which reference has already been made[4]. Coupled with this is the use of a separate data base for each fundamental type of equipment, with its specialized handler, which we have called an equipment subroutine.

As a simple example of the power of this system, the complete NODAL program given in Table 1 causes a secondary emission monitor to traverse through a beam, one step at a time from any initial position to any final position, takes a measurement at a particular time in the cycle, and types out a table of positions and values. I would like to draw your attention to the second half of statement 2.1. This EXECUTE command is used to obtain the execution of a group (in this case group 3) of the program in another computer (number 8) using the present value of some variable (P). The REMIT command in line 3.1 causes the return of the value of A to the original program.

In the paper on the CPS Booster system, Dr. Schindl pointed out the difficulties they had run into trying to commission the machine and the software at the same time. An interpreter helps a lot in such circumstances, as the subroutines can be tested with the prototype equipment and difficulties sorted out before the whole machine is finished. Almost all our technicians can program in NODAL, and as there are quite a few computers around already, they are using them to test out both prototype and production units.

Thus we will get quite a bit of experience with practical use of the software even before the accelerator is assembled.

There was some discussion on the relative merits of interpreters at the last conference of this series, and some of the participants thought that interpreters were fine for machine development, but that programs for the regular running of the machine should be compiled, so that the operator would not be tempted to change anything.

I wonder if there has been any change in this opinion since then. The Brookhaven system seems to come half way between the two. The assembly language systems in the PDP 8's with their command lists and execute lists are like rather complicated subroutines that could be called by compiled Fortran statements. However the powerful PDP 10 allows rapid recompilation and so a lot of the advantages of an interpreter are obtained, but this can only be done with a comparatively large central computer.

Incidentally, it has been pointed out to me that you can usually tell if a control man started his career in the computer field or as an engineer. If he is a supporter of interpreters it is highly likely that he started as an engineer!

Summing up, I will stick my neck out and prophesy that the next generation of accelerators will have control systems based on multicomputer layouts, using CAMAC for an appreciable part of the interface. The operator will communicate with the system through touch screens, knobs and tracker balls, and the software will be based on the use of an interpreter for a high level control language,

References

1. "The Impact of Computer Control on the Performance of the ISR", P. Wolstenholme, Paper 7-16.

2. "Use of a General Purpose Time-shared Computer in Accelerator Control", M.Q. Barton et al. Paper 7-13.

3. "Initial Experience with a Multiprocessor Control System", K.B. Mallory, Paper 7-19.

4. "The Computer Control System for the SPS", J.T. Hyman, Paper 7-15.

5. "A Compact Programmable Control Panel for Computer Control Systems", B.L. Hartway, IEEE Transactions on Nuclear Science, Volume NS-20, Number 3, June 1973.

6. "Experience with 'Touch Panel Control at SLAC", W.C. Struven, IEE Transactions on Nuclear Science, Volume NS-20, Number 3, June 1973.

7. "The Operator Interface of the 300 GeV Accelerator", F. Beck, Paper 7-14.

8. "Users Assessment of the Computer Controls System of the CERN PS Booster", G. Baribaud et al., Paper 7-12.


```
1.1 ASK "INITIAL POSITION=" IP "FINAL POSITION=" FP

1.2 SET P=IP; EXECUTE (8) 3.2 P

1.3 FOR P=IP+1,FP; DO 2

1.4 END

2.1 WAIT EVENT(4);EXECUTE (8) 3 P

2.2 TYPE "POSITION=" P-1 "CHARGE=" A

3.1 SET A=MINSCN(2); REMIT A

3.2 SET MINSCN(2,ØPOS)=P
```

TABLE I

DISCUSSION

Bruce L. White (University of British Columbia): How much accelerator down time can be attributed to either computer failures or software failures *as* a proportion of the totai down time?

Crowley-Milling: Some of the papers do have some information on this and it varies quite considerably from laboratory to laboratory but in most cases it is a very, very small proportion of the total time once the initial teething troubles have been overcome. As you've heard, in some *cases* there are considerable teething troubles, in other cases there are relatively minor ones, but I don't think anyone can get away without teething troubles.

Lee Teng (NAL): At NAL, our experience is that down time due to computer hardware and software failure is less than 10% of down time.

Peter Wolstenholme (CERN): It ranges from about 2.2% for the ISR to about 10%.

Alfred Maschke (BNL): I'm personally in favor of interpreters but they have one drawback in that they don't interface well with an enormous amounl of the existing FORTRAN subroutines. Have you a solution for that problem?

Crowley-Milling: This is one of the problems for laburntories that have built up large FORTRAN libraries, or are you meaning the computational programs?

Mnschke: The most difficult programs lo write, frequently the I/O things that when you buy a display unit, the manufacturer will provide you with a quarter-million-dollar FORTRAN program tu display it.

Crowley-Milling: Well, one of the advantages of using CAMAC for your main interface from the system is that you can approach the interface problems in a uniform way and this solves quite a lot of problems.

Shigeki Mori (NAL): How many cables carry other than digital signals?

Crowley-Milling: The multiplex system I described has an analog highway and for analog measurements where the highest precision is not required, the multiplex switches the analog signals onto the highway where they are fed into an ADC in the CAMAC and then they become digital from there. The other type of analog signal is the analog wave form signal where we have a switching system under computer control for switching the various analog signals from the various distant buildings to the central control area. So there's that analog system and there's also the analog measurement system.

Gregory Loew (SLAC): In your future system at CERN, what happens if one of the computers that's controlling part of the ring fails?

Crowley-Milling: We have, wherever possible, tried to make the hardware on the principle that it carries on doing what it was told to do previously until it's told to do something different. So that in manycases, it's a case of if a computer went out, that part of the system wouldcontinue to run although, of course, you wouldn't get warning signals back or your surveillance system wouldn't be in operation. But there are other regions, for example the computer controlling the main power supply where it is feeding out information every ten milliseconds, where if that goes down, you're off.

USER'S ASSESSMENT OF THE COMPUTER CONTROLS SYSTEM OF THE CERN PS BOOSTER

G. Baribaud, G. Benincasa, A. Daneels, P. Heymans,
C. Metzger, F. Pedersen, M. Rabany, K. Schindl and J. Stark

MPS Division, CERN, Geneva, Switzerland

Summary and Introduction

The CERN PS Booster' (PSB) was designed to be completely computer-controlled and no manual back-up was foreseen. The physical construction of the four-ring PSB necessitates simultaneous operation of different parts of the accelerator and therefore requires a multi-entry software facility. A significant feature of this facility is the data base, which links the software to the hardware of the accelerator and also leads to an increase in the versatility of tests and operation. The evolution of the system from its conception, through the phases of commissioning and running-in, each with its different needs, to the present operational stage is described. Attention is drawn to the lessons that have been learnt during the first two years of exploitation. The initial phases were made more difficult because it was impossible to separate completely effects due to the commissioning of the controls system and the first tests of the accelerator. However, the investment in this first phase gave rise to substantial benefits as soon as basic settings for the PSB were found. The current phase of operation typifies some of the problems involved with simultaneous development of a machine and its computer-controls system. There is a certain conflict between those who have to operate the machine as it is and those who want to develop the control system further. Most aspects of the system have worked satisfactorily from the start, but some have been less reliable. However, it is hoped that the effort which is being given to the hardware will allow more sophisticated tasks, such as closed-loop control, to be carried out.

Computer-Controls System

The basic computer configuration')[3] for the Linac, PSB, and CPS (Fig. 1) includes an IBM 1800 with 48K of core memory (16-bit words) operating under MPX (Multi-programming System), and several peripheral devices (two PDS-1 minicomputers to drive alphanumerical and graphical displays and a Varian 620i satellite to generate analog functions). A 4K partition is dedicated to each accelerator where application programs are housed. Core resident programs go into higher level partitions called Special Areas, shared with other users. A larger partition of 6.5K, called Variable Core (VCORE) is used for background programming and for execution of long or special programs called on interrupt (Interrupt Core Loads) when requested by a partition. The more important application programs in use are listed in Table 1. The total length of programs is about 350K words; 20 man-years were required to define, write, debug, and optimize these programs. Most programs refer to the data base' (∿ 700 process variables) which was introduced to avoid conflicting control from the various operator consoles: three midi-consoles (Fig. 2) (for the injection line, RF, and transfer line), a central maxi-console (Fig. 3) concentrating control of all subsets, and a mobile console, used for hardware tests in the equipment rooms (Fig. *4)*. The control and data acquisition of the four PSB rings are largely independent of each other but are synchronized with the Linac and the CPS. The essential components of the control system are assessed in Table 2.

Problems During Running-In

At present the system works as specified. While certain parts were satisfactory from the start, others had teething troubles, though not more than would be expected for a system of such newness and complexity. Two types of problems are discussed, those which turned out to be more serious than anticipated and those which had not been fully foreseen.

When deciding that there would be no manual back-up from the Main Control Room (MCR), it was realized that if one of the major components of the control system failed, the accelerator could no longer be controlled. (In view of the expense of full manual back-up, the risk was nevertheless taken.) Thus the situation of sometimes not being able to change a parameter setting by computer was a major handicap until reliability improved sufficiently.

Trouble was caused by the front-end equipment (transmission system, converters, power supplies) in the early stages of running-in. This was mainly due to trying to start up the accelerator at the scheduled time although some of the construction staff had moved to another project before they had reached the testing stage of their equipment. It was only with the first beam in the machine that the control system could be fully tested out, and therefore it had to be accepted that the last part of the running-in of the software coincided with the running-in of the PSB.

As for the multi-user computer system itself, computer crashes caused by program development occasionally disturbed the PSB program under execution. Since less program development occurs now, this is less noticeable. Besides this, the data base on disk was sometimes erroneously overwritten. The situation has been improved by introducing protection in the form of a software indicator. A long-standing puzzle has been solved only recently. An injection line magnet changed its value when no-one was working with it. It shared, by error, its control address with an ejection dipole (controlled from a different midi-console). There is no protection against this, but a checking program has been written.

Three problems arose in connection with the function generator, which has been in heavy use since the beginning. Firstly, some operators found it clumsy to use (possibly because of insufficient contact during the design). As a remedy, for some functions (choice of Q-values during cycle) an automatic setting procedure has since been implemented. Secondly, up till now, there has been no digital acquisition of a complete function. This will be rectified. Finally, if the Varian computer breaks down, the PSB stops. A back-up Varian has recently arrived.

Finally, the human element played its role in determining the speed of running-in. To the operators, not only the accelerator but also the control system was completely new, and they were unaware of the full capabilities of computer-assisted control. For some of them, accustomed to controlling a machine by hand, confrontation with a control system, supposedly easier but in practice more difficult during the early stages of running-in, led to psychological problems.

Among the problems not fully foreseen were the following. Initially, the information on the status of the elements was not displayed continuously. When a power supply tripped, the operator would notice this through its effect on the beam but there was no immediate information from the control system on such an event. This has been overcome with the introduction of the Status Display and the Repetitive Varilog on the midi-consoles (see Fig. 2 and below).

The injection line quadrupoles which are controlled by stepping motors (incremental control) were lengthy to set by hand or by program. Recently a closed loop iteration procedure program has been used successfully to set up the injection line focusing.

While the bulk of the measurement, data treatment, and display programs (which were ready at start-up) fulfilled their requirements, some modifications and additions were, on occasion, needed rapidly. This presented no particular problems, notably thanks to the close collaboration between machine and software specialists.

Aspects of Special Interest to the Users

i) During optimization from the midi-console, the operator can compare the current machine set-up with a reference set-up without, however, losing the current values (stored in a buffer on the disk-based data base). Owing to the slowness of the computer disk accesses, these subset operations are used much less frequently than had been hoped. Such an operation takes about *40* seconds. As often only a few parameters vary between different settings, the operator does not take much longer to make a comparison by tuning only these parameters. However, a subset operation regularly used is the setting from the maxi-console, for which *40* seconds is very short compared with the time for a manual setting of some hundred parameters.

ii) The voltages of the four accelerating cavities are controlled by high-speed generators. The parameters of the given mathematical function are controlled by program through the RF midi-console. This allows one to obtain a mathematically described function from the digitally controlled voltage generator just like any ordinary process variable. At present the procedure to enter changes is slow owing to limitations of the present system. A program orientated more towards advanced machine experiments is being developed and will include a facility to reduce the voltage slowly during the cycle to obtain a constant bucket area.

iii) Watchdog programs fall into three categories. Firstly, whenever a status changes, the number of parameters that are OFF (power supply disconnected) and NOT READY (down) is displayed on the midi-console (Fig. 2). Secondly, there are programs called at regular intervals: a) Vacuum Survey displays an alarm message forewarning vacuum specialists of possible breakdowns; b) RF Voltage Generator Survey checks the memories of the Voltage Generator and displays and resets those that have varied; c) Repetitive Varilog warns the operators of parameters drifting away from reference values. A problem with the Varilog is that only one reference value exists on disk and different operators require different reference values -- a fixed theoretical value, a value gained from experience, or a value taken when the beam was running well. Finally a statistics program compiles beam histograms'.

iv) The Booster electronic equipment is located in the Booster building (about *400* metres from the MCR), and it is there that various calibrations and adjustments have to be made. Originally the results could be observed only on the maxi-console in the MCR, which implied, in addition, communication between the MCR and the operator working on the electronics. It was decided to introduce a second, mobile, maxi-console in the Booster building. It can be connected, through a single cable, to the computer network from any one of seven different points. This allows the operator to move the console close to the equipment being tested. The mobile console offers the same facilities as the maxi-console in the MCR, so the 'computer-control-acquisition' loop can be thoroughly checked locally. The console is regarded as an extremely useful tool by those responsible for PSB systems.

v) The data base may be updated and modified via the interactive display by means of a special program. Users quickly learned how to check or modify characteristics such as conversion factors, status bit coordinates, maximum values, permissible variations, etc. They had the possibility of fitting the relevant data bank parameters to reality, masking a status bit, etc., within a few minutes. Whole runs might otherwise have been lost: Thus we found that the risk of having vital parameters changed by inexperienced operators is small compared to the advantages of a flexible data base for program development and accelerator operation.

Conclusions and Outlook

At this stage the correctness of the major options (use of existing IBM 1800, addition of a satellite for real-time work, choice of multi-access consoles, introduction of a data base, no manual back-up, addition of the mobile console) are confirmed by our good experience. The midi-consoles remain an easy to handle setting-up tool. The maxi-console is used for more complicated tasks. We are less sure whether we should not have already introduced an interpreter facility (not available when the control system was defined). We expect this to be particularly useful for machine experiments. While nearly all PSB parameters are computer controlled and/or acquired, there remain a few (important) exceptions. We expect to complete their computerization in the framework of the expansion of the PS computer system. At the same time we plan to expand the PSB system's monitoring and fault analysis facilities. Like any other system, the computer control system needed running-in. This progressed more quickly and easily where there was close co-operation between the control engineers, PSB system specialists, the programmers, and the operations team. Most of the authors were newcomers to the field; now that we are familiar with computer controls we are looking forward to using the extended capabilities of the expanded system under construction.

Acknowledgements

We are greatly indebted to the former and present members of the CO/CCI Group, in particular E. Asseo, H. van der Beken and J. Bosser, who designed and built most of the PSB computer control system and are now working on its expansion. C. Bovet has defined the machine physics content of a large number of application programs and contributed to their implementation. Constructive criticism by the PSB operating team has led to numerous developments, K.H. Reich suggested substantial improvements to the manuscript.

References

1. The PSB Staff, this conference.

2. E. Asseo et al., Proc. Particle Accelerator Conference, Chicago, 1971 [IEEE Trans. Nuclear Sci. 18, No. 3, 354 (1971)].

3. G. Benincasa et al., Proc. IEE Conf. on Software for Control, Warwick, 1973 (IEE Conference Publ. No. 102), p. 57.

4. A. Daneels, Proc. National Computer Conference, Chicago, 1974, to be published.

5. K.H. Reich, Some thoughts on the data acquisition and control systems for the CPS Booster, CERN Internal Note SI/Note DL/69-5 (1969).

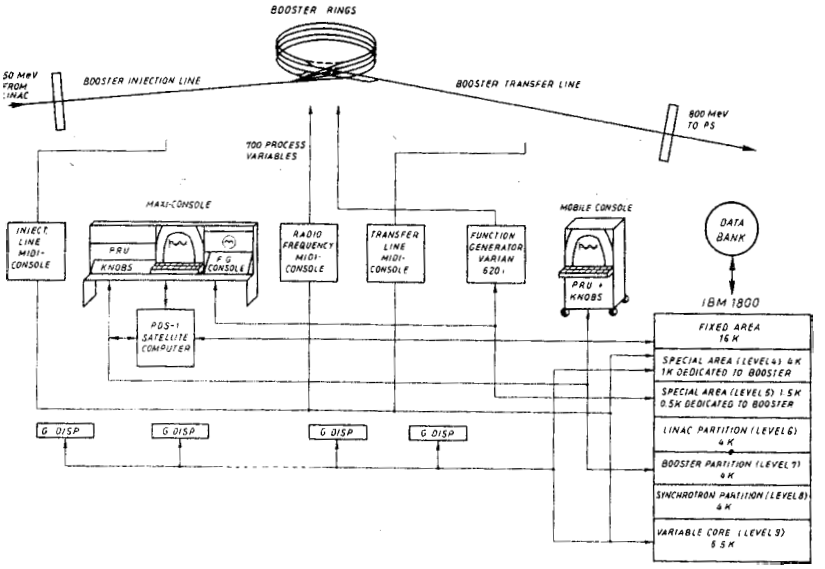


Fig. 1 On-line operation facilities at the PS Booster

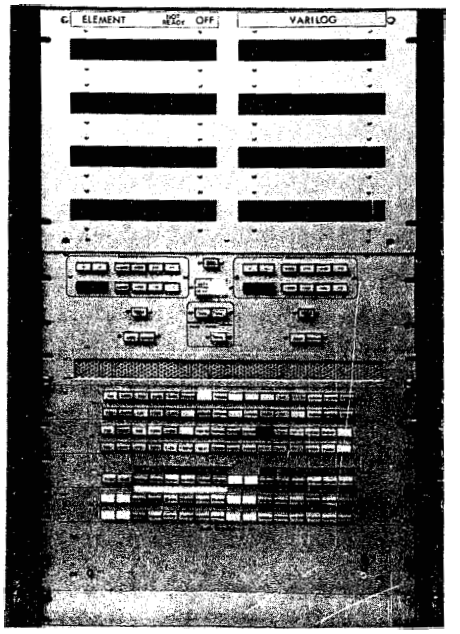


Fig. 2 A midi-console

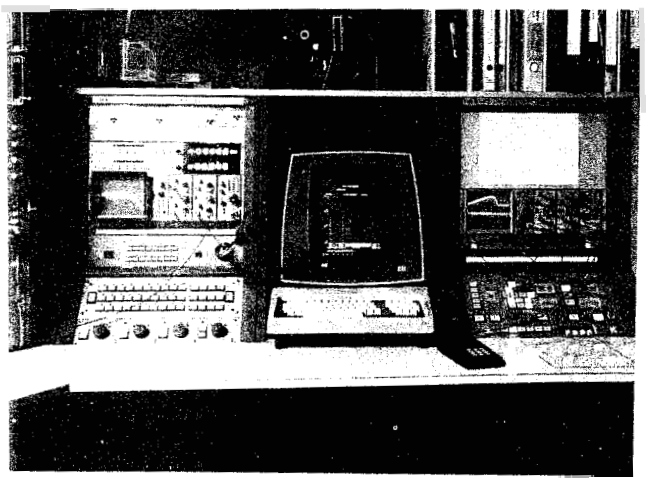


Fig. 3 The maxi-console

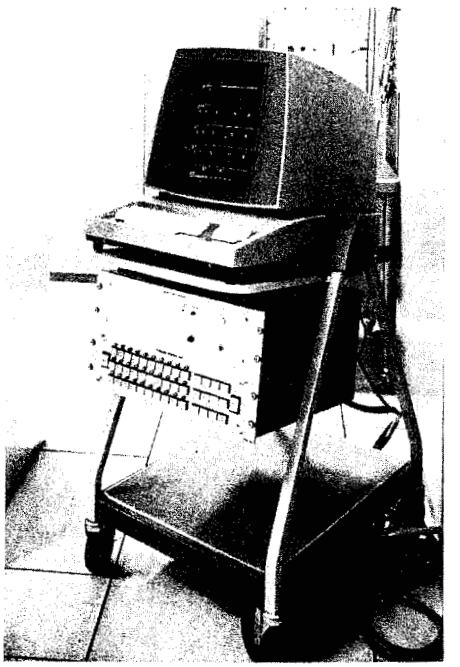


Fig. 4 The mobile console

TABLE 1 COMPUTER PROGRAMS

No.	Program name and description	Frequency of call/week	Length of time/ call (C= continuous)	Further uses (see below)	Input media (see below)	Output media (see below)	Refers to data base	Length (K words on disk)
	GENERAL OPERATION PROGRAMS							
1	MIDI-CONSOLE (see Table 2)	300	5 sec	HT	M,D	M	YES	15
2	KNOBS	50	15 min	HT	P,KNOBS	P	YES	27
3	STATISTICS. PSB intensity	21	8 h		P	L,D	NO	10
4	LOG. parameter print-out	50	2 min	ME,HT,ST	P	L	YES	16
5	VARILOG, Display of parameters outside tolerance	10	3 min	ME,HT,ST	P	P	YES	10
6	STATUS DISPLAY on PDS-1	40	30 sec	ME,HT	P	P	NO	6
7	GENERAL DISPLAY (see Table 2)	LOO	C	ME	Push-buttons	Nixies	NO	3
8	REPETITIVE VARILOG. Watchdog	10 min	30 sec	ME	P	M,D,P	NO	6
9	TRANSFER LINE PICK-UPS CALIB.	2	3 min	HT,ME	P	P,T,D	NO	5
10	SETTING, of 12 PSB sub-sets	10	30 sec	HT	P	P	YES	57
11	PARAMeter behaviour display	20	5 min	ME,HT	P	P,T	(YES)	9
12	VACUUM, Past and present state of pressure in pumps	30	10 sec	HT	P,Vacuum panel	P,L	NO	15
13	RF VOLTAGE GENERATOR	5	10 rnin	ME	M	P,M	YES	16
14	FUNCTION GENERATOR (see Table 2)	20	10 min	ME	F.G. Console	Oscilloscope	NO	1
	BEAM OBSERVATION PROGRAMS							
15	LINAC SPECTROMETER	30	30 sec		P	Television	(YES)	7
16	LINAC EMITTANCE	20	30 sec		P	Television	NO	4
17	Q-MEASUREMENT in both planes	30	10 min	ME	P,Q-meas panel	P,T,L	NO	5
18	ORBIT DISPLAY (with dipoles control and Q-calculation)	50	10 min	ME	P,RU-panel	P,D,L, Cards	YES	38
19	IONIZATION BEAM SCANNER (IBS) Evaluation of beam profile	15	5 min	ME,HT	P,IBS-panel	P,L,D	NO	33
20	800 MeV LINE MEASUREMENTS Spectrometry and emittance	10	10 min	ME	P,800 MeV-panel	P,T, Cards	YES	16
	CONTROL SYSTEM DIAGNOSTICS (HARDVARE AND SOFTWARE)							
21	UPDATE DATA BANK	15	2 min	OP	P,D	P,D	YES	7
22	READ DISK	20	30 sec		P,D	P	NO	2
23	REPETITIVE RF VOLTAGE SURVEY	2 hours	2 min		P	P,T	YES	3
24	RING PICK-UPS HARDWARE TEST	1	10 min	OP	P,RU-panel	P,RU-panel	NO	3
75	MIDI-CONSOLE HARDWARE TEST	1	5 min		P,M	M	NO	2
26	KNOBS HARDWARE TEST	1	5 min		P,KNOBS	P	NO	1
	MISCELLANEOUS FAULT RECOVERY							
27	RESTART PARTITION	1	30 sec		P,IBM switches	IBM 1800	NO	1
28	RESTART PDS-1	4	30 sec		PRU button	P	NO	1
29	ENABLE FUNCTION GENERATOR	2	10 sec		PRU button	F.G.	NO	1
30	COLD START MIDI-CONSOLE	2	30 sec		PRU button	M,P	NO	1

OP = Operation, MP = Machine experiments, HT = Hardware Test, ST = Software Test

T = Typewriter, L = Lineprinter, M = Midi-console, P = PDS-1, D = Disk

Table 2 Survey of the PSB control system

Item	Purpose and reasons for choice	Performance expected	Assessment in March 1974
IBM 1800 (in MCR)	Process control computer (already used by CPS). Use by PSB implied i) no delay in making choice and ordering a new computer; ii) profit from CPS knowledge and experience.	i) Almost all elements effectively controllable and acquirable from MCR. ii) Watchdog and statistics programs. iii) Hardware tests' and calibration facilities.	All performance aims atrained. However, sharing the existing computer led to some constraints, particularly program length.
Alphanumerical and graphical display (in MCB and at PSB)	Centralized interactive console driven by IMLAC PDS-1 mini-computer.	i) To allow fast on-line interaction with programs. ii) To display results of programs in an easily understandable form.	Good for alphanumerics but should be improved for graphical displays. Hard copy facility very much appreciated.
Varian 620i (at PSB) with special console (in MCR)	Flexible generation of up to *48* analog functions in real time.	Interactive creation and modification of functions from the console.	i) Performs as expected. ii) Sampling of function incomplete.
Three midi-consoles (in MCR)	To allow simultaneous control of three PSB sub-sets without syntax handling; simultaneous control of two selected parameters of a sub-set (increase, decrease, inversion of polarity, ON/OFF).	i) Possibility of linear coupling of variables. ii) Common operation on all parameters of the entire sub-set. iii) Display of information on parameters under display and watchdog programs.	i) Very useful in setting-up periods. ii) Watchdog programs are a useful diagnostic tool. iii) Slow in operation, owing to repetition rate (twice per acceleration cycle) and disk access time on IBM. iv) Too many buttons (120) for operator comfort.
KNOBS (in MCR and at PSB)	Four incremental encoders with which one can control most of the PSB parameters from a central point.	i) Ability to form special couplings. ii) Ability to work alongside other programs, e.g. beam quality measurement programs.	Vesy useful during steady operation and for machine experiments.
General display (in MCR)	Twenty Nixie displays distributed over the control room. Already used by CPS.	Cycle-to-cycle display of manually selected parameters such as Q-values, efficiencies, mean radial position.	Gives an over-all view of the machine. Name of displayed parameter difficult to read.
Program Request Unit (in MCR and at PSB)	Push-button matrices from which i) programs can be called into core; ii) options can be exercised in running programs. Already used by CPS.	i) Queueing of programs. ii) Easy to handle by operators. iii) Flashing light to show which program is running.	Performance expectations attained. With increasing number of programs, limited number of buttons led to: i) regrouping of several programs in one button; ii) too rigid nomenclature for the option buttons.
BCER console (at PSB)	Alphanumerical and graphical display and Program Request Unit. A facility for local hardware testing in the Booster building.	To give most of the facilities of the central console.	Turned out to be indispensable for maintenance and calibration. Shares computer access with central console.
Data base	Up-to-date image of the current accelerator state covering most PSB variables (∿ 700) with their characteristics.	Easy to use for setting and other application programs. Automatic updating of current control values. Easy modification of parameter specifications.	Its flexibility has been greatly appreciated, especially during the running-in period, but misuse possible.
STAR	16-bit parallel data transmission system for acquisition and control. Already used by the CPS. Designed for use over long distances.	i) Reliable transmission in range of 20 to 100 K words per sec. ii) Random addressing of up to 1024 process variables per call.	i) In general, meeting requirements. ii) Connection to specific electronic systems is very simple. iii) Diagnostic equipment to speed up fault localization is being improved.

USE OF A GENERAL-PURPOSE TIME-SHARED COMPUTER IN ACCELERATOR CONTROL

M.Q. Barton, B.B. Culwick, **J.A.** Curtiss, J.J. Dabrowski
R.S. Frankel, W.E. Harrison, F.R. Martin, J.D. Smith,
R.J. Warkentien, I. Weitman

Brookhaven National Laboratory
Associated Universities, Inc.
Upton, L.I., N.Y.

Summary

A general purpose real-time data acquisition and control system implemented on a PDP-10 time shared computer and interfaced to devices via PDP-8 peripheral processors and a serial transmission scheme has been constructed. The design objectives of Fortran coded time-shared access to the accelerator have been achieved under the manufacturer's monitor with the addition only of shareable device handlers. The time-sharing monitor has allowed the development and operation of alternative control systems in parallel with continued use of an earlier system. Program development has been facilitated by the convenient access provided by the operating system and the multiple terminals available for programming and testing.

Objectives

Computer control and monitoring of the Brookhaven AGS dates from 1965. A system of control terminals interfaced to dual PDP-8's with disc storage was developed and served usefully in accelerator operation and physics studies of the machine. With the completion of the AGS conversion, it became apparent that exploitation of the machine could be greatly aided by suitable computerization of instrumentation and control of the accelerator. At this time it was also recognized that such computerization requires very significant efforts in manpower if effective results are to be achieved in a reasonable period of time. Two ways in which this burden could be alleviated were proposed 1) implementation of the control and monitoring programs to a great degree in Fortran, **2)** implementation of the system in a time-sharing environment.

The first of these points is not seriously disputed at this time. No matter how efficient the individual, experienced analyst, the range of talent which can usefully be brought to bear on a problem and the speed of implementation are both greatly increased by use of the high level and universally spoken language. The second point is only slightly more subtle. The many and varied activities around the accelerator are obviously facilitated by independent access to computational power but the total integration of the system and interchange of information are simplified in a single machine. Both possibilities are provided by a medium scale general-purpose time-shared computer. This paper will discuss the implementation of an accelerator control system based on such a machine.

Configuration

The time-shared computer selected as the basis for the operating system is a Digital Equipment Corp. PDP-10. Among other reasons for the selection of this machine were principally the amply demonstrated capability of the time-shared operating system and the prior existence of two machines of this class in the Accelerator Department. A more difficult decision, given the objectives which included control of the accelerator complex from a single location, was the selection of direct device communication from the PDP-10 or interfacing to the hardware devices via a small computer. It was decided to interpose the small computer for the following reasons:

1. The PDP-10 manufacturer's time-shared operating system is designed around time responses of the order of terminal needs. To impose on this monitor the real-time needs of the AGS, while not impossible, would nullify many of the time sharing advantages. By interposing a small computer or computers operating synchronously with the AGS it would be possible to allow the PDP-10 to operate asynchronously under its normal scheduling algorithm.

2. The totality of the PDP-10 monitor is impressive in both bulk and complexity. By divorcing the real-time code procedures from the PDP-10 it was possible to develop these independently of the monitor. The alternative of "user mode" 1/O development or actual incorporation of the necessarily complex service routine into monitor development versions would be both laborious and hazardous to the system. There would be no time-sharing for the system developers: Definition of a reasonably simple service routine for data communication with the small computer allowed development of the small machine code without "bombing" the PDP-10 monitor.

3. Demanding real-time requirements in one area of the AGS would preclude the provision of such responses to other areas if operation were from a single processor. Such conflicts are rather unpredictable in some areas of accelerator operation and at some periods in the AGS cycle. This leads to the desirability of increased processor power which is conveniently allowed by multiple small computers assigned to specific hardware groupings.

4. An extension of the arguments of **3)** is the dedicated processor assigned to function generation or fast switching as a functional part of accelerator hardware as distinct from monitoring or supervisory control. The possibility of implementation of dedicated processors controlled by the PDP-10 is included by adopting similar approaches for all input-output.

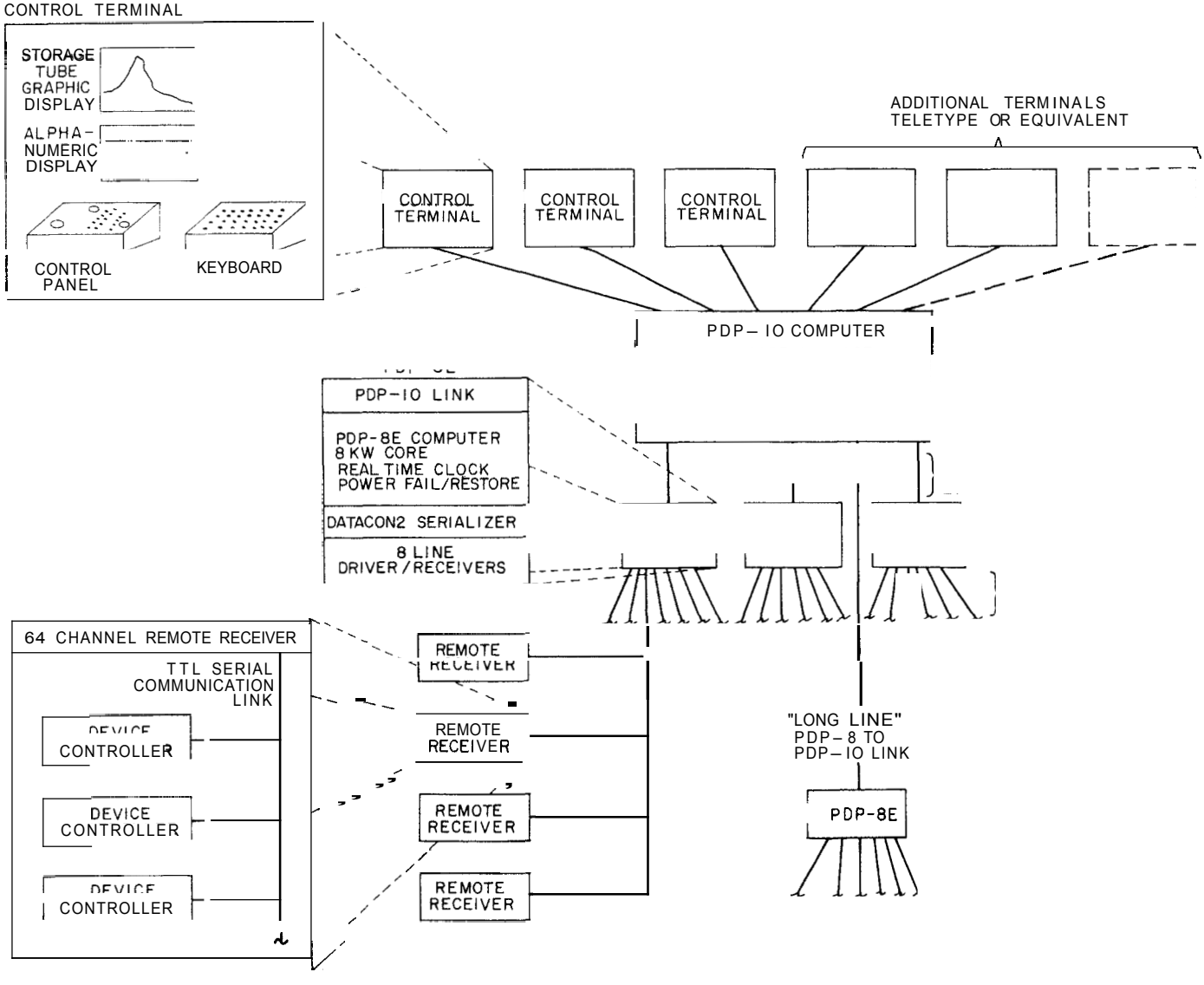
5. As will be described later, hardware facilities for communication within the system are by means of relatively slow, serial pulse trains. Any device requiring high speed computer response would require an alternative parallel interface. For consistency with the above arguments this should not be directly on the PDP-10 but requires an intermediate processor which could then be located near to the data source or sink.

6. Some consideration has been given to hardware redundancy. Spare or redundant small processors can be provided but this is hardly an advantage for a system which includes them over one without them! Operational systems to continue during a PDP-10 failure are possible using the small processors but must be at a much reduced scale. Also, a significant effort is required to produce this system for what is likely to be a small reward. Thus although this offers some advantage in principle we believe this to be slight in practice.

The sum of the above arguments has persuaded us that the "peripheral processor'' approach has sufficient merit to justify its selection over a directly interfaced design. The peripheral processor selected is the PDP-8E. This decision was based to some extent on historical precedent but has justification in the price, modern physical design and local expertise in coding, cross assemblers, etc.

The remainder of the selected configuration consists of a serial transmission scheme using a single co-axial cable connection to distributed locations for control of hardware devices. The principle is that electronics be located as close to the physical control point as allowed by the radiation environment but long traditions of multiple parallel cables have only been overcome to a modest degree.

The overall configuration is shown in Fig. 1.



PDP-8E Monitor

In order to implement a system with the desired properties in the configuration described above, it was necessary to impose severe restrictions upon the processing allowed to be performed within the PDP-8. To preserve the programmer's flexibility it was necessary that all logical decisions as well as all arithmetic calculation be made in the PDP-10. Thus the PDP-8's function only as sophisticated input/output devices rather than processors. Nevertheless, to make these devices useful in a dynamic environment required that input and output buffers and 1/O sequences be completely dynamic. An attempt has been made to generalize the input/output operation in the only dimension by which real-time differs from batch or time-share ie. time. Input/Output operations are characterized by a device address, a list, a time and a priority. The time is specified in milliseconds after the start of an AGS pulse. The priority is one of four values representing the real time criticality of the operation and is used by the monitor to resolve conflicts in 1/O requests. In particular the lowest priority causes the monitor to ignore the time and perform the operations as soon as higher priority requests permit.

One further complexity was introduced to improve the efficiency of repeated operations. A request to the PDP-8 is divided into two operations. The first step in an **1/O** operation is to define a COMMAND LIST which is transmitted to the PDP-8. This list is stored until overwritten or explicitly deleted. The commands within a list may then be performed by transmitting an EXECUTE LIST specifying a command list and a time and priority at which to execute it. More than one command list may be executed as defined in one execute list or the same command list may be repeated at two or more times. On completion of the operations specified in'an execute list, the PDP-10 is called and the service routine within the PDP-10 schedules the calling job to run again. Multiple (currently *4)* user access to the PDP-8's is provided to allow flexibility in the assigning of devices to PDP-3 channels.

Higher Level Organization

Presently a number of Fortran time sharing programs have been written which access machine data via the system described. The Fortran interface to machine data is quite convenient and allows programs to be written without concern for the real-time aspects of data acquisition. When the execute list has been transmitted to the PDP-3, the program can issue an input request and pass into an 1/0 wait state, or preferably suspend until awakened by the completion of the requested operations.

Operations within the PDP-8 are currently restricted *to* a single AGS pulse with longer time scale operations integrated in the PDP-10. Design is now proceeding on a system to provide file organized data and operat*ions* control for major areas of the machine from a single operations console. It is planned that an operator will maintain general control of machine operations with additional diagnostic activities and studies conducted Erom other terminals.

System E tension

The present system allows operations initiated by the PDP-10 and completed in the peripheral processor during one AGS pulse. It is envisaged that some repetitive functions in the machine will be allowed by repeating operations within the PDP-8 from pulse tu pulse. Such tasks might include function generation, elementary monitoring functions, etc. They would be initiated by a program in the PDP-10 and would notify the program of problems beyond the elementary level. They could be coded to continue if the PDP-10 stopped. It is not planned to extend the PDP-8 capabilities appreciably beyong this level to avoid placing restrictions on the access and decision making functions. However, some extension of the list processing facilities will be required to interface the PDP-8 monitor to some non-standard devices in existing machine *equipment.* This will be done by defining additional list formats.

Hardware

The control system equipment which connects the PDP-HE' s to controlled devices is called collectively DATACON2. The basic data transmission scheme is a transformer coupled phase encoded bipolar signal on a single co-axial line. Each transmission consists of a frame pulse followed by a key bit, 32 data hits and a parity check bit sent to devices. The data is self-clocked. An addressed device responds, after some delay allowed for internal processing, with a similar pattern but phase reversed to distinguish a reply from a message, Remote device? cuntain high impedance receivers of which 100 may be bridged on the line. Repeaters are required every 2000 feet and allow the number of receivers to be increased to the addressing limit of 256 stations per line. Signal details are given in Fig. 2.

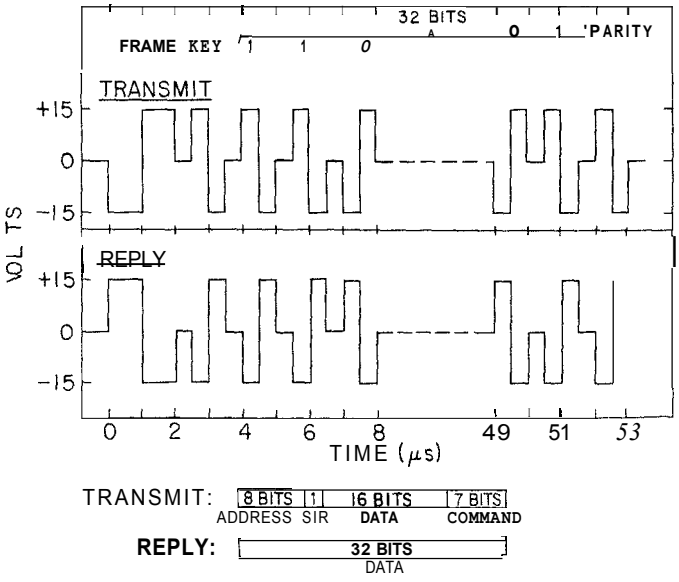


FIG. 2–DATACON2 WAVEFORMS AND WORD FORMATS

The single line technique minimizes hardware and cabling while giving a data rate of 600K bits/s which is a good match to an interrupt driven I/O service routine in the PDP-8E. The frame pulse serves as a "clear arid initialize" to all receivers. The key bi! which is always logical one indicates completion of a transmission when it reaches the end of a shift register. The parity bit is used for conventional data checking. The system provides for a suitable signalling rate with high noise immunity and excellent isolation.

The same transmission technique has been adapted to couple the PDP-10 to PDP-8 computers. Two bi-directional lines are used to provide Cull duplex transmissions with interrupt **response** control. TTL pulse trains are used for distances up to a few feet. Beyond this distance the phase encoded format is adopted *using* the drivers and receivers developed !or the device control system.

The general purpose remote receiver is capable of communicating with up to 64 device controllers, As distinct from other systems using fast parallel data transmission at remote locations and serial transmission between locations, the DATACON2 system uses serial transmission throughout. The remote receiver functions to perform some system overhead of address decoding, parity checking, etc., tu convert the phase encoded signal to TTL levels and to generate a clock signal, The data is then transmitted, still as a serial train, to the device control cards where it is clocked into shift registers. After a few microseconds for settling tin ACCEPT pulse is generated. The addressed device, which lies at the intersection of two lines generated by two 3 bit to 8 line decoders in the remote receiver, processes data and returns a REPLY pulse. The "crate controller" then generates a REPLY CLOCK and strobes data from the device cards, converts it to phase encoded form and transmits it on the line. This approach, while not fully bussed within a remote crate, minimizes the intercard wiring and is almost free of cross talk problems. A non-trivial checkout

advantage of the serial scheme is that very few lines need be checked to identify a problem.

This system is used as a general purpose means of device control and monitoring. For some large power supplies where serious noise problems and isolation requirements were encountered, a dedicated receiver approach in which the only external connection is via the coupling transformer has been developed. Excellent isolation is achieved allowing control voltages and monitored signals to be referenced to the local ground.

About a dozen standard device control modules have been developed for the common applications of self-contained device control and subsystems. These include power supply controllers, predetermined timers, scalers, and stepping motor controllers. The standard devices also include so-called system components, A/D converter and multiplexers, which permit monitoring of analog signals either associated with controlled equipment or independently generated.

All monitoring within the system is performed on a polling basis. Extension to interrupt operation would be straightforward utilizing a second co-axial line but has not been found useful at this point.

Acknowledgements

Significant contributions to the hardward system have been made by D. Easler, V. Kovarik, R. Scheetz and G. Smith.

DISCUSSION

Is the Datacom transmission system a commercial system?

Barton: No, it was developed at Brookhaven. I believe the specifications are in a paper presented in a previous National Conference. I'm not sure.

James Halbig **(LASL):** Recently we have run into an interesting problem where we were sending out a command and asking for data in the same area, and since they were running into each other too fast, it bombed the command and we were having very weird things happening. I notice with only three PDP-8's, have you run into this problem yet or are your command ingestion processes fast enough so that you haven't run into these situations?

Barton (rephrasing the question): Do we have a problem with overloading of the Datacom rates and overlapping of commands? No, the system is free of that. It can't happen.

Halbig: Is it protected by the system, you say?

Barton: No transmission can go out until you've got the reply from the previous one. The minicomputer software is run on the interrupt system so that it can't try to send another one until it's got the previous one back. There's also a time-out so that if you fail to get a reply at all, it won't hang up; it will give you an error bit in the system and for that type of problem, it's worked out very well.

THE OPERATOR INTERFACE OF THE 300 GeV ACCELERATOR

F. Beck

CERN Lab II, Geneva, Switzerland

The new CERN accelerator is controlled through a large computer network with the help of a specially designed real-time interpretive language. This has enabled the problem of designing an operator interface to be separated from that of producing control mechanisms.

The paper discusses the appearance of this interface, and some of the facilities which it will provide for machine operators.

Introduction

The new accelerator to be built by CERN will be almost exclusively computer-controlled. That is, all remotely-controllable or remotely-monitored functions of the machine can be accessed by executing suitable interpretive statements in one more central computers. It is not the purpose of this paper to describe the mechanism of this control (see paper by T. Hyman in these proceedings), but rather to explain how it has enabled us to make certain very desirable innovations at the operator interface.

Purpose of the Control Room

The control room is used for two distinct functions when the accelerator is running :

One is to supervise the machine when it is running and to make small operational adjustments. At such times there may well be only one operator in the control room, The other use of the control room is for the so-called machine physics studies, where several groups of workers may be operating more or less independently on different parts of the accelerator. A third use of the control room is when the accelerator is temporarily shut down. Safety requirements dictate the need for some hard-wired circuits, but these can be augmented by computer control to give extra flexibility when the computer is available.

The Consoles

The machine physics and supervision functions can be fulfilled by supplying a number of consoles with controls and displays on them. Each console is interfaced to the control system by means of its own computer, and the consoles are interchangeable in every way, taking their individual functions on a temporary basis from the control program currently loaded. This interchangeability means that the breakdown of one console or its computer reduces the flexibility of the rest of the system, but leaves it workable.

The committment to identical facilities on each console places a premium on multi-purpose equipment, and strictly excludes any item specifically dedicated to one piece of hardware on the accelerator. The number of consoles is not difficult to decide. In view of the price of having a computer per console, it should be as small as possible. The requirement to have several teams working at once implies several consoles. Three was decided on as a practical compromise.

Control-room layout

Thus we arrive at a central control complexwith three identical consoles and a personnel access desk, and a computer room next door containing the central part of the control equipment, including eight mini-computers (three console computers, a display computer, a library computer, a computer to handle alarms, a service computer, and one which does message-switching for the whole control system). The control room itself, except for a silent printer and some wall displays, contains nothing else. Fig. 1 gives the general layout.

Design of the Console

The console itself is designed to allow access to everything by a seated operator. There is a nearly vertical surface for diplays, a nearly horizontal surface for controls, and a table-top. Everything is in 19-inch rack units for convenience, and the console is arranged in a gentle curve with 20° between successive rack elements. With five units in the curve an operator sitting at the middle unit can see and reach everything and two or three people can stand behind him, or he can move over for a colleague to sit beside him. It was proved to be possible to design the console so that the table-top can clear the operator's knees, and for him simultaneously to see wall-displays and other consoles over the displays on his own. Fig. 2 shows the general form of the console which will be used.

Two multi-purpose devices enable us to keep the number of controls on the console small. One is a general purpose knob which can be changed underprogram control to one of various types of control devicesand the other is a set of touch-buttons with programmable legends which can be used to choose from a programmable selection of possibilities with a touch of the finger.

Displays

The general-purpose displays are standard TV monitors, some in colour and some in black and white. All pictures are in the form of 625-line, 50 frame-per-second raster signals, and are driven from an external synchronisation line. Addition of certain pictures is possible, up to three pictures contributing to any monitor input. Possible sources of pictures are CCTV, dot-pictures on 1024 x 625 mesh from scan converters, a computer-driven cursor and 64 x 24 character arrays in up to four colours. Picture-sources and monitorsare connected to a computer-controlled video crossbar with summing amplifiers, and the effect of this is to enable the operator to allocate any screen for the output of his program. This picture can subsequently be moved or copied on operator request to any other screen in the system, as well as to remote lines and to a printer (See Fig. 3).

The program which does the video switching is driven by the programmable touch buttons, but the monitors are identified by a single button under each. Thus on touching the button marked "move", the operator is presented with the question "which picture do you want to move?" and then by the question "where do you want to move this picture?". In each case identification is done, if possible, by pressing the identifying button under the screen in question. When this is not possible, as with moves to remote buildings or to a printer, a touch-button is temporarily dedicated to each such purpose.

Hard Copy

Hard copy is obtained by channeling the chosen signal to a special device which traps each TV line sequentially in a *1024* - bit buffer and uses the next TV frame time to read it into a computer, which prints it on a xerographic dot-printer. In the absence of buffering, which is not currently envisaged, only one picture at a time may be requested on the general-purpose printer, which is silent. A frame will take about 10 seconds to print.

Wall Displays

In addition to the displays on the console, displays are also provided on the wall. Projection TV has been considered, but requires a rather low ambient light level as well as having a rather restricted life. At the moment large TV monitors are being considered. These can be in colour, and by supplying two or three on the front wall and one especially for visitors looking in on the double height control room from windows on the top floor, it may be possible to avoid the use of projection TV. Information which changes only rarely may be displayed on indicators of the airport "flap" type, which can now be obtained in a relatively silent version with a full 64-character facility. We are still looking into alternative methods of displaying large characters.

Analog Signals

The general layout of the consoles and the electrical interconnections between the components is shown in Fig. 3. The four-beam oscilloscopes available on each console can be connected to chosen remote lines by a computer-controlled switch, the operator can make such connections by means of a touch panel dedicated to this purpose, and a display gives the names of the signals currently connected.

Ambient Conditions

Accoustical disturbances to the operator's concentration will be avoided where possible. The air conditioning system is isolated from the control room by concrete walls without doors, except for the necessary under-floor and over-ceiling ducts. By careful use of the pressure difference from this system it is hoped to dispense with the use of coolingfans in most, if not all of the equipment in the consoles. A xerographic printer has been found which is silent. The typing machine on the safety desk will be chosen with this characteristic in view. The walls and floor of the control room will have finishes chosen for sound absorption.

Lighting will in general be at a low level, in order to allow the displays to have their maximum effect. A light-lock system using circularly polarized light and suitable filters over the display screens is being investigated. This, if successful would enable the desk tops and the printer to be adequately illuminated without destroying thecontrast of the displays.

Use of the System

The major test of the control room and its system is - will it allow an accelerator to be controlled? The answer, judging from experience of systems of this kind at NAL, SLAC, LAMPF and elsewhere, is that the degree of control available can be made to approach that of a hard-wired system but not to equal it.

Using the knob, the ball, the touch-buttons and the graphics system, a program for the control and monitoring of a subsystem can be written quite quickly. Such a program will be written in interpretive language, usually by a worker engaged with the subsystem, rather than by a central controls programmer. A general selection program makes all such subsystems available at the touch of a button.

The real-time monitor in each console computer makes it practical to launch a monitoring or data-collecting program which will run while the operator performs other operations, reporting its results on one of the many screens in the system. At all times an alarm computer processes reports of unusual conditions and transmits them to a dedicated screen on each console. Thus the operator can have an overview of the entire accelerator while he is studying one subsystem.

Will the system work?

Most individual components of the control-room system have now been tested singly. The interpretive language and its hardware interfaces work. All components of the graphics system have been demonstrated. The message transfer system connecting the console computer to the rest of the system, including the library and graphics facilities which are properly part of it, is the only component which is at the current state of the art, but its specification is very conservative.

The greatest risk inherent in asystem of this kind is the basic one that the overall reliability of such a lot of electronic hardware may be below a tolerable level. This risk is known, and attempts have been made to reduce it by various features of the design. There are undoubtedly those who regret the passing of the old type of control room, with its racks of specialised controls each dealing with a subsystem. With a machine of this size, even if it were economically realisable, theindications are that a control system of this type will in the end actually prove to be more convenient for the operator seeking either an overview of the whole machine or control of particular parts of it.

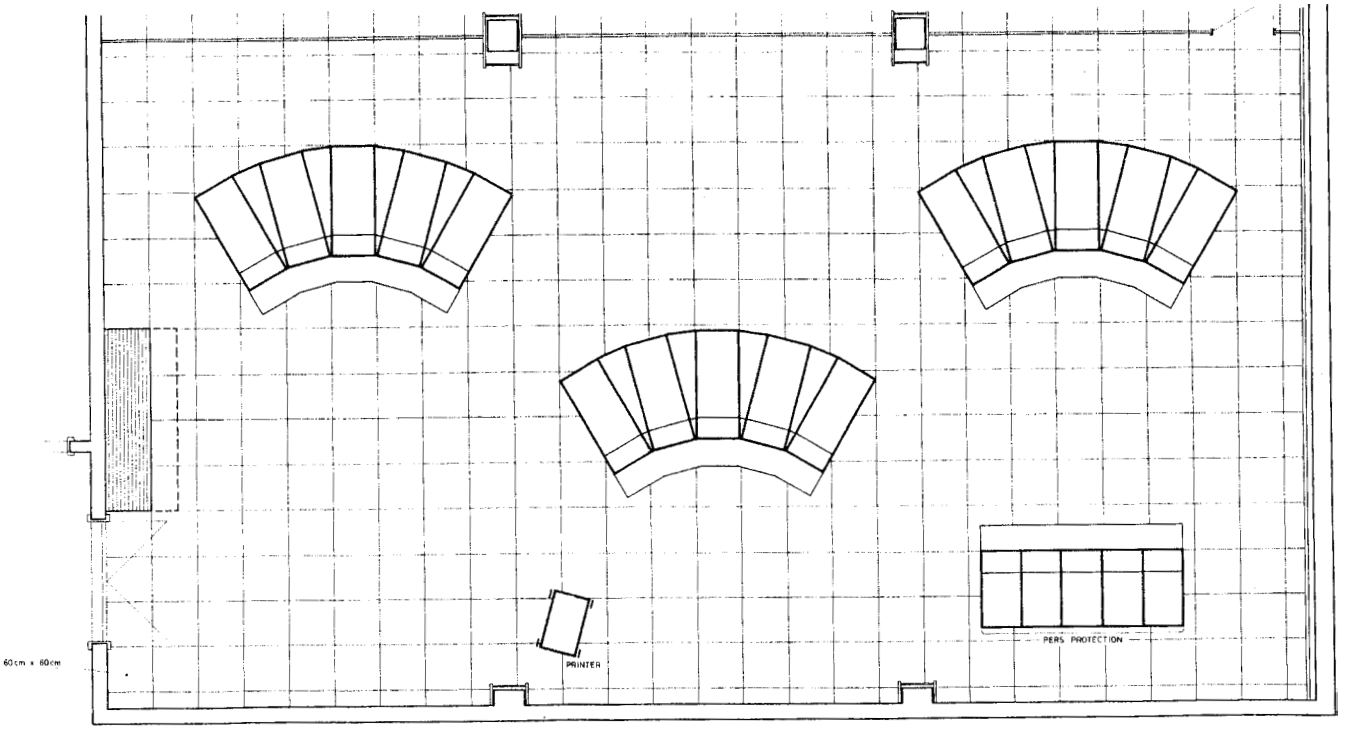


Fig. 1 General Layout of **Control** Room

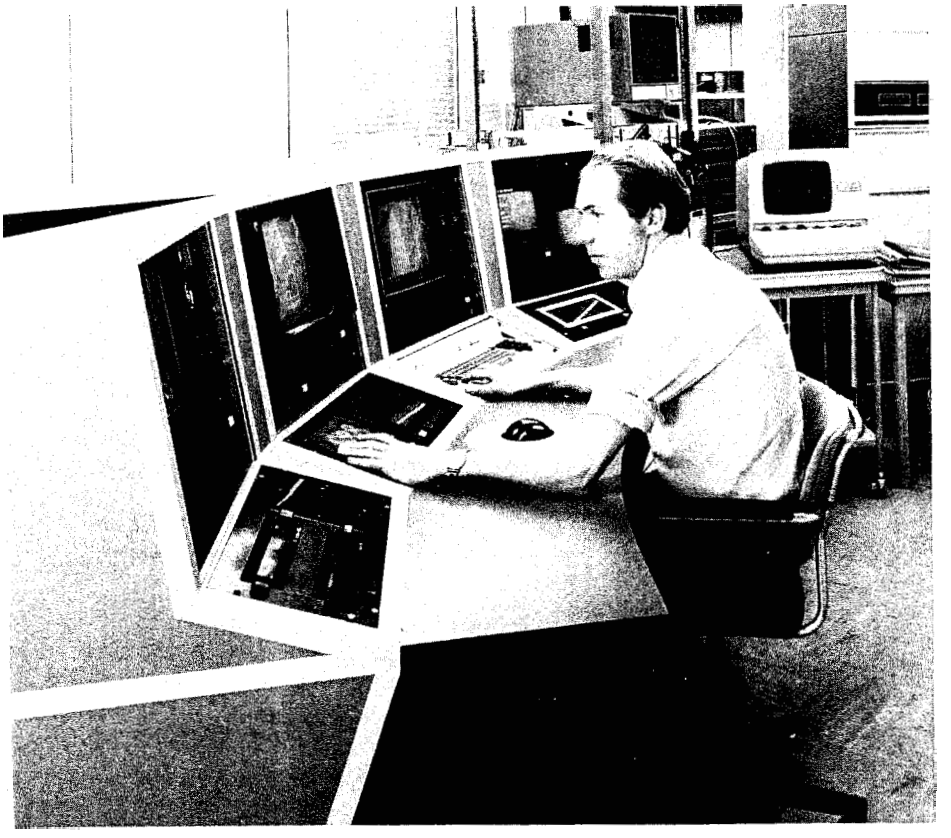


Fig. 2 General Form of **Console**

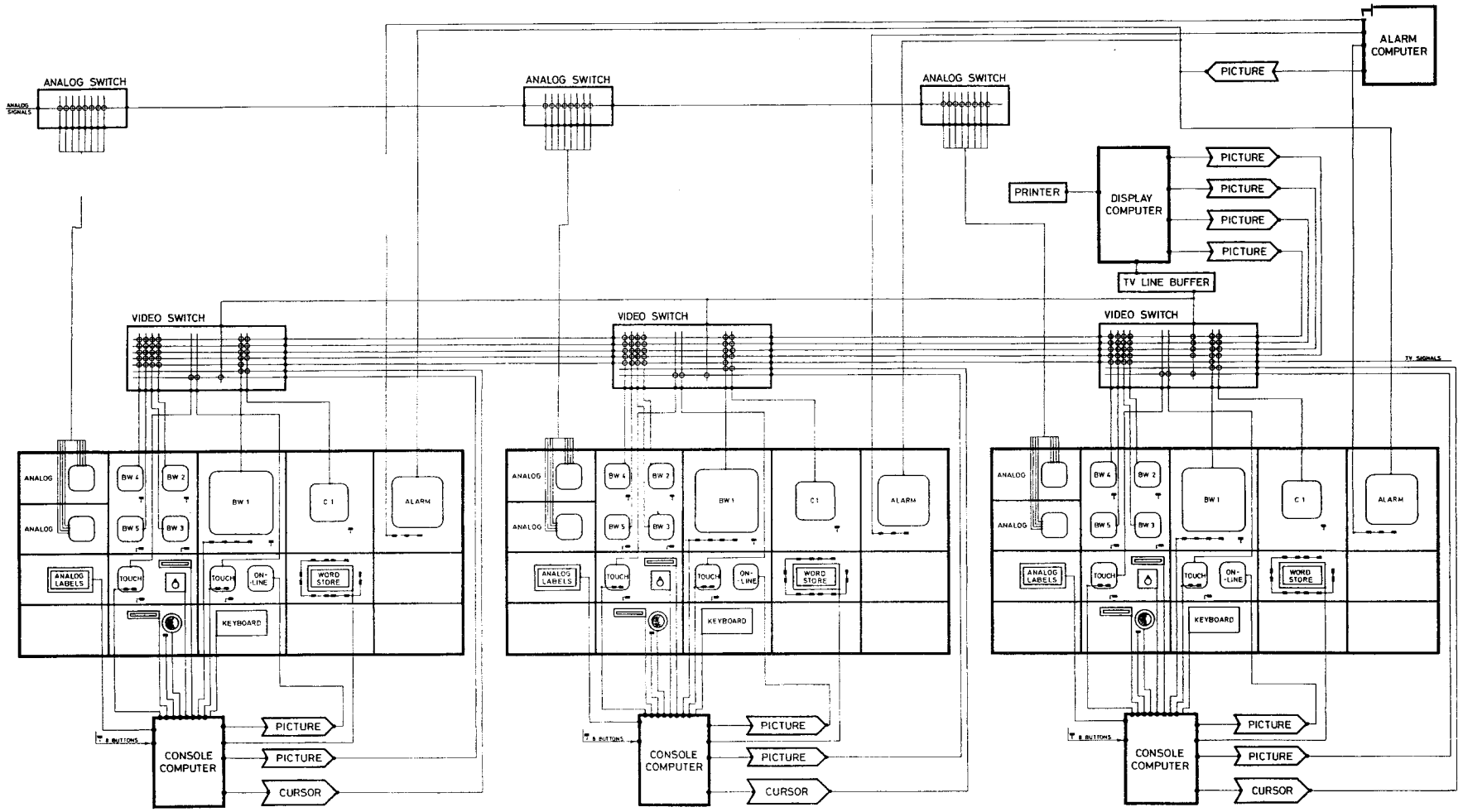


Fig. 3 General Layout of Consoles and Electric Interconnections between Components

THE COMPUTER CONTROL SYSTEM FOR THE SPS

J.T. Hyman

CERN Lab II, Geneva, Switzerland

Summary

The aim in the design of the control system for the SPS has been to give the operators and machine physicists an integrated system capable of providing sophisticated control facilities but yet retaining simplicity of use for normal operations.

Twenty four minicomputers are used in the system with CAMAC input/output and a fast multiplex system to provide the interface to the SPS equipment. The inter-computer communication is over serial data links through a store and forward message transfer system.

The software is based on the use of an interpreter in conjunction with a small real-time executive. A comprehensive addressing scheme, with segmented data tables is used in preference to a large monolithic structure.

Introduction

Two factors influenced the design of the computer control system, namely, the physical size of the machine - with the large number of pieces of equipment to be controlled and the determination to liberate the power of modern computers from the past software barrier at the user level. Figure 1 shows the phsysical layout of the site and gives an idea of the distributed nature of the control system.

Experience elsewhere had demonstrated that the use of Interpretive software (where source statements are interpreted directly at run-time and not pre-compiled or assembled) would do much to provide the flexibility needed for the commissioning, machine development and operational phases of the machine[1]. By careful consideration of all the steps involved in the software, it has been possible to provide an extremely powerful but easy to learn and use control language - NODAL, which retains good real-time response through the use of assembly language programs for critical operations.

In all, *24* modern *16* bit computers (NORD-10 manufactured by Norsk Data Elektronikk, Oslo) are distributed around the site. Each is connected via a fast serial data link to a packet switching message transfer system employing a further NORD-10 computer, Some of the computers perform specific functions while others provide general control and surveillance facilities. A simplified diagram of the system is shown in figure 2 and the functions listed in Table 1. The hardware and the software have been developed very much in parallel to the benefit of both tht two disciplines and the rate at which implementation has been possible.

Computer	ore(k)	rum(k)	Other Periphs.	unction
GP1 - *6*	16	*64*	TTY, VDU	General Acquisition and control in BA's
Extraction North/West	*24*	128	TTY, VDU PT-R/P MT cassette	Control of Extraction systems
Power Supply	*24*	128	TTY, VDU PT-R/P MT cassette	Control of Power Suppl & Function Generators
Radio Frequency	*24*	128	TTY, VDU PT-R/P MT cassette	RF system
Beam Line North/Wes BA80/WRB2 Injection	*16*		TTY	Control of Primary Beams
BA81	*16*	64		Control of North Expt. Area. User Interface
CPS	16			Interface to CPS
Console	24			Console and Operator Interface
Display	16		Special Character Controllers Printer	Display Generation
Alarm	16	*256*		Analysis of Alarms
Service	*64*	2 x *512*	2 X Discs TTY, VDU PT-R/P Printer M. Tape	Number Crunching Program Development
Library	16	*2* x *512*	*2* X Discs	System . Library Data Bank

Hardware

Several features of the NORD-10 make the computer particularly suitable for the SPS application[2].

i) fast microprogram including all operator communications and floating point operations

ii) availability in a range of sizes from 8K up to 64K words of core store

iii) separate internal and fully buffered external input/output busses - the latter with full interrupt facilities

iv) full set of operating registers for each of the 16 hardware interrupt levels - context switching in 1.5 μs.

v) the ability to have a large number (512 theoretically!) of true cycle-stealing DMA channels (1 M word/second interleaved throughput)

vi) good well proved software (compatible with the earlier NORD-1)

These computers are interfaced to the SPS equipment in the manner shown in figure 3. The primary interface is provided by CAMAC using a crate controller interface developed by CERN in collaboration with the computer manufacturers[3]. The controller provides direct vector addressing of interrupts, DMA (with an additional module) and an Autonomous Function Control (allowing traffic on the CAMAC crate dataway independent of the computer). Some SPS equipment is controlled and read directly by the CAMAC, notably the fast beam monitors. All interrupts from the SPS equipment pass via the CAMAC system. Both commercially available CAMAC modules and specially designed ones are used.

All other equipment is connected via a secondary interface in the form of a General Purpose Multiplexer, designed by CERN, and controlled itself by four CAMAC modules as shown in figure 3[4]. A basic concept of the multiplexer is that of having one module to provide all of the setting and monitoring facilities necessary for the full control of the piece of equipment connected. By careful choice of the number of different on/off controls, digital acquisition words, analogue acquisition channels and status check bits for each module design, the number of different types has been kept below 20. The modules use photo-coupler or reed-relay outputs to eliminate unwanted earth loops. As distinct from the CAMAC system, where the plug-in module address is associated with its position in the crate, the multiplex modules carry their own local (i.e. with: in a crate) address decoders. Serial transmission at a rate of approximately 1 M Baud over twisted pairs is used between the MPX Control Units and the remote stations. The distribution of general timing signals (derived from SPS Event + N ms delay) is also conveniently performed through the G.P. MPX[5].

The only control circuits between the various buildings, apart from those required for synchronisation between the SPS and its injector (the CERN PS) and those for the power supply, are provided by the Data Links and Message Transfer System. To provide adequate security in the transmission both cross parity checks within each word and longitudinal parity (checksum) techniques are employed. The data link for each computer uses two quads (a video pair + an audio pair in each direction) of a 6 quad or pod cable (of the type used for domestic television distribution). Data is carried in serial form over the video pairs, leaving and entering the computers via DMA. There is a handshake for each block of data together with other control information over the audio pairs using PI/O computer entry and interrupts. Facilities are provided in the system, using the hardware operator communication of the NORD-10 micro processor, to bootstrap the remote computers from the central library system.

In addition to the hardware described above, the operator interface in the Main Control Room uses some special devices. The operator interface is described in a separate paper presented at the Conference[6].

Software

Very great store was placed on the availability of good basic software when the choice of computer was being made. Specific requirements for the system were stated as:-

1) A sophisticated monitor supporting assemblers, interactive editor, linker etc.

2) A small real-time executive capable of accepting input for scheduling tasks from programs running under its control.

These two requirements are satisfied by the NORD-10 software in the form of TSS - a multi-user time sharing system and the SINTRAN II real-time executive, which is capable of working with a drum system or in a core-only environment. All of the relevant SINTRAN commands are available from NODAL so that program scheduling can be carried out on-line.

NODAL itself has been developed at CERN and has a powerful set of commands[7]. These can be used either:-

a) Immediately -

```
SET MBV(2) = 154
```

which will set the current in Vertical Bending Magnet 2 to 154 amps.

b) Programmed -

```
1.1 FOR INJPHS = 5,15;DO 2
1.2 END

2.1 TYPE INJPHS
2.2 TYPE BCT(4)!
```

which will type the reading of Beam Current Transformer 4 over a range of INJection PHase. Comprehensive mathematical functions are available and special commands exist which allow one computer to send a NODAL program to another computer and for this latter to send back the results of running the program received.

In the examples, MBV, INJPHS and BCT are the names of system variables and are used by NODAL *to* find entry into the appropriate Equipment Subroutines. These subroutines are written in assembly language and each contains its own data table (with entries for property of interest i.e. nominal value, current value, status etc). One equipment subroutine can be used for

all equipment of the same type. By avoiding a large monolithic data base, it is possible to add new equipment to the system with the minimum of trouble and without changing what already exists and is proved.

Considerable thought has been given to the detailed way in which access is achieved to the required piece of equipment. An equipment numbering scheme has been developed where information redundant to later addressing operations is replaced successively by further data. This scheme has made possible full unambiguous addressing of all equipment throughout the SPS within the *16* bits available. Data table accesses are reduced to simple indexed operations[8]. The equipment subroutine approach and the addressing scheme are shown in outline in figure *4*.

To provide the necessary program priority, two main task buffers are provided in the NODAL-SINTRAN SYSTEM. The lowest level buffer is provided for interactive use while the second is for system programs. A third small high priority buffer is provided for immediate commands passed down the data links. In addition to programs written in NODAL, assembly language programs can be run directly under SINTRAN with, in computers with drums, swapping of core-loads.

Two schemes will be used for surveillance of the SPS. The first of these will be the normal periodic scan which will be implemented as time initiated tasks (either NODAL or assembly language) under SINTRAN. The second will use a special DMA scan facility built into the G.P. MPX. This latter scan will soak up any idle time the computers have. Any errors discovered from either of the scans - or from program errors detected by the NODAL interpreter will be noted in an Error "Bucket". This will be sent to the Alarm computer once per machine cycle (or when full).

The Message Transfer System software is designed to be completely transparent to the users and to allow any computer to communicate with any other[9]. Messages will be divided into *64* word blocks to facilitate coupling to the overall and local filing schemes. Each block will be preceded by a *4* word leader as shown below.

Source Computer	Destination
Priority	Word count
Directive *	
Program Name	

* Directive gives information to destination computer as to type of message.

The whole MTS works on a store and forward principle and will look to each satellite computer rather like a mag-tape unit (with about the same data rate). The MTS software will run under SINTRAN and programs will be available for traffic analysis.

The software for the operator interface has been designed in such a way that the maximum use is made of the NODAL-SINTRAN system used in the remote satellite computers. The "drivers" required for the special interface hardware are implemented as either NODAL functions or as CALLS to assembly language subroutines.

References

1. K9 Computer Software System - P. Adams RHEL/R240 Rutherford Laboratory, Chilton, Didcot, England.
2. NORD-10 Reference Manual - A/S Norsk Data Elektronikk, Oslo.
3. A multicontroller Approach to CAMAC for the SPS Control System - M. Collins, R. Rausch CERN report Lab II-CO/73-1
4. G.P. MPX Equipment for Analogue and Digital Acquisition and Digital Command for the SPS Computer Control System - R. Rausch, J.M. Sainson, R. Wilhelm CERN report Lab II-CO/73-2
5. The SPS Timing System - C.G. Beetham, R. Rausch CERN report tab II-CO/Int/CC/74-2
6. The Operator Interface of the 300 GeV Accelerator - F. Beck, This Conference Publication No. *7-14*.
7. Preliminary Programming Information for the SPS Control System - J.T. Hyman, G. Shering CERN report Lab II-CO/Int/CC/73-5
8. System Variables - M.C. Crowley-Milling CERN report Lab II-CO/Int/OO/73-8
9. Technical Specification for the Data Links and Message Transfer System for the SPS (Amendment) CERN Lab II-CO/SPEC/73-18

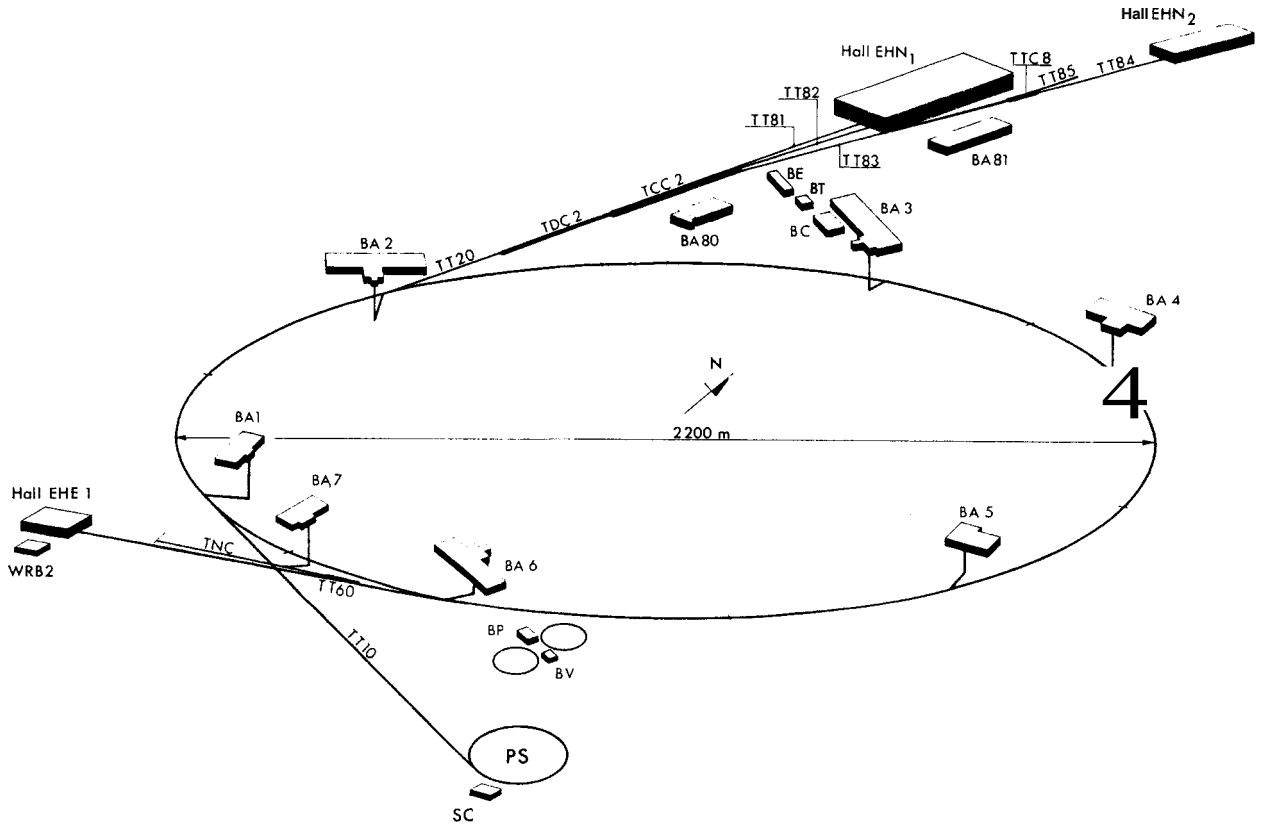


FIG. 1 SPS SITE LAYOUT

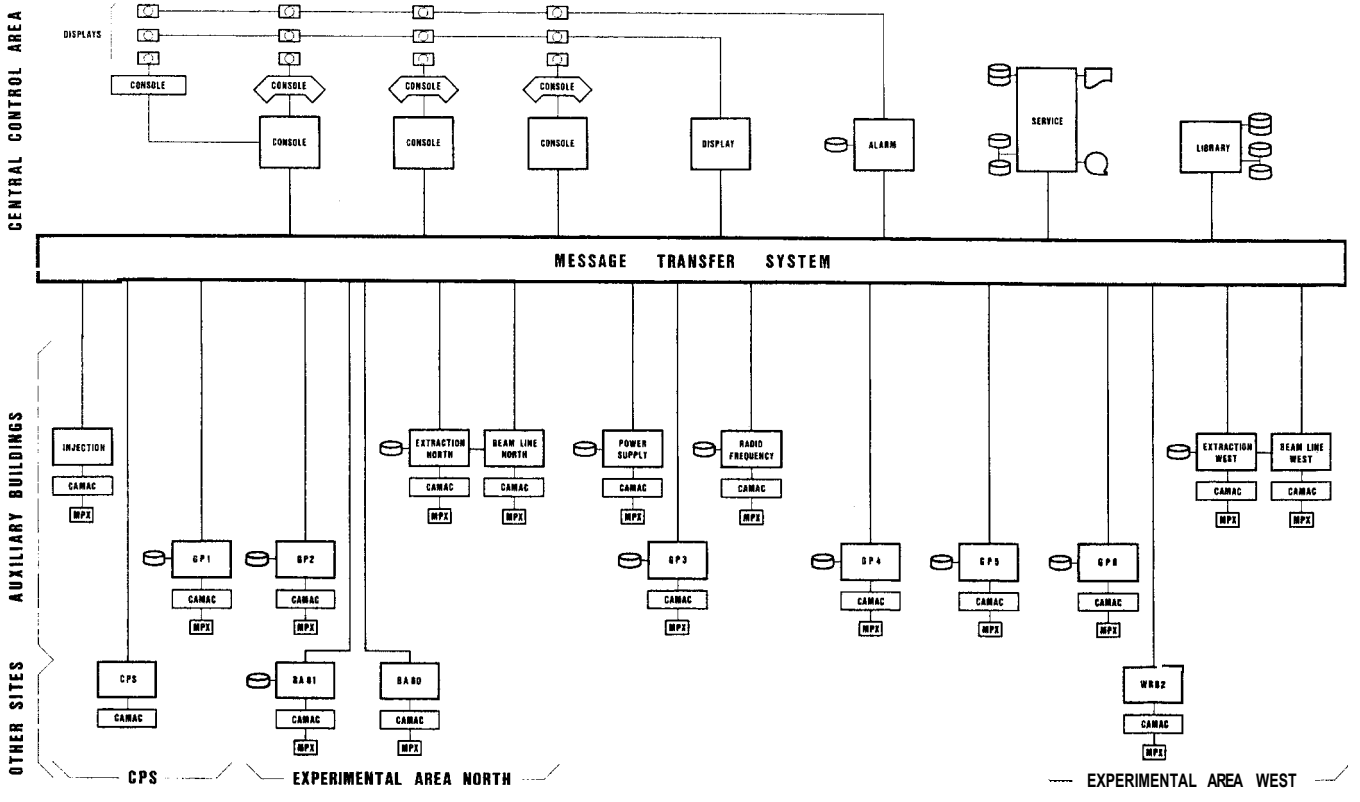


FIG. 2 SPS CONTROL COMPUTERS

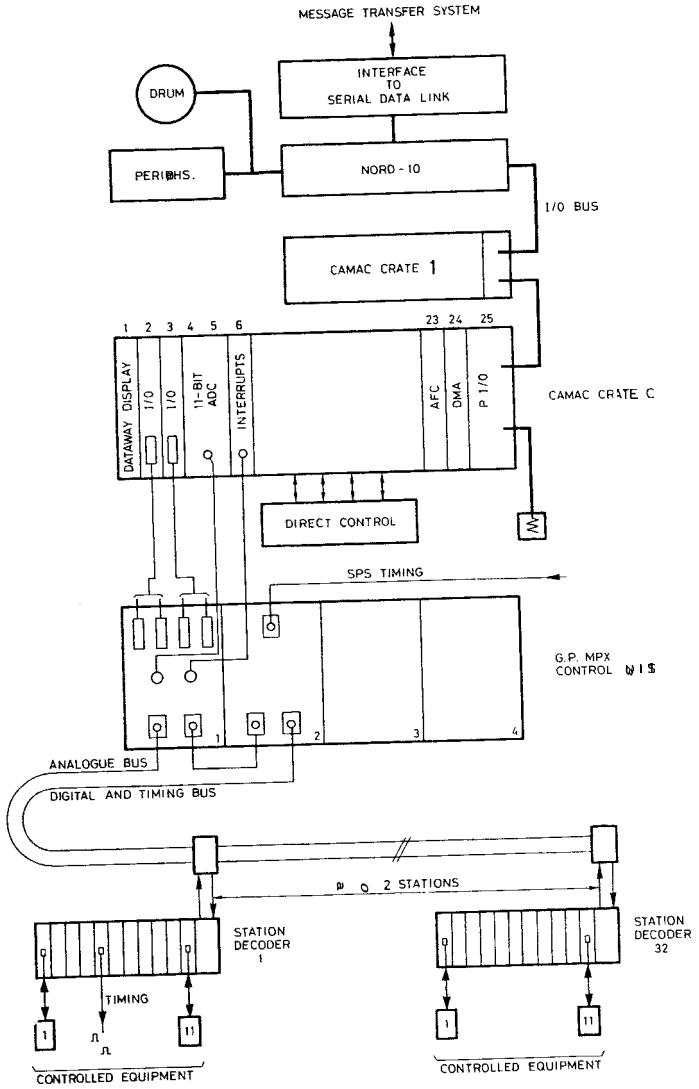


FIG. 3 COMPUTER / SPS EQUIPMENT INTERFACE

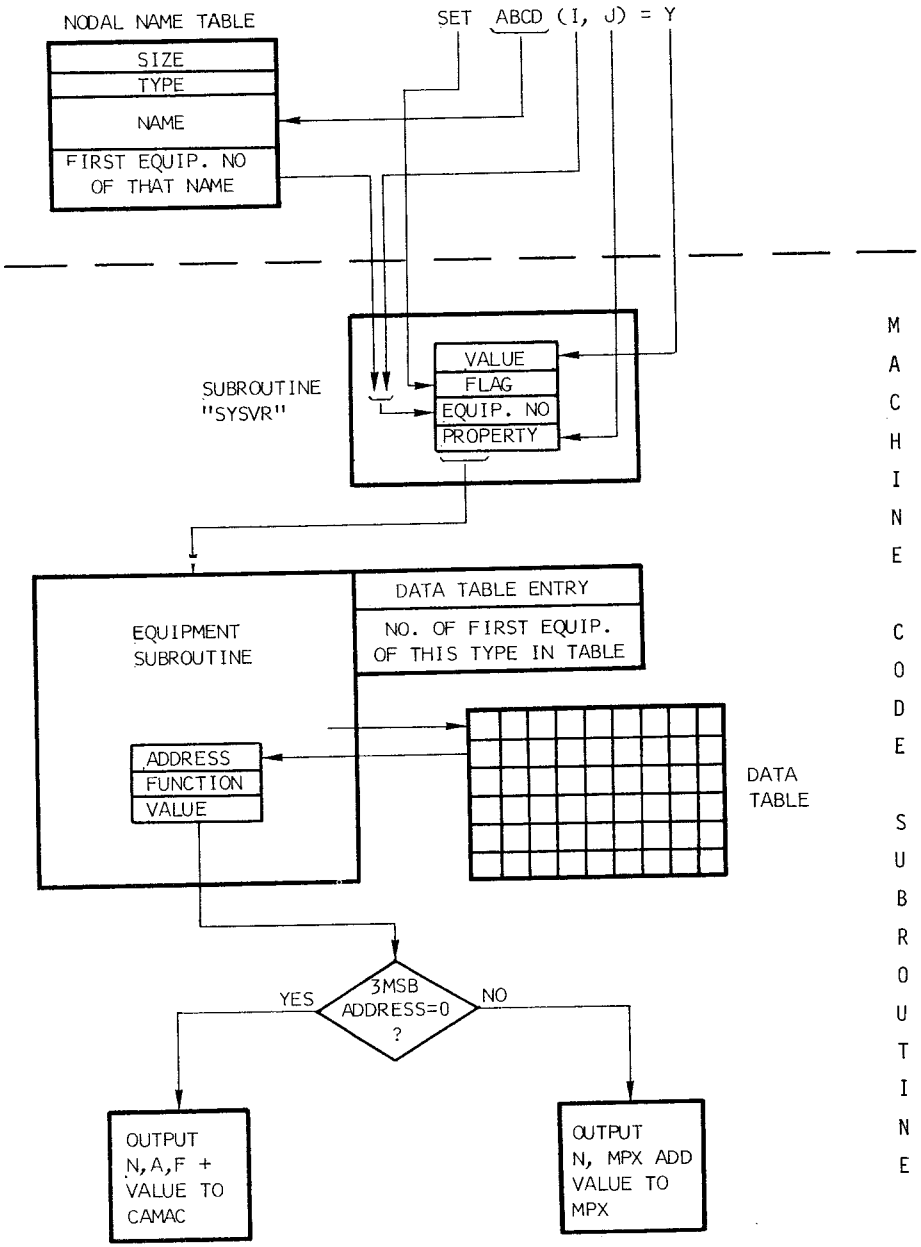


FIG. 4 EQUIPMENT SUBROUTINE APPROACH

THE IMPACT OF COMPUTER CONTROL ON THE PERFORMANCE OF THE CERN INTERSECTING STORAGE RINGS

P. Wolstenholme

CERN

Geneva, Switzerland

Summary

The ISR control system has now developed to a state in which it relies heavily for both routine operation and machine development on the control computer. This gives significant benefits in security of operation, as well as easing the task of controlling a very complex installation. The computer has enabled the machine development team to concentrate on beam studies, without worrying overmuch about calibrations and reliability of individual components, so that they have been able in three years to surpass the original design objectives.

1. Initial Objectives

The basic design document for the Intersecting Storage Rings was the design study published in 1964. Planning of the control computer system started in 1967, at about the same time as the excavation work in the ring tunnel.

At that date, although some process plants were being controlled by computer, the experience in accelerator laboratories of computer control was not very encouraging. Small computers were only just changing in technology from discrete to integrated circuits, and the high reliability we not take for granted had not been proved.

Furthermore, the large proton storage rings would be unique, and it was feared that a long and arduous commissioning period might be needed to achieve any sort of useful performance. The computer system could not be allowed to present its own commissioning problems at the same time.

The computer system was therefore planned as a complement to the manual facilities, to be installed in parallel and used whenever its performance was superior.

In designing control systems for both computer and manual control, a number of compromises had to be accepted. For example, digital-to-analog converters for control of beam transfer line power supplies were made to accept decimal settings. Extensive general purpose control systems were ruled out, in favour of individual solutions for particular groups of hardware. To minimise the cost of the control system and to avoid undue duplication, the design principle adopted was of data transmission systems linking the control room to remote equipment buildings, having both a computer connection and a manual control panel in the control room. The bulk of the expense was in the command link and in the remote equipment, and as these were common to the manual and computer controls, they could be developed and tested in parallel with the computer system.

The equipment initially selected for computer control was that in which sheer quantity appeared likely to overwhelm operators, and in which individual monitoring or adjustment was inappropriate or excessively laborious. The main examples selected were power supply adjustment, in which nearly 300 power units had to be set, beam observation (e.g. of the closed orbit) and vacuum system supervision. This latter choice surprised some people at the time, but turned out to be very important indeed. The vacuum system had 300 pumps and a similar number of gauges, making an over-all appreciation of the vacuum situation difficult without reasonably sophisticated data reduction and presentation.

Flexibility of the computer software was taken very seriously and an elaborate file structure was adopted for all data, even when it seemed fixed, rather than incorporating coefficients into the programs. In this way, very drastic changes to machine operating conditions could be introduced without revisions to programs. This approach contrasted markedly with the suggestion made in the ISR design study for a function generator controlling tune through the pole-face windings, and is one of the key elements in the success of the computer system.

The mixture of manual and computer controls precluded a control room layout based on two or three computer consoles, and the solution adopted was to insert computer terminals in three positions in the operating area, which was nevertheless kept fairly small.

A long-term objective of complete computer control was agreed, to provide a framework for gradual development of the system, and all controls and instrumentation were designed with the future computer connection in mind.

In 1968, the problems and costs of setting up a network of computers appeared considerable. The gradual implementation coupled with a requirement for flexibility to meet unforeseen requirements caused us to choose a single computer of reasonably high power: a 24-bit machine with a 1-microsecond core store cycle. A fast-access disc store and a graphic display system were also specified. To permit continuous hardware and software development, as well as to assure a high level of serviceability, a second computer was included. The order was placed in November 1968 and the computers delivered 12 months later.

2. Early Experience

Tests of the first part of the beam transfer line from the CPS started in May 1970, and at the end of that month the Storage Ring Control Room (SRC) was first used. The computer had been installed some six months previously, and was used to take data from pick-up electrodes and compute beam positions. This work continued for the rest of the year. As the beam transfer system was commissioned, the power supply

setting and checking programs were put into operation, and in September when the TT1 transfer line was first tested over its 350 m length, the magnet currents were set by computer, and a STEER command, requesting the computer to adjust the beam position at a particular luminescent screen, made the next proton pulse pass right through the line.

In November, some tests were performed on one storage ring, and in the following January both rings were put into operation. Initial tests were at low momentum (15 GeV/c) at which the magnet profile should have given the design conditions. During the next few months, working points in the Q_H-Q_V diagram were tested, followed by working lines. By April 1971 there was data for ten lines stored in the computer for 15 GeV/c and rather fewer for other momenta. After quite an amount of trouble with the power supply control system, it settled down to become reliable and the development of working lines went ahead smoothly. A suite of programs was made available for manipulation of the machine tune, and development progressed rapidly[1].

During the same period, orbit measurement and correction facilities were put into operation. It was realised that the orbit measurements could not be used as a basis for setting up collision of the beams at the intersections, and a procedure was established for sweeping the two beams vertically across each other at the intersection, and monitoring the interaction rate. This permitted a steering resolution to better than 0.5 mm and also provided a measurement of effective beam height and hence of luminosity.

From the very beginning, steering in the beam transfer system was performed through the computer, which was told to make certain corrections at particular monitor positions, and worked out which correction element to use and by how much to change it. At the injection point to a storage ring the adjustments are very delicate, as the residual betatron oscillations about the closed orbit must be minimised. As the manual estimation of injection errors was rather subjective, and because of the four adjustments required per ring (angle and position, referred to a standard point, in radial and vertical senses) an automatic procedure was instituted, performing in a few minutes an operation which initially could take up to an hour. This closed-loop adjustment by the computer remains a major task at present, and efforts are continuing to improve its accuracy, which limits ISR luminosity directly.

Later in the year, currents of a few amps were stored in the ISR, and the vacuum was found to be very critical in limiting the current achievable. The computer had been connected to monitor pump currents and gauges because of the immense complexity and size of the vacuum system, and because the calculation of true pressure for each Bayard-Alpert u.h.v. gauge required an elaborate calibration sequence. Soon, programs which had been expected ro run a few times a day were in operation every 15 seconds, monitoring pressure rises at the beams were stacked, and the programs had to be revised to allow them to run even faster. The computer terminal installed by the vacuum racks in a corner of the control room became the centre of attention.

By the end of 1971 the computer was performing many of the operational and machine-development functions, and since then its use has been extended and consolidated.

3. Beam Control

Many essential functions of the computer may be grouped under this one heading, which will be discussed as an illustration of our current position.

Periodically, after a long shut-down or a realignment, a major orbit correction is needed. The procedure for orbit measurement is assigned to a set of push-buttons, and the measurement is made on five successive pulses from the CPS and averaged. If a correction is thought necessary a data file is sent to the CERN central computers for analysis, and a list of corrections is sent back to the ISR for application by the control computer. A further check of the corrected orbit is made, and this is normally satisfactory[2].

At the start of each run, when beams are to be set up for physics, the orbit is again checked and the small errors in vertical position at each intersection are taken out. This establishes a reasonably accurate collision of the beams when they are later stacked.

The main magnets and the correction windings have been set up to standard values selected from many alternative tables stored in the computer, and provided that injection has been optimised, the stacks can be built up. If a high luminosity is required, the "8C" working line may have been selected: this calls for adjustment of the working line at intervals while the stack is being established, so as to compensate the curvature introduced by space charge[3].

Alternatively, the stack may be established at 26 GeV/c, and then accelerated (by phase-displacement) to 31.4 GeV/c. In this case a dialogue is established between the programs which progressively alter the main magnetic field and correction winding currents, and the radio-frequency system, the whole procedure being automatic[4].

A luminosity check is commonly required, and in this case we either perform a high-accuracy calibration at one intersection region, or a steering adjustment at about six of our intersection points simultaneously. At first, the orbit bumps were introduced by means of equal energisation of two magnets (per ring) placed approximately one quarter-wavelength upstream and downstream of each intersection, but now we use four-magnet bumps which have minimum second-order effects outside the intersection of interest, and we also correct the coefficients from our knowledge of the actual betatron wavelengths at central orbit, The bump amplitude can be perturbed by space-charge effects, and these are also compensated for.

When it became necessary to minimise background by altering the angle at which the beams passed through the intersection, a set of coefficients was calculated and the existing program was able to handle the manoeuvre, replacing millimetres by milliradians.

By means of the standard procedures outlined above, we have been able to establish beams of the required characteristics, with low decay rates, at any required energy, and to place them exactly in the intersection region, to achieve high luminosity, as a routine operation. To illustrate the effort this represents, it can be remarked that there are 35 programs for dealing with the set of 200 ISR power supplies (excluding beam transfer and experimental magnets) and there are 87 data files of settings for these power supplies stored in the

computer memory. To relate this to the over-all project, the total number of programs available to run on the control computer exceeds *400*.

4. Faults

When dealing with an intricate machine, the question of fault-finding is important. In the computer system, all control programs have been made to follow a rigorous protocol. First, status signals are examined, to see whether the requested actions may be performed. If conditions are incorrect, the operator is warned. Next, it is usual to check on present settings and to calculate the new settings: the details vary with the system. The correction is then made, and after a short delay a new series of measurements and checks is initiated. Sometimes a fine adjustment is required, and this can be automatic, but if it seems excessive the operator is warned of a possible calibration problem.

This may seem very obvious, but it is one of the major differences between digital computer control and pure hardware control, in which checking of outputs is rare. There are several available techniques for achieving the sort of coordinated adjustment of multiple outputs which we often need, the digital differential analyser being admirably suited to present-day technology, but the computer retains the great advantage of reporting on failures in the external world and becoming obviously paralysed by internal failures.

In a project such as the Intersecting Storage Rings, where a simple test of new operating conditions may easily require two hours, security of operation is of the greatest importance in facilitating machine development. One must be quite certain that perturbations introduced are exactly those desired and that their amplitudes are recorded.

It is fair to state that, although in such a complex machine as the ISR we have had our share of hardware faults, the computer has very often signalled and identified these at once, so avoiding waste of time checking a large mass of equipment to localise the fault, or worse still continuing in blissful ignorance.

A further aspect of computer operation is the routine supervision of equipment, with the aim of reporting on failures and drifts. At the ISR we have about 30 programs dealing with various classes of equipment, which run at appropriate intervals during the standby periods, filling, physics experimental runs, and machine development. These programs report to an alarm printer. This is a little unconventional, in that control computers in accelerators or nuclear power stations often use cathode-ray display tubes for alarm presentation. At the ISR, perhaps on account of the very long time cycle of refilling the machine, we have chosen to print all alarm messages and to keep them for some time.

5. Operator Communication

At present, we have four computer terminals in the control room. Each has a key-board, a small printer and a text display screen. These facilities are supplemented by a graphics display system with two screens, four fast printers (for alarms, logging of routine happenings, vacuum and general purposes) and various data processing peripherals.

At each terminal, so as to ease the task of the operator, there is a set of 12 buttons: four of these are for special purposes such as stopping the program currently executing at that terminal, and eight are general-purpose buttons to which can be assigned any named file of eight commands. At present we have 165 such files of commands in the computer store, and the system is intensively used.

One noticeable omission is the knob. We have no digital computer-linked knobs at present. The characteristics of the storage ring seem to make knob-twiddling undesirable: there are very few control knobs in the entire control room. When an adjustment is desired, it is usually necessary to calculate its magnitude and then to apply it exactly, and it may well be an elaborate quantity involving setting of *40* parameters in a smoothly coordinated fashion.

6. Conclusion

At the ISR, computer control is well established, to the extent that the simpler routine operations would be virtually impossible without it, and complex operations now common would be ruled out altogether.

As our knowledge of the machine improves, and as the machine performance is pushed ever higher, the flexibility and security achieved by computer techniques becomes ever more important.

In three years of operation, the storage rings have been brought to performance levels exceeding the design objectives, and the operational procedures now handled as routine are in advance of early predictions. The computer has played a vital role in permitting the accelerator physicists to concentrate on studying the beams without being confused by irregular or unknown behaviour of the hardware. The development time saved by adopting this tool can only be guessed, but must certainly be appreciable.

7. Acknowledgements

I must express my appreciation of the hard work and continued enthusiasm, despite many early discouragements and difficulties, of the staff of what is now the ISR Computer Group, and also for the co-operation and trust of the entire staff of the ISR Division.

8. References

1. J.P. Gourber: "Adjustment of Working Lines in the ISR." 8th Int. Conf. on High Energy Accelerators (1971).

2. B. Autin and P.J. Bryant: "Closed Orbit Manipulation and Correction in the ISR. ibid.

3. P.J. Bryant: "Dynamic Compensation During Stacking of the Detuning Caused by Space Charge Effects." Paper presented at this conference.

4. K.N. Henrichsen and M.J. de Jonge: "Acceleration by Phase Displacement in the ISR." Paper presented at this conference.

DIGITAL CONTROL OF RECTIFIER FIRING ANGLES FOR THE ZERO GRADIENT SYNCHROTRON (ZGS) RING MAGNET POWER SUPPLY*

Martin J. Knott, Lloyd G. Lewis, and Herbert H. Rabe
Argonne National Laboratory
Argonne, Illinois

Abstract

The heart of the new control system for the ZGS ring magnet power supply is a counter that counts from 0 to 3600 each voltage cycle of the main generator. This provides an electrical degree scale that is synchronized with the generator voltage wave by a phase-lock feedback loop. Digital gates compare the number in the counter with the desired angle forfiring each of the 12 rectifier phases. At eauality, a pulse is generated and applied to the control grids of the appropriate mercury vapor rectifiers. Fast digital arithmetic adder circuits upclate the desired firing angles for each of the 12 phases in response to commands from the ZGS programmer and in response to feedback signals from beam spill monitors and from $\dot{B}$ pickup coils on the ring magnet. Separate digital arithmetic adders and selectors provide individual adjustment of each phase in order to reduce low frequency ripple. This system has greatly reduced 50-, 100-, and 150-cycle ripple on the ring magnet field on flattop and on porches, has provided fast action to permit spill control when the RF accelerating cavity is off, and has provided stable operation in full rectify for the accelerating part of the ZGS cycle.

Introduction

The new slow resonance extraction system for the ZGS provides two simultaneous beams that have *no* RF structure. The system accomplishes this by turning off the RF accelerating cavity early in flattop and then, after the beam has debunched, by moving the beam to the $\nu_r = 2/3$ extraction point with the ring magnet control system. The rate of extraction is then controlled through manipulation of the ring magnet field.

This magnetic spill mode places specific demands on the control system for the ring magnet power supply. One of these demands is that the system must be able to rapidly change the voltage applied to the ring magnet. The required speed and accuracy are determined by the amount of beam steering needed to start and maintain the extraction at a selected rate.

A second demand is that the control system for the ring magnet minimizes the generation of low frequency ripple. This is important because the ripple produces modulation of the extracted beam intensity.

An additional requirement is that the ring magnet control system be capable of operating in full rectify; that is with natural commutation from phase to phase. This provides the minimum accelerating time and the desired conditions for beam injection into the ZGS.

ZGS Ring Magnet

The ZGS ring magnet circuit contains eight magnets and eight power supplies connected in a series circuit with four-fold symmetry.[1] The result is the equivalent of a 12-phase supply in each quadrant of the ring magnet.

The rectifiers in each of these eight supplies are mercury vapor tubes. The excitation arc operates continuously so that firing control is provided by two grids placed between the cathode arc and the anode.

Each of the eight supplies is provided with a low pass LC filter. The filter has a rolloff of 40 dB/decade and a corner frequency of about 40 Hz. The filter is underdamped with a damping ratio of about 0.3.

Ripple Amplitudes

Ripple amplitudes produced by the ZGS ring magnet power supply were measured in two ways. The first was to use the fast gauss clock in the ZGS programmer. The clock output was sent to a digital-to-analog (D—A) converter and to an oscilloscope. The gauss pictures from the oscilloscope showed that most of the ripple produced by the original analog control system was at low frequencies. Amplitudes at ~ 50 cycles (generator frequency) were of the order of 1 or 2 G. The 12th harmonic was not readily observed on this display.

The second method was to look at the dc voltage across one pair of ring magnets. This was a more convenient signal for ripple studies since the relative amplitudes of the several harmonics were more favorable for measurement.

The relatively large low frequency ripple (at less than the 12th harmonic) results from a variety of causes. One cause is the incorrect spacing of rectifier firing pulses. A second cause is the characteristics of the low pass filter which attenuates poorly at the low frequencies. Additional causes include possible errors in the number of turns on the polyphase transformer windings, variations in the leakage inductance from one phase winding to another, lack of symmetry in circuit resistances, and imbalances between phases of the generator voltage.

The effects of some of these causes of low frequency ripple can be cancelled on flattop by properly retarding or advancing the firing time of one or several of the 12-phase rectifiers with respect to the others. From this, it is apparent that exactly uniform spacing of the firing pulses to the rectifiers will not produce minimum ripple.

Firing Accuracy

The bias voltages to the unijunctions in the original firing control system were readjusted to produce a significant change in the ripple at the generator frequency. These changes in firing angles were measured with the digital phase-angle meter used for routine monitoring of the ZGS ring magnet supply.

The data showed that substantial reductions in the low frequency ripple could be obtained if the firing

*Work performed under the auspices of the U. S. Atomic Energy Commission.

angles of the 12-phase rectifiers were reproducible to 1/10 of an electrical degree. This is far beyond the accuracy and stability of conventional analog ramp type control systems. For this reason, a digital control system was designed and installed at the ZGS.

Rectifier Grid Drive

The control of firing angles to 0.1° electrical corresponds to controlling the turn-on of a rectifier to about 5 μs. Any variation in the turn-on time of a single rectifier must be smaller than this if the control accuracy is to be achieved. In a similar way, variation in the average time delay from one rectifier to another must be shorter than 5 μs.

High voltage switch-transistors were used to provide the drive to the grids of the rectifier tubes. The firing pulse from the control circuit was coupled through a well insulated pulse transformer to a drive module that operated at rectifier cathode potential. The 1/2 μs pulse was lengthened to 4 ms by a single shot amplifier located at cathode potential. This lengthened pulse was applied to switch-transistors that supplied the grid drive signal.

The grids were switched to *t300* V with respect to the cathode with a rise time of 600 ns. Under these conditions, the tube turn-on was about 1 μs at low currents and also at high currents when the tube was first used. At high currents, the time delay and the jitter increased during the first two minutes. At equilibrium, the delay varied from a minimum of about *2* μs to a maximum of about 5 μs. We believe that this increase in turn-on delay is caused by outgassing of the electrodes under high current loads.

Turn-off of the rectifier by removal of the positive anode voltage left a plasma in the space between the grids and the cathode arc. This caused grid currents that lasted long enough to influence the next turn-on. For this reason, a switch-transistor was used to clamp grid #1 to a negative bias when the tube was off. This bias swept out the ions left in the interelectrode space in about 1/2 ms.

Number System and Logic

The digital parts of the control system shown in the block diagram of Fig. 1 use the binary number system. This was chosen since the input from the ZGS programmer is in one's complement form and because of convenience in construction.

The DISPLAY system uses LED numeric display elements driven by a binary coded decimal counter. This is convenient for checkout by the maintenance personnel.

The digital logic utilizes 7400 series TTL-MSI integrated circuits. About 250 integrated circuit chips are mounted in dual in-line packages and are interconnected by wire-wrap wiring. The propagation delays for this logic series vary from package to package but are of the order of a few tens of ns.

Phase Lock Loop

The generator voltage wave varies in frequency during the ZGS cycle and is very distorted. Rectifier commutation produces notches in the generator voltage wave that are as large as 25% of the peak voltage. For this reason, a zero crossing type of reference is not suitable even when the input wave is heavily filtered. This is true because the filters that were tried produced variable phase shifts and/or large transients when entering flattop and invert. The phase-lock loop shown in the upper right portion of Fig. 1 was found to operate satisfactorily.

In this loop, a dc tachometer voltage from the main generator and the output voltage from the filter are added in an operational amplifier. The resultant voltage drives a voltage-to-frequency (v—f) converter that produces a sawtooth wave. This sawtooth drives a binary that divides the frequency by two and produces a square wave with ±10 V output levels.

It is well known that the mathematical product of two sine waves of the same frequency but different phases produces a dc component plus a second harmonic component. The dc component depends on the phase difference between the two sine waves.

In a similar way, the product of a square wave and a distorted sine wave of the same period produces a dc component that is a function of the phase difference between the two waves. This fact is utilized in the loop in Fig. 1 by feeding the distorted sine wave from the generator bus and the square wave from the frequency divider to a transconductance type analog multiplier. The output which contains dc and ac components is fed to the low-pass filter to complete the feedback loop.

This loop would operate without the dc tachometer input; but since the maximum loop gain is finite, the phase difference between the ac reference and the square wave in locked operation would vary with generator speed. The dc tachometer input amplitude is adjusted so that the dc output of the filter is nearly zero in the locked condition. In this way, the phase difference between the ac reference and the square wave is made very nearly 90° and independent of generator speed.

Main Counter Loop

The MAIN COUNTER and its associated feedback loop are shown in the upper left part of Fig. 1. The function of this counter is to provide a digital degree scale that has 360.0° per generator cycle and that is phase synchronized with the square wave from the phase-lock loop. Its operation is described below.

The dc tachometer voltage, shown in the upper left of Fig. 1, is multiplied by a constant in the SERVO CONTROL. The product is then applied to the input of the v—f converter. The gain constant is adjusted to give very nearly 160 counts per electrical degree of the generator wave. In this way, the main counter receives very nearly 16 x 3600 counts each generator cycle, without the feedback loop's correction. This makes the action of the feedback loop almost independent of generator speed.

The main counter is provided with gates that clear the counter to zero each time the total count reaches 16 x 3600. The gates generate a ROLLOVER pulse at the same time that the counter is cleared. No other input clears the counter, thus assuring 360.0° per main counter cycle.

The main counter is synchronized with the phase-lock loop in the following way. The positive-going edge of the square wave from the phase-lock loop ÷ 2 loads a register with the number from the main counter. This number is then subtracted from a reference number, obtained by adding a BIAS to the number contained in the RECTIFY D.S. digital switch. This difference is the digital servo-loop error signal and represents the amount that the main counter is ahead or behind the reference square wave from the phase-lock loop. The difference is loaded into a second register that feeds a d—a converter, thus furnishing a voltage error signal.

This voltage error signal feeds a proportional and an integral network in the servo control. The effect is to speed up or slow down the v—f converter *so* that the number transferred from the main counter is equal to the reference number.

Full Rectify Adjustment

The main counter control loop contains a reference number that may be changed to adjust the firing pulse times for full rectify. At full rectify (000.0° from the programmer), the RECTIFY D.S. is changed in 0.1° increments until the firing pulses are correctly timed. The digital phase angle meter is used to check this. At correct adjustment, the RECTIFY D.S. plus the BIAS has a nominal value of 180.0°. Small variations are caused by the effects of noise on the phase-lock loop.

Preset Counter

Under ideal conditions at full rectify, rectifier #1 turns on when the number in the main counter is 30°, rectifier #2 when the number is 60°, etc., and rectifier #12 when the number is 360°. At invert, each rectifier turn-on is delayed up to 155° so that several of the rectifier turn-on angles will occur in the following cycle of the main counter. The logic problems associated with this situation are avoided by using the PRESET COUNTER shown below the main counter in Fig. 1.

The preset counter counts by 0.1° steps and has a range of 819.1°. It is not cleared to zero but is preset to the number in the main counter at a specific time each cycle. The PRESET CONTROL logic operates so that in effect, the time for the presetting is after rectifier #12 has turned on and also is after the rollover of the main counter. If rollover has not occurred before turn-on of rectifier #12, the preset control in effect locks out the unwanted comparator output pulses generated between the time of rectifier #12 turn-on and the time of rollover.

The range of the preset counter and the method of presetting it require that the "B" input to the comparator has the following ranges:

Rectifier #1 varies from 15° to 200°
Rectifier #2 varies from 45° to 230°
Rectifier #3 varies from 75° to 260°
. . . . . .
Rectifier #12 varies from 345° to 530°

Lag Register

In normal operation, the ZGS programmer makes the major part of the changes in rectifier firing angles. This is done through the programmer input to the SELECTOR at the bottom of Fig. 1. The number of degrees of firing delay is put in the 0005 register at any time. The number is then transferred to the 0005' register under internal timing control.

The number in the LAG REGISTER is subtracted from the number in the 0005' register. The difference is divided by 256 and the quotient added to the initial value of the number in the lag register. The lag register then approaches the number in the 0005' register along a digitally generated "exponential." The time constant is controlled by the RATE logic and is selected from the ZGS programmer. The output "L" is thus made to change slowly enough to prevent arc faults in the rectifiers and to prevent distortions in the ring magnet field that would reduce the beam intensity.

Under fault conditions, the safety interlocks switch the selector from programmer input to a steady invert angle.

Maximum Invert Angle

The rectifier arc fault rate is dependent on the amount of firing delay used. Less delay is permissible at high magnet currents than at low currents. The control system is therefore provided with logic that limits the firing delay.

The MAXIMUM INVERT adjustment digital switch is shown at the lower left of Fig. 1. The hold button on the register permits changes during operation of the ring magnet. The digital switch angle is added to a fixed 108.8° to get the total maximum angle.

The CURRENT COMPENSATION input at the lower left of Fig. 1 is a voltage obtained from a magnet current transductor. This voltage is fed to a sample and hold (S/H) and then to an a–d converter. The number in the associated register is proportional to magnet current. The amplifier gain may be changed to adjust the amount of compensation.

The current compensation angle is subtracted from the maximum invert angle to give a limit "M" that varies with magnet current. This value "M" and the lag register number "L" go to a COMPARATOR and SELECTOR that make the number at "G" equal to the smaller of these two inputs to the comparator.

Phase Counter

The phase counter (φCNT), located in the lower right of Fig. 1, controls the distribution of firing pulses to the several rectifiers and determines the angular increments between the rectifier firings. The operation is as follows.

Consider the φCNT to be in the first of its 12 states. The counter output and DECODE gates condition DRIVER #1 to transmit the next comparator pulse to rectifier #1. The counter output causes the 30°INC generator output "C" to be zero and connects D. S. 1 digital switch to the E input to the adder. The output of this adder can be adjusted between 0° and 30° by adjusting D. S. 1.

If the programmer input is 0^{o} (full rectify) and if the FEEDBACK is not in use ($F=15^{o}$), the B input to the comparator may be from 15^{o} to 45^{o} depending on the D.S. 1 setting.

As soon as the number in the preset counter equals or exceeds the number B, a comparison pulse is generated. This pulse is transmitted to rectifier #1 and causes the ϕCNT to advance to the second state.

In this second state, D.S. 2 digital switch is connected by the selector to output E and driver #2 is conditioned. In this case, the 30^{o}INC generator output has a value of 30.0^{o}.

This process continues to fire each of the 12 rectifiers in the proper sequence. The ϕCNT is self-synchronizing at startup of the system because of the equal to or greater than action of the comparator.

Feedback

The digital control system is provided with a fast channel that may be used in conjunction with other control systems such as the $\dot{B}$ feedback control and the external beam intensity control.

The feedback system, located at the bottom of Fig. 1, consists of an input amplifier, a S/H, an a–d converter, and a register (REG). The input voltage range is -20 to t20 V. The a–d converter has an output range of 0^{o} to 30.0^{o}. When the feedback input is not in use. the REG is held at 15.0^{o}.

Model

Dynamic checks of the digital control of the rectifier firing angles are done through use of the MODEL. This model contains two small 6-phase transformers supplied from the generator bus. One transformer has a delta primary and the other a wye connected primary. The secondaries connect to 12 small photo-coupled SCR's that are operated by the 12 drivers of Fig. 1. The rectified voltage is fed to an operational amplifier analog model of the ZGS passive filter and ring magnet system. Magnet voltage, magnet current, and current through the filter inductor are available. Model current and magnet voltage are transmitted to the power house display system for the operators' inspection.

Discussion

The control system has been in routine use since November 1973. Initial startup was with all the digital switches, D.S. 1 - D.S. 12, set for equal intervals between rectifier firings. No particular problems with arcbacks were encountered.

Readjustments of the individual rectifier angles were made to minimize ripple. This was done with the aid of the control computer using the PHASOR[2] program. The amplitudes of the first, second, and third harmonics were reduced to values that were about a factor of 20 smaller than with the old analog ramp control system. This was done without the feedback input.

The amplitude of the sixth harmonic could be minimized but remained large. The minimum was fairly broad, and the values of D.S. 1 - D.S. 12 indicated that the delta and wye connected transformers did not produce voltage waves that are 30^{o} apart. It appears that the angles are about 28^{o}.

The feedback connection is used with the B coil on the ring magnet to control the slope of the magnet flat-top for energy loss extraction. In this mode, increased ripple amplitudes appear on the ring magnet voltage. These are at low frequencies and are not reproducible from cycle to cycle. It appears that low frequency noise is picked up in the $\dot{B}$ system. Even so, the ripple is less than with the old control system.

The feedback input is used during resonant extraction to control the extraction rate.[3] The signal is supplied from beam monitoring devices to magnetically program the beam position during extraction.

Acknowledgments

Many people have enthusiastically contributed to the digital firing control system project. Their efforts have made the system operational in a remarkably short time.

We wish to thank Mr. Ray Kickert for his efforts, especially during the measurements of the dynamic characteristics of the mercury vapor rectifiers and during debugging and testing of the system.

The ring magnet power group, under Mr. George West, did an outstanding job of constructing many of the circuit modules and making the many changes in the control and interlock circuits. We wish to thank P. Bertucci, L. Johns, P. Roth, E. Kulovitz, W. Welch, and the whole ring magnet power group.

References

1. J. F. Sellers, E. F. Frisby, W. F. Praeg, and A, T. Visser, Ring Magnet Power System for the Zero Gradient Synchrotron, 1965 Particle Accelerator Conference, Washington, D. C., March 10 to 12, 1965, IEEE Transactions on Nuclear Science, Volume NS-12, No. 3, p. 338 (1965)

2. Lloyd G. Lewis and Anthony D. Valente, Argonne National Laboratory, PHASOR: A Control Computer Method for Displaying Amplitude and Phase of Ripple Components in the Ring Magnet Voltage, IXth International Conference on High Energy Accelerators, Stanford, California, May 2 to 7, 1974.

3. Y. Cho, E. A. Crosbie, L. G. Lewis, C. W. Potts, and L. G. Ratner, Argonne National Laboratory, Slow Resonance Extraction of Two Simultaneous Beams without RF Structure, IXth International Conference on High Energy Accelerators, Stanford, California, May 2 to 7, 1974.

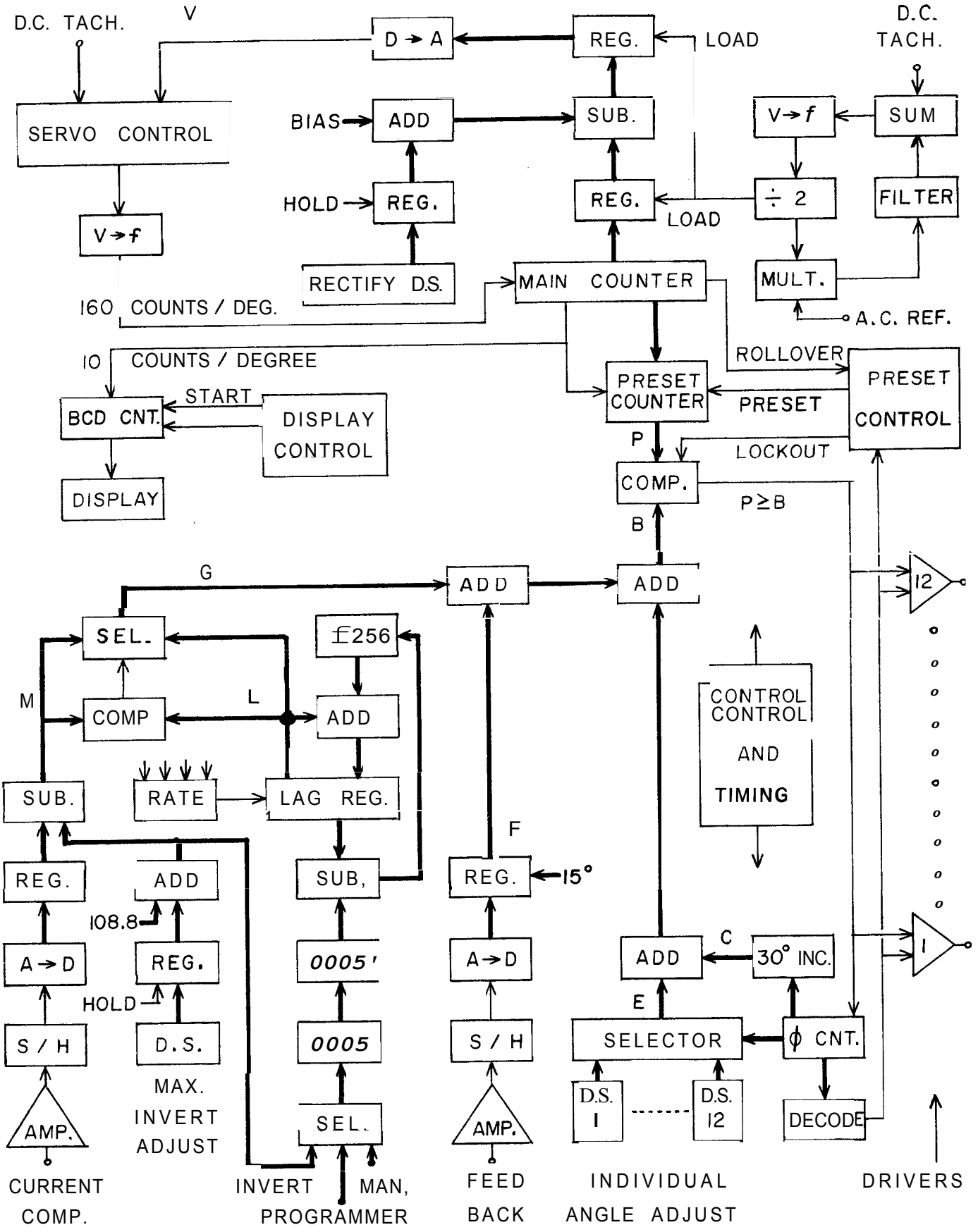


FIG. 1 – DIGITAL FIRING ANGLE CONTROL SYSTEM BLOCK DIAGRAM

PHASOR: A CONTROL COMPUTER METHOD FOR DISPLAYING AMPLITUDE AND PHASE OF RIPPLE COMPONENTS IN THE RING MAGNET VOLTAGE*

Lloyd G. Lewis and Anthony D. Valente
Argonne National Laboratory
Argonne, Illinois

Abstract

Deviations of 12-phase generator-transformer-rectifier systems from ideal performance result in the generation of ring magnet ripple at the fundamental and at low harmonics of the generator frequency. Analysis and display of the amplitude and phase of each of these harmonic components makes it possible for the systems engineer to minimize the ripple by readjusting the control system. The Zero Gradient Synchrotron (ZGS) control computer samples both the filtered voltage on the ring magnet and a reference voltage produced by a phase-lock loop connected to the generator bus. Data are taken during a selected interval of the *ZGS* cycle and are then analyzed. Computer driven graphic displays plot the raw ripple data, amplitude and phase bar graphs for each harmonic component, reconstructed ripple data for checking, and graphs for comparing ripple components under different operating conditions. Numerical information is also displayed. The PHASOR program corrects the phase angles for the phase shifts produced by the ZGS passive filter. These corrected angles indicate which of the 12-phase firing angles should be retarded or advanced to reduce the ripple.

Introduction

Power supplies for synchrotron ring magnets usually consist of phase-controlled rectifiers operated from an ac power line or from ac generators. The number of ac phases is often high to minimize the ripple. The ripple on the magnet is reduced even more in some systems by inserting a low-pass filter between the rectifiers and the ring magnet.

In a 12-phase system with a low-pass filter, the amplitude of the ripple component at the fundamental frequency of the power line may exceed the amplitude of the 12th harmonic. This is caused in part by the filter's attenuation being larger at the higher frequency. Additional causes include errors in the number of turns on the polyphase transformer windings, variation in the leakage inductance from one phase winding to another, lack of symmetry in circuit resistances, and imbalances between phases of the power line or generator.

The magnitude of the low frequency ripple components may be reduced on flattop by properly retarding or advancing the firing time of each of the 12-phase rectifiers with respect to the others.

Proper adjustment of the firing delays of each of the 12 phases is extremely difficult by trial and error methods and an optimum is difficult to determine by eye. For these reasons, analytical methods are required.

A swept frequency spectrum analyzer was used in an attempt to analyze the ripple during a 700 ms flattop of the ZGS ring magnet. At the low ripple frequencies, 50-600 Hz, the sweep rate for the required resolution was so low that an analysis could not be performed in the length of the flattop, In addition, no phase angle information is given by such an instrument.

The ZGS control computer system was used in conjunction with the program PHASOR to analyze the ripple and display the results. The program is of the interactive type where the computer operator directs the logic flow after observing the results of each section of the program.

Data Input

The reference for all phase angles was a square wave produced by a phase-lock loop that had one phase of the generator voltage as its input. This loop acted as a filter for the distortions in the generator voltage wave and gave sharp indications of corresponding points in each generator voltage cycle. The loop was adjusted so that the positive-going square wave transitions were at 90° on the generator voltage sine wave and were independent of generator voltage and frequency.

This square wave, shown in Fig. 1A, was the input to an analog integrator that was voltage limited at ± 10 V. The waveform from this is shown in Fig. 1B. The rise and fall times were adjusted to be slightly longer than the control computer data sampling interval. In this way, the computer was assured of one data point on the rise even through the computer was not synchronized to the generator.

The second input to the ZGS control computer data station was a voltage containing the magnet ripple information. It was obtained by capacitively coupling the voltage which was across one quadrant of the ring magnet to an amplifier with a high common mode rejection. Zener diode networks eliminated most of the dc component.

Data Taking

The manual keyboard at the computer driven scope was used to specify the point in the ZGS cycle lor the start of data taking (e.g. 250 ms after the start of flattop). The keyboard was then used to enter the number of data samples of the ripple voltage that are to be taken. The computer then generates requisitions for all of the data points. Measurements are made at 100 us intervals and alternate between the reference wave and the ripple wave.

When the operator pushes the DISPLAY NEW SET key, a new set of data is taken on the next *ZGS* cycle. These data are then displayed on the scope screen. Figure 3 top plots the samples taken on the reference wave. The points that are circled are on the rising and falling slopes of the reference. Figure 3 bottom plots the samples taken on the ripple wave.

*Work performed under the auspices of the U. S. Atomic Energy Commission.

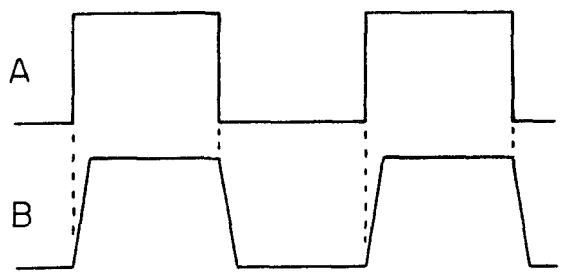


Fig. 1 Phase Lock Loop Waveforms

The computer operator, by inspection of the scope display, determines that the amplitude range of the data is acceptable and that enough points are taken. He may then proceed to analyze the data by pushing the ANALYZE button on the scope.

Analysis

A finite, periodic function V(t) may be written as

$$V(t) = \sum_{n} \left(A_n \cos n\omega t + B_n \sin n\omega t \right) \qquad (1)$$

where

$$n = 0, 1, 2, 3 \ldots \text{ and } \omega = \frac{2\pi}{\tau}$$

and the coefficients are given by

$$A_n = \frac{2}{\tau} \int_{-\frac{\tau}{2}}^{+\frac{\tau}{2}} V(t) \cos n\omega t \, dt \qquad (2)$$

$$n = 0, 1, 2 \ldots$$

$$B_n = \frac{2}{\tau} \int_{-\frac{\tau}{2}}^{+\frac{\tau}{2}} V_t \sin n\omega t \, dt$$

where $B_0 = 0$ and A_0 = twice the dc value of the signal.

If we make k measurements during one period of the function V(t), we may approximate the integrals (2) and (3) by the following:

$$a = \frac{2}{k} \sum_{d=1}^{k} V_d \cos(r\theta_d) \quad r = 0, 1, 2, 3 \ldots \qquad (4)$$

$$b = \frac{2}{k} \sum_{d=1}^{k} V_c \sin(r\theta_d) \qquad (5)$$

$$\text{Then } V(t) = \frac{1}{2} a_0 + a_1 \cos \omega t + a_2 \cos 2\omega t + \ldots + b_1 \sin \omega t + b_2 \sin 2\omega t + \ldots \qquad (6)$$

or

$$V(t) = \frac{1}{2} a_0 + c_1 \sin(\omega t + x_1) + c_2 \sin(\omega t + x_2) + \ldots \qquad (7)$$

where

$$c_r = \sqrt{a_r^2 + b_r^2} \text{ and } x = \arctan\left(\frac{b_r}{a_r}\right) \qquad (8)$$

with the restriction $-180^\circ \le x_r \le +180^\circ$.

The first step in the analysis is to assign an angle θ_d to each of the data points. The computer searches the reference wave data points, Fig. 3 top, to locate all the positive-going edges. It counts the number of data points in each cycle and calculates the fractional intervals at the beginning and end of each cycle. These fractional intervals are calculated from the position of the circled points, Fig. 3 top. The total number of intervals is then divided into 360 to get the number of degrees per interval. θ_d for the first data point in each cycle and the frequency of each cycle are displayed on the scope screen. A value of θ_d for each data point is then assigned.

The computer uses the equations (4), (5), and (8) to compute the amplitude and phase of the first 12 harmonic components. The sums, equations (4) and (5), may be extended over more than one cycle if the operator so specifies.

The phase angles, x_r of equation (7), are then corrected for the phase shifts produced by the ZGS passive filter, shown in Fig. 2. The results give the phase angle of each frequency component at the output of the rectifier.

Display Derived Ripple

The operator may push the DISPLAY DERIVED RIPPLE button to check the computation. In this mode, the computer uses the phases and amplitudes of the ripple components derived from the data to calculate V(t) at each value of θ_d. The graph is shown in Fig. 3 center. The amplitudes and phase angles of the components are given in the table at the bottom of Fig. 3.

A measure of the error is given by a number labelled FIT. This number is found by taking the difference between each measured ripple voltage and the voltage calculated from the phases and amplitudes of the ripple. This difference is divided by the measured voltage at each point and the ratio is squared. The number FIT is one minus the mean of this ratio.

Graph Phasor Set

The operator may see the results of the harmonic analysis by pushing a button labelled GRAPH PHASOR SET. This activates a subroutine that constructs the graphic display that is shown in Fig. 4.

The top lines on the right of Fig. 4 give the date and time of day for starting to take the set of data. The remaining lines on the right give the point in the ZGS cycle at which the data taking began. In this case it was 400.0 ms after the start of block 16 (flattop).

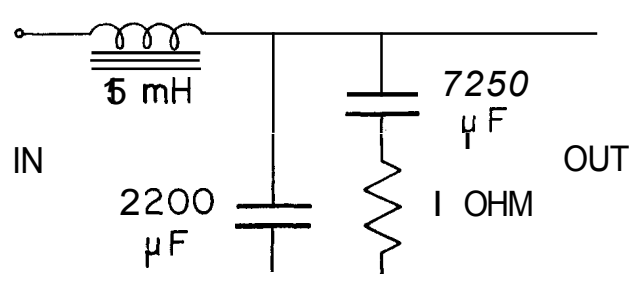
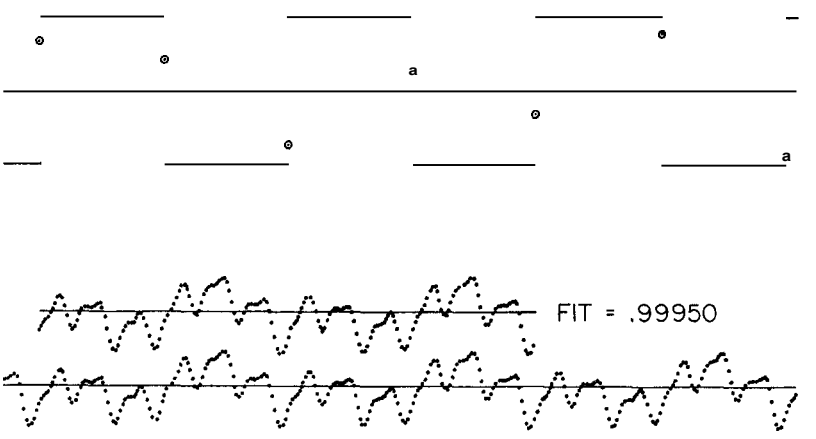


Fig. 2 ZGS Passive Filter



PHASOR

15 NOV. 1973
21 : 04 : 36

START AT 16 400.0
300 SAMPLES TAKEN

2 PERIOD ANALYSIS

	HZ	1ST THETA
1	50.15	4.82
2	50.10	2.28

ALPHA	SET		AMP.	PHASE		AMP.	RETAINED SET PHASE	ALPHA	SET	
0	0	0	-.2	0	dc	0	0	0	0	0
			1.1	29.3	1	0	0			
0	0	0	1.1	-111.7	2	0	0	0	0	0
			.2	-112.0	3	0	0			
0	0	0	.3	-130.1	4	0	0	0	0	0
			.1	-145.9	5	0	0			
0	0	0	1.4	- 76.6	6	0	0	0	0	0
			.1	- 82.1	7	0	0			
0			.0	138.0	8	0	0	0		
			.0	11.1	9	0	0			
			.0	47.8	10	0	0			
			.0	- 5.9	11	0	0			
			.6	15.6	12	0	0			

Fig 3. Display New Set and Derived Ripple

Three hundred data samples were taken and *two* periods were analyzed. The first period had a frequency of 50.15 Hz, while the second had 50.10 Hz. This difference is caused by the slowing down of the generator during the ZGS cycle. The angle θ_d for the first data point in each cycle was 4.82° and 2.27°.

The top graph gives the reconstructed ripple data that was calculated from the amplitudes and phases of the derived ripple components. The FIT number is also given. This graph is included in Fig. 4, as well as in Fig. 3, for identification purposes and because many people get a better "feel" for the data from an analog type display.

The upper bar graph of Fig. 4 plots the dc component and the amplitudes of the first 12 harmonics of the generator frequency. The vertical scale for this plot is shown above and to the left of the bar graph. The scale factor in volts per inch is changeable at will through the scope keyboard. These amplitudes are for the filtered voltage applied to the ring magnet.

The lower bar graph of Fig. 4 plots the phase angles x_r for the first 12 harmonics. The range of angles is fixed at ±180° to -180° in accordance with the restriction on x_r in equation (8). These angles have been corrected for the phase shifts produced by the passive filter of Fig. 2. They are, therefore, the phase angles of the harmonic components at the output of the rectifiers. This is done to make it possible to determine which rectifier firing angles should be retarded or advanced to reduce the amplitudes of the ripple components.

The lower part of Fig. 4 lists several sets of numeric data. The column in the center lists dc and phases 1-12. The *two* columns to the left of center give the amplitudes in volts and the phase angles in degrees for the 12 phases and the amplitude of the dc component. These are the values used to calculate the derived ripple plotted at the top of Fig. 4.

The table of numbers at the lower left records the alpha angle settings for the 12 phases and in addition, the full rectify setting. These are the settings of the ZCS control system that produced the ripple reconstructed at the top of Fig. 4. The numbers are in octal code and represent deviations from the ideal uniform spacing of rectifier firing angles. These numbers are recorded in the exact format in which they appear on the control panel of the digital firing angle control system.

These numbers are entered through the use of the ENTER/MODIFY ALPHA SET subroutine, and can be used by the operator when desired.

Retained Set

The operator may save a set of results, such as that presented in Fig. 4, by pushing the button labelled RETAIN THIS PHASOR **SET.** This activates a subroutine that stores the information in computer memory for comparison with future data.

The operator may then analyze a new set of data and call for GRAPH PHASOR SET. The result is the generation of a display such as shown in Fig. 5.

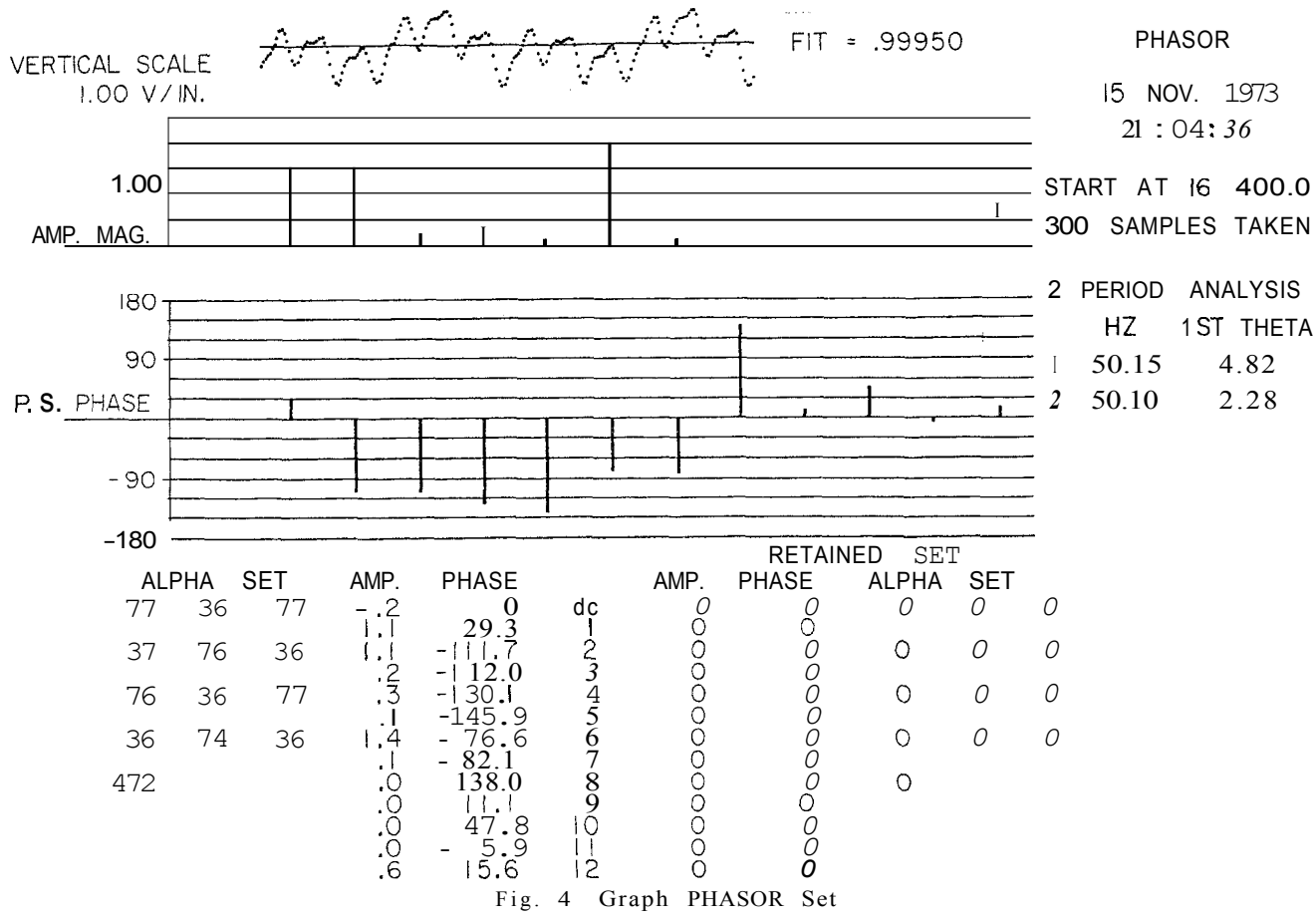


Fig. 4 Graph PHASOR Set

The numeric information at the top right of Fig. 5 is similar to that of Fig. 4 except it is for the new set of data. The derived ripple curve and the FIT number are also for the new set of data.

The bar graph for the amplitude now has two lines at each harmonic location. The left line in each pair gives the amplitude of that harmonic component in the new set of data, while the right line in each pair gives the amplitude of that harmonic component in the retained set. In this way, the amplitudes may be compared visually *to* determine the effect of the changes in the firing angles.

The bar graph for the phases also has a pair of lines at each harmonic location. The left line in each pair gives the phase angle for that harmonic component in the new set of data, while the right line gives the phase angle of that harmonic component in the retained set.

The numeric information, at the bottom of Fig. 5 on the right, gives the amplitude and phase angles for the retained set and in addition the alpha set that produced them, The numeric information, at the bottom on the left, gives the amplitude and phase angles for the new set of data and the corresponding alpha set.

output

The program PHASOR is an interactive one so that most of the output is through visual observation of the computer driven scope display. Several options in the interaction can produce copies of the scope display on 8½" x 11" photographic paper. These include:

COPY NEW SET -- similar to Fig. 3,
COPY LEFT SHIFTED -- that portion of Fig. *3* that was analyzed,
COPY DERIVED -- derived ripple,
COPY PHASOR & ALPHA SET -- similar to Fig. 4, 5.

The 'hard-copy" unit can produce a print in about ten seconds. No line printer output is provided.

Calibration

The effects produced by changes in rectifier firing angle were experimentally investigated. For example, the firing angle of phase number 1 was advanced several electrical degrees to produce a large ripple on flattop. PHASOR was then used to measure the amplitude and phase of the harmonic components of the ripple thus produced. This procedure was repeated for several combinations of changes in firing angles of selected rectifiers.

The calibration data were useful in predicting which of the 12 rectifier groups should have their firing angles altered to reduce a given observed ripple.

Discussion

Analyses of ripple data were made for a variety of firing angle combinations during the calibration runs and for many actual operating conditions while ripple reduction adjustments were made. In all cases, the bar graphs similar to Figs. 4 and 5 showed very small or no amplitudes for the 5th, 7th, 8th, 9th, 10th, and 11th harmonics. The phase angles computed for these

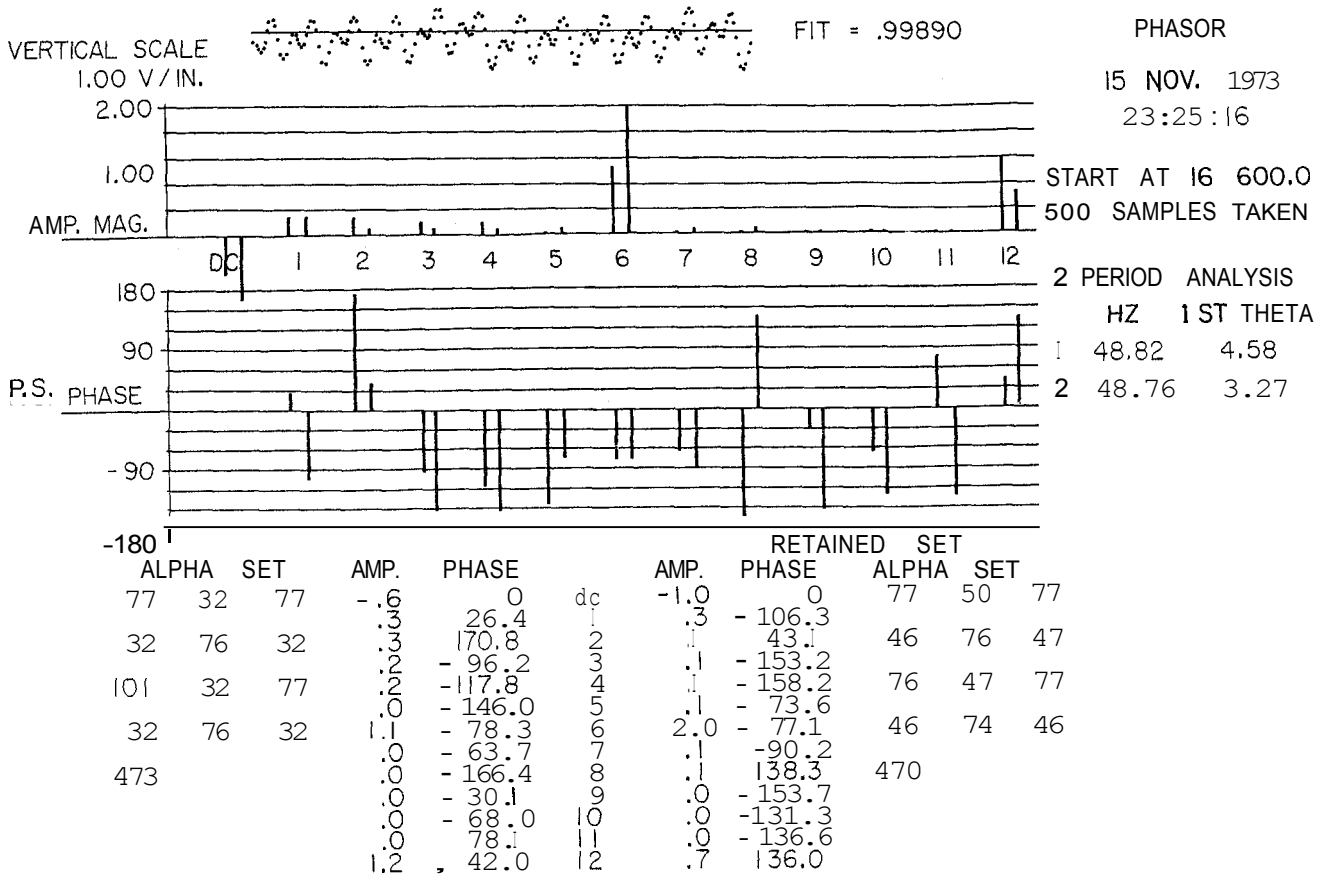


Fig. 5 Graph PHASOR Set With Retained Set for Comparison

harmonic components varied widely from one data set to the next which leads us to the conslusion that these harmonic components are largely the result of "noise" or inaccuracies in the input data.

We were not able to find a combination of rectifier firing angles that produced large or significant amounts of 5th, 7th, 8th, 9th, 10th, and 11th, harmonics. We therefore have amplitude and phase meaurements at harmonic numbers 1, 2, 3, 4, 6, and 12 for a total of 12 measurements.

The control system has adjustments for each of the 12 phases but only 11 of these are independent variables as far as ripple is concerned. The 12th phase control and the "full rectify" control adjust the slope of the flattop. This slope is adjusted to zero before the ripple measurements are made.

Some thought was given to writing a program that would compute new firing angle settings from the ripple component amplitudes and phase angles. There appear to be enough measurements to permit the solving of a set of 12 equations. No adequate algorithm for this was developed in the very limited effort expended.

Inspection of the problem indicates that the ripple may be reduced one component at a time. This is the procedure used.

A perfect rectifier system will produce only the 12th harmonic, therefore this cannot be eliminated or effectively reduced by adjusting firing angles. On the other hand, the 6th harmonic can be increased or decreased in only one way. That is, all even numbered phases should be advanced an equal amount and all odd numbered phases retarded by the same amount. This method reduced the 6th harmonic amplitude to a minimum but would not make it vanish. The data indicate that the phase shift between our delta and wye connected transformers is only 28° rather than the theoretical 30°.

The first harmonic amplitude may be reduced by changing all of the 12 angles. In this case, the changes are distributed sinusoidally with the peak of the distribution determined by the phase angle of the 1st harmonic of the ripple. The 2nd harmonic may be reduced by a similar procedure except that the sinusoid for the distribution is the 2nd harmonic.

This program was used successfully to reduce the flattop ripple at the ZGS with the distributions for alpha angle changes determined manually. It is hoped that additional subroutines can soon be added to permit the computer to calculate the alpha settings that will minimize the ripple.

INITIAL EXPERIENCE WITH A MULTI-PROCESSOR CONTROL SYSTEM

K. B. Mallory
Stanford Linear Accelerator Center
Stanford, California

The SLAC accelerator has now been controlled through a system of two linked computers far a year. In the first four months of 1974 nine additianal CPU's have been linked into the system. Figure 1 shows the present configuration. It is time to review the problems encountered in computer-control of the accelerator and to discuss their solutions--installed, pending and proposed.

BACKGROUND

When SLAC was built, an SDS-925 computer was installed in the switchyard's data assembly building, now the Main Control Center (MCC). Its functians were to monitor interlocks and to control a few of the switchyard magnets. There was no cmputer asssciated with the accelerator itself. Four years later a PDP-9 was installed in the Central Control Roam (CCR) to log klystron performance and to help automatically select spare klystrons to replace failures. By making maximum use of existing relay multiplexers the PDP-9 was csnnected to nearly all accelerator control, analog and status signals within six months. As a result, however, it vas limited to executing sne control or analog readsut at a time.

It was then proposed functionally to move CCR to MCC by linking the computers and using "touch-panel" displays (Refs. 1,2), without physically moving hardware. The pattern generator for defining multiple-beams was the last interface to be completed, early in 1973. Operations from MCC started shortly thereafter.

INITIAL PERFORMANCE

From the outset, nearly all of the accelerator control and monitoring signals could be made available at the touch panel display units. Operators designed their own panels, using a convenient software "panel compiler". However, the system could only operate control at a time, just as was the case at a single control position In CCR. It presented analog signals only when the operator explicitly asked for them by name. Its only alarm annunciator was a "scroll" of the last fifteen messages resulting from detected changes. Since a major fault is normally followed by a number of consequent faults, the most important message often was rolled off the "scroll" before the operator realized anything had happened.

In our operating system (*Ref.* 3), *each* status change and button-push creates one or more tasks. The PDP-9 can handle up to roughly 50 or more tasks at a time; the 925 can support twice as *many*. Nevertheless, there are many occasions when multiple changes create far too many tasks for the system to manage which, at first, caused many system crashes. The solution was to cause various kinds of tasks to be deleted before the system was swamped. To give an extreme example, rist so rare as we would like, a fault can occasionally dump the entire RF system. This causes some 800 status changes to appear at the PDP-9 within two or three seconds. When *too many status* changes occur, the PDP-9 stops reporting individual changes and instead, with a single task, sends a total update of accelerator status to the 925. Similarly, *most* messages across the link can be aborted if there are too many tasks already in the system.

Since the computer system essentially replaces a pre-existing manual control system, there has been considerable pressure to "give us back what we had before." The annunciator problem was the first to bo attacked. There are now several new programs that (1) display the status of all 245 klystrons on one panel, (2) display status of a system (e.g. personnel protection or vacuum) and soon, (3) display a list of accelerator faults in order of priority. This last list displays current status, rather than changes, and is thus independent of occasional missed tasks, (4) multiple scrolls so that messages of different types can be directed to different displays.

RECENT IMPROVEMENTS

These software changes have made the system mare reliable and have imprsved its operation, but software alone cauld do nothing about the me-at-2-time control and very little about the slaw analog acquisition. The original proposal far improving controls required 30 special-purpose pracessors in the gallery, with circuits to store a command and then drive local relays while the PDP-9 transmitted control signals to other sectors. These processors at first were very complicated; but even when all of the timing and much of the special lsgic was deleted, they cost as much as putting a computer into every fourth sector, and increased the amount of work to be done by the PDP-9. Since an analog multiplex system and a method to restructure the addressing of some of the control channels were also desired, the special-purpsse processors never got off the drawing board. We bought nine PDP-8's instead.

The first of the PDP-8's arrived a year ago. An executive program similar to the one in the PDP-9 and 925 had been written and tested in a simulator in the IBM 360. A terminal-emulator prsgram was written for the PDP-8; it asked the 360's text-editor Cor a binary "listing" of the executive program, loaded it into core, and we were in business. By August, the eight gallery processors had been linked to the one in CCR, in October the link into the PDP-9 was established, and we were waiting primarily for fabrication and installation of interface hardware in the gallery. (Fig. 2) Programs to control the new hardware rind a program in the PDP-9 to store the PDP-8 programs on its disk were completed this winter. During this conference we have installed remote restart switches, as a pacifier to the operators who know that any system can go down occasionally.

By the end of this conference, when the accelerator is being started up, we expect eight of the nine computers to be fully operational, and to have 28 channels of control to the accelerator instead of the one we had before. The ninth csmputer is being used to test the analog multiplexing hardware as it comes out of the shop. We expect to have a form of analog multiplex system operating in September.

DEVELOPMENTS FOR THE FUTURE

I suggesred above that we were restructuring our control addresses. The original control addressing scheme required the operator first ti select a sector and then push a button for the desired control signal. When we installed pulsed beam guidance, we subdivided individual control addresses for adjusting up to six preset levels of a device. For manual operations, pushing one butt-n at a time, it made no difference to an operator what the addressing hierarchy might be in the hardware.

But we now have three independent operating positions in the Main Control Room, and arc talking *about*

adding automatic controls that might be initiated by the computer. The operator now selects which beam he wishes to tune on his touch panel (subdevice address). Then he selects what function he wishes to control (control address, e.g. beam loading or vertical steering). Finally he selects the particular location (sector) where he will make his adjustment. Thus our addressing logic has been turned completely upside-down. In particular, far instance, the controls for beam current and spectrum sharpening of all beams share three control addresses at the injector, which are accessed only by one of the new PDP-8 channels. Thus operators could still find themselves interfering with each other.

We plan to install special interfaces to allow parallel control of selected multilevel devices. The first was scheduled for installation in July, but it now appears that parallel control for "phase closure" (spectrum sharpening) and for fine energy control *may* become operational before the end of May.

When the analog multiplexing system comes into operation, a new problem will arise: the amount of link traffic is expected to be at best doubled, perhaps trebled from what it is now. Two pstential solutions are being studied -- a mare-efficient message-switching system for the PDP-8 in CCR (which will not do much to reduce link traffic from the PDP-9 to the 925) or a new data link, for analog signals only, direct from the PDP-8's t>an auxiliary processor at the 925.

Eventually, we will prsbably have to replace the 925, reliable though it be now. We are proposing to install new minicomputers to buffer several of the 1/0 devices now connected to the 925, and later to connect them to a new major processor which can first share and later, if necessary, take over the tasks of the veteran - the original cmputer installed for control of the BSY at SLAC.

REFERENCES

1. D. Fryberger and R. Johnson, "An Innovation in Control Panels for Large Computer Systems," Particle Accelerator Conference, Chicago, Illinois, March 1971.

2. S. Howry et al., "SLAC Control Room Consolidation - Software Aspects," Particle Accelerator Conference, Chicago, Illinois, March 1971.

3. S. Howry, "An Operating System for Process Control," 3rd ACM Symposium on Operating Systems Principles, Stanford, October 1971.

4. K. B. Mallory, "Some Effects of (Now Having) Computer Control for the Stanford Linear Accelerator Center," Particle Accelerator Conference, San Francisco, California, March 1973.

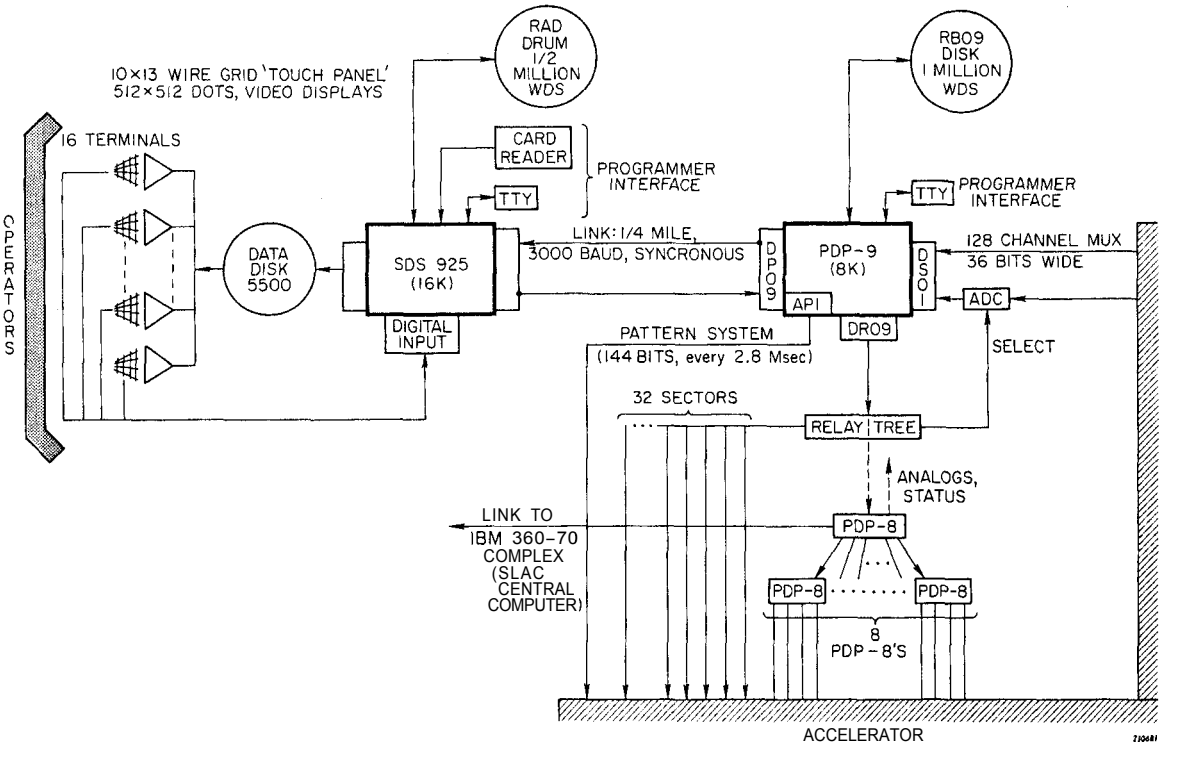


Fig. 1

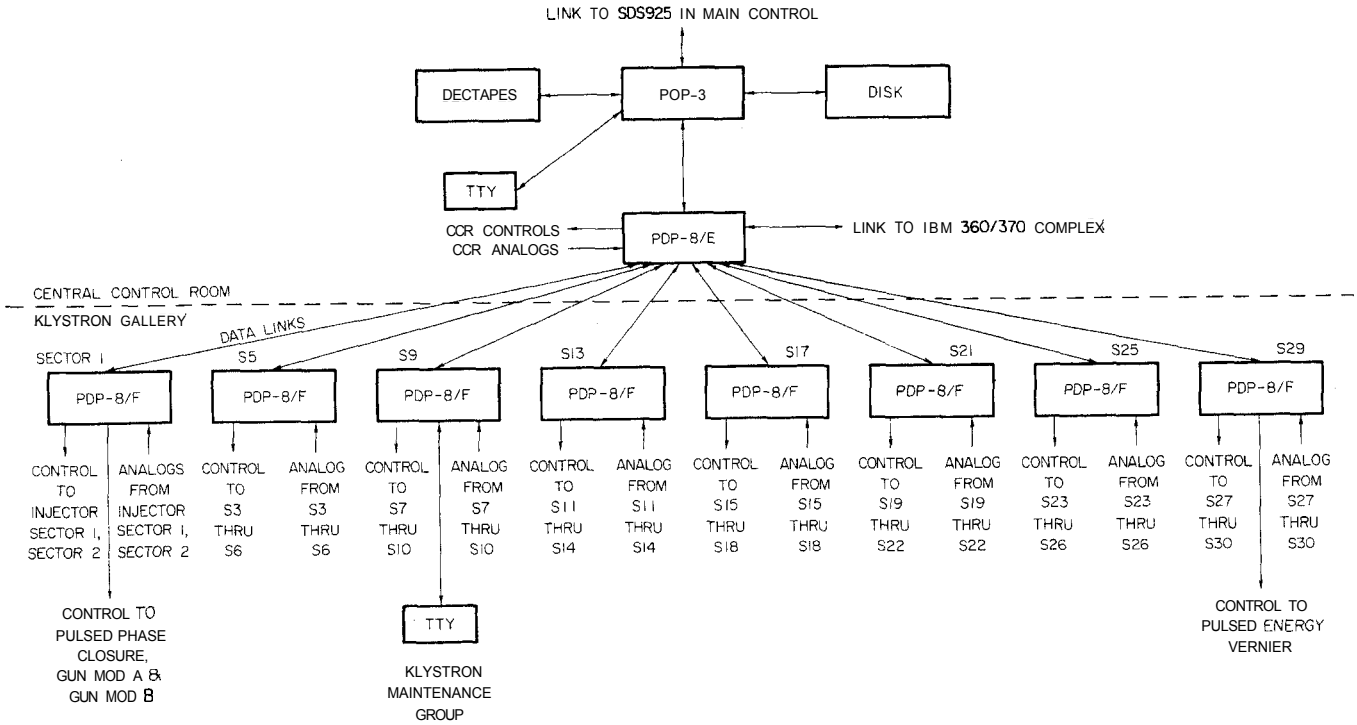

LINK TO SDS925 IN MAIN CONTROL
DECTAPES
POP-3
DISK
TTY
CCR CONTROLS
CCR ANALOGS
PDP-8/E
LINK TO IBM 360/370 COMPLEX
CENTRAL CONTROL ROOM
KLYSTRON GALLERY
DATA LINKS
SECTOR 1
S5
S9
S13
S17
S21
S25
S29
PDP-8/F
CONTROL TO INJECTOR SECTOR 1, SECTOR 2
ANALOGS FROM INJECTOR SECTOR 1, SECTOR 2
CONTROL TO S3 THRU S6
ANALOG FROM S3 THRU S6
CONTROL TO S7 THRU S10
ANALOG FROM S7 THRU S10
CONTROL TO S11 THRU S14
ANALOG FROM S11 THRU S14
CONTROL TO S15 THRU S18
ANALOG FROM S15 THRU S18
CONTROL TO S19 THRU S22
ANALOG FROM S19 THRU S22
CONTROL TO S23 THRU S26
ANALOG FROM S23 THRU S26
CONTROL TO S27 THRU S30
ANALOG FROM S27 THRU S30
CONTROL TO PULSED PHASE CLOSURE, GUN MOD A & GUN MOD B
TTY
KLYSTRON MAINTENANCE GROUP
CONTROL TO PULSED ENERGY VERNIER

Fig. 2

THE CPS IMPROVEMENTS 1965-1973
AN ASSESSMENT

THE CPS STAFF
CERN, Geneva, Switzerland

Summary

In 1965, plans were made to increase the beam intensity delivered by the CPS by a factor of ten or more. The first stage, involving a new power supply for the main magnet and more than doubling the cycle repetition rate, was completed in 1968. In the second stage, which is now essentially complete, the major items was the construction of an 800 MeV slow-cycling booster injector. Many other modifications were included. The Linac current had to be increased by an order of magnitude to supply the Booster, and the higher beam intensities required a more powerful RF accelerating system. Besides the 800 MeV injection elements, quadrupole lenses were installed to avoid longitudinal dilution at transition, and multipoles to counteract instabilities. In addition, the chamber vacuum was improved by a factor of ten, shielding and radiation resistance increased where necessary, and beam-equipment interaction reduced. Adequate instrumentation and control facilities had to be provided, and the efficiency of fast and slow extraction systems improved. Perturbations due to various collective phenomena had to beovercome.

The performance obtained during the first physics runs is reported.

1. Introduction

After a few years of operation, the CPS had reached a maximum intensity of 1 Tp/pulse* and, in view of space-charge effects, a further factor of two seemed the most that could be expected. The motor-generator set supplying the main magnet limited the duty cycle to a typical value of 10%at 19 GeV/c (200 ms flat-top with a 2 s repetition time) and even less at higher energies (100 ms flat-top every 3 s at 24 GeV/c). The experimental facilities comprised two halls, with a total area of 4000 m^2, fed by internal targets and a single fast extraction channel.

In 1964, an improvement programme was launched with the object of increasing the average accelerated beam intensity by a factor of 10 to 15[1]. This was to be achieved in two stages :

i) raising the repetition rate to gain a factor of 2 or 3, depending on energy and flat-top length, by constructing a new magnet power supply;

ii) raising the injection energy (factor ∿ 5 in intensity per pulse). Two possible methods were investigated in detail; a 200 MeV Linac[2] and a 600 MeV twin slow cycling booster synchrotron[3], A comparative study[4] showed that although both schemes could produce the required intensity increase, the higher space-charge limit of the booster allowed a greater potential for future development. Further studies finally led to an 800 MeV booster with 4 superposed rings[5]. In addition to the new injector, this part of the programme involved a number of complementary improvements to the 50 MeV Linac and the main proton synchrotron, which are detailed below.

* Tp = 10^{12} protons (Teraproton).

The programme was balanced by a comparable expansion of experimental areas and facilities (West Hall with the Omega spectrometer and the Big European Bubble Chamber (BEBC) and neutrino facility with Gargamelle), which took place simultaneously.

2. Main Magnet Power Supply

The new power supply[6] was designed to more than double the duty cycle.

The magnet voltage was increased from 5.4 to 10.8 kV, which approximately halved the rise and fall times of the magnetic field. In order to avoid increasing the maximum voltage to ground, limited by the winding insulation, a second rectifier set was inserted in the middle of the magnet circuit, with the output voltages of both rectifier sets symmetrical to ground. Keeping the same maximum current (6400 A) as before, the higher magnet voltage implies a higher peak power, namely 95 MVA in place of 46 MVA.

The increase in duty cycle raises the average power and the losses in the magnet. Mean power rose from 18 to 46 MVA and power dissipation in the magnet from 1.6 to 3 MW. The magnet cooling system had to be adapted to the new conditions.

The new power supply has a more flexible control system, which provides a wider choice of magnet cycles, including the possibility of two "flat-tops" at different energies. The distribution of accelerated protons between users is thereby simplified; a common example of such a complex cycle is : acceleration to 26.3 GeV/c, ejection of 4 bunches to ISR, deceleration to 24 GeV/c, then slow extraction shared with an internal target over a 400 ms burst.

The reduction obtained in the ripple voltage (20 V peak to peak instead of 100) and the better reproducibility of the magnet field ($4\ 10^{-4}$) are important factors in producing a satisfactory slow extracted beam.

Reliability has proved to be very good (2 h downtime per 1000 hours of operation in 1973).

An important additional implication was the need to increase the mean power and the rate of rise of the auxiliary power supplies. These modifications were carried out progressively, and still continue today, as each auxiliary sub-system proves to be a bottle-neck for an increase in the machine overall efficiency and has, in its turn, to be matched to the main power supply capability or modified to improve the control of beam dynamics effects.

3. Linac

Since the original 50 MeV Linac had also to serve as injector for the new Booster synchrotron, its performance required substantial improvement. This involved increasing the pulse length to 100 μs, for multiturn injection up to 15 turns; more current (100 mA) within a specified emittance and energy spread (30 π mm mrad

and ± 150 keV); and a higher repetition rate (2 s^{-1}) so that alternate pulses could be sent down a pair of new beam measuring lines. Besides increasing the duty cycle of several components (ion source, pre-accelerator, pulsed quadrupoles, etc.), a major problem was cavity beam loading and its compensation. This was tackled by installing for each of the three tanks an additional RF amplifier using more powerful tubes. However, the beam loading compensation is very difficult to adjust with adequate stability for long pulses at peak intensity, and it has been necessary to limit the beam to 50 mA, to achieve stable operation and reproducible beam quality.

4. 800 MeV Injection System

After injection at 50 MeV from the Linac and acceleration in the Booster, the 800 MeV beam is injected into the PS over one turn, and the bunches are trapped directly in synchronized buckets. The injection system together with the associated beam observation devices and low energy magnetic corrections is described elsewhere[7]. An incoming beam within the specified characteristics is trapped with barely detectable losses.

5. Accelerating System

The reduction of the magnetic field rise time also implies an increase of the energy gain per turn, and it was initially intended to achieve this with a set of three additional narrow-band second-harmonic cavities'. These would have been switched on 80 ms after injection when a remaining frequency swing of only 10%was needed to reach top energy. Although prototype units were developed and successfully tested with the beam, the project was dropped when, during the second stage of the improvement programme, it became clear that the whole RF system would have to be rebuilt.

An additional requirement was the desire to be able to trap the 20 Booster bunches in 10 of the PS buckets as a means of increasing the ISR luminosity. After investigating several alternatives[8], it was decided to build a new acceleration system capable of coping both with the faster rate of rise brought about by the new magnet power supply (section 2) and the higher beam intensity.

The new RF system[10] comprises ten units spaced around the ring. Each unit has two identical ferrite-tuned cavity resonators, working over the frequency range 2.5 - 10 MHz, providing a peak accelerating voltage of 2 x 10 kV. The available power output is 90 kW per unit, which is adequate, under the worst conditions, for an intensity of 1.5 Tp per PS bucket. The pair of resonators is connected in parallel, which simplifies tuning current control and allows a larger tolerance for the power tube output capacitance. The accelerating gaps are short-circuited by vacuum relays at the end of the acceleration phase of the cycle, so that they show a low impedance to the beam and re-bunching is avoided.

The power amplifier is a neutralized 70 kW tetrode, operating with grounded cathode in class B. It is housed in the cavity compartment to provide isolation between the varying cavity impedance and the feed cable, and is built as a plug-in assembly for rapid exchange; the rest of the system is in the centre of the ring where it is always accessible. All sub-assemblies are easily interchangeable and, apart from the final stages, fully transistorized.

The beam control system has also been replaced to meet the more stringent operational requirements (automatic phase programme, adapted pick-up sensitivity, beam-derived frequency programme, synchronization with the Booster, single bunch acceleration).

6. Vacuum System

It has long been known that residual gas could be a source of beam instabilities, and therefore set a lower limit on ultimate performance than simple gas scattering effects would indicate. Furthermore, the prospect of increased radiation damage, and therefore reduced reliability of vacuum seals made of organic materials, was an additional reason for redesigning the vacuum system[11].

The 82 oil diffusion pump groups have been replaced by about 130 sputter-ion pumps (200 or 400 ℓ/s pumping speed according to the local load) and 14 turbomolecular pump groups (260 ℓ/s) for pumping down to the 10^{-5} Torr range. All the rubber seals have been replaced by metallic types, and new bellows-sealed valves installed.

The completion of this project has reduced the mean pressure by a factor of ten, namely from 2-3 10^{-6} Torr down to 2-3 10^{-7} Torr. Recent beam dynamics experiments[12] have shown that at the intensity level of 2 Tp/p a return to the old pressure level immediately lowered the intensity by 50%. It should also be noted that, in spite of the longer pump down time, the time lost due to vacuum system faults has gone down from 20 h to 10 h per 1000 h of operation.

7. Extraction Systems

Efficient sharing of accelerated protons between an increasing number of users demanded the development of new extraction systems and components. Limitation of the intensity permissible on internal targets, to avoid both overheating of the target head and radiation damage to adjacent components, places a premium upon methods of slow extraction which can simultaneously share the beam without unduly increasing losses. A resonant extraction system of this kind is now in operation[13]. Generally, the use of higher intensities implies the necessity for improvements in extraction efficiency.

This problem has been tackled in two ways; firstly, by the development of extraction system components with wider apertures for the same deflecting power; secondly, by the use of devices ahead of the extractor magnet which enhance the separation of the protons-to-be-ejected whilst providing the minimum obstruction in the machine aperture (septa). Brief descriptions of these components follow.

i) A Full Aperture Kicker (FAK), to replace the plunging partial aperture devices which could only handle beam of pre-booster dimensions.
The new system consists of 9 ferrite transmission line magnet modules of 15 Ohm characteristic impedance. With a pulse voltage of 40 kV (80 kV on the pulse generator), the flux density in the 53 mm gap is 630 Gauss and the total kick strength at 26 GeV/c gives a displacement of 19 mm at the septum extractor magnet location with a 55 ns (10 to 90%) rise time. These parameters have been chosen taking into consideration the expected larger transverse emittance and the longer bunch length of the high intensity beam. The system was commissioned in 1973 and has performed well up to

26 GeV/c (nearly 100%efficiency) with the maximum beam injected so far (6 Tp/p).

ii) Electrostatic septum deflector as first stage of the slow extraction beam channels".
This unit has a 0.1 mm molybdenum foil grounded anode (the septum) with an anodized aluminium cathode. Field strengths of 100 to 110 kV/cm are currently achieved over a 10 to 20 mm gap. No adverse effects are observed when the proton beam hits the septum even at 6 Tp/p, but it is necessary to avoid grazing the cathode.
Among the major difficulties was the effect of secondary ions, which had to be screened off to avoid excessive sparking, and electromagnetic coupling of the septum with the beam, which had to be damped to avoid exciting strong beam oscillations.
The successful operation of the electrostatic septum was the main factor in reducing slow extraction losses to 3-5%[16].

iii) As intermediate element in the slow extraction channel, a 1.5 mm thick septum magnet[17], capable of giving a 1.5 mrad deflection (0.115 T at 24 GeV/c), was built and installed, and has been operating reliably for two years.

iv) Large aperture septum extractor magnets are being developed to accommodate the bigger beams. A vertical aperture of 30 mm (instead of 15-20 mm) is now necessary. For slow extraction, the 10%duty cycle initially specified had to be raised to 30% to match the capability of the new main magnet power supply (section 2).
The 30x50mm aperture magnet for fast and slow extraction from a long straight section has three 76 cm modules with 6 and 9 mm septa giving 30 mrad deflection (0.9 and 1.3 T at 26 GeV/c); although performing electrically and magnetically as intended, it has suffered from several mechanical failures (water/vacuum seals and has had to be modified.
Large aperture magnets for fast extraction from a short straight section[19] (30 x 45 mm aperture with a 19 mrad deflection at 26 GeV/c given by 1.8 T) are being built and will be installed this year. Because of their vertical dimensions, these new models can no longer fit between the upper and lower main magnet coils, and therefore have to be significantly shorter (105 instead of 140 cm).

8. Corrections for Beam Quality Preservation

The low-energy corrections are discussed elsewhere[7], as well as the y-transition jump system to avert longitudinal blow-up when passing through transition" energy.

At energies above transition, two types of correction are used :

i) programmed octupoles increase the spread in betatron frequencies in order to avoid the vertical head-tail instability. This effect is discussed in another paper[21]. It is expected to become stronger with increasing intensity. More powerful and more compact lenses (to fit into the restricted straight section space) have been built[22].

ii) the RF voltage is carefully programmed to provide enough Landau damping to suppress longitudinal instabilities[23].

In addition it is intended to install pulsed sextupoles in the near future, in order to program chromaticity and thus reduce the growth rate of the head-tail instability. The use of pulsed quadrupoles to correct the betatron tune dynamically during acceleration is also planned.

Extensive research into the coupling characteristics of various machine components which might interact with the beam is being conducted[24].

9. Instrumentation and Controls

The CPS instrumentation has been a key element in understanding beam behaviour and in obtaining rather rapidly the performance summarized in section 11 below. The main techniques used in the PS ring and for extraction systems have been reviewed elsewhere[25]. The special devices developed for the injection of the Booster beam are described in ref. 7.

In parallel with the improvements to the major components of the CPS, a control system centered around an IBM 1800 has been built up. This computer system serves the Booster and many sub-systems of the Linac and PS. Computer driven consoles with interactive control are used by the operating staff in the Main Control Room[26].

A multi-computer system is being built around several intercommunicating PDP-11/45[27], to facilitate operation under the even more demanding future conditions.

10. Radiation Problems and Beam Dumping

Although the proportion of accelerated protons wasted has been steadily reduced by increasing efficiency in their distribution, the increase in intensity has nevertheless created problems because of radiation damage; the higher levels of induced activity render "in situ" maintenance more difficult.

Most of the organic materials near the beam have been replaced by metal, ceramic or oxide-coated components, designed for faster servicing and quicker exchange. The major source of concern was the main PS magnet[28]. Several units have already had to be replaced, the weak points being the adhesive holding the laminations together and the poleface windings. The magnet blocks can be mechanically clamped, but the poleface windings will have to be replaced by a new version. An evaluation of the situation in the experimental areas of the CPS with regard to induced activity and radiation damage has also been made[29].

The roof shielding above targets was reinforced, and the earth shielding over the remainder of the ring increased to the structural load limit. An evaluation of the effects of various modes of operation on site radiation has been made, and this is one of the criteria used in establishing long-term programmes. There is a continued effort to keep down unnecessary losses.

In the operation of an accelerator such as the CPS, a certain amount of beam dumping is inevitable. This occurs, for example, during beam studies, or when one part of a complex distribution cycle has to be temporarily suppressed.

The CPS lattice makes it very difficult to design

an efficient general purpose fast dumping system, capable of absorbing the total expected intensity (10 Tp/p) for several hours, as has been done for newer machines such as the ISR, NAL or the SPS.

The policy[30] is therefore to use the external beam channels as often as possible for this purpose, and to provide a dump in each of them. Nevertheless, internal dumping cannot altogether be avoided. Internal dump targets, capable of localizing the losses in a limited region of the machine and of withstanding the thermal stresses caused by the higher intensity are being designed, and the feasibility of a fast dumping kicker is being investigated.

11. Performance

The peak intensity reached so far, as a result of the improvement programme, is over 6 Tp/pulse at 26 GeV/c. A much more important outcome is that the PS has been operating stably for regular scheduled high energy physics runs, at 26 GeV/c with 5 to 6 Tp/p at a 2 s repetition time. The beam was extracted by the full-aperture kicker system with losses barely above the threshold level of the beam loss monitoring system.

A longitudinal emittance of 9 mrad* (in units of RF radians x $\Delta p/m_o c$) was maintained at 6 Tp/p from trapping at 800 MeV up to transfer to the ISR at 26 GeV/c, thanks to the y-transition jump system. With the octupole corrections and the programming of the RF voltage along the cycle, all the harmful instabilities can be kept under control.

There is still some transverse mismatch and dilution during the first phase of acceleration due to the (not yet quite optimum) matching of the Booster-PS transfer line, to differences between the beam from the four PSB rings, and to the present somewhat limited flexibility of the low field corrections.

There are no measurable injection losses when the PSB beam is reduced to the specified emittance (E_V = 12 π mm mrad; E_H = 33 π mm mrad at the CPS entrance), i.e. during machine studies, but when it is not collimated, injection losses of about 10% have been observed.

It is not planned to use high intensity beam for "counter physics" experiments until the East experimental area is re-arranged in 1975[31] but slow extraction has been tested, and, although not optimized, showed losses of only 7 to 10%.

The PS beam is at present distributed over some 20'000 m^2 of experimental areas, and to the ISR. Later, the machine will also act as injector for the 400 GeV SPS under construction nearby.

Typical cycles in current use have a 2.5 s repetition time, with fast extraction at 26 GeV/c for the ISR and bubble chambers, followed by a 500 ms flat-top at 24 GeV/c for counter experiments.

* 1 rad = 15.6 eVs for the CPS.

References

1. Germain, P., Contribution to CERN/SPC/189, "Studies in progress on possible improvements to the PS and its experimental equipment", October 1964.
   - Standley, P.H., "The CPS improvement programme", Proc. of 5th Int. Conf. on High Energy Accel., Frascati, 1965, pp. 80-85.
2. Taylor, C.S., private communication.
3. Hardt W., "Slow cycling injection method for intensity improvement of the CPS (TART Scheme)", Proc. of 5th Int. Conf. on High Energy Accel., Frascati, 1965, pp. 151-153.
4. Barbalat O (editor), "Comparison between two possible CPS injectors", CERN internal report DIR/TM/14, 1966, and CERN/SPS-227, 1966.
5. *MPS* Staff, "The second stage CPS improvement study", CERN internal report MPS/Int. DL/B 67-19.
   - Bovet C., Reich K.H., "The CERN proton synchrotron Booster", Proc. of 6th Int. Conf. on High Energy Accel.. Cambridge, 1967, pp. 315-319.
   - PSB Staff, "The CERN PS Booster, Design expectations confronted with reality, t-o years after start-up", Proc. of this Conference.
6. Bayard O., "La nouvelle alimentation de l'aimant du synchrotron à protons du CERN", CERN 71-10 (Part 1) and 71-20 (Part 2), 1971.
7. D. Boussard et al, "Injection and trapping of the beam at 800 MeV in the CERN PS", Proc. of this Conference.
8. Fischer H., "Proposed accelerating units for doubling the rise of the magnetic field at 80 ms after injection" CERN internal report MPS/RF/64-13.
9. Pirkl W., "Price estimates for 12 different versions of a new CPS accelerating system", CERN internal report MPS/RF 67-4.
10. Pirkl W., private communication.
11. Riboni P., "PS vacuum system improvement", CERN internal note MPS/ML/Note 69-3.
12. Möhl D., "Effect of vacuum pressure on beam instabilities", CERN internal note MPS/DL/Note 72-34.
13. Kubischta W., "Multiple target extraction sharing scheme at the CPS", Proc. of 8th Int. Conf. on High Energy Accel., CERN, Geneva, 1971, pp. 110-112.
14. Fiander D.C., "A design proposal for a full aperture kicker system for the CPS", CERN internal note MPS/SR/Note 71-3.
15. Bleeker J et al., "Development of an electrostatic septum at CERN", Proc. of 5th Int. Symp. on Discharges and Electrical Insulation in Vacuum, Poznan, 1972.
16. Kubischta W., private communication.
17. Bloess D., "Specification for the thin septum magnet for slow ejection 16", CERN internal note MPS/SR/Note 70-3.

18. Keyser R.L., "The development of large aperture septum magnets for slow ejection", CERN internal report MPS/SI/Int. MAE 72-5.

19. Bertolotto R., "Proposition pour la construction de nouveaux aimants à septum pour l'éjection rapide", CERN internal note MPS/SR/Note 72-4.

20. Hardt W., "Gamma-transition-jump scheme of the CPS", Proc. of this Conference.

21. -Gareyte J., Sacherer F., "Head-tail type instabilities in the CERN PS and Booster", Proc. of this Conference.
-Sacherer F., "Transverse bunched beam instabilities - Thaory", Proc. of this Conference.
-Möhl D., Schönauer H., "Landau damping by nonlinear space-charge forces and octupoles", Proc. of this Conference.

22. Gyr M., "Studies on the PS octupoles", CERN internal note MPS/SR/Note 71-16/Corr.

23. Boussard D., Gareyte J., "Damping of the longitudinal instabilities in the CERN PS", Proc. of 8th Int. Conf. on High Energy Accel., CERB, 1971, pp. 317-320.

24. -Möhl D., "Equipment responsible for transverse beam instability in the PS", CERN internal note MPS/DL/Note 74-6.
-Faltens H, Umstätter H.H., "Longitudinal couplings impedances at insulated PS vacuum chamber flanges", CERN internal note MPS/LIN/Note 74-5.

25. Agoritsas A. et al, 'Techniques for measuring beam parameters", Proc. of 2nd USSR National Conf. on Part. Accel., Moscow, 1970.

26. Carpenter B., "Experiments with interactive control software at the CERN PS", Proc. of IEE Conf. on Software for Control, Warwick, England, 1973.

27. Madsen J.H.B., "The expansion of the PS control system", CERN internal note MPS/CO/Note 72-42.

28. Gouiran R., "La radioactivité de l'aimant du CPS et son influence sur la maintenance de l'anneau - Statistiques et prévisions", CERN internal report CERN/MPS/SR 73-5.

29. Coet P., "The work in highly radioactive experimental areas of the PS", CERN internal report CERN/MPS/MU-EP/72-2.

30. Steinbach Ch., "Beam dumping, the situation in January 1974", CERN internal note MPS/OP/Note 74-4.

31. Hoffmann L., "East hall transformation project", CERN internal note MPS/MU/Note EP/73-12/Rev.

SIMULTANEOUS STEERING OF H^+ AND H^- BEAMS AT LAMPF*

by

K. R. Crandall and W. E. Jule

University of California
Los Alamos Scientific Laboratory
Los Alamos, New Mexico

Summary

Based on analysis and computer simulations, it has become apparent that two kinds of doublet steering are necessary for linear acceleration of H^+ and H^- beams simultaneously. The respective advantages of steering by electrically "tilting" and "displacing" a system of doublets are described. Single dipole steering for simultaneous beams and the effect of the earth's magnetic field on oppositely charged beams is also considered. Finally, the implementation of this kind of steering at LAMPF is discussed.

Theory

Conventional steering superposes a dipole field to counteract any mechanical misalignment of a quadrupole. If one is dealing with a single quadrupole, this steering field can be applied in a manner which electrically moves the magnetic center of the quadrupole from its mechanical center to the correct design position. In Fig. 1 are shown force versus displacement diagrams for focussing and defocussing quads. A particle displaced a distance, x, from the quad center would feel a force, f,, as defined by the solid line. A steering field superposed on the quad field simply translates the solid line to the dashed line, and moves the magnetic center of the quad to point B. This type of displacement works for beams of opposite charge, since, while a quadrupole changes from focussing (F) to defocussing (D) when the sign of the beam changes, the steering field also reverses direction, The situation becomes more complicated when one considers two quadrupoles positioned close together which act as a doublet. In the standard approach, a series steering coil is wound on the two quadrupoles and the same steering field *is* applied to both magnets. From the above argument *on* how to electrically displace a quadrupole's magnetic center, one might conclude that equal fields applied in this way would electrically displace the doublet (both magnets are housed in the same case). Fig. 2 shows that this type of steering does not produce the desired effect.

Dipole steering fields applied in this way will electrically "tilt" the doublet, not displace it. This kind of steering, which we will call "tilted doublet steering" (TDS), works well for a single beam, but Fig. 2 shows that oppositely charged beams feel equal and opposite forces in traversing a tilted doublet; one beam would be steered onto the machine axis while the oscillation amplitude of the other beam is increased.

This difficulty can be overcome in the following manner. Consider only the horizontal plane for simplicity and consider a doublet which is FD for a positively charged beam. The force diagrams for this arrangement are shown in Fig. 3. It is evident that an electrical displacement of the doublet from A to B requires that equal and opposite forces be applied to the quadrupoles. We can accomplish this by applying equal and opposite steering fields to the ends of the doublet. This is called "displaced doublet steering" (DDS).

Now consider the force diagrams (Fig. *4)* for a negatively charged beam. The first quadrupole is now D and the second quadrupole is F and the steering fields reverse their signs. So we see that DDS electrically corrects for misalignments of the doublet for negatively as well as positively charged beams. Hence the most versatile steering coil configuration is one which allows independent dipole fields to be superposed in both planes on each quadrupole. If economics, or other considerations dictate less versatile configurations of steering magnets, or the associated position sensing equipment, analytic techniques are effective in determining the best steering strategy.

Practice

At LAMPF there are 134 quadrupoles in the Alvarez linac and 103 doublets in the side-coupled structure. Since it would require two power supplies per quadrupole for electrical alignment, it is reasonable to investigate steering configurations which minimize transverse oscillations for a small number of steering positions. Hence, the first goal during construction is to attain the best doublet alignment possible. The doublets in the side-coupled structure are aligned to $\pm$ .007" and $\pm$ .4mr. Numerical simulations show that a .010" displacement has approximately the same effect as a 0.25mr doublet axis tilt. The alignments in the side-coupled linac are comparable to these, and hence it is necessary to have a combination of TDS and DDS.

In the side-coupled structure, one doublet per module is wired to provide a combination of TDS and DDS. However, each doublet has steering in only one plane. Based on numerical simulations, which also consider the number and location of position monitors, it has been found that steering in one plane in two sucessive modules and then in the other plane for the next two modules (i.e., the pattern is HHVV and then repeats) is an effective configuration.

The effect of the earth's magnetic field has also been considered. It is shown in reference 1 that the earth's field displaces the equilibrium orbit. Experimental results imply that this displacement is 0.15 cm in the side-coupled structure. The equilibrium orbit is displaced equally and oppositely for oppositely charged beams, hence to minimize transverse oscillations, it is necessary to steer so that the beams are positioned at their respective equilibrium orbits rather than at the design center of the linac.

In the Alvarez linac, there is not enough position information to establish that an off axis equilibrium orbit exists. However, it is expected that the effect of the earth's field would be small because of the steel in the tank wall which is not present in the side-coupled linac.

If one wishes to do effective steering, the position information should not be separated from the steering

*Work performed under the auspices of the U. S. Atomic Energy Commission.

magnet by too many intervening quadrupoles. If there are many misaligned quadrupoles before the position information, then the position information is not very useful. The best configuration seems to be to have position information in two successive cells after the steering magnet.

Acknowledgement

I would like to thank Don Swenson for suggesting the use of the force diagrams.

References

1. D. A. Swenson and K. R. Crandall, Los Alamos Scientific Laboratory, Private Communication, July, 1968.

2. D. A. Swenson, Los Alamos Scientific Laboratory, Private Communication, August 1968.

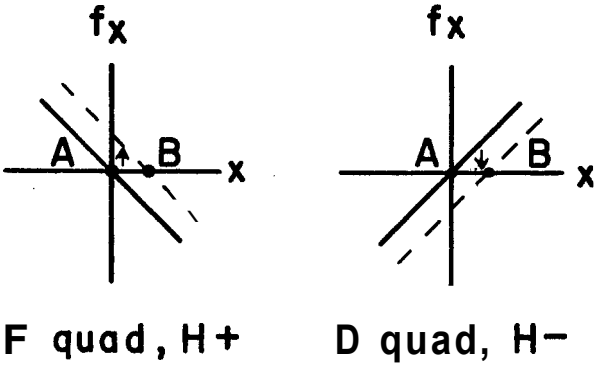


FIG. I

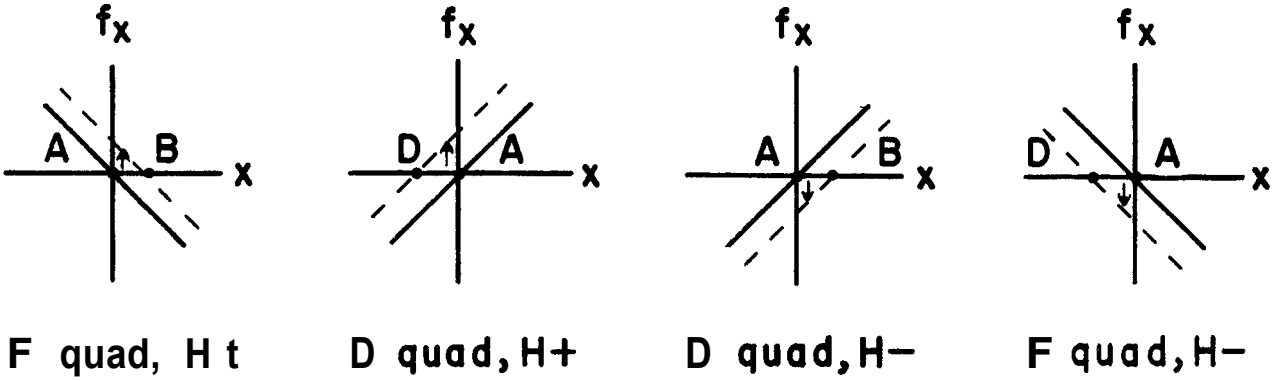


FIG. 2

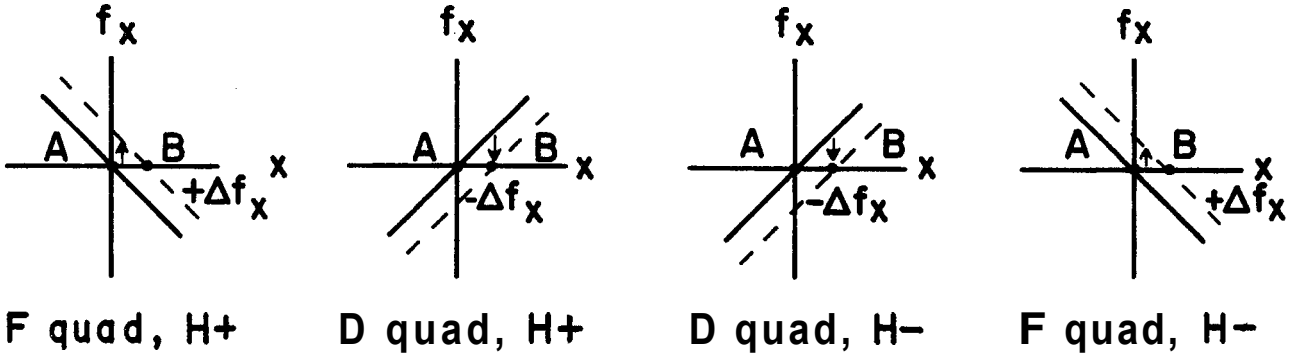


FIG. 3

FIG. 4

FUSION REACTIONS IN COLLIDING BEAMS*

John P. Blewett
Brookhaven National Laboratory
Upton, N.Y. 11973

Abstract

Two colliding beam configurations are presented in which fusion reactions can take place between deuterons and tritons. The first is a linear system in which the ion beams travel in the same direction and are focused by a collinear electron beam. In the second configuration the ions travel in a spiral path in a strong magnetic field and are focused by electrons travelling along the lines of force of the magnetic field. The first system yields very little power but the second appears to merit further attention.

1. Introduction

Students of controlled thermonuclear reactions tend to divide feasibility experiments using electromagnetic containment into "ordered" and "equilibrium" systems. The latter category includes virtually all of the magnetically contained plasma systems with which we are familiar. The former category, to which I propose to address myself, is generally regarded with disfavor; it is expected to reduce itself speedily to an equilibrium system by space-charge forces and by coulomb scattering. Furthermore, it usually includes a disproportionate amount of stored energy which, after the order in the system is lost, cannot be recovered.

In this paper I shall present two ordered systems. To the first all the above objections apply. The second seems to be less objectionable, and I present it herewith in the hope that some one will consider it further.

Many fusion reactions are possible candidates for use in production of power. The favorite, on which I shall concentrate, is:

Deuteron + triton → α particle + neutron + 17 MeV. This reaction goes at a relatively low temperature; the reaction cross section has a maximum of about 5 barns at about 100-keV energy for a deuteron bombarding a triton at rest. Most of the energy produced – about 14 MeV – accompanies the neutron.

First, we review briefly the arithmetic of fusion reactions in colliding beams. We consider colliding beams of deuterons with density ρ_D travelling at velocity v_D and tritons with density ρ_T travelling at velocity v_T. Densities are in coulomb per cubic meter; velocities are in meters per second.

In one cubic meter of the triton beam there are $6 \times 10^{18}\ \rho_T$ ions. These present to the deuteron beam a cross section of $6 \times 10^{18}\ \rho_T\sigma$, where σ is the fusion cross section. The rate of arrival of deuterons in the triton system is $6 \times 10^{18}\ \rho_D(v_D - v_T)$ per second. Hence the number of collisions per second per cubic meter is

$$36 \times 10^{36}\ \rho_T\rho_D\sigma(v_D - v_T) \qquad (1)$$

and the fusion energy liberated is

$$36 \times 10^{36}\ \rho_T\rho_D\sigma(v_D - v_T)E \text{ watts per cubic meter,} \qquad (2)$$

where E is the fusion energy liberated per collision.

For 100-keV deuterons bombarding tritons at rest the cross section σ has a maximum value of about 5×10^{-28} m^2. The fusion energy liberated per collision is 17 MeV or 2.7×10^{-12} joules. We assume that the velocities of deuterons and tritons correspond to a relative energy of about 100 keV, whence $v_D - v_T = 3 \times 10^6$ m/sec. We assume further that the densities of the two beams are equal so that $\rho_D = \rho_T = \rho_o$. With these assumptions we find that the fusion power is

$$1.46 \times 10^5\ \rho_o^2 \text{ watts per cubic meter.} \qquad (3)$$

If, for example, the system is to yield a fusion power of 1 megawatt per cubic meter, the charge density required is 2.6 coulombs per cubic meter, or about 1.5×10^{13} ions per cubic centimeter.

2. Linear Colliding Beams

The first example we present will be linear colliding beams. The results to be presented will be so absurd that the example will have value only as an indication of problems to be solved.

Suppose that two collinear beams of deuterons and tritons are brought into collision, each having a velocity of 1.5×10^6 m/sec. Going somewhat beyond the state of the art, we assume that both are 1000-ampere beams and that both have cross sections of 1000 square centimeters. This leads to a charge density of 6.7×10^{-3} coulombs per cubic meter and hence, to a fusion yield [from Eq. (3)] of 6.5 watts per cubic meter, or of 0.65 watts per meter of distance along the colliding beams. This seems a depressingly small yield, particularly when we realize that almost 60 MW have gone into producing the two colliding beams.

To improve the situation we make two changes:

a) We will make the two beams travel in the same direction at much higher energy.

b) The beams will be focused by an electron beam travelling in the opposite direction.

By these means the beam will be concentrated in a small cross section and the power level will be increased to more interesting levels.

It will be required that the deuterium and tritium ions differ in velocity by 3×10^6 m/sec as noted in the Introduction. Also the ions will be required to have the same energy so that both beams can come from the same ion source and so that the unreacted ions in both beams can be retarded by the same field to regain their kinetic energy.

These two requirements set velocities of 1.6×10^7 and 1.3×10^7 m/sec for deuterons and tritons respectively; both will have an energy of about 2 MeV.

Space charge and current fields produce a repulsive radial force in the ion beam of

$$E_r - vB_\theta = 2\ Ir(1 - \beta^2)/(\varepsilon_o \beta c r_o^2) \text{ volts/m} , \qquad (4)$$

*Work performed under the auspices of the U.S. Atomic Energy Commission.

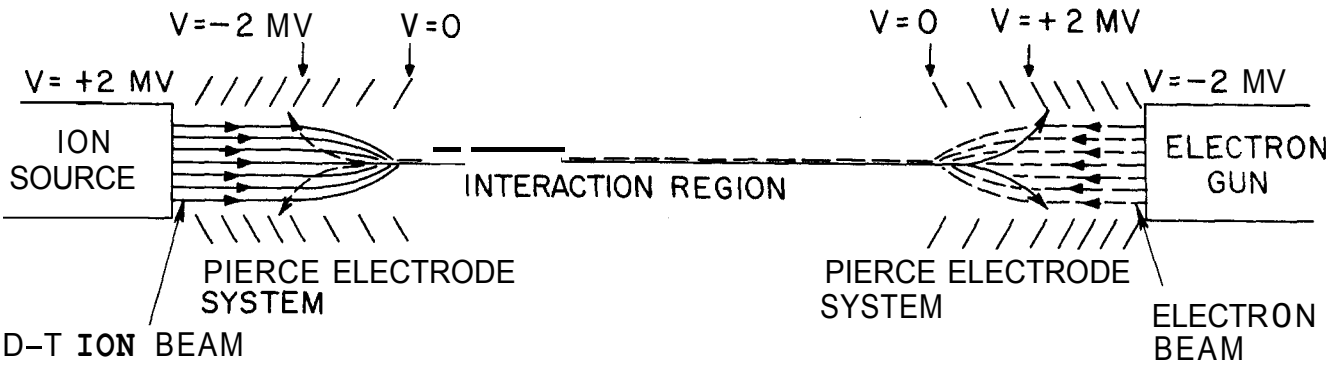


Fig. 1. Linear colliding beam system.

where I is total current (2000 amperes),
βc is ion velocity (about 1.5 X 10')
ϵ_o is the dielectric constant of free space (1.1×10^{-10} F/m)
r_o is the radius of the beam.

Approximately this force is

$$E_r - vB_\theta = 1200\ Ir/r^2 \text{ volts/m} \qquad (5)$$

If a relativistic electron beam of I_e amperes is now introduced, collinear with the ion beam but travelling in the opposite direction, it will contribute a focusing force of

$$2I_e r(1+\beta\beta_e)/(\epsilon_o \beta_e c r_o^2) \cong 60\ I_e r/r_o^2 \text{ volts/m}, \qquad (6)$$

where $\beta_e c$ is the electron velocity (assumed approximately equal to c). The internal forces in a relativistic beam approximately cancel each other and the electron beam will experience a focusing force due to the ion beam of approximately the strength given by Eq. (5). If the inward forces on ions and electrons are set equal, the electron current required proves to be about 80,000 amperes.

Under the forces just discussed, both beams will collapse to a small diameter determined by the original values of their emittances. If we assume (optimistically) an emittance of 100π cm·mrad for the ion beam, the final beam radius proves to be 1.4 mm. The charge density in each ion beam is about 11 coulombs/m^3 and the fusion power is now 17 MW/m^3. But the beam has become so small that the actual power generated per meter of beam is barely over 100 watts.

In Fig. 1 we present a configuration of electrodes for the linear colliding beam system. This arrangement makes possible the generation of 2-MeV beams of ions and electrons and the deceleration of both beams for recovery of the energy stored. One can safely conclude from the parameters just presented that such a system will never be built.

3. Proposed Configuration

What evidently is required to make a colliding beam system viable is a method for storing the ion beams until they interact. If this can be done the input ion currents become quite reasonable. For an output of 1 MW of fusion power all that is required is an input of 60 mA each of deuterons and tritons.

We note further that a prime requirement of the system is that it include strong restoring forces which will prevent coulomb scattered ions from leaving the system before they have time to take part in a fusion reaction.

The system to be proposed includes coincident deuteron and triton beams of the same momentum circulating in approximately circular paths in a rather high magnetic field, focused by a cylindrical beam of electrons travelling along the lines of force of the field. Figure 2 is a cross-section sketch of the geometry.

To satisfy the relative velocity criterion and to have the same momentum the deuteron energy must be 845 keV; the triton energy will be 564 keV. The deuteron velocity will be 9×10^6 m/sec; the triton velocity will be 6×10^6 m/sec. In a field of 6 tesla, the radius of curvature of these beams will be 3.0 cm.

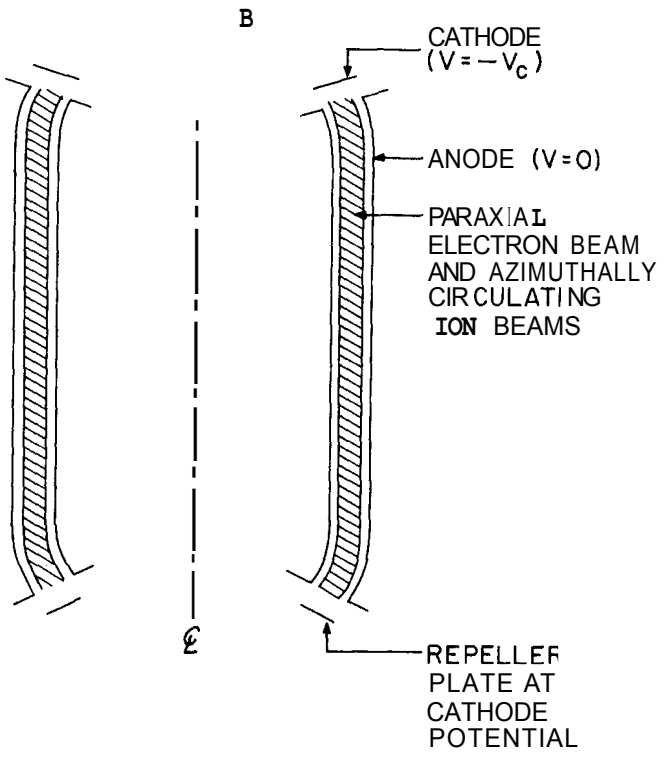


Fig. 2. Cross section through cylindrical colliding beam system.

4. Dynamics of the Electron Beam

We consider first the behavior of the electron

beam in the absence of the ion beams. The potential distribution in the beam must satisfy Poisson's equation

$$\frac{1}{r}\frac{\partial}{\partial r}\left(r\,\frac{\partial V}{\partial r}\right)+\frac{\partial^2 V}{\partial z^2}=\frac{4\pi\rho}{\epsilon}\ . \tag{7}$$

How the space-charge forces distribute themselves depends on two factors:

First is the boundary conditions. If, for example, we choose to concentrate the space-charge forces in the z-direction we use the continuity of space-charge condition and arrive at the classical $z^{4/3}$ potential distribution. In the present case, however, we choose to eliminate or at least minimize z-variations of potential due to space-charge fields; we can accomplish this by introducing electrodes which hold the outer and inner boundaries of the beam at zero potential (see Fig. 2). Now the primary potential distribution is radial and we can forget the second term on the left-hand side of Eq. (7).

The second factor to be considered is the dependence of electron energy on the potential distribution. If the electrons travel without deviation along the lines of force of the magnetic field, the high retarding space-charge field in the center of the beam will increase the density of the space charge in that region and this fact will need to be taken into account in the solution of Poisson's equation. This problem we shall bypass, and still hope to obtain significant results, by assuming that the electron source has infinitesimal radial extent but that, due to its finite emittance, all electrons are circulating about the lines of force of the magnetic field. The electron orbits will be considered further later in this section. This assumption will permit us to assume a charge density independent of radius and will simplify the solution of Poisson's equation. This solution, with the conditions that it must vanish at the inner radius (r_1) and the outer radius (r_2) of the beam, is rather easily obtained. It is:

$$V=\frac{\pi\rho}{\epsilon}\left\{r^2-\frac{(r_2^2-r_1^2)\ln r+r_1^2\ln r_2-r_2^2\ln r_1}{\ln(r_2/r_1)}\right\}\ . \tag{8}$$

If we assume that the radial extent of the electron beam is small we can simplify the expression for the potential by setting

$$r=r_o(1+\delta)$$
$$r_1=r_o(1-$$
$$r_2=r_o(1+\delta_2)\ .$$

Here r_o is a radius lying near the middle of the beam, to be defined more precisely later. With these assumptions, neglecting higher orders of the δ's, Eq. (5) becomes:

$$V=\frac{2\pi\rho\ r_o^2(\delta+\delta_1)(\delta-\delta_2)}{\epsilon} \tag{9}$$

The maximum value of V, to this order of approximation, will be for $\delta=(\delta_2-\delta_1)/2\ (\cong 0)$.

For example we assume an electron layer 1 mm thick extending from $r_1=2.95$ cm to $r_2=3.05$ cm. For reasons to be presented later we choose a value of ρ of 11.7 coulombs per cubic meter that leads to fusion yields of 20 MW/m^3; substituting for ϵ the value 1.11×10^{-10} F/m we find that the maximum value of the potential is 165,000 volts. Evidently the primary energy of the electron beam must be a little above this,

The motion of individual electrons is described by the following equations of motion:

$$m\ddot{r}-mr\dot{\theta}^2=eE_r+er\dot{\theta}B_z \tag{10}$$

$$\frac{1}{r}\frac{d}{dt}(mr^2\dot{\theta})=-e\dot{r}B_z \tag{11}$$

$$\dot{z}=\pm\sqrt{2eV_c/m}\ . \tag{12}$$

Here

E_r = [from (9)] $\dfrac{2\pi\rho r_o}{\epsilon}(2\delta+\delta_1-\delta_2)$ (13)

B_z = constant (6 T for the example to be considered)

V_c = cathode potential (greater than 165 kV in the example given).

The plus or minus sign in Eq. (12) depends on whether the electron is on a primary or reflected path.

From (11)

$$\dot{\theta}=-\frac{eB_z}{2m}\left(1-\frac{r_o^2}{r^2}\right)\ , \tag{14}$$

where r_o is the radius, somewhere near the middle of the electron sheet, where $\dot{\theta}=0$. If we write $r=r_o(1+\delta)$ etc., Eq. (14) becomes

$$\dot{\theta}=-\frac{eB_z\delta}{m}\ . \tag{15}$$

Substituting (15) in (10) we obtain

$$mr_o\ddot{\delta}-mr_o(1+\delta)\left(\frac{eB_z\delta}{m}\right)^2=\frac{2\pi\rho r_o e}{\epsilon}(2\delta+\delta_1-\delta_2)-\frac{e^2B_z^2r_o}{m}\delta(1+\delta)\ . \tag{16}$$

Keeping only first order terms (16) becomes

$$\delta+\delta\left|\left(\frac{z}{\quad}\right.\right.\qquad\qquad$$

A first integration gives

$$\dot{\delta}^2+\delta^2\left[\left(\frac{eB_z}{m}\right)^2-\frac{4\pi\rho e}{\epsilon m}\right]=\frac{4\pi\rho e}{\epsilon m}\delta(\delta_1-\delta_2)+\text{integration constant.} \tag{18}$$

If $\delta=0$ for $\delta=\delta_2$ then the integration constant has the value

$$\delta_2\left[\left(\frac{eB_z}{m}\right)^2\delta_2-\frac{4\pi\rho e}{\epsilon m}\delta_1\right]$$

and

$$\dot{\delta}^2+(\delta-\delta_2)\left\{(\delta+\delta_2)\left(\frac{eB_z}{m}\right)^2-\frac{4\pi\rho e}{\epsilon m}(\delta+\delta_1)\right\}=0\ .$$

The other value for which $\dot{\delta}=0$ must be given by

$$\delta=\frac{-\left(\frac{eB_z}{m}\right)^2\delta_2+\frac{4\pi\rho e}{\epsilon m}\delta_1}{\left(\frac{eB_z}{m}\right)^2-\frac{4\pi\rho e}{\epsilon m}} \tag{19}$$

Evidently singularities will appear in this relation, and the electron sheet will become unstable if $(4\pi\rho/\epsilon)\cdot(m/eB_z^2)$ approaches unity. For the example we

have assumed (B_z = 6 T, ρ = 11.7 coulombs/m^3), this dimensionless quantity has the value 0.21 and the value of δ given by (19) is 0.26 δ_1 - 1.26 δ_2. If $\delta_1 \cong \delta_2$, the other value of δ for which δ = 0 is approximately - δ_1.

For those familiar with the notation of plasma physics, the quantity $(4\pi\rho/\epsilon)(m/eB_z^2)$ can be recognized as an analog of the plasma β function which is a measure of the ratio of plasma pressure to magnetic pressure. In a plasma @ must be kept below unity.

5. Dynamics of the Deuteron and Triton Beams

We assume, initially, that a small number of deuterons and tritons are injected into the space-charge field calculated in the preceding section for the electron sheet. These ions are to move in a flat spiral with negligible velocity in the z-direction. The method of injection into this orbit will be described in the next section.

Motion of the ions will be governed by

$$m_i \ddot{r} - \frac{m_i v_i^2}{r} = eE_r + ev_i B_z \quad , \qquad (20)$$

where m_i is the ion mass,
v_i is the ion velocity, given by $m_i v_i = - B_z e r_o$,
E_r is given by (13) above.

In the coordinates of the preceding section (20) becomes

$$\left(\frac{\quad}{\quad}\right) \frac{\quad}{1+\delta} = \frac{\quad}{\epsilon m_i} (2\delta + \delta_1 - \delta_2) - \left(\frac{\quad}{m_i}\right) \quad , \qquad (21)$$

whence

$$\ddot{\delta} + \delta \left[\left(\frac{B_z e}{m_i} \right)^2 - \frac{4\pi\rho e}{\epsilon m_i} \right] = \frac{2\pi\rho e}{\epsilon m_i} (\delta_1 - \delta_2) \qquad (22)$$

whose solution is

$$\delta = \delta_o \sin(\omega t + \varphi) - \frac{2\pi\rho e}{2} (\delta_1 - \delta_2) \quad ,$$

where

$$\omega^2 = \left(\frac{B_z e}{m_i} \right)^2 - \frac{4\pi\rho e}{\epsilon m_i}$$

δ_o and φ are determined by initial conditions.

We note that, since ρ represents the density of an electron space charge, the two terms in ω^2 both have the same sign. For deuterons

$$\omega = (8.33 \times 10^{16} + 6.33 \times 10^{19})^{\frac{1}{2}} = 7.96 \times 10^9 \quad .$$

The wavelength of this "betatron oscillation" is 0.71 mm (for deuterons). For tritons, ω = 6.50 x 10^9 and the betatron wavelength is 0.87 mm. This very short wave oscillation has its frequency determined almost completely by the density of the electronic space charge.

The very strong restoring force provided by the electron cloud should be effective in restoring to their orbits, ions that have undergone coulomb scattering either by other ions or by electrons. This topic is not analyzed in this report but must be given attention in future studies of this device.

6. Ion Injection

Deuterons and tritons are to be injected in such a fashion that they will continue to circulate in the magnetic field and will be unable to escape. During injection they will be given as little axial momentum as possible. Escape of ions at the ends of the devices will be prevented by a local increase in magnetic field The local increase in axial field will be accompanied by introduction of a radial field component which will serve to reverse the paraxial velocity of the ion beam. Field bumps of this type will be included at both ends of the device as indicated in Fig. 2.

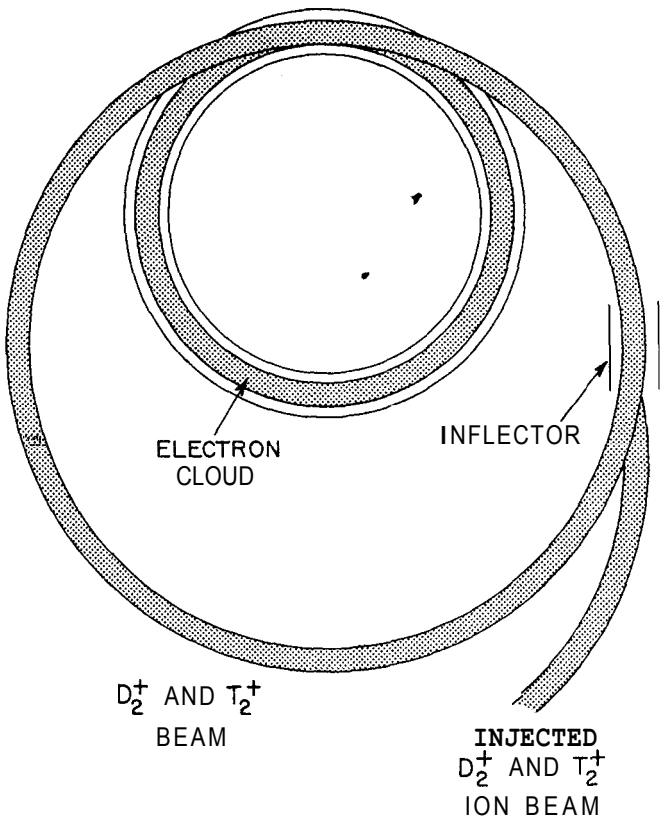


Fig. 3. Injection for cylindrical colliding beam system.

Several methods of injection will occur to the reader. One possible method is illustrated in Fig. 3. This method utilizes molecular ions which pass through an inflector to be deflected onto an orbit that intersects the electron cloud. Something of the order of 10%of the molecular beam should be stripped by electron collisions to become atomic ions which then will switch to orbits through the electron cloud (we assume a stripping cross section of the order of 10^{-16} cm^2). The remainder of the molecular ions will continue on circular orbits and return to the inflector. To prevent their loss by a second deflection, they will make their first entry into the inflector with a small component of paraxial velocity. The inflector is to have a finite axial extent and the paraxial velocity of the ions will be such as to allow the beam to miss the inflector on the second and later revolutions. Thus the molecular beam will re-enter the electron cloud several times

until virtually all of the beam has been reduced to atomic ions. This scheme has the virtue of allowing continuous injection. Pulsed injection procedures may, however, prove to be simpler and less demanding of extra magnetic field volume.

Another possible injection method would involve injection of neutral atoms produced by acceleration and stripping of negative ions. These techniques are well established for use in injection into the AGS. The neutral atom beam would be injected tangent to the electron cloud where a fraction of the order of 10% would be ionized and proceed on the desired circular orbits.

The procedure for initially combining the deuteron and triton beams into a single beam involves electrostatic deflection. The two beams, having the same momenta but different energies can be combined by deflection in an electrostatic field.

7. Procedure with High Density Lon Beams

The preceding sections dealt with the motion of ion beams of low intensity in a dense sheet of electrons. It has been shown that, to the first order, the motion of both electrons and ions is stable. There are large restoring forces on the ions which can serve to counteract the undesirable effects of coulomb scattering.

If, now, the electron density is doubled and the ion density is raised to the level of the original electron density, the net density and the electric field pattern will be unchanged. Only the distribution of B_z will be affected by the circulating ion current. For the densities quoted, B_z will drop by about 0.1 T through the thickness. This drop is too small to affect perceptibly the electron or ion motions.

The procedure to increase density would be to raise the injected ion currents. The potential maximum in the electron sheet would then drop and the electron current supply would automatically add electrons to restore the maximum value of the potential.

When the ion density has reached 11.7 coulombs/m^3, the fusion reactions will yield 3600 watts of fusion power per meter length of the system. The deuteron and triton supplies are required to provide only about 200 μA each to maintain this yield.

It would appear that the procedure of pushing ion current and electron current up, maintaining a constant difference between their charge densities, can be continued indefinitely to yield higher and higher levels of fusion power. No doubt, however, instabilities will put a stop to this. The point at which this happens will be difficult to predict theoretically and might more easily be determined experimentally.

DISCUSSION

V. Kelvin Neil (LLL): Your atoms are held in the device electrostatically rather than magnetically?

Blewett: *Yes.*

V. Kelvin Neil: And each one of these reactions which you're trying to get produces the helium?

Blewett: Yes.

V. Kelvin Neil: And the helium is also then electrostatically held? I'm trying to get to one of the problems in TOKOMAC where the helium is contained and, in effect, quenches the reaction.

Blewett (restating the question): The containment system is essentially an electrostatic containment system and that one of the products of the reaction would be a helium ion and will the helium ions do the same poisoning of the reaction as they do in TOKOMAC reactors? I don't think I can give a very good answer to that, except to say that the helium ions have about 4 MeV of energy which should be enough to kick them out of this region.

Leon Katz (University of Saskatchewan): Is this being proposed as a source of energy or as a source of neutrons for breeders?

Blewett: These are *sort* of interchangeable, aren't they? I should say that it is being proposed only as an experiment.

Arie Van Steenbergen (BNL): Charge exchange injection of accelerators is not an established fact.

WILL NEGATIVE HYDROGEN ION SOURCES SOON REPLACE PROTON SOURCES IN HIGH ENERGY ACCELERATORS?*

Th. Sluyters and K. Prelec
Brookhaven National Laboratory
Upton, New York

Although charge exchange injection into circular accelerators and storage rings has been proposed quite some time ago, the application of this attractive method has not been widespread because of low intensities of negative hydrogen beams available until recently. For synchrotrons and storage rings multiturn injection of protons via stripping of negative ions offers a better and simpler alternative to the present injection schemes by increasing the phase space density of the coasting beam. For cyclotrons injection of protons via stripping of relatively high energy neutral particles (obtained by partial stripping of negative ions) may alleviate the space charge problem during the early part of acceleration. However, beam intensities of negative hydrogen ions obtained by direct extraction from standard sources such as duoplasmatrons and Penning sources were seldom higher than several milliamperes, which was not sufficient for most of present circular accelerators. Indirect method of producing negative ion beams via charge exchange of protons, although at that time promising with respect to the intensity, had a disadvantage of yielding beams of a too low quality and requiring a too complex mechanical structure.

During the last year or *so* several papers and reports appeared describing two new approaches to the production of negative hydrogen beams extracted directly from a plasma. One of them was the hollow discharge duoplasmatron,[1,4,5] developed from a standard source by placing a rod along the main axis and reaching into the anode discharge region. A 100 μs pulsed beam of 6 mA was obtained with a normalized emittance less than 0.1 cm-mrad. An accompanying electron current of 0.5 A, a relatively low ion current density of 0.1 A/cm^2 and a high arc current of 100 A were features still to be improved.

The second approach was the use of the racetrack magnetron.[2,3,4] Even when operated with hydrogen gas only, the source yielded considerably higher H^- currents than a duoplasmatron. From an extraction slit of 1 mm × 10 mm, pulsed H^- currents ranged up to 75 mA, which corresponds to a current density of 0.75 A/cm^2. Even higher densities were obtained when cesium was injected into the source. The maximum reported[3] current density was 3.7 A/cm^2. These high current densities have been explained by an efficient production of negative ions at the cathode surface, especially when covered by a layer of cesium, and by decreasing the distance negative ions have to travel between the cathode and the extraction slit.

Prototypes of both sources have been built at BNL. With the hollow discharge duoplasmatron and hydrogen as the operating gas up to 8 mA of H^- current was obtained, corresponding to an ion current density of 0.25 A/cm^2. The normalized emittance was 0.3 cm-mrad and the pulse length 1 ms.

A significant improvement was achieved by injecting cesium through the hollow center tube. The beam intensity increased to 18 mA and the emittance remained about the same.

Two models of a magnetron source were also built at BNL. While the first of them already showed a behavior similar to the original source, there were several weak points in the construction and a new improved model was designed. By using a narrow extraction slit (0.5 mm × 10 mm) and with hydrogen as the operating gas, extracted H^- currents reached 17 mA, with normalized emittances in two directions of 0.44 and 0.60 cm-mrad at an extraction voltage of 8 kV. A dramatic change was observed after cesium was injected into the source. The extracted current of negative hydrogen ions increased to 100 mA, which corresponds to a current density of 2.0 A/cm^2. The normalized emittance measured in the direction of the extraction slit was 1.2 cm-mrad.

The new developments in the production of negative ion beams from sources using the direct extraction method have made their application more attractive in several fields. Current densities and phase space areas are becoming comparable to those of standard proton sources presently used in preaccelerators. Achievement of such characteristics seems to eliminate one of the main objections to the charge exchange injection into circular accelerators.

Acknowledgments

The assistance of many AGS staff members is greatly appreciated, especially V. Buchanan, R. Larson and L. Repeta in the design of the sources, power supplies and diagnostics and R. Clipperton and E. McKenna for the technical assistance and every-day operation of the ion source laboratory.

References

1. V.P. Golubev, G.A. Nalivaiko, and S.G. Tsepakin, Proc. Proton Linear Accel. Conf. (Los Alamos Report No. \$4-5115, 1972), p. 356.
2. Iu.I. Bel chenko, G.I. Dimov, and V.G. Dudnikov, Novosibirsk Report No. 66-72, 1972 (in Russian).
3. Iu.I. Bel'chenko, G.I. Dimov, V.G. Dudnikov, and A.A. Ivanov, Novosibirsk Report No. 81-72, 1972 (in Russian).
4. K. Prelec and Th. Sluyters, Rev. Sci. Instrum. 44, 1451 (1973).
5. Th. Sluyters and K. Prelec, Nucl. Instrum. Methods 113, 299 (1973).

* Work performed under the auspices of the U.S. Atomic Energy Commission.

ISABELLE DESIGN STUDY OF INTERSECTING STORAGE ACCELERATORS*

H. Hahn
Brookhaven National Laboratory
Upton, New York

Summary. The present status of the ISABELLE design study for 200 x 200 GeV proton Intersecting Storage Accelerators at Brookhaven is presented. The most prominent features of this machine are the high center-of-mass energy of at least *400* GeV, the high luminosity of up to 10^{33} cm^{-2}sec^{-1}, the flexibility of the experimental insertions, and the use of superconducting magnets for bending and focusing of the beams. A general description of the design considerations and the main parameters is given. The possibility of future options, in particular the addition of a 15-GeV electron ring, is discussed.

I. Introduction

The advantage of using colliding beams to overcome the relativistic limitation in achieving the highest center-of-mass energies rather than beams from conventional accelerators striking stationary targets had been recognized early in accelerator history by Wideröe.[1] The original work at MURA on the stacking of many pulses[2] in each beam was fundamental for the achievement of adequate luminosity, and led directly to the design of the CERN ISR[3] which is at present the only proton-proton colliding beam device.

The construction of storage rings at the Brookhaven AGS had been considered previously in response to the recommendations made by the Ramsey panel.[4,5] A summer study was held at Brookhaven in 1963 to discuss the relative merits of accelerators and storage rings.[6] It was concluded that storage rings at AGS energies would be feasible, and a fir t parameter list for colliding beams was worked out.' At the same time it was pointed out by Jones[7] that storage rings of two or three times the circumference of the AGS could be used to accelerate the stacked protons to higher energies from 70 to 100 GeV. However, finally a decision was made not to construct storage rings, because it was thought that they lacked the versatility of a single proton accelerator of the same equivalent energy.

The idea of building storage rings at Brookhaven was revived in 1970 by Blewett[8] and this time it was greeted with enthusiasm. It soon received the endorsement of the Fitch committee which recommended that BNL apply its pioneering development work in superconducting magnets to build two proton intersecting storage accelerating rings to operate in the neighborhood of 200 GeV.[9] A study group was set up under Mills which issued a preliminary design study[10] (the "Gray Book") in 1972. The ISABELLE design has undergone a number of metamorphoses as documented in a series of publications.[10-15] However, the study has now advanced to a point where a revised version of the "Gray Book" is being edited.[16] A construction proposal will be submitted to the AEC in the near future. If funded in FY 1976 the ISA could be operational in 1981 providing an exciting facility for particle physics research.

The LSA design incorporates a series of innovations which will make it the frontier of high energy physics and accelerator technology. Its most prominent features are the high center-of-mass energy of *400* GeV, the high luminosity of up to 10^{33} cm^{-2}sec^{-1}, the flexibility of the experimental insertions, and the use of superconducting magnets for bending and focusing of the beam. This paper describes the present status of the ISABELLE design study, explains the basic design choices which had to be taken, gives a qualitative description of the machine components and the final parameter list, and concludes with an outlook on possible future additions to the basic proton-proton rings.

*Work performed under the auspices of the U.S. Atomic Energy Commission.

II. Basic Design Choices

Center-of-Mass Energy

The usefulness of the machine under consideration depends on many factors. One of these, the center-of-mass energy (usually designated by $\sqrt{s}$), is the single most important parameter in particle physics. The *400* GeV center-of-mass energy of the ISA is equivalent to that of a conventional accelerator of 86 TeV. In the U.S., the NAL accelerator, at *400* GeV, provides a center-of-mass energy of 28 GeV. The highest center-of-mass energies presently available is at the CERN ISR with an energy of 61 GeV. This is equivalent to a 2 TeV accelerator. The ISA will allow almost an order of magnitude increase in center-of-mass energy.

The choice of the ISA design energy is less obvious than that of the Bevatron, which was conceived to produce antiprotons. Current theoretical ideas give some indication as to the minimum energy desirable for the next machine. Simplifying greatly, one may state that there are two energy scales which a new machine should reach or exceed.[17] The first is set by the energy for which the strength of weak interactions equals that of electromagnetic interactions. Theories which would unify the Fermi theory of weak interactions and quantum electrodynamics have been proposed and postulate the existence of intermediate vector bosons (W), with rest masses above 37 GeV. Storage rings with 100 x 100 GeV would be adequate to produce these particles. In fact, the failure to observe W-production at center-of-mass energies larger than 100 GeV would cause difficulty for theories of this class. Another energy scale is given by the unitarity limit which for lepton-lepton interactions is about 300 GeV, but for hadron interactions may be near 600 GeV. It is clear, that with the weak, electromagnetic and strong interactions beginning to have the same effective strength at ISA energies, substantial new physics can be expected to appear before reaching the unitarity limit.

Another approach to choose the design energy would be to look at the historical progress of the accelerator field. The traditional step in center-of-mass energy has been a factor of *4* (AGS to NAL) to 8 (CERN PS to ISR). This would indicate a desired energy range from about 100 x 100 GeV to 250 x 250 GeV. The design energy of 200 GeV would thus appear to be justified from most points of view.

Luminosity

A design parameter as important as the energy is the luminosity of storage rings. The luminosity is determined by parameters of the machine such as the circulating current, beam emittance, geometry of the beam crossing region, tolerable beam-beam tune shift, etc. The design luminosity of the ISA has been fixed at

10^{33} cm^{-2}sec^{-1} per interaction region.

The ISA luminosity is expected to be more than two orders of magnitude above the values currently achieved at the CERN proton storage rings. This high value can be obtained by exploiting low-beta insertions, head-on (or small angle) collisions of the protons and, especially, the small emittance and high phase space density of the AGS at Brookhaven. An informative expression for the optimum luminosity of proton storage rings has been derived by Keil,[18]

$$L_{opt} = \frac{4}{3}\gamma\left(\frac{I^-}{e\,c\,r_p}\,\frac{\pi}{3}\,\frac{\epsilon_{inv}}{\ell}\,\Delta\nu_{max}\right)^{\frac{1}{2}}$$

which is obtained by adjusting the amplitude function at the crossing point to the value

$$\beta^*_{opt} \cong \left(\frac{ec}{8r_p I}\,\frac{\epsilon_{inv}}{\pi}\,\ell\Delta\nu_{max}\right)^{\frac{1}{2}} .$$

Here I is the current stacked in one ring, $\epsilon_{inv} = \beta\gamma\epsilon$ is the invariant transverse emittance which is assumed equal in the horizontal and vertical planes, ℓ is the unshielded free space between magnets around the collision region, $\Delta\nu_{max}$ is the linear tune shift due to the space-charge forces of the beam-beam interactions, e is the electronic charge, c is the velocity of light and, r_p is the classical proton radius.

The luminosity depends strongly on the current which can be stored and, in the case of the ISA, accelerated. An estimate of the more serious current limitations due to the beam induced gas pressure rise[19] and the transverse resistive wall instability (CERN's brick wall effect[20]) indicates that 10 A is a realistic figure for the ISA. The beam-beam tune shift tolerable in proton storage rings is not firmly established, but there seems to be agreement that $\Delta\nu_{max} \cong 5 \times 10^{-3}$ is a conservative limit. The present design provides a free space between magnets of ℓ = 40 m; this value could easily be halved at a later time if higher luminosities should be desired. The optimum luminosity depends directly on the emittance achievable; the AGS, with an $\epsilon_{inv} \cong 12.5\ \pi\ 10^{-6}$ m·rad, is ideally suited as an injector for a proton storage ring. The optimum luminosity in the ISA is obtained with β^*_{opt} = 0.7 m and reaches the level of $L_{opt} = 3 \times 10^{33}$ cm^{-2}sec^{-1}, a value which is comfortably above the design requirement.

Experimental Insertions

The anticipated experiments at the ISA differ in their specific requirements as to luminosity, tolerable momentum spread, shape and size of the crossing region, radiation background, etc. A number of experiments have been conceptually designed and the constraints on the experimental insertions have been established. It was concluded that only the small-angle scattering experiment requires an unusual straight section configuration to provide the desirable angular resolution of 25 μrad or better. Most experiments studied can be performed adequately in a general-purpose experimental insertion with a total of 40 m of free space around the crossing point and adjustable optical parameters. To preserve complete four-fold symmetry during commissioning of the machine, all four experimental insertions will be made identical. After having gained experience with the operation of the ISA, it will be possible to introduce other experimental insertions, also fully matched but in all likelihood no longer identical, which are better suited to experiments with special requirements. This concept provides considerable flexibility in the layout of the experiments, approaching that of a conventional accelerator.

Superconducting Magnets

The use of superconducting magnets has a significant impact on the expected performance of the ISA. The study of performance limitations due to collective effects indicates that most limitations become worse for a machine with a large radius and small vacuum chamber dimensions. Superconducting magnets are beneficial on both accounts:

i) Operation at fields of 40 kG, as assumed in the ISA design, reduces the machine radius by a factor of two when compared to a conventional machine of equal maximum energy. Superconducting 40 kG magnets using commercially available NbTi composite wires have been built and operated at Brookhaven, reliably and economically.[21,22]

ii) Operation of large-gap conventional magnets is prohibitive in terms of the electric power consumption. Economically designed conventional magnets limit the luminosity of storage accelerators, otherwise comparable to the ISA, to values of about 10^{32} cm^{-2}sec^{-1} which is an order or magnitude below the present design value.[23]

The use of superconducting magnets obviously necessitates the generation and maintenance of a low-temperature environment, 4.5 K in the case of NbTi conductors. The need for a dewar, refrigerator and liquid helium distribution system presents an economic burden which must be compensated for by savings in the construction cost due to the smaller tunnel size, vacuum equipment, and other field-dependent items, but also by savings due to reduced operating cost owing to lower electric power consumption. A comparison of the ISA with the low-luminosity conventional magnet ISA described in Ref. 23 shows that the initial capital expenditures would be at most 10% Less for the conventional magnet ISA. The annual electric power consumption, on the other hand, is clearly in favor of the superconducting machine: 35 GWh vs 90 GWh/year. At the rate of 2.8¢/kWh predicted for December 1974 this represents an annual savings of about $1.5 M in operating funds.

Performance and economical considerations point towards the superconducting solution. In arriving at a decision, the advantages must be balanced against the risk inherent in the application of a new technology. Superconducting magnet technology has advanced to a point that the performance of magnets, i.e. their peak field, field quality, and random errors due to fabrication tolerances, can be predicted with an accuracy equal to that for conventional magnets. Questions regarding the behavior of superconducting magnets in radiation environments have been proven manageable based on the experience gained from the operation of the 8° bend in the high-intensity proton beam to the North Area of the AGS.[22] Refrigeration systems of the capacity required have demonstrated their reliability in commercial use. It is our judgment that the technical know-how for the execution of thisproject is at hand.

Further advances in this field conceivably in time for the construction of the ISA are anticipated from the development of new materials of the A15 type such as Nb_3Sn or Va_3Ga which would bring 60 kG magnets into reach. These would be translated into an increase of the energy of about 300 GeV and a further reduction of the electric power consumption without essentially changing the financial scope of the project,

III. General Description

Ring Structure

The geometric configuration of the storage accelerator is essentially that of a circle expanded by four,

symmetrically located experimental straight sections, in which the beams are brought together in a horizontal small-angle or collinear collision region (Fig. 1). The total circumference of the rings is 2690 m corresponding to exactly 3-1/3 times the circumference of the AGS. Shown in Fig. 1 are the four experimental halls to be constructed from the start around the four collision points. The ISA consists of two intersecting magnet rings located one above the other in a common tunnel, the cross section of which is shown in Fig. 2. The AGS will be used as the source of 28.5 GeV protons which will be ejected into the beam line now feeding the North Area and the 7 ft bubble chamber, and which would be extended to the proposed location of the ISA. The area north of the AGS is reasonably level and the Brookhaven site provides ample space for future expansion.

The separated function lattice structure initially will have complete four-fold symmetry. The regular part of the ring contains *48* normal cells. The regular cell structure is broken into octants by adding four 250 m long (200 m straight) experimental insertions and four 110 m long (50 m straight) service insertions with the latter satisfying the machine requirements of injection, fast protective ejection, rf system, etc. The vertical separation of the beams will be 46 cm allowing a common dewar for the magnets of the upper and lower rings. The elements of a typical half cell are shown in Fig. 3. On the other hand, both rings are electrically and magnetically separated to permit experiments with unequal energies and to accommodate the antiproton option.

The normal cell uses a simple FODO sequence with two 4.25 m long (iron face-to-face) dipoles and one 1.3 m long (iron face-to-face) quadrupole per half cell. The total length of a normal cell is 25.40 m leaving a distance between magnets of about 1 m. The maximum amplitude function, horizontally and vertically, is β_{max} = *43* m and the maximum horizontal momentum dispersion is X_p = 1.7 m in the normal cell.

The service insertions are fully matched to the regular lattice and exhibit zero dispersion in the center while keeping the amplitude function at low values, $\beta_{vmax} \leq 110$ m (Fig. *4*).

Conflicting design requirements prohibit the use of a unique insertion for all experiments and a number of fully-matched experimental insertions have been worked out in detail: A general purpose modest-beta insertion, a high luminosity low-beta insertion, a small-angle elastic scattering insertion, and a multipurpose spectrometer insertion where the beams interact within a bending magnet. Initially, during the commissioning of the ISA, four general purpose modest-beta insertions (β_v^* = 6 m) will be installed to keep β_{max} to safe values, say below 300 m. Luminosities of 5×10^{32} cm^{-2}sec^{-1} at each crossing point should be achievable. In this insertion the crossing angle is adjustable from 0 to 6 mrad by means of horizontal steering magnets. To achieve the design luminosities a low-beta insertion (β_v^* = 2.2 m, X_p = 0 m) will be required imposing higher β_{max} and larger chromaticity (Fig. *5*). Further improvements in luminosity resulting from an even lower beta (the theoretical optimum is β_v^* = 0.7 m) and shorter free space between magnets, down to 20 m, are conceivable.

Beam Transfer

A number of schemes for transferring the AGS beam at 28.5 GeV to the ISA have been studied. The method of energy stacking now used at the CERN ISR has been adopted in view of its numerous advantages:

i) Operation of the AGS can be optimized for highest transverse phase-space density (instead of highest intensity) which is a prerequisite to achieving the highest luminosities. The intensity in the ISA is then simply built up by a larger number of AGS pulses.

ii) No modifications or additions to the AGS are required. Prior to ejection the total rf peak voltage in the AGS will be reduced from *400* kV to approximately 36 kV in order to match the AGS bunch shape to the bucket of the ISA stacking system. Existing equipment for fast ejection of the beam to the North Area would be retained for the beam transfer to the ISA.

iii) Aperture requirements for injection purposes are well matched to the available vacuum chamber aperture of 8 cm which has been determined by vacuum considerations.

The beam transport equipment from the AGS to the ISA is more economical if conventional magnets are used since it only needs to be energized during the stacking process. The ISA stacking rf system operates on the same frequency as the AGS *(4.45* MHz) and is designed for a peak voltage of 12 kV. To prevent self-bunching and dilution of the stacked protons, the impedance seen by the beam must be kept below 100 Ω, which is achieved by an appropriate feedback system.[24] The AGS pulse, with its intensity reduced to 2.3×10^{12} protons in 10 bunches, is captured directly by the stacking system, decelerated, slowly debunched and deposited into the unbunched stack. The AGS pulse fills only a fraction (⅓) of the ISA circumference; dilution of the stack is prevented by designing a stacking rf system with suppressed buckets. The design current of 10 A (or 5.6×10^{14} protons) will be reached in about one hour by repeating this cycle 250 times or more. Assuming a total longitudinal phase space dilution of 2 (which according to the CERN-ISR experience is not unrealistic) the momentum spread of the stacked beam will be $\Delta p/p = 0.7\%$, and its dimensions 2.0 × 0.8 cm in horizontal and vertical direction respectively. Estimates show that the design current of 10 A does not exceed the limits set by coherent transverse instabilities,[25] and the beam induced pressure rise,[26] if appropriate precautions are taken.

Acceleration System

In order to accelerate the stacked beam it will be rebunched by an rf system operating at the second harmonic, f = 223 kHz. Adiabatic rebunching can be done, in principle, without phase-space dilution or loss of particles but the 700 Ω impedance of the acceleration rf system necessitates a rebunching in the relatively short time of about 100 msec and some degradation of the beam must be expected (note that the accelerating gaps are shorted during the stacking procedure). The peak rf voltage, which is determined by the momentum spread of the stacked beam to be *40* kV, is provided by four ferrite loaded cavities. The energy gain per turn of 12.5 keV during the 2 minute acceleration cycle is well within the capabilities of the rf system. No insurmountable difficulties with accelerating the beam of 10 A are expected: The choice of the 2nd harmonic should make the beam essentially stable against longitudinal bunched beam instabilities;[27] estimates of the transverse resistive wall instability indicate that the bunched beam will remain stable if the unbunched beam was stable; diffusion from a repeated crossing of the 5th order resonance during the acceleration cycle was numerically computed and found to be inconsequential, 3rd or 4th order resonances, however, must be avoided at all times even when the momentum spread (and tune spread) is increased to about 2% as a result of the bunching.[28] After the acceleration cycle, the rf is switched off, the cavities are shorted again, and the beam is allowed to debunch retaining the 0.3% momentum spread of the bunched beam.

Superconducting Magnet and Dewar System

A program to develop superconducting magnets for use in accelerators and beam transport lines has been going on at Brookhaven for ten years and has led to the construction of dipole models which satisfy most of the important design criteria of the ISA magnets. The experience gained from the two identical 1 m long ISA models[21] and the two 1.8 m long dipoles for the so-called 8° bend[22] used in the extracted primary proton beam line to the AGS neutrino area will be described elsewhere in this paper. As will be substantiated there, the results have provided conclusive information concerning the question of stability, magnetic field precision (i.e. systematic errors), reproducibility (i.e. random errors), reliability, and behavior in a radiation environment.

Stability of the magnets, with the absence of quenching (transition to the normal state) or training effects (higher fields can be reached only after repeated quenching), is essential in the application of superconducting magnets to accelerators. The Brookhaven magnets have shown a remarkable degree of stability and, in fact, operation in the resistive region above the short sample critical current (defined by a resistivity of 10^{-12} Ω-cm), has been possible.

Systematic deviations from field uniformity (actually the dipoles will need a sextupole term for adjustment of the chromaticity) must be avoided at all field levels encountered during operation (6 to 40 kG). One requires roughly that the prescribed field shape of the magnets is accurate to within a few parts in 10^5 over the entire aperture of the vacuum chamber (8 cm diameter representing 67% of the magnet coil aperture). Systematic errors which are the same from magnet to magnet, may be introduced by the conductor arrangement, by the construction of the coil ends, by iron saturation effects, by diamagnetic effects in the superconductor itself, and by rate-dependent eddy currents. Saturation and magnetization effects are field dependent and require special attention. The results from the various models indicate that a single sextupole tuning coil is sufficient to compensate all important magnet errors. However, additional tuning coils must be incorporated to provide full control over the working line in the presence of space-charge effects.

Random errors, or deviations from magnet to magnet, are mainly caused by fabrication tolerances in the position of the conductors or the concentricity of the coils in the iron shield, by a nonsymmetrical gap in the median plane of the iron shield, and possibly by other causes. Closed orbit deviations, gradient errors and imperfection stopbands are caused by random errors. Briefly, one requires differences in the dipole fields of $\Delta B/B \leq 5 \times 10^{-4}$ rms and in the quadrupole gradients of $\Delta G/G \leq 10^{-3}$ rms. Estimates of the permissible random field errors indicate that tolerances on the conductor position of ≤ 50 μm rms are required. Measurements confirmed that these tolerances can be achieved with the particular construction technique employed in the ISA models. Multipurpose correction windings will be installed in all magnets to provide compensation of random field errors at least up to the decapole component.

The reliability of superconducting magnets, that is the absence of changes over long operating periods or changes due to thermal cycling, is being tested in an ongoing life test; after 5000 pulses simulating 10 years of normal ISA operation no indication of changes has been detectable.

The effects of radiation on the materials used in the magnet construction certainly requires consideration The critical current density of NbTi is essentially unaffected by particle fluxes up to[29,30] $10^{17}/cm^2$ so that it is unlikely that the superconductor will be degraded in normal operation. Care must be taken to avoid plastics which are most sensitive to radiation damage; epoxy-impregnated fiberglass will, therefore, be used almost exclusively in the windings. Quenches may be initiated by localized heating from beam spills, but the 8° bending magnet has demonstrated that a properly cooled magnet is able to withstand a fair amount of beam heating without destruction of the superconducting state. An accidental beam spill of the entire stored beam may present a serious problem, this being the case for superconducting and normal magnets alike.

The study of the recent literature on superconducting magnets proves that a number of different designs have been successfully employed. At Brookhaven two alternate styles, the window-frame and the cosine magnets, have been tried. In order to be definite, the design and cost estimate of the ISA have been based on the cosine magnet. It is well known that a pure dipole field is provided by coils of circular cross section with a cosine current density distribution. In the actual construction, shown in Fig. 6, the ideal current distribution is approximated by six current blocks per quadrant, of different azimuthal widths, but equal current density. Exact positioning of the blocks is determined in a way to suppress the five lowest harmonics. The current blocks are built up with a single layer of wide flat braid (about 2.1 cm x 0.05 cm). The braid is composed roughly of 100 twisted composite wires, 0.3 mm in diameter, each containing, typically, *400* superconducting NbTi filaments of 10 μ diameter. The wires in the braid have a CuNi jacket to increase the coupling resistance between wires and thus decrease eddy current effects to tolerable levels during pulsing. The iron core tightly surrounds the coil, and as an integral part of the construction, must also be at liquid helium temperature. The physical length of the dipoles is 4.25 m, that of the quadrupoles is 1.3 m. The inner diameter of the coil is 12 cm, the outer diameter of the iron is 40 cm. The stored energy per dipole is 465 kJ at 40 kG, there are 256 dipoles per ring, and the total stored energy is about 120 MJ per ring. Since the vacuum chamber is warm, adequate thermal insulation must be installed between the vacuum chamber and the magnet coil. Special requirements on this insulation are established by the need for outgassing the vacuum chamber at 2000 C.

Two magnets, one from the upper and one from the lower ring, will be contained in one dewar (Fig. 7). This configuration has the advantages that all vacuum joints are directly accessible for leak tests at room temperature, but it may lead to higher heat loads unless special precautions are taken. Heat loads from current leads will be minimized by having cold connections between all dipoles of one octant of the ISA ring. In this arrangement, the current in the dipoles can be chosen almost arbitrarily. In the ISA dipole it is 3.3 kA at full field to keep voltages induced during a quench within tolerable bounds. However, for the purpose of magnet protection during a quench, it is necessary to provide current leads from every other magnet which are connected to shunting diodes. Since these leads are normally not in use, they can be designed for lower current carrying capacity (here 1000 A). The quadrupoles will be designed for a current of 500A at the highest gradient of *6.6* kG/cm and a pair of leads for each quadrupole is foreseen.

The ISA design calls for *40* kG superconducting magnets. This choice is based on the present-day availability of NbTi filamentary superconducting wires from commercial sources in this country and the experience with magnet models at Brookhaven and at

other laboratories. It is conceivable that improvements of magnet design and construction techniques will result in magnets which can be operated reliably at 60 kG. The reduced current carrying capability of NbTi superconductor at 60 kG must be compensated by a larger conductor cross section resulting in increased superconductor cost. But, since the superconductor represents only a fraction of the total magnet cost, the price increase for 60 kG is not significant when compared to the total cost of the project. Work is in progress to test the concept for 60 kG magnets.[31] The prospects for early development of new superconducting materials, such as Nb_3Sn or V_3Ga, are encouraging. These materials would have an impact on the ISA design in two ways: First, their high critical temperature (18 K in the case of Nb_3Sn versus 9.5 for NbTi) makes operation at temperatures in the range from 8 - 9 K possible, resulting in substantial savings in the electric power consumption of the refrigeration system. Second, the critical current of these materials is higher by an order of magnitude considerably simplifying the design of 60 kG magnets. Filamentary Nb_3Sn or Va_3Ga wires are not yet available commercially in the U.S. because these compounds are brittle and must be fabricated in ways different from the drawing process used for NbTi. A diffusion technique has been developed at Brookhaven by which conductor samples have been produced.[32] In view of their great potential, the development of Nb_3Sn conductors will be emphasized and the construction of a 1 m long dipole model using this material has been initiated. First results from Nb_3Sn magnets are expected in less than a year. A final decision on the choice of the magnet for the ISA can he delayed until one year after approval of the project without affecting the orderly progress of the construction.

Refrigeration System

All components of the refrigeration system required to generate the cold environment for the superconducting magnets are conventional as to their design which is similar to that used in large helium liquefiers in gas fields. Their sizes are comparable to the industrial liquid nitrogen or natural gas liquefiers which have an established record of reliability. The operating temperature of the superconducting magnets was specified at ≤ 4.5 K which can only be achieved by pool boiling of liquid helium. Some consideration has been given to the optimum choice of the operating temperature. Earlier studies of the GESSS (General European Superconducting Synchrotron Study)-group[33] seemed to favor lower temperatures down to 3.5 K. Our analysis showed, however, that the greater cost and complexity of a refrigeration system designed for subatmospheric pressure does not seem to be commensurate with the gains made possible in the magnetic design. Furthermore, operation at lower temperatures increases the electric power consumption, thus providing a compelling argument for temperatures at or above 4.2 K.

The refrigeration system of the ISA must function in a variety of situations: normal operation, cooldown, bake-out of vacuum chamber, etc. The system's requirements are set by the normal operating condition with all magnets excited to full field. The total accelerator heat load in this case is about 20 kW, of which only 15% represents excitation-dependent ohmic losses. The total refrigerator capacity of 23 kW is provided by a system consisting of a central six-unit four-stage compressor station and eight 2.9 kW refrigerator cold boxes which are installed close to each octant. The refrigerator units are designed with four expansion engines, with the final expansion employing either a wet engine or a Joule-Thompson valve. The electric power requirements at the compressor motors are 9.5 MW with J-T valves or 7.5 MW if wet engines are used. Since available information about the reliability of wet engines is insufficient it is planned to install a parallel J-T valve, which could be put into operation if the wet engine fails. For greatest operational simplicity, the refrigeration system is designed entirely without liquid nitrogen usage. A total of 136 000 liters of liquid helium is contained in the filled dewars of the ISA. Nevertheless, it will be possible to cool and fill the entire ISA in less than 1 week,

The response of the refrigeration system to a number of faults has been analyzed in detail and precautions to prevent possible loss of refrigerant have been incorporated into the design:

i) The quench of a single magnet may lead to a quenching of all magnets in one half-cell which are cryogenically coupled. The release of the 1.8 MJ during the quench will result in the evaporation of 800 liters of liquid helium which will be vented into a low-pressure buffer device, The dewars will be refilled and ready for operation after about ½ hour.

ii) Shutdown of one of the 8 refrigerator units can be tolerated during normal operation of the ISA, since the system was sized so that 7 units are adequate to carry the Pull load. The helium distribution system is interconnected around the entire ring, and the computer control system assures equal loads in the refrigerator units.

iii) Unscheduled loss of electric power would cause transfer of the liquid helium to liquid storage vessels by pressure build-up in the dewars. A loss of 15% of the helium must be expected if the electric power remains off for longer than 10 hours. By providing an emergency diesel-powered compressor this loss of refrigerant can be prevented.

iv) The worst fault would occur if the protective beam dump fails and the beam with its 20 MJ energy is spilled into the magnets. This would evaporate, in a short time, over 8000 liters of liquid helium which could not be recovered.

Magnet Power Supply

The demands on the magnet power supply are modest as a result of the slow two-minute acceleration cycle. The total energy stored in the bending magnets of each ring is about 120 MJ. Therefore, a 2 MVA rated power supply is adequate. With the peak dipole current of 3.3 kA the required power supply voltage is about 600 V. These are ideal parameters for solid-state rectifiers-inverters. The power supply will be a six-phase SCR system including a passive inductance-capacitance filter to reduce the ripple to the required $\Delta I/I \leq 10^{-6}$. The quadrupoles, sextupole and correction element windings, and the magnets in the experimental insertions, will be supplied by similar power supplies at much lower power levels.

The large total stored energy makes it important to include fault protection in case of a magnet quench. For this purpose shunting power diodes are included across the magnets in each dewar. These operate below their voltage threshold for current conduction under normal operation but provide a current path in case of a quench.

Vacuum System

The density of residual gas molecules in proton storage rings must be lower by several orders of magnitude than in conventional accelerators. This is necessary to reduce beam blow-up from multiple Coulomb scattering or inelastic nuclear scattering and the accom anying background radiation. The design, therefore, calfs for a pressure of 10^{-10} Torr in the circular

quadrants of the ring and 10^{-11} Torr in the experimental insertions. Electrons and negative ions trapped in the Coulomb field of the beam must be removed with suitable clearing electrodes.

Experience with the CERN ISR shows that the most serious current limitation is set by the beam-induced gas pressure rise (pressure bump phenomena).[19] Qualitatively, this effect is caused by ionized residual gas molecules being propelled electrostatically against the vacuum chamber and liberating adsorbed molecules in sufficient quantity to increase the gas pressure. At some value of the current, this pressure leads, avalanche-like, to the destruction of the beam. For the geometry of the ISA vacuum system (8 cm i.d. circular vacuum chamber, 5 m distance between pumps, each with 500 ℓ/sec pumping speed) the theory26 yields the limit $\eta I_{cr} \leq 30$ A where η is the desorption coefficient. The desorption coefficient of typical chamber materials at room temperature depends, predominantly, on the bake-out temperature and the surface condition. A desorption coefficient of $\eta < 3$ (permitting $I > 10$A) is expected with a bake-out temperature of 200° C and an argon discharge cleaning prior to assembly. The use of a vacuum chamber operating at liquid helium temperatures has been considered, but adandoned in view of experiment indicating desorption coefficients of several thousand.[35] Experiments to simulate the pressure bump effect are in progress and will allow an early verification of the assumptions used in the design of the ISA vacuum system.

The ISA vacuum chamber will be made of aluminum whose good thermal conductivity will prevent cold spots in the center of the cold magnets. The good electrical conductivity will alleviate resistive wall instabilities. The pumping will be provided by conventional Ti-sublimation pumps and ion-sputter pumps for non-getterable gases. The dewar construction provides direct access to all vacuum joints and pumps resulting in an almost conventional UHV system.

Control System

It is planned to operate the whole ISA-AGS accelerator complex from a central control center. This maximizes the information interchange between the two accelerator systems and minimizes the operating crew required. The various functions encountered in the operation of the machines, such as data collection, analysis and display, beam monitoring, or execution of operator instructions will be carried out by a carefully designed computer-based control system. If computers are considered as integral parts of the control system from the inception, a powerful system of great flexibility at relatively moderate cost will result.

ISA Shielding

Many of the considerations regarding the shielding requirements of conventional accelerators are equally applicable to storage rings. There are, however, important differences which had to be taken into account in the layout of the ISA shielding. Adequate shielding is required here for radiation protection against accidental beam spills, whose location and occurrence are unpredictable. The basic requirement is that a person outside of the shield will not receive a radiation dose exceeding 100 mrem in the worst case of 10^{15} protons dumped at any point. This will be satisfied by an earth cover extending to 160 m in any tangent direction in the plane of the accelerator and providing 6 m of earth in any transverse direction over the ring tunnel. The skyshine dose at the site boundary has been estimated to be 10^{-3} mrem per 10^{15} protons dumped. It is concluded that an off-site point would never accumulate the permissible annual dose equivalent of 1 mrem. At the end of its useful life span of typically one day, the beam will be dumped in a controlled fashion into a beam stop consisting of a metal block shield 4 m long and 1 m wide. Special requirements in regard to shielding will exist in the experimental areas, which are not related to safety considerations and can, therefore, be worked out after the machine has been put into operation.

IV. Future Options

A number of options have been investigated which could be added to the basic ISA at a later stage. The most attractive from the standpoint of physics research would be the addition of a facility for ep collisions.[36,37] Electrons would first be accelerated to 4 GeV in the AGS, they would then be accelerated to 15 GeV, providing high center-of-mass energies for ep collisions. This second acceleration could take place in an additional electron ring located either inside the ISA tunnel or, to minimize interference with the ongoing pp work, in a separate tunnel to the east of the ISA. Another more economical possibility is to accelerate the electrons in one of the ISA rings. The vacuum chamber in one, or perhaps both, ISA rings would be designed to allow water cooling on one side to carry away the large amounts of energy radiated from the electron beam. However, further studies are required to ascertain the feasibility of this approach. It is estimated that the luminosity of ep collisions would be greater than 10^{33} $cm^{-2}sec^{-}$ at electron energies up to 7 GeV (cm energy = 75 GeV) and then drop to 5×10^{31} $cm^{-2}sec^{-1}$ at the maximum electron energy of 15 GeV (cm energy = 109 GeV).

Special care was taken in the design of the basic ISA so as not to preclude the deuteron and antiproton option. Acceleration and storage of deuterons[38] should not present any particular problems and would make it possible to study proton-neutron and neutron-neutron cross sections with luminosities of about 7×10^{32} $cm^{-2}sec^{-1}$. Antiprotons39 can be produced by using one ring as a 200 GeV accelerator and the other as storage ring, providing $p\bar{p}$ collisions with a luminosity approaching 10^{29} $cm^{-2}sec^{-1}$.

V. A Two-Stage Approach to ISABELLE

A preliminary design study of a 100 GeV storage accelerator has been carried out in sufficient detail to provide the information required for a rough cost estimate.[40] In a situation where available funds limit the size of a project it may be necessary to consider a proton storage ring of lower energy and lower luminosity. The minimum energy of the next generation proton storage rings should represent a reasonable step beyond the CERN ISR and permit to test the region where the strength of weak and electromagnetic interactions are about equal. The opinion has been expressed that an ISA capable of 100 x 100 GeV at a luminosity of 10^{32} $cm^{-2}sec^{-1}$ is admittedly less attractive than the full ISABELLE but nevertheless fully justifiable in terms of the physics as presently understood and a natural step towards a superconducting 300 GeV ISA. The particular design was therefore done for a storage ring using the ISA tunnel. Here it is indicated to use conventional magnets at about 15 kG, with the exception of the 70 or so dipoles in the experimental insertions which should be superconducting to assure an optimum insertion design. The estimates show that the conversion penalty would be smaller than 20% of the ISABELLE cost. More objectionable, the physics program would have to be interrupted during a one year period.

Table I. Main ISABELLE Parameters

FINAL ENERGY	200 x 200 GeV
-Equivalent Accelerator	*86* TeV
LATTICE (four-fold symmetry)	
-Circumference ($3\text{-}1/3 \times C_{AGS}$)	*2690* m
-Experimental insertion length (straight)	*4 x 250 (200)* m
-Multipurpose insertions (straight)	*4* x 110 *(50)* m
-Normal cell length	*48* x *25.40* m
-Vertical distance between orbits	*0.46* m
-Distance between magnets D-D (iron-iron)	0.90 m
-Distance between magnets D-Q (iron-iron)	1.0 m
GENERAL PURPOSE EXPERIMENTAL INSERTIONS (horizontal crossing, adjustable parameters)	
$-\beta^*_v$	*2-6* m
$-\beta^*_h$	5-10 m
-Maximum β	1000 - 300 m
-Total free space around crossing point	*40* m
-Crossing angle	*0-6* m
-Interaction length	< 1 m
MAGNET SYSTEM	
-Bending field at 200 GeV	*40* kG
at *28.5* GeV	*5.9* kG
-Number of normal dipoles/ring	*256*
-Dipole length magnetic	4.11 m
physical (iron-iron)	*4.25* m
-Peak current in dipole	*3.3* kA
-Stored energy at *40* kG/dipole	*465* kJ
-Vacuum chamber aperture (warm bore)	*8* cm
-Main coil i.d.	*12* cm
-Operating temperature (pool boiling)	≤ *4.5* K
-Quadrupole gradient	*6.6* kG/cm
-Peak current in quadrupole	*500* A
-Stored energy/quadrupole	30 kJ
-Quadrupole length magnetic	1.16 m
physical (iron-iron)	*1.30* m
CRYOGENIC SYSTEM	
-Total heat load at *4.5* K	≈ *20* kW
-Total refrigeration capacity	*8 x 2.9* kW
-Power requirements of compressors	*7.5* MW
-Total liquid helium	*136 000* liter
INJECTION	
-AGS energy	*28.5* GeV
-Number protons/AGS pulse (10 bunches)	2.3×10^{12}
-AGS emittance $\epsilon_h = \epsilon_v$	$0.4\ \pi \times 10^{-6}$ m·rad
-Longitudinal phase space per bunch, A	*0.36* eV·sec
-ISA current/ring	10 A
-Number protons/ring	5.6×10^{14}
-Number AGS pulses stacked	≈ *250*
-Stacked beam size	*2.0* cm x *0.8* cm
-Momentum spread	*0.7* %
-rf frequency stacking system	*4.45* MHz
-rf voltage	*12* kV
-Impedance (with feedback)	*400 (40)* Ω
ACCELERATION	
-Duration	2 min
-rf frequency (h = *2)*	*223* kHz
-Energy gain/turn	*12.5* kV
-Peak rf voltage	*40* kV
-Momentum spread at 200 GeV	0.3 %
LUMINOSITY	
L_{pp} (200 GeV, unbunched, β^*_v = *2* m, $\Delta\nu_{max} = 5 \times 10^{-3}$)	≥ 10^{33} cm-2sec-1
-$p\bar{p}$ option, $L_{p\bar{p}}/L_{pp}$	≤ 10^{-4}
-dp option, L_{dp}/L_{pp}	≅ *0.7*
-dd option, L_{dd}/L_{pp}	≅ **0.7**
-ep option	
Maximum e-energy	*15* GeV
Number of electrons	8.2×10^{12}
Maximum luminosity at 7 GeV-electrons	10^{33} cm^{-2}sec^{-1}
Luminosity at *15* GeV-electrons	5×10^{31} cm^{-2}sec^{-1}

Acknowledgments

This paper is adapted from the new ISABELLE design study report and thus summarizes the work of many members of the Brookhaven Accelerator Department. The study was coordinated by the ISA Parameter Committee composed of H. Hahn, Chairman, M.Q. Barton, J.P. Blewett, R.W. Chasman, E.D. Courant, J.G. Cottingham, G.K. Green, M. Month, M. Plotkin, I. Polk, R.R. Rau, J. Sandweiss, R.P. Shutt, and J. Spiro. The physics input to the design study was provided by the ISA Experimental Coordinating Group under the guidance of J. Sandweiss and R.P. Shutt, co-chairman, with C. Baltay, E.W. Beier, D. Berley, A.S. Carroll, W.E. Cleland, G.T. Danby, R.M. Edelstein, E. Engels, G. Finocchiaro, K.J. Foley, M.L. Good, P. Grannis, H. Jostlein, J. Kirz, J.T. Lach, D.M. Lazarus, L.M. Lederman, W. Lee, Y.Y. Lee, S.J. Lindenbaum, I.R. Linscott, R.I. Louttit, A.K. Mann, J.N. Marx, A. Maschke, J. Orear, S. Ozaki, R.B. Palmer, R.F. Peierls, J. Peoples, R.H. Phillips, L. Rosenson, C. Rubbia, J.S. Russ, N.P. Samios, W. Selove, L.W. Smith, G.A. Snow, M.W. Strovink, S.C.C. Ting, F. Turkot, C.L. Wang, W.J. Willis and the ex-officio members H.W.J. Foelsche, H. Hahn, V. Radeka, R.R. Rau, A.M. Thorndike, and J. Weneser. Further direct contributions to the design study were made by H.J. Halama, C. Lasky, H. McChesney, P. Mohn, W. Moore, G. Morgan, G. Parzen, E.C. Raka, W.B. Sampson, A. Schlafke, Th. Sluyters, and A. van Steenbergen, but also by many members of the Brookhaven Accelerator Department whose names had to be omitted here. Last but not least, the design study profited enormously from the comments made by our colleagues from universities and other accelerator centers during and after the 1972 Summer Study. It is a pleasant duty to thank the many contributors without whose efforts there would not be an ISABELLE design report.

References

1. R. Wideroe, BRD Patent 876279 (priority September 8, 1943).
2. J.W. Kerst, F.T. Cole, H.R. Crane, L.W. Jones, J.L. Laslett, T. Ohkawa, A.M. Sessler, K.R. Symon, K.M. Terwilliger, and N.W. Wilson, Phys. Rev. 102, 590 (1956).
3. K. Johnsen, Nucl. Instrum. & Meth. 108, 205 (1973).
4. E.D. Courant, BNL Report EDC-51 (1963).
5. J.P. Blewett, Proc. Intern. Conf. High Energy Accelerators, Dubna 1963, p. 75.
6. J.W. Bittner, Ed., Proc. 1963 Summer Study on Storage Rings, Accelerators and Experimentation at Super-High Energies, Brookhaven 1963.
7. L.W. Jones, ref. 5, p. 300.
8. J.P. Blewett, BNL Reports AADD-169 (1970) and AADD-175 (1971).
9. V.L. Fitch, Chairman, J.P. Blewett, R.L. Cool, E.D. Courant, M.L. Good, G.K. Green, V.W. Hughes, L.M. Lederman, S.J. Lindenbaum, F.E. Low, A.K. Mann, B.D. McDaniel, F.E. Mills, A. Pevsner, R.R. Rau, N.P. Samios, R.D. Sard, M. Schwartz, R. Serber, J.C. Street, A.M. Thorndike, M.G. White, and W.J. Willis.
10. J.P. Blewett and H. Hahn, Eds., BNL Report 16716 (1972).
11. J.P. Blewett. Proc. 8th Intern. Conf. High-Energy Accelerators, CERN 1971, p. 501.
12. E.D. Courant, Proc. 3rd All-Union Conf. Charged Particle Accelerators, Moscow, 1972, Vol. 1, p. 367.
13. F.E. Mills, IEEE Trans. Nucl. Sci. NS-20, No. 3, 1036 (1973).
14. J.P. Blewett, Proc. US-Japan Seminar High-Energy Accelerator Science, Tokyo and Tsukuba, 1973 (in press).
15. R.R. Rau, Comments on Nuclear and Particle Physics, (in press).
16. H. Hahn and M. Plotkin, Eds., "Design Study of 200 GeV Intersecting Storage Accelerator" (in press).
17. T.D. Lee, Phys. Today 25, No. 4, 23 (1972).
18. E. Keil, Report CERN/ISR-TH/73-48 (1973).
19. E. Fischer, ref. 12, p. 101.
20. K. Hubner, E. Keil, and B. Zotter, ref. 11, p. 295.
21. W.B. Sampson, P.F. Dahl, A.D. McInturff, K.E. Robins, this conference.
22. J. Allinger, G. Danby, B. DeVito, H.W.J. Foelsche, S.Y. Hsieh, J.W. Jackson, and A.G. Prodell, this conference.
23. W.J. Willis, G. Danby, H. Hahn, H.J. Halama, A.W. Maschke, M. Month, G. Parzen, and I. Polk, BNL Report CRISP 74-6 (1974).
24. E. Keil and B. Zotter, Particle Accelerators, 3, 11 (1972).
25. M. Month and K. Jellett, Nucl. Instrum. & Meth. 113, 453 (1973).
26. O. Grobner and R.S. Calder, ref. 13, p. 760.
27. F. Sacherer, ref. 13, p. 825.
28. R. Chasman, A. Garren, R. Gluckstern, and F.E. Mills, this conference.
29. K. Wohlleben, J. Low Temp. Phys. 13, 269 (1973).
30. W. Maurer, ref. 12, p. 222.
31. J. Allinger, G. Danby, and J. Jackson, this conference.
32. M. Suenaga and W.B. Sampson, Appl. Phys. Lett. 20, 443 (1972).
33. D.B. Thomas, ref. 12, p. 176.
34. S.K. Erents and G.M. McCracken, J. Appl. Phys. 44, 3139 (1973).
35. J.W. Bittner and H.J. Halama, ref. 12, p. 191.
36. R. Chasman and G.A. Voss, ref. 13, p. 777.
37. R. Chasman, Proc. DESY Seminar ep and ee Storage Rings, Hamburg 1973 (in press).
38. S. Ohnuma and Th. Sluyters, Proc. 1972 Proton Linear Accelerator Conf., Los Alamos, p. 191.
39. C. Baltay, R. Chasman, H.W.J. Foelsche, H. Hahn, M. Month, and A. van Steenbergen, this conference.
40. M. Month, L.N. Blumberg, R. Chasman, J. Claus, H. Hahn, H.J. Halama, G.H. Morgan, G. Parzen, I. Polk, E.C. Raka, and J. Spiro, BNL Report CRISP 74-8 (1974).

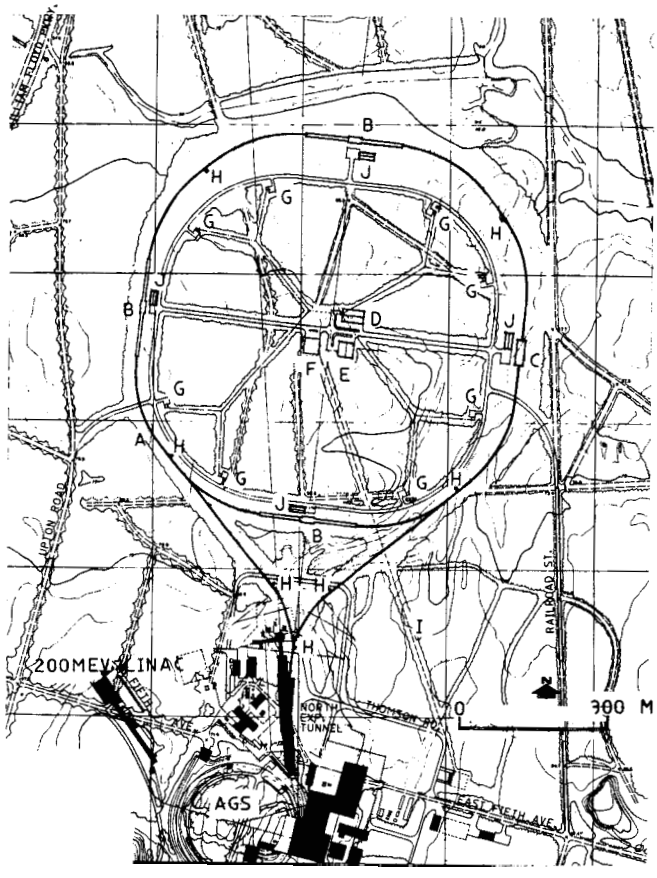


Fig. 1. ISA Site Plan. Legend: A-main magnet enclosure, B-large experimental halls, C-small experimental hall, D-compressor building, E-service building, F-69 kV substation, G-refrigerator buildings, H-exit buildings, 1-69 kV overhead line, J-assembly buildings.

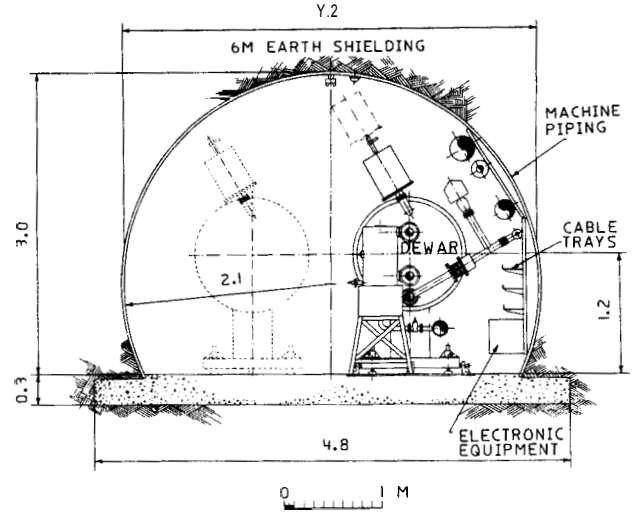


Fig. 2. Tunnel cross section (dimensions in m).

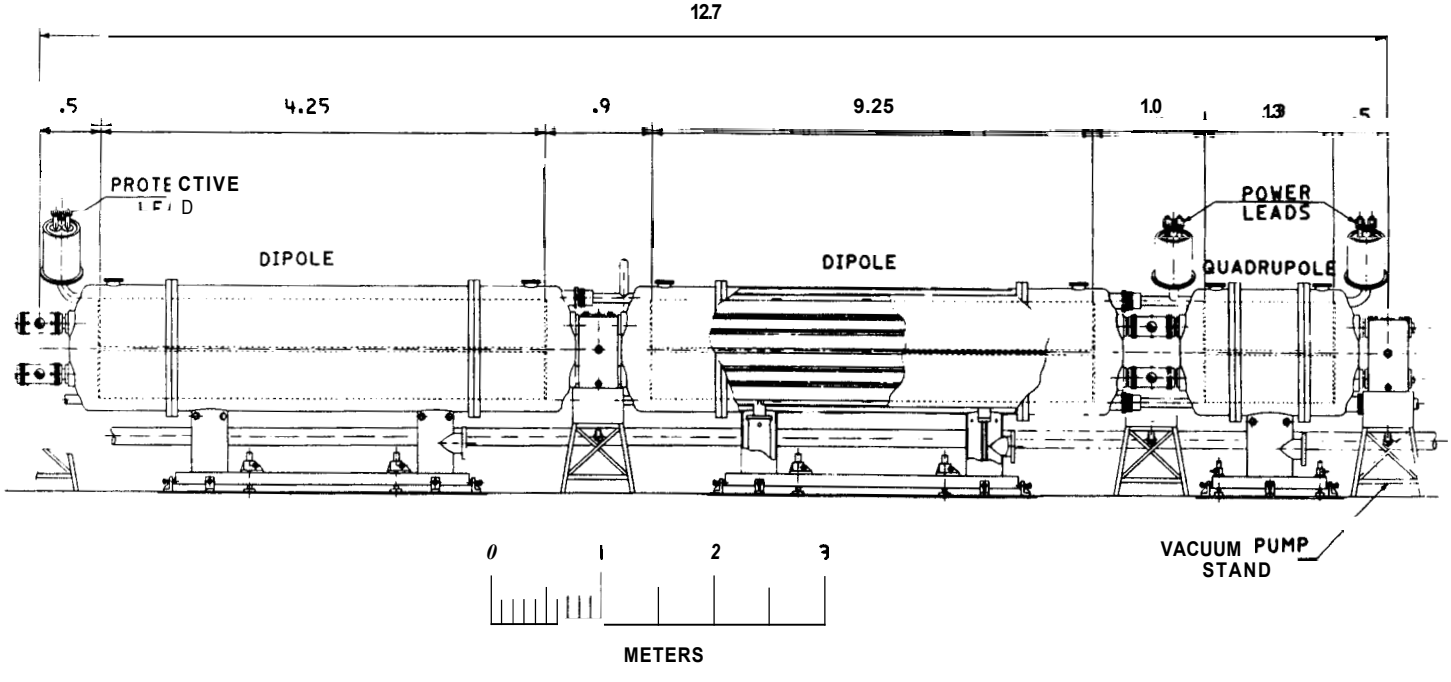


Fig. 3. Components of normal half cell (dimensions in m).

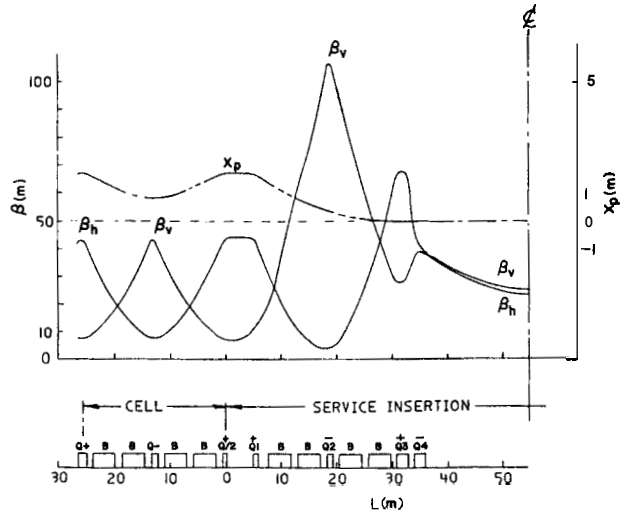


Fig. 4. Normal cell and service insertion.

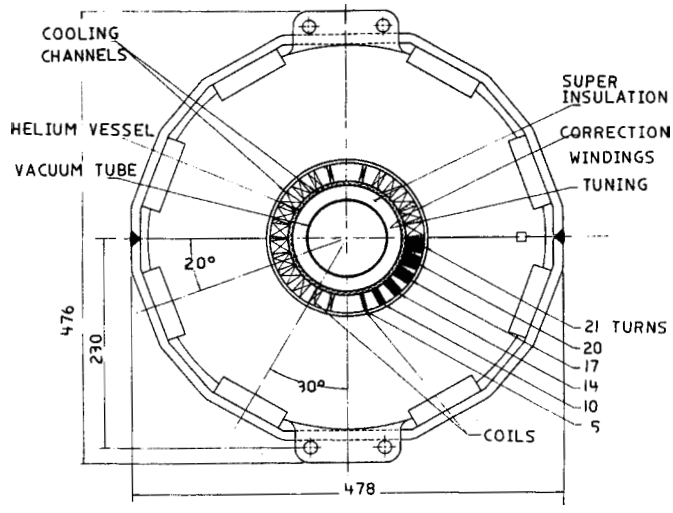


Fig. 6. Cross section of ISA dipole (dimensions in mm). Main parameters are aperture 8 cm, main coil i.d. *12* cm, main coil o.d. 16.2 cm, iron core i.d. 16.85 cm, iron core o.d. *40.6* cm, length *4.25* m, weight *4280* kg, current 3300 A at *40* kG.

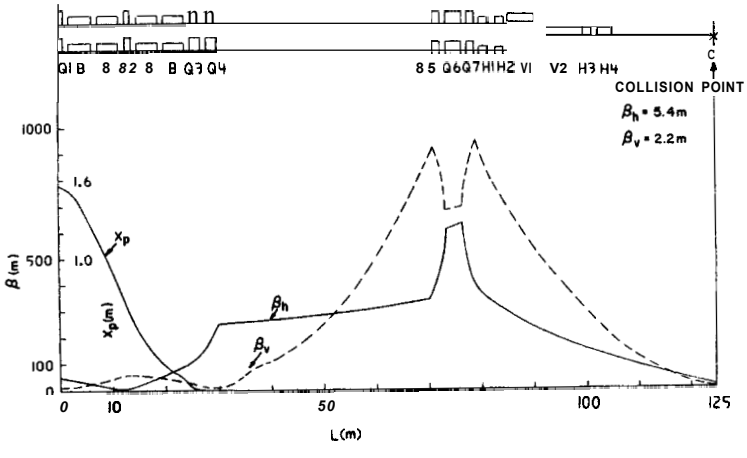


Fig. 5. Low-beta insertion. The same magnet configuration with modified quadrupole settings can be used as general-purpose modest-beta insertion.

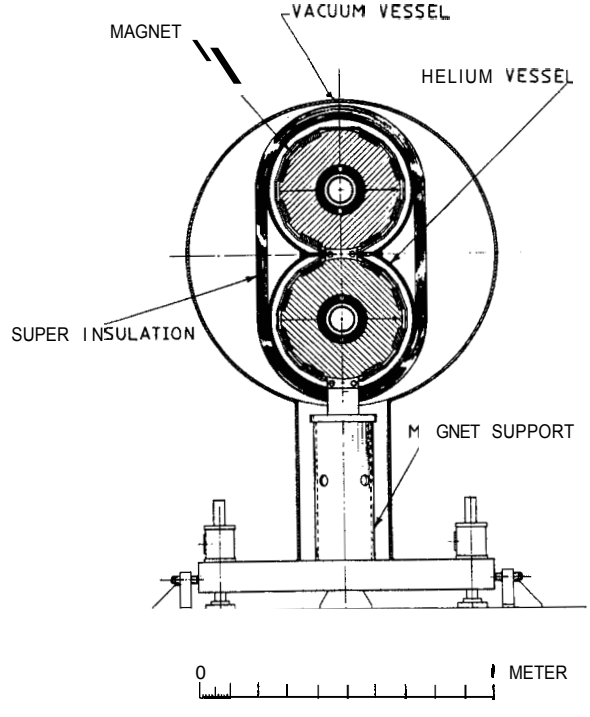


Fig. 7. Dewar cross section.

Paul Reardon (NAL): Have you done vacuum experiments in your prototype magnets?

Harold Hahn (BNL): No, but we have a very intensive vacuum program separate from the magnet program. When we still were thinking of a cold vacuum tube, we developed cryosorption pumps and tested their behavior with very good results. The design has changed in the meantime and we are now investigating the outgassing rate of aluminum after various treatments like argon discharge, bake-out at a certain temperature, and chemical polishing. We are convinced that the outgassing rate of aluminum after a heat treatment at 200° C is about an order of magnitude lower than required in the ISA. We have not yet completed a simulation experiment of the pressure bump phenomena. Results from this experiment should be available, I think, in summer.

Mark Barton (BNL): I would like to comment on Reardon's question. The vacuum problem has not been examined in the magnet, but the warm bore feature has. The Model II has warm bore.

Reardon: The bake-out of this special superinsulation is really an interesting question.

Hahn: The bake-out would be done, of course, while the machine is not in operation. Therefore, the heat leak from the bake-out can be compensated by the lack of a heat leak from the current leads. At least from the point of straight heat load, there is no problem.

Martin Donald (Rutherford): Do you have to cross transition energy?

Hahn: No. The transition energy is below the injection.

Rolfe Wideroe (SIN): Did you say how much the first phase of the project will cost?

Hahn: I didn't mention the cost. It will be official very soon; it's 126.5 million dollars.

Kjell Johnsen (CERN): You have in each beam a stored energy of about 20 MJ. Have you thought about how to get rid of it as a whole and what precautions do you take against dumping small fractions of it into the superconducting magnets?

Hahn: The present design foresees an internal beam dump, essentially the same system you have in the ISR. I would suspect that the real machine will be equipped with an external dump while keeping the internal beam dump as a protective device. We are aware of the importance of the beam dump. Does that answer your first question?

Johnson: I guess so, but our internal beam dump would explode if 20 MJ were dumped into it.

Hahn: To solve the problem caused by beam loss, we will use beam scrapers at well chosen locations around the ring. We have many straight sections far away from the experimental insertions and the idea is to scrape and dump small amounts of the beams at these locations. In addition, the experience with our superconducting magnets exposed to a full intensity beam from the AGS has shown that they can tolerate more radiation than at least some people thought they could.

Richard B. Neal (SLAC): I heard about a phased approach to ISABELLE. Could you describe what you have in mind?

Hahn: Clearly what we have in mind is what I have been describing today. Any other approach would have to be suggested by financial limitations by the AEC or some other "force majeure." But I think it could be implemented easily if required, and we have discussed a 100-GeV machine in the same ISA tunnel with conventional magnets to be replaced later by superconducting magnets. At this time, one would go most likely to 60-kg magnets and 300 GeV. The obvious question in such an approach is the conversion penalty which we estimate at not more than 20% of the total initial project. It also would provide us with magnets already usable for the electron ring. The interruption of the experimental program might be more serious, of course, and I would like to state again that what we want to build is what I have described in this talk.

David Thomas (Rutherford): This is a comment on magnets. In my talk, I said that all magnets are bad and I stick by that. I think no superconducting magnet will operate exactly at the design field and therefore one hasn't really licked the design problem. But having said that, I would like to put the record straight by saying the best of the bad designs on the basis of the performance specifications given here is certainly the Brookhaven magnet.

DESIGN AND STATUS OF EPIC

EPIC Machine Design Study Group of the
Rutherford* and Daresburyt Laboratories, United Kingdom

Presented by G H Rees

Introduction

The origins of EPIC date from the time when a study was undertaken of possible future machines for the national high energy physics laboratories in Britain. The new facilities were to replace the Rutherford and Daresbury accelerators NIMROD and NINA at the end of their useful lives. A few people from the two laboratories evaluated some storage ring machine designs[1], and one such design was described in an internal report[2]. This was based on a proposal made by Pellegrini et al. at the 1971 International Accelerator Conference[3].

The studies were given further impetus in the Autumn of 1972 by visits to the Stanford Linear Accelerator Centre of Professor Flowers, the then chairman of the British Science Research Council and Dr Stafford, director of the Rutherford Laboratory. The thoughts of Professors Panofsky and Richter of SLAC on the physics potential of high energy electron-positron and electron-proton colliding beam systems were communicated to their visitors. Before the end of 1972 an EPIC machine design study group had been established. From the outset it was a combined study between Rutherford and Daresbury Laboratories, for it was appreciated that only by pooling the resources of the two high energy laboratories would it be possible to realise a complex of the size of EPIC.

The first nine months of 1973 were spent obtaining approximate cost estimates for a two ring machine complex, with a number of different options envisaged for the actual construction stages[4]. The complex consisted of a single conventional magnet ring providing electron-positron colliding beams at incident momenta up to 14 GeV/c, together with a second ring housed in the same tunnel which would be capable of accelerating and then storing high energy protons. The second magnet ring was evaluated both for superconducting missing magnet schemes and for conventional magnets. As an electron-proton colliding beam system the peak proton momentum for a full superconducting ring was 200 GeV/c. During the initial design and costing, the study group recognised the machine design uncertainties in predicting the luminosity for the electron-proton colliding beams.

The costings are given in Table 2 of the following section, and were reported at the DESY Storage Ring Symposium of October 1973. At about that time it was decided to concentrate the studies towards a more accurate evaluation of the single ring electron-positron system. The two ring scheme for electron-proton interactions, though now only a long term objective, is still considered an essential feature in the design of the initial ring.

By October 1974 the revised evaluation of the electron-positron ring will be completed. A machine proposal will then be submitted for approval to the Science Research Council, seeking funding to allow completion of a 14 GeV electron-positron storage ring by 1981.

Electron-Positron-Proton Initial Feasibility Study.

EPIC has many features in common with the early design of PEP, which was reported [4] at the 1973 US Accelerator Conference. A schematic diagram of the proposed EPIC complex is shown in Figure 1. The two ring colliding beam system has four interaction regions, each of which is 17 m maximum in length. The rings are contained in a common tunnel, with the proton ring magnets situated vertically above the magnets of the electron machine. A system of vertical bending magnets brings the separate paths of the electrons and protons into coincidence over the central regions of the long straight sections.

In Figure 2 is shown a proposed lay out of the machine at the Rutherford Laboratory. The use of as much as possible of the existing laboratory facilities has been taken into account. The present linac buildings, the Nimrod magnet hall, main control room and two experimental halls are all planned to be used in the few facility. The 100 MeV electron linac, positron converter and 200 MeV positron linac will be located in the hall that presently houses the Nimrod 15 MeV proton linac. The Nimrod magnet hall will house a debuncher for the 200 MeV positrons together with the linac-booster beam transfer lines. The booster will be sited in its own shielding enclosure, half in and half out of one of the existing experimental halls. Most of the components for the transfer lines from the booster to EPIC will be available from existing experimental hall equipment.

The proposed lay out of the components in an insertion is shown in Figure 3, and typical lattice β-functions in the insertion in Figure 5. The range of the minimum β_H values at the centre of the insertion is 0.4 to 1.2 m in the e-ring and 1.0 to 2.5 m in the p-ring. Correspondina values for β_V are 0.1 m to 0.3 m in the e-ring and 0.4 to 1.0 m in the p-ring. Collinear crossings of the electron and proton beams in the insertions are brought about by vertical bending magnets. The bend angles in the dipoles nearest to the interaction region are 3.7° for the electrons and there is a large associated radiation loss. The choice of such a large bend angle is made to enable the proton-ring high-6 quadrupoles to be located as close as possible to the centre of the insertion.

The maximum design luminosity for collisions between 14 GeV/c electrons and 100 GeV/c protons is approximately $5\ 10^{31}\ cm^{-2}\ sec^{-1}$, but with a measure of uncertainty because of the incomplete understanding of the effects of the beam-beam interaction. There is no damping mechanism for the betatron and synchrotron oscillations for the protons, and it remains to establish the maximum allowable space charge forces on the protons in the collision regions of storage rings. Parameters relevant to the initial feasibility study are given in Table 1, where the luminosity estimates correspond to the maximum momentum particles.

*J R J Bennett, H C Brooks, M H R Donald, D A Gray, M R Harold, J D Lawson, J D Lewin, B G Loach, J R M Maidment, G H Rees, P F Smith and W A Smith

†E A Hughes, N Marks, D E Poole, M W Poole, V P Suller, G Saxon, T Swain, K Tarry and D J Thompson

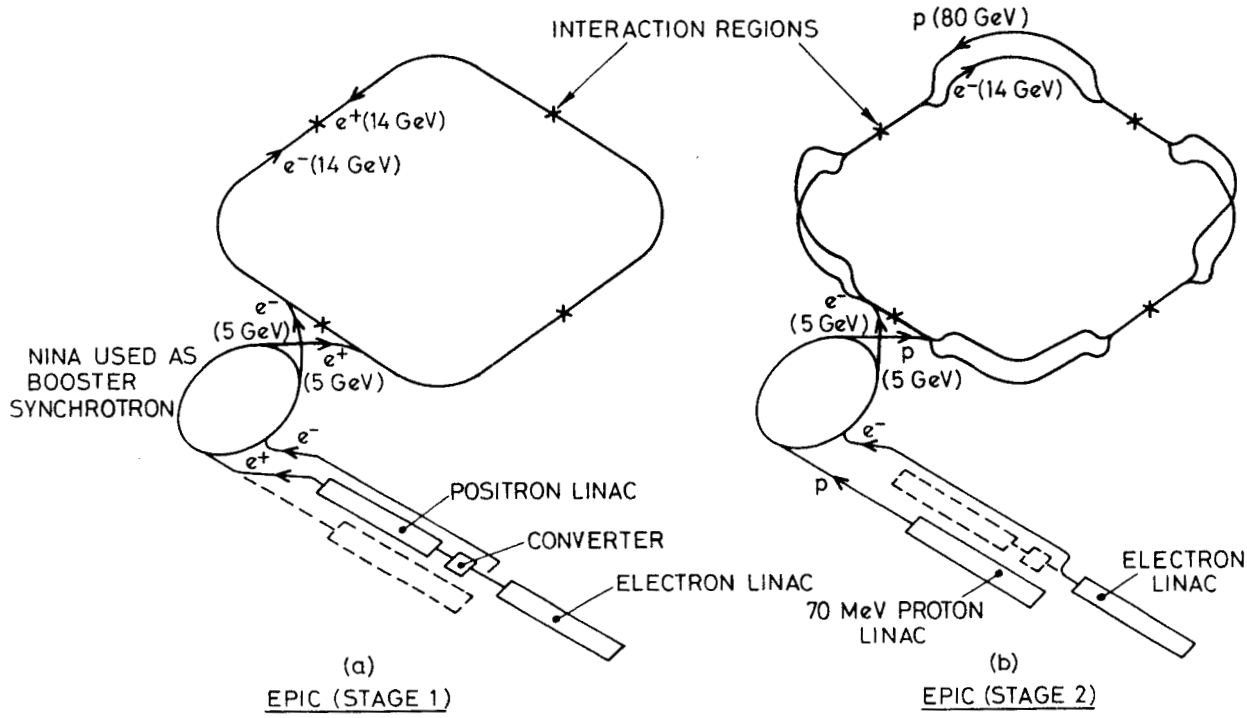


FIG.I. SCHEMATIC DIAGRAM OF EPIC (STAGE 1) FOR e^+e^- COLLISIONS AND EPIC (STAGE 2) FOR e p COLLISIONS

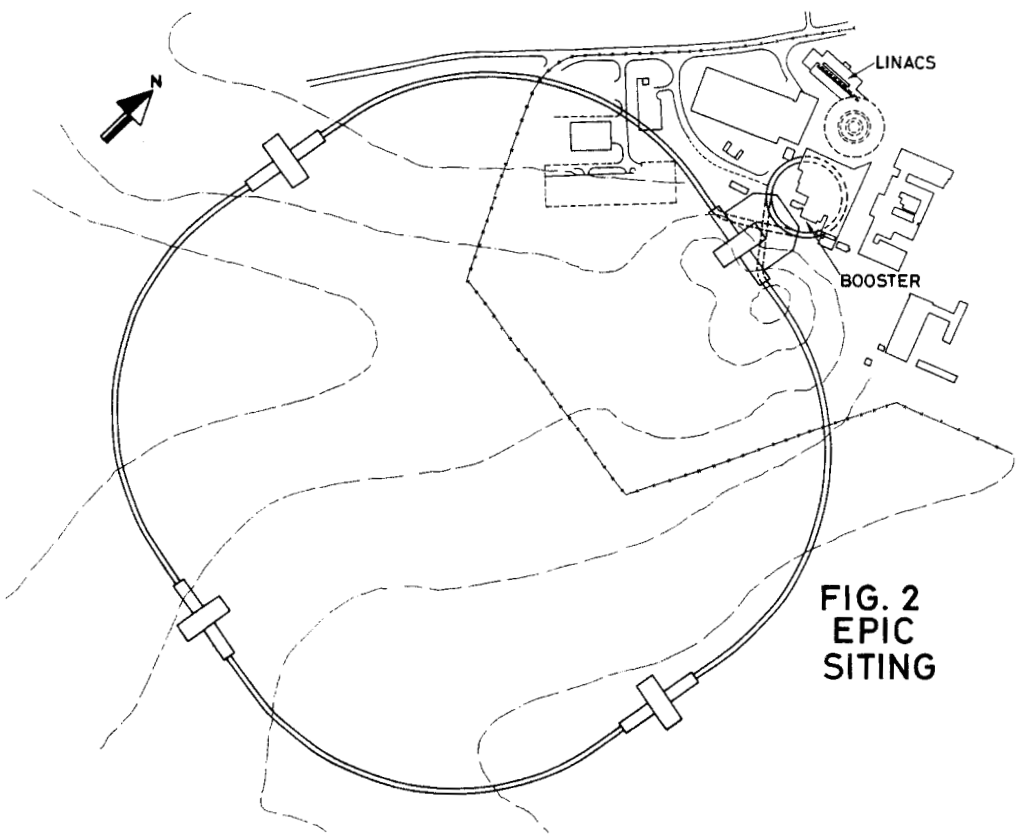


FIG. 2
EPIC
SITING

TABLE 1 - Selected Parameters
(Half-Full S/c Ring for Protons)

Ring circumference (metres)		2122.3	
No. of Interaction Regions		4	
Interaction region lengths (metres)		17.0	
Long st. section lengths (metres)		141.4	
No. of normal magnet cells		56	
No. of dispersion matching sections		8	
Machine tunes, Q		15.1-19.4	
	e-ring		p-ring
Maximum momentum (GeV/c)	14		100
Bending radius (metres)	168.1		74.5
Peak RF Voltage (Megavolts)	42.8		4.0
Peak radiated power (Megawatts)	2.5		0.0
No. of bunches/ beam for e-p	8		8
No. of particles/ bunch for e-p	$5\ 10^{11}$		$7.5\ 10^{11}$
e-p Luminosity ($cm^{-2}\ sec^{-1}$/Xn.)		$\sim 5\ 10^{31}$	
No. of bunches/ beam for e+ - e-	2		
No. of particles/ bunch for e+ - e-	$5\text{-}8\ 10^{11}$		
e+ - e- Luminosity ($cm^{-2}\ sec^{-1}$/Xn.)		$\sim 5\ 10^{31}$	

Preliminary investigation has shown that the vertical bending units may be used as spectrometer magnets for the detection of proton fragments which emerge from the electron-proton interactions at small angles. It is possible to place detection systems behind the common vertical dipoles which are downstream of the collision region for the proton ring. The shaded area of Figure 4 is an acceptance plot for the small angle fragments. The region marked (A) is related to an additional detector array installed normal to the beams at the location (A) of Figure 3. Similarly, (B) is realised by the use of a long septum magnet and further detectors at the corresponding point (B) in this figure. The use of machine components as spectrometer magnets is a feature missing from the PEP[5] and ISABELLE[7] e-p proposals.

A powerful RF accelerating system compensates for the synchrotron radiation energy losses of the electrons (and positrons). This leads to very short bunch lengths. For electron-positron collisions there are two bunches in each beam so that separation of the beams prior to collision is necessary only at the intersection regions. In the case of an electron-proton system there is the choice of using either bunched or unbunched proton beams. Provided that the problem of satisfactory bunch compression can be obtained and sustained for protons there are many advantages for the bunched option. The most important of these is the reduction in the total number of protons, easing the shielding requirements and the protection problems for superconducting magnet rings. In the EPIC design the choice is made of eight proton bunches together with eight electron bunches. The scheme for the required proton bunch compression is described in reference 2, and a method for separating the electrons and protons in the intersection region in reference 8.

Synchronisation is an essential feature of the collisions between bunched electron and proton beams. The increase of proton velocity with energy requires compensating path lengths in the particle orbits. Schemes considered for EPIC include: radial steering of the proton beam together with a number of different vertical 'dog-leg' insertions in the electron ring[9], continuously variable 'dog-leg' insertions[10] and moving the proton high-β quadrupoles to allow the electron energy to be changed at a given proton energy. Synchronisation becomes progressively more difficult at the lower proton energies and in the EPIC feasibility study the lowest proton momentum is restricted to 55 GeV/c.

A modified form of the Daresbury accelerator, NINA, will serve as a booster for EPIC. The combined function magnets are adequate for accelerating particles to a peak momentum of 5 GeV/c. The NINA repetition rate will be reduced from 53 Hz to 4 Hz, and an additional RF system will be installed. During the feasibility study it was considered that the booster could serve as an injector for electrons, positrons and protons. To this end, the gamma transition of the lattice was arranged to assist with proton bunch compression. Now there are reservations that the protons can be accelerated successfully in the presence of the electron RF systems. If a separate booster is developed for protons, it might also cater for deuterons. There is a strong physics case for studying electron-deuteron collisions[11] in EPIC in conjunction with electron-proton studies. However, the entire question of whether or not to use bunched proton beams must be reassessed if there is the additional requirement of providing deuteron beams.

The lattice design of EPIC is influenced by the need to provide an electron-positron radial beam size that satisfies luminosity requirements. It has been found that, to provide adequate values in the e-ring of gamma transition and radial beam size, it is necessary to provide a number of combined function magnets in a predominantly separated-function lattice. In each superperiod, two such units are included amongst the sixty bending magnets. This lattice feature is shown in Figure 6, together with the horizontal dispersion matching sections.

An important consideration for the electron-proton colliding beams is the choice of the radial to vertical beam aspect ratio at the interaction region. The ratio is chosen at four to one. If a choice had been made of a smaller ratio, the vertical magnet apertures would have been undesirably large, particularly as the conventional ring in the feasibility design had to cater for the possibility of storing 80 GeV/c protons in addition to 14 GeV/c electrons. This feature allowed for a possible proton-proton colliding beam option. The effect of horizontal-vertical space charge coupling between the electron and proton beams has not been assessed, but it is realised that this could affect the luminosity estimates. At electron energies below 14 GeV, the natural beam size may be too small, and two possible schemes have been considered to

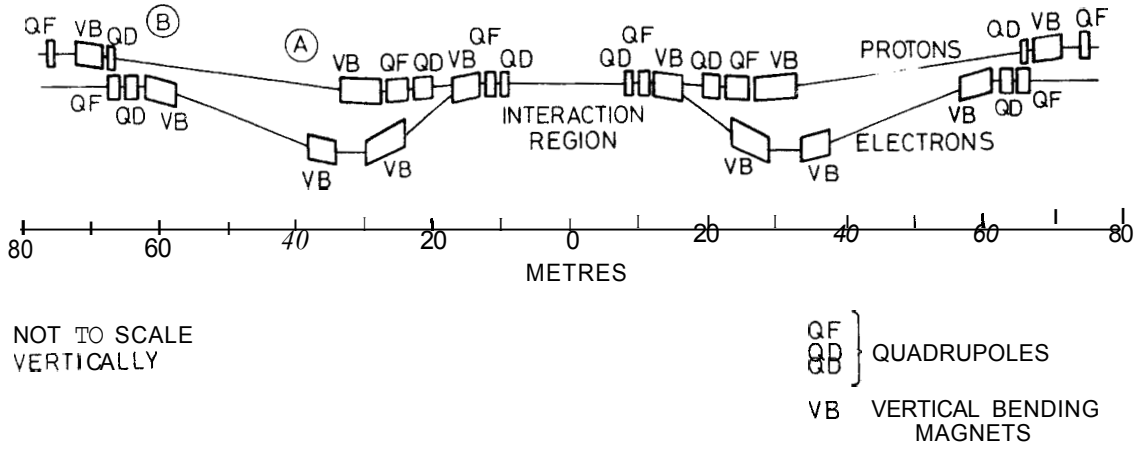


FIG. 3. e – p INTERACTION REGION GEOMETRY

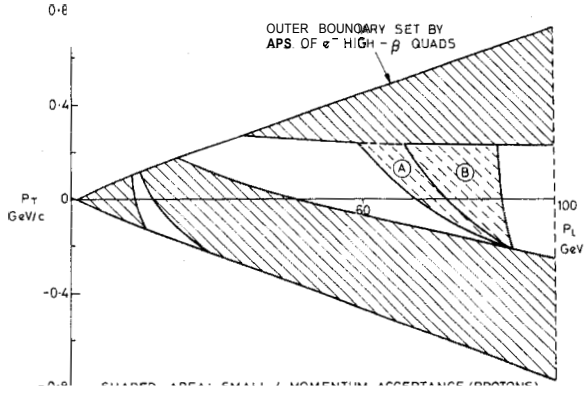


FIG. 4.

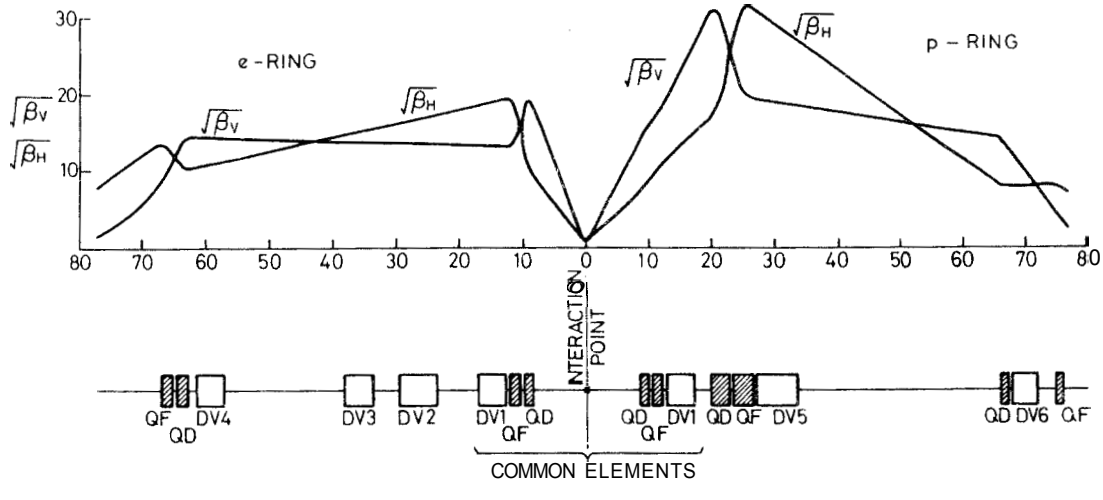


FIG. 5. e – p INSERTION (N.B BOTH RINGS ARE SYMMETRICAL ABOUT THE INTERACTION POINT)

overcome this effect. These include reducing the Q values of the machine and a further adjustment in the radial damping. If satisfactory enhancement is introduced, the luminosity will scale approximately as the product of the energies of the incident particles.

The approximate costings of the various options of the feasibility study are given in Table 2.

TABLE 2 - 1973 Cost Estimates of EPIC Options

Option	Rings	Cost
14 GeV e^+ - e^- Ring	Conventional (C)	£19.6M
14 GeV e- - 80 GeV p	C + C	£35.1M
14 GeV e^- - 100 GeV p	C + Half-Full S/c	£43.7M
14 GeV e^- - 200 GeV p	C + Full S/c	£56.5M

Revised Design of Electron-Positron Ring

The ring circumference has been extended by 3% to provide increased straight section lengths. This will ease the design of a future proton ring in the event that it is built with all conventional magnet units.

The dipole magnets now proposed for the single ring are low field units, and costing is proceeding on the basis of using C-magnets. The open end of the C will face radially inwards to simplify the design of the vacuum system.

The magnet lattice has a high chromaticity as a consequence of the high β-values in the long insertions. The full range of the beam momentum spread is also large to ensure an adequate beam lifetime. To correct for the chromaticity, provision is made in the lattice to include sextupoles near to every quadrupole. Studies of the distribution and strengths of these sextupoles are still continuing and are proving to be a major design problem. Present studies treat the problem in linear approximation, but subsequent studies will include tracking over many machine revolutions.

As in the feasibility study the space between the high-β quadrupoles, which is completely free for experimental equipment, is set at 17 m. This may be revised if necessary as the insertion is longer than is required for the design of the electron-positron ring alone. However, there are restrictions on the maximum allowed β-values in the insertion, and the premium to be paid for increasing the central region is a decrease in the luminosity.

The variable damping feature has been mentioned in the previous section. Referring to Figure 6, the modified damping is introduced by combined-function focussing units, indicated DI/QF. On either side of these units are quadrupoles which may be adjusted to vary the local dispersion while still preserving the dispersion matching. Details of the scheme are given in reference 12. The damping time constant of the horizontal betatron oscillations of the electrons and positrons is given by:

$$T_x = [\, J_x P_\gamma / 2E \,]^{-1}$$

where P_γ is the average rate of synchrotron radiation energy loss, E is the energy of the circulating electrons or positrons and J_x, the partition coefficient, is a function of the magnet lattice. The horizontal beam size varies inversely as the square root of the coefficient, J_x. In a separated-function magnet lattice J_x is approximately equal to 1, while in the EPIC electron-positron ring it is adjusted to be approximately 0.4.

The beam aspect ratio at the interaction region is now under review. Recent studies of the beam-beam interaction for e^+ - e^- collisions indicate that a larger ratio than the previously considered value of four to one might be acceptable. These studies are reported in a subsequent section. The possible advantage for EPIC in increasing the beam aspect ratio is that the maximum horizontal β-value could then be decreased.

The revised ring parameters are given in Table 3. The luminosity will scale as E^2, provided satisfactory beam sizes are obtained by adjustments of machine tune and damping.

TABLE 3 - EPIC Electron-Positron Ring

Ring circumference (m)	2191.6
Long st. section lengths (m)	154.3
Maximum momentum (GeV/c)	14
Injection momentum (GeV/c)	4.8
Range of machine tunes, Q	15 1-19.4
Bending radius (m)	71.9
Max. energy loss/turn (MeV)	19.8
Peak RF Voltage (MV)	30.0
No. of bunches/beam	2
Max. no. of particles/bunch	$8\ 10^{11}$
Peak synch. rad'n. power (MW)	1.39
Rms. mom. spread at 14 GeV/c	$8\ 10^{-4}$
Rms. bunch length (cm)	1.8
Rms. bet. amp. (cm) at β_x = 42 m	0.33
Max. luminosity (cm^{-2} sec^{-1}/Xn.)	$\sim 5\ 10^{31}$

Injection Scheme for Electrons and Positrons

The specification for the total filling time of the EPIC ring is 15 minutes for two bunches of electrons and two bunches of positrons, with the maximum number of particles per bunch set at $8\ 10^{11}$. At the injection momentum of 4.8 GeV/c, the damping time constant of the radial betatron motion is approximately 0.6 sec, so that the maximum rate for filling an individual EPIC bunch is of the order of once per second. Accordingly, if individual bunches are filled in sequence, the repetition rate of the booster injector must be approximately 4 Hz, and the number of particles per booster pulse must be at least 10^9.

The scheme proposed to inject a full booster beam pulse into a single EPIC bunch is the following. The booster accelerates eight bunches, which are subsequently ejected bunch-by-bunch, one after every revolution period of the main ring. There is an interchange of the radial and vertical beam emittances in the transfer line, followed by radial multi-turn injection into EPIC. A requirement for this scheme is that the circumference of the booster is related to that of EPIC by the ratio $8/(2n+1)$, where n is an integer. The chosen value of n is 35.

The straight sections of NINA are increased in length when it is used as a booster for EPIC. The harmonic number, h, of the existing RF system is thus altered, and the ring size is adjusted to make the new value of h equal 336, a number which is

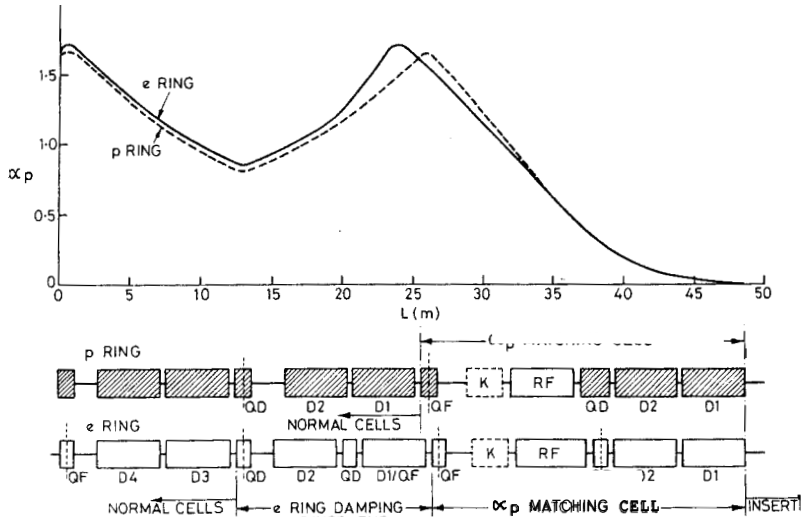


FIG. 6.
e-- p RINGS - α_p MATCHING SECTIONS - e RING DAMPING ADJUSTMENT

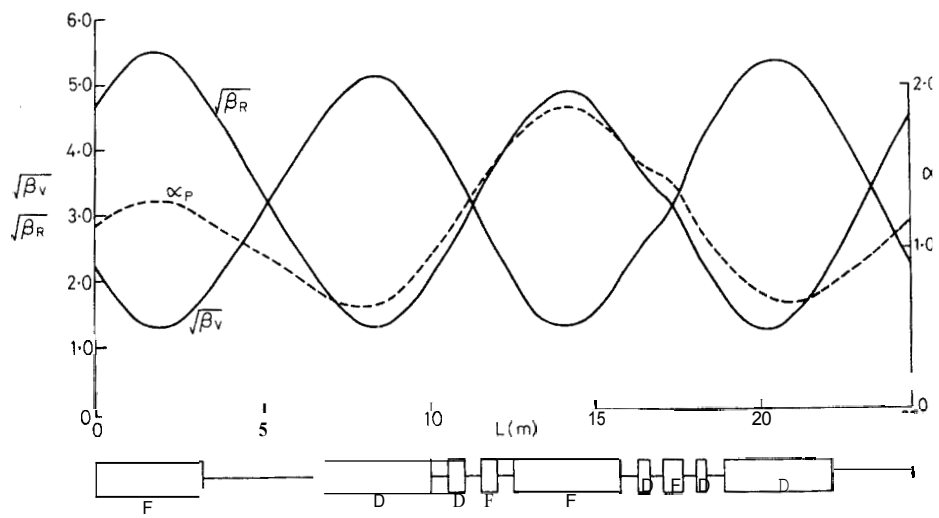


FIG.7. NINA BOOSTER-NORMAL PERIOD

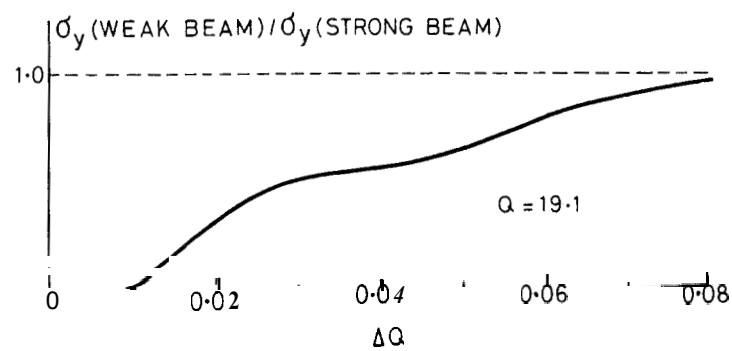


FIG. 8. BEAM-BEAM HORIZONTAL-VERTICAL COUPLING IN EPIC

divisible by 8. A second RF system is installed, with h = 48, to assist in initial trapping and bunch compression.

A further gain in overall capture efficiency is obtained by modulating the gun of the proposed 100 MeV electron linac injector[13]. Modulation at 9.71 MHz, with 10 nanosecond pulse lengths, leads to the filling of the required 8 booster bunches. This proposal is important for obtaining the required fluxes of injected positrons. If the average current in the electron linac is set at 400 mA for positron production, the peak current during the 10 ns pulses becomes 4A. The electron energy at the positron converter will be modulated by more than 10% during the pulse, but the output energy of the subsequent 200 MeV positron linac can be correctly stabilised.

It is planned to reduce the momentum spread of the 200 MeV positrons by means of a debuncher and correcting cavity. A scheme is under study which is similar to the one installed at the 300 MeV electron linac of Mainz University[14]. Studies of trapping in the booster indicate that the input momentum spread should be approximately $\pm$ 3.5 10^{-3}.

The proposed modifications for NINA include a new magnet power supply, the second RF system, new injection and fast extraction systems and the introduction of quadrupole doublets and combined function triplets into the magnet lattice. The lattice design is shown in Figure 7. The doublets introduce a range of Q-tuning, while the triplets provide damping of the horizontal betatron motion of the electrons and positrons. The damping magnets have a D-profile and are arranged to form a triplet of zero total bend by the use of a reversed field in the central unit.

The magnetic field in the booster has a reduced rate of rise at injection, an intermediate flat at a field level corresponding to 2.25 GeV/c and a flat top of approximately 20 ms duration. Trapping, and acceleration to 2.25 GeV/c are undertaken by the lower frequency RF system. During the intermediate flat, the beam damps in phase sufficiently to be captured by the high voltage, high frequency RF system, which then completes acceleration to 4.8 GeV/c. The beam phase is adjusted during the flat top for synchronisation with the EPIC main ring.

Electron-Positron RF System

Design is proceeding on the basis of a peak energy gain per turn in EPIC of 30 MeV, developed in 42 m of accelerating structure. At 14 GeV/c the energy loss per turn in synchrotron radiation is 19.8 MeV. The RF over-voltage provides a beam lifetime of 10^5 s for loss out of the phase stable region due to quantum fluctuation effects.

Beam loading of the RF cavities by the two electron and two positron bunches is being analysed in a manner similar to that proposed by Keil[15]. The tightly bunched beams excite the RF cavities not only at the fundamental resonant mode but also at the higher cavity modes. This is a consequence of having appreciable harmonic components of beam current up to quite high frequencies, together with a close spacing of the harmonics. The amplitude of the harmonics varies as $e^{-(\omega\Delta)^2/2}$, where Δ is the rms bunch duration. The spacing of the harmonics is at twice the bunch repetition frequency. Beam-cavity and beam-equipment interactions will affect the equilibrium bunch lengths and the synchrotron motion, and these effects remain to be determined.

The design of the RF system is thus provisional, and there may be future changes in the choice of RF harmonic number and type of accelerating structure. The present choice of harmonic number is 2944, corresponding to an RF frequency of 402.7 MHz. The proposed standing wave accelerating structure is of the type developed at Los Alamos for LAMPF, but at approximately half the frequency. The inner aperture of the proposed cavity is of diameter 12 cm. The re-entrant nose cones are adjusted to optimise the transit-time corrected shunt impedance (approximately 30 MΩ/m). As discussed in reference 16 there is mechanical complexity in Los Alamos type structures at 400 MHz. The addition of the side-mounted cavities, that give the resonant coupling and $\pi/2$ mode operation, is complicated by the cavity size.

There will be four RF buildings, one associated with each superperiod of the machine. These buildings will provide access for installing and removing ring components. The installed RF power at each building will be approximately 1 MW, CW. The accelerating structure adjacent to an RF building will be subdivided into two sections of approximate length 5 m. The number of feeder points for the 5 m sections will be determined by power characteristics of windows. In the event that the peak energy of the storage ring is subsequently increased, further RF buildings and accelerating structures will be installed.

Normal Cells

Each of the four superperiods contains 14 normal cells which are of a separated-function FODO design of length 24.8 m. Each half-cell contains two dipoles, a quadrupole, a sextupole, a correction dipole and a beam monitor.

The dipoles for the electron-positron ring are 4.5 m long while the quadrupoles are 1.0 m. There is a spacing of 0.4 m between the two dipoles of a half-cell. One section of vacuum chamber extends through the two dipoles, and a shorter section threads through the quadrupole, sextupole and correction dipole. Two pumping ports are included in the longer section, while the shorter section has a length of bellows and a beam monitor. An aluminium chamber is proposed as in the SPEAR design, with the necessary cooling channel along the length of the outer wall. There will be distributed pumps within the vacuum chamber in the dipoles.

Insertions

No vertical bending magnets are required in the insertions of the electron-positron ring. The quadrupoles are arranged as in the electron-proton configuration, Each half of an insertion has a pair of high-β quadrupoles together with a pair of matching quadrupoles. These doublets generate the low-β values at the centre of the insertion and provide betatron motions which are matched to those in the normal cells.

In one of the long insertions there are two injection systems, one for the electrons and one for the positrons. Each system has an injection septum magnet together with upstream and downstream fast kicker magnets.

Other elements contained in the long insertions are the RF systems, electrostatic beam separation plates, correction dipoles, sextupoles, octupoles and skew quadrupoles. The insertion sextupoles will be distributed relative to the chromaticity correction sextupoles so as to minimise third order resonances.

Beam-Beam Computer Simulation

A computer program has been developed that evaluates the motion of a weak beam in the presence of a strong beam for the case of electron-positron beam-beam interactions. The dimensions of the strong beam are assumed fixed, with Gaussian distributions in the two transverse phase planes. Representative particles of the weak-beam are introduced with the same radial distribution as the strong beam but with small initial vertical motions.

The program tracks particles of the weak beam through successive superperiods of the storage ring, assuming no magnet imperfections in the lattice components. For each superperiod transit, estimates are obtained for the radiation damping, the fluctations of the quantum excitations and the linear and non-linear forces of the beam-beam interaction. Random number generators are used to derive the quantum excitation terms. A number of different approximations have been used for the beam-beam space charge forces, but all have given essentially the same results. The possibility is now being considered of extending the program to include the added effects of imperfections in the ring magnets.

Initial tracking studies have been made for EPIC Q values of 19.1. Results are given in Figure 8 for a radial to vertical beam aspect ratio in the strong beam of four to one. The horizontal axis of the graph is the parameter ζ, which is approximately equal to the tune shift per interaction, ΔQ. The radial size of the weak beam remains unchanged, but the vertical dimension grows to reach that of the strong beam for $\Delta Q = 0.08$. Luminosity estimates for EPIC assume ΔQ values of 0.04.

A second set of results has been obtained for the same Q values but with a different beam aspect ratio for the strong beam. The aspect ratio at the collision region has been changed to 16:1 by doubling the radial dimension and halving the vertical. Though σ_y (strong), the rms beam height of the strong beam, is halved, it is found that σ_y (weak) again approaches the value of σ_y (strong) when ΔQ reaches 0.08. It is of interest to note that the beam-beam limits of operating storage rings occur at ΔQ values of this magnitude.

Results have also been obtained for EPIC Q values of 18.1. At this tune, the effect of the linear term in the space charge force is equivalent to reducing the minimum B-function at the point of collision. The simulation becomes approximate and the results difficult to interpret. Preliminary results indicate a reduced vertical growth of the weak beam at the interaction point, but an appreciable vertical size at the high-β quadrupoles.

Summary

The present status of the EPIC machine design has been outlined in this report. By October 1974 an improved cost estimate will be obtained for a 14 GeV electron-positron storage ring. The physics case for EPIC and a machine proposal will then be submitted to the Science Research Council, seeking funds to allow the ring to be built by 1981.

References

1 D A Gray (Editor). Proceeding of the Daresbury-Rutherford Accelerator Working Party, Rutherford Report RHEL.R 252 (1972) p.34.

2 G H Rees. Initial design aspects of storage rings as a possible future UK facility, Rutherford Report DRAG/SR1 (internal note), May 1972.

3 C Pellegrini et al., A high energy proton-electron-positron colliding beam system, Proceedings 8th International Conference on High Energy Accelerators, CERN(1971) p. 153.

4 M R Harold & G H Rees, Some EPIC parameters of interest to experimentalists, EPIC Report EPIC/MC/12 (internal note), March 1973.

5 T Elioff et al., Proton-Electron-Positron Design Study. Proceedings of the 1973 Particle Accelerator Conference, IEEE Trans. Nucl. Sc. NS-20, No.3 1039 (1973).

6 R Bangerter et al., PEP Lattice Design. Proceedings of the 1973 Particle Accelerator Conference, IEEE Trans. Nucl. Sc. NS-20, No. 3 786 (1973).

7 R Chasman & G A Voss. ISABELLE e-p Option. Proceedings of the 1973 Particle Accelerator Conference, IEEE Trans. Nucl. Sc. NS-20, No. 3 777 (1973).

8 J R M Maidment. Beam separation in the EPIC II e-p option. EPIC Report EPIC/MC/30 (internal note), August 1973.

9 G H Rees. Energy variation for e-p collisions in EPIC II. EPIC Report EPIC/MC/18 (internal note), May 1973.

10 J D Lewin. Path length adjustment for energy variations in EPIC. EPIC Report EPIC/MC/22 (internal note), June 1973.

11 P V Landshoff. Some physics questions about deep inelastic e-p. EPIC Report EPIC/WP3/3 (internal note), June 1973.

12 G H Rees. EPIC Updated: variable damping and tunes in the e± ring. EPIC Report EPIC/MC/39 (internal note), January 1974.

13 G Saxon. Injection Schemes for EPIC. EPIC Report EPIC/MC/41 (internal note), January 1974.

14 H Herminghaus & K Kaiser. Design, construction and performance of the energy compressing system of the Mainz 300 MeV electron linac. Nucl. Instr. & Methods, 113, (1973) p.189-194.

15 E Keil. The interaction between tightly bunched beams and RF cavities. CERN/ISR-TH/74-15. March 1974.

16 M A Allen & P B Wilson. Linac type RF structures for high energy storage rings. SLAC-PUB-1142, October 1972.

Phil Morton (SLAC): What is included in your cost estimate—salaries and so forth, or what?

Grahame Rees (Rutherford): No, never include salaries.

Matthew Allen (SLAC): The shunt impedance figures for the cavities seem awfully high. Are you sure of that number?

Rees: We assumed copper cavities, not aluminum cavities, and these were values obtained from Los Alamos type computer programs.

Allen: Losses in the coupling slots will reduce the value below the computed values.

Rees: Perhaps we have been a bit conservative in power estimates because of the large amount we've allowed for power dissipated in the higher modes—we've allowed as much as for the fundamental mode. I agree, we might have to evaluate this.

Ednor Rowe (University of Wisconsin): What fraction of the Dower loss due to svnchrotron radiation occurs in the dog legs in the interaction region?

Rees: About **30** - 40% at top energy.

Ernest Michaelis (CERN): Do you plan to vary the proton energy or is it fixed?

Rees: The usual way we thought to change energy would be to keep the ratio of electron and proton momenta constant so that the particles always come out of the vertical bending magnets at the same angle. We also thought it desirable to change the energies of the beams independently. This would be quite difficult in our design because one then has to change the position of the proton quadrupoles. But since the displacements required aren't large, this could be set up before a run at a given energy.

Melvin Month (BNL): You said that the synchrotron frequency goes up to a dangerous level if the tune drops below 15. Could you explain that statement?

Rees: Synchrotron frequencies are reaching 10% of the revolution frequency which has always been considered an undesirably high value. So we will have to look seriously at betatron-synchrotron coupling at modes higher than this.

THE PROTON-ELECTRON-POSITRON PROJECT - PEP*

L. Smith

LBL-SLAC Joint Study Group
Berkeley and Stanford, California

Introduction

In the summer of 1971, a group of physicists at LBL and SLAC, including visitors from CERN and Frascati, made an inquiry into the feasibility of a new colliding beam complex capable of producing collisions at higher energies than hitherto envisaged between electrons and positrons and also between electrons and protons and positrons and protons. They concluded that such a facility, which would consist of an electron storage ring and a proton storage ring, was quite possible and that no known physical limitation of the behavior of stored beams would prevent the achievement of luminosities sufficient to yield useful reaction rates for many important high-energy interactions. To illustrate these conclu ions, a conceptual design was described and analyzed.[1] The physics importance was later forcefully emphasized by an LBL-SLAC Physics Study Group.[2]

Subsequently, the collaborative study between LBL and SLAC grew, involving more people as the concepts and designs became more refined. A combination of a 15 GeV electron-positron ring and a 200 GeV superconducting proton ring, referred to as PEP, emerged as the preferred design. In the meantime, other laboratories began studying similar or related ideas in both the U. S. and Europe and their representatives came together at SLAC and LBL in the summer of 1973 to exchange ideas and work on common problems. By the end of 1973, a version of PEP suitable for location on the SLAC site had been developed and the two laboratories entered into a formal agreement to jointly propose and construct the electron-positron portion of the system, in a manner compatible with the subsequent addition of the proton ring to achieve the full PEP capability. This paper will describe the full PEP complex as presently visualized; the accompanying paper by John Rees[3] will describe the specific electron-positron system for which a formal proposal for construction is presently being submitted.

physics Potential

For electron-proton collisions with the maximum energies of the preferred design, the center-of-mass energy is 110 GeV which is the same as that which would be available with a 6000 GeV beam from a conventional accelerator incident on a stationary hydrogen target (there is no economically feasible way of reaching these energies with a conventional accelerator). The facilities of the present proposal are designed to be compatible with this addition. The future electron-proton system, together with the presently proposed electron-positron system, would comprise a total facility of unique capability for particle physics research which is briefly outlined below.

(a) Deep Inelastic Lepton Scattering ($e^-(e^+)p \rightarrow e\text{-}(e^+) + \text{hadrons}$)

Inelastic electron-proton scattering plays an essential and unique role in the investigation of the structure of the hadrons. The known electromagnetic field generated by the scattered electron interacts with the local electromagnetic current of the proton and thus can probe the structure of the nucleon at arbitrarily small distances. This local interaction is in sharp contrast to hadron-hadron scattering in which the basic interaction between the particles is more complex. By varying the energy and angle of the scattered electron it is possible to "tune" or vary the virtual photon's mass Q^2 over a large range. In particular, it is possible to achieve virtual photon masses whose square is negative and whose magnitude is much greater than the proton mass and therefore allows for collisions in an asymptotic region not available in accelerators using a fixed mass projectile.

Experiments on inelastic scattering at SLAC, where both the mass and energy of the virtual photon are large, have yielded profound and unexpected results. These results show that the cross sections do not depend independently on both the mass and energy of the photon, but instead on their ratio. This "scaling" behavior has led to major new concepts in our understanding of hadronic structure in terms of a possible substructure within the hadron that is composed of point-like constituents (partons). The greatly enhanced center-of-mass energy of a PEP facility would extend the measurements of deep inelastic scattering far into the unknown region. With the example parameters used here the virtual photon energy would reach to 6000 GeV and its mass to 110 GeV compared to an energy of 20 GeV and a mass of 5 GeV at the present SLAC frontier.

Confirmation of the scaling behavior at these larger values of energy and mass would give support to these new ideas while observation of violations of scaling would indicate a new energy scale for hadronic phenomena perhaps associated with the production of new particles and of a "size" for the constituents themselves. This point is emphasized by the surprising results of the recent SPEAR experiments in the time-like region which do not support these ideas of the quark-parton model, and in this respect make the further study of the inelastic electron reactions even more intriguing. Other general and fundamental features to be studied for large photon masses include the applicability of Regge theory analyses, the validity of sum rules based on current algebra, and the "fragmentation" of very massive virtual photons into jets of secondary hadrons.

Besides the electromagnetic inelastic electron scattering, it will. be possible to observe the effects caused by weak neutral current of the type discovered in the recent CERN and NAL neutrino experiments. The effects of the neutral current would be observable as parity violations, charge conjugation violation, and possibly electromagnetic scaling violations. Since both energy and momentum transfer are easily determined, detailed knowledge as to the nature of these neutral current effects will be possible.

Thus, this unique feature of a PEP facility, the study of deep inelastic scattering, will yield results on one of the most significant problems in particle physics.

* Work supported by the U. S. Atomic Energy Commission.

(b) Weak Interactions ($ep \rightarrow \nu_e$ + hadrons)

If the scaling phenomena observed in deep inelastic scattering is assumed to hold also for the weak interactions, as would be implied at least in part by the conserved vector current (CVC) idea, then with the Fermi theory one is led to the conjecture that the total weak interaction cross section will continue to grow quadratically with the center-of-mass energy. This has the startling consequence that at energies in the PEP region the weak interactions with their inherent violation of parity and strangeness would have grown in strength to be comparable to the electromagnetic interactions. In fact in the region of the largest momentum transfer accessible for the particular example of PEP parameters used in this study, the scaling hypothesis indicates that the deep inelastic electromagnetic cross section is smaller than the weak process.

Experiments with PEP will show either that the weak interaction is no longer "weak" or that the Fermi theory in its simple form breaks down. The discovery of a failure in the Fermi theory would in itself be of the first magnitude in importance; additionally one could then entertain hopes of discovering the mechanism of breakdown. If a W boson, for example, were the source of a major failure of Fermi theory, its mass might be sufficiently low ($\approx$ 30 GeV) that W particles could be produced by PEP.

Thus, the exploration of weak interactions at PEP energies will present some of the most exciting possibilities for new discoveries. Information from experiments in this area could lead also to unifying principles for the basic forms of elementary particle interactions.

General Description

The goal of PEP is to provide collisions at energies ranging from 30 to 110 GeV in center-of-mass energy for electrons and protons, and from 10 to 30 GeV for electrons and positrons. A luminosity of 10^{32} $cm^{-2}sec^{-1}$ at the top energies, to be achieved simultaneously at a number of interaction points, is deemed adequate to support a vigorous and varied experimental program in both e-p and e^+e^- physics. In order to achieve that luminosity with a relatively modest number of stored particles, we have chosen to use bunched beams in head-on collision. The head-on collision scheme appears also to be more advantageous for experimental detectors as well as affording a greater simplicity in the insertion structure. We have furthermore adopted a six sided configuration, which provides five areas for physics experiments and one for accelerator physics investigations and monitoring.

The geometrical configuration of the two rings is shown schematically in Fig. 1. The six collision points are at the centers of 20 meter long straight sections at each crossing of the rings. The electron ring is placed alternately above and below the plane of the proton ring; this pattern eliminates vertical dispersion in the circular portions of the electron ring, and the attendant and undesirable quantum-excitation contribution to vertical emittance, and eliminates the need for a series of quadrupoles in the sloping sections (see Fig. 2) of the electron ring. As a result, the required insertions are shortened, overcrowding of magnet elements is avoided, and the electron path length can be varied in these sections to provide synchronization with the protons over the projected range of proton energies (50 to 200 GeV).

The circular arcs of both rings are made up of 48 conventional FODO cells (8 per sextant) operating at a nominal phase advance of about 90° per cell at maximum beam energies. In addition to insuring positive damping for the electrons, the separated function scheme simplifies the design of the super-conducting magnets in the proton ring and, in both rings, permits a wide range of focusing conditions useful for controlling beam size. To achieve matching between cells and insertions for the variety of conditions required in the interaction region, the quadrupoles in the insertions, the normal cells, and in the two cells on each side of each insertion are independently controlled.

The insertions, as presently conceived, are shown in Fig. 2, along with the adjacent cells. Starting from the interaction point, both beams go through the doublet, $Q_{1,2}$, which consists of conventional steel quadrupoles and which is strong enough to focus the electrons and/or positrons, but has little effect on the protons. The bending magnet, B_1, also conventional, serves to separate the two beams, deflecting the light particles toward the elevation of their next sextant. The small deflection given to the protons is compensated by three vertical bending magnets ($B_{2,3,4}$), which restore the protons to the median plane. The angle of deflection provided by B_1 is adjustable to permit the variation in total circumference of the electron ring needed for synchronization at different proton energies. On the basis of single particle beam dynamics, the subsequent bending magnets in the electron line could be wide aperture magnets fixed permanently in position. However, the electro-magnetic fields generated by a high-intensity beam in such a vacuum chamber configuration might make that scheme infeasible, in which case it would be necessary to move magnets or the vacuum chamber in this region when the proton energy is to be changed.

In the proton line, the doublet, $Q_{3,4}$, consists of super-conducting quadrupoles which focus the protons. Beyond $Q_{3,4}$ is a 28 meter long straight section; these straight sections, twelve in all, will be used to accommodate rf systems, injection hardware and other beam components. The twelve 20 meter long straight sections directly above or below in the electron ring will serve the same purposes for the light particles.

The choice of 20 meters free space around the interaction point represents a compromise between the desire for as much room as possible for experimental equipment and the machine physics requirement that β_{max} should be as small as possible because of aperture, chromaticity, and tolerance considerations. It appears that the straight section space assigned to major accelerator hardware is more than adequate; if this is really the case, one or more of the insertions could be modified to meet particular experimental requirements by extending the interaction region at the expense of the adjoining 28 and 20 meter straight sections. The vertical separation of 80 centimeters between the two rings appears to be adequate to accommodate the necessary equipment in both rings. The tunnel size adopted for the Stage I proposal[4] would permit the further addition of another electron ring, a feature which might prove to be extremely valuable in light of the fact that current experimental results are indicating that electron-electron collisions at high energy would yield significant additional information. A second electron ring would also make it possible to achieve higher luminosities for the e^+e^- system at lower energies by permitting an increased number of bunches.

Figure 3 shows an overall view of the rings on the SLAC site. We include it here only to give a general impression, since it is, of course, identical to the layout proposed for Stage I and will be discussed in detail in the following paper. Figure 4 shows tunnel cross sections in alternate sextants of the ring.

Operating Parameters

Tables I and II give the lattice parameters and typical operating parameters. Figures 5 and 6 show the betatron and off-momentum functions for the high energy mode of Table II. In contrast to an electron-positron system, in which emittances are determined by the Lattice configuration and particle energy (and the limitations on performance imposed by the beam-beam interaction are known empirically, if not understood theoretically), one must make assumptions concerning the behavior of protons in order to arrive at a set of operating parameters for an electron-proton system. Regarding emittances, there is sufficient experience with high energy accelerators to provide reasonable figures, but regarding the beam-beam effect, there is as yet no indication of the ultimate limitations. We must assume, however, that protons are subject to the same harmful effect, and, in the absence of radiation damping, are probably more sensitive than are electrons. We have therefore taken as design criteria that the linear beam-beam tune shift should not exceed 0.05 for the electrons (based on actual experience) or 0.005 for protons, the latter figure having also some justification on theoretical grounds.

The performance is then limited by this criterion, as in well-designed electron rings, and the interaction point parameters are determined by maximizing luminosity consistent with the above tune shifts while minimizing β_{max}, chromaticity, and restricting the total number of particles used. The number of protons required (3.6×10^{13}) is small compared to the number stored in the ISR (6×10^{14}), but it should be remembered that in our case they must be accelerated from a low energy and collected into short bunches. Thus, the intensity achieved at Brookhaven (10^{13}) and the design goal at Batavia (5×10^{13}) are better standards for comparison.

The assumed transverse emittances are somewhat larger than those achieved in existing synchrotrons, but here again the beam-beam limit precludes any advantage in striving for greater brightness.

The chromaticity is sufficiently low that it can be controlled by using two sextupoles in each of the FODO cells in both sings. This distribution is smooth enough to eliminate serious nonlinear resonances near the chosen working points while providing necessary control over head-tail instabilities.

Injection, Acceleration, and Bunching

The electrons or positrons would be handled in the same way as in Stage I, as described in the next paper. It should be noted that the vertical bends required to separate the rings in the full PEP configuration cause an increase in synchrotron radiation, so that, for the full configuration more rf power will be required.

For the protons, the procedure is more complicated. Referring to Table II, 24 bunches, each with 1.5×10^{12} protons, are required. The present concept is to accelerate 1.5×10^{12} protons first to about 5 GeV in a small proton synchrotron located, possibly, at the present SPEAR site, and then transfer them by single turn extraction to an existing bucket at the 96th harmonic in the PEP proton ring. This process would be repeated 24 times, filling every fourth bucket in the main ring. The protons would then be accelerated to the appropriate energy and the rf voltage increased until the bunches are short enough to fit into buckets at four times higher frequency (h = 384, f = 53 MHz). At this frequency, the voltage would be raised to compress the bunches to the desired length. Assuming a longitudinal emittance of 10π cm in ($\Delta\$ /, \Delta z$) units, the final voltage would be about 6 MeV/turn for σ_ℓ = 25 cm.

Since this value of σ_ℓ is much less than the minimum-β values for the protons, the luminosity is not sensitive to proton bunch length but, unfortunately, the beam-beam tune shifts are sensitive since the electrons or positrons may encounter protons in regions of higher electron-ring-β if the proton bunches are longer. The voltage needed in the proton ring depends strongly on both longitudinal emittance and required bunch length; a final choice of voltage will require careful consideration of achievable emittance and the parametric dependence of the beam-beam effect.

After the proton bunches are formed, the electrons would be introduced into their ring already synchronized in azimuth and perhaps separated laterally in order to prevent particles from meeting each other except at low-β points. How long this situation can be maintained for experiments is difficult to predict for the electron-proton system, but judging from electron ring experience, we anticipate a need to refill every few hours. The remaining protons would be decelerated as far as possible and then dumped.

Machine Components

The electron-ring system would differ very little from that described in the next paper. The proton ring would have a number of unique features, some of which are described. below.

(a) Superconducting Magnet System

The magnet design incorporates intrinsically stable, fine filament, NbTi super-conductor. Cross sections of the magnets are shown in Fig. 7. The ultra-high vacuum region is enclosed by a nonmagnetic beam tube, upon which the multi-layered coil is wound. Circular symmetry is used in all inner regions to yield the best structural and magnetic properties.

The cryostat is continuous through a half-sextant of the ring with surrounding evacuated thermal insulation, an 80° temperature shield, and finally a room-temperature vessel. Helium at 4.4°K is introduced at the center of a sextant and forced in both directions to the ends, from whence it flows back at reduced temperature and pressure in the outer annular region of the cry stat, acting as a counter-flaw heat exchanger.? The only additional element in the tunnel is the transfer line from the surface, where the rest of the refrigeration equipment is housed. This scheme minimizes interference between refrigeration components and tunnel hardware, particularly with experimental apparatus near the interaction region.

The heat leak at 4.4°K is assumed to be 1.2W/meter, and that from room temperature to 80% is taken to be 2.5W/meter. Allowance is made for two pairs of electrical leads for the dipoles, six for the quadrupoles and, in addition, for quench leads and auxiliary beam equipment. The additional heat load due to eddy current heating and beam induced currents appears to be much less. The total load at 4.4°K is about 1500W per

sextant, requiring some 600 kW of installed power capacity at each of the six stations. The magnet power supply circuit would parallel the refrigeration system.

(b) Vacuum System in the Proton Ring

Much attention has been given in the recent past to the question of warm-bore versus cold-bore vacuum systems. A cold-bore system has many attractive features--continuous cryo-pumping surfaces, no need for baking, simple design and minimal running cost, for example. On the other hand, desorption coefficients as high as 10^5 from cold surfaces have been reported, which raises the possibility of a run-away phenomenon similar to that which has affected operation of the ISR. Analyses of cryo-systems carried out independently at LBL and Rutherford indicate that pumping speed is probably adequate to maintain good vacuum and so we have tentatively chosen to follow the cold-bore route for the proton ring. In the neighborhood of the interaction regions the pumping capacity would probably have to be increased, perhaps by a permanent electro-deposit of porous silver or by a replaceable condensation of CO_2. Gas loads that could enter from the electron ring or pass from the straight sections into magnet sections can be intercepted by short lengths of tubular cryo-pumps that are easily cycled.

(c) Radio-Frequency Systems

Because of the limited vertical clearance, special problems arise in designing the rf systems. In the electron ring, fortunately, a cost optimization study leads to a choice of about 350 MHz for the frequency, and, as a result, the cavities are small enough to clear the proton ring. In the proton ring, the frequencies of the accelerating and bunching systems are 13 and 53 MHz, respectively, the bunching frequency being determined by requiring that the final desired bunch length should occupy about one-fourth of the bucket length. It is visualized to use a single set of structures in the proton *ring* for both modes; it would consist of a number of tubes which would act as frequency modulated drift tubes during acceleration and initial bunching and as half wave transmission lines at the higher frequency. The requirement of 6 MeV/turn could be met by using 17 tubes, occupying a total length of 50 meters and consuming about 2 MW of parer in the CW mode. They would be located in two of the 28 meter straight sections, separated in azimuth from the electron rf straight sections.

Conclusion

The design presented in this paper is subject to further modification and optimization. The procedure has been to evolve a conceptual design on which to base the Stage I proposal, and to consider detailed design of the final PEP complex only to the point of satisfaction that the two are indeed compatible. An obvious next step is to demonstrate the feasibility of a superconducting accelerator and storage ring; the LBL project, ESCAR,[6] is directed toward that end, including also the development of a suitable vacuum system. There are numerous questions in beam dynamics, particularly in the area of collective effects, which require additional study before we can feel confident that the operating specifications can be realized. This work will continue in parallel with the detailed work required for the construction of Stage I.

It is believed that the total PEP complex will provide one of the most important facilities for future research in high energy particle physics. In addition to the extremely important physics results[3] expected from the electron-positron collisons, the provision for electron (or positron) collisions with protons, outlined here, will permit an enormous extension of parameters in traditional electron machine experiments (inelastic electron scattering, photoproduction, etc.,), and in addition will open the field of weak interactions to practical experimentation with a well-understood, well-controlled probe--the electron.

Acknowledgment

The work reported here is that of the members of the LBL-SLAC Joint Study Group. The author is their spokesman.

References

1. C. Pellegrini, J. Rees, B. Richter, M. Schwartz, D. Möhl, and A. Sessler, Proceedings of the VIII International Conference on High Energy Accelerators, CERN, 1971, p. 153.

2. Particle physics with Positron-Electron-Proton Colliding Beams, LBL-SLAC Study Group, LBL-750 or SLAC-146, April 1972.

3. J. Rees, The PEP Electron-Positron Ring, Proceedings of the IX International Conference on High Energy Accelerators, Stanford, May 1974.

4. A Prooosal for a Positron-Electron Colliding Beam Storage Ring Project, SLAC-LBL Joint Study Group, April 1974.

5. Refrigeration System for the NAL Energy Doubles, Cryogenic Consultants Incorporated, April 26, 1973 (unpublished).

6. T. Elioff, et al., Experimental Superconducting Accelerator Ring (ESCAR), Proceedings of the IX International Conference on High Energy Accelerators, Stanford, May 1974.

TABLE I

Lattice Parameters

Average Radius	R	345		m.
Number Of Interactlon Points	N_I	6		
Radius of Circular Sextant	R_n	220		m.
Straight Insertion Length	L_s	130.5		m.
Interaction Region Free Space	L_I	20		m.
Vertical Separatlon of Rings	h	0.8		m.
Number Of Cells	N_c	48		
Cell Length	L_c	28.8		m.
		Protons	Electrons	
Dipole Length	ℓ_d	4.96	5.56	m.
Quadrupole Length	ℓ	1.20	0.78	m.
Dipole Peak Field	B_o	44	2.94	kG
Quadrupole Peak Gradient	$\lvert B'_o \rvert$	560	55.4	kG/m.

TABLE II

Operating Parameters

		High-Energy Mode		Low-Energy Mode		
		Proton	Electron	Proton	Electron	
Momentum	P	200	15	50	5	GeV/C
Number of Particles	$10^{-13}N$	3.6	0.7	3.6	1.06	
Number of Bunches	n_B	24	24	40	48	
Beam Power Radiated	P_B	--	4.9	--	2	MW
Luminosity/crossing	$\mathcal{L}$			2.1×10^{31}		$cm^{-2}s^{-1}$
Momentum Width = $\left(\frac{\Delta p}{p}\right)_{rms}$	σ	.047	.094	.188	.031	%
Bunch Length (rms)	σ_ℓ	25	2.6	25	2.6	cm
Interaction Point:						
rms beam width	σ_x^*	.064	.067	.128	.117	cm
rms beam height	σ_y^*	.021	.012	.043	.021	cm
β-function horizontal	β_x^*	3.25	1.05	3.3	3.2	m
β-function vertical	β_y^*	1.42	0.34	1.45	1.05	m
Dispersion	$\eta_x^* = \eta_y^*$	0	0	0	0	
Normalized Emittance (95% beam)						
Horizontal	$\beta\gamma\epsilon_x/\pi$	.016	7.52	.016	2.51	cm-rad
Vertical	$\beta\gamma\epsilon_y/\pi$	.004	.752	.004	.251	cm-rad
Beam-Beam Tune Shift						
Horizontal	$\Delta\nu_x$	.002	.045	.002	.050	
Vertical	$\Delta\nu_y$	.005	.049	.005	.050	
Betratron Function (Max)	β_{max}	771	352	750	100	m
Chromaticity	$\xi = -\left(\frac{p}{\nu}\right)\left(\frac{d\nu}{dp}\right)$					
Horizontal	ξ_x	4.1	3.8	4	4	
Vertical	ξ_y	3.7	5.0	4	4	
Betatron Tune	$\nu_x = \nu$	15.75	15.75	15.75	12.75	
Dipole Field (Cells)	B_0	44.0	2.94	11.0	.98	kG
Quadrupole Gradient (Cells)	$\lvert B'_0 \rvert$	560	55.4	140	15.0	kG/m
Transition Energy	γ_T	14.5	13.2	14.5	10	

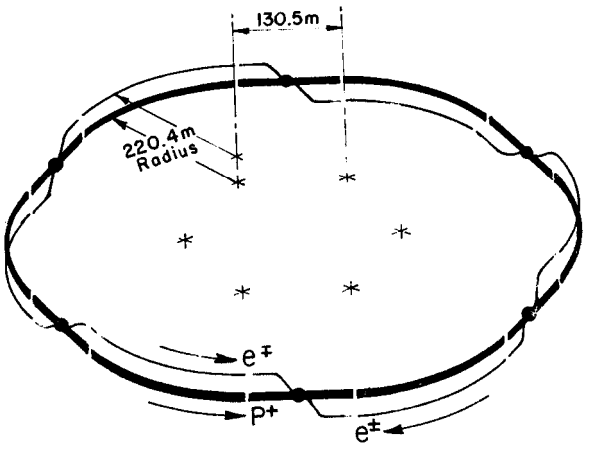


Fig. 1. PEP schematic.

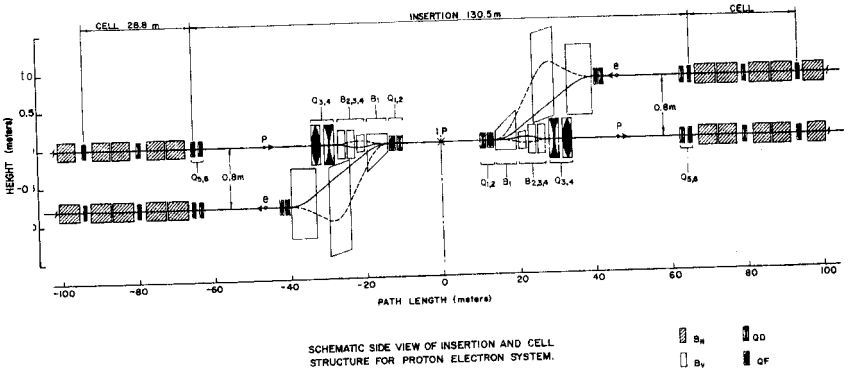


Fig. 2. Schematic side view of insertion and cell structure for proton electron system.

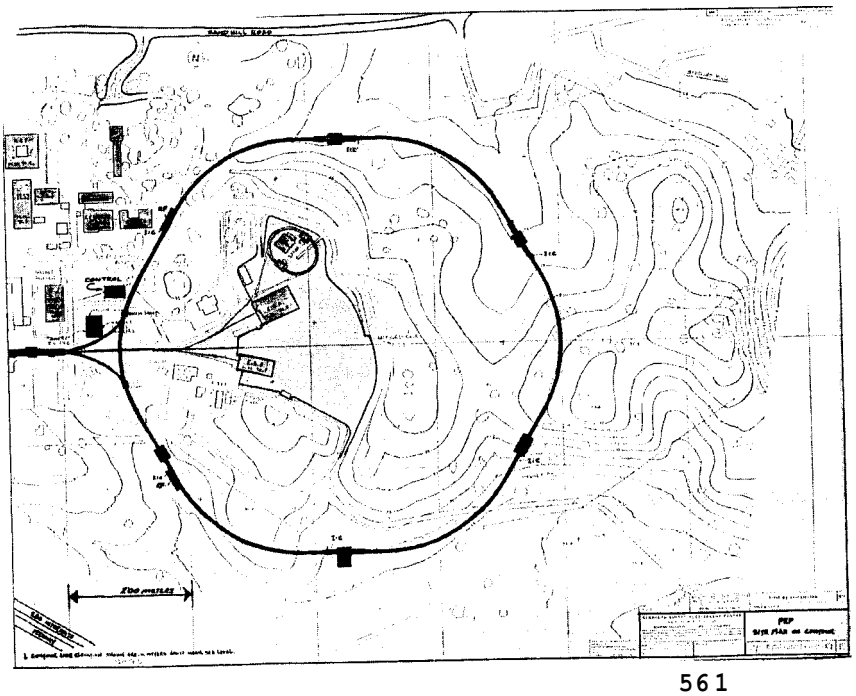


Fig. 3. Aerial view of SLAC site.

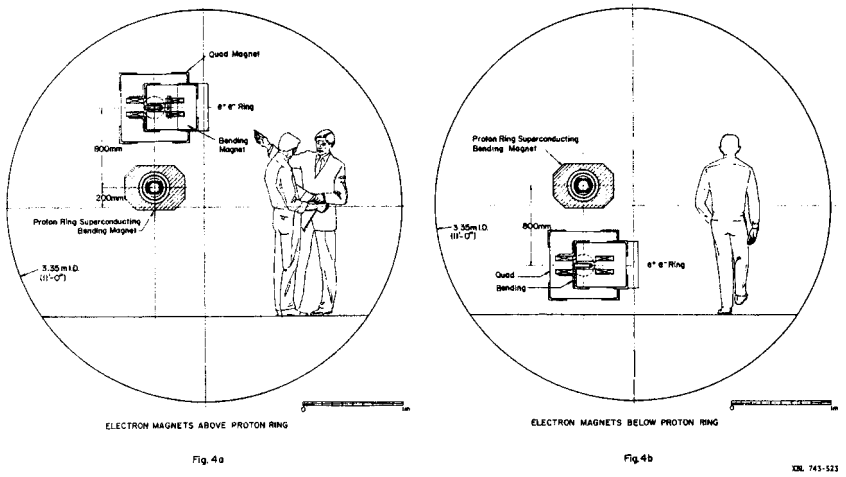


Fig. 4. Tunnel cross sections.

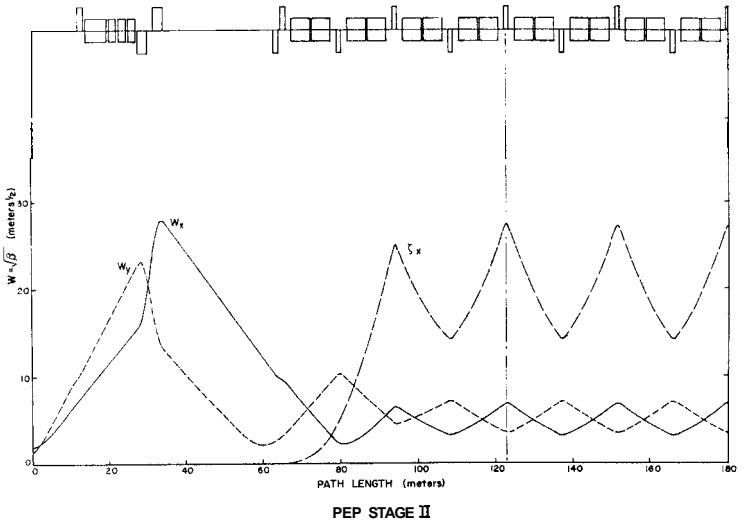


Fig. 5. Proton betatron functions through half sextant.

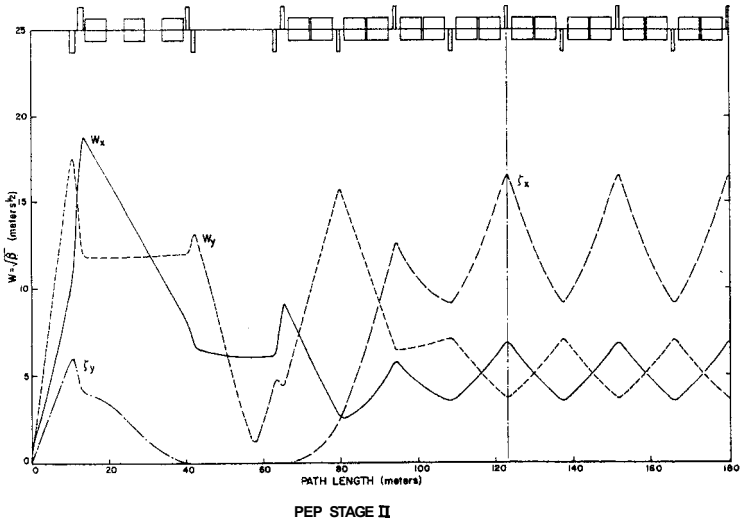
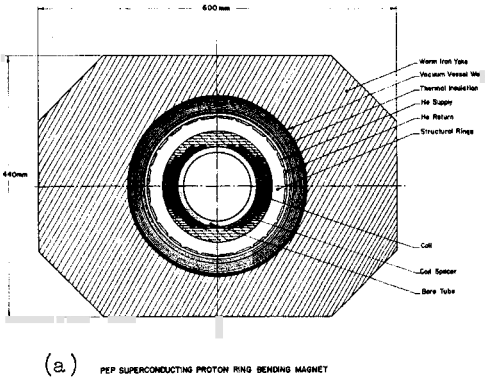


Fig. 6. Electron betatron functions through half sextant.



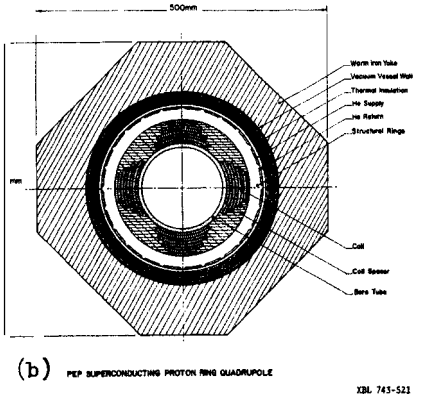


Fig. 7. (a) PEP superconducting proton ring bending magnet.
(b) PEP superconducting proton ring quadrupole.

Alessandro Ruggiero **(NAL):** Do you have any idea of the stability of a bunched proton beam at this current level and would you expect bunch lengthening phenomena?

Lloyd Smith (LBL): We don't know. This is an example for the reasons why we wanted to put off the proton part of this proposal for some time. There are many things of this nature that have to be understood. I think it was quite clear from some of the talks given yesterday that we will have to be extremely careful about the environment and coupling impedances. All this remains to be worked out.

Lee Teng (NAL): I have two questions about the general ring geometry. First, I noticed that you crossed over on the inside for electron-positron injection and, second, your straight sections are quite a bit shorter than those in other devices, especially for 20-GeV protons.

Smith: The short straight sections follow directly from the cross-over feature. It's one virtue of this design that we can get rid of a lot of magnets in that region, leading to a shortening of that insertion. About the first subject, John Rees will talk.

John Rees (SLAC): I'd like to answer it now. The injection as done in most electron-positron storage rings places some very tender elements at the mercy of synchrotron radiation and cooling is the outstanding problem. It is completely solved by injecting from the inside. The arrangement of the beam crossing over or under and then bringing it in parallel is a straightforward mechanical problem.

David Gray (Rutherford): What energy variation are you allowing in the e-p mode of operation?

Smith: You saw the two extreme cases in the so-called typical operating parameters 15 on 200 and 5 on 50 GeV.

Gray: Can you match the circulation times over that energy range?

Smith: Yes, that's pretty much what determines the range. In the insertion, there is actually a loop up and back to push it as far as possible.

Darrell Drickey **(UCLA):** Isn't it, in principle, possible to increase luminosity by going, for example, to 5 on 200 GeV?

Smith: It's quite possible. I emphasize again that the operating parameters would actually run over a whole range. I might say that because protons and electrons behave differently, it is not possible to construct simple scaling laws as in electron rings and the mentioned energies represent the best combinations we could come up with, again blaming the $\Delta\nu$ being independent of gamma.

THE PEP ELECTRON-POSITRON RING -- PEP STAGE I*

J. R. Rees
LBL-SLAC Joint Study Group
Berkeley and Stanford, California

Summary

The first stage of the positron-electron-proton (PEP) colliding-beam system which has been under joint study by a Lawrence Berkeley Laboratory-Stanford Linear Accelerator Center team for the past two years, will be the electron-positron storage ring. The physics justification for the e^+e^- ring is summarized briefly and the proposed facility is described. The ring will have six arcs having gross radii of about 220 m and six interaction regions located at the centers of straight sections about 130 m long. The longitudinal distance left free for experimental apparatus around the interaction regions will be 20 m. The range of operating beam energies will be from 5 GeV to 15 GeV. The design luminosity at 15 GeV will be $10^{32}cm^{-2}s^{-1}$, and the luminosity will vary approximately as the square of the beam energy. Alternative methods under consideration for adjusting the beam cross-section are discussed. The designs of the storage ring subsystems and of the conventional facilities including the experimental halls at the interaction regions are described.

1. Introduction

In the preceeding report presented to this Conference by L. Smith, the evolution of the PEP system was described.[1] In the autumn of 1973, following the 1973 PEP Summer Study, the two cooperating laboratories, LBL and SLAC, reached the conclusion that the electron-positron storage ring component of the system, operated at beam energies up to 15 to 20 GeV and capable of yielding high luminosity in electron-positron collisions, was a straightforward extension of techniques already successfully used in several laboratories and that such a ring could be designed and built immediately with confidence. For the proton ring, superconducting-magnet technology offered the promise of achieving high beam energy with economical size and with low power consumption; however, there appeared to be some technical uncertainties yet to be resolved. In the meantime electron-positron rings operating in Europe and the U.S. had revealed that a wealth of new and previously unexpected high-energy physics information concerning the structure of elementary particles, both leptons and hadrons, was forthcoming from electron-positron collisions. These experiments suggested that it was urgent to move on higher energies than those available from existing machines.

With these facts in mind, LBL and SLAC jointly decided to propose the immediate design and construction of the 15-GeV electron-positron storage ring, PEP Stage I, and to defer the proposal of the proton storage ring until further development of superconducting technology had taken place. The two laboratories agreed to locate PEP at SLAC and to design the electron-positron ring and its housing to be compatible with the future addition of a 200-GeV proton ring such as that described in the preceding paper.[1] The two universities signed an agreement in February, 1974, outlining joint financial and management arrangements for the project.

The main component of the proposed facility is an electron-positron storage ring having six bending arcs and six long straight sections. The major diameter of the ring is about 700 m and the radius of the arcs is about 220 m. The facility is shown in Fig. 1. The electrons and uositrons are produced in the SLAC linac and introduced into the storage ring via two beam transport paths emanating from the end of the two-mile

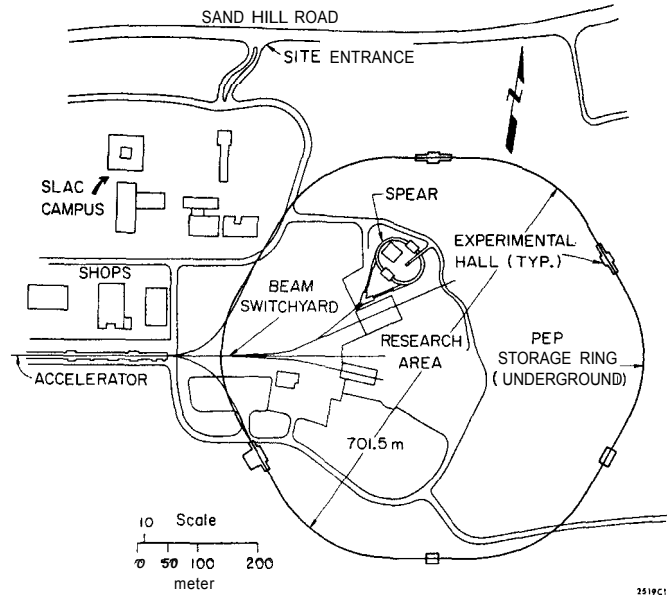


Fig. 1. Layout of the PEP ring superimposed on an aerial view of the SLAC site.

accelerator and joining the storage ring in the northwest and southwest straight sections. Beam of energies up to 15 GeV can be injected and stored, and, at a future date, components could be added to permit stored-beam energies as high as 20 GeV. Also provisions are made in the design of the ring housing so that a synchrotron-radiation research facility could be added in the future.

The energy lost from the beams by synchrotron radiation is restored by a high-power radiofrequency accelerating system which employs klystrons to drive the accelerating structure at a frequency of about 360 MHz and which is capable of delivering several megawatts of power to the beams. Since this power appears as synchrotron radiation which strikes the outer wall of the (mostly aluminum) vacuum chamber, that wall will be water-cooled. The radiation-desorbed gases will be pumped away very rapidly by means of long, narrow sputter-ion pumps located in the vacuum chamber in the bending magnets directly alongside the beams to sustain pressures of about 10^{-8} Torr which must be maintained in the vacuum chamber to achieve adequate beam lifetimes (several hours) and low experimental background counting rates.

The proposed storage ring is designed to generate a luminosity of $10^{32}cm^{-2}s^{-1}$ per interaction region at a beam energy of 15 GeV. This luminosity appears adequate to support a vigorous experimental program. To achieve this performance, it is necessary to store a current of about 100 mA in each beam. Based on the expected performance of the SLAC two-mile accelerator in filling SPEAR II,[2] the filling time for PEP will be ten to fifteen minutes, which is a comfortably short period compared to the storage time of several hours, and ensures that storage ring operations will consume only a small fraction of the linear accelerator beam time.

The fundamental limitation on the performance of existing electron-positron storage rings is the transverse beam-beam limit which imposes an upper limit on

* Work supported by the U.S. Atomic Energy Commission

the current density of the beams where they collide.[3] The magnetic guide field of PEP is designed to attain the specified performance, as described in Section 3, within the limitations established by this instability.

Each counter-rotating beam will be concentrated into three bunches, each a few centimeters long, equally spaced around the ring, and the bunches will collide only at the centers of the six long straight sections. Five of these interaction regions will be housed in experimental halls of various designs for high-energy physics experiments. These designs are discussed in Section 4. The sixth interaction region (northwest) will be reserved for accelerator physics measurements and experiments.

The construction schedule calls for completion of the facility four years after full authorization so that experimental physics could begin in 1980 if full authorization occurs in 1976. The total cost is estimated to be $53.3 million plus escalation.

2. High-Energy Physics with Electron-Positron Colliding Beams

High-energy electron-positron colliding-beam storage rings have opened up a new physical region for the study of elementary particles and their interactions, the region in which a state of pure energy is produced by the annihilation of the colliding electron and positron. This state comes into being only when a particle strikes its anti-particle and therefore does not occur when primary beams from conventional accelerators strike material targets or when protons collide with protons in a proton-proton storage ring system. The energy can rematerialize into combinations of all of the presently known elementary particles. Thus data can be obtained about the structure and interactions of these particles in a new experimental regime.

The results from entering this new region have been surprising and profound. As the energies of the colliding beams have been increased, the results of experiments done with them have become more and more difficult to understand in terms of present models of elementary-particle structure and interactions. Most recently, new experiments from the SPEAR facility at SLAC and the CEA facility in Cambridge have given results which flatly contradict the predictions of the theoretical ideas involving substructure within the nucleon which had been so successful in explaining a host of experiments done with conventional accelerators, and the resolution of this contradiction seems certain to lead to a far deeper understanding of elementary-particle physics. With the PEP storage ring we shall extend the available reaction energy in electron-positron collisions to 30 GeV, thus greatly expanding our reach into the annihilation region.

The range of experimental studies opened up by PEP is extremely rich and varied, spanning the entire field of elementary-particle physics including the strong interactions, the electromagnetic interactions and the weak interactions. In the field of strong interactions, reactions leading to mesons and nucleons in the final state will reveal new and vital information about the structure and sub-structure of the elementary particles. For example, a conceptually simple experiment, the measurement of the total reaction cross section for producing strongly interaction particles by electron-positron collisions, tests some very basic hypotheses about the structure of the particles produced. These hypotheses have failed the tests of experiments with the present generation of electron-positron rings, and experiments at higher energy may demand entirely new theoretical constructs.

In the field of pure electromagnetism, processes with only electrons, mu-mesons and gamma rays as reaction products can be studied. The theory of the electromagnetic interaction, quantum electrodynamics, is the only successful field theory in particle physics in the sense that all experimental tests to date agree with its predictions. PEP will greatly increase the energy limits to which this theory can be tested. Particularly exciting is the fact that, if present trends in the hadron production observed in e^+e^- colliding beams continue to the maximum PEP energy, and if our present concepts of the way these reactions take place have any validity, then quantum electrodynamics must break down in the PEP energy region.

In the study of the weak interaction, PEP will open new vistas. For example, the colliding electron-positron pair can transform itself into a mu-meson pair either by the weak or by the electromagnetic interaction, and the energy-dependences of these two processes are such that the weak interaction amplitude becomes more and more competitive with the electromagnetic amplitude the higher the energy. At PEP energies, the interference between the two should become observable. Particle physicists are now seeking a unified picture of the weak and electromagnetic interactions and PEP offers the possibility of testing various unifying concepts from a new experimental vantage point.

Theoretical calculations based on current ideas and models indicate that luminosities in the range $10^{31}cm^{-2}s^{-1}$ to $10^{32}cm^{-2}s^{-1}$ are required to carry out a comprehensive program of studies in weak, strong and electromagnetic interactions.

In summary, PEP offers the possibility of the study of a very broad range of fundamental questions in particle physics in a new and presently inaccessible energy region. The mysteries unveiled in the present generation of electron-positron colliding-beam facilities lead us to expect new phenomena to be uncovered with this device. These experiments, together with the complementary experiments with protons, neutrinos and mesons at the highest-energy proton accelerators, offer great promise of leading to a new depth of understanding of elementary particles and the fundamental laws of physics.

3. Description of the Electron-Positron Storage Ring

Magnetic Focusing System for the Storage Ring

Tables of Parameters. Table 1 presents a summary of general parameters and lattice parameters of the PEP e^+e^- storage ring, and Table 2 gives typical beam parameters for 15-GeV operation. Emittances are defined as (σ_β^2/β).

Table 1

Genera1 Parameters

Beam Energy, E		
Nominal Maximum	**15**	**GeV**
Minimum	**5**	**GeV**
Design Luminosity per Interaction Region, $\mathscr{L}_{max}$		
At 15 GeV	$10^{32}cm^{-2}s^{-1}$	
Below 15 GeV	$10^{32}(E/15)^2cm^{-2}s^{-1}$	
Nominal Crossing Angle, 2δ	**0**	**radians**
Number of Interaction Regions		
Total (superperiodicity)	**6**	
Available for High-Energy Physics	**5**	
Reserved for Machine Physics Studies	**1**	
Number of Stored Bunches, N_b	**3**	
Available Length at Each Interaction Region	**20**	**m**

Lattice Parameters

Straight Section Length	**130.416**	**m**
Gross Radius of Arcs	**220.337**	**m**
Magnetic Bending Radius	**169.916**	**m**
Maximum Diameter of Ring	**701.505**	**m**
Circumference of Ring	**2166.912**	**m**
Cell Length	**28.842**	**m**
Total Number of Cells	**48**	
Number of Standard Cells	**36**	
Effective Length of Bending Magnets	**5.561**	**m**
Effective Length of Cell Quadrupoles	**0.780**	**m**
Bending Field at 15 GeV	**2.9447**	**kG**
Maximum Quadrupole Field at Bore Radius	**<7.5**	**kG**

Table 2

Typical Beam Parameters at 15 GeV

Total Betatron Tunes			
Horizontal	18.75		
Vertical	18.75		
Momentum Compaction	0.00455		
Transverse Damping Time	0.00823		s
x-y Coupling Coefficient	0.280		
Horizontal Emittance	2.3	x 10^{-5}	cm-rad
Vertical Emittance	1.8	x 10^{-7}	cm-rad
Number of Stored Particles (each beam)	4.44	x 10^{12}	
Synchrotron Radiation Power (each beam)	2.6		MW
Linear Tune Shifts per Interaction Region			
Horizontal, $\Delta\nu_x$	0.06		
Vertical, $\Delta\nu_y$	0.06		
Luminosity (each interaction region), $\mathscr{L}$	1.0	x 10^{32}	$cm^{-2}s^{-1}$
Cell Parameters			
Horizontal Phase Advance	97.0°		
Vertical Phase Advance	82.3°		
Maximum Horizontal Beta	48.2		m
Maximum Vertical Beta	50.2		m
Maximum Momentum Dispersion	2.24		m
Interaction Region Parameters			
Horizontal Beta, β_x^*	4.0		m
Vertical Beta, β_y^*	0.20		m
Momentum Dispersion, η^*	-0.73		m
Beam Size (r.m.s.)			
Horizontal Betatron, σ_x^*	0.096		cm
Horizontal Dispersion, σ_{xE}^*	0.072		cm
Total Horizontal, σ_x^*	0.12		cm
Total Vertical, σ_y^*	0.006		cm

Choice of General Parameters. The primary design goals set for the PEP storage ring were: (1) to cover the range of beam energies from 5 GeV up to 15 GeV in order to provide a range of center-of-mass energies extending approximately from those expected to be available at other smaller e^+e^- colliding-beam machines up to those available at the largest proton accelerators; (2) to maintain luminosities around $10^{32}cm^{-2}s^{-1}$ over this range in order to provide experimentally useful reaction rates with the expected cross sections; (3) to furnish an adequate number and variety of experimental halls (interaction regions) to permit a vigorous and varied national program of experimentation and (4) to ensure compatibility of the housings and experimental halls with the possible future addition of a superconducting 200-GeV proton storage ring for e-$ collisions, another 15-GeV electron ring for e-e- or e e collisions, or both additional rings. These goals together with the size, shape and geophysical characteristics of of potential locations at SLAC led us to the choice of the six-sided storage ring shown in Fig. 1. With a radiofrequency power of about 5 MW available to the beams and with the arrangements for controlling the cross-sectional area of the beams described below, the storage ring should achieve a peak luminosity of $10^{32}cm^{-2}s^{-1}$ at a beam energy E of 15 GeV, and a variation of luminosity approximately proportional to E^2 below that energy. It may also be possible to operate the storage ring at energies somewhat higher than 15 GeV with reduced luminosity. The design-luminosity curve is shown in Fig. 2.

The arc radius and the straight-section length are the two most influential parameters in determining the performance of the storage ring. The arc radius should be as large as possible to minimize synchrotron radiation power. Component-free drift spaces 20 m long centered at the interaction regions have been reserved for experimental purposes. The rest of the space in the straight section is used for injection systems, rf

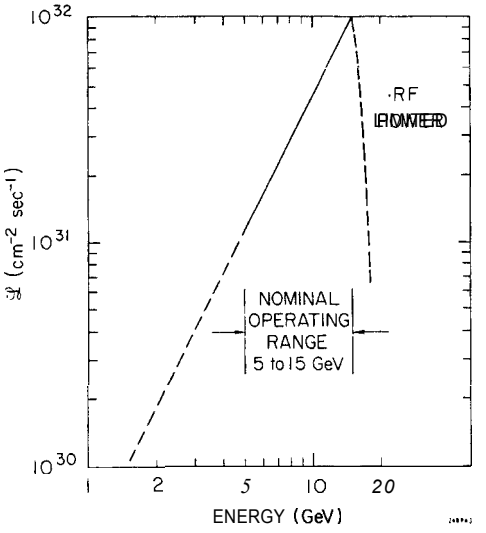


Fig. 2. Design luminosity as a function of beam energy showing the nominal operating range and the upper limit imposed by the available rf power.

cavities and various beam-control elements.

In order to attain high luminosity, it is necessary to collide intense beams within a small cross-sectional area. However, the number of particles which can be collided within a given area is limited by the incoherent beam-beam interaction;[3] this limit is usually characterized by the small-amplitude vertical and horizontal tune shifts $\Delta\nu_y$ and $\Delta\nu_x$. It is well known that, when beam currents are limited by the beam-beam interaction, the maximum theoretical luminosity $\mathscr{L}_{max}$ may be increased if the beam size is enlarged. If one operates a storage ring at different energies under the same focusing configuration, the transverse beam dimensions vary directly as energy E, the maximum (tune-shift-limited) number of storage particles as E^3; thus the luminosity varies as E^4 and drops off very rapidly at lower energies. If, however, the focusing configuration is changed as the energy is lowered in such a way that beam size remains essentially constant, approximately filling the aperture, then the maximum number of stored particles varies as E and luminosity as E^2. This E^2 luminosity is quite acceptable, because most reaction cross sections increase at lower energies. Above the design energy, luminosity will be rf-power-limited, and will drop precipitously, cutting off at an energy of around 18 GeV.

Several different methods for beam size control will be provided. These include varying the momentum dispersion function at the interaction point as in SPEAR,[2] unmatching the momentum dispersion function so that it does not repeat periodically from cell to cell and varying the betatron tune.[4] Vertical size will be adjusted by means of variable horizontal-vertical betatron-oscillation coupling. Using combinations of these techniques, it should be possible to reach, or at least approach, the luminosity shown in Fig. 2 at all operating energies.

Variation of the betatron tune gives a contribution to $\mathscr{L}_{max}$ which varies as ν_{xA}^{-3}, where ν_{xA}^{-3} is that part of the radial tune which comes from the bending arcs. Momentum dispersion at the interaction region gives a contribution proportional to η^{*2}/β_x^*, where η^* and β_x^* are respectively the momentum dispersion function and the betatron amplitude function at the interaction point. An unmatched dispersion function η gives a luminosity increment proportional to η_1^2/β_x^* where η_1 is a measure of the mismatch in the bending cells.

A lattice in which the arcs consist of doublet

cells and are joined by comparatively simple insertions was chosen.[5] Preliminary studies showed that the natural beam size would be about right to give the peak design luminosity if the bending part of the lattice contained between *40* and 50 cells operating with a betatron phase advance per cell of around 90° in both the horizontal and vertical planes. For convenience, the number of cells was chosen to be *48,* or eight cells per 60-degree arc. The nominal phase advance of 90° per cell allows considerable latitude in varying the tune, since doublet cells work reasonably well at phase advances from below 45° to above 135°. A conventional separated-function bending cell, shown in Fig. 3, provides independent control of the total betatron tunes

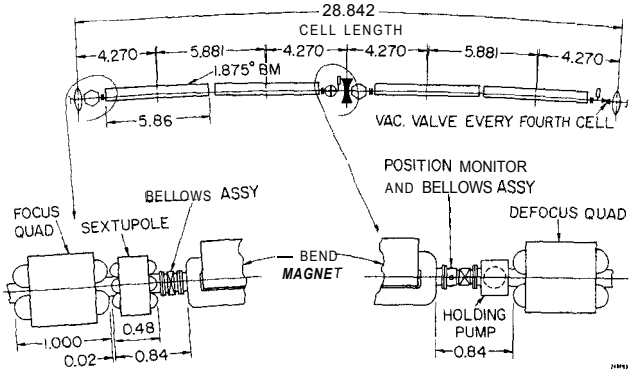


Fig. 3. A standard cell is shown between the quadrupole centerlines. Dimensions are in meters.

ν_x and ν_y by means of the independently controllable focusing and defocusing quadrupoles. The spaces between the quadrupoles and bending magnets provide room for various devices including the sextupoles, which are necessary to control chromaticity.

Each insertion consists of a straight section, shown in Fig. *4,* of approximately *130* m in length, and

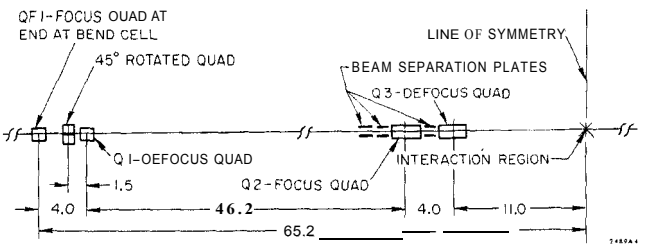


Fig. *4.* The straight insertion, which is symmetric about the interaction point, is shown from the centerline of the cell quadrupole to the interaction point. Dimensions are in meters.

two modified bending cells which have standard dimensions but independently-powered quadrupoles. Suitable configurations have been found over a considerable range of values of tunes, $\beta_x^*, \beta_y^*, \eta^*$ and η_1 (the η-mismatch amplitude). These configurations include ranges for the various beam-enlargement schemes which are adequate to produce the design luminosity over the designated operating range of 5 to 15 GeV. Solutions which are favorable for injection also have been found.

Apertures and Magnet Design

The "beam-stay-clear", or minimum unobstructed lateral region around the design orbit, is a roughly elliptical figure with diameters

$$a_i = 20\,\sigma_i + 2\ \text{cm}$$

where a_i is the vertical or horizontal aperture diameter, σ_i is the vertical or horizontal rms beam radius and the subscript denotes the particular location on the circumference. The factor of 20 allows sufficient, but not overly conservative, clearance to give good beam lifetimes according to experience at SPEAR; the additional *2* cm is a margin for orbit distortions and misalignments. The actual bore clearance of the magnets will include an additional allowance for vacuum chamber walls, installation tolerances and for a possible bake-out mantle.

The magnet system is being designed to minimize the installed cost plus 10-years' operating cost at 15 GeV. Prudent attention was given to reducing energy consumption. The magnets themselves will be capable, nevertheless, of operation at *20* GeV. Laminated magnets were selected for the main ring elements in order to minimize capital costs and to ensure sufficient uniformity magnet-to-magnet.

Radiofrequency System

General. The energy radiated per turn by a 15-GeV electron circulating in the PEP ring is 26 MeV. In order to achieve a reasonable quantum lifetime, an overvoltage which depends on the lattice parameters and radiofrequency is required. At a frequency of 358 MHz (chosen for reasons discussed below), a peak rf voltage of *44* MV is sufficient. In order to reach the design luminosity of $10^{32}\text{cm}^{-2}\text{s}^{-1}$, the required circulating current is 100 mA for this same lattice. The radiated power is therefore 2.6 MW per beam, or 5.2 MW total. In addition, another 2.0 MW is dissipated in the rf structure. At lower energies, the rf power requirements are lower.

It is proposed that the required rf power of 7.2 MW be supplied by *24* klystrons, each delivering a CW output power of 300 kW to an accelerator section 2.1 m in length, comprising five cavities. The accelerator sections will be arranged in two groups of 12 sections each, located at the ends of the southern-most straight section, shown in Fig. 1. Allowing space between sections for flanges, bellows, etc., the overall length of each group will be about 30 m. Rf power will be supplied to the cavities through waveguides running down vertical penetrations from the klystrons which will be housed above ground for ease of maintenance. A list of the principal parameters for the rf system is given in Table 3.

Table 3

General Rf System Parameters

Frequency	358.6	MHz
Energy Loss per Turn	26	MeV
Peak Rf Voltage[1]	*44*	MV
Particles per Beam	*4.4* x 10^{12}	
Circulating Current per Beam	100	mA
Synchrotron Radiation Power (total)	5.2	MW
Total Accelerating Structure Length	60	m
Active Accelerating Structure Length	50	m
Total Shunt Impedance (V_p^2/P_c)	950	MΩ
Total Cavity Power Dissipation	2.0	MW
Total Rf Power	*7.2*	MW
Conversion Efficiency at Design Current[2]	*70*	%
Number of 300-kW Klystrons	*24*	
Total Power Input to Rf Power Supplies[3]	11	MW

[1] For a quantum lifetime of 12 hours.

[2] Ratio of radiated power to total rf power.

[3] Based on klystron efficiency of 70% and a power supply efficiency of 95%

Choice of Frequency. Although operation at frequencies below 100 MHz has some advantages, the attainable shunt impedance per unit length of the cavities is low. In order to attain the high peak voltages required for PEP using such cavities, the length of the rf structure would need to be several hundred meters. By using a higher frequency, the geometric shape of the cavities can be optimized and the shunt impedance per unit length can be increased dramatically. On the other hand, as the operating frequency is increased, the overvoltage ratio (peak voltage divided by the synchrotron radiation loss per turn) required to give a reasonable quantum lifetime also increases. Taking these two competing factors into account, it can be shown that there is a rather broad optimum for PEP in the frequency region 100 to 400 MHz.

Within this frequency region, economic and engineering considerations dominate the choice of frequency. The structure diameter, weight and cost become unreasonably large below about 200 MHz. A careful study of the comparative advantages of klystrons vs gridded tubes indicated that klystrons were superior to tetrodes with respect to initial and annual operating costs, reliability and expected life. Klystron size and cost are lowest at the upper end of the 100-400 MHz frequency range. This factor, together with the decrease in structure costs with increasing frequency, led to a choice of 358 MHz for both PEP and SPEAR II.[2] Before PEP is constructed, operational experience with the new SPEAR II rf system will have served as a test of the proposed design.

System Design. Further details on the PEP rf system design are described in another report to this Conference.[6]

Vacuum System

Introduction. The vacuum system proposed for PEP will be similar in design, construction and operation to the system currently in successful use at SPEAR.[7] The vacuum chamber in the bending magnets will be an 11-m-long, 6061-T4 aluminum extrusion with an internal cross section, shown in Fig. 5, designed to accommodate

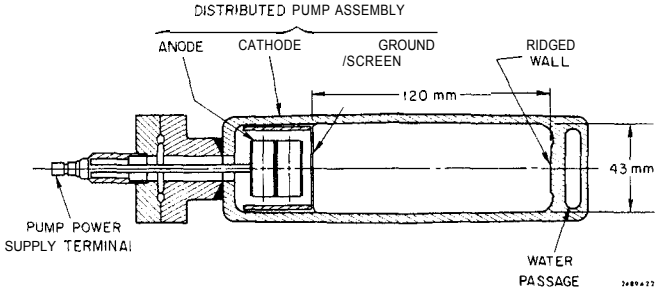


Fig. 5. Cross section of the vacuum chamber for the bending magnets. The vacuum pump which operates in the fringing-field region of the magnet is shown with one of the high-voltage terminals.

the beam-stay-clear region required by beam dynamics. The synchrotron-radiation absorbing wall will be approximately 10 mm thick. The absorbing surface will be ridged as in the SPEAR chambers in order to minimize the synchrotron-radiation-induced gas desorption. A cell vacuum chamber will consist of two bending magnet chambers and two quadrupole chambers. The quadrupole chambers will accommodate the required expansion bellows, position monitors, gauging, etc.

Synchrotron Radiation. The surfaces which are subjected to synchrotron radiation require cooling. At 15 GeV and 100 mA dc in each beam, the total power radiated per beam will be 2.6 MW. The maximum linear heat flux is 35 W/cm for a single electron or positron beam and 45 W/cm for both beams. The synchrotron radiation consists of photons with a spectral energy distribution up to well above 80 keV.

The main gas load during operation is due to synchrotron-radiation-induced desorption which is dominated by a two-step process in which a photoelectron is ejected from the vacuum chamber wall by a synchrotron-radiation photon and subsequently desorbs a gas molecule upon reentering the wall. This gas load is concentrated in the arcs where the synchrotron radiation is produced. Data from SPEAR indicate that it is conservative to extrapolate the desorption rate linearly with beam energy. The total photon desorbed gas load for the entire ring is estimated to be 10^{-5} Torr-ℓ/mA-s at 15 GeV.

Vacuum Pumps. The vacuum system is conductance-limited in the bending magnet chambers where the bulk of the outgassing occurs. Distributed sputter-ion pumps of the type which were developed and used for SPEAR will therefore be installed inside the vacuum chamber within the bending magnets. These pumps are rated at 300 ℓ/s per m of pump length. Commercially available 100-ℓ/s ion pumps will be mounted at each quadrupole and will maintain the system at a base pressure of 1×10^{-9} Torr without a stored beam. Based on the above estimate for the total gas load, the maximum pressure will be 5.0×10^{-8} Torr and the average pressure will be 2.5×10^{-8} Torr.

In the insertions, which will be fabricated of 300-series stainless steel tubing, the main gas load will be due to thermal outgassing. Initially, a system of commercially available ion pumps will be installed to maintain an average pressure of 5×10^{-9} Torr. Extra pumping ports will be provided so that added pumps could lower the average pressure in the insertions to 5×10^{-10} Torr if required by experimental conditions.

Electron and Positron Injection

The six PEP interaction regions are illuminated by three equally-spaced bunches in each beam which are filled selectively by gating the SLAC linac gun. The rf frequency of 358 MHz implies that the rf phase (time) acceptance will be of the order of nanoseconds.[7] A special new electron gun has been installed on the two-mile accelerator to provide very high peak currents in the short (−1.4 ns) pulses necessary for injection into both SPEAR II and PEP. Figure 6 is a plot showing the PEP filling time vs injection energy. The line shows the predicted injection times based on a conservative 50% injection efficiency and the expected yields of electrons and positrons with the new gun. For good operating efficiency, the filling time should not exceed ten or fifteen minutes. From Fig. 6, it can be seen that this can be achieved at energies above approximately 10 GeV up to the maximum positron energy from the two-mile accelerator, which coincidentally is 15 GeV, the design energy of the ring. The maximum injection repetition rate, which is used at the highest injection energies, is 360 pps, the full SLAC rate. At lower filling energies, the damping rates of horizontal betatron oscillations and the energy oscillations require that the filling repetition rate be reduced. The design of the injection system permits the filling of an adjacent bunch while a previously injected bunch is damping, and the curve in Fig. 6 reflects this mode of operation.

For storage ring operation at energies below reasonable injection energies, especially below 10 GeV, the beam will be stored at the injection energy and then the ring magnets will be ramped down to the operating energy.

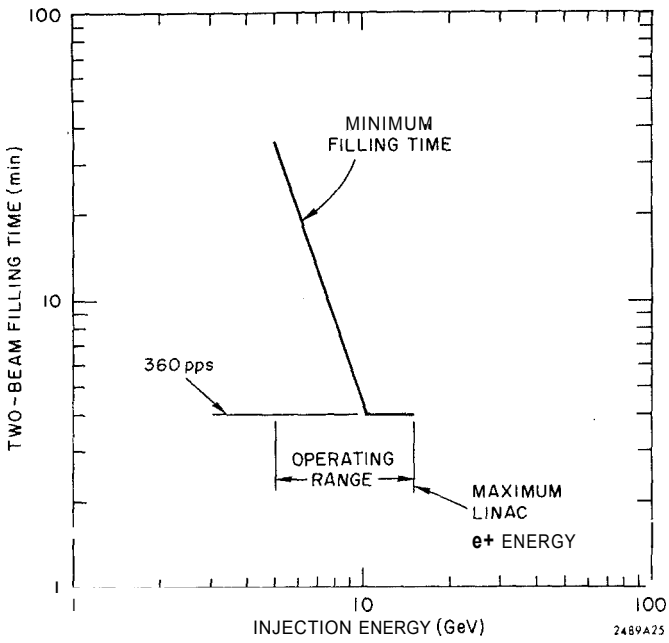


Fig. 6. Filling time vs injection energy. Filling time is the time required to fill both the electron and positron beams to a current of 100 x E(GeV)/15 mA from a beam of 20 mA e^+ and 40 mA e^- in a 1.4 ns pulse with 50% capture efficiency.

Instrumentation Monitoring and Control

The storage ring system, like the linear accelerator, is too spread out for a single data-collection point to be practical. Data will, therefore, be collected at a number of places, edited and compressed as much as possible and then transmitted to the control room. The control room will be located to permit a short path for direct transmission of fast monitoring signals from the injection lines. To reduce the amount of cabling, signals generated within the bending sextants will be wired to instrumentation racks in the nearest data center. Interlock signals will be summarized and then wired directly to the equipment they must control. The remaining signals will be edited by a small computer and sent by serial link to the control room.

The central element of the control system will be a "large mini-computer" which will provide task synchronization between the peripheral elements and manage intercommunication. It need not have elaborate computational ability. It will have three types of "peripherals". The first type is the "data-collection" computer, at least one per interaction area, which provides all connections to the real world. The second type is the console manager which provides all operator interfaces. The third peripheral will be a moderately-sized computational computer which will carry out large-scale calculations and provide file management and programming aids.

Control of Beam Instabilities

Transverse Instabilities. In the design of this storage ring it has been assumed that the maximum luminosity obtainable is determined by the beam-beam incoherent limit and that it is possible to store beams of sufficient intensity to reach this limit. The various transverse instabilities that can occur with large bunched beams and can jeopardize their storage may be categorized into three types: those that are determined by the average circulating current, those that are present because there are multiple bunches in the ring and those that depend upon the peak current in a single bunch.

The present PEP design appears to be rather conservative in requiring an average single-beam current of 100 mA in three bunches. Many electron storage rings have stored such currents at much lower energies where the transverse instabilities are generally much more troublesome. While multiple-bunch transverse instabilities have been predicted, they have not been observed in rings having only a few bunches. Also, because the bunch spacing in PEP is large and fixed, it seems feasible to build a feedback system to damp each bunch individually. The only multiple-bunch motion that has been observed in SPEAR is the coherent motion between two colliding beams. This coupled motion does not seem to be of major concern and its effect is ameliorated by use of electric quadrupoles which are planned for inclusion in the PEP lattice.

The head-tail instability has been the most important single-beam transverse instability observed in electron storage rings and it has been controlled through the chromaticities. In the PEP design it will be possible to vary the value of the chromaticity by means of the sextupole fields which are distributed throughout the lattice without producing destructive non-linear resonances.

The peak current required in PEP is not substantially different from that already attained in single beams in SPEAR.

Longitudinal Instabilities. The six circulating bunches in PEP will have six coherent normal modes. The in-phase oscillations of the bunches can be controlled by a feedback loop coupling a signal picked up from the beam back to a varactor-diode phase modulator in the input drive to one or more of the klystron groups. In order to damp the other five possible modes, a high-frequency cavity will be installed to split the synchrotron oscillation frequencies.

Three potential longitudinal instabilities which can arise out of the b am-beam interaction have been suggested and studied.[1] The first occurs only when the colliding beams cross at an angle, which is not the case in PEP. The second is due to a non-zero value of the η-function at the interaction region η^*. It places an upper limit of the value of η^* above that at which PEP will operate. The third occurs when the bunch length is large compared to the value of the β-function at the interaction region. This will not be the case in PEP.

A potential problem in the design of the PEP rf system is the additional power loss due to the excitation of higher-order cavity modes. Both theoretical and experimental approaches are planned in attacking this problem, and it is expected that by proper structure design, the enhanced power loss due to the excitation of higher-order cavity modes can be held to a tolerable level.

4. Physical Plant

Ring Housing and Shielding

The ring will be located symmetrically about the axis of the SLAC two-mile accelerator with the western-most point approximately 100 m downstream from the end of the accelerator. The terrain slopes downward from the accelerator axis in both north and south directions so that the interaction regions, which are off the axis, will generally lie in areas of lower elevation. Some segments of the ring will be in areas low enough to permit cut-and-cover construction. Those parts deeper underground will require bored tunnels.

The ring, which is horizontal, will be housed in a tunnel at an elevation of approximately 65 m above mean sea level. It crosses under the SLAC beam switchyard about 11 m below the accelerator beam. As shown in Fig. 1, the ring will circumscribe the present research yard. The beam transport tunnels, through which electrons and positrons are brought into the ring, will start at the end of the linear accelerator and branch away and downward, crossing over the ring to insertion points from the inside of the ring, as shown in Fig. 1.

The electron-positron storage ring will be positioned high in the tunnel and suspended from the concrete lining. The tunnel design provides for eventual inclusion of a proton ring. The proton storage ring would occupy a middle height and the electron-positron storage ring would be remounted to alternate above and below it, crossing it in a vertical plane at the interaction points. In the bored tunnel areas a circular housing will be constructed *3.3* m in diameter, as shown in Fig. 7. A rectangular section *3.3* m wide by 2.7 m

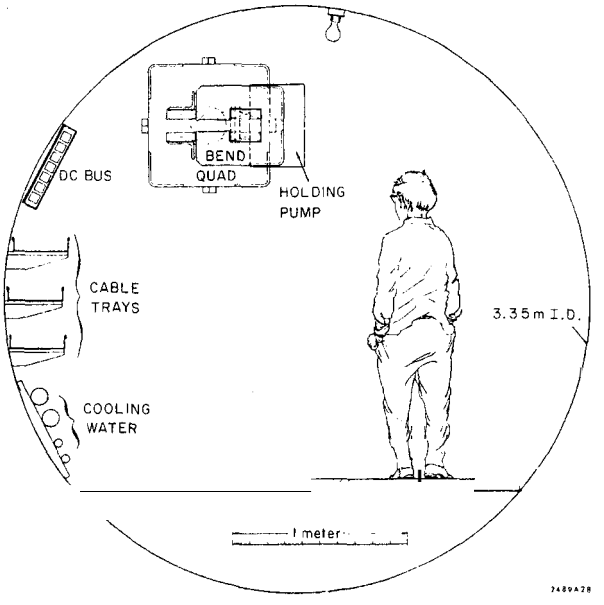


Fig. 7. Cross section of the PEP housing.

high is planned in the cut-and-cover areas. The access aisle will be on the outside of the ring. Because the production of neutrons by proton interactions is some three orders of magnitude greater than that due to electron interactions, and, in addition, because the energy of stored protons will be about 200 GeV as compared to 15 GeV for the stored electrons and positrons, the total shielding requirements will be determined by beam losses from the future proton storage ring.

Experimental Areas

The planned site for PEP offers convenient access to five of the six interaction regions. Thus, it is proposed that five experimental areas be developed in a manner suitable for experiments in the first stage of PEP. The sixth one will have access for only relatively small experimental setups such as those needed for accelerator physics and luminosity monitoring.

The complement of experimental areas is regarded as typical; however, a Summer Study will be held in 1974 on the subject of PEP experimentation, and the details of the experimental areas may change.

The primary constraint on the experimental areas, imposed by the magnet configuration, is the length of the interaction region drift section, which will be 20 m. This is the distance between the final focusing elements of the storage ring and is the space in which most experimental equipment will be mounted.

It is proposed that two of the experimental areas be of the basic design shown in Fig. 8. These so-called

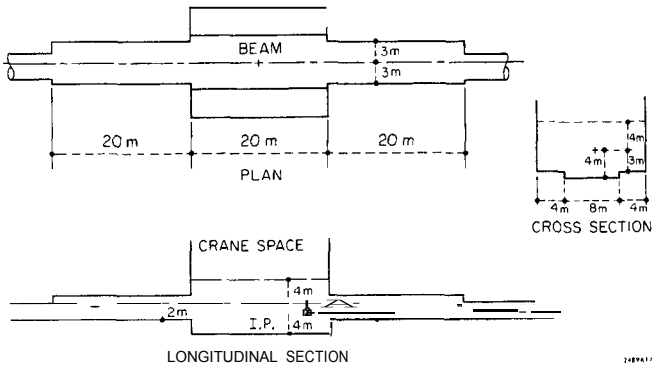


Fig. 8. "Standard" interaction area with alcove.

"Standard" areas are seen as general purpose facilities which will accommodate many of the experiments planned for PEP, including those involving a future proton ring. The basic design consists of an 8-meter-by-20-meter pit with 4 m of clearance above and below the beam Line. On either side of the pit is a platform *4* m wide and *3* m below beam elevation and extending along the beam line are 20-meter alcoves 6 m wide. These dimensions are determined by examining some of the experiments envisaged for standard areas, such as tests of quantum electrodynamics, various studies of hadron production and searches for weak interaction effects.

The third area will have the same transverse dimensions as that described above, but the pit will be extended along the beam direction to a total length of *30* m and the forward-angle alcoves will be omitted. This extension is provided mainly for weak interaction experiments where there may be significant interference between the single-photon exchange amplitude and weak amplitude in the forward direction for processes such as muon pair production. Rather involved forward-angle experiments providing for ranging out muons (using 10-15 m of iron) to measure their polarization are accommodated by this area.

The fourth experimental area is the largest and could be dedicated to a large 4π-steradian magnetic detector or some other large device as yet unconceived. The layout of the experimental pit area at the interaction region is largely determined by the geometry of a large cylindrical magnetic detector similar to the one in current use at SPEAR, except with a superconducting coil and possibly also provisions for calorimetry to give additional information on energetic hadrons. The pit region has clearances of ± 6 m vertically, and horizontally 8 m and 12 m on either side of the center line.

The fifth area is designated with an eye to future potential expansion. Initially, it will have the same dimensions as the Standard experimental area except that the alcoves will be omitted. In addition, the ends of the pits will be made in such a manner that either one or both can later be easily extended to provide additional experimental space downstream of the proton beam for various possible e-p devices.

Power and Cooling

The maximum power demand of the electron-positron

storage ring and experimental apparatus is estimated to be 26 MW. The installed capacity will be 36 MW. While the distribution system can provide 3 MW to each of the five experimental areas, it is expected that the total experimental-equipment load will not exceed 5 MW at any time.

Except for experimental areas, low-conductivity water (LCW) will be provided for the installed power capacity. One megawatt of cooling capacity will be installed at each experimental area. Cooling will be done by relatively small local LCW systems exchanging heat with cooling tower water which will be distributed around the ring to cool the closed-loop LCW systems.

Acknowledgements

The work reported in this paper is that of the members of the LBL-SLAC Joint Study Group; the author is only their spokesman. Special thanks, however, are due W. B. Herrmannsfeldt and C. S. Nissen.

References

1. L. Smith, "The Proton-Electron-Positron Project - PEP", invited paper at this conference.
2. J. Paterson, "SPEAR, Status and Future Developments", invited paper at this conference.
3. F. Amman, IEEE Trans. Nucl. Sci. NS-20, No. 3, 858 (1973).
4. R. H. Helm, M. J. Lee and J. M. Paterson, report to this conference;
   M. Bassetti, report to this conference.
5. R. H. Helm and M. J. Lee, report to this conference.
6. M. A. Allen and P. B. Wilson, report to this conference.
7. U. Cummings et al., J. of Vac. Sci. and Tech. 8, *348* (Jan.-Feb. 1971).

DISCUSSION

Alessandro Ruggiero (NAL): The proposed ring encircles the present research yard. Do you anticipate any interference with potential expansion of the research yard or any other conflict?

John Rees (SLAC): The answer is no, we don't expect to expand the research yard in the easterly direction because the huge backstop is required to stop the radiation from the linear accelerator and the level of the storage ring is way below ground there and does not interfere with the normal operation in any way. We even expect to be able to tunnel under the linac without disturbing it except when we have *to* open the enclosure to bring out the injection beams. Dr. Panofsky points out that the linac works well at a magnitude 5 earthquake and the same can be said for SPEAR. We had a stored beam and it didn't even dump.

Melvin Month (BNL): Is the luminosity quoted per interaction region and has each bunch **six** interactions per revolution ?

Rees: Yes. The revolution is quoted per interaction region **and** each bunch has six interactions per revolution. Being in the same plane, they can't get by each other.

ISABELLE ANTIPROTON OPTION*

C. Baltay
Columbia University, New York, New York
R. Chasman, H.W.J. Foelsche, H. Hahn, M. Month, and A. van Stienbergen
Brookhaven National Laboratory
Upton, New York

Summary: The possibility of colliding antiprotons in ISABELLE has been investigated. Protons are accelerated on the second harmonic to 200 GeV in one of the rings and are extracted into a bypass during flat top, The 30 GeV antiprotons from a target placed at a low-β point in this bypass are transported to the second ring where they are injected and matched into a bucket of a 10th harmonic rf system. This procedure is repeated until all the buckets are filled. The antiprotons are then accelerated to 200 GeV. Protons are now stacked in the first ring in the opposite direction, accelerated to 200 GeV and made to collide with the antiprotons. $p-\bar{p}$ luminosities up to $\sim 10^{29}$ cm^{-2}sec^{-1} seem feasible.

Introduction

The attractiveness for intersecting storage rings such as ISABELLE would be further enhanced if they would provide interactions of a variety of particles besides proton-proton interactions. Ever since the ISABELLE Summer Study some design effort has been directed towards exploring such possibilities. As a result several options have emerged and special care was taken in the basic ISABELLE design to allow for their addition at a later time at minimum cost. The antiproton option, to be described here, involves accelerating and storing a $\sim$ 1 mA antiproton beam and colliding it at 200 GeV with 10 A ISABELLE proton beam. A pp luminosity of the order of 10^{29} cm^{-2}sec^{-1} is obtained.

Choice of Method

Various methods of accumulating large antiproton densities in storage rings have been studied in the past.

The most straightforward mechanism for $\bar{p}$-production is to target protons outside the storage ring and to inject the produced antiprotons into the ring. In this case the number of antiprotons collected in the ring depends on the production cross section as well as on the longitudinal and transverse acceptances of the ring. In previous studies, such a procedure alone has resulted in rather small p intensities. To increase those, several methods have been suggested involving repeated injection made possible by transverse phase-space damping or, in other words, by overcoming the limitations imposed by Liouville's theorem. Budker[2] proposed to damp the transverse oscillations of the antiprotons by means of Coulomb collisions with a high quality beam of electrons traveling with the antiprotons. This is technologically complex and not very efficient for the ISABELLE parameters. Recently, van de Meer[3] put forward the idea of damping betatron oscillations by detecting and compensating statistical variations of the beam center. This so-called stochastic cooling is being investigated experimentally at the ISR, but its usefulness is limited by rf noise problems.

A somewhat different way of obtaining a high antiproton intensity is to use antiprotons originating in $\bar{\Lambda}$ decay and again avoid the constraints of Liouville's theory.[4] The antihyperons would be produced at a target in the vicinity of the storage ring and would produce antiprotons by decay in flight inside the aperture. However, in order to reach high intensities with this method, injection times of the order of days are required. Furthermore, very high radiation levels would result near the injection point.[5]

In the ISABELLE antiproton option none of the above-mentioned technically difficult methods are used. A relatively high intensity of circulating antiprotons (— 1 mA) is obtained in the following way: Protons (~ 10 A) are accelerated to 200 GeV in one of the rings by a second harmonic rf system and, while still bunched, extracted in a single turn into a bypass. The 30 GeV antiprotons from a target placed at a low-β point in this bypass are transported to the second ring, where they are injected and stacked in a bucket of a tenth harmonic rf system. This procedure is repeated until all ten buckets are filled, whereafter the antiprotons are accelerated to 200 GeV. Protons are now stacked in the first ring in the opposite direction accelerated to 200 GeV and made to collide with the antiprotons.

Antiproton Intensity

The antiproton yield, for a primary proton energy of 200 GeV, has recently been measured.[6] It has a plateau around 30 GeV with $d^2\sigma/d\Omega dp \approx 0.5$ $\bar{p}$ per interaction/sr (MeV/c). For small forward angles (<10 mrad) the number of 30 GeV antiprotons that can be stacked in the ISA ring is given by:

$$N_{\bar{p}} \cong \frac{d^2\sigma}{d\Omega dp} N_p \frac{C_{ISA}}{M_p \ell_B} \Delta\Omega \Delta p \eta_t \eta_s \quad . \qquad (1)$$

Here N_p is the number of protons in the ISA,

M_p is the number of proton bunches,

C_{ISA} is the ISA circumference,

ℓ_B is the proton bunch length at 200 GeV (antiproton bunch length at 30 GeV),

$\Delta\Omega$ (in steradians) is the solid angle at the target, inside of which antiprotons will be accepted by the ISA ring,

Δp (in GeV/c) is the momentum spread which will be accepted in the ring at 30 GeV,

η_t is the target efficiency including the effect of $\bar{p}$ interactions within the target, and

η_s is the stacking efficiency.

The solid angle $\Delta\Omega$ of the acceptable $\bar{p}$ beam is given by:

$$M = \pi a' b' \quad ,$$

* Work performed under the auspices of the U.S. Atomic Energy Commission.

where a' and b'are half angles of divergence. These are related to the horizontal and vertical betatron acceptances, A_h and A_v, of the machine by

$$a' = \frac{A_h}{\pi a} \quad \text{and} \quad b' = \frac{A_v}{\pi b} ,$$

a and b being the effective half sizes of the $\bar{p}$ source at the target. The effective source dimensions must include an allowance for the divergence of the $\bar{p}$ beam over the finite length, ℓ_t, of the target. It is advantageous, in principle, to make the physical width of the target (or the proton beam size) as small as possible to get close to the limits $a_{min} = \ell a'/2$ and $b_{min} = \ell b'/2$. However, practical considerations limit the effective source dimensions to $a = \sqrt{2} a_{min}$ and $b = \sqrt{2}\, b_{min}$ leading to

$$\Delta\Omega = \frac{\sqrt{2}\left(A_h A_v\right)^{+\frac{1}{2}}}{\ell_t}$$

Substituting in Eq. (1), one gets

$$N_{\bar{p}} \cong \frac{d^2\sigma}{d\Omega dp} N_p \frac{C_{ISA}}{M_p \ell_B} \frac{\sqrt{2}\left(A_h A_v\right)^{\frac{1}{2}}}{\ell_t} \Delta p \eta_s \eta_t \quad . \qquad (2)$$

Betatron and momentum acceptances are closely related to the available aperture, which should be as large as possible for maximum $N_{\bar{p}}$. For antiprotons the available aperture can be made larger than that assumed for protons, considering the low $\bar{p}$ intensity ($\sim$ 1 mA). Space-charge effects will be negligible in this case and one can let the beam fill the vacuum chamber horizontally, Furthermore, beam loading problems do not exist. One can use a low cost, rf accelerating system of higher frequency and voltage than what is used for the proton beam. This in turn will make it possible to stack the antiprotons azimuthally rather than in momentum space, gaining both in available aperture and stacking efficiency. At the same time, the voltage can be made high enough so that the rf system will be able to accommodate as large a momentum spread as the vacuum chamber will accept.

Protons in the ISA are accelerated on the second harmonic frequency, resulting in two circulating bunches. On flat top, during which the protons are extracted, 70% of the particles in one bunch lie within 1/10 of the circumference. The antiprotons, produced by the protons, will have the same bunch structure. One of the antiproton bunches will be injected, in the second ring, into a bucket of a 10th harmonic rf system with an efficiency of 70%. Ten ISA proton pulses (the second $\bar{p}$ bunch from each ISA pulse will be dumped) are required to fill the ten buckets with antiprotons.

The horizontal aperture of 8 cm is subdivided in the following way at *30* GeV, assuming a momentum spread of *2.5%* and a horizontal acceptance $A_h = 2\pi \times 10^{-6}$ m.rad (which is matched to the production cone):

Betatron amplitude:	1.9 cm
Phase oscillation amplitude $[X_p(\Delta p/p)]$:	*4.3* cm
Sagitta:	*1.3* cm
Reserve:	*0.5* cm
Total:	8.0 cm

A *4.4* cm long iridium target has an optimum target efficiency of $\eta_t = 1/3$. With these numbers and taking $A_v = A_h$ and $C_{ISA}/M_p\ell_B = 5$, one gets

$$\Delta\Omega = 2 \times 10^{-4} \text{ and } \frac{N_{\bar{p}}}{N_p} \cong 8 \times 10^{-5}$$

Extraction and Targeting of Primary Proton Beam

The 200 GeV proton beam will be extracted in the south experimental insertion (Figs, 1 and 2). The quadrupole magnets in this insertion will be rearranged to give slowly varying β-functions in the central part ($\beta_h \sim 12$ m, $\beta_v \sim 25$ m at the center) and to leave a free space of 100 m there. In the beginning of this 100 m drift space, a 1 mrad horizontal kicker magnet will be installed. The time between proton bunches is about *4* psec so that only very moderate demands are put on the kicker rise time. After a 10 m drift space following this kicker, the beam will be sufficiently displaced to enter the array of 3 septum magnets listed in Table I. They are followed by a *24* m drift space at the end of which the beam will enter a 60 mrad achromatic bend, followed by a triplet that will focus the beam at the target 5 m away. The target is located at a distance of $\sim$ *3.5* m from the ISA ring, which leaves adequate space for shielding,

The beam spot size at the target is only $\sim 0.25 \times 0.25$ mm^2 corresponding to $\beta = 0.60$ m. The target will most likely explode from the exposure to 6×10^{14} protons and will have to be replaced for each proton pulse,

Table I. Septum Magnets

Septum	Unit	1	2	*3*
Length	(m)	1	1.5	*1.5*
Deflection	(mrad)	1.8	*4.0*	*4.0*
Peak field	(kG)	*12*	18	18
Gap height	(cm)	*1.5*	*1.5*	1.5
Septum thickness	(mm)	*2.5*	*5*	5
Peak current	(kA)	15	22.5	22.5
Current density	(kA/cm^2)	40	30	*30*

Antiproton Beam Transport

Antiprotons emerging from the target will be focused by a strong, large aperture, room temperature triplet located 3 m downstream from the target. Thereafter, they will enter a 21 mrad bending magnet, which will separate them from the protons that were transmitted by the target. The protons will continue into a beam dump while the antiprotons will go into an achromatic bend from which they will emerge parallel to the ISA ring. Two quadrupole doublets will now match the antiproton beam into a transport channel that runs in parallel with the ISA ring and which simulates an ISA octant, with room temperature magnets.

Antiproton Injection and Acceleration

The antiprotons will be injected into the ISA by a fast kicker at the injection insertion ordinarily used for protons. (The rise time of this kicker has to be $\sim$ 150 nsec which is well within the present state of art.) They will be captured and matched into a bucket of a 10th harmonic (1.12 MHz) rf system. The peak voltage per turn required for matching is $\sim$ 150 kV, which is also suitable for 2 min acceleration to 200 GeV, using a synchronous phase of 5°. Because of the low antiproton intensity, the rf system can have high impedance resulting in low power demands.

$\bar{p}$-p Luminosity

The expected luminosity for p-$\bar{p}$ collisions has been calculated. It is limited by beam-beam interaction and it has been assumed that the maximum permissible tune shift for the antiprotons is $\Delta\nu = 0{,}005$. For a 1.7 mrad horizontal crossing geometry with $\beta_v = 2.5$ m and $\beta_h = 5$ m at the intersection point, assuming a 10 A proton beam with an emittance of $0.4\pi\ 10^{-6}$ m.rad at 30 GeV, one gets

$$L_{p\bar{p}} \simeq 8 \times 10^{28} cm^{-2} sec^{-1}$$

Acknowledgments

The authors are greatly indebted to Dr. G.K. Green for valuable discussions.

References

1. ISABELLE Design Study, in press.
2. G.I. Budker, Sov. J. Atomic Energy, 22, 438 (1967)
3. S. van der Meer, Report CERN/ISR-PO/72-31, (1972).
4. G.K. O'Neill, Princeton-Pennsylvania Accelerator Report PPAD 415D (1961).
5. K. Hübner, Report CERN/ISR-TH73/-19 (1973).
6. W.F. Baker, et al., NAL-Pub-74/13-EXP (submitted to Phys. Rev. Lett;) (1974).

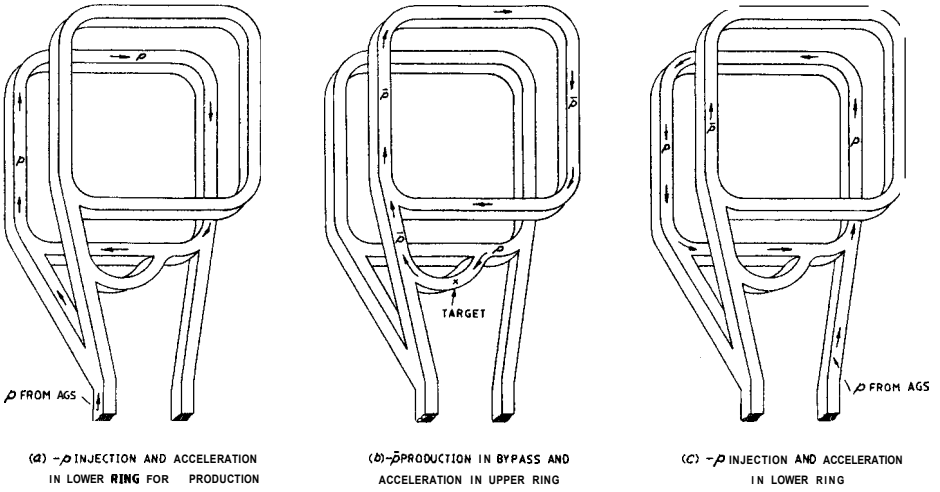


Fig. 1.

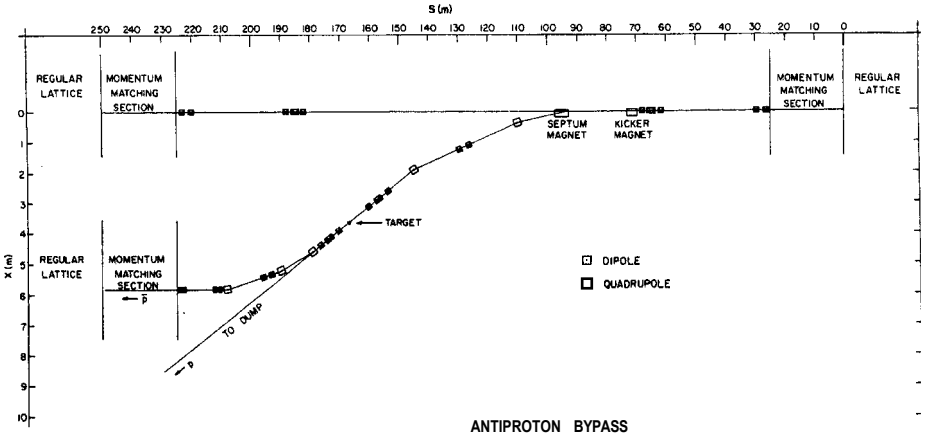


Fig. 2.

Andrei Kolomensky (Lebedev Institute): What is the main limitation for increasing the luminosity: Is it a tune process or something else?

Renate Chasman (BNL): It's the tune. The antiprotons will see a very dense proton beam and will experience the ordinary beam-beam interaction.

Kolomensky : So this figure 0.005 is the main limitation?

Chasman: Yes.

James Allaby (CERN): At what energy are the antiprotons injected?

Chasman: At **30** GeV, where the yield reaches a plateau so that the intensity is really proportional to the momentum bite.

Marshal King (Rutherford): The bypass presumably is superconducting. Have you thought about the effects of scattering downstream of the target, particularly in comparison with the dipole value?

Chasman: No, the entire bypass from the target downstream will be at room temperature.

SLED. A METHOD OF DOUBLING SLAC's ENERGY*

Z. D. Farkas, H. A. Hogg, G. A. Loew and P. B. Wilson

Stanford Linear Accelerator Center
Stanford University, Stanford, California 94305

Introduction

Over the past few years, several schemes for making significant increases in the energy of the SLAC beam have been proposed. Two of the proposals, namely the use of superconducting accelerating sections[1] and recirculation of the beam for a second pass through the existing accelerator,[2] have been abandoned for technical and economic reasons after extensive investigation. An on-going method of gradually raising the beam energy is the development and installation of 30- and 40-MW klystrons by the SLAC Klystron Group. It is clear, however, that the accelerator would have to be completely refitted with klystrons producing about 100 MW in order that the present machine energy be approximately doubled. While such an approach is not inconceivable,[3] the realization of such klystrons and the modulators needed to drive them would require further years of development and a high initial capital investment.

Since the accelerator energy is determined by the peak RF input power, and since many experiments are not now limited by average beam power, it was felt that some method for enhancing peak RF power at the expense of RF pulse width might be the answer for increasing SLAC's energy without at the same time increasing the average input power consumption. Standard pulse compression schemes were considered and rejected. One approach that seemed to hold promise, however, came as a result of our experience at SLAC with superconducting cavities. In the course of making measurements on superconducting cavities, it is a common observation that the power radiated from a cavity that is heavily overcoupled approaches four times the incident generator power immediately after the generator has been switched off. Normally this radiated power travels as a reverse wave back toward the generator. There are, however, several microwave networks which can direct this radiated power into an external load; for instance, two identical cavities attached to a 3-db coupler, as shown in Fig. 1. Using overcoupled cavities, we have in principle a

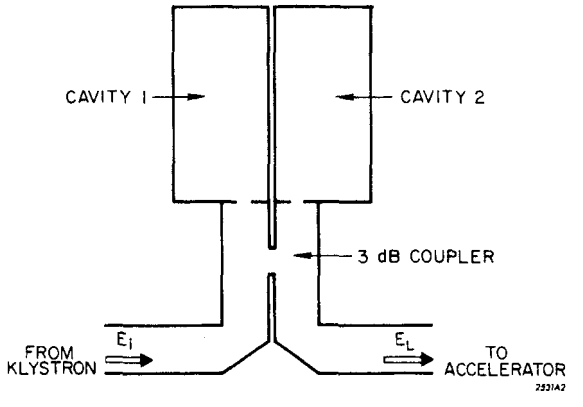


FIG. 1--Schematic drawing of the SLED microwave network.

power multiplier which can enhance peak power by up to a factor of four. This is accomplished, of course, at the expense of pulse width, since the radiated power decays away with a time constant given by the cavity filling time. A further development which enhances the viability of the SLED concept is the observation that if the RF source is reversed in phase rather than simply being switched off, the peak power can be increased by up to a factor of nine. How this comes about is described qualitatively in the following section.

Qualitative Description of SLED

In the case of the present SLAC accelerator, klystrons provide a 2.5 psec RF output pulse which travels, through a waveguide directly into the accelerating sections as indicated schematically at the top of Fig. 2. In the case of SLED, the

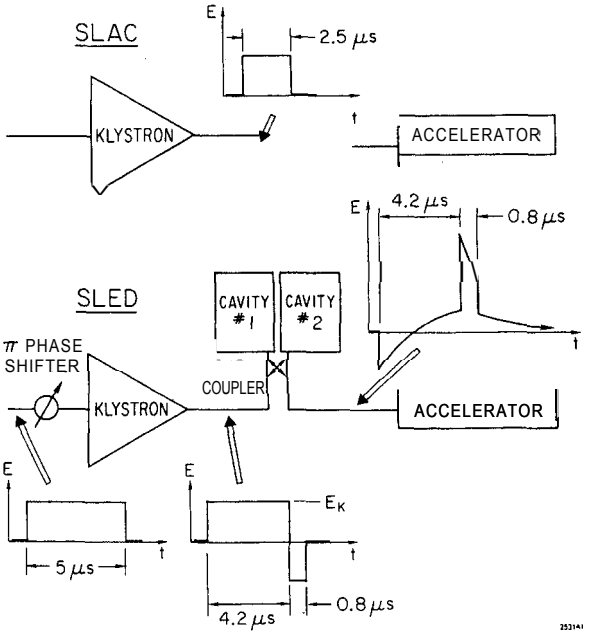


FIG. 2--A comparison of the present SLAC and SLED RF systems.

high-power waveguide system is broken near the klystron and the power divider/dual-cavity assembly shown schematically in Fig. 1 is inserted. The cavities are assumed to be identical and tuned to resonance. After the RF pulse is turned on, the fields in the cavities build up and a wave of increasing amplitude is radiated from the coupling apertures of each cavity. The two emitted waves combine so as to add at the accelerator port of the 3-db coupler, while they cancel at the klystron port. In addition to the wave emitted from the cavities, a wave travels directly from the klystron to the accelerator. This direct wave, which is just the wave that would appear at the accelerator if both cavities were detuned, is opposite in phase to the combined emitted waves. If the cavities are overcoupled, the emitted wave grows in time to an amplitude which is larger than the direct wave. The net field at the input to the accelerator, which is the sum of the direct and emitted waves, then goes through a phase reversal as shown at the right-center of Fig. 2. One accelerator filling time (0.8 psec) before the end of the RF pulse, the π phase shifter reverses the phase of the output wave from the klystron as shown by the waveform at the bottom of Fig. 2. Immediately after this phase reversal, the emitted and direct waves add in phase at the accelerator, since the emitted wave (which is proportional to the stored fields in the cavities) cannot change instantaneously. Therefore, when the klystron phase is reversed, the field at the input to the accelerator increases by two units (assigning one unit to the

*Work supported by the U. S. Atomic Energy Commission.

direct wave, E_K), since at any instant the load wave is the sum of the direct and emitted waves. Following the phase reversal, the fields in the cavities (and hence the emitted wave also) decrease rapidly as the cavities try to charge up to a new field level of opposite phase. The resultant wave at the accelerator decreases also, as is shown qualitatively in Fig. 2. At the end of the RF pulse, the direct wave goes to zero and the emitted wave only is present at the accelerator. It then decays to zero with a time constant given by the cavity filling time.

Theory

In order to understand the theory of SLED in detail, it is helpful to consider the transient behavior of the reflected and stored fields for a single resonant cavity. As discussed previously, the field which would normally be reflected back toward the generator in the case of a single resonant cavity is directed into the load by means of the microwave network shown in Fig. 2. In analyzing the behavior of a single cavity, it is convenient to consider the net reflected field as the superposition of a wave E_e emitted from the coupling aperture, and a reverse wave E_K which is equal in magnitude to the incident wave E_i from the generator (klystron), and which is reflected from the waveguide-cavity interface with a 180^o-phase reversal. If at any instant the generator is turned off, the field traveling away from the cavity is equal to E_e, which in turn is proportional to the stored field inside the cavity at that time. If, on the other hand, at any instant the cavity could be emptied of stored energy (by, for example, instantaneously detuning it) then the reverse wave traveling back toward the generator would be just E_K. By conservation of power,

$$P_K = P_L + P_c + dW_c/dt \quad ,$$

where P_K is the incident power, P_L is the net reflected power (the power delivered to the load in the case of the SLED network shown in Fig. 2), P_c is the power dissipated in the cavity and W_c is the energy stored in the cavity at time t. *Using* $P_c = \omega W_c/Q_0$, together with the fact that power is proportional to the square of the field, ($P = kE^2$), the above relation becomes

$$E_K^2 = (E_e + E_K)^2 + E_e^2/\beta + (2Q_0/\omega\beta)E_e dE_e/dt \quad .$$

A cavity coupling coefficient β has also been defined, such that $kE_e^2 = \beta P_c$. If at any instant the generator is turned off, β is given by the ratio of the power emitted from the coupling aperture to the power dissipated in the cavity walls. If we now introduce the cavity filling time $T_c = 2Q_L/\omega = 2Q_0/[\omega(1+\beta)]$, the preceding expression can be rearranged to give

$$T_c dE_e/dt + E_e = -\alpha E_K \quad , \qquad (1)$$

where $\alpha = 2\beta/(1+\beta)$.

Equation (1) can now be solved for the generator waveform E_K shown at the top of Fig. 3. For convenience, we take E_e to be initially positive, and since initially E_e and E_K must be opposite in phase, we take E_K to be -1. At time t_1 the phase of the generator wave is reversed, and $E_K = +1$. At time t_2 the incident power is turned off. By solving Eq. (1), the following expressions for the emitted field in the three time intervals A, B and C shown in Fig. 3 are obtained:

$$E_e(A) = -\alpha e^{-\tau} + \alpha \quad ; \qquad E_{e_1} = -\alpha e^{-\tau_1} + \alpha \quad ; \qquad (2a)$$

$$E_e(B) = \gamma e^{-(\tau-\tau_1)} - \alpha \quad ; \qquad E_{e_2} = \gamma e^{-(\tau_2-\tau_1)} - \alpha \quad ; \qquad (2b)$$

$$E_e(C) = E_{e_2} e^{-(\tau-\tau_2)} \qquad (2c)$$

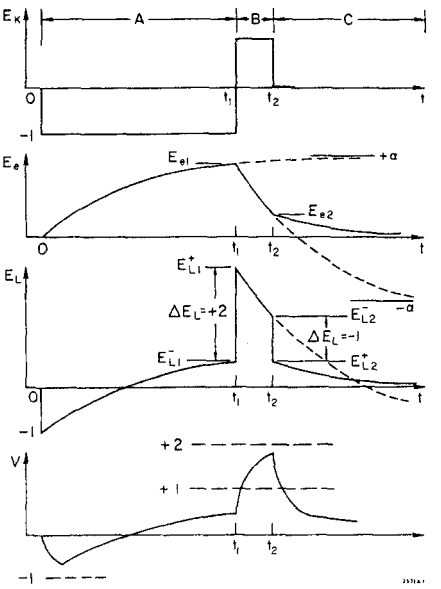


FIG. 3--Direct wave E_K, emitted wave E_e, and net load wave E_L for SLED.

where $\tau \equiv t/T_c$, $\gamma \equiv \alpha(2 - e^{-\tau_1})$ and E_{e_1} and E_{e_2} are the values of E_e at t_1 and t2. The variation in E_e as a function of time is shown in Fig. 3 for the case $\beta = 5$, $\tau_1 = 2$ and $\tau_2 = 2.4$. The load waveform, given by $E_L = E_K + E_e$, is also shown in Fig. 3. The load fields are:

$$E_L(A) = E_e(A) - 1 = -\alpha e^{-\tau} + (\alpha - 1) \qquad (3a)$$

$$E_L(B) = E_e(B) + 1 = \gamma e^{-(\tau-\tau_1)} - (\alpha - 1) \qquad (3b)$$

$$E_L(C) = E_e(C) = \left[\gamma e^{-(\tau_2-\tau_1)} - \alpha\right] e^{-(\tau-\tau_2)} \qquad (3c)$$

The field on a traveling-wave constant-gradient accelerating section is given by $E(z,t) = E[0, t - \Delta t(z)]$, where $\Delta t(z)$ is the length of time it takes for a wave to propagate from the input of the structure to position z on the structure. For a constant-gradient structure, in which the group velocity varies linearly with z according to $v_g(z) = v_{g0}(1 - gz/L)$, the propagation time to position z is given by

$$\Delta t(z) = \int_0^z \frac{dz}{v_g(z)} = \int_0^z \frac{dz}{v_{g0}(1 - gz/L)} \quad .$$

Defining $z' = z/L$, where L is the length of the accelerating structure, and integrating the above expression, we obtain

$$\Delta t(z') = T_a[\ln(1 - gz')/\ln(1 - g)] \qquad (4)$$

where $T_a = \Delta t(1) = (L/gv_{g0})\ln[1/(1-g)]$ is the filling time for the structure. The field $E(z,t)$ along the structure is now obtained by substituting $t - T_a[\ln(1 - gz')/\ln(1-g)]$ for t in Eqs. (3). The result is:

$$E(A) = -\alpha e^{-\tau} f(z') + (\alpha - 1) \qquad (5a)$$

$$E(B) = \gamma e^{-(\tau-\tau_1)} f(z') - (\alpha - 1) \qquad (5b)$$

$$E(C) = \left[\gamma e^{-(\tau_2-\tau_1)} - \alpha\right] e^{-(\tau-\tau_2)} f(z') \qquad (5c)$$

where $f(z') = (1 - gz')^{\nu}$ and $\nu = (T_a/T_c)[\ln(1-g)]^{-1}$.

In using these relations, the fact must be taken into account that there are discontinuities in the field along the accelerating structure corresponding to discontinuities at

times $t_d = 0$, t_1 and t_2 in the field as a function of time at the input to the structure. In general, a field discontinuity will occur at a position z'_d along the structure for a discontinuity at time t_d in the waveform at z=0, where

$$z'_d = (1/g)\left[1 - (1-g)^{(t'-t'_d)}\right] \quad . \tag{6}$$

This expression is obtained by solving Eq. (4) for z', defining also a normalized time by $t' = t/T_a$, and setting $At = t - t_d$. For example, in the time interval $0 < t < t_1$, the field is zero for $z' > z'_d$, where z'_d is obtained using $t'_d = 0$ in Eq. (6). For $z' < z'_d$, the field is given by Eq. (5a).

The accelerating voltage is now obtained by integrating the field from z' = 0 to z' = 1, taking into account the location of the field discontinuities and using the appropriate fields given by Eqs. (5) up to and following each discontinuity. Thus the energy gain V for the interval $t_1 < t < t_2$ is given by

$$V = \int_0^{z'_{d_1}} E(B)\, dz' + \int_{z'_{d_1}}^{1} E(A)\, dz' \quad ,$$

where z'_{d_1} is given by Eq. *(6)* with $t'_d = t'_1$. The energy gain is by definition unity after one filling time for a direct wave $E_K = 1$, which would be present with the cavities detuned. Since f(z') is common to all of the energy gain integrals, the calculation is simplified by defining

$$F_1(z'_d) = \int_0^{z'_d} f(z')\, dz' = \left[1 - (1-gz'_d)^{1+\nu}\right]\left[g(1+\nu)\right]^{-1} \quad ;$$

$$F_2(z'_d) = \int_{z'_d}^{1} f(z')\, dz' = \left[(1-gz'_d)^{1+\nu} - (1-g)^{1+\nu}\right]\left[g(1+\nu)\right]^{-1}$$

Thus, during $t_1 < t < t_2$,

$$V = \gamma e^{-(\tau-\tau_1)} F_1(z'_d) - (\alpha-1) z'_{d_1}$$

$$- \alpha e^{-\tau} F_2(z'_d) + (\alpha-1)(1-z'_{d_1})$$

Similar expressions can be derived for time intervals A and C. A plot of the normalized energy gain as a function of time is given at the bottom of Fig. 3. The maximum energy is obtained after one filling time, by letting $t = t_1 + T_a$ (or $t' = t'_1 + 1$) and $z'_{d_1} = 1$. For this special case,

$$V_{max} \equiv M = \gamma\, e^{-T_a/T_c}\left[1 - (1-g)^{1+\nu}\right]\left[g(1+\nu)\right]^{-1} - (\alpha-1) \quad . \tag{7}$$

Further details of the SLED theory are given by Farkas[4] and Wilson.[5] The effect of cascading several of the microwave networks shown in Fig. 1 was calculated[4] in the hope of obtaining flatter output pulses and perhaps still higher values for the energy multiplication factor. Somewhat flatter output pulses were predicted, but not higher multiplication factors in the examples investigated. The possibility cannot be ruled out, however, that other more favorable configurations might be found.

Choice of Parameters

An analysis of Eq. (7) shows that the maximum energy gain M approaches 3 if $\beta \gg 1$, $T_c \gg T_a$ and $t_1 \gg T_c$. Since $T_c(1+\beta) = 2Q_0/\omega$, it is impossible to have both a large filling time and a large coupling coefficient unless the unloaded Q of the cavities can be made arbitrarily large. However, the unloaded Q of a practical room-temperature resonator is limited to about 10^5. The RF pulse length is also limited by practical considerations. The present pulse length, t of SLAC is 2.5 psec. It is reasonable to consider doubling %is pulse length to 5.0 psec. Figure 4 shows the

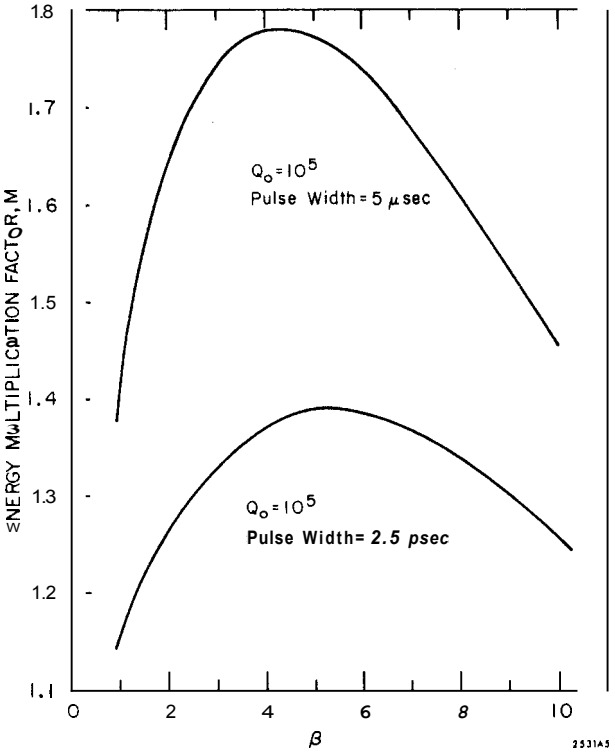


FIG. 4--Energy multiplication factor as a function of cavity coupling coefficient.

energy multiplication factor as a function of the cavity coupling coefficient for these two pulse lengths with $Q_0 = 10^5$. It is seen that the energy gain is maximum for a coupling coefficient in the range $\beta = 4$ to 5. Figure 5 shows the energy multiplication factor M as a function of unloaded Q for various values of RF pulse length, and Fig. *6* gives M as a function of pulse length for various values of Q_0. The coupling coefficient has been optimized at each point on the curves in both figures to give the maximum energy gain. It is seen that the longer the pulse length and the higher the unloaded Q, the greater is the energy gain.

As a result of a number of practical and economic considerations, the parameters proposed for SLED are $Q_0 = 10^5$, $t_2 = 5.0$ psec and $\beta \approx 4.5$. The energy multiplication factor for these values is 1.78. Figure 7 shows the RF power output from the SLED microwave network as a function of time for these parameters. The "pulse compression" effect of the SLED network is clearly seen.

Beam Loading

Figure 8 shows the unloaded relative energy gain as a function of time in the region of peak energy for the SLED parameters as chosen in the previous section. It is clear that the pulse length of a beam accelerated near peak energy will necessarily be short compared to the structure filling time. The unloaded energy is seen to be increasing as a function of time as peak energy is approached. By turning on the beam prior to reaching peak energy, the transient energy droop due to beam loading can be used to produce a rough compensation for the rising unloaded energy gain, resulting in a considerably tighter energy spectrum. For SLAC, the transient beam

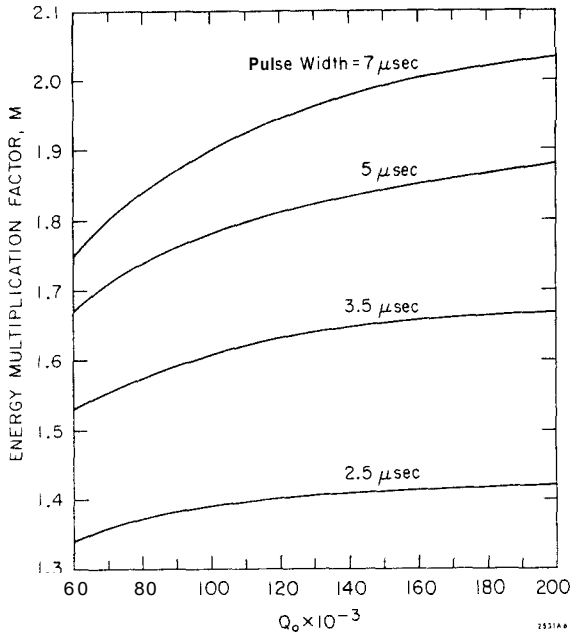


FIG. 5--Energy multiplication factor as a function of unloaded Q.

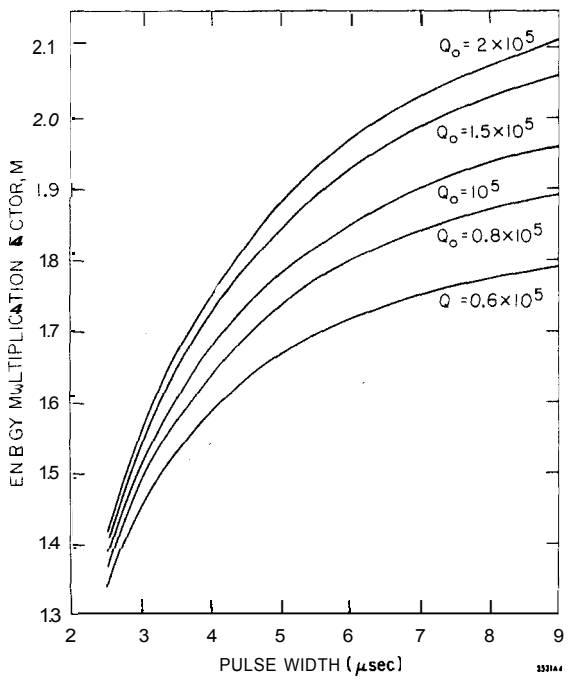


FIG. 6--Energy multiplication factor as a function of pulse width.

loading voltage is given, to the accuracy required here, by

$$V_b(MV) = 35iP\left[2\Delta t/T_a - (\Delta t/T_a)^2\right] ,$$

where i_p is in milliamperes and Δt is the time after the beam has been switched on. Figure 8 also shows the transient variation in the relative beam loading as a function of time for a maximum unloaded energy of 46 GeV and a peak current of 200 mA, assuming that the beam is switched on 0.35 psec before the peak energy is reached. The curve of the resultant beam energy shows that beam loading compensation has reduced the variation in energy gain over this time interval from 10%to about 24%. Table I gives the

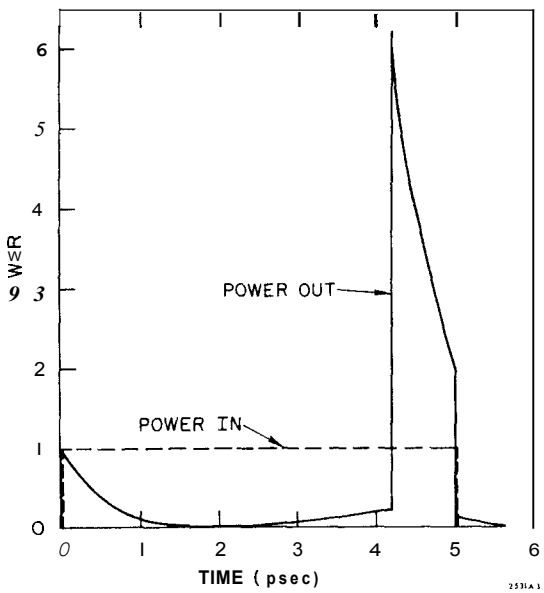


FIG. 7--Input power to and output power from the SLED microwave network as a function of time,

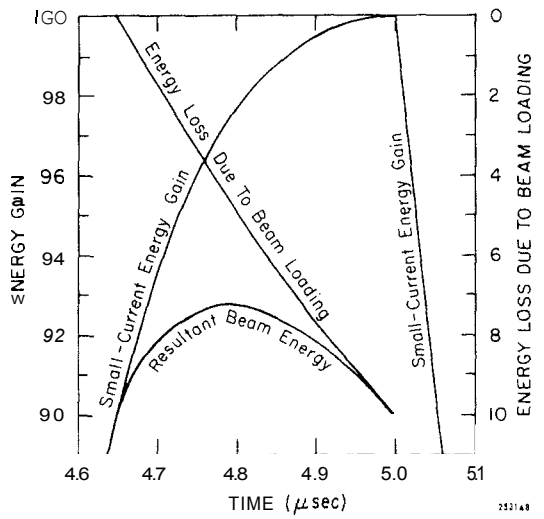


FIG. 8--Unloaded energy gain, energy droop due to beam loading and resultant beam energy for a beam pulse length of 0.35 μsec.

loaded energy V, the peak current i_p, the average current i_{ave} and the energy spectrum width $\Delta V/V$ for various values of the beam pulse length T_b. For each value of T_b, the peak current has been chosen so that the beam energy is the same at the beginning and end of the pulse. The maximum unloaded energy is taken as 46 GeV, which would be obtained from the SLAC linac for an energy multiplication factor of 1.78 and a klystron power of 30 MW. A repetition rate of 180 pps has been assumed in computing the average current.

By shaping the current pulse as a function of time, the energy spectrum widths can in principle be reduced considerably below the values given in Table I for a constant pulse current. Likewise, by advancing the triggers to a fraction of the klystrons along the machine, the peak current for a given beam pulse length can be reduced below the values shown in Table I while still maintaining a tight energy spectrum. The peak pulse current for SLED will in practice be limited by beam breakup. For the present SLAC focusing

Table I

SLED Beam Loading Characteristics (30 MW klystrons)

T_b (μsec)	V (GeV)	i_P (mA)	i_{ave} (μA)	$\Delta V/V$ (%)
0	46.0	0	0	0
0.10	45.8	**31**	**0.6**	**0.15**
0.15	45.4	54	1.5	0.4
0.20	44.8	80	2.9	0.7
0.25	44.0	110	4.9	**1.1**
0.30	43.0	143	**7.7**	1.7
0.35	41.8	181	11.4	2.4
0.40	40.3	224	16.2	3.3

configuration and beam energy, beam breakup limits the peak current to 160 mA for a beam pulse length of 0.3 psec. At a final energy of 40 GeV, a pulse current on the order of 250 mA could be accelerated at this pulse length, assuming a reasonable increase in the strength of the focusing along the accelerator.

In Table 11, the parameters for the present SLAC accelerator and for SLED are summarized for a beam-loaded

Table II

Comparison of SLED and Present SLAC Parameters

		Present SLAC (30 MW klystrons)	SLED (30 MW klystrons)	SLED (40 MW klystrons)
Unloaded Energy	(GeV)	26	46	53
Loaded Energy	(GeV)	23.5	41.5	48
Repetition Rate	(pps)	360	180	180
RF Pulse Length	(μsec)	2.6	5.0	5.0
Beam Pulse Length	(μsec)	1.6	0.36	0.36
Average Current	(μA)	40	12.5	14.5
Peak Current	(mA)	*10*	190	220
Electrons per Pulse		7×10^{11}	4.5×10^{11}	5×10^{11}
Duty Cycle		6×10^{-4}	6.5×10^{-5}	6.5×10^{-5}
Energy Spread	(%)	~1.0	< 1.0*	< 1.0*
Average Beam Power	(kW)	950	520	700

*Assumes current pulse shaping (e g , 230 mA for the first half of the pulse, then 160 mA for the second half for the case of *30* MW klystrons) *For* constant peak current, estimated energy spread is 2 5%.

energy 10% below the unloaded energy. Parameters for SLED are given for both **30** and 40 MW klystrons; at the time SLED becomes operational, the average peak klystron power per station is expected to lie between these limits.

SLED Cavity Design

As noted in the previous sections, cavities with Q_0 on the order of 10^5 are needed to obtain **a** power multiplication factor high enough to be of interest. This Q_0 can be ob- obtained in copper cavities operating at or somewhat above room temperature if a higher-order resonant mode is employed. Considerations of cost, mechanical stability and frequency separation of competing modes make it desirable to choose the mode with the smallest cavity volume for a specified Q_0. Modes which are members of the TE_{01n} family have this desirable characteristic. The value n=5 was chosen as optimum for our purposes. The ratio of diameter D to length L for the cavity remained to be determined. **A** value of D/L less than unity (which gives maximum Q_0) was chosen on the basis of material availability. A smaller diameter also reduces the deformation of the end-plates due to atmospheric pressure loading. The exact ratio (D/L = 0.611) was selected to maximize frequency separation from competing modes. The TM_{115} mode, which is normally degenerate with the TE_{015} mode, was lowered approximately 24 MHz by cutting a circular groove at the outer diameter in one end-plate. This groove does not disturb the TE_{015} mode field pattern or frequency. In summary, the selected parameters for the SLED prototype cavity are:

Diameter = 20.51 cm
Length = 33.59 cm
*Q_0 = 1.08×10^5

*Theoretical Q for copper at f_0 = 2856 MHz

The rate of change of frequency with temperature is -48 kHz/°C for copper construction.

Preliminary analysis has indicated that a cavity tuning error of 10 degrees is acceptable. Assuming $Q_0 = 10^5$ and $\beta = 5$, the loaded Q is $Q_L = 1.6 \times 10^4$. Thus the cavity half-bandwidth, $\frac{1}{2}$BW, is approximately 90 kHz . If Af is the difference between the driving frequency and the cavity resonant frequency, the cavity tuning angle is given by $\psi = \tan^{-1}[\Delta f/(\frac{1}{2}BW)]$. Thus, if ψ is to be limited to ±10 degrees, Af must not be greater than 16 kHz. From the tuning rate with temperature given above, this implies that the cavity temperature must be held constant to within 1/3°C. The existing accelerator cooling water system holds temperature fluctuations to better than ±0.15°C, which would appear to be adequate. However, the RF power dissipated inside each cavity, which is calculated to be about 2 kW average for a 30 MW klystron source, will raise the metal temperature on the order of 1.4°C. This temperature change will shift the resonant frequency by 67 kHz and introduce a tuning error of 37 degrees. Although the cavities may be pre-tuned to 2856 MHz at the equilibrium temperature with the RF power on, there will still be a phase- and amplitude-drift period during warm-up following each RF shutdown. The severity **of** this problem will be gauged during prototype tests. The concept of a mechanically temperature-compensated cavity has been suggested and will be tried if necessary.

A cross-sectional drawing of the prototype assembly is shown in Fig. 9. The cavity cylinders are made from copper forgings, machined to 9.5 mm wall thickness. The inner surface finish is better than 0.15 microns **(RMS)**. Water-cooling tubes are brazed on in pairs covering the five zones of maximum heat dissipation along each cylinder. The cavities are fine-tuned by distorting the thin-wall end-plate using a differential screw. The tuning range is approximately ±1 MHz. Coupling between the cavity and waveguide magnetic fields is achieved through circular apertures in the end-plates. A 2.77 cm diameter aperture in a 4.06 mm thick wall gives the desired β value for $Q_0 = 10^5$.

It is anticipated that there will be frequent need to run the accelerator in the present non-SLED mode; that is, with the flat-topped RF pulse from the klystron transmitted without distortion to the accelerator. This can be done by detuning the SLED cavities, which then appear as short-circuits across two ports of the 3-db hybrid coupler. Under these conditions, the klystron pulse is transmitted through the SLED network without significant reflection or loss. The design requirements placed upon the detuner are quite severe. Primarily, when it is moved from the "detuned" to the "tuned" position, it must return the cavity to the same resonant frequency to within a few kilohertz. Also, in the "tuned" position, it must not degrade the cavity Q_0 nor introduce any frequency modulation due to mechanical vibration. A prototype detuner has been designed which consists

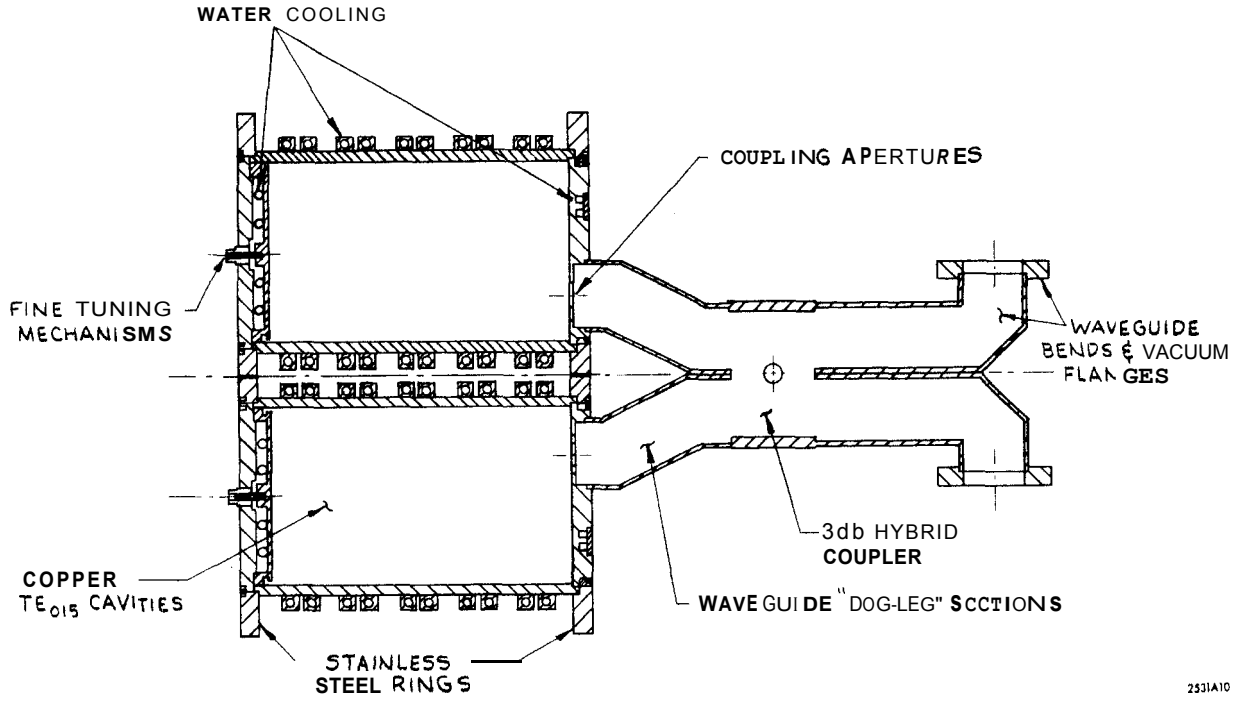


FIG. 9--Assembly drawing of the prototype microwave network for SLED.

of a stainless steel needle 1.52 mm in diameter inserted into the TE_{015} cavity through a 2.03 mm hole in the cavity wall. This hole enters the cavity on a current node and thus causes negligible perturbations of f_0 and Q_0. The needle enters at an angle such that when fully inserted, its tip reaches a circle of maximum azimuthal E field. In this way a detuning of 18 MHz, or approximately 100 bandwidths, is achieved. In its fully retracted position, the needle is decoupled by at least 90 db from the cavity fields and has no residual effect upon f_0 and Q_0.

The SLED prototype assembly described above has performed very well in low-power tests at room temperature. The "detuned" and "tuned" output waveforms follow very closely the "Power In" and "Power Out" curves, respectively, shown in Fig. 7. High-power tests into a matched load are presently in progress. In September of this year, the prototype cavity-hybrid unit will be installed as shown in Fig. 10 on a klystron station near the accelerator injector to allow tests to be made with a beam.

If SLED is to be a viable means for increasing the energy of the SLAC linac, it must be shown that the klystrons can operate satisfactorily at the 5.0 psec RF pulse length and 180 pps repetition rate required. Initial tests at the longer pulse length indicate that the klystron fault rate is somewhat higher than is the case at the present 2.5 psec pulse length, but there is no evidence that the klystrons will not operate satisfactorily under the SLED conditions.

SLED Modes of Operation and Physics Possibilities

Boosting the energy of the present SLAC accelerator into the 40- to 50-GeV range by means of SLED makes available a number of new operating modes for the machine and a corresponding variety of possibilities for the high energy physics program. The full exploitation of the SLED idea requires that all 245 high-power klystron stations be equipped with microwave cavity networks; new pulse-forming networks and pulse transformers must be added to the modulators as well. The combination of these two features gives

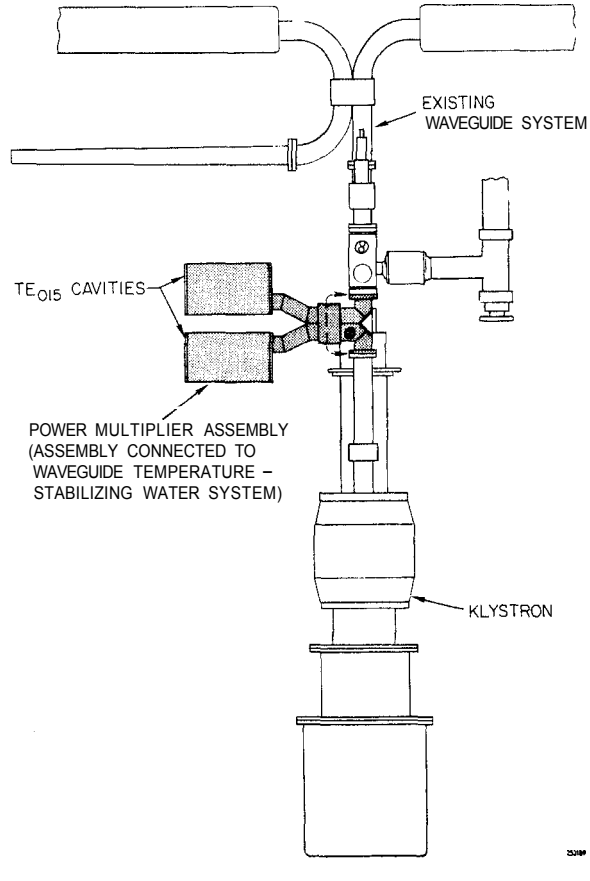


FIG. 10--Proposed installation of the SLED microwave network at a typical station in the Klystron Gallery.

a 5 psec RF pulse at the output of each klystron and boosts its effective peak power from 30 to 100 *MW*. This enhancement in peak power is achieved at the cost of reducing the repetition rate from 360 pps to 180 pps and the beam duty cycle by a factor of 10. The present plan is to make these modifications reversible. The cavity detuners which have been described above can be inserted in a fraction of a second. This results in a possible machine operating mode at the present energy (–23 GeV) but with a beam pulse length of 4.2 psec, giving an improvement in duty cycle over present operation (at 360 pps) of over 30%. This mode of operation cannot be interlaced on a pulse-to-pulse basis with the SLED high-energy mode, but is obtainable after a short switch-over time. It will be used for phasing the machine, possibly for injection of 1.5 GeV electrons and positrons into SPEAR, and for –20 GeV beams for experiments such as LASS (Large Aperture Solenoidal Spectrometer). An alternate method of obtaining low-energy beams might be to inject electrons on an early part of the energy gain waveform. Early injection will be made possible by not installing SLED cavities on the injector klystrons, thereby having a flat 5 psec RF pulse available for capture. When the present mode of operation at 360 pps needs to be restored, this will be done by halving the lengths of the new pulse-forming networks in the modulators. The switch-over might be done by remote control. Even if done manually, the operation should not take more than an hour or so for the entire machine. It is important to point out that none of these modes of operation require an increase in average power for the accelerator above the –25 *MW* that is presently used.

A full discussion of the physics possibilities opened by SLED is beyond the scope of this report. Only a few general remarks will be made here. It appears that End Station A would continue to be the main experimental center for electron scattering and photoproduction physics. In order to bend the 40- to 50-GeV beams into the A-line, three out of the five 0.1° pulsed magnets at the apex of the beam switchyard (BSY) would be replaced by stronger magnets and power supplies. The eight 3° bending magnets which make up the 24° A-bend would also be replaced by stronger magnets. The A-beam dump magnets used for photon experiments would be upgraded. What modifications would be made in the spectrometers is not yet clear.

The main "ecological" change in the research yard would take place in the mix of experiments between End Stations B (ESB) and C (ESC), For higher-energy RF-separated $K^{\pm}$ and antiproton beams, there is insufficient drift distance behind ESB in the Research Yard. For this reason, it has been proposed that the RF separators be moved to the present C-beam, which would be rebuilt with the target moved up by about 100 m. This change might eventually cause LASS and/or the bubble chamber to be moved to the C-beam. The K^{o}-decay experiments in ESB may not require higher energies than at present (and therefore no modifications), but production experiments with K^{o}'s may be exploitable. It is also possible that higher-energy primary e^{-} or photon beams may be of interest to LASS in its present location (or in ESC). In any case, upgrading the 12° B-line would be fairly inexpensive because one would simply add some of the 3° magnets available from the A-line. ESC, on the other hand, would be more drastically modified, but at relatively low cost since no large-angle bends would be involved. The proposed plan would be to create three independent channels by means of a magnetic slit located downstream of the present tune-up dump. The pulsed magnets at the apex of the BSY would aim the electron beam from the accelerator into any one of these three channels. The central beam would be charged (separated beams mentioned above), and the other two would be neutral. One of these neutral beams might consist of photons derived from the collision of electrons with a beam of photons from a laser or from coherent bremsstrahlung; it would be used by the streamer chamber. The other might be a K^{o} beam.

The present cost estimates for SLED (at FY 1974 rates, excluding project indirects, design and engineering, and contingency) break down roughly as follows:

Microwave System	$\sim$1 M
Modulator Modifications	~1.9 M
Instrumentation and Control	–0.5 M
Beam Switchyard Modifications	–1.6 M
Total	$ 5.0 M

Acknowledgements

The authors acknowledge the work that has been carried out by the SLAC Klystron Group, under J. Lebacqz, to test and evaluate the performance of the SLAC klystrons at the longer pulse length required by SLED. C. Olson and the Accelerator Electronics Group have made design and engineering studies of the modifications required to increase the pulse length of the SLAC modulators, and have carried out those modifications on an initial unit for long pulse klystron tests. A. Lisin and R. Sandkuhle have been responsible for the mechanical design of the SLED prototype assembly. Fabrication and scheduling were directed by H. Zaiss. K. Mallory has studied the instrumentation and control problems associated with SLED, and D. Walz has investigated the changes required to upgrade the beam switchyard. J. Murray and L. Keller with many others have studied the high energy physics possibilities opened up by SLED. H. Deruyter has been responsible for all microwave measurements involved in the development and testing of the cavity-hybrid microwave network.

References

1. P. B. Wilson et al., Particle Accelerators 1, 223 (1970).
2. W. B. Herrmannsfeldt et al., Proc of the 8th Int. Conf. on High Energy Accelerators (CERN-Scientific Information Service, Geneva, 1971), p. 563.
3. G. A. Loew, "Electrons, the Energy Crisis and the Possibilities of RF power," SLAC RLA Note 52, Stanford Linear Accelerator Center, Stanford University, Stanford, California (June 1973), unpublished.
4. Z. D. Farkas, "Power Multiplier," Technical Note SLAC-TN-73-8, Stanford Linear Accelerator Center, Stanford University, Stanford, California (September 1973), unpublished.
5. P. B. Wilson, "SLED: A Method for Doubling SLAC's Energy," Technical Note SLAC-TN-73-15, Stanford Linear Accelerator Center, Stanford University, Stanford, California (December 1973), unpublished.

DISCUSSION

Herbert Lengeler (CERN): How are you going to realize a cavity at room temperature with a Q value of 10^5?

Farkas: We use a TE_{115} cavity which just happens to have a Q of 10^5. It's not very big, 8 inches in diameter and 13 inches high.

Helmut Herminghaus (Mainz): Couldn't you have rather severe mismatch during some part of the pulse and if so, how are the klystrons protected?

Farkas: Yes, that is something we worry about. As I mentioned in the talk, the reasons for the 3DB hybrid is to take all the energy reflected from the cavities and channel it into the accelerator section. Another possibility of

separating incident from reflected power at any place would be to use circulators which obviously is not practical at these very high power levels. There is yet another possibility, using resonant rings, which poses other problems.

Andrei Kolomensky (Lebedev Institute): You have three times less average current and you inject less current?

Farkas: Right, we inject over a shorter time.

Kolomensky: Why don't you use some current to excite the cavities? Put the total current at 40 mA and use some of it for excitation.

Farkas: I don't know whether we can use that current. However, it might not be entirely useless. As a matter of fact, there is acceleration at other times than during the 0.2 to 0.3 μs interval of peak acceleration and you might use current at those times for some other purpose.

Raphael Littauer (Cornell): What is the estimated cost of the SLED project?

Farkas: Five million dollars, about two for the cavities and network, another two for modifying the modulators, and about one million for instrumentation and control, including the switchyard.

A PRELIMINARY DESIGN OF TRI-RING INTERSECTING STORAGE ACCELERATORS IN NIPPON, TRISTAN

Tetsuji Nishikawa
National Laboratory for High Energy Physics
Oho-machi, Tsukuba-gun
Ibaraki-ken, Japan

Introduction

When the present KEK proton synchrotron project was originally proposed, it was expected to bring up the Japanese high-energy physics program to the present frontier of the world high energy physics. However, a shortcut of the budget forced the project to start with a lower energy accelerator and extend it to a higher energy range. Thus the future extension of the presently constructing 12 GeV proton synchrotron is taken into consideration even at the initiation of the present project?) Several possible extension schemes such as a large conventional synchrotron in the energy region of 80 ~ 100 GeV have been considered as a long range plan of the KEK project. At present, however, the future plan of the KEK synchrotron is concentrated on *a* plan of tri-ring intersecting storage accelerators for various types *of* colliding beam experiments as $e^{\pm}p$, pp, $e^{+}e^{-}$ and $\bar{p}p$ at very high center of mass energies. This project is nicknamed as TRISTAN (Tri-Ring Intersecting Storage Accelerators in Nippon) and a preliminary design study is undertaken in the KEK Accelerator Department in cooperation with the university scientists and the cryogenic specialists. This is a report on the present status of the preliminary design study of the TRISTAN.[2)]

Outline of TRISTAN

The site of KEK is a land area of approximately 220 hectares in Tsukuba District, Japan. The present 12 GeV proton synchrotron project is in progress at the middle of the site, so that there remains a space enough to build a larger ring with more than 2 Km in its circumference. Thus, as ISABELLE:) PEP,[4)] and EPIC[5)] projects, with a superconducting magnet system we will be able to construct a proton storage ring of 150 ~ 200 GeV inside the site boundary.

The presently constructing synchrotron will be used as the injector of the storage accelerator. Since, however, to raise up the proton energy from 12 GeV to a 100 GeV range a large superconductor magnetization is required, the application of superconducting magnets to the storage accelerator would suffer from technical difficulties unless a new superconducting technique could be developed. Therefore, we are planning to install another conventional ring in the same enclosure as a booster between the present synchrotron and the superconducting rings. It accelerates protons to about 50 GeV and its guiding field is inverted in order to provide the protons for another intersecting ring so as to run in opposite direction. The conventional ring will also be used as an electron or a positron storage ring after it acted *as* a proton booster between the present main ring and the superconducting rings. Furthermore, as a future option, this ring may be used to produce antiproton beams which will be accelerated and stored in one of the superconducting rings. So we will be able to carry out various types of colliding beam experiments as pp, $e^{\pm}p$, $e^{+}e^{-}$, $p\bar{p}$ and $e^{\pm}\bar{p}$ by choosing different sets of three rings. The particles accelerated in a ring which is free of colliding beam experiments can be extracted toward an experimental hall and used for stationary target experiments.

A preliminary outline plan of the TRISTAN is shown in Fig.1. Two diamond-shape rings (solid lines) are superconducting proton rings intersecting each other at four interaction points in a horizontal plane. The conventional ring (broken line) will be installed above or below the two superconducting rings and intersect them vertically at the beam-transfer or interacting points. Several experimental halls for stationary target experiments are also shown.

Table I. PRELIMINARY PARAMETERS OF TRISTAN pp RINGS

Injection Energy	12-50 GeV
Maximum Final Energy(Each Ring)	180 GeV
Number of Intersecting Points	4
Average Radius(Curved Section)	204 m
Long Straight Section Length	150 m
Short Straight Section Length	30 m
Total Circumference(6×12 GeV Ring)	2035 m
Maximum Magnetic Field	50 kG
Total Stored Energy	-70 MJ
Acceleration Time	-100 sec
Number of Betatron Oscillations	22.25
Cell Structure Separated Function	FODO
Number of Cells(Each Ring)	80
Cell-Length	-16.4 m
Full Vacuum Chamber Aperture	6 cm
Crossing Angle	40 mrad
Total Charge(Each Ring)	6×10^{14}
Circulating Current(Each Ring)	15 A
Luminosity(180 GeV)	7.5×10^{31} $cm^{-2}sec^{-1}$
Maximum Luminosity for Collinear Crossing	10^{34} $cm^{-2}sec^{-1}$

TRISTAN pp System

A set of preliminary parameters of TRISTAN pp rings is given in Table I. The average radius of TRISTAN rings is taken as six-times of the present main ring or approximately 324 m.

First, six pulses from the present main ring are injected into the TRISTAN conventional ring to fill up its total circumference leading to 6×10^{13} particles per turn. Then the protons are accelerated upto about 50 GeV and transfered into one of the superconducting rings. From the expected beam characteristics of the present synchrotron, the emittances of the 50 GeV beam would be 0.4 and 2.8 πmm·mrad in vertical and horizontal directions, respectively. Using a set of skew quadrupoles in the beam transport line, we interchange horizontal and vertical phase space of the 50 GeV beam before injection. By means of transverse stacking method we can accommodate some ten pulses of the 50 GeV beam in a useful half-aperture of about 3 cm. Thus 6×10^{14} protons or a 15 A proton beam will be stacked and accelerated in each superconducting ring. The filling time needed for the whole stacking process is about 100 seconds for each, and acceleration takes place in the following ~100 seconds. The vertical and horizontal emittances at 180 GeV are estimated to be $\varepsilon_V \approx 0.8$ πmm·mrad and $\varepsilon_H \approx 0.35$ πmm·mrad.

In Fig.2 and Fig.3 we show the proposed lattice for TRISTAN superconducting rings with the cell structure of a separated function FODO system. Taking the length of each long straight section as 150 m, we get the average radius of curved section as 204 m. The total cell number of 80 is chosen with betatron oscillation frequen-

cy in neighborhood of 20 and the phase advance of each cell of about 90°. A quadrant of each ring consists of 19 normal cells and one half bending-magnet cell (HBM cell). As is shown in Fig.2, the HBM cell of either ring is located in the down- (or up-) stream in a quadrant of two intersecting rings. Thus the superperiod of each ring is 2 forming a diamond-shape lattice in which each diamond crosses another diamond at a crossing angle of 2°14'. However, the crossing angle can be taken at any degrees by using an appropriate set of deflecting magnets in the position of the missing magnets of the HBM cells or in the long straight sections. In these lattice configurations, we can obtain proton energies of 150 GeV at the bending field of 40 kG and 180 GeV at 50 kG.

The luminosity for a horizontal crossing of the unbunched beams is given by

$$L_{pp} \simeq \frac{fN_p^2}{b_p \theta C} ,$$

where N_p is the total number of protons stored in each ring, $2b_p$ the full vertical beam height, θ the crossing angle, C the circumference and f the revolution frequency. Letting $N_p = 6 \times 10^{14}$, $b_p = \sqrt{\varepsilon_v \cdot \beta_v} = 0.9$ mm (β_v = 1m), θ = 2°14' and C = 2035 m, we obtain

$$L_{pp} = 7.5 \times 10^{31} cm^{-2} sec^{-1} .$$

If we use a quasi-collinear crossing of the bunched beams, then the luminosity will be improved leading to the maximum luminosity corresponding to the maximum allowable tune shift of Avo,

$$L_{pp\ max} = \frac{\beta_p \gamma_p}{2 r_p} \Delta\nu_0 \doteqdot 10^{34} \quad cm^{-2} sec^{-1} , \quad (1)$$

where we take the 8-function as $\beta_p (\beta_v = \beta_H)$ = 1m, γ_p = 190 (180 GeV), the classical proton radius $r_p = 1.5 \times 10^{-18}$ m and $\Delta\nu_0$ = 0.02. In this expression, the proton bunch length ℓ_p is assumed to be $\ell_p << 2\beta_p$.

Table II

PRELIMINARY PARAMETERS OF TRISTAN ep RINGS

Maximum Electron Energy	17 GeV
Maximum Proton Energy	180 GeV
Length of Interaction Region	150 m
Bending Radius (Electron)	124 m
Maximum Bending Field (Electron)	4.5 kG
Total Circumference	2035 m
Center of Mass Energy	110 GeV
R.F. Frequency (Electron)	~1200 MHz
Maximum R.F. Voltage (Electron)	100 MV/turn
Electron Current	30 mA
Power radiated by Electrons	1.5 MW
Maximum Luminosity	1.5×10^{31} $cm^{-2} sec^{-1}$
Crossing Angle	$\lesssim$30 mrad
Injector	1 GeV Electron Linac
Injection Field (Electron)	265 G

TRISTAN ep SYSTEM

In Table II are shown preliminary design parameters of TRISTAN ep system. The center of mass energy of the ep colliding system is 110 GeV with the electron energy of 17 GeV and the proton energy of 180 GeV.

We have considered several schemes for storage of electrons including its injector and RF acceleration system. Because of strong synchrotron radiation along a curved orbit, energy and intensity of the electron beam is limited by feasible RF techniques. In this respect, of the schemes proposed the one preferable is that in which an electron linac is used both as the injector and the ring RF acceleration system!) The total length of the electron linac is about 100 m and it is installed in one of the long straight sections of the TRISTAN conventional ring. As the injector the linac works at a pulsed operation and provides about 10^{12} electrons with a single turn injection. Immediately after this the electron linac is turned into a ring RF system which works, in a sense, at a CW operation. The energy loss per turn for an electron circulating the storage ring is about 35 MeV for a 15 GeV beam and 50 MeV for a 17 GeV Including effect of quantum fluctuations, about twice of these figures are required for the RF peak voltage. Considering the power and aperture requirements, we tentatively choose the RF frequency of the linac at L-band region and divide the total length into 10 sections. With a shunt impedence of about 50 MΩ/m, values of necessary RF power are listed in Table III both for the injector and the storage ring operations. It is shown that RF power tubes with a peak RF power of ~30 MW and with an average power of ~350 kW are required, which, however, would not be far beyond from the present available techniques.

In addition to the RF power requirements, some problems associated with this system should be mentioned. First, the linac RF system has the advantage of achieving a 100 % RF capture of the injected beam. However, about 200 mA·μs peak current of the linac at injection is required for providing a 30 mA circulating current in the ring since the revolution frequency of electrons is 150 kHz. This figure is around the maximum current achieved up to the present in the existing linacs. Furthermore, for obtaining a higher luminosity it is favorable that the electron bunches are arranged so as to be separated from one another at a distance equal to the separation of proton bunches. During the period of synchrotron accelerations, the RF acceleration voltage has to be programmed in a range from some hundred kV to a hundred MV. For this, we probably need to excite each section successively with a feed-back RF control system. In addition, a transverse focusing system along the linac should be matched to the ring lattice system. Preliminary orbit analysis shows that the transverse motion is quite feasible throughout the whole process including injection, acceleration and storage. Finally, if we wish to storage positrons as well as electrons in the same ring, we may need to build another relatively small ring which is provided for injection of positrons at a sufficient intensity.

Table III RF POWER OF ELECTRON LINAC PROPOSED FOR TRISTAN INJECTOR AND RF ACCELERATING SYSTEM

Function	Injector	Storage Ring RF (15 GeV)	Storage Ring RF (17 GeV)
Energy Gain	1 GeV	35 MeV	50 MeV
Operation Mode	Pulsed	CW	CW
Peak RF Voltage (Each Section)	100 Mv	6MV	10 MV
Wall Loss (Each Section)	20 Mw	70 kW	200 kW
Beam Loading (Each Section)	10 MW	100 kW	150 kW
RF Power (Each Section)	30 MW	170 kW	350 kW
Total Power	300 MW	1.7 MW	3.5 MW

The maximum luminosity for ep colliding experiments will be determined by the maximum allowable tune shift for electrons per intersection. For a quasi-collinear crossing, following relations between the length parameters may be assumed as a practical case.

i) The electron bunch length is short enough while the possible shortest proton bunch length could be 0.3 m.

ii) The β function are assumed to be $\beta_V = \beta_H$ and vary as $\beta_{e,p}(s) = \beta_{e,p} + \frac{s^2}{\beta_{e,p}}$ in the interaction region. The β-function for the electron ring at the center of the interaction region is much shorter than that for the proton ring or $\beta_e << \beta_p$.

iii) The proton bunch length (or the length of the interaction region of an unbunched proton beam), ℓ_p, could be longer than or comparable to the β_e value, while it is short enough compared to the β_p value, i.e. $2\beta_e \lesssim \ell_p << 2\beta_p$.

iv) The electron beam radius is narrower than the proton beam radius.

On the assumption of these relations, it is shown[1] that the tune shift, $\Delta\nu_e$, has a minimum when the following condition is satisfied between the proton bunch length (or the interaction length) and the electron-ring β-function as

$$\ell_p = 2\sqrt{3}\,\beta_e \quad . \tag{2}$$

Taking $\Delta\nu_{e\ min} = \Delta\nu_0$ (maximum allowable tune shift), we can obtain an expression for the maximum luminosity,

$$L_{ep\ max} = \frac{fN_e\gamma_e}{4\beta_e r_e}\,\Delta\nu_0 \ , \tag{3}$$

where N_e is the total number of stored electrons and r_e the classical electron radius. It is noted here the luminosity is one half of the usual expression for extremely short bunches, because the proton bunch length (or the optimum interaction length of an unbunched proton beam) is longer than β_e-value (see equ.(1)). For an unbunched proton beam as given in the pp colliding system, the optimum interaction length is estimated to be $\ell_p = 1$ m and, from equ.(2), the optimum β_e-value is about 0.3 m. Letting $f = 1.5 \times 10^5$ Hz, $N_e = 1.3 \times 10^{12}$ (30 mA), $\gamma_e = 3.3 \times 10^4$ (17 GeV), $r_e = 2.8 \times 10^{-15}$ m and $\Delta\nu_0 = 0.025$, we get

$$L_{ep}\ (\text{unbunched p}) \fallingdotseq 5 \times 10^{30}\ \text{cm}^{-2}\text{sec}^{-1} \ .$$

If we can bunch the proton beam as short as 0.3 m, then the corresponding optimum β_e-value is about 0.1 m and the maximum luminosity will become three-times higher, or

$$L_{ep\ max} \fallingdotseq 1.5 \times 10^{31}\ \text{cm}^{-2}\text{sec}^{-1} \ .$$

Time Schedule and Possible Phase I Project

The time schedule and cost estimates of the TRISTAN project should depend upon many unknown factors as the operation experience of the present machine, the future development of accelerator arts, the national economy, the man-power plan, the supply and power problems, etc. A tentative schedule presently seen is as follows:

1973 ~ 1975	Design study and fundamental research on superconducting magnets.
1975	Completion of the present machine.
1975 ~ 1977	Developments of superconducting magnets for storage rings and technical feasibility study.
1978	Construction started
1982	Completion of the conventional ring.
1985	Completion of the superconducting rings.

A rough total construction cost is estimated to be around 10^4 M yen, and, since this figure may be beyond a growth rate of our research budget, we had better divide the TRISTAN project into two stages, Phase I and Phase II. At present, we are considering two possible courses on the process from Phase I to Phase II. The one is that in which we construct the conventional ring in Phase I and use it as a storage accelerator both for protons and electrons. The construction of the accelerator enclosure for the whole project should also be included in Phase I. The conventional ring will accelerate protons to some ten GeV and electrons over ten GeV. Besides, this ring itself may be used as a 12 GeV electron-proton colliding beam machine. In this option, electrons as a starter are injected, accelerated and stored at about 13 GeV. Subsequently, 12 GeV protons accelerated by the presently constructing synchrotron are injected and stored in the same ring rotating in opposite direction. By a small momentum difference or an application of an electric field, we could separate electron and proton orbits except the interaction regions, so that we can devise a bypass or an interacting region without difficulty (Fig.4)[2]. The ep colliding experiments at 25 GeV in center of mass energy will be performed with a maximum attainable luminosity of about $10^{31}\ \text{cm}^{-2}\text{sec}^{-1}$.

The other course from Phase I to Phase II is to build double conventional rings in Phase I and replace one of them by a superconducting ring in Phase II. By means of taking this course, we can perform ep colliding experiments at a center of mass energy as high as 50 ~ 60 GeV; i.e. the energy at which weak processes involving neutrinos would become comparable to electromagnetic processes or large momentum-transfer strong interactions. Design of accelerator and the experimental facilities in Phase I will also become simple and more flexible, provided a little additional construction money should be financed.

Acknowledgement

Many colleagues in the KEK Accelerator Department and other laboratories have contributed to promote the design study reported here. In particular, the discussions with Professor K. Huke, Institute for Nuclear Study, University of Tokyo, Professor K. Kikuchi and Dr. T. Suzuki, KEK Accelerator Department should be acknowledged.

References

1. T. Nishikawa: Proc. 9th Intn'l Conf. on High Energy Acc., SLAC, 1974, p.

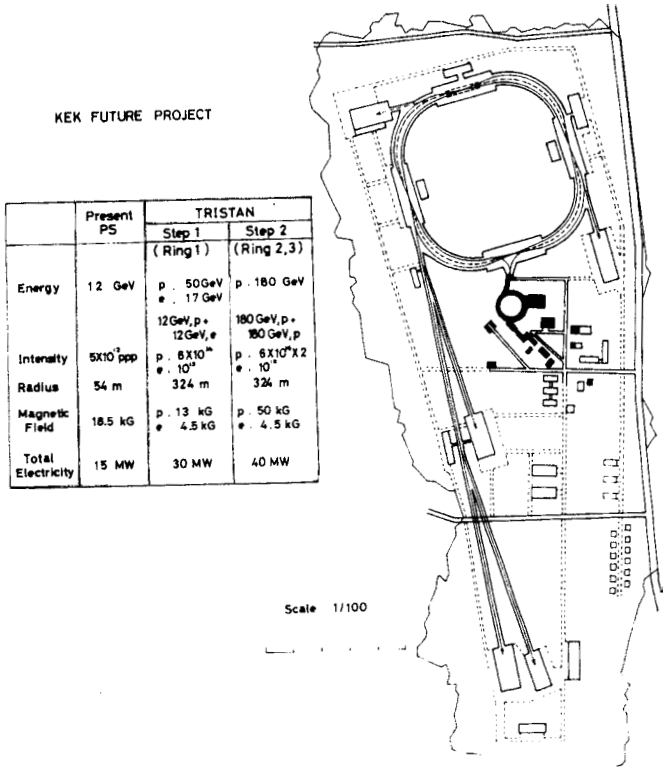
2. T. Nishikawa: Proc. U.S.-Japan Seminar on High Energy Accelerator Science, 1973, KEK, p.209

3. 200-GeV Intersecting Storage Accelerators, ISABELLE, A Preliminary Design Study, ed. by J.P. Blewett and H. Hahn, Brookhaven Rept. BNL 16716, May 1972

4. The LBL-SLAC Storage Ring Study Group: Proton-Electron Positron Design Study, IEEE Trans. NS-20 (1973) 1039, see also Pellegrini et al., Proc. of 8th Intn'l Conf. on High Energy Acc., 1971, CERN, p.153

5. D.A. Gray: Proc. U.S.-Japan Seminar on High Energy Accelerator Science, 1973, KEK, p.492

6. A Similar idea is proposed by I. Sato: Genshikaku Kenkyu 17 (1972) *441* (a Japanese Circular published from Institute for Nuclear Study, University of Tokyo)



	Present PS	TRISTAN	
		Step 1 (Ring 1)	Step 2 (Ring 2,3)
Energy	12 GeV	p . 50GeV e . 17GeV	p . 180 GeV
Intensity	$5X10^{12}$ ppp	12GeV,p+ 12GeV,e p . $8X10^{10}$ e . 10^{12}	180GeV,p+ 180GeV,p p . $6X10^{10}X2$ e . 10^{11}
Radius	54 m	324 m	324 m
Magnetic Field	18.5 kG	p . 13 kG e . 4.5kG	p . 50 kG e . 4.5 kG
Total Electricity	15 MW	30 MW	40 MW

Fig.1 Plan View of TRISTAN

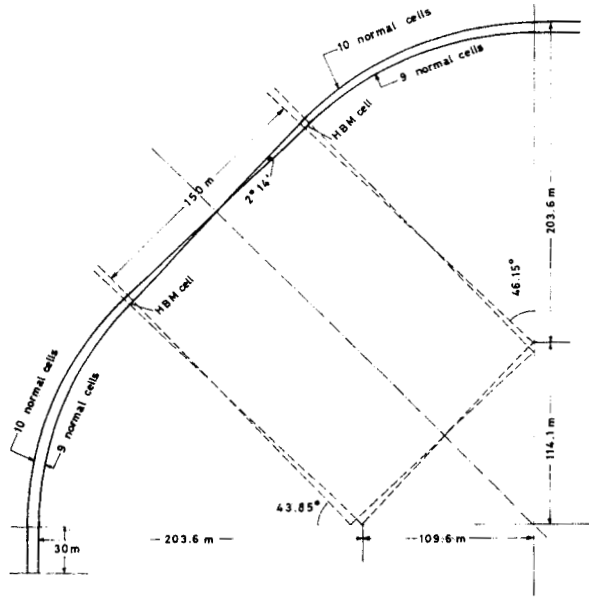
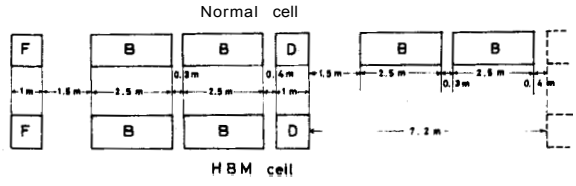
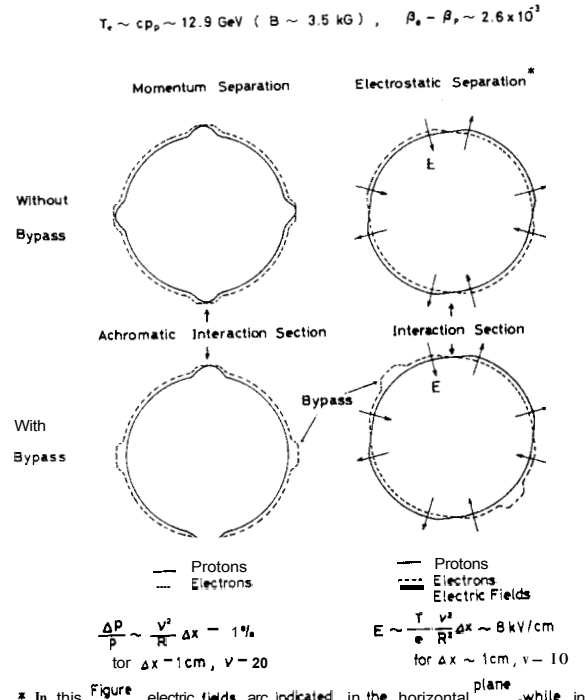


Fig.2 Quadrant of TRISTAN pp Rings



Cell Lrngth		16.4 m
Cell Numbers	Normal cell	76
	HBM cell	4
Radius of Curvature in Bending Magnet		124.0 m
Maximum BM Field (180 GeV)		50 kG
Maximum QM Gradient (180 GeV)		10.4 kG/cm
Phase Advance per cell		82° 7'
β Functions and X_p in regular cell		
β_{max}		26 m
β_{min}		6 m
$(X_p)_{max}$		2.4 m

Fig.3 Cell Structure of TRISTAN pp Rings



* In this Figure , electric fields arc indicated in the horizontal plane .while in practice one had better apply in the vertical directions .

Fig.4 Possible Single Ring ep Colliding Beam System for TRISTAN Phase I.

THE SUPER-ADONE ELECTRON-POSITRON STORAGE RING DESIGN

F. Amman, M. Bassetti, A. Cattoni, R. Cerchia, V. Chimenti, D. Fabiani, A. Marra, M. Matera, C. Pellegrini, M. Placidi, M. A. Preger, A. Renieri, S. Tazzari, F. Tazzioli and G. Vignola

Laboratori Nazionali di Frascati del CNEN

Frascati, Italy

Abstract.

The results of a design study[1] for a high energy electron-positron storage ring to be built at the Frascati National Laboratories are summarized.

1. - Introduction.

Super-Adone (SA) is a 10 GeV single-ring machine. Luminosity per crossing is $5\times10^{31} \div 10^{32}$ in the energy range from 5 to 10 GeV with one bunch per beam; multi-bunch operation is envisaged, to increase luminosity at energies lower than 5 GeV.

The design aim is to achieve good performances at relatively low cost; the following assumptions have been made: maximum RF power transferred to the beam 1.4 MW; maximum current per beam 200 mA; approximate linear tune shift per crossing 0.08; two interaction regions; maximum number of bunches per beam eight.

The limit on the current per beam is imposed by filling time since it is assumed to use ADONE as a booster with relatively minor changes to its injector.

The experimental regions are only two. The addition of two more experimental regions would increase costs (two more experimental halls, two more special "low-β" insertions) while four experimental apparatus would anyway not be able to run at the same time in the single bunch mode. At present it is considered more convenient to design the experimental halls in such a way as to guarantee a fast turn-over time for the experiments installed on the machine, rather than to have more straight sections.

As far as beam behaviour in a storage ring is concerned, the operation of existing storage rings allows to draw the following conclusions:

1) operation with charges per bunch of a few 10^{11} $e^{\pm}$ per bunch and peak currents of about 30 A has been achieved;
2) coherent single beam instabilities have been interpreted and cured;
3) the transverse incoherent beam-beam limit[2] is reasonably well explained by current models and numerical computations: the maximum linear tune shift per crossing obtained is about 0.08 (ADONE and SPEAR); a possible explanation for the γ^7 luminosity dependence observed at ADONE at energies lower than 1 GeV, could be a diffusion process in competition with radiation damping; the interpretation is not inconsistent with existing data, and would give, for Super-ADONE, the $\gamma^{7\div4}$ law for luminosity at energies below 2 GeV;
4) anomalous bunch lengthening has not been, so far, clearly interpreted, and although some light has come from the recent SPEAR results[3], extrapolation to new machines and higher peak currents is still difficult;
5) low-β operation has been proved possible and in agreement with expectation[5,10];
6) experimental information on the longitudinal beam-beam limit is not complete[2]; data obtained with ADONE will be used in the following (although the actual limit might be somewhat higher).

The most relevant difference between the new generation of storage rings and the present one, is the required charge per bunch which is typically one order of magnitude higher; this represents the major unknown of these projects and requires careful studies to determine possible coherent losses in RF structures and bunch lengthening effects. The operation of DORIS and SPEAR II will cast some light on these phenomena and will allow to bridge at least part of the gap in terms of charge per bunch and peak current.

Another problem of the new generation of storage rings is the accumulation of intense positron beams in a single bunch; it turns out that an injection system consisting of a linear injector and a booster is the most convenient solution to keep filling times within tolerable limits and to avoid saturation in the stored current.

2. - Design criteria.

The very strong dependence of radiation loss on energy ($\propto E^4$), at fixed bending radius makes the optimum radius a sharply peaked function of energy. The solution described here has not been carefully optimized and corresponds to an energy somewhat higher than the optimum value for the bending radius chosen.

Assuming that the maximum value of the approximate linear tune shift due to beam-beam interaction, ξ_m, is a constant, the specific luminosity (for $\beta_z \leq \beta_x$) at the beam-beam limit, is given by

$$L/I = 2.17\times10^{32}\ \xi_m E \quad \frac{1}{\beta_z} \quad (cm^{-2}s^{-1}A^{-1}) \qquad (1)$$

with β_z in m; k, in the present design, ranges from 1.07 to 1.2 (in general: $k_{max} = 2$ for $\beta_x = \beta_z$ at crossing).

Equ. (1) shows that specific luminosity depends only on the operating energy and the minimum β, ξ_m being constant. The β value cannot be made much smaller than the bunch length for the assumed value of ξ_m; very small β's at the crossing entail very large values of the same quantity in the quadrupoles adjacent to the straight section, with the consequent complications of large aperture and very high sensitivity to errors in the focusing field.

We assume $\beta_z = 0.2$ m; from ADONE and SPEAR results we take $\xi_m = 0.08$ and obtain, with k=1.1.

$$L/I = 0.95 \times 10^{32} E_{GeV} \ (cm^{-2}s^{-1}A^{-1}) \qquad (2)$$

In the choice of the total current per beam three variables have to be taken into account:

a) maximum RF power to the beams;
b) maximum current that can be stored in a reasonable time;
c) limit set by the transverse and longitudinal beam-beam effects on the beam transverse density.

Point b) sets an absolute limit on the maximum luminosity that can be achieved with a given injection system; a) influences the luminosity at the maximum energy and c) luminosity at low energies, both through economical factors (cost of the RF power and cost of the ring aperture). For a luminosity of 5×10^{31} cm^{-2} s^{-1} at 10 GeV, 50 mA per beam are required, and the RF power transferred to the two beams is 1.4 MW; at constant RF power to the beams and at a total current per beam smaller than 200 mA the allowed beam current is :

$$I = 50 \times (10/E_{GeV})^4 \text{ mA} \qquad \text{for } E \geq 7 \text{ GeV},$$

$$I \leq 200 \text{ mA} \qquad \text{for } E < 7 \text{ GeV}.$$

Transverse and longitudinal beam-beam effects limit the current per beam to :

$$I = 48.7 \cdot h \cdot \xi \ \frac{E^3_{GeV}}{H^*} \qquad (3)$$

where h is the number of bunches per beam and H^* is a quantity depending on the ring magnetic structure and related to the r.m.s. beam radial dimension σ_x at the interaction point; in the optimum condition of $\xi_x = \xi_z = \xi_m$, and for negligible coupling :

$$\sigma_x = a^p \sqrt{2 \beta_x H^*} \propto E \sqrt{\beta_x H^*}$$

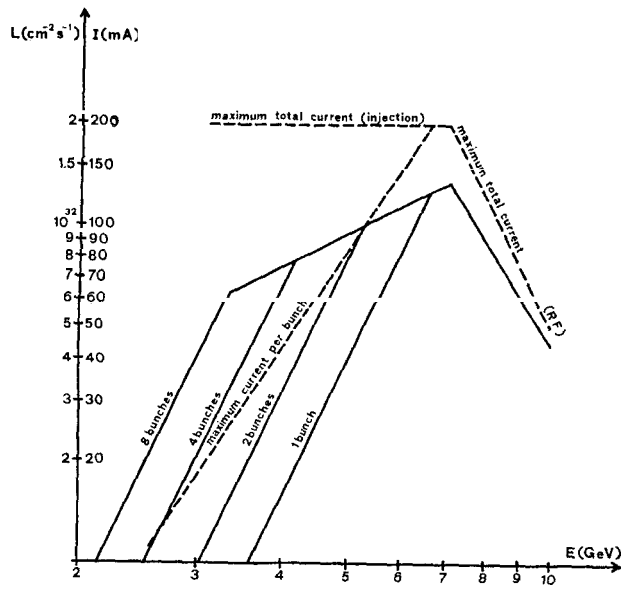
Eqs. (1) and (3) show that for a given magnetic structure (i.e. given H^*) and number of bunches, the luminosity L is proportional to E^4; if one wants to keep I constant, and therefore obtain $L \propto E$, the product hH^* has to vary like E^{-3}. A possible choice is that of varying the number of bunches; in a double ring the method is easy and the most convenient; in a single ring multiple bunch operation is conceivable, with an upper limit for the number of bunches per beam of 4 to 8.

Many different ways have been devised to increase H^*:

a) use of high dispersion function ψ at the crossing, within the longitudinal beam-beam limit[6];
b) variation of the betatron wavenumber Q_x with energy[7,8];
c) use of special magnetic lattices that allow a continuous variation of H^*[9].

The present design is based on method a) and multibunch operation, with vertically separated beams (except in the interaction regions) and $h \leq 8$. Method b) makes injection somewhat more complicated, while method c) may turn out to be the most flexible and convenient; a more systematic analysis is needed to make the final choice.

A plot of the expected luminosity versus energy is shown in Fig. 1.



Fig, 1 - Luminosity and current dependence on energy.

As far as injection is concerned, an injection system consisting of a linac and an intermediate energy booster has many advantages : the number of pulses injected on the same stored beam is small (order of $10^2 \div 10^3$); the number of pulses to be transferred from the booster to the main ring is quite low (order of 10') so that the booster energy need not *to* be very high; the linac energy can be in the 500-1000 MeV range.

In the present design it is foreseen to use ADONE as a booster, operating with six bunches that can be individually extracted; to keep the total filling time within one hour, or one tenth of the lifetime in the main ring at 1.5 GeV, the linac energy has to be increased to 500 MeV with the addition of 4 accelerating sections (two klystrons).

The overall positron filling time is about 45 minutes for 200 mA of positrons and the electron filling time is about 10 minutes. The damping time for betatron oscillations in the main ring is 1.3 sec at 1.5 GeV which allows a maximum repetition rate for successive injection pulses on the same RF bucket of 1 pulse per second.

3. - Lattice description.

The lattice consists of 24 normal cells and 2 low-β insertions each containing 8 magnets: the magnetic elements of a half-insertion are shown in Fig. 2. The experimental straight section is 7 m long, and the distance between its center and the first magnet is 18.1 m. Each half-insertion has 10 independent quadrupoles and 4 magnets.

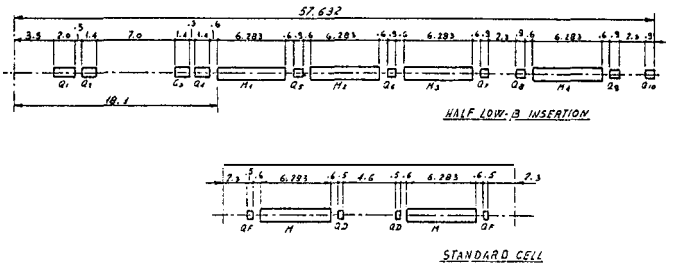


Fig. 2 - Magnetic structure.

The standard cell structure

$$\frac{0}{2}; QF; M; QD; 0; QD; M; QF; \frac{0}{2}$$

is symmetric with respect to the center of the 4.6 m straight section; most of the straight sections are occupied by RF cavities, and all of them contain a sextupole for the correction of chromaticity. Optimization of luminosity as a function of energy requires ψ^2/β_x at the crossing point $(\psi^2/\beta_x)_I$, the number of bunches per beam (h), and the coupling between radial and vertical betatron oscillations (ε) to be adjustable.

Four values of $(\psi^2/\beta_x)_I$ have been chosen, which define four configurations S_A, S_B, S_C, S_D, the number of bunches can be 1, 2, 4, 8 and ε is varied continuously within a given configuration ($\varepsilon_{min} \cong 0.2$). The optical parameters of the standard cell end of the low-β insertion for the 4 configurations S_A, S_B, S_C, S_D are given in Table I.

TABLE I

E_m = 10 Gev τ_x^o = 4.3 msec $\tau_x = \tau_x^o(E_m/E)^3$ $\sigma_x = \sigma_x^o(E/E_m)$ ν_x = 9.2

$A = A^o(E/E_m)^2$ τ_z^o = 4.1 msec $\tau_z = \tau_z^o(E_m/E)^3$ $\sigma_z = \sigma_z^o(E/E_m)$ ν_z = 9.2

σ_p^o = 1.1 x 10^{-3} τ_y^o = 2.0 msec $\tau_y = \tau_y^o(E_m/E)^3$ $\sigma_p = \sigma_p^o(E/E_m)$

Configuration	$a = \frac{\Delta l}{l}\frac{\Delta E}{E} \times 10^3$	β_x^I (m)	β_z^I (m)	ψ^I (m)	H (m)	H* (m)	$A^o \times 10^6$ (m)	σ_x^o out of coupling: cross-sing point (mm)	σ_x^o out of coupling: max (mm)	σ_x^o on coupling: cross-sing point (mm)	σ_x^o on coupling: max (mm)	σ_z^o on coupling: cross-sing point (mm)	σ_z^o on coupling: max (mm)	$C_x = \frac{\Delta\nu_x}{\nu_x}\frac{\Delta E}{E}$	$C_z = \frac{\Delta\nu_z}{\nu_z}\frac{\Delta E}{E}$
S_A	1.5	1.00	.20	0	.31	.31	.72	.8	9.7	.6	6.9	.26	6.4	- 2.1	- 2.4
S_B	1.3	1.00	.20	.98	.26	.74	.60	1.3	9.3	1.2	6.8	.24	6.3	- 2.1	- 2.4
S_C	1.3	2.16	.20	2.33	.26	1.52	.62	2.7	10.8	2.6	8.6	.24	4.8	- 2.3	- 3.5
S_D	1.2	1.25	.20	2.90	.54	3.91	1.28	3.3	15.0	3.2	11.9	.35	6.9	- 2.9	- 3.6

Figs. 3 and 4 shows the optical functions β_x, β_z and ψ for configurations S_A and S_D respectively.

While it is not possible to pass continuouslyfrom S_A and S_B to S_C and S_D, it is possible to pass from S_A to S_B and from S_C to S_D: only two injection configurations are therefore needed. The two injection structures have β_z^I = 1 m and ψ^I = 0.

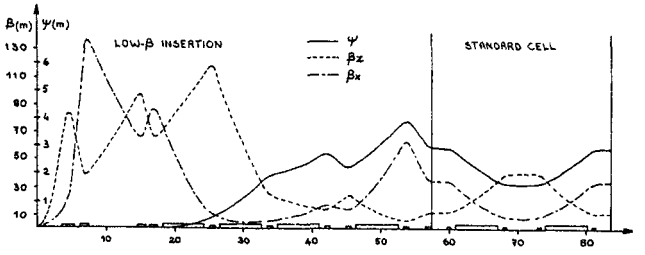


Fig. 3 - Optical functions for configuration **SA.**

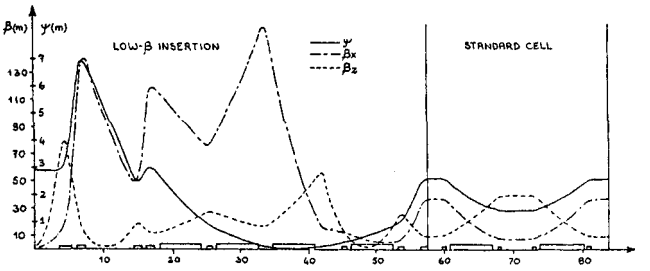


Fig. 4 - Optical functions for configuration S_D.

Operation with more than one bunch per beam can be obtained by separating the beams at all crossing points in the vertical plane (except for the experimental straight sections) using three independent pairs of electrostatic plates in each quarter of the machine.

There will be three kinds of quadrupoles having the following half-apertures (A): A = 105 mm (Q_2, Q_6); A = 90 mm (Q_3, Q_4, Q_5, Q_9); A = 75 mm (Q_1, Q_7, Q_8, Q_{10} and periodic cell) and two different kinds of magnets (the 16 low-β insertion magnets(b), and the 48 magnets of the periodic cells(a)), having the following characteristics:

	Gap height	Useful field region	total gap width
(a)	110	120	285
(b)	150	170	425

All magnets and quadrupoles will have laminated structures, assembled from precision-punched steel laminations. Magnets will be of the "C" type for ease of access and to make vacuum chamber assembly easier. With laminated cores "C"-type magnets are cheaper than "H"-type ones.

4. - Injection system.

For injection it is proposed to use ADONE as a booster. Injection in ADONE will be at 0.5 GeV over six equally spaced (58 ns) bunches which can be individually extracted after acceleration to 1.5 GeV.

A schematic diagram of the injection equipment connecting SA to the Linac/Adone facility is shown in Fig. 5.

Extraction from ADONE requires a slow "bumper", a fast kicker magnet and two septum magnets. The kicker magnet will occupy one of the interaction straight sections. The beam transport system both matches the ADONE emittance to the acceptance of **SA** and allows for a compensated deflection in the vertical plane. The overall system is achromatic to first order.

For injection into SA a perturbed closed orbit is excited by means of a bumper coil (EB) located in the high β_x section preceding the (I)sections, and switched off with two similar coils (SB) in the following high β_x sections. To achieve a complete compensation, in position and angle, of the perturbed closed orbit, two correcting bumps (CB) will be put in sections (I) near the deflectors D_1, D_2.

The same bump excites the perturbations for both injected beams making the overall number of oc-

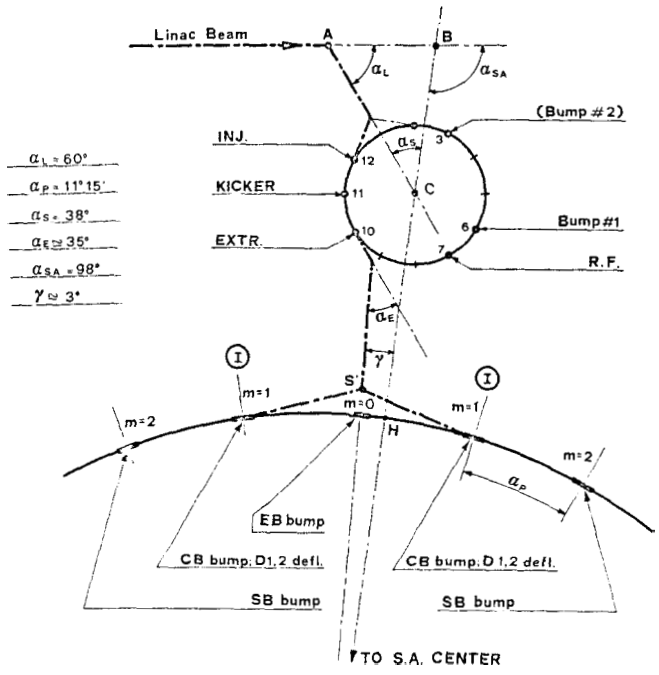


Fig. 5 - Injection system.

cupied high-β_x sections equal to 5.

The final deflection onto the right injection orbit is accomplished by means of two pairs of septum deflectors D_1, D_2 placed in sections (I).

5. - Radiofrequency system.

A reasonable choice for the RF frequency is 102.8 MHz, twice the frequency of the new ADONE RF system. At 102.8 MHz, 20 MV per turn are needed to ensure the required beam lifetime. We assume the shunt impedance per cavity to be 3 MΩ and the maximum voltage per cavity *to* be 0.36 MV. There are therefore 56 cavities (two per straight section). The power lost in the cavities is 1.2 MW at 20 MV, and power to the beam is 1.4 MW at 10 GeV, totalling 2.6 MW.

The cavities are normal reentrant resonators, under vacuum. Cavities only will be placed in the tunnel, while power amplifiers (one per cavity) will be located in nearby buildings and connected to the cavities through power coaxial cables.

6. - Vacuum system.

The system is designed for an average pressure of 10^{-9} Torr, with two 200 mA beams at 10 GeV. Pressure in the experimental sections will be 10^{-10} Torr.

The vacuum chamber material is S. S. AISI 304 L; its surface area is: chamber 13.4×10^6 cm^2, cavities 5×10^6 cm^2; the volume is: chamber 16×10^3 liters, cavities 90×10^3 liters.

Details on the required vacuum equipment, which includes distributed pumping in all magnets, can be found in the following 'parameter summary'.

Parameter summary.

Beam

Energy (GeV)	5	7	10
Luminosity $\times 10^{-32}$ (cm^{-2}s^{-1})	0.96	1.3	0.43
Current (mA)	200	200	50
Number of bunches per beam	4	1	1
Radiation loss per turn (MeV)	0.86	3.3	13.8
R. m. s. dimensions at interaction point (mm)			
radial uncoupled	1.6	0.9	0.8
radial coupled	1.6	0.85	0.6
vertical coupled	0.17	0.16	0.3
azimuthal [radiation]	50	70	75
Lifetime (hours)	~21	~14	~9

Magnetic structure

Central orbit length (m)	857
Average radius (m)	136.51
Experimental straight section total length (m)	2 x 7
Number of periodic cells	24
Periodic structure	0/2-F-B-D-0-D-B-F-0/2
Period length (m)	26.166
Bending magnet radius (m)	64
Bending magnet length (m)	64 x 6.283
Maximum field (Tesla)	0.52
Periodic cell quad length (m)	96 x 0.5
Maximum gradient (Tesla/m)	5
Weight (Tons) magnets	Fe 900 Cu 120
quadrupoles	Fe 185 Cu 40
Magnet gap aperture (cm^2)	
periodic cell	28.5 x 11
insertion	42.5 x 15
Quadrupole maximum inner radius (cm)	
periodic cell	7.5
insertion	10.5

Focusing characteristics

Periodic cell	$\beta_{x,z}$ (m)	max	35÷37; 39÷41
		min	8÷9 ; 10÷12
	ψ(m)	max	2.90÷3.10
		min	1.60÷1.80
	α R (m)		1.61÷2.08
Insertion	$\beta_{x,z}$ (m)	max	140÷170; 80÷140
	ψ(m)	max	3.5÷7
Interaction point	$\beta_{x,z}$ (m)		1.0÷2.2; 0.2
	ψ(m)		0÷2.9
Natural chromaticity :	radial		-2.16 -2.9
	vertical		-2.4÷ -3.6
Betatron frequency :	radial		9.2
	vertical		9.2
Revolution frequency (MHz)			0.35

Radiofrequency system

Frequency (MHz)	103
Harmonic number	294
Number of cavities	56
Number of amplifiers	56 (2x28)
Maximum power to the beam (MW)	2 x 0.7
Total R.F. power (MW)	2.6
Peak voltage (MV)	20

Vacuum system

Number of 200 l/s Ti-pumps	120
Number of 270 l/s turbomolecular pumps	32

Distributed pumps :	
pumping speed (l/s.cm)	10
length (m)	400
Pressure with beam in the experimental straight section (Torr)	10^{-10}

Injection

Extracted beam emittance (mmxmrad):	
horizontal	~5
vertical	3
Average injection rate (A/hour)	e^+ 0.2; e^- 1÷2
Injection energy in SA (GeV)	1.5
Injection energy in Adone (GeV)	0.5
Injection rate in Adone (p.p. s.)	5

7. - Buildings and utilities.

The tunnel will be built under ground between section 1 and section 5; the remaining part will be built at surface level. Two experimental halls ($20x40m^2$ x x 16 m height) will cover the experimental sections.

The maximum required electric power is 25 MVA including spare power, and is no problem,

The required cooling water flow is about 12.5 l/sec and could also be easily available.

A simple building, serving the machine and plants, will collect the electric, water, cooling, heating and conditioning stations tohether with the' machine services; control and data rooms will be put in a connected building.

The RF final stages will be accomodated in a different building.

8. - Higher energy ring.

A very preliminary study of the maximum dimersion ring that can be built in the Frascati National Laboratories area shows that a circular ring with mean radius of 340 in (or a race-track with a total length of about 2. 500 m) is feasible.

The storage ring energy could be 15-16 GeV, and the corresponding energy loss per turn would be (25-33) MeV/turn; the RF power transferred to the beams, required to obtain a luminosity of $5x10^{31}$ $cm^{-2}s^{-1}$ at the maximum energy would be (1.75÷2.3) MW. The injection system discussed above could be adequate, if a slight reduction in luminosity ($8x10^{31}$ max, at 10÷11 GeV) is accepted.

References

I - Super-Adone, Internal document of the Italian Institute of Nuclear Physics (INFN) and of the Frascati National Laboratories (1973).

2 - F. Amman, Beam-beam limits, 1973 Particle Accelerator Conference, IEEE Trans. on Nuclear Science NS-20, 858 (1973).

3 - M. A, Allen et al., Some observations on bunch lengthening at SPEAR, Report SPEAR-171 (1974).

4 - F. Amman et al., Remarks on two beam behaviour of the 1.5 GeV electron positron storage ring Adone, Proc. VIII Intern. Conf. on High Energy Accelerators, CERN (1971).

5 - SPEAR storage ring group, Operating resultsfrom SPEAR, 1973 Particle Accelerator Conference, IEEE Trans. on Nuclear Science NS-20, 752 (1973).

6 - SLAC storage ring group, The SLAC storage ring project SPEAR, Proc. VIII Intern. Conf. on High Energy Accelerators, CERN (1971), pag. 145.

7 - J. Rees et al., Preliminary design of a 15 GeV electron-positron variable tune storage ring, Report SPEAR-167 (1973).

8 - G. H. Rees et al., Variable damping and tunes in the e- ring, Report EPIC/MC/39 (1974).

9 - M. Bassetti, Resonant methods for beam size control in storage rings, This Conference.

10 - R. Averill et al., Colliding electron and positron beams in the CEA bypass, Proc. VIII Intern. Conf. on High Energy Accelerators, CERN (1971), pag. 140.

DISCUSSION

John Rees (SLAC): When you put more than one bunch in each orbit, how do you keep them apart except at the interaction region?

Sergio Tazzari (Frascati): We have a system of electrostatic plates that allows us to separate them.

James M. Paterson (SLAC): This is the same question put a different way. When you have multi-bunching and have the bunches separated in the other part of the ring, what is the typical beta function where the bunches pass?

Tazzari: The maximum beta function on the standard cell is about 50 meters.

Kjell Johnsen (CERN), Session Chairman: I thank the last speaker and I'd also like to thank the other speakers. I think many realistic projects have been presented to us this morning. It's probably too much to hope that all will be funded before we meet again at the Accelerator Conference, but I think we should hope, and have good reason to hope, that a few will have been started before the next conference.

BUNCHED BEAM INTERSECTING STORAGE ACCELERATORS FOR PROTON-PROTON COLLISIONS*

M. Month
Brookhaven National Laboratory
Upton, New York

Abstract

A set of parameters suitable for the operation of a bunched beam storage device for head-on proton-proton collisions is developed. The use of superconducting magnets allows a high energy/circumference ratio as well as a high magnet aperture/power consumption ratio as compared to conventional magnet designs. Using the AGS as injector, a beam-beam limited luminosity of 10^{32} cm^{-2} sec^{-1} at *200* GeV can be achieved using "single-turn" injection, this a consequence of the high intensity (0.7 A), low density AGS beam. The beam-beam tune shift limit is taken to be 5×10^{-3}. Acceleration from 30 to 200 GeV in *2.3* min. is obtained with a *27* MHz, *33* kV (peak) rf system with modest power dissipation. Various parameters, e.g. tune, chromaticity, nonlinear detuning and synchrotron frequency are discussed in terms of their influence on beam stability. In particular, the longitudinal stability of the bunches, the phase area growth due to rf noise, the transverse resistive wall instability, the head-tail effect, and beam stability against nonlinear resonances, specifically those arising from the beam-beam interaction, are discussed. It is found that the parameter set proposed is consistent with beam stability against these effects.

1. Introduction

We propose a pair of intersecting storage accelerators capable of colliding bunched proton beams head-on.[1] We will discuss the performance of such a device in terms of attainable energy and luminosity. The energy that is achievable follows directly from the choice of the ring circumference and the dipole magnetic field. The luminosity, on the other hand, is determined by the average current, the value of β^* at the collision point, the bunch length, and the beam-beam tune shift. Thus, we have 6 primary parameters upon which the ultimate performance is based.

Actually, we must consider a third performance characteristic, the beam lifetime, by which we mean the time during which there exist collisions providing usable experimental information. We can interpret this characteristic in terms of a luminosity duty factor. Since a deteriorating beam must be dumped and then the rings refilled, we can define the duty factor as the fraction of total operating time that beams capable of giving acceptable data persist.

We must ask, therefore: How much time during a given operating period will a beam be utilized for experimental purposes? And how much time will be spent dumping and refilling? The answer to the first question is the beam lifetime, which involves an understanding of various beam stability phenomena. The answer to the second is related to practical considerations: that is, it is the specific time required for dumping, obtaining a new beam, injecting, and setting up for collisions.

As we will see, the basic thrust of our suggestion will be a bunched beam with low momentum spread and large betatron emittance. This immediately differentiates our design from momentum stacked storage devices, such as the CERN ISR, used for colliding coasting proton beams.[2] In this latter case, large momentum spread is required for beam stability, small betatron emittance to maximize luminosity. In the bunched beam case, we want a small momentum spread in order to control linear tune spread at small values and we want large emittance to keep the transverse beam density low so that the beam-beam limit is not exceeded, Thus, for bunched beams, the preferred stacking mode is in betatron phase space. However, given the AGS as an injector, we find that the beam characteristics are not too far removed from optimal. We therefore suggest, for an initial design, the extremely simple operating procedure of taking the AGS bunches as they are, transferring them to the storage device (of course, we need as many AGS pulses as is required to fill the circumference of the ISA), accelerating and colliding them. That is, we suggest initially a no-stacking-operating mode.

To be specific, we will use for our lattice, the configuration proposed for the BNL ISA project.[3] This provides the basis for obtaining three fundamental parameters: the circumference, the vacuum chamber aperture, and the attainable energy. The particular values for these parameters are intimately tied to the question of whether to use a conventional magnet design or a superconducting one. Disregarding the technical feasibility of the superconducting design, which is extensively discussed in Ref. (3), the latter, superconducting magnet choice has two distinct advantages. First, there is the obvious fact that for a given machine radius, the higher magnetic field gives a higher energy. Secondly, for a given power consumption (in the superconducting design, heat leaks require power dissipation), the conventional design is severely limited by magnet gap, meaning greatly reduced vertical aperture as compared to the superconducting magnet design. As will become apparent, the larger aperture significantly improves beam stability and performance, the latter ultimately translating into higher luminosity. For this study, we will adopt a somewhat large aperture, which greatly simplifies the design effort. This implies the use of superconducting magnets, unless, of course, there is a willingness to lift the stringent limitation on magnet power consumption, thereby allowing the gap of the conventional dipoles to substantially increase.

Although we will not consider vacuum pumping and electron clearing here, we point out that requirements on these functions should be substantially reduced by the low average current and bunch structure.

In Section **2**, we discuss the performance capability of the bunched beam ISA, specifically the energy and luminosity. In Section **3**, the matching conditions for the bunched beam transfer are given, and we consider the acceleration and storage of the beam, including the stability of the bunches. Section *4* will deal with the nonlinear beam-beam interaction. As we will see, the synchrotron motion coupled with the beam-beam interaction imposes a strong constraint on the linear tune spread (e.g. that tune spread arising from momentum spread through the machine chromaticity). This connects the nonlinear constraints with transverse beam stability arising from collective beam effects. As it turns out, both the harmful consequences of the beam-beam nonlinearities and the transverse instabilities can both be suppressed by having a nonlinear tune spread in addition to the linear one. Both these aspects will be discussed together in Section *4*. Table I provides a list of parameters that are developed over the length of this paper.

* Work performed under the auspices of the U.S. Atomic Energy Commission.

TABLE I. PARAMETERS FOR A BUNCHED BEAM ISA

Basic Parameters	
Average Radius, R (m)	*428.2*
Final Energy, E (GeV)	*201.4 (302.1)*
Magnetic Field, B (kG)	*40 (60)*
Average Current, I (A)	*0.72*
β at Collision Point, β*(m)	*3.0*
Beam-Beam Tune Shift, $\Delta\nu_{bb}$	5×10^{-3}
Luminosity Per Collision Region (cm^{-2} sec^{-1})	1.04×10^{32} *(1.56 x 10^{32})*
Lattice†	
Vertical Beam Separation (cm)	*46.0*
FODO Cell Length (m) (no.)	*25.7 (48)*
Maximum β (m)	*43.0*
Maximum Dispersion $X_{p,max}$ (m)	*1.7*
Multipurpose Insertion (straight) Length (m) (no.)	*40.0 (4)*
Experimental Insertion (straight) Length (m) (no.)	*200.0 (4)*
Dipole Filling Factor in Curved Portions	*61%*
Bending Magnet Length (m) (no.)	*4.11 (256)*
Symmetry	*4*
Beam Transfer and Rf Parameters	
Kicker Rise Time (μsec) (Inj. & Ej.)	0.22
V_{rf} (Peak Voltage/Turn, kV)	*32.7*
f_{rf} (Frequency, MHz)	*26.8*
Bunching Factor, B, During Storage (Length/Separation)	*0.063* (15.78:1)
Q (Quality Factor)	*70*
$\|Z_s\|$ (Shunt Impedance) (kΩ)	*20*
Rf Power (kW)	*26.7*
Acceleration Time (min.)	*2.29*
Synchrotron Wave Number, ν_s	1.39×10^{-4}
Beam Characteristics at Injection (Matched From AGS)	
AGS Intensity (Protons Per Pulse)	1.2×10^{13}
Protons Per Bunch, N_B	10^{12}
AGS Longitudinal *95%* Emittance (eV-sec/bunch)	1.0
AGS Transverse *95%* Emittance (Area/π at *30* GeV, rad.m)	*2.35 x* 10^{-6}
Injection Energy (GeV)	*30*
Total Fractional Momentum Spread	*2.04* $\times 10^{-3}$
Bunching Factor, B, at Injection	*0.093* (10.81:1)
Beam and Chamber Characteristics	
At Cell β_{max}, β_{max}= 43.0m, X_p=1.7m, Vertical Half Beam Size (cm) *(30, 201.4* GeV), b	*1.00, 0.39*
Horizontal Half Beam Size (cm) *(30, 201.4* GeV), a	*1.17, 0.43*
Total Fractional Momentum Spread (Final Energy)	*4.45* $\times 10^{-4}$
Total Bunch Length (m) *(4* X rms length)	*4.26*
Central Tune	*19.381*
Chromaticity (u' = pdν/dp) (Final Energy)	+ *2.25*
Linear Tune Spread (via Chromaticity) (Final Energy)	
Nonlinear Tune Spread (Detuning Effect)	10^{-2}
Space Charge Tune Shift *(30, 201.4* GeV)	*6.64* $\times 10^{-4}$, 2.18 x 10^{-5}
Chamber Radius, r (cm)	*4.0*

†See Ref. (3).

2. Performance: Energy and Luminosity

Energy

The attainable energy is simply determined from the amount of circumference available for bending and the maximum dipole field. Subtracting the straight parts of the circumference (used for injection, ejection, rf stations, and experiments), and using a *61%* dipole filling of the curved portions[3], we have,

$$p(\mathrm{GeV/c}) = 5.035\ B(\mathrm{kG}) \quad . \tag{2.1}$$

This means at a *40* kG field, the maximum energy is *201.4* GeV, while for a *60* kG field, this increases to *302.1* GeV.

Luminosity

Under certain conditions, the luminosity and the limiting beam-beam tune shift can be very simply expressed. If the beams are nearly round in the transverse plane and if the rms bunch length is sufficiently less than the value of β*, then we have[4] for the luminosity, L, and tune shift, Δ_{bb},

$$L = \left(\frac{I}{e}\right) \frac{\gamma}{r_p} \frac{\Delta\nu_{bb}}{\beta^*} \ , \tag{2.2}$$

$$\Delta\nu_{bb} = \frac{r_p \beta^* N_B}{4\gamma a b} \ , \tag{2.3}$$

where a,b are the horizontal and vertical 1/2 beam sizes *(95%* sizes), γ is the energy in proton mass units, e is the electron charge, r_p is the classical proton radius, I is the average beam current, and N_B is the number of protons per bunch. The bunch length constraint is

$$\ell_p < 4\ \beta^* \quad . \tag{2.4}$$

Neglecting the small horizontal size arising from dispersion, we see that for a given beam-beam limit, *(2.3)* fixes the transverse bunch density. If we take $\Delta\nu_{bb}$ = 5×10^{-3}, and γ = *214.7*, we find

$$\frac{N_B}{\epsilon} = 2.62 \times 10^{18}\ \mathrm{m}^{-1} \quad .$$

The number of protons per bunch, corresponding to an average current of *0.72* A, is $N_B = 10^{12}$. This is a reasonable assumption as to what the AGS, as an injector, can provide. This then gives a required emittance, ε = *0.38* $\times 10^{-6}$ rad.m (at *201.4* GeV). This corresponds to ε = *2.35* $\times 10^{-6}$ rad.m at 30 GeV, which is in fact very close to the measured AGS emittance.[5] Using I = *0.72* A, and β* = *3* m, then L = *1.04* $\times 10^{32}$ cm^{-2} sec^{-1}. The *95%* bunch length is restricted to ℓ < 12 m, which is well within our design bunch length.† The emittances assumed correspond to beam sizes small compared to our design vacuum chamber radius.

The possibility of increasing the luminosity exists, but involves complications. The current can be increased by injecting more than one turn in betatron phase space, complicating our simple one turn matched transfer scheme. The value of β* can be reduced; however, this ultimately has the effect of increasing the chromaticity and making quadrupole tolerances more stringent. It further requires a lower bunch length, which means higher voltage and power consumption. Thirdly, for the bunched beam, it is conceivable, because of the small linear tune spread, that the beam-beam tune shift limit is larger than 5×10^{-3}. That is, by placing the beam in tune space far from low order resonances (e.g. away from *4* through 10), the beam-beam limit may be less than for stacked coasting beams, where

because of the large linear tune spreads, low order resonances (e.g. 5th) must be nearby.[6] To take advantage of this possibility however, what is required is a higher transverse beam density, i.e. for the same current, a lower emittance.

3. Beam Transfer and Rf Parameters

For an ISA circumference 3-1/3 times the circumference of the AGS, 40 AGS bunches would be needed to fill the ISA.[3] If 4 AGS pulses are used, each contributing 10 bunches (with 2 removed), the fast kicker requirement in the AGS is relaxed. In the ISA, the rise time of the fast kicker is determined by the distance between bunches, d. Since, in the AGS, we have 12 equally spaced bunches, the distance between bunches is $d = C_{AGS}/12 = 67.3$ m, since $C_{AGS} = 807.2$ m. Thus, the ISA kickers must be capable of rising and falling in roughly $t_r = d/c = 0.22$ μsec. The matched bunches will be injected in one of the multipurpose insertions, as shown in Ref. (3).

If we transfer matched bunches in stationary buckets, the matching condition is

$$\left(Vh\right)_{ISA} = \left(Vh\right)_{AGS} \frac{\eta_{ISA} R^2_{ISA}}{\eta_{AGS} R^2_{AGS}} \qquad (3.1)$$

where $\eta = \frac{1}{\gamma_t^2} - \frac{1}{\gamma_{INJ}^2}$, γ_t is the transition energy (in proton mass units), γ_{INJ} is the injection energy, V is the peak rf voltage, and h is the harmonic number of the respective rf systems. With $V_{AGS} = 384$ kV/turn, $h_{AGS} = 12$, $\eta_{AGS} = 0.0137$, $R_{ISA} = \frac{10}{3} R_{AGS}$, and $\eta_{ISA} = 0.0021$ (i.e. $\gamma_t = 18$, $\gamma_{INJ} = 32$), we have, for matching

$$\left(Vh\right)_{ISA} = 7848.2 \text{ kV/turn} \quad . \qquad (3.2)$$

From the point of view of bunched beam stability, it is desirable to have a high frequency rf system (i.e. high h).[7] However, this, coupled with the matching constraint (3.2), which would require a "lower" voltage, means that the bucket rapidly shrinks around the bunch. Thus, given the matching constraint, there is a limit on h. The bucket area is given by

$$A_b = \frac{4\sqrt{2}\sqrt{E_o}}{\pi\sqrt{\pi} f} \sqrt{\frac{V\gamma}{\eta h^3}} \quad , \qquad (3.3)$$

where f is the revolution frequency and E_o is the proton rest energy.

To clarify this point about high rf frequency (i.e. high harmonic number, h), we will develop the current limit arising out of the bunched beam space charge frequency shift, which is the most stringent limit on current. If the chamber wall is perfectly conducting, then the image force induced on the beam is non-resistive. Although no growth can result, a non-resistive force can drive the beam into a condition of latent instability, which could then be activated by the chamber resistivity or resonant structures in the ring. The condition for the current limit can be derived from the Landau damping criterion which states essentially that the frequency shift resulting from the force must be less than the spread in synchrotron frequency for the bunches, or[8]

$$\frac{\Delta\omega_{sc.}}{\Omega_s} < \frac{S}{4\Omega_s} \quad , \qquad (3.4)$$

where $\Delta\omega_{sc}$ is the space charge frequency shift, $\Omega_s = 2\pi f \upsilon_s$ is the central synchrotron frequency, υ_s is the synchrotron wave number, and S is the spread in synchrotron frequency in a bunch. If the bunches are well within the bucket, then S comes primarily from the octupole component of the synchrotron force, i.e.,

$$\frac{S}{\Omega_s} = \frac{\pi^2 h^2 B^2}{16 M^2} \quad , \qquad (3.5)$$

where M is the number of (equally spaced) bunches (note that $h \geq M$), and B is the bunching factor (length/separation). The real space charge frequency shift can be written,[7]

$$\frac{\Delta\omega_{sc}}{\Omega_s} = (0.152) \frac{\pi^3 E_o Z_o}{16 f^2} \frac{g_c I B}{\gamma\eta A^2 M^2} \quad , \qquad (3.6)$$

where I is the average beam current, A is the invariant bunch area (in eV-sec), Z_o is the free space impedance ($Z_o = 377$ ohms), g_c is a geometrical factor,

$$g_c = 1 + 2\ell n (r/b) \quad , \qquad (3.7)$$

and r,b are the vacuum chamber radius and beam radius respectively. Taking $r/b \approx 4$, we obtain from (3.4),

$$I < 4.9 \times 10^{-3} \gamma\eta A^2 h^2 B \quad , \qquad (3.8)$$

which is dependent on h, not M. For elliptical bunches, the peak voltage, V, and bunching factor, B, are related by,

$$Vh = \frac{8 f^2}{\pi^3 E_o} \frac{\eta A^2 M^4}{\gamma B^4} \quad . \qquad (3.9)$$

At injection, taking M = 40, A = 1.0 eV-sec (a realistic value for the AGS at $N_{AGS} \approx 1.2 \times 10^{13}$ ppp),[5] and Vh from (3.2), we find from (3.9), $B^{-1} = 10.81$. If $h = M$, the current limit from (3.8) is $I < 0.049$ A, which is more than an order of magnitude less than the design current of 0.72 A. To stabilize the beam at injection, we use a higher rf frequency. Taking $h = 6M = 240$ (corresponding to an rf frequency, $f_{rf} = 26.76$ MHz), the current limit increases to $I < 1.76$ A. The matching peak voltage can be found from (3.2): V = 32.7 kV/turn. The bucket area at injection is, from (3.3), $A_b = 1.68$ eV-sec, which results in a bucket filling of $A/A_b = 60\%$.

The process of increasing h and decreasing V is clearly an effective stabilizing technique. After matching, the voltage can be increased (adiabatically) in order to decrease the bucket filling factor. Then, of course, the bunches become tighter and the current limit is slightly reduced.

At high energy, the current limit is greatly increased. With $\gamma = 214.7$, $\eta = 0.0031$, we find $B^{-1} = 15.78$, $A_b = 2.13$ eV-sec, giving a bucket filling of 47%, and a space charge current limit, $I < 11.9$ A.

It is thus clear that in the storage phase, the limitation to bunch stability derives from the interaction with resonant structures.[7] For each such structure, there will be a limit on its shunt impedance. For example, consider a structure, capable of inducing a dipole mode beam oscillation at a frequency, $f_{RES} \approx 50$ MHz, near the "critical frequency". We find a shunt impedance limit, $R_s < 3$ kΩ. However, for such a structure, if the shunt impedance is 100 Ω above the limit, we estimate a growth time on the order, $\tau \approx 10$ sec. Such a short growth time reflects the importance of achieving the required stability limit for each resonant structure.

The bunch characteristics during storage can be found from:

(1) bunch length, $\ell_p = \frac{2\pi RB}{M}$, **(3.10)**

(2) total momentum spread,

$$\frac{\delta p}{p} = \frac{2\pi\nu_s B}{M\eta} \qquad (3.11)$$

(3) central synchrotron frequency,

$$\nu_s = (Vh\eta/2\pi\gamma E_o)^{\frac{1}{2}} \qquad (3.12)$$

Using V_{rf} = 32.7 kV/turn, f_{rf} = 26.8 MHz (h = 240), B^{-1} = 15.78 (A = 1.0 eV-sec), we have ν_s = 1.39 X 10^{-4}, ℓ_p = 4.26 m, $\Delta p/p$ = 4.45 X 10^{-4}.

After matching, the 40 bunches in the ISA can be directly accelerated. Acceleration is governed by the equation

$$p = eV \sin\phi \quad f \quad , \qquad (3.13)$$

where ϕ_s is the rf stable phase angle. Thus, the time to accelerate an amount δp is

$$\delta t = \frac{\delta p}{f\ eV\ \sin\phi_s} \quad . \qquad (3.14)$$

With $\delta p = p_{Final} - p_{INJ}$ = 171.4 GeV/c, V = 32.7 kV, and $\phi_s = 20^o$, we have δt = 2.29 min.

The proton bunches must be stored for long periods of time in order to sustain a high luminosity duty factor. Since there is negligible radiation damping of synchrotron oscillations for protons, rf noise, which can couple to this motion, can induce a diffusive growth in the synchrotron amplitude. In particular, we will limit ourselves here to an estimate of the longitudinal phase space area growth due to fluctuations in the rf voltage. It has been shown that for a mean square voltage fluctuation

$$\langle u^2 \rangle = \left\langle \left(\Delta V/V\right)^2 \right\rangle \quad , \qquad (3.15)$$

the mean diffusion time for growth of the synchrotron amplitude is [9]

$$\tau = \frac{h}{\pi f\ Q\ \nu_s^2 \langle u^2 \rangle} \quad , \qquad (3.16)$$

where Q is the quality factor for the accelerating cavity. If we take h = 240, $\langle u^2 \rangle$ = 0.76 X 10^{-6} (corresponding to an error in stable phase angle of 0.05 degrees), f = 111.5 kHz, ν_s = 1.39 X 10^{-4}, and Q = 70 (consistent with a shunt impedance, R_s = 20 kΩ and a peak beam current, I_{peak} = 11.4 A), we find a growth time on the order of years.

4. Tune, Tune Spread and the Beam-Beam Interaction

The fundamental limit to the performance of a storage device arises from the fact that during collisions, the electromagnetic forces between two sufficiently intense beams induce beam growth and ultimately beam loss at the aperture boundary. A measure of the strength of the interaction is the beam-beam linear tune shift, Δ_{bb}, although the beam-beam interaction is in fact a highly nonlinear one. There is disagreement about whether the observed beam loss can be explained using traditional resonance concepts or whether some new multiresonance picture must be used, with resonances combining to cause quasi-random, i.e. diffusion-type beam behavior. We are not here concerned with this aspect of the beam-beam interaction. We simply accept the existence of such a limit, though we might mention the point that if the beam-beam limit is tune sensitive" as appears to be the case and, further, if closeness to low order nonlinear resonances (i.e. of order 4 or 5, rather than 11 or 12) enchances the loss phenomenon, then bunched beams could have a beam-beam limit higher than coasting beams since the tune spread is far less and the working line (really a working point in the bunched beam case) can be set away from the low order resonances. Thus, we choose a rather conservative beam-beam limit, Δ_{bb} = 5 X 10^{-3}. But, since our working point can be removed from all resonances up to, say, the 13th order, then it is not inconceivable that for bunched proton beams, the limit would be considerably higher.

However, with bunched beams, particles execute synchrotron motion. Through the machine chromaticity, this time variation of momentum translates into a dynamic tune oscillation. Particles can thus "pass through" high order resonances and the possibility of "lock-in" emerges.[9] The beam-beam interaction is by far the most dangerous source of nonlinear resonances," and we will therefore attempt to set up stability criteria for these nonlinearities in the presence of synchrotron motion. We will do *so* by treating the nonlinear resonances in the traditional manner as isolated entities. In doing this, we are making the implicit assumption that the dynamic tune variation caused by the synchrotron motion does not significantly alter the beam-beam limit, or that, in any case, we are operating below the true limit.

The basic stabilization criteria are related to (1) control of the central tune away from the "low" order nonlinear resonances, (2) maintenance of small linear tune spread (equivalent to the maximum tune variation per synchrotron period) for essentially the same reason, (3) introduction of sufficient nonlinear detuning (e.g., 0th azimuthal harmonic octupole), and (4) an upper bound on the resonance excitation strength. We confine ourselves to one-dimensional resonances. Analogous criteria for coupling resonances are more complicated, but not conceptually different.

The tune of the ISA is $\nu \sim$ 19-20. If our particular choice is ν = 19.3810, then we are very close to a 21st order resonance (8/21). The nearest resonances of lower order are the 13th (5/13) and the 8th (318). The distance from these resonances are 0.0036 and 0.006 respectively. This gives us a feeling for the required control on ν spread, $\overline{\Delta\nu}$. With $\overline{\Delta\nu} = 10^{-3}$, we can essentially neglect these resonances. Note that this type of control is required during collisions where the high order resonances may be dangerous. Thus, we need such control only under static magnetic and rf conditions.

Although tune control as described here might be sufficient to stabilize a beam against beam-beam nonlinearities, we can place some limit on resonance excitation in the event that in practice the tune control is not as fine as prescribed. To derive the nonlinear stability criteria, we will use the quasi-static (adiabatic) picture of "lock-in" or "particle trapping". Under such circumstances, we can derive two simple constraints. First, by including sufficient nonlinear detuning, any particle trapped will not reach an aperture. If we let Δ_{NL} represent the nonlinear (octupole) detuning strength at the rms beam amplitude, then the amplitude range for "lock-in" is given approximately by

$$\Delta\epsilon = \frac{\overline{A_L}}{\Delta_{NL}} \epsilon_B \quad , \qquad (4.1)$$

where ϵ_B is the rms beam emittance, and $\Delta\epsilon$ is the "lock-in" range in emittance units. If we have $\Delta_{NL} = 10^{-2}$ and $\overline{\Delta_L} = 10^{-3}$, then we see that the range $\Delta\epsilon$ is 1/10 of the beam emittance. It should also be remembered that since trapped particles do not reach an aperture limit, they simply oscillate within the range $\Delta\epsilon$ and, to lowest order, there is no effect of the nonlinear "lock-in"

process on the beam.

The condition *(4.1)* is independent of the exciting resonance. For strong excitation strengths, this will cease to be the case. One can picture the effect in the particle phase space. Unstable fixed points, which for small excitation widths are outside the machine aperture, begin to move toward the beam. When they are near the beam, particle motion becomes dominated by these unstable fixed points and the particles will begin to move on outward (in amplitude) moving trajectories. To prevent this, we set a limit on the resonance excitation width, Δ (evaluated at the beam rms emittance):[5]

$$\Delta < \Delta_{NL} \left(\frac{\epsilon_B}{\epsilon_{AP}}\right)^{(p-4)/2} , \qquad (4.2)$$

where ϵ_{AP} is the emittance corresponding to the aperture, and p is the order of the resonance ($p > 4$). For $\Delta_{NL} = 10^{-2}$, this condition will be easily satisfied, even for the strong beam-beam interaction.

For a weak resonance (Δ_e small) or high synchrotron frequency, our adiabatic assumption will begin to break down. Actually, we can picture this breakdown qualitatively as follows: If the tune variation is slow, the particle trapping is efficient. As the tune rate increases, the buckets trapping the particles move through the phase space faster and become "leaky". The trapping efficiency of these buckets decreases. However, since the bucket motion within the phase space is a distance in amplitude only a fraction of the beam size, we expect no significant distortion of the beam distribution.

With the parameters we have chosen, we find that for the beam-beam interaction, adiabatic conditions essentially do prevail--the adiabatic condition being

$$\bar{\Delta}_L \lesssim 2\pi \Delta_e \Delta_{NL}/\nu_s , \qquad (4.3)$$

where ν_s is the synchrotron wave number, and where it is understood that *(4.3)* represents an "order-of-magnitude" criterion.

Using the calculations for resonance excitation widths given in Ref. (12), we can give an example of the use of the foregoing expressions for a typical case. Take the 10th order resonance, with $\Delta_e = 10^{-3}\,\Delta_{bb}$. With $\Delta_{bb} = 5 \times 10^{-3}$, $\Delta_e = 5 \times 10^{-6}$. If we have the aperture at $\epsilon_{AP} = 10\,\epsilon_B$, *(4.2)* for $p = 10$ is $\Delta_e < 10^{-5}$. This means that for the 10th order resonance, the unstable fixed points are outside the aperture, but not by much. The implication of this is that if the beam-beam tune shift increases, and if Δ_{NL} remains the same, these unstable fixed points will enter the machine vacuum chamber. Thus, the aperture limit, or sink for particle loss, will occur inside the chamber. Of course, this is only a real limit on Δ_{bb} if we are forced to choose a tune in the vicinity of this resonance and if Δ_{NL} is not large enough.

We conclude that the group of parameters $\{\bar{\Delta}_L = 10^{-3}, \Delta_{NL} = 10^{-2}, \Delta_{bb} = 5 \times 10^{-3}, \nu_s = 1.39 \times 10^{-4}\}$ represents a consistent, stable set.

Because the transverse density varies along the bunch, the space charge tune shift is coupled to the synchrotron motion and therefore adds to the tune variation during synchrotron motion. The circular geometry implies no image contribution at the chamber center. We therefore have for the incoherent tune shift,[13]

$$\Delta\nu_{sc} = \left(\frac{I}{e}\right) \frac{r_p R}{\pi\nu f B \gamma^3} \frac{1}{b(a+b)} . \qquad (4.4)$$

With $I = 0.72$ A, $R = 428.2$ m, $\nu = 19.381$, $B^{-1} = 15.78$, $\gamma = 214.7$, $a = 0.43$ cm, $b = 0.39$ cm, we have $\Delta\nu_{sc} = 2.18 \times 10^{-5}$. This is negligible as a contribution to the range of tune through a synchrotron period.

Since we have stated both linear and nonlinear tune spreads, we must examine their consistency with stability against the transverse resistive wall instability.[14] Landau damping stabilization can be derived from linear and/or nonlinear tune spread. Note that the synchrotron frequency is sufficiently small that the linear tune and tune spread are well defined characteristics in the adiabatic sense and the latter provides an effective means of Landau damping. In this case, we can write two separate expressions for the required spread, one relating to image forces created in the chamber and the other dependent on the beam characteristics. Of course, both must be satisfied. We have, approximately, for the criterion dependent only on the image force,

$$\delta\nu > \frac{4 r_p R^{5/2}}{e\nu\gamma r^3} I \sqrt{\frac{2\epsilon_o \rho_e}{c|k-\nu|}} , \qquad (4.5)$$

where $\delta\nu$ is the full width of the betatron tune distribution, k is the azimuthal mode number ($k > \nu$), r is the chamber radius, ρ_e is the chamber resistivity (in ohm-m), and ϵ_o is the free space dielectric constant ($\epsilon_o = 10^{-9}/36\pi$ sec/ohm-m); while the beam dependent criterion is approximately,

$$\delta\nu > \frac{4 r_p R^2 I}{e\nu c \gamma^3 B b^2} , \qquad (4.6)$$

where b is the 1/2 beam size.

Take k = 20 (lowest mode), $\rho_e = 1.6 \times 10^{-8}$ ohm-m (Aluminum), and $r = 4$ cm, then (4.5) gives at injection ($\gamma = 32$) $\delta\nu > 1.03 \times 10^{-4}$. At high energy, the criterion becomes $\delta\nu > 1.54 \times 10^{-5}$. For the beam dependent term, we require $\delta\nu > 2.88 \times 10^{-3}$ at injection; while at high field, the fall-off with γ is rapid, leading to the requirement $\delta\nu > 9.15 \times 10^{-5}$. Thus, the linear tune spread, $\bar{\Delta}_L = 10^{-3}$ will be more than adequate during storage. At injection, effective damping of the resistive wall instability will result if we combine the linear tune spread with the rather large nonlinear spread, $\Delta_{NL} = 10^{-2}$.

The head-tail instability•• is stabilized (1) by having positive chromaticity and (2) by having sufficient nonlinear tune spread. Our design value, $\nu = +2.5$, stabilizes azimuthal oscillation modes up to the 8th at injection and higher at the final energy. The large nonlinear tune spread, $\Delta_{NL} = 10^{-2}$, means that the beam should be stable against the head-tail effect for all modes.

5. Conclusions

We have developed a set of parameters suitable for the operation of a bunched beam storage device for head-on proton-proton collisions. The use of superconducting magnets allows a high energy/circumference ratio as well as a high magnet aperture/power consumption ratio as compared to conventional magnet designs. With the AGS as injector, we can achieve a respectable luminosity with "single-turn" injection as a consequence of the high intensity, low transverse density AGS beam. At an energy of 200 GeV, and an average current of 0.72 A, our estimated beam-beam limited luminosity is 10^{32} cm^{-2} sec^{-1}. The beam-beam tune shift limit has been taken to be 5×10^{-3}. Acceleration from 30 to 200 GeV in 2.3 min can be obtained with a 27 MHz, 33 kV (peak) rf system with modest power dissipation.

Beam stability plays an especially important role in storage ring design. Various parameters, e.g. tune, chromaticity, nonlinear detuning and synchrotron frequency have been discussed in terms of their influence on beam stability. In particular, we have considered the longitudinal stability of the bunches, the phase area growth due to rf noise, the transverse resistive wall instability, the head-tail effect, and beam stability against nonlinear resonances, specifically those arising from the beam-beam interaction. We have found our proposal parameter set to be consistent with beam stability against these effects.

References

1. M. Month, BNL Informal Report, CRISP 73-20 (1973).
2. "The Design Study of Intersecting Storage Rings (ISR) for the CERN Proton Synchrotron", CERN Report AR/Int. SG/64-9 (1964).
3. "200-GeV Intersecting Storage Accelerators-ISABELLE", A Preliminary Design Study, BNL Report 16716 (1972); and subsequent revised edition, 1974, to be published.
4. M. Sands, Stanford University Report, SLAC-121 (1970).
5. The AGS parameters have been obtained privately from M.Q. Barton, J.C. Herrera, E.C. Raka and A. van Steenbergen.
6. M. Month, BNL Informal Report, CRISP 73-24 (1973).
7. M. Month, BNL Informal Report, CRISP 73-23 (1973).
8. F.J. Sacherer, Proc. 1973 Particle Accelerator Conference, San Francisco, p. 825, March 1973.
9. E. Hartwig, V.K. Neil, and R.K. Cooper, Proc. 1973 Particle Accelerator Conference, San Francisco, p. 833, March 1973.
10. See, for example: SPEAR Storage Ring Group, p. 752; and Orsay Storage Ring Group, p. 768, Proc. 1973 Particle Accelerator Conference, San Francisco, March 1973.
11. A. Schoch, CERN Report, CERN 57-23 (1958).
12. E. Keil, CERN Reports CERN/ISR-TH/72-7 and 72-25 (1972).
13. L.J. Laslett, Proc. 1963 Summer Study on Storage Rings at Super-High Energies, (J.W. Bittner, ed.), BNL Report 7534, p. 324 (1963).
14. L.J. Laslett, V.K. Neil and A.M. Sessler, Rev. Sci. Instrum. 36, 436 (1965).
15. C. Pellegrini, Frascati Report, LNF-69/45 (1969); M. Sands, SLAC Reports SLAC-TN-69/8, 69/10 (1969); and B. Zotter, CERN Report, CERN/ISR-TH/69-60 (1969).

INSERTIONS FOR COLLIDING-BEAM STORAGE RINGS

W.W. Lee and L.C. Teng
National Accelerator Laboratory*
Batavia, Illinois

Abstract

A new approach is presented for the design of the beam-collision straight sections of high-energy colliding-beam storage rings. Interchangeable special function lattice insertions are used to obtain local beam characteristics at the collision point to meet the requirements of individual experiments. Other insertions are used to adjust the phase advance and the orbit-length dispersion to optimize the performance of the rings. These insertions are modularized in length and matched to one another in optics and dispersion functions so that they can be inserted or joined together with maximum flexibility. Examples are given for 1000 GeV-1000 GeV superconducting magnet proton storage rings.

Introduction

The magnet rings of colliding-beam storage rings can be considered as being composed of two types of sections serving different functions. These can roughly be identified as the inactive curved sections and the active straight sections. In straight sections beams are injected and made to collide, and experiments are performed. Curved sections serve only to transport the beams from one straight section to the next. The design of the inactive curved sections is based only on beam stability and economy, and is generally the concern of the accelerator builders alone; whereas the design of the active straight sections is crucial to both the builders and the users.

The conventional procedure for designing the straight sections is to first assemble the builders and the users in study sessions. Plans of all conceivable colliding-beam experiments are made. Each straight section is designed for one or a group of these hypothetical experiments. These straight sections are then incorporated as integral parts of the magnet lattice of the storage rings. In contrast, for conventional experiments using the external beam from an accelerator, because of the flexibility in the interposing beam lines the design of specific experiments have much less influence on the design of the magnet lattice. We suggest here a parallel interpretation of colliding-beam experiments which restores to some degree the decoupling between the machine and the experiments and leads to a different approach for design of the straight sections in storage rings.

When the beam in a storage rings exits from a curved section it can be considered as having been extracted from the machine. A tailor-made line is provided to transport the "external" beam to the experimental target (the collision point) for the specific experiment. After going through the very thin target (the other beam) the beam unaffected by the target is transported "back" by another tailor-made beam line to be reinjected and recirculated in the following curved section. The design approach suggested by this interpretation consists in modularizing and specializing segments (insertions) of the straight-section ("external") beam lines of storage rings in such a way that all segments are mutually matched and hence mutually interchangeable, Specific modules are joined together to transport the beams to the Collision point with the characteristics appropriate to the specific experiment. Other appropriate modules joined together then transport the beam onward to the next curved section properly matched for recirculation. In this manner the flexibility in the external beam lines of an accelerator could, to a large extent, be retained for the straight-section beam lines of storage rings. The parallelism is broken only by the needs of recirculation which impose the following additional constraints on the straight-section beam lines for storage rings:

(a) For an accelerator the length of the external beam line is to some extent flexible. For storage rings the length of the straight-section beam line constrained between curved sections is fixed.

(b) The phase advance in the transport line which is of little consequence for the external beam of an accelerator must be considered for the straight-section beam lines of storage rings.

(c) We need a standard recirculating line which simply transports the beam across a straight section and properly matched for recirculation without "targeting" for experiments.

(d) Since the target is the other beam the same consideration of matching and recirculation applies also to the "target" beam.

Examples

To demonstrate the practicality of this approach we will use as an example two 1000-GeV proton colliding-beam storage rings using superconducting magnets. In each ring the curved sections are composed of 100 curved separated-function FODO cells each 60 m long and having a phase advance of 90°. The parameters of such a cell are given in Fig. 1. The curved sections of the two rings are assumed to be stacked one above the other with a vertical separation of 0.3 m between beams. In or near the beam-collision point it is likely that some quadrupoles will be used in common by both beams. These quadrupoles will have opposite focal actions on the two beams traveling in opposite directions. Thus, the

*Operated by Universities Research Association, Inc. under contract with the U.S. Atomic Energy Commission.

simplest lattice arrangement is such that all adjacent quadrupoles between the two rings have opposite focal actions on the two beams, hence the same field-gradient polarity.

As initial steps in the development of this approach we assume:

(a) The simplest standard recirculating line would consist of straight cells formed by leaving out the dipoles in the curved FODO cells. A series of a multiple of 4 of these straight cells would have unity transfer matrices in both the horizontal and the vertical planes and would hence match both optics and dispersion. The straight-section length could therefore be 240 m, 480 m, etc.

(b) The lengths of the modular insertions should be multiples of the half-cell length of 30 m. Since the length of the straight sections is fixed insertions should be kept as short as possible.

(c) As standard transport elements for the straight-section beam lines we will use 1.1 m quadrupoles and 6.2 m dipoles. These turn out to be convenient choices of lengths. The currents in these magnets are adjusted to give the required strengths in the same manner as for transport elements in external beam lines of accelerators.

(d) Although not demanded in principle, matching for recirculation would be greatly simplified if the phase advances in the horizontal and the vertical planes are identical in all insertions. This is automatically guaranteed by making all insertions antisymmetric such that the two planes are longitudinal reflections of each other.

We now give a few examples of specific insertions. Optics and dispersion matching is obtained by first using the "thin" version of the computer program MAGIC' in which all magnet elements are assumed to be of zero length. The results are then used as trial input to the "thick" version of the program to give the final physical parameters. For simplicity, when several standard transport elements must be strung together to give the required strength we have not included the short drift spaces between the elements necessary to accommodate the end structures and connections.

A. Dispersion Modifying Insertion

As examples we give here two zero-dispersion insertions (dispersion function = η = 0) which reduce the horizontal dispersions at the ends of curved sections to zero. If the curved section ends in an F quadrupole where the dispersion is large the insertion would have to be 2 cells in length and look like that shown in Fig. 2. Four 24.67 mrad dipoles introduced into the normal straight cells produce a local horizontal orbit displacement of 0.740 m and a horizontal dispersion to cancel that from the curved section. There does not seem to be any advantage in modifying the optics by rearranging the quadrupoles. If the curved section ends in a D quadrupole where the dispersion is small the insertion could be reduced to 1½ cell long by first modifying the optics in the insertion (still matched to that of normal cells at the ends) and then introducing four 12.44 mrad dipoles. The local orbit displacement is reduced to 0.228 m. This insertion is shown in Fig. 3. Identical insertions would be used in reverse at the downstream end of the straight sections to rematch dispersion for recirculation.

Conventionally, zero dispersion in the straight section is obtained by modifying the ends of the curved sections as an integral part of the ring lattice. These insertions illustrate the basic departure of the present approach. They can be inserted or withdrawn freely without affecting the operation of the ring.

B. Beam-Size Modifying Insertion

As an example we show in Fig. 4 a low-β insertion (β = amplitude function). This insertion is conventional except that it is antisymmetric, matched to the normal cell optics at the ends, and has a length modularized to 2½ cell lengths. The 8-value β^* at the central collision point is 1 m in both planes. The total free drift space on either side of low-β point is 25 m long. The free drift-space length could be substantially increased for higher low-β values. For extremely long drift spaces the insertion would be 3½ cells in length. Presumably several insertions with different β^* values (including high-β values) would be needed.

C. Phase Adjusting Insertion

To make it possible to freely interchange insertions having different phase advances we need an insertion with a phase advance which is adjustable over a wide range. Evidently this insertion would be used to adjust the betatron tune of the ring. In other cases one may also use it to adjust the phase advance across a single straight section to a desired value. An example of this insertion which is antisymmetric and matched to the normal cell optics is shown in Fig. 5. The phase advance is adjustable from 100° to 300°. The field-gradient settings of the quadrupoles are plotted against the phase advance. It should be possible to program these curves into the control computer so that the phase advance can be adjusted by turning a single knob.

D. Orbit-Length Dispersion Adjusting Insertion

This is an obvious companion to the phase adjusting insertion. To be useful the insertion should be rather long. The simplest would be a 4-cell long antisymmetric insertion with 360° phase advance. By varying the field-gradients of the quadrupoles but keeping the phase advance at 360° one can very the orbit-length dispersion $\frac{\Delta \ell}{\ell} / \frac{\Delta p}{p}$ without affecting the optics and dispersion matching at the ends. No example is given for this simple insertion. The utility of this insertion is less obvious than that of the phase adjusting insertion, but clearly it could be used to adjust the transition energy of the ring.

E. Beam Crossing ("Targeting") Insertion

The beams traveling in opposite directions in the two rings stacked one on top of the other are separated by 0.3 m. These two beams can be displaced vertically to come together to collide head on in a half-cell by three vertical dipoles as shown in Fig. 6. These dipoles must have a vertical good field aperture of more than 50 mm. It is likely that the standard transport dipoles turned vertical would have an adequate aperture. Several remarks should be made for this insertion.

(1) This insertion is generally followed by a beam size modifying insertion. The vertical dipoles in this insertion should be trimmed to give the appropriate small beam separation and angle at the entrance to the following insertion such that the beams would cross each other at the proper location (e.g. the low-β point) and at the desired small angle. Furthermore, the vertical dipoles could easily have an adequate trimming range to accommodate either the cross-over geometry (the upper beam becomes the lower beam in the following curved section) or the no-cross-over geometry.

(2) The small vertical dispersion introduced by the vertical bends will make the distance over which the beams collide longer hence extending further away from the low-β point. The resulting reduction in luminosity is generally quite small, especially if the horizontal dispersion is made zero in the collision region.

(3) This short insertion occupying only a drift space is not a true insertion in the dispersion-optical sense. In some cases it can be merged into the ends of other insertion, i.e. the vertical dipoles can be placed in a drift space of adequate length in any insertion.

With the sample insertions given above we can now put together an example of a complete straight-section beam line. To get the maximum luminosity we would want zero-dispersion and low-β at the beam-collision ("targeting") point. This could be obtained from the string of insertions shown in Fig. 7. The total length is 7½ cells or 450 m.

Similar exercises in putting together other complete straight-section beam lines indicate that a straight-section length of 4 cells or 240 m (in 1000-GeV storage rings) is too short for full exploitation of the flexibility inherent in this scheme. A straight-section length of 8 cells (480 m) or greater would be more appropriate. This study also shows that the straight-section length should be measured in terms of the betatron oscillation wave length in the curved section which is in turn governed by the available dipole and quadrupole strengths for the specified beam energy. One wave length is too short, two or more wave lengths would be adequate.

An obvious criticism for this design approach is that the flexibility is bought at the expense of longer straight sections. However, comparison with conclusions of design studies for Isabelle and PEP indicates that, in fact, the additional length required is rather small. Recalling the parallelism invoked in the Introduction we observe further that even with the slightly longer length these straight-section beam lines are much shorter than the conventional external beam lines of an accelerator at the same energy. This parallelism also provides a basis for the choice of the number of straight sections. Accelerator facilities in which experiments are performed mainly in external beams typically have 4-6 external beam lines. A similar number of straight sections in a colliding-beam storage ring facility is thus appropriate.

References

1. M.J. Lee, W.W. Lee and L.C. Teng, "Magnet Insertion Code (MAGIC)", Note-61, 1973 PEP Summer Study Report (1973).

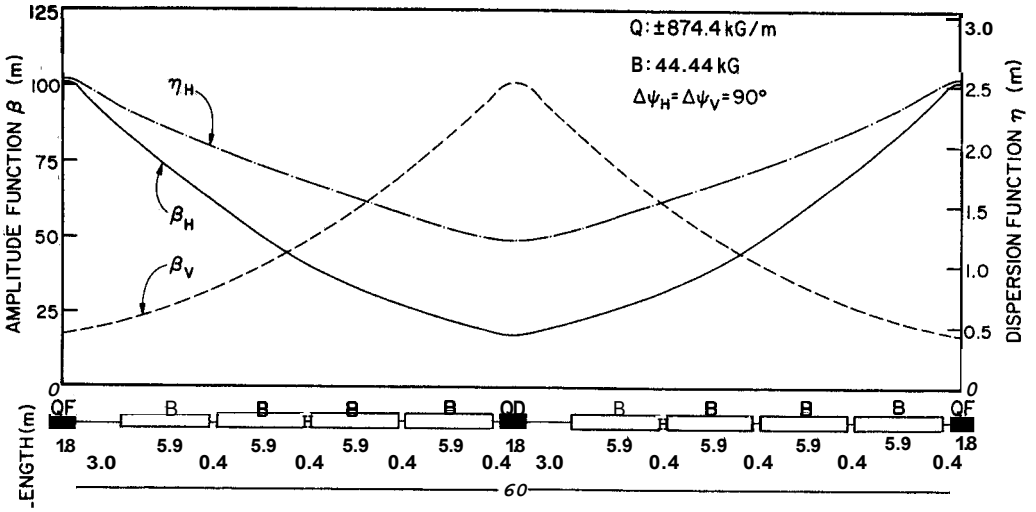


Figure 1. Normal curved cell

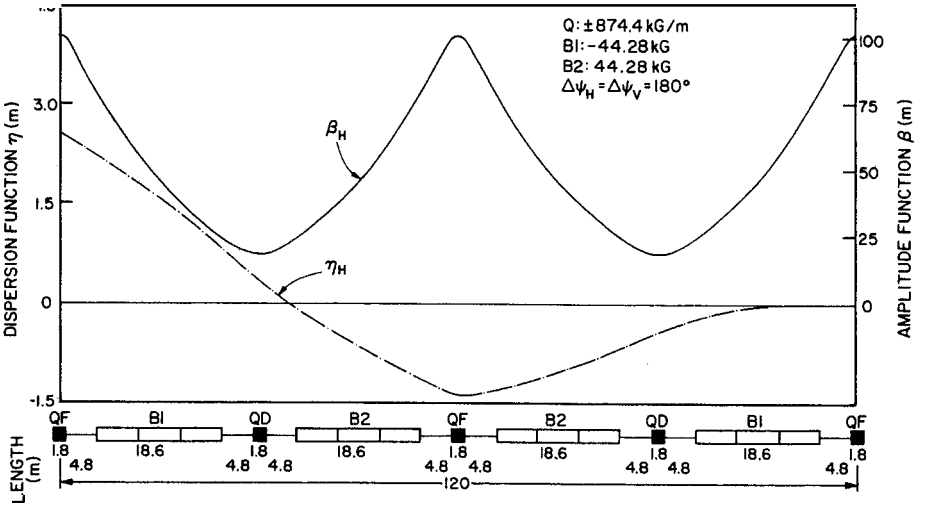


Figure 2. Zero-dispersion insertion (F type)

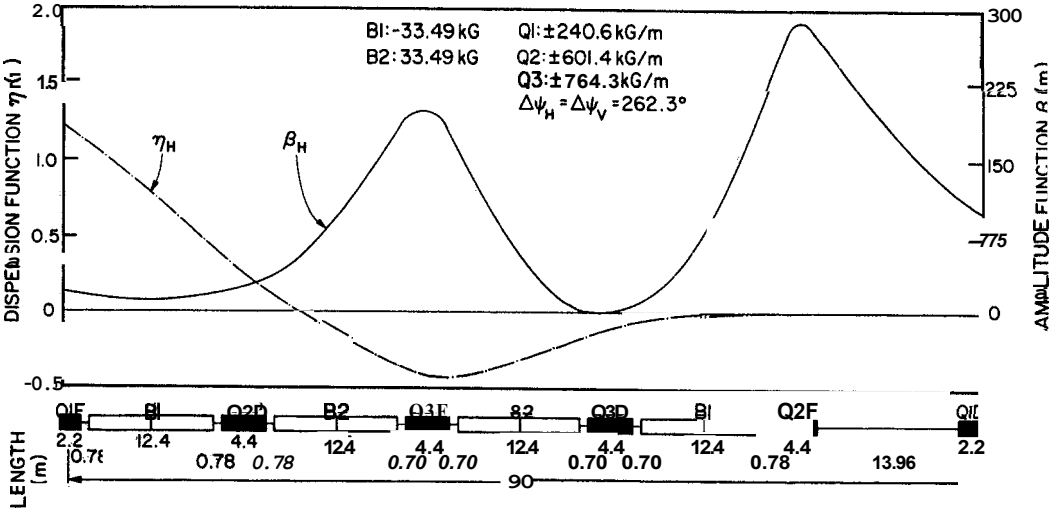


Figure 3. Zero-dispersion insertion (D type)

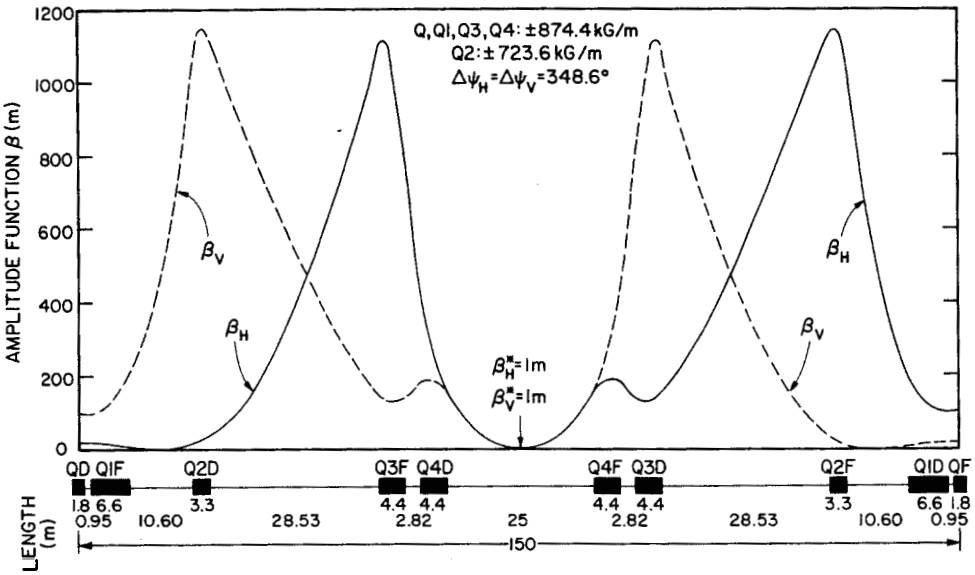


Figure 4. Low-β insertion

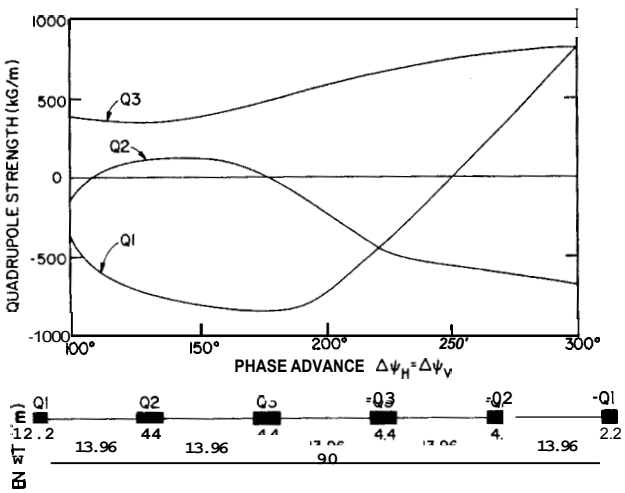


Figure 5. Phase adjusting insertion

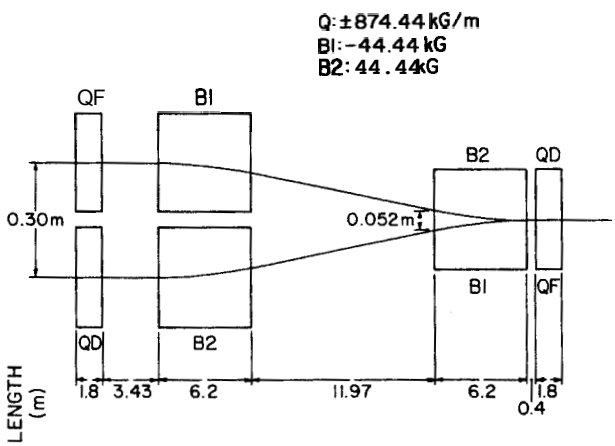


Figure 6. Beam crossing insertion

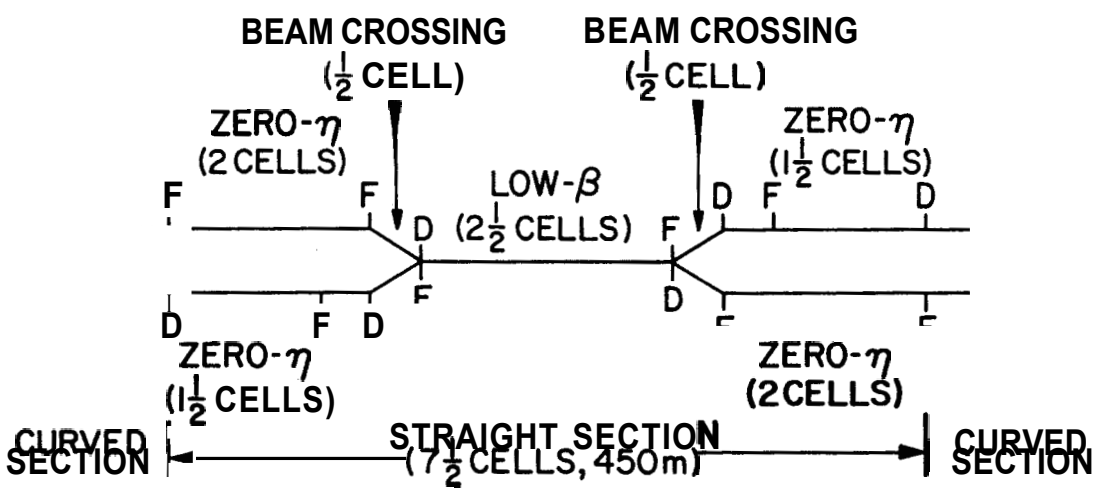


Figure 7. High luminosity straight section

-RESONANCE CROSSING IN A PROTON SYNCHROTRON; APPLICATION TO ISABELLE*

R. Chasman
Brookhaven National Laboratory
Upton, New York

A. Garren
Lawrence Berkeley Laboratory
Berkeley, California

R.L. Gluckstern
University of Massachusetts
Amherst, Massachusetts

and

F.E. Mills
National Accelerator Laboratory
Batavia, Illinois

Summary. We have investigated the effect on the transverse properties of a beam in the presence of a nearby nonlinear resonance, periodic variation of the betatron tune as a result of synchrotron oscillations leading to periodic resonance crossing, and a zeroth harmonic octupole term (or other multipole) which makes the betatron frequency depend on transverse amplitude. Depending on whether the product of the resonance strength and the zeroth harmonic octupole component is small or large, one gets one of the following two pictures for fast resonance crossing: a) A pattern of resonances and side bands the side bands being separated by ν_s/n (ν_s is the synchrotron frequency, n the order of the resonance). Detailed consideration of the betatron phase change between consecutive crossings leads to prediction of an odd-even dependence of the beam growth on the side band number. Computer runs yield phase-space trajectories which confirm these predictions in detail. b) A diffusion-like process, the betatron tune shift between crossings resulting from the amplitude change now being larger than the spacing of side bands. The diffusion picture also holds whenever ν_s/n is smaller than the betatron tune stability. These effects are observed in computer runs and lead to design tolerances for the resonance terms. When nonlinearities are present that are larger than these tolerances, azimuthally distributed multipoles have to be introduced to tune out the resonances. The multipole distributions required to do so have been calculated.

Introduction

In a proton storage ring accelerator such as ISABELLE~large currents (~ 10 A) are accelerated for times of the order of minutes. The beam must have a spread both in momentum and betatron frequency to stabilize against longitudinal and transverse instabilities. The spread in betatron frequency is achieved by a momentum dependent ν-value or chromaticity. Under these conditions the w-value of individual particles will vary periodically with time while the beam is accelerated, as a result of synchrotron oscillations. This leads to repeated crossings of those nonlinear resonances included in the particles v-swing. During acceleration the excitation of nonlinear resonances is due primarily to magnet imperfections because the beams in the two rings are separated and the relatively Large nonlinear effects originating in beam-beam interaction are absent.

The present paper deals with the transverse beam behavior under the following conditions: a) A nearby single nonlinear resonance, due to magnet nonlinearities, b) periodic variation of the betatron tune as a result of synchrotron oscillations leading to periodic crossing of the nonlinear resonance, c) a zeroth harmonic octupole term which makes the betatron frequency depend on the transverse amplitude.

Several authors[2,3] have dealt with the transverse motion of particles under similar conditions. However, their treatments are generally limited to a single synchrotron period and fail to make detailed predictions for the transverse beam behavior resulting from many repeated resonance crossings. In this paper, theory and computer simulations have been extended to cover many synchrotron periods. All calculations are one-dimensional, but a generalization to both transverse dimensions is straightforward. Fast crossings only (see below) have been considered.

Theory

General Case

The one-dimensional equation of the betatron motion of a particle in a nonlinear perpendicular field B in a synchrotron is given by:

$$\frac{d^2x}{ds^2} + K(s)x = \frac{1}{\rho}\left(b_2x^2 + b_3x^3 + b_4x^4 + \ldots.\right) \qquad (1)$$

Here $B = B_0(1 + b_1x + b_2x^2 + b_3x^3 + b_4x^4 + \ldots.)$, K(s) includes the linear part of B and ρ is bending radius. Introducing the variables $\eta = \beta^{-\frac{1}{2}}x$ and $\sigma = \frac{1}{\nu}\int ds/\beta$ one gets[4]:

$$\frac{d^2\eta}{d\sigma^2} + \nu^2\eta = \frac{\nu^2\beta^{3/2}}{\rho}\sum_{n=3,\ldots} b_{n-1}\beta^{(n-1)/2}\eta^{n-1}$$

where β is the Courant-Snyder β-function and ν is the betatron tune.

An additional transformation to amplitude phase variables I and φ given by $I = \eta'^2/\nu^2 + \eta^2$, $\varphi = -$ arctg $\eta'/\nu\eta$ (or $\eta = \sqrt{I}\cos\varphi$, $\eta' = -\sqrt{I}\nu\sin\varphi$) yields

$$I' = -\frac{2\sqrt{I}\nu\sin\varphi}{\rho}\sum_{n=3,\ldots} b_{n-1}\beta^{(n+2)/2}\eta^{n-1}$$

$$\varphi' = \nu - \frac{\nu\cos\varphi}{\rho\sqrt{I}}\sum_{n=3,\ldots} b_{n-1}\beta^{(n+2)/2}\eta^{n-1}\ .$$

One can set $\eta = \sqrt{I}\cos\varphi$ on the right-hand side of these expression and gets:

Work performed under the auspices of the U.S. Atomic Energy Commission.

$$I' = -\frac{2\nu}{\rho}\sin\varphi \sum_{n=3,\ldots} b_{n-1}\beta^{(n+2)/2} I^{n/2}\cos^{n-1}\varphi$$

$$\varphi' = \nu - \frac{\nu}{\rho}\cos\varphi \sum_{n=3,\ldots} b_{n-1}\beta^{(n+2)/2} I^{(n-2)/2}\cos^{n-1}$$

Near an isolated nonlinear resonance of order n, $\nu = r/n + \Delta_o$ where r is an integer and $\Delta_o \ll 1/n$. Fourier analyzing the nonlinear field coefficients $b_i = \Sigma b_{ir}\cos r(\theta + \theta_r)$, keeping only the octupole zeroth harmonic component and neglecting rapidly oscillating terms one obtains in the smooth approximation with $\beta = R/\nu$ and $\sigma = \theta$ (R is the average radius of the machine, θ the regular length):

$$I' = -\frac{2\nu}{}\left(\frac{R}{}\right)^{(n+2)/2} I^{n/2}\sin[n\varphi - r(\theta+\theta_-)]$$

$$\varphi' = \nu - \frac{\nu}{2^n\rho}\left(\frac{R}{\nu}\right)^{(n+2)/2} b_{n-1,r} I^{(n-2)/2}\cos[n\varphi - r(\theta+\theta_r)].$$

Substituting $\chi = n\varphi - r(\theta+\theta_r)$, $B_n = -\nu/(2^n\rho)(R/\nu)^{(n+2)/2} b_{n-1,r}$ and $A = -(3\nu/8\rho)(R/\nu)^3 b_{3,0}$ one finally gets:

$$I' = 2B_n I^{n/2}\sin\chi \qquad (2a)$$

$$\chi' = (n\nu - r) + nAI + nB_n I^{(n-2)/2}\cos\chi \,. \qquad (2b)$$

For a constant betatron tune these equations lead to the usual invariant of motion for a nonlinear resonance. Fixed points are obtained from $I' = 0$, $\chi' = 0$. The nonlinear resonance widths are given by $\pm B_n I^{(n-2)/2}$. In the appendix, a Hamiltonian, valid for any order resonance, is derived from which Eq. (2) can be obtained. More exact expressions for B_n and A are also given.

The θ-dependence of ν will be written as

$$\nu(\theta) = \frac{r}{n} - \frac{\Delta}{n}(\cos\nu\theta - \cos\nu_s\theta_o) \,,$$

where $A > 0$, Δ/n is the half-swing of the betatron frequency ν and ν_s is the synchrotron frequency. Δ_o/n, defined as $\Delta/n\cos\nu_s\theta_o$, is the difference between the average frequency $r/n \mp \Delta/n\cos\nu_s\theta_o$ and the resonance frequency r/n. $\nu(\theta)$ will be **equal** to r/n whenever $\theta = \pm\theta_o + 2j(\pi/\nu_s)$ where j is any integer and $0 \le \nu_s\theta_o \le \pi$.

Setting $\chi_\pm = \chi(\pm\theta_o)$, where χ_+ and χ_- are the values of χ at the upward and downward resonance crossings, one has near $\theta = \pm\theta_o$:

$$\chi = \chi_\pm + \chi''_\pm \frac{(\theta \mp \theta_o)^2}{2}$$

Assuming the condition for fast crossing in which $n\nu$ varies much more rapidly than the two other terms, nAI and $nB_n I^{(n-2)/2}\cos\chi$, on the right-hand side of Eq. (2b), one can write $\chi'' = \nu_s\Delta\sin\nu_s\theta$, $\chi''_\pm = \chi''(\theta_\pm) = \pm\nu_s\Delta\sin\nu_s\theta_o$. The change ΔI and $\Delta\chi$ in I and χ during one synchrotron period (assuming AI is small) are then obtained from Eq. (2) in the following way:

$$\Delta I = 2B_n I^{n/2}\left[\int_{-\infty}^{\infty}\sin\left[\chi_+ + \chi''_+\frac{(\theta-\theta_o)^2}{2}\right]d\theta + \int_{+\infty}^{\infty}\sin\left[\chi_- + \chi''_-\frac{(\theta+\theta_o)^2}{2}\right]d\theta\right] .$$

$$\Delta\chi = (\Delta_o + nAI)\frac{2\pi}{\nu_s} + nB_n I^{(n-2)/2}\left[\int_{-\infty}^{+\infty}\left[\chi_+ + \chi''_+\frac{(\theta-\theta_o)^2}{2}\right]d\theta + \int_{+\infty}^{-\infty}\cos\left[\chi_- + \chi''_-\frac{(\theta+\theta_o)^2}{2}\right]d\theta\right] .$$

Evaluation of the integrals in the expressions of AI and $\Delta\chi$ leads to

$$\Delta I = 4CB_n I^{n/2}\cos\left(\frac{\chi_+ - \chi_-}{2} + \frac{\pi}{4}\right)\sin\frac{\chi_+ + \chi_-}{2}$$

$$\Delta\chi = (A + nAI)\frac{2\pi}{\nu_s} + 2CB_n I^{(n-2)/2}\cos\left(\frac{\chi_+ - \chi_-}{2} + \frac{\pi}{4}\right)\cos\frac{\chi_+ + \chi_-}{2} .$$

where $C = \sqrt{\dfrac{2\pi}{\nu_s\Delta\sin\nu_s\theta_o}}$.

Noticing that $\Delta\chi_+ = \Delta\chi_- = \Delta\chi$, one can go to a new variable $\bar{\chi} = (\chi_+ + \chi_-)/2$, leading to

$$AI = 4CB_n I^{n/2}\cos\left(\frac{\chi_+ - \chi_-}{2} + \frac{\pi}{4}\right)\sin\bar{\chi} \qquad (3a)$$

$$\Delta\bar{\chi} = (\Delta_o + nAI)\frac{2\pi}{\nu_s} + 2CB_n I^{(n-2)/2}\cos\left(\frac{\chi_+ - \chi_-}{2} + \frac{\pi}{4}\right)\cos\bar{\chi} \qquad (3b)$$

I and $\bar{\chi}$ get impulses at $\theta = \pm\theta_o + 2\pi j/\nu_s$. One can therefore write $I'(\theta)$ in the following way:

$$I'(\theta) = 2\frac{\nu_s}{2\pi}CB_n I^{n/2}\sum_{j=-\infty}^{\infty}\left\{\sin\left[\chi_+^i + \frac{2\pi j}{\nu_s}\Delta_o + \alpha(\theta) + \frac{\pi}{4}\right]\delta\left(\theta - \theta_o - \frac{2\pi j}{\nu_s}\right) + \sin\left[\chi_-^i + \frac{2\pi j}{\nu_s}\Delta_o + \alpha(\theta) + \frac{\pi}{4}\right]\delta\left(\theta + \theta_o - \frac{2\pi j}{\nu_s}\right)\right\} .$$

Here χ_+^i and χ_-^i are the initial values of χ_+ and χ_-, $\alpha'(\theta) = nAI + nB_n I^{(n-2)/2}\cos\chi$ and $\alpha(\theta) = \int_o^\theta \alpha'(\theta)d\theta$. After some manipulation of the 6-functions one finally gets with $F_j = \cos[(\chi_+^i - \chi_-^i)/2 + \pi/4 - (\Delta_o - \nu_s j)\theta_o]$:

$$I'(\theta) = 4\frac{\nu_s}{2\pi}CB_n I^{n/2}\sum_j F_j\sin[\bar{\chi}^i + (\Delta_o - \nu_s j)\theta + \alpha(\theta)]. \qquad (4a)$$

Similarly it can be shown that

$$\bar{\chi}'(\theta) = \Delta_o + nAI + 2\frac{\nu_s}{2\pi}CB_n I^{(n-2)/2}\sum_j F_j\cos[\bar{\chi}^i + (\Delta_o - \nu_s j)\theta + \alpha(\theta)]. \qquad (4b)$$

Side Band Approximation

In the case that $\Delta_o = \nu_s\ell + \varepsilon$, where $\varepsilon \ll \nu_s$ and $\alpha'(\theta) \sim$ const, the term with $j = \ell$ in Eq. (4a and b) will always be the slowest varying one, permitting the neglect of the other more rapidly oscillating terms. With the additional transformation $\Phi = \bar{\chi} + \nu_s\ell\theta$, one gets:

$$I' = 4\frac{\nu_s}{2\pi}CB_n I^{n/2}F_\ell\sin\Phi \qquad (5a)$$

$$\Phi' = (\Delta_o - \ell\nu_s) + nAI + 2\frac{\nu_s}{2\pi}CB_n I^{(n-2)/2}F_\ell\cos\Phi \,. \qquad (5b)$$

These equations are now identical in form to those which were obtained earlier for $\nu(\theta) =$ const (see 2a and b) with the exception that $(\nu - r/n)$ has been replaced by $\Delta_o - \ell\nu_s$ and B_n by $2(\nu_s/2\pi)CB_nF_\ell$. Varying the betatron tune with the synchrotron frequency hence causes the resonance at $\nu = r/n$ to be replaced by a series of resonances (or side bands) at $\nu = r/n + \nu_s\ell/n$ where *d* is any

integer. The width of these resonances are $\pm 2(\nu_s/2\pi)$ $CB_nF_\ell I^{(n-2)/2}$ compared to $B_nI^{(n-2)/2}$ obtained at $\nu=r/n$ in the case of $\nu(\theta)$ = const. In the side approximation then the particle motion will follow invariants in I,Φ phase space given by

$$\text{Const.} = (\Delta_o - \ell\nu_s)I + \frac{nAI^2}{2} 2\frac{\nu_s}{2\pi} CB_nF_\ell I^{n/2} \cos\Phi \quad . \qquad (6)$$

Fixed points are obtained from $I' = 0$, $\Phi' = 0$. The dependence of the side band width $\pm 2(\nu_s/2\pi)$ $CB_nF_\ell I^{(n-2)/2}$ on the side band order ℓ is contained in $\sin \nu_s\theta_o$ and Fg. While $\sin \nu_s\theta_o$ varies monotonically with ℓ, F_ℓ exhibits an odd-even dependence for side bands near—the central resonance, which comes from the fact that Y changes by $\sim \pi/2$ when ℓ changes by 1.

Diffusion Approximation

The assumption used to obtain the side band picture was $\alpha'(\theta)\approx$const, where $\alpha'(\theta)=nAI+nB_nI^{(n-2)/2}\cos\chi$. If $\Delta\alpha'(\theta)$ the change in $\alpha'(\theta)$ over one synchrotron period, is comparable to ν_s, then terms with different j's will dominate in the sums in Eq. (4a and b) at different values of θ and one cannot approximate these sums by the same $j=\ell$ term at all values of θ. To first order in $B_nI^{(n-2)/2}$, $\Delta\alpha'(\theta)\approx nA\Delta I$. Taking ΔI from Eq. (3a) one gets that $\Delta\alpha'(\theta)\ll\nu_s$ implies $|4ACB_nI^{n/2}|\ll\nu_s$ and one expects that the side band picture should no longer be valid if $|4ACB_nI^{n/2}|\geq\nu_s$. In order to see how the amplitude I will vary with θ or (time) in this regime one has to go back to Eq. (3a) which gives the change in I over one synchrotron period. If one assumes that will now vary randomly with θ (or time) one gets a diffusion-like rms-type growth of I expressed by: $dI^2/dt = (\Delta I)^2\nu_s/T_{rev}$, where T_{rev} is the revolution time around the machine and $(\Delta I)^2$ is the average value of $(\Delta I)^2$. One obtains for the doubling time t_d for the rms value of I:

$$t_d = \frac{\alpha_n \Delta T_{rev}}{8B_n^2 I_o^{n-2}\pi} \qquad (7)$$

where $\alpha_n = \frac{4^{1-n/2} - 1}{1 - n/2}$ and I_o is the initial value for I.

As can be seen from Eq. (7) t_d is independent of the synchrotron frequency and the zeroth harmonic octupole component and inversely proportional to the square of the resonance width. However, ν_s and A (or $b_{3,0}$) enter into the condition $|4ACB_nI_o^{n/2}|\geq\nu_s$ under which diffusion-type emittance growth can occur.

Computer Calculations

Computer calculations have been performed aimed at testing the theoretical predictions for the transverse beam behavior presented in the previous section. Some results obtained in these simulations will be given below.

The transverse particle motion corresponding to a single machine revolution was calculated by a linear transformation followed by a nonlinear kick. The ν-value entering the linear transformation, varied with time with the synchrotron frequency and was shifted by an amount $-(3\nu/8\rho)(R/\nu)^3 b_{3,0} I$, where I is the particle amplitude.

The following parameters were kept fixed in all computer runs: R = 382 m, ρ = 167 m, A/n = 0.03 and ν_s = 0.001. The resonance betatron tunes were kept close to 21.

Figures 1 through 4 refer to a third order resonance. In Fig. 1 particle trajectories in I, Φ space are shown for four different average betatron tunes corresponding to $\nu = 1/3(r + \ell\nu_s)$ where r = 62 and ℓ = 0,1,2 and 3. The zeroth harmonic octupole component is small and the side band picture should hold. The trajectories clearly follow invariants of the form given in Eq. (6). This figure also exhibits the odd-even dependence of F_ℓ on ℓ, which was mentioned earlier, and the amplitudes corresponding to the stable fixed points agree well with theory. Similar trajectories are shown in Fig. 2 for different average betatron tunes slightly off the central band and again seem to verify the predictions expressed in Eq. (6).

In Fig. 3 the amplitude of a single particle is plotted as function of revolution number for different values of the zeroth harmonic octupole component $b_{3,0}$. The initial amplitude is 2×10^{-6} m in all runs. When $b_{3,0}$ is small the particle amplitude varies periodically with time as can be expected from the phase-space trajectories shown in Figs. 1 and 2. However, when the $b_{3,0}$ is increased, the simple periodic time dependence deteriorates and a more random behavior sets in, indicating that the side band picture no longer holds. The necessary condition, stated earlier in this paper for the side band model to be valid was $|4ACB_nI^{n/2}| \ll \nu_s$. With the numerical values used here this is equivalent to $|b_{3,0}| \ll 10\ m^{-3}$, in good agreement with the results shown. In Fig. 4 the rms amplitude of 10 particles starting out with $I = 2 \times 10^{-6}$ m but different values of $\bar{\chi}$ is plotted as function of revolution number under similar conditions. When $b_{3,0}$ is small the rms amplitude fluctuates with time but no growth pattern can be seen. For large octupole components the diffusion picture predicts an amplitude doubling time of 1.4 sec, corresponding to 175 000 revolutions. This is in fair agreement with the numerical results shown here for a statistical sample of only 10 particles.

Results obtained with a fifth order resonance are contained in Figs. 5 and 6. Particle trajectories in the I, Φ phase plane, obtained with a small zeroth harmonic octupole component, are shown in Fig. 5 for three different average betatron tunes, $\nu = 1/5(r + \ell\nu_s)$, corresponding to r = 104 and ℓ = 0,1 and 2. The odd-even dependence of the factor Fg entering into the expression for C in Eq. (6) is again obvious. For the conditions referring to Fig. 5 an unstable fixed point exists, but it occurs at an amplitude above the range of I included there. Figure 6 shows the rms amplitude of 10 particles as function of revolution number for a small and large value of $b_{3,0}$. As in the case of a third order resonance, no steady rms amplitude growth can be seen for the small zeroth harmonic octupole term while a diffusion-type growth shows up when this term becomes large. Again, the amplitude doubling time is within the range of theoretical predictions.

Discussions of Results and Application to ISABELLE

Both theoretical and numerical calculations presented in this paper indicate that fast crossing of nonlinear resonances with an amplitude dependent betatron tune leads to two different patterns of transverse beam behavior.

When the effective betatron tune (including the amplitude dependent part) is constant within a range small compared to ν_s/n, particles move along phase-space trajectories predicted by a simple resonance theory involving side bands. For a given nonlinear resonance strength one can then limit the transverse beam growth by adjusting both the distance of the average Linear betatron tune to the nearest side band and the strength of the zeroth harmonic octupole component. In the case that the variation of the effective betatron tune is of the order ν_s/n and more, the beam no longer follows the resonance pattern. A diffusion-like emittance growth sets in, which one should be able to avoid by resonance compensation.

In an ideal machine, where the average linear betatron tune is constant, the variation of the effective ν-value comes from its amplitude dependent part. One then gets diffusion-like behavior only when a large zeroth harmonic octupole (or other multipole which makes the betatron frequency depend on transverse amplitude") component exists. Nonideally, however, there most probably will be a variation in the average linear betatron tune and for small values of ν_s one will have beam growth even in the absence of strong octupoles. Computer results, not shown here, confirm this.

In ISABELLE ν_s is of the order of 10^{-5} and, even with weak octupoles, one might get diffusion-like beam growth from nonlinear resonance crossings. The emittance doubling times have been calculated from Eq. (7) for different order resonances assuming the nonlinearities that are to be expected in the ISABELLE magnets. The results are given in the following table together with the nonlinear field coefficients:

n	b^r_{n-1}	t_d(sec)
3	0.005 m^{-2}	0.58
4	0.095 m^{-3}	680
5	1.7 m^{-4}	7.4×10^5
6	31.2 m^{-5}	1.0×10^9
7	521 m^{-6}	2.8×10^{12}

For an acceleration time of a few minutes nonlinear resonances of the order 5 and higher appear harmless. The third and fourth integral resonances can be avoided by proper placement of the working line and no resonance compensation seems to be required.

Acknowledgments

The authors wish to thank Dr. Lloyd Smith for valuable discussions regarding resonance compensation.

Appendix

Equations for Transverse Motion in Angle-Action Variables with Resonant Perturbations when the Tunes Vary Due to Synchrotron Oscillations

For completeness we include a derivation of the equations for amplitude and phase in the vicinity of a single resonance that, we believe, clarifies the proper arguments to use in thetrigonometric functions of the relevant Fourier coefficients, and that takes account of the slow variation of the tunes due to the synchrotron oscillations. The treatment applies to any resonance, horizontal, vertical, or coupled.

We start with a Hamiltonian for the motion of x,z, $p_x = dx/ds$, $p_z = dz/ds \equiv x_1, x_2, p_1, p_2$ in terms of the path length s, where x and z are the horizontal and vertical displacements from the instantaneous closed orbit. We have[5]

$$H = H^{(0)} + H', \quad H^{(0)} = \frac{1}{2}\Sigma\,(p_i^2 + K_i x_i^2),$$

$$H = \sum_{n=2}^{\infty} H^{(n)}, \quad H^{(n)} = \frac{B_o}{B\rho} \sum_{L+M=n} \frac{n!}{L!M!n}\, c^M_{n-1} x^L z^M .$$

The K_i and c^M_{n-1} are defined in terms of median-plane expansions of the magnetic field

$$B(x,z=0) = B_o(1 + b_1 x + b_2 x^2 + \ldots),$$
$$B(x,z=0) = B_o(a_0 x + a_2 x^2 + \ldots),$$
$$K_x = \frac{B_o b_1}{B\rho} - \frac{1}{\rho_o^2}, \quad K_z = -\frac{B_o b_1}{B\rho};$$

$$c^M_{n-1} = \left[(-1)^{M/2} b_{n-1},\ (-1)^{(M+1)/2} a_{n-1} \right] \text{ for M even, odd.}$$

We then replace x_i, p_i by phase and amplitude variables Ψ_i, J_i using the (instantaneous) betatron functions β_i, α_i (Ref. 4):

$$x_i = \sqrt{2J_i\beta_i}\cos\Psi_i, \quad p_i = -\sqrt{2J_i/\beta_i}\,(\sin\Psi_i + \alpha_i\cos\Psi),$$

by use of the generating function $F_1 = -\Sigma(x_i^2/2\beta_i)(\tan\Psi_i + \alpha_i)$. The transformation equations $p_i = \partial F_1/\partial x_i$, $J_i = -\partial F_1/\partial\Psi_i$, $H_1 = H + \partial F_1/\partial s$ and the relations $d\beta_i/ds = -2\alpha_i$, $d\alpha_i/ds = K_i\beta_i - (1+\alpha_i^2)/\beta_i$, give $H_1 = \Sigma(J_i/\beta_i) + H'(\Psi_i, J_i)$. We investigate the resonance arising from the $x^L z^M$ term in H' that oscillates as $\cos\Psi_{\ell m}$, where

$$\Psi_{\ell m} = \ell\Psi_x + m\Psi_z; \quad \ell = L, L-2, \ldots; \ \ell \geq 0; \ m = M, M-2, \ldots, -M.$$

This term has the form $h\, c^M_{n-1}(J_x\beta_x)^{L/2}(J_z\beta_z)^{M/2}\cos\Psi_{\ell m}$, with h a constant. It causes a resonance when the tunes $\nu_i = \nu_i^o$, where $\nu^o_{\ell m} \equiv \ell\nu_x^o + m\nu_z^o = r$ = integer.

We now make a second transformation to variables μ_i, $\bar{J}_i$:

$$\mu_i = \Psi_i - \Phi_i, \quad \Phi_i = \int ds \left[\frac{1}{2\pi}\left(\frac{\nu_i}{R} \right) \right], \quad \bar{J}_i = J_i .$$

in which ν_i depends on s due to the synchrotron oscillations. The generating function, $F_2 = \Sigma J_i(\Psi_i - \Phi_i)$, gives $\mu_i = \partial F_2/\partial\bar{J}_i$, $J_i = \partial F_2/\partial\Psi_i$, $H_2 = H_1 + \partial F_2/\partial s$. In addition we change to $\theta = s/R$ as independent variable and get

$$H_2(\mu_i, J_i, \theta) = \Sigma(\nu_i - \nu_i^o)J_i + R\,h\,c^M_{n-1}(J_x\beta_x)^{L/2}(J_z\beta_z)^{M/2}\cos(\mu_{\ell m} + \Phi_{\ell m})$$
$$\mu_{\ell m} = \ell\mu_x + m\mu_z, \quad \Phi_{\ell m} = \ell\Phi_x + m\Phi_z .$$

Since μ_i, J_i vary slowly we average the other factors over one turn, and obtain

$$H_2(\mu_i, J_i) = \Sigma(\nu_i - \nu_i^o)J_i + D^{LM}_{\ell m} J_x^{L/2} J_z^{M/2}\cos(\mu_{\ell m} + \gamma^{LM}_{\ell m}),$$

where $$D^{LM}_{\ell m} = \left[\left(A^{LM}_{\ell m} \right)^2 + \left(B^{LM}_{\ell m} \right)^2 \right]^{\frac{1}{2}},$$

$$\gamma^{LM}_{\ell m} = \tan^{-1}\left(B^{LM}_{\ell m}/A^{LM}_{\ell m} \right),$$

$$\left\{A^{LM}_{\ell m}, B^{LM}_{\ell m}\right\} = Q^{LM}_{\ell m}\frac{B_o}{B\rho}\int_o^{2\pi R} ds\, c^M_{n-1}\beta_x^{L/2}\beta_z^{M/2}\left\{\cos\Phi_{\ell m}, \sin\Phi_{\ell m}\right\}$$

$$Q^{LM}_{\ell m} = \epsilon_{\ell m}(n-1)!/\left[2^{n/2}\pi \left(\frac{L+\ell}{2}\right)!\left(\frac{L-\ell}{2}\right)!\left(\frac{M+m}{2}\right)!\left(\frac{M-m}{2}\right)! \right],$$
$$n = L + M$$

and $\epsilon_{\ell m} = \frac{1}{2}$ if $\ell = m = 0$; $\epsilon_{\ell m} = 1$ otherwise. To suppress the resonance, $c^M_{n-1}(s)$ must lead to $D^{LM}_{\ell m} \approx 0$.

*For example a sextupole to second order.

Finally we transform to variables $\bar{\mu}_i, \bar{J}_i$:

$$\bar{\mu}_1 = \mu_{\ell m} + \gamma^{LM}_{\ell m} = \ell\mu_x + m\mu_z + \gamma^{LM}_{\ell m}, \quad \bar{\mu}_{12} = m\mu_x - \ell\mu_z,$$

$$\bar{J}_1 = (\ell J_x + m J_z)/(\ell^2 + m^2), \quad \bar{J}_2 = (m J_x - \ell J_z)/(\ell^2 + m^2),$$

using the generating function $F_3 = (\ell\mu_x + m\mu_z + \gamma^{LM}_{\ell m})\bar{J}_1 + (m\mu_x - \ell\mu_z)\bar{J}_2$. The new Hamiltonian is

$$H_3(\mu_i, J_i, \theta) = \Sigma(\bar{\nu}_i - \mathrm{Ti})\bar{J}_i +$$

$$D^{LM}_{\ell m}(\ell\bar{J}_1 + m\bar{J}_2)^{L/2}(m\bar{J}_1 - \ell\bar{J}_2)^{M/2}\cos\bar{\mu}_1$$

$$\bar{\nu}_1 = \ell\nu_x + m\nu_z, \quad \bar{\nu}_2 = m\nu_x - \ell\nu_z, \quad \bar{\nu}^o_1 = \nu_{\ell m} = r = \text{integer}.$$

Since H_3 is independent of μ_2, J_2 is a constant, and the equations for μ_1, J_1 are $d\mu_1/d\theta = \partial H_3/\partial J_1$, $dJ_1/d\theta = -\partial H_3/\partial\mu_1$.

For the multiple crossing of a horizontal resonance: L = ℓ = n, M = m = 0, in the presence of a 0-th harmonic octupole term, the motion follows from the Hamiltonian

$$H_3(\bar{\mu}_1, \bar{J}_1, \theta) = (n\nu_x - r)\bar{J}_1 + D^{n0}_{n0}(n\bar{J}_1)^{n/2}\cos\bar{\mu}_1 + D^{40}_{00}(n\bar{J}_1)^2 .$$

The equations of motion, Eq. (2), are obtained from H_3 by substituting

$$\bar{J}_1 = J_x/n = I/2n, \quad \bar{\mu}_1 = \chi, \quad B_n = nD^{n0}_{n0}/2^{n/2}, \quad A = D^{40}_{00} .$$

As for the phases $\Phi_{\ell m}$ that enter the formulas for $A^{LM}_{\ell m}$, $B^{LM}_{\ell m}$, if we evaluate them at the resonance, then $\Phi_i = \int_o^s (ds/\beta_i)$ which is the Courant-Snyder phase σ_i. If we evaluate them at another momentum, say P_1, then $\Phi_i = \nu_i(\sigma_i - \theta) + \nu^o_i\theta$. The term $\nu_i(\sigma_i - \theta)$ oscillates about zero in each period on the lattice; the $\nu^o_i\theta$ term contributes $r\theta$ to $\Phi_{\ell m}$, which is the factor often used, incorrectly, in place of the complete $\Phi_{\ell m}$. It is probably safe to ignore the variation of $D^{LM}_{\ell m}$ with momentum, but all of the terms involved must be taken at one momentum value in evaluating this number.

References

1. H. Hahn and M. Plotkin, Eds. "Design Study of 200 GeV Intersecting Storage Accelerators" (in press).

2. A.A. Kolomensky and A.N. Lebedev, Theory of Cyclic Accelerators, Chapter 3, 38 (1966).

3. M.H.R. Donald, RHEL/M/NIM (1973). (See also other references in this paper)

4. E.D. Courant and H.S. Snyder, Ann. Phys. 3, 1-48 (1958).

5. G. Guignard, CERN Report CERN/SI/Int. DL/70-3 (1970).

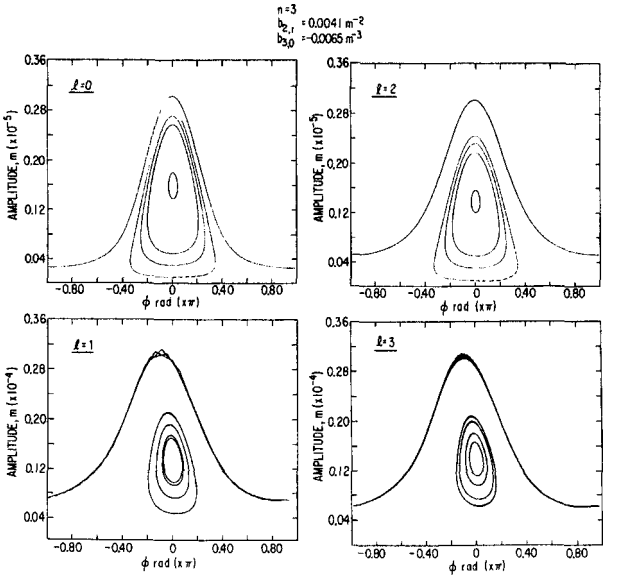


Fig. 1. Particle trajectories in I-Φ space for different side bands of a third order resonance. (Note the difference in vertical scale for even and odd band.)

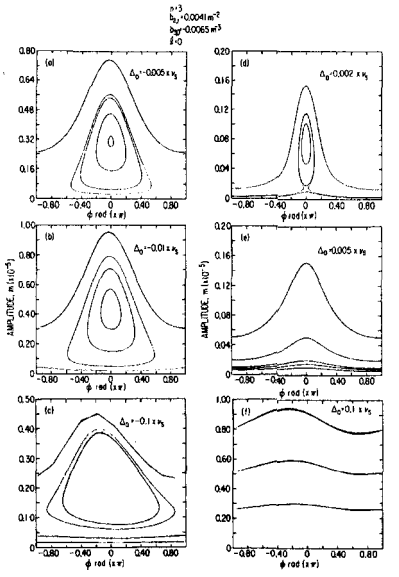


Fig. 2. Particle trajectories in I-Φ space near the central (ℓ = 0) side band of a third order resonance.

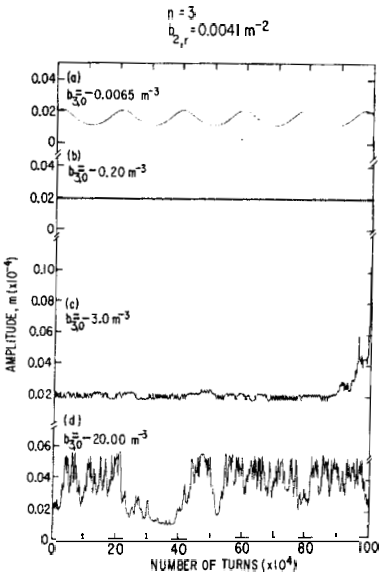


Fig. 3. Single particle amplitude as function of revolution number, for different zeroth harmonic octupole components, near a third order resonance.

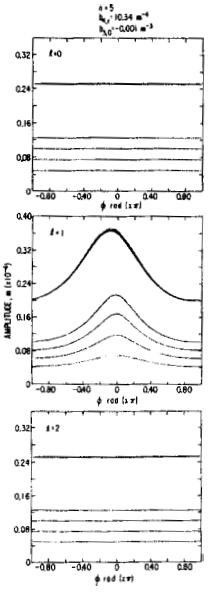


Fig. 5. Particle trajectories in I-Φ phase space for different side bands of a fifth order resonance.

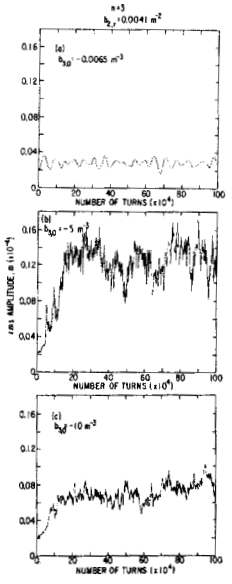


Fig. 4. rms amplitude of 10 particles as function of revolution number, for different zeroth harmonic octupole components, near a third order resonance.

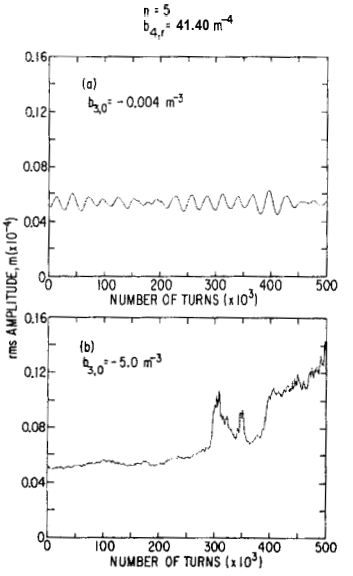


Fig. 6. rms amplitude of ten particles as function of revolution number, for different zeroth harmonic octupole components, near a fifth order resonance.

MAIN RING MAGNET SYSTEM OF KEK PS

A. Ando, K. Endo, T. Kasuga, M. Kihara and E. Takasaki
National Laboratory for High Energy Physics
Oho-machi, Ibaraki, Japan

Summary

Results of the field measurement on the quadrupole and bending magnets for the main ring of KEK 12 GeV proton accelerator are shown. The design of secondary magnets is reported.

Introduction

The main ring of the KEK 12 GeV proton accelerator is the separated function synchrotron with the four long straight sections? There are *48* bending magnets and 56 quadrupole magnets in the ring, and two quadrupole magnets and one bending magnet, which serve as the reference magnets for the main ring B-clock system, are set up in the power house.

All magnets have already been set into the tunnel by March and the precise alignment is now going on. The magnetic field measurement on the quadrupole magnet was performed before installed into the tunnel. On the bending magnet, however, the field measurement is in progress inside the main ring tunnel.

The design of the secondary magnets has already finished. The following secondary magnets are installed in the main ring; the horizontal and vertical steering magnets, the trimming quadrupole magnets, the skew quadrupole magnets, the sextupole magnets, and the octupole magnets.

The steering magnets are always used in dc excitation. The other correction magnets are also energized by dc power supplies in the initial operation of the main ring, so as to provide correction only at injection, although magnets themselves are designed to permit future pulsed operation with the full excitation at the maximum energy. All magnets are excited by individual power supplies to generate harmonics with changeable amplitude and phase.

In this report, the results of the field measurements on the quadrupole and bending magnets, and the design of the secondary magnets are given.

Magnetic Field Measurements

Quadrupole magnet

Magnetic field measurements were performed on 60 quadrupole magnets before installed in the main ring tunnel. As the basic measurements on each magnet, the excitation curve of the field gradient, the transversal distributions of the field gradient at the center of magnet and the effective gradient length $(1/B')\int B'ds$ on the magnet axis were measured at eight excitation levels from 0.13 kG/cm to *2.04* kG/cm.

These field measurements were done under the dynamic operation by using two digital integrators connected with the conventional twin coils and the reference coil. The long coil 10 cm long was used for measurements of the effective gradient length. In order to check the stability of the measuring system, one particular magnet was chosen as the standard magnet, on which the above-mentioned quantities were frequently measured. The results of this measurement have shown the rms statistical error to be less than 0.02 % for both the field gradient and the effective gradient length at all excitation levels.

The remanent field was also measured by the Hall generator after exciting the magnet up to 2.0 kG/cm. The relative error for the remanent field gradient is less than *4* %, and the accuracy in its absolute value is estimated to be at most 7 %.

The radial distributions of the effective gradient length on the standard magnet are shown in Fig.1. As the result of the multipole expansion, the effective gradient length contains the 12th multipole as the main higher component, rather than the octupole as shown in Table 1. It is the particular feature of using the oriented steel that the higher multipole components in the effective length do not change appreciably with the field strength.

The histograms of the field gradient, the effective gradient length and the integral of field gradient $\int B'ds$ are shown in Fig.2. The average value and the standard deviation for these quantities are given in Table 2. The fluctuation in $\int B'ds$, which is the most interesting quantity from the viewpoint of the operation of the machine, is less than 8×10^{-4} at all excitation levels.

The average value of the remanent field gradient is *0.58* G/cm with the fluctuation of *0.04* G/cm. This fluctuation corresponds to 3×10^{-4} at injection field of 150 G/cm. In Table 2, the effect of the remanent field is added to the field gradient produced by the exciting current, for B' = 0.128 kG/cm.

Bending magnet

Magnetic measurements on the *48* bending magnets have not yet been finished. In this section, the measured results on one bending magnet are reported.

The bending magnet is measured under the dynamic operation by using the same measuring system as that for the quadrupole magnet. The remanent field is also measured by the Hall generator after pulsing the magnet up to 17.5 kG.

As reported in the previous paper: a slight amount of gradient exists in the field produced by the exciting current. The k-value at the injection field is -0.017 m^{-1} and it decreases with increasing field strength to reach an almost constant value of -0.005 m^{-1} above a certain field level. This variation of the field gradient may be attributed to the systematic gap opening during welding, the gap deformation due to the magnetic force and the core saturation.

The remanent field on the magnet centerline is 6.6 G and the gradient is 12 G/m. This can be partly cancelled by the field gradient produced by the exciting current (i.e. B' = −25.5 G/m at the injection field).

The radial distribution of the effective length was measured at 1.5, 7.5, 12.2 and 15.8 kG along the coordinate system shown in Fig.3. At low fields, the integral of the field strength over the central part of magnet is little dependent on the radial position. Therefore, the multipole components included in the effective length are mainly governed by the contribution from the fringing field at both ends. Above the medium fields, however, the field integral over the central part of the magnet is dependent on the position. The multipole components included in the effective length are listed in Table 3.

Although the power supply capability limited the maximum excitation to 15.8 kG for full scale magnet, we have roughly estimated the effective length from the data of the half-length magnet. The effective length for the half-length magnet is 1614.9 mm and the sextupole coefficient a_2/a_0 is $-1.2\ m^{-2}$. Considering that the sextupole component of the field strength at the magnet center is $-1.1\ m^{-2}$, the sextupole component included in the effective length for the full scale magnet can be approximated to be $a_2/a_0 = -1.13\ m^{-1}$.

Design of Secondary Magnets

The secondary magnets consist of 56 steering magnets, 16 trimming quadrupole magnets, 8 skew quadrupole magnets, 8 sextupole magnets and 16 octupole magnets. They are installed in the midi straight sections after F and D quadrupole magnet, in such a manner that they have the same superperiodicity as the main lattice.

Although strict tolerances were imposed on the main magnets, the variation in field strength and the misalignment of magnets yield the closed orbit distortion, which is estimated to be 13 mm in the horizontal plane and 6 mm in the vertical plane. Also, the variation in the field gradient and the field imperfections caused by the fringing field and the saturation effect excite the linear and non-linear resonances.

In Table 4 are summarized the principal parameters of the secondary magnets, and the proposed location for these magnets is shown in Fig.4. The secondary magnets are energized by dc power supplies, in the initial operation of the accelerator, to provide the correction only at injection. However, these magnets except for the steering magnet are made of laminated cores to permit future pulsed operation.

Steering magnet and closed orbit correction

The closed orbit distortion is caused by misalignment and random variation in field strength of the main magnets. The correction is done by the steering magnets at injection, and the displacement of the main quadrupole magnets at high fields.

The steering magnets are placed after every quadrupole magnet; 28 horizontal steering magnets follow the main F quadrupoles and 28 vertical ones the main D quadrupoles. The position of the closed orbit is measured with 56 beam position monitors which are fixed at the downstream end of every main quadrupole magnet. The field strength of the steering magnets listed in Table 4 is sufficient for providing the local closed orbit bump less than the half-aperture in both planes.

Current of the steering magnets is ad'usted with a method based on the least squares theory? The correcting deflections represented by a vector $\vec{\theta}$ are related to the measured distortion $\vec{x}$ in the following form;

$$\vec{x} + A\vec{\theta} = 0 , \qquad (1)$$

where A is a matrix constructed from the betatron oscillation variables. Since the solution of the above equation suffers from sensor error, besides A has no inverse matrix, it is relevant to treat eq.(1) as the least square problem in which the norm $||\vec{x} + A\vec{\theta}||^2$ is minimized. After simple manipulations, we get

$$\vec{B} + M\vec{\theta} = 0 ,$$

where $\vec{B} = A^T\vec{x}$ and $M = A^TA$. The matrix M is symmetric and has real and non-negative eigenvalues. The eigenvectors with low eigenvalue give only minor effects on the closed orbit and can be deleted from the solution?

In Fig.5 the eigenvalues are arranged in order of their dominant frequency, showing a resonant sensitivity to distortions with frequency near the ν value.

Fig.6 shows examples of closed orbit correction, assuming that the original closed orbit has the distorted sinusoidal form with frequency of 7.25. The effect of monitor failure has been studied by letting the distortion at thefailedmonitor be zero. In order to reduce the maximum closed orbit distortion by a factor of 2 or 3, it is sufficient to select 10 eigenvectors even in the presence of 3 failed monitors.

The closed orbit correction at high fields is performed in the similar way by replacing the deflection $\vec{\theta}$ by the displacement of the main quadrupole magnets and constructing a new matrix A.

The power supplies for the steering magnets will permit independent control of individual current. A block diagram for this system is shown in Fig.7. Information such as magnet location and current is transmitted to each power supply in the digital form through transmission lines. Each magnet current is changed after converting the digital settings into an analogue value.

Trimming quadrupole magnet

The trim quadrupole magnets are used for independent tuning of the horizontal and vertical betatron frequencies and exciting the 15th harmonic to cancel the stopband of the half integer resonance at $\nu = 7.5$. The error quadrupole field comes from the variations in the gradient length $\int B'ds$ of the quadrupole magnet and the k-value in the bending magnet.

Correcting sextupole and octupole magnets may be the source of gradient error when the excursion of closed orbit from the center of magnets is present. Similarly, the higher multipole components in the bending magnet yield the same effect.

In the "fine tuning" mode, the trim quadrupole should not excite any harmonics in the neighbourhood of $2\nu_x$ and $2\nu_z$, such as 14th, 15th and 16th. As the trim quadrupoles have the same periodicity as the main lattice, the harmonics of multiple of 4 are excited. To eliminate the 16th harmonic, the current of the quadrupoles in one superperiod must be properly modulated. Although the complete elimination is impossible with 4 quadrupoles, the stopband can be suppressed to 0.08 for the tune shift $\Delta\nu = 0.1$, for the proposedarrsngement. Since the betatron frequencies can be tuned by the main quadrupoles, the trim quadrupoles are used for fine tuning of $\Delta\nu$ less than 0.2.

The stopband width which is expected from the gradient error in the main magnets is 0.016, assuming the variation of 30 % in the k-value of the bending magnet (Table 5). At 12 GeV, however, the closed orbit excursion (5 mm rms) in the bending magnet produces the stopband width of the same amount. Contribution from the correcting sextupole magnets may be even larger. In the "15th excitation" mode, two quadrupole pairs at the opposite side of the ring are excited with the same gradient but in opposite sign, so as not to excite such harmonics as Oth, 14th and 16th. In order to change the amplitude and phase of the 15th harmonic independently in both planes, eight quadrupoles are used to generate cos and sin functions.

The trim quadrupole magnets are designed to be excited up to 4 T/m, which corresponds to the tune shift $\Delta\nu = 0.1$ for the maximum energy. At first, however, the trim quadrupoles are excited by dc power supplies up to 0.7 T/m which will provide the tune shift $\Delta\nu = 0.2$ at

the injection field. The required strength for the 15th harmonic excitation is smaller than this, so that both modes are easily superimposed.

Skew quadrupole magnet

Sources of the skew quadrupole field are the roll of the quadrupole magnets and the vertical closed orbit deviation in the presence of the sextupole field. If an increase of 10 % in emittance due to the coupling oscillation at $\nu_x = \nu_z$ is allowed, the tolerable limit is given by $B'_x = 1.6 \times 10^{-5}$ T/m at injection and 1.9×10^{-4} T/m at 12 GeV, for $\nu_x - \nu_z = 0.005$. These values correspond to the average roll error of 10^{-5} rad.

The main quadrupole magnets were settled in the tunnel with the roll error less than 10^{-4}. Here, assuming the mean value of roll error to be 5×10^{-5}, the required strength of the skew quadrupole field is obtained as listed in Table 4. Such field is provided by the special windings on the octupole magnet described later.

Sextupole magnet

Sextupole magnets are used for narrowing the stopband of the third order resonance and compensating the chromatic aberration. Source of the sextupole field is mainly the fringing field and the saturation effect in the bending magnet. The sextupole field produced by eddy current in the vacuum chamber is less important in our case because the injection field is high.

The stopband width for each resonance line, which is estimated by using the data of the field measurement, is summarized in Table 5. Here we assumed the roll error of the bending magnet is 10^{-4} rad. As seen in the table, the dangerous resonance is $3\nu_x = 22$ which is near the working point.

The tune shift due to momentum error is $\Delta\nu_x = -0.04$ and $\Delta\nu_z = -0.02$ for $\Delta p/p = 0.3$ % at injection. At 12 GeV, it becomes $\Delta\nu_x = -0.002$ and $\Delta\nu_z = 0$ since $\Delta p/p = 0.1$ %. To compensate this tune shift, especially $\Delta\nu_x$, eight sextupole magnets are used. The required strength is given in Table 4. The field strength required to cancel the 22nd harmonic of sextupole field is smaller than that for compensation of the tune shift.

Octupole magnet

Octupole magnets are used for narrowing the stopband of the fourth order resonance induced by both magnetic imperfections and the space charge force.

The main source of the octupole component is the fringing field and saturation effect of the main quadrupole magnet. Amplitude dependent tune shift due to the octupole field is less than 10^{-3} for the horizontal emittance of $\varepsilon_H = 80\ \pi$ mm-mrad. The stopband width is given in Table 5.

In the presence of momentum spread, the betatron frequency oscillates around a central ν value by virtue of the synchrotron oscillation. When the beam crosses the fourth order resonance lines many times during the acceleration period, the horizontal and vertical emittance growth occurs. Since the growth rate at each traversal of the stopband depends on its width, it should be eliminated by the correcting octupole magnets.

Octupole magnets are also used to provide octupole field with appropriate amplitude and phase for the half integer resonant extraction.

The coupled motion induced by space charge forces drives $2\nu_x - 2\nu_z = 0$ resonance which will result in the emittance blow-up! This can be compensated by the octupole field with the zeroth harmonic. For the intensity of 5×10^{12} protons in the ring, the required strength is 30 G/cm^3 at 12 GeV. This field strength is sufficient for the correction of field error and the half integer resonant extraction.

Acknowledgements

The authors wish to thank Professor T. Nishikawa for many fruitful discussions and continuous support. Thanks are due to Messrs. A. Araki, T. Igarashi and S. Ochiai for preparing the field measurement equipments and carrying out the numerical computation.

References

1. K. Endo and M. Kihara, Proc. 4th Int'l Conf. on Magnet Technology, BNL, 1972, p.363.

2. M. Kihara, Proc. U.S.-Japan Seminar on High Energy Accelerator Science, Tokyo and Tsukuba, 1973, p.134.

3. G.R. Lambertson and L.J. Laslett, Proc. 5th Int'l Conf. on High Energy Accelerators, Frascati, 1965, p.26.

4. G. McD. Bingham, NAL internal report TM-200 (1970).

5. A.G. Ruggiero, NAL internal report TM-348 (1972).

6. B.W. Montague, CERN 68-38 (1968).

7. G. Guignard, CERN 70-24 (1970).

Table 1. Multipole coefficients for the effective gradient length of the quadrupole magnet ($\ell_G = \sum_{n=0}^{14} a_n x^n$)

B' (kG/cm)	0.128	1.777	1.927
a_0 (mm)	615.48	604.15	602.70
a_1/a_0 (m^{-1})	0.029	0.018	0.013
a_2/a_0 (m^{-2})	0.16	-0.21	-0.39
a_3/a_0 (m^{-3})	-11.7	6.1	8.4
a_4/a_0 (m^{-4})	-2040	-2360	-2300
a_5/a_0 (m^{-5})	5100	-20200	-22800

Table 2. Average values and standard deviations of $\frac{dB}{dx}$, L_G and $\int\frac{dB}{dx}ds$ for the quadrupole magnet

$\frac{dB}{dx}$ (kG/cm)	$\sigma(\frac{dB}{dx})$ (%)	L_G (mm)	$\sigma(L_G)$ (%)	$\int\frac{dB}{dx}ds$ (kG)	$\sigma(\int\frac{dB}{dx}ds)$ (%)
0.128	0.047	615.66	0.050	7.832	0.059
1.268	0.058	610.65	0.055	77.40	0.075
1.777	0.058	603.76	0.076	107.26	0.079
1.927	0.050	602.24	0.088	116.02	0.047

Table 3. Multipole coefficients for the effective length of the bending magnet

$$(\ell_B = \sum_{n=0}^{5} a_n x^n)$$

B	(kG)	1.5	7.5	12.2	15.8
a_0	(mm)	3257.0	3254.4	3243.7	3228.8
a_1/a_0	(m^{-1})	-0.0067	-0.0037	-0.0043	0.002
a_2/a_0	(m^{-2})	-0.24	-0.18	-0.24	-0.47

Note that, as seen in Fig.3, the fluctuation in measured values at 1.5 kG is somewhat larger.

Table 4. Principal parameters of the secondary magnets

	Number	Length (m)	Field strength at injection	Field strength at 12 GeV	Power supply
Steering magnet					
horizontal	28	0.15	920 G	-	dc
vertical	28	0.15	370 G	-	dc
Trim quadrupole	16	0.15	70 G/cm	0.4 kG/cm	pulsed
Skew quadrupole	8	0.2	9 G/cm	100 G/cm	pulsed
Sextupole magnet	8	0.4	8 G/cm^2	190 G/cm^2	pulsed
Octupole magnet	16	0.2	0.25 G/cm^3	30 G/cm^3	pulsed

Table 5. Total stopband width

N	n_1	n_2	injection	12 GeV		
2	2	0	0.016	0.008	$\langle \Delta B'/B' \rangle = 8\times10^{-4}$ for QM	
	1	1	1.8×10^{-6}	5.7×10^{-7}	$\langle \Delta B' \rangle$ = 8 G/m (inj)	} for BM
	0	2	0.016	0.008	30 G/m (12 GeV)	
3	3	0	0.027	0.039	B'' = 0.07 T/m^2 (inj)	} for BM
	2	1	3.3×10^{-6}	4.6×10^{-6}	4 T/m^2 (12 GeV)	
	1	2	0.033	0.046		
	0	3	1.2×10^{-6}	1.7×10^{-6}		
4	4	0	1.4×10^{-3}	1.5×10^{-4}	B''' = 0.6 T/m^3 (inj)	} for QM
	3	1	4.7×10^{-8}	4.4×10^{-9}	8 T/m^3 (12 GeV)	
	2	2	6.3×10^{-4}	5.7×10^{-5}		
	1	3	3.3×10^{-8}	3.1×10^{-9}		
	0	4	3.3×10^{-4}	3.3×10^{-5}		

Roll error is assumed to be 5×10^{-5}rad and 10^{-5}rad for QM and BM. < > means rms error.

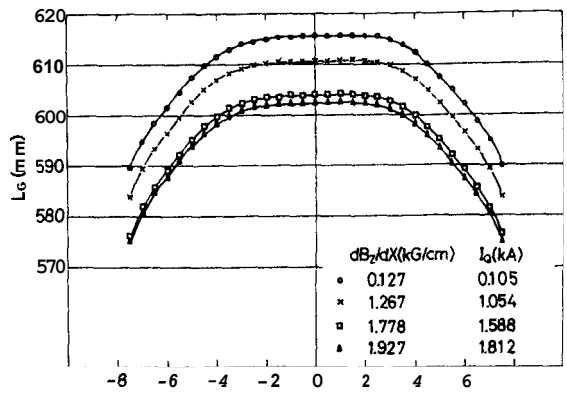


Fig.1 Radial distributions of the effective gradient length of the quadrupole magnet.

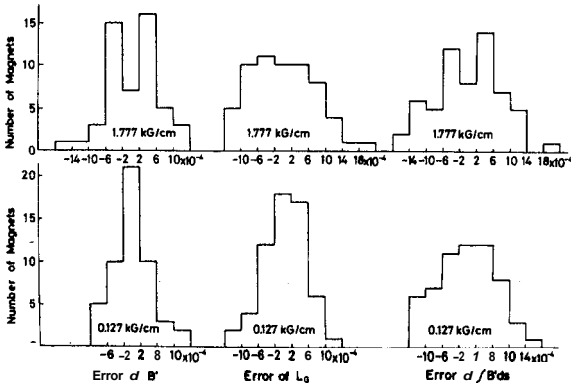


Fig.2 Deviations in $\frac{dB}{dx}$, L_Q and $\int \frac{dB}{dx} ds$ of the quadrupole magnet.

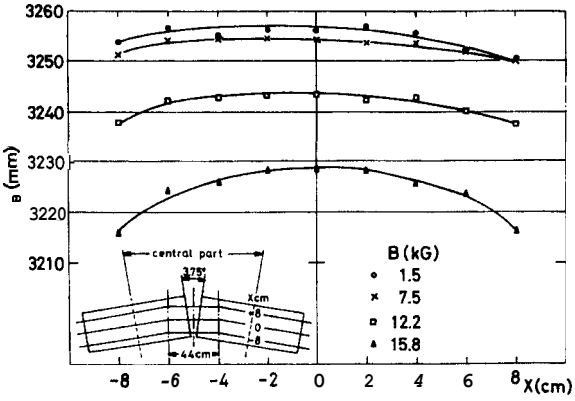


Fig.3 Radial distributions of the effective length of the bending magnet.

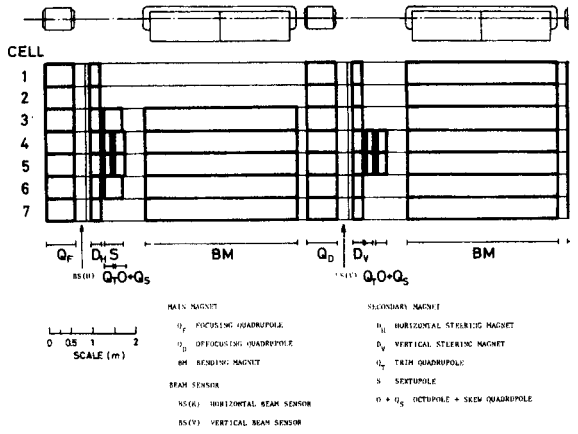


Fig.4 Secondary magnet locations.

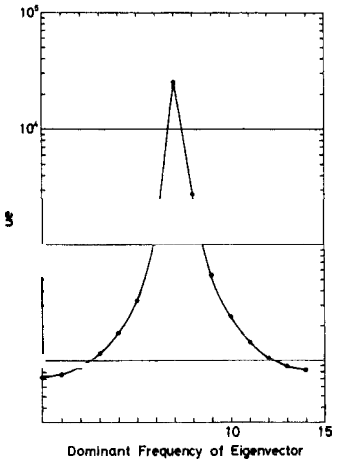


Fig.5 Eigenvalues arranged in order of dominant frequency of eigenvectors. They are doubly degenerated except for both ends.

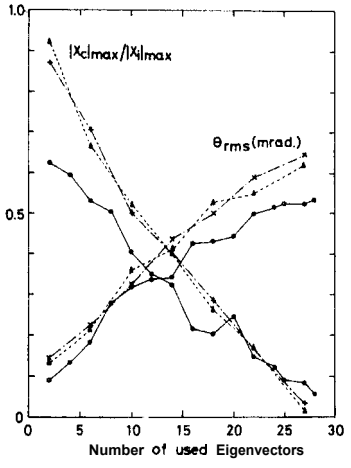


Fig.6 Ratio of the maximum orbit distortion after and before correction, and rms value of correcting deflections as the function of number of used eigenvectors. Solid lines: no monitor failure. Dotted lines: three monitors in failure. Dash-dotted lines: three consecutive monitors in failure.

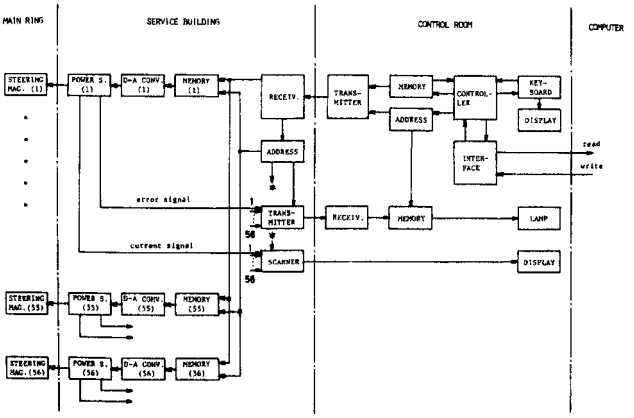


Fig.7 Block diagram of the control system for the steering magnet power supply.

SATURNE II : PROPOSAL OF A RENOVATED PROTON FACILITY AT SACLAY

H. Bruck, J. -L. Laclare, G. Leleux
Section d'Optique Corpusculaire, Centre d'Etudes Nucldaires de Saclay
and the "GERMA" group*

Abstract.

The Saclay proton synchrotron Saturne will be transformed into a strong focusing machine to be used essentially for nuclear spectroscopy. The advantages of a circular machine for such a purpose are underlined. The shortcomings of weak focusing are analysed and essential parameters of the transformed machine are given.

1 - Generalities.

The Saclay proton synchrotron Saturne is 16 years old. But there are still long range programs for use of this machine in the field of nuclear physics, with heavier or polarized particles, for medical purposes, but mostly for proton nuclear spectroscopy.

For the latter purpose, a circular machine, even when compared to the Linac in Los Alamos, seems also attractive. It has less intensity but higher energy and less energy dispersion. Furthermore, the extraction mechanism analyses the energy, making therefore a separate energy analyser unnecessary.[1,2]

	$\bar{I}$	E_c	$\Delta p/p$ total	$\Delta p/p$ analysed
Los Alamos	$6.\,10^{15}$	0.8 GeV	10^{-2}	----
Saturne II (expected)	$2.\,5.\,10^{12}$	2.7 GeV	$3.\,10^{-4}$	

At present, the beam gets progressively unreliable with intensities approching $N_{acc} \longrightarrow 10^{12}$ accelerated protons, the horizontal emittance of the extracted beam being $(\varepsilon_x)_{ext} \sim 30\ \pi$ mrd. mm.

More particles in a much smaller emittance are expected from a modern machine.

It has been decided to renovate Saturne. Preliminary studies led to the recommandation to keep the present 20 MeV injector, the magnet power supply and the building, but to set up a new strong focusing, separated function magnet structure around the old magnet (fig. 1). Construction of this machine has started and will be completed in 1977. The cost is evaluated at $33.\,6\ 10^6$ french francs. The expected performance characteristics of the transformed machine are :

	(old machine) Saturne I	(new machine) Saturne II
E_c	3 GeV	2.7 GeV
N_{acc} at 1 GeV	$\lesssim 10^{12}$	$2.\,5\ 10^{12}$
T_c	3 sec	0.9 sec
A	15 %	30 %
$\frac{dN_{ext}}{d\mathcal{E}_x}$ x 5 π mrd. mm	$3.\,10^{10}$	$2.\,25\ 10^{12}$
$\left(\frac{\Delta p}{p}\right)_{ext}$	$2.\,10^{-3}$	some 10^{-4}

for meaning of symbols see section 3.

2 - Essential improvement factors.

Apparently the difficulties to get a reliable beam of high intensity in the present machine are related to resistive wall instabilities and to enlargement of the beam by betatron resonances.[3] The importance of these effects is inherent in the weak focusing principle : in order to get a beam steady with respect to transverse resistive instability, the betatron wave numbers ν_x and ν_z have to cover finite domaines $\delta\nu_{x,z} \gtrsim (\Delta\nu_{sc})_{x,z}$, where $\Delta\nu_{sc}$ is the space charge displacement of the wave numbers. Therefore with growing intensity the required values of $\delta\nu_x$ and $\delta\nu_z$ grow and cover a growing number of resonance lines.

Now, not only at given beam density, $\delta\nu_x$ and $\delta\nu_z$ are large in a weak focusing machine (because $\Delta\nu_{sc} \propto 1/\nu$), covering many resonance lines, but at given magnet field quality, the band width of these lines is also much larger than in a strong focusing machine.

In renovating Saturne, it therefore appears as most essential to introduce strong focusing with as high as possible wave numbers. A strong focusing separated function structure has been designed having betatron wave numbers $\nu_x = \nu_z = 3.6$, physical radius R = 16.8m and long straight sections, each ~10m long as required for easy extraction (fig. 1).

* "Groupe d'Etude et de Rdalisation de la Machine" in charge of future development and carrying the proposal into effect. This group comprises staff members of CEA and IN2P3 ; R. Vienet is in charge of this group.

Comparing the old machine to the new one at the same relative field errors $\langle \delta B' \rangle / B$; $\langle \delta B'' \rangle / B$; $\langle \delta B''' \rangle / B$, the respective theoretical stop band width are reduced to 1/50 ; 1/6 ; 1/10.

Because of its higher wave numbers, this machine furthermore accelerates polarized protons without crossing low harmonic depolarizing resonances.[4]

Another essential improvement of performance characteristics will result from further reducing magnet field fluctuations.

Owing to strong and only slowly decreasing eddy currents inside the 10 mm thick iron sheets of the present magnet core, the field strength would be depressed at beginning of extraction flat top by $\Delta B/B = 10^{-2}$ with time constant $\tau \sim 1/10$ sec, whereas a field constant to at least 10^{-5} is required. This defect will be cured by an entirely new magnet, decided upon for various reasons and having sheet thickness of 1.5 mm.

Furthermore, the ripple of the power supply is at present $\Delta I/I$ = some 10^{-3} during field rise and $\Delta I/I$ = some 10^{-4} during flat top, whereas ten times less must be achieved. The appropriate technology has not been decided upon yet. Use of the present magnet as a filter is contemplated.

3 - Parameters.

a) Orbit. "Missing magnet" lattice.

Maximum kinetic energy(proton)	E_c = 2.7 GeV
Physical radius	R^c = 16.8 m
Magnet radius	ρ = 6.34 m
4 long straight sections, each of length	L = 10.3 m
Magnet field index	n = 0
Maximum quadrupole strength	$(G\ell)_F$ = 4.12 T
	$(G\ell)_D$ = 4.49 T
Betatron wave numbers	$\nu_x \approx \nu_z \approx 3.6$
Natural wave number dispersion	$k = d\ /(dp/p)$
	k_x = - 4.8 ; k = - 4.8
Orbit parameters	$(\beta_x)_M$ = 17.4 m ; $(\beta_x)_m$ = 1.47 m
	$(\beta_z)_M$ = 16.0 m ; $(\beta_z)_m$ = 1.78 m
Momentum compaction	α = 0.017
Local momentum compaction	Rg_M = 6.77 m ; Rg_m = - 4.76 m

b) Injection.

Energy(protons)	E_i = 20 MeV
Number of turns	n_i = 200
Injected number of particles	N_i = $6.\ 10^{12}$
Space charge displacement at injection	$(\Delta\nu_{ce})_x$ = 0.17
	$(\Delta\nu_{ce})_z$ = 0.17
Emittances	$(\mathscr{E}_x)_i$ = 90 π mrd. mm
	$(\mathscr{E}_z)_i$ = 200 π mrd. mm
Energy dispersion	$(\Delta p/p)_i = \pm 8.\ 10^{-3}$
Maximum beam dimensions	$(x_M)_i = \pm 8.2$ cm ; $(z_M)_i = \pm 6.8$ cm

c) Acceleration.

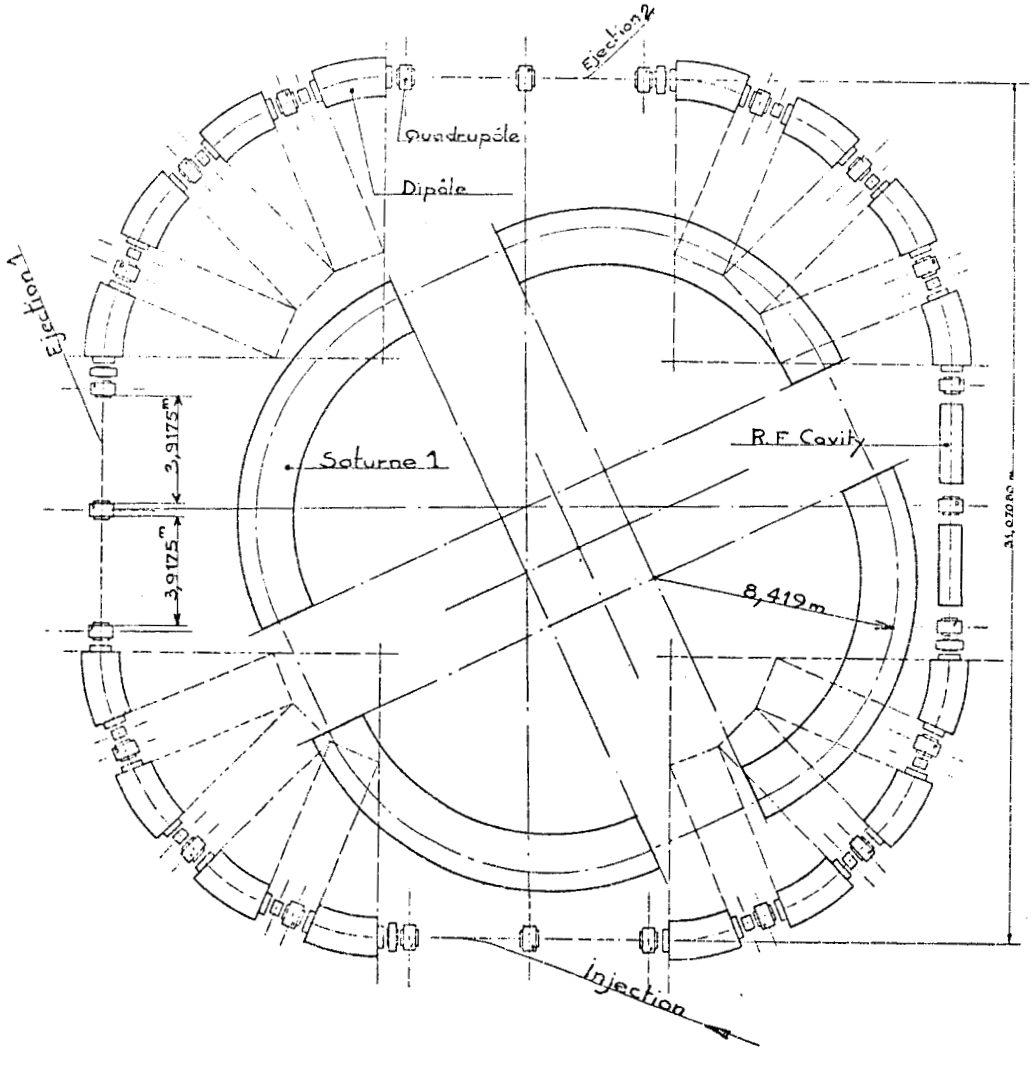
Peak voltage	$\hat{V}_{RF}$ = 14 kV
Harmonic number	k_{RF} = 3
Speed of magnet field rise	$\dot{B}$ = 3.5 T s^{-1}
Number of accelerated particles	N_{acc} = 2.5. 1012
Kinetic transition energy	$E_{c,tr}$ = 6.36 GeV

d) Extraction (1 GeV)

Number of particles	$N_{ext} = 2.25.10^{12}$
Emittances (total)	$(\mathcal{E}_x)_{ext} \leq 7\ \pi$ mrd. mm ; $(\mathcal{E}_z)_{ext} = 25\ \pi$ mrd. mm
Energy dispersion (total)	$(\Delta p/p)_{ext} \gtrsim \pm 145\ 10^{-4}$
Energy resolution	$(\Delta p/p)_{res} \simeq 10^{-}$
Duration of one cycle	$T_c \approx 0.9$ sec
of flat top	$\tau \approx 0.3$ sec
Duty cycle	$A \approx 30\ \%$

References.

1. R. Beurtey and J. Faure, Private communication.
2. H. Bruck, J.-L. Laclare and G. Leleux, General properties of slowly extracted beam, present proceedings.
3. J. Faure, G. Leleux and R. Vienet, Instabilities detected in Saturne, present proceedings.
4. J. Faure, A. Hilaire and R. Vienet, Acceleration of polarized protons in Saturne, Particle Accelerators *3* (1972) pp 225.



THE ELECTRON PULSE STRETCHER EROS

N. R. Heese and R. Servranckx
Saskatchewan Accelerator Laboratory,
University of Saskatchewan, Saskatoon, Canada, S7N 0W0

1. Introduction

The Electron Ring of Saskatoon is designed as a pulse stretcher whose purpose is to bring the duty factor of the 250 MeV electron linear accelerator at Saskatoon from a value of 6.25×10^{-4} to a value of 0.8 or more. The ring, into which the 1 μs long linac pulse is injected, is a racetrack shape of 73 m circumference. The electrons are then slowly extracted between linac pulses utilizing a resonance phenomenon. The reader is asked to consult Refs. 1 and 2 for a complete description of the design.

2. Optimization of the Design

In 1973 an optimization of the design, as regards to cost, was undertaken. It appeared immediately that the most expensive elements of the design were the quadrupoles and hexapoles, particularly those of the curved sections. Their aperture was over 10 inches. As suggested by K. Brown of SLAC, we examined the possibility of increasing the horizontal tuning, ν_x, from a value of 3 1/3 to 5 1/3. The change might reduce the aperture required since the chromatic excursion is proportional to $1/\nu_x^2$. However, to achieve this, we had to change the structure and increase the number of units in the curved sections and also modify the structure of the straight sections. Figure 1 shows the present layout of the ring: A more detailed analysis of the considerations involved in the modification can be found in Ref. 3.

Figure 2 shows the graphs of the beam dynamic functions β_x, β_z and the chromatic excursion function $g = dx_{co}/d\delta$, where x_{co} denotes the closed orbit, $\delta = p - p_o/p_o$, p is the momentum of the particle, and p_o is the nominal momentum.

A further delicate adaptation of the straight and curved sections allowed a reduction in the aperture of all quadrupoles by a factor of at least two.

3. Monochromatic Extraction

The extraction process adopted is based on the 1/3 resonance which has been extensively described in the literature (see Ref. 1). Previous to this an achromatic extraction process was considered. A modification of the chromatic parameters of the ring enabled us to achieve a monochromatic extraction of the beam.

The area of the extraction triangle is plotted on the graph in Fig. 3. From this graph it can be seen that the particles along the curved segment from B to C are extracted. They cover an energy spread of 0.08%. If by some deceleration process (radiation, RF, betatron core) the stable particles of the beam can lose energy with time, they will be extracted at the same energy and within the same energy spread while the tuning of the machine remains constant.

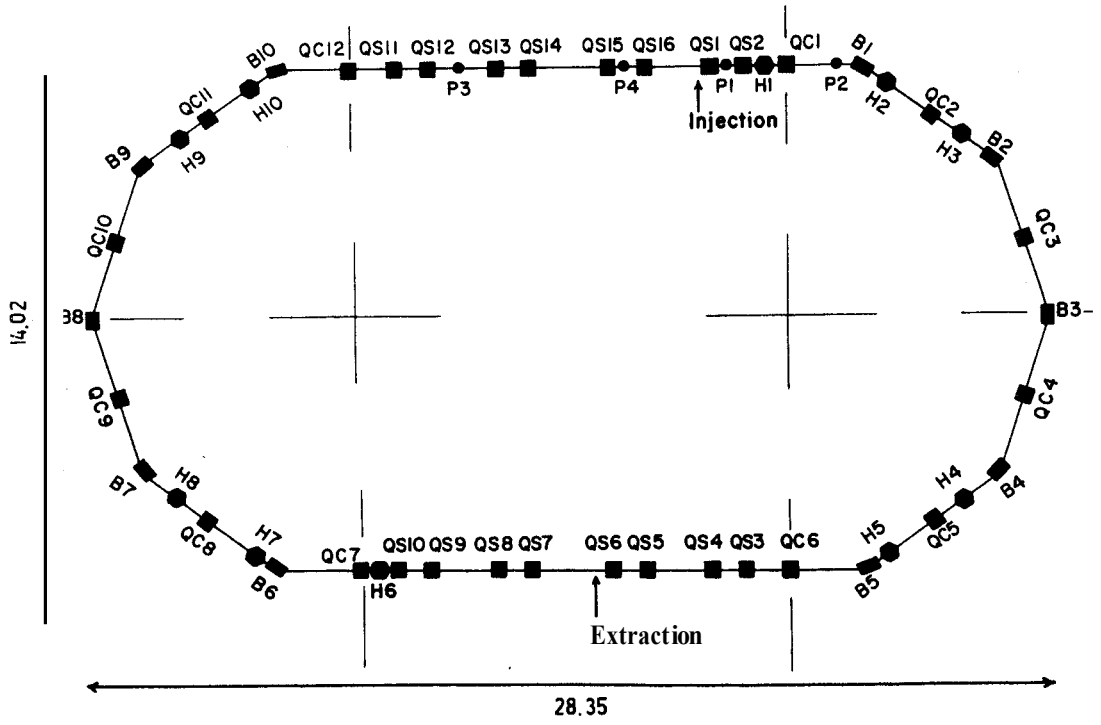


Fig. 1 EROS ring layout

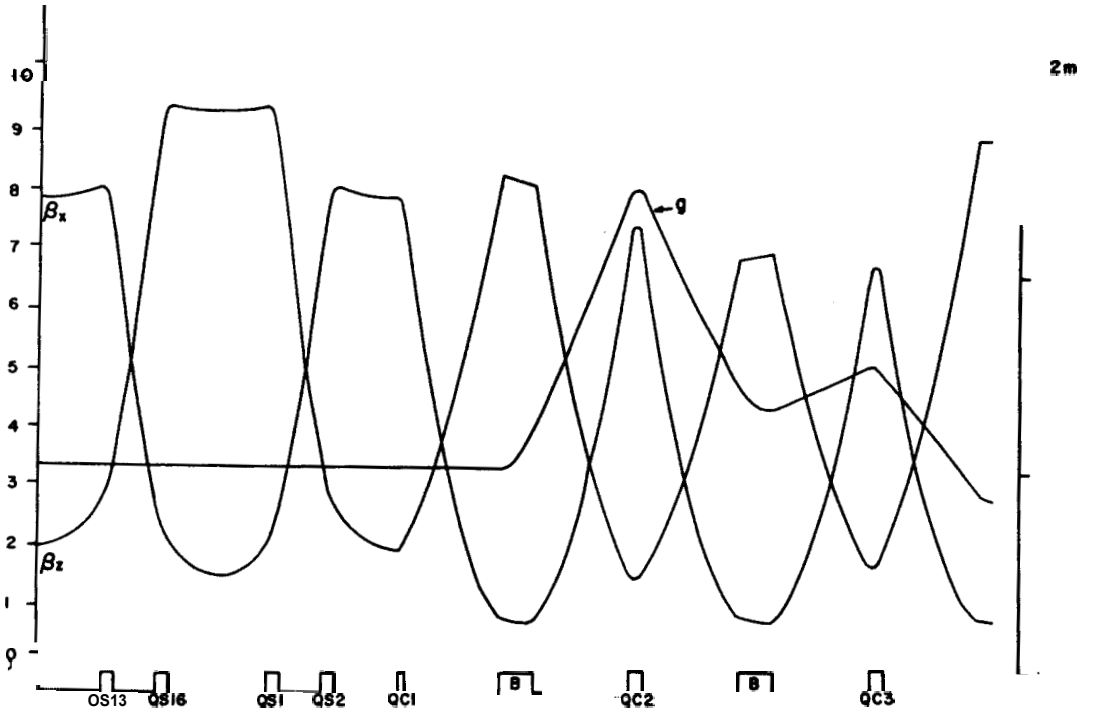


Fig. 2 β_X, β_Z, g-function in half a curved section.

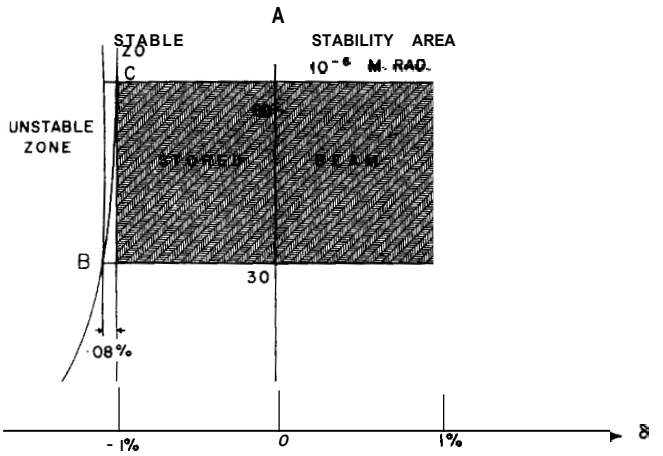


Fig. 3 Area of extraction triangle.

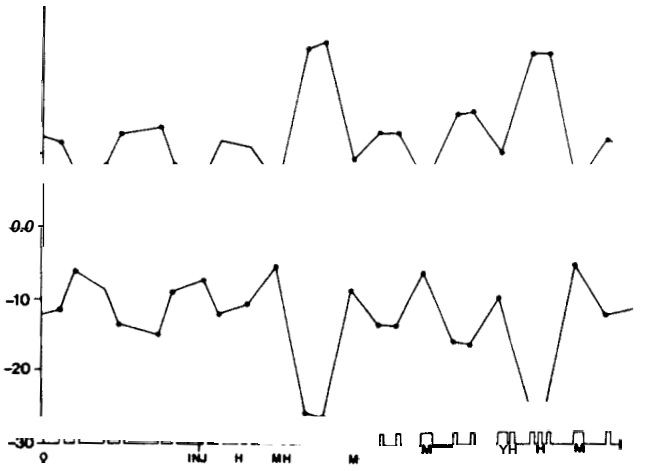


Fig. 4 Stored beam horizontal envelope.

Detailed calculation of particle tracing[4] shows this process works very well and leads to a beam size much in favor of the monochromatic extraction. The beam obtained by this extraction process is expected to have the following characteristics:

Energy range	150 to 250 MeV
Energy spectrum	0.08%
Beam emittance - horizontal	3 mm-mrad
- vertical	25 mm-mrad

The beam envelopes around the ring are as shown on Figs. 4, 5 and 6. In such an extraction the ring acts as a monochromator.

Extraction of the particles results from energy loss due to synchrotron radiation. The energy loss per turn is given by

$$\Delta E(\text{keV}) = 88.5 \frac{E^4(\text{GeV})}{m} .$$

Assuming the energy spread is 1%, the energy to be lost for complete extraction is $\Delta E(\text{keV}) = 1 \times 10^4\ E(\text{GeV})$. The number of turns needed to lose this energy is then

$$N = \frac{1 \times 10^4\ R(m)}{88.5\ E^3(\text{GeV})} = 113 \frac{R(m)}{E^3(\text{GeV})} .$$

Table 1 illustrates some values for our ring (remember R = 1 m). Since the ring is 73 m long, one turn takes 243.3 ns so that the total time (T) for full extraction can be computed and the allowable maximum repetition rate (Rm) for complete extraction is obtained easily (the accelerator natural repetition rate is 625 pps).

A pulsed betatron core could be used to increase the energy loss. The technical feasibility of this device is being studied.

We are also examining the use of a radio frequency cavity to achieve the required loss. One possible method is similar to that used on the ISR at CERN where they managed to accelerate particles by moving empty RF buckets through the beam.

Table 1
Radiation Losses and Repetition Rate in EROS

E (GeV)	ΔE_{tot} (MeV)	N	T (ms)	Rm (pps)
0.1	0.058	113 × 103	27.5	36.4
0.15	0.294	33 × 103	8.0	125
0.2	0.931	14 × 103	3.4	294
0.25	2.27	7.2 × 103	1.75	571
0.3	4.71	4.2 × 103	1.02	980

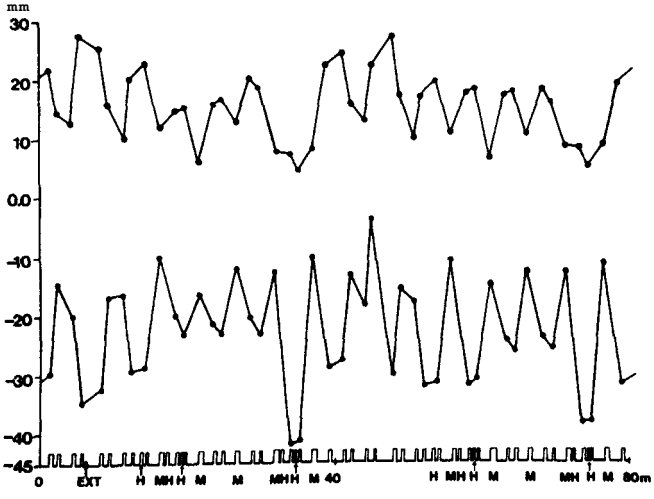


Fig. 5 Horizontal envelope during extraction.

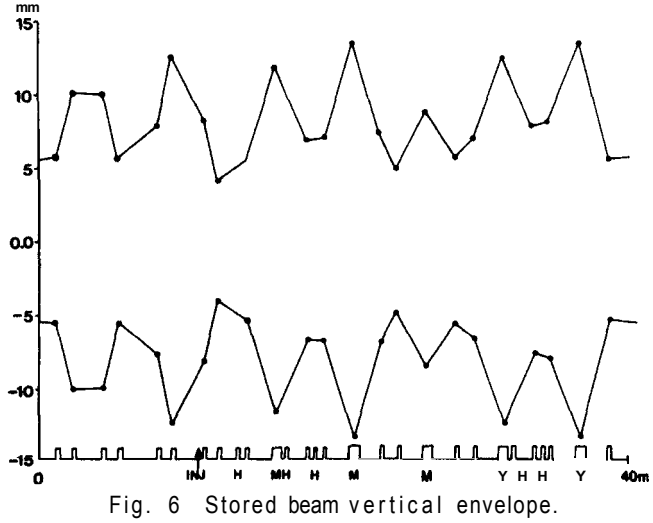


Fig. 6 Stored beam vertical envelope.

4. Main Magnetic Components of EROS

The perturbation of the ring design effected in 1973 by the presence of Karl Brown had a vast and beneficial impact on the magnetic components. The apertures of the quadrupoles and hexapoles were reduced from 10 inches in some parts of the ring to a uniform 4 inches all around. The bending magnets, although increasing in number from eight to ten were reduced considerably in size which allowed us to design them as rectangular units. The aim of the magnet design has been to achieve the required performance while keeping the construction as simple as possible.

Bending Magnets

Table 2 shows the parameters that must be satisfied for the bending magnets. Using a gap height of 5 cm (leaving a little room for error in the placement of the vacuum box and anticipating larger vertical oscillations during tune-up), it was found that a pole width of 17.78 cm (7 in.) would be more than adequate, provided small rectangular shims were used at the sides of the pole to extend the width of the useable field. The computer program TRIM5 was used extensively in the magnet design, and Fig. 7 shows a cross section of the proposed magnet, with the shaded area in the gap depicting the region of acceptable field levels (as ascertained by TRIM). The iron length of the magnet was evaluated using fringing fields given by TRIM and

Table 2
Bending Magnet Requirements

Field required for 250 MeV	8333 G
Deflection angle	36°
Effective length	61.808 cm
Poleface entrance angle	18°
Poleface exit angle	18°
Field index	0
Beam envelope in bending magnets:	
Max. vertical space occupied by beam	2.80 cm
Max. horizontal space occupied by beam	3.51 cm (including extraction)
Sagitta of 36° bend	4.90 cm
Width of good field required	8.41 cm
Definition of "good field"	± 0.05%
Power supply stability	± 0.005% (long term)
Field difference between any two magnets	< 0.1%

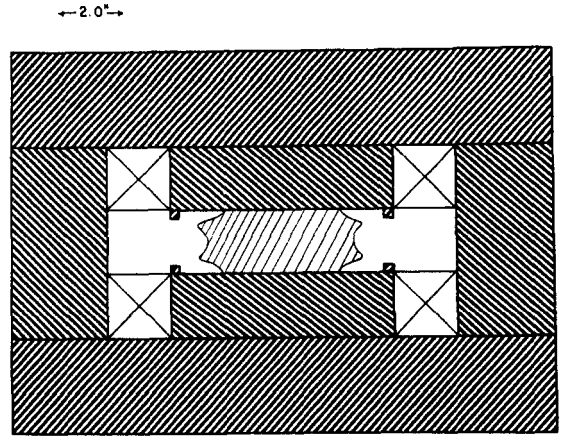


Fig. 7 Cross section through bending magnet.

Table 3
Quadrupole Requirements

1)	Strength	$-1.828\ m^{-2}$
	Effective length	0.25 m
	Aperture	12.7 cm (5 in.) diam.
	Max. field gradient	15,233 G/m
	Max. poletip inductance	967.4 G
	Number required	8
	Designation	5 QS 1.2
2)	Strength	$1.922\ m^{-2}$
	Effective length	0.25 m
	Aperture	12.7 cm (5 in.) diam.
	Max. field gradient	16,017 G/m
	Max. poletip inductance	1016.9 G
	Number required	8
	Designation	5 QS 1.2
3)	Strength	$1.778\ m^{-2}$
	Effective length	0.25 m
	Aperture	12.7 cm (5 in.) diam.
	Max. field gradient	14,817 G/m
	Max. poletip inductance	941.0 G
	Number required	4
	Designation	5 QC 1.2
4)	Strength	$3.556\ m^{-2}$
	Effective length	0.25 m
	Aperture	12.7 cm (5 in.) diam.
	Max. field gradient	29,633 G/m
	Max. poletip inductance	1882.0 G
	Number required	8
	Designation	5 QC 2.4
	Total integrated harmonic content at 4 in. aperture	1%
	Field difference between any two quadrupoles (tracking)	< 0.1%
	Power supply stability	± 0.005% (long term)

Table 4
Sextupole Requirements

1)	Strength	$-6.0\ m^{-3}$
	Effective length	0.2 m
	Aperture	12.7 cm (5 in.) diam.
	Poletip inductance	242 G
	Number required	2
	Designation	5 S .4
2)	Strength	$-7.65\ m^{-3}$
	Effective length	0.2 m
	Aperture	12.7 cm (5 in.) diam.
	Poletip inductance	305.7 G
	Number required	4
	Designation	5 S .4
3)	Strength	$0.318\ m^{-3}$
	Effective length	0.2 m
	Aperture	14.0 cm(5.5 in.)diam.
	Effective poletip inductance (these are air-core magnets)	15.6 G
	Number required	4
	Designation	5.5 S .016
	Total integrated harmonic content permissible at 4 in. aperture	10%
	Magnetic field stability	0.1%

a simple ray tracing program, and it turned out to be 56.64 cm. The flux in the return yoke was 13.6 kG at a thickness of 7.5 cm; the reluctance of the iron was 3% of the total, and the magnet requires 35,000 At at maximum field.

Quadrupoles

Table 3 shows the requirements for quadrupole magnets. Although an aperture of 10 cm would have been sufficient to handle the maximum extent of the beam in the ring, the aperture was increased to 12.7 cm for two reasons: (i) since the ring is designed to handle electrons of 100 MeV or less, the poletip inductance of the quads at this energy would have been very low (300 gauss or less), and remanent field problems would probably be encountered which would jeopardize the fine tuning of the ring. (ii) The first harmonic produced in a quadrupole due to the non-infinite extent of the magnet and to the non-hyperbolic shape of the poles is the 12-pole (n = 6, which decreases with the fifth power of the radius as one moves inward), thus an increase in aperture to 12.7 cm would considerably decrease the harmonic content at the normalizing aperture of 10 cm. The pole pieces can thus be cut from 6 inch diameter circular steel rods, which simplifies the construction considerably. Further reduction of harmonic content can be achieved by careful assembly and machining, chamfering the pole-edges at the exit and entry planes of the magnet and using mirror-plates (field-clamps) with adjustable studs.[6] Prototype magnet tests will reveal if these steps are necessary.

To meet ring tuning requirements, the quadrupoles must be driven in four groups (three groups of eight magnets and one group of four). The poles of all the magnets of one group must therefore be driven in series by one power supply. Since we wanted to avoid high voltages, we decided to use small water-cooled coils of low impedance.

Sextupoles

The requirements for sextupoles are outlined in Table 4. It can be seen that the poletip inductance of the iron magnets is quite low even after an increase in aperture; thus for low energy operation, remanent field problems could occur. Only experience will show the necessity of adding a degaussing cycle to the power supplies that drive them. Harmonic content should not be a problem, due to the increased aperture in both the iron-core and air-core magnets. The magnet coils are air-cooled and all of the magnets in each of the three groups indicated in Table 4 will be driven in series.

References

[1] R. Servranckx, Proceedings of the International Conference on Photonuclear Reactions and Applications, Asilomar, Calif., p.1039 (1973).
[2] Saskatchewan Accelerator Laboratory, Internal Reports SAL-RING-16 to -25, -27 (unpublished).
[3] Saskatchewan Accelerator Laboratory, Internal Report SAL-RING-28 (unpublished).
[4] R. Servranckx, Particle Accelerators (in press).
[5] J. S. Colonias and J. H. Cole, Proceedings of the International Symposium on Magnet Technology, Stanford University, p.188 (1965).
[6] W. V. Hassenzahl, Proceedings of the International Conference on Magnet Technology, Brookhaven, p.469 (1972).

PRELIMINARY DESIGN CONSIDERATIONS FOR THE STAGE I PEP LATTICE+

R. H. Helm and M. J. Lee

Stanford Linear Accelerator Center
Stanford University, Stanford, California 94305

Description and Summary

A general description of the proposed PEP e^+e^- storage ring may be found elsewhere[1,2] and in these Proceedings.[3] In the present paper, we discuss the lattice and its operating characteristics in more detail, show how the design luminosity and other criteria may be met and outline the limits of the operative regions of the beam parameters in several modes of operation.

The relevant design parameters are:

Beam Energy, E (each beam)	5 to 15 GeV
Luminosity per Interaction Regions at 15 GeV, $\mathscr{L}$	10^{32} cm^{-2}sec^{-1}
Number of Superperiods (number of interaction regions)	6
Number of Stored Bunches, N_b (each beam)	3
Available Length per Interaction Region	20 m
Length of Straight Sections	130.416 m
Gross Radius Arcs	220.337 m

Figure 1 depicts schematically the basic elements of the lattice as presently conceived and shows typical betatron and dispersion functions. The 60° arc of each superperiod contains eight cells, of which six are standard while in the two end cells the quadrupoles are independently variable. The structure is symmetric about the interaction points and about the centers of the 60° arcs. The proposed Stage I of PEP lies in a horizontal plane, although a future Stage II option with an added 200 GeV proton ring would involve vertical as well as horizontal bends.[4] Qualitatively speaking, the four independent quadrupoles in the straight sections Q3, Q2, Q1 and QF1 (see Fig. 1) provide matching of the betatron functions from the interaction point to the cells; the two modified cell quadrupoles QD1 and QF2 provide for dispersion matching; and the two sets of standard cell quadrupoles QD and QF allow adjustment of the betatron tunes.

Design Requirements

Luminosity Considerations. In order to define the lattice requirements imposed by the luminosity specification, we consider an idealized situation in which the stored e^+ and e^- beams are equal, and the coupling between horizontal and vertical betatron oscillations is adjusted so that the horizontal and vertical beam-beam tune shifts are equal ($\Delta\nu_x = \Delta\nu_y = \Delta\nu$). It then follows from simplified theory[5,6] that

$$\mathscr{L}_{max} = \frac{\pi}{r_e^2 m_e^2} f_0 N_b (\Delta\nu)^2 E^2 \left(\frac{1}{\beta_y^*} + \frac{1}{\beta_x^*}\right)\left(\epsilon_0 + \frac{\eta^{*2}}{\beta_x^*}\frac{\sigma_E^2}{E^2}\right). \quad (1)$$

Further, if the bending magnets are of equal strength and zero-gradient,

$$\mathscr{L}_{max} = \frac{55\pi}{32\sqrt{3}} \frac{\hbar c/e^2}{r_e m_e^4} \frac{f_0 N_b (\Delta\nu)^2 E^4}{P0} \left(\frac{1}{\beta_y^*} + \frac{1}{\beta_x^*}\right) \left(\langle \overline{H} \rangle + \frac{1}{2}\frac{\eta^{*2}}{\beta_x^*}\right), \quad (2)$$

where $\mathscr{L}_{max}$ is the maximum luminosity at the beam-beam tune shift $\Delta\nu$, $\hbar c/e^2 = 137.0$, r_e is the classical electron radius, m_e is the electron rest energy, f_0 is the orbital frequency, N_b is the number of bunches in each beam, E is the energy of each beam, β_x^* and β_y^* are the horizontal and vertical betatron functions at the interaction point, $\epsilon_0\pi$ is the total transverse emittance (i.e., the sum of the areas in radial and vertical phase space), η^* is the dispersion function at the interaction point, σ_E/E is the relative energy spread due to quantum excitation,, ρ_0 is the magnetic radius of the bending magnets and $\langle H \rangle$ is defined by

$$\langle \overline{H} \rangle = \frac{1}{2\pi\rho_0} \sum \int_i \frac{1}{\beta_x} \left[\eta^2 + (\beta_x \eta' - \frac{1}{2}\beta_x' \eta)^2\right] ds \quad (3)$$

where $\int_i$ denotes integration over the i-th bending magnet and Σ denotes summation over all bending magnets.

The luminosity is limited by the maximum tolerable beam-beam tune shift which is typically $\Delta\nu_{max} = 0.025$ to 0.08 per interaction point in e^+e^- storage rings.[7,8] It is evident from Eqs. (1) and (2) that the interaction betatron functions should be as small as possible. The minimum value of β_y^* has been chosen to be around 0.2 meters because it is felt that the maximum β-value at the nearest quadrupole, 10 meters from the interaction point, should be not much greater than 500 meters in order to keep apertures and chromaticity within tolerable bounds. The minimum value permitted for β_x^* is considerably larger because of the D-F configuration of the Q3-Q2 doublet. (See Fig. 1.) As will be seen later, useful ranges of β_x^* for the present design lie in the range of ~3 to 5 meters.

Aperture Limitation. Equation (2) shows that for a fixed lattice, luminosity varies as E^4 and therefore falls off very rapidly at low energy. However, it is possible to modify the lattice so that the beam size is kept essentially constant as a function of energy; then luminosity varies only as E^2, as may be seen from Eq. (1). In the PEP design, the apertures are chosen for the design energy and luminosity at 15 GeV and the luminosity is therefore aperture-limited at lower energies with an approximate E^2 dependence.

Beam Enlargement. Several schemes for beam enlargement* have been studied for lower energy operation. Some of the important features of these schemes are described below.

(1) Variable Tune. It can be shown that, approximately, $\epsilon_0 \propto N_c \psi_{xc}^{-3} E^2$ where N_c is the number of bending cells and ψ_{xc} is the horizontal betatron phase advance per cell.[2]

† Work supported by the U. S. Atomic Energy Commission.

* For another discussion of beam enlargement see Ref. 9.

Thus in order to keep ϵ_0 constant for different energies we wish to make the lattice operable over some range of values of ψ_{xc}. In this design study we have considered only cases with $\nu_x \times \nu_y$ and also have assumed that the vertical tunes should be just slightly above an integer or half-integer per superperiod.[10,11] This means that for the PEP lattice with superperiodicity of 6, the desirable tunes are, e.g., $\nu_{x,y} \approx 12, 15, 18, 21, \cdots$. In the present PEP design, the horizontal phase advance in the straight insertion is always close to 360°, so that the design values of phase advance per cell are $\psi_{xc} \approx 45^0, 62.5^0, 90^0, 112.5^0, \cdots$.

(2) Energy Disperiosn (High η^*). A variable value of the interaction point dispersion function η^* alters the luminosity limit through the factor η^{*2}/β_x^* [Eqs. (1)and (2)]. This scheme has been used successfully, e.g. at SPEAR.[7]

(3) Mismatched Dispersion Function. In common practice the momentum dispersion function is matched so that it repeats periodically from cell to cell in the standard cells. We may, however, for low energy operation mismatch the dispersion function in the standard cells as described by

$$\eta(s) = \eta_0(s) + \eta_1(s),$$

where $\eta_0(s)$, the matched dispersion function, is periodic from cell to cell, and $\eta_1(s)$, the mismatch component, is oscillatory at the betatron wavelength. As is shown elsewhere, this results in an increase in the function $\langle \overline{H} \rangle$, described roughly by[6]

$$\langle \overline{H} \rangle = \frac{1}{\beta} (\eta_{0s}^2 + \eta_1^2 \qquad (4)$$

where the subscript s denotes the symmetry point (midpoint) of the bending arc. That is, the emittance is quadratic in the mismatch amplitude.

A fourth method of beam enlargement, mismatching the betatron function β_x, also affects the quantity $\langle \overline{H} \rangle$. This scheme was considered briefly in the PEP study but seemed to offer no obvious advantages. It may be studied further if serious difficulties arise in other schemes.

Another possible method of beam enlargement consists of altering the damping partition number J_x, since $\epsilon_0 \alpha \langle \overline{H} \rangle / J_x$. In order to avoid complexity and expense, no special insertion is planned for damping modification as is planned in EPIC.[12] However, it still would be possible to vary J_x by varying the rf frequency from its nominal value; it may be shown that the PEP lattice would require a frequency change of about 2 parts in 10^5, resulting in a maximum orbit shift of less than a centimeter, to reduce J_x to zero.

Since the variable tune and the dispersion-mismatch methods increase the transverse emittance they increase the aperture requirements everywhere in the lattice. The high-η^* method, on the other hand, enlarges the beam in only the few quadrupoles nearest the interaction points, which may be a significant advantage in terms of sensitivity to orbit distortions. However it has been shown that the high-η^* configurations may lead to a longitudinal instability if η^* is too large.[8]

We expect that practical operating configurations will consists of combinations of variable-tune and high-η^*, or of high-η^* and mismatched-η, although other combinations may prove useful. Some of these configurations are discussed in a later section.

First Order Design

Summary of Constraints. The lattice requirements that have been discussed so far imply that the values of β_x^*, β_y^*, η^* and the tunes ν_x and ν_y should be independently adjustable. In addition, the symmetry of the ring requires that the slopes of the betatron and dispersion functions vanish at the interaction regions; i.e., $\beta_x'^* = \beta_y'^* = \eta'^* = 0$. Thus, eight mathematical constraints are imposed on the focusing strengths, requiring at least eight independently variable sets of quadrupoles. A number of other important constraints must also be considered. A twenty meter drift space is required for experiments at each interaction region. The maximum values of the p-functions and η-function must be kept everywhere within reasonable bounds in order to minimize aperture requirements and to reduce chromaticity and other aberrations. Magnetic field values must be kept within conservative limits. Furthermore, sufficient drift space must be reserved for various components such as rf cavities, injection components (septum magnets and kickers), rotated quadrupoles, sextupoles, beam monitors and control devices, electrostatic plates for separating the beams and so on.

The geometry of the ring has been fixed by considerations discussed in Ref. (1). Once the quadrupole locations have been fixed and the quadrupole strengths have been specified to satisfy the eight mathematical constraints mentioned above, it will not always be possible for all configurations to satisfy the additional constraints imposed by aperture and quadrupole strength limits. Hence in the present study we have mapped out the regions of beam parameters within which all of the constraints are satisfied. Some of the results will be described in a later section.

Computational Methods. Solutions for the quadrupole settings under a variety of focusing configurations as specified by the values of β_x^*, β_y^*, η^*, η_s, ν_x and ν_y have been found by use of the magneto-optic programs MAGIC[13] and TRANSPORT.[14] MAGIC employs thin-lens approximations for the transport elements, but has great flexibility and speed, and has been used to survey a wide range of configurations. TRANSPORT has been used to obtain more precise thick-lens solutions in a number of cases, and the beam tracing program SYNCH[15,16] has been used to generate emittances, beam sizes, luminosities, etc., from the TRANSPORT solutions. In all cases which have been checked, the thin-lens MAGIC results* agree with the thick-lens TRANSPORT-SYNCH results to within 5 to 10% in betatron functions, damping rates, emittance and luminosity.

Typical Configurations. The MAGIC program has been used to survey a large number of possible configurations. Some of the interesting results are shown in Figs. 2 through 6.

*Figures 2, 3 and 4 show the operative regions in the (β_x^*, η^*) plane at several different tunes in the matched-η mode. The tunes of 18.75, 15.75 and 12.75 have been chosen for illustrative purposes; in practice, of course, ν_x and ν_y would be split to avoid the linear coupling resonance, and neither would be exactly on the quarter integer. The operative regions in these plots are limited by regions in which either the beam size becomes too large (aperture limit) or in which there are no mathematical solutions to the non-linear set of equations which relate the constraints to the variable quadrupole strengths. The luminosity contours are plotted for the nominal energies of 15, 10 and 5 GeV, respectively; the beam-beam tune shifts per interaction region are assumed to be $\Delta\nu_x = \Delta\nu_y = 0.06$. Note that the design luminosities given by $\mathscr{L}_{max} \alpha E^2$ are respectively 1.0, 0.44 and 0.11 (in units of 10^{32}cm^{-2}sec^{-1}) for 15, 10 and 5 GeV. For other values of tune shift and energy the value of luminosity may be scaled according to Eq. (2).

The luminosity contours and boundaries of the operative region in the (β_x^*, η^*) plane may be shifted somewhat by different choices of β_y^*.

* In the computation a pair of thin lenses is used for each quadrupole magnet with a short focal length such as Q2 and Q3. The thin lenses are symmetrically located about the center of the magnet and separated by 1/2 of magnet length.

Table I shows values of some of the beam and machine parameters for three typical matched-q configurations, as obtained by TRANSPORT and SYNCH.

Figure 5 illustrates the operative region in the (η_s, η^*) plane for the mismatched-q mode of operation, for $\nu = 18.75$, $\beta_x^* = 4.0$ m and $\beta_y^* = 0.2$ m. The contours represent the energies at which $\mathscr{L}_{max} = 10^{32}(E/15\ \mathrm{GeV})^2$ (in $\mathrm{cm}^{-2}\mathrm{sec}^{-1}$) at tune shifts of $\Delta\nu_x = \Delta\nu_y = 0.06$. Note that the full design energy range of 5 to 15 GeV is covered in one continuous region of the (η_s, η^*) plane, but that non-zero values of η^* as well as η-mismatch are required at the lower energies. In the right-hand portion of Fig. 5, the beam size at the interaction point is dominated by the dispersion term for configurations near the lower operative boundary, and by emittance (enhanced by the η-mismatch) near the upper boundary.

Figure 6 shows how the parameters Q (momentum compaction) $\sigma_{x\beta}$, σ_{xE}, and the energy for design luminosity vary with the η-mismatch, along the particular path designated as Path A in Fig. 5.

Second-Order Design

Chromaticity. Sextupole magnets will be placed near some of the standard cell quadrupoles in order to control the chromaticity. The uncorrected chromaticities when the tunes are around 18 are $\xi_x \approx -35$, $\xi_y \approx -100$ where the definition is

$$\xi = E_0 \frac{\partial \nu}{\partial E} .$$

Overcorrection of the chromaticities by 10 to 20% will probably be used as at SPEAR, in order to take advantage of the fast damping effect for coherent oscillations.[17] The sextupole strengths required for this correction have been found to be quite modest.

Non-linear Stopbands. The sixfold symmetry of the ring will tend to produce large sextupole Fourier coefficients with indices which are multiples of 6. These will strongly excite the stopbands at tunes 12 and 18. To suppress these coefficients we probably will need additional sextupoles in the straight sections; e.g., near QF1 and Q3.

Damping Variation with Frequency. The damping partition numbers (J_X and J_E) for an off-energy particle are determined by the value of the quantity

$$D = D_0 + D_E \frac{\Delta E}{E_0} + \cdots ,$$

where, for a machine using rectangular zero-gradient bending magnets,[18]

$$|D_0| << 1$$

and

$$D_E \approx \frac{2\oint \eta^2 G^2 ds}{\oint B^2 ds} ,$$

in which G is the local quadrupole gradient and B is the bending field. The damping rates,

$$\alpha_x \propto J_x = 1 - D \qquad \text{and} \qquad \alpha_E \propto J_E = 2 + D$$

are affected very little by the natural energy spread of the beam because AE goes through many synchrotron oscillations during a damping period. However, if the equilibrium closed orbit is shifted by a change in orbital frequency (or equivalently rf frequency), we have

$$D_f \equiv f_0 \frac{\partial D}{\partial f_0} = - \frac{D_E}{\alpha}$$

or

$$D \approx - \frac{D_E}{\alpha} \frac{\Delta f_0}{f_0}$$

where Q is the momentum compaction factor. Thus a shift in the rf frequency does affect the damping rate.

In the matched PEP configurations, we typically have $D_E \sim 250$ to 300, with α ranging from -0.004 at tune 18 to -0.02 at tune 12. Hence the frequency change to produce $D \sim 1$ is $\Delta f_0/f_0 \gtrsim 2 \cdot 10^{-5}$. In the unmatched-configurations, however, D_E can be an order of magnitude greater, and the frequency stability required to keep the damping rate constant may be a problem.

Conclusions

The present version of the PEP lattice is capable of reaching the theoretical design luminosity by means of several alternative operating configurations, at least according to first-order theory. Investigation of non-linear effects may further delimit the choice of favorable operating configurations.

Acknowledgments

Many of the features of the lattice design originated with A. Garren, W. Herrmannsfeldt, P. Morton, B. Richter and J. Rees. We are indebted to A. King and B. Woo for computer programming assistance.

References

1. PEP Study Group, A Proposal for a Positron-Electron Colliding Beam Storage Ring Project, ed. J. Rees and W. B. Herrmannsfeldt, Stanford Linear Accelerator Center Report No. 171, Stanford Linear Accelerator Center, Stanford, Calif. (1974).
2. J. Rees and B. Richter, "Preliminary Design of a 15-GeV Electron-Positron Variable-Tune Storage Ring," PEP-NOTE 69, 1973 PEP Summer Study Report (unpublished).
3. J. Rees, "The PEP Electron Positron Ring — PEP Stage I," invited paper to this conference.
4. L. Smith, "The Proton-Electron-Positron Project — PEP," invited paper to this conference.
5. M. Sands. "The Phvsics of Electron Storage Rings, an Introduction," Proceedings of the International School of Physics "Enrico Fermi", Course XLVI, ed. B. Touschek (Academic Press, 1971); also Stanford Linear Accelerator Center Report No. 121.
6. R. H. Helm, M. J. Lee and J. M. Paterson, "Beam Enlargement by Mismatching the Energy-Dispersion Function," published report to this conference.
7. J. Paterson, "SPEAR, Status and Future Developments," invited paper to this conference.
8. F. Amman, "IEEE Trans. Nucl. Sci. NS-20 No. 3, 858 (1973).
9. M. Bassetti, "Beam Dimension Control in Storage Rings," CNEN, Frascati Laboratories, published report to this conference.
10. M. Bassetti, Proceedings of V International Conference on High Energy Accelerators, Frascati, 709 (1965).
11. B. Richter, "Design Considerations for High Energy Electron-Positron Storage Rings," Proceedings of the International Symposium on Electron and Positron Storage Rings (1966).
12. G. H. Rees, "Aspects of PEP as Compared to EPIC," PEP-NOTE 51, 1973 PEP Summer Study (unpublished).
13. M. J. Le. M. W. Lee and L. C. Teng, "Magnet Insertion Code," PEP NOTE 61, 1973 PEP Summer Design Study (unpublish).
14. K. L. Brown, and S. K. Howry, "TRANSPORT/360 A Computer Program for Designing Charged Particle Beam Transport System," Stanford Linear Accelerator Center Report No. 91 (1970).

15. A. A. Garren and A. S. Kenney, "A Computer Program for Synchrotron Design and Orbit Analysis," Internal note LBL 1968 (unpublished).
16. J. S. Colonias, "Particle Accelerator Design; Computer Programs," Book, Academic Press (1974).
17. *SPEAR* Group, "Fast Damping of Transverse Coherent Dipole Oscillations in SPEAR," published report to this conference.
18. H. Wiedemann, "Scaling of FODO-CELL Parameters," PEP-NOTE 39, 1973 PEP Summer Study (unpublished).

TABLE I

Typical Beam Parameters

		5 Gev	10 Gev	15 GeV	
Total Betatron Tune					
Horizontal	ν_x	12.75	15.75	18. 75	
Vertical	ν_y	12.75	15.75	18. 75	
Momentum Compaction		0. 01668	0. 00759	0.00455	
Transverse Damping Time	τ_x, τ_y	0.222	0.0278	0. 00823	sec
x-y Coupling Coefficient	κ	0.249	0.294	0.280	
Horizontal Emittance	ϵ_x	1.730×10^{-5}	2.149×10^{-5}	2.297×10^{-5}	cm-rad
Vertical Emittance	ϵ_y	1.072×10^{-6}	1.858×10^{-6}	1.796×10^{-6}	cm-rad
Number of Stored Particles (each beam)	N	1.252×10^{12}	3.055×10^{12}	4.44×10^{12}	
Synchrotron Radiation Power (each beam)	P_{rad}	0.0090	0.353	2.596	MW
Linear Tune Shifts per Interaction Point					
Horizontal	$\Delta\nu_x$	0. 06	0.06	0. 06	
Vertical	$\Delta\nu_y$	0. 06	0. 06	0. 06	
Luminosity (each interaction point)	$\mathscr{L}$	0.117×10^{-32}	0.462×10^{32}	1.008×10^{32}	$cm^{-2}sec^{-1}$
Cell Parameters					
Horizontal Phase Advance	ψ_x	48.9^o	72.9^o	97.0^o	
Vertical Phase Advance	ψ_y	29.9^o	56.5^o	82.3^o	
Maximum Horizontal Beta	$\beta_{x\,max}$	50.1	45.1	48.2	m
Maximum Vertical Beta	$\beta_{y\,max}$	78.8	53.9	50.2	m
Maximum Momentum Dispersion	η_{max}	6.38	3.34	2.24	m
Interaction Region Parameters					
Horizontal Beta	β_x^*	4.6	4.0	4.0	m
Vertical Beta	β_y^*	0.16	0.20	0.20	m
Momentum Dispersion	η^*	-2.40	-1.20	-0.73	m
Horizontal Beam Size (betatron)	$\sigma_{x\,\beta}^*$	0. 0892	0.0927	0.0959	cm
Horizontal Beam Size (dispersion)	$\sigma_{x\,E}^*$	0. 0789	0.0789	0.072 0	cm
Horizontal Beam Size (total)	σ_x^*	0.1191	0.1217	0.1199	cm
Vertical Beam Size	σ_Y^*	0.00414	0.00610	0. 00600	cm

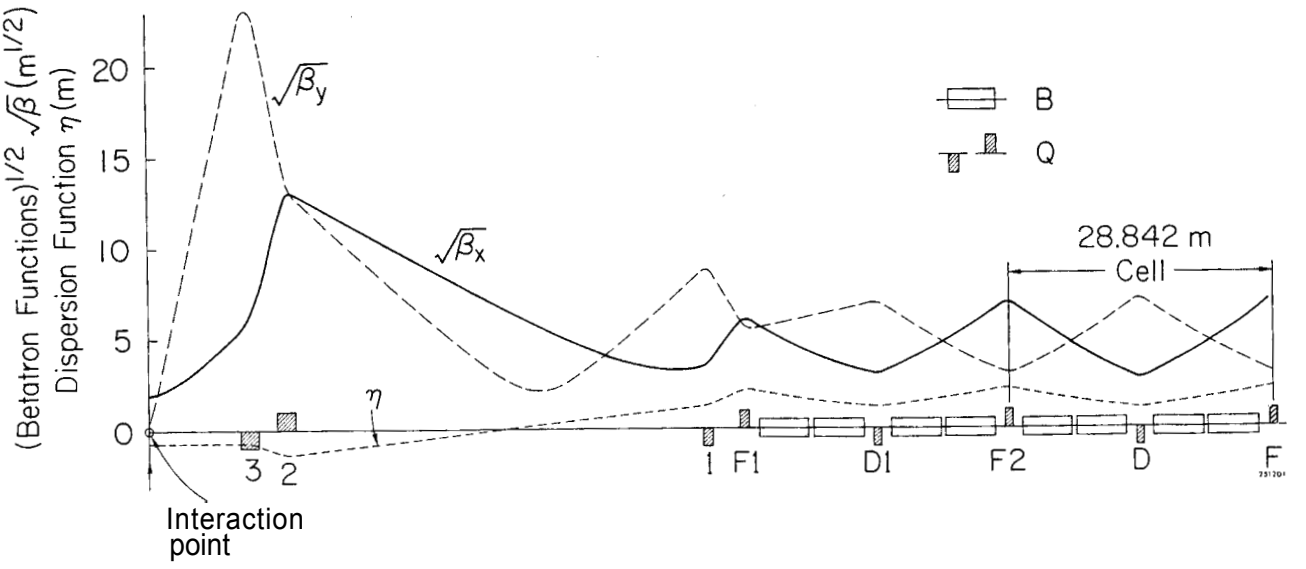


FIG. 1--Schematic of PEP lattice. The typical betatron functions shown are for a matched-q configuration (see text for definition) with $\beta_x^* = 4.0$ m, $\beta_y^* = 0.2$ m, $\eta^* = -0.73$ m, $\nu_x = \nu_y = 18.75$.

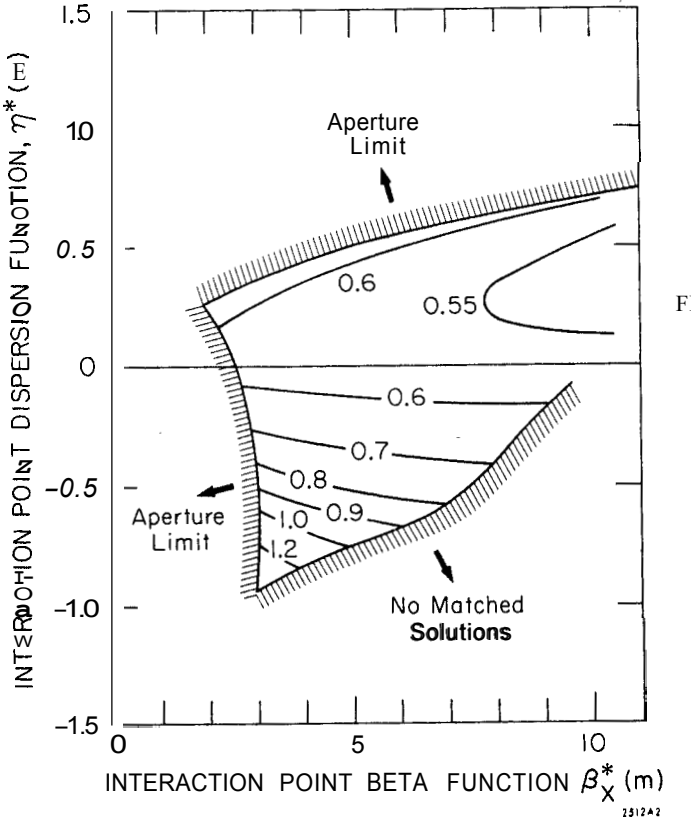


FIG. 2--Matched-η mode operative region in the (β_x^*, η^*) plane with $\nu_x = \nu_y = 18.75$, $\beta_y^* = 0.20$ m. The contours are luminosities in units of 10^{32}cm^{-2} sec^{-1}, computed at energy E = 15 GeV and beam-beam tune shifts $\Delta\nu_x = \Delta\nu_y = 0.06$.

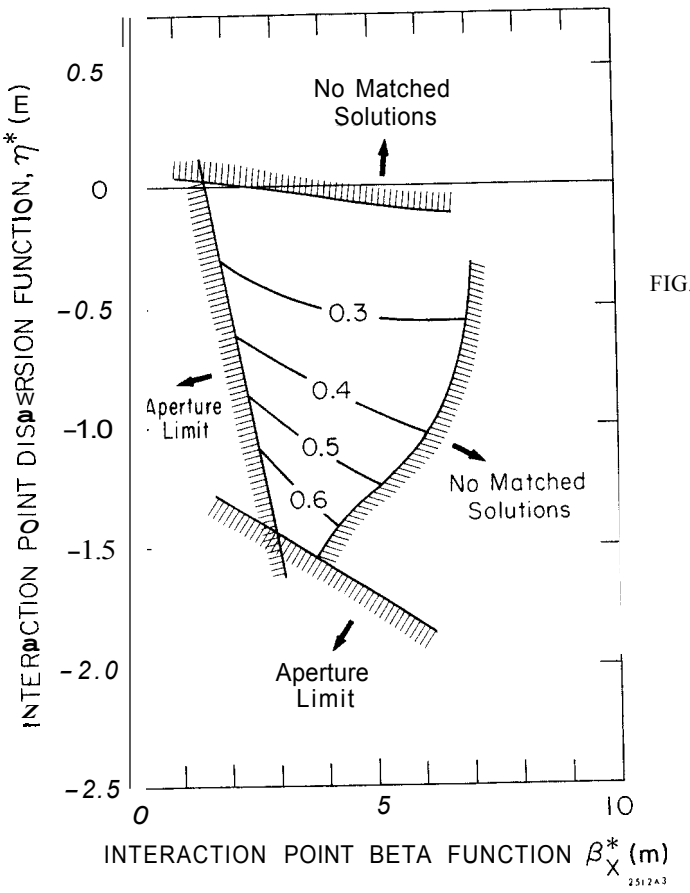
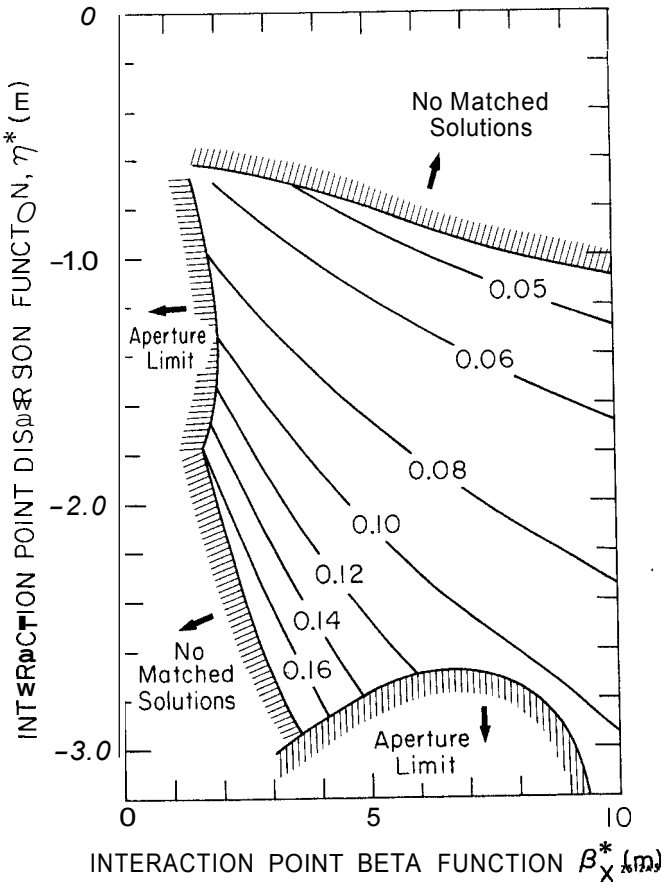


FIG. 3--Matched-η mode operative region in the (β_x^*, η^*) plane with $\nu_x = \nu_y = 15.75$, $\beta_y^* = 0.18$ m. The contours are luminosities in units of 10^{32} cm^{-2} sec^{-1}, computed at energy E = 10 GeV and beam-beam tune shifts $\Delta\nu_x = \Delta\nu_y = 0.06$.

FIG. 4--Matched-η mode operative region in the (β_x^*, η^*) plane with $\nu_x = \nu_y = 12.75$, $\beta_x^* = 0.16$ m. The contours are luminosities in units of 10^{32}cm^{-2} sec^{-1} computed at energy E = 5 GeV and beam-beam tune shifts $\Delta\nu_x = \Delta\nu_y = 0.06$.



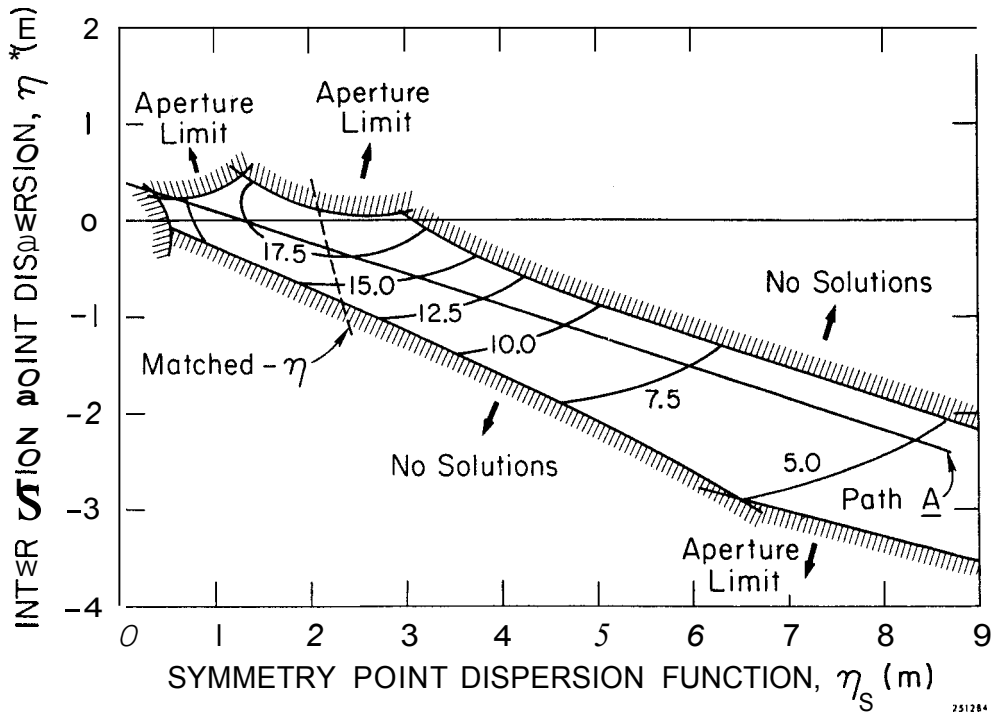


FIG. 5--Mismatched-η mode operative regions in the (η_S, η^*) plane with $\nu_x = \nu_y = 18.75$, $\beta_x^* = 4.0$ m, $\beta_y^* = 0.20$ m. The contours are the energies E_L (GeV) corresponding to luminosities given by $\mathscr{L}_{max} = 10^{32}(E_L/15\ \text{GeV})^2$ (in units of $\text{cm}^{-2}\text{sec}^{-1}$), with $\Delta\nu_x = \Delta\nu_y = 0.06$. The dashed curve labeled "η-matched", near $\eta_S = 2$, represents solutions for which the dispersion function is periodic within the standard cells. The line labeled "Path A" is for reference in Fig. 6.

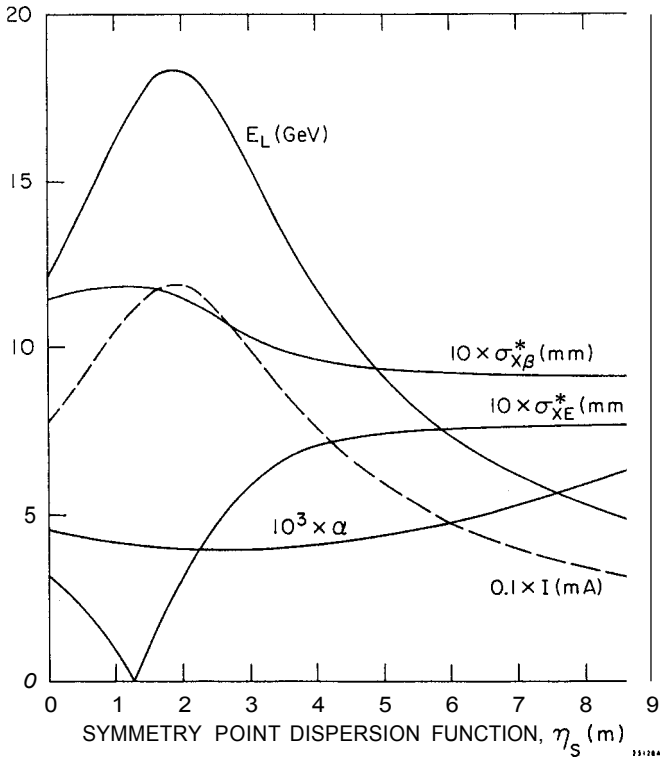


FIG. 6--Variation of beam parameters for different mismatched-η configurations along Path A in Fig. 5 $\sigma_{x\beta}$ is rms beam amplitude due to betatron motion; σ_{xE} is rms beam amplitude due to compaction factor; and I is the current in each beam and $\mathscr{L}_{max} = 10^{32}(E_L/15\ \text{GeV})^2$.

DESIGN CONSIDERATIONS FOR A HIGH ENERGY ELECTRON POSITRON STORAGE RING

H. Wiedemann
Deutsches Elektronen-Synchrotron DESY
Hamburg, Germany

The successfull operation of the electron positron storage ring - SPEAR - in the multi-GeV-range encouraged the accelerator physicist to think about the next generation of storage rings for energies Of more than 10 GeV. We have learned from the presently working storage rings that it seems not practical to assume an artificial beam enlargement as an essential design aspect. As is well known this artificial beam enlargement was needed to get high luminosities at medium energies where the beam intensities are limited by the beam beam interaction at the collision points. Therefore we have to find other means to increase the luminosity in this energy regime. One possible way is to vary the focusing of the periodic cell structure of a storage ring with energy, thus varying the quantum excitation of betatron oscillations [1),2)]. This brings us to the point where we should discuss more general the influence of the beam optics in the periodic cell structure on relevant storage ring parameters. In this note this influence on the energy will be discussed. This can be done in rather general terms since the special design of the long straight section on both sides of the interaction point has no effect on the beam parameters except the amplitude functions at the point where the beams collide. For these amplitude functions we assume values which we know can be realized. Throughout this note we assume only one ring where the two beams counterrotate in the same vacuum pipe and collide head on in the interaction points.

I. Storage Ring Parameters for Numerical Calculations

For numerical calculations in this note we assume the following storage ring parameters which are close to parameters assumed in different laboratories for electron-positron storage ring studies of the next generation:

circumference of the ring	C	= 2304 m
bending radius	ρ	= 206.8 m
average radius of the arcs	R	= 256.7 m
installed rf-power	P_{rf}	= 5.0 MW
totallength of cavities (copper)	L_c	= 240 m
shunt impedance of the cavities at 500 Mc	R_c	= 10 MΩ/m

II. Maximum Energy of the Storage Ring

The maximum energy of a storage ring is given when the total installed rf-power is dissipated in the cavities. These cavity losses depend on the cavity length, the shunt impedance per unit length, the rf-frequency and on the necessary rf-voltages as given by the focusing of the periodic cell structure.

The amount of cavity length depends on the amount of money one wants to spend for them. It is not intended to use this length as a parameter here but rather use one length for which the necessary free length in a ring of 2 km circumference can be realized. The shunt impedance per unit length for 500 Mc is conservatively assumed to be 10 MΩ/m which could be increased somewhat using other than iris structures e.g. trift tube cavities. Since the production of the latter are more costly one has to find a cost optimum for the product $R_c \cdot L_c$. The effect of the rf-frequency has been studied in detail [3)] with the result of a very flat optimum in the range of 200 to 700 Mc depending somewhat on the energy for which the design is made. In this note we assume 500 Mc. For these rf-parameters the maximum achievable energies as a function of focusing power are calculated. The focusing is varied by varying the cell length keeping the phase advance per cell constant at 90°. This 90° degree phase advance per cell is an essential for the multibunch operation which is discussed later. Characterising the focusing by the transition energy γ_{tr} the maximum achievable energies using copper rf-cavities are shown in fig.1. It becames clear from fig.1 that the transition energy should be about 20 or larger in order not to loose to much energypotential of the ring. However, the gain between $\gamma_{tr} = 20$ and $\gamma_{tr} = 30$ is only 1 GeV if we use copper cavities.

Designing storage rings of the next generation it might be reasonable also to have a look at the next generation technology which in our case means superconducting cavities. In this case the energy isn't limited by cavity losses any more but by the minimum reasonable luminosity which falls off like E^{-10} in this energy regime. If we exchange the 240 m copper cavities by 240 m of superconducting cavities the maximum energy for a luminosity of $L = 10^{31}\ cm^{-2}sec^{-1}$ is computed and shown in fig.2. Here we find a rather steep increase in energy versus transition energy which calls for the maximum reasonable focusing.

III. Luminosity

It has been shown that increased focusing in the periodic cell structure leads to higher achievable energies. This is a true reflection of the fact that at a fixed energy in the rf-power limited case an increased focusing also results in higher luminosities (fig.3).

At lower energies however, there is the problem of the beam beam incoherent limit. So far it was assumed that each beam is made up by only one bunch or in case of more than two interaction points by half as many bunches as there are interaction points. In this case the bunches meet only at the interaction points and nowhere else in the arcs where the beta-functions and by this the beam beam effect is larger. In fig.3 the circles ○ show the maximum luminosities for one bunch. For energies lower than those indicated by the crosses the beam beam effect is effective. Here the luminosity scales like $L \sim A \cdot \gamma^2$, where A is the beam cross section at the interaction point. If natural beam sizes are used - $A \sim \gamma^2$ - the luminosity scales like $L \sim \gamma^4$. To avoid this fast drop of the luminosity toward lower energies the variation of the focusing was proposed [1)2)]. In this note another mode of operation is proposed.

For this we divide the whole energy regime into three parts:

1) J. Rees, B. Richter, Preliminary design of a 15 GeV Electron-Positron Variable Tune Storage Ring, PEP-Note 69; 1973 PEP-Summer-Study
2) H. Wiedemann, e-p Luminosity for different energies in PEP, PEP-Note 58, 1973 PEP-Summer-Study
3) M. Allen, G. Rees, CRISP-Note 72-68, Brookhaven

1. The rf-power limited regime

Here the luminosity is given by: [4]

$$(1)\quad L_1 = \frac{1}{4e^2 f}\,\frac{P_B^2}{U^2 R\cdot B}$$

where: P_B the rf-power available per beam, U the energy loss per turn, f the revolution frequency; A the beam cross section and B the number of bunches. It is clear that the number of bunches should be as small as possible e.g. B = 1. Also the beam cross section should be minimized which requires strong focusing as has been already discussed. Using the scaling laws for FODO-Cell structures [5] the luminosity scales like $L_1 \sim \gamma_{tr}^4$.

2. The rf-power and tune shift limited regime

In this case the beam current per bunch is limited by the incoherent beam beam effect.

$$(2)\quad \Delta\nu = \frac{r_e}{2ef}\,\frac{I\beta}{\gamma AB} = \frac{r_e}{2ef}\,\frac{P_{rf}}{\gamma U}\cdot\frac{\beta}{AB} \le 0.05$$

(β: amplitude function at the interaction point, B number of bunches).
Together with eq. (1) the luminosity is given by

$$(3)\quad L_2 = \frac{f\Delta\nu^2}{r_e^2}\,\frac{A}{\beta^2}\,B\gamma^2$$

Since we assume natural beam sizes the number of bunches B has to be varied according to eq.(2) like:

$$(4)\quad B = \frac{r_e}{2ef}\,\frac{P_{rf}}{\gamma U}\,\frac{\beta}{A} \sim \gamma^{-7}$$

If we find a way to increase the number of bunches considerably the luminosity scales like $L_2 \sim \gamma^{-3}$ in this regime. Here we neglected the rf-cavity losses. Since it seems very advantageous to increase the number of bunches, a way to do this is discussed in this note. As a result of this discussion we find a maximum number of bunches B_{max} which is much smaller than the harmonic number.

3. The tune shift limited regime

At lower energies where we always have the maximum number of bunches the total beam current is limited only by the incoherent beam beam limit and the luminosity is given by:

$$(5)\quad L_3 = \frac{f\Delta\nu^2}{r_e^2\beta^2}\,\gamma^2 AB_{max}$$

Since there is no easy way to have many bunches and a variable focusing the beam sizes are given by the quantum excitation e.g. $A \sim \gamma^2$ and the luminosity then scales as $L_3 \sim \gamma^4$.

Since this multi bunch mode requires only a phase advance of 90° per cell in the arcs the luminosity can be increased at very low energies by turning off every second quadrupole in the arcs thus increasing the cell length by a factor of two. By this the product $A\cdot B_{max}$ can be increased as will be shown later. In principle this can be continued to increase the luminosity at very low energies but doing so the aperture limit is reached very fast.

4) M. Sands, Physics of Electron Positron Storage Rings, SLAC-121

5) H. Wiedemann, Scaling of FODO-Cell Parameters, PEP-39, 1973 PEP-Summer-Study

IV. Beam Separation

If we use many bunches per beam we have to separate them outside the interaction points. This can be done with an appropriate number of electrostatic separating plates. Many and strong fields however, are needed if we do not match the separation to the focusing structure of the ring. Since there is a small beam beam effect left even if the beams are separated one would like to have the points where the bunches meet at similar places from the beam optics point of view. The easiest way of separating the two beams is given in the case where the phase advance per cell is just 90°. An electrostatic field introduces a regular closed orbit oscillation with a wavelength equivalent to two cell lengths (fig.4). The distance between bunches cames out to be one cell length or a multiple of that length. While for the arcs only one separating plate on either end is needed one may need some more in the straight sections due to the nonregular structure there.

The circumference of the storage ring has to be a multiple of the cell length. Also the distance from any "pass by point" in the arcs to the interaction point has to be a multiple of one half cell length.

In the numerical example a transition energy of γ_{tr} = 31 is realized by a cell length of L = 14.4 m. The maximum number of bunches then is 160.

V. Beam-Beam-Effect

Even with beam separation there is still an electromagnetic interaction of one beam on the particles of the other beam the socalled long range forces. It is well known from experience of running storage rings that the beam separation has to be large compared to the standard beam width (a horizontal beam separation is considered). In this note a beam separation is assumed large enough that one beam sees only a force from the other beam which falls off like the inverse of the separation, $F \sim 1/x$. This means the separation x is at least $10\sigma_x$. For that large separations the linear tune shift turns out to be: [6]

$$(6)\quad \delta\nu = 9.6\times10^{-9}\,\frac{\beta_x I\cdot C}{cp\ x^2}$$

where β is the betatron amplitude at the "pass by points", I the total beam current in amps, C the ring circumference, cp the beam energy and x the beam separation (C,β,x in meters).

To achieve the shown luminosity in fig.3 for γ_{tr} = 31, a maximum current of I = 140 ma at 15 GeV and β_x = 11.1 m at a pass by points the linear tune shift is $\delta\nu\cdot x^2 = 0.023\ cm^2$. For a separation of x = 1 cm which is equivalent to a separation of $x = 20.5\ \sigma_x$ the total linear tune shift outside the interaction points is only $\delta\nu = 0.023$. The total beam beam effect at a separation of $x \approx 20\ \sigma_x$ is very much reduced to a mere linear tune shift which can easy be corrected by electrostatic quadrupoles. The nonlinear part of the beam beam effect can be neglected for the magnitude of separation discussed here [6].

The total aperture requirement in this case is only $A = x + 14\ \sigma_x = 17$ mm. This seems very little however, one needs more at higher energies. At 22 GeV which is the highest energy where the beams have to be

6) SPEAR-Group, Beam Beam Coupling in SPEAR, Proceedings of this conference

separated the standard width is σ_x = 0.71 mm. A separation of x = 1 cm corresponds still to 14 σ_x and the aperture requirement is only A = 20 mm. This small aperture requirements show that the beam separation may be easily increased to twice the assumed value to be safe.

At energies below 15 GeV it is advantageous to double the cell length by turning off every second quadrupole which gives a γ_{tr} = 15.4. Here the maximum number of bunches is 80 and the maximum current at 12 GeV is I = 290 ma. With β_x = 33.2 m and x = 2 cm corresponding to 10 σ_x the linear tune shift is $\delta\nu$ = 0.044. In this case the maximum luminosity is 2×10^{32} $cm^{-2}sec^{-1}$ for a total installed rf-power of 5 MW (fig.3).

VI. Conclusion

To achieve the highest possible energy for a given installed rf-power the focusing in the periodic cell structure should be as strong as possible. For lower energies where the beam beam effect is effective the total beam current can be pushed up by filling many bunches in one beam, which requires beam separation outside the interaction points. The total linear tune shift due to long range forces is small. Even with beam separation the required apertures seem not to be excessive due to the small beam sizes produced by the strong focusing.

Acknowledgement

The author wishes to thank G.A. Voss for many helpfull discussions.

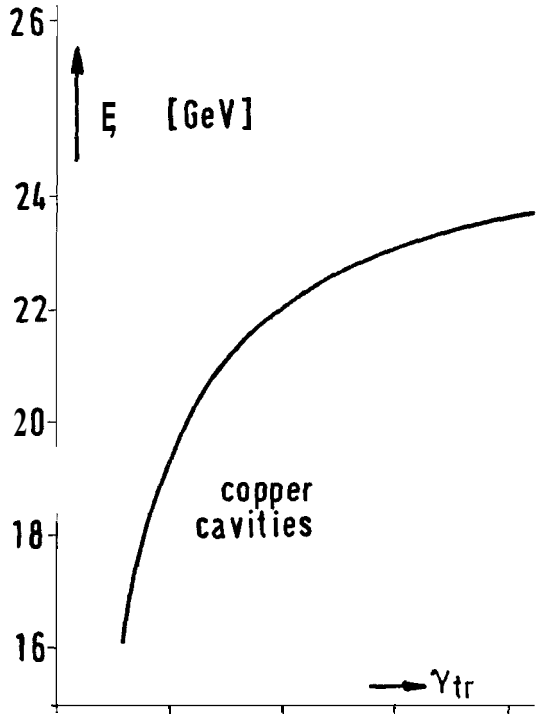


Fig.1: Maximum storage ring energy vs transition energy,

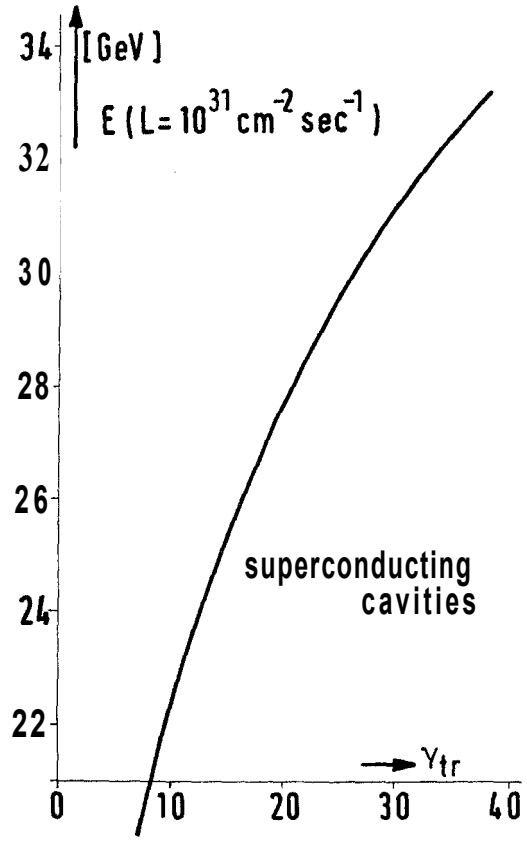


Fig.2: Maximum energy for a luminosity of L = 10^{31} $cm^{-2}sec^{-1}$ vs. transition energy.

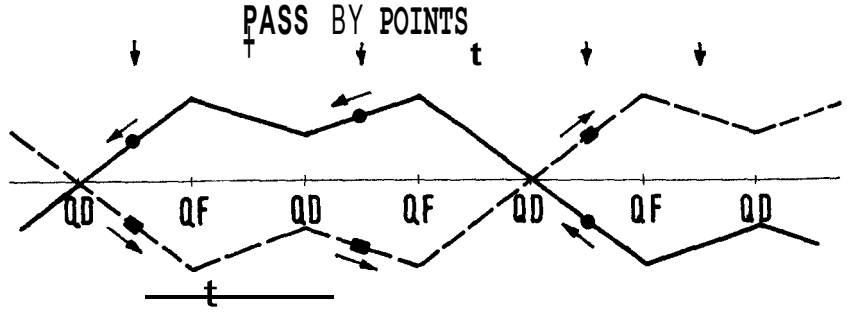


Fig.4: Separation of the beams in the multibunch mode.

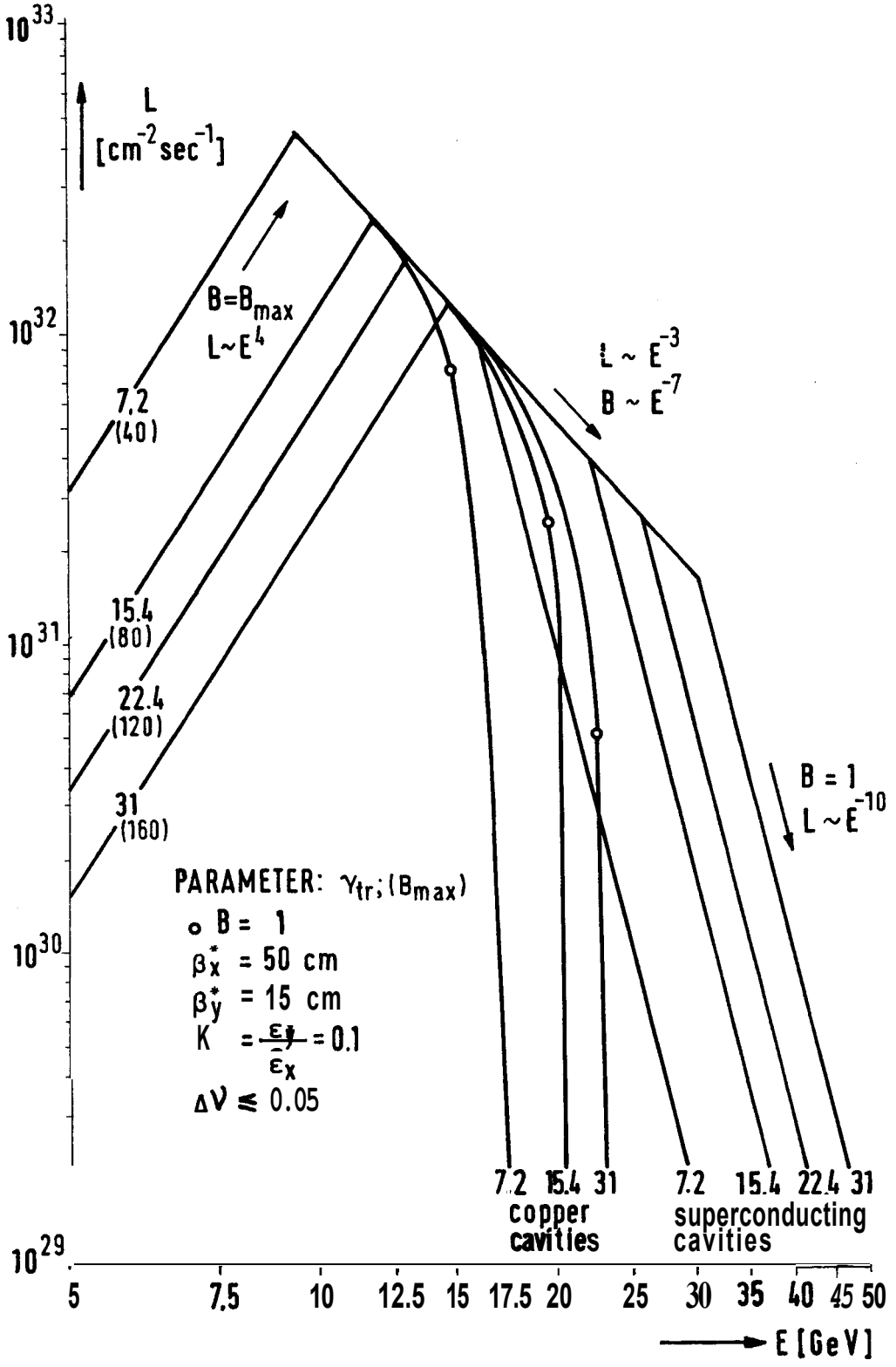


Fig.3: Luminosities for different transition energies and numbers of bunches.

HIGH-INTENSITY STORAGE RINGS FOR MESON FACTORY

Batskikh G.I., Vasiliev A.A., Kuzmin A.A., Meshcherov R.A.,
Murin B.P., Rybalko V.S.

Radiotechnical Institute of the USSR Academy of Sciences
Moscow, USSR

Stavisskiy Yu.Ya.

Institute of Physics and Energetics

Abstract

Design aspects and basic parameters of storage rings are considered. Storage rings are designed to stretch and to bunch the beam of the high-intensity linac-meson factory. Continuous beam as well as intense short (25 nsec) proton pulses are provided. Beam duty factor varies from 10^{-5} approximately up to 1. Peak current of stored beam reaches 50 A.

A 600-MeV Linac (meson factory) will provide at its output high intensity beams of accelerated protons and negative hydrogen ions H^- with macropulse current of 50 mA and 5 mA respectively, repetition rate of 100 Hz and duty factor of 1% [1]. In future it is supposed to increase H^--ions current up to the value of proton current.

In some physics experiments, where counters are used, high beam pulse intensity is not acceptable due to counting channels overloading. For such experiments it is desirable to have a time-stretched beam with duty factor aproaching 100%. At the same time a number of important applications is based on pulsed modes of accelerator operation, when practically the whole beam intensity is concentrated in short bursts. To such applications one can attribute.

1. Neutron physics
2. Study of fast processes, induced by protons, mesons, neutrons.
3. Rare process experiments limited by background, not assosiated with the accelerated beam.

In connection with the development of the atomic power production and adjacent technology, the role of applied neutron studies is increased.

The most effective methods of neutron studies are based on the "time of flight" technique, wich needs pulsed neutron sources of high intensity. From this point of view the linac current macropulse duration (100 psec) is too large, and it is necessary to use some equipment to form short intense bursts.

This report describes the principles of construction and main parameters of storage rings [2] wich will make it possible to change linac beam duty factor in wide range and to provide both practically continuous beam and intense short pulses of 25 nsec.

Storage ring-buncher

For neutron experiments based on the "time of flight" technique, it is supposed to use a strong focusing storage ring of relatively small diameter. The magnet system of such a storage ring-buncher should first of all be compact, and at the same time it should provide sufficient space for various systems, necessary for beam injection, bunching, diagnostics and extraction.

Fig. 1 shows the chosen structure of the magnet period, the amplitude functions βx, βz and the closed orbit displacement for an off-momentum particle $(\Delta p/p=0.01)$. The magnet period consists of three strong fo-

cusing magnets, placed side by side (a triplet with combined functions of focusing and bending fields), and a free straight section of 2.38 m length.

Fig. 2 presents layout of main systems and components of the storage ring–buncher. The magnet system comprises 11 periods of the mentioned type. In free straight sections one can see the components of the charge-exchange injection and fast extraction system, RF bunching cavities and scrapers for removing the beam "halo". In this figure there are also shown the main components of the systems for beam diagnostics and correction.

For the chosen circumference the proton revolution period is equal to 200 nsec. The injected H^--beam macropulse duration equals to 100 μsec, that is the charge–exchange injection occupies 500 turns.

The H^--beam is supposed to be bunched at the linac input and to be accelerated in groups of bunches, the frequency of groups being equal to 40 MHz. Each group at the same time consists of five bunches in correspondence with the frequency of the 1-st linac stage accelerating field (~200 MHz). In order to avoid excessive momentum spread of stored protons and, consequently increase of beam radial dimension, it is expedient to choose the frequency of the bunching voltage in the storage ring–buncher equal to 200 MHz. In this case each bunch will be injected into a single bucket of RF field, each five filled buckets being accompanied by five empty ones. Thus four 25–nsec groups of bunches are stored within the chamber of the storage ring.

In order to decrease the amplitude of the RF cavity voltage, a debuncher is installed at the output of the linac. The debuncher decreases the injected beam momentum spread down to $\pm$0.1%.

The main problem of the injection is the heating of the charge–exchange carbon film target, installed at some distance from the chamber axes. In order to decrease the heating it is necessary to limit the time of the stored beam passage through the target. It is achieved by two pulsed magnets which provide beam bump at the target position. When the magnets are switched on the beam orbit is shifted onto the target. At the end of the injection cycle the pulsed magnets are switched out and their magnetic fields decrease down to zero simultaneously during 10-20 μsec. Thus an adiabatic and at the same time relatively fast removal of stored beam from the charge–exchange target is provided. Calculations demonstrate, that the carbon target temperature will increase by 1200-1500°C per one injection cycle at the injected beam pulse of 50 mA. During intervals between injection cycles the target is qooled down by heat radiation, but the target maximum temperature can tise up to 2000-2500°C. That is why a possibility is provided to change the target after each injection cycle, for instance, by using a set of films, mounted on a rotating disc [3].

In the storage ring–bunchex two independent extraction lines are provided.Fast extraction of the beam or the single group of bunches into each line is achieved by two kickers and a septum magnet (Fig. 2). The distance between kickers equals to half of the wavelength of betatron oscillations, so kicker pulses have opposite polarities. A matched two–units ferrite deflector with travelling wave is used as a kicker magnet.These units are powered from special pulsed generators including a double pulse forming line and a shock ferrite line. Hydrogen thyratrons are supposed to be used as current switches.

The chosen storage ring structure makes it possible to use different modes of fast extraction. The minimum burst duration (25 nsec) is provided when extraction repetition rate is 400 Hz. High value of peak and average power, commutated in the pulsed generators, are needed for small rise and decay time in kickers (20 nsec) and for high repetition rate of cycles. Thus the extraction system is one of the most complicated and powerful systems of the storage ring–buncher.

During designing of the vacuum chamber and RF system the main attention will be paid to the problem of the intense beam interaction

with RF cavities and other chamber components.

The pumping system must provide 10^{-8} torr pressure within the chamber. The main parameters of the storage ring–buncher are presented in Table I.

TABLE I

Main parameters of the storage ring–buncher

N,N:	Parameter	Unit	Value
1.	Energy of stored protons	MeV	600
2.	Orbit length	m	47.5
3.	Number of magnet periods	-	11
4.	Betatron oscillation number	-	2.75
5.	Induction of magnetic field on the equilibrium orbit	kG	72
6.	Radius of orbit curvature	m	3.39
7.	Magnetic field index	-	19.3
8.	Proton revolution period	nsec	200
9.	Injected H^--beam duration	μsec	100
10.	Injection cycles repetition rate	Hz	100
11.	H^--beam pulse current	mA	5–50
12.	Charge-exchange target thickness (carbon)	$\mu gr/cm^2$	200
13.	Charge-exchange injection efficiency	%	95
14.	Proton current in storage ring	A	2.4–24
15.	Incoherent betatron frequency shift due to space-charge effect	-	0.02–0.2
16.	Injected beam emittance	rad.m	$1.7\pi.10^{-5}$
17.	Stored beam emittance		
	a) horizontal	rad.m	$5\pi.10^{-5}$
	b) vertical	rad.m	$4\pi.10^{-5}$
18.	Vacuum chamber aperture		
	a) horizontal	cm	12
	b) vertical	cm	7

The stored beam is extracted from the storage ring–buncher on the external uranium target in pulses with duration and repetition rate near to optimum for neutron experiments. In future it is supposed to store protons during two injection cycles by very careful design of the main systems of the storage ring. Thus the stored beam intensity can go up to 50 A.

Construction of storage ring–buncher in the meson factory complex will provide pulsed neutron sources with neutron fluxes exceeding those of the best installations, now operating or being under construction.

Storage ring–stretcher

A possibility to stretch the meson factory beam by means of a special storage ring–stretcher was discussed earlier [2]. The main parameters of such an installation are presented in Table II. In the storage ring–stretcher a passibility is provided to store intense beams at different energies in the range of 300–600 MeV with following slow extraction during the intervals between linac acceleration cycles. Thus a practically continuous beam with duty factor of 98–99% is achieved.

In the storage ring–stretches it is also supposed to use very thin internal targets, which will be repeatedly crossed by the stored beam. This will make if possible to perform thorough study of nuclear reactions by observation of the yield of heavy nuclei with short tracks in the target.

A peculiar feature of the storage ring–stretcher magnet system is its four matched straight sections, the total. length of which equals aproximately to the half ring circumference. In two of them, where charge–exchange target of the injection system and internal targets for nuclear-physics experiments are installed, there is a deep minimum of the amplitude function in both transverse directions with values of $\beta_{min}=0.1\beta_{av}$, where β_{av} – average value of amplitude function in normal period. Thus the influence of the multiple scattering of protons in the target on the stored beam emittance is essentially reduced.

TABLE II

Main parameters of the storage ring-stretcher

N, N:	Parameter	Unit	Value
1.	Energy of stored protons	MeV	300–600
2.	Orbit length	m	236
3.	Extracted beam mean intensity	A	45
4.	Duty factor	%	98
5.	Proton current in the storage ring	A	0.38–0.46
6.	Number of turns injected	-	80–100
7.	H^--beam pulse current	mA	5
8.	Momentum spread (after debuncher)	%	± 0.2
9.	Charge-exchange target thickness	$\mu gr/cm^2$	120–180
10.	Charge-exchange efficiency	%	93
11.	Emittance increase due to the multiple passage through the target	rad.m	$(0.2-0.13)2.5\pi \cdot 10^{-5}$
12.	Number of magnet structure superperiods	-	2
13.	Number of normal periods (structure with separated functions)	-	16
14.	Number of matched sections	-	4
15.	Maximum magnetic field induction in dipole magnets	kG	8.864
16.	Field gradient in quadrupole lenses	kG/m	50.6
17.	Betatron oscillation number	-	5.75
18.	Vacuum chamber aperture		
	a) in bending magnets		
	horizontal	cm	15
	vertical	cm	7
	b) in quadrupoles-circular	cm	15

The most effective method of educing particle losses at extraction without increase of the vacuum chamber aperture in the main part of the ring is introduction of special matched straight section where maximum of β-function in the extraction plane is much more than the amplitude function value in the main structure. The storage ring-stretcher has two such straight sections ($\beta_{max} \simeq 5\beta_{av}$), and an electrostatic septum of the extraction system is installed in one of them.

For slow extraction the 3-d order ($Q_x = m/3$) nonlinear resonance excited by the m-th harmonic of the sextupole component of the magnetic field, is supposed to be used. A specific feature of the storage ring-stretcher slow extraction is the significant effect of the space-charge forces on the process of resonant excitation. Particles, oscillating with increasing amplitude, are moving in an essentially nonlinear field of the central beam region, remaining in the nonlinear resonance separatrix. This induces nonlinear frequency shift, which essentially reduces the orbit separation at septum at the beginning of extraction. In order to reduce these limitations and achieve the extraction efficiency near to 100% a special octupole correction is introduced in the storage ring-stretcher. A possibility of a partial compensation of the stored beam space-charge by means of electrons is also under consideration.

While choosing the parameters of the storage ring-stretcher, the future possibility to use it for development of *an* accelerating complex based on the linac in order to rase the proton energy up to 5-6 GeV by a superconducting linac or by a "fast" proton synchrotron with charge-exchange injection is also taken into consideration.

The authors are grateful to V.A.Aksenov, N.Ya.Basalaeva, V.A.Vizir, A.I.Dzergach, N.I.Kuzmina, V.A.Osipova, V. A. Skuratov and A. P. Fedotov for several discussions.

References

1. Murin B.P. "Proc.of the 8-th Int.Conf.on High-Energy Acc.", CERN, Geneva, 1971, p.540.
2. Batskikh G.I. et al. "Proc.of the III Soviet Union Conf.on Acc.of charged particles" (in Russian) Moscow, 1973, v.II, p.249.
3. Gorka A.J. IEEE Trans. on Nucl. Sci. v.NS-20, N 3, 1973, p. 387.

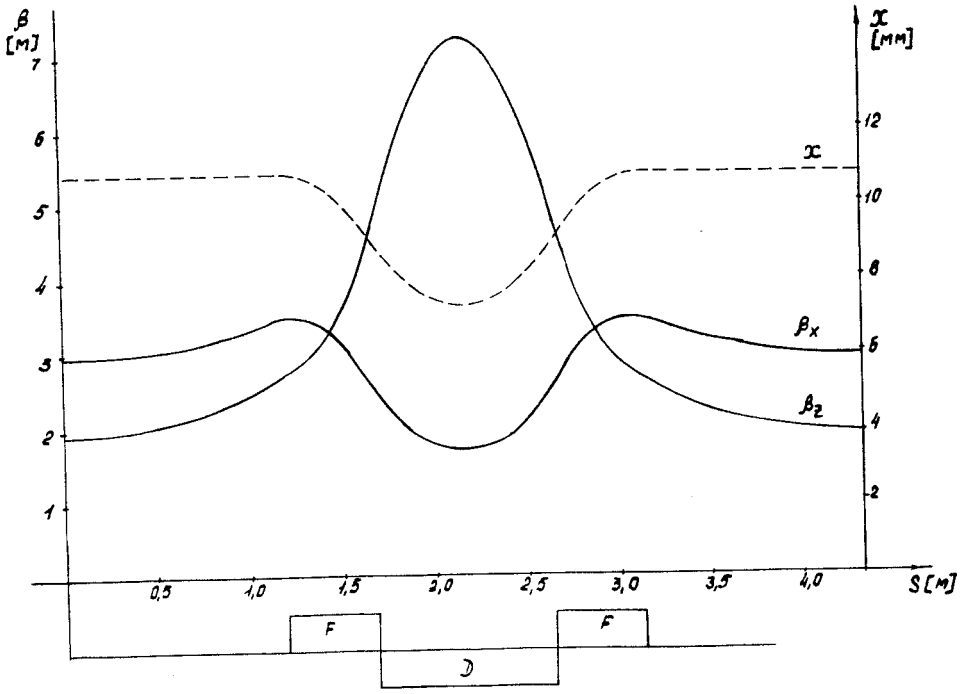
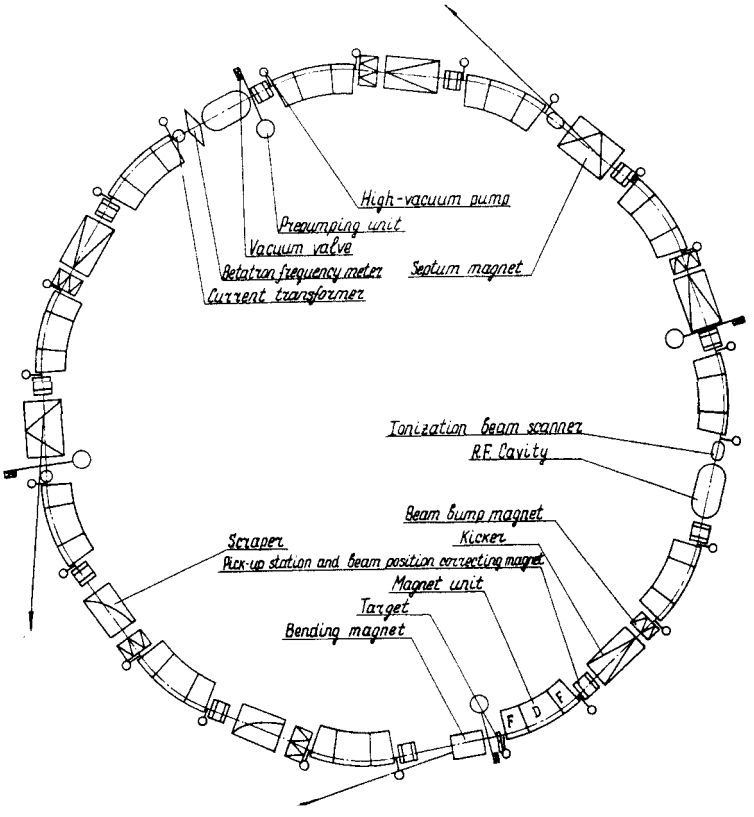


Fig. 1. Magnet period structure and calculated parameters of betatron oscillations (F, D - focusing and defocusing magnets, βx, βz - amplitude functions for horizontal and vertical oscillations, X - closed orbit displacement for particles with $\Delta p/p=0.01$).



Pig. 2. Layout of the main components of the storage ring-buncher

TRENDS OF THE DEVELOPMENT OF STRONG CURRENT CYCLIC ACCELERATORS - MESON FACTORIES

V.P.Dzhelepov, V.P.Dmitrievsky, V.V.Kolga
Joint Institute for Nuclear Research, Dubna, USSR

I.Introduction

The available experimental results and the requirements of the modern theory of various nuclear processes in the energy region below 1?GeV convincingly show that it is necessary to further increase the intensities of both primary proton beam and secondary particle beams (neutron, pion and muon ones) produced by accelerators[1].

A group of scientists of the Laboratory of Nuclear Problems, JINR, has been studying 700-900 MeV strong current proton cyclic accelerators.

Here the basic results as well as the conclusions on these studies are given. The future development of this branch of accelerators has been considered on the present day level. The results of investigations on linear accelerators are compared.

II.Strong Current Phasotrons

The beam intensities of the 500-1000 MeV operating phasotrons are within 1-3 μA.

The current limit at such intensities appears in the accelerator central region where the axial rigidity dependent on the magnet system is minimal, while the beam particle density(χ) is maximal. In order to consider the theoretically possible ways of increasing phasotron intensities, let us analyze the expression determining the phasotron beam current

$$I = e \times R \dot{R} \propto Z \Delta t/T \qquad (1)$$

In the nonrelativistic approximation the limit particle densities determined by the accelerator magnet system

$$\chi = \frac{\varepsilon_0}{m_0} Q_z^2 B^2 \qquad (2^*)$$

does not depend on the accelerator regime. Here m_0 is the rest mass of the given particle, ε_0 is the vacuum dielectric permiability, α is a bunch angular width determined by the angular size of the separatrix.

The axial size of the beam (Z)is determined by the effective aperture of the magnetic field, which does not exceed some cm in the area of the shimmed fringing field. The magnitude $R\dot{R} = \frac{E\dot{E}}{e^2c^2B^2(1+n)}$ is proportional to the voltage amplitude over the accelerating electrode (V) and is practically independent of the magnetic field configuration since $0.25 > |n| > 0$ for all phasotrons, where $n = \frac{R}{B}\frac{dB}{dR}$.

The efficiency of capturing to the accelerator phasotron regime which depends on the capture time(Δt) vs the modulation period (T) is determined by the phase mode and is increased proportionally to V/K, where

$$K = -\frac{E}{\omega}\frac{d\omega}{dE} = 1 - \frac{\nu^2}{1+n}\frac{1}{\beta^2},$$

* B is the induction of the magnetic field in T, Q is the axial frequency of free oscillations for the beam whose amplitude is small compared to the transversal dimensions.

For phasotrons having the azimuthally homogeneous magnetic field the magnitude "n" is varied in the above range and the magnitude K is practically the same along the radius for all the accelerators of the given energy.

Thus, the problem of increasing the phasotron intensity is only to increase the amplitude of the accelerating voltage across the dee since the limit particle density in the central region (X) does not depend on the character of the magnetic field variation (2).

This method for increasing the intensity has been used for CERN phasotron conversion[2], where the intensity may be increased according to the $V^{3/2}$ as it follows from (1).

The second important improvement of phasotrons is to increase the beam extraction efficiency which is based on the use of current and iron-current magnetic channels. The septum (the thickness of the front plate) of such channels does not exceed 3 to 6 mm, which provides the 50-60% coefficient of beam extraction from the accelerator chamber when using the regenerative system.

Such channels are under development now for the CERN, Columbia University[4] and Dubna[5] phasotrons.

As the analysis of expression (1) shows, there is another way to increase phasotron intensities which consists in approximating the structure of the phasotron magnetic field to that of the isochronous cyclotron. The degree of this approximation is characterized numerically by the parameter "K" whose value for the increasing average magnetic field along the radius is always smaller than unity.

The increasing of the value "K" along with increasing the capture efficiency results in decreasing the range of accelerating frequency B_0/B_c times, where B_0 and B_c are the induction in the centre of the accelerator before and after the magnetic system conversion (with the fixed final particle energy).

This reduction of the frequency range considerably simplifies the problem of increasing the amplitude of the accelerating voltage across the dee which is the basic problem for phasotrons having the azimuthally homogeneous field, when rearranging the frequencies of the accelerating voltage about $f_0/f_K \approx 2$, the mechanical units of the frequency rotary capacitor puts the limit to obtaining the required voltage amplitudes. The increase of the average induction of the magnetic field along the phasotron radius to a necessity of using the space variation of the field intensity in order to provide the axial stability of particles in acceleration.

The stability theories for such field structures have been described in many publications[6]. The spiral structures of magnetic fields are used in the conversion of the Dubna phasotron and the Nevis Laboratories (New York) on0 too. The theoretical consideration shows that the application of spiral structure magnetic fields as a means for increasing

the current of accelerated particles is quite promising. This principle can be used for creating accelerators having the quasi-continuous regime of acceleration. This regime is possible for the case when the law of varying the average induction of the magnetic field along the radius is quite close to the isochronous field. If B_i is a function corresponding to the isochronism of closed orbits for the whole energy range, B is the deviation from this law in the phasotron regime of acceleration along the radius, it is easy to see that with $K < 1$ we have

$$\frac{\Delta B}{B_i} = \frac{1}{2} K \eta_i \qquad (3)$$

where

$$\eta_i = \frac{\beta^2}{1-n^2}$$

If K is not larger than

$$K \leq \zeta \frac{eV}{E\beta^2} \qquad (4)$$

where ζ is the factor of the unity scale, we have the quasi-continuous phasotron regime of acceleration[8].

The main peculiarities of such cyclotron-phasotron regime of acceleration are its non-critical behaviour towards the amplitude of the accelerating voltage (within inequality (4)) and the extremely narrow band of frequency modulation:

$$\frac{\Delta f}{f} = \frac{1}{2} K \beta^2 \qquad (5)$$

which in many cases can be achieved by means of electronics.

Now there are no available experimental results on the abovesaid acceleration regime.

III. Strong Current Isochronous Cyclotrons

The abovesaid possibilities which can be expected from the phasotron method of acceleration allow even nowadays to increase the average particle current in such accelerators up to 20-50 μA.

The approximation to the cyclotron-phasotron regime will increase this limit about an order of magnitude. A further increase of intensity in phasotrons having a Ω-shaped magnet meets principal limitations which are due to the effects of the beam space charge.

In order to reduce this limit a new type of accelerators, the so-called strong-focusing cyclotron[9], has been suggested at the Laboratory of Nuclear Problems and a possibility of combining the isochronism of closed orbits and strong focusing*) has been proven[10] for the wide energy range.

The basic results of theoretical studies are as follows. In the magnetic fields of the type:

$$B_z = B(r)\left[1 + \varepsilon F(r,\gamma)\right] \qquad (6)$$

where ε is the field variation widths, $F(r,\gamma)$ is the periodic functions on r and γ is the dynamics of particle motion in azimuthally-homogeneous fields.

The main features are as follows:

a) the increase of maximal energy of transversal oscillations with a fixed amplitude (rigidity increase);

b) the comparison of accelerated particle pulses which results in the increase of the pulse range in the given volume of the magnetic field;

c) the weakening of the relations between ion rotation on closed orbits and stability conditions.

These theoretical conclusions have been confirmed by two models of the isochronous cyclotron with spiral structure magnetic field constructed at the Laboratory of Nuclear Problems, Dubna, USSR.

The first model was used to accelerate deuterons up to 12 MeV, the minimal r.f. amplitude across the dee was only 2 kV [11].

Thus, the possibility of cyclic acceleration during over 2000 revolutions was confirmed experimentally at the present day level of shimming and magnetic field stabilization. The general view of the pole piece of this accelerators is shown in Fig. 1.

The second model, an electron strong focusing cyclotron, was aimed at experimental testing the possibility to accelerate the proton beam in the cyclotron regime up to 100 mA. The general view and model windings are shown in Figs. 2 and 3.

In a static case the dynamic similarity of the proton and the electron in the magnetic field is based on the motion equation:

$$\frac{d\bar{\beta}}{dt} = e\left[\bar{\beta}\cdot\frac{\bar{B}}{m}\right], \quad \bar{\beta} = \frac{\bar{v}}{c} \qquad (7)$$

and hence

$$\left(\frac{\bar{B}}{m}\right)_e = \left(\frac{\bar{B}}{m}\right)_p \qquad (8)$$

for the whole range of the velocity module $|\bar{v}|$

The Coulomb field and the acceleration process taken into account make this similarity criterion more complicated. However, for each limiting mechanism it can be formulated at the confidence level of the effect under study. Thus, if one assumes that the basic effect limiting the beam density is the transversal repulsion by the Coulomb field, then with the equal strength and geometry of the beam the similarity criterion for this effect will be

$$\frac{i_p}{i_e} = \frac{V_p f_p}{V_e f_e}. \qquad (9)$$

With the current of 1 mA [12] produced by the electron model of the strong focusing cyclotron, as it follows from ref.[9], it is possible to generate currents up to 200-300 mA without the "transversal" space charge effect limitation.

The limit beam intensity of 100 mA below 1 GeV results in the appearence of a number of specific problems. Among them is the problem of 100% beam extraction from the accelerator chamber, since the beam achieves hundreds MW.

The effect of expanding the closed orbits in the periodic magnetic field [13] will allow to solve this problem. This effect is based on the dependence of the closed orbit expansion (ρ/L $d\rho/dL$) upon the magnetic field

*) The strong focusing magnetic system is that for which Q_r and Q_z are larger than unity.

variation ($\mathcal{E}(z)$, $d\mathcal{E}/dz$) where $\mathcal{L}$ is the length of the closed orbit.

In the magnetic fields of (6) type the main radius of the closed orbit for the particle having the momentum P is obtained from the expression

$$P = e\,B\,(R_m)\,R_m\,\lambda, \qquad (10)$$

where R_m is the mean radius of the closed orbit; λ is the parameter determined by the Periodic (N) part of the field structure (6) and can be as follows:

$$\lambda = \frac{1}{2} + \sqrt{\frac{1}{4} + \frac{\mathcal{E}^2}{2N^2}\left(\frac{1}{2} + n + \frac{d\mathcal{E}}{d(z/z)}\right)_{z=R_m}} \qquad (11)$$

When determining the length of the closed orbit by means of the mean radius from (11) it follows that

$$\frac{\rho}{\mathcal{L}}\frac{d\mathcal{L}}{d\rho} = \frac{1}{1 + n + \frac{z}{\lambda}\frac{d\lambda}{dz}\Big|_{z=R}} \qquad (12)$$

The result shows the possibility of considerable controlling the coefficient of orbit expansion near the following values:

$$\frac{R}{\lambda}\frac{d\lambda}{dz}\Big|_{z=R_m} \approx -(1+n)_{z=R_m}$$

In the static regime the separation of closed orbits is increased 20–50 times. Thus, this regime allows to expand the closed orbit without varying the shape of the beam emittance When the resonance method of extraction[14] is used, as is known, the shape of emitaance is changed.

The dynamic regime of this effect differs somewhat from the static one, however, the main conclusion on the possibility of increasing the energy step of the closed orbit 20–50 times is conserved.

A further important problem of such strong-focusing accelerators is the efficiency For powers of the accelerated beam close to 100 MeV this efficiency will be completely determined by the r.f. power. The contributions of all auxiliary energy systems (the magnet, the vacuum system, etc.) are negligibly small. The efficiency of modern lamp generators in the frequency range of interest is 70-75%[15]. The r.f. losses in cavities with the amplitude of 200–400 kV of accelerating voltage are not larger than 50–200 KW and this is negligibly small compared to that transferred to the beam. Thus, the efficiency of the ring isochronous cyclotron with strong focusing must be close to that of the r.f. generator.

The similar parameters of the accelerated beam can be obtained at proton linear accelerators of continuous operation. It is known that the best linear proton accelerators even at present have pulse currents of about 200 mA[16]. However, pulse losses for such accelerators are 40 MW[17], which considerably affects the accelerator efficiency and the cooling systems in the continuous acceleration regime.

Both for ring and linear machines there arises a problem of phasing the accelerating cavities at large beam loads. This problem, to our mind, can be solved considerably easier for ring machines than for linear ones due to some reasons:

a) the number of cavities is 50-100 times smaller;
b) the amplitude of accelerating voltage is several times smaller;
c) the cavity self frequency is small.

These considerations have been laid in the basis of the studies in the development of the 800 MeV strong-focusing cyclic meson factory - a "supercyclotron", the proton beam intensity being 10–100 mA.

A linear accelerator of continuous operation is assumed to be used as an injector for this accelerator[18].

IV. "K" Meson Generators

The absence of dynamic similarity of orbits in isochronous cyclotrons considerably complicates their use in the 1.6 GeV energy region. The attempt to pass integral resonance in particle acceleration is due to considerable increase of the r.f. power system of the accelerator which should provide in this case the energy gain scores MeV at each turn. The creation of the system of some successive accelerators of the energy gain 1 GeV raises the whole cost too much.

However, there is a certain possibility to be considered separately, if the problem of strong current K-meson factories becomes important. This possibility is also based on the properties of closed orbits in the periodic structures having the magnetic field variation $\mathcal{E}(r)$.

The main contribution to the violation of dynamic similarity in acceleration is made by the variation of "n", which is determined by the requirement of isochronism in closed orbits

Usually for isochronous cyclotrons a direct problem is put forward: with increasing the mean value of the induction field along the accelerator radius the mean value of the induction field along the accelerator radius the proper F function (see (6)) is chosen such that the space stability should appear. However, for smaller changes of "β" a reverse problem is possible when the condition n = constant is the basic requirement with which the dynamic similarity of orbits is obtained (Q_r, Q_z = const.). In this case the condition of isochronims of closed orbits is based on the choice of the function F and is determined by the variation of the shape and the coefficient of stackening closed orbits at various radii:

$$\frac{\lambda_0}{\lambda}\left(\frac{\sigma}{\sigma_0}\right)^{n+1} = \frac{\sigma_0}{\sigma}\left(\frac{\beta}{\beta_0}\right)^{n} \qquad (13)$$

where $\sigma = \frac{1}{\sqrt{1-\ldots}}$; $L = 2\pi R_m \sigma$, σ is the coefficient of orbit lengthening due to the periodic field structure.

As has been shown in ref.[19] such a possibility exists and can be implemented in strong current K.meson factories.

V. Conclusion

The present paper is not intended for covering all the variety of problems arising in the development of strong current meson factories. It concerns the basic, in the

authors' opinion, problems on particle acceleration physics. A lot of technical problems have not been touched upon. However, the experience of developing meson factories shows that they can be solved at the present day level.

Table 1

Accelerated proton energy (MeV)	600	Number of accelerating gaps	8
Accelerated proton current (MA)	10-100	Voltage across the cavity(kV)	250
Injected proton energy (MeV)	50	R.F. Power (MW)	76
Axial oscillation frequency	1.3-1.4	Number of sectors	8
Radial oscillation frequency	$2r\ Q_z > 1$	Yoke magnet diamter (cm)	1900
Injection radius (cm)	240	Magnet height (cm)	560
Mean field at the injection radius (Gauss)	4270	Magnet weight (t)	3450
Full radius (cm)	650	Magnet power supply (KW)	1750
Mean field at the injection radius (G)	7500	R.F. losses in cavities (kW)	1000
Energy gain per revolution (MeV)	2.0	Beam power (MW)	8-80
Ion rotation rate (MHz)	6.2	Efficiency of beam extraction from the accelerator chamber (%)	100
Acceleration voltage frequency(MHz)	49.6	Beam intensity losses in acceleration	10^{-4}

References

1. V.G.Vasilkov,V.I.Goldansky,V.P.Dzhelepov, V.P.Dmitrievsky. JINR Publication P9-5285(1970).
2. G.Brianti,E.G.Michaelis, SC Improvements, Rep. M53(1966).
3. V.P.Dmitrievsky, B.I.Zamolodchikov, V.V.Kolga. AE, 9,303,1960.
4. K.Ziegler, E.Martin, R.Cohen. V Int.Cyc. Conf., Oxford (1969) p.226.
5. N.L.Zaplatin, A.F.Chesnov.Proc.III Nation. Conf. on Accelerators,Moscow,1972.
6. V.P.Dzhelepov, V.P.Dmitrievsky,B.I.Zamolodchikov,V.V.Kolga. UFN,85,651,1965.
7. John A.Matrin. V Int. Cyc. Conf. (1969)p.3 R.Cohen, E.Martin, S.Rainwater,K.Schneider, K.Ziegler,S.Ohnuma.V Int.Cyc.Conf. Oxford (1969)p.699.
8. V.P.Dzhelepov, V.P. Dmitrievsky. Proc. III National Conf. on Accelerators, Moscow,1972
9. V.P.Dzhelepov et al. Int.Conf. on Isochronous Cyclotrons. Gatlinburg,USA (1966)p.215.
10. V.N.Anosov,A.A.Glazov,Yu.N.Denisov et al. AE,25,539(1968).
11. A.A.Glazov,V.I.Danilov,V.P.Dzhelepov et al. 8, No. 3,189 (1960).
12. A.A.Glazov,V.P.Dzhelepov et al. JINR Publication P9-6214(1972).
13. V.P.Dmitrievsky,V.V.Kolga,N.I.Polumordvinova. JINR Publication P9-6733(1972).
14. W.Jogo.V Int.Cyc.Conf.,Oxford(1969)p.159. J.Reginald Richardson,M.K.Craddock,Oxford (1969)p.85.
15. K.L.Erdman,R.Roirier,O.K.Fredriksson, S.F.Welton,W.A. Grundman. VI Int.Cyc.Conf. Vancouver,1972.
16. I.Kapchinsky, V.A.Batalin,A.A.Kolomiets, B.K. Kondratiev,R.P.Kuida,PTW, 5,17(1972).
17. D.C.Hagerman,IEEE Trans.on Nucl.Sci., NS.13(4)p.277.
18. V.A.Teplikov,A.P.Maltsev,S.M.Ermakov, A.V.Zotov,V.A.Yurchenko. IFVE Ing-68-35-K (1968).
19. V.P. Dmitrievsky, V.V.Kolga, N.I. Polumordvinova. the VIIIth International Confer. on High Energy Accelerators. CERN (1971), p.518.

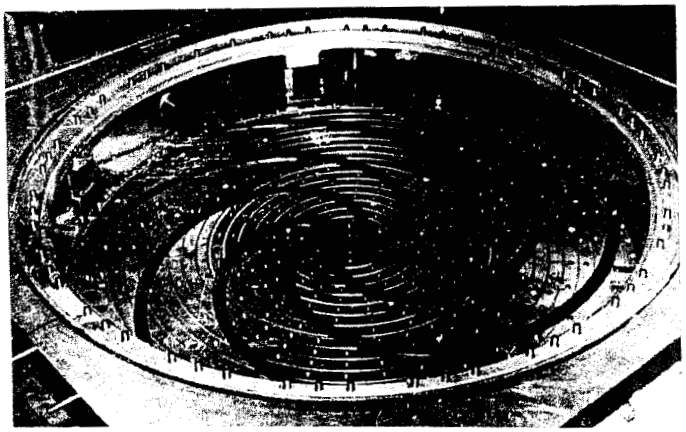
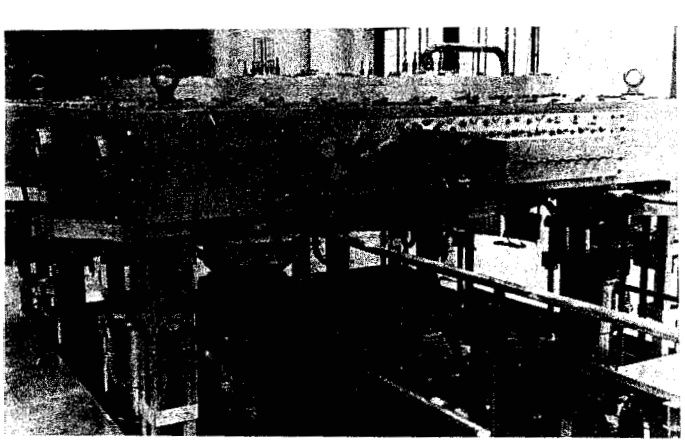
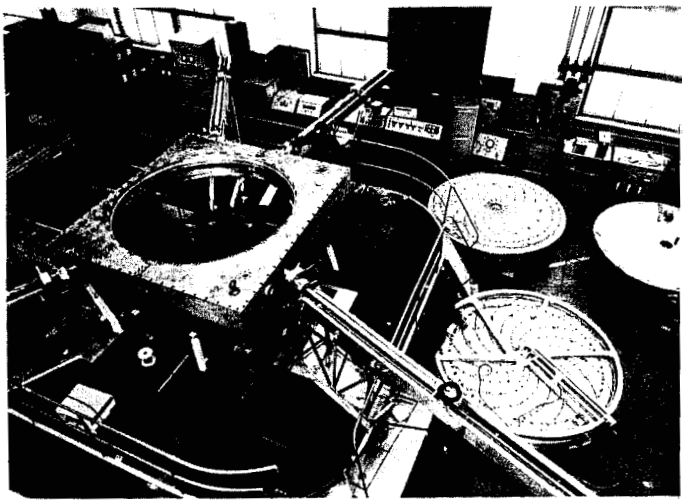


Fig. 1
The general view of the accelerator pole piece





Figs. 2, 3
The general model view and the model windings

FIRST BEAM TESTS WITH THE 590 MeV RING CYCLOTRON AT SIN

J. -P. Blaser, H. A. Willax

'Swiss Institute for Nuclear Research, Villigen, Switzerland

Abstract

At the beginning of this year a few tests were performed with the SIN ring cyclotron, the first isochronous cyclotron accelerating protons successfully in CW-mode to truly relativistic energies ($\gamma = 1.6$ 3). The extracted proton beams, though still low in intensity, were used for production of pions at an external target. The results of these early tests are presented and discussed.

Introduction and Brief History of the Project

In the early sixties studies were started at ETH (Swiss Federal Institute of Technology in Zurich) about a high intensity proton accelerator in the "intermediate energy" range (0.5 - 1 GeV). The idea was to develop research in the overlapping region of nuclear and particle physics by making available very intense beams of pions and muons. This new field, also potentially rich in applications, e. g., chemistry, solid state physics, biology and medicine, was considered very suitable for a new national research facility in Switzerland in order to continue a valuable tradition in nuclear physics and to stimulate participation at CERN. A small team at the physics department of ETH investigated different accelerator types primarily for production of pion beams of high intensity and good experimental quality. [1] In 1962 - 1963, a proposal for a double stage isochronous cyclotron, a "meson factory", capable of providing 500 MeV p in an external CW beam of up to 100 μA, was worked out. [2]

The concept of a ring cyclotron with separated magnets, several re-entrant RF cavities providing high accelerating voltages and "free sections" inserted between the magnets, appeared beneficial for the following reasons: At proposed energies the loss of beam within the machine and beam transport systems has to be minimized. Optimal beam transmission through the accelerator and high extraction efficiency are main design goals. The large operating radius of the ring combined with a high energy gain per particle revolution lead to the high extraction efficiency achievable in such a machine. [3] Good focusing properties of small gap magnets as well as possibilities for tailoring the beam before injection aid beam transmission. The "open structure" eases maintenance and repairs of activated machine components.

In the meantime, a committee of CERN member states (ECFA) had recommended a series of future accelerators in Europe. Complementing large projects to be realized on an international scale, smaller accelerators in national centers were considered as essential backup for the international effort to assure the scientific resources, available at the universities. Among these proposals a "meson factory" along the line of the ETH studies was proposed.

Results of early beam dynamics studies and model work on main components of the proposed accelerator were encouraging enough to submit a project proposal to the Swiss Government in 1965. A development and construction budget of 92 MSfr. was granted in 1966. The decision on starting construction, however, was delayed until late 1968, when a practical solution was worked out for a modification of the first cyclotron stage (the injector cyclotron) to a multiparticle variable energy machine. In the design of this cyclotron, two modes of operation had to be considered:

a) the injector mode, in which a 72 MeV p beam of high quality and intensities up to 100 μA had to be delivered at 50 MHz pulse frequency (the correct frequency for full acceptance in the ring cyclotron), and
b) the variable energy mode providing beams of d, He_3, a, heavy ions and polarized p and d to be directly used for nuclear physics experiments.

The difficult task of building this machine was taken up by Philips-Company Eindhoven in fall of 1968.

At that time the development of main components of the ring cyclotron, carried out by the cyclotron group of ETH [4] had progressed *so* far that procurement could be started. The laboratory became an annex institution of ETH with the name SIN (Swiss Institute for Nuclear Research). In 1969, after good results with full scale prototypes of a main magnet and an accelerating cavity had been achieved and after a thorough beam dynamical study [5] indicated stability limits, it was decided to increase the final energy from 520 to 590 MeV without altering the design geometry of the ring cyclotron as frozen in 1967. A calculated risk was taken with this decision since it entailed two possible problems:

1) The betatron oscillations had to pass the condition of the non-linear coupling resonance $\nu_r = 2\,\nu_z$ at least twice at rather high energies, and
2) the magnets (already in process of being ordered) had to provide more flux, so that critical areas in the yoke cross section became saturated.

In spring of 1969 the building construction program started at Villigen with a tight schedule; the initial assembly work of both accelerators began by summer 1971. A carefully scheduled mounting and testing period of two years lead to the final assembly of the machines by summer 1973. Already in fall 1972 the testing and debugging of subsections of the ring machine were started' (1/4 ring tests). The final corrections of the magnetic field by careful shimming of the individual magnet sectors required special efforts in summer 1973, concentrated around the injection and extraction region where perturbing effects of magnetic beam guiding elements had to be compensated. While the injector cyclotron [7] achieved first internal beam on August 1, 1973 without the extraction elements installed, the ring cyclotron and beam transport systems were made ready for first beam tests scheduled for October 1973. A delay in the fabrication of the magnetic deflector coil of the injector cyclotron's extraction system brought a 3 month delay in testing the accelerator system with proper beam (72 MeV p at 50 MHz). In November 1973, a few preliminary tests of the beam transport system and injection into the ring were performed successfully with low energy particles (20 and 17 MeV p, 33 MeV d) which could be extracted from the first stage cyclotron without the magnetic deflector coil being mounted.

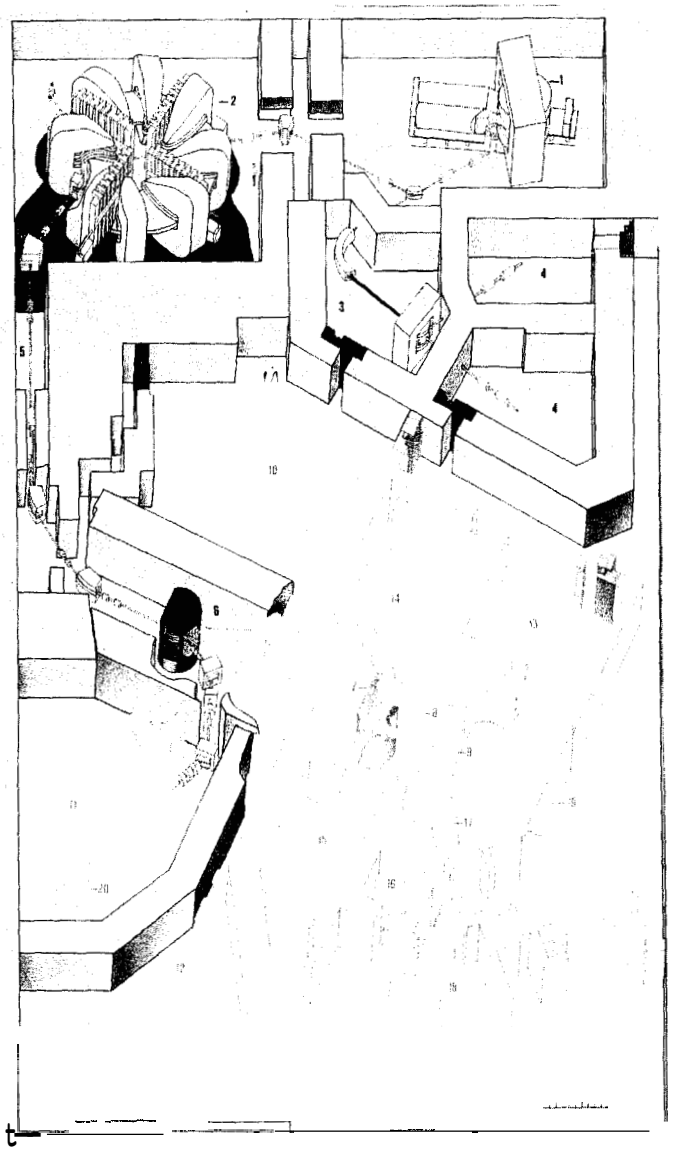


Fig. 1 SIN Experimental Hall
Scheme of the status of assembly during the first test period between January and April 1974 is marked by heavier contours. The lighter contours demonstrate the assembly goals of the end of 1974.

1) Injector cyclotron (2. 5 m pole diam)
2) Ring cyclotron (15 m outer diam)
3) Analyzing system for low energy beams
4) Experimental areas for low energy beams
5) 590 MeV p beam line
6) Pion production target "M" (thin target)
7) Local shielding for thick target "E"
8) Secondary beam bending magnet
9) Beam dump
10) Experimental area for pion work
11) Experimental area, used for first pion detection and experiments (πM3)
12) Low intensity p beam (future)
13, 14) Pion experimental area
15) Biomedical pion beam area
16) Muon experimental area
17) Superconducting muon channel
18) Muon experimental area
19) Opening for neutron beam
20) μ -neutrino mass experiment

With the beginning of this year an experimental p beam of proper injection energy (between 70. 5 and 72 MeV) and pulse frequency (50.7 MHz) could be extracted at intensities of 1 - 2 μA. This test beam was used in six major test runs to learn about the principle functioning of the accelerator system, the two last runs also including the use of the first pion production target with one secondary beam transport channel (πM3).

Beam Tests with the SIN Ring Cyclotron

In Fig. 1 is seen the status of assembly in the experimental hall of SIN Villigen during the first test period between January and April 1974. The injector cyclotron, during this period still under responsibility of Philips, is shown in Fig. 2. Its properties and technical features are described elsewhere.[7] For the initial tests with a p beam of approximately correct injection energy and a pulse frequency corresponding to the 3rd harmonic mode, this machine still had an improvised shorting bar, providing the 50 MHz resonant structure within the main vacuum chamber. It had to be separately mounted and manually adjusted to the right position for the exact isochronous frequency (theoretical value 50.680 MHz). The magnetic deflector coil, the second essential element of the beam extraction device, had just been installed in December 1973. Operational experience on extracted beam and its quality still had to be gained in the time period discussed below. The ring cyclotron, as described elsewhere[6] and shown in Fig. 3, was already equipped with all essential elements, including beam probes and deflection devices. A double set of carbon collimators limiting the free vertical beam aperture to 25 mm at injection radius and to 15 mm over a radial range from 490 to 590 MeV were installed for protection of critical components. There was no operational experience yet on the long term stability of all four cavities working simultaneously, or the RF induced perturbing signals on the probes.

The first experimental test runs were handicapped by the following factors:
- limited time periods of simultaneous operation of all accelerating cavities in use, with interruptions when a cavity fell back into a multipactoring condition. In the course of the runs, however, the average "on-off"-

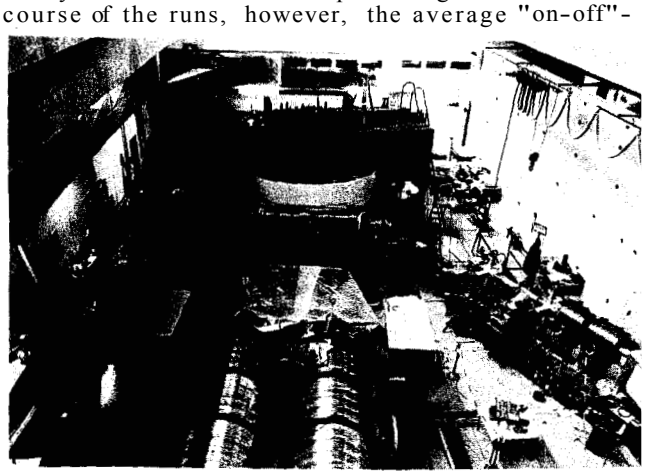


Fig. 2 Injector Cyclotron
Situation shortly before final assembly in summer 1973. The dee (under plastic cover) and the connected RF resonators for variable frequency are withdrawn from the main vacuum chamber.

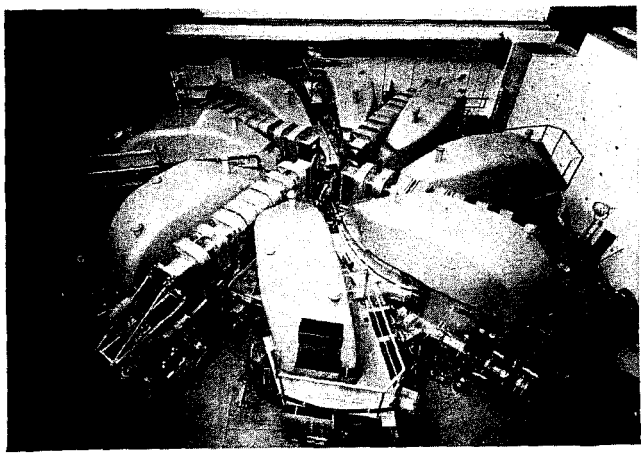


Fig. 3 590 MeV Ring Cyclotron
Situation during final assembly in summer 1973. Between the eight 250 t sector magnets are four RF cavities providing voltages up to 650 kV at 50 MHz. The extraction beam path (right foreground) is being installed.

time ratio changed from typically 50 % to 90 % taken over 20 hours, with periods of uninterrupted operation of up to 6 hours.
- perturbing signals on probe current readings, induced by the cavities operating at high voltages. Some of the effects could be eliminated or diminished during the course of the tests.
- uncertainities in the absolute value of the energy of the injector beam of ± 1 MeV, and uncertainities in the reproduction of the injector settings, leading to a defined energy and optical beam characteristics. Those changes in initial conditions usually caused time consuming experimental search for the proper settings of the beam transport system and the ring injection parameters.
- fluctuations in intensity and (sometimes) in the intensity distribution within the useful emittance, especially noticed when the ion source of the injector was set for low intensities. This effect, in many cases, made optimizations on certain parameter settings very time consuming.

In the first night of tests with a 1 μA beam of the proper injection energy (= 72 MeV) and the required pulse frequency (50.7 MHz) on January 11/12, 1974, the beam transfer from the injector to the center of the ring cyclotron could be accomplished with a 60 - 70 % transmission. Before injection into the ring, the proper position of the main injection elements first had to be determined. The vertical alignment of the beam was found to be critical. We succeeded in detecting the beam over the first 5 to 7 accelerated revolutions. However, coherent oscillations of 10 - 15 mm amplitude in both directions were observed. In the following night (January 12/13, 1974), the settings of injection parameters were improved. RF pickup on two essential probes made measurements difficult. With the remaining, unaffected probe, the beam was finally detected over the range from 72 - 92 MeV. Fig. 4 shows the radial intensity distribution taken by the 1 mm radial differential probe. Except for the two innermost revolutions the turn spacing corresponds to a "peak to peak" accelerating voltage in each cavity of 480 kV. This is within the 10 % uncertainity of the voltage calibration of the cavities, which were set for 500 kV.

In the second test run of January 17/18, the failure of an RF power feed-through made it necessary to attempt acceleration in the ring with three cavities only. Even though under those conditions (with the injection elements adjusted to an "uncentered" equilibrium orbit) the problem of the first internal beam clearing all obstacles is not trivial, this run was successful. With a 1 - 1.5 μA beam delivered from the injector, the transmission through the beam line could be brought up to 80 - 90 %. At injection a typical loss of 20 % had to be taken into account. Immediately after the centering problems had been solved experimentally, a beam of up to 0.7 μA could be brought out to approximately 540 MeV without trim-coil corrections to the main field. Some trim-coil adjustments were necessary to take the beam further out. A current of 0.4 μA was achieved at 570 MeV. However, a drastic decrease in beam intensity, starting about 2 cm before extraction radius, could not be overcome. At the nominal extraction radius, 5 - 10 nA of circulating beam remained. The attempt to extract part of that beam was successful: 4 nA of 585 MeV p were measured at the temporary beam dump, installed in the cyclotron vault 5 m downstream from the last extraction magnet. The reason for the drastic intensity drop shortly before extraction radius was found during the following visual inspection of the ring. Vertical beam clipping had occured due *to* a Paulty mount of a single trim-coil plate in one sector magnet. This fault was quickly repaired and the broken RF feed-through was replaced by a spare unit.

For the third major beam experiment on February 7/8, the injector beam quality had improved, and higher beam intensities could be achieved. With a stable 1.5 μA beam delivered from the injector and the four ring cavities operating stably over periods of several hours, transfer and injection of the beam into the ring presented no basic problems. Even though some initial coherent beam oscillations in the ring could not completely be eliminated, a 0.2 - 0.3 μA beam was accelerated to extraction radius, the transmission from injection to extraction being approximately 75 %. About 80 % of this beam was extracted and measured at the temporary external beam dump in the cyclotron vault. For a short time the injector beam intensity was increased, and 0.6 μA were registered at this beam dump.

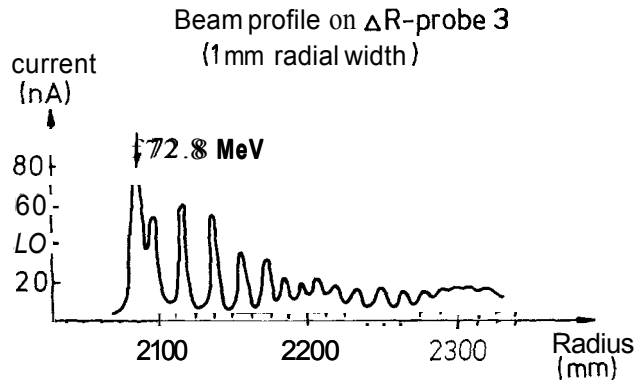


Fig. 4 Profile of separated beam revolutions as measured with a differential beam probe of 1 mm when acceleration from 72 to 92 MeV was achieved for the first time.

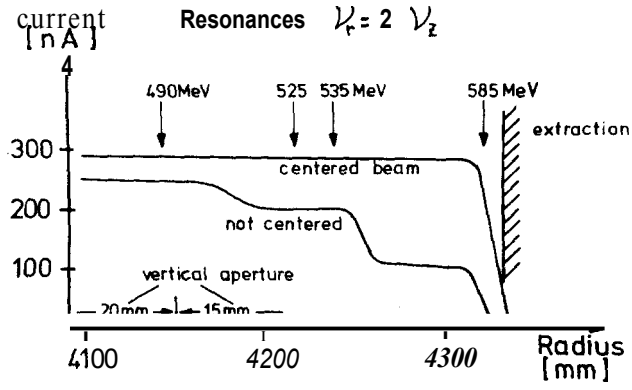


Fig. 5 Radial beam profiles at high energies. This plot shows the internal beam current versus radius for a well centered and a non-centered beam. Initially, the beam was injected excentrically into the ring cyclotron, giving radial oscillations of about 15 mm amplitude. These radial oscillations were converted into vertical oscillations at the coupling resonance $\nu_r = 2\ \nu_z$ which occurs at four different energies before extraction. Due to the small vertical aperture of beam collimators there resulted a noticeable beam loss after each crossing of a resonance. After centering the injected beam by adjusting the electrostatic inflector voltage no beam loss was observed.

The fourth experiment, carried through on February 15, was mainly aimed at closer investigations of the ring internal beam behaviour. With a typically 0.5 - 1 μA beam, the build-up of coherent beam oscillations and their effect on total transmission through the ring was measured. The following results could be stated:

- A first harmonic horizontal field component on the order of a few G in the magnetic field near injection radius causes difficulties with the vertical alignment of the beam in the ring.
- Depending on the centering of the beam at injection (initiating coherent horizontal oscillations), the transmission of beam to extraction radius may be affected by the coupling resonance $\nu_r = 2\nu_z$ which, in our case, without trim-coil corrections, occurs at energies of 490, 525 and 535 MeV. In Fig. 5 beam intensity profiles versus machine radius are shown for the two typical cases of a well centered beam, and a beam with initial coherent radial amplitude of ∿ 15 mm.

For the beam tests on February 23/24 and March 16/17, the p beam line of 40 cm length, leading from the ring to the first pion production target (housed in heavy local shielding) was installed and operable. The first pion channel πM3 with the length of 15 m was also ready for transmitting beam (see Fig. 1). During tune-up on February 23, again one cavity of the ring cyclotron failed due to a fault in the grid circuit of the power amplifier. With three cavities operating stably at operating voltages between 450 and 500 kV per cavity, a loss of 30 - 40 % at injection had to be taken into account. A coherent radial oscillation had to be eliminated by excitation of pole face windings in two adjacent magnets. Since the main goal of the experiment was the first production of pions in an external target, not much time was spent to optimize injection parameters. A beam of 0.1 - 0.2 μA was brought to extraction radius and with an extracted beam of 50 - 100 nA, the 590 MeV p beam line was tested for the first time. The beam immediately was brought on target, a 0.5 cm carbon plate. Due to a slight misalignment of a temporary collimator the transmission in the p beam line could not be improved beyond 50 % that day, However, with a 50 - 100 nA beam on target in a spot size of ∿ 1 cm^2, the first pions were detected behind the pion channel, which was set to a momentum of 300 ± 3 MeV/c. In more than six hours of beam on target, several very informative first measurements on pion production rates, π - μ - e ratios and the effectiveness of shielding could be made. After readjustments of the machine settings and an increase of injector beam intensity to ∿ 5 PA, a beam of 0.8 - 1 μA was extracted from the ring and 0.3 μA were used on target for a short while.

For the following test on March 16/17, all four RF cavities were operational. For injection, acceleration and extraction, no pole face windings had to be used. However, this time the injector beam showed a large horizontal emittance (probably due to a large dispersion). 50 % of the beam available at the injection point were lost within the injection channels of the ring (whereas the transmission through those channels was more than 80 - 90 % in previous runs). Intensities had to be kept low for this reason. For a period of almost 12 hours, beam of varying intensities between 50 - 300 nA was delivered for optimization of the 590 MeV p beam line (which could be brought up to over 90 % in rather short time) and for pion production on target M. The emittance of the 590 MeV beam was measured to be typically:
$A_x = \pi$ x 12 mm mrad, $A_z = \pi$ x 4 mm mrad. A result of measurements on the pion range taken after the pion channel (set for 200 MeV/c) is shown in Fig. 6.

Towards the end of this experimental "production run", the intensity of the injector beam increased to 10 μA. With a circulating beam of 4 - 5 μA on the first orbit in the ring, a 2 μA beam of 590 MeV was extracted and used for a short time on target M for measurements on background radiation.

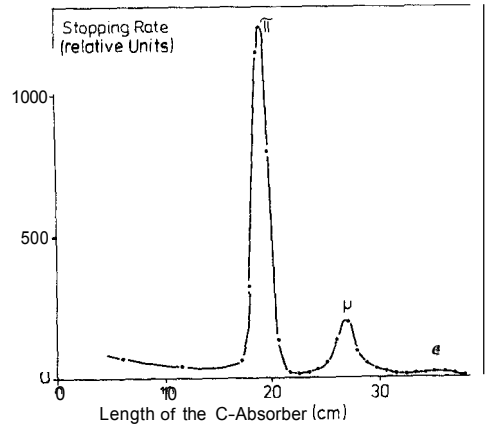


Fig. 6 Differential Range Curve (p_π = 200 MeV/c)
A range curve was taken as a quick test of the predicted momentum resolution and intensity of the pion beam in the πM3 area. The predictions were confirmed within 30 %.

p intensity	: 200 nA during 1 1/2 h
pion production target	: 0.96 g/cm^2 of carbon
pion stop rate	: 370 stops/s in 1.4 g/cm^2 of carbon
momentum resolution	: 2 % FWHM

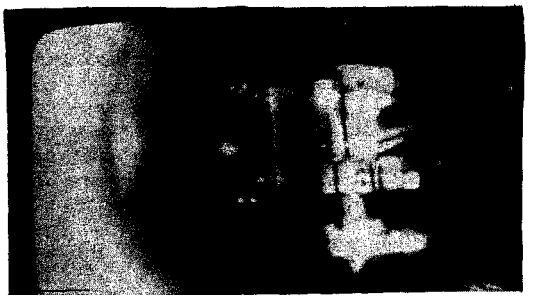


Fig. 7 590 MeV p Beam
Trace of a 1 μA p beam observed through TV on a movable quartz plate in front of the entrance to the second internal deflection element of the ring cyclotron (a magnetic quadrupole channel of 15 mm free aperture). The spot size is about 6 mm x 8 mm. This beam is well separated from the internal circulating beam, having passed the electrostatic deflector channel 45° upstream. The quadrupole channel had to be positioned slightly above midplane for good transmission through the following elements.

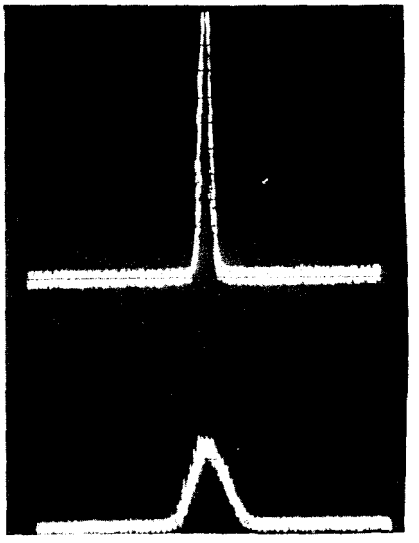


Fig. 8 590 MeV p Beam
The intensity distribution of 1 μA beam in the horizontal plane, measured by two "profile monitors" (metal plates of 1 mm thickness sweeping through the beam), about 3 and 6 m after extraction from the ring.(Calibration on abscissa in cm).

After this preliminary test period, in which the injector cyclotron under the responsibility of Philips has produced valuable test beam with increasing reliability and quality, this machine was prepared for acceptance tests. On March 26, 1974 for the first time it produced slightly more than 100 μA extracted beam in the injector mode. On April 18, measurements on the beam extracted from this machine at 72 MeV and 50.65 MHz showed the following results:

Current	: 105 μA
Emittance A_x, A_z	: Π x 5 mm mrad (80 % of beam)
Energy spread Δ E	: 200 keV (FWHM)
Phase width	: 20° RF at 50.65 MHz

Further Procedure

While the definite version of the 50 MHz shorting bar system is being installed in the injector at present, the ring is being prepared for the next operating period scheduled at the end of May 1974. During the summer of this year the following main activities are planned:

- Education and training of personnel for operation and maintenance of the accelerator system.

- Beam development on both accelerators with the special aim of improvement of the total transmission.

- Delivery of low intensity beam (up to a few μA) on pion production target M (thin target) for pion experiments.

- Installation of target E (thick target), the corresponding secondary beam lines and the beam dump.

After a longer shut-down in the late summer of 1974, it is expected to bring the whole facility to a condition where more than 10 μA can be usefully produced.

Acknowledgment

As the main reason for a first success in the start-up of this accelerator facility we consider the excellent work and high motivation of all the staff members involved during its development, construction and beginning operation, as well as their dedication to their tasks, which often were difficult. We hope the spirit of this great team can be kept up during the difficulties of beginning operation. The great effort of some industrial firms which undertook to supply us with reliable components of unconventional features needs to be mentioned as an essential part of the success. We thank our authorities for their confidence and steady support in all phases of the project.

References

1. J. P. Blaser and K. Steimel
Nucl. Instr. and Methods 18/19, p. 417 (1962)

2. H.A. Willax
CERN 63-19, p. 386 (1963)

3. G. Tripard, W. Joho
Nucl. Instr. and Methods 79, p. 293 (1970)

4. H.A. Willax
Proc. Oxford Cyclotron Conference, p. 58 (1969) (Butterworth, 1971)

5. W. Joho, Thesis (May 1970)
"Extraction of a 590 MeV Proton Beam from the SIN Ring Cyclotron" (SIN Report TM-11-8)

6. H. A. Willax
IEEE Trans. Nucl. Sci., NS 20 (3), p. 202 (1973)

7. A. Baan et al
IEEE Trans. Nucl. Sci., NS 20 (3), p. 257 (1973)

BASIC DESIGN CONSIDERATIONS ON AN ELECTRON BEAM STRETCHER

H. Herminghaus
Institut fur Kernphysik, D-6500 Mainz, West-Germany

This paper gives a brief description of some less conventional schemes for injection, extraction and spill out control to be used with an electron beam pulse stretcher ring.

In designing an electron beam stretcher for the 300 MeV Electron Linac of Mainz University the **main** effort was made to get low transversal beam emittance of the extracted beam and to provide some means for flattening the beam intensity. To be compatible with later recycling of the linac the stretcher should be able to operate up to 600 MeV. The magnet ring will mainly consist of two 180^{o} bending systems connected by two long straight sections. In this paper, however, only some as we think rather unconventional details will be discussed.

Since the emittance of the extracted beam is in part determined by the emittance of the circulating beam we consider it to be of advantage to use a longitudinal stacking in order to keep the emittance as small as possible. The stacking procedure is as follows: The beam is swept between two deflecting cavities of mutual distance L through the aperture of a focussing lens, the focal length of which is L/4. By correct phasing of the RF the beam will not move downstream the device (Fig. 1). The linac beam is fed in obliquely through the first deflector and bent to a regular orbit by

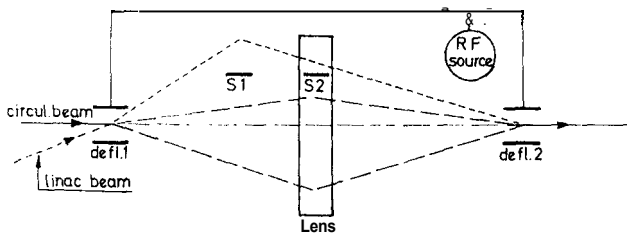


FIG. 1--longitudinal stacking scheme.

means of two septa. In this manner it is achieved that injection is not affected by the performance of the RF, provided only that the beam passes behind the septa at inflection and in front of it at the successive turns. This scheme should work with reasonable margins for bunch lengths of less than 10^{o} over 6 turns of injection. To preserve the bunch structure sufficiently during injection the momentum compaction factor should be less than 10^{-3} if an energy range of **2.5%** is to be captured. After about 100 turns after injection the original bunch structure may be considered to be totally lost. It is reckoned with a maximum injected linac beam of 170 mA, leading to a maximum circulating beam of about 1 A.

For extraction at some location of the ring dispersion will be provided and it shall have there a large horizontal but small vertical β-function. This gives a flat beam, the position of which is dependent of energy (Fig. 2). At the low

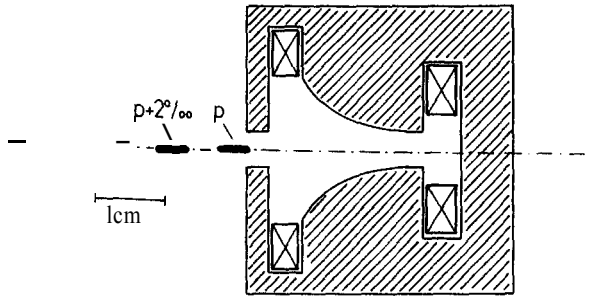


FIG. 2--Semiquadrupol used for extraction. Beam dimension and dispersion in correct scale.

energy side a small semiquadrupole is situated inside the vacuum (gap width about 5 mm). If the energy of the beam is lowered slowly it drifts into the gap of the semiquadruple and is bent out subsequently. Final extraction is done by a magnetic septum a few meters downstream. The semiquadrupole is acting at a small fraction of the beam at a time only, causing a large Q-shift there of about 0.15 over a few mm. It is believed that this extraction scheme is scarcely affected by field errors in the ring.

The extraction has been computed by tracing many particles by a computer program, taking into account a field distribution in the semiquadrupole as measured at a conductive paper model. Figure 3 gives an example for such a computation. The extracted phase space shown had been obtained

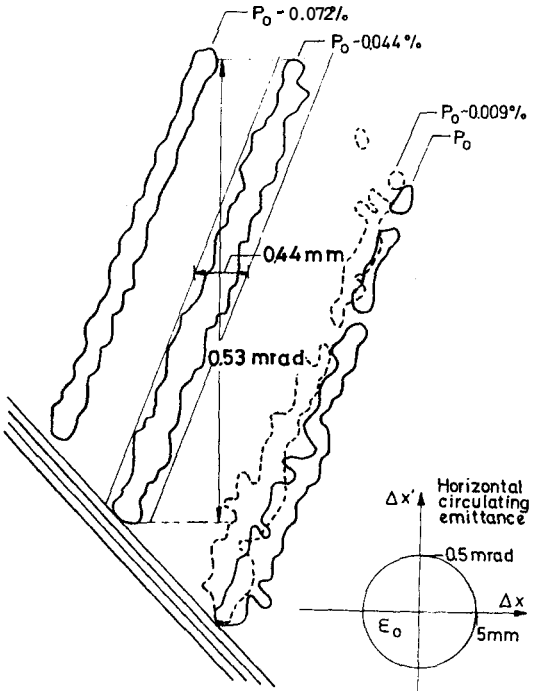


FIG. 3--Phase space of extracted beam at location of semiquadrupole. Each area encloses electrons of equal energy. The beam at lower left represents the shadow of the septum. The dimensions of the phase space areas as indicated by arrows in the figure represent **3%** of the circulating emittance. Dispersion is assumed to be **4.5** cm/%. Total momentum spread of extracted beam is less than 0.08%.

with $Q_H = 0.15$, $Q_V = 0.26$, all other parameters as indicated in the figure. The emittance of any monochromatic part of the extracted beam is about 3% or less of the emittance of the circulating beam in horizontal direction, while vertically the emittance is enlarged by a factor of about **1.3.** Extraction efficiency is about 90%. Since all monochromatic parts can be arranged to be of equal length and parallel in phase space as shown in Fig. **3** they can easily be brought to complete coincidence by a chromatic deflection system. So the overall emittance is substantially less than the emittance of the injected linac beam.

The slow energy shift necessary for extraction may be done by synchrotron radiation loss at an energy range of

about 250 to 330 MeV.[1] Below 250 MeV the electrons lose their energy too slowly. This may be cured by inserting a small accelerator cavity in the ring which will periodically accelerate and decelerate the electrons. Those particles that have suffered enough deceleration will be extracted, the others will remain in the ring until, by a small phase slip per turn, these will meet a decelerating field, too. The process is controlled by proper variation of both amplitude and phase of the RF, thus providing flattening of the extracted beam intensity. At energies higher than 330 MeV, the following scheme may be used to compensate for too quick energy loss by synchrotron radiation: In a RF separator structure there are always transversal and axial forces related by

$$F_{tr} \sim j \cdot \text{grad } F_{ax} \ ,$$

j indicating a 90° phase shift in time.[2] Thus, the inflecting device shown in Fig. 1 may be converted into an accelerating mechanism by inserting a third cavity between the two others. This cavity should be phased in such a way that particles which have suffered maximum deflection in the first cavity meet the accelerating field off axis in the middle one at its maximum value. In this case, any closed orbit particle being deflected at all will be accelerated. By providing a certain RF phase slip between turns a very smooth acceleration of all closed orbit particles may be achieved and it is easily estimated that even for particles undergoing betatron oscillations the energy gain comes to an average rather quickly. Thus, the device described may be used to accelerate an unbunched beam. Though the achievable acceleration is very modest, it is sufficient in our case to compensate the radiation loss which amounts to about 6 keV per turn for electrons at 600 MeV with 2 m bending radius. The RF power requirement of the deflector cavities is in our case mainly determined by the necessity to avoid transverse beam instabilities and amounts to several tens of kilowatts each. Moreover, the interaction of the beam with the two outer deflectors tends to disturb the proper distribution of RF power in these cavities. It is desirable, therefore, to find a similar mechanism using less cavities. At the moment, schemes are investigated in which the setup of a small betatron oscillation by the transverse field of the RF separator mode is used subsequently for acceleration by the axial field of the same mode in a second cavity.

I *am* greatly indebted to Messrs. K. H. Kaiser, W. Manz and H. Schier for their great help in doing the numerical computations.

REFERENCES

1. R. Servranckx, Proc. Int. Conf. on Photonuclear Reactions and Applications, Asilomar, Calif., March 1973, p. 1039.
2. H. Hahn, Rev. Sci. Instr., Vol.34 No.10 (1963) p.1094.

THE NEXT STEP: ACCELERATORS VERSUS STORAGE RINGS

Leon M. Lederman
Columbia University, New York, New York, 10027

The reason I was willing to accept the invitation of Dick Neal to come here was largely because of the opportunity it gave me to collectively pay homage to the community of accelerator scholars for all the magnificent instruments which have been provided to me and presumably the users I represent here. Perhaps he picked me because I am old enough to have been through so many of these things, starting with a Nevis Cyclotron, and progressing through the Cosmotron and the AGS, and recently, the ISR, and the Fermi National Accelerator Lab with even occasional forays to the Bevatron and PPA. The teamwork of the users and the builders is part of our profession. We work hard in mutual stimulation. You make the machines, and we try to use them so well that the need for more machines becomes self-evident. Both of us, of course, working so that Gell-Mann and his friends become more and more famous. (That is not really fair. It is really an unholy trinity, engaged in a more or less honorable endeavor, the significance of which for history and for the future we do not have to elaborate here.)

My subject is to put the thing in perspective, and I have a slide here for people who do not travel so much. This is a picture of the Fermi National Accelerator Laboratory (Fig. 1) where I have been spending most of my time. Let me just

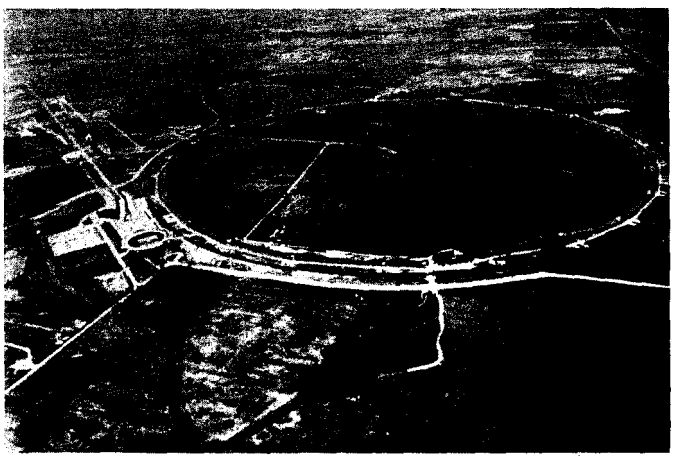


FIG. 1--Air view of the Fermi National Accelerator Laboratory.

say that I am very poorly prepared for these remarks, largely because of the fault of some of you here. I had planned to prepare this talk in some detail during the breakdowns of the FNAL accelerator, and for the last six weeks or so there have been so few.. .. It is really a thing of great beauty. We sit three kilometers from the accelerator and watch a beam sit steadily on a target which is only about 0.4 mm in transverse dimension, and with a duty cycle and intensity which is just positively embarrassing. This is, though, the last word in accelerators, and I always wondered what future archeologists might make of this — and to illustrate that I have another slide, which might surprise you (Fig. 2). It is clear to me the mystery of Stonehenge is solved! Some of you might even appreciate the next figure (Fig. 3), which shows how this was built. You see your progenators, the accelerator builders of an early day — I do not know if you recognize anybody.

In considering my assignment, The Next Step, I decided to be as general as I could, considering configurations that are thinkable in my lifetime as a physicist, which might not last more than another fifteen or twenty years. In reviewing

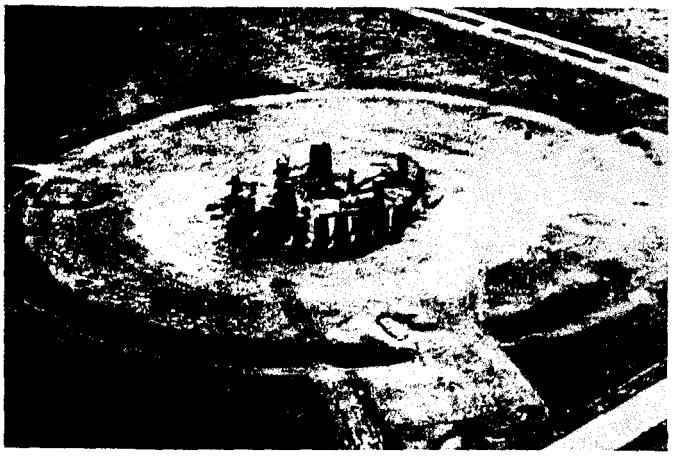


FIG. 2--Air view of Stonehenge.



FIG. 3--Construction of Stonehenge.

the history, there were always two arguments used for a new accelerator. One was to answer existing questions of the kind Gell-Mann reviewed for us in beautiful detail, and the other was that the accelerator should permit the kind of exploration that has always led to totally new questions — even undreamed of, like CP violation, or strangeness, or some of the many other discoveries that were made in a totally

surprising context. And both these steps are quite important. I might give an example of something which is a little bit out of context of here, but something I would like to bring to the attention of this gifted group. Some of us, a few years ago, wrote little notes on the interest that might accrue to collisions of high energy uranium with uranium. I wrote such things, stimulated by some work we did with antiproton production far below thresholds, a nuclear physics question, and then I read a note by Francis Farley, who took off on some speculations of Cocconi about the virtues of complexity. These are highly speculative things, and therefore there was no dream that one should actually spend real money on accelerating uranium to very high energies. But recently, starting from very abstract theoretical ideas, Lee and Wick have produced a nuclear physics theory which has greatly stimulated the idea of going to many GeV per nucleon. It is just these kinds of connections — remote connections — which have made our subject so interesting.

Let me now talk about more relevant things. I was asked to talk about storage rings versus accelerators, And much to my surprise, I found that the ISR has been, in a sense, too successful. Because if one looks at the current listing of unfunded projects, one finds six storage rings — that is something people are thinking about — five are electrons, one is a proton-proton storage ring, and no conventional accelerators! How could this be? What happened to the conventional accelerator? Is a new, conventional accelerator unthinkable in the time scale of the next ten-fifteen years? Thus, in the time I had to prepare this, I considered whether this is a wise thing — is it wise to forgo the opportunity for conventional accelerators?

In Fig. 4, we have a review of all possible experiments, trying not to omit anything. We have lepton-lepton, lepton-hadron, hadron-hadron interactions. We write "storage" where it seemed obvious that a storage ring was the right thing, and "accelerator or storage" when that is possible, and accelerator clearly when you require secondary beams. Now it could be that $p\bar{p}$ could also go in storage rings, but that is somewhat of a quibble. Here is then an almost complete list of the kinds of experiments you can do unless somebody finds something which is different from a hadron or a lepton. (I teach physics for poets, and I got an examination paper last week in which a hadron was defined as "a no longer active particle physicist.")

lepton-lepton	lepton-hadron	hadron-hadron
e^+e^-, e^-e^- : S	ep A or S	pp A or S
	PP A	$\bar{p}p$, πp, Kp, Yp : A
	νp A	

S = Storage
A = Accelerator

But there are alternative reactions, e.g.

$$\mu^+ + Z \to \mu^+ + \mu^- + \mu^+ + Z \text{ (tridents)}$$
$$e + \mu + Z$$
$$\nu + Z \to \mu^+ + \mu^- + \nu + Z \quad \Big\} \text{ A}$$

or

$$p + p \to \ell^+ + \ell^- + \text{junk} \qquad \text{A or S}$$

FIG. 4--All possible experiments to do at accelerators and storage rings.

There are alternative reactions (Fig. 4) sometimes, which are not totally obvious, but which permit the study of lepton-lepton scattering using nuclei as observers — this works if the incident energy is high enough. There are also some interesting experiments certainly, like neutrinos going to muon pairs, and other experiments which involve lepton-lepton interactions, as we will see, where the leptons come out of some complex and maybe not so pretty initial state.

In looking at these experiments, one must remember that there are deep interconnections — for example, there are three which study hadronic electricity: the e^+e^- goes to hadrons, which is of enormous current interest today — it is worked on at SPEAR; the deeply inelastic scattering; and perhaps electron pairs coming out of what you have in the way of hadrons, say proton-proton collisions. If you want to test the complete theory of the electrical structure of hadrons, presumably you need information on all three kinds of reactions. And then, again, looking at e^+e^- goes to hadrons, the data look very much like pp goes to hadrons. The hadronic things coming out look so much like the yields we see at the ISR, that clearly there is an important connection, and that further investigations of both will have *to* go hand-in-hand.

I will now survey briefly a set of experiments which one would like to do. Most of these are extrapolations of currently active experiments. The extrapolations of expected cross sections are made here in these next few charts, on the basis of data at lower energies, on the basis of models, and sometimes dimensional scaling, and then maybe sometimes on the basis of just nothing at all. In contrasting storage rings and accelerators, I take 5 TeV as a thinkable accelerator, largely because it fits on the Fermi National Accelerator site — and has roughly the same relation to a thinkable storage ring (and here we have had a great deal of thought) as ISR and FNAL, which are the complimentary accelerators we are working with today. And clearly, as we study FNAL and ISR, and the relationships of the two kinds of experiments, we will learn more about the validity of the kind of comparison I am doing now. So my thinkable accelerators from the point of view of hadron collisions are a storage ring of at least 200 GeV against 200 GeV, for Super ISR, and say roughly 5 TeV for Super FNAL. These are arbitrary numbers, if you like, but thinkable in the time frame of the next ten or so years and at costs which very probably do not exceed the annual construction costs we have already inflicted on the U. S. taxpayers. I have made up a report card, Table I, (this being the end of the semester),

TABLE I

Report Card

	Super ISR (SISR)	Super FNAL (SNAL)
• $\sqrt{s}$	$\geq$ 400	~ 100
• usable $\sqrt{s}$	depends	100
• usable luminosity[a]	$\to 5 \times 10^{7}$	10^{12} [b]
• dwell time[c]	B-	B+
• experimental area's flexibility, cost	A	C-
• particle identification	B-	A?
• backgrounds	D	D
• secondary beams	F	P
• interaction of expt. and machine	C-	A-
• sociology	B	A+

Table I (cont'd)

(a) But don't forget Fermi motion.

(@) Only for pp experiments.

(c) Compromises — energy, intensity, special tricks, unequal energies.

---

where some entries are in the form of numbers and some are just letter grades. In some cases, we use the pass-fail option. The first entry is $\sqrt{s}$ which is a ridiculous notation for the energy available in the collision. Super ISR is listed as more than 400 GeV and Super FNAL (5 TeV) about 100 GeV. But I also made a note here, "Do not forget about Fermi motion", because for some special experiments 100 GeV can go surprisingly high paying a price in luminosity. Another entry is usable energy in the center of mass. Usable energy is not always all of the available energy and this depends, again, very much on the kind of experiment you do, and also on what comes next, which is luminosity. I think it is fair to say that a conventional accelerator can probably exploit the full energy available, 100 GeV. It has not yet been established at FNAL, but we will see that it is not terribly far away. For the ISR, whether you can use the full square root of s depends upon what you are talking about. Certainly for the exploration of totally new physics, production processes, it does not seem as if you will ever use the full energy unless luminosities are much, much higher than are being talked about. On the other hand, for tests of scaling, where you have various scaling parameters, for example $2p/\sqrt{s} \equiv x$, you want to make this vary over a very large range — then the mere fact that energy is available is useful.

The next entry in Table I is luminosity and I took for this what might be plausible, namely a beam of a few 10^{13} ppp which gives $\sim 10^{12}$ interactions per second for SNAL. For the Super ISR, I assumed $\sim 10^{33}\ \text{sec}^{-1}$, which gives 5×10^{7} interactions per second. That is luminosity. On the other hand, usable luminosity is a different thing. Usable luminosity for a conventional accelerator is relevant to experiments using primary protons which, if we look at FNAL, is a small fraction of all the experiments. Most of the luminosity at NAL is being used to generate secondary particles. That is how you can compensate for the fact that you have to build a 5 TeV machine to get a mere 100 GeV available. You make lots of secondary particles. Of course at the ISR you use the full luminosity — to date only $\sim 5 \times 10^{5}$ interactions/sec. Experimental techniques for surviving at the projected SISR rates are in principle on hand but have yet to be proved practical.

Again, even in pp experiments, it is not at all clear that the full luminosity at NAL is usable. At NAL recently, when the beam intensity reached 10^{13} particles, it was at times embarrassing, because if the proper experiments, for example neutrino experiments, are not running, even though the beam is split many ways, there are many experiments that cannot use the full luminosity. The apparatus just does not work. It is not easy to make full use of primary protons at the full intensity — you have to use tricks. However, it has been done in special cases and the important thing to note is that the intensity is there,

There are other entries like dwell time — how long do you sit to do an experiment. You sit as the ISR a long time because there are lots of compromises. Since you have many experiments around the ring, if one experiment wants high energy, and another experiment wants low energy, clever as the people at the ISR are, they have not yet been able to change the energy as one goes from one crossing region to the other. (I have a lot of confidence in them, and I expect that one of these days, they will solve the problem.) But until they do, it is a problem and so you have meetings at which one has to make a compromise, and at the ISR it is usually what Carlo Rubbia wants. To get your particular spectrum of conditions you have to wait a long time. Someone every once in a while comes in and he says, "I only want 1 A today." If he is convincing, we have to wait; there's the usual compromise. Now at NAL, for example, there is the new technique of the front porch, where several energies might be available at one time; this can certainly be a great help, and source intensities are no problem — many more groups can more or less control their own intensity, although that still needs some improvements. SNAL gets good grades for this.

Then there are things like experimental areas and flexibility, which are really quite a problem at a conventional accelerator. The bigger the accelerator, the bigger the problem. The experimental areas are complex, and costly, and not nearly as flexible as people hoped, certainly for NAL. Whereas relatively, I think, the experimental areas at the ISR are fairly simple — they are much smaller, physically, and more easy to rearrange. They also cost less.

Particle identification in doing experiments is a problem. Using a many TeV beam, if one scales Cerenkov counters, for example, one finds enormous lengths. A several mile long Cerenkov counter boggles the mind a bit. On the other hand, there may be other techniques that are, or may become much more useful at SNAL, e.g., the relativistic rise in the ionization loss, or perhaps transition radiation; there are techniques which are being developed and there is clearly a lot of interaction between instrumentation and the exploitation of accelerators. Particle identification at the ISR is easy in the forward direction because you can use Cerenkov counters of moderate length. Here, what is relevant is that at SNAL you are dealing with particles of many TeV, whereas at SISR one deals with particles of merely 100 GeV; now we have learned how to deal with those particles. On the other hand, the need to exploit the limited luminosity at ISR requires large aperture equipment and this means that it is much more difficult, say, at 90°, to do particle identification; most of the good particle identifiers have small apertures.

Backgrounds: Well, I find everywhere I go there are lots of backgrounds. I do not give good marks to any machine. This is probably my problem. Maybe electron machines are better. On the other hand, most of the cross sections I will show you that are of interest at NAL, or SNAL, are a much smaller fraction of the total cross section than they would be at SISR; so just the energy gives you a better grade for ISR's.

There is one thing that gives ISR types a bad grade, and that is the interaction of the experiment and the machine — what I call "real life at the ISR". You are very much coupled in with the machine at an ISR. It is well known that you cannot keep these clumsy experimentalists away from the machine, and every once in a while they knock something over, and the machine goes out for months — that is hard to avoid. Whereas at NAL, close contact between experimentalists and the accelerator proper is at a minimum.

Sociology in Table I just means how many physicists can you employ, and it is amazing how well the ISR does. But that is also because it is in Europe, where large groups were pioneered. We once counted 200 Ph.D.'s working at one time, and I do not think that NAL can beat that, although in principle it should. So I gave that a better mark anyway.

Well, now I want to sort of back up this report card with some information. The effect of Fermi motion, if you like, or essentially the nuclear physics boost you get from hitting a nucleus instead of a free proton, scaled up from the work we did at PPA and the Bevatron to NAL, is given in Fig. 5. In one collision out of 10^{5}, the 28 GeV that is usually available from a 450 GeV accelerator goes way up to 40 or 50 GeV. This is not an unmixed blessing, It is interesting for certain explorations if you have a good signal you can then ask about

a particle whose mass is 40 GeV. The same considerations will enable SNAL to go to ~ 140 GeV.

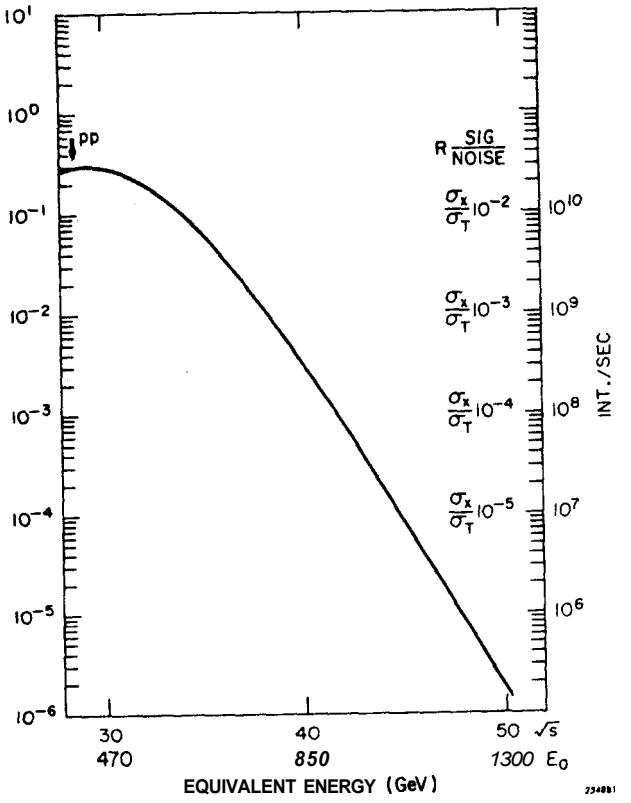


FIG. 5--"Fermi motion boost" at NAL (450 GeV).

I talked about usable luminosity, or using luminosity that is available. Let me *go* through a quick history of the ISR to illustrate this. Shown in Fig. **6** is a charged particle spectrometer, the Saclay-Strassbourg spectrometer, which has produced some nice results on charged-particle yields at 90^{o}. You see the crossing region and you see the spark chambers and the magnet, more spark chambers, and other identifiers. The total solid angle of this apparatus is of the order of 0.01 steradian. I would like to contrast it with another approach at the ISR, which was the so-called CCR experiment, which insisted on having *a* very large coverage, about 1.0 steradian on each side, This experiment was interested in large, transverse momentum π^{o}'s, and tracked a yield curve out to a transverse momentum of ~ 9 GeV. It stopped running at the end of 1972, and here it is in 1974 and the spectrometers, of which there are several working at the ISR (one is shown in Fig. 7), have still not really gone beyond about 4 or 5 GeV, to my knowledge. *So* the use of the luminosity is not a trivial thing, and one pursues this problem.

Here is a picture of what our groups hopes to do next at the **ISR,** which is essentially a 2π spectrometer (Fig. 8). This is a now super-conducting magnet, with spark chambers inside, and glass outside to look at γ rays, and a wall thickness of only –1 radiation length, so that one does not disturb the photons too much. This would help the ISR in achieving luminosity times solid angle, which might *go* up by a factor of ~ 50 or so above the previous generation of experiments.

The same sort of thing happens at NAL. The next figure, Fig. 9, is useful for comparing SNAL against the SISR. Here is a Cronin-Piroue data on production of pions. Note that they have, in fact, a rather small aperture but still they are able, with some trouble, to achieve cross sections of the order of $<10^{-37}$. In terms of exhausting the kinematic limit you see data out to $x_{\perp} \sim 0.7$ where the maximum value of the accelerator is 1; you see they are not too far away.

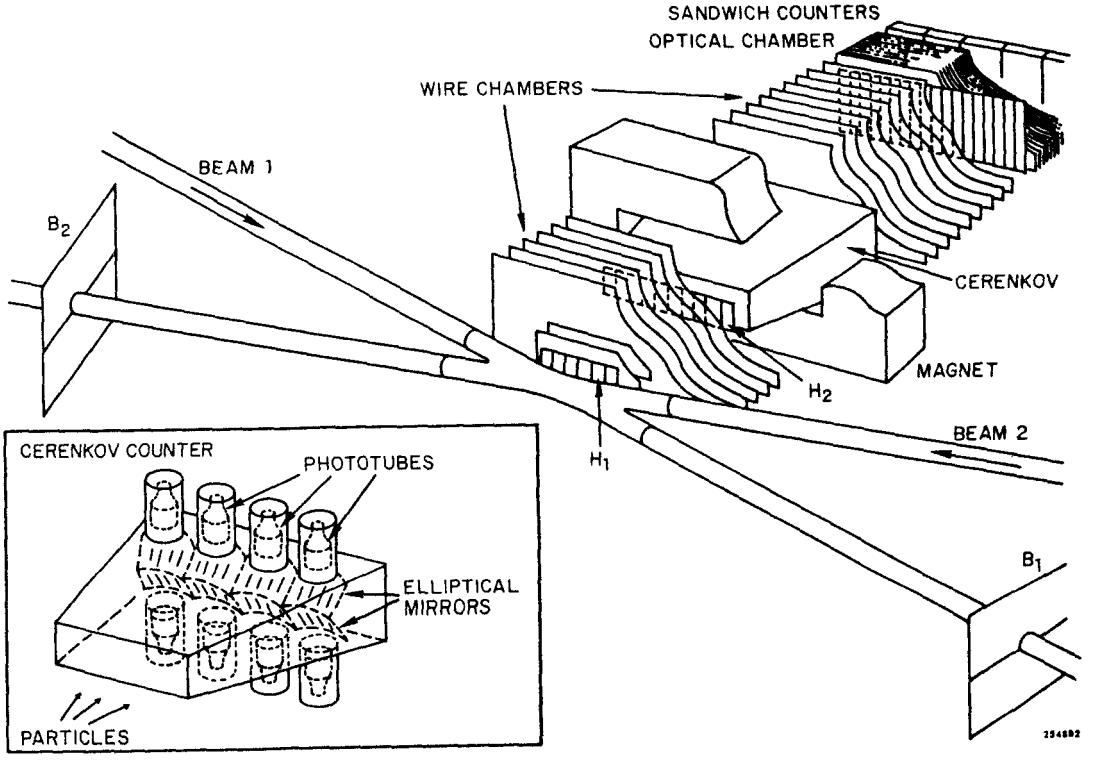


FIG. 6--The Saclay-Strassbourg Spectrometer at ISR.

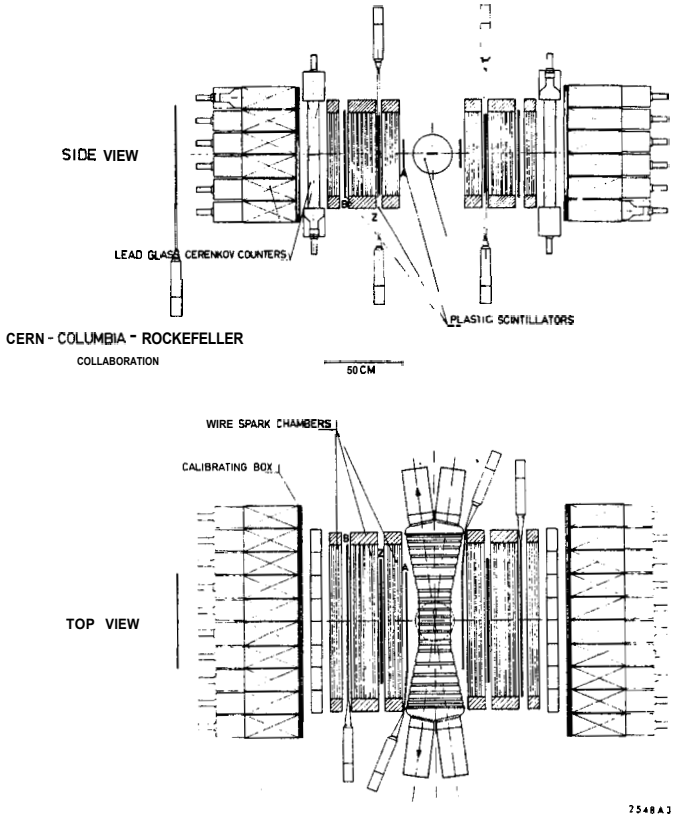


FIG. 7--The CCR Experiment Spectrometer at ISR.

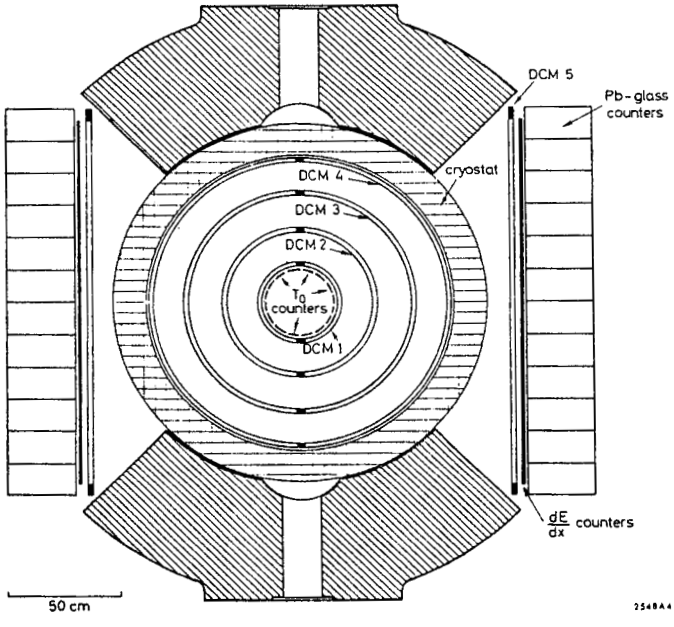


FIG. 8--A planned 2π Spectrometer at ISR.

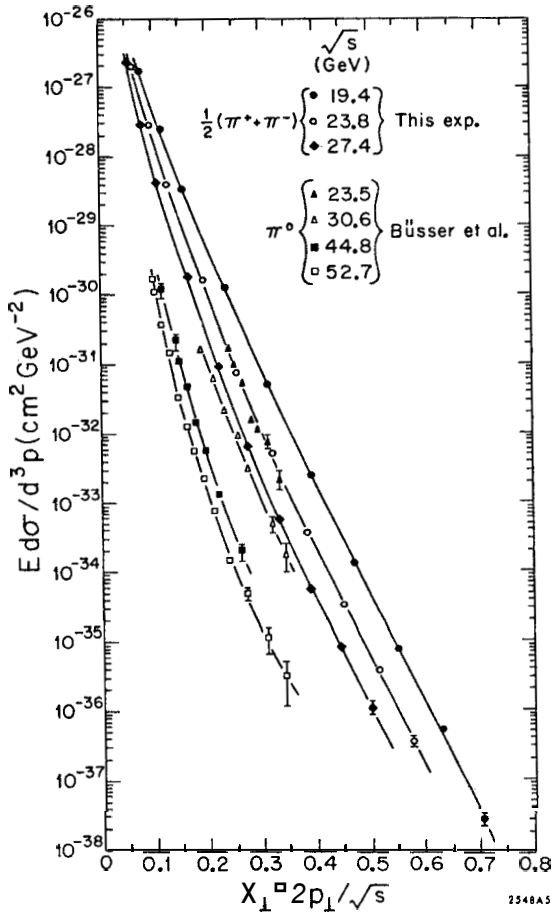


FIG. 9--Cronin-Piroue data on pion production.

And this is a very early NAL experiment. The comparison with data taken at ISR is given in Fig. 9, where even though the ISR energy is much higher, the luminosity is such that with a reasonably good solid angle, one could not go above $x_\perp \sim 0.4$. This is a good example. Energy you have, but limited luminosity prevents you from exploiting it fully. Of course, that was one stage. One hopes one will be able to go on, in both experiments. We will always be more inhibited at the ISR. This is the luminosity price.

Now let me go on to some other experiments. Figure 10 is the famous rising total cross sections. There is some bubble chamber data from NAL and there are the famous ISR experiments showing this rising cross section. New data from the total cross section group at NAL have experimental points which also show a rise with statistical errors in this region of the order of one or two-tenths of a percent. So here, again, you see a comparison between an ISR experiment where you have difficult experiments with fairly large error bars, but a big handle in s, as opposed to very precise experiments over a more limited range of s. What is even more interesting about the NAL approach is that they also have cross sections (Fig. 11, 12), for π's K's, and antiprotons, incidentally all of which look as if they were rising

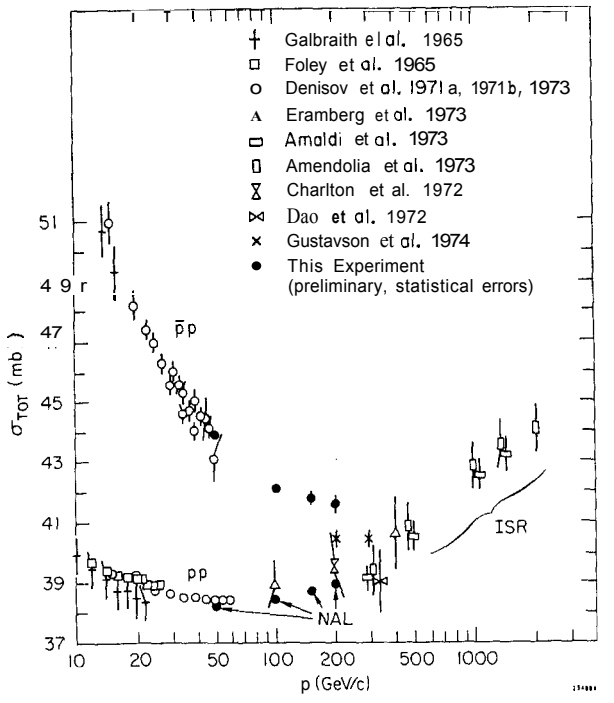


FIG. 10--The proton-proton total cross section.

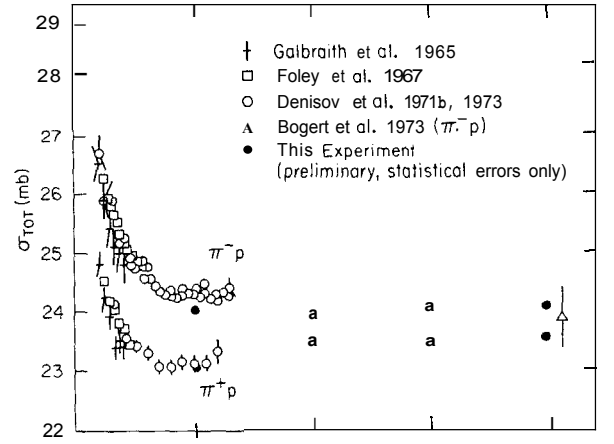


FIG. 11--The $\pi^{\pm}$p total cross sections.

in this region. And it seems to me that in any incisive elucidation of this phenomenon, the need for secondary particle cross sections is also important. And perhaps I ought to leave this as a question: would theory be totally happy having only the proton-proton data?

The next Figure **(13)** deals with an extrapolation of total *cross* sections under various current theories and some possible SNAL and SISR "results". Following this (Fig. **14)** is a multiplicity extrapolation and then (Fig. **15)** a slope parameter in elastic scattering. The "stretch" in rapidity for ISR, SNAL and SISR in two current models is given in Fig. 16. Here was a clear ISR break since the NAL parameter s cannot extend far enough — only the ISR could discover the "central plateau".

Let me go on to some other experiments, and extrapolations thereof. Figure 17 is a strong interaction experiment which is a continuation of high p perpendicular, proton plus proton goes to pion plus anything. This is an extrapolation of

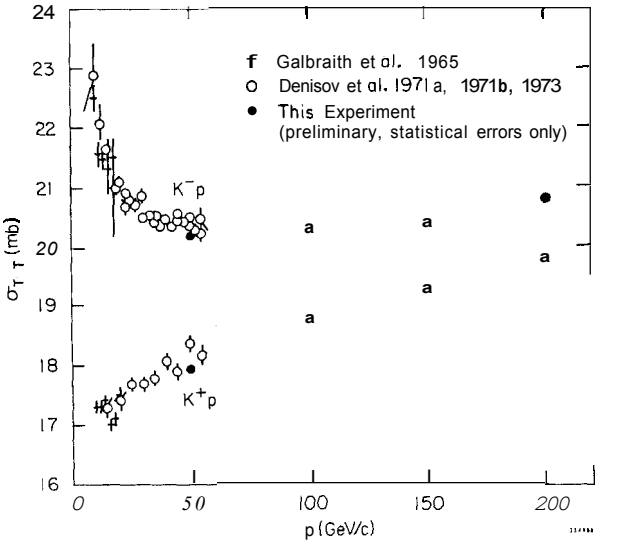


FIG. 12--The $K^{\pm}$p total cross sections.

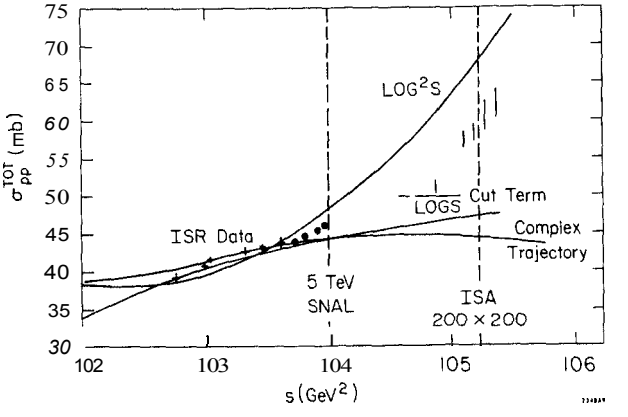


FIG. 13--Model-dependent extrapolation of the proton-proton total cross section.

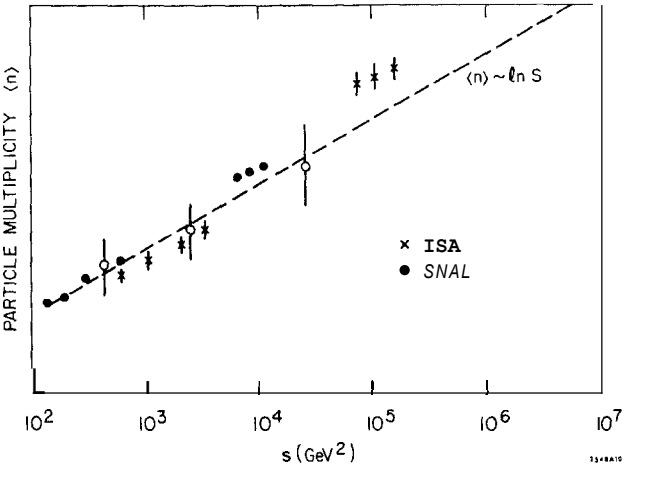


FIG. 14--ℓn s extrapolation of the particle multiplicity.

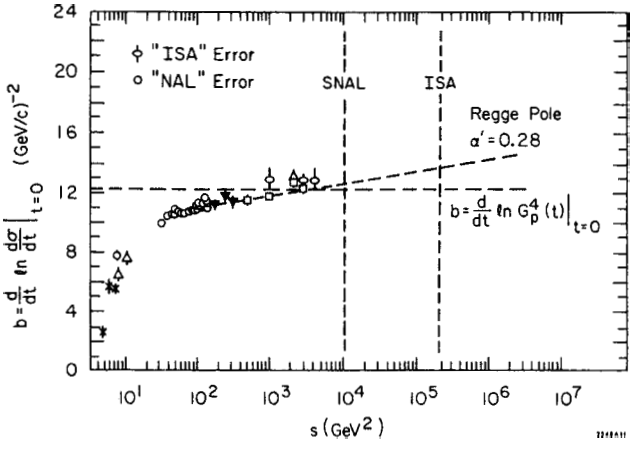


FIG. 15--Slope parameter in proton-proton elastic scattering.

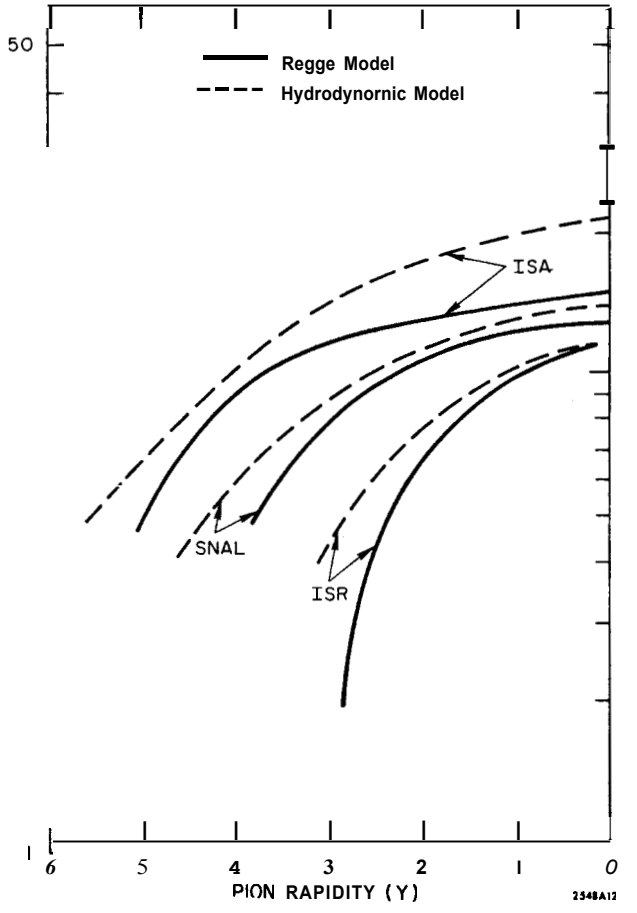


FIG. 16--Two model-dependent extrapolations of the pion rapidity distribution at ISR, Super NAL, and ISA.

ISR data, to SNAL and SISR and you see that 20 GeV/c is observable if one can go to cross sections like 10^{-39}, and I think that is certainly possible for SNAL. On the other hand, for an ISR I think it is very hard to go say, below 10^{-37}, but this also gets to ~20 GeV/c.

The two machines in this particular piece of physics, where the s dependence is not very dramatic, are roughly equivalent. SNAL however permits additional information to come from incident pions, kaons, and $\bar{p}$'s. On the other hand, one of the things which is most intriguing to me in high

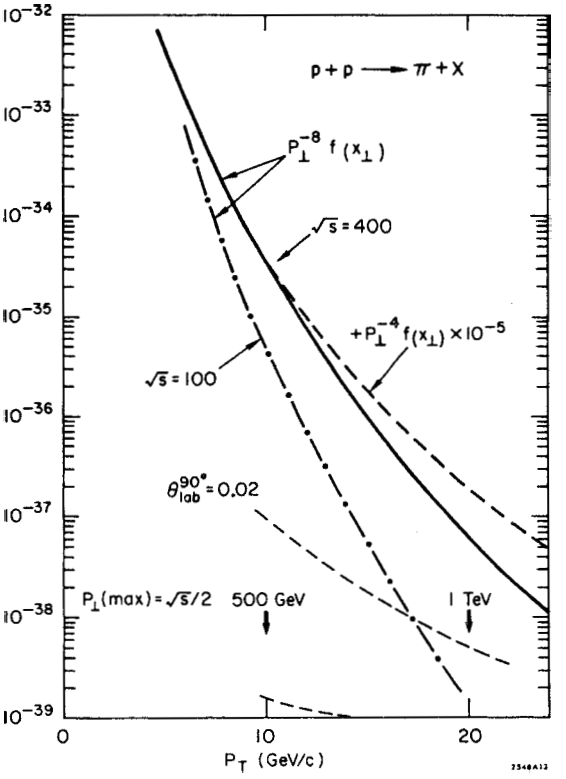


FIG. 17--Cross sections at $\theta_{cm} = 90^0$ for inclusive production of π mesons, as a function of the transverse momentum of the π meson.

$P_\perp$ phenomena is the possibility of observing interference effects between strong and electromagnetic, or between strong and weak interactions. One does not really know where those interference effects take place — they may take place near $P_\perp \sim 15$ GeV/c, or maybe a little bit beyond. And here you might, then, look at strong interactions for violation of discrete symmetries in order to detect such interference. You might look for, say, parity violation, and so on. For that reason, you are certainly led to a greater interest in the high energy. And that will be primarily true, in general, for weak interactions.

Figure 18 shows another way to look at it. This is a sort of kinematic region from the point of view of testing any scaling laws for deep inelastic stuff, and clearly SISR takes you out a long way in s; on the other hand, SNAL covers a big chunk too.

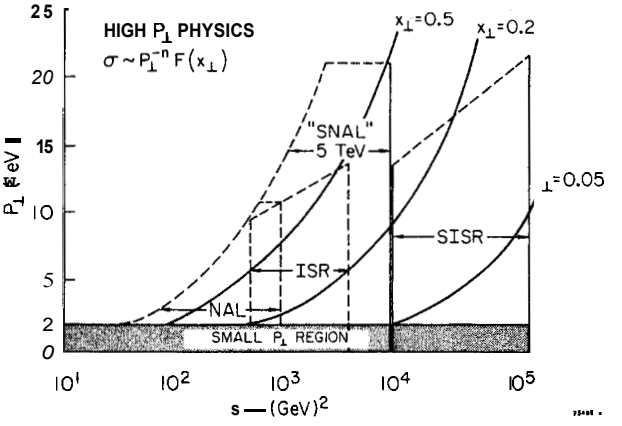


FIG. 18--Regions in s(GeV^2) and $P_\perp$ (GeV) available to NAL, ISR, Super NAL, and Super ISR.

Figure 19, shows a case of looking at electromagnetic interactions with proton machines, again in a large storage ring, one can (if one believes in these extrapolations which are admittedly model dependent, maybe totally wrong, but which are at least thinkable) explore masses, look for things

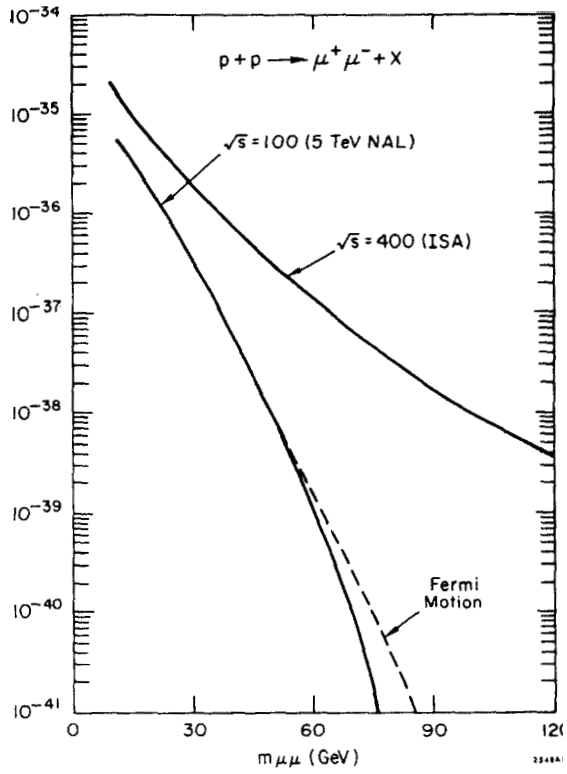


FIG. 19--Electromagnetic interactions with a proton machine; μ-pair production at a 5 TeV NAL and ISA.

up to enormously large masses, because again if we can reach 10^{-37} we seem to have sensitivity out to about 60 GeV of mass. Again, though, if you look down here at 10^{-39}, you see that you have about the same limit with a conventional accelerator. Why would you want to do this sort of thing? Well, there are several reasons. One is, you would like to look for bumps, you would like to look for the Z_0's, and a Z_0 on a background of this kind would presumably show up as some resonance in the effective mass of $\mu\mu$ or ee or whatever lepton pair you look for. Also, if the continuum does have some size which can be measured, one wants to answer questions of scaling, and you might also want to calibrate the search for intermediate bosons, which presumably have the same hadronic part but an interesting and new leptonic part. Figure 20 shows one of a long series of things that can be made with the virtual photon flux discovered in Fig. 19. These are heavy leptons. These curves are steep and so SISR, for the first time, really takes over (up to $m_L \sim 80$ GeV). Other "things" calibrated by Fig. 19 are quarks, monopoles and, in fact, anything that can be pair produced at say, PEP. We DO NOT discuss the relative experimental problems without bullet proof vests.

We now come to what could be the most interesting point: weak interactions, The main point about pp collisions is, of course, that you have such high energy. Somehow we have to be freed of the tyranny of doing neutrino physics. At the moment we are stuck with it, but it may be that one can never do weak interactions with protons because the effective signal is too small. One does not know yet. In perhaps two or three years, one will know whether this is a feasible reaction. There are two ends here: one is actual production of the intermediate boson, and the other is weak interactions without an intermediate boson.

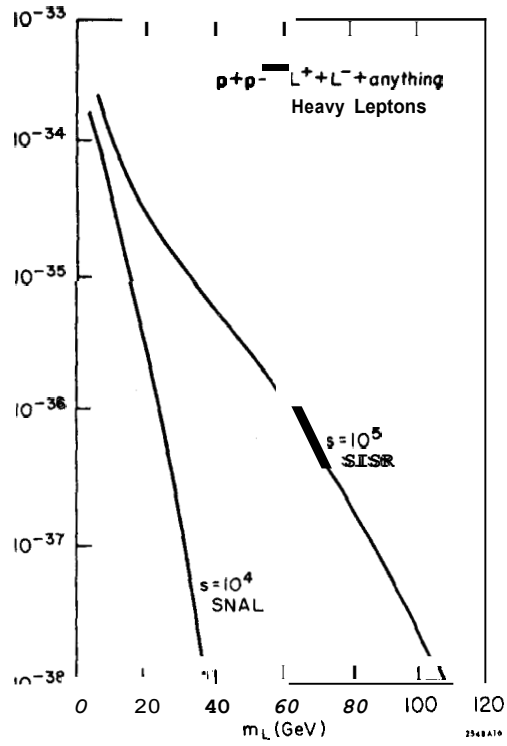


FIG. 20--Heavy lepton production as a function of lepton mass at Super NAL and Super ISR.

Figure 21 shows that, at $\sqrt{s}$ = 400 you have a signal which might be measurable out to beyond $Q^2 = (100\ \text{GeV})^2$. Remember that in number of events, one multiplies by 10

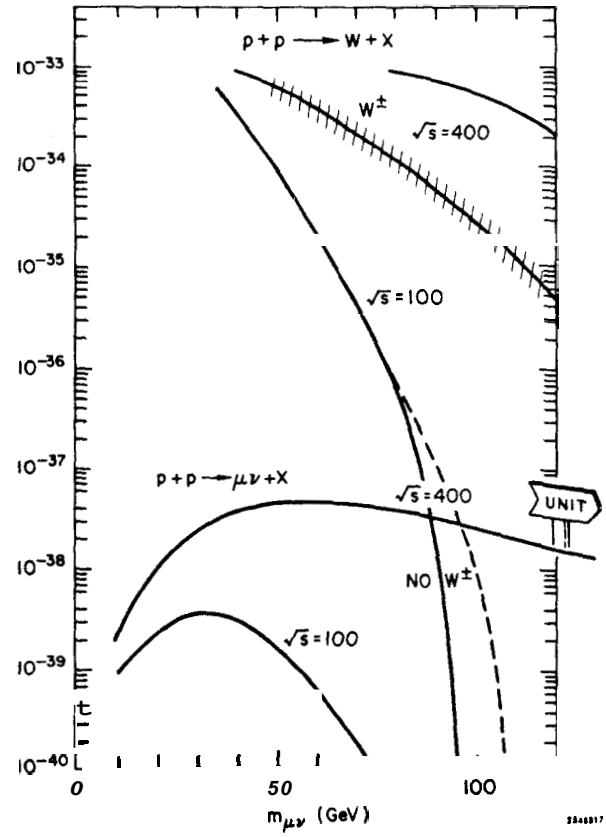


FIG. 21--Production of W boson or $\mu\ \nu$ in proton-proton scattering.

if one takes a reasonable bite in Am. So there are of the order of a hundred events per day, and one can track this thing out and answer one of the crucial questions of weak interactions as to what happens at very, very high values of the effective lepton mass. Strictly, there is no unitarity limit in this reaction. On the other hand, one knows that for a four fermion interaction at a center of mass energy of some hundreds of GeV, unitarity breaks down. Whatever physics intercedes should show up in a reaction of this kind at high masses. That is the force of this kind of research. All of this is to say that ISR's may be useful for weak interactions. They may even be useful for such esoteric things as neutral currents, e.g., interference between virtual Z^0 and γ's to produce lepton pairs. We know NAL type machines can also study these questions, but not much beyond ~ 50 GeV. Experimentally, there is reasonable hope that backgrounds of ~100 GeV/c transverse momentum objects from non-weak sources will be manageable. Missing transverse momentum signalling a neutrino will also be helpful.

We now go to the report card about secondary beams. There is simply an enormous amount of stuff that still wants to be done at the next level of energies. For example (see Fig. 22), elastic scattering of secondary particles, total cross sections, hyperon interactions, high $P_\perp$ events for not

1. π, K, $\bar{p}$ elastic
2. π, K, $\bar{p}$ total
3. hyperon-nucleon scattering
4. high $P_\perp$ for $\pi p \rightarrow$ hadron + anything
5. resonances $Kp \rightarrow$ hadron +anything
6. K^0 physics pp — hadron+ anything

$\sqrt{s}$ ~ 80 GeV

7. muon beams — 10^7/sec up to 3 TeV

   μp scattering

   Brems. (QED)

   μ^* Prod.

   Universality etc.
8. electron beams — prob. similar
9. y-beams, even polarized!
10. neutrino beams E_ν — 2 TeV

    very high σ will permit

    more civilized detectors

    But: shielding! up ve!

FIG. 22--Secondary beam possibilities at Super NAL.

only protons but also the other particles because the quantum number effects may be revealing. The resonances are things which have to be pursued and which with storage rings will be very difficult. There is K^0 physics, and maybe some elucidation of the CP problem, maybe that we are stuck with K mesons and have to do more experiments of that kind. Then going to electromagnetic interactions there are photon beams of interesting intensity and these may even be polarized by crystal techniques. There are muon beams of the order of 10^7/sec, up to perhaps 3 TeV. Now that should be a very beautiful thing for scattering, for tests of QED, at center of mass energies of the order of 100 GeV, for perhaps searches for heavy leptons, and tests of μe universality. And for some sort of clue to the Bjorken formula we saw before. Presumably at these accelerators you could also make electron beams, like muon beams, with similar intensities. Then, of course, in weak interactions there are neutrino beams, and to have a 2 or 3 TeV neutrino beam with the consequently much higher cross sections might permit more civilized detectors, detectors which may not be so big. There is, of course, the problem of shielding, which I have not solved with these high energy machines, but somebody will solve them.

Let me discuss electron-proton scattering. I did say that ep can be done two ways — storage mechanism or via conventional accelerator. One usually looks at a kinematic domain, q^2 vs u where we compare a 15 GeV e against 200 GeV p storage ring solution to the problem, with muon beams of 3 TeV. Using 10^7 muons and a reasonable target I get a muon luminosity of 5×10^{33}, roughly get a factor of 50 improvement over storage ring in luminosity. Off hand, in Fig. 23, it looks as if a very large kinematic range is

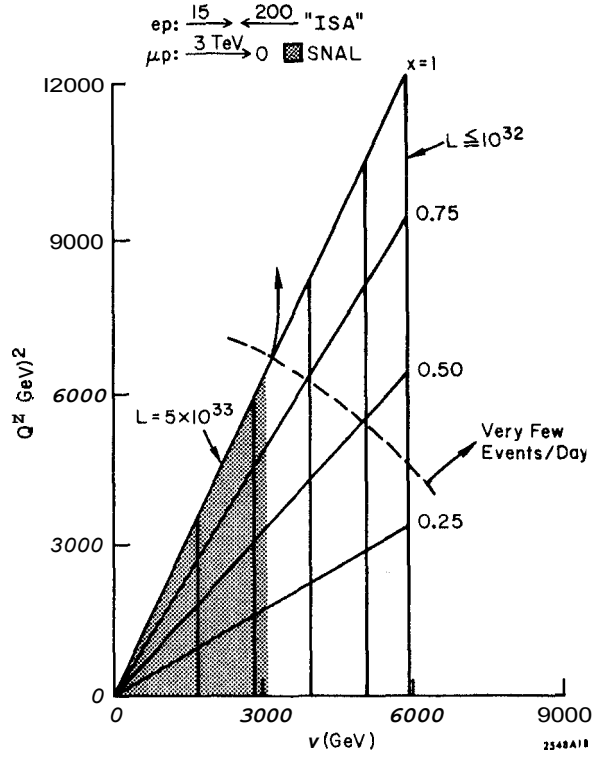


FIG. 23--Availalbe ν (GeV) - Q^2 (GeV^2) regions in lepton-proton scattering: comparison of ep storage ring (ISA) and μp conventional accelerator (Super NAL).

exposed by ep storage rings. On the other hand, if one looks at the numbers, one finds that in a large part of this plot the number of events per day is very small. So if one says, "Well, one can do good physics with a very small number of events per day", then of course the whole thing is relevant. If one says, "You really cannot learn anything very incisive from a very small number of events per day", then the two experiments look more competitive, with greater flexibility, e.g. in secondary particle detection, going to the muon approach.

I briefly considered alternatives to the e^+e^- storage question and could only come up with the "Fermi accelerator" Fig. 24 to compete with 15 GeV × 15 GeV e^+e^-. Conventional magnets are used. Rumor has it that Wilson wants the real estate for 100 kG superconducting magnets. This way he would feel challenged. For storage rings of course.

My conclusions are that a ~ 10 year program must include both proton storage rings and a fixed target proton accelerator. The graphs here indicate that a good match would have the Super ISR with ~ 6 -10 times the $\sqrt{s}$ as



FIG. 24

a "conventional" Super-NAL, that is, the example I chose finds the two machines too closely matched. Costs become a crucial matter. We need e^+e^-, and probably in the form of storage rings. As NAL and ISR develop, in the next few years we will see how sound the comparisons made here turn out. I hope that in the next few years, also, that we will find enough things to shake what I thought was the great complacency of Gell-Mann in saying that he sees in the air the ultimate theory. I hope we can spoil that. We will surely try.

DISCUSSION

Murray Gell-Mann,(California Institute of Technology): Can you give some idea of the cost?

Lederman: You want to know how much a 5 TeV accelerator will cost. I have no idea. I don't think a reasonable estimate is possible. I can give you a number that no one can prove that's impossible, a number like 200 million dollars can not be proven an impossible number.

PERSPECTIVES ON COLLIDING BEAMS

E. Keil
CERN
Geneva, Switzerland

Summary

The design and performance of colliding beam devices is restricted by two different kinds of limitations: those due to technology and funds, and those due to space charge phenomena. Among the technological limitations are maximum magnetic fields, RF power, and the stored energy of the beams. The space charge limits are determined by single-beam and beam-beam phenomena, such as the stability of coherent longitudinal and transverse oscillations, or the incoherent beam-beam tune shift. The aim in the design of a colliding beam device is to achieve the best possible luminosity within all these limits. Procedures for determining appropriate machine parameters which include all constraints from the beginning, have been developed. The resulting parameter sets will be compared to those of machines under study at present. The design procedures also allow predictions how the parameters and luminosity of future colliding beam devices would change if some or all of the technological limitations were to occur at a different level.

1. Introduction

The beam dynamics and technology on which the design of storage rings is based are essentially the same for both electron and proton machines. There are, however, important differences such as synchrotron radiation. The discussion will be presented under two main headings

- electron storage rings
- proton storage rings.

Since no electron-proton machine has as yet been built it would appear too early to make predictions for the parameters of the next generation of these machines.

For each kind of machine, the requirements which have to be satisfied in order to achieve a high luminosity will be reviewed first. They can be cast into a series of design equations which link their design parameters. It turns out that a fairly detailed picture can be obtained by choosing a rather small number of parameters. Their choice is guided by extrapolation and scaling from existing machines. Finally, examples of machines beyond those presently contemplated will be shown which are designed according to these principles.

2. Electron storage rings

The principles for the design of an electron storage ring have been known for a long time[1]. The storage ring SPEAR[2] has been designed accordingly. The operating experience with ADONE[3] and SPEAR' has recently led to some changes in the design principles[5] which are being incorporated in the design of the electron-positron part of PEP[6]. The following presentation follows essentially Ref. 5. It is assumed that the electron and positron bunches collide head-on, i.e. they follow the same trajectory in opposite directions in the vicinity of the interaction point.

2.1 Luminosity and beam-beam tune shift

Apart from the energy of the colliding particles, the luminosity per intersection L is the most important parameter of a storage ring as far as its usefulness for colliding beam physics is concerned. It is given by

$$L = \frac{N^2 f}{4\pi k \sigma_x^* \sigma_Y^*} \tag{1}$$

N is the total number of particles in one beam, f is the revolution frequency, σ_x^* and σ_Y^* are the rms beam horizontal (x) and vertical (y) radii at the interaction point, k is the number of bunches in one beam. In (1), the rms bunch half length σ_ℓ does not appear because it has been assumed that it is smaller than the amplitude functions β_x^* and β_Y^* at the intersection point.

The beam-beam interaction at the crossing points is usually accompanied by the electromagnetic effect of one beam on the other. It has become customary to describe the strength of this essentially non-linear perturbation by the linear tune shift given to particles close to the axis of the other beam.

The beam-beam tune shifts in the two directions are given by

$$\Delta Q_y = \frac{N r_e \beta_y^*}{2\pi k\, (\sigma_x^* + \sigma_y^*)\, \sigma_y^* \gamma} \tag{2}$$

$$\Delta Q_x = \frac{N r_e \beta_x^*}{\pi k\, (\sigma_x^* + \sigma_y^*)\, \sigma_x^* \gamma} \tag{3}$$

Here, r_e is the classical electron radius and γ is the usual relativistic parameter,

The recent treatment[5] differs from the previous one[1] by assuming head-on collisions and, consequently using products of beam radii in (2) and (3). This reflects the experimental observation in ADONE[3] and in SPEAR' that crossings at an angle do not yield a higher luminosity although in this case the product of beam radii is replaced by a - bigger - effective beam cross section.

It is most instructive to eliminate one power of N, from (1) by using (2). This manipulation yields

$$L = \frac{N f \gamma \Delta Q}{2 r_e \beta_y^*} \tag{4}$$

It has been assumed that $\sigma^* >> a_Y^*$.

Equation (4) holds for any N and any ΔQ_y provided that the approximations used in its derivation are satisfied. However, it gains its full significance by interpreting it in the following manner: if ΔQ_y is replaced by its maximum permissible value ΔQ, and if the beam dimensions at the interaction point are chosen such that (2) and (3) hold then (4) gives the maximum luminosity which can be achieved in an electron storage ring with N electrons in each beam.

It is interesting to note how little one has to know about a storage ring in order to estimate its luminosity. The maximum beam-beam tune shift ΔQ is believed to be a universal constant. There are two lower limits for β_y^*, the bunch length and high values of β_y at the ends of the intersection region which are a consequence of low values of β_y^*. The most important outstanding parameter is N which is entirely determined by single beam phenomena.

Looked upon in a different way, *(4)* is just a formal expression which relates the luminosity to a small number of as yet unknown parameters. All the difficulties of designing storage rings are hidden in these parameters.

2.2 Synchrotron radiation

In electron machines the synchrotron radiation is by far the most important single beam phenomenon. The power loss P which has to be compensated is given by[1]:

$$P = \frac{4\pi}{3} r_e m_e c^2 \gamma^4 N f \rho^{-1} \qquad (5)$$

Here ρ is the bending radius of the electron beam and $m_e c^2$ is the electron rest mass. It is customary in electron storage ring design to use *(5)* to eliminate Nf from *(4)*. In this case the luminosity becomes:

$$L = \frac{3}{8\pi} \frac{\Delta Q \, \rho \, P}{r_e^2 m_e c^2 \gamma^3 \beta_y^*} \qquad (6)$$

The interpretation of this equation is the same as that of *(4)*.

Clearly, there are many space charge phenomena in electron storage rings which have caused difficulties in their initial operation, but, which on the whole have been overcome later on. For this reason, they have not been included in the design procedure.

2.3 Design procedure

2.3.1 Outline

For a given energy y, the luminosity (6) depends only on *4* parameters: ΔQ, ρ, P, β_y^*. Fixing all of them determines L. If R/ρ is fixed, N follows from (5). Fixing k and imposing upper limits on ΔQ_y and ΔQ_x, gives, from *(2)* and (3), upper limits on $\beta_y^*/(\sigma_x^* \sigma_y^*)$ and on β_x^*/σ_x^{*2}. These expressions are taken at the interaction point. In order to obtain a machine design, they have to be related to the beam size and lattice parameters in the normal machine lattice. If one assumes that there are no dispersive elements - and also no dispersion matching - between the machine lattice and the interaction point, then the ratio β_x/σ_x^2 is an invariant. It is, in fact, given by quantum fluctuations in synchrotron radiation and becomes approximately[1]

$$\frac{\sigma_x^{*2}}{\beta_x^*} = \frac{\sigma_x^2}{\beta_x} = \frac{3 C_q}{2} \cdot \frac{R}{Q^3} \frac{\gamma^2}{\rho} \qquad (7)$$

where $C_q = 3.84 \times 10^{-13}$ m. Since all parameters in (7) except Q are known, this equation determines the maximum Q-value Q_{max} in the machine lattice. The actual value of Q must be smaller than Q_{max} and be compatible with the requirements on the working point.

In addition, there is the contribution to Q from the insertions which is not included here.

For a given Q and a chosen phase advance per period, the parameters of the period are completely determined, such as β_{max}, β_{min}, length, and quadrupole focal length. The radial beam size in the cells follows from (7). To complete the description of the machine, $\sigma_{y_{max}}$ and β_x^* are still to be determined. They are related by (2) and the usual scaling of σ and β, $\sigma \sim \beta^{1/2}$:

$$\frac{\beta_y^*}{a_x^* \sigma_y^*} = \frac{\beta_{max}}{\sigma_{x_{max}} \sigma_{y_{max}}} \left(\frac{\beta_y^*}{\beta_x^*} \right)^{1/2} \qquad (8)$$

If r is defined so that $\sigma_{y_{max}} = r \sigma_{x_{max}}$, (2), (7) and (8) can be manipulated to give

$$r^2 \beta_x^* = \beta_y^* \left(\frac{Q}{Q_{max}} \right)^6 \qquad (9)$$

Since only the product $r^2 \beta_x^*$ is fixed by (9), r and hence the vertical beam size can be chosen freely, and β_x^* fixed afterwards to maximize the luminosity. In order to save vertical aperture, $\sigma_{y_{max}}$ is fixed at $\sigma_{y_{max}} = 1$ mm, resulting in a vertical aperture A_y of *40* mm, half of which is for closed orbit errors. Allowing 20 $\sigma_{y_{max}}$ for the beam gives a good beam lifetime and ample allowance for the change in the beam size due to the beam-beam interaction. The horizontal aperture A_x is determined in the same way.

The peak RF voltage V required is determined by the radiation loss/electron U which follows from the total power P and the number of electrons. V has to be higher than U by the overvoltage ratio q required to achieve a given quantum lifetime τ_q. The latter is related to the damping time τ_s by a pair of transcendental equations[1].

2.3.2 Results

A machine designed according to the procedure just described is the preliminary design of a 15 GeV electron-positron storage ring[5] which is compatible with the current PEP design[6]. Its parameters are summarized in Table I.

In order to demonstrate where electron storage ring design may lead to in the future, the parameters of this machine are scaled to an even higher energy. Consider a step in energy by a factor $10^{1/2}$, i.e. from 15 to about 50 GeV. In order to keep the luminosity constant which is the bare minimum in view of the rapid decrease of most of the cross sections involved, the radius of the machine is assumed to go up by a factor of $10^{3/4}$, and the RF power by a factor $10^{3/4}$. This choice fixes the machine design apart from the RF parameters which are chosen to yield a constant quantum lifetime. The results are also shown in Table I.

TABLE 1

Comparison of electron storage ring parameters

E/GeV	15	50
$L/cm^{-2}s^{-1}$	10^{32}	10^{32}
R/m	220	1240
R_0/m	318	1790
ρ	0.75R	0.75R
ΔQ_y	0.06	0.06
ΔQ_x	$\leq$ 0.06	$\leq$ 0.06
k	2	2
f/kHz	150	26.7
β_y*/m	0.2	0.2
P/MW	2.77	15.6
σ_x^{*2}/β_x/cm	$\geq 5.4 \times 10^{-5}$	3.0×10^{-5}
$\sigma_x^*\sigma_y^*/\beta_y$/cm	$\geq 5.4 \times 10^{-5}$	3.0×10^{-5}
N	4.25×10^{12}	7.56×10^{12}
Q	10	27
β_{max}/m	59	127
β_{min}/m	10.1	21.8
$\sigma_{x_{max}}$/mm	6.3	6.2
$\sigma_{y_{max}}$/mm	1	1
β_x*/m	5.21	6.21
A_x/mm	146	144
A_y/mm	40	40
τ_s/ms	3.7	3.7
τ_q/s	10^4	10^4
U/MeV	27	480
q	2.2	1.36
V/MV	60	650

It may be seen that a machine at 50 GeV energy requires a very large RF voltage and RF power, and that it has a very large radius. This may indicate that the technological limit for electron storage is below 50 GeV. Since this limit is so much influenced by synchrotron radiation it appears rather difficult to overcome.

3. Proton storage rings

Practical experience on proton storage rings is available from a single machine, the ISR[7]. In addition, there have been a few design studies[8,9,10], but there is no established design procedure for this type of machine. Below, an outline of such a procedure is presented. It is assumed that the proton beams are unbunched and collide at a small angle.

3.1 Luminosity and beam-beam tune shift

When the proton beams collide at an angle such that they are well separated at the ends of the free intersection space, the luminosity L obtained is given by:

$$L = \frac{c\lambda^2}{\pi^{\frac{1}{2}}\sigma^*\alpha_0} \tag{10}$$

Here c is the velocity of light, λ is the line (number) density of protons, and α_0 is the crossing angle. It has been assumed that the rms beam radii σ_x^* and σ_y^* are equal to σ^*.

Under the same assumptions, the beam-beam tune shift in the x direction is:

$$\Delta Q = \left(\frac{2}{\pi}\right)^{\frac{1}{2}} \frac{\lambda r_p \beta^*}{\gamma\sigma^*\alpha_0} \tag{11}$$

Here, r_p is the classical proton radius and β^* is the value of β_x and β_y at the interaction point. It has been assumed that the crossing takes place in the vertical plane. In this case $|\Delta Q_y| \leq |\Delta Q_x|$ always holds for a round beam.

The above expressions are all approximations. They are valid for beams which are well separated at the end of the free space around the intersection point, and for values of β^* which are not too small. The optimum choice of β^* will be discussed below. Accurate formulae for round beams[11,12] and for elliptic beams[13] are available.

If the tune shift (11) is again used to replace one power of A in (10) the following formula is obtained:

$$L = \frac{c\gamma\ \lambda\ \Delta Q_x}{2^{\frac{1}{2}}\ r_p\ \beta^*} \tag{12}$$

Although this is valid for all values of λ and ΔQ_x it may again be interpreted as an expression for the maximum value of the luminosity which can be obtained in a proton machine, if the crossing angle and/or the beam dimensions are adjusted so that (11) holds with ΔQ_x replaced by its maximum permissible value.

It can be shown[12] that the luminosity L reaches an asymptotic value when β^* decreases, and that $\frac{2}{3}$ of that luminosity are obtained when β^* is chosen as follows:

$$\beta^* = \left(\frac{\Delta Q_x E_t\ \ell}{8\pi\ \lambda\ r_p}\right)^{\frac{1}{2}} \tag{13}$$

Here $E_t = 4\pi\beta\gamma\sigma^{*2}/\beta^*$ is the normalised transverse emittance, and ℓ is the free length around the interaction point. With the choice (13) for β^* the luminosity becomes:

$$L = \frac{4}{3} c\gamma \left(\frac{\pi\lambda^3\ \Delta Q_x}{E_t\ \ell\ r_p}\right)^{\frac{1}{2}} \tag{14}$$

3.2 Single beam limits

In proton machines there is no one phenomenon which is clearly more important than all the others. Therefore it is appropriate to include many of them in the design procedure right from the start and to let the latter itself find out which are the most important. The discussion below is based on present knowledge of these phenomena, i.e. any new developments which may make them less severe are not taken into account.

3.2.1 Incoherent tune shift

In the highly relativistic limit where the contribution of the direct space charge effect to the incoherent tune shift is negligible compared to the contribution of images, the standard formula[14] may be written as follows:

$$\Delta Q_I = \frac{N r_p R}{\pi Q \gamma}\left(\frac{E_1}{h^2} + \frac{\rho}{R}\,\frac{E_2}{g^2}\right) \tag{15}$$

Here, h is the half aperture of the vacuum chamber and g is the half height of the magnet gap, and magnets are supposed to occupy only a fraction ρ/R of the circumference. E_1 and E_2 are image field coefficients which depend on the shape of the vacuum chamber and magnet polepieces, respectively. For the parallel plate geometry of a separated function machine one has[14]:

$$E_1 = \frac{\pi^2}{48} \qquad E_2 = \frac{\pi^2}{24} \tag{16}$$

Assuming that g and h are equal and calling the half aperture b, (15) can be brought into the form:

$$\Delta Q_I = \left(\frac{\pi^2}{24}\,\frac{r_p E_p}{e^2 c^2}\right)\frac{I}{B_M b^2}\cdot\frac{R}{Q}\,\frac{R}{\rho}\left(1 + \frac{2\rho}{R}\right) \tag{17}$$

Here $E_p = m_p c^2$ is the rest energy of the protons and B_M is the field strength in the bending magnets. The somewhat strange form of (17) is chosen because it will turn out to be rather convenient to write the design constraints in a form which links the beam dynamics parameters directly to engineering parameters which by experience only take values within rather narrow limits.

It will turn out throughout that the aperture of the vacuum chamber and hence of the magnets is not determined by the space required for the beam proper or for closed orbit errors, but is necessary to remove the walls far enough from the beam so that their effects become small. This, naturally, leads to a circular or nearly circular vacuum chamber. Its cross section should have as few variations as possible in order to avoid the inductive impedances and the cavity resonances associated with them.

In the case of a beam centered in an exactly circular chamber the first term in the bracket vanishes. Hence (17) is pessimistic. This has been confirmed by a recent calculation[15] of the image field coefficient E_1 for a beam with an arbitrary position in an elliptic chamber.

In the design of a storage ring one wants the single beam tune shift to be below a given limit. Hence (17) is a design constraint which the machine parameters must satisfy. In particular, it may be considered as an equation for the current I_q which can be stored in a machine.

3.2.2 Transverse resistive wall instability

The resistive wall instability[16] is the best known example of a transverse coherent instability. The stability criterion can be expressed in the following form[17]:

$$|Z_\perp| \le \frac{E_p}{e}\,\frac{\pi Q}{IR}\left|(n-Q)\eta + Q'\right|\frac{\Delta p}{m_p c} \tag{18}$$

Here the amplitude function has already been replaced by its average value R/Q, $\eta = \gamma_t^{-2} - \gamma^{-2}$, γ_t is the γ-value at transition, $Q' = dQ/dp/p$ is the absolute chromaticity and Δp is the momentum spread in the beam. The above equation must be satisfied for the total transverse impedance $Z_\perp$ in the machine, for all combinations of I and $\Delta p/m_p c$ which occur during its filling, and for every $n > Q$. If stacking in momentum space is used, as in the ISR, then I and $\Delta p/m_p c$ grow roughly in proportion and in (18) may be interpreted as the total current and the total momentum spread in the beam.

In the special case of the resistive wall impedance the following expression applies, neglecting the smaller capacitive impedance:

$$|Z_\perp| = 2^{\frac{1}{2}}\, R\, Z_0\, \delta/b^3 \tag{19}$$

Here Z_0 is the impedance of free space and δ is the skin depth measured at the frequency $\omega = (n-Q)\,c/R$ and hence:

$$|Z_\perp| = \frac{2}{b^3}\left(\frac{R^3 Z_0}{(n-Q)\sigma}\right)^{\frac{1}{2}} \tag{20}$$

σ is the conductivity of the vacuum chamber material. At low mode numbers n, just above Q, the Q' term in (18) dominates and the tune spread required to Landau damp the instability becomes:

$$\delta Q = Q'\,\frac{\Delta p}{p} \ge \frac{2}{\pi c}\left(\frac{Z_0 E_p}{ec}\right)^{\frac{1}{2}}\frac{R}{Q}\left(\frac{R}{\rho B_M}\right)^{3/2}\frac{I}{b^3}\left(\frac{\gamma}{(n-Q)\sigma}\right)^{\frac{1}{2}} \tag{21}$$

In a real machine, the tune spread which can be accommodated is below a given limit. Hence (21) is another design equation for it, giving the current I_t which is transversely stable.

In an actual machine there are many more transverse impedances apart from the resistivity of the vacuum chamber walls. In principle, all have to be included in the stability considerations and designed accordingly. However, there is this difference between isolated objects and the vacuum chamber that the former can be modified as required whereas the latter cannot easily be changed.

In the ISR, a transverse feedback system has been used successfully[18] to counteract the effect of the wall impedance for the two lowest modes. A similar system could also be used in future machines.

3.2.3 Longitudinal resistive wall instability

The traditional stability criterion for the resistive wall instability[19] can be written in the following form[20,21]:

$$\left|\frac{Z}{n}\right| \le \left(\frac{E_p}{e}\right)\frac{\eta}{I\gamma}\left(\frac{\Delta p}{m_p c}\right)^2 \tag{22}$$

Here Z is the tolerable coupling impedance, and n is the mode number. Ap is the full width of the momentum spread at half height of the distribution function. Again, *(22)* must be fulfilled for all combinations of I and Ap which occur during the filling process. When stacking in momentum space is used the most severe conditions apply to the beginning of the filling.

For a beam in a circular vacuum chamber of radius b, the coupling impedance, neglecting the small capacitive contribution and putting in the worst n = 1, is given by:

$$\left|\frac{Z}{n}\right| = \frac{1}{b}\left(\frac{RZ_0}{\sigma}\right)^{\frac{1}{2}} \qquad (23)$$

Assuming that the current/pulse is I_p, the momentum spread necessary for longitudinal stability of a single pulse becomes, combining *(22)* and *(23):*

$$\left(\frac{\Delta p}{m_p c}\right)^2_s = \left(\frac{Z_0 R}{\sigma}\right)^{\frac{1}{2}} \frac{e}{E_p} \frac{I_p Q^2 \gamma}{b} \qquad (24)$$

In the derivation it has been assumed that $\gamma >> \gamma_t$ and hence $\eta \simeq Q^{-2}$ has been used.

If one assumes that the aperture taken by the momentum spread of the stacked beam should not exceed the vacuum chamber radius b (this leaves another radius b for manipulations, betatron oscillations, closed orbit distortions etc.), then one can calculate an upper limit I_ℓ for the stored current which is longitudinally stable:

$$I_\ell = \frac{bQ^2 I_p \gamma}{R(\Delta p/m_p c)_s} \qquad (25)$$

This is the third design constraint for a proton machine. In an actual machine there are many more longitudinal impedances apart from the resistivity of the vacuum chamber, the most conspicuous of these being the shunt impedance of the RF system. The RF system of the ISR contains a feedback loop[22] which reduces its shunt impedance at the cavity resonances by a large factor. The elements in question must be designed so that their total impedance is small compared with the vacuum chamber walls or their impedances have to be included.

3.2.4 Synopsis of single beam limits

Many single beam phenomena have been considered which limit the total current which can be stored in a proton storage ring. There are even more phenomena which have not been mentioned at all. Hopefully, they are less restrictive than those mentioned. However, the important thing to be demonstrated was that one should adopt an open-ended approach to the design of these large machines which has been shown here by way of a few examples.

3.3 Technical limits on proton storage rings

The question arises whether there are technical phenomena in proton machines which take the place of the synchrotron radiation in electron machines. It turns out that the stored energy in the beam may be such a phenomenon. It will be considered below.

Furthermore, all the collective effects mentioned have in common that, when the other parameters are fixed, then the aperture radius b must be bigger than some limit. Hence, for a given wavelength there is always an aperture radius b for which the machine works,

The question arises quite naturally whether there are upper limits to the aperture. It turns out that the maximum poletip field of the quadrupoles is one of them.

3.3.1 Stored energy in the beam

If one considers proton machines at several hundred GeV energy and with several amperes of circulating current one finds that the stored energy of the beams may take values which are much bigger than those in the ISR[23] or the large proton synchrotrons at NAL or at CERN. It therefore appears most suitable to include it as a design constraint. It is given by the following expression:

$$W = 2\pi\left(\frac{m_p c}{e}\right)^2 \frac{R}{\rho} \frac{I\gamma^2}{B_M} \qquad (26)$$

There are two reasons why the stored energy in the beam may be dangerous. In emergency cases, the beam must be deflected in a beam dump system by fast ejection and the whole energy in the beam is deposited in a long thin cylinder of material creating problems of local heating and stress. Water has been suggested as a possible material for the absorber[24].

In superconducting machines, in particular, the beam power deposited near to the vacuum chamber is equal to the stored beam energy divided by the beam lifetime. If this power has to be removed at cryogenic temperatures it may constitute a significant heat load. Attempts to localize the beam loss have not yet been successful in the ISR.

The stored energy equation *(26)* may be considered as an equation for the maximum current I_W which can be stored in a machine.

3.3.2 Limits on the quadrupole strength

Calculating the properties of a separated function FODO lattice in thin lens approximation[5], one finds that for 90° phase advance per period the focal length of the quadrupoles is given by

$$f = \ell_p/2\sqrt{2} \qquad (27)$$

Here R_p is the length of a period which is related to R/Q by

$$\ell_p = \frac{\pi}{2}\frac{R}{Q} \qquad (28)$$

The relation between focal length and gradient is

$$f = \frac{B\rho}{\ell_Q}\left(\frac{dB}{dx}\right)^{-1} = \frac{B\rho}{\ell_Q}\frac{b}{B_Q} \qquad (29)$$

where Bp is the magnetic rigidity of the protons, and ℓ_Q is the length of the quadrupoles, and B_Q is their field at a distance b from their centre. Since the value of R/ρ has already been used in several places, the quadrupole length ℓ_Q cannot exceed the space left free by bending magnets. One can introduce an adjustable

parameter C_Q which just describes the fraction of the straight sections in a period occupied by the quadrupoles.

The above formulae can be combined and manipulated to finally take the form:

$$b = \left(\frac{ec}{E_p}\right)\frac{\pi^2}{2^{\frac{1}{2}}16}\left(\frac{R}{Q}\right)^2 \frac{B_Q C_Q}{\gamma}\left(1 - \frac{\rho}{R}\right) \qquad (30)$$

In a real machine, an upper limit for B_Q is determined by the type of magnets used for the construction of the magnet lattice. Therefore (30) is an upper limit for the aperture radius b, and as such it complements the design equations given by the collective phenomena.

It may be considered a fortunate accident that the upper limit for b (30) increases more steeply with R/Q than the lower limits for b determined by the collective phenomena (17) and (21). Hence there is always a solution to the combined equations.

3.4 Proton storage ring design

3.4.1 Outline of the procedure

The design equations (17), (21), (25), (26) and (30) involve only 16 parameters which can be grouped as follows:

i) Machine energy γ

ii) Injected beam parameters, given by injector: I_p, E_t, $(\Delta p/mpc)_i$

iii) Magnet lattice parameters R/ρ, B_M, B_Q, C_Q, b, W_{max}

iv) Space charge parameters σ, n-Q, δQ_{max}, ΔQ_{1max}

v) Intersection parameters ℓ, ΔQ_{2max}

The most transparent way of proceeding consists in choosing first these parameters, then to calculate the maximum currents I_q, I_t, I_ℓ, I_n permitted by (17), (21), (25), (26) and the corresponding luminosities. This yields a clear picture of which luminosity can be obtained with a given set of machine parameters. It is then quite easy to choose a good set of parameters for which many more derived quantities can be obtained.

3.4.2 Choice of parameters

The choice of the parameters must be guided by extrapolation and scaling from existing proton synchrotrons and storage rings. As examples, machines will be used which are under study at CERN, using the CERN SPS as an injector, and therefore operating with known and fixed injected beam parameters. The choice of the magnet lattice parameters R/ρ, %, B_Q, C_Q can be guided by a comparison with the large proton synchrotrons at NAL and CERN, for a conventional copper-steel magnet system. For the supraconducting magnet system, parameters in the vicinity of the ISABELLE proposal[25] are used.

The aperture radius b and the stored energy in the beam W_{max} are used as parameters for the time being. They will be fixed later.

The choice of the vacuum chamber material fixes σ, the conductivity. It is advantageous to work in the half-integral range of Q just above an integer. Hence n-Q = 3/4. Experience with the ISR suggests that non-linear resonances must be avoided in order to obtain a good lifetime of the stored beam, and a low background from beam-wall events in the experiments. The working space in the tunes is restricted to the range between the 5th order resonances at $Q = n + 3/5$ and the 3rd order resonances at $Q = n + 2/3$. This leaves a free space of $\Delta Q = 1/15$ which includes the 8th order resonances at $Q = n + 5/8$.

This free space must be large enough to include the tune spread required for transverse stability, the tune spread in the single beam and the sum of all the tune spreads due to the beam-beam interactions. Replacing the tune spreads by the corresponding tune shifts yields roughly

$$\Delta Q \geq \delta Q_{max} + \Delta Q_{1_{max}} + N_2\, \Delta Q_{2_{max}} \qquad (31)$$

Here N_2 is the number of crossing points. On the basis of this argument, the values $\delta Q_{max} = \Delta Q_{1max} = 0.02$ were used in the examples.

The maximum permissible value ΔQ_{2max} for the beam-beam tune shift has been the subject of much speculation[26,27,28]. Experimental information from the ISR suggests that no bad effects are observable with $\Delta Q_2 \simeq 7 \times 10^{-4}$ if the tunes are chosen as described above. In addition, a special experiment at 2 GeV/c[29] has shown that there is no detectable lifetime reduction for a beam lifetime of about 30 minutes at $\Delta Q_2 \simeq 5 \times 10^{-3}$. In this experiment the short lifetime was entirely due to single beam effects, most likely intra-beam scattering[30,31]. An experiment using a non-linear lens to simulate the second beam has not yet given conclusive results.

Choosing $\Delta Q_{2max} = 0.005$ has become standard practice[6,25,32].

Choosing the same size of the working region as in the ISR and the standard value for the beam-beam tune shift is not necessarily a satisfactory method of extrapolation. An argument against this choice is that a beam-beam effect which is an order of magnitude stronger will excite non-linear resonances more strongly and hence the invisible 8th order resonances may become harmful. There are two arguments in favour of this scaling: Firstly, future machines will have a higher luminosity than the ISR at roughly the same number of protons, and are, therefore, relatively less sensitive to beam-wall background. Secondly, the "feeding" of particles into the resonances by intra-beam scattering is slower at higher energies. The balance between the arguments against and in favour of the choices made can only be arrived at by more detailed calculations.

The last parameter to be fixed was the free length around the crossing points. It was chosen as ℓ = 30 m.

3.4.3 Results

Using these parameters, the stored current and the luminosity were calculated, employing the accurate formulae[12] for the beam-beam tune shift and the luminosity. The results are displayed in Figs. 1 to 4. The energy (γ) is used as abscissa. Each graph contains 4 sets of curves. One set has W as a variable parameter, the other 3 sets the aperture radius b; they apply to the single beam tune shift, and the transverse and longitudinal stability limits. For smaller values of y, the longitudinal phase space density limit may be independent of b.

This means that the momentum spread of the injected beam is stable and hence no aperture dependent blow-up is required.

It may be seen that usually the single beam tune shift and the stored energy in the beam present the most serious limitations. A superconducting machine needs a smaller stored energy in the beam and a smaller aperture radius b for the same luminosity than a conventional copper-steel magnet machine.

Proton machines in the energy range up to 1000 GeV which correspond to accelerators in the energy range up to *2130* TeV appear to be technically feasible. However, they are very large and correspondingly expensive.

In order to simplify the presentation, the operation at only one energy has been considered. This excludes machines such as ISABELLE[25] in which the stored beam has to be accelerated to the design energy, and the operation of a given machine over an extended energy range. Both these problems can **be** tackled within the formalism presented by scaling the parameters y, B_M and B_Q accordingly. It turns out that the stored current is proportional to γ when the tune of the machine is kept constant. According to *(14)* this would result in a luminosity variation like $\gamma^{5/2}$. The operating range of the machine can be extended towards lower energies by using a larger aperture than is required at maximum energy.

3.4.4 Specific machines

On the basis of the results displayed in Figs. 1 to *4* a parameter list for a *400* GeV/c conventional machine has been worked out which is being used to design this machine in more detail. It is shown in Table 11. All the derived parameters can be obtained from the formulae given earlier in this paper. For comparison, I have included the parameters of a superconducting machine with the same energy and luminosity. In these machines, round numbers were chosen for the aperture such that the actual values of AQ, and δQ were below the limits imposed.

The important conclusion from Table II is that it is possible to design stable machines with a good luminosity. They compare favourably with the ISR because the collective effects are of the same order of magnitude and the luminosity is much higher.

Comparing the conventional and superconducting machines in Table II shows that in the latter one reaches the same luminosity with a smaller radius, aperture and stored energy.

Much work still has to be done before the feasibility of these machines can be established, in particular in the following areas: design of intersection regions, RF acceleration, beam transfer from the SPS and injection, beam dumping, and site layout.

TABLE II

Comparison of *400* GeV proton storage ring parameters using conventional and superconducting magnet

		conv,	s.c.	
Maximum momentum	p	*400*	*400*	GeV/c
Maximum field in bending magnets	B_M	1.8	*4.0*	T
Maximum poletip field in quadrupoles	B_Q	*0.6*	2.0	T
Circumference factor	R/ρ	*1.3*	*1.6*	
Bending radius	ρ	*741*	*333*	m
Average radius	R	*964*	*533*	m
Quadrupole filling factor	C_Q	*0.5*	*0.2*	
Aperture radius	b	*30*	*20*	mm
Average wavelength	R/Q	*36.4*	*17.9*	m
Betatron wavenumber	Q	*26.5*	29.8	
Phase advance/period	μ	π/2	*n12*	
Period length	a_P	*57.2*	28.1	m
Quadrupole length	a_Q	*3.3*	*1.1*	m
Injected current/pulse	I_P	*0.07*	*0.07*	A
Injected phase space density	D	1.3×10^{20}	1.3×10^{20}	m^{-3}
Injected normalised beam emittance	E_t	$30\pi\cdot10^{-6}$	$30\pi\cdot10^{-6}$	m
Stored current	I	*5*	*5*	A
Number of injector pulses		*72*	*72*	
Stored energy in the beam	W_B	*40*	22	MJ
Single beam tune shift	ΔQ_1	0.015	0.008	
Vacuum chamber conductivity	σ	10^6	10^6	A/Vm
Resistive wall mode number	n-Q	*0.75*	*0.75*	
Required tune spread in beam	δQ	*0.007*	*0.005*	
Total stored momentum spread	Δp/p	3.6×10^{-3}	4.2×10^{-3}	
Free length in crossing regions	ℓ	*30*	*30*	m
Amplitude function at crossing point	β_0	*2.0*	*2.0*	m
Rms beam radius at crossing point	σ_0	*0.2*	*0.2*	mm
Beam-beam tune shift/crossing	ΔQ_2	0.005	*0.005*	
Crossing angle	α	1	1	mrad
Luminosity/crossing	L		10^{33}	$cm^{-2}s^{-1}$

4. Conclusions

A comparison between the extrapolations for electron and proton machines in Tables I and II shows that an electron machine at 50 GeV is significantly bigger than a proton machine at 400 GeV. This is even more true when one considers the superconducting version of the latter. Hence, there is a distinct difference in the maximum energy which one can hope to achieve in electron and proton machines. Whether this difference is significant or not must be decided on the basis of experiments which can be performed with these machines.

References

1) M. Sands in "Physics with Intersecting Storage Rings", editor B. Touschek, Academic Press, New York (1971)

2) J. Rees et al., 8th Int. Conf. High Energy Acc., CERN, 143 (1971)

3) F. Amman, 8th Int. Conf. High Energy Acc., CERN, 63 (1971)

4) H. Wiedemann et al., 1973 Particle Acc. Conf., San Francisco, 838 (1973)

5) J. Rees and B. Richter, SPEAR-167 (1973)

6) L. Smith, this conference

7) K. Johnsen, this conference

8) Proton-Proton Colliding-Beam Storage Rings for the Natl. Acc. Lab., Design Study 1968

9) J.P. Blewett and H. Hahn, editors, BNL 16716 (1972)

10) A.N. Skrinsky et al., 8th Int. Conf. High Energy Acc., CERN, 72 (1971)

11) E. Keil, C. Pellegrini and A.M. Sessler, to be published in Nucl. Instr. and Meth.

12) E. Keil, Nucl. Instr. and Meth. 113, 333 (1973)

13) B.W. Montague, private communication

14) L.J. Laslett, BNL 7534, 324 (1963)

15) B. Zotter, Report CERN/ISR-TH/74-11 (1974)

16) L.J. Laslett, V.K. Neil, A.M. Sessler, Rev. Sci. Instr. 36, 436 (1965)

17) H.G. Hereward, private communication

18) L. Thorndahl and A. Vaughan, 1973 Particle Acc. Conf., San Francisco, 807 (1973)

19) V.K. Neil and A.M. Sessler, Rev. Sci. Instr. 36, 429 (1965)

20) V.K. Neil, D.L. Judd and L.J. Laslett, Rev. Sci. Instr. 32, 267 (1961)

21) E. Keil and W. Schnell, Report CERN/ISR-TH-RF/69-48 (1969)

22) F.A. Ferger and W. Schnell, USSR 2nd Natl. Conf. Particle Acc., Moscow, Vol. 2, 128 (1972)

23) A. Delizée et al., 7th Int, Conf. High Energy Acc., Yerewan, Vol. 2, 183 (1969)

24) B.W. Montague, private communication

25) H. Hahn, this conference

26) B.V. Chirikov, Inst. of Nucl. Phys., Novosibirsk, Preprint 267, Section 4.3 (1969)

27) E. Keil, 8th Int. Conf. High Energy Acc., CERN, 372 (1971)

28) L.J. Laslett, this conference

29) K. Hübner, this conference

30) C. Pellegrini, Frascati Report LNF-68/1 (1968)

31) A. Piwinski, this conference

32) G.H. Rees, this conference

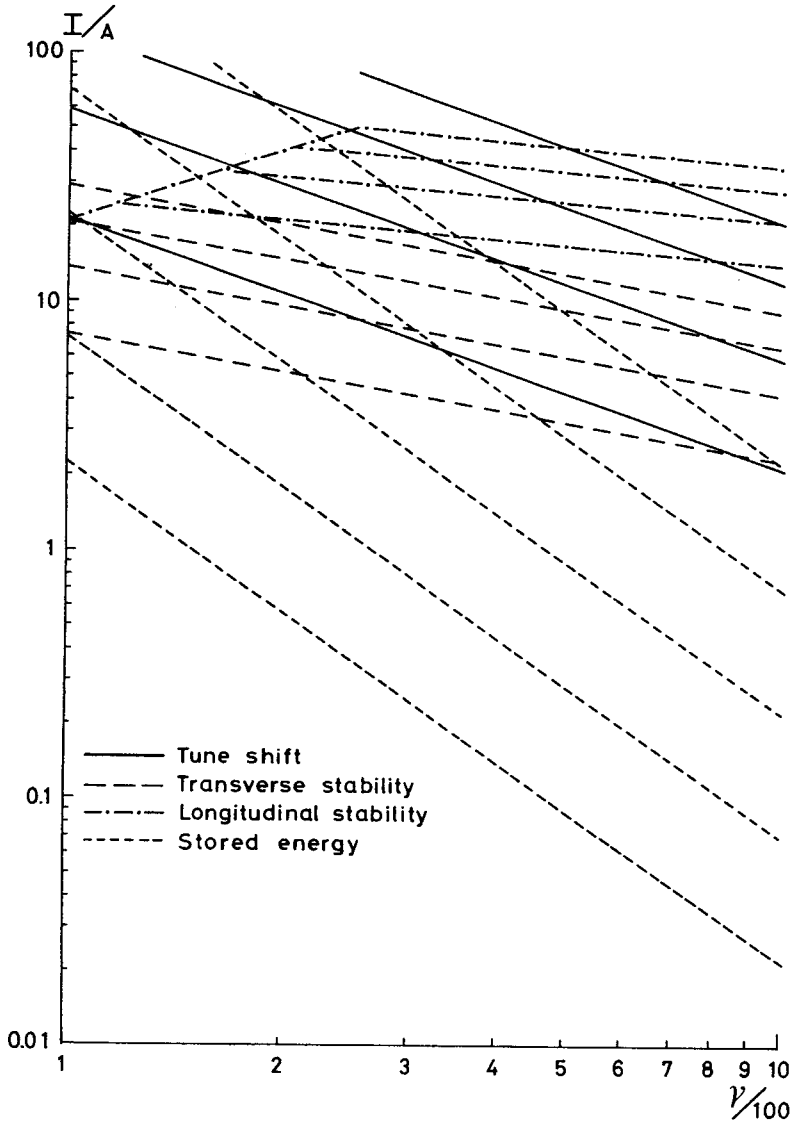


Fig 1 - Circulating current I vs energy γ

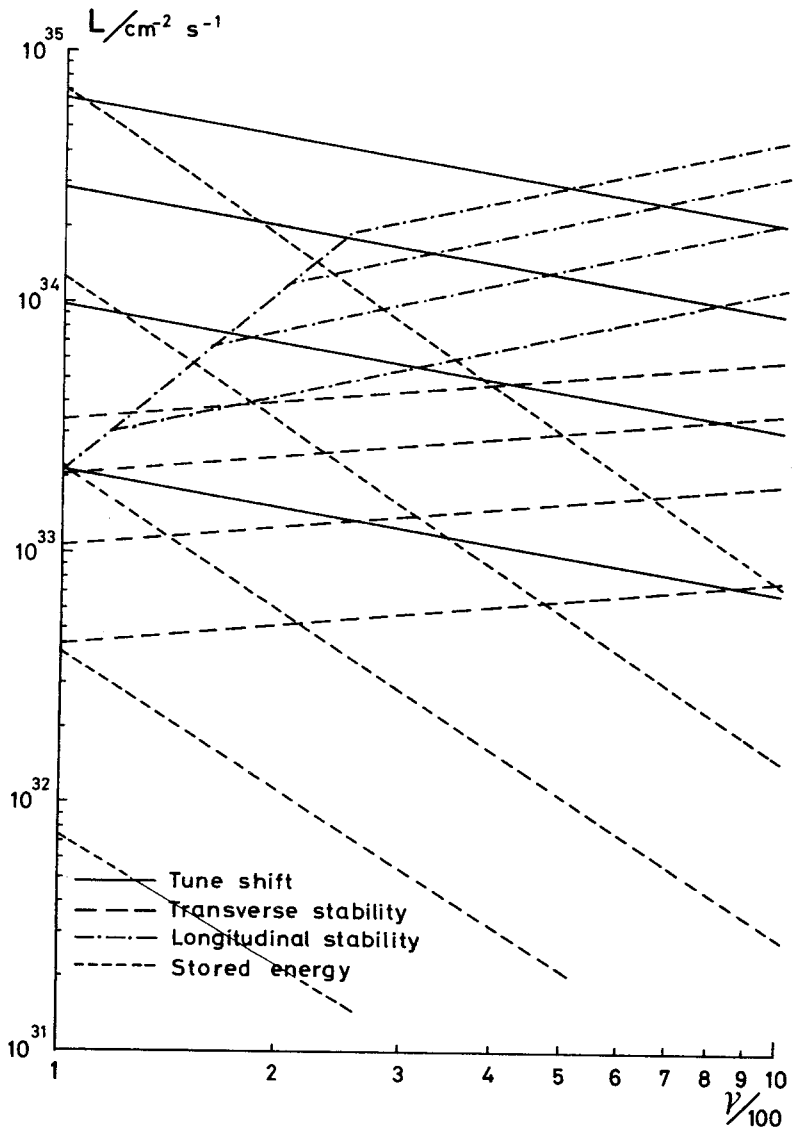


Fig 2 - Luminosity/crossing L vs. energy γ

The parameters used in the figures are: $R/\rho = 1.3$, $B_M = 1.8$ T, $B_Q = 0.6$ T, $C_Q = 0.5$, $n\text{-}Q = 0.75$, $\ell = 30$ m, $\Delta Q_1 = 0.02$, $\Delta Q_2 = 0.005$, $\delta Q = 0.02$, $\Delta(\beta\gamma)_i = 0.013$, $E_t = 29.6\pi \times 10^{-6}$ m, $\sigma = 10^6$ A/Vm, $I_p = 70$ mA. The curves for tune shifts, transverse and longitudinal stability are drawn for an aperture radius b = 20, 30, 40, 50 mm. The curves for the stored energy in the beam are drawn for W = 1, $10^{\frac{1}{2}}$, 10, $10^{3/2}$, 100 MJ.

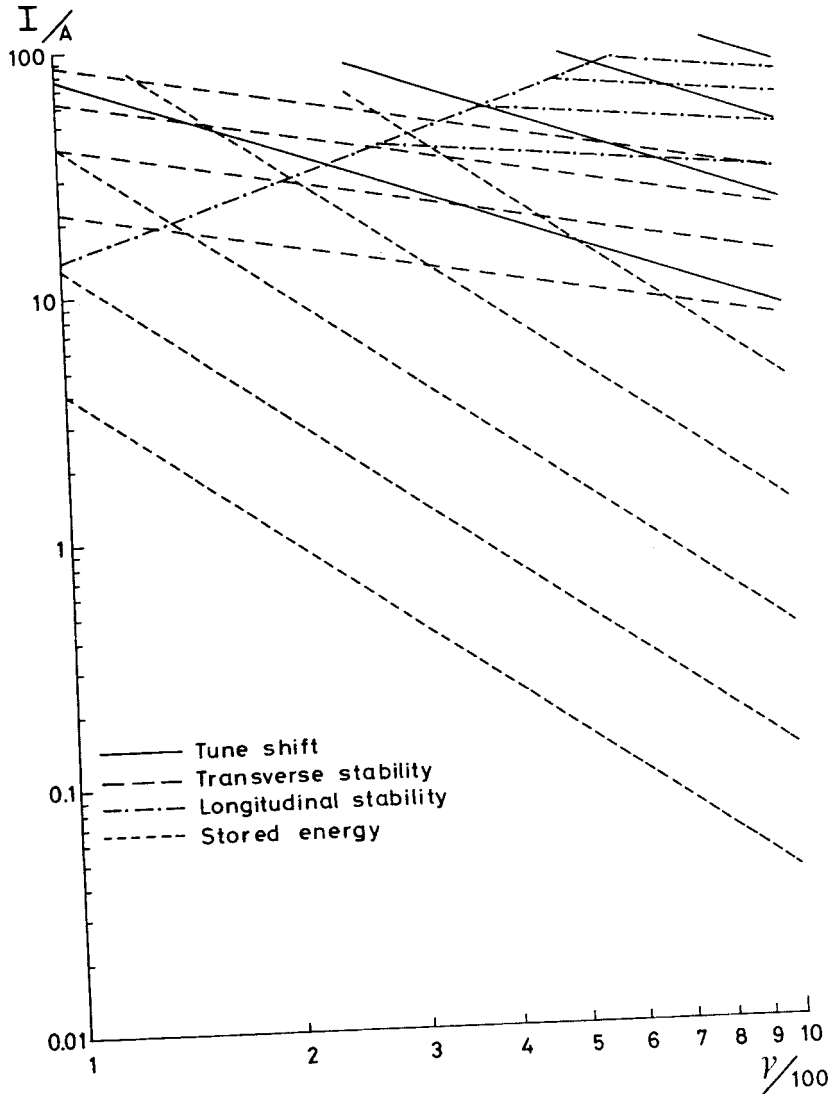


Fig. 3 - Circulating current I vs energy γ

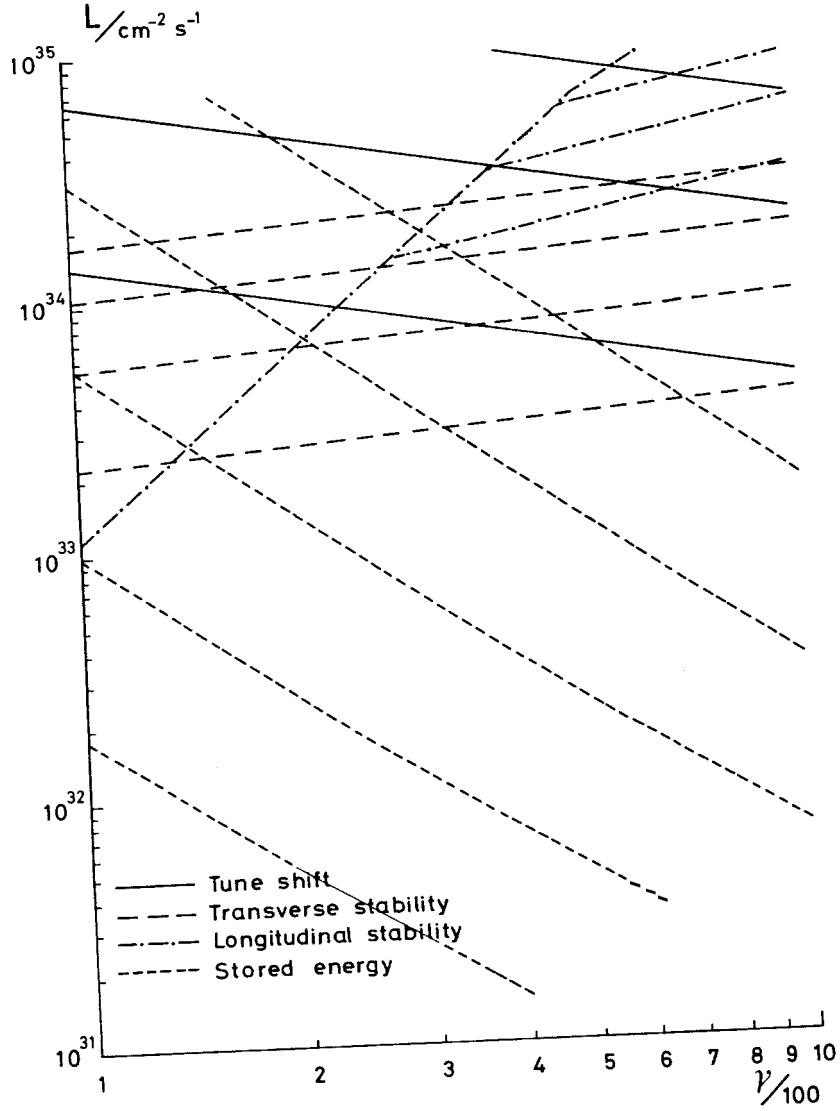


Fig. 4 - Luminosity / cross section L vs energy γ

The parameters used in the figures are: $R/\rho = 6$ $B_M = 4$ T, $B_Q = 2$ T, $C_Q = 0.2$, $n\text{-}Q = 0.75$, $\ell = 30$ m, $\Delta Q_1 = 0.02$, $\Delta Q_2 = 0.005$, $\delta Q = 0.02$, $\Delta(\beta\gamma)_i = 0.013$, $E_t = 29.6\pi \times 10^{-6}$ m, $\sigma = 10^6$, $I_p = 70$ mA. The curves for tune shifts, transverse and longitudinal stability are drawn for an aperture radius b = 20, 30, 40, 50 mm. The curves for the stored energy in the beam are drawn for $W = 1, 10^{\frac{1}{2}}, 10, 10^{\frac{3}{2}}, 100$ MJ.

Rae Stiening (NAL): How does one avoid 5th-order resonances—in other words, can you make magnets of good quality at that high energy?

Keil: That is a good question. I'll answer the second part first. I don't think that the magnet tolerances influence the order of resonances which one can stand in a machine more than the beam-beam effects in the machine; that is to say that if you make a lousy magnet, then you may get single-beam difficulties. However, if you want to run the machine as a colliding beam device, then the two-beam situation is bound to be worse even under these conditions.

Matt Allen (SLAC): Just an engineering detail—the 50-GeV machine would need about 1 km of RF cavities. The wall losses would be about 20 MW for copper cavities. This might be a possible application for superconducting cavities which would require a lot of niobium.

SYNCHROTRON RADIATION SOURCES

S.P.Kapitza (presented by V. V. Elyan)
Institute for Physical Problems
Moscow, USSR

Summary. Synchrotrons and storage rings as synchrotron radiation sources in the vacuum ultraviolet and soft X-ray region are discussed. Comparative consideration of several special projects of dedicated SR storage rings is given.

Synchrotron radiation (SR) is well known to the accelerator community mainly as an unwelcome refuse of synchrotrons and electron storage rings. Following the modern trend in utilizing all products that appear in an industrial process much use has been recently found for this by-product of accelerator technology.

SR spans a very broad band of the electromagnetic spectrum practically starting in the infrared and usually terminating somewhere in the X-ray region. Certainly from the point of view of energy 10 keV quanta, even 100 keV ones cannot compete with the GeV's and TeV's that tend to dominate the minds of those present. But it is the technology and expertize developed for high energy physics that compels us to consider SR sources. Thus a new challenge to the accelerator designer is open and a new dimension for the use of high energy particle accelerators is added in providing a most powerful tool of research in a diverse number of fields.

May be it is this diversity of applications that presents one of the major difficulties, for we could certainly leave the development of this field to the future user who could make the decision, what sort of machine is considered to be the best. But when a number of fields from solid state physics to biology, from diagnostic medicine to astrophysics are involved, who then should take the lead? In this case I think it is for the machine builder to get an understanding of the users' needs and by combining them with the current possibilities of accelerator technology make the proper step in building a new machine. Before considering this next step I will start with reminding you of the main properties of SR.

SR is primarily produced when a fast electron with an energy $E \gg E_0 = mc^2$ is deflected in a strong magnetic field H. Radiation is emitted tangentially to the orbit and is spacially confined to a small angle $\vartheta \approx 1/\gamma = E_0/E$ typically less than 1 mrad for energies above 1 GeV. The spectrum is continuous, passing through the millimeter, submillimeter, IR, optical, UV into the X-ray region. The number of quanta gradually decreases with photon energy ξ as $\xi^{1/3}$ up to a Cut off frequency, where the spectrum is rapidly terminated, The cut of wave length λ_{max} is determined by the electron energy E (GeV) and the radius R(m)

$$\lambda_{max} = \frac{1{,}7R}{\gamma^3} \qquad (1)$$

We will consider λ_{max} the wave length at the maximum of the power spectrum as the main parameter of the SR spectrum, rather than the critical wave length $\lambda_c = 2{,}42\,\lambda_{max}$ introduced in most theoretical papers on SR.

SR is highly polarized, its plane of polarisation being that of the orbit. In a full revolution of a charge $\frac{2\pi}{137}\cdot\gamma$ quanta are emitted with a total radiation loss of ΔE

$$\Delta E\,(\text{kev}) = 88{,}5\,\frac{E^4\,(\text{Gev})}{R\,(\text{m})} \qquad (2)$$

Thus the SR power is $P_s = I\,\Delta E$, where I is the electron beam current. For all practical purposes the electron spin and quantum phenomena do not affect the SR spectrum, although the beam cross section is determined by quantum fluctuations. The classical electrodynamic theory is in full agreement with all observations and the appropriate treatment can be found in most modern textbooks (see also [1]).

SR from a high energy electron beam presents a source of highly collimated, polarized radiation with a well defined continuous spectrum. Its spectral intensity in the UV and X-ray region is far greater than that of any other sources. Moreover, even in the infrared the intensity is higher than that of heated bodies usually used as sources in IR spectroscopy. These well defined properties of SR have led to consider an electron beam radiating in a magnetic field as a primary radiation standard, being at 1 GeV more or less similar to a black body at a temperature $\sim 10^7$°. SR standards are finding use in calibrating UV and X-ray instruments for space astronomy.

Most of the work with SR has been done on existing synchrotrons and storage rings. This extensive experience is well summed up in a number of conference reports [2] and references can be found in an extensive bibliography [3]. The first experiments were mainly done parasitically on large synchrotrons, the most prominent being the DESY 7 GeV synchrotron at Hamburg. Later a substantial project had also been started at Daresbury on the NINA 4 GeV synchrotron where a national SR facility is now operating.

Although much work is still being done on most electron synchrotrons, SR facilities are now provided also on the large modern electron storage rings. The Stanford SR Project (SSRP) at SPEAR described in detail elsewhere in these Proceedings [4] provides a national US facility mainly for the W and X-ray region with a high flux down to 1 Å. Up to seven experiments can share a beam run, which accepts 11,5 mrad SR emitted horizontally. A broad ranging program of research will be pursued including studies of UV and X-ray photoelectron spectroscopy, extended X-ray absorption edge fine structures, X-ray diffraction on biological system, Compton scattering X-ray absorption, X-ray induced luminiscence, sub-nanosecond time constant measurements on solids, chemical kinetic studies and UV reflectivity, thus covering most of the problems requiring the short wavelength part of the SR spectrum.

A most powerful facility is to be provided at the DESY-DORIS storage ring, where

two large SR bunkers are built in addition to those that were primarily used on the DESY synchrotron. One of these new bunkers is operated by the European Molecular Biology Organization (EMBO) and will be devoted to studies of complex biological structures - enzimes, muscles, etc.

Parasitic SR facilities are also envisaged on the new 1,7 GeV DCI storage ring at *Orsay* (France) operated by the Laboratoire pour l'Utilisation du Rayonnement Electromagnetique (LURE) group, working at present on the 550 MeV ACO ring. From 1975 ACO will be used only for SR work.

In the Soviet Union at Novosibirsk SR work is actively being done both on the 670 MeV VEPP-2M storage ring and the large VEPP-3 complex. A summary of data on these machines that all provide parasitic SR facilities is given in the first half of Table I.

The work on these machines will certainly lead to rapid and immediate progress in the whole field of SR research. This will provide for a new opportunity to reaccess the merits of various SR sources and will contribute to the demands that a SR source should comply with, although even now we can consider these demands and envisage the parameters of a dedicated SR source.

The future SR source will certainly be a storage ring. Work on storage rings has shown them to be ideal sources of radiation. They are fret: from vibrations that so complicates experiments on large synchrotrons, provide great spacial and temporal stability of the beam, little if *any* radiation danger, which is a constant hazard on lar e synchrotrons. On large synchrotrons the R beam is practically available some 20 to 30 meters from the beam, when with storage rings work in the immediate vicinity of the machine is possible.

At present the only storage ring fully committed to SR work is the Wisconsin Tantalus I facility[7]. Its remarkable success in the SR field down to ~100 Å has led to a project of converting the old 180 MeV NBC synchrotron into a 240 MeV storage ring, described in more detail in these Proceedings[8]. The conversion will include a 10 MeV injector microtron, a new vacuum chamber, coils and supplies necessary for the operation of the synchrotron as a storage ring. A 300 MeV SR storage ring is being currently built in Japan. These SR sources will provide for work in the low energy part of the spectrum, down to ~100 Å, whereas the large colliding beam machines will be supplying the shorter wave lengths down to ~1 Å.

The next step is the design of dedicated SR storage rings, producing SR down to the shortest limit of practical importance should now be considered. A critical accessment of λ_{max} in this case leads one to the conclusion that 1,5 ÷ 1 Å is the limiting value, this figure being of crucial importance for the design of a SR storage ring.

The next parameter of importance in the design is the magnetic field. Modern trends in the designing of high energy synchrotrons and storage *rings* favor low fields. In the case of SR sources just the opposite is right- the field should be as high as possible.

The storage ring is best conceived as a separated function machine[7]. Moreover, the separation of functions takes a step futher by introducing special magnets designed solely for the production of SR. These multiple gap magnets - wigglers were first introduced to increase SR damping in the CEA colliding beam experiment. Now these magnets operated at as high a field as reasonable will be used as a local means of generating SR. Thus the magnetic system is to be made up of bending dipole magnets, focussing quadrupoles and SR magnets, plus auxiliary magnets for tuning the system and compensating higher order gradients. The focussing lattice of the magnetic system is of rather straightforward design that allows one to adjust the β-function and ν_z and ν_x within certain margins. The main bending magnets are to be of the C-type where access to the vacuum chamber and SR light tubes is simpler. This concept is used in all three major projects of SR sources which we will now consider in more detail (see Table I).

The most ambitious project is the 2 GeV electron storage ring, proposed by the Daresbury laboratory group to take place of the NINA synchrotron 8,9. This large storage ring is designed to run with a 1 A current and will certainly be the most powerful dedicated SR source with 240 kw in SR power. Using a 5 T superconducting wiggler insert the λ_{max} can be shifted down from 2,5 Å to 0,8 Å with a corresponding increase in flux. The design of superconducting wigglers using the available superconducting cables is quite straightforward for fields up to 5 T and may be 6 T. Future developments will make the construction of wigglers with fields up to 10 T possible.

At least 10 beam lines are envisaged with the machine that will use most of the support facilities of the NINA synchrotron. The SR storage ring is suitably placed in the hall that at present houses the main NINA magnet. The injector to the storage ring is to be a booster 500 MeV synchrotron with electrons primarily accelerated by a 8 MeV microtron or linear accelerator.

Next one should mention the Tantalus II, the first large dedicated SR facility, a project that was proposed by the Wisconsin University Group[10]. At first this project tnat draws much from the experience gained with the 240 MeV Tantalus I ring was designed for 960 MeV, but later the energy was increased to 1760 MeV with a corresponding increase in size[11]. The bending field *is* rather low 1,2T and nigh field wiggler sections are also envisaged. The circulating current is to be 100 mA and the injector to the storage ring will be a 35 MeV microtron.

The project proposed in the design study by *our* group at the Institute for Physical Problems follows a similar pattern.[12] It is to be a separated function machine operating at 1,35 GeV with a rather high bending field of 1,8 T. As a next step in the development program superconducting high field section8 are also suggested. We plan for a 100 mA circulating current and propose to use a 30 MeV microtron injector. The general design has some similarity to the VEPP-2M storage ring and will draw on the experience with that machine.

In comparing the intensity of SR sources it is important to note that the effective SR luminosity is directly proportional to the current, rather than the number of particles

circulating, and inversely proportional to the beam hight. The beam cross section is ultimately dependent on the beam current, tuning of the ring and coupling of vertical and horizontal motion, so it is rather difficult to calculate the effective SR luminosity of a storage ring and the flux finally enter ing the detector of the experimental set up. That is why only the total SR power is given in Table I without taking into account the beam size and the divergence of the electron beam in the SR storage ring as determined by its β -function, To get an idea of the intensities available, recent experiments on VEPP-3 have shown that with only a 20 mA stored beam and operating at 3 m from the electron beam at least a 100 fold decrease in exposure time was obtained in a comparative experiment on molecular biology X-ray structure work at 1,5 A that was to determine the relative merit of storage rings as compared to modern high intensity fine focus rotating anode X-ray tubes. The optical brightness of the electron beam SR source can be enhanced by adjusting the local β value so that the beam will converge at the point of origin of the SR. The image of the radiating beam can be transported by an optical ellipsoid mirror reflecting X-rays at grazing incidence and leading to a great increase in flux available for experiments.

The vacuum systems of all projects propose to use the now standard all metal techniques developed on storage rings that can lead to an expectant beam life time of some hours at high energies and beam currents, requiring a base pressure of 10^{-9} torr.

Berillium windows can be used to separate the storage ring vacuum system for X-rays shorter than 4 7 Å. For experiments with longer wave lengths up to 1050 Å where optical LiF windows become transparent a common vacuum system for the user and the machine becomes necessary. It may be worth noting that much surface physics and other work also demands ultra high vacuum conditions, compatible with that of a storage ring, and appropriately dealt with in all the design studies.

We thus see that all these projects have much in common, the differences mainly stemming from prototypes used and technical circumstances of secondary importance that govern the detailed decisions made.

These projects do not approach the limit of modern storage ring design, for both in current and energy they are surpassed by the most advanced existing electron storage rings, where the operation is futher complicated by all the problems brought in by a colliding beam experiment.

These specialized storage rings may be Considered as radiation devices where the active body is a highly confined relativistic electron beam. It is fascinating to inquire on other possibilities of inducing this highly excited state of matter to radiate. One of these possibilities is the undulator, consisting of an extended region of a periodic magnetic field. If the period of the field along the beam is ℓ , the wiggling motion of the electron leads to a dipole radiation whose wave length is primarily determined by a Doppler effect shortening

$$\lambda = \frac{\ell}{2\gamma^2} \sim \frac{\ell}{1-\beta\cos\vartheta} \qquad (3).$$

For a 2 GeV electron and $\ell = 1$cm , $\lambda = 3$Å. For a pure dipole radiation pattern the magnetic field has to be less than the field that produces the same SR, in this case less than 0,6 T. At higher fields the radiation pattern is complicated by local synchrotron radiation, that can also be considered as Doppler shifted multiple radiation. In the case of strong fields the momentary synchrotron radiation pattern manages to develop and the whole device can be considered really to be a wiggler. Unfortunately the radiation from the undulator is not monochromatic, being broadened by the angular Doppler effect factor.

It has also been suggested to use Compton scattering from laser beams. In this case the scattered beam wave length is primarily determined by a formula similar to (3)

$$\lambda \approx \frac{\lambda_\ell}{4\gamma^2} \qquad (4).$$

Thus for a CO_2 c.w. laser of $\lambda_\ell = 10^{-3}$ cm and already with a beam of electron at E = 100 MeV one obtains λ = 0,6 Å. The angular dependence term again leads to a rather broad spectrum, influenced also by the angular convergence of the laser beam as determined by the diffraction pattern of the optical beam forming system in setting up a spacial standing wave pattern interacting with the stored electron beam.

Unfortunately the intensity from all these c.w. devices is not large. Without going into detailed calculations it is worth noting that all processes considered could really be thought of as different cases of Compton scattering. Compton effect is the basic interaction of an electromagnetic field with the free electron. SR radiation can also be considered as Compton scattering in a frame of reference where the electromagnetic wave has been transformed to a constant magnetic field. At present a constant magnetic field provides the greatest macroscopic density of electromagnetic energy and thus it is the best means for producing scattered radiation, in this case SR. May be in the future high power c.w. laser technology will provide a better opportunity but at present superconducting coils seem to be the best way of producing the high field interacting with the electron.

Certainly the most fascinating thing to do would be to make coherent synchrotron radiation, but no one has yet suggested a way of doing this with fast electrons, although devices that can be considered as SR lasers, or rather masers, operating in the millimeter and submillimeter band have been described.

SR storage rings at present should be considered as a multiple purpose broad band sources of radiation. For this new generation of machines one can suggest the building of a rather simple storage ring that will lead to immediate progress in a diverse number of fields. Moreover, in analysing the possibilities of these facilities it seems that the new techniques and instrumentation which will have to be developed will demand more effort and even greater expenses than the design and operation of a SR storage ring. Mirror for collecting and focussing the SR from the orbits have to be designed. New monochromators will have to be developed, new opportunities in X-ray diffraction work explored. The pola-

risation of SR may lead to new possibilities in ESCA work, as better monochromatisation will lead to greater details in the electron spectrum studied. The benefit of the fine adjustment of the wave length near the K-edge of a scattering atom may lead to methods of determining the phase of the diffracted wave in X-ray crystal studies, eliminating the phase ambiguity in reconstructing the structure. I will not dwell on the possibilities of greatly enhancing the contrast in medical diagnostic work that seems so promising by operating near the K-edge of iodine, iron or other elements, nor on the fascinating development of a novel X-ray scanning microscope.

Much will depend on the extent to which SR research will develop and will the necessity in a SR storage ring lead to recognize it as a facility similar to nuclear research reactors, powerful electron microscopes, etc.

It will be greatly surprising if a source of radiation many orders of magnitude more powerful will not lead to new departures in science and may be the most exciting uses of SR are still not recognized for it is in principle impossible to plan for the unknown.

In all dedicated storage ring projects considered the primary flux and intensity of SR will be less-than 'that immediately available in existing high power storage rings, operating as centralized facilities, producing may be the shortest wave length and/or the greatest flux. But parasitic operation will always limit the opportunities of an enterprising experimentalist, for in these conditions it is difficult to adjust the β - function or introduce special SR magnets without drastically interfering with the intricate adjustments needed for colliding beam experiments. A dedicated machine offers greater freedom for SR research, freedom that will surely lead to new and unexpected developments.

The SR storage ring is a specialized machine. a source of auanta that can be aptly called a photon factory. In spite of its size and complexity it will certainly produce more photons at a cheaper price than any existing device. From a human point of view atoms and molecules, not to speak of the complex structures discovered in modern molecular biology in these fields are just as fundamental as the remote depths of space and inanimate matter penetrated by our most powerful machines of research: telescopes and accelerators. In SR one can see a novel agent that strangely unites these frontiers of scientific adventure made possible by the advances of modern technology.

Storage Rings as SR Sources Table 1.

Facility	E GeV	H T	$\lambda_{max.}$ A	I mA	ΔE keV	P_{SR} kw	$R_{bend.}$ m	D m
SPEAR	2,5	0,65	2	250	270	65	12,7	60
DORIS	1,75 3,5	0,48 0,96	5,3 0,65	6000 200	70 1100	420 220	12,1	55
D C I	1,8	1,6	1,5	500	240	120	3,8	30
VEPP-3	2,25	1,26	1,2	200	375	75	6	23,6
Tantalus I	0,24	1,5	90	10	0,55	0,0055	0,54	3
N B S	0,24	0,96	140	100	0,35	0,035	0,83	3
VEPP-2M	0,67	1,8	10	100	15	1,5	1,22	5,7
Tantalus II	1,76	1,24	2	100	180	20	4,5	26
New NINA	2	1,2	1,6	1000	240	240	5,55	30
I P P	1,35	1,8	2,4	100	110	10	2,5	10

REFERENCES

1. A.A.Sokolov and I.M.Ternov. Synchrotron Radiation, Pergamon Press, 1960.
2. Notes of the Annual SR Users Group Conference published by the SR Center, Physical Sciences Laboratory. University of Wisconsin, 1968-1973.
3. DPNL Synchrotron Radiation Bibliography, 1972.
4. H.Winick. The Stanford Synchrotron Radiation Project (SSRP), These Proceedings, 1974.
5. E.M.Rowe and F.E.Mills. Tantalus I: A dedicated storage ring SR source, Particle Acc., 211-227, 4, 1973.
6. E.M.Rowe, M.A.Green. W.S.Trzeciak, W.R.Winter Jr. The conversion of the NBS 180 MeV electron synchrotron to a 240 MeV storage ring for SR research, These Proceedings, 1974.
7. S.Kapitza. Synchrotron radiation as a new tool of research, in Russ., Priroda, 10, 1971. See also Proc. III All-Union Part. Acc.Conf.,Moscow, oct.,1972,v.I,pp.11-16.
8. P.J.Thompson. DNPL, TM-105, 1973.
9. D.J.Thompson, G.Saxon, N.Marks, V.P.Suller and T.E.Swain. A 2 GeV 1A electron storage ring dedicated to the production of SR. These Proceedings, 1974.
10. E.Rowe et al. IEEE Trans.on Nucl.Sci.NS-18, 3,210-212, 1971.
11. E.Rowe. Proc. III All-Union Part.Acc.Conf., Moscow, October 1972, v.1, pp. 25-30.
12. S.Kapitza, L.Lugansky, L.Zikin. Design study of a 1,35 GeV synchrotron radiation source, Proc. III All-Union Part.Acc.Conf., Moscow, October 1972, v.1, pp.82-84.

ASTROPHYSICS AND ELEMENTARY PARTICLE PHYSICS*

Remo Ruffini†
Joseph Henry Laboratories, Princeton University, Princeton, New Jersey 08540

ABSTRACT

Recent developments of relativistic astrophysics allow the observation of regimes in which all existing field theories have never been tested. In the description of these regimes, unreachable in any experiment performed in a laboratory on the Earth, our current knowledge of electrodynamics or elementary particle physics has to be extrapolated by many orders of magnitude. For the first time, we are able to observe phenomena in which a fully relativistic treatment of gravitational interactions is mandatory.

1. INTRODUCTION

There is a major difference between astrophysics and usual experimental physics. In the usual experiments performed in a laboratory on the Earth, a physical phenomenon is isolated from all kinds of inessential and competing processes and reproduced in its most simple and clear form in order to be directly submitted to measurement and inquiry. Once the possibility of a new physical phenomenon is theoretically envisaged, a suitable experiment is designed in order to focus on this specific process. The strength and power of an experiment is such that on the basis of its result, the theory is confirmed or disproved. The success of an experiment is greater the most scientists succeed in focusing on a direct and clear measurement of the effect under consideration. In this interplay between the theory and the experiment and their possible feedback lies the entire dynamics of human scientific knowledge as postulated by Galileo.

In astrophysics, this program cannot be applied straightforwardly, mainly because some of the phenomena we are interested in do take place on time scales much too long to be recorded by a human observer (the lifetime for the thermonuclear evolution of a star of one solar mass is expected to be $\sim 10^{10}$ years!) and the size of the "objects" under investigation involves masses orders of magnitude larger than that of the earth ($M_\odot \sim 2 \times 10^{33}$ gr mass of a galaxy $\sim 10^{12} M_\odot$, estimated mass of a quasar $\sim 10^{10}$ Mg). The corresponding densities and pressures reach limits unthinkable in any earth-bound experiment (the core of a massive neutron star can reach hundred times nuclear densities).

However, although the approach is here different, yet the final result, namely the "isolation" of a specific phenomenon in an "experiment" is quite the same. In astrophysics, we are dealing with a very large number of entities (10^{12} stars in a galaxy, 10^4 galaxies in a cluster of galaxies, etc.). Between these entities, we can make classifications and divide them with respect to some "equivalence relation" into "equivalence classes." In the case of stars, e.g., these equivalence relations can be the mass, the luminosity, the surface temperature, the radius of the star, any special periodicity or any combination of these parameters. From these classifications, a certain regular pattern often emerges and relations can be established between the different equivalence classes. By far the most successful of these classifications in the case of stars has resulted in the Hertzsprung-Russel diagram. In the case of stars after the endpoint of thermonuclear evolution, a corresponding diagram is currently being constructed from a direct observation of pulsars and binary x-ray sources.

One of the greatest successes of theoretical astrophysics has been to relate through detailed theoretical models the regular pattern appearing in the classification with the temporal evolution of a star. It is difficult to overemphasize the importance of this essential step. Thanks to this, it is then possible to reconstruct the effective evolution of a single star by observing stars belonging to different equivalence classes. Although, therefore, we will never be able to follow each star (or galaxy or quasar) through its evolution, we can in principle, by looking at a large enough sample of stars, find one which at the moment of observation indeed performs for us the "experiment" we are interested in, in order to isolate and probe a new physical phenomenon. This, in a few words, is the methodology which govern the dynamics in the processes of acquiring knowledge in astrophysics.

The recent enormous success of this entire field of research stems from the very important interplay between so many different experimental techniques ranging from observatories working at radio and optical wavelengths on the Earth and telescopes for γ and x-ray observations on artificial Earth satellites, to the field of burst astronomy which is still in its infancy. Still all these observations would have produced very small progress if a deep theoretical understanding of these experimental data would not have occurred simultaneously—that is, if the theoretical framework would not have made comparable progress. Essential in the interplay between theoretical work and experimental research has been a very effective use of numerical analysis on computers which on one side has allowed a drastic reduction in the time of analysis of the experimental results and on the theoretical side has enabled one to overcome at once some of the gravest difficulties in the solution of the field equations governing the phenomena.

In particular, in the last forty years, the profound progress made in nuclear physics has allowed one to gain a much deeper understanding of thermonuclear evolution of stars. It has also become clear that during its entire thermonuclear evolution, a star radiates on the order of a few percent of its mass by burning light elements (H, He) into heavier elements. Only in the last four or five years, however, it has become clear that by far the most energetic epoch of the life of a star is reached after the exhaustion of its thermonuclear sources of energy has occurred and the star has undergone gravitational collapse. The interest in the latest stages of the evolution of a star is also dictated by the large amount of the new physical processes expected to be encountered in the description of gravitationally collapsed objects. Magnetic fields of the order of 10^{12} gauss are expected to be developed in the magnetosphere of a neutron star. During the few milliseconds in which gravitational collapse occurs of the order of 10^{57} nucleons are expected to undergo at once transformations dominated by weak interactions of the form

$$e^- + p \rightarrow n + \nu_e$$
$$n \rightarrow p + e^- + \bar{\nu}_e$$
$$e^+ + n \rightarrow p + \bar{\nu}_e$$

The neutron star, expected to be the outcome of this process, has an average density which can be as high as ten times nuclear densities. This density, together with the fact that the material in the star is degenerate ($T = 0$), implies that the Fermi energy of the particles is so high as to generate all the resonances and particle spectra observed in earth-bound accelerators (CERN or other). The other aspect, of course, which has generated so much interest, stems from

*Summary of a talk delivered at the International Accelerator Conference at the *Stanford* Linear Accelerator Center, May 1974. An extended version is to appear in the "American Scientist."

†Work partially supported by NSF Grant GP30799X to Princeton University.

the possibility of being for the first time ultrarelativistic gravitational fields at work and have not only the first clear evidence for the existence and possibility of a direct detection of gravitational radiation but also the formation of a completely collapsed object or a "black hole." We have, therefore, the opportunity of testing the validity, under a variety of regimes, of the two best field theories known in theoretical physics: Maxwell's theory of electromagnetism and Einstein's theory of gravitation. On the other hand, we have the possibility of learning much new physics about the weak and strong interactions from the analysis of neutronization of matter and the equilibrium configurations of neutron stars.[1,2]

In all these respects, the process of gravitational collapse and the physics of gravitationally collapsed objects has an enormous potential for a deeper understanding of nature and physical processes. A comparable amount of knowledge could be gained, in principle, only from another phenomenon: the collapse or the initial explosion of the Universe itself.

2. THE BASIC THEORETICAL WORKS ON GRAVITATIONAL COLLAPSE

The entire area of research of the physics of collapsed objects was started by a few fundamental works both in the theoretical and experimental fields. Nothing can illustrate better the motivation behind these pioneering theoretical works than the words of Landau[3] at the beginning of his classic paper, "On the Theory of Stars," "The astrophysical methods usually applied in attacking the problems of stellar structure are characterized by making physical assumptions chosen only for the sake of mathematical convenience . . . It seems reasonable to try to attack the problem of stellar structure by methods of theoretical physics, i.e., to investigate the physical nature of stellar equilibrium. For that purpose we must at first investigate the statistical equilibrium of a given mass without generation of energy . . ."

This way of attacking the problem of the equilibrium configuration of a star at the endpoint of thermonuclear evolution by using the tools of quantum mechanics and Fermi statistics was first proposed by R. H. Fowler[4] and E. C. Stoner[5] but it was not until the decisive contributions of Chandrasekhar' and Landau[7] that the central role played by special relativity in the solution of this problem was recognized. The understanding of this key factor led directly to the novel concept of a critical mass against gravitational collapse.

We can here summarize the main points of the reasoning that led to this conclusion. The description of a star in this approach follows very much along the lines of the Thomas-Fermi treatment of an atom.[7] In the model of the atom, the electrons are described by a degenerate Fermi gas constrained to a finite volume by the Coulomb attraction of the nucleus.[4]

At the endpoint of thermonuclear evolution, the composition of a star is expected to be of nuclei embedded in a gas of electrons (all the orbitals having been detroyed by the great compression of the material, white dwarf star $\rho \sim 10^5$ gr/cm) or, alternatively, a gas of neutrons, protons, and electrons in beta equilibrium (the matter having undergone neutronization under the effect of pressure, neutron star $\rho \sim 10^{15}$ gr/cm^3). In both cases, the material of the star is simply describable by a degenerate Fermi gas, constrained to a finite volume by the self-gravitation of the system. The pressure to keep the system from collapsing is simply given, in both cases, by the quantum pressure due to the Pauli exclusion principle.[7] In the case of the white dwarf stars, the pressure is mainly due to the gas of degenerate electrons while the nuclei mainly contribute to the density distribution; in the case of neutron stars, both pressure and density are generated by the gas of neutrons.[1,2]

The main formulae can be obtained most straightforwardly.

For a degenerate Fermi gas, the density of particles is simply given by

$$n = \frac{N}{V} = \frac{8\pi}{h^3} p^2 \, dp$$

and the Fermi momentum

$$P_F = \left(3\pi^2 \hbar^3 N/V\right)^{1/3} .$$

The kinetic energy of a particle is given by

$$E = p^2/2m . \qquad (1)$$

The total energy is then, simply,

$$\int_0^{P_F} \frac{4\pi}{h^3} \frac{p^4}{} \, dp$$

and the pressure[8]

$$P = -\partial E/\partial V = \left(3\pi^2\right)^{2/3} \left(\hbar^2/5m\right) (N/V)^{5/3} \qquad (2)$$

If, however, the kinetic energy at the top of the Fermi sea becomes comparable to the rest energy of the particle, then the particle energy is no longer given by Eq. (1) but by the usual relativistic relation

$$E = c\left(p2 + m2\,c2\right)^{1/2}$$

or in the extreme relativistic regime by

$$E = c\,p . \qquad (3)$$

The pressure is then in this limit given by

$$P = -\partial E/\partial V = \left(3\pi^2\right)^{1/3} (\hbar c/4) (N/V)^{4/3} \qquad (4)$$

The increase of pressure corresponding to an increase in density is clearly much smaller in Eq. (4) than in Eq. (2). To have clearly understood and expressed this relativistic softening of the equation of state and have focussed the essential role the transition to a relativistic regime plays in the physics of a degenerate star have been the basic contribution of S. Chandrasekhar[6] and L. Landau,[3] which led to the revolutionary concept of a critical mass against gravitational collapse.

There exists, therefore, a fundamental difference between the theoretical description of an atom and that of a degenerate star. Never do the electrons in an atom reach energy so relativistic as to be in the regime described by Eq. (4). Their pressure, given by Eq. (2), reacts to a density change in such a way as always to balance the attractive effects of the electromagnetic field of the nucleus. In a star at the endpoint of thermonuclear evolution, on the contrary, the conditions under which Eq. (4) applies are always reached if the star is massive enough as a direct consequence of the non-screening and long-range character of gravitational interactions. The more massive the star is, the more it contracts, the more the spatial volume of the phase space occupied by the system is reduced and correspondingly the volume in the momentum space expanded[8] so that the Fermi momentum of the system can always reach relativistic regimes. In the transition from Eq. (2) to Eq. (4), the pressure dependence on the density softens considerably and the system is not able to hold itself up in equilibrium, then gravitationally collapses. Practically in free fall the star should shrink down to a point, Landau said, if some new physical phenomena would not occur!

Following these pioneering works, the systematic analysis and detailed computations of the configurations of equilibrium of white dwarfs were presented by S. Chandrasekhar[9] and the ones for neutron stars by R. J. Oppenheimer and G. M. Volkoff.[10] The value of the critical mass for white dwarfs was found to be $M_{crit} \simeq 1.39\ M_\odot$, the one for neutron stars $M_{crit} \sim 0.7\ M_\odot$.

What was the relation of these theoretical works with reality? White dwarf stars had indeed been observed for many years[11] and the theoretical work of Chandrasekhar was in splendid agreement with experiments. For the discovery of neutron stars, we have to wait still a few decades (see Section 3). The key idea leading to their identification was presented as far back as 1934 by Baade and Zwicky[12] in a very compact paper.

"With all reserve we advance the view that supernovae represent the transitions from ordinary stars into neutron stars which in their final stages consist of extremely closely packed neutrons."[12]

It was not until 1939 with the work of Oppenheimer and Snyder[13] that attention was focussed not on the stable equilibrium configurations of degenerate matter (neutron stars and white dwarfs) but on the process of gravitational collapse itself. Then for the first time it became self-evident how the analysis of this phenomenon was so important and revolutionary for our understanding of the nature of space and time. It became clear that the phenomenon of gravitational collapse with its processes of time dilatation, light deflection, and gravitational red shifts, was a most unique place where a fully relativistic theory of gravitation could be seen at work and the validity of general relativity confronted with experimental evidence. The work of Oppenheimer and Snyder appears today one of the most important cornerstones of relativistic astrophysics and one of the most mature and profound works ever written in gravitation physics. In that paper, the authors not only give the basis for the entire field of what will be later known as "black hole" physics, but they also give a fully analytic solution of the collapse of a cloud of dust (pressure zero or free fall, very good approximation to a realistic gravitational collapse) with a detailed analysis of the self-closure of the system from a faraway observer as a consequence of the general relativistic effects.

Still more time was needed *to* realize that the process of gravitational collapse was the ideal place to generate a theoretically detectable amount of gravitational radiation.[14] The reason for this delay is simply explained: Since the first days of general relativity, Einstein himself[15,16] had shown that gravitational fields, like any other relativistic mass zero field, had to propagate with the speed of light and that energy could be carried by gravitational waves. It was not conceived, however, even by a gedanken process, how gravitational radiation could indeed be detected. This key, a fundamental contribution, was made by Joseph Weber in 1960.[17] It was in a much detailed article[18] and in an extensive book[19] that Weber presented not only the main principles on which the detectability of gravitational radiation should be based, but also presented the technical details on the ground of which a detector of gravitational radiation could be built. This detector was made operational by Joseph Weber himself.[1] The relevance of this paper, quite apart from its impact on experimental techniques, has been also very large in generating in the theoretical field, in the following years, much thinking on astrophysical processes to produce detectable amounts of gravitational radiation.

With this paper, we can conclude the set of "heroic" works which were destined to open a new era in relativistic astrophysics.

3. THE DISCOVERY OF COLLAPSED OBJECTS

After the flourishing of the fundamental theoretical works between 1931 and 1939, the progress of relativistic astrophysics was dramatically slowed down due to many diverse social and scientific interests. It was not until 1957 that work in this field started again to develop, thanks mainly to the contributions of Ambartsumian,[20] Cameron,[21] Wheeler,[22] Zel'dovich,[23] and their students and collaborators. The major emphasis in their work was directed toward critically reconsidering the assumptions made in the classical works of Oppenheimer and his students.[10,13] Alternative models of neutron stars were advanced, the emphasis being directed at times toward a better treatment of the surface layers, at times toward the understanding of the role played by nuclear interactions in the treatment of the core. Different models lead to different ranges of masses, radii, and density distributions for the neutron stars' equilibrium configurations.[14]

Slowly the maturity of a "critical" interest of research was regained and new fresh ideas started again to flourish.

In 1962 a new program of research started by R. Giacconi, H. Gursky, F. Paolini, and B. Rossi gave the first evidence for the existence of x-ray sources outside the solar system. In 1964 Zel'dovich[24] following an earlier suggestion of Shklovsky developed a model giving a clear evidence for the possibility of x-ray generation by a plasma accreting into a neutron star. Then in 1968, Shklovsky[25] presented a totally new and original idea: Scorpius XI, the first and most powerful source of x-rays observed in the galaxy is most likely, Shklovsky suggested, a close binary system in which one of the members is a neutron star and the other member a cool dwarf star. "A stream of gas flowing out of the second component is permanently incident on the neutron star," this accreting material enormously compressed should then emit x-rays; "the optical object accompanying the x-ray source might be a cool dwarf star with half of its surface heated by a strong flux of hard x-rays from the source." As we shall see, this article will become a few years later the leading work for the understanding of one of the most exciting discoveries of modern astrophysics: the binary x-ray sources.

1968 is the year *in* which an enormous momentum is gained in this entire field of research.. .the first clear evidence for the existence of neutron stars is given. This conclusion clearly follows from the discovery of pulsars[26,27] and the observation of the pulsar NP0532 at the center of the Crab Nebula.[28] The hypothesis advanced in 1939 by Baade and Zwicky[12] of the possible connection between neutron stars and supernova remnants is spectacularly confirmed. This discovery naturally led to an in-depth search for pulsars inside our own galaxy; of the order of 105 of them are kept today under constant observation and much has been learned about their pulsed radiation, spectra, and time variabilities.[29] Unfortunately the theoretical feedback has not yet been as strong as one could have possibly wished. One of the most important by-products of the discovery of pulsars has been, however, to have dramatically brought back to the attention of a large section of theoretical and experimental astrophysicists the basic issues of the physics of gravitationally collapsed objects.

The clear evidence for the existence of neutron stars, together with the unavoidability of the existence of a critical mass against gravitational collapse,[30] made the existence of "black holes" inside our galaxy inescapable. On the other side, the theoretical picture to be expected at this ultimate endpoint of gravitational collapse appeared more and more complex and presented fundamental issues on the physical processes occurring in these ultrarelativistic regimes.[31,32]

From all this naturally developed the need for launching a realistic effort in order to detect and differentiate the two families of collapsed objects: neutron stars and black holes. The simple idea was advanced by Ruffini and Wheeler[32] of capitalizing on the Shkovsky accretion picture not only in the case when a neutron star is a member of a close binary system but also in the case where a black hole attracts and pulls material from the companion star. The short time variability of the x-ray source and the statistical analysis involved would then be a most powerful tool for the determination of the "form factor" of a black hole.[14]

The discovery and systematic analysis of the binary x-ray sources started in 1971 by the group led by Riccardo Giacconi[33] using the Uhuru satellite came in the most mature moment to have the maximum exploitation and better theoretical

understanding of the experimental results.[34] The success of this discovery has been certainly enhanced by the resonance with so many different observational techniques.[35,36]

In the theoretical field, the feedback of these observations has been very impressive. Essential to the understanding of these binary systems is first of all the understanding of the process of gravitational collapse itself through which these systems have to be formed.[37] On the other side, to understand the process of x-ray emission, a fully relativisitic magnetohydrodynamics has to be developed[38] together with more classical analysis of disc-like structures around the collapsed object in equilibrium under the two opposite effects of gravitational attraction and centrifugal forces.[39-41] The physics of binary star systems is essential in reaching the understanding of the evolution of these binary systems.[42] An accurate analysis of the gravitational and electromagnetic structure of the collaped objects is essential for the understanding of the "core" of these x-ray sources. Finally, criteria to differentiate between the two classes of collapsed objects are much needed.[34]

The great progress currently being made in all these theoretical fields, together with the possibility of having in the forthcoming year, satellites with x- and γ-ray telescopes with larger collecting areas and better time resolutions, as well as pointing facilities, make one hope that in the next five, or at most, ten years, a complete understanding of the final configuration of gravitationally collapsed stars will be gained.

Each one of these X-ray binaries is much like a high-energy accelerator. Here the acceleration process is done by gravity and we have to infer from the scattering of the imploding material the "form factor" of the collapsed object.

If we now turn from this program of research to be achieved in the next few years to a much larger program on longer time scales, two different directions of research naturally present themselves to our attention. The first is clearly to try to directly observe the transition from a normal star into a collapsed object by observing "the moment of gravitational collapse." See Figure 1. This program points to the clear need for developing an entirely new branch of theoretical and experimental astrophysics, what we should call "burst astronomy." In this sense, the recent results obtained by I. Strong,[44] the preliminary work of K. Lande and at the University of Torino,[45] the large effort being made in building a new, more sensitive, set of gravitational wave detectors at the Universities of Louisiana, Rome, and Stanford[46] can only be viewed with the greatest expectation and excitement.

The second direction points toward even a larger program: capitalize on what we are learning in the physics of collapsed objects for gaining a deeper knowledge of the fundamental field equations governing physical processes. It is conceivable that the analysis of these fully relativistic processes will be of great help in the understanding of other apparently disconnected fields of physics, like, e.g., elementary particle physics. It is very likely that this will be by far the most exciting long-range frontier!

References

1. For a review of the current status of the theoretical and experimental research in this field, we suggest Black Holes, Gravitational Waves and Cosmology by M. Rees, R. Ruffini, and J. A. Wheeler, Gordon and Breach, New York, London, 1974, or
2. Neutron Stars, Black Holes and Binary x-ray Sources, H. Gursky and R. Ruffini, eds., Reidel, Dordrecht, Holland, 1974.
3. L. D. Landau, "On the Theory of Stars," Phys. Zeit. der Sowiet 1, 285 (1932).
4. R. H. Fowler, "On Dense Matter," Mont. Not. of RAS XXXVII, 114 (1926).
5. E. C. Stoner, "The Limiting Density in White Dwarf Stars," Philosophical Magazine 77, 63 (1929).
6. S. Chandrasekhar, Mon. Not. of RAS 91, 456 (1931).
7. See, e.g., L. D. Landau and E. M. Lifshitz, Mecanique Quantique, MIR, Moscow, 1971.
8. See, e.g., L. D. Landau and E. M. Lifshitz, Physique Statistique, MIR, Moscow, 1970.
9. S. Chandrasekhar, Mont. Not. of RAS 95, 207 (1935).
10. R. J. Oppenheimer and G. M. Volkoff, Phys. Rev. 55, 374 (1939).
11. See, e.g., A. S. Eddington, The Internal Constitution of Stars, Cambridge University Press, 1926.
12. W. Baade and F. Zwicky, Phys. Rev. 45, 138 (1934).
13. J. R. Oppenheimer and R. Snyder, Phys. Rev. 56, 455 (1939).
14. See, e.g., R. Ruffini, "Neutron Stars, Black Holes and Binary X-ray Sources," invited talk at the 1973 Solvay Conference on Relativistic Astrophysics.
15. A. Einstein, Sitzber. Preuss. Akad. Wiss., 588 (1916).
16. A. Einstein, Sitzber. Preuss. Akad. Wiss., 154 (1918).
17. J. Weber, Phys. Rev. 117, 306 (1960).
18. J. Weber, General Relativity and Gravitational Waves, Interscience Pub., Inc., New York, 1961.
19. See, e.g., J. Weber, Phys. Rev. Letters 18, 795 (1964).
20. See, e.g., V. A. Ambartsumian and G. S. Saallyou, Soviet Astr. 6, 601 (1961) and references mentioned there.
21. A. G. W. Cameron, "Neutron Star Models," Astrophys. J. 130, 884 (1959).
22. See, e.g., J. A. Wheeler et al. report at the Solvay Conference, 1958.
23. See, e.g., Ya. B. Zel'dovich, Soviet Phys. J.E.T.P. 14, 1143 (1962).
24. Ya. B. Zel'dovich, Soviet Phys. Dokl. 9, 246 (1964).
25. I. S. Shklovskii, Soviet Astron. 11, 749 (1968).
26. A. Hewish et al., Nature 217, 709 (1968).
27. T. Gold, Nature 218, 731 (1968).
28. D. H. Staelim, E. C. Reifenstein, Science 162, 1481 (1968).
29. See, e.g., E. Groth, "Observational Properties of Pulsars" in ref. 2.
30. The unavoidability of the existence of a critical mass for the equilibrium configurations of neutron stars has been proved independently from any detail of the equation of state at nuclear or supranuclear densities by C. Rhoades and R. Ruffini, Phys. Rev. Letters 32, 324 (1974).
31. R. Penrose, Rivista del Nuovo Cimento, Numero Speciale, Vol. I, 1969.
32. R. Ruffini and J. A. Wheeler, Physics Today 24, 30 (1971).
33. See, e.g., R. Giacconi in "Binary X-ray sources," invited talk delivered at the Solvay conference on relativistic astrophysics, in press, 1974.
34. See, e.g., R. Ruffini, "The Physics of Gravitationally Collapsed Objects" in ref. 2.
35. See, e.g., P. Boynton, "Optical Observations of X-ray Sources" in ref. 2.
36. See, e.g., R. H. Hjellming, Ap. J. Letters 182, L29 (1973).
37. See, e.g., S. Colgate, "Supernovae" in ref. 2.
38. See, e.g., ref. 34 and references mentioned therein.
39. V. F. Schwartzman, Astron. Z. 15, 377 (1971).
40. J. E. Pringle and M. Rees, Astron. and Astrophys. 21, 1 (1972).
41. Shakura and Sunyaev, Astron. and Astrophys.
42. See, e.g., R. P. Kraft, "Evolution of Binary Systems: Neutron Stars and Black Holes" in ref. 2.
43. See, e.g., R. B. Partridge, "Burst Astronomy" in ref. 2.
44. See I. Strong, "Cosmic Gamma-Ray Bursts" in ref. 2.
45. See, e.g., Editorial Report in Physics Today, July 1974.
46. See, e.g., W. Fairbank et al, in the Proceedings of the Varenna Summer School, 1972, B. Bertotti, ed., Academic Press, New York, 1974.
47. B. Paczynski, Annual Review of Astron. and Astrophys. 9, 183, 1971, and references mentioned therein.
48. W. D. Arnett, Astrophys. and Space Sci. 5, 180 (1969).

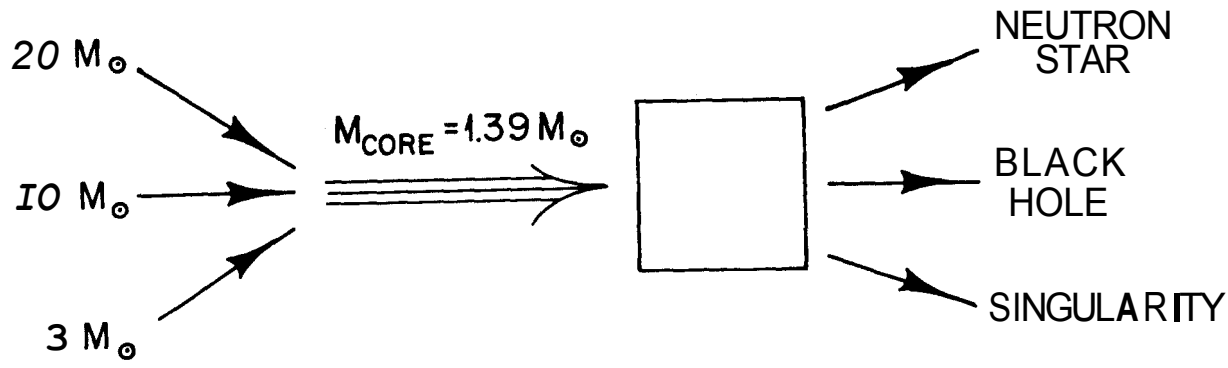


Fig. 1

Figure 1. Recent theoretical work by Arnett[47] and Paczinsky[48] has shown that stars in a large range of masses $2 \lesssim M/M_{\odot} \lesssim 50$ toward the endpoint of their thermonuclear evolution develop a degenerate core of white dwarf material. Once this core reaches the critical value of 1.39 $M_{\odot}$ (Chandrasekhar limit), the star undergoes gravitational collapse. It is extremely important to prove by experimental evidence the validity of this theory postulating a "standard" starting point for the process of collapse to occur. The "moment of gravitational collapse," much shorter than a second, leads the collapsing core either to a neutron star or to a black hole or to a still theoretically unconceived configuration which we label most generally as a "singularity." The key factor in determining which of the different outcomes will in fact occur appears to be more and more controlled by the value of the critical mass of neutron stars.[13]

A 2 GeV 1A ELECTRON STORAGE RING DEDICATED TO THE PRODUCTION OF SYNCHROTRON RADIATION

DARESBURY SYNCHROTRON RADIATION SOURCE DESIGN GROUP*
Daresbury Laboratory,
Daresbury, Warrington, England

Summary

An electron storage ring is being designed to replace the 5 GeV electron synchrotron NINA as a source of synchrotron radiation. The new machine will be used solely for this purpose and its design is being optimized to the needs of the experimenters. The characteristic wavelength of the radiation will be 4 Å and the flux at that wavelength about 3 x 10^{13} photons/s/mr (horizontal) in 0.1% bandwidth. Design considerations include long beam lifetime, small source size and large available solid angle for most beam lines. Assuming a bending field of 1.2 T the beam in the storage ring will have an energy of 2 GeV and the design value of the circulating current will be 1 A. The mean radius will be about 15 m and there will be at least 10 beam lines. Superconducting wavelength shifters or "wigglers" can be incorporated to extend the usable spectrum on two beam lines to 0.1 Å. The new machine will fit into the existing buildings at Daresbury.

Introduction

At the present time, the 5 GeV electron synchrotron NINA provides two synchrotron radiation beam lines supporting nine experiments. These are parasitic on the high energy physics programme, which is expected to cease in about four years' time. To continue to provide a synchrotron radiation facility it is estimated that a purpose-built dedicated source will not only be more suitable but will be cheaper to operate than a high energy synchrotron, saving the capital cost after about five years of operation. Studies have therefore been carried out to determine the requirements and feasibility of such a machine and a detailed design is now emerging.

Specification

A considerable proportion of experiments use radiation down to 1 Å (0.1 nm) in wavelength, and a few such as scattering experiments and radiometry require wavelengths down to 0.1 A or less.

For reasons of intensity, duty cycle, beam stability, and access, the source should clearly be a storage ring, and it has therefore been designed for a characteristic wavelength (λ_c) of about 4 Å, with the understanding that wavelength shifters[1,2] (or "wigglers") will be inserted in two straight sections to provide shorter wavelengths.

High intensity is most important for many experiments and is necessary to justify the facility. This design will provide 3 x 10^{13} photons/s/mr (horizontal) in 0.1% bandwidth at 4 Å wavelength and 5 x 10^{13} at the spectrum peak (10 Å). With a 1.2 T bending field and a 2 GeV beam this will require a circulating current of 1A. Other user requirements are: small beam cross section at the tangent points (~ 2 mm^2); lifetime of stored beam at least 8 hours; facility to circulate only one bunch, for time-resolved measurements in the nanosecond region (at reduced mean intensity); and space for at least 10 beam lines of up to 40 mr horizontal aperture and with good access whilst a beam is circulating (but not necessarily whilst filling).

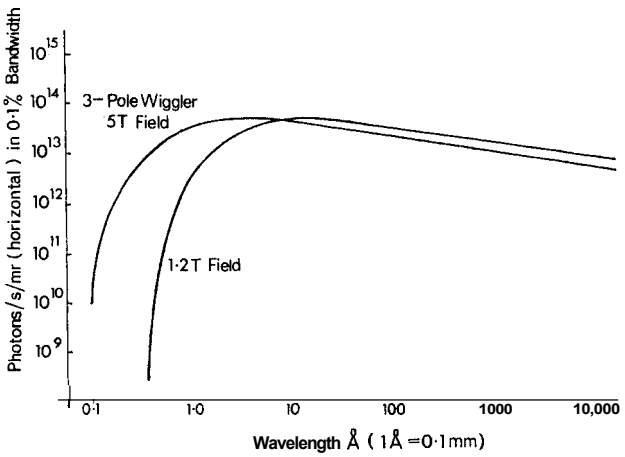


Fig.1 shows the spectra[3] for the two types of beam line.

Some Machine Design Features

Choice of energy and field

Unlike an accelerator or storage ring used for high energy physics, in a synchrotron radiation source it is the characteristic wavelength λ_c rather than the energy which is a prime parameter. The number of photons/s/mr (horizontal) in 0.1% bandwidth at a wavelength λ is given by[3] $N = F(\lambda/\lambda_c)$ x beam energy (GeV) x beam current (A), where F is an algebraic function involving no other machine parameters, and $\lambda_c = 18.6/BE^2$ where B is the bending field (T) and E is the energy (GeV).

If the dipole magnetic field is increased, the radiation spectrum can be kept constant by decreasing the particle energy, which results in a reduction in the bending radius and integrated field length of the magnets, though it is also necessary to increase the circulating beam current. The reduction in integrated field length decreases both the capital and running costs of the magnets, and it has been found[4] that the combined costs are a minimum when a dipole field of about 1.7 T is chosen. Above this value saturation effects dominate the magnet design and cause the costs to increase sharply. However the loss of aperture, also due to pole saturation, at fields above 1.4 T cannot be tolerated in an electron storage ring, and the final choice of field will be in the region of 1.2 to 1.3 T. At such levels the loss of aperture *is* small, and the total magnet cost is only 6% above optimum. The higher energy and lower circulating current benefit the r.f. system through reduction of beam loading and provide better high energy flux from a given wiggler magnet. For 1.2 T the energy will be 2 GeV and the bending radius 5.55 m.

*The principal persons concerned with the machine design are:

D. J. Thompson (project leader), V.R. Atkins, J.C. Hopkins, E.A. Hughes, A. Jackson, J.B. Lyall, N. Marks, P. Moore, D.E. Poole, M.W. Poole, G. Saxon, V.P. Suller, T.E. Swain, K. Tarry, D.G. Taylor, B. Trickett.

The magnet lattice

Having chosen the energy and bending radius, the magnet lattice must be selected. A separated function design is essential in a storage ring to provide radial damping. An 8-cell FBODBO lattice (F, D = quadrupoles, B = dipole, O = straight) was chosen for the following reasons :-

it gives good access to the synchrotron radiation,

it has adequate length and numbers of straight sections,

it has economy of components,

it provides ease of chromaticity correction,

it requires reasonable quadrupole field gradients,

the triplet lattice is anti-damping to electrons with relatively small energy deviations.

The requirement for 2.3 m of clear space in each straight section, after allowance for sextupoles, then fixed the mean radius.

There will be 16 sextupole magnets, individually energized, for chromaticity control and for local sextupole field correction. Other correction elements include skew quadrupoles and an octupole magnet.

Stability considerations restrict the Q-values to less than 3.5 Within this region the structure resonances centred on $Q_V = Q_R = 2^2/_3$ (i.e. p = 8) dominate the diagram and need to be avoided. The regions centred on $Q_V = Q_R = 2\%$ and 3% are reasonably free of lower order resonances and in the injection process allow the maximum flexibility in kicker timing. As 2% is much further from the stability limit it is preferred for the storage ring to operate in the region $2\frac{1}{4} < Q_{\cdot} Q_R < 24$. However, the cross-sectional dimensions of the damped beam, which are determined by the quantum excitations resulting from synchrotron radiation emission, and therefore increase with energy, are smaller for a given lattice when operated at higher Q_R values. For this reason the storage ring will be operated at the highest feasible Q_R value. The storage ring will have the capability of operating at any point within the stable area in the Q-diagram so that subject to injection limitations the tune can be changed to find the optimum working point.

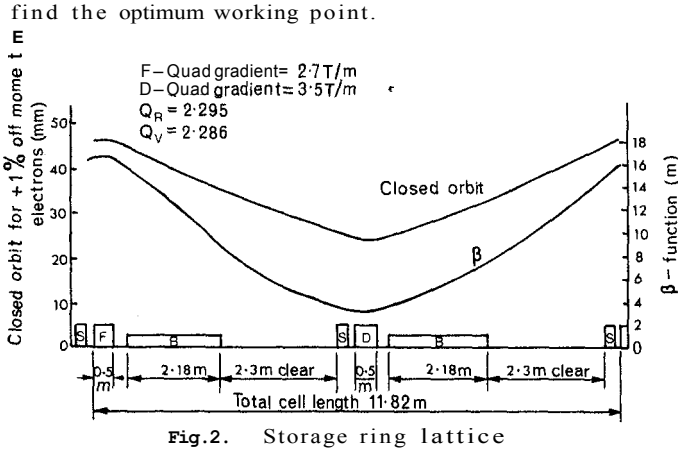


Fig.2. Storage ring lattice

The lattice parameters assuming $Q_V \sim Q_R \sim 2.25$ are shown in fig.2.

The sixteen dipole bending magnets have a magnetic length of 2.18 m and are of a 'C core' design. Whilst this design has a smaller good field aperture and is more susceptible to saturation effects than the 'H' or 'window frame' designs, it is required in order to allow the connection of a large number of beam lines including those from "wigglers". The magnets will be built from thick laminations rather than machined from solid blocks. This not only allows complete shuffling of the steel but also eliminates the small eddy currents which occur in a solid magnet when rise times of the order of a few minutes are used.

The sixteen quadrupoles will also be laminated and there will be separate power supplies for the dipoles and for the focusing and defocusing magnets so as to control the radial and vertical Q values separately.

Injector

In order to accumulate a high circulating current it is essential to inject many pulses into the storage ring. The injection energy must therefore be high enough for radial damping of betatron oscillations to take place between injection pulses. An energy of 600 MeV has been chosen, giving a damping time constant of 400 ms and an adequate Touschek lifetime of 50 mins.

The injection method is a conventional multi-turn system using a septum magnet and a fast localized orbit bump produced by two fast kickers. The exact rate at which injection can take place is determined by the acceptance aperture of the storage ring, the emittance of the 600 MeV beam and the radial Q value at injection. These parameters are not yet finalized, but so far it appears that injection can be at a rate of up to 6 Hz when Q_R is in the vicinity of 2%.

The 600 MeV electrons for injection into the storage ring will be provided by a linear accelerator in the range 10-15 MeV followed by a booster synchrotron. This will have a mean radius one third that of the storage ring. Extraction and transfer to the storage ring will take place over three turns though it is not considered necessary for each injected pulse to fill the storage ring uniformly.

Extraction from the booster will be by a simple shaving technique with a fast orbit bump and a septum magnet. With a circulating current of 20 mA in the booster this will lead to electrons being accumulated in the storage ring at between 1 and 5 mA per pulse, and at a transfer rate of 5 Hz the 1000 mA stored beam will be reached in ~ 3 minutes.

Alternatively efficient single-turn extraction using an integer resonance system could be developed.

The booster synchrotron is a combined function machine of the FODO type to provide maximum length of useful straight section. It too will contain 8 unit cells and the field on the equilibrium orbit will be 0.785 T. Each magnet will bend through an angle of $22\frac{1}{2}^{\circ}$ and will be curved. The bending radius is 2.546 m and the gaps in the central orbit between the individual laminated blocks reduced by inserting profiled, laminated steel packets, bonded to the nearest magnet block.

The repetition rate of the booster will be 10 Hz, but injection into the storage ring can be at any submultiple by appropriate pulsing of the gun. At 10 Hz it is calculated that both the dipole and sextupole fields due to eddy currents in the corrugated stainless steel vacuum vessel (wall thickness 0.2 mm) will be acceptably small.

The radio-frequency system

Since the beam loss due to synchrotron radiation at 2 GeV, 1A is 255 kW the r.f. system forms a major part of the storage ring equipment. Factors to be taken into account in the design of such a system are i) quantum lifetimes with implications in the choice of cavity voltage in the storage mode; and ii) stability of operating conditions with heavy beam loading. It is also necessary to limit the synchrotron oscillation frequency, particularly at injection.

The radiated beam power will be increased by about 10% if two "wigglers" are added (without reducing the beam current). The total power requirement will therefore be around 400 kW. It is judged prudent not to exceed 50 kW per cavity window, so that there will be 8 separate single cell cavities. In order to maintain the low shunt impedance (10-15 MΩ) required from stability and beam loading considerations at an acceptable peak voltage, the unconventional technique of fabricating the cavities from stainless steel will be adopted, although this increases the difficulty of achieving a high coupling factor to the feeder waveguide. The cavity frequency is not finally decided but will be either 428 MHz or 499 MHz depending mainly on economic considerations relating to r.f. power sources.

For resistive matching the coupling β is $1 + P_b/P_c$ where P_b is the radiated power and P_c is the power dissipated in the cavities. Reactive compensation of the beam loading induced voltage is obtained by detuning the cavity by an amount

$$\Delta f = \frac{f_o I_o \cos \phi_s ZT^2 \ell}{2Q_o V_{ep}} = \frac{f_o P_b \cot \phi_s}{2Q_o P_c}$$

where I_o is the mean beam current, V_{ep} is the effective peak cavity voltage, $ZT^2\ell$ is the total transit time corrected shunt impedance and ϕ_s is the phase angle of the beam relative to the voltage zero.

Ideally the beam loaded cavity should present a match to the amplifier at all energies and beam currents. This can only be achieved if both the cavity tuning and the coupling factor are varied and it is hoped to go some way towards achieving this. It is necessary to work with a system stable in the presence of coherent synchrotron oscillations. To ensure this the 'stability factor' δ must be less than unity. For the resistively matched system $\delta = 1/(1 + 2P_c/P_b)$ which is always less than one if there are cavity losses. If the beam loaded cavity is not resistive then the more general expression for stability is

$$1 + \tan 2\psi - \frac{I \tan \psi \, ZT^2 \ell}{(1 + \beta) V_{ep} \cos \phi} > 0$$

where ψ is the detuning angle. It may be noted that stability is aided by over coupling (high β) and by detuning to a higher frequency (high tan $) than would give exact compensation.

At injection (600 MeV) the beam builds up in small increments to 1A. The beam power is low so stability is easy to achieve. However the beam induced voltage is high and a large cavity detuning must be used. To keep this to a reasonable amount a high cavity voltage must also be employed, with due regard, however, to the frequency and amplitude of the synchrotron oscillations.

On accelerating to 2 GeV the radiated power increases. It is proposed to vary the voltage, the coupling and the detuning during acceleration and fig.3 shows a suitable programme.

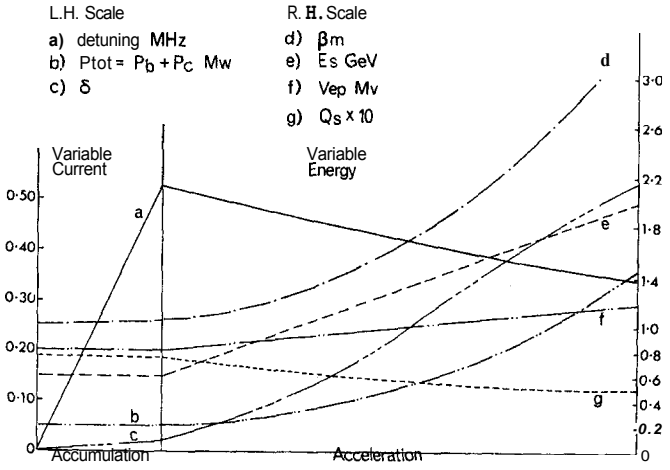


Fig. 3. R.f. parameters

Other Design Features

Vacuum. The high value of radiated power in the storage ring (255 kW excluding wiggler losses) dictates a well-cooled vacuum chamber. Because of the large number of branches, ease of fabrication of complex shapes is essential and stainless steel will be used. Because of lifetime considerations, the emphasis will be on a clean bakeable vacuum system, giving a pressure of 10^{-9} torr at full beam current. There will be differential pumping between the storage ring and each experimental beam line, and in the transfer path from the booster synchrotron. There will be distributed ion-pumping in the dipole magnets giving at least 1000 ℓ/s pumping speed per dipole.

Radiation. Personnel safety presents a problem in that the users must be able to set up equipment whilst a beam is circulating, and be in close proximity to their equipment whilst data-taking. Radiation levels around a storage ring are inherently low except whilst filling, at which time the building will be evacuated. By using scrapers and an emergency beam dump it can be arranged that most of the beam is lost in pre-determined areas which are adequately shielded. The remainder of the ring will have a modest shield wall of lead, iron or concrete, and the vacuum chamber will be designed to prevent high energy photons from going down the beam lines to experiments.

Single Bunch Operation. This will be required by experimenters interested in measurement of lifetimes of excited states. It will provide 300 ns between pulses. It will require a low frequency chopper to inject a short burst of pulses into the synchrotron, followed by a higher frequency device (∿ 35 MHz) to reduce this to a single bunch. Using a suitable synchronizer to trigger the extraction system, a single bunch will be stacked in the storage ring.

Controls. The whole machine complex will be controlled through a network of computers. At the lowest level, three minicomputers, one each for linac, booster synchrotron and storage ring, will be interfaced to the plant via CAMAC. All local controls will operate via these to permit independent testing of the three accelerators. These minicomputers will be connected via parallel data links to a more powerful machine forming the central control facility. This machine will contain the main database for the system, and will support two identical control consoles, aided by a fourth minicomputer. It will also be linked to an on-line task in the Daresbury central computer, an IBM 370/165, which will make very powerful computation facilities available

on-line for accelerator physics work.

The Wavelength Shifter or "Wiggler"

To accommodate the small number of users who require radiation between 0.1 Å and 0.8 Å it is intended to insert "wiggler" magnets[1,2] into straight sections in the storage ring lattice. In view of the development of superconducting technology it is certainly feasible to provide a sufficiently high field over the full aperture. The use of large numbers of poles in these magnets to enhance the radiation intensity is undesirable because of the large increase in r.f. power required. Use of a small number of poles with the highest fields practicable is to be preferred, as this benefits the user at short wavelengths most economically. It is therefore intended initially to use only three poles in each wiggler magnet and to design for a peak field of 5 T. Recent improvements in superconducting coil design indicate that fields in excess of 6 T may eventually be realised, and this will enhance the intensity at 0.1 Å by an order of magnitude. Design work on a superconducting wiggler magnet is proceeding at the Rutherford Laboratory of the Science Research Council. These magnets will be full aperture so as not to affect injection or beam lifetime, but will only be energized after the beam has been stored and accelerated.

Installation

The layout (fig.4) has been chosen with three things in mind - to provide for many experiments with good access, to allow the maximum amount of installation to proceed prior to the cessation of high-energy physics using NINA, and to minimise civil engineering work. All these points result in the storage ring being placed approximately centrally in the "Inner Hall" of the NINA building. At least one quarter of the ring can be constructed without interfering with the operation of NINA. Reduction of the high energy physics experimental areas from five to three will release sufficient space to build the injector (perhaps without all its shielding), and at the same time other space will become available for controls and for some of the ancillary plant before NINA closes down.

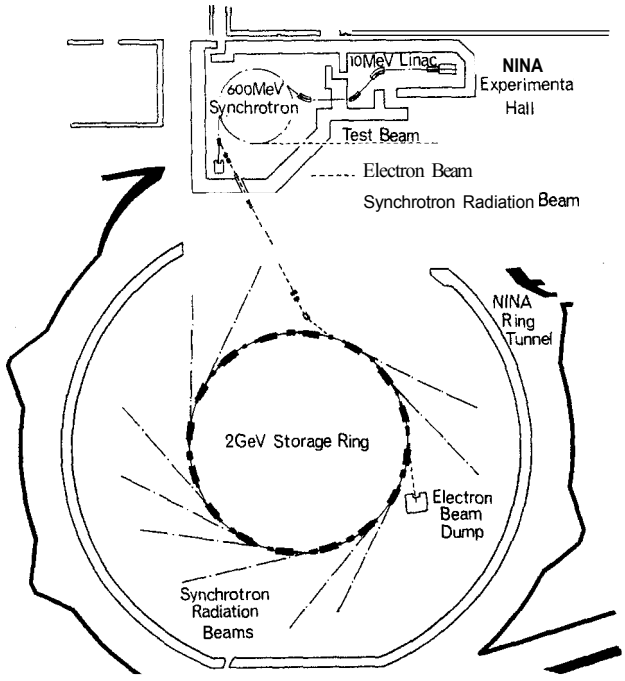


Fig.4. Layout

Parameter List

Injector

Energy	10-15 MeV
Energy spread (maximum)	± 0.5%
Emittance (maximum)	10^{-5} m-r
Current (within above limits)	20 mA

Booster Synchrotron

Peak energy	600 MeV
current	20 mA (∿ 10^{10} e-/pulse)
Peak magnetic field on orbit	0.785 T
Bending radius	2.546 m
Mean orbit radius	5.02 m
Betatron Q-value, both planes	2.25
Period structure	FODO (Comb. Func. Lattice)
No. of periods	8
Field index in F-sector	-5.2
Field index in D-sector	6.2
Field gradient in F	2.04% per cm
Field gradient in D	2.44% per cm
Magnetic length of sector magnet	1.0 m
Aperture	120x35 mm (approx.)
Repetition rate	10 Hz
R.f, frequency	428 MHz or 499 MHz
R.f. power	< 1 kW peak

Storage Ring

Energy	2 GeV
Characteristic wavelength	3.88 Å
Maximum current	1 A (∿ 2 x 10^{12} e- stored)
Beam lifetime at maximum current	8 hours
Peak magnetic field	1.2 T
Bending radius	5.55 m
Mean orbit radius	15.05 m
Betatron Q-value (either plane)	2.0 - 3.5
Peak quadrupole gradient	4.5 T/m
Period structure	FBODBO (Sep. Func. Lattice)
No. of periods	8
Dipole magnetic length	2.18 m
Quadrupole magnetic length	0.5 m
No. of sextupoles/period	2
Clear length of straight section	2.3 m (approx.)
Good field aperture	150x40 mm (approx.)
Maximum pressure with 1A beam	torr
Vacuum chamber aperture	200 x 45 mm
Distributed pumping capacity/dipole	1000 l/s
Radiation damping time, 600 MeV	440 ms (radial betatron)
Touschek lifetime, at 600 MeV	50 min
Radiation loss from normal dipoles, at 2 GeV	255 keV/turn
R.f. frequency	428 MHz or 499 MHz
Total r.f. power	∿ 400 kW
No. of cavities	8
Cavity material	Stainless steel
Cavity shunt impedance (transit time corrected)	1.25 to 2.0
Q_s	∿ 0.05

Programme

The official design study of the dedicated Synchrotron Radiation Source will be complete by the end of 1974. It is expected to show that the capital cost will be about £2M (1973 prices). Approval for construction will then be sought, and if the present ideas for the NINA programme turn out to be correct, the SRS

will come into operation during 1979.

References

1. W.S. Trzeciak. "A "wavelength shifter" for the University of Wisconsin electron storage ring". IEEE Trans. Nucl. Sci. NS-18, (1971) 213.

2. R.J. Averill, R.D. Hays and H. Mieras. "Wiggler magnet design". CEAL-TM-199 (January 1973).

3. V.P. Suller. "Comparative Synchrotron Radiation Spectra". Daresbuq Laboratory Internal Report, DL/TM 118 (December 1973).

4. N. Marks and M.W. Poole. "The choice of dipole magnetic field for the SRS". Daresbuq Laboratory Internal Report to be published.

THE STANFORD SYNCHROTRON RADIATION PROJECT (SSRP)†

H. Winick
Stanford University
Stanford, California 94305

Summary

The Stanford Synchrotron Radiation Project is a new national facility for UV and X-ray research using synchrotron radiation from the storage ring SPEAR. This ring now operates in colliding beam mode with E (stored beam energy) varying from 1.5 to 2.5 GeV and with 15 to 45 mA in each beam. Improvements in mid-1974 will raise the energy to $\gtrsim 4$ GeV with expected currents of up to 100 mA in each beam. The critical energy of the synchrotron radiation spectrum varies as E^3 and is 11 keV for E = 4 GeV. Up to seven experiments can share a beam run which accepts 11.5 mrad of radiation. The UV and soft x-radiation are deflected at grazing incidence on ultrasmooth platinum plated copper blocks and focused on custom built, high vacuum, high resolution monochromators. X-radiation above about 3.5 keV emerges from a 630μ thick beryllium window assembly. Sensors in the beam run detect high pressure or contamination and cause valves to close isolating the beam runs from each other and from the SPEAR vacuum system. Shielding and interlocks permit experimenters to adjust their equipment with beam shutters closed and to be within about 1 m of their equipment during operation with shutters open. A broad ranging program of research will be pursued including studies of UV and x-ray photo-electron spectroscopy, extended x-ray absorption edge fine structure, x-ray diffraction on biology systems, compton scattering, x-ray absorption x-ray induced luminescence, sub-nanosecond time constant measurements on solids, and UV reflectivity.

Introduction

SSRP utilizes synchrotron radiation from circulating electrons in the storage ring SPEAR. SSRP has been funded since June 1973 by the National Science Foundation and is administered by the W. W. Hansen Laboratories of Physics at Stanford University. SPEAR is a high energy electron-positron colliding beam storage ring located at the Stanford Linear Accelerator Center (SLAC), funded by the Atomic Energy Commission. Prospective users of SSRP should contact the Director, Professor S. Doniach or the Deputy Director, Professor W. Spicer, at the W. W. Hansen Laboratories of Physics.

SSRP is open to all qualified users. Experimental proposals are reviewed by the Director, advised by a Proposal Review Panel, outside referees, and the SSRP staff. Early submission of proposals is recommended. SLAC exercises control over radiation safety and also sets vacuum standards for experiments which will connect on-line to the SPEAR Vacuum System.

Characteristics of SPEAR

Some basic synchrotron radiation relationships are given in Table I. Additional synchrotron adiation relationships are given by Rowel and Winick.[1] The storage ring SPEAR has been described in the literature.[3] The particular parameters of SPEAR that are relevant to synchrotron radiation are listed in Table II. The spectral distribution of the radiation is shown in Fig. 1. The data given in Table II and Fig. 1 are obtained using the result of Mack.[4] SPEAR has a bending radius of 12.7 m The radiation is highly polarized with the E vector in the plane of the acceleration.

BASIC SYNCHROTRON RADIATION RELATIONSHIPS

ELECTRON ENERGY:	E (GeV)
RADIUS OF CURVATURE:	R (METERS)
ELECTRON CURRENT:	I (AMPERES)

$$\frac{\Delta E}{\text{TURN-ELECTRON}} = 88\frac{E^4}{R}\ (\text{keV});\ \epsilon_c = 2.2\frac{E^3}{R}\ (\text{keV})$$

$$\text{TOTAL RADIATED POWER} = 88\frac{E^4}{R} \times I(\text{kW})$$

$$\text{EMISSION ANGLE} \approx \frac{1}{\gamma} = \frac{mc^2}{E} = 2 \times 10^{-4} \text{ at } 2.5 \text{ GeV}$$

$$\frac{N_\gamma}{\text{TURN-ELECTRON}} \approx \frac{\Delta E/\text{TURN-ELECTRON}}{\epsilon_c} = 40E$$

TABLE I

SPEAR now operates for colliding beam experiments with one RF bunch per beam at energies up to 2.5 GeV per beam (limited by RF voltage). The current is limited by the maximum allowable incoherent tune shift ($\Delta\nu \approx .05$) due to beam-beam interaction. This limit increases with increasing energy. With the present SPEAR operational configuration, the currents corresponding to this limit are shown in Table II. Machine studies on SPEAR are in progress to increase the beam cross-section at the interaction point so that larger currents and larger interaction rates (luminosity) can be achieved, especially at the lower energies. Larger currents can of course be stored in a single beam (over 200 mA has been stored in one electron bunch and even more is possible if more of the 40 RF bunches are filled) but present plans call for synchrotron radiation operation only during colliding beam experimental runs. The water-cooling of the SPEAR vacuum chamber is adequate for synchrotron radiation losses of up to 150 kW per beam.

The beam decays with a lifetime that depends on

†Supported by National Science Foundation Grant No. GH 39525, in cooperation with the Stanford Linear Accelerator Center and the Atomic Energy Commission.

energy and current. At2.5 GeV the lifetime is 2 hours with 45 mA in each beam and increases to 4 hours with 30 mA per beam. Typically it takes 15 to 30 minutes to fill SPEAR with 2 beams, followingwhich beams are stored and made to collide for several hours, after which the cycle is repeated.

PARAMETERS OF SPEAR

	UNTIL 7/74	AFTER 11/74
ACCELERATING FREQ. (MHz)	51	358
PULSE DURATION (10^{-10} sec) (FWHM)	8 to 16	1 *to* 2.4
ORBITAL FREQ. (MHz)	1.28	1.28

E_e (GeV)	1.5	2.0	25	3.0	3.5	4.0	4.5
I, (mA)	20	25	45	*50*	75	75	45
RADIATION LOSS (kW)	0.70	2.8	12	28	78	135	130
ϵ_c (keV)	0.58	1.4	2.7	4.7	7.4	11	15.7

TRANSVERSE ELECTRON BEAM SIZE AND DIVERGENCE AT SYNCHROTRON RADIATION SOURCE POINT (TYPICAL AT 2.5 GeV)

	x (mm)	x'(mrad)	y (mm)	y'(mrad)
FWHM	3.22	0.566	1.59	0.266

TABLE II

During the summer of 1974 themagnetpower supplies and the RF system will be modified to permitbeam storage up to 4.2 GeV or more. The new RF system will produce 500 kW at 358 MHz. The present RF system produces 160 kW at 51 MHz. Higher colliding beam currents are possible at thehigherenergiesreachinganexpected peak of 100 mA at 3.8 GeV. Above 3.8 GeV the expected beam current falls off due to RF voltage limits. In addition to the dramatic improvement the higher currents and energy will make in synchrotron radiationpower and critical energy, ϵ_c, as shown in Table II, the higher frequency will reduce the synchrotron radiation light pulse to $\sim 10^{-10}$ sec **makingpossibleexperiments** requiring fast time correlations.

Plan of the Synchrotron Radiation Facility

A **prefabricatedsteelbuilding** 12 m wide, 24 m long and 7.3 m high has been constructed adjacent to SPEAR as shown in Fig. 2 and Fig. 3. **The** building is well insulated and temperature controlled and has a thick (30 cm) concrete floor for stability. Vibration sources (such as compressors) arelocated outside the building and decoupled from the building and floor.

About 11.5 mradians of synchrotron radiation, corresponding to 15 cm of curved path in a SPEAR bending magnet, emerges tangentially into a high vacuum pipe. This horizontal fan of radiation is split three ways by reflection at grazing incidence on two remotely movable ultra-smooth platinum-plated copperblocks[5] placed 6.5 m from the source point. One of these mirrors intercepts the outer 2 mrad of synchrotronradiation at a horizontal grazingangleof incidence of 2° resulting in a horizontally focused 4° deflected beam containing photons with energy up to about 2 keV. A plane mirror intercepts the inner 3 to 6 mrad atavertical grazing angle of incidence of 4° causing the beam to rise at 8° from the median plane. This rising beam contains photons up to 300 eV. Since SPEAR can produce up to 25 W of synchrotron radiation per mrad these mirrors are cooled thermoelectrically.

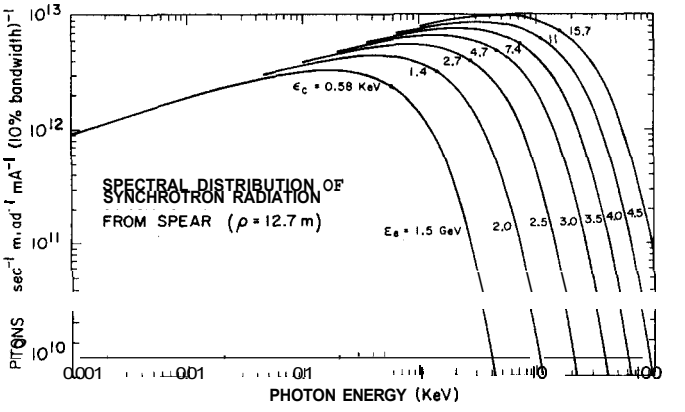


Figure 1

The central part of the beam contains 3 to 10 mrad of radiation which is not deflected by mirrors. This radiationproceedsdownthehigh vacuum beam pipe, passes through a pair of water-cooled 65μ thick beryllium foils and exits from the vacuum system 10.5 m from the source point through a pair of 250μ beryllium windows. Significant transmission begins at about 3.2 keV. Thiswindow system has been used successfully over extended running periods with SPEAR operating at 2.4 GeV with currents up to 50 mA. In-vacuum water-cooled carbon foils[6] are being considered to handle the higher power densities that will be present when SPEAR operates at higher energy.

After emerging from the SPEAR vacuum system the x-rays travel in a helium atmosphere intoashielded area in which several crystal monochromators andexperiments will be installed. Some of these direct the monochromatic radiation upwards to an upper level experimental area as shown in Fig. 3 and Fig. 4.

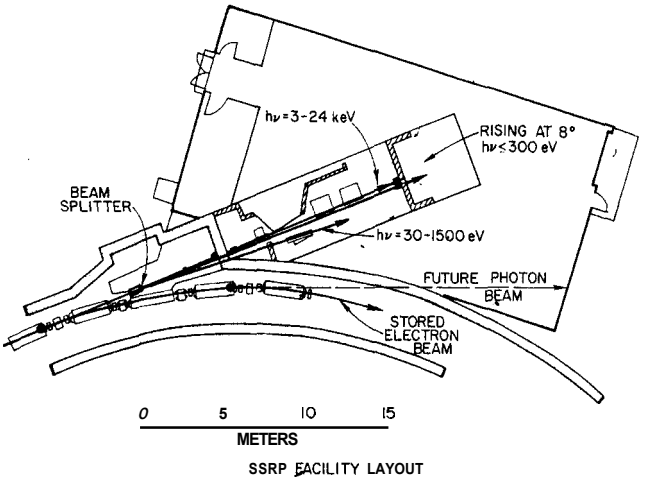


Figure 2

An elevated concrete slab 4.5 m wide, 12 m long, and 2.4 m above the floor serves as a second level for installing experimental apparatus. The rising 8° beam line vacuum pipe penetrates this slab as shown in Fig. 3. Electrical services, compressed air, helium and water services are installed at several locations along the perimeter of the slab. Vacuum controls, radiation protection controls, and signals to and from the SPEAR and SLAC control rooms are centralized in an adjacent control room.

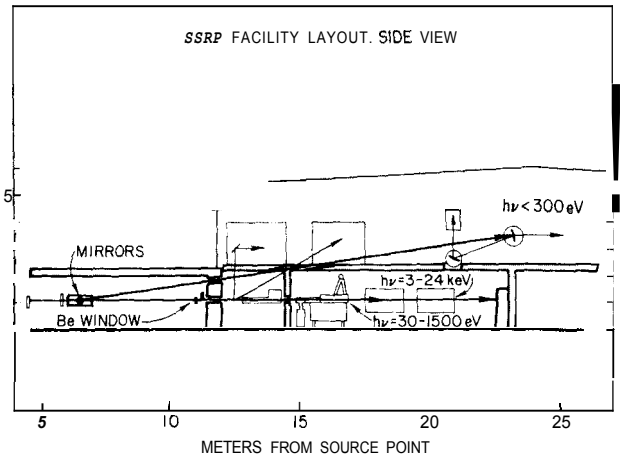


Figure 3

The synchrotron radiation beam can be independently steered so that it can be reproduced spatially, correcting for variations that may occur from run to run, or variations that may be required for positioning the two collidingbeaminteraction points. This is accomplished by powering steering coils some of which are arranged in pairs to produce local orbit distortions (beam bumps) in the vicinity of the synchrotron radiation source point.

Vacuum System

The vacuum system is built to SLAC specifications[7] and is all metal and bakable. Thecentral beam pipe extends to 10.5 m from the source terminating at the beryllium window assembly within the SPEAR tunnel. The 4° and 8° beam runs continue in vacuum in the synchrotron radiation buildingandextend to 16 m and 23 m from the source point.

All metal ultra-highvacuumgate valves isolate the beam runs fromeachother and from the SPEAR vacuum system. Synchrotron radiation strikes only water-cooled surfaces and movable water-cooled absorbers may be remotely inserted to block the radiation.

Ionization gauges and fast sensors[8] are used to detect leaks and desorption diodes[9] sense contamination. These devices are monitored by a vacuum control system which causes valves to close automatically in the event of vacuum problems. Fast isolation from SPEAR is provided by a vane which closes in 30 msec.[10]

Radiation Protection System

A systemofbeam stoppers, a permanent magnet, radiation monitors and interlocked gates is installed to protect personnel fromexposure to synchrotron radiation or the high energy radiation that could result in the worse case event that injected or stored beams are lost in SPEAR in certain criticallocations. With appropriate beam stoppers closed, occupancyis safe in the immediate vicinity of experiments during all phases of SPEAR operation. With beam stoppers open experimenters are able to occupy areas within about 1 m of beam lines. Access to the SPEAR tunnel and to the primary x-ray beam line in the SSRP building is remotely controlled by SLAC operators. Access to smallsecondarybeam areas is experimenter controlled.

Status of the Project

At this writing (April 1974) a pilot project beam run has been in operation since July, 1973, providing radiation to an x-ray photo-electron spectroscopy (XPS) experiment and an extended x-ray absorption fine structure (EXAFS) experiment. This equipment is now being removed and the full facility with all beam runs, control systems, personnel protection systems, shielding, etc., is being installed. Operation with five experiments is planned for May and June, 1974. Following this the SPEAR ring will be down for several months for the improvement program which will allow storage of beams with energy in excess of 4 GeV. Some synchrotron radiation shouldbeavailable in the latter part of 1974 and routine operation for colliding beam and synchrotron radiation experiments is scheduled to commence in late 1974 or early 1975.

Experimental Program

X-ray Beam Line (hν > 3 keV)

Several different groups will set up spectrometers using the x-rays available in the main beam line. The activities in this beam line include:

X-ray Photo-Electron Spectroscopy (XPS). A 3-crystal monochromator designed to produce intense radiation at 8.0 keV with a bandwidth of 0.1 eV has been built by P. Pianetta of Stanford and has been operated in a double crystal configuration. A high vacuum sample chamber and electron energy analyzer built by I. Lindau of Stanford isalsocomplete. Theequipment was used in a pilot project x-ray beam and has produced its first data on the 4f levels of metallic gold.[11] A broad-ranging program of research in the fields of solid state materials science, inorganic and organic chemistry will be led by W. Spicer, I. Lindau and S. Doniach of Stanford.

Extended X-ray Absorption Fine Structure (EXAFS). Initially one EXAFS channel-cut single crystal x-ray spectrometer with associated detectors and data processing equipment is being assembled. Several investigators (including A. Bienenstock, S. Doniach, S. Hunter, B. Kincaid, and M. Weissbluth of Stanford, D. Sayers and E. Stern of the University of Washington, F. Lytle of the Boeing Aerospace Company and P. Eisenbergerof the Bell Telephone Research Laboratories) will use EXAFS studies to determine the radial structure functions associated with specific elemental constituents inavarietyof complex materials including gases, liquids, glasses and certain complex crystalline materials in which the environment of one particular kind of atom is important; e.g., the iron atom in hemoglobin.

X-ray Diffraction. A group from the California Institute of Technology (J. Baldeschweiler, R. Stroud, and N. Webb) are building a focusing monochromator with low angle diffraction camera for x-ray diffraction studies of biological systems including time dependent diffraction. Samples to be studied include proteins, enzymes, muscle, and membrane systems.

A group consisting of K. Hodgson and E. Shooter of Stanford and L. Jensen of the University of Washington,

Seattle, are proposing to install a diffractometer at the focus of the monochromator to do structural studies on protein single crystals.

Compton Scattering. P. Eisenberger of the Bell Telephone Research Laboratories is planning to build a triple axis monochromator - energy analyzer system to measure x-ray inelastic scattering. This is planned for use in SPEAR II (early 1975). Among other measurements that of the Comptonprofile in solids and molecular systems gives very detailed information aboutelectronic charge distributions which can be used to test specific theories of chemical bonding.

4° Beam Line ($25 < h\nu < 2500$ eV). A flexible facility, entered around a specially designed grazing incidence monochromator with a fixed exit slit, will be set up in this beam line under the direction of F. C. Brown, R. Bachrach, and S. Hagstrom of the Xerox Research Center at Palo Alto and Stanford University. A beam splitting mirror will provide about 2 mrad to this line, focused in the horizontal direction. Research on this beam line will include studies on high resolution soft x-ray absorption spectroscopy, x-ray induced luminescence, photo-emission spectroscopy by time of flight measurement and subnanosecond time constant measurements on solids.

8° Rising Beam Line ($h\nu < 300$ eV). A specially adapted ultra-high vacuum normal incidence monochromator for this energy range is now being built by the McPherson Company under subcontract from China Lake for installation in the beam run. A group from the Michelson Laboratory at China Lake, led by V. Rehn (others include A. Baer, T. Donovan, D. Kyser, and J. Stanford), in collaboration with a Stanford group, will make reflectivity and photo-emission measurements. Differential reflectivity (electro- and piezo-reflectance) measurements are being planned.

Acknowledgments

The dedication of the SSRP staff, R. Dannemiller, A. Golde, and B. Salsburg, together with Mark Baldwin of SLAC, has been vital to the progress of this project. Invaluable assistance has Seen received from many others at SLAC, particularly R. Baker, W. Basinger, M. Beck, R. Filippi, G. Fischer, A. Gallagher, F. Generali, F. Hall, J. Harris, E. Hoyt, B. Humphrey, J. Jurow, R. Larsen, R. Melen, J. Miljan, R. Messimer, W. Milner, H. Morales, J. Paterson, J. Pope, W. Porter, R. Robbers, W. Savage, T. Taylor, A. Tseng, G. Warren, and J. Wehner, The beam line vacuum system was drawn with meticulous care by F. Johnson. Our debt is particularly great to N. Dean for the genuine interest, guidance and support he provided.

References

1. Ednor M. Rowe, IEEE Trans. Nucl. Sci. NS-20, no. 3, p. 973, June 1973.
2. Herman Winick, IEEE Trans. Nucl. Sci. NS-20, no. 3, p. 984, June 1973.
3. J. M. Paterson, Proc. of this Conference. *Also* B. Richter, Proc. of 1973 Particle Accel. Conf., San Francisco. IEEE Trans. on Nucl. Sci. NS-20, No. 3, p. 752, June 1973.
4. R. A. Mack, Spectral and Angular Distribution of Synchrotron Radiation, CEAL-1027 (1966).
5. S. Holmes, A. Klugman, and P. Kraatz: Applied Optics, 12, No. 8, p. 113, Aug. 1973.
6. E. W. Hoyt and P. Pianetta, SLAC TN-73-10, Sept. 1973.
7. M. Baldwin and J. Pope, SLAC TN-73-13, Oct. 1973.
8. G. W. McClure, Appl. Phys. L 2, No. 12, p. 233, (1963).
9. E. Garwin, E. Hoyt, J. Jurow, M. Rabinowitz, Proc. 4th International Vacuum Congress, Apr. 1968, Manchester, England.
10. This fast closing vane is of the type used on the ISR at CERN and was kindly supplied to us by CERN.
11. I. Lindau, P. Pianetta, S. Doniach and W. Spicer, X-ray Photo-Emission Spectroscopy at the Stanford Synchrotron Radiation Project. Accepted for publication in Nature.

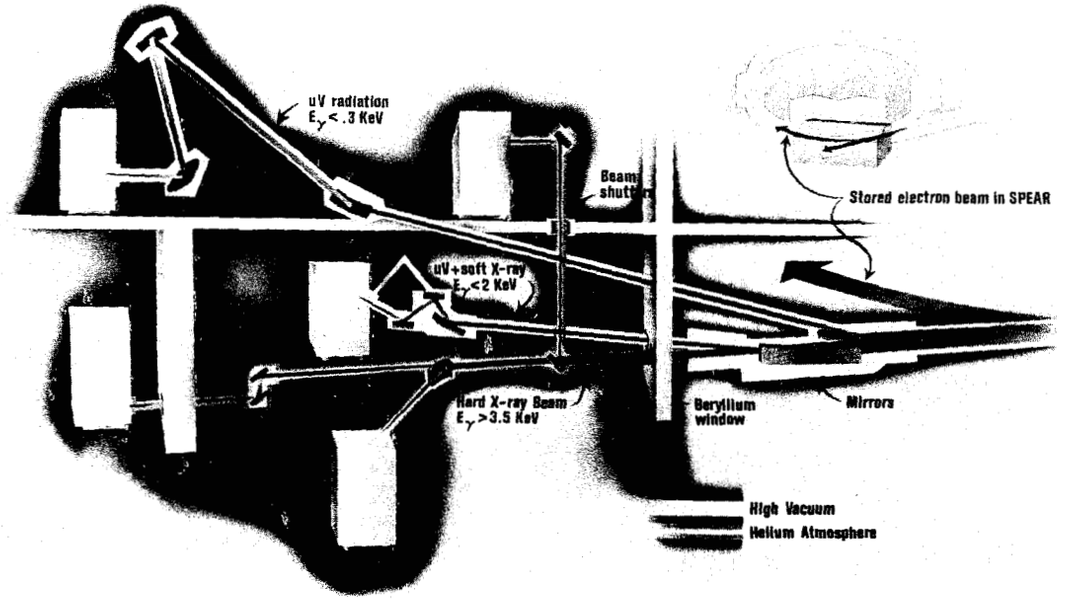


Figure 4

THE CONVERSIONOFTHE NBS 180 MEV ELECTRON SYNCHROTRON TO A 240 MEV ELECTRON STORAGE RING FOR SYNCHROTRON RADIATION RESEARCH

E. M. Rowe, M. A. Green, W. S. Trzeciak, and W. R. Winter, Jr.
Physical Sciences Laboratory - University of Wisconsin
Stoughton, Wisconsin

Introduction

The National Bureau of Standards 180 MeV electron synchrotron was used for the first investigations of the optical and electronic properties of solids, liquids, and gases utilizing synchrotron radiation1 . Since the time of this pioneering work, other sources of far greater brightness such as DESY, the Tokyo Synchrotron, and Tantalus I have come into use as synchrotron radiation sources. Thus several years ago, it became evident that in order to maintain a viable vacuum ultraviolet and soft x-ray research program at the NBS utilizing this machine as a synchrotron radiation source a considerable increase in source brightness would be necessary.

Two alternatives were considered. The first of these was to increase the beam brightness through a hundredfold increase in beam current, from 1 mA to 100 mA, by means of a new injector operating at 6 MeV. The machine would have remained a synchrotron and, hence, the duty factor would remain unchanged, i.e. no more than 0.2 assuming that useful synchrotron radiation is produced only at electron energies between 150 and 180 MeV and sinusoidal magnet excitation. The beam cross section area would have been 3π mm^2 at an absolute minimum at full energy and current because only adiabatic damping could occur in this mode of operation.

Operation of the synchrotron as an electron storage ring was then considered. In this mode of operation a beam cross sectional area of less than 0.65π mm^2 could be expected after damping, and the duty factor would be 1.0. A brightness figure of merit, defined by $S = ID/A$, where I is the beam current, D is the duty factor, and A is the electron beam cross sectional area, can be used to compare the two alternatives. Taking a circulating current of 10 mA, and the storage mode duty factor of 1, gives a value for $S = 1.54$ mA/mm^2. A similar calculation for synchrotron operation at 100 mA circulating yields $S = 2.1$ mA/mm^2. Thus, 10 mA at 180 MeV, which represents minimal operation of the machine as a storage ring, would give about the same brightness as synchrotron operation at a very high beam current. Further, whereas 100 mA operation of the machine as a synchrotron is the best that could be expected, operation of the machine as a storage ring would probably not be limited to beam currents of 10 mA. In addition, with relatively simple modifications, the machine energy could be raised, probably to as much as to 240 MeV, which would result in a considerable increase in the range and intensity of the synchrotron radiation spectrum. Finally, the storage mode of operation also offered 10^{-9} to 10^{-10} torr internal pressures and close access to the machine by the investigators; that is right up to the vacuum chamber. These are qualities of synchrotron radiation sources that have come to be expected by vacuum ultraviolet and soft x-ray experimentalists.[2] On the basis of these considerations, the decision was made to proceed with the conversion project.

I. Scope of the Conversion Project

During the study of the conversion project, it became clear that the only component of the original machine that could be preserved was the magnet. Other components such as the magnet coils, radio frequency system, magnet power supply and vacuum chamber could not be used in the converted machine.

Furthermore, the field index of the synchrotron magnet was greater than 3/4, a condition that leads to overdamping of the synchrotron motion and, therefore, antidamping of the radial motion[3]. Thus, besides a higher energy injector and injection system, the project required a vacuum chamber capable of supporting vacuua in the 10^{-9} - 10^{-10} range, a radio frequency system and accelerating cavity, magnet coils and magnet power supply and, finally, means for adjusting the field index of the magnet to a value below .75.

Interestingly, increasing the source brightness of the synchrotron by the first alternative would also have required a new vacuum chamber, accelerating cavity and magnet correction coils. Subsequently, investigation of the condition of the synchrotron indicated that the main magnet coils would also have to be replaced because of their advanced state of deterioration.

A plan view of the converted synchrotron is shown in Fig. 1, and operating parameters are given in Table I. In what follows, the components necessary for the conversion project will be described.

Table I

Converted Synchrotron Parameters

MAGNET	
Field Index	0.70
Radial Tune	0.54
Vertical Tune	0.83
Field at Injection	0.044T
Field at 180 (240) MeV	0.73 (1.0) T
Orbit Radius	0.84 M
Useful Radial Aperture	5.00 cm
Useful Vertical Aperture	2.50 cm
INJECTION	
Type	Multi-turn
Source	10 MeV Microtron
Inflector	Shorted Coaxial Line, 0.15 T, Nominal
Pulsed Field Bump	1.1×10^{-3} TM, Turning Off in 0.12 μsec
RF SYSTEM	
Frequency	113.6 MHz
Harmonic Number	2
Number of Cavities	1
Maximum Volts Per Turn	10 kV
Maximum Power Available	3 kW

Table I (cont'd.)

VACUUM SYSTEM	
Construction	Stainless Steel, Bakeable
Pumps	One 200 ℓ/sec Sputter Ion Holding Pump Plus Sixteen 50 Liter Sputter Ion Pump Elements Mounted Internally
Pressure (average, without beam)	5×10^{-10} Torr

II. Injector

Based on experience gained during the development of the 44 MeV microtron previously constructed at the Physical Sciences Laboratory as an injector for Tantalus I, the decision was made to employ a 10 MeV microtron as the injector for the converted synchrotron. The operating parameters of this machine are given in Table II.

Table II

Microtron Parameters

Accelerating Frequency	2.998	kmHz
Cavity Gradient	515	$kVcm^{-1}$
Repetition Rate	15-60	Hz
Energy Gain Per Turn	1	MeV
Number of Turns	10	
Beam Pulse Length	1	μsec
Pulse Beam Current	30	mA
Vertical Emittance	< 0.13	π mrad cm
Radial Emittance	< 1.1	π mrad cm

The microtron, shown in Fig. 2 with its beam transport line, is mounted vertically so as to present its small vertical emittance to the radial admittance of the converted synchrotron in order to simplify multi-turn injection. Pumping is supplied by four internally mounted sputter ion elements operating in the magnet fringe field. The base pressure achieved with this system is 3×10^{-8} torr.

Radio frequency power for the microtron is supplied by a two MW tunable magnetron (English Electric Valve Co. M5015) driven by a conventional storage line and thyratron modulator. The radio frequency system consists of the magnetron, a 25 db isolator, a remotely controlled attenuator and a dual 70 db directional coupler. The use of the attenuator allows adjustment of cavity excitation while the magnetron operates at fixed output power for frequency stability.

Electrons are supplied by a LaB_6 pellet 2 mm in diameter mounted in a tantalum support which is also the cathode heater. Cathodes, which have a lifetime of approximately 100 hours, can be replaced in less than one hour inclusive of the time required to achieve operating vacuua (10^{-6} torr) in the microtron.

The accelerating cavity is of cylindrical geometry and is constructed of OFHC copper. An unloaded Q of 11,000 was obtained for the cavity in spite of the fact that the front and back cover plates are simply bolted on. A cavity coupling coefficient of $\beta = 3.5$ permits pulse beam currents in excess of 50 mA.

Electrons are extracted from the microtron by means of a compensated iron channel on the tenth orbit with nearly 100% efficiency. The operation of this microtron is characterized by simplicity, reliability and, above all, stability.

III. Beam Transport System

The beam transport system consists of two quadrupole doublets, a beam stop mounted at the focus of the first doublet and a chopper positioned upstream from the beam stop. The chopper deflects the electron beam so as to miss a 5 mm aperture in the beam stop by means of a DC electric field. During injection a radio frequency electric field, synchronized with the storage ring radio frequency accelerating system, is superimposed on the DC field so that approximately 100 pulses of 2.5 nsec length pass through the beam stop aperture to the next doublet and, thence, to the inflector.

IV. Inflector and Pulse Bump System

In order to achieve the design circulating beam current, multi-turn injection will be carried out. The coaxial inflector produces a field of .15 T which is sufficient to bend the electrons through $\pi/4$ radians against the magnetic field of the storage ring and place them on an orbit 2 cm displaced outward from the central orbit. Excitation for the inflector is provided by a thyratron discharging a capacitor through a 48:1 low leakage inductance matching transformer. The current flowing through the inflector during the pulse is 7550 amperes. The current pulse is sinusoidal and its length is 50 psec.

Located diametrically opposite from the inflector is a pulsed magnetic bump capable of displacing the orbit by two cm at the inflector. During injection the bump is pulsed, displacing the orbit so as to be tangential to the inflector. During the decay of the bump field the orbit moves back to its unperturbed position. The time required for the bump field to decay is .12 μsec, during which time twelve beam pulses will be injected. Assuming 25% efficiency for injection and capture, stored beam currents of greater than 15 mA should be possible with a microtron beam current of 30 mA.

The bump field is produced by a thyratron discharging a two section energy storage line of 10Ω impedance through the bump inductance. A capacitor and a 10Ω resistor terminate the circuit and thus reflections are eliminated. Fig. 3 shows the bump structure and Fig. 4 shows the bump magnetic field as a function of time.

V. Vacuum System

In order to achieve the required 10^{-9} range pressures in the storage *ring* vacuum chamber an all stainless steel system is required. Space limitations in the magnet do not permit bellows, thus the chamber will be a rigid annulus of 1.66 meters mean diameter with a 20 cm × 9 cm rectangular cross section. Sixteen dual sputter ion pump elements will be mounted along the inner wall of the vacuum chamber to handle the synchrotron radiation induced outgassing under stored beam conditions.

To pass photon beams for the two research areas to be serviced by the storage ring, a total of eleven, 4 cm diameter ports, tangential to the central orbit, will be provided. As an aid to injection system adjustment, one of these ports will be positioned so as to allow observation of a BeO_2 scintillator plate which may be positioned by remote control, either directly in front of the inflector so

as to intercept the injected beam or further in so as to intercept the injected beam after one revolution.

VI. Radio Frequency System

The electron revolution frequency in the storage ring is 56.8 MHz. In order that the accelerating cavity, which must be mounted internal to the vacuum chamber, not take up an unduly large portion of the circumference of the vacuum chamber, second harmonic operation of the accelerating system has been chosen. The accelerating cavity, which is a $\lambda/4$ coaxial resonator, is constructed of OFHC copper and exhibits an unloaded Q in excess of 2000. Provisions for cavity tuning by means of a remotely controlled capacitance probe near the accelerating gap have been included and the cavity is water-cooled. The cavity is also shown in Fig. 3.

The power amplifier is a conventional push-pull tetrode amplifier capable of 3 kW output. This is sufficient power to drive the accelerating cavity to voltages in excess of 10 kV. At a beam energy loss of approximately 350 eV per turn at 240 MeV this accelerating potential will insure adequate lifetime against quantum fluctuations and Touschek effect. Beam loading of the cavity at currents as high as 100 mA are not expected to be a problem.

VII. Magnet Correction Coils

To reduce the field index of the synchrotron magnet to a value below 3/4, four pair of coils will be mounted on the magnet pole faces. These coils will be energized independently to maintain a field index of 0.70 over the whole range of magnet excitation. The maximum MMF required of any of the compensating coils is 3000 ampere turns; however, field measurements indicate that at fields greater than about .8 T the current flow in the coils must reverse due to saturation effects in the magnet. Since the rate of rise of the magnet field between injection and full energy will be rather low (0.1 T sec^{-1}), a system utilizing relays rather than bipolar supplies will be used to reverse the polarity of the compensating coils.

Excitation of the compensating coils will be controlled by signals derived from the magnet current.

VIII. Main Magnet Coils and Power Supply

At an energy of 180 MeV the synchrotron magnetic field was at the central orbit .73 T. Since the original coils could not operate continuously at the excitation necessary to produce this field, new field coils were necessary. Because of this and because compensating coils to control the field index were also required, the decision was made to construct field coils capable of operating at an excitation sufficient to produce a field of 1.2 T at the central orbit. Thus, the maximum energy that will actually be reached by the converted synchrotron will depend on the capability of the compensating coils to control the field index.

The magnet coils are excited by an SCR controlled, current regulated power supply. Peak voltage and current ratings of this supply are 1250 amperes at 400 volts. Long term current regulation of the supply is ± 0.01% against line and load fluctuations combined. The control signals for the magnet power supply are generated by digital techniques, thus computer control of the converted synchrotron will be possible.

IX. Current Status of the Conversion Project

The 10 MeV microtron and most of the electron beam transport system are complete and have been tested. The main magnet coils and the compensating coils are also complete. The vacuum chamber and radio frequency accelerating system are under construction. Installation at the National Bureau of Standards of the major components of the converted synchrotron is scheduled to begin in June 1974.

References

1. Madden, R. P. and Codling, K., New Autoionizing Atomic Energy Levels in He, Ne, and Ar, Phys. Rev. Letters, 10, 516 (1963).

2. Rowe, E. M. and Mills, F. E., Tantalus I: A Dedicated Storage Ring Synchrotron Radiation Source, Particle Accelerators 1973, Vol. 4, pp. 211-227.

3. Bruck, H., Accélérateurs Circulaires de Particules, Presses Universitaires de France, 1966, Chap. 24.

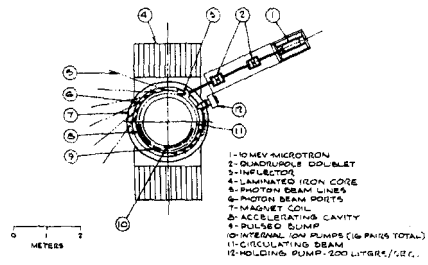


FIG. 1--Plan view of converted synchrotron,

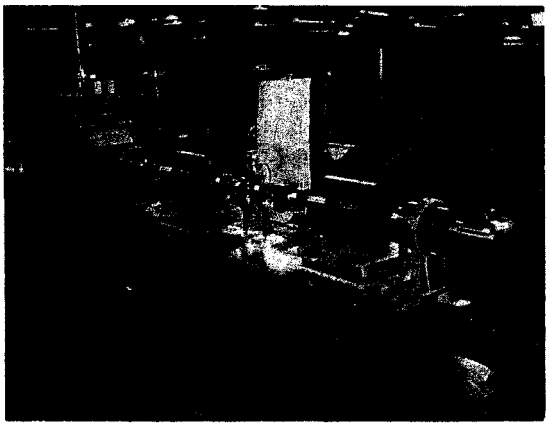


FIG. 2--10 MeV Microtron and beam transport line. Units shown are (from left to right) microtron, steering magnet, chopper, quadrupole doublet, beam stop, beam current monitor transformer, quadrupole doublet and steering magnet.

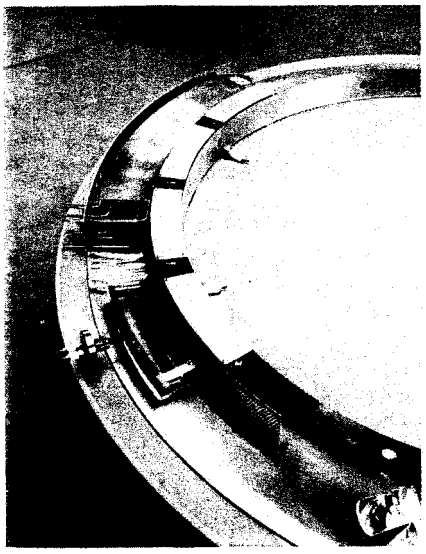


FIG. 3--Section of vacuum chamber during construction showing pulse bump, internal sputter-ion pump elements and radio frequency accelerating cavity.

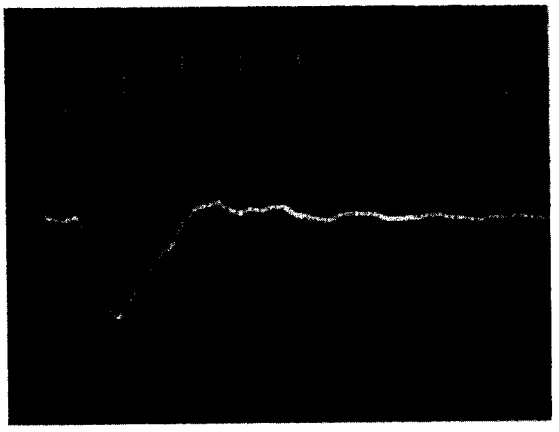


FIG. 4--Pulse bump magnetic field as a function of time. Sweep speed 10^{-7} sec cm^{-1}.

LIST OF PARTICIPANTS BY COUNTRY

AUSTRIA
CERN
Werner Kubischta

International Atomic Energy Agency
Alexander V. Shalnov

CANADA
University of British Columbia
Michael K. Craddock
Bruce L. White

Atomic Energy of Canada, Limited
J.A. Hulbert
Carl H. Westcott

McGill University
Robert B. Moore

University of Saskatchewan
Leon Katz
Roger Servranckx

CERN
James V. Allaby
Frank Beck
Philippe Bernard
Roy Billinge
M. Hildred Blewett
Franco Bonaudi
Michael Crowley-Milling
Fritz Ferger
Hans Fischer
Jacques Gareyte
Werner Hardt
Mervyn Hine
J. Trevor Hyman
Willibald Jentschke
Kjell Johnsen
Eberhard Keil
Herbert Lengeler
Ernest G. Michaelis
Boris Milman
Karl H. Reich
Lorenzo Resegotti
Frank Sacherer
Karl Heinz Schindl
Wolfgang Schnell
Brian Southworth
Peter Wolstenholme

FRANCE
Institute National De Physique
Andre Chabert
Jean Yoccoz

Universite Paris-Sud, Centre D'Orsay
Paul Brunet
Jean Buon
Pierre Lehmann
Marie Paule Level
Pierre Marin
Henri Zyngier

Centre D'Etudes Nucleaires De Saclay
Gaston Bronca
Henri Bruck
Jean Faure
Maurice Gouttefangeas
Marcel Jablonka
Jean-Louis Laclare
Jean-Marie Lefebvre
Francis Netter

EAST GERMANY
Karl-Marx-Universitat
Johannes Ranft

WEST GERMANY
Physikalisches Institut, Bonn
Dirk Husmann
Wolfgang Paul
Helmut Piel

Max-Planck-Institut fur Plasmaphysik
Claus Andelfinger
Peter Merkel

DESY
Donatus Degele
Arno Febel
Horst Gerke
Guenter Hemmie
Anton Piwinski
Klaus Steffen
Gustav-Adolf Voss

Institute fur Experimentelle, Karlsruhe
Anselm Citron
Helmut Krauth
Michael Kuntze
Peter Turowski

Institute fur Kernphysik, Mainz
Helmut Herminghaus

GREECE
N. R. C. Demokritos
Tassos A. Filippas

ITALY
Laboratori Nazionali Di Frascati
Ubaldo Bizzarri
Aldo Cattoni
Massimo Placidi
Alberto Renieri
Sergio Tazzari
Angelo Turrin

JAPAN
National Laboratory for High Energy Physics
Motohiro Kihara
Yoshitaka Kimura
Tetsuji Nishikawa

Institute for Nuclear Study, University of Tokyo
Hiroshi Tsujikawa
Kazuo Huke

NETHERLANDS
I. K. O.
Conrad De Vries

SWEDEN
Chalmers Technical University
Gosta Brogren

SWITZERLAND
Swiss Institute for Nuclear Research
Jean-Pierre Blaser
Rolf Wideroe

UNITED KINGDOM
Daresbury Nuclear Physics Laboratory
Alick Ashmore
David E. Poole
Michael W. Poole
David J. Thompson

Rutherford High Energy Laboratory
James R. J. Bennett
Peter Clee
Martin H. R. Donald
David A. Gray
N. Marshall King
Alfred R. Mortimer
Grahame Rees
David B. Thomas

Hammersmith Hospital
Geoffrey Burton

UNITED STATES OF AMERICA
Argonne National Laboratory
Lowell M. Bollinger
Edwin A. Crosbie
Tat K. Khoe
Robert L. Kustom
Lloyd G. Lewis
Ronald L. Martin
Lazarus G. Ratner
James Simpson

Austin Research Associates Corporation
Millard L. Sloan

Brookhaven National Laboratory
Mark Q. Barton
John Blewett
Renate W. Chasman
Gordon T. Danby
George Kenneth Green
Harold Hahn
Alfred W. Maschke
Melvin Month
George Parzen
Eugene C. Raka
R. Ronald Rau
William B. Sampson
Theodorus J. M. Sluyters
Julius Spiro
Arie Van Steenbergen

California Institute of Technology
Murray Gell-Mann

Lawrence Berkeley Laboratory
University of California
Robert Avery
Warren Chupp
Bruce Cork
Tom Elioff
Robert J. Force
Alper Garren
William Gilbert
Michael Green
Hermann Grunder
Walter Hartsough
Edward Hartwig
John M. Hauptman
Paul Hernandez
David Judd
John A. Kadyk
Dennis Keefe
Glen Lambertson

UNITED STATES OF AMERICA (cont'd)
Lawrence Berkeley Laboratory
University of California
L. Jackson Laslett
Christoph Leemann
Kenow Lou
Richard Mobley
Richard Morgado
Jack Peterson
Joseph B. Rechen
Frank Selph
Andrew M. Sessler
Lloyd Smith
John W. Staples
Lynn Stevenson
Jack Tanabe
Ralph Thomas
Ferdinand Voelker
William Wenzel

Lawrence Livermore Laboratory
University of California
V. Kelvin Neil

University of California, Los Angeles
Darrell Drickey

University of California, Santa Cruz
Matthew Sands

Columbia University
Leon Lederman

Laboratory of Nuclear Studies
Cornell University
Joseph L. Kirchgessner
Raphael M. Littauer
Boyce McDaniel
Gerald Rouse
Ronald M. Sundelin
Maury Tigner

Harvard University
Karl Straucb

University of Illinois
Alfred O. Hanson

Meson physics Facility
Los Alamos Scientific Laboratory
Donald C. Hagerman
James Halbig
Willard E. Jule
Edward Knapp
James E. Spencer

University of Maryland
Martin P. Reiser
Gus T. Zorn

University of Massachusetts
Robert Gluckstern

Cyclotron Laboratory
Michigan State University
Henry G. Blosser

National Accelerator Laboratory
Francis Cole
Donald A. Edwards
Helen Edwards

UNITED STATES OF AMERICA (cont'd)
National Accelerator Laboratory
H. Eugene Fisk
James E. Griffin
Edward Hubbard
Philip V. Livdahl
Frederick E. Mills
Shigeki Mori
Shoroku Ohnuma
Curtis W. Owen
Robert Peters
Paul Reardon
Alessandro Ruggiero
Rae Stiening
Lee C. Teng
Donald E. Young

Oak Ridge National Laboratory
Charles M. Jones
Robert S. Livingston

Physics International
Bruce Ecker
Sidney Putnam

Princeton University
Remo Ruffini
Milton G. White

Plasma Theory Division
Sandia Laboratories
Glenn Kuswa
Craig L. Olson

Stanford Linear Accelerator Center
Stanford University
Matthew A. Allen
Joseph Ballam
Karl Brown
Joseph K. Cobb
Kenneth F. Crook
Sidney D. Drell
Z. David Farkas
Gerhard E. Fischer
John L. Harris
Richard H. Helm
William B. Herrmannsfeldt
Harry A. Hogg
Roland F. Koontz
Charles J. Kruse
Jean V. Lebacqz
Martin J. Lee
Alexander V. Lisin
Gregory A. Loew
Kenneth B. Mallory
Roger H. Miller
Philip L. Morton
Richard B. Neal
Wolfgang K. H. Panofsky
James M. Paterson
Vernon G. Price
Daryl D. Reagan
John R. Rees
Burton Richter
Andrew P. Sabersky
Steven J. St. Lorant
Richard Taylor
Dieter Walz
Alan Wilmunder
Perry B. Wilson

UNITED STATES OF AMERICA (cont'd)
Stanford High Energy Physics Laboratdry,
Stanford University
Ilan Ben-Zvi
Robert Hofstadter
Michael S. McAshan
Roy E. Rand
H. Alan Schwettman
Todd Smith
John P. Turneaure
Herman Winick

U. S. Atomic Energy Commission
Division of Physical Research
John Teem
George Wheeler
William A. Wallenmeyer

National Bureau of Standards
Center for Radiation Research
James E. Leiss

Texas Instruments
Richard Sah

University of Wisconsin
Ednor M. Rowe

Yale University
Klaus Peter Schuler

UNION OF SOVIET SOCIALIST REPUBLICS
Institute of High Energy Physics
Serpukov
Yuri Ado

Institute of High Energy Physics, Moscow
USSR Academy of Sciences
Nicolai V. Lazarev
Leonid Ivanovich Sokolov

Joint Institute for Nuclear Research, Moscow
Vatali P. Dmitrievsky
Vladislav P. Sarantsev

P. N. Lebedev Institute, Moscow
USSR Academy of Sciences
Andrei A. Kolomensky

Physical Engineering Institute, Moscow
USSR Academy of Sciences
Oleg A. Valdner

Radiotechnical Institute, Moscow
USSR Academy of Sciences
Vladimir V. Elyan

LIST OF PARTICIPANTS - ALPHABETICALLY

Yuri Ado
Institute of High Energy Physics
Moscow District
Serpukov, USSR

James V. Allaby
NP Division - CERN
1211 Geneva 23
Switzerland

Matthew Allen
Stanford Linear Accelerator Center
P.O. Box 4349
Stanford, California 94305

Claus Andelfinger
Max Planck Institut Fur
Plasmaphysik
8046 Garching
Germany

Alick Ashmore
Daresbury Nuclear Physics
Laboratory
Daresbury, Near Warrington
Lancs., Great Britain

Robert Avery
Lawrence Berkeley Laboratory
University of California
Berkeley, California 94720

Joseph Ballam
Stanford Linear Accelerator Center
P.O. Box 4349
Stanford, California 94305

Mark Q. Barton
Brookhaven National Laboratory
Upton, Long Island
New York 11973

Frank Beck
Laboratory II - CERN
1211 Geneva 23
Switzerland

James R. J. Bennett
Rutherford High Energy
Laboratory
Chilton, Didcot
Berkshire, England

Ilan Ben-Zvi
Stanford High Energy Physics
Laboratory
Stanford University
Stanford, California 94305

Philippe Bernard
TC Division - CERN
1211 Geneva 23
Switzerland

Roy Billinge
Laboratory - CERN
1211 Geneva 23
Switzerland

Ubaldo Bizzarri
Laboratori Nazionali Di Frascati
Box 70
Frascati 00044, Italy

Jean-Pierre Blaser
Ecole Polytechnique Federale
Institut De Physique
CH-5234 Villigen, Switzerland

John Blewett
Brookhaven National Laboratory
Upton, Long Island
New York 11973

M. Hildred Blewett
ISR - CERN
1211 Geneva 23
Switzerland

Henry G. Blosser
Cyclotron Laboratory
Michigan State University
East Lansing, Michigan 48823

Lowell M. Bollinger
Argonne National Laboratory
9700 South Cass Avenue
Argonne, Illinois 60439

Franco Bonaudi
ISR - CERN
1211 Geneva 23
Switzerland

Gosta Brogren
Chalmers Technical University
Gothenburg, Sweden

Gaston Bronca
Centre d'Etudes Nucleaires
de Saclay
BP no. 2
F-91-Gif-sur-Yvette, France

Karl Brown
Stanford Linear Accelerator Center
P.O. Box 4349
Stanford, California 94305

Henri Bruck
Centre d'Etudes Nucleaires
de Saclay
BP no. 2
F-91-Gif-sur-Yvette, France

Paul Brunet
Lab. de l'Accelerateur Lineaire
Universite Paris-Sud, Centre
d'Orsay, Batiment 200
F-91405 Orsay, France

Jean Buon
Lab. de l'Accelerateur Lineaire
Universite Paris-Sud, Centre
d'Orsay, Batiment 200
F-91405 Orsay, France

Geoffrey Burton
Hammersmith Hospital
Synchrotron Unit
London, England

Aldo Cattoni
Laboratori Nazionali Di Frascati
Box 70
Frascati 00044, Italy

Andre Chabert
Institut National de Physique
11, Rue Pierre-et-Marie-Curie
F-75231 Paris Cedex 5, France

Renate W. Chasman
Brookhaven National Laboratory
Upton, Long Island
New York 11973

Warren Chupp
Lawrence Berkeley Laboratory
University of California
Berkeley, California 94720

Anselm Citron
Institut Fur Experimentelle
Kernphysik
Postf. 3640
Karlsruhe, Germany

Peter Clee
Rutherford High Energy
Laboratory
Chilton, Didcot
Berkshire, England

Joseph Cobb
Stanford Linear Accelerator Center
P.O. Box 4349
Stanford, California 94305

Francis Cole
National Accelerator Laboratory
P.O. Box 500
Batavia, Illinois 60510

Bruce Cork
Lawrence Berkeley Laboratory
University of California
Berkeley, California 94720

Michael K. Craddock
Physics Department
University of British Columbia
Vancouver 8, British Columbia

Kenneth Crook
Stanford Linear Accelerator Center
P.O. Box 4349
Stanford, California 94305

Edwin A. Crosbie
Argonne National Laboratory
9700 South Cass Avenue
Argonne, Illinois 60439

Michael Crowley-Milling
CERN
1211 Geneva 23
Switzerland

Gordon T. Danby
Brookhaven National Laboratory
Upton, Long Island
New York 11973

Donatus Degele
DESY
Notkestieg 1
Hamburg 52, Germany

Conrad De Vries
I. K. O. Oosterringdijk 18
Amsterdam-0, Netherlands

Vitali P. Dmitrievsky
Joint Institute for Nuclear Res.
101000 Moscow Head Post Office
P.O. Box 79, USSR

Martin H. R. Donald
Rutherford High Energy
Laboratory
Chilton, Didcot
Berkshire, England

Sidney D. Drell
Stanford Linear Accelerator Center
P.O. Box4349
Stanford, California 94305

Darrell Drickey
Department of Physics
University of California
Los Angeles, California 90024

Bruce Ecker
Physics International
2700 Merced St.
San Leandro, California 94577

Donald A. Edwards
National Accelerator Laboratory
P.O. Box500
Batavia, Illinois 60510

Helen Edwards
National Accelerator Laboratory
P.O. Box500
Batavia, Illinois 60510

Tom Elioff
University of California
Lawrence Berkeley Laboratory
Berkeley, California 94720

Vladimir V. Elyan
Radiotechnical Institute
USSR Academy of Sciences
125083, Moscow, USSR

David Farkas
Stanford Linear Accelerator Center
P.O. Box 4349
Stanford, California 94305

Jean Faure
Centre d'Etudes Nucleaires
de Saclay
BP no. 2
F-91-Gif-Sur-Yvette, France

Arno Febel
DESY
Notkestieg 1
Hamburg 52, Germany

Fritz Ferger
ISR - CERN
1211 Geneva 23
Switzerland

Tassos A. Filippas
N. R. C. Mocritus
Aghia Paraskevi-Attikis
Athens, Greece

Gerhard E. Fischer
Stanford Linear Accelerator Center
P.O. Box 4349
Stanford, California 94305

Hans Fischer
TC Division - CERN
1211 Geneva 23
Switzerland

H. Eugene Fisk
National Accelerator Laboratory
P.O. Box 500
Batavia, Illinois 60510

Robert J. Force
Lawrence Berkeley Laboratory
University of California
Berkeley, California 94720

Jacques Gareyte
MPS Division - CERN
1211 Geneva 23
Switzerland

Alper Garren
University of California
Lawrence Berkeley Laboratory
Berkeley, California 94720

Murray Gell-Mann
California Institute
of Technology
Pasadena, California 91109

Horst Gerke
DESY
Notkestieg 1
Hamburg 52, Germany

William Gilbert
University of California
Lawrence Berkeley Laboratory
Berkeley, California 94720

Robert Gluckstern
University of Massachusetts
Amherst, Massachusetts 01002

Maurice Gouttefangeas
Centre d'Etudes Nucleaires
de Saclay
BPno. 2
F-91-Gif-Sur-Yvette, France

David A. Gray
Rutherford High Energy
Laboratory
Chilton, Didcot
Berkshire, England

George Kenneth Green
Brookhaven National Laboratory
Upton, Long Island
New York 11973

Michael Green
Lawrence Berkeley Laboratory
University of California
Berkeley, California 94720

James E. Griffin
National Accelerator Laboratory
P.O. Box 500
Batavia, Illinois 60510

Hermann Grunder
University of California
Lawrence Berkeley Laboratory
Berkeley, California 94720

Donald C. Hagerman
Los Alamos Scientific Laboratory
Meson Physics Facility
Los Alamos. New Mexico 87544

Harold Hahn
Brookhaven National Laboratory
Upton, Long Island
New York 11973

James Halbig
Los Alamos Scientific Laboratory
Meson Physics Facility
Los Alamos, New Mexico 87544

Alfred O. Hanson
University of Illinois
Urbana, Illinois 61801

Werner Hardt
MPS Division - CERN
1211 Geneva 23
Switzerland

John Harris
Stanford Linear Accelerator Center
P.O. Box 4349
Stanford, California 94305

Walter Hartsough
University of California
Lawrence Berkeley Laboratory
Berkeley, California 94720

Edward Hartwig
University of California
Lawrence Berkeley Laboratory
Berkeley, California 94720

John M. Hauptman
Lawrence Berkeley Laboratory
University of California
Berkeley, California 94720

Richard Helm
Stanford Linear Accelerator Center
P.O. Box 4349
Stanford, California 94305

Guenter Hemmie
DESY
Notkestieg 1
Hamburg 52, Germany

Helmut Herminghaus
Institut Fur Kernphysik
Postf. 3980
Mainz, Germany

Paul Hernandez
Lawrence Berkeley Laboratory
University of California
Berkeley, California 94720

William Herrmannsfeldt
Stanford Linear Accelerator Center
P.O. Box 4349
Stanford, California 94305

Merrvyn Hine
CERN
1211 Geneva 23
Switzerland

Robert Hofstadter
Stanford High Energy Physics
Laboratory
Stanford University
Stanford, California 94305

Harry Hogg
Stanford Linear Accelerator Center
P.O. Box4349
Stanford, California 94305

Edward Hubbard
National Accelerator Laboratory
P.O. Box500
Batavia. Illinois 60510

Kazuo Huke
Institute for Nuclear Study
University of Tokyo
Tanashi, Tokyo, 188, Japan

J. A. Hulbert
Atomic Energy of Canada, Limited
Chalk River Nuclear Laboratories
Accelerator Physics Branch
Chalk River, Ontario, Canada

Dirk Husmann
Physikalisches Institut
Nussallee 12
Bonn, Germany

Trevor Hyman
Laboratory - CERN
1211 Geneva 23
Switzerland

Marcel Jablonka
Centre d' Etudes Nucleaires
de Saclay
BP No. 2
F-91-Gif-Sur-Yvette, France

Willibald Jentschke
CERN
1211 Geneva 23
Switzerland

Kjell Johnsen
ISR - CERN
1211 Geneva 23
Switzerland

Charles M. Jones
Oak Ridge National Laboratory
Oak Ridge, Tennessee 37830

David Judd
Lawrence Berkeley Laboratory
University of California
Berkeley, California 94720

Willard E. Jule
Los Alamos Scientific Laboratory
Meson Physics Facility
Los Alamos, New Mexico 87544

John A. Kadyk
University of California
Lawrence Berkeley Laboratory
Berkeley, California 94720

Leon Katz
Accelerator Laboratory
University of Saskatchewan
Saskatoon, Saskatchewan S7N OWO
Canada

Denis Keefe
University of California
Lawrence Berkeley Laboratory
Berkeley, California 94720

Eberhard Keil
CERN
1211 Geneva 23
Switzerland

Tat K. Khoe
Argonne National Laboratory
9700 South Cass Avenue
Argonne, Illinois 60439

Motohiro Kihara
National Laboratory for High
Energy Physics
Oho-Machi, Tsukuba-Gun
Ibaraki-Ken, 300-32, Japan

Yoshitaka Kimura
Energy Physics
Oho-Machi, Tsukuba-Gun
Ibaraki-Ken, 300-32, Japan

N. Marshall King
Rutherford High Energy
Laboratory
Chilton, Didcot
Berkshire, England

Joseph L. Kirchgessner
Laboratory of Nuclear Studies
Cornell University
Ithaca, New York 14850

Edward Knapp
Los Alamos Scientific Laboratory
Meson Physics Facility
Los Alamos, New Mexico 87544

Andrei A. Kolomensky
Lebedev Physical Institute
USSR Academy of Sciences
Leninsky Prospect 53
Moscow, USSR

Roland Koontz
Stanford Linear Accelerator Center
P.O. Box 4349
Stanford, California 94305

Helmut Krauth
Institut Fur Experimentelle
Kernphysik
Postf. 3640
Karlsruhe, Germany

Charles Kruse
Stanford Linear Accelerator Center
P.O. Box4349
Stanford, California 94305

Werner Kubischta
CERN
1211 Geneva 23
Switzerland

Michael Kuntze
Institut Fur Experimentelle
Kernphysik
Postf. 3640
Karlsruhe, Germany

Robert L. Kustom
Argonne National Laboratory
9700 South Cass Avenue
Argonne, Illinois 60439

Glenn Kuswa
Sandia Laboratories
Division 5245
Albuquerque, New Mexico 87115

Jean-Louis Laclare
Centre d'Etudes Nucleaires
de Saclay
BPno. 2
F-91-Gif-Sur-Yvette, France

Glen Lambertson
Lawrence Berkeley Laboratory
University of California
Berkeley, California 94720

L. Jackson Laslett
Lawrence Berkeley Laboratory
University of California
Berkeley, California 94720

Nicolai V. Lazarev
Institute for Theoretical &
Experimental Physics
Moscow, USSR

Jean Lebacqz
Stanford Linear Accelerator Center
P.O. Box 4349
Stanford, California 94305

Leon Lederman
Physics Department
Columbia University
Irvington-On- Hudson
New York 10025

Martin Lee
Stanford Linear Accelerator Center
P.O. Box 4349
Stanford, California 94305

Christoph Leemann
Lawrence Berkeley Laboratory
University of California
Berkeley, California 94720

Jean-Marie Lefebvre
Commissariat A l'Energie Atomique
B-P-2 cen-Saclay 91-Gif
Yvette, France

Pierre Lehmann
Lab. del'Accelerateur Lineaire
Universite Paris-Sud, Centre
d'Orsay, Batiment 200
F-91405 Orsay, France

James E. Leiss, Director
National Bureau of Standards
Center for Radiation Research
Washington, D. C. 20234

Herbert Lengeler
NP Division - CERN
1211 Geneva 23
Switzerland

Marie Paule Level
Lab. de l'Accelerateur Lineaire
Universite Paris-Sud- Centre
d'Orsay, Batiment 200
F-91405 Orsay, France

Lloyd G. Lewis
Argonne National Laboratory
9700 South Cass Avenue
Argonne, Illinois 60439

Alexander Lisin
Stanford Linear Accelerator Center
P.O. Box 4349
Stanford, California 94305

Raphael M. Littauer
Laboratory of Nuclear Studies
Cornell University
Ithaca, New York 14850

Philip V. Livdahl
National Accelerator Laboratory
P.O. Box 500
Batavia, Illinois 60510

Robert S. Livingston
Oak Ridge National Laboratory
Oak Ridge, Tennessee 37830

Gregory A. Loew
Stanford Linear Accelerator Center
P.O. Box 4349
Stanford, California 94305

Kenow H. Lou
Lawrence Berkeley Laboratory
University of California
Berkeley, California 94720

Michael S. Mc Ashan
Stanford High Energy Physics
Laboratory
Stanford University
Stanford, California 94305

Boyce McDaniel
Laboratory of Nuclear Studies
Cornell University
Ithaca, New York 14850

Kenneth Mallory
Stanford Linear Accelerator Center
P.O. Box 4349
Stanford, California 94305

Pierre Marin
Laboratoire de l'Accelerateur
Lineaire
Batiment 200
Orsay, France

Ronald L. Martin
Argonne National Laboratory
9700 South Cass Avenue
Argonne, Illinois 60439

Alfred W. Maschke
Brookhaven National Laboratory
Upton, Long Island
New York 11973

Peter Merkel
Max-Planck-Institut Fur
Plasmaphysik
8046 Garching
Germany

Ernest G. Michaelis
MSC Division - CERN
1211 Geneva 23
Switzerland

Roger Miller
Stanford Linear Accelerator Center
P.O. Box 4349
Stanford, California 94305

Frederick E. Mills
National Accelerator Laboratory
P.O. Box 500
Batavia, Illinois 60510

Boris Milman
Laboratory II - CERN
1211 Geneva 23
Switzerland

Richard Mobley
Lawrence Berkeley Laboratory
University of California
Berkeley, California 94720

Robert B. Moore
Foster Radiation Laboratory
McGill University
Montreal, Quebec
Canada

Melvin Month
Brookhaven National Laboratory
Upton, Long Island
New York 11973

Richard Morgado
Lawrence Berkeley Laboratory
University of California
Berkeley, California 94720

Shigeki Mori
National Accelerator Laboratory
P.O. Box 500
Batavia, Illinois 60510

Alfred R. Mortimer
Rutherford High Energy
Laboratory
Chilton, Didcot
Berkshire, England

Phil L. Morton
Stanford Linear Accelerator Center
P.O. Box 4349
Stanford, California 94305

Richard B. Neal
Stanford Linear Accelerator Center
P.O. Box 4349
Stanford, California 94305

V. Kelvin Neil
Lawrence Livermore Laboratory
University of California
Livermore, California 94550

Francis Netter
Centre d'Etudes Nucleaires
de Saclay
BPno. 2
F-91-Gif-Sur-Yvette, France

Tetsuji Nishikawa
National Laboratory
Of High Energy Physics
Oho-Machi, Tsukaba-Gun
Iboraki-Ken, Japan

Shoroku Ohnuma
National Accelerator Laboratory
P.O. Box 500
Batavia, Illinois 60510

Craig L. Olson
Plasma Theory Division
Sandia Laboratories
Albuquerque, New Mexico 87115

Curtis W. Owen
National Accelerator Laboratory
P.O. Box 500
Batavia, Illinois 60510

Wolfgang K. H. Panofsky
Stanford Linear Accelerator Center
P.O. Box 4349
Stanford, California 94305

George Parzen
Brookhaven National Laboratory
Upton, Long Island
New York 11973

James Paterson
Stanford Linear Accelerator Center
P.O. Box 4349
Stanford, California 94305

Wolfgang Paul
Physikalisches Institut
Nussallee 12
D 5300
Bonn, Germany

Robert Peters
National Accelerator Laboratory
P.O. Box 600
Batavia, Illinois 60510

Jack Peterson
University of California
Lawrence Berkeley Laboratory
Berkeley, California 94720

Helmut Piel
University of Wuppertal
Wuppertal, Germany

Anton Piwinski
DESY
Notkestieg 1
Hamburg 52, Germany

Massimo Placidi
CERN
1211 Geneva 23
Switzerland

David E. Poole
Daresbury Nuclear Physics Lab.
Keckwick Lane
Daresbury, Warrington, 3WA4 4AD
England

Michael W. Poole
Daresbury Nuclear Physics Lab.
Keckwick Lane
Daresbury, Warrington, 3WA4 4AD
England

Vernon G. Price
Stanford Linear Accelerator Center
P.O. Box 4349
Stanford, California 94305

Sidney Putnam
Physics International
2700 Merced St.
San Leandro, California 94577

Eugene C. Raka
Brookhaven National Laboratory
Upton, Long Island
New York 11973

Roy E. Rand
Stanford High Energy Physics
Laboratory
Stanford University
Stanford, California 94305

Johannes Ranft
Sektion Physik
Karl-Marx-Universitat
DDR-701 Leipzig
Linnestr. 5, East Germany

Lazarus G. Ratner
Argonne National Laboratory
9700 South Cass Avenue
Argonne, Illinois 60439

R. Ronald Rau
Director, Physics Department
Brookhaven National Laboratory
Upton, Long Island
New York 11973

Daryl Reagan
Stanford Linear Accelerator Center
P.O. Box 4349
Stanford, California 94305

Paul Reardon
National Accelerator Laboratory
P.O. Box 500
Batavia, Illinois 60510

Joseph B. Rechen
Lawrence Berkeley Laboratory
University of California
Berkeley, California 94720

Grahame Rees
Rutherford High Energy
Laboratory
Chilton, Didcot
Berkshire, England

John Rees
Stanford Linear Accelerator Center
P.O. Box 4349
Stanford, California 94305

Karl H. Reich
MPS Division - CERN
1211 Geneva 23
Switzerland

Martin P. Reiser
University of Maryland
College Park, Maryland 20742

Alberto Renieri
Laboratori Nazionali Di Frascati
Box 70
Frascati 00044, Italy

Lorenzo Resegotti
ISR - CERN
1211 Geneva 23
Switzerland

Burton Richter
Stanford Linear Accelerator Center
P.O. Box4349
Stanford, California 94305

Gerald Rouse
Laboratory of Nuclear Studies
Cornell University
Ithaca, New York 14850

Ednor M. Rowe
University of Wisconsin
P.O. Box6
Stoughton, Wisconsin 53589

Remo Ruffini
Physics Department
Princeton University
P.O. Box 708
Princeton, New Jersey 08540

Alessandro Ruggiero
National Accelerator Laboratory
P.O. Box 500
Batavia, Illinois 60510

Andrew Sabersky
Stanford Linear Accelerator Center
P.O. Box 4349
Stanford, California 94305

Frank Sacherer
CERN
1211 Geneva 23
Switzerland

Richard Sah
Texas Instruments
P.O. Box 5012 Station Z
Dallas, Texas 75222

William B. Sampson
Brookhaven National Laboratory
Upton, Long Island
New York 11973

Matthew Sands
University of California
Santa Cruz, California 95060

Vladislav P. Sarantsev
Joint Institute for Nuclear Res.
101000 Moscow Head Post Office
P.O. Box 79, USSR

Karl Heinz Schindl
MPS Division - CERN
1211 Geneva 23
Switzerland

Wolfgang Schnell
ISR - CERN
1211 Geneva 23
Switzerland

Klaus Peter Schuler
Yale University
New Haven, Conneticut 06520

H. Alan Schwettman
Stanford High Energy Physics Laboratory
Stanford University
Stanford, California 94305

Frank Selph
University of California
Lawrence Berkeley Laboratory
Berkeley, California 94720

Roger Servranckx
Accelerator Laboratory
University of Saskatchewan
Saskatoon, Saskatchewan S7N OWO
Canada

Andrew M. Sessler, Director
University of California
Lawrence Berkeley Laboratory
Berkeley, California 94720

Alexander V. Shalnov, Director
Div. of Research and Laboratories
International Atomic Energy Agency
P.O. Box590
A1011 Vienna, Austria

James Simpson
Argonne National Laboratory
9700 South Cass Avenue
Argonne, Illinois 60439

Millard L. Sloan
Austin Research Associates Corp.
600 W. 28th St.
Austin, Texas 78705

Theodorus J. M. Sluyters
Brookhaven National Laboratory
Upton, Long Island
New York 11973

Lloyd Smith
University of California
Lawrence Berkeley Laboratory
Berkeley, California 94720

Todd Smith
Stanford High Energy Physics Laboratory
Stanford University
Stanford, California 94305

Leonid Ivanovich Sokolov
Institute for Theoretical & Experimental Physics
Moscow, USSR

Brian Southworth
Editor, CERN Courier
CERN
1211Geneva 23, Switzerland

James E. Spencer
Los Alamos Scientific Laboratory
Meson Physics Facility
Los Alamos, New Mexico 87544

Julius Spiro
Brookhaven National Laboratory
Upton, Long Island, New York 11973

John W. Staples
Lawrence Berkeley Laboratory
University of California
Berkeley, California 94720

Klaus Steffen
DESY
Notkestieg 1
Hamburg 52, Germany

Lynn Stevenson
University of California
Lawrence Berkeley Laboratory
Berkeley, California 94720

Rae Stiening
National Accelerator Laboratory
P.O. Box 500
Batavia, Illinois 60510

Steven St. Lorant
Stanford Linear Accelerator Center
P.O. Box 4349
Stanford, California 94305

Karl Strauch
Harvard University
Cambridge, Massachusetts 02138

Ronald M. Sundelin
Laboratory of Nuclear Studies
Cornell University
Ithaca, New York 14850

Jack Tanabe
Lawrence Berkeley Laboratory
University of California
Berkeley, California 94720

Sergio Tazzari
Laboratori Nazionali Di Frascati
Box 70
Frascati 00044, Italy

Richard Taylor
Stanford Linear Accelerator Center
P.O. Box 4349
Stanford, California 94305

John Teem, Director
Division of Physical Research
U. S. Atomic Energy Commission
Germantown, Maryland 20545

Lee C. Teng
National Accelerator Laboratory
P.O. Box 500
Batavia, Illinois 60510

David B. Thomas
Rutherford High Energy Laboratory
Chilton, Didcot
Berkshire, England

Ralph Thomas
Lawrence Berkeley Laboratory
University of California
Berkeley, California 94720

David J. Thompson
Daresbury Nuclear Physics Lab.
Keckwick Lane
Daresbury, Warrington, 3WA4 4AD
England

Maury Tigner
Laboratory of Nuclear Studies
Cornell University
Ithaca, New York 14850

Hiroshi Tsujikawa
Institute for Nuclear Study
3-2-1, Midori-Cho, Tanashi
Tokyo, 188, Japan

Peter Turowski
Institut fur Experimentelle Kernphysik
Postf. 3640
Karlsruhe, Germany

John P. Turneaure
Stanford High Energy Physics Laboratory
Stanford University
Stanford, California 94305

Angelo Turrin
Laboratori Nazionali Di Frascati
Box 70
Frascati 00044, Italy

Oleg A. Valdner
Physical Engineering Institute
Imeni A. F. I offe
USSR Academy of Science
Moscow, USSR

Arie Van Steenbergen
Brookhaven National Laboratory
Upton, Long Island
New York 11973

Ferdinand Voelker
Lawrence Berkeley Laboratory
University of California
Berkeley, California 94720

Gustav-Adolf Voss
Desy
Notkestieg 1
Hamburg, 52, Germany

William A. Wallenmeyer
Asst. Dir., High Energy Physics
Division of Physical Research
U. S. Atomic Energy Commission
Washington, D C. 20545

Dieter Walz
Stanford Linear Accelerator Center
P. O. Box4349
Stanford, California 94305

William Wenzel
University of California
Lawrence Berkeley Laboratory
Berkeley, California 94720

Carl H. Westcott
Atomic Energy of Canada, Limited
Chalk River Nuclear Laboratories
Accelerator Physics Branch
Chalk River, Ontario, Canada

George Wheeler
Division of Physical Research
U. S. Atomic Energy Commission
Germantown, Maryland **20545**

Bruce L. White
University of British Columbia
Vancouver 8, British Columbia
Canada

Milton G. White
Princeton University
P.O. Box 708
Princeton, New Jersey **08540**

Rolf Wideroe
Swiss Institute for Nuclear Research
CH **5234** - Villigen
Switzerland

Alan Wilmunder
Stanford Linear Accelerator Center
P.O. Box **4349**
Stanford, California **94305**

Perry B. Wilson
Stanford Linear Accelerator Center
P.O. Box **4349**
Stanford, California **94305**

Herman Winick
Stanford High Energy Physics
Laboratory
Stanford University
Stanford. California **94305**

Peter Wolstenholme
ISR - CERN
1211 Geneva **23**
Switzerland

Jean Yoccoz
Institut National de Physique
11, Rue Pierre-et-Marie-Curie
F-75231 Paris Cedex **5,** France

Donald E. Young
National Accelerator Laboratory
P.O. Box **500**
Batavia, Illinois **60510**

Gus T. Zorn
University of Maryland
College Park, Maryland **20742**

Henri Zyngier
Lab. de l'Accelerateur Lineaire
Universite Paris-Sud, Centre
d'Orsay, Batiment **200**
F-91405 Orsay, France

CATALOGUE
of
High Energy Accelerators

FOREWORD

It has become customary to issue an up-to-date catalogue of the parameters and performance of high-energy accelerators at the time of the International Accelerator Conferences. Accordingly, we have sent out data sheets to the various laboratories, requesting their cooperation in obtaining this information. The forms are identical to those used for the 1971 CERN conference and we thank M. H. Blewett for her kind permission to use them again.

We would like to express our warmest thanks to all those who have returned the filled-out data sheets that include considerable new information.

Unfortunately, sheets for a few of the machines were not returned to us, at least by the publication deadline. Rather than publish out-of-date or incorrect material, we have not included any data for these machines. (They are shown with an asterisk in the Table of Contents.)

In contrast to previous years, you will find in this catalogue a new section listing parameters of a few new major projects that are not yet funded. Realizing that such information is at best tentative, reply to our questionnaire was left as an option for the laboratories contacted and is therefore in no way complete. Further, the authors of these pages which were returned wish us to emphasize that their data is subject to change; however, we feel that this information may reflect the direction in which the High Energy Accelerator field is currently moving.

G. E. Fischer
Ruth Thor Nelson

Note added for revised Proceedings edition:

Since the Conference, we have received two additional data sheets. They are included in this revised Proceedings edition of the Catalogue of High Energy Accelerators. Several data sheets remain outstanding. We regret that we are unable to include a complete listing of the data sheets in this revised edition.

Editors
July 1974

CONTENTS

Page

I. Proton Synchrotron (E ≥ 1 GeV) and Boosters

1. CERN, Geneva, 400-GeV PS - SPS 709
2. CERN, Geneva, 28-GeV PS - CPS 710
3. CERN, Geneva, 0.8-GeV Rooster for CPS - PSB 711
4. France, CEA Saclay, 3-GeV PS - Saturne 712
5. Japan, Nat. Lab. Tsukuba, 10-GeV PS 713
6. Japan, Nat. Lab. Tsukuba, 0.5-GeV Booster for 10-GeV PS 714
7. UK, Rutherford, 8-GeV PS - Nimrod 715
8. USA, Argonne, 12.7-GeV PS - ZGS 716
9. USA, Argonne, 0.2-GeV Booster for ZGS 717
9A. USA, Argonne, 0.5-GeV Booster for ZGS 718
10. USA, Brookhaven, 33-GeV PS - AGS 719
11. USA, Lawrence, 6.2-GeV PS - Bevatron 720
12. USA, NAL Batavia, 200/500-GeV PS 721
13. USA, NAL Batavia, 8-GeV Booster for 200/500-GeV PS 722
14. USSR, IHEP Serpukhov, 76-GeV PS 723
15. USSR, ITEP Moscow, 10-GeV PS 724
16. USSR, JINR Dubna, 10-GeV Synchrophasotron 725
17. USSR, RI Moscow, 1-GeV Cybernetic Accelerator 726

II. Electron Synchrotrons (E ≥ 1 GeV)

1. German Fed. Rep., Bonn, 2.5-GeV Synchrotron 727
2. German Fed. Rep., Hamburg, 7.5-GeV Synchrotron - DESY 728
3. Italy, Frascati, 1.1-GeV Synchrotron 729
4. Japan, INS Tokyo, 1.3-GeV Synchrotron 730
5. Sweden, Lund, 1.2-GeV Synchrotron 731
6. UK, Daresbury, 5.2-GeV Synchrotron - Nina 732

Page Page

II. Electron Synchrotrons (E ≥ 1 GeV) Cont.

7. USA, Cornell, 12-GeV Synchrotron 733
8. USSR, Tomsk, 1.5-GeV Synchrotron - Syrius (*)
9. USSR, Yerevan, 6.1-GeV Synchrotron - ARUS (*)

III. Electron Linear Accelerators (E ≥ 1 GeV)

1. France, Orsay, 2-GeV Linear Accelerator 734
2. USA, HEPL Stanford, 1.2-GeV Mark III Linear Accelerator 735
3. USA, HEPL Stanford, 2-GeV Superconducting Mark III Linear Accelerator 736
4. USA SLAC Stanford, 22-GeV Linear Accelerator 737
5. USSR Kharkov, 2-GeV Linear Accelerator 738

IV. Proton Linear Accelerator (E ≥ 500 MeV)

1. USA, Los Alamos, 800-MeV Proton Linear Accelerator - LAMPF 739

V. Proton Linear Accelerators used as Injectors for Synchrotrons

1. CERN, Geneva 50-MeV injector for CPS (*)
2. France, Saclay, 20-MeV injector for Saturne 740
3. Japan, Nat. Lab. Tsukuba, 20-MeV injector for 8-GeV PS 741
4. UK, Rutherford, 15-MeV injector for Nimrod 742
4A. UK, Rutherford, 70-MeV injector for Nimrod 743
5. USA, Argonne, 50-MeV injector for ZGS (Polarized) 744
5A. USA, Argonne, 50-MeV injector for ZGS (Unpolarized) 745
6. USA, Brookhaven, 200-MeV injector for AGS 746
7. USA, NAL Batavia, 200-MeV injector for 200/500-GeV PS 747
8. USA, Lawrence, 19-MeV injector for Bevatron 748
8A. USA, Lawrence, 50-MeV injector for Bevatron 749
8B. USA, Lawrence, 8.5-MeV SuperHILAC injector for Bevatron 750

Page Page

V. Proton Linear Accelerators used as Injectors for Synchrotrons Cont.

9. USSR, IHEP Serpukhov, 100-MeV injector for 76-GeV PS 751
10. USSR, ITEP Moscow, 24.6-MeV injector for 10-GeV PS 752
11. USSR, JINR Dubna, 9.4-MeV injector for Synchrophasotron (*)

VI. Storage Rings

1. CERN, Geneva, 10 to 28-GeV, proton-proton - ISR 753
2. France, Orsay, 1.8-GeV, electron-positron - DCI 754
3. France, Orsay, 0.5-GeV, electron-positron - ACO 755
4. German Fed. Rep., Hamburg, 3-GeV electron-positron - DORIS 756
5. Italy, Frascati, 1.5-Gev, electron-positron - ADQNE 757
6. USA, SLAC Stanford, 2.6-GeV, electron-positron - SPEAR 758
7. USA, Wisconsin, 0.24-GeV, electron (storage only) - Tantalus I 759
8. USSR, Novosibirsk, 25-GeV, proton-antiproton - VAPP-4 (*)
9. USSR, Novosibirsk, 3-GeV, electron-positron - VEPP-3 (*)
10. USSR, Novosibirsk, 1.8-GeV, antiproton (storage) - NAP (*)

VII. Unfunded Projects

1. Italy, Frascati, Super Adone, 10-12 GeV, electron-positron storage ring 760
2. UK, Daresbury, 2-GeV, electron storage ring for synch. rad. 761
3. UK, Rutherford-Daresbury, 14-GeV, electron-positron storage ring - EPIC 762
4. USA, Argonne, 12-GeV, Superconducting Stretcher Ring (ZGS - SSR) 763
5. USA, Brookhaven, 200-GeV, proton-proton storage rings -ISABELLE 764
6. USA, LBL-SLAC, 15-GeV, electron-positron storage ring PEP - Stage I 765
7. USA, Wisconsin, 1.7-GeV, electron storage ring for synch. rad Tantalus II 766

NAME OF MACHINE: CERN SPS
INSTITUTION: CERN Laboratory II
LOCATION: Geneva - Pays de Gex (F)

PERSON IN CHARGE: J.B. Adams
DATA SUPPLIED BY: G. von Holtey
DATE: January 1974

HISTORY AND STATUS

CONSTRUCTION STARTED (date): 1971
FIRST BEAM OBTAINED OR GDAL (date): end of 1976
TOTAL COST OF FACILITY: 1150 MSF
FUNDED BY: 11 Member States of CERN
TOTAL ACCELERATOR STAFF (now): 360
ANNUAL OPERATING BUDGET: -

ACCELERATOR PARAMETERS

Physical Dimensions (Mean)

RING DIAM. 2200 m; Tunnel sect. Ø = 4 m
MAGNET 80x44 cm; Mag. Gap 15 x 4.5 cm
"DONUT" 14.5x4.5 cm; Aperture 11.0 x 4.3 cm

Injector System

TYPE: improved CPS
OUTPUT (max) 10^{13} ppp at 10 to 14 GeV/c
BEAM EMITTANCE (10 GeV/c) H:2.6π V:3.3π mm-mrad
INJECTION PERIOD 23 usec, or 1 turns
INFLECTOR TYPE: pulsed magnetic kicker

Magnet System

FOCUSING TYPE: AG separate function
No. MAG. UNITS 744+216 length (ea) 6.26/3.085 m
STRAIGHT SECT. 216 Total S.S. Length - m
FOCUSING ORDER: FODO
BETATRON OSC. FREQ. ν_x 27.6 ν_y 27.55
FIELD, AT INJ. 450 G, at max 1a kG
RISE TIME 3.4 sec; Flat-top time 0.7to2.0sec
MAG. WEIGHT (tons) Fe 13500, Cu 1400
POWER INPUT (MW) PEAK 135 MEAN 36

Acceleration System

HARMONIC No. 4620 No. Cavities 2
RF RANGE: 200.2 MHz
ORBIT FREQ.
ENERGY GAIN: 3.6 MeV/turn
RADIATION LOSS - keV/turn
RF POWER INPUT (kW) PEAK 1.0 MW

Other Rekvant Parameters or Notable Features

ACCELERATOR PERFORMANCE

	Normal (or Goal)	Maximum Achieved
ENERGY (GeV)	400	
RESOLUTION ΔE/E (%)		
REPET. RATE (pulse/sec)*	0.17(0.11)	
PULSE WIDTH		
DUTY FACTOR, macroscopic (%)*	12 (22.5)	
INTERNAL BEAM (part/pulse)	10^{13}	
(part/sec) *	$1.7\ 10^{12}$	($1.1\ 10^{12}$
CURRENT (mA)	69.5	
BEAM EMITTANCE (mm-mrad)	0.2 π	
SCHEDULED OPERATION (hr/wk)	-	

"ON BEAM" - % OF SCHEDULED TIME

Some Typical External and Secondary Beams

PARTICLE	FLUX (part/sec)	BEAM AREA (cm^2)	ENERGY (GeV)	AEIE (%)

RESEARCH PROGRAM

TOTAL EXPERIMENTAL AREA ca 27000 m^2
BEAM LINES TO Stations
STATIONS SERVED AT SAME TIME
BEAM SEPARATORS SPECTROMETERS
ON-LINE COMPUTERS WITH Inputs
BUBBLE CHAMBERS, in-house Users'
TOTAL POWER INSTALLED FOR RESEARCH MW
No. USER GROUPS: in-house outside
TOTAL RESEARCH STAFF, in-house outside
ANNUAL RESEARCH BUDGET, in-house
SCHEDULED RESEARCH TIME, hours/week

RECENT IMPROVEMENTS OR MODIFICATIONS TO MACHINE

* for 0.7 sec (2.0 sec) flat top.

Published Articles Describing Machine

The 300 GeV Programme, CERN/1050, January 1972.

NAME OF MACHINE: CERN Proton Synchrotron (CPS)
INSTITUTION: European Organization for Nuclear Research
LOCATION: eyrin, Geneva, Switzerland

PERSON IN CHARGE: G.L. Munday
DATA SUPPLIED BY: O. Barbalat - L. Hoffmann
DATE: February 1974

HISTORY AND STATUS

CONSTRUCTION STARTED (date): 1955
FIRST BEAM OBTAINED, OR GOAL (date): November 24, 1959
TOTAL COST OF FACILITY: 200 MFr.Sw. (1954-1959)
FUNDED BY: CERN Member States
TOTAL ACCELERATOR STAFF (now): 460
ANNUAL OPERATING BUDGET***: 52 MFr.Sw.

ACCELERATOR PARAMETERS

Physical Dimensions (Mean)
RING DIAM. 200 m; Tunnel sect. 6 x 6 m
MAGNET 1.16,0.94 m; Mag. Gap 10.0 x 15.0 cm
"DONUT" 7.4 x15.0cm; Aperture 7.0 x 14.6 cm

Injector System
TYPE: Linac or Booster
OUTPUT: 50/300 mA at 50/800 MeV
BEAM EMITTANCE: 20 x 20 π / 30 x 13 π mn-mrad
INJECTION PERIOD: 20/2.5 μsec, or 3/1 turns
INFLECTOR TYPE: electrostatic dc and pulsed magnetic kicker or septum and pulsed kicker

Magnet System
FOCUSING TYPE: AG Field index, n= 288
No. MAG. UNITS: 100 Length (ea): 4.26 m
STRAIGHT SECT.: 100 Total S.S. Length: 188 m
FOCUSING ORDER: FOFDOD
BETATRON OSC. FREQ. ν_H: 6.25 ν_V: 6.25
FIELD, AT INJ.: 147 G, at max: 14 kG
RISE TIME: 0.7-1.0 sec; Flat-top time: 0.5-0.7 sec
MAG. WEIGHT (tons) Fe: 3000, Cu: 130
POWER INPUT (MW) PEAK: 41 MEAN: 2.8

Acceleration System
HARMONIC NO.: 20 NO. Cavities: 10
RF RANGE: 2.9 to 9.55 MHz
ORBIT FREQ. RANGE: 0.145 to 0.478
ENERGY GAIN: (max) 80
RADIATION LOSS: keV/turn
RF POWER INPUT (kW) PEAK: 1000 MEAN: 300

Other Relevant Parameters or Notable Features
*** Including developments, Linac and Booster

ACCELERATOR PERFORMANCE

	Normal (or Goal)	Maximum Achieved
ENERGY (GeV)	25	28
RESOLUTION ΔE/E (%)	± 0.05	
REPET. RATE (pulse/sec)	~ 0.5	
PULSE WIDTH		
DUTY FACTOR, macroscopic (%)	20-25	
INTERNAL BEAM (part/pulse)	$1.5 \cdot 2 \cdot 10^{12}$	$5 \cdot 6 \cdot 10^{12}$ (with Booster)
(part/sec)	10^{12}	$3 \cdot 10^{12}$
CURRENT (mA)		
BEAM EMITTANCE (mn-mrad)	1 π	
SCHEDULED OPERATION (hr/wk)	145 (excluding yearly shutdown)	
"ON BEAM" 91 % OF SCHEDULED TIME		

Sane **Typical External a d Secondary Beams**

PARTICLE	FLUX (part/sec)	BEAM AREA (cm²)	ENERGY (GeV)	ΔE/E (%)	
Slow ejected protons	$0.5 \cdot 10^{12}$	0.1	24	1.0	on 3 targets
π^-	$4 \cdot 10^5$	1	6	4	
π^+	$1.2 \cdot 10^6$	2	6	2	
$p^+ \pi^+$	$1.6 \cdot 10^6$	2	15	2	
K^+	$2.4 \cdot 10^4$	3	2.8	1.75	
K^-	$2 \cdot 10^3$				

RESEARCH PROGRAM

TOTAL EXPERIMENTAL AREA: 20.000 m²
BEAM LINES TO: 17 + ISR + 3 tests Stations
STATIONS SERVED AT SAME TIME: 10 + ISR + tests
SEPARATED BEAMS: 10 SPECTROMETERS: 10
ON-LINE COMPUTERS: 13
BUBBLE CHAMBERS, in-house: 3 Users':
TOTAL POWER USED FOR RESEARCH: 27 MW (average)
No, USER GROUPS: mixed 15+5 outside: 15 + 40**
TOTAL RESEARCH STAFF: in-house: 190 outside: 620 + 500 **
ANNUAL RESEARCH BUDGET, in-house:
SCHEDULED RESEARCH TIME, hours/week: 125

** Bubble chamber picture analysis

RECENT IMPROVEMENTS OR MODIFICATIONS TO MACHINE
- 800 MeV Booster Injector
- Transformations for use as SPS injector

* For the whole of CERN

PUBLISHED ARTICLES DESCRIBING MACHINE

Regenstreif,E., CERN 59-29,CERN 60-26, CERN 62-3.
Hine,M.G.N., Int. Conf. Instrum. for High Energy Accel.,LRL,Sept.60,214-222.
Lapostolle,P.,Onde électrique 40, 489-504(1960).
Adams,J.B., Nature 185,568-72(1960).
Germain,P.,Industries Atomiques 7, 9-10/61-73(1963).
Reich, K.H., Kerntechnik 3, (8)345-55(1961).
Hereward,H.G.,Nucl.Instr.Meth.20,9-11(1963).
Standley,P.H.,Fourth Int.Conf.High Energy Acc. Dubna 1963,99-109 (USAEC Conf.114)
Fifth Int.Conf.High En.Acc.Frascati,1965,80-85.
Eaconnier et al. Seventh Int.Conf.High En.Acc. Erevan 1969, 565-575.
Baconnier et al. U.S.Nat.Acc.Conf.Chicago 1971.

PUBLISHED ARTICLES (cont.)

PS Staff, Ninth Int. Conf. High Energy Accelerators Stanford 1974

NAME OF MACHINE Booster for the CPS (PSB) PERSON IN CHARGE K.H. Reich
INSTITUTION CERN, European Org. Nucl. Res. DATA SUPPLIED BY H. Koziol, K.H. Reich
LOCATION Meyrin, Geneva, Switzerland DATE 8th March 1974

HISTORY AND STATUS

CONSTRUCTION STARTED (date) January 1968
FIRST BEAM OBTAINED. OR GOAL (date) May 1972
TOTAL COST OF FACILITY 60 MFr (Swiss)
FUNDED BY CERN Member States
TOTAL ACCELERATOR STAFF (now) 72
ANNUAL OPERATING BUDGET 8 MFr (including develop.)

ACCELERATOR PARAMETERS

Physical Dimensions (Mean) (width x height)
RING DIAM. 50 m; Tunnel sect. 4.05 x 5.15 m
MAGNET 0.7 x 1.52m Gap 24.1 x 7.0 cm
"DONUT" x cm; Aperture [1] x cm

Injector System
TYPE Improved CERN PS Linac
OUTPUT 50 mA at 50 MeV
BEAM EMITTANCE 30π×30π (95% of beam) mn-mrad
INJECTION PERIOD 100 μsec, or 4 x 15 turns
INFLECTOR TYPE magnetic (1 for multiturn, 1 for monoturn)

Magnet System [2]
FOCUSING TYPE AG, sep. functions; triplets
No. MAG. UNITS 32 Length (ea) (mag.) 1.618 m
STRAIGHT SECT. [3] Total S. s Length [3] m
FOCUSING ORDER ½L1, B, L2, F, L3, D, L4, F, L5, B, ½L1
BETATRON OSC. FREQ. ν_H 4 to 5 ν_V 4 to 5.3
FIELD, AT INJ. 1253 G, at max 5.93 kG
RISE TIME 0.60 sec; Flat-top time 0.08 sec
MAG. WEIGHT (tons) Fe 580, Cu 34.6 (B+F+D)
POWER INPUT (MW) PEAK 5.6 [4] MEAN 1.64 [4]

Acceleration System
HARMONIC NO. 5 No. Cavities 1 per ring
RF RANGE 2.997 8.033 MHz
ORBIT FREQ. 0.599 1.607 MHz
ENERGY GAIN 1 keV/t
RADIATION LOSS – keV/turn
RF POWER INPUT (kW) PEAK 4 x 7 Mean 4 x 4

Other Relevant Parameters or Notable Features 4 rings stacked on top of each other. Bending magnets and quadrupoles combined to 4-gap units. Linac beam switched to 4 rings by vertical deflector. At 800 MeV the 4 beams are ejected sequentially and combined by vertical bending septum and kicker magnets.

Publications describing machine:
Proc. Int. Accelerator Conferences:
VI (Cambridge): Bovet, Reich (p.315)
VII (Yerevan): Bigliani et al. (p.433)
VIII (Geneva): Bovet et al. (p.102, 380)
IX (1974): Baribaud et al.; Reich
Proc. Nat. Accelerator Conference:
4th (Chicago): Asseo et al; Bigliani; Bigliani et al; Brückner; Koziol, Reich; Rufer, Unterlerchner; Sacherer, Sherwood.
5th (San Francisco): Bovet; Baribaud, Metzger; Rabany.
Publ. (cont.) Int. Conf. Magnet Technology:
3rd (Hamburg): Asner et al. (p.418)
4th (Brookhaven): Pahud (p.718).

ACCELERATOR PERFORMANCE

(present, at 800 MeV)	Normal (or Goal)	Maximum Achieved
ENERGY (GeV)	0.800	
RESOLUTION	$\Delta p/p \pm 1.3 \times 10^{-3}$	
REPET. RATE (pulse/sec)	as CPS, max 0.87	
PULSE WIDTH	4 x 0.622	
DUTY FACTOR, macroscopic (%)	$2.16\ 10^{-4}$ %	
INTERNAL BEAM (part/pulse)	7×10^{12} ppp	
(part/sec)	(goal 1.3×10^{13} ppp)	
CURRENT (mA)	400 mA	

BEAM EMITTANCE (nm-mrad) H: 28π; V: 13π
SCHEDULED OPERATION (hr/wk) 1974 : ∿ 3000 h
"ON BEAM" % OF SCHEDULED TIME

Some Typical External and Secondary Beams

PARTICLE	FLUX (part/sec)	BEAM AREA (cm^2)	ENERGY (GeV)	ΔE/E (%)
CPS INJECTOR				

RESEARCH PROGRAM

TOTAL EXPERIMENTAL AREA m²
BEAM LINES TO Stations
STATIONS SERVED AT SAME TIME
BEAM SEPARATORS SPECTROMETERS
ON-LINE COMPUTERS WH Inputs
BUBBLE CHAMBERS, in-house Users'
TOTAL POWER INSTALLED FOR RESEARCH MW
No. USER GROUPS: in-house outside
TOTAL RESEARCH STAFF, in-house outside
ANNUAL RESEARCH BUDGET, in-house
SCHEDULED RESEARCH TIME, hours/week

RECENT IMPROVEMENTS OR MODIFICATIONS TO MACHINE

Mobile console in PSB equipment rooms giving full access to central control computer.

[1]

	section	apert. (und. vac.)
in bend. mag.	13.8x6.8	13.2x6.1
in triplet	13.8x12.4	13.5x12.1
in L1	Ø 12.3	Ø 12.0

[2] Data for quadrupoles

	F	D
number	32	16
magn. length (m)	0.50	0.88
bore radius	0.06	
gradient (T/m)	0.81 (inj)	
	3.83 (max)	

[3] L_1: 16x2.54m; L_2, L_5: 16x0.28m; L_3, L_4: 16x0.59m;

[4] At output of power supply.

NAME OF MACHINE SATURNE
INSTITUTION C.E.A.
LOCATION SACLAY - FRANCE

PERSON IN CHARGE GOUTTEFANGEAS
DATA SUPPLIED BY
DATE JAN. 1974

HISTORY AND STATUS

CONSTRUCTION STARTED (date) 1955
FIRST B E N OBTAINED. OR GOAL (date) August 1958
TOTAL COST OF FACILITY In 1957 - 87 MF
FUNDED BY C.E.A
TOTAL ACCELERATOR STAFF (now) 192
ANNUAL OPERATING BUDGET

ACCELERATOR PARAMETERS

Physical Dimensions (Mean)

RING DIAM. 22 m; Tunnel sect. m
MAGNET 1.77 2 m; Mag. Gap 17.5 × 52.75 cm
"DONU" 0.648 cm; Aperture 10.6 × 34 cm

Injector System.

Linac
OUTPUT (max) 40mA at 20 MeV
BEAM EMITTANCE 18 mA in 2,8 π mm-mrad
INJECTION PERIOD 600 µsec, or 550 turns
INFLECTOR TYPE. electrostatic V=100 KV E = 66.6 KV/cm

Magnet System

FOCUSING TYPE Weak
No. MAG. UNITS 4 Length (ea) 13.255 m
STRAIGHT SECT. 4 Total S.S. Length 16 m
FOCUSING ORDER
BETATRON OSC. FREQ. ν_H 0.721 ν_V 0.884
FIELD. AT INJ. 771 G, at max 15 kG
RISE TIME 0.87 sec; Flat-top time 0.5 sec
MAG. WEIGHT (tons) Fe 1x080, Cu 55
POYER INPUT (MW) PEAK 24 MEAN 1

Acceleration System

HARMONIC No. 2 NO. Cavities 1
RF RANGE 1.6 8.44 MHz
ORBIT FREQ.
ENERGY GAIN 1.16
RADIATION LOSS keV/turn
RF POUER INPUT (kW) PEAK 36 6

Other Relevant **Parameters** or **Notable Features**

acceleration of deutons
5.10^{11} d/pulse at 2,3 GeV

Published Articles Describing Machine

Onde electrique n° 387 (juin 59)

ACCELERATOR PERFORMANCE

	Normal (or Goal)	Maximum Achieved
ENERGY (GeV)	3	3
RESOLUTION ΔE/E ◀■▶	3.4	
REPET. RATE (pulse/sec)	0.22 with Flat top	
PULSE UIDTH	0.45	
DUTY FACTOR, macroscopic (%)	9	
INTERNAL BEAM (part/pulse)	$1.2 10^{12}$	$1.6 10^{12}$
(part/sec)	$2,6 10^{12}$	$3,5 10^{11}$
CURRENT (mA)		
BEAH EHITTANCE (mm-mrad)	π x28 / π x8	
SCHEDULED OPERATION (hr/wk)	130	168

"ON BEAM" 71 % OF SCHEDULED TIME

Some Typical External and Secondary Beams

PARTICLE	FLUX (part/sec)	BEAM AREA (cm²)	ENERGY (GeV)	ΔE/E (%)
π+	$.6x10^5$	16	2	2
p	$6x10^{10}$	25x12 *	3	0.2
F	$8x10^{10}$	10x15 *	1	0.05
d	$4.4x10^{10}$		2.7	
α	$2x10^9$	350x150 *	0.7	
n	$.5x10^7$	28	2 GeV/c	

RESEARCH PROGRAM (* emittance n 10^{-6})

TOTAL EXPERIHENTAL AREA 3480 m²
BEAH LINES TO 0 Stations
STATIONS SERVED AT SAME TIME 3
BEAM SEPARATORS 0 SPECTROMETERS 2
ON-LINE COMPUTERS WITH 8 Inputs
BUBBLE CHAMBERS. in-house Users'
TOTAL POUER INSTALLED FOR RESEARCH 22 MW
No. USEK GROUPS: in-house 2 outside 12
TOTAL RESEARCH STAFF, in-house outside
ANNUAL RESEARCH BUDGET. in-house
SCHEDULED RESEARCH TIME, hours/week 93

RECENT IMPROVEMENTS OR MODIFICATIONS TO MACHINE

- acceleration of particles a $1,2\ 10^{11}$ α/pulse at 1.2 GeV/A
- a superconducting quadrupole doublet OGA permits to increase the number of pions by a factor 4
- A renovation of Saturne is being studied. With a new nasnet and the same injector, one should obtain $1,10^{12}$ p/s external in 3 mmmrad at 1 GeV (max. energy 2.7 - 3 GeV)

NAME OF MACHINE 10 GeV Proton Synchrotron
INSTITUTION Nat.Lab.for High Energy Phys.
LOCATION Tsukuba, Japan

PERSON IN CHARGE T. Nishikawa
DATA SUPPLIED BY
DATE March. 1974

HISTORY AND STATUS

CONSTRUCTION STARTED (date) April, 1971
FIRST BEAM OBTAINED. OR GOAL (date) 1975
TOTAL COST OF FACILITY 4×10^9 Yen
FUNDED BY Javanese Government
TOTAL ACCELERATOR STAFF (now) 65
ANNUAL OPERATING BUDGET 5×10^8 Yen

ACCELERATOR PARAMETERS

Physical Dimensions (Mean)
RING DIAM. 108 m; Tunnel sect. 4.0 x 4.7 m
MAGNET 85 x 70 m; Mag. Gap 5.6 x 14 cm
"DONUT" 5.0 x 14 cm; Aperture 5.0 x 14 cm

Injector System
TYPE 20 MeV Linac + 500 MeV Booster
OUTPUT (max) 1.6×10^{-3} at 500 MeV
BEAM EMITTANCE 75π(H) x 10π(V) mn-mrad
INJECTION PERIOD 5×10^5 μsec, or 9 turns
INFLECTOR TYPE magnetic

Magnet System
TYPE AG separated function
No. MAG. UNITS 48(bng) Length (ea) 3.2 (bng) m
STRAIGHT SECT. 4(long) Total S.S. Length 48.4(ℓ) m
FOCUSING ORDER FODO
BETATRON OSC. FREQ. ν_H 7.25 ν_V 7.25
FIELD. AT INJ. 1.5 kG, at max. 13 (17.5) kG
RISE TIME 0.5(0.85) sec; Flat-top time 0.5 sec
MAG. WEIGHT (tons) Fe 680, Cu 30
POWER INPUT (MW) PEAK 13(25) MEAN 4.5(8.6)

Acceleration System
HARMONIC No. 9 No. Cavities 3
RF RANGE 6.0 to 7.9 MHz
ORBIT FREQ. 0.67 to 0.88
ENERGY GAIN 12.6
RADIATION LOSS 19.1 (16.7) keV/turn
RF POWER INPUT (kW) PEAK 46 mean 26.5

Other Relevant Parameters or Notable Features

ACCELERATOR PERFORMANCE

	Normal (or Goal)	Maximum Achieved
ENERGY (GeV)	8 (12)	
RESOLUTION ΔE/E (%)	0.2 (0.1)	
REPET. RATE (pulse/sec)	1/2	
PULSE WIDTH	0.4	
DUTY FACTOR, macroscopic (%)	25	
INTERNAL BEAM (part/pulse)	$>2 \times 10^{12}$	(10^{13})
(part/sec)	$>10^{12}$	(5×10^{12})
CURRENT (mA)	>280	(1415)
BEAM EMITTANCE (mn-mrad)	$13\pi \times 1.7\pi$	($9\pi \times 1.2\pi$)
SCHEDULED OPERATION (hr/wk)		

"ON BEAM" ____ % OF SCHEDULED TIME

Some **Typical External and Secondary Beams**

PARTICLE	FLUX (part/sec)	BEAM AREA (cm^2)	ENERGY (GeV)	ΔE/E (%)

RESEARCH PROGRAM

TOTAL EXPERIMENTAL AREA 3500 m^2
BEAM LINES TO 3 Stations
STATIONS SERVED AT SAME TIME
BEAM SEPARATORS 3 SPECTROMETERS 2
ON-LINE COMPUTERS WITH 2 Inputs
BUBBLE CHAMBERS, in-house 1 Users'
TOTAL POWER INSTALLED FOR RESEARCH 11 MW
No. USER GROUPS: in-house 3 outside 9
TOTAL RESEARCH STAFF, in-house 25 outside 60
ANNUAL RESEARCH BUDGET. in-house
SCHEDULED RESEARCH TIME. hours/week

RECENT IMPROVEMENTS OR MODIFICATIONS TO MACHM

Published Articles Describing Machine

NAME OF MCHINE Booster Synchrotron for 10-GeV PS

INSTITUTION Nat. Lab. for High Energy Phys.

LOCATION Tsukuba, Japan

PERSON IN CHARGE T. Nishikawa

DATA SUPPLIED BY T. Nishikawa

DATE March. 1974

HISTORY AND STATUS

CONSTRUCTION STARTED (date) April, 1971

FIRST BEAM OBTAINED. OR GOAL (date) 1974

TOTAL COST OF FACILITY

FUNDED BY Japanese Government

TOTAL ACCELERATOR STAFF (now) 10

ANNUAL OPERATING BUDGET

ACCELERATOR PARAMETERS

Physical Dimensions (Mean)

RING DIAM. 6 m; Tunnel sect. m

MAGNET 0.7 x 0.8 m; Mag. Gap 7.2 x 14.0 cm

"DONUT 7.0 x 16. cm; Aperture 5.6 x 14.0 cm

Injector System

TYPE Linac

OUTPUT (max) 100 mA at 20 MeV

BEAM EMITTANCE 10π (norm.) mn-mrad

INJECTION PERIOD 5.5 μsec, or turns

INFLECTOR TYPE magnetic

Magnet System

FOCUSING TYPE combined function

No. MAG. UNITS 8 Length (ea) 2.6 m

STRAIGHT SECT. 8 Total S.S. Length 17 m

FOCUSING ORDER FDDFO

BETATRON OSC. FREQ. ν_u 2.25 ν_v 2.25

FIELD, AT INJ. 1.97 G, at max 11.0 kG

RISE TIME 0.025 sec; Flat-top time - sec

MAG. WEIGHT (tons) Fe 88.1, Cu 6.57

POWER INPUT (MW) PEAK MEAN 0.5

Acceleration System

HARMONIC No. 1 No. Cavities 1

RF RANGE 1.616 to 6.077 MHz

ORBIT FREQ. 1.616 to 6.027

ENERGY GAIN max. 7

RADIATION LOSS keV/turn

RF POWER INPUT (kW) PEAK 60 mean 40

Other Rekvant Parameters or Notable Features

ACCELERATOR PERFORMANCE

	Normal (or Goal)	Maximum Achieved
ENERGY (GeV)	0.5	
RESOLUTION ΔE/E (%)	0.3	
REPET. RATE (pulse/sec)	20	
PULSE WIDTH	0.06 μs	
DUTY FACTOR, macroscopic (%)	1.2×10^{-6}	
INTERNAL BEAM (part/pulse)	0.5×10^{12}	(2×10^{12})
(part/sec)	1×10^{13}	(4×10^{13})
CURRENT (mA)	480	(1900)
BEAM EMITTANCE (mn-mrad)	75π(H)x10π(V)	
SCHEDULED OPERATION (hr/wk)		

"ON BEAM" % OF SCHEDULED TIME

Some Typical External and Secondary Beams

PARTICLE	FLUX (part/sec)	BEAM AREA (cm^2)	ENERGY (GeV)	ΔE/E (%)

RESEARCH PROGRAM

TOTAL EXPERIMENTAL AREA m^2

BEAM LINES TO Stations

STATIONS SERVED AT SAME TIME

BEAM SEPARATORS SPECTROMETERS

ON-LINE COMPUTERS WITH Inputs

BUBBLE CHAMBERS. in-house Users'

TOTAL POWER INSTALLED FOR RESEARCH MW

No. USER GROUPS: in-house outside

TOTAL RESEARCH STAFF, in-house outside

ANNUAL RESEARCH BUDGET, in-house

SCHEDULED RESEARCH TIME, hours/week

RECENT IMPROVEMENTS OR MODIFICATIONS TO MACHINE

Published Articles Describing Machine

NAME OF MACHINE NIMROD

INSTITUTION RUTHERFORD LABORATORY
LOCATION CHILTON, DIDCOT, BERKS., UK

PERSON IN CHARGE D A GRAY

DATA SUPPLIED BY D A GRAY
DATE January 1974

HISTORY AND STATUS

CONSTRUCTION STARTED (date) 1957
FIRST BEAM OBTAINED. OR GOAL (date) August 1963
TOTAL COST OF FACILITY £10M to first operation
FUNDED BY Science Research Council
TOTAL ACCELERATOR STAFF (now) 330 incldg expl area
ANNUAL OPERATING BUOGET ~ £8M (Lab. total)

ACCELERATOR PARAMETERS

Physical Dimensions (Mean)
RING DIAM 53.27 m; ~~Machine Room~~ Machine Room 61 x 9 m
MAGNET 3.15 x 2.74 m; Mag. Gap 116 x 28.4 cm
"DONUT" x cm; Aperture 100 x 20 cm

Injector System
TYPE Alvarez linac
OUTPUT (max) 45 at 14.9
BEAM EMITTANCE At 18 mA 100% in 50 mn-mrad
INJECTION PERIOD 350 µsec, or 120 turns
INFLECTOR TYPE Electrostatic

Magnet System
FOCUSING TYPE Weak n = 0.6
No. MAG. UNITS 8 Length (ea) 14.751 m
STRAIGHT SECT. 8 Total S.S. Length 30.44 m
FOCUSING ORDER -
BETATRON OSC. FREQ. ν_H 0.71 ν_V 0.87
FIELD, AT INJ. 299 G, at max 14.2 kG
RISE TIME 0.75 sec; Flat-top time Up to 0.95 sec
MAG. WEIGHT (tons) Fe 7,000 , Cu 250
POWER INPUT (MW) PEAK 160 MEAN 2.5

Accelcration System
HARMONIC NO. 4 No. Cavities 1 unit 2 gaps
RF RANGE 1.416 7.980 MHz
ORBIT FREQ. .354 to 1.995 MHZ
ENERGY GAIN 5.5 keV/turn
RADIATION LOSS Negligible keV/turn
RF POWER INPUT (kW) PEAK 45 Mean 20

Other Rekvant Parameters or Notable Features
a) Vacuum vessel is double glass-epoxy laminate system.
b) Magnet is C-tpe with field correction using 'crenellations'.

Published Articles Describing Machine
i) Nimrod - A 7 GeV proton synchrotron. Ruth. Lab. Report NIRL/R/44 (1965).
ii) The work of the Rutherford Laboratory 1972. Ruth. Lab. Report RHEL/R270 (1973).

ACCELERATOR PERFORMANCE

	Normal (or Goal)	Maximum Achieved
ENERGY (GeV)	7.1	8.0
RESOLUTION ΔE/E (%)	0.015	
REPET. RATE (pulse/sec)	22	
PULSE WIDTH (ms)	450	
DUTY FACTOR, macroscopic (%)	20	
INTERNAL BEAM (part/pulse)	3×10^{12} P	4.2×10^{12} *
(part/sec)	1.1×10^{12}	1.7×10^{12}
CURRENT (mA)	-	-
BEAM EMITTANCE (mm-mrad)		
SCHEDULED OPERATION (hr/wk)	120 average for research and machine development.	

"ON BEAM" 88 % OF SCHEDULED TIME for research.

Some Typical External and Secondary Beams

PARTICLE	FLUX (part/sec)	BEAM AREA (cm²)	Momentum ENERGY (GeV)	ΔE/E (%)	
P	4.5×10^{11}	0.1	7.8	0.7	Zxtracted beam.
π^-, π^+	5×10^7		1-4	2-10	
	4×10^7	6	0.2	10	
K^+	3×10^3		1.0-2.0	2	
$K^\pm$	6×10^3 (K^-)		0.4-1.0	6	

RESEARCH PROGRAM

TOTAL EXPERIMENTAL AREA 7300 m²
BEAM LINES TO 9 Stations
STATIONS SERVED AT SAME TIME 9
BEAM SEPARATORS SPECTROMETERS
ON-LINE COMPUTERS WITH Inputs
BUBBLE CHAMBERS. in-house 0 Users'
TOTAL POWER INSTALLED FOR RESEARCH 24 12 MW
No. USER GROUPS: in-house 4 outside
TOTAL RESEARCH STAFF, in-house x outside 141
ANNUAL RESEARCH BUDGET, in-house -
SCHEDULED RESEARCH TIME, hours/week 94 average in 1973

RECENT IMPROVEMENTS OR MODIFICATIONS TO MACHINE

*
1) Second-harmonic cavity commissioned in 1973 gave 40% increase.
Characteristic of cavity:
Harmonic No.8. Drift tube acceleration.
RF Voltage 8 kV peak.
RF power kW 21 peak 12 mean.

2) New 70 MeV injector being built ready for 1975. Should give x 5 beam.

NAME OF MACHINE Zero Gradient Synchrotron
INSTITUTION Argonne National Laboratory
LOCATION Argonne, Illinois USA

PERSON IN CHARGE Ronald L. Martin
DATA SUPPLIED BY Ronald L. Martin
DATE February 1974

HISTORY AND STATUS

CONSTRUCTION STARTED (date) June 1959
FIRST BEAM OBTAINED. OR GOAL (date) Sept. *1963*
TOTAL COST OF FACILITY $50 M
FUNDED BY US AEC
TOTAL ACCELERATOR STAFF (now) 230
ANNUAL OPERATING BUDGET $10.5 M

ACCELERATOR PARAMETERS

Physical Dimensions (Mean)
RING DIAM. 54.7 m; Tunnel sect. 12.7 x 10.4 m
MAGNET 1.4 x 2.6 m; Mag. Gap *14.6* x 136.5 cm
"DONUT" 14.6 x 82.2 cm; Aperture 13.3 x 81.3 cm

Injector System
TYPE Linac
OUTPUT (max) 40 mA at 50 MeV
BEAM EMITTANCE 25 π mm-mrad
INJECTION PERIOD *100* μsec, or 60 turns
INFLECTOR TYPE dc magnetic

Magnet System field index,
FOCUSING TYPE weak n = 0 (wedge foc)
No. MAG. UNITS *8* Length (ea) *16.3* m
STRAIGHT SECT. *8* Total S.S. Length 41.45 m
FOCUSING ORDER
BETATRON OSC. FREQ. ν_H 0.83 ν_V 0.81 (at inj)
FIELD, AT INJ. 482 G, at max 21.5 kG
RISE TIME 0.85 sec; Flat-top time 0-1 sec
MAG. WEIGHT (tons) Fe 4700, Cu 68
POWER INPUT (MW) PEAK 110 MEAN 10

Acceleration System
HARMONIC NO. 8 No. Cavities 1 (3 gaps)
RF RANGE *4.4* to 14.0 MHz
ORBIT FREQ. *0.55* to *1.75* MHz
ENERGY GAIN 10 keV/turn
RADIATION LOSS keV/turn
RF POWER INPUT (kW) P E A K 6 0 Mean 30

Other Relevant Parameters *or* Notable *Features*

Only high energy synchrotron using wedge focusing

ACCELERATOR PERFORMANCE

	Normal (~~on Goal~~)	Maximum Achieved
ENERGY (GeV)	12.0	*12.7*
RESOLUTION ΔE/E (%)	±0.01	±0.01
REPET. RATE (pulse/sec)	0.30	0.5
PULSE WIDTH (sec)	0.70	1.0 (max flattop)
DUTY FACTOR, macroscopic (%)	20	20
INTERNAL BEAM (part/pulse) $\times 10^{12}$	2.5	3.8
(part/sec) $\times 10^{12}$	*0.8*	1.5
CURRENT (mA)	700	1000
BEAM EMITTANCE (mm-mrad) (int)	25 π	150 π
SCHEDULED OPERATION (hr/wk)	80	135 ave for year

"ON BEAM" 90 % OF SCHEDULED TIME

Some Typical External and Secondary Beams

PARTICLE	FLUX (part/sec)	BEAM AREA (cm^2)	ENERGY (GeV)	ΔE/E (%)
π	10^5	1	0.5-8	±(0.75-2)
K	10^3	1	*0.5-6*	±2
K^0	2×10^5	*200*	0.2-2.5	
n	10^6	6	2-11	

RESEARCH PROGRAM

TOTAL EXPERIMENTAL AREA 13000 m^2
BEAM LINES TO 17 Stations
STATIONS SERVED AT SAME TIME 13 peak, 7 average
BEAM SEPARATORS 4 SPECTROMETERS 1
ON-LINE COMPUTERS WITH 5 Inputs
BUBBLE CHAMBERS, in-house 1 Users' 0 (*1* streamer chamber)
TOTAL POWER INSTALLED FOR RESEARCH 30 MW
No. USER GROUPS: in-house 5 outside *30*
TOTAL RESEARCH STAFF, in-house outside
ANNUAL RESEARCH BUDGET, in-house $3.5 M
SCHEDULED RESEARCH TIME, hours/week 120 ave.

RECENT IMPROVEMENTS OR MODIFICATIONS TO MACHINE

2 simultaneous external beams
Resonant Extraction - 90% *(40* psec - *700* msec)
Titanium vacuum chamber installed *1972*
Polarized protons to *8.5* GeV/c *1973*
70% polarization - 5 x 10^8/pulse internal
200 MeV injection from booster *1974*

Published Artkles **Describing** Machine

L.C. Teng, "Status of the Argonne 12.5-BeV Zero Gradient Synchrotron," Dubna - *1963* Proceedings, **pp.** 223-232.

NAME OF MACHINE ZGS Booster Synchrotron I
PERSON IN CHARGE Ronald L. Martin
INSTITUTION Argonne National Laboratory
DATA SUPPLIED BY James D. Simpson
LOCATION Argonne, Illinois USA
DATE February 1974

HISTORY AND STATUS

Former 2.2 GeV Cornell Electron Syn.
CONSTRUCTION STARTED (date)
FIRST BEAM OBTAINED, OR GOAL (date) October 1971
TOTAL COST OF FACILITY
FUNDED BY US AEC (Development and AI)
TOTAL ACCELERATOR STAFF (now) 8
ANNUAL OPERATING BUDGET

ACCELERATOR PARAMETERS

Physical Dimensions (Mean)
RING DIAM. 12 m; Tunnel sect. ____ ____ m
MAGNET 0.40x0.55m; Mag. Gap 3.5 x 10.0 cm
"DONUT" 2.5 x8.0 cm; Aperture 2.8 x 6.4 cm

Injector System
TYPE Linac (H^- Ion)
OUTPUT (max) 5mA at 50 MeV
BEAM EMITTANCE 25 mn-mrad
INJECTION PERIOD 200 μsec, or 300 turns
INFLECTOR TYPE None. Strips H to H^+ after injection.

Magnet System
FOCUSING TYPE AG field index, n = 26.1
No. MAG. UNITS 12 Length (ea) 3.16 m
STRAIGHT SECT. ____ Total S.S. Length 13.2 m
FOCUSING ORDER ODFO
BETATRON OSC. FREQ. ν_x 3.375 ν_y 3.375
FIELD, AT INJ. 1.7 kG, at max 3.5 kG
RISE TIME 16 m sec; Flat-top time ____ sec
MAG. WEIGHT (tons) Fe 60, Cu 2.7
POWER INPUT (MW) PEAK ____ MEAN 0.15

Acceleration System
HARMONIC NO. 1 No. Cavities 1
RF RANGE 1.8 to 3.3 MHz
ORBIT FREQ.
ENERGY GAIN 5.5 (max)
RADIATION LOSS ____ keV/turn
RF POWER INPUT (kW) PEAK 50

Other Rekvant Parameters or Notable Features

ACCELERATOR PERFORMANCE

	Normal (or Goal)	Maximum Achieved
ENERGY (GeV)	0.2	0.2
RESOLUTION AEIE (%)		
REPET. RATE (pulse/sec)	30	
PULSE WIDTH		
DUTY FACTOR, macroscopic (%)		
INTERNAL BEAM (part/pulse)	10^{12}	1.5×10^{11} (accel)
(part/sec)		
CURRENT (mA)		
BEAM EMITTANCE (mn-mrad)	5.0 π	
SCHEDULED OPERATION (hr/wk)		

"ON BEAM" ____ % OF SCHEDULED TIME

Some Typical External and Secondary Beams

PARTICLE	FLUX (part/sec)	BEAM AREA (cm^2)	ENERGY (GeV)	AEIE (%)

RESEARCH PROGRAM

TOTAL EXPERIMENTAL AREA ____ m^2
BEAM LINES TO ____ Stations
STATIONS SERVED AT SAME TIME ____
BEAM SEPARATORS ____ SPECTROMETERS ____
ON-LINE COMPUTERS WITH ____ Inputs
BUBBLE CHAMBERS, in-house ____ Users' ____
TOTAL POWER INSTALLED FOR RESEARCH ____ MW
No. USER GROUPS: in-house ____ outside ____
TOTAL RESEARCH STAFF, in-house ____ outside ____
ANNUAL RESEARCH BUDGET, in-house ____
SCHEDULED RESEARCH TIME, hours/week ____

RECENT IMPROVEMENTS OR MODIFICATIONS TO MACHINE

Published Articles Describing Machine

R. L. Martin, Proceedings 1971 Particle Accelerator Conference, Chicago, Illinois, "The Argonne ZGS Booster," p. 957.

NAME OF MACHINE ZGS Booster Synchrotron II
INSTITUTION Argonne National Laboratory
LOCATION Argonne, Illinois USA

PERSON IN CHARGE Ronald L. Martin
DATA SUPPLIED BY James D. Simpson
DATE February 1974

HISTORY AND STATUS Procurement begun

CONSTRUCTION STARTED (date) February 1974
FIRST BEAM OBTAINED. DR GOAL (date) January 1976
TOTAL COST OF FACILITY
FUNDED BY US AEC (AI)
TOTAL ACCELERATOR STAFF (now) 8
ANNUAL OPERATING BUDGET

ACCELERATOR PARAMETERS

Physkal Dimensions (Mean)
RING DIAM. 13.7 m; Tunnel sect. m
MAGNET x m; Mag. Gap 3.1 x 10 cm
"DONUT" x cm; Aperture x cm

Injector System
TYPE Linac (H^- Ion)
OUTPUT (max) 5 mA at 50 MeV
BEAM EMITTANCE 2.5 mn-mrad
INJECTION PERIOD 250 μsec, or 400 turns
INFLECTOR TYPE None. Strips H^- to H^+ after injection.

Magnet System
FOCUSING TYPE AG
No. MAG. UNITS Length (ea) m
STRAIGHT SECT. Total S.S. Length 19.8 m
FOCUSING ORDER FDFODO
BETATRON OSC. FREQ. ν_H 2.2 ν_V 2.32
FIELD, AT INJ. 2.8 kG, at max 10 kG
RISE TIME 16 m sec; Flat-top time sec
MAG. WEIGHT (tons) Fe , Cu
POWER INPUT (MW) PEAK MEAN

Acceleration System
HARMONIC NO. 1 No. Cavities 2
RF RANGE 2.2 to 5.3 MHz
ORBIT FREQ.
ENERGY GAIN 10 keV/turn (max)
RADIATION LOSS keV/turn
RF POWER INPUT (kW) PEAK 80

Other Rekvrnt Parameters or Notable Features

ACCELERATOR PERFORMANCE

	Normal (or Goal)	Maximum Achieved
ENERGY (GeV)	0.5	
RESOLUTION ΔE/E (%)		
REPET. RATE (pulse/sec)	60	
PULSE WIDTH		
DUTY FACTOR, macroscopic (%)		
INTERNAL BEAM (part/pulse)	5×10^{12}	
(part/sec)		
CURRENT (mA)		
BEAM EMITTANCE (mn-mrad)		
SCHEDULED OPERATION (hr/wk)		

"ON BEAM" % OF SCHEDULED TIME

Some Typical External and Secondary Beams

PARTICLE	FLUX (part/sec)	BEAM AREA (cm^2)	ENERGY (GeV)	AEIE (%)

RESEARCH PROGRAM

TOTAL EXPERIMENTAL AREA m^2
BEAM LINES TO Stations
STATIONS SERVED AT SAME TIME
BEAM SEPARATORS SPECTROMETERS
ON-LINE COMPUTERS WITH Inputs
BUBBLE CHAMBERS, in-house Users'
TOTAL POWER INSTALLED FOR RESEARCH MW
No. USER GROUPS: in-house outside
TOTAL RESEARCH STAFF, in-house outside
ANNUAL RESEARCH BUDGET, in-house
SCHEDULED RESEARCH TIME, hours/week

RECENT IMPROVEMENTS OR MODIFICATIONS TO MACHINE

Published Articles Describing Machine

NAME OF MACHINE: Alternating Gradient Synchrotron

INSTITUTION LOCATION: Brookhaven National Laboratory, Upton, New York

PERSON IN CHARGE: R.R. Rau

DATA SUPPLIED BY: A. van Steenbergen

DATE: January 28, 1974

HISTORY AND STATUS

CONSTRUCTION STARTED (date): 1953

FIRST BEAM OBTAINED, OR GOAL (date): July 29, 1960

TOTAL COST OF FACILITY: $30.65 M

FUNDED BY: USA-AEC

TOTAL ACCELERATOR STAFF (now): 538

ANNUAL OPERATING BUDGET: $17 M

ACCELERATOR PARAMETERS

Physical Dimensions (Mean)

RING DIAM. 256.9 m; Tunnel sect. 5.49 x 5.49 m

MAGNET 0.84, 0.99 m; Mag. Gap 5.67 x 31.75 cm

"DONUT" 7.9 x 17.4 cm; Aperture 6.35 x 13.33 cm

Injector System

TYPE: Alvarez Linear Accelerator

OUTPUT (max) 100 at 200.3

BEAM EMITTANCE 10 π mn-mrad

INJECTION PERIOD ≤150 μsec, or ≤ 30 turns

INFLECTOR TYPE: pulsed magnetic

Magnet System

FOCUSING TYPE: AG

No. MAG. UNITS 240 Length (ea) 2.28, 1.90, resp. m

STRAIGHT SECT. * Total S.S. Length 270 m

FOCUSING ORDER: (F/2)o(F/2)(D/2)o(D/2)

BETATRON OSC. FREQ. ν_H 8.75 ν_V 8.75

FIELD AT INJ. 251 G, at max 13.1 kG

RISE TIME 0.45 sec; Flat-top time 1.0 sec

MAG. WEIGHT (tons) Fe 4000, Cu 400

POWER INPUT (MW) PEAK 30 MEAN 2.4

Acceleration System

HARMONIC NO. 12 No. Cavities 12 double

RF RANGE 2.52 4.46 MHz

ORBIT FREQ. 0.210 0.380

ENERGY GAIN 192

RADIATION LOSS - keV/turn

RF POWER INPUT (kW) PEAK 1000

Other Relevant Parameters or Notable Features

* 24 X 3 m; 72 X 1.5 m; 144 X 0.6 m

ACCELERATOR PERFORMANCE

	Normal (or Goal)	Maximum Achieved
ENERGY (GeV)		33
RESOLUTION ΔE/E (%)		0.1
REPET. RATE (pulse/sec)		0.5
PULSE WIDTH		1.2 sec flat top
DUTY FACTOR, macroscopic (%)		50
DUTY FACTOR, macroscopic (#)		6 10^{12} ~0.1
INTENSITY (part/sec)		
CURRENT (mA)		
BEAM EMITTANCE (mm-mrad)		0.8 π x 3.0 π
SCHEDULED OPERATION (hr/wk)		(6d/7d)
"ON BEAM" 100 % OF SCHEDULED TIME		

Some Typical External and Secondary Beams

PARTICLE	FLUX (part/sec)		ENERGY (GeV)	ΔE/E (%)
FEB, Protons	6 10^{12}		28	0.2
SEB, Protons	4 10^{12}		28	0.2
K^+, K^-	10^5, 4 10^4		3	±
K^+, K^-	3 10^5, 10^5		1	±
π			3	± 2
$\frac{n}{K^0}$	3 10^7 / 10^6		3-20	

RESEARCH PROGRAM

TOTAL EXPERIMENTAL AREA 15000 m^2

BEAM LINES TO 10 Stations

STATIONS SERVED AT SAME TIME

BEAM SEPARATORS 12 SPECTROMETERS 6

ON-LINE COMPUTERS WITH 2 2 0 Inputs

BUBBLE CHAMBERS, in-house 2 Users' MW

TOTAL POWER INSTALLED FOR RESEARCH 54

No. USER GROUPS: in-house 5 outside 63 involved

TOTAL RESEARCH STAFF, in-house 138 outside -

ANNUAL RESEARCH BUDGET, in-house $5.

SCHEDULED RESEARCH TIME, hours/week 4 weeks 500 hrs.

RECENT IMPROVEMENTS OR MODIFICATIONS TO MACHINE

50-MeV Linac injector replaced by 200-MeV Linac. New magnet system power supply and rf system for doubling repetition rate. New ring vacuum system. Magnet system modularized. New external beam branches, SEB system. Addition of third FEB system for ν physics area.

Published Articles Describing Machine

G.K. Green, E.D. Courant, "The Proton Synchrotron," Handbuck der Physik *44, 218-340 (1959).*

NAME OF MCHINE Bevatron
INSTITUTION Lawrence Berkeley Laboratory
LOCATION Univ. of Calif., Berkeley, Calif.

PERSON IN CHARGE Edward J. Lofgren
DATA SUPPLIED BY Kenneth C. Crebbin
DATE February, 1974

HISTORY AND STATUS

CONSTRUCTION STARTED (date) 1949
FIRST BEAM OBTAINED, OR GOAL (date) Feb. 1954
TOTAL COST OF FACILITY $31 M
FUNDED BY USAEC
TOTAL ACCELERATOR STAFF (now) 135
ANNUAL OPERATING BUDGET ~$5.4 M

ACCELERATOR PARAMETERS

Physical Dimensions (Mean)

RING DIAM. 38.23 m; Tunnel sect. ——— -- m
MAGNET 6.1x2.75 m; Mag. Gap 152 × 30 cm
"DONUT" -- x -- cm; Aperture 112 × 25 cm

Injector System

** TYPE Cockroft-Walton and Linac
OUTPUT (max) 25 (*) (mA) at 19.2 (4.8/Amu) MeV
BEAM EMITTANCE 25 mm-mrad
INJECTION PERIOD 600 μsec, or 300 turns
INFLECTOR TYPE 3 Magnet Achromatic + E.S

Magnet System

FOCUSING TYPE Weak Field index n=0.67
No. MAG. UNITS 144 Length(ea) 0.66 m
STRAIGHT SECT. 4 Total S.S. Length 6.1 m
FOCUSING ORDER -----
BETATRON OSC. FREQ. ν_H 0.647 ν_V 0.922
FIELD, AT INJ. 417 G, at max 15.53 kG
RISE TIME 1.7 sec; Flat-top time 0.3 ±2.0 sec
MAG. WEIGHT (tons) Fe 9700, Cu 347
POWER INPUT (MW) PEAK 121 MEAN 6.0

Acceleration System

HARMONIC No. 1 No. Cavities 1 (2 gaps)
RF RANGE 0.24 2.50 MHz
ORBIT FREQ. .497 (.252) to 2.47 (2.41) MHz
ENERGY GAIN 1.5 (0.75) KeV/turn
RADIATION LOSS ——— keV/turn
RF POWER INPUT (kW) PEAK ——— ----

( ) Values for 1 Amu others for protons

Other Relevant Parameters or Notable Features

** Four injector systems. See appropriate one for more details.

ACCELERATOR PERFORMANCE

	Normal (or Goal)	Maximum Achieved
ENERGY (GeV)	5.4-6.1	6.2 (2.75/Amu)
RESOLUTION AEIE (%)	~0.02	~0.03
REPET. RATE (pulse/sec)	~0.2	0.29
PULSE WIDTH	1.5 sec at 5.4 GeV	
DUTY FACTOR, macroscopic (%)	25	
INTERNAL BEAM (part/pulse)	4×10^{12}	6.0×10^{12}
(part/sec)	0.75×10^{12}	1.5×10^{12}
CURRENT (mA)	1.9×10^{3}	2.4×10^{3}
BEAM EMITTANCE (inn-mrad)	~330 radial	
SCHEDULED OPERATION (hr/wk)	158	

"ON BEAM" 87 % OF SCHEDULED TIME

Some Typical External and Secondary Beams

PARTICLE	* FLUX (part/sec)	BEAM AREA (cm^2)	ENERGY (GeV)	ΔE/E (%)
P	4.5×10^{11}	0.18	6.2	~0.03
^{2}H	$\sim 3.8 \times 10^{10}$	Minimum	5.5	~.02
^{4}He	$\sim 3.8 \times 10^{9}$	at	11.0	~.02
^{12}C	$\sim 1.9 \times 10^{7}$	Peak	33.0	~.02
^{14}N	$\sim 1.0 \times 10^{7}$	Field	38.5	~.02
^{16}O	$\sim 3.8 \times 10^{6}$	———	44.0	~.02
^{20}Ne	$\sim 1.9 \times 10^{4}$	———	55.0	~.02

"These values for the 19.2 (4.8/Amu) injector.

RESEARCH PROGRAM

TOTAL EXPERIMENTAL AREA ~7000 m^2
BEAM LINES TO 5 Prim (6 sec from 2 Prim) Stations
STATIONS SERVED AT SAME TIME 3 prim + 6 sec.
BEAM SEPARATORS 11 SPECTROMETERS ---
ON-LINE COMPUTERS 3-PDP-5; 2-PDP-8; 1-PDP-9; 2-PDP-11
BUBBLE CHAMBERS, in-house 0 Users' 0
TOTAL POWER INSTALLED FOR RESEARCH 21 MW
No. USER GROUPS: in-house 10 outside 22
TOTAL RESEARCH STAFF, in-house ——— outside ———
ANNUAL RESEARCH BUDGET. in-house ———
SCHEDULED RESEARCH TIME, hours/week % 142

RECENT IMPROVEMENTS OR MODIFICATIONS TO MACHINE

Installation of cryogenic vacuum pumping reduced base pressure to ~3×10^{-7} Torr from 2×10^{-6} Torr and reduced pumpdown time required to reach full beam intensity.

With the completion of the Bevalac project, there will be three different injectors available for the Bevatron,

Published Articles Describing Machine

1) F.G.H. Lothrop, D.M. Evans, Digital Control of Bevatron Accel. Cycle, Vol. NS-18 Number 3, June 1971.
2) D.M. Evans, et al, Bevatron Guide Field Control, Vol. NS-18 Number 3, June 1971.
3) R.A. Byrns, J.T. Tanabe, The Bevatron Cryopump, Vol. NS-20 Number 3, June 1973.
4) K.C. Crebbin et al, First Phase of Heavy Ion Acceleration at the Bevatron, Vol. NS-20 Number 3, June 1973.

NAME OF MACHINE 200/500 GeV Synchrotron
INSTITUTION National Accelerator Lab.
LOCATION Batavia, Illinois U. S. A.

PERSON IN CHARGE P. J. Reardon
DATA SUPPLIED BY F. T. Cole/H. L. Allen
DATE March 1. 1974

HISTORY AND STATUS

CONSTRUCTION STARTED (date) 1969
FIRST BEAM OBTAINED, OR GOAL (date) March 1, 1972
TOTAL COST OF FACILITY $230M
FUNDED BY USAEC
TOTAL ACCELERATOR STAFF (now) 275
ANNUAL OPERATING BUDGET

ACCELERATOR PARAMETERS

Physical Dimensions (Mean)

RING DIAM. 2000 m; TunRel sect. 3.05 2.44 m
MAGNET 0.64x0.35 m; Mag. Gap 13 x 5.2 cm
"DONUT" 12.7 x 5.2 cm; Aperture 12.5 x cm

Injector System

TYPE 8-GeV Booster
OUTPUT (max) 350 at 8-GeV
BEAM EMITTANCE 3π mm-mrad
INJECTION PERIOD twelve 1.6 μsec pulses in 0.8 sec. μsec, or turns
INFLECTOR TYPE Electromagnetic

Magnet System

FOCUSING TYPE AG field index, n = sep fn
No. MAG. UNITS 1014 Length (ea) 6.1 m
STRAIGHT SECT. 50.9 Total S.S. Length 305.4 m
FOCUSING ORDER Q OBBBB Q OBBBB(FODO)
BETATRON OSC. FREQ. ν_H F 19.25 ν_V D 19.25 (300 GeV)
FIELD. AT INJ. 396 G, at max 13.5 kG
RISE TIME 2.4 sec; Flat-top time 1 sec
MAG. WEIGHT (tons) Fe 8000 Cu 850
POWER INPUT (MW) PEAK 60 MEAN 36

Acceleration System

HARMONIC NO. 1113 No. Cavities 15
RF RANGE 53.08 53.10 MHz
ORBIT FREQ. 0.04769 to 0.04771
ENERGY GAIN 2.6 MeV/turn
RADIATION LOSS keV/turn
RF POWER INPUT (kW) PEAK 1800

Other Relevant Parameters or Notable **Features**

ACCELERATOR PERFORMANCE

	Normal (or Goal)	Maximum Achieved
ENERGY (GeV)	300	400
RESOLUTION ΔE/E (%)	1/6	(1/12 at 400 G
REPET. RATE (pulse/sec)	1 sec	1/4 at 200 Ge 1 sec at 300 G
PULSE WIDTH	16%	25% a
DUTY FACTOR, macroscopic (%)	5 x 10^{12}	7 x 1(at 300 GeV
INTERNAL BEAM (part/pulse)		
(part/sec)		
CURRENT (mA)	0.	1.0
BEAM EMITTANCE (mn-mrad)	0.1π	0.1π
SCHEDULED OPERATION (hr/wk)	140 (overall average)	

"ON BEAM" 60 % OF SCHEDULED TIME

Some Typical External and Secondary Beams

PARTICLE	FLUX (part/sec)	(cm²)	(GeV)	(%)
π, K	10^7 @ 150	1	to 200	0.1 - 2.1
π, K	10^7 @ 100	1	to 200	0.014 - 1.0
n	10^8/cm²	up	to 300	
K^o	10^6/c			
ν	10^6/m²	up	to 200	5
μ	10^6 @ 150	1	to 150	2
p	Extracted	1	0 - 400	

* Approx. flux 10^{13} interacting protons @ 300 GeV

TOTAL EXPERIMENTAL AREA 10,500 m²
BEAM LINES TO 6 Primary Targets plus 2 Internal Target Stations
STATIONS SERVED AT SAME TIME 7
BEAM SEPARATORS 0 SPECTROMETERS

ON-LINE COMPUTERS WITH Inputs
BUBBLE CHAMBERS, in-house 2 Users n
TOTAL POWER INSTALLED FOR RESEARCH 35
No. USER GROUPS: in-house 15 outside 100
TOTAL RESEARCH STAFF, in-house 120
ANNUAL RESEARCH BUDGET, in-house $5M

RECENT IMPROVEMENTS OR MODIFICATIONS TO MACHINE

Published **Articles Describing Machine**

1. Operating results from NAL, D. E. Young, National Accelerator Conference, IEEE Transactions NS-203, **p.** 191, (1973).

NAME OF MACHINE Booster Synchrotron — PERSON IN CHARGE P. J. Reardon
INSTITUTION National Accelerator Lab. — DATA SUPPLIED BY E. L. Hubbard
LOCATION Batavia, Illinois, U.S.A. — DATE March 1, 1974

HISTORY AND STATUS

CONSTRUCTION STARTED (date) 1969
FIRST BEAM OBTAINED, OR GOAL (date) 1971
TOTAL COST OF FACILITY $17,000,000
FUNDED BY USAEC
TOTAL ACCELERATOR STAFF (now) (Part of NAL
ANNUAL OPERATING BUDGET Accelerator Div.)

ACCELERATOR PARAMETERS

Physical Dimensions (Mean)
RING DIAM. 151 m; Tunnel sect. 3.0 2.4 m
MAGNET 46 x 33 m; Mag. Gap 15.2 x 5.7 cm
"DONUT" none cm; Aperture 16.5 x 4.2 cm

Injector System
TYPE Linear Accelerator
OUTPUT (max) 80 mA at 203 MeV
BEAM EMITTANCE 10π mn-mrad
INJECTION PERIOD 8 μsec, or 3 turns
INFLECTOR TYPE Wire Septum

Magnet System
FOCUSING TYPE Alternating Gradient
No. MAG. UNITS 96 Length (ea) 3.04 m
STRAIGHT SECT. 24 Total S.S. Length 144 m
FOCUSING ORDER FOFDOOD
BETATRON OSC. FREQ. ν_H 6.72 ν_V 6.78
FIELD, AT INJ. 490 G, at max 6.7 kG
RISE TIME .033 sec; Flat-top time none sec
MAG. WEIGHT (tons) Fe 250, Cu 36
POWER INPUT (MW) PEAK 1.8 MEAN 1.3

Acceleration System
HARMONIC No. 84 No. Cavities 16
RF RANGE 30.3 52.8 MHz
ORBIT FREQ. 0.36 0.63 k Hz
ENERGY GAIN 600 keV/turn max
RADIATION LOSS keV/turn
RF POWER INPUT (kW) PEAK 880

Ocher Rekvant Parameters or Notable Features

ACCELERATOR PERFORMANCE

	Normal (or Goal)	Maximum Achieved
ENERGY (GeV)	8	8
RESOLUTION ΔE/E (%)	0.1	
REPET. RATE (pulse/sec)	15	15
PULSE WIDTH (μsec)	1.6	1.6
DUTY FACTOR, macroscopic (%)		
INTERNAL BEAM (part/pulse)	(4 x 10^{12})	1 x 10^{12}
Part/main-ring cycle	(5 x 10^{13})	1 x 10^{13}
CURRENT (mA)	380	100
BEAM EMITTANCE (mn-mrad)	6.5π	
SCHEDULED OPERATION (hr/wk)	164	164

"ON BEAM" 95 % OF SCHEDULED TIME

Some Typical External and Secondary Beams

PARTICLE	FLUX	BEAM AREA (cm²)	ENERGY (GeV)	AEIE (%)
p	1 x 10^{13}	0.3	8	
(Particles/main-ring cycle - main-ring cycle time varies from 3 to 12 sec.)				

RESEARCH PROGRAM

TOTAL EXPERIMENTAL AREA none m²
BEAM LINES TO Stations
STATIONS SERVED AT SAME TIME
BEAM SEPARATORS SPECTROMETERS
ON-LINE COMPUTERS WITH Inputs
BUBBLE CHAMBERS, in-house Users'
TOTAL POWER INSTALLED FOR RESEARCH MW
No. USER GROUPS: in-house outside
TOTAL RESEARCH STAFF, in-house outside
ANNUAL RESEARCH BUDGET, in-house
SCHEDULED RESEARCH TIME, hours/week

RECENT IMPROVEMENTS OR MODIFICATIONS TO MACHINE

Published Artkles Describing Machine

1. Booster Synchrotron, E. L. Hubbard, ed., National Accelerator Lab. Report TM-405 (1973)

2. The NAL Booster Synchrotron Magnet Power Supply Servo, A. R. Donaldson and R. A. Winje, National Accelerator Conference, IEEE Transactions NS-20, 3, p. 409, (1973)

3. Synchronous Transfer of Beam from the NAL Fast Cycling Booster Synchrotron to the NAL Main Ring System, J. A. Dinkel, J. E. Griffin, E. L. Hubbard, R. E. Peters, and L. C. Teng. National Accelerator Conference, IEEE Transactions NS-20, 3, p. 409, (1973)

76-GeV IHEP

NAME OF MACHINE Proton Synchrotron — PERSON IN CHARGE Yu.M.Ado

INSTITUTION Institute of High Energy Ph. — DATA SUPPLIED BY E.F.Trojanov

LOCATION Serpukhov, USSR — DATE February, 1974

HISTORY AND STATUS

CONSTRUCTION STARTED (date) 1962

FIRST BEAM OBTAINED, OR GOAL (date) October, 1967

TOTAL COST OF FACILITY —

FUNDED BY —

TOTAL ACCELERATOR STAFF (now) —

ANNUAL OPERATING BUDGET —

ACCELERATOR PARAMETERS

Physical Dimensions (Mean)

RING DIAM. 472 m; Tunnel sect. 6 × 8 m

MAGNET — × — m; Mag. Gap — × — cm

"DONUT" 195×11.5m; Aperture 17 × 11.5 cm

Injector System

TYPE Linac

OUTPUT (max) 120 mA at 100 Mev

BEAM EMITTANCE 10π (90%) (norm) mn-mrad

INJECTION PERIOD 36 μsec, or 3 turns

INFLECTOR TYPE electrostatic

Magnet System

FOCUSING TYPE AG Field Index n=443

No. MAG. UNITS 120 Length (ea) 72x10.4+48x9.3m

STRAIGHT SECT. 120 Total S.S. Length 287.5 m

FOCUSING ORDER F O D O

BETATRON OSC. FREQ. ν_x 9.80 ν_y 9.85

FIELD AT INJ. 76 G, at max 13 kG

RISE TIME 2.5 sec; Flat-top time 2 sec

MAG. WEIGHT (tons) Fe 20,000, Al 700

POWER INPUT (MW) PEAK 80 MEAN 15

Acceleration System

HARMONIC No. 30 No. Cavities 52

RF RANGE 2.6 to 6.1 MHz

ORBIT FREQ. 0.086 to 0.202 MHz

ENERGY GAIN 180 kev/turn

RADIATION LOSS — keV/turn

RF POWER INPUT (kW) PEAK 300 mean 80

Other Relevant Parameters or Notable Features

There are 12 superperiods and in each there are 2 long straight sections, each 4.86m long,

Published Articles Dercribing Machine

ACCELERATOR PERFORMANCE

	Normal (or Goal)	Maximum Achieved
ENERGY (GeV)	70	76
RESOLUTION ΔE/E (%)	0.03	—
REPET. RATE (pulse/sec)	1/8	—
PULSE WIDTH	—	2.0sec
DUTY FACTOR, macroscopic (%)	25	—
INTERNAL BEAM (part/pulse)	2.2×10^{12}	~~2.7×10^{11}~~ 10^{12}
(part/sec)	2.7×10^{11}	~~3.4×10^{11}~~
CURRENT (mA)	—	—
BEAM EMITTANCE (mn-mrad)	1π	—

SCHEDULED OPERATION (hr/wk) 90(average for year)

"ON BEAM" — % OF SCHEDULED TIME

Some **Typical External and Secondary Beams**

PARTICLE	FLUX (part/pulse)	BEAM AREA (cm²)	ENERGY (GeV)	AEIE (%)
π^-	10^4-10^6	4	30-65	1
$\pi^+ + p$	10^6	1	40-70	2
π^-	$>10^6$	1	20-50	1
e	10^4-10^6	4	20-45	2
K^+	5-10	-	17-40	0.25
$\bar{p}$	5-10^6	-	10-25	0.5
μ^-	$>10^6$	900	20-40	—

RESEARCH PROGRAM

TOTAL EXPERIMENTAL AREA 23,300 m²

BEAM LINES 13 Stations

STATIONS SERVED AT SAME TIME —

BEAM SEPARATORS 2 SPECTROMETERS 5

ON-LINE COMPUTERS WITH 5 Inputs

BUBBLE CHAMBERS, in-house — Users' 2

TOTAL POWER INSTALLED FOR RESEARCH 30 MW

No. USER GROUPS: in-house 6 outside 6

TOTAL RESEARCH STAFF, in-house-outside —

ANNUAL RESEARCH BUDGET, in-house —

SCHEDULED RESEARCH TIME, hours/week —

RECENT IMPROVEMENTS OR MODIFICATIONS TO MACHINE

Fast beam extraction system is operating on 3 directions.

There is neutral beam with intensity 10^6-107 ppp.

NAME OF MACHINE ITEP P.S.
INSTITUTION ITEP
LOCATION Moscow, USSR

PERSON IN CHARGE Goldin L.L.
DATA SUPPLIED BY Goldin L.L.
DATE February 1974

HISTORY AND STATUS

CONSTRUCTION STARTED (date) 1956 1961 1973*
FIRST BEAM OBTAINED. OR GOAL (date)
TOTAL COST OF FACILITY
FUNDED BY
TOTAL ACCELERATOR STAFF (now)
ANNUAL OPERATING BUDGET

ACCELERATOR PARAMETERS

Physical Dimensions (Mean)

RING DIAM. 30 m; Tunnel sect. ____ ____ m
MAGNET 2 x 2 m; Mag. Gap ____ x ____ cm
"DONUT" ____ x ____ cm; Aperture 11 x 8 cm

Injector System

TYPE Linear Accelerator
OUTPUT (max) 200mA at 24.6 MeV
BEAM EMITTANCE 60 nm-mrad
INJECTION PERIOD 4 μsec, or 1 turns
INFLECTOR TYPE lectrostatic

Magnet System

FOCUSING TYPE Strong
No. MAG. UNITS 96 Length (ea ... I,910 m
STRAIGHT SECT. 2.35 M Total S.S. Length 37.6 m
FOCUSING ORDER FODFODFODFDFD
BETATRON OSC. FREQ. ν_H 9.3 ν_V 9.
FIELD. AT INJ. 240 G, at max 12 kG
RISE TME 0.8 sec; Flat-top time 0.3 sec
MAG. WEIGHT (tons) Fe 3000, Cu 500
POWER INPUT (MW) PEAK ____ MEAN 3.5 MWT

Acceleration System

HARMONIC No. ____ No. Cavities 5
RF RANGE 1.09 - 4.77 Mc
ORBIT FREQ. 0.252 - 1.19
ENERGY GAIN 15 KeV
RADIATION LOSS ____ keV/ rn
RF POWER INPUT (kW) PEAK 12-KW/cavity

Other Rekvant **Parameters or Notable Features**

ACCELERATOR PERFORMANCE **

	Normal (or Goal)	Maximum Achieved
ENERGY (GeV)	10	10.4
RESOLUTION ΔE/E (%)		
REPET. RATE (pulse/sec)		
PULSE WIDTH		
DUTY FACTOR, macroscopic (%)		
INTERNAL BEAM (part/pulse)		
(part/sec)		
CURRENT (mA)		
BEAM EMITTANCE (nm-mrad)		
SCHEDULED OPERATION (hr/wk)		

"ON BEAM" ____ % OF SCHEDULED TIME

Some Typical External a d Secondary Beams

PARTICLE	FLUX (part/sec)	BEAM AREA (cm^2)	ENERGY (GeV)	AEIE (%)

RESEARCH PROGRAM

TOTAL EXPERIMENTAL AREA 7000 m^2
BEAM LINES TO ____ Stations
STATIONS SERVED AT SAME TIME ____
BEAM SEPARATORS ____ SPECTROMETERS ____
ON-LINE COMPUTERS WITH ____ Inputs
BUBBLE CHAMBERS, in-house ____ Users' ____
TOTAL POWER INSTALLED FOR RESEARCH ____ MW
No. USER GROUPS: in-house ____ outside ____
TOTAL RESEARCH STAFF, in-house ____ outside ____
ANNUAL RESEARCH BUDGET, in-house ____
SCHEDULED RESEARCH TIME, hours/week ____

RECENT IMPROVEMENTS OR MODIFICATIONS TO MACHINE

* After reconstruction

** The accelerator is in tne course of ajustement after reconstruction.

Published Artkles Describing Machine

NAME OF MACHINE 10 GeV proton Synchrophazotron — PERSON IN CHARGE A.M.Baldin
INSTITUTION Joint Inst.for Nucl. Research — DATA SUPPLIED BY I.N.Semenyushkin
LOCATION Dubna, USSR — DATE July 1971

HISTORY AND STATUS

CONSTRUCTION STARTED (date) ~~1952~~ ~~1957~~
FIRST BEAM OBTAINED, OR GOAL (date)
TOTAL COST OF FACILITY
FUNDED BY
TOTAL ACCELERATOR STAFF (now)
ANNUAL OPERATING BUDGET

ACCELERATOR PARAMETERS

Physical Dimensions (Mean)
RING DIAM. 72 m; Tunnel sect. ____ × ____ m
MAGNET 7.5.5.3 m; Mag. Gap 40 × 200 cm
"DONUT" ____ × ____ cm; Aperture 35 × I20 cm

Injector System
TYPE Linac
OUTPUT (max) I.0 at 9.4
BEAM EMITTANCE Π IO mm-mrad
INJECTION PERIOD 350 usec, or 50 turns
INFLECTOR TYPE electrostatic

Magnet System
FOCUSING TYPE weak field Index, n=0.66
No. MAG. UNITS 48 Length (ea) 3.7 m
STRAIGHT SECT. 4 Total S.S. Length 32 m
FOCUSING ORDER
BETATRON OSC. FREQ. ν_H 0.626 ν_V 0.892
FIELD, AT INJ. I50 G, at max I2.(kG
RISE TIME 3.0 sec; Flat-top time 0.1
MAG. WEIGHT (tons) Fe 36000, Cu 2.700
POWER INPUT (MW) PEAK I40 MEAN I3

Acceleration System
HARMONIC NO. I No. Cavitie I
RF QANGE. 0.2 to • MHz
ORBIT FREQ. 0.2 to I.45
ENERGY GAIN 2.4
RADIATION LOSS ____ keV/turn
RF POWER INPUT (kW) PEAK 500 I50

Other Relevant Parameters or Notable Features

Published Articles Dercribing Machine

ACCELERATOR PERFORMANCE

	Normal (or Goal)	Maximum
ENERGY (GeV)	IO	
RESOLUTION AEIE (%)	0.08	Achieved 0.II
REPET. RATE (pulse/sec)		0.5
PULSE WIDTH		
DUTY FACTOR, macroscopic (%)	IO	
INTERNAL BEAM (part/pulse)	x10^9 I.0	I2
(part/sec)	x10^9 I.0	I5
CURRENT (mA)	T5Π	v) 80Π (H)
BEAM EMITTANCE (mn-mrad)		
SCHEDULED OPERATION (hr/wk)		I20

"ON BEAM" 90 % OF SCHEDULED TIME

Some Typical External and Secondary Beams

PARTICLE	FLUX (part/sec)	BEAM AREA (cm^2)	ENERGY (GeV)	ΔE/E (%)
Π⁻	~10^4	5	2-7	±I
Π⁺	~10^3	5	2-5	±I
Sep. K,p				
Π⁺	n		I-5	±2

RESEARCH PROGRAM

TOTAL EXPERIMENTAL AREA 2700 m^2
BEAM LINES TO ____ Stations
STATIONS SERVED AT SAME TIME 3
BEAM SEPARATORS ____ SPECTROMETERS ____
ON-LINE COMPUTERS WITH ____ Inputs
BUBBLE CHAMBERS, in-house I Users' I
TOTAL POWER INSTALLED FOR RESEARCH 26
No. USER GROUPS: in-house-outside
TOTAL RESEARCH STAFF, in-house ____ outside
ANNUAL RESEARCH BUDGET, in-house
SCHEDULED RESEARCH TIME, hours/week

RECENT IMPROVEMENTS OR MODIFICATIONS TO MACHM

acceleration of deuterons up to IO GeV I=IO pulse, He^2_4 up to 20 BeV I=10^7 ~/p

Slowly extraction of beem from synchrophazotron (τ =400 msec, efficiency 94%;)

NAME OF MACHINE 1 GeV Model of Cybernetic Accelerator
INSTITUTION Radiotech.Inst.of Ac.Sci
LOCATION Moscow, USSR
PERSON IN CHARGE G.I.Batskikh
DATA SUPPLIED BY G.I.Batskikh
DATE

HISTORY AND STATUS

CONSTRUCTION STARTED (date) 1961
FIRST BEAM OBTAINED, OR GOAL (date) 1967
TOTAL COST OF FACILITY
FUNDED BY
TOTAL ACCELERATOR STAFF (now) 12 p.
ANNUAL OPERATING BUDGET

ACCELERATOR PARAMETERS

Physical Dimensions (Mean)

RING DIAM. 17 m; Tunnel sect. ____ ____ m
MAGNET ____ x ____ m; Mag. Gap ____ x ____ cm
"DONUT" ____ x ____ cm; Aperture 1,6 x 2,2 cm

Injector System

TYPE Van de Graaf
OUTPUT (max) 5 mA at 1.0 MeV
BEAM EMITTANCE 10 π mn-mrad
INJECTION PERIOD ____ μsec, or 1 turns
INFLECTOR TYPE electrostatic

Magnet System

FOCUSING TYPE strong n=191,3
No, MAG. UNITS 100 Length (ea) ____ m
STRAIGHT SECT. ____ Total S.S. Length ____ m
FOCUSING ORDER FODO
BETATRON OSC. FREQ. ν_H 6,25 ν_V 6,25
FIELD, AT INJ. 250 G, at max 10 kG
RISE TIME 0,5 sec; Flat-top time ____ sec
MAG. WEIGHT (tons) Fe 12, Cu 4
POWER INPUT (MW) PEAK ____ MEAN 30 kW

Acceleration System

HARMONIC No. 5 No. Cavities 13
RF RANGE 1,25 to 25 MHz
ORBIT FREQ. 0,25 to 5,0 MHz
ENERGY GAIN max 2 kV
RADIATION LOSS ____ keV/turn
RF POWER INPUT (kW) PEAK ____ ____

Other Rekvant Parameters or Notable Features

Published Artkks Describing Machine

ACCELERATOR PERFORMANCE

	Normal (or Goal)	Maximum Achieved
ENERGY (GeV)	1	1.0
RESOLUTION ΔE/E (%)		
REPET. RATE (pulse/sec)	0,5	
PULSE WIDTH	0,5 sec	
DUTY FACTOR, macroscopic (X)		
INTERNAL BEAM (part/pulse)	1 x 10 ~~10~~	
(part/sec)		
CURRENT (mA)		
BEAM EMITTANCE (mn-mrad)		
SCHEDULED OPERATION (hr/wk)		

"ON BEAM" ____ % OF SCHEDULED TIME

Sane Typical External and Secondary Beams

PARTICLE	FLUX (part/sec)	BEAM AREA (cm^2)	ENERGY (GeV)	ΔE/E (%)

RESEARCH PROGRAM

TOTAL EXPERIMENTAL AREA ____ m^2
BEAM LINES TO ____ Stations
STATIONS SERVED AT SAME TIME ____
BEAM SEPARATORS ____ SPECTROMETERS ____
ON-LINE COMPUTERS WITH ____ Inputs
BUBBLE CHAMBERS. in-house ____ Users' ____
TOTAL POWER INSTALLED FOR RESEARCH ____ MW
No. USER GROUPS: in-house ____ outside ____
TOTAL RESEARCH STAFF, in-house ____ outside ____
ANNUAL RESEARCH BUDGET. in-house ____
SCHEDULED RESEARCH TIME, hours/week ____

RECENT IMPROVEMENTS OR MODIFICATIONS TO MACHINE

NAME OF MACHINE Bonn 2.5 GeV Synchrotron
INSTITUTION Physikal. Institut d. Univ.
LOCATION D-53 Bonn, Nussallee 12

PERSON IN CHARGE K.H. Althoff, G. Knop, G. Noldeke, W. Paul
DATA SUPPLIED BY D. Husmann
DATE 22.1.1974

HISTORY AND STATUS

CONSTRUCTION STARTED (date) April 1965
FIRST BEAM OBTAINED, OR GOAL (date) March 1967
TOTAL COST OF FACILITY DM 12.3×10^6
FUNDED BY Federal Rep. of Germany and State of Nordrhein-Westfalen
TOTAL ACCELERATOR STAFF (now) 19
ANNUAL OPERATING BUDGET 1.8×10^6

ACCELERATOR PARAMETERS

Physical Dimensions (Mean)
RING DIAM. 22.15 m; Tunnel sect. 2.2 x 4.1 m
MAGNET 695.74 m; Mag. Gap 6 x 20 cm
"DONUT" 4.2 x 12.5 cm; Aperture 4 x ____ cm

Injector System
TYPE Linac
OUTPUT (max) 250 at 25
BEAM EMITTANCE 3 inn-mrad
INJECTION PERIOD 1 μsec, or 5 turns
INFLECTOR TYPE septum magnet

Magnet System
$n = +23.26$
FOCUSING TYPE AG
No. MAG. UNITS 12 Length (ea) 4.005 m
STRAIGHT SECT. 12 Total S.S. Length 21.48 m
FOCUSING ORDER OFDO
BETATRON OSC. FREQ. ν_μ 3.4 ν_V 3.4
FIELD AT INJ. 110 G, at max 11 kG
RISE TIME 8.8 sec; Flat-top time ____ sec
MAG. WEIGHT (tons) Fe 133, Cu 10
POWER INPUT (MW) PEAK .80 MEAN ____

Acceleration System
HARMONIC No. 116 No. Cavities 1 or 2
RF RANGE 499.67 MHz
ORBIT FREQ. 4.3074
ENERGY GAIN 330 keV/turn
RADIATION LOSS max. 325 keV/turn
RF POWER INPUT (kW) PEAK 80 mean 40

Other Rekvant Parameters or Notable Features

ACCELERATOR PERFORMANCE

	Normal (or Goal)	Maximum Achieved
ENERGY (GeV)	2.3	2.5
RESOLUTION AEIE (%)		0.5
REPET. RATE (pulse/sec)		50
PULSE WIDTH	max.	1 msec
DUTY FACTOR, macroscopic (%)	max.	5
INTERNAL BEAM (part/pulse)		4×10^{10}
(part/sec)		2×10^{12}
CURRENT (mA)		0.32 μA
BEAM EMITTANCE (inn-mrad)		1
SCHEDULED OPERATION (hr/wk)		150

"ON BEAM" 85 % OF SCHEDULED TIME

Some Typical External and Secondary Beams

PARTICLE	FLUX (part/sec)	BEAM AREA (cm^2)	ENERGY (GeV)	AEIE (%)
e^-	10^{12}	0.1	.5 - 2.3	.5
γ	5×10^{11}	eff. qu. at 2.1 GeV		

RESEARCH PROGRAM

TOTAL EXPERIMENTAL AREA 1100 m^2
BEAM LINES TO 6 Stations
STATIONS SERVED AT SAME TIME 2
BEAM SEPARATORS - SPECTROMETERS ____
ON-LINE COMPUTERS 2 with 7 Inputs (total)
BUBBLE CHAMBERS, in-house - Users' -
TOTAL POWER INSTALLED FOR RESEARCH 1.2 MW
No. USER GROUPS: in-house 8 outside 4
TOTAL RESEARCH STAFF, in-house x outside 5
ANNUAL RESEARCH BUDGET, in-house 2.5×10^6
SCHEDULED RESEARCH TIME, hours/week 150

RECENT IMPROVEMENTS OR MODIFICATIONS TO MACHINE

Ejection of electrons up to 2.3 GeV
On line computer with CAMAC interface

Published Articles Describing Machine

K.H. Althoff et al. : The 2.5 GeV Electron Synchrotron of the University of Bonn, Nuclear Instr. a. Meth. 61 (1968), 1 - 30

NAME OF MACHINE DESY

INSTITUTION Deutsches Elektronen-Synchrotron

LOCATION Hamburg, Germany

PERSON IN CHARGE H. Schopper

DATA SUPPLIED BY H. Kumpfert

DATE January 1974

HISTORY AND STATUS

CONSTRUCTION STARTED (date) 1959

FIRST BEAM OBTAINED, OR GOAL (date) February 1964

TOTAL COST OF FACILITY 110 MDM (orig.constr.costs)

FUNDED BY Federal Government, City of Hamburg

TOTAL ACCELERATOR STAFF (now) 80

ANNUAL OPERATING BUDGET 6 MDM

ACCELERATOR PARAMETERS

Physical Dimensions (Mean)

RING DIAM. 100.84 m; Tunnel sect. 3.7 x 8.8 m

MAGNET 0.77 x 0.69 m; Mag. Gap 5.6(8.8) x 14.4 (9.0) cm

"DONUT" ___ x ___ cm; Aperture 3.8(7.0) x 120(10.0) cm

Injector System

TYPE Electron/Positron* Linacs**

OUTPUT (max) 200 mA(e^-) at 300 - 500 MeV

BEAM EMITTANCE 2 π mm-mrad

INJECTION PERIOD 1 μsec, or 1 turns

INFLECTOR TYPE septum + fast kicker magnet

Magnet System

FOCUSING TYPE AG Field Index n 69.51 (F) 70.16 (D)

No. MAG. UNITS 48 Length (ea) 4.15 m

STRAIGHT SECT. 48 Total S.S. Length 117.6 m

FOCUSING ORDER FODO

BETATRON OSC. FREQ. ν_y 6.29 ν_x 6.23

FIELD AT INJ. 315(42) G, at max 7.9 kG

RISE TIME 9×10^{-3} sec; Flat-top time max. 3.1×10^{-3} sec

MAG. WEIGHT (tons) Fe 570, Cu 77

POWER INPUT (MW) PEAK ___ MEAN 1.7

Acceleration System

HARMONIC No. 528 No. Cavities 16

RF RANGE 499.666 to 499.645 MHz

ORBIT FREQ. 0.9463

ENERGY GAIN max. 1250 keV/turn

RADIATION LOSS max. 8830 keV/turn

RF POWER INPUT (kW) PEAK 1000 mean 700

Other Relevant Parameters or Notable Features

"Positron Data: 1.6 mA ($|\frac{\Delta E}{E}| \leq \frac{1}{2}$ %) at 380 MeV

**The old 40 MeV-Electron Linac (140 mA max.) is still in use

Published Articles Describing Machine

Die Atomwirtschaft. July 1964

Proc, 1973 US Particle Accelerator Conference, San Francisco, (Improvements)

DESY Annual Reports

ACCELERATOR PERFORMANCE

	Normal (or Goal)	Maximum Achieved
ENERGY (GeV)	7..4	7.5
RESOLUTION ΔE/E (X)	± 0.25	± 0.25
REPET. RATE (pulse/sec)	50	50
PULSE WIDTH	3.1	3.1
DUTY FACTOR, macroscopic (%)	15.4	15.4
INTERNAL BEAU (part/pulse)	$4 \times 10^{**}$	5×10^{11}
(part/sec)	2×10^{13}	2.5×10^{13}
average CURRENT (mA)	64	80
BEAM EMITTANCE (mm-mrad)		
SCHEDULED OPERATION (hr/wk)	168	

"ON BEAM" 90 - 95 % OF SCHEDULED TIME

Some Typical External and Secondary Beams

PARTICLE	FLUX (part/sec)	BEAM AREA (cm^2)	ENERGY (GeV)	ΔE/E (%)
2 x e^-	5×10^{12}		1-7.25	± 0.25
	$\epsilon_z \approx 0.1\pi$ x mm x mrad			
or	$\epsilon_r \approx 0.5\pi$ x mm x mrad			
	50 % < η < 85 %			
2 x e+	10^{11}		1-7.25	± 0.25
3 x y				
3 x converted y (test beams)				
2 x Synchrotron Radiation				

RESEARCH PROGRAM

TOTAL EXPERIMENTAL AREA 6400

BEAM LINES TO 17 Stations

STATIONS SERVED AT SAME TIME 6 x e^- or γ + test & synchr. rad. beams

BEAM SEPARATORS ___ SPECTROMETERS 11

ON-LINE COMPUTERS WITH 20 Inputs

BUBBLE CHAMBERS: in-house ___ Users' ___

TOTAL POWER INSTALLED FOR RESEARCH 23 MW

No. USER GROUPS: in-house: 3 outside: 2 mixed: 9

TOTAL RESEARCH STAFF: ~~in-house~~ ~~outside~~ 275

ANNUAL RESEARCH BUDGET: in-house 7.5 MDM

SCHEDULED RESEARCH TIME, hours/week 136

RECENT IMPROVEMENTS OR MODIFICATIONS TO MA

- flat top operation (duty factor 15.4 %)
- 2 e^+/e^- beams (fast extraction) for DORIS
- max. circulating currents (e^-) up to 80 mA average as compared to 30 mA
- e^+ beams (slow extraction) for use in normal e- -experimental areas
- additional p^+-acceleration capability expected for 1915

NAME OF MACHINE Electron Synchrotron
INSTITUTION Laboratori Naz.dl CNEN
LOCATION Frascati - Italy

PERSON IN CHARGE Ubaldo Bizzarri
DATA SUPPLIED BY " "
DATE Febr**u**ary 1974.

HISTORY AND STATUS

CONSTRUCTION STARTED (date) January 1956
FIRST BEAM OBTAINED, OR GOAL (date) Feb.9, 1959
TOTAL COST OF FACILITY $ 2.0 M
FUNDED BY CNEN
TOTAL ACCELERATOR STAFF (now) 30
ANNUAL OPERATING BUDGET 150.000

ACCELERATOR PARAMETERS

Physical Dimensions (Mean)
RING DIAM. 8.74 m; Tunnel sect. _____ _____ m
MAGNET 096x08 m; Mag. Gap 8.6 x 23 cm
"DONUT" 7.7x21 cm² Aperture 5.7 x 19.2 cm

Injector System
TYPE Microtron
OUTPUT (max) 30 at 12.4
BEAM EMITTANCE H:8 mn-mrad
INJECTION PERIOD 2 μsec, or 100 *turns*
INFLECTOR TYPE Electrostatic

Magnet System
FOCUSING TYPE weak FIELD INDEX 0.61
No. MAG. UNITS 4 Length (ea) 5.65 m
STRAIGHT SECT. 4 Total S.S. Length 27.4 m
FOCUSING ORDER _____
BETATRON OSC. FREQ. ν_H _____ ν_V _____
FIELD, AT INJ. 110 G. at max 10.2 I
RISE TIME 23 sec; Flat-top time _____ _____ sec
MAG. WEIGHT (tons) Fe 100, Cu 10.
POWER INPUT (MW) PEAK _____ MEAN 0.150
Accelerator System Magnet supply LC Resonant

HARMONIC No. 4 No. Cavities 1
Rf RANGE 43.7 MHz
10.9
ORBIT FREQ.
ENERGY GAIN ~4
RADIATION LOSS- max-25 keV/turn
RF POWER INPUT (kW) PEAK 10 MEAN 4

Other Relevant Parameters or Notable Features

ACCELERATOR PERFORMANCE

	Normal (or Goal)	Maximum Achieved
ENERGY (GeV)		1.1
RESOLUTION ΔE/E (%)		0.1
REPET. RATE (pulse/sec)		20
PULSE WIDTH		4 msec
DUTY FACTOR, macroscopic (%)		8
INTERNAL BEAM (part/pulse)		$2 \div 5.10^{10}$
(part/sec)		$4 \div 10.10^{11}$
CURRENT (mA)		
BEAM EMITTANCE (mm-mrad)		20H 4V
SCHEDULED OPERATION (hr/wk)		141

Extracted bean
"ON BEAM" 75% % OF SCHEDULED TIME

Some Typical External and Secondary Beams

PARTICLE	FLUX (part/sec)	BEAM AREA (cm²)	ENERGY (GeV)	ΔE/E (%)
e⁻	2.10^{11}		0.5÷1	<0.5
γ	$1.3.10^{11}$	1Qeq	0.4÷1	
γ	$0.5.10^{11}$	Qeq	1	
*				

* 30-50% polarized

RESEARCH PROGRAM

TOTAL EXPERIMENTAL AREA _____ m²
BEAM LINES TO 5 Stations
STATIONS SERVED AT SAME TIME 1
BEAM SEPARATORS _____ SPECTROMETERS 1
BEAM SEPARATORS _____ _____ Inputs
ON-LINE COMPUTERS YES
BUBBLE CHAMBERS, in-house 2 Users' _____
TOTAL POWER INSTALLED FOR RESEARCH 2.5 MW
No USER GROUPS. in-house 3 outside 7
TOTAL RESEARCH STAFF, in-house 18 outside 44
ANNUAL RESEARCH BUDGET, in-house _____
SCHEDULED RESEARCH TIME, hours/week 141

RECENT IMPROVEMENTS OR MODIFICATIONS TO MACHINE

Published Articles Describing Machine

- Proc . 2nd UN Conf. Peaceful Uses Atomic Energy Geneva 1958, Paper 15/8/1374, UN, NEw York (1958)
- Nuovo Cimento Suppl. 3, 324 (1959)
- Nuovo Cimento Suppl. 24 (1962)
- Lettese al Nuovo Cimento Vol. 1, 16, 820 (1969)
- Frascati Reports (available on request)

NAME OF MACHINE 1.3 GeV Electron Synchrotron PERSON IN CHARGE K. Huke
INSTITUTION Inst.for Nuclear Study, Univ. DATA SUPPLIED BY K. Huke
LOCATION Tanashi, Tokyo, Japan of Tokyo DATE February 1974

HISTORY AND STATUS

CONSTRUCTION STARTED (date) 1957 January
FIRST BEAM OBTAINED. OR GOAL (date) 1961 (750 MeV)
TDTAL COST OF FACILITY ~ $2M*
FUNDED BY Japanese Government
TOTAL ACCELERATOR STAFF (now) 14
ANNUAL OPERATING BUDGET ~ $ 0.1M*
*(salaries not included)

ACCELERATOR PARAMETERS

Physical Dimensions (Mean)
RING DIAM. 10.9 m; Tunnel sect. 2.8 × (dia)14 m
MAGNET 0.7 x 0.53 m; Mag. Gap 5.4 × 15 cm
"DONUT 4.5 x 15 cm; Aperture 3.5 × 11 cm

Injector System
TYPE Linac
OUTPUT (max) 100 mA at inflector 9 MeV
BEAM EMITTANCE 8 mn-mrad
INJECTION PERIOD 1 μsec, or 10 turns
INFLECTOR TYPE Electro-static plate and pulsed magnets for multi-turn.

Magnet System
FOCUSING TYPE AG
No. MAG. UNITS 8 Length (ea) 3.14 m
STRAIGHT SECT. 8 Total S.S. Length 9.60 m
FOCUSING ORDER 1/2 O, 1/2 D,F, 1/2 D, 1/2 O
BETATRON OSC. FREQ. ν_H ~ 2.25 ν_V ~ 2.25
FIELD, AT INJ. 80 G, at max 11 kG
RISE TIME 20~19 msec; Flat-top time --- sec
MAG. WEIGHT (tons) Fe 53, Cu 79
POWER INPUT (MW) PEAK stored MEAN 0.402
0.18 MJ

Acceleration System
HARMONIC No. 16 No. Cavities 1
RF RANGE ~ 138 fixed MHz
ORBIT FREQ. ~ 8.6
ENERGY GAIN peak 10
RADIATION LOSS 64 (max) keV/turn
RF POWER INPUT (kW) PEAK 20 MEAN 4 ~ 5

Other Relevant Parameters or Notable Features

ACCELERATOR PERFORMANCE

	Normal (or Goal)	Maximum Achieved
ENERGY (GeV)	1.3	1.3
RESOLUTION ΔE/E (X)	0.1	0.1
REPET. RATE (pulse/sec)	22.5	22.5
PULSE WIDTH	1.3	6(max)
DUTY FACTOR, macroscopic (%)	~ 5	10
INTERNAL BEAM (part/pulse) ×10^10	2	4 at 1 GeV
(part/sec) ×10^11	4	8 at 1 GeV
CURRENT (mA)	30	60
BEAM EMITTANCE (mn-mrad)	5	5
SCHEDULED OPERATION (hr/wk)	144	168

"ON BEAM" 95 % OF SCHEDULED TIME

Some Typical External and Secondary Beams

PARTICLE	FLUX (part/sec)	BEAM AREA (cm²)	ENERGY (GeV)	ΔE/E (%)
e^-	4×10^{11}	0.6×0.8	1	0.3
γ	$e\times10^{10}$	2.2 (at 3.1 m from radiator)	1.14	brems.
Soft X-ray				

RESEARCH PROGRAM

TOTAL EXPERIMENTAL AREA 1000 m²
BEAM LINES TO 3 (two γ, one e & γ) Stations
STATIONS SERVED AT SAME TIME max 2
BEAM SEPARATORS none SPECTROMETERS 4(25.18.5,6 tons)
ON-LINE COMPUTERS WITH 2 (TOSBAC 40) Inputs
BUBBLE CHAMBERS, in-house 0 Users' 1
TOTAL POWER INSTALLED FOR RESEARCH 0.45 MW
No, USER GROUPS: in-house 2 outside 5
TOTAL RESEARCH STAFF, in-house 16 outside *
ANNUAL RESEARCH BUDGET, in-house ~ $ 0.05M
SCHEOULED RESEARCH TIME, hours/week 132

RECENT IMPROVEMENTS OR MODIFICATIONS TO MACHINE

Epoxy-resin doughnuts were replaced by thin stainless steel bellows.
Add a fast extraction system to supply electrons to the 300 MeV storage ring.

Published Articles Describing Machine

1. H. Kumagai, et al., Japanese J. appl. Phys. 1 (1962) 66.
2. Annual Reports from 1960 to 1973, Institute for Nuclear Study, University of Tokyo.
3. K. Huke, et al., Japanese J. appl. Phys. 7 (1968) 1274.

NAME OF MACHINE Lund Electron Synchrotron
INSTITUTION Univ of Lund. Inst of Phys
LOCATION Lun Sweden

Facility: Bengt Forkman
PERSON IN CHARGE Machine: Rune Alvinsson
DATA SUPPLIED BY Rune Alvinsson
DATE January 22, 1974

HISTORY AND STATUS

CONSTRUCTION STARTED (date) 1957
FIRST BEAM OBTAINED, OR GOAL (date) Dec. 1960
TOTAL COST OF FACILITY ~ $ 1 M excl. buildings
FUNDED BY Swedish Atom. Research Council
TOTAL ACCELERATOR STAFF (now) 8
ANNUAL OPERATING BUDGET ~ $ 30 000 excl. salaries

ACCELERATOR PARAMETERS

Physical Dimensions (Mean)

RING DIAM. 10.8 m; Tunnel sect. _____ _____ m
MAGNET 0.55x0.39 m; Mag. Gap 4.6 × 13.5 cm
"DONUT" 4 × 7 cm; Aperture 3.6 × 6.5 cm

Injector System

TYPE Microtron
OUTPUT (max) 75 mA at 10 MeV
BEAM EMITTANCE Hor. 20, vert. 50 mm-mrad
INJECTION PERIOD 5 μsec, or 40 turns
INFLECTOR TYPE Electrostatic

Magnet System

FOCUSING TYPE AG
No. MAG. UNITS 16 Length (ea) 1.4 m
STRAIGHT SECT. 16 Total S.S. Length 11.2 m
FOCUSING ORDER FOFDOD
BETATRON OSC. FREQ. ν_H 1.77 ν_V 1.77
FIELD, AT INJ. 100 G, at max. 11.0 kG
RISE TIME 0.04 sec; Flat-top time _____ sec
MAG. WEIGHT (tons) Fe 24, Cu 11.2
POWER INPUT (MW) PEAK _____ MEAN 0.185

Acceleration System

HARMONIC NO. 45 No. Cavities 2
RF RANGE 399.10 MHz
ORBIT FREQ. 8.87 MHz
ENERGY GAIN max. 60
RADIATION Loss max. 50 keV/turn
RF POWER INPUT (kW) PEAK 12 MEAN 3

Other Relevant Parameters or Notable Features

ACCELERATOR PERFORMANCE

	Normal (or Goal)	Maximum Achieved
ENERGY (GeV)		1.2
RESOLUTION ΔE/E (%)		
REPET. RATE (pulse/sec)	12.5	
PULSE WIDTH		5 msec.
DUTY FACTOR, macroscopic (%)		6
INTERNAL BEAM (part/pulse)		2.4×10^{10} (0.8 GeV)
(part/sec)		3×10^{11} (- " -)
CURRENT (mA)		50 (- " -)
BEAM EMITTANCE (m-mrad)		
SCHEDULED OPERATION (hr/wk)	120	

"ON BEAM" 85 - 90 % OF SCHEDULED TIME

Some Typical External and Secondary Beams

PARTICLE	FLUX (part/sec)	BEAM AREA (cm^2)	ENERGY (GeV)	ΔE/E (%)
bremsstr.				
synchr. light				

RESEARCH PROGRAM

TOTAL EXPERIMENTAL AREA 300 m^2
BEAM LINES TO 4 Stations
STATIONS SERVED AT SAME TIME 4
BEAM SEPARATORS _____ SPECTROMETERS ~
ON-LINE COMPUTERS WITH 2x16 bit digital inputs
BUBBLE CHAMBERS, in-house 1 Users' 0
TOTAL. POWER INSTALLED FOR RESEARCH 0.8 MW
No. USER GROUPS: in-house 3 outside _____
TOTAL RESEARCH STAFF, in-house x outside _____
ANNUAL RESEARCH BUDGET, in-house $ 25 000 excl. salaries
SCHEDULED RESEARCH TIME, hours/week 112

RECENT IMPROVEMENTS OR MODIFICATIONS TO MACHINE

Published Articles Describing Machine

Wernholm, O., Arkiv för Fysik 27, 527 (1964)

NAME OF MACHINE NINA
INSTITUTION DARESBURY LABORATORY
LOCATION DARESBURY, WARRINGTON, U.K.

PERSON IN CHARGE PROFESSOR A. ASHMORE
DATA SUPPLIED BY D. J. THOMPSON
DATE 21ST JANUARY, 1974

HISTORY AND STATUS

CONSTRUCTION STARTED (date) NOVEMBER, 1963
FIRST BEAM OBTAINED, OR GOAL (date) 2nd DECEMBER 1966
TOTAL COST OF FACILITY £4.5.10^6
FUNDED BY SCIENCE RESEARCH COUNCIL
TOTAL ACCELERATOR STAFF (now) 110 (inc. exp area)
ANNUAL OPERATING BUDGET £1.2 M

ACCELERATOR PARAMETERS

Physical Dimensions (Mean)

RING DIAM. 70 m; Tunnel sect. 6.7 x 5.8 m
MAGNET — x — m; Mag. Gap — x — cm
"DONUT" 17.3 x 5.0 m; Aperture 15.0 x 4.4 F cm
13.5 7.0 11.2 6.1 D

Injector System

TYPE IRIS LOADED WAVEGUIDE LINAC
OUTPUT (max) 500 at 43
BEAM EMITTANCE 3.2 mn-mrad
INJECTION PERIOD 0.73 μsec, or 1 turns
INFLECTOR TYPE PULSED MAGNETIC

Magnet System

FOCUSING TYPE AG
No. MAG. UNITS 40 Length (ea) 3.2625 m
STRAIGHT SECT. 3.5m Total S.S. Length 90 m
FOCUSING ORDER 1.0 m FODO
BETATRON OSC. FREQ. ν_H 5.21 ν_V 5.26
FIELD, AT INJ. 69 G, at max 7.45* kG
RISE TIME 9m sec; Flat-top time — sec
MAG. WEIGHT (tons) Fe 360, Cu 40
POWER INPUT (MW) PEAK — MEAN 0.95

Acceleration System

HARMONIC No. 300 NO. Cavities 5
RF RANGE 407.88 MHz
ORBIT FREQ. 1.76 MHz
ENERGY GAIN 470 (max.) keV/turn
RADIATION LOSS 2700* keV/turn
RF POWER INPUT (kW) PEAK 480 Mean 150 (rating)

Other Rekvmt Parameters or Notable Features

ACCELERATOR PERFORMANCE

	Normal (or Goal)	Maximum Achieved
ENERGY (GeV)	1.0 to 5.0	5.2
RESOLUTION ΔE/E (%)	—	—
REPET. RATE (pulse/sec)	53	—
PULSE WIDTH	2 msec	3 msec
OUT-FACTOR, macroscopic (%)	7	11
INTERNAL BEAM (part/pulse)	8.10^{10}	$2.4.10^{11}$
(part/sec)	4.10^{12}	$1.2.10^{13}$
CURRENT (mA)	18	54
BEAM EMITTANCE (mn-mrad)	—	

SCHEDULED OPERATION (hr/wk) 168 hrs/wk 5 wks in 7
"ON BEAM" 82 % OF SCHEDULED TIME for research

Some Typical External and Secondary Beams

PARTICLE	FLUX (part/sec)	BEAM AREA (cm²)	ENERGY (GeV)	AEIE (%)
Electron	2.10^{12}	0.6	1.0-5.0	—
Photon	3.10^{11}	4.0	0.8-5.0	—
Tagged Photon	10^6	1.0	0.25-4.5	

Two synchrotron radiation beams (λ_c = 0.94 Å*)

RESEARCH PROGRAM**

TOTAL EXPERIMENTAL AREA 3000 m²
BEAM LINES TO 5 (inc. test beam) Stations
STATIONS SERVED AT SAME TIME 3 (inc. test beam)
BEAM SEPARATORS — SPECTROMETERS 5
ON-LINE COMPUTERS 6
BUBBLE CHAMBERS, in-house — Users' —
TOTAL POWER INSTALLED FOR RESEARCH 15 MW
No. USER GROUPS: in-house 2 outside 6
TOTAL RESEARCH STAFF, in-house 35 outside 88
ANNUAL RESEARCH BUDGET, in-house £2.2 M
SCHEDULED RESEARCH TIME, hours/week Year 5900 in 1973
00 in 1976

RECENT IMPROVEMENTS OR MODIFICATIONS TO MACHINE

Published Articles Describing Machine

A.W. MERRISON, CONTEMPORARY PHYS. 8, 4 (1967), p.373
DNPL Reports 1-6 and Annual Reports

* Refers to 5.0 GeV

** Excluding Synchrotron Radiation Facility

NAME OF MACHINE: Cornell 12 GeV Electron Synchrotron
INSTITUTION: Cornell University
LOCATION: Ithaca, N.Y.

PERSON IN CHARGE: Maury Tigner
DATA SUPPLIED BY: M. Tigner
DATE: January, 1974

HISTORY AND STATUS

CONSTRUCTION STARTED (date): April, 1965
FIRST BEAM OBTAINED, OR GOAL (date): May, 1967
TOTAL COST OF FACILITY: $11.5 M
FUNDED BY: National Science Foundat.
TOTAL ACCELERATOR STAFF (now): 45
ANNUAL OPERATING BUDGET: $1 M

ACCELERATOR PARAMETERS

Physical Dimensions (Mean)
RING DIAM. 250 m; Tunnel sect. 2 x 3 m
MAGNET 20 x .29 m; Mag. Gap 2.5/3.7 x 10 cm
"DONUT": none cm; Aperture 2.5 x 5.5 cm

Injector System
TYPE: Varian S-Band TW Linac
OUTPUT (max) 100 MA at 150 MeV
BEAM EMITTANCE .15 mn-mrad
INJECTION PERIOD 2.5 usec. or 1 turns
INFLECTOR TYPE: Pulse Magnetic

Magnet System
FOCUSING TYPE: Alternating Gradient
No. MAG. UNITS 192 Length (ea) 3.4 m
STRAIGHT SECT. 6 Total S.S. Length 48 m
FOCUSING ORDER: FDDF
BETATRON OSC. FREQ. ν_H 10.75 ν_V 10.75
FIELD, AT INJ. 50 G, at max kG
RISE TIME 8×10^{-3} sec; Flat-top time - see
MAG. WEIGHT (tons) Fe 1800, Cu 25
POWER INPUT (MW) PEAK - MEAN 1

Acceleration System
HARMONIC No. 6
RF RANGE: fixed 714 MHz
ORBIT FREQ. 0.205 MHz
ENERGY GAIN 6 MeV/turn, Max.
RADIATION LOSS 1.8×10^{-4} keV/turn
RF POWER INPUT (kW) PEAK 1500

Other Relevant Parameters or Notable Features

ACCELERATOR PERFORMANCE

	Normal (or Goal)	Maximum Achieved
ENERGY (GeV)	12	12.2
RESOLUTION ΔE/E (%)	.5	.5
REPET. RATE (pulse/sec)	60	60
PULSE WIDTH	2×10^{-3} sec.	2×10^{-3} s
INTERNAL BEAM (part/pulse)	10^{11}	3×10^{10}
(part/sec)	6×10^{12}	1.8×10^{11}
DEAM EMITTANCE (mn-mrad)	-	-
SCHEDULED OPERATION (hr/wk)	144	144

"ON BEAM" 85 % OF SCHEDULED TIME

Some Typical External and Secondary Beams

PARTICLE	FLUX (part/sec)	BEAM AREA (cm^2)	ENERGY (GeV)	ΔE/E (%)
γ	10^{11}	1	12	-
ℓ	10^{12}	.5	12	

RESEARCH PROGRAM

TOTAL EXPERIMENTAL AREA 1400 m²
BEAM LINES TO 5 Stations
STATIONS SERVED AT SAME TIME 2
BEAM SEPARATORS -; SPECTROMETERS 2
ON-LINE COMPUTERS WITH 2 Inputs
BUBBLE CHAMBERS, in-house none Users' none
TOTAL POWER INSTALLED FOR RESEARCH 3 MW
No. USER GROUPS in-house 4 outside 4
TOTAL RESEARCH STAFF, in-house 25 outside 20
ANNUAL RESEARCH BUDGET, in-house $1.8 M
SCHEDULED RESEARCH TIME, hours/week 135

RECENT IMPROVEMENTS OR MODIFICATIONS TO MACHINE

Published Articles Dercribing Machine

NAME OF MACHINE: Orsay Electron Linear Accelerator
INSTITUTION: Lab. Accelerateur Linéaire *
LOCATION: ORSAY (France)

PERSON IN CHARGE: P. BRUNET
DATA SUPPLIED BY: P. BRUNET
DATE: February 1974

HISTORY AND STATUS

CONSTRUCTION STARTED (date): 1956
FIRST BEAM OBTAINED, OR GOAL (date): 1959
TOTAL COST OF FACILITY: 10^8 F fr
FUNDED BY: National Ministry of Education
TOTAL ACCELERATOR STAFF (now): 50
ANNUAL OPERATING BUDGET: 1.5×10^6 F

ACCELERATOR PARAMETERS

Physical Dimensions

ACCELERATOR LENGTH: 360 m, DIAM.:
TUNNEL SIZE (L×H×W): m^3

Injection System

TYPE: Electron Buncher
OUTPUT: 1000 mA AT 12(1.5μs), 20(0.02μs) MeV
BEAM EMITTANCE: 5 mm-mrad
INJECTION PERIOD: 1.5 μs 50 RF cycles

Acceleration System

No. SECTIONS: 1 + 38 length (ea): 6 m
FIELD MODE: π/2 FREQUENCY: 2999 MHz
GROUP VELOCITY: Tapered c; Phase Vel: ~ 1.0 c
WAVE TYPE: TM-01 FILLING TIME: 0.7 and 0.9 μsec
SHUNT IMPEDANCE (MΩ/cm): 0.45
ATTENUATION (Np/m): 0.54 and 0.92 (total) to 2.7
IRIS, aperture: 1.8 cm, thickness: 3 mm
IRIS SPACING (cm): 2.5
10 150 and 11 800
POWER UNITS No.: 39 TYPE: Klystrons
POWER RATING (MW/unit): 25 and 20
FEED SPACING (m): 6
RF POWER DEMAND (MW) PEAK: 860 MEAN: 0.13

Focusing System

doublets and triplets
QUADRUPOLES, No.: 13 sets SPACING: 6 to 25 m
GRADIENTS: 11 T/m

Other Relevant Parameters or Notable Features

e^- → e+ converter after
16 sections e.g. ≃ 1.0 GeV

ACCELERATOR PERFORMANCE

	Normal (or Goal)	Maximum Achieved
electrons		
ENERGY (GeV)	2.3	2.1
ENERGY GAIN (MeV/m)	10	10
RESOLUTION ΔE/E (%)		
REPET. RATE (pulse/sec)	1.25 to 50	50
PULSE WIDTH (μs)	0.02&1.5	1.5
DUTY FACTOR, macroscopic (%)	10^{-4}&8.10^{-3}	8.10^{-3}
BEAM CURRENT (μA)	7.5	7.5
BEAM EMITTANCE (inn-mrad)	0.3	

positrons	ACO	DCI
ENERGY (GeV)	0.25	1.3
ENERGY GAIN (MeV/m)	10	10
RESOLUTION ΔE/E (%)	2	2
REPET. RATE (pulse/sec)	50	50
PULSE WIDTH (μs)	1.5	0.02
DUTY FACTOR, macroscopic (%)	8×10^{-3}	10^{-4}
BEAM CURRENT (μA)	2.5×10^{-2}	3×10^{-3}
BEAM EMITTANCE (inn-mrad)	6π	1.6π

Some Typical External and Secondary Berms

PARTICLE	FLUX (part/sec)	BEAM AREA (cm^2)	ENERGY (GeV)	ΔE/E (%)
e^-	1×10^{13}	0.2	1.8	1
e+	3×10^9	0.8	0.25	7 (ACO)

RESEARCH PROGRAM (Linac only)

TOTAL EXPERIMENTAL AREA: 250 m^2
BEAM LINES TO: 5 Stations
STATIONS SERVED AT SAME TIME: 2
BEAM SEPARATORS: 0 SPECTROMETERS: 1
ON-LINE COMPUTERS WITH: Inputs
BUBBLE CHAMBERS, in-house: outside:
TOTAL POWER INSTALLED FOR RESEARCH: MW
No. USER GROUPS, in-house: outside:
TOTAL RESEARCH STAFF, in-house: outside:
ANNUAL RESEARCH BUDGET, in-house:
SCHEDULED RESEARCH TIME, hours/week:

Published Articles Describing Machine

Onde Electrique (juillet 1969)

Recent or Planned Modifications to Machine

- Linac beams are not directly used for physics experiments any more, but only for injection in storage rings : ACO in 74, DCI and ACO in 75.
- The last experimental remaining room can handle a 500 MeV e^- or e^+ beam.

* Université PARIS-SED
Dependent on I.N.2.P.3 (Institut National de Physique Nucléaire et de Physique des Particules).

NAME OF MACHINE Mark III Electron Linear Accelerator
INSTITUTION High Energy Physics Lab.
LOCATION Stanford University, Stanford, Calif. 94305

PERSON IN CHARGE Professor R. Hofstadter
DATA SUPPLIED BY Professor M. [illegible] Yearian
DATE March 1974

HISTORY AND STATUS

CONSTRUCTION STARTED (date) 1949
FIRST BEAM OBTAINED, OR GOAL (date) 1953(280'); 1964(310')
TOTAL COST OF FACILITY $3.5 M (Accel. only)
FUNDED BY [illegible]6-69; ONR, AEC, AFOSR
TOTAL ACCELERATOR STAFF (now) See Note A
ANNUAL OPERATING BUDGET See Note A

ACCELERATOR PARAMETERS

Physical Dimensions

ACCELERATOR LENGTH 100 m, DIAM. 10 cm
TUNNEL SIZE (L×H×W) 150 m (variable H&W) m³

Injection System

TYPE Oxide cathode gun
OUTPUT 300 mA AT 80 keV MeV
BEAM EMITTANCE m-mrad
INJECTION PERIOD 1.5 μs RF cycles

Acceleration System

No. SECTIONS 31 length(ea) 3.0m
FIELD MODE 2π/3 FREQUENCY 2856 MHz
GROUP VELOCITY .01c; Phase Vel. 1.00 c
WAVE TYPE TM 01 FILLING TME 0.83 μsec
SHUNT IMPEDANCE (MΩ/cm) 360
ATTENUATION (Np/m) 0.19
IRIS, aperture 1.9-2.6 cm, thickness 5.8 mm
IRIS SPACING (cm) 3.50
Q 13 500
POWER WITS, No. 31 TYPE Klystrons
POWER RATING (MW/unit) 20
FEED SPACING (m) 3
RF POWER DEMAND (MW) PEAK 600 MEAN 0.1

Focusing System

QUADRUPOLES, No. 4 pairs SPACING variable
GRADIENTS plus magnetic lenses

Other Relevant Parameters or Notable Features

Note A: Mark III in process of phasing out; staff and operating budget minimal.

*1969 - present - NSF

Published Articles Describing Machine

1. General Description: M. Ghodorow et al., Rev. Sci. Instr. 26, 134 (1955).

ACCELERATOR PERFORMANCE

	Normal (or Goal)	Maximum Achieved
electrons		
ENERGY (GeV)		1.2
ENERGY GAIN (MeV/m)		
RESOLUTION ΔE/E (%)		0.4 - 1.0
REPET. RATE (pulse/sec)		0.1 - 120
PULSE WIDTH		0.8 - 1.3 μsec
DUTY FACTOR, macroscopic (%)		1.6×10^{-2}
BEAM CURRENT (μA)		5
BEAM EMITTANCE (mm-mrad)		
positrons		
ENERGY (GeV)		1
ENERGY GAIN (MeV/m)		
RESOLUTION ΔE/E (%)		1
REPET. RATE (pulse/sec)		60
PULSE WIDTH		1 μsec
DUTY FACTOR, macroscopic (%)		0.6×10^{-2}
BEAM CURRENT (μA)		0.2×10^{-3}
SEAM EMITTANCE (mm-mrad)		

Some Typical External and Secondary Beams

PARTICLE	FLUX (part/sec)	BEAM AREA (cm²)	ENERGY (GeV)	ΔE/E (%)
e^-	3×10^{13}	0.3	1	0.1
e^+	10^9	0.3	0.8	0.5
γ	Depends on radiation thickness			

RESEARCH PROGRAM

TOTAL EXPERIMENTAL AREA 1760 m²
BEAM LINES TO 5 Stations
STATIONS SERVED AT SAME TIME 1
BEAM SEPARATORS None SPECTROMETERS 4
ON-LINE COMPUTERS WITH 3 Inputs
BUBBLE CHAMBERS, in-house None outside
TOTAL POWER INSTALLED FOR RESEARCH 3 MW
No. USER GROUPS, in-house outside
TOTAL RESEARCH STAFF, in-house outside
ANNUAL RESEARCH BUDGET, in-house
SCHEDULED RESEARCH TIME, hours/week
(See Note A)

Recent or Planned Modifications to Machine

NAME OF MACHINE Superconducting Mark III Electron Linac
INSTITUTION High Energy Physics Lab.
LOCATION Stanford Univ., Stanford, Ca 94305
PERSON IN CHARGE Mason R. Yearian, Acting Director
DATA SUPPLIED BY R. E. Rand
DATE March 1074

HISTORY AND STATUS

CONSTRUCTION STARTED (date) 1969
FIRST BEAM OBTAINED, OR GOAL (date) 1976
TOTAL COST OF FACILITY $10 M
FUNDED BY ONR & NSF
TOTAL ACCELERATOR STAFF (now) 57 + 13 students
ANNUAL OPERATING BUDGET $ 1 M

ACCELERATOR PARAMETERS

Physical Dimensions
ACCELERATOR LENGTH 150 m, DIAM. Dewar 90 cm
TUNNEL SIZE (L×H×W) 180 x 4 x 4 m³

Injection System
TYPE Superconducting Buncher & Pre-accelerator
OUTPUT 0.1 mA AT 8 MeV
BEAM EMITTANCE 0.5π mm-mrad
INJECTION PERIOD CW μs RF cycles

Acceleration System
No. SECTIONS 8 length(ea) 6 m
FIELD MODE π 12 FREQUENCY 1300 MHz
GROUP VELOCITY 1 c; Phase Vel. 1 c
WAVE TYPE TM-01 FILLING TIME μsec
SHUNT IMPEDANCE (MΩ/cm)
ATTENUATION (Np/m)
IRIS, aperture cm, thickness mm
IRIS SPACING (cm)
Q 10^{10} – 10^{11}
POWER UNITS, No. 8 TYPE Klystron
POWER RATING (MW/unit) 0.015
FEED SPACING (m) 6
RF POWER DEMAND (MW) PEAK 0.36 MEAN 0.36

Focusing System
QUADRUPOLES, No. , SPACING
GRADIENTS

Other Relevant Parameters or Notable Features

Operating temperature = 1.85°K

ACCELERATOR PERFORMANCE

	Normal (or Goal)	Maximum Achieved
electrons		
ENERGY (GeV)	0.7 - 2	
ENERGY GAIN (MeV/m)	12.3	
RESOLUTION AEIE (%)	0.01	
REPET. RATE (pulse/sec)		
PULSE WIDTH		
DUTY FACTOR, macroscopic (%)	100	
BEAM CURRENT (μA)	100	
BEAM EMITTANCE (mn-mrad)	0.1	
positrons		
ENERGY (GeV)		
ENERGY GAIN (MeV/m)		
RESOLUTION ΔE/E (%)		
REPET. RATE (pulse/sec)		
PULSE WIDTH		
DUTY FACTOR, macroscopic (%)		
BEAM CURRENT (μA)		
BEAM EMITTANCE (mn-mrad)		

Some Typical External and Secondary Beams

PARTICLE	FLUX (part/sec)	BEAM AREA (cm²)	ENERGY (GeV)	AEIE (%)
e^-	10^{9}	0.05	2	0.01

RESEARCH PROGRAM

TOTAL EXPERIMENTAL AREA 3000 m²
BEAM LINES TO 5 Stations
STATIONS SERVED AT SAME TIME 1
BEAM SEPARATORS SPECTROMETERS 2
ON-LINE COMPUTERS WITH Inputs
BUBBLE CHAMBERS, in-house outside
TOTAL POWER INSTALLED FOR RESEARCH 6 MW
No. USER GROUPS, in-house outside
TOTAL RESEARCH STAFF, in-house outside
ANNUAL RESEARCH BUDGET, in-house
SCHEDULED RESEARCH TIME, hours/week

Published Articles Describing Machine

Suelzle, L. R., IEEE Trans., June 1971, to be published.

Recent or Planned Modifications to Machine